

December 21, 2017

Docket Nos.: 52-025
52-026

ND-17-2074
10 CFR 50.90
10 CFR 52.63

U.S. Nuclear Regulatory Commission
Document Control Desk
Washington, DC 20555-0001

Southern Nuclear Operating Company
Vogtle Electric Generating Plant Units 3 and 4
Request for License Amendment and Exemption:
Containment Pressure Analysis (LAR-17-043)

Ladies and Gentlemen:

Pursuant to 10 CFR 52.98(c) and in accordance with 10 CFR 50.90, Southern Nuclear Operating Company (SNC), the licensee for Vogtle Electric Generating Plant (VEGP) Units 3 and 4, requests an amendment to Combined License Numbers NPF-91 and NPF-92, for VEGP Units 3 and 4, respectively. The requested amendment includes changes to the Updated Final Safety Analysis Report (UFSAR) in the form of departures from the incorporated plant-specific Design Control Document (DCD) Tier 2* and Tier 2 information and related changes to the VEGP Units 3 and 4 COL Appendix A and COL Appendix C (and corresponding plant-specific DCD Tier 1) information. Pursuant to the provisions of 10 CFR 52.63(b)(1), an exemption from elements of the design as certified in the 10 CFR Part 52, Appendix D, design certification rule is also requested for the plant-specific Tier 1 material departures.

SNC previously communicated to the staff our intent to submit a License Amendment Request (LAR) for Containment Reanalysis in letter ND-14-1282, "Schedule of Technical Documentation to Support Future License Amendment Request for Containment Reanalysis," dated August 28, 2014 (ML14241A271). In that letter, SNC confirmed our commitment, made at a public meeting between Nuclear Regulatory Commission (NRC) and AP1000 stakeholders on July 23, 2014 (ML 14192A803), to make several technical documents that will support the submittal available for NRC review prior to LAR submittal. These technical documents have previously been made available to the Staff and included calculations/analyses for: heat sinks, WGOTHIC evaluation model, mass and energy releases, steam line break containment integrity, and loss of coolant accident containment integrity.

In addition, the minimum backpressure analyses and WCAP-15846, "WGOTHIC Application to AP600 and AP1000", Revision 5 (2016), were made available for the Staff's review in support of the LAR submittal by letter ND-17-0893, "Schedule of Technical Documentation to Support Future

License Amendment Request for Containment Reanalysis Updated,” dated May 24, 2017 (ML17144A400).

The requested amendment involves changes to incorporate the results of the updated analyses within the information presented in COL Appendix A, COL Appendix C (and corresponding plant-specific Tier 1) and the UFSAR.

Enclosure 1 provides the description, technical evaluation, regulatory evaluation (including the Significant Hazards Consideration Determination), and environmental considerations for the proposed changes in the License Amendment Request (LAR).

Enclosure 2 provides the background and supporting basis for the requested exemption.

Enclosure 3 provides the proposed changes to the VEGP 3&4 licensing basis documents, except for the proposed changes to the incorporated by reference WCAP-15846 which are addressed in Enclosures 5 and 6.

Enclosure 4 provides the information only changes to the VEGP 3&4 Technical Specification Bases document.

Enclosure 5 provides the tracked-changes proprietary version and technical evaluation of the incorporated by reference document APP-SSAR-GSC-587 Rev. 5 “WGOTHIC Application to AP600 and AP1000” (WCAP-15846) Revisions 1 through 5 (Proprietary).

Enclosure 6 provides the tracked-changes non-proprietary version and technical evaluation of the incorporated by reference document APP-SSAR-GSC-587 Rev. 5 “WGOTHIC Application to AP600 and AP1000” (WCAP-15846) Revisions 1 through 5 (Non-Proprietary).

Enclosure 7 provides the proprietary version of the incorporated by reference document APP-SSAR-GSC-587 Rev. 5 “WGOTHIC Application to AP600 and AP1000” (WCAP-15846) Revision 5 (Proprietary).

Enclosures 5 and 7 contain information that is considered proprietary; therefore, Enclosures 5 and 7 are requested to be withheld from disclosure to the public under 10 CFR 2.390.

Enclosure 8 provides the non-proprietary version of the incorporated by reference document APP-SSAR-GSC-588 Rev. 5 “WGOTHIC Application to AP600 and AP1000” (WCAP-15862) Revision 5 (Non-Proprietary).

An affidavit from SNC supporting withholding under 10 CFR 2.390 is provided as Enclosure 9.

Enclosure 10 is Westinghouse’s Proprietary Information Notice, Copyright Notice and CAW-17-4679, Application for Withholding Proprietary Information from Public Disclosure and Affidavit. The affidavit sets forth the basis upon which the information may be withheld from public disclosure by the Commission and addresses with specificity the considerations listed in paragraph (b)(4) of Section 2.390 of the Commission's regulations. Accordingly, it is respectfully requested that the information that is proprietary to Westinghouse be withheld from public disclosure in accordance with 10 CFR Section 2.390 of the Commission's regulations.

Correspondence with respect to the copyright or proprietary aspects of the items listed above or the supporting Westinghouse affidavit should reference CAW-17-4679 and should be addressed to James A. Gresham, Manager, Regulatory Compliance, Westinghouse Electric Company, 1000 Westinghouse Drive, Building 3 Suite 310, Cranberry Township, Pennsylvania 16066. Correspondence with respect to proprietary aspects of this letter and its enclosures should also be addressed to Brian H. Whitley at the contact information within this letter.

This letter has been reviewed and confirmed to not contain security-related information. This letter contains no regulatory commitments.

SNC requests staff approval of this license amendment by February 21st, 2019. SNC expects to implement this proposed amendment (through incorporation into the licensing basis documents; e.g., the UFSAR) within 30 days of approval of the requested changes.

In accordance with 10 CFR 50.91, SNC is notifying the State of Georgia of this LAR by transmitting a copy of this letter and enclosures to the designated State Official.

Due to the size of this submittal, this letter is being submitted with a compact disc. The compact disc contains the letter and all the enclosures.

Should you have any questions, please contact Ms. Amy C. Chamberlain at (205) 992-6361.

I declare under penalty of perjury that the foregoing is true and correct. Executed on the 21st of December 2017.

Respectfully submitted,

A handwritten signature in black ink, appearing to read "B. H. Whitley", is written over a horizontal line.

Brian H. Whitley
Director, Regulatory Affairs
Southern Nuclear Operating Company

- Enclosures:
- 1) Vogtle Electric Generating Plant (VEGP) Units 3 and 4 - Request for License Amendment: Containment Pressure Analysis (LAR-17-043)
 - 2) Vogtle Electric Generating Plant (VEGP) Units 3 and 4 - Exemption Request: Containment Pressure Analysis (LAR-17-043)
 - 3) Vogtle Electric Generating Plant (VEGP) Units 3 and 4 - Proposed Changes to the Licensing Basis Documents (LAR-17-043)
 - 4) Vogtle Electric Generating Plant (VEGP) Units 3 and 4 – Information Only Changes to the Technical Specification Basis Document (LAR-17-043)
 - 5) Vogtle Electric Generating Plant (VEGP) Units 3 and 4 – APP-GW-GLR-801, Rev. 0 “WGOTHIC Application to AP600 and AP1000” (WCAP-15846) Revisions 1 through 5 (Proprietary) (LAR-17-043) **(Withheld Information)**
 - 6) Vogtle Electric Generating Plant (VEGP) Units 3 and 4 – APP-GW-GLR-802, Rev. 0 “WGOTHIC Application to AP600 and AP1000” (WCAP-15846) Revisions 1 through 5 (Non-Proprietary) (LAR-17-043)
 - 7) Vogtle Electric Generating Plant (VEGP) Units 3 and 4 – APP-SSAR-GSC-587 Rev. 5 “WGOTHIC Application to AP600 and AP1000” (WCAP-15846) Revision 5 (Proprietary) (LAR-17-043) **(Withheld Information)**
 - 8) Vogtle Electric Generating Plant (VEGP) Units 3 and 4 – APP-SSAR-GSC-588 Rev. 5 “WGOTHIC Application to AP600 and AP1000” (WCAP-15862) Revision 5 (Non-Proprietary) (LAR-17-043)
 - 9) Vogtle Electric Generating Plant (VEGP) Units 3 and 4 – Affidavit from Southern Nuclear Operating Company for Withholding Under 10 CFR 2.390 (LAR-17-043)
 - 10) Vogtle Electric Generating Plant (VEGP) Units 3 and 4 – Westinghouse Authorization Letter CAW-17-4679, Affidavit, Proprietary Information Notice and Copyright Notice

cc:

Southern Nuclear Operating Company / Georgia Power Company

Mr. S. E. Kuczynski (w/o enclosures)

Mr. M. D. Rauckhorst

Mr. D. G. Bost (w/o enclosures)

Mr. M. D. Meier (w/o enclosures)

Mr. D. H. Jones (w/o enclosures)

Mr. D. L. McKinney (w/o enclosures)

Mr. T. W. Yelverton (w/o enclosures)

Mr. B. H. Whitley

Mr. J. J. Hutto

Mr. C. R. Pierce

Ms. A. G. Aughtman

Mr. D. L. Fulton

Mr. M. J. Yox

Mr. E. W. Rasmussen

Mr. J. Tupik

Mr. W. A. Sparkman

Ms. A. C. Chamberlain

Ms. A. L. Pugh

Mr. J. D. Williams

Document Services RTYPE: VND.LI.L00

File AR.01.02.06

Nuclear Regulatory Commission

Mr. W. Jones (w/o enclosures)

Ms. J. Dixon-Herrity

Mr. C. Patel

Ms. J. M. Heisserer

Mr. B. Kemker

Mr. G. Khouri

Ms. S. Temple

Mr. F. Brown

Mr. T. E. Chandler

Ms. P. Braxton

Mr. T. Brimfield

Mr. C. J. Even

Mr. A. Lerch

State of Georgia

Mr. R. Dunn (w/o enclosures 5 and 7)

Oglethorpe Power Corporation

Mr. M. W. Price (w/o enclosures 5 and 7)

Mr. K. T. Haynes (w/o enclosures 5 and 7)

Ms. A. Whaley (w/o enclosures 5 and 7)

Municipal Electric Authority of Georgia

Mr. J. E. Fuller (w/o enclosures 5 and 7)

Mr. S. M. Jackson (w/o enclosures 5 and 7)

Dalton Utilities

Mr. T. Bundros (w/o enclosures 5 and 7)

Westinghouse Electric Company, LLC

Mr. L. Oriani (w/o enclosures)

Mr. G. Koucheravy (w/o enclosures)

Mr. M. Corletti

Mr. M. L. Clyde

Ms. L. Iller

Mr. D. Hawkins

Mr. J. Coward

Other

Mr. S. W. Kline, Bechtel Power Corporation (w/o enclosures 5 and 7)

Ms. L. A. Matis, Tetra Tech NUS, Inc. (w/o enclosures 5 and 7)

Dr. W. R. Jacobs, Jr., Ph.D., GDS Associates, Inc. (w/o enclosures 5 and 7)

Mr. S. Roetger, Georgia Public Service Commission (w/o enclosures 5 and 7)

Ms. S. W. Kernizan, Georgia Public Service Commission (w/o enclosures 5 and 7)

Mr. K. C. Greene, Troutman Sanders (w/o enclosures 5 and 7)

Mr. S. Blanton, Balch Bingham

Mr. R. Grumbir, APOG (w/o enclosures 5 and 7)

NDDocumentinBox@duke-energy.com, Duke Energy (w/o enclosures 5 and 7)

Mr. S. Franzone, Florida Power & Light (w/o enclosures 5 and 7)

Southern Nuclear Operating Company

ND-17-2074

Enclosure 1

Vogtle Electric Generating Plant (VEGP) Units 3 and 4

Request for License Amendment:

Containment Pressure Analysis (LAR-17-043)

(Enclosure 1 consists of 29 pages, including this cover page.)

Table of Contents

1. SUMMARY DESCRIPTION
2. COMBINED DETAILED DESCRIPTION AND TECHNICAL EVALUATION
3. TECHNICAL EVALUATION (SEE SECTION 2)
4. REGULATORY EVALUATION
 - 4.1. Applicable Regulatory Requirements/Criteria
 - 4.2. Precedent
 - 4.3. Significant Hazards Consideration
 - 4.4. Conclusions
5. ENVIRONMENTAL CONSIDERATIONS
6. REFERENCES

Pursuant to 10 CFR 52.98(c) and in accordance with 10 CFR 50.90, Southern Nuclear Operating Company (SNC, or the "Licensee") hereby requests an amendment to Combined License (COL) Nos. NPF-91 and NPF-92 for Vogtle Electric Generating Plant (VEGP) Units 3 and 4, respectively.

1. SUMMARY DESCRIPTION

This license amendment request (LAR) proposes changes to the plant-specific containment integrity analyses described in Updated Final Safety Analysis Report (UFSAR) Section 6.2. Accumulated design changes within containment have necessitated recalculation of geometry input to the WGOTHIC evaluation model (EM) used for containment integrity analyses. Heat sinks, control volumes, and flow paths have been recalculated, and are in turn modeled in the WGOTHIC EM. Mass and energy (M&E) releases for Loss of Coolant Accident (LOCA) and Main Steam Line Break (MSLB) events are also recalculated. Various methodology changes are also made to the WGOTHIC methodology for the AP1000 design. These updates culminate in the recalculation of the containment integrity analyses.

Additionally, changes are proposed to Inspections, Tests, Analyses, and Acceptance Criteria (ITAAC) related to flow rate testing of the passive containment cooling system (PCS) in order to capture lessons learned from preoperational testing performed at Sanmen Unit 1.

This LAR proposes changes to the UFSAR in the form of departures from the incorporated plant-specific Design Control Document (DCD) Tier 2 licensing basis information, involves changes to UFSAR information that has been designated as Tier 2* information, changes to the plant-specific ITAAC provided as Appendix C to the Combined License (COL), changes to the plant-specific Technical Specifications (TS) provided as Appendix A to the COL, and provides the associated plant-specific TS Bases changes that would accompany the proposed changes to the plant-specific Technical Specifications. This submittal requests approval of the LAR necessary to implement these changes.

NOTE: The proposed licensing basis changes to the UFSAR, COL Appendix A, and COL Appendix C are discussed and evaluated within this LAR. However, due to the proprietary nature of the WGOTHIC methodology, the discussion and evaluation of the methodology changes are provided in proprietary and non-proprietary documents, which are included as Enclosures 5 and 6. Additionally, WCAP-15846, Revision 5 (Proprietary) and WCAP-15862, Revision 5 (Non-Proprietary) are provided as Enclosures 7 and 8 of this LAR.

2 and 3. COMBINED DETAILED DESCRIPTION AND TECHNICAL EVALUATION

The following discussion pertains to the UFSAR-described design functions associated with the changes proposed as part of this LAR.

As described in Section 6.2 of the UFSAR, the AP1000 plant containment system (CNS) is designed such that for the limiting design basis accidents (DBA), the containment peak pressure remains below the design pressure of 59 psig for the duration of the transient, and thus, meets general design criteria (GDC) 16, 38, and 50 as shown in UFSAR Table 6.2.1.1-3. This is achieved by the PCS, whose functional objective is to reduce the containment temperature and pressure following a DBA loss of coolant accident (LOCA) or main steam line break (MSLB) inside containment by removing thermal energy from the containment atmosphere. The PCS also serves as the safety-related means of transferring heat to the ultimate heat sink for design basis events and shutdowns.

As described in UFSAR Subsection 6.2.2.2.2, the major components of the PCS are the passive

containment cooling water storage tank (PCCWST), which is incorporated into the shield building structure above the containment; an air baffle, located between the steel containment vessel and the concrete shield building, which defines the cooling air flowpath; air inlets and an air exhaust, also incorporated into the shield building structure; and a water distribution system, mounted on the outside surface of the steel containment vessel, which functions to distribute water flow on the containment.

An inorganic zinc (IOZ) coating is used on the interior and exterior surface of the containment vessel (CV) shell above the operating deck elevation. Its design function is described in UFSAR Subsection 6.1.2.1.5. The IOZ coating is primarily used to help wettability, coverage, and distribution of the PCS water. The coating also affects the transfer of thermal energy from the post-accident containment atmosphere through the containment shell to the environment.

Containment integrity analyses are conducted. As described in UFSAR Subsection 6.2.1.1.1, the containment integrity analyses for the AP1000 plant employ a multi-volume lumped parameter model to study the long-term containment response to postulated LOCA and MSLB accidents, which are the limiting DBAs with respect to containment pressure. The containment integrity analyses are based on assumptions that are conservative with respect to the containment and its heat removal systems, such as minimum heat removal and maximum initial containment pressure.

UFSAR Subsection 6.2.1.1.3 describes the use of the Westinghouse-GOTHIC (WGOTHIC) computer code for modeling multiphase flow in containment transient analyses. It solves the conservation equations in integral form for mass, energy, and momentum for multicomponent flow. The momentum conservation equations are written separately for each phase in the flow field (drops, liquid pools, and atmospheric vapor). The WGOTHIC methodology is described in WCAP-15846, which is incorporated by reference (IBR) into the UFSAR, as cited in UFSAR Section 6.2 and Table 1.6-1.

The AP1000 WGOTHIC containment evaluation model (WGOTHIC EM) consists of thermal conductors (heat sinks), control volumes, flow paths, material properties, climes (a heat and mass transfer model for the containment vessel and its exterior), boundary conditions, and initial conditions. Using the WGOTHIC EM, separate input files are created for the double ended cold leg guillotine (DECLG) LOCA, double ended hot leg guillotine (DEHLG) LOCA, and MSLB peak containment pressure analyses. Mass and energy (M&E) releases are calculated and combined with the WGOTHIC EM input files to perform the containment integrity analyses. These analyses confirm that the containment peak pressure does not exceed the containment design pressure of 59 psig, thus meeting the requirements of GDCs 16 and 50. Additionally, these analyses analyze the long-term pressure response and so confirm that the design meets GDC 38.

The calculated containment peak pressure plays an important role in containment leakage rate testing (CLRT) program, for which the limits are specified in the plant-specific Technical Specifications (TS) under TS Administrative Control 5.5.8, "Containment Leakage Rate Testing Program." Leakage rate testing requirements are defined by 10 CFR 50, Appendix J, "Primary Reactor Containment Leakage Testing for Water-Cooled Power Reactors." Per TS Administrative Control 5.5.8.a, the CLRT shall follow 10 CFR 50, Appendix J, Option B; which defines P_a as the calculated peak containment internal pressure related to the design basis LOCA as specified in the TS. L_a is in turn defined as the maximum allowable leakage rate at pressure P_a as specified in the TS. Therefore, the calculated peak pressure from the containment integrity analyses establishes the limits for the CLRT program, which are specified in the TS.

The ITAACs along with Chapter 14 of the UFSAR describe the initial test program of the AP1000 plant. The overall objective of the initial test program is to demonstrate that the plant has been

constructed as designed, that the systems perform consistent with the plant design, and that activities culminating in operation at full licensed power including initial fuel load, initial criticality, and power ascension are performed in a controlled and safe manner. Testing performed as prescribed in UFSAR Subsection 14.2.9.1.4 and the ITAACs in 2.2.02 verify that the as-installed components of the PCS perform properly to accomplish their safety-related functions to transfer heat from inside containment to the environment. More specifically, as stated in UFSAR Subsection 14.2.9.1.4, "The purpose of the passive containment cooling system testing is to verify that the as-installed components perform properly to accomplish their safety-related functions to transfer heat from inside the containment to the environment, as described in subsection 6.2.2..."

In summary, the AP1000 plant containment systems are designed such that for the DBAs, the containment peak pressure remains below the containment design pressure of 59 psig for the duration of the transient. This is accomplished by a number of design features and is verified by analysis and testing.

The following subheadings and associated discussions describe the changes and associated evaluation of the activity proposed in this LAR.

3.1 Updates to WGOthic EM, WGOthic Methodology, and Resulting Containment Integrity Analyses:

The current licensing basis containment integrity analyses described in UFSAR Section 6.2 are based on the AP1000 design configuration at the time of the amended design certification (i.e., DCD Revision 19). Accumulated design changes within containment have necessitated recalculation of geometry input to the WGOthic EM used for containment integrity analyses. Heat sinks, control volumes, and flow paths have been recalculated, and are in turn modeled in the WGOthic EM. Various methodology changes are also made to the WGOthic methodology for AP1000 plant design. M&E releases for LOCA and MSLB are also recalculated. These updates culminate in the recalculation of the containment integrity analyses.

3.1.1 Updates to WGOthic EM:

The WGOthic heat sinks, control volumes, and flow paths have been recalculated and incorporated into the WGOthic EM, as discussed below.

a. Passive Containment Heat Sinks:

The WGOthic evaluation model used in the current UFSAR analysis is based in large part on conservative assumptions made originally during the development of the AP600 design. Nominal dimensions from certified for construction (CFC) drawings have been used to calculate metal volumes and surface areas for use as heat sink input to the WGOthic EM. These updated values align the WGOthic EM with the updated AP1000 design.

The total metal volume has increased by approximately 30% from the current model. Despite an overall increase in total metal volume as a result of the quantification effort, an appropriate level of conservatism is maintained in terms of the total amount of metal volume credited for heat transfer.

Despite an overall increase in total metal volume as a result of the quantification effort, an appropriate level of conservatism is maintained in terms of the total amount of metal volume credited for heat transfer. More than 10% of the metal is conservatively turned off for heat

transfer in the WGOTHIC EM and is in alignment with the original method of analysis. Additional conservatisms and limitations still exist as identified in NUREG-1793, such as:

- A 20 thousandths-of-an-inch (mil) air gap is assumed between the steel and concrete (on applicable heat sinks)
- Heat transfer to horizontal, upward-facing surfaces is not credited
- Condensation/convection on heat sinks in the dead-ended compartments below the operating deck are not credited after the blowdown period

Tier 2* UFSAR Table 6.2.1.1-10 currently identifies only the “additional heat sinks credited in the containment peak pressure evaluation” that were added to the model between Revisions 18 and 19 of the AP1000 DCD. This table is updated to summarize the range of required total volume (minimum and maximum) of metal heat sinks inside containment as they relate to the WGOTHIC methodology and analyses. This range was defined by both peak pressure (for which a minimum amount of heat sinks is conservative) and minimum backpressure (for which a maximum amount of heat sinks is conservative) analyses.

The volume of material determines the total energy that the heat sinks can absorb. Most of the metal heat sinks are relatively thin and absorb a high percentage of their energy capacity before the peak pressure is reached in the DBA analyses. The surface area contribution is small and is therefore omitted from UFSAR Tier 2* Table 6.2.1.1-10.

During the effort to re-quantify heat sinks, the individual steel types of each heat sink were identified. Additional granularity is therefore added to the new model regarding these steel types. The current UFSAR model contains three steel groups (carbon steel, group A carbon steel, and stainless steel), whereas the new model contains six steel groups (groups A, B, C, and D carbon steel; groups J and K stainless steel). ASME Boiler and Pressure Vessel Code, Section 2, Part D material properties are used in the model. As the ASME values are defined as typical, an uncertainty of -10% is applied to both the thermal conductivity and heat capacity. The inputs for the steel properties vary as a function of temperature (previously input as constant values). These refinements to the model provide for higher analytical accuracy. These changes are reflected in the markups to UFSAR Table 6.2.1.1-8.

Consistent with the expectations of SRP Chapter 6.2 and to provide additional granularity for the updated UFSAR Table 6.2.1.1-10, Table 6.2.1.1-11 is added to the UFSAR to identify the heat sinks (general location, material type, surface area, volume, and effective thickness) which are credited in the containment peak pressure analyses. This information has been moved from Section 13 of WCAP-15846 to the UFSAR as WCAP-15846 has been updated to focus only on methodology and is not intended to include the analytical input values. Accordingly, UFSAR Subsection 6.2.1.1.3, current paragraph nine, which provides a discussion of heat sinks, is modified to reference new Table 6.2.1.1-11 instead of WCAP-15846, Section 13.

Updates to the licensing basis for the recalculation of heat sinks are reflected in markups to UFSAR Subsection 6.2.1.1.3, Tables 6.2.1.1-8, 6.2.1.1-10, and new Table 6.2.1.1-11.

b. Control Volumes:

The total containment volume is divided into and modeled as separate control volumes in the WGOTHIC EM. The WGOTHIC control volumes are defined by their volume, hydraulic

diameter, pool area, elevation, and height. These control volumes represent both physical volumes and virtual volumes. Physical volumes correspond to compartments and rooms with physical separations such as walls, floors, and ceilings. The majority of these volumes exist below or at the operating deck level. Several physical control volumes exist above the operating deck; these are primarily due to the steam generator compartments as well as the pressurizer compartment.

The majority of the above deck volume is a large open space without any physical boundaries. This is modeled with lumped parameter control volumes. These are virtual volumes which have been carefully developed to prohibit any buoyancy driven flow in the WGOTHIC EM.

The recalculated containment free volume remains $2.06\text{E}06 \text{ ft}^3$, which is consistent with that contained in the current UFSAR model (a negligible increase of 270 ft^3). The prior calculation of containment free volume was based on many conservative assumptions and estimates, and the updated volume is based on a more detailed itemization of control volumes; therefore the change in containment heat sinks does not correlate on a one-for-one basis with the change in containment free volume. The containment volume presented in Table 6.2.1.1-2 of the UFSAR therefore remains unchanged.

Changes also include renodalization of the annulus downcomer and riser from torus control volumes to quadrant-specific control volumes. Additionally, the pressurizer compartment is now modeled as two separate control volumes in order to align the WGOTHIC EM with the updated AP1000 design.

There are no direct changes to the licensing basis due to the recalculation of control volumes; however, these changes are reflected in the updates to the underlying analyses.

c. Flow Paths:

The WGOTHIC EM control volumes previously discussed are connected by one or more flow paths. Flow paths represent physical openings between two volumes such as doorways, penetrations, stairwells, etc., but can also represent connections between control volumes which are not defined by physical boundaries.

Four categories of flow paths relevant to the containment integrity analyses are defined:

- Flow paths through the annulus, outside of containment.
- Flow paths linked to boundary conditions to model elements such as break flow.
- Flow paths between control volumes above deck; these are “virtual” flow paths that are not defined by real physical boundaries.
- Flow paths inside containment that are constrained by physical boundaries.

The flow paths outside of containment and those linked to boundary conditions are calculated directly in the WGOTHIC EM calculation; these have not changed. Flow paths inside containment that are constrained by physical boundaries are recalculated based on CFC drawings.

3.1.2 Updates to M&E Releases:**a. LOCA M&E Releases:**

LOCA M&E releases are discussed in UFSAR Subsection 6.2.1.3 and have been recalculated using the approved methodology described in WCAP-10325-P-A. The calculation documents the analyses performed for the blowdown phase of a double-ended hot leg guillotine (DEHLG) and the double-ended cold leg guillotine (DECLG) break LOCA, which is the limiting event for containment peak pressure. The calculation also documents the long-term M&E release analysis for the DECLG case. Although the DEHLG case yields higher initial integrated blowdown energy releases, the DECLG case is limiting for long-term response. This is because the DEHLG break location effectively isolates the steam generator in the broken loop, decreasing the total long-term M&E releases, therefore reducing the post-blowdown containment pressure response.

In addition, a change is made to the description in UFSAR Subsection 6.2.1.3.2.2, "Description of Blowdown Model." The SATAN-VI code input contains a generic assumption of a constant, overall heat transfer coefficient of 375 Btu/hr-ft²-°F which causes an unrealistic spike in the break compartment temperature towards the end of blowdown. The code should instead use a natural convection, vapor heat transfer coefficient on the primary side when superheated steam flow is expected to occur near the end of blowdown. The vessel would essentially be filled with 100% steam, and the convective term in the overall heat transfer coefficient would become the controlling parameter. The DEHLG LOCA SATAN run is therefore modified to use the reduced, natural convection heat transfer coefficient (37 Btu/hr-ft²-°F) when the quality of the vessel is greater than 99% steam; this is more representative of the superheated releases at the end of the DEHLG blowdown. This change is reflected in UFSAR Subsection 6.2.1.3.2.2.

Various parameters in Table 6.2.1.3-8 are updated as a result of the overall calculation update. These include the nominal vessel inlet temperature (537.2°F to 535.5°F), nominal vessel outlet temperature (610.0°F to 612.2°F), and steam pressure (881.0 psia to 870.0 psia).

As stated above, the DECLG case is limiting for peak pressure and the long-term containment response. UFSAR Table 6.2.1.3-9 provides the long-term DECLG break mass and enthalpy releases for both the two-phase mixture and steam. As seen in the revision to UFSAR Table 6.2.1.3-9, the updated DECLG break blowdown ends at 30.2 seconds. Meanwhile, the DEHLG break blowdown ends at 19.6 seconds, as reflected in UFSAR Table 6.2.1.3-10. The DEHLG case results in a slightly lower total mass release and a higher total energy release for the blowdown phase. Although there are no specific acceptance limits for the M&E releases, they are a key transient input for the containment integrity analyses.

Updates to the licensing basis due to the information on LOCA M&E releases above are reflected in the markups to UFSAR Subsection 6.2.1.3.2.2, Tables 6.2.1.3-8, 6.2.1.3-9, and 6.2.1.3-10, and Figures 6.2.1.3-1 to 6.2.1.3-4.

b. MSLB M&E Releases:

MSLB M&E releases are discussed in UFSAR Subsection 6.2.1.4 and have been recalculated. The calculation documents the analysis of steam line break double-ended

rupture (DER) cases at various power levels to determine the M&E releases inside containment for use in the revised containment integrity analysis.

An additional penalty to the analysis is taken whereby energy from the metal of the faulted steam generator is transferred to the fluid in the faulted steam generator as the fluid temperature drops below the metal temperature. In the current analysis, only steam generator metal that comes in contact with the primary side coolant is included. The revised analysis includes steam generator metal that only comes in contact with the secondary side fluid, as well. This conservatively accounts for an additional source of energy. This additional conservatism is reflected in revised text in UFSAR Subsection 6.2.1.4.1.7. A corresponding editorial change is also made in the same section in order to provide the new listing of effects that are included.

The analysis is performed at a range of initial power levels because no single power level can be predefined as a worst case initial condition due to opposing effects of conservatism. For example, at higher power levels, there is less initial water/steam in the steam generator, which is a benefit. However, at higher power levels, there is also a greater initial feedwater flow rate, higher feedwater temperature, more decay heat, and a greater heat transfer rate from the primary side, which are penalties. The power levels that are specifically analyzed are 101%, 70%, 30%, and 0%. For the purpose of containment peak pressure, the 30% power case was determined to be limiting. The results of the 30% power case are provided in UFSAR Table 6.2.1.4-2. For completeness, new Table 6.2.1.4-3 is added to also show the M&E release results of the full power (101%) case. The 101% power case continues to provide the limiting containment peak temperature at any power level. Although there are no specific acceptance limits for the M&E releases, they are the key transient input for the containment integrity analysis.

Updates to the licensing basis due to the information on MSLB M&E releases above are reflected in the markups to UFSAR Subsection 6.2.1.4.1.7 and Tables 6.2.1.4-2, 6.2.1.4-3, and 6.2.1.4-4.

3.1.3 Updates to WGOthic Methodology:

The currently approved containment integrity methodology is defined in WCAP-15846 (APP-SSAR-GSC-587) Revision 1, as modified by APP-GW-GLR-096 Revision 3. The non-proprietary version is WCAP-15862 (APP-SSAR-GSC-588). A revision to the proprietary and non-proprietary versions of this methodology document has been made to incorporate the contents of APP-GW-GLR-096 and other assessments of outstanding design debt identified in APP-GW-GLR-139, as well as an update to the methodology used in the latest containment integrity analyses.

The methodology update necessitates changes to various licensing basis sections to reflect the new document revision (UFSAR Table 1.6-1, Subsection 6.2.2.3, Subsection 6.2.7, and Subsection 6A.5).

The majority of the changes to the methodology document occur in Chapter 13 of WCAP-15846, which describes the plant geometry and nodalization used in the WGOTHIC EM. Due to the proprietary nature of the methodology itself, the full discussion on the methodology changes and a comprehensive description of WCAP-15846 changes between Revisions 1 through 5 and associated technical evaluation is provided in a proprietary (APP-GW-GLR-801, Revision 0) and non-proprietary document (APP-GW-GLR-802), which are provided as Enclosures 5 and 6 of this

LAR, respectively. Additionally, WCAP-15846, Revision 5 (Proprietary) and WCAP-15862, Revision 5 (Non-Proprietary) are provided as Enclosures 7 and 8 of this LAR.

3.1.4 Updates to Containment Integrity (Containment Peak Pressure) Analyses:

a. LOCA Peak Pressure:

The LOCA containment integrity analysis has been recalculated to incorporate the aforementioned changes. The peak containment pressure decreased from 58.3 psig to 58.1 psig for the limiting DECLG break. The peak containment vapor temperature decreased from 411.3°F to 385.8°F for the DEHLG break. The updated containment pressure and temperature does not result in a change to the limiting profiles assumed in the equipment qualification testing program. The results of the reanalysis show increased margin with respect to the 59 psig acceptance criterion.

The LOCA peak containment pressure occurs for the DECLG case with minimum passive core cooling system (PXS) flows. The DECLG break peak pressure is calculated to be 58.1 psig and the peak temperature to be 357.8°F. The containment design pressure is 59 psig and so the GDC 16 and GDC 50 criteria continue to be met. The reanalyzed DECLG containment pressure and temperature curves for 5,000 seconds are used to update UFSAR Figures 6.2.1.1-5 and 6.2.1.1-6. The DECLG containment pressure and temperature curves for 3 days are used to update UFSAR Figures 6.2.1.1-7 and 6.2.1.1-8.

The DEHLG peak pressure is calculated to be 49.8 psig and the peak temperature is calculated to be 385.8°F. The DEHLG containment pressure and temperature curves for 100 seconds are used to update UFSAR Figures 6.2.1.1-9 and 6.2.1.1-10.

The revised peak pressure values for both the DECLG and DEHLG breaks are also reflected in UFSAR Tables 6.2.1.1-1 and 6.2.1.1-3.

GDC 38 requires that the containment pressure be reduced to below half of design pressure (29.5 psig) within 24 hours. Due to the revised pressure profiles, UFSAR Table 6.2.1.1-3 is updated to reflect that the DECLG pressure is reduced to below 27 psig after 24 hours, continuing to satisfy this requirement.

Updates to the licensing basis due to the information on LOCA peak containment pressure analyses above are reflected in markups to UFSAR Subsection 6.2.1.1.3, Tables 6.2.1.1-1 and 6.2.1.1-3, and Figures 6.2.1.1-5 to 6.2.1.1-10. Markups are also made to TS Administrative Control 5.5.8.

b. MSLB Peak Pressure:

The MSLB containment integrity analysis has been recalculated to incorporate the aforementioned changes. The peak containment pressure decreased from 58.2 psig to 57.2 psig for the DER initiated from 30% power. The peak containment vapor temperature increased from 374.7°F to 383.6°F for the DER initiated from 101% power. The updated containment pressure and temperature does not result in a change to the limiting profiles assumed in the equipment qualification testing program. The results of the reanalysis show increased margin with respect to the 59 psig acceptance criterion.

The steam line break peak containment pressure is calculated to be 57.2 psig from the 30% power case, which remains below the containment design pressure of 59 psig and so the GDC 16 and GDC 50 criteria continue to be met. The 30% power MSLB containment pressure curve for 5,000 seconds is used to update the UFSAR Figure 6.2.1.1-1.

The peak containment vapor temperature is 383.6°F from the 101% power case. The 101% power MSLB containment temperature curve for 5,000 seconds is used to update the UFSAR Figure 6.2.1.1-2.

The revised peak pressure values for both the 30% power and 101% power cases are also reflected in UFSAR Tables 6.2.1.1-1 and 6.2.1.1-3.

Updates to the licensing basis due to the information on SLB peak containment pressure analyses above are reflected in markups to UFSAR Subsection 6.2.1.1.3, Tables 6.2.1.1-1 and 6.2.1.1-3, and Figures 6.2.1.1-1 and 6.2.1.1-2.

3.1.5 Criterion Allowing for Analysis Showing that As-Tested Performance of the PCS is Greater than that Assumed in the Peak Pressure Analyses:

In addition to the general updates to align the analyses with the updated design, supplementary licensing basis changes are proposed in order to capture lessons learned from preoperational testing conducted at Sanmen Unit 1. More specifically, an additional ITAAC criterion is proposed which would allow for analysis showing that as-tested performance of the PCS is greater than that assumed in the peak pressure analyses as a result of PCS water flow testing.

ITAAC 2.2.02.07a.ii Acceptance Criteria requires that “When tested and/or analyzed with the flow paths delivering and an initial water level at 27.4 + 0.2, - 0.00 ft., the PCCWST water inventory provides greater than or equal to 72 hours of flow, and the flow rate at 72 hours is greater than or equal to 100.7 gpm.” During PCS preoperational testing at Sanmen Unit 1, the water flow rate from the PCCWST to the containment shell met the required 100.7 gpm up to 71.5 hours, but fell below 100.7 gpm at 72 hours. Thus, the ITAAC acceptance criterion was not met.

The as-tested delivered flow rates were compared to the minimum safety analysis delivered flow rates showing that although the flow at 72 hours did not meet the minimum 72 hour flow rate, the system (including uncertainties) performed better than expected during the initial part of the transient, i.e., the time of peak containment pressure and temperature.

A clarification is therefore added to the ITAAC to explain that if the 100.7 gpm value at 72 hours acceptance criterion is not met, justification will be provided to ensure that the actual performance of the PCS is greater than assumed for the peak pressure analyses and thus, that the plant remains safe. This change is reflected in ITAAC 2.2.02.07a.i and 2.2.02.07a.ii. Additionally, UFSAR Subsection 6.2.2.4.2 restates these same commitments, and thus the additional acceptance criterion is also added.

3.1.6 Clarification of the Heat Transfer Elevation and Changes Related to Inorganic Zinc Application

ITAAC 3.3.00.02g states that the containment vessel provides a heat transfer surface for containment at elevations greater than 7 feet above the operating deck. Technically this is correct;

however, the design commitment implies that the CV surface from the operating deck up to 7 feet above does not provide a credited heat transfer surface. In practice, this portion of the CV is credited as transferring heat from inside containment to the atmosphere, consistent with the methodology that the NRC has reviewed and approved as part of the current containment integrity analyses. An editorial clarification is therefore made to prevent misinterpretation, thus necessitating NRC approval of the clarification to the ITAAC. This change has no technical impact and is reflective of the current and revised analyses.

Licensing changes are proposed to ITAAC 2.2.02.07b.iii, ITAAC 3.3.00.02g, Tier 1 Section 3.3 Item 2.g) as well as Tier 2 Subsections 6.1.2.1.1 and 6.1.2.1.5 and Tier 2 Tables 6.1-2 (Note 9) and 14.3-2. These changes have been included in the revised containment integrity analyses and so are now proposed for incorporation into the licensing basis.

3.1.7 Updates to LOCA Minimum Containment Backpressure:

Starting from the updated WGOTHIC peak pressure containment EM, the minimum containment backpressure transient for the small break loss of coolant accident (SBLOCA) and large break loss of coolant accident (LBLOCA) is recalculated. The LBLOCA minimum containment backpressure is described in UFSAR Subsection 6.2.1.5. The SBLOCA and post-LOCA long-term core cooling analyses are described in UFSAR Subsections 15.6.5.4B and 15.6.5.4C, respectively.

For the purpose of LOCA analyses, it is conservative to minimize the containment backpressure, which maximizes the amount of reactor coolant system (RCS) inventory lost from the reactor vessel, therefore maximizing temperature of the fuel cladding. A conservative multiplier of 2.1 on the WGOTHIC heat sink surface area and volume is used in current minimum containment backpressure analysis supporting the UFSAR. However, a finalized and more detailed quantification of the containment passive heat sinks has been performed (described above); therefore, continuing to apply a factor of 2.1 to the re-quantified heat sinks would be overly conservative. The new analyses therefore use a multiplier of 1.35, which is based on the estimated deviation of the quantified metal and unquantified structures, while still maintaining an appropriate amount of additional conservatism. This change is reflected in UFSAR Subsection 6.2.1.5.3.

As part of the update, various initial conditions were updated, which are described in UFSAR Subsection 6.2.1.5.2. Initial pressure is decreased from 14.7 psia to 14.5 psia, containment temperature is decreased from 90°F to 50°F, and relative humidity is increased from 99% to 100%. Each of these changes is conservative to the overall analysis.

The current analysis utilizes the guidance in Branch Technical Position CSB 6-1, "Minimum Containment Pressure Model for PWR ECCS Performance Evaluation", Reference 8 in UFSAR Subsection 6.2.7 (note that the referenced branch technical position has been replaced by BTP 6-2) for material properties of passive heat sinks. However, it was determined that the heat sink material properties should instead be based on ASME Boiler and Pressure Vessel Code (B&PVC), Section II, Part D (+10%) properties rather than the general properties identified in BTP 6-2, which has both conservative and non-conservative effects. This is consistent with the material properties used for the SBLOCA minimum backpressure analysis. For example, the BTP 6-2 thermal conductivity is notably non-conservative for Group A carbon steel (30% to 40% lower than the ASME values), which is approximately half of the metal in the WGOTHIC model. The heat capacity for Group A carbon steel used in the revised analysis is conservative for the containment

shell throughout the transient. The generic guidance is not preferred to the detailed information that has been collected associated with the revised heat sinks for this plant design. The in-text citation of CSB 6-1/BTP 6-2 is therefore deleted from UFSAR Subsection 6.2.1.5.3 and from the reference list in UFSAR Subsection 6.2.7. A sentence is also added to UFSAR Subsection 6.2.1.5.3 to instead reflect the use of ASME material property data including a +10% uncertainty for the heat sink material properties.

Updates to the licensing basis due to the information on the LBLOCA minimum backpressure analyses above are reflected in markups to UFSAR Subsections 6.2.1.5, 6.2.1.5.2, 6.2.1.5.3, and 6.2.7, Table 6.2.1.5-1, and Figure 6.2.1.5-1.

Assessment of Peak Clad Temperature (PCT) Impacts on LOCA:

As previously discussed, starting from the updated WGOTHIC peak pressure containment EM, the minimum containment backpressure transient for SBLOCA and LBLOCA are recalculated. These revisions to the LOCA WGOTHIC minimum containment backpressure models and analyses constitute the changes associated with the post-Core Reference Report (WCAP-17524-P-A) design change rebaseline evaluation. The design change rebaseline evaluation addressed AP1000 plant design changes which occurred since the AP1000 Core Reference Report LBLOCA and SBLOCA analyses were performed. The Core Reference Report was incorporated by VEGP 3&4 as Amendment 52 (ML16201A440). The design changes impacting LBLOCA and SBLOCA as part of that analysis effort included numerous passive core cooling (PXS), vessel model, RCS, and secondary system changes.

A LBLOCA rebaseline evaluation was performed and results in a PCT penalty of +54°F. The current analysis of record (AOR) for the LBLOCA event documented in UFSAR Subsection 15.6.5.4C results in a PCT of 1936°F. Additional PCT penalties were reported in the calendar year 2016 Annual 10 CFR 50.46 Report (ND-17-0457, ML17102A521). These included a PCT penalty of +11°F for the revised heat transfer multiplier distributions, and a PCT penalty of +23°F for the error in burst strain application. With the addition of the +54°F PCT increase due to the culmination of the LBLOCA rebaseline effort with the completion of the minimum backpressure model update, the current licensing basis PCT will be 2024°F, which continues to demonstrate margin to the 2200°F 10 CFR 50.46 acceptance criteria.

A SBLOCA rebaseline evaluation was performed and results in a PCT penalty of +243.5°F. The current AOR for the SBLOCA event documented in UFSAR Subsection 15.6.5.4B results in a PCT of 663.5°F. Additional PCT penalties were reported in the calendar year 2016 Annual 10 CFR 50.46 Report (ND-17-0457). These included a PCT penalty of +32°F due to the NOTRUMP bubble rise/drift flux model inconsistencies and a PCT penalty of +13°F from the impact of a reduction in the second and third stage ADS control valves and fourth stage ADS squib valve minimum effective flow areas documented in VEGP 3&4 LAR-16-012 (ND-16-0984, ML16207A340) and approved as Amendment 62. Additionally, a PCT penalty of +144°F from changes to the ADS Stages 1 through 4 and IRWST injection line resistances is included in VEGP 3&4 LAR-17-009 (ND-17-0443, ML17090A209). With the addition of the +243.5°F PCT increase due to the culmination of the SBLOCA rebaseline effort with the completion of the minimum backpressure model update, the current licensing basis PCT will be 1096°F, which continues to demonstrate margin to the 2200°F 10 CFR 50.46 acceptance criteria.

3.1.8 Clarifications/Consistency/Editorial Changes

In addition to the changes described above, other clarifications and editorial consistency changes are proposed. These include:

- a. UFSAR Subsection 6.2.1.1.3 discusses the design evaluation of the containment system. Current paragraph nine transitions from the discussion of the heat sinks to a discussion of IOZ coatings. This discussion is replaced by a simplified and more concise bullet stating that “the thermal conductivity of inorganic zinc is reduced by a factor of two relative to the minimum test requirements. The conditions for use of this reduction factor identified in Section 4 of Reference 37 are met.” A new paragraph is also added to identify that IOZ is modeled on the containment vessel (inside and outside) and IOZ plus an epoxy top coat for the containment vessel below the operating deck inside of containment. These changes have no technical impact and are reflective of the current and revised analyses.
- b. WCAP-15846 Sections 13.2 and 13.9 discuss the model using nominal cold dimensions. Therefore, the following statement is added to UFSAR Subsection 6.2.1.1.3 after the heat sink discussion: “The free volume inside the containment is calculated using nominal, cold dimensions. This conservatively neglects the thermal expansion of the containment vessel at elevated temperatures.” This change is simply a relocation of information pertaining to the existing methodology. This change has no technical impact and is reflective of the current and revised analyses.
- c. UFSAR Subsection 6.2.1.1.3 discusses the design evaluation of the containment system. Current paragraph nine continues the general discussion of the model, specifically the heat sinks. An introductory paragraph is added, as new paragraph seven, which provides a reference to UFSAR Table 6.2.1.1-10, which summarizes the required volume of steel inside containment to validate the heat sink input used in the revised analyses (both peak pressure and minimum pressure). Note that the change to UFSAR Tier 2* Table 6.2.1.1-10 is described in the “Heat Sink” section of this licensing change package. This change has no technical impact beyond what is discussed elsewhere for UFSAR Table 6.2.1.1-10 and is reflective of the revised analyses.
- d. UFSAR Subsection 6.2.1.1.3 discusses the design evaluation of the containment system. The sixth paragraph summarizes the analyses performed for the MSLB events, and provides statements regarding the analyses for a spectrum of break sizes and power levels. Although individual break sizes were evaluated for the AP600 design, a full double-ended pipe rupture is the limiting MSLB scenario; this largest break size causes the highest release rate from the break (fastest blowdown), creating the most challenging scenario for the containment integrity analysis (highest peak pressure). The statement regarding the AP1000 plant analyses being performed for different break sizes is therefore not appropriate and is revised by removing the reference to the representative pipe break size spectrum. As reflected in the current and revised analyses, the full double-ended MSLB is analyzed at different power levels, and so a statement to that end is added to UFSAR Subsection 6.2.1.1.3. This change has no technical impact and is reflective of the current and revised analyses.
- e. UFSAR Subsection 6.2.1.4.3 describes the “Containment Response Analysis” for the MSLB event. This section points to UFSAR Subsection 6.2.7 Reference 36 (“Evaluation of the Effect of AP1000 Enhanced Shield Building Design on the Containment Response

and Safety Analysis”) as documenting the steam line break analysis. However, Reference 36 contained only an evaluation of the shield building changes on the steam line break analysis for DCD Revision 19. Since the containment response following a main steam line break is described in UFSAR Subsection 6.2.1.1, as well as the steam line break undergoing a full reanalysis (which incorporates the enhanced shield building design) the reference to Reference 36 is no longer needed and so is deleted from this section. Therefore, Reference 36 is also deleted from UFSAR Subsection 6.2.2.3 and 6.2.7. This change has no technical impact beyond what is discussed elsewhere for the update to the MSLB M&E release analysis.

- f. UFSAR Subsection 6.2.1.4.3.2 describes the “Mass and Energy Release Data” for the MSLB analysis. The second sentence refers to Table 6.2.1.4-2 for the “mass and energy release data for the cases that produce the highest containment pressure and temperature in the containment response analysis.” However, the “data” should more specifically refer to the “analysis results”, as this is what is provided by Table 6.2.1.4-2. This change, in turn, makes the statement “in the containment response analysis” redundant and unnecessary and so is deleted. Additionally, a change is made to this sentence to specify that this is for the steam line break (as opposed to LOCA). The pluralization for “cases” and “produce” are also changed since the Table provides data for the highest containment pressure analysis and is a single case. Another phrase is also added to refer the reader to Table 6.2.1.4-3 for the analysis results of the case which produces the highest containment temperature. These changes have no technical impact and are reflective of the current and revised analyses.
- g. UFSAR Subsection 6.2.1.5 describes the “Minimum Containment Pressure Analysis for Performance Capability Studies of Emergency Core Cooling System (PWR).” As evidenced by the current first sentence, this section currently only describes the LBLOCA backpressure with no reference to SBLOCA. For completeness, a new paragraph is added to state that the minimum containment backpressure analyses are also performed for the SBLOCA and post-LOCA long term cooling analyses; references to the appropriate sections in Chapter 15 are also provided. Accordingly, the first three sentences of Subsection 6.2.1.5 are deleted (as they pertain to and imply the section is solely related to LBLOCA). These changes have no technical impact and are reflective of the current and revised analyses.

UFSAR Subsection 6.2.1.5 describes the “Minimum Containment Pressure Analysis for Performance Capability Studies of Emergency Core Cooling System (PWR).” The fourth sentence is updated to clarify that an analysis is performed to establish a “minimum” containment pressure boundary condition as well as including a cross-reference to the appropriate section in UFSAR Chapter 15 which uses the minimum containment pressure boundary condition. Note that UFSAR Subsection 6.2.7 Reference 8 is not an appropriate reference in the current UFSAR sentence and has been deleted. These changes have no technical impact and are reflective of the current and revised analyses.

- h. UFSAR Subsection 6.2.1.5.1 describes the “Mass and Energy Release Data” for the minimum backpressure analyses. The first sentence states that the M&E releases during the blowdown portion of the DECLG are presented in Table 6.2.1.5-1. However, as part of the revised analysis, the time-frame over which the M&E release results is provided has now been extended to cover the whole duration. Therefore, “...during the blowdown portion only of...” is replaced with “for” since the table now presents both blowdown and

post-blowdown. This change has no technical impact beyond what is discussed elsewhere for the update to the minimum backpressure analysis.

- i. UFSAR Subsection 6.2.1.5.1 describes the “Mass and Energy Release Data” for the minimum backpressure analyses. The last sentence states that “...the mass/energy releases during the reflood phase of the subject break are not considered. This produces a conservatively low containment pressure result for use as a boundary condition in the WCOBRA/TRAC large break LOCA analysis.” However, both the current and revised analyses do consider the M&E during reflood (see Table 14-1 and Section 14.3 of WCAP-15846 Revisions 1 and 5). This clarification to the license is not a change in the analytical approach, but a clarification to the description of the approach in the UFSAR. This change has no technical impact and is reflective of the current and revised analyses.
- j. UFSAR Subsection 6.2.1.5.3 describes “Other Parameters” used in the minimum backpressure analyses. The next to last sentence of the first paragraph states, “To further minimize containment pressure, containment purge was assumed to be in operation at time zero and air is vented through both the 15 inch diameter (16 inch, Sch. 40 piping) containment purge supply and exhaust lines until the isolation valves have fully closed.” This level of detail for pipe/valve design is excessive and unnecessary for this UFSAR section, and so the dimensions are deleted. These values are not crucial considerations from which the NRC Staff based the original safety evaluation on, nor are they crucial to the understanding of the events. Retaining the specification of “containment purge supply” line in the existing UFSAR text is sufficient detail for this application. Further, SRP Section 6.2.1 does not state that this level of detail shall be included in the UFSAR. This change has no technical impact and is reflective of the current and revised analyses.
- k. UFSAR Subsection 6.2.1.5.3 describes “Other Parameters” used in the minimum backpressure analyses. The last sentence of the first paragraph states that “These valves [referring to the containment purge supply and exhaust isolation valves] were modeled to close 12 seconds after the 8 psig closure setpoint was reached.” The specific closure time and setpoint value is not appropriate for inclusion in the licensing basis and so is removed; the setpoint value is instead replaced with the appropriate setpoint signal used to close the valves (i.e. Replace “8 psig closure” with “High-2 containment pressure”). Additionally, text is added to note that a delay time is incorporated with the High-2 setpoint in the analysis to account for purge valve closure time. These values are not crucial considerations from which the NRC Staff based their original safety evaluation on, nor are they crucial to the understanding of the events. Further, SRP Section 6.2.1 does not state that this level of detail shall be included in the UFSAR. This change has no technical impact and is reflective of the current and revised analyses.
- l. UFSAR Subsection 6.2.1.1.3 discusses the design evaluation of the containment system. The first and second paragraphs begin to discuss the modeling of the containment; the third paragraph then delves into the details of the analysis with respect to “Heat conduction from the dry to wet section...” This text is out of place and is moved to the end of Subsection 6.2.1.1.3 as the new second-to-last paragraph. Additionally, this aspect of the analysis is elaborated on in the updated paragraph by relating it to the applicable acceptance criteria and providing a reference to the associated Chapter 15 section and Table 6.2.1.1-3 containing the results; this additional clarifying text is moved from current paragraph nine of UFSAR Subsection 6.2.1.1.3, which is focused on heat sinks. Lastly,

Note 1 is added to Table 6.2.1.1-3 related to this clarification. This change has no technical impact and is reflective of the current and revised analyses.

- m. UFSAR Subsection 6.2.1.1.1 discusses the “Design Basis” of the containment system. The third paragraph identifies that “the single failure postulated for the containment pressure/temperature calculations is the failure of one of the valves controlling the cooling water flow for the PCS. Failure of one of these valves would lead to cooling water flow being delivered to the containment vessel through two of three delivery headers. This results in reduced cooling flow for PCS operation. No other single failures are postulated in the containment analysis.” However, both the current and revised analyses assume only one of the three PCS cooling water flow paths is available, which is more conservative than the two implied by the current text. To reflect this conservatism, as is already stated by the existing UFSAR Table 6.2.2-3, UFSAR Subsection 6.2.1.1.1 is clarified by replacing the last sentence regarding “No other single failures are postulated in the containment analysis” with the following: “However, as stated in Table 6.2.2-3, only one flowpath is necessary to meet the minimum containment cooling requirements, and only one flowpath is assumed in the containment integrity analyses.” Note that this licensing change package also adds a similar statement to UFSAR Table 6.2.1.1-3 as Note 2 for consistency. This change has no technical impact and is reflective of both the current and revised analyses.
- n. A discrepancy exists between a value cited in UFSAR Table 6.2.2-1 for the percentage of wetted coverage of the containment shell circumference at 72 hours and the value used in the supporting containment pressure analysis. Specifically, UFSAR Table 6.2.2-1 states that the wetted coverage of the containment shell circumference at 72 hours is 41.6%. However, a review of the updated supporting containment pressure analysis reports a wetted coverage of 41.7% for the containment shell circumference, noting that the actual value used for wetted coverage is 41.65%. This discrepancy is attributed to rounding of the analyzed value and has no technical consequence on the results of containment pressure analysis. Therefore, a change to UFSAR Table 6.2.2-1 to specify the wetted coverage of the containment shell circumference at 72 hours as 41.7% is proposed for consistency with the updated containment pressure analysis as part of this activity.
- o. UFSAR Subsection 6.2.1.4.3.2 describes the “Mass and Energy Release Data” for the MSLB event. The first sentence refers to “...the spectrum of breaks analyzed”. As discussed earlier, however, only the full DER is analyzed at various power levels since it bounds other break sizes previously analyzed for the AP600 design. Therefore, “spectrum of breaks” is replaced with “cases” to reflect that the event is analyzed for different cases which vary the initial power level. This change has no technical impact and is reflective of the current and revised analyses.

List of Proposed Licensing Basis Changes

Table 3-1 delineates the changes to the licensing basis being requested as part of this LAR.

Table 3-1: List of Licensing Basis Changes

UFSAR Section/Subsection/Table/Figure	LAR ID	Change
Tier 1 Table 2.2.2-3 ITAAC Number 2.2.02.07a.i	3.1.5	Add "or a report exists and concluded that the as-measured flow rates bound the 72-hours containment peak pressure results"
Tier 1 Table 2.2.2-3 ITAAC Number 2.2.02.07a.ii	3.1.5	Add "or a report exists and concluded that the as-measured flow rates bound the 72-hours containment peak pressure results"
Tier 1 Table 2.2.2-3 ITAAC Number 2.2.02.07b.iii	3.1.6	Remove "above 7"
Tier 1 Section 3.3 Item 2.g	3.1.6	Remove "greater than 7 feet"
Tier 1 Table 3.3-6 ITAAC Number 3.3.00.02g	3.1.6	Remove "greater than 7 feet"
Table 1.6-1 (6.2)	3.1.3	Revise WCAP-15846 from Rev 1 to Rev 5
Table 1.6-1 (6A)	3.1.3	Revise WCAP-15846 from Rev 1 to Rev 5
Subsection 6.1.2.1.1	3.1.6	Remove "greater than 7' above the operating deck"
Subsection 6.1.2.1.5	3.1.6	Remove "greater than 7' above the operating deck"
Table 6.1-2	3.1.6	Remove note 9 from Containment shell, Inside Surface (IOZ).
Table 6.1-2	3.1.6	Delete note 9.
Subsection 6.2.1.1.1	3.1.8.m	Replace "No other single failures are postulated in the containment analysis" with "However, as stated in Table 6.2.2-3, only one flowpath is necessary to meet the minimum containment cooling requirements, and only one flowpath is assumed in the containment integrity analyses."
Subsection 6.2.1.1.3	3.1.8.l	Moved discussion on "dry to wet" to the end of Section 6.2.1.1.3 as the new second-to-last paragraph. Provide reference to the related

UFSAR Section/Subsection/Table/Figure	LAR ID	Change
		Chapter 15 section and Chapter 6 Table 6.2.1.1-3 containing the results. This additional clarifying text is moved from current paragraph nine of UFSAR Section 6.2.1.1.3, which is focused on heat sinks.
Subsection 6.2.1.1.3	3.1.8.d	Delete "representative pipe break spectrum." Add statement regarding analyses at different power levels.
Subsection 6.2.1.1.3	3.1.1.a 3.1.8.c	Add introductory paragraph providing reference to Table 6.2.1.1-10.
Subsection 6.2.1.1.3	3.1.8.a	Replace existing IOZ paragraph to identify that IOZ is modeled.
Subsection 6.2.1.1.3	3.1.8.b	Add sentence regarding the free volume inside containment being calculated using nominal, cold dimensions.
Subsection 6.2.1.1.3	3.1.4.a 3.1.4.b	Add statements pertaining to where the results of the analyses are presented in the licensing basis (i.e., Figure 6.2.1.1-5, -6, etc.)
Subsection 6.2.1.3.2.2	3.1.2.a	Add clarifying statement that "The only exception to the Reference 4 methodology is that the overall heat transfer coefficient between the primary side of the reactor coolant system metal and the fluid is adjusted when there is no liquid in the system to prevent an unrealistically high temperature for the steam release".
Subsection 6.2.1.4.1.7	3.1.2.b	Add that "Energy from the metal of the faulted steam generator is also transferred to the fluid in the faulted steam generator as the fluid temperature drops below the metal temperature."
Subsection 6.2.1.4.1.7	3.1.2.b	Clarify that "The effects of the reactor coolant system metal, the steam generator metal, and the energy in the fluid from the intact steam generator are included..." as opposed to "The effects of both the reactor coolant system metal and the reverse steam generator heat transfer are included..."
Subsection 6.2.1.4.3	3.1.8.e	Remove "documented in Reference 36. The containment response analysis is..."
T2 Section 6.2.1.4.3.2	3.1.8.o	Replace "spectrum of breaks" with "cases".
Subsection 6.2.1.4.3.2	3.1.8.f	Replace "data" with "analysis results".
Subsection 6.2.1.4.3.2	3.1.8.f	Clarify that Table 6.2.1.4-2 provides the mass and energy release analysis results for the "steam line break case that produces the highest containment pressure and Table 6.2.1.4-3 provides the mass and energy release analysis results for the steam line break case that produces the highest containment" temperature...
Subsection 6.2.1.4.3.2	3.1.8.f	Delete "in the containment response analysis."

UFSAR Section/Subsection/Table/Figure	LAR ID	Change
Subsection 6.2.1.5	3.1.8.g	Delete "The containment backpressure used for the AP1000 cold leg guillotine and split breaks for the emergency core cooling system (ECCS) analysis presented in Subsection 15.6.5 is described. The minimum containment backpressure for emergency core cooling system performance during a loss-of-coolant accident is computed using the <u>WGOTHIC</u> computer code. Subsection 6.2.1.1 demonstrates that the AP1000 containment pressurizes during large break LOCA events."
Subsection 6.2.1.5	3.1.7 3.1.8.g	Delete Reference 8
Subsection 6.2.1.5	3.1.8.g	Add "Minimum containment pressure analyses are also performed to provide the containment backpressure boundary condition for small-break LOCA (Section 15.6.5.4B) and post-LOCA long-term cooling analyses (Section 15.6.5.4C). A multi-node <u>WGOTHIC</u> containment model described in WCAP-15846 (Reference 20) is used."
Subsection 6.2.1.5.1	3.1.8.h	Replace "during the blowdown portion only of" with "for"
Subsection 6.2.1.5.1	3.1.8.i	Delete "Note that the mass/energy releases during the reflood phase of the subject break are not considered. This produces a conservatively low containment pressure result for use as a boundary condition in the WCOBRA/TRAC large break LOCA analysis."
Subsection 6.2.1.5.2	3.1.7	Change initial pressure from 14.7 psia to 14.5 psia.
Subsection 6.2.1.5.2	3.1.7	Change initial containment temperature from 90°F to 50°F.
Subsection 6.2.1.5.2	3.1.7	Change relative humidity from 99 percent to 100 percent.
Subsection 6.2.1.5.3	3.1.7	Change "Passive heat sink surface areas were increased by a factor of 2.1 times the values presented in Reference 20." with "Passive heat sink surface areas were increased by a factor of 1.35 relative to the heat sinks developed for the peak containment evaluation model as described in Reference 20."
Subsection 6.2.1.5.3	3.1.7	Replace "Material properties were biased high (density, conductivity, and heat capacity) as indicated in CSB 6-1 (Reference 8)." with "The thermal conductivity and volumetric heat capacity of steel materials were increased by 10% from the ASME standard to increase heat removal."
Subsection 6.2.1.5.3	3.1.8.j	Delete "15 inch diameter (16-inch, Sch. 40 piping)"

UFSAR Section/Subsection/Table/Figure	LAR ID	Change
Subsection 6.2.1.5.3	3.1.8.k	Delete "12 seconds".
Subsection 6.2.1.5.3	3.1.8.k	Replace "8 psig closure" with "High-2 containment pressure". Additionally, text is added to note that a delay time is incorporated with the High-2 setpoint in the analysis to account for purge valve closure time.
Subsection 6.2.2.3	3.1.8.e	Delete Reference 36
Subsection 6.2.2.4.2	3.1.5	Add "or a report exists and concludes that the as-measured flow rates bound the 72 hour containment peak pressure and temperature results."
Subsection 6.2.7	3.1.7	Delete Reference 8 (not used)
Subsection 6.2.7	3.1.3	Revise WCAP-15846 from Rev 1 to Rev 5
Table 6.2.1.1-1	3.1.4.a 3.1.4.b	Update calculated values for breaks.
Table 6.2.1.1-3	3.1.4.a 3.1.4.b	Update calculated pressure results.
Table 6.2.1.1-3	3.1.4.a 3.1.8.l	Change "22 at 24 hrs" to "<27 after 24 hrs ₍₁₎ "
Table 6.2.1.1-3	3.1.8.l	Add note 1: "Analysis without crediting heat conduction from dry to wet sections on containment shell".
Table 6.2.1.1-3	3.1.8.m	Change "Two of Three Trains of PCS Water Supply" to "Two of Three PCS Water Supply Flowpaths ₍₂₎ ".
Table 6.2.1.1-3	3.1.8.m	Add note 2: "Table 6.2.2-3 notes that operation of only one of three flowpaths is necessary to meet minimum containment cooling requirements."
Table 6.2.1.1-8	3.1.1.a	Update table in its entirety for material properties used in the <u>WGOTHIC</u> containment evaluation model
Tier 2* Table 6.2.1.1-10	3.1.1.a	Update table in its entirety for heat sinks inside containment
New Table 6.2.1.1-11	3.1.1.a	Add new table for heat sinks credited in the peak containment pressure analyses
Table 6.2.1.3-8	3.1.2.a	Update values for Nominal Vessel Inlet Temperature °F (537.2 to 535.5), Nominal Vessel Outlet Temperature °F (610.0 to 612.2), and Steam Pressure psia (881.0 to 870.0).
Table 6.2.1.3-9	3.1.2.a	Update long-term DECL break mass and energy releases
Table 6.2.1.3-10	3.1.2.a	Update table for blowdown DEHL break mass and energy releases

UFSAR Section/Subsection/Table/Figure	LAR ID	Change
Table 6.2.1.4-2	3.1.2.b	Update table for MSLB DER mass and energy releases from 30% power level
Table 6.2.1.4-3	3.1.2.b	Update table for MSLB DER mass and energy releases from full power level
Table 6.2.1.4-4	3.1.2.b	Update values for Nominal Steam Temperature °F (525.0 to 525.5) and Nominal Feedwater Enthalpy BTU/lbm (419.3 to 419.4)
Table 6.2.1.5-1	3.1.7	Update table for minimum containment pressure mass and energy releases for LBLOCA
Table 6.2.2-1	3.1.8.n	Update table value for wetted coverage (% of circumference) at 72 hours from 41.6 to 41.7.
Figure 6.2.1.1-1	3.1.4.b	Update figure for containment pressure response for full DER MSLB – 30% power
Figure 6.2.1.1-2	3.1.4.b	Update figure for containment response for full DER MSLB – 101% power
Figure 6.2.1.1-5	3.1.4.a	Update figure for containment pressure response for DECLG LOCA
Figure 6.2.1.1-6	3.1.4.a	Update figure for containment temperature response to DECLG LOCA
Figure 6.2.1.1-7	3.1.4.a	Update figure for new containment pressure response for DECLG LOCA – 3 days
Figure 6.2.1.1-8	3.1.4.a	Update figure for containment temperature response for DECLG LOCA – 3 days
Figure 6.2.1.1-9	3.1.4.a	Update figure for containment pressure response – DEHLG LOCA
Figure 6.2.1.1-10	3.1.4.a	Update figure for containment temperature response for DEHLG LOCA
Figure 6.2.1.3-1	3.1.2.a	Update figure for DECLG integrated break flow
Figure 6.2.1.3-2	3.1.2.a	Update figure for DECLG LOCA integrated energy released
Figure 6.2.1.3-3	3.1.2.a	Update figure for DEHLG integrated break flow
Figure 6.2.1.3-4	3.1.2.a	Update figure for DEHLG LOCA integrated energy released
Figure 6.2.1.5-1	3.1.7	Update figure for minimum containment pressure for DECLG LOCA
Subsection 6A.5	3.1.3	Revise WCAP-15846 from Rev 1 to Rev 5
Table 14.3-2	3.1.6	Remove "above 7' above the operating deck"
TS 5.5.8	3.1.4.a	Update peak pressure results (58.3 to 58.1).
WCAP-15846	3.1.3	WCAP-15846 is incorporated by reference into the VEGP Units 3 & 4 UFSAR and is updated from Revision 1 to Revision 5. The changes between Revision 1 to Revision 5 are included in Enclosure 5 (Proprietary) and Enclosure 6 (Non-Proprietary) to this LAR. Additionally, WCAP-15846, Revision 5 (Proprietary) and WCAP-15862,

UFSAR Section/Subsection/Table/Figure	LAR ID	Change
		Revision 5 (Non-Proprietary) are provided as Enclosures 7 and 8 of this LAR.

In summary, the AP1000 plant containment systems are designed such that for DBAs, the containment peak pressure remains below the design pressure of 59 psig for the duration of the transient. This is accomplished by a number of design features and is verified by analysis and testing.

The current licensing basis containment integrity analyses described in UFSAR Section 6.2 is based on the AP1000 design configuration at the time of the amended design certification (i.e., DCD Revision 19). Accumulated design changes within containment have necessitated recalculation of geometry input to the WGOTHIC EM used for containment integrity analyses. Heat sinks, control volumes, and flow paths have been recalculated, and are in turn modeled in the WGOTHIC EM. M&E releases for LOCA and MSLB are also recalculated. These updates culminate in the recalculation of the containment integrity analyses. These analyses were done in accordance with the revised WGOTHIC methodology for the AP1000 plant design, the changes to which are evaluated in Enclosures 5 (proprietary) and 6 (non-proprietary) of this LAR, respectively.

Changes are also proposed to the ITAAC 2.2.02.07a.i and 2.2.02.07a.ii to explain that if the 100.7 gpm value at 72 hours acceptance criteria is not met, justification will be provided to demonstrate that the actual performance of the PCS is greater than assumed for the peak pressure analyses and illustrate that the plant remains safe.

A clarification change is also proposed to ITAAC 3.3.00.02g to clarify that the portion of the containment vessel from the operating deck up to 7 feet above the operating deck is also credited as transferring heat from inside containment to the atmosphere, consistent with the methodology that the NRC has reviewed and approved as part of the current containment integrity analyses. This change has no technical impact and is reflective of the current and revised analyses.

The proposed changes do not require a change to procedures or method of control that adversely affects the performance of the PCS safety-related or nonsafety-related design functions as described in the UFSAR. The physical design and operation of the PCS, including as-installed inspections, testing, and maintenance requirements, as described in the UFSAR are not changed, and thus there are no changes to procedures or method of control required to address the proposed changes to the licensing basis. The proposed changes maintain the design function of the PCS to ensure that for DBAs, the containment peak pressure remains below the design pressure of 59 psig for the duration of the transient, and thus, meets GDC 16, 38, and 50.

An impact review determined these proposed changes do not affect or require any change to the AP1000 plant Probabilistic Risk Assessment (PRA) presented in UFSAR Chapter 19, including the Fire PRA, results and insights (e.g., core damage frequency and large release frequency). The proposed changes maintain the design function of the PCS to ensure that for DBAs, the containment peak pressure remains below the design pressure of 59 psig for the duration of the transient, and thus, meets GDC 16, 38, and 50. The physical design and operation of the PCS, including as-installed inspections, testing, and maintenance requirements, as described in the

UFSAR are not changed, and thus there are no changes to the AP1000 PRA required to address the proposed changes to the licensing basis. No new postulated failures of the PCS are required in the PRA model. Therefore, there are no changes required to initiating event frequencies and system logic models of the PRA, including the Seismic Margins Analysis. The existing PRA conclusions remain valid.

There are no radiation zone changes or radiological access control changes required due to the proposed changes. The physical design and operation of the PCS, including as-installed inspections, testing, and maintenance requirements, as described in the UFSAR are not changed, and thus there are no changes required to the radiation protection design features described in UFSAR Section 12.3.

There are no fire area changes required because of these proposed changes. The physical design and operation of the PCS, including as-installed inspections, testing, and maintenance requirements, as described in the UFSAR are not changed, and thus there are no changes required to the fire protection analysis described in UFSAR Appendix 9A.

There is no change to the risk-significant designation of SSCs within the Design Reliability Assurance Program as described in UFSAR Table 17.4-1, as the physical design and operation of the PCS, including as installed inspections, testing, and maintenance requirements, as described in the UFSAR are not changed.

The proposed changes do not affect the containment, control, channeling, monitoring, processing or releasing of radioactive and non-radioactive materials. No effluent release path is affected. The types and quantities of expected effluents are not changed. Therefore, radioactive or nonradioactive material effluents are not affected.

The proposed changes do not affect plant radiation zones, controls under 10 CFR 20, and expected amounts and types of radioactive materials, as the physical design and operation of the PCS, including as-installed inspections, testing, and maintenance requirements, as described in the UFSAR are not changed. Therefore, individual and cumulative radiation exposures do not change.

The proposed changes do not affect the results of the aircraft impact assessment described in UFSAR Subsection 19F.4 since there are no changes to the structures credited in that assessment.

4. REGULATORY EVALUATION

4.1 Applicable Regulatory Requirements/Criteria

10 CFR 52.98(f) requires NRC approval for any modification to, addition to, or deletion from the terms and conditions of a COL. This activity involves changes to Tier 2* information and to the COL Appendix A Technical Specifications, associated with the proposed changes to UFSAR Tier 2 information; therefore, this activity requires an amendment to the COL. Accordingly, NRC approval is required prior to making the plant-specific changes in this license amendment request.

10 CFR 52, Appendix D, Section VIII.B.5.a allows an applicant or licensee who references this appendix to depart from Tier 2 information, without prior NRC approval, unless the

proposed departure involves a change to or departure from Tier 1 information, Tier 2* information, or the Technical Specifications, or requires a license amendment under paragraphs B.5.b or B.5.c of the section. This activity involves changes to Tier 2* information and to the COL Appendix A Technical Specifications, associated with the proposed changes to UFSAR Tier 2 information and thus requires prior NRC approval.

10 CFR 50, Appendix A, General Design Criteria (GDC) 16, *Containment Design*, requires that the reactor containment and associated systems are provide an essentially leak-tight barrier against the uncontrolled release of radioactivity to the environment and to assure that the containment design conditions important to safety are not exceeded for as long as postulated accident conditions require. This is confirmed by analysis via the revised containment integrity analyses, which show margin to the containment design pressure.

10 CFR 50, Appendix A, GDC 38, *Containment heat removal*, requires, in part, that a system to remove heat from the reactor containment is provided. The system safety function shall be to reduce rapidly, consistent with the functioning of other associated systems, the containment pressure and temperature following any loss-of-coolant accident and maintain them at acceptably low levels. This is confirmed by analysis via the revised containment integrity analyses, which show that accident pressure is reduced by half within 24 hours.

10 CFR 50, Appendix A, GDC 50, *Containment design basis*, requires that the reactor containment structure, including access openings, penetrations, and the containment heat removal system are designed so that the containment structure and its internal compartments can accommodate, without exceeding the design leakage rate and with sufficient margin, the calculated pressure and temperature conditions resulting from any loss-of-coolant accident. This margin shall reflect consideration of (1) the effects of potential energy sources which have not been included in the determination of the peak conditions, such as energy in steam generators and as required by § 50.44 energy from metal-water and other chemical reactions that may result from degradation but not total failure of emergency core cooling functioning, (2) the limited experience and experimental data available for defining accident phenomena and containment responses, and (3) the conservatism of the calculational model and input parameters. These aspects are considered in the revised containment integrity analyses.

4.2 Precedent

None.

4.3 Significant Hazards Consideration

This change proposes updates to the plant-specific containment integrity analyses described in the UFSAR and COL Appendix A Technical Specification. Heat sinks, control volumes, and flow paths have been recalculated, and are in turn modeled in the WGOTHIC evaluation model (EM). Various methodology changes are also made to the WGOTHIC methodology for the AP1000 plant design. Mass and energy (M&E) releases for LOCA and MSLB are also recalculated. These updates culminate in the recalculation of the containment integrity calculations. Additionally, changes are proposed to ITAAC acceptance criteria related with flow rate testing of the passive containment cooling system (PCS) in order to capture lessons learned from testing at Sanmen Unit 1.

An evaluation to determine whether or not a significant hazards consideration is involved with the proposed amendment was completed by focusing on the three standards set forth in 10 CFR 50.92, "Issuance of amendment", as discussed below:

4.3.1 Does the proposed amendment involve a significant increase in the probability or consequences of an accident previously evaluated?

Response: No

This change proposes updates to the plant-specific containment integrity analyses. Heat sinks, control volumes, and flow paths have been recalculated, and are in turn modeled in the WGOTHIC evaluation model (EM). Various methodology changes are also made to the WGOTHIC methodology for the AP1000 plant design. Mass and energy (M&E) releases for LOCA and MSLB are also recalculated. These updates culminate in the recalculation of the containment integrity calculations. Additionally, changes are proposed to ITAAC acceptance criteria related to flow rate testing of the passive containment cooling system (PCS) in order to capture lessons learned from testing at Sanmen Unit 1.

The proposed changes do not adversely affect the operation of any systems or equipment that initiate an analyzed accident or alter any structures, systems, and components (SSC) accident initiator or initiating sequence of events. The proposed changes do not adversely affect the physical design and operation of the passive containment cooling system (PCS) including as-installed inspections, testing, and maintenance requirements, as described in the UFSAR. Therefore, the operation of the PCS is not adversely affected. A loss of coolant accident (LOCA) and a main steam line break (MSLB) are considered and identified as the limiting events for the AP1000 design with respect to containment peak pressure and temperature. However, the proposed changes do not adversely affect the probability of either a LOCA or MSLB from occurring. Therefore, the probabilities of the accidents previously evaluated in the UFSAR are not affected.

The proposed changes do not adversely affect the ability of the PCS to perform its design functions. The design of the PCS continues to meet the same regulatory acceptance criteria, codes, and standards as required by the UFSAR. In addition, the proposed changes maintain the capabilities of the PCS to mitigate the consequences of an accident and to meet the applicable regulatory acceptance criteria. The proposed changes do not adversely affect the prevention and mitigation of other abnormal events, e.g., anticipated operational occurrences, earthquakes, floods and turbine missiles, or their safety or design analyses. Therefore, the consequences of the accidents evaluated in the UFSAR are not affected.

Therefore, the proposed amendment does not involve a significant increase in the probability or consequences of an accident previously evaluated.

4.3.2 Does the proposed amendment create the possibility of a new or different kind of accident from any accident previously evaluated?

Response: No

This change proposes updates to the plant-specific containment integrity analyses. Heat sinks, control volumes, and flow paths have been recalculated, and are in turn modeled in the WGOTHIC EM. Various methodology changes are also made to the WGOTHIC methodology for the AP1000 plant design. M&E releases for LOCA and MSLB are also recalculated. These updates culminate in the recalculation of the containment integrity calculations. Additionally, changes are proposed to ITAAC acceptance criteria related to flow rate testing of the passive containment cooling system PCS in order to capture lessons learned from testing at Sanmen Unit 1.

The proposed changes would not introduce a new failure mode, fault, or sequence of events that could result in a radioactive material release. The proposed changes do not alter the design, configuration, or method of operation of the plant beyond standard functional capabilities of the equipment. Therefore, this activity does not allow for a new fission product release path, result in a new fission product barrier failure mode, or create a new sequence of events which results in significant fuel cladding failures.

Therefore, the proposed amendment does not create the possibility of a new or different kind of accident from any accident.

4.3.3 Does the proposed amendment involve a significant reduction in a margin of safety?

Response: No

This change proposes updates to the plant-specific containment integrity analyses. Heat sinks, control volumes, and flow paths have been recalculated, and are in turn modeled in the WGOTHIC EM. Various methodology changes are also made to the WGOTHIC methodology for the AP1000 plant design. M&E releases for LOCA and MSLB are also recalculated. These updates culminate in the recalculation of the containment integrity calculations. Additionally, changes are proposed to ITAAC acceptance criteria related to flow rate testing of the passive containment cooling system (PCS) in order to capture lessons learned from testing at Sanmen Unit 1.

Safety margins are applied at many levels to the design and licensing basis functions and to the controlling values of parameters to account for various uncertainties and to avoid exceeding regulatory or licensing limits. The proposed changes maintain existing safety margins, and in some cases, provide additional margin. The proposed changes maintain the capabilities of the PCS to perform its design functions. Therefore, the proposed changes satisfy the same design functions in accordance with the same codes and standards as stated in the UFSAR. These changes do not adversely affect any design code, function, safety analysis, safety analysis input or results, or design/safety margin. No safety analysis or design basis acceptance limit/criterion is challenged or exceeded by the proposed changes, and no margin of safety is reduced.

Therefore, the proposed amendment does not involve a significant reduction in a margin of safety.

Based on the above, it is concluded that the proposed amendment does not involve a significant hazards consideration under the standards set forth in 10 CFR 50.92(c), and, accordingly, a finding of “no significant hazards consideration” is justified.

4.4 Conclusions

Based on the considerations discussed above, (1) there is reasonable assurance that the health and safety of the public will not be endangered by operation in the proposed manner, (2) such activities will be conducted in compliance with the Commission's regulations, and (3) the issuance of the amendment will not be inimical to the common defense and security or to the health and safety of the public. The above evaluations demonstrate that the proposed changes can be accommodated without an increase in the probability or consequences of an accident previously evaluated, without creating the possibility of a new or different kind of accident from any accident previously evaluated, and without a significant reduction in a margin of safety. Having arrived at negative declarations with regard to the criteria of 10 CFR 50.92, this assessment determined that the proposed change does not involve a Significant Hazards Consideration.

5. ENVIRONMENTAL CONSIDERATIONS

This change proposes updates to the plant-specific containment integrity analyses described in the UFSAR and COL Appendix A Technical Specification. Heat sinks, control volumes, and flow paths have been recalculated, and are in turn modeled in the WGOTHIC EM. Various methodology changes are also made to the WGOTHIC methodology for the AP1000 plant design. M&E releases for LOCA and MSLB are also recalculated. These updates culminate in the recalculation of the containment integrity calculations. Additionally, changes are proposed to ITAAC acceptance criteria related to flow rate testing of the PCS in order to capture lessons learned from testing at Sanmen Unit 1.

A review has determined that the anticipated effects on facility construction and operation following implementation of the requested amendment meets the eligibility criteria for categorical exclusion set forth in 10 CFR 51.22(c)(9), in that:

(i) There is no significant hazards consideration

As documented in Section 4.3, Significant Hazards Consideration, of this license amendment request, an evaluation was completed to determine whether or not a significant hazards consideration is involved by focusing on the three standards set forth in 10 CFR 50.92, "Issuance of amendment". The Significant Hazards Consideration determined that (1) the proposed amendment does not involve a significant increase in the probability or consequences of an accident previously evaluated; (2) the proposed amendment does not create the possibility of a new or different kind of accident from any accident previously evaluated; and (3) the proposed amendment does not involve a significant reduction in a margin of safety. Therefore, it is concluded that the proposed amendment does not involve a significant hazards consideration under the standards set forth in 10 CFR 50.92(c), and accordingly, a finding of "no significant hazards consideration" is justified.

(ii) There is no significant change in the types or significant increase in the amounts of any effluents that may be release off site

The proposed changes in the requested amendment would not adversely affect the design or function of any structure, system, component (SSC). The proposed changes are unrelated to any aspect of plant construction or operation that would introduce any change to effluent types (e.g., effluents containing chemicals or biocides, sanitary system effluents, and other effluents), or adversely affect any plant radiological or non-radiological effluent release quantities. Furthermore, the proposed changes do not adversely affect any effluent release

path or diminish the functionality of any design or operational features that are credited with controlling the release of effluents during plant operation. Therefore, it is concluded that the proposed amendment does not involve a significant change in the types or a significant increase in the amounts of any effluents that may be released offsite.

(iii) There is no significant increase in individual or cumulative occupational radiation exposure.

The proposed changes in the requested amendment would not adversely affect the design or function of any structure, system, component (SSC). Plant radiation zones (in UFSAR Section 12.3) are not affected, and controls under 10 CFR 20 preclude a significant increase in occupational radiation exposure. Therefore, the proposed amendment does not involve a significant increase in individual or cumulative occupational radiation exposure.

Based on the above review of the proposed amendment, it has been determined that anticipated construction and operational effects of the proposed amendment do not involve (i) a significant hazards consideration, (ii) a significant change in the types or significant increase in the amounts of any effluents that may be released offsite, or (iii) a significant increase in individual or cumulative occupational radiation exposure. Accordingly, the proposed amendment meets the eligibility criteria for categorical exclusion set forth in 10 CFR 51.22(c)(9). Therefore, pursuant to 10 CFR 51.22(b), no environmental impact statement or environmental assessment need be prepared in connection with the proposed amendment and proposed exemption.

6. REFERENCES

None.

Southern Nuclear Operating Company

ND-17-2074

Enclosure 2

Vogtle Electric Generating Plant (VEGP) Units 3 and 4

Exemption Request:

Containment Pressure Analysis (LAR-17-043)

(Enclosure 2 consists of 7 pages, including this cover page.)

1.0 PURPOSE

Southern Nuclear Operating Company (the Licensee) requests a permanent exemption from the provisions of 10 CFR 52, Appendix D, Section III.B, *Design Certification Rule for the AP1000 Design, Scope and Contents*, to allow a plant-specific departure from elements of the certification information in Tier 1 of the plant-specific AP1000 Design Control Document (DCD). The regulation, 10 CFR 52, Appendix D, Section III.B, requires an applicant or licensee referencing Appendix D to 10 CFR Part 52 to incorporate by reference and comply with the requirements of Appendix D, including certified information in DCD Tier 1. The Tier 1 information for which a plant-specific departure and exemption is being requested is to make editorial changes to promote consistency in Tier 1 information.

This request for exemption will apply the requirements of 10 CFR 52, Appendix D, Section VIII.A.4 to allow departures from Tier 1 information due to the following proposed consistency and editorial changes to the system-based design descriptions, as described below.

Table 1: List of Tier 1 Licensing Basis Changes

UFSAR Section/Subsection/Table/Figure	Change
Tier 1 Table 2.2.2-3 ITAAC No. 2.2.02.07a.i	Add "or a report exists and concluded that the as-measured flow rates bound the 72-hours containment peak pressure results"
Tier 1 Table 2.2.2-3 ITAAC No. 2.2.02.07a.ii	Add "or a report exists and concluded that the as-measured flow rates bound the 72-hours containment peak pressure results"
Tier 1 Table 2.2.2-3 ITAAC No. 2.2.02.07b.iii	Remove "above 7"
Tier 1 Section 3.3 Item 2.g)	Remove "greater than 7 feet"
Tier 1 Table 3.3-6 ITAAC Number 3.3.00.2g	Remove "greater than 7 feet"

This request will provide for the application of the requirements for granting exemptions from design certification information, as specified in 10 CFR Part 52, Appendix D, Section VIII.A.4, 10 CFR 52.63, §52.7, and §50.12.

2.0 BACKGROUND

The Licensee is the holder of Combined License Nos. NPF-91 and NPF-92, which authorize construction and operation of two Westinghouse Electric Company AP1000 nuclear plants, named Vogtle Electric Generating Plant (VEGP) Units 3 and 4, respectively.

Accumulated design changes within containment have necessitated recalculation of geometry input to the WGOTHIC EM used for containment integrity analyses. Heat sinks, control volumes, and flow paths have been recalculated and are in turn modeled in the WGOTHIC EM. Various methodology changes are also made to the WGOTHIC methodology for the AP1000 plant. Mass and energy (M&E) releases for LOCA and MSLB are also recalculated to address changes to the current design. These updates culminate in the revisions of the containment integrity analyses. As a result of the redefined WGOTHIC EM, the containment minimum backpressure analysis is also recalculated. In addition, supplementary updates have been made to capture lessons learned from the passive containment cooling system (PCS) testing conducted at Sanmen Unit 1.

An exemption from elements of the AP1000 certified (Tier 1) design information to allow a departure from the design description is requested.

3.0 TECHNICAL JUSTIFICATION OF ACCEPTABILITY

An exemption is requested to depart from AP1000 generic Design Control Document (DCD) Tier 1 material in regard to the AP1000 by making updates to capture lessons learned from the PCS testing conducted date at Sanmen Unit 1. This update adds criterion to illustrate that the plant remains safe and the actual performance of the PCS is greater than assumed for the peak pressure analyses should the individual flow acceptance criterion not be met. The proposed exemption would allow a change to the plant-specific Tier 1 ITAAC information.

The proposed changes to the description information presented in plant-specific Tier 1 are at a level of detail that is consistent with the information currently provided therein. The proposed changes neither adversely impact the ability to meet the design functions of the structures, systems, and components (SSCs) nor involve a significant decrease in the level of safety provided by the structures, systems, or components. Because the proposed editorial changes are consistent with plant-specific DCD Tier 2 information and the underlying plant design, the changes do not physically affect an SSC. The proposed changes to information in plant-specific DCD Tier 1 continue to provide the detail necessary to implement the corresponding ITAAC. Further, application of the current generic certified design information in Tier 1 as required by 10 CFR Part 52, Appendix D, Section III.B, in the particular circumstances discussed in this request would not serve the underlying purpose of the rule due to the apparent editorial inconsistencies with the existing design information provided in Tier 2 of the plant-specific DCD.

4.0 JUSTIFICATION OF EXEMPTION

10 CFR Part 52, Appendix D, Section VIII.A.4 and 10 CFR 52.63(b)(1) govern the issuance of exemptions from elements of the certified design information for AP1000 nuclear power plants. Since SNC has identified consistency and clarification changes to the Tier 1

information as discussed in Enclosure 1 of the accompanying License Amendment Request, an exemption from the certified design information in Tier 1 is needed.

10 CFR Part 52, Appendix D, and 10 CFR 50.12, §52.7, and §52.63 state that the NRC may grant exemptions from the requirements of the regulations provided six conditions are met: 1) the exemption is authorized by law [§50.12(a)(1)]; 2) the exemption will not present an undue risk to the health and safety of the public [§50.12(a)(1)]; 3) the exemption is consistent with the common defense and security [§50.12(a)(1)]; 4) special circumstances are present [§50.12(a)(2)]; 5) the special circumstances outweigh any decrease in safety that may result from the reduction in standardization caused by the exemption [§52.63(b)(1)]; and 6) the design change will not result in a significant decrease in the level of safety [Part 52, App. D, VIII.A.4].

The requested exemption to allow editorial and consistency changes to the description of the components satisfies the criteria for granting specific exemptions, as described below.

1. This exemption is authorized by law

The NRC has authority under 10 CFR 52.63, §52.7, and §50.12 to grant exemptions from the requirements of NRC regulations. Specifically, 10 CFR 50.12 and §52.7 state that the NRC may grant exemptions from the requirements of 10 CFR Part 52 upon a proper showing. No law exists that would preclude the changes covered by this exemption request. Additionally, granting of the proposed exemption does not result in a violation of the Atomic Energy Act of 1954, as amended, or the Commission's regulations.

Accordingly, this requested exemption is "authorized by law," as required by 10 CFR 50.12(a)(1).

2. This exemption will not present an undue risk to the health and safety of the public

The proposed exemption from the requirements of 10 CFR 52, Appendix D, Section III.B would allow changes to elements of the Tier 1 DCD to depart from the AP1000 certified (Tier 1) design information. The plant-specific Tier 1 will continue to reflect the approved licensing basis for VEGP Units 3 and 4, and will maintain a consistent level of detail with that which is currently provided elsewhere in Tier 1 of the DCD. Therefore, the affected plant-specific Tier 1 ITAAC will continue to serve its required purpose.

Because the changes will not alter the operation of any plant equipment or system's ability to perform their design function, these changes do not present an undue risk to existing equipment or systems. The changes do not introduce any new industrial, chemical, or radiological hazards that would represent a public health or safety risk, nor do they modify or remove any design or operational controls or safeguards that are intended to mitigate any existing on-site hazards. Furthermore, the proposed changes would not allow for a new fission product release path, result in a new fission product barrier failure mode, or create a new sequence of events that would result in significant fuel cladding failures. Accordingly, these editorial and consistency changes do not present an undue risk from any new equipment or systems.

Therefore, the requested exemption from 10 CFR 52, Appendix D, Section III.B would not present an undue risk to the health and safety of the public.

3. The exemption is consistent with the common defense and security

The exemption from the requirements of 10 CFR 52, Appendix D, Section III.B would correct editorial and consistency errors, as presented in plant-specific Tier 1 information, thereby departing from the AP1000 certified design information. The proposed exemption will enable performance of the ITAAC associated with these changed elements, by reflecting the revised design information in the text, tables and figures that are referenced in these ITAAC. The exemption does not alter or impede the design, function, or operation of any plant structures, systems, or components (SSCs) associated with the facility's physical or cyber security, and therefore does not affect any plant equipment that is necessary to maintain a safe and secure plant status. The proposed exemption has no impact on plant security or safeguards.

Therefore, the requested exemption is consistent with the common defense and security.

4. Special circumstances are present

10 CFR 50.12(a)(2) lists six "special circumstances" for which an exemption may be granted. Pursuant to the regulation, it is necessary for one of these special circumstances to be present in order for the NRC to consider granting an exemption request. The requested exemption meets the special circumstances of 10 CFR 50.12(a)(2)(ii). That subsection defines special circumstances as when "Application of the regulation in the particular circumstances would not serve the underlying purpose of the rule or is not necessary to achieve the underlying purpose of the rule."

The rule under consideration in this request for exemption is 10 CFR 52, Appendix D, Section III.B, which requires that a licensee referencing the AP1000 Design Certification Rule (10 CFR Part 52, Appendix D) shall incorporate by reference and comply with the requirements of Appendix D, including Tier 1 information. The VEGP Units 3 and 4 COLs reference the AP1000 Design Certification Rule and incorporate by reference the requirements of 10 CFR Part 52, Appendix D, including Tier 1 information. The underlying purpose of Appendix D, Section III.B is to describe and define the scope and contents of the AP1000 design certification, and to require compliance with the design certification information in Appendix D.

The proposed editorial and consistency changes do not impact the ability of any SSCs to perform their functions or negatively impact safety. Accordingly, this exemption from the certification information will enable the licensee to safely construct and operate the AP1000 facility consistent with the design certified by the NRC in 10 CFR 52, Appendix D.

Therefore, special circumstances are present, because application of the current plant-specific certified design information in Tier 1 as required by 10 CFR Part 52, Appendix D, Section III.B in the particular circumstances discussed in this request is not necessary to achieve the underlying purpose of the rule.

5. The special circumstances outweigh any decrease in safety that may result from the reduction in standardization caused by the exemption.

Based on the nature of the changes to the plant-specific Tier 1 information and the understanding that these changes resolve editorial inconsistencies within the licensing basis, it is likely that other AP1000 licensees will request this exemption. However, if this is not the case, the special circumstances continue to outweigh any decrease in safety from the reduction in standardization because the design functions of the systems associated with this request will continue to be maintained. The proposed editorial and consistency changes are departures from information in the plant-specific AP1000 DCD. This exemption request and the associated mark-ups demonstrate that there is a minimal change from the plant-specific AP1000 DCD, minimizing the reduction in standardization and consequently the safety impact from the reduction.

Therefore, the special circumstances associated with the requested exemption outweigh any decrease in safety that may result from the reduction in standardization caused by the exemption.

6. The design change will not result in a significant decrease in the level of safety.

The requested exemption revises the plant-specific DCD Tier 1 information by correcting editorial and consistency issues in various systems. The changes for consistency and clarity do not affect any safety-related equipment or function, and the design functions of the associated systems continue to be met. Because these functions continue to be met, there is no reduction in the level of safety.

Therefore, the requested exemption does not involve a design change that would result in a significant decrease in the level of safety.

5.0 RISK ASSESSMENT

A risk assessment was not determined to be applicable to address the acceptability of this proposal.

6.0 PRECEDENT

None identified.

7.0 ENVIRONMENTAL CONSIDERATION

A review has determined that the proposed amendment would change a requirement with respect to installation or use of a facility component located within the restricted area, as defined in 10 CFR 20, or would change an inspection or surveillance requirement. However, the proposed exemption does not involve (i) a significant hazards consideration, (ii) a significant change in the types or a significant increase in the amounts of any effluents that may be released offsite, or (iii) a significant increase in individual or cumulative occupational radiation exposure. Specific justification is provided in Section 5 of the corresponding license amendment request. Accordingly, the proposed exemption meets the eligibility criteria for categorical exclusion set forth in 10 CFR 51.22(c)(9). Therefore, pursuant to 10

CFR 51.22(b), no environmental impact statement or environmental assessment need be prepared in connection with the proposed exemption.

8.0 CONCLUSION

The proposed consistency changes to DCD Tier 1 are necessary to revise information in design descriptions in plant-specific Tier 1 information. The exemption request meets the requirements of 10 CFR 52.63, 10 CFR 52.7, 10 CFR 50.12, 10 CFR 51.22 and 10 CFR 52 Appendix D. Specifically, the exemption request meets the criteria of 10 CFR 50.12(a)(1) in that the request is authorized by law, presents no undue risk to public health and safety, and is consistent with the common defense and security. Furthermore, approval of this request does not result in a significant decrease in the level of safety, presents special circumstances, does not present a significant decrease in safety as a result of a reduction in standardization, and meets the eligibility requirements for categorical exclusion.

9.0 REFERENCES

None.

Southern Nuclear Operating Company

ND-17-2074

Enclosure 3

**Vogtle Electric Generating Plant (VEGP) Units 3 and 4
Proposed Changes to the Licensing Basis Documents
(LAR-17-043)**

Note:

Added text is shown as bold **Blue Underline**
Deleted text is shown as bold **~~Red Strikethrough~~**

(Enclosure 3 consists of 76 pages, including this cover page)

COL Appendix A, Technical Specification Changes

Technical Specification 5.5.8 Containment Leakage Rate Testing Program is revised as follows:

...

- b. The calculated peak containment internal pressure for the design basis loss of coolant accident, Pa, is ~~58.3~~58.1 psig. The containment design pressure is 59 psig.

...

COL Appendix C and Plant-Specific Tier 1 Changes

COL, Appendix C, Inspections, Tests, Analyses and Acceptance Criteria (ITAAC) Number 135 and 136 Acceptance Criteria and corresponding Plant Specific Tier 1 Subsection 2.2.2 Passive Containment Cooling System Table 2.2.2-3 are revised as follows:

Table 2.2.2-3 Inspections, Tests, Analyses, and Acceptance Criteria				
No.	ITAAC No.	Design Commitment	Inspections, Tests, Analyses	Acceptance Criteria
				...
135	2.2.02.07a.i	7.a) The PCS delivers water from the PCCWST to the outside, top of the containment vessel.	i) Testing will be performed to measure the PCCWST delivery rate from each one of the three parallel flow paths.	i) When tested, each one of the three flow paths delivers water at greater than or equal to: * * * <u>– or a report exists and concludes that the as-measured flow rates bound the 72-hour containment peak pressure and temperature results.</u>

Table 2.2.2-3 Inspections, Tests, Analyses, and Acceptance Criteria				
No.	ITAAC No.	Design Commitment	Inspections, Tests, Analyses	Acceptance Criteria
136	2.2.02.07a.i i	7.a) The PCS delivers water from the PCCWST to the outside, top of the containment vessel.	ii) Testing and or analysis will be performed to demonstrate the PCCWST inventory provides 72 hours of adequate water flow.	ii) When tested and/or analyzed with all flow paths delivering and an initial water level at $27.4 + 0.2, - 0.00$ ft, the PCCWST water inventory provides greater than or equal to 72 hours of flow, and the flow rate at 72 hours is greater than or equal to 100.7 gpm <u>or a report exists and concludes that the as-measured flow rates bound the 72-hour containment peak pressure and temperature results.</u>
				...

COL, Appendix C, ITAAC Number 140 Acceptance Criteria and corresponding Plant Specific Tier 1 Subsection 2.2.2 Passive Containment Cooling System Table 2.2.2-3 are revised as follows:

Table 2.2.2-3 Inspections, Tests, Analyses, and Acceptance Criteria				
No.	ITAAC No.	Design Commitment	Inspections, Tests, Analyses	Acceptance Criteria
				...
140	2.2.02.07b. iii	7.b) The PCS wets the outside surface of the containment vessel. The inside and the outside of the containment vessel above the operating deck are coated with an inorganic zinc material.	iii) Inspection of the containment vessel interior coating will be conducted.	iii) A report exists and concludes that the containment vessel interior surface is coated with an inorganic zinc coating above 7' above the operating deck.
				...

COL Appendix C and corresponding Plant-specific Tier 1 Section 3.3, Buildings, Design Description, item 2.g) are revised as follows:

...

g) The containment vessel ~~greater than 7 feet~~ above the operating deck provides a heat transfer surface. A free volume exists inside the containment shell above the operating deck.

...

COL Appendix C, ITAAC Number 775 Design Commitment and corresponding Plant Specific Tier 1 Subsection 3.3, Buildings, Table 3.3-6 item 2.g) are revised as follows:

Design Commitment	Inspections, Tests, Analyses	Acceptance Criteria
		...
2.g) The containment vessel greater than 7 feet above the operating deck provides a heat transfer surface. A free volume exists inside the containment shell above the operating deck.	The maximum containment vessel inside height from the operating deck is measured and the inner radius below the spring line is measured at two orthogonal radial directions at one elevation.	The containment vessel maximum inside height from the operating deck is 146'-7" (with tolerance of +12", -6"), and the inside diameter is 130 feet nominal (with tolerance of +12", -6").
		...

Plant-Specific Tier 2 Changes

UFSAR Table 1.6-1 is revised as follows:

DCD Section Number	Westinghouse Topical Report Number	Title
		...
6.2
	WCAP-15846 (P) WCAP-15862	<u>WGOTHIC Application to AP600 and AP1000, Revision 1, March 2004Revision 5, September 2016</u>
		...
...		
6A	WCAP-15846 (P) WCAP-15862	<u>WGOTHIC Application to AP600 and AP1000, Revision 1, March 2004Revision 5, September 2016</u>
		...

UFSAR Subsection 6.1.2.1.1 is revised as follows:

...

The coating used on the inside surface of the containment shell, ~~greater than 7' above the operating deck,~~ supports the transfer of thermal energy from the post-accident atmosphere inside containment to the containment shell. Passive containment cooling system testing and analysis have been performed with a coating. This coating is classified as a Service Level I coating.

...

UFSAR Subsection 6.1.2.1.5 is revised as follows:

...

The inorganic zinc coating used on the inside surface of the containment shell, ~~greater than 7' above the operating deck,~~ supports the transfer of thermal energy from the post-accident atmosphere inside containment to the containment shell. Passive containment cooling system testing and analysis have been performed with an inorganic zinc coating. This coating is classified as Service Level I coating.

...

UFSAR Table 6.1-2 (Sheet 1 of 2) AP1000 Coated Surfaces, Containment Shell and Surfaces Inside Containment is revised as follows:

...

Surface	Boundary	Surface Material	Coating	Coating Functions/Safety Classifications		Coating Classification (1)
...						
Containment Shell, Inside Surface	Shell surfaces above the operating floor	Carbon Steel	Inorganic Zinc Coating	1 Promote wettability 2 Heat conduction (9) 3 Nondetachable 4 Inhibit corrosion	1 Safety (2) 2 Safety 3 Safety 4 Safety	Safety – Service Level I
	Shell surfaces below the operating floor	Carbon Steel	Inorganic Zinc Coating with Epoxy Top Coat	1 Nondetachable (inorganic zinc only) 2 Inhibit corrosion 3 Enhance radioactive decontamination (epoxy only) 4 Ensure setting (epoxy only)	1 Safety 2 Safety 3 Nonsafety 4 Safety	Safety – Service Level I
...						

UFSAR Table 6.1-2 (Sheet 2 of 2) AP1000 Coated Surfaces, Containment Shell and Surfaces Inside Containment is revised as follows:

...

Notes:

* * *

~~9. Heat conduction is supported as described in Subsections 6.1.2.1.1 and 6.1.2.1.5.~~

UFSAR Subsection 6.2.1.1.1 is revised as follows:

...

The single failure postulated for the containment pressure/temperature calculations is the failure of one of the valves controlling the cooling water flow for the PCS. Failure of one of these valves would lead to cooling water flow being delivered to the containment vessel through two of three delivery headers. This results in reduced cooling flow for PCS operation. ~~No other single failures are postulated in the containment analysis.~~ However, as stated in Table 6.2.2-3, only one flowpath is necessary to meet the minimum containment cooling requirements, and only one flowpath is assumed in the containment integrity analysis.

...

UFSAR Subsection 6.2.1.1.3 is revised as follows:

...

To model the passive cooling features of the AP1000, several assumptions are made in creating the plant decks. The external cooling water does not completely wet the containment shell, therefore, both wet and dry sections of the shell are modeled in the WGOthic analyses. The analyses use conservative coverage fractions to determine evaporative cooling- ~~as~~

~~Heat conduction from the dry to wet section is considered in the analysis. The combination of passive containment cooling system coverage area and heat conduction from the dry to wet sections is~~ explained in Chapter 7 of Reference 20. ~~An analysis is also performed for the limiting LOCA event without considering heat conduction from the dry to wet section.~~ The analyses conservatively assume that the external cooling water is not initiated until 400 seconds (~~Reference 36~~ Chapter 7, Reference 20) into the transient, allowing time to initiate the signal and to fill the headers and weirs and to develop the flow down the containment side walls. The effects of water flowing down the shell from gravitational forces are explicitly considered in the analysis.

The containment initial conditions of pressure, temperature, and humidity are provided in Table 6.2.1.1-2.

For the LOCA events, two double-ended guillotine reactor coolant system pipe breaks are analyzed. The breaks are postulated to occur in either a hot or a cold leg of the reactor coolant system. The hot leg break results in the highest blowdown peak pressure. The cold leg break results in the higher post-blowdown peak pressure. The cold leg break analysis includes the long term contribution to containment pressure from the sources of stored energy, such as the steam generators. The LOCA mass and energy releases described in ~~Subsection 6.2.1.3~~ are used for these calculations.

For the MSLB event, a ~~representative pipe break spectrum is analyzed. Various break sizes and power levels are~~ double-ended pipe rupture is analyzed at several power levels with the WGOthic code. The MSLB mass and energy releases described in ~~Subsection 6.2.1.4~~ are used for these calculations.

The results of the LOCA and MSLB postulated accidents are provided in [Table 6.2.1.1-1](#). A comparison of the containment integrity acceptance criteria to General Design Criteria is provided in [Table 6.2.1.1-3](#).

The containment pressure response for the peak pressure steam line break case is provided in [Figure 6.2.1.1-1](#). The containment temperature response for the peak temperature steam line break case is provided in [Figure 6.2.1.1-2](#).

[Table 6.2.1.1-10 summarizes the required volume of steel inside containment to validate the heat sink input and methodology for the WGO THIC containment analyses. It includes requirements for analyses that minimize heat sinks \(the peak containment pressure analyses\) and ones that maximize heat sinks \(the minimum containment pressure analyses\).](#)

The [passive methodology for calculating the](#) internal containment heat sink data used in the WGO THIC analyses is presented in [Reference 20](#), Section 13. [Heat sinks include and updated in Reference 36. Data for both metallic and concrete structures. Table 6.2.1.1-11 lists the heat sinks that are credited for heat transfer in the containment evaluation model for peak containment pressure analyses.](#) ~~heat sinks are presented. Additional heat sink data utilized in the containment peak pressure analysis, as updated in Reference 36, are identified in Table 6.2.1.1-10. These additional heat sinks are characterized as metal gratings with material type and minimum required surface area and volume within the subcompartment defined in Table 6.2.1.1-10. The containment pressure and temperature responses to a double-ended cold leg guillotine are presented in Figures 6.2.1.1-5 and 6.2.1.1-6 for the 24 hour portion of the transient and Figures 6.2.1.1-7 and 6.2.1.1-8 for the 72 hour transient. A separate analysis for the double-ended cold leg guillotine LOCA event, without considering heat conduction from the dry to wet section, results in somewhat higher containment pressure in the long term, but still below 50 percent of design pressure at 24 hours. This separate analysis confirms the assumption in Subsection 15.6.5.3.3 of reducing the containment leakage to half its design value at 24 hours. The containment pressure and temperature response to a double-ended hot leg guillotine break are presented in Figures 6.2.1.1-9 and 6.2.1.1-10. The physical properties of the heat sink materials corresponding to the heat sink information used in the containment peak pressure evaluation (Reference 20 and updated in Reference 36) are presented in Table 6.2.1.1-8. These properties represent~~ [are inputs to the containment peak pressure evaluation, and in some cases, reflect consistent with the methodology specified in Reference 20 Section 13, including: For inorganic zinc, the properties specified in Table 6.2.1.1-8, Reference 36, and Table 13-49 of Reference 20, are determined to be conservatively used and the associated reductions identified in subsection 10.2.1 and Table 13-132 of Reference 20 are not used for this input parameter. The thermal conductivity value for the inorganic zinc coating in Table 6.2.1.1-8 represents the thermal conductivity value used in the containment integrity analysis. This is the minimum design requirement value after reduction by a factor of two to account for degradation due to aging.](#)

- [The thermal conductivity and volumetric heat capacity of the steel materials are reduced by 10% per the ASME standard to account for variability of alloy content.](#)
- [The thermal conductivity of inorganic zinc is reduced by a factor of two relative to the minimum test requirement. The conditions for use of this reduction factor identified in Section 4 of Reference 37 are met.](#)
- [Emissivity is reduced by 10% and is only credited on the outer surface of the containment vessel, baffle, and shield building. Emissivity inside containment is ignored.](#)

Carbon steel and concrete heat sinks inside containment are modeled with a coating of epoxy on the exposed surface. The containment vessel is modeled with an inorganic zinc coating inside and outside containment. The containment vessel below the operating deck has both inorganic zinc coating and an epoxy top coating.

The free volume inside the containment is calculated using nominal, cold dimensions. This conservatively neglects the thermal expansion of the containment vessel at elevated temperatures.

The containment pressure and temperature responses to a double-ended cold leg guillotine break are presented in Figures 6.2.1.1-5 and 6.2.1.1-6 for the first 5000 seconds, which shows the peak portion of the containment transients and Figures 6.2.1.1-7 and 6.2.1.1-8 for the 3-day transients. The containment pressure and temperature response to a double-ended hot leg guillotine break are presented in Figures 6.2.1.1-9 and 6.2.1.1-10. A separate analysis for the double-ended cold leg guillotine LOCA event, without considering heat conduction from the dry to wet section, results in somewhat higher containment pressure in the long term, but still below 50 percent of design pressure at 24 hours. This separate analysis confirms the assumption in subsection 15.6.5.3.3 of reducing the containment leakage to half its design value at 24 hours as shown in Table 6.2.1.1-3.

The instrumentation provided outside containment to monitor and record the containment pressure and the instrumentation provided inside containment to monitor and record temperature are found in **Section 7.5**.

UFSAR Subsection 6.2.1.3.2.2 is revised as follows:

...

A description of the SATAN-VI model that is used to determine the mass and energy released from the reactor coolant system during the blowdown phase of a postulated LOCA is provided in **Reference 4**. Significant correlations are discussed in this reference. The only exception to the Reference 4 methodology is that the overall heat transfer coefficient between the primary side of the reactor coolant system metal and the fluid will be adjusted when there is no liquid in the system to prevent an unrealistically high temperature for the steam release.

UFSAR Subsection 6.2.1.4.1.7 is revised as follows:

...

Similarly, the heat stored in the metal of the reactor coolant piping, the reactor vessel, and the reactor coolant pumps is transferred to the primary coolant as the plant cooldown progresses. This energy also is available to be transferred to the steam generator with the broken line. Energy from the metal of the faulted steam generator is also transferred to the fluid in the faulted steam generator as the fluid temperature drops below the metal temperature.

The effects of ~~both the reactor coolant system metal and the reverse steam generator heat transfer, the steam generator metal, and the energy in the fluid from the intact steam generator~~ are included in the results presented.

UFSAR Subsection 6.2.1.4.3 is revised as follows:

...

The WGOTHIC Computer Code ([Reference 20](#)) is used to determine the containment responses following the steam line break, which is ~~documented in Reference 36. The containment response analysis is~~ described in [Subsection 6.2.1.1](#).

UFSAR Subsection 6.2.1.4.3.2 is revised as follows:

...

Using [References 5, 6, 31 and 32](#) as a basis, mass and energy release data are developed to determine the containment pressure-temperature response for the [spectrum of breaks cases](#) analyzed. [Table 6.2.1.4-2](#) provides the mass and energy release ~~data analysis results for the steam line break cases~~ that ~~produce~~[produces](#) the highest containment pressure and [Table 6.2.1.4-3](#) provides the mass and energy release analysis results for the steam line break case that ~~produces the highest containment~~ temperature ~~in the containment response analysis~~. [Table 6.2.1.4-4](#) provides nominal plant data used in the mass and energy releases determination.

UFSAR Subsection 6.2.1.5 is revised as follows:

...

~~The containment backpressure used for the AP1000 cold leg guillotine and split breaks for the emergency core cooling system (ECCS) analysis presented in Subsection 15.6.5 is described. The minimum containment backpressure for emergency core cooling system performance during a loss-of-coolant accident is computed using the WGOTHIC computer code. Subsection 6.2.1.1 demonstrates that the AP1000 containment pressurizes during large break LOCA events. An analysis is performed to establish a containment pressure boundary condition applied to the WCOBRA/TRAC code. (Reference 8). A single-node containment model is used to assess containment pressure response. Containment internal heat sinks used heat transfer correlations of 4 times Tagami during the blowdown phase followed by 1.2 times Uchida for the post-blowdown phase. The calculated containment backpressure is provided in Figure 6.2.1.5-1. Results of the WCOBRA/TRAC analyses demonstrate that the AP1000 meets 10 CFR 50.46 requirements (Reference 7).~~

[Minimum containment pressure analyses are also performed to provide the containment backpressure boundary condition for small break LOCA \(Section 15.6.5.4B\) and post-LOCA long-term cooling analyses \(Section 15.6.5.4C\). A multi-node WGOTHIC containment model described in WCAP-15846 \(Reference 20\) is used.](#)

UFSAR Subsection 6.2.1.5.1 is revised as follows:

...

The mass and energy releases to the containment ~~during the blowdown portion only off~~or the double-ended cold-leg guillotine break (DECLG) transient are presented in ~~Table 6.2.1.5-1~~, as computed by the WCOBRA/TRAC code.

The mathematical models which calculate the mass and energy releases to the containment are described in ~~Subsection 15.6.5~~. A break spectrum analysis is performed (see references in ~~Subsection 15.6.5~~) that considers various break sizes and Moody discharge coefficients for the double-ended cold leg guillotines and splits. Mixing of steam and accumulator water injected into the vessel reduces the available energy released to the containment vapor space, thereby minimizing calculated containment pressure. ~~Note that the mass/energy releases during the reflood phase of the subject break are not considered. This produces a conservatively low containment pressure result for use as a boundary condition in the WCOBRA/TRAC large break LOCA analysis.~~

UFSAR Subsection 6.2.1.5.2 is revised as follows:

...

Initial containment conditions were biased for the emergency core cooling system backpressure analysis to predict a conservatively low containment backpressure. Initial containment conditions include an initial pressure of ~~14.7~~14.5 psia, initial containment temperature of ~~90~~50°F, and a relative humidity of ~~99~~100 percent. An air annulus temperature of 0°F is assumed. The initial through-thickness metal temperature of the containment shell is assumed to also be 0°F.

UFSAR Subsection 6.2.1.5.3 is revised as follows:

...

Containment parameters, such as containment volume and passive heat sinks, are biased to predict a conservative low containment backpressure. The containment volume used in the calculation is conservatively set to 1.1 times the free volume of the AP1000 containment Evaluation Model. Passive heat sink surface areas were increased by a factor of ~~2.1 times the values presented in~~ 1.35 relative to the heat sinks developed for the peak containment evaluation model described in Reference 20. Material properties were biased high (density, conductivity, and heat capacity) as indicated in CSB 6-1 (Reference 8). The thermal conductivity and volumetric heat capacity of the steel materials were increased by 10% from the ASME standard to increase heat removal. No air gap was modeled between the steel liner and base concrete of jacketed concrete heat sinks. The outside surface of the containment shell was maintained at 0°F throughout the calculation. To further minimize containment pressure, containment purge was assumed to be in operation at time zero and air is vented through both the ~~15-inch diameter (16-inch, Sch. 40 piping)~~ containment purge supply and exhaust lines until the isolation valves have fully closed. These valves were modeled to close ~~12 seconds~~ after the ~~8-psig closure~~ High-2 containment pressure setpoint was reached and after an associated delay to account for valve closure time.

UFSAR Subsection 6.2.2.3 is revised as follows:

...

The shield building air inlets were changed as part of the enhanced shield building design. The impact of these changes on the containment pressure analyses is small, and the conclusions remain valid. The analyses provided in **Subsection 6.2.1** include the air inlet changes ~~(Reference 36)~~.

UFSAR Subsection 6.2.2.4.2 is revised as follows:

...

The inventory within the tank is verified to provide 72 hours of operation from the minimum initial operating water level with a minimum flow rate over the duration in excess of 100.7 gpm or a report exists and concludes that the as-measured flow rates bound the 72 hours containment peak pressure and temperature results. The flow rates are measured utilizing the differential pressure across the orifices within each standpipe.

...

UFSAR Subsection 6.2.7 is revised as follows:

...

8. ~~Branch Technical Position CSB6-1, "Minimum Containment Pressure Model for PWR-ECGS Performance Evaluation."~~ Not used.

...

20. WCAP-15846 (Proprietary) and WCAP-15862 (Non-Proprietary) "WGOTHIC Application to AP600 and AP1000," ~~Revision 1, March 2004~~ Revision 5, September 2016.

...

Table 6.2.1.1-1 Summary of Calculated Pressures and Temperatures is revised as follows:

**Table 6.2.1.1-1
Summary of Calculated Pressures and Temperatures**

Break	Peak Pressure (psig)	Available ¹ Margin (psi)	Peak Temperature (°F)
Double-ended hot leg guillotine	50.4 49.8	8.6 9.2	411.3 385.8
Double-ended cold leg guillotine	58.3 58.1	0.7 0.9	295.7 357.8
Full main steam line DER, 30% power, MSIV failure	58.2 57.2	0.8 1.8	373.2 381.8
Full main steam line DER, 101% power, MSIV failure	54.2 54.4	4.8 4.6	374.7 383.6

Note:

1. Design Pressure is 59 psig

Table 6.2.1.1-3 Results of Postulated Accidents is revised as follows:

**Table 6.2.1.1-3
Results of Postulated Accidents**

Criterion	Acceptance Criterion Value	Lumped DEHLG LOCA Value	Lumped DECLG LOCA Value	30% Power MSLB Value	External Pressurization Value
GDC 16 & GDC 50 Design Pressure	<59.0 psig	50.4 49.8 psig	58.3 58.1 psig	58.2 57.2 psig	
GDC 38 Rapidly Reduce Containment Pressure	< 29.5 psig		22 at 24 hrs < 27 psig after 24 hrs ⁽¹⁾		
GDC 38 & 50 External Pressure	< 1.7 psid				1.63
GDC 38 & GDC 50 Containment Heat Removal Single Failure	Most Severe	Two of Three Trains-of PCS Water Supply <u>Flowpaths</u> ⁽²⁾	Two of Three Trains-of PCS Water Supply <u>Flowpaths</u> ⁽²⁾	Two of Three Trains-of PCS Supply <u>Flowpaths</u> ⁽²⁾	

Notes:

1. Analysis without crediting heat conduction from dry to wet sections on containment shell.
2. Table 6.2.2-3 notes that operation of only one of three flowpaths is necessary to meet minimum containment cooling requirements.

ND-17-2074

Enclosure 3

Proposed Changes to the Licensing Basis Documents (LAR-17-043)

Replace Table 6.2.1.1-8 Physical Properties of Passive Heat Sinks⁽³⁾ in its entirety with the following Table:

<u>Table 6.2.1.1-8</u> <u>Material Properties Used in the WGO THIC Containment Evaluation Model</u>				
<u>Material</u>		<u>Thermal Conductivity (BTU/hr-ft-°F)</u>	<u>Volumetric Heat Capacity (BTU/ft³-°F)</u>	<u>Emissivity</u>
<u>Epoxy</u>		<u>0.1875</u>	<u>26.25</u>	<u>N/A</u>
<u>Inorganic zinc</u>		<u>0.302</u>	<u>22.825</u>	<u>0.54⁽¹⁾</u>
<u>Baffle aluminum</u>		<u>13.4</u>	<u>28.443</u>	<u>0.81⁽¹⁾</u>
<u>Concrete</u>		<u>0.83</u>	<u>26.6</u>	<u>0.81⁽¹⁾</u>
<u>Air</u>	<u>0°F</u>	<u>0.0131</u>	<u>0.020736</u>	<u>N/A</u>
	<u>250°F</u>	<u>0.0192</u>	<u>0.020988</u>	<u>N/A</u>
	<u>500°F</u>	<u>0.0246</u>	<u>0.021427</u>	<u>N/A</u>
<u>Group A Carbon Steel</u>	<u>70°F</u>	<u>31.4</u>	<u>44.9</u>	<u>N/A</u>
	<u>100°F</u>	<u>31.2</u>	<u>46.2</u>	<u>N/A</u>
	<u>150°F</u>	<u>30.8</u>	<u>48.0</u>	<u>N/A</u>
	<u>200°F</u>	<u>30.3</u>	<u>49.6</u>	<u>N/A</u>
	<u>250°F</u>	<u>29.7</u>	<u>50.8</u>	<u>N/A</u>
	<u>300°F</u>	<u>29.1</u>	<u>51.9</u>	<u>N/A</u>
<u>Group B Carbon Steel</u>	<u>70°F</u>	<u>24.6</u>	<u>46.4</u>	<u>N/A</u>
	<u>100°F</u>	<u>24.8</u>	<u>47.8</u>	<u>N/A</u>
	<u>150°F</u>	<u>25.0</u>	<u>49.6</u>	<u>N/A</u>
	<u>200°F</u>	<u>25.0</u>	<u>51.4</u>	<u>N/A</u>
	<u>250°F</u>	<u>24.8</u>	<u>52.7</u>	<u>N/A</u>
	<u>300°F</u>	<u>24.6</u>	<u>54.0</u>	<u>N/A</u>
<u>Group C Carbon Steel</u>	<u>70°F</u>	<u>21.3</u>	<u>46.5</u>	<u>N/A</u>
	<u>100°F</u>	<u>21.2</u>	<u>47.1</u>	<u>N/A</u>
	<u>150°F</u>	<u>21.2</u>	<u>48.4</u>	<u>N/A</u>
	<u>200°F</u>	<u>21.2</u>	<u>49.9</u>	<u>N/A</u>
	<u>250°F</u>	<u>21.1</u>	<u>51.1</u>	<u>N/A</u>
	<u>300°F</u>	<u>21.1</u>	<u>52.5</u>	<u>N/A</u>
<u>Group D Carbon Steel</u>	<u>70°F</u>	<u>18.9</u>	<u>46.3</u>	<u>N/A</u>
	<u>100°F</u>	<u>18.9</u>	<u>47.1</u>	<u>N/A</u>
	<u>150°F</u>	<u>19.1</u>	<u>48.7</u>	<u>N/A</u>
	<u>200°F</u>	<u>19.2</u>	<u>49.9</u>	<u>N/A</u>
	<u>250°F</u>	<u>19.3</u>	<u>51.1</u>	<u>N/A</u>
	<u>300°F</u>	<u>19.4</u>	<u>52.2</u>	<u>N/A</u>
<u>Group J Stainless Steel</u>	<u>70°F</u>	<u>7.7</u>	<u>51.3</u>	<u>N/A</u>
	<u>100°F</u>	<u>7.8</u>	<u>51.5</u>	<u>N/A</u>
	<u>150°F</u>	<u>8.1</u>	<u>52.6</u>	<u>N/A</u>
	<u>200°F</u>	<u>8.4</u>	<u>53.7</u>	<u>N/A</u>
	<u>250°F</u>	<u>8.6</u>	<u>54.7</u>	<u>N/A</u>
	<u>300°F</u>	<u>8.8</u>	<u>55.1</u>	<u>N/A</u>
<u>Group K Stainless Steel</u>	<u>70°F</u>	<u>7.5</u>	<u>53.1</u>	<u>N/A</u>
	<u>100°F</u>	<u>7.5</u>	<u>53.4</u>	<u>N/A</u>
	<u>150°F</u>	<u>7.7</u>	<u>54.5</u>	<u>N/A</u>
	<u>200°F</u>	<u>7.9</u>	<u>54.6</u>	<u>N/A</u>
	<u>250°F</u>	<u>8.2</u>	<u>55.7</u>	<u>N/A</u>
	<u>300°F</u>	<u>8.4</u>	<u>55.8</u>	<u>N/A</u>
<u>Notes:</u> 1. <u>Emissivity is only credited outside containment</u>				

Replace Table 6.2.1.1-10 [DATA FOR ADDITIONAL HEAT SINKS CREDITED IN THE CONTAINMENT PEAK PRESSURE EVALUATION]* in its entirety with the following Table:

<u>Table 6.2.1.1-10</u>	
<u>[Plant Requirements for Metal Heat Sinks Inside Containment]*</u>	
<u>Region</u>	<u>Metal Volume (ft³) (minimum – maximum)</u>
<u>Above the operating deck</u>	<u>4973 – 7279</u>
<u>Inside SG/Pressurizer compartments</u>	<u>1002 – 1677</u>
<u>Below the operating deck</u>	<u>5246 – 8255</u>
<u>Total</u>	<u>11,811⁽³⁾ – 17,211</u>
<u>Notes:</u> <u>1. Does not include the containment vessel.</u> <u>2. Only includes structures and equipment that are typically less than or equal to containment ambient temperature.</u> <u>3. The total minimum volume includes an additional 590 ft³ of metal inside containment.</u>	

Insert new Table 6.2.1.1-11 Heat Sinks Credited in the Peak Containment Pressure Analyses as follows:

<u>Table 6.2.1.1-11</u> <u>Heat Sinks Credited in the Peak Containment Pressure Analyses</u>				
<u>Description</u>	<u>Material</u>	<u>Surface Area (ft²)</u>	<u>Metal Volume (ft³)</u>	<u>Metal Effective Thickness (in)</u>
<u>Above the Operating Deck</u>				
<u>Containment vessel above the operating deck</u>	<u>Carbon Steel C</u>	<u>62,988</u>	<u>8,986</u>	<u>1.625 and 1.750</u>
<u>Polar crane bridge and trolley</u>	<u>Carbon Steel B</u>	<u>9,000</u>	<u>1,936</u>	<u>2.581</u>
<u>Crane girder</u>	<u>Carbon Steel C</u>	<u>11,509</u>	<u>1,190</u>	<u>1.241</u>
<u>Circular walkway at 162'</u>	<u>Carbon Steel B</u>	<u>11,903</u>	<u>349</u>	<u>0.351</u>
<u>Upper manway platforms at 166' above SG rooms and ADS platform at 166' and 176.88' over pressurizer compartment</u>	<u>Carbon Steel B</u>	<u>13,060</u>	<u>238</u>	<u>0.219</u>
<u>Internal stiffener</u>	<u>Carbon Steel C</u>	<u>2,320</u>	<u>232</u>	<u>1.198</u>
<u>Integrated head stands</u>	<u>Carbon Steel B</u>	<u>692</u>	<u>170</u>	<u>2.940</u>
<u>Recirculation unit platforms at 153' (CH53, CH57)</u>	<u>Carbon Steel B</u>	<u>9,056</u>	<u>176</u>	<u>0.242</u>
<u>Outer SG compartment walls (loop B)</u>	<u>Carbon Steel B, Concrete</u>	<u>1,808</u>	<u>139</u>	<u>0.922</u>
<u>Outer SG compartment walls (loop A)</u>	<u>Carbon Steel B, Concrete</u>	<u>1,572</u>	<u>105</u>	<u>0.800</u>
<u>Outer pressurizer walls</u>	<u>Carbon Steel B, Concrete</u>	<u>1,117</u>	<u>77</u>	<u>0.832</u>
<u>Stairs outside SG compartments</u>	<u>Carbon Steel B</u>	<u>4,394</u>	<u>74</u>	<u>0.201</u>
<u>Attachment plates above the operating deck</u>	<u>Carbon Steel C</u>	<u>678</u>	<u>62</u>	<u>1.090</u>
<u>Ring duct</u>	<u>Carbon Steel A</u>	<u>9,024</u>	<u>117</u>	<u>0.155</u>
<u>Recirculation duct and supports</u>	<u>Carbon Steel A</u>	<u>3,823</u>	<u>53</u>	<u>0.166</u>
<u>ADS module</u>	<u>Carbon Steel C</u>	<u>1,856</u>	<u>58</u>	<u>0.373</u>
<u>Inside SG Compartments and Pressurizer Compartment</u>				
<u>Inner SG room walls (loop B)</u>	<u>Carbon Steel B, Concrete</u>	<u>6,838</u>	<u>364</u>	<u>0.639</u>
<u>Inner SG room walls (loop A)</u>	<u>Carbon Steel B, Concrete</u>	<u>5,738</u>	<u>314</u>	<u>0.656</u>

Table 6.2.1.1-11
Heat Sinks Credited in the Peak Containment Pressure Analyses

<u>Description</u>	<u>Material</u>	<u>Surface Area (ft²)</u>	<u>Metal Volume (ft³)</u>	<u>Metal Effective Thickness (in)</u>
<u>Inner pressurizer compartment walls</u>	<u>Carbon Steel B, Concrete</u>	<u>2,958</u>	<u>150</u>	<u>0.608</u>
<u>Lower manway platforms at 104'-7" in SG compartments</u>	<u>Carbon Steel B</u>	<u>3,631</u>	<u>113</u>	<u>0.375</u>
<u>Tubesheet platforms at 116'-6" in SG compartments</u>	<u>Carbon Steel B</u>	<u>3,979</u>	<u>33</u>	<u>0.100</u>
<u>Steel plate at 95'-6" in SG compartment (loop B)</u>	<u>Stainless Steel K</u>	<u>239</u>	<u>27</u>	<u>1.370</u>
<u>Flow-Through Compartments Below the Operating Deck</u>				
<u>Containment vessel below operating deck</u>	<u>Carbon Steel C</u>	<u>10,381</u>	<u>1,514</u>	<u>1.750</u>
<u>CMTs</u>	<u>Carbon Steel C</u>	<u>2,109</u>	<u>1,187</u>	<u>6.754</u>
<u>Floor framing below operating deck</u>	<u>Carbon Steel A</u>	<u>9,236</u>	<u>495</u>	<u>0.643</u>
<u>Platform at 118'-6" between maintenance floor and maintenance floor mezzanine</u>	<u>Carbon Steel B</u>	<u>27,703</u>	<u>439</u>	<u>0.190</u>
<u>Columns in maintenance floor room</u>	<u>Carbon Steel B</u>	<u>2,255</u>	<u>330</u>	<u>1.754</u>
<u>Curved IRWST wall</u>	<u>Stainless Steel K</u>	<u>4,110</u>	<u>219</u>	<u>0.639</u>
<u>Walls in maintenance floor and maintenance floor mezzanine</u>	<u>Carbon Steel B, Concrete</u>	<u>9,029</u>	<u>372</u>	<u>0.493</u>
<u>Walls in reactor coolant drain tank (RCDT) room and vertical access (VA) room</u>	<u>Carbon Steel B, Concrete</u>	<u>2,966</u>	<u>133</u>	<u>0.538</u>
<u>Platforms at 83' and 107', and stairs in VA room</u>	<u>Carbon Steel B</u>	<u>3,131</u>	<u>37</u>	<u>0.140</u>
<u>Ceiling of maintenance floor mezzanine, Q-deck</u>	<u>Carbon Steel B, Concrete</u>	<u>5,552</u>	<u>28</u>	<u>0.060</u>
<u>Ceiling of maintenance floor mezzanine, steel plate (south)</u>	<u>Carbon Steel A, Concrete</u>	<u>514</u>	<u>13</u>	<u>0.293</u>
<u>Ceiling of pressurizer spray valve room</u>	<u>Carbon Steel B, Concrete</u>	<u>199</u>	<u>8</u>	<u>0.500</u>
<u>Dead-end Compartments Below the Operating Deck</u>				
<u>Accumulators</u>	<u>Carbon Steel C</u>	<u>1,616</u>	<u>264</u>	<u>1.959</u>
<u>PXS compartments walls</u>	<u>Carbon Steel B, Concrete</u>	<u>5,492</u>	<u>261</u>	<u>0.569</u>
<u>Upper refueling room walls</u>	<u>Stainless Steel K, Concrete</u>	<u>5,191</u>	<u>218</u>	<u>0.503</u>
<u>Platforms in PXS compartments</u>	<u>Carbon Steel B</u>	<u>6,404</u>	<u>158</u>	<u>0.296</u>

<u>Table 6.2.1.1-11</u> <u>Heat Sinks Credited in the Peak Containment Pressure Analyses</u>				
<u>Description</u>	<u>Material</u>	<u>Surface Area (ft²)</u>	<u>Metal Volume (ft³)</u>	<u>Metal Effective Thickness (in)</u>
<u>CVS compartment walls</u>	<u>Carbon Steel B, Concrete</u>	<u>2,869</u>	<u>120</u>	<u>0.500</u>
<u>Demineralizers, reactor coolant filters in CVS compartment</u>	<u>Stainless Steel J</u>	<u>364</u>	<u>109</u>	<u>3.599</u>
<u>IRWST ceiling</u>	<u>Stainless Steel K, Concrete</u>	<u>2,174</u>	<u>87</u>	<u>0.479</u>
<u>PXS compartments ceiling</u>	<u>Carbon Steel A, Concrete</u>	<u>1,668</u>	<u>70</u>	<u>0.500</u>
<u>Lower refueling room walls</u>	<u>Stainless Steel K, Concrete</u>	<u>1,164</u>	<u>66</u>	<u>0.681</u>
<u>CVS compartment ceiling</u>	<u>Carbon Steel A, Concrete</u>	<u>679</u>	<u>28</u>	<u>0.500</u>
<u>Hatches over PXS, CVS Rooms</u>	<u>Carbon Steel D</u>	<u>62</u>	<u>17</u>	<u>3.294</u>

Revise Table 6.2.1.3-8 Basis for Long-Term Analysis as follows:

**Table 6.2.1.3-8
Basis for Long-Term Analysis**

Number of Loops	2
Active Core Length (ft)	14.0
Core Power, license application (MWt)	3400
Nominal Vessel Inlet Temperature (°F)	537.2 535.5
Nominal Vessel Outlet Temperature (°F)	640.0 612.2
Steam Pressure (psia)	881.0 870.0
Rod Array	17 x 17
Accumulator Temperature (°F)	120.0
Containment Design Pressure (psia)	73.7

Replace Contents of Table 6.2.1.3-9 (all Sheets) Long-Term DECL Break Mass and Energy Releases with the following:

Table 6.2.1.3-9 (Sheet 1 of 12)

**Long-Term DECL Break
Mass and Energy Releases**

Time (sec)	Two-Phase		Steam	
	Mass (lbm/sec)	Enthalpy (Btu/lbm)	Mass (lbm/sec)	Enthalpy (Btu/lbm)
0.00000	0.00	0.00	0.00	1172.85
0.00108	40052.87	533.75	0.00	1172.85
0.10110	59368.22	536.62	0.00	1172.85
0.20117	66300.29	536.89	0.00	1172.85
0.30142	66447.67	536.95	0.00	1172.85
0.40126	65675.65	537.00	0.00	1172.85
0.50145	65274.95	537.18	0.00	1172.85
0.60133	65290.12	537.55	0.00	1172.85
0.70130	65183.67	538.11	0.00	1172.85
0.80144	64916.35	538.88	0.00	1172.85
0.90103	64703.12	539.95	0.00	1172.85
1.00122	64778.19	541.41	0.00	1172.85
1.10107	63859.23	543.18	0.00	1172.85
1.20134	62704.81	545.26	0.00	1172.85
1.30148	61608.59	547.41	0.00	1172.85
1.40117	60696.70	549.57	0.00	1172.85
1.50101	59585.89	551.90	0.00	1172.85
1.60141	58359.48	554.43	0.00	1172.85
1.70131	56787.10	556.83	0.00	1172.85
1.80125	55305.59	558.86	0.00	1172.85
1.90137	54805.09	560.74	0.00	1172.85
2.00120	53523.86	562.60	0.00	1172.85
2.10115	51899.58	564.36	0.00	1172.85

Table 6.2.1.3-9 (Sheet 2 of 12)

**Long-Term DECL Break
Mass and Energy Releases**

Time (sec)	Two-Phase		Steam	
	Mass (lbm/sec)	Enthalpy (Btu/lbm)	Mass (lbm/sec)	Enthalpy (Btu/lbm)
2.20135	50470.83	566.26	0.00	1172.85
2.30124	48836.67	568.63	0.00	1172.85
2.40170	46760.05	570.30	0.00	1172.85
2.50110	45835.40	570.67	0.00	1172.85
2.60114	45719.77	570.44	0.00	1172.85
2.70114	43403.61	570.20	0.00	1172.85
2.80148	42788.61	571.01	0.00	1172.85
2.90154	41342.36	571.84	0.00	1172.85
3.00113	40211.11	572.79	0.00	1172.85
3.10107	38847.30	573.56	0.00	1172.85
3.20165	37459.63	574.16	0.00	1172.85
3.30125	36707.64	574.64	0.00	1172.85
3.40140	35554.13	574.74	0.00	1172.85
3.50164	33912.53	574.51	0.00	1172.85
3.60102	32445.79	574.15	0.00	1172.85
3.70124	31442.01	573.68	0.00	1172.85
3.80133	30850.86	573.12	0.00	1172.85
3.90137	30538.16	572.52	0.00	1172.85
4.00213	30402.98	572.04	0.00	1172.85
4.20089	30215.90	571.36	0.00	1172.85
4.40010	29884.56	570.88	0.00	1172.85
4.60029	29237.21	569.91	0.00	1172.85
4.80091	28863.69	569.12	0.00	1172.85

Table 6.2.1.3-9 (Sheet 3 of 12)

**Long-Term DECL Break
Mass and Energy Releases**

Time (sec)	Two-Phase		Steam	
	Mass (lbm/sec)	Enthalpy (Btu/lbm)	Mass (lbm/sec)	Enthalpy (Btu/lbm)
5.00095	28500.04	568.75	0.00	1172.85
5.20029	27991.45	568.29	0.00	1172.85
5.40047	27617.14	567.86	0.00	1172.85
5.60072	26880.06	567.43	0.00	1172.85
5.80010	25514.01	567.46	0.00	1172.85
6.00037	24438.77	568.10	0.00	1172.85
6.20107	23755.47	568.80	0.00	1172.85
6.40077	23353.56	570.18	0.00	1172.85
6.60037	24088.35	574.19	0.00	1172.85
6.80035	22164.93	578.28	0.00	1172.85
7.00004	22614.22	581.76	0.00	1172.85
7.20050	22660.07	587.32	0.00	1172.85
7.40063	21703.27	593.51	0.00	1172.85
7.60053	21990.12	598.58	0.00	1172.85
7.80031	21794.29	601.95	0.00	1172.85
8.00010	20967.93	606.91	0.00	1172.85
8.20042	20881.43	612.68	0.00	1172.85
8.40037	20555.65	617.72	0.00	1172.85
8.60062	20196.66	623.44	0.00	1172.85
8.80051	19882.25	628.99	0.00	1172.85
9.00018	19753.14	632.83	0.00	1172.85
9.20122	19392.43	635.04	0.00	1172.85
9.40127	18955.06	636.58	0.00	1172.85

Table 6.2.1.3-9 (Sheet 4 of 12)

**Long-Term DECL Break
Mass and Energy Releases**

Time (sec)	Two-Phase		Steam	
	Mass (lbm/sec)	Enthalpy (Btu/lbm)	Mass (lbm/sec)	Enthalpy (Btu/lbm)
9.60057	18125.94	643.16	0.00	1172.85
9.80034	17308.72	655.66	0.00	1172.85
10.00008	16528.22	674.84	0.00	1172.85
10.20015	15595.19	700.74	0.00	1172.85
10.40041	15312.81	707.39	0.00	1172.85
10.40102	15311.00	707.41	0.00	1172.85
10.40164	15309.15	707.43	0.00	1172.85
10.60060	14926.83	708.59	0.00	1172.85
10.80003	14921.74	707.14	0.00	1172.85
11.00059	14498.78	713.57	0.00	1172.85
11.20005	14065.62	725.27	0.00	1172.85
11.40030	13746.99	726.15	0.00	1172.85
11.60079	13378.70	725.68	0.00	1172.85
11.80077	13108.47	723.62	0.00	1172.85
12.00002	12817.73	725.37	0.00	1172.85
12.20002	12608.56	728.61	0.00	1172.85
12.40202	12228.65	731.29	0.00	1172.85
12.60080	11936.85	732.84	0.00	1172.85
12.80058	11684.11	734.81	0.00	1172.85
13.00048	11398.79	742.13	0.00	1172.85
13.20050	11185.74	745.24	0.00	1172.85
13.40083	10918.00	748.36	0.00	1172.85
13.60040	10702.65	750.83	0.00	1172.85

Table 6.2.1.3-9 (Sheet 5 of 12)

**Long-Term DECL Break
Mass and Energy Releases**

Time (sec)	Two-Phase		Steam	
	Mass (lbm/sec)	Enthalpy (Btu/lbm)	Mass (lbm/sec)	Enthalpy (Btu/lbm)
13.80071	10588.34	754.34	0.00	1172.85
14.00069	10461.08	753.58	0.00	1172.85
14.20110	10350.79	748.85	0.00	1172.85
14.40163	10338.33	743.29	0.00	1172.85
14.60172	10339.87	739.95	0.00	1172.85
14.80216	10168.76	736.39	0.00	1172.85
15.00154	10107.50	731.33	0.00	1172.85
15.20132	10037.27	730.64	0.00	1172.85
15.40209	9805.80	731.18	0.00	1172.85
15.60198	9668.46	729.18	0.00	1172.85
15.80174	9572.84	729.82	0.00	1172.85
16.00165	9332.89	732.42	0.00	1172.85
16.20099	9168.69	732.14	0.00	1172.85
16.40111	9045.69	733.75	0.00	1172.85
16.60064	8823.68	736.75	0.00	1172.85
16.80135	8656.43	737.69	0.00	1172.85
17.00245	8501.97	740.04	0.00	1172.85
17.20278	8305.69	743.04	0.00	1172.85
17.40007	8132.45	745.16	0.00	1172.85
17.60291	7951.18	748.11	0.00	1172.85
17.80012	7753.09	751.70	0.00	1172.85
18.00106	7538.37	755.57	0.00	1172.85
18.20078	7305.90	759.71	0.00	1172.85
18.40101	7057.74	763.21	0.00	1172.85

Table 6.2.1.3-9 (Sheet 6 of 12)

**Long-Term DECL Break
Mass and Energy Releases**

Time (sec)	Two-Phase		Steam	
	Mass (lbm/sec)	Enthalpy (Btu/lbm)	Mass (lbm/sec)	Enthalpy (Btu/lbm)
18.60187	6816.10	765.94	0.00	1172.85
18.80066	6587.07	768.24	0.00	1172.85
19.00116	6420.48	774.60	0.00	1172.85
19.20154	6201.37	780.97	0.00	1172.85
19.40130	5931.44	787.59	0.00	1172.85
19.60026	5703.61	791.54	0.00	1172.85
19.80112	5474.96	795.15	0.00	1172.85
20.00183	5247.80	797.78	0.00	1172.85
20.20207	5037.97	798.71	0.00	1172.85
20.40037	4844.34	796.50	0.00	1172.85
20.60103	4673.24	792.34	0.00	1172.85
20.80154	4507.68	785.42	0.00	1172.85
21.00033	4359.90	775.95	0.00	1172.85
21.20061	4213.90	765.34	0.00	1172.85
21.40038	4075.02	753.86	0.00	1172.85
21.60041	3941.72	741.54	0.00	1172.85
21.80051	3813.73	728.79	0.00	1172.85
22.00092	3691.21	715.52	0.00	1172.85
22.20055	3573.81	702.02	0.00	1172.85
22.40015	3460.34	688.27	0.00	1172.85
22.60085	3349.67	674.29	0.00	1172.85
22.80028	3240.79	660.43	0.00	1172.85
23.00123	3134.87	646.66	0.00	1172.85
23.20025	3032.48	632.75	0.00	1172.85

Table 6.2.1.3-9 (Sheet 7 of 12)

**Long-Term DECL Break
Mass and Energy Releases**

Time (sec)	Two-Phase		Steam	
	Mass (lbm/sec)	Enthalpy (Btu/lbm)	Mass (lbm/sec)	Enthalpy (Btu/lbm)
23.40130	2934.25	618.77	0.00	1172.85
23.60062	2839.94	605.26	0.00	1172.85
23.80059	2785.80	590.53	0.00	1172.85
24.00032	2738.35	576.48	0.00	1172.85
24.20023	2690.76	563.10	0.00	1172.85
24.40037	2646.22	550.81	0.00	1172.85
24.60079	2595.15	538.42	0.00	1172.85
24.80099	2539.13	526.24	0.00	1172.85
25.00086	2484.05	514.43	0.00	1172.85
25.20027	2428.62	503.09	0.00	1172.85
25.40063	2373.34	492.10	0.00	1172.85
25.60067	2316.52	481.47	0.00	1172.85
25.80048	2260.36	471.09	0.00	1172.85
26.00093	2204.96	461.22	0.00	1172.85
26.20012	2150.27	451.77	0.00	1172.85
26.40032	2095.19	442.78	0.00	1172.85
26.60063	2041.33	433.95	0.00	1172.85
26.80110	1987.93	425.53	0.00	1172.85
27.00110	1932.88	417.43	0.00	1172.85
27.20147	1875.86	409.77	0.00	1172.85
27.40054	1816.27	402.49	0.00	1172.85
27.60094	1763.81	394.91	0.00	1172.85
27.80020	1734.80	386.34	0.00	1172.85
28.00090	1703.80	378.17	0.00	1172.85

Table 6.2.1.3-9 (Sheet 8 of 12)

**Long-Term DECL Break
Mass and Energy Releases**

Time (sec)	Two-Phase		Steam	
	Mass (lbm/sec)	Enthalpy (Btu/lbm)	Mass (lbm/sec)	Enthalpy (Btu/lbm)
28.20081	1659.91	370.23	0.00	1172.85
28.40000	1602.77	362.72	0.00	1172.85
28.60056	1529.80	355.96	0.00	1172.85
28.80117	1438.61	351.27	0.00	1172.85
29.00084	1301.55	331.87	0.00	1172.85
29.20008	1046.95	320.22	0.00	1172.85
29.40028	846.42	293.61	0.00	1172.85
29.60048	740.78	369.07	0.00	1172.85
29.80038	390.68	290.99	0.00	1172.85
30.00017	76.52	291.27	0.00	1172.85
30.20022	0.00	291.27	0.00	1172.85
30.30000	0.00	1172.85	0.00	1172.85
30.70000	0.00	1172.85	0.00	1172.85
31.60000	0.00	1172.85	110.15	1172.85
39.98990	0.00	1172.85	277.76	1172.85
44.26170	44.77	332.98	309.91	1172.85
51.11270	151.51	201.99	306.69	1172.85
55.33040	206.47	188.62	304.53	1172.85
60.08680	260.73	181.68	302.04	1172.85
64.61610	303.35	178.72	300.29	1172.85
69.75980	344.91	177.00	298.26	1172.85
75.64790	383.82	176.25	295.90	1172.85
79.69800	404.01	176.38	294.29	1172.85
86.42560	430.39	177.08	292.30	1172.85

Table 6.2.1.3-9 (Sheet 9 of 12)

**Long-Term DECL Break
Mass and Energy Releases**

Time (sec)	Two-Phase		Steam	
	Mass (lbm/sec)	Enthalpy (Btu/lbm)	Mass (lbm/sec)	Enthalpy (Btu/lbm)
91.00040	444.22	177.71	290.93	1172.85
95.00040	453.98	178.34	289.72	1172.85
101.00040	464.97	179.37	287.88	1172.85
105.00040	474.33	179.63	286.81	1172.85
111.00040	474.91	181.29	285.44	1172.85
119.00040	479.52	182.62	283.41	1172.85
132.23300	471.78	185.81	280.19	1172.85
150.00000	458.14	189.29	275.62	1172.85
153.03100	452.32	190.28	274.92	1172.85
159.50000	446.63	191.35	273.67	1172.85
185.00000	407.43	197.56	269.12	1172.85
190.00000	397.85	199.07	268.28	1172.85
192.00000	210.98	247.43	277.12	1172.85
201.00000	336.81	1172.85	178.25	1172.85
210.10000	0.00	1172.85	203.18	1172.85
215.04000	0.00	1172.85	306.42	1172.85
225.14500	5.35	1172.85	294.70	1172.85
251.34600	0.00	1172.85	290.12	1172.85
262.10700	0.00	1172.85	301.34	1172.85
278.62500	0.00	1172.85	288.52	1172.85
299.44900	78.64	339.18	272.67	1172.85
319.81500	0.00	1172.85	282.61	1172.85
341.55800	0.00	1172.85	288.11	1172.85
357.38100	0.00	1172.85	281.99	1172.85

Table 6.2.1.3-9 (Sheet 10 of 12)

**Long-Term DECL Break
Mass and Energy Releases**

Time (sec)	Two-Phase		Steam	
	Mass (lbm/sec)	Enthalpy (Btu/lbm)	Mass (lbm/sec)	Enthalpy (Btu/lbm)
380.08900	0.00	1172.85	213.98	1172.85
401.34000	66.05	333.10	206.10	1172.85
422.89000	101.14	289.75	207.95	1172.85
439.29700	60.86	337.13	198.55	1172.85
461.72200	111.06	277.12	199.40	1172.85
482.52000	70.43	317.00	197.45	1172.85
503.31800	58.46	333.71	192.82	1172.85
518.91600	75.95	305.41	189.44	1172.85
539.71400	76.76	302.01	188.86	1172.85
560.51200	54.02	335.33	183.08	1172.85
581.30900	76.29	297.85	179.47	1172.85
602.10700	81.14	289.73	173.60	1172.85
648.90200	76.26	290.30	166.19	1172.85
701.67700	82.14	277.68	160.57	1172.85
749.38800	79.12	275.91	154.02	1172.85
801.38200	84.06	264.97	149.41	1172.85
848.61900	78.26	266.39	143.76	1172.85
898.37400	85.11	253.96	139.52	1172.85
947.83100	76.92	257.74	133.90	1172.85
1002.89100	83.57	245.17	122.89	1172.85
1150.00000	72.37	243.43	112.79	1172.85
1201.00000	303.14	146.76	112.79	1172.85
1251.00000	314.82	157.69	111.17	1172.85
1300.00000	314.73	155.46	108.24	1172.85

Table 6.2.1.3-9 (Sheet 11 of 12)

**Long-Term DECL Break
Mass and Energy Releases**

Time (sec)	Two-Phase		Steam	
	Mass (lbm/sec)	Enthalpy (Btu/lbm)	Mass (lbm/sec)	Enthalpy (Btu/lbm)
1310.00000	314.96	154.98	107.65	1172.85
1531.16000	321.76	145.34	95.87	1172.85
1750.00000	330.97	137.47	86.56	1172.85
1984.63000	332.53	131.38	78.21	1172.85
3997.77000	321.57	112.70	47.86	1172.85
6009.01000	294.32	110.59	39.01	1172.85
6512.70000	284.52	110.60	37.89	1172.85
7518.20000	270.41	110.58	35.95	1172.85
8022.81000	262.54	110.62	35.06	1172.85
9980.83000	232.36	111.06	32.69	1172.85
10000.00000	232.06	111.06	32.67	1172.85
10500.00000	224.18	111.25	32.30	1172.85
11000.00000	216.31	111.46	31.95	1172.85
11500.00000	208.39	111.69	31.59	1172.85
11756.12000	204.33	111.81	31.42	1172.85
11806.12000	198.63	207.23	36.30	1172.85
11856.12000	0.00	1171.70	36.26	1171.70
13000.00000	0.00	1171.70	35.35	1171.70
15005.00000	0.00	1171.70	33.78	1171.70
20005.80000	0.00	1171.70	31.27	1171.70
26007.30000	0.00	1171.70	29.77	1171.70
30007.90000	0.00	1171.70	28.77	1171.70
36008.10000	0.00	1171.70	27.11	1171.70
40000.00000	0.00	1171.70	26.02	1171.70
60000.00000	0.00	1171.70	23.27	1171.70

Table 6.2.1.3-9 (Sheet 12 of 12)

**Long-Term DECL Break
Mass and Energy Releases**

Time (sec)	Two-Phase		Steam	
	Mass (lbm/sec)	Enthalpy (Btu/lbm)	Mass (lbm/sec)	Enthalpy (Btu/lbm)
1000000.00	0.00	1171.70	8.63	1171.70
1500000.00	0.00	1171.70	7.25	1171.70
2000000.00	0.00	1171.70	6.39	1171.70
4000000.00	0.00	1171.70	4.53	1171.70

Replace Contents of Table 6.2.1.3-10 (all Sheets) Blowdown DEHL Break Mass and Energy Releases with the following:

Table 6.2.1.3-10 (Sheet 1 of 5)

**BLOWDOWN DEHL BREAK
MASS AND ENERGY RELEASES**

Time (sec)	Two-Phase		Steam	
	Mass (lbm/sec)	Average Enthalpy (Btu/lbm)	Mass Flow (lbm/sec)	Enthalpy (Btu/lbm)
0.00000	0.00	0.00	0.00	1172.85
0.00109	105,570.69	640.36	0.00	1172.85
0.10123	84,276.91	643.74	0.00	1172.85
0.20147	69,536.27	648.87	0.00	1172.85
0.30212	66,459.53	648.51	0.00	1172.85
0.40115	63,767.37	647.50	0.00	1172.85
0.50117	61,780.84	646.07	0.00	1172.85
0.60163	60,568.67	644.59	0.00	1172.85
0.70199	59,836.05	643.37	0.00	1172.85
0.80156	59,097.35	642.66	0.00	1172.85
0.90127	58,145.00	642.15	0.00	1172.85
1.00142	57,238.52	642.77	0.00	1172.85
1.10124	56,197.23	644.53	0.00	1172.85
1.20146	55,077.32	645.55	0.00	1172.85
1.30111	54,566.21	646.09	0.00	1172.85
1.40180	54,386.15	647.10	0.00	1172.85
1.50106	53,769.79	647.80	0.00	1172.85
1.60162	52,685.67	647.41	0.00	1172.85
1.70104	51,506.02	645.71	0.00	1172.85
1.80114	50,609.82	644.03	0.00	1172.85
1.90174	50,184.90	643.59	0.00	1172.85
2.00150	49,725.24	643.29	0.00	1172.85
2.10118	49,161.41	643.89	0.00	1172.85
2.20155	48,229.62	645.79	0.00	1172.85
2.30103	47,263.74	647.48	0.00	1172.85

Table 6.2.1.3-10 (Sheet 2 of 5)

**BLOWDOWN DEHL BREAK
MASS AND ENERGY RELEASES**

Time (sec)	Two-Phase		Steam	
	Mass (lbm/sec)	Average Enthalpy (Btu/lbm)	Mass Flow (lbm/sec)	Enthalpy (Btu/lbm)
2.40113	46,518.36	648.54	0.00	1172.85
2.50111	46,092.72	648.26	0.00	1172.85
2.60141	45,621.89	646.13	0.00	1172.85
2.70168	45,100.39	643.63	0.00	1172.85
2.80172	44,605.49	641.15	0.00	1172.85
2.90173	44,144.54	638.98	0.00	1172.85
3.00164	43,675.82	637.47	0.00	1172.85
3.10145	43,218.53	636.62	0.00	1172.85
3.20168	42,709.16	636.15	0.00	1172.85
3.30109	42,224.10	635.20	0.00	1172.85
3.40161	41,851.30	633.69	0.00	1172.85
3.50202	41,572.59	632.18	0.00	1172.85
3.60144	41,230.11	631.98	0.00	1172.85
3.70164	40,821.18	633.63	0.00	1172.85
3.80150	40,275.80	635.07	0.00	1172.85
3.90150	39,842.81	638.19	0.00	1172.85
4.00100	39,426.69	638.75	0.00	1172.85
4.20138	39,081.20	636.41	0.00	1172.85
4.40048	39,248.60	629.12	0.00	1172.85
4.60221	39,552.56	621.60	0.00	1172.85
4.80261	40,044.99	614.28	0.00	1172.85
5.00037	34,131.29	647.30	0.00	1172.85
5.20026	34,081.91	641.02	0.00	1172.85
5.40054	34,072.49	632.55	0.00	1172.85
5.60033	33,996.78	628.40	0.00	1172.85

Table 6.2.1.3-10 (Sheet 3 of 5)

**BLOWDOWN DEHL BREAK
MASS AND ENERGY RELEASES**

Time (sec)	Two-Phase		Steam	
	Mass (lbm/sec)	Average Enthalpy (Btu/lbm)	Mass Flow (lbm/sec)	Enthalpy (Btu/lbm)
5.80062	33,868.08	624.58	0.00	1172.85
6.00047	33,694.00	621.26	0.00	1172.85
6.20044	33,486.38	619.01	0.00	1172.85
6.40091	32,744.20	620.51	0.00	1172.85
6.60074	32,303.09	621.00	0.00	1172.85
6.80014	31,604.74	621.00	0.00	1172.85
7.00181	31,339.32	618.53	0.00	1172.85
7.20150	30,952.43	616.40	0.00	1172.85
7.40211	30,470.86	615.61	0.00	1172.85
7.60157	30,019.92	614.03	0.00	1172.85
7.80114	29,402.10	613.35	0.00	1172.85
8.00274	28,766.97	613.62	0.00	1172.85
8.20091	28,022.33	614.27	0.00	1172.85
8.40064	27,170.14	616.22	0.00	1172.85
8.60026	26,248.56	618.43	0.00	1172.85
8.80142	25,251.81	623.03	0.00	1172.85
9.00012	24,695.39	624.65	0.00	1172.85
9.20300	23,232.10	632.39	0.00	1172.85
9.40008	22,325.42	638.48	0.00	1172.85
9.60128	21,729.93	641.25	0.00	1172.85
9.80116	20,355.91	652.80	0.00	1172.85
10.00109	19,420.14	662.24	0.00	1172.85
10.20236	18,471.76	672.91	0.00	1172.85
10.40117	17,602.76	682.03	0.00	1172.85
10.60151	16,610.39	694.91	0.00	1172.85

Table 6.2.1.3-10 (Sheet 4 of 5)

**BLOWDOWN DEHL BREAK
MASS AND ENERGY RELEASES**

Time (sec)	Two-Phase		Steam	
	Mass (lbm/sec)	Average Enthalpy (Btu/lbm)	Mass Flow (lbm/sec)	Enthalpy (Btu/lbm)
10.80100	15,628.61	713.20	0.00	1172.85
11.00240	14,721.95	731.75	0.00	1172.85
11.20062	13,821.05	752.20	0.00	1172.85
11.40229	12,889.32	775.73	0.00	1172.85
11.60122	11,975.66	802.31	0.00	1172.85
11.80212	11,077.56	833.25	0.00	1172.85
12.00010	10,210.87	868.52	0.00	1172.85
12.20059	9,346.99	910.42	0.00	1172.85
12.40039	8,498.21	955.06	0.00	1172.85
12.60095	7,826.42	977.10	0.00	1172.85
12.80059	7,371.91	986.44	0.00	1172.85
13.00077	6,967.45	997.64	0.00	1172.85
13.20054	6,562.39	1,014.23	0.00	1172.85
13.40073	6,181.01	1,032.01	0.00	1172.85
13.60048	5,830.31	1,047.88	0.00	1172.85
13.80018	5,505.98	1,060.91	0.00	1172.85
14.00022	5,206.85	1,065.11	0.00	1172.85
14.20054	4,944.17	1,065.64	0.00	1172.85
14.40083	4,611.19	1,078.60	0.00	1172.85
14.60032	4,336.69	1,092.23	0.00	1172.85
14.80049	4,095.19	1,103.57	0.00	1172.85
15.00012	3,818.80	1,124.39	0.00	1172.85
15.20081	3,569.39	1,147.25	0.00	1172.85
15.40035	3,336.41	1,165.94	0.00	1172.85
15.60040	3,120.28	1,182.81	0.00	1172.85

Table 6.2.1.3-10 (Sheet 5 of 5)

**BLOWDOWN DEHL BREAK
MASS AND ENERGY RELEASES**

Time (sec)	Two-Phase		Steam	
	Mass (lbm/sec)	Average Enthalpy (Btu/lbm)	Mass Flow (lbm/sec)	Enthalpy (Btu/lbm)
15.80093	2,913.39	1,199.27	0.00	1172.85
16.00065	2,726.75	1,211.13	0.00	1172.85
16.20058	2,526.63	1,204.33	0.00	1172.85
16.40032	2,350.66	1,209.98	0.00	1172.85
16.60035	2,222.36	1,210.26	0.00	1172.85
16.80092	2,096.17	1,205.95	0.00	1172.85
17.00019	1,946.13	1,201.30	0.00	1172.85
17.20081	1,797.79	1,203.22	0.00	1172.85
17.40079	1,663.12	1,206.03	0.00	1172.85
17.60039	1,531.49	1,205.92	0.00	1172.85
17.80081	1,399.92	1,209.32	0.00	1172.85
18.00075	1,246.94	1,214.97	0.00	1172.85
18.20019	1,095.75	1,222.13	0.00	1172.85
18.40124	984.45	1,219.68	0.00	1172.85
18.60070	850.38	1,218.35	0.00	1172.85
18.80042	687.47	1,216.49	0.00	1172.85
19.00044	535.47	1,222.79	0.00	1172.85
19.20009	426.42	1,231.82	0.00	1172.85
19.40032	269.60	1,236.30	0.00	1172.85
19.60049	0.00	0.00	0.00	1172.85

Replace Table 6.2.1.4-2 (all Sheets) Mass and Enthalpy Release Data for the Case of Main Steam Line Full Double Ended Rupture from 30% Power Level with Faulted Loop Main Steam Line Isolation Valve Failure that Produces Highest Containment Pressure in its entirety with the following:

Table 6.2.1.4-2 (Sheet 1 of 2)

**MAIN STEAM LINE DOUBLE
ENDED RUPTURE MASS AND ENERGY RELEASES FROM 30% POWER LEVEL**

<u>Time (sec)</u>	<u>Mass (lbm/sec)</u>	<u>Enthalpy (Btu/lbm)</u>
<u>0.00</u>	<u>11468.30</u>	<u>1188.58</u>
<u>0.01</u>	<u>17637.10</u>	<u>1188.60</u>
<u>0.50</u>	<u>11865.20</u>	<u>1189.62</u>
<u>0.60</u>	<u>10839.60</u>	<u>1189.81</u>
<u>2.39</u>	<u>9088.22</u>	<u>1192.77</u>
<u>4.76</u>	<u>6977.98</u>	<u>1195.62</u>
<u>7.10</u>	<u>4973.83</u>	<u>1197.61</u>
<u>7.11</u>	<u>2402.15</u>	<u>1197.62</u>
<u>9.51</u>	<u>2311.41</u>	<u>1198.55</u>
<u>19.01</u>	<u>1881.93</u>	<u>1202.24</u>
<u>23.81</u>	<u>1699.56</u>	<u>1203.37</u>
<u>28.61</u>	<u>1543.11</u>	<u>1204.06</u>
<u>33.31</u>	<u>1411.22</u>	<u>1204.38</u>
<u>39.41</u>	<u>1267.86</u>	<u>1204.47</u>
<u>44.61</u>	<u>1169.42</u>	<u>1204.38</u>
<u>49.81</u>	<u>1084.97</u>	<u>1204.18</u>
<u>55.11</u>	<u>1009.94</u>	<u>1203.88</u>
<u>60.31</u>	<u>945.58</u>	<u>1203.51</u>
<u>65.51</u>	<u>889.21</u>	<u>1203.10</u>
<u>70.71</u>	<u>839.97</u>	<u>1202.66</u>
<u>81.11</u>	<u>759.10</u>	<u>1201.75</u>
<u>91.51</u>	<u>694.97</u>	<u>1200.81</u>
<u>101.91</u>	<u>642.42</u>	<u>1199.87</u>
<u>112.31</u>	<u>598.45</u>	<u>1198.95</u>
<u>122.81</u>	<u>560.75</u>	<u>1198.06</u>
<u>133.21</u>	<u>528.62</u>	<u>1197.22</u>
<u>143.61</u>	<u>500.83</u>	<u>1196.42</u>
<u>164.41</u>	<u>455.33</u>	<u>1194.93</u>

Table 6.2.1.4-2 (Sheet 2 of 2)

MAIN STEAM LINE DOUBLE

ENDED RUPTURE MASS AND ENERGY RELEASES FROM 30% POWER LEVEL

<u>Time (sec)</u>	<u>Mass (lbm/sec)</u>	<u>Enthalpy (Btu/lbm)</u>
<u>185.31</u>	<u>419.91</u>	<u>1193.56</u>
<u>206.11</u>	<u>391.98</u>	<u>1192.33</u>
<u>226.91</u>	<u>369.44</u>	<u>1191.27</u>
<u>247.81</u>	<u>350.46</u>	<u>1190.33</u>
<u>289.41</u>	<u>319.78</u>	<u>1188.67</u>
<u>331.11</u>	<u>295.40</u>	<u>1187.26</u>
<u>372.81</u>	<u>276.49</u>	<u>1186.05</u>
<u>414.51</u>	<u>260.24</u>	<u>1184.91</u>
<u>456.21</u>	<u>246.00</u>	<u>1183.82</u>
<u>539.51</u>	<u>222.09</u>	<u>1181.80</u>
<u>622.81</u>	<u>201.03</u>	<u>1179.82</u>
<u>706.21</u>	<u>183.96</u>	<u>1178.08</u>
<u>753.51</u>	<u>167.56</u>	<u>1180.19</u>
<u>770.01</u>	<u>160.58</u>	<u>1181.96</u>
<u>786.61</u>	<u>151.83</u>	<u>1184.83</u>
<u>796.21</u>	<u>145.40</u>	<u>1187.30</u>
<u>803.21</u>	<u>139.83</u>	<u>1189.63</u>
<u>815.61</u>	<u>128.28</u>	<u>1195.13</u>
<u>823.81</u>	<u>117.54</u>	<u>1199.98</u>
<u>828.01</u>	<u>110.64</u>	<u>1202.88</u>
<u>836.21</u>	<u>94.84</u>	<u>1209.36</u>
<u>844.51</u>	<u>77.41</u>	<u>1216.98</u>
<u>848.71</u>	<u>60.78</u>	<u>1221.36</u>
<u>850.51</u>	<u>46.64</u>	<u>1223.19</u>
<u>851.41</u>	<u>38.93</u>	<u>1224.05</u>
<u>852.01</u>	<u>32.47</u>	<u>1224.58</u>
<u>852.71</u>	<u>19.65</u>	<u>1225.19</u>
<u>852.81</u>	<u>11.58</u>	<u>1225.30</u>
<u>852.91</u>	<u>2.62</u>	<u>1150.35</u>
<u>1000.01</u>	<u>2.62</u>	<u>1150.35</u>

Replace Table 6.2.1.4-3 Not Used with the following Tables (multiple sheets):

~~Table 6.2.1.4-3~~ — Not Used

Table 6.2.1.4-3 (Sheet 1 of 2)

**MAIN STEAM LINE DOUBLE
ENDED RUPTURE MASS AND ENERGY RELEASES FROM FULL POWER LEVEL**

<u>Time (sec)</u>	<u>Mass (lbm/sec)</u>	<u>Enthalpy (Btu/lbm)</u>
<u>0.00</u>	<u>9488.34</u>	<u>1195.03</u>
<u>0.01</u>	<u>14673.17</u>	<u>1195.04</u>
<u>0.49</u>	<u>10265.53</u>	<u>1195.51</u>
<u>0.53</u>	<u>10146.34</u>	<u>1195.54</u>
<u>2.12</u>	<u>8728.07</u>	<u>1196.69</u>
<u>7.11</u>	<u>4914.85</u>	<u>1197.03</u>
<u>7.12</u>	<u>2470.30</u>	<u>1196.90</u>
<u>9.11</u>	<u>2431.47</u>	<u>1197.32</u>
<u>11.11</u>	<u>2344.55</u>	<u>1198.22</u>
<u>18.91</u>	<u>1939.20</u>	<u>1201.83</u>
<u>22.91</u>	<u>1767.69</u>	<u>1202.99</u>
<u>26.91</u>	<u>1621.85</u>	<u>1203.75</u>
<u>30.81</u>	<u>1499.85</u>	<u>1204.20</u>
<u>40.31</u>	<u>1267.30</u>	<u>1204.47</u>
<u>45.31</u>	<u>1173.99</u>	<u>1204.39</u>
<u>50.11</u>	<u>1097.11</u>	<u>1204.22</u>
<u>59.81</u>	<u>975.89</u>	<u>1203.69</u>
<u>69.61</u>	<u>882.49</u>	<u>1203.04</u>
<u>79.41</u>	<u>809.49</u>	<u>1202.35</u>
<u>89.21</u>	<u>751.10</u>	<u>1201.65</u>
<u>99.01</u>	<u>702.44</u>	<u>1200.93</u>
<u>118.61</u>	<u>624.39</u>	<u>1199.51</u>
<u>138.21</u>	<u>564.93</u>	<u>1198.16</u>
<u>157.81</u>	<u>518.99</u>	<u>1196.95</u>
<u>177.31</u>	<u>483.30</u>	<u>1195.89</u>
<u>196.91</u>	<u>454.74</u>	<u>1194.91</u>

Table 6.2.1.4-3 (Sheet 2 of 2)

**MAIN STEAM LINE DOUBLE
ENDED RUPTURE MASS AND ENERGY RELEASES FROM FULL POWER LEVEL**

<u>Time (sec)</u>	<u>Mass (lbm/sec)</u>	<u>Enthalpy (Btu/lbm)</u>
<u>236.11</u>	<u>411.54</u>	<u>1193.20</u>
<u>275.31</u>	<u>379.33</u>	<u>1191.74</u>
<u>314.41</u>	<u>353.51</u>	<u>1190.48</u>
<u>353.61</u>	<u>331.84</u>	<u>1189.34</u>
<u>376.81</u>	<u>305.86</u>	<u>1191.91</u>
<u>388.41</u>	<u>289.54</u>	<u>1194.76</u>
<u>400.01</u>	<u>269.11</u>	<u>1199.84</u>
<u>405.81</u>	<u>256.10</u>	<u>1203.69</u>
<u>411.61</u>	<u>240.27</u>	<u>1208.68</u>
<u>417.41</u>	<u>220.56</u>	<u>1215.05</u>
<u>423.21</u>	<u>196.05</u>	<u>1222.95</u>
<u>429.01</u>	<u>167.41</u>	<u>1232.28</u>
<u>437.51</u>	<u>119.88</u>	<u>1248.03</u>
<u>439.11</u>	<u>98.02</u>	<u>1251.23</u>
<u>439.81</u>	<u>90.27</u>	<u>1252.49</u>
<u>440.61</u>	<u>82.50</u>	<u>1253.87</u>
<u>443.51</u>	<u>57.13</u>	<u>1258.36</u>
<u>444.31</u>	<u>49.36</u>	<u>1259.44</u>
<u>445.01</u>	<u>41.86</u>	<u>1260.34</u>
<u>445.71</u>	<u>33.21</u>	<u>1261.19</u>
<u>446.01</u>	<u>28.91</u>	<u>1261.54</u>
<u>446.21</u>	<u>25.55</u>	<u>1261.78</u>
<u>446.31</u>	<u>23.51</u>	<u>1261.89</u>
<u>446.41</u>	<u>20.64</u>	<u>1262.01</u>
<u>446.51</u>	<u>2.62</u>	<u>1150.35</u>
<u>500.01</u>	<u>2.62</u>	<u>1150.35</u>

Table 6.2.1.4-4 Plant Data Used for Mass and Energy Releases Determination is revised as follows:

**Table 6.2.1.4-4
Plant Data Used for Mass and Energy Releases Determination**

Plant data for all cases:		
Power, Nominal Rating (MWt)		3415
Nominal RCS Flow (GPM)		299,880
Nominal Full Load T _{avg} (°F)		573.6
Nominal RCS Pressure (psia)		2250
Nominal Steam Temperature (°F)		525.0 <u>525.5</u>
Nominal Feedwater Enthalpy (BTU/lbm)		419.3 <u>419.4</u>

Replace Table 6.2.1.5-1 (multiple sheets) Minimum Containment Pressure Mass and Energy Releases in its entirety with the following Tables (multiple sheets):

Table 6.2.1.5-1 (Sheet 1 of 20)

**MINIMUM CONTAINMENT PRESSURE MASS AND ENERGY RELEASES FOR LARGE
BREAK LOCA**

<u>Time (sec)</u>	<u>Mass Release (lbm/s)</u>	<u>Energy Release (BTU/s)</u>
<u>0.00</u>	<u>0.00</u>	<u>0</u>
<u>0.01</u>	<u>7942.87</u>	<u>4197068</u>
<u>0.51</u>	<u>57956.40</u>	<u>30282500</u>
<u>1.01</u>	<u>56472.40</u>	<u>29608220</u>
<u>1.51</u>	<u>54084.40</u>	<u>28449280</u>
<u>2.01</u>	<u>48999.30</u>	<u>25903610</u>
<u>2.51</u>	<u>44669.40</u>	<u>23773360</u>
<u>3.01</u>	<u>40136.20</u>	<u>21554050</u>
<u>3.51</u>	<u>36059.80</u>	<u>19555650</u>
<u>4.01</u>	<u>32343.80</u>	<u>17726170</u>
<u>4.51</u>	<u>30080.20</u>	<u>16651800</u>
<u>5.01</u>	<u>28154.80</u>	<u>15805980</u>
<u>5.51</u>	<u>26326.81</u>	<u>15014160</u>
<u>6.01</u>	<u>24527.91</u>	<u>14256040</u>
<u>6.51</u>	<u>22846.03</u>	<u>13563570</u>
<u>7.01</u>	<u>21582.36</u>	<u>13025710</u>
<u>7.51</u>	<u>20192.85</u>	<u>12407740</u>
<u>8.01</u>	<u>18986.50</u>	<u>11890100</u>
<u>8.51</u>	<u>17871.42</u>	<u>11359050</u>
<u>9.01</u>	<u>17076.27</u>	<u>10930030</u>
<u>9.51</u>	<u>16328.68</u>	<u>10479370</u>
<u>10.01</u>	<u>15748.25</u>	<u>10165630</u>
<u>10.51</u>	<u>15138.17</u>	<u>9823398</u>
<u>11.01</u>	<u>14561.62</u>	<u>9486835</u>
<u>11.51</u>	<u>13474.22</u>	<u>9024197</u>
<u>12.01</u>	<u>13680.55</u>	<u>8910145</u>
<u>12.51</u>	<u>13179.21</u>	<u>8612196</u>

Table 6.2.1.5-1 (Sheet 2 of 20)

**MINIMUM CONTAINMENT PRESSURE MASS AND ENERGY RELEASES FOR LARGE
BREAK LOCA**

<u>Time (sec)</u>	<u>Mass Release (lbm/s)</u>	<u>Energy Release (BTU/s)</u>
<u>13.01</u>	<u>12104.41</u>	<u>8178315</u>
<u>13.51</u>	<u>11928.12</u>	<u>7962325</u>
<u>14.01</u>	<u>11331.71</u>	<u>7630674</u>
<u>14.51</u>	<u>10285.89</u>	<u>7140065</u>
<u>15.01</u>	<u>9612.06</u>	<u>6800880</u>
<u>15.51</u>	<u>8890.77</u>	<u>6437936</u>
<u>16.01</u>	<u>8397.32</u>	<u>6117610</u>
<u>16.51</u>	<u>8110.99</u>	<u>5827232</u>
<u>17.01</u>	<u>7989.51</u>	<u>5551450</u>
<u>17.51</u>	<u>7776.17</u>	<u>5249230</u>
<u>18.01</u>	<u>7400.69</u>	<u>4907268</u>
<u>18.51</u>	<u>7127.20</u>	<u>4601066</u>
<u>19.01</u>	<u>6709.37</u>	<u>4279012</u>
<u>19.51</u>	<u>6386.74</u>	<u>3978181</u>
<u>20.01</u>	<u>6115.01</u>	<u>3705914</u>
<u>20.51</u>	<u>5776.52</u>	<u>3425902</u>
<u>21.01</u>	<u>5517.91</u>	<u>3180462</u>
<u>21.51</u>	<u>5273.02</u>	<u>2963178</u>
<u>22.01</u>	<u>4939.00</u>	<u>2748973</u>
<u>22.51</u>	<u>4605.24</u>	<u>2551896</u>
<u>23.01</u>	<u>4470.27</u>	<u>2376817</u>
<u>23.51</u>	<u>3941.49</u>	<u>2159592</u>
<u>24.01</u>	<u>3651.01</u>	<u>2028490</u>
<u>24.51</u>	<u>3112.96</u>	<u>1831021</u>
<u>25.01</u>	<u>2948.30</u>	<u>1674552</u>
<u>25.51</u>	<u>2559.77</u>	<u>1528877</u>
<u>26.01</u>	<u>2458.65</u>	<u>1408223</u>

Table 6.2.1.5-1 (Sheet 3 of 20)

**MINIMUM CONTAINMENT PRESSURE MASS AND ENERGY RELEASES FOR LARGE
BREAK LOCA**

<u>Time (sec)</u>	<u>Mass Release (lbm/s)</u>	<u>Energy Release (BTU/s)</u>
<u>26.51</u>	<u>2948.44</u>	<u>1371068</u>
<u>27.01</u>	<u>2746.30</u>	<u>1290115</u>
<u>27.51</u>	<u>1786.07</u>	<u>1043598</u>
<u>28.01</u>	<u>2712.07</u>	<u>1012782</u>
<u>28.51</u>	<u>2910.33</u>	<u>1083228</u>
<u>29.01</u>	<u>2233.45</u>	<u>918945</u>
<u>29.51</u>	<u>1450.78</u>	<u>729919</u>
<u>30.01</u>	<u>1211.72</u>	<u>620407</u>
<u>30.51</u>	<u>1589.06</u>	<u>589646</u>
<u>31.01</u>	<u>2324.34</u>	<u>657795</u>
<u>31.51</u>	<u>511.11</u>	<u>385601</u>
<u>32.01</u>	<u>327.07</u>	<u>257183</u>
<u>32.51</u>	<u>229.93</u>	<u>170637</u>
<u>33.01</u>	<u>138.97</u>	<u>118111</u>
<u>33.51</u>	<u>38.78</u>	<u>49703</u>
<u>34.01</u>	<u>30.85</u>	<u>39557</u>
<u>34.51</u>	<u>24.61</u>	<u>28213</u>
<u>35.01</u>	<u>32.26</u>	<u>28358</u>
<u>35.51</u>	<u>24.41</u>	<u>20639</u>
<u>36.01</u>	<u>7.67</u>	<u>6232</u>
<u>36.51</u>	<u>63.33</u>	<u>50679</u>
<u>37.01</u>	<u>17.81</u>	<u>22853</u>
<u>37.51</u>	<u>13.02</u>	<u>16607</u>
<u>38.01</u>	<u>9.73</u>	<u>12441</u>
<u>38.51</u>	<u>0.00</u>	<u>0</u>
<u>39.01</u>	<u>3.26</u>	<u>2928</u>
<u>39.51</u>	<u>65.55</u>	<u>53687</u>

Table 6.2.1.5-1 (Sheet 4 of 20)

**MINIMUM CONTAINMENT PRESSURE MASS AND ENERGY RELEASES FOR LARGE
BREAK LOCA**

<u>Time (sec)</u>	<u>Mass Release (lbm/s)</u>	<u>Energy Release (BTU/s)</u>
<u>40.01</u>	<u>67.34</u>	<u>72602</u>
<u>40.51</u>	<u>62.30</u>	<u>67887</u>
<u>41.01</u>	<u>49.03</u>	<u>58542</u>
<u>41.51</u>	<u>43.45</u>	<u>52364</u>
<u>42.01</u>	<u>17.96</u>	<u>22932</u>
<u>42.51</u>	<u>15.20</u>	<u>19131</u>
<u>43.01</u>	<u>33.83</u>	<u>37590</u>
<u>43.51</u>	<u>25.45</u>	<u>21467</u>
<u>44.01</u>	<u>29.94</u>	<u>24662</u>
<u>44.51</u>	<u>33.10</u>	<u>29509</u>
<u>45.01</u>	<u>28.30</u>	<u>26896</u>
<u>45.51</u>	<u>24.91</u>	<u>23758</u>
<u>46.01</u>	<u>72.50</u>	<u>78140</u>
<u>46.51</u>	<u>56.34</u>	<u>68242</u>
<u>47.01</u>	<u>40.06</u>	<u>48849</u>
<u>47.51</u>	<u>106.92</u>	<u>118490</u>
<u>48.01</u>	<u>26.54</u>	<u>28205</u>
<u>48.51</u>	<u>57.76</u>	<u>61793</u>
<u>49.01</u>	<u>166.99</u>	<u>188706</u>
<u>49.51</u>	<u>142.10</u>	<u>153683</u>
<u>50.01</u>	<u>122.34</u>	<u>133270</u>
<u>50.51</u>	<u>104.57</u>	<u>118432</u>
<u>51.01</u>	<u>94.50</u>	<u>106009</u>
<u>51.51</u>	<u>114.97</u>	<u>125648</u>
<u>52.01</u>	<u>304.27</u>	<u>327915</u>
<u>52.51</u>	<u>438.18</u>	<u>353398</u>
<u>53.01</u>	<u>217.91</u>	<u>238944</u>

Table 6.2.1.5-1 (Sheet 5 of 20)

**MINIMUM CONTAINMENT PRESSURE MASS AND ENERGY RELEASES FOR LARGE
BREAK LOCA**

<u>Time (sec)</u>	<u>Mass Release (lbm/s)</u>	<u>Energy Release (BTU/s)</u>
<u>53.51</u>	<u>208.85</u>	<u>243504</u>
<u>54.01</u>	<u>196.84</u>	<u>229968</u>
<u>54.51</u>	<u>170.84</u>	<u>200237</u>
<u>55.01</u>	<u>143.16</u>	<u>168668</u>
<u>55.51</u>	<u>108.35</u>	<u>123758</u>
<u>56.01</u>	<u>96.07</u>	<u>110132</u>
<u>56.51</u>	<u>145.71</u>	<u>166951</u>
<u>57.01</u>	<u>184.00</u>	<u>199601</u>
<u>57.51</u>	<u>148.14</u>	<u>159282</u>
<u>58.01</u>	<u>111.16</u>	<u>129618</u>
<u>58.51</u>	<u>103.14</u>	<u>115094</u>
<u>59.01</u>	<u>59.11</u>	<u>70920</u>
<u>59.51</u>	<u>121.13</u>	<u>133279</u>
<u>60.01</u>	<u>192.10</u>	<u>221407</u>
<u>60.51</u>	<u>274.36</u>	<u>259082</u>
<u>61.01</u>	<u>217.48</u>	<u>222919</u>
<u>61.51</u>	<u>140.77</u>	<u>164224</u>
<u>62.01</u>	<u>113.46</u>	<u>131276</u>
<u>62.51</u>	<u>81.97</u>	<u>95753</u>
<u>63.01</u>	<u>125.53</u>	<u>146907</u>
<u>63.51</u>	<u>277.75</u>	<u>267057</u>
<u>64.01</u>	<u>279.66</u>	<u>259800</u>
<u>64.51</u>	<u>202.16</u>	<u>222185</u>
<u>65.01</u>	<u>181.19</u>	<u>194112</u>
<u>65.51</u>	<u>125.69</u>	<u>141746</u>
<u>66.01</u>	<u>97.86</u>	<u>111750</u>
<u>66.51</u>	<u>155.16</u>	<u>176333</u>

Table 6.2.1.5-1 (Sheet 6 of 20)

**MINIMUM CONTAINMENT PRESSURE MASS AND ENERGY RELEASES FOR LARGE
BREAK LOCA**

<u>Time (sec)</u>	<u>Mass Release (lbm/s)</u>	<u>Energy Release (BTU/s)</u>
<u>67.01</u>	<u>224.14</u>	<u>242392</u>
<u>67.51</u>	<u>230.40</u>	<u>234200</u>
<u>68.01</u>	<u>180.98</u>	<u>207383</u>
<u>68.51</u>	<u>155.58</u>	<u>181044</u>
<u>69.01</u>	<u>129.63</u>	<u>148391</u>
<u>69.51</u>	<u>134.89</u>	<u>158826</u>
<u>70.01</u>	<u>179.41</u>	<u>202659</u>
<u>70.51</u>	<u>189.19</u>	<u>217939</u>
<u>71.01</u>	<u>189.94</u>	<u>212600</u>
<u>71.51</u>	<u>200.16</u>	<u>215380</u>
<u>72.01</u>	<u>155.87</u>	<u>182233</u>
<u>72.51</u>	<u>144.58</u>	<u>165043</u>
<u>73.01</u>	<u>152.39</u>	<u>171976</u>
<u>73.51</u>	<u>193.73</u>	<u>218892</u>
<u>74.01</u>	<u>213.02</u>	<u>246071</u>
<u>74.51</u>	<u>207.90</u>	<u>243728</u>
<u>75.01</u>	<u>285.04</u>	<u>276724</u>
<u>75.51</u>	<u>218.60</u>	<u>234337</u>
<u>76.01</u>	<u>174.99</u>	<u>194687</u>
<u>76.51</u>	<u>168.67</u>	<u>191156</u>
<u>77.01</u>	<u>230.41</u>	<u>262908</u>
<u>77.51</u>	<u>220.33</u>	<u>257748</u>
<u>78.01</u>	<u>328.67</u>	<u>299957</u>
<u>78.51</u>	<u>269.62</u>	<u>271423</u>
<u>79.01</u>	<u>194.11</u>	<u>220457</u>
<u>79.51</u>	<u>190.95</u>	<u>218188</u>
<u>80.01</u>	<u>213.99</u>	<u>244892</u>

Table 6.2.1.5-1 (Sheet 7 of 20)

**MINIMUM CONTAINMENT PRESSURE MASS AND ENERGY RELEASES FOR LARGE
BREAK LOCA**

<u>Time (sec)</u>	<u>Mass Release (lbm/s)</u>	<u>Energy Release (BTU/s)</u>
<u>80.51</u>	<u>236.23</u>	<u>267305</u>
<u>81.01</u>	<u>260.53</u>	<u>279713</u>
<u>81.51</u>	<u>223.30</u>	<u>258393</u>
<u>82.01</u>	<u>217.44</u>	<u>254964</u>
<u>82.51</u>	<u>205.88</u>	<u>242910</u>
<u>83.01</u>	<u>238.23</u>	<u>259684</u>
<u>83.51</u>	<u>243.58</u>	<u>275560</u>
<u>84.01</u>	<u>234.26</u>	<u>269102</u>
<u>84.51</u>	<u>228.11</u>	<u>268944</u>
<u>85.01</u>	<u>220.56</u>	<u>262949</u>
<u>85.51</u>	<u>211.33</u>	<u>251832</u>
<u>86.01</u>	<u>218.36</u>	<u>259571</u>
<u>86.51</u>	<u>248.80</u>	<u>284213</u>
<u>87.01</u>	<u>260.76</u>	<u>296727</u>
<u>87.51</u>	<u>262.52</u>	<u>299547</u>
<u>88.01</u>	<u>264.89</u>	<u>298182</u>
<u>88.51</u>	<u>820.35</u>	<u>304725</u>
<u>89.01</u>	<u>1658.45</u>	<u>387314</u>
<u>89.51</u>	<u>419.25</u>	<u>332530</u>
<u>90.01</u>	<u>465.12</u>	<u>307753</u>
<u>90.51</u>	<u>798.98</u>	<u>323657</u>
<u>91.01</u>	<u>1564.18</u>	<u>392925</u>
<u>91.51</u>	<u>1681.45</u>	<u>488011</u>
<u>92.01</u>	<u>524.80</u>	<u>328926</u>
<u>92.51</u>	<u>715.87</u>	<u>302892</u>
<u>93.01</u>	<u>916.00</u>	<u>331695</u>
<u>93.51</u>	<u>1609.64</u>	<u>395641</u>

Table 6.2.1.5-1 (Sheet 8 of 20)

**MINIMUM CONTAINMENT PRESSURE MASS AND ENERGY RELEASES FOR LARGE
BREAK LOCA**

<u>Time (sec)</u>	<u>Mass Release (lbm/s)</u>	<u>Energy Release (BTU/s)</u>
<u>94.01</u>	<u>1483.75</u>	<u>445986</u>
<u>94.51</u>	<u>796.83</u>	<u>367070</u>
<u>95.01</u>	<u>567.18</u>	<u>323061</u>
<u>95.51</u>	<u>846.66</u>	<u>343109</u>
<u>96.01</u>	<u>1008.32</u>	<u>354410</u>
<u>96.51</u>	<u>1583.02</u>	<u>418731</u>
<u>97.01</u>	<u>846.20</u>	<u>359939</u>
<u>97.51</u>	<u>559.47</u>	<u>324035</u>
<u>98.01</u>	<u>651.65</u>	<u>321456</u>
<u>98.51</u>	<u>736.91</u>	<u>339803</u>
<u>99.01</u>	<u>916.43</u>	<u>329098</u>
<u>99.51</u>	<u>1519.14</u>	<u>410810</u>
<u>100.01</u>	<u>720.12</u>	<u>338623</u>
<u>100.51</u>	<u>508.98</u>	<u>313605</u>
<u>101.01</u>	<u>751.29</u>	<u>332987</u>
<u>101.51</u>	<u>709.66</u>	<u>337150</u>
<u>102.01</u>	<u>1026.40</u>	<u>342413</u>
<u>102.51</u>	<u>1501.55</u>	<u>485867</u>
<u>103.01</u>	<u>1509.55</u>	<u>443226</u>
<u>103.51</u>	<u>1615.99</u>	<u>389899</u>
<u>104.01</u>	<u>709.60</u>	<u>343936</u>
<u>104.51</u>	<u>298.47</u>	<u>290818</u>
<u>105.01</u>	<u>405.18</u>	<u>307500</u>
<u>105.51</u>	<u>236.00</u>	<u>257365</u>
<u>106.01</u>	<u>214.57</u>	<u>244634</u>
<u>106.51</u>	<u>196.03</u>	<u>225879</u>
<u>107.01</u>	<u>211.49</u>	<u>243737</u>

Table 6.2.1.5-1 (Sheet 9 of 20)

**MINIMUM CONTAINMENT PRESSURE MASS AND ENERGY RELEASES FOR LARGE
BREAK LOCA**

<u>Time (sec)</u>	<u>Mass Release (lbm/s)</u>	<u>Energy Release (BTU/s)</u>
<u>107.51</u>	<u>209.45</u>	<u>241604</u>
<u>108.01</u>	<u>212.12</u>	<u>244237</u>
<u>108.51</u>	<u>211.72</u>	<u>243033</u>
<u>109.01</u>	<u>231.93</u>	<u>255782</u>
<u>109.51</u>	<u>221.98</u>	<u>254250</u>
<u>110.01</u>	<u>230.22</u>	<u>261121</u>
<u>110.51</u>	<u>221.28</u>	<u>253187</u>
<u>111.01</u>	<u>220.14</u>	<u>254614</u>
<u>111.51</u>	<u>219.87</u>	<u>253850</u>
<u>112.01</u>	<u>222.09</u>	<u>256551</u>
<u>112.51</u>	<u>228.52</u>	<u>255866</u>
<u>113.01</u>	<u>225.70</u>	<u>254820</u>
<u>113.51</u>	<u>230.06</u>	<u>256396</u>
<u>114.01</u>	<u>232.07</u>	<u>259134</u>
<u>114.51</u>	<u>221.75</u>	<u>256236</u>
<u>115.01</u>	<u>220.54</u>	<u>255640</u>
<u>115.51</u>	<u>208.33</u>	<u>246119</u>
<u>116.01</u>	<u>217.96</u>	<u>249376</u>
<u>116.51</u>	<u>203.44</u>	<u>239316</u>
<u>117.01</u>	<u>233.75</u>	<u>262602</u>
<u>117.51</u>	<u>231.74</u>	<u>261453</u>
<u>118.01</u>	<u>212.96</u>	<u>251032</u>
<u>118.51</u>	<u>945.18</u>	<u>291332</u>
<u>119.01</u>	<u>1704.73</u>	<u>351147</u>
<u>119.51</u>	<u>1072.30</u>	<u>370636</u>
<u>120.01</u>	<u>805.66</u>	<u>318168</u>
<u>120.51</u>	<u>1629.05</u>	<u>366554</u>

Table 6.2.1.5-1 (Sheet 10 of 20)

**MINIMUM CONTAINMENT PRESSURE MASS AND ENERGY RELEASES FOR LARGE
BREAK LOCA**

<u>Time (sec)</u>	<u>Mass Release (lbm/s)</u>	<u>Energy Release (BTU/s)</u>
<u>121.01</u>	<u>1601.92</u>	<u>368274</u>
<u>121.51</u>	<u>876.85</u>	<u>344974</u>
<u>122.01</u>	<u>953.84</u>	<u>345943</u>
<u>122.51</u>	<u>1061.37</u>	<u>345113</u>
<u>123.01</u>	<u>2077.05</u>	<u>361856</u>
<u>123.51</u>	<u>1155.47</u>	<u>400824</u>
<u>124.01</u>	<u>735.68</u>	<u>308794</u>
<u>124.51</u>	<u>1068.45</u>	<u>328982</u>
<u>125.01</u>	<u>1486.66</u>	<u>389182</u>
<u>125.51</u>	<u>1532.30</u>	<u>376918</u>
<u>126.01</u>	<u>1054.35</u>	<u>378053</u>
<u>126.51</u>	<u>355.16</u>	<u>300169</u>
<u>127.01</u>	<u>985.78</u>	<u>370905</u>
<u>127.51</u>	<u>1033.92</u>	<u>331664</u>
<u>128.01</u>	<u>1622.16</u>	<u>383545</u>
<u>128.51</u>	<u>1509.10</u>	<u>437329</u>
<u>129.01</u>	<u>886.90</u>	<u>351995</u>
<u>129.51</u>	<u>335.52</u>	<u>289093</u>
<u>130.01</u>	<u>567.94</u>	<u>261593</u>
<u>130.51</u>	<u>1353.63</u>	<u>358127</u>
<u>131.01</u>	<u>1597.91</u>	<u>353608</u>
<u>131.51</u>	<u>250.38</u>	<u>256082</u>
<u>132.01</u>	<u>183.70</u>	<u>215997</u>
<u>132.51</u>	<u>182.98</u>	<u>211803</u>
<u>133.01</u>	<u>188.64</u>	<u>218584</u>
<u>133.51</u>	<u>189.25</u>	<u>220139</u>
<u>134.01</u>	<u>187.08</u>	<u>215705</u>

Table 6.2.1.5-1 (Sheet 11 of 20)

**MINIMUM CONTAINMENT PRESSURE MASS AND ENERGY RELEASES FOR LARGE
BREAK LOCA**

Time (sec)	Mass Release (lbm/s)	Energy Release (BTU/s)
134.51	208.59	225750
135.01	189.82	213258
135.51	186.80	214116
136.01	182.34	209390
136.51	183.58	209779
137.01	181.74	207033
137.51	176.95	201679
138.01	195.32	207464
138.51	169.57	191895
139.01	199.69	206952
139.51	175.63	196657
140.01	174.02	195324
140.51	169.66	190497
141.01	154.86	176102
141.51	166.87	176534
142.01	142.95	162974
142.51	145.92	165928
143.01	142.22	163605
143.51	140.98	163470
144.01	135.00	157359
144.51	130.69	152796
145.01	143.00	154391
145.51	129.44	150373
146.01	131.26	152180
146.51	126.54	149938
147.01	120.20	146381
147.51	121.14	147390

Table 6.2.1.5-1 (Sheet 12 of 20)

**MINIMUM CONTAINMENT PRESSURE MASS AND ENERGY RELEASES FOR LARGE
BREAK LOCA**

<u>Time (sec)</u>	<u>Mass Release (lbm/s)</u>	<u>Energy Release (BTU/s)</u>
<u>148.01</u>	<u>118.77</u>	<u>145198</u>
<u>148.51</u>	<u>137.33</u>	<u>152053</u>
<u>149.01</u>	<u>125.19</u>	<u>149500</u>
<u>149.51</u>	<u>125.34</u>	<u>151325</u>
<u>150.01</u>	<u>123.63</u>	<u>151903</u>
<u>150.51</u>	<u>121.18</u>	<u>149714</u>
<u>151.01</u>	<u>123.87</u>	<u>153456</u>
<u>151.51</u>	<u>142.83</u>	<u>161818</u>
<u>152.01</u>	<u>123.52</u>	<u>152431</u>
<u>152.51</u>	<u>137.71</u>	<u>164398</u>
<u>153.01</u>	<u>138.42</u>	<u>165917</u>
<u>153.51</u>	<u>143.37</u>	<u>169283</u>
<u>154.01</u>	<u>144.04</u>	<u>170853</u>
<u>154.51</u>	<u>146.94</u>	<u>172510</u>
<u>155.01</u>	<u>157.46</u>	<u>180972</u>
<u>155.51</u>	<u>182.18</u>	<u>194506</u>
<u>156.01</u>	<u>182.68</u>	<u>199083</u>
<u>156.51</u>	<u>240.23</u>	<u>226854</u>
<u>157.01</u>	<u>186.17</u>	<u>201397</u>
<u>157.51</u>	<u>188.78</u>	<u>207869</u>
<u>158.01</u>	<u>177.53</u>	<u>197204</u>
<u>158.51</u>	<u>182.14</u>	<u>199744</u>
<u>159.01</u>	<u>170.94</u>	<u>193739</u>
<u>159.51</u>	<u>175.02</u>	<u>193991</u>
<u>160.01</u>	<u>183.89</u>	<u>202184</u>
<u>160.51</u>	<u>178.53</u>	<u>200576</u>
<u>161.01</u>	<u>180.58</u>	<u>202006</u>

Table 6.2.1.5-1 (Sheet 13 of 20)

**MINIMUM CONTAINMENT PRESSURE MASS AND ENERGY RELEASES FOR LARGE
BREAK LOCA**

<u>Time (sec)</u>	<u>Mass Release (lbm/s)</u>	<u>Energy Release (BTU/s)</u>
<u>161.51</u>	<u>176.12</u>	<u>199661</u>
<u>162.01</u>	<u>178.24</u>	<u>202356</u>
<u>162.51</u>	<u>183.29</u>	<u>206040</u>
<u>163.01</u>	<u>187.97</u>	<u>205289</u>
<u>163.51</u>	<u>192.60</u>	<u>207365</u>
<u>164.01</u>	<u>188.51</u>	<u>207204</u>
<u>164.51</u>	<u>180.04</u>	<u>204996</u>
<u>165.01</u>	<u>177.20</u>	<u>203222</u>
<u>165.51</u>	<u>177.24</u>	<u>203394</u>
<u>166.01</u>	<u>179.82</u>	<u>205213</u>
<u>166.51</u>	<u>191.01</u>	<u>210737</u>
<u>167.01</u>	<u>202.91</u>	<u>222624</u>
<u>167.51</u>	<u>185.70</u>	<u>209773</u>
<u>168.01</u>	<u>201.58</u>	<u>219384</u>
<u>168.51</u>	<u>700.89</u>	<u>213031</u>
<u>169.01</u>	<u>1432.73</u>	<u>284625</u>
<u>169.51</u>	<u>722.96</u>	<u>282295</u>
<u>170.01</u>	<u>575.47</u>	<u>275907</u>
<u>170.51</u>	<u>705.57</u>	<u>272191</u>
<u>171.01</u>	<u>1397.11</u>	<u>321115</u>
<u>171.51</u>	<u>1406.78</u>	<u>306333</u>
<u>172.01</u>	<u>1180.97</u>	<u>318445</u>
<u>172.51</u>	<u>1451.68</u>	<u>326298</u>
<u>173.01</u>	<u>847.43</u>	<u>302801</u>
<u>173.51</u>	<u>751.32</u>	<u>271505</u>
<u>174.01</u>	<u>1484.65</u>	<u>298434</u>
<u>174.51</u>	<u>1442.95</u>	<u>361325</u>

Table 6.2.1.5-1 (Sheet 14 of 20)

**MINIMUM CONTAINMENT PRESSURE MASS AND ENERGY RELEASES FOR LARGE
BREAK LOCA**

<u>Time (sec)</u>	<u>Mass Release (lbm/s)</u>	<u>Energy Release (BTU/s)</u>
<u>175.01</u>	<u>306.30</u>	<u>258039</u>
<u>175.51</u>	<u>754.45</u>	<u>290941</u>
<u>176.01</u>	<u>1234.32</u>	<u>321950</u>
<u>176.51</u>	<u>1756.73</u>	<u>314456</u>
<u>177.01</u>	<u>846.52</u>	<u>320401</u>
<u>177.51</u>	<u>750.78</u>	<u>285970</u>
<u>178.01</u>	<u>1352.84</u>	<u>375378</u>
<u>178.51</u>	<u>1523.54</u>	<u>329154</u>
<u>179.01</u>	<u>1610.91</u>	<u>489664</u>
<u>179.51</u>	<u>539.67</u>	<u>286078</u>
<u>180.01</u>	<u>747.77</u>	<u>308665</u>
<u>180.51</u>	<u>1370.97</u>	<u>351393</u>
<u>181.01</u>	<u>1627.21</u>	<u>324214</u>
<u>181.51</u>	<u>355.67</u>	<u>296933</u>
<u>182.01</u>	<u>748.64</u>	<u>299398</u>
<u>182.51</u>	<u>1313.10</u>	<u>372028</u>
<u>183.01</u>	<u>1602.96</u>	<u>368136</u>
<u>183.51</u>	<u>1550.98</u>	<u>345203</u>
<u>184.01</u>	<u>1200.60</u>	<u>358644</u>
<u>184.51</u>	<u>1566.80</u>	<u>362057</u>
<u>185.01</u>	<u>567.66</u>	<u>310741</u>
<u>185.51</u>	<u>759.46</u>	<u>306641</u>
<u>186.01</u>	<u>1582.28</u>	<u>358212</u>
<u>186.51</u>	<u>805.19</u>	<u>309261</u>
<u>187.01</u>	<u>1606.31</u>	<u>377818</u>
<u>187.51</u>	<u>753.33</u>	<u>326692</u>
<u>188.01</u>	<u>848.18</u>	<u>318199</u>

Table 6.2.1.5-1 (Sheet 15 of 20)

**MINIMUM CONTAINMENT PRESSURE MASS AND ENERGY RELEASES FOR LARGE
BREAK LOCA**

<u>Time (sec)</u>	<u>Mass Release (lbm/s)</u>	<u>Energy Release (BTU/s)</u>
<u>188.51</u>	<u>1765.10</u>	<u>384565</u>
<u>189.01</u>	<u>754.14</u>	<u>309859</u>
<u>189.51</u>	<u>1345.61</u>	<u>397944</u>
<u>190.01</u>	<u>1756.46</u>	<u>369226</u>
<u>190.51</u>	<u>925.16</u>	<u>368732</u>
<u>191.01</u>	<u>670.60</u>	<u>329144</u>
<u>191.51</u>	<u>784.74</u>	<u>311315</u>
<u>192.01</u>	<u>2049.53</u>	<u>372920</u>
<u>192.51</u>	<u>1470.02</u>	<u>508289</u>
<u>193.01</u>	<u>611.38</u>	<u>320418</u>
<u>193.51</u>	<u>756.78</u>	<u>328536</u>
<u>194.01</u>	<u>879.90</u>	<u>312220</u>
<u>194.51</u>	<u>1098.97</u>	<u>378667</u>
<u>195.01</u>	<u>1744.50</u>	<u>365532</u>
<u>195.51</u>	<u>701.02</u>	<u>343283</u>
<u>196.01</u>	<u>662.32</u>	<u>323679</u>
<u>196.51</u>	<u>832.72</u>	<u>334816</u>
<u>197.01</u>	<u>1646.10</u>	<u>379766</u>
<u>197.51</u>	<u>893.81</u>	<u>335562</u>
<u>198.01</u>	<u>1714.79</u>	<u>373751</u>
<u>198.51</u>	<u>611.19</u>	<u>333258</u>
<u>199.01</u>	<u>609.68</u>	<u>320394</u>
<u>199.51</u>	<u>859.92</u>	<u>338769</u>
<u>200.01</u>	<u>1607.56</u>	<u>389751</u>
<u>200.51</u>	<u>847.96</u>	<u>336163</u>
<u>201.01</u>	<u>1726.12</u>	<u>374152</u>
<u>201.51</u>	<u>469.76</u>	<u>312506</u>

Table 6.2.1.5-1 (Sheet 16 of 20)

**MINIMUM CONTAINMENT PRESSURE MASS AND ENERGY RELEASES FOR LARGE
BREAK LOCA**

<u>Time (sec)</u>	<u>Mass Release (lbm/s)</u>	<u>Energy Release (BTU/s)</u>
<u>202.01</u>	<u>487.49</u>	<u>317122</u>
<u>202.51</u>	<u>613.81</u>	<u>324092</u>
<u>203.01</u>	<u>833.89</u>	<u>325131</u>
<u>203.51</u>	<u>1259.87</u>	<u>410487</u>
<u>204.01</u>	<u>1625.88</u>	<u>385435</u>
<u>204.51</u>	<u>1483.54</u>	<u>513440</u>
<u>205.01</u>	<u>334.19</u>	<u>297833</u>
<u>205.51</u>	<u>254.25</u>	<u>275754</u>
<u>206.01</u>	<u>251.45</u>	<u>276027</u>
<u>206.51</u>	<u>240.26</u>	<u>268651</u>
<u>207.01</u>	<u>242.13</u>	<u>267065</u>
<u>207.51</u>	<u>245.12</u>	<u>268164</u>
<u>208.01</u>	<u>243.47</u>	<u>265902</u>
<u>208.51</u>	<u>237.91</u>	<u>263708</u>
<u>209.01</u>	<u>234.71</u>	<u>258062</u>
<u>209.51</u>	<u>231.02</u>	<u>257222</u>
<u>210.01</u>	<u>226.45</u>	<u>253802</u>
<u>210.51</u>	<u>232.31</u>	<u>254552</u>
<u>211.01</u>	<u>223.84</u>	<u>249586</u>
<u>211.51</u>	<u>216.30</u>	<u>243441</u>
<u>212.01</u>	<u>213.96</u>	<u>238951</u>
<u>212.51</u>	<u>215.87</u>	<u>240067</u>
<u>213.01</u>	<u>215.05</u>	<u>237629</u>
<u>213.51</u>	<u>219.00</u>	<u>238554</u>
<u>214.01</u>	<u>226.80</u>	<u>244094</u>
<u>214.51</u>	<u>223.98</u>	<u>241160</u>
<u>215.01</u>	<u>214.93</u>	<u>234096</u>

Table 6.2.1.5-1 (Sheet 17 of 20)

**MINIMUM CONTAINMENT PRESSURE MASS AND ENERGY RELEASES FOR LARGE
BREAK LOCA**

<u>Time (sec)</u>	<u>Mass Release (lbm/s)</u>	<u>Energy Release (BTU/s)</u>
<u>215.51</u>	<u>210.14</u>	<u>230933</u>
<u>216.01</u>	<u>202.37</u>	<u>225065</u>
<u>216.51</u>	<u>196.68</u>	<u>219516</u>
<u>217.01</u>	<u>200.69</u>	<u>219035</u>
<u>217.51</u>	<u>184.67</u>	<u>208066</u>
<u>218.01</u>	<u>185.29</u>	<u>209360</u>
<u>218.51</u>	<u>181.72</u>	<u>207222</u>
<u>219.01</u>	<u>186.53</u>	<u>210264</u>
<u>219.51</u>	<u>193.14</u>	<u>213581</u>
<u>220.01</u>	<u>190.57</u>	<u>208299</u>
<u>220.51</u>	<u>178.65</u>	<u>199749</u>
<u>221.01</u>	<u>175.16</u>	<u>196941</u>
<u>221.51</u>	<u>164.34</u>	<u>188476</u>
<u>222.01</u>	<u>163.08</u>	<u>188061</u>
<u>222.51</u>	<u>158.73</u>	<u>183780</u>
<u>223.01</u>	<u>160.78</u>	<u>186829</u>
<u>223.51</u>	<u>167.31</u>	<u>185445</u>
<u>224.01</u>	<u>160.04</u>	<u>181597</u>
<u>224.51</u>	<u>154.22</u>	<u>179787</u>
<u>225.01</u>	<u>152.87</u>	<u>177243</u>
<u>225.51</u>	<u>163.79</u>	<u>186478</u>
<u>226.01</u>	<u>159.82</u>	<u>182491</u>
<u>226.51</u>	<u>169.10</u>	<u>190870</u>
<u>227.01</u>	<u>166.42</u>	<u>186909</u>
<u>227.51</u>	<u>169.19</u>	<u>189283</u>
<u>228.01</u>	<u>167.97</u>	<u>188685</u>
<u>228.51</u>	<u>162.80</u>	<u>183799</u>

Table 6.2.1.5-1 (Sheet 18 of 20)

**MINIMUM CONTAINMENT PRESSURE MASS AND ENERGY RELEASES FOR LARGE
BREAK LOCA**

<u>Time (sec)</u>	<u>Mass Release (lbm/s)</u>	<u>Energy Release (BTU/s)</u>
<u>229.01</u>	<u>163.17</u>	<u>183882</u>
<u>229.51</u>	<u>166.72</u>	<u>185166</u>
<u>230.01</u>	<u>163.60</u>	<u>183083</u>
<u>230.51</u>	<u>166.08</u>	<u>185501</u>
<u>231.01</u>	<u>185.01</u>	<u>198040</u>
<u>231.51</u>	<u>171.17</u>	<u>190371</u>
<u>232.01</u>	<u>170.02</u>	<u>189413</u>
<u>232.51</u>	<u>167.32</u>	<u>187192</u>
<u>233.01</u>	<u>165.87</u>	<u>187133</u>
<u>233.51</u>	<u>162.23</u>	<u>184680</u>
<u>234.01</u>	<u>162.12</u>	<u>184239</u>
<u>234.51</u>	<u>163.65</u>	<u>185256</u>
<u>235.01</u>	<u>170.11</u>	<u>190998</u>
<u>235.51</u>	<u>172.03</u>	<u>191517</u>
<u>236.01</u>	<u>176.57</u>	<u>195559</u>
<u>236.51</u>	<u>177.90</u>	<u>195105</u>
<u>237.01</u>	<u>179.11</u>	<u>196781</u>
<u>237.51</u>	<u>177.36</u>	<u>194796</u>
<u>238.01</u>	<u>184.55</u>	<u>203196</u>
<u>238.51</u>	<u>175.43</u>	<u>193499</u>
<u>239.01</u>	<u>180.92</u>	<u>198347</u>
<u>239.51</u>	<u>186.38</u>	<u>201952</u>
<u>240.01</u>	<u>187.65</u>	<u>204156</u>
<u>240.51</u>	<u>206.22</u>	<u>215759</u>
<u>241.01</u>	<u>189.12</u>	<u>203103</u>
<u>241.51</u>	<u>193.57</u>	<u>210875</u>
<u>242.01</u>	<u>193.46</u>	<u>207113</u>

Table 6.2.1.5-1 (Sheet 19 of 20)

**MINIMUM CONTAINMENT PRESSURE MASS AND ENERGY RELEASES FOR LARGE
BREAK LOCA**

<u>Time (sec)</u>	<u>Mass Release (lbm/s)</u>	<u>Energy Release (BTU/s)</u>
<u>242.51</u>	<u>198.81</u>	<u>213650</u>
<u>243.01</u>	<u>201.22</u>	<u>217114</u>
<u>243.51</u>	<u>197.74</u>	<u>212561</u>
<u>244.01</u>	<u>206.62</u>	<u>221578</u>
<u>244.51</u>	<u>203.31</u>	<u>217715</u>
<u>245.01</u>	<u>208.59</u>	<u>223702</u>
<u>245.51</u>	<u>203.91</u>	<u>219671</u>
<u>246.01</u>	<u>208.89</u>	<u>222208</u>
<u>246.51</u>	<u>212.31</u>	<u>225805</u>
<u>247.01</u>	<u>212.32</u>	<u>225398</u>
<u>247.51</u>	<u>214.35</u>	<u>227594</u>
<u>248.01</u>	<u>214.15</u>	<u>226651</u>
<u>248.51</u>	<u>217.36</u>	<u>228825</u>
<u>249.01</u>	<u>222.31</u>	<u>234267</u>
<u>249.51</u>	<u>217.86</u>	<u>229171</u>
<u>250.01</u>	<u>223.83</u>	<u>235041</u>
<u>250.51</u>	<u>220.16</u>	<u>231207</u>
<u>251.01</u>	<u>240.82</u>	<u>243903</u>
<u>251.51</u>	<u>253.81</u>	<u>247226</u>
<u>252.01</u>	<u>436.89</u>	<u>265598</u>
<u>252.51</u>	<u>276.84</u>	<u>260077</u>
<u>253.01</u>	<u>829.62</u>	<u>316490</u>
<u>253.51</u>	<u>314.26</u>	<u>270224</u>
<u>254.01</u>	<u>236.27</u>	<u>246359</u>
<u>254.51</u>	<u>314.74</u>	<u>268735</u>
<u>255.01</u>	<u>272.12</u>	<u>261657</u>
<u>255.51</u>	<u>252.32</u>	<u>253658</u>

Table 6.2.1.5-1 (Sheet 20 of 20)

**MINIMUM CONTAINMENT PRESSURE MASS AND ENERGY RELEASES FOR LARGE
BREAK LOCA**

<u>Time (sec)</u>	<u>Mass Release (lbm/s)</u>	<u>Energy Release (BTU/s)</u>
<u>256.01</u>	<u>277.28</u>	<u>262941</u>
<u>256.51</u>	<u>342.11</u>	<u>256883</u>
<u>257.01</u>	<u>755.60</u>	<u>308477</u>
<u>257.51</u>	<u>411.16</u>	<u>280874</u>
<u>258.01</u>	<u>646.77</u>	<u>293049</u>
<u>258.51</u>	<u>592.41</u>	<u>299836</u>
<u>259.01</u>	<u>276.26</u>	<u>264083</u>
<u>259.51</u>	<u>697.14</u>	<u>280918</u>
<u>260.01</u>	<u>1081.61</u>	<u>351122</u>
<u>260.51</u>	<u>708.00</u>	<u>303184</u>
<u>261.01</u>	<u>917.67</u>	<u>334397</u>
<u>261.51</u>	<u>542.69</u>	<u>321954</u>
<u>262.01</u>	<u>249.78</u>	<u>263198</u>
<u>262.51</u>	<u>347.78</u>	<u>287660</u>
<u>263.01</u>	<u>560.89</u>	<u>302627</u>
<u>263.51</u>	<u>682.74</u>	<u>309234</u>
<u>264.01</u>	<u>837.97</u>	<u>332817</u>

UFSAR Table 6.2.2-1 Passive Containment Cooling System Performance Parameters is revised as follows:

**Table 6.2.2-1
 Passive Containment Cooling System Performance Parameters**

...				...
PCCWST Water Elevation (Note 3) (feet)	Nominal Flow (Note 5) (gpm)	Minimum Flow (Note 6) (gpm)	Safety Analysis Flow (gpm)	Wetted Coverage (Note 3) (% of circumference)
* * *				
At 72 hours	105	102	100.7 @ 72 hours	41.6 41.7

...

Replace UFSAR Figure 6.2.1.1-1 AP1000 Containment Response for Full DER MSLB – 30% Power with the following:

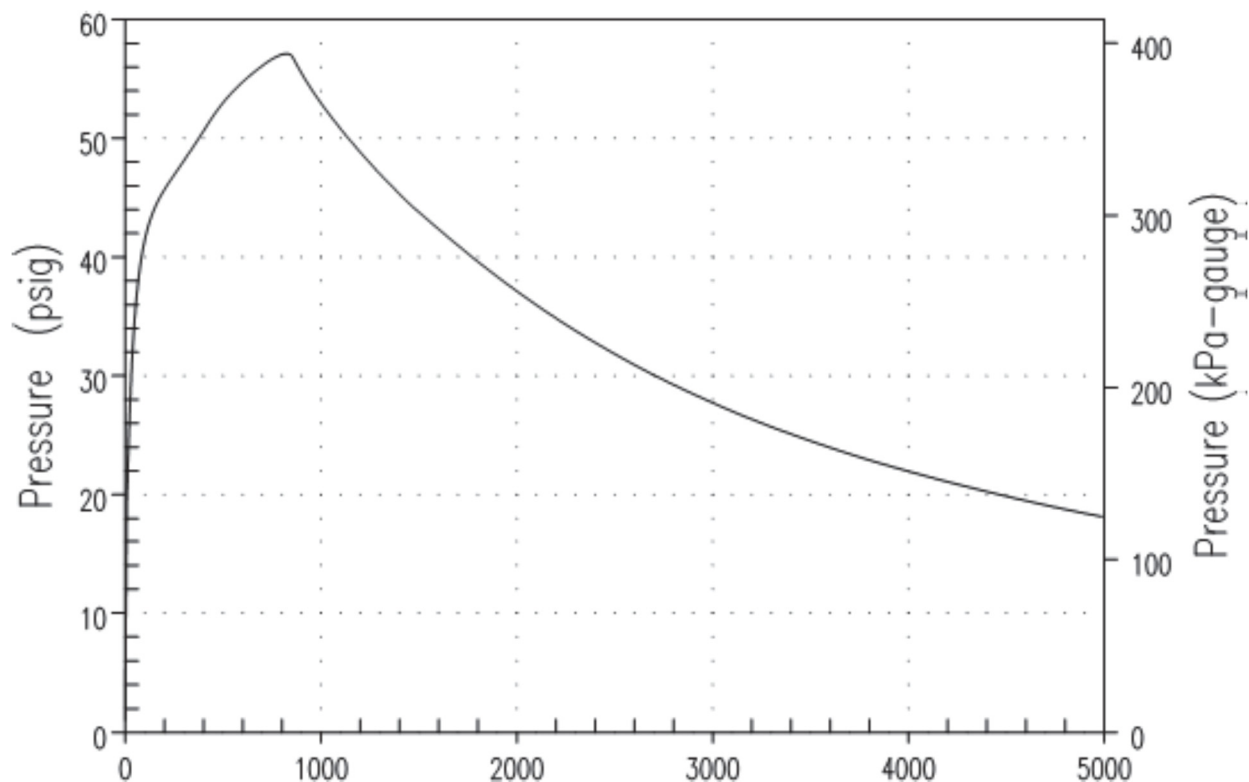


**Figure 6.2.1.1-1
AP1000 Containment Pressure Response for Full DER MSLB – 30% Power**

Replace UFSAR Figure 6.2.1.1-2 AP1000 Containment Response for Full DER MSLB – 101% Power with the following:

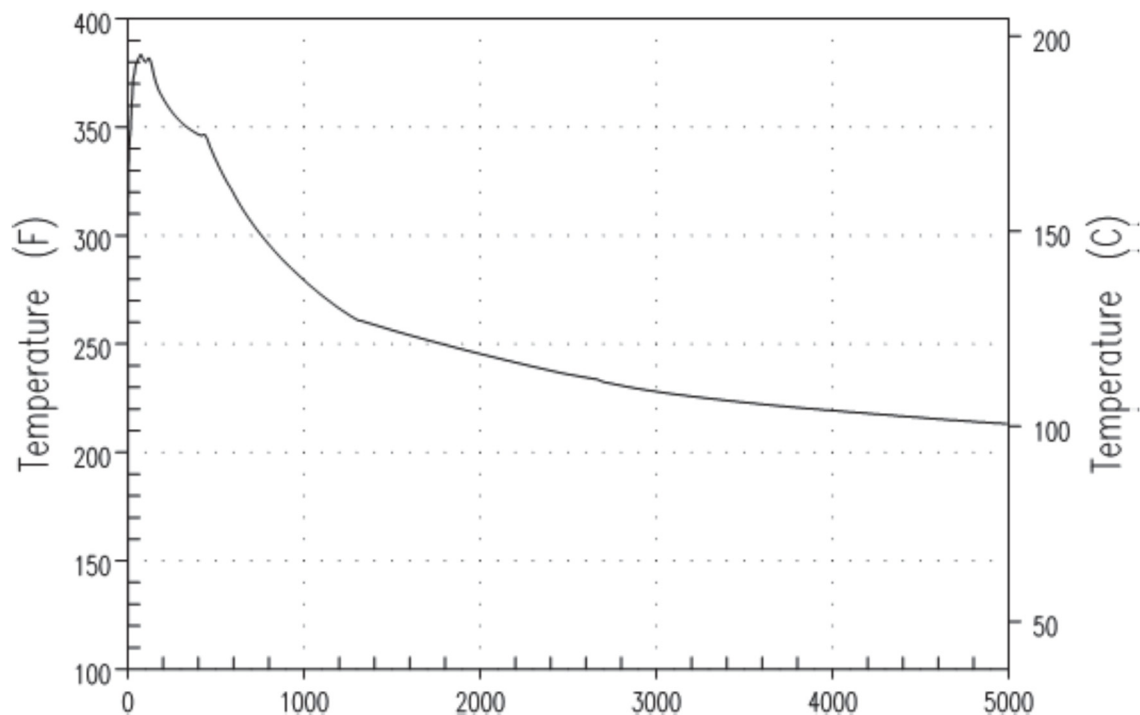


**Figure 6.2.1.1-2
AP1000 Containment Temperature Response for Full DER MSLB – 101% Power**

Replace UFSAR Figure 6.2.1.1-5 AP1000 Containment Response for DECLG LOCA with the following:

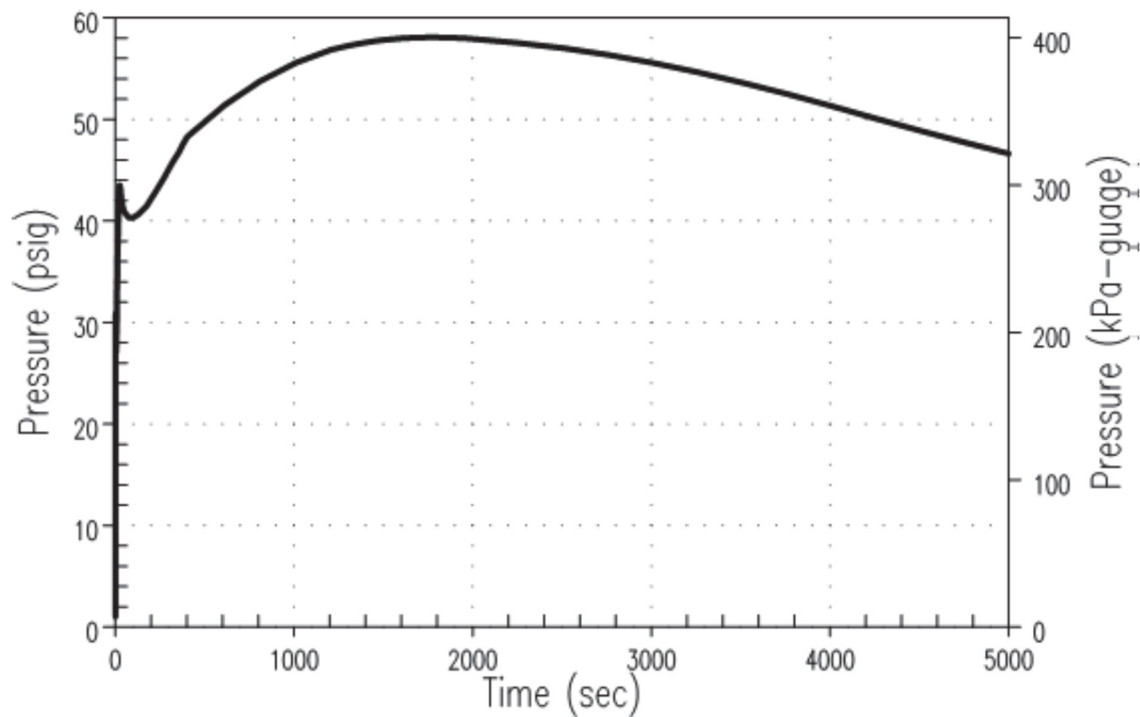


**Figure 6.2.1.1-5
AP1000 Containment Pressure Response for DECLG LOCA- 5000 sec**

Replace UFSAR Figure 6.2.1.1-6 AP1000 Containment Temperature Response for DECLG LOCA with the following:

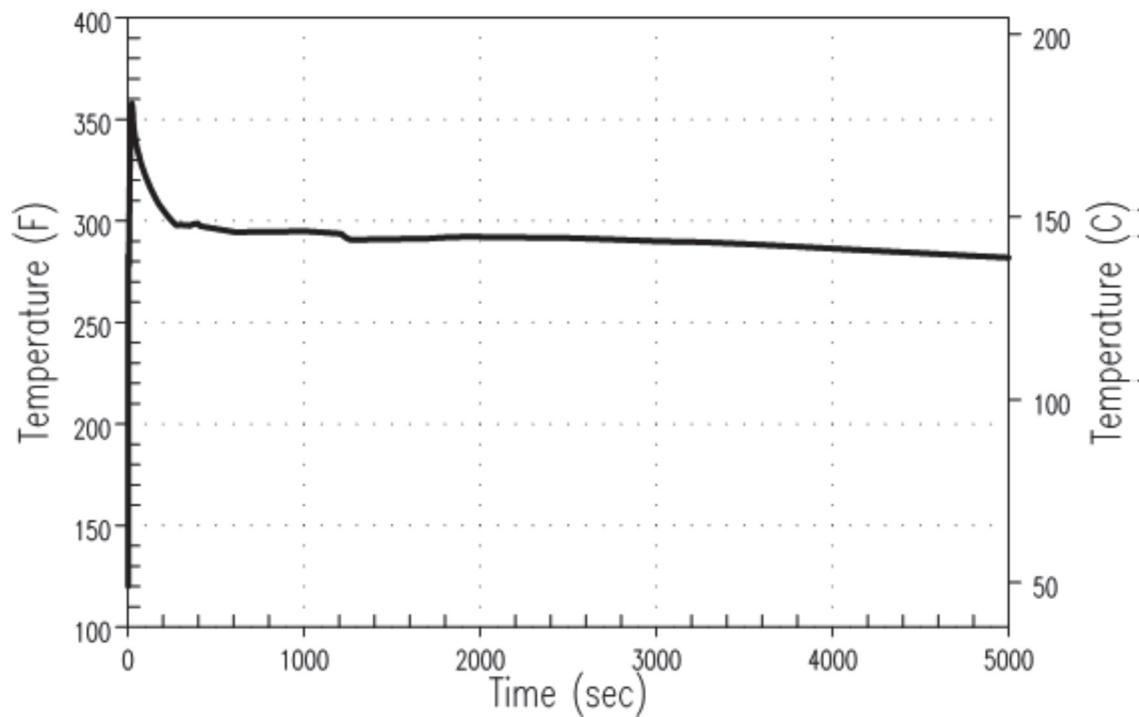


**Figure 6.2.1.1-6
AP1000 Containment Temperature Response to DECLG LOCA- 5000 sec**

Replace UFSAR Figure 6.2.1.1-7 AP1000 Containment Pressure Response for DECLG LOCA – 3 Days with the following:

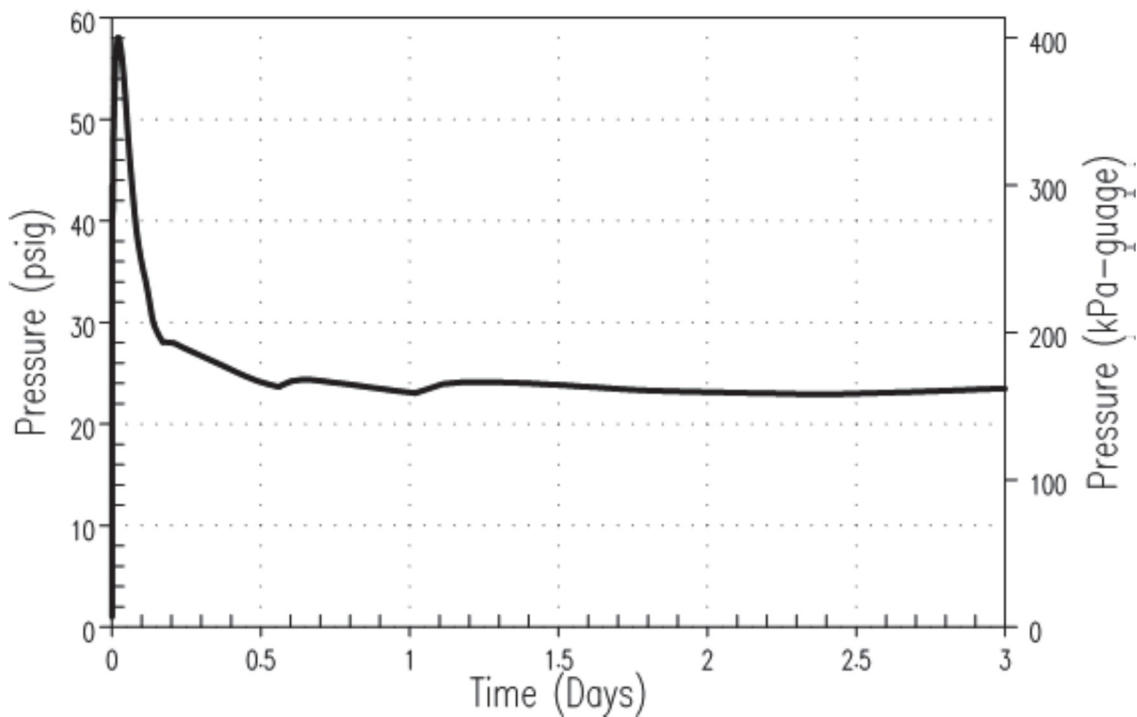
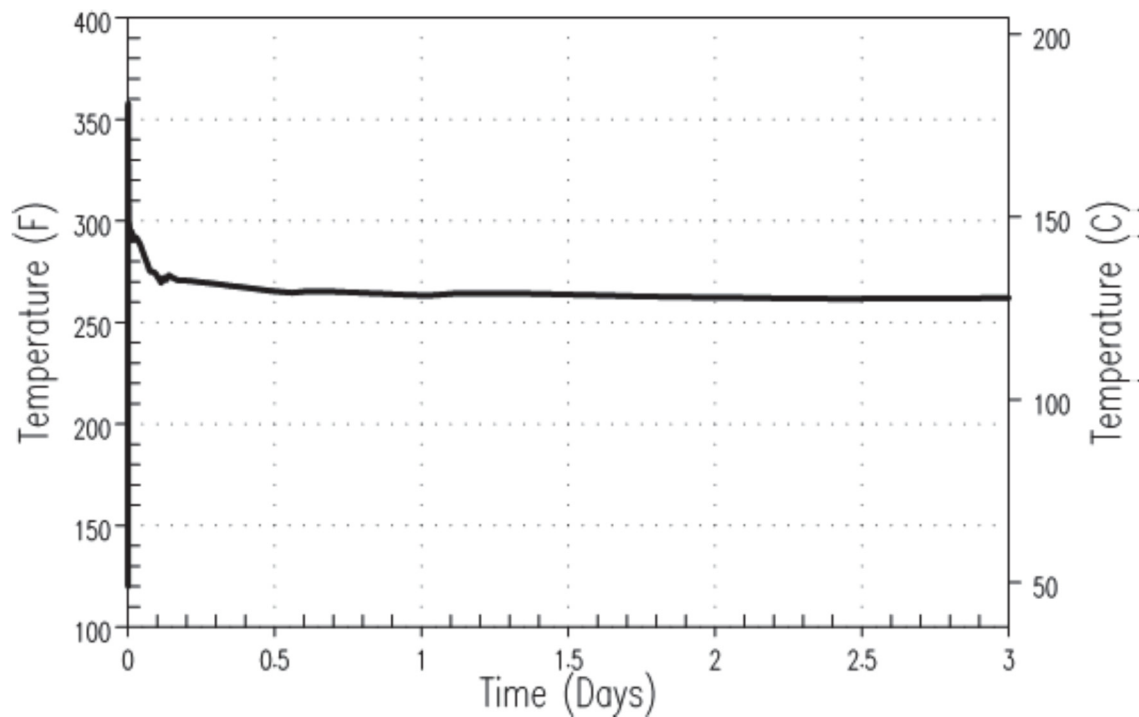


Figure 6.2.1.1-7

AP1000 Containment Pressure Response for DECLG LOCA – 3 Days

Replace UFSAR Figure 6.2.1.1-8 AP1000 Containment Temperature Response for DECLG LOCA – 3 Days with the following:



**Figure 6.2.1.1-8
AP1000 Containment Temperature Response for DECLG LOCA – 3 Days**

Replace UFSAR Figure 6.2.1.1-9 AP1000 Containment Pressure Response for DECLG LOCA with the following:

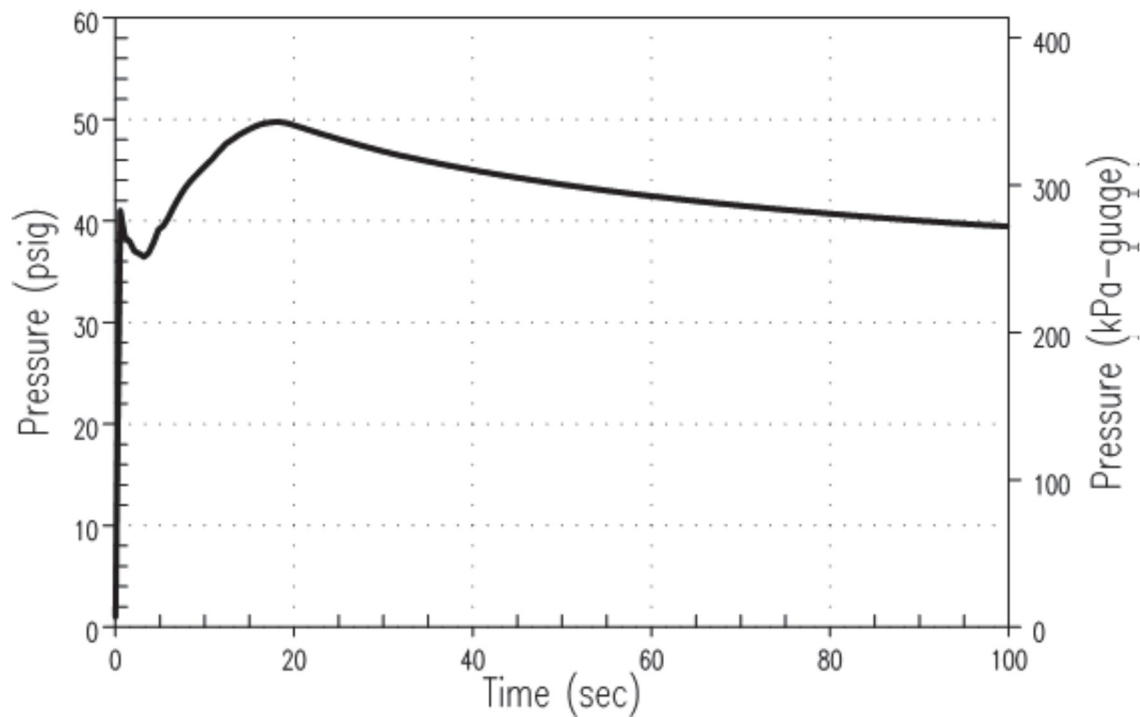


**Figure 6.2.1.1-9
AP1000 Containment Pressure Response – DEHLG LOCA**

Replace UFSAR Figure 6.2.1.1-10 AP1000 Containment Response for DECLG LOCA with the following:

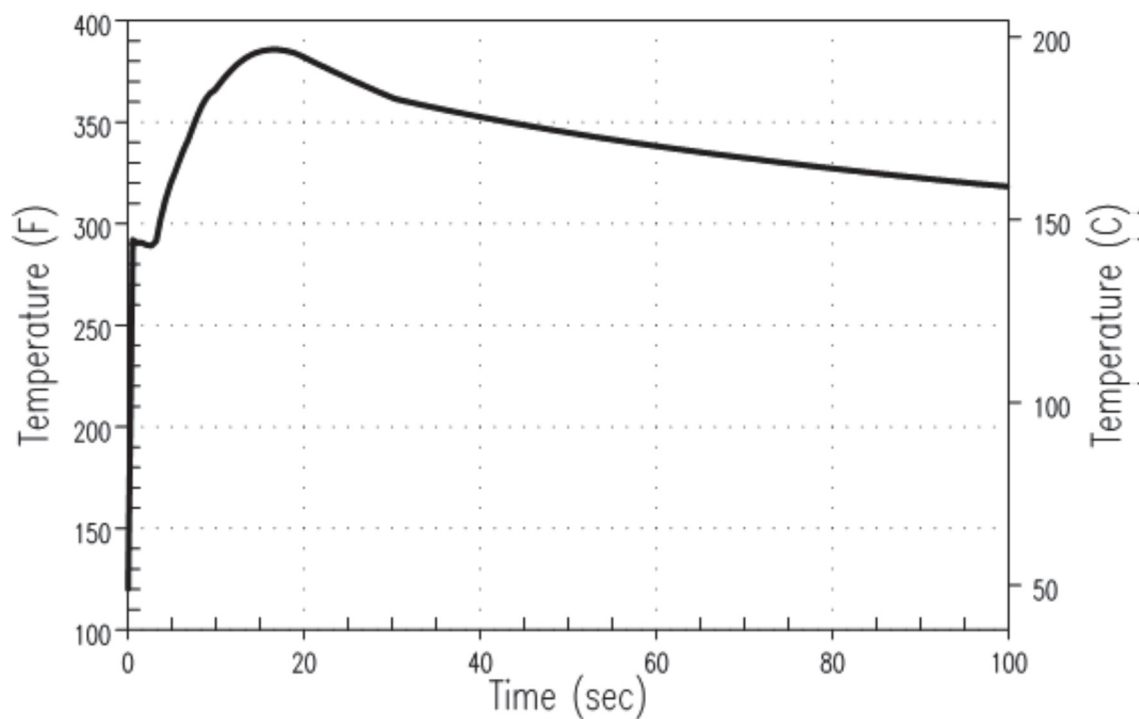


**Figure 6.2.1.1-10
AP1000 Containment Temperature Response for DEHLG LOCA**

Replace UFSAR Figure 6.2.1.3-1 AP1000 DECLG Integrated Break Flow with the following:

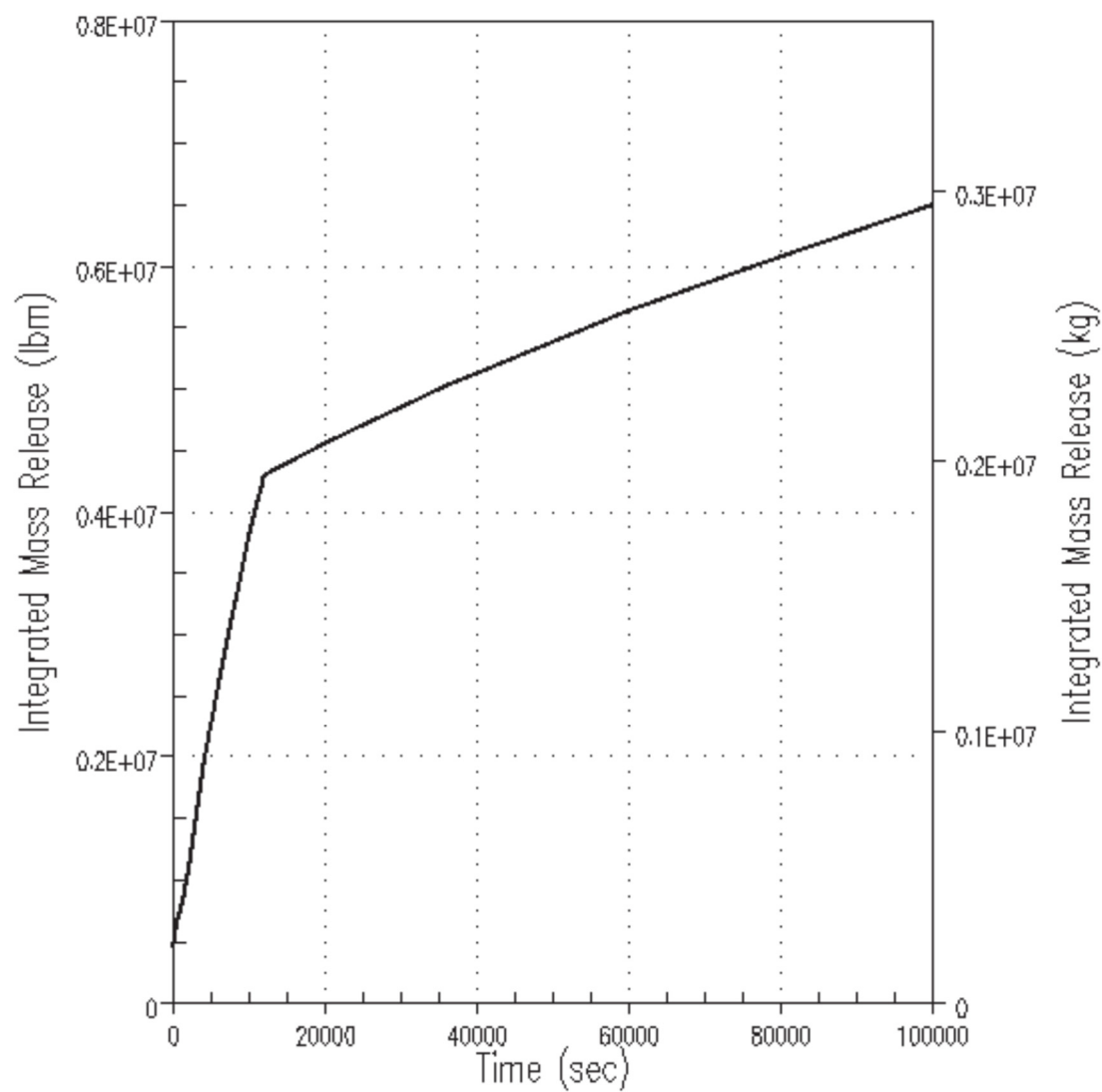


**Figure 6.2.1.3-1
AP1000 DECLG Integrated Break Flow**

Replace UFSAR Figure 6.2.1.3-2 AP1000 DECLG LOCA Integrated Energy Released with the following:

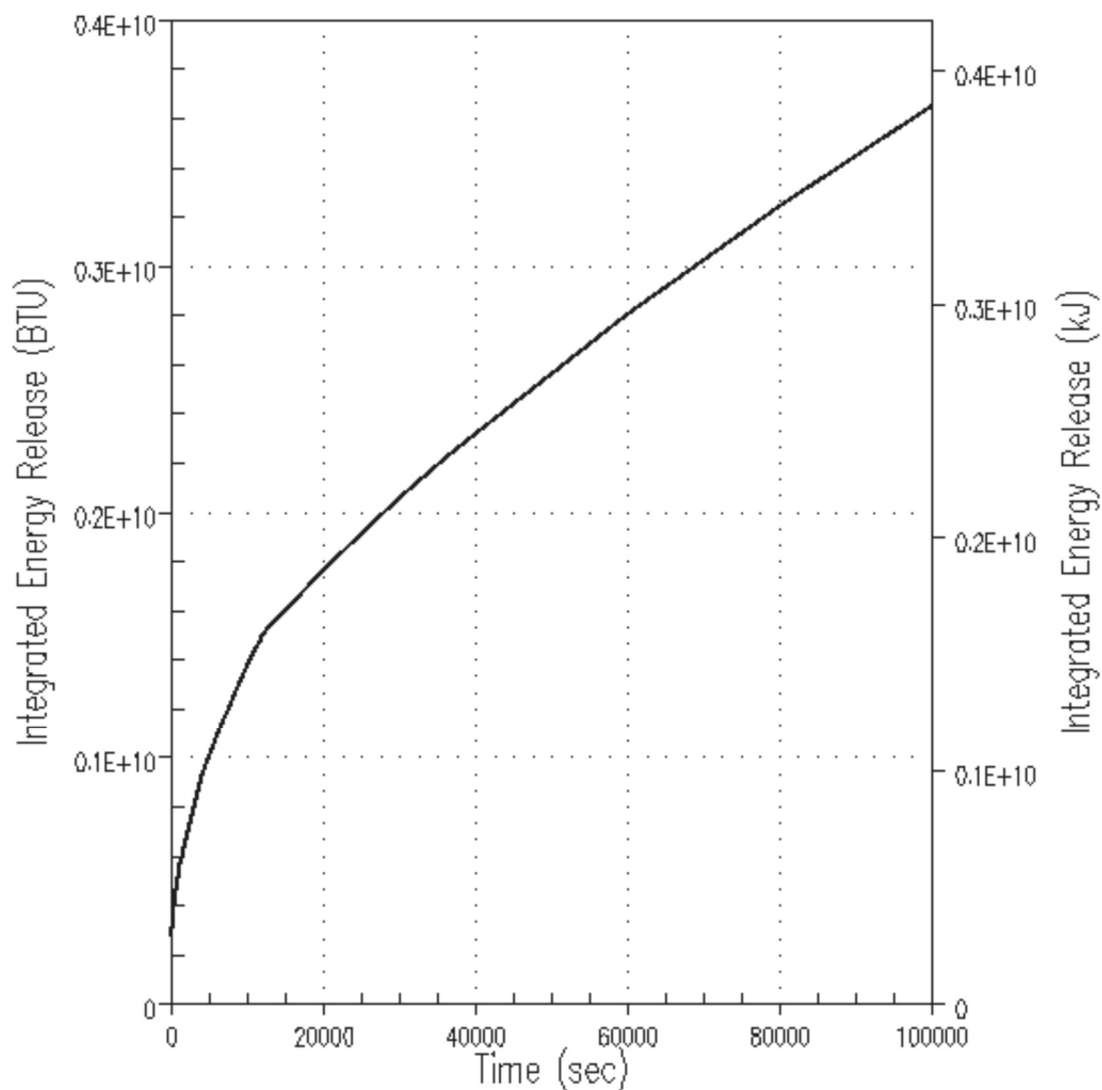


**Figure 6.2.1.3-2
AP1000 DECLG LOCA Integrated Energy Released**

Replace UFSAR Figure 6.2.1.3-3 AP1000 DECLG Integrated Break Flow with the following:

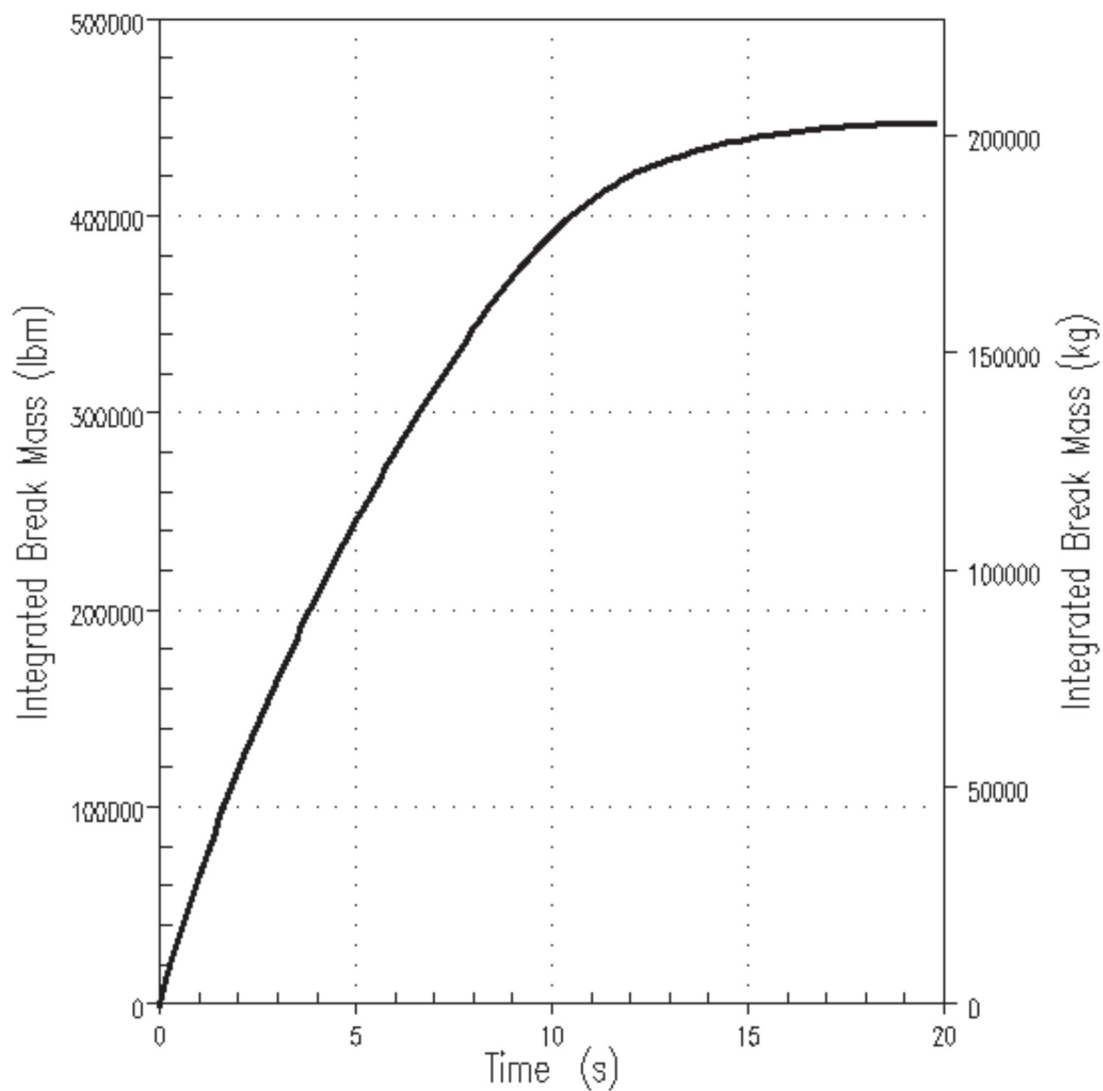


**Figure 6.2.1.3-3
AP1000 DEHLG Integrated Break Flow**

Replace UFSAR Figure 6.2.1.3-4 AP1000 DECLG Integrated Energy Released with the following:

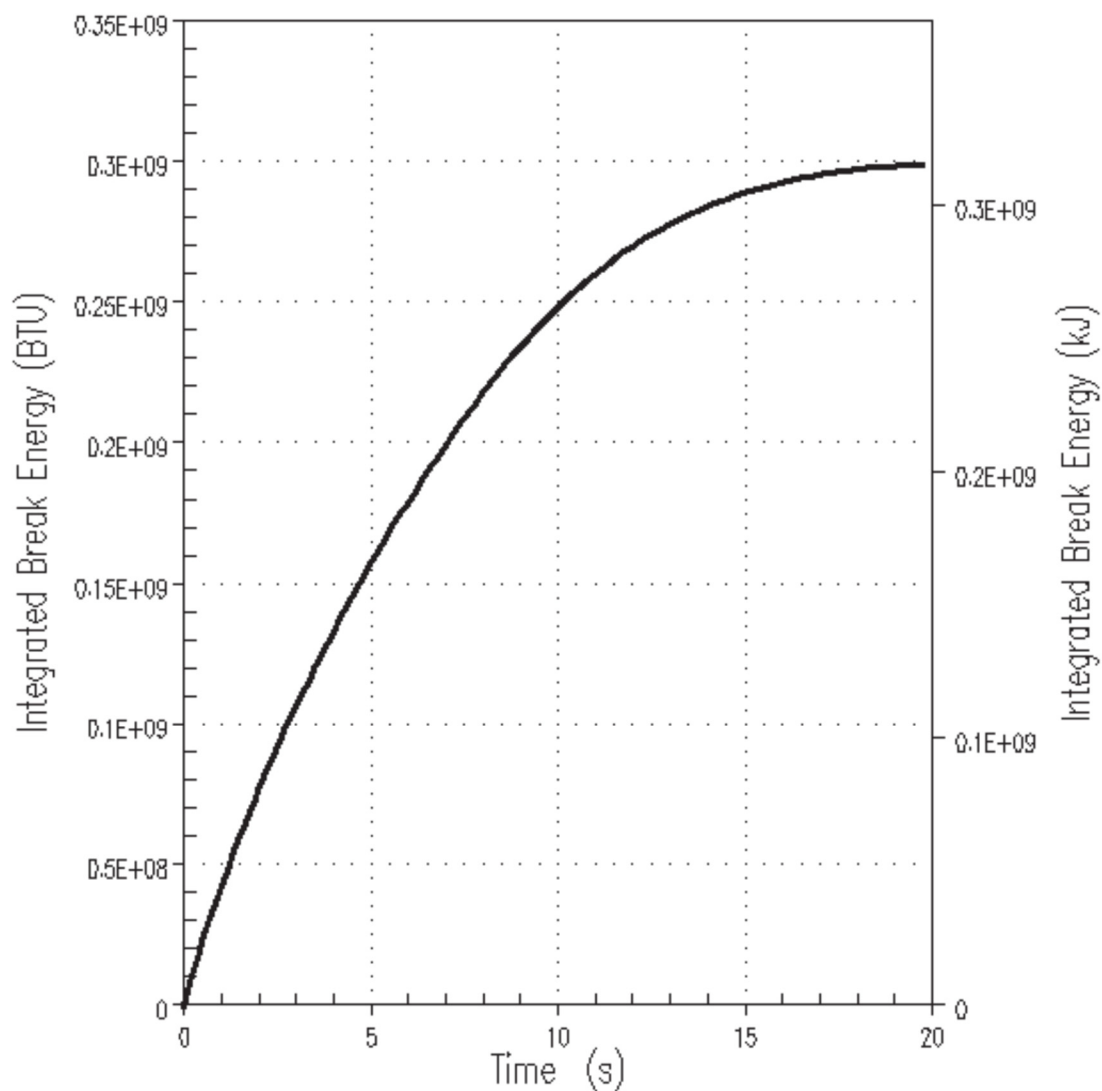


**Figure 6.2.1.3-4
AP1000 DEHLG LOCA Integrated Energy Released**

Replace UFSAR Figure 6.2.1.5-1 AP1000 Minimum Containment Pressure for DECLG LOCA with the following:

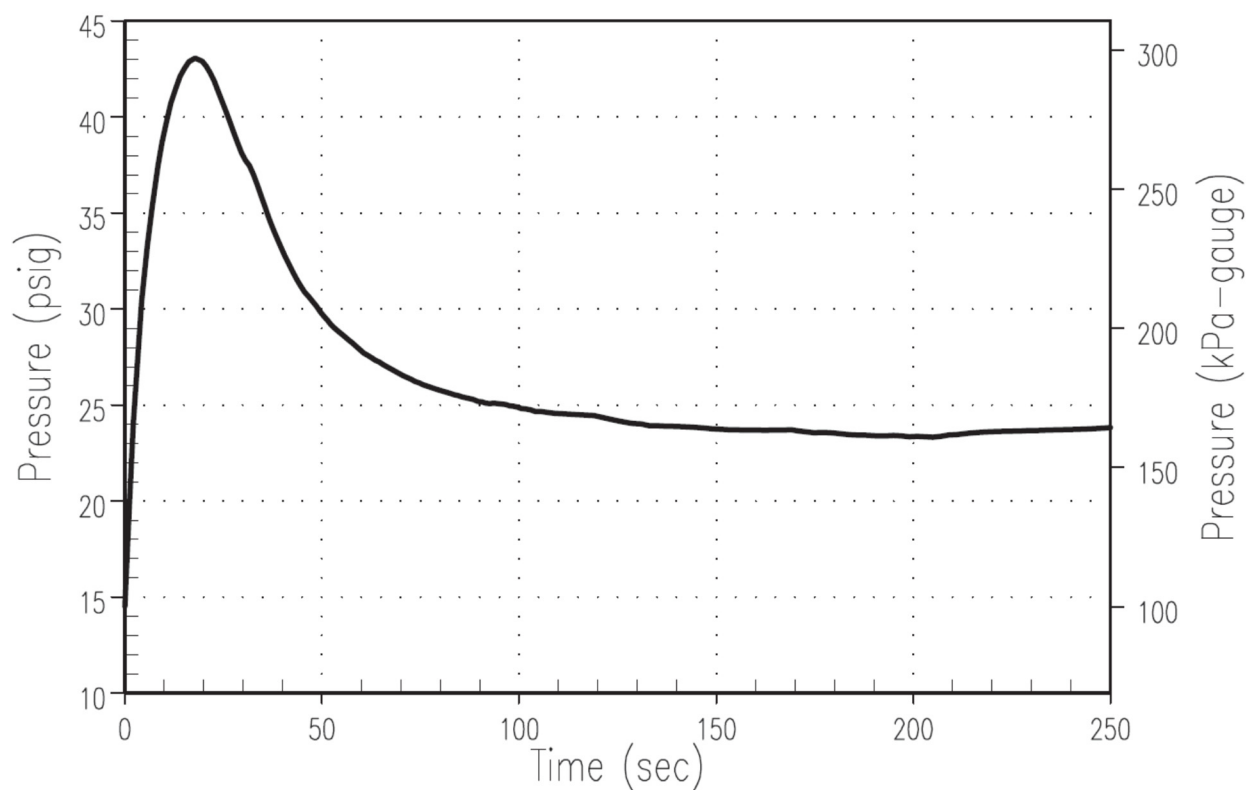


**Figure 6.2.1.5-1
AP1000 Minimum Containment Pressure for DECLG LOCA**

UFSAR Section 6A.5 References is revised as follows:

...

2. WCAP-15846 (Proprietary) and WCAP-15862 (Non-Proprietary) "WGOTHIC Application to AP600 and AP1000," ~~Revision 1, March 2004~~ [Revision 5, September 2016](#).

...

UFSAR Table 14.3-2 (Sheet 3 of 17) Design Basis Accident Analysis is revised as follows:

**Table 14.3-2 (Sheet 3 of 17)
Design Basis Accident Analysis**

Reference	Design Feature	Value
* * *		
Table 6.1-2	The exterior of the containment vessel (above plant elevation 135' 3") and the interior of the containment vessel (above 7' above the operating deck) is coated with an inorganic zinc coating.	
* * *		

Southern Nuclear Operating Company

ND-17-2074

Enclosure 4

**Vogtle Electric Generating Plant (VEGP) Units 3 and 4
Information Only Changes to the Technical Specification Bases Document
(LAR-17-043)**

Note:

Added text is shown as bold **Blue Underline**
Deleted text is shown as bold **~~Red Strikethrough~~**

(Enclosure 4 consists of 2 pages, including this cover page)

Technical Specification Bases 3.6.4 Containment Pressure is revised as follows:

...

The initial pressure condition used in the containment analysis was 15.7 psia (1.0 psig). This resulted in a maximum peak pressure from a LOCA, P_a of ~~58.3~~58.1 psig. The containment analysis (Ref. 1) shows that the maximum peak calculated containment pressure results from the limiting LOCA. The maximum containment pressure resulting from the worst case LOCA, P_a , does not exceed the containment design pressure, 59 psig.

....

Southern Nuclear Operating Company

ND-17-2074

Enclosure 5

Vogtle Electric Generating Plant (VEGP) Units 3 and 4

**APP-GW-GLR-801, Rev. 0 “WGOTHIC Application to AP600 and AP1000” (WCAP-15846)
Revisions 1 through 5 (Proprietary)**

(LAR-17-043)

(Withheld Information)

(Enclosure 5 consists of 1081 pages, excluding this cover page.)

Southern Nuclear Operating Company

ND-17-2074

Enclosure 6

Vogtle Electric Generating Plant (VEGP) Units 3 and 4

**APP-GW-GLR-802 Rev. 0 “WGOTHIC Application to AP600 and AP1000” (WCAP-15846)
Revisions 1 through 5 (Non-Proprietary)
(LAR-17-043)**

(Enclosure 6 consists of 1081 pages, excluding this cover page.)

DOCUMENT COVER SHEET

DOCUMENT NO. APP-GW-GLR-802	REVISION 0	PAGE 1 of 1081	OPEN ITEMS N
DOCUMENT STATUS: DES		AP1000 SAFETY CLASS: NA	Westinghouse Acceptance of AP1000 Design Partner Document by: N/A (Print Full Name) (Signature/Date)
LICENSING REVIEW STATUS: Not Required			
PLANT APPLICABILITY: <input type="checkbox"/> All AP1000 Plants except: <input checked="" type="checkbox"/> Only the following plants: SV3, SV4, VS2, VS3, BN3, BN4, HA2, HA3, LN1, LN2, TP6, TP7, WL1, WL2, APP			

ALTERNATE DOCUMENT NUMBER: None

ORIGINATING ORGANIZATION: Westinghouse Electric Company

TITLE: LAR-79 Supplementary Information for Updates to WGOTHIC Methodology (Non-Proprietary)

DCP/DCA/SUPPLEMENTS/EDCR # INCORPORATED IN THIS DOCUMENT REVISION:
None

ATTACHMENTS:
None

PARENT DOCUMENT: None

☒ © 2017 WESTINGHOUSE ELECTRIC COMPANY LLC, ALL RIGHTS RESERVED – WESTINGHOUSE NON-PROPRIETARY CLASS 3

All Class 3 Documents require the following two approvals in lieu of a Form 36.

LEGAL REVIEW

Ray Kuyler

SIGNATURE / DATE (If processing electronic approval select option)

Electronically Approved***

PATENT REVIEW

Edward L. Schmiech

SIGNATURE / DATE

Electronically Approved***

☐ © 2017 WESTINGHOUSE ELECTRIC COMPANY LLC, ALL RIGHTS RESERVED – WESTINGHOUSE PROPRIETARY CLASS 2

This document is the property of and contains Proprietary Information owned by Westinghouse Electric Company LLC and/or its affiliates, subcontractors and/or suppliers. It is transmitted to you in confidence and trust, and you agree to treat this document in strict accordance with the terms and conditions of the agreement under which it was provided to you. Handle this document in accordance with applicable procedures for filing and transmittal. Any unauthorized use of this document is prohibited.

*NOTE: This selection is only to be used for Westinghouse generated documents.

☐ © 2017 WESTINGHOUSE ELECTRIC COMPANY LLC, ALL RIGHTS RESERVED and/or
© 2017 WESTINGHOUSE AP1000 BUSINESS PARTNER, ALL RIGHTS RESERVED
WESTINGHOUSE PROPRIETARY CLASS 2 and/or WESTINGHOUSE BUSINESS PARTNER PROPRIETARY (SEE ATTACHED DOCUMENT)

This document is the property of and contains Proprietary Information owned by Westinghouse Electric Company LLC and/or is the property of and contains Proprietary Information owned by the Westinghouse Business Partner identified in the document attached hereto and/or their affiliates, subcontractors and suppliers. It is transmitted to you in confidence and trust, and you agree to treat this document in strict accordance with the terms and conditions of the agreement under which it was provided to you. Any unauthorized use of this document is prohibited.

☐ SUPPLIER OR THIRD PARTY PROVIDED INFORMATION – File And Protect Using Policies For Westinghouse Proprietary Class 2 Information

This document is the property of and contains Proprietary Information owned by a Supplier/Third Party to Westinghouse Electric Company, LLC. Treat this document in strict compliance with applicable procedures and the terms and conditions under which it was provided. Any unauthorized use of this document is prohibited.

ORIGINATOR(S) W2-6.1-100.pdf Anthony J. Schoedel	SIGNATURE / DATE (If processing electronic approval select option) Electronically Approved***	
REVIEWER(S) W2-6.1-100.pdf Michael J. Patterson	SIGNATURE / DATE Electronically Approved***	
	SIGNATURE / DATE	
	SIGNATURE / DATE	
VERIFIER(S) W2-6.1-100.pdf Jason J. Eisenhauer	SIGNATURE / DATE Electronically Approved***	Verification Method: Independent Review
APPLICABILITY REVIEWER N/A	SIGNATURE / DATE	
RESPONSIBLE MANAGER* W2-6.1-100.pdf Zachary S. Harper	SIGNATURE / DATE Electronically Approved***	

*Approval of the responsible manager signifies that the document and all required reviews are complete, the appropriate proprietary class has been assigned, electronic file has been provided to the EDMS, and the document is released for use.

This document may contain technical data subject to the export control laws of the United States. In the event that this document does contain such information, the Recipient's acceptance of this document constitutes agreement that this information in document form (or any other medium), including any attachments and exhibits hereto, shall not be exported, released or disclosed to foreign persons whether in the United States or abroad by recipient except in compliance with all U.S. export control regulations. Recipient shall include this notice with any reproduced or excerpted portion of this document or any document derived from, based on, incorporating, using or relying on the information contained in this document.

***Electronically approved records are authenticated in the electronic document management system.

Westinghouse Non-Proprietary Class 3

Record of Revisions

Revision	Changes
0	Initial issue.

Changes to WGOTHIC Methodology for the AP1000 Plant (WCAP-15846)

Originator: Anthony J. Schoedel
Structural and Mechanical Licensing

Reviewer: Michael J. Patterson
Plant Analysis & Licensing

Verifier : Jason J. Eisenhauer
Plant Analysis & Licensing

Manager: Zachary S. Harper
Structural and Mechanical Licensing

December 2017

Changes to WGOTHIC Methodology for the AP1000 Plant (WCAP-15846)

Table of Contents

Executive Summary.....	5
1. Summary Description	5
2 and 3. Detailed Description and Technical Evaluation	6
WCAP-15846-P, Rev. 5 Showing Tracked Changes from Revisions 1 through 4.....	36

AP1000 is a trademark or registered trademark of Westinghouse Electric Company LLC, its affiliates and/or its subsidiaries in the United States of America and may be registered in other countries throughout the world. All rights reserved. Unauthorized use is strictly prohibited. Other names may be trademarks of their respective owners.

Executive Summary

The current licensing basis containment integrity analyses described in Section 6.2 of the Updated Final Safety Analysis Report (UFSAR) is based on the design configuration at the time of the amended AP1000 design certification (i.e., DCD Revision 19). Accumulated design changes within containment have necessitated recalculation of geometry input to the WGOTHIC evaluation model (EM) used for the containment integrity analyses.

Heat sinks, control volumes, and flow paths have been recalculated, and are in turn modeled in the WGOTHIC EM. Mass and energy (M&E) releases for design basis accidents (DBA), loss of coolant accidents (LOCA) and main steam line breaks (MSLB), are also recalculated. Various methodology changes are also made to the WGOTHIC methodology for the AP1000 plant design. These updates culminate in the recalculation of the containment integrity analyses, which are proposed for incorporation into the licensing basis via Westinghouse License Amendment Request (LAR) 079 (WEC LAR-079).

The licensing basis changes to the UFSAR, Combined License (COL) Appendix A, and COL Appendix C are discussed and evaluated within WEC LAR-079. However, due to the proprietary nature of the WGOTHIC methodology, the discussion and evaluation of the methodology changes are included as Attachments 1 (proprietary) and 2 (non-proprietary) of WEC LAR-079, respectively.

This document structure was developed in order to support the AP1000 plant Licensees' submittals for WEC LAR-079 to the U.S. Nuclear Regulatory Commission (NRC) for the overall update to the containment integrity analyses, while also ensuring the appropriate protection of the Westinghouse intellectual property.

1. Summary Description

This LAR proposes changes to the plant-specific containment integrity analyses described in UFSAR Section 6.2. Accumulated design changes within containment have necessitated recalculation of geometry input to the WGOTHIC EM used for containment integrity analyses. Heat sinks, control volumes, and flow paths have been recalculated, and are in turn modeled in the WGOTHIC EM. M&E releases for LOCA and MSLB are also recalculated. Various methodology changes are also made to the WGOTHIC methodology for the AP1000 plant design. These updates culminate in the recalculation of the containment integrity safety analyses.

This LAR proposes changes to the UFSAR in the form of departures from the incorporated plant-specific Design Control Document (DCD) Tier 2 licensing basis information, involves changes to UFSAR information that has been designated as Tier 2* information, involves changes to the plant-specific Inspections, Tests, Analyses, and Acceptance Criteria (ITAAC) provided as Appendix C to the COL, involves changes to the plant-specific Technical Specifications provided as Appendix A to the COL. This submittal requests approval of the license amendment necessary to implement these changes.

2 and 3. Detailed Description and Technical Evaluation

The currently licensed containment integrity methodology is defined in WCAP-15846, as modified by APP-GW-GLR-096 Revision 3. The non-proprietary version is WCAP-15862. Revisions to the proprietary and non-proprietary versions of this methodology document have been made to incorporate the contents of APP-GW-GLR-096 and other assessments of outstanding design debt directly, as well as update the methodology as used in the latest containment integrity analyses.

The update to the methodology document itself in turn necessitates changes to various licensing basis sections to reflect the new document revision (UFSAR Table 1.6-1, Section 6.2.7, and Section 6A.5). The latest revision of WCAP-15846 that is being proposed for incorporation into the licensing basis is Revision 5.

Revisions 2 and 3 of WCAP-15846 included only errata pages which updated the PCS flowrates in Table 13-125 and Figure 13-93 during the AP1000 design certification (i.e., DCD Revision 19). These revisions did not constitute full revisions, but instead were limited to the update of Table 13-125 and Figure 13-93; these changes are now superseded with the latest revision. The majority of the changes to the document occurred as part of Revision 4, with a few remaining items (e.g., PCS water stripping due to baffle supports and clarifications to the MSLB event) made in Revision 5. The marked up Revision 5 provides traceability for the cumulative set of changes since Revision 1.

The majority of the changes to the WGOTHIC methodology occur in Chapters 7 and 13 of WCAP-15846, which describe the method for calculating PCS water evaporation and the plant geometry and nodalization used in the WGOTHIC EM, respectively. These two chapters contain the actual methodology of the containment integrity analyses and are evaluated accordingly. Additionally, a majority of the proposed changes in these two chapters are editorial and non-technical in nature. Changes are also made to Chapters 1, 3, 4, 5, 6, 9, 10, and 14 for various reasons. Table 1 provides a description and evaluation of the changes in each of the modified Chapters of WCAP-15846.

Table 1: Description and Evaluation of Changes to WCAP-15846

Revision 1		Revision 5		Page(s)	Detailed Description of Changes	Technical Evaluation of Changes
Title	Chapter/ Section/ Subsection	Title	Chapter/ Section/ Subsection			
Introduction	1	Introduction	1	1-1	No changes	No changes
Objective	1.1	Objective	1.1	1-1	The “Objective” section has been completely rewritten to better explain the purpose of the containment EM, a summary of the lumped parameter modeling approach, and the history of the development of the document.	These changes are editorial in nature and are made to improve reader understanding of the intention of the document as a whole. The overarching objective of the document (to describe the methodology used to develop the AP1000 design containment integrity EM) is unchanged. There is no technical impact due to these changes.
N/A	N/A	Report Overview	1.2	1-1 – 1-3	The “Report Overview” is a newly added section which replaces the “Applications Report Content Summary” (old section 1.4). Various changes to the text are also made to better explain the contents of each chapter.	These changes are editorial in nature and are made to conform with changes to the document as a whole. This section provides an outline of the document. There is no technical impact due to these changes.
AP600 Containment DBA Reports	1.2	AP600 Containment EM Documentation	1.3	1-3 – 1-11	An introductory paragraph is added to the “AP600 Containment EM Documentation” section. Additionally, text pertaining to the AP600 design containment EM has been consolidated into this section and placed into an appropriate subsection, whereas previously, it was distributed throughout Chapter 1 (e.g. old section 1.5 is moved to new section 1.3.2, 1.2.2 is moved to 1.3.3, etc.). Also, Figure 1-1 has been modified to more fully show the relationship of the supporting documentation to the EM and SSAR analyses.	The previous structure of Chapter 1 had elements of the AP600 design interspersed throughout a majority of the sections. With this document intended to primarily provide the AP1000 design methodology, the AP600 design-specific discussions and discussions of testing, scaling, etc., as applied to the AP600 plant are therefore consolidated into this section. There is no technical impact due to these changes.
AP1000 Containment DBA Reports	1.3	AP1000 Containment EM Documentation Updates	1.4	1-11 – 1-12	An introductory paragraph is added to the “AP1000 Containment EM Documentation Updates”, which summarizes the updates made from the AP600 design EM and how the applicability of the AP600 design EM was determined for the AP1000 design EM. The text is largely unchanged, but various editorial changes are made to conform with AP1000 naming conventions (e.g. AP1000 “plant”).	The addition of the introductory paragraph is made in order to transition the discussion from the AP600 design (as discussed in section 1.3) to the AP1000 plant containment EM. This change, as well as the other changes in this section, is editorial in nature. There is no technical impact due to these changes.
Applications Report Content Summary	1.4	N/A	N/A	N/A	Old section 1.4 is moved to new section 1.2, as described above.	See discussion on new section 1.2.
Use of LST and Validation Results	1.5	N/A	N/A	N/A	Old section 1.5 is moved to section 1.3, as described above.	See discussion on new section 1.3.
Interface with DCD Calculations	1.6	Interface with Plant Licensing Calculations	1.5	1-13	This section is largely unchanged. It has been retitled to reflect that it supports “plant licensing calculations” as opposed to “DCD calculations”. The bullets have been reordered, and additional bullets added (related to heat sinks and their modeling).	The reordering of bullets is editorial in nature. Additionally, other editorial changes are made (e.g. include “containment” before “EM”, change “DCD” to “SSAR”). Three additional bullets are added to explicitly identify these items (surface area and thickness for heat sinks, material properties, containment free volume); these items have been and continue to be “inputs” to the EM, but were not previously listed. Therefore, this clarification does not constitute a change to the methodology. There is no technical impact due to these changes.
Conclusions	1.7	Conclusions	1.6	1-13	Old section 1.6.1 addressed the previous change in code versions (v4.1 to v4.2). The topic of code changes is now discussed in section 3.2, and includes discussion on the recent update from v4.2 to v4.3.	See discussion on section 3.2.
				1-13	Old section 1.6.2 briefly discussed the changes from the AP600 to AP1000 EM, which has been moved to section 1.3.6.	See discussion on section 1.3.6.
References	1.8	References	1.7	1-13 – 1-14	References have been corrected to follow the appropriate convention. Additionally, new references 10 and 11 have been added for completeness.	These changes are editorial in nature. There is no technical impact due to these changes.
Test and Analysis Process Overview and High and Medium	2	Test and Analysis Process Overview and High and Medium Ranked	2	2-1	No changes	No changes

Revision 1		Revision 5		Page(s)	Detailed Description of Changes	Technical Evaluation of Changes
Title	Chapter/ Section/ Subsection	Title	Chapter/ Section/ Subsection			
Ranked Containment Phenomena		Containment Phenomena				
Introduction	2.1	Introduction	2.1	2-1 – 2-2	No changes	No changes
Element 1 – AP600 PCS Requirements and Code Capabilities	2.2	Element 1 – AP600 PCS Requirements and Code Capabilities	2.2	2-3	No changes	No changes
Element 2 – Assess Code Versus Tests and Important Processes	2.3	Element 2 – Assess Code Versus Tests and Important Processes	2.3	2-3 – 2-6	Editorial change to Table 2-1 (capitalized “Note”)	The change is editorial in nature. There is no technical impact due to this change.
Element 3 – Assess Uncertainties and Develop Bounding Models	2.4	Element 3 – Assess Uncertainties and Develop Bounding Models	2.4	2-6 – 2-7	No changes	No changes
Element 4 – Perform DBA Calculations and Compare to Success Criteria	2.5	Element 4 – Perform DBA Calculations and Compare to Success Criteria	2.5	2-8	No changes	No changes
Conclusions	2.6	Conclusions	2.6	2-8	No changes	No changes
References	2.7	References	2.7	2-8	No changes	No changes
Overview of WGOTHIC	3	Overview of WGOTHIC	3	3-1	No changes	No changes
Introduction	3.1	Introduction	3.1	3-1	Editorial change to specify “containment” vessel.	The change is editorial in nature. There is no technical impact due to this change.
				3-1	Editorial change to replace “describes” with “summarizes”.	The change is editorial in nature. There is no technical impact due to this change.
Overview of the Code Development and Validation	3.2	Overview of the Code Development and Validation	3.2	3-1	Editorial change to define acronym for evaluation model (EM).	The change is editorial in nature. There is no technical impact due to this change.
				3-4	Add heaters, coolers, and valves to the existing list of components.	These items are added to the list of components that the GOTHIC code has the option to model. These additions clarify the capabilities of GOTHIC. This change is a clarification made for completeness. There is no technical impact due to this change.
				3-4	Change sentence pertaining to “mitigation” systems found in “many” containments.	This sentence previously stated “any typical containment”. Neither the AP600 plant, nor the AP1000 plant containment designs are “typical” however, and so this change better represents the capability of GOTHIC and how the code can be applied to containment designs. This change is editorial in nature. There is no technical impact due to this change.
				3-4	Correction to the description related to modeling of components in GOTHIC not being used in the (peak pressure) analyses	Contrary to the previous statement, <u>WGOTHIC</u> has been and continues to be used to model components that are not within the passive safety systems for the minimum backpressure analyses. This statement is therefore corrected to that end. This correction has no impact on the analysis or methods used for the analysis. There is no technical impact due to this change.
				3-4	Editorial change to define acronym for electric power research institute (EPRI)	The change is editorial in nature. There is no technical impact due to this change.
				3-4	Editorial change to add “these”.	The change is editorial in nature. There is no technical impact due to this change.
				3-8	Change to expand on figure showing evolution of <u>WGOTHIC</u> code from 1997 to 2014 (versions 4.1 to 4.3.1).	This figure is an extension of the existing figure, and identifies the significant changes in the <u>WGOTHIC</u> code from 1997 to 2014, as

Westinghouse Non-Proprietary Class 3

Revision 1		Revision 5		Page(s)	Detailed Description of Changes	Technical Evaluation of Changes
Title	Chapter/ Section/ Subsection	Title	Chapter/ Section/ Subsection			
						discussed in the text of section 3.2 (page 3-11).
				3-9	Editorial change to define acronym for Carolina’s Virginia Tube Reactor (CVTR).	The change is editorial in nature. There is no technical impact due to this change.
				3-9	Editorial change to define acronym for Numerical Applications, Inc. (NAI).	The change is editorial in nature. There is no technical impact due to this change.
				3-9	Editorial change to underline “W” in <u>WGOTHIC</u> .	The change is editorial in nature. There is no technical impact due to this change.
				3-9	Editorial change to delete a space (between “dimension” and “less”).	The change is editorial in nature. There is no technical impact due to this change.
				3-9	Added statement pertaining to specific dimensionless numbers.	The listing of the dimensionless numbers is consistent with the referenced Table 3-3, and so this change does not represent a technical change, but a restatement of existing information. There is no technical impact due to this change.
				3-9	Added statement pertaining to the results of the key scaling groups for the enhanced shield building design (newly added as Reference 3.7).	This statement is taken verbatim from APP-GW-GLR-096, Revision 3, which evaluated the effects of the enhanced shield building design on the containment peak pressure analyses and was reviewed as part of design certification. The inclusion of this information directly in WCAP-15846 does not represent a technical change, but a restatement of existing information. There is no technical impact due to this change.
				3-10	Editorial change to add “results”	The change is editorial in nature. There is no technical impact due to this change.
				3-10	Added discussion pertaining to evolution of <u>WGOTHIC</u> code from 1997 to 2001 (versions 4.1 to 4.2a).	This addition provides a general discussion of the changes made to the <u>WGOTHIC</u> code that was ultimately used in the analyses supporting DCD Revision 19. Therefore, this information does not represent a technical change, but instead describes the history of the certified design. There is no technical impact due to this change.
				3-11	Added discussion pertaining to evolution of <u>WGOTHIC</u> code from 2001 to 2014 (versions 4.2a to 4.3.1).	Various changes and corrections were made to the <u>WGOTHIC</u> code from 2001 to 2014. This includes: Transferring from UNIX to LINUX (v4.2b), correction of mass error (v4.2b.1), Automated evaporation-limited PCS flow calculations (v4.3), Correction of wet clime dry out calculation (v4.3.1), and Addition of 2-D conduction multiplier option to automated evaporation-limited PCS flow calculation (v4.3.1). Each of these code updates was done under Westinghouse’s 10 CFR 50 Appendix B program, and underwent the appropriate verification and validation testing to ensure that the analytical results were valid.
The WGOTHIC Clime Model	3.3	The WGOTHIC Clime Model	3.3	3-12	Included column to show percent differences between original shield building design and enhanced shield building design.	This information is taken directly from APP-GW-GLR-096, Revision 3, which evaluated the effects of the enhanced shield building design on the containment peak pressure analyses and was reviewed as part of design certification. The inclusion of this information directly in WCAP-15846 does not represent a technical change, but a restatement of existing information. There is no technical impact due to this change.
				3-14	Clarification that in <u>WGOTHIC</u> , a time-dependent water flow rate boundary “can be” specified for each conductor surface of the top clime in a wet stack (previously stated that it “is” specified).	The discussion in section 3.3 pertains to the <u>WGOTHIC</u> code capability rather than to the application of the code to the AP1000 plant containment EM, and so it is more appropriate to state “can be” to express the possibility of, as opposed to stating “is”, which conveys a definitive use. There is no technical impact due to this change.

Westinghouse Non-Proprietary Class 3

Revision 1		Revision 5		Page(s)	Detailed Description of Changes	Technical Evaluation of Changes
Title	Chapter/ Section/ Subsection	Title	Chapter/ Section/ Subsection			
				3-14	Added discussion related to PCS evaporation limited option added as part of <u>WGOTHIC</u> version 4.3.	A discussion is added which states that for the automated evaporation-limited option, the wet and dry stacks are paired. This is a statement of code capability rather than a change to the application of the code to the AP1000 plant containment EM, which is discussed in sections 7.5 and 13.5. There is no technical impact due to this change.
General Clime Equations	3.4	General Clime Equations	3.4	3-16	Added introductory paragraph explaining that with <u>WGOTHIC</u> version 4.3, there are now two means of modeling the PCS water flow rate and coverage (related to calculation of the evaporation-limited PCS flow rate).	This paragraph is added to better introduce the two different options for modeling the PCS water flow rate and coverage. The automated evaporation-limited PCS flow rate option as a code capability is discussed in section 3.4.2, and as applied to the AP1000 plant containment EM, in section 7.5.2.2. There is no technical impact due to this change.
				3-16	Editorial corrections to equation 3-1 to reflect the appropriate characters (e.g. ∂ , =, -).	The change is editorial in nature. There is no technical impact due to this change.
				3-16	Added statement to elaborate on structure of equation 3-2 related to positive/negative terms.	The added statement clarifies the use of positive/negative terms in the existing equation 3-2. There is no technical impact due to this change.
				3-16	Editorial corrections to equation 3-2 to reflect the appropriate characters (e.g. -, =, +).	The change is editorial in nature. There is no technical impact due to this change.
				3-17	Editorial correction for name of film heat capacity term (correct term is specific heat).	The change is editorial in nature. There is no technical impact due to this change.
				3-18	Editorial corrections to equation 3-3 to reflect the appropriate characters (=).	The change is editorial in nature. There is no technical impact due to this change.
				3-18	Editorial corrections to equation 3-4 to reflect the appropriate characters (e.g. -, ∂ , etc)	The change is editorial in nature. There is no technical impact due to this change.
				3-18	Add a definition for k_{wall} .	The change is editorial in nature. There is no technical impact due to this change.
				3-18	Clarification to text regarding energy “entering/leaving” the film surface.	This addition covers the inverse of what was previously discussed (i.e. energy leaving the film surface is energy entering the atmosphere, and vice-versa). There is no technical impact due to this change.
				3-18	Editorial corrections to equation 3-5 to reflect the appropriate characters (e.g. -, ∂ , =, +)	The change is editorial in nature. There is no technical impact due to this change.
				3-18	Add a definition for $T_{surf,1}$	The change is editorial in nature. There is no technical impact due to this change.
				3-18	Specify value of Stefan-Bolzman constant.	The change is editorial in nature. There is no technical impact due to this change.
				3-18	Editorial corrections to equation 3-6 to reflect the appropriate characters (e.g. -, ∂ , =, +)	The change is editorial in nature. There is no technical impact due to this change.
				3-18	Editorial corrections to equation 3-7 to reflect the appropriate characters (e.g. -, ∂ , =, +)	The change is editorial in nature. There is no technical impact due to this change.
				3-19	Editorial corrections to equation 3-8 to reflect the appropriate characters (e.g. -, ∂ , =, +)	The change is editorial in nature. There is no technical impact due to this change.
				3-19	Editorial corrections to equation 3-9 to reflect the appropriate characters (e.g. -, ∂ , =, +)	The change is editorial in nature. There is no technical impact due to this change.
				3-19	Editorial corrections to equation 3-10 to reflect the appropriate characters (e.g. -, ∂ , =, +)	The change is editorial in nature. There is no technical impact due to this change.
				3-19	Editorial corrections to equation 3-11 to reflect the appropriate characters (e.g. -, ∂ , =, +)	The change is editorial in nature. There is no technical impact due to this change.
				3-19	Add definitions of ρ_{wall} , $c_{p,wall}$, ΔX_{wall}	Although these terms were used in the existing equation 3-11,

Westinghouse Non-Proprietary Class 3

Revision 1		Revision 5		Page(s)	Detailed Description of Changes	Technical Evaluation of Changes
Title	Chapter/ Section/ Subsection	Title	Chapter/ Section/ Subsection			
						they were not previously defined. There is no technical impact due to this change.
				3-19	Add reference to Figure 3-5.	The change is editorial in nature. There is no technical impact due to this change.
				3-19	Clarify film “thickness”	δx_{film} is defined as “fil thickness” on page 3-17, and so reference to this term is update to be consistent with that definition. There is no technical impact due to this change.
				3-19	Editorial corrections to equation 3-12 to reflect the appropriate characters (e.g. -, ∂ , =, +)	The change is editorial in nature. There is no technical impact due to this change.
				3-19	Rephrased sentence regarding film convective energy transport being neglected.	The change is editorial in nature. There is no technical impact due to this change.
				3-19	Corrected description of equation 13 to state that the outer quarter of the film thickness is defined (as opposed to the outer half), consistent with the equation itself as evidenced by the $\partial x_{\text{film}}/4$ term.	This change corrects the description of equation 3-13 as described in the text, but makes no changes to the equation itself. There is no technical impact due to this change.
				3-20	Corrected description of numerical error as a result of neglecting transport in the control volumes, which is estimated to be less than 20 percent for the completely evaporated film (as opposed to 20 percent of the total energy transport).	The discussion leading up to the modified sentence repeatedly refers to the “completely evaporated film”. The discussion previously concluded that the numerical error is less than 20 percent of the total energy transport, which is not an equivalent to the completely evaporated film. This statement is therefore corrected.
				3-21 – 3-24	[$]^{a,c}$
Integration of the Westinghouse Clime Model into GOTHIC	3.5	Integration of the Westinghouse Clime Model into GOTHIC	3.5	3-25	Clarification is added to state that the clime model provided in Figure 3-7 is a ‘standard’ model.	There can be variations of the clime model, and so the existing text is clarified to be referring to the ‘standard’ model that is shown in Figure 3-7. There is no technical impact due to this change.
				3-25, 3-27	[$]^{a,b,c}$
References	3.6	References	3.6	3-28	Reference 7 is added to reflect in-text citation in section 3.2.	Due to the timing of the development of WCAP-15846 Revision 1 and APP-GW-GLR-096 Revision 3 (Reference 7), Reference 7 was a standalone document and was not referenced in WCAP-15846 Revision 1. With the latest revision of WCAP-15846, some of the contents of Reference 7 are incorporated into

APP-GW-GLR-802 Revision 0

© 2017 Westinghouse Electric Company LLC

Page 12 of 1081

Westinghouse Non-Proprietary Class 3

Revision 1		Revision 5		Page(s)	Detailed Description of Changes	Technical Evaluation of Changes
Title	Chapter/ Section/ Subsection	Title	Chapter/ Section/ Subsection			
						of the value used in the analysis is based on the technical specifications and site parameters (and skewed in the conservative direction. Further, Table 5-1 itself is modified to add a column providing indication of the direction of conservatism for each parameter. There are no technical impacts due to these changes.
				5-1	The ambient outside relative humidity and temperature are clarified by explicitly stating they are based on maximum wet bulb temperature.	These clarifications better describe what these values represent and do not change the manner in which they were actually selected. There are no technical impacts due these changes.
Initial Containment Humidity	5.3	Initial Containment Humidity	5.3	5-4	No changes	No changes
Initial Containment Pressure	5.4	Initial Containment Pressure	5.4	5-4 – 5-6	No changes	No changes
Initial Containment Temperature	5.5	Initial Containment Temperature	5.5	5-7 – 5-8	No changes	No changes
Ambient Humidity	5.6	Ambient Humidity	5.6	5-9	Clarification is added to specify that the statement pertaining to upper limit of ambient humidity is for the AP600 plant.	The change is editorial in nature. There is no technical impact due to this change.
Ambient Temperature	5.7	Ambient Temperature	5.7	5-11 – 5-13	No changes	No changes
Sensitivity to Drop Modeling Assumptions	5.8	Sensitivity to Drop Modeling Assumptions	5.8	5-14	No changes	No changes
Conclusions	5.9	Conclusions	5.9	5-14 – 5-15	No changes	No changes
Meteorological Effects on PCS Performance	6	Meteorological Effects on PCS Performance	6	6-1	No changes	No changes
Introduction	6.1	Introduction	6.1	6-1	No changes	No changes
Wind-Induced Turbulence	6.2	Wind-Induced Turbulence	6.2	6-1 – 6-6	No changes	No changes
Recirculation of Chimney Effluent	6.3	Recirculation of Chimney Effluent	6.3	6-6 – 6-8	No changes	No changes
N/A	N/A	Applicability to the AP1000 Shield Building Design	6.4	6-8	New section 6.4 has been added to discuss the implications of meteorological effects on the enhanced shield building design that was incorporated into the AP1000 DCD Revision 19. This discussion is derived from APP-GW-GLR-096, Revision 3. The conclusions of this evaluation are not changed or modified in any way, but are now incorporated into WCAP-15846.	This change is consistent with the contents of APP-GW-GLR-096, Revision 3 and so does not represent “new” information. The change is editorial in nature. There is no technical impact due to this change.
Conclusions	6.4	Conclusions	6.5	6-9	No changes	No changes
References	6.5	References	6.6	6-9	APP-GW-GLR-096, Revision 3 is added as reference 6.3, consistent with the discussion added to section 6.4.	The change is editorial in nature. There is no technical impact due to this change.
Basis and Method for Calculating the PCS Water Evaporation Rate for the AP600 and AP1000 DBA Evaluation Models	7	Basis and Method for Calculating the PCS Water Evaporation Rate for the AP600 and AP1000 DBA Evaluation Models	7	7-1	No changes	No changes
Executive Summary	--	N/A	--	N/A	The executive summary is deleted in its entirety.	The executive summary provided a summary of the contents of chapter 7, but was largely redundant and unnecessary. It has therefore been deleted in its entirety. Additionally, the executive summary was deleted because it was inconsistent with the format of other sections; no other section has an executive summary. There is no technical impact due to this change.

Westinghouse Non-Proprietary Class 3

Revision 1		Revision 5		Page(s)	Detailed Description of Changes	Technical Evaluation of Changes
Title	Chapter/ Section/ Subsection	Title	Chapter/ Section/ Subsection			
Introduction	7.1	Introduction	7.1	7-1	The definition of PCS is added.	The change is editorial in nature. There is no technical impact due to this change.
				7-1	There are three flow paths from the PCCWST to the top of the containment shell. The description is therefore updated to reflect that there are three parallel valves.	This text is corrected to reflect that there are three parallel valves/flow paths. This change is consistent with the current design and current and revised analyses. There is no technical impact due to this change.
				7-1	The sentence pertaining to the pressure signal which opens the PCCWST valves previously identified as generic “high pressure” signal. This is clarified to specify the “high-2 containment” pressure signal.	The “high pressure” signal is referred to generically, but is replaced with the setpoint name (high-2). There is no technical impact due to this change.
				7-1	An editorial change is made, changing “input to” to “for”.	The change is editorial in nature. There is no technical impact due to this change.
				7-2	The “PCS film coverage model” is no longer separate from the <u>WGOTHIC</u> EM (as described in 7.5.2.2) and so conforming changes are made to that end.	As applied to the AP1000 plant containment EM, the PCS film coverage is now automated and integral to the <u>WGOTHIC</u> code. There is no technical impact due to this change.
				7-2	An editorial change is made to update reference to section 7.2.5 (instead of 7.5.2.2).	The change is editorial in nature. There is no technical impact due to this change.
Water Application and Distribution	7.2	Water Application and Distribution	7.2	7-3	[] ^{a,c}
				7-3	[] ^{a,c}
				7-4	The definition of LST is added.	The change is editorial in nature. There is no technical impact due to this change.
				7-8	[] ^{a,c}
				7-9	Clarifications are made to remove “about” before each of the referenced PCS water flow rate test values. Additionally, changes are made with respect to the AP1000 plant identity guidelines.	These changes are editorial in nature. There are no technical impacts due to these changes.
				7-9	Figure 7-2 is moved such that it appears after the paragraph in which it is referenced.	The change is editorial in nature. There is no technical impact due to this change.
				7-10	[
				7-10 – 7-11] ^{a,c}
				7-12	[] ^{a,c}
				7-13	New section 7.2.6 is added to discuss the addition of a new assumption to the model, which removes all of the PCS water film that interacts with the baffle supports on the vertical portion of the containment vessel (also discussed in 7.5.2.3).	During PCS flow testing, losses were observed in the form of water stripped from the containment vessel due to the interaction with the baffle supports. Therefore, the methodology now conservatively assumes that all of the PCS water film interacting with the baffle supports on the vertical portion of the containment

Westinghouse Non-Proprietary Class 3

Revision 1		Revision 5		Page(s)	Detailed Description of Changes	Technical Evaluation of Changes
Title	Chapter/ Section/ Subsection	Title	Chapter/ Section/ Subsection			
						vessel is lost and so is not credited for heat removal. This assumption is conservatively made based on observed phenomena.
Water Coverage Basis	7.3	Water Coverage Basis	7.3	7-14	Redundant discussion related to the PCS evaporation limited flow is removed.	Section 7.3 is intended to describe the bases for the film flow rate and film stability limit, with the PCS film coverage model as a whole being described in section 7.5. There is no technical impact due to this change.
				7-15	Clarifications added with respect to the estimate at 220 gpm bounding the test data at 100 gpm.	The text is clarified to prevent misinterpretation. There is no technical impact due to this change.
				7-16	Editorial changes are made with respect to the AP1000 plant identify guidelines.	These changes are editorial in nature. There are no technical impacts due to these changes.
				7-16	Acronym for the small scale test is added.	The change is editorial in nature. There is no technical impact due to this change.
				7-16	Editorial change to split a single sentence into two sentences.	The change is editorial in nature. There is no technical impact due to this change.
				7-16	Table number changed to "Table 7-11"	This change is editorial in nature. There is no technical impact due to this change.
Effect of Two-Dimensional (2-D) Heat Conduction Though the Containment Shell	7.4	Effect of Two-Dimensional (2-D) Heat Conduction Though the Containment Shell	7.4	7-18	Editorial change to make a sentence read better (re-ordered wording).	The change is editorial in nature. There is no technical impact due to this change.
				7-18	Modeling of two-dimensional heat conduction is updated to discuss using multipliers applied to the PCS evaporation rate or to the overall heat and mass transfer coefficients.	This discussion better explains how the effects of circumferential two-dimensional heat conduction are considered. The multiplier on the PCS evaporation flow is the existing technique used in the post-processing spreadsheet, and the heat and mass transfer coefficient multiplier is introduced as a technique which has been built into the <u>WGOTHIC</u> code for evaporation-limited PCS flow modeling.
				7-19	Text is moved.	The change is editorial in nature. There is no technical impact due to this change.
				7-19	The title of section 7.4.2 is updated ("Inside and Outside" is deleted, and "2-D" is added).	Although section 7.4.2 still addresses the 'inside and outside' heat transfer boundary conditions, the title is updated to reflect that the discussion pertains to the 2-D conduction model. The change is editorial in nature. There is no technical impact due to this change.
				7-19	In referring to containment pressure ranges, "Steady-state" is replaced with "constant".	The sentence is corrected to remove redundancy (previously read "steady-state calculations of the PCS heat transfer process performed at steady-state...". The change is editorial in nature. There is no technical impact due to this change.
				7-19	Editorial change from "are" to "were".	The change is editorial in nature. There is no technical impact due to this change.
				7-19	Clarified that heat transfer "rates" are calculated by <u>WGOTHIC</u> in the containment analysis.	This change is made to ensure consistency with how "heat transfer" is referred to (i.e. as "heat transfer rates", earlier in the same sentence). The change is editorial in nature. There is no technical impact due to this change.
				7-20	Corrected a typographical error (deleted a semicolon).	The change is editorial in nature. There is no technical impact due to this change.
				7-20	Replaced "2-D" with "two-dimensional".	The change is editorial in nature. There is no technical impact due to this change.
				7-20	Editorial change to update reference to section 7.4 (from 7.5.1.3).	The change is editorial in nature. There is no technical impact due to this change.
				7-20 – 7-21	The discussion regarding <u>WGOTHIC</u> under-predicting net radiation and convection from dry surface, and the use of ANSYS in estimating	The change is editorial in nature. There is no technical impact due to this change.

Revision 1		Revision 5		Page(s)	Detailed Description of Changes	Technical Evaluation of Changes
Title	Chapter/ Section/ Subsection	Title	Chapter/ Section/ Subsection			
					the amount of conservatism, is moved from what was previously section 7.5.2.3.	
				7-21	The statement regarding the use of the multiplication factor being used for the evaporation limited PCS flow is deleted and replaced with the paragraph after equation 7-1, which clarifies that the factor was used in the spreadsheet calculation as described in 7.5.2.1.	This clarification specifies the applicability of the multiplier as being limited to the spreadsheet calculation. There is no technical impact due to this change.
				7-22	Deleted extraneous hyphens.	The change is editorial in nature. There is no technical impact due to this change.
				7-22 – 7-27	Figures 7-6 through 7-11 are moved immediately after the text in 7.4.4.	The change is editorial in nature. There is no technical impact due to this change.
				7-28 – 7-29	New section 7.4.5 is added to describe the enhanced overall heat and mass transfer due to 2-D conduction (existing 7.4.5, “Insights from the PCS Large-Scale Testing”, is moved to 7.4.6). 7.4.5 now describes modeling the effect of 2-D heat conduction as used with the evaporation-limited PCS option incorporated into the WGOthic code (discussed in section 7.5.2.2). This change also adds plots of normalized total wet and dry heat transfer (2-D/1-D Conduction) vs. wetted fraction and 2-D conduction multiplier as a function of wetting fraction as Figure 7-12 and Figure 7-13, respectively.	The 2-D conduction multiplier is an option that can be credited when the PCS flow film is narrowed (i.e. begins to dry out) along the sidewall of the containment surface. This calculation was previously done as part of the iterative spreadsheet calculation of the PCS evaporation-limited flow. As applied to the revised AP1000 plant analysis, however, the calculation is done as part of the automated PCS evaporation-limited calculation as part of WGOthic. In this method, the multiplier is applied to the overall heat transfer rate, as opposed to the evaporation flux in the spreadsheet calculation. Additionally, the multiplier is now applied when the second standpipe of the PCCWST is uncovered. The automated method for enhancing the effects of circumferential 2-D heat conduction is developed from the same analyses that are the bases for the spreadsheet method, and so this alternate method remains valid.
				7-30	Editorial change to delineate “Table 7-4 and Table 7-5” instead of “Tables 7-3 and 7-4”.	The change is editorial in nature. There is no technical impact due to this change.
				7-31	Change table number to “Table 7-4”.	The change is editorial in nature. There is no technical impact due to this change.
				7-32	Change table number to “Table 7-5”.	The change is editorial in nature. There is no technical impact due to this change.
The Containment Evaluation Model Treatment of Water Coverage	7.5	The Containment Evaluation Model Treatment of Water Coverage	7.5	7-32	7.5 is simplified and rewritten to serve as an ‘introductory’ section. The relevant text is now addressed in 7.5.2.1	The change is editorial in nature. There is no technical impact due to this change.
				7-32	Redundant text is removed from 7.5.1 (the third, fourth, fifth, and sixth sentences). This information is already included in the first bullet at the end of 7.5.1.	The change is editorial in nature. There is no technical impact due to this change.
				7-33	Equation 7-2 is clarified. More specifically, it is updated to reflect that the parameters are a function of Z, and further, that there is a multiplier present in the equation which identifies the fraction of the surface that is wet.	The change is editorial in nature. There is no technical impact due to this change.
				7-33	Editorial corrections to equation 7-2 to reflect the appropriate characters (e.g. =).	The change is editorial in nature. There is no technical impact due to this change.
				7-33	Editorial corrections to equation 7-3 to reflect the appropriate characters (e.g. =, +).	The change is editorial in nature. There is no technical impact due to this change.
				7-33	Editorial corrections to the equations presented in the first bullet to reflect the appropriate characters (e.g. =, +).	The change is editorial in nature. There is no technical impact due to this change.
				7-33	A reference to Section 7.5.1.1 is added to the second bullet.	The change is editorial in nature. There is no technical impact due to this change.
				7-33	The film flow rate is specified to be a function of Z.	The change is editorial in nature. There is no technical impact due to this change.
				7-33	Editorial corrections to equation 7-4 to reflect the appropriate	The change is editorial in nature. There is no technical impact

Westinghouse Non-Proprietary Class 3

Revision 1		Revision 5		Page(s)	Detailed Description of Changes	Technical Evaluation of Changes
Title	Chapter/ Section/ Subsection	Title	Chapter/ Section/ Subsection			
					characters (e.g. =).	due to this change.
				7-33	Editorial corrections to equation 7-5 to reflect the appropriate characters (e.g. =).	The change is editorial in nature. There is no technical impact due to this change.
				7-33	Editorial corrections to equation 7-6 to reflect the appropriate characters (e.g. =).	The change is editorial in nature. There is no technical impact due to this change.
				7-34	Editorial corrections to equation 7-7 to reflect the appropriate characters (e.g. =, -).	The change is editorial in nature. There is no technical impact due to this change.
				7-34	Editorial corrections to equation 7-8 to reflect the appropriate characters (e.g. =, -).	The change is editorial in nature. There is no technical impact due to this change.
				7-34	Editorial corrections to equation 7-9 to reflect the appropriate characters (e.g. =, -).	The change is editorial in nature. There is no technical impact due to this change.
				7-34	Editorial corrections to equation 7-10 to reflect the appropriate characters (e.g. =, -).	The change is editorial in nature. There is no technical impact due to this change.
				7-34	Editorial corrections to equation 7-11 to reflect the appropriate characters (e.g. =, -).	The change is editorial in nature. There is no technical impact due to this change.
				7-34	Editorial corrections to equation 7-12 to reflect the appropriate characters (e.g. =).	The change is editorial in nature. There is no technical impact due to this change.
				7-34	Editorial corrections to equation 7-13 to reflect the appropriate characters (e.g. =, -).	The change is editorial in nature. There is no technical impact due to this change.
				7-34	Editorial corrections to equation 7-14 to reflect the appropriate characters (e.g. =, -).	The change is editorial in nature. There is no technical impact due to this change.
				7-34	Equations 7-15 and 7-16 are deleted, along with the text describing their use when mass flux is not constant.	The change is editorial in nature. There is no technical impact due to this change.
				7-34	The term W (film flow per unit width) is replaced with W_0f , which becomes the wetted width.	W is defined as the width of the wetted surface (film flow per unit width), which itself is a function of W_0 (the containment circumference) and f (the wetted fraction of the circumference). In other words, W is equivalent to W_0f . W is replaced with W_0f throughout section 7.5.1 for more granularity of the equation set. There is no technical impact due to this change.
				7-35	The title of 7.5.2 is changed from “WGOTHIC Model” to a more descriptive “Interaction of the PCS Film Coverage Model with WGOTHIC”.	The change is editorial in nature. There is no technical impact due to this change.
				7-35	An introductory paragraph is added to section 7.5.2 to provide an introduction to the two methods of applying the PCS film coverage (the spreadsheet method and the automated method).	The change is editorial in nature. There is no technical impact due to this change.
				7-35	References to the AP600 design and AP1000 design climes are provided (sections 4.4 and 13.5, respectively).	The change is editorial in nature. There is no technical impact due to this change.
				7-35	The “Wetted Perimeter Inputs” discussion from 7.5.2.1 is absorbed into 7.5.2.	The change is editorial in nature. There is no technical impact due to this change.
				7-35	Two instances of table number changing to “Table 7-6”	This change is editorial in nature. There is no technical impact due to this change.
				7-36	A paragraph is added to provide a ‘summary’ of 7.5.2.	The change is editorial in nature. There is no technical impact due to this change.
				7-36 – 7-37	Section 7.5.2.1 now describes the spreadsheet calculation of the PCS film coverage. This content is taken from what was previously in sections 7.5.1.3 and 7.5.2.2. The methodology, as provided in the previous version, is clarified with respect to the effects of two-dimensional conduction.	There is no new information or methodology in this section, which is instead a relocation of existing information from elsewhere in the prior revision of the document. The change is editorial in nature. There is no technical impact due to this change.
				7-37 – 7-38	[

Westinghouse Non-Proprietary Class 3

Revision 1		Revision 5		Page(s)	Detailed Description of Changes	Technical Evaluation of Changes
Title	Chapter/ Section/ Subsection	Title	Chapter/ Section/ Subsection			
				7-38 – 7-39	Section 7.5.2.3 is added to further describe the application of PCS water stripping from baffle supports (also described in section 7.2.6).	During PCS flow testing, losses were observed in the form of water stripped from the containment vessel due to the interaction with the baffle supports. Therefore, the methodology now conservatively assumes that all of the PCS water film interacting with the baffle supports on the vertical portion of the containment vessel is lost and so is not credited for heat removal. This assumption is conservatively made based on observed phenomena.
				7-39	The discussion on dry convection and radiation heat transfer predictions is moved in its entirety to section 7.4.3.	The change is editorial in nature. There is no technical impact due to this change.
Summary of Supporting Tests and Selected Analysis	7.6	Summary of Supporting Tests and Selected Analysis	7.6	7-39	Added “plant” to conform with the AP1000 plant identity guidelines.	The change is editorial in nature. There is no technical impact due to this change.
				7-40	Table number changed to “Table 7-7”	This change is editorial in nature. There is no technical impact due to this change.
				7-40	Table number changed to “Table 7-8”	This change is editorial in nature. There is no technical impact due to this change.
				7-40	“LST” is removed from the title.	The change is editorial in nature. There is no technical impact due to this change.
				7-42	Table number changed to “Table 7-7.” The title of Table 7-7 is clarified to include the definition of “STC” as the Westinghouse Science and Technology Center.	The change is editorial in nature. There is no technical impact due to this change.
				7-43	Table number changed to “Table 7-8”	This change is editorial in nature. There is no technical impact due to this change.
				7-44	Updated in-text reference to “Figure 7-14”.	The change is editorial in nature. There is no technical impact due to this change.
				7-45	Figure number changed to “Figure 7-14”	This change is editorial in nature. There is no technical impact due to this change.
				7-46	Table number changed to “Table 7-9”	This change is editorial in nature. There is no technical impact due to this change.
				7-47	Table number changed to “Table 7-9”	This change is editorial in nature. There is no technical impact due to this change.
				7-48	Table number changed to “Table 7-9”	This change is editorial in nature. There is no technical impact due to this change.
				7-49	Three instances of table number changing to “Table 7-9”	This change is editorial in nature. There is no technical impact due to this change.

Revision 1		Revision 5		Page(s)	Detailed Description of Changes	Technical Evaluation of Changes
Title	Chapter/ Section/ Subsection	Title	Chapter/ Section/ Subsection			
				7-49	Table number changed to “Table 7-11”	This change is editorial in nature. There is no technical impact due to this change.
				7-49	Added “plants” to conform with the AP1000 plant identity guidelines.	The change is editorial in nature. There is no technical impact due to this change.
				7-50	Two instances of table number changing to “Table 7-10”	This change is editorial in nature. There is no technical impact due to this change.
				7-50	Table number changed to “Table 7-11”	This change is editorial in nature. There is no technical impact due to this change.
				7-51	Table number changed to “Table 7-11”	This change is editorial in nature. There is no technical impact due to this change.
				7-51	Replaced “a DBA” with a more concise “LOCA or secondary line break inside containment”.	The change is editorial in nature. There is no technical impact due to this change.
				7-52	Clarification is added to explain that the containment shell properties provided were preliminary and do not reflect the specific values used in the latest containment integrity analyses, and further, that the process used to develop these preliminary values remains valid.	The containment shell heatup analysis is used in a sensitivity study on the importance of the time at which PCS flow is put on the containment dome. This sensitivity used preliminary containment shell material properties, which are revised as part of the analysis; specifically, the containment vessel thermal conductivity is now lower than previously used. A lower thermal conductivity, however, results in longer timing. A shorter time is conservative, and so the 33-second delay described in section 7.7.3 remains valid and conservative.
				7-53	Additional detail is added to differentiate results of the AP1000 plant analyses (which weren’t previously provided) from those of the AP600 plant analyses. Specifically, it is described that heat-up is faster and that steady-state coverage is not established until ~400 seconds, but the external shell surface stays below 212°F in the DECL LOCA analysis.	The previous revision of WCAP-15846 did not describe results of the AP1000 plant analysis for when the steady-state coverage is achieved, but only identified that for the AP600 plant analysis. This additional discussion provides the same information for the AP1000 plant analysis. Specifically, it is stated that steady-state coverage is achieved at almost 400 seconds, at which time the external surface is well below the 212°F boiling point.
				7-53	Three instances of table number changing to “Table 7-12”	This change is editorial in nature. There is no technical impact due to this change.
				7-53	Additional discussion is added for the AP1000 plant steamline break, which describes that there is greater/faster heatup of the containment gas and shell than the LOCA event.	This discussion is added to differentiate the behavior of the MSLB event from the LOCA in terms of the heatup of the containment shell. It also helps to lead into the discussion pertaining to the ability of the water fil to wet and rewet a “hot, dry surface...with the inorganic zinc coating.” This behavior existed in the previous analysis and is not a result of the revision; however, it is now being explicitly mentioned.
AP600 Containment DBA Evaluation Model Film Coverage Sensitivities	7.7	AP600 Containment DBA Evaluation Model Film Coverage Sensitivities	7.7	7-54	Table number changed to “Table 7-12”	This change is editorial in nature. There is no technical impact due to this change.
				7-54	Figure number changed to “Figure 7-15”	This change is editorial in nature. There is no technical impact due to this change.
				7-54	The acronym for “loss of coolant accident” is spelled out.	The change is editorial in nature. There is no technical impact due to this change.
				7-55	Figure number changed to “Figure 7-15”	This change is editorial in nature. There is no technical impact due to this change.
				7-55	Figure number changed to “Figure 7-16”	This change is editorial in nature. There is no technical impact due to this change.
				7-55	Figure number changed to “Figure 7-17”	This change is editorial in nature. There is no technical impact due to this change.
				7-56	Figure number changed to “Figure 7-18”	This change is editorial in nature. There is no technical impact due to this change.

Revision 1		Revision 5		Page(s)	Detailed Description of Changes	Technical Evaluation of Changes
Title	Chapter/ Section/ Subsection	Title	Chapter/ Section/ Subsection			
				7-56	The acronym for “in-containment refueling water storage tank” is spelled out.	The change is editorial in nature. There is no technical impact due to this change.
				7-57	Figure number changed to “Figure 7-16”	This change is editorial in nature. There is no technical impact due to this change.
				7-58	Figure number changed to “Figure 7-17”	This change is editorial in nature. There is no technical impact due to this change.
				7-59	Figure number changed to “Figure 7-18”	This change is editorial in nature. There is no technical impact due to this change.
				7-60	Figure number changed to “Figure 7-19”	This change is editorial in nature. There is no technical impact due to this change.
				7-60	Figure number changed to “Figure 7-20”	This change is editorial in nature. There is no technical impact due to this change.
					Table number changed to “Table 7-12”	This change is editorial in nature. There is no technical impact due to this change.
				7-61	Figure number changed to “Figure 7-19”	This change is editorial in nature. There is no technical impact due to this change.
				7-62	Figure number changed to “Figure 7-20”	This change is editorial in nature. There is no technical impact due to this change.
Conclusions and Summary	7.8	Conclusions and Summary	7.8	7-64	The discussion on ‘bounding assumptions and conservatisms for the operational characteristics of the PCS delivering and applying water to the containment surface’ has been moved to Section 13.5.2.	The change is editorial in nature. There is no technical impact due to this change.
Nomenclature	7.9	Nomenclature	7.9	7-65	No changes	No changes
References	7.10	References	7.10	7-66	Added references 7.13 and 7.14.	Reference 7.13 (Perry’s Chemical Engineers’ Handbook) is added related to the time to establish steady state water coverage. Reference 7.14 (AP1000 Containment Vessel Inner Surface Condensate Return Test Facility Description Report) is added related to the discussion in 7.2.6 on water stripping from baffle supports.
Physics of Liquid Films on the AP600 Containment Shell	7A	Physics of Liquid Films on the AP600 and AP1000 Containment Shells	7A	7.A-1 – 7.A-17	No changes	No changes
Containment Pressure Sensitivity During Blowdown	8	Containment Pressure Sensitivity During Blowdown	8	8-1	No changes	No changes
Introduction	8.1	Introduction	8.1	8-1	No changes	No changes
Method	8.2	Method	8.2	8-1	No changes	No changes
Analysis	8.3	Analysis	8.3	8-2	No changes	No changes
Conclusions	8.4	Conclusions	8.4	8-2 – 8-4	No changes	No changes
Circulation and Stratification Within Containment	9	Circulation and Stratification Within Containment	9	9-1	A change is made to how the maximum temperature curve is developed for the equipment qualification envelope. It was previously stated (also in Section 1.6) that only the temperature from the break location was used, to bound temperature distribution effects. However, the peak temperature does not always occur at the break location. Therefore, temperatures from locations inside containment are considered when developing the EQ temperature curve. This maintains the intent of bounding temperature distribution effects.	The method of selecting the maximum temperature from control volumes at each time step provides for a more accurate determination of an appropriate equipment qualification envelope. It was previously assumed to occur within the break compartment, which is not the case. Therefore this change provides a more accurate means of determining the EQ envelope.
Introduction	9.1	Introduction	9.1	9-4	A change is made to how the maximum temperature curve is developed for the equipment qualification envelope. It was previously stated (also in Section 1.6) that only the temperature from	The method of selecting the maximum temperature from control volumes at each time step provides for a more accurate determination of an appropriate equipment qualification

Westinghouse Non-Proprietary Class 3

Revision 1		Revision 5		Page(s)	Detailed Description of Changes	Technical Evaluation of Changes
Title	Chapter/ Section/ Subsection	Title	Chapter/ Section/ Subsection			
					the break location was used, to bound temperature distribution effects. However, the peak temperature does not always occur at the break location. Therefore, temperatures from locations inside containment are considered when developing the EQ temperature curve. This maintains the intent of bounding temperature distribution effects.	envelope. It was previously assumed to occur within the break compartment, which is not the case. Therefore this change provides a more accurate means of determining the EQ envelope.
Large-Scale Test Results	9.2	Large-Scale Test Results	9.2	9-20 – 9-27	No changes	No changes
Circulation and Stratification Assessment for the Loss-of-Coolant Accident	9.3	Circulation and Stratification Assessment for the Loss-of-Coolant Accident	9.3	9-42	Editorial change to update reference to a section in Chapter 13, which is revised as described below.	The change is editorial in nature. There is no technical impact due to this change.
Main Steamline Break (MSLB)	9.4	Main Steamline Break (MSLB)	9.4	9-42 – 9-45	No changes	No changes
Conclusions	9.5	Conclusions	9.5	9-45 – 9-46	No changes	No changes
References	9.6	References	9.6	9-47	No changes	No changes
Thermal and Circulation Effects of Drops During a LOCA	9.A	Thermal and Circulation Effects of Drops During a LOCA	9.A	9.A-1 – 9.A-3	No changes	No changes
Effects of Stratification on Heat Sink Utilization	9.B	Effects of Stratification on Heat Sink Utilization	9.B	9.B-1 – 9.B-13	No changes	No changes
Additional Information on Containment Circulation and Stratification	9.C	Additional Information on Containment Circulation and Stratification	9.C	9.C-1 – 9.C-233	No changes	No changes
Basis for Assuming Homogeneous Bulk Conditions for AP600 and AP1000 Containment Pressure Design Basis Analysis	9.D	Basis for Assuming Homogeneous Bulk Conditions for AP600 and AP1000 Containment Pressure Design Basis Analysis	9.D	9.D-1 – 9.D-36	No changes	No changes
Nominal Inputs and Correlations Sensitivities	10	Nominal Inputs and Correlations Sensitivities	10	10-1	No changes	No changes
Introduction	10.1	Introduction	10.1	10-1	No changes	No changes
Sensitivity Study Results	10.2	Sensitivity Study Results	10.2	10-5	An editorial change is made to section 10.2.1 to provide the acronym for “evaluation model”.	The change is editorial in nature. There is no technical impact due to this change.
				10-5	“Carbo-zinc”, which is a name-brand product, is changed to a more generic “Inorganic Zinc” to align with how it is described directly within the licensing basis and elsewhere in WCAP-15846.	The change is editorial in nature. There is no technical impact due to this change.
				10-5	The specific value for conductivity of IOZ is added.	Table 13-49 of WCAP-15846 Revision 1 previously identified the values for emissivity and conductivity. It is now added to the text in Section 10.2 since these were the values used in the sensitivity study but are not input values for the EM.
				10-5	A change is made is made to clarify that this is a historical sensitivity, not a commitment to reduce thermal conductivity by a factor of 4 for	The change is editorial in nature. There is no technical impact due to this change.

Westinghouse Non-Proprietary Class 3

Revision 1		Revision 5		Page(s)	Detailed Description of Changes	Technical Evaluation of Changes
Title	Chapter/ Section/ Subsection	Title	Chapter/ Section/ Subsection			
					the EM. A reference to section 13.4.1 is added, which points the reader to a discussion on thermal conductivity of coatings in the AP1000 EM.	
Conclusions	10.3	Conclusions	10.3	10-9	No changes	No changes
References	10.4	References	10.4	10-9	No changes	No changes
Timestep Sensitivity	11	Timestep Sensitivity	11	11-1	No changes	No changes
Introduction	11.1	Introduction	11.1	11-1	No changes	No changes
Methodology	11.2	Methodology	11.2	11-1	No changes	No changes
Results	11.3	Results	11.3	11-1 – 11-3	No changes	No changes
Summary	11.4	Summary	11.4	11-3 – 11-5	No changes	No changes
References	11.5	References	11.5	11-6	No changes	No changes
Sensitivity to Clime Noding	12	Sensitivity to Clime Noding	12	12-1	No changes	No changes
Introduction	12.1	Introduction	12.1	12-1 – 12-4	No changes	No changes
Model Descriptions	12.2	Model Descriptions	12.2	12-4 – 12-7	No changes	No changes
Results	12.3	Results	12.3	12-8 – 12-11	No changes	No changes
Summary	12.4	Summary	12.4	12-11	No changes	No changes
References	12.5	References	12.5	12-11	No changes	No changes
Description of AP1000 Plant Geometry in WGOthic Evaluation Model	13	Description of AP1000 Plant Geometry in WGOthic Evaluation Model	13	13-1	No changes	No changes
Introduction	13.1	Introduction	13.1	13-1	The introduction is completely rewritten to serve as a true introduction. Previously, the section went into miscellaneous details of the analysis, and their relation to the AP600 plant methodology. This extraneous and repetitive information is therefore removed from the “introduction.” Some of the information relevant to the control volumes is moved to section 13.2. Further, references to pertinent sections of the document are provided, consistent with this section serving as an introduction.	These changes are editorial in nature and are made to improve reader understanding of the intention of the chapter as a whole. The overarching objective of the chapter (to describe the methodology used to develop the AP1000 plant containment integrity EM) is unchanged. There is no technical impact due to these changes.
N/A	N/A	AP1000 Plant WGOthic Evaluation Model Control Volumes	13.2	13-2 – 13-11	[

Revision 1		Revision 5		Page(s)	Detailed Description of Changes	Technical Evaluation of Changes
Title	Chapter/ Section/ Subsection	Title	Chapter/ Section/ Subsection			
]a,c
				13-12 – 13-14	[
]a,c
				13-15	[
N/A	N/A	AP1000 Evaluation Model Flow Paths	13.3	13-15	[]a,c
				13-16 – 13-31	[]a,c
AP1000 Plant Geometry in WGOthic Model	13.2	N/A	N/A	N/A	Section 13.2 is replaced by new sections 13.2 (control volumes) and 13.3 (flow paths).	
Conductor Type Descriptions	13.3	AP1000 Evaluation Model Thermal Conductors	13.4	13-32 – 13-33	[

Westinghouse Non-Proprietary Class 3

Revision 1		Revision 5		Page(s)	Detailed Description of Changes	Technical Evaluation of Changes
Title	Chapter/ Section/ Subsection	Title	Chapter/ Section/ Subsection			
] ^{a,c}
				13-34 – 13-46	[] ^{a,c}
				13-47 – 13-48	[] ^{a,c}
				13-48	Also included in section 13.4.1 is discussion of a new reduction factor (2) relative to the minimum test requirement based on Addendum 1 of WCAP-15846, which is now referenced specifically within this WCAP (as opposed to being a stand-alone addendum).	The thermal conductivity of inorganic zinc is reduced by a factor of two relative to the minimum test requirement. Although a sensitivity documented in section 10.2.1 assumed a factor of four degradation in the thermal conductivity to address the effects of oxidation, later work in reference 13.7 has shown that thermal conductivity will not decrease substantially as the coating ages, and may even increase slightly. The factor of two provides margin for variations in the coating composition and structure, corrosion product composition, and measurement uncertainties.
				13-49 – 13-50	[] ^{a,c}

Westinghouse Non-Proprietary Class 3

Revision 1		Revision 5		Page(s)	Detailed Description of Changes	Technical Evaluation of Changes
Title	Chapter/ Section/ Subsection	Title	Chapter/ Section/ Subsection			
Clime Noding Descriptions	13.4	AP1000 Plant WGOTHIC Evaluation Model Climes	13.5	13-51	[] ^{a,c}
				13-51	[] ^{a,c}
				13-51	[] ^{a,c}
				13-51	[] ^{a,c}
				13-51	[] ^{a,c}
				13-51	[] ^{a,c}
				13-52	[] ^{a,c}
				13-53	[] ^{a,c}
				13-54	[] ^{a,c}
				13-54	[] ^{a,c}
				13-56 – 13-57	[

Revision 1		Revision 5		Page(s)	Detailed Description of Changes	Technical Evaluation of Changes
Title	Chapter/ Section/ Subsection	Title	Chapter/ Section/ Subsection			
						^{a,c}
				13-58	Section 13.5.2 now includes a discussion on passive cooling system flow, which was previously contained in section 13.4.3.	The change is editorial in nature. There is no technical impact due to this change.
				13-58	Various changes are made, including general rewording, the addition of references to other sections in the document, and clarification that PCCWST draindown is confirmed through plant testing. It is further clarified that the minimum delivered flowrate is based on only one of the three water flow paths being open.	General wording changes and references to other sections are editorial in nature. The statement regarding PCCWST draindown being confirmed through plant testing is consistent with the description of PCS testing in UFSAR Chapter 14. The clarification that flowrate is based on one of three water paths is consistent with the prior and revised analyses. These changes are consistent with other portions of the licensing basis and so are editorial in nature. There is no technical impact due to these changes.
				13-58	The definition of “evaporation-limited” is deleted in this section, as it is already defined in section 7, where it is discussed in more detail.	The change is editorial in nature. There is no technical impact due to this change.
				13-58	A statement is added pertaining to the fact that there are now two options for calculating evaporation-limited flow (e.g. automated and spreadsheet) as discussed in Section 7.5.2 and that no evaporation of the film is credited prior to development of steady state PCS water coverage as discussed in section 7.2.5.	The changes are editorial in nature. There is no technical impact due to these changes.
				13-58	Under the “Initial Temperature of Containment Shell” parameter of Table 13-6, the statement “Conservatively bounds initial temperature profile of shell” is deleted.	Use of the maximum containment shell temperature identified in the Technical Specifications ensures that the analysis remains valid for plant conditions that are in conformance with the Technical Specifications. Although this is intended to “conservatively bound initial temperature profile of shell”, the statement is not an accurate characterization of the relationship.
				13-58	Under the “Applied External Film Flow Rate” parameter of Table 13-6, it is clarified that water flow rate is based on one of three PCS discharge valves being open.	The clarification that flowrate is based on one of three PCS discharge valves being open is consistent with the prior and revised analyses. This change is consistent with other portions of the licensing basis and so is editorial in nature. There is not technical impact due to these changes.
				13-58	Under the “Film Coverage Fraction” parameter of Table 13-6, the basis is clarified.	The basis previously pointed the reader to Chapter 7 without any additional elaboration. The basis is now specified (in addition to the reference to Chapter 7 being provided). The change is editorial in nature. There is no technical impact due to this change.
				13-58	Under the “PCS Coating Properties” parameter of Table 13-6, the reduction factor of IOZ is updated to reflect coatings test requirements. Further, the name-brand Carbo-Zinc is replaced with “inorganic zinc”.	“Carbo-zinc”, which is a name-brand product, is changed to a more generic “Inorganic Zinc” to align with how it is described directly within the licensing basis. This change is editorial in nature. There is no technical impact due to this change.
				13-58	Under the “PCS Emissivity” parameter of Table 13-6, “inorganic zinc” is specified, and it is changed to 90% of “the coatings test requirement”.	The basis was previously 90% of the “nominal values”. However, as discussed in section 13.4.1, emissivity is reduced by 10% of the “coating test requirement” and is only input to credit radiation in the clime modeling of the outer surface of the containment vessel, the baffle and the shield building.
				13-59	Under the “PCS Initial Delay Time” parameter of Table 13-6, the specific times are replaced by what those times actually represent.	Development of steady state PCS water coverage is discussed and identified in section 7.2.5, as per the reference. This change is editorial in nature. There is no technical impact due to this change.

Revision 1		Revision 5		Page(s)	Detailed Description of Changes	Technical Evaluation of Changes
Title	Chapter/ Section/ Subsection	Title	Chapter/ Section/ Subsection			
				13-59	Section 13.5.3 now includes a discussion on condensate film stripping, which was previously contained in section 13.4.4.	The discussion on condensate film stripping is relocated. This change is editorial in nature. There is no technical impact due to this change.
				13-59	[] ^{a,c}
				13-59	[
Initial and Boundary Conditions	13.5	AP1000 Plant WGOTHIC Evaluation Model Initial and Boundary Conditions	13.6	13-61	Editorial changes are made to section 13.6 related to the “model” being more appropriately referred to as the <u>WGOTHIC</u> containment evaluation model. A change to a referenced section (13.6.1) is also made consistent with the overall restructuring of the chapter.	This change is editorial in nature. There is no technical impact due to this change.
				13-61	Section 13.6.1 now includes a discussion on initial conditions, which was previously contained in 13.5.1. The first paragraph is rearranged (e.g. the statement about the initial conditions being based on sensitivity studies is moved to later in the first paragraph), with editorial changes made (e.g. “described” to “summarized”).	These changes are editorial in nature. There is no technical impact due to these changes.
				13-61	The statement regarding the PCS downcomer being modeled with a particular flow path and interfacing with particular volumes is removed.	This statement is not necessary for the discussion on initial conditions. Flow paths are discussed in section 13.3. This change is editorial in nature. There is no technical impact due to this change.
				13-61	The “listing” of outside initial conditions in the text is clarified by expanding the list to explicitly provide not just the “PCS downcomer”, but the annulus region, the chimney region, and the surrounding environment.	The expanded list provides a more complete description of what the outside containment initial conditions represents. This change is editorial in nature. There is no technical impact due to this change.
				13-61 – 13-62	The “value” columns from the tables providing the outside and inside containment initial conditions (Tables 13-7 and 13-8) are removed since the tables contain a reference to where the values are located elsewhere within the licensing basis (i.e. site parameters or Technical Specifications).	This change is editorial in nature. There is no technical impact due to this change.
				13-61	Under the “External Atmosphere Temperature” parameter of Table 13-7, the “maximum safety air temperature limit” is clarified to be the “maximum dry bulb air temperature limit”.	This change is editorial in nature. There is no technical impact due to this change.
				13-61	Under the “External Total Pressure” parameter of Table 13-7, the basis for value is clarified to be the standard atmospheric pressure (previously stated only as “standard”).	This change is editorial in nature. There is no technical impact due to this change.
				13-61	Under the “External Atmosphere Pressure Ratio (Relative Humidity)” parameter of Table 13-7, the repetitive values are omitted from the basis since there is already a reference from which the values correspond to (i.e. site parameters).	This change is editorial in nature. There is no technical impact due to this change.
				13-61	A new parameter is explicitly listed for the “External PCS Film Flow Temperature”. Although this was previously modeled (and with the maximum PCCWST temperature from the Technical Specifications), it was not listed in the table and so is now included for completeness.	This change is editorial in nature. There is no technical impact due to this change.

Westinghouse Non-Proprietary Class 3

Revision 1		Revision 5		Page(s)	Detailed Description of Changes	Technical Evaluation of Changes
Title	Chapter/ Section/ Subsection	Title	Chapter/ Section/ Subsection			
				13-62	In Table 13-8, the “Initial Heat Sink Temperature” parameter is combined with the existing “Internal Atmosphere Temperature” row; further, “Containment Shell” (temperature) is listed as one of the parameters within this row for completeness.	These changes are editorial in nature. There is no technical impact due to these changes.
				13-62	Under the “Internal Total Pressure” parameter of Table 13-8, editorial changes are made (“at” to “to” and removal of unnecessary “DCD Chapter 16” after “Technical Specifications”).	These changes are editorial in nature. There is no technical impact due to these changes.
				13-62	Under the “Relative Humidity-Humidity” parameter of Table 13-8, the specific value of “0%” is instead replaced with the basis for the value, as the table is intended to provide.	This change is editorial in nature. There is no technical impact due to this change.
				13-62	Under the “IRWST Liquid Volume Fraction” parameter of Table 13-8, an editorial change is made to remove the unnecessary “DCD Chapter 16” after “Technical Specifications”.	These changes are editorial in nature. There is no technical impact due to these changes.
				13-62	Under the “IRWST Water Temperature” parameter of Table 13-8, an editorial change is made to remove the unnecessary “DCD Chapter 16” after “Technical Specifications”.	These changes are editorial in nature. There is no technical impact due to these changes.
				13-62	Section 13.6.2 now includes a discussion on boundary conditions, which was previously contained in 13.5.2. The first paragraph is rewritten to serve as an introduction to the section. A general definition of a ‘boundary condition’ is provided as well as how boundary conditions are applied within the model (i.e. through forcing functions). The two types of boundary conditions (flow and pressure) are defined and described.	These changes are editorial in nature. There is no technical impact due to these changes.
				13-62	Tables 13-128 and 13-129 previously listed forcing functions that define boundary conditions. The forcing functions that are used in either the LOCA or MSLB events are now discussed in the text within section 13.6.2, and so the tables are removed.	These changes are editorial in nature. There is no technical impact due to these changes.
				13-62	Figures 13-94 through 13-104 previously provided curves of the forcing functions as applied to the “base cases” done as part of the previous analysis. The behavior of each of the applicable forcing functions is now qualitatively described in the text within section 13.6.2, and so the figures are removed.	These changes are editorial in nature. There is no technical impact due to these changes.
				13-62	[] ^{a,c}
				13-63	[] ^{a,c}
				13-63	[] ^{a,c}
				13-63	[] ^{a,c}
				13-63	[] ^{a,c}

Westinghouse Non-Proprietary Class 3

Revision 1		Revision 5		Page(s)	Detailed Description of Changes	Technical Evaluation of Changes
Title	Chapter/ Section/ Subsection	Title	Chapter/ Section/ Subsection			
						} ^{a,c}
				13-63	[} ^{a,c}
				13-64	[} ^{a,c}
				13-64	[} ^{a,c}
				13-64	[} ^{a,c}
				13-64	[} ^{a,c}
				13-64	[} ^{a,c}
AP1000 Containment Evaluation Model Summary	13.6	N/A	N/A	N/A	The contents of what was previously contained in section 13.6 have been moved to the appropriate location in sections 13.2, 13.3, 13.4, and 13.5.	These changes are editorial in nature. There is no technical impact due to these changes.
Summary of Evaluation Model Transient Calculations	13.7	Summary of Evaluation Model Transient Calculations	13.7	13-65	Previously, section 13.7 contained “This section provides representative Evaluation Model (EM) results for two limiting containment overpressure design basis accidents (DBAs), typical of those provided in the DCD. The results provided here do not define the containment peak pressure used as a licensing basis; licensing-specific results are provided in the DCD.” This is replaced with “This section provides an overview of the accident progression for the two limiting containment DBAs. The descriptions provided here do not define the containment peak pressure used as a licensing basis; licensing-specific results are provided in the DCD.” Section 13.7 is therefore modified to serve as an overview of the LOCA and MSLB analyses. The paragraphs in section 13.7 are modified to that end, and figures 13-116 through 13-123, which provide results, are removed.	Although representative results were previously provided, the relevant information is the licensing basis analysis, which was always contained directly in the DCD and UFSAR. To that end, representative results are irrelevant and are thus removed from WCAP-15846. The description of section 13.7 is therefore updated to reflect this. As the updated analytical results are still provided in the UFSAR, there is no technical impact due to these changes.
				13-65	The LOCA sequence is moved from Table 13-135 to a bulleted list	The timing for each of the steps in the LOCA sequence is no

Revision 1		Revision 5		Page(s)	Detailed Description of Changes	Technical Evaluation of Changes
Title	Chapter/ Section/ Subsection	Title	Chapter/ Section/ Subsection			
					within section 13.7.1.	longer specified in WCAP-15846, as they are already provided in the UFSAR. These changes are editorial in nature. There is no technical impact due to these changes.
				13-65 – 13-66	Various changes are made to section 13.7.1 (LOCA) to reflect removal of analytical results from WCAP-15846, instead making general reference to the analytical results as presented in the proposed licensing basis.	Although representative results were previously provided, the relevant information is the licensing basis analysis, which was always contained directly in the DCD and UFSAR. To that end, representative results are irrelevant and are thus removed from WCAP-15846. The description of section 13.7 is therefore updated to reflect this. As the updated analytical results are still provided in the UFSAR, there is no technical impact due to these changes.
				13-67	Various changes are made to section 13.7.2 (MSLB) to reflect removal of analytical results from WCAP-15846, instead making general reference to the analytical results as presented in the proposed licensing basis.	Although representative results were previously provided, the relevant information is the licensing basis analysis, which was always contained directly in the DCD and UFSAR. To that end, representative results are irrelevant and are thus removed from WCAP-15846. The description of section 13.7 is therefore updated to reflect this. As the updated analytical results are still provided in the UFSAR, there is no technical impact due to these changes.
WGOthic Containment Minimum Pressure Calculation for Small-Break LOCA and Long-term Cooling	13.8	WGOthic Containment Minimum Pressure Calculation for Small-Break LOCA and Long-term Cooling	13.8	13-67	Editorial changes are made to include acronyms for SBLOCA and LTCC, and to specify that the WGOthic Evaluation Model used to determine the peak containment pressure for design basis events uses assumptions that are biased to maximize the containment pressure.	These changes are editorial in nature. There is no technical impact due to these changes.
				13-67	Similar to the changes made to section 13.7, analytical results are no longer included in WCAP-15846, but are instead provided in the licensing basis. To that end, the outdated results and figures and tables showing those results are removed.	Although representative results were previously provided, the relevant information is the results of the licensing basis analysis, which was always contained directly in the DCD and UFSAR. To that end, representative results are irrelevant and are thus removed from WCAP-15846. The description of section 13.7 is therefore updated to reflect this. As the updated analytical results are still provided in the UFSAR, there is no technical impact due to these changes.
				13-68	[]
				13-69	Table 13-136 previously provided a list of “Assumptions for Minimum Pressure Calculation”, which included the assumptions for both the peak pressure evaluation model as well as the minimum pressure model. Since the intention of the table (now Table 13-9) is to provide the assumptions for the minimum pressure calculation, the column for the peak pressure evaluation model is deleted. This information is contained in preceding sections.	Information in Table 13-9 covering the peak pressure model is redundant to the information included in the discussions on the peak pressure model. It was originally intended to convey that many of the assumptions are biased in the opposite direction of the minimum pressure model. However, this fact is described at the beginning of section 13.8. If the reader requires information on the assumptions of the peak pressure model, then they refer to the appropriate section. This deletion effectively removes redundant information that can be found elsewhere. There is no technical impact due to this change.
				13-69	The “Mass and Energy” parameter is deleted from Table 13-9.	Mass and Energy isn’t an assumption, but is a calculated value.

Westinghouse Non-Proprietary Class 3

Revision 1		Revision 5		Page(s)	Detailed Description of Changes	Technical Evaluation of Changes
Title	Chapter/ Section/ Subsection	Title	Chapter/ Section/ Subsection			
						Conservatism with respect to the M&E calculation for minimum back pressure are described in UFSAR section 6.2.1.5.1 and the analytical results are provided in Table 6.2.1.5-1.
				13-69	A parameter is added for “Heat sinks” to Table 13-9.	The prior minimum backpressure analysis had all heat sinks credited, but this was not explicitly identified in the table. There is no technical impact due to this change.
				13-69	The parameter for “inner shell heat transfer correlation – blowdown” is replaced with a more encompassing “Heat transfer correlation”. Additionally, the assumption is changed from “Uchida increased by 20% for small-break LOCA” to “Uchida increased by 20%”.	Consistent with section 13.8 addressing SBLOCA and Table 13-9 identifying “assumptions for SBLOCA minimum pressure calculations”, there is no need to specify “for small-break LOCA” under the assumption. This change is editorial in nature. There is no technical impact due to this change.
				13-69	The parameter for passive heat sink structural air gaps is clarified to be in steel-jacketed concrete walls and is changed to “not modeled” as opposed to “ignored”.	This change clarifies that the existing tabular parameter for passive heat sink structural air gaps pertains to steel-jacketed concrete walls. This clarification does not represent a change to parameter described in the approved methodology as cited in the UFSAR. Additionally, the change from the description of the parameter from “ignored” to “not modeled” is editorial in nature and does not represent a technical change. There is no technical impact due to this change.
				13-69	The material properties parameter is clarified to specify which material properties (i.e. volumetric heat capacity and thermal conductivity).	This change clarifies that the volumetric heat capacity and thermal conductivity are the parameters used in the minimum backpressure analysis to bias the analysis for maximum heat removal. As such, this change does not represent a technical change and is consistent with the approved methodology.
				13-69	A parameter is added for passive containment cooling system flow rates.	The intent of Table 13-9 (old Table 13-136) is to identify the bounding assumptions in the minimum pressure analysis. As such, the parameter for passive containment cooling system flow rates is added to Table 13-9 to indicate that maximum system specified flows are conservative for the application of the minimum pressure analysis. This assumption is consistent with the existing analysis and does not constitute a technical change to the method by which the analysis is performed.
				13-69	A parameter is added for “PCS water temperature”.	The intent of Table 13-9 (old Table 13-136) is to identify the bounding assumptions in the minimum pressure analysis. As such, the parameter for PCS water temperature is added to Table 13-9 to indicate that minimum PCS water temperature is modeled to maximum evaporative cooling in the analysis. This assumption is consistent with the existing analysis and does not constitute a technical change to the method by which the analysis is performed.
				13-69	The “fan coolers” parameter is clarified to start at 10 minutes after event initiation.	The parameter for “fan coolers” is clarified for the minimum pressure analysis to assume to start 10 minutes after event initiation. Originally, this parameter simply stated that the fan coolers were assumed to operate, but provided no indication of when during the event operation was assumed to initiate.
				13-69	The “containment purge” parameter is clarified to be open initially, and then shuts on an “S” signal.	The parameter for “containment purge” is clarified to be open initially, and then is assumed to shut on an automatic safeguards actuation signal (i.e., “S” signal). Originally, this parameter only indicated that containment purge would shut on the “S” signal, but provided no indication as to whether it was initially open. There is no technical change associated with the clarification.

Westinghouse Non-Proprietary Class 3

Revision 1		Revision 5		Page(s)	Detailed Description of Changes	Technical Evaluation of Changes
Title	Chapter/ Section/ Subsection	Title	Chapter/ Section/ Subsection			
				13-69	The “initial conditions” parameter is broken into initial pressure inside containment, humidity inside containment, temperature inside containment, and environment temperature.	The “initial conditions” parameter in Table 13-9 (old Table 13-136) indicated that these conditions were biased to minimize initial air quantity. However, as “initial conditions” in the application of the minimum backpressure analysis is not indicative of a singular condition, this parameter is updated in Table 13-9 to itemize initial condition biases for “initial pressure inside containment,” “initial humidity inside containment,” “initial temperature inside containment,” and “initial environment temperature.” The “initial pressure inside containment” parameter is set to the minimum operating air pressure defined by Technical Specifications. The “initial humidity inside containment” is maximized to minimize initial air quantity. The “initial temperature inside containment” is set to the maximum operating air temperature defined by Technical Specifications. And the “initial environment temperature” is minimized based on maximum containment shell differential defined by Technical Specifications. As such, this change acts to clarify individual initial condition parameters biases for the application of the minimum pressure analysis and does not constitute a technical change.
N/A	N/A	Conclusions	13.9	13-70 – 13-71	A new section is added to provide a summary of the key elements of methodology for the peak containment pressure analyses. These key elements are described further in their corresponding sections, as referenced in section 13.9.	As indicated in the detailed description of the change, this new section provides a summary conclusion of the key elements of the methodology for the peak containment pressure analyses. As such, there is no technical change related to the method of evaluation previously unevaluated in this additional text.
References	13.9	References	13.10	13-72	Reference 13.2 (AP600 DCD) is deleted. The GOTHIC user manual is added as the new Reference 13.2.	Reference to the AP600 DCD (old reference 13.2) is no longer cited in Chapter 13 and is instead replaced with reference to the GOTHIC user manual (new reference 13.2) which is referenced in updated Section 13.3 for the in text citation for the heights of vertical flow paths. Reference to the AP600 DCD is legacy information for which the development of the AP1000 plant methodology was based on. As the updated methodology is applicable to the AP1000 design and adequately describes the method by which containment integrity analyses are performed for the AP1000 plant, the old reference to AP600 DCD is no longer necessary and can be deleted in Chapter 13.
					Reference 13.5 is added (WCAP-14326) for the basis of heat and mass transfer correlations.	Detail is added to the discussion related to the AP1000 design clime conductor modeling in Section 13.5.1. Specifically, discussion related to the basis for the heat and mass transfer coefficients and conservative multiplication factors are described for the climes modeling. To aid this discussion, reference to WCAP-14236 is included as an in-text citation in Section 13.5.1 and so is added to the list of references for Chapter 13 as new Reference 13.5. This change is made to provide a basis for the application of the aforementioned conductor parameters and does not constitute a reduction in detail from the existing methodology.
					Reference 13.6 is added (WCAP-10325) for the LOCA mass and energy release methodology.	Description of the Base Case LOCA Boundary Condition is provided in updated Section 13.6.2.1. WCAP-10325 is included as an in-text citation (as new Reference 13.6) in this updated section to support discussion of the treatment of the refill phase of the LOCA transient as being consistent with the Westinghouse

Revision 1		Revision 5		Page(s)	Detailed Description of Changes	Technical Evaluation of Changes
Title	Chapter/ Section/ Subsection	Title	Chapter/ Section/ Subsection			
						long term M&E release methodology. As such, inclusion of WCAP-10325 is warranted to the list of references in Chapter 13 and is included as new Reference 13.6. This change is made to provide a basis for aspects of the text updated in Section 13.6.2.1 and does not constitute a reduction in detail from the existing methodology.
					Reference 13.7 is added (WCAP-15846 Addendum 1) for the thermal conductivity model of IOZ.	Updates to the text in Section 13.4.1 for Thermal Conductor Type Descriptions include discussion related the thermal conductivity of inorganic zinc coatings and associated degradation of thermal conductivity considering the effects of oxidation. As part of this text update, reference to WCAP-15846 (new Reference 13.7) is cited to document investigation into the IOZ coating thermal conductivity degradation effects. As such, the addition of WCAP-15846 is warranted to the list of References in Chapter 13, and is included as new Reference 13.7. This change is made to provide a basis for the text update describing the effects of IOZ coatings over time and does not constitute a reduction in detail from the existing methodology.
					Various editorial changes are made to the reference listing in section 13.10, including deletion of authors and relocating the “revision.”	These changes are editorial in nature. There are no technical impacts due to these changes.
LOCA Mass and Energy Release Calculation Methodology	14	LOCA Mass and Energy Release Calculation Methodology	14	14-1	No changes	No changes
Introduction	14.1	Introduction	14.1	14-1 – 14-2	No changes	No changes
Blowdown Mass and Energy Release Calculation	14.2	Blowdown Mass and Energy Release Calculation	14.2	14-2	No changes	No changes
Post-Blowdown Mass and Energy Release Calculation	14.3	Post-Blowdown Mass and Energy Release Calculation	14.3	14-3	An editorial change is made to update the reference to Figure 14-1 (rather than 14.3-1).	The change is editorial in nature. There is no technical impact due to this change.
				14-3	An editorial change is made to describe the performance of two sensitivities in the past-tense.	The change is editorial in nature. There is no technical impact due to this change.
				14-3	[J ^{a,c}
				14-3, 14-5	[

Westinghouse Non-Proprietary Class 3

Revision 1		Revision 5		Page(s)	Detailed Description of Changes	Technical Evaluation of Changes
Title	Chapter/ Section/ Subsection	Title	Chapter/ Section/ Subsection			
] ^{a,c}
				14-7	Editorial corrections to the release rate equation to reflect the appropriate characters (e.g. -, ∂, =, +).	
				14-8	[
Comparison of SATAN/Spreadsheet Releases with WCOBRA-TRAC Calculated Releases	14.4	Comparison of SATAN/Spreadsheet Releases with WCOBRA-TRAC Calculated Releases	14.4	14-11	A clarification is added to explicitly state that the <u>W</u> COBRA/TRAC code uses a best estimate approach to calculating the LOCA M&E releases.	This change represents a clarification to the existing Section 14.4 text to state that the <u>W</u> COBRA/TRAC codes LOCA M&E releases are a “best estimate” for the comparison to the SATAN/spreadsheet method. This does not constitute a technical change, rather is simply a clarification of the existing methodological approach.
				14-11	The M&E release comparison provided is not based on the current or revised <u>W</u> GOTHIC EM, but instead is based on representative information. It is therefore clarified that a “representative comparison” is provided.	This change represents a clarification to the existing Section 14.4 text to state that a representative comparison of the blowdown mass and energy releases are shown in the associated figures in Section 14.4. This is consistent with the comparison described in the existing methodology, and is simply clarified in the updated methodology to be clear that the comparison is not based on the current or revised <u>W</u> GOTHIC EM. This change has no technical impact as is provided for clarity.
				14-11	For completeness, “releases” is added after “mass and energy”.	The change is editorial in nature. There is no technical impact due to this change.
				14-11	Editorial changes are made to update the figure numbers.	The change is editorial in nature. There is no technical impact due to this change.
				14-11 – 14-14	Editorial changes are made to include figure titles.	The change is editorial in nature. There is no technical impact due to this change.
] ^{a,c}
Summary and Conclusions	14.5	Summary and Conclusions	14.5	14-16	A summary table is added, which provides a list of input parameters, major assumptions, and the basis for the inputs/assumptions.	

Westinghouse Non-Proprietary Class 3

Revision 1		Revision 5		Page(s)	Detailed Description of Changes	Technical Evaluation of Changes
Title	Chapter/ Section/ Subsection	Title	Chapter/ Section/ Subsection			
						with respect to UFSAR LOCA Chapter 15 results or represents conservative inputs resulting with respect to the resulting outputs of the analysis.
References	14.6	References	14.6	14-16	No changes	No changes

Westinghouse Non-Proprietary Class 3

WCAP-15846-P, Rev. 5 Showing Tracked Changes from Revisions 1 through 4

1-1

1 INTRODUCTION

1.1 OBJECTIVE

This report describes the methodology that is used to develop a containment evaluation model (EM) to perform the containment design basis accident (DBA) analyses for the Westinghouse advanced passive plants, in particular the AP1000® plant design. The containment EM is used to calculate a conservative containment pressure transient response for the DBA events and to specify conditions for equipment qualification (EQ). The containment DBA events include the response to a double-ended rupture (DER) in the reactor coolant system (RCS), leading to a loss of coolant accident (LOCA), and a double-ended main steam line break (MSLB).

The methodology makes use of the lumped parameter modeling approach. The lumped parameter modeling approach is based on over 30 years of nuclear industry experience. International tests at various scales have identified limitations in this approach that are due primarily to the oversimplification of the momentum formulation. Conservative biases have been applied to various models for the important phenomena in the containment EM to account for these limitations and allow a conservative calculation of the containment pressure response.

The passive containment DBA analysis methodology was originally developed and validated for the AP600 plant design; this information was documented in WCAP-14407 (Reference 1.10). The AP600 containment DBA analysis methodology was reviewed and approved by the Nuclear Regulatory Commission (NRC), as documented in NUREG-1512.

Westinghouse increased the power level of the passive plant design soon after the AP600 design was certified. The original AP1000 containment design was very similar to the AP600, therefore WCAP-14407 was updated to include a description of the AP1000 containment EM and the document was re-numbered as WCAP-15846. Subsequent revisions of WCAP-15846 were issued to incorporate additional information requested by the NRC during the review of the AP1000 containment analyses. The AP1000 containment DBA analysis methodology was reviewed and approved by the NRC, as documented in NUREG-1793 (Reference 1.11).

The AP1000 containment EM has been updated to incorporate a number of plant design changes that have been made since the original version of NUREG-1793 was issued. The software has also been updated to change operating systems, increase array sizes, add optional capabilities, and correct code errors. This latest revision of WCAP-15846 includes a description of the updated AP1000 containment EM.

1.2 REPORT OVERVIEW

Section 2 contains a summary of the containment EM development process. Each step or element in the process is briefly described. Section 3 presents an overview of the Westinghouse-GOTHIC (Generation of Thermal Hydraulic Information for Containment) code package. The WGOTHIC features, development history, and validation programs are briefly described. The models and features that were added by Westinghouse to adapt GOTHIC to model the passive containment cooling system (PCS) are also described.

Deleted: The computer code used for both the AP600 and AP1000 containment pressure design basis accident (DBA) analyses is WGOTHIC. WGOTHIC is used to calculate a conservative containment pressure transient response and to specify temperatures for equipment qualification. The containment DBA analysis makes use of the lumped parameter approach which is based on 30 years of nuclear industry experience. The industry experience has identified lumped parameter limitations and biases that are due primarily to the oversimplification of the momentum formulation. Limitations and biases have been identified based on international tests at different scales (Section 9). Biases and conservatism are applied to models for important phenomena in the WGOTHIC Evaluation Model to develop a bounding methodology, so that containment pressure is conservatively estimated.¶ This report describes specific modeling and defines methods used to develop conservative input for the WGOTHIC code to create a bounding Containment Evaluation Model. Using design parameters specified in the Design Control Document (DCD), the licensing basis Containment Evaluation Model is used to calculate the design basis pressures and temperatures reported in the DCD. (See Section 1.6 for a discussion of updates made for DCD calculations.¶)

Moved (insertion) [2]

Deleted: high and medium ranked phenomena. This section describes the process used to develop the bounding Containment Evaluation Model.

Deleted: , and those phenomena that were determined to be of high or medium rank are presented, with a summary of how those phenomena are addressed by the WGOTHIC Evaluation Model.¶

Deleted: (See Section 1.5 for summary of WGOTHIC code updates for DCD analysis.)

1-2

Section 4 presents the methodology and assumptions that were used to develop the AP600 containment EM. Because the AP6000 containment EM was used for the sensitivity studies in this report, the model input is also provided; this includes free volumes, elevations, heat sink characteristics, and boundary conditions. Graphics are included which aid in visualizing both the AP600 layout and the WGOthic model of the AP600 plant.

Section 5 contains a number of sensitivity cases varying the initial conditions assumed for the design basis analyses. These include sensitivities on initial containment humidity, initial containment pressure, initial containment temperature, outside humidity, outside temperature, and break boundary condition drop size assumptions. Except as noted specifically for a sensitivity study, all sensitivities in this report are based on the AP600 containment EM that is described in Section 4. This section provides the basis for choosing the conservative initial conditions that are assumed in the DBA analyses.

Section 6 describes the effects of meteorological changes on the performance of the PCS. The effects of PCS effluent entrainment into the PCS inlet are evaluated. In addition to recirculation, the effects of wind on PCS performance are identified. The results of these studies show that wind effects are beneficial to containment cooling since they augment the natural draft velocity that develops during PCS operation. The effluent recirculation due to inversions or strong winds is shown to have a negligible effect on PCS performance and containment pressure response.

Section 7 describes the methodology for modeling the PCS water flow rate and water coverage area input for the containment EM. Based on conservatively bounded liquid film test data from various tests, the water coverage area and evaporation rate are conservatively calculated, and only the amount of water which evaporates is applied to the EM. Thus, there is a conservative bound on the amount of evaporative cooling credited in the EM. The implementation of evaporation limited PCS flow in the EM conservatively under-predicts the subcooled liquid film heat removal from containment. The basis for the delay time in the application of the evaporation limited PCS flow and other input parameters are presented. Sensitivities to the water coverage area and other input parameters are presented to demonstrate the conservatism in the method.

Section 8 compares the AP600 blowdown pressurization transient from a multi-volume containment model that includes the PCS heat and mass transfer methodology to a single volume containment model that is based on Standard Review Plan (SRP) methodologies. The single volume model uses a thermal conductor and the Uchida heat transfer correlation to model heat transfer through the containment shell. This comparison shows that there is very little difference in the results between the two models for the blowdown phase of the transient. The results of a heat sink sensitivity case are also presented.

Section 9 addresses circulation and stratification within the AP600 containment. Circulation and stratification can be affected by break location, orientation, and type, in addition to nodding assumptions. The effects of circulation and stratification inside the containment are assessed for an MSLB and the various time phases (i.e., blowdown, refill, peak pressure, and long-term) of a LOCA. The effects of circulation above the operating deck for both the AP600 and AP1000 plant were also examined in Reference 1.9, Section 4.2. Based on these results, biases have been incorporated into the containment EM as described in Sections 4, 9, and 13.

Deleted: geometric input for the WGOthic design basis Evaluation Model of the AP600 using design inputs specified in this report. In this section, the code inputs are described for the AP600 model geometry. The code inputs include

Deleted: The methodology defined in this section is used for the Evaluation Model. (See Section 1.6 and Appendices 4.A and 4.B for input model updates for the DCD analysis.)

Deleted: base case Evaluation Model

Deleted: for

Deleted: In this section t

Deleted: studied

Deleted: supplies

Deleted: calculating

Deleted: applied

Deleted: C

Deleted: valuation

Deleted: odel

Deleted: ing

Deleted:

Deleted: valuation

Deleted: odel

Deleted: valuation

Deleted: odel

Deleted: applied

Deleted: valuation

Deleted: odel

Deleted: also

Deleted: film as well as the coverage areas

Deleted: which

Deleted: used to determine the water coverage

Deleted: presents

Deleted: the sensitivity of

Deleted: . The PCS model that uses climes is compared to a single volume model of the AP600 created

Deleted: WGOthic conductors to model the containment shell instead of the clime model and uses the

Deleted: instead of the Westinghouse-developed ...

Deleted: A sensitivity to

Deleted: s during blowdown is

Deleted: C

Deleted: valuation

Deleted: odel

Deleted: and 9

1-3

Section 10 evaluates the conservatism contained in some of the EM assumptions made for the design basis LOCA and MSLB analyses that are intended to maximize the peak pressure. The conservatism in the heat and mass transfer correlation biases, the initial conditions inside and outside of containment, PCS water temperature, material properties, steel-concrete gap, external annulus loss coefficient, dead-ended compartment modeling biases, and the LOCA mass and energy releases are described in a step-wise fashion. The final result is a reasonable estimate of the conservatism that is included in the AP600 containment EM. The calculated containment peak pressure occurs at the end of the LOCA blowdown phase for the sensitivity case with more realistic assumptions and is approximately 11.5 psi lower than the peak pressure that is calculated with the AP600 containment EM. A similar sensitivity for the net effect of parameters important in the MSLB analysis is also provided.

Section 11 evaluates the sensitivity of the containment EM to changes in the calculated time step size. The time step selection logic was modified to reduce the calculated time step by one-half and by one-quarter in separate cases. The results of these sensitivity cases show that the solution is stable, in that the pressure transients did not change appreciably as the time step size was reduced. This result supports the conclusion that the time step logic used in the WGOthic code is acceptable.

Section 12 evaluates the sensitivity of the predicted containment pressure transient to changes in the PCS noding. The PCS noding structure that is used to represent volumes, elevations, and azimuthal segments in the external annulus, as well as the numerical mesh pattern through conductors are found to be acceptable.

Section 13 presents the methodology and assumptions that are used to develop the AP1000 containment EM. It has been updated to reflect the finalized design and will be used to perform the licensing basis analyses in Section 6.2 of the Standard Safety Analysis Report (SSAR).

Section 14 presents the LOCA mass and energy release data, which is a key input for the containment DBA analysis. Some of the codes and models that are used to calculate the LOCA mass and energy release input data for non-passive plant design containment DBA analysis are not appropriate to be used for the passive plant design. Therefore, Section 14 describes the methodology and assumptions that are used to calculate the LOCA mass and energy release input data for the passive plant containment EM.

1.3 AP600 CONTAINMENT EM DOCUMENTATION

The AP600 containment EM has been developed using a process that is similar to the evaluation model development and assessment process that is described in DG-1096. The draft regulatory guidance describes an acceptable process to develop an evaluation model for the SSAR Chapter 15 accident analyses. It is also considered to also be applicable for the development of a containment EM for the Chapter 6 analyses of the SSAR. Although it was drafted after the development of the AP600 containment EM, it outlines the same principles that were used for the AP600 EM.

As shown in Figure 1-1, this report fits into the framework of licensing documentation which defines the containment DBA methods. A brief summary of the various reports follows.

Deleted: describes

Deleted: valuation

Deleted: odel

Deleted: i

Deleted: In this section, the

Deleted: for

Deleted: quantification

Deleted: contained in the

Deleted: valuation

Deleted: odel in the above parameter. Based on these sensitivities, there is approximately 13 psi of margin in the AP600 design basis analysis second

Deleted: as compared to the nominal case second peak. Since the nominal case maximum pressure occurs during

Deleted: , there

Deleted: of margin in the maximum calculated

Deleted: between

Deleted: design basis case and the nominal case. It should be noted that the nominal case only credits conservatisms that can be readily quantified.

Deleted: describes

Deleted: WGOthic

Deleted: is

Deleted: examines

Deleted: clime

Deleted: Results support the noding

Deleted: geometric input for the WGOthic design basis Evaluation Model of the

Deleted: using design inputs specified in this report. In this section, the code inputs are described for the AP1000 model geometry. The code inputs include free volumes, elevations, heat sink characteristics, and boundary conditions. Graphics are included which aid in visualizing both the AP1000 layout and the WGOthic model of the AP1000. The methodology defined in this section is used for the licensing basis DCD Evaluation Model.

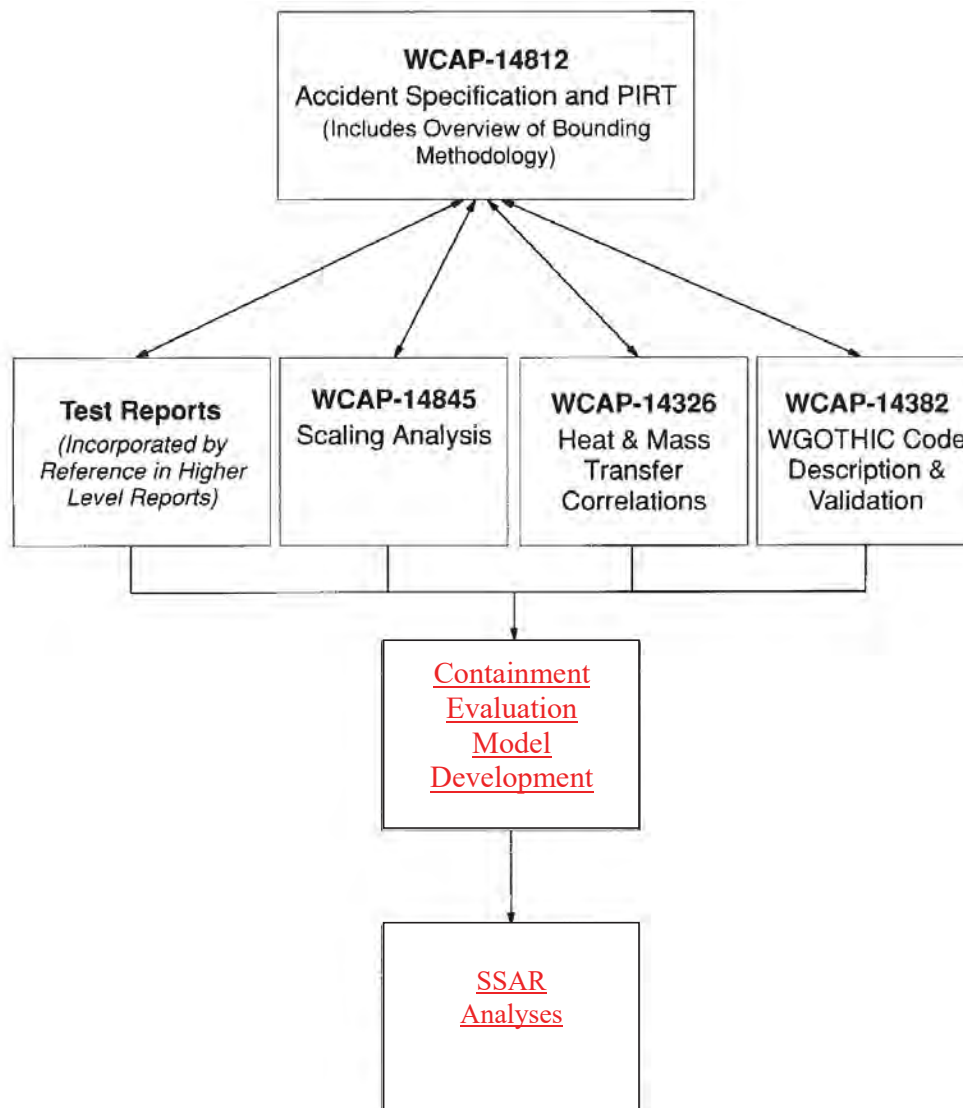
Deleted: The methodology specified in the above sections is used, together with design inputs specified in Section 1.6, to perform the licensing basis calculations in Section 6.2 of the DCD.

Deleted: DBA REPORTS

Deleted: Following is a

Deleted: purposes of the AP600 containment DBA

1-4



Moved (insertion) [3]

Figure 1-1. Relationship of AP600 Containment DBA Reports

1-5

1.3.1 Accident Specification and Phenomena Identification and Ranking Table Report

The containment DBA analyses consider the LOCA and MSLB events. To be able to model the PCS for these events, the EM must be able to model:

- The transport of break mass and energy (steam) to the containment shell.
- The condensation of steam on the inside surface of the containment shell.
- The transport of the condensate film on the inside surface of the containment shell.
- The conduction of heat through the containment shell.
- The transport and heating of the applied liquid film on the outside surface of the containment shell.
- Evaporation from the applied liquid film on the outside surface of the containment shell, and
- The natural draft cooling air flowing through the downcomer, riser and chimney of the shield building.

WCAP-14812 (Reference 1.1) describes the containment and PCS, defines DBA accident scenarios, identifies success criteria, and ranks the importance of phenomena that must be considered when developing the containment EM. A cross-reference to relevant tests and test data reports is also included.

A systematic process has been followed to identify and rank phenomena, including input and review by members of industry, academia, and regulatory authorities. The following information is provided in WCAP-14812 for each phenomenon:

- Phenomena identification ranking table (PIRT) ranking
- Basis for PIRT ranking
 - Test results
 - Scaling results
 - Sensitivity studies
 - Expert review
- How phenomena are implemented in the containment EM
- Justification of containment EM treatment of phenomenon
 - Test experience
 - Modeling guidance
 - Sensitivity studies
- Containment EM treatment of uncertainty

Deleted: ¶

Moved (insertion) [5]

Deleted: Both the AP1000 and AP600 employ a Passive Containment Cooling System (PCS). The ...

Deleted: •

Deleted: •

Deleted: •

Deleted: •

Deleted: •

Deleted: •

Deleted: •

Deleted: passive containment cooling system ...

Deleted: ¶

Moved (insertion) [4]

Deleted: •

Deleted: •

Deleted: •... How phenomena are implemented ...

Deleted: •... Justification of containment ...

Deleted: •... Containment Evaluation ...

Test Reports
(Incorporated by
Reference in High
Level Reports)

Moved up [31]:

1-6

1.3.2 Testing

In the mid-1980s, Westinghouse developed the large scale test (LST) facility to provide steady-state heat and mass transfer data for a geometrically similar model of the AP600 containment vessel. The test vessel was 1/8 geometric scale. The focus was on long-term transient behavior, because that is where the passive containment design, with no credited active heat removal system, differed significantly from the current containment test databases. Because of limitations of scale (power-to-volume and power-to-area ratios, and steam supply), the LST matrix was selected to vary boundary conditions parametrically to obtain data over a range of parameters. Specific passive containment pressure transients were not simulated with the LST.

The LST was designed to provide steady-state heat and mass transfer data in an integral setting, that is, with external evaporation and internal condensation acting simultaneously, for a geometrically similar model of the AP600 containment vessel (Reference 1.5, Section 3.2.4.2). The use of the LST has been supported through the application of scaling methodologies that evolved during the 1990s. The LST data have been used to validate the system scaling equation that is used to support the identification and ranking of phenomena (Reference 1.2, Section 10.2).

Local data from the LST is used to support validation of the condensation correlation applied to the inner steel shell surface (Reference 1.3, Section 3.9) and to examine potential stratification effects in an enclosed volume in an integral setting with external cooling (Section 9). Water coverage and film stability data were used to develop a bounding model to address the effects of film stability (Section 7). External dry heat transfer data have been used to supplement convective heat transfer data (Reference 1.3, Section 3.5).

Local data from the LST have been combined with other separate effects tests (SETs) and integral effects tests (IETs) at different scales to provide supporting data for the following phenomena:

- Dry external riser annulus heat transfer
- External liquid film stability
- Internal condensation mass transfer
- Internal stratification

The LST matrix was developed to contain parametric variations that examined various extremes and combinations of boundary condition effects. In this way, the LST was ranged similarly to a SET.

In addition to the more obvious matrix test parameters, such as steam flow, experience with the international containment test database pointed to the need to examine the effects of boundary condition parameters on distributions of non-condensables inside containment. A brief overview of the parametric variations included in the LST matrix (Reference 1.6, Tables 1.3-1, 1.3-2, and 1.3-3) follows.

- The LST matrix was designed to cover a range of pressure. Air and helium were used as non-condensables, and steam was used as the working fluid. Therefore, the important thermodynamic properties of the containment atmosphere in both the AP600 and AP1000 plant are preserved.

Moved (insertion) [6]

Deleted: <#>USE OF LST AND VALIDATION RESULTS¶

Deleted: as an integral test

Deleted: have

Deleted: ¶
As discussed in subsection 1.2.2, I

Deleted: s

Deleted: •

Deleted: •

Deleted: •

Deleted: •

Deleted: <#>LST Matrix Tests¶

Deleted: The following provides a

Deleted: •

1-7

- Water flow rates, and thus shell coverage, were varied to obtain various degrees of coverage and to examine water film behavior through complete dryout on the sidewall. In addition to quantitative recorded test data, videotapes and engineering notes were taken to characterize the qualitative behavior of the liquid film.
- The matrix was defined to address the effect of external cooling on stratification which has been suggested in international tests (Appendix 9.C). For example, LST 219.1 applied water to the external shell surface starting from dry conditions. To gain further insight, additional parametric variation of external transients were examined in LST 214.1, 215.1, 216.1, 221.1, by suddenly varying water coverage and air flow rates during the course of a test. This is in addition to the test-to-test parametric variations in external conditions.
- Transients initiated by a larger initial steam flow rate, relative to the steady-state tests, were included. The LST did not include "blowdown" mass flow rates scaled to the AP600 or APL000 design due to limitations on steam supply. The LST high initial steam flow transients (LST 220.1, 221.1, 222.1, 222.2) include the influence of an initial rapid pressurization on the subsequent quasi-steady heat and mass transfer rates. The transients also provided code validation of transient performance with reductions in steam flow.
- Tests were included to examine the influence of break elevation and momentum (LST 222.1, 222.2, 222.3, and 222.4) to support evaluation of the various LOCA and MSLB break locations and orientations.
- Tests with initial vacuum (LST 223.1) and initially pressurized to two atmospheres (LST 224.1, 224.2) were included to range the effect of non-condensable gas in the containment.
- Tests were included to provide parameter variations specifically to validate elements of the Evaluation Model. These parameter variations were external loss coefficient (LST 215.1); natural convection (LST 206.1, 211.1, 214.1, 215.1) instead of running the fan at various speeds to replace the external density head; and circumferential variations in inlet blockage (LST 215.1).
- In the containment DBA, there is no appreciable source of hydrogen to containment (Reference 1.1, Section 4.4.2E). As part of the DBA testing program, data were taken to supplement the literature for postulated severe accidents. Helium was introduced into the LST primarily to study the effects of additional non-condensable gases. Helium was shown to be a good simulant of hydrogen in the German Heissdampfreaktor (HDR) tests. Sampling of the non-condensable gas concentration (LST 212.1, 217.1, 218.1, 219.1, 220.1, 221.1, 222.1, 222.2, 222.3, 222.4, 223.1, 224.1, and 224.2) was included at four elevations, including the helium content measurement where applicable.

Deleted: •

Deleted: •

Deleted: •

Deleted: "blowdown" steam flow rate,

Deleted: blowdown

Deleted: •

Deleted:

Deleted:

Deleted:

Deleted:

Deleted: •

Deleted: content

Deleted: •

Deleted: versus

Deleted: used

Deleted: •

Deleted: s

Deleted: tent

1.3.3 Scaling Report

WCAP-14845 (Reference 1.2) describes how scaling has been used to derive the appropriate non-dimensional parameters and their ranges to examine phenomena for bottom-up model validation for the AP600 design. SETs are identified and the test parameter ranges compared to AP600 ranges to show sufficiency of the test database for application to containment DBAs. Scaling has been used to assess the use of the LST to supplement the smaller scale separate effects data (Reference 1.2, Sections 10.1 and 11.3). Scaling is also used to identify distortions in the LST facility. These distortions must then be addressed in the bounding methodology.

The scaling analysis in WCAP-14845 (Reference 1.2) satisfies the three stated objectives for AP600 containment pressure scaling. The conclusions of the scaling analysis are:

1. Support Development of Bounding Methodology (PIRT Confirmation)

The scaling analysis confirmed the identification in the PIRT (Reference 1.1, Table 4-1) of high ranked phenomena. The high ranked phenomena inside containment are the break source, gas compliance (storage of mass and energy in the gas volume of the containment atmosphere), and condensation on the shell and heat sinks. The high ranked phenomena outside containment are evaporation of the external liquid film and the PCS natural circulation flow rate. In addition, the scaling analysis confirmed the PIRT ranking of lower order phenomena including convection and radiation heat transfer, liquid film conductance, and liquid film energy transport.

The high ranked phenomena and the parameters that most strongly affect them are the ones that must be bounded in the evaluation model. Phenomena and how they are bounded in the evaluation model are described in Section 4.4 of Reference 1.1.

The net effect of these is an evaluation model that bounds all the dominant processes so as to produce the maximum pressure response.

2. Specify Individual Model Constitutive Relations.

The range of AP600 dimensionless groups for each of the separate effects test database has been shown to be adequately covered.

Appropriate constitutive relations and models were identified for each of the dominant phenomena and parameters in 1 above:

Condensation and evaporation are modeled using conventional free and forced convection mass transfer relationships, characterized by Reynolds, Grashof, and Schmidt numbers. The range of these dimensionless variables necessary to cover AP600 operation was defined and separate effects tests were identified and used to validate the selected mass transfer correlations. The range of dimensionless variables in the data were shown to encompass the expected range of operation in AP600.

Deleted: Use of LST Separate Effects Data

Deleted: Separate effects test data from the LST is used to support validation of the condensation correlation applied to the inner steel shell surface (Reference 1.3, Section 3.9) and to examine potential stratification effects in an enclosed volume in an integral setting with external cooling (Section 9). Water coverage and film stability data were used to develop a bounding model to address the effects of film stability (Section 7). External dry heat transfer data have been used to supplement convective heat transfer data (Reference 1.3, Section 3.5).

Moved up [4]: As a convenient vehicle for Model approach, the following information is provided in WCAP-14812 for each phenomenon:¶

- Phenomena identification ranking table (PIRT) ranking¶

- Basis for PIRT ranking¶
 - <#>Test results¶
 - <#>Scaling results¶
 - <#>Sensitivity studies¶
 - <#>Expert review¶

- How phenomena are implemented in the Evaluation Model¶
- Justification of Evaluation Model treatment of phenomenon¶

- <#>Test experience¶
- <#>Modeling guidance¶
- <#>Sensitivity studies¶

- Evaluation Model treatment of uncertainty¶
- <#>Scaling Report¶

The application of scaling to a specific methodology is related to the type of analysis being performed and the regulatory needs to be satisfied. The regulations require supporting documentation for the use and sufficiency of the database to develop bounding models for the full-scale AP600 containment pressure transient. The objectives for the scaling of the AP600 pressure transient and the approximately 1/8 geometric scale test vessel, called the Large-Scale Test (LST), are derived from regulations and regulatory guides. WCAP-14845 (Reference 1.2) describes how scaling has been used to derive the appropriate non-dimensional parameters and their AP600 ranges to examine phenomena for bottom-up model validation. Separate Effects Tests (SETs) are identified and the test parameter ranges compared to AP600 ranges to show sufficiency of the test database for application to containment DBAs. ...

Deleted: <#>LST Confirmation of Phenomena¶

The LST data have been used to validate the system scaling equation used to support the identification and ranking of phenomena (Reference 1.2, Section 10.2).¶

As a convenient vehicle for defining the Evaluation Model approach, the following information is provided in WCAP-14812 for each phenomenon:¶

- Phenomena identification ranking table (PIRT) ranking¶

- Basis for PIRT ranking¶
 - <#>Test results¶
 - <#>Scaling results¶
 - <#>Sensitivity studies¶
 - <#>Expert review¶

1-9

3. Investigate Use of LST to Validate Elements of the Bounding Evaluation Model

Steady state heat and mass transfer correlations have been shown to be applicable for the AP600 double-ended cold-leg guillotine (DECLG) LOCA and MSLB DBA pressure transients. The LST was used as a source of separate effects data to validate condensation and evaporation mass transfer, film stability, and circulation and stratification models as discussed under 1 and 2 above. Component level distortions in the LST were addressed by using local measurements of temperature, concentration, and velocity from the LST, and by supplementing the LST data with data from other sources when the range of LST parameters was insufficient to cover AP600 operation.

The scaling analysis shows the three dominant system level phenomena for the transient phase are the break source energy addition, the gas volume, and the heat sink surface area dependent condensation energy removal rate. The scaling analysis shows that the LST system level phenomena are distorted in the transient phase relative to AP600, but are well-scaled in the quasi-steady phase.

The LST is therefore not used as a system level representation of AP600 transient pressure response. However, the steady-state LST data is acceptable for use as separate effects data for the following models:

- Internal condensation
- Internal above-deck steam distribution
- External dry heat transfer
- External water coverage (film stability)

1.3.4 Heat and Mass Transfer Correlations Report

WCAP-14326 (Reference 1.3) documents the analytical and experimental bases for heat and mass transfer correlations associated with:

- Condensation mass transfer
- Evaporation mass transfer
- Convective heat transfer
- Liquid film thermal resistance

For modeling convenience, an explicit representation of the liquid film thermal resistance is modeled, with condensation or evaporation occurring at the film surface. This is in contrast to the more traditional approach of combining mass transfer and liquid film resistance and then using the solid surface temperature. The explicit representation allows clearer treatment of elements of uncertainty in mass transfer and liquid film over the AP600 range of conditions.

Deleted: loss-of-coolant accident (

Deleted:)

Deleted: main steam line break (

Deleted:)

Deleted: ¶
The use of the LST in support of code validation is summarized in Section 1.4.¶

Deleted: •

Deleted: •

Deleted: •

Deleted: •

1-10

1.3.5 WGOTHIC Code Description and Validation

WCAP-14382 (Reference 1.4) documents the implementation of the “climes” subroutines in the GOTHIC code. Climes are used to represent heat and mass transfer on the containment shell, shield building, and baffle. The report shows validation comparisons to the LST using both lumped parameter and distributed parameter models, identifies lumped parameter biases and competing effects based on the LST calculations, and describes the derivation of nodding guidance for the AP600 containment EM.

Verification and validation of the code changes has been completed for each code version update.

WGOTHIC verification and validation has been completed using calculations of separate effects tests (Reference 1.4, Section 4 and Reference 1.3, Sections 3.1 and 3.3). An assessment of the effects of a WGOTHIC Solver Upgrade from 1.2 (used in Reference 1.4) to 4.1 has shown that code validation conclusions remain valid (Reference 1.7).

Deleted: valuation

Deleted: odl

Deleted: WGOTHIC v

1.3.6 Evaluation Model Development

The containment DBA analysis approach is based on the lumped parameter formulation. The lumped parameter containment EM does not resolve internal velocity and concentration fields due to its simplified momentum model and large lumped volumes.

Analyses of the LST have been completed using the WGOTHIC lumped parameter momentum formulation. In the LST calculations, nominal properties and nominal test boundary and initial conditions are used to isolate the biases inherent in the computer code, independent of conservatism included in the EM. This allows the examination of the known lumped parameter biases, and quantification of the effects of compensating errors in lumped parameter results. The method to address the lumped parameter biases, as well as the method that is used to address phenomena for the containment EM are documented (Reference 1.1, Section 4.4).

Comparisons between preliminary versions of the containment EM and the system level LST response show that pressure is reasonably well predicted, with a modest conservative margin. Examination of LST WGOTHIC lumped parameter results identified the existence of competing internal effects in which the excessive velocities predicted by the lumped parameter model over-predict the velocity component of mass transfer, while over-mixing under-predicts the steam concentration component of mass transfer. Consequently, these competing effects in predictions must be addressed in the containment EM. The effect of over-predicted velocities was resolved by using only free convection for internal heat and mass transfer, thereby eliminating velocity from the condensation correlation. The over-mixing issue was resolved by examining and biasing the effects of circulation and stratification in the containment EM, as discussed in Section 9.

Deleted: SSAR

1-11

The sensitivity calculations in this report were performed with WGOthic Solver version 4.1 and plant geometry described in Section 4. An evaluation of the effects of WGOthic Solver version 4.2 and AP600 input modifications that changed the credited heat sinks was performed to show that the changes to internal containment parameters do not affect the case-to-case sensitivities that were used to select the limiting extremes for internal initial and boundary conditions. Since the internal heat sinks reach their maximum thermal effectiveness well before the DECLG LOCA peak pressure is reached, the changes do not significantly impact the sensitivities that were used to select limiting scenarios for circulation and stratification. The small change to internal pressure, and thus the related small change to internal temperature boundary condition for the containment shell, does not affect the sensitivities for clime vertical nodding and conductor mesh. Similarly, the changes do not affect external condition case-to-case results. The changes also do not invalidate the time step study. Therefore, the sensitivities performed in this report, remain valid for the updated AP600 containment EM.

1.4 AP1000 CONTAINMENT EM DOCUMENTATION UPDATES

Both the AP1000 and AP600 plant designs employ a passive containment cooling system. The AP1000 containment structure is taller, but maintains the same diameter and internal layout as the AP600. A detailed comparison of the AP600 and AP1000 plant designs is provided in WCAP-15612 (Reference 1.8).

The code capability requirements (see Section 1.3.1) for the AP1000 containment EM are the same as AP600. Westinghouse developed special subroutines to mechanistically calculate the heat and mass transfer and to track the liquid films for the PCS. These subroutines were appended to the GOTHIC version 4.0 code to create WGOthic version 4.2.

To determine the applicability of using the WGOthic code (version 4.2) and the AP600 containment EM methodology for performing the AP1000 containment DBA analyses, Westinghouse:

- Reviewed the AP600 containment PIRT (WCAP-14812) for application to the AP1000 plant design.
- Reviewed the AP600 containment scaling analysis (WCAP-14845) for application to the AP1000 plant design, and
- Compared the test data ranges of the important dimensionless parameters for heat and mass transfer and water coverage with the operating range for the AP1000 plant.

The AP600 containment PIRT was reviewed to determine if there were any new phenomena or any change in the importance ranking of the existing phenomena with respect to the AP1000 containment and RCS design changes. This review was documented in WCAP-15613 (Reference 1.9, Section 2.6). No new phenomena were identified and there were no significant changes in the ranking of phenomena as a result of the AP1000 design changes.

An LST scaling assessment was performed for the AP1000 plant design and compared with AP600 (Reference 1.9, Section 4.2). Due to its relatively low and constant steam injection flow rate, the LST was not well scaled to model the blowdown transient for either AP600 or AP1000 plant designs. The

Deleted: The methodology in the WGOthic Application Report is used, along with design input specified in Section 1.6, to perform the licensing basis DBA containment calculations reported in the AP600 SSAR, Chapter 6.2.¶

Deleted: 600

Deleted: DBA REPORTS

Moved up [5]: Both the AP1000 and AP600 employ a Passive Containment Cooling System (PCS). The AP1000 containment structure is taller, but maintains the same diameter and internal layout as the AP600. A detailed comparison of the AP600 and AP1000 plant designs is provided in WCAP-15612 (Reference 1.8).¶
The capability requirements for the AP1000 Containment Evaluation Model are the same as AP600. To be able to model the PCS, the Evaluation Model must be able to model:¶
• The transport of break mass and energy (steam) to the containment shell¶
• The condensation of steam on the inside surface of the containment shell¶
• The transport of the condensate film on the inside surface of the containment shell¶
• The conduction of heat through the containment shell¶
• The transport and heating of the applied liquid film on the outside surface of the containment shell¶
• Evaporation from the applied liquid film on the outside surface of the containment shell and¶
• The natural draft cooling air flowing through the downcomer, riser and chimney of the shield building.

Deleted: .¶

Deleted: Containment

Deleted: valuation

Deleted: odel

Deleted: •

Deleted: •

Deleted: •

Deleted: reactor coolant system (

Deleted:)

1-12

steady-state LST data were determined to be acceptable for use as a source of separate effects test data for internal condensation, above-deck steam distribution, external heat transfer, and external water coverage.

The ranges of the dimensionless parameters for the heat and mass transfer correlations were examined to determine if the existing test data covered the **AP1000** operating range (Reference 1.9, Section 4.2). The test data covered the upper range of the **AP1000** dimensionless parameters for the heat and mass transfer correlations in the important riser region of the annulus. Therefore, the correlations were also considered to be valid for the **AP1000** containment EM.

Experimental test data and correlations were reviewed to determine if the increase in containment height would affect the circulation within the open volume above the operating deck. Both the correlations and test data suggest that increasing the containment height would increase the turbulence and improve the mixing (see Section 9.C).

An alternate analysis methodology was used to independently assess the degree of mixing in the open volume above the operating deck. Detailed, 2-dimensional slice Computational Fluid Dynamics (CFD) models representing this region were constructed for both the AP600 and the **AP1000 plants** (Reference 1.9, Section 4.2). The flow and velocity patterns for the AP600 and **AP1000 plants** were very similar. Both models predicted cold falling plumes near the walls and a hot rising plume near the center of the volume. Except for the small layers very close to the walls and within the central plume, the temperature profile within the volume was nearly uniform. Therefore, based on the experimental test data, correlations, and results from the alternate analysis approach, the well-mixed assumption for this region was also considered to be valid for the **AP1000 containment EM**.

The operating ranges of the liquid film coverage parameters for AP600 and **AP1000 plant designs** were compared to the composite PCS test data. The test data covered the operating range of the important film coverage parameters (minimum film Reynolds number and maximum heat flux) for both AP600 and **AP1000 plants**. Therefore, the constant coverage area input values and the model for calculating the evaporation-limited PCS water flow rate input that was used for AP600 are also applicable to the **AP1000 plant**.

In summary, both the AP600 and **AP1000 plant designs** employ the same passive containment cooling system design features so the events and phenomena to be analyzed in the **AP1000 containment EM** are the same as the AP600. The range of important dimensionless parameters from the PCS test data covers the operating range of both the AP600 and **AP1000 plants**, so the **WGOTHIC** heat and mass transfer correlations remain acceptable. Since the containment designs are similar and since the heat and mass transfer correlations remain acceptable, **WGOTHIC** source code changes were not needed for the **AP1000 containment EM**. Therefore, a containment **EM** that uses the same bounding methodology that was accepted by the NRC for the AP600 was also accepted for the **AP1000 plant (Reference 1.11)**.

Deleted: valuation

Deleted: odel

Deleted: n

Deleted: C

Deleted: valuation

Deleted: odel

Deleted: C

Deleted: valuation

Deleted: odel

Deleted: a

Deleted: required

Deleted: C

Deleted: valuation

Deleted: odel

Deleted: evaluation model

Deleted: should

Deleted: be

Deleted: able

1-13

1.5 INTERFACE WITH PLANT LICENSING CALCULATIONS

The licensing basis containment DBA pressure analysis reported in Section 6.2 of the SSAR is performed with the containment EM, defined by the methodology described herein. The following design inputs are required as input to the containment EM:

- Conservatively calculated mass and energy releases as a function of time, using approved methodology (SSAR 6.2.1.3.2 for LOCA and Section 6.2.1.4 for MSLB).
- Appropriate Technical Specification and Site Interface Parameters for initial and boundary conditions (SSAR 16.1, Section 3.6 and 2.3).
- PCS delivered flow as a function of time assuming at least one Passive Containment Cooling Water Storage Tank (PCCWST) drain valve fails to open.
- The surface area and effective thickness of metal and concrete structures that are credited as heat sinks.
- The thermal conductivity and heat capacity of the heat sink materials and the coatings, and
- The containment free volume.

Any deviations from the AP1000 standard passive plant design will be addressed by changing the associated input values that are calculated with the methodology defined by the containment EM, as documented herein. The results of the containment EM are used for containment design pressure evaluation and equipment qualification condition specifications, as reported in Chapter 6 and Appendix 3D of the SSAR. The calculated peak containment pressure from the containment EM has sufficient margin to bound uncertainty in important parameters. The calculated pressure and temperature response from the containment EM can be used to determine the envelope for equipment qualification.

1.6 CONCLUSIONS

This report defines a methodology which calculates a conservative peak containment pressure as well as pressure and temperature envelopes that are appropriate for the equipment qualification of the passive containment design. The containment EM methodology is cross referenced to PIRT phenomena in Reference 1.1, Section 4.4. The licensing basis DBA calculation is presented in Section 6.2 of the SSAR.

1.7 REFERENCES

- 1.1 WCAP-14812, Rev. 2, "Accident Specification and Phenomena Evaluation for AP600 Passive Containment Cooling System," April 1998.
- 1.2 WCAP-14845, Rev. 3, "Scaling Analysis for AP600 Containment Pressure During Design Basis Accidents," March 1998.

Deleted: <#>APPLICATIONS REPORT CONTENT SUMMARY¶
<#>The Introduction outlines the containment DBA analysis approach, summarizes the use of the LST, and shows how the Evaluation Model methods are incorporated in the containment DBA analysis reported in SSAR 6.2 for long-term loss-of-coolant accidents (LOCA) and main steamline breaks (MSLB). Subsequent sections document elements of the methodology, as follows.¶

Moved up [2]: Section 2 contains a summary of

Moved up [6]: USE OF LST AND

Deleted: DCD

Deleted: DCD

Deleted: WGOETHIC

Deleted: valuation

Deleted: odel

Deleted: valuation

Deleted: odel methodology

Deleted: •

Moved (insertion) [7]

Deleted: ••

Deleted: DCD

Deleted: DCD

Deleted: .

Deleted: •

Deleted: DCD

Deleted: .

Deleted: failure of

Deleted: .

Moved up [7]: •• Conservatively calculated

Deleted: valuation

Deleted: odel

Deleted: DCD

Deleted: Evaluation Model methodology consid

Deleted: of the break room node is the maximum

Deleted: envelopes to bound the effects of

Deleted: <#>Upgrade of WGOETHIC Versi

Deleted: yields

Deleted: calculation

Deleted: . Evaluation Model

Deleted: DCD

Deleted: Rev. 2,

Deleted: Revision

1-14

1.3 WCAP-14326, [Rev. 3](#), “Experimental Basis for the AP600 Containment Vessel Heat and Mass Transfer Correlations,” April 1998.

Deleted: 2

Deleted: Rev. 2,

1.4 WCAP-14382, “WGOTHIC Code Description and Validation,” May 1995.

1.5 WCAP-14141, [Rev. 1](#), “AP600 Test and Analysis Plan for Design Certification,” April 1995.

Deleted: Rev. 1,

1.6 WCAP-14135, [Rev. 1](#), “Final Data Report for PCS Large-Scale Tests, Phase 2 and Phase 3,” April 1997.

Deleted: Rev. 1,

1.7 WCAP-14967, “Assessment of Effects of WGOTHIC Solver Upgrade from Version 1.2 to 4.1,” September 1997.

1.8 WCAP-15612, “**AP1000** Plant Description and Analysis Report,” December 2000.

Deleted: M. Corletti et al.,

1.9 WCAP-15613, “**AP1000** PIRT and Scaling Assessment,” February 2001.

[1.10 WCAP-14407, Rev. 2, “WGOTHIC Application to AP600,” April 1998.](#)

[1.11 NUREG-1793, Final Safety Evaluation Report Related to Certification of the AP1000 Standard Design,” September 2011.](#)

2 TEST AND ANALYSIS PROCESS OVERVIEW AND HIGH AND MEDIUM RANK CONTAINMENT PHENOMENA

2.1 INTRODUCTION

The Evaluation Model for the passive containment cooling system (PCS) design basis accident (DBA) has been developed using elements of scaling (top-down and bottom-up modeling of the integrated components), testing, and analysis (bottom-up phenomenological models and evaluations), similar to the methodology for Code Scaling Applicability and Uncertainty (Reference 2.1). Results have been used to identify bounding models and input values for use in the DBA Evaluation Model. The results of the DBA analyses provide conservative predictions of design basis transient pressure and temperature response for the containment.

The development of the PCS DBA methodology has followed an approach which can be organized into the four elements shown in Figure 2-1. The elements include tasks, that together provide a structured, traceable, and practical method for

- Specifying the scenario
- Identifying phenomena important to the transient
- Evaluating data and scale effects
- Documenting and validating the computer code
- Assessing margins and uncertainties
- Developing and applying the Evaluation Model

The process is represented by a once-through flow diagram for simplicity. The actual process included many iterations between the various tasks. For example, to better represent the observations of the large-scale containment test (LST) dome temperature distribution, due to the subcooling of the film applied to the LST, the initial WGOTHIC code version used in 1992 was augmented by the addition of a model for convective heat transport for the liquid film. In addition, extensive review by representatives of regulatory agencies, industry, and academia were incorporated into the process (Reference 2.2). The end result is documentation which describes the PCS DBA Evaluation Model and its bases in an auditable, traceable manner. Following is a brief description of the four elements of the process used to develop the methodology.

2-2

PCS Test and Analysis Process Overview

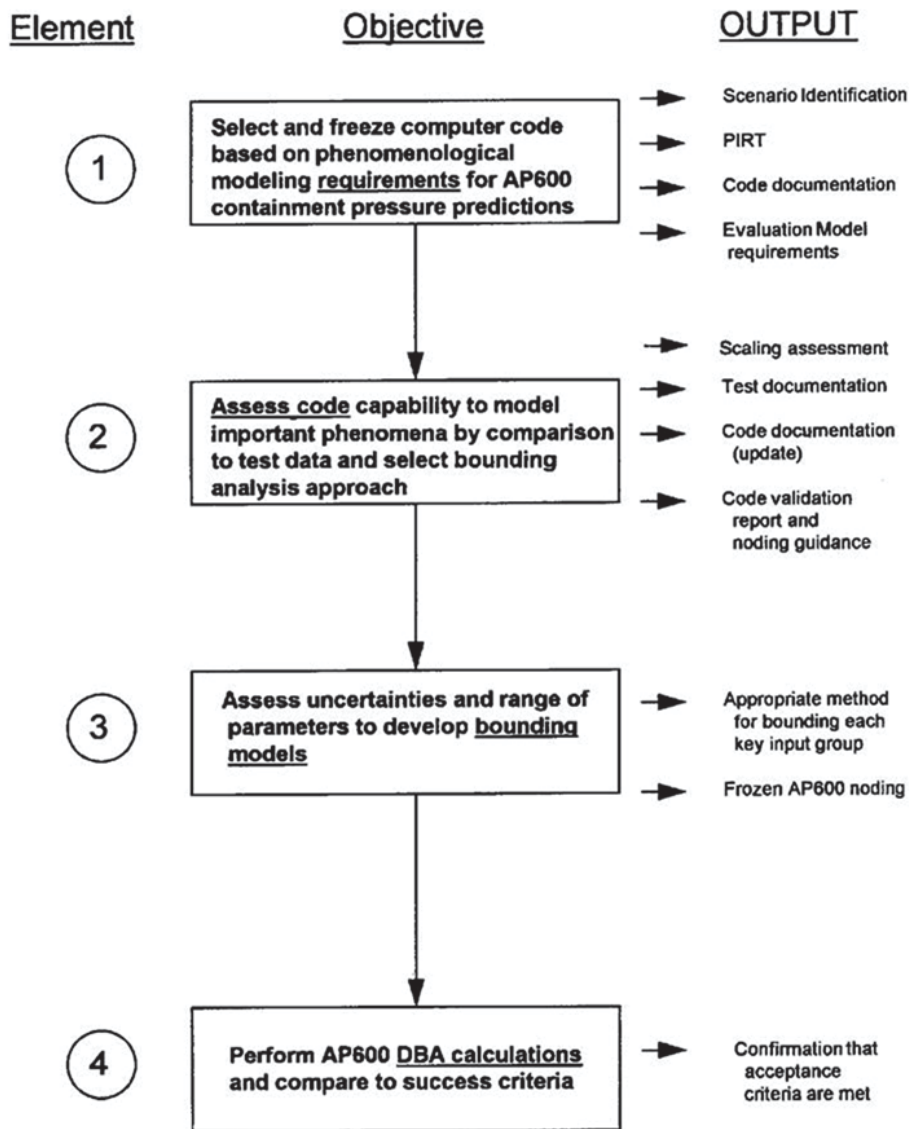


Figure 2-1. PCS Test and Analysis Process Overview

2.2 ELEMENT 1 – PCS REQUIREMENTS AND CODE CAPABILITIES

The PCS DBA methodology development process began with a review of the AP600 design and DBA scenarios and an identification of phenomena important for AP600 containment pressurization. From this review, an initial test program was defined and a computer code was selected.

A PIRT was developed to identify the key thermal-hydraulic phenomena which govern the transients of interest. The PIRT (Reference 2.2, Section 4) ranks phenomena according to their relative importance to the particular transient phase of interest. The PIRT process included input and review by representatives of academia and regulatory authorities, and cross-functional Westinghouse technical reviews. The bases for high, medium, and low rankings are documented in the PIRT. A key result of the PIRT is that the dominant phenomenon for transferring heat from the containment is mass transfer – condensation on the inside and evaporation on the outside. The mass and energy release boundary condition imposed on the problem is the primary driver of the containment pressure response, and is ranked high. For the loss-of-coolant accident (LOCA) scenario, pressurization is mitigated primarily by internal volume compliance during blowdown, and by internal heat sinks below deck, from blowdown through the transition period when the PCS cooling begins to dominate and turns the pressure around. PCS heat removal dominates the long-term LOCA response. The main steamline break (MSLB) transient is mitigated primarily by volume compliance and internal heat sinks. A summary of the high and medium ranked phenomena is shown in Table 2-1. As described in Reference 2.10, Section 2.6, the **AP1000** design changes do not affect the PIRT or the results of the AP600 PIRT confirmation that are documented in Reference 2.9.

In parallel with bottom-up phenomena evaluations, the WGOTHIC computer code was selected, upgraded, and frozen to allow explicit modeling of many of the phenomena identified in the initial review. As the scaling analysis and testing programs progressed, code upgrades were completed to better model experimental results according to guidelines consistent with computer code lifecycle management. Hand calculations and spreadsheets were used to verify correct programming of the upgrades as documented within the Westinghouse QA program. Documentation of the code used in the Evaluation Model consists of base GOTHIC 4.0 documentation (Refs. 2.3, 2.4, 2.5) and upgrades to create WGOTHIC 4.2 (Section 3).

2.3 ELEMENT 2 – ASSESS CODE VERSUS TESTS AND IMPORTANT PROCESSES

Analyses and computer code validations were used identify the most appropriate models and biases to use in the PCS DBA Evaluation Model. The PCS test results were documented, including separate effects (Reference 2.6) and integral effects (Reference 2.7). The PCS test data and other data from the literature were used to provide input to code validation (Reference 2.8). Validation was used to study how the oversimplification inherent in the lumped parameter WGOTHIC model applies to the AP600. The lumped parameter limitations lead to the potential for compensating errors, so that a methodology to bound the effects of compensating errors was identified (Reference 2.8, page 8-9). The effect of lumped parameter momentum formulation and noding on WGOTHIC results was an important output of validation. Insight from validation was used to develop a bounding Evaluation Model in Element 3.

2-4

A scaling evaluation of AP600 was performed (Reference 2.9) which provided additional confirmation of the PIRT phenomena and ranking. Scaling identified the appropriate non-dimensional parameters, the effects of facility scales, and the ranges of parameters expected in AP600. Scaling was also used to identify distortions in the LST facility and to evaluate the effect of distortions on the use of the LST for studying lumped parameter code biases.

The results of scaling, testing, and code validation were used to establish a bounding analysis approach for each of the PIRT phenomena, documented in Reference 2.2, Section 4.4.

Table 2-1. Phenomena Identification and Ranking Table – Summary of High and Medium Ranked Phenomena

Phenomenon*		Effect on Containment	Pi Groups	Where Addressed
Break Source Mass and Energy (1A)		The mass and energy source for containment pressurization.	$\pi_{p,g,brk,enth}$ $\pi_{p,g,brk,work}$ $\pi_{p,work,d}$ $\pi_{p,work,p}$	Scaling Analysis
Gas Compliance (2C)		Stores mass and energy in atmosphere, increasing pressure.	$\pi_{p,\tau}$	Scaling Analysis
Initial Conditions Inside (4A, 4B, 4C)		Temperature, humidity, pressure affect non-condensables and energy storage.	parameter	Initial Conditions Section 5
Containment Solid Heat Sinks (3), Pool (5), Drops (1), and Shell (7)		Store energy (and remove mass from atmosphere) reducing pressure.	$\pi_{p,g,j}$ $\pi_{p,work,j}$	Scaling Analysis
	Internal Heat Sink Conduction (3D, 5E, 7F) and Heat Capacity (3E, 5A, 7G)	Limits conduction heat transfer into heat sinks, shell, or pool, and through shell. Stratification in the break pool can affect the effective heat capacity of the pool.	parameter	Scaling Analysis
	Heat Transfer Through Horizontal Liquid Films (3C)	Water on and non-condensable gases near upward facing horizontal surfaces limit heat and mass transfer to horizontal heat sinks.	parameter	Scaling Analysis

2-5

Table 2-1. Phenomena Identification and Ranking Table – Summary of High and Medium Ranked Phenomena (cont.)

Phenomenon*		Effect on Containment	Pi Groups	Where Addressed
Condensation Mass Transfer (3F, 5B, 7C)		The first-order transport process that removes mass and energy from the containment gas.	$\pi_{p,work,j}$	Scaling Analysis
	Break Source Direction and Elevation (1B), Momentum (1C), and Density (1D)	Direction, elevation, density, and momentum can dominate circulation and affect condensation rate.	parameter	Circulation and Stratification, Section 9
	Circulation and Stratification (2A)	Intercompartment Flow (Circulation) and stratification can affect the distribution of steam (and non-condensables) near heat sinks for condensation heat removal.	parameters	
	Intercompartment Flow (2B)			
	Source Fog (2D)		parameter	
Evaporation Mass Transfer (7N)		First-order transport process that removes mass and energy from the evaporating external shell.	$\pi_{e,fg,esx}$ $\pi_{p,g,brk,work}$ $\pi_{p,work,d}$ $\pi_{p,work,p}$	Scaling Analysis
	PCS Natural Circulation (9A, 13A)	Convective air flow provides convective heat and mass transfer from containment shell.	parameter	Scaling Analysis
	Liquid Film Flow Rate (8A), Water Temperature (8B), Film Stability (8C)	Affects the upper limit for water coverage on the external shell and amount of water available for evaporation.	parameter	Film Stability, Section 7
Liquid Film Energy Transport (7E, 7M)		<i>Inside:</i> Carries condensation energy to the IRWST and break pool. <i>Outside:</i> Absorbs energy rejected by the external shell surface.	$\pi_{e,f,if}$ See Note 1	Scaling Analysis
Convection Heat Transfer (3G, 7H, 10A, 10B)		A second order transport process that removes energy from the containment gas, and from the external shell.	$\pi_{p,q,j}$ $\pi_{e,q,esx} + \pi_{e,q,dsx}$ Note 2	Scaling Analysis

Deleted: note

Table 2-1. Phenomena Identification and Ranking Table – Summary of High and Medium Ranked Phenomena (cont.)

Phenomenon*	Effect on Containment	Pi Groups	Where Addressed
Radiation Heat Transfer (3H, 7I)	A second order transport process that removes energy from the containment gas and from the external shell.	$\pi_{p,q,j}$ $\pi_{e,q,esx} + \pi_{e,q,dxx}$ Note 2	Scaling Analysis
Baffle Conduction (10D) and Baffle Leakage Paths (10G)	Conduction through the baffle into downcomer volume and leakage paths can influence the external natural circulation flow rates.	$\pi_{e,q,bf}$, $\pi_{e,q,bfx}$ None for leakage	PIRT Sections 4.4.10D and 4.4.10G

* Indicators in parentheses refer to phenomena in the “Phenomena Identification and Ranking According to Effect on Containment Pressure” (Reference 2.2, Table 4-1).

Notes:

- The fraction of the internal condensation carried away by the liquid film is defined by the ratio: $\pi_{e,f,j}/(\pi_{e,f,j} + \pi_{e,f,g,j})$, for each heat sink j. The fraction of the external shell heat rejection that goes into the subcooled heat capacity of the external liquid is defined by the ratio: $\pi_{e,q,ssx}/(\pi_{e,q,ssx} + \pi_{e,q,esx} + \pi_{e,q,fg,esx} + \pi_{e,q,dxx})$. The pi group values for AP600 are presented in Reference 2.9, Section 8.
- Inside containment $\pi_{p,q,j}$ represents the pressure effect of sensible heat transfer. The sensible heat transfer is approximately 1/2 radiation heat transfer and 1/2 convection heat transfer. Outside containment $\pi_{e,q,esx} + \pi_{e,q,dxx}$ represents the sum of the dry and evaporating shell sensible heat transfer, that is approximately 1/2 radiation heat transfer and 1/2 convection heat transfer.

2.4 ELEMENT 3 – ASSESS UNCERTAINTIES AND DEVELOP BOUNDING MODELS

Uncertainties were assessed, and together with the results of code validation, were used to develop a method of applying the WGOTHIC lumped parameter formulation to create a bounding DBA Evaluation Model. Key results are summarized as follows.

It is worthwhile noting how representative high-ranked phenomena are addressed for the AP600 PCS in the context of understanding this overview. In this regard, some background on lumped parameter containment codes follows, and then a summary is given of how uncertainties are handled for two representative phenomena, the heat and mass transfer rate correlations, and circulation and stratification.

The application of WGOTHIC lumped parameter formulation for the PCS Evaluation Model has been justified by conservatively addressing lumped parameter biases (Appendix 9C, Section 9.C.3.4). Lumped parameter containment codes have been used for nuclear power plant licensing calculations for over 30 years. Limitations of the lumped parameter approach for containment modeling are documented in the literature. Generally, lumped parameter codes can reasonably predict global parameters, such as pressure, but the lumped parameter formulation oversimplifies physics when local details are important. For containment analysis, details within a volume are important when the physics of stratification within a volume or entrainment into jets or plumes is important. Coupling of the WGOTHIC lumped parameter nodes, with one or more distributed parameter volumes to gain some resolution of the details within a

volume, can increase the accuracy of the solution. However, while distributed parameter calculations were used to help understand test results, the use of such more detailed models was not practical for PCS DBA calculations due to computing requirements.

Complex thermal hydraulic models may produce results that match or bound test data but may also include compensating errors. Sufficient data were obtained on the important variables in the LST to isolate compensating errors in the lumped parameter model. Studies of LST calculations have shown that the compensating errors in lumped parameter calculations arise from offsetting effects of steam concentration and velocity. Because the jet source is numerically expanded to uniformly fill the volume flow area in a lumped parameter node, numerical entrainment leads to high predicted velocities in the above-deck region and a resultant homogenization of the containment. Mixing of non-condensables from the below-deck region in the LST penalizes PCS heat transfer because the non-condensables from below-deck penalize condensation rates. Overpredicting velocities benefits PCS heat transfer because of forced convection enhancement. In the Evaluation Model, the competing effects are addressed by using only free convection inside containment, thereby eliminating the influence of velocity overprediction. This results in a bounding prediction relative to the potential for compensating errors.

After developing an understanding of lumped parameter model performance, bounding approaches to address important phenomena, summarized in Table 2-1, were developed. Uncertainties are addressed by quantifying a bias and distribution for a phenomenon or by studying the range of expected containment conditions and establishing an upper bound approach. Examples of the two approaches follow, using mass transfer correlation and circulation and stratification.

Separate effects tests (SETs) and LST data have been used to select appropriate heat and mass transfer correlations from the literature and develop biases to bound the data (Reference 2.6, Section 4.5). A lower bound for heat transfer through the containment shell to the ultimate heat sink is therefore used.

One of the more complex issues is the coupling of circulation and stratification, break direction and momentum, and intercompartment flow, and the impact of those parameters on internal heat sink utilization. Circulation and stratification are complex physical processes that are not easily solved by numerical methods. Since both the AP600 and AP1000 rely on passive cooling by natural circulation, there are no active systems to force the atmosphere to homogenize. Based on a study of plausible break scenarios (mass and energy, momentum, direction, and elevation), bounding, or extreme cases are identified for further study. The extreme cases are studied using first principles calculations and sensitivities to specific flow patterns of interest. The lumped parameter plant model, with above-deck noding based on noding frozen for the LST evaluations, is used to calculate the containment response for the specified flow patterns. Based on the sensitivities, a limiting scenario is chosen for use as the PCS DBA to bound the impact on mass transfer of the strongly coupled phenomena. Biases are introduced with lumped parameter compartment nodes to bound the effects of stratification, and an assessment of stratification effects on PCS heat removal through the shell shows that no net penalty on heat removal from the above-deck region need be applied. This is discussed in more detail in Section 9 (See Table 9-1).

Similar evaluations have led to the definition of a bounding Evaluation Model for important phenomena identified in the PIRT and documented in Reference 2.2 Section 4.4.

2.5 ELEMENT 4 – PERFORM DBA CALCULATIONS AND COMPARE TO SUCCESS CRITERIA

The Evaluation Model was developed as previously described to produce conservative, bounding pressure transients for each accident phase. The acceptance criteria are that the peak pressure must remain below the design pressure and pressure should be rapidly reduced, consistent with assumptions in radiological release calculations, which is typically interpreted as the pressure at 24 hours should be less than one half of the design pressure. Documentation is provided in Reference 2.2 that shows for each phenomenon:

- Relevant model in the code
- Test basis
- Report references
- Summary report conclusions
- Validation basis summary
- How validation results are used
- How uncertainty is addressed

2.6 CONCLUSIONS

A structured, traceable approach has been followed to develop the PCS DBA Evaluation Model. The PIRT has been used to develop a bounding Evaluation Model and the PIRT has been used as the basis for a road map to relevant supporting information for each phenomenon.

2.7 REFERENCES

- 2.1 Boyack, B.E., et al., "An Overview of the Code Scaling, Applicability, and Uncertainty Evaluation Methodology," Nuclear Engineering and Design, Volume 119 (1990) No. 1, May 1990, pp 1-15.
- 2.2 WCAP-14812, "Accident Specification and Phenomena Evaluation for AP600 Passive Containment Cooling System," Rev. 2, April 1998.
- 2.3 NTD-NRC-95-4563, "GOTHIC Version 4.0 Documentation," September 21, 1995.
- 2.4 NTD-NRC-95-4577, "Updated GOTHIC Documentation," October 12, 1995.
- 2.5 NTD-NRC-95-4595, "AP600 WGOTHIC Comparison to GOTHIC," November 13, 1995.
- 2.6 WCAP-14326, "Experimental Basis for the AP600 Containment Vessel Heat and Mass Transfer Correlations," Rev. 2, April 1998.
- 2.7 WCAP-14135, "Final Data Report for PCS Large-Scale Tests, Phase 2 and Phase 3," Rev. 1, April 1997.
- 2.8 WCAP-14382, "WGOTHIC Code Description and Validation," May 1995.

2-9

- 2.9 WCAP-14845, "Scaling Analysis for AP600 Containment Pressure During Design Basis Accidents," Rev. 3, March 1998.
- 2.10 WCAP-15613, "**AP1000** PIRT and Scaling Assessment," February 2001.

3-1

3 OVERVIEW OF WGOTHIC

3.1 INTRODUCTION

The passive containment cooling system (PCS) phenomena were identified and ranked by order of importance in determining the containment vessel pressure in a phenomena identification and ranking table (PIRT). The important phenomena are summarized in Section 2. Existing containment analysis codes were reviewed to determine which most closely met the requirements identified in the PIRT. Although none of the codes met all of the requirements, the GOTHIC code package (Reference 3.1) was selected for further development based on its validation history and modeling capability. This section provides an overview of the GOTHIC code and summarizes the changes made to the GOTHIC solver program to incorporate the special heat and mass transfer correlations, liquid film tracking, and the wall-to-wall radiation model for performing design basis analyses for PCS-type containments.

Deleted: describes

3.2 OVERVIEW OF THE CODE DEVELOPMENT AND VALIDATION

The GOTHIC code is a state-of-the-art program for modeling multi-phase flow. The GOTHIC code has been developed through a long history from other qualified thermal-hydraulic computer codes (as shown in Figure 3-1).

GOTHIC consists of three separate programs, the preprocessor, solver, and postprocessor. The preprocessor allows the user to rapidly create and modify an input model. The solver performs the numerical solution for the problem. The postprocessor, in conjunction with the preprocessor, allows the user to rapidly create graphic and tabular outputs for most parameters in the model.

The GOTHIC solver program calculates the solution for the integral form of the conservation equations for mass, momentum, and energy for multi-component, two-phase flow. The conservation equations are solved for three fields: continuous liquid, liquid drops, and the steam/gas phase. The three fields may be in thermal non-equilibrium within the same computational cell. This would allow the modeling of subcooled drops (for example, containment spray) falling through an atmosphere of saturated steam. The gas component of the steam/gas field can be comprised of up to eight different non-condensable gases with mass balances performed for each component. Relative velocities are calculated for each field, as well as the effects of two-phase slip on pressure drop. Heat transfer between the phases, surfaces, and the fluid are also allowed.

The GOTHIC solver program is capable of performing calculations in three modes. A model can be created in the lumped-parameter nodal-network mode, the two-dimensional distributed parameter mode, or the three-dimensional distributed parameter mode. Each of these modes may be used within the same model (as shown in Figure 3-2). The lumped parameter nodal-network mode is used for the containment Evaluation Model (EM).

3-2

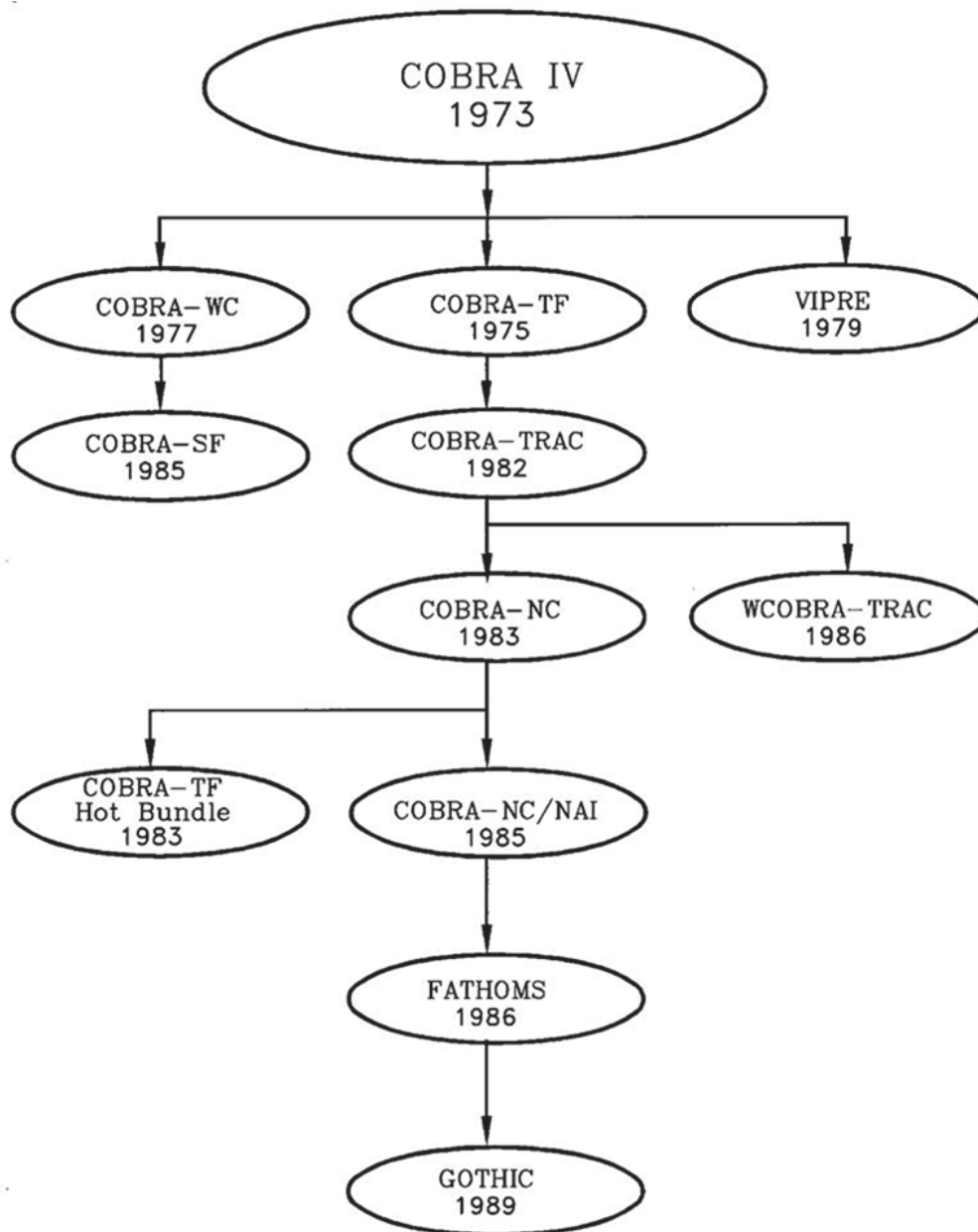


Figure 3-1. Summary of GOTHIC Historical Development

3-3

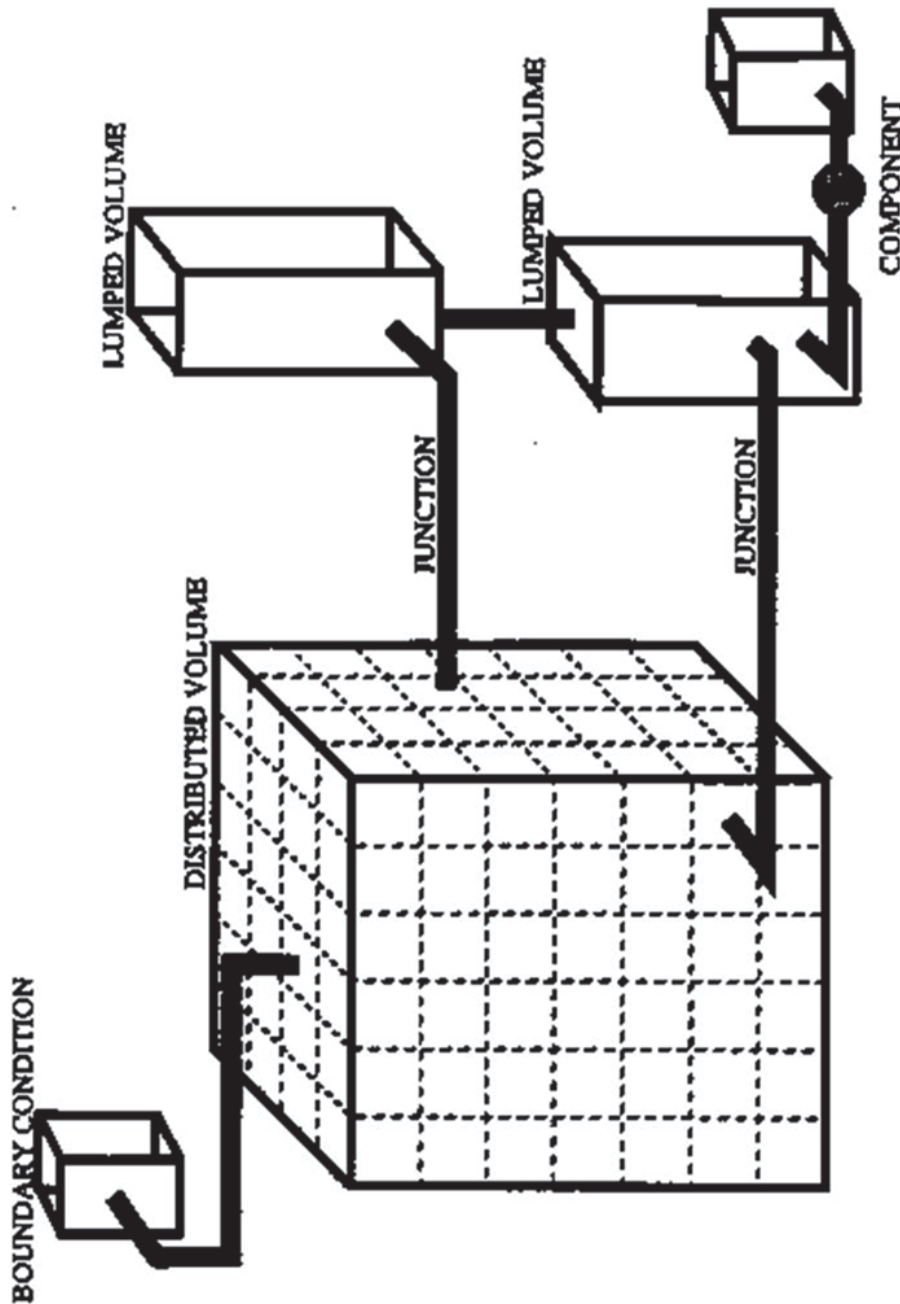


Figure 3-2. GOTHIC Modeling Features

3-4

The GOTHIC code also contains the options to model a large number of structures and components. These include, but are not limited to, heated and unheated conductors, heaters, coolers, pumps, fans, valves, and a variety of heat exchangers, and ice condensers. These components can be coupled to represent the various mitigation systems found in many containments. However, they are not used in the AP600 or AP1000 peak containment pressure analyses to model any of the passive safety systems.

The GOTHIC code has an extensive validation history, which was an important consideration in the selection of the code for further development for modeling of the PCS. The GOTHIC code validation program includes both a comparison of code-calculated results with analytical solutions to specified standard problems and a comparison of code-calculated results with experimental data. The results of the Electric Power Research Institute (EPRI)-sponsored GOTHIC code validation program are presented in Reference 3.1, Enclosure 1. Table 3-1 lists some of the tests used in the GOTHIC code validation program. The phenomenological models validated by each test are cross-referenced and presented in Table 3-2. In addition, industry experience using GOTHIC in the lumped parameter mode, as well as attempts to improve results using multi-dimensional analyses, are described in Appendix 9.C.3.

Westinghouse purchased Version 3.4c of the GOTHIC code in 1991 and began modifying it to include mechanistic convection heat and mass transfer correlations, a liquid film tracking model, a one-dimensional wall conduction model, and wall-to-wall radiant heat transfer to model heat removal by the PCS. The code, with these modifications, is called Westinghouse-GOTHIC and is abbreviated as WGOTHIC.

The WGOTHIC development history is shown in Figure 3-3. The PCS heat and mass transfer models developed by Westinghouse were incorporated into the GOTHIC version 3.4c pre-processor and solver programs to create the WGOTHIC version 1.0 pre-processor and solver programs in 1993.

Between 1991 and 1993, while Westinghouse was developing the PCS heat and mass transfer models, GOTHIC version 3.4d underwent an EPRI-sponsored peer review. The purpose of the review was to establish a reference point for placing the GOTHIC code package under a 10 CFR 50, Appendix B Quality Assurance Program. The peer design review group reviewed the documentation, coding, convergence, pre-/post-processor, code qualification package, and the code's adequacy for containment analysis. The conclusions from the review are presented in Section 2.2 of the GOTHIC Design Review Final Report (Reference 3.2).

Overall, the GOTHIC containment analysis package was found to be adequate for containment analyses, and that the code package offered the ability to provide more accurate and mechanistic results than with other currently available containment codes. This conclusion was qualified with the statements that the nodal and junction treatment, as well as the range of the qualification database, need to be justified for each intended application; as was done via the large-scale (LST) and separate effects tests (SETs) (Reference 3.3) and various scale integral tests (Appendix 9.C.3) used to qualify WGOTHIC.

Deleted: any typical

Deleted: ;

Deleted: .

Deleted: t

Deleted: T

Deleted: typically

Deleted:

Deleted: described in this report

3-5

Table 3-1. GOTHIC Validation Tests

Battelle-Frankfurt Tests D-1, D-15, D-16	Modeling: 7 lumped parameter volumes, junctions Phenomena: Blowdown transients, subcompartment pressurization, wall differential pressures
Battelle-Frankfurt Test 6	Modeling: 1 distributed parameter volume (55 cells), conductors, junctions Phenomena: Hydrogen transport by convection and diffusion
Battelle-Frankfurt Tests 12, 20	Modeling: Combination of 5 lumped and 1 distributed parameter volumes (2 cells), conductors, junctions Phenomena: Hydrogen transport by convection and diffusion
Battelle-Frankfurt Tests C-13, C-15	Modeling: 10 lumped parameter volumes, conductors, junctions Phenomena: Main steamline break, pressure/temperature response
Hanford Engineering Development Laboratory Tests HM-5, HM-6	Modeling: 1 distributed parameter volume (300 cells), conductors, junctions Phenomena: Hydrogen mixing in a large, simulated containment
Light Water Reactor Aerosol Containment Experiments Tests LA-5, LA-6	Modeling: Combination of 1 lumped and 1 distributed parameter (2 cells) volumes, conductors, junctions Phenomena: Severe accident response to sudden containment failure
Marviken Full-Scale Containment Tests 17, 24	Modeling: 21 lumped parameter volumes, conductors, junctions Phenomena: Pressurized high temperature steam blowdown
Carolina's Virginia Tube Reactor Tests 3, 4, 5	Modeling: 2 lumped volume and a 2 distributed parameter volume (20 cells) models, conductors, junctions Phenomena: Steam blowdowns (T31.5 includes hydrogen/helium)
Heissdampfreaktor Tests V21.1, T31.1, T31.5, V44	Modeling: 37 lumped parameter volumes, conductors, junctions Phenomena: Steam blowdowns (T31.5 includes hydrogen/helium)

3-6

Table 3-2. GOTHIC Phenomenological Models Validated by Test

Item	BFMC	HEDL	LACE	MARV	CVTR	HDR
Fluid momentum	X		X	X		
Energy transport	X		X	X		
Non-condensable gases	X	X	X	X	X	X
Equations of state	X		X	X		
Pressure response	X	X	X	X	X	X
Temperature response	X	X	X	X	X	X
Humidity response	X	X	X	X	X	X
Hydrogen transport	X					
Energy sources	X	X	X		X	X
Subcompartment analysis	X			X		
High energy line breaks	X					
PWR standard containment			X			
BWR pressure suppression				X		
Fluid/structure interaction	X					
Conductors	X					
Subdivided volumes	X					
Turbulence	X					
3-D calculations	X	X		X		

3-7

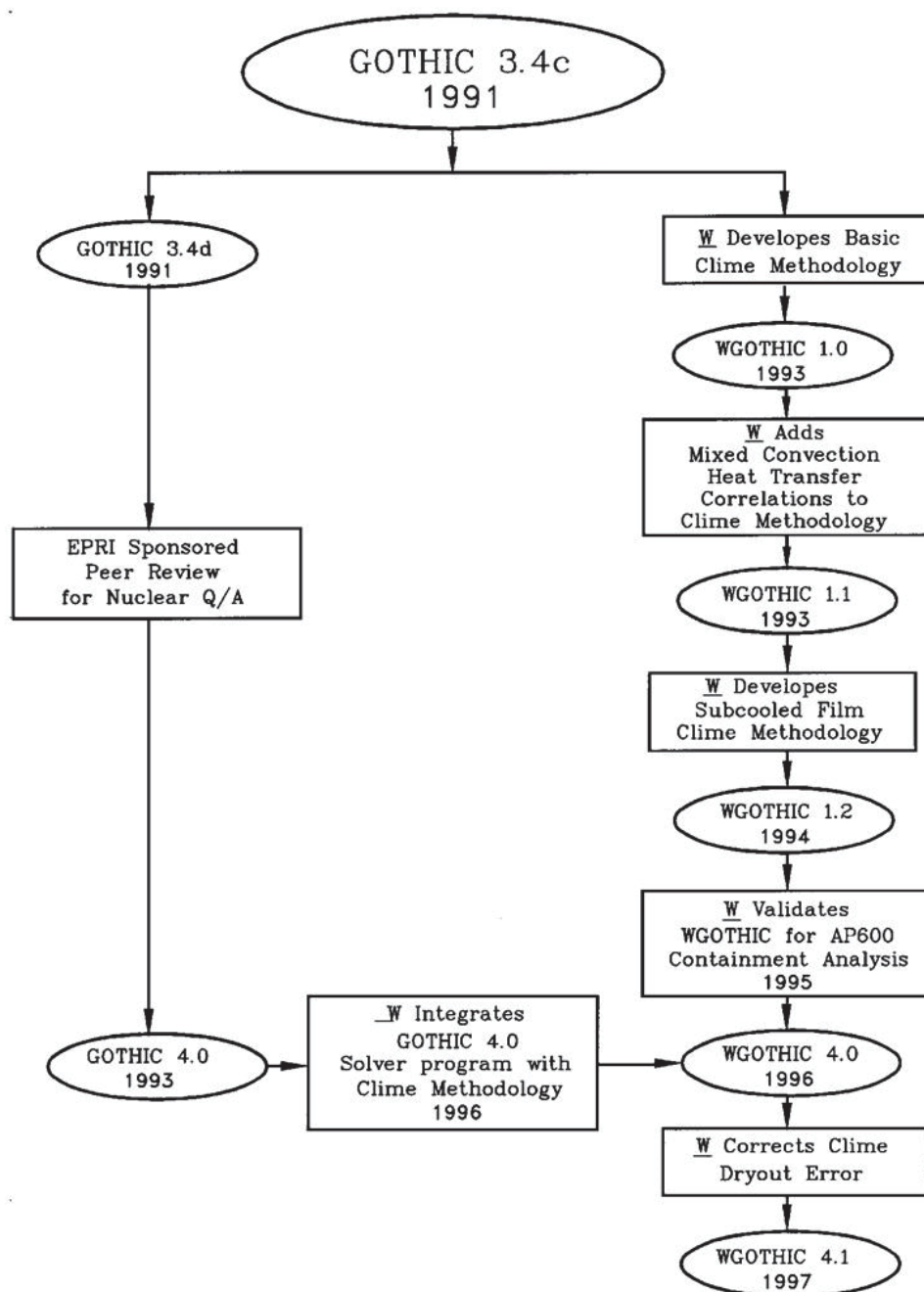


Figure 3-3. Summary of WGOTHIC Historical Development (Page 1 of 2)

3-8

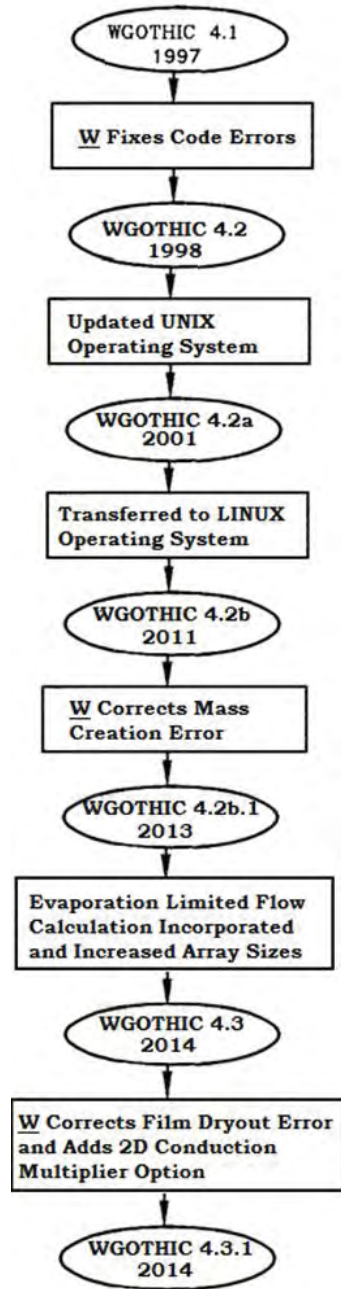


Figure 3-3. Summary of WGOthic Historical Development (Page 2 of 2)

Deleted: cont.

3-9

The review group had three recommendations. The first was the addition of dynamic memory allocation, so that the code would not need to be recompiled for different sizes of models. The second was the inclusion of an iterated Newton method to aid in convergence. The third was to incorporate a fog model to simulate condensation of vapor when regions go from superheated to saturated.

As described in Reference 3.4, the conclusions and recommendations from the GOTHIC design review also apply to WGOTHIC. None of the recommended changes were incorporated in WGOTHIC. The first recommendation, dynamic memory allocation, wasn't incorporated in WGOTHIC, since it is a user convenience option and does not affect the solution technique. The second recommendation, to include an iterated Newton solution option to aid in convergence, was not incorporated in WGOTHIC, since satisfactory convergence was supported by the comparisons presented in the GOTHIC code qualification test report (Reference 3.1) and the WGOTHIC validation report (Reference 3.3). The third recommendation, to include a fog model, was not incorporated in WGOTHIC because it was concluded that, based on the GOTHIC Carolina's Virginia Tube Reactor (CVTR) qualification test case results (Reference 3.1) and an assessment of fog modeling as it relates to the AP600 (Reference 3.5, Sections 4.4.2D and 4.4.9C), it is conservative with respect to the prediction of containment temperature and pressure to not include the fog model.

Westinghouse updated the PCS models to account for subcooled films and incorporated the GOTHIC software error corrections that were provided by Numerical Applications, Inc. (NAI) to create WGOTHIC pre-processor version 2.0 and solver version 1.2 in 1994. Westinghouse validated this version of WGOTHIC for performing AP600 analyses in 1995 (Reference 3.3). The WGOTHIC validation program consisted of four parts:

1. The subset of GOTHIC validation tests that was identified as sensitive in the original acceptance tests was rerun with WGOTHIC. These tests were run with the same input options selected in the original GOTHIC validation calculation (that is, the PCS models were not exercised) to determine if any of the code changes made to incorporate the PCS models would affect the transient results. This comparison is presented in Appendix D of Reference 3.3. It shows that the code changes Westinghouse made to incorporate the PCS models do not affect the GOTHIC calculation results.
2. The PCS model one-dimensional conduction equation solution technique was validated by comparison with an analytical solution for a test problem. This comparison is presented in Section 4.1 of Reference 3.3. The code calculated results match the analytical solution.
3. The PCS model heat and mass transfer correlations were validated by comparison with separate effects test data from the Westinghouse Flat Plate Tests, the Westinghouse Large-Scale Tests, the Wisconsin Condensation Tests, and publicly available published reports. These comparisons are documented in Reference 3.6. The range of the important dimensionless parameters from the test program bounds both the AP600 and **AP1000** operating range, as shown in Table 3-3. The dimensionless parameters compared are the Prandtl number (Pr), the Schmidt number (Sc), the Reynolds Number (Re), and the Grashof Number (Gr). The percent differences reported for the enhanced shield building design (Reference 3.7) of the key scaling groups are small and negative indicating the PCS air flow path design changes are expected to slightly reduce the **AP1000** operating range from the previous shield building design. Therefore, the correlations are acceptable for modeling heat and mass transfer in both the AP600 and **AP1000** PCS.

Deleted:

Deleted: W

Deleted:

3-10

4. WGOTHIC, including the PCS models and nodalization, was verified to be coded correctly by comparison with transient test data from the Westinghouse Large-Scale tests. Comparison with steady state test data from the LSTs assessed the ability of WGOTHIC to represent internal flow fields and noncondensable gas distributions and to calculate the net heat removal from the vessel in an integral system. The comparisons provided insight for the applicability of documented lumped parameter biases (Appendix 9.C.3) that are applied to the AP600 and **AP1000** containment Evaluation Models and identified a bounding approach to address compensating errors. This comparison is presented in Section 8 of Reference 3.3. Section 9, Table 9-1 summarizes how lumped parameter biases have been addressed.

In 1996, the source code for the PCS heat and mass transfer models for WGOTHIC solver version 1.2 and pre-processor version 2.0 was incorporated into the GOTHIC solver and pre-processor version 4.0 source code to create the WGOTHIC version 4.0 pre-processor and solver programs. This was done to incorporate all of the GOTHIC design review code changes into WGOTHIC.

A series of verification tests, including the most sensitive GOTHIC code qualifications test cases, were run to validate WGOTHIC version 4.0. The results of the GOTHIC code qualification test cases that were run using the WGOTHIC version 4.0 all compared very well with the results obtained using GOTHIC version 4.0, indicating that the incorporation of the Westinghouse PCS model did not significantly affect the GOTHIC calculations.

Version 4.1 of the WGOTHIC pre-processor, solver, and post-processor programs was created in 1997 to correct an error that was discovered in the PCS heat and mass transfer model and several other non-calculational code problems. The error caused the PCS heat removal to be over-predicted at the point of dryout. Verification test cases performed using WGOTHIC version 4.1 demonstrated that the dryout error was corrected. Version 4.1 of WGOTHIC has been used for all of the analysis results presented in this report except as specifically noted for sensitivity studies in Section 11.

Deleted: c

Version 4.2 of the WGOTHIC code was created in 1998 to correct several errors that were discovered while using version 4.1. One error was caused by mixing both single and double precision variables within function and subroutine argument lists. Another error prevented the calculation of opposed mixed convection heat and mass transfer in the PCS. A third error was related to the cell centered velocity that is used in the clime heat and mass transfer calculations. It was determined that these errors did not have a significant effect on the code calculated output results; however, the code was updated to correct the errors and increase array dimensions to allow larger models to be created. Verification test cases that were performed using WGOTHIC version 4.2 demonstrated that the errors were corrected. Also, the changes that were made to create version 4.2 did not affect the results from the validation cases that were performed with version 4.1.

Version 4.2 was updated to Version 4.2a when the version of the UNIX operating system was upgraded in 2001. This version was used for the **AP1000** Design Control Document (DCD) analyses, Revision 15 through Revision 19.

3-11

Version 4.2a was updated to version 4.2b when the code was transferred from the UNIX operating system to the LINUX operating system in 2011. Version 4.2b.1 was created in 2013 to correct an error that would cause a small increase in the system mass over time. Although this error would not adversely affect the SSAR analyses, when integrated over several days, the mass error could become significant and affect the calculated results. The code output was also updated to allow the change in the mass and energy balances to be more easily tracked throughout the transient.

Version 4.3 of WGOTHIC was created in 2014 to incorporate an option to allow the evaporation-limited PCS flow calculations that are described in Section 7.5 to be automated within the code. This version also increased the array sizes, to allow more thermal conductor types, flow paths, and plot output time steps, along with providing plot output in binary files that can be read by another plotting program. These changes were made to improve the user experience and allow even larger models to be created. Validation testing of version 4.3 identified an error in the wet clime dry out calculation that affected the condensation rate inside containment. The error was introduced in version 4.2b.1 and only affected the version 4.3 results when the automated evaporation-limited PCS flow calculation option was not selected. No SSAR analyses were performed with version 4.3.

Version 4.3.1 was created in 2014 to correct the clime dry out error that was discovered during validation of version 4.3 and to add a 2-D conduction multiplier option to the automated evaporation-limited PCS flow calculation. The 2-D conduction multiplier that is used within WGOTHIC is described in Section 7.4.

Subsequent code version updates will be made to address changes in computing platforms, correction of errors, and updates to enhance the user experience without it being a change in methodology. Therefore, updates will not be made to this document unless a methodology-changing code change is made.

3-12

Table 3-3. Operating Range Comparison for AP600 and AP1000 Heat and Mass Transfer Parameters

Heat Transfer Correlation	Parameter	Composite of Test Data	AP600 Range	AP1000 Range	Percent Change for Enhanced AP1000 Shield Building	
Internal Free Convection: $h = 0.13 k/(v^2/g)^{1/3} [\Delta\rho/\rho]^{1/3} Pr^{1/3}$	$\Delta\rho/\rho$	0.08 to 0.55	<0.40	<0.42	N/A	Deleted: AP1000
	Pr	0.72 to 0.90	0.72 to 0.90	0.72 to 0.90	N/A	Formatted: Centered
	Sc	~0.52	~0.52	~0.52	N/A	Formatted: Centered
External Mixed Convection: $Nu_{force} = 0.023 Re_d^{0.8} Pr^{1/3}$ $Nu_{free} = 0.13 (Gr_d Pr)^{1/3}$ For Opposed Mixed Convection: $Nu_{mix} = (Nu_{force}^3 + Nu_{free}^3)^{1/3}$ For Assisted Mixed Convection: $Nu_{mix} = \text{Max} \{ (Nu_{free}^3 - Nu_{force}^3)^{1/3}, Nu_{free}, 0.75 * Nu_{force} \}$	Re_d Riser	<120000 evap. <500000 dry	<189000	<210000	-15%	Formatted: Centered
	Re_d Downcomer		<151000	<190000	-7.0%	Formatted: Centered
	Re_d Chimney		<1400000	<1800000	-13.0%	Formatted: Centered
	Gr_d Riser	<7.0x10 ¹⁰ evap. <1.0x10 ¹¹ dry	<1.2 x 10 ⁹	<1.5 x 10 ⁹	-4.7%	Formatted: Centered
	Gr_d Downcomer		<6.2 x 10 ⁹	<2.1 x 10 ¹⁰		Formatted: Centered
	Gr_d Chimney		<2.1 x 10 ¹²	<8.0 x 10 ¹²	2.9%	Formatted: Centered
	Pr	~0.72	~0.72	~0.72		Formatted: Centered
	Sc	~0.52	~0.52	~0.52		Formatted: Centered
Liquid Film Heat Transfer: $Nu_{turb} = 0.0038 Re^{0.4} Pr^{0.65}$ $Nu_{wavy\ laminar} = 0.822 Re^{-0.22}$	Re	<20000	<3200	<3500		Formatted: Centered
	Pr	1.77 to 5.9	1.5 to 3.0	1.5 to 3.0		Deleted: 1 Formatted: Centered

3.3 THE WGOTHIC CLIME MODEL

A solution technique that includes wall-to-wall radiation at the conditions expected for the passive plant design necessitates a close coupling of the participating walls. This coupling is accomplished by assigning boundaries that define the portions of the various walls that radiate to one another. Consistent with the basic formulation implemented for the GOTHIC code that considers conductors or heat sinks to be energy sink or source terms, code modifications that include wall-to-wall radiant heat transfer can be thought of as the addition of a special type of conductor group. This special conductor type or group consists of a set of walls that radiate to each other and interface with GOTHIC fluid cells through mass and energy source terms. The term *clime*, meaning *region*, is used to differentiate and distinguish this special conductor type from those already existing in GOTHIC terminology.

For the passive containment model, a clime is a horizontal slice of the containment structure consisting of the following:

[

] ^{a,c}

A representative three-conductor clime is shown schematically in Figure 3-4. The internal containment vessel volume, riser air flow channel volume, downcomer air flow channel volume, and environment volume are separate computational cells or fluid volumes in the model. The shell, baffle, and shield building walls are one-dimensional conductors representing solid wall structures between the

3-14

computational cells. These conductors are further subdivided into regions of different materials with different mesh sizes. Each conductor surface may have a liquid film present (not shown) depending on thermodynamic conditions.

The climes are stacked vertically through the PCS to model the effects of changing properties both inside and outside the containment shell. Usually there are at least two stacks of climes a wet stack and a dry stack. The only difference between a wet and dry stack is that a time-dependent, water flow rate boundary condition can be specified for each conductor surface of the top clime in a wet stack. Because condensation can occur on either wet or dry conductor surfaces, an initially dry stack of climes could contain some wet conductor surfaces and/or a partially wet conductor surface due to condensation. Likewise, an initially wet stack of climes could contain some dry conductor surfaces and/or a partially dry conductor surface due to evaporation. However, for the evaporation-limited option that was incorporated into WGOthic version 4.3, the wet and dry clime stacks are paired. As the water evaporates from the outside of the containment vessel wall wet clime, the corresponding area is moved to the dry clime. There can still be condensation on the inside surface of both a wet and a dry clime. See Section 7.5 and Section 13.5 for more information on the implementation of the clime modeling in the AP1000 containment EM.

Deleted: is

The user must specify values for the area and circumferential perimeter for each conductor of each clime in both the wet and dry stacks. The input values for the area and circumferential perimeter for the clime conductors in the wet stacks are based on measurements of the water coverage from the full-scale Water Distribution Tests. The PCS film coverage model, which conservatively bounds results from several test facilities, is described in Section 7.

The WGOthic clime model calculates the temperature, flow rate, and thermal resistance of the water films on the various conductor surfaces of a clime. Liquid mass is conserved whenever the film reaches the bottom clime in a stack or a conductor surface dries out. The clime model takes the film flow rate from each conductor surface of the previous clime in the stack as input, then adds the local condensation rate, or subtracts the local evaporation rate to determine the output water flow rate on each of its corresponding conductor surfaces. Any liquid film remaining on the conductor surfaces of the last clime in a stack is added to the liquid field of the GOTHIC cell in contact with the conductor surface, or an alternate drain cell specified by user input.

Dryout occurs when either the film flow rate is low enough or the heat flux is high enough to result in complete evaporation of the film before it can exit the conductor. The clime model calculates the evaporation heat and mass transfer and the location of the dryout elevation; the remainder of the conductor surface below the dryout elevation is treated as a dry surface.

3-15

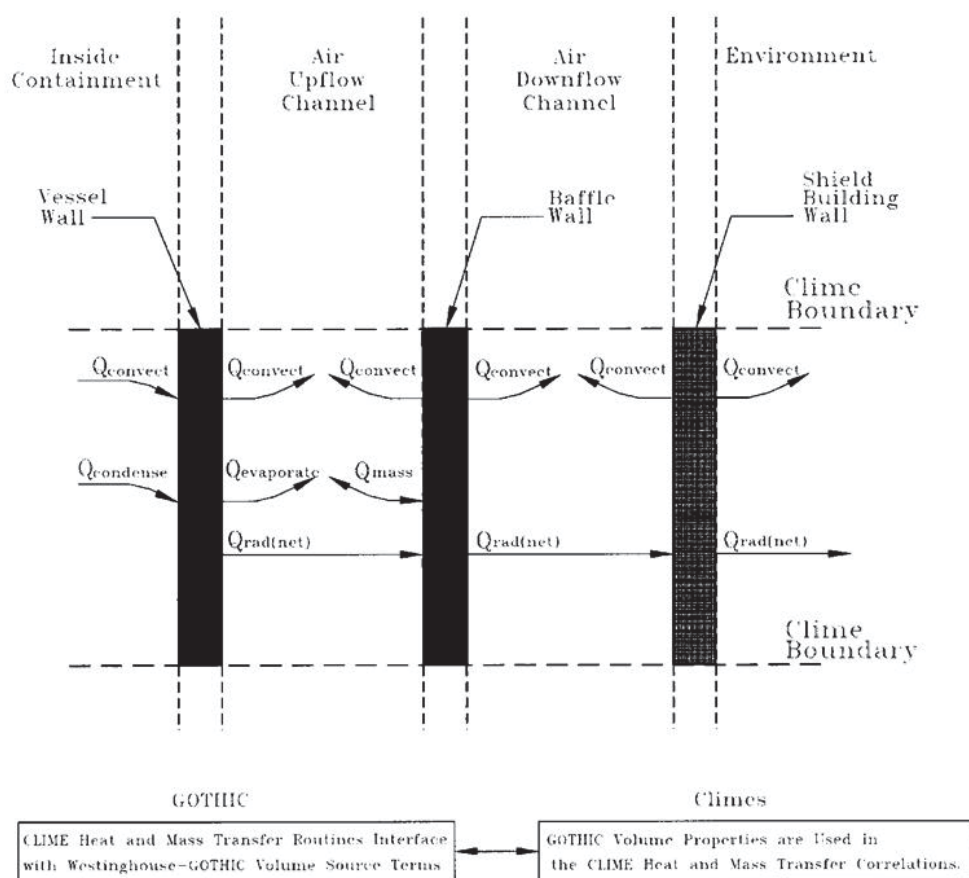


Figure 3-4. Westinghouse-GOTHIC Clime Wall Source Term Models

3.4 GENERAL CLIME EQUATIONS

Starting with WGOthic version 4.3, there are two options for modeling the PCS water flow rate and coverage. In the first option, the user specifies constant values for the area and wetted perimeter of the wet and dry climes, and an external calculation is performed to determine the evaporation-limited PCS flow rate. This is the standard coverage model option; it typically requires several iterations to converge and is consistent with all previous versions of WGOthic. In the second option, the user specifies the water coverage fraction for the first two climes as a function of the PCS flow rate (assuming no evaporation), and the evaporation-limited PCS flow rate is calculated within WGOthic. This is the automated evaporation-limited PCS flow and coverage model option. The general clime equations for both options are described next.

3.4.1 Standard PCS Flow and Coverage Model Option

The energy equation for the film must balance the heat from the wall into the film, the heat conduction through the film, and the heat and mass transfer from the film surface to the ambient, with the change in energy of the flowing film. Assuming constant fluid properties over the node surface, one-dimensional film flow along the wall, one-dimensional conduction across the film, and that the viscous dissipation term can be neglected, the general energy transport equation for the film can be written in terms of temperature as:

$$\frac{\partial T}{\partial t} = \frac{k}{\rho c_p} \frac{\partial^2 T}{\partial x^2} - V_z \frac{\partial T}{\partial z} \quad (3-1)$$

For computational purposes, the water film is divided into 3 control volumes as shown in Figure 3-5. The boundary control volume of the film includes the outer 1/2 layer of the wall and its temperature equals the wall temperature. The outer surface of the outer control volume touches the atmosphere and its temperature is coupled to the temperature of the atmosphere through the heat and mass transfer boundary layer correlations. The temperature in the central control volume represents the average heat stored in the film. Note that all convected energy is transported in the central control volume. This simplification improves numerical stability.

By convention, mass and energy entering a control volume are assigned positive values and mass and energy leaving a control volume are assigned negative values. Referring to Figure 3-5, the central control volume has a thickness of $\delta x_{film}/2$ and the film energy transport equation for this control volume can be expressed in a finite difference form as follows:

$$\frac{T_{avg} - T_{avg,old}}{\Delta t} = \frac{4k_{film}}{\rho_{film} c_{p,film}} \frac{T_{surf,1} - 2T_{avg} + T_{wall,1}}{\delta x_{film}^2} + V_z \frac{T_{in} - T_{out}}{\Delta z} \quad (3-2)$$

3-17

where,

k_{film}	=	film thermal conductivity (Btu/ft-sec-°F)
δx_{film}	=	film thickness (ft)
$c_{p,\text{film}}$	=	film specific heat (Btu/lbm-°F)
ρ_{film}	=	film density (lbm/ft ³)
T_{in}	=	inlet temperature of film at the top of the clime (°F)
T_{out}	=	exit temperature of film at the bottom of the clime (°F)
T_{avg}	=	temperature of the center of the film (°F)
$T_{\text{wall},1}$	=	temperature of first wall node (°F)
$T_{\text{surf},1}$	=	film surface temperature (°F)
Δz	=	height of the clime (ft)
v_z	=	film velocity (ft/sec)

Deleted: capacity

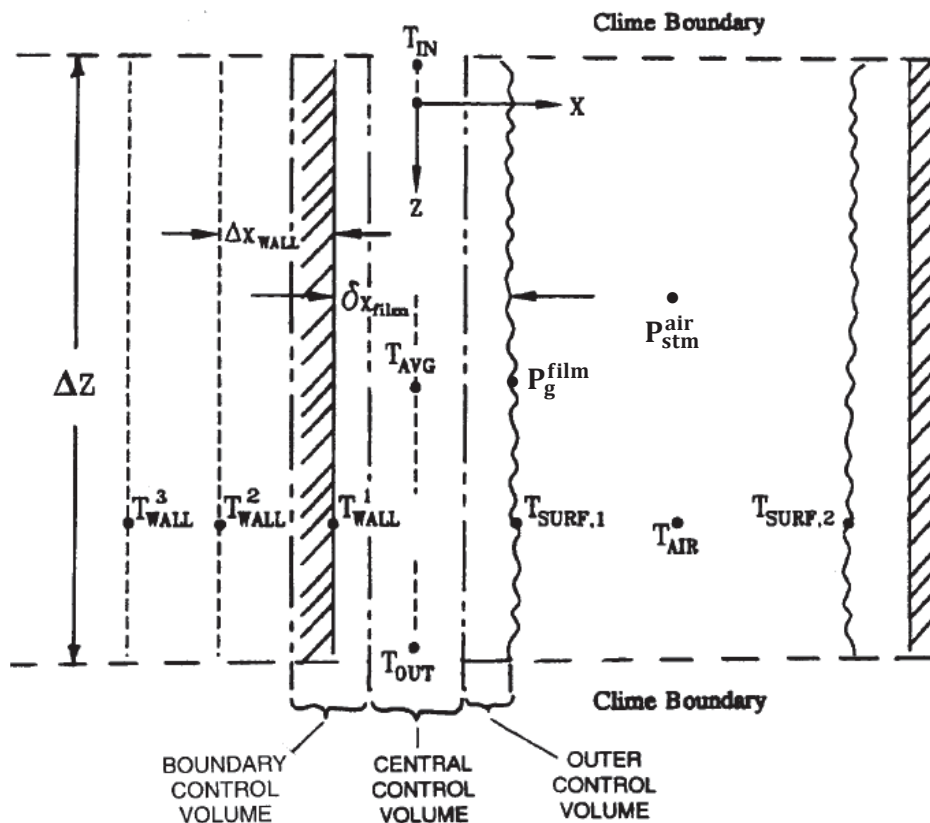


Figure 3-5. Clime Finite Difference Model Definitions

3-18

The film inlet temperature is given, either from a boundary condition or from the outlet temperature of the preceding clime in the stack. To ensure stability, the film outlet temperature is defined to be the same as the average temperature.

$$T_{out} = T_{avg} \quad (3-3)$$

The inner film surface boundary condition forces the heat flux from the outer surface of the conductor wall to equal the heat flux into the film. The solid film interface boundary condition is:

$$-k_{wall} \left. \frac{\partial T}{\partial x} \right|_{wall} = -k_{film} \left. \frac{\partial T}{\partial x} \right|_{film} \quad (3-4)$$

where k_{wall} is the wall thermal conductivity (Btu/ft-sec-°F).

The outer film surface boundary condition equates the energy leaving the outer film layer surface to the energy entering the atmosphere. The energy entering/leaving the film surface may leave/enter the atmosphere through a combination of convection, evaporation, and radiation. The outer film surface boundary condition is:

$$-k_{film} \left. \frac{\partial T}{\partial x} \right|_{film} = h_c (T_{surf,1} - T_{air}) + h_M h_{fg} (p_g^{film} - p_{stm}^{air}) + \epsilon \sigma (T_{surf,1}^4 - T_{surf,2}^4) \quad (3-5)$$

where,

h_c	=	convection heat transfer coefficient from the film to the air (Btu/sec-ft ² -°F)
$T_{surf,1}$	=	<u>film surface temperature in (°F) in first right term, in (°R) in the last term</u>
T_{air}	=	air temperature (°F)
h_M	=	mass transfer coefficient (lbm/sec-ft ² -psi)
h_{fg}	=	latent heat of vaporization of the film (Btu/lbm)
p_{stm}^{air}	=	partial pressure of steam in the air (psi)
p_g^{film}	=	saturation pressure of steam at the film surface temperature, $T_{surf,1}$ (psi)
ϵ	=	emissivity of film surface
σ	=	Stefan-Bolzman constant <u>$= 4.761 * 10^{-13}$ (Btu/sec-ft²-°R)</u>
$T_{surf,2}$	=	temperature of second radiative surface (°R)

The four film equations are:

$$\frac{T_{avg} - T_{avg,old}}{\Delta t} = \frac{4k_{film}}{\rho_{film} c_{p,film}} \frac{T_{surf,1} - 2T_{avg} + T_{wall,1}}{\delta x_{film}^2} + V_Z \frac{T_{in} - T_{out}}{\Delta z} \quad (3-6)$$

$$-k_{wall} \left. \frac{\partial T}{\partial x} \right|_{wall} = -k_{film} \left. \frac{\partial T}{\partial x} \right|_{film} \quad (3-7)$$

3-19

$$-k_{\text{film}} \frac{\partial T}{\partial x} \Big|_{\text{film}} = h_c (T_{\text{surf},1} - T_{\text{air}}) + h_M h_{fg} (p_g^{\text{film}} - p_{\text{stm}}^{\text{air}}) + \varepsilon \sigma (T_{\text{surf},1}^4 - T_{\text{surf},2}^4) \quad (3-8)$$

$$T_{\text{out}} = T_{\text{avg}} \quad (3-9)$$

The wall conduction equation is tightly coupled to these film equations. For points within the wall, the conduction equation is simply a one-dimensional partial differential equation:

$$\frac{\partial T}{\partial t} = \frac{k}{\rho c_p} \frac{\partial^2 T}{\partial x^2} \quad (3-10)$$

By replacing the derivatives with finite differences, this partial differential equation is replaced with a system of algebraic equations. The subscript “n” identifies the point (node) at which the derivatives are to be calculated.

$$\frac{T_{\text{wall},n} - T_{\text{wall},n,\text{old}}}{\Delta t} = \frac{k_{\text{wall}}}{\rho_{\text{wall}} c_{p,\text{wall}}} \frac{T_{\text{wall},n+1} - 2T_{\text{wall},n} + T_{\text{wall},n-1}}{\Delta x_{\text{wall}}^2} \quad (3-11)$$

where,

$$\begin{aligned} \rho_{\text{wall}} &= \text{wall density (lbm/ft}^3\text{)} \\ c_{p,\text{wall}} &= \text{wall specific heat (Btu/lbm-}^\circ\text{F)} \\ \Delta x_{\text{wall}} &= \text{wall node thickness (ft)} \end{aligned}$$

This equation, along with Equations (3-6 through 3-9), can be considered to be the system of equations for a clime.

Although the differential boundary condition Equation (3-7) is mathematically complete and correct, numerical stability in a finite difference formulation is improved by defining an alternate control volume containing the boundary between solid and liquid. As shown in Figure 3-5, the boundary control volume is defined to contain the wall material from the surface to a point halfway between the surface and the first internal calculational point (that is, between wall nodes 1 and 2) into the control volume and the inner quarter of the film thickness. A single energy balance equation for the boundary control volume is:

$$\left[\rho_{\text{wall}} c_{p,\text{wall}} \frac{\Delta x_{\text{wall}}}{2} + \rho_{\text{film}} c_{p,\text{film}} \frac{\delta x_{\text{film}}}{4} \right] \frac{dT_{\text{wall},1}}{dt} = k_{\text{wall}} \frac{T_{\text{wall},2} - T_{\text{wall},1}}{\Delta x_{\text{wall}}} - 2k_{\text{film}} \frac{T_{\text{wall},1} - T_{\text{avg}}}{\delta x_{\text{film}}} \quad (3-12)$$

The film convective energy transport has been neglected for the boundary control volume. Because the film velocity at the wall is zero, the effect of neglecting this is small. A similar control volume and heat flux equation is defined for the outer quarter of the film thickness to model the air/film interface. In this case, the film surface heat flux is the sum of the convection, radiation, and mass transfer heat fluxes.

$$\rho_{\text{film}} c_{p,\text{film}} \frac{\delta x_{\text{film}}}{4} \frac{dT_{\text{surf}}}{dt} = 2k_{\text{film}} \frac{T_{\text{avg}} - T_{\text{surf}}}{\delta x_{\text{film}}} - h_c (T_{\text{surf},1} - T_{\text{air}}) - h_M h_{fg} (p_g^{\text{film}} - p_{\text{stm}}^{\text{air}}) - \varepsilon \sigma (T_{\text{surf},1}^4 - T_{\text{surf},2}^4) \quad (3-13)$$

Deleted: This

Deleted: ,

Deleted: Note that we neglect

Deleted: half

Deleted: outer

Deleted: layer

Deleted: in Equation (3-8)

3-20

Most of the convective energy transport by the film as it flows down the shell is carried in the central flow region of the film. At the wall, the film velocity is zero so there is little transport next to the wall even though the temperature gradient is greatest there. At the film surface, the vertical temperature gradient is smallest because the film surface temperature is strongly coupled to the surrounding atmosphere which has a relatively small vertical temperature gradient.

In the WGOTHIC Containment Evaluation Model, most of the water film on the outside of the containment is expected to evaporate. The latent heat of evaporation of water is around 1000 Btu/lbm. Compare this with the heat required to heat water from its initial temperature to the dewpoint temperature of the surrounding air which is around 20-50 Btu/lbm. At most, the subcooling of a completely evaporating film accounts for about 5 percent of the total energy removal. The numerical error introduced by neglecting the transport in the control volumes at the wall and on the film surface is estimated to be less than 20 percent ~~for the completely evaporated film~~. Thus, the total energy imbalance introduced by neglecting these transport terms is less than 1 percent of the total energy removal from containment.

Deleted: of

Deleted: total energy transport

On the inside of containment, the water film temperature is very closely tied to the partial pressure of steam. During the large-scale tests, the internal steam concentration vertical gradient was observed to be nearly zero. The numerical error in the transport equation on the inside is smaller than the 1 percent of total energy on the outside of containment.

In principle, the effects of the numerical modeling assumptions could be reduced more by including the film surface vertical convective energy transport term. During the development of the model, this term was included and appeared to be linked to an instability that arose through the interaction between the transport energy and the non-linear radiation and convective heat and mass transfer models. As a result, a decision was made to accept the small numerical error to maintain the stability of the model.

The second numerical assumption made is that the film instantly covers the containment as soon as film flow is introduced in the code, i.e., no tracking of a film front is performed. The film flow is initiated by a high-pressure signal inside containment. At this time, the outer surface of the containment is still cold. It takes several minutes for the film to entirely cover the containment. It also takes about 10-15 minutes for the outer surface of the containment to heat sufficiently for the heat and mass transfer models to start to have any effect. As a result, by the time evaporation could contribute to heat removal, the containment would be covered with water anyway. The only other time that this could have an impact on transient results would be if there is a step change in the flow. Given that the transient involving large changes in the film flow occur over a period of more than a day, the error in assuming an instantaneous step change instead of a change over several minutes can be considered to be small. In addition, it can be compensated for by ramping the flow rate over a period of several minutes instead of introducing the step change.

Equations 3-6, 3-9, and 3-11 through 3-13 represent the complete system of equations for a clime as used in WGOTHIC. See Sections 4 and 13 for a description of how climes are implemented for the AP600 and **AP1000** Containment Evaluation Models.

3-21

3.4.2 Automated Evaporation-Limited PCS Flow and Coverage Option

The equations above have been modified for the automated evaporation-limited PCS flow and coverage option. This option was originally intended to model 2D heat conduction between the wet and dry sections of the containment shell. However, some problems were encountered during the code development process, so a 1D conduction solution using the DLSODE solver with an optional 2D conduction heat transfer multiplier has been incorporated in WGOETHIC version 4.3. The 2D conduction heat transfer multiplier option is described in Section 7.6.

L

3-22

L

L^{a,c}

L^{a,c}

3-23

L

J^{a,c}

3-24

a,c

Figure 3-6. Wetting Fraction vs. Elevation

3.5 INTEGRATION OF THE WESTINGHOUSE CLIME MODEL INTO GOTHIC

The Westinghouse clime model is composed of a set of subroutines. These subroutines were added to the GOTHIC solver program to create the WGOTHIC solver program. The GOTHIC solver program logic was modified to incorporate the clime model as follows:

- A call to the subroutine that reads the clime input was added
- A call to the subroutine “gshell”, the main calling routine for the clime model, was added
- A call to the subroutine that generates the clime output was added

The standard clime model flow control outline is shown in Figure 3-7. Subroutine “gshell” is the main calling routine for the other subroutines of the clime model. Separate subroutines in the clime model compute the heat and mass transfer coefficients between the conductor surfaces and the corresponding volumes, the surface-to-surface radiation heat transfer, the conductor wall temperature distribution, and the changes to the source terms for the GOTHIC mass and energy conservation equations.

The flow control outline for the automated evaporation-limited PCS flow and coverage model option is shown in Figure 3-8. Subroutine “gshell2” is the main calling routine for the other subroutines in this model. Note, the 2D conduction solution logic has not yet been implemented. If the 2D conduction multiplier option is selected, those multipliers are calculated and applied to the heat and mass transfer coefficients that are input to the DLSODE solver.

The interface between the clime model and GOTHIC takes place through the source terms for the GOTHIC mass and energy conservation equations. The GOTHIC vapor mass and energy source terms are updated to include the mass and energy transfer due to convection, radiation, evaporation, and condensation within the climes. The GOTHIC liquid mass and energy source terms are updated to include the liquid mass and energy transfer due to runoff or stripping of the liquid film from the climes.

Deleted: 6

3-26

a,b,c

Figure 3-7. Clime Routines Flow Control Outline

WCAP-15846-P, Revision 5
APP-SSAR-GSC-587, Revision 5

September 2016

3-27

a,b,c

Figure 3-8. Clime Routines Flow Control Outline

3-28

3.6 REFERENCES

- 3.1. Westinghouse Letter NTD-NRC-95-4563, B.A. McIntyre to Quay (NRC), "GOTHIC Version 4.0 Documentation," September 21, 1995.
- 3.2. Westinghouse Letter NTD-NRC-95-4462, N.J. Liparulo to T.R. Quay (NRC), EPRI Report RA-93-10, "GOTHIC Design Review, Final Report," May 15, 1995.
- 3.3. WCAP-14382, "WGOTHIC Code Description and Validation," M. Kennedy, et al., May 1995.
- 3.4. Westinghouse Letter NTD-NRC-95-4595, B.A. McIntyre to Quay (NRC), "AP600 WGOTHIC Comparison to GOTHIC," November 13, 1995.
- 3.5. WCAP-14812, Rev. 2, "Accident Specification and Phenomena Evaluation for AP600 Passive Containment Cooling System," April 1998.
- 3.6. WCAP-14326, Rev. 2, "Experimental Basis for the AP600 Containment Vessel Heat and Mass Transfer Correlations," F. Delose, et al., April 1998
- 3.7. [APP-GW-GLR-096, Rev. 3, "Evaluation of the Effect of the AP1000® Enhanced Shield Building Design on the Containment Response and Safety Analyses," R. Ofstun, June 13, 2011.](#)

Deleted: GENERAL CLIME EQUATIONS **<#>Clime Equations Without Evaporation-** **Limited PCS Flow Option¶**

The energy equation for the film must balance the heat from the wall into the film, the heat conduction through the film, and the heat and mass transfer from the film surface to the ambient, with the change in energy of the flowing film. Assuming constant fluid properties over the node surface, one-dimensional film flow along the wall, one-dimensional conduction across the film, and that the viscous dissipation term can be neglected, the general energy transport equation for the film can be written in terms of temperature as:¶

$$\frac{\partial T}{\partial t} = \frac{k}{\rho c_p} \frac{\partial^2 T}{\partial x^2} + v_z \frac{\partial T}{\partial z} \quad (3-1)¶$$

For computational purposes, the water film is divided into 3 control volumes as shown in Figure 3-5. The boundary control volume of the film includes the outer 1/2 layer of the wall and its temperature equals the wall temperature. The outer surface of the outer control volume touches the atmosphere and its temperature is coupled to the temperature of the atmosphere through the heat and mass transfer boundary layer correlations. The temperature in the central control volume represents the average heat stored in the film. Note that all convected energy is transported in the central control volume. This simplification improves numerical stability. Referring to Figure 3-5, the film energy transport equation can be expressed in a finite difference form as follows:¶

$$\frac{T_{avg} - T_{avg,old}}{\Delta t} = \frac{4k_{film}}{\rho_{film} c_{p,film}} \frac{T_{surf,i} - 2T_{avg} + T_{wall,i}}{\delta x_{film}^2} + v_z \frac{T - T_{out}}{\Delta z} \quad (3-2)¶$$

where,¶

k_{film} = film thermal conductivity (Btu/ft-sec-°F)¶

δx_{film} = film thickness (ft)¶

$C_{p,film}$ = film heat capacity (Btu/lbm-°F)¶

ρ_{film} = film density (lbm/ft³)¶

T_{in} = inlet temperature of film at the top of the clime (°F)¶

T_{out} = exit temperature of film at the bottom of the clime (°F)¶

T_{avg} = temperature of the center of the film (°F)¶

$T_{wall,i}$ = temperature of first wall node (°F)¶

$T_{surf,i}$ = film surface temperature (°F)¶

Δz = height of the clime (ft)¶

v_z = film velocity (ft/sec)¶

...

4-1

4 DESCRIPTION OF AP600 PLANT GEOMETRY IN WGOTHIC EVALUATION MODEL

All information in this section is for the AP600 Evaluation Model. The model described herein is referenced in other sections of this report for sensitivities and comparison to test data. See Section 13 of this report for the AP1000 WGOTHIC Evaluation Model information.

This entire section (4) is proprietary to Westinghouse Electric Company. (a,c)

a,c

4-2

a,c

WCAP-15846-P, Revision 5
APP-SSAR-GSC-587, Revision 5

September 2016

4-3

a,c

WCAP-15846-P, Revision 5
APP-SSAR-GSC-587, Revision 5

September 2016

4-4

a,c

WCAP-15846-P, Revision 5
APP-SSAR-GSC-587, Revision 5

September 2016

4-5

a,c

WCAP-15846-P, Revision 5
APP-SSAR-GSC-587, Revision 5

September 2016

4-6

a,c

WCAP-15846-P, Revision 5
APP-SSAR-GSC-587, Revision 5

September 2016

4-7

a,c

WCAP-15846-P, Revision 5
APP-SSAR-GSC-587, Revision 5

September 2016

4-8

a,c

WCAP-15846-P, Revision 5
APP-SSAR-GSC-587, Revision 5

September 2016

4-9

a,c

WCAP-15846-P, Revision 5
APP-SSAR-GSC-587, Revision 5

September 2016

4-10

a,c

WCAP-15846-P, Revision 5
APP-SSAR-GSC-587, Revision 5

September 2016

4-11

a,c

WCAP-15846-P, Revision 5
APP-SSAR-GSC-587, Revision 5

September 2016

4-12

a,c

WCAP-15846-P, Revision 5
APP-SSAR-GSC-587, Revision 5

September 2016

4-13

a,c

WCAP-15846-P, Revision 5
APP-SSAR-GSC-587, Revision 5

September 2016

4-14

a,c

WCAP-15846-P, Revision 5
APP-SSAR-GSC-587, Revision 5

September 2016

4-15

a,c

WCAP-15846-P, Revision 5
APP-SSAR-GSC-587, Revision 5

September 2016

4-16

a,c

WCAP-15846-P, Revision 5
APP-SSAR-GSC-587, Revision 5

September 2016

4-17

a,c

WCAP-15846-P, Revision 5
APP-SSAR-GSC-587, Revision 5

September 2016

4-18

a,c

WCAP-15846-P, Revision 5
APP-SSAR-GSC-587, Revision 5

September 2016

4-19

a,c

WCAP-15846-P, Revision 5
APP-SSAR-GSC-587, Revision 5

September 2016

4-20

a,c

WCAP-15846-P, Revision 5
APP-SSAR-GSC-587, Revision 5

September 2016

4-21

a,c

WCAP-15846-P, Revision 5
APP-SSAR-GSC-587, Revision 5

September 2016

4-22

a,c

WCAP-15846-P, Revision 5
APP-SSAR-GSC-587, Revision 5

September 2016

4-23

a,c

WCAP-15846-P, Revision 5
APP-SSAR-GSC-587, Revision 5

September 2016

4-24

a,c

WCAP-15846-P, Revision 5
APP-SSAR-GSC-587, Revision 5

September 2016

4-25

a,c

WCAP-15846-P, Revision 5
APP-SSAR-GSC-587, Revision 5

September 2016

4-26

a,c

WCAP-15846-P, Revision 5
APP-SSAR-GSC-587, Revision 5

September 2016

4-27

a,c

WCAP-15846-P, Revision 5
APP-SSAR-GSC-587, Revision 5

September 2016

4-28

a,c

WCAP-15846-P, Revision 5
APP-SSAR-GSC-587, Revision 5

September 2016

4-29

a,c

WCAP-15846-P, Revision 5
APP-SSAR-GSC-587, Revision 5

September 2016

4-30

a,c

WCAP-15846-P, Revision 5
APP-SSAR-GSC-587, Revision 5

September 2016

4-31

a,c

WCAP-15846-P, Revision 5
APP-SSAR-GSC-587, Revision 5

September 2016

4-32

a,c

WCAP-15846-P, Revision 5
APP-SSAR-GSC-587, Revision 5

September 2016

4-33

a,c

WCAP-15846-P, Revision 5
APP-SSAR-GSC-587, Revision 5

September 2016

4-34

a,c

WCAP-15846-P, Revision 5
APP-SSAR-GSC-587, Revision 5

September 2016

4-35

a,c

WCAP-15846-P, Revision 5
APP-SSAR-GSC-587, Revision 5

September 2016

4-36

a,c

WCAP-15846-P, Revision 5
APP-SSAR-GSC-587, Revision 5

September 2016

4-37

a,c

WCAP-15846-P, Revision 5
APP-SSAR-GSC-587, Revision 5

September 2016

4-38

a,c

WCAP-15846-P, Revision 5
APP-SSAR-GSC-587, Revision 5

September 2016

4-39

a,c

WCAP-15846-P, Revision 5
APP-SSAR-GSC-587, Revision 5

September 2016

4-40

a,c

WCAP-15846-P, Revision 5
APP-SSAR-GSC-587, Revision 5

September 2016

4-41

a,c

WCAP-15846-P, Revision 5
APP-SSAR-GSC-587, Revision 5

September 2016

4-42

a,c

WCAP-15846-P, Revision 5
APP-SSAR-GSC-587, Revision 5

September 2016

4-43

a,c

WCAP-15846-P, Revision 5
APP-SSAR-GSC-587, Revision 5

September 2016

4-44

a,c

WCAP-15846-P, Revision 5
APP-SSAR-GSC-587, Revision 5

September 2016

4-45

a,c

WCAP-15846-P, Revision 5
APP-SSAR-GSC-587, Revision 5

September 2016

4-46

a,c

WCAP-15846-P, Revision 5
APP-SSAR-GSC-587, Revision 5

September 2016

4-47

a,c

WCAP-15846-P, Revision 5
APP-SSAR-GSC-587, Revision 5

September 2016

4-48

a,c

WCAP-15846-P, Revision 5
APP-SSAR-GSC-587, Revision 5

September 2016

4-49

a,c

WCAP-15846-P, Revision 5
APP-SSAR-GSC-587, Revision 5

September 2016

4-50

a,c

WCAP-15846-P, Revision 5
APP-SSAR-GSC-587, Revision 5

September 2016

4-51

a,c

WCAP-15846-P, Revision 5
APP-SSAR-GSC-587, Revision 5

September 2016

4-52

a,c

WCAP-15846-P, Revision 5
APP-SSAR-GSC-587, Revision 5

September 2016

4-53

a,c

WCAP-15846-P, Revision 5
APP-SSAR-GSC-587, Revision 5

September 2016

4-54

a,c

WCAP-15846-P, Revision 5
APP-SSAR-GSC-587, Revision 5

September 2016

4-55

a,c

WCAP-15846-P, Revision 5
APP-SSAR-GSC-587, Revision 5

September 2016

4-56

a,c

WCAP-15846-P, Revision 5
APP-SSAR-GSC-587, Revision 5

September 2016

4-57

a,c

WCAP-15846-P, Revision 5
APP-SSAR-GSC-587, Revision 5

September 2016

4-58

a,c

WCAP-15846-P, Revision 5
APP-SSAR-GSC-587, Revision 5

September 2016

4-59

a,c

WCAP-15846-P, Revision 5
APP-SSAR-GSC-587, Revision 5

September 2016

4-60

a,c

WCAP-15846-P, Revision 5
APP-SSAR-GSC-587, Revision 5

September 2016

4-61

a,c

WCAP-15846-P, Revision 5
APP-SSAR-GSC-587, Revision 5

September 2016

4-62

a,c

WCAP-15846-P, Revision 5
APP-SSAR-GSC-587, Revision 5

September 2016

4-63

a,c

WCAP-15846-P, Revision 5
APP-SSAR-GSC-587, Revision 5

September 2016

4-64

a,c

WCAP-15846-P, Revision 5
APP-SSAR-GSC-587, Revision 5

September 2016

4-65

a,c

WCAP-15846-P, Revision 5
APP-SSAR-GSC-587, Revision 5

September 2016

4-66

a,c

WCAP-15846-P, Revision 5
APP-SSAR-GSC-587, Revision 5

September 2016

4-67

a,c

WCAP-15846-P, Revision 5
APP-SSAR-GSC-587, Revision 5

September 2016

4-68

a,c

WCAP-15846-P, Revision 5
APP-SSAR-GSC-587, Revision 5

September 2016

4-69

a,c

WCAP-15846-P, Revision 5
APP-SSAR-GSC-587, Revision 5

September 2016

4-70

a,c

WCAP-15846-P, Revision 5
APP-SSAR-GSC-587, Revision 5

September 2016

4-71

a,c

WCAP-15846-P, Revision 5
APP-SSAR-GSC-587, Revision 5

September 2016

4-72

a,c

WCAP-15846-P, Revision 5
APP-SSAR-GSC-587, Revision 5

September 2016

4-73

a,c

WCAP-15846-P, Revision 5
APP-SSAR-GSC-587, Revision 5

September 2016

4-74

a,c

WCAP-15846-P, Revision 5
APP-SSAR-GSC-587, Revision 5

September 2016

4-75

a,c

WCAP-15846-P, Revision 5
APP-SSAR-GSC-587, Revision 5

September 2016

4-76

a,c

WCAP-15846-P, Revision 5
APP-SSAR-GSC-587, Revision 5

September 2016

4-77

a,c

WCAP-15846-P, Revision 5
APP-SSAR-GSC-587, Revision 5

September 2016

4-78

a,c

WCAP-15846-P, Revision 5
APP-SSAR-GSC-587, Revision 5

September 2016

4-79

a,c

WCAP-15846-P, Revision 5
APP-SSAR-GSC-587, Revision 5

September 2016

4-80

a,c

WCAP-15846-P, Revision 5
APP-SSAR-GSC-587, Revision 5

September 2016

4-81

a,c

WCAP-15846-P, Revision 5
APP-SSAR-GSC-587, Revision 5

September 2016

4-82

a,c

WCAP-15846-P, Revision 5
APP-SSAR-GSC-587, Revision 5

September 2016

4-83

a,c

WCAP-15846-P, Revision 5
APP-SSAR-GSC-587, Revision 5

September 2016

4-84

a,c

WCAP-15846-P, Revision 5
APP-SSAR-GSC-587, Revision 5

September 2016

4-85

a,c

WCAP-15846-P, Revision 5
APP-SSAR-GSC-587, Revision 5

September 2016

4-86

a,c

WCAP-15846-P, Revision 5
APP-SSAR-GSC-587, Revision 5

September 2016

4-87

a,c

WCAP-15846-P, Revision 5
APP-SSAR-GSC-587, Revision 5

September 2016

4-88

a,c

WCAP-15846-P, Revision 5
APP-SSAR-GSC-587, Revision 5

September 2016

4-89

a,c

WCAP-15846-P, Revision 5
APP-SSAR-GSC-587, Revision 5

September 2016

4-90

a,c

WCAP-15846-P, Revision 5
APP-SSAR-GSC-587, Revision 5

September 2016

4-91

a,c

WCAP-15846-P, Revision 5
APP-SSAR-GSC-587, Revision 5

September 2016

4-92

a,c

WCAP-15846-P, Revision 5
APP-SSAR-GSC-587, Revision 5

September 2016

4-93

a,c

WCAP-15846-P, Revision 5
APP-SSAR-GSC-587, Revision 5

September 2016

4-94

a,c

WCAP-15846-P, Revision 5
APP-SSAR-GSC-587, Revision 5

September 2016

4-95

a,c

WCAP-15846-P, Revision 5
APP-SSAR-GSC-587, Revision 5

September 2016

4-96

a,c

WCAP-15846-P, Revision 5
APP-SSAR-GSC-587, Revision 5

September 2016

4-97

a,c

WCAP-15846-P, Revision 5
APP-SSAR-GSC-587, Revision 5

September 2016

4-98

a,c

WCAP-15846-P, Revision 5
APP-SSAR-GSC-587, Revision 5

September 2016

4-99

a,c

WCAP-15846-P, Revision 5
APP-SSAR-GSC-587, Revision 5

September 2016

4-100

a,c

WCAP-15846-P, Revision 5
APP-SSAR-GSC-587, Revision 5

September 2016

4-101

a,c

WCAP-15846-P, Revision 5
APP-SSAR-GSC-587, Revision 5

September 2016

4-102

a,c

WCAP-15846-P, Revision 5
APP-SSAR-GSC-587, Revision 5

September 2016

4-103

a,c

WCAP-15846-P, Revision 5
APP-SSAR-GSC-587, Revision 5

September 2016

4-104

a,c

WCAP-15846-P, Revision 5
APP-SSAR-GSC-587, Revision 5

September 2016

4-105

a,c

WCAP-15846-P, Revision 5
APP-SSAR-GSC-587, Revision 5

September 2016

4-106

a,c

WCAP-15846-P, Revision 5
APP-SSAR-GSC-587, Revision 5

September 2016

4-107

a,c

WCAP-15846-P, Revision 5
APP-SSAR-GSC-587, Revision 5

September 2016

4-108

a,c

WCAP-15846-P, Revision 5
APP-SSAR-GSC-587, Revision 5

September 2016

4-109

a,c

WCAP-15846-P, Revision 5
APP-SSAR-GSC-587, Revision 5

September 2016

4-110

a,c

WCAP-15846-P, Revision 5
APP-SSAR-GSC-587, Revision 5

September 2016

4-111

a,c

WCAP-15846-P, Revision 5
APP-SSAR-GSC-587, Revision 5

September 2016

4-112

a,c

WCAP-15846-P, Revision 5
APP-SSAR-GSC-587, Revision 5

September 2016

4-113

a,c

WCAP-15846-P, Revision 5
APP-SSAR-GSC-587, Revision 5

September 2016

4-114

a,c

WCAP-15846-P, Revision 5
APP-SSAR-GSC-587, Revision 5

September 2016

4-115

a,c

WCAP-15846-P, Revision 5
APP-SSAR-GSC-587, Revision 5

September 2016

4-116

a,c

WCAP-15846-P, Revision 5
APP-SSAR-GSC-587, Revision 5

September 2016

4-117

a,c

WCAP-15846-P, Revision 5
APP-SSAR-GSC-587, Revision 5

September 2016

4-118

a,c

WCAP-15846-P, Revision 5
APP-SSAR-GSC-587, Revision 5

September 2016

4-119

a,c

WCAP-15846-P, Revision 5
APP-SSAR-GSC-587, Revision 5

September 2016

4-120

a,c

WCAP-15846-P, Revision 5
APP-SSAR-GSC-587, Revision 5

September 2016

4-121

a,c

WCAP-15846-P, Revision 5
APP-SSAR-GSC-587, Revision 5

September 2016

4-122

a,c

WCAP-15846-P, Revision 5
APP-SSAR-GSC-587, Revision 5

September 2016

4-123

a,c

WCAP-15846-P, Revision 5
APP-SSAR-GSC-587, Revision 5

September 2016

4-124

a,c

WCAP-15846-P, Revision 5
APP-SSAR-GSC-587, Revision 5

September 2016

4-125

a,c

WCAP-15846-P, Revision 5
APP-SSAR-GSC-587, Revision 5

September 2016

4-126

a,c

WCAP-15846-P, Revision 5
APP-SSAR-GSC-587, Revision 5

September 2016

4-127

a,c

WCAP-15846-P, Revision 5
APP-SSAR-GSC-587, Revision 5

September 2016

4-128

a,c

WCAP-15846-P, Revision 5
APP-SSAR-GSC-587, Revision 5

September 2016

4-129

a,c

WCAP-15846-P, Revision 5
APP-SSAR-GSC-587, Revision 5

September 2016

4-130

a,c

WCAP-15846-P, Revision 5
APP-SSAR-GSC-587, Revision 5

September 2016

4-131

a,c

WCAP-15846-P, Revision 5
APP-SSAR-GSC-587, Revision 5

September 2016

4-132

a,c

WCAP-15846-P, Revision 5
APP-SSAR-GSC-587, Revision 5

September 2016

4-133

a,c

WCAP-15846-P, Revision 5
APP-SSAR-GSC-587, Revision 5

September 2016

4-134

a,c

WCAP-15846-P, Revision 5
APP-SSAR-GSC-587, Revision 5

September 2016

4-135

a,c

WCAP-15846-P, Revision 5
APP-SSAR-GSC-587, Revision 5

September 2016

4-136

a,c

WCAP-15846-P, Revision 5
APP-SSAR-GSC-587, Revision 5

September 2016

4-137

a,c

WCAP-15846-P, Revision 5
APP-SSAR-GSC-587, Revision 5

September 2016

4-138

a,c

WCAP-15846-P, Revision 5
APP-SSAR-GSC-587, Revision 5

September 2016

4-139

a,c

WCAP-15846-P, Revision 5
APP-SSAR-GSC-587, Revision 5

September 2016

4-140

a,c

WCAP-15846-P, Revision 5
APP-SSAR-GSC-587, Revision 5

September 2016

4-141

a,c

WCAP-15846-P, Revision 5
APP-SSAR-GSC-587, Revision 5

September 2016

4-142

a,c

WCAP-15846-P, Revision 5
APP-SSAR-GSC-587, Revision 5

September 2016

4-143

a,c

WCAP-15846-P, Revision 5
APP-SSAR-GSC-587, Revision 5

September 2016

4-144

a,c

WCAP-15846-P, Revision 5
APP-SSAR-GSC-587, Revision 5

September 2016

4-145

a,c

WCAP-15846-P, Revision 5
APP-SSAR-GSC-587, Revision 5

September 2016

4-146

a,c

WCAP-15846-P, Revision 5
APP-SSAR-GSC-587, Revision 5

September 2016

4-147

a,c

WCAP-15846-P, Revision 5
APP-SSAR-GSC-587, Revision 5

September 2016

4-148

a,c

WCAP-15846-P, Revision 5
APP-SSAR-GSC-587, Revision 5

September 2016

4-149

a,c

WCAP-15846-P, Revision 5
APP-SSAR-GSC-587, Revision 5

September 2016

4-150

a,c

WCAP-15846-P, Revision 5
APP-SSAR-GSC-587, Revision 5

September 2016

4-151

a,c

WCAP-15846-P, Revision 5
APP-SSAR-GSC-587, Revision 5

September 2016

4-152

a,c

WCAP-15846-P, Revision 5
APP-SSAR-GSC-587, Revision 5

September 2016

4-153

a,c

WCAP-15846-P, Revision 5
APP-SSAR-GSC-587, Revision 5

September 2016

4-154

a,c

WCAP-15846-P, Revision 5
APP-SSAR-GSC-587, Revision 5

September 2016

4-155

a,c

WCAP-15846-P, Revision 5
APP-SSAR-GSC-587, Revision 5

September 2016

4-156

a,c

WCAP-15846-P, Revision 5
APP-SSAR-GSC-587, Revision 5

September 2016

4-157

a,c

WCAP-15846-P, Revision 5
APP-SSAR-GSC-587, Revision 5

September 2016

4-158

a,c

WCAP-15846-P, Revision 5
APP-SSAR-GSC-587, Revision 5

September 2016

4-159

a,c

WCAP-15846-P, Revision 5
APP-SSAR-GSC-587, Revision 5

September 2016

4-160

a,c

WCAP-15846-P, Revision 5
APP-SSAR-GSC-587, Revision 5

September 2016

4-161

a,c

WCAP-15846-P, Revision 5
APP-SSAR-GSC-587, Revision 5

September 2016

4-162

a,c

WCAP-15846-P, Revision 5
APP-SSAR-GSC-587, Revision 5

September 2016

4-163

a,c

WCAP-15846-P, Revision 5
APP-SSAR-GSC-587, Revision 5

September 2016

4-164

a,c

WCAP-15846-P, Revision 5
APP-SSAR-GSC-587, Revision 5

September 2016

4-165

a,c

WCAP-15846-P, Revision 5
APP-SSAR-GSC-587, Revision 5

September 2016

4-166

a,c

WCAP-15846-P, Revision 5
APP-SSAR-GSC-587, Revision 5

September 2016

4-167

a,c

WCAP-15846-P, Revision 5
APP-SSAR-GSC-587, Revision 5

September 2016

4-168

a,c

WCAP-15846-P, Revision 5
APP-SSAR-GSC-587, Revision 5

September 2016

4-169

a,c

WCAP-15846-P, Revision 5
APP-SSAR-GSC-587, Revision 5

September 2016

4-170

a,c

WCAP-15846-P, Revision 5
APP-SSAR-GSC-587, Revision 5

September 2016

4-171

a,c

WCAP-15846-P, Revision 5
APP-SSAR-GSC-587, Revision 5

September 2016

4-172

a,c

WCAP-15846-P, Revision 5
APP-SSAR-GSC-587, Revision 5

September 2016

4-173

a,c

WCAP-15846-P, Revision 5
APP-SSAR-GSC-587, Revision 5

September 2016

4-174

a,c

WCAP-15846-P, Revision 5
APP-SSAR-GSC-587, Revision 5

September 2016

4-175

a,c

WCAP-15846-P, Revision 5
APP-SSAR-GSC-587, Revision 5

September 2016

4-176

a,c

WCAP-15846-P, Revision 5
APP-SSAR-GSC-587, Revision 5

September 2016

4-177

a,c

WCAP-15846-P, Revision 5
APP-SSAR-GSC-587, Revision 5

September 2016

4-178

a,c

WCAP-15846-P, Revision 5
APP-SSAR-GSC-587, Revision 5

September 2016

4-179

a,c

WCAP-15846-P, Revision 5
APP-SSAR-GSC-587, Revision 5

September 2016

4-180

a,c

WCAP-15846-P, Revision 5
APP-SSAR-GSC-587, Revision 5

September 2016

4-181

a,c

WCAP-15846-P, Revision 5
APP-SSAR-GSC-587, Revision 5

September 2016

4-182

a,c

WCAP-15846-P, Revision 5
APP-SSAR-GSC-587, Revision 5

September 2016

4-183

a,c

WCAP-15846-P, Revision 5
APP-SSAR-GSC-587, Revision 5

September 2016

4-184

a,c

WCAP-15846-P, Revision 5
APP-SSAR-GSC-587, Revision 5

September 2016

4-185

a,c

WCAP-15846-P, Revision 5
APP-SSAR-GSC-587, Revision 5

September 2016

4-186

a,c

WCAP-15846-P, Revision 5
APP-SSAR-GSC-587, Revision 5

September 2016

4-187

a,c

WCAP-15846-P, Revision 5
APP-SSAR-GSC-587, Revision 5

September 2016

4-188

a,c

WCAP-15846-P, Revision 5
APP-SSAR-GSC-587, Revision 5

September 2016

4-189

a,c

WCAP-15846-P, Revision 5
APP-SSAR-GSC-587, Revision 5

September 2016

4-190

a,c

WCAP-15846-P, Revision 5
APP-SSAR-GSC-587, Revision 5

September 2016

4-191

a,c

WCAP-15846-P, Revision 5
APP-SSAR-GSC-587, Revision 5

September 2016

4-192

a,c

WCAP-15846-P, Revision 5
APP-SSAR-GSC-587, Revision 5

September 2016

4-193

a,c

WCAP-15846-P, Revision 5
APP-SSAR-GSC-587, Revision 5

September 2016

4-194

a,c

WCAP-15846-P, Revision 5
APP-SSAR-GSC-587, Revision 5

September 2016

4-195

a,c

WCAP-15846-P, Revision 5
APP-SSAR-GSC-587, Revision 5

September 2016

4-196

a,c

WCAP-15846-P, Revision 5
APP-SSAR-GSC-587, Revision 5

September 2016

4-197

a,c

WCAP-15846-P, Revision 5
APP-SSAR-GSC-587, Revision 5

September 2016

4-198

a,c

WCAP-15846-P, Revision 5
APP-SSAR-GSC-587, Revision 5

September 2016

4-199

a,c

WCAP-15846-P, Revision 5
APP-SSAR-GSC-587, Revision 5

September 2016

4-200

a,c

WCAP-15846-P, Revision 5
APP-SSAR-GSC-587, Revision 5

September 2016

4-201

a,c

WCAP-15846-P, Revision 5
APP-SSAR-GSC-587, Revision 5

September 2016

4-202

a,c

WCAP-15846-P, Revision 5
APP-SSAR-GSC-587, Revision 5

September 2016

4-203

a,c

WCAP-15846-P, Revision 5
APP-SSAR-GSC-587, Revision 5

September 2016

4-204

a,c

WCAP-15846-P, Revision 5
APP-SSAR-GSC-587, Revision 5

September 2016

4-205

a,c

WCAP-15846-P, Revision 5
APP-SSAR-GSC-587, Revision 5

September 2016

4-206

a,c

WCAP-15846-P, Revision 5
APP-SSAR-GSC-587, Revision 5

September 2016

4-207

a,c

WCAP-15846-P, Revision 5
APP-SSAR-GSC-587, Revision 5

September 2016

4-208

a,c

WCAP-15846-P, Revision 5
APP-SSAR-GSC-587, Revision 5

September 2016

4-209

a,c

WCAP-15846-P, Revision 5
APP-SSAR-GSC-587, Revision 5

September 2016

4-210

a,c

WCAP-15846-P, Revision 5
APP-SSAR-GSC-587, Revision 5

September 2016

4-211

a,c

WCAP-15846-P, Revision 5
APP-SSAR-GSC-587, Revision 5

September 2016

4-212

a,c

WCAP-15846-P, Revision 5
APP-SSAR-GSC-587, Revision 5

September 2016

4-213

a,c

WCAP-15846-P, Revision 5
APP-SSAR-GSC-587, Revision 5

September 2016

4-214

a,c

WCAP-15846-P, Revision 5
APP-SSAR-GSC-587, Revision 5

September 2016

4-215

a,c

WCAP-15846-P, Revision 5
APP-SSAR-GSC-587, Revision 5

September 2016

4-216

a,c

WCAP-15846-P, Revision 5
APP-SSAR-GSC-587, Revision 5

September 2016

4-217

a,c

WCAP-15846-P, Revision 5
APP-SSAR-GSC-587, Revision 5

September 2016

4-218

a,c

WCAP-15846-P, Revision 5
APP-SSAR-GSC-587, Revision 5

September 2016

4-219

a,c

WCAP-15846-P, Revision 5
APP-SSAR-GSC-587, Revision 5

September 2016

4-220

a,c

WCAP-15846-P, Revision 5
APP-SSAR-GSC-587, Revision 5

September 2016

4-221

a,c

WCAP-15846-P, Revision 5
APP-SSAR-GSC-587, Revision 5

September 2016

4-222

a,c

WCAP-15846-P, Revision 5
APP-SSAR-GSC-587, Revision 5

September 2016

4-223

a,c

WCAP-15846-P, Revision 5
APP-SSAR-GSC-587, Revision 5

September 2016

4-224

a,c

WCAP-15846-P, Revision 5
APP-SSAR-GSC-587, Revision 5

September 2016

4-225

a,c

WCAP-15846-P, Revision 5
APP-SSAR-GSC-587, Revision 5

September 2016

4-226

a,c

WCAP-15846-P, Revision 5
APP-SSAR-GSC-587, Revision 5

September 2016

4-227

a,c

WCAP-15846-P, Revision 5
APP-SSAR-GSC-587, Revision 5

September 2016

4-228

a,c

WCAP-15846-P, Revision 5
APP-SSAR-GSC-587, Revision 5

September 2016

4-229

a,c

WCAP-15846-P, Revision 5
APP-SSAR-GSC-587, Revision 5

September 2016

4-230

a,c

WCAP-15846-P, Revision 5
APP-SSAR-GSC-587, Revision 5

September 2016

4-231

a,c

WCAP-15846-P, Revision 5
APP-SSAR-GSC-587, Revision 5

September 2016

4-232

a,c

WCAP-15846-P, Revision 5
APP-SSAR-GSC-587, Revision 5

September 2016

4-233

a,c

WCAP-15846-P, Revision 5
APP-SSAR-GSC-587, Revision 5

September 2016

4-234

a,c

WCAP-15846-P, Revision 5
APP-SSAR-GSC-587, Revision 5

September 2016

4-235

a,c

WCAP-15846-P, Revision 5
APP-SSAR-GSC-587, Revision 5

September 2016

4-236

a,c

WCAP-15846-P, Revision 5
APP-SSAR-GSC-587, Revision 5

September 2016

4-237

a,c

WCAP-15846-P, Revision 5
APP-SSAR-GSC-587, Revision 5

September 2016

4-238

a,c

WCAP-15846-P, Revision 5
APP-SSAR-GSC-587, Revision 5

September 2016

4-239

a,c

WCAP-15846-P, Revision 5
APP-SSAR-GSC-587, Revision 5

September 2016

4-240

a,c

WCAP-15846-P, Revision 5
APP-SSAR-GSC-587, Revision 5

September 2016

4-241

a,c

WCAP-15846-P, Revision 5
APP-SSAR-GSC-587, Revision 5

September 2016

4-242

a,c

WCAP-15846-P, Revision 5
APP-SSAR-GSC-587, Revision 5

September 2016

4-243

a,c

WCAP-15846-P, Revision 5
APP-SSAR-GSC-587, Revision 5

September 2016

4-244

a,c

WCAP-15846-P, Revision 5
APP-SSAR-GSC-587, Revision 5

September 2016

4-245

a,c

WCAP-15846-P, Revision 5
APP-SSAR-GSC-587, Revision 5

September 2016

4-246

a,c

WCAP-15846-P, Revision 5
APP-SSAR-GSC-587, Revision 5

September 2016

4-247

a,c

WCAP-15846-P, Revision 5
APP-SSAR-GSC-587, Revision 5

September 2016

4-248

a,c

WCAP-15846-P, Revision 5
APP-SSAR-GSC-587, Revision 5

September 2016

4-249

a,c

WCAP-15846-P, Revision 5
APP-SSAR-GSC-587, Revision 5

September 2016

4-250

a,c

WCAP-15846-P, Revision 5
APP-SSAR-GSC-587, Revision 5

September 2016

4-251

a,c

WCAP-15846-P, Revision 5
APP-SSAR-GSC-587, Revision 5

September 2016

4-252

a,c

WCAP-15846-P, Revision 5
APP-SSAR-GSC-587, Revision 5

September 2016

4-253

a,c

WCAP-15846-P, Revision 5
APP-SSAR-GSC-587, Revision 5

September 2016

4-254

a,c

WCAP-15846-P, Revision 5
APP-SSAR-GSC-587, Revision 5

September 2016

4-255

a,c

WCAP-15846-P, Revision 5
APP-SSAR-GSC-587, Revision 5

September 2016

4-256

a,c

WCAP-15846-P, Revision 5
APP-SSAR-GSC-587, Revision 5

September 2016

4-257

a,c

WCAP-15846-P, Revision 5
APP-SSAR-GSC-587, Revision 5

September 2016

4-258

a,c

WCAP-15846-P, Revision 5
APP-SSAR-GSC-587, Revision 5

September 2016

4-259

a,c

WCAP-15846-P, Revision 5
APP-SSAR-GSC-587, Revision 5

September 2016

4-260

a,c

WCAP-15846-P, Revision 5
APP-SSAR-GSC-587, Revision 5

September 2016

4-261

a,c

WCAP-15846-P, Revision 5
APP-SSAR-GSC-587, Revision 5

September 2016

4-262

a,c

WCAP-15846-P, Revision 5
APP-SSAR-GSC-587, Revision 5

September 2016

4-263

a,c

WCAP-15846-P, Revision 5
APP-SSAR-GSC-587, Revision 5

September 2016

4-264

a,c

WCAP-15846-P, Revision 5
APP-SSAR-GSC-587, Revision 5

September 2016

4-265

a,c

WCAP-15846-P, Revision 5
APP-SSAR-GSC-587, Revision 5

September 2016

4-266

a,c

WCAP-15846-P, Revision 5
APP-SSAR-GSC-587, Revision 5

September 2016

4-267

a,c

WCAP-15846-P, Revision 5
APP-SSAR-GSC-587, Revision 5

September 2016

4-268

a,c

WCAP-15846-P, Revision 5
APP-SSAR-GSC-587, Revision 5

September 2016

4-269

a,c

WCAP-15846-P, Revision 5
APP-SSAR-GSC-587, Revision 5

September 2016

4-270

a,c

WCAP-15846-P, Revision 5
APP-SSAR-GSC-587, Revision 5

September 2016

4-271

a,c

WCAP-15846-P, Revision 5
APP-SSAR-GSC-587, Revision 5

September 2016

4-272

a,c

WCAP-15846-P, Revision 5
APP-SSAR-GSC-587, Revision 5

September 2016

4-273

a,c

WCAP-15846-P, Revision 5
APP-SSAR-GSC-587, Revision 5

September 2016

4-274

a,c

WCAP-15846-P, Revision 5
APP-SSAR-GSC-587, Revision 5

September 2016

4-275

a,c

WCAP-15846-P, Revision 5
APP-SSAR-GSC-587, Revision 5

September 2016

4-276

a,c

WCAP-15846-P, Revision 5
APP-SSAR-GSC-587, Revision 5

September 2016

4-277

a,c

WCAP-15846-P, Revision 5
APP-SSAR-GSC-587, Revision 5

September 2016

4-278

a,c

WCAP-15846-P, Revision 5
APP-SSAR-GSC-587, Revision 5

September 2016

4-279

a,c

WCAP-15846-P, Revision 5
APP-SSAR-GSC-587, Revision 5

September 2016

4-280

a,c

WCAP-15846-P, Revision 5
APP-SSAR-GSC-587, Revision 5

September 2016

4-281

a,c

WCAP-15846-P, Revision 5
APP-SSAR-GSC-587, Revision 5

September 2016

4-282

a,c

WCAP-15846-P, Revision 5
APP-SSAR-GSC-587, Revision 5

September 2016

4-283

a,c

WCAP-15846-P, Revision 5
APP-SSAR-GSC-587, Revision 5

September 2016

4-284

a,c

WCAP-15846-P, Revision 5
APP-SSAR-GSC-587, Revision 5

September 2016

4-285

a,c

WCAP-15846-P, Revision 5
APP-SSAR-GSC-587, Revision 5

September 2016

4-286

a,c

WCAP-15846-P, Revision 5
APP-SSAR-GSC-587, Revision 5

September 2016

4-287

a,c

WCAP-15846-P, Revision 5
APP-SSAR-GSC-587, Revision 5

September 2016

4-288

a,c

WCAP-15846-P, Revision 5
APP-SSAR-GSC-587, Revision 5

September 2016

4-289

a,c

WCAP-15846-P, Revision 5
APP-SSAR-GSC-587, Revision 5

September 2016

4-290

a,c

WCAP-15846-P, Revision 5
APP-SSAR-GSC-587, Revision 5

September 2016

4-291

a,c

WCAP-15846-P, Revision 5
APP-SSAR-GSC-587, Revision 5

September 2016

4-292

a,c

WCAP-15846-P, Revision 5
APP-SSAR-GSC-587, Revision 5

September 2016

4-293

a,c

WCAP-15846-P, Revision 5
APP-SSAR-GSC-587, Revision 5

September 2016

4-294

a,c

WCAP-15846-P, Revision 5
APP-SSAR-GSC-587, Revision 5

September 2016

4-295

a,c

WCAP-15846-P, Revision 5
APP-SSAR-GSC-587, Revision 5

September 2016

4-296

a,c

WCAP-15846-P, Revision 5
APP-SSAR-GSC-587, Revision 5

September 2016

4-297

a,c

WCAP-15846-P, Revision 5
APP-SSAR-GSC-587, Revision 5

September 2016

4-298

a,c

WCAP-15846-P, Revision 5
APP-SSAR-GSC-587, Revision 5

September 2016

4-299

a,c

WCAP-15846-P, Revision 5
APP-SSAR-GSC-587, Revision 5

September 2016

4-300

a,c

WCAP-15846-P, Revision 5
APP-SSAR-GSC-587, Revision 5

September 2016

4-301

a,c

WCAP-15846-P, Revision 5
APP-SSAR-GSC-587, Revision 5

September 2016

4-302

a,c

WCAP-15846-P, Revision 5
APP-SSAR-GSC-587, Revision 5

September 2016

4-303

a,c

WCAP-15846-P, Revision 5
APP-SSAR-GSC-587, Revision 5

September 2016

4-304

a,c

WCAP-15846-P, Revision 5
APP-SSAR-GSC-587, Revision 5

September 2016

4-305

a,c

WCAP-15846-P, Revision 5
APP-SSAR-GSC-587, Revision 5

September 2016

4-306

a,c

WCAP-15846-P, Revision 5
APP-SSAR-GSC-587, Revision 5

September 2016

4-307

a,c

WCAP-15846-P, Revision 5
APP-SSAR-GSC-587, Revision 5

September 2016

4-308

a,c

WCAP-15846-P, Revision 5
APP-SSAR-GSC-587, Revision 5

September 2016

4-309

a,c

WCAP-15846-P, Revision 5
APP-SSAR-GSC-587, Revision 5

September 2016

4-310

a,c

WCAP-15846-P, Revision 5
APP-SSAR-GSC-587, Revision 5

September 2016

4-311

a,c

WCAP-15846-P, Revision 5
APP-SSAR-GSC-587, Revision 5

September 2016

4-312

a,c

WCAP-15846-P, Revision 5
APP-SSAR-GSC-587, Revision 5

September 2016

4-313

a,c

WCAP-15846-P, Revision 5
APP-SSAR-GSC-587, Revision 5

September 2016

4-314

a,c

WCAP-15846-P, Revision 5
APP-SSAR-GSC-587, Revision 5

September 2016

4-315

a,c

WCAP-15846-P, Revision 5
APP-SSAR-GSC-587, Revision 5

September 2016

4-316

a,c

WCAP-15846-P, Revision 5
APP-SSAR-GSC-587, Revision 5

September 2016

4-317

a,c

WCAP-15846-P, Revision 5
APP-SSAR-GSC-587, Revision 5

September 2016

4-318

a,c

WCAP-15846-P, Revision 5
APP-SSAR-GSC-587, Revision 5

September 2016

4-319

a,c

WCAP-15846-P, Revision 5
APP-SSAR-GSC-587, Revision 5

September 2016

4-320

a,c

WCAP-15846-P, Revision 5
APP-SSAR-GSC-587, Revision 5

September 2016

4-321

a,c

WCAP-15846-P, Revision 5
APP-SSAR-GSC-587, Revision 5

September 2016

4-322

a,c

WCAP-15846-P, Revision 5
APP-SSAR-GSC-587, Revision 5

September 2016

5-1

5 INITIAL AND BOUNDARY CONDITIONS

5.1 INTRODUCTION

The purpose of this section is to describe a series of sensitivity analyses performed using the AP600 containment model to examine the effect of initial conditions on containment pressure response for the LOCA and MSLB events. Sensitivity evaluations are performed on initial containment humidity, pressure, and temperature, as well as ambient (outside containment) humidity and temperature. In addition, a sensitivity to drop modeling assumptions – a boundary condition for LOCA – is presented in this section.

Initial conditions assumed in the WGOTHIC Evaluation Model are conservatively set to maximize containment pressure response and are consistent with Technical Specifications and site interface parameter limits. Initial conditions assumed in the sensitivity evaluations are set at the opposing end of the Technical Specifications and site interface parameter limits for all sensitivity cases in this section except for the external temperature sensitivity, which was examined over a more limited range to be consistent with the film temperature range.

5.2 INITIAL CONDITION SENSITIVITY CASES

The initial conditions considered in the sensitivity studies are summarized in Table 5-1. The relative humidity inside containment is set to 0% for the containment EM. The input for the other initial conditions for the plant licensing analyses will be defined by the Technical Specifications and site parameters, in the direction of conservatism determined by these sensitivities.

Table 5-1. Initial Conditions

Initial Condition	Reference Value	Sensitivity Value	Direction of Conservatism for Evaluation Model
Containment Relative Humidity, %	0	100	Low
Containment Pressure, psia	15.7	14.5	High
Containment Temperature, °F	120	50	High
Ambient (Outside) Relative Humidity (Based on maximum wet bulb temperature coincident with maximum dry bulb temperature), %	22	0	High
Ambient (Outside) Temperature (Based on maximum dry bulb temperature), °F	115	40	High
Water Film Temperature on Outside Shell Surface, °F	120	40	High

Deleted: . The reference values for the initial condition parameters were selected in the Evaluation Model to maximize peak containment pressure ba (...)

Deleted: reference value in Table 5-1 corresponds to what is used in the Evaluation Model.

Deleted: ¶

Deleted: Sensitivity Case

Formatted: Superscript

Deleted: and dry bulb s

Deleted: (Based on 80°F wet bulb temperature at 115°F) 100% Relative Humidity is the maximum value when the ambient temperature is 40°F

Deleted: ,

Formatted: Left, Indent: Left: 0.25"

5-2

The sensitivity cases considered for the LOCA and MSLB transients are summarized in Table 5-2 with the initial condition parameters assumed in each case. Only values noted in Table 5-2 were varied in each of the cases. The reference cases for the LOCA and MSLB are described in Sections 4.5.2.1 and 4.5.2.2, respectively. The mass and energy releases are the same for all LOCA and MSLB cases. A summary of the pressure results are summarized in Table 5-3 for the LOCA and Table 5-4 for the MSLB. A discussion of each sensitivity case is provided in the following sections.

Table 5-2. Initial Conditions Sensitivity Analysis Cases

Case	Inside Containment					Outside Containment		
	Transient	T-air (°F)	P (psia)	RH (%)	T-ht. sink (°F)	T-air (°F)	T-film (°F)	RH (%)
Reference		120	15.7	0	120	115	120	22
1	LOCA	120	15.7	100	120	115	120	22
2	LOCA	120	14.5	0	120	115	120	22
3	LOCA	50	15.7	0	50	115	120	22
4	LOCA	120	15.7	0	120	115	120	0
5	LOCA	120	15.7	0	120	40	40	100
6	LOCA	120	15.7	0	120	40	40	0
7	LOCA	120	15.7	0	120	115	40	22
8	MSLB	120	15.7	100	120	115	120	22
9	MSLB	120	14.5	0	120	115	120	22
10	MSLB	50	15.7	0	50	115	120	22
11	MSLB	120	15.7	0	120	115	120	0
12	MSLB	120	15.7	0	120	40	40	100
13	MSLB	120	15.7	0	120	40	40	0
14	MSLB	120	15.7	0	120	115	40	22

5-3

Table 5-3. Summary of Pressure Results for LOCA Initial Condition Sensitivity Studies

	Peak Pressure during Blowdown (psig)	Peak Post-Blowdown Pressure (psig)	Pressure at 24 Hours (psig)
Eval. Model	34.4	43.9	18.9
Case 1	34.0	42.5	16.6
Case 2	33.0	42.1	17.2
Case 3	35.2	42.5	19.4
Case 4	34.4	43.9	18.9
Case 5	34.4	43.7	16.6
Case 6	34.4	43.7	16.6
Case 7	34.4	43.7	16.6

Table 5-4. Summary of Pressure Results for MSLB Initial Condition Sensitivity Studies

	Peak Pressure (psig)
Evaluation Model	44.8
Case 8	43.6
Case 9	42.9
Case 10	44.6
Case 11	44.7
Case 12	44.7
Case 13	44.7
Case 14	44.7

5.3 INITIAL CONTAINMENT HUMIDITY

The purpose of this sensitivity analysis is to illustrate the effect of initial containment humidity on containment pressure response. Initial humidity affects the initial mass of air in the containment and the concentration of air inside containment during the accident. In general, the presence of non-condensable gases reduces the effectiveness of internal heat sink structures to absorb energy, since the condensing vapor must diffuse through the gas before it can condense on the surface.

The upper and lower bounds on relative humidity are 100 percent and 0 percent, respectively. The minimum, initial containment relative humidity (0 percent) is used for the Evaluation Model, since this value produces a higher peak containment pressure. The maximum relative humidity (100 percent) is assumed for the sensitivity case in order to quantify the effect of initial containment relative humidity on containment pressure response.

The sensitivity of containment pressure to initial containment humidity is illustrated in Figure 5-1 for the LOCA (Case 1) and Figure 5-2 for the MSLB (Case 8). The sensitivity and reference cases are compared, corresponding to 100 percent and 0 percent relative humidity, respectively. A higher containment pressure response is predicted for zero percent relative humidity than for the sensitivity case at 100 percent relative humidity. The effect of relative humidity on containment pressure is explained by the influence of air on the rate of condensation on internal heat sink structures, and the additional mass of air in containment. Lower relative humidity corresponds to lower vapor partial pressure and hence, to lower water vapor concentration. Since the total initial pressure is fixed, the partial pressure and, therefore, the concentration of air is greater at 0 percent than at 100 percent relative humidity. The higher mass of air also contributes to the pressurization as it heats up in thermal equilibrium with the steam. A greater quantity of air in the condensing vapor also results in greater resistance to heat transfer, since the vapor must diffuse through the gas before it can condense on the surface. This factor reduces the overall heat removal capability of internal heat sink structures, and results in greater containment pressures for the initial 0 percent relative humidity case.

5.4 INITIAL CONTAINMENT PRESSURE

Initial containment pressure directly affects the containment pressure response. The range of initial containment pressures is bounded by the Technical Specifications limits. The initial internal containment pressure is set to the maximum Technical Specifications limit of 15.7 psia (1.0 psig) in the Evaluation Model. The lower bound (sensitivity case) initial containment pressure is set at the minimum Technical Specification limit of 14.5 psia (-0.2 psig).

The sensitivity of containment pressure to the initial containment pressure is shown in Figure 5-3 for the LOCA (Case 2) and Figure 5-4 for the MSLB (Case 9). As expected, greater initial containment pressure results in greater containment pressure response throughout the transient. A higher initial pressure results in a greater mass (and hence concentration) of air and results in higher containment pressures.

5-5

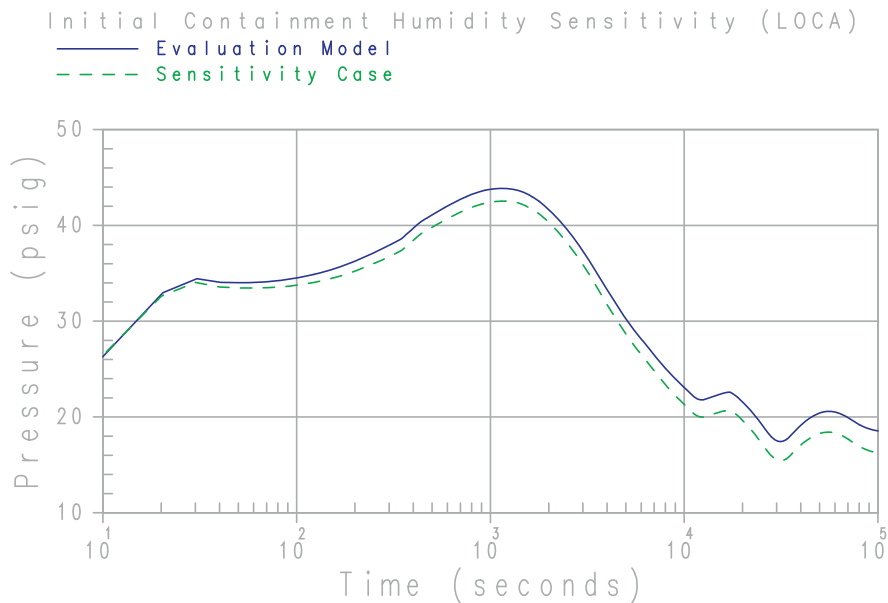


Figure 5-1. Case 1 – Initial Containment Humidity Sensitivity – LOCA

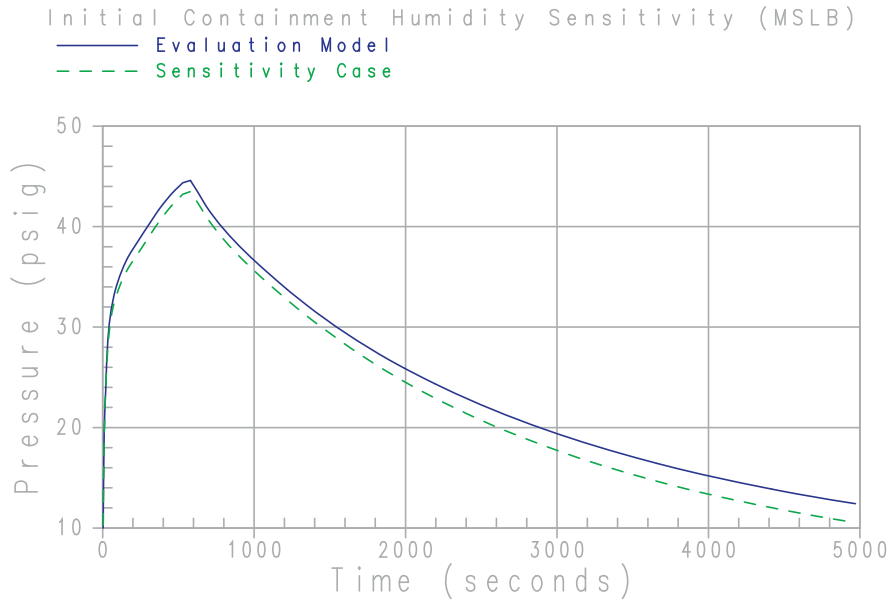


Figure 5-2. Case 8 – Initial Containment Humidity Sensitivity – MSLB

5-6

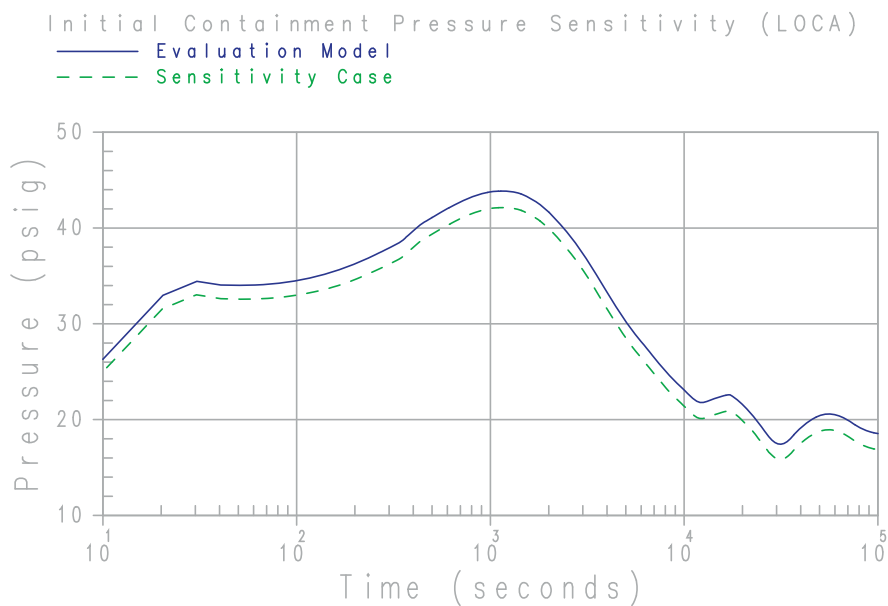


Figure 5-3. Case 8 – Initial Containment Humidity Sensitivity – MSLB

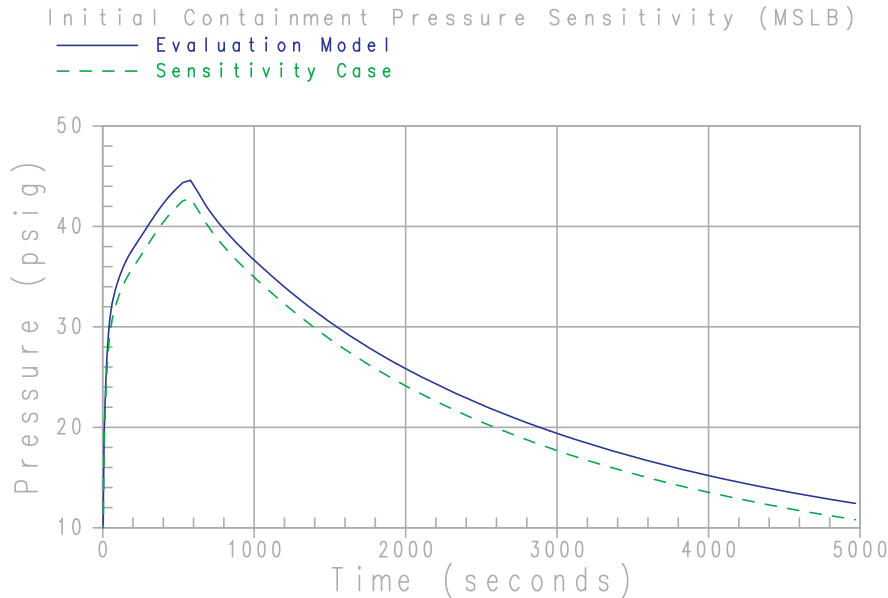


Figure 5-4. Case 9 – Initial Containment Pressure Sensitivity – MSLB

5.5 INITIAL CONTAINMENT TEMPERATURE

The purpose of this sensitivity analysis is to quantify the effect of initial containment temperature on containment pressure response. Containment air, internal heat sink, and containment shell initial temperature are simultaneously varied. A change in the initial air temperature affects the concentration of air inside containment. A change in the initial containment heat sink temperature directly affects the heat absorption capacity of these structures.

The initial containment temperature is set to the maximum Technical Specification limit of 120°F in the Evaluation Model. The lower bound (sensitivity case) initial containment temperature is set to a value of 50°F.

The sensitivity of containment pressure to initial containment temperature is shown in Figure 5-5 for the LOCA (Case 3) and Figure 5-6 for the MSLB (Case 10). As indicated, a higher peak containment pressure is predicted for the Evaluation Model case at 120°F, than for the sensitivity case at 50°F initial temperature. As illustrated in Figure 5-5, the pressure is higher for the 50°F initial temperature case during the blowdown phase of the transient, lower at the time of maximum pressure, and higher beyond approximately 5000 seconds. For the MSLB case shown in Figure 5-6, the peak pressure is slightly lower for the 50°F initial temperature case, but is higher during the initial pressure rise and beyond approximately 2000 seconds.

This pressure response behavior is predominately due to two competing influences: (1) the effect of initial temperature on the amount of air in the containment, and (2) the effect of initial temperature on the heat absorption capacity of internal heat sink structures. A lower initial temperature results in a higher air mass which contributes to the pressurization as the containment heats up. The increased concentration inhibits condensation of vapor on internal heat sinks and results in higher containment pressures. In contrast, a lower initial temperature results in increased heat absorption capacity of internal heat sinks that tend to lower containment pressures. Initially the non-condensable gas concentration factor dominates, and the sensitivity case exhibits a slightly higher containment pressure. When the heat absorption capacity of internal heat sinks becomes the more dominant factor, a higher containment pressure results for the Evaluation Model case. As the internal heat sinks saturate, the air concentration factor again becomes the governing influence, and the pressure for the sensitivity case exceeds that for the Evaluation Model. The Evaluation Model uses the maximum temperature assumption in order to maximize the more limiting post-blowdown peak containment pressure.

5-8

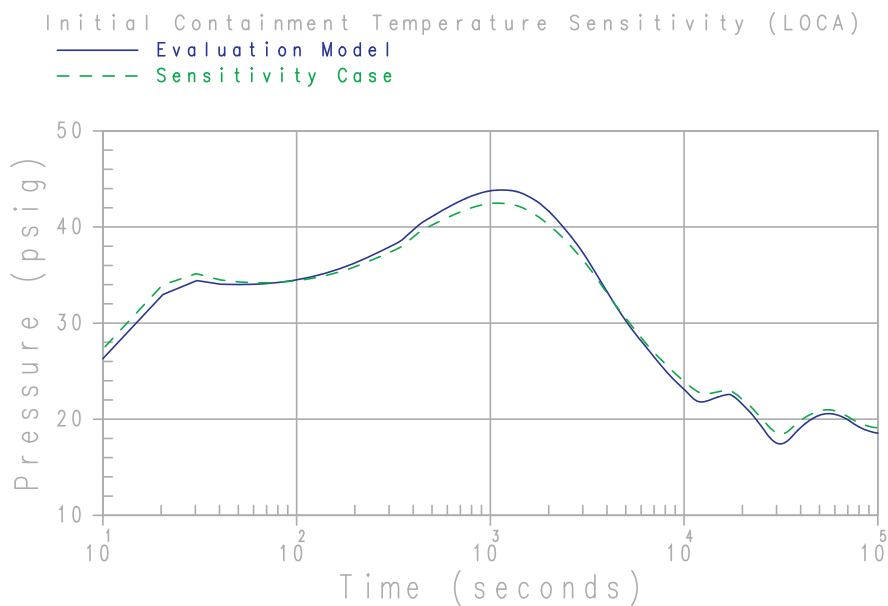


Figure 5-5. Case 3 – Initial Containment Temperature Sensitivity – LOCA

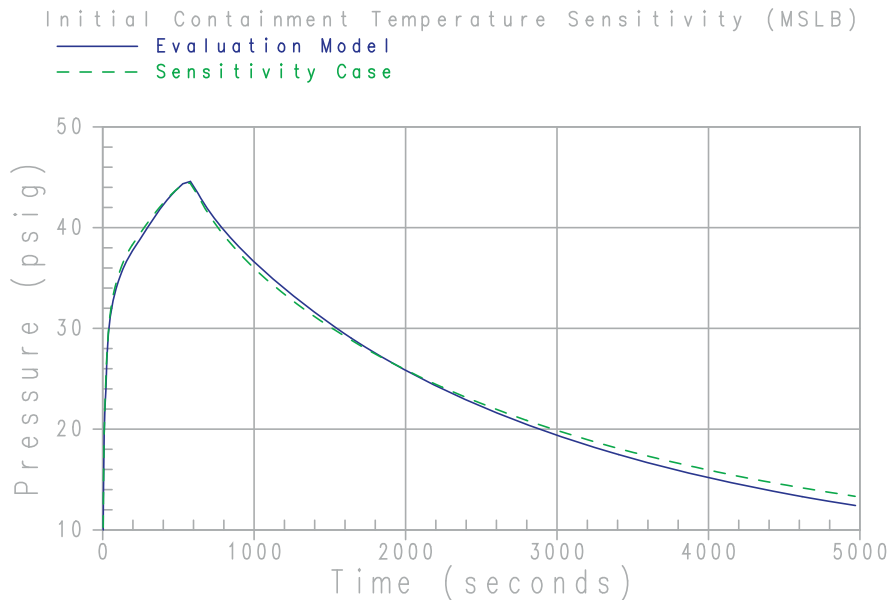


Figure 5-6. Case 10 – Initial Containment Temperature Sensitivity – MSLB

5.6 AMBIENT HUMIDITY

Heat is removed from the containment atmosphere by condensation and convection heat transfer to the shell, where it is conducted through the shell and rejected to the atmosphere on the outside of containment. Heat rejection to the atmosphere is achieved by convection to the buoyant cooling air, radiation to the baffle, and evaporation of the external PCS film to the cooling air. Evaporation of PCS water is the most significant of these heat removal mechanisms. Evaporation mass transfer is driven by the concentration gradient, or equivalently, the vapor partial pressure difference between the film and riser air. Changes in ambient or outside atmospheric conditions (e.g., relative humidity) can influence, to some degree, the vapor partial pressure difference. The purpose of this sensitivity analysis is to evaluate the effect of ambient humidity on containment pressure response.

The upper limit of ambient humidity is defined by the site interface parameters to be a maximum wet bulb temperature of 80°F for the AP600 plant. This corresponds to a relative humidity of 22 percent when the ambient temperature is 115°F. These boundary conditions are assumed in the Evaluation Model.

Two sets of sensitivities to relative humidity are presented. The first provides a comparison of the Evaluation Model to the case with 0 percent relative humidity at an ambient temperature of 115°F. The second sensitivity compares relative humidity of 0 percent and 100 percent at an ambient temperature of 40°F.

The sensitivity of containment pressure to ambient humidity is depicted in Figure 5-7 for the LOCA (Case 4) and Figure 5-8 for the MSLB (Case 11). The sensitivity and reference cases are compared corresponding to 0 and 22 percent relative humidity, respectively. These figures illustrate that containment pressure is not sensitive to initial inlet humidity. This result is consistent with the small effect of inlet humidity on the main factors governing the process of evaporation between the wetted shell and the riser air flow. The rate of evaporation is principally driven by the concentration gradient or, equivalently, the difference in vapor partial pressure between the film interface and the bulk air mixture. The partial pressure of vapor at the film interface is equal to the saturation pressure at the film temperature. Because the concentration of water vapor in the bulk air mixture is small in comparison, the partial pressure gradient is essentially given by the saturation pressure at the film interface. Consequently, initial inlet humidity has no significant effect on the rate of film evaporation or on containment pressure.

The sensitivity performed at 40°F, comparing 0 and 100 percent relative humidity, exhibited the same behavior, indicating almost no sensitivity to ambient humidity. A comparison of Case 5 to Case 6 for LOCA, and Case 12 to Case 13 for MSLB indicates a nearly identical pressure response. A comparison plot for these cases is not provided. The differences in these cases compared to the Evaluation Model are due to ambient temperature differences which are discussed in the Section 5.7.

5-10

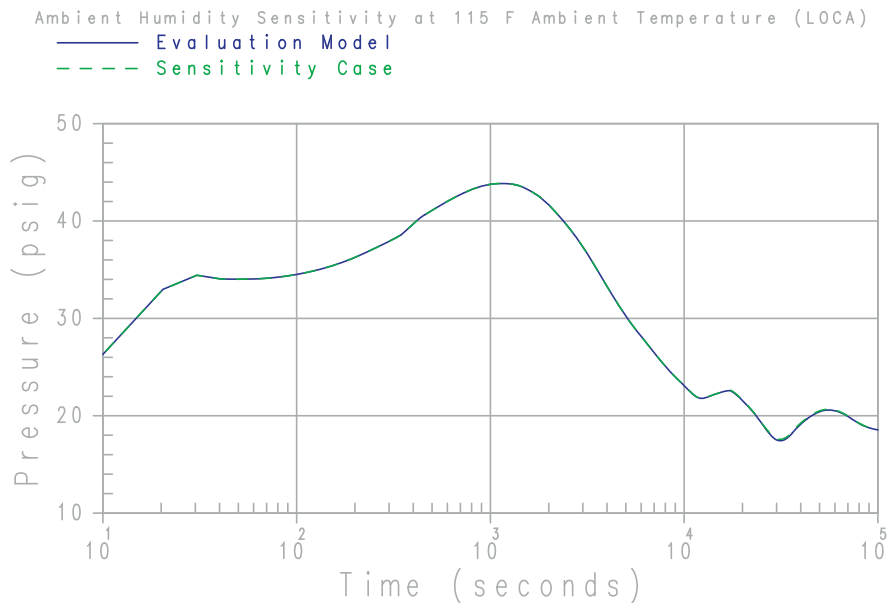


Figure 5-7. Case 4 – Ambient Humidity Sensitivity at 115°F Ambient Temperature – LOCA

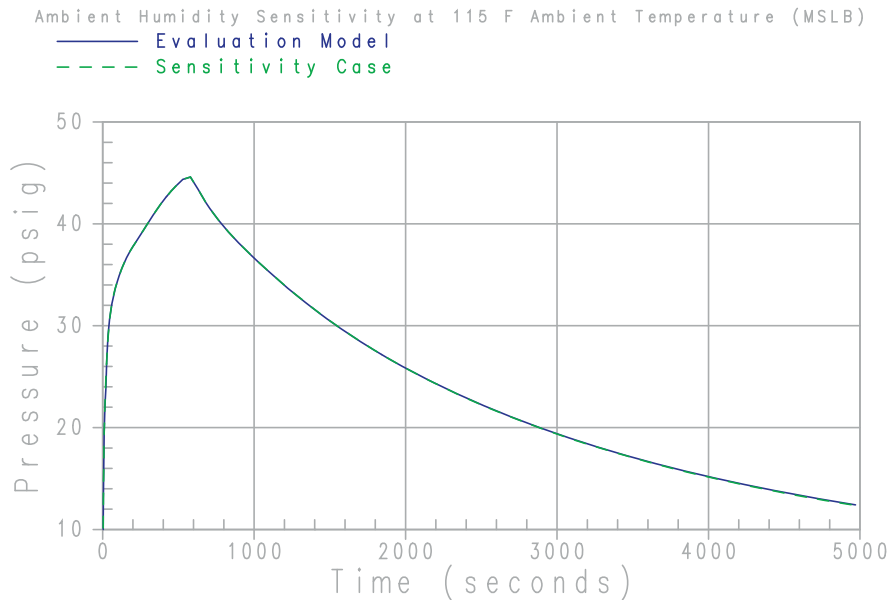


Figure 5-8. Case 11 – Ambient Humidity Sensitivity at 115°F Ambient Temperature – MSLB

5.7 AMBIENT TEMPERATURE

The purpose of this sensitivity analysis is to illustrate the effect of ambient temperature on containment pressure response. Cooling air and PCS water temperature are simultaneously and independently varied in order to investigate the effects. A change in the ambient air temperature primarily affects heat rejection by convection to the riser air flow. A change in the PCS water temperature affects the amount of energy absorbed by sensible heating.

The site interface parameter limits on ambient air temperature are 115°F and -40°F. The minimum PCS water temperature is limited by the Technical Specifications to a value of 40°F. Since a higher ambient temperature and PCS water temperature produces a slightly greater containment pressure, the maximum ambient temperature (115°F) and PCS water temperature (120°F) are assumed for the Evaluation Model. The temperature for both inlet air and PCS water (sensitivity case) is set equal to 40°F.

The sensitivity of containment pressure to ambient temperature is shown in Figure 5-9 for the LOCA (Case 5) and Figure 5-10 for the MSLB (Case 12). As indicated, lower containment pressures are predicted for the sensitivity case at lower ambient temperatures late in the transient for the LOCA case. There is little impact on the peak pressure or pressure early in time. The containment pressure for an MSLB is less sensitive to external conditions and therefore, there is a smaller impact on pressure for the entire transient.

The reduction in the long-term pressure is primarily attributed to liquid subcooling with a small contribution due to forced convection heat transfer effects. The external liquid film absorbs sensible heat from the point of PCS flow application to the point where significant film evaporation occurs. The subcooled heat capacity is dependent on water source temperature and external water flow rate. A lower source temperature results in greater subcooled heat capacity of the external film and, hence, more energy removed from containment. Forced convection heat transfer exists in the riser post-wetting as a result of the high buoyancy-driven air flow rate. The rate of energy transfer by forced convection is dependent on the heat transfer coefficient and the temperature difference between the liquid film and bulk air. Of these parameters, the temperature difference is influenced to a greater extent by bulk air temperature. A lower bulk air temperature results in greater forced convection heat transfer and, therefore, more energy removal from containment. The combined energy absorbed by liquid subcooling and forced convection represents a small fraction of the total energy removed from containment. Consequently, lowering the ambient air and source water temperatures to 40°F results in more total energy removed from containment, and, therefore, results in a decrease in containment pressure relative to the Evaluation Model.

Case 7 (LOCA) and Case 14 (MSLB) considered only the change in PCS water temperature, shown in Figures 5-11 and 5-12, respectively. These cases confirm that the air temperature impact is less important than the PCS water temperature.

5-12

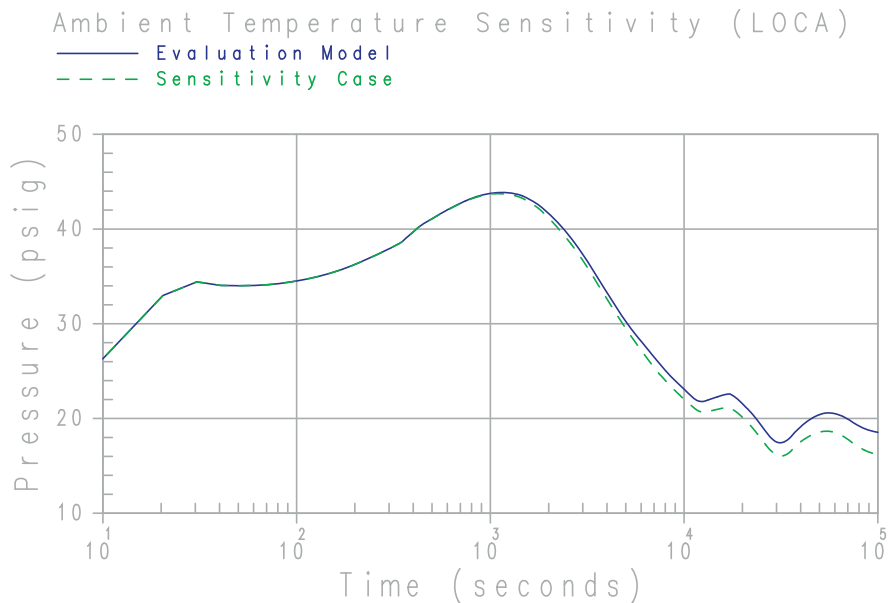


Figure 5-9. Case 5 – Ambient Temperature Sensitivity – LOCA

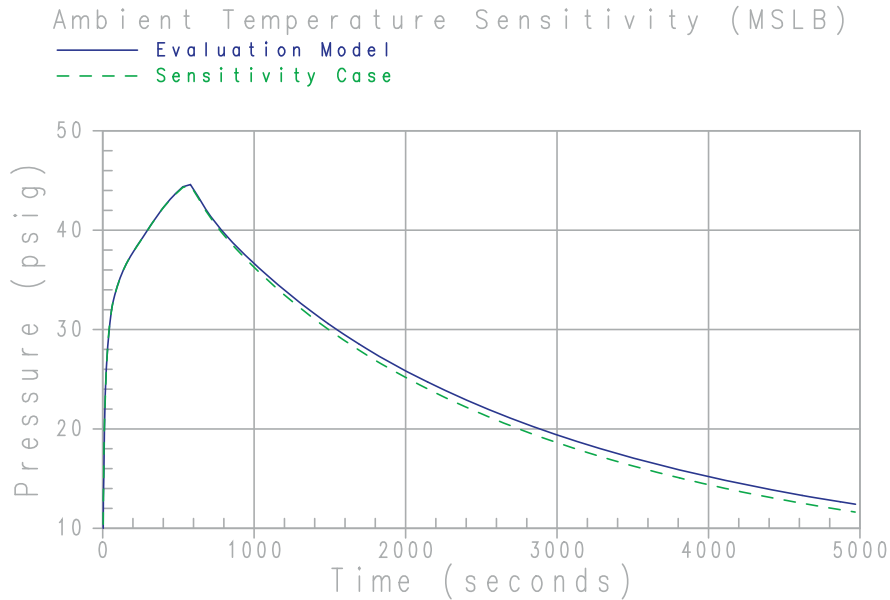


Figure 5-10. Case 12 – Ambient Temperature Sensitivity – MSLB

5-13

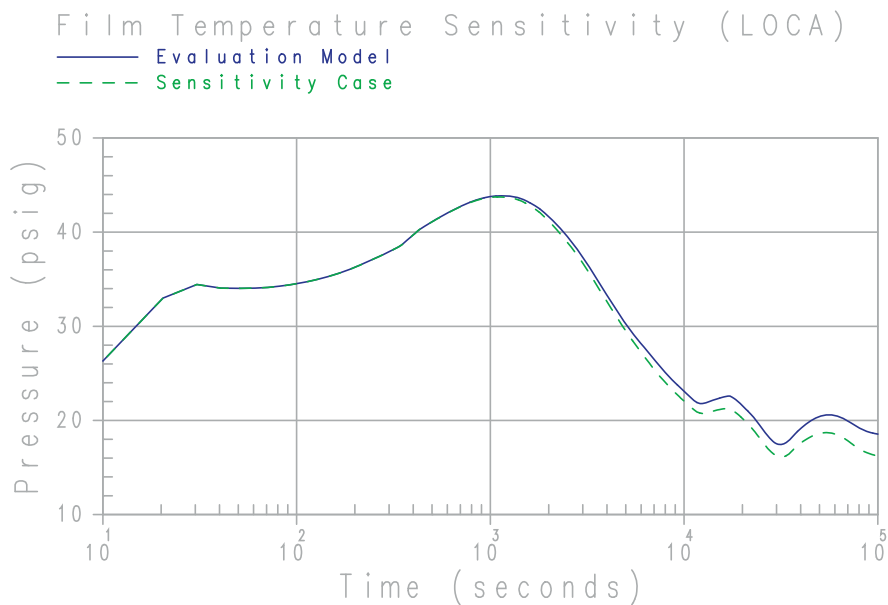


Figure 5-11. Case 7 – Film Temperature Sensitivity – LOCA

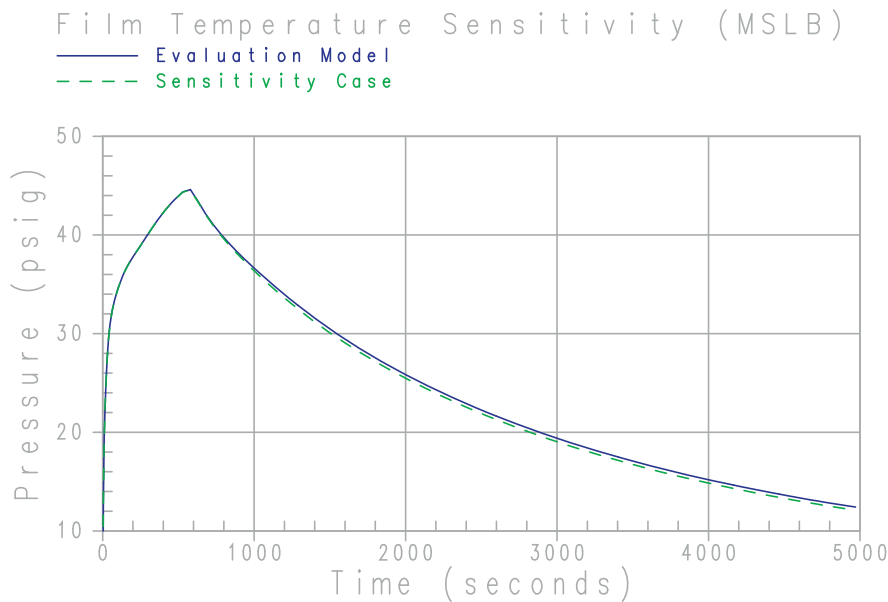


Figure 5-12. Case 14 – Film Temperature Sensitivity – MSLB

5.8 SENSITIVITY TO DROP MODELING ASSUMPTIONS

During a LOCA blowdown, the liquid and entrained droplets enter the atmosphere saturated at the containment total pressure where they are exposed to the containment gas mixture of air and steam at the steam partial pressure. Since the liquid and drops are initially superheated, they evaporate quickly to reach thermal equilibrium with the gas mixture. A sensitivity study was performed for the LOCA to determine the impact of the modeling assumption in WGOTHIC of the fraction of liquid converted to drops on the containment pressure. The mass released during the MSLB does not contain droplets.

The fraction of liquid assumed to be turned into droplets during the LOCA blowdown was varied from 0 to 100 percent. These sensitivities showed that the impact of assuming no droplets released, had a significant impact on the calculated pressure response compared to the cases where droplets were modeled. With no droplets assumed, the blowdown pressure was higher, but the peak pressure was lower. However, the sensitivity to the assumed fraction of droplets was very weak above a level of approximately 5 percent. The drops are strongly coupled to the containment atmosphere temperature due to the large surface area of the drops. The presence of drops in the atmosphere at approximately the 5 percent level maintains the atmosphere in a saturated condition and the presence of additional drops has little impact on containment pressure.

This sensitivity indicates that it is important to model the presence of drops in the containment atmosphere but the specific fraction assumed has a minor impact on the resulting pressure. The containment pressure response for assumed droplet fractions of 0 and 100 percent along with the Evaluation Model assumptions for drops (discussed in Section 4.5.2.1) is illustrated in Figure 5-13.

5.9 CONCLUSIONS

A series of sensitivity analyses has been carried out using the AP600 containment model to determine the effect of initial conditions on containment pressure response for the LOCA and MSLB events. Sensitivity evaluations were performed on initial containment humidity, pressure, and temperature, as well as ambient humidity and temperature and PCS water (film) temperature. These sensitivities demonstrate that the initial conditions assumptions in the Evaluation Model result in a conservative prediction of containment pressure. The containment pressure is more sensitive to internal conditions than to ambient conditions. The sensitivity to internal conditions is due primarily to the effect of these conditions on the amount of air in the containment.

A sensitivity was performed for the LOCA to determine the impact of the drop modeling assumption in WGOTHIC on the calculated containment pressure. The results show that it is important that the droplet formation be modeled, but at fractions above approximately 5 percent, the fraction assumed to be released as drops has a small impact on the calculated pressure.

5-15

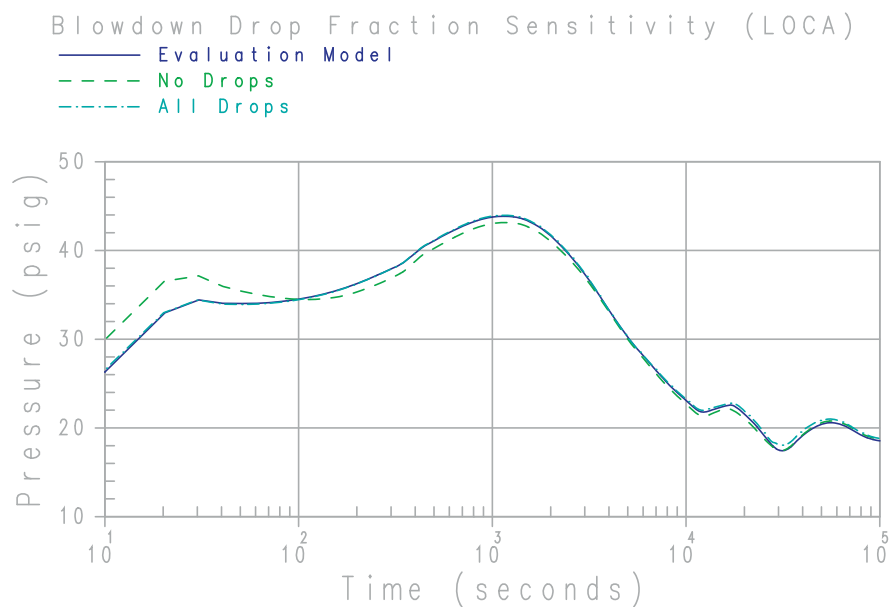


Figure 5-13. Blowdown Drop Fraction Sensitivity – LOCA

6 METEOROLOGICAL EFFECTS ON PCS PERFORMANCE

6.1 INTRODUCTION

Meteorological conditions which could be postulated to degrade the performance of the PCS design have been investigated. The design includes, within the chimney, a shield plate which protects the containment surface from direct impingement of rain. Screens on the PCS inlets and around the entrance to the chimney protect the PCS from birds or larger debris which may be blown by wind. Meteorological effects that are evaluated, are wind-induced turbulence and the potential for recirculation due to wind or temperature inversions. This chapter shows that the assumption of a quiescent atmosphere in the evaluation model conservatively neglects enhancements to heat and mass transfer due to wind. It is also shown that the potential effects of recirculation produce a negligible effect on containment pressure.

6.2 WIND-INDUCED TURBULENCE

6.2.1 Summary of Wind Tunnel Tests

A goal of the containment building design is that wind not adversely impact heat removal from the building. The PCS is designed for wind to either have a nominal effect on PCS flow (wind neutral) or enhance PCS flow (wind positive). To verify the wind positive performance, a series of wind tunnel tests were performed. The wind tunnel tests, performed at the Boundary Layer Wind Tunnel Laboratory at the University of Western Ontario (UWO), were designed to test the aerodynamic response of air flow past the AP600 containment under a variety of conditions. The tests occurred in four phases.

Phase 1 testing (~1:100 scale) examined the effects of various design options on the wind-induced pressures. In Phase 1 testing, although the flow through the building annulus was not modeled, the pressure difference between inlets and chimney, ΔP , was measured. The inlet-minus-chimney ΔP is the pressure driving flow through the PCS, and a pressure coefficient, c_p , is defined based on free stream wind velocity and ΔP :

$$\Delta P = \frac{1}{2} c_p \rho_{amb} V_{roof}^2$$

where,

ρ_{amb} = ambient air density
 V_{roof} = free stream wind velocity

In Phase 2 tests, the air flow path was modeled for two different building designs: the most wind-neutral design found in Phase 1 testing and the current design of the building. The purpose of the Phase 2 testing was to provide information for the design of the baffle wall. Buoyancy was not considered in the wind tunnel tests, since the driving pressure due to buoyancy amounts to only about 1 to 5 percent of the wind-induced driving pressure for the design wind cases.

At the end of Phase 2 of the wind tunnel program, several questions remained. In Phase 3, analysis was used to address the potential effects of wind and thermal inversion on recirculation of the chimney effluent back into the inlet, using available literature from mechanical and natural draft cooling towers.

Three additional questions were addressed with testing in Phase 4. The first question regards the effect of Reynolds number on the results. Reynolds number effects could only be addressed definitively by testing a larger model (1:30 scale) in a higher wind speed tunnel, such that the Reynolds numbers were in the same range as expected full-scale values. The second question was the effect of a tornado wind profile (near uniform) on the results. Tornado profile effects could be obtained using the same test model as in previous phases, but with a uniform flow model. The third question addressed the blockage effects of a hyperbolic cooling tower relative to the UWO wind tunnel size. Cooling tower blockage could be addressed by testing the model in a larger wind tunnel where blockage would be small.

The final question, the effect of severe terrain, was the subject of Phase 4 testing, in which a smaller scale (1:800 scale) was chosen to allow modeling of larger areas around the site.

Test results indicated that the AP600 design was wind positive for average PCS flow. The testing included a variety of terrain and conditions, including open country terrain, tornado loading, modeling of the cooling tower(s), and simulation of several types of severe terrain. Open country terrain yielded the most beneficial results for PCS heat removal, indicating a significant contribution to PCS air flow due to wind-induced driving pressures. The effect of the cooling tower, however, was to reduce static pressure at both the chimney and the inlets, resulting in lower mean wind ΔP . Thus, the likelihood of flow in the PCS changing direction (flow reversal) was greater when the plant was in the wake of the cooling tower, giving the least positive mean PCS driving force due to wind.

The three Phase 4 severe terrain scenarios included an escarpment with mountain backdrop, a river valley site, and a river valley site with two cooling towers. Each terrain scenario caused durations and magnitudes of negative wind ΔP , which could lead to flow reversals within the PCS flow path.

The wind-positive response of the PCS has been shown (Reference 6.1) to be beneficial for containment heat removal for the limiting terrain configuration. Increased wind speed drives more flow through the PCS annulus and increases heat and mass transfer coefficients. Three questions have been addressed regarding the results of the wind tunnel tests:

- The model scale aerodynamic response versus full-scale response
- The effects of wind-induced flow oscillations on PCS heat removal and containment pressure response
- The effect of near-zero average wind ΔP for certain wind angles in some of the severe terrain tests

Due to the shape of the containment shield building (sharp edges initiate flow separation), the model-to-full-scale aerodynamic response is relatively insensitive to model size in the range tested. A review of the literature has indicated that pressure oscillations in heat transfer generally improve heat transfer rates. In addition, time constants associated with the containment shell and internal volume minimize any benefit or penalty on containment pressure due to oscillations. The effect of wind-induced pressure oscillations has been evaluated with simple calculations.

6.2.2 Tracking of a Wind-Driven Particle

Using the measured pressure coefficients, density of air, and design wind speed of 214 mph, wind ΔP was calculated and converted into annulus velocities using the momentum equation, which balances the driving force with the unrecoverable losses. Figure 6-1 presents the calculated path of the first element to travel from the inlet to the outlet of the PCS. Figure 6-1 also presents the path of the element neglecting the wind, and using an assumed buoyancy-driven annulus velocity of 15 ft/sec. Note that the wind-driven element shows a net positive flow response to pressure oscillations (net flow is from the inlet to the chimney).

6.2.3 Containment Time Constants

A review of the literature has indicated that oscillating flows generally increase heat transfer. The effect of the wind ΔP oscillations on the containment post-LOCA pressure response is limited by time constants associated with the containment shell and the containment volume. The shell time constant gives the response of the containment shell to changes in its environment. Using a lumped mass approach, the time constant compares the thermal capacitance of the shell to the heat removal rate from its surface and has a value of about []^{a,c}. The shell time constant is significantly higher than the frequency of pressure fluctuations, which are on the order of several seconds for high wind speed cases. The time constants show that the thermal response of the containment shell is sufficiently slow so that high speed oscillations will not significantly affect PCS heat removal. At lower wind speeds, oscillations are much slower. However, at lower wind speeds, the wind ΔP is much lower. As wind speed reduces, the wind ΔP decreases rapidly, as a function of the square of the wind velocity. Thus, oscillations will not have a significant impact on PCS heat removal. Since PCS heat removal is relatively unaffected, containment pressure response to a postulated LOCA will not be significantly affected by pressure oscillations. Thus, heat transfer fluctuations occur relatively faster than the ability of the wall material to transmit oscillations through the shell.

6-4

a,b

Figure 6-1. Particle Path through the AP600 PCS with and without Wind

6.2.4 Wind-Induced Oscillation Effect on Heat Transfer Coefficient

Pressure fluctuations affect the heat transfer coefficient on the containment surface. In particular, oscillations result in short periods where the heat transfer coefficient may be lower than the value assumed in the no-wind case, followed by periods of higher heat transfer coefficients. The heat transfer response to wind oscillations has been investigated using a 1-D plane wall conduction model. The conduction model was used to estimate the effect of pressure oscillations on heat transfer through the containment shell. The model simulates the containment shell and a liquid water film on the outside of the shell. The 1-D conduction model was subjected to the heat and mass transfer coefficient on the outside of the plane wall calculated from the time-varying annulus velocity. Only forced convection correlations were used, so that heat and mass transfer rates on the outside of the plane wall approached zero as annulus velocities approached zero. The use of a forced convection correlation is conservative since, even as velocities in the annulus pass through zero, heat transfer would still occur. To further impose a conservative bias in the calculation, heat and mass transfer rates on the outside of the wall were assumed to be zero whenever the annulus velocity was negative.

6-5

The response of the containment shell to the imposed velocity was calculated. Figure 6-2 presents the surface temperature of the inside of the plane wall versus time. The figure compares the response of the wall to the annulus velocity oscillations versus the response assuming a steady buoyancy-driven annulus velocity. Note that, despite neglecting heat removal from the wall during periods of negative annulus velocity, the temperature of the inside of the plane wall is still about the same as a typical steady velocity case, showing that the response of the containment shell is limited by the time constants discussed in previous sections.

a,b

Figure 6-2. 1D Containment Shell Model Inside Temperature Results

6.2.5 WGOTHIC Evaluation Model Basis

The wind tunnel testing of the AP600 indicates that the average wind ΔP tends to be positive under a variety of conditions. Wind flowing towards and over the containment building will tend to increase average flow rates through the PCS. The wind-induced flow rate increase will improve heat transfer rates in the PCS.

In addition to the open-country terrain, several highly turbulent severe terrain scenarios were tested to obtain data on the AP600 subjected to limiting site conditions. For the severe terrain, positive wind ΔP that averages near zero may be seen. In addition, the wind ΔP tends to oscillate, giving periods of negative wind ΔP . Negative pressures indicate the possibility of flow reversals within the PCS annulus. Assessment of the current literature has indicated that flow oscillations will tend to increase heat transfer primarily by enhancing mixing across the riser annulus flow channel. While periods of negative pressure may result in short periods of flow reversal within the annulus, the literature indicates that turbulent conditions may continue to exist. Turbulent conditions would continue to provide significant heat transfer

rates despite the oscillating flow. Time constants were calculated for the containment shell which indicated that the shell time constants were of significantly higher magnitude than the period of the pressure oscillations. Thus the pressure oscillations in the annulus would be damped in their effects on the containment heat removal rates at the inside of the containment shell. A 1-D conduction model of the containment shell, subjected to oscillating heat transfer rates, was solved using the wind Δp from a particularly turbulent angle of the limiting test site. The 1-D conduction calculation used the forced convection correlation to conservatively determine heat transfer rates in the annulus. Heat transfer was also assumed to be zero when the flow reversed. The results of the calculation indicate a slight benefit in PCS heat removal and containment pressure due to wind for the limiting case. The effect of the containment shell was to dampen the oscillations occurring on one side of the shell. Thus, a conservative calculation of the passive containment response to a LOCA could assume a quiescent atmosphere.

6.3 RECIRCULATION OF CHIMNEY EFFLUENT

After the PCS cooling air flow passes over the containment shell surface, the air and evaporated water exhaust through an opening in the roof of the shield building and through the chimney. The potential for recirculation of the chimney effluent back to the PCS inlets, due to temperature inversions or strong winds has been evaluated (Reference 6.2) through a review of literature and shows the negligible effect of a conservatively high assumed recirculation.

6.3.1 Summary of Literature Review

Many references were found in the literature to address potential recirculation due to strong winds or thermal inversions. References are available for natural draft hyperbolic cooling towers, typically hundreds of feet tall, and for mechanical draft cooling towers, typically 10 to 20 feet tall.

Strong winds can cause the formation of a recirculation cavity on the leeward side of a building or cooling tower. It was found that there are some intermediate wind speeds which can be sufficient to bend the plume horizontally, yet not strong enough to carry all the effluent away. Analytical and experimental research in the literature was conducted to determine the extent of the recirculation cavity behind a natural draft cooling tower and its effect on the plume. Curves are provided in the literature based on a normalized temperature difference that indicates the increase in the mixed mean ambient inlet temperature due to mixing with the plume. Such curves suggest a maximum normalized temperature increase of 10 percent for recirculation. Similar studies for mechanical draft towers suggest recirculation of 3 to 7 percent reaching a maximum of 15 percent.

Thermal inversions, and combinations of wind and temperature inversions were cited. Results showed that an inversion, by itself, does not induce the downflow necessary to recirculate chimney effluent. Adverse inversion conditions are associated with calm or light winds. Using simplified plume rise equations, the approximate effluent conditions resulted in plume rise above the shield building chimney for stable atmospheric conditions (inversions). The plume rise was sufficient to raise the plume, in light wind, above the recirculation zone of structures the size of those associated with the passive containment design. Consequently, the maximum expected recirculation would be determined from the strong wind case.

Based on the literature review and evaluations of the AP600, the upper limit for recirculation of the passive containment chimney effluent is []^{a,c}. To account for the uncertainty in choosing a value for recirculation, the more conservative value of []^{a,c} has been assessed, which would result in the mixed mean ambient inlet temperature increasing from the safety analysis basis of 115°F to []^{a,c}.

6.3.2 Evaluation of Effect of Recirculation

The effect of a recirculation ratio of []^{a,c} has been assessed with WGOTHIC sensitivity calculations. The base case calculation used an inlet temperature of 115°F and inlet humidity of 20 percent. Two sensitivities were run: one with only the inlet temperature increased, based on the recirculation ratio, and one with both the inlet temperature and inlet humidity increased. Results show that the pressure transient is insensitive to temperature and humidity in this range due to the self-regulating performance of the PCS.

The base case used for recirculation sensitivity differs from the evaluation model in the details of internal nodding, azimuthal segregation of the annulus into quadrants, modified mass and energy releases, the use of 22 percent relative humidity, an initial PCS flow profile starting at 220 gpm, and in the use of nominal heat and mass transfer correlations. Since these sensitivity results are used to examine relative effects of changes in the annulus inlet conditions, the sensitivity results are judged to provide a reasonable estimate of the potential effect of recirculation. The base case chimney outlet temperature reaches a maximum of []^{a,c} at about 2100 seconds and decreases almost linearly to []^{a,c} at about 8700 seconds, after which it gradually reduces to []^{a,c} at 24 hours. For simplicity, a conservative assessment of the potential effect can be based on an assumed chimney outlet temperature of []^{a,c}, which includes []^{a,c} to account for the increase in outlet temperature when the inlet temperature is increased in the sensitivity run. Using the definition of the recirculation ratio, the mixed mean inlet temperature, accounting for the effect of effluent recirculation, is

$$T_{in} = T_{\infty} + R (T_{out} - T_{\infty})$$

$$_{in} = 115 + []^{\text{a,c}}$$

So the inlet temperature to be assumed in the sensitivity cases is []^{a,c} which is applied for all annulus quadrants, consistent with the definition of R from the literature. The first sensitivity case used a constant []^{a,c} inlet temperature and essentially unchanged inlet humidity []^{a,c}. Results from the sensitivity show that the pressure transient changed by a negligible (<0.1 percent) amount due to the []^{a,c} increase in inlet temperature, and confirmed the initial guess for the corresponding increase in outlet temperature. The second sensitivity included the increase in inlet temperature combined with the inlet humidity set to 98 percent. Again, there is a negligible effect on the containment pressure. The lack of sensitivity of the pressure response is due to the self-regulating performance of the PCS. By comparing the annulus conditions in going from 20 to 98 percent inlet humidity, it is seen that the annulus mass flow rate increased by about []^{a,c}. The higher mass flow increases the capacity to move vapor out of the annulus and is due to the increase in vapor pressure at the annulus outlet from []^{a,c} of the approximately 14.7 psia total pressure. Since steam density is more sensitive to temperature increases than air density is, and steam density is less than air density at annulus conditions, the increased steam content provides a greater

density driving head for flow through the annulus. The increased mass flow results in a greater velocity through the annulus, which increases the PCS mass transfer coefficient. Thus, the mass flow increase offsets increases in inlet humidity. Similar, self-regulating performance results from an increase in inlet temperature alone.

It may be expected that an increase in inlet humidity would suppress the evaporation rate from the film. Such an effect is actually small since the driving force for evaporation is the difference between the vapor pressure of the film and the bulk saturation pressure in the annulus. Since the vapor pressure of the film is on the order of ten times that of the annulus, a relatively large percentage change to annulus humidity corresponds to a relatively small percent of the driving force.

Sensitivities to the effects of increasing both inlet temperature and humidity to account for potential recirculation show that there is a negligible effect on the containment pressure transient.

6.3.3 WGOTHIC Evaluation Model Basis

Since the effect of effluent recirculation is negligible, the WGOTHIC evaluation model does not consider any additional penalty due to recirculation.

6.4 APPLICABILITY TO THE AP1000 SHIELD BUILDING DESIGN

The AP1000 shield building design increases the structural integrity, enhances the overall seismic safety margin, and simplifies construction. Some of the design changes impact the air flow rate through the PCS.

[^{a,c} In the AP1000 air inlet design, a steel structure containing the fixed, always open louvers and screens has been added around the top of the shield building. The flow area through the modified louvers and screens is higher than what was through the original louvers, screens and inlet ducts. After passing through the screens, the air enters the common plenum that is formed by the steel structure and the outside of the concrete shield building and continues through the air inlet ducts. The air inlet ducts are arranged in two rows, and uniformly distributed around the circumference of the shield building. The flow area through the air inlet ducts is lower than it was through the original louvers, screens and inlet ducts. As in the previous design, air exiting these ducts enters a common plenum inside the shield building which transitions to the outer flow annulus.

The AP1000 shield building design increases the overall resistance of the PCS flow path, reducing the natural circulation flow rate through the PCS air flow path. The impact of this change on the test results and scaling were examined. The operating range of the AP1000 heat and mass transfer correlations is shown in Table 3-3. The percent differences caused by these design changes on the key scaling groups are small and negative indicating the AP1000 PCS air flow path design is expected to slightly reduce the AP1000 operating range. The wind tunnel tests included variations of the shield building design and concluded that the criteria of wind aiding in natural circulation of the PCS would be met. Therefore, the range of test data that was used to validate the AP1000 PCS heat and mass transfer correlations remains acceptable and the conclusions in this section remain valid (Reference 6.3).

6.5 CONCLUSIONS

Wind-induced pressure oscillations have been shown to provide a benefit to PCS heat removal because of the wind-positive design; that is, wind induces more heat removal than a quiescent atmosphere. The effects of recirculation due to thermal inversions or strong winds has been shown to have a negligible impact on PCS heat removal. The WGOTHIC evaluation model bounds the postulated effects with no input modifications.

6.6 REFERENCES

- 6.1 NTD-NRC-95-4467, J. Narula, "Analysis of AP600 Wind Tunnel Testing for PCS Heat Removal," June 2, 1995.
- 6.2 NTD-NRC-94-4166, R. Haessler, "AP600 Passive Containment Cooling System Letter Reports," June 10, 1994.
- 6.3 APP-GW-GLR-096, Revision 3, R. Ofstun, "Evaluation of the Effect of the AP1000® Enhanced Shield Building Design on the Containment Response and Safety Analyses," June 13, 2011.

7-1

7 BASIS AND METHOD FOR CALCULATING THE PCS WATER EVAPORATION RATE FOR THE AP600 AND AP1000 CONTAINMENT DBA EVALUATION MODELS

7.1 INTRODUCTION

The energy released to the containment atmosphere following a postulated design basis high energy line break is removed from the exterior containment shell surface by a combination of convection and radiation from dry surface areas and by convection, radiation, and water evaporation from wetted surface areas, to a naturally circulating air stream. The energy removal due to water evaporation dominates the passive containment cooling system (PCS) total heat removal and is a function of the PCS flow rate, the wetted area, and the external shell temperature. Since these parameters vary with time, the energy removal rate due to evaporation also varies with time.

The containment shell outer surface is wetted with water that is stored in a tank located above the containment. Piping and three parallel valves provide a flow path from the tank to the top of the containment shell. The valves open upon receipt of a high-2 containment pressure signal, allowing water from the tank to drain by gravity through the piping to a central distribution bucket located above the center of the containment shell. This water flow fills the distribution bucket, overflows out onto the dome, and spreads outward on the nearly horizontal surface at the top of the containment shell. As the applied water spreads outward from the center of the dome, it runs down the increasingly sloped dome surface where it is collected and redistributed by weirs located at the ~24-foot and ~51-foot radius of the dome. These water distribution weirs reapply the collected water at a regular uniform spacing around the containment shell perimeter.

The PCS water flow rate into the distribution bucket and onto the containment surface is controlled by the inlet elevations of standpipes within the PCS water storage tank. As the tank drains and each standpipe is uncovered, the PCS flow to the containment surface is reduced in a step-wise fashion. The standpipes are located so that the PCS flow results in sufficient heat removal to match the decreasing rate of heat release to the containment, and to achieve the desired decrease in containment pressure.

Because the ability of the PCS to remove heat at a given containment pressure (temperature) is largely dependent on the amount of water applied and the surface area that is wetted, the method of water application and the behavior/stability of the liquid film are important. Therefore, this section describes the testing and analyses utilized to define a conservative water flow rate for the WGOTHIC Evaluation Model, including:

1. Water distribution testing used to demonstrate the weir design and how the resulting wetted surface area is affected by the applied water flow rate and surface irregularities in the containment shell structure.
2. PCS testing performed with heated wetted surfaces to determine how the water film is affected by post-accident containment operating conditions, including the steel shell surface temperature, the water film temperature, the water film mass flux (mass flow rate per foot of wetted perimeter, hereafter referred to simply as film flow rate), and cooling air flow velocity.

Deleted: ¶

Deleted: two

Deleted: input to

7-2

3. The method used to predict the containment shell wetted area and water film behavior conservatively compares with test data in order to conservatively calculate the amount of water than can be evaporated from the containment shell.
4. The method used to calculate the effect of heat conduction, the circumferential direction though the steel containment shell (2-D conduction), on the water evaporation rate from the surface with vertical wet stripes.

The liquid film application, flow rate, area wetted, and film behavior are factors in the conservative determination of the amount of supplied water that evaporates from the shell. The methodology bounds data from tests of an unheated, full-scale portion of the containment dome and 4 feet of sidewall, and from various scale heated tests. The evaporation-limited PCS water flow rate for the WGOthic Containment Evaluation Model is calculated using a simple model that is consistent with test observations and uses as inputs the parameters Γ_{dist} and Γ_{min} which are selected to conservatively bound test data. Γ_{dist} represents the film flow rate (mass flow rate per unit wetted perimeter) of water applied by the weir distribution system at the second weir. Γ_{min} represents the minimum stable film flow rate, below which water coverage is assumed to decrease, and is selected to bound heated film stability test data. The database from which conservative values for Γ_{dist} and Γ_{min} are determined is discussed, as well as how these parameters are implemented into the model.

The Evaluation Model conservatively neglects heat removal during the initial period from the first spillage from the bucket to the time when steady-state coverage has developed on the containment shell (Section 7.2.5). The time to develop steady-state coverage is conservatively estimated. The effects of surface temperature during the initial application are also addressed (Section 7.6.5).

The supporting tests for water coverage are shown to span the range of AP600 and AP1000 non-dimensional parameters, so that the database is sufficient.

7.2 WATER APPLICATION AND DISTRIBUTION

The wetting characteristics of the containment coating and the application and distribution of water onto the containment steel shell outer surface are important design features of the passive containment design. The containment is covered with an inorganic zinc coating, and an assembly of devices on the containment dome are used to collect and redistribute water to maximize the containment surface wetted area at a given delivered water flow rate.

The Phase 3 Water Distribution Test (Reference 7.2) was performed to demonstrate the operation of the prototype of the AP600 water distribution devices on a full-scale sector of the containment dome. Other PCS tests were performed to quantify the heat removal capability of the PCS. The test results provided information to understand and characterize the behavior of water films on the outside of the containment surface. In addition to the containment coating and the water distribution devices, other parameters that characterize the water film behavior are the delivered water flow rate, the water film flow rate (per foot of wetted perimeter), the water film temperature, and the evaporative heat flux. The film Reynolds number provides a dimensionless measure of the film flow rate, and the Marangoni number is a dimensionless measure of heat flux. The range of dimensioned and dimensionless parameters for PCS testing used to understand and characterize containment surface wetting are summarized in Table 7-1.

Deleted: evaluated

Deleted: "PCS film coverage model," separate from the WGOthic Evaluation Model. This model permits a

Deleted: , considering the aspects of water application, and film behavior and stability. The resulting amount of water is input to the WGOthic Evaluation Model.¶

Deleted: input

Deleted: 5.2.2

7-3

Table 7-1. Ranges of the Film Coverage Parameters in the PCS Tests

a,c

7.2.1 Containment Shell Surface Coating

The containment shell surface is covered with an inorganic zinc coating for corrosion protection. Prototypical coated surfaces were obtained for testing by following the manufacturers' specifications for preparation of the metal surface and for application of the coating for each test article in the tests described in Sections 7.2.3 and 7.6.

- The surface was prepared for coating application according to the coating manufacturer's requirements by sandblasting to a white metal surface finish. The coating was then sprayed onto the surface to a thickness range within the required specification of 4 to 10 mils. Coating thickness measurements were taken to verify that the coating thickness was within specification.
- Local or spot recoating of the surfaces was performed if the surface of the test article was affected by changes to the facility, such as the installation of additional instrument penetrations.

Although no specific aging simulation of the surfaces was performed prior to testing, matrix tests were performed over a period of time using the original coated surface, where aging of the surfaces occurred due to operation and exposure to the environment. For example, the small-scale tests vessel was erected in 1986 and tests were performed until late 1992 using the same test vessel with the original coating. The **large-scale test (LST)** matrix tests were conducted from late 1991 until the end of 1993 and further operation took place through 1996, with the original coating. An estimate of the equivalent service time cannot be evaluated since a large number of tests were performed during this period. In each test facility, no noticeable degradation of the surface was noted during the testing.

In consideration of the above, the surfaces tested are considered prototypic of the AP600 and **API1000** containment shell exterior surfaces. Measurement and/or observations of film coverage on the prototypical surface were made in each of the PCS tests.

7.2.2 PCS Water Distribution Weir Description and Operation

An assembly of devices for distributing the water applied to the containment shell is provided to maximize the outside surface area of the containment shell that is wetted during PCS operation. The PCS water distribution devices include a distribution bucket located above the center of the containment dome, eight divider plates that extend radially from the center of the dome to the first set of water distribution weirs, the first set of water distribution weirs located []^{a,c}, and the second set of water distribution weirs located []^{a,c}.

The PCS water is delivered to the water distribution bucket at the center of the containment dome. The bucket has 16 vertical slots, such that two slots meter water flow to each of the eight pie-shaped segments on the dome created by the eight divider plates that originate at the distribution bucket and extend radially along the surface of the dome to the first distribution weir ring. These divider plates are required because the center of the dome is relatively flat, and maldistribution of flow due to localized imperfections in plate welds or alignment, or variations in the slope at the center of the dome could otherwise occur. Thus, the dividers distribute the water applied to each one-eighth dome segment and to the corresponding one of eight weir assemblies that comprise the first ring of weirs.

7-5

The first weir ring consists of eight weir assemblies located []^{a,c}. This radial position is just below [

] ^{a,c} Each of the eight first weir assemblies consist of two water collection dams that direct the applied water, in its one-eighth segment from the dome center, into a collection box. Each of the eight collection boxes meters flow to two distribution troughs, one on either side of the collection box. Each distribution trough meters the water from the collection box back onto the dome surface via nine V-notches spaced at 1-foot intervals. The eight weir assemblies are installed with the distribution boxes end-to-end, so that each forms one-eighth of the weir ring [

] ^{a,c}

The second weir ring is located [] ^{a,c}. This assembly again corrects any uneven distribution of flow that may have occurred below the first weir ring due to weld discontinuities or deviations in the dome shape from the ideal shape. Also, since the containment dome is steeply sloped at this radial position, the water applied by this second weir ring is not significantly affected by local surface imperfections or deviations from ideal shape, since gravity rather than allowable surface variations becomes controlling. Thus, the second weir ring creates an even distribution over the rest of the dome and the vertical portion of the containment shell. The second weir ring consists of sixteen weir assemblies; each with two collection dams, a collection box, and two distribution troughs. The 16 weir assemblies are again arranged end-to-end to form a distribution system that completely circles the containment. Water that runs down the dome from each of the 16 distribution troughs in the first weir ring is collected by the dams, flows into the collection box, and is metered to two distribution troughs. [] ^{a,c}

Figure 7-1 is an illustration of a weir assembly. The dams collect all the water flowing from above them and direct this water into their corresponding collection box. As the water rises in the collection boxes, it overflows via three V-notches on either side of the top of the box, effectively dividing the collected water into six equal portions. Each portion of the water overflowing through the six collection box V-notches, flows into one of the three parallel flow channels in each of the two distribution troughs. As the parallel flow channels fill with water, each flow channel overflows via another set of V-notches arranged equidistantly along the back wall (facing the containment axial center-line) of the distribution trough, onto the containment shell. The eight weir assemblies comprising the first weir rang, have [

] ^{a,c} Note that in each weir assembly the spacing of the two streams, one on either side of the collection box, is greater than the uniform V-notch spacing along the distribution boxes.

7-6

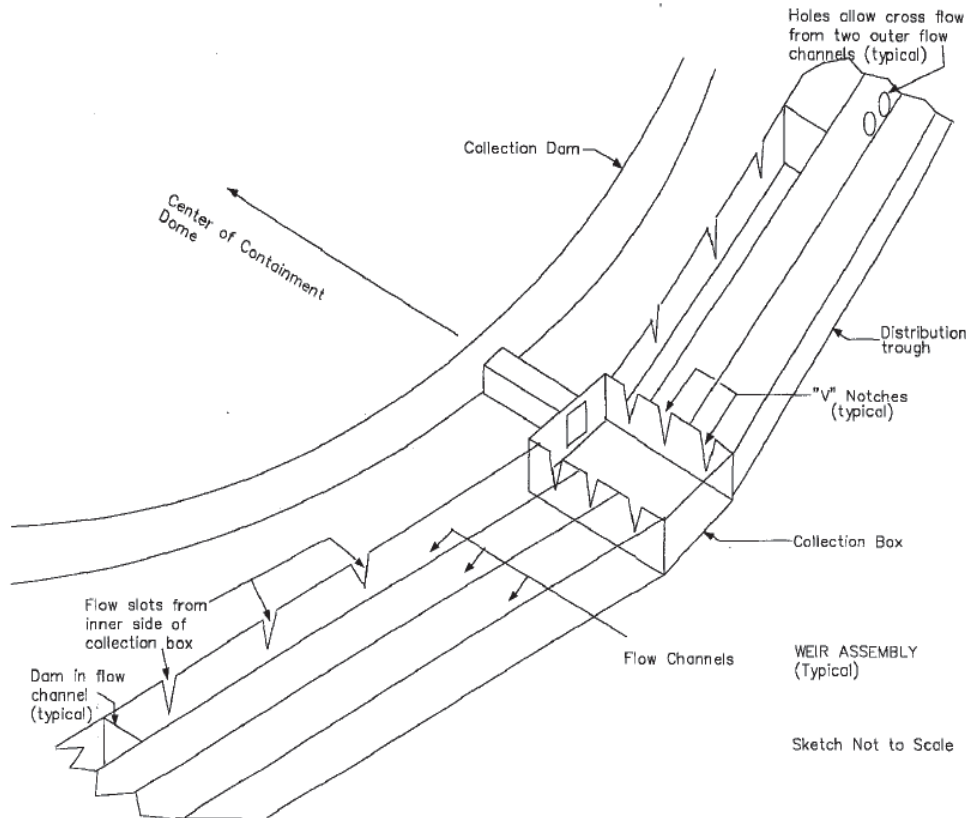


Figure 7-1. Illustration of PCS Water Distribution Weir Assembly

All components of the water distribution system are seismic category I, and designed to withstand thermal and pressure expansion/contraction of the containment without failure. The system is capable of functioning adequately during PCS accident operation under extreme low or high ambient temperatures. The weir distribution systems are constructed of stainless steel to limit concerns over blockage due to corrosion products or paint/coating degradation. The water distribution weir system is designated a safety class C component based on its containment cooling function.

7.2.3 PCS Water Distribution Testing Results

The Water Distribution Test (Reference 7.2) was used to determine the effectiveness of water distribution devices, to determine the water coverage as a function of the flow rate on the prototypical surface, and to determine the time to establish steady-state coverage. A full-scale test section, representing a 1/8 sector of the containment dome to the ~50 foot radius and a 1/16 sector of the full containment dome and a 4-foot long portion of the vertical sidewall, was built. The test section included both meridional and circumferential joints, with the maximum allowable plate misalignment, and was coated with the

7-7

prototypic inorganic zinc coating. Testing included simulation of the maximum allowable deviation in dome shape from ideal shape, by tilting the distribution troughs.

There was no source of heat to simulate mass and energy removal by evaporation for these tests. Two water distribution weir designs were tested. The final weir design was tested in Phase 3 of the Water Distribution Test (Reference 7.2) and is the weir described in Section 7.2.2.

These tests demonstrated that the water coverage just below the weirs consisted of discrete streams after the water was collected, redistributed, and re-applied at a fixed spacing around the containment dome perimeter by the water distribution weirs. These individual streams were sufficiently wide at the higher applied flows (35 and 27.5 gpm) to join just below the weirs and provide high water film coverage over the portion of the test section below the weir. However, at reduced applied water flow rates, the streams were sufficiently narrow in width that the water coverage consisted of vertical alternating wet and dry stripes. [

] ^{a,c}

The water coverage was measured just above the second weir (at the 49-ft radius) and at the springline (65-ft radius at the top of the vertical sidewall). Measurements of stripe widths accounted for only the traverse where flowing water was observed, not the wider wetted traverse. The Phase 3 test data are summarized in Table 7-2, where the wetted perimeter of the flowing water was observed and is listed as a percent of total area or water coverage.

Table 7-2. Summary of the Phase 3 Water Distribution Test

^{a,c}

7-8

The coverage listed at 49-ft and 65-ft are the measured coverage just above the second weir and at the springline and for the water flow rates delivered in Phase 3 of the Water Distribution Test. The coverage decreases as the delivered flow rate decreases. The flow rate was not adjusted to account for the water lost at sampling points upstream of the springline. The correction would increase the water coverage percentages slightly.

The surface area that was wetted at a flow rate of 27.5 gpm (equivalent to 220 gpm on the full dome) was estimated to be []^{a,c} from the top of the dome down to the first weir, based on a review of the video tapes for the Phase 3 Water Distribution Tests. About []^{a,c} of the vessel was wet between the first and second weirs, and the entire vessel was wet at the bottom of the test section.

This test also demonstrated the time required to fill the prototypic water distribution devices and establish steady-state water coverage on the containment shell at a PCS flow rate equivalent to 220 gpm. []

[]^{a,c} Since the initial PCS-delivered flow rate has been increased, the time required to achieve steady-state water coverage will be decreased, as discussed in Section 7.2.5.

7.2.4 Delivered PCS Water Flow Rate versus Time

The AP600 and AP1000 minimum delivered PCS water flow rates are shown as a function of time in Figure 7-2. The minimum delivered PCS water flow rate was calculated assuming only one of the parallel PCS tank discharge valves is open. This assumption reduces the gravity-driven flow rate by []^{a,c} since flow orifices in the discharge lines limit the flow rate from the tank.

Deleted: a single failure of

Deleted: to

Deleted: single failure

The amount of water required for evaporative heat removal from the PCS shell decreases as the core decay heat decreases. Therefore, the PCS flow rate is designed to vary with time. The gravity-driven flow rate decreases as the water level in the PCS tank decreases. A series of standpipes are located within the PCS tank. The delivered PCS water flow rate decreases substantially whenever the water level falls below the top of a standpipe.

7.2.5 Time to Establish Steady State Water Coverage

Some period of time is required to establish steady state water coverage after the PCS has been actuated. This is an important input for the containment Evaluation Model. The delivered PCS water must fill the distribution bucket, two sets of distribution dam/weirs, and then cover the vertical containment shell.

The time needed to establish steady state water coverage was observed on the video tape recording of the 220 gpm equivalent full-scale PCS flow Water Distribution test. []

[]^{a,c}

7-9

As shown in Figure 7-2, the initial delivered PCS water flow rate is about twice as high as the tested value (440 gpm for AP600 and 469 gpm for the AP1000 plant). Therefore, the time to establish steady state water coverage will be less than measured in the Water Distribution tests.

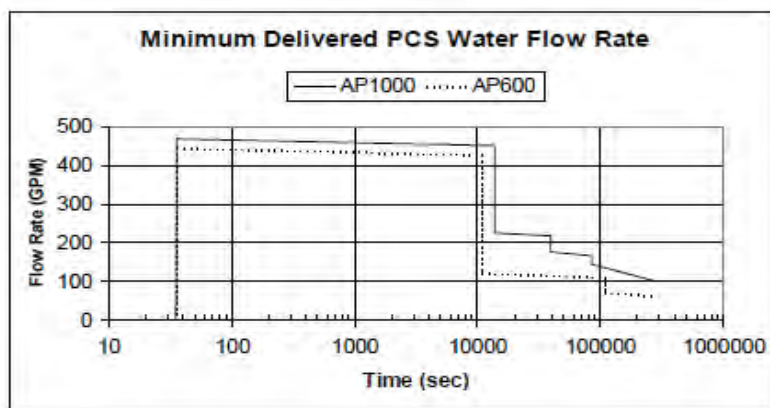


Figure 7-2. Minimum Delivered PCS Water Flow Rate from the Bucket

A simple analytical model was developed to estimate the weir outflow rates for a constant 440 gpm PCS water flow rate. The results are shown in Figure 7-3. This figure helps illustrate the various components of the time needed to establish steady state flow from the bucket, first, and second weirs. The steady state water coverage delay time input values for the AP600 and AP1000 containment Evaluation Models are based on the actual prototype test results, rather than these calculations.

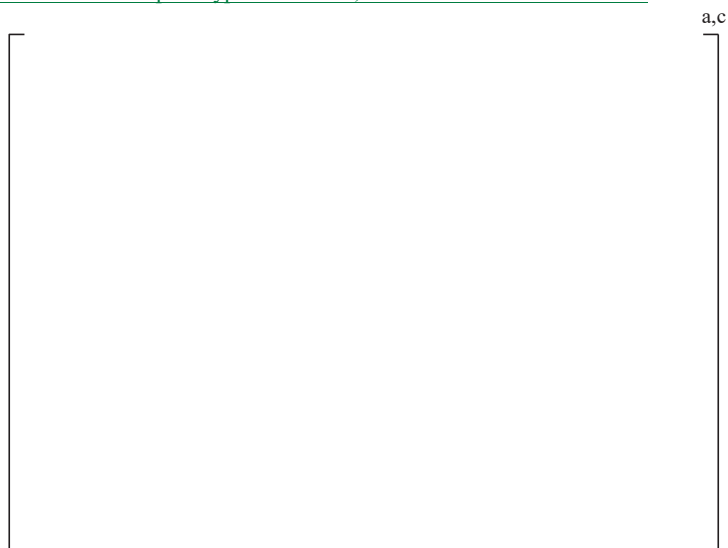


Figure 7-3. Weir Outflow

Deleted: about

Deleted: about

Moved down [8]: A simple analytical model was developed to estimate the weir outflow rates for a constant 440 gpm PCS water flow rate. The results are shown in Figure 7-3. This figure helps illustrate the various components of the time needed to establish steady state flow from the bucket, first, and second weirs. The steady state water coverage delay time input values for the AP600 and **AP1000** containment Evaluation Models are based on the actual prototype test results, rather than these calculations.¶

Moved down [9]: The time to establish steady state coverage is the sum of the valve stroke time, the time to fill the lines and distribution bucket, the time to fill and spill over the two sets distribution dam/weirs, and the time to cover the vertical containment shell. The PCS discharge valve stroke time is 20 seconds and the time to fill the lines and bucket at 440 gpm was calculated to be 17 seconds. As described above, about 10 minutes after flow initiation, a steady state flow and coverage pattern was observed in the 220 gpm equivalent full-scale PCS flow Phase 3 Water Distribution test. Therefore, for AP600, the steady state coverage delay time input value is calculated to be $20 + 17 + 600 \times 220 / 440 = 337$ seconds.¶

Moved (insertion) [8]

7-10

The time to establish steady state coverage is the sum of the time for the valve to open, the time to fill the lines and distribution bucket, the time to fill and spill over the two sets distribution dam/weirs, and the time to cover the vertical containment shell. The opening of the PCS isolation valve must bound electronic delays and the maximum valve stroke time. The higher flowrate for the AP600 and AP1000 plants allows the bucket to fill up faster, which can be scaled from the test results based on [

Moved (insertion) [9]

Deleted: stroke time

Deleted: discharge

Deleted: is 20 seconds and the time to fill the lines and bucket at 440 gpm was calculated to be 17 seconds

] ^{a,c}

As described above, about [^{a,c} after flow initiation, a steady state flow and coverage pattern was observed in the 220 gpm equivalent full-scale PCS flow Phase 3 Water Distribution test. To estimate the time to fill the weirs and fully wet the containment sidewall for AP600 analyses, the test results were scaled [

] ^{a,c}

The AP1000 containment diameter, dome geometry, and water distribution system are the same as AP600, but the initial delivered PCS water flow rate for the AP1000 plant is higher at 469 gpm. [

Deleted: the containment sidewall is 25.5 feet higher. Also,

Deleted: is higher

Deleted: ,

Deleted: gpm. vs. 440 gpm. Since the water distribution system is the same, scaling the AP600 steady state coverage delay time input value by the change in flow rate yields:

$$t_{PCS-AP1000} = t_{STROKE} + t_{PCS-AP600} * Q_{PCS-AP600} / Q_{PCS-AP1000}$$

where,

$t_{PCS-AP1000}$ is the time to reach steady state coverage for AP1000

$t_{PCS-AP600}$ is the time to reach steady state coverage for AP600

$m_{PCS-AP1000}$ is the initial PCS flow for AP1000, 469 gpm

$m_{PCS-AP600}$ is the initial PCS flow for AP600, 440 gpm

t_{STROKE} is the valve stroke time, 20 seconds.

Using this information, $t_{PCS-AP1000} = 20 + 317 * 440 / 469 = 317.4$ seconds. The

] ^{a,c}

7-11

[

] ^{a,c}

Using a relationship between average film Reynolds numbers, the time to fill the weirs and wet the surface of the containment vessel can be determined. The steady state water coverage on the containment surface was estimated to occur within [] ^{a,c} for the test. Removing the time for the valve to open and the time to fill the bucket, the remaining [] ^{a,c} represents the time the film took to fill the weirs and wet the surface of the containment vessel. For the AP1000 design, this is scaled as follows: [

] ^{a,c}

Table 7-3 summarizes the time to reach steady state coverage. The total time is used in the Evaluation Model as a delay after the high-2 containment pressure setpoint is reached. No PCS water is credited until after the delay.

7-12

Table 7-3. Summary of Time to Reach Steady State Coverage

a,c

7.2.6 PCS Water Stripping from Baffle Supports

During pre-operational passive PCS flow tests, some water was observed as “raining” in the annulus rather than flowing down the containment vessel. It was postulated that this was due to stripping of the PCS water as it hit the baffle supports that are attached to the exterior surface of the containment vessel. To conservatively account for the loss of PCS water due to this effect, the safety analysis methodology was altered to remove all PCS water that interacts with the baffle supports on the cylindrical portion of the containment vessel. The assumptions and bases are summarized below.

Testing was performed for condensate return inside containment (Reference 7.14). The test facility consisted of a large, flat plate that could be positioned at an angle relative to the horizontal to simulate locations on the inside of the AP1000 containment dome (i.e. 0-deg would represent the very top of the dome, and 90-deg would represent the vertical wall). The purpose of these tests was to determine the behavior of a liquid condensate film. While the tests were designed to simulate conditions inside the containment, some of the conclusions are applicable to the issue of film stripping by the baffle supports on the outside the containment.

A key conclusion from these tests was that the condensate losses from attachment plates that are located on the vertical wall are essentially zero as the film that contacts the support beams tends to flow around the beam and remain on the plate. The water film bypassed supports and remained attached to the containment vessel wall for the 90-deg test. This phenomenon was also observed at the bottom of the dome up to 86-deg inclination where film contacting the support beam tended to flow downward away from the wall and was lost. It should be noted that the film flow rates for the condensate on the inside of the containment vessel are significantly less than those expected on the outside, and this could result in higher losses on the outside. In addition, condensation on the relatively colder surfaces inside the containment vessel could impact the film behavior differently than evaporation off the relatively hot surface outside the containment vessel. However, these concerns are addressed by the bounding assumption of removing all of the PCS water film that interacts with the baffle supports on the vertical portion of the containment vessel. This bounding assumption also covers all other uncertainties regarding the non-uniformity of the evaporating PCS film.

Additional assumptions based on the condensation test observations:

- For obstructions on the dome section of the containment vessel that are angled upward (less than 90-deg), the water film would not separate from the obstruction, but would instead run over it. For the case of the baffle supports, the first row of supports is located on the dome above the spring line. Any water that might splash off this row would fall vertically downward and impact the dome below the support. Therefore, no losses are assumed for this row.
- Water film that interacts with the longitudinal welds along the supports will remain on the containment vessel wall. This is consistent with what was observed in the Phase 2 condensation tests, and is not expected to be affected by higher PCS water flow rates.
- Water that passes a row of baffle supports re-establishes into a uniform film flow that is reduced by the amount that is assumed to be stripped by the supports. Evaporation is also reducing the PCS water on the containment vessel wall.

7-14

7.3 WATER COVERAGE BASIS

The PCS film coverage model was developed to calculate the amount of water that evaporates from the AP600 shell, consistent with conservative models for film stability. The “film flow rate,” represented by the parameter Γ , is the water mass flow rate divided by the circumferential wetted perimeter, that is, $\Gamma = \dot{m}/W$. Water is distributed on to the containment shell by a series of streams around the circumference. At the high initial delivered PCS flow rate, these streams merge into a continuous film. After the first stand pipe uncovers and the delivered PCS flow rate decreases, the streams remain separate and flow down as stripes from the weirs. The stripes start with a film flow rate, Γ_{dist} and flow down the wall at a constant width until evaporation causes the film flow rate to reach the film stability limit, Γ_{min} . Once Γ_{min} is reached, film stability causes the width of the stripe to reduce as additional evaporation takes place. The bases for Γ_{dist} and Γ_{min} are presented in this section.

Deleted: Inputs to the PCS film coverage model are the delivered PCS flow rate, the sidewall height and diameter, and an estimated evaporation mass flux. The output from the model is the evaporation rate from the containment shell. The evaporation-limited PCS water flow rate is input to the WGOthic Containment Evaluation Model, rather than the total delivered PCS flow rate. The WGOthic code calculation is used to determine an average evaporation mass flux that is input to the PCS film coverage model. Thus, an iteration is required. The iteration is made to converge on the conservative side, i.e., the evaporation flux input to the PCS film coverage model is underestimated. This results in an overestimated amount of water runoff, and therefore underestimates the evaporation-limited PCS water flow rate input to the WGOthic Containment Evaluation Model. ¶
¶
The PCS film coverage model described in Section 7.5 assumes there is no evaporation from the center of the dome to the second weir. The surface area for evaporation is modeled as a right circular cylinder with the same area as the containment shell surface below the second weir. ¶
¶

7-15

7.3.1 Water Distribution Film Flow Rate, Γ_{dist}

Values of water coverage at the springline were measured in Phase 3 of the Water Distribution Test (Reference 7.2). The data, presented in Figure 7-4, show the coverage increased with the total water flow rate to []^{a,b} percent coverage at 220 gpm, then increased to []^{a,b} percent at 280 gpm. Thus, a model that limits the coverage at the top of the side wall to []^{a,c} percent bounds the test data at flow rates greater than 280 gpm. Modeling the coverage at lower flow rates with a value of $\Gamma_{\text{dist}} = []^{\text{a,b}}$ lbm/hr-ft is a good estimate at 220 gpm and bounds the test data at 100 gpm and 55 gpm as shown in the figure below.

Deleted: for lower flow rates

a,b

Figure 7-4. Comparison of Water Distribution Model to Phase 3 Water Distribution Test Results

7-16

The room temperature, isothermal Water Distribution Test data are applicable to both AP600 and AP1000 plants. The basis for using the data is that the water applied to the shell beyond the second weir during actual PCS operation is heated to the shell temperature while flowing down to the second weir. The AP600 scaling analysis estimated less than 1600 ft² of heat transfer surface area is required to heat up the subcooled water, whereas there is 4400 ft² of wetted surface area above the second weir (Reference 7.8, Section 7.6.6). Consequently, heated water is applied to a heated shell at approximately the same temperature at the second weir, so the water and shell are nearly isothermal, as in the Water Distribution Test. The decreased stability exhibited by the application of cold water to a hot surface (References 7.10 and 7.12) is not an issue in this case, so it is assumed that the coverage measured in the cold, isothermal tests is conservative for the nearly isothermal application below the second weir in both AP600 and AP1000 plant designs.

The room temperature (65° to 68°F) Water Distribution Test coverage's are a conservative basis for Γ_{dist} due to the effect of increased temperature on the film properties. The film spreads where the water spills from the weir V-notch and impinges on the shell surface. The spreading is a momentum-dominated process that is opposed by friction and surface tension. At higher temperatures, the film viscosity is decreased by a factor of 2 to 3, and the surface tension is decreased by 15-20 percent, while the impingement momentum is essentially unchanged. The reduction of the friction and surface tension both allow the film to spread more at high temperature than at low temperature.

7.3.2 Minimum Film Flow Rate, Γ_{min}

Observations of the evaporating film flow on heated surfaces show the film flows in constant width stripes until evaporation causes the film flow rate to reach a minimum value, Γ_{min} after which, the film width narrows with additional evaporation. Most of the LST, small scale test (SST), and Westinghouse Flat Plate tests produced constant width stripes, or constant coverage. The lowest values of film flow rate, Γ , either were above Γ_{min} , or at most were close to Γ_{min} . Consequently, the film measurement data for each of the tests is a record of values of $\Gamma \geq \Gamma_{min}$. Several of the lowest measured values of Γ are presented in Figure 7-5.

A conservative upper limit for the minimum stable film flow rate, Γ_{min} , is needed for the PCS film coverage model. The minimum stable film flow rate increases as the heat flux increases. As demonstrated by the work of Bohn and Davis (Reference 7.10). The Westinghouse test data cover a heat flux range that is greater than the maximum expected operating value for both the AP600 and AP1000 plants (see Table 7-11). A constant Γ_{min} value of []^{a,c} lbm/hr-ft was selected to bound the various Westinghouse test data as shown in Figure 7-5. The comparison presented in Figure 7-5 shows this value to be much higher than the lowest stable measured Γ values of each test.

Deleted: , a

Deleted: 9

Deleted: Table 7-10

7-17

a,c

Figure 7-5. Determination of Gamma-Min from LST, SST, and Flat Plate Data

7-18

7.4 EFFECT OF TWO-DIMENTIONAL (2-D) HEAT CONDUCTION THROUGH THE CONTAINMENT SHELL

The PCS transfers heat from the containment atmosphere to the outside environment. Cooling water is applied to the outside surface of the shell to facilitate the heat removal process by evaporation of the applied water. Early in the postulated event, the water applied to the shell exterior provides at least []^{a,b} percent coverage of the external surface. As the transient progresses, the applied flow rate is reduced and the water coverage of the external surface area of the shell is reduced as discussed in Sections 7.2 and 7.3.

As evidenced by test data, the flow distribution weirs develop alternating wet and dry vertical “stripes” on the containment surface. These stripes become clearly segregated as the applied water flow rate is reduced. Heat removal from the wetted areas is greater than from the dry areas and results in the wetted surface area being cooler than the dry surface (evaporative cooling in the wetted area is much greater than convection and radiation from the dry surface). This temperature difference results in heat conduction in the circumferential direction through the thickness of the containment shell. Thermal energy is conducted from the hotter dry stripe areas into the adjacent portions of the containment shell cooled by a wet stripe. The transfer of additional thermal energy to the wet stripe increases the temperature of the wetted steel which increases the water film temperature, which increases the water evaporation rate, the containment heat removal rate, and the use of the delivered water.

Since the water evaporation rate calculated by WGOTHIC only considers heat conduction in the radial direction through the containment steel shell, the effects of circumferential two-dimensional heat conduction can be credited by using multipliers applied to the PCS evaporation rate or the overall heat and mass transfer coefficients. A description follows of the method used to calculate the effect of circumferential two-dimensional heat conduction on the water evaporation. Section 7.5 describes how this is applied in the PCS film coverage model to calculate the evaporation-limited PCS water flow rate input for the Containment Evaluation Model.

7.4.1 Geometry of the Wet and Dry Vertical Stripes on the Containment Outside Steel Surface

The Water Distribution Tests, as discussed in Section 7.2.3, showed the outside surface of the containment shell will be partially wet when the PCS-delivered water flow rate is reduced below the high initial flow rate. At cold, unheated conditions, the observed side wall wetting was []^{a,c} percent with 100 gpm and []^{a,c} percent with 55 gpm equivalent delivered PCS flow. The limited percentages of wetted area were a consequence of the water being applied to the surface at discretely spaced locations, and the fact that the water spread to a stream width that resulted in a bounding Γ_{dist} of []^{a,b} lbm/hr-ft. Therefore, the observed stream width and wetted surface areas were directly proportional to the water flow rate. At these lower flow rates, the stream widths were observed to be less than the distance between weir slots and therefore alternating, vertical, dry and wetted stripes formed down the containment below the second distribution weir.

Deleted: in temperature

Deleted: the overall heat and mass transferevaporation rates calculated by WGOTHIC arecan be enhanced by considering

Deleted: ¶

Formatted: Highlight

7-19

The occurrence of alternating wet and dry vertical stripes on the containment outside surface was also documented on a hot surface with evaporation in progress in the PCS large-scale test (Reference 7.7). In the LST, with heat transfer occurring, wet stripes were observed to flow vertically at constant width to the bottom of the sidewall unless almost all of the applied water was evaporated.

Moved (insertion) [1]

In the Water Distribution Test, the streams initiated by the second (lower) set of weirs had a center-to-center spacing on the vertical sidewall that corresponded to the spacing of applied water streams at the weir, multiplied by the ratio of the containment radius at the sidewall to the radius at the weir. For example, the 6-inch weir slot spacing at the ~50-foot radius of the dome produced stripes at a spacing of ~8-inches at the sidewall radius of 65 feet.

Moved up [1]: rated.

Deleted: rated.

This evaluation of the effects of two-dimensional conduction on the wet steel surface temperature, and resulting water evaporation rate was based on the same alternating wet and dry stripe pattern and spacing produced by the weir(s) in the water distribution test. However, the location of the second weir ring and the weir ring slot spacing used were updated to correspond to the AP600 plant. Specifically, the weir slots on the backwall of the distribution troughs in the second weir ring are at the 50.7 foot radius, and the spacing between weir slots is 6.5 inches. This results in an 8.35-inch center-line to center-line stripe spacing at the vertical sidewall. In addition, a wider dry stripe directly under the 16-weir collection boxes was taken into account.

7.4.2 Heat Transfer Boundary Conditions for the 2-D Conduction Model

Deleted: Inside and Outside

The boundary conditions used in the two-dimensional heat conduction model were established by a series of one-dimensional, steady-state calculations of the PCS heat transfer process performed at constant containment pressures ranging from 10 psig to 65 psig (24.7 to 79.7 psia). These calculations were performed using the same heat and mass transfer correlations as used in WGOTHIC. The heat transfer and the temperature differences from the steam/air mixture inside containment through the steel shell, and from the wet and dry outside containment surfaces to the air were provided. The heat transfer and temperature differences were used to establish heat transfer coefficients for each containment pressure condition for both the inside heat transfer to the inside water film, and for the outside heat transfer from the outside water film. These heat transfer coefficients were reduced based on the conservative multiplication factors (Reference 7.11, WCAP-15326, Rev. 1) applied in WGOTHIC, and were then further decreased to account for the water film and paint layer conductivities and thicknesses. The outside heat transfer coefficient versus the outside steel shell temperature obtained for each pressure condition for the wetted surface, was fitted using a second degree polynomial for use in the conduction model. A constant dry surface heat transfer coefficient (with a fixed outside cooling air temperature) that accurately modeled the pressure conditions analyzed, established the outside heat transfer boundary conditions. These boundary conditions were reviewed to assure that the heat transfer rates at all containment pressure/temperature conditions were higher than the corresponding heat transfer rates calculated by WGOTHIC in the containment analysis. This assures that any increase in heat transfer, as compared to the heat transfer with only radial conduction through the containment steel shell, is underpredicted.

Deleted: steady-state

Deleted: are

7-20

7.4.3 2-D Conduction (ANSYS) Model Description

The effect of circumferential conduction through the AP600 steel containment shell on the shell surface temperatures and the resulting effects on the condensing heat transfer on the inside surface, the evaporative heat transfer on outside wetted surfaces, and the convective heat transfer from the dry outside surface, were quantified using the ANSYS computer code. The ANSYS computer code is a multi-purpose, finite element program that has been used commercially since 1970. For this calculation ANSYS revision 5.3 was used.

Deleted: ;

The ANSYS calculation was a two-dimensional, thermal, steady-state analysis of a periodic half-cell (cross-section) that consisted of a two-dimensional block []^{a,c} thick and []^{a,c} wide; corresponding to the AP600 containment steel shell thickness and the spacing of water streams at the containment sidewall perimeter imposed by the PCS water distribution weirs. A thermal conductivity of 24 Btu/hr-ft-°F was used for the steel material. Adiabatic boundary conditions were used for the right and left side of the half-cell model to represent symmetry and periodicity of the cell.

For each steady-state containment pressure analyzed, a half-cell model was established for each water coverage fraction ranging from 0.05 to 0.95. The nodding density was increased on each side of the wet/dry interface on the outside surface to increase the accuracy of the heat transfer calculation near the wet/dry interface.

In addition to these partially wetted half-cell models, the heat transfer with a completely wetted and complete dry half-cell model was analyzed for each containment pressure using the same inside and outside boundary conditions. Since the half-cell has a 1-D solution when fully wet or dry, these cases provide the heat flux with only radial condition through the containment shell. The heat flux rate results of these fully wetted and fully dry cases were used to normalize the heat flux rate obtained from the partially wetted cases, where two-dimensional heat conduction occurs.

Deleted: 2-D

The ANSYS two-dimensional heat conduction results show that the temperature of the dry surface area is decreased compared to the dry surface temperature when only one-dimensional radial heat conduction is used. This results in less radiation and convection from the dry regions. Although WGOTHIC utilizes one-dimensional radial heat conduction, the dry area convection and radiation is not overpredicted because WGOTHIC must use a wet surface area that corresponds to the evaporated water flow rate calculated by the PCS film coverage model. The evaporated water flow rate calculated by the PCS film coverage model includes the enhanced evaporation characterized by the multiplier, M (Section 7.4). Thus, WGOTHIC must use more cooler wet surface area to evaporate the water flow rate from the PCS film coverage model. This results in less hotter dry surface area, and therefore, WGOTHIC underpredicts the net radiation and convection from the dry surface.

Moved (insertion) [12]

Deleted: 5.1.3

7-21

The WGOTHIC conservatism can be estimated using values from the ANSYS two-dimensional calculation, which is the best representation of the heat conduction through the shell. It is assumed the WGOTHIC temperatures and heat fluxes are the same as ANSYS one-dimensional cases.

- At containment pressures of 15 and 25 psig, and with 50 percent wet coverage, the two-dimensional ANSYS model predicts dry heat transfer (radiation and convection) is 73 and 82 percent respectively, of the one-dimensional value. WGOTHIC will predict 67 percent of the one-dimensional dry heat transfer, since it reduces the dry surface area available by 33 percent.
- For the same containment pressures, at 25 percent wet coverage, the two-dimensional model predicts the actual dry heat transfer (radiation and convection) is 83 to 91 percent of the one-dimensional value. WGOTHIC will predict 57 percent of the one-dimensional dry heat transfer, since it reduces the dry surface area by 43 percent. Thus, WGOTHIC again predicts less dry energy removal than two-dimensional model predicts.

It is concluded that the WGOTHIC model predicts less dry heat transfer than the two-dimensional ANSYS model.

7.4.4 Enhanced Evaporation due to 2-D Conduction

The heat flux from the wetted portion of the half-cell model was compared with the wetted heat flux that occurs when only radial heat conduction (one-dimension) is assumed. Figure 7-6 shows the water evaporation rate with two-dimensional conduction versus the fraction of wetted area, normalized to the evaporation rate, calculated with only radial heat conduction (one-dimensional) outward through the steel shell, for containment pressures of 10, 15, 20, and 25 psig. These calculational results are bounded by the following polynomial expression:

$$[\quad]^{a,c} \quad (7-1)$$

where,

- M = the wetted area heat transfer rate enhancement or multiplication factor
x = fraction of containment surface wetted, = W/W_o

This multiplication factor is applied to the average evaporation flux from WGOTHIC in the spreadsheet calculation of the evaporation-limited PCS flow discussed in Section 7.5.2.1 to approximate the effects of 2-D conduction. Although there may be notable dry stripes at the lower elevations of the containment shell throughout the transient, the 2-D conduction multiplier is not credited until the PCS flowrate from the bucket has decreased such that the film width is narrowed below []^{a,c} along the entire sidewall.

Deleted: which is used in an external the PCS film coverage model to determine the evaporation-limited PCS applied water flow rate that is input to WGOTHIC (See Section 7.5):

7-22

Several additional plots to illustrate the effect of two-dimensional conduction on the PCS heat transfer process are provided for the 20 psig containment pressure, 25 percent wetted case. A temperature distribution contour plot is shown for the ANSYS half-cell model in Figure 7-7, with the surface inside containment at the top of the page. Figure 7-8 shows the thermal flux from the inside to outside surface (x direction), perpendicular to the containment shell, and Figure 7-9 shows the total heat flux (x, y directions) that occur in the steel shell. Figure 7-10 and Figure 7-11 show the thermal flux distribution on the outside and inside surface of the wall, respectively.

Deleted: -

Deleted:

Deleted: -

a,c

Figure 7-6. Normalized Water Evaporation Rate (2-D/1-D) versus Overall Containment Wetted Fraction

7-23

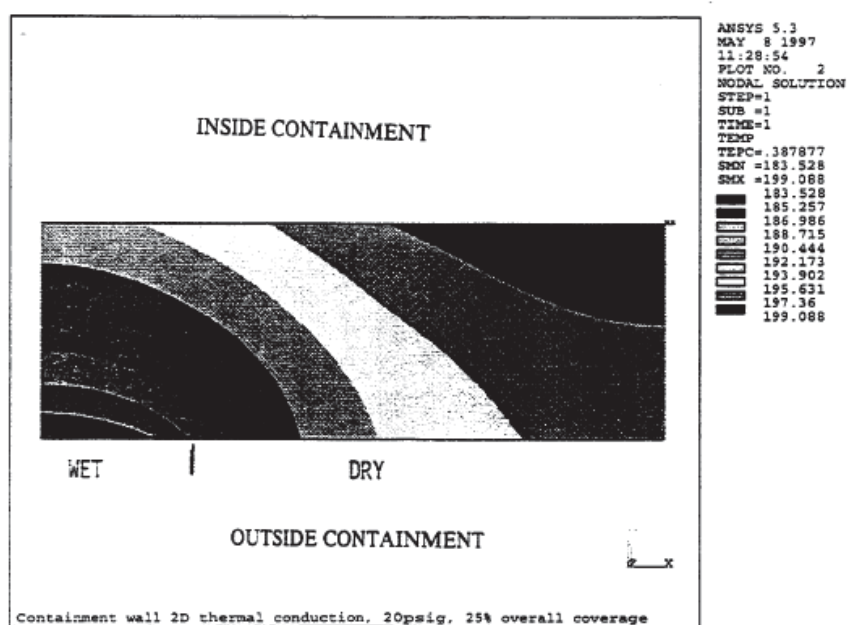


Figure 7-7. Containment Steel Shell Temperature Gradient (°F) with 2-D Heat Conduction;
20 psig, 25% Wetted

7-24

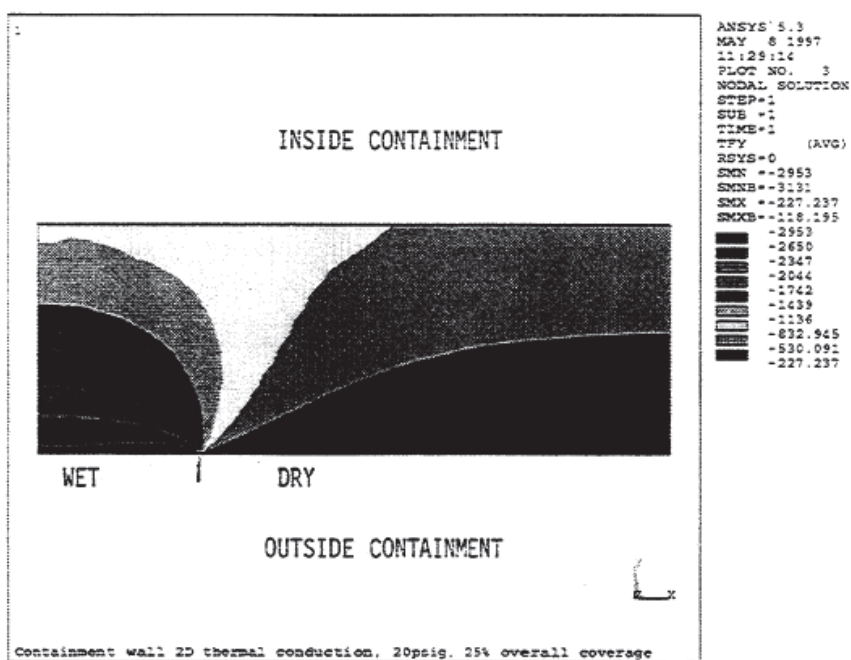


Figure 7-8. Containment Steel Shell Thermal Flux Gradients (Btu/hr-ft²) in Y-Direction; 20 psig, 25% Wetted

7-25

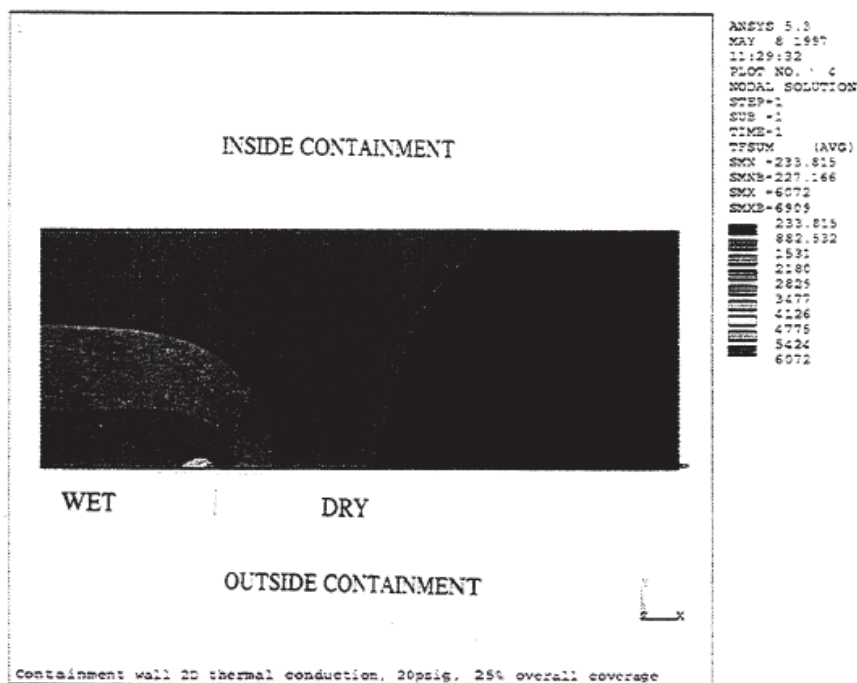


Figure 7-9. Containment Steel Shell Total Thermal Flux (Btu/hr-ft²); 20 psig, 25% Wetted

7-26

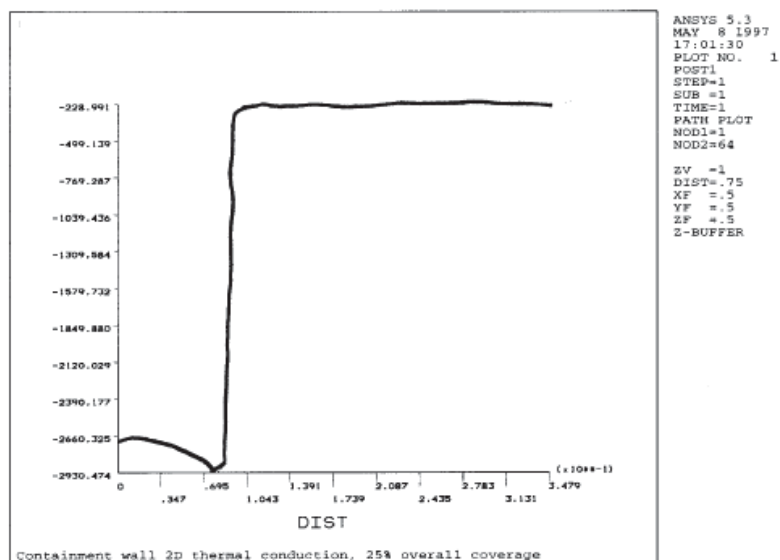


Figure 7-10. Thermal Flux in Y-Direction on Outside Surface of Containment Wall [Btu/hr-ft²]

7-27

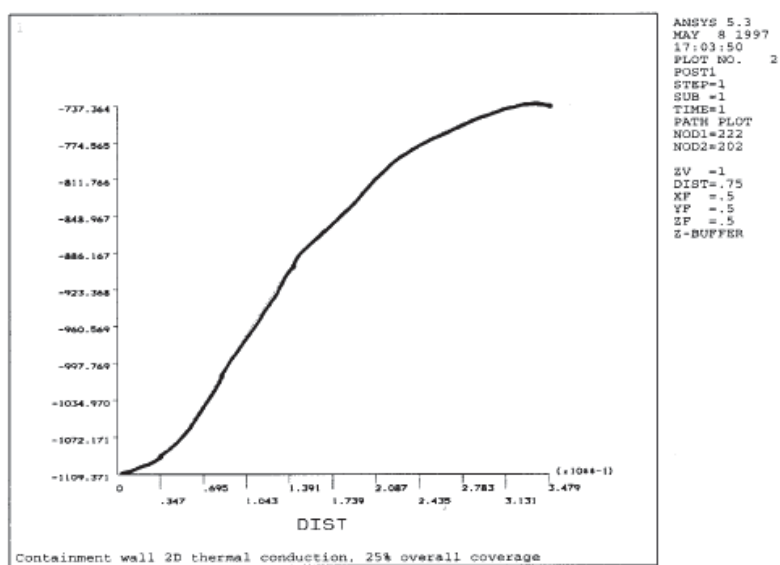


Figure 7-11. Thermal Flux in Y-direction on Inside Surface of Containment Wall [Btu/hr-ft²]

7-28

7.4.5 Enhanced Overall Heat and Mass Transfer Due to 2-D Conduction

As described in Section 7.4.4, the evaporation rate from the containment shell can be enhanced by including the effects of circumferential 2-D heat conduction by using a factor to increase the evaporation-limited PCS flowrate based on the fraction of the containment surface that is wetted. An alternate approach is to incorporate the effects of 2-D heat conduction by applying a multiplier on the overall heat transfer rate. The information in this section is developed from the same analyses that are the basis for the PCS evaporation factor in Section 7.4.4.

The conduction of heat from the hot dry region into the cooler wetted region of the containment shell will increase the overall heat transfer rate through the shell. Figure 7-12 shows the total heat transfer rate (wetted and dry areas combined) versus the fraction of wetted area, normalized to the heat transfer rates calculated with only radial heat conduction (one-dimensional) outward through the steel shell. [

1^{a,c}

a,c

Figure 7-12 Normalized Total Wet and Dry Heat Transfer (2-D/1-D Conduction) vs. Wetted Fraction

7-29

This alternate approach of modeling the effect of 2-D heat conduction is used with the evaporation-limited PCS option incorporated into the WGOETHIC code discussed in Section 7.5.2.2. Figure 7-13 shows [

$\gamma^{a,c}$

a,c

Figure 7-13. 2-D Conduction Multiplier as a Function of Wetting Fraction

7-30

7.4.6 Insights from the PCS Large-Scale Testing

The large-scale PCS heat transfer tests were largely conducted with high water coverage fractions such that circumferential conduction would have little or no effect on the water evaporation rate. An exception is test run RC050C of matrix tests 213.1. A clear indication of 2-D conduction effects is seen by comparing the results of RC050C with test run RC048C of matrix test 212.1. In these tests, the containment pressure and other boundary conditions were essentially the same, with the exception that the amount of water applied to the external surface of the test vessel was []^{a,b} gpm in test RC048C and only []^{a,b} gpm in test RC050C.

The reduced water flow rate in test RC050C resulted in a reduction in the wetted area observed at the bottom of the test vessel sidewall, []^{a,b} percent for test RC050C versus []^{a,b} percent for test RC048C. In spite of the reduced wetted area in test RC050C, the total heat removed from the test vessel and the amount of water evaporated in this test was equal to test RC048C.

Furthermore, the lower portion of the vertical sidewall in test run RC050C was wetted with []^{a,b}. This stripe geometry is similar to that observed in the water distribution test discussed in Section 7.2.3 and assumed for the 2-D conduction model.

A comparison of the LST vessel shell wall temperatures for these two test runs using the thermocouple pairs (one thermocouple at the inside wall surface matched to a thermocouple at the outside wall surface), used to derive local heat flux rates, provides insight to the effect of circumferential conduction. [Table 7-4](#) and [Table 7-5](#) provide comparisons of the inside and outside LST shell temperatures, and the local heat flux derived from the temperature difference across the 7/8-inch thick steel shell; for the two lowest elevations on the LST sidewall.

[Table 7-4](#) shows that at the Level D elevation in test run RC048C all the inside and outside wall temperatures are relatively uniform. This indicates that the outer wall is wetted at all the thermocouple pair locations. The average outside wall surface temperature is []^{a,b} °F, and the average local heat flux is []^{a,b} Btu/hr-ft² based on the thermocouple pair ΔTs. In comparison, only four of seven outside wall thermocouples appear to be wetted in test run RC050C (dry outside wall temperatures are very high, []^{a,b} °F, and the wall ΔT is small). In this test run the average wetted outside wall temperature is []^{a,b} °F, and the average wetted local heat flux is []^{a,b} Btu/hr-ft².

Similarly, [Table 7-5](#) shows that at the Level E elevation (just above the runoff collection gutter) the test run RC048C uniformly wetted outside wall average temperature is []^{a,b} °F and the average heat flux is []^{a,b} Btu/hr-ft². In comparison, test run RC050C which is []^{a,b} percent wetted at this elevation; indicates that only two of the outside wall thermocouples are clearly wetted, and the average wetted outside wall temperature is []^{a,b} °F and the average heat flux is []^{a,b} Btu/hr-ft². Note that the test run RC050C thermocouples at the 240° circumferential location show an outside wall temperature and heat flux that is intermediate to the clearly wetted or dry locations. This thermocouple pair may be adjacent to a wet stripe, where circumferential heat conduction would cause these observed intermediate temperatures and ΔT.

These tables show that with the striped water coverage on the outside surface, the wall temperatures and heat flux of the wet portions of the shell are higher than when the outside surface is completely wet.

Deleted: Table 7-3

Deleted: Tables 7-3

Deleted: Table 7-4

Deleted: Table 7-3

Deleted: Table 7-4

7-31

Table 7-4. Elevation D Heat Flux Comparison from PCS Large-Scale Tests RC048C and RC050C

Deleted: 3

a,c

7-32

Table 7-5. Elevation E Heat Flux Comparison from PCS Large-Scale Test RC048C and RC050C

Deleted: 4

[illegible]

Deleted: The PCS heat removal at a given containment pressure is largely determined by how much of the delivered water evaporates. Heat removal is maximized if all the water delivered to the shell evaporates.¶ Consequently, the determination of how much water evaporates from the containment shell is necessary to determine the containment heat removal. The flow rate of water that runs off the shell is the difference¶ between the delivered water flow rate and the evaporation rate.¶

Formatted: Underline

Deleted: The PCS film coverage model eliminates the need for the WGOOTHIC code to determine the wetted area as a function of time. The use of the evaporation-limited PCS flow to calculate containment pressure introduces conservatism because it discounts sensible heating of any runoff flow, and because a heat flux lower than the heat flux calculated by WGOOTHIC is used to calculate the amount of water evaporated.¶

As the water coverage of the containment shell decreases due to the decrease in the delivered PCS flow rate with time, alternate wet and dry stripes are formed on the containment shell exterior surface and twodimensional (radial and circumferential) heat conduction is established in the containment shell. Accounting for two-dimensional conduction increases the temperature of the wetted steel surface, and therefore also increases the temperature of the liquid film, over what is calculated for one-dimensional (radial) conduction only. The increase in the temperature of the liquid film, in turn, results in the evaporation of more water, reducing the calculated runoff from the shell. Section 7.5.1.3 describes how the increase in water evaporation effectiveness of the PCS is accounted for in the PCS film coverage model, when both radial and circumferential heat conduction are important in the steel containment shell.

7.5 THE CONTAINMENT EVALUATION MODEL TREATMENT OF WATER COVERAGE

The containment Evaluation Model includes a PCS film coverage model that determines the wetted area on the outside of the containment vessel. It accounts for the reduction in the wetted area down the side of the containment vessel as the PCS flowrate changes, due to the decreasing flowrate as the standpipes in the PCCWST uncover and due to the evaporation of the water. The model also determines the amount of PCS water that does not evaporate, and excludes the sensible heating of this runoff flow. Section 7.5.1 describes the equations that determine the wetted fraction, and Section 7.5.2 describes the implementation and interaction with the WGOthic code.

7.5.1 PCS Film Coverage Model

The PCS film coverage model, which is used to calculate the rate at which water evaporates from the sidewall of the containment shell, is described in this section. The model assumes water is delivered to the sidewall consistently with the initial distribution spreading data described in Section 7.3.1.

7-33

The PCS film coverage rate model starts with a simple definition that relates the total film flow rate, \dot{m} ; the containment circumference, W_o ; the wetted fraction of the circumference, or the fraction of the surface that is wet, f ; and the film flow, or mass flow rate per unit width, Γ . Each of these is a function of the parameter Z , the distance below the top of the sidewall. The equation is:

$$\dot{m}(Z) = \Gamma(Z)W_o f(Z) \quad (7-2)$$

which, rearranged, also defines Γ . The derivative of the mass flow rate with respect to vertical distance is also used. Using the chain rule for derivatives:

$$\frac{d\dot{m}}{dz} = W_o f \frac{d\Gamma}{dz} + \Gamma W_o \frac{df}{dz} \quad (7-3)$$

The wetted coverage and runoff flow rate are calculated based on the following assumptions and boundary conditions:

- The delivered PCS water flow rate boundary condition at the top of the sidewall, \dot{m}_{on} is presented in Figure 7-2. The initial film flow rate at the top of the sidewall is specified to be $\Gamma = \dot{m}_{top}/(W_o f)$, $f = [\quad]^{a,c}$. For delivered flow rates less than $[\quad]^{a,b}$ gpm, the film flow rate at the top of the sidewall is specified to be $\Gamma_{dist} = [\quad]^{a,b}$ lbm/hr-ft. The other boundary condition, the width of coverage at the top is determined from $W_o f_{top} = W_o f_{\Gamma} f = [\quad]^{a,c}$ or $W_o f_{top} = \dot{m}/\Gamma_{dist}$ depending on the delivered flow rate.
- The water is assumed to flow in constant width stripes below each weir slot as long as the film flow rate Γ remains greater than Γ_{min} . The film flow rate decreases due to evaporation as the film travels down the sidewall. The constant width coverage model is described in Section 7.5.1.1.
- After the film flow rate reaches Γ_{min} , evaporation is assumed to cause the stripe width to narrow while Γ remains constant at Γ_{min} .

7.5.1.1 Constant Width Coverage

After the water distribution is established at the top of the sidewall by the weir, the film evaporates at mass flux, $\varphi_m(Z)$, as it flows down the shell in stripes of constant width. The basis for the constant width stripe is the observations of the stripes on the LST, and the physical explanation in Appendix 7.A-3. For a constant wetted fraction $df/dZ = 0$, and $d\Gamma/dZ = \varphi_m(Z)$. The rate of change equations for \dot{m} , Γ , and $W_o f$ for the constant width portion of the wetted area are:

$$\frac{d\dot{m}}{dz} = -\varphi_m(Z)W_o f \quad (7-4)$$

$$\frac{d\Gamma}{dz} = -\varphi_m(Z) \quad (7-5)$$

$$W_o \frac{df}{dz} = 0 \quad (7-6)$$

7-34

With the boundary conditions listed above, and Equations 7-4, 7-5, and 7-6, the water mass flow rate, \dot{m} , and the film flow rate, Γ , can be calculated for the constant width evaporation portion of the coverage. For the case with $\phi_m = \text{constant}$, the simple analytical expression for the mass flow rate is:

$$\dot{m}(Z) = \dot{m}_{top} - \phi_m W_o f_{top} Z \quad (7-7)$$

Equation (7-4) can be written in terms of difference equations for a numerical solution where $\Delta \dot{m} = \dot{m}_2 - \dot{m}_1$, $\Delta Z = Z_2 - Z_1$, and ϕ_m is a variable:

$$\Delta \dot{m} = -W_o f_{top} \phi_m \Delta Z \quad (7-8)$$

or

$$\dot{m}_2 = \dot{m}_1 - W_o f_{top} \phi_m (Z_2 - Z_1) \quad (7-9)$$

Knowing \dot{m} , the film flow rate is determined from Equation (7-2) where $\Gamma = \Gamma_{dist} = \dot{m}_{top} / (W_o f)$.

The value of Z when Γ reduces to Γ_{min} is Z_{min} . The value of Z_{min} can be determined from Equation (7-7) when ϕ_m is constant:

$$Z_{min} = \frac{(\dot{m}_{top} / W_o f_{top}) - \Gamma_{min}}{\phi_m} \quad (7-10)$$

7.5.1.2 Constant Γ_{min} Coverage

When $\Gamma = \Gamma_{min}$, the ~~wetted~~ width, $W_o f$, begins to narrow, while Γ_{min} is maintained at a constant value. The resulting ~~rate of~~ change equations for \dot{m} , Γ , and $W_o f$ for this portion of the stripe are:

$$\frac{d\dot{m}}{dz} = -\phi_m(Z) W_o f(Z) \quad (7-11)$$

$$\frac{d\Gamma}{dz} = 0 \quad (7-12)$$

$$\frac{df}{dz} = -\frac{\phi_m(Z) f(Z)}{\Gamma(Z)} \quad (7-13)$$

When $\phi_m = \text{constant}$ and $\Gamma = \Gamma_{min} = \text{constant}$, the solution to Equation 7-13 is the simple exponential function:

$$f(Z) = f_{top} e^{-\phi_m(Z - Z_{min}) / \Gamma_{min}} \quad (7-14)$$

Knowing from Equation (7-14), the mass flow rate at any Z is simply calculated from Equation (7-2). The runoff flow rate is $\dot{m}_{off} = W_o f_{bot} \Gamma_{min}$, where $W_o f_{bot}$ is the wetted circumference at the bottom of the containment shell, $Z = Z_{max}$.

By inspection of Equation (7-14), it is noted that $W_o f$, the ~~wetted width~~, is always greater than zero. Thus, for constant values of ϕ_m and Γ_{min} , Equation (7-14) always predicts some water runs off the wall without

Deleted: stripe

Deleted: W

Deleted: When ϕ_m is not constant with height, the analytical expression for W depends on the functional form of ϕ_m and a general expression is written for numerical integration where ϕ_m is calculated for each Z :
 $\Delta \dot{W} = -W_o f_{top} \phi_m \Delta Z$

Deleted: W

Deleted: or (7-16),

Deleted: film flow per unit width

7-35

evaporating. However, from experimental observations, all the water delivered to the containment shell is evaporated for some transient conditions. Thus, the preceding calculation method is conservative in its execution.

7.5.2 Interaction of the PCS Film Coverage Model with WGOETHIC

There are two processes that can be used to implement the PCS film coverage model. The first is a spreadsheet that is used iteratively with WGOETHIC runs. The second is fully contained within the WGOETHIC code. This section provides an overview of the WGOETHIC clime modeling as it relates to the PCS flow modeling followed by detailed summaries of the two process for determining the PCS film coverage and the evaporation-limited flowrate.

The WGOETHIC code uses a special type of heat conductor called a “clime” to model the convection, radiation, conduction, evaporation, and condensation heat and mass transfer processes from the inside of containment to the outside of containment. Each clime consists of a horizontal slice of the shell, riser, baffle, downcomer, and shield building of the PCS. []^{a,c} climes are used to represent the PCS in the AP600 containment design basis accident (DBA) Evaluation Model. []^{a,c} climes are used to represent the PCS in the AP1000 containment DBA Evaluation Model. Details of the climes in the WGOETHIC AP600 containment model are described in Section 4.4; the clime portion of the WGOETHIC AP1000 containment Evaluation Model is described in Section 13.5.

The maximum wetted area for each clime is input to the WGOETHIC model. The wetted area input values for the WGOETHIC Model are based on the measured water coverage values from the Phase 3 Water Distribution Tests on the dome, and []^{a,c} percent of the shell circumference wetted on the sidewall. The wetted area for the top of the dome down to the first weir is estimated from the video tapes of the Phase 3 Water Distribution Test. The wetted coverage area change over the diverging area between the first and second weirs. The wetted perimeter specified for this region is based on the average of the value just below the first weir and the minimum measured value just above the second weir. The wetted perimeter does not change much over the steeply sloped region between the second weir and the top of the vertical sidewall. The wetted perimeter input values are the same for each clime representing the vertical sidewall.

The percent of the perimeter wetted is summarized in Table 7-6. The values listed represent the measurements at the []^{a,c} flow rate (which is equivalent to a []^{a,c} PCS water flow rate). The use of these wetted perimeter percentages for the higher initial PCS flow rate is a conservatism in the containment Evaluation Model.

Table 7-6. Clime Wetted Perimeter and Basis for WGOETHIC Evaluation Model

Clime	Percentage	Location	Method of Determination
[] ^{a,c}		[] ^{a,c}	Visual inspection and calculation
[] ^{a,c}		[] ^{a,c}	Measured
[] ^{a,c}		[] ^{a,c}	Measured

Deleted: WGOETHIC Model

Deleted: The WGOETHIC AP600 containment model is described in detail in Section 4. The WGOETHIC AP1000 Containment Model is described in detail in Section 13. Features specific to water coverage are discussed in this section.¶

Deleted: 4

Moved (insertion) [10]

Deleted: perimeter

Deleted: The clime model allows the waterto flow at constant width until it reaches the next lower clime, or it evaporates entirely. When it evaporates entirely before reaching the bottom of the clime, the code tracks the distance traveled and breaks the clime vertically into wet and dry portions with temperatures calculated using the appropriate wet or dry heat and mass transfer models.

Deleted: perimeter

Deleted: Use of the evaporation-limited PCS water flow rate from the film coverage model as input to the WGOETHIC model, as described in Section 7.5.1, eliminates the need to vary the wetted perimeter input values with time. The sensitivity analyses, presented in Section 7.6, demonstrate that this approach is conservative as compared to using the actual PCS film flow rate with variable coverage area.¶

Moved (insertion) [11]

Deleted: perimeter value

Deleted: and wetted perimeter

Deleted: ¶
The WGOETHIC model uses the following input to compute the evaporation heat removal rate from the shell: the evaporation-limited PCS water flow rate, the PCS water temperature, and the area and wetted perimeter for each clime. The vertical variation in the wetted perimeter and the resulting wetted area were conservatively calculated in the PCS film coverage model, so the WGOETHIC code does not calculate the change in these values as a function of time or position. Rather, the evaporation-limited PCS water flow rate is determined in the PCS film coverage area model, and is input to WGOETHIC to account for changes in the evaporation rate due to anticipated changes in the coverage area with time and location on the shell. The WGOETHIC code uses wetted perimeter inputs for each clime as described in Section 7.5.2.1. ¶
The evaporation-limited PCS flow rate that is input to the WGOETHIC code is calculated in the PCS film coverage model described in Section 7.5.1. The application of the PCS flow is assumed to be dela...

Moved up [10]: The wetted perimeter for each WGOETHIC model. The clime model allows the water¶

Moved up [11]: The wetted perimeter value for the top of the dome down to the first weir is estimated from the video tapes of the Phase 3 Wa...

Deleted: 5

Deleted: 5

7-36

The application of the PCS water flow is delayed based on the estimated time required to reach steady-state coverage at the full delivered PCS flow rate, as described in Section 7.2.5. No PCS water is credited until after the time that the containment sidewall is wet to the bottom elevation. The evaporation-limited PCS flow rate is calculated by the PCS film coverage model, using either the spreadsheet process or the option within WGOthic, as described in Section 7.5.2.1 and Section 7.5.2.2, respectively. Section 7.5.2.3 addresses the PCS water stripping from the baffle supports on the vertical surface of the containment vessel that was described in Section 7.2.6.

7.5.2.1 Spreadsheet Calculation of the PCS Film Coverage

The equations developed in Section 7.5.1 are solved in a spreadsheet for both one-dimensional and two-dimensional shell heat transfer. The use of the spreadsheet is an iterative process that requires preliminary WGOthic runs that assume a PCS flowrate, then the evaporation flux from WGOthic is determined, and that flux is used as input to the spreadsheet.

The containment evaluation model uses the following input to compute the evaporation heat removal rate from the shell: the evaporation-limited PCS water flow rate, the PCS water temperature, and the wetted area for each clime. The vertical variation in the wetted perimeter and the resulting wetted area are conservatively calculated by the PCS film coverage model; the WGOthic code does not calculate the change in these values as a function of time or position. The evaporation-limited PCS flow rate that is determined by the PCS film coverage model spreadsheet calculation must be input to WGOthic to account for changes in the evaporation rate due to anticipated changes in the coverage area with time and location on the shell.

The clime model allows the water to flow at constant width until it reaches the next lower clime, or it evaporates entirely. When it evaporates entirely before reaching the bottom of the clime, the code tracks the distance traveled and breaks the clime vertically into wet and dry portions with temperatures calculated using the appropriate wet or dry heat and mass transfer models.

Iteration between WGOthic runs and the PCS film coverage model spreadsheet is necessary to converge on the same evaporation rate in both. The iteration proceeds as follows:

1. An average evaporation mass flux, ϕ_m , at selected times is determined from the WGOthic output for climes below the second weir by summing the evaporation mass from each wet clime and dividing it by the total wetted area for each time step.
2. The evaporation mass flux, ϕ_m , is input to the spreadsheet, which solves the equations presented in Section 7.5.1. At each time step, the delivered flowrate is applied to the top of the containment shell, and the evaporation rate and PCS film width is tracked down the elevation of the sidewall. The run-off flow at the bottom is excluded, and \dot{m}_{evap} , the evaporation-limited PCS flowrate, is defined.
3. The evaporation-limited PCS flowrate calculated by the spreadsheet is compared to the PCS flowrate that was credited in the WGOthic run at each time step. Iterations are done until the flowrates are similar, with it being conservative for the spreadsheet \dot{m}_{evap} to be greater than or equal to the PCS flowrate input in the WGOthic run. If this condition is not met, a revised

Deleted: An i

Deleted: and the WGOthic model

Deleted: ¶

Deleted: between the PCS film coverage model spreadsheet and the WGOthic calculations

Deleted: heat

Deleted: wet

Deleted: .

Deleted: The evaporation rate, m_{evap} is calculated in the spreadsheet for each time using Equations (7-7 and (7-14) for problems with constant evaporation mass flux, and Equations (7-8) and (7-15) for problems with variable evaporation flux.

Deleted: WGOthic is run with m_{evap} from the spreadsheet and the calculated results are used to define ϕ_m for input to Step 2 to recalculate the water evaporation rate.

7-37

evaporation-limited PCS flowrate is used as input to WGOETHIC and a new iteration round is performed.

The above process is done for the entire transient, with the evaporation-limited flow rate calculated at each selected time step.

The spreadsheet calculation has an option to include the effects of two-dimensional conduction. During the initial high flow PCS period, only one-dimensional heat transfer is credited. However, as the standpipes in the PCCWST uncover, the delivered PCS flow rate is reduced and the wetted circumference at the top of the containment shell is predicted to decrease. The effects of two-dimensional conduction are not credited until the uncovering of the second standpipe, which occurs several hours after the start of PCS flow.

The two-dimensional conduction model discussed in Section 7.4 calculated the evaporation rate for a range of wet stripe widths for both one-and two-dimensional conduction. The calculation used the same overall temperature difference (and steam partial pressure difference) between the bulk containment and the bulk riser as boundary conditions for both cases. The effective heat transfer coefficients, for mass transfer, were determined for each case. The comparison shows for a given stripe width, the enhancement of the evaporation rate when the real physical case of two-dimensional conduction is considered. It was found that the enhancement varied with stripe width, but had little effect on the overall temperature difference between the bulk containment and riser. Consequently, the family of curves representing the bulk temperature difference were lower bounded, thereby eliminating the dependence on the bulk temperature difference. The only dependent variable is the wet stripe width. The enhancement of evaporation is characterized by the multiplier, M, that is a polynomial function of the wet stripe width. M is defined by Equation 7-1. The multiplier, M is used in the spreadsheet as a multiplier on ϕ_m to produce a better estimate of the actual evaporation flux from the film stripes and the evaporation-limited PCS flow rate that is used as input to the containment evaluation model.

7.5.2.2 WGOETHIC Automated Evaporation-limited PCS Flow Model

Starting with version 4.3, the WGOETHIC code includes an option to implement the evaporation-limited PCS flow model. This option automates the iterative process that is needed with the PCS film coverage model to calculate the evaporation-limited PCS flow rate. With the evaporation-limited PCS flow option, the PCS flow delivered from the bucket is input by the user. The code then performs the function of the spreadsheet described above, accounting for the narrowing of the water stripes down the containment shell and not crediting the sensible heating of the runoff flow. The incorporation of this calculation into the WGOETHIC code has the advantage of removing the manual iterations between the code and the spreadsheet. In addition, the WGOETHIC code more accurately calculates the evaporation-limited flowrate, without having differing margin at each time step, which occurs with the spreadsheet calculation and iteration.

Deleted: When the WGOETHIC calculated values of ϕ_h are sufficiently close to, but higher than, the values assumed for input to the spreadsheet under Step 2, the solution is converged. That is because a higher heat flux input to the spreadsheet will predict more water evaporated. The use of the lower evaporation rate input results in WGOETHIC pressure predictions that are slightly high.

[

] a,c

7-38

L

$\Gamma^{a,c}$

In summary, the evaporation-limited PCS flow option in WGOthic eliminates the need for an analyst to manually perform iterations between the code and a spreadsheet. The spreadsheet calculation does not converge the same at each time step or for each run, and causes varying margin between the credited PCS flow and the WGOthic evaporation calculation. The evaporation-limited flow option in WGOthic takes away this variability, using criteria that establish the same degree of conservatism each time step. The automated code option also does quadrant-specific calculations rather than the spreadsheet tracking the evaporation for the containment as a whole. The top clime, which is the dome region of the containment vessel, is specified with a wetted fraction of $\Gamma^{a,c}$ in the WGOthic input for both PCS evaporation-limited calculation, but the spreadsheet calculation $\Gamma^{a,c}$ of the top clime. A factor to credit the effects of 2-D conduction between wet and dry stripes is available as an option that can be turned in both the spreadsheet and the option built in to WGOthic. The factor is similar, but the spreadsheet applies it as a direct multiplier on the evaporation rate while the evaporation-limited PCS flow option puts a multiplier on the heat flux.

7.5.2.3 Application of PCS Water Stripping from Baffle Supports

As discussed in Section 7.2.6, some of the PCS water was observed as “raining” in the annulus rather than flowing down the containment vessel during a pre-operational PCS flow test. To conservatively account for this

7-39

effect, termed as rainout, the safety analyses will not credit any PCS water that encounters the baffle supports on the cylindrical portion of the containment vessel. It is assumed that PCS water hits the baffle supports in proportion to the fraction of the containment vessel circumference that is obstructed by the baffle supports, and that all of this PCS water is lost. The elevation of the baffle support affects the amount of rainout as the PCS flowrate decreases at lower elevation because of evaporation. In addition, the wetted fraction, which may decrease at lower elevations, affects the rainout because if a baffle support is in a dry stripe, there will obviously be no rainout due to the baffle support. Both the PCS flowrate and wetted fraction change not only down the elevation of the containment, but these parameters vary throughout the safety analysis transients. Thus, rainout is not modeled as a single fraction but is a transient factor that is expected to range between $[]^{a,c}$ and $[]^{a,c}$ of the PCS flow.

The rainout calculation tracks the PCS water for each quadrant as a function of elevation. The rainout at higher elevations, evaporation, narrowing of water stripes (see Section 7.5.1.2), and the changing wetted fraction are accounted for in determining how much PCS water hits a set of baffle supports. Because this issue arose after the evaporation-limited model was incorporated into WGOETHIC, the detailed rainout calculation was developed to interface only with this model (Section 7.5.2.2). The evaporation and wetted fraction of each clime is calculated by WGOETHIC and is used to calculate the rainout flowrate based on the geometric information (number, width, and location) of the baffle supports. The PCS flow delivered from the bucket to the top of the containment vessel, which is a WGOETHIC input, is reduced by the rainout flowrate. Although the water is stripped from the containment at various elevations, the rainout-adjusted PCS flowrate is used as the bucket-delivered PCS flowrate input to WGOETHIC. This method ignores the rainout water for all elevations, which has a small conservative effect on the wetted fraction and dryout calculations.

The evaporation-limited PCS flowrate that is credited for heat removal excludes any sensible heat removal by the water that runs off. [

]

7.6 SUMMARY OF SUPPORTING TESTS AND SELECTED ANALYSIS

This section provides a summary of the PCS tests and data that are relevant to water film coverage and film behavior, and which support the Evaluation Model. In addition Section 7.6.4 provides an estimate of the range of film coverage parameters that can occur in the AP600 and AP1000 plants, and compares this parameter range to a composite of the ranges tested.

Section 7.6.5 summarizes an estimate of the heatup of the AP600 and AP1000 containment shell versus time. This heatup versus time is utilized in the sensitivity study of PCS flow initiation time presented in Section 7.7.3.

7.6.1 Westinghouse Wet Flat Plate Test

The primary purpose of the Westinghouse wet flat plate test was to generate heat and mass transfer data for evaporative cooling with parameters that bound the expected conditions on the AP600 containment

Deleted: 7.5.2.3 Dry Convection and Radiation Heat Transfer Predictions¶

Moved up [12]: The ANSYS two-dimensional heat conduction results show that the temperature of the dry surface area is¶ decreased compared to the dry surface temperature when only one-dimensional radial heat conduction is¶ used. This results in less radiation and convection from the dry regions. Although WGOETHIC utilizes¶ one-dimensional radial heat conduction, the dry area convection and radiation is not overpredicted because WGOETHIC must use a wet surface area that corresponds to the evaporated water flow rate calculated by the PCS film coverage model. The evaporated water flow rate calculated by the PCS film coverage model includes the enhanced evaporation characterized by the multiplier, M (Section 7.5.1.3). Thus, WGOETHIC must use more cooler wet surface area to evaporate the water flow rate from the PCS film coverage model. This results in less hotter dry surface area, and therefore, WGOETHIC underpredicts the net radiation and convection from the dry surface.¶

¶ The WGOETHIC conservatism can be estimated using values from the ANSYS two-dimensional calculation, which is the best representation of the heat conduction through the shell. It is assumed the WGOETHIC temperatures and heat fluxes are the same as ANSYS one-dimensional cases.¶

¶ At containment pressures of 15 and 25 psig, and with 50 percent wet coverage, the two-dimensional¶ ANSYS model predicts dry heat transfer (radiation and convection) is 73 and 82 percent¶ respectively, of the one-dimensional value. WGOETHIC will predict 67 percent of the¶ one-dimensional dry heat transfer, since it reduces the dry surface area available by 33 percent.¶

¶ For the same containment pressures, at 25 percent wet coverage, the two-dimensional model predicts¶ the actual dry heat transfer (radiation and convection) is 83 to 91 percent of the one-dimensional¶ value. WGOETHIC will predict 57 percent of the one-dimensional dry heat transfer, since it reduces¶ the dry surface area by 43 percent. Thus, WGOETHIC again predicts less dry energy removal than¶ two-dimensional model predicts.¶ It is concluded that the WGOETHIC model predicts less dry heat transfer than the two-dimensional ANSYS model.

Deleted: ¶

7-40

shell. A secondary purpose was to observe the film hydrodynamics including possible formation of dry patches due to surface tension instabilities. The test article is described in Reference 7.3.

Tests were performed in two orientations, vertical (to represent the sidewall) and 15 degrees from horizontal (to represent the upper portion of the dome) with various combinations of air velocity, film flow rate, and heat flux. A stable, wavy laminar water film was formed easily on the hot, coated, steel surface, even in the vertical orientation. A description of the test section and results from the various tests are given in Reference 7.3. The test data are summarized in [Table 7-7](#).

Deleted: Table 7-5

Two of the heated flat plate tests were run with very low film flow rates at relatively high heat flux (6000-8000 BTU/hr-ft²) to force the film to completely evaporate before reaching the end of the test section. The observations given in Reference 7.3 state the following: "The upper part was 80 percent wetted and fingers of water film extended down 4 feet to within 2 feet of the end of the heated plate. The bottom of the fingers slowly moved up and down. The dry patch between fingers was between 1/4-inch and 1-1/2 inches wide. As the width varied in time, the lateral, slow flow of liquid could be seen feeding the thinnest parts of evaporating film. These two tests showed that the end point of water films on the containment would still be stable film evaporation, even with very thin films and high heat fluxes."

7.6.2 Small-Scale Tests

The small-scale tests were designed to provide heat and mass transfer data for both the inside and outside of the test vessel. The test apparatus consisted of a 3-foot diameter, 24-foot high steel pressure vessel filled with air at atmospheric pressure into which steam was supplied to maintain various pressures. Water was applied to the external surface to simulate evaporation in the PCS annulus. The pressure vessel was surrounded by a clear, plexiglass shield that formed a 15-inch wide annulus for either forced or natural circulation-driven air flow and allowed observation of the applied external film flow.

The tests were conducted with varying steam supply flow rates, water film flow rates, water film temperatures, cooling air flow rates, and cooling air inlet temperature and humidity. Instrumentation was provided to measure internal steam condensation rates, external water evaporation rates, inner and outer wall temperatures, film temperatures, air velocity, temperatures, and humidity. A summary of the test data from Reference 7.4 (for tests with measured water coverage) is provided in [Table 7-8](#).

Deleted: Table 7-6

The following observations and conclusions (with respect to the water film) were drawn from these tests:

- A stable, uniform, wavy laminar film was formed on the inorganic zinc-coated steel surface using simple weirs.
- The film remained stable and uniform on the vertical sidewall of the vessel at average evaporating heat fluxes in the range of those expected on the AP600.

7.6.3 Large-Scale Tests

Deleted: (LSTs)

The Westinghouse large-scale PCS test facility was built to provide heat and mass transfer test data for a geometrically similar model of the AP600 containment vessel. The tests provided experimental data used for evaluating the physics in containment, determining the relative importance of various parameters that

7-41

affect heat and mass transfer, and validating computer codes and models. The following provides a discussion focused on the use of LST data to develop a bounding film coverage model.

Three series of tests were run at the Westinghouse large-scale PCS test facility. The steady-state pressure, annulus air flow rate, external water flow rate, injected steam flow rate, injection velocity, location and orientation, and non-condensable gas concentration were varied between the tests. Test conditions were selected to provide heat and mass transfer validation over a range of post-accident containment operating conditions for the AP600.

Table 7-7. Summary of Westinghouse Science and Technology Center (STC) Heated Flat Plate Tests

 $\overline{a,c}$ [illegible]

7-43

Table 7-8. Summary of Small-Scale Tests

Deleted: 6

a,c

The large-scale PCS test facility is a 20-foot tall, 15-foot diameter pressure vessel that simulates the AP600 containment vessel. The geometry is approximately a 1/8-scale of the AP600 containment vessel. A plexiglass cylinder is installed around the vessel to form the air cooling annulus. Air flows upward through the annulus via natural convection to cool the vessel, resulting in condensation of the steam inside the vessel. A fan is located at the top of the annulus shell to provide the capability to induce higher air velocities than can be achieved with purely natural convection. Water is applied to the elliptical dome surface by two rings of J-tubes. This method of application resulted in a series of spaced, wavy laminar flow stripes. At low test pressures the stripes spread within a few inches of their application point to form a continuous wavy laminar film. At high pressure the continuous film separated to form discrete stripes.

7-44

The following important observations with respect to film behavior were made during the tests:

- The J-tubes resulted in a non-uniform distribution of water on the surface of the LST, similar to that observed in the Water Distribution Test.
- Some J-tubes dripped and others had noticeably lower flow rates. This resulted in some regions of the dome and sidewall that were just wet or had a very low film flow rate.
- As the pressure and temperature increased inside the pressure vessel, dry spots first began to form in the wet, but low flow regions on the dome and sidewall.
- With increased pressure and heat flux, the dry spots grew vertically (both upward from the gutter and downward from the dome, between dripping or low flow J-tubes), separating the original continuous film into wavy laminar flow stripes. At higher heat fluxes, dry spots also formed just below, and in line with the J-tube location. A typical coverage pattern for high heat flux and high flow rate is shown in Figure 7-14.
- The central, wavy laminar flow region of the individual film stripes was surrounded by a region of laminar flow (with no visible waves). The thickness of the laminar flow region appeared to continually decrease out to the very edge (or bottom) of the film stripe.
- The widths of both the wavy laminar and laminar flow regions of the stripe were observed to decrease with increasing heat flux. At high flow rates, the width of the stripe was observed to remain relatively constant with elevation as the film flowed down the vertical sidewall. At lower flow rates, the stripe width was observed to taper uniformly with elevation as the film flowed down the vertical sidewall.
- The film stripes remained stable (i.e., they did not split or bunch up to form thick, narrow rivulets) as they evaporated on the vertical sidewall.

Deleted: 6

7-45

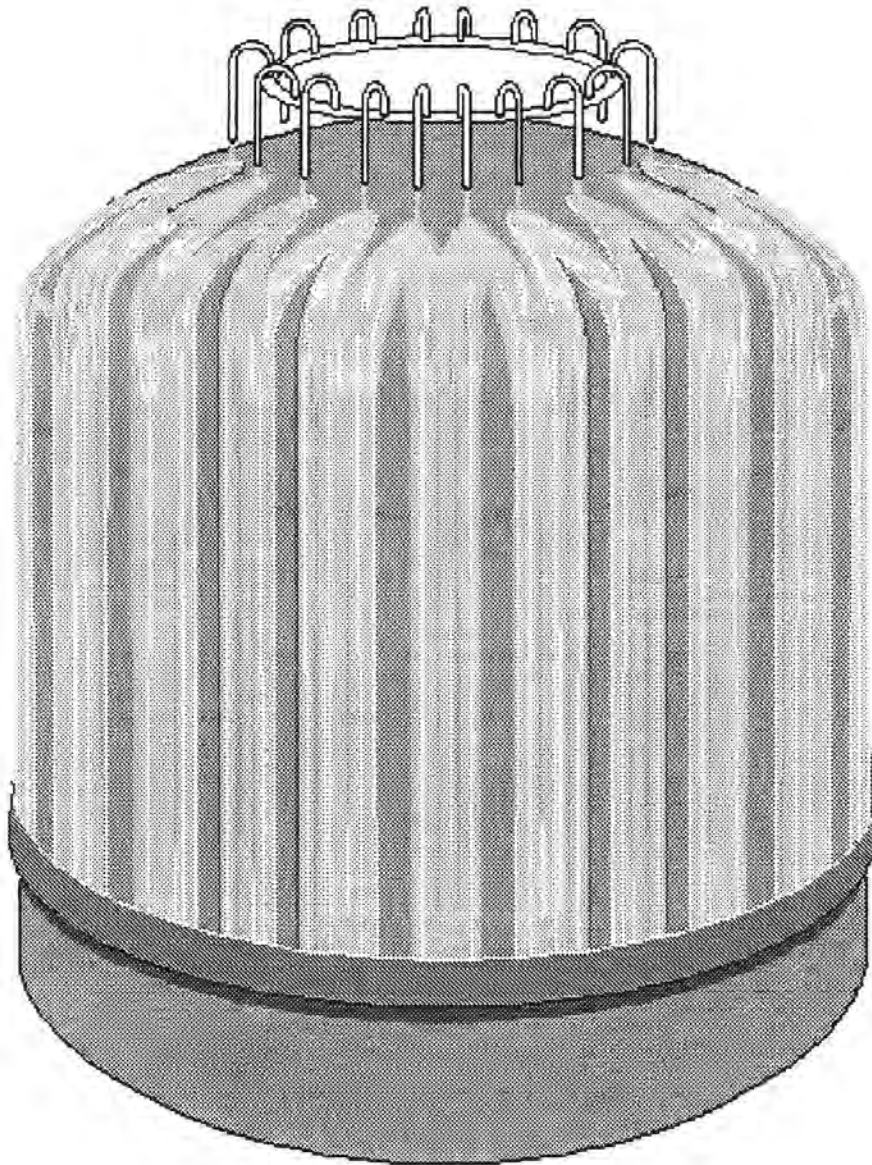


Figure 7-12. Large-Scale Test Water Coverage Pattern

Deleted: 12

7-46

The applied PCS flow rate was observed to vary or oscillate at a slow but regular period during some tests. This phenomenon was the result of sharing a common water source with a boiler feedwater valve that opened every two minutes, thereby reducing the PCS flowrate to the J-tube header. From observations made during testing, the flow oscillations had an effect on the water coverage fraction; it was most noticeable at the bottom of the sidewall. The length of the narrow film stripes and the width of the wider film stripes both decreased when the flow was observed to decrease. The dryout point of the narrow film stripes was observed to rise up and fall down the sidewall as the flow oscillated. At no time were the stripes observed to become unstable due to the oscillations; the process remained well-behaved and repeated itself with the periodicity of the applied flow.

After the Baseline LSTs were completed, instrumentation was added so the transient inlet and outlet cooling water flow rates could be measured and recorded by the data acquisition system. All of the Phase 2 and Phase 3 tests, with the exception of the blind test, (220.1, RC062) were included in the evaluation. The steam injection location, velocity, and initial pressure were much different in the Phase 3 tests, and subsequently, the level of stratification within the vessel was different than the Phase 2 tests. The differences in stratification resulted in changes in the coverage from the top to the bottom of the vessel; the top was less well covered than the bottom during some of the Phase 3 tests. The test numbers that were evaluated are listed in [Table 7-9](#).

Deleted: Table 7-7

Measurements of the dry stripes on the vessel were taken just above the gutter during the defined steady-state periods of each test. The time the measurement was recorded on the data sheets for each test. This could have been either the time the measurement was started or finished. In test 221.1B, the time of measurement does not match with the stated steady-state time period. The test engineer postulated the recorded time to be one hour off, i.e., 12:45 was recorded as 1:45 by mistake. The following assesses the effects of variations in flow during the time taken to record coverage data at the gutter.

From recorded test data the maximum and minimum exit mass flow rates were determined over the approximate time the wetted perimeter measurement was made. The time taken to perform these measurements was related to the number of dry stripes; more stripes took longer to measure. A 15-minute band on either side of the stated time of measurement was used in this evaluation to bound the time it took to make the measurement.

The maximum and minimum exit film flow rates were calculated by dividing the maximum and minimum mass flow rate by the measured wetted perimeter value. Because the film flow rate is calculated by dividing the mass flow rate by the wetted perimeter, if the wetted perimeter were slightly less than measured (due to a reduction in the mass flow rate), the film flow rate would be higher than calculated with this method.

Table 7-9. Summary of Large-Scale Tests

a,c

[illegible]

7-48

Table 7-9. Summary of Large-Scale Tests (cont.)

Deleted: 9

a,c

[illegible]

7-49

Similarly, if the wetted perimeter were slightly higher than measured (due to an increase in the mass flow rate), the film flow rate would be lower. In either case, the difference between the maximum and minimum film flow rates would be smaller than calculated. The maximum and minimum film flow rates for the tests are tabulated in [Table 7-9](#).

Deleted: Table 7-7

An evaluation of the LST data (Reference 7.5) yielded some additional important conclusions with respect to film coverage and heat removal:

- Evaporation is the primary mode of heat removal from the outside of the vessel. Sensible heating of the subcooled liquid film, convection, and radiation are second order.
- Striped film coverage provided better heat removal than forced quadrant coverage for the same wetted coverage.
- The highest heat flux occurred near the top of the dome at the elevation where the external film was applied for all of the wetted LSTs (except the horizontal, high-velocity, steam jet injection case). Although the dome represents about 30 percent of the heat transfer surface area, approximately 40 percent of the total heat removal occurred on the dome and 60 percent on the cylindrical sidewalls.
- Injection of high-velocity steam (similar to a steamline break) resulted in a well-mixed vessel (both above and below the operating deck), and thus, a relatively uniform wall temperature and heat flux over the evaporating surface.

The test data related to water coverage from References 7.6 and 7.7 are summarized in [Table 7-9](#). Tests 207.1, 207.3, 208.1, 216.1A, and 216.1B were conducted with water coverage by quadrants and are not representative of AP600 conditions and are therefore excluded from the table. The data of [Table 7-9](#) are used to develop a bounding film stability model as described in Section 7.3.2.

Deleted: Table 7-7

Deleted: Table 7-7

7.6.4 Estimated Range of Film Coverage Parameters

The estimates for the maximum and minimum values for the range of AP600 and **AP1000** film coverage parameters during a DBA are calculated using the simple approach described below. The range of film coverage parameters is compared with the range of the PCS tests and is shown in [Table 7-11](#).

Deleted: Table 7-9

To determine a maximum sidewall film flow rate, none of the initial PCS water is assumed to evaporate on the dome. Measurements from the unheated, Phase 3 Water Distribution Tests indicate that approximately []^{a,c} percent of the perimeter at the top of the sidewall will be wetted with 220 gpm, assuming this same wetted parameter at the higher actual PCS delivered flow rate results in an estimated maximum sidewall film flow rate of []^{a,c} lbm/hr-ft for AP600 and **AP1000 plants** respectively. The maximum sidewall Re_{film} would be []^{a,c} respectively at the estimated maximum 200°F film temperature. The liquid film Reynolds numbers range up to []^{a,c} in the test data (Reference 7.11).

7-50

The shell heat flux provides the boundary conditions for the evaporating film. The steady-state, shell average heat flux and film temperature were estimated for the subcooled, evaporating, and dry portions of the shell, assuming an initial ambient air and film temperature of 120°F. These estimates were made at the containment design pressure to bound conditions at the expected DBA peak pressure and at half containment design pressure, for conditions representative of 24 hours after blowdown. The results are presented in [Table 7-10](#).

Deleted: Table 7-8

Table 7-10. Estimated Shell Heat Flux and Film Temperature

Deleted: 8

Containment Pressure (psig)		Avg. Subcooled		Avg. Evaporating		Avg. Dry	
		Heat Flux (BTU/hr-ft ²)	Film Temp (°F)	Heat Flux (BTU/hr-ft ²)	Film Temp (°F)	Heat Flux (BTU/hr-ft ²)	Shell Temp(°F)
AP1000	59	9500	160	4800	195	400	275
AP600	45	7500	155	3800	190	320	250
AP1000	29.5	6000	150	2800	180	290	240
AP600	22.5	3500	150	1500	170	165	215

To account for stratification, the maximum wet shell heat flux is estimated to be 50 percent higher than the average subcooled value. The minimum wet shell heat flux would be 0 BTU/hr-ft².

The initial PCS film temperature will be between 40°F and 120°F. The 120°F value is used in the DBA Evaluation Model to minimize the benefit of heat removed by heating the subcooled film. The film temperature will increase as the film flows down the dome. The maximum evaporating film temperature was estimated to be less than 212°F.

The resulting estimated range of the AP600 film parameters during a DBA is summarized in [Table 7-11](#) and compared with the composite test data range.

Deleted: Table 7-9

The test data parameter ranges are sufficient for evaluating the film stability model. It is important for the test data to cover the higher range of heat flux and the lower range of the sidewall film Reynolds number for evaluating the film stability model. Films with high Reynolds number values on low heat flux surfaces are more stable than films with low Reynolds number values on high heat flux surfaces. The maximum tested heat flux is almost 50% higher than the estimated maximum **AP1000** value. Tests were run at low film flow rates and to dryout, so the lower range of film Reynolds numbers are also covered.

7-51

Table 7-11. Comparison of the Range of Film Coverage Parameters

Deleted: 9

7.6.5 Containment Shell Heatup Analysis

This section summarizes an analysis of the heatup of the containment shell versus time. This analysis will be utilized in the sensitivity study on the importance of the time at which PCS flow is put on the containment dome following a DBA (see Section 7.7.3).

The shell surface temperature begins to increase following a LOCA or secondary line break inside containment. The time for the dry outer shell to reach a given temperature is a function of the internal containment gas temperature, the internal energy transfer coefficient, and the shell thickness. The time can be calculated using the properties of the steel shell and Figure 4-8 from Kreith (Reference 7.9).

Deleted: a DBA

The initial shell temperature is assumed to be 120°F. The time for the dry external shell surface temperature to reach the boiling point (212°F) can be calculated with the following input:

$$\begin{aligned} T &= 212^{\circ}\text{F (external shell surface temperature)} \\ T_i &= 120^{\circ}\text{F (initial shell temperature)} \\ T_{\infty} &= 250^{\circ}\text{F (internal containment gas temperature for AP600)} \\ T_{\infty} &= 270^{\circ}\text{F (internal containment gas temperature for AP1000)} \\ \zeta &= (T - T_{\infty}) / (T_i - T_{\infty}) \end{aligned}$$

So, $\zeta = 0.292$ for AP600 and $\zeta = 0.387$ for AP1000.

The Biot number is given by

$$Bi = h * L / k$$

where,

h is the heat transfer coefficient on the inside wall, Btu/hr-ft²-°F
 k is the thermal conductivity of the shell

and

7-52

L is the shell thickness

The Fourier number is given by

$$Fo = \alpha * t / L^2$$

where,

α is the thermal diffusivity and is given by

$$\alpha = k / (\rho * c_p)$$

ρ is the shell density

c_p is the shell specific heat

and

t is the time to reach the target temperature

The properties of the steel shell are given below:

k	=	23.6 BTU/hr-ft-°F (AP1000)
	=	25 BTU/hr-ft-°F (AP600)
L	=	[0.1458] ^{ac} ft (AP1000)
	=	[0.1354] ^{ac} ft (AP600)
—	=	490 lbm/ft ³
c_p	=	0.107 BTU/lbm-°F (AP1000)
	=	0.104 BTU/lbm-°F (AP600)

By assuming a heat transfer coefficient on the inside wall, the Biot number is calculated then used to determine the Fourier number and the time for the outer surface to reach 212°F.

h (BTU/hr-ft ² -°F)	1/Bi		Fo		t (sec)	
	AP600	AP1000	AP600	AP1000	AP600	AP1000
5	36.9	32.4	43	28	5792	4373
10	18.5	16.2	22	18	2963	2811
50	3.7	3.2	5	3.5	673	547
100	1.8	1.6	2.6	2.2	350	344

The shell internal heat transfer coefficient is likely in the range of 50-100 BTU/hr-ft²-°F. Thus, the external shell surface temperature is estimated to reach 212°F between 350 and 670 seconds for AP600 and between 340 and 550 seconds for the AP1000 plant. The containment shell material properties in the AP1000 WGOthic EM differ from the preliminary values listed above, but this calculation remains a valid illustration of the time for the outside of the containment vessel to reach 212°F. A lower thermal conductivity results in longer timing.

7-53

The WGOthic AP600 Evaluation Model calculated shell surface temperatures at the top of the dome, before application of the PCS film, can be compared to the hand calculated results. During the initial 5.5 minutes of the transient, the containment gas temperature (and therefore the maximum possible internal shell surface temperature) is maintained at about 250°F by condensation on the heat sinks inside containment. The dome surface temperature is predicted to be 174°F at 337 sec, and without external water is projected to reach 212°F at 500 sec, which is in reasonable agreement with the estimates above. The heatup rate from the WGOthic calculation is about 0.2°F/sec and falls between the 50 and 100 BTU/hr-ft²-°F internal energy transfer coefficient values assumed in the hand calculation.

The calculated temperature increase in the AP600 dry external shell surface is compared to water coverage events as a function of time in [Table 7-12](#).

Deleted: Table 7-10

At the maximum time delay for initial water application to the shell (36 seconds, from [Table 7-12](#)), the outer shell temperature is calculated to increase less than 4°F. The temperature increase of the dry portion of the outer shell is less than 70°F at the time the weirs are filled and steady-state coverage is established (337 seconds, from [Table 7-12](#)). Therefore, the external shell surface temperature is less than 190°F at the time steady-state coverage is established for the AP600 plant. For the AP1000 plant, the calculations above show that the heat-up will be a little faster and the steady-state coverage is not established until almost 400 seconds, but the external shell surface temperature remains well below 212°F at this time in the DECL LOCA analysis.

Deleted: Table 7-10

Deleted: Table 7-10

For a steamline break DBA postulated to occur at the highest elevation of the steamline inside containment and with no liquid entrained in the break effluent, there is a greater heatup of the containment gas and the containment shell than discussed above for the LOCA event. Application of the calculational method above, for an inside containment gas temperature of approximately 350°F, predicts the outside of the containment shell is 212°F before 200 seconds. The AP1000 steamline break analysis confirms this timing. However, water coverage is not adversely affected by application of the film to a hot, dry, shell surface. Both the STC wet flat plate tests and the LSTs verified the ability of the water film to wet and rewet a hot, dry surface (temperature exceeding 240°F) with the inorganic zinc coating. Video tape records of the Westinghouse wet flat plate tests show the initial wetting, dryout, and re-wetting of a hot, dry plate in both a vertical and inclined position. The dry plate temperature was estimated to be about 240°F (based on the maximum heating fluid temperature). An applied wavy laminar film quickly covered the hot, dry plate. As the flow rate was reduced, the waves in the film became smaller and eventually disappeared. The plate remained visibly wet until after the film flow was turned off, then dry patches appeared and grew in circumference as the plate dried out. Video tapes also show the initial wetting of the LST vessel. The measured shell surface temperature was about 260°F at the time the water was applied. The film front was observed to “sizzle” as it quickly advanced downward and covered the surface of the elliptical dome.

Deleted: ¶
W

7-54

Table 7-3. Transient Dry Shell Temperature Increase

Deleted: 10

Event	Time (sec)	Increase in Dry, External Shell Temp. (°F)
Signal Actuation	0	0
Valve Strokes Open	20	0
Piping Fills	34	2
Bucket Fills & Spills	36	4
Weirs are filled and steady-state coverage is established	337	68

7.7 AP600 CONTAINMENT DBA EVALUATION MODEL FILM COVERAGE SENSITIVITIES

Sensitivity analyses performed with the AP600 containment DBA Evaluation Model are provided in this section. The model's sensitivity to the PCS film flow rate and water coverage are studied. An estimate of the conservatism in the assumed time delay for PCS film application is also studied.

7.7.1 Sensitivity of the Evaluation Model to the Input PCS Film Flow Rate

Calculations were performed using the WGOTHIC code with the AP600 containment Evaluation Model described in Section 4. The delivered PCS flow rate presented in Figure 7-2 was applied to the WGOTHIC model. Sensitivity calculations were performed by decreasing the input PCS flow rates to 75, 60, 50, and 25 percent of the nominal value. Recalling that the time it takes to fill the headers and weirs is inversely proportional to the film flow rate, the time of film application was adjusted in each case to account for the decreased film flow rate. The water wetted perimeter input value was kept the same for each case, assuring the difference in calculational results was due only to applied PCS flow.

Figure 7-15 presents the change in peak containment pressure as a function of percent change in applied PCS flow rate. As expected, the peak containment pressure increases as PCS flow rate decreases from its nominal value. Decreasing the PCS flow rate results in the following;

Deleted: 13

- The time of film application is increased.
- The heat removed from the containment to heat the cool applied PCS water is reduced.
- The amount of evaporation from the containment shell decreases.

The containment pressure increase is very modest until the applied flowrate is significantly decreased. This is because the initial decreases in applied flow only decrease the runoff flow rate, the amount of water evaporated remains constant.

7.7.2 Sensitivity to the Water Coverage Area

A sensitivity study was performed to determine the effect that the PCS water coverage area has on the AP600 peak containment pressure for a DBA loss of coolant accident (LOCA) as calculated by WGOTHIC. The AP600 containment Evaluation Model described in Sections 4 and 7.5 was used to

7-55

perform the calculations with only one-dimensional heat conduction through the shell. The sensitivity study considered a range of sidewall water coverage fractions from 20 to 100 percent. These input coverage fractions were kept constant over the entire transient. The delivered PCS water flow rate shown in Figure 7-2 was used in each case.

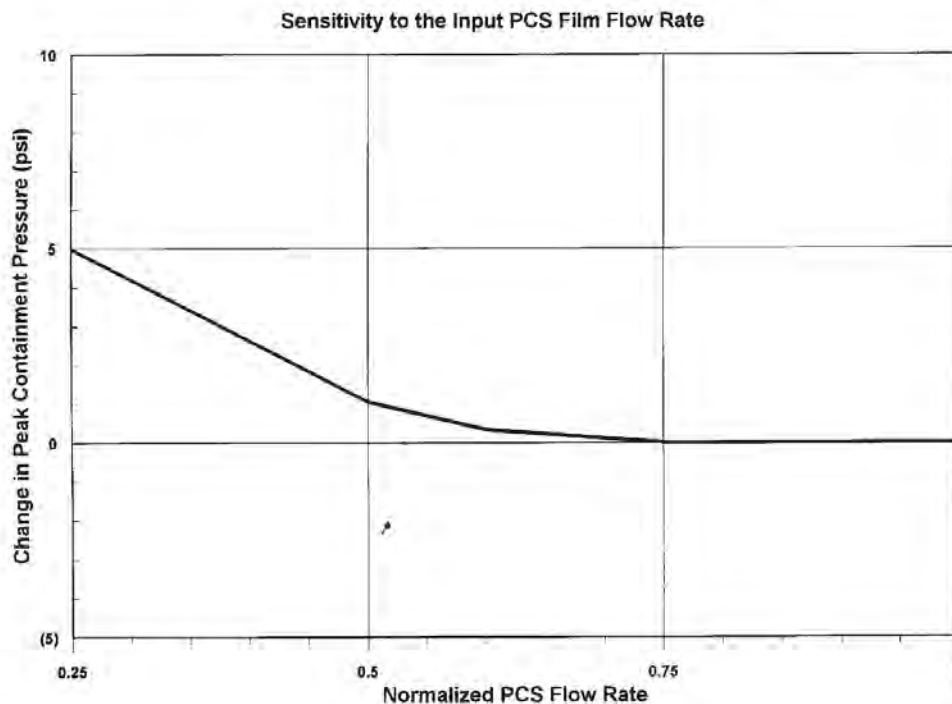


Figure 7-13. Sensitivity to the Input PCS Film Flow Rate

The transient pressure comparison is shown in Figure 7-16. As the water coverage fraction decreases, the peak containment pressure increases. For the 100 percent coverage case, the peak pressure is about 43 psig. The containment design pressure limit, 45 psig, is exceeded at 70 percent and lower coverage.

Decreasing the coverage fraction results in a decrease in the amount of evaporation at a given containment pressure (temperature). As the coverage fraction decreases, the reduced evaporative heat removal causes the containment pressure to increase until the evaporation rate per unit area increases sufficiently to remove enough heat to match the energy input into containment.

The transient PCS runoff flow rate is shown in Figure 7-17. The runoff flow rate is the difference between the PCS delivered flow rate and the evaporation rate. As the input coverage area decreases, the amount of evaporated water decreases and the runoff flow increases.

Deleted: 13

Deleted: 14

Deleted: 15

7-56

Figure 7-18 presents a comparison of the pressure transients for the 50 and 100 percent coverage cases to the Evaluation Model.

Deleted: 16

The level in the PCS water storage tank drops below the first standpipe at about 10,800 seconds causing a substantial reduction in the PCS flow rate (from 423 gpm to 123 gpm). For the 100 and 50 percent coverage cases, this results in a large decrease in the runoff flow rate, but no change in the evaporation rate, which is dictated by the containment pressure (temperature). Note that all the delivered water is not being used. Pressure continues to decrease, although at a slower rate in both the constant coverage cases since in both cases evaporation is removing more heat than is being released to containment. But in the Evaluation Model, the containment pressure increases when the delivered flow decreases. This occurs because the PCS film coverage model decreases the wetted perimeter, (i.e., the wetted surface area is decreased in accordance with the decrease in the applied water flow rate). The increase in pressure reflects the increase in the evaporation rate required to achieve a balance between the heat removed from and the heat input to the containment. Therefore, the Evaluation Model containment pressure approaches the same pressure as the 50 percent fixed coverage case. Pressure then begins to decrease again when the evaporative heat removed at the area dictated by the delivered flow rate exceeds the heat input.

At about 40,000 seconds, the in-containment refueling water storage tank (IRWST) is predicted to empty. After the IRWST empties, the flow for core cooling is provided by the sump, which is assumed to be at saturation. Since most of the internal heat sinks (except concrete) are saturated, the PCS is the primary heat sink at this time and must now absorb the energy that had previously been absorbed by sensible heat addition to the cool IRWST water. The containment pressure increases until the heat removal rate (primarily evaporation from the PCS) exceeds the heat generation rate. The pressures for all three cases remained below the 24-hour goal of 1/2 design pressure.

7-57

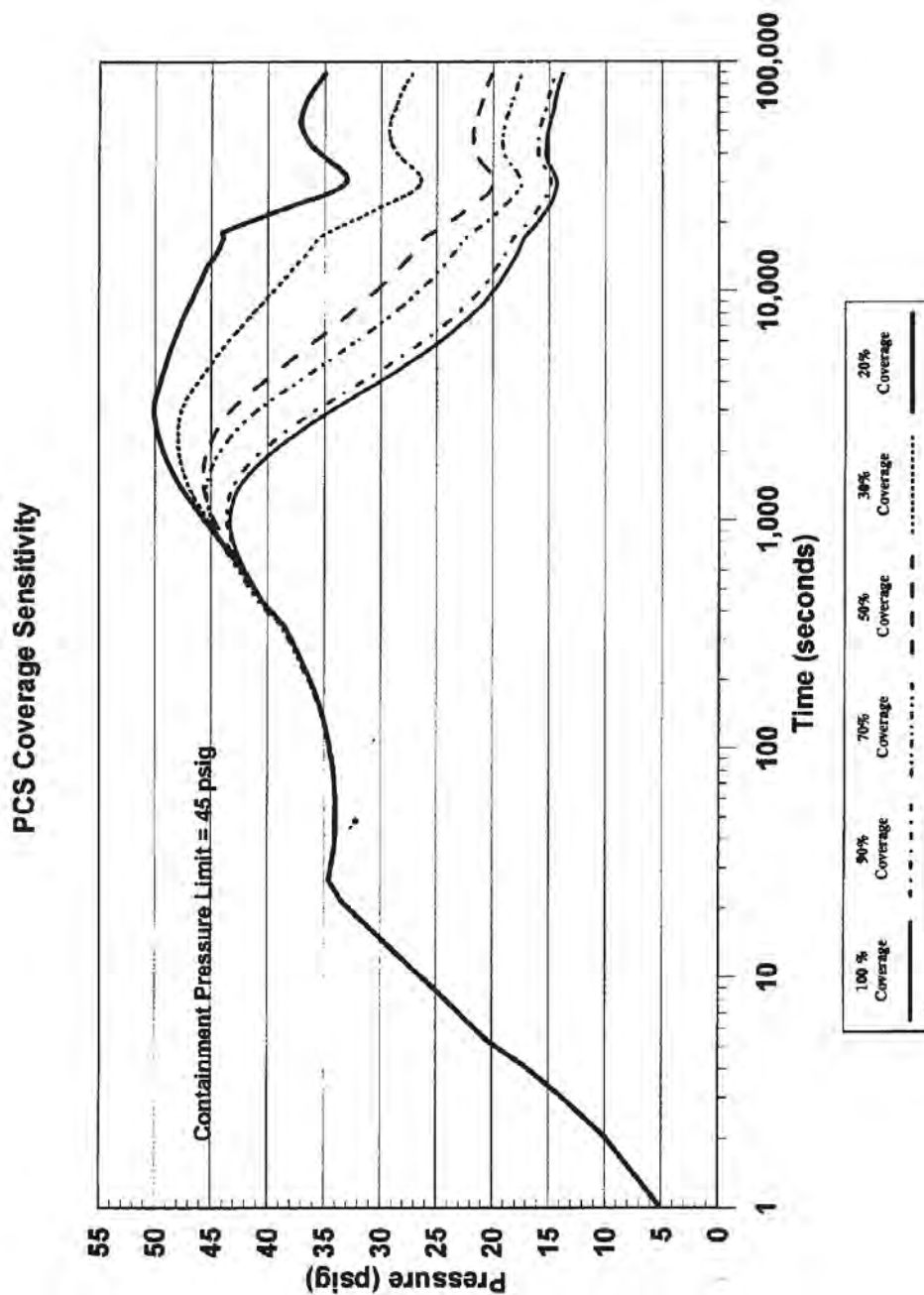


Figure 7-14. Comparison of Peak Containment Pressure as Function of PCS Coverage Area

Deleted: 14

7-58

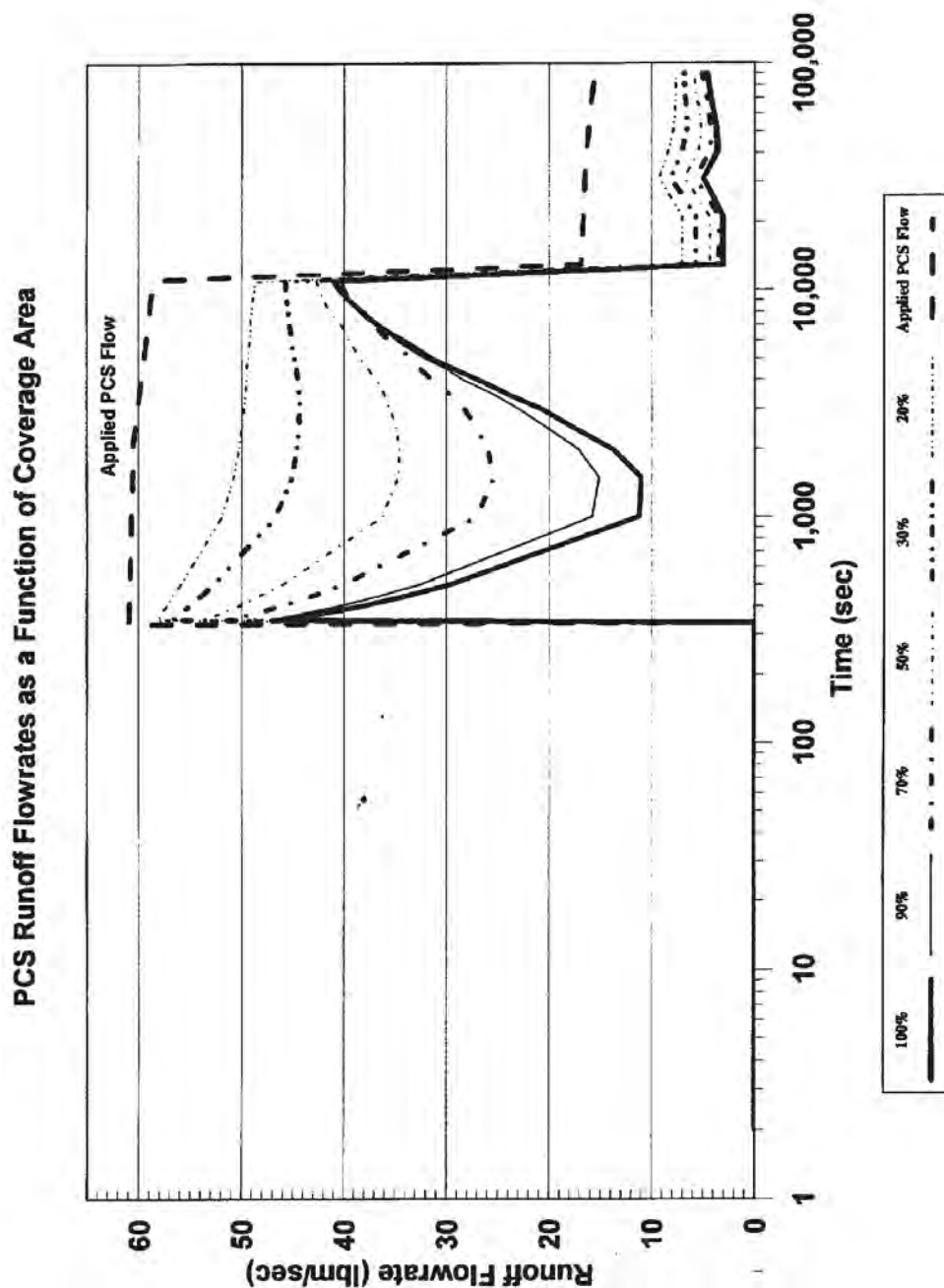


Figure 7-15. PCS Runoff Flow Rates as a Function of Coverage Area

Deleted: 15

7-59

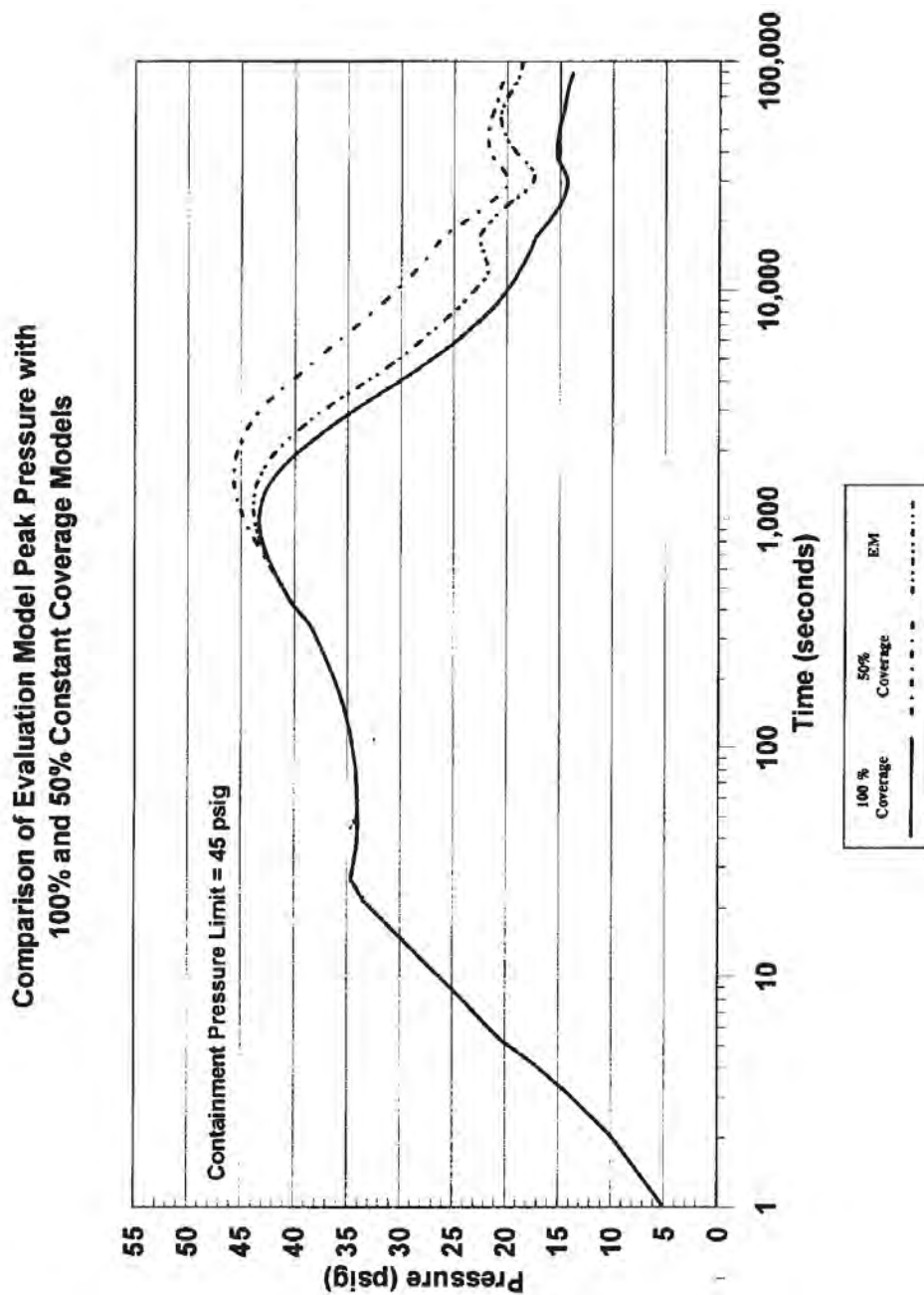


Figure 7-16. Comparison of Evaporation Model Peak Pressure with 100% and 50% Constant Coverage Models

Deleted: 16

The transient runoff flow rate for these three cases is shown in Figure 7-19. The runoff flow rate for the 50 percent coverage case is higher than the 100 percent coverage case. The lower evaporative heat removal in this case results in a sustained higher containment energy content and subsequently higher pressure. Note that there is virtually no runoff flow in the Evaluation Model case since the water coverage portion of the model limits the applied water to the amount that can evaporate.

Deleted: 17

7.7.3 Conservatism in the Assumed Time Delay for Application of the PCS Film

A delay in application of the PCS film is assumed in the DBA Evaluation Model to cover the time it takes to fill the weirs and establish steady-state coverage, as described in Section 7.2. The coverage delay time is conservative in that it neglects energy removal from the shell while steady-state film coverage is being developed. The following assessment shows the amount of conservatism in the predicted energy removal is small.

To quantify the amount of energy removal neglected during the development of steady-state film coverage, the WGOTHIC calculation used to access the heatup of the containment shell, described in Section 7.6 was extended to 1,800 seconds. The heat removal results from this case with the water film applied at 337 seconds were compared to the results from a second case in which the assumed water coverage delay time was reduced to 35 seconds. The same input water coverage fractions were used in both cases.

Note that the WGOTHIC Evaluation Model assumes that steady-state water coverage develops instantaneously after a specified time required to fill the weirs and develop steady-state coverage. The 35-second delay case is a more realistic estimate of the film application delay time for the top of the dome, but will overestimate heat removal from the rest of the dome and sidewall. Therefore, only the heat removal from the top of the dome will be compared for the two cases to estimate the effect on heat removal.

Figure 7-20 compares the integrated energy removal rate from the top of the dome as a function of time. There is very little difference in the energy removal rates for either case. This is because the time required to significantly heat the containment external shell is much greater than the 33-second delay time for water application. Recall that, from Table 7-12, the external shell surface is calculated to heat up about 68°F after ~5 minutes when steady flow conditions develop.

Deleted: 18

Deleted: Table 7-10

The energy release difference at the lower portions of the dome and sidewalls will be even less. Therefore, the assumed water coverage delay time, although conservative, has a minor effect on containment pressure.

7-61

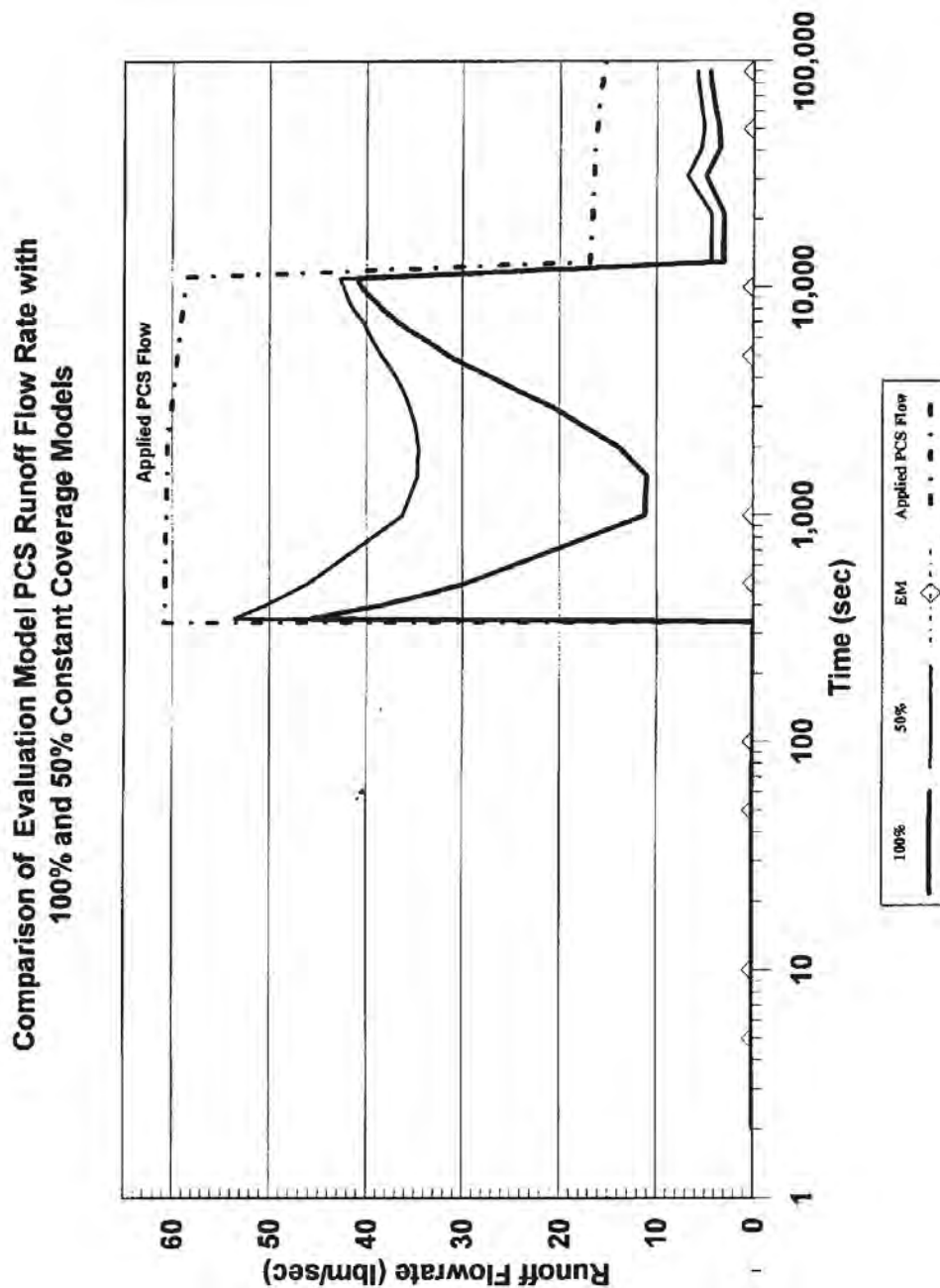


Figure 7-17. Comparison of Evaporation Model PCS Runoff Flow Rate with 100% and 50% Constant Coverage Models

Deleted: 17

7-62

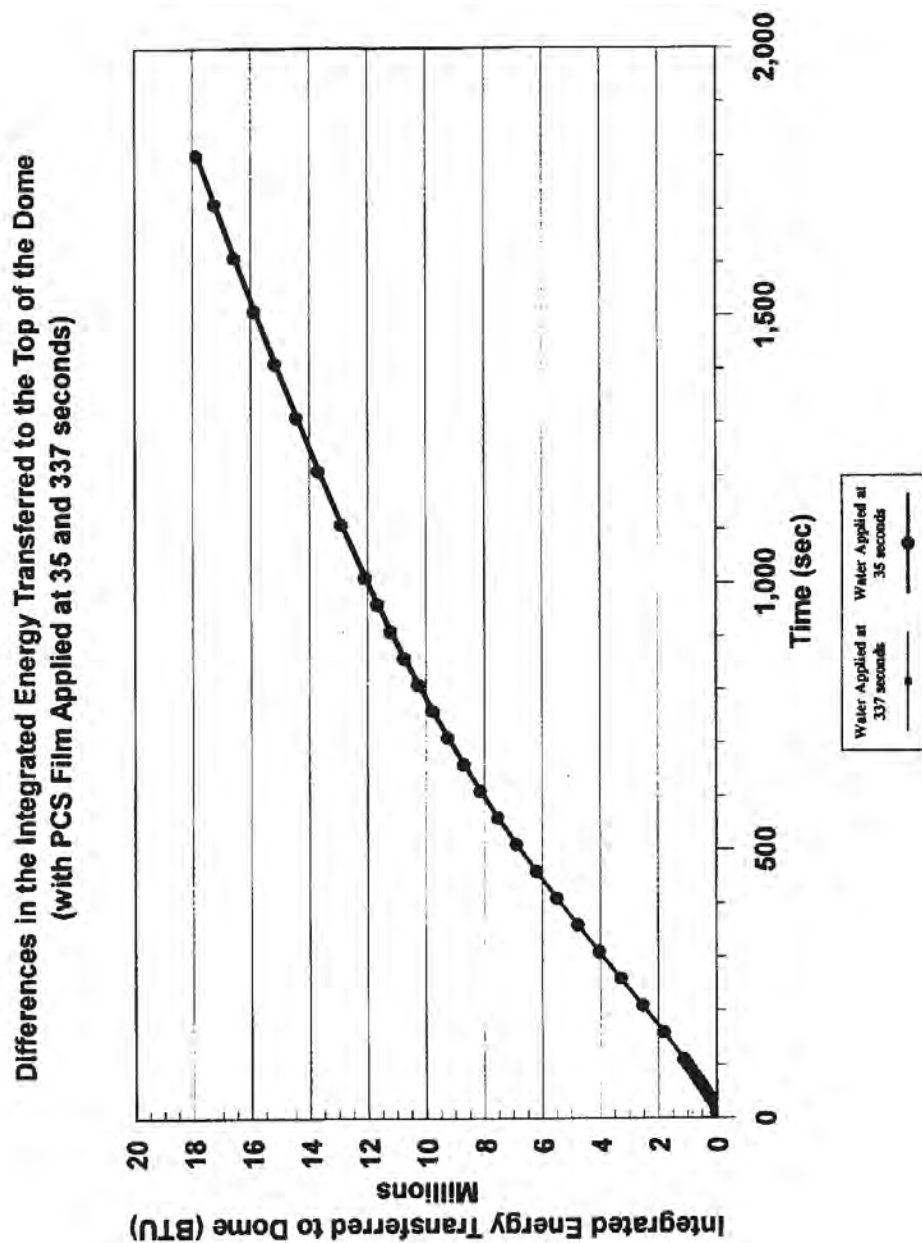


Figure 7-20. Difference in the Integrated Energy Transferred to the Top of the Dome
(with PCS Film Applied at 35 and 337 Seconds)

Deleted: 18

7.8 CONCLUSIONS AND SUMMARY

The basis and calculational method used to determine the amount of water that is evaporated from the AP600 containment steel shell during the operation of the passive containment water cooling system is conservative; both with respect to the individual elements of the WGOTHIC code and the PCS film coverage model, as well as the method of combining these elements in the Evaluation Model.

The amount of water that can be evaporated is the important input parameter to the WGOTHIC portion of the Evaluation Model. The amount of water evaporated determines the effectiveness of the PCS in limiting peak containment pressure, as well as the capability of the PCS to reduce and maintain low containment pressure following postulated limiting design basis events.

The basis for determining the evaporation-limited PCS flow rate input for WGOTHIC has been developed based on PCS test data and observations, and includes the following:

- The portion of the containment shell perimeter that is wetted versus the amount of water being delivered from the PCS water storage tank to the containment dome has been based on data from the Phase 3 Water Distribution Test. This test was performed with prototypic water distribution devices on a full sized segment of the dome and top of sidewall. The relationship of wetted perimeter to delivered flow is conservatively bounded by the linear equation,

$$\Gamma_{\text{dist}} = \text{Delivered Flow/Wetted Perimeter}$$

where,

$$\Gamma_{\text{dist}} \text{ is a constant} = [\quad]^{\text{a,c}} \text{ lbm/hr-ft for PCS flow rates less than 220 gpm}$$

The wetted perimeter used in the PCS film coverage model is limited to []^{a,c} percent of the containment circumference.

- The several PCS tests performed with hot evaporating surfaces have demonstrated that the value for Γ_{dist} obtained with cold water on a cold surface conservatively bounds the Γ_{dist} that will occur with heated water on a heated surface during operation of the PCS.
- In the heat flux range of PCS operation, water streams on the containment surface are observed to become narrower in width only when most of the water in the stream has been evaporated. The Evaluation Model uses a Γ_{min} of []^{a,c} lbm/hr-ft, as the film flow rate at which water streams will become narrower. This minimum film flow rate conservatively bounds the observed minimum film flow rates observed in the PCS tests over the entire range of anticipated heat fluxes.
- Water or streams of water on the containment below the second water distribution weir ring and on the vertical containment sidewall are always observed to flow downward, following the natural fall line of the dome surface.

7-64

The calculational methods for determining the amount of water evaporated have been developed and are consistent with or conservatively bound PCS test data and observations, and include the following:

- The evaporation of water due to the conduction of heat in the circumferential direction through the containment steel shell has been calculated for the alternating, vertical, wetted and dry stripes that were observed in the PCS testing at reduced delivered water flow rates.
- The reduction in dry surface convective and radiative heat transfer that is calculated to occur with alternating, vertical, wet and dry stripes on the containment shell has been determined to be conservatively considered in the WGOTHIC portion of the Evaluation Model.

Bounding assumptions and conservatisms for the operational characteristics of the PCS delivering and applying water to the containment surface have been incorporated in the Evaluation Model as summarized in Section 13.5.2.

Deleted: including:

7.9 NOMENCLATURE

Dimensionless Groups

Biot Number:

$$Bi = \frac{\text{Convection}}{\text{Conduction}} = \frac{h \cdot L}{k}$$

Marangoni Number:

$$Ma = \frac{\text{Surface Tension Force}}{\text{Viscous Force}} = \frac{\partial \sigma}{\partial T} * \frac{\partial T}{\partial L} * \frac{\delta^2}{\mu * \alpha}$$

Reynolds Number:

$$Re = \frac{\text{Momentum Force}}{\text{Viscous Force}} = \frac{4 * \Gamma}{\mu}$$

Parameters

g	=	gravitational constant
h	=	convection heat transfer coefficient
k	=	conductivity
L	=	characteristic length,
\dot{m}	=	mass flow rate
M	=	multiplier representing the ratio of 2-D to 1-D heat transfer
q''	=	surface heat flux
T	=	film temperature;
W	=	width of water film stripe
Z	=	vertical distance from top of sidewall

Greek Characters

α	=	thermal diffusivity,
β	=	surface angle of inclination relative to horizontal
Γ	=	film flow rate = mass flow rate per unit width of film,
δ	=	film thickness,
ρ	=	liquid density
σ	=	liquid surface tension
ϕ	=	heat or mass flux
θ	=	contact angle between the surface and film
μ	=	liquid viscosity

7.10 REFERENCES

- 7.1 A. T. Pieczynski, W. A. Stewart, WCAP-13884, "Water Film Formation on AP600 Reactor Containment Surface," February 1988.
- 7.2 J. E. Gilmore, WCAP-13960, "PCS Water Distribution Phase 3 Test Data Report," December 1993.
- 7.3 W. A. Stewart, A. T. Pieczynski, L. E. Conway, WCAP-12665 Rev. 1, "Tests of Heat Transfer and Water Film Evaporation on a Heated Plate Simulating Cooling of the AP600 Reactor Containment," April 1992.
- 7.4 R. E. Batiste, WCAP-14134, "AP600 Passive Containment Cooling System Integral Small-Scale Tests Final Report," August 1994.
- 7.5 R. P. Ofstun and D. R. Spencer, PCS-T2R050, "Large-Scale Test Data Evaluation," May 1995, Westinghouse Electric Corporation.
- 7.6 F. E. Peters, WCAP-13566, "AP600 1/8th Large-Scale Passive Containment Cooling System Heat Transfer Test Baseline Data Report," October 1992.
- 7.7 F. E. Peters, WCAP-14135, Rev. 1, "Final Data Report for PCS Large-Scale Tests, Phase 2 and Phase 3," April 1997.
- 7.8 D. R. Spencer, WCAP-14845, Rev. 3, "Scaling Analysis for AP600 Containment Pressure During Design Basis Accidents," March 1998.
- 7.9 Frank Kreith, "*Principles of Heat Transfer*," 3rd Edition, 1973.
- 7.10 M. S. Bohn and S. H. Davis, "Thermocapillary breakdown of Falling Liquid Films at High Reynolds Numbers," *International Journal of Heat and Mass Transfer*, Vol. 36, pp 1875-1881 (1993).
- 7.11 F. Delose, R. P. Ofstun, D. R. Spencer, WCAP-14326, Rev. 2, "Experimental Basis for the AP600 Containment Vessel Heat and Mass Transfer Correlations," April 1998, Westinghouse Electric Corporation.
- 7.12 T. Fujita and T. Ueda, "Heat Transfer to Falling Liquid Films and Film Breakdown Parts I and II," *International Journal of Heat and Mass Transfer*, Vol. 21, pp. 97-108 and 109-118 (1978).
- 7.13 D.W. Green, R.H. Perry: "Perry's Chemical Engineers' Handbook", (8th Edition) McGraw-Hill, 2008.
- 7.14 TFD-FSE-15-1, Revision 0, "AP1000® Containment Vessel Inner Surface Condensate Return Test Facility Description Report," May 2015.

7.A-1

APPENDIX 7.A PHYSICS OF LIQUID FILMS ON THE AP600 AND AP1000 CONTAINMENT SHELLS

7.A.1 INTRODUCTION

The total evaporation from the external shell is the parameter of interest for mass transfer, the dominant means of removing heat from the containment. Total evaporation is equal to the integral of the mass flux over the covered, or wetted, area. The mass flux for a given set of parameters (surface and film temperature, film flow rate, annulus conditions) is given by correlations presented in Reference 7.A.1. The subject of this appendix is the wetted area of the external shell surface, and how the wetted area is limited by film stability effects.

Note that the initial application of water to the external surface at safety analysis basis surface temperatures is discussed in Section 7.6.5, so that quasi-steady water coverage is assumed to be established in the discussions of this appendix.

The introduction and Section 7.2 provide a brief overview of the PCS design, as it relates to film stability considerations. The test program is discussed in Section 7.6, where it is shown that the range of non-dimensional parameters for AP600 and **AP1000** is adequately covered in the test program. Subsequent Appendix 7A sections give a summary of literature findings on film stability, a discussion of the contact wetting angle that addresses the wettability of the coated surface in the context of surfaces studied in the literature, and a description of LST observed liquid film behavior for high and low flow tests. The physics summarized in this appendix were considered in the development of the PCS film coverage model. The PCS film coverage model is biased to conservatively bound test data that include cold full-scale tests and smaller-scale heated surface tests.

The double dam-weir system is designed to evenly distribute the PCS water onto the surface of the dome. The elliptical shape of the dome and corresponding area divergence helps spread the stripes of water flowing from the individual V-notches in the weirs. Water coverage on the top of the dome is the most difficult to quantify, but water coverage on this portion of the dome is also the least important to the successful operation of the PCS; the area between the top of the dome and the second weir is only about 20 percent of the total shell external surface area and is neglected in the PCS film coverage model calculation of the evaporation-limited PCS flow rate input for the WGOTHIC model.

The distribution system applies water to the shell in discrete, evenly spaced streams. Water from the PCCWST discharge header falls into a bucket suspended just above the center of the dome. Slots on the side of the bucket allow water to spill at discrete locations around the circumference onto the containment dome. From there, the water flows outward and downward, spreading due to the area divergence, until it is collected and redistributed by a series of two weir rings. Weir outflow rates as a function of time, including the initial filling of the bucket and dams, are shown in Figure 7-3. The method of water application, by weir slots, induces discrete water streams that can remain discrete at low PCS water flow rates and merge to form continuous circumferential water coverage at higher PCS water flow rates.

7.A-2

The initial application of water flowing from a weir slot hits the surface and spreads until surface tension and skin friction dissipate the momentum. If the film is significantly subcooled relative to the surface at that point, thermocapillary effects (see Section 7.A.2.2) may also affect how wide the stripe is as it flows down from the point of application. The PCS water distribution system employs two weir rings on the dome. By the time the water exits the second weir ring, the water has been heated to a temperature relatively close to that of the shell, so that thermocapillary effects are less important. Therefore, the focus for film stability is on evaporating film stability.

Evaporation of the PCS water results in a reduction of the mass flow rate as the film advances down the containment structure from the second weir. As the mass flow rate decreases, the wetted perimeter of the stable film also changes. From observation of tests, the wetted perimeter typically decreases only after the mass flow rate decreases below a certain point. The physical processes that limit the amount of stable film coverage on the containment shell are discussed in this appendix.

7.A.2 SUMMARY OF GENERAL LIQUID FILM BEHAVIOR

This section provides a summary of available literature on models and data for liquid films and provides a discussion of the various aspects of liquid film behavior.

7.A.2.1 Literature Summary

The study of movement in a fluid interface has been studied over 150 years. In studying the spreading of a drop of alcohol on the surface of water, British engineer and physicist James Thompson correctly explained the phenomena as a surface-tension-driven flow. The name of Italian physicist Carlo Marangoni has been associated with two distinct but related surface effects. The first is motion in a fluid interface caused by local variations in interfacial tension which were, in turn, caused by differences in composition or temperature. The second phenomenon is a conjugate of the first; it is the departure from equilibrium surface tension that is produced by the extension or contraction of an interface. Both of these phenomena are important to the understanding of the behavior of liquid films.

The stability of liquid films has been studied by many analysts and experimenters within the last 50 years. These studies may be grouped in two general categories;

1. Determining the minimum flow rate required to rewet a stable dry patch.
2. Examining the thermocapillary breakdown of a thin film.

Films are generally categorized as saturated films or subcooled films, due to differences in stability, or wetting performance. Films that are applied at or near the temperature of the surface are typically referred to as "saturated films." Such films, when applied to heated surfaces as is done on AP600 and **AP1000**, have a significant evaporation component and are thus called "evaporating films." Norman and McIntyre (Reference 7.A.2) reported data showing that a large increase in the minimum film wetting rate was required as the temperature difference between the surface and film was increased (that is, subcooling of the liquid film relative to the surface was increased). Hallet (Reference 7.A-3) also observed this phenomenon and developed a film breakdown correlation that was related to the film surface tension difference, the wave number, and the heat transfer coefficient. Fujita and Ueda (Reference 7.A-4) measured the breakdown of both subcooled and saturated liquid films on heated, vertical, polished,

7.A-3

stainless steel tubes. A comparison of the results from their tests also showed that the highly subcooled films are unstable at flow rates several times higher than that observed for saturated films. More recently, Bohn and Davis (Reference 7.A-5) measured the breakdown of subcooled water films on heated, vertical, polished, stainless steel tubes and developed a film breakdown correlation that was dependent on thermocapillary effects. Thus, there is clearly a basis for separately considering film stability for subcooled and evaporating films.

The conclusion that thermocapillary effects influence the early breakdown of subcooled films is based on the following. Subcooled films having liquid temperatures much lower than the solid surface temperature absorb heat, causing the film temperature to increase. Evaporating films that are more nearly in thermal equilibrium with the solid surface, transfer mass and energy from the film surface to the gas atmosphere. Thus, one explanation for the apparent reduced stability of subcooled films is the existence of significantly higher temperature gradients through the film that give rise to increased thermocapillary forces (see Section 7.A.2.2).

The manner in which data has been presented in the literature is also of interest. In general, the surface heat flux is recognized as the dominant independent parameter, and properties have a strong influence on film behavior. The literature presents data most often as film flow rate (mass flow rate per unit wetted perimeter) versus heat flux. To account for the effect of viscosity on wettability, the Westinghouse test data reduction uses film Reynolds number as the dependent parameter, with surface heat flux as the independent parameter.

The performance of the coated surface to be used for AP600 and **AP1000** can be compared to the performance of the typical surfaces studied in the literature, polished steel and polished copper. The use of polished materials in laboratory tests allows careful characterization of the important parameter, the wetting angle. The coated surface does not lend itself to characterization of a single local wetting angle (Section 7.A.3.2). Therefore, the data for film flow rate versus heat flux give an appropriate means of comparison of film stability data. Stable film flow rates on the order of 20 to 50 lbm/hr-ft are noted on the LST and other test surfaces, even with heat fluxes up to 10,000 Btu/hr-ft². Comparison to Fujita-Ueda data shows that the coated surface is significantly better at wetting, and is less sensitive to heat flux than the polished surfaces.

The list of papers reviewed and considered for application to the containment Evaluation Model is extensive and will not be given here. However, in a summary article (Reference 7.A-6), Bankoff provided an extensive list of relevant papers. The current state of the art is focused on the "moving contact line," which was also considered for application to the containment Evaluation Model, but is generally not very practical for engineering application.

7.A-4

7.A.2.2 Thermocapillary Effect

Based on discussions with Bankoff (Reference 7.A-8), the thermocapillary effect is a result of the variation of surface tension with temperature in moving from the contact line to the free film surface (see Figure 7.A-1). For a stable stripe shape, the forces in the horizontal direction must sum to zero. The surface tension decreases as temperature increases, so the minimum stable film flow rate has to be greater to prevent the hotter liquid at the surface from causing the film stripe width to contract. The thermocapillary effect on the force balance is sometimes estimated (as in Equation 7.A-2) by replacing the actual $\sigma(T)$ function with a much simpler function using the temperature drop through the film which can be related to the heat flux as

$$\sigma_{surf} - \sigma_{film} \geq \sigma_{surf} - \left(\sigma_{surf} + \frac{d\sigma}{dT} * \Delta T_{film} \right) \geq - \frac{d\sigma}{dT} * \frac{q''}{k_{film}}$$

This simplification becomes increasingly inaccurate as the film subcooling increases, since the sensible temperature increase of the film invalidates the approximation q''/k , used to estimate the film surface temperature.

Overall, investigators have identified momentum, surface tension, body (hydrostatic) force, thermocapillary, and vapor thrust as the dominant forces affecting film stability. These forces are typically expressed as functions of flow rate, heat flux, fluid properties, and wetting angle. Vapor thrust can be neglected in AP600 and AP1000 because the heat flux is low, less than 10,000 BTU/hr-ft². Consequently, film stability may be considered to be controlled by a balance between momentum, surface tension, hydrostatic, and thermocapillary forces.

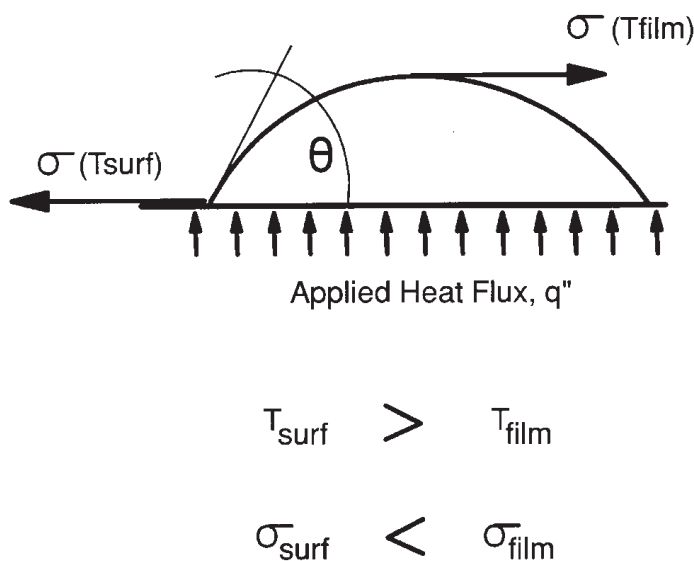


Figure 7.A-1. Variation in Surface Tension over the Surface of a Heated Liquid Film

7.A-5

7.A.2.3 Available Theoretical Analytical Models

The available analytical theoretical models have not been found to be practical for determining the film coverage on the passive containment design. Rather, the Evaluation Model includes a film coverage model that is consistent with the physics of liquid films, and is developed to provide a conservatively bounded total water coverage. However, models proposed in the literature can be used to gain insight into film behavior.

The Zuber-Staub model (Reference 7.A-7) considers the stability of a dry patch located within a uniform, flowing film, i.e., the inability of the liquid film to rewet the dry patch. The mathematical formulation of the model includes three of the dominant terms identified above: momentum, surface tension, and thermocapillary. The model uses a vertical force balance at the tip of a postulated dry patch to determine the minimum uniform film thickness required to rewet the dry patch. This minimum film thickness is a function of the surface heat flux, the film properties (including the contact angle between the film and surface).

One of the Zuber-Staub formulations treats the film thickness as the dependent parameter from which film stability criteria can be derived. Although film thickness is not easily measured, film thickness is related to the film flow rate through continuity. Therefore, the discussions that follow will treat the film flow rate as the controlling parameter from which film stability criteria may be derived.

According to the Zuber-Staub model, if the film flow rate is greater than the minimum stability value, any dry patch created in the film would be washed over and would readily disappear after formation due to the momentum of the flowing film. Conversely, if the film flow rate was equal to or less than the minimum stability value, a dry patch, if formed, would be predicted to be stable (i.e., the film would not be able to recover the dry patch). The Zuber-Staub model does not consider the effects of waves in recovering the dry patch.

The concept of a force balance can be used to develop insight into controlling parameters for film stability. A force balance more specific to the passive containment design that includes momentum, surface tension, thermocapillary, and body forces (and thus, surface inclination angle, β) to account for spreading on the inclined surface of the elliptical dome, but neglects the vapor thrust term, may be written in terms of the film flow rate, Γ . Since the relationship is for a stable film width, equilibrium between the various forces is assumed. If the film flow rate is greater than the value of Γ in the equation, the film will wash over any dry patch which happens to form. The equation, which can be used to examine the minimum stable film flow, Γ_{min} , is:

$$\frac{1}{15} * \left(\frac{9 * g * \sin \beta * \Gamma_{min}^2}{\rho * \mu} \right)^{\frac{2}{3}} + \left(\frac{3 * \rho * g^2 * \cos(\beta)^3 * \mu * \Gamma_{min}}{8 * \sin \beta} \right)^{\frac{1}{3}} = \frac{\sigma * (1 - \cos \theta)}{\left(\frac{3 * \mu * \Gamma_{min}}{g * \sin \beta * \rho^2} \right)^{\frac{1}{3}}} - \frac{d\sigma}{dT} * \frac{q''}{k} * \cos \theta \quad (7.A-2)$$

7.A-6

Note that the formulation given above assumes a laminar film with uniform film thickness and does not consider the effect of waves in wavy laminar flow. Waves in wavy laminar flow typically have a peak to valley distance of about 3 times the average film thickness, but occupy only a small fraction of the flowing volume. Waves carry momentum as they pass, but do not significantly affect the calculated average film thickness. Waves will wash through the region of flowing film, effectively wiping out any history effect of the method of application or other upstream effects. Therefore, film stability can be considered to be a local phenomenon, governed by local force balances at the point of interest on the contact line.

Equation 7.A-2 predicts higher values for the minimum stable film flow rate on surfaces that wet poorly, that is, those that have large contact angles, than for surfaces that wet readily. For surfaces that are heated, heat flux is destabilizing. The equation also shows that as the film heats up, it becomes more stable due to property changes.

Since the theoretical models available in the literature are not practical for determining the film coverage on the passive containment design, the insight gained from examining those approaches is used to support development of an empirical bulk coverage model. That is, the film stability can be characterized using a criterion for a minimum film flow rate, Γ_{\min} , that will maintain a stable stripe. Data from tests at different scales, wherein the range of AP600 and AP1000 dimensionless parameters is sufficiently covered, can be used to empirically derive a bounding value for Γ_{\min} . As discussed in 7.A.2.1, data can be represented using the film flow rate, and plotted against the dominant independent parameter, heat flux.

7.A.3 CONTACT ANGLE AND SURFACE WETTABILITY

A discussion of contact angles in general and observations from test coupons are provided to gain insight into the performance of the coated surface relative to surfaces in the literature. Finally, factors which can affect surface wettability are discussed.

7.A.3.1 Advancing and Receding Contact Angles

The place where the wet and dry regions intersect is called the contact line. For example, in a liquid film flowing down a wall in a constant width stripe, the contact lines are the two vertical lines defining the width of the stripe. The contact angle is defined as the angle between the solid and the liquid surface at the contact line. The contact angle between a water film and the surface to which it is applied is an indication of the surface wettability. Typically, better wetting occurs on surfaces with small contact angles. In practice, contact angles are measured for both advancing and receding films. Usually the two values are quite different, with the advancing contact angle being much larger than the receding contact angle. The relation between contact angle and velocity is qualitatively depicted in Figure 7.A-2. Of interest is the hysteresis between advancing and receding contact angles. There is actually a range of stable contact angles for a static contact line. Thus, if a droplet starts out by spreading, such as when it is dropped onto the surface, it will spread to a diameter governed by the advancing contact angle. Then as the droplet evaporates, it may be expected to remain at a constant diameter, with the contact line anchored, until the mass lost contracts the droplet such that the receding contact angle is reached. Further evaporation would then cause the droplet diameter to decrease.

7.A-7

It is general practice to measure contact angles of a liquid on a smooth or polished surface, such as glass or polished steel having surface profiles measured in microns. High magnification is used to measure the contact angle as it meets the surface. The surface on the external containment shell is an inorganic zinc coating applied on a carbon steel structure. The surface of the inorganic zinc coating is not smooth, having a surface profile of several mils. With a surface profile of several mils, the magnified image shows significant peaks and valleys, making it impossible to measure a single contact angle that is applicable over the entire surface. Thus, the significance of a representative contact angle for the organic zinc coating used for the exterior of the containment shell is diminished. The interest is on bulk coverage performance over a large surface area, so larger scale integral tests are used. It is desired, however, to understand and relate the bulk wetting performance of the coated surface to that of surfaces in the literature. Therefore, measurements were taken to characterize a bulk static contact angle on the prototypic surface by observing a drop on sample coupons under various conditions as described below.

7.A.3.2 Static Contact Angle Measurements of Coated Surface

The bulk contact angle for a drop of water was measured as a function of temperature and age of the surface coating selected for the AP600 and AP1000. Two samples were prepared for these measurements. The first test coupon was supplied to Westinghouse by the coating vendor. This sample was prepared by the vendor and was not subjected to weathering. The second sample was a 12-in² section of a steel plate that was painted by Westinghouse and weathered for two years.

7.A-8

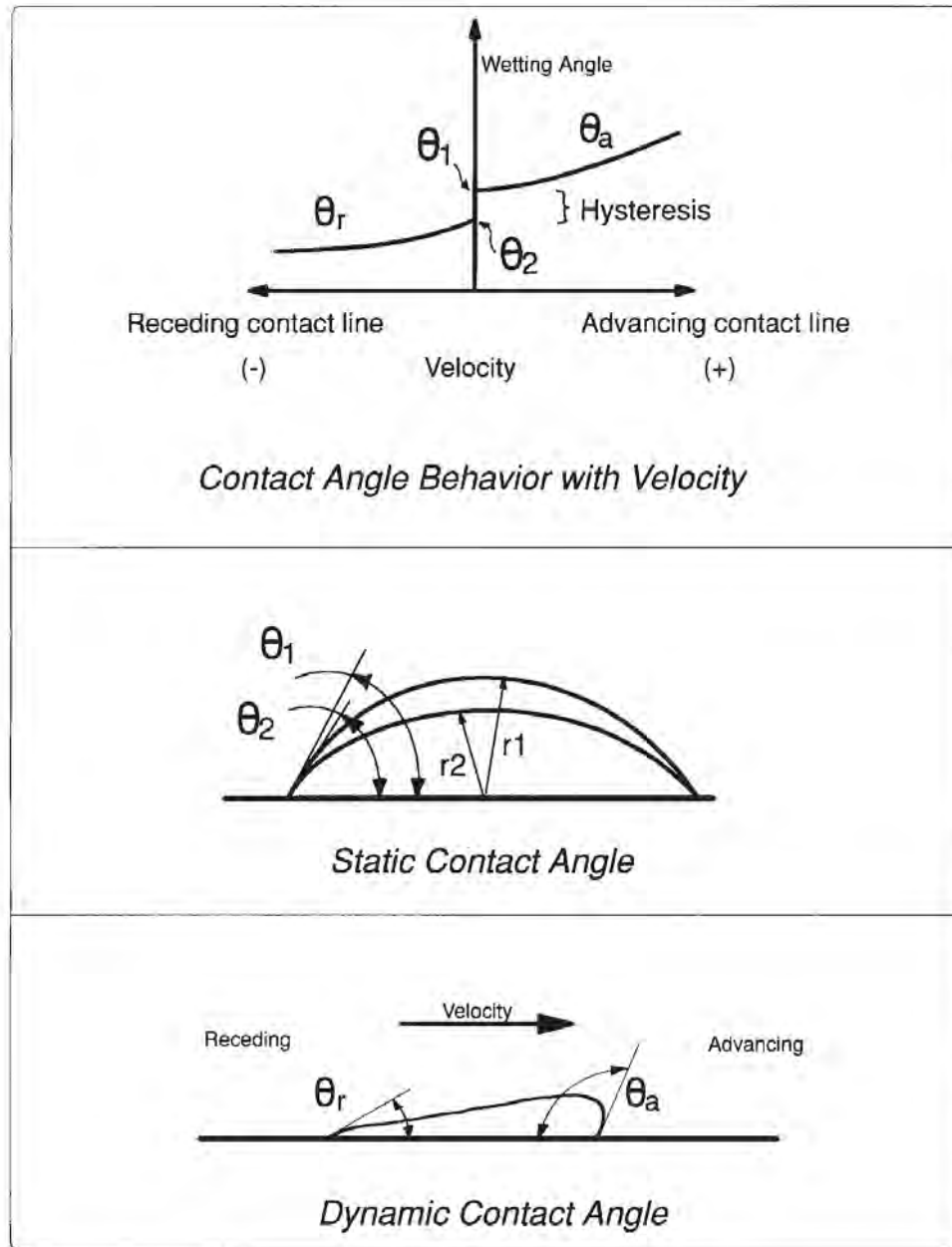


Figure 7.A-2. Typical Qualitative Contact Angles for Advancing and Receding Contact Lines

7.A-9

The following procedure was used to determine the static contact angle for both samples at ambient conditions:

- The test coupons were cleaned per coating vendor specifications and dried.
- The test coupon was placed in a horizontal position.
- A drop of water was placed on the test coupon.
- Using an optical comparator, the average angle between the sample surface and the drop at the interface.
- Measurements were repeated using several drops to ensure repeatability and consistency in the measurements.

Additional measurements were taken with the test coupons held at different temperatures. This was done to evaluate the effect of the surface temperature on the contact angle. The test coupons were heated with either hot water or a heat gun.

The static contact angle measurements taken are summarized in Table 7.A-1. They show that the contact angle for inorganic zinc coated surface decreases both with an increase in age and an increase in temperature. At high temperatures, the contact angle was observed to be initially larger than that observed for lower temperatures. It was observed, however, that the drops quickly spread and flattened out to a quasi-steady shape, thereby reducing the measured contact angle.

From the measurements listed in Table 7.A-1, it is concluded that a representative bulk or average contact angle for the inorganic zinc coated containment shell surface is between []^{a,c} for a new surface, and between []^{a,c} after just two years of weathering.

Table 7.A-1. Summary of Test Results to Determine Static Contact Angle

Description of Test	Contact Angle	
	Weathered Sample	Unweathered Sample
1. Room Temperature, T=80°F	24°	30°
2. Heated, T=110°F	23°	33°
3. Heated, T=180°F t=0 sec	28°	53°
t=15 sec	23°	44°
t=30 sec	20°	35°
t=60 sec	20°	28°

7.A-10

A small drop of water spread around on the inorganic zinc-coated surface was not observed to contract, or snap back into a drop. This observation indicates that the receding contact angle for this surface is nearly zero. These observations also suggest that the film breakdown to form a dry spot occurs at a lower film Reynolds number than the critical Reynolds number for rewetting.

Static wetting angle measurements indicate that the coated surface is clearly more wettable than surfaces reported in the literature, and based on the force balance it is expected to be less sensitive to heat flux.

7.A.3.3 Relative Magnitude of Surface Tension Effects

A solid surface will be wet with liquid if the free surface energy of the solid is greater than the free surface energy of the liquid. Surface tension, σ , is defined as the work required to expand the surface of a liquid by a unit of area. It is a measure of the strength of the intermolecular forces in the fluid, similar to the latent heat of vaporization.

Hydrogen bonding is the strongest type of intermolecular force. Liquid water has relatively strong intermolecular forces due to the strong hydrogen bonds; 80 percent of the intermolecular attraction in water is attributed to hydrogen bonding. In a water molecule, the electrons spend more time in the vicinity of the oxygen atom than the hydrogen atoms because oxygen is more electro-negative than hydrogen (3.5 versus 2.1 for hydrogen on a scale of 4.0). This results in an electric dipole within the molecule. For this reason water is said to be a polar molecule.

As its temperature increases, the mean spacing between molecules in a liquid increases, causing the density to decrease and a reduction in the intermolecular forces. Therefore, both surface tension, σ , and the latent heat of vaporization, h_{fg} , decrease with increasing liquid temperature. For example, the surface tension of water is about 4.97×10^{-3} lbf/ft and the latent heat of vaporization is about 1054 BTU/lbm at room temperature. The value of these two parameters decreases to 4.0×10^{-3} lbf/ft and 970 BTU/lbm, respectively, at 212°F.

7.A.3.4 Factors Affecting Surface Wettability

The wetting of a solid surface by water is improved by reducing the surface tension of the water (by use of a wetting agent such as a detergent), by making the surface more porous (to improve the spreading by capillary action), or by using a polar surface (increasing the intermolecular forces between the surface and the polar liquid water). The use of a surfactant was examined during the Water Distribution Tests. It was found that surfactants offered no effective improvement in coverage. This has been postulated to be due to the turbulence of the flowing film which would not allow the surfactant to influence the surface of the film significantly. The porosity of the inorganic zinc coating is believed to be the primary factor affecting wetting early in the coating's life, adding a significant capillary effect at the contact line. It was postulated that the buildup of polar molecules (e.g., oxides of zinc) on the solid surface improved its wettability with age. Photographs were taken of both new and weathered surface coating samples using a scanning electron microscope with an energy dispersive X-ray spectrometer to identify the chemical species present on the surface. More oxides of zinc were found on the weathered surface than the new surface, supporting the hypothesis that the increase in wetting is due to the surface becoming more polar as it ages.

A buildup of some surface contaminants can result in a reduction in wettability. The worst surface contaminant for the inorganic zinc coating is silicone; it has both low surface energy and low polarity. Sources of silicone in air pollution are rare. Other surface contaminants that could result in reduced wetting include hydrocarbons such as oils, members of the PTFE family (Teflon), polypropylene, and polyethylene residues. To combat surface contaminants, the coatings vendor has developed and made available a standard cleaning procedure and a specially developed detergent that emulsifies these types of surface contaminants so they can be washed away.

Although the number of potential contaminants that would adversely affect wetting of the inorganic zinc coating surface is probably limited to a dozen or so, it would be very difficult to analytically predict the wetting degradation over time. The degradation of surface wettability would have to be estimated as a function of the concentration of each potential contaminant, the deposition rate of each as a function of the local or worst case atmospheric conditions, and the assumption that the degradation is additive, etc. Therefore, periodic in-service inspections will be performed to look for corrosion and surface contaminant buildups to assure surface wettability. The frequency and procedures for testing and the minimum acceptance criteria prior to cleaning the surface are defined in the Reliability Assurance Program.

7.A.3.5 Summary of Wetting Angle Assessment

The contact angle between a water film and the surface to which it is applied is an indication of the surface wettability. Although the surface provided by the inorganic zinc coating applied to the external surface of the containment is not smooth relative to other materials used to measure contact angles such as glass or polished steel, measurements were taken to characterize a bulk static contact angle of a spreading film on the prototypic surface to relate to literature data. The static angle was measured by observing the spreading of a drop on two coupons, one weathered and one not weathered, under ambient and heated conditions. Results showed that a surface weathered for two years is significantly more wettable []^{a,b} than surfaces for which data exists in the literature (in the range of 60 degrees).

7.A.4 DESCRIPTION OF LST OBSERVATIONS

LST observations to characterize wetting behavior were made during shakedown tests, video tapes were recorded, and sketches were made for the test records. During these shakedown tests, quasi-steady heat flux and water flow rate conditions were achieved, and then water flow was slowly valved down in stages with constant steam flow. At each stage, when quasi-steady conditions again were reached, observations and notes were taken. Subsequent similar cycles were done at several steam flows (heat fluxes). The objective was to observe the behavior of the liquid film as it varied from a moderately high flow down to nearly complete evaporation. Since the majority of the LST matrix tests were run with a high flow rate, the qualitative discussion starts with a description of water coverage on a high flow test. Finally, the water coverage on a low flow test is described. Observations are consistent with the physics of liquid films discussed above.

7.A-12

7.A.4.1 High Flow LST

As discussed in Section 7.6.3, the water is applied to the shell in stripes around the circumference of the test vessel. Stripe widths for a given steady state test were relatively constant, varying by fractions of an inch as the delivered flow rate varied (see Section 7.6.3). Based on Reynolds number, the flow regime is wavy laminar, which has been confirmed by test observations. The wavy laminar regime is discussed in the literature. A simple sketch is provided in Figure 7.A-3, showing qualitative characteristics observed for a representative film stripe on a heated LST surface with a high flow rate. High flow rate LST typically exhibited constant width stripes, as discussed further below. Stripe widths varied from an inch or an inch or less to complete circumferential coverage, depending on the test delivered flow and heat flux. Within a stripe, the majority of the width is flowing water with wavy laminar conditions. In that portion, waves are generated by upstream disturbances and advance down the stripe with a velocity faster than the average film speed, consistent with continuity flow theory. The waves generally alternate with slight left and right horizontal velocity components.

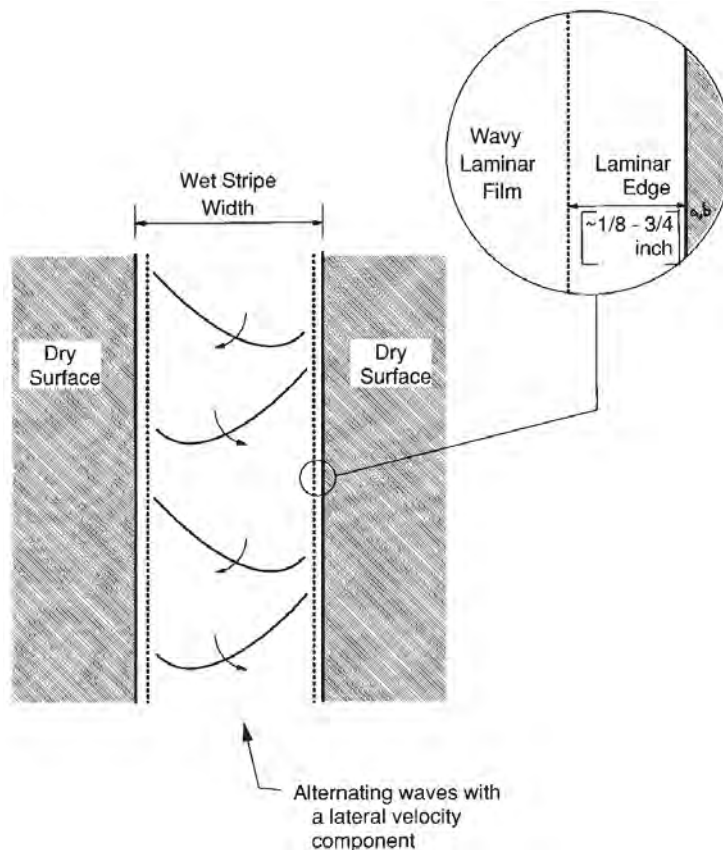


Figure 7.A-3. Sketch of Qualitative Wave Laminar Film Flow Characteristics on Heated LST Shell Water Stripe

Water stripe edges exhibited a narrow []^{a,b} region of laminar flow. Visual observation indicated that the edges were wetted but not obviously flowing. When an obstruction was placed within a wet edge, a “bow wave” built up above the obstruction, confirming that indeed liquid was flowing downward in that region. The film flow, and thus thickness, in that region is small enough that viscous forces damp out any disturbances. For example, the waves are damped by viscous forces in the stripe edge. Note that the laminar edge was also observed to occur on stripes which narrowed as their film flow rates decreased due to evaporation. This indicates that there is a very thin layer near a stripe edge, or in fact the equivalent wetting angle at the contact line is very small. This is consistent with the consideration in 7.A.3 that the receding wetting angle likely governs film stability of an evaporating stripe on the containment shell.

Since the water is applied as stripes at the dome with J-tubes (see Figure 7.A-4), and there is significant liquid film subcooling over much of the LST dome for high flow tests, the width of stripes that reach the vertical sidewall is less than can be supported by a stable film at the given film flow rate. Therefore, it can be postulated that the initial width at the top of the vertical sidewall is sufficiently greater than the evaporating film stability limit and that evaporation from the stripes does not cause the receding contact angle to be reached. Rather the film stripes in high flow LST tests are believed to remain within the region of hysteresis over the entire height, consistent with the observed constant width stripes.

7.A.4.2 Low Flow LST

Figure 7.A-5 shows a composite of typical film characteristics on a portion of the LST shell at relatively low flows typical of the water flow applied to LST 213.1. The tests described here have film flows that are low enough that evaporation causes the receding contact angle to be reached, and further evaporation leads to narrowing of the stripes.

As for the high flow LST, the water is delivered to the vessel shell surface via J-tubes, as a subcooled film. The application method and subcooled film stability set the initial stripe width, similar to the high flow tests. However, the film heats up to become an evaporating film before it reaches the sidewall. Observations were made of shakedown tests at conditions (steam flow, external water flow) similar to those for LST 213.1. During the initial setup prior to heating the vessel, the film flow was established and gradually valved down. As very low flows were reached, some J-tubes were seen to stop delivering water before others, indicating that there was some asymmetry in delivered flow per stream. This is consistent with observations of heated tests that indicated stripe widths and vertical extents varied around the circumference of the vessel.

In Figure 7.A-5 the width of the two outer stripes shown remain approximately constant down to a certain elevation, varying only as the delivered flow rate varied. At some elevation on the sidewall, which may be different for different stripes, the film width began to narrow until the gutter was reached.

For some stripes, shown as the two innermost stripes in Figure 7.A-5, the delivered flow was low enough that the stripes completely evaporated before reaching the gutter elevation.

7.A-14

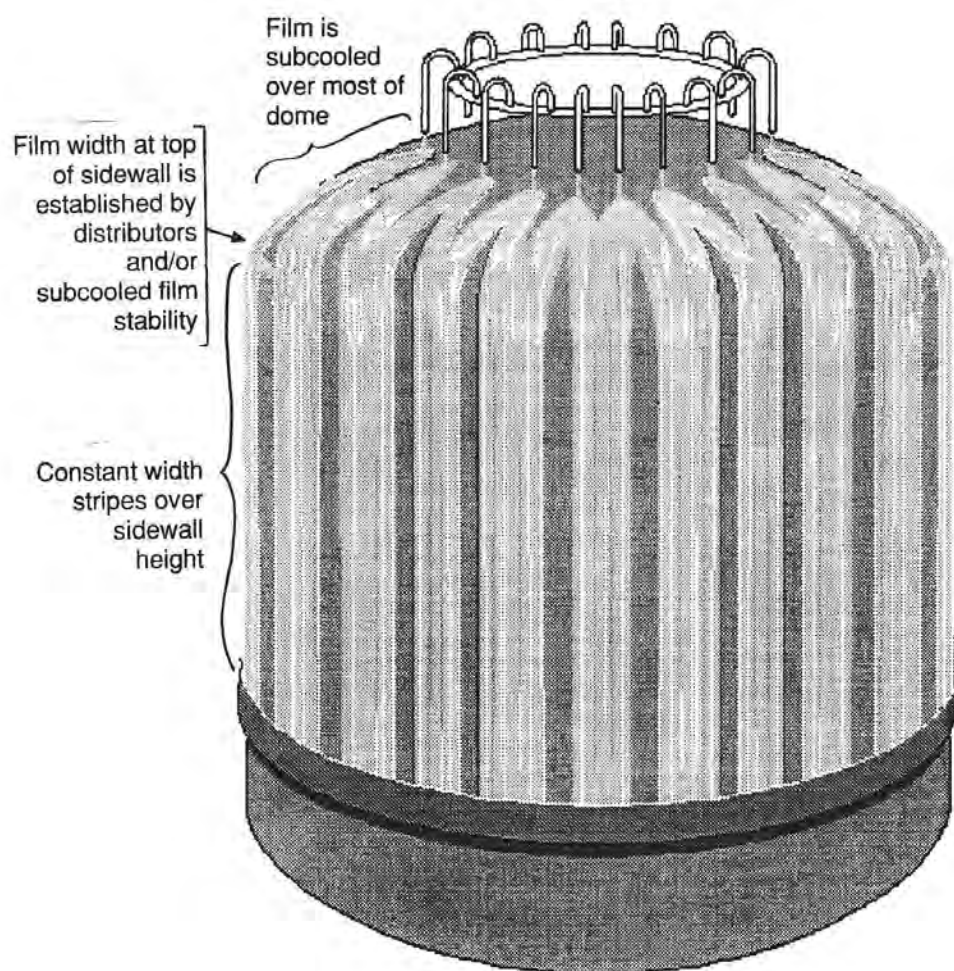


Figure 7.A-4. Large-Scale Test Water Coverage Pattern at High PCS Flows

7.A-15

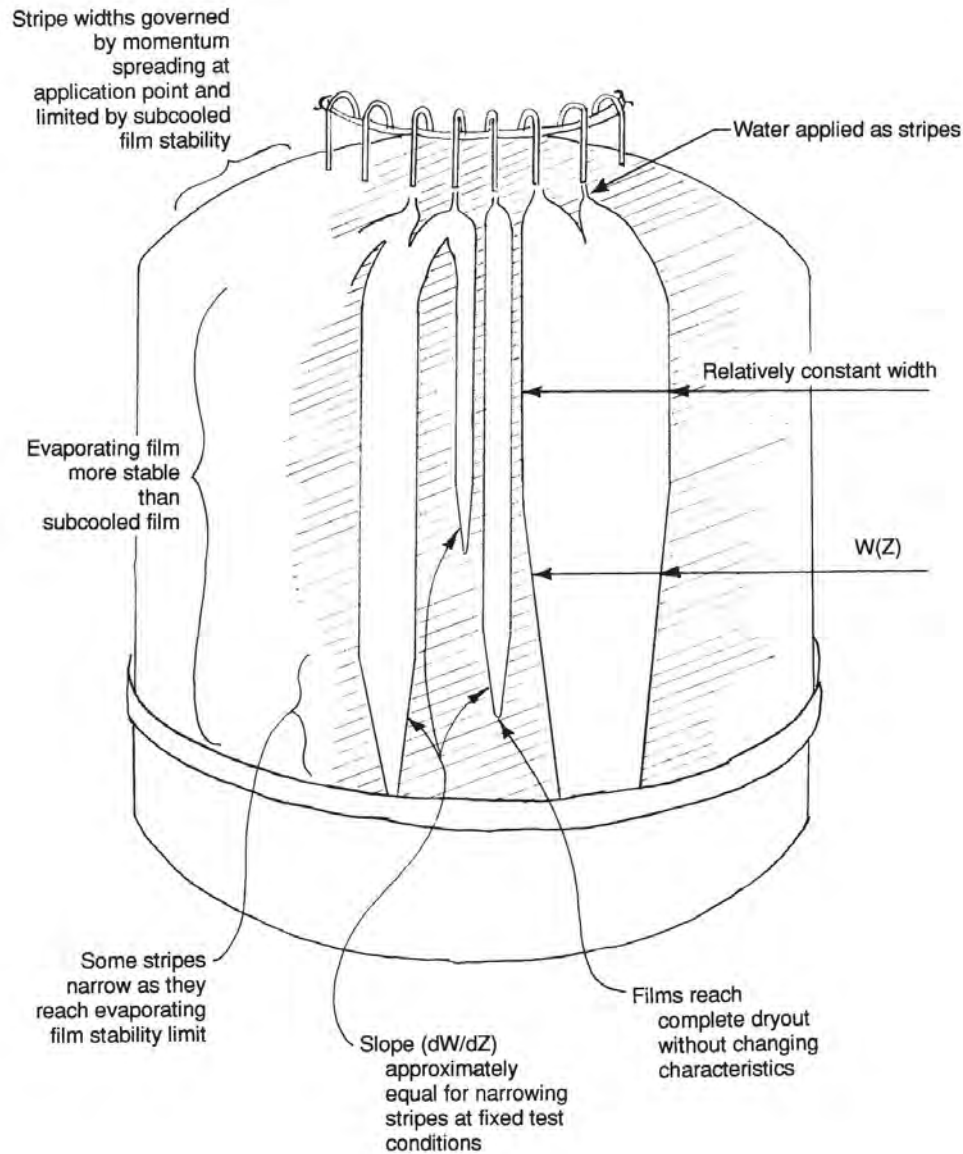


Figure 7.A-5. Sketch of LST Observation of Vessel Exterior at Water Flows Similar to LST 213.1 Showing Complete Dryout of Some Stripes

7.A-16

The slope of the changing width as a function of height, dW/dZ , was carefully observed. Qualitative observation indicated that the dW/dZ of each stripe around the circumference was nearly constant at a specific quasi-steady-state test condition.

Of most interest in these tests, relative to water coverage, is the fact that stripes that evaporated completely did so without changing their characteristics near the point of complete dryout. Thus, for the surface tested, the liquid films did not snap, or draw up, into a thick film. The edges of the film, including the bottom edge remained as wavy laminar film up to within a fraction of an inch from the edge, including the lower edge. As the water flow rate was valved down, the bottom edge moved gradually up, and when the flow was increased to its original value, the vertical extent of the stripe returned to a consistent elevation. Therefore, the film was well behaved as it completely evaporated.

7.A.5 CONCLUSIONS

A comparison of coated surface data with polished surface data from the literature shows the coated surface is more wettable.

Models from the literature are not sufficiently developed to be considered reliable. The literature provides an indication of the appropriate parameters to study film breakdown data: Re_{film} or Γ and heat flux. A practical approach taken to bound the data from the various tests is to establish a minimum stable film flow rate, Γ , that can be used to define a minimum coverage.

History effects are washed out by waves, so breakdown can be considered to be a local phenomenon. Therefore, LST (Section 7.6.3), SST (Section 7.6.2), and heated flat plate tests (Section 7.6.1) can be said to represent the bottom portions of liquid film stripes on the containment shell that dry out due to evaporation.

Observations of tests are explained based on physics of liquid films on heated surfaces. At high enough applied flows, the applied stripe maintains constant width until the film stability limit is reached, governed by the receding contact angle, then the stripe begins to narrow consistent with the minimum film flow rate required to maintain a stable film.

Observations of tests show that complete dryout occurs while maintaining a stable stripe geometry, gradually decreasing in width until it disappears.

7.A.6 REFERENCES

- 7.A.1 WCAP-14326, Revision 2, "Experimental Basis for the AP600 Containment Vessel Heat and Mass Transfer Correlations," April 1998.
- 7.A.2 W. S. Norman and V. McIntyre, "Heat Transfer to a Liquid Film on a Vertical Surface," *Trans. Inst. Chem. Engrs.* Vol. 38, pp 301-307 (1960).
- 7.A.3 V. A. Hallett, "Surface Phenomena Causing Breakdown of Falling Liquid Films During Heat Transfer," *International Journal of Heat and Mass Transfer*, Vol. 9, pp 283-294 (1966).

7.A-17

-
- 7.A-4 T. Fujita and T. Ueda, "Heat Transfer to Falling Liquid Films and Film Breakdown Parts I and II," *International Journal of Heat and Mass Transfer*, Vol. 21, pp 97-108 and 109-118 (1978).
- 7.A-5 M. S. Bohn and S. H. Davis, "Thermocapillary breakdown of Falling Liquid Films at High Reynolds Numbers," *International Journal of Heat and Mass Transfer*, Vol. 36, pp 1875-1881 (1993).
- 7.A-6 S. G. Bankoff, "Dynamics and Stability of Thin Heated Liquid Films," *Transactions of the ASME – Journal of Heat Transfer*, Vol. 112, pp 538-546, (1990).
- 7.A-7 N. Zuber and F. W. Staub, "Stability of Dry Patches Forming in Liquid Films Flowing over Heated Surfaces," *International Journal of Heat and Mass Transfer*, Vol. 9, pp 897-905 (1966).
- 7.A-8 Dr. S. G. Bankoff, discussions held at Westinghouse Science and Technology Center during observations of LST, 1996.

8 CONTAINMENT PRESSURE SENSITIVITY DURING BLOWDOWN

8.1 INTRODUCTION

The purpose of performing the single-node WGOTHIC analysis is to show that the containment pressure during the blowdown phase (predicted using the WGOTHIC code) is essentially the same as if Standard Review Plan (SRP) methodologies were utilized for the analysis. This comparison supports the use of WGOTHIC during the analysis of the blowdown phase of the transient, since it is expected that the presence of external heat removal from the containment shell during the first 50 seconds of the transient has little impact on the pressure transient. The containment shell time constant is long, as compared to the transient time, and passive cooling system (PCS) film flow is assumed to be delayed until well after the end of blowdown.

The purpose of performing the sensitivity to heat sinks during blowdown is to confirm that volume compliance is the dominant means of mitigating pressure increase during blowdown.

8.2 METHOD

The AP600 evaluation model (EM) described in Section 4 was used for comparison in this study. The EM was converted to a single-node containment model, consistent with SRP 6.2.1 methodology and comparable to the licensed Westinghouse methodology by the following input modifications:

- All of the climes were removed.
- All of the flow paths, except for those associated with the mass and energy release forcing functions, were deleted. The mass and energy forcing functions were not changed.
- All control volumes which represent the outside containment regions were deleted.
- A single-node containment control volume, containing all of the thermal conductors from the base case and the two mass and energy release forcing functions, was created.
- A conductor representing the containment shell was added to the single-node containment control volume.
- The Uchida heat transfer correlation with revaporization was used on the shell and conductors.

The EM was modified to eliminate heat removal from the containment gas volume by internal heat sinks and the steel shell. The only modification to the EM was to delete all thermal conductors within containment and to effectively eliminate the clime conductors for the shell itself by assuming an adiabatic inner surface.

8.3 ANALYSIS

The blowdown phase pressure results for the single-node analysis are compared to the EM containment pressure in Figure 8-1.

The blowdown phase pressure response without heat sinks is compared to the EM results in Figure 8-2.

8.4 CONCLUSIONS

The conclusion of the blowdown nodding sensitivity is that the single-node model (utilizing SRP 6.2.1 methodologies) essentially provides the same results during the blowdown phase as the EM.

The conclusion of the sensitivity to eliminating heat sinks during blowdown shows a relative pressure increase at the end of blowdown of only 3.6 psi relative to the EM. This compares to the EM pressure increase of about 33 psi during the blowdown phase, which confirms the dominant pressure mitigation during blowdown is energy storage due to pressure increase of the volume, or volume compliance.

8-3

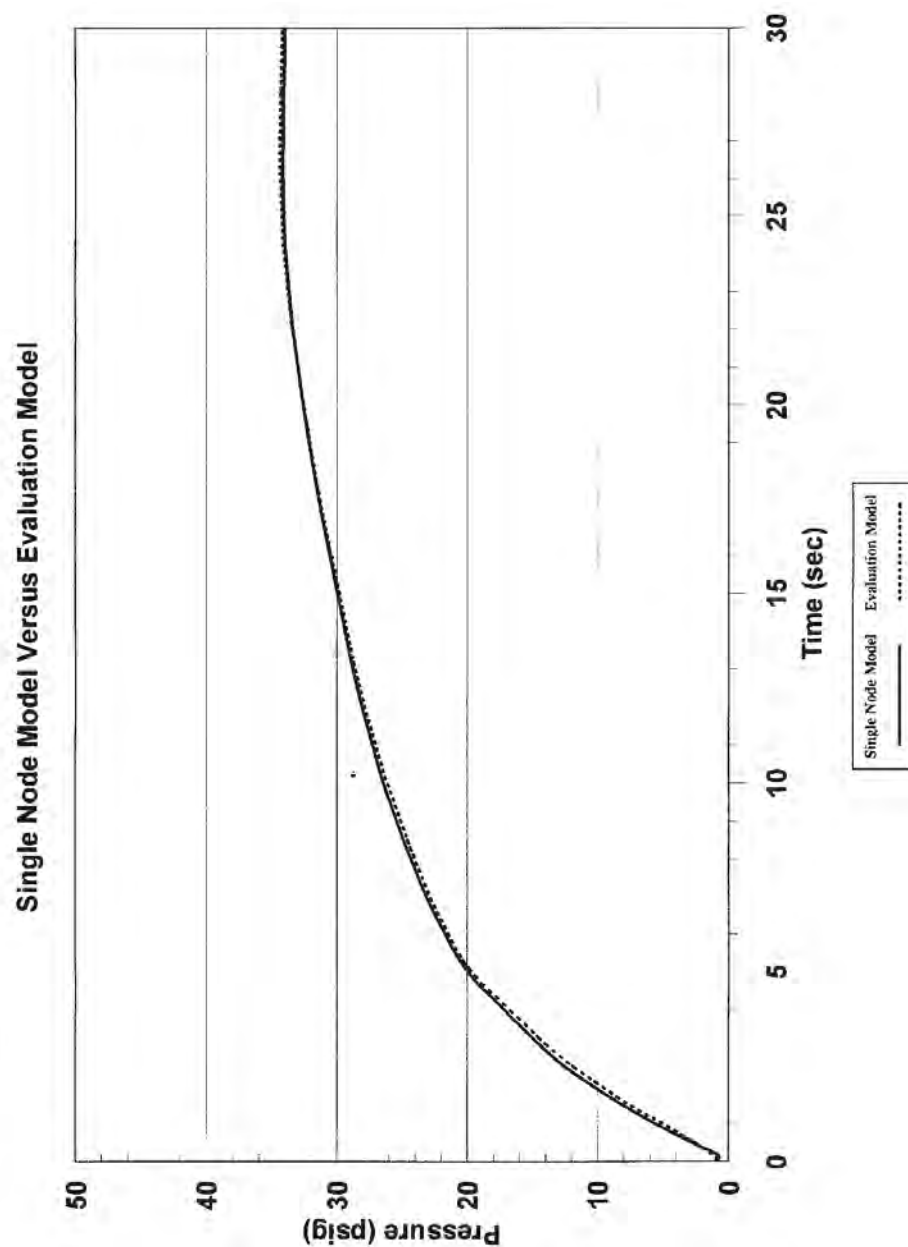


Figure 8-1. Comparison of Single-Node Model with EM Pressure Curve

8-4

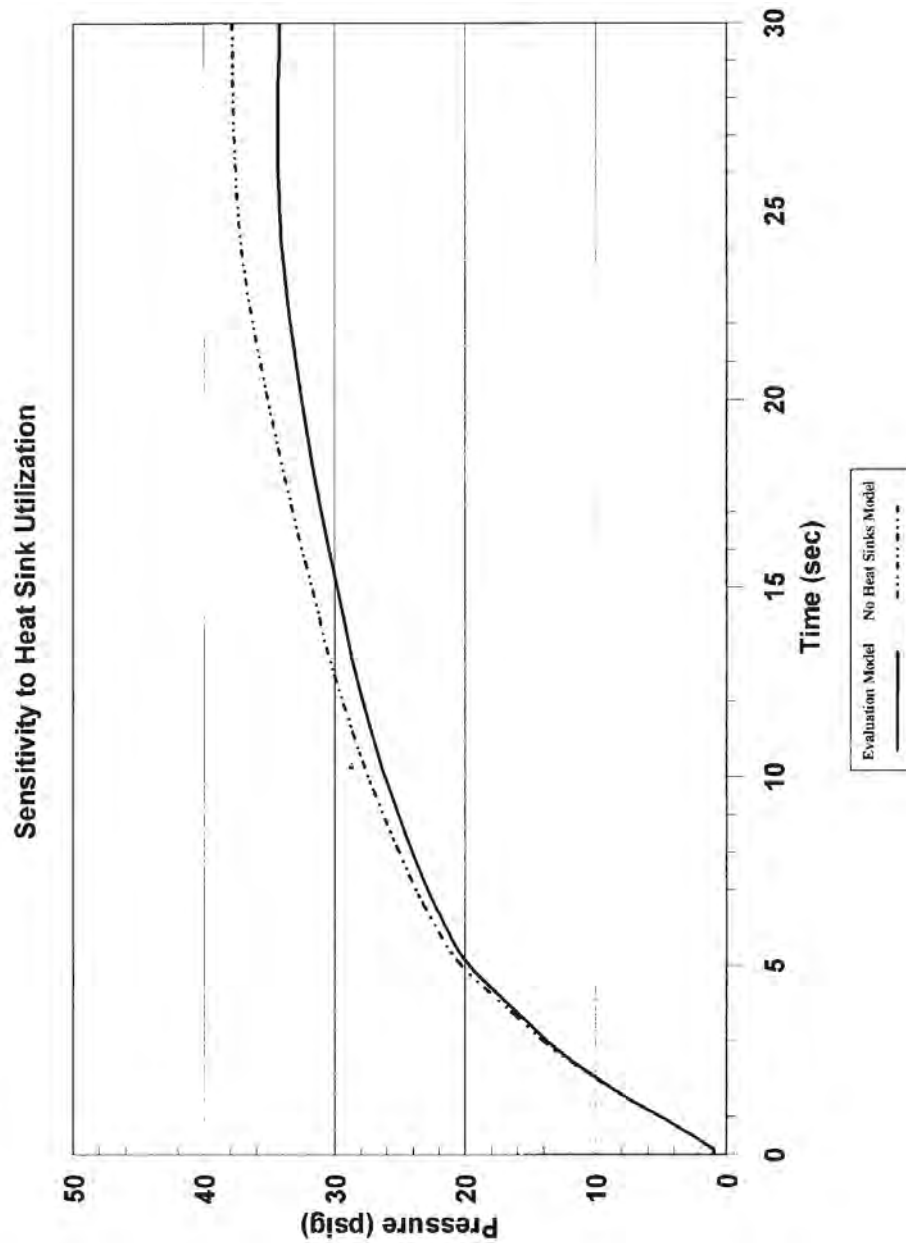


Figure 8-2. Comparison of Response with No Heat Sinks to EM Response

9 CIRCULATION AND STRATIFICATION WITHIN CONTAINMENT

Design basis accident (DBA) evaluations of AP600 and **AP1000** containment pressurization transients follow an approach that bounds uncertainties in parameters important for containment response. In this regard, the assessment of circulation and stratification examined a range of possible break elevations, orientations, and momentum to determine the worst case set of assumptions. A summary of the evaluation results and a cross reference to supporting subsections is given in Table 9-1.

The effect of break parameters on mass transfer to heat sinks, the dominant means of pressure mitigation, is evaluated. The evaluation results in both the selection of a limiting scenario for large-scale circulation, and also a conservative handling of potential effects of stratification. The objective is to perform a bounding, or worst case analysis. The effects of circulation and stratification do not lend themselves readily to quantification of a bias and distribution for uncertainty, such as would be done for a best-estimate analysis. For example, it would be very difficult to quantify the probability of a break being directed in any particular direction. Rather the simplest DBA approach is to examine the range of possible break conditions, to select a limiting scenario, and use modeling techniques to bound the potential for reduced heat sink mass transfer.

For equipment qualification (SSAR Appendix 3D.5.5.1.5), the simple bounding approach is taken which uses the maximum temperature from all control volumes inside containment at each time step. This bounds the effects of temperature distributions. For containment pressure, the evaluation in this section has been performed, summarized as follows.

Deleted: the maximum temperature in the break compartment/containment as input to the qualification envelope. This temperature is the maximum value in containment

Deleted: .

The containment pressure transient is potentially affected by parameters which influence the dominant heat removal mechanism, mass transfer. Mass transfer has as its primary parameters steam concentration, and, in the case of forced convection conditions, velocity. Large-scale circulation and entrainment into jets or plumes can drive circulation and can affect local values of steam concentration and velocity near heat transfer surfaces. Jet and plume entrainment within compartments or the above-deck region can also result in stratification, or the existence of a vertical steam concentration gradient. Therefore, an assessment of the effects of circulation and stratification should focus on how the steam concentration and velocity are affected. Since the Evaluation Model assumes only free convection inside the containment, the potential benefit of forced convection, when it exists, is neglected. Therefore, the assessment can be further focused on the potential effects on steam concentration distributions.

For the main steamline break (MSLB), the containment vessel shell never becomes the dominant heat removal mechanism before break releases are over; therefore, known biases inherent in the lumped parameter Evaluation Model are used to minimize the internal heat sink effectiveness. Lumped parameter model biases, supported with LST comparisons, are used to impose a conservative break release boundary condition location in the Evaluation Model for MSLB pressure responses.

For the loss of coolant accident double-ended cold leg guillotine break (LOCA DECLG), temporal partitioning has been used to further refine the evaluation for blowdown (0-30 sec.), refill (30 to 90 sec.), peak pressure (90 to 1200 sec.), and long-term (1200 sec. and beyond). During blowdown, volume pressurization is the dominant energy absorber, so the details of mixing and stratification effects are not dominant. During the long-term, the passive containment cooling system (PCS) is the dominant heat removal mechanism, so that increasing the concentration of noncondensables in the above-deck region

would reduce the PCS heat removal capability and result in higher calculated containment pressures. The peak pressure period, where both the below-deck heat sinks and the PCS surface are significant contributors, has been assessed by examining extreme release scenarios and examining the range of conditions to select a limiting scenario for peak pressure. The evaluation includes a logical sorting and organization of extreme break scenarios that are quantified by various analytical models and selected experimental results. The analytical models include hand calculations and the use of the WGOTHIC AP600 Containment Evaluation Model for sensitivities to the range of the extreme break scenarios considered.

Entrainment into a jet or plume and large-scale, density-driven circulation between compartments can force some degree of homogenization between and within compartments. Entrainment into a jet or plume can reduce the vertical density gradient occurring due to stratification because of the induced circulation. The assessment of large-scale circulation and compartment density gradients is summarized below.

Large-scale circulation is evaluated by examining a range of extreme release scenarios, including break location, elevation, orientation, and momentum. A limiting, large-scale circulation scenario for the peak pressure period can be shown to result from the assumption of dissipation of the break momentum within the steam generator compartment, at the elevation of the primary system pipe. The scenario is limiting because other scenarios were shown to have improved heat sink utilization, and thus lower peak pressures. For example, the extreme postulated scenario of an undissipated forced jet exiting the upper steam generator compartment opening would drive significantly more convection on the steel shell (PCS) surface, and data indicates that the kinetic energy exiting the steam generator compartment would drive circulation below deck. Mass transfer would be greater than that for a buoyant plume. For a buoyant source and a break low in containment, it is reasonable to use a lumped parameter formulation to model the large-scale, or intercompartment circulation. A review of possible release locations and the expected circulation patterns led to the selection of four potentially limiting cases for further evaluation. The lumped parameter WGOTHIC AP600 Containment Evaluation Model was then used to examine those potentially limiting buoyant source release locations. Results from the sensitivity cases were consistent with the expected circulation patterns in each case, which supports the use of the WGOTHIC lumped parameter model for those sensitivities. Results also showed that the postulated scenarios examined a wide range of possible transient evolutions of steam concentrations throughout the dominant circulating compartments. An assumption of a buoyant release within the broken steam generator compartment reduced the steam access to a large fraction of heat sinks compared to the other locations for a buoyant release, which reduced below-deck heat sink effectiveness and led to the maximum calculated containment pressure.

The use of lumped parameter models can introduce a bias in heat and mass transfer calculations when details within a compartment or region may be important. The simplified momentum formulation can lead to overmixing when multiple lumped parameter nodes are used to represent a single region, such as is done for the above-deck region in the Evaluation Model. Thus, density gradients larger than those predicted by the model in the above-deck region are expected and are assessed independently from the Evaluation Model. The calculation uses a single calculational node to represent each below-deck compartment. The single node representing each compartment allows only an average value of steam concentration for that compartment. For both above- and below-deck regions, density gradients larger than those predicted by the Evaluation Model are evaluated to gain insight into the effects of extreme gradients on heat sink utilization. Showing how sensitive the heat sink utilization is to extreme gradients

provides greater confidence that the simplifications inherent in the Evaluation Model have been conservatively bounded.

Since stratification within compartments is not considered explicitly in the WGOTHIC lumped parameter model, it has been evaluated for its effect on total compartment heat sink utilization. The potential for degraded heat sink effectiveness has been examined using a simple calculation for the vertical heat sink distribution and an extreme vertical density gradient. Results show that the total heat sink effectiveness within a compartment or region is affected by the assumed vertical gradients. Evaluations also showed that mass transfer to upward facing surfaces in circulating compartments may be degraded very early in the transient, and heat sink effectiveness within dead-ended compartments may be overestimated by the lumped parameter model after blowdown. Biases have been introduced into the Evaluation Model to bound these effects.

The conclusion of the circulation and stratification assessment provides specific guidelines for the Evaluation Model to bound the effects. The guidelines are summarized in Table 9-1, noted in the conclusions in Section 9.5, and are implemented as noted in Section 4 in the Special Modeling Assumptions subsection for each compartment or region.

9.1 INTRODUCTION

The rupture of the primary system or main steamline piping has the potential to release a significant amount of mass and energy into the containment atmosphere. The passive containment is designed to withstand a loss-of-coolant accident (LOCA) or a main steamline break (MSLB) through a combination of a high containment design pressure and passive heat removal mechanisms. The passive heat removal systems include energy absorption by internal heat sinks as well as heat removal by the passive containment cooling system (PCS).

A containment analysis is performed to verify the adequacy of the containment heat removal mechanisms to maintain post-accident containment pressure below the design limit. In this regard, the WGOTHIC code (Reference 9.1) has been developed as the containment code for performing the design basis containment analysis. Appropriate Evaluation Models (Sections 4 and 13) have been created. These models consider important input parameters such as mass and energy releases, containment volume, internal heat sinks, and PCS heat removal to calculate post-LOCA and post-MSLB containment pressure and temperature response.

To obtain a conservative containment analysis, the effects of circulation and stratification must be bounded by the Evaluation Model. Circulation and stratification are natural processes that occur inside the passive containment during postulated containment pressurization transients and have been identified as important phenomena to be addressed in support of the Evaluation Model for containment pressure calculations (Reference 9.2). The circulation and stratification that occur during a high energy pipe break transient, have the potential to reduce heat and mass transfer rates by transporting and concentrating noncondensables. The degradation of heat and mass transfer may reduce the effectiveness of the heat sinks and the PCS at mitigating the peak containment pressure. The effects of circulation and stratification must be addressed to justify the approach used in the containment Evaluation Model.

9-4

This section presents an overview of the effects of circulation and stratification for the containment Evaluation Model for the LOCA and MSLB events. The evaluation results are summarized in Table 9-1. As the table shows, the LOCA and MSLB events are evaluated separately. The LOCA event is divided into four temporal phases based on heat sink utilization: the blowdown phase, the refill phase, the peak pressure phase, and the long-term phase. During each of these phases, important phenomena, such as mass and energy release rates, break source direction, and heat removal mechanisms are considered for impact on circulation and stratification. Unlike the LOCA events, the MSLB events are not divided into temporal phases. The MSLB is characterized by a single, high-intensity blowdown phase. However, different piping rupture locations are considered in the MSLB evaluation.

Table 9-1. Circulation and Stratification Evaluation Summary

Element	Summary of Evaluation	Relevant PIRT Parameter ⁽¹⁾	WCAP-14407 Section Reference
General Approach			
	Circulation and stratification evaluated because of the potential to degrade heat sink effectiveness via the condensation parameters: <ul style="list-style-type: none"> Steam concentration Velocity 	Circulation/stratification (2A), condensation (3F, 7C)	9.0
	High kinetic energy sources, such as during LOCA blowdown and MSLB result in forced convection component of mass transfer	Circulation (2A), condensation (3F)	9.0
	Effects of velocity eliminated in calculation by assuming only free convection internally. Focus, therefore, is on impact of circulation and stratification on steam and noncondensible distributions	Circulation/stratification (2A)	9.0
	Equipment qualification temperature is conservatively taken from the <u>maximum temperature from all control volumes inside containment to bound the effects of temperature distributions</u> (containment pressure is therefore, the focus of the evaluation in Section 9)	Circulation/stratification (2A)	9.0
	For the DBA LOCA, volume compliance is the primary pressure mitigator during blowdown, internal heat sinks and the containment steel shell are the primary mitigators during the peak pressure phase, and the steel shell surface is the dominant mitigator during the long-term phase	Gas compliance (2C), condensation (3F, 7C)	9.0, 9.3, 9.3.2.1, 9.3.2.4
	For the DBA MSLB, the internal heat sinks are the dominant pressure mitigators.	Condensation (3F)	9.0, 9.4.3

Deleted: break compartment

9-5

Table 9-1. Circulation and Stratification Evaluation Summary (cont.)

Element	Summary of Evaluation	Relevant PIRT Parameter ⁽¹⁾	WCAP-14407 Section Reference
Test Data (cont.)			
A. Method to Address Distortions in the LST for Circulation and Stratification Assessment	Power to volume ratio: using only quasi-steady-state data for circulation and stratification, therefore, no impact of this distortion on these results.	Stratification (2A), int. heat sink conduction (3D), shell conduction (7F)	9.2.3
	Power to area ratio: <ul style="list-style-type: none"> Steam flow was ranged and external boundary conditions were ranged Considering the matrix of the LST, a range of power-to-area (or condensation rate) ratios were considered, which minimizes the degree of the distortion Distortion addressed by considering stratification and condensation data from LST matrix tests and supplementing LST with assessment of international test data for stratification 	Circulation/Stratification (2A)	9.2.3, 1.4.1
	Circulation path impact on <i>circulation</i> : cannot use the LST data for assessment of circulation. Addressed by supplementing LST with assessment of international test data for circulation	Circulation (2A), intercomp flow (2B)	9.2.3
	Circulation path impact on <i>stratification</i> : <ul style="list-style-type: none"> Lack of LST SG compartment circulation results in LST stratification more extreme than if a circulation path existed Addressed by supplementing LST with assessment of using international test data for stratification 	Stratification (2A), intercomp flow (2B)	9.2.3

9-6

Table 9-1. Circulation and Stratification Evaluation Summary (cont.)

Element	Summary of Evaluation	Relevant PIRT Parameter ⁽¹⁾	WCAP-14407 Section Reference
Test Data (cont.)			
B. Usage of LST Data for Circulation and Stratification Assessment	LST above-deck separate effects style data for condensation and stratification is considered	Mass and energy (1A), direction and elevation (1B), momentum (1C), Circulation/stratification (2A)	9.2.1, 9.2.2
	LOCA – applicable tests had diffuser under the SG, reference case had elevated diffuser. Key LST result – above-deck stratification data used to support development of a bounding stratification gradient for evaluation of heat sink utilization for peak pressure/long-term phases	Stratification (2A)	9.2.1
	MSLB – applicable tests had elevated 3" pipe pointing vertically/horizontally. Key LST results – kinetic energy drives circulation below-deck, forced convection significantly enhances mass transfer (factor of 1 to 10 over shell surface relative to free convection mass transfer)	Circulation/stratification (2A)	9.2.2
Lumped Parameter Biases Implemented in <u>WGOTHIC</u> Evaluation Model			
A. International/ Industry Experience	Lumped-parameter modeling uses a simplified momentum formulation, which biases calculated pressure with respect to circulation and stratification. These biases are evaluated and bounded by the Evaluation Model.	Circulation/stratification (2A)	9.1.2
	NUPEC modeling experience is applied to Evaluation Model compartment flow connections, resulting in reasonably predicted circulation patterns.	Circulation (2A) Inter-compartment Flow (2B)	9.2.4, Appendix C Section 9.C.3

9-7

Table 9-1. Circulation and Stratification Evaluation Summary (cont.)

Element	Summary of Evaluation	Relevant PIRT Parameter ⁽¹⁾	WCAP-14407 Section Reference
Lumped Parameter Biases Implemented in <u>W</u>GOTHIC Evaluation Model (cont.)			
B. LOCA Biases	The effects of stratification on heat sink utilization are negligible for compartments experiencing downflow of heavier ambient atmosphere mixture	Stratification (2A)	9.3.1.1
	<ul style="list-style-type: none"> Dead-ended compartments with no assumed thermal gradients stratify Condensation and convective heat transfer turned off in dead-ended compartments after 30 seconds 	Stratification (2A)	9.3.2.1
	<ul style="list-style-type: none"> Effect of stratification on steel shell condensation assessed with extreme gradient Stratification effect bounded by removing upward facing surface of operating deck as a heat sink 	Stratification (2A)	9.3.1.1
	<ul style="list-style-type: none"> Effect of stratification on heat sinks in a below-deck compartment assessed with extreme gradient CMT room (most heat sinks) evaluated for case in which LOCA plume is rising in room Stratification effect bounded by removing floor as heat sink (bias applied in all compartments regardless of assumed break location) 	Stratification (2A)	9.3.1.3
C. MSLB Biases	LST data indicates: <ul style="list-style-type: none"> Kinetic energy drives some circulation below-deck Forced convection is driven by high kinetic energy jet above-deck No significant stratification above-deck, therefore no bias required 	Circulation/stratification (2A)	9.4.2

9-8

Table 9-1. Circulation and Stratification Evaluation Summary (cont.)

Element	Summary of Evaluation	Relevant PIRT Parameter ⁽¹⁾	WCAP-14407 Section Reference
Lumped Parameter Biases Implemented in <u>WGOTHIC</u> Evaluation Model (cont.)			
C. MSLB Biases (cont.)	<p>Lumped parameter model code biases:</p> <ul style="list-style-type: none"> • Evaluation Model places break node at operating deck level minimizing circulation and steam access to below-deck heat sinks • Momentum dissipated in each node (Evaluation Model uses only free convection) • Density-driven circulation as plume rises resulting in relatively homogeneous region above modeled break node <ul style="list-style-type: none"> – Results in steam-rich region above modeled break node and steam-deficient region below modeled break node, which bounds effects of stratification – Conservatively, the LOCA stratification biases are included for the MSLB Evaluation Model 	Circulation/stratification (2A)	9.4.2

9-9

Table 9-1. Circulation and Stratification Evaluation Summary (cont.)

Element	Summary of Evaluation	Relevant PIRT Parameter ⁽¹⁾	WCAP-14407 Section Reference
LOCA Evaluation Results			
A. Considerations by Time Phase for Evaluation Model	<p>LOCA blowdown (0 to 30 seconds):</p> <ul style="list-style-type: none"> • Blowdown pressurizes compartments and drives significant circulation above and below-deck • Lumped parameter modeling adequate for pressure-driven flow • Containment pressure insensitive to nodding (multi-node vs. one-node model) • Low sensitivity to heat sinks because volume storage is dominant pressure mitigator • Fr indicates significant forced convection on steel shell, Evaluation Model conservatively assumes only free convection • Steam driven into dead-ended compartments. Assuming thermally uniform heat sinks results in no circulation, therefore, condensation and convection heat transfer in dead-ended compartments neglected after 30 seconds. 	<p>Intercompartment Flow (2B)</p> <p>Gas compliance (2C)</p> <p>Break source momentum (1C)</p>	9.3.2, 9.3.2.1, 9.2.2

9-10

Table 9-1. Circulation and Stratification Evaluation Summary (cont.)

Element	Summary of Evaluation	Relevant PIRT Parameter ⁽¹⁾	WCAP-14407 Section Reference
LOCA Evaluation Results (cont.)			
A. Considerations by Time Phase for Evaluation Model (cont.)	LOCA refill (30 to 90 seconds): <ul style="list-style-type: none"> Break releases are negligible Containment depressurizes during this phase Conservatively ignore containment pressure reduction by neglecting this phase to maximize initial pressure for the peak pressure phase 	Break source mass and energy (1A)	9.3.2.2
	LOCA peak pressure (90 to 1200 seconds): <ul style="list-style-type: none"> Steam source location changes to ADS Stage 4 valves in both SG compartments at approximately 1000 seconds Condensation on steel shell becomes dominant heat removal mechanism towards end of peak pressure phase Compartment filling reduces heat transfer for affected compartments during peak pressure phase and long-term phase (compartment filling is modeled by code) 	Break source (1B, 1C)	9.3.2.3

9-11

Table 9-1. Circulation and Stratification Evaluation Summary (cont.)

Element	Summary of Evaluation	Relevant PIRT Parameter ⁽¹⁾	WCAP-14407 Section Reference
LOCA Evaluation Results (cont.)			
A. Considerations by Time Phase for Evaluation Model (cont.)	<p>LOCA long-term (1200 seconds to 24 hours):</p> <ul style="list-style-type: none"> Condensation on steel shell remains dominant heat removal mechanism WGOTHIC predicted steam gradient becomes essentially homogeneous in less than 24 hours, excluding the SG compartments (due to ADS Stage 4 valves releasing steam) Evaluation using extreme stratification gradient shows nearly negligible increase in heat removal by the steel shell relative to homogeneous steam concentration case – bounded by removing the non-grating operating deck floors Evaluation using extreme stratification gradient shows a decrease in heat removal by the below-deck compartment heat sinks relative to the homogeneous steam concentration case – bounded by removing the compartment floor. 	<p>Condensation (7C) Break pool filling (5F) Stratification (2A)</p>	<p>9.3.2.4</p> <p>9.3.1.3</p>

9-12

Table 9-1. Circulation and Stratification Evaluation Summary (cont.)

Element	Summary of Evaluation	Relevant PIRT Parameter ⁽¹⁾	WCAP-14407 Section Reference
LOCA Evaluation Results (cont.)			
B. Range of Break Scenarios and Effects	Jet dissipated in SG East compartment <ul style="list-style-type: none"> Limiting scenario Post-blowdown flow into CMT room is downward with steam/air mixture 	Break source (1B, 1C)	9.3.1.1, 9.3.2.5
	Undissipated jet in SG East compartment <ul style="list-style-type: none"> Forced convection above-deck improves condensation on containment shell Significant kinetic energy-driven circulation below-deck Minimal stratification in above-deck region 	Break source (1B, 1C)	9.3.1.2
	Jet to RCDT cavity – dissipated plume rises in CMT North room <ul style="list-style-type: none"> Good steam access to below-deck room with most internal heat sinks 	Break source (1B, 1C)	9.3.1.3
	Jet to RCDT cavity – dissipated plume rises in SG West compartment <ul style="list-style-type: none"> Same scenario as dissipated jet rising in SG East compartment 	Break source (1B, 1C)	9.3.1.3
	Jet dissipates in RCDT cavity <ul style="list-style-type: none"> Flow split based on flow area and loss coefficients Better steam access to CMT room and SG West compartment compared to break in SG East compartment 	Break source (1B, 1C)	9.3.1.3

9-13

Table 9-1. Circulation and Stratification Evaluation Summary (cont.)

Element	Summary of Evaluation	Relevant PIRT Parameter ⁽¹⁾	WCAP-14407 Section Reference
LOCA Evaluation Results (cont.)			
C. Sensitivity Cases Run with the Evaluation Model	Break locations (all located low in containment): <ul style="list-style-type: none"> • Jet undissipated in SG East compartment – forced convection benefit on steel shell assessed to estimate effect of undissipated jet • Jet dissipated in SG East compartment – limiting case for maximum containment pressure • Jet into RCDT cavity - plume rises in CMT North room • Jet dissipated in RCDT cavity – plume rise determined by flow path resistances 	Intercompartment Flow (2B)	9.3.2.5
	Loss coefficients: <ul style="list-style-type: none"> • Loss coefficients for several flow paths changed to modify blowdown-predicted flow direction • Modeled dissipated jet in SG East compartment • End of blowdown conditions changed with negligible change to maximum containment pressure 	Intercompartment Flow (2B)	9.3.2.1

9-14

Table 9-1. Circulation and Stratification Evaluation Summary (cont.)

Element	Summary of Evaluation	Relevant PIRT Parameter ⁽¹⁾	WCAP-14407 Section Reference
LOCA Evaluation Results (cont.)			
C. Sensitivity Cases Run with the Evaluation Model (cont.)	<p>Thermal and circulation effects of drops:</p> <ul style="list-style-type: none"> • Drops only created during LOCA blowdown • Thermal effects <ul style="list-style-type: none"> – 5 percent drop formation enough to saturate containment atmosphere – 0 percent drops less limiting for maximum containment pressure – Negligible change in containment pressure between 100 percent drops and Evaluation Model (approximately 50 percent drops) • Circulation effects examined for 0 and 100 percent drop formation <ul style="list-style-type: none"> – Presence of drops increases density of atmosphere increasing relative buoyancy of plume – Containment atmosphere entrainment into plume is significant for both 0 and 100 percent cases 	<p>Break source droplet/ liquid flashing (1E)</p> <p>Stratification (2A)</p> <p>Intercompartment Flow (2B)</p> <p>Containment volume fog (2D)</p>	<p>9.2.3.6</p> <p>5.8</p> <p>9.2.3.6</p>

9-15

Table 9-1. Circulation and Stratification Evaluation Summary (cont.)

Element	Summary of Evaluation	Relevant PIRT Parameter ⁽¹⁾	WCAP-14407 Section Reference
LOCA Evaluation Results (cont.)			
D. Conclusions	<ul style="list-style-type: none"> Evaluation Model with dissipated break in SG East compartment is the limiting scenario <ul style="list-style-type: none"> Calculated containment pressure is not very sensitive to break location due to heat sink utilization prior to maximum pressure Biases included in Evaluation Model to bound effects of stratification 		9.2.3.5, 9.5
MSLB Evaluation Results			
A. Break Location Scenarios and Effects	<ul style="list-style-type: none"> Selected based on routing of steamline pipe MSLB above-deck <ul style="list-style-type: none"> High kinetic energy release with relatively short duration, which drives circulation below the source High Fr number (comparison provided to LST Fr number) LST data indicates forced convection enhancement to mass transfer (only free convection modeled) Break in MSLB Evaluation Model located in node just above-deck, which limits steam access to below-deck heat sinks 	Stratification (2A) Intercompartment Flow 2B) Break source (1B, 1C)	9.4, 9.4.1, 9.4.1.1, 9.4.2

9-16

Table 9-1. Circulation and Stratification Evaluation Summary (cont.)

Element	Summary of Evaluation	Relevant PIRT Parameter ⁽¹⁾	WCAP-14407 Section Reference
MSLB Evaluation Results (cont.)			
A. Break Location Scenarios and Effects (cont.)	<ul style="list-style-type: none"> MSLB in CMT North room <ul style="list-style-type: none"> Break in CMT room would significantly dissipate due to equipment in room and rise as a plume CMT room contains most of the internal heat sinks Good steam access to CMT room heat sinks, therefore case is expected to be less limiting 		9.4.1.2
B. Sensitivity Cases	<ul style="list-style-type: none"> MSLB located just above deck MSLB in CMT North room 		9.4.3
C. Conclusions	<ul style="list-style-type: none"> MSLB in CMT North room calculated containment pressure significantly less limiting MSLB located just above-deck used for the MSLB Evaluation Model 		9.4.3, 9.5

Note:

- PIRT parameters are identified in Reference 9.2, Table 4-1

9.1.1 Definitions

Several terms used to discuss circulation and stratification are defined, as they relate to containment analysis.

Stratification is a state characterized by strata, or horizontal layers, of different density. Stratification is stable when the lower layers are increasingly dense due to composition and/or temperature. The term stratification does not indicate the magnitude of the density gradient.

Mixing is a collective term for convective transport processes that reduce temperature and/or concentration differences within a volume or between volumes. Convective transport processes in containment include jets, plumes, wall layers, turbulent diffusion, and entrained flow. Molecular diffusion also contributes to mixing but is considerably less effective than convection, except in boundary layers. Diffusion also contributes to mixing in stratified conditions.

9-17

Circulation is a term used to describe gross, overall convective flow patterns that occur on a compartment scale and on a large scale (or containment scale). The compartment-scale circulation is due to wall layers, jets, plumes, and entrained flow. The large-scale circulation is due to interactions between compartments induced by pressure, density, elevation, and momentum differences such as intercompartment flow. The break source jet or plume can induce both compartment-scale and large-scale circulation.

Segregation is a state characterized by a different air/steam concentration in one compartment than in another. For example, the heavier air may reach different concentrations in separate compartments, especially the dead-ended compartments if the intercompartment circulation is low.

9.1.2 Lumped Parameter Biases and Capabilities

Lumped parameter biases and capabilities have been identified based on industry experience, as documented in the literature (Appendix 9.C, Section 9.C.3.4). The documented experience base includes facilities at different geometric scales, from that of the LST to nearly full-scale AP600 height (Appendix 9.C, Figure 9.C-24). The lumped parameter biases and capabilities, summarized below, have been reported consistently across the range of facilities, indicating that the biases and capabilities are applicable to the Containment Evaluation Model. The consistency across scales also indicates that the LST facility is a reasonable basis on which to study the biases and capabilities as they apply to AP600, reported in WCAP-14382 (Reference 9.1). The following provides a summary of the method used in the development of the Containment Evaluation Model to address each documented bias and capability.

1. Single node models were not capable of modeling stratification, or the passing of a stratification front through horizontal vents.

[

] ^{a,c}

9-18

2. Sump liquid level and sump temperature were not well predicted

[

] ^{a,c}

3. Some codes produced results which were not correct due to missing or oversimplifying buoyancy terms

[

] ^{a,c}

4. To account for recirculation flows, the applied lumped parameter model used double junctions in the horizontal direction. (This did not help in the case of an elevated release and resulting stratified containment.)

See discussion for item 3 above regarding the impact of lumped volume static pressure profile on the use of double junctions in the Evaluation Model. All of the LOCA cases have releases in the lower compartments (below the operating deck). This break location results in good circulation throughout containment. The main steamline break releases contain high kinetic energy. Therefore, the break node used in the lumped parameter model is a node that minimizes kinetic energy driven circulation to below-deck heat sinks, thus overestimating calculated containment pressure.

5. For releases low in containment, typical for the LOCA DECLG, the lumped parameter model well-predicted pressure, temperature, and helium concentrations inside the compartments, which were affected by the global circulation loop, while predictions needed improvements to account for postulated circulation effects inside dead-ended compartments

9-19

[

] ^{a,c}

6. Scenarios with homogeneous containment atmosphere (like HDR E11.4 and E11.5) can be simulated successfully with lumped parameter models. (Such conditions typically result from breaks located within the bottom 20 percent of the containment height.)

See discussion for item 5 regarding the use of lumped parameter models for bounding design basis analyses.

7. Circulation effects due to sump boiling (releases generated at the bottom of containment) were well-simulated.

Sump boiling is not a consideration for containment DBA, since long-term primary system energy rejection is through the ADS Stage 4 valves and the sump is therefore a relatively insignificant heat source.

8. The order of magnitude of computed velocities matches data and it can be concluded that trends in the direction of the flow are predicted well; however, predicted velocities differ by as much as a factor of two.

Calculated velocities using lumped parameter codes are strongly dependent on the noding used. Experience with validating the WGOTHIC lumped parameter model of the LST (Reference 9.1, Section 8.2) shows that the noding used can result in calculated velocities that differ from measured by an order of magnitude, showing that the particular test facility and noding used can have a strong influence on calculated velocities. Therefore, a bounding approach is used in the WGOTHIC Evaluation Model, as follows. The effects of predicted velocities in the containment pressure transient are eliminated by considering only free convection heat and mass transfer in the containment. This conservatively biases the Evaluation Model when forced convection would occur during the LOCA blowdown and the MSLB transients.

9. The lumped parameter method does not have the capability to predict the hydrogen distribution in a stratified containment atmosphere, as in HDR E11.2 with high-positioned release. In a break scenario with buoyant plume (released at about 50 percent of containment height), the steam and gas transport to the lower parts of the containment were over-predicted. (Artificial limitation of convective flows by decreasing flow areas improved predicted concentrations in the lower regions, but overestimated the containment pressure in upper compartments.)

Hydrogen distribution predictions are not a consideration for containment DBA (Reference 9.2, Section 4.4.2E).

9.2 LARGE-SCALE TEST RESULTS

In the passive containment design, interest is focused on how much the jet kinetic energy affects gradients inside containment. If the jet kinetic energy is sufficient to disrupt stable stratification, it may also be sufficiently energetic to virtually eliminate vertical gradients in the upper containment volume and to induce circulation between the above-deck and below-deck regions. The Westinghouse Large-Scale Test (LST) data was used to understand the effect of jet kinetic energy on stratification gradients above the operating deck.

The Westinghouse large-scale PCS test facility was built to provide integral test data for a geometrically similar model of the AP600 containment vessel and PCS. The tests provide experimental data that can be used for evaluating the physics in containment, determining the relative importance of various parameters that affect heat and mass transfer, and validating computer codes. Three series of tests (References 9.5 and 9.6) were run at the Westinghouse large-scale PCS test facility. The steady-state pressure, annulus air flow rate, water coverage, steam flow rate, injection velocity, location and orientation, and noncondensable gas concentration were varied between the tests.

It is desirable to use a Froude number formulation that relates momentum phenomena in both the AP600 and the LST to permit scaled inferences between the tests and the AP600. A volumetric Froude number can be defined as the square of the jet Reynolds number, divided by the containment Grashof number:

$$Fr_v = \frac{\rho_a * U_o^2 * d_o^2}{g * (\rho_a - \rho_o) * H^3}$$

where,

ρ_a	=	density of ambient containment
U_o	=	velocity of jet at source
d_o	=	hydraulic diameter of jet at source
g	=	gravitational acceleration
ρ_o	=	density of jet source
H	=	height of volume above steam source

The following sections first describe test configurations as they represent LOCA and MSLB configurations and then provide data that can be used to examine gradients in the above-deck region.

9.2.1 LOCA Configuration

Twenty-five LSTs were conducted in the LOCA configuration with the diffuser located under the steam generator model. A diffuser was used to provide a uniform velocity profile. The tests do not apply to the LOCA blowdown phase, but they do apply to the peak pressure and long-term phases. The volumetric Froude numbers ranged from approximately 5×10^{-6} to 5×10^{-3} . Steam concentrations just above the deck and below the deck near the bottom of the vessel are presented in Figure 9-1, which can be used to see test-to-test variation in above-deck gradients. The plotted values are the ratios of the measured local steam partial pressure to the partial pressure of steam assuming perfect mixing. A value of 1.0 indicates perfect mixing. The values show the above-deck ratios generally range from 0.6 to 1.0 and below-deck values

range from 0.1 to 0.4. The below-deck values are an indication of the distortion in the LST due to lack of a simulated steam generator compartment flow path. The distortion leads to an air-rich mixture in the LST below-deck.

Stratification data for LSTs with the diffuser under the simulated steam generator compartment are shown in Figure 9-2 through Figure 9-25. Tests have been grouped by steam flow and plotted so that the temperature axis spans the same range for all the tests to simplify test-to-test comparison. For each group of tests, three plots are shown. First is the azimuthally-averaged temperature data from thermocouples located one inch inside the vessel shell, called the “fluid thermocouples.” Data is available from nine elevations above the operating deck; fluid thermocouple data was not taken below the deck. Second is a plot of the saturation temperature obtained based on the third plot of measured steam mole fractions, or pressure ratio ($p_{\text{stm}}/P_{\text{vessel}}$).

Also, a reference test to examine the physics of stratification (test 222.2), with an elevated diffuser, is included as Figure 9-26 through Figure 9-28. These test data are reviewed in Section 9.2.3 to develop insight into an appropriate bounding stratification gradient.

9.2.2 MSLB Configuration

Phase 3 of the LST program included a series of tests designed to simulate a main steamline pipe rupture. LST data from baseline and Phase 2 tests suggested that noncondensable concentrations increase dramatically below the elevation of steam injection with considerable steam mixing above the operating deck. One could postulate that the effect of the higher steamline elevation could be to create a larger volume of rich air mixture which extends above the operating deck, and reduces the active heat transfer area. Test series 222 addressed the impact of the elevation and direction of the steamline break on the response of the test vessel and included a high flow transient to a steady-state condition. The kinetic energy available in an MSLB is seen to be an important parameter.

The four configurations in this test series were:

- 222.1 Low velocity steam flow from under the operating deck
- 222.2 Low velocity steam flow above the operating deck (a reference condition to examine the physics, not a realistic AP600 configuration)
- 222.3 High velocity steam flow with horizontal discharge above the operating deck
- 222.4 High velocity steam flow above the operating deck directed upward

Stratification data for LSTs with high kinetic energy above the operating deck are shown in Figure 9-29 through Figure 9-34 also grouped by steam flow, and showing measured internal fluid temperature, saturation temperature, and measured steam pressure ratio, as described in Section 9.2.1 for the LOCA configuration. These data are referenced in the development of a bounding MSLB Evaluation Model (Section 9.4.2).

To understand the effects of kinetic energy on circulation and stratification, it is useful to note the stratification pattern observed for a test with a buoyant source (low Froude number) versus a test with a high Froude number. For example, test 222.4 can be used to assess the effects of steam releases with Froude numbers representative of an MSLB occurring above the steam generator. Test 222.4 is compared to test 222.2, which had a similar setup, but a diffuser was used to provide a low velocity elevated steam source.

The elevated buoyant source in test 222.2 produced a significantly stratified vessel, with very little steam penetration below the elevation of the break. In contrast, the high kinetic energy-elevated source of test 222.4 induced a substantial amount of circulation in the test vessel, including substantial steam ingress into the below-deck regions. The decrease in the steam concentration stratification for test 222.4 compared to test 222.2 is due to the high kinetic energy of the injected fluid because that is the only significant difference between the two tests.

Mass transfer data from LSTs with high velocity jets (forced convection) has been compared to that from the low velocity diffuser under the simulated steam generator (dominated by free convection) in Reference 9.9, Figure 3.9-5. The referenced figure includes shell condensation data above the operating deck for the elevated high momentum source LST compared to the mean of such data from the diffuser under the steam generator. The elevated diffuser LST is not included in the referenced figure due to its atypical condition of a low Froude number elevated source - the elevated releases which may be postulated for an MSLB are of a higher Froude number similar to that of the tests for which data are plotted, as described earlier in this section. Results indicate that in the LST forced convection effects enhanced the mass transfer rate by a factor of 1 to a factor of 10 in the direction the jet is directed.

9.2.3 Method to Address Distortions in LST Stratification Data

Internal momentum effects were distorted in the LST due to the lack of a simulated flow path for entrainment near the bottom of the steam generator compartment. Thus in the LOCA DECLG configuration, the LST effectively stratified into two regions – separated at the elevation of the steam generator compartment exit (Section 9.2.1). Therefore, the LST cannot be used to examine intercompartment circulation.

There is also a system level distortion in the LST with respect to power-to-volume and power-to-area (Reference 9.7, Section 11). Since only quasi-steady state data for circulation and stratification were used, there is no impact of power-to-volume distortion on this evaluation. The LST quasi-steady data was taken with a range of break flow rates, and the external wall boundary condition was ranged using controllable variables (turning external water and fan on and off). The internal release configuration also allowed varying the release elevation, momentum, and direction. Initial noncondensable content ranged from near vacuum to two atmospheres. Thus the LST provides a valuable database to examine the physics of potential stratification mechanisms that may be postulated to occur in a passive containment.

Because of the momentum-related distortions in the LST, available international test data has been reviewed (Appendix 9.C, Section 9.C.2) to supplement the database for examining stratification effects. The supplementing of LST data with additional tests at various scales, combined with the use of LST matrix tests, sufficiently addresses the system level power-to-area distortion. The following summarizes conclusions that may be drawn from LST and the international databases, leading to the selection of an extreme stratification gradient to be considered in thermal calculations of Appendix 9.B.

It is desired to gain insight into vertical steam concentration gradients that may occur within the region above the operating deck and within compartments below-deck during a LOCA. (The bounding approach for an MSLB is given in Section 9.4.2.) The region above the operating deck in the LST can be considered to be an enclosure with a plume and wall boundary layers (Appendix 9.C, Section 9.C.1.4.1). The relevant vertical profile data is presented in Figure 9-2 through Figure 9-25. Comparisons of internal fluid thermocouple data (1-inch inside the vessel wall) and steam concentration measurements show that the gas is within a few degrees of saturation, so that the vertical temperature profiles provide a good measure of the vertical steam concentration gradient during the LSTs. Clearly, for the diffuser under the steam generator model, there is only about a 3 to 12°F temperature gradient from the steam generator exit elevation to the dome. The plotted data is at the fluid thermocouple location. A review of the internal rake temperature data shows that the bulk fluid vertical temperature difference is equal to or several degrees less than that given by the fluid thermocouples.

Comparison of the vertical temperature profile from the elevated diffuser case in the LST (Figure 9-26) shows that the stratification in the above-deck region is more pronounced than that in any of the tests with the LOCA configuration. Such stratification from an elevated diffuser is similar to that observed in the CVTR tests (Appendix 9.C, Section 9.C.2.3) which had a similarly elevated, low momentum source. Tests in the much larger HDR and NUPEC facilities indicate that stratification gradients from diffuse releases low in containment in fact produce temperature gradients above the operating deck similar in magnitude to those quoted above in the LST with a low diffuser. However, because of the distortions in LST mentioned above and uncertainties in transferring stratification data from HDR and NUPEC to AP600 and **AP1000**, an extreme stratification gradient, well beyond that which would occur in a containment with natural convection and a low elevation release, has been considered for thermal calculations.

The steam concentrations used for thermal calculations presented in Appendix 9.B assume a three region distribution — nearly pure steam at the top (steam fraction 0.98), the average value at the middle (steam fraction 0.63), and the balance of the air content at the bottom (steam fraction 0.28). The elevated diffuser case in the LST shows a steam pressure ratio (equal to steam mole fraction) of 0.10 near the operating deck and 0.90 under the dome. The distribution chosen is consistent with that indicated by the LST elevated diffuser, considering that the Appendix 9.B calculation represents an average steam concentration calculated for AP600 transient conditions. It should be noted that the LST elevated diffuser test produces an extreme, or bounding, test configuration for the real situation of a buoyant plume released low in containment, such as for the LOCA DECLG post-blowdown. Thermal calculations in Appendix 9.B are used to develop appropriate biases to bound the effects of stratification within the AP600 and **AP1000** lumped parameter compartment nodes and the above-deck region.

9.2.4 Application of Modeling Methods Developed for NUPEC M-4-3 Lumped Parameter Model

The following is a brief summary of the experience gained in developing the WGOTHIC lumped parameter model of the NUPEC natural circulation test, M-4-3, and application of the experience to development of the WGOTHIC lumped parameter Evaluation Model. Justification is provided for using the lumped parameter Evaluation Model for performing sensitivity studies. The sensitivities are used to examine the effects of circulation in containment from a LOCA DECLG.

NUPEC Lumped Parameter Modeling Experience

Actual circulation was interpreted based on data provided by NUPEC for the detailed time history for gas temperature and hydrogen concentration as well as a video of processed data to aid visualization.

As shown in Figure 9.C-55 (flow pattern) and Figure 9.C-61 (data for one circulation loop) of Appendix 9.C, the break flow rose from the affected steam generator loop, spread through the upper portion of the large vertical opening into the adjacent steam generator loop, and rose from those two compartments into the dome. The large-scale natural convection loop continued with continuity driving circulation down through the opposite steam generator compartments and other openings through the operating deck, and then down to the level of the break release. From the break release level, the convection loop was closed by entrainment into the rising plume. This result is consistent with results of international tests at several scales and is rather simple and straightforward. However, careful development of the lumped parameter noding structure is necessary to allow the code to predict the observed qualitative behavior, as follows.

It should first be noted that for the M-4-3 calculations, best estimate condensation correlations were used to better isolate the biases of lumped parameter noding on predicted parameter distributions and the effect of those biases on containment pressure.

For general application of WGOTHIC lumped parameter, it is necessary that the vertical noding be defined by a set of horizontal planes that cut through the entire modeled region, as described in Reference 9.4, Section 16.12.1. This is done to prevent artificial flows driven solely by the method used to estimate a static pressure profile using the single value of density available within a lumped parameter cell. The successful elimination of such artificial circulation is confirmed when a new model is developed by running a null problem (uniform temperatures in heat sinks and volumes, and no heat or mass source) and verifying that there is no predicted circulation.

9-25

[

] ^{a,c}

Application of NUPEC Test Experience to Containment Evaluation Model

The Evaluation Model has been verified to have no significant artificial flows in a null problem. In the further development of the WGOTHIC lumped parameter nodding used in the containment pressure Evaluation Model, experience with the NUPEC tests was used qualitatively in representing the CMT compartment.

[

] ^{a,c}

9-26

Table 9-2. AP600 Flow Areas Connecting to North and South CMT Compartments (excluding Dead-Ended Compartment Connections)

[illegible]

a,c

9-27

[Model changes were implemented based on the NUPEC M-4-3 modeling experience as follows. The CMT compartment was divided into two nodes joined at the narrow section by a flow path, with the intent of allowing flow to rise up from the side connected to the steam generator compartments. Circulation patterns still did not match expectations, since calculated circulation patterns suddenly changed at several times during the transient. The horizontal connection between the two CMT nodes was then split into two vertically-aligned, horizontal connections similarly to modeling the adjacent steam generator compartments in NUPEC. The double junction allows countercurrent flow through the connections between North and South CMT nodes. For each sensitivity case then, the plume was calculated to rise from the assumed break room(s) and flow passed down through the remaining openings in the operating deck to close the circulation loop with the rising plume.

The flow connections to the CMT North include a connection at the floor elevation in the CMT room to the RCDT Cavity (See Figure 9-47 node 102). The floor connection provides a path for entrainment of the heavier bulk mixture into the CMT North. Based on similarity to NUPEC as discussed above, it can be expected that break flow entering CMT North will rise and spread horizontally to rise from CMT South. The physical situation suggests that the lighter mixture from both CMT nodes would indeed rise from both CMT compartments. Thus, with the final Evaluation Model, results of the circulation sensitivities performed fit well with the simple qualitative observations discussed above.

Because the NUPEC tests are not exactly prototypical of the AP600 and **AP1000** intercompartment connections, there is some uncertainty in judging the correctness of the various calculated circulation patterns. However, as discussed above, the circulation patterns are reasonable based on expectations developed from a review of international larger scale tests. It can be concluded that it is reasonable to split the CMT at the pinch point into North and South nodes, and to treat the results of the lumped parameter calculation as valid sensitivities for a spectrum of circulation patterns.

Examination of the circulation patterns and steam concentration distributions of the sensitivity studies shows that a range of steam concentration time histories in the various compartments is calculated. From the range of sensitivities, an assessment can be made of the potential effects of circulation on containment pressure. The effect on pressure arises due to variations in internal solid heat sink usage for various transient distributions of steam. As discussed in Section 9.3.2.5, results of the sensitivities are used to select a limiting circulation scenario.

The acceptability of the CMT modeling method is based on the qualitative circulation being reasonable based on test experience, as described above. The lumped parameter formulation is generally accepted as reasonable for predicting total pressure when breaks are located relatively low in containment (Appendix 9.C, Section 9.C.3.4). On this basis, it is judged that the lumped parameter Evaluation Model is a reasonable tool to perform the sensitivity studies for various postulated LOCA DECLG break positions relatively low in containment.]^{a,c}

9.3 CIRCULATION AND STRATIFICATION ASSESSMENT FOR THE LOSS-OF-COOLANT ACCIDENT

The rupture of primary system piping can lead to a significant release of mass and energy into the containment. A containment analysis is performed to verify the ability of the passive containment systems to mitigate the consequences of a hypothetical LOCA. The WGOTHIC code, in conjunction with the Containment Evaluation Model, is used for the containment analysis. The effects of circulation and stratification must be bounded by the containment analysis calculations to ensure a conservative containment analysis. For purposes of evaluating the effects of circulation and stratification on the LOCA containment analysis, the LOCA event is divided into four temporal phases: the blowdown phase, the refill phase, the peak pressure phase, and the long-term phase, based on Section 3.4.2.2 of Reference 9.2.

The blowdown phase is the period immediately following the rupture of the primary system piping: For the design basis event, a double-ended, cold leg guillotine (DECLG) break is assumed, which results in the complete severance of the pipe. This phase is characterized by a rapid depressurization of the reactor coolant system (RCS), as the RCS inventory is expelled into the containment volume. The containment gas volume rapidly pressurizes due to the tremendous release of mass and energy. This phase is short in duration (about 30 seconds) and ends when the RCS pressure has equilibrated with containment.

The refill phase immediately follows blowdown. After blowdown, the accumulators refill the lower plenum of the reactor with a high flow rate of cold water. The resulting steam and water flow rates from the break are very low and increase with time. The mass and energy release rates are two orders of magnitude less than the blowdown rates, and can be approximated as 0 from approximately 30 to 90 seconds into the event. With a negligible steam source rate and a high condensation rate, the containment pressure drops by a few psi from its peak at the end of blowdown to the end of the refill phase at approximately 90 seconds. (It should be noted that the Evaluation Model used for sensitivity studies conservatively neglects the refill period.)

The phase following refill is the peak pressure phase. During the beginning of the peak pressure phase, a continuing pressurization of the containment building accompanies the release of mass and energy. Containment pressurization is mitigated by the containment volume and the presence of the substantial number of heat sinks inside containment. Hot steam condenses on the cold steel and concrete surfaces, which transfers energy into the heat sinks. As this phase continues, the temperature of the internal heat sinks increases and their effectiveness is reduced. By this time, however, water flow onto the containment shell has initiated. The PCS provides the path to the ultimate heat sink, and represents the only assumed path through which energy can be removed from inside the containment building. A key feature of the peak pressure phase is the second, more limiting, pressure peak. The combination of internal heat sinks and the PCS act to limit the containment pressurization, and containment pressure begins to drop. Later in this phase, the PCS becomes clearly dominant. The peak pressure phase extends from 90 seconds to about 1500 seconds when the containment pressure reaches its peak. During this phase, ADS Stage 4 actuates and becomes the source of mass and energy release.

The long-term phase is the period after the peak pressure occurs out to twenty-four hours and beyond. During the long-term phase, core decay heat continues to create steam, which exits the fourth stage automatic depressurization system (ADS) as a buoyant plume. The containment continues to depressurize

as a result of energy removed by the PCS. As containment pressure drops, internal heat sinks may begin to reject some of their heat back into the containment atmosphere. Thus the long-term phase depressurization is governed by PCS heat removal.

To facilitate an understanding of the relative positions of the various compartments, a simplified AP600 compartment diagram is provided in Figure 9-36. Figure 9-36 shows the relative location of various important compartments, such as the steam generator compartment, the core makeup tank (CMT) compartment, and the above-deck volume. Noding used to represent these compartments within the Evaluation Model is described in Section 4. The compartment features are discussed in Section 4 and summarized in Table 3-1 of Reference 9.2.

Figure 9-35 presents a diagram of the CMT compartment. The CMT room contains most of the below-deck containment heat sinks (approximately 52 percent of below-deck heat sinks by area). Although 48 percent of the heat sinks are not in the CMT room, no other single below-deck compartment contains as many heat sinks. Also, the CMT room is the largest (volume) of the below deck compartments and contains many flow paths. These flow paths mean that the CMT room is of significant importance with respect to both above- and below-deck circulation patterns. Therefore, the effect of circulation and stratification on heat sink utilization in the CMT room plays an important part in the transient pressure mitigation.

9.3.1 LOCA Break Scenarios

The DECLG rupture is the design basis LOCA event for the AP600 and AP1000. The circulation and stratification patterns associated with this break will depend on the direction of the break jet momentum. Although leak-before-break has been implemented, the conservative design basis analysis evaluation assumes the broken pipe can be pointed in any direction from its nominal position. Three scenarios may be postulated: the jet momentum is locally dissipated in the steam generator compartment, the jet exits undissipated up through the steam generator compartment, or the jet momentum is dissipated in the reactor coolant drain tank (RDCT) cavity (stairwell).

9.3.1.1 Jet Momentum Locally Dissipated in Steam Generator Compartment

During the blowdown phase, a tremendous amount of mass is released as shown in Figures 4-96 and 4-98 of Section 4.5.2 for AP600. For the case where the jet momentum is locally dissipated, the source flow rate is so high that it increases the local pressure by several psi. This results in a high-pressure source in the break compartment, with the fluid flow distribution governed by the relative resistances through flowpaths. This forces the source mixture through the RDCT cavity, CMT room, the steam generator compartments, and into the above-deck volume. Pressurization will also drive steam into dead-ended compartments during blowdown (See subsection 9.3.2.1). As the event progresses into the peak pressure phase, the source flow rate drops by two orders of magnitude. The jet momentum locally dissipates. This brings the source flow velocity to near zero, including a local pressure increase that is the same order of magnitude as the buoyant forces. The pressure source may be opposed or aided by buoyancy in other flow paths. The resulting flow pattern is the solution to the flow in a network with buoyancy and heat/mass transfer in the network branches. Superimposed on the large-scale flow, the mixture within a given compartment is most likely stratified (Reference 9-8).

Within compartments, the gas may stratify with air concentrating in lower regions and steam concentrating in upper regions, resulting in a vertical steam concentration gradient. If the circulation is sufficient to entrain significant bulk mixture, the gradient may be expected to be small. Entrainment-driven circulation rates in the CMT room are shown, for example, in Section 9.3.1.3. Significant circulation occurs over the height of the CMT room.

Stratification is expected in the containment based on LST data. Low Froude numbers during the long-term indicate a low kinetic energy buoyant plume source. This type of plume is not sufficiently energetic to disrupt stratification. The physics of buoyant plumes and wall layers leads to the existence of recirculating stratification (Appendix 9.C, Section 9.C.1.4.1) in the above-deck region. Plumes rise from the release point and entrain significant volume of mixture as they rise. The heavier bulk air/steam mixture is drawn through the top of the CMT and other deck openings and through compartments to be entrained into the rising plume. Stratification is assumed to have a negligible impact on heat removal in compartments which experience the already air-rich downflow. A very conservative assessment of the effects of stratification on heat removal through the steel shell by the PCS has been performed (Appendix 9.B). An extreme stratification gradient is assumed, to bound the potential for distortions in test data (9.2.3). The homogeneous case total heat sink utilization results are nearly equal to those for the stratified case, with the homogeneous case giving less than 0.5 percent less instantaneous heat removal rates. A simple bias of removing operating deck floors is included in the Evaluation Model to bound this effect.

The containment pressure was calculated for this case using the WGOTHIC AP600 Evaluation Model, (Section 4). It was assumed that the jet was dissipated in the East steam generator compartment, so no specific break orientation was modeled. The break was located in Volume []^{a,c} at elevation []^{a,c}. The results are discussed in Section 9.3.2.5.

9.3.1.2 Jet Directed Up With No Dissipation

A jet directed upward, that passes through the steam generator compartment undissipated, is considered unlikely. Releases are initially from the break and, later in the transient, releases exit from the fourth stage ADS and the break pipe is covered with liquid. The containment design calls for a steel plate to cover half the flow area in the steam generator compartment above the cold leg pipe and ADS Stage 4 valves. This plate and other structures in the steam generator compartment such as gratings, supports, and the steam generator itself make it doubtful that the break jet could pass through the steam generator compartment unobstructed. Despite the improbability of this scenario, it will be considered as an extreme case to support the selection of a limiting scenario for circulation and stratification.

For the case in which a jet is postulated to pass undissipated up through the steam generator compartment, there is no entrainment into the Steam Generator compartment due to chimney or momentum effects because these effects would act to dissipate the jet. An undissipated jet would enter the above-deck region at the top of the Steam Generator compartment with approximately the same diameter as the broken cold leg pipe. This scenario is similar to two of the LST MSLB configuration tests 222.3 and 222.4. To assess the effects relative to the mass transfer in the above-deck region, volumetric Froude numbers (Fr_v) for the undissipated jet are determined and compared to the LST. An examination of the magnitude of AP600 pressure improvements is provided with sensitivities, relative to condensation results discussed in Reference 9.9, Section 3.9.

For a LOCA DECLG, a postulated undissipated jet will have the same mass flow rate as the design basis LOCA DECLG exiting the top of the steam generator compartment. The two cases differ in the flow area and exit velocity. For the design basis case, the flow area is the area at the top of the Steam Generator compartment. For the undissipated jet, the flow area is the area of the cold leg pipe. For a constant mass flow rate, the product of the flow area times the exit velocity will be equal for the two cases ($U_{DECL} \times A_{DECL} = U_{UNDIS} \times A_{UNDIS}$, where U is the velocity, A is the area, subscript _{DECL} designates the design basis case, and subscript _{UNDIS} designates the undissipated jet case). Fr_v defined in Section 9.2 is proportional to $U^2 d^2$, and is therefore proportional to $U^2 A^2$. For the two cases, the other terms in the Fr_v equation will be the same and $Fr_{v-UNDIS}$ can be expressed in terms of Fr_{v-DECL} , using $U_{DECL} \times A_{DECL} = U_{UNDIS} \times A_{UNDIS}$. The relationship is $Fr_{v-UNDIS} = Fr_{v-DECL} (A_{DECL} / A_{UNDIS})^2$. The area of the top of the Steam Generator compartment is approximately $[]^{a,c}$, and the area of the cold leg pipe is approximately $[]^{a,c}$. This results in $Fr_{v-UNDIS} \approx Fr_{v-DECL} \times []^{a,c}$.

Reference 9.7, Section 6.5.2 presents Fr_v as a function of time for the design basis LOCA in Figure 6-2. At 24 hours Fr_v is approximately 3E-06 (the minimum value during the transient excluding the refill phase). For an undissipated jet, Fr_v is estimated to be 3E-06 x $[]^{a,c}$ which equals $[]^{a,c}$. This value is at the lower end of the LST Fr range in the MSLB configuration as shown in Reference 9.7, Figure 6-3. For such high values of Fr , data from the LST in the MSLB configuration (Section 9.2.2) shows that there is minimal deviation from a homogeneous steam concentration in the above-deck region. For the MSLB, Reference 9.9, Figure 3.9-5 shows that use of the Evaluation Model free convection correlation underpredicts condensation on shell surfaces by a factor of $[]^{a,c}$ for the LST. A multiplier of $[]^{a,c}$ is a reasonable factor to assess based on the data. To address postulated uncertainty in scaling the LST condensation results to AP600, a range of potential forced convection benefits in AP600 shell heat transfer are considered by examining the sensitivity of predicted containment pressure to condensation multipliers in the Evaluation Model. A sensitivity study examined the effects on containment pressure of using condensation multipliers of $[]^{a,c}$. These sensitivity cases show that taking credit for improved condensation provides a significant benefit in the calculated containment pressure. The results are discussed in Section 9.3.2.5.

9.3.1.3 Jet into RCDT Cavity (Stairwell)

During the blowdown phase, a jet into the RCDT cavity will create a pressure source in the RCDT cavity compartment. As with the jet dissipation in the East steam generator compartment, the high-pressure source will force fluid through all available openings. The source mixture will flow into the above-deck volume through both the CMT room and steam generator compartments. Following the blowdown phase, the source will rise from the RCDT cavity as a buoyant plume and split, based upon flow areas and resistances, with part of the flow rising through the West steam generator compartment and the remaining fluid flowing through the CMT compartment.

The post-blowdown flow split between the West steam generator and the CMT compartment will depend on flow areas and loss coefficients associated with both flow paths. A range of flow splits can be postulated varying from all the fluid rising through the steam generator compartments to all of the fluid rising through the CMT room and everything in between.

The first scenario is an extreme case which postulates that all the fluid rises through the West steam generator compartment. This scenario is identical to the scenario that assumes the jet momentum is locally dissipated in the East steam generator compartment. The case of the jet momentum dissipated in the East steam generator compartment is discussed in Section 9.3.1.1. The buoyant plume rising from the RCDT cavity into the West steam generator compartment is essentially the same scenario.

The second scenario is a split of the flow entering the RCDT cavity, with part of the break flow rising through the West steam generator compartment and part rising through the CMT compartment. The flow split is dependent on the relative flow path resistances. In this scenario, both the steam generator compartments and the CMT compartment would be subjected to a steam-rich break plume. The CMT and steam generator compartments contain the majority of the below-deck heat sinks. The flow split will result in good heat sink utilization subjecting both the steam generator compartments and the CMT compartment to the steam source. Thus, the case with the jet momentum dissipated in the RCDT cavity and a plume flow split between the CMT and steam generator compartments, will not be limiting. This is confirmed in the sensitivity calculations of Section 9.3.2.5.

The third scenario is an extreme case which postulates that the plume from the RCDT cavity rises into the CMT room. For this scenario, the buoyant plume rises from the floor to the ceiling of the CMT room, entraining gas from the bulk concentration present in the CMT room. An examination of entrainment into a CMT plume can be used to gain insight into the potential for stratification.

Calculation of CMT Room Plume Entrainment Rates

For the case of the LOCA jet being dissipated in the CMT room, the rate of entrainment of mixture in the CMT into the incoming break flow plume, Q_e , can be estimated based on the work of Peterson (Reference 9.15). In particular, Peterson gives the following relation for the volumetric entrainment rate into a buoyant plume,

$$Q_e = k_\mu * B^{1/3} * z^{5/3} \quad (9-1)$$

where k_μ is a constant equal to approximately 0.15, z is the height of the plume, and B is the buoyancy flux, given by:

$$B = g * \frac{(\rho_a - \rho_o)}{\rho_a} * Q_b \quad (9-2)$$

In this equation, g is acceleration due to gravity, ρ_a and ρ_o are the ambient fluid and injected fluid densities respectively, and Q_b is the volumetric flow rate from the plume source.

Substitution of equation (9-2) into equation (9-1) gives:

$$Q_e = k_\mu * \left[g * \frac{(\rho_a - \rho_o)}{\rho_a} * Q_b \right]^{1/3} * z^{5/3} \quad (9-3)$$

The ratio of entrained flow to break flow is therefore:

$$\frac{Q_e}{Q_b} = k_\mu * \left[g * \frac{(\rho_a - \rho_o)}{\rho_a} * \frac{1}{Q_b^2} \right]^{1/3} * Z^{5/3} \quad (9-4)$$

AP600 break flow rates for a LOCA DECLG at transient times of 460 seconds and 1,000 seconds are 1,070 ft³/sec and 266 ft³/sec respectively for steam. The injected fluid density is taken as the density of saturated steam at the CMT room pressure. These densities are 0.128 lb/ft³ (based on 54.6 psia at 460 seconds) and 0.135 lb/ft³ (based on 58 psia at 1,000 seconds). Ambient fluid density is taken as the total density of gas mixture in the CMT room at the times of interest. Inspection of the WGOTHIC output, from the sensitivity case which modeled the break in the CMT room (see Section 9.3.2.5), indicates densities of 0.158 lb/ft³ at 460 seconds and 0.165 lb/ft³ at 1,000 seconds in the CMT room. The height of the CMT room is 28.1 feet. Based on this data the applicable entrainment ratios, Q_e/Q_b , are 0.68 at $t=460$ seconds, and 1.7 at $t = 1000$ seconds.

An entrainment-driven circulation time constant for the CMT room is calculated by dividing the entrainment flow rate into the volume of the CMT. From above Q_e/Q_b is 0.68 when Q_b is 1066 ft³/sec and 1.7 when Q_b is 266 ft³/sec. Solving for Q_e gives a range of 725 to 452 ft³/sec for the entrainment rate. The volume of the CMT room is approximately 157200 ft³ and the resulting circulation time constant ranges from 217 seconds to 348 seconds (3.6 to 5.8 minutes). This range is relatively short compared to the time of ADS Stage 4 actuation (approximately 1000 seconds), when the steam source is relocated to the steam generator compartments.

Assessment of CMT Room Entrainment Circulation

The entrainment rate for this case is relatively large, increasing to over a factor of two relative to break flow later in time. Thus, a significant amount of CMT room mixture is entrained into the break as the plume rises to the ceiling. It may be concluded that vertical concentration gradients in the CMT room would be relatively small due to circulation within the room. It also may be concluded that the break flow circulates within the room, significantly increasing the room average steam concentration. Thus, high steam concentrations are expected in the CMT room compared to other break scenarios. The high steam concentrations for this scenario will result in high heat sink utilization for heat sinks in this important room.

With such low density mixture in the North CMT room, the chimney effect induces flow to the room from connecting flow paths at the floor elevation. Connecting flow paths from the Section 4 Evaluation Model are []^{a,c}, horizontally connecting to the steam generator compartments, and until the liquid level closes the path, []^{a,c} from the RCDT cavity (see Figure 9-47). The density head over almost 30 feet of height outside the CMT room strongly drives circulation through the CMT and upward in this scenario, suggesting that the flow should rise from the North CMT room into the above-deck region. There is little resistance to flow navigating past the CMT room pinch point to access the ceiling openings on the South CMT room opposite the stairwell, suggesting that flow would spread as it rises into the South CMT room, and then rise from all CMT deck openings. It is known from studies of building fires that very little pressure driving force is necessary to drive horizontal flow in a stratified room (References 9.10, 9.11, 9.12).

The effect of stratification on heat sink utilization is also evaluated. Room pressure, temperature, and steam concentrations were input into a separate calculation to assess the potential effect of stratification in the CMT room. For the calculation, the CMT room was divided vertically into three equal sections. Using free convection heat and mass transfer correlations, room heat sink energy removal was calculated for a room with a homogeneous steam concentration. The applied steam fraction was .63. For the second scenario, the CMT room was subjected to a stratified condition. The top region was assumed to be nearly all steam (steam fraction = 0.98), the middle region was assumed to have a nominal steam fraction (0.63), and the bottom region steam fraction was determined by conserving the total amount of steam in the total volume (0.28). Figure 9.B-3 shows the energy absorbed by the heat sinks in the CMT room for; 1) a stratified steam concentration with the CMT floor included, 2) a homogeneous steam concentration with the CMT floor included, and 3) a homogeneous steam concentration without the CMT floor included. As Figure 9.B-3 shows, the homogeneous concentration with the floor results in the most energy absorbed in the CMT room (top curve). The curve for the stratified concentration with the floor is close to the curve for the homogeneous concentration without the floor. The curve for the homogeneous concentration without the floor is more conservative (less energy absorbed) after 2000 seconds. Given the relative closeness of these two curves, and considering the extreme cases they represent, it is concluded that the lumped parameter Evaluation Model (which uses a homogeneous steam concentration in each volume) without floors provides a reasonably conservative model for heat sink utilization, accounting for the thermal effects of potential stratification. Information on the heat sink utilization calculations is presented in Appendix 9.B.

The break scenario with a buoyant plume flowing into the CMT compartment will not be a limiting scenario. The evaluation of this scenario has shown only small vertical concentration gradients are expected in the CMT compartment while a bias has nevertheless been implemented by removing the floor. Furthermore, high steam concentrations are expected in this compartment due to the large amount of entrainment and subsequent circulation driven by the break plume. The high steam concentrations will yield improved heat sink usage in this room. The scenario discussed in Section 9.3.1.1, with the jet momentum dissipated in the steam generator compartment, will have lower steam concentrations in the CMT room. Thus, the break scenario with a buoyant plume flowing into the CMT compartment will be bounded by the case with the break jet locally dissipated. To further confirm this conclusion, the results of a WGOTHIC analysis using the AP600 Containment Evaluation Model (Section 4), for a buoyant plume flowing into the CMT compartment, are discussed in Section 9.3.2.5. The analysis confirms that the buoyant plume rising into the CMT compartment is not a limiting scenario.

9.3.2 WGOTHIC Containment Evaluation Model for LOCA

The WGOTHIC Containment Evaluation Model uses lumped parameter nodding. Lumped parameter nodding simplifies the calculation by assuming homogeneous conditions in each network node. Lumped parameter formulation uses what may be called a scalar form of the momentum equations as follows. Here, momentum flow into each volume is parallel to the junction, and the terms perpendicular to the junction are discarded while junction momentum is dissipated within the volume. Momentum orientation is not tracked, and no turning losses are represented. During the LOCA blowdown phase, the high break mass flow pressurizes the steam generator compartment and flow exits based on relative loss coefficients. Such pressure-driven flows are reasonably modeled by the lumped parameter node-network formulation. Lumped parameter reasonably represents buoyancy and pressure-driven flows and the resulting large-scale circulations. The effects of stratification within each compartment or region can then be

superimposed on the large-scale circulation solution. The Containment Evaluation Models are described in Section 4 (AP600) and Section 13 (AP1000).

Comparison of lumped parameter GOTHIC results to test data, has shown lumped parameter nodding to be acceptable for LOCA breaks occurring in low zones of containment. Reference 9.13 discusses the test results and subsequent GOTHIC evaluation of the German Heissdampfreaktor (HDR) hydrogen mixing and distribution experiment E11.5. This experiment simulated a large-break LOCA in the lowest region of the HDR containment. The authors conclude that accident scenarios initiated by large-break LOCAs in the low zones of containments can be reliably predicted by the GOTHIC lumped parameter model using only a modest number of nodes (Appendix 9.C, Section 9.C.3.3). The DBA LOCA case models the break in []^{a,c} (lower East steam generator compartment) at the []^{a,c} elevation.

The conclusions concerning the use of a lumped parameter for low breaks modeled by GOTHIC, can be readily applied to WGOTHIC because of the similarity between the two codes. WGOTHIC is a descendant of the GOTHIC code. The difference between the two codes relates to the heat and mass transfer correlations applied to WGOTHIC by Westinghouse, to model the PCS phenomena for the passive containment design. Thus, since the LOCA scenarios of interest are breaks in the lower region of containment, it is reasonable to use WGOTHIC lumped parameter to model these events.

As discussed previously, the LOCA event is divided into four phases: the blowdown phase, the refill phase, peak pressure phase, and the long-term phase. These phases are discussed in Subsections 9.3.2.1 through 9.3.2.4.

9.3.2.1 Blowdown Phase (0 to 30 seconds)

The lumped parameter solution during blowdown is a node-network solution, governed by pressure differences and flow resistances between nodes. The mass and energy release in the Evaluation Model acts as a high-pressure source that forces the steam out through flowpaths connected to the source node. The Evaluation Model also assumes only free convection on inner containment surfaces. Based on high kinetic energy during blowdown (Reference 9.7, Figure 6-2) significant enhancement to mass transfer due to forced convection occurs (Section 9.2.2). The steam is driven into the below-deck region and the above-deck volume. Figure 9-37 shows the calculated steam concentration of various containment regions during the blowdown phase, using the Evaluation Model described in Section 4 with a dissipated break in the SG East compartment.

The paragraphs in this subsection describe several sensitivity cases and an evaluation performed to examine various aspects of the blowdown phase. The first sensitivity case examines the effect of modeling a containment with a homogeneous steam concentration on the calculated containment pressure. The second sensitivity case examines the effect of removing all internal heat sinks on the calculated containment pressure. Following this sensitivity case, an evaluation of heat sink utilization in dead-ended compartments is performed. The final sensitivity case examines the effect of varying the flow pattern and steam concentrations on the calculated containment pressure.

To show the relative insensitivity to stratification, or heat and mass transfer coefficient during blowdown, a comparison is needed between the containment pressure response predicted by this node-network solution, and the containment response predicted for a homogeneous containment. Section 8, Figure 8-1 compares the LOCA blowdown pressure results of a one-node WGOTHIC AP600 model to the node-network solution. The one-node model assumes the same total containment volume and containment heat sinks as the multi-node model. Both models predict essentially identical containment pressure responses during the blowdown phase. Therefore, the details of the flow connections and heat mass transfer rates for the multi-node Evaluation Model are not important with respect to the containment pressure results because volume compliance is the dominant pressure mitigator during blowdown.

During the blowdown phase, the mass and energy release is mitigated primarily by containment volume via the rapid pressurization of the containment building. Figure 8-2 shows a comparison of the AP600 Evaluation Model results for the blowdown phase versus an identical model with all internal heat sinks removed. At the end of blowdown (30 seconds), the difference between these two cases is about 3 psi, accounting for only 10 percent of the pressurization. Thus, in the Evaluation Model, the blowdown mass and energy release increases containment pressure by about 35 psi, while the containment heat sinks absorb approximately 3 psi worth of energy. Clearly, the dominant mechanism during blowdown is the pressurization of containment.

The heat sink effectiveness in the presence of a stratification gradient is evaluated in Appendix 9.B. To conservatively account for the reduced effectiveness of heat sinks in lower room areas, floors are eliminated in the WGOTHIC Containment Evaluation Model throughout the transient.

The effectiveness of heat sinks in dead-ended compartments is also evaluated. Since only one opening exists for these compartments, interaction with overall containment volume is expected to be minimal unless the compartments have non-uniform temperatures. During blowdown, these compartments pressurize along with the rest of containment. Steam/air mixture from the bulk containment volume flows into the dead-ended compartments during the initial pressurization. Once pressurized, additional steam/air flow into the dead-ended compartments only occurs to make up for steam condensing in the compartment. Analysis of the Nuclear Power Engineering Corporation (NUPEC) natural circulation test, M-4-3, showed that asymmetric heating of dead-ended compartment walls can lead to natural circulation flows within the compartment (Reference 9.14). However, a conservative evaluation of dead-ended compartments would consider no thermally driven circulation. In such a case, inside the compartments, the condensation of steam leaves behind a heavier air-rich mixture. The air flows to the bottom and blankets the lower heat sinks. The poor circulation within the dead-ended compartments leaves the air-rich layer relatively undisturbed. As steam continues to condense, the air-rich layer continues to build up and will result in significant stable stratification within the dead-ended compartments. Although the heat sinks in the dead-ended compartments will contribute somewhat to containment heat removal, to conservatively bound the effects of stratification, condensation and convection on the heat sinks in the dead-ended compartments are neglected after 30 seconds in the Evaluation Model.

Based on the results of the evaluation, it has been demonstrated that blowdown pressure history is relatively insensitive to the effects of circulation and stratification. The internal heat sinks do heat up during blowdown, however, as discussed above, containment volume pressurization is the dominant mechanism for absorbing the energy released. Since volume pressurization is the governing process, blowdown pressure response is not sensitive to circulation and stratification effects. The Evaluation

Model utilizes a conservative lower estimate of containment free volume. Thus, the uncertainties in heat and mass transfer or stratification, and flow path effects, do not significantly impact the LOCA blowdown pressure history and the Evaluation Model adequately models the LOCA blowdown phase.

To assess the effects of varying the steam concentrations and flow rates on the calculated containment pressure, a sensitivity was performed which varied several loss coefficients in the Evaluation Model. This sensitivity shows how changes in conditions during the blowdown phase affect the later phases and, in particular, the calculated containment pressure. For this sensitivity, the AP600 Containment Evaluation Model (Section 4), with a dissipated jet in the SG East compartment, was used and the loss coefficients [

] ^{a,c} Figure 9-38 shows the pressure transient for this sensitivity case. The maximum calculated pressure is 43.8 psig, which is 0.1 psi less than the 43.9 psig reported in Section 9.3.2.5.

Circulation plots for this sensitivity case are presented in Figure 9-39 through Figure 9-42. Compared to the circulation plots for the dissipated jet in the SG East compartment (Figure 9-47 through Figure 9-50), the effects of the revised loss coefficients are evident. At 20 seconds, Figure 9-39 shows that most of the break flow goes from the SG East compartment to the SG West compartment, and through the RCDT cavity to the North CMT room. At 1000 seconds (Figure 9-40), flow is rising from both SG compartments and a steam/air mixture is flowing down into the North and South CMT volumes. Figure 9-48, shows flow rising only from the SG East compartment. At 1550 and 80050 seconds (Figure 9-41 and Figure 9-42) the ADS Stage 4 valves are the source of the steam releases and the flow patterns are similar to those in Figure 9-49 and Figure 9-50. This sensitivity altered the flow patterns and steam concentrations early in the transient by changing some of the flow path loss coefficients. The change in calculated maximum pressure was negligible.

9.3.2.2 Refill Phase (30 to 90 seconds)

The refill phase immediately follows blowdown. After blowdown, the accumulators refill the lower plenum of the reactor with a high flow rate of cold water. The resulting steam and water flow rates from the break are very low and increase with time. The mass and energy release rates are two orders of magnitude less than the blowdown rates, and can be approximated as 0 from approximately 30 to 90 seconds into the event. With a negligible steam source rate and a high condensation rate, the containment pressure drops by a few psi from its peak at the end of blowdown to the end of the refill phase at approximately 90 seconds. For the calculation of maximum containment pressure, the Evaluation Model conservatively neglects the refill period.

9.3.2.3 Peak Pressure (90 to 1200 seconds)

During the peak pressure phase, the location of the steam releases changes from the break to the ADS Stage 4 valves in both steam generator compartments. The Evaluation Model includes this change in steam release location. In addition, the lower compartments begin to fill with liquid from the break. The reduced heat transfer area due to filling is accounted for in the Evaluation Model. Figure 9-43, for a jet dissipated in the SG East compartment, shows that the condensation on the steel becomes the dominant mechanism for heat removal towards the end of the peak pressure phase.

The evaluation of break scenarios in Section 9.3.1 led to the conclusion that the case with jet momentum dissipated in the steam generator compartment may lead to stratification within compartments after the blowdown phase. Given this possibility, it is necessary to show that the Evaluation Model bounds the possible effects of this stratification. Lumped parameter models assume no gradients within each volume of the network. Thus, in the Evaluation Model, all heat sinks within a compartment volume see identical environmental conditions. In contrast, actual conditions may lead to a stratified compartment with a region of higher steam concentration on top and lower steam concentration near the bottom. For the effects of stratification on heat sink utilization, the most significant heat sinks are the above-deck region (containment shell) and the CMT room (steel and jacketed concrete). The compartment features are discussed in Sections 4 and 13 and summarized in Table 3-1 of Reference 9.2. In Section 9.3.1.3, the CMT room was assessed for its sensitivity to stratification. In this calculation, heat sink usage was calculated for a homogeneous room and a severely stratified room. A bias has been defined to bound the potential effects of stratification in compartments as discussed in 9.3.1.3. In Section 9.3.1.1, the containment shell was assessed for its sensitivity to stratification. A bias has been defined to bound the potential effects of stratification above-deck as discussed in Section 9.3.1.1. Appendix 9.B discusses the calculations performed.

Based upon the results of the evaluation, a method to bound circulation and stratification effects for the peak pressure phase has been developed. In the Evaluation Model, all floors are neglected throughout the transient and condensation and convection on all heat sinks in dead-ended compartments are neglected after 30 seconds (refer to Section 9.3.2.1).

9.3.2.4 Long-Term Phase (1200 seconds to 24 hours)

Figure 9-43 shows the condensation on the steel shell remains the dominant mechanism for heat removal during the long-term. The results shown are from the AP600 Containment Evaluation Model (Section 4) with a dissipated jet in the SG East compartment. During early portions of the transient, internal heat sinks are the primary path of containment heat removal. As the transient progresses, the temperature of the heat sinks increases and their heat removal effectiveness is reduced. PCS heat removal, which dominates in the long-term, is dependent on steam concentrations. The effects of stratification on the containment shell heat removal have been evaluated in Section 9.3.1.1 and a bias of removing operating deck floors has been included in the Evaluation Model.

In addition, WGOTHIC predicts a slight gradient between the upper and lower compartments (excluding dead-ended compartments). Figure 9-44 shows WGOTHIC predicted steam concentrations for various compartments in the AP600, using the Evaluation Model (Section 4) with a dissipated jet in the SG East compartment. As Figure 9-44 shows, at 24 hours WGOTHIC predicts a homogeneous above-deck region. However, WGOTHIC predicts a slightly lower steam concentration below the operating deck, excluding the SG compartments which continue to have steam release through the ADS Stage 4 valves.

The trend over time for the WGOTHIC calculations leads to a very small steam density gradient between above- and below-deck compartments. The WGOTHIC predicted average steam concentration above the operating deck is approximately 0.47 at 24 hours. Below the operating deck, the average is approximately 0.46 at 24 hours excluding the SG compartments. The calculated steam concentration for a homogeneous condition between the above-deck region and the below-deck open compartments is approximately 0.468. There is a negligible change between the WGOTHIC calculated above-deck steam concentration and the

calculated homogeneous concentration (excluding dead-ended and SG compartments). Since the predicted stratification is slight, and since the volume of the above-deck regions is significantly greater than the below-deck open compartments, mixing the above-deck volume with the below-deck open compartments does not significantly change the above-deck steam concentrations. Thus, the WGOTHIC predictions as the transient calculation passes through 24 hours are essentially similar to the assumption of a homogeneous containment. It is conservative to not include the steam generator compartment steam concentration in the homogeneous calculation.

It is concluded that WGOTHIC predicts a slight segregation between the above- and below-deck regions, but the deviation from the homogeneous assumption is insignificant. Based upon the results of the evaluation, it has been shown that the Evaluation Model adequately bounds the effects of circulation and stratification during the long-term phase.

9.3.2.5 Evaluation Model Results

Sensitivities have been performed using the lumped parameter AP600 Containment Evaluation Model (Section 4) for several postulated, plausible break locations. An evaluation of the sensitivities leading to selection of a limiting scenario for design basis accident calculations follows.

It has been determined that to bound circulation and stratification effects, floors are neglected throughout the transient, and condensation and convection on all heat sinks in the dead-ended compartments are neglected after blowdown. The stratification of steam and air within compartments may reduce heat sink effectiveness. These biases are included in the Evaluation Model used to perform sensitivities.

Undissipated Jet Rising in SG East Compartment

The postulated, undissipated jet directed up the Steam Generator compartment results in increased heat and mass transfer, possibly as high as a factor of []^{a,b} over the steel shell surface based on the LST, compared to that using the free convection correlation in the Evaluation Model, as discussed in Section 9.3.1.2. To estimate the potential benefit for AP600, the heat transfer coefficient multipliers for the inner surfaces of the clime conductors (that is, only the steel shell mass transfer is enhanced) were increased to []^{a,c} times the Evaluation Model values. The Evaluation Model with the break in the steam generator East compartment was used for the sensitivity cases. The postulated, undissipated jet will only occur until the ADS Stage 4 valves are opened at approximately 1000 seconds. Therefore the containment pressure response is plotted for the first 1000 seconds of the LOCA. The containment pressure sensitivity results are shown in Figure 9-45, along with the Evaluation Model results. The results show that the pressure response during the blowdown phase is the same for all cases. This is expected because volume compliance is the dominant pressure mitigator during blowdown (Section 9.3.2.1). Compared to the Evaluation Model results at 1000 seconds, the calculated containment pressure for the []^{a,c}. These results show that a substantial benefit in containment pressure is gained when the heat transfer coefficient is increased to account for the forced convection from an undissipated jet. Therefore, this case will be less limiting than the other postulated break scenarios in which the jet is dissipated.

Dissipated Jet Rising in SG East Compartment

Another postulated break scenario, the design basis case, is a dissipated jet in the SG East compartment (Volume 107, elevation 100 ft.). Figure 9-46 shows the results of the WGOTHIC AP600 Containment Evaluation Model which includes the circulation and stratification biases. Assuming the break momentum is dissipated in the broken loop steam generator compartment, a maximum containment pressure of 43.9 psig is calculated, which is below the design pressure of 45 psig. The pressure transients for compartments directly connected to the SG East compartments are shown in Figure 9-46A. Figure 9-47 through Figure 9-50 show the circulation pattern predicted by WGOTHIC for this case at different times during the transient. The figures show the Evaluation Model flow path connections for the below-deck volumes, the flow rates and directions, volume steam pressure ratio, and liquid level. Figure 9-51 is a depiction of each of the flow connections to the above-deck volumes. In subsequent figures, total flows through the ceiling of each compartment are shown for simplicity. Flow paths that have been grouped have the same flow direction. Figure 9-47 presents data at 20 seconds which is near the end of blowdown. Flow is forced into all of the below-deck volumes and into the above-deck volumes from the East and West steam generator compartments and the North and South CMT rooms. Figure 9-48 presents data at 1000 seconds which is near the time of maximum pressure and prior to ADS Stage 4 valve actuation. Flow to the dead-ended compartments has stopped. The general circulation pattern is fluid from the break flowing up through the SG East compartment while a steam/air mixture is drawn into and through the SG West compartment, the North and South CMT rooms, and the RCDT cavity into the SG East compartment. At 1500 seconds, Figure 9-49 shows the change in circulation pattern due to the actuation of the ADS Stage 4 valves. The steam releases flow up through both steam generator compartments while a steam/air mixture is drawn into and through the CMT rooms and the RCDT cavity. This flow pattern develops less than 2 minutes after ADS Stage 4 activation. Figure 9-50 shows the circulation pattern near 24 hours. The flow rate out of the ADS Stage 4 valves is approximately one-fourth of the flow at 1500 seconds. The flow pattern remains out of the SG compartments and into the CMT rooms, however, flow through the RCDT cavity has ceased, due to liquid level rising above the top of the flow path.

Plume Rising in CMT Room

In Section 9.3.1.3, the LOCA with jet dissipation in the RCDT cavity was postulated. It was postulated that the entire buoyant plume rises into the North CMT compartment. The evaluation concluded this scenario was not limiting because of the higher steam concentrations expected in the CMT compartment, which would result in better internal heat sink utilization. Furthermore, the evaluation concluded that the relative steam densities would drive the steam to navigate the bend in the CMT compartment. This would lead to a steam-rich environment for the heat sinks in the south end of the CMT room opposite the stairwell. To confirm that this scenario is not bounding, a WGOTHIC calculation was performed using the AP600 Containment Evaluation Model (Section 4). The calculation assumed a LOCA where the jet plume dissipates and rises into the North CMT compartment. This was simulated by applying the break boundary conditions to the North CMT node (Volume 6, elevation 107 ft.), the only change made to the Evaluation Model. The circulation and stratification biases of neglecting floors throughout the transient and condensation and convection in dead-ended compartments following blowdown were included. The containment pressure results of this evaluation are shown in Figure 9-52. The maximum pressure was calculated to be 43.7 psig. As expected, this pressure is below the previous scenario where momentum is dissipated in the East steam generator compartment. The circulation pattern predicted by WGOTHIC is shown in Figure 9-53 and Figure 9-54.

Figure 9-53 presents data at 1000 seconds which is near the time of maximum pressure and prior to ADS Stage 4 valve actuation. Compared to Figure 9-48 (break in SG East compartment), Figure 9-53 shows flow out of the North and South CMT rooms into the above-deck region, while a steam/air mixture flows down into both SG compartments and up through the RCDT cavity into the North CMT room. Figure 9-54, at 1400 seconds, shows the change in flow pattern due to ADS Stage 4 valve actuation. The flow rates and pattern are similar to those in Figure 9-49, as expected. Figure 9-55 shows the heat sink utilization for this sensitivity case. As expected, Figure 9-55 shows a greater CMT room (Volumes 6 and 104) heat sink utilization than that shown in Figure 9-43 for a break in the SG East compartment. Both figures show that the PCS shell is the dominant heat sink at the time of maximum containment pressure and beyond.

Plume Rising in RCDT Cavity

In Section 9.3.1.3, a LOCA with jet dissipation in the RCDT cavity was postulated. This scenario assumed the break flow splits between the CMT and steam generator compartments. The evaluation concluded that good below-deck heat sink utilization is expected because of the high steam concentrations in the CMT and steam generator compartments. A WGOTHIC calculation was performed for this scenario using the AP600 Containment Evaluation Model (Section 4). The calculation simulated the flow split by placing the break boundary condition directly in the RCDT cavity []^{a,c}. The circulation and stratification biases were included. The pressure prediction from the evaluation is shown in Figure 9-56. The maximum pressure was calculated to be 43.4 psig. This pressure is below both of the previously discussed sensitivities. The WGOTHIC predicted circulation pattern is shown in Figure 9-57 and Figure 9-58.

Figure 9-57 presents data at 1000 seconds which is near the time of maximum pressure and prior to ADS Stage 4 valve actuation. With the break in the RCDT cavity, the bulk flow distribution is based on the path areas and loss coefficients. Consequently, at 1000 seconds, the steam flow from the break goes up through the CMT rooms, while a steam/air mixture flows down through both SG compartments and into the North CMT room and RCDT cavity. Figure 9-58, at 1500 seconds, shows the change in flow pattern due to ADS Stage 4 valve actuation. The flow rates and pattern are similar to those in Figure 9-49, as expected. Figure 9-59 shows the heat sink utilization for this sensitivity case. Compared to Figure 9-43 for a break in the SG East compartment, Figure 9-59 shows a small delay in the heat absorption from the SG East compartment and the CMT rooms. The heat absorption from the SG West compartment starts a little sooner in Figure 9-59. The effects are due to the break location differences. Consistent with the other cases, Figure 9-59 shows that the PCS shell is the dominant heat sink at the time of maximum containment pressure and beyond.

9.3.2.6 Evaluation of Drops During a LOCA

Drops, or fog particles, are created when the blowdown break source steam velocity is large enough to disperse a fraction of the break liquid along with the gas. As discussed in Reference 9.2, Section 4.4.2D and Reference 9.7, Section 7.1, drops will be formed during the LOCA blowdown phase. For the post-blowdown phases of a LOCA and for the main steamline break (MSLB), there will not be any significant drop formation. The thermal and circulation effects of drops on LOCA containment pressure are examined in Appendix 9.A and summarized below.

Drop fall times for various size drops were determined in Appendix 9.A, which only account for the gravitational effects on the drops. Fall times range from seconds to hours depending on the drop size and fall height. This provides an indication that the drops will exist long enough that their effect on containment pressure must be considered. In addition, Appendix 9.A estimated plume entrainment rates for 0 percent and 100 percent of the break liquid converted to drops. The entrainment rates and subsequent circulation time

constant for both 0 and 100 percent drops show that a large fraction of the containment volume will be entrained in the plume within a few minutes, which is relatively short compared to the time to reach maximum pressure (at approximately 1200 seconds), and very short compared to long-term cooling. A relatively large entrainment rate within the above-deck region indicates that the steam density gradients above-deck are not large whether drops exist or not. Therefore, the presence of drops will not significantly affect the general circulation and stratification patterns in the containment atmosphere.

Section 5.8 shows the results of sensitivity cases to assess the Evaluation Model treatment of the thermal effects of drops with respect to containment pressure. The results that show the Evaluation Model assumption of 50 percent of the break liquid being converted into drops provides essentially the same containment maximum calculated pressure as assuming 100 percent of the liquid is converted into drops.

The 50 and 100 percent drop fractions are both more limiting with respect to maximum pressure than assuming none of the break liquid is converted into drops.

The formation of drops during the LOCA blowdown phase is a physically real phenomenon which may influence the maximum containment pressure calculated by the Evaluation Model. Drop formation increases the effective density of the containment atmosphere due to the close coupling between small drops and gas by shear forces, making the post-blowdown releases relatively more buoyant. A small percentage ($\geq 5\%$) of the blowdown break liquid formed into drops is sufficient to saturate the containment atmosphere, at which point, additional drop density has a minor thermal effect. The Evaluation Model treatment of drops, as described in Section 4.5.2.1 and Section 13.6.2.1, provides a sufficiently bounding calculation for maximum and long-term containment pressure.

Deleted: 5

9.4 MAIN STEAMLINE BREAK (MSLB)

The main steamline transports steam from the steam generators within the containment building to the turbine generators in the auxiliary building. The main steamline path begins at the top of the steam generator, where it bends 180° and follows a downward path to the CMT room. In the CMT room, the steamline bends 90°, crosses through the CMT room, and exits the building through a penetration in the

containment shell. Rupture of the main steamline inside containment would release high energy steam into the containment. To confirm the design adequacy of the containment, various MSLB scenarios are examined to develop a conservative model accounting for the effects of circulation and stratification in the containment pressure calculations.

9.4.1 Break Locations

An evaluation of circulation and stratification must allow for the consideration of possible break locations. For the MSLB, two distinct break locations may be postulated: a break in the steamline above the operating deck or a break in the steamline in the CMT compartment.

9.4.1.1 MSLB Above the Operating Deck

An MSLB above the operating deck could occur anywhere in the steamline piping from the top of the steam generator to the operating deck penetration into the CMT compartment.

The design basis MSLB mass and energy releases for containment pressure assume a 1.388 ft² break (due to integral flow limiters). The MSLB event is characterized by a high energy release of short duration. Reference 9.7, Figure 6-3 shows the calculated Froude numbers for the event compared to Froude numbers calculated for the LST. The high Froude numbers indicate a high kinetic energy source which is expected to drive circulation above and below the jet source elevation. High Froude numbers also indicate that a significant forced convection enhancement to mass transfer occurs during an MSLB.

An examination of releases from smaller sized breaks in main steamlines indicates that the reduction in mass flow is more than offset by the reduction in exit flow area. Therefore, the larger size breaks have the lowest Froude numbers. The double-ended rupture MSLB has the limiting combination of mass and energy release and Froude numbers.

9.4.1.2 MSLB in the CMT Compartment

A steamline rupture in the CMT compartment would propel a high momentum steam jet into the CMT room. Since the break is within an enclosed compartment, momentum from the jet would be dissipated by the equipment, walls, floors, and ceilings of the CMT room. The effect would create a pressure source in the CMT compartment with the fluid following the path of resistance through the node network into adjacent compartments and the above-deck volume.

The steam source in the CMT compartment will create a steam-rich environment for this room which contains many heat sinks. The high steam concentration will result in excellent heat sink utilization for this scenario.

The MSLB in the CMT compartment case is bounded by the scenario of an MSLB occurring above the operating deck. While the break above the operating deck does produce substantial circulation, the steam concentrations in the CMT compartment will not approach the steam levels for a break directly within the CMT room. Thus, the MSLB in the CMT compartment is not the bounding scenario. To confirm this conclusion, Section 9.4.3 presents the results of a WGOTHIC analysis for a break in the

CMT compartment. As expected, the containment peak pressure is lower for the MSLB in the CMT compartment than for an MSLB above the operating deck.

9.4.2 WGOTHIC Containment Evaluation Model for MSLB

In creating an appropriate and conservative Evaluation Model, it is necessary to understand how the code handles circulation, to bias the model to produce bounding but reasonably representative results. Investigation of the lumped parameter AP600 Containment Evaluation Model (Section 4) has shown that this nodding structure tends to mix upwards from the break elevation.

The lumped parameter calculational bias may be attributed to the use of multiple, relatively large lumped parameter nodes to represent the above-deck region in the Evaluation Model. Lumped parameter formulation uses what may be called a scalar form of the momentum equations, as follows. Here, momentum flow into each volume is parallel to the junction, and the terms perpendicular to the junction are discarded while junction momentum is dissipated within the volume. Momentum orientation is not tracked, and no turning losses are represented. This momentum dissipation is the characteristic of the lumped parameter nodding which results in the calculated stratification above/below the jet. With momentum diffused throughout the volume node, the vigorous circulation from the high kinetic energy jet does not occur in the model. Circulation above the jet source in the lumped parameter model is driven by the density head terms in the momentum equation which cannot drive flow below the source. Thus, lumped parameter nodding predicts a steam-rich atmosphere above the assumed source elevation, and a steam-deficient atmosphere below this source elevation (simulating stratification).

With an understanding of both the physics, and lumped parameter model biases, a WGOTHIC representation is constructed which conservatively represents the accident scenario. The high kinetic energy of the MSLB will tend to circulate steam through the above-deck portion of the containment vessel and lead to forced convection conditions for the shell. The lumped parameter Evaluation Model, however, calculates a steam-rich region above the injection point and an air-rich region below this point. Figure 9-60 shows the steam concentration results of a WGOTHIC MSLB calculation using the AP600 Containment Evaluation Model with the source entering []^{a,c}, which is just above the operating deck (refer to Section 4.5.2.2). The model predicts a small steam density gradient above-deck, consistent with the expectation of only small gradients in the AP600, based on LST data (see Section 9.2.2). Evaluation has shown that the effect on shell mass transfer of even extreme stratification, beyond that expected for the AP600 or **AP1000** (see Section 9.3.1.3), is very small. Very little steam penetrates into the below-deck region in the model. Steam access into the below-deck compartments in the model is governed only by the volume pressurization. As the mass and energy releases pressurize the above-deck region, a steam/air mixture from above-deck is pushed into the below-deck compartments. The use of the WGOTHIC lumped parameter model, with an injection point just above the operating deck, results in a conservative Evaluation Model for the steam line break as a result of reduced steam access to the below-deck heat sinks. The reduced steam access is due to the momentum dissipation in the model which reduces the calculated circulation to the nodes below the operating deck. The Evaluation Model neglects any heat and mass transfer contribution from forced convection, so above-deck velocity predictions become unimportant. Mass transfer is seen to be underestimated by as much as a factor of []^{a,c} on the steel shell surface relative to forced convection in the LST. To add an additional conservative bias, the stratification heat sink biases developed for LOCA scenarios are also included

9.4.3 MSLB Sensitivity Results

Based on an evaluation of circulation and stratification, an MSLB Evaluation Model has been constructed to bound circulation and stratification effects. The limiting MSLB scenario assumes a pipe break above the operating deck. In this scenario, test data indicates that the high kinetic energy source jet induces circulation above and below the jet elevation, including substantial steam penetration into below-deck compartments. The lumped parameter Evaluation Model, that bounds circulation and stratification, places the break source directly above the operating deck []^{a,c}. This results in a well-circulated upper region with little steam access to the heat sinks below the operating deck. To further bound circulation and stratification effects, stratification heat sink biases developed for LOCA scenarios are included (see Table 9-1). Figure 9-61 shows the results of the AP600 WGOTHIC MSLB Evaluation Model described above. A containment peak pressure of 44.8 psig is calculated, which is below the design pressure of 45 psig.

In Section 9.4.1.2, the MSLB in the CMT compartment scenario was evaluated, concluding that increased circulation below the operating deck would reduce the calculated containment pressure. This scenario was determined not to be the limiting scenario, because of the high steam concentrations expected in the CMT compartment. The high steam concentration would result in improved heat removal rates by the heat sinks in the CMT compartment. To confirm this hypothesis, a WGOTHIC analysis was performed for a break in the CMT compartment []^{a,c}. As with the break above the operating deck, LOCA stratification biases were included. Figure 9-62 shows the results of the WGOTHIC calculation. A containment peak pressure of 43.2 psig is calculated, which is 1.6 psi less than the peak pressure for the MSLB above the operating deck. As expected, the Evaluation Model predicts the MSLB above-deck to be the limiting location.

9.5 CONCLUSIONS

A WGOTHIC Containment Evaluation Model is used which considers circulation and stratification in the calculation of LOCA and MSLB containment pressures and temperatures. The effects of circulation and stratification on the calculated containment pressure have been examined, and biases have been defined for the Evaluation Model. The Evaluation Model input deck and specific biases are described in Sections 4 and 13. In addition, break locations have been examined for LOCA and MSLB to determine the limiting location for each transient with respect to calculated containment pressure.

The following biases have been incorporated into the Evaluation Model for the LOCA analysis based on the circulation and stratification evaluations documented in this section:

- Heat and mass transfer from floors of compartments and the operating deck have been removed to bound the potential reduction in heat transfer due to stratification. Refer to Sections 9.3.1.1, 9.3.1.3, and Appendix 9.B.
- Condensation and convective heat transfer in dead-ended compartments are turned off after 30 seconds (i.e., after blowdown) to bound the potential reduction in heat transfer due to stratification. The basis for this bias is provided in Section 9.3.2.1.

- The lumped parameter Evaluation Model considers only free convection for internal heat sinks and shell surfaces and, therefore, conservatively neglects the increase in mass transfer to the containment steel shell due to forced convection during blowdown. Refer to Section 9.3.2.1.

Ranges of LOCA break locations and jet directions were evaluated to determine the limiting case with respect to containment pressure. The limiting scenario is the DECLG break in the East steam generator compartment with the jet momentum locally dissipated. Other break locations, or jet directions, result in increased heat sink utilization which results in lower calculated containment pressures. Based on the results presented in Section 9.3.5.2, the calculated maximum LOCA containment pressure from a dissipated jet is not very sensitive to the break location since internal heat sinks “reach maximum effectiveness” well before the time of maximum pressure.

The following biases have been incorporated into the Evaluation Model for the MSLB analysis based on the circulation and stratification evaluations documented in this section:

- The break is placed in a node at the operating deck level to minimize circulation and steam access to below-deck heat sinks, which bounds the potential reduction in heat transfer in below-deck compartments due to stratification. This is discussed in Section 9.4.2.
- The lumped parameter Evaluation Model considers only free convection for internal heat sinks and shell surfaces and, therefore, conservatively neglects the increase in mass transfer to the containment steel shell due to forced convection during the entire transient. Refer to Section 9.4.2.
- The above listed LOCA biases (relative to floors and dead ended compartments) have been included in the MSLB Evaluation Model to further conservatively bound potential reductions in heat transfer due to stratification. Refer to Section 9.4.3.

Based on the routing of the steamline pipe, two MSLB locations were evaluated; a break above the operating deck and a break in the CMT room. As discussed in Section 9.4.3, the break above-deck resulted in the higher calculated containment pressure. The break in the CMT room had increased heat sink utilization in the CMT room which resulted in the lower calculated containment pressure.

The above biases are incorporated into the Evaluation Model as described in Sections 4.2 and 13.2, subsections entitled “Special Modeling Assumptions.” Therefore, the effects of circulation and stratification have been conservatively bounded in the WGOTHIC containment pressure calculations.

9.6 REFERENCES

- 9.1 WCAP-14382, "WGOTHIC Code Description and Validation," May 1995.
- 9.2 WCAP-14812, "Accident Specification and Phenomena Evaluation for AP600 Passive Containment Cooling System," Revision 2, April 1998.
- 9.3 NTD-NRC-95-4563, "GOTHIC Version 4.0 Documentation, Enclosure 2: Technical Manual," September 21, 1995.
- 9.4 NTD-NRC-95-4563, "GOTHIC Version 4.0 Documentation, Enclosure 3: User Manual," September 21, 1995.
- 9.5 WCAP-13566, "AP600 1/8th Large-Scale Passive Containment Cooling System Heat Transfer Test Baseline Data Report," October 1992.
- 9.6 WCAP-14135, "Final Data Report for PCS Large-Scale Tests, Phase 2 and Phase 3," Revision 1, April 1997.
- 9.7 WCAP-14845, "Scaling Analysis for AP600 Containment Pressure During Design Basis Accidents," Revision 3, March 1998.
- 9.8 Wolf, L., Gavrilas, M., Mun, K., 1996, "Overview of Experimental Results for Long-Term, Large-Scale Natural Circulations in LWR-containments after Large LOCAs," DOE - Project, Order Number: DE-AP07-96ID10765, University of Maryland at College Park, July 1996.
- 9.9 WCAP-14326, "Experimental Basis for the AP600 Containment Vessel Heat and Mass Transfer Correlations," Revision 2, April 1998.
- 9.10 Jaluria, Y. "Buoyancy Driven Wall Flows in Enclosure Fires," Twenty-first Symposium (International) on Combustion, The Combustion Institute, 151-157 (1986).
- 9.11 Goldman, D., Jaluria, Y., "Effect of Opposing buoyancy on the Flow in Free and Wall Jets," Journal of Fluid Mechanics, 166, 41-56 (1986).
- 9.12 Jaluria, Y., Cooper, L.Y., "Negatively Buoyant Wall Flows Generated in Enclosure Fires," Progress in Energy and Combustion Science, 15, 159-182 (1989).
- 9.13 Fisher, K., Schall, M., and Wolf, M., "Simulations of GOTHIC Large-Scale Containment Experiments," published by Battelle Ingenieurtechnik GmbH, October 1995.
- 9.14 Ofstun, R.P., Woodcock, J., Paulsen, D.L., "Westinghouse – GOTHIC Modeling of NUPEC's Hydrogen Mixing and Distribution Test M-4-3," Third International Conference on Containment Design and Operation, October 1994, Toronto, Canada.
- 9.15 Peterson, P.F., "Scaling and Analysis of Mixing in Large Stratified Volumes," International Journal of Heat and Mass *Transfer*, Vol. 37, Suppl. 1, pp 97-106, 1994.

9-48

a,c

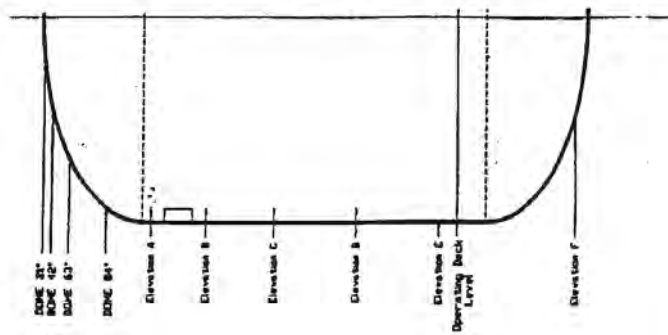


Figure 9-1. Measured Steam Concentrations for LST

9-49

a,c

**Figure 9-2. LST with Diffuser Under Steam Generator – Steam Flow 0.11-0.17 lb/sec –
Internal Fluid Temperature – Group 1**

9-50

a,c

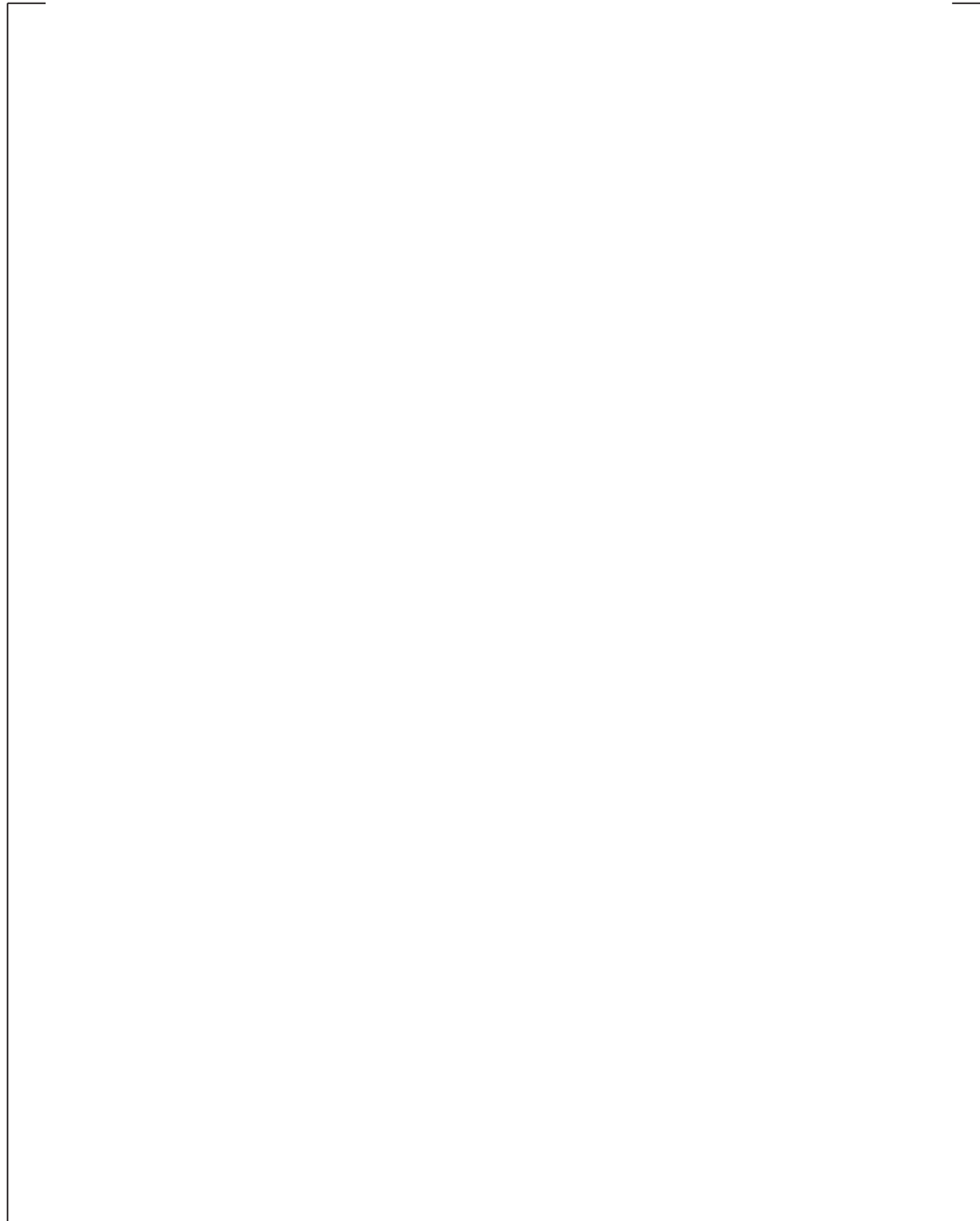


Figure 9-3. LST with Diffuser Under Steam Generator – Steam Flow 0.11-0.17 lb/sec – Saturation Temperature – Group 1

9-51

a,c

**Figure 9-4. LST with Diffuser Under Stream Generator – Steam Flow 0.11-0.17 lb/sec –
Internal Steam Pressure Ratio – Group 1**

9-52

a,c

**Figure 9-5. LST with Diffuser Under Steam Generator – Steam Flow 0.11-0.17 lb/sec –
Internal Fluid Temperature – Group 2**

9-53

a,c

Figure 9-6. LST with Diffuser Under Steam Generator – Steam Flow 0.11-0.17 lb/sec – Saturation Temperature – Group 2

9-54

a,c

**Figure 9-7. LST with Diffuser Under Steam Generator – Steam Flow 0.11-0.17 lb/sec –
Internal Steam Pressure Ratio – Group 2**

9-55

a,c

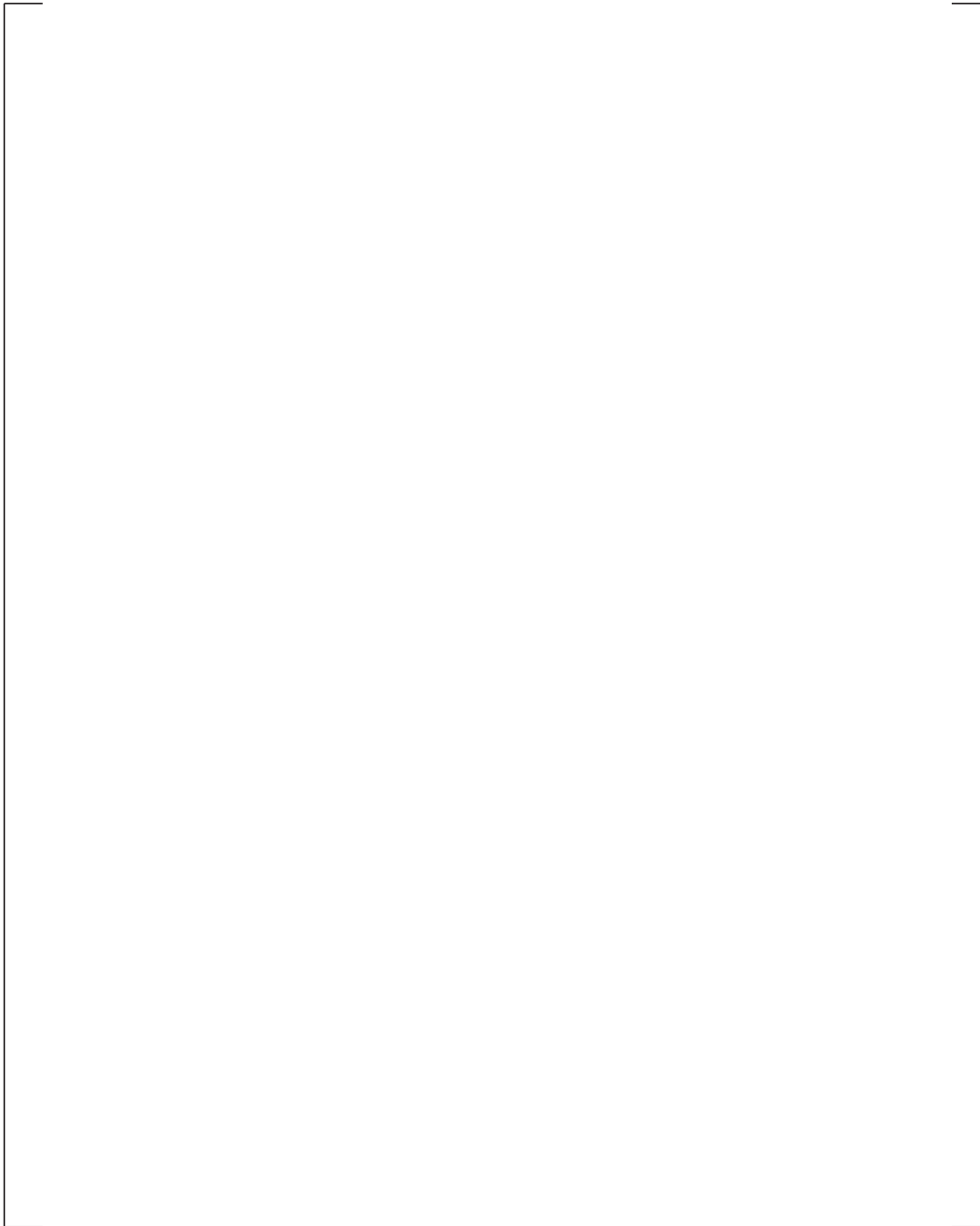


Figure 9-8. LST with Diffuser Under Steam Generator – Steam Flow 0.270.36 lb/sec – Internal Fluid Temperature

9-56

a,c

Figure 9-9. LST with Diffuser Under Steam Generator – Steam Flow 0.27-0.36 lb/sec – Saturation Temperature

9-57

a,c

**Figure 9-10. LST with Diffuser Under Steam Generator – Steam Flow 0.27-0.36 lb/sec –
Internal Steam Pressure Ratio**

9-58

a,c

**Figure 9-11. LST with Diffuser Under Steam Generator – Steam Flow 0.49-0.62 lb/sec –
Internal Fluid Temperature – Group 1**

9-59

a,c

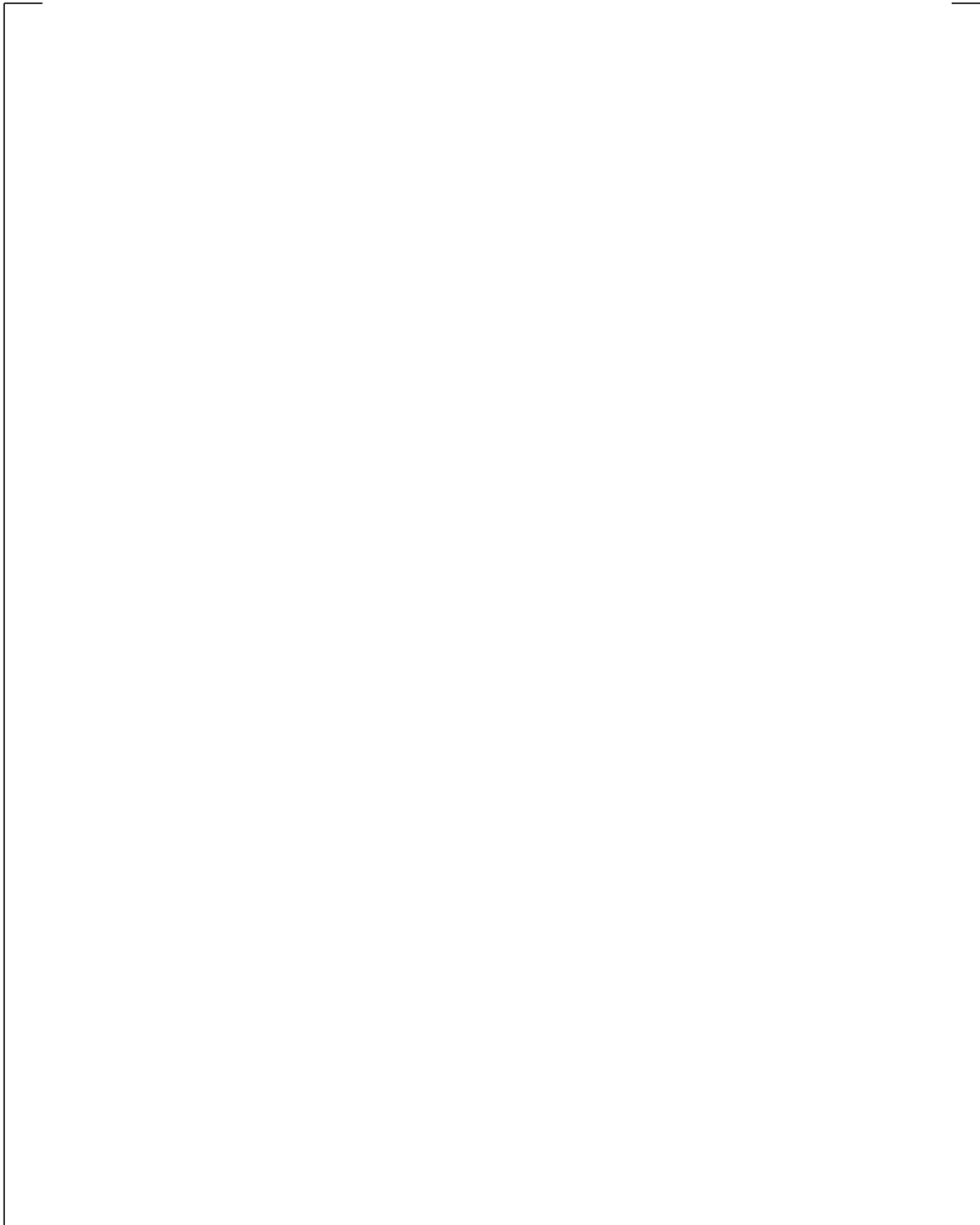


Figure 9-12. LST with Diffuser Under Steam Generator – Steam Flow 0.49-0.26 lb/sec – Saturation Temperature – Group 1

9-60

a,c

Figure 9-13. LST with Diffuser Under Steam Generator – Steam Flow 0.49-0.62 lb/sec – Internal Steam Pressure Ratio – Group 1

9-61

a,c

**Figure 9-14. LST with Diffuser Under Steam Generator – Steam Flow 0.49-0.62 lb/sec –
Internal Fluid Temperature – Group 2**

9-62

a,c

Figure 9-15. LST with Diffuser Under Steam Generator – Steam Flow 0.49-0.62 lb/sec – Saturation Temperature – Group 2

9-63

a,c

**Figure 9-16. LST with Diffuser Under Steam Generator – Steam Flow 0.49-0.62 lb/sec –
Internal Steam Pressure Ratio – Group 2**

9-64

a,c

**Figure 9-17. LST with Diffuser Under Steam Generator – Steam Flow 0.76-0.84 lb/sec –
Internal Fluid Temperature**

9-65

a,c

Figure 9-18. LST with Diffuser Under Steam Generator – Steam Flow 0.76-0.84 lb/sec – Saturation Temperature

9-66

a,c

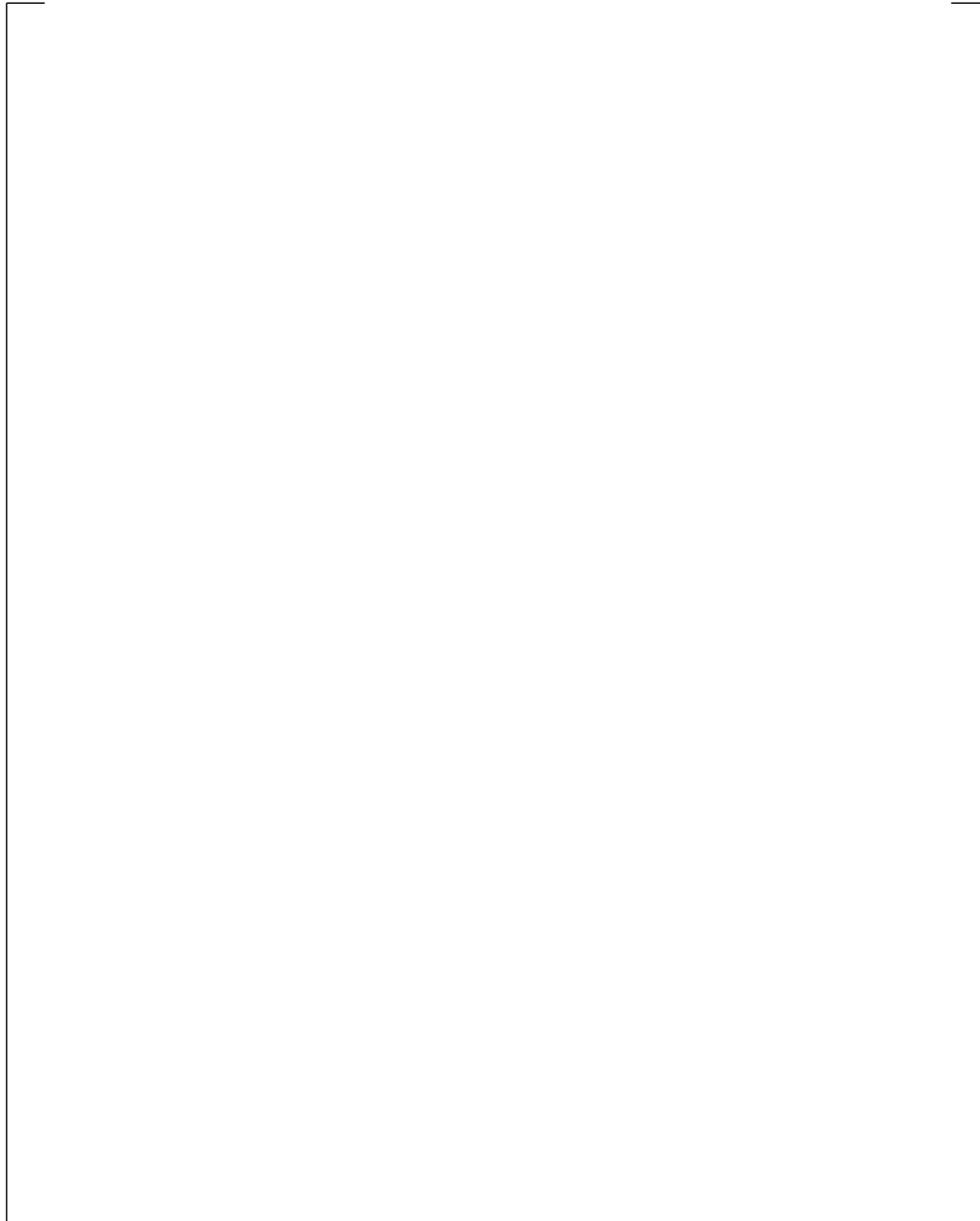


**Figure 9-19. LST with Diffuser Under Steam Generator – Steam Flow 0.76-0.84 lb/sec –
Internal Steam Pressure Ratio**

9-67

a,c

**Figure 9-20. LST with Diffuser Under Steam Generator – Steam Flow 1.10-1.20 lb/sec –
Internal Fluid Temperature**

9-68

a,c

Figure 9-21. LST with Diffuser Under Steam Generator – Steam Flow 1.10-1.20 lb/sec – Saturation Temperature

9-69

a,c

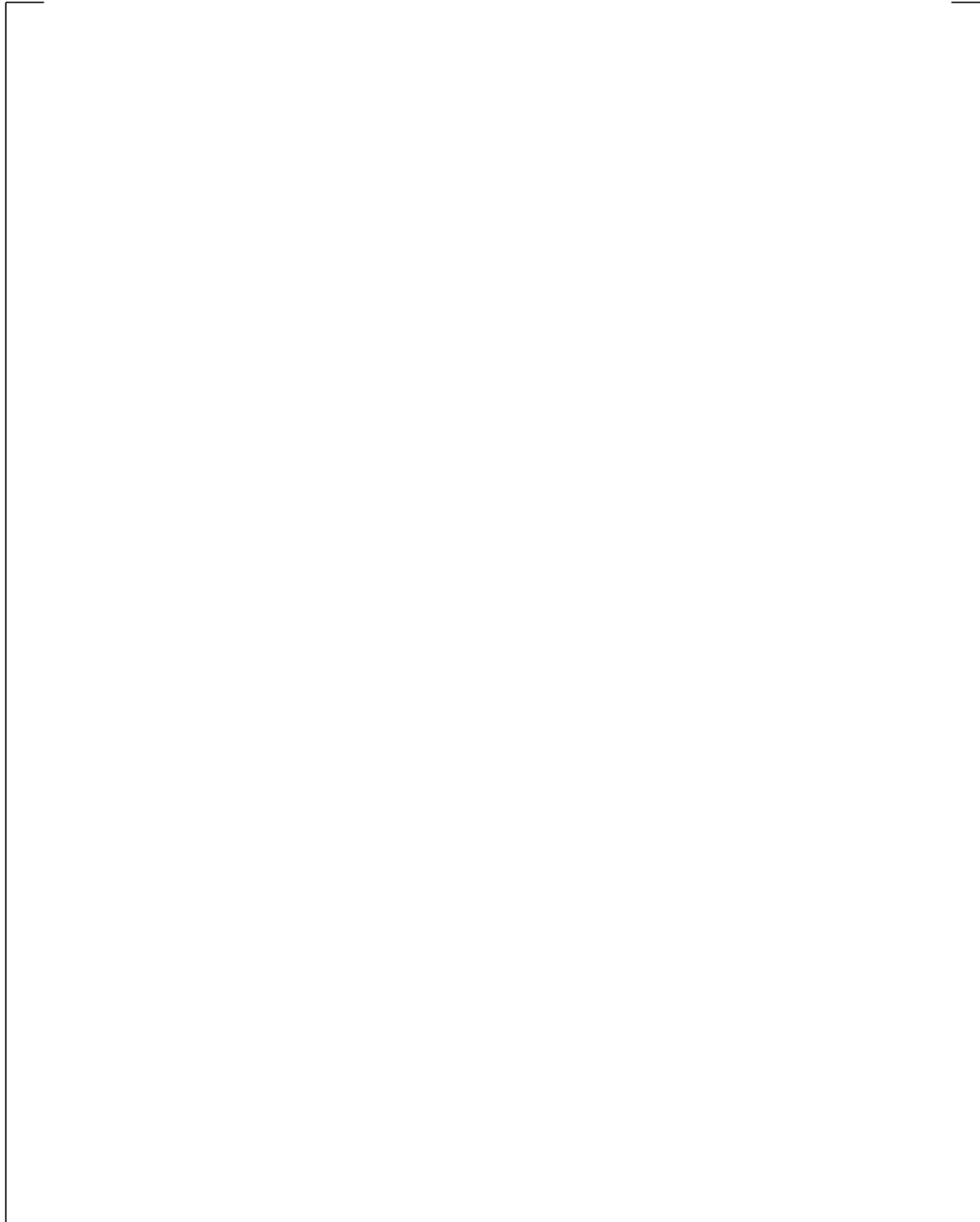


**Figure 9-22. LST with Diffuser Under Steam Generator – Steam Flow 1.10-1.20 lb/sec –
Internal Steam Pressure Ratio**

9-70

a,c

Figure 9-23. LST with Diffuser Under Steam Generator – Steam Flow 1.54-1.68 lb/sec – Internal Fluid Temperature

9-71

a,c

Figure 9-24. LST with Diffuser Under Steam Generator – Steam Flow 1.54-1.68 lb/sec – Saturation Temperature

9-72

a,c

**Figure 9-25. LST with Diffuser Under Steam Generator – Steam Flow 1.54-1.68 lb/sec –
Internal Steam Pressure Ratio**

9-73

a,c

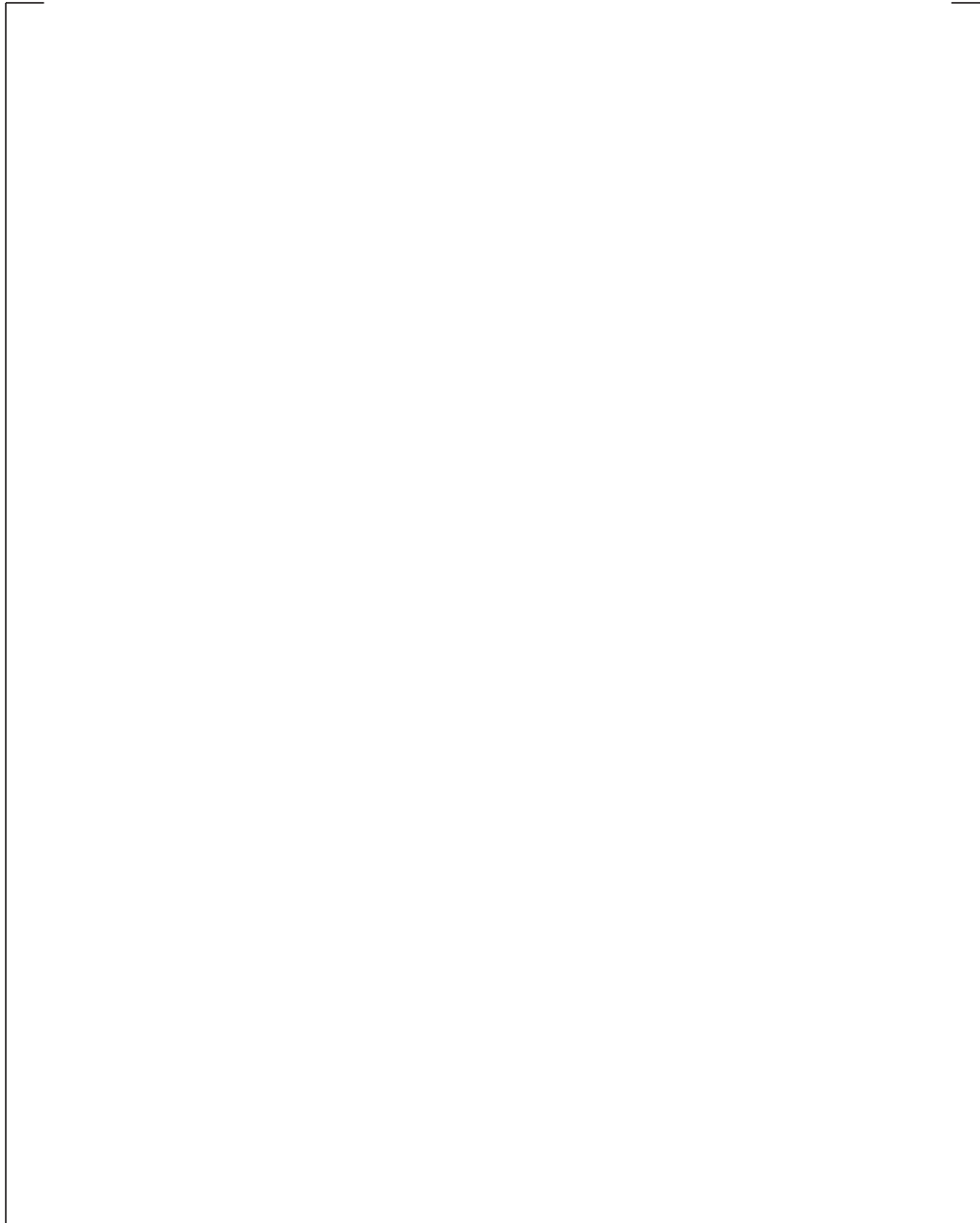


**Figure 9-26. LST with Diffuser Up 6 Feet – Steam Flow 0.76 & 1.68 lb/sec –
Internal Fluid Temperature**

9-74

a,c

**Figure 9-27. LST with Diffuser Up 6 Feet – Steam Flow 0.76 & 1.68 lb/sec –
Saturation Temperature**

9-75

a,c

**Figure 9-28. LST with Diffuser Up 6 Feet – Steam Flow 0.76 & 1.68 lb/sec –
Internal Steam Pressure Ratio**

9-76

a,c

Figure 9-29. LST with Steam Injection: 3 Inch Pipe – Steam Flow 0.76 – 0.95 lb/sec – Internal Fluid Temperature

9-77

a,c

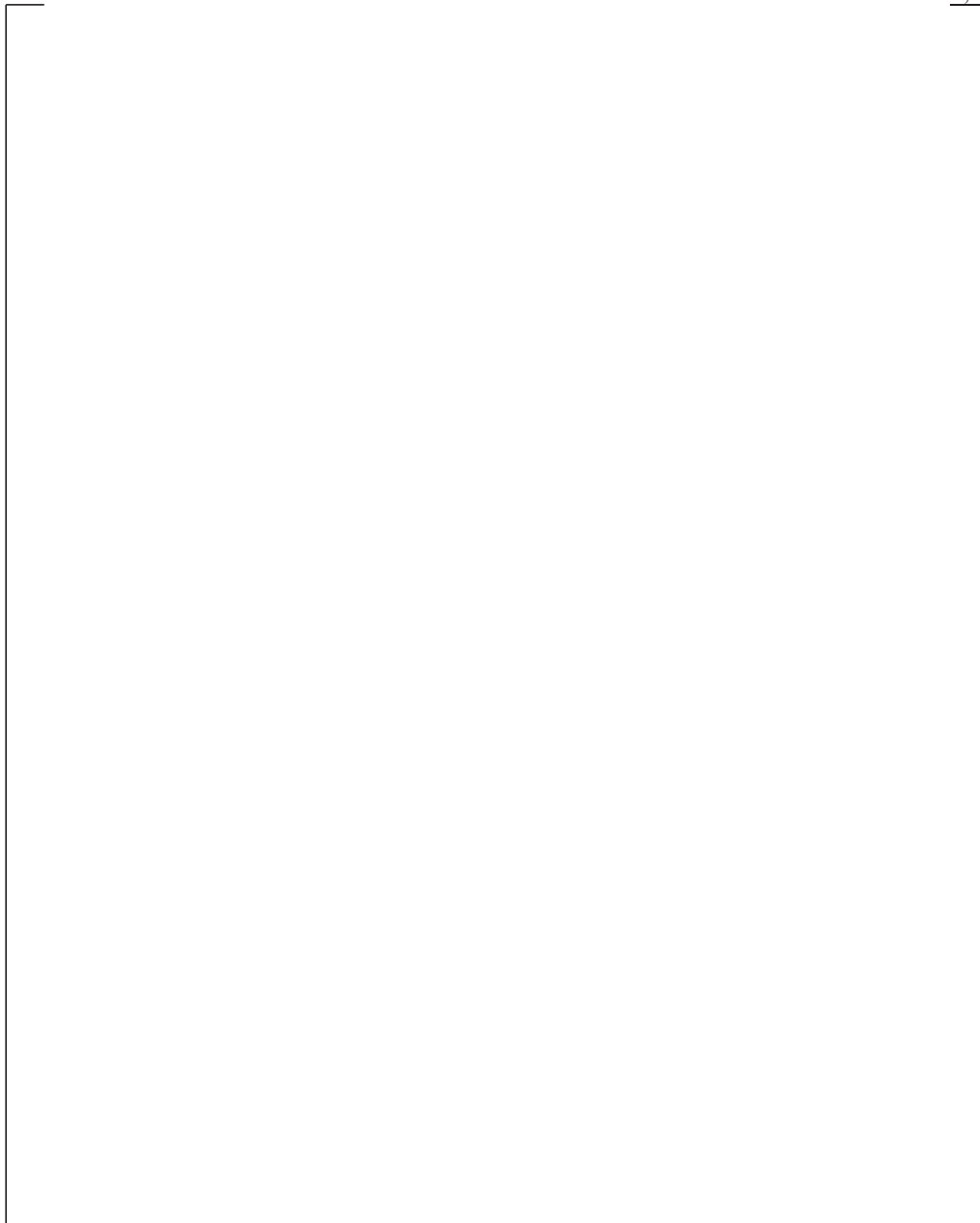


Figure 9-30. LST with Steam Injection: 3 Inch Pipe – Steam Flow 0.76 – 0.95 lb/sec – Saturation Temperature

9-78

a,c

**Figure 9-31. LST with Steam Injection: 3 Inch Pipe – Steam Flow 0.76 – 0.95 lb/sec –
Internal Steam Pressure Ratio**

9-79

a,c

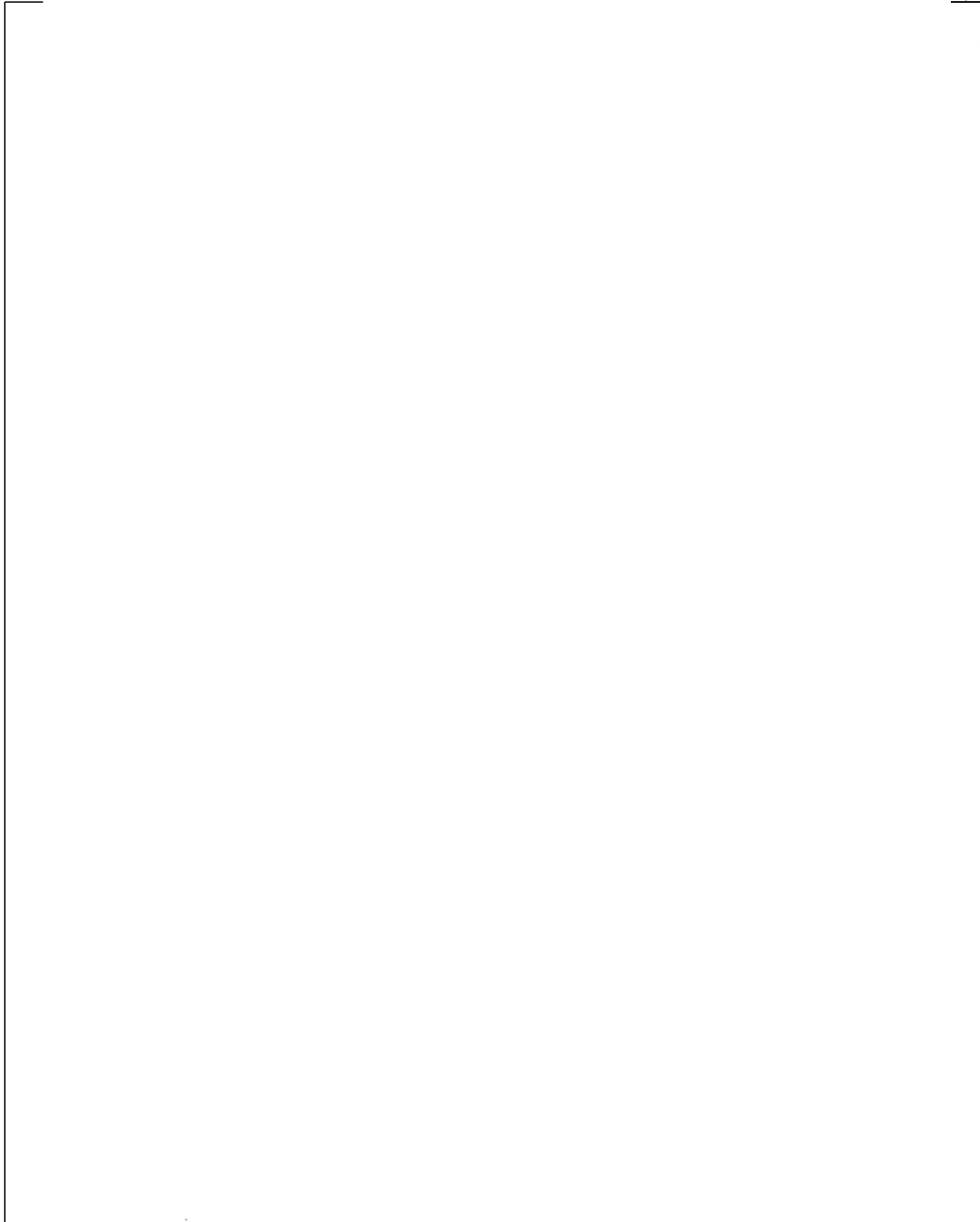


**Figure 9-32. LST with Steam Injection: 3 Inch Pipe – Steam Flow 1.25 – 1.31 lb/sec –
Internal Fluid Temperature**

9-80

a,c

Figure 9-33. LST with Steam Injection: 3 Inch Pipe – Steam Flow 1.25 – 1.31 lb/sec – Saturation Temperature

9-81

a,c

**Figure 9-34. LST with Steam Injection: 3 Inch Pipe – Steam Flow 1.25 – 1.31 lb/sec –
Internal Steam Pressure Ratio**

9-82

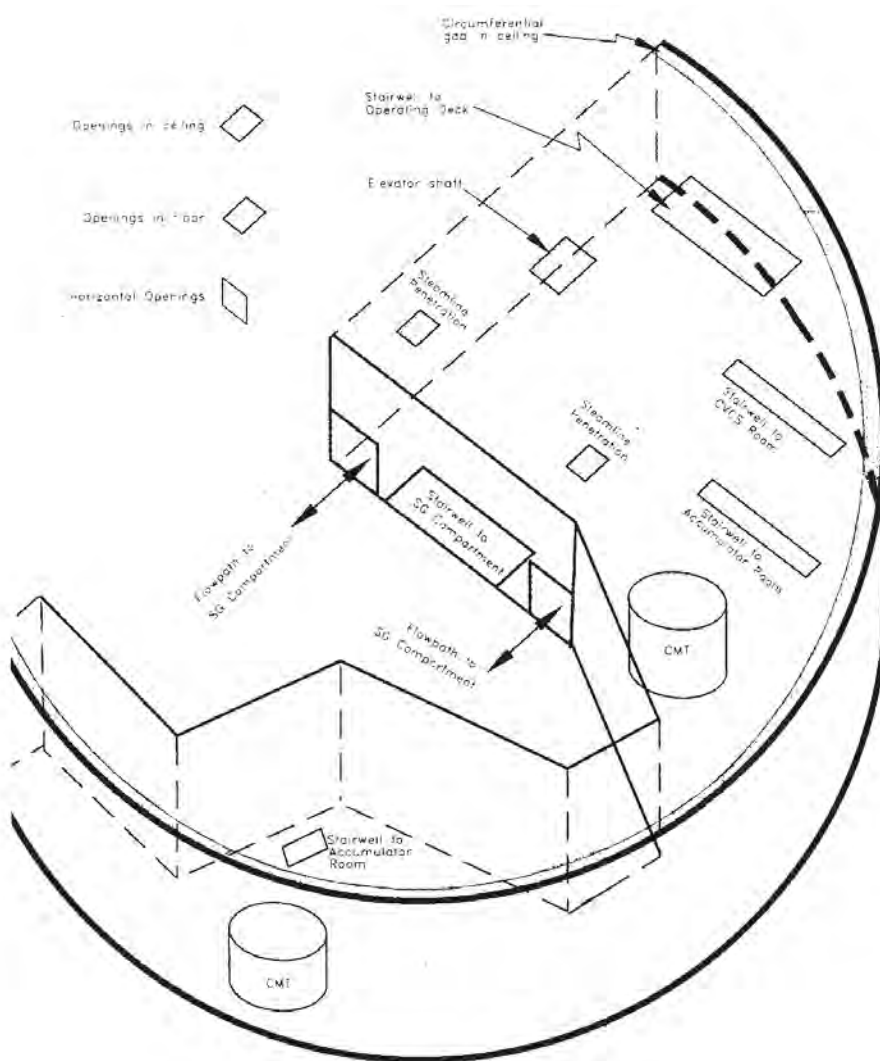


Figure 9-35. CMT Compartment Layout

9-83

a,c

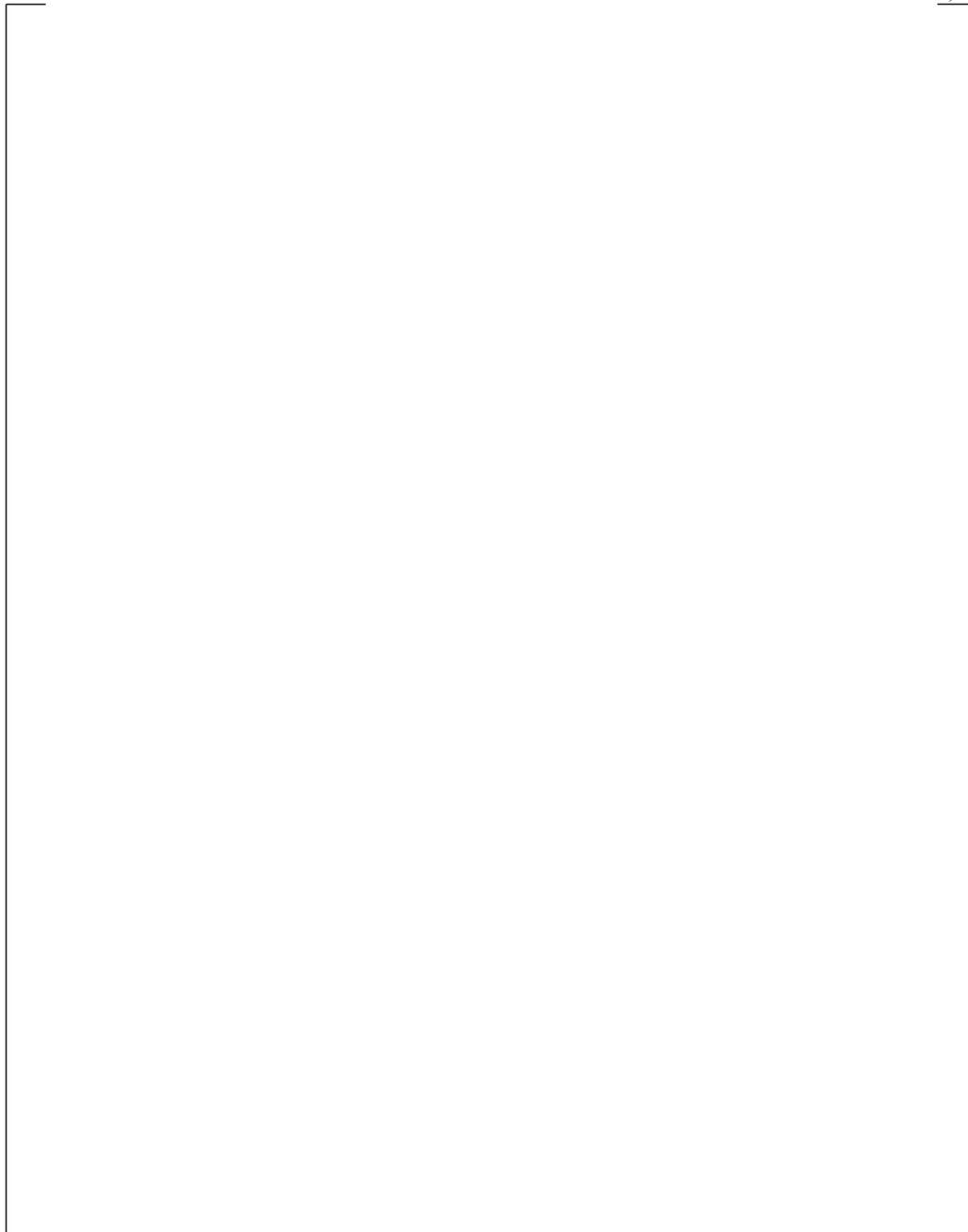
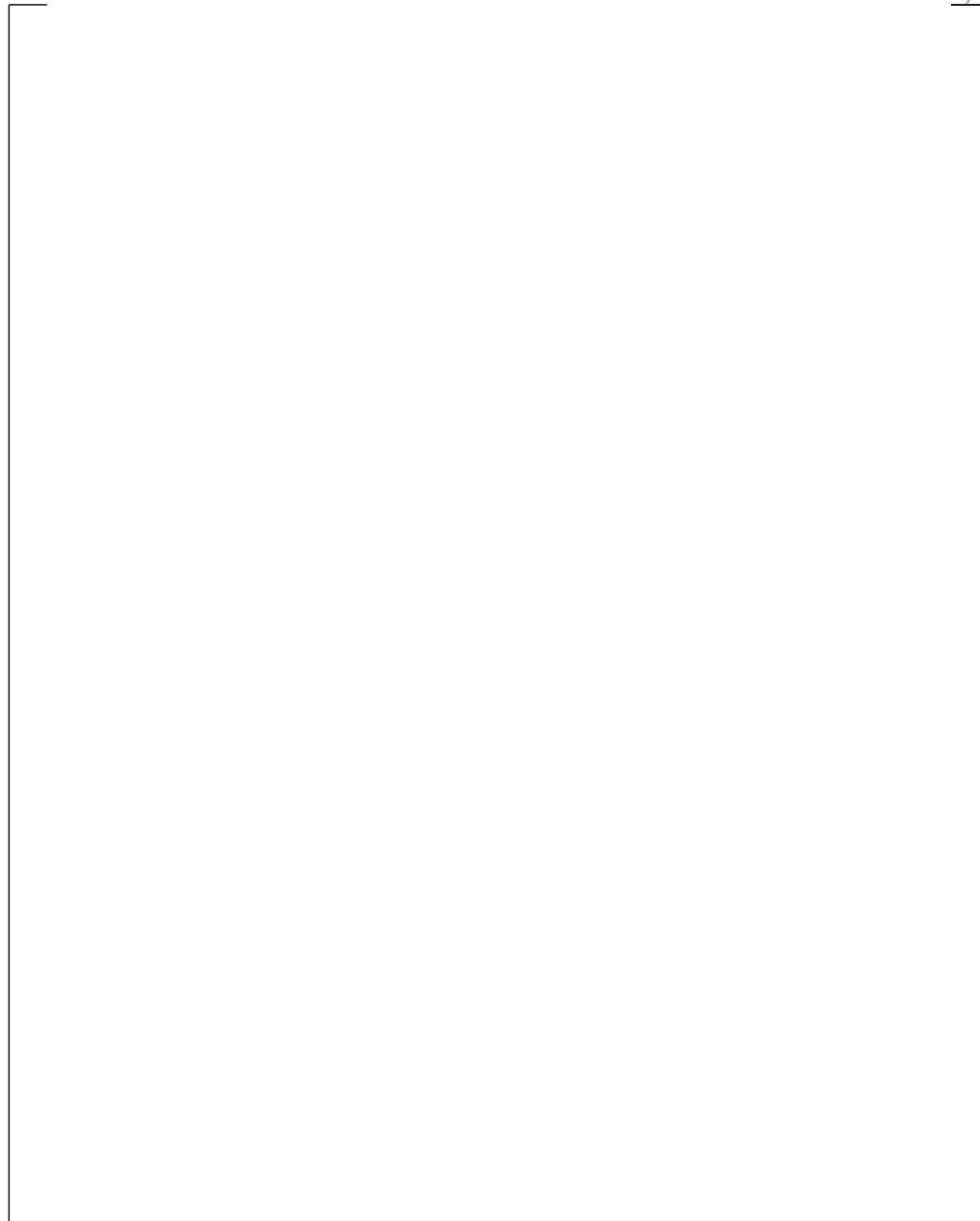


Figure 9-36. Simplified AP600 Containment Diagram

9-84

a,c



**Figure 9-37. WGOTHIC Calculated LOCA Blowdown Steam Pressure Ratio for Jet Momentum
Dissipated in SG East Compartment**

9-85

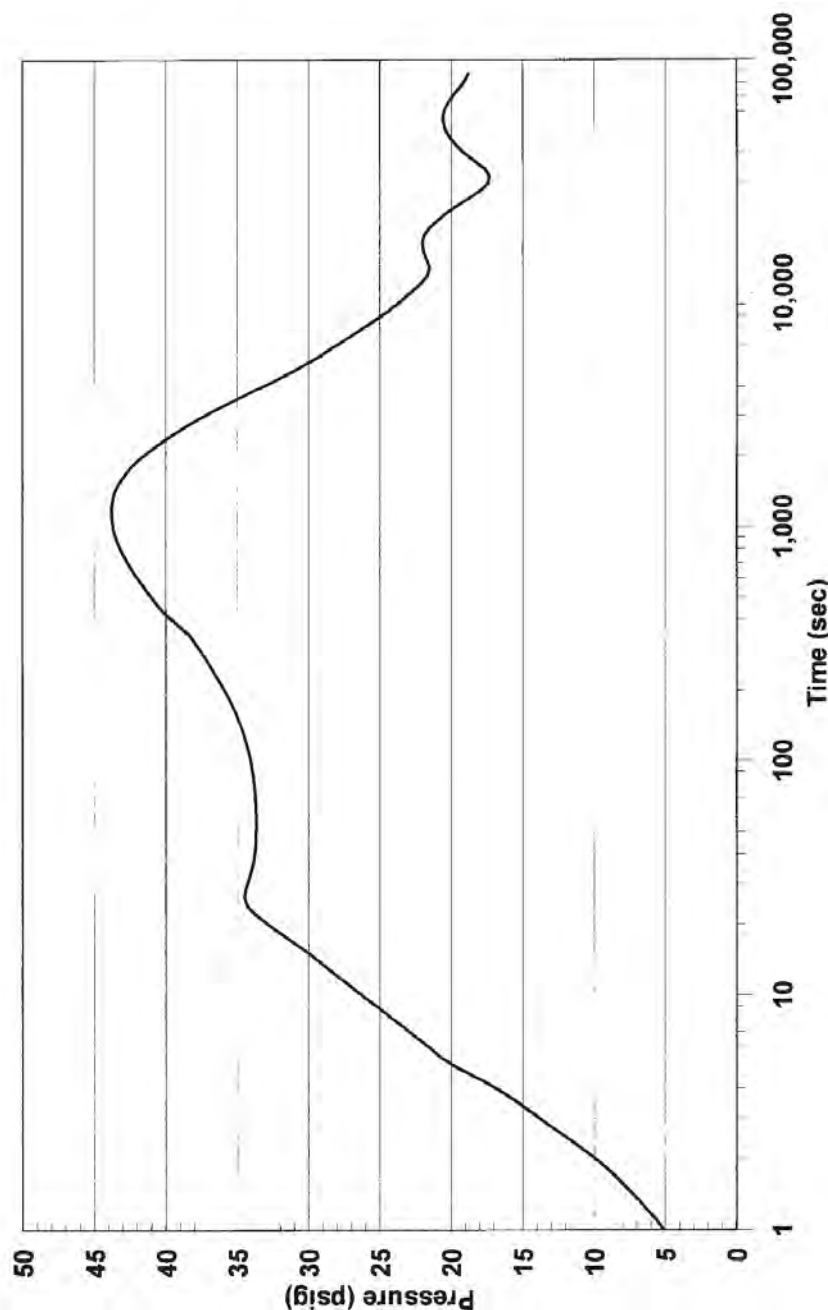


Figure 9-38. WGOthic Calculated AP600 Containment Pressure – Sensitivity to Loss Coefficients for LOCA Jet Momentum Dissipated in SG East Compartment

9-86

a,c

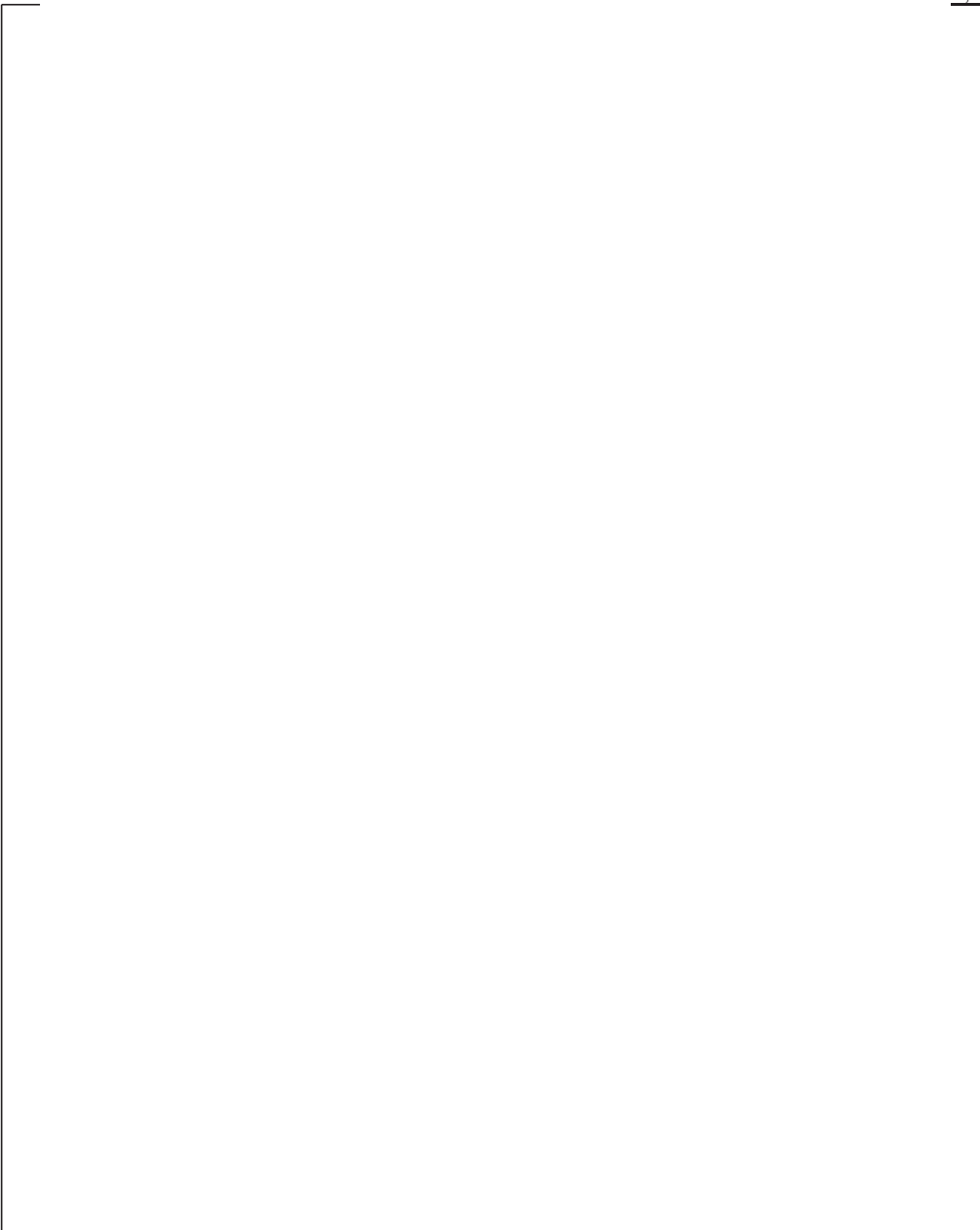


Figure 9-39. WGOTHIC Calculated Flow Pattern – Sensitivity to Loss Coefficients for LOCA Jet Momentum Dissipated in SG East Compartment at 20 Seconds

9-87

a,c

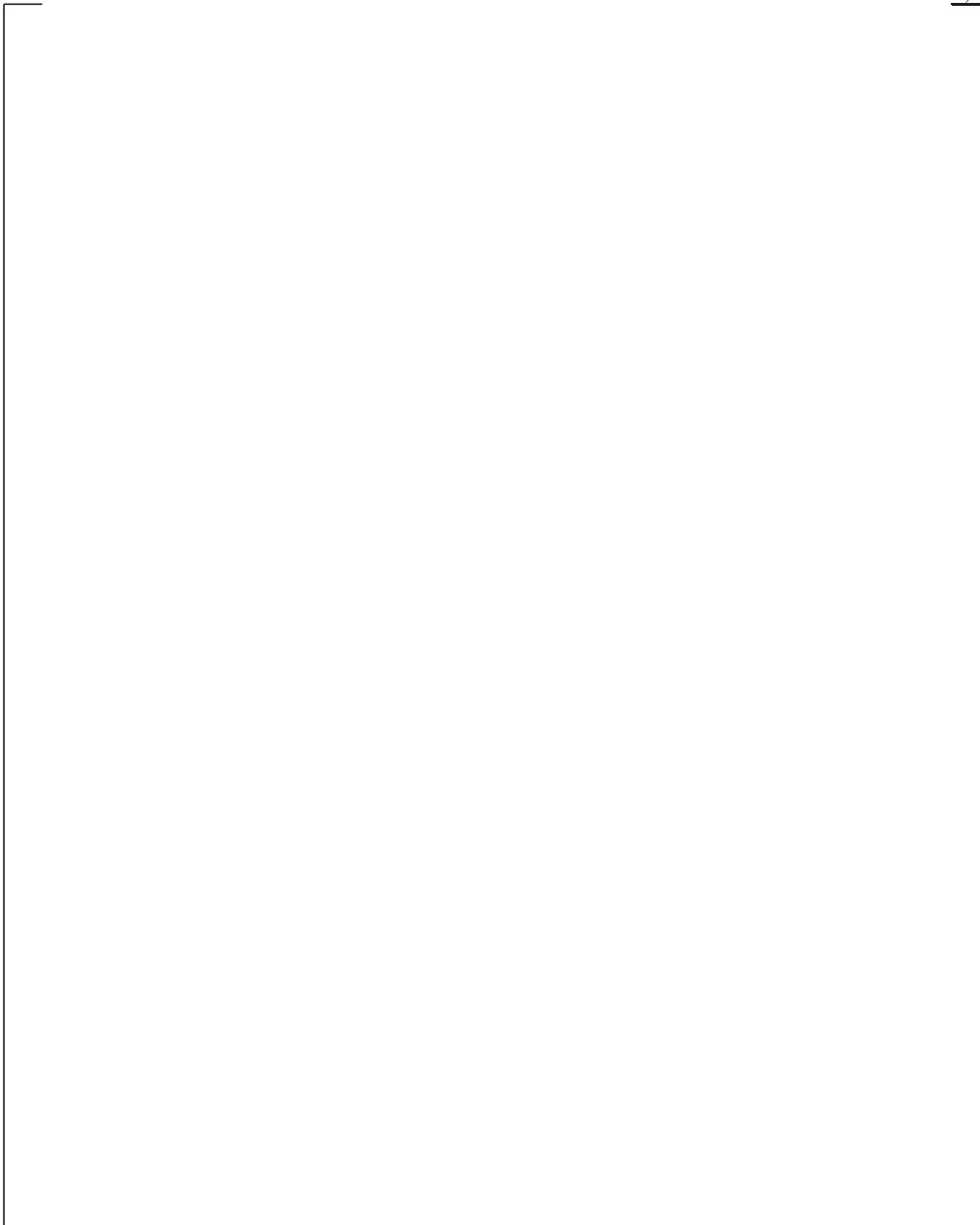


Figure 9-40. W Gothic Calculated Flow Pattern – Sensitivity to Loss Coefficients for LOCA Jet Momentum Dissipated in SG East Comp. at 1000 Seconds

9-88

a,c

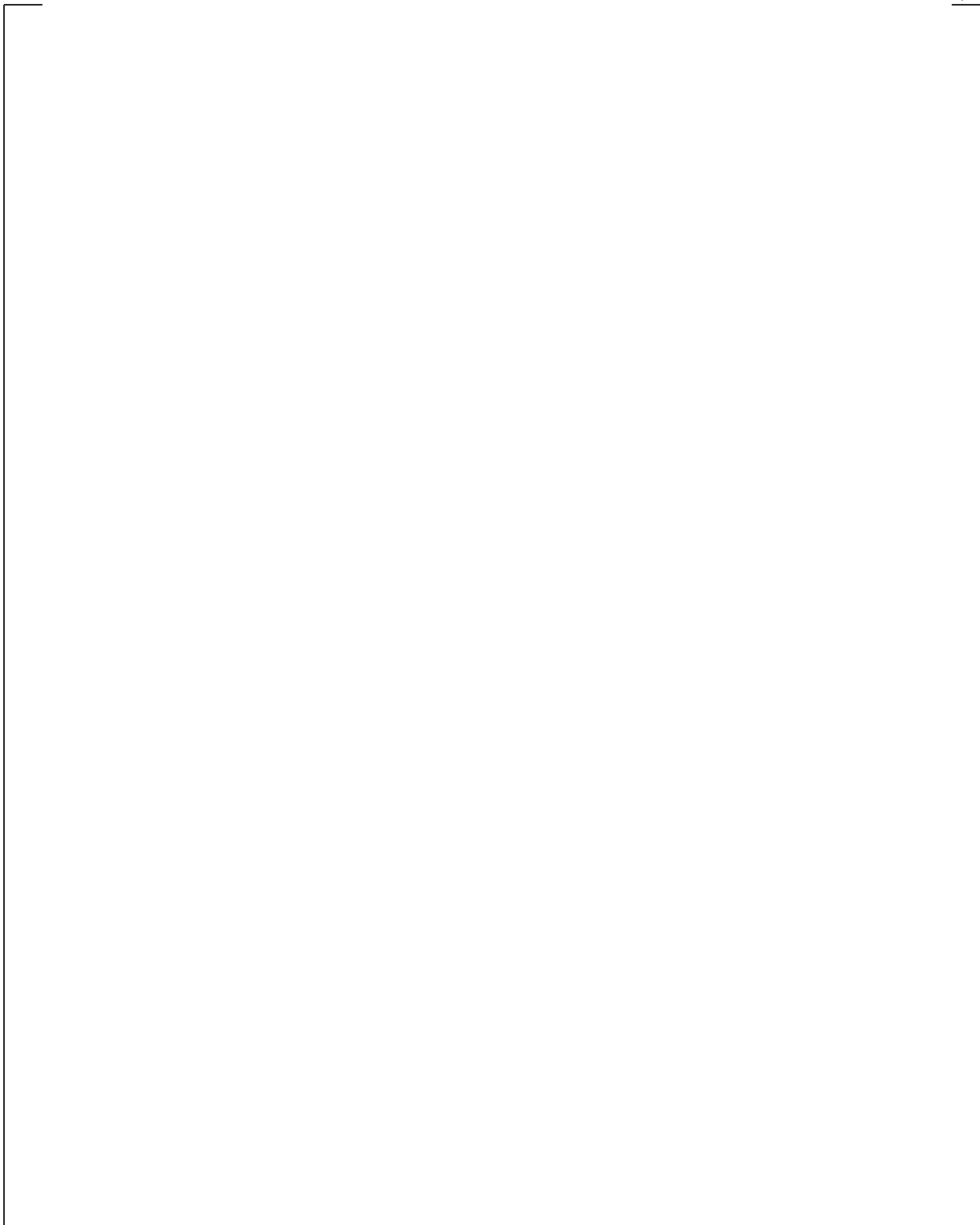


Figure 9-41. WGOTHIC Calculated Flow Pattern – Sensitivity to Loss Coefficients for LOCA Jet Momentum Dissipated in SG East Comp. at 1550 Seconds

9-89

a,c

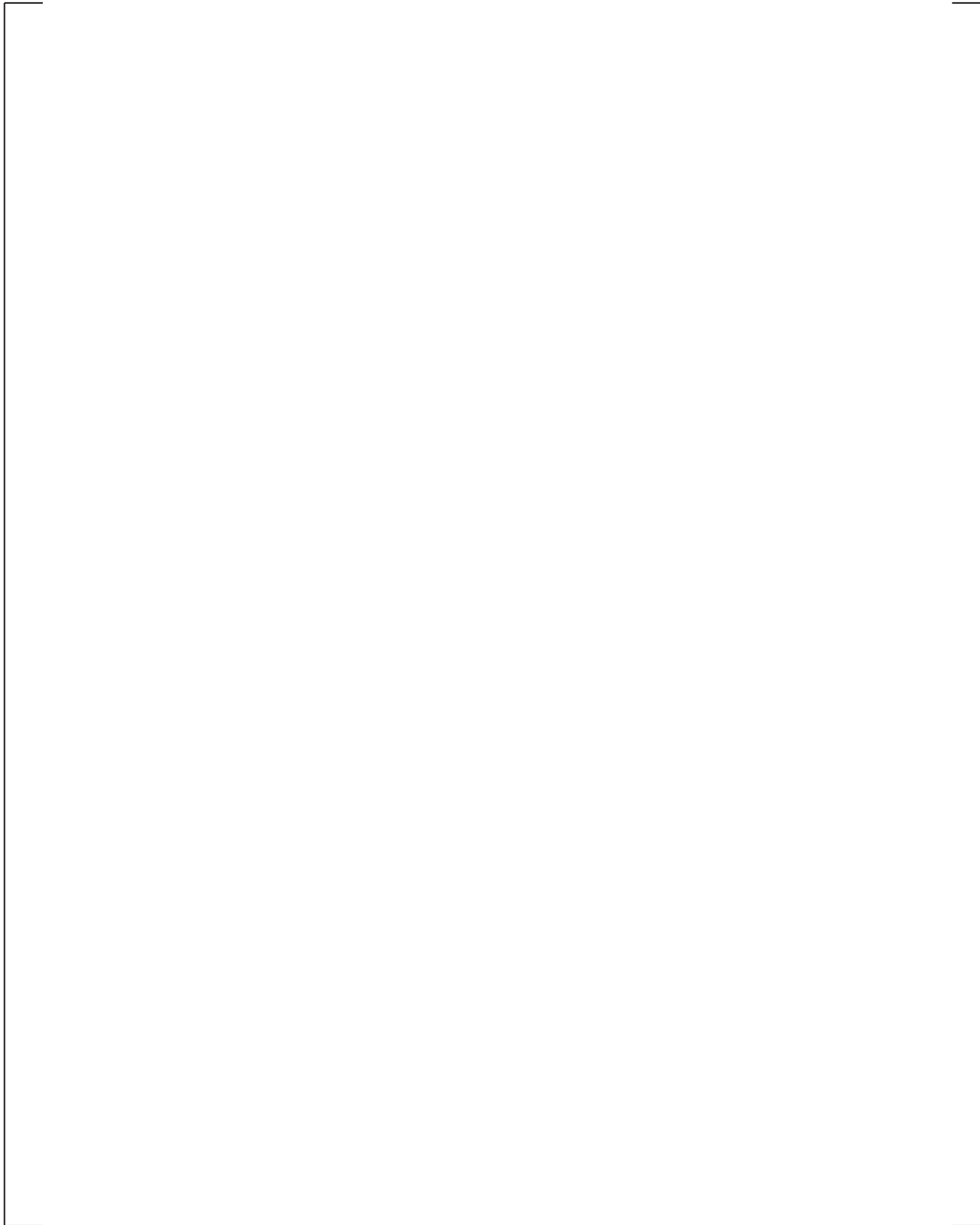


Figure 9-42. WGOTHIC Calculated Flow Pattern – Sensitivity to Loss Coefficients for LOCA Jet Momentum Dissipated in SG East Comp. at 80050 Seconds

9-90

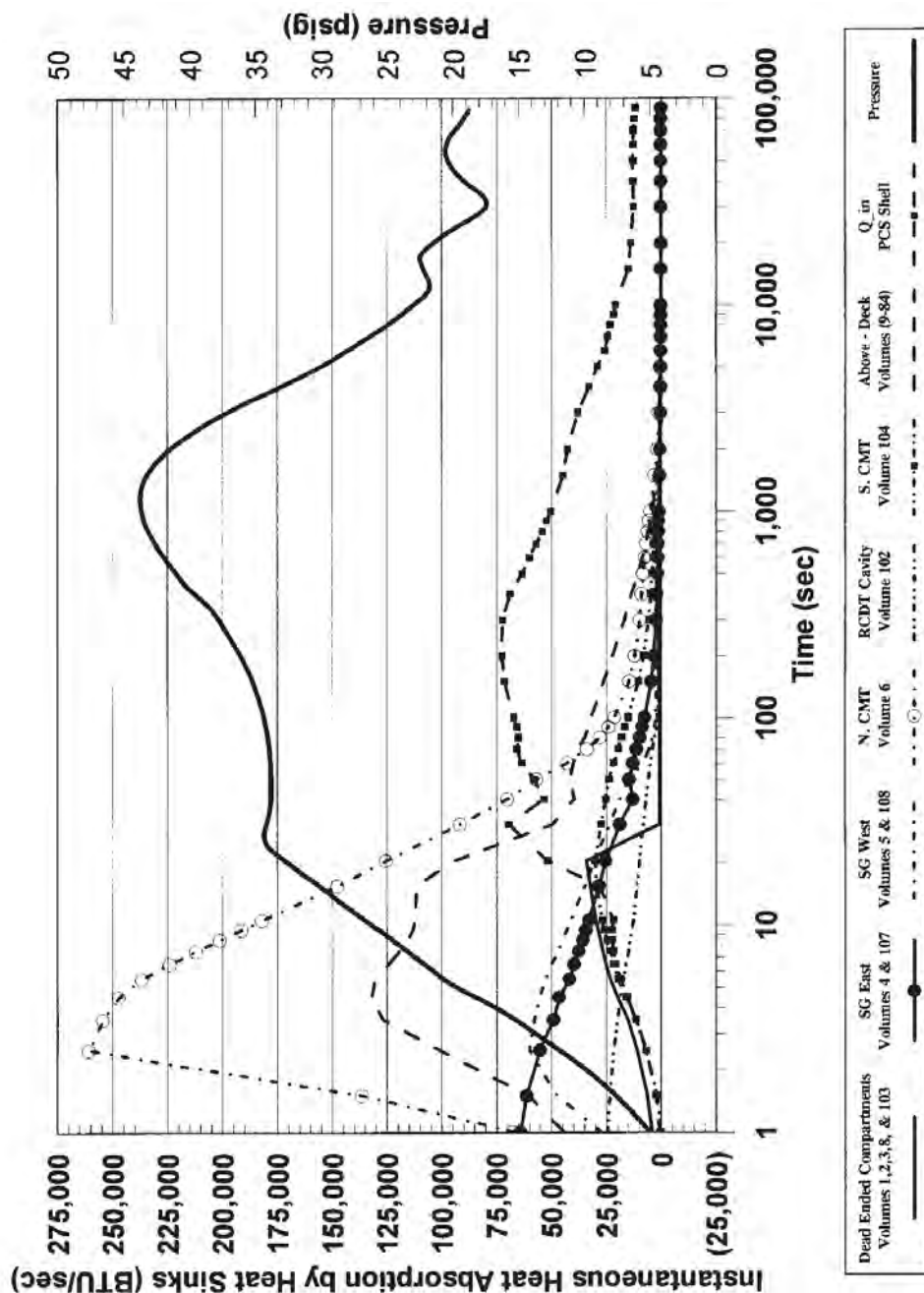


Figure 9-43. WGOthic Calculated AP600 Containment Heat Removal Rates – LOCA Jet Momentum Dissipated in SG East Compartment

9-91

a,c

Figure 9-44. WGOTHIC Calculated AP600 Containment Steam Pressure Ratio for LOCA Jet Momentum Dissipated in SG East Compartment

9-92

a,c

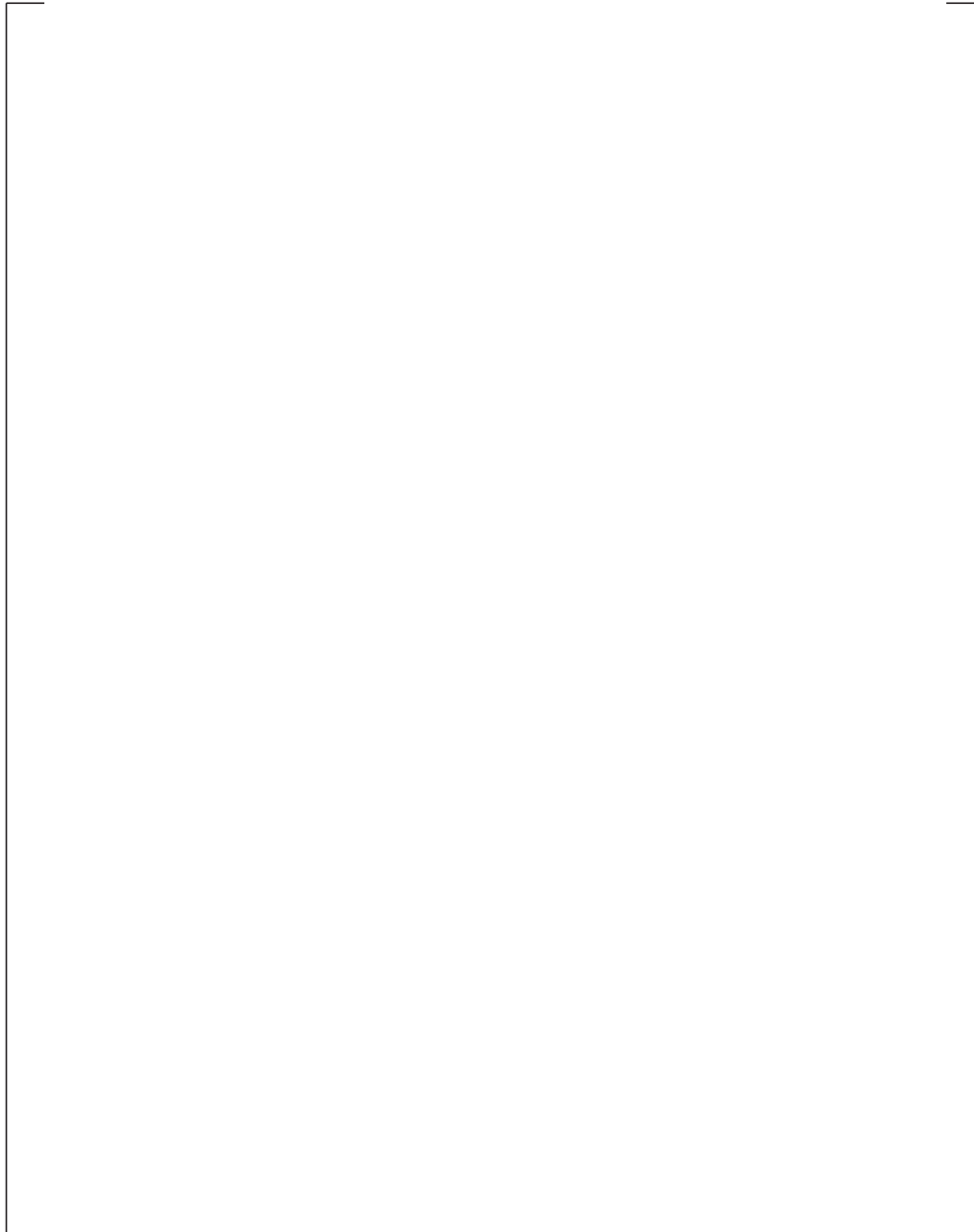


Figure 9-45. WGOTHIC Calculated AP600 Cont. Pressure – Sensitivity to Heat Transfer Coefficient for Study of Undissipated Jet Effects During a LOCA

9-93

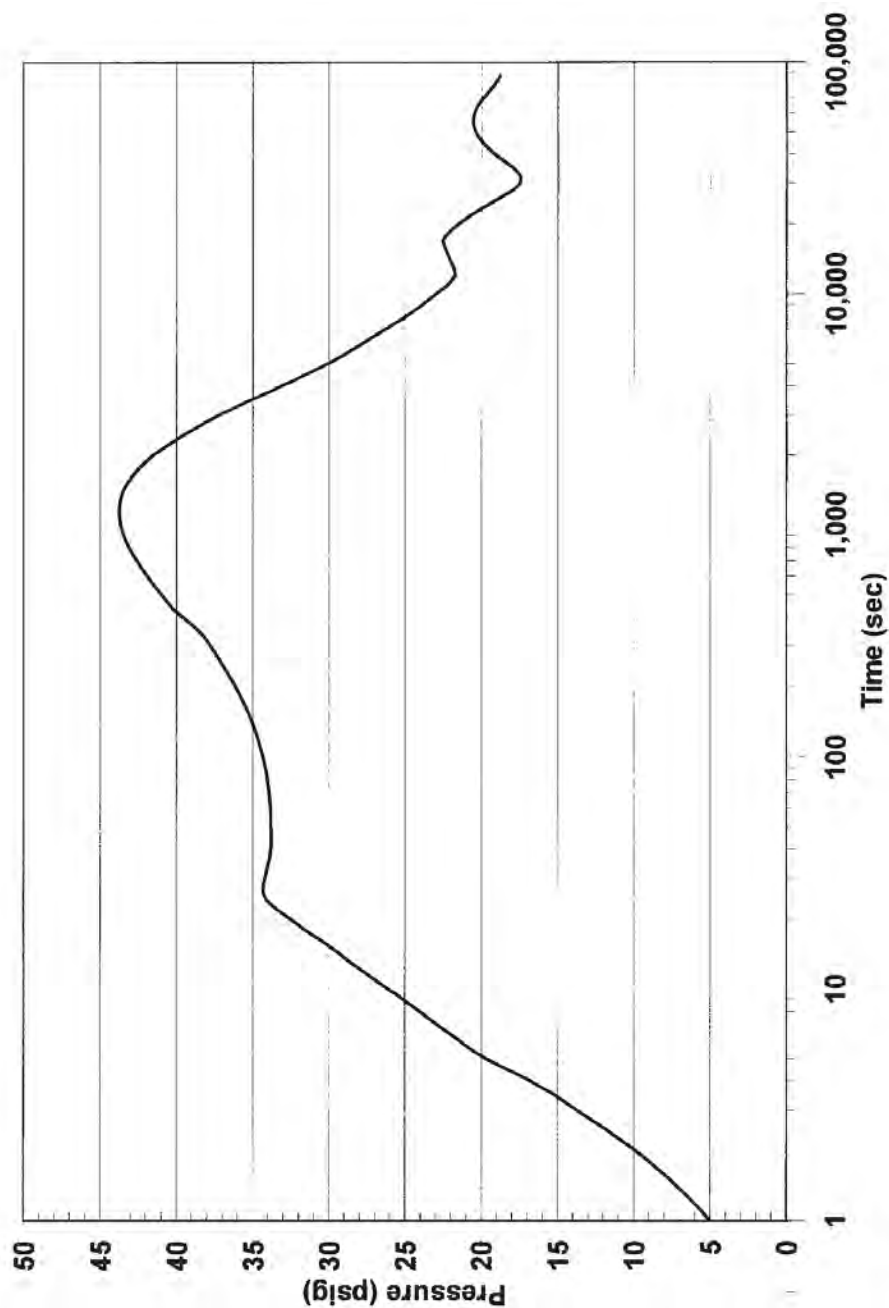


Figure 9-46. WGOTHIC Calculated AP600 Containment Pressure – LOCA Jet Momentum Dissipated in SG East Compartment

9-94

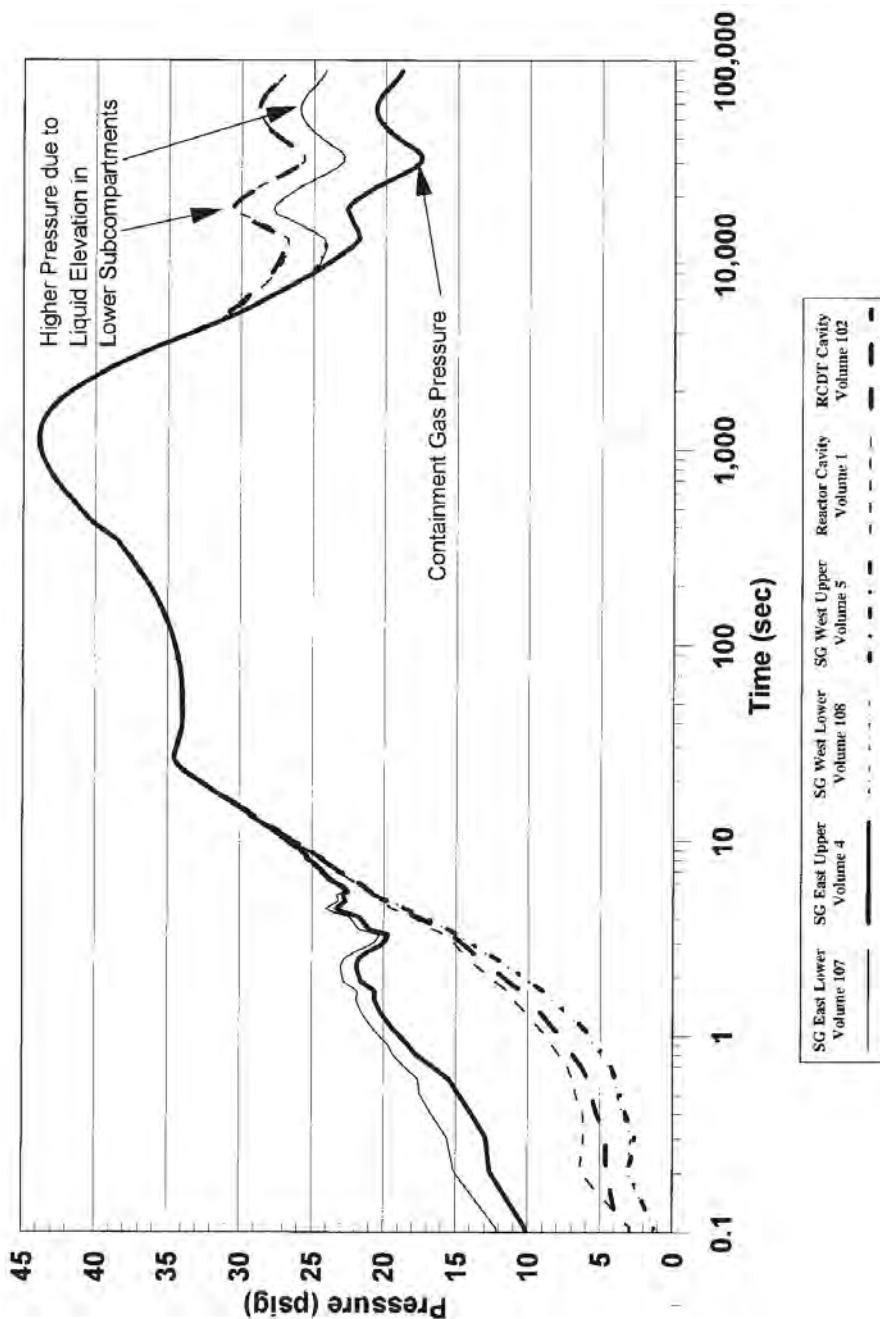


Figure 9-46A. WGOthic Calculated AP600 Containment Below-Deck Compartment Pressure for LOCA Jet Momentum Dissipated in SG East Compartment

9-95

a,c

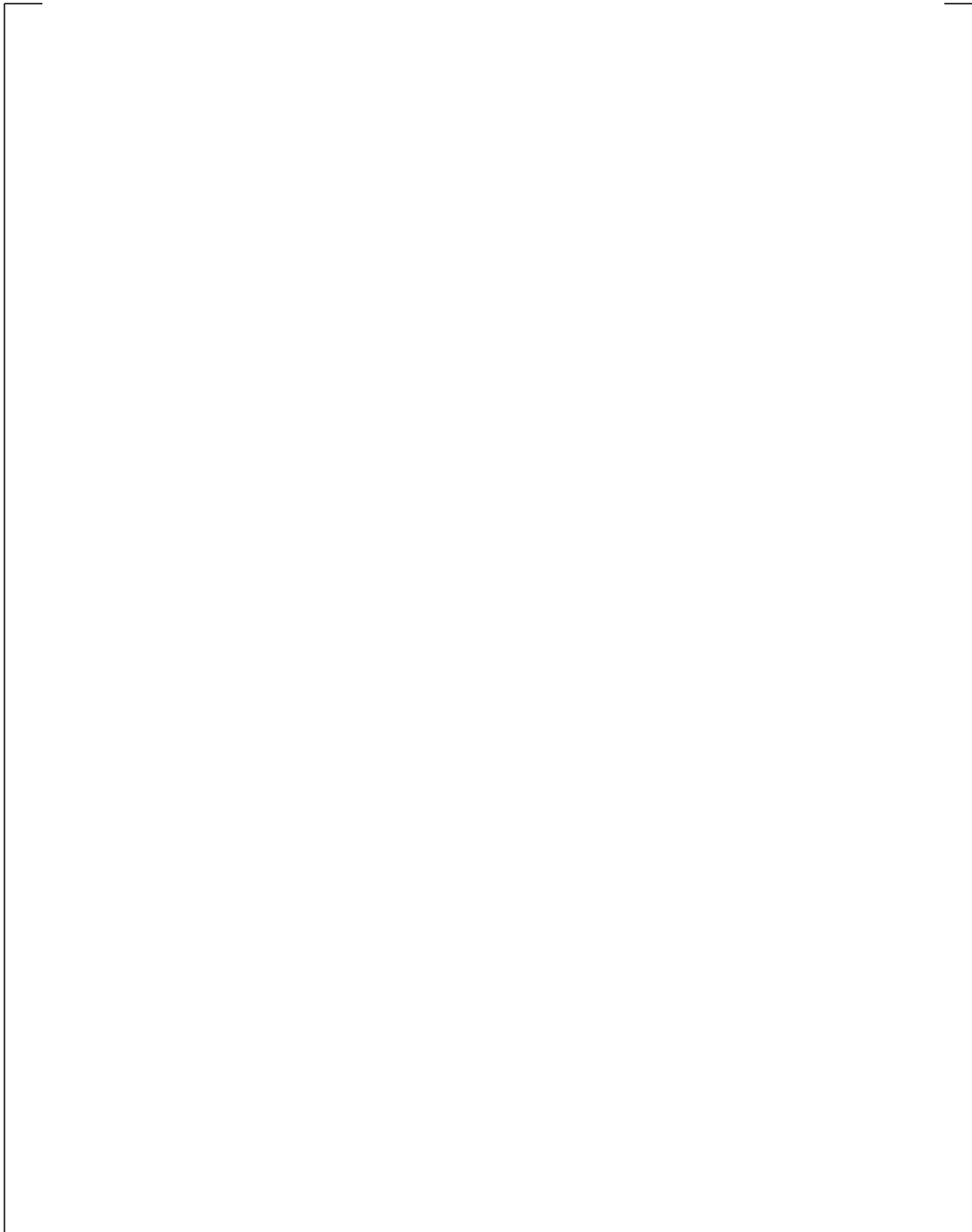


Figure 9-47. WGOTHIC Calculated Flow Pattern – LOCA Jet Momentum Dissipated in SG East Compartment at 20 Seconds

9-96

a,c

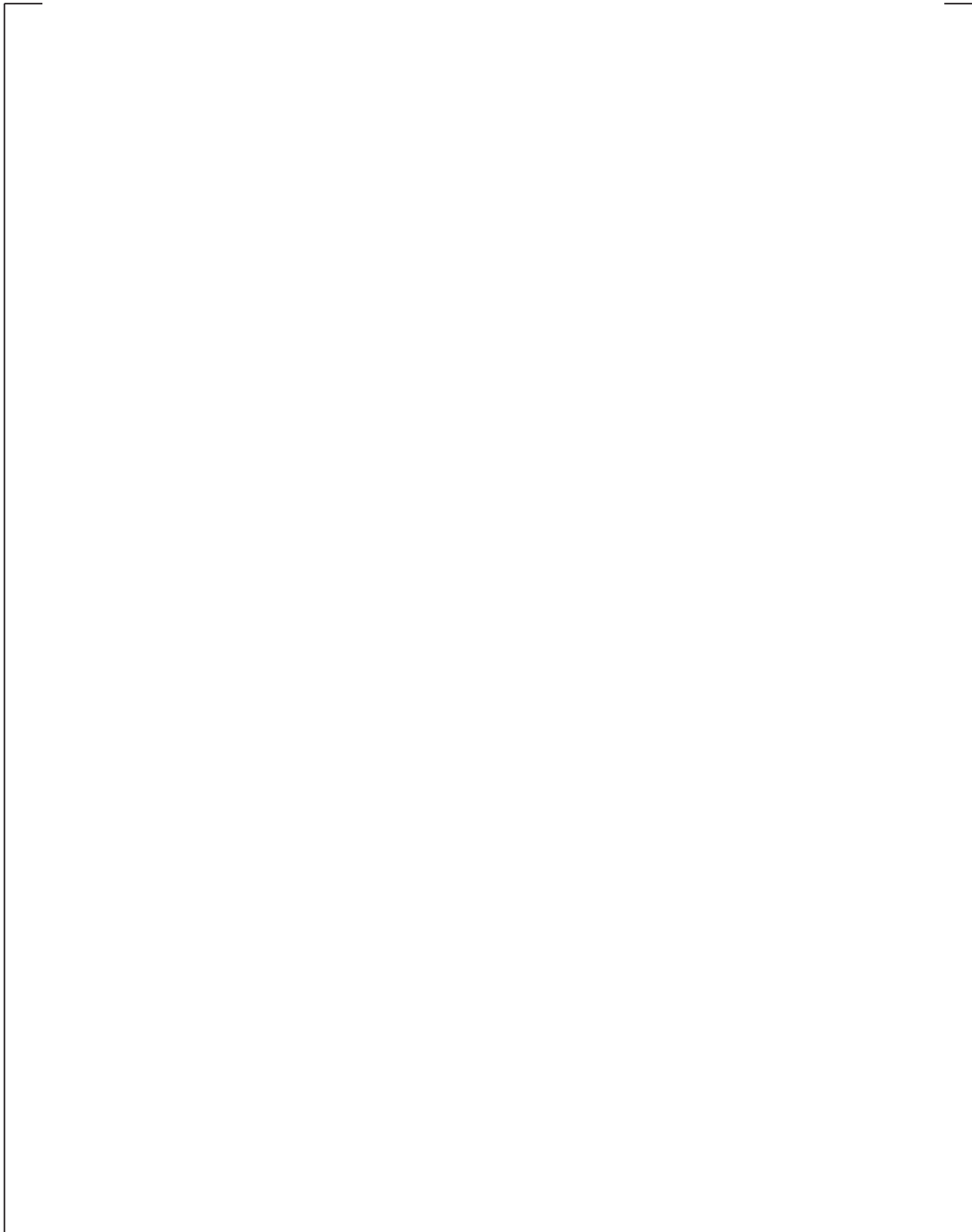


Figure 9-48. WGOTHIC Calculated Flow Pattern – LOCA Jet Momentum Dissipated in SG East Compartment at 1000 Seconds

9-97

a,c

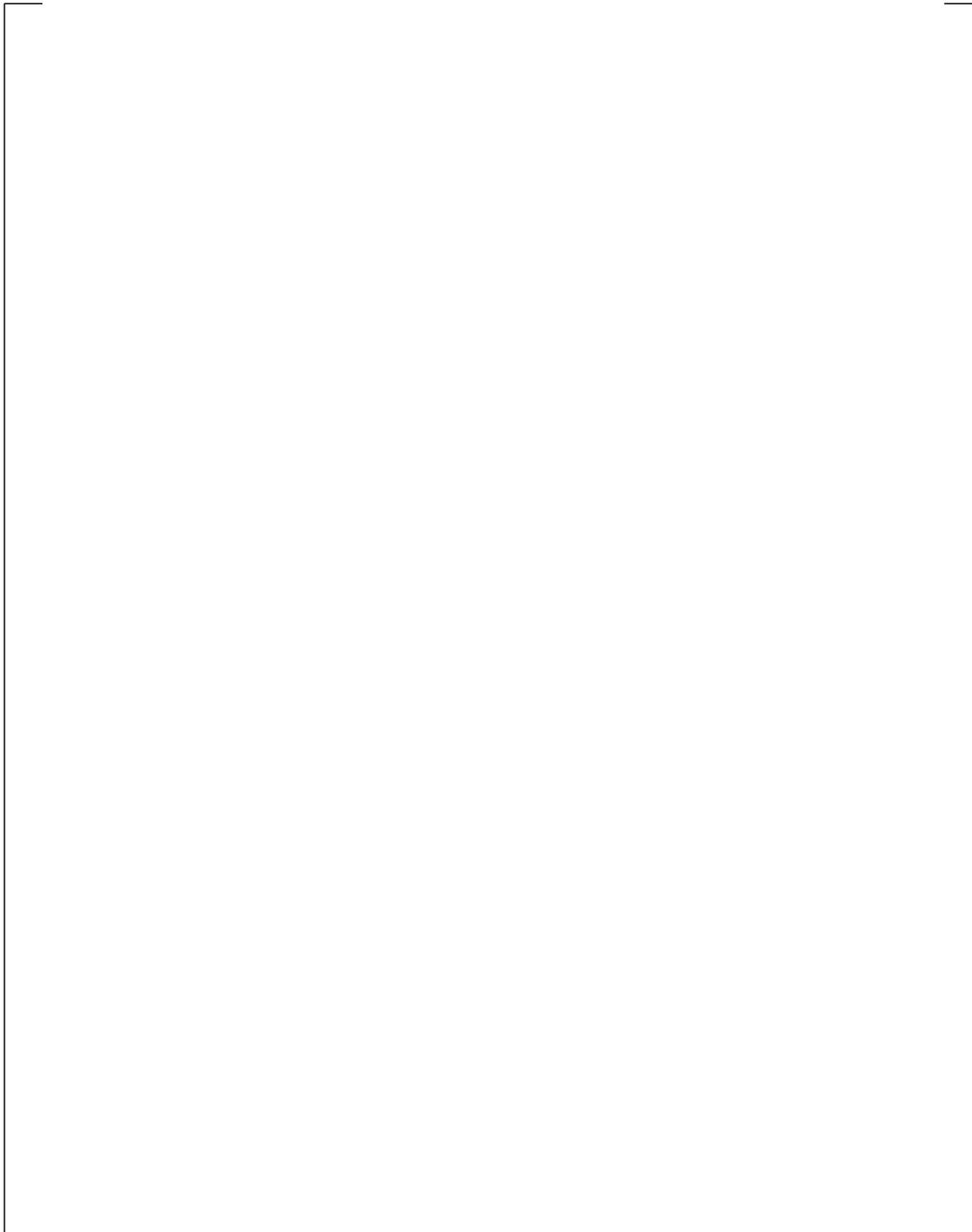


Figure 9-49. WGOTHIC Calculated Flow Pattern – LOCA Jet Momentum Dissipated in SG East Compartment at 1500 Seconds

9-98

a,c

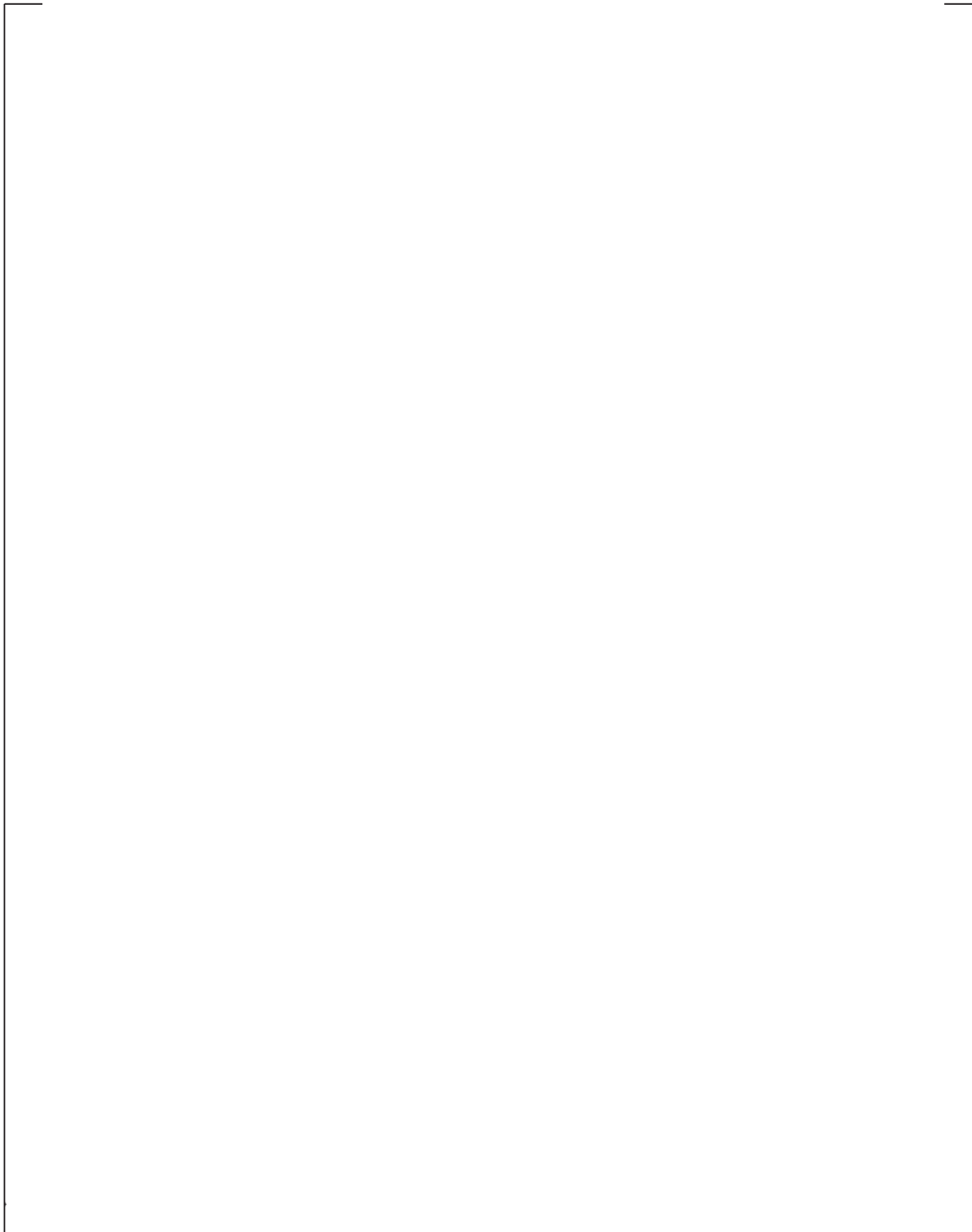


Figure 9-50. W Gothic Calculated Flow Pattern – LOCA Jet Momentum Dissipated in SG East Compartment at 8000 Seconds

9-99

a,c

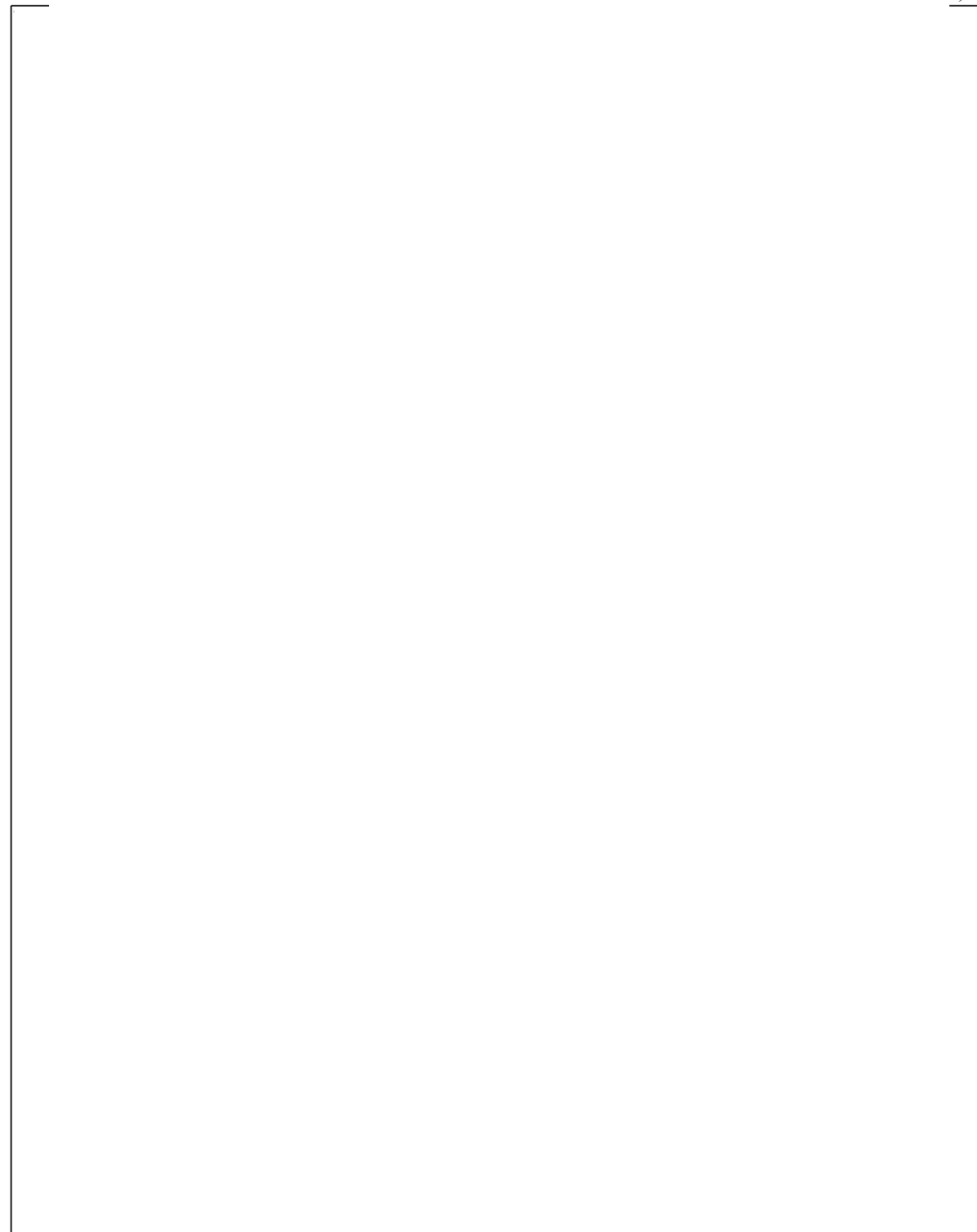


Figure 9-51. Details of WGOTHIC Flow Paths to Above-Deck Region from CMT, Refueling Canal, and IRWST

9-100

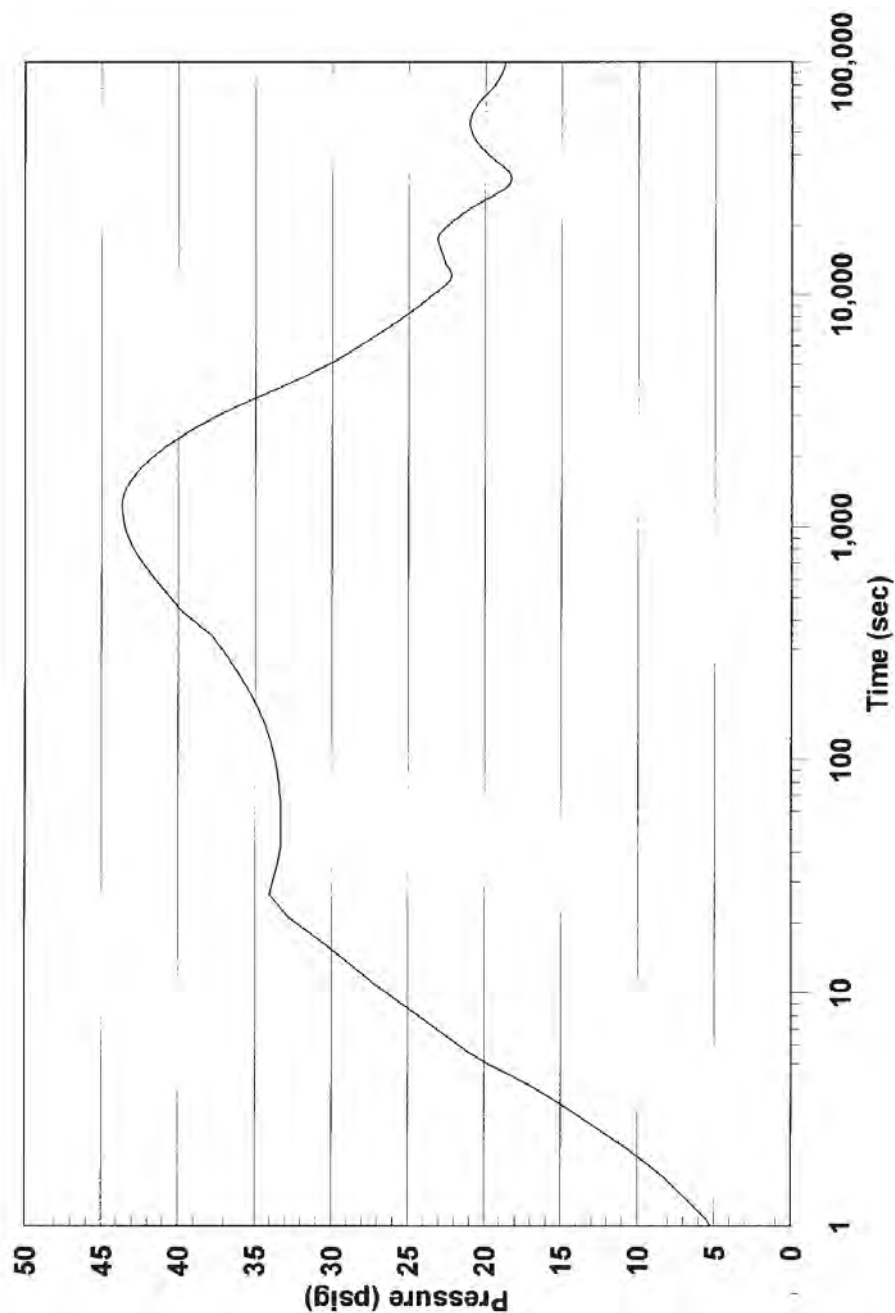


Figure 9-52. WGOTHIC Calculated AP600 Containment Pressure – LOCA Plume Rising into CMT Room

9-101

a,c

Figure 9-53. WGOTHIC Calculated Flow Pattern – LOCA Plume Rising into CMT Room at 1000 Seconds

9-102

a,c

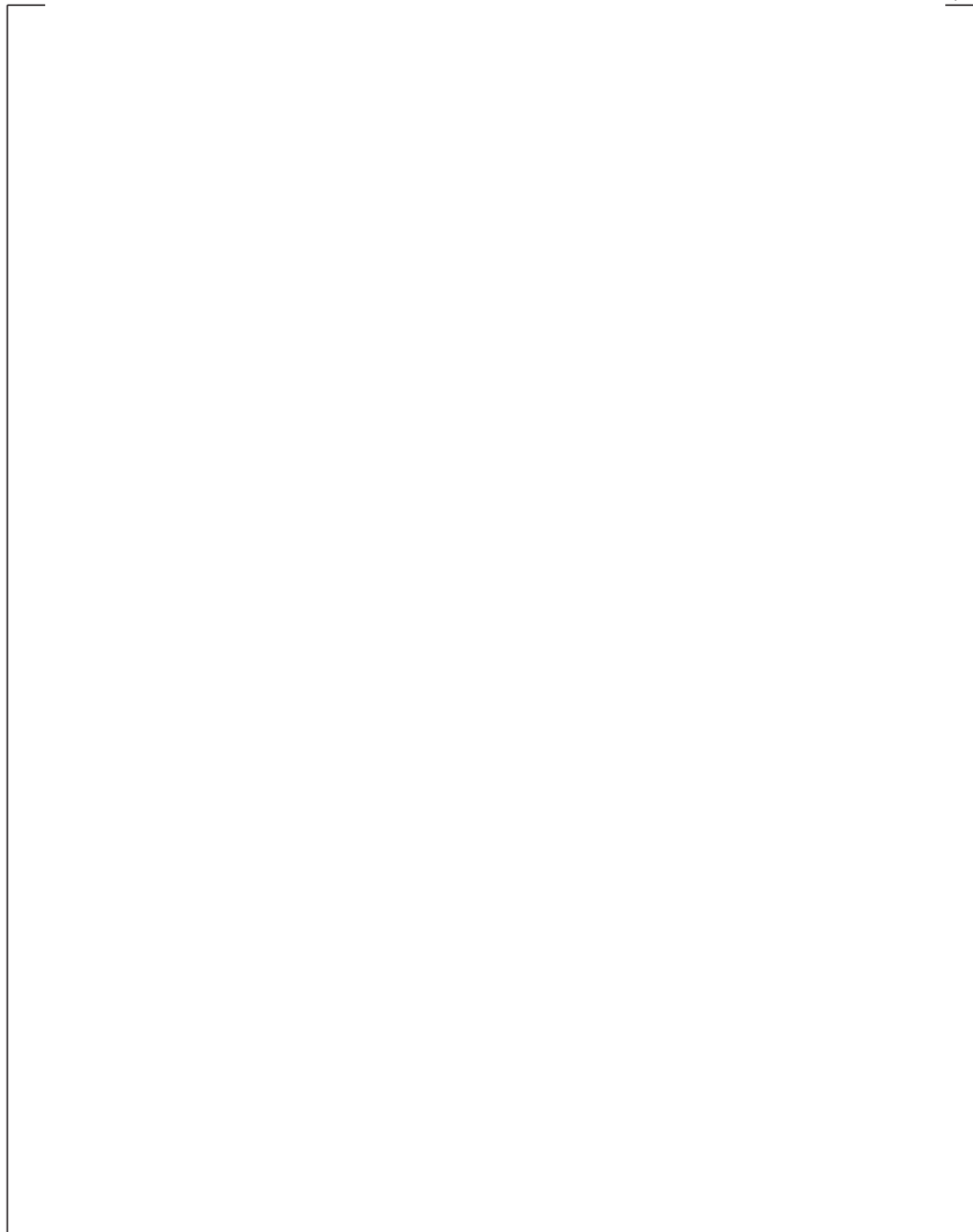


Figure 9-54. WGOTHIC Calculated Flow Pattern – LOCA Plume Rising into CMT Room at 1400 Seconds

9-103

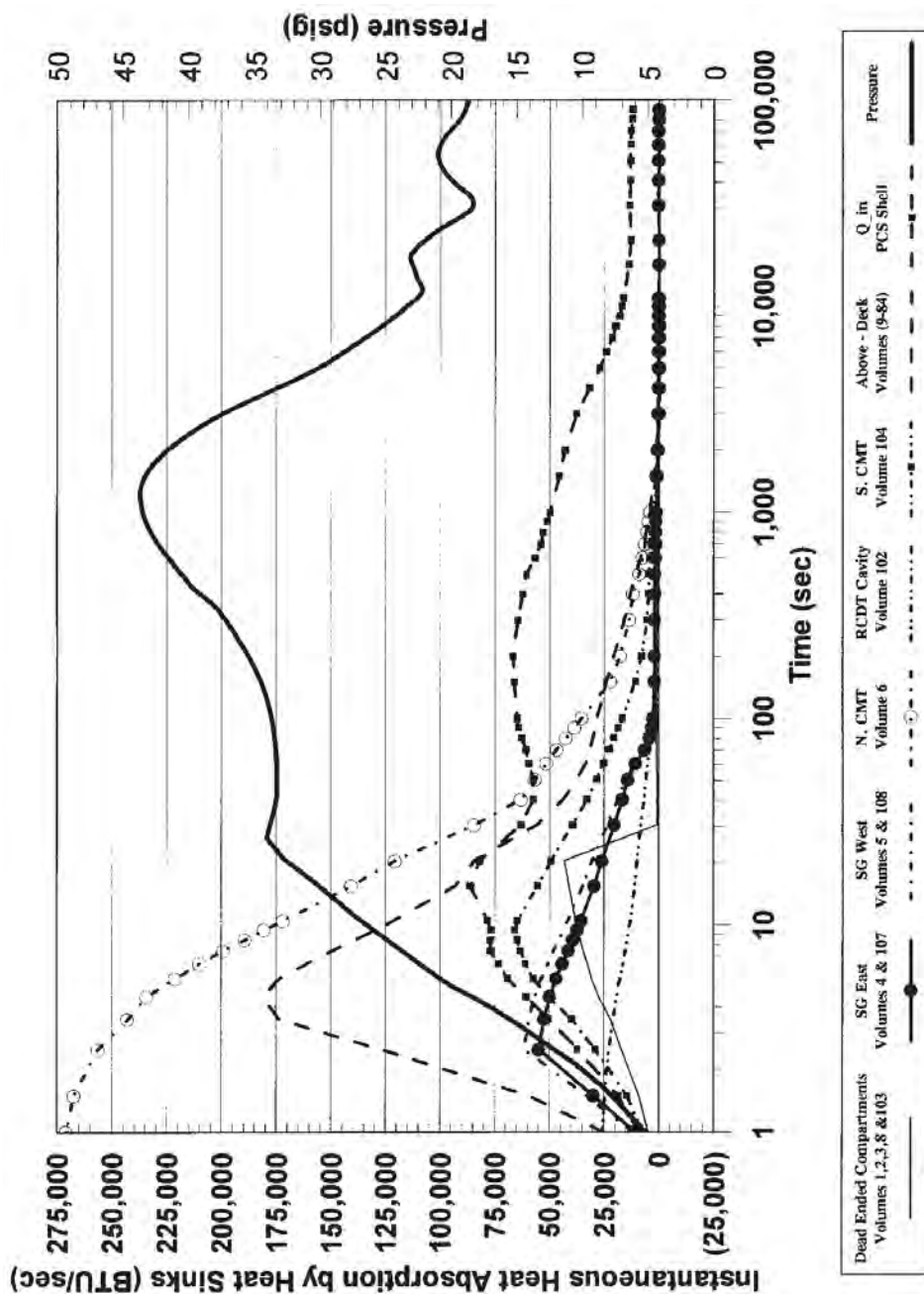


Figure 9-55. WGOthic Calculated AP600 Containment Heat Removal Rates – LOCA Plume Rising into CMT Room

9-104

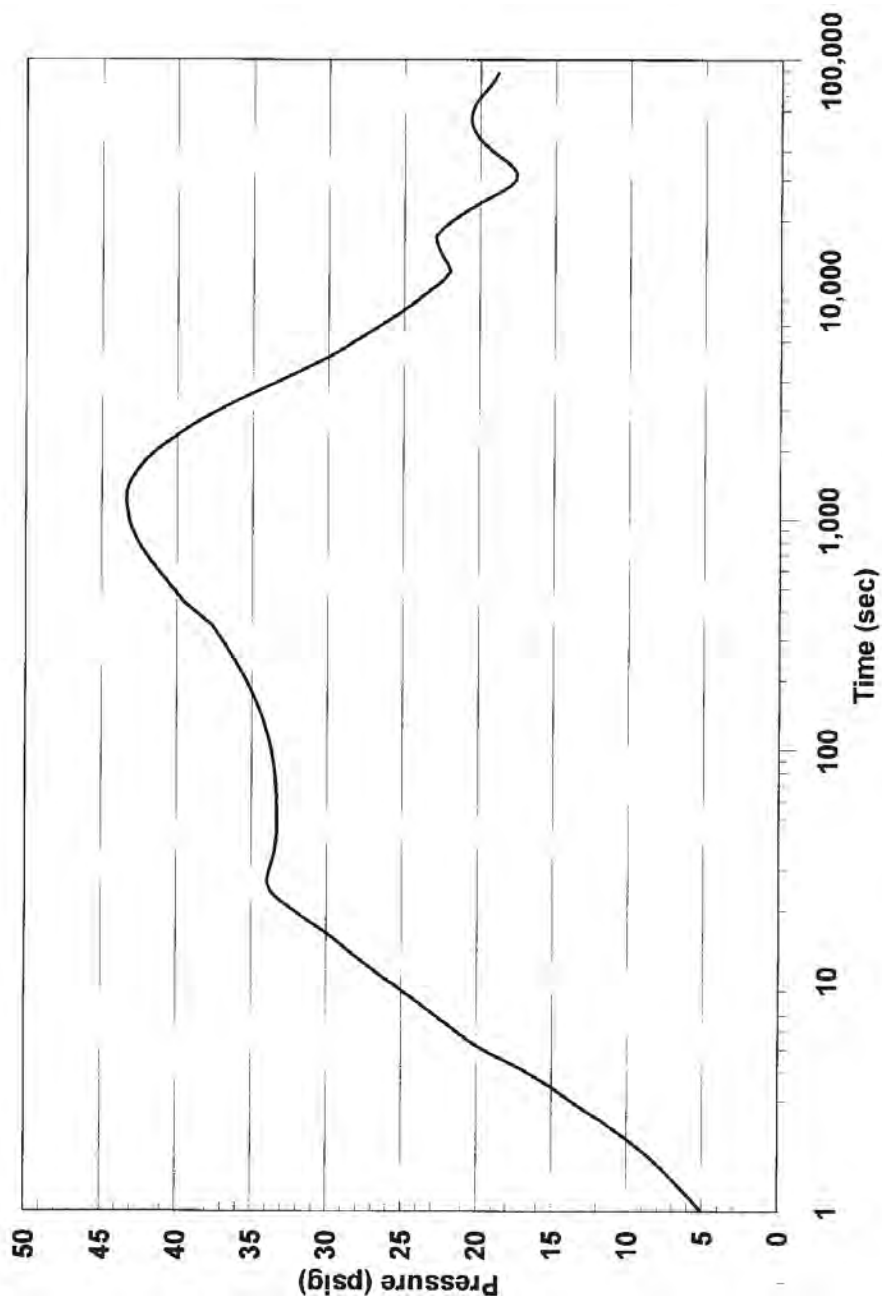


Figure 9-56. WGOTHIC Calculated AP600 Containment Pressure – LOCA Plume Rising into CMT Room and SG Compartments

9-105

a,c

Figure 9-57. WGOTHIC Calculated Flow Pattern – LOCA Plume Rising into CMT Room and SG Compartment at 1000 Seconds

9-106

a,c

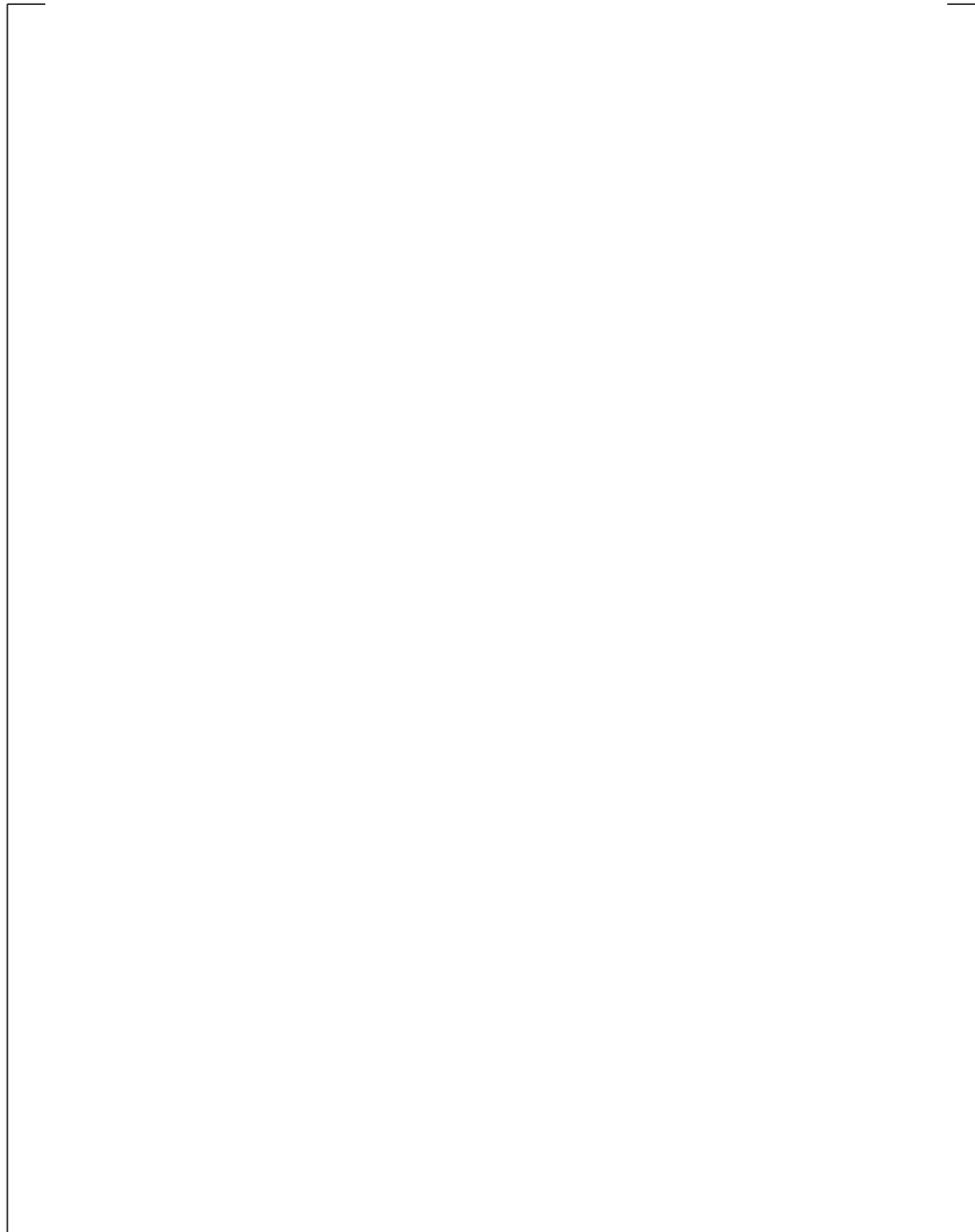


Figure 9-58. WGOTHIC Calculated Flow Pattern – LOCA Plume Rising into CMT Room and SG Compartments at 1500 Seconds

9-107

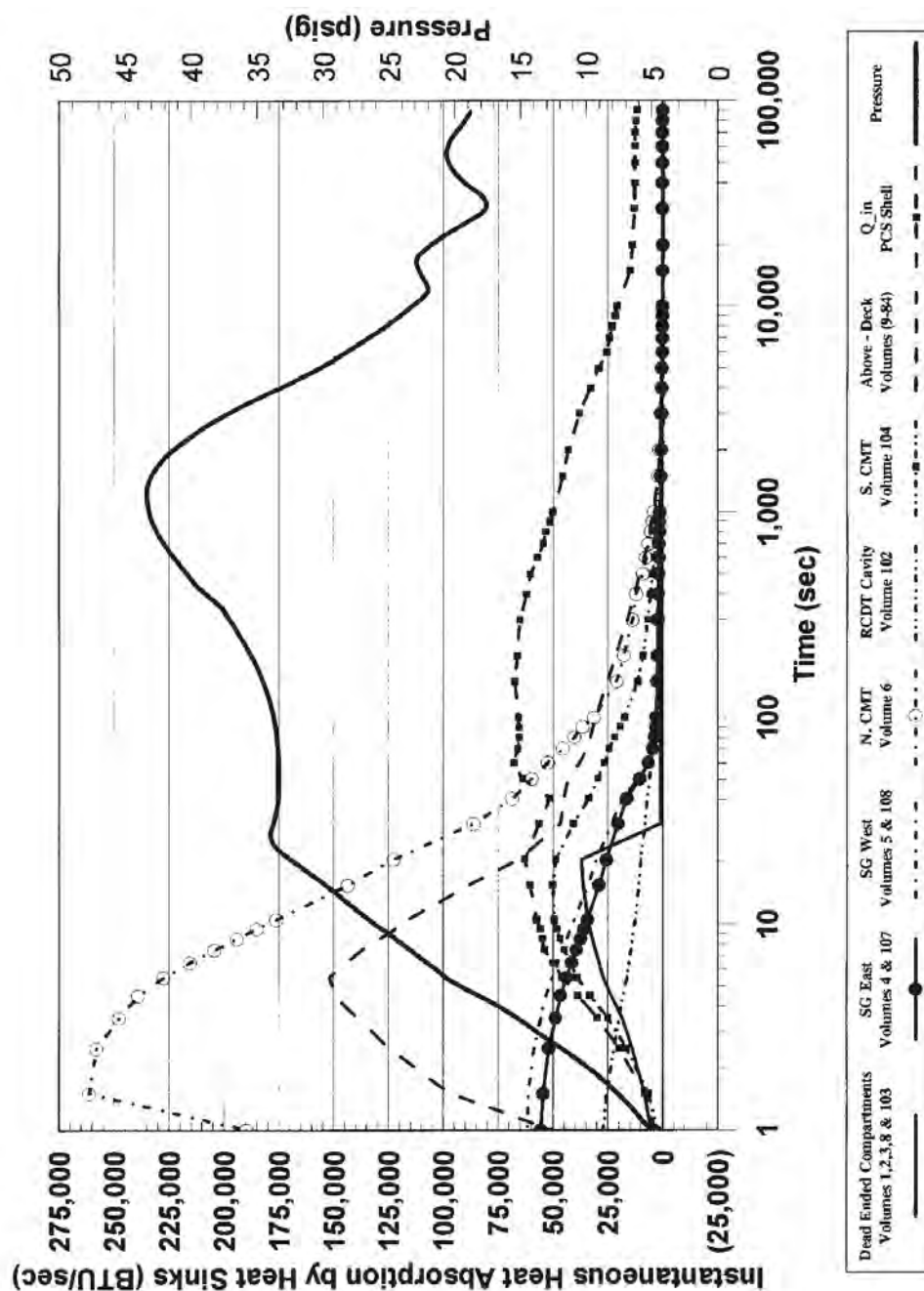
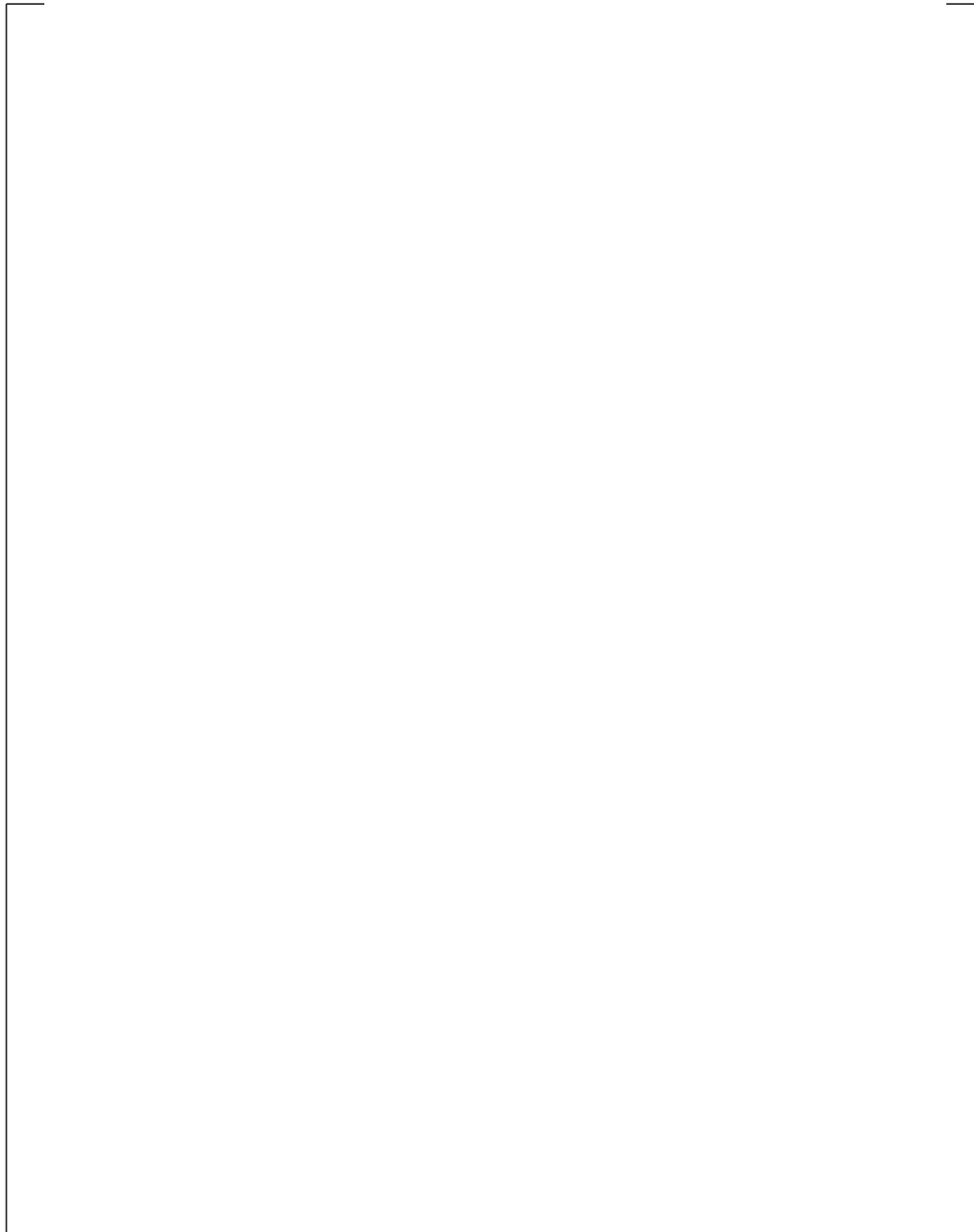


Figure 9-59. WGOthic Calculated AP600 Containment Heat Removal Rates – LOCA Plume Rising into CMT Room and SG Compartments

9-108

a,c



**Figure 9-60. WGOTHIC Calculated AP600 Containment Steam Pressure Ratio for
MSLB Above-Deck**

9-109

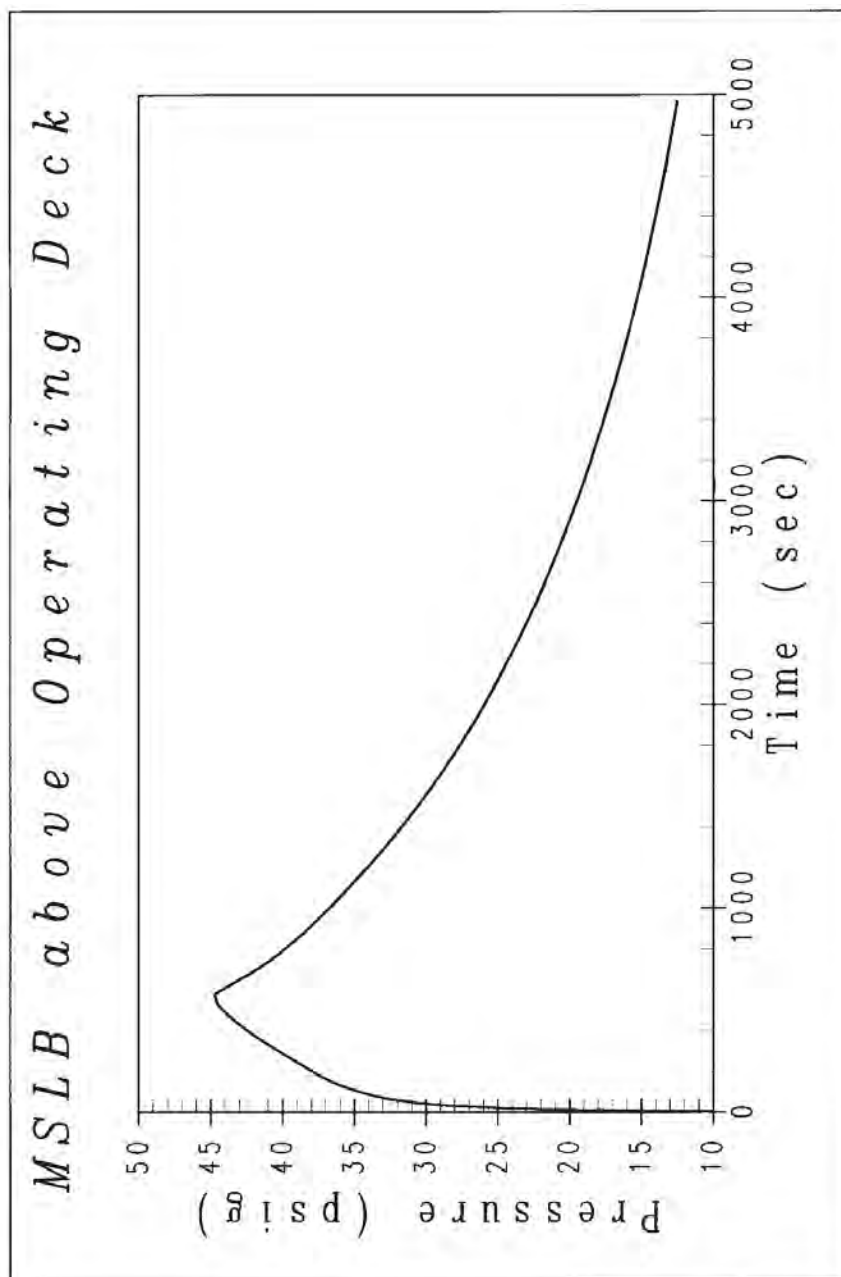


Figure 9-61. WGOTHIC Calculated AP600 Containment Pressure – MSLB Above Operating Deck

9-110

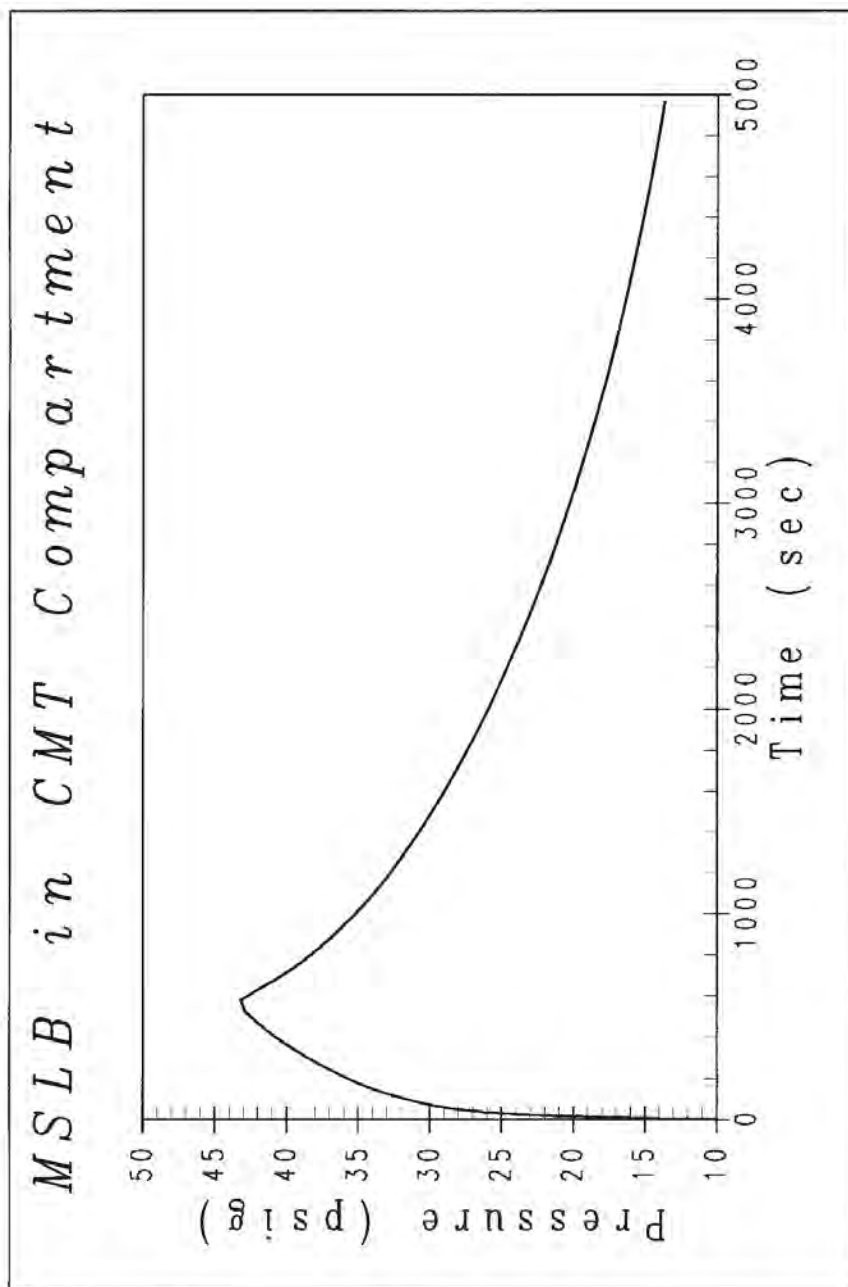


Figure 9-62. WGOTHIC Calculated AP600 Containment Pressure – MSLB in CMT Room

9.A-1

APPENDIX 9.A THERMAL AND CIRCULATION EFFECTS OF DROPS DURING A LOCA

Drops, or fog particles, are created when the blowdown break source steam velocity is large enough to disperse a fraction of the break liquid along with the gas. As discussed in Section 4.4.2D of Reference 9.A.1 and Section 7.1 of Reference 9.A.2, drops will be formed during the LOCA blowdown phase. For the post-blowdown phases of a LOCA and for the MSLB, there will not be any significant drop formation. The thermal and circulation effects of drops on LOCA containment pressure are examined in this section.

The limiting DBA analysis LOCA is a DECLG break. The source flow from the reactor side of the break has more energy than the source flow from the steam generator side of the break, so more drops are expected from the reactor side. During blowdown, a range of drop sizes will be produced. The percentage of liquid converted to drops will also be within some range, the theoretical limits being 0 and 100 percent, although it is anticipated that a significant fraction of the liquid will form drops.

Many factors affect the length of time that the drops will be present in the atmosphere, such as shear coupling to the moving gas, coalescence, de-entrainment at walls and other surfaces, and the drop size (affecting its fall time). To estimate the fall time for various size drops, a simple calculation was performed which only accounts for the gravitational effects on the drops. Using the terminal velocity versus drop diameter information in Section 7.6 of Reference 9.A.3, fall times range from seconds to hours depending on the drop size and fall height. Table 9.A-1 shows estimated fall times for drops with diameters of 0.001, 0.01, and 0.1 inches. This provides an indication that the drops will exist long enough that their effect on containment pressure must be considered.

Table 9.A-1. Estimated Drop Fall Times

Drop Size (in)	Terminal Velocity (ft/sec)	Fall Time (sec)	
		30 ft	100 ft
0.001	.08	375	1250
0.01	8	3.8	12.5
0.1	20	1.5	5

Thermal Effects

The drops flash when they enter the containment atmosphere, reaching saturation very quickly. Section 7.1 of Reference 9.A.2 estimates 3.5 percent of a given drop flashes to steam. Section 7.1 also estimates that the drop diameter only decreases 5 percent due to evaporation in later phases. The drops are strongly coupled to the containment atmosphere temperature due to the large surface area of the total drop population. This strong coupling results in the drop temperature closely following the containment atmosphere temperature as it changes during the transient. Sensitivities using WGOTHIC show that if 5 percent or more of the liquid is converted into drops, then the containment atmosphere will be saturated

9.A-2

quickly. Given the high velocity of the blowdown releases, much greater than 5 percent is anticipated to be converted into drops. With the atmosphere saturated, thermal effects such as superheating will not occur and the effect of larger drop fractions does not significantly affect the pressure response. The effects of drops on the Evaluation Model calculation of containment pressure is investigated with a sensitivity study described in Section 5.8.

Circulation and Stratification Effects

The presence of drops increases the density of the containment atmosphere, which makes the post-blowdown steam release relatively more buoyant. An estimate of the effect of drops on circulation and stratification is made by calculating the plume entrainment rate and resulting circulation time constant for the conditions at the end of the blowdown phase of the DBA LOCA. As discussed in Section 7.1 of Reference 9.A.2, well-accepted models are not available to predict the mass of the drops created during blowdown, so the bounds of 0 percent and 100 percent of the liquid will be considered.

To estimate the volume entrained into the plume (Q_{ent} , in ft³/sec), Peterson's equations (Reference 9.A.4) can be used:

$$Q_{ent} = 0.15 * B^{1/3} * Z^{5/3}$$

where,

- Z = elevation (ft.)
- B = $g * Q_{st} * (\rho_{amb} - \rho_{st}) / \rho_{amb}$
- g = gravitational acceleration = 32.2 ft/sec²
- Q_{st} = volumetric steam flow (ft³/sec)
- ρ_{amb} = containment ambient density (lbm/ft³)
- ρ_{st} = steam density (lbm/ft³)

The entrainment is calculated for a height of 100 feet above the top of the steam generator compartment, so Z = 100 ft. The steam release at the beginning of the peak pressure phase is estimated to be 1870 ft³/sec (Q_{st}). For the case assuming 0 percent of the liquid is released as drops, the $(\rho_{amb} - \rho_{st}) / \rho_{amb}$ term is approximately 0.275. For the case assuming 100 percent of the liquid is released as drops, the density term is approximately 0.60. Using the above equation, the estimated entrainment rate is $Q_{ent} = 8239$ ft³/sec (0 percent drops) and 10695 ft³/sec (100 percent drops). The estimated entrainment at the end of blowdown is approximately four times the steam flow (Q_{st}) for the case without drops, and slightly less than six times the steam flow for the case with drops.

Knowing the entrainment rate, a circulation time constant can be calculated for the containment free volume. This time constant will change with time, but it provides an indication of the amount of circulation expected for the releases after the refill phase. The circulation time constant is the volume divided by the entrainment rate, and for 0 percent drops it is 206 seconds and for 100 percent drops it is 159 seconds. It should be noted that the estimated times conservatively neglect volumetric entrainment into the wall layers. These time constants increase as the steam flow decreases, but this estimation shows that a large fraction of the containment volume will be entrained in the plume within a few minutes, which is relatively short compared to the time to reach maximum pressure (at approximately

1200 seconds), and very short compared to long-term cooling. A relatively large entrainment rate within the above-deck region indicates that the steam density gradients above-deck are not large whether drops exist or not. Therefore, the presence of drops will not significantly affect the general circulation and stratification patterns in the containment atmosphere.

Evaluation Model Drop Sensitivity Study

The AP600 Containment Evaluation Model, with the jet dissipated in the steam generator compartment, was used to determine the effect of drops on the calculation of containment pressure. The treatment of drops in the AP600 Containment Evaluation Model is described in Section 4.5.2.1. The Evaluation Model converts all of the liquid from the reactor side of the break to drops, and none of the liquid from the steam generator side of the break. Sensitivity cases were analyzed for comparison to the Evaluation Model results. The sensitivity cases are discussed in Section 5.8. One case modeled no drop formation and one case modeled 100 percent of the liquid converted into drops.

The containment pressure, as a function of time, was calculated for the sensitivity case. The maximum containment pressure, calculated with the Evaluation Model, is greater than the maximum pressure calculated assuming no drop formation. The presence of drops does have a slight influence on the Evaluation Model pressure calculation. Drop formation is expected during the blowdown phase and the sensitivity study indicates that drop formation should be modeled to provide a bounding calculation for containment pressure.

Conclusions

The formation of drops during the LOCA blowdown phase is a physically real phenomenon that may influence the maximum containment pressure calculated by the Evaluation Model. Drop formation increases the density of the containment atmosphere making the post-blowdown releases relatively more buoyant. A small percentage of the blowdown break liquid formed into drops is sufficient to saturate the containment atmosphere, at which point additional drop density has a minor thermal effect. The Evaluation Model treatment of drops provides a sufficient bounding calculation for maximum and long-term containment pressure.

References

- 9.A.1. WCAP-14812, "Accident Specification and Phenomena Evaluation for AP600 Passive Containment Cooling System," Revision 2, April 1998.
- 9.A.2. WCAP-14845, "Scaling Analysis for AP600 Containment Pressure During Design Basis Accidents," Revision 3, March 1998.
- 9.A.3. NTD-NRC-95-4563, "GOTHIC Version 4.0 Documentation, Enclosure 2: Technical Manual," September 21, 1995.
- 9.A.4. Peterson, P., "Scaling and Analysis of Mixing in Large Stratified Volumes," *International Journal of Heat and Mass Transfer*, Vol. 37, Supplement 1, pp 97-106, 1994.

9.B-1

APPENDIX 9.B EFFECTS OF STRATIFICATION ON HEAT SINK UTILIZATION

9.B.1 INTRODUCTION

An analysis was performed to determine the impact of stratification on the relative effectiveness of containment heat sinks during a postulated LOCA. Models were developed to study transient heat conduction effects for steel and concrete structures under a variety of containment atmosphere boundary conditions. The models were then used to determine the effects of stratification of steam in the containment atmosphere on heat sink utilization in the CMT room and in the above-deck region.

9.B.2 HEAT SINK ANALYSIS

The condensation heat transfer in the containment atmosphere has been characterized as a function of the steam fraction, and has been used as boundary conditions to determine the transient heat absorption rate of the heat sink structures. The results of these analyses are used to estimate the relative effects of stratification on the heat sinks located on the PCS steel shell and in the CMT room.

The purpose of the analysis is to obtain relative effects of stratification for reasonably representative conditions to assess the magnitude of the bias. An extreme stratification gradient is assumed from which the relative effect of stratification on total heat sink energy removal in a region can be assessed. A bias is developed to bound the non-conservative effects of stratification.

9.B.3 CONDENSATION BOUNDARY CONDITIONS

These sensitivity calculations are performed to examine the relative effect of a gas mixture that is homogeneous (as in a lumped parameter node) and a gas mixture that is stratified. To keep the calculations simple, boundary conditions are assumed constant with time, and the following homogenous atmosphere conditions are assumed:

$$\begin{aligned} T_{\text{atm}} &= 276^{\circ}\text{F} \\ P_{\text{atm}} &= 59.7 \text{ psia} \\ f_{\text{st}} &= 0.63 \text{ (homogeneous steam mole fraction)} \end{aligned}$$

These parameters represent approximately time-averaged values over the first hour of the LOCA, since the CMT room steam concentration is relatively constant (Figure 9-44).

The heat transfer from the containment atmosphere and the structure is assumed to be dominated by condensation so that convection and radiation are neglected. The condensation heat transfer is determined by first determining the mass transfer for turbulent free convection (Reference 9.B.1, Section 4.3):

$$m'' = 0.13 * \left[\frac{\rho_{\text{stm}} * D_v * \Delta P_{\text{stm}}}{\left(\frac{v^2}{g} \right)^{1/3} * P_{\text{lm,air}}} \right] * \left[\frac{\Delta \rho * S_c}{\rho} \right]^{1/3} \quad (9.B-1)$$

9.B-2

where,

- \dot{m}'' is the condensation mass flux
- ρ_{stm} is the density of steam at the total pressure and boundary layer temperature
- ΔP_{stm} is the difference in the steam partial pressure atmosphere - surface
- ν is the mixture kinematic viscosity
- g is gravity
- $P_{\text{lm,air}}$ is the log mean pressure difference atmosphere - surface
- $\Delta \rho$ is the mixture density difference atmosphere - surface
- ρ is the bulk mixture density
- Sc is the mixture Schmidt number (typically ~0.51)
- and D_v is the air-steam diffusion coefficient which is given by (Reference 9.B-1, Section 4.3.2)

$$D_v = 0.892 * \frac{14.2 \text{ psi}}{P} * \left(\frac{T_{\text{surf}} + T_{\text{atm}}}{2 * 460^\circ \text{R}} \right)^{1.81} \quad (9.B-2)$$

The steam partial pressure in the atmosphere is given by:

$$P_{\text{stm,atm}} = f_{\text{st}} * P \quad (9.B-3)$$

where f_{st} is the steam mole fraction in the atmosphere and P is the total pressure.

The steam partial pressure at the condensing surface is given by:

$$P_{\text{stm,atm}} = f_{\text{st}} * P \quad (9.B-4)$$

where P_{sat} is the saturation pressure corresponding to T_{surf} .

The log mean pressure difference between the atmosphere air pressure and the air pressure at the surface is given by:

$$P_{\text{lm-air}} = \frac{(P_{\text{air-surf}} - P_{\text{air-atm}})}{\ln\left(\frac{P_{\text{air-surf}}}{P_{\text{air-atm}}}\right)} \quad (9.B-5)$$

where $P_{\text{air-surf}}$ is the air partial pressure at the heat sink surface, $P - P_{\text{stm-surf}}$ and $P_{\text{air-atm}}$ is the air partial pressure in the atmosphere, $(1 - f_{\text{st}}) * P$.

The densities of air and steam at the atmospheric and surface pressures and temperatures are determined from the ideal gas law.

9.B-3

To determine the effect of the steam fraction, three distinct regions based on equal volume are assumed. The top region is assumed to be nearly all steam with $f_{st-top} = 0.98$. The middle region is assumed to be at the nominal conditions with $f_{st-mid} = 0.63$. The bottom region steam fraction is determined by conserving the total amount of steam in the total volume.

$$f_{st-bot} = 3 * f_{st-nom} - f_{st-top} - f_{st-mid} = 0.28 \quad (9.B-6)$$

Applying these three steam mole fractions along with the above containment atmosphere conditions, a relationship can be determined for the condensation heat transfer coefficient as a function of heat sink surface temperature. An equivalent condensation heat transfer coefficient is calculated from m'' for use as a boundary condition for heat sink condensation, described later. The equivalent condensation heat transfer coefficient is calculated by:

$$h_{cond} = \frac{m'' * h_{fg}}{(T_{atm} - T_{surf})} \quad (9.B-7)$$

where h_{fg} is the difference between the steam and liquid saturation enthalpy. The relationships for equivalent heat transfer coefficient are shown graphically Figure 9.B-1.

The condensation heat transfer coefficient varies considerably with respect to the steam fraction in the containment atmosphere, f_{st} , and the surface temperature, T_{surf} . For each steam fraction, the heat transfer coefficient increases with increasing T_{surf} until the saturation temperature that corresponds to the steam partial pressure at the surface is reached. At this point the condensation heat transfer drops to zero, and is zero for all surface temperatures greater than this temperature.

For the case of $f_{st} = 0.98$, $T_{sat} = 291^\circ\text{F}$, which is greater than the containment atmosphere temperature. Thus, the condensation heat transfer coefficient increases with surface temperature and no cutoff is reached. For the case of $f_{st} = 0.63$, $T_{sat} = 264^\circ\text{F}$, and the heat transfer coefficient drops to zero at this temperature. For the case of $f_{st} = 0.28$, 217°F , the heat transfer coefficient drops to zero.

9.B-4

9.B.4 HEAT CONDUCTION MODELS

Several models were developed to calculate heat transfer to the heat sinks. These include:

- Steel structures of varying thickness
- Concrete structures
- Steel-jacketed concrete structures
- Steel containment shell

A description of each model is given as follows.

Steel Structures

The one-dimensional model consists of a 1 ft. by 1 ft. section of steel, modeled by ten nodes of equal thickness, representing one-half the heat sink thickness. For example, for a one-half inch thick steel plate, the model has ten nodes, each 0.025 in. thick. A convective boundary condition is applied to one surface, while the other surface is assumed to be adiabatic. Connections between the nodes are defined by the area of the interface (1 ft²), and the distance from the node center to the interface (0.0125 in.). The properties for steel are listed below:

$$\begin{aligned}\rho &= 490.7 \text{ lbm/ft}^3 \\ C &= 0.107 \text{ Btu/lbm-}^\circ\text{F} \\ k &= 30 \text{ Btu/hr-ft-}^\circ\text{F}\end{aligned}$$

A zero-volume node is attached to the steel at the surface exposed to the atmosphere. The boundary conditions for the three steam fractions are described in the previous section.

Concrete Heat Sinks

The concrete heat sinks have much lower thermal conductivity and are modeled differently than the steel heat sink. The thermal properties of the concrete are given as:

$$\begin{aligned}\rho &= 140 \text{ lbm/ft}^3 \\ C &= 0.19 \text{ Btu/lbm-}^\circ\text{F} \\ k &= 0.83 \text{ Btu/hr-ft-}^\circ\text{F}\end{aligned}$$

Once again, ten nodes are used to represent one-half the concrete thickness. For this case, the nodes are not equal volume with the nodes nearest the convecting surface having small thicknesses, and the thickness increasing geometrically as the nodes progress inward to the adiabatic boundary. The thicknesses are summarized for each node in Table 9.B-1.

9.B-5

Table 9.B-1. Concrete Model Nodal Thickness

		a,c

As for the steel model, Node #1 is connected to a zero-volume surface node, which is in turn connected to the boundary temperature. The heat transfer coefficient is defined in the previous section as a function of the surface temperature for the three steam fractions considered.

Steel-Jacketed Concrete Heat Sinks

The steel-jacketed concrete heat sinks combines the two-foot thick concrete model previously described with a one-half inch steel plate. The condensation boundary condition is attached to the outside of the steel plate, that is represented by 10 nodes, 0.05 in thick. The inside steel node is attached to the first concrete node with an assumed gap of 0.036 in. The gap conductance is given by

$$h_{\text{gap}} = \frac{k_{\text{mix}}}{\delta_{\text{gap}}} \quad (9.B-8)$$

where δ_{gap} is the gap thickness

and k_{mix} is the thermal conductivity of the containment atmosphere mixture

$$k_{\text{mix}} = 0.5 * (k_{\text{air}} + k_{\text{stm}}) \quad (9.B-9)$$

For $T_{\text{atm}} = 276^{\circ}\text{F}$, and $f_{\text{st}} = 0.5$, $k_{\text{mix}} = 0.03 \text{ Btu/hr-ft}^{\circ}\text{F}$, and $h_{\text{gap}} = 10 \text{ Btu/hr-ft}^2\text{-}^{\circ}\text{F}$.

The concrete is represented by 10 nodes with thicknesses shown in Table 9.B-1.

9.B-6

Steel Containment Shell

The steel containment shell model is somewhat more complex in that the inside boundary condition is the same as the other models while the outside boundary condition is not adiabatic, but is representative of the outer shell evaporative heat transfer. The steel shell is assumed to be []^{a,c} thick. For this case, a []^{a,c}. The inner-most node is connected to a zero-volume node upon which the condensation boundary condition is assumed. The outer-most node is also connected to a zero-volume node upon which an evaporation boundary condition is assumed. The outside boundary temperature is assumed to be an average between the inlet air temperature at the bottom of the Passive Containment Cooling System annulus, and the outlet air temperature at the top.

$$T_{\text{air-avg}} = 142^{\circ}\text{F}$$

and $h_{\text{evap}} = 113 \text{ Btu/hr-ft}^2\text{-}^{\circ}\text{F}$

Note that the assumption of a constant value of h over the entire shell surface is very conservative, since in the stratified case, the shell adjacent to the steam-rich top would heat up and significantly increase the evaporation rate on the outside. No credit is taken in this analysis for the associated increase in external heat transfer coefficient.

For this model, there is a short period of time during which the shell heats up from the initial temperature. After this time, a steady-state condition is established as heat is transferred at a nearly constant rate from the inside to the outside of the shell.

9.B.5 RESULTS

For each of the models described above, three transient calculations were performed representing each of the three steam fraction conditions. The results of these calculations were used to examine heat absorption effects for each of the conditions. Since the models represent one square foot of heat sink area, the results can be used to estimate the heat sink behavior in a typical room by multiplying the integrated heat removal by the total area for a particular heat sink type.

Containment Steel Shell Heat Sink Stratification Sensitivity

Figure 9.B-2 shows the heat removal rate for the containment shell. The areas for the top, middle, and bottom of the shell are not weighted equally (as in Equation 9.B-10). The volume of the containment above the operating deck is divided into three regions of equal volume, and the associated surface area for each volume is used. For the AP600 containment,

Elevation of operating deck	=	135.25 ft
Elevation of spring line	=	218.71 ft
Elevation of top of dome	=	256.4 ft
Containment radius	=	65 ft
Gas Volume in dome	=	336,963 ft ³
Surface area of dome	=	15,552 ft ²
Total volume of gas above deck	=	1.45 x 10 ⁶ ft ³

9.B-7

The two lower regions both consist of a cylindrical gas volume = 481,582 ft³. This corresponds to a cylindrical section 36.28 feet in length with a surface area = 14,776 ft². The upper region gas volume is also 481,582 ft³, and consists of the dome and a cylindrical section 11.1 feet in length. The total surface area associated with this volume is 19,898 ft².

Thus, the equivalent integrated heat removal rate through one square foot of the shell is weighted by surface area as

$$Q_{3Region} = \frac{(19,898 * Q_{Top} + 14,776 * Q_{Mid} + 14,776 * Q_{Bot})}{49,450} \quad (9.B-10)$$

The results show that the higher weighting of the upper, steam-rich region nearly compensates for the lower heat removal rates in the bottom region, and the heat removal rate is slightly (~0.5% after 200 seconds) higher for the homogeneous case.

Results for the steel shell assessment are presented in terms of instantaneous rate since the external boundary condition never allows the steel to saturate. The results also allow interpretation of stratification effects during the quasi-steady, long-term, while the steel shell is the dominant heat sink and the balance between instantaneous source and sink heat rates governs the containment pressure. Since the stratification penalty on the steel shell heat removal rate is nearly negligible, a simple bias is introduced into the Evaluation Model by removing the non-grating operating deck floors to bound the effect. The stratification effect is exaggerated due to the use of an extreme gradient, well beyond what has been observed in the LST (Section 9.2.1 and 9.2.3) and in the international containment database (Appendix 9.C.2).

Simulated Room Heat Sink Stratification Sensitivity

These models were applied to heat sinks which reasonably represent the AP600 CMT room. The heat sinks for the AP600 CMT room (North and South sections) are summarized in Table 9.B-2.

Table 9.B-2. AP600 Assumed Room Heat Sink Distribution

Heat Sinks in Simulated Room	Thickness	Surface Area	Region
Steel-Jacketed Concrete – Ceiling (single-sided)	0.5 in. / 24 in.	5398.87 ft ²	Top
Steel-Jacketed Concrete – Floors (single-sided)	0.5 in. / 24 in.	5601.44 ft ²	Bottom
Steel-Jacketed Concrete – Walls (double-sided)	0.5 in. / 24 in.	4596.11 ft ²	1/3 in each region
Steel-Jacketed Concrete – Wall (double-sided)	0.5 in / 48 in	673.99 ft ²	1/3 in each region
Concrete – Bulk (double-sided)	48 in.	3287.36 ft ²	1/3 in each region
Steel – CMT (single-sided)	4.874 in.	1848.8 ft ²	1/3 in each region
Steel – Containment Shell Wall (single-sided)	1.57 in.	11385.53 ft ²	1/3 in each region

9.B-8

Table 9.B-2. AP600 Assumed Room Heat Sink Distribution (cont.)

Heat Sinks in Simulated Room	Thickness	Surface Area	Region
Steel – Columns (double-sided)	0.39 in.	1656.5 ft ²	1/3 in each region
Steel – Floor Grating (double-sided)	0.39 in.	3781.69 ft ²	1/3 in each region
Steel – Elevator (double-sided)	0.2 in.	218.96 ft ²	1/3 in each region
Steel – Platform (double-sided)	0.144 in.	11254.2 ft ²	1/3 in each region
Steel – Stair & Rails (double-sided)	0.132 in.	181.59 ft ²	1/3 in each region

As was discussed previously, each heat sink was analyzed using three different steam fractions representing the top, middle, and bottom thirds of the room which is a bounding gradient when the plume rises through the CMT compartment. There is expected to be no significant stratification penalty in the CMT room with downflow in the Evaluation Model, where the plume rises from the steam generator compartment. For each individual heat sink, a homogeneous case and three-region averaged result was obtained for a 1 ft² section of the heat sink. The energy removal by each heat sink is determined by calculating the heat removal for 1 ft², and multiplying by the appropriate surface area.

Where appropriate, the heat sinks that are located in a specific volume (i.e., ceilings and floors) are not averaged for the three-region, but are analyzed solely with the steam fraction of that volume. This becomes important for the ceilings since these heat sinks are located within the high steam fraction volume and higher heat transfer is expected when the room is stratified. The opposite is expected when considering floors. Refer to Table 9.B-2 for the region designation.

Figure 9.B-3 shows the integrated heat removal by all the heat sinks in the CMT room for a one hour transient. As will be discussed below, the stratification bias for this case is a function of the total energy absorbed. This is because the adiabatic boundary condition results in heat sinks reaching a maximum thermal absorption governed by the saturation temperature for the given steam concentration in a volume. Therefore, results for this scenario are presented in terms of integrated total heat absorption.

The results show the CMT room heat sinks including the floors for the homogeneous and stratified cases. In addition, the case where the floors are not included for the homogeneous case is also shown. The stratified, three-region results are lower than the homogeneous case results by 10-15% when all heat sinks are considered. The homogeneous case with floors excluded is slightly conservative when compared to the stratified case with the floors included. Thus, the combination of assuming homogeneous conditions and neglecting the floors in the total heat sink area results in total heat sink utilization that is neutral at the time of peak pressure, and over the longer term is slightly conservative relative to the expected conditions.

9.B-9

The assessment of stratification effects is very conservative because a conservatively low benefit for the uppermost region is used, and the gradient is much more extreme than what has been observed in the LST (9.2.1 and 9.2.3) and in the international containment database (Appendix 9.C.2). The choice of stratified conditions to examine for this sensitivity are conservative and the results bound other, less extreme postulated stratification gradients. The room temperature is assumed to be 276°F in the stratified case, the same temperature as in the base case homogeneous room. One could, for example, postulate a less extreme, thermodynamically consistent, gradient of 0.77 for the top, 0.63 for the middle, and 0.49 for the bottom. The saturation temperature for a region at 59.7 psia and a steam mole fraction of 0.98 (psat of 58.5 psia) is 291°F. The upper region then would be about 15°F hotter than assumed. Therefore, the upper region conditions are thermodynamically inconsistent in a way that minimizes heat absorption in the upper region of the room, and thus maximizes the stratification bias.

The bias for the CMT room is governed by the air content in the lowest region. Results indicate that steel heat sinks, and the steel on jacketed concrete, reach a maximum for integrated heat absorption well within the one-hour time frame of the calculation. The concrete continues to absorb heat over a very long term, on the order of days. However, the transient skin temperature of concrete increases due to its relatively poor thermal conductivity and a gap between the steel jacket and concrete reduces concrete effectiveness, so that the magnitude of concrete heat absorption is not significant relative to the steel. The integrated heat absorption by heat sinks is then primarily a function of the maximum bulk steel temperature rise, which is related to the saturation temperature of the adjacent region. While a less severe assumed stratification gradient would result in less rapid heat absorption by sinks in the upper region, the upper heat sinks would still reach their maximum well within the one-hour time frame. The lower region integrated heat absorption is limited by the saturation temperature for the assumed steam concentration. Therefore, the stratification bias is controlled by the lower region steam concentration and is maximized by the assumption of the extreme stratification gradient.

Since the exaggerated effect of stratification for the case of a plume rising through the CMT shows a bias on total integrated heat removal, a bias is introduced into the Evaluation Model by removing heat sinks associated with floors in compartments. As an additional conservatism, that bias is retained for the Evaluation Model with a plume rising through the steam generator compartment, as well as all sensitivity cases performed, even though most situations result in downflow through the CMT compartment.

For the case of the steel containment shell above the operating deck, the dome surface area weights the upper, steam-rich volume more heavily than the lower volumes, and compensates for the lower heat removal rates. Thus, the homogeneous case results are nearly equal to those for the stratified case, with the homogeneous case giving less than 0.5% less instantaneous heat removal rates. A simple bias of removing operating deck floors is included in the Evaluation Model to bound this effect.

9.B-10

9.B.6 CONCLUSIONS

For the case of the steel containment shell above the operating deck, the dome surface area weights the upper, steam-rich volume more heavily than the lower volumes, and compensates for the lower heat removal rates. Thus, the homogeneous case results are nearly equal to the stratified case, with the homogeneous case giving less than 0.5 percent less instantaneous heat removal rates. A simple bias of removing operating deck floors is included in the Evaluation Model to bound this effect.

The results of the heat sink utilization analysis for below-deck compartments indicate that in general, the assumption of homogeneous compartment volumes predicts higher overall heat removal by the heat sinks compared to stratified volumes. This is primarily due to the propensity of the condensation heat transfer to fall off as the heat sink surface temperature approaches the local saturation temperature in the lower steam fraction volumes. Stratification gradients are not expected to be nearly as extreme as assumed in this evaluation. The results of the homogeneous case gives 15-20% higher integrated heat removal than the stratified results. Therefore, a bias is introduced in the Evaluation Model to account for this difference, implemented by removing heat sinks representing floors from the Evaluation Model.

References

- 9.B-1. WCAP-14845, "Scaling Analysis for AP600 Containment Pressure During Design Basis Accidents," Revision 3, March 1998.

9.B-11

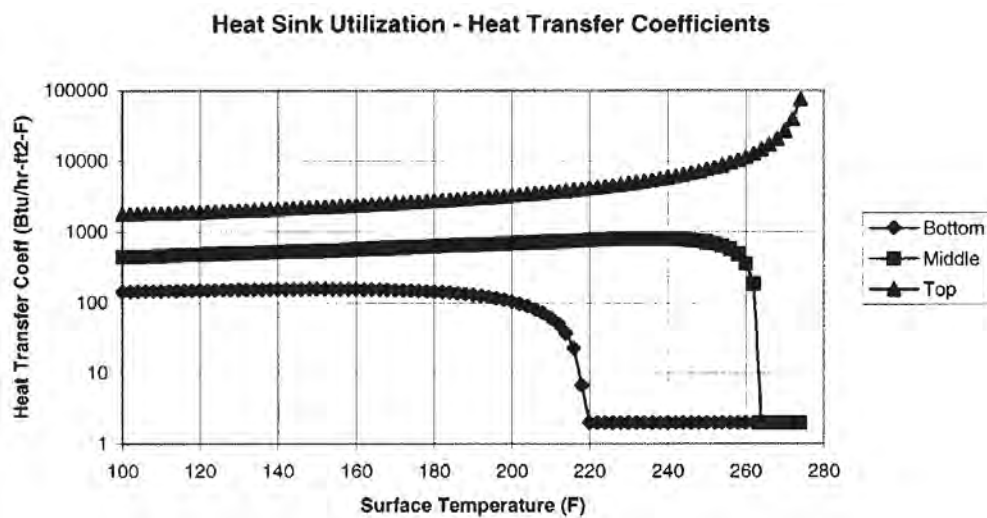


Figure 9.B-1. Condensation Heat Transfer Coefficients vs. T_{surf}

9.B-12

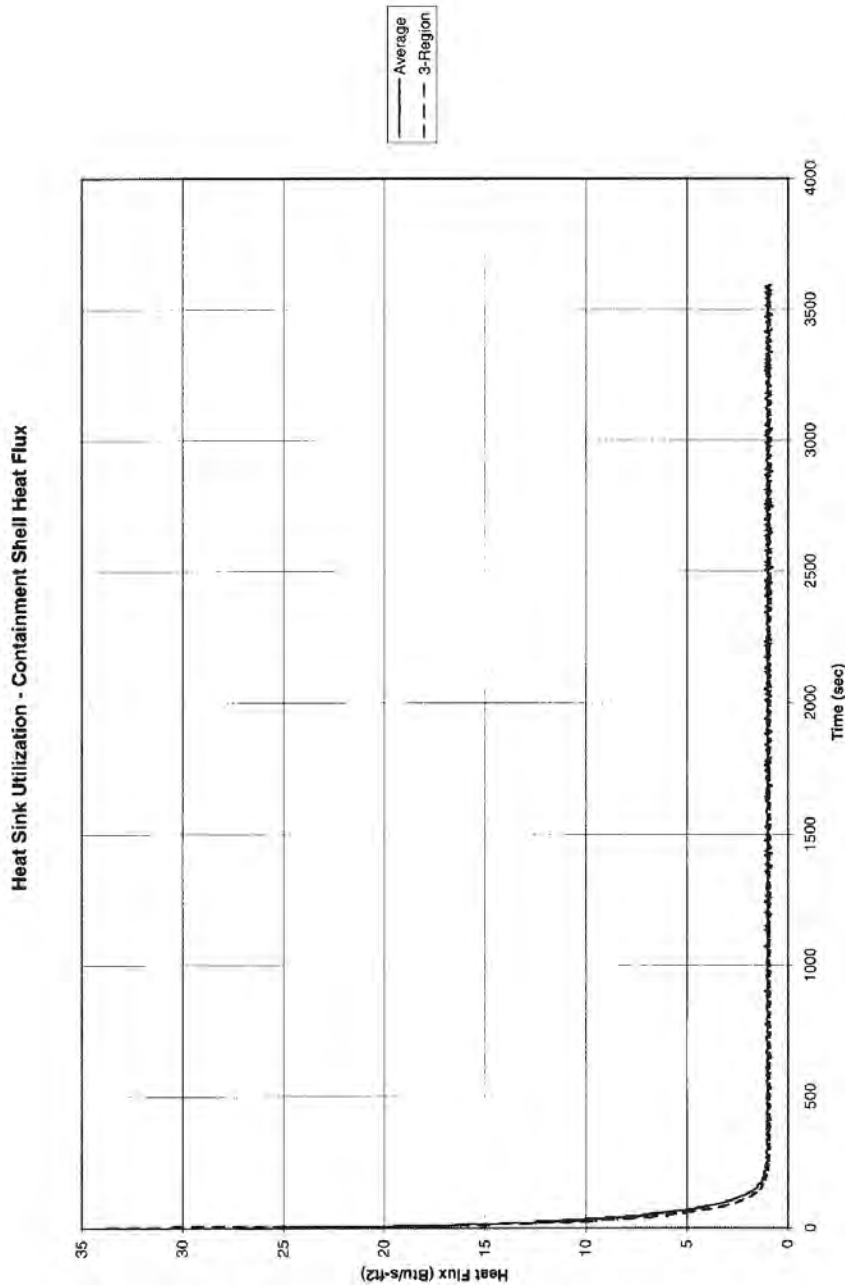


Figure 9.B-2. Containment Shell Heat Sink Results

9.B-13

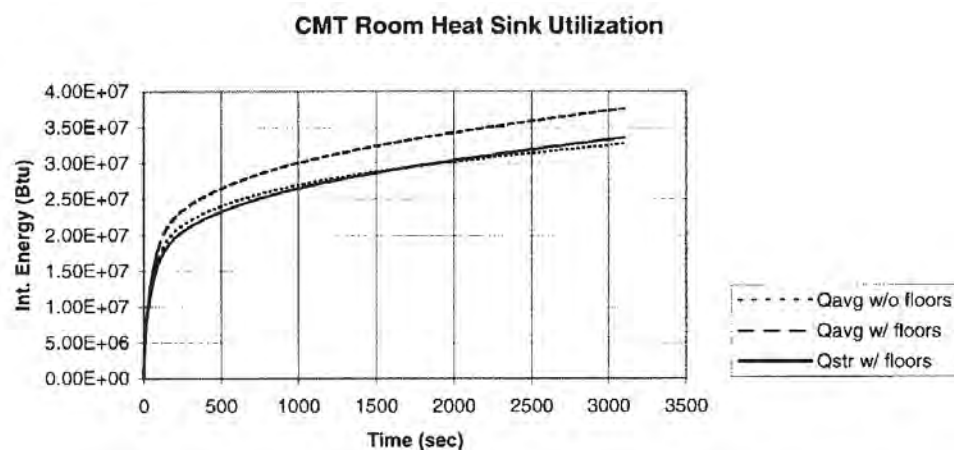


Figure 9.B-3. CMT Room Heat Sink Results

9.C-1

APPENDIX 9.C ADDITIONAL INFORMATION ON CONTAINMENT CIRCULATION AND STRATIFICATION

9.C.1 DEVELOPMENT OF EXPECTED FLOW PATTERNS FOR AP600 AND AP1000 BASED ON SEPARATE FLOW TESTS IN ENCLOSURES

9.C.1.1 Stratification Phenomena

Stratification is the formation of horizontal layers of constant density. Stratified layers are stable if the density of the layers decreases in the upward vertical direction (the gradients of density are negative in z direction according to Figure 9.C-1a) and if forced convection mixing is not sufficiently strong to disrupt the stable fluid layers.

Another more general definition of stratified conditions is that gradients of density in the horizontal direction are small, except in jets, buoyant plumes, and small regions near the vertical walls inside boundary layers (wall jets). In most of the volume, the density gradients in z direction are negative, while inside the jets, wall jets, and buoyant plumes they could be positive (see Figure 9.C-1b).

Stratification occurs as a consequence of the temperature or concentration gradients in the vertical direction. Increasing temperatures or decreasing concentrations of heavier mixture components with increasing elevation promote stratification. The existence of flow structures, such as jets, plumes, and vertical wall boundary layers, decreases the "steepness" of the vertical density gradients.

Examples of stratified conditions are numerous. Stratified layers are observed as large-scale geophysical phenomena (in lakes, sea, and oceans, in atmosphere - stratus clouds), as well as inside the enclosures. For example, warmer air tends to gather below ceilings in energy storage devices, nuclear reactors, solar collectors, and enclosures under the influence of the spread of fire and smoke.

This appendix discusses the stratification phenomena inside a nuclear reactor containment. Possible reasons for the stratification will be specified. Stratification may occur if:

1. The upper boundary is at the higher temperature than the lower boundary (see Figure 9.C-2 a), as well as for other similar combinations of temperature boundary conditions at the outside and inside surfaces (see Figure 9.C-2 b – d).
2. A higher concentration of the heavier or lighter components of the mixtures is maintained (by injecting and removing) near the lower or upper boundaries of the enclosure, respectively.
3. A lighter fluid is released (permanently, or from time to time) and captured below the ceiling of the containment.
4. The release point of the lighter/heavier fluid is closer to the top/bottom.
5. The shape of the enclosure promotes stratification (tall elongated enclosure).

9.C-2

6. The distribution of the non-complete vertical partitions suppresses fluid flow in the upper portions of the enclosure.
7. The distribution and size of the horizontal openings suppresses the fluid flow in vertical direction.
8. The internal heat sources (sinks) are positioned in the upper (lower) portions of the enclosure.

Under the conditions above (or a combination of them), the stratification may be stable. The presence of stratified layers inhibits circulation, that otherwise could be induced by a jet, plume, or boundary layers. The conduction and diffusion, heat and mass transfer processes, respectively, are dominant. As a result, the overall heat and mass transfer decreases and the heat transfer through the containment shell is slowed.

One way to avoid the stratification is to generate fluid flow patterns inside the enclosure using forced convection. Additional devices such as fans, sprays, or nozzles are necessary, as well as associated power supplies and controls.

Since the AP600 and AP1000 rely on a passive containment cooling system (PCS), only the effects of fluid circulation due to the interaction of natural convection with the stratified field are discussed.

Modifications to the shape of the enclosure, the distribution and size of the internal partitions, and the openings could be made to avoid stratification. A different distribution of heat sources could also be applied to generate natural convection effects. The fluid flows due to natural convection promote better circulation inside the enclosure. The introduction of jets may also interrupt stably stratified layers through better mixing of the layers of various densities and concentrations. With a jet stratification may become unstable or, at least, the vertical gradient reduced. With only natural convection if the generated buoyancy forces are strong enough, the entire volume of the enclosure will be affected, resulting in the relatively uniform values of temperature and concentration fields. Natural convection heat transfer is dominant and the more intensive circulation improves the transfer of heat from the containment. Natural convection flow effects are generated spontaneously due to the gravity (buoyancy forces) when heated sources exist, so that additional control and other devices are not necessary.

9.C.1.1.1 Static Stratification

Static stratification occurs if the upper horizontal boundary of the domain is maintained at a higher temperature than lower boundary, as in Fig. 9.C.1-1a. Stratification also occurs if the concentration of heavy components is low in the mixture in the upper portion of the domain. The fluid layers are undisturbed and fluid motion is negligible. The temperature or density distribution in the vertical direction is linear. Heat transfer is predominantly governed by conduction, while mass transfer is driven by diffusion. The formed fluid layers are stable and communicate only with the neighboring upper and lower layers. The resulting heat and mass transfer rates are low.

Corresponding experimental results are found in Akino et al., 1989 and Hiller et al., 1988. In both papers, stable stratified layers are identified using various colors reflected by liquid crystals (suspended in the fluid).

9.C-3

Static stratification exists inside a containment vessel if the temperature distribution of the vertical walls is the same as in the surrounding stratified fluid (adiabatic vertical walls, as in Fig 9.C.1-1a). Since, the top of the passive containment, as well as the vertical walls, are exposed to the surrounding air and cooled by natural convection, stable stratification is not present. Even small temperature differences between the air inside and outside the containment produce large Grashof (Rayleigh) numbers, due to the height of the containment ($H_f=109$ ft). For example, a temperature difference of 9°F between the air at the deck level and the air below the dome ceiling results in $Gr_f = 2.2 \cdot 10^{13}$. This is in the range of chaotic turbulent flow, characterized by upward and downward plumes (see experimental results by Akino et al., 1989).

Static stratified layers are also generated by releasing a lighter gas, e.g., steam or hydrogen, into the upper portion of the containment and capturing the gas beneath the dome.

Hydrogen distribution experiments performed in the HDR facility, test group E11, combine high hydrogen release rates with superheated steam injection into the containment (see Wolf et al., 1994a). A comparison of influences of the axial break and gas release positions is obtained with E11.2 (high release position) and E11.4 (low release position) experiments. Although these two specific experiments simulate severe accident scenarios, comparison of results from the two experiments provides insights into the physics of stratification. The tests are characterized by boundary conditions that can promote circulation (especially test E11.4). They also show that relatively small concentration gradients can exist in the presence of circulation.

Steam release from small breaks generates thermal stratification for break positions located at the higher level, with the hot zone above the break locations. Two mechanisms are used to break up the established thermal stratification. The first mechanism used subsequent steam releases at positions lower than the original release to break up the established thermal stratification. This mechanism did not produce homogeneously mixed conditions. The second method is the application of external sprays on the upper dome. This causes condensation on the inner surface and a decrease in the temperature in the upper part of the dome. Convective flows form and affect the whole volume of the dome and lower compartments, resulting in a completely homogenized atmosphere.

As in the HDR E11.2 experiment, condensation on the dome of the passive containment breaks up stratification. The condensation on the vertical walls also contributes to breaking of stratified layers and to entrainment in the vertical boundary layers. The circulation inside the containment affects the lower compartments and promotes circulation due to the natural convection.

The shape of an enclosure could also promote stratification. One example is natural convection inside romb shaped enclosures (see Figure 9.C-3). Stratification is generated if the upper vertical side is at a high temperature and the inclined top and bottom sides are adiabatic (see, Dzodzo, 1993). The overall heat and mass transfer are suppressed by the presence of the stratified fluid in the upper and lower corners of the romb shaped enclosures. When the boundary conditions are reversed, i.e., the lower vertical side is at the higher temperature, the entire volume of the enclosure is effected by circulation. Heat transfer is intensified and stratified layers are not present in the upper and lower corners. A comparison of experimentally and numerically obtained temperature and velocity fields for these two cases is presented in Figure 9.C-4. An overview of the numerical results for various angles of the romb (parallelogram-shaped) enclosures, Prandtl numbers, and aspect ratios is presented by (Hyun and Choi, 1990).

Although the top of the passive containment is somewhat conical in shape, stratification in the upper portion of the dome would not exist because of the natural convection due to the lower temperatures of the ceiling and vertical walls. Stratification effects are promoted if the containment ceiling is insulated or at a higher temperature.

The distribution of the internal heat sources in the upper part and heat sinks in the lower part of enclosures promotes the formation of the stratified layers (see Figure 9.C-2 b, c, d). Examples of the influence of the position and distance between the heat source and heat sink are provided by A. Kurosawa et al., 1993 and C. J. Ho et al., 1994. An example of the influence of an array of discrete heat sources on natural convection is presented by T. J. Heindel et al., 1995.

Vertical non-complete partitions inside an enclosure contribute to the stratification. If the non-complete vertical partition is positioned near the ceiling, flow in the upper part of the enclosure is obstructed and a stagnant stratified region near the ceiling is formed (see Hanjalic et al., 1996, and Nowak and Novak, 1994 for examples of the two-dimensional numerical simulation, and T. Fusegi et al., 1992, for the three-dimensional simulation). This is of special interest for the analysis of the spread of fire and smoke inside the buildings. Such partitions do not exist above the operating deck level in the passive containment.

Narrow horizontal openings between upper and lower compartments also suppress circulation and cause stratification. The results of a two-dimensional numerical simulation (R. Frederick and A. Valencia, 1995) show the influence of the size of the horizontal openings on the natural convection inside the vertically connected enclosures.

The potential for stratification in compartments below the operating deck of containments, due to the various sizes of the openings is also studied (see Reference Wolf et al., 1994b).

9.C.1.1.2 Stratification and Circulation

Figure 9.C-1b illustrates conditions where a portion of an enclosure is stratified and other portions are affected by strong recirculation zones and currents. Due to the circulation effects, shallow vertical density gradients are present inside the stratified portion of the enclosure volume.

Convective heat and mass transfer that results from communication between the stratified and flow-affected zones, contributes to the mixing between the zones with different temperatures, concentrations, and densities. Flow inside the enclosure is promoted by the existence of the entraining wall layers (which are a consequence of the heat transfer), penetrating jets, and buoyant plumes (see Reference, Peterson, 1994 and Figure 9.C-1b).

To gain insight into passive containment physics, we will start with small-scale enclosure examples and progress to larger scale.

9.C.1.1.2.1 Interaction of Wall Jets (Boundary Layers) with Stratified Layers

One example of interaction of wall jets with stratified layers is the natural convection inside a square enclosure (see Figure 9.C-5). The opposite vertical walls of the enclosure are at the different temperatures and the horizontal walls are adiabatic (see Markatos and Pericleous, 1984 and Figure 9.C-5a). With high Rayleigh numbers (over 10^6), $Pr=0.71$, turbulent flow exists inside the enclosure. Velocity and temperature gradients are large in the boundary layers. Velocities have maximum values near the walls, while inside the core of the enclosure they are small. The temperature (density) field in the core of the enclosure is stratified (see Figure 9.C-5). Communication exists between the boundary layer region and core of the enclosure through the vortices (see Figure 9.C-5b), which change in number, position, and intensity for various temperature differences between the opposite walls (various Ra numbers). Temperature gradients are highest in the boundary layers near the vertical and horizontal walls (see Figure 9.C-5c). For the laminar convection ($Ra=10^{+4}$ and $Ra=10^{+5}$), the temperature difference between the highest and lowest points at the vertical axis of the stratified core is $0.6*(T_h - T_c)$, while for the turbulent regime ($Ra=10^{+8}$, 10^{+12} , 10^{+16}) it is $0.4*(T_h - T_c)$. The decrease in the vertical temperature gradients inside the stratified core for the turbulent regime is the result of higher velocities and stronger circulation inside the cavity. The temperature field inside the core of the enclosure is stratified, while recirculation due to convection inside the enclosure is predominantly near the walls. Despite the presence of the stratified core, for high Ra numbers, a fluid particle travels the entire enclosure (due to the convection) and contributes to better mixing and decreases the vertical gradients inside the core.

The increase of the Rayleigh number corresponds with a decrease in the thickness of the boundary layers, an increase in the temperature gradients inside the boundary layers, and an increase in the heat transfer rate. The dependence of the average Nusselt numbers on the Rayleigh numbers is presented in Figure 9.C-6.

A similar two-dimensional flow pattern and stratified temperature (density) field is also obtained between two opposite vertical line jets (see Figure 9.C-7) as discussed in Baines and Turner, 1969.

A numerical analysis (Markatos and Pericleous, 1984) is performed for a two-dimensional plane, assuming that the influence of the front and back walls of real three-dimensional enclosures is not significant. For Rayleigh numbers greater than 10^6 , the $k-\epsilon$ turbulence model is used. Due to time-averaging, the numerical results do not show either the instability mechanisms during the transition from laminar to turbulent flow, or the resulting oscillations that would result from solving the time dependent Navier-Stokes equations.

Experimental and numerical results for three-dimensional enclosures are provided by Hiller et al. 1989, Mallinson and de Vhal Davis, 1977, respectively. The results indicate that observed vortices, which affect mixing inside the core of the enclosure, communicate between the front and back walls through the middle of the enclosure, thus enhancing mixing due to three-dimensional circulation effects (see Figure 9.C-8).

9.C-6

Reviews of various aspects of confined convective flows, including the interactions between boundary layers near the bounding walls and core and the effects of the cavity aspect ratio, inclination angle, and thermal boundary conditions on flow patterns, are presented by Ostrach 1972, 1982, Catton, 1978, Hoogendoorn, 1986 and Allard, 1992. A state of the art review of the analyses of two-dimensional and three-dimensional transient effects on the natural convection flows in sidewall heated enclosures is presented by T. Fusegi and J. M. Hyun, 1994.

R. J. Janssen and R.A.W.M Henkes, 1995 simulated the instability mechanisms and the transition from laminar to turbulent (oscillatory and finally chaotical) flow regimes inside a two-dimensional square enclosure with differentially heated vertical walls and adiabatic horizontal walls by solving the time-dependent Navier-Stokes equations. The results indicate that the transition from laminar to chaotic flow (for $Pr < 2.0$) is through periodic and quasi-periodic flow regimes. The periodic, quasi-periodic and chaotic flow regimes are established for Prandtl number 0.71 and Rayleigh numbers $2 \cdot 10^8$, $3 \cdot 10^8$ and $7.5 \cdot 10^8$. Internal waves corresponding to fluctuations in the temperatures at $Ra = 2 \cdot 10^8$ are presented in Figure 9.C-9. The temperature differences in the entire core of the enclosure are small, $0.004 \cdot (T_h - T_c)$. The predicted temperature differences inside the core of the enclosure are much smaller than those predicted by $k-\epsilon$ turbulence model (Markatos and Pericleous, 1984). This indicates that temperature gradients inside the boundary layers are greater (isotherms inside the thermal boundary layer are not presented in Figure 9.C-9) and heat transfer is more intensive than calculated by $k-\epsilon$ model.

Two instability mechanisms influence the transition to turbulent (chaotical) flow regime. The first instability is a Kelvin-Helmholtz type instability (as in a plane jet with inflection points in the velocity profile) in the fluid layer exiting from the corners (where the vertical boundary layers are turned horizontal). The second source of the instability is related to the instability in the boundary layer near the vertical walls. The instability inside the enclosure vertical boundary layers is mechanically (shear) driven. Both regions of the instability origins (hot and cold intrusions from corners and boundary layer waves) are presented in the Figure 9.C-10 (from S. Armfield and R. Janssen, 1996). The figure presents temperatures for the initial solution, i.e., immediately after setting the left and right vertical boundaries to $\Delta T/2$ and $-\Delta T/2$, respectively. For values of Rayleigh numbers greater than 10^9 , the turbulent oscillatory and chaotical flow affects the stratified layers inside the core of the enclosure. If the radius ($H_v = 65$ ft) of the containment is taken as a characteristic length (as a distance between the hot buoyant jet plume in the center and cold vertical wall boundary layers), a 9°F temperature difference results in a Grashof number $Gr_v = 4.7 \cdot 10^{12}$.

9.C.1.1.2.2 Interaction of Jets or Plumes with the Stratified Layers

The penetration of a stratified layer by a jet is another example where a portion of an enclosure is stratified and another portion is affected by strong recirculating zones (Figure 9.C-1b). Depending upon the strength of the jet and the depth of the stratified layers, portions of the enclosure are affected by interaction between the jet and stratified layers. A portion of the stratified fluid is entrained by the jet, decreasing the average jet velocity. The jet penetrates upward (Garra and Patrick, 1983, So and Aksoy, 1993, and Porterie et al., 1996), or downward (Markatos and Pericleous, 1984, see Figure 9.C-5 b and c near the cool wall). A negatively buoyant jet, as presented in Kapoor and Jaluria, 1993, is also possible.

The upward penetrating jet is of interest for LOCA or MSLB accident scenarios. Scaling and analysis of mixing in large stratified volumes for the cases of upward penetrating jets is presented by Peterson, 1994. If the strength of the jet is strong enough, it produces fluid flow below the ceiling. After reaching the vertical side walls, the flow results in downward negatively buoyant jets (see Figure 9.C-11 a and b).

The downward, negatively buoyant penetrating jet (Kapoor and Jaluria, 1993, see Figure 9.C-11a and Figure 9.C-11b) is of interest for the analysis of the flow patterns inside the upper-deck region (Figure 9.C-11a), as well as for the compartments below the dome floor (Figure 9.C-11b). If the strength of the negatively buoyant jet is not high, it is not able to reach compartments below the deck. The direction of the flow changes as presented in Figure 9.C-11a. The redirection of the flow causes additional entrainment of the surrounding fluid, thus contributing towards the increase of the circulation (and mixing) inside the upper-deck region. The correlations for entrainment rates in the negatively buoyant jets are presented in Kapoor and Jaluria, 1993.

If the strength of the negatively buoyant jets is high, it is able to penetrate into the below-deck compartments. There are indications from large-scale tests conducted by Westinghouse (tests 222.3 and 222.4, 3-inch pipe, elevated 6 ft, pointed at the wall and up, respectively, see F. E. Peters, WCAP-14135, July 1994) which simulate the MSLB, that the entire volume of the containment has almost the same steam concentration. This occurs despite the fact that formation of the global circulation loop between the lower-deck compartments and upper dome regions is not possible. An explanation is that the kinetic energy of the jets is high enough to provide downward penetration of the negatively buoyant jets into the below-deck compartments.

Depending upon the distribution of compartments below the dome floor and the number, size and distribution of openings between the compartments and the dome region, various flow patterns are possible inside the compartments. A portion of the downward vertical plumes produced by natural convection (wall boundary layers) or the negatively buoyant jets produced by strong vertical upward penetrating jet into the dome region enters horizontal openings in the compartments, thus promoting circulation and flow inside the compartments below the deck. Fluid flows upward to the dome through other compartment horizontal openings to preserve overall mass continuity and to close the global circulation loop (see Figure 9.C-11b).

9.C-8

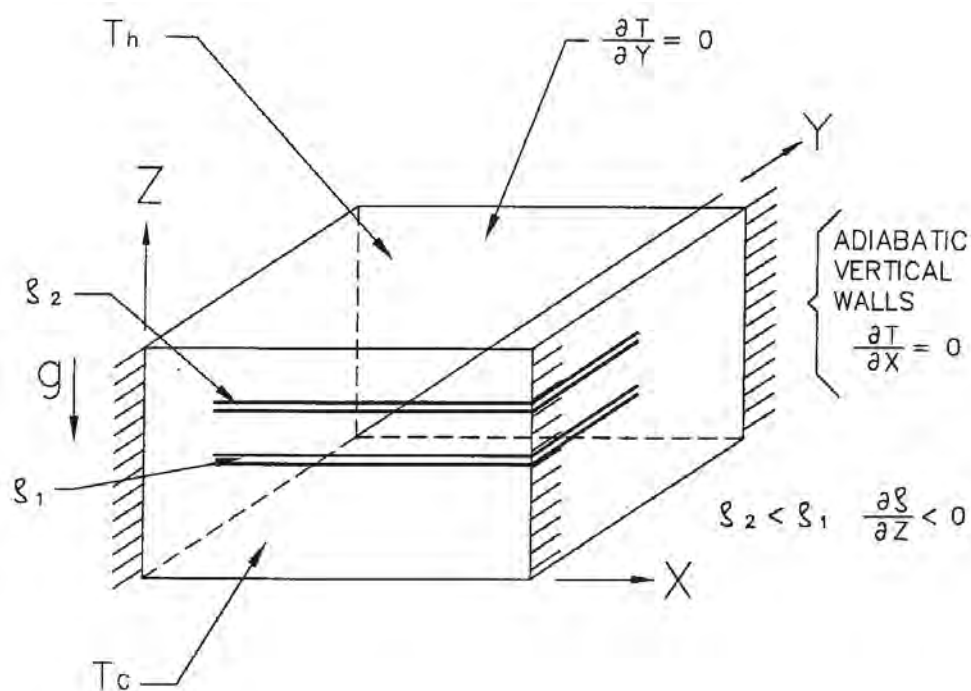
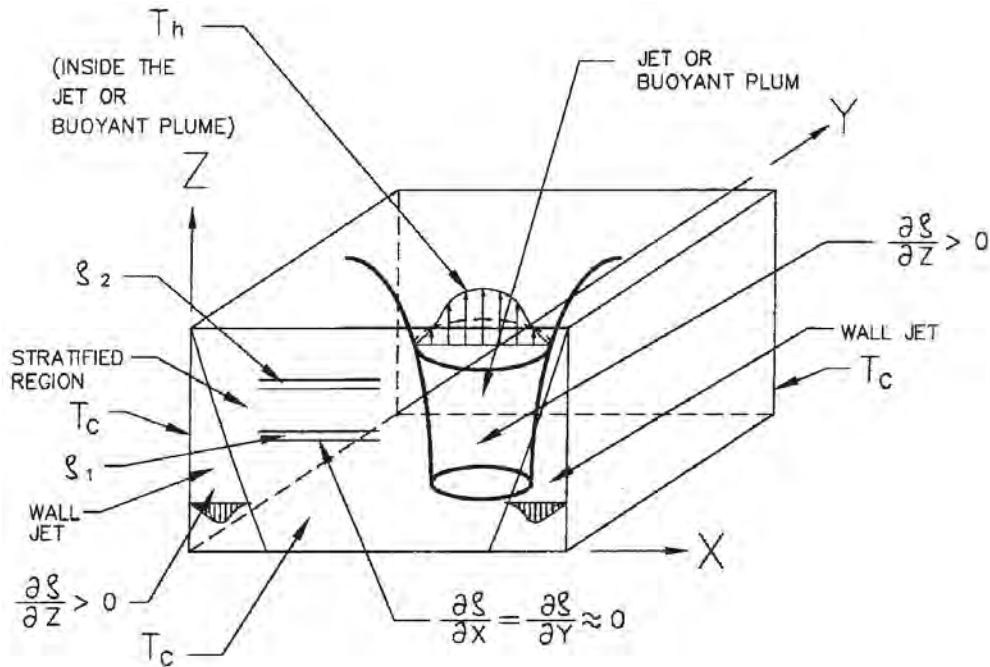


Figure 9.C-1a. The Formation of the Horizontal Layers of the Constant Density Due to the Stratification

9.C-9



STRATIFIED REGIONS $\left(\frac{\partial \rho}{\partial X} = \frac{\partial \rho}{\partial Y} = 0, \frac{\partial \rho}{\partial Z} < 0 \right)$ AND

JET REGIONS $\left(\frac{\partial \rho}{\partial X} \neq 0, \frac{\partial \rho}{\partial Y} \neq 0, \frac{\partial \rho}{\partial Z} > 0 \right)$ INSIDE

THE ENCLOSURE.

Figure 9.C-1b. Interaction of Jets, Plumes and Wall Boundary Layers with Stratified Regions

9.C-10

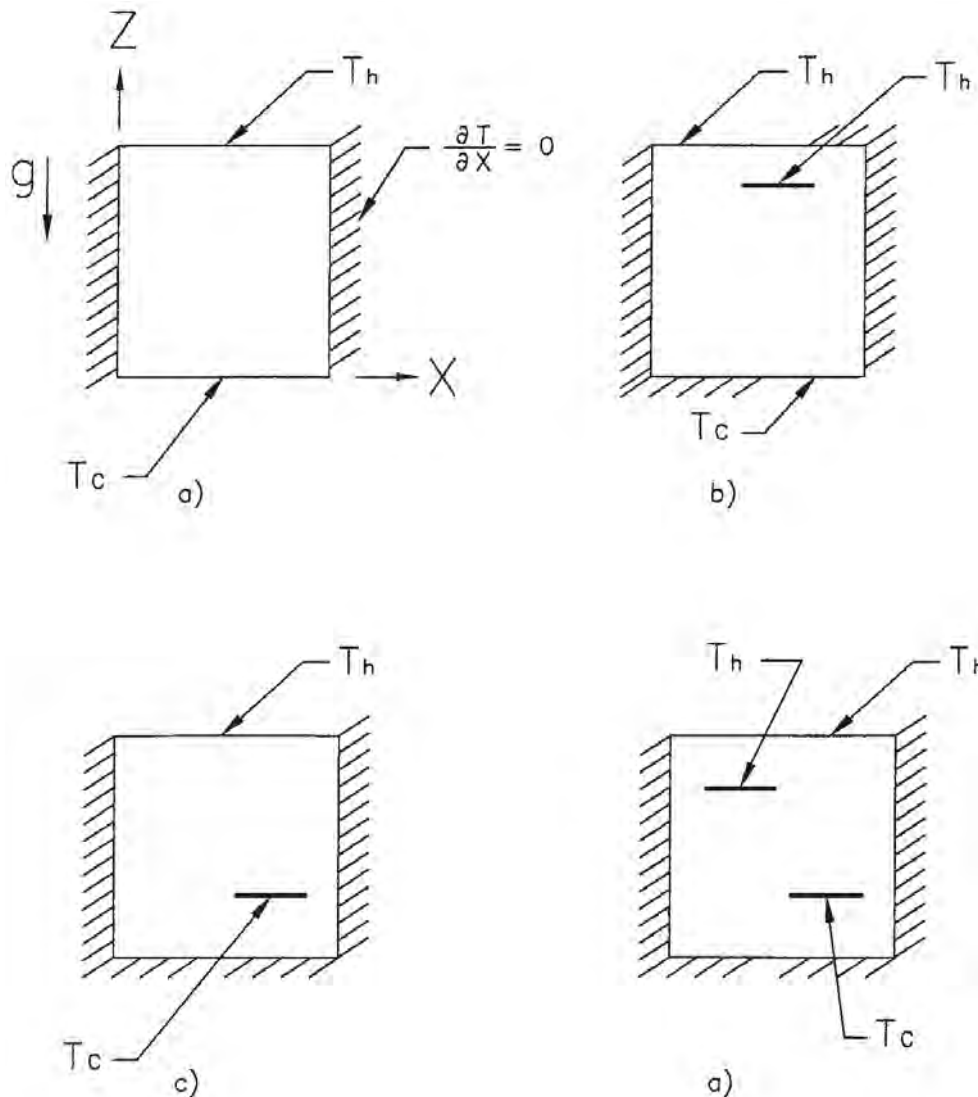


Figure 9.C-2. Combination of the Constant Temperature Boundary Conditions at the Outside and Inside Surfaces which will Produce Stratification Inside the Enclosure

9.C-11

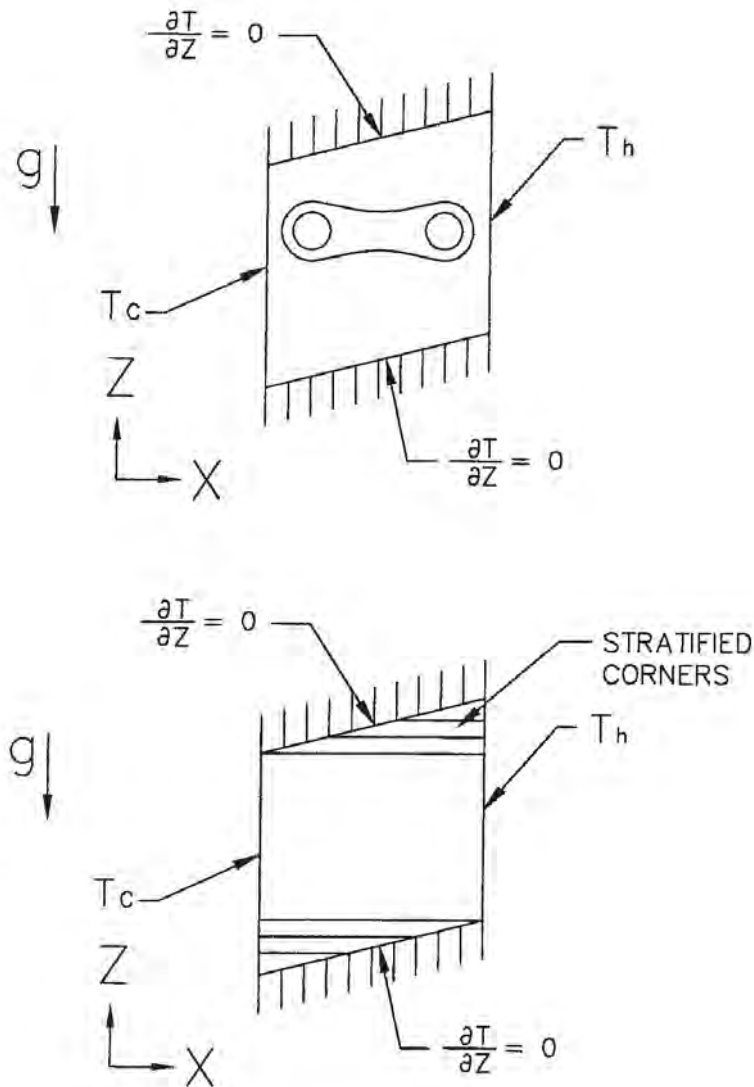


Figure 9.C-3. Stratification Inside the Upper and Lower Corners of the Romb-Shaped Enclosure

Example of the Stratification Caused by the Shape of the Enclosure and Distribution of the Boundary Conditions

9.C-12

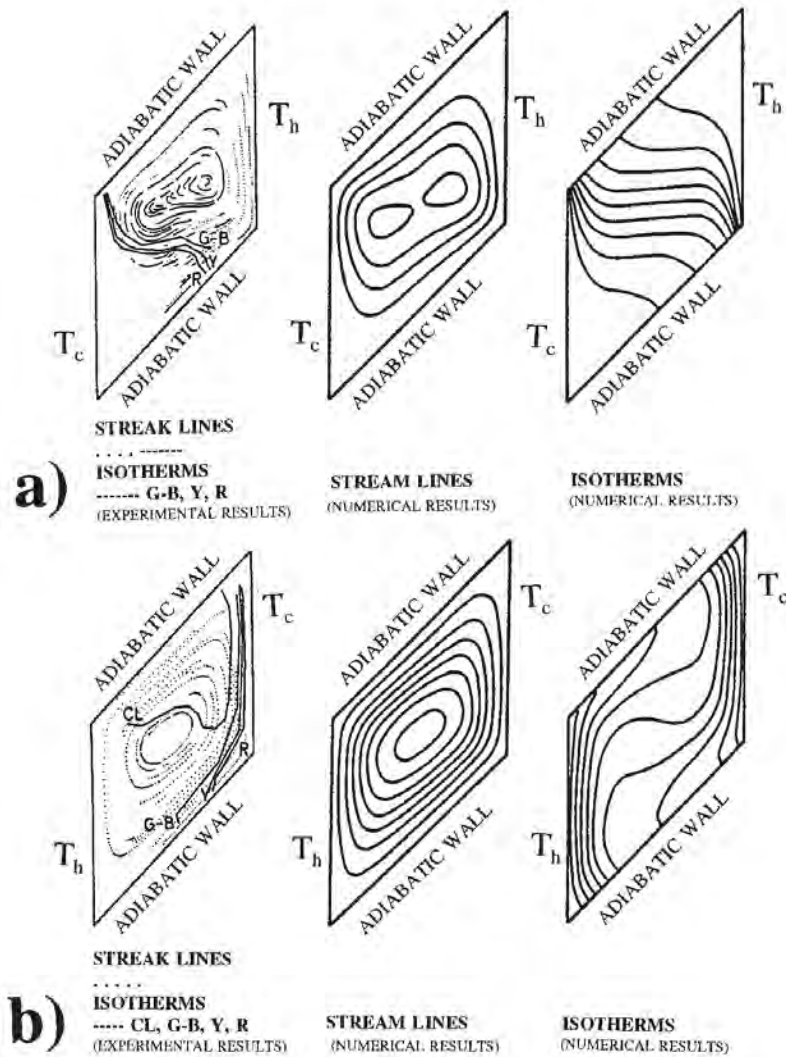
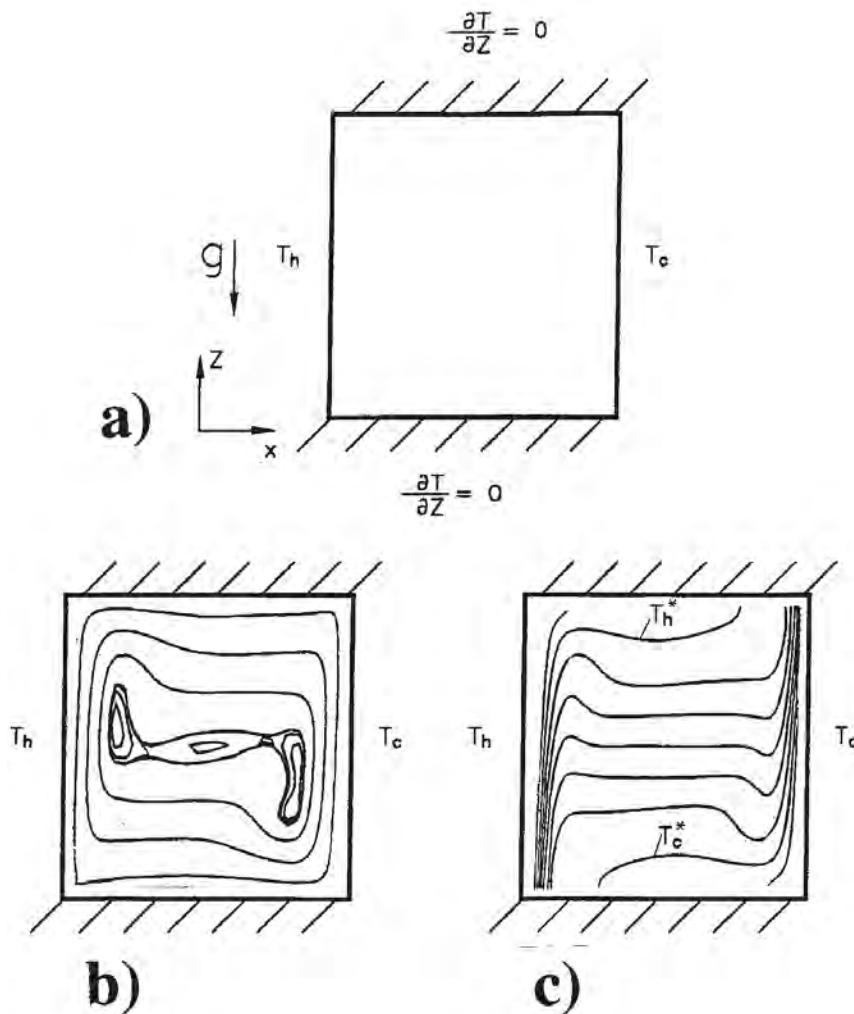


Figure 9.C-4. Experimental and Numerical Results for the Romb-Shaped Enclosure with the Romb Angle 44° and $Ra=3.5 \times 10^4$, $PR=5270$

- a) results for the upper vertical wall at the higher temperature
- b) results for the lower vertical wall at the higher temperature

(Reprinted from: M.B. Dzodzo, "Visualization of laminar natural convection in romb-shaped enclosures by means of liquid crystals," in Imaging in transport processes (ed. S. Sideman and K. Hijikata), Begel House, Inc., 1993, pp. 183-193)

9.C-13



**Figure 9.C-5. a) The Square Enclose with Vertical Walls at the Different Temperatures and Horizontal Walls Adiabatic
b) Streamlines for $Ra=106$ and $Pr=0.71$,
c) Isotherms for $Ra=106$ and $Pr=0.71$**

“Reprinted from N.C. Markatos and K.A. Pericleous/Laminar and Turbulent Natural Convection in an Enclosed Cavity, Int. J. Heat Mass Transfer, Vol. 27, No. 5, pp. 755-772, 1984, Copyright 1984, Figure 9.C.5(d) and 6(d), with kind permission from Elsevier Science Ltd, The Boulevard, Langford Lane, Kidlington OX51GB, UK”

9.C-14

Ra	10^3	10^4	10^5	10^6	10^8	10^{10}	10^{12}	10^{14}	10^{16}
Nu	1.108	2.201	4.430	8.754	32.045	156.85	840.13	3624.4	11226

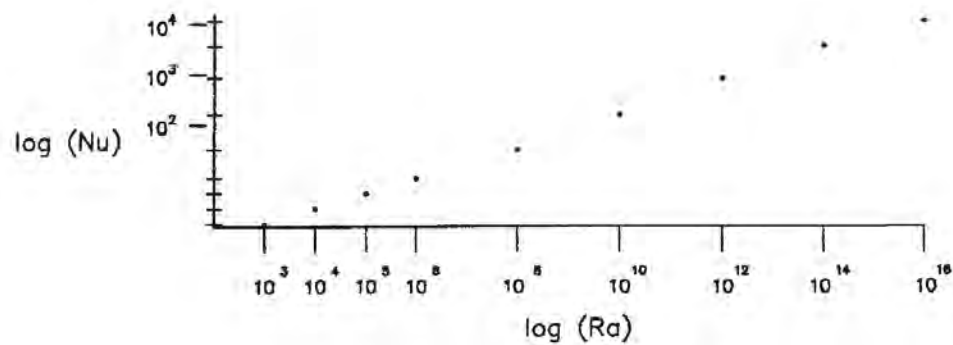


Figure 9.C-6. Average Nusselt Numbers as a Function of the Rayleigh Numbers for the Square Enclosure with Opposite Vertical Walls at the Different Temperatures and $Pr=0.71$ (air)

(according to N.C. Markatos and K.A. Pericleous/Laminar and Turbulent Natural Convection in an Enclosed Cavity, Int. J. Heat Mass Transfer, Vol. 27, No. 5, pp. 755-772, 1984)

9.C-15

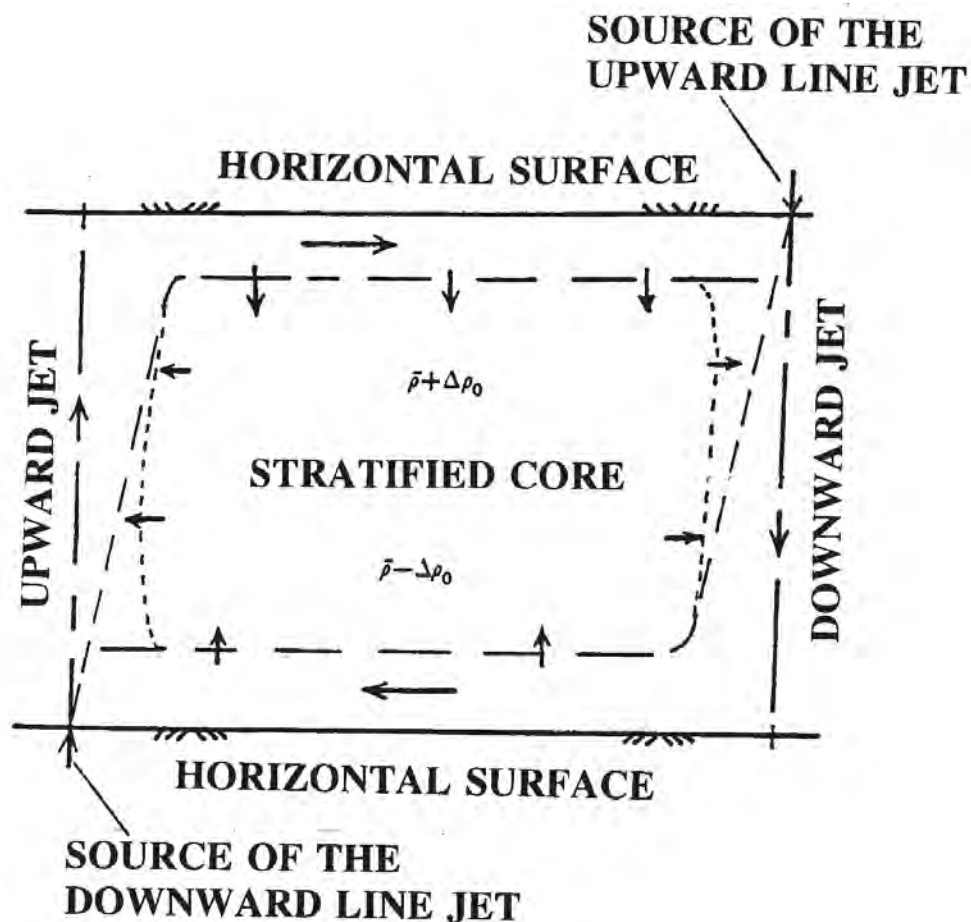


Figure 9.C-7. Formation of the Stratified Core in Between Two Opposite Vertical Line Jets
(after Baines and Turner, 1969)

“Reprinted with the permission of Cambridge University Press from Baines W.D. and Turner, J.S./Turbulent buoyant convection from a source in a confined region, Journal of Fluid Mechanics, Vol. 37, 1969; pp. 51-80, Copyright 1969, Figure 9.C.10”

9.C-16

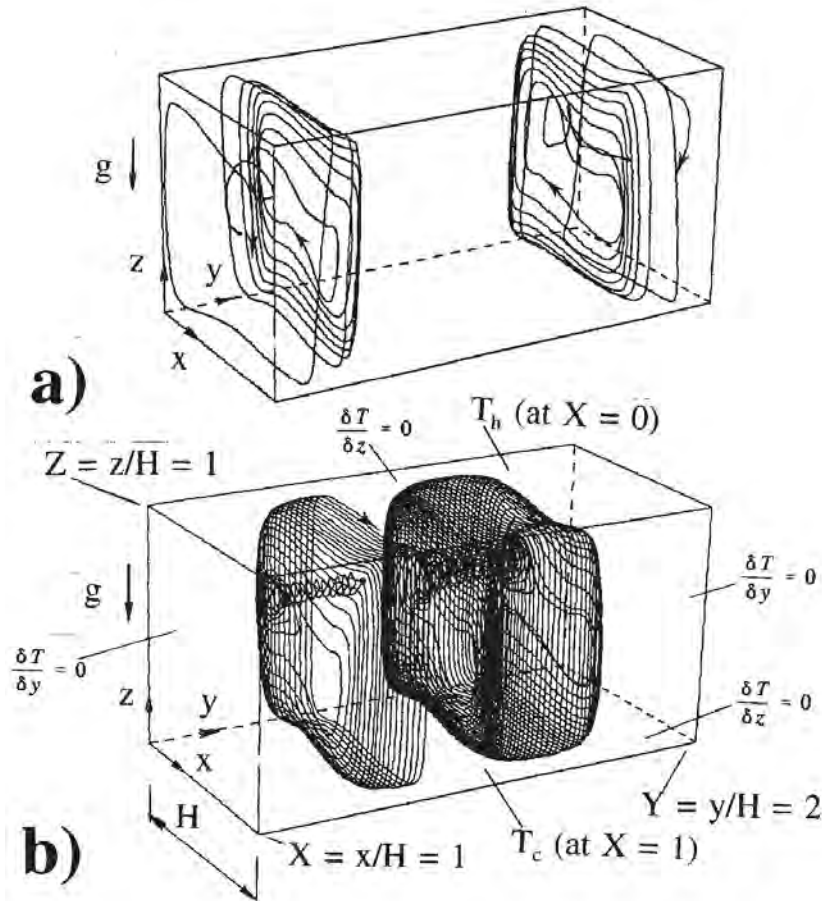


Figure 9.C-8. Flow in an Enclosure with Vertical Opposite Walls at Different Temperatures (Ra=105, PR=0.71)

- a) forward flow (towards $Y=0$ and $Y=2$) – streamlines through the points ($X=0.5, Y=0.1, Z=0.49$) and ($X=0.5, Y=1.9, Z=0.49$)
- b) reverse flow (towards $Y=1.0$) – streamlines through the points ($X=0.3, Y=0.8, Z=0.65$) and ($X=0.3, Y=1.2, Z=0.65$) after (Mallinson and de Vahl Davis, 1977)

“Reprinted with the permission of Cambridge University Press from Mallinson G.D. and G. de Vahl Davis/Three-dimensional natural convection in a box; a numerical study, Journal of Fluid Mechanics, Vol. 83, 1977; pp. 1-31, Copyright 1977. Figure 9.C.8”

9.C-17

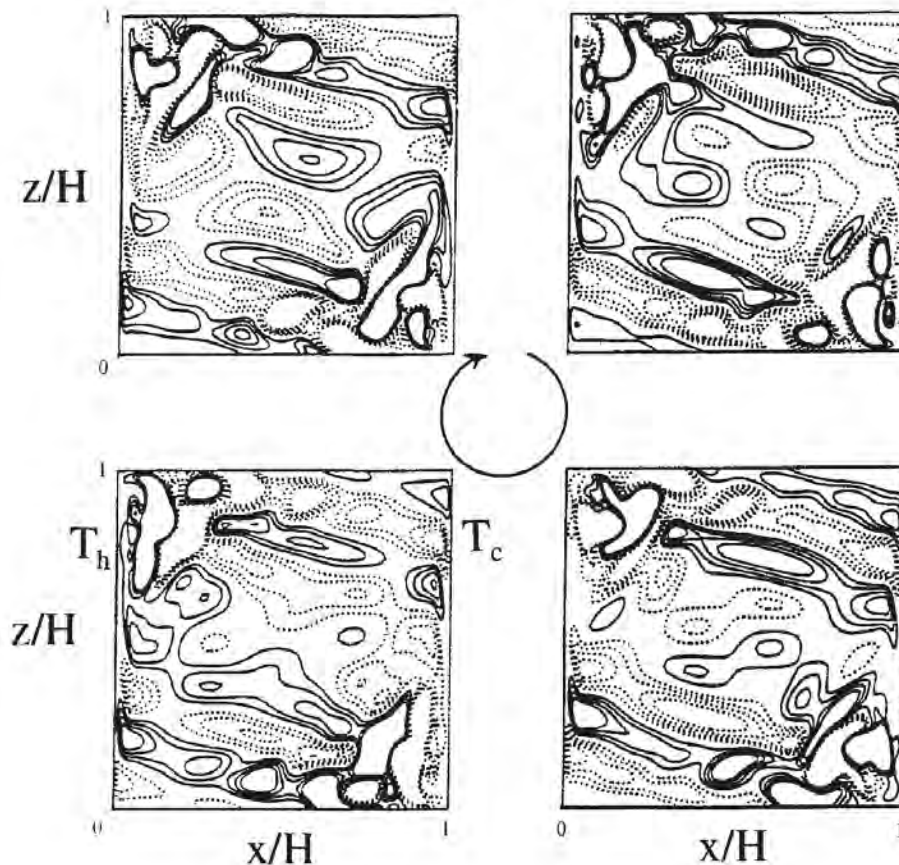


Figure 9.C-9. Internal Waves in the Square Cavity – Fluctuations in the Temperature Field at $Ra=2 \cdot 10^8$ and $PR=0.71$ (air)

Circle with the arrow (in the middle) presents the direction of the consecutive temperature fields. Contour lines correspond to $\pm 0.0005 \Delta T$, $\pm 0.001 \Delta T$, $\pm 0.0015 \Delta T$ and $\pm 0.002 \Delta T$ (the dotted contour lines correspond to negative values, where $T_h = \Delta T/2$ and $T_c = -\Delta T/2$). (After Janssen and Henkes, 1995)

“Reprinted with the permission of Cambridge University Press from Janssen, R.J.A. and R.A.W. Henkes/Influence of Prandtl number on stability mechanisms and transition in a differentially heated square cavity, Journal of Fluid Mechanics, Vol. 290, 1995; pp.319-344, Copyright 1995, Figure 9.C.4”

9.C-18

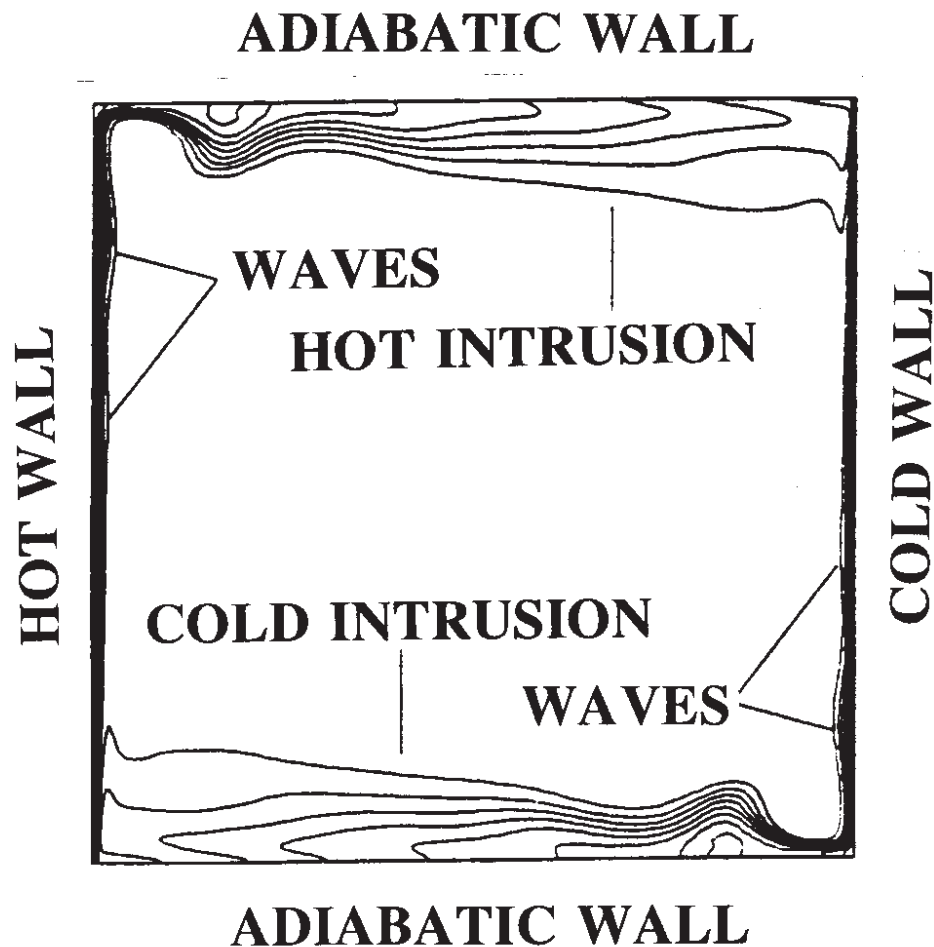


Figure 9.C-10. Temperature for the Initial Solution with the Hot and Cold Intrusions and Boundary Layer Waves Presented (after Armfield and Janssen, 1996)

“Reprinted with permission from Int. J. Heat and Fluid Flow, Vol. 17, S. Armfield and R. Janssen/A direct boundary-layer stability analysis of steady-state cavity convection flow, pp. 539-546, 1996. Elsevier Science Inc.”

9.C-19

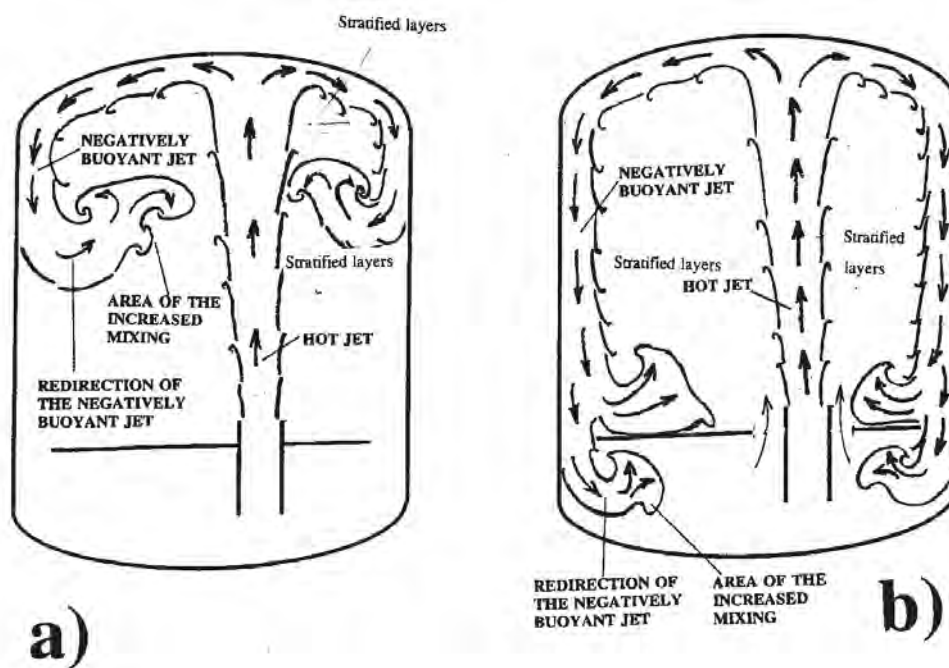


Figure 9.C-11. Formation of the Downward Negatively Buoyant Jets

- a) Negatively buoyant jet redirected inside the dome region
- b) Negatively buoyant jet penetrating the below deck region

9.C-20

9.C.1.1.3 References

1. Akino, N., Kunugi, T., Shiina, Y., Seki, M. and Okamoto, Y. (1989)
"Natural convection in a horizontal silicone oil layer in a circular cylinder heated from below and cooled from above," (in Japanese), Trans. Jpn. Soc. of Mech. Eng. 55 509 no. 1989-1), no. 88-0901 B: 152-158, 1989.
2. Allard, F., (1992)
"Effects of thermal boundary conditions on natural convection in thermally driven cavities," in-Turbulent Natural Convection in Enclosures, A Computational and Experimental Benchmark Study, (Eds.) R.A.W.M Henkes and C.J. Hoogendoorn, Editions Europeennes Thermique et Industrie, Paris, pp. 234-256.
3. S. Armfield and R. Janssen (1996)
"A direct boundary-layer stability analysis of steady-state cavity convection flow" Int. J. Heat and Fluid Flow, Vol. 17, No. 6, December 1996.
4. W.D. Baines and J.S. Turner (1969)
"Turbulent buoyant convection from a source in a confined region" J. Fluid Mech., Vol. 37, part 1, pp. 51-80.
5. Catton, I., (1978)
"Natural convection in enclosures" Proc. 6th Int. Heat Transfer Conf., Vol. 6, pp. 13-31.
6. Dzodzo M. B., (1993)
"Visualization of laminar natural convection in romb-shaped enclosures by means of liquid crystals" in "Imaging in transport processes", (ed. S. Sideman and K. Hijikata), Chapter 15, pp. 183-193., Begel House, Inc., 1993.
7. R. Frederick and A. Valencia, (1995)
"Natural Convection in Central Microcavities of Vertical Pinned Enclosures of very High Aspect Ratios," Int. J. Heat and Fluid Flow, Vol. 16, No. 2, April 1995, pp. 114-124.
8. T. Fusegi, J. M. Hyun, K. Kuwahara, (1992)
"Numerical simulations of natural convection in a differentially heated cubical enclosure with a partition" Int. J. Heat and Fluid Flow, Vol. 13, No. 2, June 1992, pp 176-183.
9. T. Fusegi, T. M. Hyun, (1994)
"Laminat and Transitional Natural Convection in an enclosure with complex and relistic conditions," Int. J. Heat and Fluid Flow, Vol. 15, No. 4, August 1994, pp. 258-268.
10. A. D. Garrad and M.A. Patrick, (1983)
"The velocity field produced by a submerged jet directed upwards at a free surface" Int. J. Heat Mass Transfer, Vol. 26, No. 7, pp. 1029-1036.

9.C-21

11. K. Hanjalic, S. Kernjeres and F. Durst, (1996)
“Natural convection in partitioned two-dimensional enclosures at higher Rayleigh numbers”
Int J. Heat Mass Transfer, Vol. 39, No. 7, pp. 1407-1427, 1996
12. T. J. Heindel, S. Ramadhyani, and F. P. Incropera (1995)
“Conjugate natural convection from an array of discrete heat sources: part 1 – two and three-dimensional model validation” Int. J. Heat and Fluid Flow, Vol. 16, No. 6, December 1995, pp. 01-510.
13. Hiller W.J., Koch St., Kowalewski T.A., (1988)
“Simultane erfassung von temperatur und geschwindigkeitsfeldern in einer thermischen konvektionsstromung mit ungekapselten flussigkristalltracern, DGLR - Workshop, 2D-Mesttechnik, 1988.
14. Hiller W.J., Koch St., Kowalewski T.A., (1989)
“Three-dimensional structures in laminar natural convection in a cube enclosure” Exp. Therm. Fluid Sci., Vol. 2, pp. 34-44.
15. C. J. Ho, Y. T. Cheng and C. C. Wang, (1994)
“Natural convection between two horizontal cylinders inside a circular enclosure subjected to external convection” Int. J. Heat and Fluid Flow, Vol. 15, No. 4, August 1994, pp 299-306.
16. Hoogendoorn, C.J., (1986)
“Natural convection in enclosures” Proc. 8th Int. Heat Transfer Conf., Vol. 1, pp. 111-120.
17. J.M. Hyun and B.S. Choi, (1990)
“Transient natural convection in a parallelogram-shaped enclosure,” Int. J. Heat and Fluid Flow, Vol. 11, No. 2, June 1990, pp. 129-134.
18. R. J. A. Janssen and R.A.W.M. Henkes, (1995)
“Influence of Prandtl number on instability mechanisms and transition in a differentially heated square cavity,” J. Fluid Mech., Vol. 290, pp. 319-344., 1995
19. K. Kapoor and Y. Jaluria, (1993)
“Penetrative convection of a plane turbulent wall jet in a two-layer thermally stable environment: a problem in enclosure fires” Int. J. Heat Mass Transfer, Vol. 36, No. 1, pp. 155-167, 1993.
20. A. Kurosawa, N. Akino, T. Otsuji, S. Kizu, K. Kobayashi, K. Iwahori, T. Takeda and Y. Ito, (1993)
“Fundamental study on thermo-hydraulic phenomena concerning passive safety of advanced marine reactor” Journal of Nuclear Science and Technology, Vol 30 [2], pp. 131-142, February 1993.
21. G.D. Mallinson and G. de Vahl Davis, (1977)
“Three-dimensional natural convection in a box: a numerical study” J. Fluid Mech., Vol. 83, pp. 1-31.

9.C-22

22. N.C. Markatos and K.A. Pericleous, (1984)
“Laminar and turbulent natural convection in an enclosed cavity” Int. J. Heat Mass Transfer, Vol. 27, No. 5, pp. 755-772.
23. E. S. Nowak and M. H. Novak, (1994)
“Vertical partitions in slender rectangular cavities” Int. J. Heat and Fluid Flow, Vol. 15, No. 2, April 1994, pp. 104-110.
24. Ostrach, S., (1972)
“Natural convection in enclosures” Advances in Heat Transfer, Vol. 8, Academic Press, New York, pp. 161-227.
25. Ostrach, S., (1982)
“Natural convection heat transfer in cavities and cells” Proc. 7th Int. Heat Transfer Conf., Vol 1, pp.365-379.
26. F.E. Peters, (1994)
WCAP-14135, “Final Data Report for PCS Large-Scale Tests, Phase 2 and Phase 3,” Revision 1, April 1997.
27. P.F. Peterson, (1994)
“Scaling and analysis of mixing in large stratified volumes” Int. J. Heat Mass Transfer, Vol. 37, Suppl. 1, pp. 97-106.
28. B. Porterie, M. Larini, F. Giroud and J.C. Loraud (1996)
“Solid-propellant fire in an enclosure fitted with a ceiling safety-vent” Int. J. Heat Mass Transfer, Vol. 39, No. 3, pp. 575-601.
29. R.M. C So and H. Aksoy, (1993)
“On vertical turbulent buoyant jets” Int. J. Heat Mass Transfer, Vol. 36, No. 13, pp. 3187-3200.
30. L. Wolf, H. Holzbauer, T. Cron, (1994a)
“Detailed Assessment of the HDR-Hydrogen Mixing Experiments E11” International Conference on New Trends in Nuclear System Thermohydraulics, Pisa, Italy, May 30th – June 2nd, Vol. 2, pp. 91-103.
31. L. Wolf, H. Holzbauer, M. Schall, (1994b)
“Comparisons between multi-dimensional and lumped-parameter Gothic-containment analyses with data” International Conference on New Trends in Nuclear System Thermohydraulics, Pisa, Italy, May 30th – June 2nd, Vol. 2, pp. 321 – 330.

9.C.1.2 Circulation Phenomena

Circulation processes inside enclosures are the result of natural or forced convection effects. Forced convection inside an enclosure is promoted using devices such as fans, nozzles, or sprays of liquid droplets. PCS applications are of primary interest, since no credit is taken for active systems in the design basis analysis.

A review of possible flow patterns due to natural convection effects is presented. Natural convection is generated if:

1. The upper boundary is at a lower temperature than the lower boundary or opposite vertical boundaries are at different temperature, as well as for other similar combinations of temperature boundary conditions (or imposed heat flux conditions) at the outside and inside surfaces.
2. A higher concentration of the lighter or heavier components of a mixture is maintained near the lower or upper boundaries of the enclosure, respectively.
3. A lighter fluid is released (permanently, or from time to time) from a source which is closer to the bottom of the enclosure.
4. The shape of the enclosure promotes natural convection (together with the distribution of other boundary conditions).
5. The distribution and size of the horizontal and vertical internal openings allows or enhances (as with a chimney or staircase effects) the formation of fluid flow patterns due to the natural convection.
6. If the internal heat sources (sinks) are positioned in the lower (upper) portions of the enclosure.

Under the conditions above (or a combination of them), natural convection causes circulation inside the enclosure. The convection increases the intensity of heat and mass transfer, therefore increasing the heat released from the containment. The intensity of heat transfer depends upon the location of the heat sinks and sources, which can exchange positions due to the transient effects. The velocity and temperature profiles inside the formed boundary layers (wall jets) influence the rate of heat transfer due to the convection. Wall jets entrain the surrounding atmosphere and contribute to better mixing. In the regions with a higher steam concentration, the increase in the heat transfer rate and the effects of entrainment occur due to the condensation inside the boundary layers.

Another contributing factor that promotes circulation inside an enclosure is the interaction of the enclosure atmosphere with the penetrating buoyant plumes or jets and wall layers. In the case of a containment vessel, the plumes or jets could be generated by a LOCA or MSLB. If the break position is inside a narrow corridor or surrounded by additional equipment, the kinetic energy of the jet is dissipated and steam rises in the form of a buoyant plume. The rising plume entrains the surrounding gas and results in circulation inside the volume of the enclosure.

If the break position is open and the jet is directed upward, both the kinetic energy of the jet and the buoyancy forces contribute to penetration into the atmosphere. The higher speeds of the jet affect a greater portion of the volume and both entrainment of the surrounding gas and circulation is stronger.

9.C.1.2.1 Circulation Phenomena Due to the Presence of Boundary Layers (Wall Jets) and Buoyant Plumes Formed as a Consequence of Natural Convection Effects

Natural convection flow is the most often generated by different temperatures or heat fluxes imposed on the boundaries of an enclosure. Various distributions on the boundaries produce various flow patterns and temperature fields.

Section 9.C.1.1 discusses boundary temperature distributions (upper/lower horizontal plates at the higher/lower temperatures) that produce static stratification. Section 9.C1.2 discusses the case where vertical opposite sides are at constant, but different temperatures. If Rayleigh numbers are greater than 10^4 , this condition produces a recirculated region near the walls and a stratified core of the enclosure.

Figure 9.C-12 presents a case known as Rayleigh-Benard convection. The upper horizontal boundaries are at the lower temperatures (or cooled). The flow patterns formed depend upon the temperature difference and geometry of the enclosure (in fact the value of the Rayleigh number).

For the smaller Ra numbers, vortical cells are formed. An increase in the Ra numbers produces a greater number of vortical cells that start to oscillate, periodically changing the size and intensity. A further increase in the Ra number results in chaotic flow, and produces vertical plumes which reach the opposing horizontal sides of the enclosure. The flow patterns and possible bifurcations produced during the transition from the laminar to turbulent (chaotical) flow regimes are described in Koschmieder, 1993, Yang, 1988, and Ozawa et al., 1992. Some experimental results (flow patterns and temperature fields) are presented for laminar flow regimes by M. Dzodzo et al., 1994 and M.J. Braun et al., 1993. Flow patterns for turbulent and chaotic flow between two horizontal plates at different temperatures are described in Akino et al., 1989.

Flow in the Hele-Shaw cell is presented as an example of natural convection between two horizontal plates. A Hele-Shaw cell has a square cross-section, but it is narrow in one of the horizontal directions so that three-dimensional convection effects are suppressed (see Figure 9.C-13). The upper and lower horizontal sides are at the lower and higher temperatures, respectively.

Consecutive flow patterns and temperature fields for a Hele-Shaw cell with various Rayleigh numbers are presented in Figure 9.C-14 (after Buhler et al., 1987). If the value of the Rayleigh number is greater than 4×10^6 , oscillatory flow patterns with four vortical cells are present. The large and small vortices expand and contract periodically (see Figure 9.C-14). At high Rayleigh numbers (above 5.9×10^7), a reverse transition from the oscillatory to the steady flow patterns occurs. This phenomena is probably due to suppressed three-dimensional convection effects.

9.C-25

For cubic or cylindrical enclosures, with the upper and lower horizontal surfaces at the lower and higher temperatures, respectively, three-dimensional convection effects produce turbulent (chaotical) flow (see Figure 9.C-15). In the paper by Akino et al., 1989, the turbulent flow regime starts at a Rayleigh number of 2×10^6 ($Pr = 200$). For fluids with a Prandtl number close to one, the transition to turbulent flow regime occurs at a smaller Rayleigh number ($Ra \sim 10^4$).

The flow pattern consists of vertical buoyant plumes detached from the horizontal sides. The vertical plumes reach opposite sides of the enclosure and generate opposing plumes (see Figure 9.C-16). Temperature gradients near the horizontal surfaces are high, while temperatures in the core of the containment are almost uniform. Figure 9.C-17a illustrates an example where the temperature in the middle of the enclosure oscillates between 26 and 29°C with $Ra = 9.38 \times 10^7$ ($T_h = 35^\circ\text{C}$ and $T_c = 20^\circ\text{C}$). The highest temperature is registered during the rise of the hot plume and the lowest temperature is registered during the downward penetration of the cold plume. The amplitude of the temperature oscillations in the middle of the enclosure is three degree Celsius. The temperature interval between 26 and 29°C represents $0.2 \times (T_h - T_c)$ or 20 percent of the maximum temperature difference. The temperature in the middle of the enclosure is $(27.5^\circ\text{C}) \pm 1.5^\circ\text{C}$.

Rayleigh-Benard convection is relevant to the containment. In the case of a LOCA or MSLB, the upper portion of the dome and vertical sides are cooled. If the temperature below the ceiling is 9°F lower than temperature of the incoming steam (at the deck level), the Grashof number (based on the height of the containment, $H_c = 109$ ft) is $Gr_i = 2.2 \times 10^{13}$. This Grashof number is in the range of the chaotic flow, with the upward and downward plumes (because $Gr_i > 10^4/0.71$).

Maintaining the vertical walls of the containment at the lower temperature also promotes downward vertical plumes near the walls due to separation of the vertical boundary layers (see Figure 9.C-17b).

9.C.1.2.2 Circulation Phenomena Due to the Interaction With the Hot Buoyant Plumes and Jets

The presence of a hot buoyant plume or a jet of the hot steam during a LOCA or MSLB contributes to the circulation of the containment atmosphere by entraining the surrounding air and other gases. In the case of jet inflow, additional entrainment and circulation are generated by the jet kinetic energy.

Depending upon the strength (initial velocity and mass flow) and direction of the plume or jet, various flow patterns inside the containment are possible. Interaction of the vertical downward plumes generated due to the natural convection (cooling of the shell) produce turbulent flow. This results in good mixing of the dome atmosphere. Examples of vertical plumes and jets are presented by Garrad and Patrick, 1983, So an Aksoy, 1993, and Porterie et al. 1996. The scaling and analysis of circulation in large stratified volumes is presented by Peterson, 1994.

9.C-26

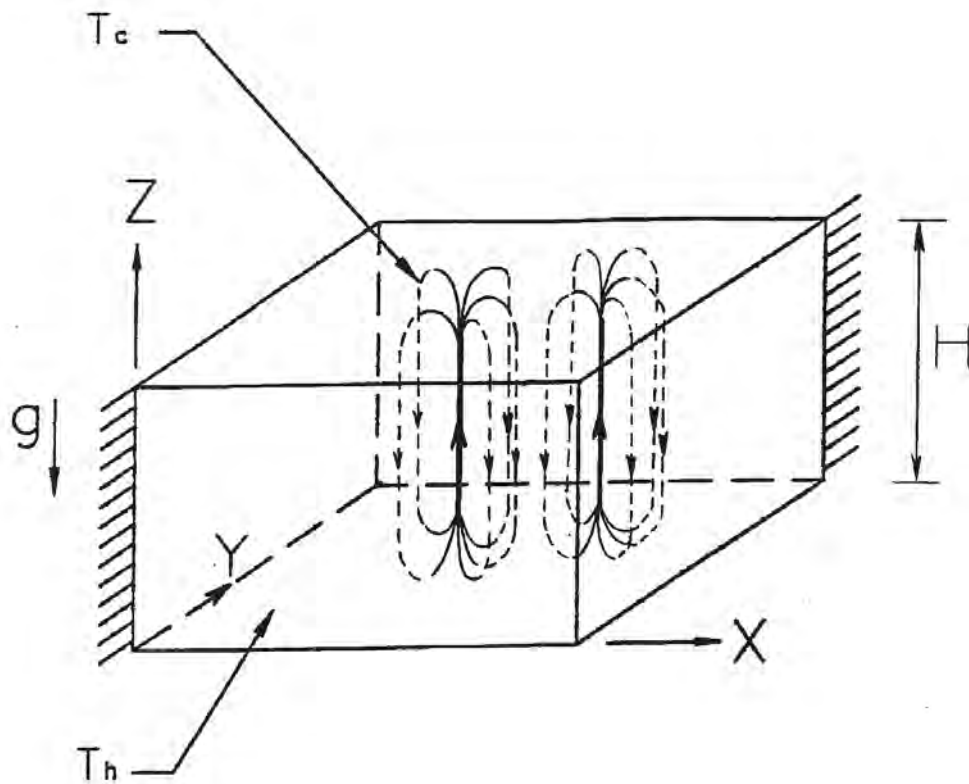


Figure 9.C-12. Rayleigh-Benard Convection Example

9.C-27

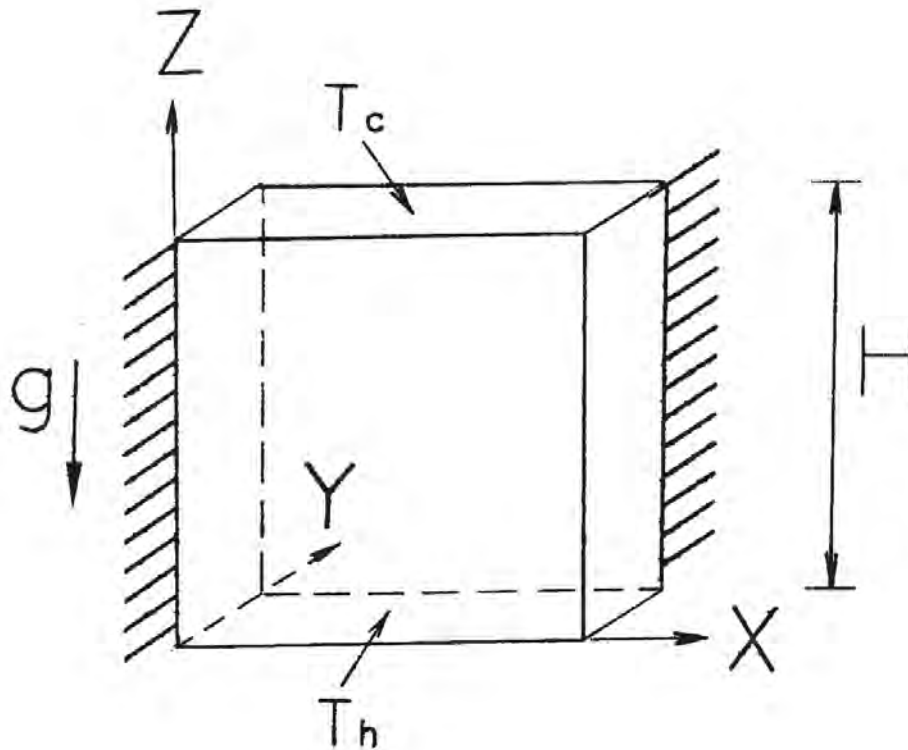


Figure 9.C-13. Hele-Shaw Cell

9.C-28

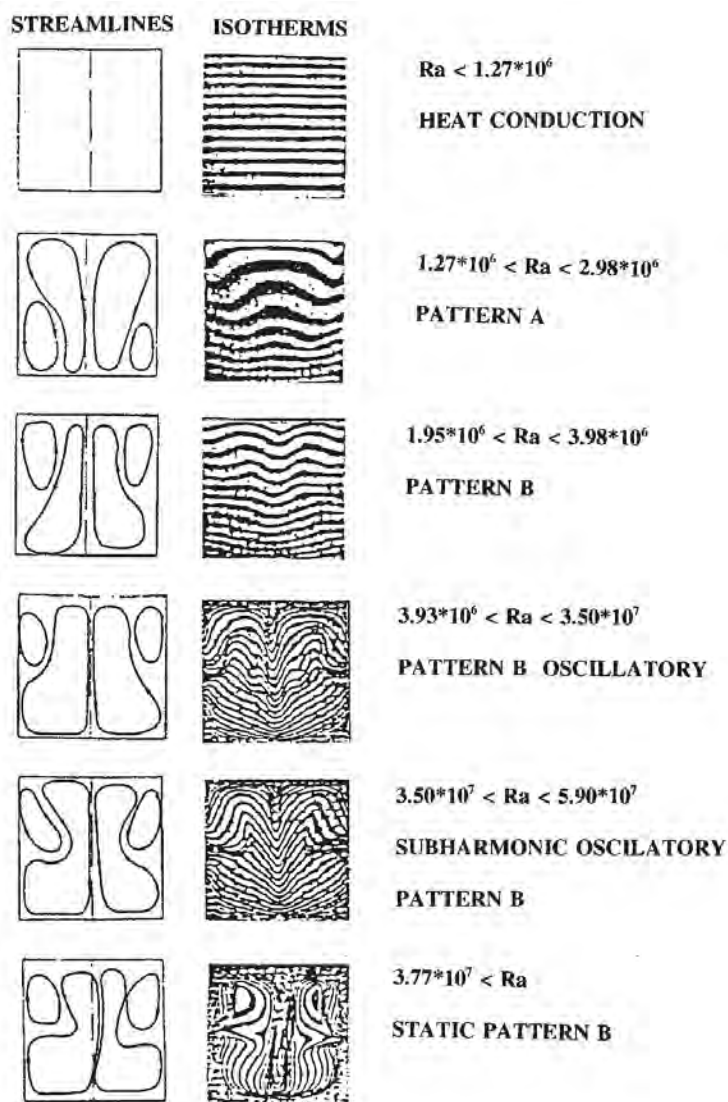
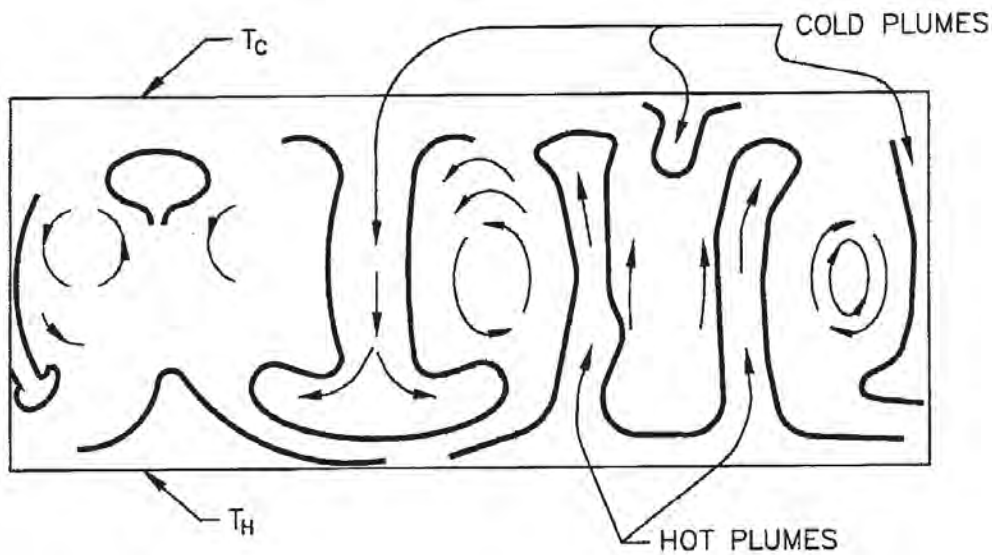


Figure 9.C-14. Steady and Oscillatory Convection in Hele-Shaw Cell (after Buhler et al., 1987)

“Reprinted from L. Buhler, P. Ehrhard, C. Gunther, U. Muller and G. Zimmermann/Natural convection in vertical gaps heated at the lower side – an experimental and numerical study, HTD-Vol.94, AMD-Vol. 89, Bifurcation Phenomena in Thermal Processes and Convection, Winter Annual Meeting of the American Society of Mechanical Engineers, Boston, Massachusetts, December 13-20, 1987”

9.C-29



**Figure 9.C-15. Turbulent (Chaotical) Flow without Hot and Cold Plumes Interactions
(Plane Cross-Section of the Three-Dimensional Enclosure is Presented)**

(according to Figure 6 in N. Akino, T. Kunugi, Y. Shiina, M. Seki, Y. Okamoto/Natural convection in a horizontal silicone oil layer in a circular cylinder heated from below and cooled from above," Trans. Jpn. Soc. Of Mech. Eng. 55 509 no. 1989-1), no. 88-0901 B;, pp. 152-158, 1989 – with permission from Norio Alkino)

9.C-30

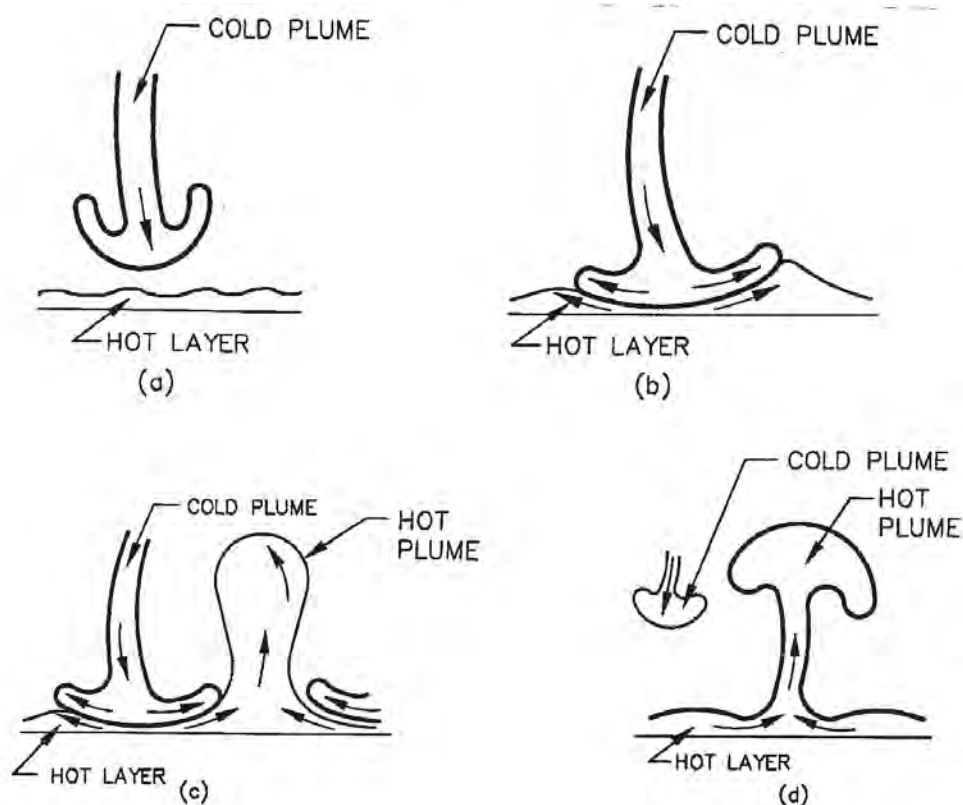


Figure 9.C-16. Interaction of Hot and Cold Plumes (after Aqino et al., 1989)

(according to Figure 12 in N. Akino, T. Kunugi, Y. Shiina, M. Seki, Y. Okamoto/Natural convection in a horizontal silicone oil layer in a circular cylinder heated from below and cooled from above," Trans. Jpn. Soc. of Mech. Eng. 55 509 no. 1989-1), no. 88-0901 B:, pp. 152-158, 1989 – with permission from Norio Akino)

9.C-31

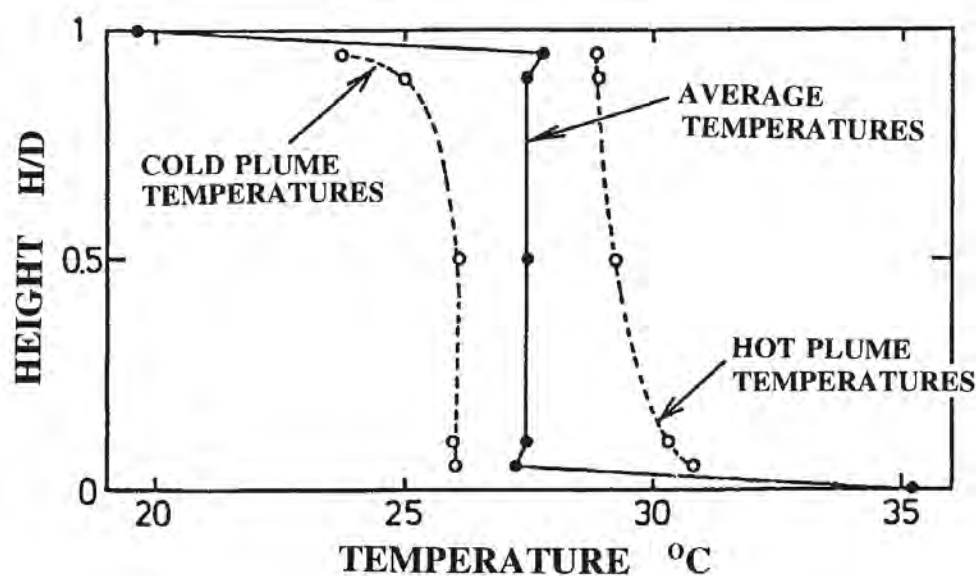


Figure 9.C-17a. Vertical Temperature Distribution inside the Cylindrical Enclosure with Lower and Upper Horizontal Plate at Higher and Lower Temperatures, Respectively ($Ra = 9.38 \times 10^7$, $Pr = 200$)

(according to Figure 14 in N. Akino, T. Kunugi, Y. Shiina, M. Seki, Y. Okamoto/Natural convection in a horizontal silicone oil layer in a circular cylinder heated from below and cooled from above," Trans. Jpn. Soc. of Mech. Eng. 55 509 no. 1989-1), no. 88-0901 B; pp. 152-158, 1989 – with permission from Norio Akino)

9.C-32

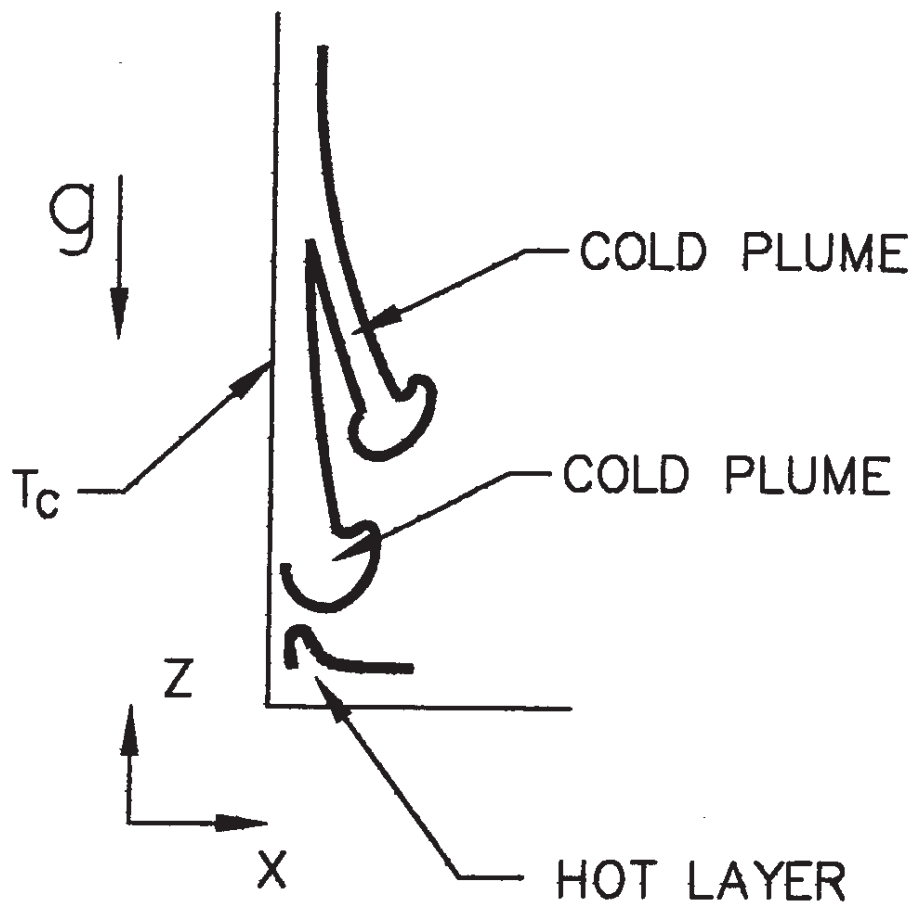


Figure 9.C-17b. Generation of the Cold Plumes Due to the Brake (Separation) of the Vertical Boundary Layers Near the Cold Vertical Walls

9.C-33

9.C.1.2.3 References

1. N. Akino, T. Kunugi, Y. Shina, M. Seki, Y. Okamoto, (1989)
“Natural Convection in a Horizontal Silicone Oil Layer in a Circular Cylinder Heated from Below and Cooled from Above” Nippon Kikai Gakkai Ronbunchyu, 55 Vol. 509 (1989-1), pp. 152 – 158.
2. M. J. Braun , M. B. Dzodzo, S. B. Lattime, (1993)
“Automatic computer based non-intrusive temperature measurements in laminar natural convection using thermochromic liquid crystals in enclosures with variable aspect ratio” FED-Vol. 172, Experimental and numerical flow visualization, The 1993 ASME Winter Annual Meeting, New Orleans, Louisiana, November 28 – December 3, 1993, pp. 111-119.
3. L. Buhler, P. Erhard, G. Gunther, U. Muller, G. Zimmermann, (1987)
“Natural convection in vertical gaps heated at the lower side – an experimental and numerical study. In: Bifurcation Phenomena in Thermal Processes and Convections (eds.H.M. Bau, L.A. Bertram, S.A. Lorpela) ASME, HTD-Vol. 94/AMD-Vol.89, 67-74.
4. M. Dzodzo, M.J. Braun, S.B. Lattime, (1994)
“A non-intrusive computer automated investigation of natural convection using thermochromic liquid crystals and comparison with numerical simulation” (ed. G.F. Hewitt) Proceedings of The Tenth International Heat Transfer Conference, Brighton, UK, Volume 2, 2-MT-6, pp. 225-230.
5. A.D. Garrad and M.A. Patrick, (1983)
“The velocity field produced by submerged jet directed upwards at a free surface”, Int. J. Heat Mass Transfer, Vol. 26, No. 7, pp. 1029-1036.
6. E. L. Koschmieder, (1993)
“Benard Cells and Taylor Vorticies” Cambridge University Press
7. M. Ozawa, U. Muller, I. Kimura and T. Takamori, (1992)
“Flow and temperature measurements of natural convection in a Hele-Shaw cell using a thermo-sensitive liquid-crystal tracer” Experiments in Fluids, Vol 12, pp. 213-222.
8. P.F. Peterson, (1994)
“Scaling and analysis of mixing in large stratified volumes” Int. J. Heat Mass Transfer, Vol. 37, Suppl. 1, pp. 97-106.
9. B. Porterie, M. Larini, F. Giroud and J.C. Loraud, (1996)
“Solid-propellant fire in an enclosure fitted with a ceiling safety-vent” Int. J. Heat Mass Transfer, Vol. 39, No. 3, pp. 575-601.
10. R.M.C. So and H. Aksoy, (1993)
“On vertical turbulent buoyant jets” Int. J. Heat Mass Transfer, Vol. 36, No. 13, pp. 3187-3200.
11. K.T. Yang, (1988)
“Transitions and Bifurcations in Laminar Buoyant Flows in Confined Enclosures” J. of Heat Transfer, November 1988, Vol. 110, pp. 1191-1204.

9.C-34

9.C.1.3 Important Dimensionless Groups

9.C.1.3.1 Important Dimensionless Groups for Stratification and Circulation Phenomena Inside Enclosures

For natural convection, the ratio of the buoyancy to viscosity forces is the most important dimensionless group. The Grashof number defines the ratio of the buoyancy to viscosity forces:

$$Gr = \frac{g * \beta * (T_h - T_c) * H^3}{\nu^2} = \frac{g * (\rho_c - \rho_h) * H^3}{\rho_c * \nu^2}$$

Natural convection correlations often use the Rayleigh number instead of Grashof number, where the Rayleigh number Ra is defined as:

$$Ra = \frac{g * \beta * (T_h - T_c) * H^3}{\alpha * \nu} = \frac{g * (\rho_c - \rho_h) * H^3}{\rho_c * \alpha * \nu} = Gr * \frac{\nu}{\alpha} = GrPr$$

Using the Rayleigh number reduces the number of dimensionless groups in the correlations for natural convection. The appearance of Prandtl number inside some correlations could be avoided.

The Prandtl number is based on fluid properties, i.e., the ratio of kinematic viscosity to thermal diffusivity.

$$Pr = \frac{\nu}{\alpha}$$

When considering the interaction between the hot buoyant plume and the cold vertical wall boundary layer, the Grashof and Rayleigh numbers are defined with H_v as the characteristic length.

$$Gr_v = \frac{g * (\rho_v - \rho_o) * H_v^3}{\rho_v * \nu^2}$$

This applies to flows generated inside the enclosures with the opposite vertical walls at the different temperatures. It also applies to flow caused by two opposing vertical jets (between the two horizontal plates). The AP600 and **AP1000** have a combination of the two cases.

Upward flow is caused by the buoyant plume, while downward flow is caused by the lower temperatures of the vertical wall. If the initial kinetic energy of the plume is small, this Grashof number gives an indication of the formed flow pattern and heat transfer due to the two opposing vertical flow paths. The formation of a recirculating stratified core between the vertical jets is related to this parameter as well.

9.C-35

When considering the interaction between the cold ceiling and the hot rising plume (at the bottom of the enclosure), the height of the upper-deck region H_t can be used as a characteristic length. The Grashof number is:

$$Gr_t = \frac{g * (\rho_t - \rho_o) * H_t^3}{\rho_t * \nu^2}$$

The value of this Grashof number indicates the status of the Rayleigh-Benard convection. If the values are above 10^4 , it is possible to form periodic vertical downward plumes which detach from the ceiling.

The conditions described above interact. The overall flow pattern is expected to be a superposition of the flow patterns described for enclosures with horizontal and vertical temperature gradients. The prevailing flow pattern is estimated from the ratio of the two Grashof numbers already defined:

$$\frac{Gr_t}{Gr_v} = \frac{(\rho_t - \rho_o) * H_t^3 * \rho_v}{(\rho_v - \rho_o) * H_v^3 * \rho_t}$$

Note that both dimensions of the large-scale test (LST) installation (H_t and H_v) are scaled to AP600 dimensions. Therefore, if the ratio of relative densities (in vertical and horizontal directions) is the same, the flow patterns obtained in LST experiments can be applied to the AP600.

Even small temperature differences between the shell and the atmosphere inside a containment produce large Grashof numbers. For example, a temperature difference of 9°F results in $Gr_t = 2.2 * 10^{13}$ and $Gr_v = 4.7 * 10^{12}$ for $H_t = 109$ ft and $H_v = 65$ ft, respectively.

In the case of LST, a temperature difference of 9°F results in $Gr_t = 3.9 * 10^{10}$ and $Gr_v = 7.2 * 10^9$ for $H_t = 13.2$ ft and $H_v = 7.5$ ft, respectively.

If the Grashof numbers are greater than 10^8 , the Nusselt number can be obtained by applying the correlation for turbulent free convection.

For jets and buoyant plumes that penetrate the containment, the ratio of inertia forces and buoyant forces influences the entrainment of surrounding gases. If the initial velocities are high, a constant spreading angle indicates a jet. As the jet velocities decrease, upward motion results from buoyant forces. Buoyant plume behavior is indicated by different spreading angles at each level.

The Froude number represents the ratio of the inertia to gravity forces, or the ratio of kinetic energy to potential energy:

$$\frac{Gr_t}{Gr_v} = \frac{(\rho_t - \rho_o) * H_t^3 * \rho_v}{(\rho_v - \rho_o) * H_v^3 * \rho_t}$$

9.C-36

For buoyant plumes and jets, the Froude number can be defined as:

$$Fr_{j,o} = \frac{\rho_o * U_o^2}{g * (\rho_a - \rho_o) * d_o}$$

where the characteristic length is the initial diameter of the jet or plume. The source velocity and density have the subscript (o), while the ambient density has the subscript (a). The elevation of the transition from a forced jet to a buoyant plume is calculated (Peterson, 1994 and Spencer, 1997) from the expression:

$$\frac{z_{trans}}{d_o} = Fr_{j,o}^{1/4} * \left(\frac{\rho_o}{\rho_a}\right)^{1/4}$$

The ratio of the square of the jet Reynolds number to the containment Grashof number is a volumetric Froude number:

$$Fr_v = \frac{\rho_a * U_o^2 * d_o^2}{g * (\rho_a - \rho_o) * H^3}$$

If the volumetric Froude numbers are much greater than one, the inertia forces dominate. The inertia forces unstratify layers, promote circulation inside the containment, and contribute towards the better mixing.

However, Peterson, 1994, proposes that the jet or plume is not able to disturb the stratified vertical density gradients if:

$$Fr_v < \left(1 + \frac{d_o}{4 * \sqrt{2} * \alpha * H}\right)^2$$

where (α) is Taylor's jet entrainment parameter and where $\alpha = 0.05 = \text{constant}$.

For volumetric Froude numbers less than one, the inertia forces are not dominant and are not able to unstratify layers inside the containment. Therefore, the buoyancy effects are more important than inertia effects. The reciprocal value of the Froude number or Richardson number is the appropriate dimensionless group.

$$Ri_v = \frac{g * (\rho_a - \rho_o) * H^3}{\rho_a * U_o^2 * d_o^2}$$

Since inertia effects of the plume are not important (Reynolds number of the plume is small), only Grashof numbers Gr_i and Gr_v will influence the flow pattern.

9.C-37

Another important factor is the position of the jet (plume) or heat source release location. The ratio of the release point level, H_r , to the height of the containment, H_t , describes the relative position of the jet (plume) or heat source:

$$\frac{H_r}{H_t}$$

If H_r/H_t is less than 0.2, the release location is considered low. A global circulation flow pattern affecting the entire containment is most likely formed. If H_r/H_t is greater than 0.5, the release elevation is high and stratification effects may occur in a portion of the volume. The result may be that only the upper portion of the enclosure is affected by global circulation, while the lower may be stratified. Such stratification may be stagnant. In stagnantly stratified regions, no entrainment into wall boundary layers or buoyant plumes occurs, and thus little or no vertical mixing occurs, while in recirculating stratified regions vertical mixing can be strong and can greatly reduce vertical density gradients.

Specified criteria for the H_r/H_t ratio are based on the international experimental database which is presented in the next chapter.

9.C.1.3.2 References

1. P. F. Peterson, (1994), "Scaling and Analysis of Mixing in Large Stratified Volumes," Int. J. of Heat and Mass Transfer, Vol. 37, Supplement 1, pp. 97-106, 1994.
2. D. R. Spencer, (1997), "Scaling Analysis for AP600 Containments Pressure During Design Basis Accidents," WCAP-14845, Revision 3, March 1998.

9.C.1.4 Expected Flow Patterns for AP600 and AP1000

9.C.1.4.1 Simplified Representation of Circulation Regions During Post-Blowdown LOCA in AP600 and LST

The AP600 containment and the large-scale test (LST) facility include five primary flow regions (Peterson, 1997 – letter to Woodcock). The regions are presented in Figure 9.C-18 showing a control volume that extends to the condensed fluid film surfaces. This figure is useful for structuring a discussion of circulation and stratification phenomena and for relating separate effects of enclosures tests to the various regions.

The volumetric flow rates presented in Figure 9.C-18 at "quasi-steady" conditions are:

- Q_o , the steam volumetric flow rate from the break,
- Q_e , the flow rate of fluid entrained from inside the below-deck region into the steam generator compartment (equivalent to the flow rate delivered to the below-deck region due to the penetration of a portion of the wall boundary layers through the deck gap near the walls),
- Q_p , the flow rate of fluid entrained into the plume in the above-deck region,

9.C-38

- Q_w , the flow rate of fluid entrained into the vertical wall boundary layers,
- Q_v , the flow rate of steam condensed on the vertical walls (shown leaving the control volume), and
- Q_t , the flow rate of steam condensed on the dome ceiling (shown leaving the control volume)

For the quasi-steady conditions, the steam flow rate entering in the containment volume Q_o is equal to the summation of the steam flow rates condensed on the dome ceiling Q_t and vertical walls Q_v .

The distances presented in Figure 9.C-18 are:

- H_t , the distance between the jet inflow position into the upper-deck region and the dome springline elevation (in vertical direction),
- H_{EF} , the distance between the break location and the jet inflow position into the upper-deck region (in vertical direction), and
- H_v , the distance between the vertical wall and the jet center (in horizontal direction).

The definitions of the regions relate well to the separate effects of the enclosure tests.

Region I is below the operating deck level. In the AP600 and **AP1000** configuration, connections exist between the below-deck compartments and the upper-deck region (dome). These connections allow the steam jet (plume) generated-entrainment into the break compartment to produce circulation through Region I. The volumetric flow from the lower to the upper deck regions is Q_e . Jet entrainment and the slots around the circumference of the deck floor enable this circulation (see Figure 9.C-19).

In the LST – LOCA experiments, the release point is also below the operating deck level. However, the compartment containing the release is not connected with the other below-deck compartments (see Figure 9.C-20). The simulated steam generator compartment is connected only with the upper portion (dome) of the containment. Therefore, the jet injection location for the LST LOCA experiments is effectively at the top of the simulated steam generator compartment, where the flow enters the above-deck region, and entrained volumetric flow Q_e is equal to zero (see Figure 9.C-20). The atmosphere in the below-deck compartment is a stably stratified region without recirculation. The heat and mass transfer in the below deck compartments are governed primarily by molecular diffusion.

Region II is defined as the volume between the springline elevation and a horizontal line above the operating deck elevation, and between the wall boundary layers (Region IV) and the plume (Region III). Two entrainment mechanisms remove fluid from Region II. Entrainments into the vertical jet (or buoyant plume) and the wall boundary layers are compensated for by the inflows from the upper and lower horizontal boundaries. In order to preserve mass continuity and to obtain inflow into Region II, the vertical velocity components (see Figure 9.C-21) are negative and positive at the upper and lower horizontal boundaries, respectively. The fluid inside the Region II is recirculating (see Figure 9.C-22), yet has a quasi-steady dp/dz maintained by balance between the buoyancy and the two entrainment mechanisms. Therefore, Region II can be called a recirculating stratified region. The horizontal density

and concentration gradients are small, but significant recirculation flow exists due to the entrainment into the free and wall jets (see Peterson, 1997). Region II can be considered as a region where the vertical density, temperature and concentration gradients are dependent on the values of the volumetric Froude numbers (for free jets or plumes) and Grashof (Rayleigh) numbers (for wall boundary layers). This is similar to the case of an enclosure with opposite vertical walls at different temperatures (see section 9.C.1.1.2.1). The recirculation and entrainment from the Region II contributes to a decrease in the vertical temperature, density, and concentration gradients.

Region III contains free jets (plumes) which transport fluid in the vertical direction. The upward motion of a jet (or plume) produces entrainment from Region II. As a result, the jet (or plume) spreads, reduces velocity, and dilutes (decreases the temperature and concentration difference between the core of the jet and the surrounding atmosphere – Region II).

Region IV contains wall boundary layers which also provide transport in the vertical direction. The entrainment into the wall boundary layer transports steam into Region IV. The entrainment from Region II into the wall boundary layers enhances recirculation inside the Region II. This contributes to a decrease in the vertical temperature, density, and concentration gradients inside Region II.

Region V, the dome region, is between the containment ceiling and the elevation of the springline. Because the temperature of the containment ceiling is lower than the temperature of the atmosphere below the ceiling, downward flowing “ceiling plumes” are formed (see the Rayleigh-Benard convection example of section 9.C.1.2.1). The difference in the steam concentrations between the top of the Region V (immediately below the ceiling where condensation occurs) and the top of Region II are small due to the circulation (interaction) within Region V, caused by cold plumes falling from the ceiling and the hot plume reaching the ceiling of the dome. The downward plumes increase circulation and reduce gradients inside the dome, Region V. The downward “ceiling plumes” interact with the uprising plume (from the Region III). If the strength of the jet (plume) from the Region III is high, interactions occur inside Region V and the influence of the downward plumes does not spread towards the lower regions.

However, if the plume from Region III is not strong enough to produce good mixing inside Region V, the penetration of the downward “ceiling plumes” into the lower regions can disturb (from time to time) the recirculating stratified layers inside Region II. This tends to reduce the vertical gradients within Region II.

If the plume is very weak or does not exist, the vertical downward “ceiling plumes” affect the entire volume of the upper-deck region. The flow patterns formed are the result of superposition of Rayleigh-Benard convection (described for the enclosure with cold upper and hot lower surface) and recirculating stratification (described for the enclosure with opposite vertical walls at different temperatures).

The cold dome ceiling produces downward vertical plumes as in Rayleigh-Benard convection case, while cold vertical walls produce downward wall boundary layers. Due to continuity, the downward wall boundary layers tend to generate upward flow in the middle of the above-deck region. The wall boundary layer and the upward flow in the middle of the containment form a recirculation zone. Between the wall boundary layers and the upward flow in the middle of the containment, a recirculating stratified core is formed. This is similar to enclosures with opposite vertical walls at different temperatures. Note that

although there is evidence from enclosure tests that a stable non-zero vertical density gradient could exist in Region II, entrainment flows cause circulation of fluid. Region II is not considered as stagnant.

The prevailing flow pattern can be postulated (Rayleigh-Benard or recirculating stratified) from the ratio of Grashof numbers Gr_t/Gr_v [defined for vertical $\Delta\rho$ and distance H_t (for Gr_t) and horizontal $\Delta\rho$ and distance H_v (for Gr_v)]. Note that turbulent Rayleigh-Benard convection starts at $Ra_t = Gr_t Pr > 10^4$ (for $Pr = 0.71$, based on 3D enclosure experiments – see section 9.C.1.2.1), while turbulent flow (with thin boundary layers and recirculating stratified but almost homogenized core) in enclosures with vertical walls at opposite temperatures starts at $Ra_v = Gr_v Pr > 10^8$ (for $Pr = 0.71$, based on 2D numerical simulations, see section 9.C.1.1.2.1). This indicates that for small values of Rayleigh numbers ($10^4 < Ra_v$ and $Ra_t < 10^8$), Rayleigh-Benard convection is dominant. Turbulent and chaotic flow are dominated by falling vertical plumes (see Figure 9.C-15).

For higher Rayleigh numbers (Ra_v and $Ra_t > 10^8$) combined with a weak source plume, in fact smaller Rayleigh number in horizontal direction, falling vertical plumes (see Figure 9.C-15) dominate the flow patterns. For the dominant jet (or plume), or high Rayleigh number in horizontal direction (Gr_v high) and moderate Froude number, a recirculating stratified flow pattern prevails in Region II (see Figure 9.C-5). Higher and similar magnitude values of both Rayleigh numbers (in vertical and horizontal direction) result in a flow pattern that is a superposition of the two described patterns (shown in Figure 9.C-15 and Figure 9.C-5). Finally, for the case of the momentum-dominated jet (with high Froude number), the circulation flow pattern will be present in the entire volume of the containment (see Figure 9.C-11).

9.C.1.4.2 A Qualitative Model for Recirculating Stratified Region II

A qualitative model of Region II is used to address the issue of recirculating stratification and circulation (Peterson, 1997). The model is a coarse, first-principle representation of the effects of various volumetric flows and entrainment rates. It qualitatively examines the influence of various parameters on the difference in steam concentrations from the bottom to the top of the Region II (ΔX).

Because of the complexity of the physics, two simplifying assumptions are used. It is assumed that Region II is not influenced by falling plumes from Region V and that the recirculation effects inside Region II can be neglected. Both assumptions cause overestimated vertical steam gradients ΔX . Interactions between Region II and Region V that result from the penetration of the cold falling plumes (from Region V), improve mixing and decrease vertical steam gradients ΔX . Recirculation inside Region II (established experimentally and numerically inside the core of enclosures) further decreases the vertical steam gradients.

Peterson, 1997, provides the following mass conservation equation for the thin horizontal layer inside Region II with area $A(z)$ (see Figure 9.C-23:

$$\rho(z) * A(z) * dv(z) = -\rho_p(z) * u_p(z) * p_p(z)dz - \rho_w(z) * u_w(z) * p_w(z)dz$$

where $v(z)$ is the vertical velocity, and $u_p(z)$ and $u_w(z)$ are the entrainment velocities into the steam plume and wall boundary layer, respectively. The vertical coordinate is z , while p_p and p_w are the perimeters of the plume (or jet) and wall boundary layer, respectively.

9.C-41

Since molar densities are dependent only on the temperature (assuming constant pressure in the entire volume), the differences between the molar densities $\rho(z)$, ρ_p and ρ_w are small. To simplify the analysis, the equation is written without densities. A balance of the volumetric flow rates is then used for the remainder of the analysis (instead of a mass balance).

To further simplify the analysis (considering only global effects), u_p , u_w , p_p , p_w , and A are assumed to be constant, or independent of z (Peterson, 1997). This assumption results in a linear, vertical velocity distribution. Although the actual entrainment varies with height, the integrated total should be reasonably close to the average constant values.

The calculations of the entrained volumetric flow into the plume Q_p and wall boundary layer Q_w are simplified as:

$$Q_p = \int_0^H u_p(z) * p_p(z) dz = u_p * p_p * H$$

and

$$Q_w = \int_0^H u_w(z) * p_w(z) dz = u_w * p_w * H$$

respectively. The total inflow to the top and bottom of Region II (see Figure 9.C-21) provides the boundary conditions for the vertical velocities $v(0)$ and $v(H)$ at the bottom and at the top of the Region II, respectively:

$$A * v(0) = Q_w - Q_v - Q_e$$

$$A * v(H) = -(Q_v + Q_p + Q_e)$$

where Q_e is the volumetric rate of flow into the below-deck region (see Figure 9.C-18 and Figure 9.C-19). Due to mass continuity (conservation) for the below-deck region, this flow rate is equal to the volumetric flow rate (Q_e) entrained into the steam generator compartment by the steam jet (plume).

The volumetric flow rate of steam condensed on the vertical wall is Q_v . Q_t is the flow rate of steam condensed on the dome. The total steam volumetric inflow into the containment is $Q_o = Q_v + Q_t$ (see Figure 9.C-18 and Figure 9.C-23).

The linear, vertical velocity distribution in Region II is:

$$A * v(z) = (Q_w - Q_v - Q_e) - \frac{z}{H} * (Q_p + Q_w)$$

9.C-42

Downflow exists in the top part of Region II, while in the lower portion, the velocities are positive (upwards flow). This agrees with the previous discussion of Region II inflow horizontal boundaries (see Figure 9.C-21). Because the continuity-driven velocities are assumed horizontally uniform upward at the bottom and downward at the top of Region II, there will be an elevation, z , where the two meet and vertical velocity is zero. The z coordinate where the vertical velocity is zero in this model is:

$$z = \frac{Q_w - Q_v - Q_e}{Q_p + Q_w} * H$$

The average gas mole fraction in Region II is:

$$\bar{x}_g = \frac{1}{V} * \int_0^H A(z) * x_g(z) dz = \frac{1}{H} * \int_0^H x_g(z) dz$$

The mole fraction of gas at the bottom of Region II is found from a mass balance on the wall boundary layer. (Note that Q_v is the volumetric flow of steam that condenses on the vertical wall. It contains no noncondensable gas.)

$$x_g(0) = \frac{\int_0^H x_g(z) * u_w(z) * p_w(z) dz}{Q_w - Q_v} = \frac{u_w * p_w * \int_0^H x_g(z) dz}{Q_w - Q_v} = \frac{u_w * p_w * H * \bar{x}_g}{Q_w - Q_v} = \frac{Q_w * \bar{x}_g}{Q_w - Q_v}$$

Similarly the gas mole fraction at the top of the Region II is:

$$\begin{aligned} x_g(H) &= \frac{x_g(0) * Q_e + \int_0^H x_g(z) * u_p(z) * p_p(z) dz}{Q_v + Q_p + Q_e} = \frac{\frac{Q_w * \bar{x}_g}{Q_w - Q_v} * Q_e + u_p * p_p * \int_0^H x_g(z) * dz}{Q_v + Q_p + Q_e} \\ &= \frac{\frac{Q_w * \bar{x}_g}{Q_w - Q_v} * Q_e + Q_p * \bar{x}_g}{Q_v + Q_p + Q_e} \end{aligned}$$

The relative difference in the concentrations from the bottom to the top of Region II is:

$$\frac{\Delta x}{\bar{x}_g} = \frac{x_g(0) - x_g(H)}{\bar{x}_g} = \frac{Q_w}{Q_w - Q_v} - \frac{\frac{Q_w * Q_e}{Q_w - Q_v} + Q_p}{Q_v + Q_p + Q_e}$$

The final form of the equation, which is more suitable for qualitative understanding of the influence of various volumetric flow rates, is:

$$\frac{\Delta x}{\bar{x}_g} = \frac{x_g(0) - x_g(H)}{\bar{x}_g} = \frac{Q_v * (Q_w + Q_p)}{(Q_w - Q_v)(Q_p + Q_v + Q_e)}$$

The influence of the various volumetric flow rates under various assumed conditions will now be examined.

9.C-43

9.C.1.4.2.1 Case 1: Strong Plume, Wall Boundary Layer and Plume Entrainments are Equal

If the entrainment volumetric flow rates are approximately equal ($Q_p \sim Q_w$) and are large compared to Q_v and Q_c , the relative concentration difference is simplified to:

$$\frac{\Delta x}{\bar{x}_g} = \frac{x_g(0) - x_g(H)}{\bar{x}_g} \geq \frac{Q_v * (2 * Q_w)}{(Q_w * Q_w)} = \frac{2 * Q_v}{Q_w}$$

These assumptions are valid for the case of the jet-dominated flow. The large plume and wall boundary layer entrainment volumetric flow rates act to reduce the relative, vertical steam concentration gradient.

Even if the flow pattern cannot be defined as jet-dominated (i.e., the equation for the relative difference in the concentration from the bottom to the top of Region II cannot be simplified), the recirculating stratified Region II interacts with the plume and wall jets, Regions III, and IV (see Figure 9.C-23). The relative concentration difference will still decrease if the entrainments in both the wall layer Q_w and plume Q_p are large.

It has been shown (Enclosure to Westinghouse Letter NSD-NRC-97-4978, February 7, 1997) that during the quasi-steady portion of a LOCA, jet entrainment rates (Q_p) in the AP600 are about a factor of 10 greater than the condensation rate ($Q_v + Q_i$).

9.C.1.4.2.2 Case 2: Equal Entrainment into the Wall Boundary Layer Q_w and the Rate of the Steam Condensed at the Vertical Walls Q_v

A small difference between the entrainment volumetric flow rate into the wall boundary layer Q_w and volumetric flow rate of the steam condensed at the vertical walls Q_v produces an increase in the relative difference of the concentrations. If all the steam entrained into the wall boundary layer is condensed at the vertical walls, nothing is left to be redistributed through the lower horizontal boundary of Region II and contribute towards a decrease in the vertical concentration gradients.

9.C.1.4.2.3 Case 3: High Dome Condensation Rate Q_t

The volumetric flow of the steam condensed on the dome of the containment Q_t does not directly affect the relative concentration difference in Region II (it is not present in the equation). However, indirect effects are possible. If the condensation on the dome is high, the ratio of Q_t/Q_v is high, and the volumetric flow of steam condensing on the vertical walls Q_v decreases. In contrast, a small ratio of Q_t/Q_v represents an increased volumetric flow rate condensing on the vertical walls, Q_v . A decrease in the rate of steam condensing on the vertical walls Q_v (in fact the increase of steam volumetric flow rate condensing on the dome, Q_t), decreases the relative concentration difference.

9.C.1.4.2.4 Case 4: Influence of the Below Deck Entrainment Q_e

Region I also interacts with the stratified Region II. The effects of this interaction on the relative concentration difference change are captured by the Q_e term. A large below-deck entrainment, Q_e , reduces the concentration difference. In the AP600 and AP1000, below-deck entrainment contributes to a decrease in the relative concentration difference. This effect is not present in the LST case, where $Q_e = 0$.

9.C-44

9.C.1.4.2.5 Case 5: Dominant Entrainment into the Wall Boundary Layer Q_w

If $Q_v = 0.5 Q_o$, as observed in phase 3 of the LST experiments where Q_v is between $0.4Q_o$ and $0.6Q_o$ (see WCAP-14135), and if $Q_w = 2Q_p$, i.e., the wall boundary layer entrainment is twice as strong as plume entrainment (weak plume scenario), if the entrainment in the below-deck region is negligible, $Q_e=0$, and if we assume $Q_p = 10Q_o$ the relative steam concentration is:

$$\frac{\Delta x}{\bar{x}_g} = \frac{x_g(0) - x_g(H)}{\bar{x}_g} = \frac{0.5 * Q_o * (2 * Q_p + Q_p)}{(2 * Q_p - 0.5 * Q_o)(Q_p + 0.5 * Q_o + 0)} = 0.073$$

A further increase in the entrainment into the wall boundary layers causes an additional decrease in the relative difference between steam concentrations in the bottom and the top of Region II (e.g., if $Q_w=3Q_p$, the relative concentration is 0.064). The increase in the entrainment into the wall boundary layers contributes to the homogenization of the containment atmosphere.

9.C.1.4.2.6 Conclusion

The expected circulation within the AP600 and **AP1000** containment is segregated into five regions that relate to separate effects tests (SETs) in enclosures. Given the presence of the externally cooled shell, which is assumed in a DBA analysis, there are no regions of stagnant stratification in containment.

The proposed conceptual model can be used to structure the containment into regions for comparison to relevant enclosures SETs. The mathematical representation provides insight into the influence of various volumetric flows on the axial steam concentration gradients in the AP600 and **AP1000**.

9.C-45

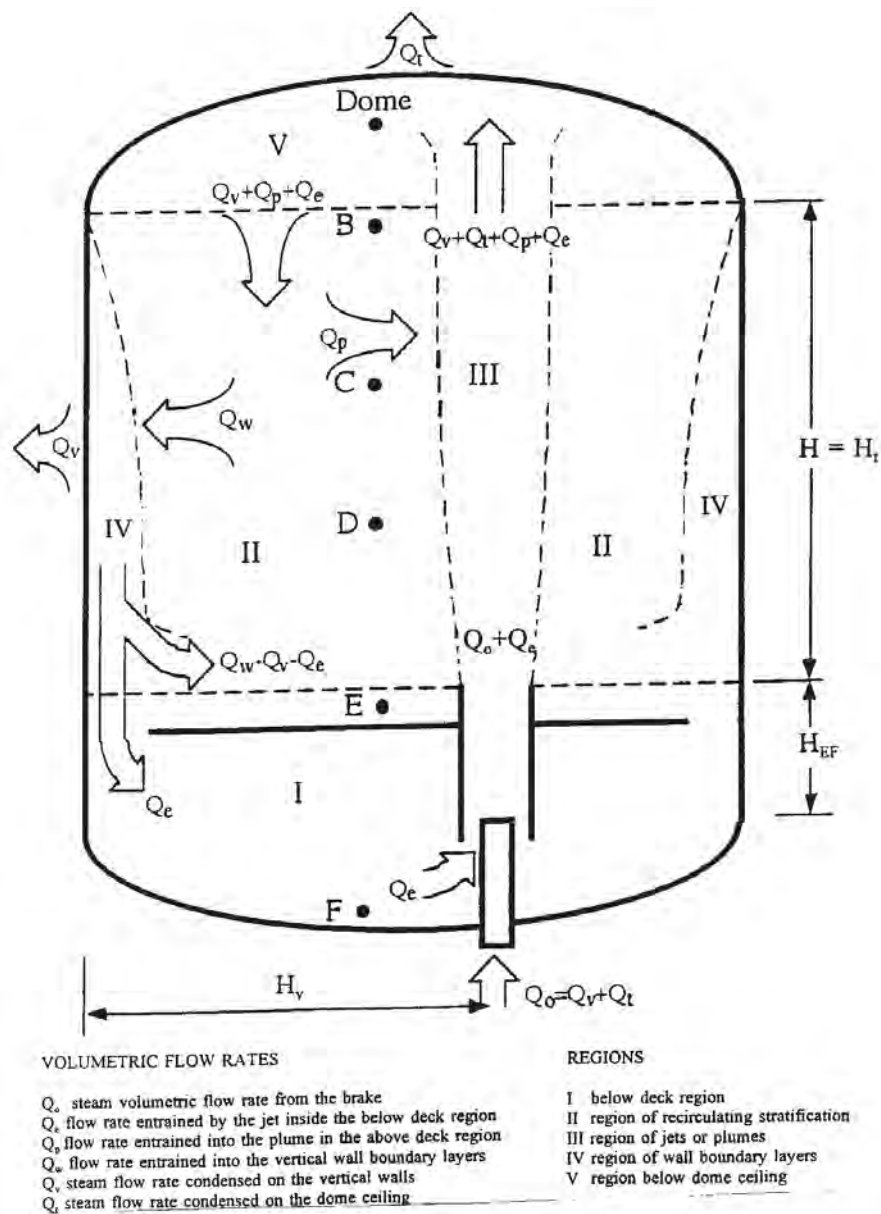


Figure 9.C-18. Primary Flow Regions and Volumetric Flow Rates for Quasi-Steady Containment Conditions

9.C-46

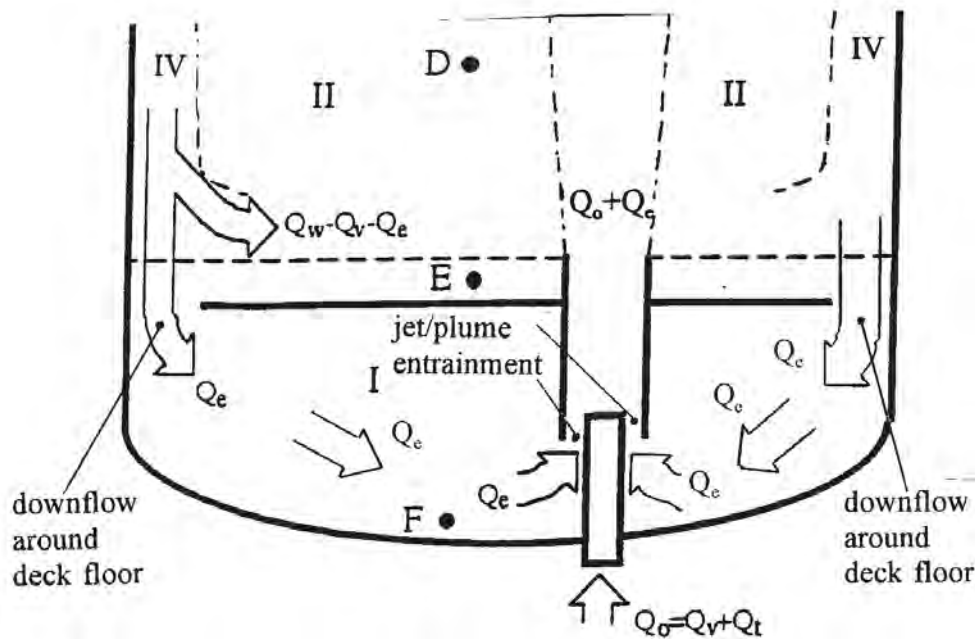


Figure 9.C-19. The Volumetric Flow between the Upper and Lower Deck Regions Q

9.C-47

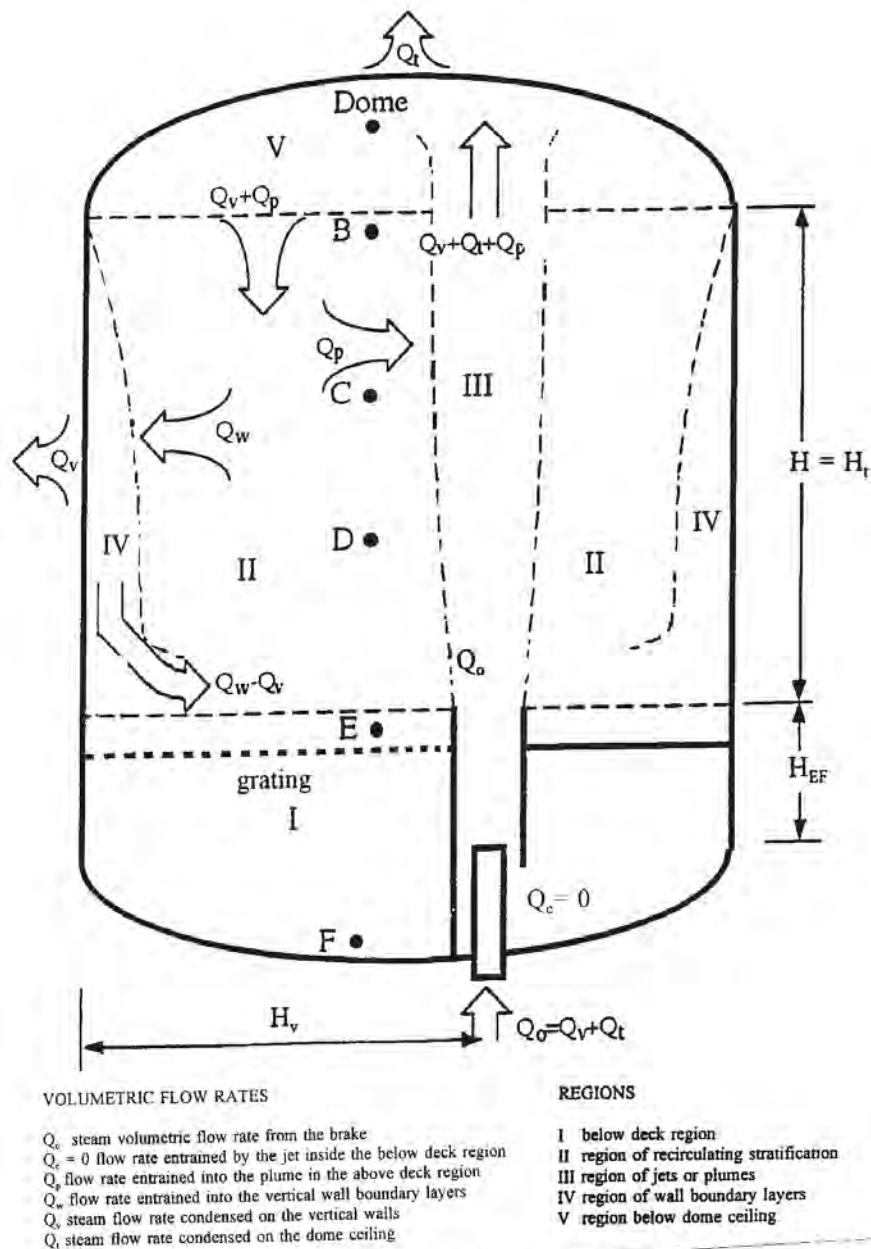


Figure 9.C-20. Primary Flow Regions and Volumetric Flow Rates for Quasi-Steady Containment Conditions in LST Case

9.C-48

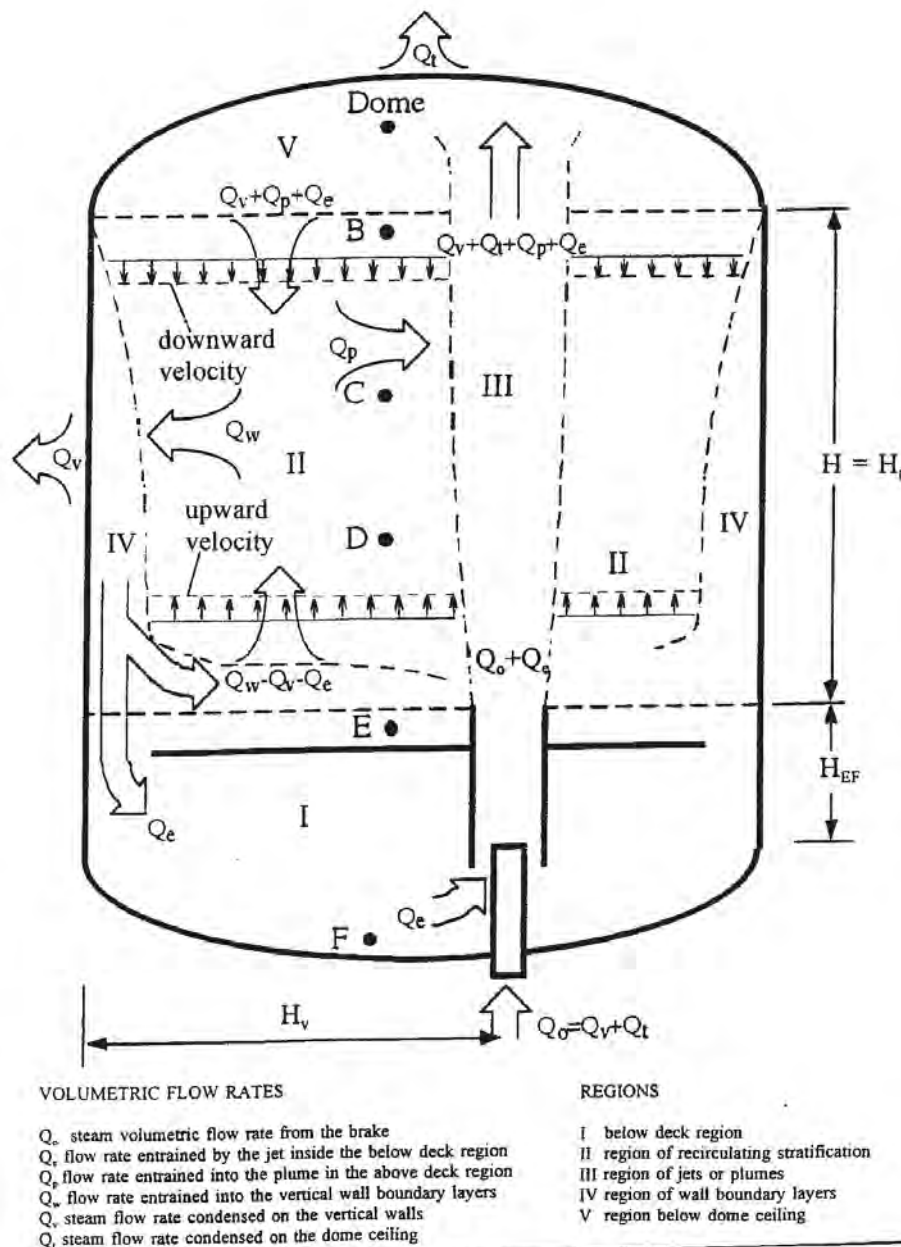


Figure 9.C-21. Inflows and Outflows from the Region II

9.C-49

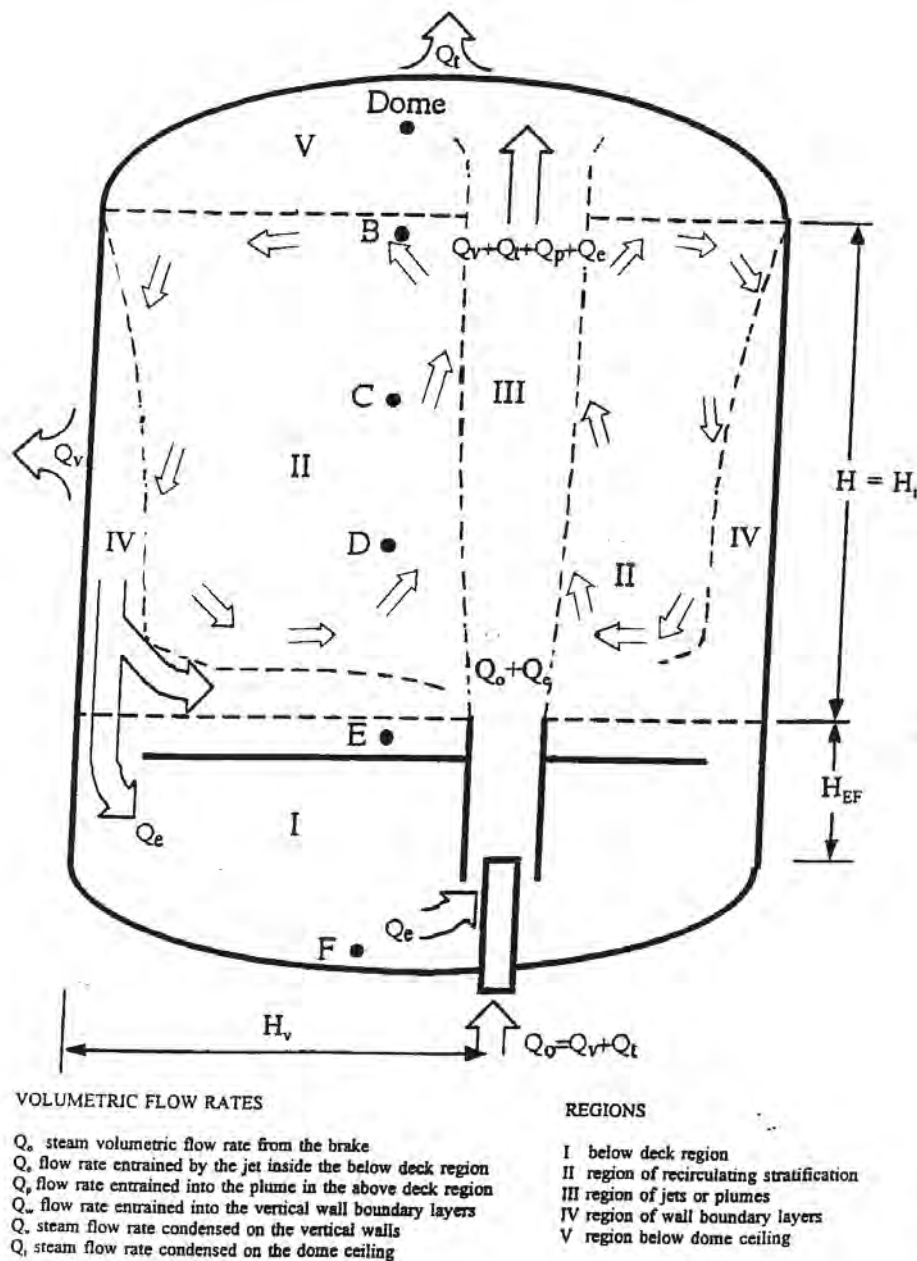


Figure 9.C-22. Recirculating Flow Paths Inside the Region II

9.C-50

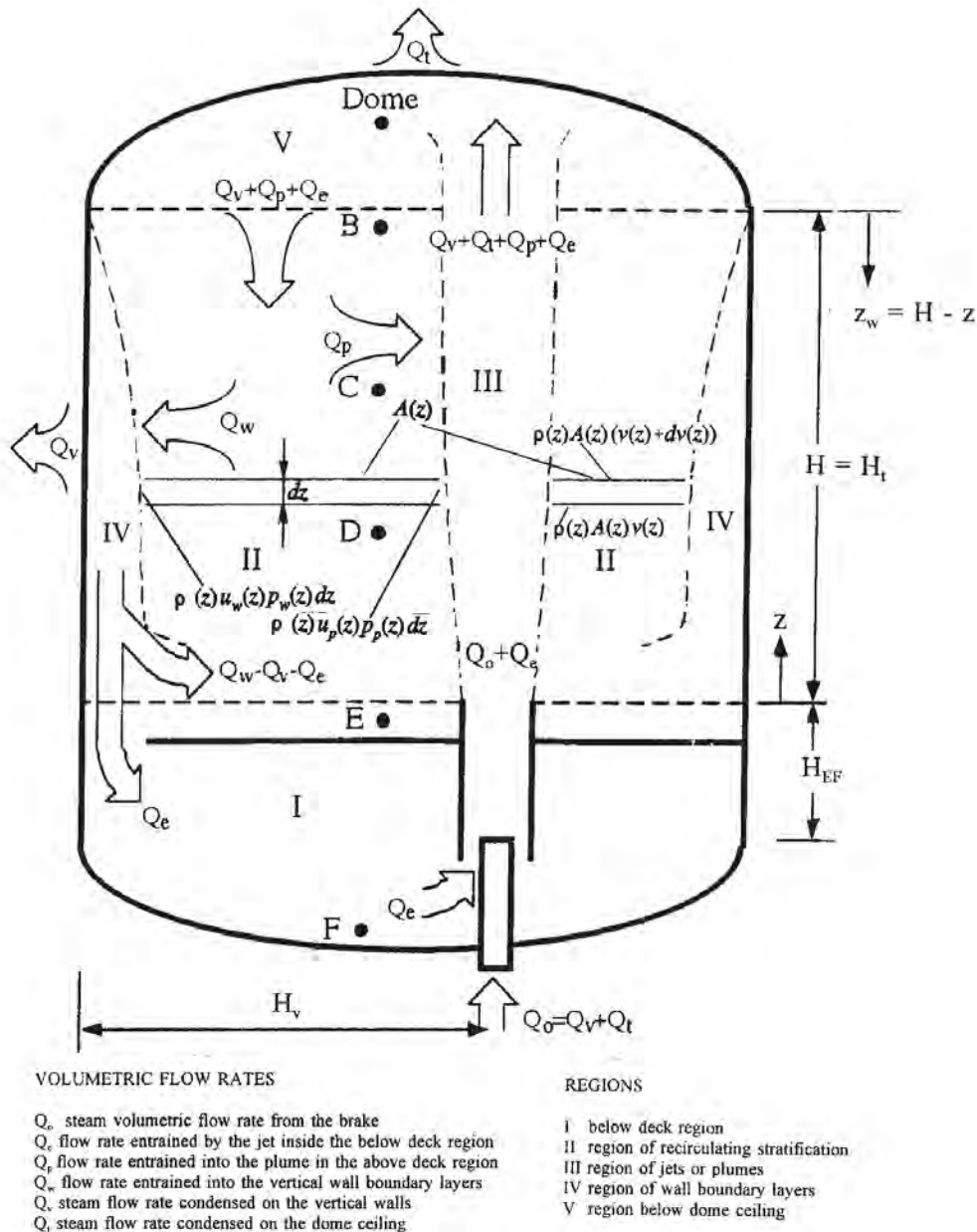


Figure 9.C-23. Mass Conservation for Thin Horizontal Layer Inside the Region II

9.C.1.4.3 References

1. P.F. Peterson, 1997
LST Mixing Model Writeup - letter to J. Woodcock, 02/24/97
2. Enclosure to Westinghouse Letter NSD-NRC-97-4978
Subject: Position paper in support of the assumption of complete mixing of aerosols in the AP600 containment atmosphere following a loss of coolant accident February 7, 1997
3. WCAP-14135, F. E. Peters, April 1997
"Final Data Report for PCS Large-Scale Tests, Phase 2 and Phase 3," Revision 1
Westinghouse Energy Systems

9.C.2 OVERVIEW OF THE INTERNATIONAL CONTAINMENT EXPERIMENTAL DATA BASE

Tests from the available international containment experimental database that are relevant to the passive containment design, are presented in this chapter. Some tests are very close to possible passive containment cases. Others are presented to emphasize the difference between the passive containment design and the test conditions that lead towards stratification.

Four experimental facilities are considered to supplement LST data. Table 9.C-1 specifies characteristics of each experimental facility and provides a comparison with the LST, the AP600 and the **AP1000**. A comparison of the sizes of various test facilities is provided in Figure 9.C-24. Scaled cross-sections of each facility are shown.

A list of the facilities and the overviewed experiments is provided in Table 9.C-2, as well as the main characteristics of each experiment.

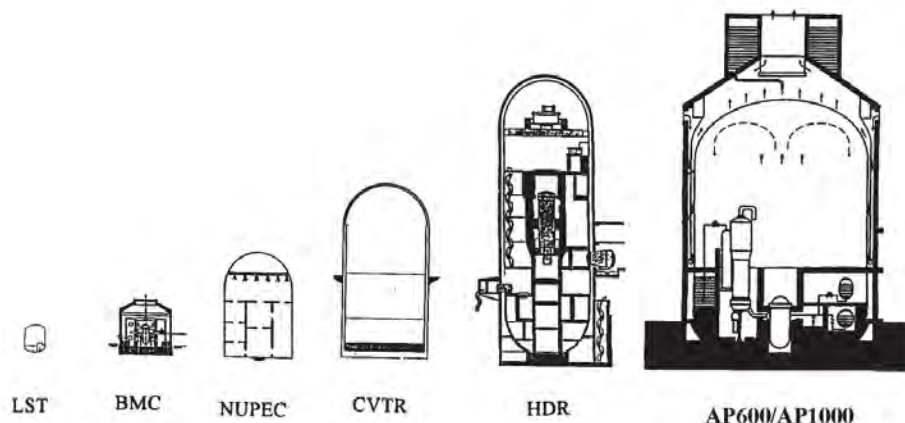


Figure 9.C-24. Comparison of Different Facilities

9.C-52

Table 9.C-1. Comparison of Various Facilities

Facility	LST	BMC	NUPEC	CVTR	HDR	AP600	AP1000
Volume m ³	83.1	640	1300 (used)	6428	11300	48710	58333
Height m	6.1	9	17.4	34.7	60	57.9	65.6
Diameter m	4.57	11.25	10.8	17.7	20	39.6	39.6
Number of compartments	3	9	25	3	62-72	11	11
Volume of the dome	79%		70%	41%	44%	81%	83%
Containment walls	steel	concrete	steel	concrete	steel shell concrete and steel	steel shell concrete and steel	steel shell concrete and steel

Table 9.C-2. Overviewed Tests from International Database

Facility	Experiment	Main Feature	Position of the Release Point and Other Relevant Data	Stratification or Circulation
BMC	F2 set First Phase	Stepwise steam addition	Release point is high Hr/Ht=0.444	Circulation through the majority of compartments, external annulus stratified
BMC	F2 set Phase 2	Inducing the natural circulation with steam injection	Steam release point is low Hr/Ht = 0.111	Circulation through the majority of compartments, external annulus stratified
BMC	F2 set Phase 3	Heater on in R6 to reverse circulation	Heat source location is low Hr/Ht = 0.111	Circulation through the majority of compartments, external annulus stratified
BMC	F2 set Phase 4	Steam injection in R6 compartment	Steam release point is low Hr/Ht = 0.111	Circulation through the majority of compartments, external annulus stratified
BMC	Test 2 Two compartments (Phase I)	Hydrogen injection, uniform initial temperature, orifice present, low feed rate	Low position of hydrogen source Hr/Ht = 0.06	Hydrogen uniformly distributed, circulation present

9.C-53

Table 9.C-2. Overviewed Tests from International Database (cont.)

Facility	Experiment	Main Feature	Position of the Release Point and Other Relevant Data	Stratification or Circulation
BMC	Test 4 Two compartments (Phase I)	Hydrogen injection, uniform initial temperature, no orifice	High position of hydrogen source $H_r/H_t = 0.57$	Concentration stratification occurs
BMC	Test 6 Two compartments (Phase I)	Hydrogen injection, stratified initial temperature, orifice present	Low position of hydrogen source $H_r/H_t = 0.06$	Stratification present, highest hydrogen concentration in the lower compartments
BMC	Test 12 Six compartments (Phase II)	Hydrogen injection in R2 room (high), uniform initial temperatures	High release point $H_r/H_t = 0.69$	Hydrogen uniformly distributed, circulation present
BMC	Test 20 Six compartments (Phase II)	Hydrogen injection in R6 room (low), stratified initial temperature	Low position of hydrogen source $H_r/H_t = 0.06$	Stratification present, highest hydrogen concentration in the lower compartments
BMC	RX4	Sump heat up and three hydrogen injections	Low position of the heat and hydrogen source $H_r/H_t = 0.0$	Circulation present, homogenization of temperature and concentrations
NUPEC	M-4-3	Simulated break inside the low steam generator compartment, steam and hydrogen release, containment shell insulated	Low position of the heat and hydrogen source $H_r/H_t = 0.0$	Circulation present during release, temperature stratifies and concentration homogenizes after the end of release
CVTR	First test without the internal water sprays	Steam release in the upper compartment, concrete shell	High position of the steam release $H_r/H_t = 0.525$	Temperature field stratifies
CVTR	The second and third test with internal water sprays	Steam release in the upper compartment, concrete shell	High position of the steam release $H_r/H_t = 0.525$	Temperature field stratifies but not as strong as in the previous case

9.C-54

Table 9.C-2. Overviewed Tests from International Database (cont.)

Facility	Experiment	Main Feature	Position of the Release Point and Other Relevant Data	Stratification or Circulation
HDR	E11.2	High positioned release point (small break) and active external spray	High position of the steam release $H_r/H_t = 0.555$	Stratification exists, external sprays promoted circulation
HDR	E11.3	Low positioned small break closed spiral stairway entrance		Global circulation pattern formed
HDR	E11.4	Low positioned release point (small break) and active external spray	Low position of the steam release $H_r/H_t = 0.18$	Global circulation formed almost uniform temperature distribution except below release point
HDR	T31.5	Simulates DBA large LOCA in the upper section of the containment	High position of the steam release $H_r/H_t = 0.526$	Temperatures and gas concentrations first stratify and latter homogenize
HDR	V21.1	Simulates DBA large LOCA in the middle section of the containment (in both staircases)	Middle position of the steam release $H_r/H_t = 0.38$	Equal heating of both staircases first suppressed circulation. Slight global circulation was generated later.
HDR	E11.5	Simulates DBA large LOCA in the lowest section of the containment with effects of dry heat release and sump boiling	Low position of the steam release $H_r/H_t = 0.18$	Global circulation due to the steam release, gas mixture injection and sump boiling contributed towards homogenization

9.C.2.1 Description of the Available Battelle Model Containment (BMC) Database

The objective of the Battelle Model Containment (BMC) tests is to obtain data to analyze design basis accidents (DBAs), hydrogen distribution, and aerosol depletion. The total volume of the containment is 640 m³ and represents 1/64 of the BIBLIS B containment. Its interior is divided into nine compartments and its walls are made of reinforced concrete. The sizes and locations of openings between the compartments can be adjusted by opening (or closing) the openings with steel plates or mobile concrete structures.

Three sets of tests are presented.

- The first set, the F2 experiments, tests natural convection as a function of release location and type of release (steam, air, dry heat).
- The second set of tests studies the influence of the initial temperature distribution, the location of hydrogen injection, the injection rates, and the size of the vent openings on hydrogen distribution, stratification and global circulation.
- The third set of tests examines the effect of sump heatup on global natural circulation.

9.C.2.1.1 Natural Convection Phenomena Inside the Multi-Compartment Containment (F2 Experiments)

The F2 experiments, performed by Kanzleiter in 1988, study natural convection inside a multi-compartment containment as a function of release location (room) and type (steam, air, dry heat). The BMC configuration used for experiment F2 is shown in Figure 9.C-25 and Figure 9.C-26. A 48-hour heatup period is the first phase of the experiment – see Figure 9.C-27, (Fischer et al., 1989, and Fischer et al., 1991). This is followed by a three-part, natural circulation phase (phases 2, 3, and 4) within the 48- to 75-hour time period see Figure 9.C-28, (Fischer et al., 1990 and Fischer et al., 1993).

An overview of the results and a comparison with analysis codes is presented by Wolf et al, 1996. Data for pressure, temperature, sump temperature, and liquid level, as well as partial steam pressure is presented for phases 1-4 (up to 75 hours).

9.C.2.1.1.1 F2 - Experiment Heatup Phase - Phase 1

Phase 1 is from 0-48 hours. A steam release inside the R2 compartment provides the heatup (see Figure 9.C-29 and Figure 9.C-27). The stepwise steam addition results in a stepwise increase of the containment pressure (see Figure 9.C-30 for GP 9117 location).

During the 48 hours of heatup, the atmosphere in the external annulus (the lower portion of R9 surrounding compartment) stratifies, Figure 9.C-31. Since there is no driving force for the circulation of steam into the lower air-rich regions of R9, the two experimental curves in Figure 9.C-31 (for temperatures GT9004 and GT9037) show that the heatup was delayed in lower positions in the external annulus behind the missile shield. The lower portion of R9 heats up over a longer period (Figure 9.C-31) because of global circulation induced by entrainment in the release. The entrainment is fed by flow from R9, R4 and R1.

Over a period of time, the atmosphere of the containment in the external annulus stratifies (after 16 hours it is already stratified). However, after 36 hours the stratification is not as pronounced, i.e., the temperature differences are not greater than 10°C in the external annulus. The initial stratification in the external annulus results from the high position of the steam release, which is inside the R2 compartment, and the closed circulation paths in the lower portion of the external annulus (see Figure 9.C-32).

The experimental curves for temperature histories of the other subcompartments (except for R4 and R3) are not presented in Wolf et al., 1996. However, consecutive phases of other experiments performed in the BMC indicate that natural circulation effects are present and contribute towards homogenization of the temperature fields among the majority of compartments. The only exception is the external annulus.

Application to the AP600 and AP1000

There is evidence that a release high in the steam generator compartment can induce global circulation flow by entrainment through the CMT room openings. It is difficult to compare time scales due to significant differences between the BMC and the passive containment compartment arrangement.

9.C.2.1.1.2 Phases 2-4 of the F2 Experiment (Natural Circulation)

After the heatup, the experiment continues through three additional phases (see Figure 9.C-27 and Figure 9.C-28 for phases 2, 3, and 4) that use the following methods to induce or amplify circulation:

- Steam injection to induce natural circulation,
- Activation of the heater to reverse circulation,
- Injection of steam to amplify reversed circulation.

Figure 9.C-28 illustrates four additional phases (5, 6, 7, and 8) that are not discussed. The circled numbers in Figure 9.C-28 represent the type of injection (see also Figure 9.C-27). The flow patterns formed during the particular injection are presented below the circled numbers. Figure 9.C-32 shows the two different locations for the steam injection, the location of the heater and the positions of the anemometers.

9.C-57

In addition to the measured velocities in the openings (see Table 9.C-3), the fluctuations in measured temperatures indicate natural circulation (see Figure 9.C-33 and Figure 9.C-34). Due to natural circulation, complex flow patterns form and temperatures in the compartments are nearly homogeneous (i.e., temperature differences are not greater than 4°C, see Figure 9.C-33 and Figure 9.C-34). The detailed temperatures and velocities during each subphase are given by Kanzleiter, 1988.

Figure 9.C-35 presents the thermodynamic states of the containment dome atmosphere at a high position ($H = 7.6$ m) during various time periods, while Figure 9.C-36 presents the conditions at a low position in the external annulus ($H = 1.0$ m). Except during air injection times, the steam partial pressure in the high position follows the shape of the total pressure curve (0.5 to 1.0 bar lower values than p_{tot}). At the low position, the steam partial pressure is almost constant (0.5 bar) after 60 hours. This indicates steam stratification inside the external annulus (lower portion of the R9 compartment) behind the missile shield.

The temperature distribution inside the external annulus is presented in Figure 9.C-37 for the second phase and in Figure 9.C-38 for the third and fourth phases. Both figures indicate stratification of the temperature fields. The temperature difference between the upper dome and the lowest position in the external annulus is 30°C at the end of the second phase and 18°C at the end of the fourth phase.

All other compartments have almost homogeneous temperatures (the greatest temperature differences are 4°C), which indicate the presence of the natural circulation (see Figure 9.C-33 and Figure 9.C-34).

The values of the measured velocities in the vent between the R3 and R6 compartments during the individual phases are presented in Table 9.C-3. The histories of the velocities in the R7-R9 and R3-R6 vent paths are presented in Figure 9.C-39 and Figure 9.C-40, respectively. The directions of the convective flow loops as a function of steam and air injections into the various compartments and the applications of the dry heater are presented in Figure 9.C-27 (arrow in R9 compartment represents positive flow loop direction). The upward (positive) velocities in Figure 9.C-39 produce a positive flow direction loop. The upward (positive) velocities in Figure 9.C-40 produce a negative flow direction loop.

The various injections and the application of the dry heat source generate natural circulation and homogenize temperatures in the majority of the containment compartments.

Table 9.C-3. Representative Velocity in [m/s] in Opening from R3 to R6 in the Different Experimental Phases of Experiment F2, Phases 2-4

	Phase No.										
	2.1	2.2	2.3	2.4	3.1	3.2	3.3	4.1	4.2	4.3	4.4
	0.35	-0.4	0.4	-0.4	+/-0.1	+/-0.1	+/-0.1	-0.35	0./0.6	0.35	-0.4

Reprinted from L. Wolf, M. Gavrilas, K. Mun, "Overview of experimental results for long-term, large-scale natural circulations in LWR-containments after large LOCAS," University of Maryland

9.C-58

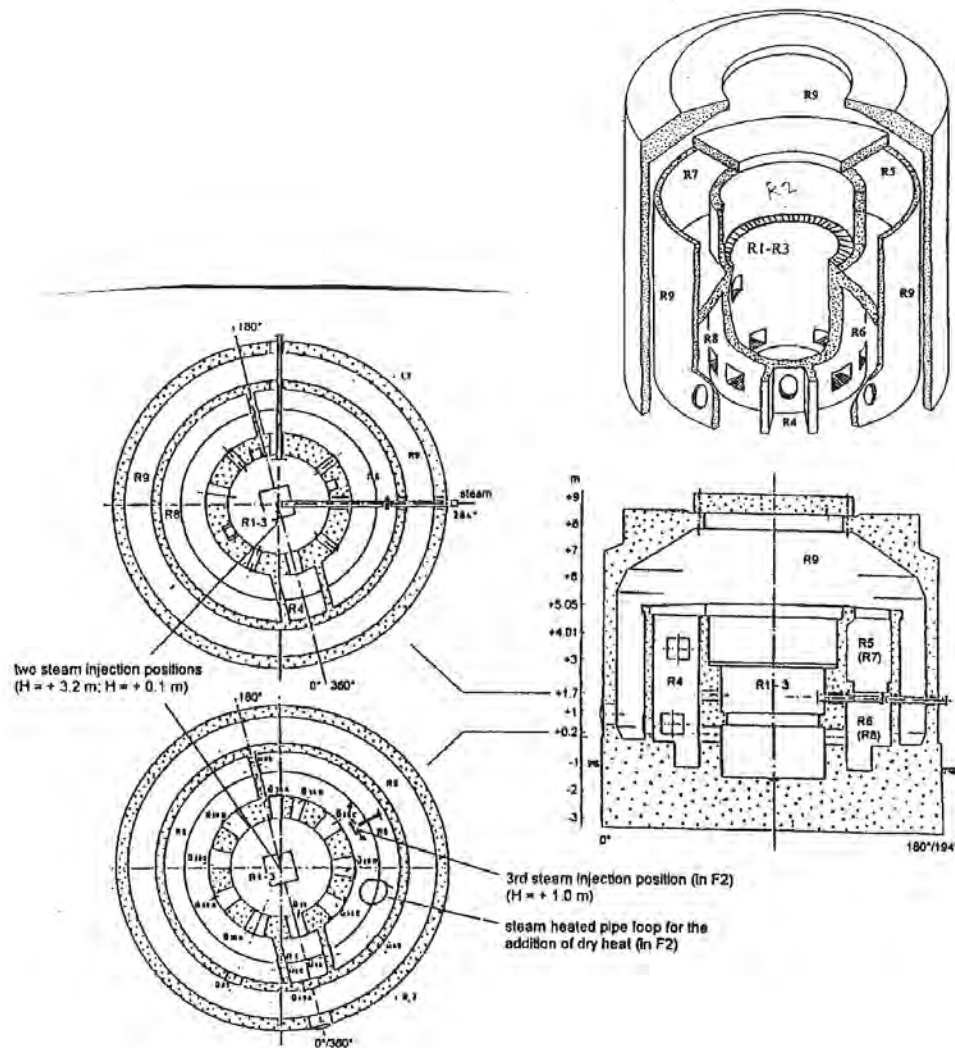


Figure 9.C-25. Model Containment: Vertical Cross-section 0/180; Horizontal Cross-sections at +0.2 m and +1.7m for Configuration in Experiment F2

(reprinted from L. Wolf, M. Gavrilas, K. Mun, "Overview of experimental results for long-term, large-scale natural circulations in LWR-containments after large LOCAs," University of Maryland at College Park, Final Report for DOE – Project, Order Number: DE-AP07-96ID10765")

9.C-59

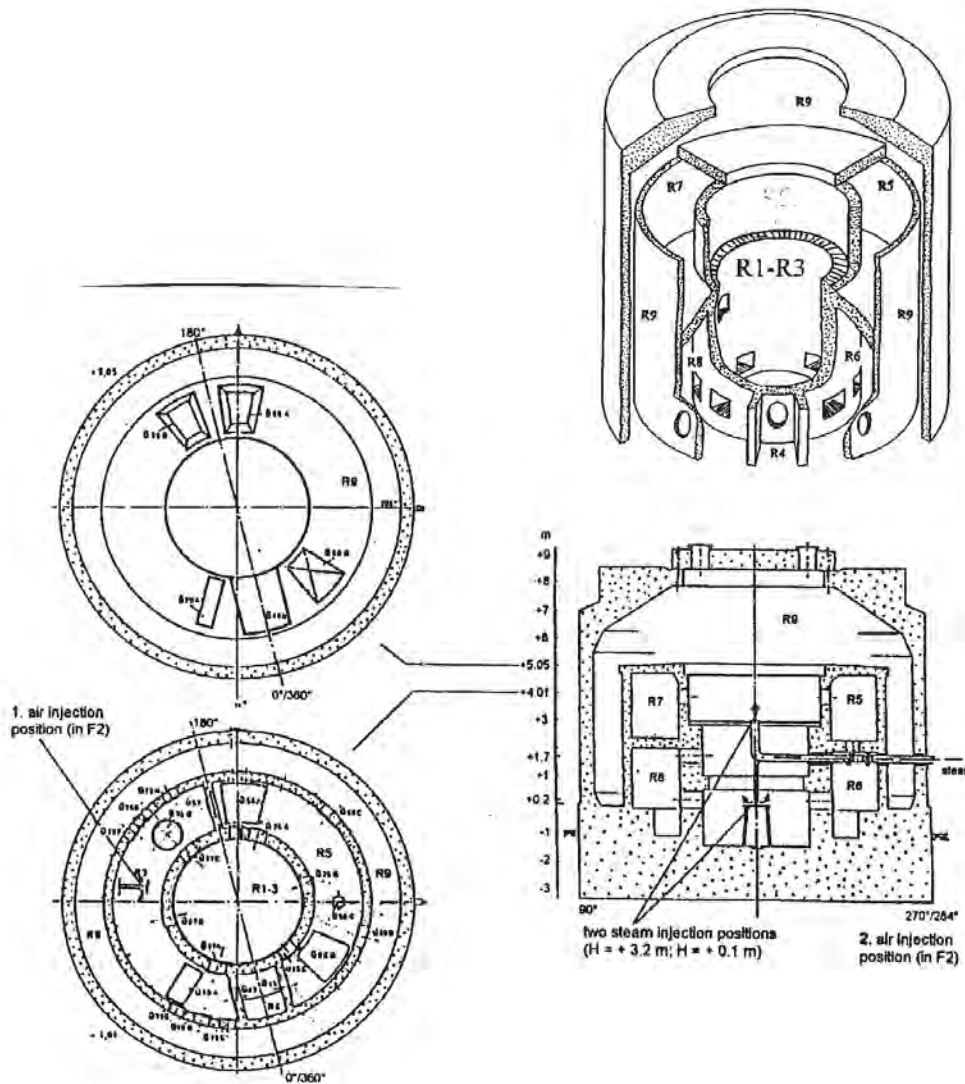


Figure 9.C-26. Model Containment: Vertical Cross-Section 0/180; Horizontal Cross-Sections at +4.01m and +5.05m for Configuration in Experiment F2

(reprinted from L. Wolf, M. Gavrilas, K. Mun, "Overview of experimental results for long-term, large-scale natural circulations in LWR-containments after large LOCAs," University of Maryland at College Park, Final Report for DOE – Project, Order Number: DE-AP07-96ID10765")

9.C-60

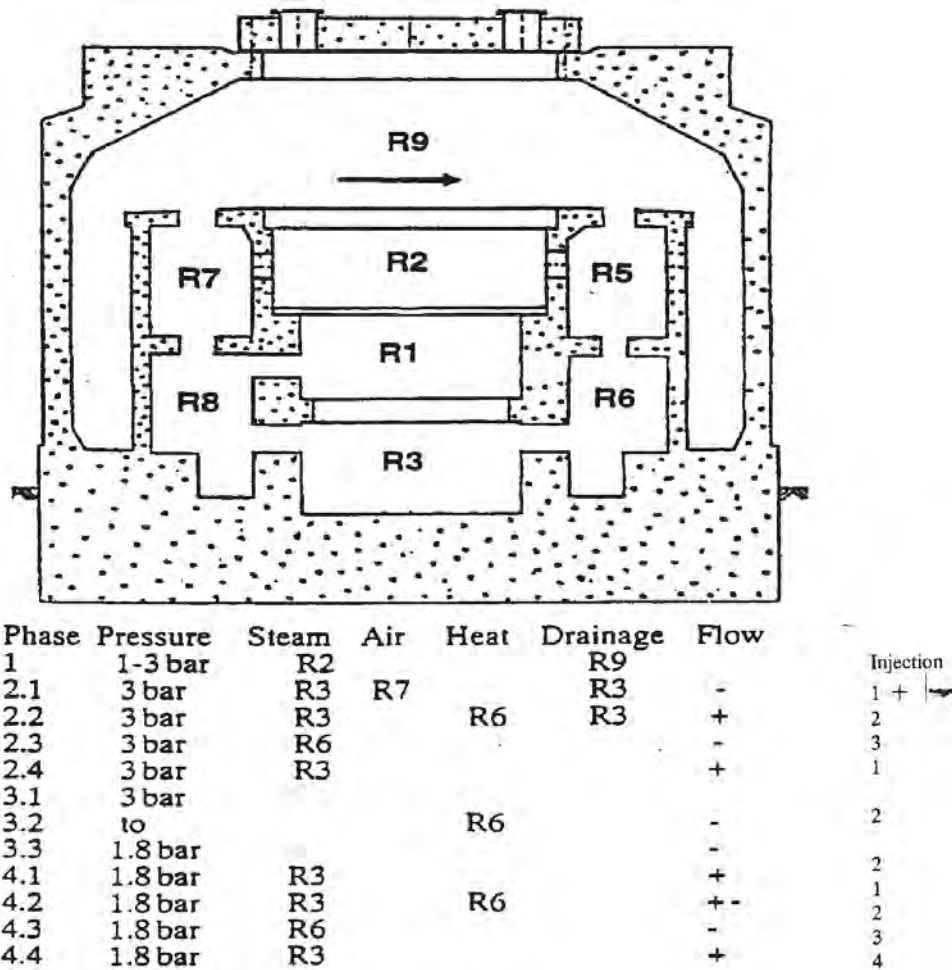


Figure 9.C-27. Injections and Convective Flow Loop Directions
(+ Sign for Flow Indicates the Same Direction of the Flow as Arrow in R9)

(reprinted from L. Wolf, M. Gavrilas, K. Mun, "Overview of experimental results for long-term, large-scale natural circulations in LWR-containments after large LOCAs," University of Maryland at College Park, Final Report for DOE – Project, Order Number: DE-AP07-96ID10765")

9.C-61

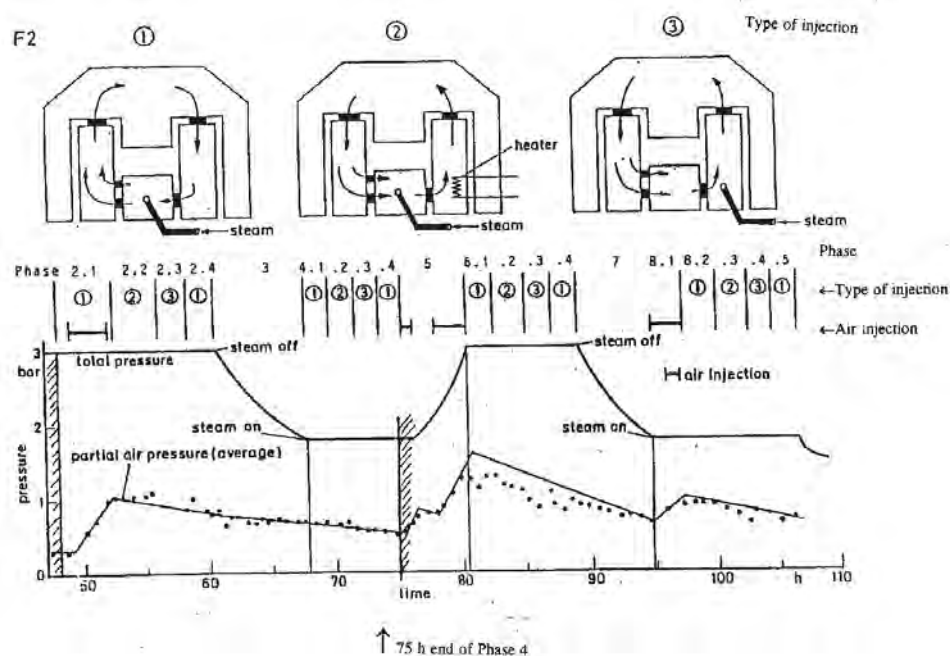


Figure 9.C-28. Experiment F2, Phase 2-8, Experimental Procedures, Total and Partial Pressures

(reprinted from L. Wolf, M. Gavrilas, K. Mun, "Overview of experimental results for long-term, large-scale natural circulations in LWR-containments after large LOCAs," University of Maryland at College Park, Final Report for DOE – Project, Order Number: DE-AP07-96ID10765")

9.C-62

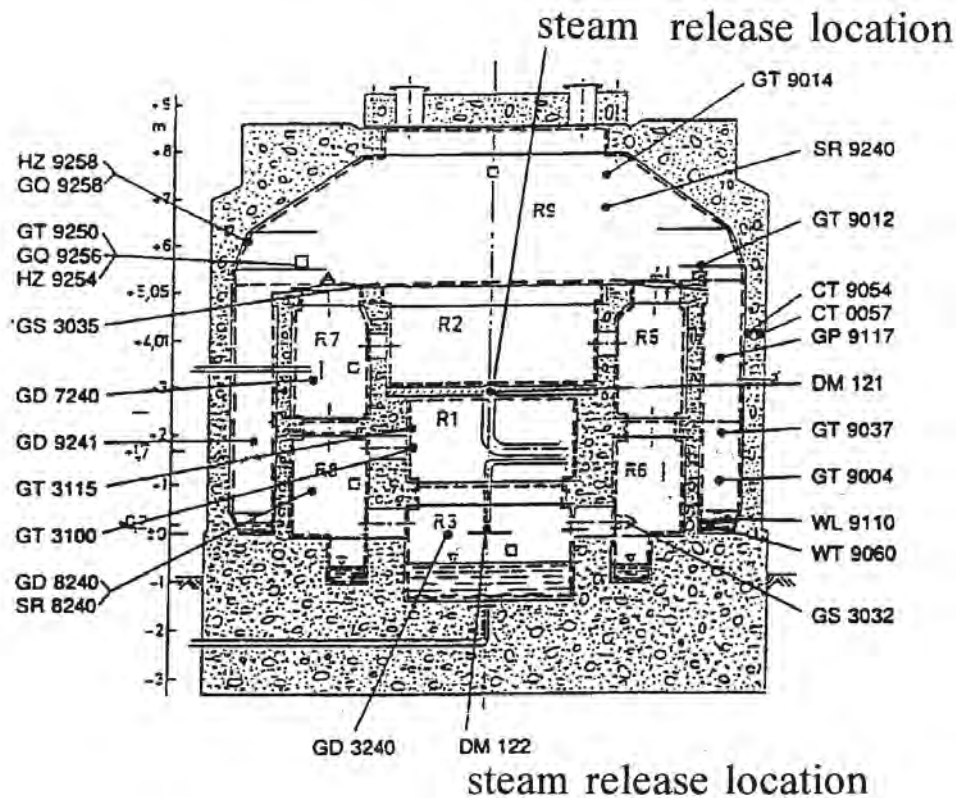


Figure 9.C-29. Number of Compartments, Locations of Measurement Transducers and Steam Releases

(reprinted from L. Wolf, M. Gavrilas, K. Mun, "Overview of experimental results for long-term, large-scale natural circulations in LWR-containments after large LOCAs," University of Maryland at College Park, Final Report for DOE – Project, Order Number: DE-AP07-96ID10765")

9.C-63

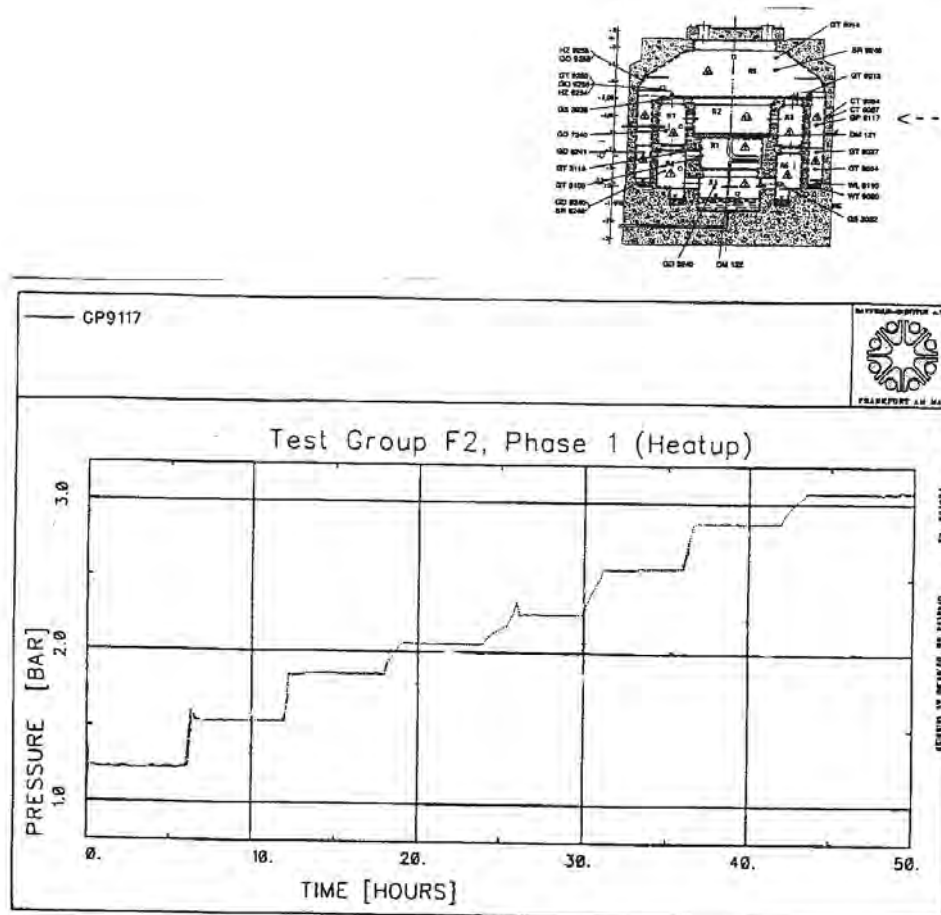


Figure 9.C-30. Test Group F2, Phase 1 (heatup), Total Pressure in the Containment

(reprinted from L. Wolf, M. Gavrilas, K. Mun, "Overview of experimental results for long-term, large-scale natural circulations in LWR-containments after large LOCAs," University of Maryland at College Park, Final Report for DOE – Project, Order Number: DE-AP07-96ID10765")

9.C-64

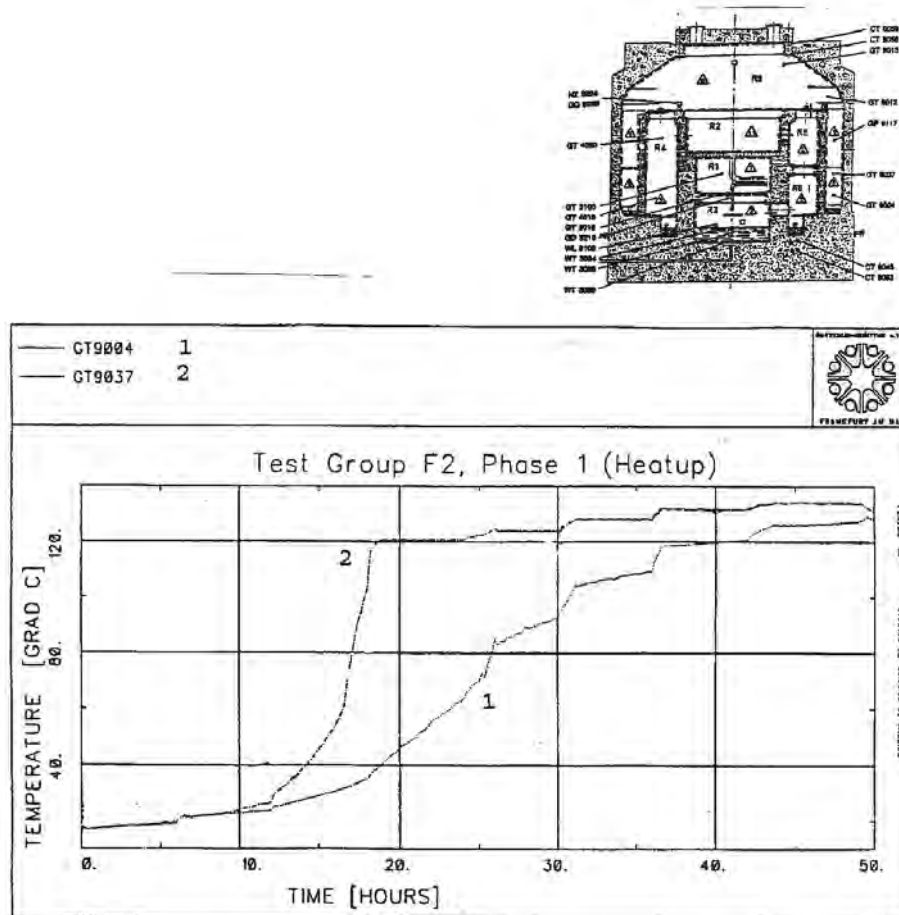


Figure 9.C-31. Test Group F2, Phase 1 (heatup), Atmospheric Temperature in the Compartment R9, H=1.0m and 2.1m.

(reprinted from L. Wolf, M. Gavrilas, K. Mun, "Overview of experimental results for long-term, large-scale natural circulations in LWR-containments after large LOCAs," University of Maryland at College Park, Final Report for DOE – Project, Order Number: DE-AP07-96ID10765")

9.C-65

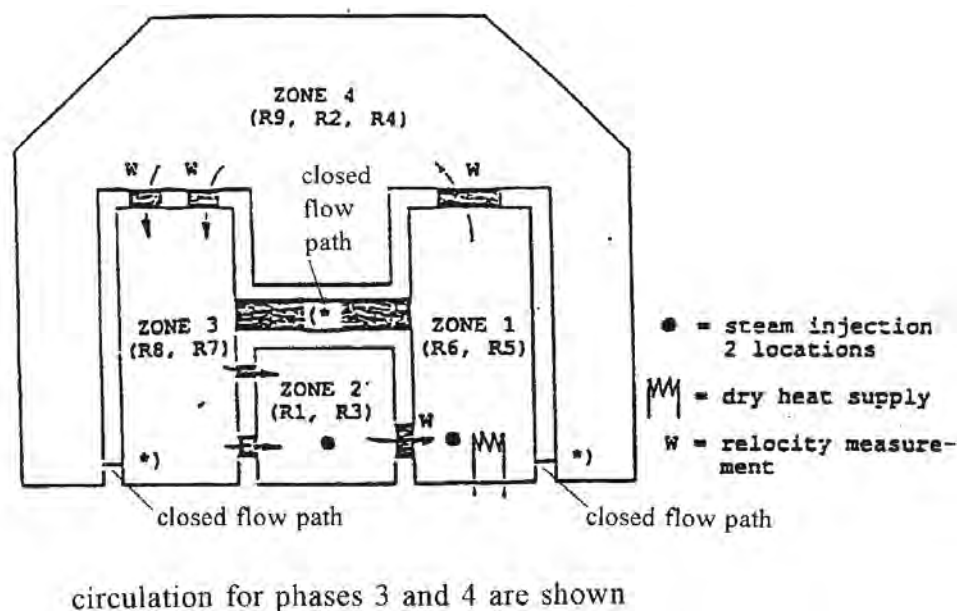


Figure 9.C-32. Scheme of Multi-Compartment Containment Geometry in Experiment F2

(reprinted from L. Wolf, M. Gavrilas, K. Mun, "Overview of experimental results for long-term, large-scale natural circulations in LWR-containments after large LOCAs," University of Maryland at College Park, Final Report for DOE – Project, Order Number: DE-AP07-96ID10765")

9.C-66

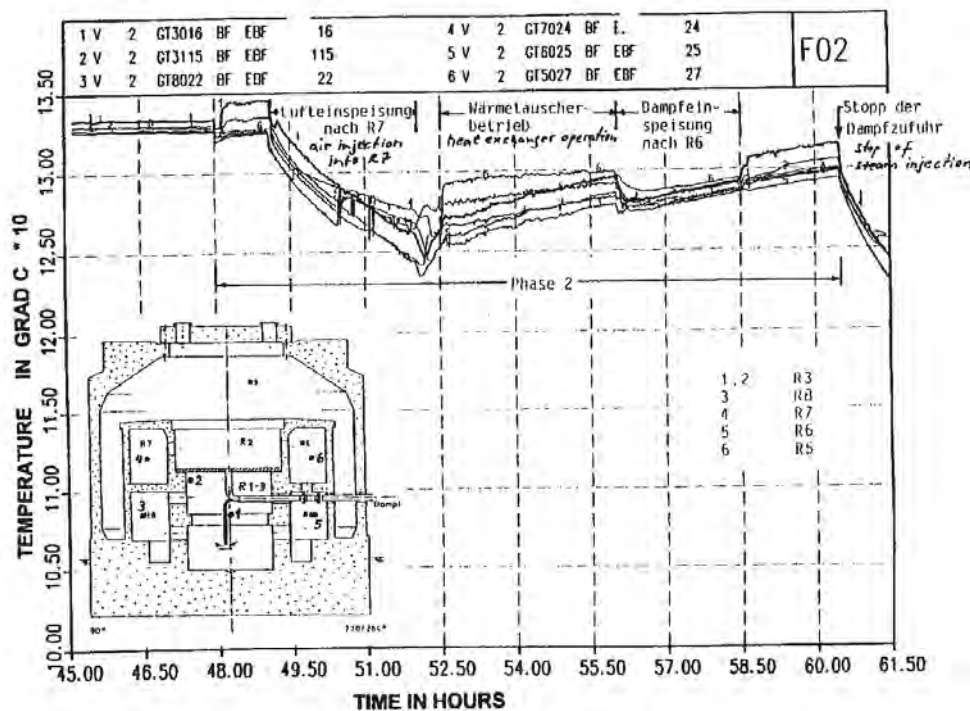


Figure 9.C-33. Test Group F2, Phase 2: Atmospheric Temperatures in Zones 1, 2 and 3 (R5 + R6, R1 + R4, R7 + R8)

(reprinted from L. Wolf, M. Gavrilas, K. Mun, "Overview of experimental results for long-term, large-scale natural circulations in LWR-containments after large LOCAs," University of Maryland at College Park, Final Report for DOE – Project, Order Number: DE-AP07-96ID10765")

9.C-67

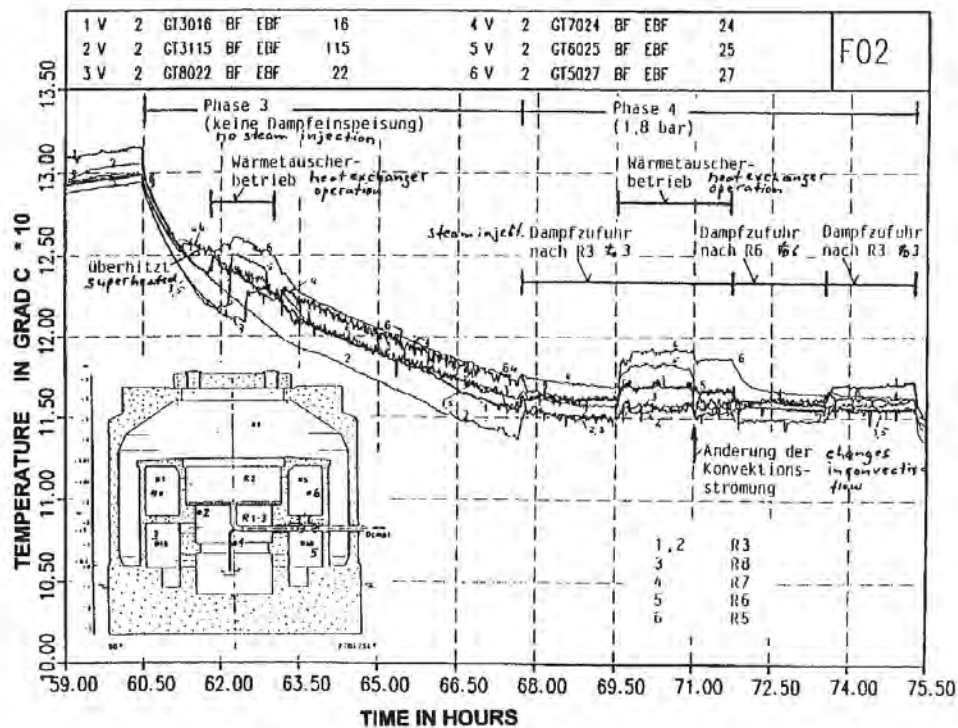


Figure 9.C-34. Test Group F2, Phase 3 and 4: Atmospheric Temperature in Zone 1, 2 and 3 (R5 + R6, R1 + R4, R7 + R8)

(reprinted from L. Wolf, M. Gavrilas, K. Mun, "Overview of experimental results for long-term, large-scale natural circulations in LWR-containments after large LOCAs," University of Maryland at College Park, Final Report for DOE – Project, Order Number: DE-AP07-96ID10765")

9.C-68

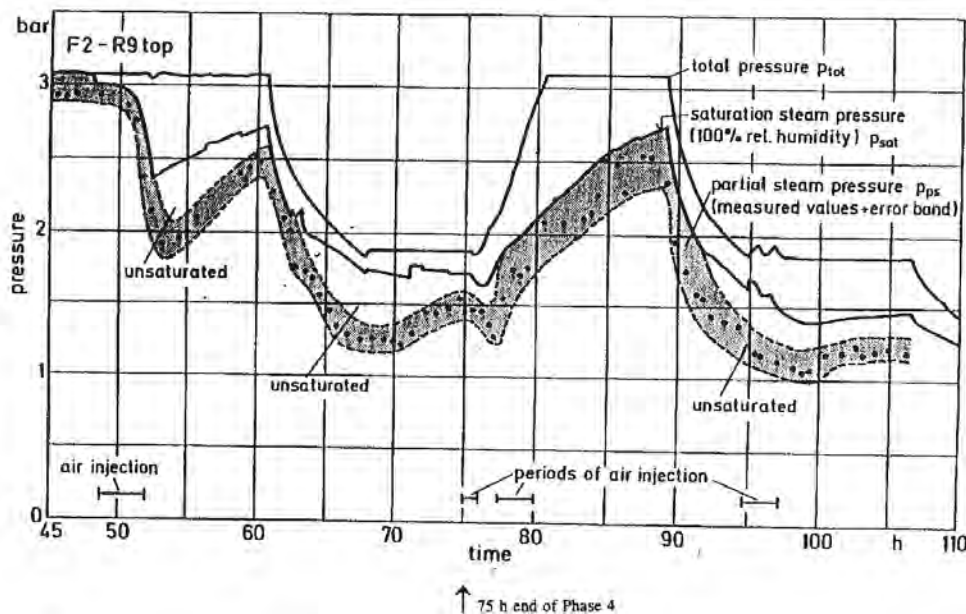


Figure 9.C-35. Thermodynamic State of Steam-Air Atmosphere in R9 top (H=7.6m)

(reprinted from L. Wolf, M. Gavrilas, K. Mun, "Overview of experimental results for long-term, large-scale natural circulations in LWR-containments after large LOCAs," University of Maryland at College Park, Final Report for DOE – Project, Order Number: DE-AP07-96ID10765")

9.C-69

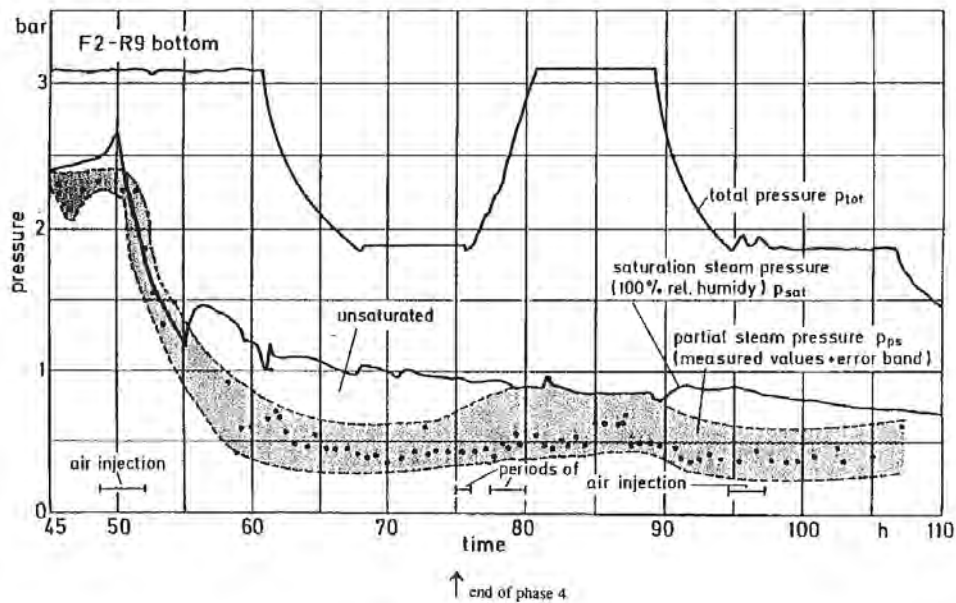


Figure 9.C-36. Thermodynamic State of Steam-Air Atmosphere in R9 Bottom (H=1 m)

(reprinted from L. Wolf, M. Gavrilas, K. Mun, "Overview of experimental results for long-term, large-scale natural circulations in LWR-containments after large LOCAs," University of Maryland at College Park, Final Report for DOE – Project, Order Number: DE-AP07-96ID10765")

9.C-70

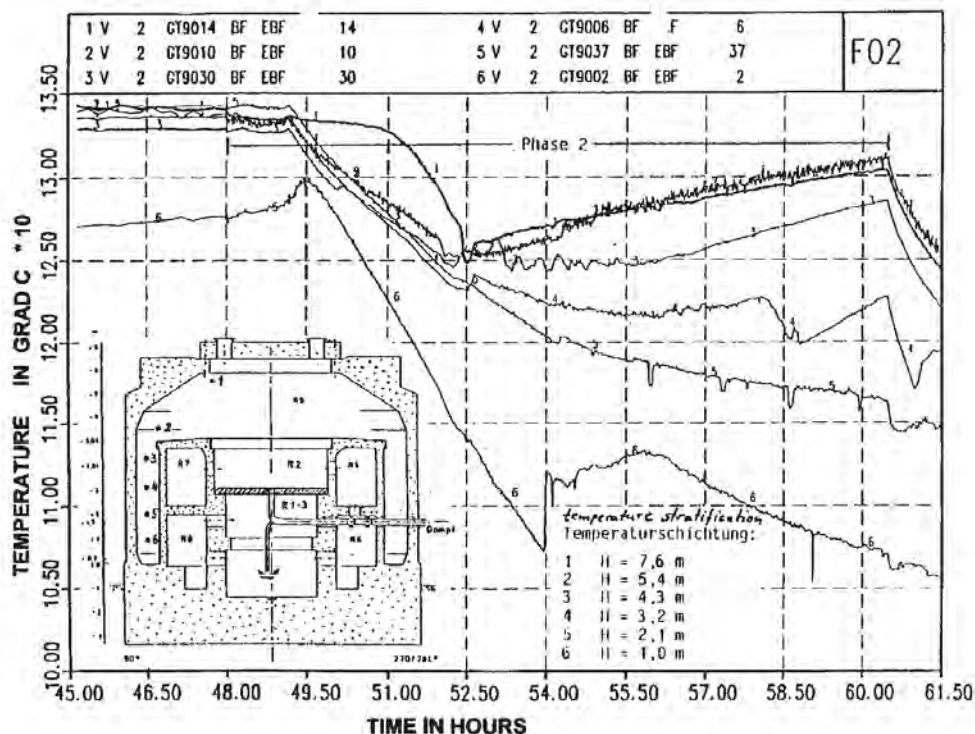


Figure 9.C-37. Test Group F2, Phase 2: Atmospheric Temperatures in R9 (Zone 4)

(reprinted from L. Wolf, M. Gavrilas, K. Mun, "Overview of experimental results for long-term, large-scale natural circulations in LWR-containments after large LOCAs," University of Maryland at College Park, Final Report for DOE – Project, Order Number: DE-AP07-96ID10765")

9.C-71

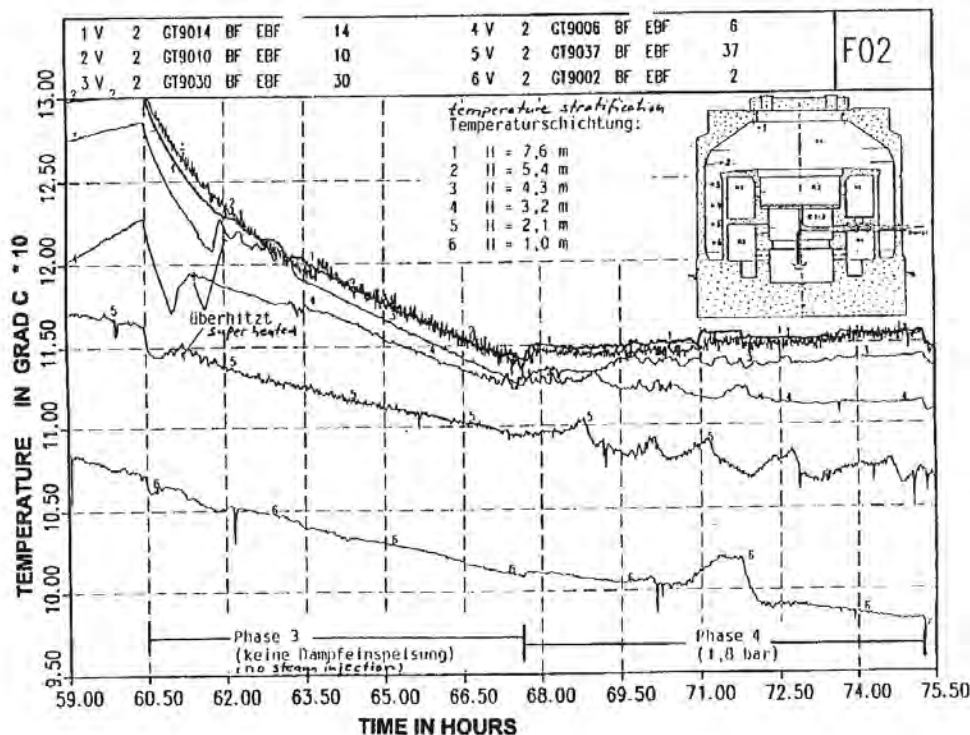


Figure 9.C-38. Test Group F2, Phase 3 and 4: Atmospheric Temperatures in R9 (Zone 4)

(reprinted from L. Wolf, M. Gavrilas, K. Mun, "Overview of experimental results for long-term, large-scale natural circulations in LWR-containments after large LOCAs," University of Maryland at College Park, Final Report for DOE – Project, Order Number: DE-AP07-96ID10765")

9.C-72

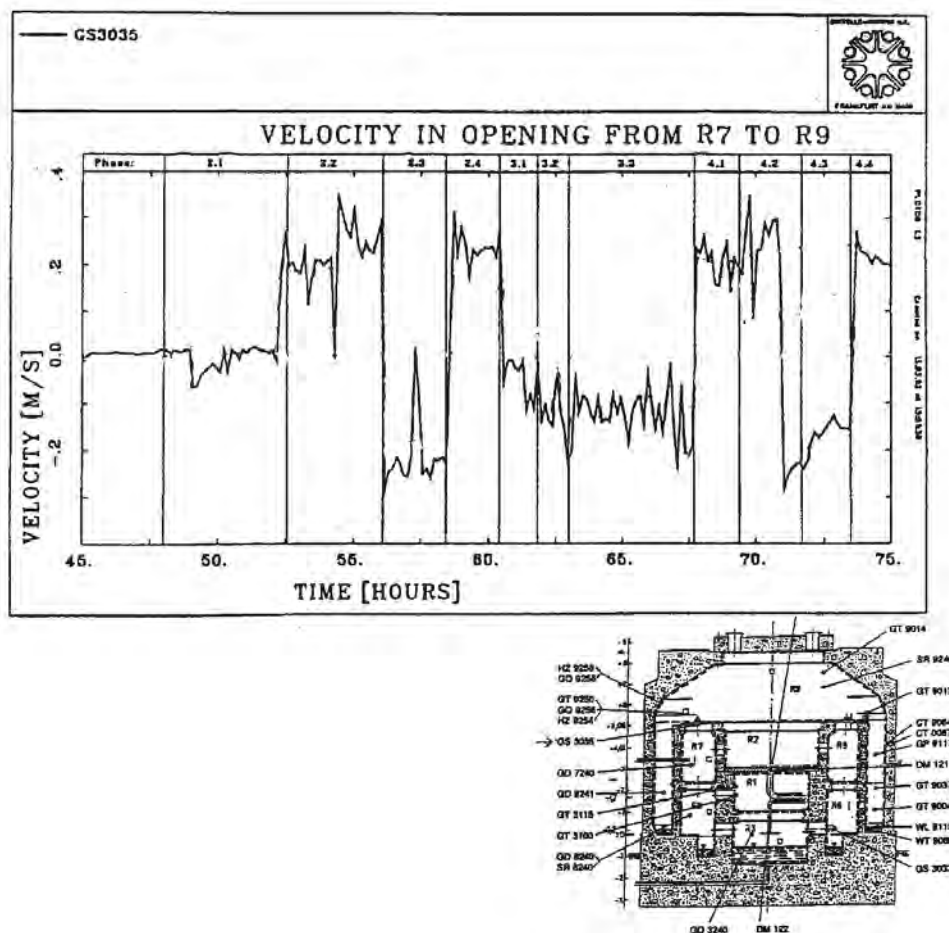


Figure 9.C-39. Velocities in Opening from Compartment R7 to Compartment R9

(reprinted from L. Wolf, M. Gavrilas, K. Mun, "Overview of experimental results for long-term, large-scale natural circulations in LWR-containments after large LOCAs," University of Maryland at College Park, Final Report for DOE – Project, Order Number: DE-AP07-96ID10765")

9.C-73

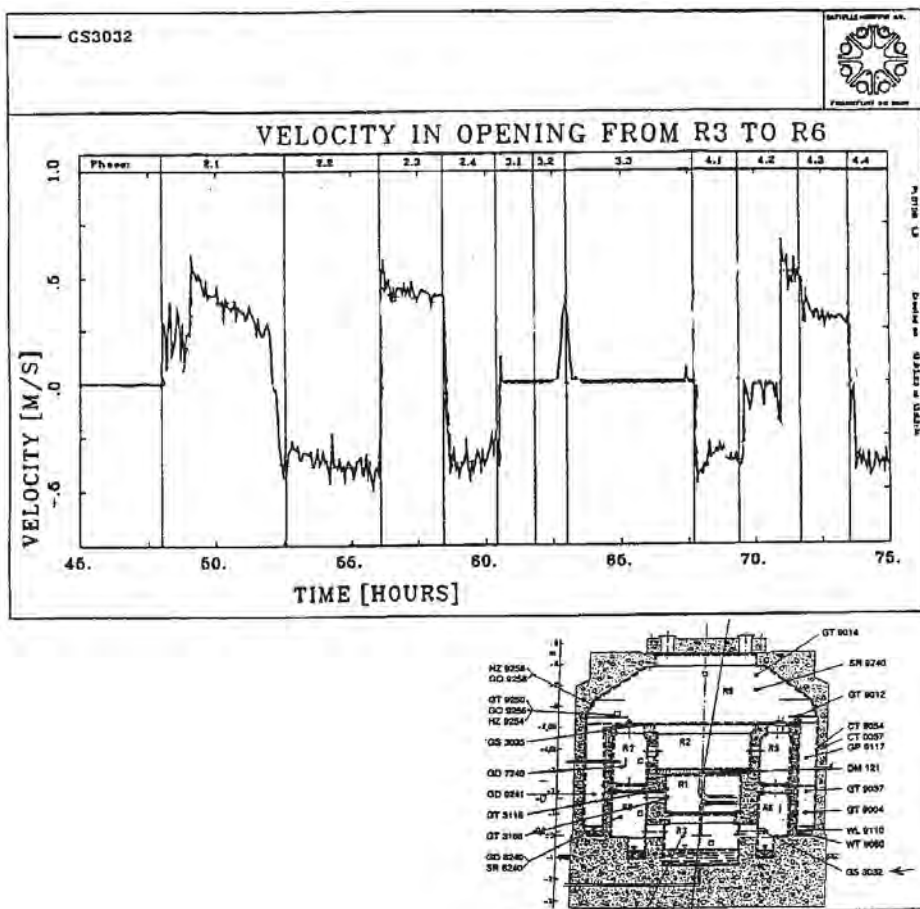


Figure 9.C-40. Velocities in Opening from Compartment R3 to Compartment R6

(reprinted from L. Wolf, M. Gavrilas, K. Mun, "Overview of experimental results for long-term, large-scale natural circulations in LWR-containments after large LOCAs," University of Maryland at College Park, Final Report for DOE – Project, Order Number: DE-AP07-96ID10765")

9.C-74

9.C.2.1.2 The Influence of Initial Temperature Distribution, Location of Hydrogen Injection, Duration of Injection, and Size of Vent Openings on the Hydrogen Distribution (BMC Tests 2, 4, 6, 12, and 20)

Another set of experimental results obtained in BMC is presented in Wolf et al., 1994. The temperature and hydrogen distribution are studied first for two compartments (Phase I) and later for the whole containment (Phase II). These experiments are not directly related to LOCA and MSLB situations, but contribute toward a better understanding of the influence of stratification and circulation phenomena on the hydrogen distribution inside containments. Although Wolf et al., 1994, compared the experimental results with the GOTHIC containment code, the comparisons are not discussed because of the non-prototypical nature of the experiment relative to the passive containment design.

The results of the experiments with only two compartments (upper and lower) are first presented by Langer et al., 1979. The total volume of the two compartments is 72 m³. The central compartments R1, R3 (form lower compartment) and R2 (upper – see Figure 9.C-25, Figure 9.C-26, and Figure 9.C-41) are used for the test. The opening size between the two compartments can be adjusted. Experiments are performed both with and without orifice (with an effective circular opening of 1 m²) between compartments R1 and R2 (see Figure 9.C-41). Uniform injection of hydrogen-nitrogen gas is provided by a flat circular plate with a diameter of 2.5 m. The upper containment is preheated with warm air for several days before the start of some experiments to provide stratification.

Tests 2, 4 and 6 (presented by Wolf et al., 1994) investigate the effects of the vertical hydrogen distribution. The measurement positions are located near the bottom (levels 1 m and 1.85 m) and at the top (levels 5 and 5.5 m) of the containment.

The experiments study the effects of

- The hydrogen injection rates
 - Test 2 has a longer time duration than test 6
- The locations of hydrogen injections
 - The hydrogen-nitrogen source is located above the pool surface in tests 2 and 6
 - The hydrogen-nitrogen source is at the 3.4 m elevation (above the mid-elevation of room R1) in test 4
- The vent flow area (between two compartments)
 - An orifice plate is present between R1 and R2 in tests 2 and 6
 - Test 4 is performed without the orifice plate

9.C-75

- The initial temperature distribution in the containment (homogeneous versus stratified)
 - A uniform temperature of 19°C is applied in test 2
 - The temperature is a uniform 22°C in test 4
 - A temperature stratification of 19°C in the R3 and R1 (lower rooms) and 35°C in the R2 (upper room) exist in test 6

The hydrogen pressure ratios at the top and bottom of the compartments are presented in Figure 9.C-42a, Figure 9.C-42b, Figure 9.C-42c for the second, fourth, and sixth experiments. A comparison of the hydrogen partial pressures shows the effects of the hydrogen release position (test 4) and the initially stratified temperature field (test 6) on the hydrogen concentration stratification.

The experimental findings presented in Wolf et al., 1994 are:

1. The hydrogen is homogeneously distributed through a compartment if the hydrogen source is at the floor and the feed rate is low, even if an orifice plate is installed (see the results for test 2, Figure 9.C-42a). Note that the feed rate in the second experiment is lower than in the fourth and sixth experiment. Also, hydrogen is released for 225 minutes in test 2 and for 125 minutes in test 4 and 6.
2. Vertical concentration stratification occurs if the source is located above the floor (see results for test 4, Figure 9.C-42b). For low kinetic energy, the diffusion process slowly equalizes concentrations.
3. If the openings between compartments are relatively small, the transport of hydrogen may be obstructed (see results for test 6, Figure 9.C-42b).
4. If an initial thermal stratification of air exists and an orifice is installed between the lower and upper compartments, the transport of the lighter H_2/N_2 gas mixture is prevented. The highest hydrogen concentrations exist in the lower, cooler part of the compartments, where circulation and mixing occurs (see results for test 6, Figure 9.C-42c). The initially stratified temperature field is provided by keeping the upper compartment R2 at a higher temperature (35°C) for several days before the start of the experiment.

Figure 9.C-42a (see results for test 2) shows that the buoyancy of the rising plume and the circulation resulting from entrainment into the introduced lighter H_2/N_2 gas mixture lead to a relatively homogenized atmosphere. Circulation and mixing are present in both the upper and lower compartments.

Test 4, with an elevated source and reasonably low kinetic energy (Fr is not reported for the tests), shows that there is no significant driving force for circulation below the break elevation. Stratification into two regions occurs, one below and one above the break elevation. The lower region is almost stagnant, while circulation and mixing is present in the upper region (see GOTHIC numerical simulation results by L. Wolf, H. Holzbauer, M. Schall, 1994).

9.C-76

In comparison, test 6, which includes an orifice between R1 and R2 and a stratified temperature field in the upper R2 compartment, shows an almost stagnant upper region. It also shows an increase in the concentration of the lighter H_2/N_2 gas mixture in the lower region (a result of the circulation and mixing in the lower regions R1 and R3). The lighter gas mixture is not able to penetrate into the upper stratified layers due to the presence of the narrow orifice. The circulation cell formed by the gas mixture injection into the lower compartments does not communicate with the stratified layers in the upper compartment (see also GOTHIC numerical simulation results by L. Wolf, H. Holzbauer, M. Schall, 1994).

Application to the AP600 and AP1000

These tests are not relevant to the passive containment design. The cold dome prevents the stratification that results from higher temperatures of either the vertical walls at the high elevations or the ceiling. In the BMC case, the higher temperatures of the wall surfaces are maintained for a long period of time due to the heat accumulated in the concrete walls (which are heated for several days before the start of the experiment). The passive containment shell is made of steel. Natural convection at the outer surface of the containment walls keeps their temperature low, so that a highly stratified initial temperature field is not possible. Even if initial stratification exists, the application of water on the outer containment surface decreases wall temperatures and causes circulation inside the containment.

9.C-77

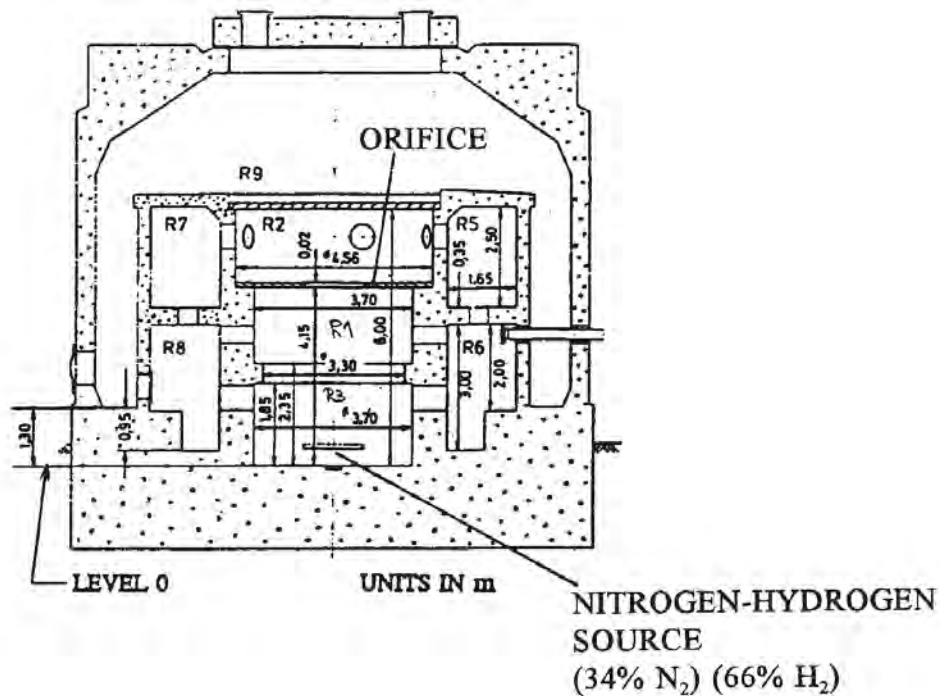
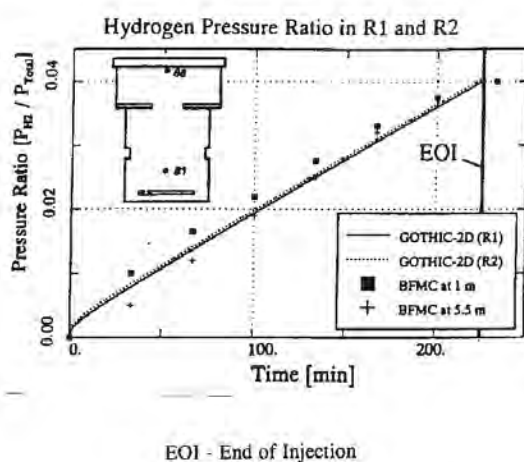


Figure 9.C-41. Vertical Cut through BMC with Orifice in Between R2 and R1

(reprinted with permission from authors from L. Wolf, H. Holzbauer, M. Schall, "Comparison between multi-dimensional and lumped-parameter GOthic-containment analyses with data," Proceedings, Volume II – Thermohydraulics of Containment and Severe Accidents, May 30th – June 2nd, 1994, pp. 321-330.)

9.C-78

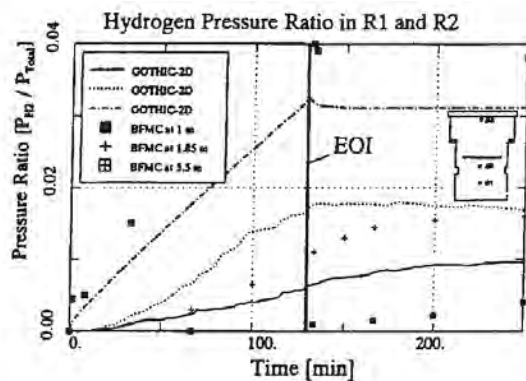


Battelle Test No. 2

Figure 9.C-42a. BMC Test No. 2: Comparison Between Experimental Data and 2-d GOETHIC Computations for Hydrogen Concentrations

(reprinted with permission from authors from L. Wolf, H. Holzbauer, M. Schall, "Comparison between multi-dimensional and lumped-parameter GOETHIC-containment analyses with data," Proceedings, Volume II – Thermohydraulics of Containment and Severe Accidents, May 30th – June 2nd, 1994, pp. 321-330.)

9.C-79



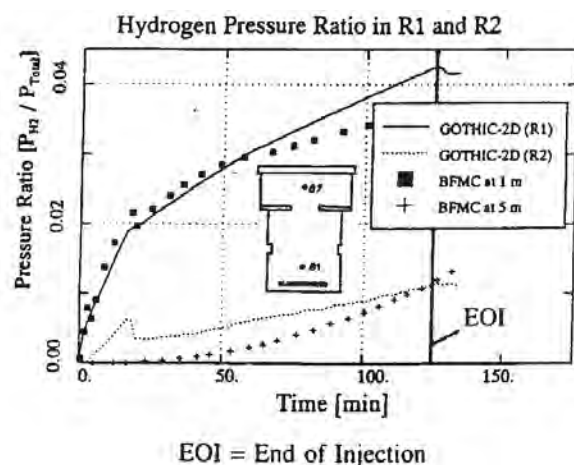
Battelle Test No. 4

EOI - End of Injection

Figure 9.C-42b. DMC Test No. 4: Comparison Between Experimental Data and 2-d GOTHIC Computations for Hydrogen Concentrations

(reprinted with permission from authors from L. Wolf, H. Holzbauer, M. Schall, "Comparison between multi-dimensional and lumped-parameter GOTHIC-containment analyses with data," Proceedings, Volume II – Thermohydraulics of Containment and Severe Accidents, May 30th – June 2nd, 1994, pp. 321-330.)

9.C-80



Battelle Test No. 6

Figure 9.C-42c. DMC Test No. 6: Comparison Between Experimental Data and 2-d GOTHIC Computations for Hydrogen Concentrations

(reprinted with permission from authors from L. Wolf, H. Holzbauer, M. Schall, "Comparison between multi-dimensional and lumped-parameter GOTHIC-containment analyses with data," Proceedings, Volume II – Thermohydraulics of Containment and Severe Accidents, May 30th – June 2nd, 1994, pp. 321-330.)

9.C-81

In the second phase (Langer and Baukal, 1982), the full model containment is used for experiments. The effects of: (1) the initial temperatures and humidities, (2) the geometry of the containment, and (3) the location and rate of hydrogen release are investigated.

The results of tests 12 and 20 are presented in Wolf et al., 1994 and are compared with the results of three GOTHIC modeling strategies. Tests 12 and 20 are performed with six compartments (R1-2, R5-8, see Figure 9.C-25 and Figure 9.C-26). The hydrogen-nitrogen mixture is injected into rooms R2 and R6 in tests no.12 and 20, respectively.

Test no. 12 is performed with a uniform initial temperature. It results in a homogenized hydrogen distribution in the containment (see Figure 9.C-43). The stratified initial temperature distribution in test 20 results in higher hydrogen distribution in the lower level compartments (R1, R6 and R8 – see Figure 9.C-44a, Figure 9.C-44b, Figure 9.C-44c). An explanation for this unexpected result is that the circulation cell formed by the injection of the lighter gas mixture is not able to penetrate upper stratified layers at the beginning of the experiment. This is similar to test 6, which includes an orifice and stratified initial temperature field in the upper compartment. After three hours, there is a tendency toward decreased gradients in the concentration field, especially between R1 and R2 compartments. This indicates that global circulation affects the upper stratified layers.

A summary of the experimental results is:

1. If the temperature field was uniform (test 12), hydrogen was homogeneously distributed inside the containments.
2. For an initially thermally stratified field (test 20), higher hydrogen concentrations are present in the lower (cooler) compartments at the beginning of the experiment.

Both groups of experiments indicate that good air circulation inside the containment (in fact a uniform temperature field) is crucial for homogeneous hydrogen distribution. Note that in the first group of tests, the stratification is obtained by preheating the upper room with warm air for several days before the start of the experiments.

A comparison between this experimental data and the numerical results obtained with GOTHIC (with lumped-parameter and multi-dimensional analyses) is presented in Wolf et. al, 1994.

9.C-82

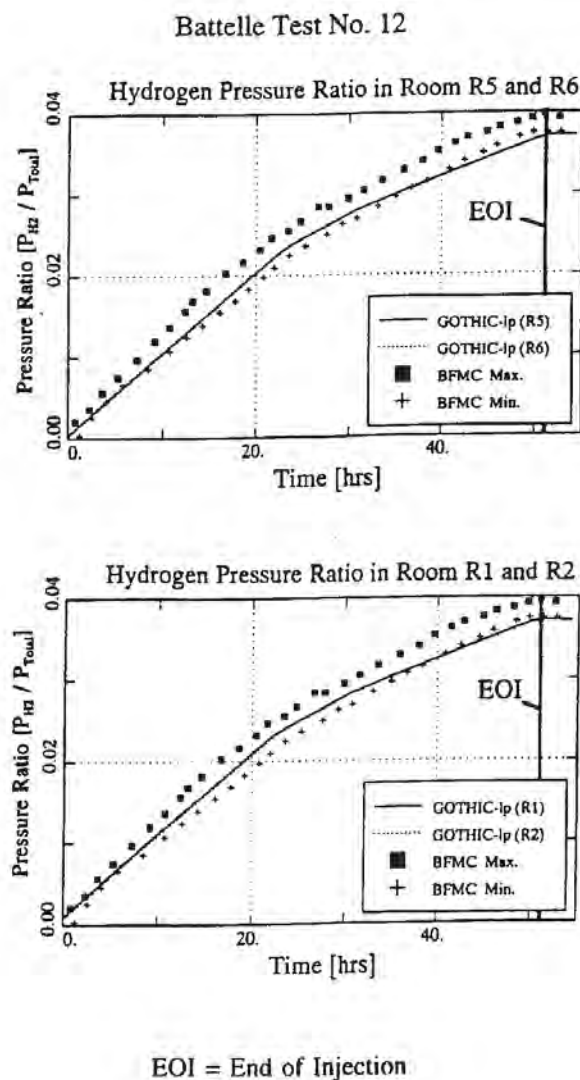


Figure 9.C-43. BMC Test No. 12: Comparison between Experimental Data and GOTHIC-lp Computations for Hydrogen Concentrations

(reprinted with permission from authors from L. Wolf, H. Holzbauer, M. Schall, "Comparison between multi-dimensional and lumped-parameter GOTHIC-containment analyses with data," Proceedings, Volume II – Thermohydraulics of Containment and Severe Accidents, May 30th – June 2nd, 1994, pp. 321-330.)

9.C-83

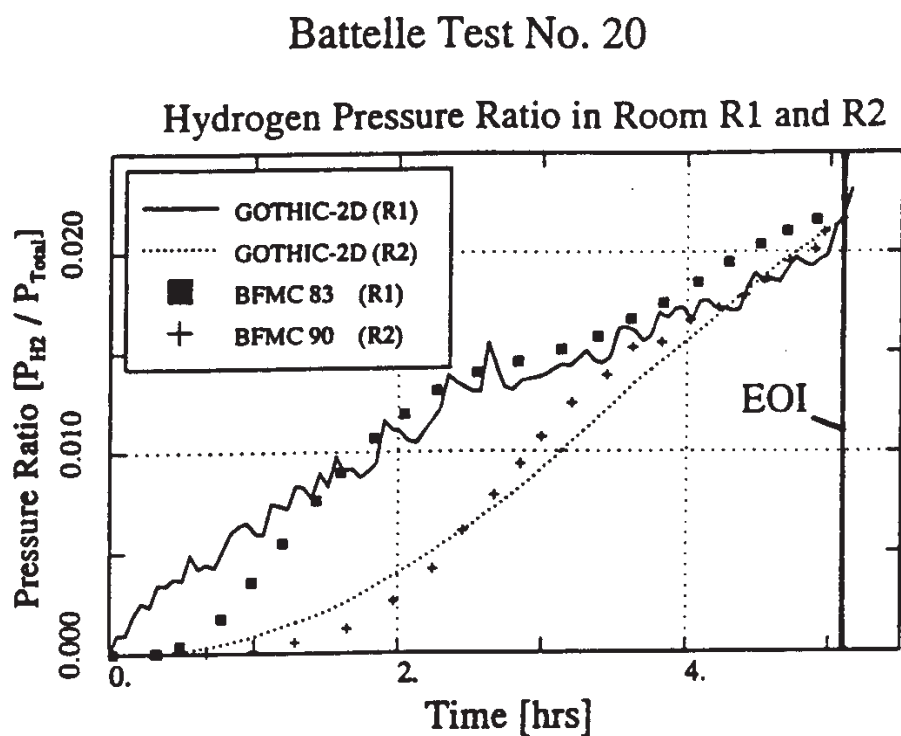


Figure 9.C-44a. BMC Test No. 20: Comparison Between Experimental Data and 2-d GOTHIC Computations for Hydrogen Concentrations

(reprinted with permission from authors from L. Wolf, H. Holzbauer, M. Schall, "Comparison between multi-dimensional and lumped-parameter GOTHIC-containment analyses with data," Proceedings, Volume II – Thermohydraulics of Containment and Severe Accidents, May 30th – June 2nd, 1994, pp. 321-330.)

9.C-84

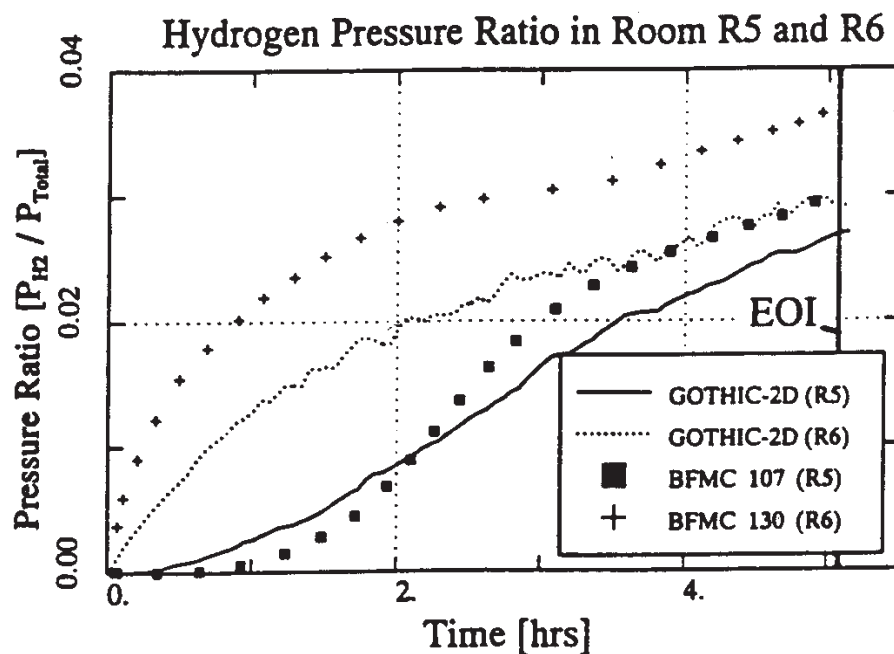


Figure 9.C-44b. BMC Test No. 20: Comparison Between Experimental Data and 2-d GOTHIC Computations for Hydrogen Concentrations

(reprinted with permission from authors from L. Wolf, H. Holzbauer, M. Schall, "Comparison between multi-dimensional and lumped-parameter GOTHIC-containment analyses with data," Proceedings, Volume II – Thermohydraulics of Containment and Severe Accidents, May 30th – June 2nd, 1994, pp. 321-330.

9.C-85

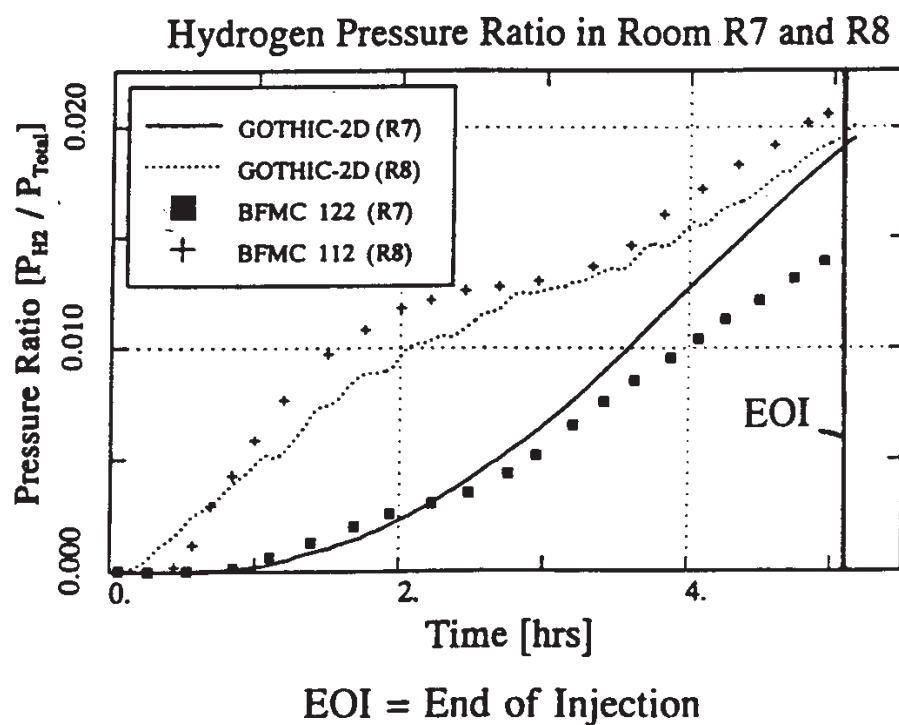


Figure 9.C-44c. BMC Test No. 20: Comparison Between Experimental Data and 2-d GOTHIC Computations for Hydrogen Concentrations

9.C.2.1.3 Effects of Sump Heatup on Global Natural Circulation (Experiments RX1 - RX5)

The third set of experiments performed in the BMC (Fischer et al., 1994 and Petersen et al., 1994) examine the effect of sump heatup on global natural circulation inside the containment. The starting and transient behavior of natural circulation for small temperature differences, the influence of natural circulation on mixing of hydrogen released during accident conditions, and the effects of stratification on the natural convection formation are also studied.

A total of five experiments are performed (RX1 to RX5) at atmospheric pressure. Temperatures are recorded in the sump, in the containment atmosphere, and in the concrete structures. The relative humidity, containment pressure, liquid sump level, velocities (in the vents), and hydrogen concentration are also measured.

The objective of long-term experiments is to establish at what sump temperature global circulation exists. During these experiments, the containment atmosphere, structure, and sump have nearly identical temperatures. Circulation effects inside the containment are already present with a sump temperature as low as 25°C. Experiments RX2 (without hydrogen injection) and RX4 (with multiple hydrogen injections) are performed as long-term tests. The respective initial and boundary conditions for all experiments are given in Table 9.C-4.

Results are provided for only the RX4 experiment, since the hydrogen distribution is available for this test. A summary of the results for the RX4 experiment, with the cold containment and multiple hydrogen injections, is presented in Wolf et al., 1996. The perspective view and cross-sections of the BMC containment, illustrating the compartment numbers and the location of the hydrogen injection, are presented in Figure 9.C-45 and Figure 9.C-46. The instrumentation plan for the RX4 test is specified in Figure 9.C-47.

At the beginning of the experiment, the temperatures of the structure range from 20-26°C. The sump temperature is 20°C (see Figure 9.C-48). Several consecutive characteristic periods evolve during the experiment. The sump heat up is divided into three periods:

1. 0 to 1:48 hr – the sump is heated to 50°C
2. 2:43 to 3:39 hr – continuation of sump heating to 60°C
3. 3:34 to 4:52 hr – continued sump heating to maintain the temperature at 60°C until the end of experiment (5 hr)

Three hydrogen injections occur:

1. 1:11-1:24 hr, 236 g of hydrogen is released
2. 2:11-2:23 hr, 215 g of hydrogen is released
3. 4:06-4:33 hr, 319 g of hydrogen is released

9.C-87

At the beginning of the sump heatup, the anemometers register velocities between 0.2-0.3 m/s (for sump temperatures 24-27°C), while at the end of the experiment, velocities are 0.6-0.8 m/s (see Figure 9.C-49). At the end, the temperature of the dome is 30°C (see Figure 9.C-50). Shaded areas in Figure 9.C-49 and Figure 9.C-50 represent periods of hydrogen injection. Velocities increase during periods of hydrogen injection.

Sump and atmosphere temperatures are presented in Figure 9.C-48, Figure 9.C-50, and Figure 9.C-51. Temperature differences in the area of the center compartment and dome are not greater than 2°C (Figure 9.C-50). The temperature difference in the external annulus is smaller than 3°C (Figure 9.C-51), indicating the presence of natural circulation effects.

Due to the natural circulation, the hydrogen distribution is almost uniform in the whole containment, see (Figure 9.C-52 and Figure 9.C-53). After two hours, the relative humidity of the whole containment atmosphere is 100 percent (see Figure 9.C-54). Even low natural circulation flows provide complete mixing of the hydrogen and steam (evaporated from sump). The heated sump provides sufficient buoyancy force for natural circulation flow.

Table 9.C-4. Test Matrix of Battelle Sump Heatup Experiments

Test No.	Containment-Atmosphere			Structure-Temperature [°C]	Sump-Temperature [°C]	H ₂ -Mass [g]
	Containment Media	Initial Temperature [°C]	Total Pressure [bar]			
RX1	air	23.5 – 28.5	1.011	24 – 26	1. ≈ 40 2. ≈ 50 3 ≈ 55 4. ≈ 60	-----
RX2	air	22 – 28.5	1.009	24.5 – 28	1. ≈ 40 2. ≈ 50 3. ≈ 60	-----
RX3	air + steam	48 – 58.5	1.008	42 – 61	60 - 100	-----
RX4	air + H ₂	24 – 27	1.014	22.5 – 26.5	1. ≈ 48 2. ≈ 60	1. 236 2. +215 3. +319
RX5	air + steam + H ₂	55 – 69	1.001	39 – 64	1. 62 – 49 2. 63 - 58	1. 371 2. +390 3. +406

(reprinted from L. Wolf, M. Gavrilas, K. Mun, "Overview of experimental results for long-term, large-scale natural circulations in LWR-containments after large LOCAS," University of Maryland at College Park, Final Report for DOE – Project, Order Number: DE-AP07-96ID10765")

9.C-88

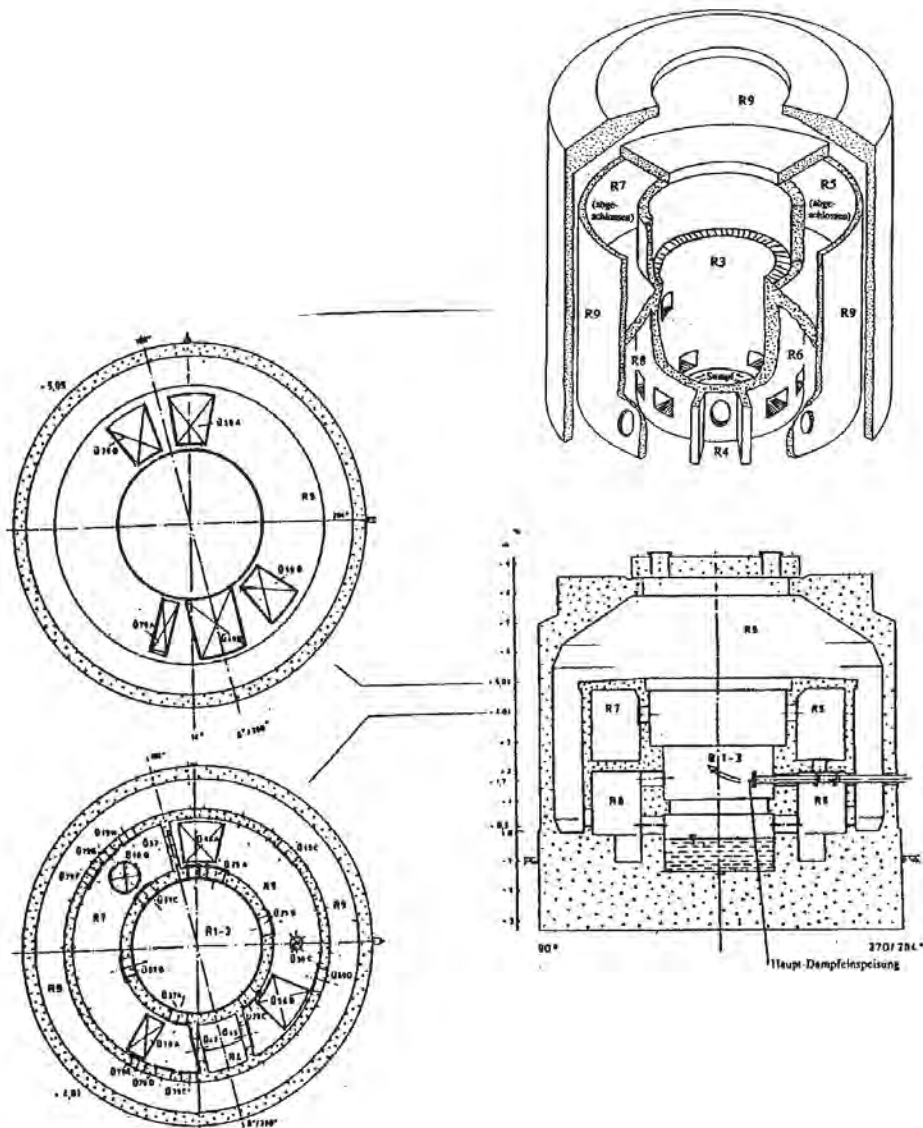


Figure 9.C-45. Perspective View, Vertical and Upper Horizontal Cross-Sections through BMC with Main Steam Feedline

(reprinted from L. Wolf, M. Gavriles, K. Mum, "Overview of experimental results for long-term, large-scale natural circulations in LWR-containments after large LOCAs," University of Maryland at College Park, Final Report for DOE – Project, Order Number: DE-AP07-96ID10765")

9.C-89

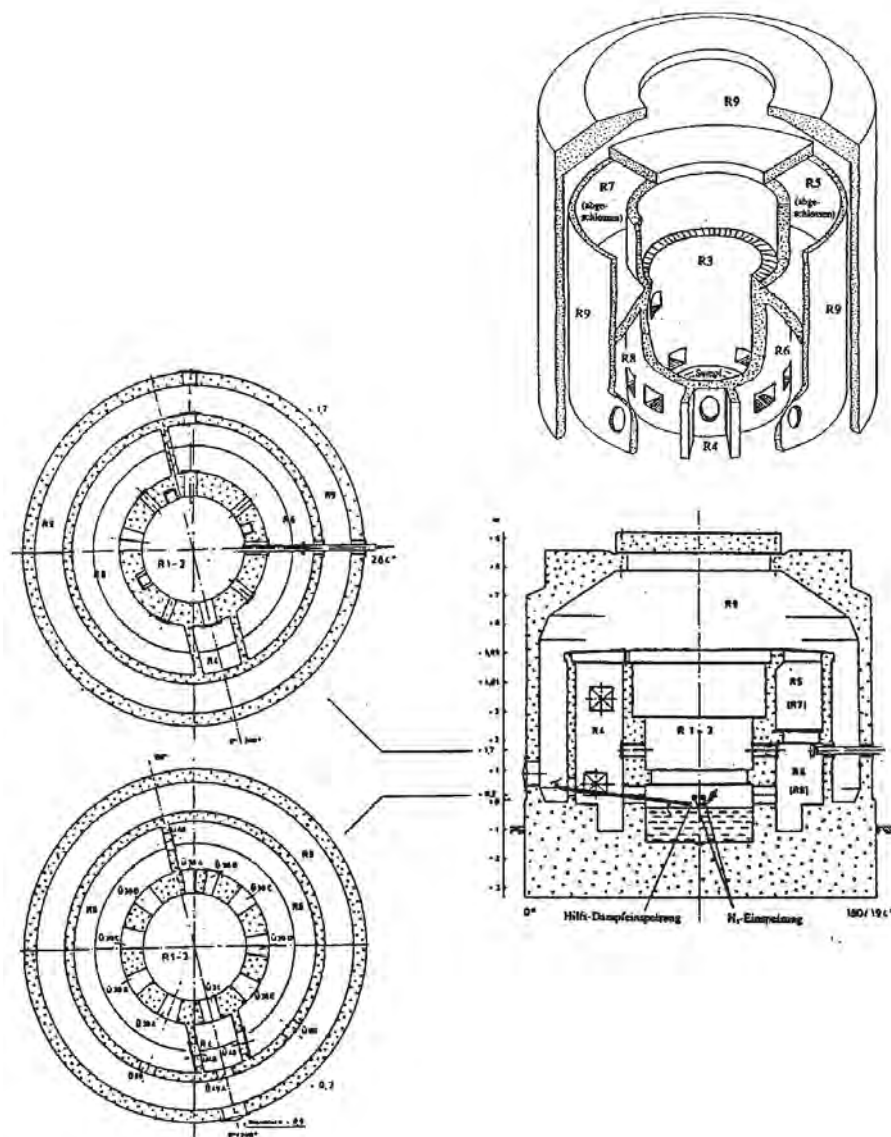


Figure 9.C-46. Perspective View, Vertical and Upper Horizontal Cross-Sections through BMC with Auxiliary Steam Feedline

(reprinted from L. Wolf, M. Gavriles, K. Mum, "Overview of experimental results for long-term, large-scale natural circulations in LWR-containments after large LOCAs," University of Maryland at College Park, Final Report for DOE – Project, Order Number: DE-AP07-96ID10765")

9.C-90

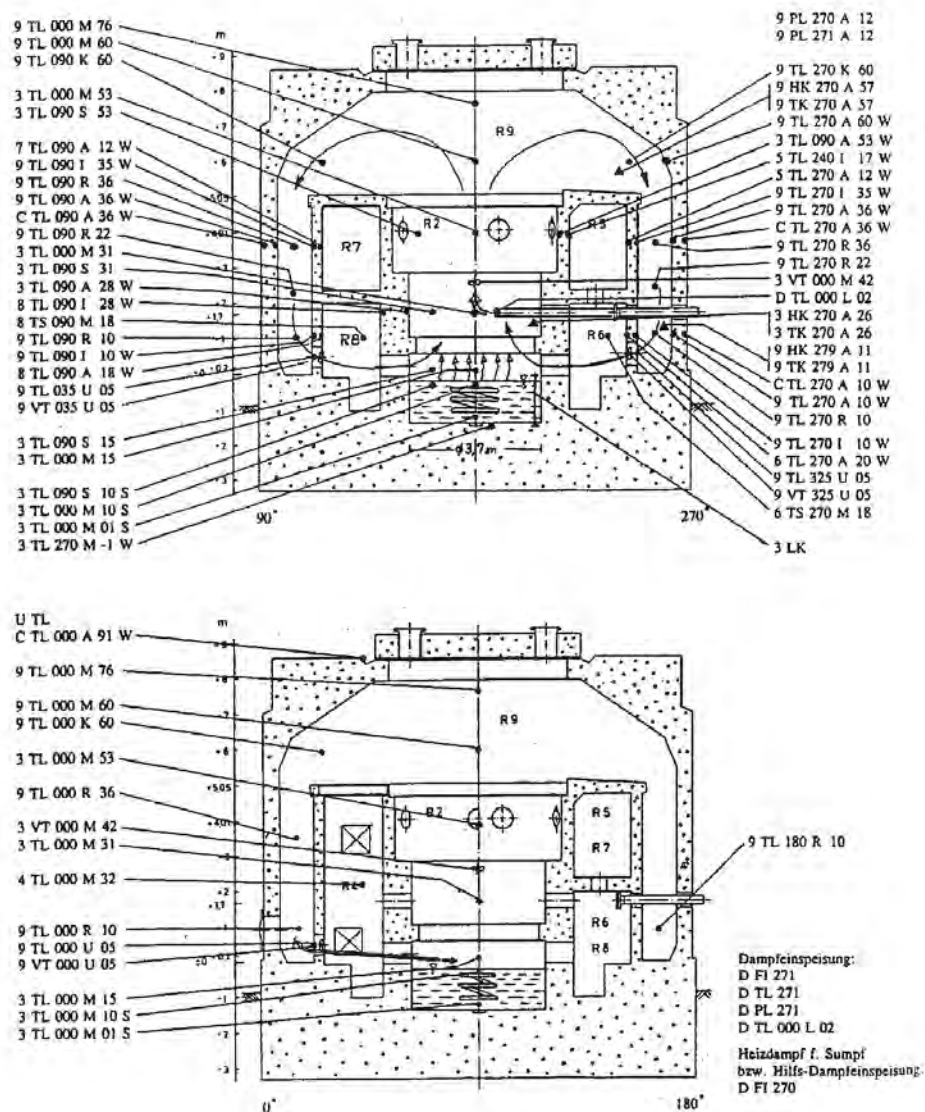


Figure 9.C-47. Instrumentation Plan for BMC – Sump Heatup Test RX4

(reprinted from L. Wolf, M. Gavrilis, K. Mum, "Overview of experimental results for long-term, large-scale natural circulations in LWR-containments after large LOCAs," University of Maryland at College Park, Final Report for DOE – Project, Order Number: DE-AP07-96ID10765")

9.C-91

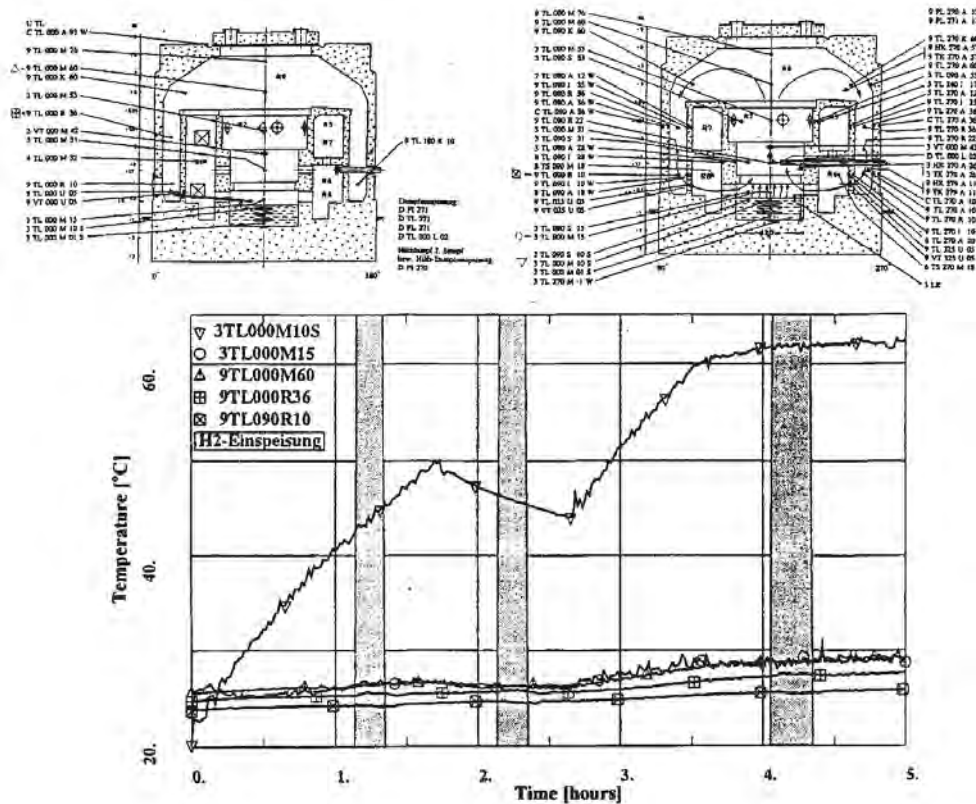


Figure 9.C-48. Battelle-Experiment RX4: Sump and Atmospheric Temperatures

(reprinted from L. Wolf, M. Gavrilis, K. Mum, "Overview of experimental results for long-term, large-scale natural circulations in LWR-containments after large LOCAs," University of Maryland at College Park, Final Report for DOE – Project, Order Number: DE-AP07-96ID10765")

9.C-92

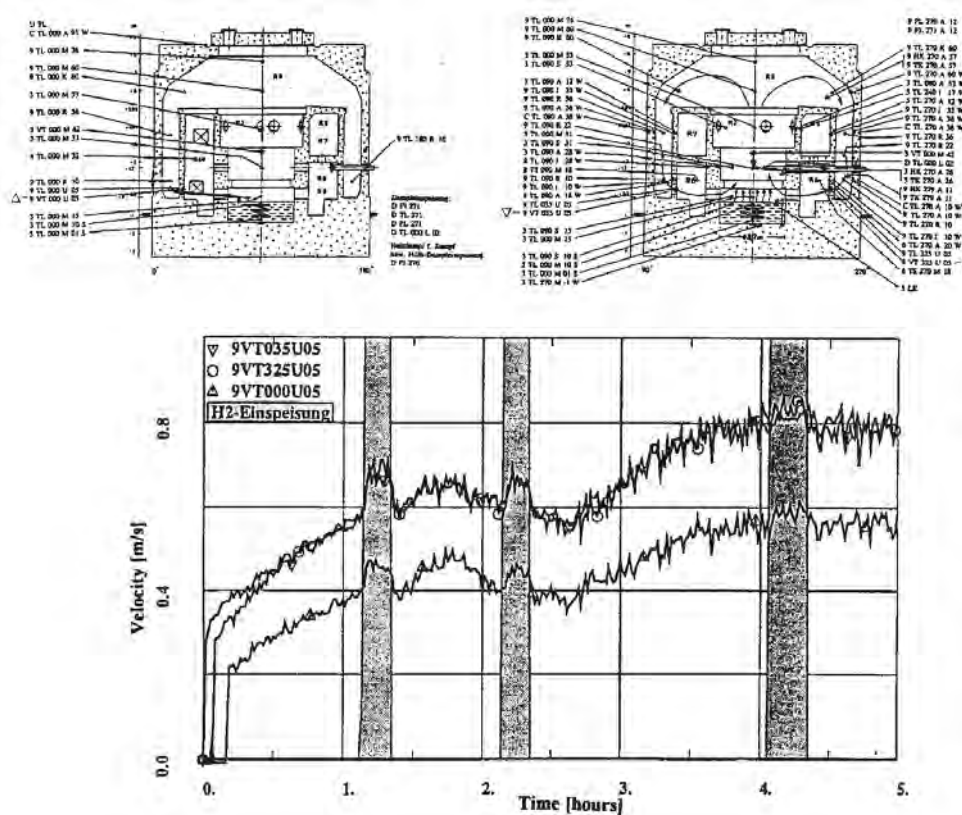


Figure 9.C-49. Battelle-Experiment RX4: Velocities in Side Vents

(reprinted from L. Wolf, M. Gavriles, K. Mum, "Overview of experimental results for long-term, large-scale natural circulations in LWR-containments after large LOCAs," University of Maryland at College Park, Final Report for DOE – Project, Order Number: DE-AP07-96ID10765")

9.C-93

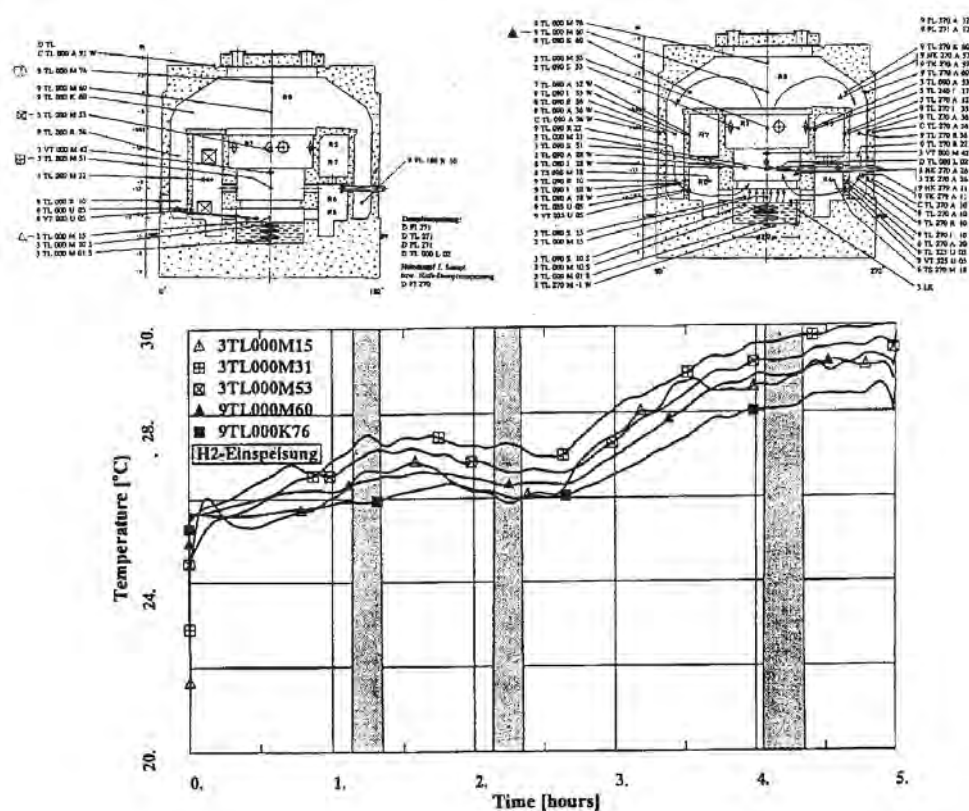


Figure 9.C-50. Battelle-Experiment RX4: Temperatures in Center Compartment and Dome

(reprinted from L. Wolf, M. Gavriles, K. Mum, "Overview of experimental results for long-term, large-scale natural circulations in LWR-containments after large LOCAs," University of Maryland at College Park, Final Report for DOE – Project, Order Number: DE-AP07-96ID10765")

9.C-94

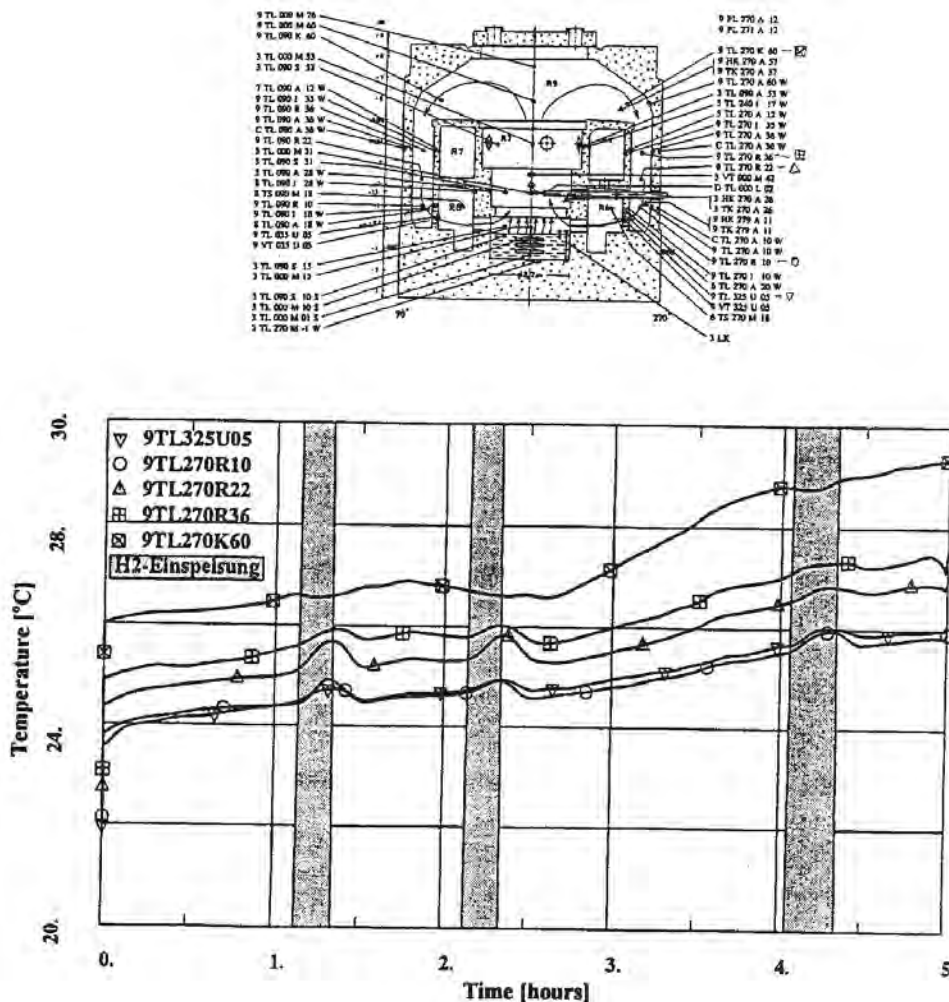


Figure 9.C-51. Battelle-Experiment RX4: Temperatures in External Annulus

(reprinted from L. Wolf, M. Gavriles, K. Mum, "Overview of experimental results for long-term, large-scale natural circulations in LWR-containments after large LOCAs," University of Maryland at College Park, Final Report for DOE – Project, Order Number: DE-AP07-96ID10765")

9.C-95

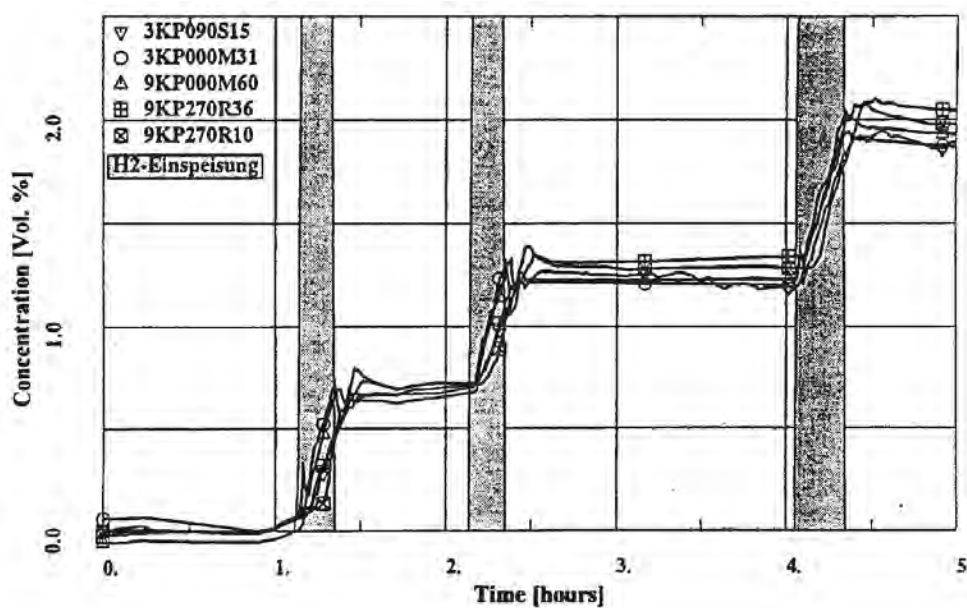


Figure 9.C-52. Battelle-Experiment RX4: Hydrogen Concentration Along Circulation Path

(reprinted from L. Wolf, M. Gavriles, K. Mum, "Overview of experimental results for long-term, large-scale natural circulations in LWR-containments after large LOCAs," University of Maryland at College Park, Final Report for DOE – Project, Order Number: DE-AP07-96ID10765")

9.C-96

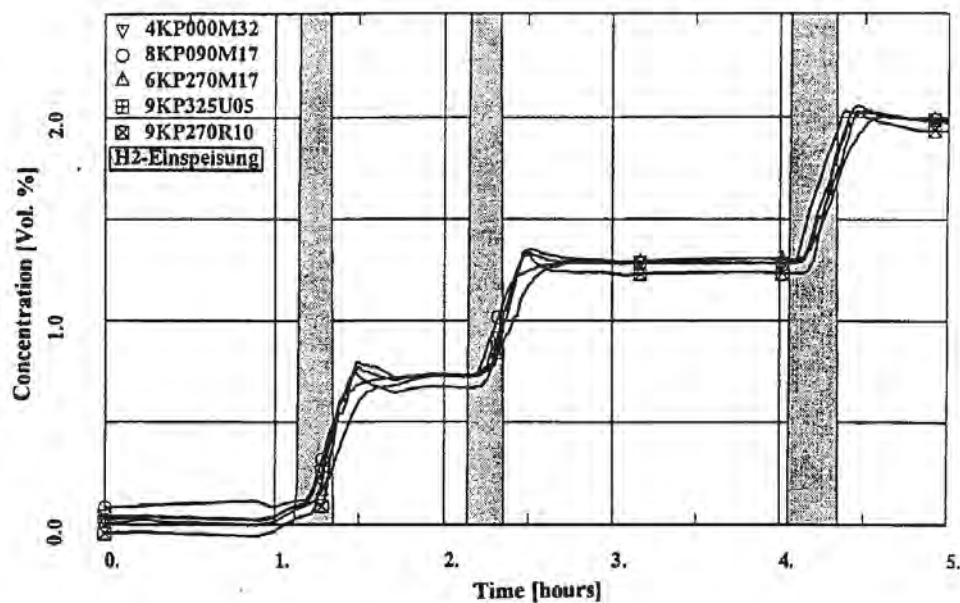


Figure 9.C-53. Battelle-Experiment RX4: Hydrogen Concentrations in Intermediate Subcompartments

(reprinted from L. Wolf, M. Gavriles, K. Mum, "Overview of experimental results for long-term, large-scale natural circulations in LWR-containments after large LOCAs," University of Maryland at College Park, Final Report for DOE – Project, Order Number: DE-AP07-96ID10765")

9.C-97

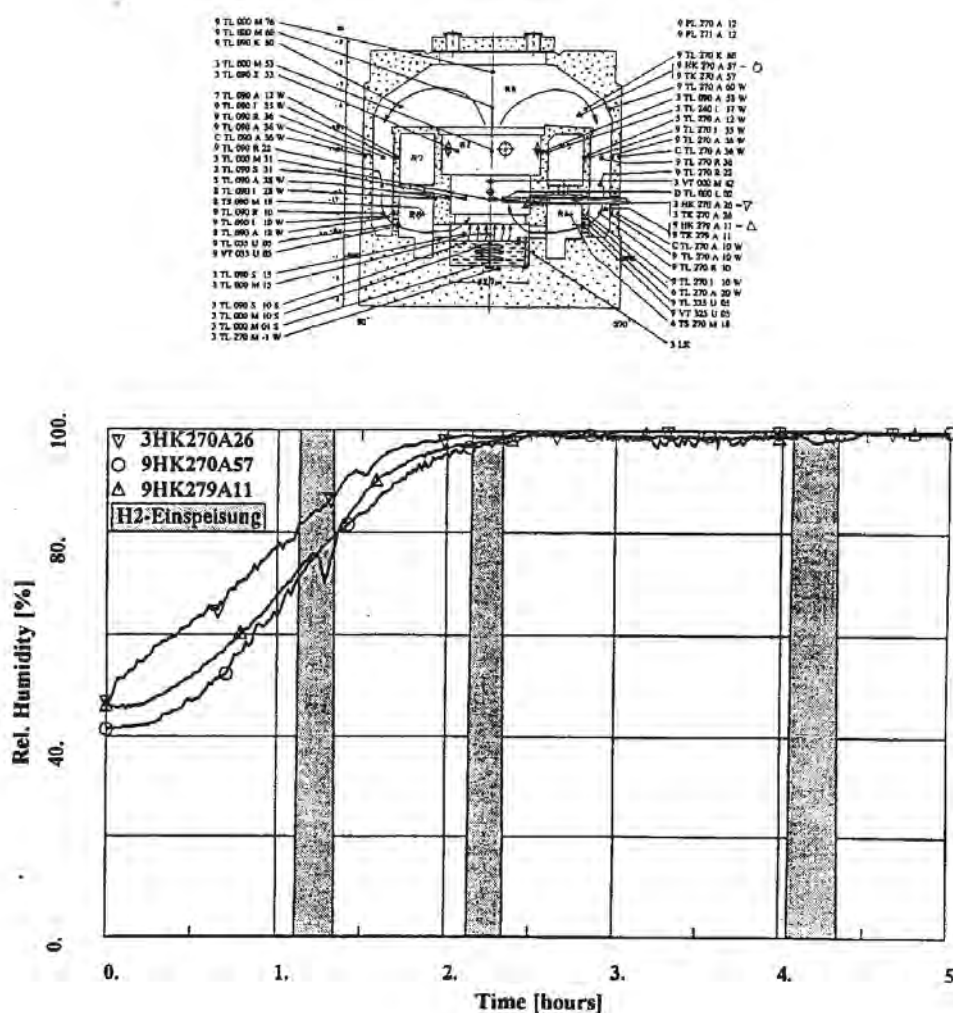


Figure 9.C-54. Battelle-Experiment RX4: Relative Humidity in the Containment Atmosphere

(reprinted from L. Wolf, M. Gavriles, K. Mum, "Overview of experimental results for long-term, large-scale natural circulations in LWR-containments after large LOCAs," University of Maryland at College Park, Final Report for DOE – Project, Order Number: DE-AP07-96ID10765")

9.C-98

9.C.2.1.4 References

1. Fischer, K., Kanzleiter, T., Schall, M., Wolf, L., 1989
“CEC Thermal-Hydraulic Benchmark Exercise on FIPLOC Verification Experiment F2 in BMC-Long-Term Heatup Phase – Specification for Phase I, Battelle-Institut e.V., Frankfurt/Main,” Germany, Sept. 1989
2. Fischer, K., T., Schall, M., Wolf, L., 1991
“CEC Thermal-Hydraulic Benchmark Exercise on FIPLOC Verification Experiment F2 in BMC-Long-Term Heatup Phase – Results for Phase I, Final Report,” EUR 13588 EN, 1991
3. Fischer, K., Kanzleiter, T., Schall, M., Wolf, L., 1990
“CEC Thermal-Hydraulic Benchmark Exercise on FIPLOC Verification Experiment F2 in BMC, Experimental Phases 2, 3, and 4 – Specification for Phase II, Battelle-Institut e.V., Frankfurt/Main,” Germany, July 1990
4. Fischer, K., T., Schall, M., Wolf, L., 1993
“CEC Thermal-Hydraulic Benchmark Exercise on FIPLOC Verification Experiment F2 in BMC, Experiment F2 in BMC, Experimental Phases – Results for Phase 2, 3 and 4, Results of Comparisons, Final Report,” EUR 14454 EN, 1993
5. Fischer, K., Hafner, W., Holzbauer, H., Kanzleiter, T., (1994)
“Experiments for Concerning Natural Convective Flows in Battelle Model Containment, Documentation of Measured Data” (In German), Battelle Ingenieurtechnik GmbH, Eschborn, Germany, Technical Report V68270.2, Oct. 1994
6. T. Kanzleiter, 1988
“FIPLOC-Verification Experiments,” (In German), Battelle-Institut e. V., Frankfurt/Main, Germany, Final Report BlEV-R-66.614-01, March 1988
7. Langer G., Jenior R., Wentlandt H.G., 1979
“Experimental investigation of the hydrogen distribution in the containment of a LWR following a LOCA” (In German), Battelle-Institut e. V., Frankfurt/Main, FRG, Report BF-R-63.363-3
8. Langer G., Baukal W., 1982
“Experimental investigation of the hydrogen distribution in a model containment (Preliminary Experiments II)” (In German), BMFT-Research Contract 150.375, Battelle-Institut e. V., Frankfurt/Main, FRG, Report BF-R-64.036-3
9. Petersen, K., Pamme, H., Seyffarth, L., Wolf, L., (1994)
“Hydrogen Mixing by Natural Convection in PWR Containments” (In German), atw 39 (1994), 758-769

9.C-99

10. L. Wolf, H. Holzbauer, M. Schall, 1994,
“Comparisons Between Multi-Dimensional and Lumped-Parameter GOTHIC Containment Analyses with Data” International Conference on New Trends in Nuclear System Thermohydraulics, Pisa, Italy, May 30th – June 2nd, Vol. 2, pp. 321 – 330.
11. L. Wolf, M. Gavrilas, K. Mun, 1996,
“Overview of Experimental Results for Long-Term, Large-Scale Natural Circulations in LWR-Containments after Large LOCAs” Final Report for DOE – Project, Order Number: DE-AP07-96ID10765, Department of Materials and Nuclear Engineering, University of Maryland at College Park, July 1996.

9.C.2.2 Description of the Available NUPEC Data Base

9.C.2.2.1 M-7-1 Test

NUPEC’s Hydrogen Mixing and Distribution Test M-7-1 is used as OECD/CSNI sponsored International Standard Problem Exercise ISP-35 (report NEA/CSNI/R(94)29) to compare and validate the performance of various computer codes. The WGOOTHIC code is included among the codes that have been compared to this test (see Reference report NEA/CSNI/R(94)29). A detailed presentation of the M-7-1 test is not provided because the test is not directly applicable to the AP600 or **AP1000**. Internal sprays, which are not used in the passive containment design, are active during the M-7-1 test. A more relevant NUPEC experiment, the M-4-3 test (Reference T. Hirose, 1993), is performed without internal sprays. This test investigates the mixing behavior of hydrogen and steam injected into the lower containment compartment.

9.C.2.2.2 M-4-3 Test

The test facility represents one quarter of a linearly scaled PWR (four-loop) containment model with 25 inner compartments. The approximate volume is 1600 m³ with a height of 17.4 m and an inner diameter 10.8 m. Of the total volume, only 1300 m³ is used. The dome compartment is approximately 70 percent of the total volume. Twenty-four smaller compartments occupy from 0.1 percent to 4 percent of the total volume. The containment walls are made of steel plates (concrete structures are not present), so that the response of the heat sinks was very fast. The external containment wall is 12 mm thick steel and is insulated. Three floors are located at the 3.2, 5.4, and 7.3 m levels. A large sump is located below the lowest floor. A gas supply system for steam and helium, a containment internal spray supply system, and measuring systems for temperature, helium concentration, and pressure are installed.

The M-4-3 test simulates a break inside the lower D loop of the steam generator compartment. This compartment is at the first level of the containment. Figure 9.C-55, Figure 9.C-56, and Figure 9.C-57 illustrate the containment compartments and their corresponding numbers on each level. Figure 9.C-55 also shows the location of the break and typical circulation patterns.

The M-4-3 test starts with a pressure of 101.35 kPa and an initial containment temperature of 30°C. A mixture of steam and helium is injected at a constant flow rate during the first 30 minutes. The mass flow rates simulating a small break are 0.33 kg/s and 0.027 kg/s for the steam and helium, respectively. The inflow temperatures are 140°C and 20°C for the steam and helium, respectively.

9.C-100

Experimental data is recorded for 2 hours. The atmosphere and wall temperatures, the helium concentrations in the various compartments, and the pressure inside the dome are recorded. The pressure inside the dome increases almost linearly during the release and reaches 1.6 bar after 30 minutes (end of the release). The total mass of the steam released is 594 kg. Following the release, pressure decreases slowly to 1.5 bar (after 2 hours – see Figure 9.C-59). The dome temperature increases from 303 to 341°K during the release and then decreases to 334°K (see Figure 9.C-59). The dome helium concentration history is presented in Figure 9.C-60.

The temperature and helium concentrations increase first near the release point and the compartments above it, indicating an upward flow direction. This is followed by increases in the dome and steam generator compartments at the opposite side of the containment, indicating a downward flow loop direction. The global circulation loop is closed in the lower level of the containment. The consecutive positions of the higher temperatures and the helium concentration fronts indicate the flow path due to the global circulation during the break release (see Figure 9.C-61, from 0 – 1800 seconds).

A comparison of the temperatures and helium concentration histories in various compartments, Figure 9.C-61, shows the direction of the formed global circulation loop during the break release. One flow path starts in compartment 8, followed by compartments 15, 21, 25 (dome), 14, and 7. Following break release, the temperature field stratifies but the temperature difference between the dome and first floor level is not greater than 14°C at the end of the experiment. After the break release, the temperatures in all the compartments slowly decrease, despite the fact that the outer surface of the containment is insulated. Figure 9.C-61b shows that the concentration in the containment starts to homogenize after the end of the release (1800 seconds). This indicates that natural circulation effects are active after the end of release.

Note that the external walls of the containment are insulated and the interior walls are made of steel. This limits their ability to accumulate energy and act as a heat sources (which would promote natural circulation) later in the test. The natural circulation that exists after the end of release is most likely formed by the presence of the hot sump at the bottom of the containment.

Throughout the test, global circulation is present inside the containment and contributes to the homogenization of the atmosphere over time.

Application to AP600 and AP1000

This test is similar to the AP600 and **AP1000** plant configurations in both the position of the injection point (break at the low level) and the geometry of the containment (70 percent of the volume is dome). However, overriding the similarities are the absence of concrete structures (able to store heat and later act as heat sources) and cooling on the outer surface of the containment shell. These features make the test very dissimilar to the passive containment design. The external cooling and the hot concrete structures, positioned in the lower portion of the passive containment produce strong global circulation and decrease the effects of thermal stratification.

9.C-101

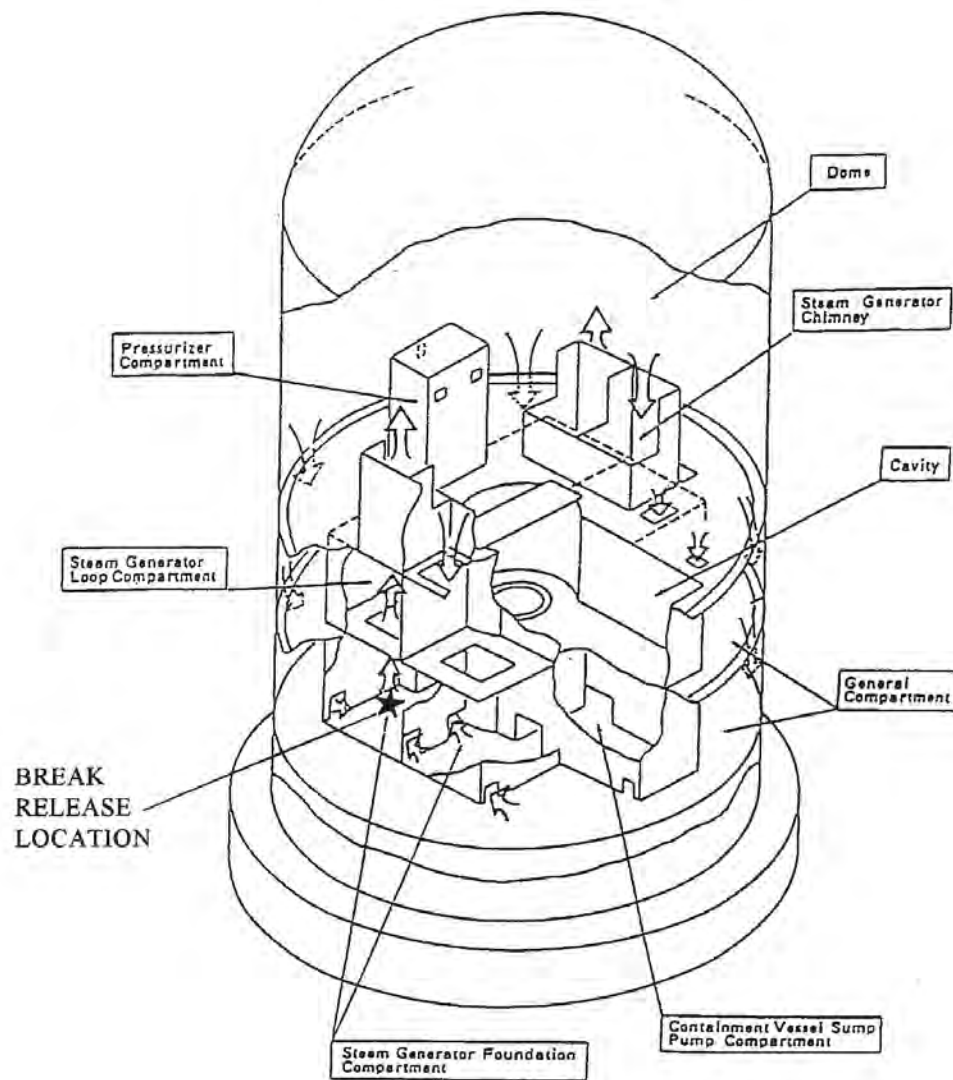


Figure 9.C-55. Model Containment used in the Test, Break-Release Position, and Circulation Flow Paths (See Arrows)

(Figure prepared according to T. Hirose documentation for M-4-3 test data, NUPEC Nuclear Power Engineering Corporation, ISP35-035, 30 April, 1993)

9.C-102

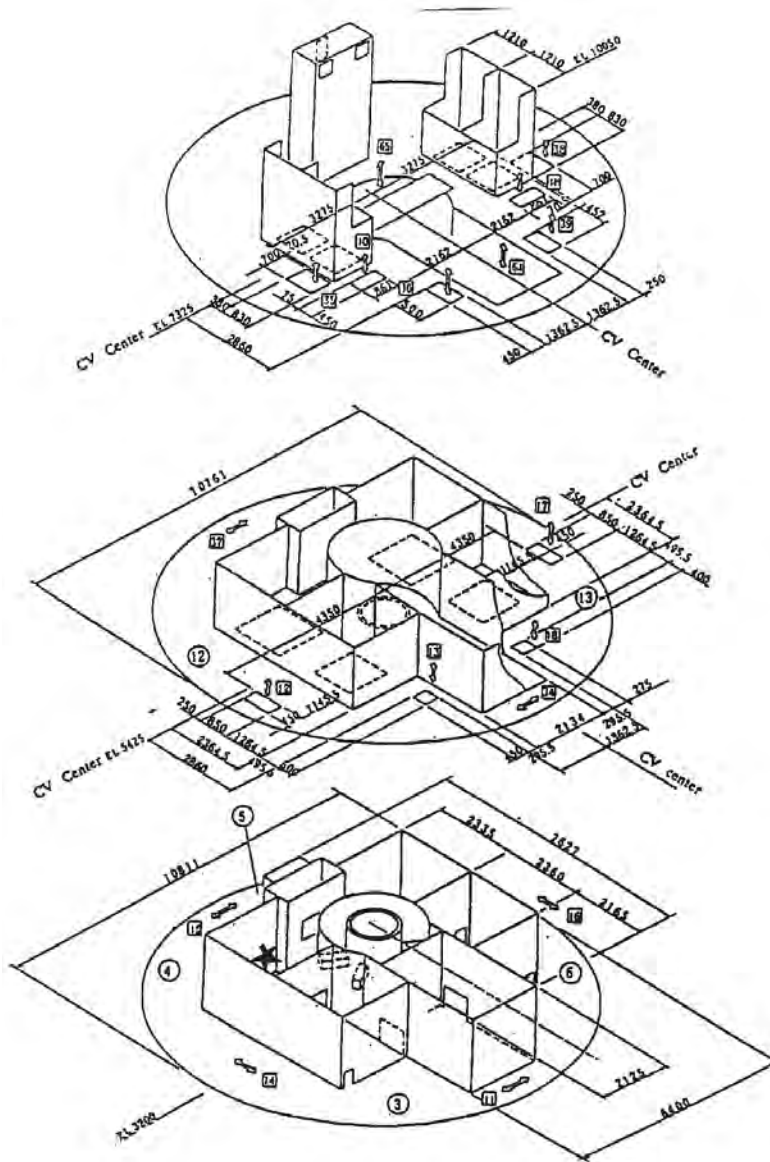


Figure 9.C-56. Detailed Arrangement of each Floor

(Figure prepared according to T. Hirose documentation for M-4-3 test data, NUPEC Nuclear Power Engineering Corporation, ISP35-035, 30 April, 1993)

WCAP-15846-P, Revision 5
APP-SSAR-GSC-587, Revision 5

September 2016

9.C-103

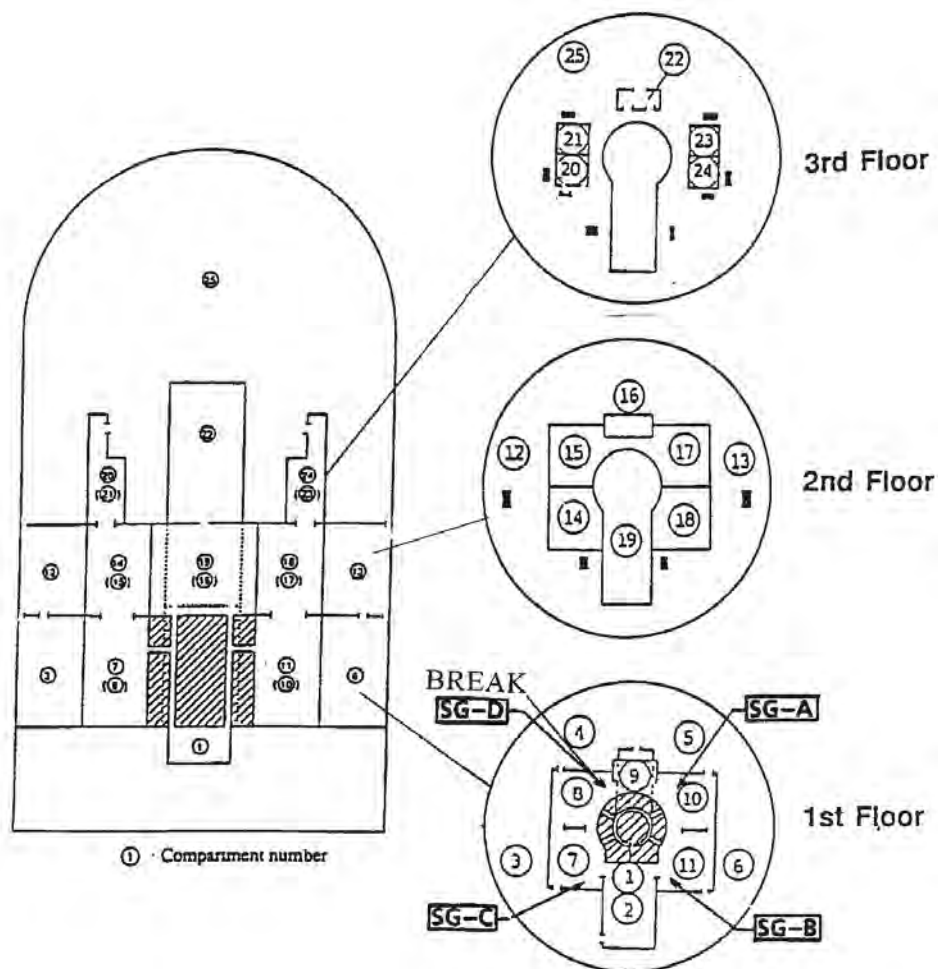


Figure 9.C-57. Distribution of the Compartments at each Floor

(Figure prepared according to T. Hirose documentation for M-4-3 test data, NUPEC Nuclear Power Engineering Corporation, ISP35-035, 30 April, 1993)

9.C-104

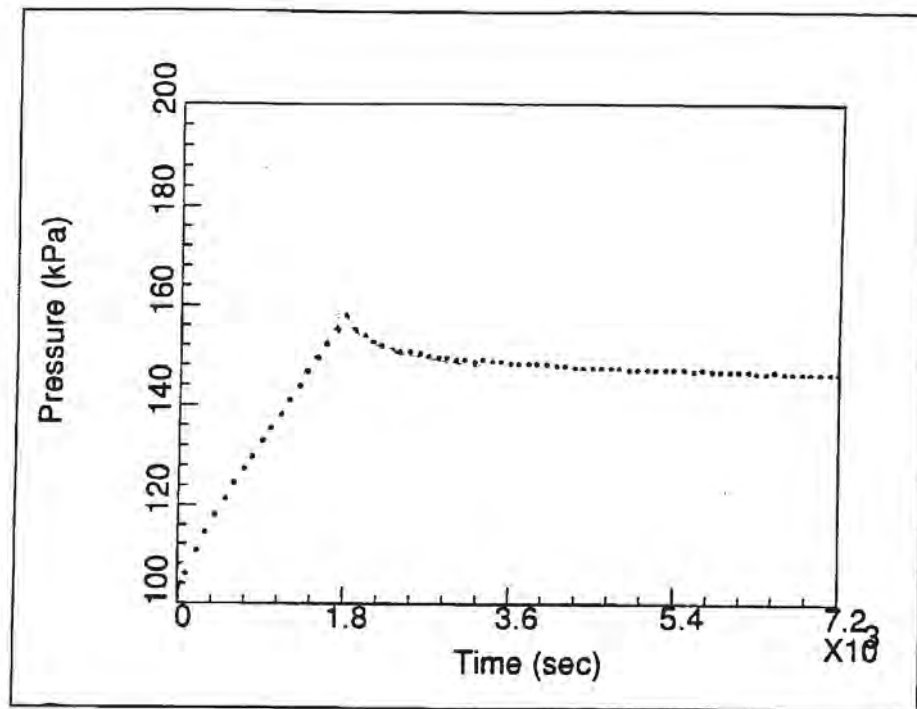


Figure 9.C-58. Pressure History

(Figure prepared according to T. Hirose documentation for M-4-3 test data, NUPEC Nuclear Power Engineering Corporation, ISP35-035, 30 April, 1993)

9.C-105

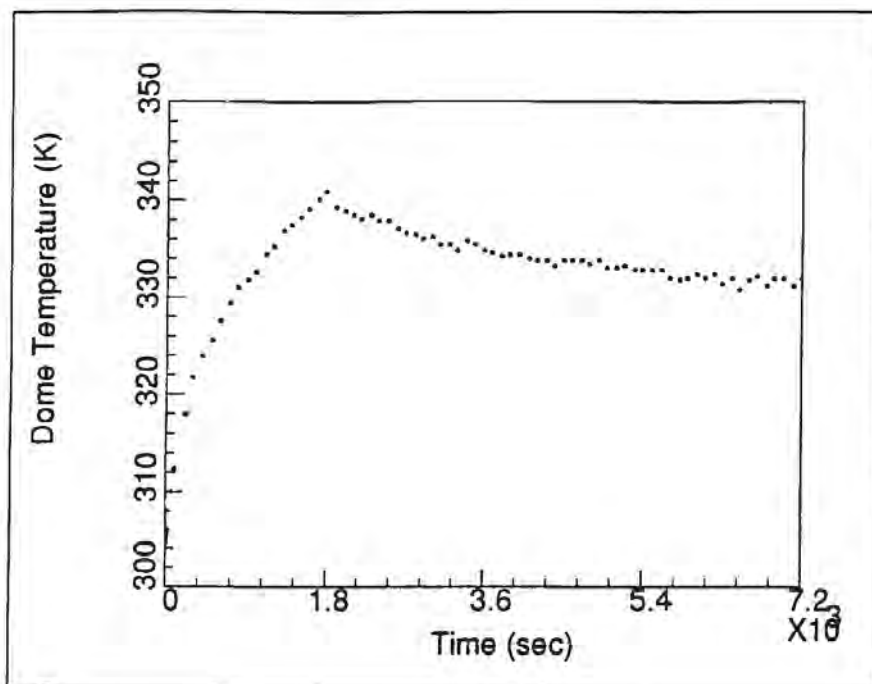


Figure 9.C-59. Dome Temperature History

(Figure prepared according to T. Hirose documentation for M-4-3 test data, NUPEC Nuclear Power Engineering Corporation, ISP35-035, 30 April, 1993)

9.C-106

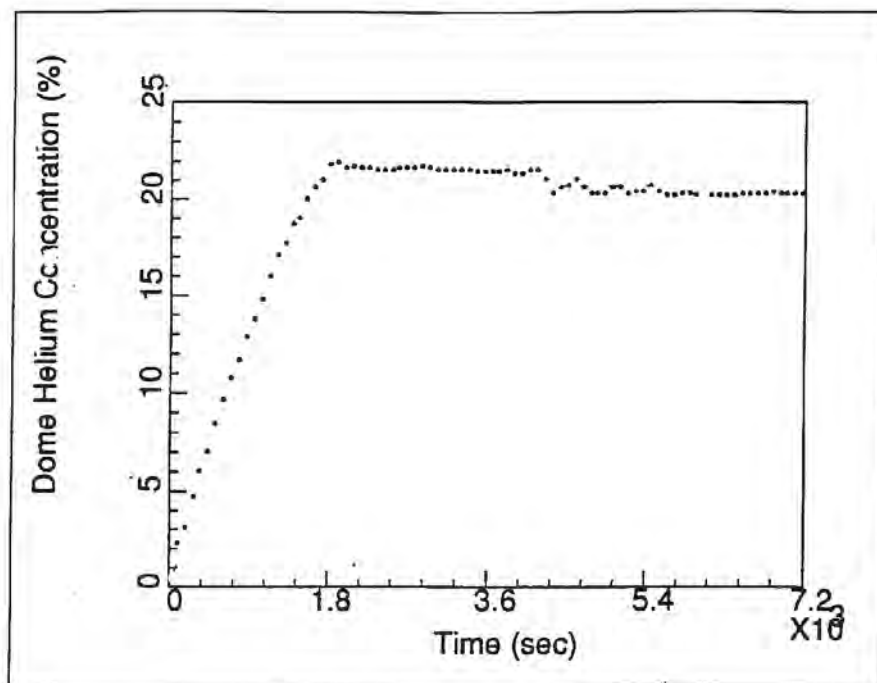


Figure 9.C-60. Dome Helium Concentration History

(Figure prepared according to T. Hirose documentation for M-4-3 test data, NUPEC Nuclear Power Engineering Corporation, ISP35-035, 30 April, 1993)

9.C-107

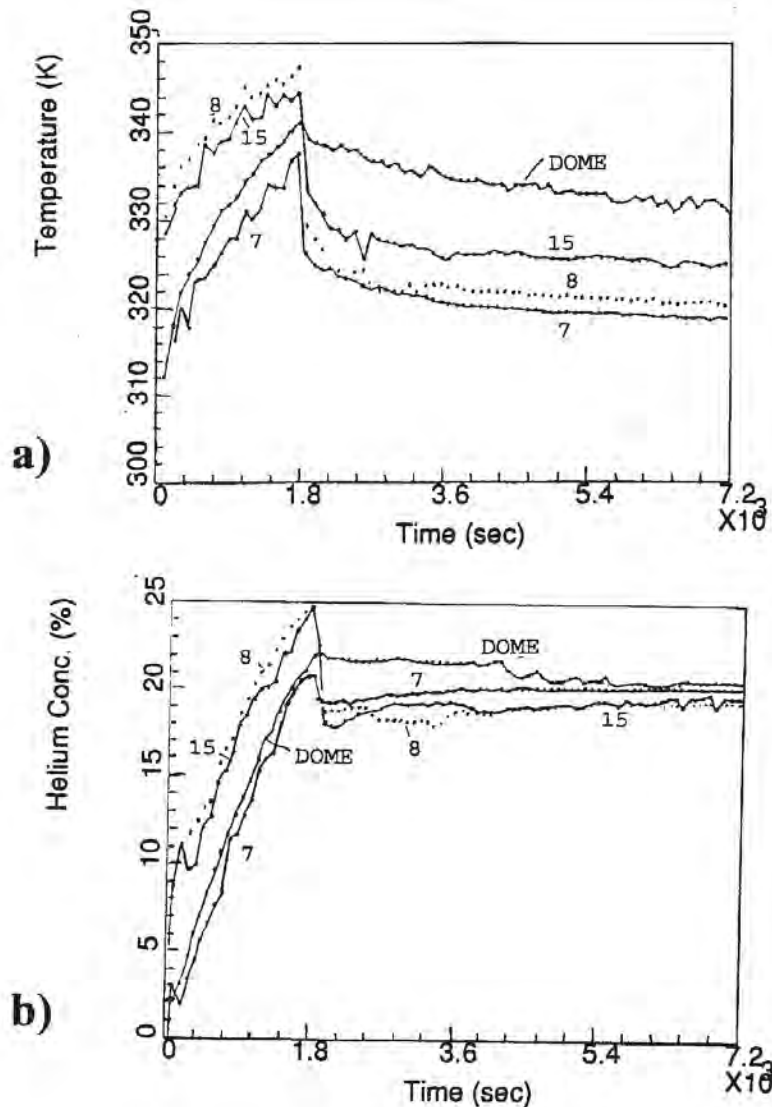


Figure 9.C-61. a) Temperature Histories for Compartments Forming a Circulation Path (8, 15, Dome and 7)
b) Helium Concentration Histories for Compartments Forming a Circulation Path (8, 15, Dome and 7)

(Figure prepared according to T. Hirose documentation for M-4-3 test data, NUPEC Nuclear Power Engineering Corporation, ISP35-035, 30 April, 1993)

9.C-108

9.C.2.2.3 References

1. NEA/CSNI/R(94)29: Final comparison report on ISP-35: NUPEC hydrogen mixing and distribution test (Test M-7-1), Committee on the safety of nuclear installations OECD Nuclear Energy Agency, December 1994
2. Tadashi Hirose (1993): Letter, floppy disk which contains the M-4-3 test data, an attached document, and a video-cassette, NUPEC Nuclear Power Engineering Corporation, ISP35-035, 30 April, 1993

9.C.2.3 Description of the Available Carolinas Virginia Tube Reactor Containment (CVTR) Database

The results of the simulated DBA of CVTR containment system are presented in (Schmitt et al., 1970). The CVTR containment is made of reinforced concrete (see Figure 9.C-62). It is cylindrical in shape with an internal diameter of 57 ft 11 - 1/2 in and an inside height of 114 ft. The cylindrical wall is 2 feet thick. At the top of the cylinder is a hemispherical dome made of 1/2-inch thick steel covered by 20.5 inches of concrete. The structure is divided in three regions (operating, intermediate, and basement). The free volume is about 227,000 ft³. A water spray system is installed at the 360 foot elevation (6 inches above the containment bend line).

Three simulated DBA tests are performed. The first test does not use the water sprays. The pressure and temperature histories are obtained to establish the effects of the sprays on pressure reduction. The remaining tests include active water sprays with flow rates 290 and 500 gpm, respectively. The water spray flow rate is adjusted by changing the total number of nozzles in the spray header. The spray flow is initiated 30 seconds after the end of steam injection and remains in operation for 12 minutes. The second and third tests are not applicable to passive containment DBA situations due to the spray effects.

Superheated steam, at approximately 10°F above the saturation temperature, is injected into the containment. The steam is released above the operating floor through a diffuser made of a 10 foot pipe installed vertically on the discharge nozzle of the steam line (see Figure 9.C-63). The end of the pipe is capped. The pipe contains approximately 126 holes (with 1-inch diameter) that direct the steam horizontally (see Figure 9.C-63). The injection continues until the containment pressure reaches 17.5 psig above the atmospheric pressure.

To obtain the containment response, measurements of the interior pressure are made using seven fast response pressure transducers and a Heise gauge. The containment atmospheric temperature is measured by 34 thermocouples and 15 resistance thermometers. Two additional thermocouples and pressure transducers are located in two partially isolated regions (the reactor header cavity and the refueling canal) to determine their thermal and pressure response. Twenty three thermocouples are positioned at the containment liner envelope and the interior surfaces to obtain the temperature response of the interior concrete sections. The heat transfer through the liner wall of the operating region of the containment is established using heat flow devices along with thermocouples that measure the temperature distribution in the cross-section of the wall. The weight of condensate collected from the selected areas of the cylindrical liner walls is also measured.

9.C-109

The mass flow rates of steam for the three DBA tests range from 360,000 to 380,000 lb/hr (see Figure 9.C-64a, Figure 9.C-64b, Figure 9.C-64c). The injection steam conditions are near to saturated conditions with an enthalpy of 1196 Btu/lb. The steam is injected in the operating region at 335 ft elevation. The duration of the release is approximately 180 seconds. The measurements are taken for approximately two hours, but only the first 50 minutes are presented in the report.

Containment pressure histories for the three DBA tests are presented in Figure 9.C-47. The influence of the spray application and the intensity of the sprays on the decrease of the containment pressure is obvious.

The containment vertical temperature profiles for various tests are presented in Figure 9.C-66, Figure 9.C-67 and Figure 9.C-68, respectively. For the first test, large vertical temperature gradients exist for the duration of the measurements (about two hours), indicating temperature stratification. The containment air recirculation system is activated one and half hours after the beginning of the first test and it decreases the vertical temperature gradients (but not so efficiently as water sprays).

The spray tests (tests 2 and 3 - which are not applicable for passive containment designs) contribute towards the uniformity of the containment atmosphere by decreasing the dome temperatures. After one hour, the dome temperatures were 177, 155, and 137°F for tests 1, 2, and 3, respectively.

One hundred minutes of test data from thermocouples mounted at the same horizontal level inside the operating region are analyzed. Significant temperature gradients are not established in the horizontal direction. This is consistent with the view that stratification gradients are mainly in a vertical direction, with negligible horizontal gradients, except near plumes and wall boundary layers.

Liner vertical temperatures are almost the same as the temperatures in the upper regions of the containment atmosphere, while they are higher than temperatures in the atmosphere of the lower regions (see Figure 9.C-69 and Figure 9.C-70 for lower regions). An explanation for the higher liner temperatures in the lower regions is that the steam, in its downward movement, passed through the annular gap near the containment wall (surrounding the operating floor) releasing heat predominantly to the wall instead of the atmosphere.

Data from six thermocouples embedded in concrete surfaces in the containment are presented in Figure 9.C-71 for the case without sprays. The operating region structures have a large temperature increase, while the basement region is almost unaffected. The results are in agreement with the atmospheric and liner temperature data and show stratification above the break elevation.

The results from two thermocouples installed in two partially isolated regions (the reactor header cavity and the fuel transfer canal) are presented in Figure 9.C-72. A small temperature increase is seen during the steam injection. After the injection, temperatures decrease very fast, resulting in the very small final temperature increase. The data also indicates that dead-ended compartments get some steam during the pressure increase.

9.C-110

The reasons for the established temperature stratification in the case of the CVTR containment test performed without internal sprays are:

- The position of the release point is above the 335 foot elevation of containment height see Figure 9.C-62). This could be considered as a release in the upper region of the containment ($H_r/H_t = 0.525$).
- The external walls and the dome of the containment were made of 23-3/4" thick concrete which accumulated a portion of the heat released in the upper regions (operational region and intermediate region – see Figure 9.C-71 for vertical temperature distribution inside the liner). The upper portions of the walls remain hot as containment cools, producing boundary conditions for a stable stratification.
- External spray cooling of the dome and walls (upper half exposed to the air) is not applied.
- The steam condensate is collected in the buckets so that weight of the condensate can be measured. This eliminated hot sump evaporation and heat source effects. The other experiments (BMC and HDR) indicate that even small temperature differences between the sump (as a heat source at the lowest level) and the containment atmosphere generate global natural circulation inside the containment.

9.C-111

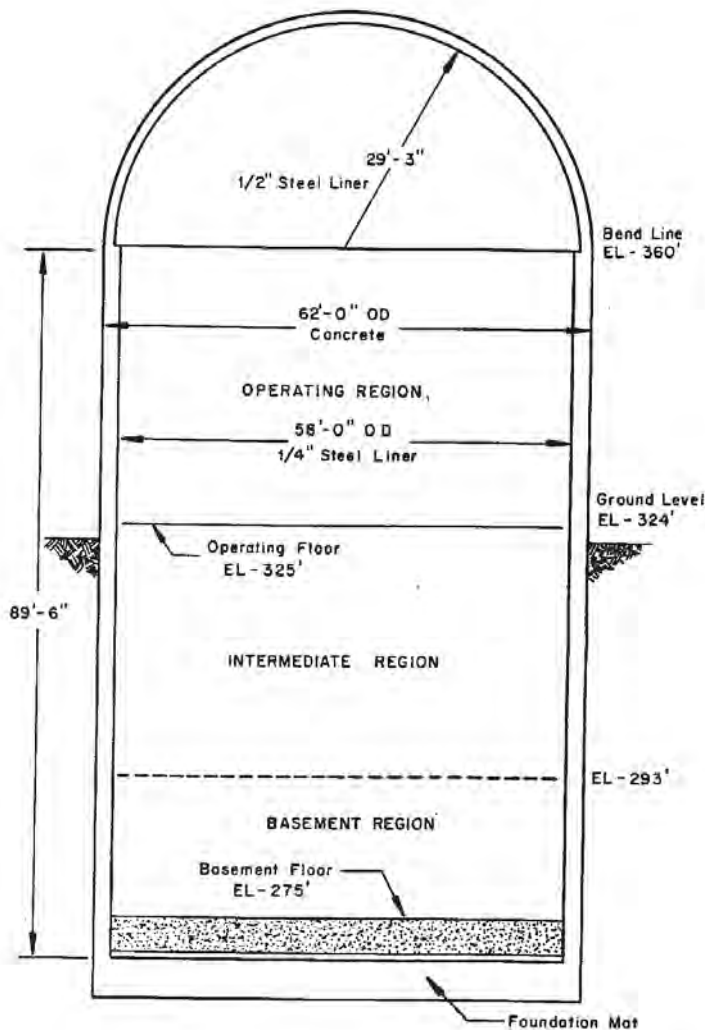


Figure 9.C-62. Carolinas Virginia Tube Reactor (CVTR) Containment Structure

(reprinted from: R.C. Schmitt, G.E. Bingham, J.A. Norberg, "Simulated design basis accident tests of the Carolinas Virginia Tube Reactor Containment – Final report," Prepared for the U.S. Atomic Energy Commission, Idaho Operations Office, Under Contract No. AT(10-1)-1230)

9.C-112

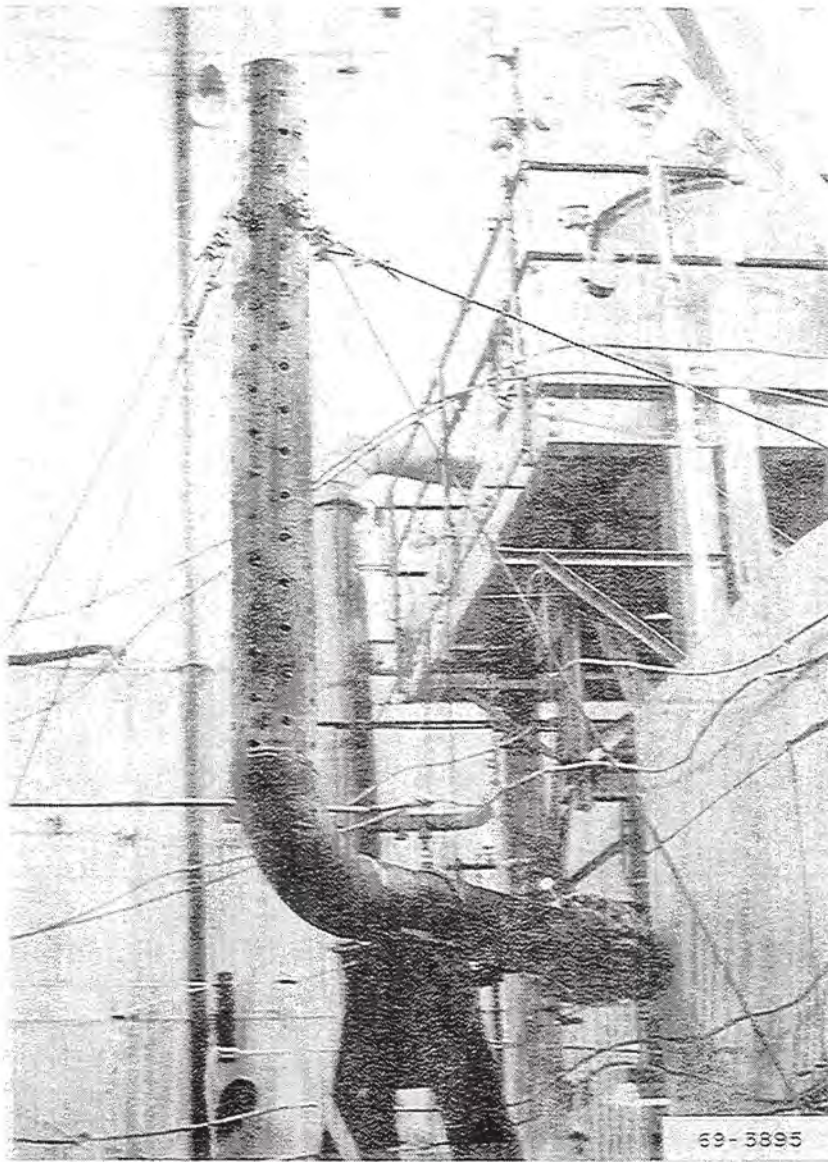


Figure 9.C-63. CVTR Steam Line Diffuser

(reprinted from: R.C. Schmitt, G.E. Bingham, J.A. Norberg, "Simulated design basis accident tests of the Carolinas Virginia Tube Reactor Containment – Final report," Prepared for the U.S. Atomic Energy Commission, Idaho Operations Office, Under Contract No. AT(10-1)-1230)

9.C-113

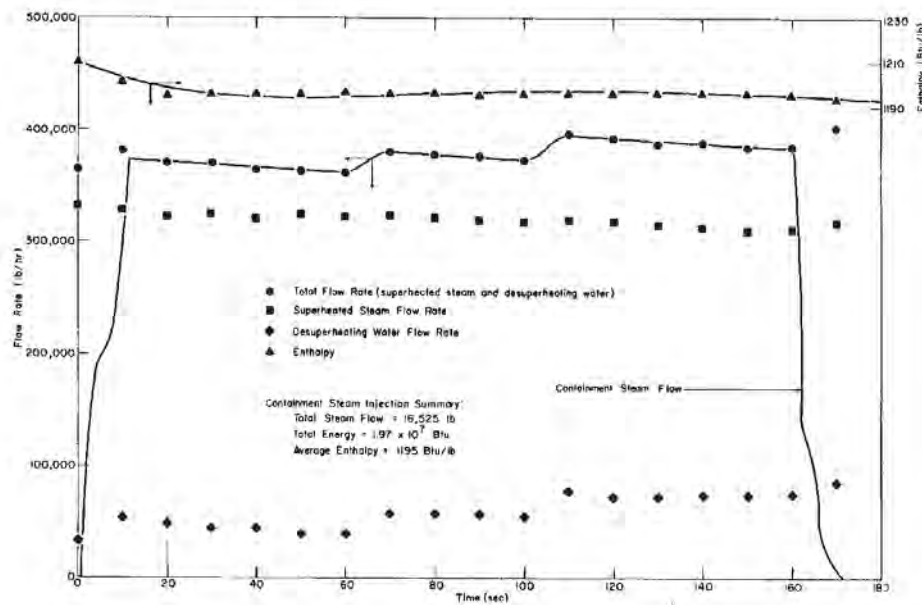


Figure 9.C-64a. Steam Injection Histories Test 1

(reprinted from: R.C. Schmitt, G.E. Bingham, J.A. Norberg, "Simulated design basis accident tests of the Carolinas Virginia Tube Reactor Containment – Final report," Prepared for the U.S. Atomic Energy Commission, Idaho Operations Office, Under Contract No. AT(10-1)-1230)

9.C-114

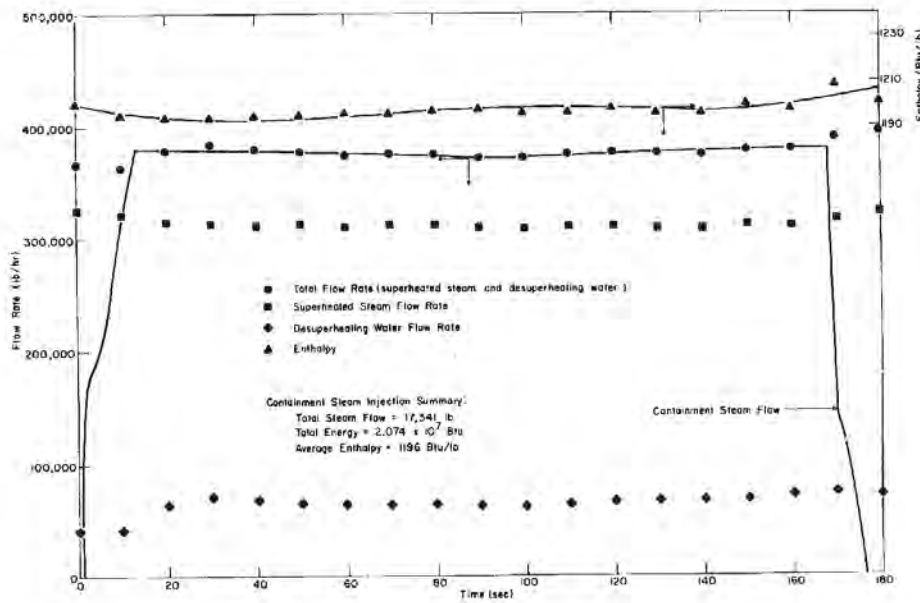


Figure 9.C-64b. Steam Injection Histories Test 2

(reprinted from: R.C. Schmitt, G.E. Bingham, J.A. Norberg, "Simulated design basis accident tests of the Carolinas Virginia Tube Reactor Containment – Final report," Prepared for the U.S. Atomic Energy Commission, Idaho Operations Office, Under Contract No. AT(10-1)-1230)

9.C-115

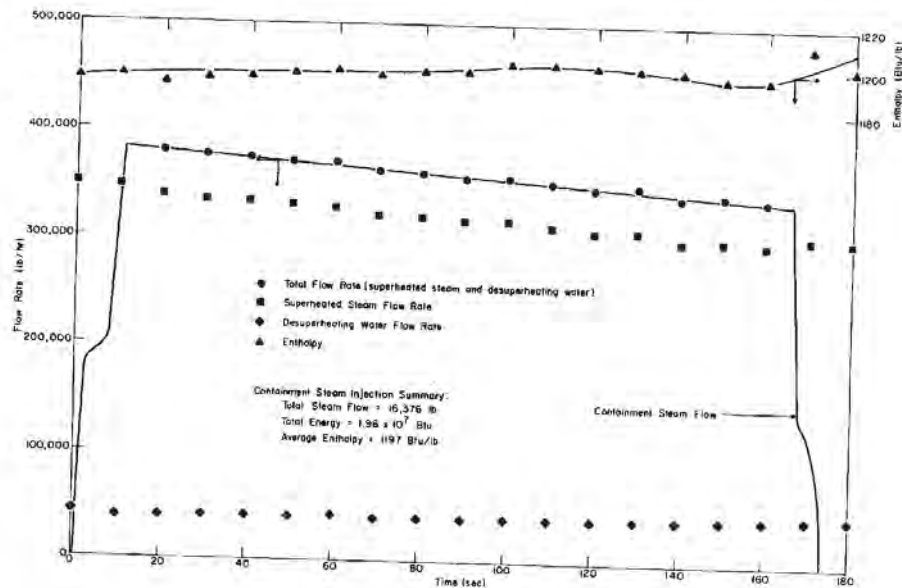


Figure 9.C-64c. Steam Injection Histories Test 3

(reprinted from: R.C. Schmitt, G.E. Bingham, J.A. Norberg, "Simulated design basis accident tests of the Carolinas Virginia Tube Reactor Containment – Final report," Prepared for the U.S. Atomic Energy Commission, Idaho Operations Office, Under Contract No. AT(10-1)-1230)

9.C-116

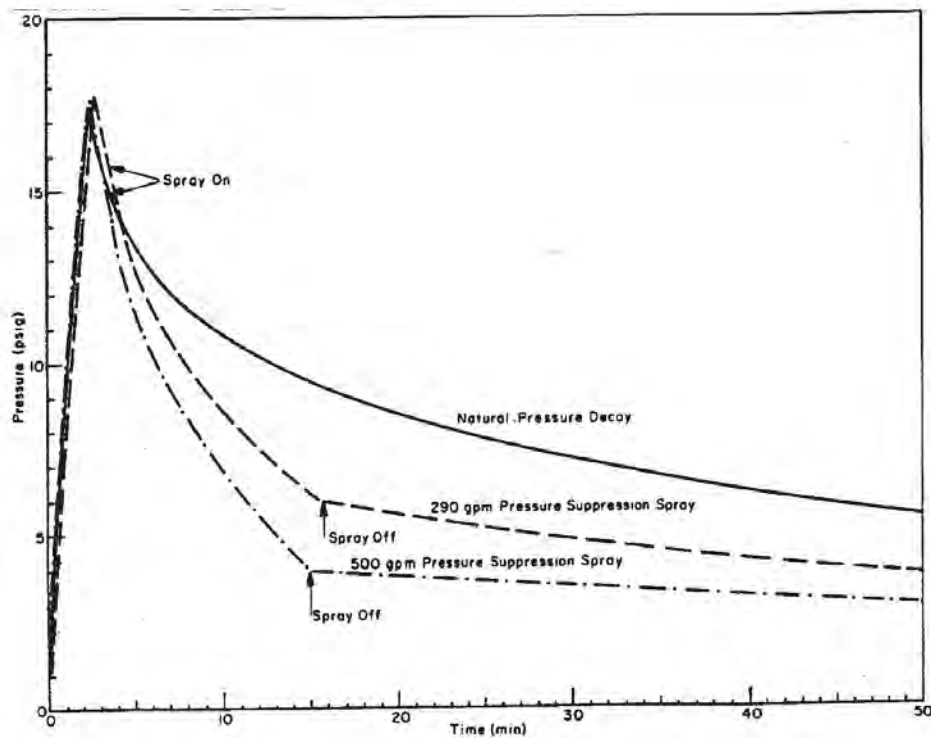


Figure 9.C-65. CVTR Containment Pressure Response (Heise Gauge)

(reprinted from: R.C. Schmitt, G.E. Bingham, J.A. Norberg, "Simulated design basis accident tests of the Carolinas Virginia Tube Reactor Containment – Final report," Prepared for the U.S. Atomic Energy Commission, Idaho Operations Office, Under Contract No. AT(10-1)-1230)

9.C-117

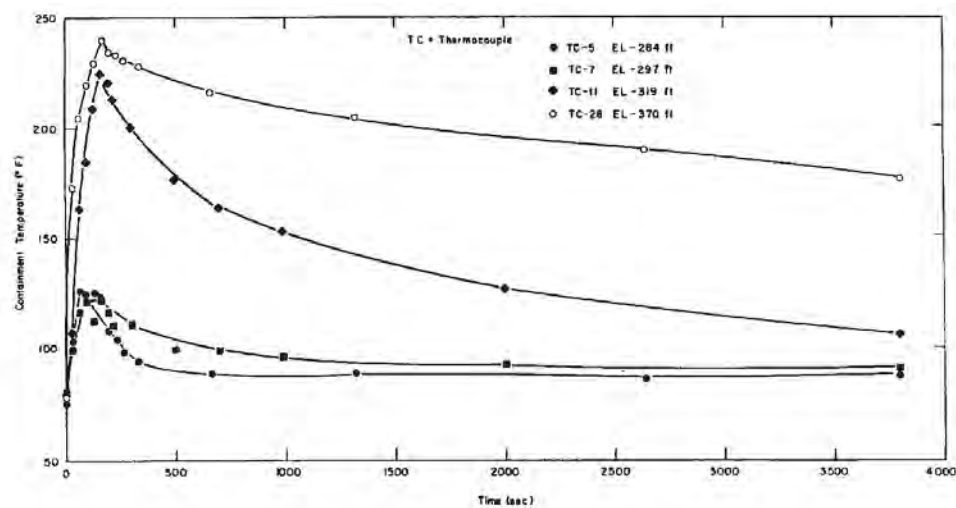


Figure 9.C-66. Atmospheric Vertical Temperature Profile, Test 1

(reprinted from: R.C. Schmitt, G.E. Bingham, J.A. Norberg, "Simulated design basis accident tests of the Carolinas Virginia Tube Reactor Containment – Final report," Prepared for the U.S. Atomic Energy Commission, Idaho Operations Office, Under Contract No. AT(10-1)-1230)

9.C-118

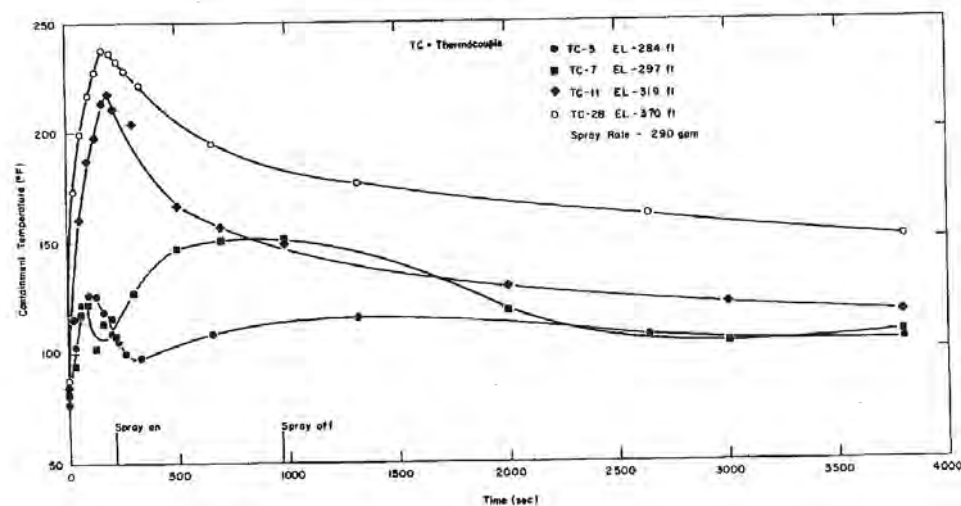


Figure 9.C-67. Atmospheric Vertical Temperature Profile, Test 2

(reprinted from: R.C. Schmitt, G.E. Bingham, J.A. Norberg, "Simulated design basis accident tests of the Carolinas Virginia Tube Reactor Containment – Final report," Prepared for the U.S. Atomic Energy Commission, Idaho Operations Office, Under Contract No. AT(10-1)-1230)

9.C-119

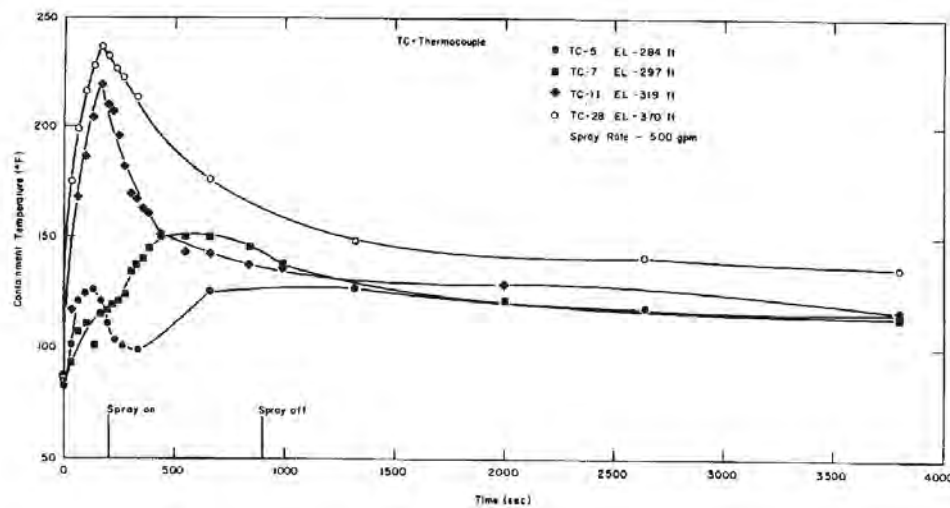


Figure 9.C-68. Atmospheric Vertical Temperature Profile, Test 3

(reprinted from: R.C. Schmitt, G.E. Bingham, J.A. Norberg, "Simulated design basis accident tests of the Carolinas Virginia Tube Reactor Containment – Final report," Prepared for the U.S. Atomic Energy Commission, Idaho Operations Office, Under Contract No. AT(10-1)-1230)

9.C-120

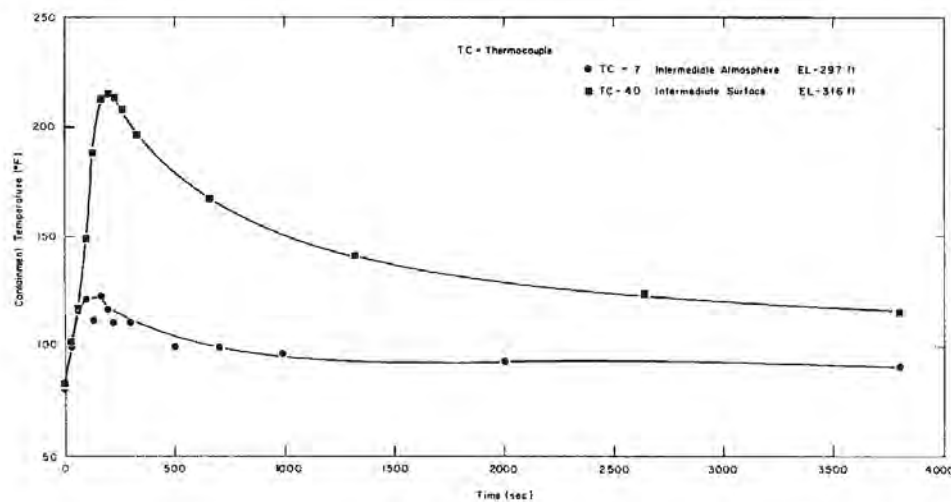


Figure 9.C-69. Surface and Atmosphere Temperatures – Intermediate Region, Test 1

(reprinted from: R.C. Schmitt, G.E. Bingham, J.A. Norberg, "Simulated design basis accident tests of the Carolinas Virginia Tube Reactor Containment – Final report," Prepared for the U.S. Atomic Energy Commission, Idaho Operations Office, Under Contract No. AT(10-1)-1230)

9.C-121

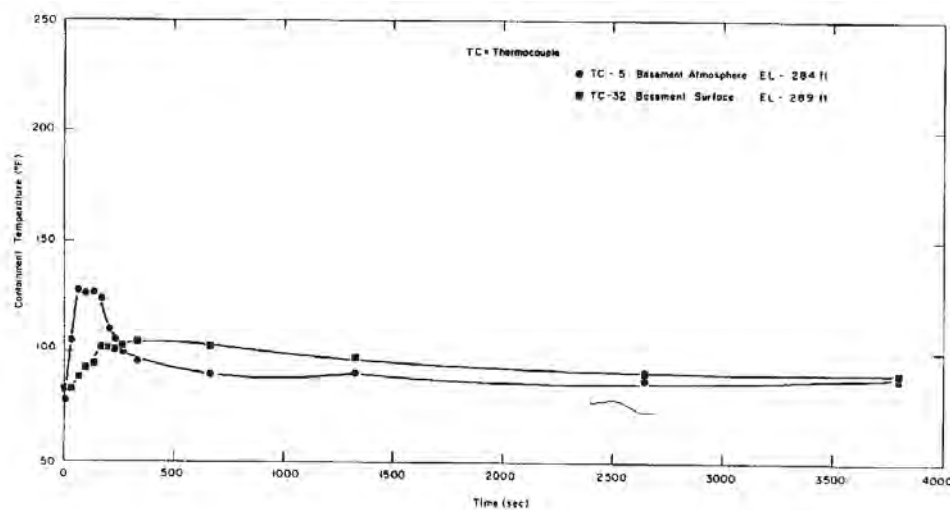


Figure 9.C-70. Surface and Atmosphere Temperatures – Basement Region, Test 1

(reprinted from: R.C. Schmitt, G.E. Bingham, J.A. Norberg, "Simulated design basis accident tests of the Carolinas Virginia Tube Reactor Containment – Final report," Prepared for the U.S. Atomic Energy Commission, Idaho Operations Office, Under Contract No. AT(10-1)-1230)

9.C-122

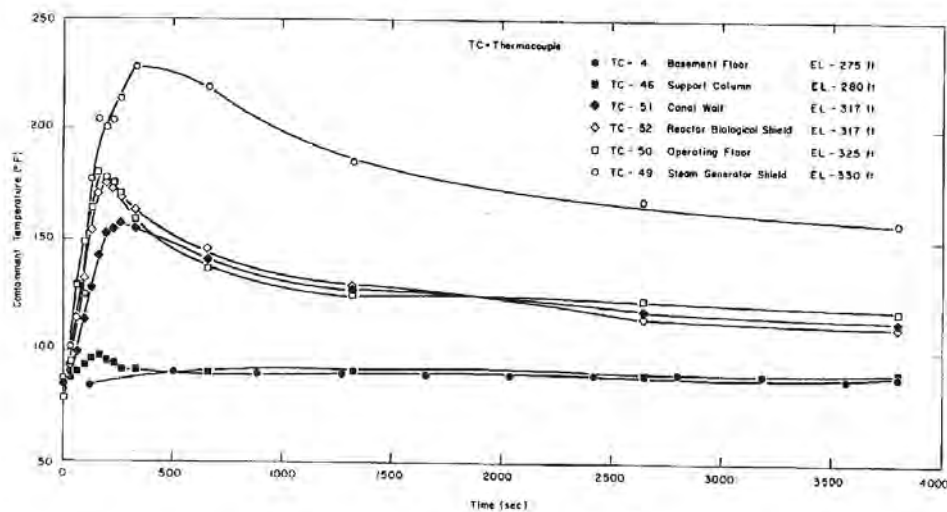


Figure 9.C-71. Concrete Surface Temperatures, Test 1

(reprinted from: R.C. Schmitt, G.E. Bingham, J.A. Norberg, "Simulated design basis accident tests of the Carolinas Virginia Tube Reactor Containment – Final report," Prepared for the U.S. Atomic Energy Commission, Idaho Operations Office, Under Contract No. AT(10-1)-1230)

9.C-123

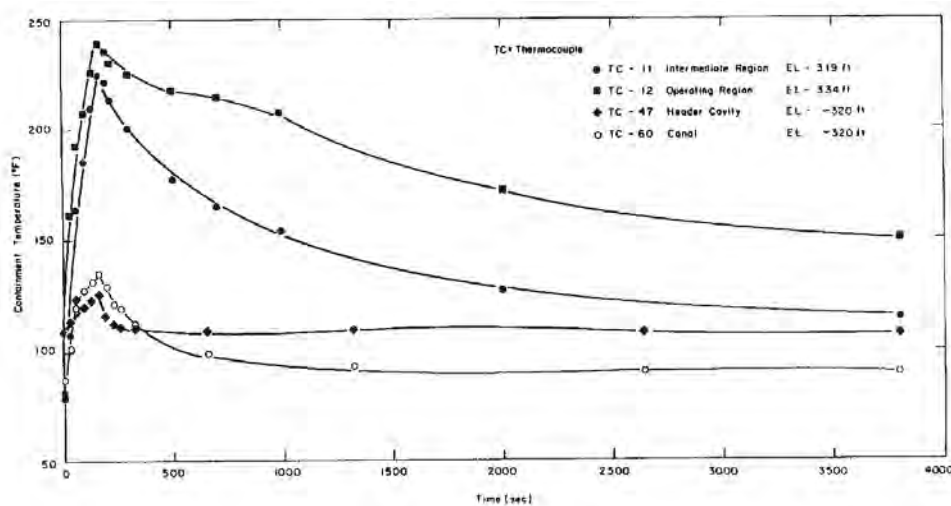


Figure 9.C-72. Isolated Containment Region Temperatures

(reprinted from: R.C. Schmitt, G.E. Bingham, J.A. Norberg, "Simulated design basis accident tests of the Carolinas Virginia Tube Reactor Containment – Final report," Prepared for the U.S. Atomic Energy Commission, Idaho Operations Office, Under Contract No. AT(10-1)-1230)

9.C.2.4 Description of the Available HDR Database

The HDR containment (Figure 9.C-73) is 20 m in diameter and 60 m high with a total free volume of 11,300 m³. It is made of steel and concrete with a total surface area of 30,000 m² available for heat transfer (condensation). The dome volume, including a crane structure, is about 42 percent of the total volume or 5,000 m³. The main and spiral staircase form the dominant vertical flow paths connecting the dome with sump. The containment can be subdivided into 62 to 72 subcompartments containing pipes, pumps, and valves etc. The subcompartments are interconnected by numerous openings. The numbers and locations of thermocouples and anemometers for the HDR-E test series are presented in Figure 9.C-74.

9.C.2.4.1 HDR E11 Test Series

Test group E11 (the hydrogen distribution and mixing experiments) is included as a part of the HDR-Safety Program Phase III that was conducted in the summer of 1989 (Cron and Schrammel, 1993). This test series simulated severe accident scenarios. The tests provide insights on DBA circulation and stratification. A review of the natural circulation flows formed in experiments E11.0 - E11.5 is presented in Wolf et al., 1996. Circulation is indicated by examination of the recorded temperatures and velocities.

Seven of the eight E11 experiments are initiated with small steam releases. The one exception, the E11.5 experiment, is initiated with a large-break, two-phase LOCA blowdown. The tests provide data for the transient and spatial distribution of the gas concentration (hydrogen/helium mixture) under various initial and boundary conditions.

The following features are considered:

- The large scale of the experimental facility and the multi-compartment geometry with a relatively large dome
- High hydrogen release rates typical of severe accidents
- Superheated steam injection into the containment - single and multiple steam and hydrogen injection phases
- Internal concrete and metal structures and surfaces
- Different axial positions for hydrogen and steam releases
- The efficiency of hydrogen mitigating features, including venting (for example blockage of one major vertical flow path)
- The impact of internal and external sprays
- Sump heat up effects
- Air heater operation effects

9.C.2.4.1.1 Experiment E11.0

Experiment E11.0 is performed with an external steam supply and without a gas mixture release. However, the external steam supply is not able to produce typical severe accident conditions. Therefore, a blowdown of the primary system is used for all other experiments. The results of E11.0 are not discussed here.

9.C.2.4.1.2 Experiment E11.1

Experiment E11.1 includes a high-positioned, small break LOCA, followed by additional steam and gas releases. The effectiveness of the internal spray for decreasing the pressure and temperature inside the containment is also tested. Since this experiment included internal sprays that are not a part of the passive containment design, the results are not discussed here.

9.C.2.4.1.3 Experiment E11.2

Experiment E11.2 also includes a high-positioned release point. However, instead of internal spray as in experiment E11.1, external spray is applied to the dome shell. A detailed presentation of this experiment is given in Wolf, Mun, Floyd, 1995. This experiment, together with E11.4, provides results used as benchmark problems to validate numerical models (Wolf et al., 1994). The verification of the GOTHIC code by Holzbauer and Wolf, 1994, is also based on E11.2 results.

Figure 9.C-75 provides the sequence of the experimental procedures. This includes the duration of the heatup and the blowdown of steam ($p=110$ bar and $T=318^{\circ}\text{C}$) in the compartment R1805 (in the main stairway at elevation 21.05-25.3 m, see Figure 9.C-74, right side). The consecutive steam and gas (mixture of 85 percent He and 15 percent H_2) injections are also presented in Figure 9.C-75. Compartment 1405, in the spiral stairway at elevation 4.5 m (see Figure 9.C-75 right side), receives steam at 770 minutes.

The change in the containment pressure with time is shown in Figure 9.C-76. The temperatures, steam concentrations, and He/ H_2 gas mixture concentrations at various axial positions of the main staircase are presented in Figure 9.C-77, Figure 9.C-78, and Figure 9.C-79, respectively. Temperature differences between the same axial positions of the two vertical flow paths (main and spiral staircases) are pronounced during the heatup phase. Later, temperature differences decrease and change signs. The crossing temperature histories in Figure 9.C-80, Figure 9.C-81, Figure 9.C-82, Figure 9.C-83 indicate a change in the flow directions.

A steep thermal gradient indicates the presence of the stratification that exists between the lower compartments and the containment dome (see Figure 9.C-84). Even an additional steam release in the lower portion of the containment (compartment R1405) at 770 minutes is not able to completely eliminate the vertical thermal gradient, although it is greatly reduced.

9.C-126

The injection of steam into the lower level, together with the effects of cooling the dome with the external spray, causes redistribution of the He/H₂ gas mixture (see Figure 9.C-79). The increase in the gas concentration in the upper part of the dome is a consequence of the steam condensation on the inside dome surface. Later, the decrease in temperatures in the upper dome promote global circulation (causing unstable stratification) and homogenize the dome atmosphere. Even after the external spray is stopped, global circulation affects the lower parts of the containment (see Figure 9.C-77, Figure 9.C-78, Figure 9.C-79). Overall, the external spray causes a reduction of 0.44 bar in the containment pressure (see Figure 9.C-76).

The application of external sprays at the dome surface promotes global circulation, homogenizes hydrogen concentrations, and decreases the containment pressure. The water film applied to the external surface of the AP600 and **AP1000** shell produces similar effects.

9.C-127

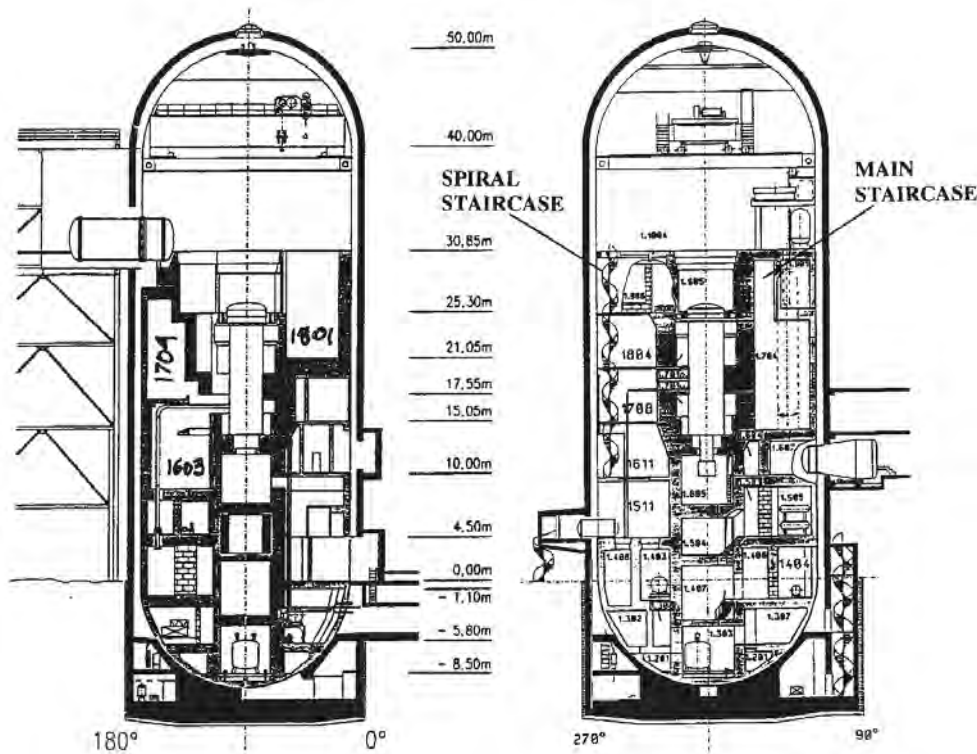


Figure 9.C-73. Cross-sections, Elevations and Numbers of Compartments of the HDR Containment, Left (180°-0°-cross-section), Right (270°-90°-cross-section)

(reprinted from: L. Wolf, K. Mun, J. Floyd, "HDR hydrogen mixing evaluation for containment safety evaluations" – Phase 1, University of Maryland at College Park, Final Report for DOE-Project Order Number: DE-AP07-95ID81401, July 1995)

9.C-128

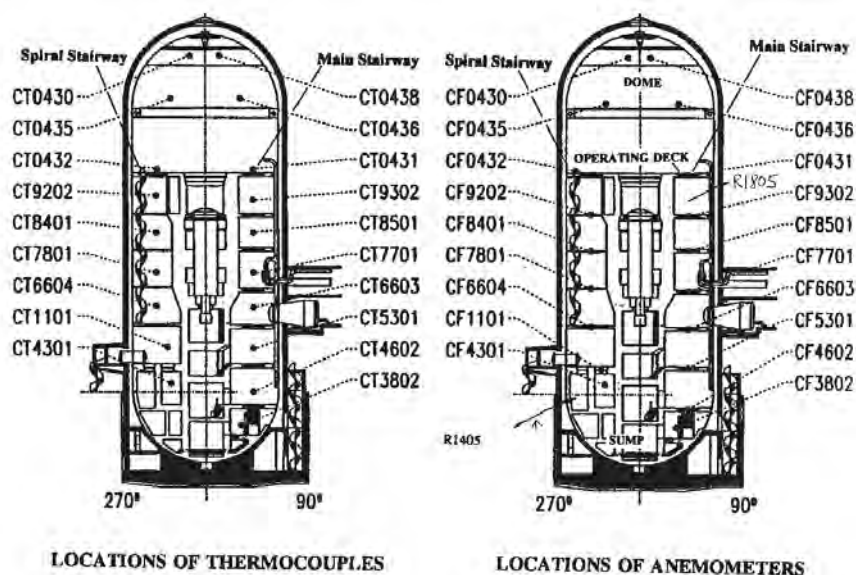


Figure 9.C-74. Locations and Enumerations of Thermocouple (left) and Anemometers (right) for HDR-E-Test Series

(reprinted from: L. Wolf, M. Gavrilas, K. Mun, "Overview of experimental results for long-term, Large-scale natural circulations in LWR-containments after large LOCAs," University of Maryland at College Park, Final Report for DOE – Project, Order Number: DE-AP07-96ID10765," July 1996)

9.C-129

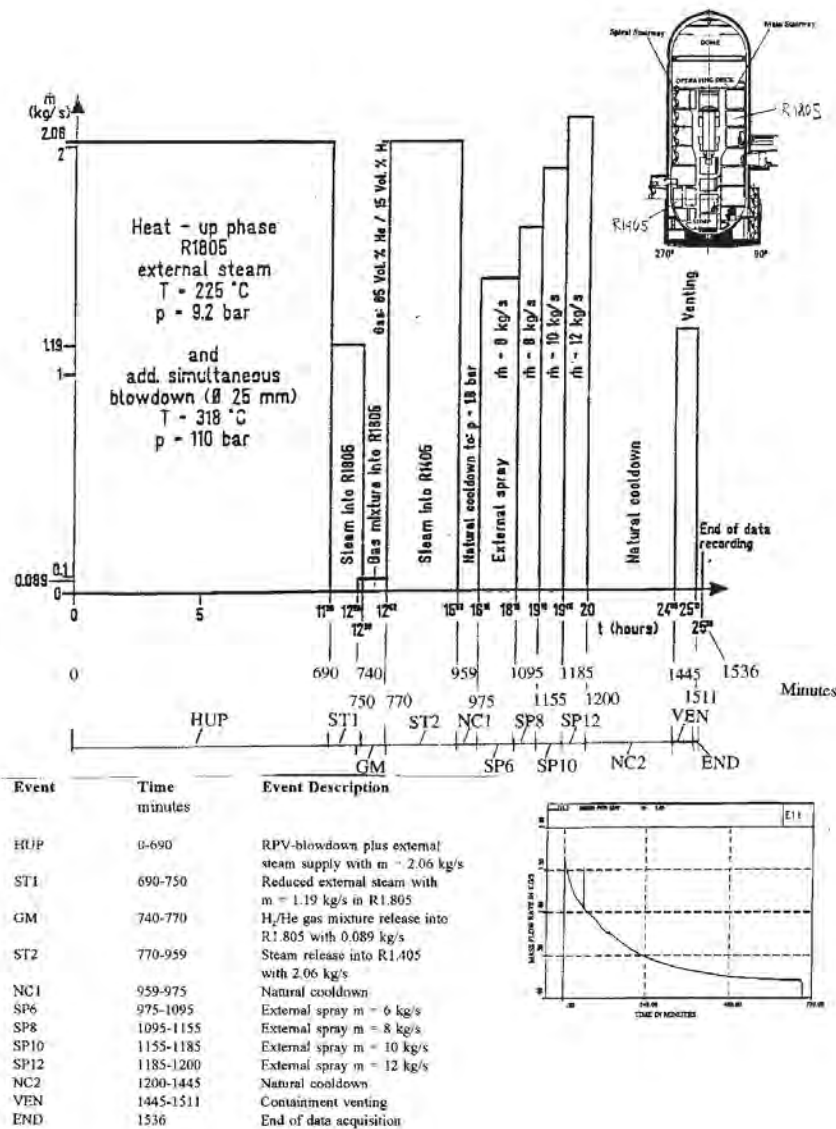


Figure 9.C-75. HDR-E11.2 Sequence of Experimental Test Procedures

(reprinted from: L. Wolf, K. Mun, J. Floyd, "HDR hydrogen mixing evaluation for containment safety evaluations" – Phase 1, University of Maryland at College Park, Final Report for DOE-Project Order Number: DE-AP07-95ID81401, July 1995)

9.C-130

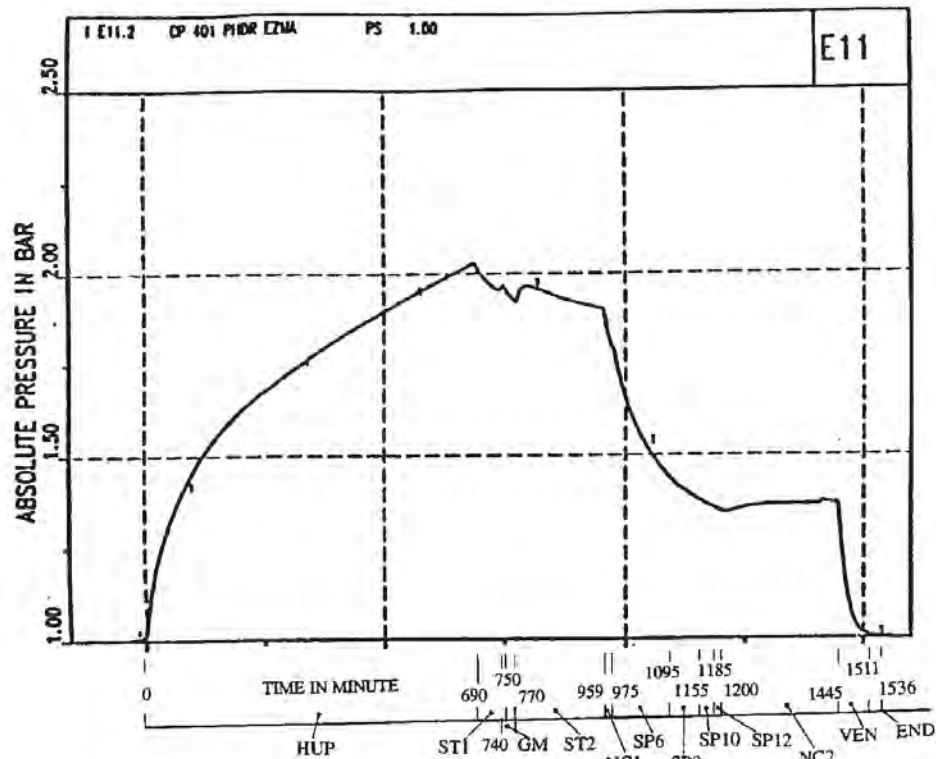


Figure 9.C-76. HDR-E11.2 Containment Pressure History

(reprinted from: L. Wolf, K. Mun, J. Floyd, "HDR hydrogen mixing evaluation for containment safety evaluations" – Phase 1, University of Maryland at College Park, Final Report for DOE-Project Order Number: DE-AP07-95ID81401, July 1995)

9.C-131

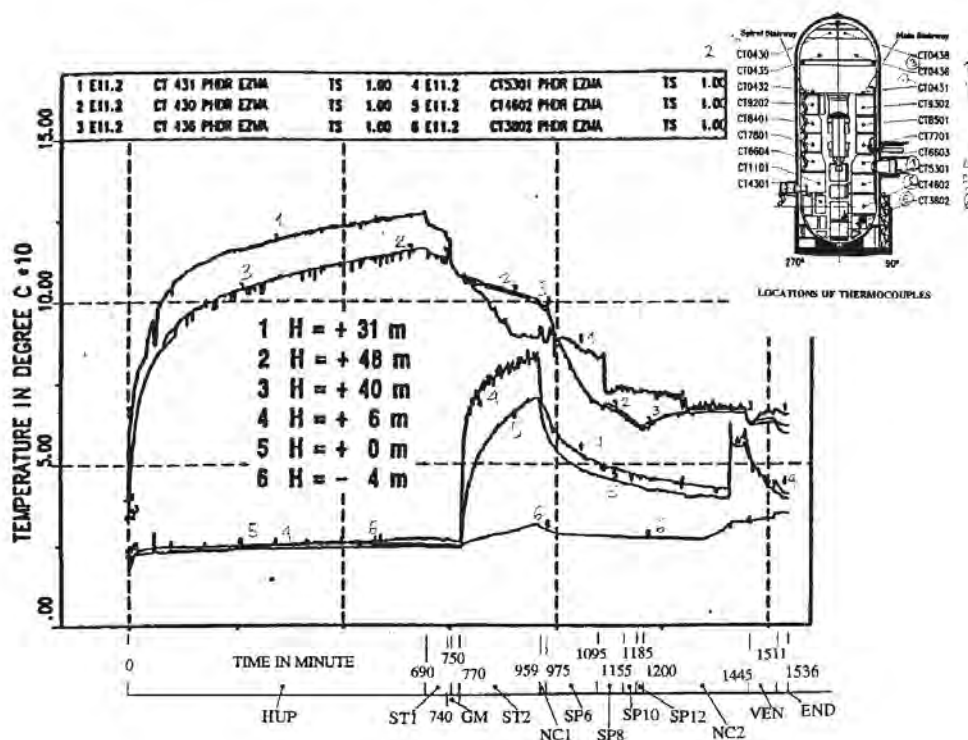


Figure 9.C-77. HDR-E11.2 Atmospheric Temperatures Along Main Stairway

(reprinted from: L. Wolf, K. Mun, J. Floyd, "HDR hydrogen mixing evaluation for containment safety evaluations" – Phase 1, University of Maryland at College Park, Final Report for DOE-Project Order Number: DE-AP07-95ID81401, July 1995)

9.C-132

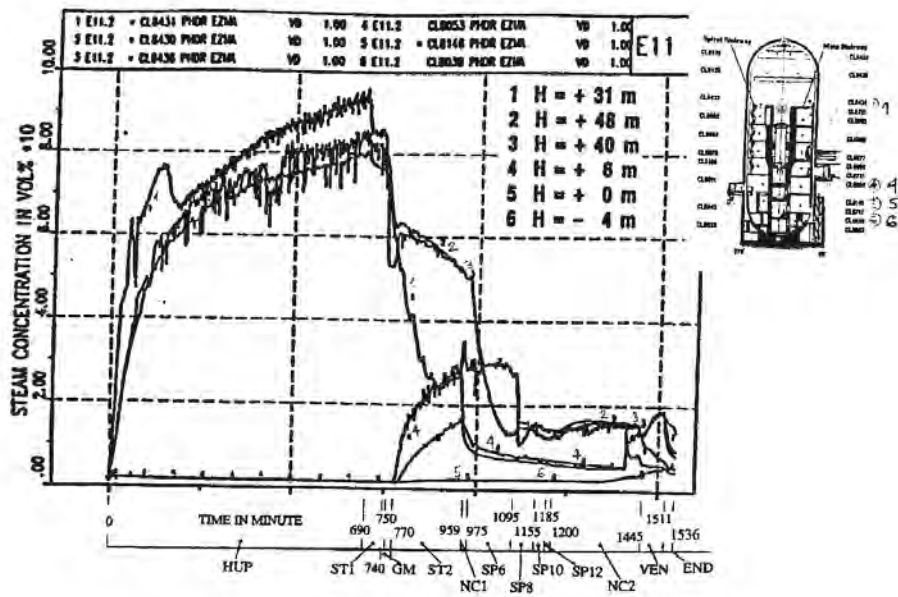


Figure 9.C-78. HDR-E11.2 Steam Concentrations Along Main Stairway

(reprinted from: L. Wolf, K. Mun, J. Floyd, "HDR hydrogen mixing evaluation for containment safety evaluations" – Phase 1, University of Maryland at College Park, Final Report for DOE-Project Order Number: DE-AP07-95ID81401, July 1995)

9.C-133

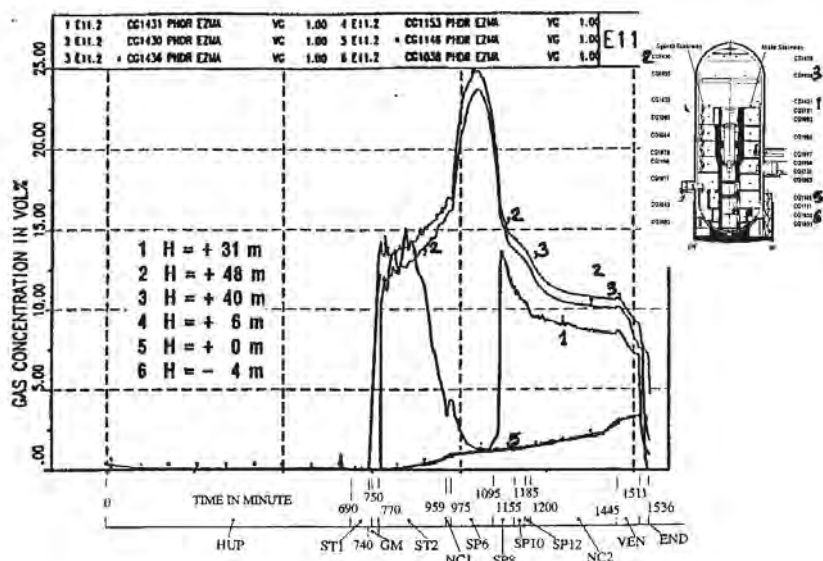


Figure 9.C-79. HDR-E11.2 H₂/He Gas Concentrations Along Main Stairway

(reprinted from: L. Wolf, K. Mun, J. Floyd, "HDR hydrogen mixing evaluation for containment safety evaluations" – Phase 1, University of Maryland at College Park, Final Report for DOE-Project Order Number: DE-AP07-95ID81401, July 1995)

9.C-134

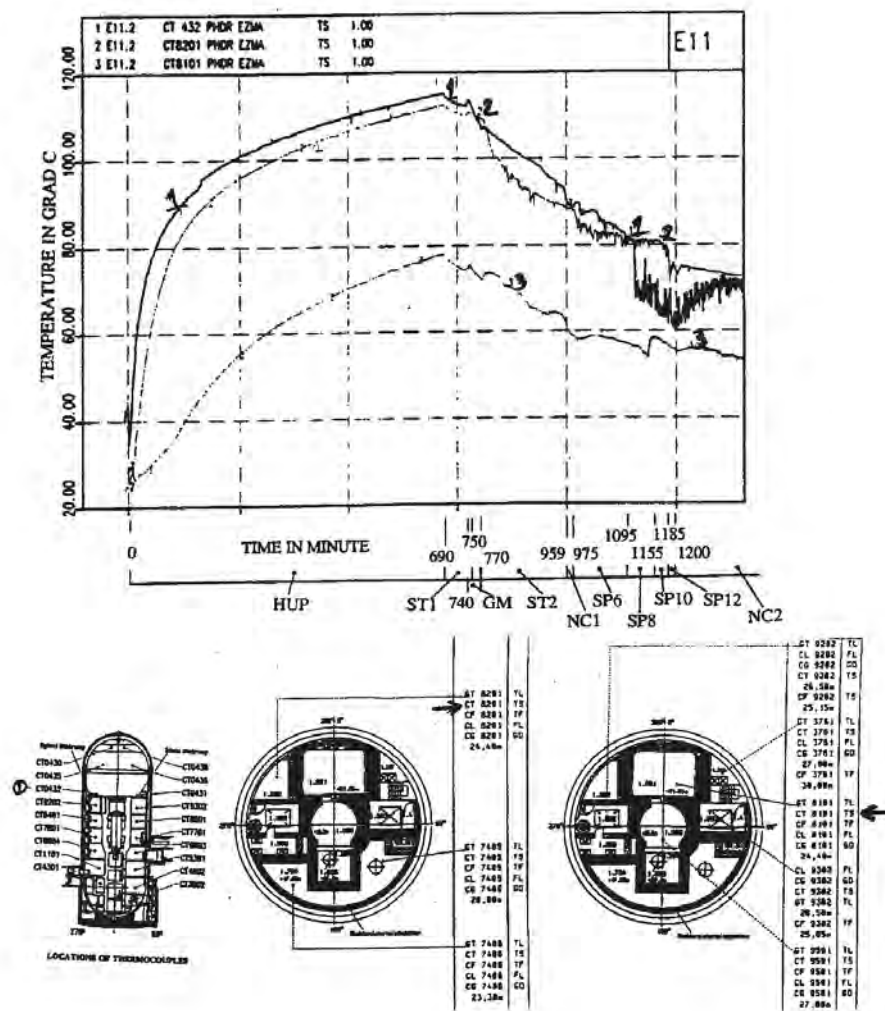


Figure 9.C-80. HDR-E11.2 Comparison Between Temperatures in Main and Spiral Stairways at +31.0 m Level

(reprinted from: L. Wolf, M. Gavrilas, K. Mun, "Overview of experimental results for long-term, Large-scale natural circulations in LWR-containments after large LOCAs," University of Maryland at College Park, Final Report for DOE – Project, Order Number: DE-AP07-96ID10765," July 1996)

9.C-135

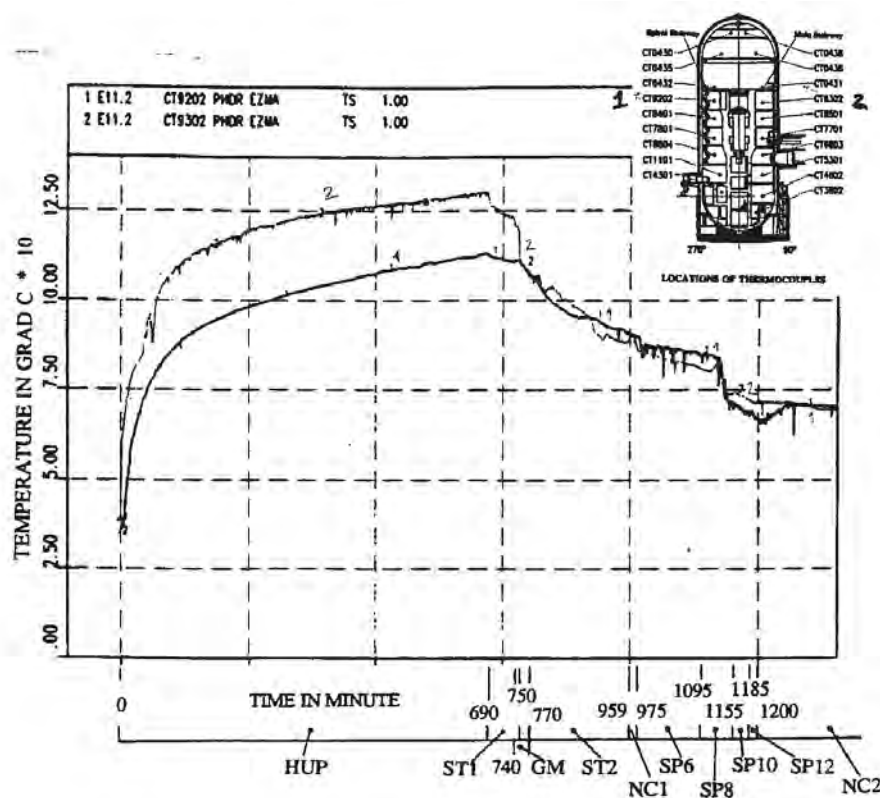


Figure 9.C-81. HDR-E11.2 Comparison Between Temperatures in Main and Spiral Stairways at +26.5 m Level

(reprinted from: L. Wolf, M. Gavrilas, K. Mun, "Overview of experimental results for long-term, Large-scale natural circulations in LWR-containments after large LOCAs," University of Maryland at College Park, Final Report for DOE – Project, Order Number: DE-AP07-96ID10765," July 1996)

9.C-136

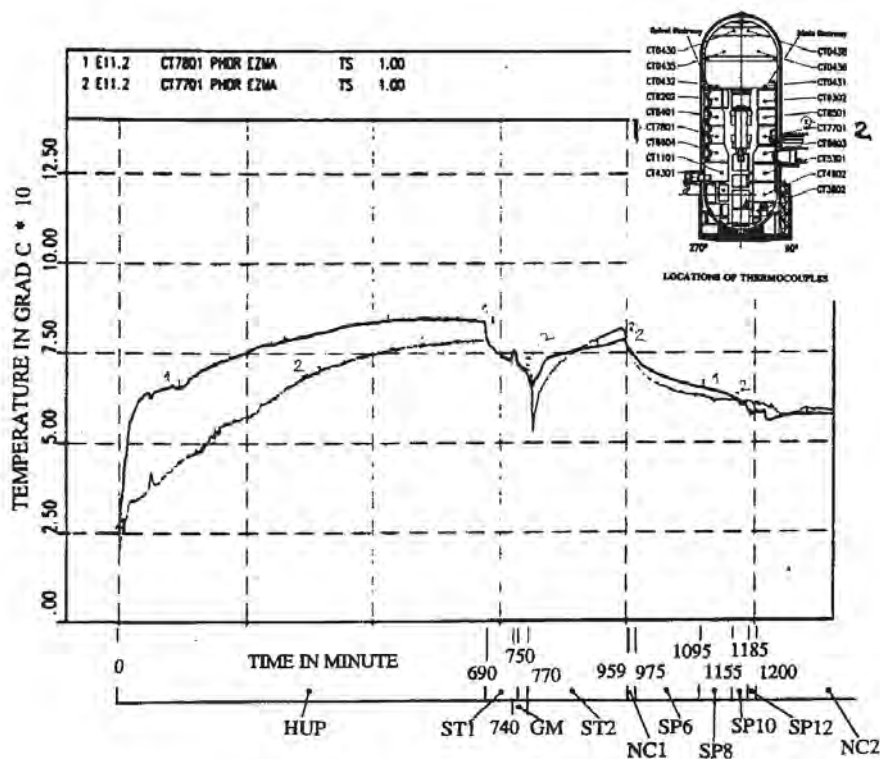


Figure 9.C-82. HDR-E11.2 Comparison Between Temperatures in Main and Spiral Stairways at +16.5 m Level

(reprinted from: L. Wolf, M. Gavrilas, K. Mun, "Overview of experimental results for long-term, Large-scale natural circulations in LWR-containments after large LOCAs," University of Maryland at College Park, Final Report for DOE – Project, Order Number: DE-AP07-96ID10765," July 1996)

9.C-137

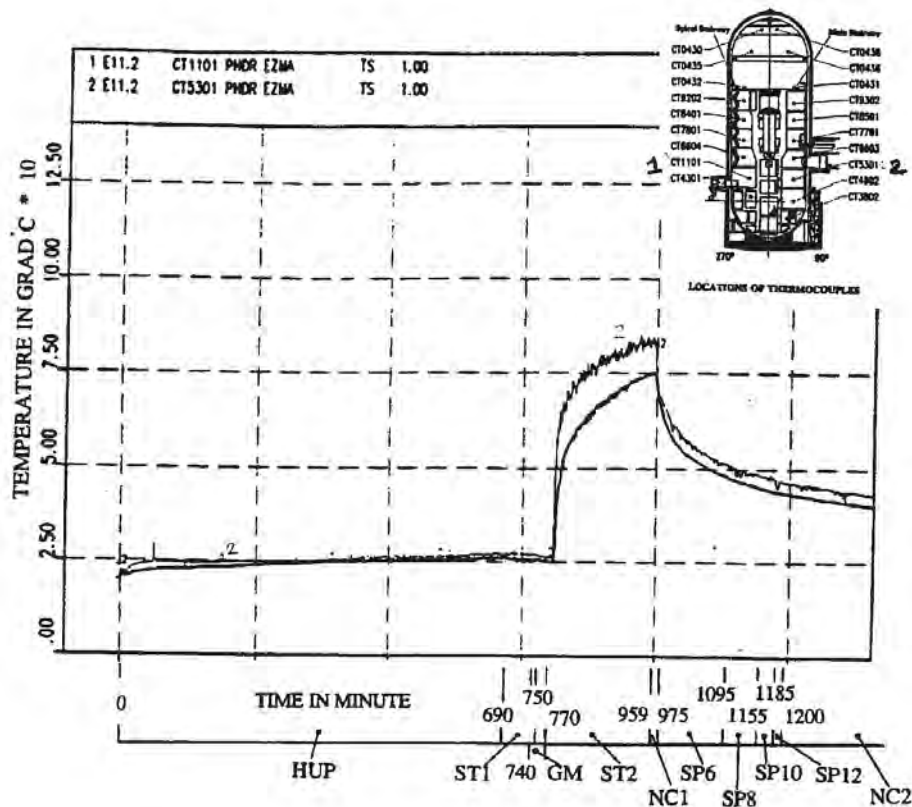


Figure 9.C-83. HDR-E11.2 Comparison Between Temperatures in Main and Spiral Stairways at +6 m Level

(reprinted from: L. Wolf, M. Gavrilas, K. Mun, "Overview of experimental results for long-term, Large-scale natural circulations in LWR-containments after large LOCAs," University of Maryland at College Park, Final Report for DOE – Project, Order Number: DE-AP07-96ID10765," July 1996)

9.C-138

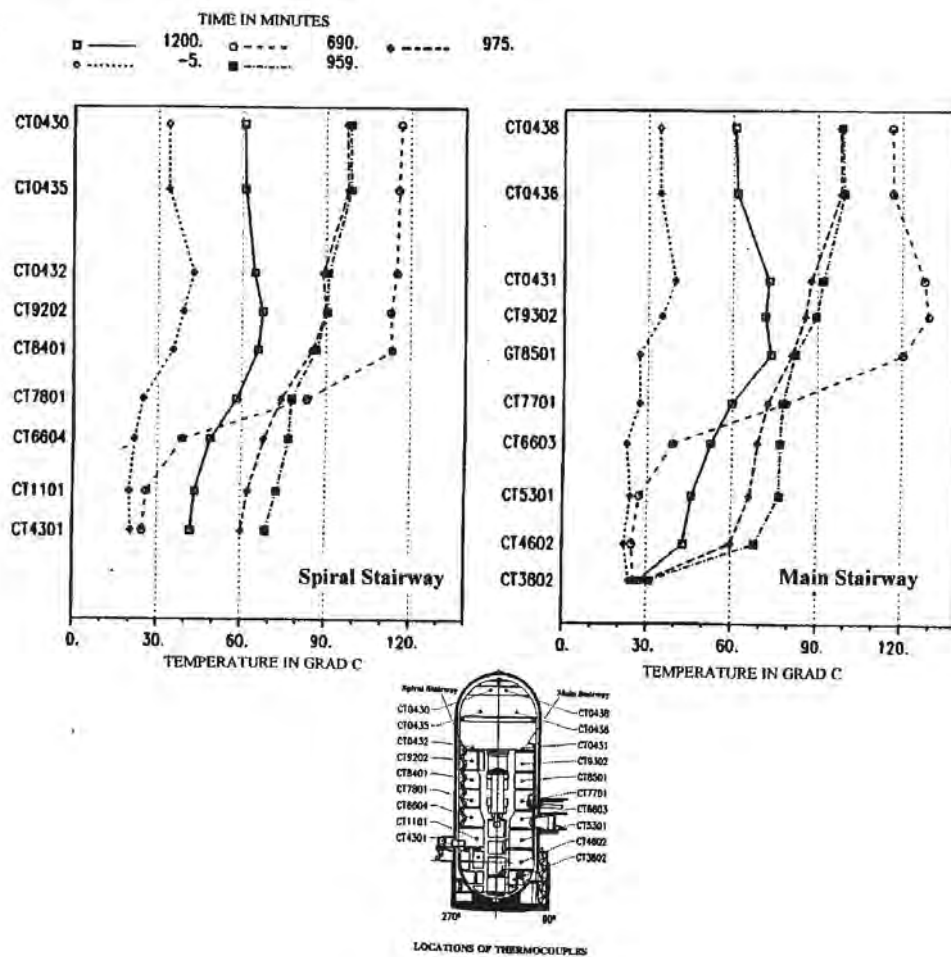


Figure 9.C-84. HDR-E11.2 Axial Temperature Profiles in Both Major Flow Paths at Specific Times, Left in Spiral Stairway, Right in Main Stairway

(reprinted from: L. Wolf, M. Gavrilas, K. Mun, "Overview of experimental results for long-term, Large-scale natural circulations in LWR-containments after large LOCAs," University of Maryland at College Park, Final Report for DOE – Project, Order Number: DE-AP07-96ID10765," July 1996)

9.C.2.4.1.4 Experiment E11.3

Experiment E11.3 includes a low-positioned small break and gas release, as well as a closed entrance to the spiral stairway at the upper-deck. Although detailed boundary conditions are not available in the literature, this case is included to qualitatively indicate the influence of the injection position on the formation of global circulation. Even with the main vertical flow path from the top of the spiral staircase to the dome closed, global circulation is generated through other horizontal connections between the compartments (see Figure 9.C-85 and Figure 9.C-86).

Temperature differences exist between the vertical axial flow channels during the heatup phase, the gas release phase, and the long cooldown period. The axial temperature profiles indicate that the temperature field was close to homogeneous with a ΔT of only 7°C, except for the region below the release, as indicated by CT8101 in Figure 9.C-87 (see Figure 9.C-87 to Figure 9.C-91).

9.C-140

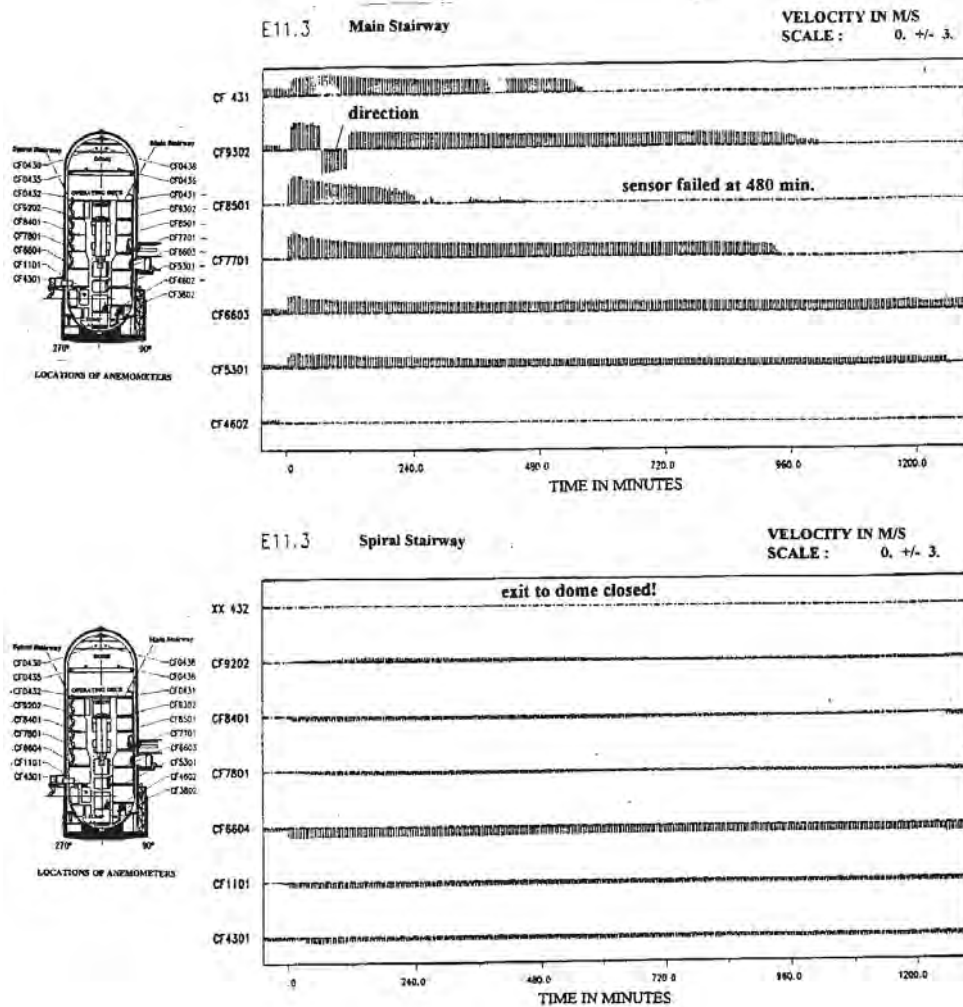


Figure 9.C-85. HDR-E11.3 Velocities in Both Major Flow Paths at Different Axial Positions During Containment Heatup

(reprinted from: L. Wolf, M. Gavrilas, K. Mun, "Overview of experimental results for long-term, Large-scale natural circulations in LWR-containments after large LOCAs," University of Maryland at College Park, Final Report for DOE – Project, Order Number: DE-AP07-96ID10765," July 1996)

9.C-141

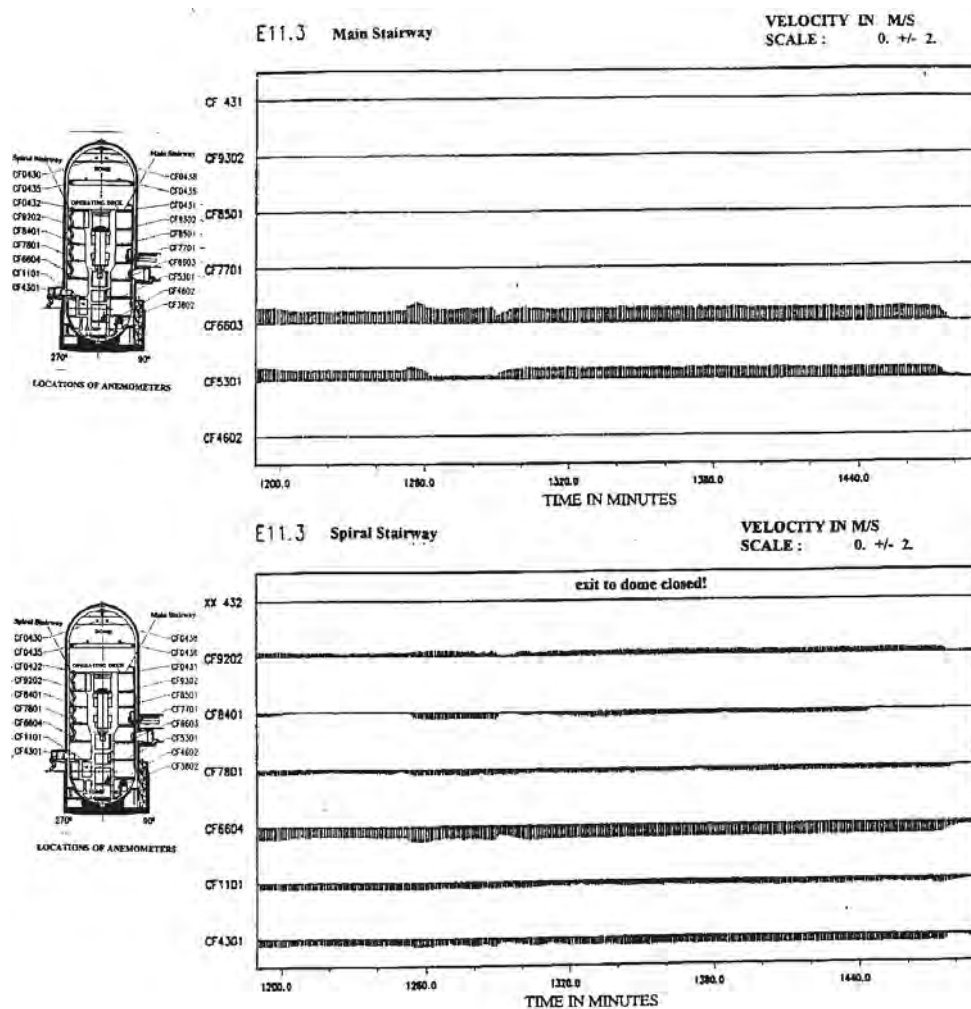


Figure 9.C-86. HDR-E11.3 Velocities in Both Major Flow Paths at Different Axial Positions During H_2/He Gas Mixture Release

(reprinted from: L. Wolf, M. Gavrilas, K. Mun, "Overview of experimental results for long-term, Large-scale natural circulations in LWR-containments after large LOCAs," University of Maryland at College Park, Final Report for DOE – Project, Order Number: DE-AP07-96ID10765," July 1996)

9.C-142

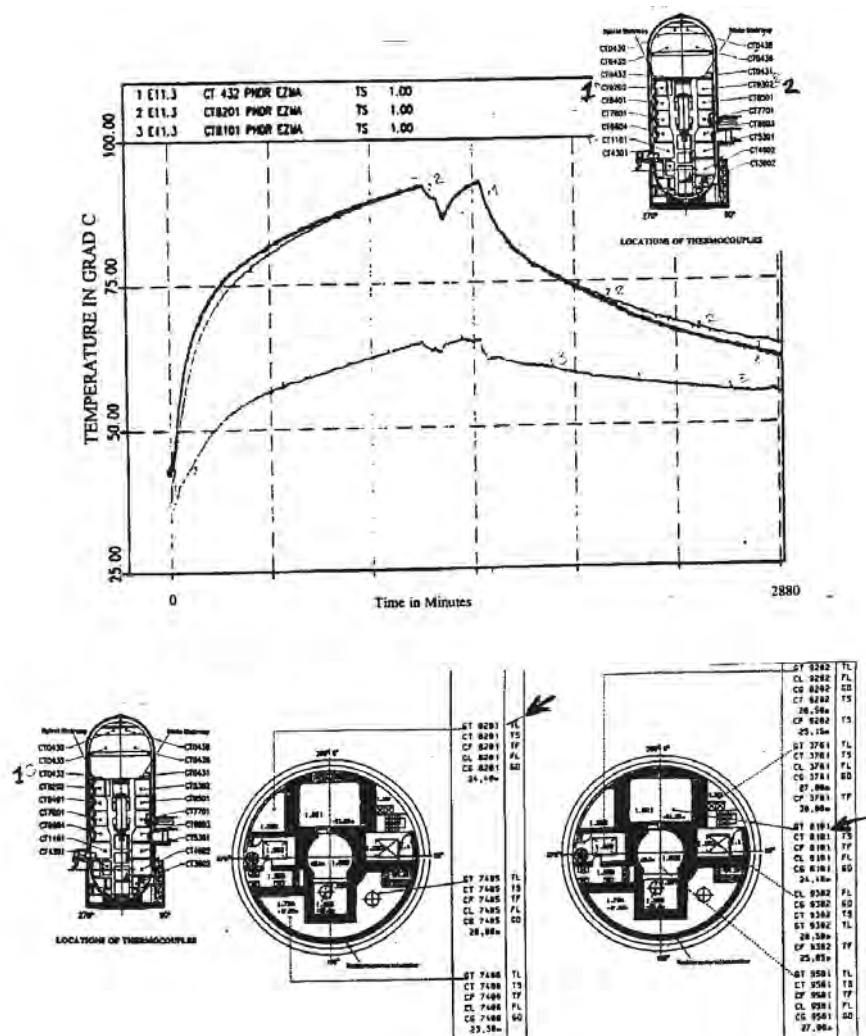


Figure 9.C-87. HDR-E11.3 Comparison Between Temperatures in Main and Spiral Stairways at +31.0 m Level

(reprinted from: L. Wolf, M. Gavrilas, K. Mun, "Overview of experimental results for long-term, Large-scale natural circulations in LWR-containments after large LOCAs," University of Maryland at College Park, Final Report for DOE – Project, Order Number: DE-AP07-96ID10765," July 1996)

9.C-143

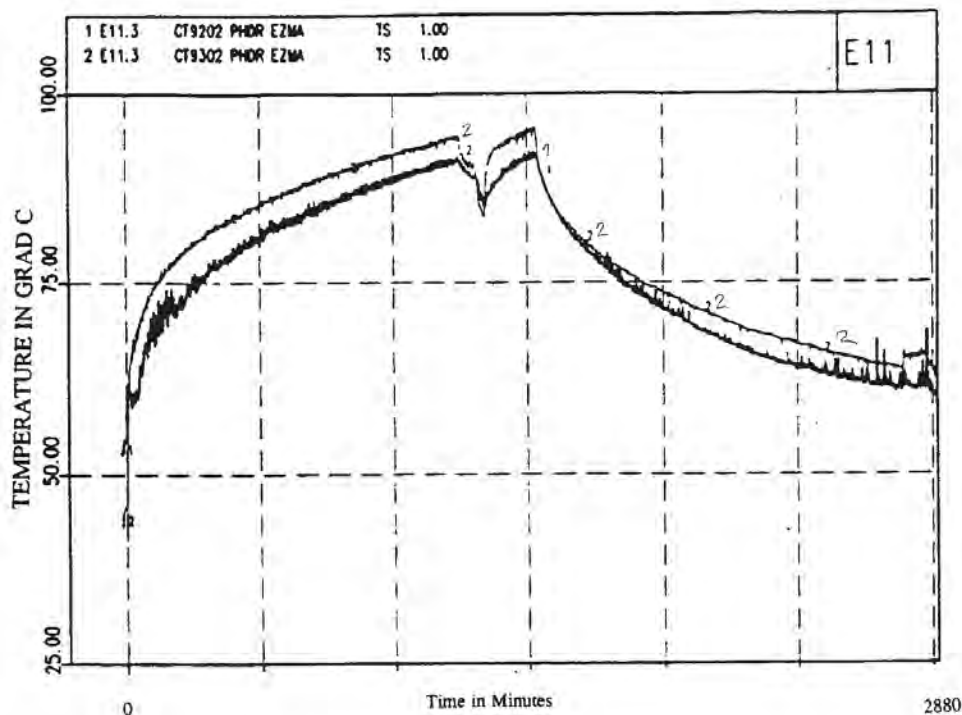


Figure 9.C-88. HDR-E11.3 Comparison Between Temperatures in Main and Spiral Stairways at +26.5 m Level

(reprinted from: L. Wolf, M. Gavrilas, K. Mun, "Overview of experimental results for long-term, Large-scale natural circulations in LWR-containments after large LOCAs," University of Maryland at College Park, Final Report for DOE – Project, Order Number: DE-AP07-96ID10765," July 1996)

9.C-144

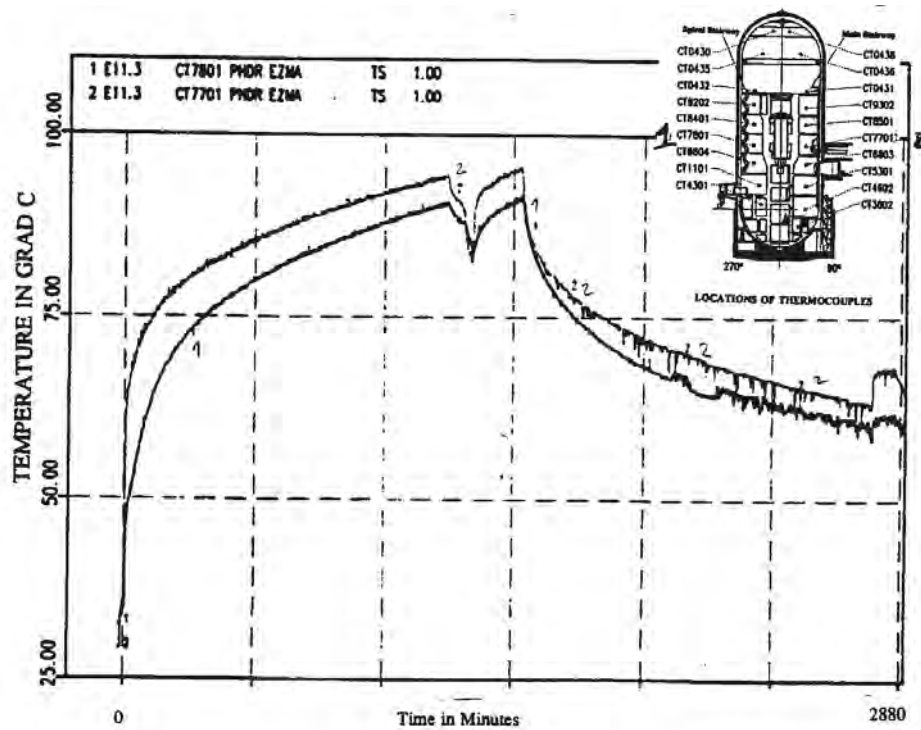


Figure 9.C-89. HDR-E11.3 Comparison Between Temperatures in Main and Spiral Stairways at +16.5 m Level

(reprinted from: L. Wolf, M. Gavrilas, K. Mun, "Overview of experimental results for long-term, Large-scale natural circulations in LWR-containments after large LOCAs," University of Maryland at College Park, Final Report for DOE – Project, Order Number: DE-AP07-96ID10765," July 1996)

9.C-145

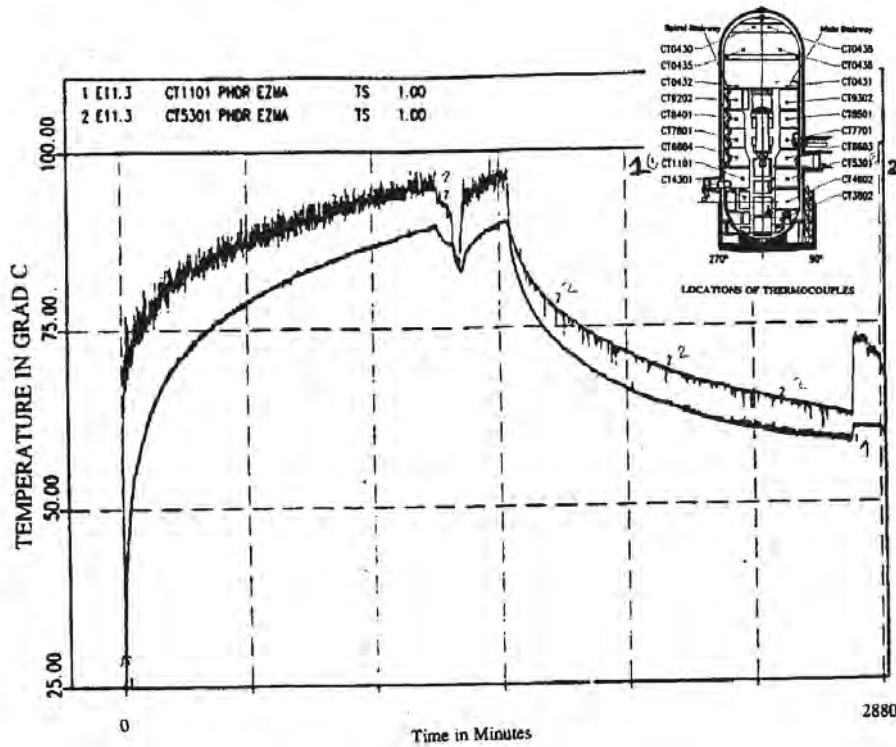


Figure 9.C-90. HDR-E11.3 Comparison Between Temperatures in Main and Spiral Stairwars at +6 m Level

(reprinted from: L. Wolf, M. Gavrilas, K. Mun, "Overview of experimental results for long-term, Large-scale natural circulations in LWR-containments after large LOCAs," University of Maryland at College Park, Final Report for DOE – Project, Order Number: DE-AP07-96ID10765," July 1996)

9.C-146

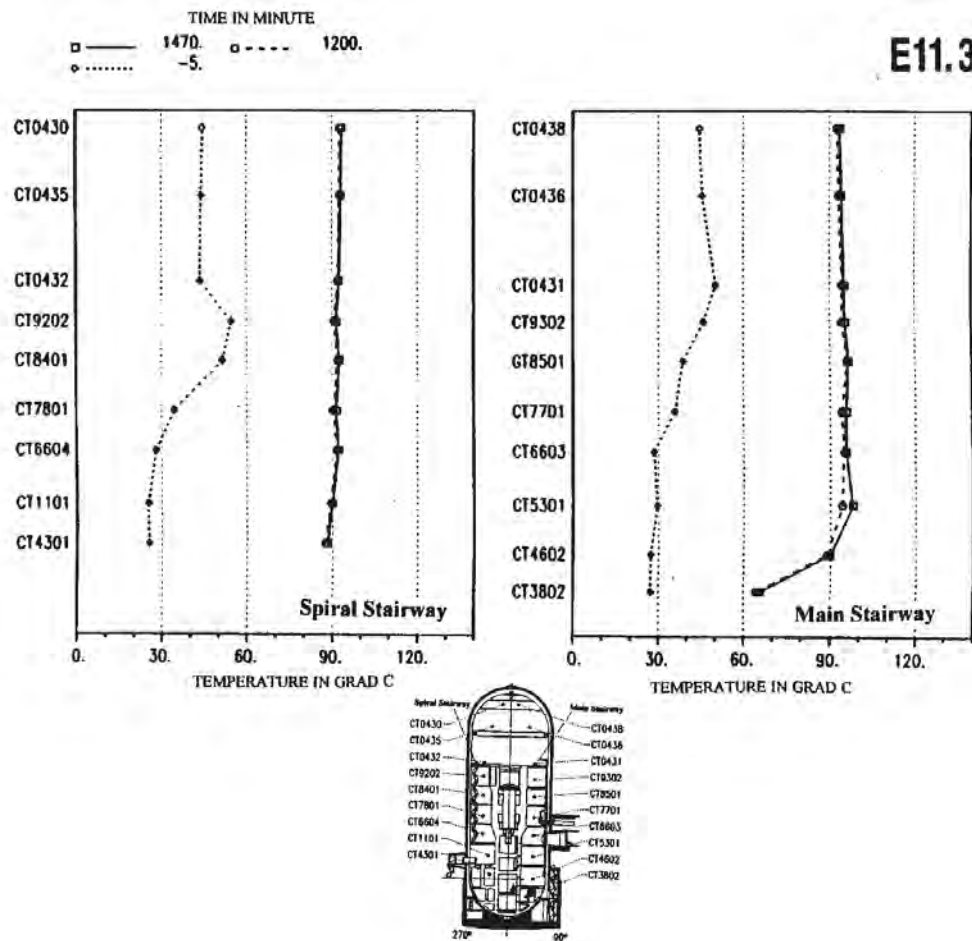


Figure 9.C-91. HDR-E11.3 Axial Temperature Profiles in Both Major Flow Paths at Specific Times, Left in Spiral Stairway, Right in Main Stairway

(reprinted from: L. Wolf, M. Gavrilas, K. Mun, "Overview of experimental results for long-term, Large-scale natural circulations in LWR-containments after large LOCAs," University of Maryland at College Park, Final Report for DOE – Project, Order Number: DE-AP07-96ID10765," July 1996)

9.C.2.4.1.5 Experiment E11.4

Experiment E11.4 includes a low-positioned break and an active external spray. The spiral stairway entrance to the dome is open. A detailed presentation of this experiment is given by Wolf, Mun, Floyd, 1995. Data from this test is used to validate various numerical containment codes (Wolf et al., 1994, Pisa and Holzbauer and Wolf, 1994, Pisa).

Figure 9.C-92 and Table 9.C-5 present the experimental procedure. This includes the duration of heatup and blowdown of steam ($p=110$ bar and $T=318^{\circ}\text{C}$ in the compartment R1405, (see Figure 9.C-74 and Figure 9.C-92) and the consecutive steam and gas injections.

The containment pressure history is shown in Figure 9.C-93. This figure shows the effects of the external spray application (after 2800 minutes) on the decrease of the containment pressure (by 0.25 bar).

Temperatures at the various axial positions in the main staircase are presented in Figure 9.C-94. Note that the shapes of the temperature curves for various levels are similar, but the values are different. Global circulation is indicated by the small temperature differences from the top to the bottom of the dome, $\Delta T=2\text{-}6^{\circ}\text{C}$, and from the dome to the sump, $\Delta T=10\text{-}26^{\circ}\text{C}$. Figure 9.C-95 and Figure 9.C-96 provide steam and gas concentration histories for the various levels in the main staircase.

During all phases of the experiment, temperature differences exist between the two vertical channels (main and spiral staircases) enabling the global circulation (see Figure 9.C-97 – Figure 9.C-100). The temperature differences decrease during the cooldown phase. As in experiment E11.3, the axial temperature distribution indicates a nearly uniform temperature profile, except below the release point (see Figure 9.C-101).

During the E11.4 test, the release into the lower-level compartment promotes global circulation and homogenizes the containment atmosphere. In addition, the application of the external sprays causes a decrease in the containment pressure (see Figure 9.C-93) and a reduction in the axial temperature gradient (see Figure 9.C-94, curves 1-6). The external spray also promotes a more uniform gas concentration (see Figure 9.C-96 from 2800 to 3000 minutes).

9.C-148

Table 9.C-5. Events for E11.4 Experiment

Event	Time (minutes)	Event Description
HUP	0-2040	RPV-blowdown plus external steam supply with $m = 2.06 \text{ kg/s}$
ST1	2040-2100	Reduced external steam with $m = 1.19 \text{ kg/s}$ in R1.405
GM1	2090-2100	H_2/He gas mixture release into R1.405 with 0.089 kg/s
ST2	2120-2180	Steam release into R1.405 with 2.06 kg/s
DH	2180-2550	Dry heat addition into R1.308
GM2	2193-2195	H_2/He gas mixture release into R1.405 with 0.2 kg/s
GM3	2195-2205	H_2/He gas mixture release into R1.405 with 0.089 kg/s
ST3	2205-2505	Start of steam release into R1.405 with $m = 1.19 \text{ kg/s}$
ST4	2550-2620	Steam release into R1.405 with $m = 2.06 \text{ kg/s}$
SUB	2620-2800	Sump boiling
NC1	2800-2805	Natural cooldown
SP6	2805-2925	External spray $m = 6 \text{ kg/s}$
SP8	2925-2985	External spray $m = 8 \text{ kg/s}$
SP10	2985-3015	External spray $m = 10 \text{ kg/s}$
SP12	3015-3016	External spray $m = 12 \text{ kg/s}$
NC2	3016-3229	Natural cooldown
VEN	3229-3300	Containment venting
END	3360	End of data acquisition

(reprinted from L. Wolf, M. Gavrilas, K. Mun, "Overview of experimental results for long-term, large-scale natural circulations in LWR-containments after large LOCAS," University of Maryland at College Park, Final Report for DOE – Project, Order Number: DE-AP07-96ID10765")

9.C-149

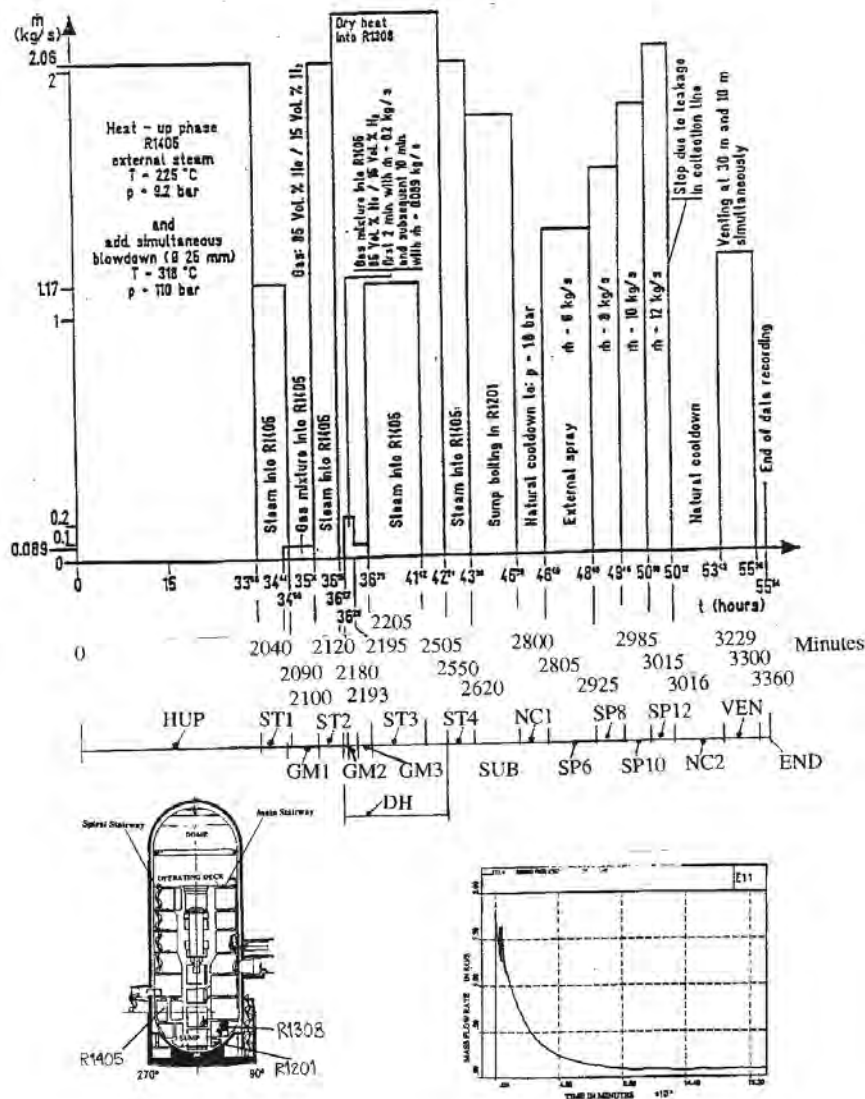


Figure 9.C-92. HDR-E11.4 Sequence of Experimental Test Procedures

(reprinted from: L. Wolf, K. Mun, J. Floyd, "HDR hydrogen mixing evaluation for containment safety evaluations" – Phase 1, University of Maryland at College Park, Final Report for DOE-Project Order Number: DE-AP07-95ID81401, July 1995)

9.C-150

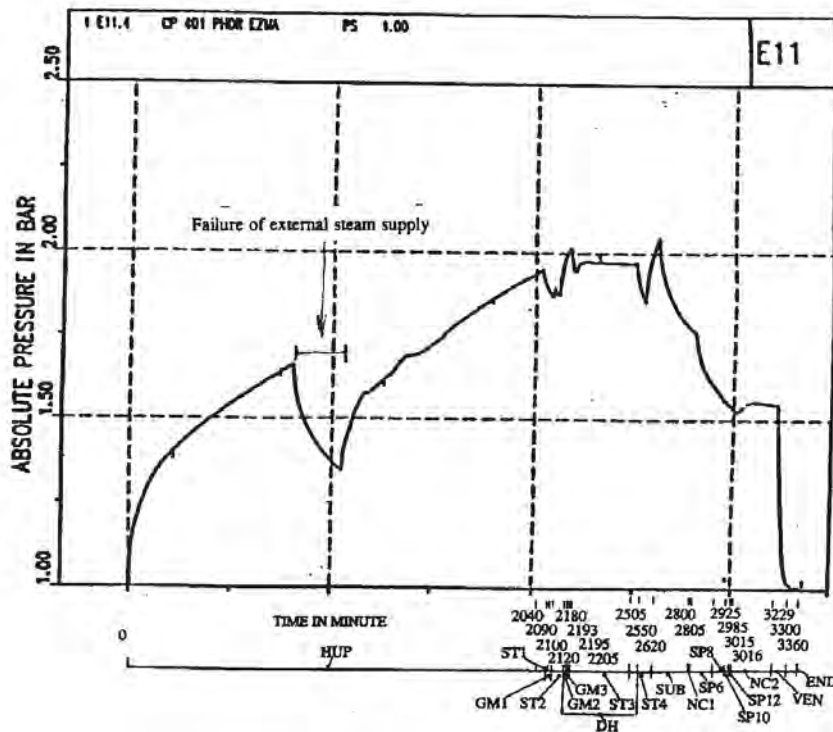


Figure 9.C-93. HDR-E11.4 Containment Pressure History

(reprinted from: L. Wolf, K. Mun, J. Floyd, "HDR hydrogen mixing evaluation for containment safety evaluations" – Phase 1, University of Maryland at College Park, Final Report for DOE-Project Order Number: DE-AP07-95ID81401, July 1995)

9.C-151

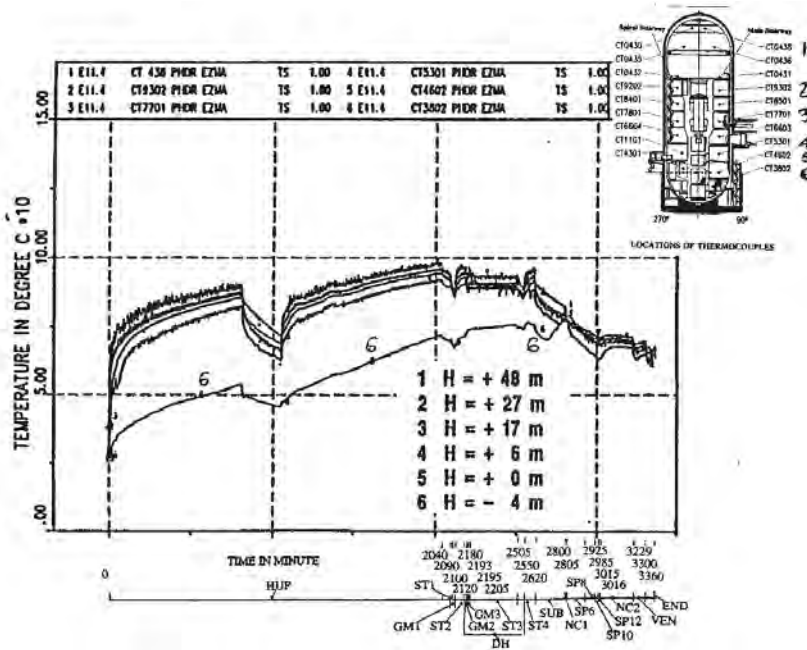


Figure 9.C-94. HDR-E11.4 Atmospheric Temperatures Along Main Stairway

(reprinted from: L. Wolf, K. Mun, J. Floyd, "HDR hydrogen mixing evaluation for containment safety evaluations" – Phase 1, University of Maryland at College Park, Final Report for DOE-Project Order Number: DE-AP07-95ID81401, July 1995)

9.C-152

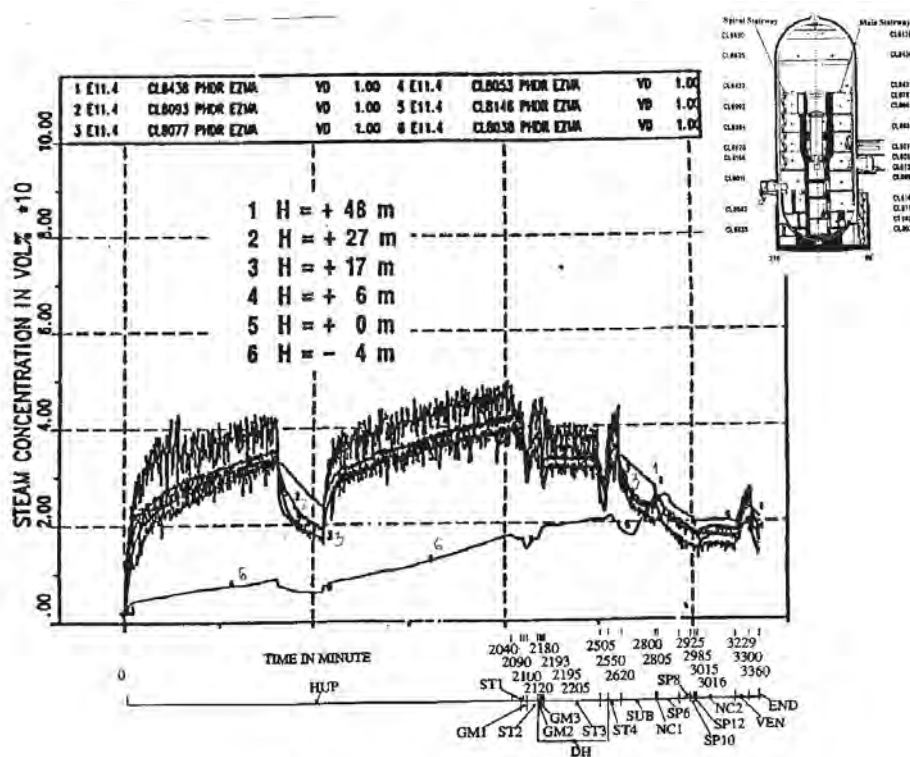


Figure 9.C-95. HDR-E11.4 Steam Concentration Along Main Stairway

(reprinted from: L. Wolf, K. Mun, J. Floyd, "HDR hydrogen mixing evaluation for containment safety evaluations" – Phase 1, University of Maryland at College Park, Final Report for DOE-Project Order Number: DE-AP07-95ID81401, July 1995)

9.C-153

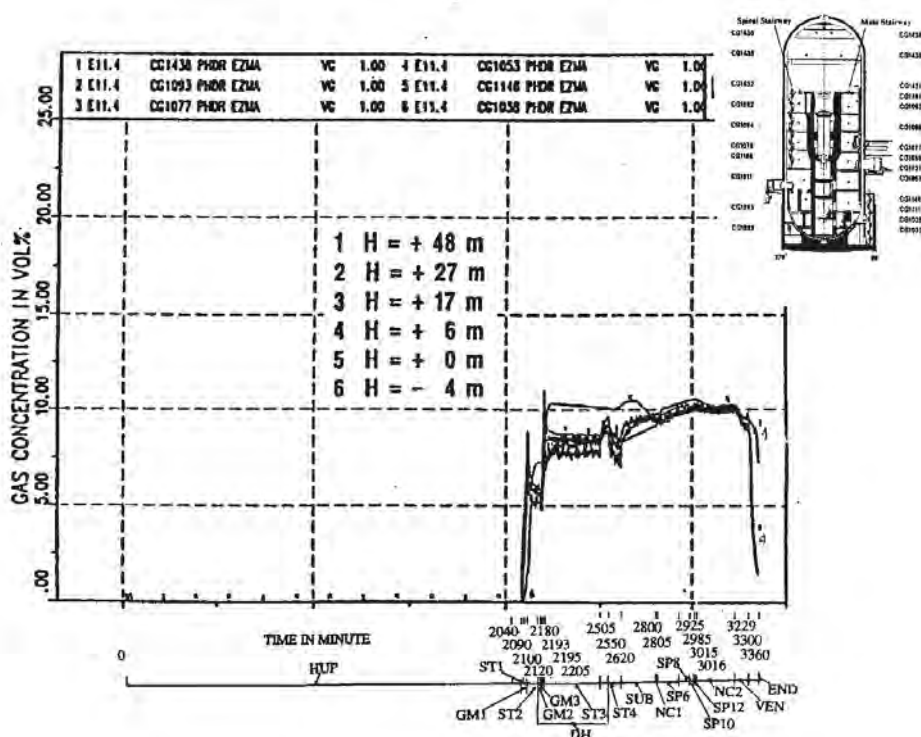


Figure 9.C-96. HDR-E11.4 H2/He Gas Concentrations Along Main Stairway

(reprinted from: L. Wolf, K. Mun, J. Floyd, "HDR hydrogen mixing evaluation for containment safety evaluations" – Phase 1, University of Maryland at College Park, Final Report for DOE-Project Order Number: DE-AP07-95ID81401, July 1995)

9.C-154

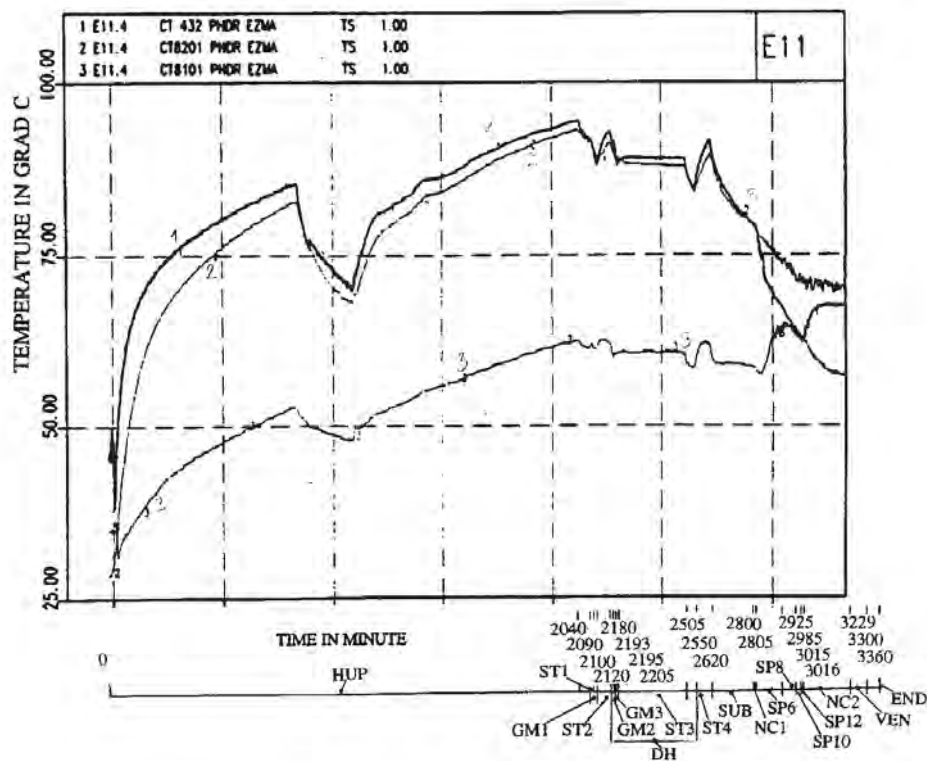


Figure 9.C-97a. HDR-E11.4 Comparison Between Temperatures in Main and Spiral Stairways at +31.0 m Level

(reprinted from: L. Wolf, M. Gavrilas, K. Mun, "Overview of experimental results for long-term, Large-scale natural circulations in LWR-containments after large LOCAs," University of Maryland at College Park, Final Report for DOE – Project, Order Number: DE-AP07-96ID10765," July 1996)

9.C-155

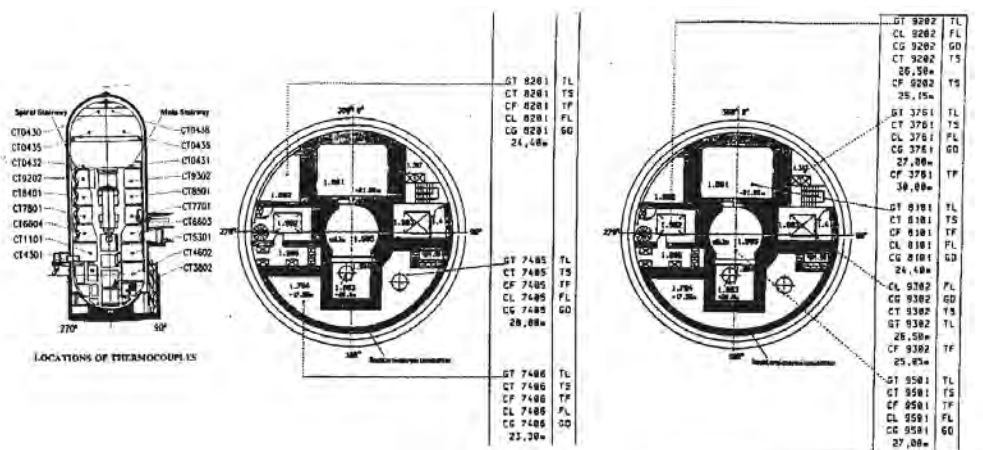


Figure 9.C-97b. HDR-E11.4 Comparison Between Temperatures in Main and Spiral Stairways at +31.0 m Level

(reprinted from: L. Wolf, M. Gavrilas, K. Mun, "Overview of experimental results for long-term, Large-scale natural circulations in LWR-containments after large LOCAs," University of Maryland at College Park, Final Report for DOE – Project, Order Number: DE-AP07-96ID10765," July 1996)

9.C-156

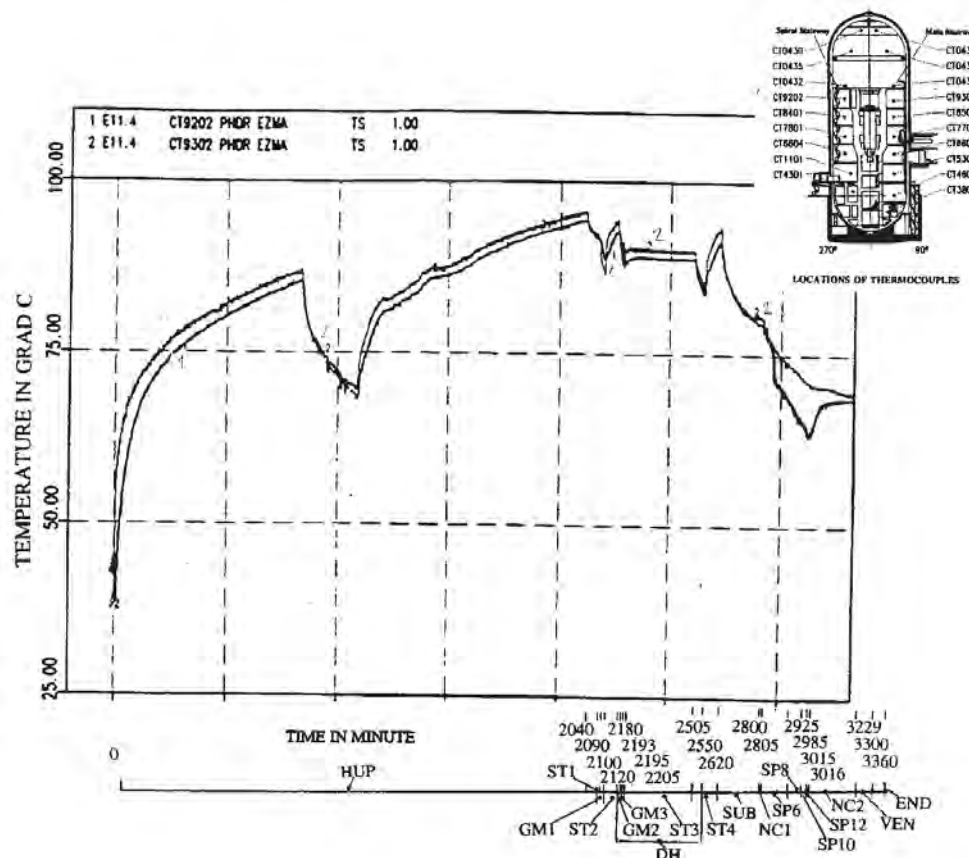


Figure 9.C-98. HDR-E11.4 Comparison Between Temperatures in Main and Spiral Stairways at +26.5 m Level

(reprinted from: L. Wolf, M. Gavrilas, K. Mun, "Overview of experimental results for long-term, Large-scale natural circulations in LWR-containments after large LOCAs," University of Maryland at College Park, Final Report for DOE – Project, Order Number: DE-AP07-96ID10765," July 1996)

9.C-157

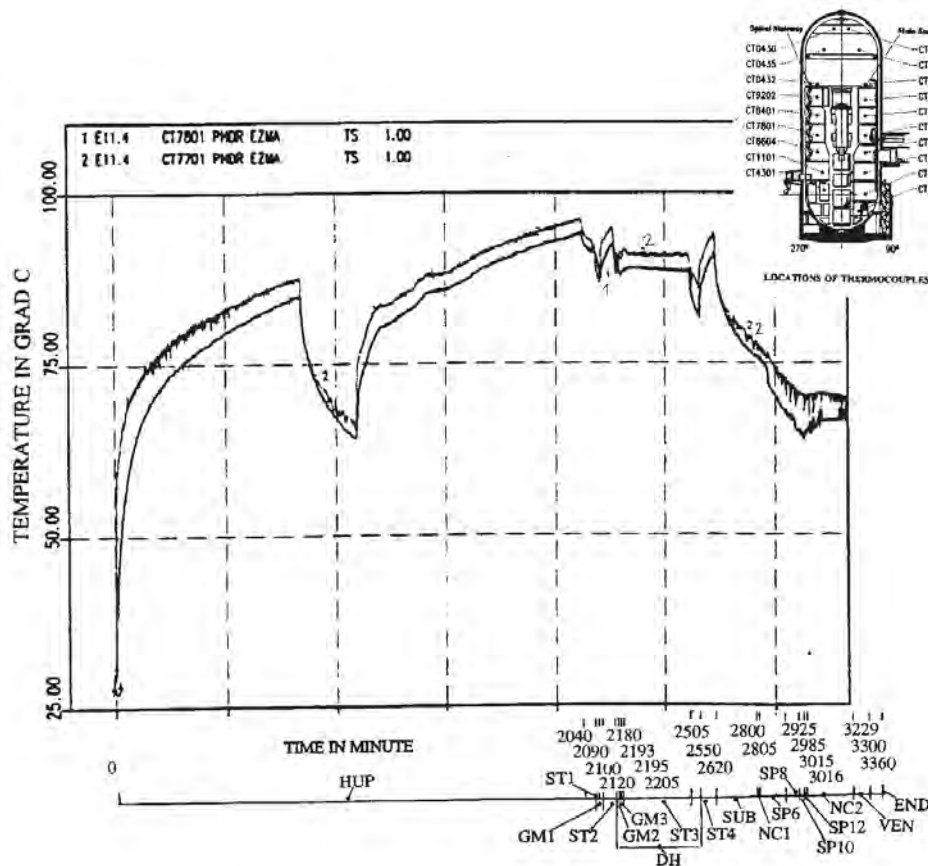


Figure 9.C-99. HDR-E11.4 Comparison Between Temperatures in Main and Spiral Stairways at +16.5 m Level

(reprinted from: L. Wolf, M. Gavrilas, K. Mun, "Overview of experimental results for long-term, Large-scale natural circulations in LWR-containments after large LOCAs," University of Maryland at College Park, Final Report for DOE – Project, Order Number: DE-AP07-96ID10765," July 1996)

9.C-158

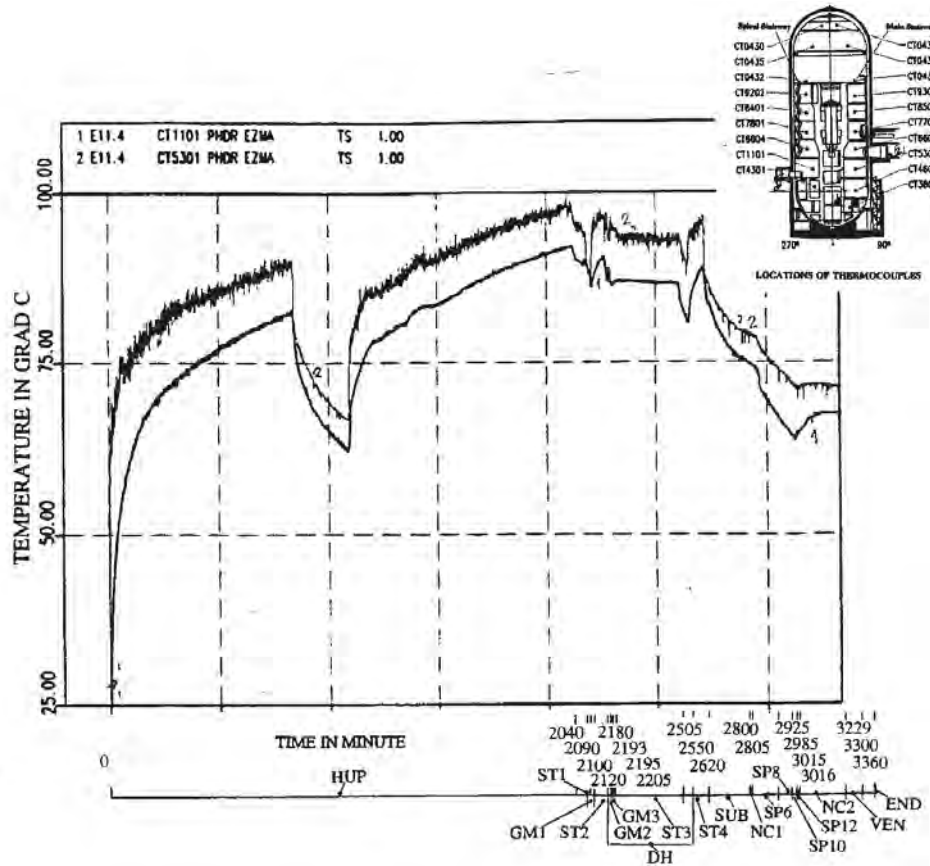


Figure 9.C-100. HDR-E11.4 Comparison Between Temperatures in Main and Spiral Stairways at +6 m Level

(reprinted from: L. Wolf, M. Gavrilas, K. Mun, "Overview of experimental results for long-term, Large-scale natural circulations in LWR-containments after large LOCAs," University of Maryland at College Park, Final Report for DOE – Project, Order Number: DE-AP07-96ID10765," July 1996)

9.C-159

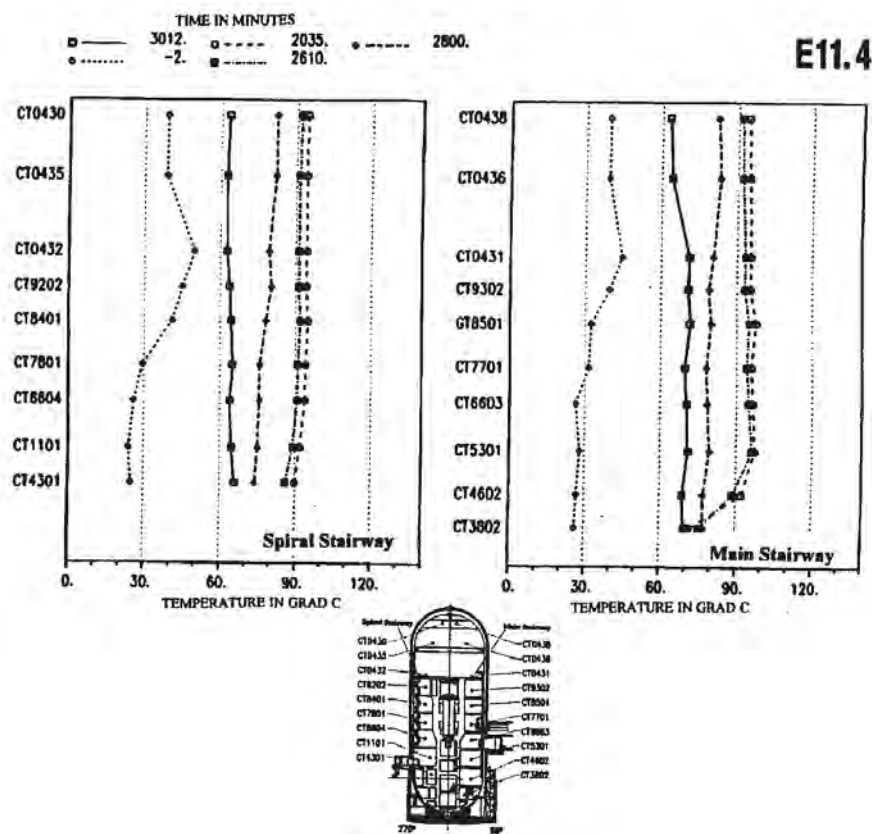


Figure 9.C-101. HDR-E11.4 Axial Temperature Profiles in Both Major Flow Paths at Specific Times, Left in Spiral Stairway, Right in Main Stairway

(reprinted from: L. Wolf, M. Gavrilas, K. Mun, "Overview of experimental results for long-term, Large-scale natural circulations in LWR-containments after large LOCAs," University of Maryland at College Park, Final Report for DOE – Project, Order Number: DE-AP07-96ID10765," July 1996)

9.C-160

9.C.2.4.1.6 Experiment E11.5

Experiment E11.5 includes a large-break LOCA at a low position, with subsequent small-break releases. The temperature differences between the vertical flow channels is large enough to obtain global natural circulation. The temperature difference changes sign at some axial positions during some phases.

A more detailed presentation of the E11.5 results will be given in the next chapter, together with the presentation of the other experiments related to large break LOCA.

Conclusions from the HDR E11 Test Series

Wolf, et al., 1996, concludes that global natural circulation patterns are established in all E11 experiments, despite the different release positions, the applications of internal and external sprays, and the changes to the flow path geometries. Also, an almost homogeneous temperature field is generated for the low position of the release points (experiments E11.3, E11.4 and E11.5). Higher release positions generated stratified temperature fields.

9.C.2.4.2 HDR Large LOCA Experimental Data Base

Experimental results for long-term, large-scale natural circulation in containments after large LOCAs presented by Wolf and Mun, 1996. An assessment of experiments T31.5, V21.1, V43, and E11.5 is provided.

Experiment T31.5 simulates a design basis large LOCA and hydrogen release in the upper section of the containment. Experiment V21.1 simulates a design basis large LOCA in the middle section of the containment, while experiment E11.5 simulates the release of steam and hydrogen in the lowest containment section. Experiment V21.1 is a subcooled blowdown, while all others use steam.

The influence of the break and hydrogen release locations on the containment atmosphere is established by comparing the results of these tests.

9.C.2.4.2.1 Experiment T31.5

The results of containment experiment T31.5 performed by Valencia, 1987 and Wenzel et al., 1987 are reported by Wolf and Valencia, 1988 and 1989. Experiment T31.5 includes a short-term, superheated steam blowdown followed by a long-term, low steam release rate and a H₂/He gas mixture injection. The short-term steam mass flow release into the room 1704 of the HDR-containment takes 25 seconds (with the approximate average flow rate of 1200 kg/s – see Figure 9.C-102). Room 1704 is at elevation 17.55-25.3 m in the upper section of the containment, near the spiral staircase (see Figure 9.C-73 and Figure 9.C-102). The large break position is at +22.3 m (about 8 m bellow the upper deck) and the blowdown pipe is pointing upward.

From 21 to 36 minutes, steam is released at an average mass flow rate 2.3 kg/s (see Figure 9.C-103). From 36 to 48 minutes, an H₂/He gas mixture is released into the containment with an approximate average mass flow rate of 0.24 kg/s (see Fig. 9.C-2-80). All the releases can be considered as steam blowdowns into a high-positioned compartment in the containment.

9.C-161

The containment pressure, temperature, hydrogen concentration, and velocities histories over 20 hours are presented in Figure 9.C-104 – Figure 9.C-108. The two pressure peaks correspond to the periods of steam injections (see Figure 9.C-104).

Temperature histories at various axial positions are presented in Figure 9.C-105. The axial temperature distribution is uniform above the break position, with the exception of local temperatures measuring the break plume. A linearly decreasing temperature (stratification) is present below the break position. The vertical temperature gradient decreases with time due to the global natural circulation, which develops both above and below the break location. The major vertical flow paths are through-compartments in the main and spiral staircases, where small temperature differences of about 5°C exist at equal heights. Horizontal connections exist at discrete elevations to provide circulation between the vertical flow paths.

The measured hydrogen concentration distributions at various times are presented in Figure 9.C-106. The H₂/He gas mixture concentration increases to a maximum value (13 percent volume, see Figure 9.C-107) in the regions above the release position. This concentration remains uniform over several hours in the upper portion of the dome (above 35 m – see Figure 9.C-107), while in the lower positions (34, 31, and 25m) it decreases after reaching maximum values. At the highest position of the dome (49 m), the decrease in the mixture concentration starts about 300 minutes after the start of the experiment and continues until about 360 minutes. After 360 minutes, the concentration above 12 m is a uniform mixture concentration of 10 percent vol. The steady-state profile of the mixture concentration is reached after 900 minutes.

For the first 12 minutes, upward and downward flows are present in the spiral and main staircases, respectively. The measured velocities are presented in Figure 9.C-108a and Figure 9.C-108b. The velocities are recorded again after the start of the steam injection (after 21 minute). Staircase flow starts again at approximately 200 minutes, at the same time that the mixture concentration in the upper portion of the containment starts to decrease. It then decreases again around 350 minutes, when upper region reaches a uniform concentration.

Interpretation of Data

Even for the case of the high release point with an initially stratified distribution, the final gas concentration through most of the containment is nearly homogenized due to the global natural circulation effects. Only a small, steady stratification gradient exists (about 1°C over the height of dome, about 18°C over 25 m below the break, gradient of about 7.5 to 8.8 percent H₂/He over the height of dome).

Applicability to the AP600 and AP1000

Since the AP600 and **AP1000** have significant cooling over the containment dome (which somewhat corresponds to the HDR dome region), additional driving forces for circulation above the operating deck exist.

9.C-162

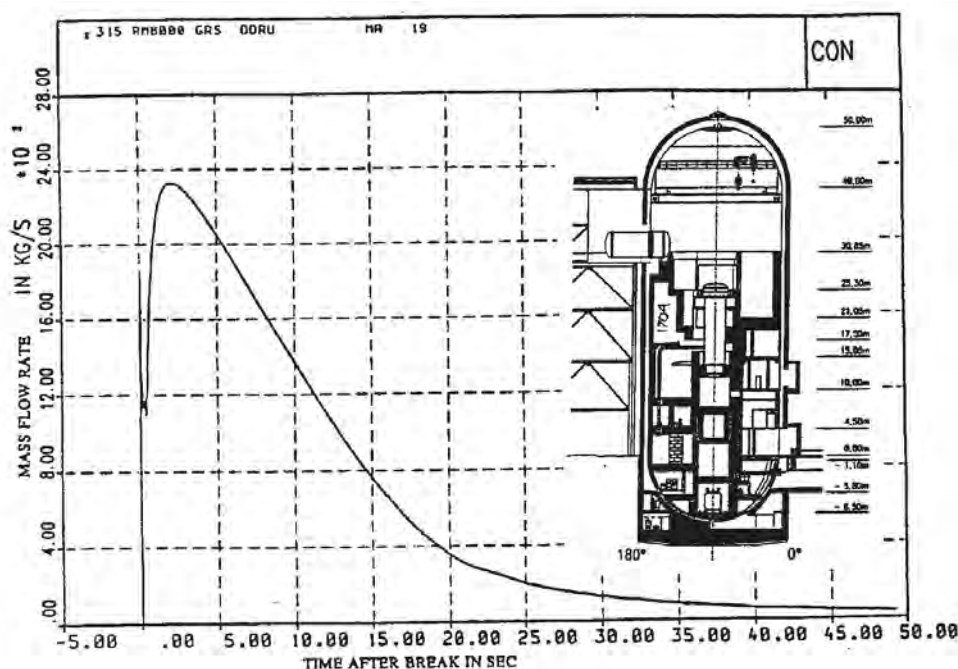


Figure 9.C-102. HDR-T31.5 Blowdown Mass Flow Rate into the Containment

(reprinted from: L. Wolf, K. Mun, "Overview of experimental results for long-term, Large-scale natural circulations in LWR-containments after large LOCAs, Vol. II: Assessment of HDR Experiments V21.1, V43, T31.5 and E11.5," University of Maryland at College Park, for DOE – Project HDR Hydrogen Mixing Evaluation for Containment Safety Evaluations natural Global Circulation, Order Number: DE-AP07-96ID10765," April 1996)

9.C-163

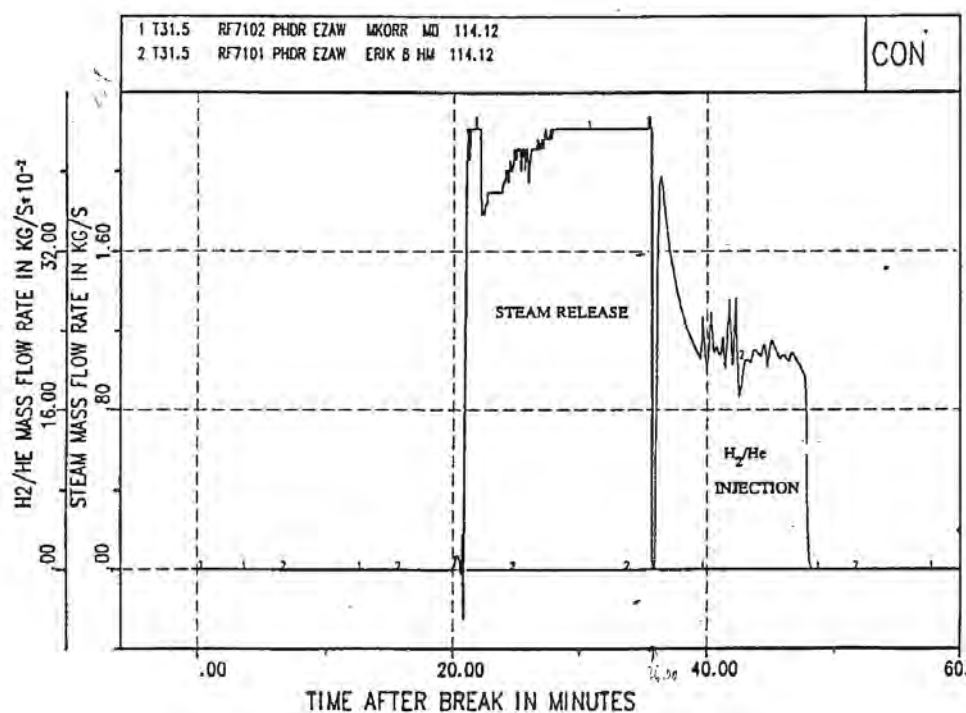


Figure 9.C-103. HDR-T31.5 Steam and H₂/He gas Mass Flow Rates into the Containment

(reprinted from: L. Wolf, K. Mun, "Overview of experimental results for long-term, Large-scale natural circulations in LWR-containments after large LOCAs, Vol. II: Assessment of HDR Experiments V21.1, V43, T31.5 and E11.5," University of Maryland at College Park, for DOE – Project HDR Hydrogen Mixing Evaluation for Containment Safety Evaluations natural Global Circulation, Order Number: DE-AP07-96ID10765," April 1996)

9.C-164

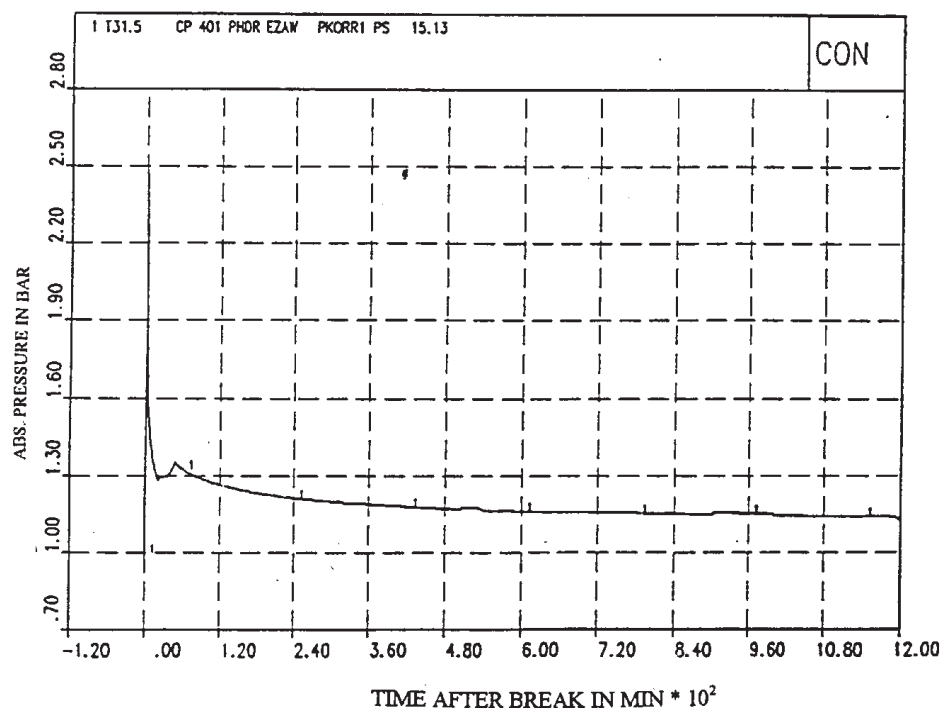


Figure 9.C-104. HDR-T31.5 Pressure History after Large LOCA over 1200 Minutes

(reprinted from: L. Wolf, K. Mun, "Overview of experimental results for long-term, Large-scale natural circulations in LWR-containments after large LOCAs, Vol. II: Assessment of HDR Experiments V21.1, V43, T31.5 and E11.5," University of Maryland at College Park, for DOE – Project HDR Hydrogen Mixing Evaluation for Containment Safety Evaluations natural Global Circulation, Order Number: DE-AP07-96ID10765," April 1996)

9.C-165

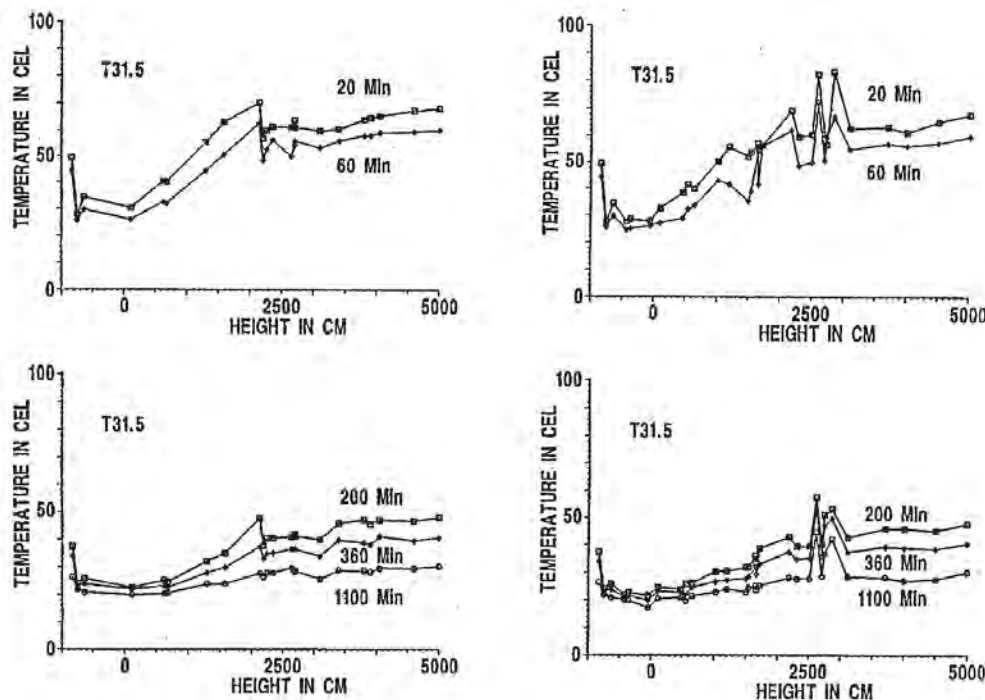


Figure 9.C-105. HDR-T31.5 Axial Temperature Profiles along Spiral Stairway (left) and Main Stairway (right) for Different Instants in Time

(reprinted from: L. Wolf, K. Mun, "Overview of experimental results for long-term, Large-scale natural circulations in LWR-containments after large LOCAs, Vol. II: Assessment of HDR Experiments V21.1, V43, T31.5 and E11.5," University of Maryland at College Park, for DOE – Project HDR Hydrogen Mixing Evaluation for Containment Safety Evaluations natural Global Circulation, Order Number: DE-AP07-96ID10765," April 1996)

9.C-166

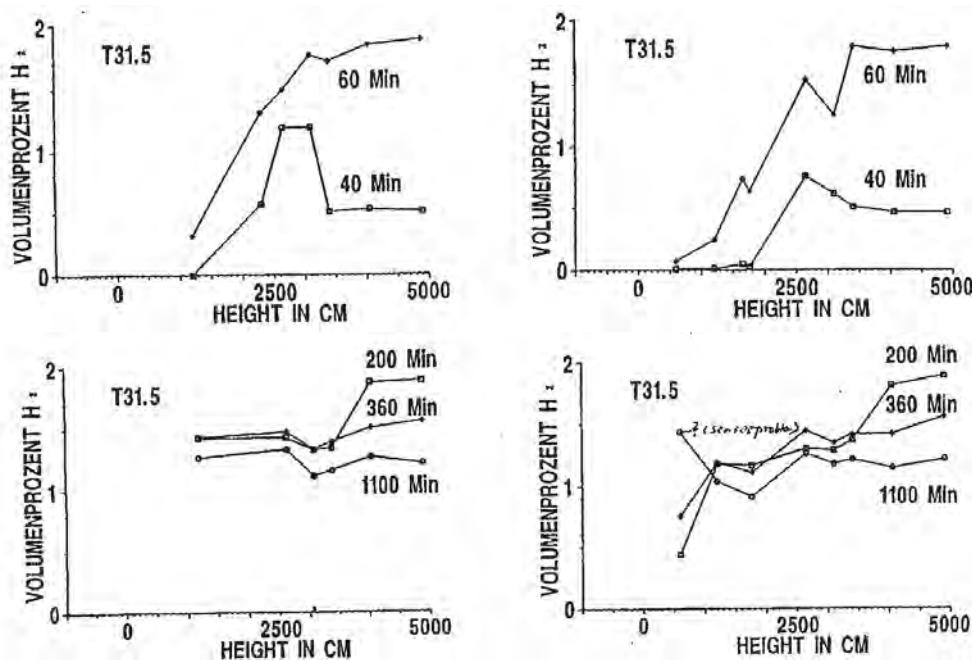


Figure 9.C-106. HDR-T31.5 Axial Gas Concentration Profiles along Spiral Stairway (left) and Main Stairway (right) in Upper Containment Region at Different Instants in Time

(reprinted from: L. Wolf, K. Mun, "Overview of experimental results for long-term, Large-scale natural circulations in LWR-containments after large LOCAs, Vol. II: Assessment of HDR Experiments V21.1, V43, T31.5 and E11.5," University of Maryland at College Park, for DOE – Project HDR Hydrogen Mixing Evaluation for Containment Safety Evaluations natural Global Circulation, Order Number: DE-AP07-96ID10765," April 1996)

9.C-167

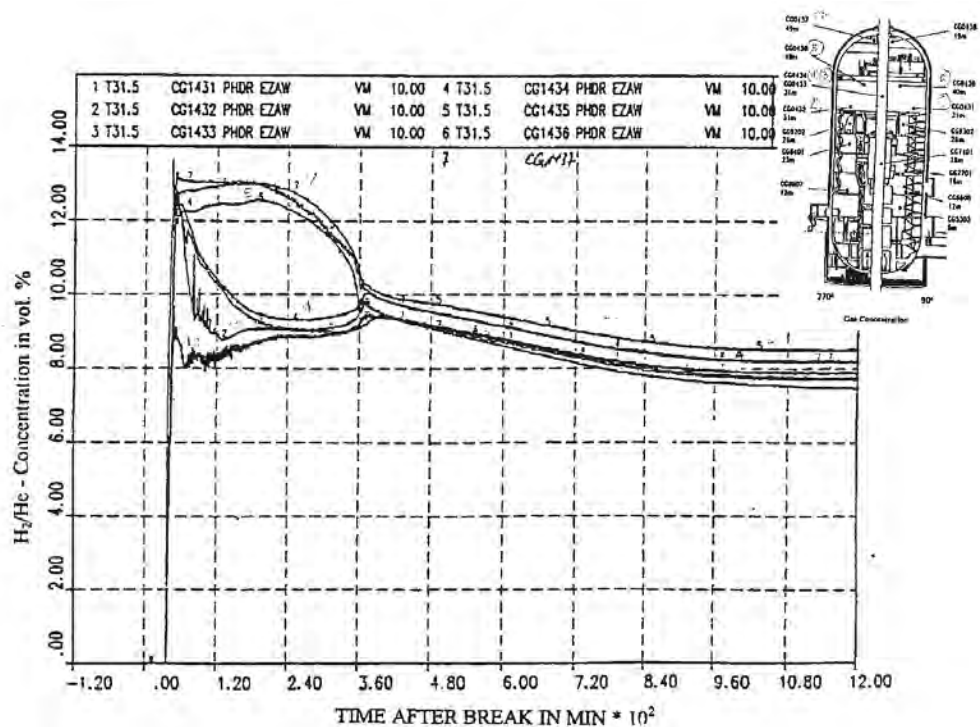


Figure 9.C-107. HDR-T31.5 Gas Concentrations Inside the Containment Dome

(reprinted from: L. Wolf, K. Mun, "Overview of experimental results for long-term, Large-scale natural circulations in LWR-containments after large LOCAs, Vol. II: Assessment of HDR Experiments V21.1, V43, T31.5 and E11.5," University of Maryland at College Park, for DOE – Project HDR Hydrogen Mixing Evaluation for Containment Safety Evaluations natural Global Circulation, Order Number: DE-AP07-96ID10765," April 1996)

9.C-168

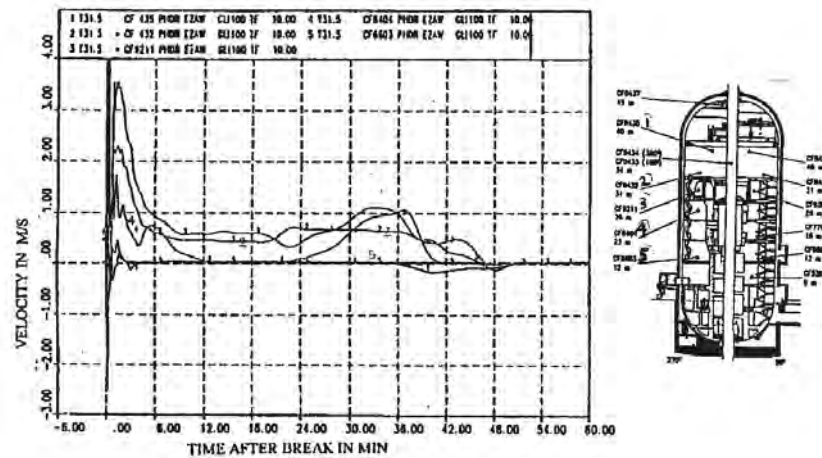


Figure 9.C-108a. HDR-T31.5 Velocities Over 60 Minutes along Spiral Stairways and Associated Dome Regions

(reprinted from: L. Wolf, K. Mun, "Overview of experimental results for long-term, Large-scale natural circulations in LWR-containments after large LOCAs, Vol. II: Assessment of HDR Experiments V21.1, V43, T31.5 and E11.5," University of Maryland at College Park, for DOE – Project HDR Hydrogen Mixing Evaluation for Containment Safety Evaluations natural Global Circulation, Order Number: DE-AP07-96ID10765," April 1996)

9.C-169

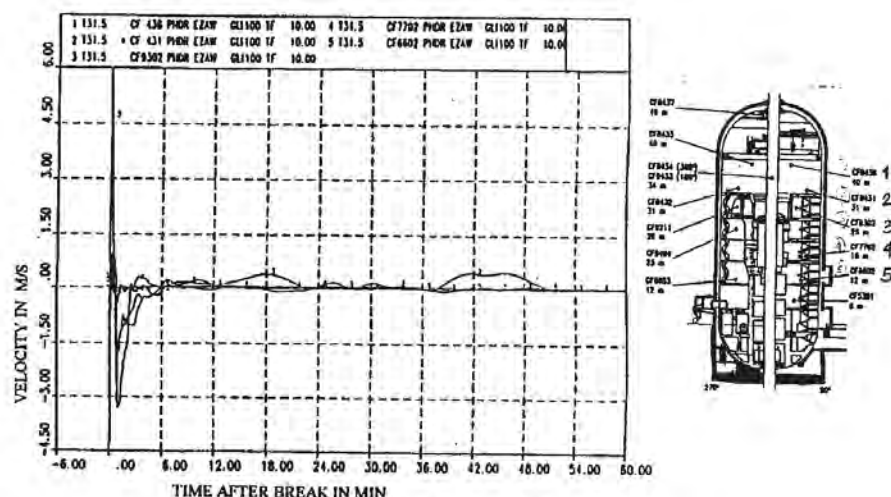


Figure 9.C-108b. HDR-T31.5 Velocities Over 60 Minutes Along Main Stairways and Associated Dome Regions

(reprinted from: L. Wolf, K. Mun, "Overview of experimental results for long-term, Large-scale natural circulations in LWR-containments after large LOCAs, Vol. II: Assessment of HDR Experiments V21.1, V43, T31.5 and E11.5," University of Maryland at College Park, for DOE – Project HDR Hydrogen Mixing Evaluation for Containment Safety Evaluations natural Global Circulation, Order Number: DE-AP07-96ID10765," April 1996)

9.C-170

9.C.2.4.2.2 Experiment V21.1

The blowdown for the V21.1 experiment (see Kanzleiter T., Valencia, L., 1984) is initiated inside the R1603 compartment, which is in the middle section of the HDR containment (see Figure 9.C-73 and Figure 9.C-109). The arrangement of reactor pressure vessel, blowdown pipe (break diameter 453 mm), and jet impingement plate for the subcooled water blowdown is shown in Figure 9.C-109. Other characteristics of the experiment are given in Table 9.C-6. The total mass and enthalpy of the exiting fluid are 50157 kg and 72320 MJ, respectively. The test could be characterized as a large break cross-section and a short-term blowdown (30 seconds). The maximum peak pressure was 3 bar because of the much higher mass and energy releases during the steam/liquid mixture blowdown (Figure 9.C-110). The transient atmospheric temperature for the dome, main and spiral stairway are presented in the Figure 9.C-111, Figure 9.C-112, and Figure 9.C-113.

At the beginning of the V21.1 experiment, the blowdown results in fairly uniform distribution of temperature in the dome (Figure 9.C-111). After about 10 seconds, a stratification gradient exists. The maximum temperature gradient over the above-deck height is 10°C at about 100 minutes. Until 420 minutes, the thermal stratification inside the dome volume exists (see Figure 9.C-111). At the end of the break release (after 30 seconds) the temperatures inside the dome are decreasing (slower near the top). After 420 minutes, temperature differences inside the dome volume are only around 2-3°C, indicating the presence of natural circulation. The natural circulation in the above-deck region acts to reduce the gradient with time.

The axial temperature distributions in the mean and spiral staircases are presented in Figure 9.C-112 and Figure 9.C-113. Immediately after the end of the blowdown, a stratification gradient develops. The transient histories of the temperatures at the same axial levels (in the spiral and main staircases) are presented in Figure 9.C-114. The large blowdown injected into the middle of the both staircases results in almost equal temperatures in both flow channels, therefore, global natural convection cannot be formed. A slightly higher temperature is recorded in the main staircase. A temperature difference of 1-2°C starts at 200 minutes and continues until 800 minutes.

Interpretation of Data

The large break with the blowdown penetrating into the middle of both staircases (mean flow paths) minimizes temperature differences among the same axial positions and suppresses the development of the natural circulation.

The small temperature differences of about 1°C (Figure 9.C-113) and the slight global natural circulation appear to be established later due to the different heat release rates of the various wall structures. These structures are heated to various temperatures during the early phase of the transient.

The large LOCA HDR tests described should be carefully applied to the passive containment design. The majority of the passive containment compartments are at the lower levels of the containment. Heating of the structures (walls, floors, and equipment) in the middle of the containment height or above is not possible because they do not exist. The formation of the stable stratified layers in the upper portion of the passive containment due to the accumulated heat (in fact the higher temperatures) in the concrete and steel structures is not possible. The temperature of the containment shell, which is the only solid structure in the upper portion of the containment, tends to be lower than the internal containment temperature. This promotes internal global circulation.

9.C-171

Application to AP600 and AP1000

Small temperature differences inside the dome, even without dome cooling or additional releases after blowdown, are sufficient to drive natural convection. This leads to more homogenous conditions over time.

Table 9.C-6. HDR-V21.1 Test Conditions

Measured Initial Conditions In Reactor Pressure Vessel	
Pressure	110.4 bar
Temperature	315 – 319°C
Liquid Level	filled
Liquid volume prior to blowdown	74.5 m ³
Liquid Mass prior to blowdown	50233 kg
Liquid level in reactor pressure vessel after blowdown	empty
Steam volume after blowdown	74.5 m ³
Steam mass after blowdown	76 kg
Mass of exiting fluid	50157 kg
Enthalpy of exiting fluid	72320 MJ
Jet impingement plate distance (LD)	2
Jet impingement plate inclination angle	0°
Break nozzle diameter	453 mm
Break nozzle length	6091 mm
Vent Flow Openings From Break Subcompartment	
UO140	open
UO143	closed
UO162	6.1 m ²
UO177	open
UO178	closed
External spray off (all the time)	

(reprinted from: L. Wolf, K. Mun, "Overview of experimental results for long-term, Large-scale natural circulations in LWR-containments after large LOCAs, Vol. II: Assessment of HDR Experiments V21.1, V43, T31.5 and E11.5," University of Maryland at College Park, for DOE – Project HDR Hydrogen Mixing Evaluation for Containment Safety Evaluations Natural Global Circulation, Order Number: DE-AP07-96ID10765," April 1996)

9.C-172

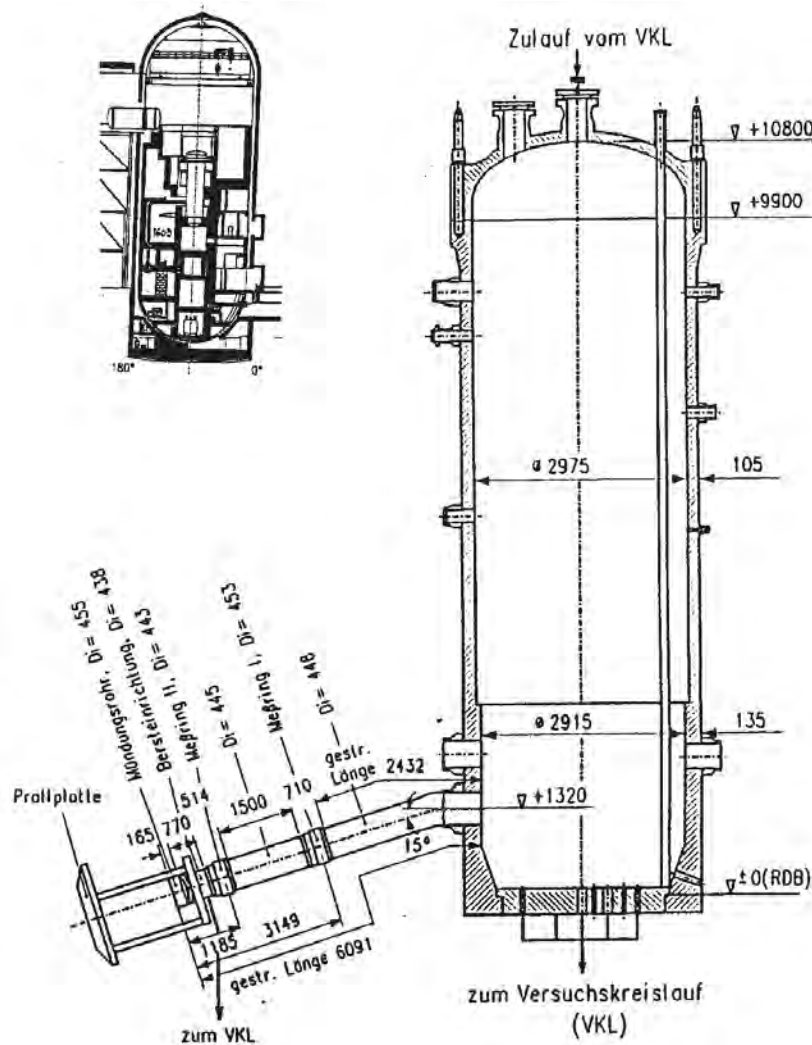


Figure 9.C-109. HDR-V21.1 Arrangement of Reactor Pressure Vessel, Blowdown Pipe and Jet Impingement Plate for Water Blowdown Test

(reprinted from: L. Wolf, K. Mun, "Overview of experimental results for long-term, Large-scale natural circulations in LWR-containments after large LOCAs, Vol. II: Assessment of HDR Experiments V21.1, V43, T31.5 and E11.5," University of Maryland at College Park, for DOE – Project HDR Hydrogen Mixing Evaluation for Containment Safety Evaluations natural Global Circulation, Order Number: DE-AP07-96ID10765," April 1996)

9.C-173

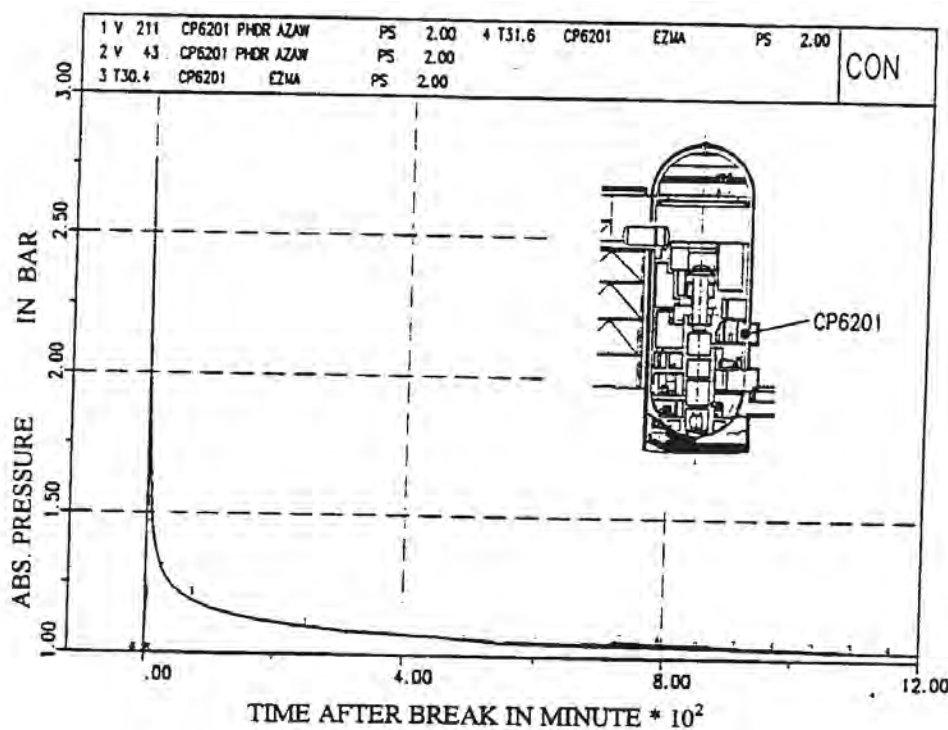


Figure 9.C-110. HDR-V21.1 Containment Pressure History

(reprinted from: L. Wolf, K. Mun, "Overview of experimental results for long-term, Large-scale natural circulations in LWR-containments after large LOCAs, Vol. II: Assessment of HDR Experiments V21.1, V43, T31.5 and E11.5," University of Maryland at College Park, for DOE – Project HDR Hydrogen Mixing Evaluation for Containment Safety Evaluations natural Global Circulation, Order Number: DE-AP07-96ID10765," April 1996)

9.C-174

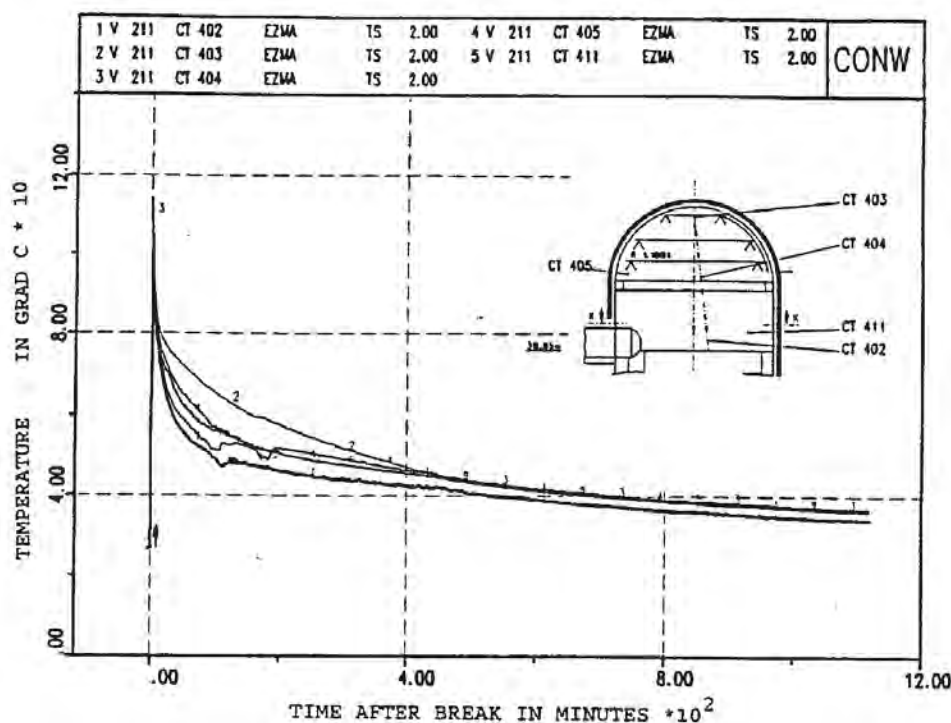


Figure 9.C-111. HDR-V21.1 Temperatures in the Containment Dome

(reprinted from: L. Wolf, K. Mun, "Overview of experimental results for long-term, Large-scale natural circulations in LWR-containments after large LOCAs, Vol. II: Assessment of HDR Experiments V21.1, V43, T31.5 and E11.5," University of Maryland at College Park, for DOE – Project HDR Hydrogen Mixing Evaluation for Containment Safety Evaluations natural Global Circulation, Order Number: DE-AP07-96ID10765," April 1996)

9.C-175

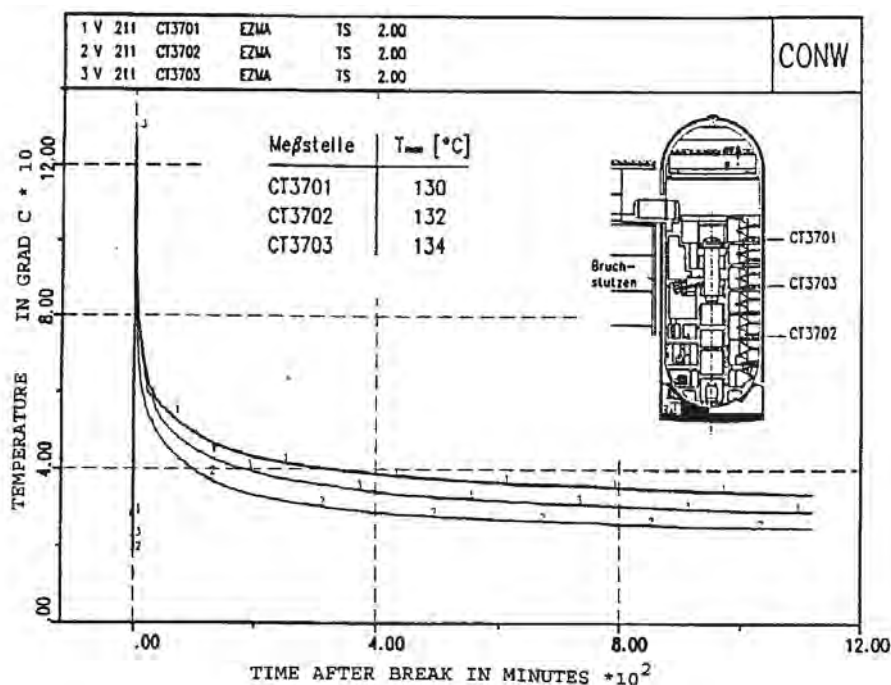


Figure 9.C-112. HDR-V21.1 Temperature Along the Main Staircase at Different Axial Positions

(reprinted from: L. Wolf, K. Mun, "Overview of experimental results for long-term, Large-scale natural circulations in LWR-containments after large LOCAs, Vol. II: Assessment of HDR Experiments V21.1, V43, T31.5 and E11.5," University of Maryland at College Park, for DOE – Project HDR Hydrogen Mixing Evaluation for Containment Safety Evaluations natural Global Circulation, Order Number: DE-AP07-96ID10765," April 1996)

9.C-176

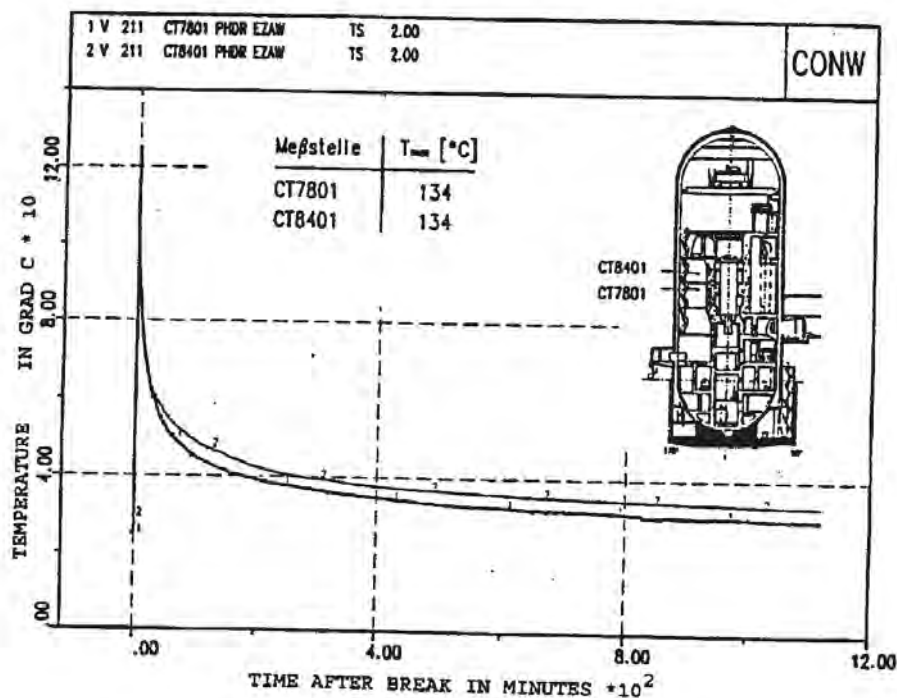


Figure 9.C-113. HDR-V21.1 Temperatures Along Spiral Staircase at Different Axial Positions

(reprinted from: L. Wolf, K. Mun, "Overview of experimental results for long-term, Large-scale natural circulations in LWR-containments after large LOCAs, Vol. II: Assessment of HDR Experiments V21.1, V43, T31.5 and E11.5," University of Maryland at College Park, for DOE – Project HDR Hydrogen Mixing Evaluation for Containment Safety Evaluations natural Global Circulation, Order Number: DE-AP07-96ID10765," April 1996)

9.C-177

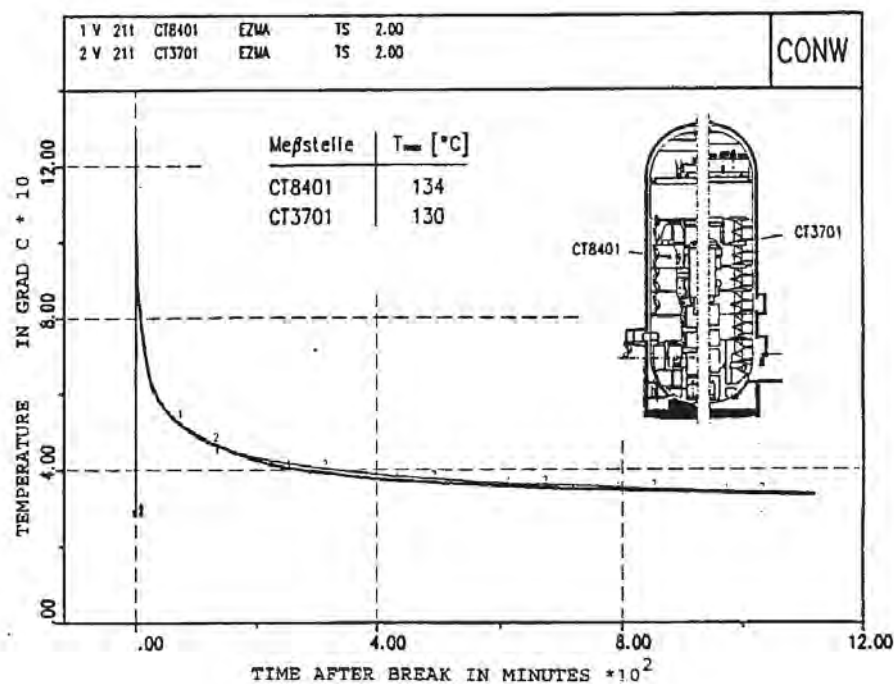


Figure 9.C-114. HDR-V21.1 Comparison Between Temperatures in Spiral Staircase (H=22.5 m) and Main Staircase (H = 25 m)

(reprinted from: L. Wolf, K. Mun, "Overview of experimental results for long-term, Large-scale natural circulations in LWR-containments after large LOCAs, Vol. II: Assessment of HDR Experiments V21.1, V43, T31.5 and E11.5," University of Maryland at College Park, for DOE – Project HDR Hydrogen Mixing Evaluation for Containment Safety Evaluations natural Global Circulation, Order Number: DE-AP07-96ID10765," April 1996)

9.C-178

9.C.2.4.2.3 Experiment E11.5

Experiment E11.5 is performed with a large break LOCA at the lowest possible position (room R1405) with subsequent small-break releases (see Figure 9.C-115). An overview of experimental results is presented by L. Wolf, K. Mun, 1996.

The containment pressure during the large break heatup phase is shown in Figure 9.C-116. At the end of the initial steam blowdown (50 seconds), the pressure reaches the peak of 2.56 bars (see Figure 9.C-116), then continuously decreases due to the condensation at the cold surfaces. Note that the external dome cooling is not applied during this experiment.

The 15-hour (900 minute) containment pressure history is presented in Figure 9.C-117. The gas release and steam injection following the initial blowdown slows the depressurization (see Figure 9.C-117). Over the time intervals 155-219 minutes, 245-545 minutes, and 695-820 minutes, the pressure slowly increases inside the containment due to the additional gas and steam releases. During the sump heating phase, the pressure first decreases and then increases. The increase in pressure coincides with the moment when the sump reaches saturated conditions and starts to evaporate. After reaching a second peak value of 1.6 bar at the end of the steam release into the subcompartment R1405, containment pressure decreases to atmospheric pressure. The containment depressurizes through the vent lines at the 0 m and 10 m elevations.

Temperatures along the main stairway during the heatup phase are presented in Figure 9.C-118. The combination of steam and gas releases during the heatup phase results in thermal stratification. This is shown by a 25°C temperature differential over the height of the containment after 80 minutes and a 12°C differential from top to bottom of the dome – see Figure 9.C-118.

Figure 9.C-119 presents the temperatures in both major flow paths (main and spiral staircases) at the same three axial positions. The temperature differences are relatively constant through time at each elevation, although smaller at the high elevations. Circulation is sufficient to keep the temperature difference between the two chimneys small (e.g., ΔT is approximately 5°C at the +16.5 elevation), for the various steam, dry heat, and sump boiling releases that occur in the lower portion of the containment.

The temperature distributions for the entire containment are presented in Figure 9.C-120 and Figure 9.C-121 over time intervals 2.0 to 75.0 minutes and 123 to 345 minutes, respectively. After the initial rise, the temperatures decrease quickly during the first 25 minutes (Figure 9.C-120). The decrease then continues at a slower rate (see Figure 9.C-121). The temperatures stratify in the main staircase, while in the spiral staircase they are almost uniform. Temperature differences between the top of the containment and the release level are approximately 10°C in the main staircase and 5°C in the spiral staircase. The temperature difference below the main stair case, between the level of the release and the bottom of the containment (between CT5301 and CT3802) is around 15°C.

The temperature decreases slowly in the upper region of the dome. The effects of the global circulation on the upper region of the dome are noticeable after the end of the steam release. This is evident from a comparison of the H₂/He concentrations during the gas mixture release (Figure 9.C-121). After the release, the temperature in the containment is relatively uniform, except for below the releases (see temperature distribution on the main stairway side).

9.C-179

During the sump heatup phase (but before the start of the boiling, 570 - 655 minutes), a convection circulation loop affects the region up to 15 m. This region has a uniform temperature gradient, while the region above is stagnant. After sump evaporation begins, the convection circulation loop affects the entire volume and homogenizes the temperatures.

The steam and gas concentrations over time correspond to the temperature distributions. Note that there are no large local changes in gas concentrations in the regions (radially) away from the two staircases, see Figure 9.C-122 and Figure 9.C-123

The flow patterns in the compartments may be inferred by comparing the velocities in the two staircases (see Figure 9.C-124, Figure 9.C-125, and Figure 9.C-126). Upward flow is recorded in both stairways at the early stage of the blowdown (first 30 seconds, see Figure 9.C-124). The upward flow in the spiral staircase is the result of the unplanned vent connection with the release point. A pressure wave destroyed the separating wall during the blowdown. This indicates that the break compartment pressurization forced flow out of all the openings in the break compartment.

After 80 seconds (end of blowdown is at 50 seconds), upward and downward flows are recorded in the main and spiral staircases, respectively (see velocities in Figure 9.C-124). During the steam releases ST1, ST2, ST3, ST4, and ST5 (see Figure 9.C-126 and Figure 9.C-127), upward flows are recorded in both staircases. During the gas mixture release phases GT1, GT2, and GT3, the flow is downwards in the spiral staircase (see Figure 9.C-126).

During the sump heatup phase the flow is upwards in the main staircase and downwards in the spiral staircase (see Figure 9.C-127). The weak circulation loop reaches the 15 m level before the start of sump boiling. After the start of sump boiling, the circulation loop extends over the total containment height and the flow velocities are higher (see Figure 9.C-127 for 655 – 695 minutes).

Various global circulation flow patterns are established during the E11.5 experiment as a result of the various steam and gas release phases, as well as the sump heatup and boiling phases. The temperatures, steam, and gas concentrations follow similar distributions. Global circulation effects contribute to reduced gradients in the vertical direction of temperature and concentration fields.

Application to AP600 and AP1000

The release position in experiment E11.5 is the closest to the possible AP600 and **AP1000** LOCA cases. However, in the HDR, chimney and heat storage effects (heat sink and source effects) along the two main flow paths cause dominant global circulation flow patterns below the operating deck. After the blowdown, the plume rises from the break compartment and entrains laterally, yielding global circulation.

In the passive containment, upward flow patterns are formed in the core of containment (depending on the break location). Downward flow is present near the vertical walls due to the relatively high cooling rates of the steel shell. The overall effects are shallower vertical density gradients in the above-deck region compared with E11.5 test. The shallow gradients are the result of the additional wall layer entrainment that is not present in HDR.

9.C-180

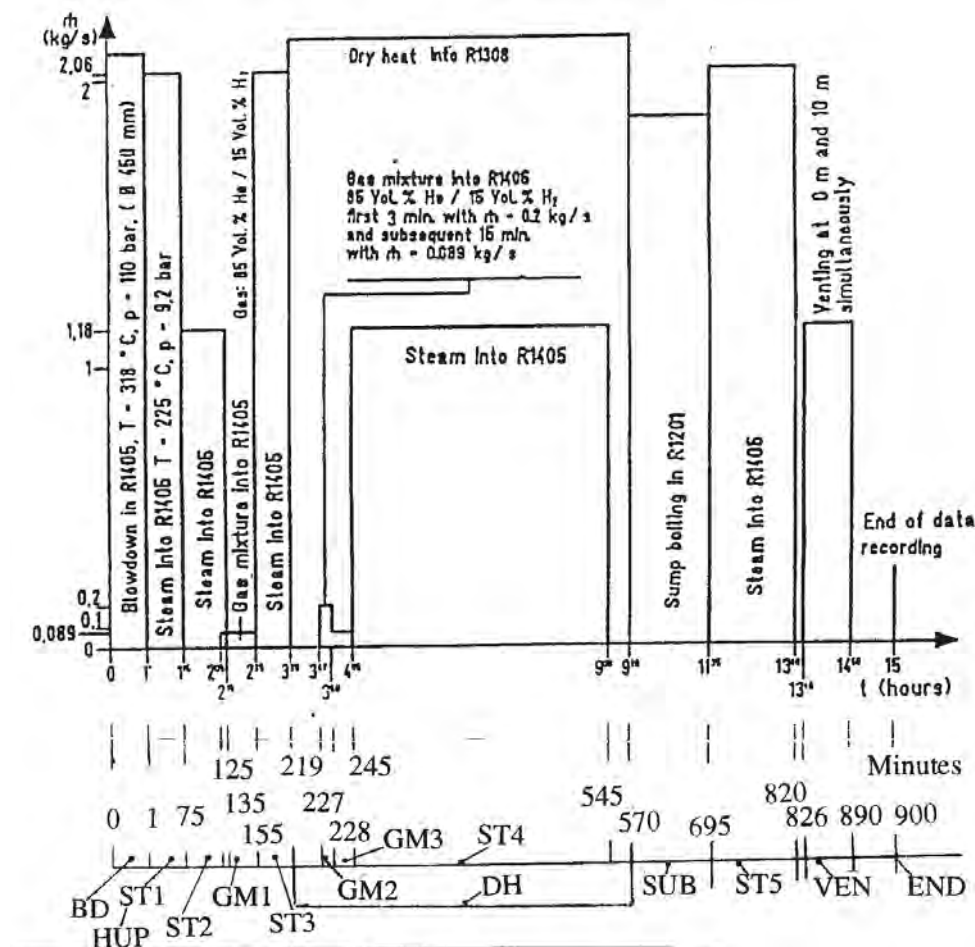


Figure 9.C-115a. HDR-E11.5 Sequence of Experimental Test Procedures

(reprinted from: L. Wolf, K. Mun, "Overview of experimental results for long-term, Large-scale natural circulations in LWR-containments after large LOCAs, Vol. II: Assessment of HDR Experiments V21.1, V43, T31.5 and E11.5," University of Maryland at College Park, for DOE – Project HDR Hydrogen Mixing Evaluation for Containment Safety Evaluations natural Global Circulation, Order Number: DE-AP07-96ID10765," April 1996)

9.C-181

Event	Time minutes	Event Description
BD	0-1	Blowdown in R1.405
HUP ST1	1-75	Steam supply with $m = 2.06 \text{ kg/s}$
ST2	75-135	Reduced external steam with $m = 1.18 \text{ kg/s}$ in R1.405
GM1	125-155	H_2/He gas mixture release into R1.405 with 0.089 kg/s
ST3	155-219	Steam release into R1.405 with 2.06 kg/s
DH	219-370	Dry heat addition into R1.308
GM2	227-228	H_2/He gas mixture release into R1.405 with 0.2 kg/s
GM3	228-245	H_2/He gas mixture release into R1.405 with 0.089 kg/s
ST4	245-545	Start of steam release into R1.405 with $m = 1.18 \text{ kg/s}$
SUB	570-695	Sump boiling
ST5	695-820	Steam release into R1.405 with $m = 2.06 \text{ kg/s}$
VEN	826-890	Containment venting
END	900	End of data acquisition

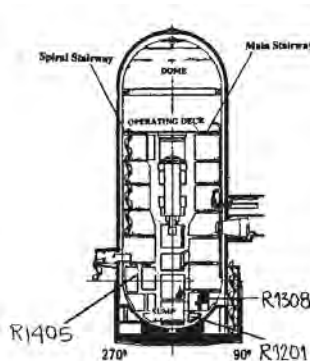


Figure 9.C-115b. HDR-E11.5 Sequence of Experimental Test Procedures

(reprinted from: L. Wolf, K. Mun, "Overview of experimental results for long-term, Large-scale natural circulations in LWR-containments after large LOCAs, Vol. II: Assessment of HDR Experiments V21.1, V43, T31.5 and E11.5," University of Maryland at College Park, for DOE – Project HDR Hydrogen Mixing Evaluation for Containment Safety Evaluations natural Global Circulation, Order Number: DE-AP07-96ID10765," April 1996)

9.C-182

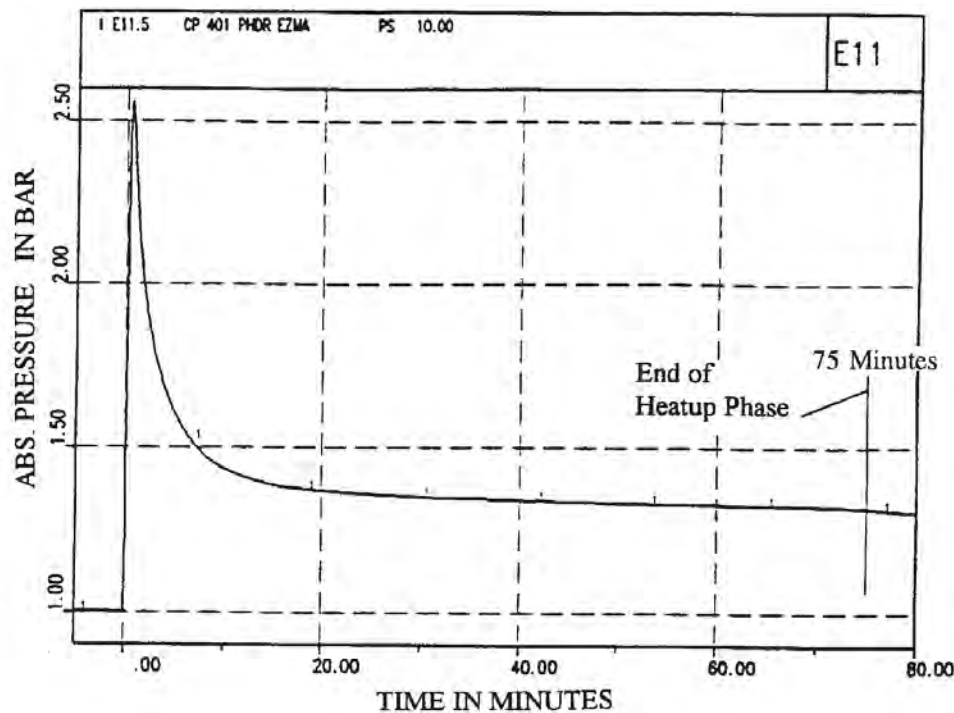


Figure 9.C-116. HDR-E11.5 Containment Pressure

(reprinted from: L. Wolf, K. Mun, "Overview of experimental results for long-term, Large-scale natural circulations in LWR-containments after large LOCAs, Vol. II: Assessment of HDR Experiments V21.1, V43, T31.5 and E11.5," University of Maryland at College Park, for DOE – Project HDR Hydrogen Mixing Evaluation for Containment Safety Evaluations natural Global Circulation, Order Number: DE-AP07-96ID10765," April 1996)

9.C-183

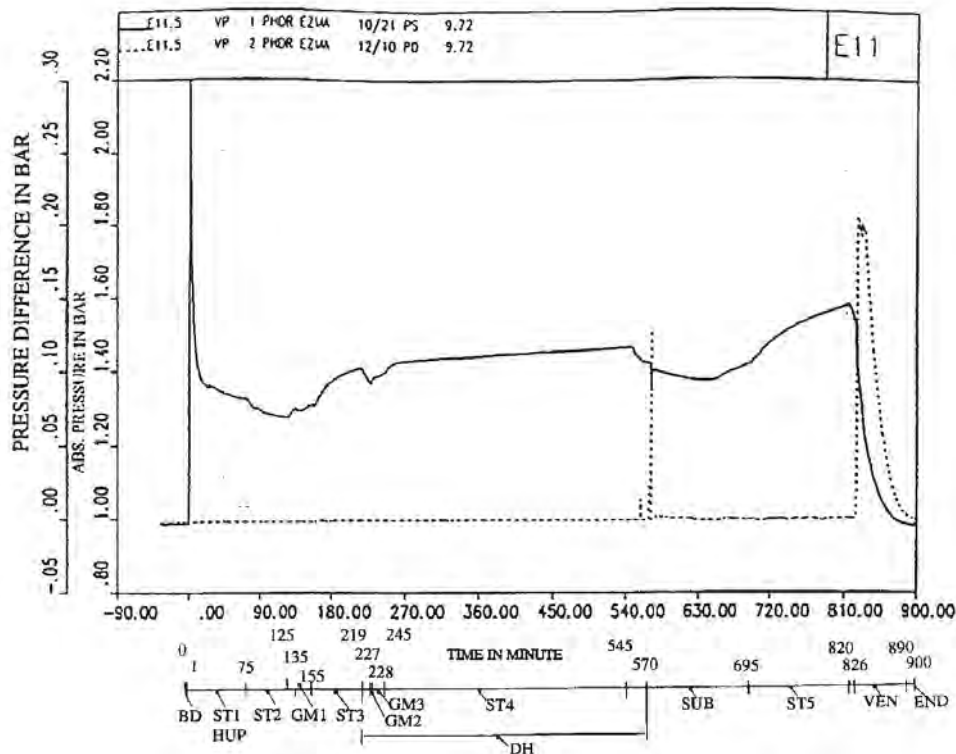


Figure 9.C-117. HDR-E11.5 Containment Pressure History

(reprinted from: L. Wolf, K. Mun, "Overview of experimental results for long-term, Large-scale natural circulations in LWR-containments after large LOCAs, Vol. II: Assessment of HDR Experiments V21.1, V43, T31.5 and E11.5," University of Maryland at College Park, for DOE – Project HDR Hydrogen Mixing Evaluation for Containment Safety Evaluations natural Global Circulation, Order Number: DE-AP07-96ID10765," April 1996)

9.C-184

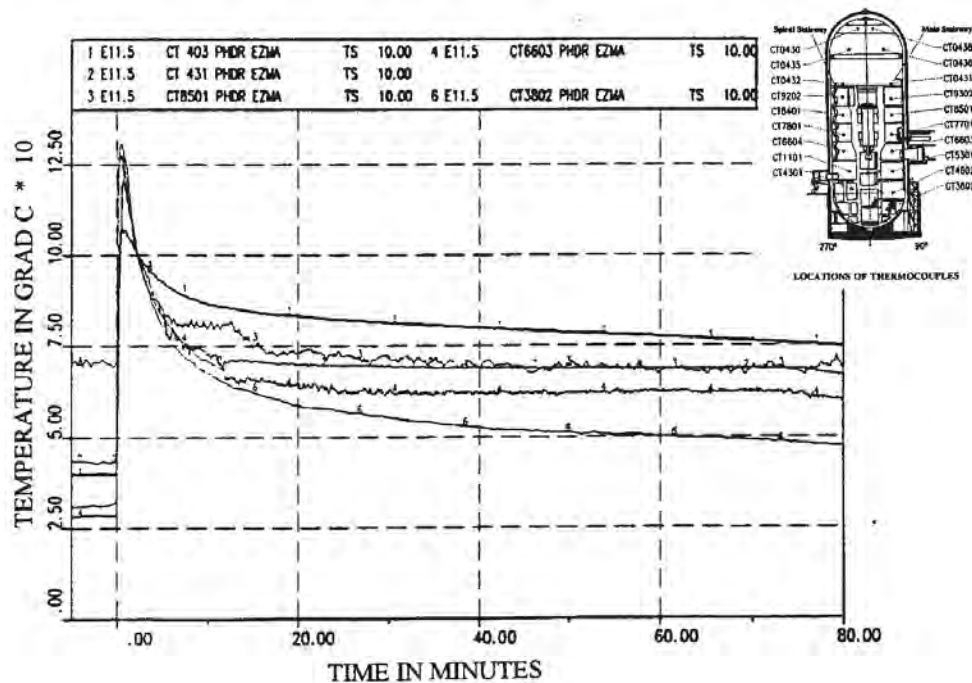


Figure 9.C-118. HDR-E11.5 Containment Temperatures Along main Stairway During Containment Heatup Phase

(reprinted from: L. Wolf, K. Mun, "Overview of experimental results for long-term, Large-scale natural circulations in LWR-containments after large LOCAs, Vol. II: Assessment of HDR Experiments V21.1, V43, T31.5 and E11.5," University of Maryland at College Park, for DOE – Project HDR Hydrogen Mixing Evaluation for Containment Safety Evaluations natural Global Circulation, Order Number: DE-AP07-96ID10765," April 1996)

9.C-185

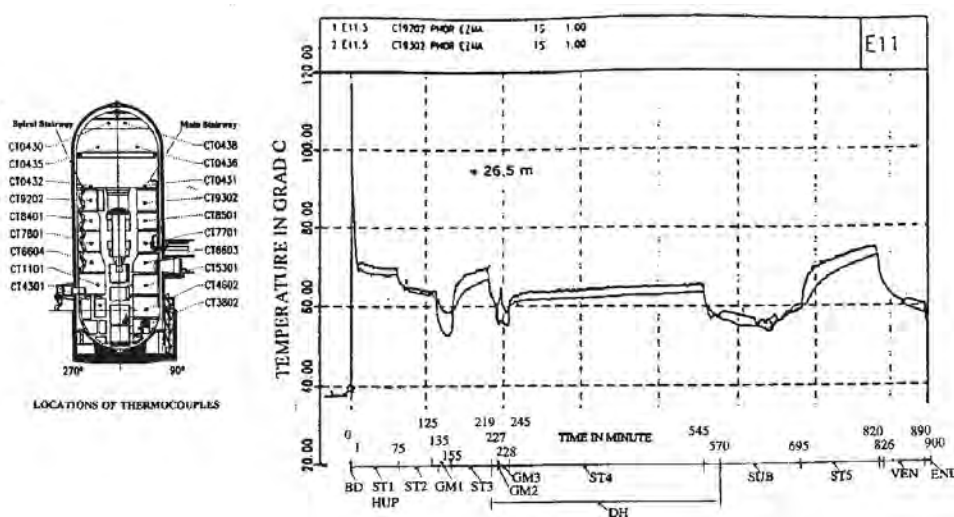


Figure 9.C-119a. HDR-E11.5 Temperatures in Both Major Flow Paths at the Same Axial Positions for Three Heights in the Containment

(reprinted from: L. Wolf, K. Mun, "Overview of experimental results for long-term, Large-scale natural circulations in LWR-containments after large LOCAs, Vol. II: Assessment of HDR Experiments V21.1, V43, T31.5 and E11.5," University of Maryland at College Park, for DOE – Project HDR Hydrogen Mixing Evaluation for Containment Safety Evaluations natural Global Circulation, Order Number: DE-AP07-96ID10765," April 1996)

9.C-186

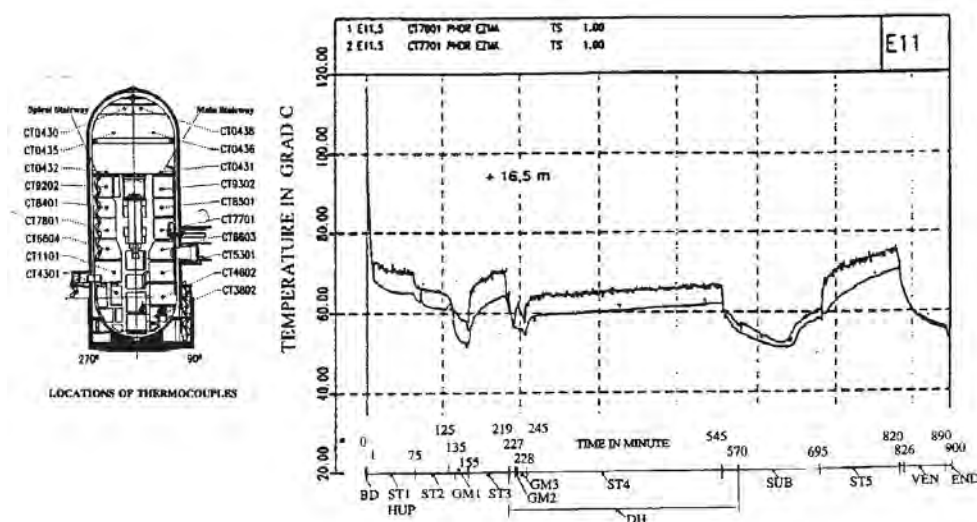


Figure 9.C-119b. HDR-E11.5 Temperatures in Both Major Flow Paths at the Same Axial Positions for Three Heights in the Containment

(reprinted from: L. Wolf, K. Mun, "Overview of experimental results for long-term, Large-scale natural circulations in LWR-containments after large LOCAs, Vol. II: Assessment of HDR Experiments V21.1, V43, T31.5 and E11.5," University of Maryland at College Park, for DOE – Project HDR Hydrogen Mixing Evaluation for Containment Safety Evaluations natural Global Circulation, Order Number: DE-AP07-96ID10765," April 1996)

9.C-187

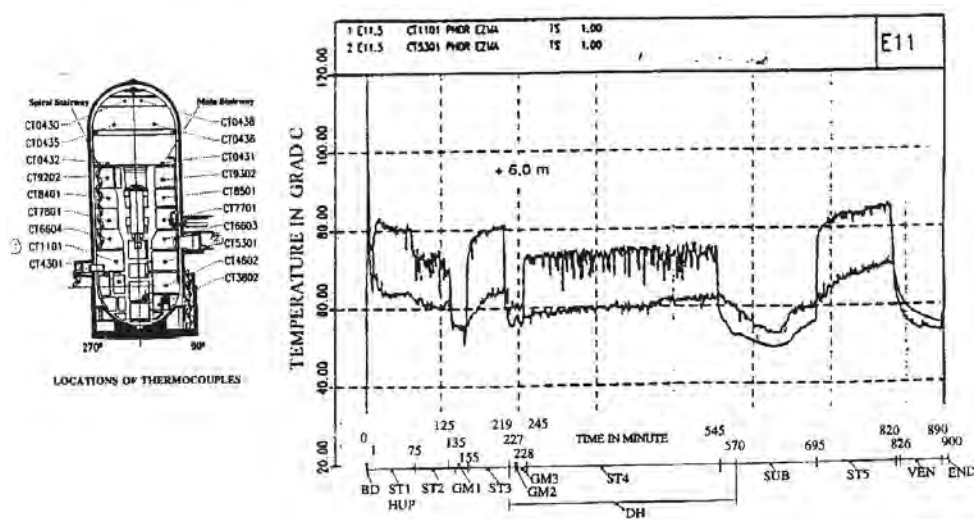


Figure 9.C-119c. HDR-E11.5 Temperatures in Both Major Flow Paths at the Same Axial Positions for Three Heights in the Containment

(reprinted from: L. Wolf, K. Mun, "Overview of experimental results for long-term, Large-scale natural circulations in LWR-containments after large LOCAs, Vol. II: Assessment of HDR Experiments V21.1, V43, T31.5 and E11.5," University of Maryland at College Park, for DOE – Project HDR Hydrogen Mixing Evaluation for Containment Safety Evaluations natural Global Circulation, Order Number: DE-AP07-96ID10765," April 1996)

9.C-188

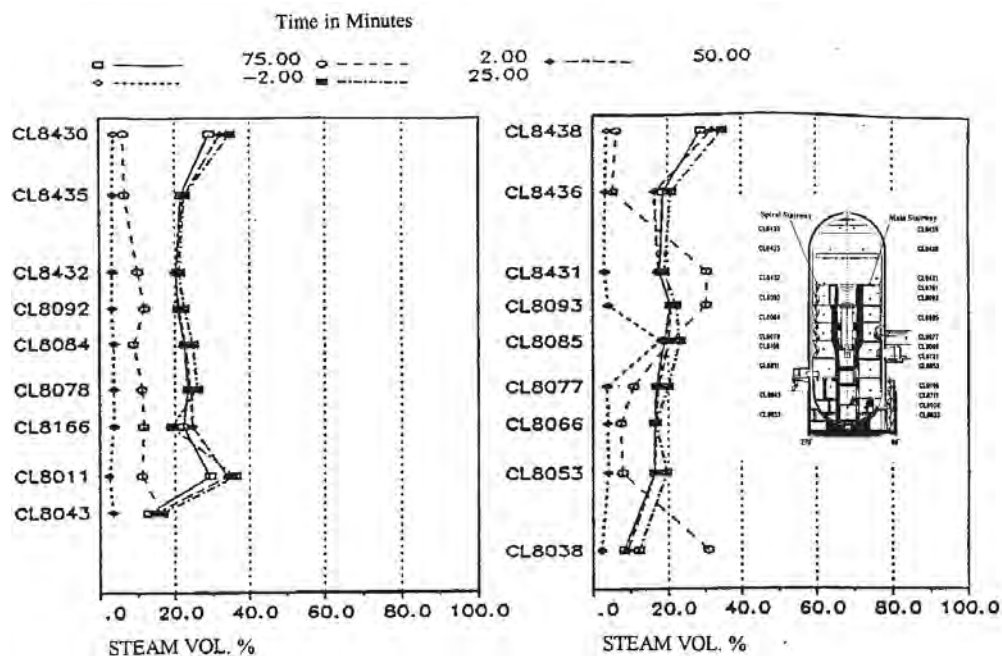


Figure 9.C-120a. HDR-E11.5 Axial Steam Concentration Profiles in Spiral (left) and Main (right) Stairways for Different Instants in time for Large Break LOCA release in Lower Containment Region

(reprinted from: L. Wolf, K. Mun, "Overview of experimental results for long-term, Large-scale natural circulations in LWR-containments after large LOCAs, Vol. II: Assessment of HDR Experiments V21.1, V43, T31.5 and E11.5," University of Maryland at College Park, for DOE – Project HDR Hydrogen Mixing Evaluation for Containment Safety Evaluations natural Global Circulation, Order Number: DE-AP07-96ID10765," April 1996)

9.C-189

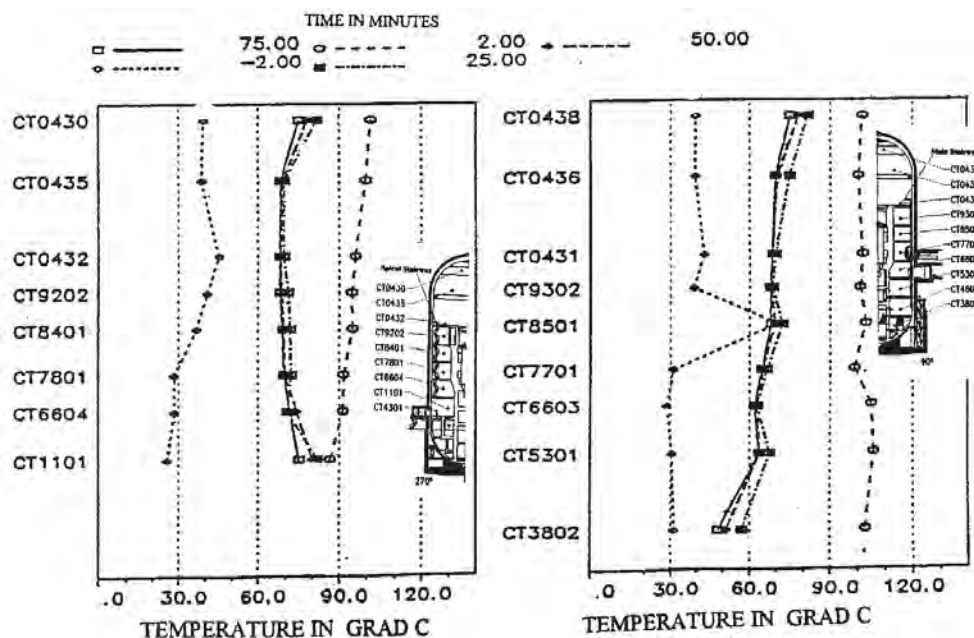


Figure 9.C-120b. HDR-E11.5 Axial Temperature Profiles in Spiral (left) and Main (right) Stairways for Different Instants in Time for Large Break LOCA Release in Lower Containment Region

(reprinted from: L. Wolf, K. Mun, "Overview of experimental results for long-term, Large-scale natural circulations in LWR-containments after large LOCAs, Vol. II: Assessment of HDR Experiments V21.1, V43, T31.5 and E11.5," University of Maryland at College Park, for DOE – Project HDR Hydrogen Mixing Evaluation for Containment Safety Evaluations natural Global Circulation, Order Number: DE-AP07-96ID10765," April 1996)

9.C-190

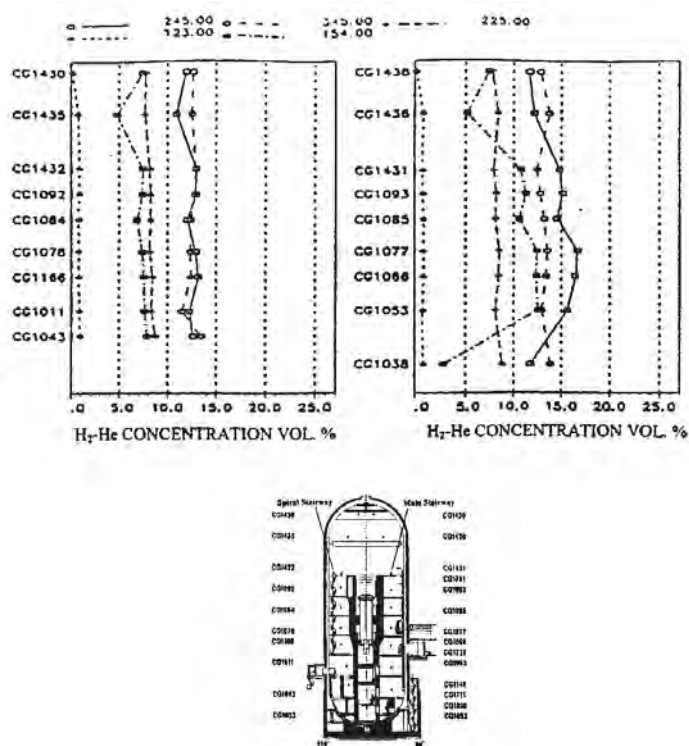


Figure 9.C-121a. HDR-E11.5 Axial H₂-He Gas Mixture Concentration Profiles along Spiral (left) and Main (right) Stairways During Gas Release Phase (Total Mass 291 kg)

(reprinted from: L. Wolf, K. Mun, "Overview of experimental results for long-term, Large-scale natural circulations in LWR-containments after large LOCAs, Vol. II: Assessment of HDR Experiments V21.1, V43, T31.5 and E11.5," University of Maryland at College Park, for DOE – Project HDR Hydrogen Mixing Evaluation for Containment Safety Evaluations natural Global Circulation, Order Number: DE-AP07-96ID10765," April 1996)

9.C-191

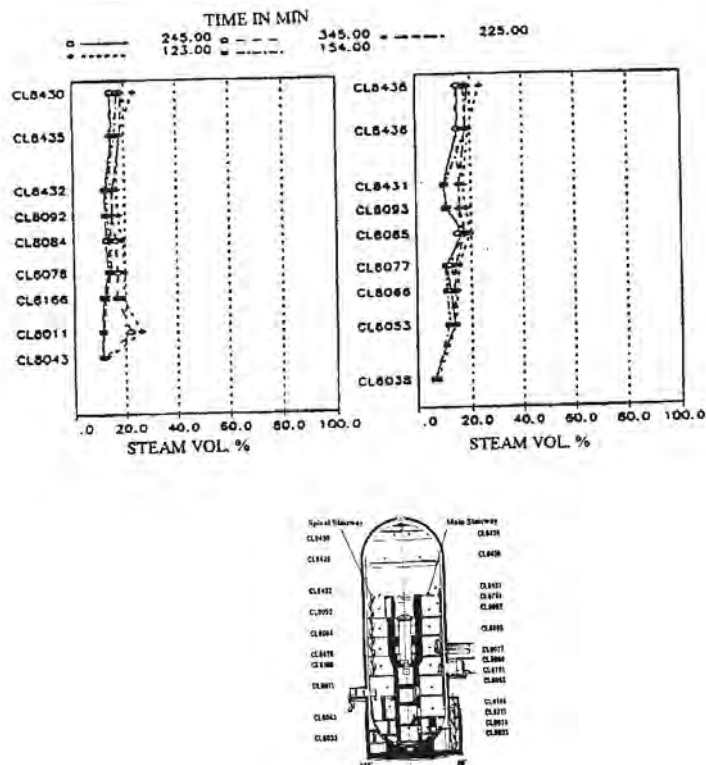


Figure 9.C-121b. HDR-E11.5 Axial Steam Concentration Profiles Along Spiral (left) and Main (right) Stairways During Gas Release Phase (Total Mass 291 kg)

(reprinted from: L. Wolf, K. Mun, "Overview of experimental results for long-term, Large-scale natural circulations in LWR-containments after large LOCAs, Vol. II: Assessment of HDR Experiments V21.1, V43, T31.5 and E11.5," University of Maryland at College Park, for DOE – Project HDR Hydrogen Mixing Evaluation for Containment Safety Evaluations natural Global Circulation, Order Number: DE-AP07-96ID10765," April 1996)

9.C-192

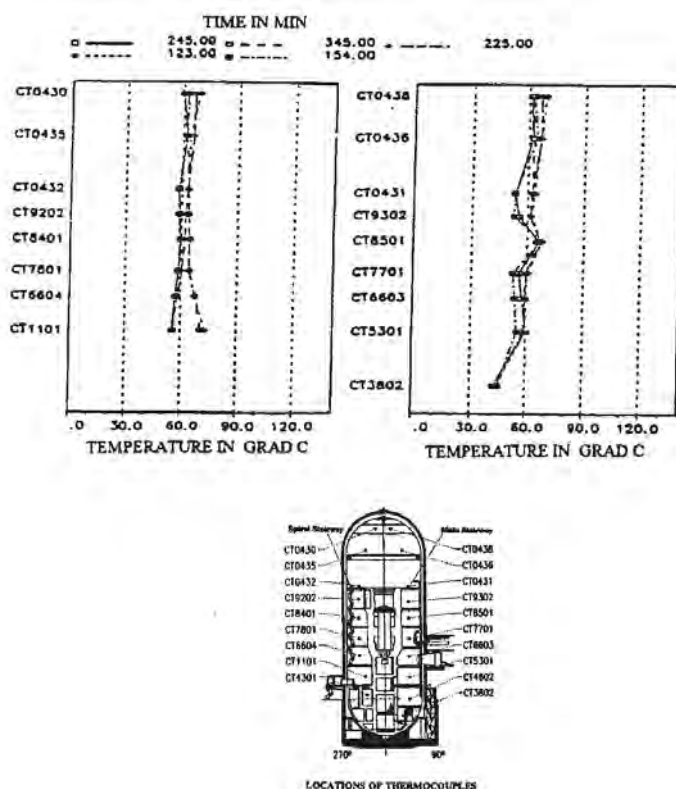


Figure 9.C-121c. HDR-E11.5 Axial Temperature Profiles Along Spiral (left) and Main (right) Stairways During Gas Release Phase (Total Mass 291 kg)

(reprinted from: L. Wolf, K. Mun, "Overview of experimental results for long-term, Large-scale natural circulations in LWR-containments after large LOCAs, Vol. II: Assessment of HDR Experiments V21.1, V43, T31.5 and E11.5," University of Maryland at College Park, for DOE – Project HDR Hydrogen Mixing Evaluation for Containment Safety Evaluations natural Global Circulation, Order Number: DE-AP07-96ID10765," April 1996)

9.C-193

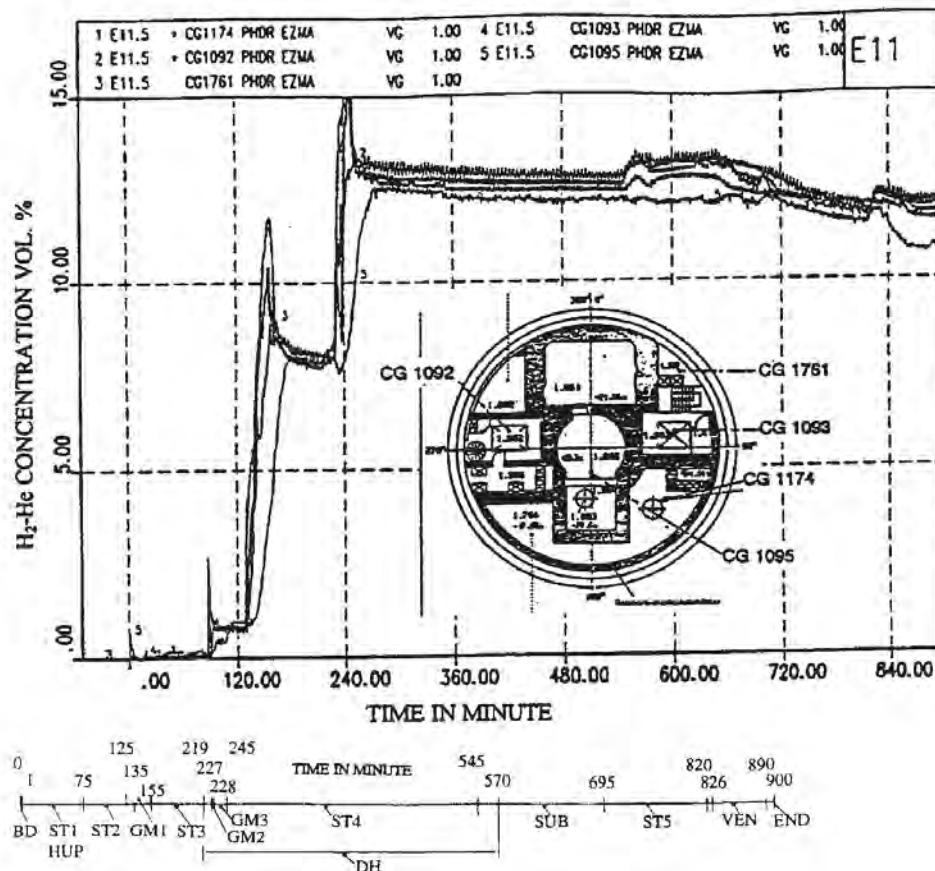


Figure 9.C-122a. HDR-E11.5 Gas Concentrations in the Major Flow Paths and in Regions and Subcompartments Away From the Stairways (H=22m up to 27 m)

(reprinted from: L. Wolf, K. Mun, "Overview of experimental results for long-term, Large-scale natural circulations in LWR-containments after large LOCAs, Vol. II: Assessment of HDR Experiments V21.1, V43, T31.5 and E11.5," University of Maryland at College Park, for DOE – Project HDR Hydrogen Mixing Evaluation for Containment Safety Evaluations natural Global Circulation, Order Number: DE-AP07-96ID10765," April 1996)

9.C-194

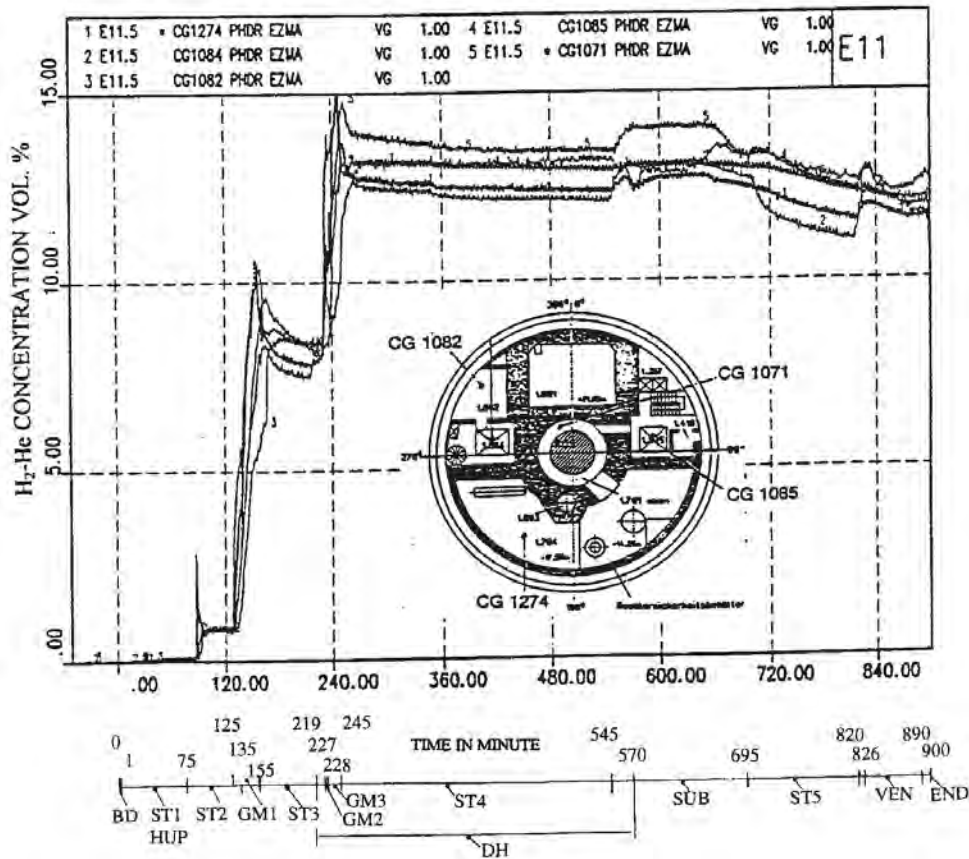


Figure 9.C-122b. HDR-E11.5 Gas Concentrations in the Major Flow Paths and in Regions and Subcompartments Away From the Stairways (H=22m up to 27 m)

(reprinted from: L. Wolf, K. Mun, "Overview of experimental results for long-term, Large-scale natural circulations in LWR-containments after large LOCAs, Vol. II: Assessment of HDR Experiments V21.1, V43, T31.5 and E11.5," University of Maryland at College Park, for DOE – Project HDR Hydrogen Mixing Evaluation for Containment Safety Evaluations natural Global Circulation, Order Number: DE-AP07-96ID10765," April 1996)

9.C-195

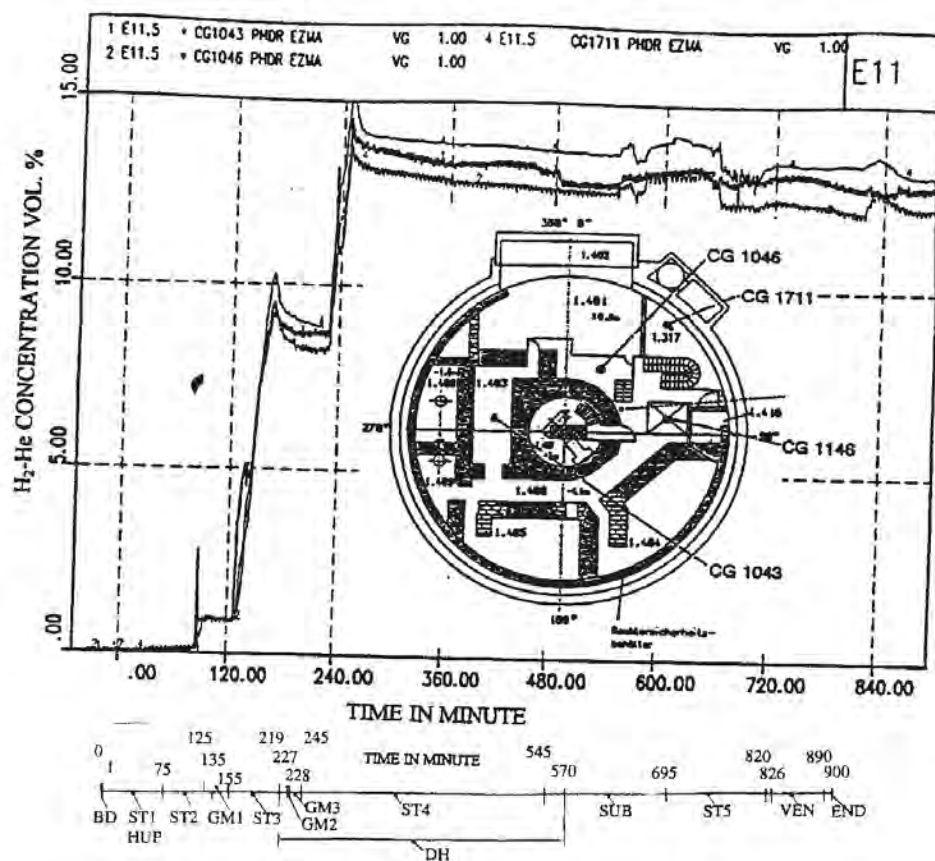


Figure 9.C-123a. HDR-E11.5 Gas Concentrations in the Major Flow Paths and in Regions and Subcompartments Away From the Stairways (H=-4.5m up to +2.0 m)

(reprinted from: L. Wolf, K. Mun, "Overview of experimental results for long-term, Large-scale natural circulations in LWR-containments after large LOCAs, Vol. II: Assessment of HDR Experiments V21.1, V43, T31.5 and E11.5," University of Maryland at College Park, for DOE - Project HDR Hydrogen Mixing Evaluation for Containment Safety Evaluations natural Global Circulation, Order Number: DE-AP07-96ID10765," April 1996)

9.C-196

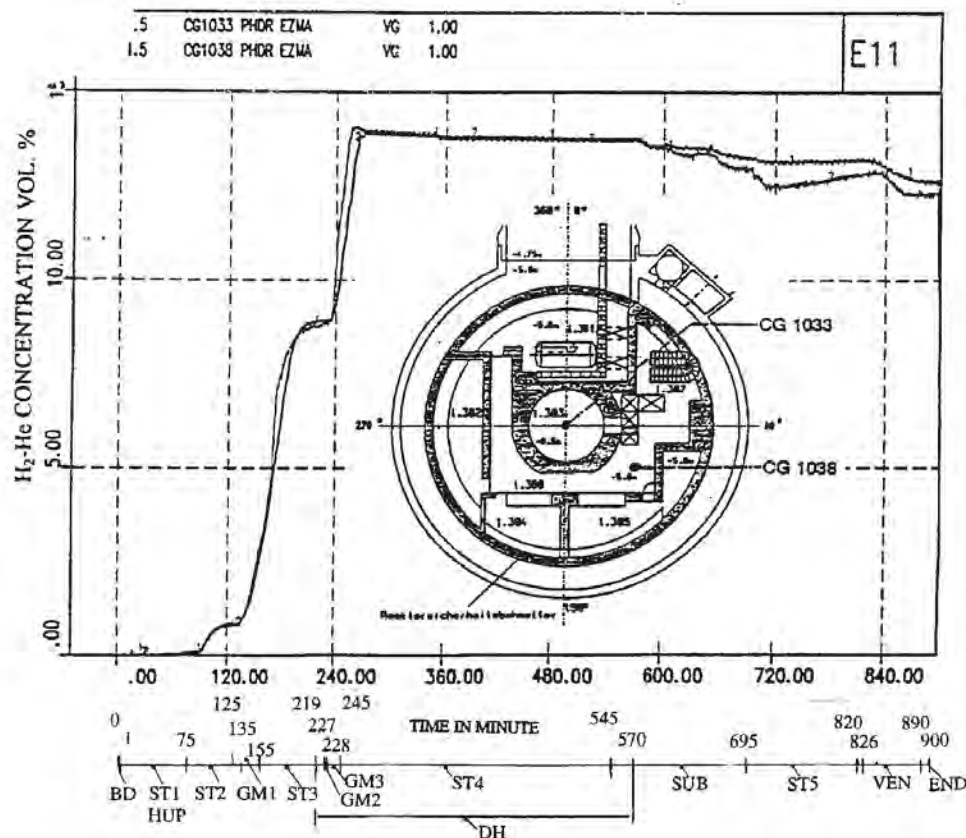


Figure 9.C-123b. HDR-E11.5 Gas Concentrations in the Major Flow Paths and in Regions and Subcompartments Away from the Stairways (H=-4.5m up to +2.0 m)

(reprinted from: L. Wolf, K. Mun, "Overview of experimental results for long-term, Large-scale natural circulations in LWR-containments after large LOCAs, Vol. II: Assessment of HDR Experiments V21.1, V43, T31.5 and E11.5," University of Maryland at College Park, for DOE – Project HDR Hydrogen Mixing Evaluation for Containment Safety Evaluations natural Global Circulation, Order Number: DE-AP07-96ID10765," April 1996)

9.C-197

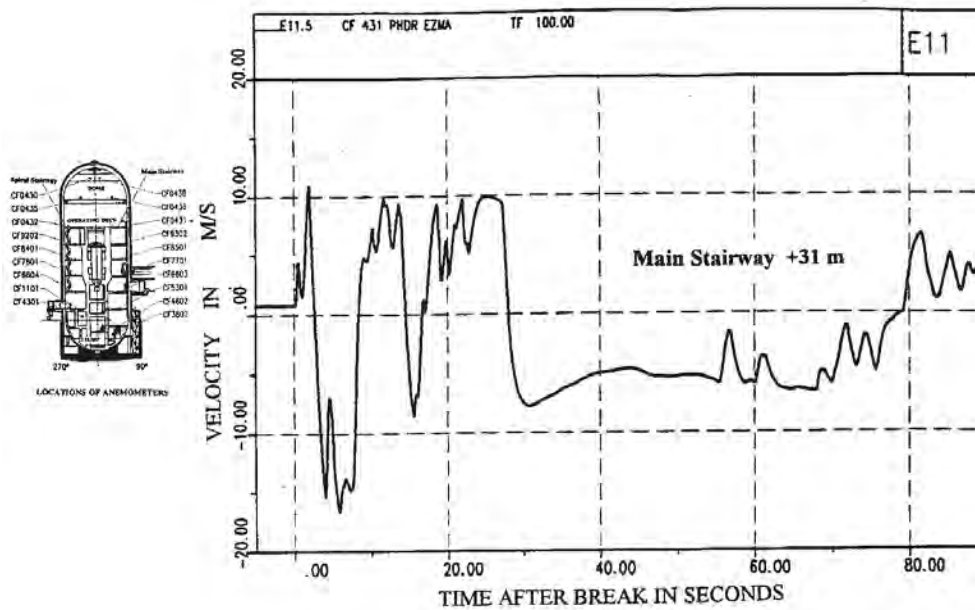


Figure 9.C-124a. HDR-E11.5 Velocities in the Main Stairway During Blowdown

(reprinted from: L. Wolf, K. Mun, "Overview of experimental results for long-term, Large-scale natural circulations in LWR-containments after large LOCAs, Vol. II: Assessment of HDR Experiments V21.1, V43, T31.5 and E11.5," University of Maryland at College Park, for DOE – Project HDR Hydrogen Mixing Evaluation for Containment Safety Evaluations natural Global Circulation, Order Number: DE-AP07-96ID10765," April 1996)

9.C-198

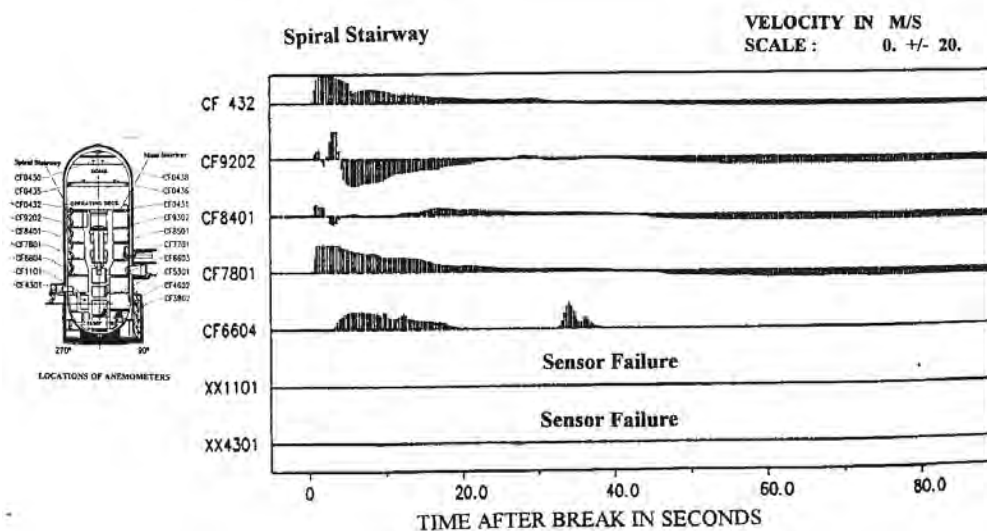


Figure 9.C-124b. HDR-E11.5 Velocities in the Spiral Stairway During Blowdown

(reprinted from: L. Wolf, K. Mun, "Overview of experimental results for long-term, Large-scale natural circulations in LWR-containments after large LOCAs, Vol. II: Assessment of HDR Experiments V21.1, V43, T31.5 and E11.5," University of Maryland at College Park, for DOE – Project HDR Hydrogen Mixing Evaluation for Containment Safety Evaluations natural Global Circulation, Order Number: DE-AP07-96ID10765," April 1996)

9.C-199

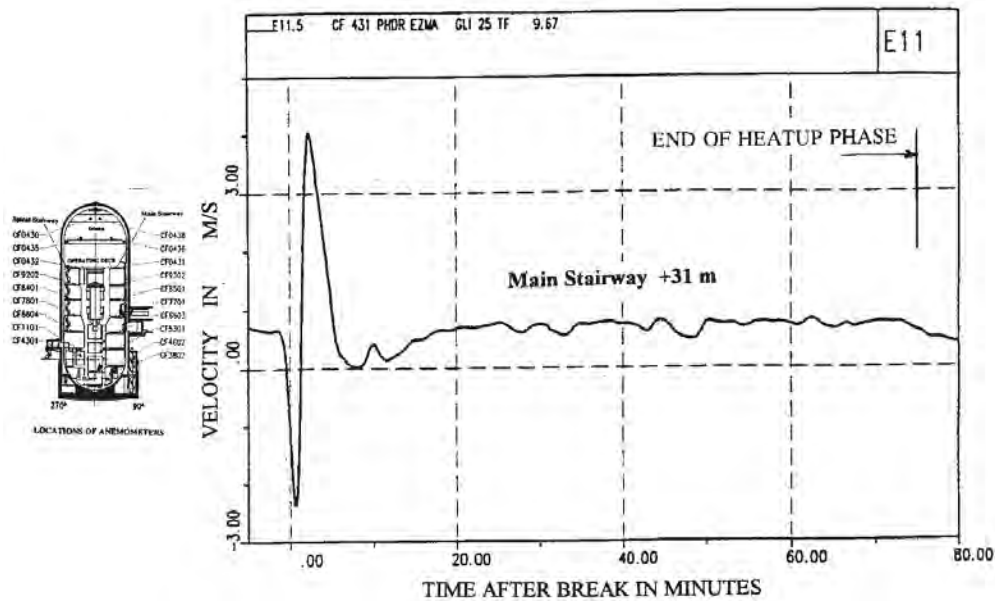


Figure 9.C-125a. HDR-E11.5 Velocities in the Main Stairway During Containment Heatup Phase

(reprinted from: L. Wolf, K. Mun, "Overview of experimental results for long-term, Large-scale natural circulations in LWR-containments after large LOCAs, Vol. II: Assessment of HDR Experiments V21.1, V43, T31.5 and E11.5," University of Maryland at College Park, for DOE – Project HDR Hydrogen Mixing Evaluation for Containment Safety Evaluations natural Global Circulation, Order Number: DE-AP07-96ID10765," April 1996)

9.C-200

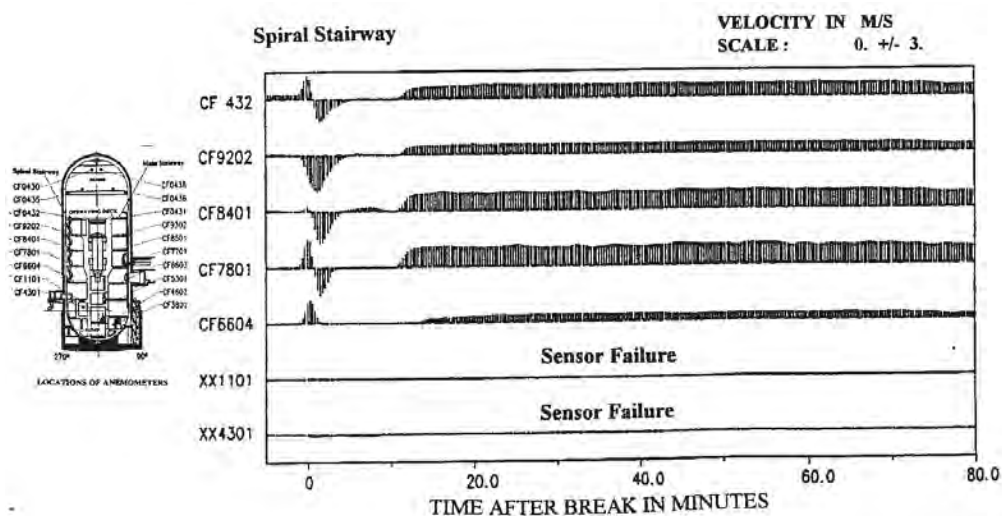


Figure 9.C-125b. HDR-E11.5 Velocities in the Spiral Stairway During Containment Heatup Phase

(reprinted from: L. Wolf, K. Mun, "Overview of experimental results for long-term, Large-scale natural circulations in LWR-containments after large LOCAs, Vol. II: Assessment of HDR Experiments V21.1, V43, T31.5 and E11.5," University of Maryland at College Park, for DOE – Project HDR Hydrogen Mixing Evaluation for Containment Safety Evaluations natural Global Circulation, Order Number: DE-AP07-96ID10765," April 1996)

9.C-201

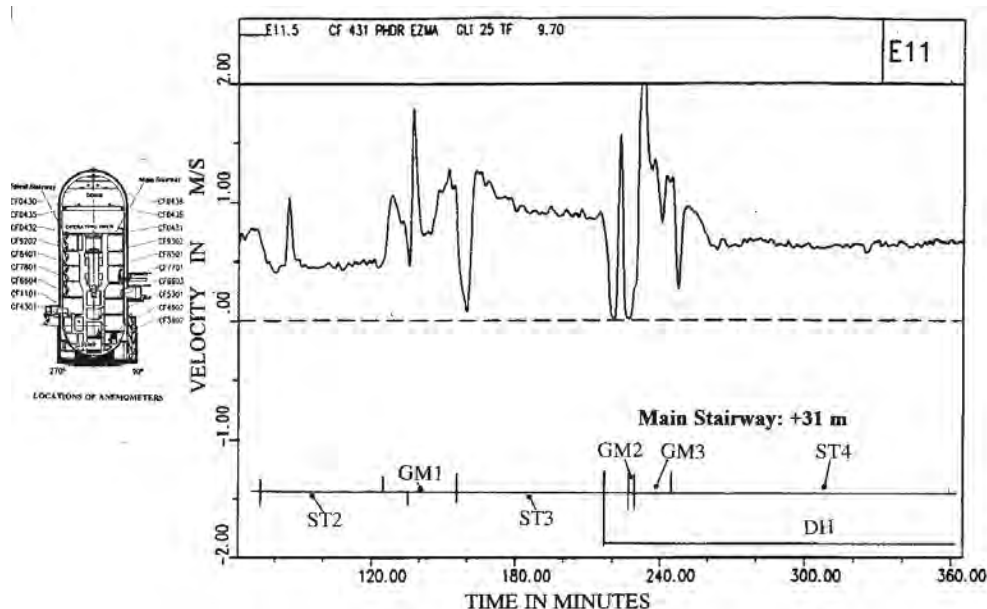


Figure 9.C-126a. HDR-E11.5 Velocities in the Main Stairway During H₂-He Gas Mixture Release Phase

(reprinted from: L. Wolf, K. Mun, "Overview of experimental results for long-term, Large-scale natural circulations in LWR-containments after large LOCAs, Vol. II: Assessment of HDR Experiments V21.1, V43, T31.5 and E11.5," University of Maryland at College Park, for DOE – Project HDR Hydrogen Mixing Evaluation for Containment Safety Evaluations natural Global Circulation, Order Number: DE-AP07-96ID10765," April 1996)

9.C-202

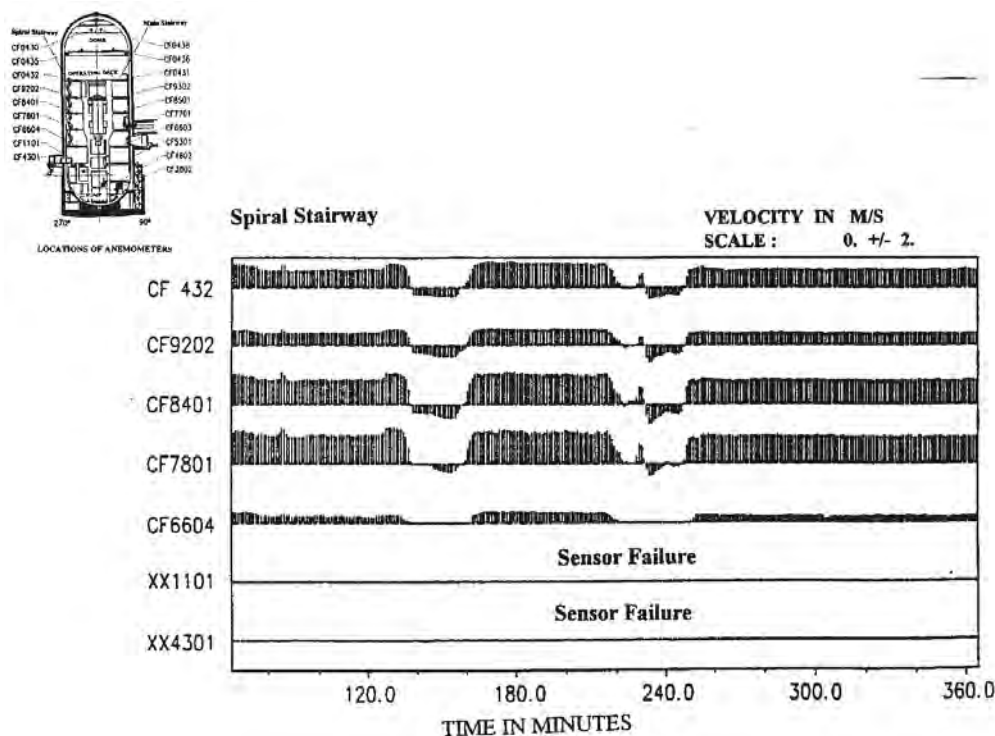


Figure 9.C-126b. HDR-E11.5 Velocities in the Spiral Stairway During H₂-He Gas Mixture Release Phase

(reprinted from: L. Wolf, K. Mun, "Overview of experimental results for long-term, Large-scale natural circulations in LWR-containments after large LOCAs, Vol. II: Assessment of HDR Experiments V21.1, V43, T31.5 and E11.5," University of Maryland at College Park, for DOE – Project HDR Hydrogen Mixing Evaluation for Containment Safety Evaluations natural Global Circulation, Order Number: DE-AP07-96ID10765," April 1996)

9.C-203

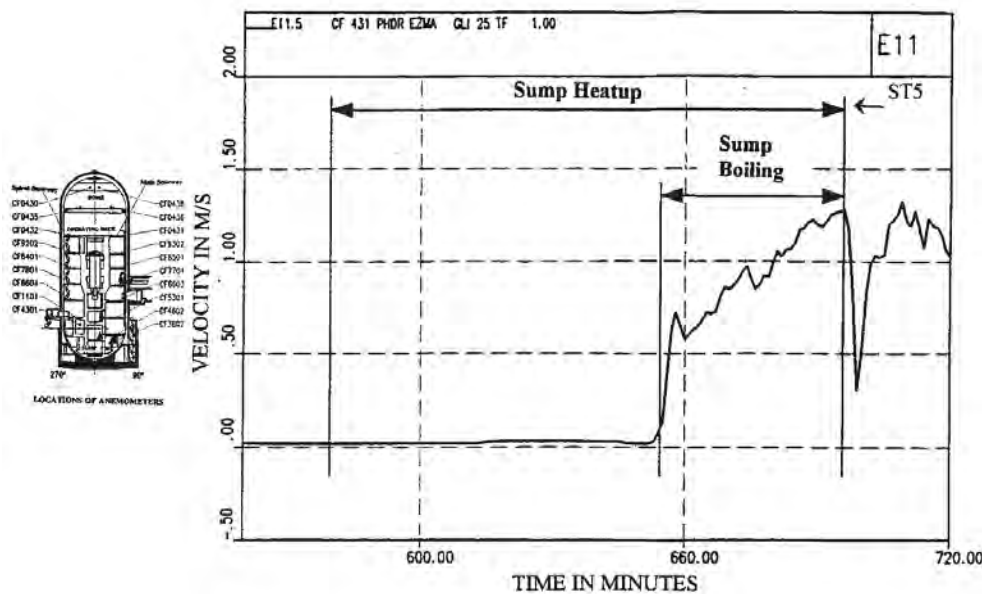


Figure 9.C-127a. HDR-E11.5 Velocities in the Main Stairway During Sump Heatup and Boiling Phase

(reprinted from: L. Wolf, K. Mun, "Overview of experimental results for long-term, Large-scale natural circulations in LWR-containments after large LOCAs, Vol. II: Assessment of HDR Experiments V21.1, V43, T31.5 and E11.5," University of Maryland at College Park, for DOE – Project HDR Hydrogen Mixing Evaluation for Containment Safety Evaluations natural Global Circulation, Order Number: DE-AP07-96ID10765," April 1996)

9.C-204

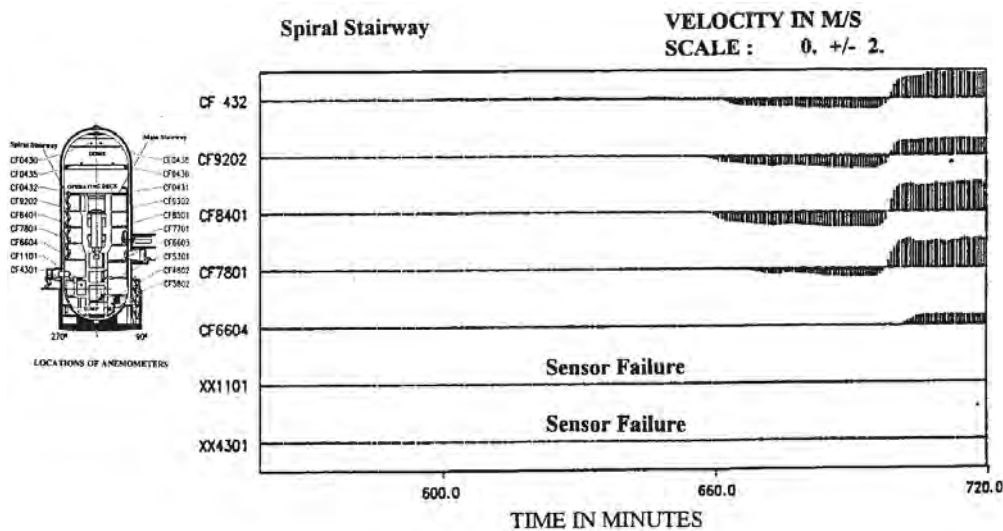


Figure 9.C-127b. HDR-E11.5 Velocities in the Spiral Stairway During Sump Heatup and Boiling Phase

(reprinted from: L. Wolf, K. Mun, "Overview of experimental results for long-term, Large-scale natural circulations in LWR-containments after large LOCAs, Vol. II: Assessment of HDR Experiments V21.1, V43, T31.5 and E11.5," University of Maryland at College Park, for DOE – Project HDR Hydrogen Mixing Evaluation for Containment Safety Evaluations natural Global Circulation, Order Number: DE-AP07-96ID10765," April 1996)

9.C-205

9.C.2.4.3 References

1. T. Cron, D. Schrammel, (1993)
“Investigations on Hydrogen Distribution in a Reactor Containment, Quick Look Report, Test Group E11, Experiments E11.0-6” (In German), PHDR Technical Report PHDR 111-92, 1993
2. H. Holzbauer, L. Wolf, (1994)
“GOTHIC verification on behalf of HDR-Hydrogen mixing experiments”
International Conference on New Trends in Nuclear System Thermohydraulics, Volume II, pp. 331-340., Pisa, Italy, May 30th - June 2nd, 1994
3. T. Kanzleiter, L. Valencia, (1984)
“Blowdown-Experiments in a Reactor Containment, Quick Look Report, Test Group CONW and COND, Experiments V21.1, V21.3, V45” (In German), Technical PHDR Report No. 49/84, Nuclear Center Karlsruhe, Germany, May, 1984
4. L. Valencia, (1987)
“Design Report, Blowdown and Hydrogen Distribution Experiments, HDR-Test Group CON, Experiments T31.4-5” (In German), PHDR-Working Report No. 3.516/87, Nov. 1987
5. H. H. Wenzel, R. Grimm, L. L’hr, (1987)
“Test Report, Blowdown and Hydrogen Distribution Experiments, HDR-Test Group CON, Experiments T31.5” (In German), PHDR-Working Report No. 3.520/88, Dec. 1987
6. L. Wolf, L. Valencia, (1988)
“Results of the Preliminary Hydrogen Distribution Experiment at HDR and Future Experiments for Phase III” 16th Water Reactor Safety Information Meeting, Gaithersburg, MD, USA, Oct. 24-27, 1988.
7. L. Wolf, L. Valencia, (1989)
“Experimental Results of the Preliminary HDR-Hydrogen Distribution Test T31.5” 4th Intl. Topical Mtg. on Nuclear Reactor Thermal-Hydraulics, Karlsruhe, Oct. 10-13, 1989, Vol. 2, pp. 967-973.
8. L. Wolf, H. Holzbauer, T. Cron, (1994)
“Detailed Assessment of the HDR-Hydrogen mixing experiments E11” International Conference on New Trends in Nuclear System Thermohydraulics, Volume II, pp. 91-103., Pisa, Italy, May 30th – June 2nd, 1994
9. L. Wolf, K. Mun, J. Floyd, (1995)
“HDR hydrogen mixing evaluation for containment safety evaluations,” Final Report, DOE-Project Order No.: DE-AP07-95ID81401, Dept. of Materials and Nuclear Engineering, University of Maryland, College Park, MD, Sept. 1995

9.C-206

10. L. Wolf, K. Mun, (1996)
“Overview of experimental results for long-term, large-scale natural circulations in LWR-containments after large LOCAS – Vol. II: Assessment of HDR Experiments V21.1, V43, T31.5 and E11.5” DOE – Project, HDR Hydrogen Mixing Evaluation for Containment Safety Evaluations Natural Global Circulation, Order Number: DE – AP07 – 96ID10765 University of Maryland at College Park, April 1996
11. L. Wolf, M. Gavrilas, K. Mun, (1996)
“Overview of experimental results for long-term, large-scale natural circulations in LWR-containments after large LOCAS” Final Report for DOE – Project, Order Number: DE - AP07 – 96ID10765 University of Maryland at College Park, July 1996

9.C.2.5 Conclusion

Eleven of the twenty experiments presented have a low release position $H_r/H_t < 0.2$. These experiments may be compared to the AP600 and **AP1000**.

They include the seven BMC experiments with a low release position (F2 set, Phase 2, 3 and 4, Test 2 – Phase I, Test 20 - Phase II and RX4), the NUPEC experiment M-4-3, and the three HDR experiments (E11.3, E11.4 and E11.5). Most of these tests (except two - BMC Test 20 and NUPAC M-4-3) have global circulation through the dome which contributes towards homogenization of temperature and concentration fields.

The two experiments with the low release position where stratification is recorded are BMC Test 20 and NUPEC M-4-3. As already noted, the stratification occurs due to the special circumstances (boundary conditions). BMC Test 20 stratifies due to the initially stratified temperature field. Upper compartments are maintained at the higher temperature for several days. Global circulation starts first in the lower compartments, resulting in higher concentrations of the released gas mixture being recorded. Later, the circulation flow path penetrates the upper thermally-stratified layers and the vertical concentration gradients are smaller.

In the M-4-3 NUPEC test, the temperature stratification occurs after the end of the release, although injected gas mixture homogenized slowly. The thermally insulated shell of the NUPEC containment could be one cause for thermal stratification. The homogenization of the gas mixture concentration indicates that some circulation inside of the containment existed, probably due to the presence of the sump.

The external cooling of the AP600 and **AP1000**, as well as the hot concrete structures positioned in the lower portion of the containment, will produce global circulation.

Seven experiments have high release positions ($H_r/H_t > 0.5$), two BMC (Test 4 and Test 12), all three CVTR experiments, and two HDR experiments (E11.2 and T31.5). Thermal stratification is present in six of the seven tests, with the exception of BMC Test 12. BMC Test 12 includes only hydrogen injection.

9.C-207

Due to the uniform initial temperature field (boundary conditions) and circulation patterns formed by hydrogen injection, the concentration field was uniform in BMC Test 12. In the second and third CVTR experiments, the application of the internal sprays decreases the pressure and vertical temperature gradients.

In HDR experiments E11.2 and T31.5, the temperature and concentration fields stratify at the beginning of the experiments. Later, the global circulation decreases the vertical gradients.

In experiment E11.2, additional steam release in the lower compartment and the application of external sprays generates global circulation and decreases vertical gradients.

A review of the tests indicates that global circulation and atmosphere homogenization will occur if:

1. The position of the steam or hydrogen release ($H_r/H_t < 0.2$) is low
2. External sprays are applied
3. Internal sprays are active
4. Openings between compartments are large
5. The temperature field is not initially stratified
6. Heat sources, such as hot concrete walls or a sump, are at the low positions
7. Compartments are connected (not dead-ended)

In the case of AP600 and **AP1000** passive containment designs, all conditions except 3) and partially 7) are satisfied.

9.C.3 APPLICATION OF LUMPED-PARAMETER CODES FOR MODELING LARGE CONTAINMENT FACILITIES

Results of codes using the lumped parameter approach are summarized in this chapter. The ability of the lumped parameter codes to model large facilities is assessed and guidelines to improve predictions are presented.

Tests from several facilities included in an international database are used to compare and validate the results of the lumped parameter containment analysis computer codes. Among the test facilities in the database are BMC, NUPEC, and HDR. Results from these experiments have been described in sections 9.C.2.1, 9.C.2.2, and 9.C.2.4, respectively.

9.C.3.1 Validation of the Lumped Parameter Containment Analysis Computer Codes Based on BMC Experimental Results

The BMC F2 tests are used to validate various containment codes (Fisher et al., 1991 and Fisher et al., 1993). BMC tests 2, 4, 6, 12, and 20 are used to compare various lumped parameter and distributed-parameter GOTHIC models (L. Wolf, H. Holzbauer, M. Schall, 1994).

9.C-208

9.C.3.1.1 F2 Experiments – Natural Convection Phenomena Inside the Multi-Compartment Containment

A comparison of the experimental results of the F2 experiments with the results of various codes is presented by L. Wolf, M. Gavrilas, K. Mun, 1996. The comparison is based on thermal-hydraulic benchmark exercises by Fisher et al., 1991 for Phase 1 and by Fisher et al., 1993 for Phases 2, 3, and 4. Many different codes including FUMO, JERICO, FIPLOC, WAVCO, CONTAIN, MELCOR, and COBRA/FATHOMS are compared. The comparisons demonstrate the state of containment code development with respect to multi-compartment thermal-hydraulics.

Figures 1.17 through 1.37 (in Wolf et al., 1996) illustrate both the experimental data and the results of various containment analysis codes for F2-Experiment Heatup Phase (Phase I) over a long period of time (48 hours). Single-node models are specified for this exercise. This results in three mean sources of deviations between measurement and code results:

1. **Single-node models are not able to model stratification** (due to the penetration of the steam front) inside the dead-end compartments.
2. **One-node lumped parameter models cannot model the stratification front passing through horizontal vents.** One-node models provide artificially perfect mixing between the connected compartments, while in reality only a portion of the vents are available for circulation.
3. **Sump liquid level and sump temperature are not predicted well due to the instantaneous transport of high temperature condensate into sump and stratification phenomena inside the sump.** (Note that the temperature of the condensate is too high.)

The influence of all three discrepancies between the experimental and numerical results can be decreased by applying a series of nodes in a vertical direction or subdivision, as in the GOTHIC distributed parameter model.

Figures 1.50 through 1.55 (in Wolf et al., 1996) compare the experimental data for the F2-Experiment Phase II with the results of various codes. All compartments except the external annulus have almost homogeneous temperatures due to the presence of the natural circulation. A comparison of the measured and predicted velocities through the vents is in agreement for the majority of the codes, which supports the conclusion (L. Wolf, M. Gavrilas, K. Mun, 1996) that containment codes based on lumped parameter models can predict fully-developed natural circulation flows.

However, some codes produced results that are not correct. It was established that the incorrect codes missed or oversimplified the buoyancy terms (see K. Fischer et al., 1993).

9.C.3.1.2 Influence of Initial Temperature Distribution, Location of Hydrogen Injection, Duration of Injection, and Size of Vent Openings on Hydrogen Distribution (BMC Tests 2, 4, 6, 12, and 20)

A comparison of the multi-dimensional and lumped parameter GOTHIC containment analyses and the BMC experimental data is presented in Wolf et al., 1994b. Tests 2, 4, and 6, described in Section 9.C.2.1.2, are performed with only the central compartments R1, R2, and R3. Only two-dimensional GOTHIC results are presented.

Three different models are used to compare the results with multi-compartment experiments 12 and 20. Test 12, which uses a uniform initial temperature distribution, results in homogenized hydrogen concentrations in the entire containment. The lumped parameter model simulates hydrogen concentration histories in the various compartments (see Figure 9 in Wolf et al., 1994b, see also Figure 9.C-43 in this appendix). **To account for recirculation flows, the applied lumped parameter model uses double-junctions in the horizontal direction.**

Test 20 has a stratified initial temperature distribution, which results in a higher hydrogen distribution in the lower rooms. The conventional lumped parameter model, with one junction connection between two subvolumes, results in a hydrogen concentration profile (in R1 and R2 rooms) that is opposite to that measured (see Figure 9 in L. Wolf, H. Holzbauer, M. Schall, 1994b). Also, the experimental results indicate a stratified hydrogen concentration during the first three hours, while the computed generated hydrogen distribution is more uniform. **The calculation performed with double-junction lumped parameter modeling (second model) does not improve results. This model also results in a high degree of hydrogen homogenization inside the containment.**

The third type of model uses a two-dimensional model (distributed parameter model) for all containment rooms except room R2 and uses double-junctions for horizontal connections. The results are presented in Figure 11 in L. Wolf, H. Holzbauer, M. Schall, 1994b and Figure 9.C-44 of this appendix. Improvement between experimental and computed results is obvious (except in the source room R6). A finer nodalization of the source compartment R6 could further improve the results, because the processes in this compartment affect the hydrogen distribution phenomena in all other portions of the containment. Therefore, a more complete momentum formulation, such as that in GOTHIC distributed parameters, is needed to accurately model H₂ distributions.

9.C-210

9.C.3.2 Validation of the Lumped Parameter Containment Analysis Computer Codes Based on Nupec Experimental Results

9.C.3.2.1 M-7-1 Test

A comparison of the M-7-1 test results with the various computer codes results is presented in report NEA/CSNI/R(94)29. The WGOTHIC (Westinghouse modified GOTHIC) code results are also included (see pages 125, 130, 135, blind test calculation results – pages 246-253, open test calculations – pages 322-327, preheating calculation - 374-378). However, the M-7-1 test is not directly applicable to the passive containment design, because internal sprays are active during the test.

9.C.3.2.2 M-4-1 Test

The experimental results of NUPEC M-4-3 test (T. Hirose, 1993) are used to validate various lumped parameter codes and to check the input geometry and boundary conditions, before applying them to blind and open comparisons with the NUPEC M-7-1 database. WGOTHIC is also compared with NUPEC M-4-3 experimental data. A comparison of the WGOTHIC results with the M-4-3 test, which is performed without internal sprays, is presented by R. P. Ofstun, J. Woodcock, D. L. Paulsen, 1994. The location of the break is at a low position in the first level of the containment. A mixture of steam and helium is injected at a constant flow rate during the first 30 minutes and experimental data is recorded for 2 hours.

A comparison of the experimentally and numerically obtained pressure of the dome is illustrated in Figure 9.C-128. Figure 9.C-129 through Figure 9.C-132 present comparisons of the temperatures and helium concentrations inside the compartments 8, 15, dome, and 7. These compartments are affected by the global circulation loop. Lumped parameter modeling methods developed for NUPEC M-4-3 are summarized in Section 9.2.4. Good agreement exists between the numerical and experimental results for the multiple, connected, lumped parameter compartments in the circulating regions.

However, a paper by R.P. Ofstun, J. Woodcock, D. L. Paulsen, 1994 shows a discrepancy between the measured and calculated (lumped parameter model) helium concentrations in dead-end compartments. Calculated values for in-core chase node and two pressurizer nodes (which are all dead-end compartments) are presented and compared with M-4-3 test data (see Figures 3-8, in R.P. Ofstun, J. Woodcock, D. L. Paulsen, 1994). The discrepancy shows that the lumped parameter model has difficulty predicting circulation effects within dead-end compartments.

It is postulated that asymmetric temperatures on the vertical walls of the dead-ended compartments induce a natural circulation within the compartment that is not modeled in the lumped parameter model. To improve the results for dead-end compartments, a WGOTHIC distributed parameter model is applied to the dead-ended compartments and interfaced to the lumped parameter model (see Figures 9 - 14 in R. P. Ofstun, J. Woodcock, D. L. Paulsen, 1994).

The lumped parameter model predicts pressure, temperature and helium concentrations inside the compartments affected by the global circulation loop. However, a distributed parameter model is necessary to improve predictions inside the dead-end compartments.

9.C-211

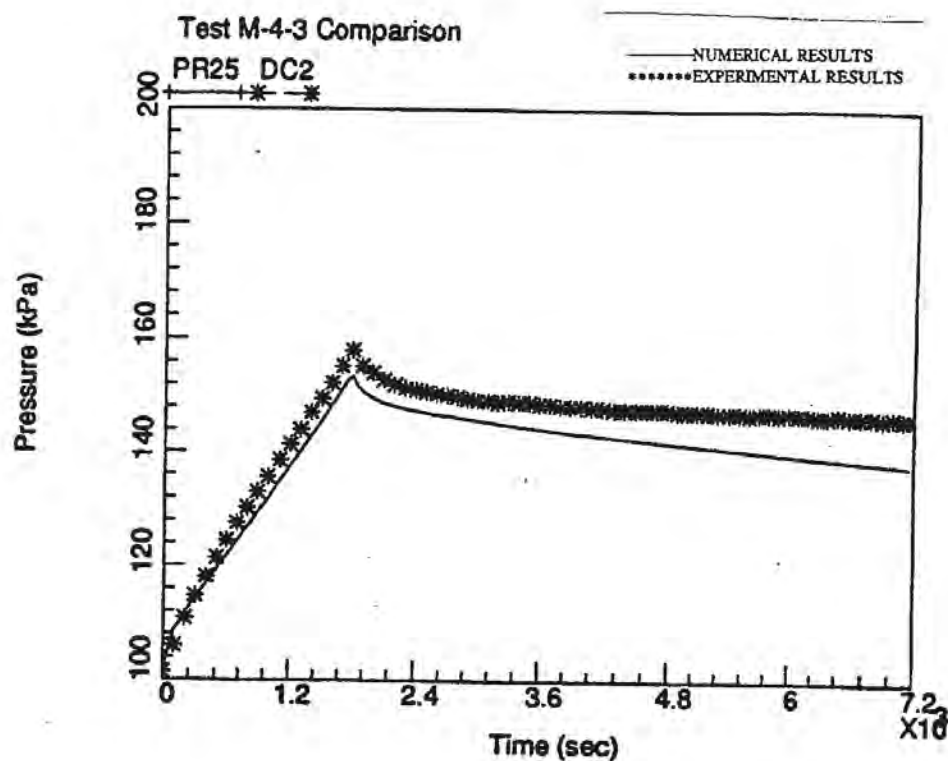


Figure 9.C-128. Dome Pressure History

(Numerical results are produced in the framework of: R.P. Ofstun, J. Woodcock, D.L. Paulsen, "Westinghouse-GOTHIC modeling of NUPEC's hydrogen mixing and distribution test M-4-3," The Third International Conference on Containment Design and Operations, Volume 1, Toronto, Canada, October 19-21, 1994)

9.C-212

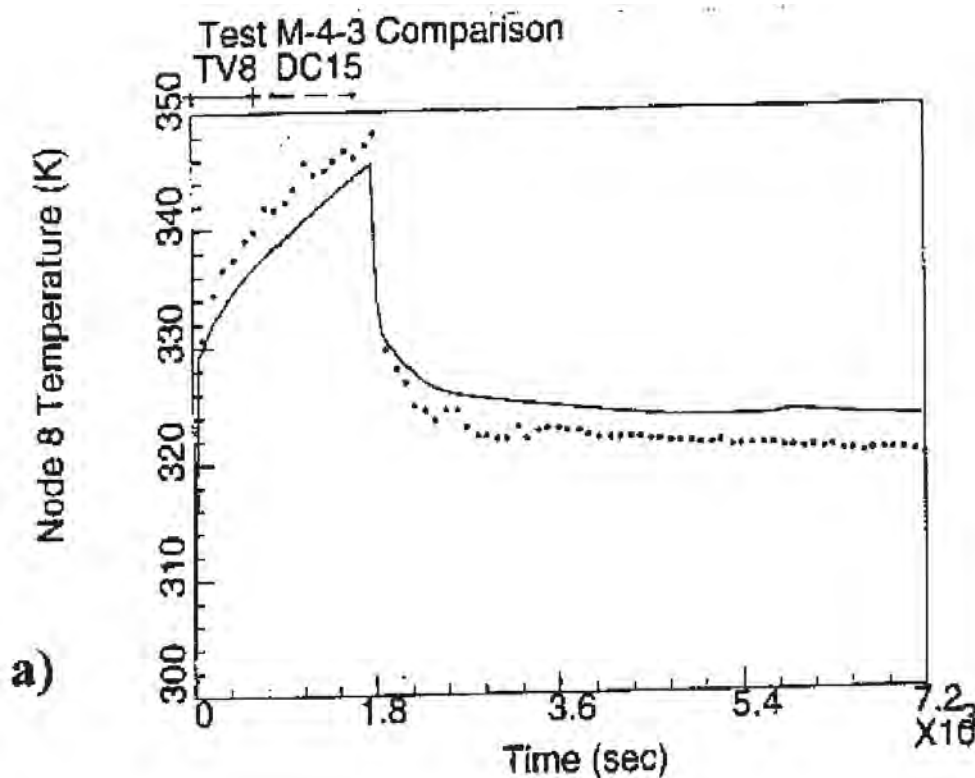


Figure 9.C-129a. Temperature History Inside Node 8

(Numerical results are produced in the framework of: R.P. Ofstun, J. Woodcock, D.L. Paulsen, "Westinghouse-GOTHIC modeling of NUPEC's hydrogen mixing and distribution test M-4-3," The Third International Conference on Containment Design and Operations, Volume 1, Toronto, Canada, October 19-21, 1994)

9.C-213

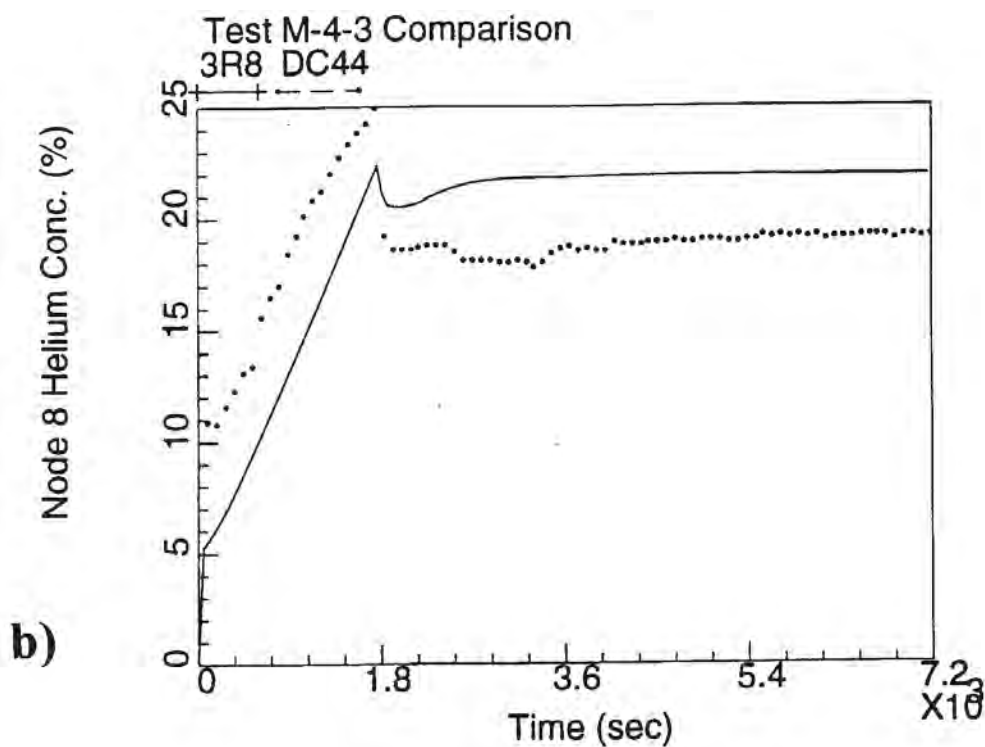


Figure 9.C-129b. Helium Concentration History Inside Node 8

(Numerical results are produced in the framework of: R.P. Ofstun, J. Woodcock, D.L. Paulsen, "Westinghouse-GOTHIC modeling of NUPEC's hydrogen mixing and distribution test M-4-3," The Third International Conference on Containment Design and Operations, Volume 1, Toronto, Canada, October 19-21, 1994)

9.C-214

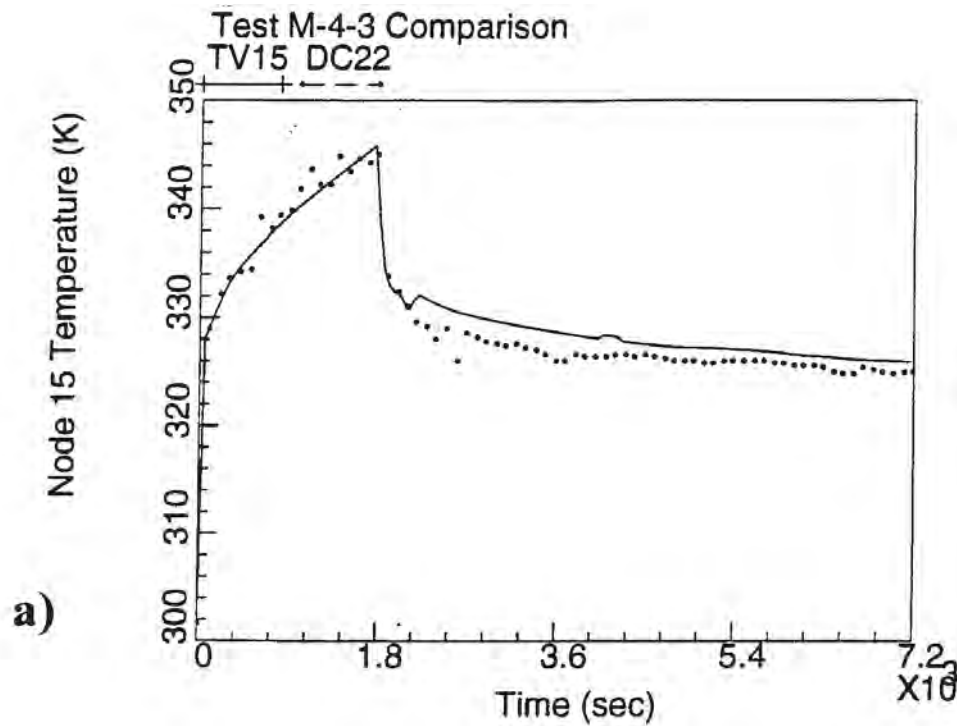


Figure 9.C-130a. Temperature History Inside Node 15

(Numerical results are produced in the framework of: R.P. Ofstun, J. Woodcock, D.L. Paulsen, "Westinghouse-GOTHIC modeling of NUPEC's hydrogen mixing and distribution test M-4-3," The Third International Conference on Containment Design and Operations, Volume 1, Toronto, Canada, October 19-21, 1994)

9.C-215

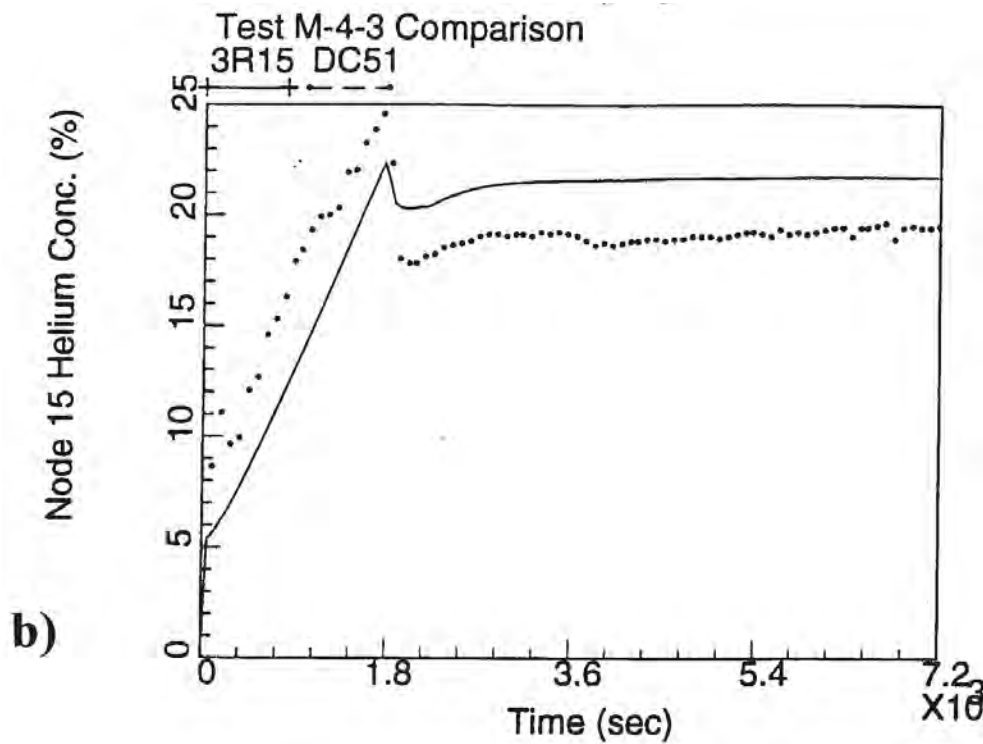


Figure 9.C-130b. Helium Concentration History Inside Node 15

(Numerical results are produced in the framework of: R.P. Ofstun, J. Woodcock, D.L. Paulsen, "Westinghouse-GOTHIC modeling of NUPEC's hydrogen mixing and distribution test M-4-3," The Third International Conference on Containment Design and Operations, Volume 1, Toronto, Canada, October 19-21, 1994)

9.C-216

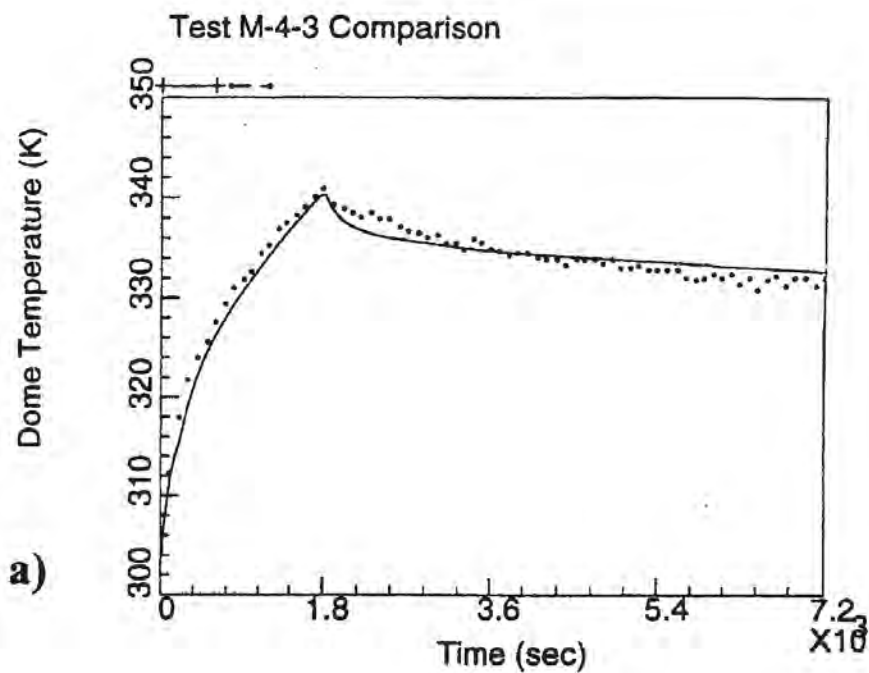


Figure 9.C-131a. Temperature History Inside Dome

(Numerical results are produced in the framework of: R.P. Ofstun, J. Woodcock, D.L. Paulsen, "Westinghouse-GOTHIC modeling of NUPEC's hydrogen mixing and distribution test M-4-3," The Third International Conference on Containment Design and Operations, Volume 1, Toronto, Canada, October 19-21, 1994)

9.C-217

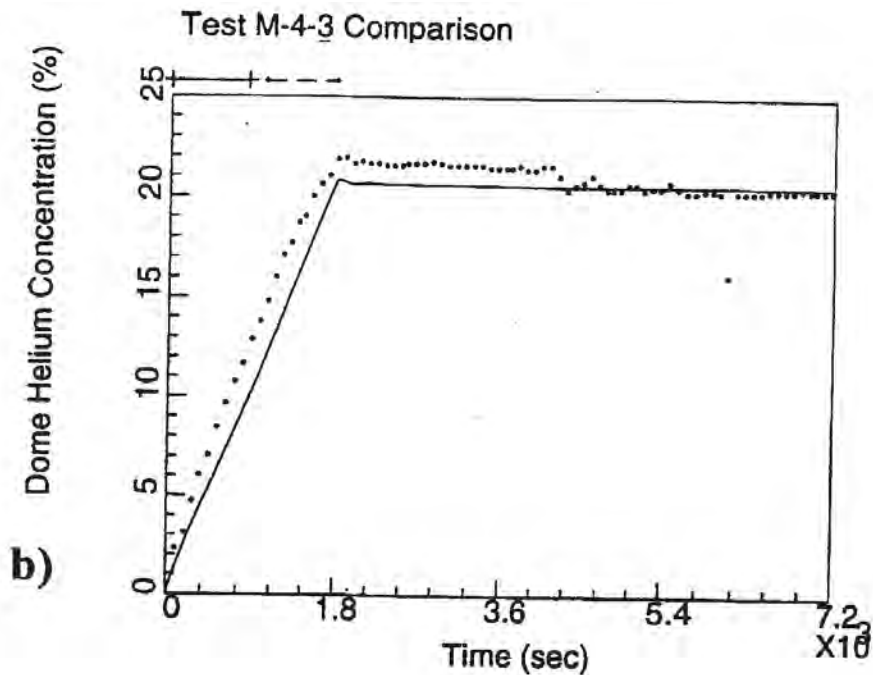


Figure 9.C-131b. Helium Concentration History Inside Dome

(Numerical results are produced in the framework of: R.P. Ofstun, J. Woodcock, D.L. Paulsen, "Westinghouse-GOTHIC modeling of NUPEC's hydrogen mixing and distribution test M-4-3," The Third International Conference on Containment Design and Operations, Volume 1, Toronto, Canada, October 19-21, 1994)

9.C-218

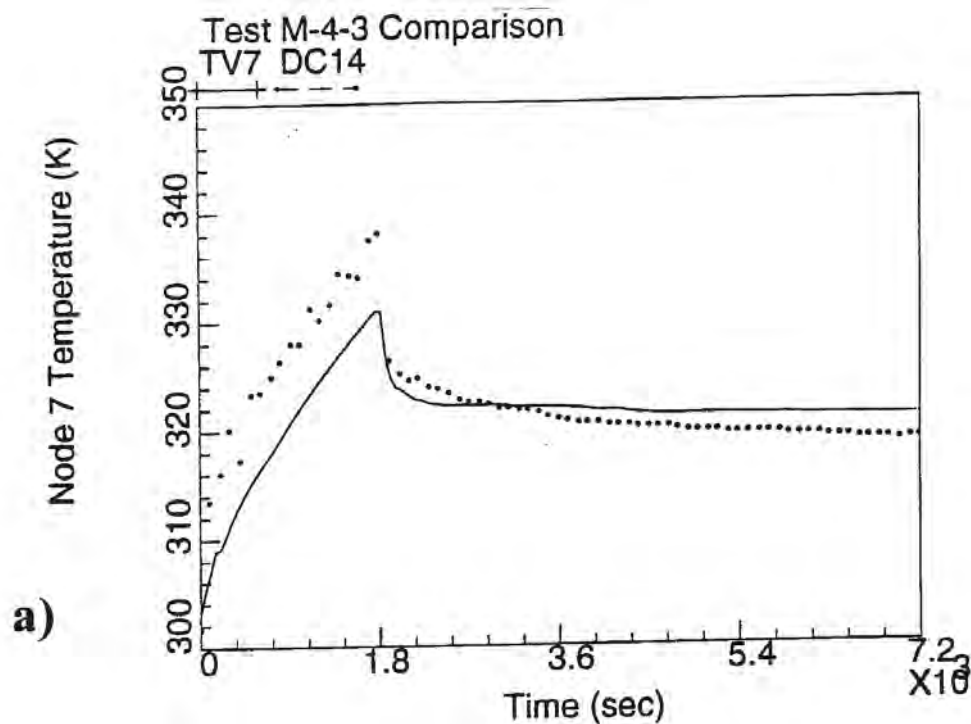


Figure 9.C-132a. Temperature History Inside Node 7

(Numerical results are produced in the framework of: R.P. Ofstun, J. Woodcock, D.L. Paulsen, "Westinghouse-GOTHIC modeling of NUPEC's hydrogen mixing and distribution test M-4-3," The Third International Conference on Containment Design and Operations, Volume 1, Toronto, Canada, October 19-21, 1994)

9.C-219

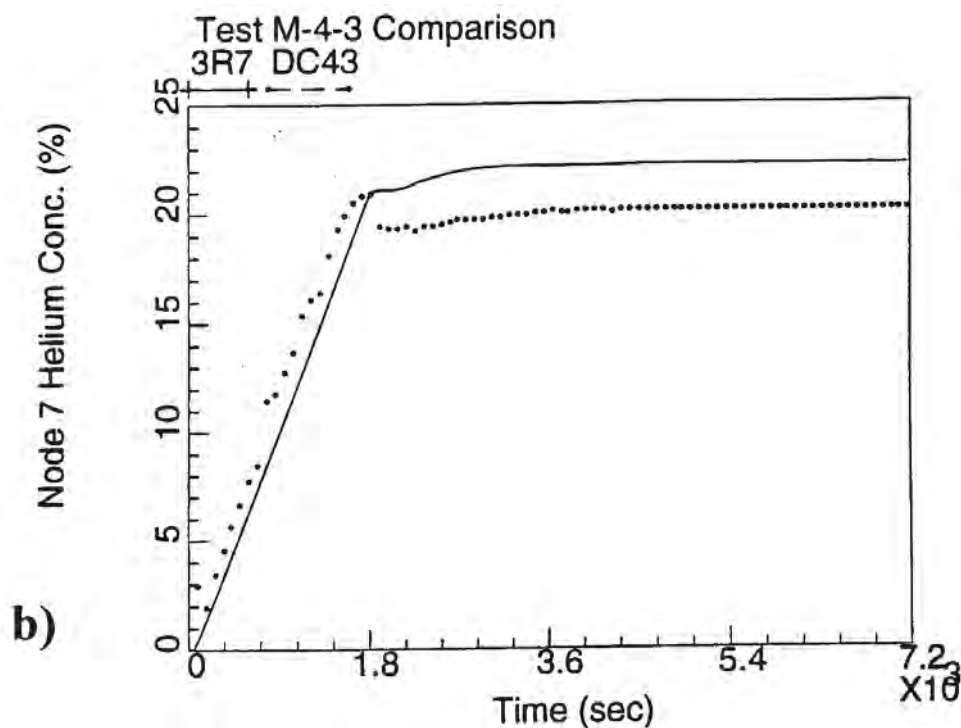


Figure 9.C-132b. Helium Concentration History Inside Node 7

(Numerical results are produced in the framework of: R.P. Ofstun, J. Woodcock, D.L. Paulsen, "Westinghouse-GOTHIC modeling of NUPEC's hydrogen mixing and distribution test M-4-3," The Third International Conference on Containment Design and Operations, Volume 1, Toronto, Canada, October 19-21, 1994)

9.C-220

9.C.3.3 Validation of the Lumped-Parameter Containment Analysis Computer Codes Based on HDR Experimental Results

Comparisons of the results of best-estimate open post-test predictions of various containment analysis computer codes (as RALOC, WAVCO, CONTAIN, MELCOR, and GOTHIC) for E11.2 and E11.4 HDR experiments presented by L. Wolf, H. Holzbauer and T. Cron, 1994a. Detailed comparisons and verifications of the blind and open GOTHIC results for the E11.2 and E11.4 HDR experiments are presented by H. Holzbauer and L. Wolf, 1994. More details about E11.2 and E11.4, and comparisons with the experimental results of large blowdown tests T31.5, V21.1, and E11.5, are presented in the report by K. Fischer, M. Schall, L. Wolf, 1995.

Following is a summary of observations from the comparison of the experiments with codes:

1. **Scenarios with homogeneous containment atmosphere (like E11.4 and E11.5) can be simulated successfully with lumped parameter models.**

The results of the E11.4 computation agree with the corrected experimental input data (open test – see Figures 17-21 in H. Holzbauer and L. Wolf, 1994).

The same conclusion is valid for accidents initiated by a large-break LOCA in the lower positions of containments, accompanied by subsequent steam and gas releases (as in E11.5). Good agreement has been achieved by the GOTHIC lumped-parameter model using a modest number of nodes (see Figures 10.9 – 10.22 in K. Fischer, M. Schall, L. Wolf, 1995). A comparison of the experimentally and numerically obtained pressure histories is presented in Figure 9.C-133. The calculated pressure history is slightly higher than the experimental results. Figure 9.C-134 presents a comparison for sump temperature. Note that the sump temperature sensor is exposed to the containment atmosphere for the first 8 hours. It is then submerged by higher sump water level. **The history of sump boiling is well simulated.** Comparisons of temperatures in main and spiral stairways at 6 m level are presented in Figure 9.C-135 and Figure 9.C-136, respectively. Gas mixture concentration comparisons for the same staircase elevation are presented in Figure 9.C-137 and Figure 9.C-138. The measured velocity in spiral stairway at 15 m elevation is presented in Figure 9.C-139. **Since the order of magnitude of the computed velocities matches the data, it can be concluded that trends in the direction of the flow are predicted well; however, predicted velocities differ by as much as factor of two.**

9.C-221

2. **The lumped parameter method is not capable of predicting the hydrogen distribution in a stratified containment atmosphere (as in E11.2 test with high-positioned release).**

The pressure history is well predicted after applying the correct steam inflow experimental data and accounting for energy sink of the sensors cooling system. Comparisons between the experimental data and the “optimized” post-test prediction for containment pressure are presented in Figure 9.C-140. GOTHIC lumped parameter results overpredict pressure by 0.25 bar (11%).

Temperatures, steam, and gas concentrations are underestimated and overestimated above and below the break location, respectively, (see Figures 7 and 8 in H. Holzbauer and L. Wolf, 1994). **Therefore, for a high-positioned release, the steam and gas transport to the lower parts of the containment are overpredicted.**

Artificial limitation of convective flows (by reduction of flow path areas) in all modeled flow paths improves the prediction of temperatures and gas concentrations in the lower containment regions (Figures. 13, 15, and 16 in H. Holzbauer and L. Wolf, 1994), but overestimates the containment pressure and temperatures in the upper containment (see results of parametric calculations NA15 and NA16, Figures 11 and 12 in H. Holzbauer and L. Wolf, 1994).

3. **Application of distributed parameter models may improve prediction of a stratified containment atmosphere (as in E11.2 test).**

A study of the influence of the number of nodes applied for a simple volume proportional to the HDR E11.2 facility volume using a distributed parameter model is presented by J.S. Narula and J. Woodcock, 1994. The authors conclude that in situations requiring detailed flow distribution in non-homogenous environments, a fine mesh may be required to obtain realistic results. A coarse mesh (small number of nodes) may reduce the accuracy of the results, despite a highly accurate containment model in all other aspects, including momentum representation.

A detailed study of the influence of the nodalization, and a comparison of the lumped parameter results with distributed parameter model results for E11.2 case are presented by K.K. Mun, 1996. This report also includes a comparison of the pressure, temperature, steam and hydrogen concentrations histories (see Figures 67 – 91 in K.K. Mun, 1996). The author concludes that, in general, the modeling approach of merging the distributed and lumped parameter models improves the prediction. However, to improve the prediction further, a proper distributed parameter nodalization for the lower break compartment and dome, together with the correct connections for the associated flow paths, are required.

All specified observations 1, 2, and 3 for GOTHIC applications are in agreement with comparisons of the results of other well-known codes (see L. Wolf, H. Holzbauer and T. Cron, 1994a).

9.C-222

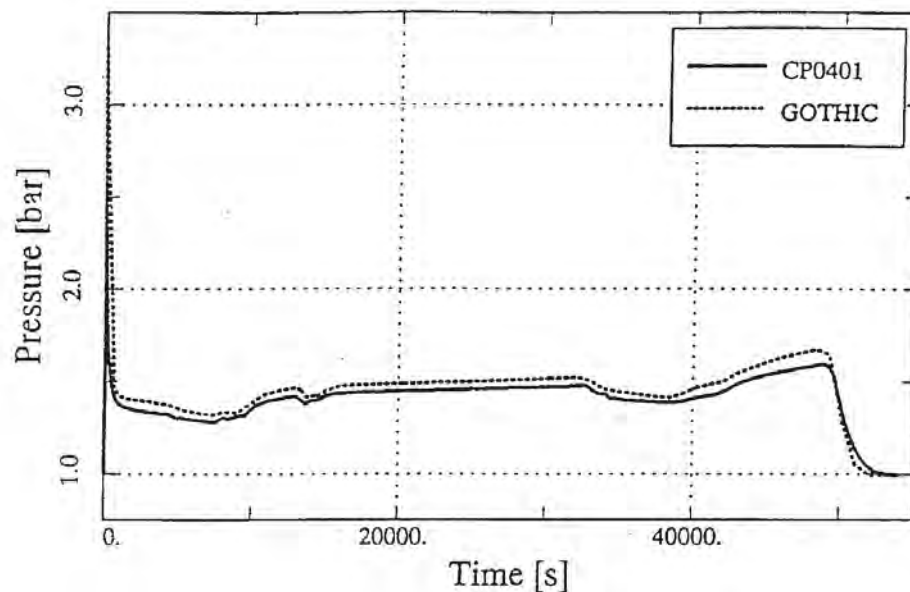


Figure 9.C-133. HDR-E11.5: Comparison Between Measured Long-Term Containment Pressure and GOTHIC Open Post-Test Prediction

Reproduced with permission from a report funded by the EPRI GOTHIC Advisory Group: K. Fischer, M. Schall, L. Wolf, "Simulations of GOTHIC Large Scale Containment Experiments," Battelle Ingenieurtechnik GnuBH, Eshborn, Fachbericht BF – V – 68317 – 01, October 1995)

9.C-223

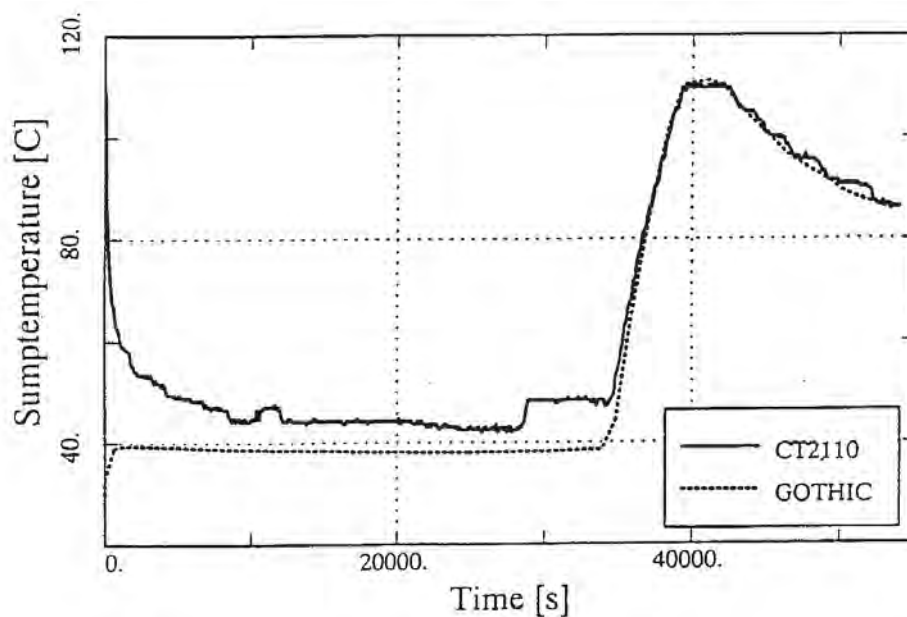


Figure 9.C-134. HDR-E11.5: Comparison Between Measured Sump Temperature and GOTHIC Open Post-Test Prediction

Reproduced with permission from a report funded by the EPRI GOTHIC Advisory Group: K. Fischer, M. Schall, L. Wolf, "Simulations of GOTHIC Large Scale Containment Experiments," Battelle Ingenieurtechnik GnuBH, Eshborn, Fachbericht BF – V – 68317 – 01, October 1995)

9.C-224

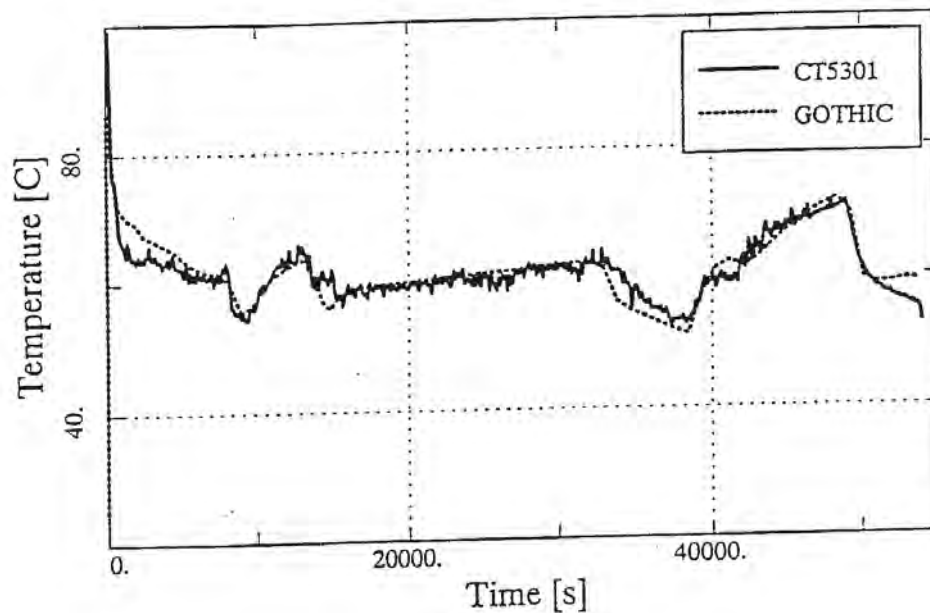


Figure 9.C-135. HDR-E11.5: Comparison Between Measured Temperature in Main Stairway (6m) and GOTHIC Open Post-Test Prediction

Reproduced with permission from a report funded by the EPRI GOTHIC Advisory Group: K. Fischer, M. Schall, L. Wolf, "Simulations of GOTHIC Large Scale Containment Experiments," Battelle Ingenieurtechnik GnuBH, Eshborn, Fachbericht BF – V – 68317 – 01, October 1995)

9.C-225

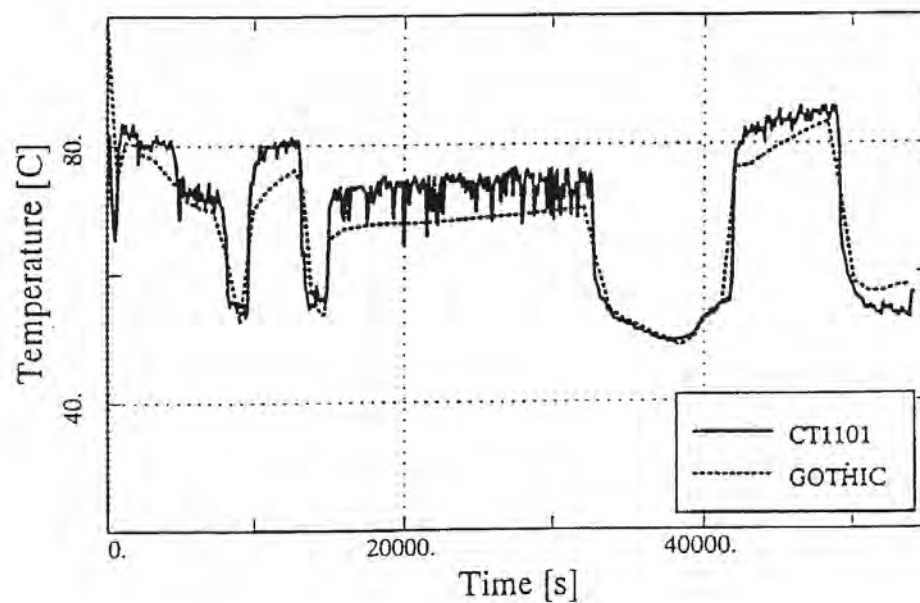


Figure 9.C-136. HDR-E11.5: Comparison Between Measured Temperature in Spiral Stairway (6m) and GOTHIC Open Post-Test Prediction

Reproduced with permission from a report funded by the EPRI GOTHIC Advisory Group: K. Fischer, M. Schall, L. Wolf, "Simulations of GOTHIC Large Scale Containment Experiments," Battelle Ingenieurtechnik GmBH, Eshborn, Fachbericht BF – V – 68317 – 01, October 1995)

9.C-226

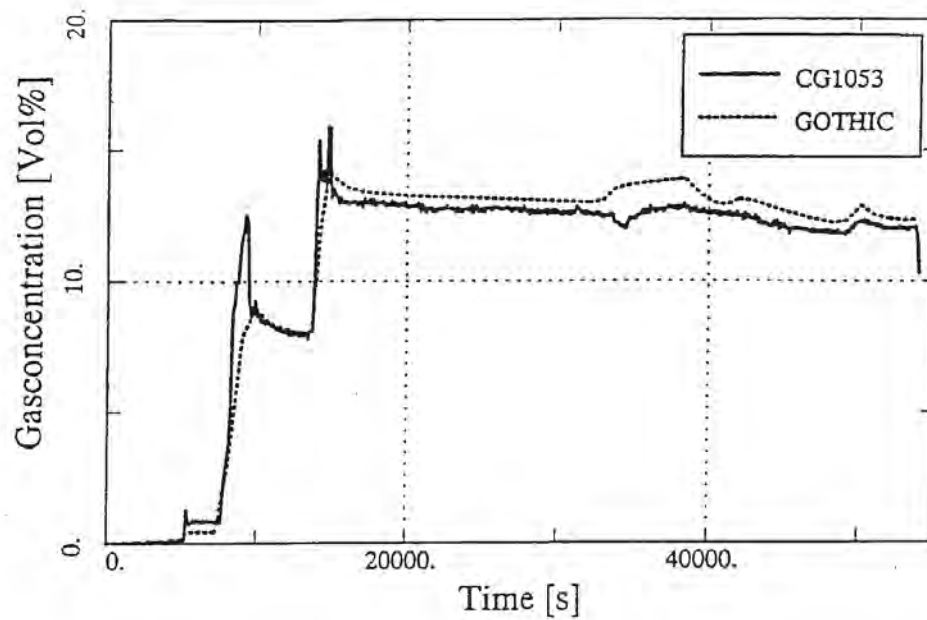


Figure 9.C-137. HDR-E11.5: Comparison Between Measured Gas Mixture Concentration in Main Stairway (6m) and GOTHIC Open Post-Test Prediction

Reproduced with permission from a report funded by the EPRI GOTHIC Advisory Group: K. Fischer, M. Schall, L. Wolf, "Simulations of GOTHIC Large Scale Containment Experiments," Battelle Ingenieurtechnik GmBH, Eshborn, Fachbericht BF – V – 68317 – 01, October 1995)

9.C-227

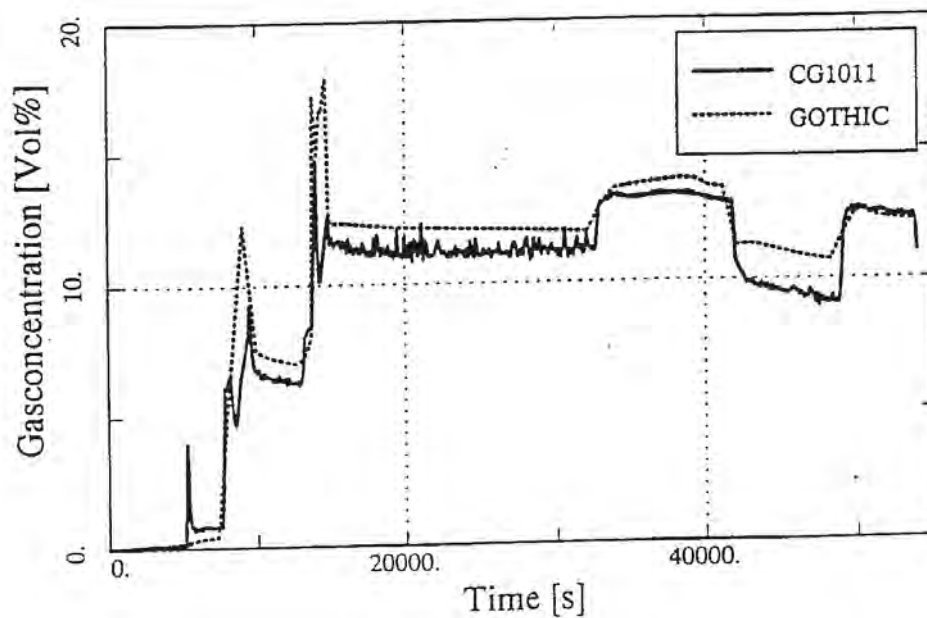


Figure 9.C-138. HDR-E11.5: Comparison Between Measured Gas Mixture Concentration in Spiral Stairway (6m) and GOTHIC Open Post-Test Prediction

Reproduced with permission from a report funded by the EPRI GOTHIC Advisory Group: K. Fischer, M. Schall, L. Wolf, "Simulations of GOTHIC Large Scale Containment Experiments," Battelle Ingenieurtechnik GnuBH, Eshborn, Fachbericht BF – V – 68317 – 01, October 1995)

9.C-228

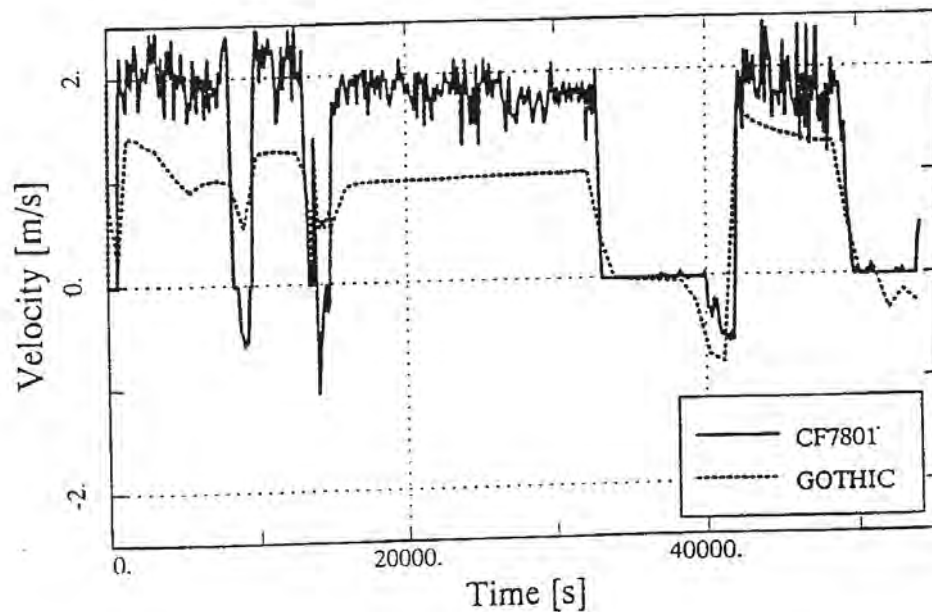


Figure 9.C-139. HDR-E11.5: Comparison Between Measured Velocity in Spiral Stairway (15m) and GOTHIC Open Post-Test Prediction

Reproduced with permission from a report funded by the EPRI GOTHIC Advisory Group: K. Fischer, M. Schall, L. Wolf, "Simulations of GOTHIC Large Scale Containment Experiments," Battelle Ingenieurtechnik GmBH, Eshborn, Fachbericht BF – V – 68317 – 01, October 1995)

9.C-229

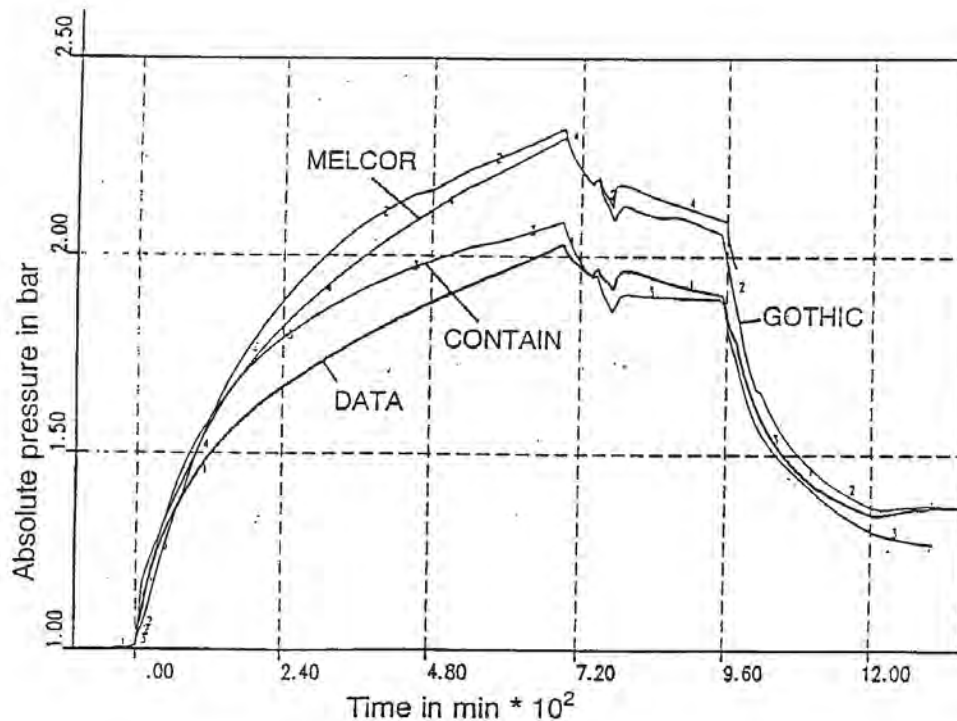


Figure 9.C-140. HDR-E11.2: Comparison Between Measured Long-Term Containment Pressure and Various "Optimized" Open Post-Test Predictions

Reproduced with permission from a report funded by the EPRI GOTHIC Advisory Group: K. Fischer, M. Schall, L. Wolf, "Simulations of GOTHIC Large Scale Containment Experiments," Battelle Ingenieurtechnik GmbH, Eshborn, Fachbericht BF – V – 68317 – 01, October 1995)

9.C-230

9.C.3.4 Conclusions

Lumped parameter models can predict pressure, and in some cases temperature, steam, and hydrogen concentrations inside the containment. Good predictions exist for the situations where the global circulation loop, which contributes towards the homogenization of atmosphere, is present inside the containment (see comparison with BMC F2 experiments and BMC test 12 experiments, NUPEC M-4-3 tests and HDR E11.4 and E11.5 tests). Additional improvements are possible if double-junctions between compartments in the horizontal direction are applied (allowing simulation of recirculation flows).

Single-node, lumped parameter models are not able to model stratification inside dead-end compartments due to the steam front penetration. They also do not include cases where the stratification front passes through horizontal vents, nor do they simulate sump liquid level, temperature, and stratification inside the sump. (See the BMC F2 experiments and the NUPEC M-4-3 results for dead-end compartments (R. Ofstun et al., 1994). The remedy can be an increase in the number of the nodes in the vertical direction or the application of distributed parameter model for dead-ended compartments (R. Ofstun et al., 1994).

For a stratified initial temperature distribution (BMC test 20) and a stratified containment atmosphere (HDR E11.2 test), the lumped parameter models do not predict the correct hydrogen distribution (they overmix the atmosphere). The artificial limitation of the size of the flow path areas in the HDR E11.2 test improved the prediction of temperatures and gas concentrations in the lower containment regions, but overestimated the containment pressure and temperatures in the upper levels.

Application of distributed parameter models may improve prediction capability. See BMC test 20 (L. Wolf, H. Holzbauer, M. Schall, 1994b; HDR E11.2 test - J. S. Narula and J. Woodcock, 1994; and K. K. Mun, 1996). All three publications conclude that proper distributed parameter nodalization for break and dome compartments is required to improve results. However, the increase of the number of nodes in all important regions of containment increases required memory and computing time beyond current practical limits.

The next step towards better space resolution and modeling would be the application of commercial CFD (Computational Fluid Dynamics) codes with built-in capabilities for multi-phase flows simulation, and multi-block, unstructured, or embedded grid options. Considering that three-dimensional transient multi-phase flow simulation would be required, only codes prepared for parallel multi-processor machines would produce results in a reasonable time. In addition, there are limitations related to noding convergence (see Gavrilas et al., 1997). Finally, an appropriate set of constitutive models (see Royle et al., 1997), such as condensation and sump evaporation, are not presently available in many CFD codes.

For the AP600 and **AP1000** with a low break release position and an established global circulation pattern that improves homogenization (see conclusion of the review of international experimental data base), a careful application of lumped parameter models could produce results which would be in agreement with test data.

9.C-231

In summary, biases that should be addressed when applying lumped parameter codes are:

1. Single-node models are not able to model stratification, or the passing of a stratification front through horizontal vents.
2. Sump liquid level and sump temperature are not predicted well.
3. Some codes produced results that are not correct due to missing or oversimplified buoyancy terms.
4. To account for recirculation flows, the applied lumped parameter model uses double junctions in the horizontal direction. (This does not help in the case of an elevated release and resulting stratified containment.)
5. For releases low in containment, typical for the AP600 and **AP1000** DECLG LOCA, the lumped parameter model predicts pressure, temperature, and helium concentrations inside the compartments that are affected by the global circulation loop. Improvements are needed to account for postulated circulation effects inside dead-ended compartments.
6. Scenarios with homogeneous containment atmosphere (HDR E11.4 and E11.5) are simulated successfully with lumped parameter models. (Such conditions typically result from breaks located below 20 percent of the containment height.)
7. Circulation effects due to sump boiling (releases generated at the bottom of containment) are well simulated.
8. The order of magnitude of computed velocities matches the experimental data. Trends in the direction of the flow are predicted well; however, predicted velocities differ by as much as a factor of two.
9. The lumped parameter method is not capable of predicting the hydrogen distribution in a stratified containment atmosphere, as in HDR E11.2 with high-positioned release. In a break scenario with a buoyant plume (released at about 50 percent of containment height), the steam and gas transport to the lower parts of the containment are over-predicted. (When convective flows are artificially limited by decreasing flow areas, predicted concentrations in the lower regions improve, but the containment pressure and temperatures in upper compartments are overestimated.)

9.C-232

9.C.3.5 References

1. Fischer, K., T., Schall, M., Wolf, L., 1991, "CEC Thermal-Hydraulic Benchmark Exercise on FIPLOC Verification Experiment F2 in BMC-Long-Term Heatup Phase – Results for Phase I," Final Report, EUR 13588 EN, 1991
2. Fischer, K., T., Schall, M., Wolf, L., 1993, "CEC Thermal-Hydraulic Benchmark Exercise on FIPLOC Verification Experiment F2 in BMC, Experiment F2 in BMC, Experimental Phases – Results for Phase 2, 3, and 4, Results of Comparisons," Final Report, EUR 14454 EN, 1993
3. K. Fischer, M. Schall, L. Wolf, 1995, "Simulations of GOTHIC Large-Scale Containment Experiments," Battelle Ingenieurtechnik GmbH, Eschborn Fachbericht BF – V - 68317 - 01, October 1995
4. M. Gavrilas, B. T. Mattingly, M.J. Driscoll, 1997, "WGOTHIC Noding and Parametric Studies of a Passively-Cooled Small Rating PWR Containment," Proceedings of the International Topical Meeting on Advanced Reactors Safety, Volume I, Orlando, Florida, June 1-5, 1997, pp. 549 – 560.
5. H. Holzbauer, L. Wolf, 1994, "GOTHIC Verification on Behalf of HDR-Hydrogen Mixing Experiments," International Conference on New Trends in Nuclear System Thermohydraulics, Volume II, pp. 331-340., Pisa, Italy, May 30th – June 2nd, 1994
6. T. Hirose, 1993, Letter, floppy disk which contains the M-4-3 test data, an attached document, and a video-cassette, NUPEC Nuclear Power Engineering Corporation, ISP35-035, 30 April, 1993
7. K. K. Mun, 1996, "Modeling of HDR Experiment E11.2 with the Distributed Parameter Feature of the GOTHIC – Code," M.S. Scholar's Paper, University of Maryland at College Park, September 1996
8. J. S. Narula, J. Woodcock, 1994, "Westinghouse – GOTHIC Distributed Parameter Modeling of HDR Test E11.2," The Third International Conference on Containment Design and Operation, Volume 1, Toronto, Canada, October 19 – 21, 1994
9. NEA/CSNI/R(94)29: Final Comparison Report on ISP-35: NUPEC Hydrogen Mixing and Distribution Test (Test M-7-1), Committee on the Safety of Nuclear Installations OECD Nuclear Energy Agency, December 1994
10. R. P. Ofstun, J. Woodcock, D. L. Paulsen, 1994, "Westinghouse - GOTHIC Modeling of HDR NUPEC'S Hydrogen Mixing and Distribution Test M-4-3," The Third International Conference on Containment Design and Operation, Volume 1, Toronto, Canada, October 19 – 21, 1994

9.C-233

11. P. Royl, Breitung, J.R. Travis, H. Wilkening, L. Seyffarth, 1977, "Simulation of Hydrogen Transport with Mitigation Using the 3D Field Code Gasflow," Proceedings of the International Topical Meeting on Advanced Reactors Safety, Volume I, Orlando, Florida, June 1-5, 1997, pp. 578 – 588.
12. L. Wolf, H. Holzbauer, T. Cron, 1994a, "Detailed Assessment of the HDR-Hydrogen Mixing Experiments E11," International Conference on New Trends in Nuclear System Thermohydraulics, Volume II, pp. 91-103., Pisa, Italy, May 30th – June 2nd, 1994
13. L. Wolf, H. Holzbauer, M. Schall, 1994b, "Comparisons Between Multi-dimensional and Lumped Parameter GOTHIC Containment Analyses with Data," International Conference on New Trends in Nuclear System Thermohydraulics, Volume II, pp. 321-330., Pisa, Italy, May 30th – June 2nd, 1994
14. L. Wolf, M. Gavrilas, K. Mun, 1996, "Overview of Experimental Results for Long-Term Large-Scale Natural Circulations in LWR-containments after Large LOCAS," DOE – Project, Order Number: DE - AP07 - 96ID10765, University of Maryland at College Park, July 1996

9.D-1

APPENDIX 9.D BASIS FOR ASSUMING HOMOGENEOUS BULK CONDITIONS FOR AP600 AND AP1000 CONTAINMENT PRESSURE DESIGN BASIS ANALYSIS

9.D.1 INTRODUCTION

During the blowdown phase of a DECLG LOCA, forced jet momentum from the break source provides vigorous mixing of steam and air inside containment. The jet momentum helps establish homogeneous conditions within a few seconds (Reference 9.D-12, Section 10.2.1.5). Consequently, treating the containment as homogeneous or well-mixed during the blowdown phase is appropriate.

After the blowdown phase, however, the physical processes are different. The forced jet momentum quickly decreases and actually ceases for a brief period during the refill phase before the break source reestablishes itself as a buoyant plume. Although the forced jet momentum ceases during the refill phase of a DECLG LOCA, wall boundary layers are quickly established, on the order of seconds (see Reference 9.D-12, Section 4.8) and according to work by Hartley, quasi-isotropic turbulence resulting from the jet momentum continues mixing enclosed volumes for some time after the source jet ceases. The turbulent wall boundary layers provide entrainment of the bulk region inside containment and hence contribute to mixing of the containment atmosphere as well.

This appendix addresses the buoyant plume, wall boundary layers, and enclosure test data as they relate to mixing inside containment during the post-blowdown time period during a DECLG LOCA.

9.D.2 APPROACH

Thermal and concentration gradients in the horizontal direction, including the boundary layer next to the shell, are addressed using results of 1) theoretical, or first principles, calculations 2) LST temperature/concentration data, and 3) separate effects enclosure test data. The wall boundary layer steam concentration profile is examined using turbulent boundary layer models. Entrainment and boundary layer profile calculations are used to estimate the magnitude of the steam concentration in the wall layer and rising plume as compared to the bulk average steam concentration at a given elevation. Test data, where available, are used to support the conclusions.

Horizontal gradients in AP600 and **AP1000** during the post-blowdown LOCA periods are addressed for the base case scenario which assumes that the source mass rises from the east steam generator compartment as a buoyant plume, having lost its momentum as it passes around the equipment and structure in the compartment.

The potential magnitude of horizontal gradients are examined in three radial regions: (1) the turbulent buoyant plume (2) the bulk region between the plume and boundary layer and (3) the turbulent boundary layer. The three radial regions are depicted in Figure 9.D-1. This three-region approach is similar to that suggested by Peterson (Reference 9.D-1). In the region-wise discussions, area fractions are developed and processes which affect horizontal temperature and concentration gradients within each region are described.

The test bases for the discussions include the LST, as well as smaller scale separate effects natural convection enclosure tests. The general interaction between the regions via entrainment is then used to summarize how the integral system performs.

9.D.3 REGION 1 HORIZONTAL GRADIENTS ADDRESSED THROUGH TURBULENT BUOYANT PLUME ANALYTICAL MODEL

Referring to Figure 9.D-1, Region 1 is comprised of the rising plume and its entrained flow. In Region 1, the concentration profile within a turbulent buoyant plume is characterized by an exponential (i.e., $e^{-57(r/z)^2}$) profile at any given elevation, with the steam concentration at the boundary of the plume equal to that of the bulk (Region 2). Such a profile is summarized by Blevins (Reference 9.D-2). The turbulent buoyant plume analytical model, based upon Reference 9.D-2, shows that the plume centerline steam concentration at the exit of the plume is within 10 percent ($0.04/(1-0.6) = 0.10$) (see Section 9.D-7) of the bulk (Region 2), assuming uniform temperature and concentration in Region 2. With the assumption that the buoyant plume develops freely to the dome region, the plume occupies about 10 percent of the cross-sectional area at the top of containment. An axisymmetric round plume with a divergent angle of 7.5 degrees from the exit of the steam generator compartment is assumed. The calculated plume equivalent diameter at the top of containment is 38 feet based on the net exit area of the trapezoidal steam generator compartment opening, the containment radius of 65 feet, and plume height of 121 feet. It is recognized that negatively buoyant plumes may descend from the dome region and limit the free development height of the positively buoyant plume. However, since this phenomenon results in an additional mixing mechanism (i.e., counter-current plume mixing of positively and negatively buoyant plumes), it is conservatively neglected in the simple analytical plume model.

9.D.4 REGION 2 HORIZONTAL GRADIENTS ADDRESSED THROUGH LST TEMPERATURE DATA AND SEPARATE EFFECTS ENCLOSURE TEST DATA

The horizontal gradients in Region 2 can be assessed based on indications from LST temperature data and separate effects enclosure test data and by examining the postulated condition of a non-uniform horizontal gradient.

The LST has been examined for evidence of horizontal gradients outside the wall boundary layer. Time-averaged thermocouple rake data for LST tests in the LOCA configuration at two different steam flows (220.1 at 0.5 lbm/sec; 217.1 at 1.0 lbm/sec) show a near-zero horizontal temperature gradient except above the steam plume and over the distance within one inch of the wall (see Figure 9.D-6 and Figure 9.D-7). Since the convective processes operating in the bulk gas region mix temperature differences and gas species at about the same rate, the observation that there is no horizontal temperature gradient also shows that there is no horizontal gas concentration gradient, and therefore, no density gradient. The data show that all of the measurable temperature drop in the vessel wall boundary layer occurs between the wall and the thermocouple located one inch away from the wall. This is consistent with boundary layer calculations which indicate that the majority (60 percent) of the gradient occurs within the first 0.25 inch of the 7-inch boundary layer at the LST operating deck level.

LST thermocouple rake data at successive, incremental data collection times, shows evidence of buoyancy forces eliminating horizontal gradients. Data from the thermocouple rake was taken every 90 seconds during the LST matrix tests. The data at some point in time may show that the temperature at a

9.D-3

measurement location may deviate less than ten degrees Fahrenheit from the horizontal average. Data at the next time interval indicate that horizontal gradients are not maintained for more than the 90-second data acquisition interval. This is evidence that a perturbation which creates a nonhomogeneous density at a given elevation also creates a local relative density driving force which tends to level out the horizontal density gradient. This is to be expected since gravity will neutralize any gradients that attempt to form, tending to result in a time-averaged flat profile.

Separate effects enclosure test data show that as the Rayleigh number, Ra , increases from 3.5×10^4 to 1×10^6 , the circulation mechanism fully transitions to turbulent, and the horizontal gradient becomes primarily concentrated in the thin wall boundary layer (Section 9.C.1.1.2.1, see for example Figure 9.C-5). These tests show that at $Ra > 10^6$, the horizontal gradient in the bulk region is nearly zero in two-dimensional enclosures. Data from three-dimensional enclosures suggest that the transition to turbulence may occur at $Ra < 10^6$, due to vortices which affect mixing inside the enclosure by communicating between the front and back walls through the middle of the enclosure. The Rayleigh number between the plume centerline and the cooled wall for both AP600 and AP1000 is 4.2×10^{12} based on a relatively low value of 9°F temperature difference. Therefore, both the AP600 and AP1000 are fully turbulent and would be expected to show little or no horizontal gradient in Region 2.

Negatively buoyant falling plumes have been shown to occur with upper horizontal surfaces cooler than the enclosure and to result in an additional mixing mechanism (Figure 9.C-15 and Figure 9.C-16) which would further homogenize the containment gases. The presence of plumes of cooler gases descending from the underside of the dome, suggested by the large vertical Grashof number on the order of 2×10^{13} , based on a relatively low temperature difference of 9°F (Section 9.C.1.3.1), are conservatively ignored.

Separate effects enclosure test data span up to Ra equal to 10^9 . Numerical studies by Markatos and Pericleous predict that the heat transfer behavior is constant (Nusselt number linearly increases with length) at increasing Ra over many decades up through Ra of 10^{16} (Figure 9.C-6), suggesting that increased heat transfer is primarily a result of thinning of the boundary layer. The implication is that the Nusselt number varies monotonically over that range, and thus no unexpected performance is introduced at higher Ra values.

In a bulk region such as Region 2 in the AP600 or AP1000, while one may not rule out some minor transient horizontal temperature or concentration gradients, a horizontal gradient outside the relatively small volumes occupied by the plume and falling wall layer is difficult to sustain at high Ra number. That is, any postulated deviation from horizontal uniformity would tend to be readily flattened by buoyant forces. Therefore, horizontal gradients may be assumed to occur solely within the plume and wall layer.

9.D.5 REGION 3 HORIZONTAL GRADIENTS ADDRESSED THROUGH TURBULENT BOUNDARY LAYER ANALYTICAL MODEL

Region 3 consists of the negatively buoyant turbulent wall boundary layer. Equations for the velocity, temperature, and air concentration boundary layer profiles are presented in Section 9.D.9. The profiles are based on turbulent boundary layer 1/7 power laws, as used by Eckert and Jackson. More recent work in the area of turbulent boundary layer profiles has led to the refinement of the boundary layer into three or more layers, such as the viscous sublayer, logarithmic-law layer, and outer layer, to attempt to increase

9.D-4

accuracy. Such multi-layer models may indeed increase the accuracy; but results show the 1/7 power profile to be reasonable to use for simple calculations.

The results of the boundary layer calculation for the LOCA post-blowdown atmosphere are compared to calculations for the LST in the LOCA configuration, that is, having a diffuser below the steam generator compartment. The LST includes the effects of both temperature and concentration as driving forces for natural convection. Conclusions regarding the thin part of the boundary layer near the wall, over which most of the gradient occurs are consistent with observations of the internal thermocouple rake data from LST.

The normalized steam concentration profile versus normalized distance through the boundary layer is plotted in Figure 9.D-2a. The parameter, C , represents local boundary layer steam concentration, and the subscripted values represent: s for surface, and b for bulk. The normalized value, η , is x/δ , where x is distance from the wall and δ is the boundary layer thickness. From Figure 9.D-2a, it can be seen that the average steam concentration in the boundary layer is only 12.5 percent lower than the steam concentration in the bulk.

The maximum boundary layer thickness has been calculated from the Eckert and Jackson style model to be less than 31 inches at the operating deck level in AP600 (assuming that a turbulent boundary layer exists for the full AP600 containment height). From the calculated profile, it is found that 60 percent of the change from bulk to wall conditions occurs over the first 2½ percent of the boundary layer, or over less than the first

inch in AP600. Furthermore, these boundary layer calculations conservatively overpredict wall layer thickness due to neglecting the effects of suction at the boundary (velocity normal toward the wall due to condensation). The boundary layer occupies less than 9 percent of the AP600 cross-sectional area at the operating deck elevation, based on the boundary layer thickness calculations and the AP600 containment radius of 65 feet. The region of significant concentration difference occupies less than 0.5 percent of the AP600 and **AP1000** cross-sectional area.

9.D.6 COMPOSITE REGION DISCUSSION

Referring to Figure 9.D-1, Region 1 is comprised of the rising plume and its entrained flow; Region 2 is the bulk region of low velocity and nearly zero horizontal temperature/concentration gradient; and Region 3 is the falling turbulent wall boundary layer and its entrained flow.

Region 1 occupies about 10 percent of the cross-section at the top, and Region 3 occupies about 9 percent of the cross-section at the bottom, the maximum cross-section for each. Thus, it is reasonable to neglect momentum-related interaction between the rising plume and the falling wall layer in simple first principles calculations. Since the plume occupies about 10 percent of the cross-sectional area at the top, and even less at lower elevations, as a first approximation the effects of the enclosure walls and dome on plume entrainment over the plume height is neglected. Similarly, with the even smaller area occupied by the falling wall layer, the effects of the enclosure are neglected when calculating wall boundary layer entrainment rates.

9.D-5

At a given instant in time, the rising plume of Region 1 is supplied to the above-deck volume from the top of the steam generator cavity. Plume entrainment calculations (Section 9.D.8) show that 5 to 14 times the source flow is entrained from Region 2 over the height of a buoyant plume above the operating deck in AP600. Therefore, the plume average steam concentration would be expected to be near that of the bulk by the time it discharges to the top of Region 2. As discussed previously, entrainment is shown to result in a centerline plume steam concentration at the top that is within 10 percent of the bulk average steam concentration.

The flow leaving Region 1 spreads horizontally and feeds Region 2 at the top. Since higher order mixing mechanisms have been neglected, by continuity, the vertical flow velocity at the top of Region 2 is a low velocity net downward flow with a steam concentration reduced by condensation and heat transfer on the dome to a value lower than the steam concentration discharged from Region 1.

In Region 3, condensation develops a liquid film over the full height of the containment shell and a negatively buoyant gas boundary layer that grows with distance down the shell. Noting that at quasi-steady conditions, the volumetric condensation rate on the wall is just equal to the source flow rate, Q_0 , wall boundary layer entrainment calculations (Section 9.D.8) show that the volume of steam condensed on the shell is only 1/6 to 1/13 of the volumetric flow rate of gas entrained into the falling wall layer. Such large entrainment rates relative to the condensation rate suggest that the average steam concentration exiting Region 3 would be near the bulk steam concentration of Region 2. These results are consistent with wall boundary layer profile calculations, discussed previously, which show that the average steam concentration through the boundary layer is only 12.5 percent below the steam concentration in the bulk.

Because global, or large-scale, circulation through the operating deck reduces stratification in the above-deck region (Section 9.C.1.4.2.4), global circulation through the operating deck is conservatively neglected for this discussion. By continuity, the flow exiting the bottom of Region 3 spreads out over the operating deck area, rising in Region 2 with a low net upward velocity and with the same steam concentration as the exit flow of Region 3. Because the top of Region 2 is fed by the plume and the bottom of Region 2 is fed by the wall layer, Region 2 will have a higher steam concentration at the top than at the bottom (neglecting negatively buoyant plumes in the dome region).

In this simplified model, as one moves from the top down in Region 2, entrainment into both the plume and the wall layer on either side of Region 2 steadily reduces the downward flow; similarly the upward flow from the bottom is reduced as one moves upward from the operating deck. There is, therefore, a neutral plane in Region 2 where the vertical velocity approaches zero.

A simplified representation summarizing horizontal gradients through the three regions, consistent with the above discussion, is shown in Figure 9.D-2b.

9.D-6

9.D.7 TURBULENT BUOYANT PLUME ANALYTICAL MODEL – SPECIES CONCENTRATION

This section addresses the assumptions, methodology, equations, and results for the turbulent buoyant plume analytical model - species concentration.

9.D.7.1 Time Period of Application

The turbulent buoyant plume analytical model is applicable in the post-refill phase (when break flow into containment is re-established) and beyond, as shown in Figure 9.D-3.

9.D.7.2 Nomenclature (See Figure 9.D-4)

u = velocity in plume
 C = concentration of air in plume
 T = temperature in plume
 u_{∞} = bulk velocity
 C_{∞} = bulk air concentration
 T_{∞} = bulk temperature
 C_{cl} = plume centerline air concentration

Subscripts:

∞ = bulk
 o = source
CL = centerline

9.D.7.3 Major Assumptions

1. Plume is turbulent and buoyant (i.e., density inside plume is less than the bulk region, Region 2).
2. Plume is not confined by wall surfaces or descending negatively buoyant plumes. It freely develops until it reaches dome region. It is recognized that descending negatively buoyant plumes may be generated in the dome region, and may limit the development height of the positively buoyant plume generated at the outlet of the steam generator compartment. However, the interaction of the positively and negatively buoyant plumes further enhances mixing, and therefore, this potential phenomenon is neglected in this simple analytical model.
3. Bulk conditions are uniform (i.e., homogeneous reservoir)
4. Plume is axisymmetric/round

9.D-7

9.D.7.4 Solution

The analytical solution to the turbulent, buoyant plume model with the above assumptions is already known, and the results are summarized in Table 9.D-1 (Reference 9.D-5, Table 9-7 – Turbulent Plumes in Constant Density Reservoirs).

9.D.7.5 Application of Turbulent Buoyant Plume Results to LST/AP600

Applying the plume centerline species concentration analytical solution, an expression for plume centerline air concentration, C_{CL} is obtained. (Note that C replaces T, and z replaces x from Table 9-7 of Reference 9.D-5)

$$C_{CL} = C_{\infty} - 11 * (Q_0 * \Delta C_0) * B^{-1/3} * z^{-5/3}$$

$$B = g * Q_0 * \left(\frac{\rho_{\infty} * \rho_{stm}}{\rho_{\infty}} \right) = \text{Buoyancy Flux}$$

where,

ΔC = Difference in concentration of air in plume and ambient
 Q_0 = Volumetric flow rate of source

Applying the above expression to LST Test 213.1B and AP600 at the same total pressure (i.e., 29.8 psia) and air concentration (i.e., 0.60), the air concentration values near the top of containment can be obtained:

For LST Test 213.1B:

$$\begin{aligned} p_{\infty} &= 29.8 \text{ psia}, p_{air} = 17.9 \text{ psia}, p_{stm} = 11.9 \text{ psia}, T_{\infty} = 218^{\circ}\text{F}, z = 13.2 \text{ ft} \\ C_{\infty} &= p_{air}/p_{\infty} = 0.60, \rho_{stm} = 0.03 \text{ lbm/ft}^3, \rho_{air} = 0.073 \text{ lbm/ft}^3, \rho_{stm,0} = 0.067 \text{ lbm/ft}^3 \end{aligned}$$

$$Q_0 = \frac{m_0}{\rho_{stm,0}} = \frac{0.54 \text{ lbm/sec}}{0.067 \text{ lbm/ft}^3} = 8 \text{ ft}^3/\text{sec}$$

$$B = 32.2 \times 8 \times 0.35 = 90.2$$

$$\frac{\rho_{\infty} - \rho_{stm,0}}{\rho_{\infty}} = 0.35$$

where,

$$\begin{aligned} \rho_{\infty} &= \rho_{air} + \rho_{stm} \\ \Delta C_0 &= C_{\infty} - 0 = 0.60 \\ \Delta C &= C_{\infty} \times 11 \times 8 \times (90.2)^{-1/3} \times (13.2)^{-5/3} = 0.16 \end{aligned}$$

9.D-8

For AP600: (assuming the same bulk air concentration as LST 213.1)

$$p_{\infty} = 29.8 \text{ psia}, p_{\text{air}} = 17.9 \text{ psia}, p_{\text{stm}} = 11.9 \text{ psia}, T_{\infty} = 202^{\circ}\text{F}, z = 110 \text{ ft}$$

$$C_{\infty} = p_{\text{air}}/p_{\infty} = 0.60, \rho_{\text{stm},0} = 0.0723 \text{ lbm/ft}^3$$

$$Q_o = \frac{m_o}{\rho_{\text{stm},0}} = \frac{15.4 \text{ lbm/sec}}{0.0723 \text{ lbm/ft}^3} = 213 \text{ ft}^3/\text{sec}$$

$$B = 32.2 \times 211 \times 0.305 = 2072$$

$$\frac{\rho_{\infty} - \rho_{\text{stm},0}}{\rho_{\infty}} = 0.305$$

$$\Delta C = 0.60 \times 11 \times 213 \times (2072)^{-1/3} \times (110)^{-5/3} = 0.04$$

Air Concentration, C_{CL} at the Top Centerline of Buoyant Plume

	Pressure (atm)	$\frac{\rho_{\infty} - \rho_{\text{stm},0}}{\rho_{\infty}}$	Q_o (ft ³ /sec)	C_{∞}	Z (ft)	B (ft ⁴ /sec ³)	ΔC	C_{CL}
LST	2	0.35	8	0.60	13.2	90.2	0.16	0.44
AP600	2	0.305	213	0.60	110	2072	0.04	0.56

9.D.7.6 Turbulent Buoyant Plume Conclusions

1. AP600 turbulent buoyant plume should provide better dilution of steam compared to LST due to the increased height above the source in AP600, and the $z^{-5/3}$ dependence for mixing/entrainment.
2. Based on the assumption of a well-mixed Region 2, the centerline concentration in the plume is close to ambient conditions for both AP600 and LST near the top of containment. Due to turbulent mixing, the average concentration in the plume should be even closer to the Region 2 bulk conditions.

9.D.8 ENTRAINMENT INTO THE BREAK PLUME AND WALL LAYER, AND THE EFFECT ON MASS TRANSFER RATE

The purpose of this calculation is to determine the volumetric entrainment rate into the break plume and into the negatively buoyant wall layer in AP600 containment during a large LOCA. The plume and buoyant wall layer entrainment models recommended by Peterson for mixing in large stratified volumes are used. The entrainment rates are used to calculate the dilution of the plume and buoyant layer to get the steam/air concentrations at the top (dome) and bottom (deck elevation) of containment. With the steam/air concentrations, the effect on the mass transfer rate in the dome region and at the operating deck level is determined.

9.D-9

9.D.8.1 Time Period of Application

The entrainment models for the buoyant plume are applicable in the post-refill period and beyond and models for the wall boundary layers are applicable to the post blowdown period and beyond, as shown in Figure 9.D-3.

9.D.8.2 Key Assumptions

- Bulk fluid (Region 2) is at a constant density

9.D.8.3 Entrainment into a Buoyant Plume

The volumetric flow rate entrained is:

$$Q_{ent} = 0.15 * B^{1/3} * Z^{5/3}$$

where,

- Z = 108 ft, the height of the plume (conservatively low value of height from steam generator cavity outlet to dome)
- B = $g Q_o(\rho_{amb} - \rho_o)/\rho_{amb}$, the buoyancy
- Q_o = the break steam volumetric flow rate
- ρ_o = the break steam density (assumed to be the saturation density at the total pressure)
- ρ_{amb} = density of the ambient gas, the same density as the entrained gas, ρ_{ent}

It is convenient to define the plume entrainment ratio:

$$r_p \equiv Q_{ent}/Q_o = 0.15 * g^{1/3} * (\Delta\rho/\rho)^{1/3} * Z^{5/3} * Q_o^{-2/3}$$

For entrainment into the plume, conservation of mass $\dot{m}_{out} = \dot{m}_{ent} + \dot{m}_o$ with $\dot{m} = Q\rho$, gives $Q_{out}\rho_{out} = Q_{ent}\rho_{ent} + Q_o\rho_o$. Conservation of mass for each species produces the relationships $Q_{out}\rho_{s,out} = Q_{ent}\rho_{s,ent} + Q_o\rho_{s,o}$ and $Q_{out}\rho_{a,out} = Q_{ent}\rho_{a,ent}$, where the s and a subscripts indicate the partial densities of the steam and air. With partial density and pressure $p_i = P/R_iT$, so mass conservation for each species becomes $Q_{out}P_{s,out}/T_{out} = Q_{ent}P_{s,ent}/T_{ent} + Q_oP_{s,o}/T_o$ and $Q_{out}P_{a,out}/T_{out} = Q_{ent}P_{a,ent}/T_{ent}$. Since the absolute temperature does not differ significantly throughout the system, the species equations can be approximated as $Q_{out}P_{s,out} = Q_{ent}P_{s,ent} + Q_oP_{s,o}$ and $Q_{out}P_{a,out} = Q_{ent}P_{a,ent}$. Note that the entrained flow is several times larger than the source flow, so the effect of the higher source temperature is not very significant. These latter equations permit the calculation of the steam and air concentration at the outlet of the plume.

Conservation of mass on a molar basis $\dot{n}_{out} = \dot{n}_{ent} + \dot{n}_o$. With $\dot{n} = \dot{Q}uA$, $\dot{Q} = P/\bar{R}T$, and $\dot{Q} = uA$, conservation of moles can be written $P_{out}Q_{out}/\bar{R}T_{out} = P_{ent}Q_{ent}/\bar{R}T_{ent} + P_oQ_o/\bar{R}T_o$. Since the total pressure, P is the same

9.D-10

for each, and the absolute temperature T only differs by a small amount, conservation of mass on a molar basis can be approximated as $Q_{out} = Q_{ent} + Q_o$.

With conservation of mass in terms of steam partial pressure, $P_{s,out} = (Q_{ent}P_{s,ent} + Q_oP_{s,o})/Q_{out}$, and $Q_{out} = Q_{ent} + Q_o$, the outlet steam partial pressure is $P_{s,out} = (Q_{ent}P_{s,ent} + Q_oP_{s,o})/(Q_{ent} + Q_o)$. Written in terms of the plume entrainment ratio r_p , $P_{s,out} = (r_pP_{s,ent} + P_{s,o})/(r_p + 1)$.

where,

\dot{m}	=	mass flow rate
\dot{n}	=	molar flow rate
\hat{n}	=	molar density
Q	=	volumetric flow rate
ρ	=	mass density
R	=	gas constant
T	=	absolute temperature

Subscripts:

a	=	air
s	=	steam
ent	=	entrained
out	=	outlet
o	=	source
stm	=	steam
bl	=	boundary layer

Values for densities and break flow rates at different times using values representative of post-refill and peak pressure are as follows:

		90 sec	1200 sec	Units
ρ_{amb}	=	0.13584	0.16325	lbm/ft ³
ρ_o	=	0.10487	0.13373	lbm/ft ³
$P_{s,o}$	=	46	60	psia
$P_{s,ent}$	=	26.94	40.30	psia
$(\rho_{amb} - \rho_o)/\rho_{amb}$	=	0.2280	0.1808	
$\dot{m}_{g,brk,o}$	=	200	45	lbm/sec
$Q_o = \dot{m}_{g,brk,o}/\rho_o$	=	1907	336.5	ft ³ /sec
$B = g Q_o(\rho_{amb} - \rho_o)/\rho_{amb}$	=	14,000	1959	ft ⁴ /sec ³
$Q_{ent} = 0.15 B^{1/3} Z^{5/3}$	=	8855	4597	ft ³ /sec
r_p	=	4.64	13.66	
$P_{s,out} = (r_pP_{s,ent} + P_{s,o})/(r_p + 1)$	=	30.32	41.64	psia

9.D-11

Solving the equations for AP600 at 90 seconds and at the time of peak pressure (1200 sec.) results in the following:

Steam Partial Pressure at Top of AP600 Plume from Entrainment Relations

Time sec	$\Delta p/\rho$	Q_o ft ³ /sec	Q_{ent} ft ³ /sec	r_p	$P_{stm,top}$ psia
90	0.2280	1,907	8,855	4.6	30.3
1200	0.1808	336.5	4,597	14	41.6

9.D.8.4 Entrainment into a Negatively Buoyant Wall Layer

The volumetric flow rate entrained is:

$$Q_{ent} = \frac{0.0979 * v * Gr_z^{2/5} p_{wall}}{(1 + 0.494 * Pr^{2/3})^{2/5} * Pr^{8/15}}$$

where,

- Z = 121 ft, the height of the wall (deck to dome)
- $Gr_z = g(\rho_{amb} - \rho_w)Z^3/(\rho_{amb}v^2)$, the Grashof number
- Pr = the Prandtl number of the boundary layer
- δ = boundary layer thickness
- $\nu = \mu/\rho$, the boundary layer kinematic viscosity based on the average of bulk and surface values of dynamic viscosity and density
- p_{wall} = the wall perimeter (πD) = 408.4 ft
- ρ_w = the total gas density adjacent to the liquid film surface
- ρ_{amb} = the density of the ambient gas, the same density as the entrained gas, ρ_{ent}
- V = volume

It is convenient to define the boundary layer entrainment ratio in terms of the entrained and condensed volumetric flow rates:

$$r_{bl} \equiv Q_{ent}/Q_{cond}$$

9.D-12

For entrainment into the boundary layer, the equations for conservation of mass $\dot{m}_{out} = \dot{m}_{ent} - \dot{m}_{cond}$, and on a molar basis $\dot{n}_{out} = \dot{n}_{ent} - \dot{n}_{cond}$ can be developed as was done for the plume. The results are the important relationships for the steam partial pressure at the outlet of the wall layer:

for volumetric flow $Q_{out} = Q_{ent} - Q_{cond}$, the outlet steam partial pressure is
 $P_{s,out} = (Q_{ent}P_{s,ent} - Q_{cond}P_{s,cond}) / (Q_{ent} - Q_{cond})$. In terms of the plume entrainment ratio r_p ,
 $P_{s,out} = (r_p P_{s,ent} - P_{s,o}) / (r_p - 1)$.

Values for densities and break flow rates at different times using representative values for post-refill (90 sec) and peak pressure (1200 sec) are as follows:

		90 sec	1200 sec	Units
ρ_{amb}	=	0.13584	0.16325	lbm/ft ³
ρ_w	=	0.19020	0.20229	lbm/ft ³
ρ_{cond}	=	0.10487	0.13373	lbm/ft ³
$P_{s,cond}$	=	46	60	psia
$P_{s,ent}$	=	26.94	40.30	psia
Pr	=	0.81	0.83	
μ	=	1.23×10^{-5}	1.24×10^{-5}	lbm/sec-ft
ρ	=	0.16302	0.18277	lbm/ft ³
$\nu = \mu/\rho$	=	7.55×10^{-5}	6.78×10^{-5}	ft ² /sec
$(\rho_w - \rho_{amb})/\rho_{amb}$	=	0.4001	0.2391	
$Gr_z = g(\rho_w - \rho_{amb})Z^3 / (\rho_{amb}\nu^2)$	=	4.00×10^{15}	2.97×10^{15}	
$1 + 0.494 Pr^{2/3}$	=	1.4293	1.4363	
Q_{ent}	=	5098	4004	ft ³ /sec
$\dot{m}_{cond} = \dot{m}_{g,brk,o} \pi_{m,es}$	=	85	40.5	lbm/sec
$Q_{cond} = \dot{m}_{cond} / \rho_{cond}$	=	810.5	302.8	ft ³ /sec
$r_{bl} = Q_{ent} / Q_{cond}$	=	6.29	13.22	
$P_{s,out} = (r_{bl}P_{s,ent} - P_{s,cond}) / (r_{bl} - 1)$	=	23.34	38.69	psia

9.D-13

Summary Tables:

Time, sec	P _{total} psia	P _{s,amb} psia	Y ft ² /sec	Δp/ρ	Gr _z	Pr	Q _{cond} ft ³ /sec
90	46	26.9	7.55x10 ⁻⁵	0.4004	4.00x10 ¹⁵	0.81	810.5
1200	60	40.3	6.78x10 ⁻⁵	0.2391	2.98x10 ¹⁵	0.83	302.8

Time, sec	Q _{ent} ft ³ /sec	r _{bl}	P _{s,bot} psia	δ _{bl} ft	V _{bl} ft ³
90	5098	6.3	23.34	2.2	63,200
1200	4004	13.221	38.69	2.3	65,500

9.D.8.5 Effect of Entrainment on Mass Transfer Rate

The condensation heat flux for given total pressure, steam partial pressure, and bulk-to-surface temperature difference is determined and used to calculate the influence of the concentration differences.

Representative bulk-to-surface temperature differences are:

		90 sec	1200 sec
T _{bulk}	=	244.2	267.7°F
T _{surf}	=	165.1	232.2°F
ΔT = (T _{bulk} - T _{surf})	=	79.1	45.5°F

The refill time phase, from 30 to 90 sec., has no source, but does have a wall layer. Refill is represented by its end state that is assumed to have the same conditions as calculated at 90 sec, except that without a plume the steam partial pressure and heat flux at the top is the same as the ambient bulk conditions.

The steam partial pressure values at the top, middle, and bottom correspond to the steam partial pressure out of the plume, the bulk steam partial pressure, and the steam partial pressure out of the wall layer.

The average heat flux is a simple, unbiased average of the top, middle, and bottom values, that is

$$\bar{q} = q_{\text{top}}/4 + q_{\text{amb}}/2 + q_{\text{bot}}/4.$$

9.D-14

Summary of Mass Transfer Effects Due to Vertical Concentration Gradients

Time sec	P _{total} psia	ΔT °F	P _{stm,top} psia	P _{stm,amb} psia	P _{stm,bot} psia	q _{top} B/sec-ft ²	q _{amb} B/sec-ft ²	q _{bot} B/sec-ft ²	\overline{q} Average B/sec-ft ²
refill	46	79	26.9	26.9	23.3	1.85	1.85	1.4	1.74
90	6	79	30.3	26.9	23.3	2.25	1.85	1.4	1.84
1200	60	43	41.6	40.3	38.7	1.5	1.4	1.3	1.4

The results in this table show that the upper estimates of vertical concentration differences in AP600 result in a 6 percent reduction on the net heat transfer to the shell during refill and less than 1 percent effect on net heat transfer during the 90 to 1200 sec time period.

9.D.8.6 Boundary Layer Thickness and Volume

The thickness of the negatively buoyant wall layer can be calculated from the integral equations presented by Peterson (Reference 9.D-1).

$$\delta_{bl} = \frac{0.565 * (1 + 0.494 * Pr^{2/3})^{1/10} * z}{Gr_z^{1/10} * Pr^{8/15}}$$

The equation can also be integrated over its height, with the simplifying assumption that all properties are constant over the height, Z. This assumption is reasonable since the Prandtl number only changes a few percent over the range of conditions inside containment, and the only other parameters are contained in the term $\Delta\rho/(\rho v^2)$ which is estimated to change less than a factor of 2 over height, and when raised to the 1/10 power has only a 7 percent effect. Consequently, the product of the integral and the circumference gives a reasonable estimate of the boundary layer volume that can be used with the entrainment rate to estimate boundary layer transit times, or fill time.

The product of the circumference and the integral of the equation above is;

$$V_{bl} = \frac{0.565 * (1 + 0.494 * Pr^{2/3})^{1/10} * (v^2/g)^{1/10} * \pi * D}{(\Delta\rho/\rho)^{1/10} * Pr^{8/15}} * \int_0^H z^{0.7} dz$$

$$= \frac{0.565 * \pi * \left(1 + 0.494 * Pr^{2/3}\right)^{1/10} * (v^2/g)^{1/10} * D * H^{1.7}}{1.7 * (\Delta\rho/\rho)^{1/10} * Pr^{8/15}}$$

9.D-15

Evaluating this equation with the values from Section 9.D.8.3;

		90 sec	1200 sec	Units
Pr	=	0.81	0.83	
v	=	7.55×10^{-5}	6.78×10^{-5}	ft ² /sec
$(\rho_w - \rho_{amb})/\rho_{amb}$	=	0.4001	0.2391	
$1 + 0.494 Pr^{2/3}$	=	1.4293	1.4363	
V (Equation 4)	=	63436	64553	ft ³

Summary Table:

AP600 Boundary Layer Volume and Fill Times

Time, sec	V, ft ³	Q_{ent} , ft ³ /sec	Boundary Layer Fill Time, sec V/ Q_{ent}
90	63436	5098	12.4
1200	64553	4004	16.1

9.D.8.7 Sublayer Penetration Time

A measure of the response time of the boundary layer temperature to a change in the environment is the sublayer penetration time. This represents the time it takes for steam to diffuse through the laminar sublayer, where most of the mass transfer resistance is located. The transient diffusion equation:

$$\frac{\partial \rho}{\partial t} = D_v \frac{\partial^2 \rho}{\partial y^2} \text{ becomes } \frac{\delta_m^2}{D_v \tau} \frac{\partial \rho^*}{\partial t^*} = \frac{\partial^2 \rho^*}{\partial y^{*2}}$$

with the substitutions:

$$\hat{\rho} = \hat{\rho}_\infty \hat{\rho}^* \quad y = \delta_m y^* t = \tau t^*$$

where,

$\hat{\rho}$	=	molar density
t	=	time
y	=	distance along the normal to the surface
δ_m	=	boundary layer thickness
D_v	=	air-steam gas diffusion coefficient
τ	=	time constant
∞	=	value at a large distance from surface
*	=	dimensionless variable

9.D-16

If the time constant is defined $\tau = \delta_m^2/D_v$, the coefficient on the left side of the dimensionless equation = 1, as required. The mass transfer sublayer thickness, δ_m , is related to the heat transfer sublayer thickness, δ_h , by $Nu/Sh = (Pr/Sc)^{1/3}$. The heat transfer sublayer thickness is $\delta_h = h/k$. Other assumed values are:

		90 sec	1200 sec	Units
h	=	2.61	2.51	Btu/hr-ft ² -°F
k	=	0.0164	0.0173	Btu/hr-ft-°F
D _v	=	0.537	0.464	ft ² /hr
Pr	=	0.81	0.83	
Sc	=	0.51	0.51	
$\delta_h = h/k$	=	0.0063	0.0069	ft
$\delta_m = \delta_h(Pr/Sc)^{1/3}$	=	0.0073	0.0081	ft
$\tau = \delta_m^2/D_v$	=	0.357	0.509	sec

Consequently, the sublayer penetration time is on the order of 1 sec or less. This is very rapid in comparison to the structure time constants that are on the order of 100 sec, and the system pressurization time constant that is on the order of 1000 sec. Even the boundary layer fill time of 16 sec is short compared to both the structure and pressure time constants.

9.D.9 TURBULENT BOUNDARY LAYER ANALYTICAL MODEL

This section addresses the assumptions, methodology, equations, and results for the turbulent boundary layer analytical model. The analytical model is not intended to be an independent verification of LST, rather, it is used to estimate boundary layer thickness and temperature/concentration profiles for AP600 containment and LST. Measured thermal/concentration boundary conditions from LST tests 217.1 and 220.1 are applied in the analytical model since these represent realistic conditions to apply to the boundary layer model.

9.D.9.1 Time Period of Application

The turbulent boundary layer analytical model (Figure 9.D-4) applies to the time period when quasi-steady conditions are established inside containment. The time period of applicability is shown in Figure 9.D-3.

9.D.9.2 Key Assumptions

- Surface is vertical flat plate
 - Containment shell radius of curvature is large so it can be treated locally as a flat plate.

9.D-17

- Velocity, temperature, concentration boundary layer profile is turbulent
 - This is appropriate since boundary layer is turbulent within a few feet of the top of the containment shell.
- Bulk (Region 2) fluid velocity $\cong 0$
 - This is true after blowdown period since the break source transitions from jet to buoyant plume and bulk containment area is large relative to plume/boundary layer.
- Condensate film is impermeable to noncondensable gases.
 - This is conservative since absorption by the film removes air from containment volume which enhances heat/mass transfer of steam.
- Condensate film is stationary relative to gas boundary layer.
 - This is appropriate since condensate film velocity is smaller than gas boundary layer velocity, and conservative because a moving film enhances heat transfer.
- Suction effect at wall is neglected.
 - This is conservative because suction thins the boundary layer.
- Thermal boundary layer thickness is the same as concentration boundary layer thickness.
 - This is appropriate since $Le^{1/3} = \left(\frac{Pr}{Sc}\right)^{1/3} \sim 1.0$.
- Saturation conditions exist at film surface.
 - This is appropriate since steam is condensing at the film surface.
- Bulk fluid (Region 2) temperature is uniform above the break source elevation.
 - Refer to LST test 217.1 and 220.1 temperature profiles in (Figure 9.D-6 and Figure 9.D-7).
- Bulk fluid (Region 2) concentration is uniform above the break source elevation.
- Surface Temperature is approximately constant for purposes of applying the simple analytical model.
- Wall heat flux is modeled as forced convection using equations from Reference 9.D-6.

9.D-18

9.D.9.3 Boundary Layer Profiles

The boundary layer profiles, used by Eckert and Jackson, are based on experimental data for turbulent boundary layers:

- Boundary Layer Velocity Profile (Reference 9.D-7, Equation 24)

$$u = U(1 - \eta)^4 * \eta^{\frac{1}{7}} \text{ where } \eta = \frac{r}{\delta}$$

where,

u = local velocity in boundary layer
 δ = boundary layer thickness
r = coordinate direction normal to condensing surface

- Boundary Layer Temperature Profile (Reference 9.D-7, Equation. 25)

$$T - T_{\infty} = (T_{\text{surf}} - T_{\infty})(1 - \eta^{\frac{1}{7}})$$

where,

T = temperature

- Boundary Layer Air Concentration Profile

$$C - C_{\infty} = (C_{\text{surf}} - C_{\infty})(1 - \eta^{\frac{1}{7}})$$

where,

C = air concentration

- Boundary Layer Thickness (Reference 9.D-8, Equation. 10.121b)

$$\delta = B * z^n$$

where,

B, n are constants to be determined

- Maximum Velocity in Boundary Layer (Reference 9.D-8, Equation. 10.121a)

$$U = A * z^m$$

A, m are constants to be determined

9.D-19

9.D.9.4 Governing Equations

- Momentum Equation

$$\frac{d \left[\int_0^\delta u * (T - T_\infty) dr \right]}{dz} = g * \int_0^\delta \beta * (T - T_\infty) dr - \frac{\tau_w}{\rho}$$

where,

τ_w	=	shear stress at condensing surface
β	=	volumetric thermal expansion coefficient
ρ	=	bulk density
g	=	local gravitation acceleration

- Energy Equation

$$\frac{d \left[\int_0^\delta u * (T - T_\infty) dr \right]}{dz} = \frac{q''_w}{\rho * C_p}$$

where,

C_p	=	specific heat at constant pressure
q''_w	=	wall heat flux

- Conservation of Mass Equation

Not used in this calculation since we are not calculating entrainment volumes/rates, but rather, temperature/concentration profiles.

- Boundary Conditions

Thermal and concentration boundary conditions are from LST tests are applied at the shell surface and in bulk (Region 2) locations because the boundary conditions are expected to be representative of AP600.

9.D.9.5 Boundary Layer Momentum Equation Development

Wall shear stress in the momentum equation is modeled using a correlation for forced turbulent convection. Eckert and Jackson argue the τ_w is similar to forced convection in the near surface region and can be represented as follows:

$$\frac{\tau_w}{\rho * U^2} = 0.0225 * \left[\frac{U * \delta}{\nu} \right]^{-1/4}$$

9.D-20

where,

ν = kinematic viscosity

$$\tau_w = 0.0225 * \rho * U^2 * \left(\frac{\nu}{U * \delta} \right)^{1/4}$$

where,

U = is a characteristic velocity interpreted by Eckert and Jackson as the maximum velocity in boundary layer.

The integral momentum equation then becomes:

$$\frac{d \left[\int_0^\delta u^2 dr \right]}{dz} = g * \int_0^\delta \beta * (T_\infty - T) dr - 0.0225 * U^2 * \left(\frac{\nu}{U * \delta} \right)^{1/4}$$

Applying turbulent velocity and thermal boundary layer profiles, it can be shown that:

$$\int_0^\delta u^2 dr = \delta \int_0^1 [U * (1 - \eta)^4 * \eta^{1/7}]^2 d\eta = 0.052315 * \delta * U^2$$

and

$$\int_0^\delta (T_\infty - T) dr = \delta * \int_0^1 (T_\infty - T_{surf}) \left(1 - \eta^{1/7} \right) d\eta = \frac{\delta}{8} * (T_\infty - T_{surf})$$

The boundary layer momentum equation becomes:

$$\frac{d}{dx} (0.052315 * U^2 * \delta) = g * \beta * (T_\infty - T_{surf}) * \frac{\delta}{8} - 0.0225 * U^2 * \left(\frac{\nu}{U * \delta} \right)^{1/4}$$

Applying Reynolds Analogy for heat/momentum transfer:

$$\frac{h}{\rho * C_p * U} = \frac{f_z}{2} * E_H \quad (\text{Reference 9.D-7, Equation 5})$$

where,

$$f_z = \text{local friction factor} = 0.045 * \left[\frac{\nu}{U * \delta} \right]^{1/4} \quad (\text{Reference 9.D-7, Equation 32})$$

E_H = ratio of turbulent eddy diffusivity of heat to that of momentum
 h = heat transfer coefficient

9.D-21

from Colburn Analogy:

$$E_H = Pr^{-2/3} \quad (\text{Reference 9.D-7, Equation 6})$$

where,

$$Pr = \text{Prandtl number}$$

Therefore,

$$\frac{h}{\rho * C_p * U} = \frac{0.045}{2} * \left[\frac{v}{U * \delta} \right]^{1/4} * Pr^{-2/3} = 0.0225 * \left[\frac{v}{U * \delta} \right]^{1/4} * Pr^{-2/3}$$

Now, since

$$q''_w = \frac{q_w}{A_{\text{surf}}} = h * (T_{\infty} - T_w)$$

heat flux can be modeled as follows:

$$\frac{q''_w}{\rho * C_p} = 0.0225 * (T_{\infty} - T_{\text{surf}}) * U * \left[\frac{v}{U * \delta} \right]^{1/4} * Pr^{-2/3}$$

where,

$$A_{\text{surf}} = \text{heat transfer surface area}$$

Now,

$$\begin{aligned} & \int_0^{\delta} u * (T - T_{\infty}) dr \\ &= \delta * \int_0^1 \left[U * (1 - \eta)^4 * \eta^{1/7} \right] (T_{\infty} - T_{\text{surf}}) \left(1 - \eta^{1/7} \right) d\eta = 0.036633 * (T_{\infty} - T_{\text{surf}}) * \delta * U \end{aligned}$$

The boundary layer energy equation becomes:

$$\frac{d}{dz} [0.03663 * (T_{\infty} - T_{\text{surf}}) * \delta * U] = 0.0225 * Pr^{-2/3} * (T_{\infty} - T_{\text{surf}}) * U * \left[\frac{v}{U * \delta} \right]^{1/4}$$

Substituting expressions for U and δ into boundary layer momentum and energy equations, differentiating the resulting equations, solve for exponents m and n by matching exponents. This procedure results in m=1/2 and n=7/10 which can also be found in Reference 9.D-8, page 335.

9.D-22

Therefore:

$$U = A * z^{\frac{1}{2}} \text{ and } \delta = B * z^{\frac{7}{10}}$$

Substituting the expressions for U and δ into boundary layer equations and performing the differentiation, we obtain:

$$\left(\frac{17}{10}\right) [0.0252315 * A^2] = 0.125 * g * \beta * (T_{\infty} - T_{\text{surf}}) - 0.0225 * A^{\frac{7}{4}} * B^{-\frac{5}{4}} * v^{\frac{1}{4}}$$

and

$$\left(\frac{6}{5}\right) [0.03663 * A] * \text{Pr}^{\frac{2}{3}} = 0.0225 * A^{\frac{3}{4}} * B^{-\frac{5}{4}} * v^{\frac{1}{4}}$$

Solving for constants A and B, an expression for boundary layer thickness can be obtained:

$$\delta = B * z^{\frac{7}{10}} = 0.565 * z * \text{Gr}_z^{-\frac{1}{10}} * \text{Pr}^{-\frac{8}{15}} * [1 + 0.494 * \text{Pr}^{2/3}]^{-1/10} \text{ (Reference 9.D-7, Equation 36)}$$

The above equation agrees with that obtained in Reference 9.D-1, Equation 18.

From the expression for δ , the velocity, thermal and concentration boundary layer profiles can be calculated, where:

$$\text{Gr}_z = \frac{g * \beta * (T_{\infty} - T_{\text{surf}}) * z^3}{\nu^2} \quad \text{(Reference 9.D-7, Equation 29)}$$

9.D.9.6 Boundary Layer Thickness Results

Rather than calculate Gr_z and δ for a mixture, the calculation is done using air or steam properties to examine the range of possible values.

AP600 Prediction (for thermodynamic properties based on LST test 217.1)

The following parametric values are associated with LST test 217.1 and are used to calculate boundary layer thicknesses below:

Location	T_{∞}	T_{surf}	Pr (air)	ν (air)
E	230°F	188°F	0.70	$0.84 \times 10^{-4} \text{ ft}^2/\text{sec}$

9.D-23

Based on AIR properties (Reference 9.D-10) and noting $\beta = 1/T$:

$$Gr_z = \frac{32.2 \frac{\text{ft}}{\text{sec}^2} * (230^\circ\text{F} - 188^\circ\text{F}) * \left(\frac{1}{690^\circ\text{R}}\right) * (110\text{ft})^3}{\left(0.84 \times 10^{-4} \frac{\text{ft}^2}{\text{sec}^2}\right)^2} = 3.7 \times 10^{14}$$

$$\delta = 0.565 * (110\text{ft}) * (3.7 \times 10^{14})^{-\frac{1}{10}} * (0.7)^{-\frac{8}{15}} * \left[1 + 0.494 * (0.7)^{\frac{2}{3}}\right]^{-\frac{1}{10}} = 30.5 \text{ in}$$

Based on STEAM properties:

$$Gr_z = \frac{32.2 * (230 - 188) * \left(\frac{1}{690}\right) * (110)^3}{(0.84 \times 10^{-4})^2} = 3.7 \times 10^{14}$$

$$\delta = 0.565 * (110\text{ft}) * (3.4 \times 10^{14})^{-\frac{1}{10}} * (1.1)^{-\frac{8}{15}} * \left[1 + 0.494 * (1.1)^{\frac{2}{3}}\right]^{-\frac{1}{10}} = 23.9 \text{ in}$$

LST Prediction (for thermodynamic properties based upon LST test 217.1)

Based on AIR properties:

$$Gr = \frac{32.2 * (230 - 188) * \left(\frac{1}{690}\right) * (13.2)^3}{(0.84 \times 10^{-4})^2} = 6.4 \times 10^{11}$$

at Point E in LST:

$$\delta = 0.565 [13.2 \text{ ft}] (6.4 \times 10^{11})^{-1/10} (0.70)^{-8/15} [1 + 0.494 (0.70)^{2/3}]^{-1/10} = 6.9 \text{ in.}$$

Based on STEAM properties ($Pr = 1.10$, $\nu = 0.87 \times 10^{-4} \text{ ft}^2/\text{sec}$):

$$Gr = \frac{32.2(230 - 188)\left(\frac{1}{690}\right)(13.2)^3}{(0.87 \times 10^{-4})^2} = 5.9 \times 10^{11}$$

at Point E in LST:

$$\delta = 0.565 * (13.2\text{ft}) * (5.9 \times 10^{11})^{-\frac{1}{10}} * (1.1)^{-\frac{8}{15}} * \left[1 + 0.494 * (1.1)^{\frac{2}{3}}\right]^{-\frac{1}{10}} = 5.4 \text{ in}$$

9.D-24

The following parametric values are associated with LST Test 220.1 and are used to calculate boundary layer thickness below:

Location	T_{∞}	T_{surf}	Pr (air)	ν (air)
E	200°F	155°F	0.70	$1.0 \times 10^{-4} \text{ ft}^2/\text{sec}$

Based on AIR properties:

$$Gr = \frac{32.2 * (200 - 155) * \left(\frac{1}{660}\right) * (13.2)^3}{(1.0 \times 10^{-4})^2} = 5.0 \times 10^{11}$$

at Point E in LST:

$$\delta = 0.565 * (13.2 \text{ ft}) * (5.0 \times 10^{11})^{-\frac{1}{10}} * (0.7)^{-\frac{8}{15}} * \left[1 + 0.494 * (0.7)^{\frac{2}{3}}\right]^{-\frac{1}{10}} = 7.1 \text{ in}$$

9.D.9.7 Concentration Profile Results

The concentration profile and integrated average in boundary layer are calculated from the turbulent analytical model for LST. The concentration at the surface is determined from inside surface temperature data and applying saturated conditions near the surface. See Figure 9.D-5 for relative measurement elevations. Radial positions are shown in Figure 9.D-6 and Figure 9.D-7.

LST Test 220.1 $P_{total} = 32 \text{ psia}$, $\dot{m} = 0.5 \text{ lbm/sec}$

Average LST Boundary Layer Air Concentration Based Upon Measured Bulk and Wall Conditions

Location	T_{surf} (measured) (°F)	T_{∞} (measured) (°F)	C_{surf} (calc)	C_{∞} (measured)	\overline{C}_{BL} (calc)
Dome	180	—	0.77	0.34	0.39
A	180	230	0.77	0.44	0.48
B	—	230	—	—	—
C	177	230	0.78	—	0.48
D	—	230	—	—	—
E	155	200	0.87	0.72	0.74

9.D-25

LST Test 217.1 $P_{\text{total}} = 43 \text{ psia}$, $\dot{m} = 1.0 \text{ lbm/sec}$

Average LST Boundary Layer Air Concentration Based Upon Measured Bulk and Wall Conditions

Location	T _{surf} (measured) (°F)	T _∞ (measured) (°F)	C _{surf} (calc)	C _∞ (measured)	\bar{C}_{BL} (calc)
Dome	200	–	0.73	0.33	0.38
A	210	260	0.67	0.35	0.39
B	207	260	0.67	–	0.39
C	205	260	0.70	–	0.395
D	198	260	0.74	–	0.40
E	188	240	0.79	0.67	0.69

Notes:

1. C_{surf} is calculated from applying Dalton's law of partial pressures, assuming saturation conditions exist at the condensing surface, and using measured surface temperatures and total pressure from LST tests.
2. \bar{C}_{BL} , which represents the average air concentration in the boundary layer, is calculated from performing an integrated average which results in $C_{BL} = (C_{\text{surf}} + 7 * c_{\infty})/8$
3. Refer to inside wall temperature data (Table 4.8-1 for LST test 217.1 and Figure 4.11-6 for LST test 220.1) in Reference 9.D-11 for surface temperature data.
4. Bulk fluid temperatures shown in the above tables represent spatially-averaged values based upon attached LST time-averaged temperature profiles for LST tests 220.1 and 217.1 at quasi-steady conditions.

9.D.9.8 Boundary Layer Concentration Profile Results – LST

1. Comparison of C_{∞} and \bar{C}_{BL} shows that the difference in air concentration is small (within 15 percent) in the radial (horizontal) direction for LST. This along with temperature profile data indicate that LST is well-mixed in the radial direction throughout the above-deck region, outside of the relatively thin laminar sublayer.
2. The measured bulk fluid temperature in both horizontal and vertical directions shows little difference (i.e. a few degrees) between the dome region and region D as seen in Figure 9.D-6 and Figure 9.D-7. There is however about 20°F difference in the bulk temperature between regions D and E, for LST test 217.1 and about 30°F difference for LST test 220.1. The data indicate some level of stratification between regions D and E, which is more pronounced in LST test 220.1. Since the LST does not have a flow connection from the simulated SG compartment, there is no global circulation. As a result, the stratification below the source elevation is not surprising.

9.D-26

3. Region E temperature/concentration is notably different than the regions above. This indicates an interface or gradient region exists between the higher temperature, steam-rich upper region (above the plane of the break) fed by the buoyant plume, and the lower temperature, air-rich region fed by the wall boundary layer.
4. Turbulent boundary layer mixing is significant such that boundary layer average properties are nearly at bulk conditions. It is expected that this will be the case for AP600.

9.D.9.9 Boundary Layer Analytical Model Results – Boundary Layer Thickness

1. The maximum boundary layer thickness calculated from the analytical model for LST turbulent boundary layer ~ 7 inches. (LST 217.1 and 220.1)
2. The maximum total boundary layer thickness calculated from the analytical model for AP600 at similar thermodynamic conditions ~ 31 inches.
3. The calculated boundary layer thicknesses are conservative because suction effects due to steam condensation at the wall were not included. It is well known that suction reduces boundary layer thickness (refer to Schlichting, Boundary Layer Theory). Therefore, actual boundary layers should be thinner than calculated.
4. The boundary layer horizontal profile is rather “flat” due to mixing effects of turbulence. Consequently, most of the horizontal boundary layer gradient is contained in the much smaller region near the condensing surface.

9.D.10 INFLUENCE OF HORIZONTAL GRADIENTS ON MASS TRANSFER COEFFICIENTS

Since only free convection is assumed throughout the design basis containment transients, the velocities calculated in the lumped parameter model are not used in calculating mass transfer rates. Therefore, justification of the approach taken for mass transfer is based on steam concentration gradients.

The horizontal concentration gradients in the post-LOCA containment atmosphere are consistent with the lumped parameter nodding and associated mass transfer coefficients used in the WGOTHIC Evaluation Model. The scale of significant concentration gradients near the wall are much less than the 2-foot thick calculation cell (node) used in the WGOTHIC Evaluation Model. Thus, the wall cell is large enough in the radial direction that cell properties can be used to represent the bulk condition for use with boundary layer heat and mass transfer correlations which are described in Reference 9.D-4.

9.D-27

9.D.11 CONCLUSION

The following conclusions apply to the containment atmosphere during the post blowdown period for a DECLG LOCA:

1. The turbulent buoyant plume (Region 1) entrains a significant volume from the bulk (Region 2) such that it is nearly at bulk thermal/concentration conditions in the dome region.
2. Based upon LST data and enclosure test data, the large bulk region (Region 2) is well-mixed horizontally and above the break source elevation, vertically as well.
3. The turbulent wall boundary layers entrain volume from the bulk region such that the average thermal/concentration in the boundary layer is nearly at bulk conditions.

9.D.12 REFERENCES

- 9.D-1 Peterson, P.F., "Scaling and Analysis of Mixing in Large Stratified Volumes," International Journal of Heat and Mass Transfer, Vol. 37, Suppl. 1, pp 97-106, 1994.
- 9.D-2 Blevins, "Jets, Plumes, Wakes, and Shear Layer," Applied Fluid Dynamics Handbook, 1984.
- 9.D-3 WCAP-14407, Rev. 2, "WGOTHIC Application to AP600," April 1998.
- 9.D-4 WCAP-14326, Rev. 2, "Experimental Basis for the AP600 Containment Vessel Heat and Mass Transfer Correlations," April 1998.
- 9.D-5 Blevins, "Jets, Plumes, Wakes, and Shear Layers," Applied Fluid Dynamics Handbook, 1984, pp. 247-251.
- 9.D-6 Eckert and Jackson, "Analysis Turbulent Free Convection Boundary Layer on a Flat Plate," NACA Report 1015, 1951.
- 9.D-7 Corradini, "Turbulent Condensation on a Cold Wall in the Presence of a Non-Condensable Gas," Proceedings on Nuclear Reactor Thermal Hydraulics, Vol. 1, 1983.
- 9.D-8 Kakac and Yener, Convective Heat Transfer, 2nd edition, CRC Press, 1995.
- 9.D-9 Kays and Crawford, Convective Heat and Mass Transfer, 3rd Edition, McGraw-Hill.
- 9.D-10 Kreith, "Principles of Heat Transfer," 3rd Edition, Appendix.
- 9.D-11 WCAP-14135, "Final Data Report for PCS Large-Scale Tests, Phase 2 and Phase 3," Revision 1, April 1997.
- 9.D-12 WCAP-14845, "Scaling Analysis for AP600 Containment Pressure During Design Basis Accidents," Revision 3, March 1998.

9.D-28

Table 9.D-1. Analytical Solution to the Turbulent Buoyant Plume Model
(Reference 9.D-5, Table 9-7)

Notation: b = half-width of the plume; i.e., transverse distance for the axial velocity to fall to one-half the centerline value; B = specific buoyancy flux, see Eqs. (9-50) and (9-54); Q = volume flow rate, per unit depth for plane plume; Q_0 = initial volume flow rate; r = radial distance from plume axis; ΔT = species concentration relative to reservoir level; ΔT_0 = initial relative species concentration; u = axial velocity; u_m = centerline axial velocity; v_e = transverse velocity of reservoir fluid into plume; x = axial distance from origin of the plume; y = transverse distance from center plane; ν = kinematic viscosity. (Refs. 9-1, 9-73.) The uncertainty in the coefficients is approximately $\pm 10\%$.

Plume Characteristic ^(a)	Plane Plume	Axisymmetric (i.e., round) Plume
1. Centerline velocity, u_m	$1.7 B^{1/3}$	$3.5 B^{1/3} x^{-1/3}$
2. Width, b	$0.097 x$	$0.11 x$
3. Axial velocity profile ^(b) , u/u_m	$e^{-74(y/x)^2}$	$e^{-57(r/x)^2}$
4. Volume flow rate, Q	$0.34 B^{1/3} x$	$0.15 B^{1/3} x^{5/3}$
5. Centerline species concentration, ΔT_m	$2.4 (Q_0 \Delta T_0) B^{-1/3} x^{-1}$	$11 (Q_0 \Delta T_0) B^{-1/3} x^{-5/3}$
6. Species concentration width, $b_{\Delta T}$	$0.13 x$	$0.10 x$
7. Species concentration profile ^(b) , $\Delta T/\Delta T_m$	$e^{-41(y/x)^2}$	$e^{-69(r/x)^2}$
8. Entrainment velocity, v_e	$0.10 u_m$	$0.041 u_m$
9. Reynolds number, $u_m b/\nu$	$0.17 \frac{B^{1/3} x}{\nu}$	$0.35 \frac{B^{1/3} x^{2/3}}{\nu}$

(a) In fully developed region.

(b) These are consistent with the corresponding width.

9.D-29

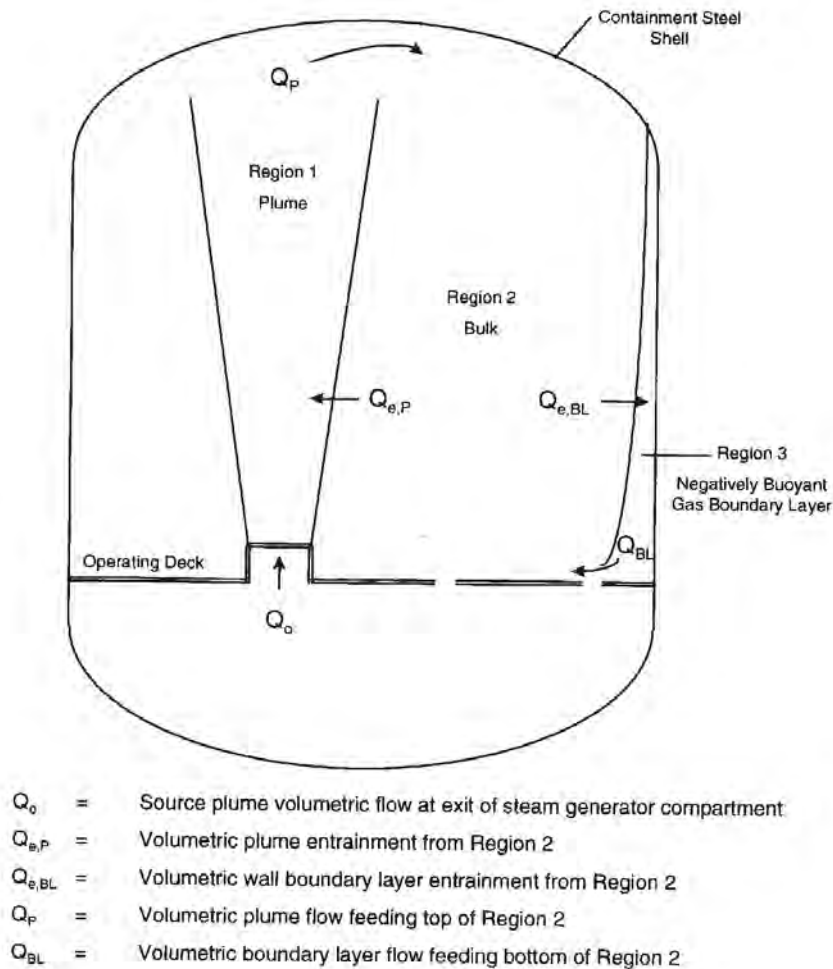


Figure 9.D-1. Interactions Between Containment Regions During Post-Blowdown LOCA (Low Momentum)

9.D-30

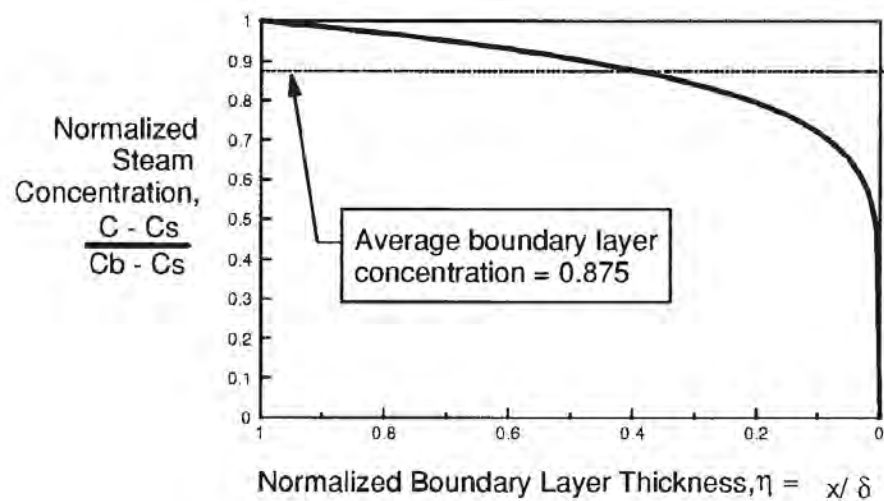


Figure 9.D-2a. Detail of Steam Concentration Distribution in Boundary Layer

9.D-31

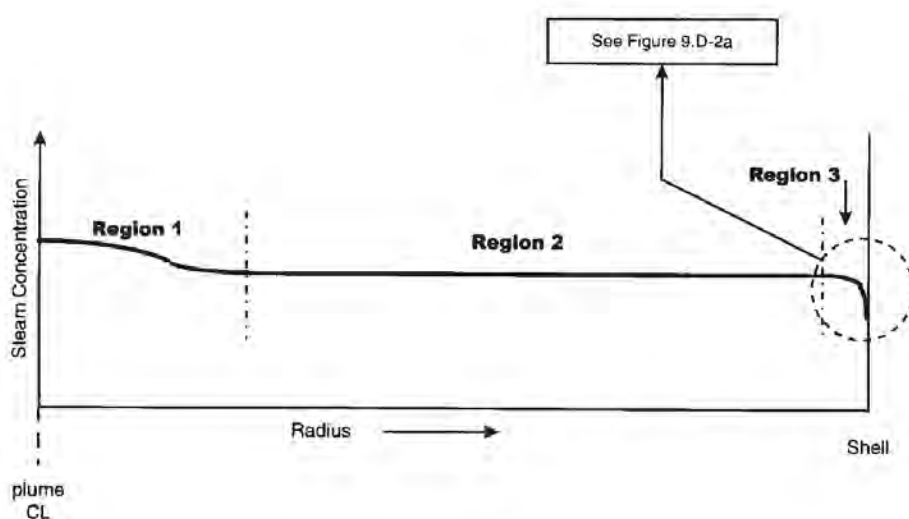


Figure 9.D-2b. Qualitative Radial Concentration Profile from Plume Centerline to Shell at Mid Elevation

9.D-32

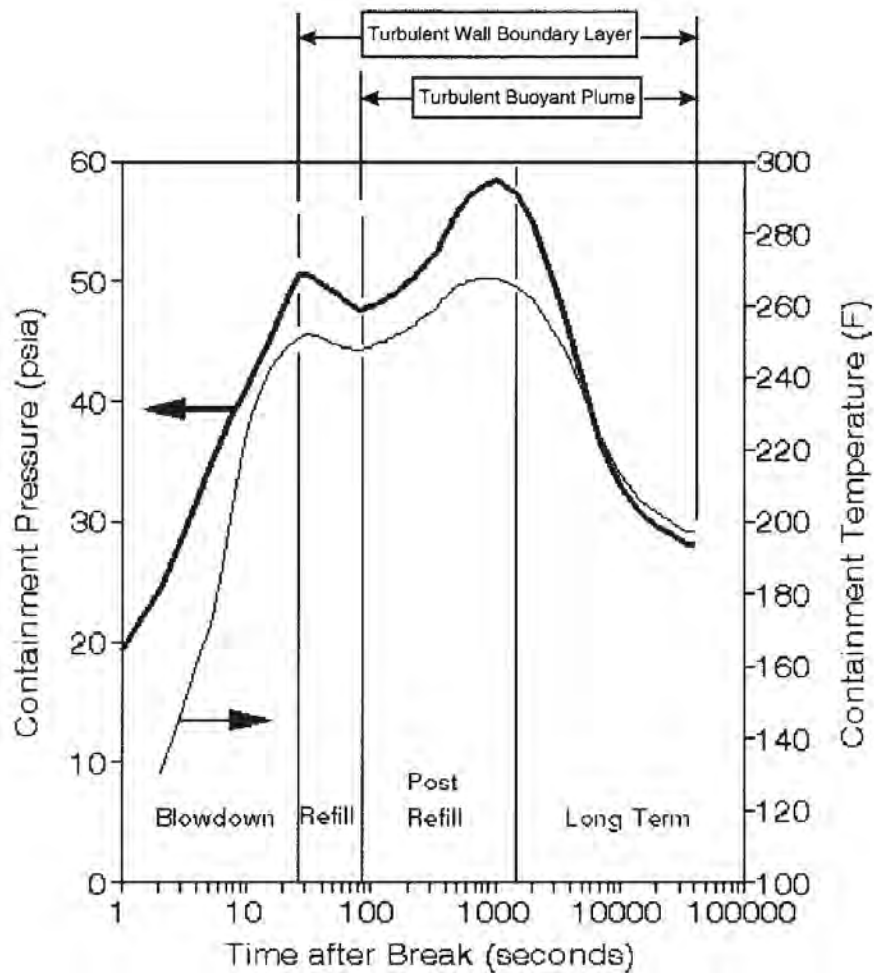


Figure 9.D-3. Period of Application of Analytical Models for Turbulent Wall Boundary Layer and Turbulent Buoyant Plume

9.D-33

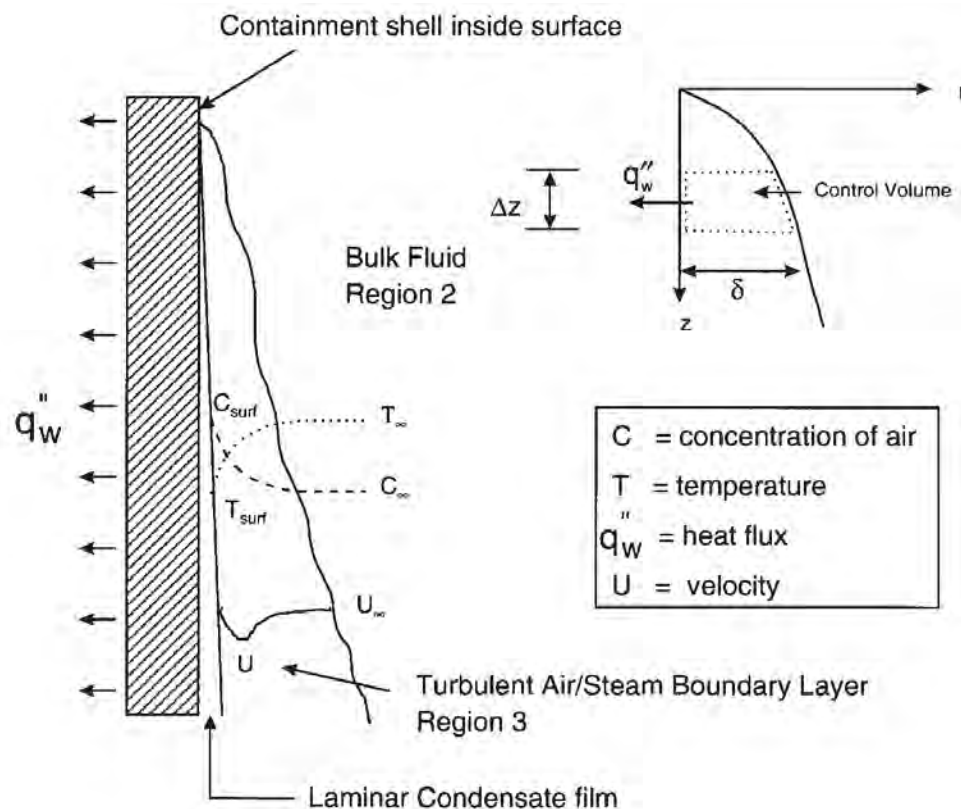


Figure 9.D-4. Turbulent Buoyant Plume Analytical Model

9.D-34

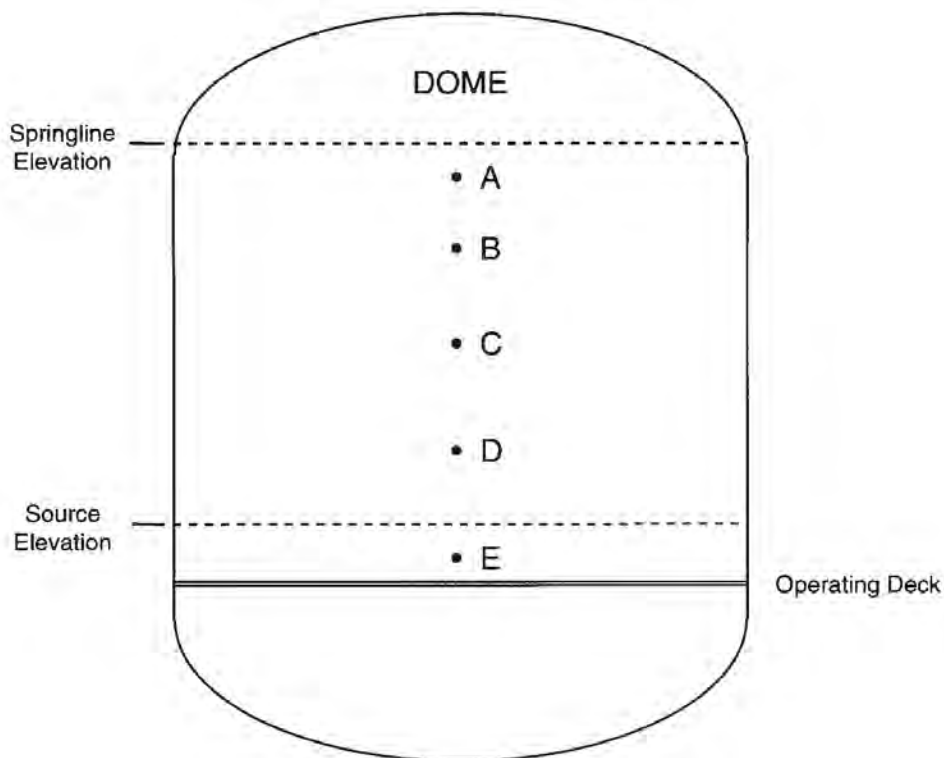


Figure 9.D-5. LST Measurement Locations

9.D-35

a,c

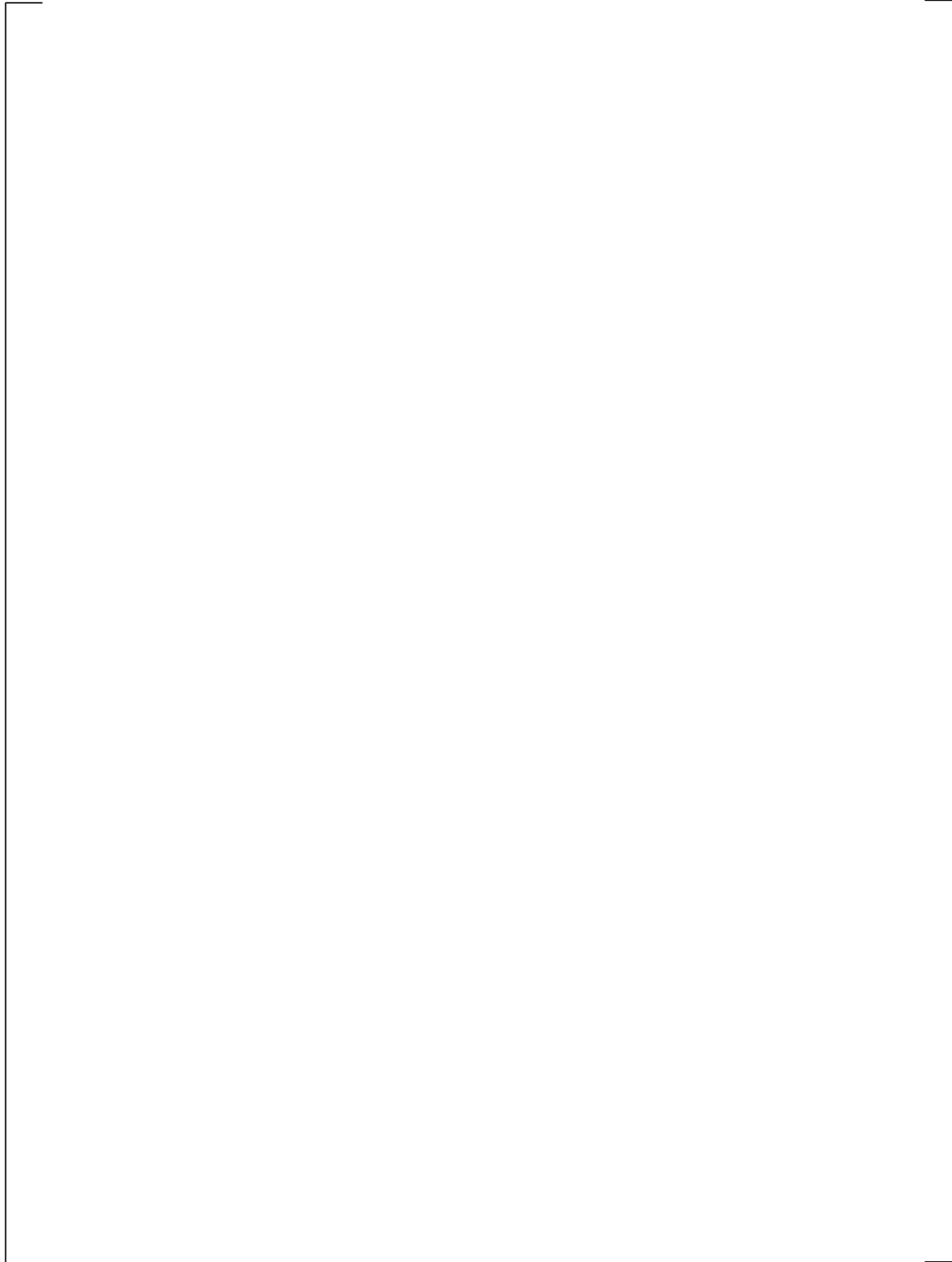


Figure 9.D-6. LST Temperature Profile – Test 220.1 @ Quasi-Steady Conditions

9.D-36

a,c

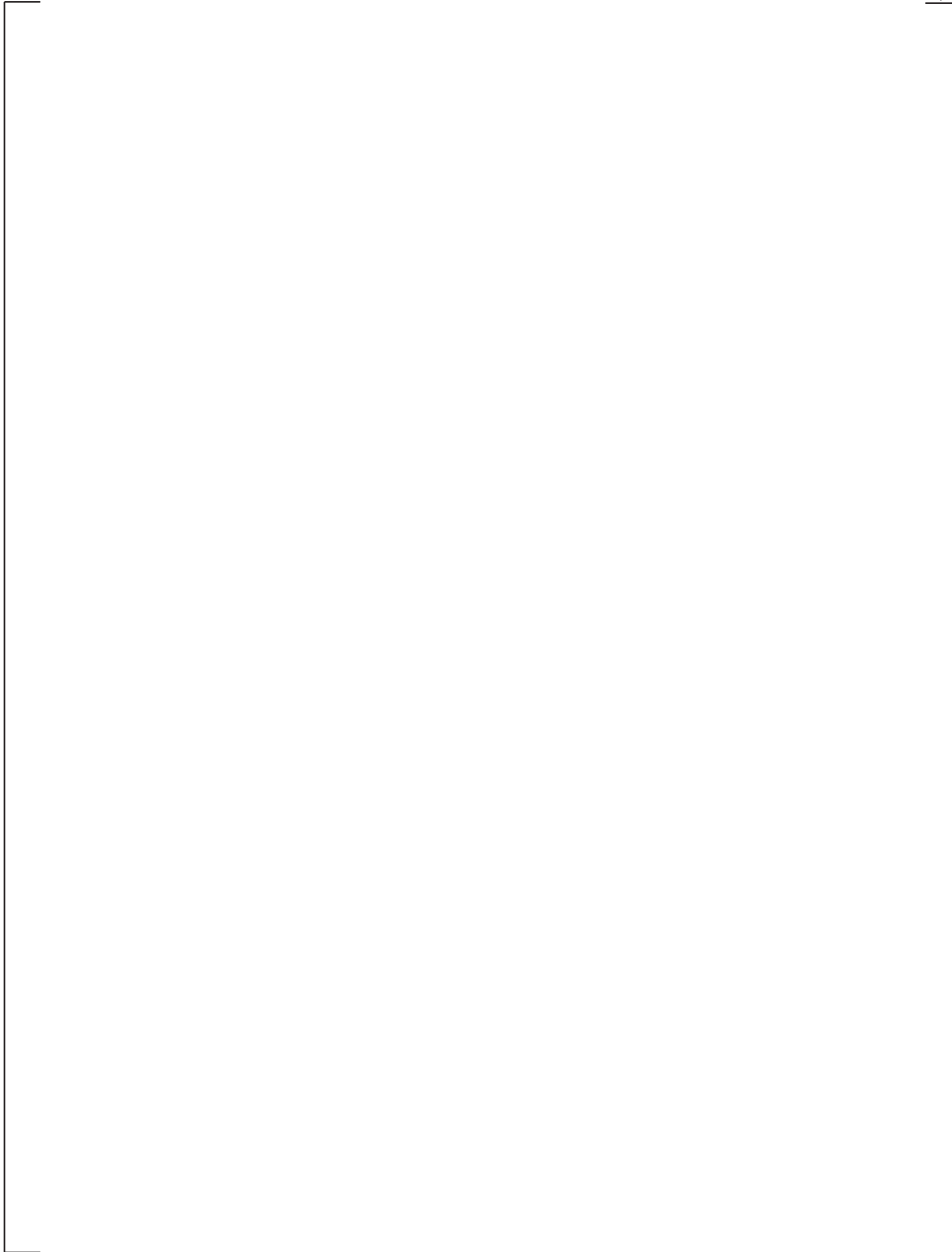


Figure 9.D-7. LST Temperature Profile – Test 217.1 @ Quasi-Steady Conditions

10-1

10 NOMINAL INPUTS AND CORRELATIONS SENSITIVITIES

10.1 INTRODUCTION

The input values for the WGOTHIC Evaluation Model have been biased to ensure a conservative prediction of containment pressure. A subset of these parameters has been selected to determine the impact of each parameter on the calculated pressure for the LOCA and MSLB transients, and to provide a quantification of the total conservatism in the Evaluation Model associated with these parameters. For these parameters, nominal values have been assumed.

Seven sensitivities were run for the LOCA transient to determine the additive sensitivity to each parameter. One sensitivity was run for the MSLB transient, which was a composite of six of the parameters investigated for the LOCA.

The results of these studies show that there is over 11.5 psi margin inherent in the AP600 Containment Evaluation Model for the LOCA peak pressure calculation due to the parameters studied. There is over 13 psi margin associated with the post-blowdown peak pressure, and for the final nominal case, the maximum pressure shifts to the blowdown phase. There is at least 4.9 psi margin in the MSLB calculation due to the parameters investigated. If nominal mass and energy releases were assumed for the MSLB case, even more margin would be shown.

10.2 SENSITIVITY STUDY RESULTS

An estimate of the amount of conservatism, quantified as the change in containment pressure and represented by some of the significant assumptions made for the Evaluation Model follows. These are not single-effect sensitivities. These results are cumulative, in that each additional modification is stacked upon those that immediately preceded it. These sensitivities provide insight into the effect of each parameter individually by comparison to the preceding case, as well as the total conservatism represented by these parameters.

The AP600 Containment Evaluation Model calculations for the LOCA and MSLB described in Section 4 were used as the basis for these studies, with the parameter changes described below, made in each succeeding case. Table 10-1 summarizes the basis for each case and the calculated pressure results for each case. Seven sensitivity cases were analyzed for the LOCA transient, as described below. Figure 10-1 shows a composite pressure curve for the LOCA cases. One MSLB sensitivity was run including all the parameters investigated for the LOCA, except for nominal mass and energy releases. Figure 10-2 shows the pressure results for the MSLB case.

10-2

Table 10-1. Nominal Inputs and Correlations Sensitivity Results

LOCA Sensitivities				
Case	Case Description	Blowdown Pressure (psig)	Post-Blowdown Peak Pressure (psig)	Pressure at 24 Hours (psig)
	AP600 Evaluation Model	34.4	43.9	18.9
1	Heat & Mass Transfer Multipliers on the Containment Shell	34.4	42.5	16.8
2	Nominal Initial and Ambient Conditions (plus case 1)	33.3	39.8	11.0
3	Nominal Clime Material Properties (plus Cases 1, 2)	33.3	39.0	10.4
4	Nominal Steel-to-Concrete Gap Thickness (plus Cases 1, 2, 3)	33.3	38.8	10.4
5	Nominal External Annulus Loss Coefficients (plus Cases 1, 2, 3, 4)	33.3	38.7	10.2
6	Condensation on Dead-Ended Compartment Heat Sinks Considered (plus Cases 1, 2, 3, 4, 5)	33.3	36.7	10.1
7	Nominal Mass and Energy Releases (plus Cases 1, 2, 3, 4, 5, 6)	32.4	30.6	9.2
	Total Conservatism Represented by Above Assumptions for LOCA Transient	2.0	13.3	9.7
MSLB Sensitivity				
Case	Case Description	Peak Pressure (psig)		
	Evaluation Model	44.8		
8	Nominal Inputs and Correlations with Conservative Mass and Energy Releases and Stratification Bias	39.9		
	Conservatism Shown	4.9		

10-3

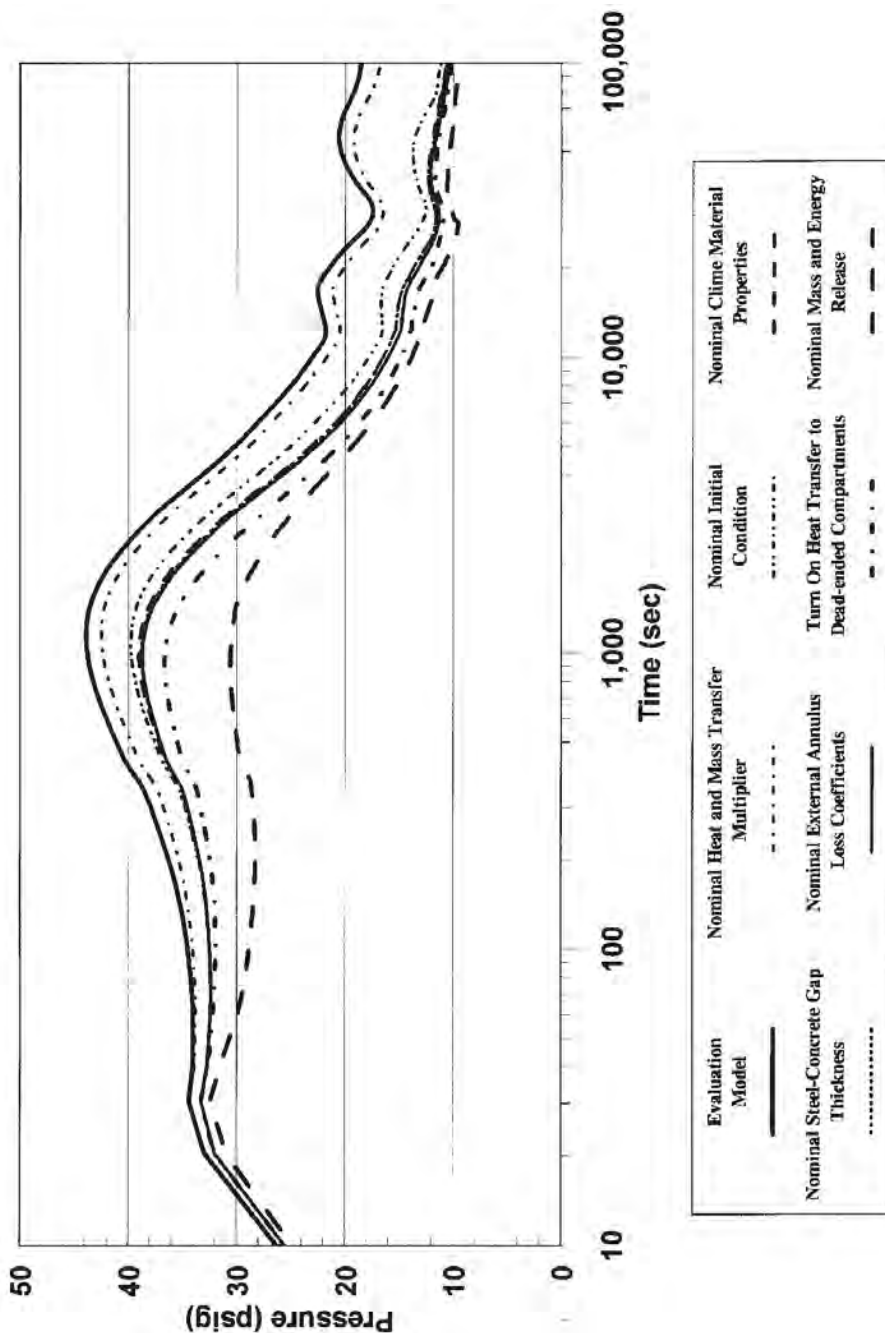


Figure 10-1. LOCA Sensitivities to Nominal Inputs and Correlations

10-4

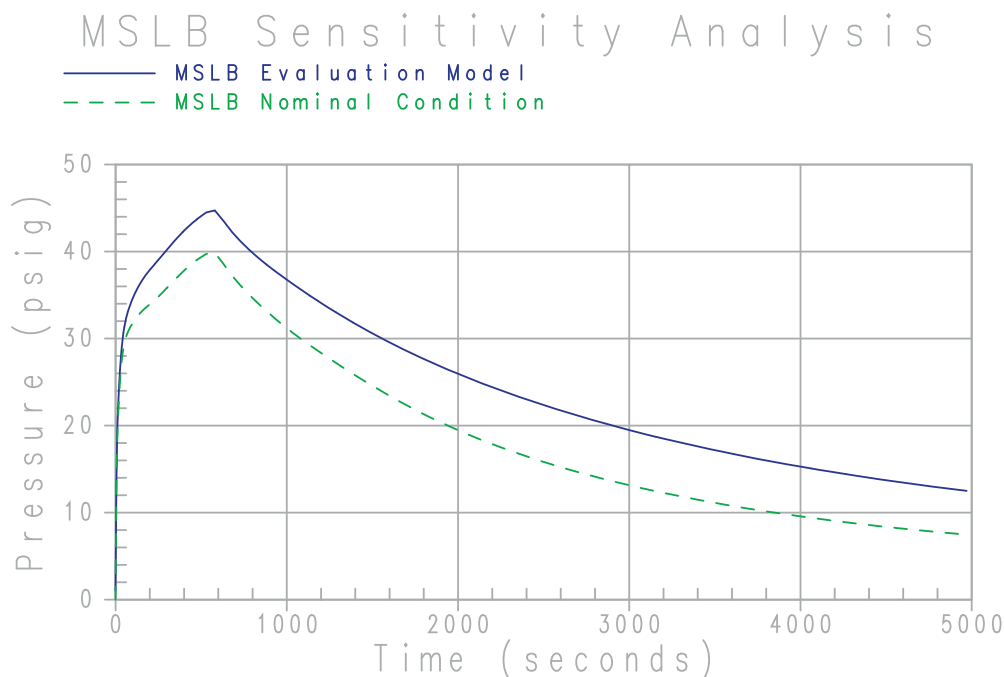


Figure 10-2. MSLB Sensitivity to Nominal Inputs and Correlations

10.2.1 Sensitivity Study Cases for LOCA

Case 1 considered nominal heat and mass transfer on the containment shell. Conservative multipliers have been applied to the heat and mass transfer coefficients calculated on the inside and outside surface of the containment shell in the Evaluation Model to ensure a conservative calculation. A multiplier of []^{a,c} is assumed on the inner surface, where free convection only is considered, and a multiplier of []^{a,c} is assumed on the outer surface, where mixed convection is considered. For this sensitivity, both multipliers were assumed to be 1.0, which represents a more nominal fit to the heat and mass transfer data with only a slight conservative bias remaining (Reference 10.1). The heat transfer regime assumptions were not changed.

The nominal heat and mass transfer modeling resulted in a 1.4 psi reduction in the post-blowdown peak pressure and a 2.1 psi reduction in the pressure at 24 hours. There was no significant impact on the peak blowdown pressure, since the heat removal from the shell has a small impact during this time period.

Case 2 considered the impact of nominal initial and ambient conditions. The parameters discussed in Section 5 were varied for this case, except they were set to a nominal set of conditions. The sensitivity case used initial conditions inside containment of 90°F, 14.7 psia, and 30 percent relative humidity as compared to 120°F, 15.7 psia, and 0 percent relative humidity in the Evaluation Model. The sensitivity case used ambient conditions of 70°F and 50 percent relative humidity compared to 115°F and 22 percent

10-5

relative humidity in the Evaluation Model. The sensitivity case PCS water temperature was set to 70°F compared to 120°F in the Evaluation Model. The initial temperature assumptions for the conductors in the containment and annulus were consistent with their environment. The individual contribution of each of these parameters is discussed in Section 5.

As discussed in Section 5, the internal containment conditions and the PCS water temperature have the most impact on containment pressure. This sensitivity case showed a 1.1 psi reduction in containment pressure during blowdown, a 2.7 psi reduction in the post-blowdown phase, and a 5.8 psi reduction at 24 hours.

Case 3 added the assumption of nominal material properties (thermal conductivity and emissivity) in the clime modeling. In the Evaluation Model (EM) the emissivities were reduced by 10 percent to bound the range found in the literature for the materials used, and the conductivity of the inorganic zinc paint was reduced by a factor of four to conservatively account for the effects of oxidation. In this sensitivity case the emissivities were increased to 0.9 (0.81 was used in the AP600 EM) and the conductivity of the inorganic zinc paint was set to its nominal value of 1.21 BTU/hr-ft-°F (0.302 BTU/hr-ft-°F was used in the AP600 EM). The factor of four decrease in the AP600 containment EM was a conservative factor based on engineering judgement rather than a mechanistic understanding of how thermal conductivity might change over time. The basis for the coatings thermal conductivity in the AP1000 containment EM is addressed in Section 13.4.1.

Deleted: carbo-

Deleted: iz

Deleted: 0.9 multiplier on the

Deleted: was removed

Deleted: carbo-

Deleted: judgement

Deleted: 2

The nominal clime property modeling resulted in a 0.8 psi reduction in the peak post-blowdown pressure and a 0.6 psi reduction in the pressure at 24 hours. There was no significant impact on the peak blowdown pressure, since the heat removal from the shell has a small impact during this time period.

Case 4 modified the assumption of the gap between the steel liner and the concrete on the applicable internal heat sinks.

The steel surface plates are one-half inch thick and are connected to each other by vertical trusses at 30-inch centers. The steel surface plates are connected to the concrete by embedding these trusses and also by six-inch long welded studs. The surface plates are stainless steel for the IRWST and refueling canal boundaries and are carbon steel elsewhere. The shear studs on the stainless steel plates are spaced at 10 inches horizontally and 8 inches vertically. The shear studs on the carbon steel plates are spaced at 10 inches horizontally and 9.6 inches vertically. The welded studs plus trusses result in a direct steel conduction path across the interface between the surface plate and the concrete. The contribution of this steel with much higher thermal conductivity has been neglected in the W Gothic Evaluation Model.

Concrete is placed into the structural modules and will initially bond to the surface plates. The wet concrete weight will load the steel plates and result in permanent outward deformation of the plates spanning between the trusses. Mechanical and thermal loading and shrinkage may break this bond due to relative motion. However, the welded studs will keep the surface plates in contact with the concrete at the stud locations and gaps between the studs would be very small. The Evaluation Model conservatively assumes a five mil gap for the steel-jacketed concrete heat sinks. A one mil gap was assumed for this sensitivity.

10-6

The results of this case show a 0.2 psi reduction in the post-blowdown peak pressure. The blowdown peak pressure was not affected significantly, since the heat capacity of the concrete has little impact on energy removal during this time. The pressure at 24 hours was not affected, since the heat sinks are effectively saturated at this time and the pressure is dictated by the balance between releases to the containment and heat removal via the PCS.

Case 5 included a modification to the pressure loss coefficient in the external annulus. The loss coefficient assumed in the Evaluation Model includes a 30 percent increase over the value derived from the test program. For this study, a loss coefficient 10 percent greater than measured was modeled.

The annulus loss coefficient has a small impact on the pressure, reducing the post-blowdown peak pressure by 0.1 psi and the pressure at 24 hours by 0.2 psi. There was no significant impact on the peak blowdown pressure since the heat removal via the PCS has a small impact during this time period.

Case 6 included the effects of heat sink utilization in the dead-ended compartments. As discussed in Section 9, condensation and convection on the heat sinks in the dead-ended compartments are not credited after blowdown to ensure a conservative treatment of their utilization. With only a small thermal asymmetry, convection would cause these heat sinks to continue to be exposed to steam after this time and would continue to provide a condensation surface. In this case, the structures were allowed to absorb energy based on conditions predicted by the WGOTHIC code. The WGOTHIC calculation limits the amount of steam entering these compartments, since circulation does not occur in lumped volumes, so the utilization of these heat sinks is not expected to be grossly over-predicted. It is therefore acceptable to include the utilization of these heat sinks in these sensitivities.

The additional heat absorption capability of the heat sinks in the dead-ended compartment, with an initial temperature of 90°F, resulted in a 2.0 psi reduction in the post-blowdown peak pressure. There was no change in the blowdown peak pressure since the Evaluation Model already considers condensation on these surfaces during blowdown. The reduction in the pressure at 24 hours was only 0.1 psi, since the heat sinks are effectively saturated at this time in both cases.

Case 7 includes the use of nominal mass and energy release rates. The nominal mass and energy release rates are compared to those used in the AP600 Evaluation Model (described in Section 4) in Figure 10-3 and Figure 10-4, respectively. The following modifications were made in the mass and energy release calculation:

- Nominal full-power temperatures and pressure without uncertainty
- Nominal RCS volume with no uncertainties (thermal expansion was considered)
- Core licensed power without adding 2 percent for calorimetric error
- Nominal core stored energy without adding 15 percent
- 1979 ANS decay heat standard without uncertainty for an 800 day average burnup

10-7

- Steam generator energy was assumed to be released over a period of one hour for the broken loop and two hours for the intact loop rather than thirty minutes and one hour, respectively
- The refill period was modeled
- No heat generation due to zirc-water reaction
- Nominal initial accumulator, CMT, and IRWST fluid temperatures were used in the post-blowdown releases

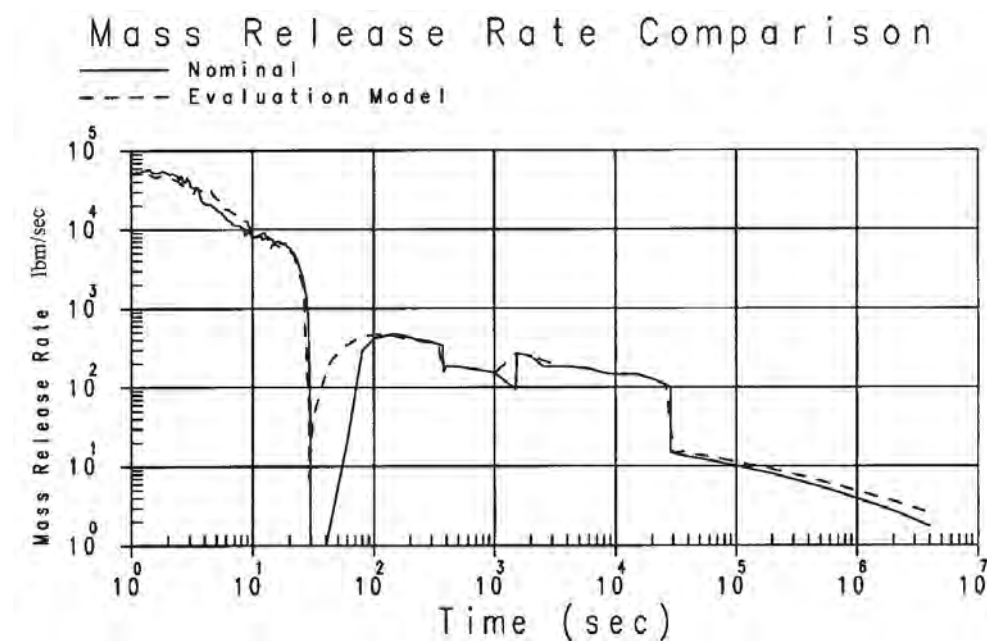


Figure 10-3. Comparison of Evaluation Model and Nominal Mass Release

10-8

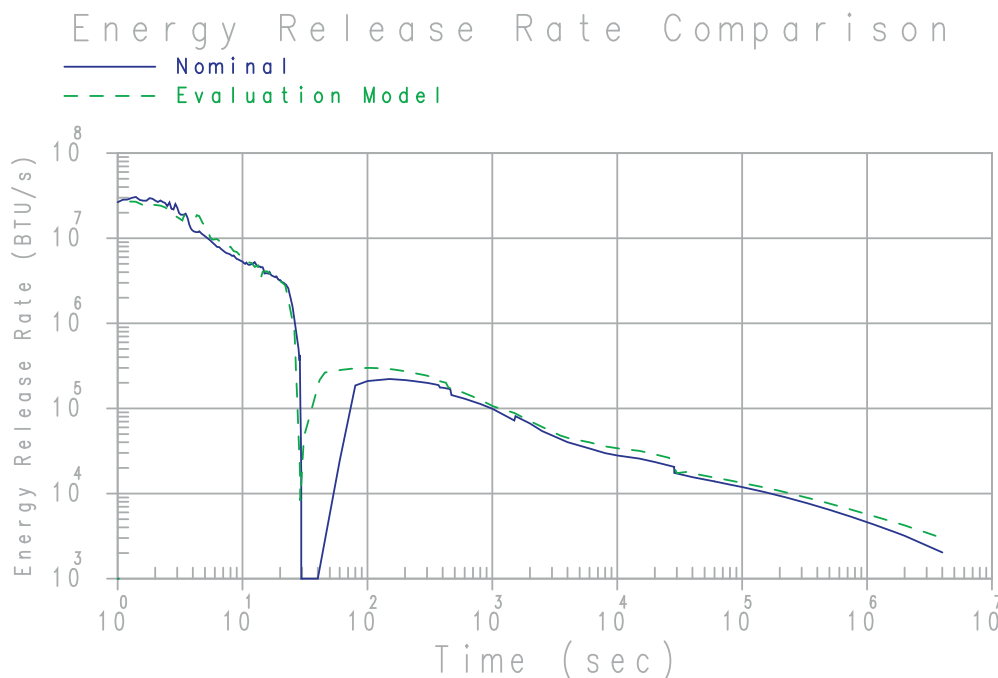


Figure 10-4. Comparison of Evaluation Model and Nominal Energy Release

This case demonstrates that the mass and energy input to the containment has the most impact on the resulting pressure and represents significant conservatism in the Evaluation Model. The blowdown peak pressure was reduced by 0.9 psi, the pressure during the post-blowdown period was reduced by 6.1 psi, and the pressure at 24 hours was reduced by 0.9 psi. The decrease in pressure is sufficient to shift the time of peak pressure for the entire transient from the post-blowdown phase to the blowdown phase. The large sensitivity during the post-blowdown phase is expected, since the mass and energy release models are deliberately biased to maximize the releases during this time in order to ensure that a conservative peak containment pressure is calculated.

10.2.2 Sensitivity Study Case for MSLB

A case was also run to provide quantification of the conservatism in some of the parameters for the MSLB transient. Case 8 included the nominal inputs and correlations embodied in cases 1 through 6 of the LOCA. Nominal mass and energy releases were not included in this calculation. The results of this case indicate that the conservative assumptions studied in the sensitivity case constitute 4.9 psi conservatism. Further reduction in containment pressure would result from the use of nominal mass and energy releases and a less conservative stratification bias. These results also do not credit the significant improvement to shell mass transfer, which would result from forced convection.

10.3 CONCLUSIONS

The results of the sensitivities in this section illustrate that the Containment Evaluation Model provides a conservative prediction of pressure. Some of the conservative nominal inputs and correlations in the Evaluation Model were removed to determine the impact on the calculated pressure for AP600 for the limiting LOCA and MSLB cases. These sensitivities are not intended to portray a best estimate calculation; other conservative features and modeling techniques have not been included that would further reduce the predicted pressure.

However, the conservatism represented by the parameters that were studied is significant. The LOCA cases investigated indicate a reduction of 2.0 psi during blowdown, 13.3 psi during the post-blowdown phase, and 9.7 psi at 24 hours. The summation of these cases switches the time of peak pressure from the post-blowdown period to the blowdown period. Comparison of the maximum pressures in the two cases shows 11.5 psi reduction in pressure. The MSLB case shows 4.9 psi margin due to nominal inputs included in this study. Incorporating other nominal conditions, such as mass and energy release rates and forced convection enhancements, would result in further pressure reduction.

10.4 REFERENCES

- 10.1 WCAP-14326, Revision 2, "Experimental Basis for the AP600 Containment Vessel Heat and Mass Transfer Correlations," April 1998.

11 TIMESTEP SENSITIVITY

11.1 INTRODUCTION

To establish WGOTHIC as an acceptable tool for use in the licensing process, it is necessary to perform a sensitivity to the time step size selected by the code. The timestep size determines how far the transient is permitted to progress from calculational step to calculational step. The algorithm that is used to determine the maximum allowable timestep size should produce a timestep value that results in a stable, suitably accurate solution without prohibitive computer execution times.

In the WGOTHIC code, the algorithm that is used to determine the maximum allowable timestep size is based on two stability criteria: the amount of time it would take to completely replace the mass within a given volume (Courant limit), and one half of the natural period of oscillation for a gravity-driven system (gravitational limit). In addition, the algorithm also includes limits on timestep growth, checks on nonphysical results, and limits on the rates of change of primary variables. These limits are all discussed in Reference 11.1, Enclosure 2, Section 12.7.

11.2 METHODOLOGY

Subroutine timstp.f in the WGOTHIC solver program contains the timestep selection algorithm. This subroutine calculates the maximum allowable timestep size that can be used in the WGOTHIC transient calculations.

Subroutine timstp.f was modified to perform the timestep sensitivity study. The maximum allowable timestep size was reduced to study the effect of using a smaller timestep on the results of the WGOTHIC transient calculations. Use of timesteps that are smaller than the maximum allowable value maintains numerical stability.

Two new versions of subroutine timstp.f were created; in WGOTHIC_S version 4.1.1, the maximum allowable timestep size was halved, and in version 4.1.2, it was quartered. The timestep selection process was not impacted by these changes and there were no other differences between the three versions of WGOTHIC_S.

The AP600 containment evaluation model input deck described in Section 4 was used for the timestep sensitivity analyses. The loss-of-coolant-accident (LOCA) transient was chosen since it contains both rapid and extended pressurization and depressurization transients. The LOCA is a long transient that relies on the PCS for a substantial amount of energy transfer to the environment.

11.3 RESULTS

The LOCA transient containment response analysis was performed with each of the three code versions. Table 11-1 indicates the number of calculational steps taken, the peak predicted pressure, and the predicted pressure at 24 hours for each code version.

11-2

Table 11-1. Timestep Sensitivity Results

WGOTHIC_S Code Version	Number of Computational Steps	Peak Pressure (psig)	Pressure at 24 Hours (psig)
Version 4.1 – 1.0* Δt	187380	43.85	18.86
Version 4.1.1 – 0.5* Δt	374414	43.76	18.88
Version 4.1.2 – 0.25* Δt	748680	43.72	18.85

The one-half timestep version of the code takes approximately twice the number of steps to complete the transient and the one-quarter-timestep version of the code takes about four times the number of steps to complete the transient. Since the timestep selection logic relies on the volume conditions at the end of each step, it is extremely difficult to get exactly twice or four times the number of steps. With the smaller timesteps, the changes in fluid conditions and other parameters used in the timestep selection process are smaller. The smaller changes permit larger timesteps to be allowed. As a result, slightly less than two times and four times the number of calculational steps are used in the modified versions of the code.

The reduced timestep versions predicted slightly lower peak pressures than the base version of the code. The predicted peak pressure for the quarter-timestep version was 0.04 psi lower than the one-half timestep version, and 0.13 psi lower than the full-timestep version. This indicates that the calculated peak pressure solution converges from above as the timestep is reduced.

In addition to the number of timesteps taken to complete the problem, the code output contains the number of times that a timestep was limited by some phenomenon. In all three cases, the timestep size was limited by either the phase change limit, the Courant limit, or the gravitational limit. Table 11-2 presents the number of times that the timestep was limited in each case.

Table 11-2. Timestep Limit Results

WGOTHIC_S Code Version	Courant Limit	Phase Change Limit	Gravitational Limit
Version 4.1 – 1.0 * Δt	4000	21	91612
Version 4.1.1 – 0.5 * Δt	8070	11	183305
Version 4.1.2 – 0.25 * Δt	16108	9	366639

During the pressurization phase of the LOCA transient, the timestep size was primarily limited by the Courant stability limit. This was not unexpected, since the volumetric break flow is so large during this phase. Since the circulation is primarily buoyancy-driven during the much longer depressurization phase, the time step size was primarily limited by the gravitational stability limit after the peak pressure was reached.

Note, the sum of the number of limiting timesteps in Table 11-2 does not add up to the total number of calculational timesteps given in Table 11-1 because, in some instances, the timestep size was not limited by any of the limits tracked in the output file. This could occur, for example, if the upper limit imposed by user input was less than the value calculated by the timestep selection algorithm.

The LOCA transient containment pressure predicted by each of the three code versions is shown in Figure 11-1. There is very little difference in the results. The transient results are further examined by comparing the differences in the predicted transient pressure from each of the three code versions. The percentage difference in the predicted transient pressure between the full-timestep version and the one-half-timestep version, and the percentage difference in the predicted transient pressure between the one-half timestep version and the one-quarter-timestep version is presented in Figure 11-2. The differences in the predicted transient pressure between successive versions of the code are very small (less than 1% over the entire 24-hour period).

11.4 SUMMARY

Two versions of WGOTHIC_S were created for this sensitivity study. The calculational timestep size was reduced to a value that was either one-half (Version 4.1.1) or one-quarter (Version 4.1.2) of the maximum allowable value calculated by the timestep selection algorithm.

A comparison of the predicted AP600 LOCA transient containment pressure response between the base version and the two versions created for the sensitivity study shows that there is very little difference in the results. Using smaller timesteps does not significantly affect the transient response. Therefore, the timestep selection algorithm produces a timestep value that results in a stable, suitably accurate solution.

Based on the timestep study results presented herein, it is concluded that the timestep selection logic for WGOTHIC_S is acceptable.

11-4

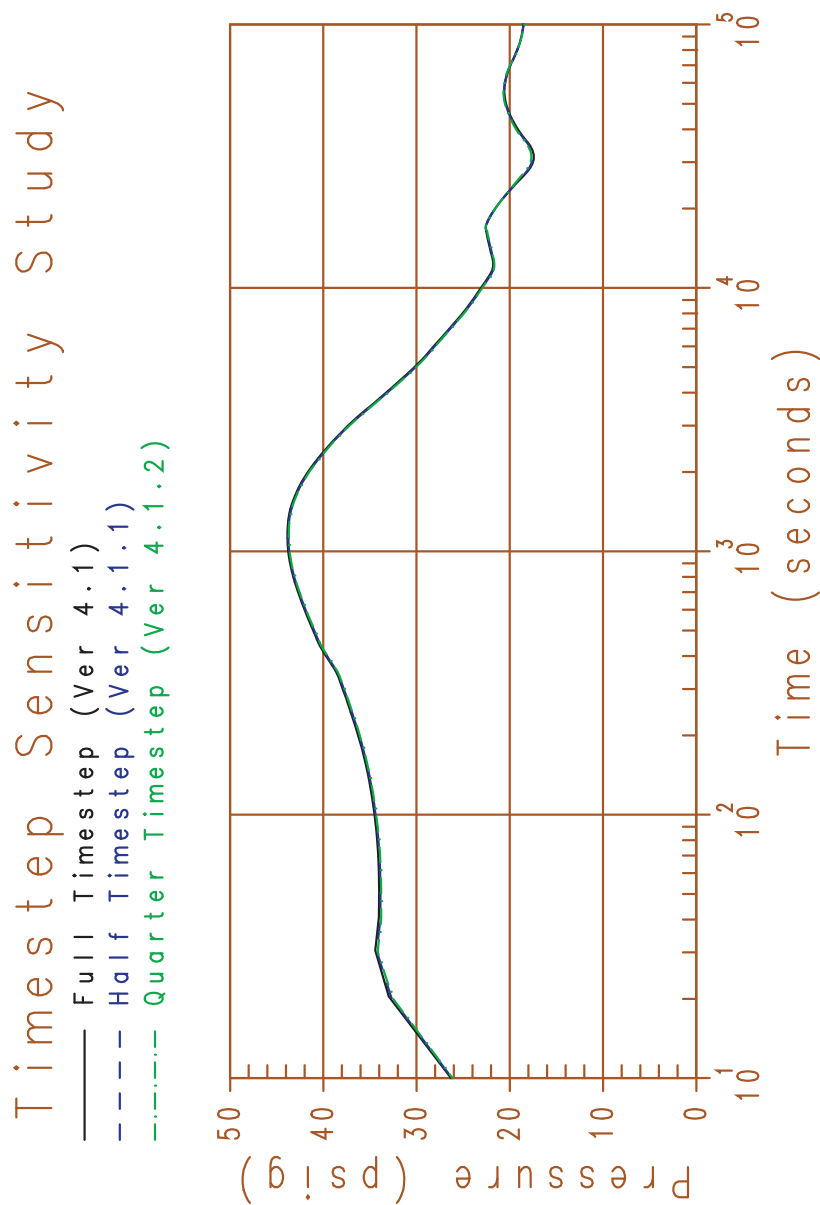


Figure 11-1. AP600 Containment LOCA Transient Pressure Prediction with Full, One-Half, and One-Quarter Timesteps

11-5

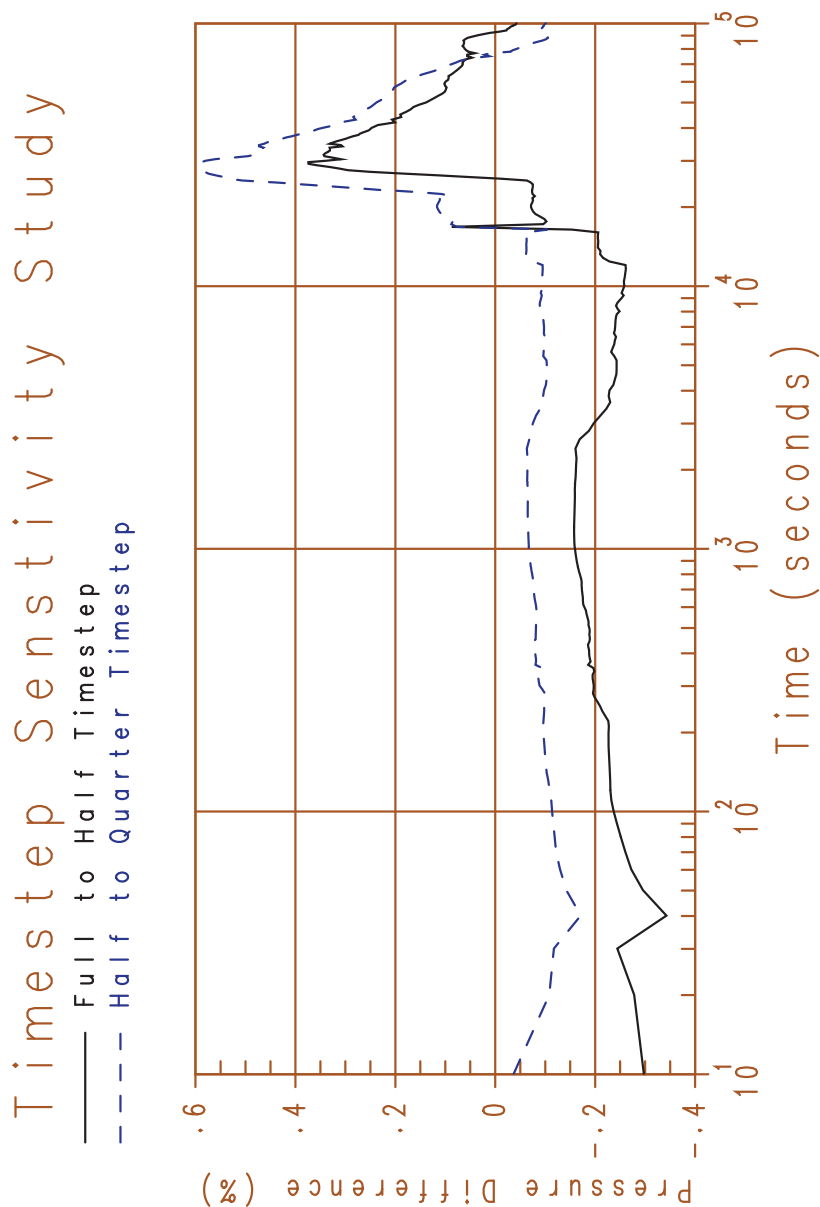


Figure 11-2. AP600 Timestep Comparison, Percentage Difference in Predicted Pressures between Successive Code Versions

11-6

11.5 REFERENCES

- 11.1 Westinghouse Letter NTD-NRC-95-4563, B. A. McIntyre to Quay (NRC), "GOTHIC Version 4.0 Documentation," September 21, 1995.

12 SENSITIVITY TO CLIME NODING

12.1 INTRODUCTION

This section provides background associated with the WGOTHIC clime model, a statement of the issue associated with the application of the clime methodology, a description of the approach developed and taken to address the issue, a summary of the results of the analyses and the conclusions drawn from a review of those analyses.

12.1.1 Background

The GOTHIC code (References 12.1 and 12.2) is a state-of-the-art program for modeling multi-phase flow for containment analysis. The code solves the integral form of the conservation equations for mass, momentum, and energy for multi-component, two-phase flow. The conservation equations are solved for three fields: continuous liquid, liquid drops, and a steam/gas phase. The three fields may be in thermal non-equilibrium within the same computational cell. Relative velocities are calculated for each field, as well as the effects of two-phase slip on pressure drop. Heat transfer between the phases, surfaces, and the fluid are also allowed.

As described in Section 3 of this report, the GOTHIC containment analysis code was modified by Westinghouse to include mechanistic convective heat and mass transfer correlations, a liquid film tracking model, a one-dimensional wall conduction model, and wall-to-wall radiant heat transfer to model heat removal by the PCS. The code with these modifications is called Westinghouse-GOTHIC, and is abbreviated as WGOTHIC.

A solution technique that includes wall-to-wall radiation at the conditions expected for the AP600 and **AP1000** plant designs necessitates a close coupling of the participating walls. This coupling is accomplished by assigning boundaries that define the portions of the various walls that radiate to one another. Consistent with the basic formulation implemented for the GOTHIC code that considers conductors or heat sinks to be energy and mass sink or source terms, code modifications that include wall-to-wall radiant heat transfer can be thought of as the addition of a special type of conductor group. This special conductor type or group consists of a set of walls that radiate to each other and interface with GOTHIC fluid cells through mass and energy source terms. The term *clime*, meaning *region*, is used to differentiate and distinguish this special conductor type from those already existing in GOTHIC terminology.

A three-conductor clime is shown schematically in Figure 12-1. For the containment model, a clime is a horizontal slice of the containment structure consisting of the steel shell, the baffle, and the shield building and liquid films which may form on those solid surfaces, and representing the following transport processes:

- The heat and mass transfer source terms from the containment volume to the shell
- Liquid film mass and energy conservation and thermal resistance on shell, baffle, or shield building surfaces

12-2

- Conduction through the shell
- Heat and mass transfer source terms from the exterior shell to the riser air flow channel
- Radiation from the exterior shell to the interior baffle
- Heat and mass transfer source terms to the interior baffle from the riser air flow channel
- Conduction through the baffle
- Heat and mass transfer source terms from the exterior baffle to the downcomer air flow channel
- Radiant heat transfer from the exterior baffle to the interior surface of the shield building
- Heat transfer source terms to the interior surface of the shield building from the downcomer air flow channel
- Conduction through the wall of the shield building
- Both radiant and convective heat transfer from the exterior surface of the shield building to the environment

As shown schematically in Figure 12-1, the internal containment vessel volume, riser air flow channel volume, downcomer air flow channel volume, and environment volume are separate computational cells or fluid volumes in the GOTHIC model. The shell, baffle, and shield building walls are one-dimensional conductors representing solid wall structures between the computational cells. These conductors are further subdivided into regions of different materials with different numerical mesh sizes.

The climes are stacked vertically through the PCS to model the effects of changing properties both inside and outside the containment shell. Usually there are at least two stacks of climes a wet stack and a dry stack. The only difference between a wet and dry stack is that a time-dependent, water flow rate boundary condition is specified for each conductor surface of the top clime in a wet stack. Because condensation can occur on either wet or dry conductor surfaces, an initially dry stack of climes could contain some wet conductor surfaces and/or a partially wet conductor surface due to condensation. Likewise, an initially wet stack of climes could contain some dry conductor surfaces and/or a partially dry conductor surface due to evaporation.

The user must specify values for the area and circumferential perimeter for each conductor of each clime in both the wet and dry stacks. The input values for the area and circumferential perimeter for the clime conductors in the wet stacks are based on measurements of the water coverage from the full-scale water distribution tests. The water coverage input calculation method for the containment Evaluation Model is described in Section 7.

The WGOTHIC clime model calculates the temperature, flow rate, and thermal resistance of the water films on the various conductor surfaces of a clime. Liquid mass is conserved whenever the film reaches the bottom clime in a stack or a conductor surface dries out. The clime model takes the film flow rate

from each conductor surface of the previous clime in the stack as input, then adds the local condensation rate, or subtracts the local evaporation rate to determine the output water flow rate on each of its corresponding conductor surfaces. Any liquid film remaining on the conductor surfaces of the last clime in a stack is added to the liquid field of the WGOTHIC cell in contact with the conductor surface, or an alternate drain cell specified by user input.

Dryout occurs when either the film flow rate is low enough or the heat flux is high enough to result in complete evaporation of the film before it can exit the conductor. The clime model calculates the evaporation heat and mass transfer and the location of the dryout elevation; the remainder of the conductor surface is treated as a dry surface.

The details of the clime equations and integration into the GOTHIC code are described in Sections 3.4 and 3.5.

12.1.2 Problem Statement

Simply stated, the objective of this effort is to demonstrate that the clime calculations are insensitive to increased numerical resolution relative to the noding pattern employed in the Evaluation Model.

12.1.3 Approach

The approach taken to address the problem statement given above is to:

- Perform sensitivity calculations using a simple two-channel annulus model with a constant temperature boundary condition. The simplified model is used to better isolate effects of clime noding. For this task, the number of climes in the model will vary from 4 to 16. Although not intended to simulate or scale to the AP600 or **AP1000** plants, this two-channel annulus model will provide for thermo-fluid conditions similar to those expected in the annulus of the passive plant, i.e., evaporation into a buoyancy-driven air flow.
- Perform sensitivity calculations with an AP600 containment model for which the number of climes, stacks, and conductor layers are varied to confirm the results of the simpler models.

12.1.4 Selected Parameters

The following thermal-hydraulic parameters are used in evaluating the comparison of various model predictions:

- Containment pressures (for the AP600 model only)
- Temperatures – cooling air and liquid film
- Heat fluxes and/or heat rates from the shell

These parameters are primary indicators of the heat transfer process and were selected as a basis for evaluating the sensitivity of the calculated results to noding patterns.

12-4

12.1.5 Success Criteria

The noding pattern used for a model may affect the results of a calculation. For the purpose of this study, the following success criteria are used to evaluate the significance of change in calculated results with increasing detail in clime noding:

- Success Criteria: The change between results calculated with two noding patterns is defined to be negligible; if:
1. The variation in results between two successive noding patterns is less than []^{a,c} percent.
 2. The variation in results from successively finer noding patterns is decreasing.

[

] ^{a,c}

Thus, the criteria listed above establish that the variation between results obtained from different noding patterns must be small, and the variation must be converging as the noding pattern is increased.

12.2 MODEL DESCRIPTIONS

The sensitivity of the thermo-fluid calculations of the WGOTHIC clime methodology to the number of nodes associated with the flow channel was investigated using a two-channel annulus model. This section presents descriptions of the model and the boundary conditions used in this investigation. This simplified two-channel model is not intended to scale to the plant. It is a simplified model with fixed boundary conditions that allows study of changes caused by clime noding detail. The fixed boundary conditions allow direct comparison of clime heat removal predictions. A detailed comparison of the results calculated for this model to those calculated in the AP600 or **AP1000** is not meaningful. However, the trends for the simple model, relative to the success criteria, are applicable to the passive plant design, as confirmed with the sensitivity calculations using an AP600 containment model as a basis (Section 12.3.2).

12.2.1 Simple Annulus Clime Model

Model Description

A simple two-channel model was developed to study the effects of increasing the number of climes over a wide range of film flow rates and film temperatures and is shown schematically in Figure 12-2. The modeled heated height was []^{a,c} feet. This height was chosen to promote the calculation of velocities in the model representative of the lower bound of the range expected for AP600. The number of climes (and corresponding annulus cells) in the heated section of the model varied between 4 and 16. Figure 12-3 presents the noding structure for the 8 clime model. The noding pattern for the 4 and 16 clime models is similar to that of the 8 clime model, having one-half and double the number of axial cells, respectively.

12-5

The annulus clime model is connected to two stacks of lumped parameter cells, similar to the Evaluation Model. One stack represents the downcomer volume and the other represents the riser volume. The volumes of the riser and downcomer are []^{a,c} cubic feet and []^{a,c} cubic feet respectively. The downcomer volume was arbitrarily selected to be about twice the value of the riser volume. A set of equally spaced elevation planes crosses both the riser and downcomer to form the two stacks of lumped parameter cells. The volume, height, and vertical flow area of each cell in the riser stack and each cell in the downcomer stack is the same.

A natural draft flow of air from the downcomer through the riser develops as the riser channel is heated. Friction acts to retard the increase in air velocity. Except for the turning location and exit, the friction lengths for each flow path are equal to the cell height. The friction lengths at the riser entrance and exit are set to one half the cell height to conserve the total friction length and fL/D values between models. Loss coefficients of []^{a,c} at the downcomer entrance and []^{a,c} at the riser outlet are used to model the form losses representative of a contraction and an expansion, respectively.

For the 8 clime model shown in Figure 12-3, a thermal conductor located within the heat source (Volume 9), provides a []^{a,c} constant temperature boundary condition for the model. A single stack of climes is used to thermally connect the heat source with the riser and downcomer volumes. There is one clime per cell in the riser. An additional clime at the bottom of the stack is used to model the runoff film flow. The last clime in the stack is connected to three dummy volumes. This modeling is used to allow the runoff from the last clime to collect in the drain volume (Volume 18) without affecting the heat removal in the active section of the annulus.

Each clime has two conductors; the first one represents a []^{a,c} thick steel plate and the other represents an acrylic cover. The perimeter and heat transfer area is the same for each conductor on all climes.

To prevent the drain volume from overfilling, it is connected to a flow rate boundary condition. The boundary flow rate for the drain volume is controlled with trips based on the liquid level in the drain volume.

These features were also included in both the 4 and 16 clime models.

12-6

Boundary Conditions

Four cases were considered for this study. The independent variables for each case are listed in Table 12-1.

Table 12-1. Input Parameters for Annulus Clime Model Sensitivity Study

a,c

The film boundary conditions are selected to cover a range of temperatures and flow rates considered typical for the passive plant. For Case 4, the film mass flow rate is reduced to force the prediction of dryout about midway down the plate. Both the downcomer and riser are connected to a fixed pressure boundary set at []^{a,c} psia.

12.2.2 AP600 Containment Model

A schematic of the AP600 containment model clime noding pattern is shown in Figure 12-24. The dashed lines represent divisions between the []^{a,c} climes (and cells) in the annulus.

The AP600 clime noding sensitivity cases were performed using a preliminary Evaluation Model input deck. The differences between the AP600 containment model that was used for these sensitivity studies and the Evaluation Model, as described in Section 4, are irrelevant to the clime noding sensitivity study because each of the sensitivity cases used this same AP600 containment model as its basis. The major differences between the sensitivity model and the Evaluation Model, are summarized below:

- The mass and energy releases in the sensitivity model are lower during the peak pressure phase and higher during the long-term phase. The different phases of the LOCA containment pressurization transient are defined in Section 3.4.2.2 of Reference 12.3. []

] ^{a,c}

12-7

- The PCS flow rate input is higher in the sensitivity model for the first three hours, but lower for the remainder of time. [

] ^{a,c}

- The internal nodding structure is different. [

] ^{a,c}

- The annulus initial conditions in the sensitivity model (15.7 psia, 120°F) are different from those in the Evaluation Model (14.7 psia, 115°F).

- [

] ^{a,c}

- The annulus loss coefficients are lower in the sensitivity model. [

] ^{a,c}

The base case AP600 containment model was modified for the clime nodding sensitivity study to examine the following effects:

- Doubling the number of climes (or vertical segments) from [] ^{a,c} to [] ^{a,c} (see Figure 12-25)
- Doubling the number of stacks (or radial segments) from [] ^{a,c} to [] ^{a,c} (see Figure 12-26)
- Doubling the number of numerical mesh points through the thickness of the clime conductors (see Figure 12-27)

As with the simple annulus model nodding study described in Section 12.2.1, the heat transfer parameters identified in Section 12.1.4 were used to evaluate the sensitivity of the calculations to changes in the nodding pattern used for the calculations. In addition, plots comparing the annulus air pressure, density and velocity profiles are included for the vertical clime nodding sensitivity comparison.

12-8

12.3 RESULTS

12.3.1 Simple Annulus Clime Model

The four test cases described in Table 12-1 of Section 12.2.1 were run using WGOTHIC Version 4.1. Transient calculations were performed until the time when little or no change in one or more governing parameters (pressure, film temperature, etc.) was predicted. Since constant boundary conditions were used, a steady-state solution was eventually reached for each case. All four cases were run out to 2000 seconds of transient time.

Plots of the predicted heat removal rate from the plate surface, shown in Figures 12-4 through 12-7, indicate that the four cases were close to steady-state conditions at the end of the 2000-second transient period. The difference between the heat rejection rates of the 4 and 8, and 8 and 16 clime models is shown in Figures 12-8 through 12-11. From these plots, it is noted that the predicted transient heat removal rate is quite insensitive to the level of clime noding detail; a change of less than 1 percent is observed for increasing the axial nodal pattern from 4 to 8 climes. The difference observed when the axial nodal pattern is increased from 8 climes to 16 is even less.

A comparison of the predicted heat removal rate from the plate surface at the end of the transient is shown in Table 12-2.

Table 12-2. Predicted Heat Removal Rates for Various Clime Noding Schemes

a,c

For the first three tests (all dry or all wet), the steady-state heat removal rate increases slightly as the number of climes is doubled from 4 to 8. Doubling the number of climes from 8 to 16 increases the heat removal rate again, but by a much smaller amount. Therefore, for these cases, the predicted heat removal rate is converging from below.

For test case 4 (half wet), the steady-state heat removal rate decreases slightly as the number of climes is doubled from 4 to 8. Doubling the number of climes from 8 to 16 also decreases the heat removal rate, but by a smaller amount. Further comparisons show that the predicted heat removal rate decreases on the top []^{a,c} feet, but increases on the bottom []^{a,c} feet of the model surface as the number of climes is increased. The decrease on the top []^{a,c} feet is larger than the increase on the bottom []^{a,c} feet. Therefore, the total predicted heat removal decreases as the number of climes increases in case 4. At the low flow rate for this test, the increased resolution of the subcooled heat flux with more climes yields a slightly lower estimate of the predicted heat removal rate.

12-9

Figures 12-12 through 12-15 compare the calculated axial heat flux profiles, and Figures 12-16 through 12-19 compare the axial film temperature profiles at time $t = 2000$ seconds, where “film temperature” for the dry case represents the surface temperature. Note, the data from the 8 and 4 clime models is represented as 2 and 4 points respectively on the plots to match the 16 points from the 16 clime model.

For the wet tests, smoother axial heat flux and film temperature profiles are calculated as the number of climes increases. In the cold film tests (cases 2 and 4), the heat flux decreases and film temperature increases as the film flows from the first clime down. In the hot film test (case 3), the heat flux increases and the film temperature decreases as the film flows from the first clime down. The heat flux remains constant after the film reaches a temperature at which evaporation dominates. For the partially wet test (case 4), the heat flux decreases rapidly and the film temperature increases to the dry surface temperature in the clime where dryout occurs.

The heat flux and surface temperature profiles are adequately represented with either 4, 8, or 16 climes for the dry test (case 1). The heat flux decreases linearly from the entrance (last clime) to the exit (first clime) of the channel while the surface temperature remains essentially constant.

Figures 12-20 through 12-23 compare the calculated axial air temperature profiles at time $t=2000$ seconds. In all tests, the air temperature increases from the entrance (last clime) to the exit (first clime) of the heated channel.

12.3.2 AP600 Containment Model

The long-term mass and energy release input and PCS flow rate input were not finalized at the time the sensitivity cases were made, therefore, sensitivity results are presented up to the time the IRWST inventory was depleted (43500 seconds). This was a sufficient transient duration to determine if the AP600 containment model would be sensitive to doubling the number of climes, the number of stacks, or the conductor mesh points.

Clime Sensitivity Results

The number of climes and volumes in the annulus of the base AP600 containment model were doubled (while maintaining the same total volume and heat transfer area) and the case was run using WGOTHIC Version 4.1. Figure 12-28 shows a comparison of the transient pressure for the double clime case with the base case. There is essentially no difference between the two cases. Figures 12-29 and 12-30 present the axial wet heat flux profile for the []^{a,c} and []^{a,c} clime cases at transient time $t=0, 30, 1500$, and 43500 seconds. The profiles are similar, but the wet heat flux profile for the []^{a,c} clime case has better resolution of the subcooled region at the top of the dome at 1500 seconds and of the dryout elevation at 43500 seconds.

Figures 12-31 and 13-32 present the axial dry heat flux profile for the []^{a,c} and []^{a,c} clime cases at transient time $t=0, 30, 1500$, and 43500 seconds. The profiles are similar.

12-10

Figures 12-33 and 12-34 present the axial external film temperature profile for the []^{a,c} and []^{a,c} clime cases at transient time t=0, 30, 1500, and 43500 seconds. The profiles are similar, but the film temperature profile for the []^{a,c} clime case has better resolution of the subcooled region at the top of the dome at 1500 seconds and of the dryout elevation at 43500 seconds.

Figures 12-35 and 12-36 present the axial external dry surface temperature profile for the []^{a,c} and []^{a,c} clime cases at transient time t=0, 30, 1500, and 43500 seconds. The profiles are similar.

Figures 12-37 and 12-38 present the axial annulus air pressure profile for the []^{a,c} and []^{a,c} clime cases at transient time t=0, 30, 1500, and 43500 seconds. The pressure quickly decreases to the boundary condition value (14.7 psia) in both cases. The pressure at the bottom of the annulus is slightly higher than at the top due the density head.

Figures 12-39 and 12-40 present the axial annulus air temperature profile for the []^{a,c} and []^{a,c} clime cases at transient time t=0, 30, 1500, and 43500 seconds. The downcomer and riser air temperatures eventually establish similar profiles. The air temperature increases slightly as it flows downward, then increases rapidly (by about 30°F at 1500 and about 18°F at 43500 seconds) in the riser as it flows upward.

Figures 12-41 and 12-42 present the axial annulus air density profile for the []^{a,c} and []^{a,c} clime cases at transient time t=0, 30, 1500, and 43500 seconds. The profiles are similar.

Figures 12-43 and 12-44 present the axial annulus air velocity profile for the []^{a,c} and []^{a,c} clime cases at transient time t=0, 30, 1500, and 43500 seconds. The profiles are similar. The air velocity decreases at the top of the riser as it enters the large open area above the dome.

Comparisons of the transient heat rate and heat releases integrated over height of the model are shown in Figures 12-45 and 12-46. Again, there is essentially no difference between the two cases.

By this comparison, it is concluded that the transient pressure and shell heat removal rates calculated by the AP600 containment model are not sensitive to the number of climes.

Stack Sensitivity Results

The number of stacks of climes in the base model were doubled (while maintaining the same total heat transfer area) and the case was run using WGOTHIC, Version 4.1. Figure 12-47 shows a comparison of the transient pressure for the double stack case with the base case. There is essentially no difference between the two cases. Comparisons of the transient heat rate and heat releases integrated over the height of the model are shown in Figures 12-48 and 12-49. Again, there is essentially no difference between the two cases.

These comparisons show the transient pressure and shell heat removal rate calculated by the AP600 containment model are not sensitive to the number of stacks.

Clime Conductor Numerical Mesh Point Sensitivity Results

The number of numerical solution mesh points through the thickness of each of the three conductors (shell, baffle, and concrete) that make up each clime in the base model was doubled and the case was run using WGOTHIC Version 4.1. Figure 12-50 shows a comparison of the transient pressure for the double mesh case with the base case. There is essentially no difference between the two cases. Comparisons of the transient heat rate and heat releases integrated over the height of the model is shown in Figures 12-51 and 12-52. Again, there is essentially no difference between the two cases.

From these comparisons, it is concluded that the transient pressure and shell heat removal rates calculated by the AP600 containment model are not sensitive to the number of numerical mesh points within the conductors that comprise each clime.

12.4 SUMMARY

12.4.1 Simple Annulus Clime Model Noding Study

A two-channel annulus model was exercised over a range of film flow rates, and film temperatures with the code calculating air velocities associated with natural draft heating. For the cases considered, increasing the number of climes was observed to have no significant effect on the predicted heat removal rate. That is, the predicted heat removal rate was insensitive to the number of clime nodes used in the model. The predicted heat removal rate converges in all cases considered. Increasing the number of climes resulted in smoother axial heat flux and film temperature profiles for the wet tests. Adequate axial heat flux and temperature profiles were predicted without increasing the number of climes for the dry cases.

12.4.2 AP600 Containment Model Clime Noding Study

Using an AP600 containment model similar to, but not exactly the same as the Evaluation Model, the effect of doubling the number of clime nodes, doubling the number of stacks, and doubling the number of conductor mesh points was studied. In each case, code calculations were found to be unaffected by the variations in the model features.

These studies demonstrate that results obtained with the AP600 containment model are not sensitive to changes in the clime and annulus noding. Therefore, it is concluded that []^{ac} climes are adequate to predict the PCS performance for the Evaluation Model.

12.5 REFERENCES

- 12.1 Westinghouse Letter NTD-NRC-95-4563, B. A. McIntyre to T. R. Quay (NRC), "GOTHIC Version 4.0 Documentation," September 21, 1995.
- 12.2 Westinghouse Letter NTD-NRC-95-4462, N. J. Liparulo to T. R. Quay (NRC), EPRI Report RA-93-10, "GOTHIC Design Review, Final Report," May 15, 1995.
- 12.3 WCAP-14812, Revision 2, "Accident Specification and Phenomena Evaluation for AP600 Passive Containment Cooling System," April 1998.

12-12

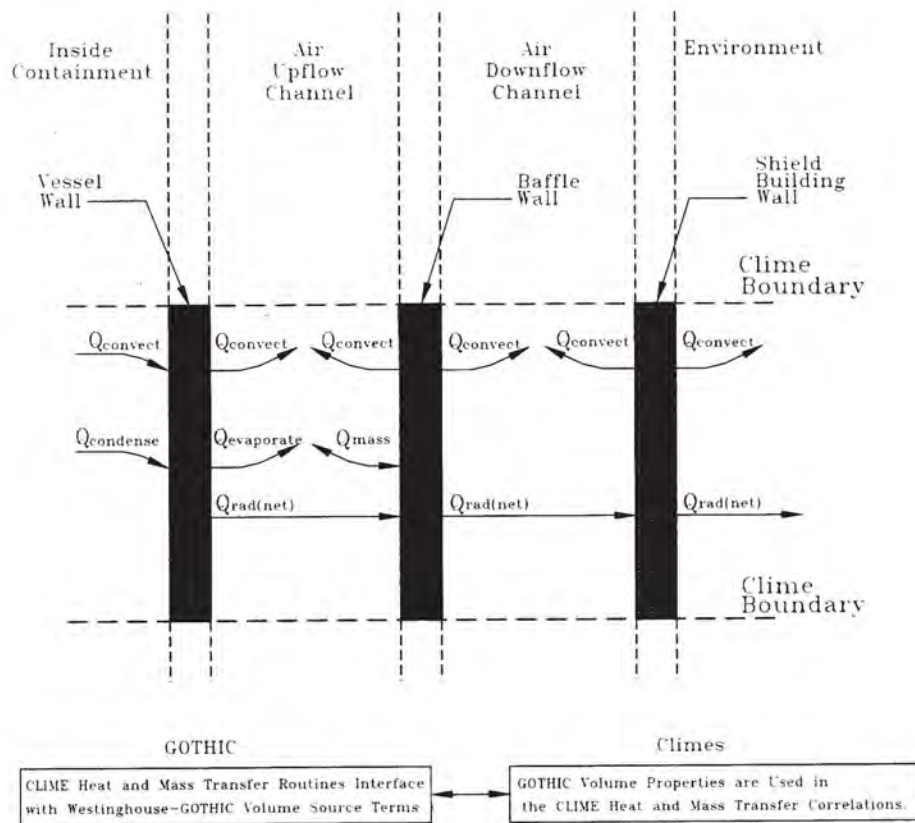


Figure 12-1. Westinghouse-GOTHIC Clime Wall Source Team Models

12-13

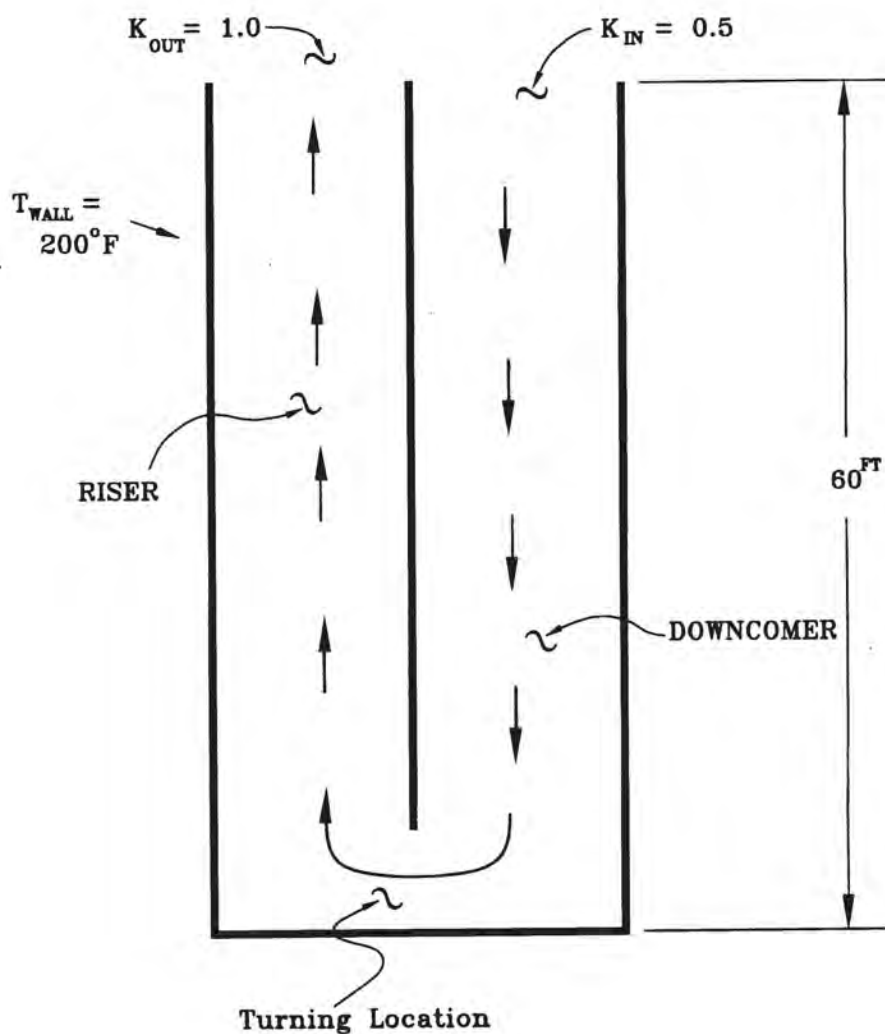


Figure 12-2. Simplified Line Diagram of Annulus Cline Model

12-14

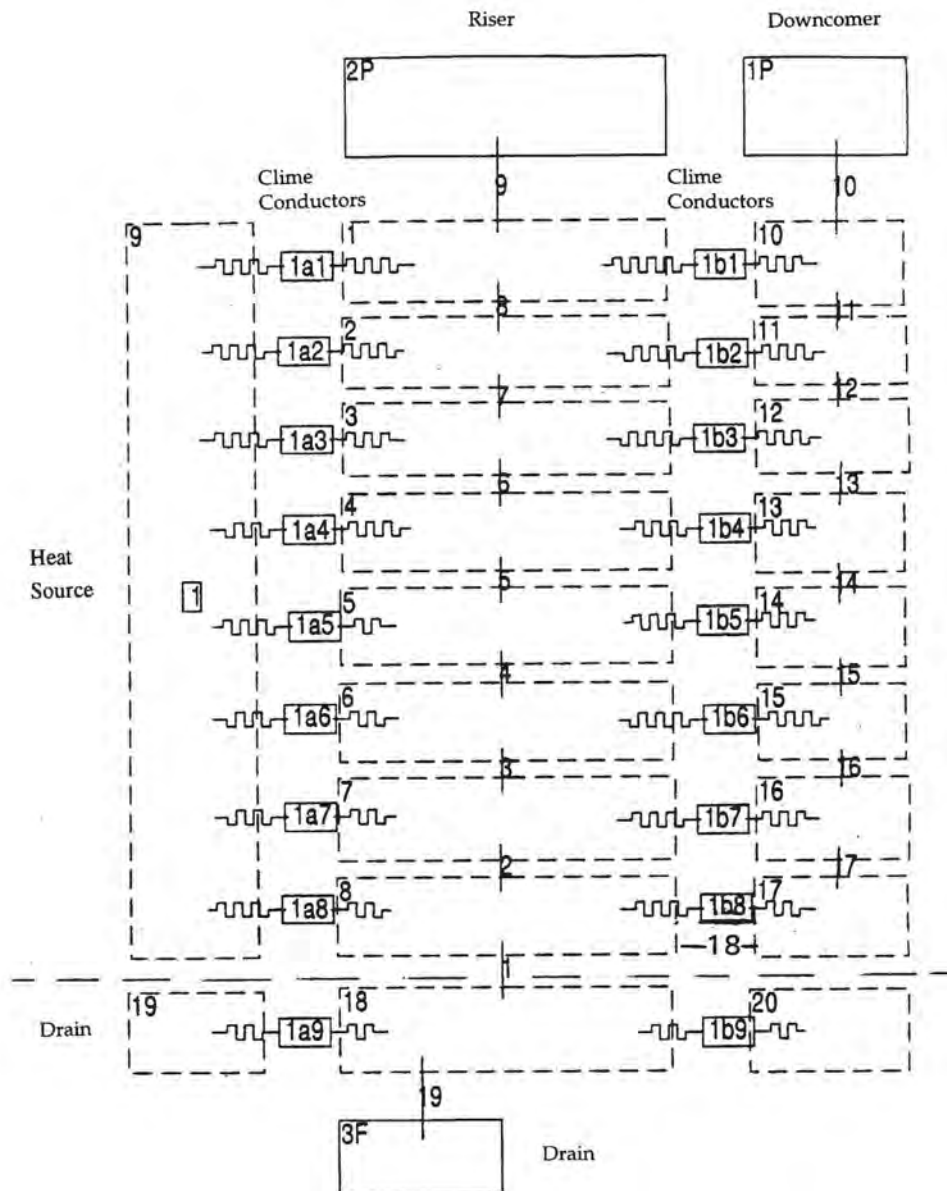


Figure 12-3. Noding Diagram, 8 Clime Node Model

12-15

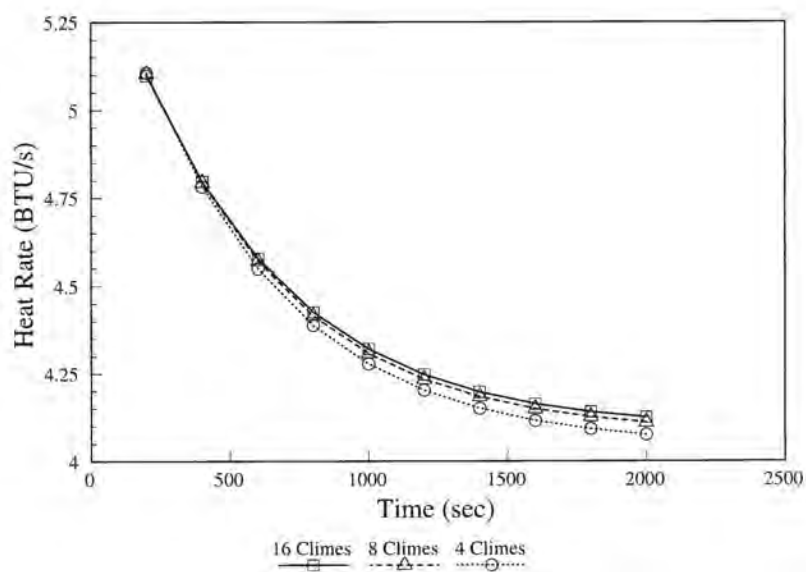


Figure 12-4. Comparison of Transient Heat Transfer Rates; Case 1

12-16

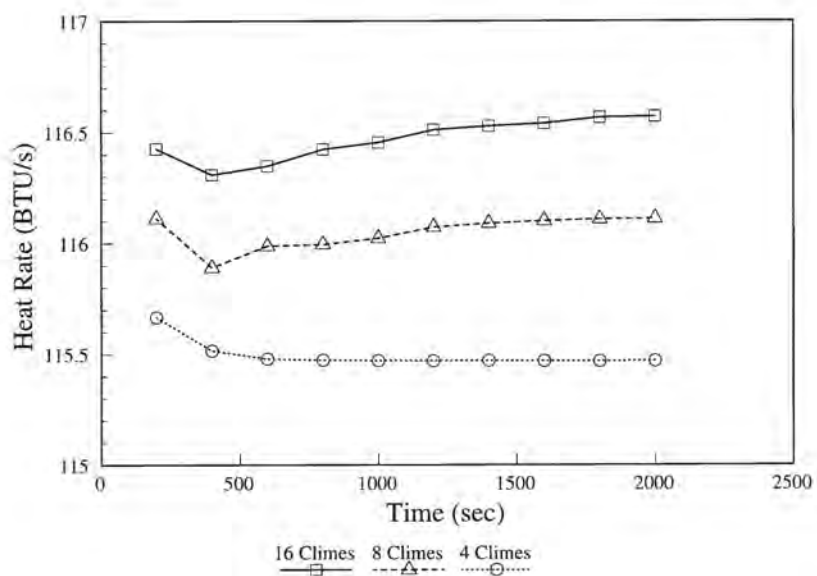


Figure 12-5. Comparison of Transient Heat Transfer Rates; Case 2

12-17

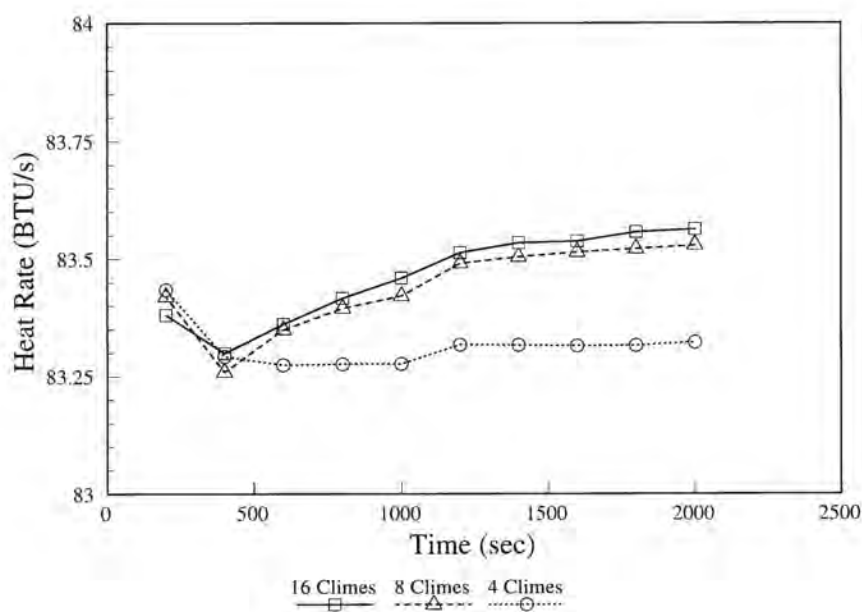


Figure 12-6. Comparison of Transient Heat Transfer Rates; Case 3

12-18

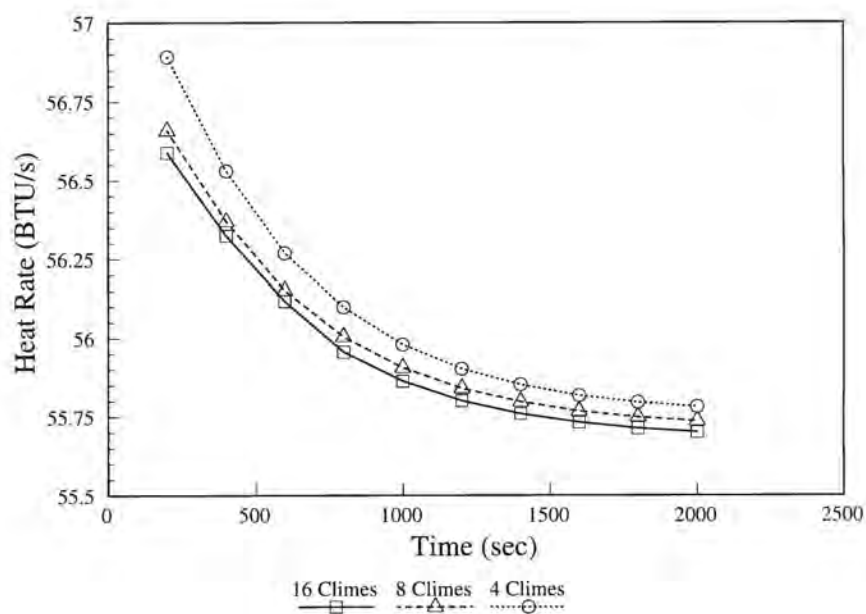


Figure 12-7. Comparison of Transient Heat Transfer Rates; Case 4

12-19

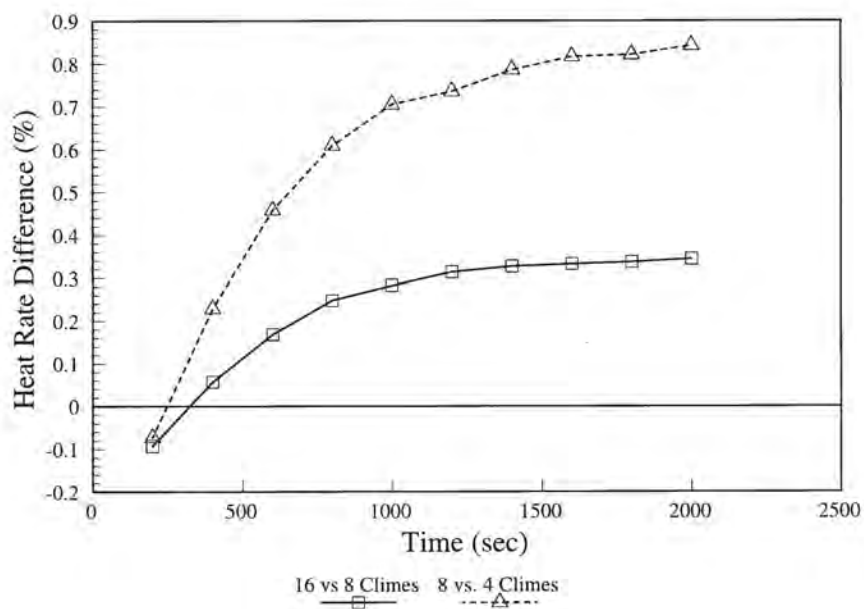


Figure 12-8. Comparison of Transient Heat Transfer Rate Differences; Case 1

12-20

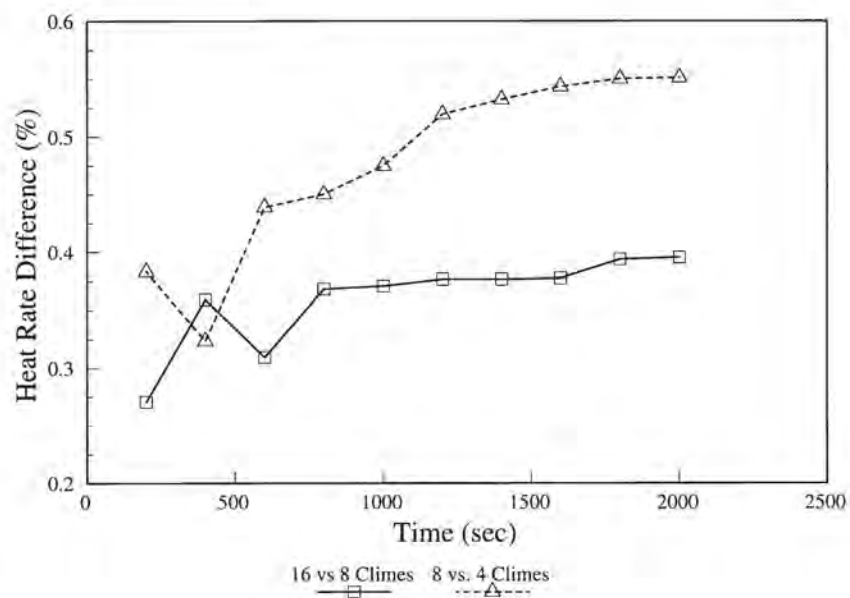


Figure 12-9. Comparison of Transient Heat Transfer Rate Differences; Case 2

12-21

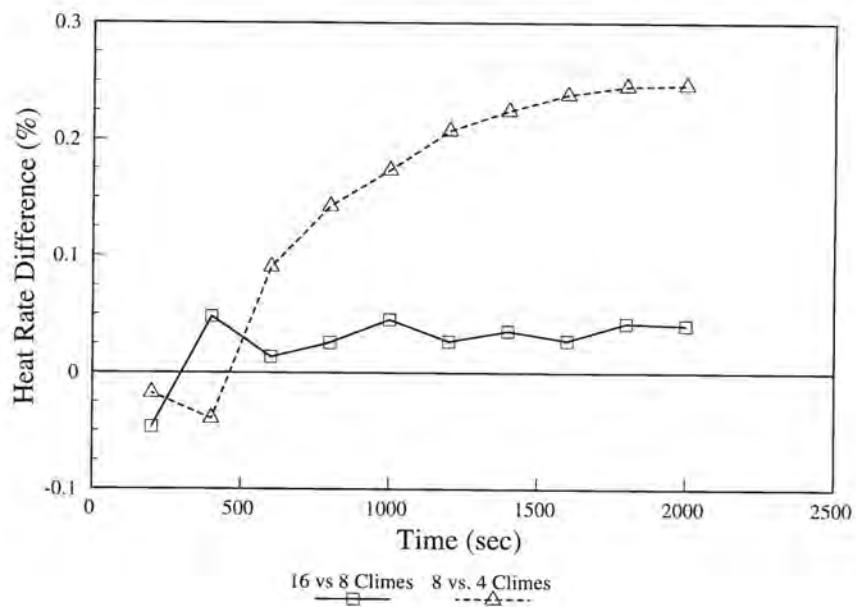


Figure 12-10. Comparison of Transient Heat Transfer Rate Differences; Case 3

12-22

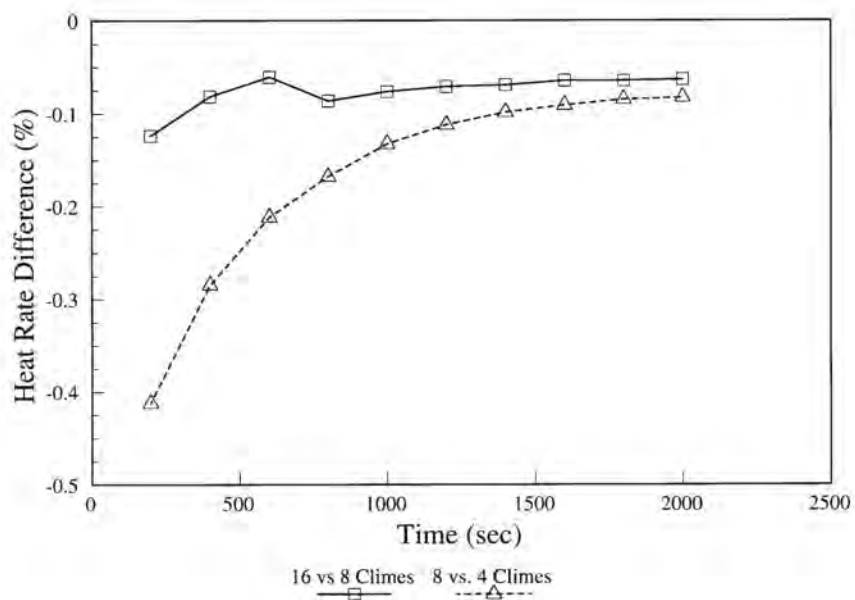


Figure 12-11. Comparison of Transient Heat Transfer Rate Differences; Case 4

12-23

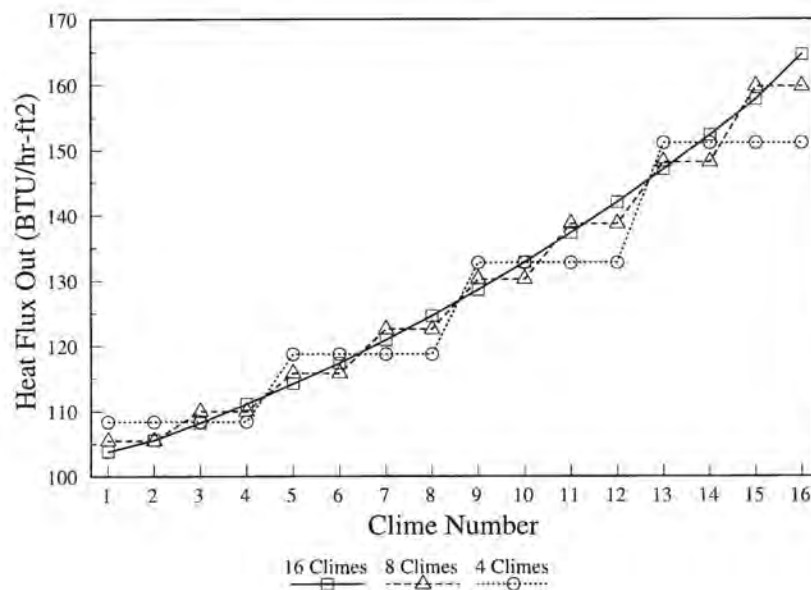


Figure 12-12. Comparison of Heat Flux Profiles; Time t=2000 Seconds; Case 1

12-24

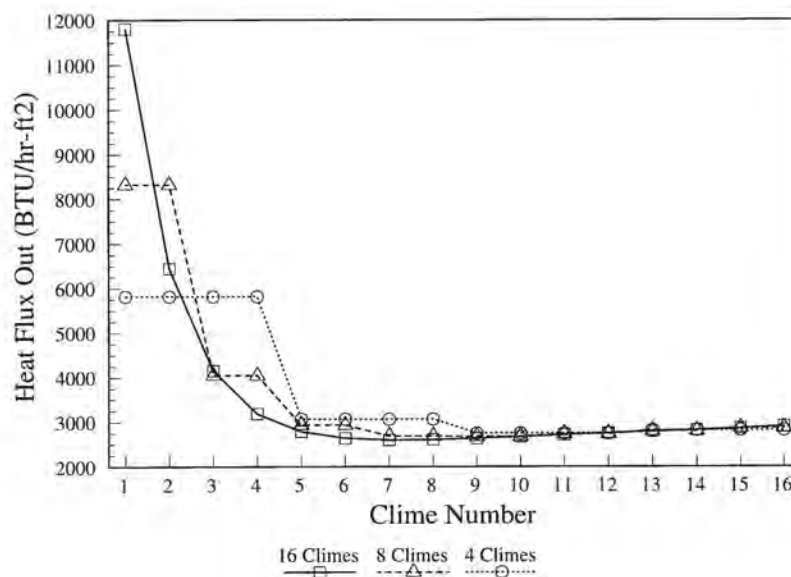


Figure 12-13. Comparison of Heat Flux Profiles; Time t=2000 Seconds; Case 2

12-25

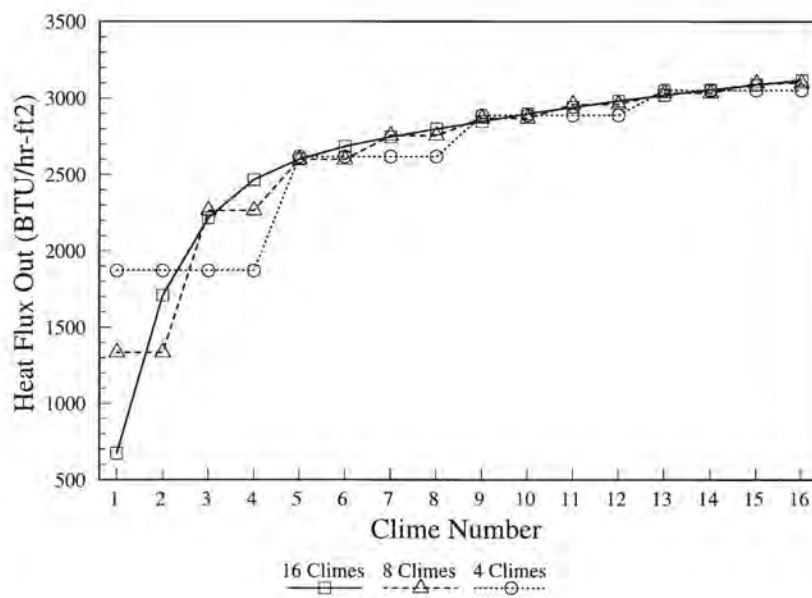


Figure 12-14. Comparison of Heat Flux Profiles; Time t=2000 Seconds; Case 3

12-26

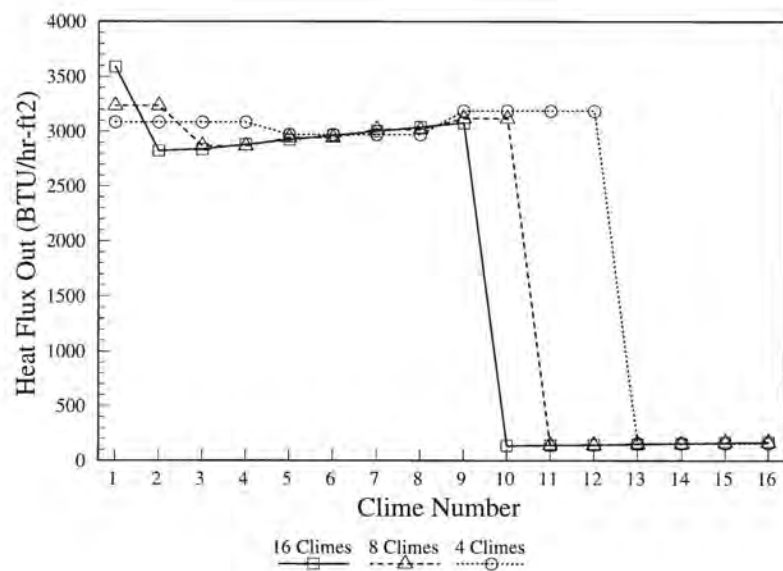


Figure 12-15. Comparison of Heat Flux Profiles; Time t=2000 Seconds; Case 4

12-27

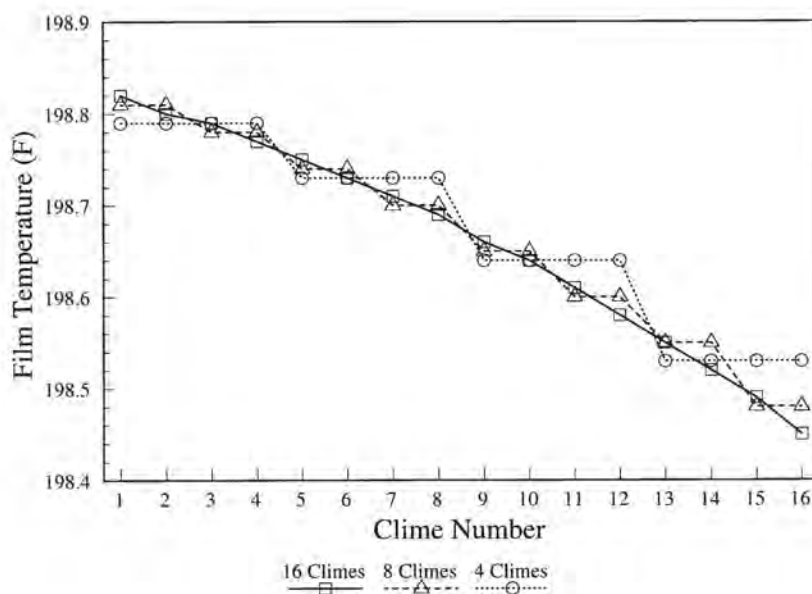


Figure 12-16. Comparison of Film Temperature Profiles; Time $t=2000$ Seconds; Case 1

12-28

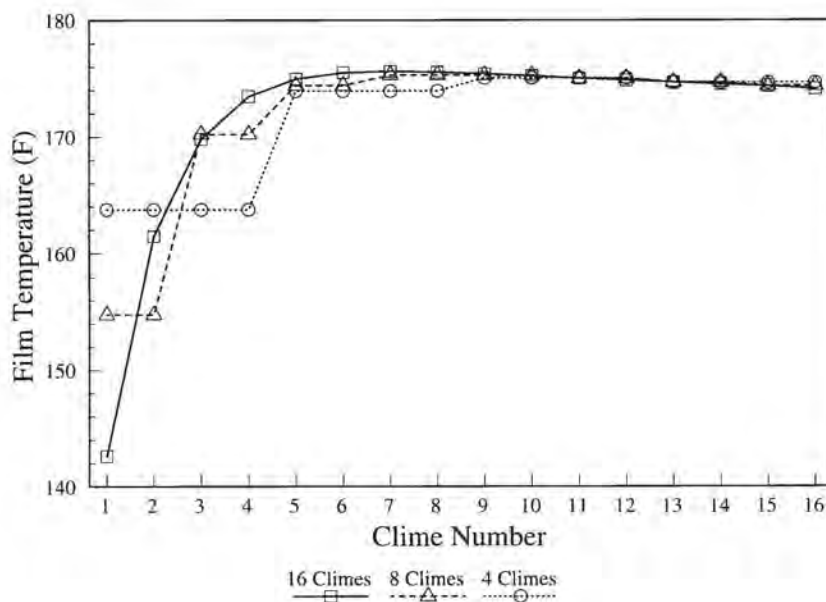


Figure 12-17. Comparison of Film Temperature Profiles; Time $t=2000$ Seconds; Case 2

12-29

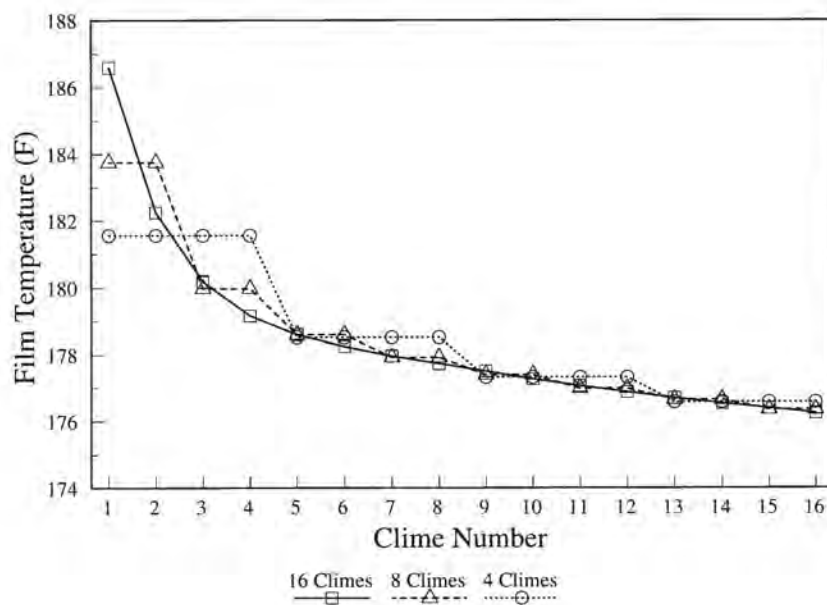


Figure 12-18. Comparison of Film Temperature Profiles; Time $t=2000$ Seconds; Case 3

12-30

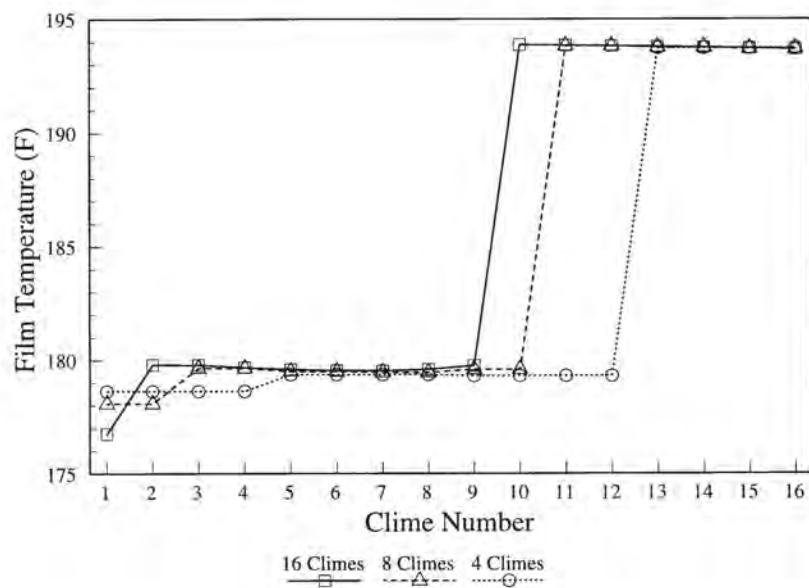


Figure 12-19. Comparison of Film Temperature Profiles; Time $t=2000$ Seconds; Case 4

12-31

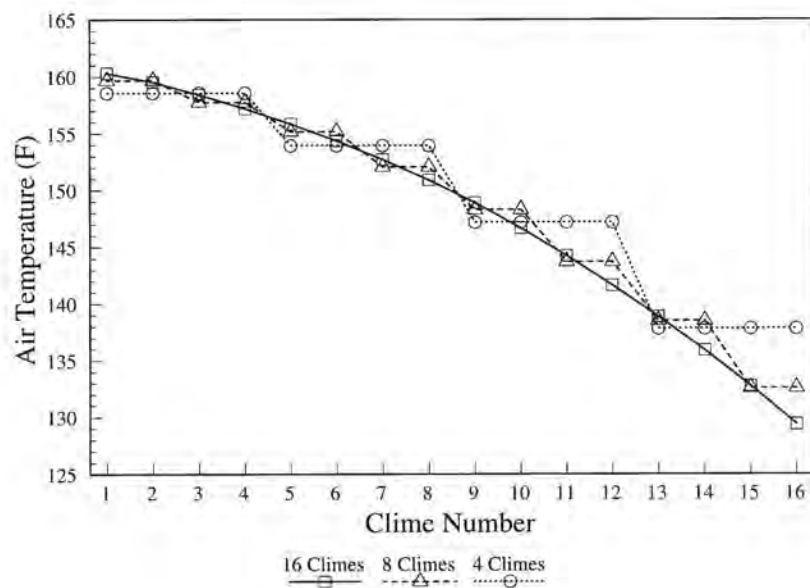


Figure 12-20. Comparison of Air Temperature Profiles; Time t=2000 Seconds; Case 1

12-32

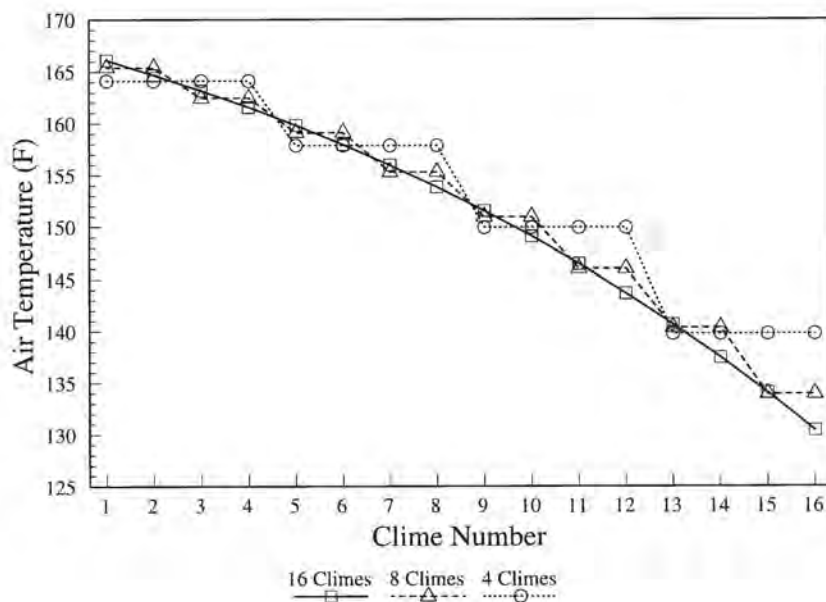


Figure 12-21. Comparison of Air Temperature Profiles; Time t=2000 Seconds; Case 2

12-33

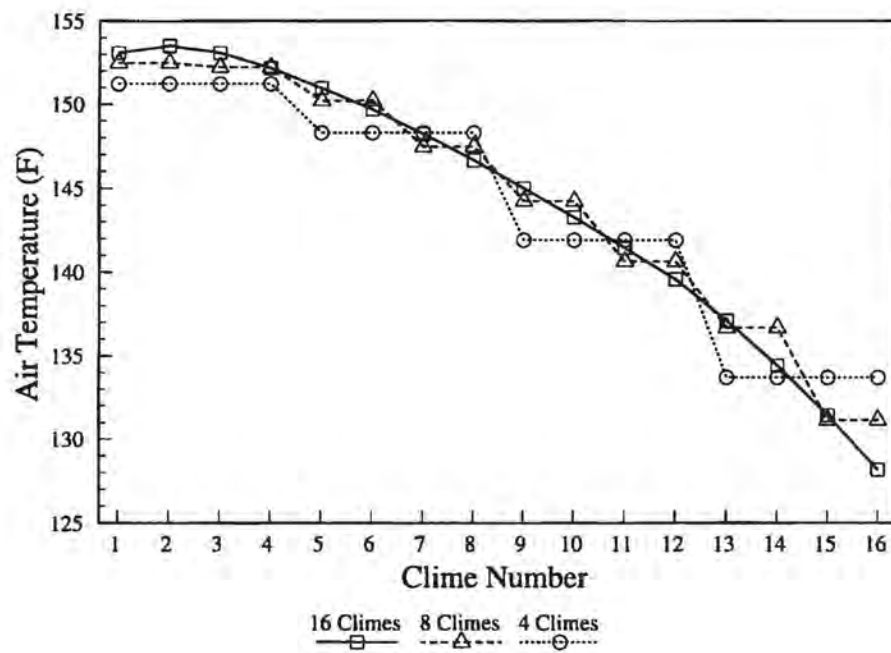


Figure 12-22. Comparison of Air Temperature Profiles; Time t=2000 Seconds; Case 3

12-34

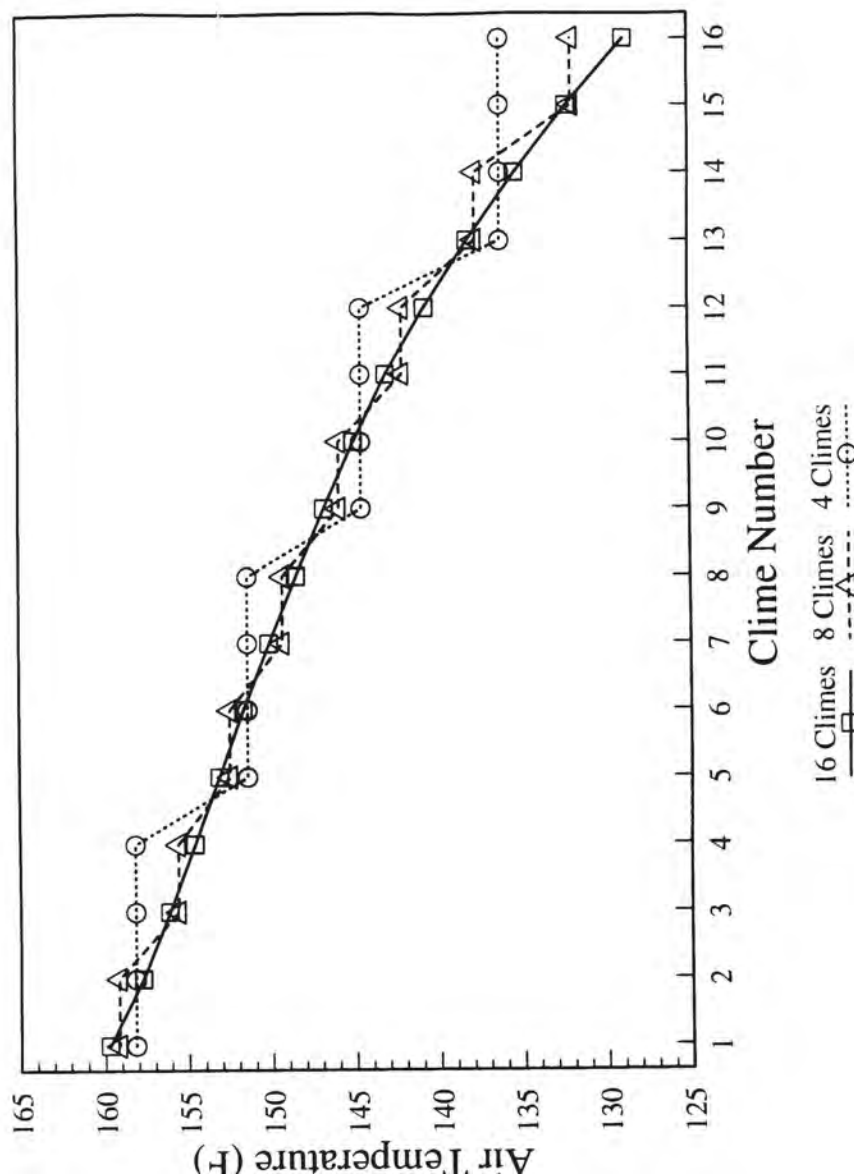


Figure 12-23. Comparison of Air Temperature Profiles; Time t=2000 Seconds; Case 4

12-35

a,c

Figure 12-24. AP600 Containment Model Clime Noding Pattern

WCAP-15846-P, Revision 5
APP-SSAR-GSC-587, Revision 5

September 2016

12-36

a,c

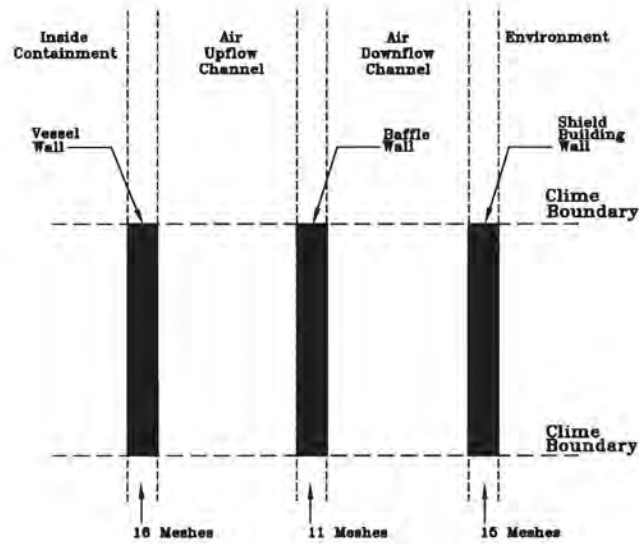
Figure 12-25. AP600 Containment Model Double Vertical Clime Noding Pattern

12-37

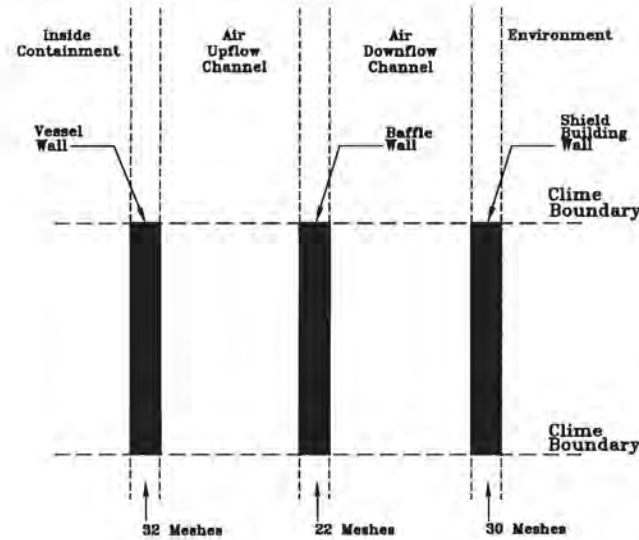
a,c

Figure 12-26. AP600 Containment Model Double Stack Clime Noding Pattern

12-38



AP600 Containment Model



AP600 Mesh Sensitivity Model

Figure 12-27. AP600 Containment Model Double Mesh Point Clime Noding Pattern

12-39

a,c

Figure 12-28. Pressure History, AP600 Containment Model; Double Clime

WCAP-15846-P, Revision 5
APP-SSAR-GSC-587, Revision 5

September 2016

12-40

a,c

Figure 12-29. Wet Heat Flux vs. Clime; AP600 Containment Model, Base Case

12-41

a,c

Figure 12-30. Wet Heat Flux vs. Clime; AP600 Containment Model, Double Clime

WCAP-15846-P, Revision 5
APP-SSAR-GSC-587, Revision 5

September 2016

12-42

a,c

Figure 12-31. Dry Heat Flux vs. Clime; AP600 Containment Model, Base Case

12-43

a,c

Figure 12-32. Dry Heat Flux vs. Clime; AP600 Containment Model, Double Clime

WCAP-15846-P, Revision 5
APP-SSAR-GSC-587, Revision 5

September 2016

12-44

a,c

Figure 12-33. Film Temperature vs. Clime; AP600 Containment Model, Base Case

12-45

a,c

Figure 12-34. Film Temperature vs. Clime; AP600 Containment Model, Double Clime

WCAP-15846-P, Revision 5
APP-SSAR-GSC-587, Revision 5

September 2016

12-46

a,c

Figure 12-35. Dry Surface Temperature vs. Clime; AP600 Containment Model, Base Case

WCAP-15846-P, Revision 5
APP-SSAR-GSC-587, Revision 5

September 2016

12-47

a,c

Figure 12-36. Dry Surface Temperature vs. Clime; AP600 Containment Model, Double Clime

WCAP-15846-P, Revision 5
APP-SSAR-GSC-587, Revision 5

September 2016

12-48

a,c

Figure 12-37. Annulus Pressure vs. Clime; AP600 Containment Model, Base Case

12-49

a,c

Figure 12-38. Annulus Pressure vs. Clime; AP600 Containment Model, Double Clime

WCAP-15846-P, Revision 5
APP-SSAR-GSC-587, Revision 5

September 2016

12-50

a,c

Figure 12-39. Air Temperature vs. Clime; AP600 Containment Model, Base Case

12-51

a,c

Figure 12-40. Air Temperature vs. Clime; AP600 Containment Model, Double Clime

12-52

a,c

Figure 12-41. Air Density vs. Clime; AP600 Containment Model, Base Case

12-53

a,c

Figure 12-42. Air Density vs. Clime; AP600 Containment Model, Double Clime

WCAP-15846-P, Revision 5
APP-SSAR-GSC-587, Revision 5

September 2016

12-54

a,c

Figure 12-43. Air Velocity vs. Clime; AP600 Containment Model, Base Case

12-55

a,c

Figure 12-44. Air Velocity vs. Clime; AP600 Containment Model, Double Clime

WCAP-15846-P, Revision 5
APP-SSAR-GSC-587, Revision 5

September 2016

12-56

a,c

Figure 12-45. Heat Rejection History Comparison, AP600 Containment Model Double Clime Sensitivity Case

WCAP-15846-P, Revision 5
APP-SSAR-GSC-587, Revision 5

September 2016

12-57

a,c

Figure 12-46. Integrated Heat Rejection Comparison, AP600 Containment Model; Double Clime Sensitivity Case

WCAP-15846-P, Revision 5
APP-SSAR-GSC-587, Revision 5

September 2016

12-58

a,c

Figure 12-47. Pressure History Comparison, AP600 Containment Model; Double Stack Sensitivity Case

12-59

a,c

Figure 12-48. Heat Rejection History Comparison, AP600 Containment Model; Double Stack Sensitivity Case

12-60

a,c

Figure 12-49. Integrated Heat Rejection Comparison, AP600 Containment Model; Double Stack Sensitivity Case

WCAP-15846-P, Revision 5
APP-SSAR-GSC-587, Revision 5

September 2016

12-61

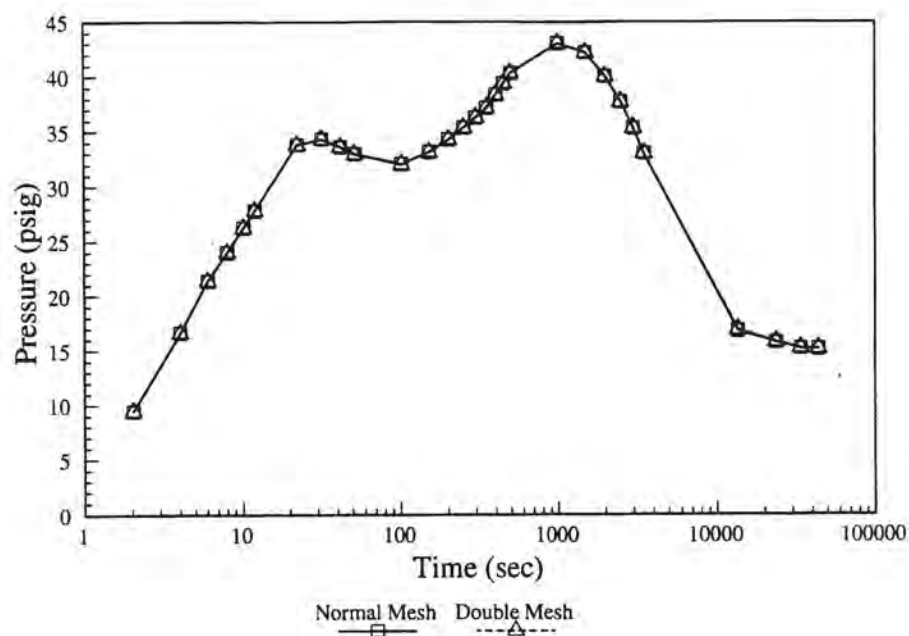


Figure 12-50. Pressure History Comparison, AP600 Containment Model; Double Mesh Sensitivity Case

12-62

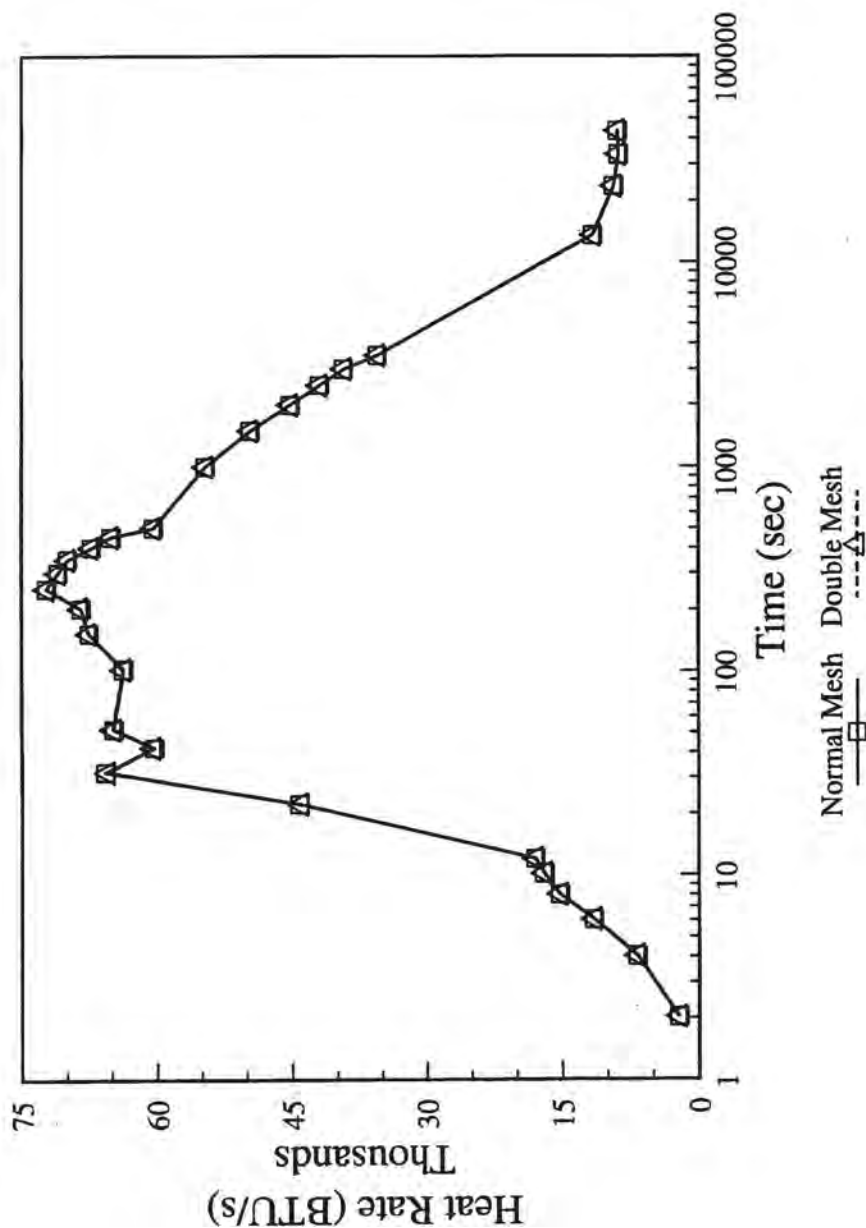


Figure 12-51. Heat Rejection History Comparison, AP600 Containment Model; Double Mesh Sensitivity Case

12-63

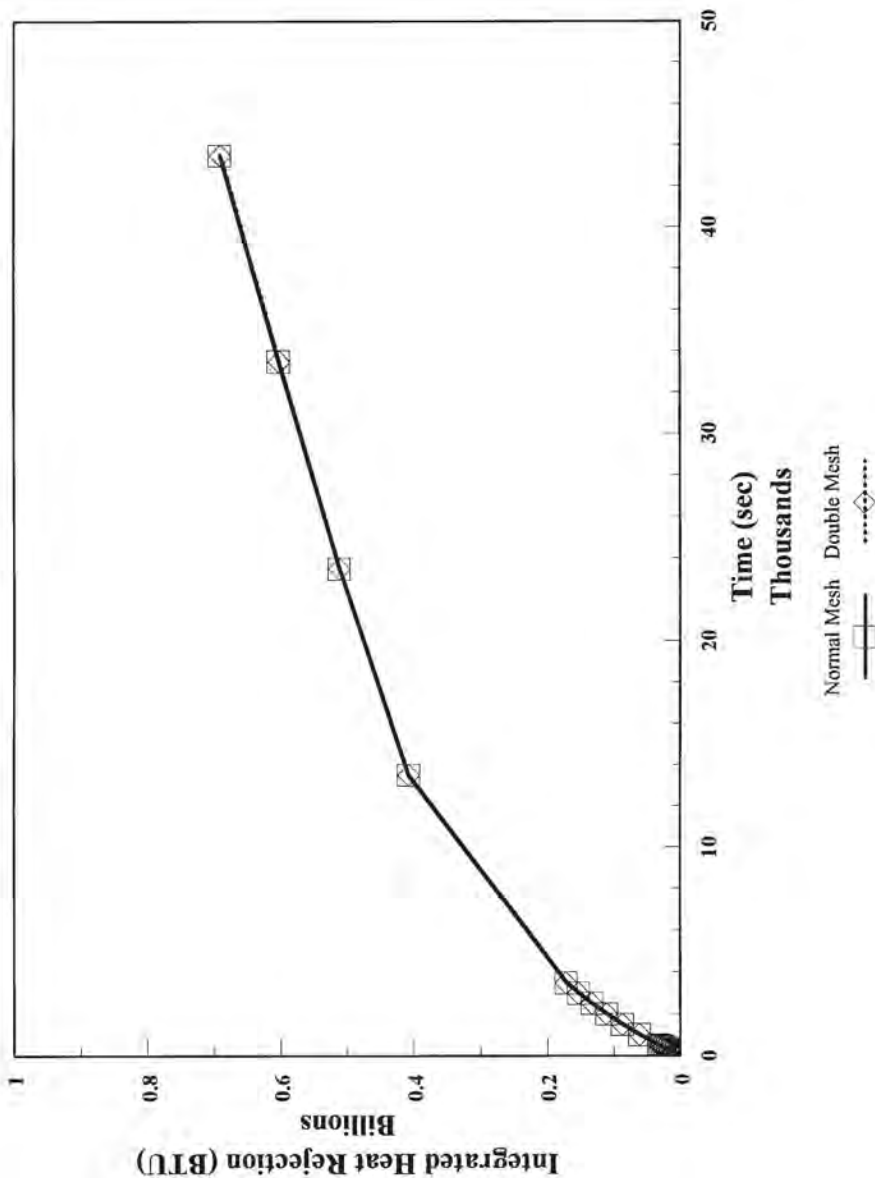


Figure 12-52. Integrated Heat Rejection Comparison, AP600 Containment Model; Double Stack Sensitivity Case

13-1

13 DESCRIPTION OF AP1000 PLANT GEOMETRY AND SUMMARY OF WGOthic EVALUATION MODEL

13.1 INTRODUCTION

The purpose of Section 13 is to describe the **AP1000** WGOthic Containment Evaluation Model (EM) that is used for containment integrity Design Basis Accident (DBA) analyses. The AP1000 Containment Evaluation Model uses the WGOthic code (Section 3) and incorporates methodologies previously discussed in this document such as passive containment cooling system (PCS), liquid film stability (Section 7), circulation and stratification (Section 9), and meteorological effects (Section 6).

The geometry of the plant is modeled with control volumes, flow paths, thermal conductors, and “climes” which are discussed in Sections 13.2, 13.3, 13.4 and 13.5, respectively. The climes are an addition to the standard GOTHIC code package that are used to model the AP1000 PCS. The climes account for the condensation/evaporation mass transfer, the convection heat transfer, the radiative heat transfer, and the tracking of the mass and thermal resistance of the condensate and evaporative films on the containment shell.

Initial conditions and boundary conditions are summarized in Section 13.6. An overview of the loss of coolant accident (LOCA) and main steamline break (MSLB) transients is provided in Section 13.7. Section 13.8 summarizes changes that are made to the peak pressure EM for small-break LOCA analyses that minimize the containment pressure transient. Section 13.9 provides a high level summary of the EM methodology.

Deleted: of the AP1000

Deleted: to be

Deleted: A

Deleted: (DBAs)

Deleted: consists of volumes, flow paths, heat sinks, material properties, heat transfer model selection, and initial and boundary conditions combined with methodologies to develop input which accounts for

Moved down [13]: The containment integrity DBAs for the AP1000 are performed with the WGOthic code package. An overview of the WGOthic code is given in Section 3. ¶
The selection of volumes and flow paths corresponds with the lumped parameter model developed for the large-scale test (LST) vessel for validation of the WGOthic code. The LST model description and guidance on application of the LST model to the full-scale AP600 model are provided in Section 6 of WCAP-14382 (Reference 13.1). Based on this guidance, the volumes and flow paths of the AP600 Containment Evaluation Model, summarized in Section 4.6 of this report, have been selected. ¶
A comparison of the AP600 and AP1000 containment model nodding structures is shown in Figure 13-1a (the AP1000 is shown on the right side of Figure 13-1a). The nodding structure below the operating deck level (135.25-ft elevation) remains the same, however, an extra horizontal slice of volumes was added above the operating deck to account for the extra 25.5-ft of elevation in the cylindrical portion of the AP1000 structure. ¶
The nodding structure for the volume above the operating deck in the AP600 containment evaluation model was developed based on the locations of the second weir, crane rail, stiffener ring, and top of the SG compartment. The elevation of the second weir was selected as a nodding boundary because of the increase in the fraction of water coverage that occurs below the second weir. The elevations of the crane rail and stiffener ring were selected as nodding boundaries since the condensed water film on the inside surface of the shell is collected and funneled back to the IRWST from these locations. The elevation of the top of the SG compartment was selected as a nodding boundary because it represents a natural location for steam to exit into the open above-deck volume from the ADS or a break that is located below the operating deck. ¶
For AP600, the volume above the top of the crane rail was divided into 3 slices of approximately equal height. The top slice extended from the top of the elliptical head to just below the elevation of the second weir. The second and third slices are of equal height. The volume between the top of the crane rail and top of the stiffener ring was divided with 2 equal height slices. The volume below the stiffener ring and the top of the operating deck was also split into 2 slices; the dividing boundary was located at the top elevation of the SG compartment. ¶
The same approach for defining the node boundaries is used in the AP1000 containment model. For the AP1000, the volume above the top of the crane rail is also divided into 3 slices. The top two slices are the same as the AP600, since the elliptical head and weir locations on AP1000 are the same. Because the crane rail is about 5-ft lower in the AP1000, the third slice ...

13-2

13.2 AP1000 PLANT WGOthic EVALUATION MODEL CONTROL VOLUMES

The WGOthic model of the AP1000 plant consists of a network of lumped parameter control volumes. Control volumes are used to represent the inner free volume of the containment, the PCS annular flow path between the shield building and containment vessel, and the environment. The AP1000 WGOthic Evaluation Model (EM) consists of [] a.c control volumes inside containment and [] a.c control volumes which represent the PCS annular flow path region. Control volumes are defined by their free volume, hydraulic diameter, pool area, elevation, and height.

The selection of volumes and flow paths corresponds with the lumped parameter model developed for the large-scale test (LST) vessel for validation of the WGOthic code. The LST model description and guidance on application of the LST model to the full-scale AP600 model are provided in Section 6 of WCAP-14382 (Reference 13.1). Based on this guidance, the volumes and flow paths of the AP600 Containment Evaluation Model, summarized in Section 4.6 of this report, were selected.

A comparison of the AP600 and AP1000 containment evaluation model nodding elevations above the operating deck (135.25 ft elevation) is shown in Figure 13-1. An extra set of volumes was added above the operating deck to account for the extra 25.5-ft of elevation in the cylindrical portion of the AP1000 structure. Other elevation divisions were shifted to be consistent with the physical basis of the divisions for AP600, as described below.

[]

[]^{a,c}

Deleted: (referred to as the "Evaluation Model")

Deleted: and computer code input specified by the methodologies in sections of this report.

Deleted: and

Deleted: passive containment cooling system (

Deleted:)

Deleted: ultimate heat sink,

Deleted: These control volumes are linked together with junctions which represent flow connections between the volumes. The inner containment volumes are connected using junctions, the outer containment volumes are connected using junctions, junctions connect to boundary conditions. The walls, major piping, and metallic structures are modeled using thermal conductors inside containment. These structures are modeled using thermal conductors. The PCS energy transfer processes are modeled using the clime model. The containment steel shell is modeled with climes, including 4 dummy climes. A listing of volumes and flow paths is provided in Section 13.6.

Moved (insertion) [13]

Deleted: The containment integrity DBAs for the AP1000 are performed with the WGOthic code package. An overview of the WGOthic code is given in Section 3. ¶

Deleted: have been

Deleted: structures

Deleted: a (the AP1000 is shown on the right side of Figure 13-1a). The nodding structure below the operating deck level (135.25-ft elevation) remains the same, however,

Deleted: a

Deleted: horizontal slice

13-3

L

J^{a,c}

13-4

L

J^{a,c}

13-5

a,c

Figure 13-1. Comparison of AP600 (left) and AP1000 (right) Above-Deck Containment Model Elevations for Nodalization

Deleted: A

Deleted: ing Structures

13-6

a,c

Figure 13-2. Plan View of Compartments Below 107' Elevation

13-7

a,c

Figure 13-3. Plan View of Compartments Immediately Below Operating Deck

WCAP-15846-P, Revision 5
APP-SSAR-GSC-587, Revision 5

September 2016

13-8

a,c

Figure 13-4. Plan View of Nodalization from 135.25' to 226' Elevation
(Pressurizer Compartment is Only Nodalized to 153' Elevation)

13-9

a,c

Figure 13-5. Plan View of Nodalization from 226' Elevation to Top of Containment

13-10

a,c

Figure 13-6. Elevation View of Nodalization (Facing North)

WCAP-15846-P, Revision 5
APP-SSAR-GSC-587, Revision 5

September 2016

13-11

a,c

Figure 13-7. Elevation View of Nodalization (Facing West)

Table 13-1. Inside Containment Volumes Listing

[illegible]

13-13

Table 13-2. Inside Containment Volumes Listing (cont.)

<u>Control Volume</u>	<u>Location</u>	<u>Elevation</u>

a,c

13-14

Table 13-3. Outside Containment Volumes Listing

[illegible]

September 2016

13-15

13.3 AP1000 PLANT WGOthic EVALUATION MODEL FLOW PATHS

The AP1000 WGOthic control volumes discussed in Section 13.2 are connected by one or more flow paths. The inlet/outlet elevations, flow area, hydraulic diameter, inertia length, friction length, and loss coefficients are required input values for each flow path.

Flow paths represent physical openings between two volumes such as doorways, penetrations, stairwells, etc., but can also represent connections between volumes not defined by physical structures. Geometric information relating to the flow paths are obtained from general arrangement drawings or nominal dimensions on more detailed drawings, where available. However, the heights of all vertical flow flowpaths are set to 0.01 ft, consistent with the GOTHIC User's Guidance (Reference 13.2), [

1^{a,c}.

The annulus region between the containment vessel and the baffle is a pathway for air to travel down the downcomer and up the riser. The air flow path is from the shield building inlet louvers downward to the annulus seal and then back upward along the external surface of the containment vessel and out of the chimney. Unrecoverable loss coefficients external to the containment are obtained from hydraulic tests of the external annular flow paths. The annulus loss coefficients are based on a 1/6 scaled test model [

1^{a,c}.

Most flow paths below the operating deck represent physical openings between room compartments while the flow paths above the operating deck are not necessarily bounded by walls and physical boundaries.

[

1^{a,c}.

Table 13-3 lists the flow paths in the AP1000 containment Evaluation Model.

13-16

Table 13-3. Flow Path Listing

[illegible]

a,c

13-17

Table 13-3. Flow Path Listing (cont.)

[illegible]

a,c

Table 13-3. Flow Path Listing (cont.)

[illegible]

a,c

13-19

Table 13-3. Flow Path Listing (cont.)

[illegible]a,c

Table 13-3. Flow Path Listing (cont.)

[illegible]a,c

Table 13-3. Flow Path Listing (cont.)

a,c

13-22

Table 13-3. Flow Path Listing (cont.)

[illegible]

a,c

13-23

Table 13-3. Flow Path Listing (cont.)

[illegible]

a,c

13-24

Table 13-3. Flow Path Listing (cont.)

[illegible]

a,c

Table 13-3. Flow Path Listing (cont.)

[illegible]

a,c

13-26

Table 13-3. Flow Path Listing (cont.)

[illegible]

a,c

Table 13-3. Flow Path Listing (cont.)

a,c

13-28

Table 13-3. Flow Path Listing (cont.)

[illegible]

a,c

13-29

Table 13-3. Flow Path Listing (cont.)

[illegible]

a,c

Table 13-3. Flow Path Listing (cont.)

a,c

13-31

Table 13-3. Flow Path Listing (cont.)

<u>Flow Path Number</u>	<u>Description</u>	<u>Control Volume A</u>	<u>Control Volume B</u>	<u>Direction of Flow</u>

a,c

13-32

13.4 AP1000 PLANT WGOthic EVALUATION MODEL THERMAL CONDUCTORS

Thermal conductors are one-dimensional slabs used to model structures that are at the ambient containment temperature and that are credited as heat sinks within the WGOthic Evaluation Model. The thermal conductors model the heat capacity of the structures, the heat transfer between the steam/gas mixture and these structures, and the heat transfer between control volumes via these structures. Any number of conductors can be assigned to a control volume. A thermal conductor can be fully contained within a control volume or it can be connected to two control volumes (e.g., walls, ceilings, floors). Thermal conductors cannot be connected to one another.

The inputs for the thermal conductors consist of the specification of the initial temperature, the exposed surface area, the thermal conductor type, and the heat transfer type. The thermal conductor type specifies the type and thickness of the material, and is further discussed in Section 13.4.1. The heat transfer type defines the characteristics of the credited heat transfer and is discussed in Section 13.4.2.

Thermal conductors are based on the metallic and concrete structures as defined on Certified for Construction drawings. [

]^{a,c}

13-33

After the exposed surface area and volume of each material of the heat sinks are quantified, the information is converted into one-dimensional slab thermal conductors. The thermal conductors are specified with a surface area applicable to side A and the same surface area applicable to side B. For walls between control volumes, the surface area input corresponds to the surface area on each side of the wall. For structures that are contained within a control volume, the surface area of side A corresponds to the total exposed surface area, and side B is turned off for heat transfer. The volumes of the materials are implicitly defined through the effective thicknesses modeled in the thermal conductor types (Section 13.4.1). In the conversion of the exposed surface area and material volume to the evaluation model input, the volume of the materials is strictly conserved; the surface area input multiplied by the material thickness always equals the calculated material volume. The exposed surface areas are also preserved, although there are instances of small adjustments:

[

1^{a,c}

The temperature of all thermal conductors inside containment is set to the maximum containment operating temperature defined in the Technical Specifications.

Table 13-4 contains a list of all thermal conductors in the **AP1000** WGOTHIC containment Evaluation Model, sorted by location. Thermal conductors that are contained fully within one control volume have the associated control volume number listed for side A and side B. Wall thermal conductors that have each side exposed to a different control volume are listed twice, once indicating the side exposed to control volume A and once indicating the side exposed to control volume B. Thermal conductors listed at the end of Table 13-4 are ones developed for AP600 and remain in the WGOTHIC input file, but which are not used in the peak containment pressure EM for the AP1000 plant. Section 13.4.1 describes the thermal conductor types and material property modeling. Section 13.4.2 describes the heat transfer coefficients of the thermal conductors modeled in the **AP1000** WGOTHIC containment Evaluation Model.

*** This record was final approved on 12/19/2017 12:02:52 PM. (This statement was added by the PRIME system upon its validation)

13-35

Table 13-4. Thermal Conductor Listing (cont.)

<u>Description</u>	<u>Thermal Conductor Number</u>	<u>Control Volume A</u>	<u>Control Volume B</u>

a,c

Table 13-4. Thermal Conductor Listing (cont.)

<u>Description</u>	<u>Thermal Conductor Number</u>	<u>Control Volume A</u>	<u>Control Volume B</u>

a,c

Table 13-4. Thermal Conductor Listing (cont.)

a,c

13-38

Table 13-4. Thermal Conductor Listing (cont.)

[illegible]

a,c

Table 13-4. Thermal Conductor Listing (cont.)

a,c

Table 13-4. Thermal Conductor Listing (cont.)

<u>Description</u>	<u>Thermal Conductor Number</u>	<u>Control Volume A</u>	<u>Control Volume B</u>

a,c

13-41

Table 13-4. Thermal Conductor Listing (cont.)

<u>Description</u>	<u>Thermal Conductor Number</u>	<u>Control Volume A</u>	<u>Control Volume B</u>

a,c

13-42

Table 13-4. Thermal Conductor Listing (cont.)

<u>Description</u>	<u>Thermal Conductor Number</u>	<u>Control Volume A</u>	<u>Control Volume B</u>

a,c

13-43

Table 13-4. Thermal Conductor Listing (cont.)

[illegible]

a,c

13-44

Table 13-4. Thermal Conductor Listing (cont.)

[illegible]

a,c

13-45

Table 13-4. Thermal Conductor Listing (cont.)

[illegible]a,c

13-46

Table 13-4. Thermal Conductor Listing (cont.)

<u>Description</u>	<u>Thermal Conductor Number</u>	<u>Control Volume A</u>	<u>Control Volume B</u>

a,c

13-47

13.4.1 Thermal Conductor Type Descriptions

The thermal conductors in the AP1000 WGOthic containment Evaluation Model are constructed of components referred to as thermal conductor types. Thermal conductor types are also used in the clime modeling discussed in Section 13.5. A thermal conductor type can be described as the cross-sectional composition of a given structure, defining both the material and effective thickness of each material. A single thermal conductor type can be used for multiple thermal conductors when the materials and thicknesses are the same. The WGOthic Evaluation Model of the AP1000 plant utilizes []^{a,c} different thermal conductor types.

A thermal conductor type consists of a number of material regions divided into subregions to model and calculate conduction through the materials. Figure 13-8 illustrates the regions and subregions of a WGOthic thermal conductor type. The thermal conductor type shown in the example consists of four separate regions of variable thickness, subregions, and material types.

The following assumptions are used in the development of the AP1000 containment Evaluation Model thermal conductor types:

- The effective thickness of each thermal conductor type material is specified so as to preserve the volume of each material when applied to the surface area input of the thermal conductor, as discussed in Section 13.4.
- Coatings are applied to carbon steel and concrete surfaces. The thickness of each layer of coating is maximized based on coatings application procedures to increase the resistance to heat transfer of the thermal conductors.

• []

[]^{a,c}

• []

[]^{a,c}

Deleted: heat sinks in the

Deleted: m

Deleted: wall

Deleted: The benefit is that these cross-sections can be used repeatedly whenever a wall of that type is modeled. The WGOthic model of the AP1000 utilizes 75 different types of wall or conductor types. These walls vary in thickness and composition.

Deleted: The walls are all constructed from a set of materials for which the properties can vary with temperature. All, except air, have been input as constants. Table 13-49 provides the list of materials and their properties. A separate entry is provided for the material properties of the paint on the inside surface of the containment. This was done in order to conservatively eliminate radiation heat transfer from the inside of containment to the shell. ¶
A wall can consist of a number of regions which are typically used to represent the different materials (e.g., epoxy paint, carbon steel) used to make the conductor type. A region may also be used to create a finely noded partition of a given material followed by another more coarsely noded region of the same material. Each region may be further subdivided with equally distributed subregions. Figure 13-88 provides an example of a WGOthic thermal conductor. The example conductor shown in the illustration consists of four separate regions of variable thickness, subregions, and material types. ¶

13-48

The properties of the materials used in the thermal conductor types are specified in the WGOTHIC Evaluation Model input. The properties used by WGOTHIC are thermal conductivity, volumetric heat capacity, and emissivity. The material properties are conservatively selected based on data available in literature and are consistent with the minimum coating test requirements. In addition the following conservatisms are applied:

- The thermal conductivity and volumetric heat capacity of all steel materials are reduced by 10% per the ASME standard to account for variability of alloy content.
- The thermal conductivity of inorganic zinc is reduced by a factor of two relative to the minimum test requirement. Although a sensitivity documented in Section 10.2.1 assumed a factor of four degradation in the thermal conductivity to address the effects of oxidation, later work in Reference 13.7 has shown that thermal conductivity will not decrease substantially as the coating ages, and may even increase slightly. The factor of two provides margin for variations in the coating composition and structure, corrosion product composition, and measurement uncertainties.
- Emissivity is reduced by 10% and is only input to credit radiation in the clime modeling of the outer surface of the containment vessel, the baffle and the shield building. All other emissivity input is set to 1E-10.

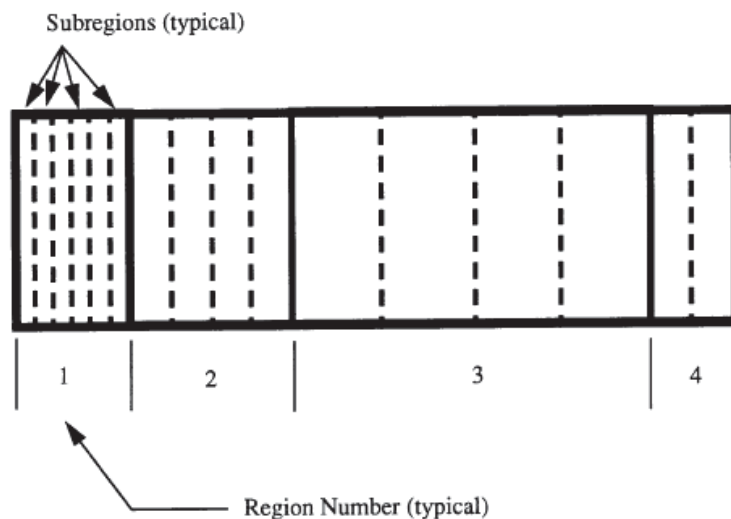


Figure 13-8. WGOTHIC Thermal Conductor Type Noding Example

13-49

13.4.2 Thermal Conductor Heat Transfer Coefficients

The heat transfer coefficient types define the surface heat transfer conditions of the thermal conductor for which they are modeled.

↓

↓^{a,c}

13-50

I

I^{a,c}

13-51

13.5 AP1000 PLANT WGOthic EVALUATION MODEL CLIMES

L

L^{a,c}

13-52

a,c

Figure 13-9. Stack Configuration for the AP1000 WGOthic EM Clime Modeling

WCAP-15846-P, Revision 5
APP-SSAR-GSC-587, Revision 5

September 2016

13-53

a,c

Figure 13-10. Clime Configuration for the AP1000 WGOthic EM

WCAP-15846-P, Revision 5
APP-SSAR-GSC-587, Revision 5

September 2016

13-54

13.5.1 Cline Conductors

L

L^{a,c}

13-55

a,c

Figure 13-11. WGOTHIC Clime Conductor Modeling

13-56

Table 13-4. Clime Modeling

a,c

[illegible]

13-57

Table 13-5. Cline Modeling (cont.)

a,c

13-58

13.5.2 Passive Cooling System Flow

One of the unique features of the AP1000 plant is the cooling water film that is applied to the external surface of the steel containment shell. As stated in Section 13.5, []^{a,c} of the AP1000 WGOthic containment Evaluation Model, have PCS flow applied to them. The PCS flow rate in the AP1000 Evaluation Model is a minimum flowrate versus time that is consistent with the minimum flowrate relative to the passive containment cooling water storage tank (PCCWST) water level at each standpipe elevation, which is confirmed through plant testing. The minimum delivered flowrate is based on only one of the passive containment cooling water flow paths being open. The amount of PCS flow credited is actually an "evaporation-limited" flow rate. The evaporation-limited PCS flow rate is derived by subtracting a conservatively calculated runoff flow rate from the total gravity-driven, delivered PCS water flow rate. The PCS film flow modeling is described in Section 7.

The PCS flow rate is input in the AP1000 WGOthic containment Evaluation Model as a time-dependent boundary condition specified through a user-defined function. Two options are available to calculate a conservative evaporation limited flow, as discussed in Section 7.5.2. No evaporation of the film is credited prior to development of steady state PCS water coverage (Section 7.2.5). Table 13-6 summarizes the basis for the PCS inputs.

Table 13-6. Basis for PCS Inputs

Input Parameter	Basis for Value in Evaluation Model
Initial Temperature of Containment Shell	Containment shell initialized uniformly to maximum Technical Specification value for containment air temperature. Reference, Technical Specification 3.6.5.
Applied External Film Flow Rate	Delivered film flow rate is based on one of three PCS tank discharge valves being open. Evaporation-limited flow is used in the Evaluation Model (Section 7).
External PCS Liquid Film Temperature	Film temperature set to upper bound of the PCCWST. This minimizes the subcooling benefit. Reference, Technical Specification 3.6.6.
Film Coverage Fraction	Maximum coverage fraction [] ^{a,c} , and reduces after the film stability limit is reached (Section 7).
PCS Coating Properties	Based on minimum coatings test requirements for most properties. Additional conservatism applied to the thermal conductivity of the Inorganic Zinc paint, crediting no more than 50% of the coatings test requirement (Section 13.4.1).
PCS Emissivity	Surface emissivity of Inorganic Zinc paint reduced to 90% of the coatings test requirement.
PCS Coatings Thickness	Maximum coating thicknesses used.

Deleted: This film is evaporated as the shell heats up following a design basis event. Evaporation of the applied film improves the heat removal capabilities of the system. In the WGOthic model

Deleted: this cooling film

Deleted: put to

Deleted: The result is a water flow rate that provides a limit on the total evaporation rate credited in the Evaluation Model, and it is this quantity, termed, "evaporation-limited PCS flow," that is used for input to the AP1000 Evaluation Model.

Deleted: development of the

Deleted: input

Deleted: evaporation-limited

Deleted: 132

Deleted: Conservatively bounds initial temperature profile of shell.

Deleted: .

Deleted: , DCD Chapter 16

Deleted: assumed single failure of one of three PCS tank discharge headers. Delivered flow is reduced by the amount predicted to run off based on water coverage model.

Deleted: applied

Deleted: to

Deleted: value of 120°F.

Deleted: t

Deleted: .

Deleted: , DCD Chapter 16.

Deleted: C

Deleted: s held constant consistent with water coverage model and evaporation-limited flow rate

Deleted: Conductivity of the Carbo-Zinc paint reduced to 25% of nominal value.

Deleted: ies

Deleted: nominal values

13-59

Table 13-6. Basis for PCS Inputs (cont.)

Input Parameter	Basis for Value in Evaluation Model
PCS Initial Delay Time	No credit is taken for partial film coverage prior to <u>the development of steady state PCS water coverage.</u> Conservatively neglects <u>any cooling from the water as coverage develops</u> (Section 7.2.5).
Internal Heat and Mass Transfer Correlation	<u>L</u> <u>J^{a,c}</u>
External Heat and Mass Transfer Correlation	<u>L</u> <u>J^{a,c}</u>

Deleted: 337 seconds after initial of the event.

Deleted: approximately 5 minutes of coverage

Deleted: d

Deleted: when

Deleted: i

Deleted: first applied and

13.5.3 Condensate Film Stripping

L

J^{a,c}

13-60

a,c

Figure 13-12. AP1000 WGOthic Evaluation Model Clime Stripping Diagram

WCAP-15846-P, Revision 5
APP-SSAR-GSC-587, Revision 5

September 2016

13-61

13.6 AP1000 PLANT WGOthic EVALUATION MODEL INITIAL AND BOUNDARY CONDITIONS

The inputs for the **AP1000 WGOthic containment Evaluation Model** also include a number of initial conditions used to define the temperatures and pressures, etc. at the beginning of the transient. Initial conditions assumed for the **AP1000 WGOthic containment Evaluation Model** have been conservatively selected to maximize the containment pressure response for the DBA analyses, and are consistent with the Technical Specifications and site interface parameters limits described in Section 13.6.1.

In addition, there are boundary conditions that are used to drive the transients being analyzed. Section 13.6.2 describes the boundary conditions used in the base case LOCA and MSLB Evaluation Model calculations.

13.6.1 Initial Conditions

The initial conditions that are assumed for the base case LOCA and MSLB analyses are summarized below. Initial conditions are specified separately for regions inside and outside of containment. The outside containment initial conditions represent the conditions at the inlet to the PCS downcomer, the annulus region, the chimney region, and the surrounding environment. Sensitivities documented in Section 5 form the basis for most of the assumed initial conditions. Table 13-7 summarizes the initial conditions outside containment. The inside containment initial conditions are presented in Table 13-8.

Table 13-7. Outside Containment Initial Conditions

<u>Input Parameter</u>	<u>Basis for Value in Evaluation Model</u>	<u>Reference to Applicable Sensitivity Studies</u>
<u>External Atmosphere Temperature</u>	<u>Set to maximum dry bulb air temperature limit defined by the site interface parameters.</u>	<u>WCAP-15846, Section 5.7</u>
<u>External Total Pressure</u>	<u>Set to standard atmospheric pressure (14.7 psia).</u>	<u>None</u>
<u>External Atmosphere Pressure Ratio (Relative Humidity)</u>	<u>A steam pressure ratio and relative humidity which bounds the limits defined by site interface parameters (wet bulb and dry bulb temperatures).</u>	<u>WCAP-15846, Section 5.6</u>
<u>External PCS Film Flow Temperature</u>	<u>Set to maximum PCCWST water temperature consistent with Technical Specification 3.6.6.</u>	<u>WCAP-15846, Section 5.7</u>

Deleted: m

Deleted: (EM)

Deleted: . Initial conditions are presented

Deleted: 5

Deleted: , below

Deleted: 5

Deleted: presents

Deleted: described

Deleted: The use of these values is based on sensitivity studies. These sensitivity studies are documented in Section 5.

Deleted: The inlet to the PCS downcomer is modeled with WGOthic flow path 233, which interfaces with the Evaluation Model Volume 98 at the 266-foot evaluation, as shown in Figure 13-86. The initial conditions at the PCS inlet, along with the basis for the Evaluation Model value and applicable references, are shown in Table 13-126.

13-62

Table 13-8. Inside Containment Initial Conditions

<u>Input Parameter</u>	<u>Basis for Value in Evaluation Model</u>	<u>Reference to Applicable Sensitivity Studies</u>
<u>Internal Atmosphere/Containment Shell/Heat Sink Temperature</u>	<u>Set to maximum Technical Specification value. This maximizes the temperature of the internal heat sinks. Reference Technical Specification 3.6.5.</u>	<u>WCAP-15846, Section 5.5</u>
<u>Internal Total Pressure</u>	<u>Set to maximum Technical Specification value. This maximizes the initial pressure and amount of air initially inside containment and retards mass transfer. Reference Technical Specification 3.6.4.</u>	<u>WCAP-15846, Section 5.4</u>
<u>Relative Humidity-Humidity</u>	<u>Set to maximize the amount of air inside containment which is noncondensable and will reduce the effectiveness of internal heat sink structures to absorb energy.</u>	<u>WCAP-15846, Section 5.3</u>
<u>IRWST Liquid Volume Fraction</u>	<u>Set at minimum Technical Specification IRWST water volume. Reference Technical Specification 3.5.6.</u>	<u>Not Applicable</u>
<u>IRWST Water Temperature</u>	<u>Set at maximum Technical Specification IRWST water temperature. This minimizes heat storage capacity. Reference Technical Specification 3.5.6.</u>	<u>Not Applicable</u>

13.6.2 Boundary Conditions

Boundary conditions provide communication between the WGOthic Evaluation Model and known conditions connected to the "boundaries" of the model. There are two types of boundary conditions, flow and pressure. Flow boundary conditions are addressed through WGOthic forcing functions and are used to prescribe flow into or out of a control volume. Flow boundary conditions are modeled on case specific bases for the LOCA and SLB cases. Pressure boundary conditions are used to model the atmosphere and/or environment attached to a fluid volume in the WGOthic model. In the AP1000 WGOthic containment Evaluation Model, pressure boundary conditions model the PCS air outlet and inlet environmental conditions. These values are consistent with those in Table 13-7.

13.6.2.1 Base Case LOCA Boundary Conditions

Deleted: Time-dependent boundary conditions were developed for both a DECLG (LOCA) and the limiting MSLB. The

Deleted: summarized in Table 13-128 (LOCA) and Table 13-129 (MSLB). Curves of the forcing functions that represent the LOCA and MSLB boundary conditions are presented in Figures 13-93 through 13-104. These figures present boundary conditions out to an accident time of 1,000,000 seconds for the LOCA, to cover the accident times of interest for both the 24-hour sensitivity cases, presented here, as well as other DBA analyses presented in the AP1000 DCD. MSLB boundary condition plots extend to an accident time of 2000 seconds, which bounds the event duration time for the limiting MSLB cases.¶
The cold leg LOCA and the MSLB accidents, as defined by these boundary conditions and the initial conditions presented in Section 13.5.1, form a set of two "base case" limiting accident sequences. Results for these base case sequences are provided in Section 13.7.

1^{a,c}

13-63

L

a.c

WCAP-15846-P, Revision 5
APP-SSAR-GSC-587, Revision 5

September 2016

13-64

↓

↓_{a,c}

13.6.2.2 Base Case MSLB Boundary Conditions

[

↓_{a,c}

13-65

13.7 SUMMARY OF EVALUATION MODEL TRANSIENT CALCULATIONS

This section provides an overview of the accident progression for the two limiting containment DBAs. The descriptions provided here do not define the containment peak pressure used as a licensing basis; licensing-specific results are provided in the DCD. Both of the transient events under consideration, double-ended cold-leg guillotine (DECLG) LOCA and MSLB, are assumed to start from the initial containment conditions presented in Section 13.6.1. The boundary conditions vary for each event and are defined in Section 13.6.2.

13.7.1 LOCA Transient Response Overview

The high level sequence of events for the containment response to a DECLG LOCA event is shown in the bulleted list below and briefly described in the text below.

- Break occurs
- Blowdown phase complete. Reflood phase begins
- Begin PCS evaporation heat removal modeling (steady state coverage assumed)
- ADS-4 actuated (steam released in upper SG compartments, IRWST drain-down begins)
- Containment peak pressure occurs
- Broken cold leg covered with water
- Water begins flooding CMT compartment
- IRWST water level equilibrates with CMT/SG compartment water levels (IRWST drain-down ends, core boil-off of sump water begins)
- PCS tank stand-pipes begin uncovering sequentially

The blowdown of RCS fluid into the containment leads to a rapid rise in the containment pressure within the first thirty seconds. Energy that is stored in the RCS metal and steam generators, along with the core decay heat is released to containment by heating and boiling of the water that is supplied by the PXS. Condensation of steam by the relatively cold metal surfaces within the containment building is initially able to maintain containment pressure following the blowdown peak pressure; however, as the internal heat sink temperatures begin to increase, condensation becomes less effective and containment pressure begins to slowly increase.

The annulus between the steel containment shell and concrete shield building is continuously cooled by a natural draft of air that flows down along the inside surface of the shield building and upward along the warmer containment shell. Condensation of steam on the inside surface of the containment shell causes the shell temperature to increase. As heat is conducted through the shell, the external shell surface

Deleted: representative Evaluation Model (EM) results

Deleted: overpressure design basis accidents (

Deleted:), typical of those provided in the DCD. The results

Deleted: ¶
¶

Deleted: loss-of-coolant accident (DECLG

Deleted:)

Deleted: main steamline break (

Deleted:)

Deleted: same

Deleted: , as

Deleted: 5

Deleted: 5

Deleted: Finally, the analysis uses the AP1000 containment EM described in Sections 13.2 and 13.3.

Deleted: given

Deleted: Table 13-135. The transient plots are shown in Figures 13-116 through 13-123.

Deleted: ¶
¶

Deleted: reactor coolant system (

Deleted:)

Deleted: , as shown in Figure 13-116.

Deleted: passive core cooling system (

Deleted:)

Deleted: at about 40 psig,

Deleted: ¶

13-66

temperature also increases. Heat transfer to the air in the riser section of the annulus causes the temperature and natural draft air flow rate to increase.

The passive PCS cooling water begins flowing onto the containment shell shortly after the initiation of the accident. As discussed in Section 7, the Evaluation Model does not credit external PCS water flow until such time as a fully-developed cooling water film forms on the containment shell. Evaporation increases the PCS heat removal capability and also increases the natural draft flow rate. The evaporation rate continues to increase as the shell temperature continues to increase.

The water level in the CMTs reaches the ADS-4 actuation setpoint at approximately 1200 seconds. After the ADS-4 relief valves open, steam generated by boiling in the core is able to vent through the large ADS-4 lines into the upper steam generator compartments inside containment. The ADS-4 actuation signal also opens valves that allow water to begin to gravity drain from the IRWST to the RCS.

At approximately 1600 seconds, the condensation rate on the containment shell and internal heat sinks exceeds the steam release rate through the LOCA break and ADS-4 flow paths and containment pressure begins to decrease.

Water spilled from the RCS has begun to fill the sump and lower steam generator compartments. The liquid levels in these compartments continue to increase as the IRWST drains to the RCS and spills from the break.

An open drain line, located between the refueling cavity and sump, allows some of the spill water to begin filling the lower refueling cavity. This helps slow the water level increase in the CMT and SG compartments. The curbs surrounding the openings to the accumulator and CVS compartments in the floor of the CMT compartment are sufficiently high to prevent water from flooding those compartments.

The IRWST gravity drain ceases after approximately 10,000 seconds when the CMT and IRWST compartment water levels equilibrate. After this, the water needed to make up for boiling in the core is supplied from the sump through the cold leg break. The flow through the open drain line between the sump and refueling cavity eventually causes the refueling cavity level to also equilibrate with the CMT and SG compartments.

The PCS flow rate decreases as the storage tank water level falls below the top of each successive stand-pipe. The first reduction in the PCS flow rate resulted in a significant reduction in the shell heat removal rate and significantly reduced the containment depressurization rate.

The containment pressure continued to slowly decrease over the remainder of the event as the only remaining energy source is the decay heat in the core. The continuous reduction in the shell evaporation rate caused the annulus air flow rate to slowly decrease and the annulus air temperature to slowly increase.

Deleted: (see Figures 13-117 and 13-118)

Deleted: ¶

Deleted: containment cooling system (

Deleted:)

Deleted: c

Deleted: m

Deleted: ; this occurs at 337 seconds.

Deleted: natural draft flow rate (see Figure 13-118), and also increases the

Deleted: (see Figure 13-119)

Deleted: ¶

Deleted: core makeup tanks (

Deleted:)

Deleted: 1500

Deleted: ¶

Deleted: 1700

Deleted: (see Figure 13-116)

Deleted: ¶

Deleted: (Figures 13-120 through 13-123)

Deleted: The water level is predicted to reach the break elevation (100-ft) at approximately 5000 seconds and the CMT floor elevation at approximately 7000 seconds.

Deleted: ¶

Deleted: steam generator (

Deleted:)

Deleted: ¶

Deleted: in-containment refueling water storage tank (

Deleted:)

Deleted: at about

Deleted: ¶

Deleted: (see Figure 13-119)

Deleted: (see Figure 13-116). Subsequent changes in the PCS flow rate were not as severe, so changes in the shell heat removal rate are not as apparent.

Deleted: ¶

Deleted: (see Figure 13-118)

Deleted: (see Figures 13-117)

13-67

13.7.2 MSLB Transient Response Overview

Steam line breaks are postulated to occur at operating conditions ranging from hot shutdown to full power. Steam generator secondary-side mass decreases with increasing power level, while both the RCS and SG secondary side energy increase as the power level increases. Because of the opposing effects of changing power level on the steam line break releases, no single power level can be identified as always being the worst case initial condition for a steam line break event. Therefore, several different power levels spanning the operating range are analyzed.

The containment response to the MSLB event is determined by the magnitude and duration of the mass and energy releases, the containment volume, steam/air circulation to the heat sinks, and time response of the heat sinks. Due to the assumption of 0% humidity as the containment initial condition and saturated vapor mass and energy releases with no liquid entrained in the break effluent, the MSLB transient is characterized by the containment atmosphere being superheated throughout the transient.

Four different power levels are analyzed for the double-ended guillotine MSLB cases. Reactor trip, main feedwater isolation and main steamline isolation occur rapidly due to a low steamline pressure signal. The PCS water on the external surface of the containment vessel is credited after a high-2 containment pressure signal and a delay to account for the development of steady state PCS water coverage. Generally, the containment pressure continues to increase until the secondary side blowdown ends due to the SG fluid inventory depleting. The containment pressure decreases rapidly as the energy continues to be transferred to the environment by the PCS.

13.8 WGOthic CONTAINMENT MINIMUM PRESSURE CALCULATION FOR SMALL-BREAK LOCA AND LONG-TERM CORE COOLING

A conservative calculation of the containment pressure is needed to provide the containment boundary conditions for the **API1000** small-break LOCA (**SBLOCA**) analysis and the long-term core cooling (**LTCC**) analysis. For these cases, containment backpressure results in enhanced gravity injection from the IRWST and the containment sump. For this reason, the WGOthic containment pressure calculation is biased to obtain the minimum containment pressure for a given event.

The WGOthic Evaluation Model is used to determine the peak containment pressure for design basis events uses assumptions that are biased to maximize the containment pressure. The minimum containment pressure model for SBLOCA and LTCC reverses many of the biases to provide a set of assumptions to minimize the containment pressure. The assumptions for the minimum containment pressure model are summarized in Table 13-9. The assumptions are to minimize the calculated containment pressure and are not necessarily physically realistic or consistent with one another. For example, the containment shell area is not actually 10% higher than nominal, but this is a conservatism applied in the analysis. Also if the containment shell surface area is greater than the nominal value, the containment volume would not increase by the same percentage, yet this is a part of the conservative assumptions.

Deleted: ¶
¶

Deleted: A break spectrum is analyzed for the MSLB event.

Deleted: with increasing

Deleted: Additionally, steam pressure and the dynamic conditions in the steam generators change with increasing power. These factors have a significant influence on both the rate of blowdown and the amount of moisture entrained in the fluid leaving the break following an event.

Deleted: a

Deleted: ¶

Deleted: nature of the secondary side releases,

Deleted: addition of superheated steam to the

Deleted: ¶
The double-ended guillotine MSLB mass and enthalpy releases for 4

Deleted: shown in Figures 13-103 and 13-104. The containment pressure transient response for these 4 cases is shown in Figure 13-124. In each case,

Deleted: is complete. The 30-percent power double-ended rupture (DER) MSLB case resulted in the highest peak pressure, 56.5 psig at about 820 seconds. No additional mass or energy is released to containment after blowdown is complete, so

Deleted: t

Deleted: internal heat sinks and

Deleted: absorb the energy

Deleted: ¶

Deleted: c

Deleted: m

Deleted: these

Deleted: uncertainties

Deleted: used in the evaluation model and the

Deleted: 136

Deleted: se

Deleted: were incorporated into the WGOthic model. The resulting pressure response curve is shown in Figure 13-125 for the double-ended DVI break event. It is recommended that a containment backpressure of 20 psia be used when analyzing the small-break LOCA up to the point of switchover to sump recirculation. For long-term cooling applications, containment backpressure of 18.5 psia was calculated at 14 days and 16 psia was calculated at 30 days.

13-68

The assumptions minimize containment pressure in the following ways.

[

1^{a,c}

13-69

Table 13-9. WGOthic Assumptions for SBLOCA Minimum Pressure Calculations

<u>Parameter</u>	<u>Minimum Pressure Model</u>
<u>Containment volume</u>	<u>Nominal increased 10%</u>
<u>Containment shell heat transfer area</u>	<u>Nominal increased 10%</u>
<u>Shell heat and mass transfer correlations</u>	<u>Biased to increase heat and mass transfer</u>
<u>Heat sinks</u>	<u>All heat sinks active</u>
<u>Passive heat sink area</u>	<u>Nominal increased by factor of 1.35</u>
<u>Heat transfer correlation</u>	<u>Uchida increased by 20%</u>
<u>I^{a,c}</u>	<u>I^{a,c}</u>
<u>Passive heat sink structural air gaps in steel-jacketed concrete walls</u>	<u>Not modeled</u>
<u>Material properties</u>	<u>Volumetric heat capacity and thermal conductivity biased for maximum heat removal</u>
<u>Passive containment cooling system flow rates</u>	<u>Maximum system specified flows</u>
<u>PCS water temperature</u>	<u>Minimum to maximize evaporative cooling</u>
<u>Passive containment cooling system</u>	<u>Assumed to start at the beginning of the event</u>
<u>Fan coolers</u>	<u>Assumed to start 10 minutes after event initiation</u>
<u>Containment purge</u>	<u>Open, shuts on automatic safeguards actuation signal</u>
<u>Initial pressure inside containment</u>	<u>Set to the minimum operating air pressure defined by Technical Specification 3.6.4</u>
<u>Initial humidity inside containment</u>	<u>Maximized to minimize initial air quantity</u>
<u>Initial temperature inside containment</u>	<u>Set to the maximum operating air temperature defined by Technical Specification 3.6.5.</u>
<u>Initial environment temperature</u>	<u>Minimized based on maximum containment shell differential defined by Technical Specification 3.6.10</u>

13-70

13.9 CONCLUSIONS

A summary of the key elements of the AP1000 containment EM methodology, as described within Section 13, is provided below.

[

] ^{a,c}

13-71

[

] ^{a,c}

13-72

13.10 REFERENCES

- 13.1 WCAP-14382, "WGOTHIC Code Description and Validation," May 1995.
- 13.2 NAI 8907-02, Rev. 4, "GOTHIC Containment Analysis Package User Manual," August 1994.
- 13.3 WCAP-14812, Rev. 2, "Accident Specification and Phenomena Evaluation for AP600 Passive Containment Cooling System," April 1998.
- 13.4 NTD-NRC-95-4563, "GOTHIC Version 4.0 Documentation," September, 1995.
- 13.5 WCAP-14326, Rev. 3 "Experimental Basis for the AP600 Containment Vessel Heat and Mass Transfer Correlations," April 1998.
- 13.6 WCAP-10325-P-A, "Westinghouse LOCA Mass and Energy Release Model for Containment Design March 1979 Version," May 1983.
- 13.7 WCAP-15846-P, Addendum 1, "Effective Thermal Conductivity Model of Inorganic Zinc Coating for Application to AP1000," October 2013.

Deleted: M. Kennedy, et al.,

Deleted: <#>AP600 Standard Safety Analysis Report (SSAR), Revision 14¶

Deleted: Revision 2,

Deleted: Westinghouse Letter

Deleted: B.A. McIntyre to Quay (NRC),

Deleted: 21

14 LOCA MASS AND ENERGY RELEASE CALCULATION METHODOLOGY

14.1 INTRODUCTION

This section describes the method used to calculate the loss-of-coolant accident (LOCA) mass and energy releases that are used to calculate the containment pressure response for the Design Basis Analysis (DBA). The method maximizes both the magnitude and the rate of the mass and energy release to containment. This introduces substantial conservatism in the prediction of the peak containment pressure and temperature response following a LOCA event.

Section 10, Figure 10-1 presents a comparison of the WGOTHIC AP600 Containment Evaluation Model sensitivity to various input values and correlations. These are not single-effect sensitivities; the results are cumulative. Each additional sensitivity case modification is stacked upon those that immediately preceded it. These sensitivities provide insight into the effect of each parameter, individually, by comparison to the preceding case, as well as the total conservatism represented by these parameters. Case 7 (the heavy dashed line in Figure 10-1) represents the effect of removing some of the conservatism in the input mass and energy releases.

For Case 7, the mass and energy release calculation input was modified as follows:

- The nominal (without adding 5°F uncertainty) full power RCS temperatures were used
- The nominal (without adding 30 psi) full power RCS pressure was used
- The nominal (without adding uncertainty) RCS volume was used
- The nominal (without adding 2% uncertainty) full core power was used
- The nominal (without adding 15%) full power core stored energy was used
- The nominal CMT, accumulator, and IRWST fluid temperatures were used.

In addition to the input changes described above, the following calculational changes were made during the post-blowdown phase:

- The 1979 ANS decay heat standard for an 800-day average burnup (without adding the 2 sigma uncertainty) was used
- The post-blowdown refill period was modeled
- The broken loop steam generator energy was assumed to be released over a 1-hour period
- The intact loop steam generator energy was assumed to be released over a 2-hour period
- No zirc-water reaction energy was added.

A comparison of the mass and energy releases for Case 7 and the AP600 Containment Evaluation Model is shown in Figures 10-3 and 10-4.

As shown in Figure 10-1, by eliminating only a portion of the conservatism in the calculation of the mass and energy releases, there is a substantial decrease in the post-blowdown peak pressure (about 6 psi). The calculated peak containment pressure is reduced from the previous case by about 4.3 psi and is shifted to the end of blowdown. The largest effect of any other single change to one of the containment model input values is a reduction of about 3 psi. Therefore, the conservatism in the mass and energy calculation outweighs any other single modeling parameter.

14.2 BLOWDOWN MASS AND ENERGY RELEASE CALCULATION

The primary differences between the conventional plant design and the passive plant design are the engineered safety features. The safety features of conventional operating plants include both passive and active systems; the AP600 and AP1000 safety features are all passive. This difference only affects the long-term inventory makeup systems, not the system behavior during the blowdown phase.

The methodology for calculating the mass and energy release to containment during the blowdown phase is not affected by the passive safety systems. The only safety system that injects water during the blowdown phase is the accumulator system; the gravity-driven core makeup tanks (CMTs) cannot inject into the common direct vessel injection line against the pressure of the gas-charged accumulators. Accumulators are included in both the passive and active plant designs and are modeled with the NRC-approved DBA LOCA mass and energy release methodology. The AP600 uses spherical accumulators, whereas currently operating Westinghouse designed plants use cylindrical accumulators. The accumulator inventory is depleted well before the time of peak pressure so any difference in discharge rate associated with the different accumulator geometry would have an insignificant effect on the calculation for peak containment pressure.

The blowdown mass and energy releases are calculated using the SATAN-VI computer code. The SATAN-VI code, associated modeling assumptions and nodding structure for the mass and energy release calculations are documented in WCAP-10325-P-A (Reference 14.1). It has been reviewed and approved by the NRC for use in calculating the blowdown mass and energy releases for Westinghouse PWR containment integrity DBA. The blowdown phenomena modeled by the SATAN VI code are the same for all Westinghouse PWRs, including the AP600 design.

The variable nodding structure of the SATAN model allows the user to simulate current and advanced reactor coolant system geometry with generalized control volumes. The standard Westinghouse PWR reactor coolant system nodding structure is modified to specifically model the passive plant reactor coolant system geometry, which includes two cold legs in the coolant loops and a direct vessel injection (DVI) line to the downcomer.

14-3

14.3 POST-BLOWDOWN MASS AND ENERGY RELEASE CALCULATION

The post-blowdown phase consists of three periods: refill, reflood, and long-term cooling. The refill period occurs just after blowdown. During the refill period, the accumulators refill the downcomer and lower plenum of the vessel with water. There are little or no releases during the refill period. The reflood period occurs just after refill. During the reflood period, the core is refilled with a 2-phase mixture of steam and water. Following reflood, the RCS fluid inventory and long-term cooling are maintained by the pumped safety injection system and recirculation system (conventional plants) or the core makeup tanks and gravity draining of the IRWST (passive plants).

The approved codes for conventional plant post-blowdown mass and energy release analyses would have had to have been significantly modified for them to have been used for passive plant analyses. Instead, a calculational method was developed to conservatively predict the AP600 and **AP1000** post-blowdown mass and energy releases in a manner that is consistent with the current approved methods for DBA. A spreadsheet was used for the calculations to simplify accounting of the mass and energy sources and releases.

Mass Sources

Figure 14-~~1~~ illustrates the basic model for the AP600 and **AP1000** post-blowdown mass and energy release calculation. All of the injection sources (accumulators, CMTs, and IRWST) are assumed to be delivered to the DVI line at a mass flow rate, m_{inject} . Flow from both accumulators refills the vessel following blowdown. The CMTs begin to inject just before the accumulators empty. The IRWST begins to gravity drain to the vessel (and spill from break) just before the CMTs empty.

The injected liquid mass flow rate delivered to the DVI line is calculated with a simplified resistance network. Two cases ~~were~~ considered initially: one with the line resistances maximized (to produce the minimum accumulator, CMT, and IRWST flow rates) and one with the line resistances minimized (to produce the maximum accumulator, CMT, and IRWST flow rates). The resistance network also calculates a flow rate around the loops and a flow rate out the broken cold leg stub, however, these are not used in the mass and energy release spreadsheet calculation. Instead, as shown in Figure 14-~~1~~, all of the injection flow that is delivered to the DVI line is assumed to pass through the core, hot legs, steam generators and out of the break. This maximizes the SG heat release rate, and is a source of conservatism in the analysis.

[

Deleted: 3-1

Deleted: are

Deleted: 1

] ^{a,c}

14-4

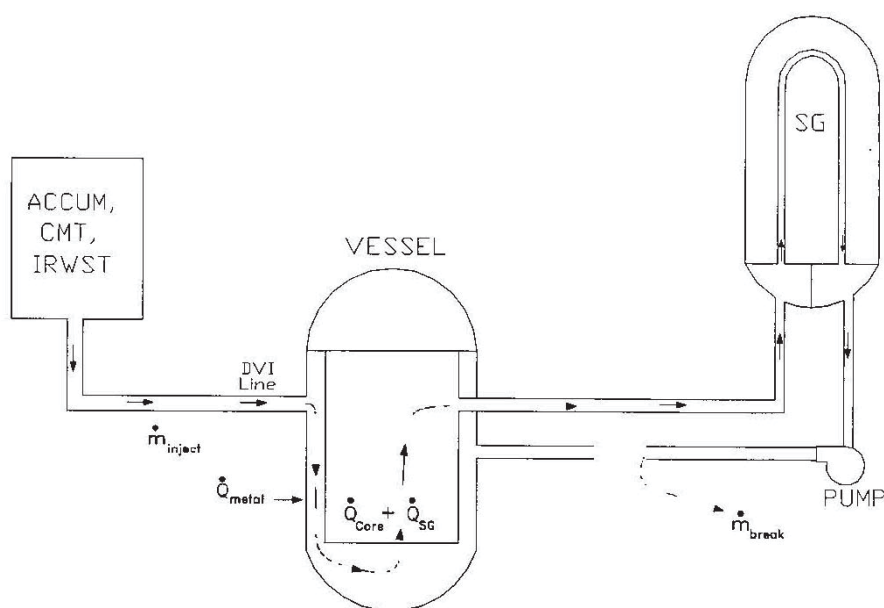


Figure 14-1. Spreadsheet Mass and Energy Release Schematic

14-5

a,c

Figure 14-2. WGOTHIC Draindown Model Noding Diagram

Energy Sources

The various sources of energy that are considered in the calculation, and their assumed release rates are summarized in Table 14-1. The release rates are biased to release energy (in the form of steam) to the containment early in the transient. The containment pressure response is dependent on the steam mass flow rate, so maximizing the steaming rate is conservative. The RCS metal energy release provides sensible heating of the injected liquid mass flow. The core decay heat and SG energy releases provide both sensible and latent heat to the injected liquid mass flow rate.

The SG equilibration time input value in the spreadsheet calculation is adjusted to maximize the steaming rate during the CMT injection phase. The SG equilibration times that are used for **AP1000** are longer than AP600 because both the core decay heat and SG stored energy are higher in the **AP1000**.

Table 14-1. DECLG LOCA Energy Release Modeling

Time Frame	Source of Energy	Energy Release Rate
Accident initiation to end of blowdown (30 seconds)	Core, RCS and SGs	SATAN VI Calculation
End of blowdown + 180 seconds	The Zr-H ₂ O Reaction Energy for 1% of the Fuel Cladding	Constant
End of blowdown to end of reflood (400 seconds)	Core stored energy	Constant
End of blowdown + SGB equilibration	SG energy - broken loop	Exponential
End of blowdown + SGI equilibration	SG energy - intact loop	Exponential
End of blowdown + 60 minutes	RCS metal energy	Exponential
End of blowdown to 72 hours	Fission Product Decay	ANS 1979 + 2 sigma

Description of Calculational Method

Three basic steps in the calculational method determine the DBA mass and energy releases as a function of time after the blowdown phase. First, the individual contributions for each of the various sources of energy are calculated. Second, the vessel internal mass and break mass flow rate are calculated. Third, the break mass flow rate is partitioned into a steam and a 2-phase component. A check for conservation of mass and energy is performed at the end of each time step. This method for calculating the mass and energy releases after the blowdown phase is described in more detail below.

14-7

Calculation of Sources of Energy

1. The 1979 decay heat standard with 2 sigma uncertainty, all U-235 fission, and 3 years full power operation is used to calculate the core decay heat energy release rate at each time step.

1. [

] ^{a,c} The core stored energy is

released at a constant rate over the reflood period.

2. The Zr-H₂O reaction energy, corresponding to 1% clad oxidation, is released at a constant rate over the first 180 seconds of the reflood period.
3. The RCS metal energy is released exponentially. Using an exponential rate is conservative since this assumes the heat transfer rate is much larger than the rate of conduction through the metal. The equation for determining the stored metal energy as a function of time is:

$$Q(t) = Q_{final} + (Q_{initial} - Q_{final}) \cdot e^{-a \cdot (t-b)}$$

where,

Q_{final}	=	stored metal heat at equilibration (BTU)
$Q_{initial}$	=	stored metal heat at the end of blowdown (BTU)
a	=	inverse of the metal time constant (sec ⁻¹)
t	=	time (sec)
b	=	end of blowdown time (sec)

therefore, the release rate is:

$$\frac{dQ}{dt} = -a \cdot (Q_{init} - Q_{final}) \cdot e^{-a \cdot (t-b)}$$

The stored metal heat and time at the end of blowdown are obtained from the SATAN output tables. The stored metal heat at equilibration, Q_{final} , is determined by the metal heat capacity and the equilibration temperature, $M^*c_p \cdot T_{eq}$. The metal heat capacity, M^*c_p , is obtained from the SATAN input tables. The RCS temperature is assumed to reach an equilibrium value at the end of the reflood period. Using an equilibration temperature, T_{eq} , of [] ^{a,c} was found to produce good agreement between the spreadsheet calculational method and the code calculated mass and energy releases for a conventional plant. This equilibration temperature value corresponds to [] ^{a,c} the AP600 containment design pressure. A higher equilibration temperature value of [] ^{a,c} is used for **AP1000** since the containment design pressure is higher than AP600. The equilibration temperature is held constant for the post-blowdown calculation.

The metal time constant is the metal heat capacity divided by the heat transfer rate. Because the heat transfer rate is variable, the time constant is arbitrarily increased to release 99% of the RCS metal energy (in excess of the equilibration temperature) over 60 minutes.

14-8

4. The steam generator stored energy at the end of blowdown is released using the same equation shown above for the RCS metal energy release rate. The stored energy and time at the end of blowdown are obtained from the SATAN output tables. The stored energy at equilibration is determined by the metal and fluid heat capacity and the equilibration temperature, $\{(M \cdot c_p)_{\text{fluid}} + (M \cdot c_p)_{\text{metal}}\} \cdot T_{\text{eq}}$. The steam generator fluid and metal heat capacity input values are obtained from the SATAN input tables.

The stored energy in the broken loop and intact loop steam generators is released at different rates. The time constants for AP600 are set to values similar to standard plant analyses. Because the **AP1000** CMT injection flow rate limits the steaming rate, the **AP1000** time constants are adjusted to provide a more mechanistic representation of the steam generator energy release relative to the available core makeup flow, and to maximize the steaming rate during the CMT injection period.

Calculation of the Vessel Liquid Mass

5. During the reflood period, the mass of liquid in the vessel is assumed to increase exponentially according to the following equation:

$$M(t) = M_{\text{final}} + (M_{\text{initial}} - M_{\text{final}}) \cdot e^{-c \cdot (t-b)}$$

where,

M_{final}	=	RCS mass at the end of reflood (lbm)
M_{initial}	=	RCS mass at end of blowdown (lbm)
c	=	inverse reflood time constant (sec^{-1})
t	=	time (sec)
b	=	end of blowdown time (sec)

At the end of the reflood period, the RCS is assumed to be at a saturation temperature of []^{a,c} for the AP600 or []^{a,c} for the **AP1000** with a vessel void fraction of []^{a,c}. These assumptions were found to produce good agreement between the spreadsheet calculational method and the code calculated mass and energy releases for a conventional plant.

The RCS liquid mass at the end of the reflood period, M_{final} , is calculated using the following equation:

$$M_{\text{final}} = V \cdot (1 - \alpha) \cdot \rho$$

where,

V	=	Vessel volume (ft^3)
α	=	Vessel void fraction at end of reflood
ρ	=	Saturated liquid density at [] ^{a,c} (lbm/ft^3)

14-9

The temperature and amount of mass in the vessel at the end of reflood are held constant throughout the long-term cooling phase. These assumptions maximize the steam release rate because there is no additional filling of the vessel and, because the temperature does not decrease, the latent heat of vaporization does not increase.

An initial value for the RCS fluid mass is given in the SATAN summary table. The RCS initial mass input for the spreadsheet calculation, $M_{initial}$, is artificially instantaneously increased to eliminate the time delay associated with refilling the downcomer and lower plenum of the vessel. Eliminating the refill period shifts the mass and energy releases earlier in time and results in an increase in the predicted peak containment pressure.

The reflood time constant is related to the vessel volume, the injected mass flow rate and the steaming rate. The time constant is set to allow the vessel mass to reach 99% of the M_{final} value in approximately 400 seconds. This time frame is consistent with reflooding times for conventional Westinghouse PWR designs with similar vessel volume and injection rates.

Calculation of the Break Vapor and 2-Phase Mass Flow Rates

Steps 7 through 10 describe the method that is used to calculate the break mass flow rate and to partition it into the vapor and 2-phase flow components for input to the WGOTHIC Containment Evaluation Model.

6. The break mass flow rate is defined as the difference between the injected mass flow rate and the time derivative of the vessel liquid mass, as shown in the equation below:

$$m_{break} = m_{inject} - c \cdot (m_{final} - m_{initail}) \cdot e^{-c \cdot (t-b)}$$

Following the end of the reflood period (400 seconds), the total flow released from the break is equal to the injected flow; no additional inventory is stored in the RCS.

7. The core inlet enthalpy is calculated by dividing the RCS metal energy release rate by the injected liquid mass flow rate, and summing this with the enthalpy of the injected flow, $h_{core} = h_{inject} + Q_{metal}/m_{inject}$. After injection stops, the core inlet enthalpy is set to a constant value. This value is based on the upper bound fluid temperature in the containment sump.

14-10

8. The total break flow rate is partitioned into a steam and a 2-phase component. Because the containment pressure is dependent on the steam release, the steam mass flow rate is maximized by assuming 95% of the core energy and all of the steam generator energy is used to produce steam. The steam and 2-phase fluid break mass flow rates are calculated using the following equations:

$$m_{steam} = \min[m_{break}, (0.95 \cdot Q_{core} + Q_{SG}) / (h_g - h_{core})]$$

$$m_{2-phase} = m_{break} - m_{steam}$$

where,

Q_{core} = Sum of the core decay heat, stored energy and Zr-H₂O reaction release rates (BTU/s)

Q_{SG} = Sum of the broken and intact SG energy release rates (BTU/s)

h_g = Steam enthalpy at the equilibration temperature (BTU/lbm)

h_{core} = Core inlet enthalpy (BTU/s)

m_{break} = Total break mass flow rate (lbm/s)

Note, because the steam enthalpy is assumed to remain constant at the equilibration temperature, the steam generator energy is used to produce additional steam release, rather than superheat the steam. This maximizes the steam release rate.

9. The enthalpy of the 2-phase break fluid is calculated using the following equation:

$$h_{2-phase} = \min[h_g, (0.05 \cdot Q_{SG}) / (m_{2-phase})]$$

where all terms have been defined previously. The limit is applied to prevent the 2-phase enthalpy from exceeding h_g when the 2-phase mass flow rate is very small.

Check for Energy Conservation

10. Conservation of energy is checked at the end of each time step. [

] ^{a,c}

14-11

14.4 COMPARISON OF SATAN/SPREADSHEET RELEASES WITH WCOBRA-TRAC CALCULATED RELEASES

The AP1000 DECL LOCA mass and energy releases calculated using the SATAN/spreadsheet method were compared to the **best estimate** WCOBRA-TRAC (WCT) code calculated results to demonstrate the amount of conservatism in the calculation. The comparison was run out 2000 seconds; this is beyond the calculated time of peak containment pressure. Although this version of the WCT code was not designed to produce LOCA mass and energy releases that would be conservative for use in calculating containment peak pressure, it should nevertheless mechanistically calculate a reasonable estimate of the releases.

A representative comparison of the blowdown mass and energy releases are shown in Figures 14-3 and 14-4. SATAN predicts a higher blowdown mass and energy release rate than WCT. The post-blowdown mass and energy comparison is shown in Figures 14-5 and 14-6. The spreadsheet method calculates a higher release rate than WCT because the spreadsheet releases the SG energy at a much higher rate than WCT.

The **representative** integrated mass and energy releases are compared in Figures 14-7 and 14-8. The SATAN/spreadsheet method predicts approximately a 50-percent higher integrated mass and energy release than WCT, by the time peak pressure occurs. This difference results in a 20 psi higher calculated peak pressure as shown in Figure 14-9.

Deleted: The

Deleted: comparison is

Deleted: 2

Deleted: 3

Deleted: 4

Deleted: 5

Deleted: 6

Deleted: 7

Deleted: 8

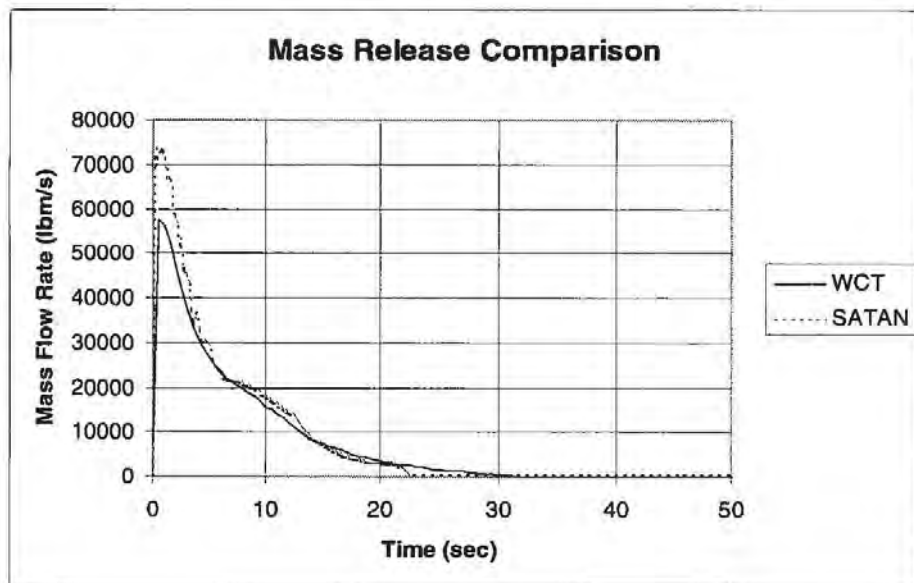


Figure 14-3. Mass Release Comparison

14-12

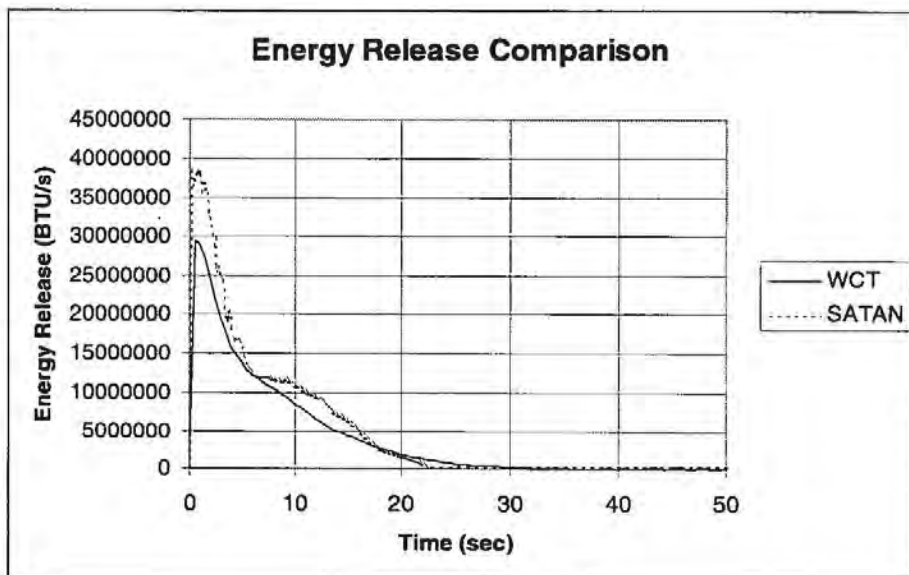


Figure 14-4. Energy Release Comparison

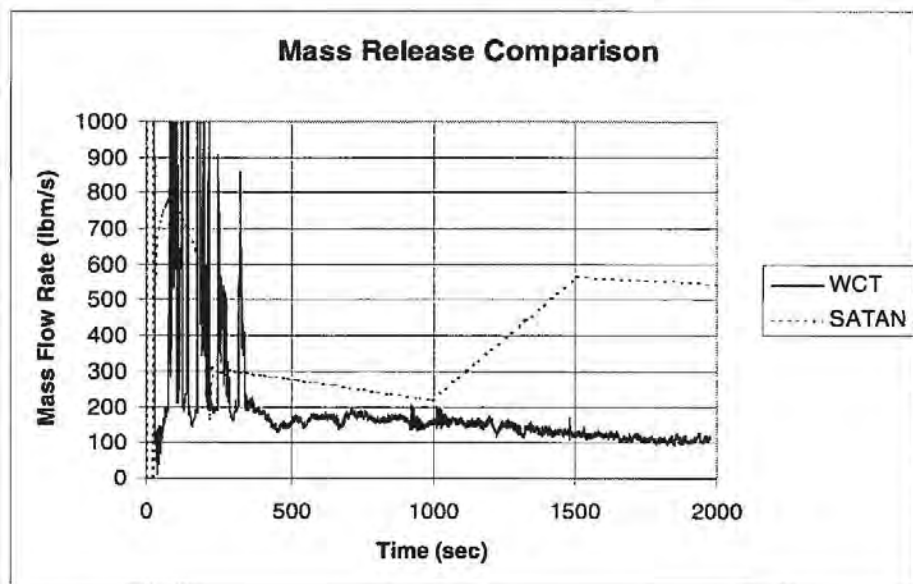


Figure 14-5. Mass Release Comparison

14-13

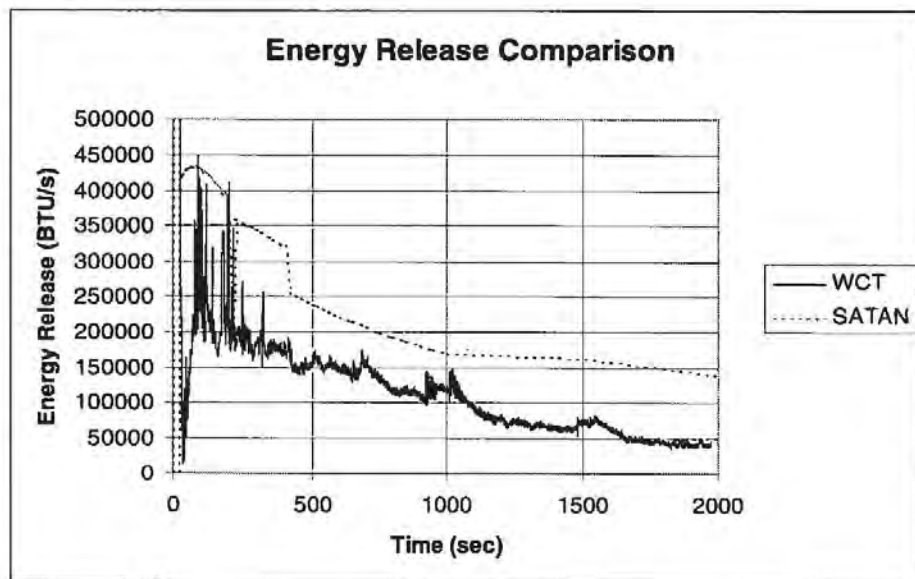


Figure 14-6. Energy Release Comparison

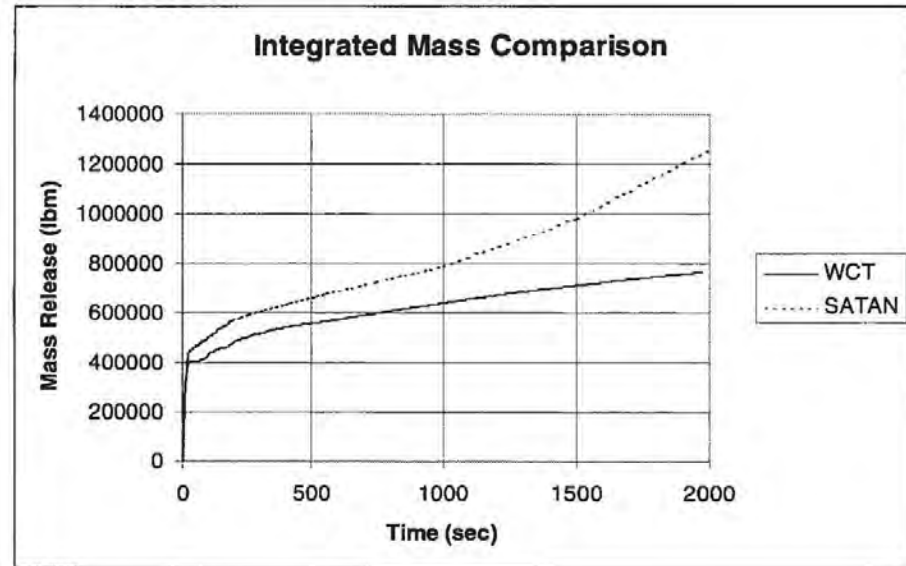


Figure 14-7. Integrated Mass Comparison

14-14

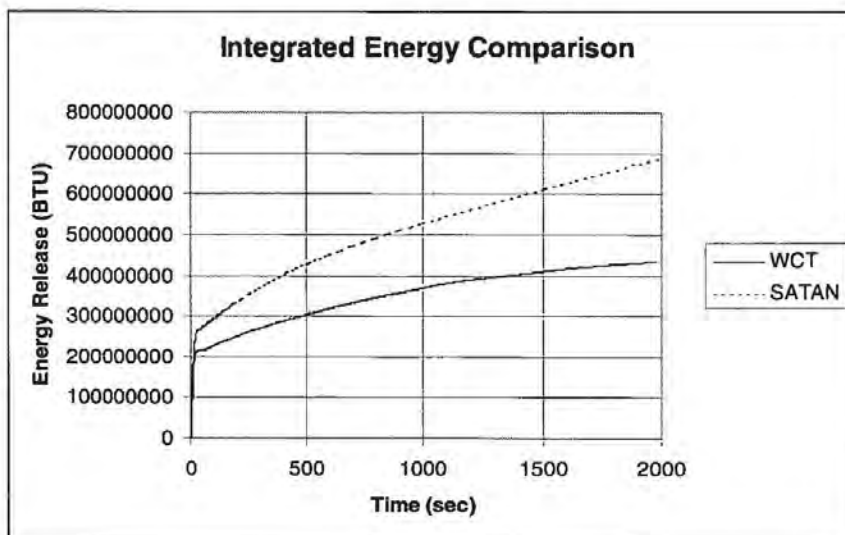


Figure 14-8. Integrated Energy Comparison

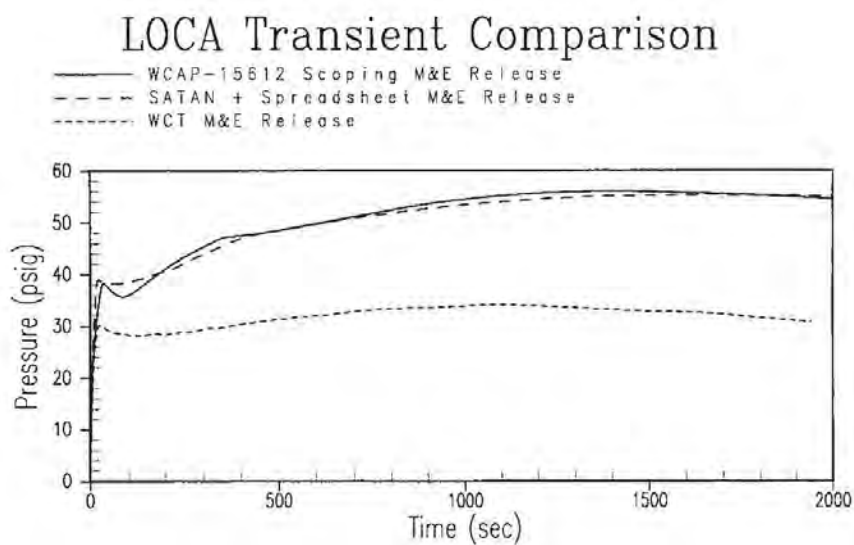


Figure 14-9. LOCA Transient Comparison

14.5 SUMMARY AND CONCLUSIONS

The methodology, used to predict mass and energy releases to the containment during the blowdown phase of the Large LOCA accident for the AP600 and **AP1000** containment DBA, is consistent with the methodology approved by the NRC for current operating plants. The approved methodology yields conservatively high total energy and energy release rates to the containment atmosphere, consistent with regulatory guidance for Design Basis Analyses.

A spreadsheet calculation method is applied to calculate the post-blowdown mass and energy releases for the AP600 and **AP1000**. Because the containment pressure is dependent on the steam release, the break steam mass flow rate is maximized in the calculation. The transient flow rates for the accumulators, CMTs and IRWST, are calculated using a resistance network. These flow rates, along with the conditions at the end of the SATAN blowdown mass and energy release analysis, are input to the spreadsheet. The spreadsheet accounts for the same sources of energy and uses similar energy release rates as the conventional plant analysis. A comparison of the releases predicted by the spreadsheet and the approved mass and energy release analysis codes/models show that the spreadsheet provides a conservatively high prediction of the release to containment. Therefore, the spreadsheet method for calculating the post-blowdown mass and energy releases used in the AP600 and **AP1000** containment analysis is consistent with the methodology approved by the NRC for current operating plants.

14-16

A summary outlining the design basis LOCA mass and energy release inputs and major assumptions is presented in Table 14-2.

Table 14-2. Basis for LOCA Mass and Energy Inputs

<u>Input Parameter</u>	<u>Basis for Value in Evaluation Model</u>
<u>RCS Initial Conditions</u>	<u>Assumed to be at the maximum expected operating temperature and pressure. Includes allowances for error and instrument dead band.</u>
<u>RCS Volume</u>	<u>RCS coolant volumes increased by 1.4% for uncertainty and 1.6% for thermal expansion. As discussed in WCAP-10325-P-A, this model conservatism is chosen to maximize the available energy in the system.</u>
<u>Core Stored Energy</u>	<u>Core stored energy conservatively increased by 15%. As discussed in WCAP-10325-P-A, Core stored energy is maximized based upon the conditions at the most limiting time in life and maximum core fluid temperature.</u>
<u>Steam Generator Mass</u>	<u>Initial mass conservatively increased by 10%. As discussed in WCAP-10325-P-A, this model conservatism is chosen to maximize the available energy in the system.</u>
<u>Initial Power Level</u>	<u>Full technical specification power, accounting for calorimetric error. As discussed in WCAP-10325-P-A, this model conservatism is chosen to maximize the available energy in the system.</u>
<u>Zirc-Water Reaction</u>	<u>1% of the zirconium conservatively assumed to react. Bounds LOCA Chapter 15 results of no appreciable zirc-water reaction.</u>
<u>Blowdown Phase Calculation Methodology LOCA Mass and Energy Release</u>	<u>SATAN 78, WCAP-10325-P-A</u>
<u>Steam Generator Heat Release</u>	<u>Exponential decay constant adjusted to maximize steaming rate during CMT injection period.</u>

14.6 REFERENCES

- 14.1 WCAP-10325-PA, "Westinghouse LOCA Mass and Energy Release Model for Containment Design March 1979 Version," May 1983.

Southern Nuclear Operating Company

ND-17-2074

Enclosure 7

Vogtle Electric Generating Plant (VEGP) Units 3 and 4

**APP-SSAR-GSC-587 Rev. 5 “WGOTHIC Application to AP600 and AP1000”
(WCAP-15846) Revision 5 (Proprietary)
(LAR-17-043)**

(Withheld Information)

(Enclosure 7 consists of 1089 pages, excluding this cover page.)

Southern Nuclear Operating Company

ND-17-2074

Enclosure 8

Vogtle Electric Generating Plant (VEGP) Units 3 and 4

**APP-SSAR-GSC-588 Rev. 5 “WGOTHIC Application to AP600 and AP1000” (WCAP-15862)
Revision 5 (Non-Proprietary)**

(LAR-17-043)

(Enclosure 8 consists of 768 pages, excluding this cover page.)

DOCUMENT COVER SHEET

DOCUMENT NO. APP-SSAR-GSC-588	REVISION 5	PAGE 1 of 768	OPEN ITEMS N
DOCUMENT STATUS: DES		AP1000 SAFETY CLASS: NA	
LICENSING REVIEW STATUS: Completed by Reference			Westinghouse Acceptance of AP1000 Design Partner Document by: N/A (Print Full Name) (Signature/Date)
PLANT APPLICABILITY:			
<input checked="" type="checkbox"/> All AP1000 Plants except: No Exceptions <input type="checkbox"/> Only the following plants:			

ALTERNATE DOCUMENT NUMBER: WCAP-15862-NP

ORIGINATING ORGANIZATION: Westinghouse Electric Company, LLC

TITLE: WGOTHIC Application to AP600 and AP1000

DCP/DCA/SUPPLEMENTS/EDCR # INCORPORATED IN THIS DOCUMENT REVISION:
APP-GW-GEE-5003

ATTACHMENTS:
N/A

PARENT DOCUMENT: N/A

☒ © 2016 WESTINGHOUSE ELECTRIC COMPANY LLC, ALL RIGHTS RESERVED – WESTINGHOUSE NON-PROPRIETARY CLASS 3

All Class 3 Documents require the following two approvals in lieu of a Form 36.

LEGAL REVIEW

J. C. Spadacene

SIGNATURE / DATE (If processing electronic approval select option)

Electronically Approved***

PATENT REVIEW

D. E. Ekeroth

SIGNATURE / DATE

Electronically Approved***

☐ © 2016 WESTINGHOUSE ELECTRIC COMPANY LLC, ALL RIGHTS RESERVED – WESTINGHOUSE PROPRIETARY CLASS 2

This document is the property of and contains Proprietary Information owned by Westinghouse Electric Company LLC and/or its subcontractors and suppliers. It is transmitted to you in confidence and trust, and you agree to treat this document in strict accordance with the terms and conditions of the agreement under which it was provided to you. Handle this document in accordance with applicable procedures for filing and transmittal. Any unauthorized use of this document is prohibited.

*NOTE: This selection is only to be used for Westinghouse generated documents.

☐ © 2016 WESTINGHOUSE ELECTRIC COMPANY LLC, ALL RIGHTS RESERVED and/or

© 2016 WESTINGHOUSE AP1000 BUSINESS PARTNER, ALL RIGHTS RESERVED

WESTINGHOUSE PROPRIETARY CLASS 2 and/or WESTINGHOUSE BUSINESS PARTNER PROPRIETARY (SEE ATTACHED DOCUMENT)

This document is the property of and contains Proprietary Information owned by Westinghouse Electric Company LLC and/or is the property of and contains Proprietary Information owned by the Westinghouse Business Partner identified in the document attached hereto and/or their affiliates, subcontractors and suppliers. It is transmitted to you in confidence and trust, and you agree to treat this document in strict accordance with the terms and conditions of the agreement under which it was provided to you. Any unauthorized use of this document is prohibited.

☐ SUPPLIER OR THIRD PARTY PROVIDED INFORMATION – File And Protect Using Policies For Westinghouse Proprietary Class 2 Information

This document is the property of and contains Proprietary Information owned by a Supplier/Third Party to Westinghouse Electric Company, LLC. Treat this document in strict compliance with applicable procedures and the terms and conditions under which it was provided. Any unauthorized use of this document is prohibited.

ORIGINATOR(S) W2-6.1-100.pdf Debra K. Ohkawa	SIGNATURE / DATE (If processing electronic approval select option) Electronically Approved***	
Michael J. Patterson	Electronically Approved***	
Richard P. Ofstun	Electronically Approved***	
Megan E. Durse	Electronically Approved***	
LICENSING REVIEWER(S) Korey L. Hosack	SIGNATURE / DATE Electronically Approved***	
REVIEWER(S) W2-6.1-100.pdf N/A	SIGNATURE / DATE N/A	
VERIFIER(S) W2-6.1-100.pdf Richard F. Wright, James H. Scobel	SIGNATURE / DATE Electronically Approved***	Verification Method: Independent Review
APPLICABILITY REVIEWER N/A	SIGNATURE / DATE N/A	
RESPONSIBLE MANAGER* W2-6.1-100.pdf Kent W. Bonadio	SIGNATURE / DATE Electronically Approved***	

*Approval of the responsible manager signifies that the document and all required reviews are complete, the appropriate proprietary class has been assigned, electronic file has been provided to the EDMS, and the document is released for use.

This document may contain technical data subject to the export control laws of the United States. In the event that this document does contain such information, the Recipient's acceptance of this document constitutes agreement that this information in document form (or any other medium), including any attachments and exhibits hereto, shall not be exported, released or disclosed to foreign persons whether in the United States or abroad by recipient except in compliance with all U.S. export control regulations. Recipient shall include this notice with any reproduced or excerpted portion of this document or any document derived from, based on, incorporating, using or relying on the information contained in this document.

*** Electronically approved records are authenticated in the electronic document management system. This record was final approved on Sep-22-2016. (This statement was added by the EDMS system to the quality record upon its validation.)

Westinghouse Non-Proprietary Class 3

WCAP-15862-NP
Revision 5

September 2016

WGOTHIC Application to AP600 and AP1000



WCAP-15862-NP
(Class 2 WCAP-15846-P, Revision 5)

APP-SSAR-GSC-588
(Class 2 APP-SSAR-GSC-587, Revision 5)

WGOTHIC Application to AP600 and AP1000

Megan E. Durse*
Richard P. Ofstun*
Debra K. Ohkawa*
Michael J. Patterson*
September 2016

Verifiers: Richard F. Wright/James H. Scobel*

Approved: Kent W. Bonadio*, Manager

This document may contain technical data subject to the export control laws of the United States. In the event that this document does contain such information, the Recipient's acceptance of this document constitutes agreement that this information in document form (or any other medium), including any attachments and exhibits hereto, shall not be exported, released or disclosed to foreign persons whether in the United States or abroad by recipient except in compliance with all U.S. export control regulations. Recipient shall include this notice with any reproduced or excerpted portion of this document or any document derived from, based on, incorporating, using or relying on the information contained in this document.

*Electronically approved records are authenticated in the electronic document management system.

Westinghouse Electric Company LLC
1000 Westinghouse Drive
Cranberry Township, PA 16066, USA

© 2016 Westinghouse Electric Company LLC
All Rights Reserved
Page 3 of 768

Note: WCAP-15862 (APP-SSAR-GSC-588) is the non-proprietary class 3 version of WCAP-15846 (APP-SSAR-GSC-587). Non-proprietary versions were not issued for the errata pages generated in May 2004. Therefore, there is no Revision 2 nor Revision 3 of this non-proprietary document.

RECORD OF REVISIONS

WCAP-15846 Revision	APP-SSAR-GSC-587 Revision	Date	Revision Description
0	0	April 2002	Original Issue
1	1	March 2004	Added Section 13.8 on minimum containment back pressure assumptions for Small Break LOCA.
1 Volume 3 Errata Pages	2	May 2004	Updated PCS flowrates in Table 13-125 and Figure 13-93 for consistency with the DCD.
1 Volume 3 Errata Pages	3	May 2004	Further updates to PCS flowrates in Table 13-125 and Figure 13-93 for consistency with the DCD.
4	4	May 2015	<p>Updated the heat sinks and nodalization for the AP1000 EM (defining the methodology without the input values), updated code version with PCS evaporation-limited flow option, and changes that had previously been reported in APP-GW-GLR-096.</p> <ul style="list-style-type: none">• Section 1: Rewritten to better explain the purpose of this document and the history of its development.• Section 3: Updated <u>W</u>GOTHIC code description beyond version 4.1.• Section 4: Removal of Appendix 4.A and 4.B that provided input values for the AP600 EM; the main body of Section 4 is retained as it defines the <u>W</u>GOTHIC model used in most of the sensitivity studies.• Section 5.1: Conclusion on the direction of conservatism and source for initial condition assumptions.• Section 6: Added discussion on the enhanced shield building design and its effect on the meteorological effects of the PCS.

RECORD OF REVISIONS (cont.)

WCAP-15846 Revision	APP-SSAR-GSC-587 Revision	Date	Revision Description
4 (cont.)	4 (cont.)		<ul style="list-style-type: none"> • Section 7: Updates to the PCS flow modeling <ul style="list-style-type: none"> – Executive summary deleted – Section 7.2.5: Changed the time to establish steady state water coverage for the AP1000 design. – Section 7.3: Moved text that is specific to the post-processing PCS evaporation-limited flow calculation to Section 7.5. – Section 7.4.3.2: Information added that was contained in old Section 7.5.2.3. – Section 7.4.5: New section that explains a heat and mass transfer factor that is an alternate approach to calculate the effects of 2-D conduction, which may be applied with the evaporation-limited PCS flow option. – Section 7.5: Introduction re-written for containment evaluation model treatment of water coverage. – Section 7.5.2: Reorganized, consolidating previous information in Section 7.5.2.1 and creating new Section 7.5.2.2 with calculation integrated into <u>WGOTHIC</u> code. • Section 9: Clarification that all locations inside containment are considered for the EQ curves • Chapter 10: Clarification of the oxidation factor put on the inorganic zinc thermal conductivity

RECORD OF REVISIONS (cont.)

WCAP-15846 Revision	APP-SSAR-GSC-587 Revision	Date	Revision Description
4 (cont.)	4 (cont.)		<ul style="list-style-type: none"> • Section 13: Simplified AP1000 plant geometry information, eliminating input values. <ul style="list-style-type: none"> – Section 13.1: Introduction is rewritten; comparison to AP600 moved to Section 13.2. – Section 13.2: Control volume information that was in Sections 13.2.*.1 and Table 13-133; total reformatting of information while removing input values. Many repetitive figures deleted and new overview figures added. – Section 13.3: Flow path information that was in Sections 13.2.*.2 and Table 13-134; total reformatting of information while removing input values. – Section 13.4: Thermal conductor information that was in Sections 13.2.*.3, 13.2.*.4 and 13.3; total reformatting of information while removing input values. – Section 13.5: Clime information that was in Section 13.4 and Table 13-132; total reformatting of information while removing input values. – Section 13.6: Initial conditions and boundary conditions that was in Section 13.5; edit of information to remove input values. Deleted conclusions section, which had summaries that were not relevant to initial conditions and boundary conditions. – Previous Section 13.6: Deleted. Summary tables and figures were moved to other sections as appropriate. – Section 13.7: Sample results edited to be overview of accident transients. – Section 13.8: Minimum back pressure input changes edited. – Section 13.9: Conclusions rewritten.

RECORD OF REVISIONS (cont.)

WCAP-15846 Revision	APP-SSAR-GSC-587 Revision	Date	Revision Description
4 (cont.)	4 (cont.)		<ul style="list-style-type: none"> Section 14: Clarifications on the details of the LOCA mass and energy release calculation Miscellaneous editorial changes are not indicated with a change bar. These are items changed for consistency with current practices, such as WGOthic to <u>W</u>GOthic, AP1000 to AP1000, Ref. to Reference, or to fix typographical errors. GAP-147 licensing review requirement satisfied by the individual GAP-147 reviews attached to each of the design changes noted on the coversheet of this document.
5	5	September 2016	<ul style="list-style-type: none"> Section 7.2.6 and Section 7.5.2.3 added to address PCS water stripping from baffle supports Section 7.6.5 clarifications made relative to the SLB event Change bars are retained from Revision 4

TABLE OF CONTENTS

RECORD OF REVISIONS	ii
LIST OF TABLES	xiv
LIST OF FIGURES	xx
1 INTRODUCTION	1-1
1.1 OBJECTIVE	1-1
1.2 REPORT OVERVIEW	1-1
1.3 AP600 CONTAINMENT EM DOCUMENTATION	1-3
1.3.1 Accident Specification and Phenomena Identification and Ranking Table Report	1-5
1.3.2 Testing	1-6
1.3.3 Scaling Report	1-8
1.3.4 Heat and Mass Transfer Correlations Report	1-9
1.3.5 <u>W</u> GOTHIC Code Description and Validation.....	1-10
1.3.6 Evaluation Model Development.....	1-10
1.4 AP1000 CONTAINMENT EM DOCUMENTATION UPDATES.....	1-11
1.5 INTERFACE WITH PLANT LICENSING CALCULATIONS	1-13
1.6 CONCLUSIONS	1-13
1.7 REFERENCES	1-13
2 TEST AND ANALYSIS PROCESS OVERVIEW AND HIGH AND MEDIUM RANK CONTAINMENT PHENOMENA.....	2-1
2.1 INTRODUCTION	2-1
2.2 ELEMENT 1 – PCS REQUIREMENTS AND CODE CAPABILITIES	2-3
2.3 ELEMENT 2 – ASSESS CODE VERSUS TESTS AND IMPORTANT PROCESSES	2-3
2.4 ELEMENT 3 – ASSESS UNCERTAINTIES AND DEVELOP BOUNDING MODELS.....	2-6
2.5 ELEMENT 4 – PERFORM DBA CALCULATIONS AND COMPARE TO SUCCESS CRITERIA.....	2-8
2.6 CONCLUSIONS	2-8
2.7 REFERENCES	2-8
3 OVERVIEW OF <u>W</u> GOTHIC.....	3-1
3.1 INTRODUCTION	3-1
3.2 OVERVIEW OF THE CODE DEVELOPMENT AND VALIDATION	3-1
3.3 THE <u>W</u> GOTHIC CLIME MODEL	3-13
3.4 GENERAL CLIME EQUATIONS	3-16
3.4.1 Standard PCS Flow and Coverage Model Option	3-16
3.4.2 Automated Evaporation-Limited PCS Flow and Coverage Option.....	3-21
3.5 INTEGRATION OF THE WESTINGHOUSE CLIME MODEL INTO GOTHIC	3-25
3.6 REFERENCES	3-28

TABLE OF CONTENTS (con't)

4	DESCRIPTION OF AP600 PLANT GEOMETRY IN <u>WGOTHIC</u> EVALUATION MODEL	4-1
4.1	INTRODUCTION	4-1
4.2	AP600 PLANT GEOMETRY IN <u>WGOTHIC</u> MODEL.....	4-2
4.2.1	Reactor Cavity Description	4-4
4.2.2	Reactor Coolant Drain Tank (RCDT) Cavity Description	4-10
4.2.3	Southeast Accumulator Cavity	4-15
4.2.4	Northeast Accumulator Cavity	4-20
4.2.5	East Steam Generator Cavity (Upper and Lower).....	4-24
4.2.6	West Steam Generator Cavity (Upper and Lower).....	4-31
4.2.7	North CMT Cavity	4-37
4.2.8	South CMT Cavity	4-49
4.2.9	Chemical and Volume Control Cavity	4-56
4.2.10	Refueling Room.....	4-60
4.2.11	Internal Refueling Water Storage Tank (IRWST).....	4-67
4.2.12	Cylindrical Central Rooms	4-73
4.2.13	Above-Deck East Steam Generator Compartment	4-78
4.2.14	Above-Deck West Steam Generator Compartment.....	4-84
4.2.15	South Inner-Half Annulus Compartment	4-91
4.2.16	North Inner-Half Annulus Compartment.....	4-97
4.2.17	North Mid-Quarter Annulus Compartment	4-105
4.2.18	West Mid-Quarter Annulus Compartment	4-112
4.2.19	South Mid-Quarter Annulus Compartment	4-120
4.2.20	East Mid-Quarter Annulus Compartment.....	4-126
4.2.21	North Outer Quarter Annulus Compartment	4-133
4.2.22	West Outer Quarter Annulus Compartment	4-138
4.2.23	South Outer Quarter Annulus Compartment	4-144
4.2.24	East Outer Quarter Annulus Compartment.....	4-150
4.2.25	East Quarter Inner Dome Compartment	4-156
4.2.26	North Quarter Inner Dome Compartment.....	4-160
4.2.27	West Quarter Inner Dome Compartment.....	4-164
4.2.28	South Quarter Inner Dome Compartment.....	4-168
4.2.29	East Quarter Outer Dome Compartment	4-173
4.2.30	North Quarter Outer Dome Compartment.....	4-177
4.2.31	West Quarter Outer Dome Compartment.....	4-181
4.2.32	South Quarter Outer Dome Compartment.....	4-185
4.2.33	Outside Containment Upflow Annulus Volumes	4-189
4.2.34	Outside Containment Downflow Annulus Volumes	4-193
4.2.35	PCS Chimney Volume	4-197
4.3	CONDUCTOR TYPE DESCRIPTIONS.....	4-199
4.4	CLIME NODING DESCRIPTION	4-213
4.4.1	Wet Stacks	4-214
4.4.2	Dry Stacks	4-234
4.4.3	Passive Cooling System Flow	4-249
4.4.4	Condensate Film Stripping	4-251

TABLE OF CONTENTS (con't)

4.5	INITIAL AND BOUNDARY CONDITIONS	4-251
4.5.1	Initial Conditions	4-251
4.5.2	Boundary Conditions	4-265
4.5.3	Conclusions	4-268
4.6	AP600 CONTAINMENT EVALUATION MODEL SUMMARY	4-270
4.7	SUMMARY OF EVALUATION MODEL TRANSIENT CALCULATIONS	4-290
4.7.1	LOCA Evaluation Model Base Case Results Summary	4-290
4.7.2	MSLB Evaluation Model Base Case Results Summary	4-294
4.8	REFERENCES	4-322
5	INITIAL AND BOUNDARY CONDITIONS	5-1
5.1	INTRODUCTION	5-1
5.2	INITIAL CONDITION SENSITIVITY CASES	5-1
5.3	INITIAL CONTAINMENT HUMIDITY	5-4
5.4	INITIAL CONTAINMENT PRESSURE	5-4
5.5	INITIAL CONTAINMENT TEMPERATURE	5-7
5.6	AMBIENT HUMIDITY	5-9
5.7	AMBIENT TEMPERATURE	5-11
5.8	SENSITIVITY TO DROP MODELING ASSUMPTIONS	5-14
5.9	CONCLUSIONS	5-14
6	METEOROLOGICAL EFFECTS ON PCS PERFORMANCE	6-1
6.1	INTRODUCTION	6-1
6.2	WIND-INDUCED TURBULENCE	6-1
6.2.1	Summary of Wind Tunnel Tests	6-1
6.2.2	Tracking of a Wind-Driven Particle	6-3
6.2.3	Containment Time Constants	6-3
6.2.4	Wind-Induced Oscillation Effect on Heat Transfer Coefficient	6-4
6.2.5	WGOTHIC Evaluation Model Basis	6-5
6.3	RECIRCULATION OF CHIMNEY EFFLUENT	6-6
6.3.1	Summary of Literature Review	6-6
6.3.2	Evaluation of Effect of Recirculation	6-7
6.3.3	WGOTHIC Evaluation Model Basis	6-8
6.4	APPLICABILITY TO THE AP1000 SHIELD BUILDING DESIGN	6-8
6.5	CONCLUSIONS	6-9
6.6	REFERENCES	6-9
7	BASIS AND METHOD FOR CALCULATING THE PCS WATER EVAPORATION RATE FOR THE AP600 AND AP1000 CONTAINMENT DBA EVALUATION MODELS	7-1
7.1	INTRODUCTION	7-1
7.2	WATER APPLICATION AND DISTRIBUTION	7-2
7.2.1	Containment Shell Surface Coating	7-4
7.2.2	PCS Water Distribution Weir Description and Operation	7-4
7.2.3	PCS Water Distribution Testing Results	7-6
7.2.4	Delivered PCS Water Flow Rate versus Time	7-8
7.2.5	Time to Establish Steady State Water Coverage	7-8
7.2.6	PCS Water Stripping from Baffle Supports	7-13

TABLE OF CONTENTS (con't)

7.3	WATER COVERAGE BASIS	7-14
7.3.1	Water Distribution Film Flow Rate, Γ_{dist}	7-15
7.3.2	Minimum Film Flow Rate, Γ_{min}	7-16
7.4	EFFECT OF TWO-DIMENSIONAL (2-D) HEAT CONDUCTION THROUGH THE CONTAINMENT SHELL	7-18
7.4.1	Geometry of the Wet and Dry Vertical Stripes on the Containment Outside Steel Surface	7-18
7.4.2	Heat Transfer Boundary Conditions for the 2-D Conduction Model	7-19
7.4.3	2-D Conduction (ANSYS) Model Description	7-20
7.4.4	Enhanced Evaporation due to 2-D Conduction	7-21
7.4.5	Enhanced Overall Heat and Mass Transfer Due to 2-D Conduction	7-28
7.4.6	Insights from the PCS Large-Scale Testing	7-30
7.5	THE CONTAINMENT EVALUATION MODEL TREATMENT OF WATER COVERAGE	7-32
7.5.1	PCS Film Coverage Model	7-32
7.5.2	Interaction of the PCS Film Coverage Model with <u>W</u> GOOTHIC	7-35
7.6	SUMMARY OF SUPPORTING TESTS AND SELECTED ANALYSIS	7-39
7.6.1	Westinghouse Wet Flat Plate Test	7-39
7.6.2	Small-Scale Tests	7-40
7.6.3	Large-Scale Tests	7-40
7.6.4	Estimated Range of Film Coverage Parameters	7-49
7.6.5	Containment Shell Heatup Analysis	7-51
7.7	AP600 CONTAINMENT DBA EVALUATION MODEL FILM COVERAGE SENSITIVITIES	7-54
7.7.1	Sensitivity of the Evaluation Model to the Input PCS Film Flow Rate	7-54
7.7.2	Sensitivity to the Water Coverage Area	7-54
7.7.3	Conservatism in the Assumed Time Delay for Application of the PCS Film	7-60
7.8	CONCLUSIONS AND SUMMARY	7-63
7.9	NOMENCLATURE	7-65
7.10	REFERENCES	7-66
APPENDIX 7.A PHYSICS OF LIQUID FILMS ON THE AP600 AND AP1000 CONTAINMENT SHELLS		7.A-1
7.A.1	INTRODUCTION	7.A-1
7.A.2	SUMMARY OF GENERAL LIQUID FILM BEHAVIOR	7.A-2
7.A.2.1	Literature Summary	7.A-2
7.A.2.2	Thermocapillary Effect	7.A-4
7.A.2.3	Available Theoretical Analytical Models	7.A-5
7.A.3	CONTACT ANGLE AND SURFACE WETTABILITY	7.A-6
7.A.3.1	Advancing and Receding Contact Angles	7.A-6
7.A.3.2	Static Contact Angle Measurements of Coated Surface	7.A-7
7.A.3.3	Relative Magnitude of Surface Tension Effects	7.A-10
7.A.3.4	Factors Affecting Surface Wettability	7.A-10
7.A.3.5	Summary of Wetting Angle Assessment	7.A-11

TABLE OF CONTENTS (con't)

7.A.4	DESCRIPTION OF LST OBSERVATIONS	7.A-11
7.A.4.1	High Flow LST	7.A-12
7.A.4.2	Low Flow LST	7.A-13
7.A.5	CONCLUSIONS	7.A-16
7.A.6	REFERENCES	7.A-16
8	CONTAINMENT PRESSURE SENSITIVITY DURING BLOWDOWN	8-1
8.1	INTRODUCTION	8-1
8.2	METHOD	8-1
8.3	ANALYSIS	8-2
8.4	CONCLUSIONS	8-2
9	CIRCULATION AND STRATIFICATION WITHIN CONTAINMENT	9-1
9.1	INTRODUCTION	9-3
9.1.1	Definitions	9-16
9.1.2	Lumped Parameter Biases and Capabilities	9-17
9.2	LARGE-SCALE TEST RESULTS	9-20
9.2.1	LOCA Configuration	9-20
9.2.2	MSLB Configuration	9-21
9.2.3	Method to Address Distortions in LST Stratification Data	9-22
9.2.4	Application of Modeling Methods Developed for NUPEC M-4-3 Lumped Parameter Model	9-24
9.3	CIRCULATION AND STRATIFICATION ASSESSMENT FOR THE LOSS-OF-COOLANT ACCIDENT	9-28
9.3.1	LOCA Break Scenarios	9-29
9.3.2	WGOTHIC Containment Evaluation Model for LOCA	9-34
9.4	MAIN STEAMLINE BREAK (MSLB)	9-42
9.4.1	Break Locations	9-43
9.4.2	WGOTHIC Containment Evaluation Model for MSLB	9-44
9.4.3	MSLB Sensitivity Results	9-45
9.5	CONCLUSIONS	9-45
9.6	REFERENCES	9-47
	APPENDIX 9.A THERMAL AND CIRCULATION EFFECTS OF DROPS DURING A LOCA	9.A-1
	APPENDIX 9.B EFFECTS OF STRATIFICATION ON HEAT SINK UTILIZATION	9.B-1
9.B.1	INTRODUCTION	9.B-1
9.B.2	HEAT SINK ANALYSIS	9.B-1
9.B.3	CONDENSATION BOUNDARY CONDITIONS	9.B-1
9.B.4	HEAT CONDUCTION MODELS	9.B-4
9.B.5	RESULTS	9.B-6
9.B.6	CONCLUSIONS	9.B-10

TABLE OF CONTENTS (con't)

APPENDIX 9.C ADDITIONAL INFORMATION ON CONTAINMENT CIRCULATION AND STRATIFICATION.....	9.C-1
9.C.1 DEVELOPMENT OF EXPECTED FLOW PATTERNS FOR AP600 AND AP1000 BASED ON SEPARATE FLOW TESTS IN ENCLOSURES	9.C-1
9.C.1.1 Stratification Phenomena.....	9.C-1
9.C.1.2 Circulation Phenomena.....	9.C-23
9.C.1.3 Important Dimensionless Groups	9.C-34
9.C.1.4 Expected Flow Patterns for AP600 and AP1000.....	9.C-37
9.C.2 OVERVIEW OF THE INTERNATIONAL CONTAINMENT EXPERIMENTAL DATA BASE	9.C-51
9.C.2.1 Description of the Available Battelle Model Containment (BMC) Database	9.C-55
9.C.2.2 Description of the Available NUPEC Data Base	9.C-99
9.C.2.3 Description of the Available Carolinas Virginia Tube Reactor Containment (CVTR) Database.....	9.C-108
9.C.2.4 Description of the Available HDR Database.....	9.C-124
9.C.2.5 Conclusion.....	9.C-206
9.C.3 APPLICATION OF LUMPED-PARAMETER CODES FOR MODELING LARGE CONTAINMENT FACILITIES.....	9.C-207
9.C.3.1 Validation of the Lumped Parameter Containment Analysis Computer Codes Based on BMC Experimental Results	9.C-207
9.C.3.2 Validation of the Lumped Parameter Containment Analysis Computer Codes Based on Nupec Experimental Results.....	9.C-210
9.C.3.3 Validation of the Lumped-Parameter Containment Analysis Computer Codes Based on HDR Experimental Results.....	9.C-220
9.C.3.4 Conclusions	9.C-230
9.C.3.5 References	9.C-232
APPENDIX 9.D BASIS FOR ASSUMING HOMOGENEOUS BULK CONDITIONS FOR AP600 AND AP1000 CONTAINMENT PRESSURE DESIGN BASIS ANALYSIS.....	9.D-1
9.D.1 INTRODUCTION	9.D-1
9.D.2 APPROACH	9.D-1
9.D.3 REGION 1 HORIZONTAL GRADIENTS ADDRESSED THROUGH TURBULENT BUOYANT PLUME ANALYTICAL MODEL	9.D-2
9.D.4 REGION 2 HORIZONTAL GRADIENTS ADDRESSED THROUGH LST TEMPERATURE DATA AND SEPARATE EFFECTS ENCLOSURE TEST DATA	9.D-2
9.D.5 REGION 3 HORIZONTAL GRADIENTS ADDRESSED THROUGH TURBULENT BOUNDARY LAYER ANALYTICAL MODEL.....	9.D-3
9.D.6 COMPOSITE REGION DISCUSSION	9.D-4
9.D.7 TURBULENT BUOYANT PLUME ANALYTICAL MODEL – SPECIES CONCENTRATION.....	9.D-6
9.D.7.1 Time Period of Application	9.D-6
9.D.7.2 Nomenclature (See Figure 9.D-4)	9.D-6
9.D.7.3 Major Assumptions	9.D-6

TABLE OF CONTENTS (con't)

9.D.7.4	Solution.....	9.D-7
9.D.7.5	Application of Turbulent Buoyant Plume Results to LST/AP600	9.D-7
9.D.7.6	Turbulent Buoyant Plume Conclusions	9.D-8
9.D.8	ENTRAINMENT INTO THE BREAK PLUME AND WALL LAYER, AND THE EFFECT ON MASS TRANSFER RATE	9.D-8
9.D.8.1	Time Period of Application	9.D-9
9.D.8.2	Key Assumptions.....	9.D-9
9.D.8.3	Entrainment into a Buoyant Plume.....	9.D-9
9.D.8.4	Entrainment into a Negatively Buoyant Wall Layer	9.D-11
9.D.8.5	Effect of Entrainment on Mass Transfer Rate	9.D-13
9.D.8.6	Boundary Layer Thickness and Volume	9.D-14
9.D.8.7	Sublayer Penetration Time	9.D-15
9.D.9	TURBULENT BOUNDARY LAYER ANALYTICAL MODEL.....	9.D-16
9.D.9.1	Time Period of Application	9.D-16
9.D.9.2	Key Assumptions.....	9.D-16
9.D.9.3	Boundary Layer Profiles.....	9.D-18
9.D.9.4	Governing Equations	9.D-19
9.D.9.5	Boundary Layer Momentum Equation Development.....	9.D-19
9.D.9.6	Boundary Layer Thickness Results	9.D-22
9.D.9.7	Concentration Profile Results	9.D-24
9.D.9.8	Boundary Layer Concentration Profile Results – LST.....	9.D-25
9.D.9.9	Boundary Layer Analytical Model Results – Boundary Layer Thickness	9.D-26
9.D.10	INFLUENCE OF HORIZONTAL GRADIENTS ON MASS TRANSFER COEFFICIENTS.....	9.D-26
9.D.11	CONCLUSION.....	9.D-27
9.D.12	REFERENCES	9.D-27
10	NOMINAL INPUTS AND CORRELATIONS SENSITIVITIES	10-1
10.1	INTRODUCTION	10-1
10.2	SENSITIVITY STUDY RESULTS	10-1
10.2.1	Sensitivity Study Cases for LOCA.....	10-4
10.2.2	Sensitivity Study Case for MSLB	10-8
10.3	CONCLUSIONS	10-9
10.4	REFERENCES	10-9
11	TIMESTEP SENSITIVITY	11-1
11.1	INTRODUCTION	11-1
11.2	METHODOLOGY	11-1
11.3	RESULTS	11-1
11.4	SUMMARY	11-3
11.5	REFERENCES	11-6

TABLE OF CONTENTS (con't)

12	SENSITIVITY TO CLIME NODING	12-1
12.1	INTRODUCTION	12-1
12.1.1	Background.....	12-1
12.1.2	Problem Statement.....	12-3
12.1.3	Approach	12-3
12.1.4	Selected Parameters.....	12-3
12.1.5	Success Criteria	12-4
12.2	MODEL DESCRIPTIONS	12-4
12.2.1	Simple Annulus Clime Model	12-4
12.2.2	AP600 Containment Model	12-6
12.3	RESULTS	12-8
12.3.1	Simple Annulus Clime Model	12-8
12.3.2	AP600 Containment Model	12-9
12.4	SUMMARY	12-11
12.4.1	Simple Annulus Clime Model Noding Study	12-11
12.4.2	AP600 Containment Model Clime Noding Study	12-11
12.5	REFERENCES	12-11
13	DESCRIPTION OF AP1000 PLANT GEOMETRY AND SUMMARY OF WGOthic EVALUATION MODEL	13-1
13.1	INTRODUCTION	13-1
13.2	AP1000 PLANT <u>W</u> GOthic EVALUATION MODEL CONTROL VOLUMES	13-2
13.3	AP1000 PLANT <u>W</u> GOthic EVALUATION MODEL FLOW PATHS	13-15
13.4	AP1000 PLANT <u>W</u> GOthic EVALUATION MODEL THERMAL CONDUCTORS	13-32
13.4.1	Thermal Conductor Type Descriptions	13-47
13.4.2	Thermal Conductor Heat Transfer Coefficients	13-49
13.5	AP1000 PLANT <u>W</u> GOthic EVALUATION MODEL CLIMES	13-51
13.5.1	Clime Conductors	13-54
13.5.2	Passive Cooling System Flow	13-58
13.5.3	Condensate Film Stripping.....	13-59
13.6	AP1000 PLANT <u>W</u> GOthic EVALUATION MODEL INITIAL AND BOUNDARY CONDITIONS.....	13-61
13.6.1	Initial Conditions.....	13-61
13.6.2	Boundary Conditions.....	13-62
13.7	SUMMARY OF EVALUATION MODEL TRANSIENT CALCULATIONS	13-65
13.7.1	LOCA Transient Response Overview	13-65
13.7.2	MSLB Transient Response Overview	13-67
13.8	<u>W</u> GOthic CONTAINMENT MINIMUM PRESSURE CALCULATION FOR SMALL-BREAK LOCA AND LONG-TERM CORE COOLING	13-67
13.9	CONCLUSIONS	13-70
13.10	REFERENCES	13-72

TABLE OF CONTENTS (con't)

14	LOCA MASS AND ENERGY RELEASE CALCULATION METHODOLOGY	14-1
14.1	INTRODUCTION	14-1
14.2	BLOWDOWN MASS AND ENERGY RELEASE CALCULATION.....	14-2
14.3	POST-BLOWDOWN MASS AND ENERGY RELEASE CALCULATION	14-3
14.4	COMPARISON OF SATAN/SPREADSHEET RELEASES WITH WCOBRA-TRAC CALCULATED RELEASES	14-11
14.5	SUMMARY AND CONCLUSIONS	14-15
14.6	REFERENCES	14-16

LIST OF TABLES

Table 2-1	Phenomena Identification and Ranking Table – Summary of High and Medium Ranked Phenomena	2-4
Table 3-1	GOTHIC Validation Tests	3-5
Table 3-2	GOTHIC Phenomenological Models Validated by Test	3-6
Table 3-3	Operating Range Comparison for AP600 and AP1000 Heat and Mass Transfer Parameters	3-12
Table 4-1	Central Cylindrical Room Parameters	4-73
Table 4-2	Flow Paths for the Cylindrical Central Volumes.....	4-74
Table 4-3	Above-Deck East Steam Generator Compartment Parameters.....	4-78
Table 4-4	Flow Paths for the Above-Deck East Steam Generator Volumes	4-78
Table 4-5	Above-Deck West Steam Generator Compartment Parameters.....	4-84
Table 4-6	Flow Paths for the Above-Deck West Steam Generator Volumes	4-85
Table 4-7	South Inner-Half Annulus Compartment Parameters	4-91
Table 4-8	Flow Paths for the South Inner-Half Annulus Volumes.....	4-91
Table 4-9	North Inner-Half Annulus Compartment Parameters	4-98
Table 4-10	Flow Paths for the North Inner-Half Annulus Volumes.....	4-98
Table 4-11	North Mid-Quarter Annulus Compartment Parameters	4-105
Table 4-12	Flow Paths for the North Mid-Quarter Annulus Volumes	4-106
Table 4-13	West Mid-Quarter Annulus Compartment Parameters	4-112
Table 4-14	Flow Paths for the West Mid-Quarter Annulus Volumes.....	4-113
Table 4-15	South Mid-Quarter Annulus Compartment Parameters	4-120
Table 4-16	Flow Paths for the South Mid-Quarter Annulus Volumes	4-125
Table 4-17	East Mid-Quarter Annulus Compartment Parameters	4-126
Table 4-18	Flow Paths for the East Mid-Quarter Annulus Volumes.....	4-127
Table 4-19	North Outer Quarter Annulus Compartment Parameters.....	4-133
Table 4-20	Flow Paths for the North Outer Quarter Annulus Volumes	4-133
Table 4-21	West Outer Quarter Annulus Compartment Parameters	4-139
Table 4-22	Flow Paths for the West Outer Quarter Annulus Volumes.....	4-139
Table 4-23	South Outer Quarter Annulus Compartments Parameters	4-144
Table 4-24	Flow Paths for the South Outer Quarter Annulus Volumes	4-145

LIST OF TABLES (cont.)

Table 4-25	East Outer Quarter Annulus Compartment Parameters	4-150
Table 4-26	Flow Paths for the East Outer Quarter Annulus Volumes.....	4-151
Table 4-27	East Quarter Inner Dome Compartment Parameters.....	4-156
Table 4-28	Flow Paths for the East Quarter Inner Dome Volumes	4-157
Table 4-29	North Quarter Inner Dome Compartment Parameters	4-160
Table 4-30	Flow Paths for the North Quarter Inner Dome Volumes.....	4-161
Table 4-31	West Quarter Inner Dome Compartment Parameters.....	4-164
Table 4-32	Flow Paths for the West Quarter Inner Dome Volumes	4-168
Table 4-33	South Quarter Inner Dome Compartment Parameters	4-170
Table 4-34	Flow Paths for the South Quarter Inner Dome Volumes.....	4-171
Table 4-35	East Quarter Outer Dome Compartment Parameters	4-173
Table 4-36	Flow Paths for the East Quarter Outer Dome Volumes	4-174
Table 4-37	North Quarter Outer Dome Compartment Parameters	4-177
Table 4-38	Flow Paths for the North Quarter Outer Dome Volumes	4-178
Table 4-39	West Quarter Outer Dome Compartment Parameters	4-181
Table 4-40	Flow Paths for the West Quarter Outer Dome Volumes	4-182
Table 4-41	South Quarter Outer Dome Compartment Parameters	4-185
Table 4-42	Flow Paths for the South Quarter Outer Dome Volumes	4-186
Table 4-43	Outside Containment Upflow Annulus Volume Parameters	4-189
Table 4-44	Flow Paths for the Outside Containment Upflow Annulus.....	4-190
Table 4-45	Outside Containment Downflow Annulus Volume Parameters	4-194
Table 4-46	Flow Paths for the Outside Containment Downflow Annulus.....	4-194
Table 4-47	PCS Chimney Volume Parameters.....	4-197
Table 4-48	Flow Paths for the PCS Chimney	4-197
Table 4-49	Conductor Material Properties.....	4-200
Table 4-50	Conductor 1 – 0.1" Thick Carbon Steel	4-200
Table 4-51	Conductor 2 – 0.03" Thick Carbon Steel	4-201
Table 4-52	Conductor 3 – 0.06" Thick Carbon Steel	4-201
Table 4-53	Conductor 4 – 0.105" Thick Carbon Steel	4-201

LIST OF TABLES (cont.)

Table 4-54	Conductor 5 – 0.1007" Thick Carbon Steel.....	4-201
Table 4-55	Conductor 6 – 0.1044" Thick Carbon Steel.....	4-201
Table 4-56	Conductor 7 – 0.158" Thick Carbon Steel.....	4-202
Table 4-57	Conductor 8 – 0.132" Thick Carbon Steel.....	4-202
Table 4-58	Conductor 9 – 0.210" Thick Carbon Steel.....	4-202
Table 4-59	Conductor 10 – 0.2448" Thick Carbon Steel.....	4-202
Table 4-60	Conductor 11 – 0.252" Thick Stainless Steel.....	4-202
Table 4-61	Conductor 12 – 0.252" Thick Carbon Steel.....	4-203
Table 4-62	Conductor 13 – 0.284" Thick Carbon Steel.....	4-203
Table 4-63	Conductor 14 – 0.404" Thick Carbon Steel.....	4-203
Table 4-64	Conductor 15 – 0.504" Thick Stainless Steel.....	4-203
Table 4-65	Conductor 16 – 0.854" Thick Carbon Steel.....	4-203
Table 4-66	Conductor 17 – 0.996" Thick Stainless Steel.....	4-204
Table 4-67	Conductor 18 – 0.81" Thick Carbon Steel.....	4-204
Table 4-68	Conductor 19 – 1.57" Thick Carbon Steel.....	4-204
Table 4-69	Conductor 20 – 1.63" Thick Carbon Steel.....	4-204
Table 4-70	Conductor 21 – 1.754" Thick Carbon Steel.....	4-204
Table 4-71	Conductor 22 – 1.998" Thick Carbon Steel.....	4-205
Table 4-72	Conductor 23 – 3.014" Thick Carbon Steel.....	4-205
Table 4-73	Conductor 24 – 4.399" Thick Stainless Steel.....	4-205
Table 4-74	Conductor 25 – 4.874" Thick Carbon Steel.....	4-205
Table 4-75	Conductor 26 – 3.0" Thick Stainless Steel.....	4-205
Table 4-76	Conductor 27 – 25.04" Thick Concrete	4-206
Table 4-77	Conductor 28 – 25.0" Thick Concrete	4-206
Table 4-78	Conductor 29 – 25.0" Thick Concrete	4-207
Table 4-79	Conductor 30 – 36.0" Thick Concrete	4-207
Table 4-80	Conductor 31 – 25.0" Thick Concrete	4-207
Table 4-81	Conductor 32 – 24.5" Thick Concrete	4-207
Table 4-82	Conductor 33 – 24.5" Thick Concrete	4-208

LIST OF TABLES (cont.)

Table 4-83	Conductor 34 – 24.5" Thick Concrete	4-208
Table 4-84	Conductor 35 – 24.5" Thick Concrete	4-208
Table 4-85	Conductor 36 – 24.0" Thick Concrete	4-208
Table 4-86	Conductor 37 – 49.0" Thick Concrete	4-209
Table 4-87	Conductor 38 – 48.5" Thick Concrete	4-209
Table 4-88	Conductor 39 – 48.5" Thick Concrete	4-209
Table 4-89	Conductor 40 – 48.5" Thick Carbon Steel.....	4-210
Table 4-90	Conductor 41 – 49.0" Thick Concrete	4-210
Table 4-91	Conductor 42 – 48.0" Thick Concrete	4-210
Table 4-92	Conductor 43 – 48.5" Thick Concrete	4-210
Table 4-93	Conductor 44 – 48.5" Thick Concrete	4-211
Table 4-94	Conductor 45 – 48.0" Thick Concrete	4-211
Table 4-95	Conductor 46 – 49.0" Thick Concrete	4-211
Table 4-96	Conductor 47 – 49.0" Thick Concrete	4-211
Table 4-97	Conductor 48 – 49.0" Thick Concrete	4-212
Table 4-98	Conductor 49 – 25.0" Thick Concrete	4-212
Table 4-99	Conductor 50 – 48.5" Thick Concrete	4-212
Table 4-100	Conductor 51 – 2.0" Thick Carbon Steel.....	4-213
Table 4-101	Conductor 52 – Dummy Baffle.....	4-213
Table 4-102	Evaluation Model Function for the AP600 PCS Film Flow	4-249
Table 4-103	Outside Containment Initial Conditions	4-251
Table 4-104	Inside Containment Initial Conditions	4-252
Table 4-105	LOCA Boundary Conditions Represented by Forcing Functions in the AP600 Evaluation Model.....	4-253
Table 4-106	MSLB Boundary Conditions Represented by Forcing Functions in the AP600 Evaluation Model.....	4-253
Table 4-107	Basis for Geometric Inputs	4-268
Table 4-108	Basis for LOCA and MSLB Mass and Energy Inputs	4-269
Table 4-109	Basis for PCS Inputs.....	4-269
Table 4-110	Containment Volumes and Heat Sinks Model Node Listing	4-270

LIST OF TABLES (cont.)

Table 4-111	Master List of Flow Paths in AP600 Evaluation Model	4-272
Table 5-1	Initial Conditions	5-1
Table 5-2	Initial Conditions Sensitivity Analysis Cases	5-2
Table 5-3	Summary of Pressure Results for LOCA Initial Condition Sensitivity Studies.....	5-3
Table 5-4	Summary of Pressure Results for MSLB Initial Condition Sensitivity Studies.....	5-3
Table 7-1	Ranges of the Film Coverage Parameters in the PCS Tests.....	7-3
Table 7-2	Summary of the Phase 3 Water Distribution Test	7-7
Table 7-3	Summary of Time to Reach Steady State Coverage	7-12
Table 7-4	Elevation D Heat Flux Comparison from PCS Large-Scale Tests RC048C and RC050C.....	7-31
Table 7-5	Elevation E Heat Flux Comparison from PCS Large-Scale Test RC048C and RC050C.....	7-32
Table 7-6	Climo Wetted Perimeter and Basis for <u>W</u> GOTHIC Evaluation Model.....	7-35
Table 7-7	Summary of Westinghouse Science and Technology Center (STC) Heated Flat Plate Tests.....	7-42
Table 7-8	Summary of Small-Scale Tests	7-43
Table 7-9	Summary of Large-Scale Tests	7-47
Table 7-10	Estimated Shell Heat Flux and Film Temperature	7-50
Table 7-11	Comparison of the Range of Film Coverage Parameters.....	7-51
Table 7-12	Transient Dry Shell Temperature Increase.....	7-54
Table 7.A-1	Summary of Test Results to Determine Static Contact Angle	7.A-9
Table 9-1	Circulation and Stratification Evaluation Summary	9-4
Table 9-2	AP600 Flow Areas Connecting to North and South CMT Compartments (excluding Dead-Ended Compartment Connections)	9-26
Table 9.A-1	Estimated Drop Fall Times	9.A-1
Table 9.B-1	Concrete Model Nodal Thickness.....	9.B-5
Table 9.B-2	AP600 Assumed Room Heat Sink Distribution.....	9.B-7
Table 9.C-1	Comparison of Various Facilities.....	9.C-52
Table 9.C-2	Overviewed Tests from International Database	9.C-52
Table 9.C-3	Representative Velocity in [m/s] in Opening from R3 to R6 in the Different Experimental Phases of Experiment F2, Phases 2-4	9.C-57

LIST OF TABLES (cont.)

Table 9.C-4	Test Matrix of Battelle Sump Heatup Experiments	9.C-87
Table 9.C-5	Events for E11.4 Experiment	9.C-148
Table 9.C-6	HDR-V21.1 Test Conditions	9.C-171
Table 9.D-1	Analytical Solution to the Turbulent Buoyant Plume Model (Reference 9.D-5, Table 9-7)	9.D-28
Table 10-1	Nominal Inputs and Correlations Sensitivity Results	10-2
Table 11-1	Timestep Sensitivity Results	11-2
Table 11-2	Timestep Limit Results	11-2
Table 12-1	Input Parameters for Annulus Clime Model Sensitivity Study	12-6
Table 12-2	Predicted Heat Removal Rates for Various Clime Noding Schemes	12-8
Table 13-1	Inside Containment Volumes Listing	13-12
Table 13-2	Outside Containment Volumes Listing	13-14
Table 13-3	Flow Path Listing	13-16
Table 13-4	Thermal Conductor Listing	13-34
Table 13-5	Clime Modeling	13-56
Table 13-6	Basis for PCS Inputs	13-58
Table 13-7	Outside Containment Initial Conditions	13-61
Table 13-8	Inside Containment Initial Conditions	13-62
Table 13-9	<u>W</u> GOTHIC Assumptions for SBLOCA Minimum Pressure Calculations	13-69
Table 14-1	DECLG LOCA Energy Release Modeling	14-6
Table 14-2	Basis for LOCA Mass and Energy Inputs	14-16

LIST OF FIGURES

Figure 1-1	Relationship of AP600 Containment DBA Reports.....	1-4
Figure 2-1	PCS Test and Analysis Process Overview	2-2
Figure 3-1	Summary of GOTHIC Historical Development	3-2
Figure 3-2	GOTHIC Modeling Features	3-3
Figure 3-3	Summary of <u>W</u> GOTHIC Historical Development (Page 1 of 2).....	3-7
Figure 3-3	Summary of <u>W</u> GOTHIC Historical Development (Page 2 of 2).....	3-8
Figure 3-4	Westinghouse-GOTHIC Clime Wall Source Term Models	3-15
Figure 3-5	Clime Finite Difference Model Definitions.....	3-17
Figure 3-6	Wetting Fraction vs. Elevation	3-24
Figure 3-7	Clime Routines Flow Control Outline	3-26
Figure 3-8	Clime Routines Flow Control Outline	3-27
Figure 4-1	Cutaway View of the 100-foot Elevation of the AP600 Including Major Components	4-4
Figure 4-2	Cutaway View of the 100-foot Elevation of the AP600 Excluding Major Components	4-5
Figure 4-3	Reactor Cavity	4-6
Figure 4-4	Reactor Cavity Cross-Section – AA	4-7
Figure 4-5	Reactor Cavity Cross-Section – BB	4-7
Figure 4-6	Reactor Coolant Drain Tank Cavity.....	4-11
Figure 4-7	Reactor Coolant Drain Tank Cross-Section – AA	4-12
Figure 4-8	Southeast Accumulator Cavity	4-16
Figure 4-9	Southeast Accumulator Cavity Cross-Section – BB.....	4-16
Figure 4-10	Northeast Accumulator Cavity	4-21
Figure 4-11	Northeast Accumulator Cavity Cross-Section – BB.....	4-21
Figure 4-12	East Steam Generator Cavity.....	4-25
Figure 4-13	East Steam Generator Cavity Cross-Section – AA.....	4-25
Figure 4-14	East Steam Generator Cavity Cross-Section – BB	4-26
Figure 4-15	West Steam Generator Cavity.....	4-32
Figure 4-16	West Steam Generator Cavity Cross-Section – AA	4-33
Figure 4-17	West Steam Generator Cavity Cross-Section – BB	4-33

LIST OF FIGURES (cont.)

Figure 4-18	North CMT Cavity.....	4-39
Figure 4-19	North CMT Cavity Cross-Section – AA.....	4-39
Figure 4-20	North CMT Cavity Cross-Section – BB.....	4-40
Figure 4-21	South CMT Cavity.....	4-50
Figure 4-22	South CMT Cavity Cross-Section – AA.....	4-51
Figure 4-23	South CMT Cavity Cross-Section – BB.....	4-51
Figure 4-24	Chemical and Volume Control Cavity	4-57
Figure 4-25	Chemical and Volume Control Cavity Cross-Section – AA	4-58
Figure 4-26	Refueling Canal	4-61
Figure 4-27	Refueling Canal Cross-Section – AA	4-62
Figure 4-28	Internal Refueling Water Storage Tank (IRWST).....	4-67
Figure 4-29	IRWST Cross-Section – AA	4-68
Figure 4-30	South Inner-Half Annulus Compartment.....	4-75
Figure 4-31	Cylindrical Central Room Cross-Section – BB	4-76
Figure 4-32	Cylindrical Central Room Cross-Section – AA	4-77
Figure 4-33	Above-Deck East Steam Generator Compartment	4-79
Figure 4-34	Above-Deck East Steam Generator Room Cross-Section – BB.....	4-80
Figure 4-35	Above-Deck East Steam Generator Room Cross-Section – AA	4-81
Figure 4-36	Above-Deck West Steam Generator Compartment	4-86
Figure 4-37	Above-Deck West Steam Generator Compartment Cross-Section – BB	4-87
Figure 4-38	Above-Deck West Steam Generator Compartment Cross-Section – AA	4-88
Figure 4-39	South Inner-Half Annulus Compartment.....	4-93
Figure 4-40	South Inner-Half Annulus Compartment Cross-Section – BB	4-94
Figure 4-41	South Inner-Half Annulus Compartment Cross-Section – AA	4-95
Figure 4-42	North Inner-Half Annulus Compartment.....	4-100
Figure 4-43	North Inner-Half Annulus Compartment Cross-Section – BB	4-101
Figure 4-44	North Inner-Half Annulus Compartment Cross-Section – AA	4-102
Figure 4-45	North Mid-Quarter Annulus Compartment	4-107
Figure 4-46	North Mid-Quarter Annulus Compartment Cross-Section – BB.....	4-108

LIST OF FIGURES (cont.)

Figure 4-47	North Mid-Quarter Annulus Compartment Cross-Section – AA.....	4-109
Figure 4-48	West Mid-Quarter Annulus Compartment.....	4-114
Figure 4-49	West Mid-Quarter Annulus Compartment Cross-Section – BB	4-115
Figure 4-50	West Mid-Quarter Annulus Compartment Cross-Section – AA	4-116
Figure 4-51	South Mid-Quarter Annulus Compartment	4-121
Figure 4-52	South Mid-Quarter Annulus Compartment Cross-Section – BB.....	4-122
Figure 4-53	South Mid-Quarter Annulus Compartment Cross-Section – AA.....	4-123
Figure 4-54	East Mid-Quarter Annulus Compartment.....	4-128
Figure 4-55	East Mid-Quarter Annulus Compartment Cross-Section – BB	4-129
Figure 4-56	East Mid-Quarter Annulus Compartment Cross-Section – AA	4-130
Figure 4-57	North Outer Quarter Annulus Compartment	4-134
Figure 4-58	North Outer Quarter Annulus Cross-Section – BB.....	4-135
Figure 4-59	North Outer Quarter Annulus Cross-Section – AA	4-136
Figure 4-60	West Outer Quarter Annulus Compartment.....	4-140
Figure 4-61	West Outer Quarter Annulus Cross-Section – BB	4-141
Figure 4-62	West Outer Quarter Annulus Cross-Section – AA.....	4-142
Figure 4-63	South Outer Quarter Annulus Compartment	4-146
Figure 4-64	South Outer Quarter Annulus Cross-Section – BB.....	4-147
Figure 4-65	South Outer Quarter Annulus Cross-Section – AA	4-148
Figure 4-66	East Outer Quarter Annulus Compartment.....	4-152
Figure 4-67	East Outer Quarter Annulus Cross-Section – BB	4-153
Figure 4-68	East Outer Quarter Annulus Cross-Section – AA.....	4-154
Figure 4-69	East Quarter Inner Dome Cross-Section – BB	4-158
Figure 4-70	East Quarter Inner Dome Cross-Section – AA	4-159
Figure 4-71	North Quarter Inner Dome Cross-Section – BB.....	4-162
Figure 4-72	North Quarter Inner Dome Cross-Section – AA.....	4-163
Figure 4-73	West Quarter Inner Dome Cross-Section – BB	4-165
Figure 4-74	West Quarter Inner Dome Cross-Section – AA	4-166
Figure 4-75	South Quarter Inner Dome Cross-Section – BB.....	4-169

LIST OF FIGURES (cont.)

Figure 4-76	South Quarter Inner Dome Cross-Section – AA.....	4-172
Figure 4-77	East Quarter Outer Dome Cross-Section – BB.....	4-175
Figure 4-78	East Quarter Outer Dome Cross-Section – AA	4-176
Figure 4-79	North Quarter Outer Dome Cross-Section – BB	4-179
Figure 4-80	North Quarter Outer Dome Cross-Section – AA.....	4-180
Figure 4-81	West Quarter Outer Dome Cross-Section – BB.....	4-183
Figure 4-82	West Quarter Outer Dome Cross-Section – AA	4-184
Figure 4-83	South Quarter Outer Dome Cross-Section – BB	4-187
Figure 4-84	South Quarter Outer Dome Cross-Section – AA.....	4-188
Figure 4-85	Outside Containment Upflow Annulus Cross-Section – BB	4-191
Figure 4-86	Outside Containment Downflow Annulus Cross-Section – BB	4-195
Figure 4-87	PCS Chimney Cross-Section – BB.....	4-198
Figure 4-88	<u>W</u> GOTHIC Conductor Noding Example	4-200
Figure 4-89	Wet/Dry Clime Modeling Diagram	4-215
Figure 4-90	Containment, Baffle, Shield Building Modeling with Climes.....	4-216
Figure 4-91	Wet Stack Clime Numbering Diagram	4-217
Figure 4-92	Dry Stack Clime Numbering Diagram	4-235
Figure 4-93	AP600 Evaluation Model LOCA Function 3: PCS Evaporation Limited Film Flow Rate	4-250
Figure 4-94	AP600 Evaluation Model LOCA Function 2: IRWST Drain Rate	4-254
Figure 4-95	AP600 Evaluation Model LOCA Function 4: Liquid Drop Model Control	4-255
Figure 4-96	AP600 Evaluation Model LOCA Function 5: Liquid Mass Break Flow.....	4-256
Figure 4-97	AP600 Evaluation Model LOCA Function 6: Liquid Break Enthalpy	4-257
Figure 4-98	AP600 Evaluation Model LOCA Function 7: Steam Mass Break Flow	4-258
Figure 4-99	AP600 Evaluation Model LOCA Function 8: Steam Break Enthalpy.....	4-259
Figure 4-100	AP600 Evaluation Model LOCA Function 11: Thermal Conductor Heat Transfer Coefficient Control	4-260
Figure 4-101	AP600 Evaluation Model LOCA Function 12: Steam Mass ADS Flow	4-261
Figure 4-102	AP600 Evaluation Model LOCA Function 13: PCS Annular Sump Drain Rate.....	4-262
Figure 4-103	Not Used.....	4-263

LIST OF FIGURES (cont.)

Figure 4-104	AP600 Evaluation Model MSLB Function 12: Steam Break Enthalpy	4-264
Figure 4-105	AP600 Evaluation MSLB Function 13: Short-Term MSLB Steam Mass Break Flow	4-264
Figure 4-106	AP600 Evaluation Model MSLB Function 13: Long-Term MSLB Steam Mass Break Flow	4-265
Figure 4-107	AP600 <u>WGOTHIC</u> Evaluation Model Section B-B	4-281
Figure 4-108	AP600 <u>WGOTHIC</u> Evaluation Model Section A-A	4-282
Figure 4-109	AP600 <u>WGOTHIC</u> Evaluation Model 135'-3" Elevation.....	4-283
Figure 4-110	AP600 <u>WGOTHIC</u> Evaluation Model 148'-0" Elevation.....	4-284
Figure 4-111	AP600 <u>WGOTHIC</u> Evaluation Model 170'-0" Elevation.....	4-285
Figure 4-112	AP600 <u>WGOTHIC</u> Evaluation Model 189'-6" Elevation.....	4-286
Figure 4-113	AP600 <u>WGOTHIC</u> Evaluation Model 209'-0" Elevation.....	4-287
Figure 4-114	AP600 <u>WGOTHIC</u> Evaluation Model 224'-9" Elevation.....	4-288
Figure 4-115	AP600 <u>WGOTHIC</u> Evaluation Model 240'-6" Elevation.....	4-289
Figure 4-116	AP600 <u>WGOTHIC</u> Evaluation Model 254'-4" Elevation.....	4-297
Figure 4-117	Below-Deck Compartments and Flowpaths	4-298
Figure 4-118a	LOCA Break Pools below the CMT Room Floor (107'-2")	4-299
Figure 4-118b	LOCA Break Pools in the Accumulator and CVS Cavities	4-300
Figure 4-119	LOCA Below-Deck Water Levels above 107'-2"	4-301
Figure 4-120	LOCA IRWST Water Level	4-302
Figure 4-121a	LOCA Pressure History: Short-Term.....	4-303
Figure 4-121b	LOCA Pressure History: Long-Term.....	4-304
Figure 4-122	LOCA Steam Concentration for East Quarter Compartments.....	4-305
Figure 4-123	LOCA Steam Concentration for West Quarter Compartments.....	4-306
Figure 4-124	LOCA Temperature Distribution for East Quarter Compartments	4-307
Figure 4-125	LOCA Temperature Distribution for West Quarter Compartments	4-308
Figure 4-126a	Temperature Distribution for Central Cylindrical Regions	4-309
Figure 4-126b	Temperature Distribution for the Dome Regions	4-310
Figure 4-127	Air Temperature Distribution in the PCS Annulus – LOCA Event	4-311
Figure 4-128	Air Flow through the PCS Annulus – LOCA Event	4-312

LIST OF FIGURES (cont.)

Figure 4-129a	LOCA Gas Circulation Pattern in the Upper East Steam Generator Compartment	4-313
Figure 4-129b	LOCA Gas Circulation Pattern in the East Outer Quarter Compartments.....	4-314
Figure 4-130a	LOCA Gas Circulation Pattern in the Upper West Steam Generator Compartment	4-315
Figure 4-130b	LOCA Gas Circulation Pattern in the West Outer Quarter Compartments.....	4-316
Figure 4-131	LOCA Gas Circulation Pattern across the Operating Deck	4-317
Figure 4-132	LOCA Steam Pressure Ratios between the CMT Room Floor and the Operating Deck.....	4-318
Figure 4-133	LOCA Steam Pressure Ratios at the Operating Deck inside the 50.975' Radius.....	4-319
Figure 4-134	MSLB Temperature Distribution	4-320
Figure 4-135	MSLB Pressure History	4-321
Figure 5-1	Case 1 – Initial Containment Humidity Sensitivity – LOCA	5-5
Figure 5-2	Case 8 – Initial Containment Humidity Sensitivity – MSLB	5-5
Figure 5-3	Case 8 – Initial Containment Humidity Sensitivity – MSLB	5-6
Figure 5-4	Case 9 – Initial Containment Pressure Sensitivity – MSLB.....	5-6
Figure 5-5	Case 3 – Initial Containment Temperature Sensitivity – LOCA	5-8
Figure 5-6	Case 10 – Initial Containment Temperature Sensitivity – MSLB	5-8
Figure 5-7	Case 4 – Ambient Humidity Sensitivity at 115°F Ambient Temperature – LOCA	5-10
Figure 5-8	Case 11 – Ambient Humidity Sensitivity at 115°F Ambient Temperature – MSLB	5-10
Figure 5-9	Case 5 – Ambient Temperature Sensitivity – LOCA.....	5-12
Figure 5-10	Case 12 – Ambient Temperature Sensitivity – MSLB.....	5-12
Figure 5-11	Case 7 – Film Temperature Sensitivity – LOCA	5-13
Figure 5-12	Case 14 – Film Temperature Sensitivity – MSLB	5-13
Figure 5-13	Blowdown Drop Fraction Sensitivity – LOCA	5-15
Figure 6-1	Particle Path through the AP600 PCS with and without Wind	6-4
Figure 6-2	1D Containment Shell Model Inside Temperature Results.....	6-5
Figure 7-1	Illustration of PCS Water Distribution Weir Assembly	7-6
Figure 7-2	Minimum Delivered PCS Water Flow Rate from the Bucket.....	7-9
Figure 7-3	Weir Outflow	7-9

LIST OF FIGURES (cont.)

Figure 7-4	Comparison of Water Distribution Model to Phase 3 Water Distribution Test Results	7-15
Figure 7-5	Determination of Gamma-Min from LST, SST, and Flat Plate Data.....	7-17
Figure 7-6	Normalized Water Evaporation Rate (2-D/1-D) versus Overall Containment Wetted Fraction.....	7-22
Figure 7-7	Containment Steel Shell Temperature Gradient (°F) with 2-D Heat Conduction; 20 psig, 25% Wetted	7-23
Figure 7-8	Containment Steel Shell Thermal Flux Gradients (Btu/hr-ft ²) in Y-Direction; 20 psig, 25% Wetted	7-24
Figure 7-9	Containment Steel Shell Total Thermal Flux (Btu/hr-ft ²); 20 psig, 25% Wetted.....	7-25
Figure 7-10	Thermal Flux in Y-Direction on Outside Surface of Containment Wall [Btu/hr-ft ²].....	7-26
Figure 7-11	Thermal Flux in Y-direction on Inside Surface of Containment Wall [Btu/hr-ft ²].....	7-27
Figure 7-12	Normalized Total Wet and Dry Heat Transfer (2-D/1-D Conduction) vs. Wetted Fraction.....	7-28
Figure 7-13	2-D Conduction Multiplier as a Function of Wetting Fraction.....	7-29
Figure 7-14	Large-Scale Test Water Coverage Pattern	7-45
Figure 7-15	Sensitivity to the Input PCS Film Flow Rate.....	7-55
Figure 7-16	Comparison of Peak Containment Pressure as Function of PCS Coverage Area.....	7-57
Figure 7-17	PCS Runoff Flow Rates as a Function of Coverage Area	7-58
Figure 7-18	Comparison of Evaporation Model Peak Pressure with 100% and 50% Constant Coverage Models	7-59
Figure 7-19	Comparison of Evaporation Model PCS Runoff Flow Rate with 100% and 50% Constant Coverage Models	7-61
Figure 7-20	Difference in the Integrated Energy Transferred to the Top of the Dome (with PCS Film Applied at 35 and 337 Seconds).....	7-62
Figure 7.A-1	Variation in Surface Tension over the Surface of a Heated Liquid Film	7.A-4
Figure 7.A-2	Typical Qualitative Contact Angles for Advancing and Receding Contact Lines	7.A-8
Figure 7.A-3	Sketch of Qualitative Wave Laminar Film Flow Characteristics on Heated LST Shell Water Stripe.....	7.A-12
Figure 7.A-4	Large-Scale Test Water Coverage Pattern at High PCS Flows.....	7.A-14

LIST OF FIGURES (cont.)

Figure 7.A-5	Sketch of LST Observation of Vessel Exterior at Water Flows Similar to LST 213.1 Showing Complete Dryout of Some Stripes.....	7.A-15
Figure 8-1	Comparison of Single-Node Model with EM Pressure Curve	8-3
Figure 8-2	Comparison of Response with No Heat Sinks to EM Response	8-4
Figure 9-1	Measured Steam Concentrations for LST.....	9-48
Figure 9-2	LST with Diffuser Under Steam Generator – Steam Flow 0.11-0.17 lb/sec – Internal Fluid Temperature – Group 1	9-49
Figure 9-3	LST with Diffuser Under Steam Generator – Steam Flow 0.11-0.17 lb/sec – Saturation Temperature – Group 1	9-50
Figure 9-4	LST with Diffuser Under Stream Generator – Steam Flow 0.11-0.17 lb/sec – Internal Steam Pressure Ratio – Group 1	9-51
Figure 9-5	LST with Diffuser Under Steam Generator – Steam Flow 0.11-0.17 lb/sec – Internal Fluid Temperature – Group 2	9-52
Figure 9-6	LST with Diffuser Under Steam Generator – Steam Flow 0.11-0.17 lb/sec – Saturation Temperature – Group 2	9-53
Figure 9-7	LST with Diffuser Under Steam Generator – Steam Flow 0.11-0.17 lb/sec – Internal Steam Pressure Ratio – Group 2	9-54
Figure 9-8	LST with Diffuser Under Steam Generator – Steam Flow 0.270.36 lb/sec – Internal Fluid Temperature	9-55
Figure 9-9	LST with Diffuser Under Steam Generator – Steam Flow 0.27-0.36 lb/sec – Saturation Temperature.....	9-56
Figure 9-10	LST with Diffuser Under Steam Generator – Steam Flow 0.27-0.36 lb/sec – Internal Steam Pressure Ratio.....	9-57
Figure 9-11	LST with Diffuser Under Steam Generator – Steam Flow 0.49-0.62 lb/sec – Internal Fluid Temperature – Group 1	9-58
Figure 9-12	LST with Diffuser Under Steam Generator – Steam Flow 0.49-0.26 lb/sec – Saturation Temperature – Group 1	9-59
Figure 9-13	LST with Diffuser Under Steam Generator – Steam Flow 0.49-0.62 lb/sec – Internal Steam Pressure Ratio – Group 1	9-60
Figure 9-14	LST with Diffuser Under Steam Generator – Steam Flow 0.49-0.62 lb/sec – Internal Fluid Temperature – Group 2	9-61
Figure 9-15	LST with Diffuser Under Steam Generator – Steam Flow 0.49-0.62 lb/sec – Saturation Temperature – Group 2	9-62
Figure 9-16	LST with Diffuser Under Steam Generator – Steam Flow 0.49-0.62 lb/sec – Internal Steam Pressure Ratio – Group 2	9-63

LIST OF FIGURES (cont.)

Figure 9-17	LST with Diffuser Under Steam Generator – Steam Flow 0.76-0.84 lb/sec – Internal Fluid Temperature	9-64
Figure 9-18	LST with Diffuser Under Steam Generator – Steam Flow 0.76-0.84 lb/sec – Saturation Temperature.....	9-65
Figure 9-19	LST with Diffuser Under Steam Generator – Steam Flow 0.76-0.84 lb/sec – Internal Steam Pressure Ratio.....	9-66
Figure 9-20	LST with Diffuser Under Steam Generator – Steam Flow 1.10-1.20 lb/sec – Internal Fluid Temperature	9-67
Figure 9-21	LST with Diffuser Under Steam Generator – Steam Flow 1.10-1.20 lb/sec – Saturation Temperature.....	9-68
Figure 9-22	LST with Diffuser Under Steam Generator – Steam Flow 1.10-1.20 lb/sec – Internal Steam Pressure Ratio.....	9-69
Figure 9-23	LST with Diffuser Under Steam Generator – Steam Flow 1.54-1.68 lb/sec – Internal Fluid Temperature	9-70
Figure 9-24	LST with Diffuser Under Steam Generator – Steam Flow 1.54-1.68 lb/sec – Saturation Temperature.....	9-71
Figure 9-25	LST with Diffuser Under Steam Generator – Steam Flow 1.54-1.68 lb/sec – Internal Steam Pressure Ratio.....	9-72
Figure 9-26	LST with Diffuser Up 6 Feet – Steam Flow 0.76 & 1.68 lb/sec – Internal Fluid Temperature	9-73
Figure 9-27	LST with Diffuser Up 6 Feet – Steam Flow 0.76 & 1.68 lb/sec – Saturation Temperature.....	9-74
Figure 9-28	LST with Diffuser Up 6 Feet – Steam Flow 0.76 & 1.68 lb/sec – Internal Steam Pressure Ratio.....	9-75
Figure 9-29	LST with Steam Injection: 3 Inch Pipe – Steam Flow 0.76 – 0.95 lb/sec – Internal Fluid Temperature	9-76
Figure 9-30	LST with Steam Injection: 3 Inch Pipe – Steam Flow 0.76 – 0.95 lb/sec – Saturation Temperature.....	9-77
Figure 9-31	LST with Steam Injection: 3 Inch Pipe – Steam Flow 0.76 – 0.95 lb/sec – Internal Steam Pressure Ratio.....	9-78
Figure 9-32	LST with Steam Injection: 3 Inch Pipe – Steam Flow 1.25 – 1.31 lb/sec – Internal Fluid Temperature	9-79
Figure 9-33	LST with Steam Injection: 3 Inch Pipe – Steam Flow 1.25 – 1.31 lb/sec – Saturation Temperature.....	9-80

Figure 9-34	LST with Steam Injection: 3 Inch Pipe – Steam Flow 1.25 – 1.31 lb/sec – Internal Steam Pressure Ratio.....	9-81
Figure 9-35	CMT Compartment Layout	9-82
Figure 9-36	Simplified AP600 Containment Diagram.....	9-83
Figure 9-37	<u>WGOTHIC</u> Calculated LOCA Blowdown Steam Pressure Ratio for Jet Momentum Dissipated in SG East Compartment	9-84
Figure 9-38	<u>WGOTHIC</u> Calculated AP600 Containment Pressure – Sensitivity to Loss Coefficients for LOCA Jet Momentum Dissipated in SG East Compartment ...	9-85
Figure 9-39	<u>WGOTHIC</u> Calculated Flow Pattern – Sensitivity to Loss Coefficients for LOCA Jet Momentum Dissipated in SG East Compartment at 20 Seconds.....	9-86
Figure 9-40	<u>WGOTHIC</u> Calculated Flow Pattern – Sensitivity to Loss Coefficients for LOCA Jet Momentum Dissipated in SG East Comp. at 1000 Seconds.....	9-87
Figure 9-41	<u>WGOTHIC</u> Calculated Flow Pattern – Sensitivity to Loss Coefficients for LOCA Jet Momentum Dissipated in SG East Comp. at 1550 Seconds.....	9-88
Figure 9-42	<u>WGOTHIC</u> Calculated Flow Pattern – Sensitivity to Loss Coefficients for LOCA Jet Momentum Dissipated in SG East Comp. at 80050 Seconds.....	9-89
Figure 9-43	<u>WGOTHIC</u> Calculated AP600 Containment Heat Removal Rates – LOCA Jet Momentum Dissipated in SG East Compartment.....	9-90
Figure 9-44	<u>WGOTHIC</u> Calculated AP600 Containment Steam Pressure Ratio for LOCA Jet Momentum Dissipated in SG East Compartment.....	9-91
Figure 9-45	<u>WGOTHIC</u> Calculated AP600 Cont. Pressure – Sensitivity to Heat Transfer Coefficient for Study of Undissipated Jet Effects During a LOCA.....	9-92
Figure 9-46	<u>WGOTHIC</u> Calculated AP600 Containment Pressure – LOCA Jet Momentum Dissipated in SG East Compartment	9-93
Figure 9-46A	<u>WGOTHIC</u> Calculated AP600 Containment Below-Deck Compartment Pressure for LOCA Jet Momentum Dissipated in SG East Compartment.....	9-94
Figure 9-47	<u>WGOTHIC</u> Calculated Flow Pattern – LOCA Jet Momentum Dissipated in SG East Compartment at 20 Seconds	9-95
Figure 9-48	<u>WGOTHIC</u> Calculated Flow Pattern – LOCA Jet Momentum Dissipated in SG East Compartment at 1000 Seconds	9-96
Figure 9-49	<u>WGOTHIC</u> Calculated Flow Pattern – LOCA Jet Momentum Dissipated in SG East Compartment at 1500 Seconds	9-97
Figure 9-50	<u>WGOTHIC</u> Calculated Flow Pattern – LOCA Jet Momentum Dissipated in SG East Compartment at 8000 Seconds	9-98
Figure 9-51	Details of <u>WGOTHIC</u> Flow Paths to Above-Deck Region from CMT, Refueling Canal, and IRWST	9-99

LIST OF FIGURES (cont.)

Figure 9-52	<u>WGOTHIC</u> Calculated AP600 Containment Pressure – LOCA Plume Rising into CMT Room	9-100
Figure 9-53	<u>WGOTHIC</u> Calculated Flow Pattern – LOCA Plume Rising into CMT Room at 1000 Seconds.....	9-101
Figure 9-54	<u>WGOTHIC</u> Calculated Flow Pattern – LOCA Plume Rising into CMT Room at 1400 Seconds.....	9-102
Figure 9-55	<u>WGOTHIC</u> Calculated AP600 Containment Heat Removal Rates – LOCA Plume Rising into CMT Room	9-103
Figure 9-56	<u>WGOTHIC</u> Calculated AP600 Containment Pressure – LOCA Plume Rising into CMT Room and SG Compartments.....	9-104
Figure 9-57	<u>WGOTHIC</u> Calculated Flow Pattern – LOCA Plume Rising into CMT Room and SG Compartment at 1000 Seconds.....	9-105
Figure 9-58	<u>WGOTHIC</u> Calculated Flow Pattern – LOCA Plume Rising into CMT Room and SG Compartments at 1500 Seconds	9-106
Figure 9-59	<u>WGOTHIC</u> Calculated AP600 Containment Heat Removal Rates – LOCA Plume Rising into CMT Room and SG Compartments.....	9-107
Figure 9-60	<u>WGOTHIC</u> Calculated AP600 Containment Steam Pressure Ratio for MSLB Above-Deck.....	9-108
Figure 9-61	<u>WGOTHIC</u> Calculated AP600 Containment Pressure – MSLB Above Operating Deck	9-109
Figure 9-62	<u>WGOTHIC</u> Calculated AP600 Containment Pressure – MSLB in CMT Room	9-110
Figure 9.B-1	Condensation Heat Transfer Coefficients vs. T_{surf}	9.B-11
Figure 9.B-2	Containment Shell Heat Sink Results.....	9.B-12
Figure 9.B-3	CMT Room Heat Sink Results	9.B-13
Figure 9.C-1a	The Formation of the Horizontal Layers of the Constant Density Due to the Stratification.....	9.C-8
Figure 9.C-1b	Interaction of Jets, Plumes and Wall Boundary Layers with Stratified Regions	9.C-9
Figure 9.C-2	Combination of the Constant Temperature Boundary Conditions at the Outside and Inside Surfaces which will Produce Stratification Inside the Enclosure.....	9.C-10
Figure 9.C-3	Stratification Inside the Upper and Lower Corners of the Romb-Shaped Enclosure	9.C-11
Figure 9.C-4	Experimental and Numerical Results for the Romb-Shaped Enclosure with the Romb Angle 44° and $Ra=3.5*10^4$, $PR=5270$	9.C-12

LIST OF FIGURES (cont.)

Figure 9.C-5	a) The Square Enclose with Vertical Walls at the Different Temperatures and Horizontal Walls Adiabatic b) Streamlines for $Ra=106$ and $Pr=0.71$, c) Isotherms for $Ra=106$ and $Pr=0.71$	9.C-13
Figure 9.C-6	Average Nusselt Numbers as a Function of the Rayleigh Numbers for the Square Enclosure with Opposite Vertical Walls at the Different Temperatures and $Pr=0.71$ (air).....	9.C-14
Figure 9.C-7	Formation of the Stratified Core in Between Two Opposite Vertical Line Jets (after Baines and Turner, 1969).....	9.C-15
Figure 9.C-8	Flow in an Enclosure with Vertical Opposite Walls at Different Temperatures ($Ra=105$, $Pr=0.71$).....	9.C-16
Figure 9.C-9	Internal Waves in the Square Cavity – Fluctuations in the Temperature Field at $Ra=2*10^8$ and $Pr=0.71$ (air).....	9.C-17
Figure 9.C-10	Temperature for the Initial Solution with the Hot and Cold Intrusions and Boundary Layer Waves Presented (after Armfield and Janssen, 1996).....	9.C-18
Figure 9.C-11	Formation of the Downward Negatively Buoyant Jets.....	9.C-19
Figure 9.C-12	Rayleigh-Benard Convection Example	9.C-26
Figure 9.C-13	Hele-Shaw Cell.....	9.C-27
Figure 9.C-14	Steady and Oscillatory Convection in Hele-Shaw Cell (after Buhler et al., 1987).....	9.C-28
Figure 9.C-15	Turbulent (Chaotical) Flow without Hot and Cold Plumes Interactions (Plane Cross-Section of the Three-Dimensional Enclosure is Presented).....	9.C-29
Figure 9.C-16	Interaction of Hot and Cold Plumes (after Aqino et al., 1989).....	9.C-30
Figure 9.C-17a	Vertical Temperature Distribution inside the Cylindrical Enclosure with Lower and Upper Horizontal Plate at Higher and Lower Temperatures, Respectively ($Ra = 9.38*10^7$, $Pr = 200$)	9.C-31
Figure 9.C-17b	Generation of the Cold Plumes Due to the Brake (Separation) of the Vertical Boundary Layers Near the Cold Vertical Walls.....	9.C-32
Figure 9.C-18	Primary Flow Regions and Volumetric Flow Rates for Quasi-Steady Containment Conditions.....	9.C-45
Figure 9.C-19	The Volumetric Flow between the Upper and Lower Deck Regions Q.....	9.C-46
Figure 9.C-20	Primary Flow Regions and Volumetric Flow Rates for Quasi-Steady Containment Conditions in LST Case	9.C-47
Figure 9.C-21	Inflows and Outflows from the Region II.....	9.C-48
Figure 9.C-22	Recirculating Flow Paths Inside the Region II	9.C-49

LIST OF FIGURES (cont.)

Figure 9.C-23	Mass Conservation for Thin Horizontal Layer Inside the Region II	9.C-50
Figure 9.C-24	Comparison of Different Facilities	9.C-51
Figure 9.C-25	Model Containment: Vertical Cross-section 0/180; Horizontal Cross-sections at +0.2 m and +1.7m for Configuration in Experiment F2.....	9.C-58
Figure 9.C-26	Model Containment: Vertical Cross-Section 0/180; Horizontal Cross-Sections at +4.01m and +5.05m for Configuration in Experiment F2.....	9.C-59
Figure 9.C-27	Injections and Convective Flow Loop Directions (+ Sign for Flow Indicates the Same Direction of the Flow as Arrow in R9)	9.C-60
Figure 9.C-28	Experiment F2, Phase 2-8, Experimental Procedures, Total and Partial Pressures.....	9.C-61
Figure 9.C-29	Number of Compartments, Locations of Measurement Transducers and Steam Releases	9.C-62
Figure 9.C-30	Test Group F2, Phase 1 (heatup), Total Pressure in the Containment	9.C-63
Figure 9.C-31	Test Group F2, Phase 1 (heatup), Atmospheric Temperature in the Compartment R9, H=1.0m and 2.1m.	9.C-64
Figure 9.C-32	Scheme of Multi-Compartment Containment Geometry in Experiment F2.....	9.C-65
Figure 9.C-33	Test Group F2, Phase 2: Atmospheric Temperatures in Zones 1, 2 and 3 (R5 + R6, R1 + R4, R7 + R8).....	9.C-66
Figure 9.C-34	Test Group F2, Phase 3 and 4: Atmospheric Temperature in Zone 1, 2 and 3 (R5 + R6, R1 + R4, R7 + R8).....	9.C-67
Figure 9.C-35	Thermodynamic State of Steam-Air Atmosphere in R9 top (H=7.6m)	9.C-68
Figure 9.C-36	Thermodynamic State of Steam-Air Atmosphere in R9 Bottom (H=1 m)	9.C-69
Figure 9.C-37	Test Group F2, Phase 2: Atmospheric Temperatures in R9 (Zone 4)	9.C-70
Figure 9.C-38	Test Group F2, Phase 3 and 4: Atmospheric Temperatures in R9 (Zone 4).....	9.C-71
Figure 9.C-39	Velocities in Opening from Compartment R7 to Compartment R9.....	9.C-72
Figure 9.C-40	Velocities in Opening from Compartment R3 to Compartment R6.....	9.C-73
Figure 9.C-41	Vertical Cut through BMC with Orifice in Between R2 and R1	9.C-77
Figure 9.C-42a	BMC Test No. 2: Comparison Between Experimental Data and 2-d GOTHIC Computations for Hydrogen Concentrations	9.C-78
Figure 9.C-42b	DMC Test No. 4: Comparison Between Experimental Data and 2-d GOTHIC Computations for Hydrogen Concentrations	9.C-79
Figure 9.C-42c	DMC Test No. 6: Comparison Between Experimental Data and 2-d GOTHIC Computations for Hydrogen Concentrations	9.C-80

LIST OF FIGURES (cont.)

Figure 9.C-43	BMC Test No. 12: Comparison between Experimental Data and GOTHIC-lp Computations for Hydrogen Concentrations	9.C-82
Figure 9.C-44a	BMC Test No. 20: Comparison Between Experimental Data and 2-d GOTHIC Computations for Hydrogen Concentrations	9.C-83
Figure 9.C-44b	BMC Test No. 20: Comparison Between Experimental Data and 2-d GOTHIC Computations for Hydrogen Concentrations	9.C-84
Figure 9.C-44c	BMC Test No. 20: Comparison Between Experimental Data and 2-d GOTHIC Computations for Hydrogen Concentrations	9.C-85
Figure 9.C-45	Perspective View, Vertical and Upper Horizontal Cross-Sections through BMC with Main Steam Feedline	9.C-88
Figure 9.C-46	Perspective View, Vertical and Upper Horizontal Cross-Sections through BMC with Auxiliary Steam Feedline	9.C-89
Figure 9.C-47	Instrumentation Plan for BMC – Sump Heatup Test RX4	9.C-90
Figure 9.C-48	Battelle-Experiment RX4: Sump and Atmospheric Temperatures	9.C-91
Figure 9.C-49	Battelle-Experiment RX4: Velocities in Side Vents.....	9.C-92
Figure 9.C-50	Battelle-Experiment RX4: Temperatures in Center Compartment and Dome	9.C-93
Figure 9.C-51	Battelle-Experiment RX4: Temperatures in External Annulus.....	9.C-94
Figure 9.C-52	Battelle-Experiment RX4: Hydrogen Concentration Along Circulation Path.....	9.C-95
Figure 9.C-53	Battelle-Experiment RX4: Hydrogen Concentrations in Intermediate Subcompartments	9.C-96
Figure 9.C-54	Battelle-Experiment RX4: Relative Humidity in the Containment Atmosphere....	9.C-97
Figure 9.C-55	Model Containment used in the Test, Break-Release Position, and Circulation Flow Paths (See Arrows)	9.C-101
Figure 9.C-56	Detailed Arrangement of each Floor.....	9.C-102
Figure 9.C-57	Distribution of the Compartments at each Floor	9.C-103
Figure 9.C-58	Pressure History.....	9.C-104
Figure 9.C-59	Dome Temperature History	9.C-105
Figure 9.C-60	Dome Helium Concentration History	9.C-106
Figure 9.C-61	a) Temperature Histories for Compartments Forming a Circulation Path (8, 15, Dome and 7) b) Helium Concentration Histories for Compartments Forming a Circulation Path (8, 15, Dome and 7)	9.C-107
Figure 9.C-62	Carolinas Virginia Tube Reactor (CVTR) Containment Structure	9.C-111
Figure 9.C-63	CVTR Steam Line Diffuser	9.C-112

LIST OF FIGURES (cont.)

Figure 9.C-64a	Steam Injection Histories Test 1	9.C-113
Figure 9.C-64b	Steam Injection Histories Test 2	9.C-114
Figure 9.C-64c	Steam Injection Histories Test 3	9.C-115
Figure 9.C-65	CVTR Containment Pressure Response (Heise Gauge)	9.C-116
Figure 9.C-66	Atmospheric Vertical Temperature Profile, Test 1	9.C-117
Figure 9.C-67	Atmospheric Vertical Temperature Profile, Test 2	9.C-118
Figure 9.C-68	Atmospheric Vertical Temperature Profile, Test 3	9.C-119
Figure 9.C-69	Surface and Atmosphere Temperatures – Intermediate Region, Test 1	9.C-120
Figure 9.C-70	Surface and Atmosphere Temperatures – Basement Region, Test 1	9.C-121
Figure 9.C-71	Concrete Surface Temperatures, Test 1	9.C-122
Figure 9.C-72	Isolated Containment Region Temperatures	9.C-123
Figure 9.C-73	Cross-sections, Elevations and Numbers of Compartments of the HDR Containment, Left (180°-0°-cross-section), Right (270°-90°-cross-section)	9.C-127
Figure 9.C-74	Locations and Enumerations of Thermocouple (left) and Anemometers (right) for HDR-E-Test Series	9.C-128
Figure 9.C-75	HDR-E11.2 Sequence of Experimental Test Procedures	9.C-129
Figure 9.C-76	HDR-E11.2 Containment Pressure History	9.C-130
Figure 9.C-77	HDR-E11.2 Atmospheric Temperatures Along Main Stairway	9.C-131
Figure 9.C-78	HDR-E11.2 Steam Concentrations Along Main Stairway	9.C-132
Figure 9.C-79	HDR-E11.2 H ₂ /He Gas Concentrations Along Main Stairway	9.C-133
Figure 9.C-80	HDR-E11.2 Comparison Between Temperatures in Main and Spiral Stairways at +31.0 m Level	9.C-134
Figure 9.C-81	HDR-E11.2 Comparison Between Temperatures in Main and Spiral Stairways at +26.5 m Level	9.C-135
Figure 9.C-82	HDR-E11.2 Comparison Between Temperatures in Main and Spiral Stairways at +16.5 m Level	9.C-136
Figure 9.C-83	HDR-E11.2 Comparison Between Temperatures in Main and Spiral Stairways at +6 m Level	9.C-137
Figure 9.C-84	HDR-E11.2 Axial Temperature Profiles in Both Major Flow Paths at Specific Times, Left in Spiral Stairway, Right in Main Stairway	9.C-138

LIST OF FIGURES (cont.)

Figure 9.C-85	HDR-E11.3 Velocities in Both Major Flow Paths at Different Axial Positions During Containment Heatup	9.C-140
Figure 9.C-86	HDR-E11.3 Velocities in Both Major Flow Paths at Different Axial Positions During H ₂ /He Gas Mixture Release	9.C-141
Figure 9.C-87	HDR-E11.3 Comparison Between Temperatures in Main and Spiral Stairways at +31.0 m Level	9.C-142
Figure 9.C-88	HDR-E11.3 Comparison Between Temperatures in Main and Spiral Stairways at +26.5 m Level	9.C-143
Figure 9.C-89	HDR-E11.3 Comparison Between Temperatures in Main and Spiral Stairways at +16.5 m Level	9.C-144
Figure 9.C-90	HDR-E11.3 Comparison Between Temperatures in Main and Spiral Stairways at +6 m Level.....	9.C-145
Figure 9.C-91	HDR-E11.3 Axial Temperature Profiles in Both Major Flow Paths at Specific Times, Left in Spiral Stairway, Right in Main Stairway.....	9.C-146
Figure 9.C-92	HDR-E11.4 Sequence of Experimental Test Procedures	9.C-149
Figure 9.C-93	HDR-E11.4 Containment Pressure History	9.C-150
Figure 9.C-94	HDR-E11.4 Atmospheric Temperatures Along Main Stairway	9.C-151
Figure 9.C-95	HDR-E11.4 Steam Concentration Along Main Stairway	9.C-152
Figure 9.C-96	HDR-E11.4 H ₂ /He Gas Concentrations Along Main Stairway	9.C-153
Figure 9.C-97a	HDR-E11.4 Comparison Between Temperatures in Main and Spiral Stairways at +31.0 m Level	9.C-154
Figure 9.C-97b	HDR-E11.4 Comparison Between Temperatures in Main and Spiral Stairways at +31.0 m Level	9.C-155
Figure 9.C-98	HDR-E11.4 Comparison Between Temperatures in Main and Spiral Stairways at +26.5 m Level	9.C-156
Figure 9.C-99	HDR-E11.4 Comparison Between Temperatures in Main and Spiral Stairways at +16.5 m Level	9.C-157
Figure 9.C-100	HDR-E11.4 Comparison Between Temperatures in Main and Spiral Stairways at +6 m Level.....	9.C-158
Figure 9.C-101	HDR-E11.4 Axial Temperature Profiles in Both Major Flow Paths at Specific Times, Left in Spiral Stairway, Right in Main Stairway.....	9.C-159
Figure 9.C-102	HDR-T31.5 Blowdown Mass Flow Rate into the Containment.....	9.C-162
Figure 9.C-103	HDR-T31.5 Steam and H ₂ /He gas Mass Flow Rates into the Containment.....	9.C-163
Figure 9.C-104	HDR-T31.5 Pressure History after Large LOCA over 1200 Minutes	9.C-164

LIST OF FIGURES (cont.)

Figure 9.C-105	HDR-T31.5 Axial Temperature Profiles along Spiral Stairway (left) and Main Stairway (right) for Different Instants in Time	9.C-165
Figure 9.C-106	HDR-T31.5 Axial Gas Concentration Profiles along Spiral Stairway (left) and Main Stairway (right) in Upper Containment Region at Different Instants in Time.....	9.C-166
Figure 9.C-107	HDR-T31.5 Gas Concentrations Inside the Containment Dome.....	9.C-167
Figure 9.C-108a	HDR-T31.5 Velocities Over 60 Minutes along Spiral Stairways and Associated Dome Regions.....	9.C-168
Figure 9.C-108b	HDR-T31.5 Velocities Over 60 Minutes Along Main Stairways and Associated Dome Regions.....	9.C-169
Figure 9.C-109	HDR-V21.1 Arrangement of Reactor Pressure Vessel, Blowdown Pipe and Jet Impingement Plate for Water Blowdown Test	9.C-172
Figure 9.C-110	HDR-V21.1 Containment Pressure History	9.C-173
Figure 9.C-111	HDR-V21.1 Temperatures in the Containment Dome.....	9.C-174
Figure 9.C-112	HDR-V21.1 Temperature Along the Main Staircase at Different Axial Positions	9.C-175
Figure 9.C-113	HDR-V21.1 Temperatures Along Spiral Staircase at Different Axial Positions	9.C-176
Figure 9.C-114	HDR-V21.1 Comparison Between Temperatures in Spiral Staircase (H=22.5 m) and Main Staircase (H = 25 m)	9.C-177
Figure 9.C-115a	HDR-E11.5 Sequence of Experimental Test Procedures.....	9.C-180
Figure 9.C-115b	HDR-E11.5 Sequence of Experimental Test Procedures.....	9.C-181
Figure 9.C-116	HDR-E11.5 Containment Pressure	9.C-182
Figure 9.C-117	HDR-E11.5 Containment Pressure History	9.C-183
Figure 9.C-118	HDR-E11.5 Containment Temperatures Along main Stairway During Containment Heatup Phase.....	9.C-184
Figure 9.C-119a	HDR-E11.5 Temperatures in Both Major Flow Paths at the Same Axial Positions for Three Heights in the Containment.....	9.C-185
Figure 9.C-119b	HDR-E11.5 Temperatures in Both Major Flow Paths at the Same Axial Positions for Three Heights in the Containment.....	9.C-186
Figure 9.C-119c	HDR-E11.5 Temperatures in Both Major Flow Paths at the Same Axial Positions for Three Heights in the Containment.....	9.C-187

LIST OF FIGURES (cont.)

Figure 9.C-120a	HDR-E11.5 Axial Steam Concentration Profiles in Spiral (left) and Main (right) Stairways for Different Instants in time for Large Break LOCA release in Lower Containment Region.....	9.C-188
Figure 9.C-120b	HDR-E11.5 Axial Temperature Profiles in Spiral (left) and Main (right) Stairways for Different Instants in Time for Large Break LOCA Release in Lower Containment Region	9.C-189
Figure 9.C-121a	HDR-E11.5 Axial H ₂ -He Gas Mixture Concentration Profiles along Spiral (left) and Main (right) Stairways During Gas Release Phase (Total Mass 291 kg).....	9.C-190
Figure 9.C-121b	HDR-E11.5 Axial Steam Concentration Profiles Along Spiral (left) and Main (right) Stairways During Gas Release Phase (Total Mass 291 kg)	9.C-191
Figure 9.C-121c	HDR-E11.5 Axial Temperature Profiles Along Spiral (left) and Main (right) Stairways During Gas Release Phase (Total Mass 291 kg)	9.C-192
Figure 9.C-122a	HDR-E11.5 Gas Concentrations in the Major Flow Paths and in Regions and Subcompartments Away From the Stairways (H=22m up to 27 m)	9.C-193
Figure 9.C-122b	HDR-E11.5 Gas Concentrations in the Major Flow Paths and in Regions and Subcompartments Away From the Stairways (H=22m up to 27 m)	9.C-194
Figure 9.C-123a	HDR-E11.5 Gas Concentrations in the Major Flow Paths and in Regions and Subcompartments Away From the Stairways (H=-4.5m up to +2.0 m).....	9.C-195
Figure 9.C-123b	HDR-E11.5 Gas Concentrations in the Major Flow Paths and in Regions and Subcompartments Away from the Stairways (H=-4.5m up to +2.0 m)	9.C-196
Figure 9.C-124a	HDR-E11.5 Velocities in the Main Stairway During Blowdown	9.C-197
Figure 9.C-124b	HDR-E11.5 Velocities in the Spiral Stairway During Blowdown.....	9.C-198
Figure 9.C-125a	HDR-E11.5 Velocities in the Main Stairway During Containment Heatup Phase	9.C-199
Figure 9.C-125b	HDR-E11.5 Velocities in the Spiral Stairway During Containment Heatup Phase	9.C-200
Figure 9.C-126a	HDR-E11.5 Velocities in the Main Stairway During H ₂ -He Gas Mixture Release Phase	9.C-201
Figure 9.C-126b	HDR-E11.5 Velocities in the Spiral Stairway During H ₂ -He Gas Mixture Release Phase	9.C-202
Figure 9.C-127a	HDR-E11.5 Velocities in the Main Stairway During Sump Heatup and Boiling Phase.....	9.C-203
Figure 9.C-127b	HDR-E11.5 Velocities in the Spiral Stairway During Sump Heatup and Boiling Phase.....	9.C-204

LIST OF FIGURES (cont.)

Figure 9.C-128	Dome Pressure History	9.C-211
Figure 9.C-129a	Temperature History Inside Node 8.....	9.C-212
Figure 9.C-129b	Helium Concentration History Inside Node 8	9.C-213
Figure 9.C-130a	Temperature History Inside Node 15.....	9.C-214
Figure 9.C-130b	Helium Concentration History Inside Node 15	9.C-215
Figure 9.C-131a	Temperature History Inside Dome.....	9.C-216
Figure 9.C-131b	Helium Concentration History Inside Dome	9.C-217
Figure 9.C-132a	Temperature History Inside Node 7.....	9.C-218
Figure 9.C-132b	Helium Concentration History Inside Node 7	9.C-219
Figure 9.C-133	HDR-E11.5: Comparison Between Measured Long-Term Containment Pressure and GOTHIC Open Post-Test Prediction	9.C-222
Figure 9.C-134	HDR-E11.5: Comparison Between Measured Sump Temperature and GOTHIC Open Post-Test Prediction	9.C-223
Figure 9.C-135	HDR-E11.5: Comparison Between Measured Temperature in Main Stairway (6m) and GOTHIC Open Post-Test Prediction.....	9.C-224
Figure 9.C-136	HDR-E11.5: Comparison Between Measured Temperature in Spiral Stairway (6m) and GOTHIC Open Post-Test Prediction.....	9.C-225
Figure 9.C-137	HDR-E11.5: Comparison Between Measured Gas Mixture Concentration in Main Stairway (6m) and GOTHIC Open Post-Test Prediction	9.C-226
Figure 9.C-138	HDR-E11.5: Comparison Between Measured Gas Mixture Concentration in Spiral Stairway (6m) and GOTHIC Open Post-Test Prediction	9.C-227
Figure 9.C-139	HDR-E11.5: Comparison Between Measured Velocity in Spiral Stairway (15m) and GOTHIC Open Post-Test Prediction.....	9.C-228
Figure 9.C-140	HDR-E11.2: Comparison Between Measured Long-Term Containment Pressure and Various “Optimized” Open Post-Test Predictions	9.C-229
Figure 9.D-1	Interactions Between Containment Regions During Post-Blowdown LOCA (Low Momentum).....	9.D-29
Figure 9.D-2a	Detail of Steam Concentration Distribution in Boundary Layer	9.D-30
Figure 9.D-2b	Qualitative Radial Concentration Profile from Plume Centerline to Shell at Mid Elevation	9.D-31
Figure 9.D-3	Period of Application of Analytical Models for Turbulent Wall Boundary Layer and Turbulent Buoyant Plume.....	9.D-32
Figure 9.D-4	Turbulent Buoyant Plume Analytical Model	9.D-33

LIST OF FIGURES (cont.)

Figure 9.D-5	LST Measurement Locations.....	9.D-34
Figure 9.D-6	LST Temperature Profile – Test 220.1 @ Quasi-Steady Conditions	9.D-35
Figure 9.D-7	LST Temperature Profile – Test 217.1 @ Quasi-Steady Conditions	9.D-36
Figure 10-1	LOCA Sensitivities to Nominal Inputs and Correlations.....	10-3
Figure 10-2	MSLB Sensitivity to Nominal Inputs and Correlations.....	10-4
Figure 10-3	Comparison of Evaluation Model and Nominal Mass Release	10-7
Figure 10-4	Comparison of Evaluation Model and Nominal Energy Release	10-8
Figure 12-1	Westinghouse-GOTHIC Clime Wall Source Team Models.....	12-12
Figure 12-2	Simplified Line Diagram of Annulus Clime Model	12-13
Figure 12-3	Noding Diagram, 8 Clime Node Model	12-14
Figure 12-4	Comparison of Transient Heat Transfer Rates; Case 1	12-15
Figure 12-5	Comparison of Transient Heat Transfer Rates; Case 2	12-16
Figure 12-6	Comparison of Transient Heat Transfer Rates; Case 3	12-17
Figure 12-7	Comparison of Transient Heat Transfer Rates; Case 4	12-18
Figure 12-8	Comparison of Transient Heat Transfer Rate Differences; Case 1	12-19
Figure 12-9	Comparison of Transient Heat Transfer Rate Differences; Case 2	12-20
Figure 12-10	Comparison of Transient Heat Transfer Rate Differences; Case 3	12-21
Figure 12-11	Comparison of Transient Heat Transfer Rate Differences; Case 4	12-22
Figure 12-12	Comparison of Heat Flux Profiles; Time t=2000 Seconds; Case 1	12-23
Figure 12-13	Comparison of Heat Flux Profiles; Time t=2000 Seconds; Case 2	12-24
Figure 12-14	Comparison of Heat Flux Profiles; Time t=2000 Seconds; Case 3	12-25
Figure 12-15	Comparison of Heat Flux Profiles; Time t=2000 Seconds; Case 4	12-26
Figure 12-16	Comparison of Film Temperature Profiles; Time t=2000 Seconds; Case 1.....	12-27
Figure 12-17	Comparison of Film Temperature Profiles; Time t=2000 Seconds; Case 2.....	12-28
Figure 12-18	Comparison of Film Temperature Profiles; Time t=2000 Seconds; Case 3.....	12-29
Figure 12-19	Comparison of Film Temperature Profiles; Time t=2000 Seconds; Case 4.....	12-30
Figure 12-20	Comparison of Air Temperature Profiles; Time t=2000 Seconds; Case 1	12-31
Figure 12-21	Comparison of Air Temperature Profiles; Time t=2000 Seconds; Case 2	12-32
Figure 12-22	Comparison of Air Temperature Profiles; Time t=2000 Seconds; Case 3	12-33

LIST OF FIGURES (cont.)

Figure 12-23	Comparison of Air Temperature Profiles; Time t=2000 Seconds; Case 4	12-34
Figure 12-24	AP600 Containment Model Clime Noding Pattern	12-35
Figure 12-25	AP600 Containment Model Double Vertical Clime Noding Pattern	12-36
Figure 12-26	AP600 Containment Model Double Stack Clime Noding Pattern	12-37
Figure 12-27	AP600 Containment Model Double Mesh Point Clime Noding Pattern	12-38
Figure 12-28	Pressure History, AP600 Containment Model; Double Clime	12-39
Figure 12-29	Wet Heat Flux vs. Clime; AP600 Containment Model, Base Case	12-40
Figure 12-30	Wet Heat Flux vs. Clime; AP600 Containment Model, Double Clime	12-41
Figure 12-31	Dry Heat Flux vs. Clime; AP600 Containment Model, Base Case	12-42
Figure 12-32	Dry Heat Flux vs. Clime; AP600 Containment Model, Double Clime	12-43
Figure 12-33	Film Temperature vs. Clime; AP600 Containment Model, Base Case	12-44
Figure 12-34	Film Temperature vs. Clime; AP600 Containment Model, Double Clime.....	12-45
Figure 12-35	Dry Surface Temperature vs. Clime; AP600 Containment Model, Base Case	12-46
Figure 12-36	Dry Surface Temperature vs. Clime; AP600 Containment Model, Double Clime.....	12-47
Figure 12-37	Annulus Pressure vs. Clime; AP600 Containment Model, Base Case	12-48
Figure 12-38	Annulus Pressure vs. Clime; AP600 Containment Model, Double Clime	12-49
Figure 12-39	Air Temperature vs. Clime; AP600 Containment Model, Base Case	12-50
Figure 12-40	Air Temperature vs. Clime; AP600 Containment Model, Double Clime	12-51
Figure 12-41	Air Density vs. Clime; AP600 Containment Model, Base Case.....	12-52
Figure 12-42	Air Density vs. Clime; AP600 Containment Model, Double Clime.....	12-53
Figure 12-43	Air Velocity vs. Clime; AP600 Containment Model, Base Case.....	12-54
Figure 12-44	Air Velocity vs. Clime; AP600 Containment Model, Double Clime.....	12-55
Figure 12-45	Heat Rejection History Comparison, AP600 Containment Model Double Clime Sensitivity Case.....	12-56
Figure 12-46	Integrated Heat Rejection Comparison, AP600 Containment Model; Double Clime Sensitivity Case.....	12-57
Figure 12-47	Pressure History Comparison, AP600 Containment Model; Double Stack Sensitivity Case	12-58
Figure 12-48	Heat Rejection History Comparison, AP600 Containment Model; Double Stack Sensitivity Case.....	12-59

LIST OF FIGURES (cont.)

Figure 12-49	Integrated Heat Rejection Comparison, AP600 Containment Model; Double Stack Sensitivity Case.....	12-60
Figure 12-50	Pressure History Comparison, AP600 Containment Model; Double Mesh Sensitivity Case	12-61
Figure 12-51	Heat Rejection History Comparison, AP600 Containment Model; Double Mesh Sensitivity Case.....	12-62
Figure 12-52	Integrated Heat Rejection Comparison, AP600 Containment Model; Double Stack Sensitivity Case.....	12-63
Figure 13-1	Comparison of AP600 (left) and AP1000 (right) Above-Deck Containment Model Elevations for Nodalization.....	13-5
Figure 13-2	Plan View of Compartments Below 107' Elevation	13-6
Figure 13-3	Plan View of Compartments Immediately Below Operating Deck	13-7
Figure 13-4	Plan View of Nodalization from 135.25' to 226' Elevation.....	13-8
	(Pressurizer Compartment is Only Nodalized to 153' Elevation).....	13-8
Figure 13-5	Plan View of Nodalization from 226' Elevation to Top of Containment.....	13-9
Figure 13-6	Elevation View of Nodalization (Facing North).....	13-10
Figure 13-7	Elevation View of Nodalization (Facing West)	13-11
Figure 13-8	<u>WGOTHIC</u> Thermal Conductor Type Noding Example	13-48
Figure 13-9	Stack Configuration for the AP1000 <u>WGOTHIC</u> EM Clime Modeling.....	13-52
Figure 13-10	Clime Configuration for the AP1000 <u>WGOTHIC</u> EM.....	13-53
Figure 13-11	<u>WGOTHIC</u> Clime Conductor Modeling	13-55
Figure 13-12	AP1000 <u>WGOTHIC</u> Evaluation Model Clime Stripping Diagram	13-60
Figure 14-1	Spreadsheet Mass and Energy Release Schematic	14-4
Figure 14-2	<u>WGOTHIC</u> Draindown Model Noding Diagram	14-5
Figure 14-3	Mass Release Comparison.....	14-11
Figure 14-4	Energy Release Comparison.....	14-12
Figure 14-5	Mass Release Comparison.....	14-12
Figure 14-6	Energy Release Comparison.....	14-13
Figure 14-7	Integrated Mass Comparison	14-13
Figure 14-8	Integrated Energy Comparison	14-14
Figure 14-9	LOCA Transient Comparison	14-14

1 INTRODUCTION

1.1 OBJECTIVE

This report describes the methodology that is used to develop a containment evaluation model (EM) to perform the containment design basis accident (DBA) analyses for the Westinghouse advanced passive plants, in particular the **AP1000**® plant design. The containment EM is used to calculate a conservative containment pressure transient response for the DBA events and to specify conditions for equipment qualification (EQ). The containment DBA events include the response to a double-ended rupture (DER) in the reactor coolant system (RCS), leading to a loss of coolant accident (LOCA), and a double-ended main steam line break (MSLB).

The methodology makes use of the lumped parameter modeling approach. The lumped parameter modeling approach is based on over 30 years of nuclear industry experience. International tests at various scales have identified limitations in this approach that are due primarily to the oversimplification of the momentum formulation. Conservative biases have been applied to various models for the important phenomena in the containment EM to account for these limitations and allow a conservative calculation of the containment pressure response.

The passive containment DBA analysis methodology was originally developed and validated for the AP600 plant design; this information was documented in WCAP-14407 (Reference 1.10). The AP600 containment DBA analysis methodology was reviewed and approved by the Nuclear Regulatory Commission (NRC), as documented in NUREG-1512.

Westinghouse increased the power level of the passive plant design soon after the AP600 design was certified. The original **AP1000** containment design was very similar to the AP600, therefore WCAP-14407 was updated to include a description of the **AP1000** containment EM and the document was re-numbered as WCAP-15846. Subsequent revisions of WCAP-15846 were issued to incorporate additional information requested by the NRC during the review of the **AP1000** containment analyses. The **AP1000** containment DBA analysis methodology was reviewed and approved by the NRC, as documented in NUREG-1793 (Reference 1.11).

The **AP1000** containment EM has been updated to incorporate a number of plant design changes that have been made since the original version of NUREG-1793 was issued. The software has also been updated to change operating systems, increase array sizes, add optional capabilities, and correct code errors. This latest revision of WCAP-15846 includes a description of the updated **AP1000** containment EM.

1.2 REPORT OVERVIEW

Section 2 contains a summary of the containment EM development process. Each step or element in the process is briefly described. Section 3 presents an overview of the Westinghouse-GOTHIC (Generation of Thermal Hydraulic Information for Containment) code package. The WGOTHIC features, development history, and validation programs are briefly described. The models and features that were added by Westinghouse to adapt GOTHIC to model the passive containment cooling system (PCS) are also described.

Section 4 presents the methodology and assumptions that were used to develop the AP600 containment EM. Because the AP600 containment EM was used for the sensitivity studies in this report, the model input is also provided; this includes free volumes, elevations, heat sink characteristics, and boundary conditions. Graphics are included which aid in visualizing both the AP600 layout and the WGOTHIC model of the AP600 plant.

Section 5 contains a number of sensitivity cases varying the initial conditions assumed for the design basis analyses. These include sensitivities on initial containment humidity, initial containment pressure, initial containment temperature, outside humidity, outside temperature, and break boundary condition drop size assumptions. Except as noted specifically for a sensitivity study, all sensitivities in this report are based on the AP600 containment EM that is described in Section 4. This section provides the basis for the conservative initial conditions that are assumed in the DBA analyses.

Section 6 describes the effects of meteorological changes on the performance of the PCS. The effects of PCS effluent entrainment into the PCS inlet are evaluated. In addition to recirculation, the effects of wind on PCS performance are identified. The results of these studies show that wind effects are beneficial to containment cooling since they augment the natural draft velocity that develops during PCS operation. The effluent recirculation due to inversions or strong winds is shown to have a negligible effect on PCS performance and containment pressure response.

Section 7 describes the methodology for modeling the PCS water flow rate and water coverage area input for the containment EM. Based on conservatively bounded liquid film test data from various tests, the water coverage area and evaporation rate are conservatively calculated, and only the amount of water which evaporates is applied in the EM. Thus, there is a conservative bound on the amount of evaporative cooling credited in the EM. The implementation of evaporation limited PCS flow in the EM conservatively under-predicts the subcooled liquid film heat removal from containment. The basis for the delay time in the application of the evaporation limited PCS flow and other input parameters are presented. Sensitivities to the water coverage area and other input parameters are presented to demonstrate the conservatism in the method.

Section 8 compares the AP600 blowdown pressurization transient from a multi-volume containment model that includes the PCS heat and mass transfer methodology to a single volume containment model that is based on Standard Review Plan (SRP) methodologies. The single volume model uses a thermal conductor and the Uchida heat transfer correlation to model heat transfer through the containment shell. This comparison shows that there is very little difference in the results between the two models for the blowdown phase of the transient. The results of a heat sink sensitivity case are also presented.

Section 9 addresses circulation and stratification within the AP600 containment. Circulation and stratification can be affected by break location, orientation, and type, in addition to nodding assumptions. The effects of circulation and stratification inside the containment are assessed for an MSLB and the various time phases (i.e., blowdown, refill, peak pressure, and long-term) of a LOCA. The effects of circulation above the operating deck for both the AP600 and **AP1000** plant were also examined in Reference 1.9, Section 4.2. Based on these results, biases have been incorporated into the containment EM as described in Sections 4, 9, and 13.

Section 10 evaluates the conservatism contained in some of the EM assumptions made for the design basis LOCA and MSLB analyses that are intended to maximize the peak pressure. The conservatism in the heat and mass transfer correlation biases, the initial conditions inside and outside of containment, PCS water temperature, material properties, steel-concrete gap, external annulus loss coefficient, dead-ended compartment modeling biases, and the LOCA mass and energy releases are evaluated in a step-wise fashion. The final result is a reasonable estimate of the conservatism that is included in the AP600 containment EM. The calculated containment peak pressure occurs at the end of the LOCA blowdown phase for the sensitivity case with more realistic assumptions and is approximately 11.5 psi lower than the peak pressure that is calculated with the AP600 containment EM. A similar sensitivity for the net effect of parameters important in the MSLB analysis is also provided.

Section 11 evaluates the sensitivity of the containment EM to changes in the calculated time step size. The time step selection logic was modified to reduce the calculated time step by one-half and by one-quarter in separate cases. The results of these sensitivity cases show that the solution is stable, in that the pressure transients did not change appreciably as the time step size was reduced. This result supports the conclusion that the time step logic that is used in the WGOTHIC code is acceptable.

Section 12 evaluates the sensitivity of the predicted containment pressure transient to changes in the PCS nodding. The PCS nodding structure that is used to represent volumes, elevations, and azimuthal segments in the external annulus, as well as the numerical mesh pattern through conductors are found to be acceptable.

Section 13 presents the methodology and assumptions that are used to develop the **AP1000** containment EM. It has been updated to reflect the finalized design and will be used to perform the licensing basis analyses in Section 6.2 of the Standard Safety Analysis Report (SSAR).

Section 14 presents the LOCA mass and energy release data, which is a key input for the containment DBA analysis. Some of the codes and models that are used to calculate the LOCA mass and energy release input data for non-passive plant design containment DBA analysis are not appropriate to be used for the passive plant design. Therefore, Section 14 describes the methodology and assumptions that are used to calculate the LOCA mass and energy release input data for the passive plant containment EM.

1.3 AP600 CONTAINMENT EM DOCUMENTATION

The AP600 containment EM has been developed using a process that is similar to the evaluation model development and assessment process that is described in DG-1096. The draft regulatory guidance describes an acceptable process to develop an evaluation model for the SSAR Chapter 15 accident analyses. It is also considered to also be applicable for the development of a containment EM for the Chapter 6 analyses of the SSAR. Although it was drafted after the development of the AP600 containment EM, it outlines the same principles that were used for the AP600 EM.

As shown in Figure 1-1, this report fits into the framework of licensing documentation which defines the passive plant containment EM. A brief summary of the various reports follows.

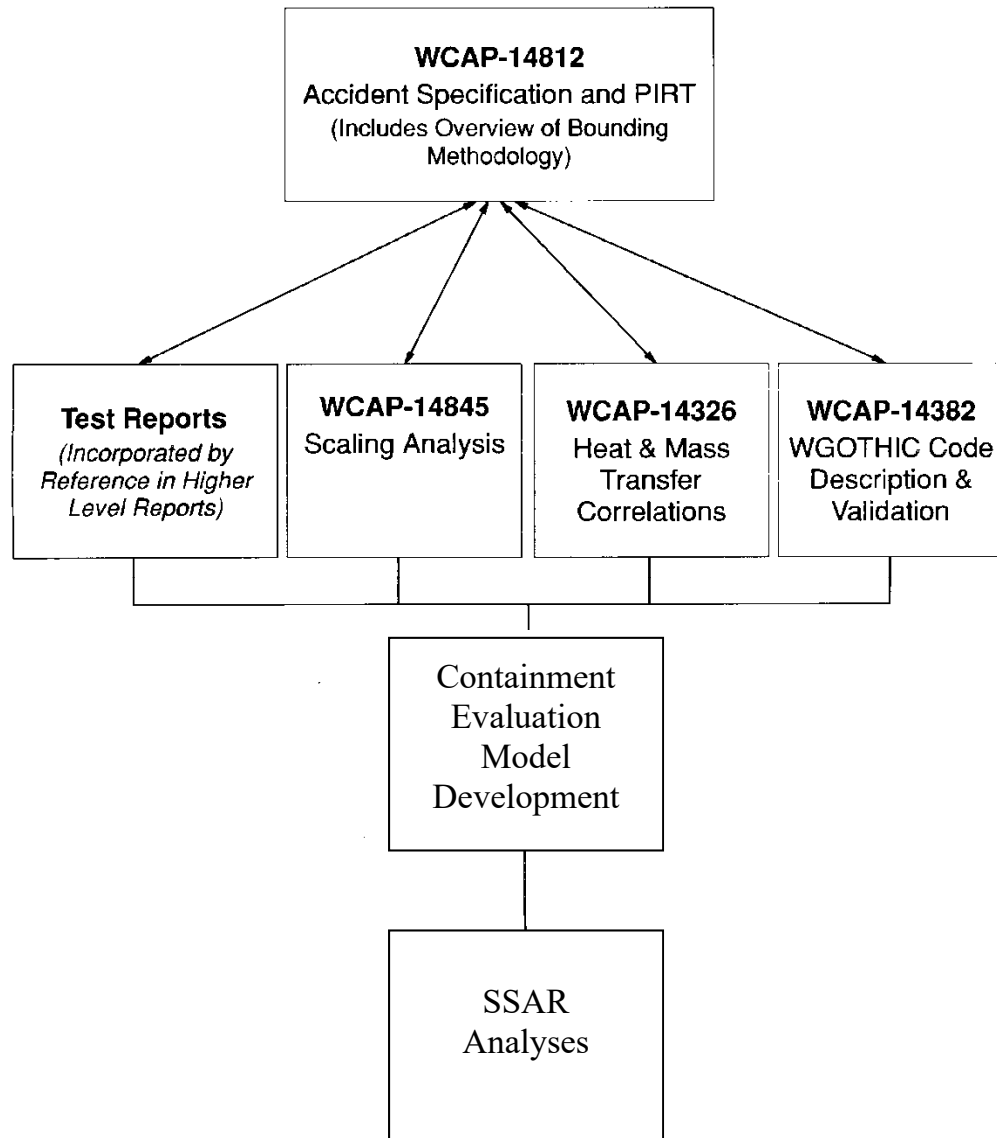


Figure 1-1. Relationship of AP600 Containment DBA Reports

1.3.1 Accident Specification and Phenomena Identification and Ranking Table Report

The containment DBA analyses consider the LOCA and MSLB events. To be able to evaluate the PCS for these events, the containment EM must be able to model:

- The transport of break mass and energy (steam) to the containment shell,
- The condensation of steam on the inside surface of the containment shell,
- The transport of the condensate film on the inside surface of the containment shell,
- The conduction of heat through the containment shell,
- The transport and heating of the applied liquid film on the outside surface of the containment shell,
- Evaporation from the applied liquid film on the outside surface of the containment shell, and
- The natural draft cooling air flowing through the downcomer, riser and chimney of the shield building.

WCAP-14812 (Reference 1.1) describes the containment and PCS, defines the DBA accident scenarios, identifies success criteria, and ranks the importance of phenomena that must be considered when developing the containment EM. A cross-reference to relevant tests and test data reports is also included.

A systematic process has been followed to identify and rank phenomena, including input and review by members of industry, academia, and regulatory authorities. The following information is provided in WCAP-14812 for each phenomenon:

- Phenomena identification ranking table (PIRT) ranking
- Basis for PIRT ranking
 - Test results
 - Scaling results
 - Sensitivity studies
 - Expert review
- How phenomena are implemented in the containment EM
- Justification of containment EM treatment of phenomenon
 - Test experience
 - Modeling guidance
 - Sensitivity studies
- Containment EM treatment of uncertainty

1.3.2 Testing

In the mid-1980s, Westinghouse developed the large scale test (LST) facility to provide steady-state heat and mass transfer data for a geometrically similar model of the AP600 containment vessel. The test vessel was 1/8 geometric scale. The focus was on long-term transient behavior, because that is where the passive containment design, with no credited active heat removal system, differed significantly from the current containment test databases. Because of limitations of scale (power-to-volume and power-to-area ratios, and steam supply), the LST matrix was selected to vary boundary conditions parametrically to obtain data over a range of parameters. Specific passive containment pressure transients were not simulated with the LST.

The LST was designed to provide steady-state heat and mass transfer data in an integral setting, that is, with external evaporation and internal condensation acting simultaneously, for a geometrically similar model of the AP600 containment vessel (Reference 1.5, Section 3.2.4.2). The use of the LST has been supported through the application of scaling methodologies that evolved during the 1990s. The LST data have been used to validate the system scaling equation that is used to support the identification and ranking of phenomena (Reference 1.2, Section 10.2).

Local data from the LST is used to support validation of the condensation correlation applied to the inner steel shell surface (Reference 1.3, Section 3.9) and to examine potential stratification effects in an enclosed volume in an integral setting with external cooling (Section 9). Water coverage and film stability data were used to develop a bounding model to address the effects of film stability (Section 7). External dry heat transfer data have been used to supplement convective heat transfer data (Reference 1.3, Section 3.5).

Local data from the LST have been combined with other separate effects tests (SETs) and integral effects tests (IETs) at different scales to provide supporting data for the following phenomena:

- Dry external riser annulus heat transfer
- External liquid film stability
- Internal condensation mass transfer
- Internal stratification

The LST matrix was developed to contain parametric variations that examined various extremes and combinations of boundary condition effects. In this way, the LST was ranged similarly to a SET.

In addition to the more obvious matrix test parameters, such as steam flow, experience with the international containment test database pointed to the need to examine the effects of boundary condition parameters on distributions of non-condensable gases inside containment. A brief overview of the parametric variations included in the LST matrix (Reference 1.6, Tables 1.3-1, 1.3-2, and 1.3-3) follows.

- The LST matrix was designed to cover a range of pressures. Air and helium were used as non-condensable gases, and steam was used as the working fluid. Therefore, the important thermodynamic properties of the containment atmosphere in both the AP600 and **AP1000** plant are preserved.

- Water flow rates, and thus shell coverage, were varied to obtain various degrees of coverage and to examine water film behavior through complete dryout on the sidewall. In addition to quantitative recorded test data, videotapes and engineering notes were taken to characterize the qualitative behavior of the liquid film.
- The matrix was defined to address the effect of external cooling on stratification which has been suggested in international tests (Appendix 9.C). For example, LST 219.1 applied water to the external shell surface starting from dry conditions. To gain further insight, additional parametric variation of external transients were examined in LST 214.1, 215.1, 216.1, 221.1, by suddenly varying water coverage and air flow rates during the course of a test. This is in addition to the test-to-test parametric variations in external conditions.
- Transients initiated by a larger initial steam flow rate, relative to the steady-state tests, were included. The LST did not include “blowdown” mass flow rates scaled to the AP600 or **AP1000** design due to limitations on steam supply. The LST high initial steam flow transients (LST 220.1, 221.1, 222.1, 222.2) include the influence of an initial rapid pressurization on the subsequent quasi-steady heat and mass transfer rates. The transients also provided code validation of transient performance with reductions in steam flow.
- Tests were included to examine the influence of break elevation and momentum (LST 222.1, 222.2, 222.3, and 222.4) to support evaluation of the various LOCA and MSLB break locations and orientations.
- Tests with initial vacuum (LST 223.1) and initially pressurized to two atmospheres (LST 224.1, 224.2) were included to range the effect of non-condensable gas in the containment.
- Tests were included to provide parameter variations specifically to validate elements of the Evaluation Model. These parameter variations were external loss coefficient (LST 215.1); natural convection (LST 206.1, 211.1, 214.1, 215.1) instead of running the fan at various speeds to replace the external density head; and circumferential variations in inlet blockage (LST 215.1).
- In the containment DBA, there is no appreciable source of hydrogen to containment (Reference 1.1, Section 4.4.2E). As part of the DBA testing program, data were taken to supplement the literature for postulated severe accidents. Helium was introduced into the LST primarily to study the effects of additional non-condensable gases. Helium was shown to be a good simulant of hydrogen in the German Heissdampfreaktor (HDR) tests. Sampling of the non-condensable gas concentration (LST 212.1, 217.1, 218.1, 219.1, 220.1, 221.1, 222.1, 222.2, 222.3, 222.4, 223.1, 224.1, and 224.2) was included at four elevations, including the helium content measurement where applicable.

1.3.3 Scaling Report

WCAP-14845 (Reference 1.2) describes how scaling has been used to derive the appropriate non-dimensional parameters and their ranges to examine phenomena for bottom-up model validation for the AP600 design. SETs are identified and the test parameter ranges compared to AP600 ranges to show sufficiency of the test database for application to containment DBAs. Scaling has been used to assess the use of the LST to supplement the smaller scale separate effects data (Reference 1.2, Sections 10.1 and 11.3). Scaling is also used to identify distortions in the LST facility. These distortions must then be addressed in the bounding methodology.

The scaling analysis in WCAP-14845 (Reference 1.2) satisfies the three stated objectives for AP600 containment pressure scaling. The conclusions of the scaling analysis are:

1. Support Development of Bounding Methodology (PIRT Confirmation)

The scaling analysis confirmed the identification in the PIRT (Reference 1.1, Table 4-1) of high ranked phenomena. The high ranked phenomena inside containment are the break source, gas compliance (storage of mass and energy in the gas volume of the containment atmosphere), and condensation on the shell and heat sinks. The high ranked phenomena outside containment are evaporation of the external liquid film and the PCS natural circulation flow rate. In addition, the scaling analysis confirmed the PIRT ranking of lower order phenomena including convection and radiation heat transfer, liquid film conductance, and liquid film energy transport.

The high ranked phenomena and the parameters that most strongly affect them are the ones that must be bounded in the evaluation model. Phenomena and how they are bounded in the evaluation model are described in Section 4.4 of Reference 1.1.

The net effect of these is an evaluation model that bounds all the dominant processes so as to produce the maximum pressure response.

2. Specify Individual Model Constitutive Relations.

The range of AP600 dimensionless groups for each of the separate effects test database has been shown to be adequately covered.

Appropriate constitutive relations and models were identified for each of the dominant phenomena and parameters in 1 above:

Condensation and evaporation are modeled using conventional free and forced convection mass transfer relationships, characterized by Reynolds, Grashof, and Schmidt numbers. The range of these dimensionless variables necessary to cover AP600 operation was defined and separate effects tests were identified and used to validate the selected mass transfer correlations. The range of dimensionless variables in the data was shown to encompass the expected range of operation in AP600.

3. Investigate Use of LST to Validate Elements of the Bounding Evaluation Model

Steady state heat and mass transfer correlations have been shown to be applicable for the AP600 double-ended cold-leg guillotine (DECLG) LOCA and MSLB DBA pressure transients. The LST was used as a source of separate effects data to validate condensation and evaporation mass transfer, film stability, and circulation and stratification models as discussed under 1 and 2 above. Component level distortions in the LST were addressed by using local measurements of temperature, concentration, and velocity from the LST, and by supplementing the LST data with data from other sources when the range of LST parameters was insufficient to cover AP600 operation.

The scaling analysis shows the three dominant system level phenomena for the transient phase are the break source energy addition, the gas volume, and the heat sink surface area dependent condensation energy removal rate. The scaling analysis shows that the LST system level phenomena are distorted in the transient phase relative to AP600, but are well-scaled in the quasi-steady phase.

The LST is therefore not used as a system level representation of AP600 transient pressure response. However, the steady-state LST data is acceptable for use as separate effects data for the following models:

- Internal condensation
- Internal above-deck steam distribution
- External dry heat transfer
- External water coverage (film stability)

1.3.4 Heat and Mass Transfer Correlations Report

WCAP-14326 (Reference 1.3) documents the analytical and experimental bases for heat and mass transfer correlations associated with:

- Condensation mass transfer
- Evaporation mass transfer
- Convective heat transfer
- Liquid film thermal resistance

For modeling convenience, an explicit representation of the liquid film thermal resistance is modeled, with condensation or evaporation occurring at the film surface. This is in contrast to the more traditional approach of combining mass transfer and liquid film resistance and then using the solid surface temperature. The explicit representation allows clearer treatment of elements of uncertainty in mass transfer and liquid film over the range of conditions.

1.3.5 WGOTHIC Code Description and Validation

WCAP-14382 (Reference 1.4) documents the implementation of the “climes” subroutines in the GOTHIC code. Climes are used to represent heat and mass transfer on the containment shell, shield building, and baffle. The report shows validation comparisons to the LST using both lumped parameter and distributed parameter models, identifies lumped parameter biases and competing effects based on the LST calculations, and describes the derivation of nodding guidance for the AP600 containment EM.

Verification and validation of the code changes has been completed for each code version update. WGOTHIC verification and validation has been completed using calculations of separate effects tests (Reference 1.4, Section 4 and Reference 1.3, Sections 3.1 and 3.3). An assessment of the effects of a WGOTHIC Solver Upgrade from 1.2 (used in Reference 1.4) to 4.1 has shown that code validation conclusions remain valid (Reference 1.7).

1.3.6 Evaluation Model Development

The containment DBA analysis approach is based on the lumped parameter formulation. The lumped parameter containment EM does not resolve internal velocity and concentration fields due to its simplified momentum model and large lumped volumes.

Analyses of the LST have been completed using the WGOTHIC lumped parameter momentum formulation. In the LST calculations, nominal properties and nominal test boundary and initial conditions are used to isolate the biases inherent in the computer code, independent of conservatism included in the EM. This allows the examination of the known lumped parameter biases, and quantification of the effects of compensating errors in lumped parameter results. The method to address the lumped parameter biases, as well as the method that is used to address phenomena for the containment EM are documented (Reference 1.1, Section 4.4).

Comparisons between preliminary versions of the containment EM and the system level LST response show that pressure is reasonably well predicted, with a modest conservative margin. Examination of LST WGOTHIC lumped parameter results identified the existence of competing internal effects in which the excessive velocities predicted by the lumped parameter model over-predict the velocity component of mass transfer, while over-mixing under-predicts the steam concentration component of mass transfer. Consequently, these competing effects in predictions must be addressed in the containment EM. The effect of over-predicted velocities was resolved by using only free convection for internal heat and mass transfer, thereby eliminating velocity from the condensation correlation. The over-mixing issue was resolved by examining and biasing the effects of circulation and stratification in the containment EM, as discussed in Section 9.

The sensitivity calculations in this report were performed with WGOTHIC Solver version 4.1 and plant geometry described in Section 4. An evaluation of the effects of WGOTHIC Solver version 4.2 and AP600 input modifications that changed the credited heat sinks was performed to show that the changes to internal containment parameters do not affect the case-to-case sensitivities that were used to select the limiting extremes for internal initial and boundary conditions. Since the internal heat sinks reach their maximum thermal effectiveness well before the DECLG LOCA peak pressure is reached, the changes do not significantly impact the sensitivities that were used to select limiting scenarios for circulation and stratification. The small change to internal pressure, and thus the related small change to internal temperature boundary condition for the containment shell, does not affect the sensitivities for clime vertical nodding and conductor mesh. Similarly, the changes do not affect external condition case-to-case results. The changes also do not invalidate the time step study. Therefore, the sensitivities performed in this report, remain valid for the updated AP600 containment EM.

1.4 AP1000 CONTAINMENT EM DOCUMENTATION UPDATES

Both the **AP1000** and AP600 plant designs employ a passive containment cooling system. The **AP1000** containment structure is taller, but maintains the same diameter and internal layout as the AP600. A detailed comparison of the AP600 and **AP1000** plant designs is provided in WCAP-15612 (Reference 1.8).

The code capability requirements (see Section 1.3.1) for the **AP1000** containment EM are the same as AP600. Westinghouse developed special subroutines to mechanistically calculate the heat and mass transfer and to track the liquid films for the PCS. These subroutines were appended to the GOTHIC version 4.0 code to create WGOTHIC version 4.2.

To determine the applicability of using the WGOTHIC code (version 4.2) and the AP600 containment EM methodology for performing the **AP1000** containment DBA analyses, Westinghouse:

- Reviewed the AP600 containment PIRT (WCAP-14812) for application to the **AP1000** plant design,
- Reviewed the AP600 containment scaling analysis (WCAP-14845) for application to the **AP1000** plant design, and
- Compared the test data ranges of the important dimensionless parameters for heat and mass transfer and water coverage with the operating range for the **AP1000** plant.

The AP600 containment PIRT was reviewed to determine if there were any new phenomena or any change in the importance ranking of the existing phenomena with respect to the **AP1000** containment and RCS design changes. This review was documented in WCAP-15613 (Reference 1.9, Section 2.6). No new phenomena were identified and there were no significant changes in the ranking of phenomena as a result of the **AP1000** design changes.

An LST scaling assessment was performed for the **AP1000** plant design and compared with AP600 (Reference 1.9, Section 4.2). Due to its relatively low and constant steam injection flow rate, the LST was not well scaled to model the blowdown transient for either AP600 or **AP1000** plant designs. The

steady-state LST data were determined to be acceptable for use as a source of separate effects test data for internal condensation, above-deck steam distribution, external heat transfer, and external water coverage.

The ranges of the dimensionless parameters for the heat and mass transfer correlations were examined to determine if the existing test data covered the **AP1000** operating range (Reference 1.9, Section 4.2). The test data covered the upper range of the **AP1000** dimensionless parameters for the heat and mass transfer correlations in the important riser region of the annulus. Therefore, the correlations were also considered to be valid for the **AP1000** containment EM.

Experimental test data and correlations were reviewed to determine if the increase in containment height would affect the circulation within the open volume above the operating deck. Both the correlations and test data suggest that increasing the containment height would increase the turbulence and improve the mixing (see Section 9.C).

An alternate analysis methodology was used to independently assess the degree of mixing in the open volume above the operating deck. Detailed, 2-dimensional slice Computational Fluid Dynamics (CFD) models representing this region were constructed for both the AP600 and the **AP1000** plants (Reference 1.9, Section 4.2). The flow and velocity patterns for the AP600 and **AP1000** plants were very similar. Both models predicted cold falling plumes near the walls and a hot rising plume near the center of the volume. Except for the small layers very close to the walls and within the central plume, the temperature profile within the volume was nearly uniform. Therefore, based on the experimental test data, correlations, and results from the alternate analysis approach, the well-mixed assumption for this region was also considered to be valid for the **AP1000** containment EM.

The operating ranges of the liquid film coverage parameters for AP600 and **AP1000** plant designs were compared to the composite PCS test data. The test data covered the operating range of the important film coverage parameters (minimum film Reynolds number and maximum heat flux) for both AP600 and **AP1000** plants. Therefore, the constant coverage area input values and the model for calculating the evaporation-limited PCS water flow rate input that was used for AP600 are also applicable to the **AP1000** plant.

In summary, both the AP600 and **AP1000** plant designs employ the same passive containment cooling system design features so the events and phenomena to be analyzed in the **AP1000** containment EM are the same as the AP600. The range of important dimensionless parameters from the PCS test data covers the operating range of both the AP600 and **AP1000** plants, so the WGOTHIC heat and mass transfer correlations remain acceptable. Since the containment designs are similar and since the heat and mass transfer correlations remain acceptable, WGOTHIC source code changes were not needed for the **AP1000** containment EM. Therefore, a containment EM that uses the same bounding methodology that was accepted by the NRC for the AP600 was also accepted for the **AP1000** plant (Reference 1.11).

1.5 INTERFACE WITH PLANT LICENSING CALCULATIONS

The licensing basis containment DBA pressure analysis reported in Section 6.2 of the SSAR is performed with the containment EM, defined by the methodology described herein. The following design inputs are required as input to the containment EM:

- Conservatively calculated mass and energy releases as a function of time, using approved methodology (SSAR Section 6.2.1.3.2 for LOCA and Section 6.2.1.4 for MSLB),
- Appropriate Technical Specification and Site Interface Parameters for initial and boundary conditions (SSAR Sections 16.1, 3.6 and 2.3),
- PCS delivered flow as a function of time assuming at least one Passive Containment Cooling Water Storage Tank (PCCWST) drain valve fails to open,
- The surface area and effective thickness of metal and concrete structures that are credited as heat sinks,
- The thermal conductivity and heat capacity of the heat sink materials and the coatings, and
- The containment free volume.

Any deviations from the **AP1000** standard passive plant design will be addressed by changing the associated input values that are calculated with the methodology defined by the containment EM, as documented herein. The results of the containment EM are used for containment design pressure evaluation and equipment qualification condition specifications, as reported in Chapter 6 and Appendix 3D of the SSAR. The calculated peak containment pressure from the containment EM has sufficient margin to bound uncertainty in important parameters. The calculated pressure and temperature response from the containment EM can be used to determine the envelope for equipment qualification.

1.6 CONCLUSIONS

This report defines a methodology which calculates a conservative peak containment pressure as well as pressure and temperature envelopes that are appropriate for the equipment qualification of the passive containment design. The containment EM methodology is cross referenced to PIRT phenomena in Reference 1.1, Section 4.4. The licensing basis DBA calculation is presented in Section 6.2 of the SSAR.

1.7 REFERENCES

- 1.1 WCAP-14812, Rev. 2, "Accident Specification and Phenomena Evaluation for AP600 Passive Containment Cooling System," April 1998.
- 1.2 WCAP-14845, Rev. 3, "Scaling Analysis for AP600 Containment Pressure During Design Basis Accidents," March 1998.

- 1.3 WCAP-14326, Rev. 3, "Experimental Basis for the AP600 Containment Vessel Heat and Mass Transfer Correlations," April 1998.
- 1.4 WCAP-14382, "WGOTHIC Code Description and Validation," May 1995.
- 1.5 WCAP-14141, Rev. 1, "AP600 Test and Analysis Plan for Design Certification," April 1995.
- 1.6 WCAP-14135, Rev. 1, "Final Data Report for PCS Large-Scale Tests, Phase 2 and Phase 3," April 1997.
- 1.7 WCAP-14967, "Assessment of Effects of WGOTHIC Solver Upgrade from Version 1.2 to 4.1," September 1997.
- 1.8 WCAP-15612, "**AP1000** Plant Description and Analysis Report," December 2000.
- 1.9 WCAP-15613, "**AP1000** PIRT and Scaling Assessment," February 2001.
- 1.10 WCAP-14407, Rev. 2, "WGOTHIC Application to AP600," April 1998.
- 1.11 NUREG-1793, Final Safety Evaluation Report Related to Certification of the AP1000 Standard Design," September 2011.

2 TEST AND ANALYSIS PROCESS OVERVIEW AND HIGH AND MEDIUM RANK CONTAINMENT PHENOMENA

2.1 INTRODUCTION

The Evaluation Model for the passive containment cooling system (PCS) design basis accident (DBA) has been developed using elements of scaling (top-down and bottom-up modeling of the integrated components), testing, and analysis (bottom-up phenomenological models and evaluations), similar to the methodology for Code Scaling Applicability and Uncertainty (Reference 2.1). Results have been used to identify bounding models and input values for use in the DBA Evaluation Model. The results of the DBA analyses provide conservative predictions of design basis transient pressure and temperature response for the containment.

The development of the PCS DBA methodology has followed an approach which can be organized into the four elements shown in Figure 2-1. The elements include tasks, that together provide a structured, traceable, and practical method for

- Specifying the scenario
- Identifying phenomena important to the transient
- Evaluating data and scale effects
- Documenting and validating the computer code
- Assessing margins and uncertainties
- Developing and applying the Evaluation Model

The process is represented by a once-through flow diagram for simplicity. The actual process included many iterations between the various tasks. For example, to better represent the observations of the large-scale containment test (LST) dome temperature distribution, due to the subcooling of the film applied to the LST, the initial WGOTHIC code version used in 1992 was augmented by the addition of a model for convective heat transport for the liquid film. In addition, extensive review by representatives of regulatory agencies, industry, and academia were incorporated into the process (Reference 2.2). The end result is documentation which describes the PCS DBA Evaluation Model and its bases in an auditable, traceable manner. Following is a brief description of the four elements of the process used to develop the methodology.

PCS Test and Analysis Process Overview

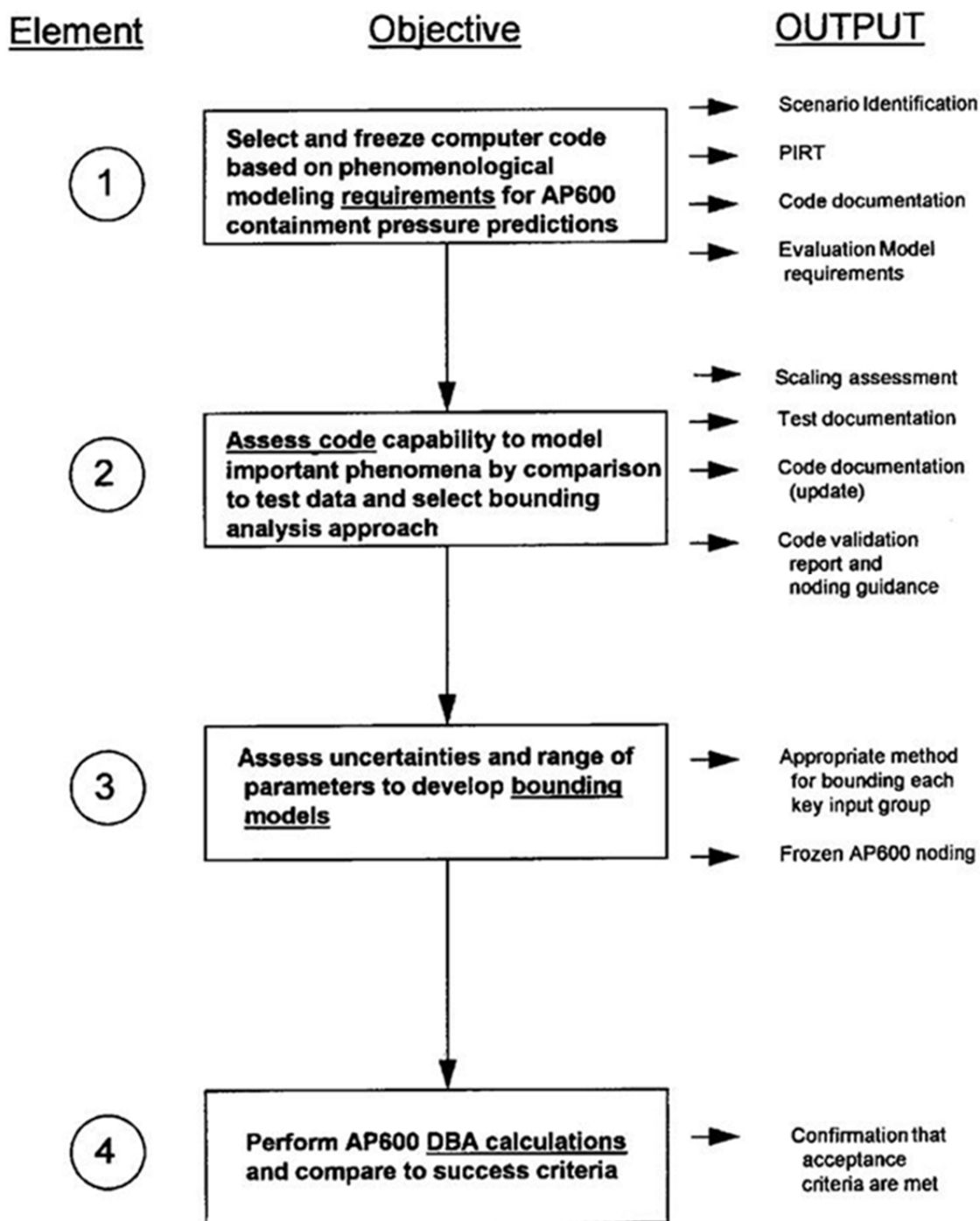


Figure 2-1. PCS Test and Analysis Process Overview

2.2 ELEMENT 1 – PCS REQUIREMENTS AND CODE CAPABILITIES

The PCS DBA methodology development process began with a review of the AP600 design and DBA scenarios and an identification of phenomena important for AP600 containment pressurization. From this review, an initial test program was defined and a computer code was selected.

A PIRT was developed to identify the key thermal-hydraulic phenomena which govern the transients of interest. The PIRT (Reference 2.2, Section 4) ranks phenomena according to their relative importance to the particular transient phase of interest. The PIRT process included input and review by representatives of academia and regulatory authorities, and cross-functional Westinghouse technical reviews. The bases for high, medium, and low rankings are documented in the PIRT. A key result of the PIRT is that the dominant phenomenon for transferring heat from the containment is mass transfer – condensation on the inside and evaporation on the outside. The mass and energy release boundary condition imposed on the problem is the primary driver of the containment pressure response, and is ranked high. For the loss-of-coolant accident (LOCA) scenario, pressurization is mitigated primarily by internal volume compliance during blowdown, and by internal heat sinks below deck, from blowdown through the transition period when the PCS cooling begins to dominate and turns the pressure around. PCS heat removal dominates the long-term LOCA response. The main steamline break (MSLB) transient is mitigated primarily by volume compliance and internal heat sinks. A summary of the high and medium ranked phenomena is shown in Table 2-1. As described in Reference 2.10, Section 2.6, the **AP1000** design changes do not affect the PIRT or the results of the AP600 PIRT confirmation that are documented in Reference 2.9.

In parallel with bottom-up phenomena evaluations, the WGOTHIC computer code was selected, upgraded, and frozen to allow explicit modeling of many of the phenomena identified in the initial review. As the scaling analysis and testing programs progressed, code upgrades were completed to better model experimental results according to guidelines consistent with computer code lifecycle management. Hand calculations and spreadsheets were used to verify correct programming of the upgrades as documented within the Westinghouse QA program. Documentation of the code used in the Evaluation Model consists of base GOTHIC 4.0 documentation (Refs. 2.3, 2.4, 2.5) and upgrades to create WGOTHIC 4.2 (Section 3).

2.3 ELEMENT 2 – ASSESS CODE VERSUS TESTS AND IMPORTANT PROCESSES

Analyses and computer code validations were used identify the most appropriate models and biases to use in the PCS DBA Evaluation Model. The PCS test results were documented, including separate effects (Reference 2.6) and integral effects (Reference 2.7). The PCS test data and other data from the literature were used to provide input to code validation (Reference 2.8). Validation was used to study how the oversimplification inherent in the lumped parameter WGOTHIC model applies to the AP600. The lumped parameter limitations lead to the potential for compensating errors, so that a methodology to bound the effects of compensating errors was identified (Reference 2.8, page 8-9). The effect of lumped parameter momentum formulation and nodding on WGOTHIC results was an important output of validation. Insight from validation was used to develop a bounding Evaluation Model in Element 3.

A scaling evaluation of AP600 was performed (Reference 2.9) which provided additional confirmation of the PIRT phenomena and ranking. Scaling identified the appropriate non-dimensional parameters, the effects of facility scales, and the ranges of parameters expected in AP600. Scaling was also used to identify distortions in the LST facility and to evaluate the effect of distortions on the use of the LST for studying lumped parameter code biases.

The results of scaling, testing, and code validation were used to establish a bounding analysis approach for each of the PIRT phenomena, documented in Reference 2.2, Section 4.4.

Table 2-1. Phenomena Identification and Ranking Table – Summary of High and Medium Ranked Phenomena

Phenomenon*		Effect on Containment	Pi Groups	Where Addressed
Break Source Mass and Energy (1A)		The mass and energy source for containment pressurization.	$\pi_{p,g,brk,enth}$ $\pi_{p,g,brk,work}$ $\pi_{p,work,d}$ $\pi_{p,work,p}$	Scaling Analysis
Gas Compliance (2C)		Stores mass and energy in atmosphere, increasing pressure.	$\pi_{p,\tau}$	Scaling Analysis
Initial Conditions Inside (4A, 4B, 4C)		Temperature, humidity, pressure affect non-condensables and energy storage.	parameter	Initial Conditions Section 5
Containment Solid Heat Sinks (3), Pool (5), Drops (1), and Shell (7)		Store energy (and remove mass from atmosphere) reducing pressure.	$\pi_{p,g,j}$ $\pi_{p,work,j}$	Scaling Analysis
	Internal Heat Sink Conduction (3D, 5E, 7F) and Heat Capacity (3E, 5A, 7G)	Limits conduction heat transfer into heat sinks, shell, or pool, and through shell. Stratification in the break pool can affect the effective heat capacity of the pool.	parameter	Scaling Analysis
	Heat Transfer Through Horizontal Liquid Films (3C)	Water on and non-condensable gases near upward facing horizontal surfaces limit heat and mass transfer to horizontal heat sinks.	parameter	Scaling Analysis

Table 2-1. Phenomena Identification and Ranking Table – Summary of High and Medium Ranked Phenomena (cont.)

Phenomenon*		Effect on Containment	Pi Groups	Where Addressed
Condensation Mass Transfer (3F, 5B, 7C)		The first-order transport process that removes mass and energy from the containment gas.	$\pi_{p,work,j}$	Scaling Analysis
	Break Source Direction and Elevation (1B), Momentum (1C), and Density (1D)	Direction, elevation, density, and momentum can dominate circulation and affect condensation rate.	parameter	Circulation and Stratification, Section 9
	Circulation and Stratification (2A)	Intercompartment Flow (Circulation) and stratification can affect the distribution of steam (and non-condensables) near heat sinks for condensation heat removal.	parameters	
	Intercompartment Flow (2B)			
	Source Fog (2D)	Affects circulation and stratification via buoyancy.	parameter	
Evaporation Mass Transfer (7N)		First-order transport process that removes mass and energy from the evaporating external shell.	$\pi_{e, fg, esx}$ $\pi_{p,g,brk,work}$ $\pi_{p,work,d}$ $\pi_{p,work,p}$	Scaling Analysis
	PCS Natural Circulation (9A, 13A)	Convective air flow provides convective heat and mass transfer from containment shell.	parameter	Scaling Analysis
	Liquid Film Flow Rate (8A), Water Temperature (8B), Film Stability (8C)	Affects the upper limit for water coverage on the external shell and amount of water available for evaporation.	parameter	Film Stability, Section 7
Liquid Film Energy Transport (7E, 7M)		<i>Inside:</i> Carries condensation energy to the IRWST and break pool. <i>Outside:</i> Absorbs energy rejected by the external shell surface.	$\pi_{e,f,if}$ See Note 1	Scaling Analysis
Convection Heat Transfer (3G, 7H, 10A, 10B)		A second order transport process that removes energy from the containment gas, and from the external shell.	$\pi_{p,q,j}$ $\pi_{e,q,esx} + \pi_{e,q,dx}$ Note 2	Scaling Analysis

Table 2-1. Phenomena Identification and Ranking Table – Summary of High and Medium Ranked Phenomena (cont.)

Phenomenon*	Effect on Containment	Pi Groups	Where Addressed
Radiation Heat Transfer (3H, 7I)	A second order transport process that removes energy from the containment gas and from the external shell.	$\pi_{p,q,j}$ $\pi_{e,q,esx} + \pi_{e,q,dx}$ Note 2	Scaling Analysis
Baffle Conduction (10D) and Baffle Leakage Paths (10G)	Conduction through the baffle into downcomer volume and leakage paths can influence the external natural circulation flow rates.	$\pi_{e,q,bf}$, $\pi_{e,q,bfx}$ None for leakage	PIRT Sections 4.4.10D and 4.4.10G

* Indicators in parentheses refer to phenomena in the “Phenomena Identification and Ranking According to Effect on Containment Pressure” (Reference 2.2, Table 4-1).

Notes:

- The fraction of the internal condensation carried away by the liquid film is defined by the ratio: $\pi_{e,f,j}/(\pi_{e,f,j} + \pi_{e,fg,j})$, for each heat sink j. The fraction of the external shell heat rejection that goes into the subcooled heat capacity of the external liquid is defined by the ratio: $\pi_{e,q,ssx}/(\pi_{e,q,ssx} + \pi_{e,q,esx} + \pi_{e,fg,esx} + \pi_{e,q,dx})$. The pi group values for AP600 are presented in Reference 2.9, Section 8.
- Inside containment $\pi_{p,q,j}$ represents the pressure effect of sensible heat transfer. The sensible heat transfer is approximately 1/2 radiation heat transfer and 1/2 convection heat transfer. Outside containment $\pi_{e,q,esx} + \pi_{e,q,dx}$ represents the sum of the dry and evaporating shell sensible heat transfer, that is approximately 1/2 radiation heat transfer and 1/2 convection heat transfer.

2.4 ELEMENT 3 – ASSESS UNCERTAINTIES AND DEVELOP BOUNDING MODELS

Uncertainties were assessed, and together with the results of code validation, were used to develop a method of applying the WGOTHIC lumped parameter formulation to create a bounding DBA Evaluation Model. Key results are summarized as follows.

It is worthwhile noting how representative high-ranked phenomena are addressed for the AP600 PCS in the context of understanding this overview. In this regard, some background on lumped parameter containment codes follows, and then a summary is given of how uncertainties are handled for two representative phenomena, the heat and mass transfer rate correlations, and circulation and stratification.

The application of WGOTHIC lumped parameter formulation for the PCS Evaluation Model has been justified by conservatively addressing lumped parameter biases (Appendix 9C, Section 9.C.3.4). Lumped parameter containment codes have been used for nuclear power plant licensing calculations for over 30 years. Limitations of the lumped parameter approach for containment modeling are documented in the literature. Generally, lumped parameter codes can reasonably predict global parameters, such as pressure, but the lumped parameter formulation oversimplifies physics when local details are important. For containment analysis, details within a volume are important when the physics of stratification within a volume or entrainment into jets or plumes is important. Coupling of the WGOTHIC lumped parameter nodes, with one or more distributed parameter volumes to gain some resolution of the details within a

volume, can increase the accuracy of the solution. However, while distributed parameter calculations were used to help understand test results, the use of such more detailed models was not practical for PCS DBA calculations due to computing requirements.

Complex thermal hydraulic models may produce results that match or bound test data but may also include compensating errors. Sufficient data were obtained on the important variables in the LST to isolate compensating errors in the lumped parameter model. Studies of LST calculations have shown that the compensating errors in lumped parameter calculations arise from offsetting effects of steam concentration and velocity. Because the jet source is numerically expanded to uniformly fill the volume flow area in a lumped parameter node, numerical entrainment leads to high predicted velocities in the above-deck region and a resultant homogenization of the containment. Mixing of non-condensables from the below-deck region in the LST penalizes PCS heat transfer because the non-condensables from below-deck penalize condensation rates. Overpredicting velocities benefits PCS heat transfer because of forced convection enhancement. In the Evaluation Model, the competing effects are addressed by using only free convection inside containment, thereby eliminating the influence of velocity overprediction. This results in a bounding prediction relative to the potential for compensating errors.

After developing an understanding of lumped parameter model performance, bounding approaches to address important phenomena, summarized in Table 2-1, were developed. Uncertainties are addressed by quantifying a bias and distribution for a phenomenon or by studying the range of expected containment conditions and establishing an upper bound approach. Examples of the two approaches follow, using mass transfer correlation and circulation and stratification.

Separate effects tests (SETs) and LST data have been used to select appropriate heat and mass transfer correlations from the literature and develop biases to bound the data (Reference 2.6, Section 4.5). A lower bound for heat transfer through the containment shell to the ultimate heat sink is therefore used.

One of the more complex issues is the coupling of circulation and stratification, break direction and momentum, and intercompartment flow, and the impact of those parameters on internal heat sink utilization. Circulation and stratification are complex physical processes that are not easily solved by numerical methods. Since both the AP600 and **AP1000** rely on passive cooling by natural circulation, there are no active systems to force the atmosphere to homogenize. Based on a study of plausible break scenarios (mass and energy, momentum, direction, and elevation), bounding, or extreme cases are identified for further study. The extreme cases are studied using first principles calculations and sensitivities to specific flow patterns of interest. The lumped parameter plant model, with above-deck noding based on noding frozen for the LST evaluations, is used to calculate the containment response for the specified flow patterns. Based on the sensitivities, a limiting scenario is chosen for use as the PCS DBA to bound the impact on mass transfer of the strongly coupled phenomena. Biases are introduced with lumped parameter compartment nodes to bound the effects of stratification, and an assessment of stratification effects on PCS heat removal through the shell shows that no net penalty on heat removal from the above-deck region need be applied. This is discussed in more detail in Section 9 (See Table 9-1).

Similar evaluations have led to the definition of a bounding Evaluation Model for important phenomena identified in the PIRT and documented in Reference 2.2 Section 4.4.

2.5 ELEMENT 4 – PERFORM DBA CALCULATIONS AND COMPARE TO SUCCESS CRITERIA

The Evaluation Model was developed as previously described to produce conservative, bounding pressure transients for each accident phase. The acceptance criteria are that the peak pressure must remain below the design pressure and pressure should be rapidly reduced, consistent with assumptions in radiological release calculations, which is typically interpreted as the pressure at 24 hours should be less than one half of the design pressure. Documentation is provided in Reference 2.2 that shows for each phenomenon:

- Relevant model in the code
- Test basis
- Report references
- Summary report conclusions
- Validation basis summary
- How validation results are used
- How uncertainty is addressed

2.6 CONCLUSIONS

A structured, traceable approach has been followed to develop the PCS DBA Evaluation Model. The PIRT has been used to develop a bounding Evaluation Model and the PIRT has been used as the basis for a road map to relevant supporting information for each phenomenon.

2.7 REFERENCES

- 2.1 Boyack, B.E., et al., “An Overview of the Code Scaling, Applicability, and Uncertainty Evaluation Methodology,” Nuclear Engineering and Design, Volume 119 (1990) No. 1, May 1990, pp 1-15.
- 2.2 WCAP-14812, “Accident Specification and Phenomena Evaluation for AP600 Passive Containment Cooling System,” Rev. 2, April 1998.
- 2.3 NTD-NRC-95-4563, “GOTHIC Version 4.0 Documentation,” September 21, 1995.
- 2.4 NTD-NRC-95-4577, “Updated GOTHIC Documentation,” October 12, 1995.
- 2.5 NTD-NRC-95-4595, “AP600 WGOTHIC Comparison to GOTHIC,” November 13, 1995.
- 2.6 WCAP-14326, “Experimental Basis for the AP600 Containment Vessel Heat and Mass Transfer Correlations,” Rev. 2, April 1998.
- 2.7 WCAP-14135, “Final Data Report for PCS Large-Scale Tests, Phase 2 and Phase 3,” Rev. 1, April 1997.
- 2.8 WCAP-14382, “WGOTHIC Code Description and Validation,” May 1995.

- 2.9 WCAP-14845, "Scaling Analysis for AP600 Containment Pressure During Design Basis Accidents," Rev. 3, March 1998.
- 2.10 WCAP-15613, "**AP1000** PIRT and Scaling Assessment," February 2001.

3 OVERVIEW OF WGOTHIC

3.1 INTRODUCTION

The passive containment cooling system (PCS) phenomena were identified and ranked by order of importance in determining the containment vessel pressure in a phenomena identification and ranking table (PIRT). The important phenomena are summarized in Section 2. Existing containment analysis codes were reviewed to determine which most closely met the requirements identified in the PIRT. Although none of the codes met all of the requirements, the GOTHIC code package (Reference 3.1) was selected for further development based on its validation history and modeling capability. This section provides an overview of the GOTHIC code and summarizes the changes made to the GOTHIC solver program to incorporate the special heat and mass transfer correlations, liquid film tracking, and the wall-to-wall radiation model for performing design basis analyses for PCS-type containments.

3.2 OVERVIEW OF THE CODE DEVELOPMENT AND VALIDATION

The GOTHIC code is a state-of-the-art program for modeling multi-phase flow. The GOTHIC code has been developed through a long history from other qualified thermal-hydraulic computer codes (as shown in Figure 3-1).

GOTHIC consists of three separate programs, the preprocessor, solver, and postprocessor. The preprocessor allows the user to rapidly create and modify an input model. The solver performs the numerical solution for the problem. The postprocessor, in conjunction with the preprocessor, allows the user to rapidly create graphic and tabular outputs for most parameters in the model.

The GOTHIC solver program calculates the solution for the integral form of the conservation equations for mass, momentum, and energy for multi-component, two-phase flow. The conservation equations are solved for three fields: continuous liquid, liquid drops, and the steam/gas phase. The three fields may be in thermal non-equilibrium within the same computational cell. This would allow the modeling of subcooled drops (for example, containment spray) falling through an atmosphere of saturated steam. The gas component of the steam/gas field can be comprised of up to eight different non-condensable gases with mass balances performed for each component. Relative velocities are calculated for each field, as well as the effects of two-phase slip on pressure drop. Heat transfer between the phases, surfaces, and the fluid are also allowed.

The GOTHIC solver program is capable of performing calculations in three modes. A model can be created in the lumped-parameter nodal-network mode, the two-dimensional distributed parameter mode, or the three-dimensional distributed parameter mode. Each of these modes may be used within the same model (as shown in Figure 3-2). The lumped parameter nodal-network mode is used for the containment Evaluation Model (EM).

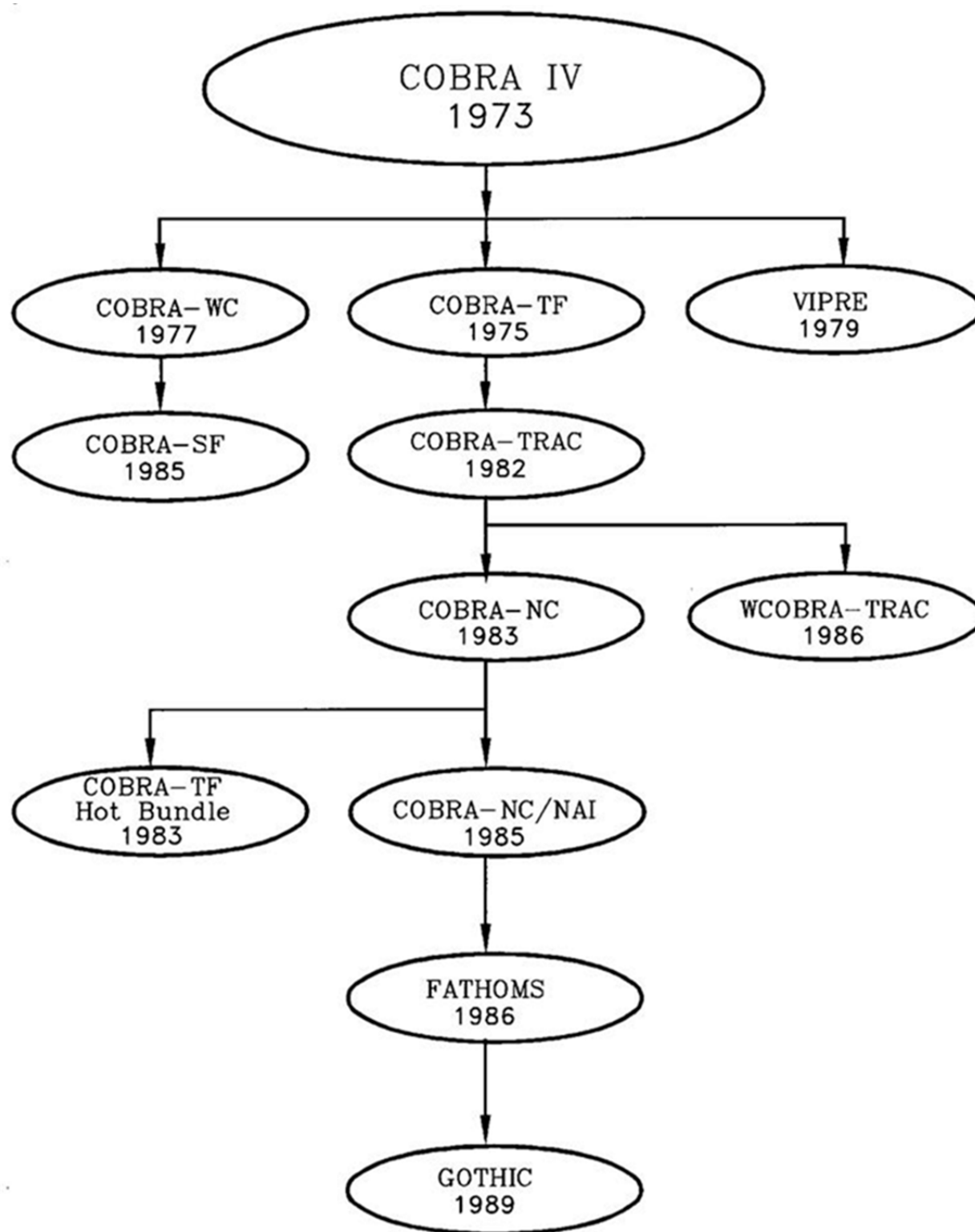


Figure 3-1. Summary of GOTHIC Historical Development

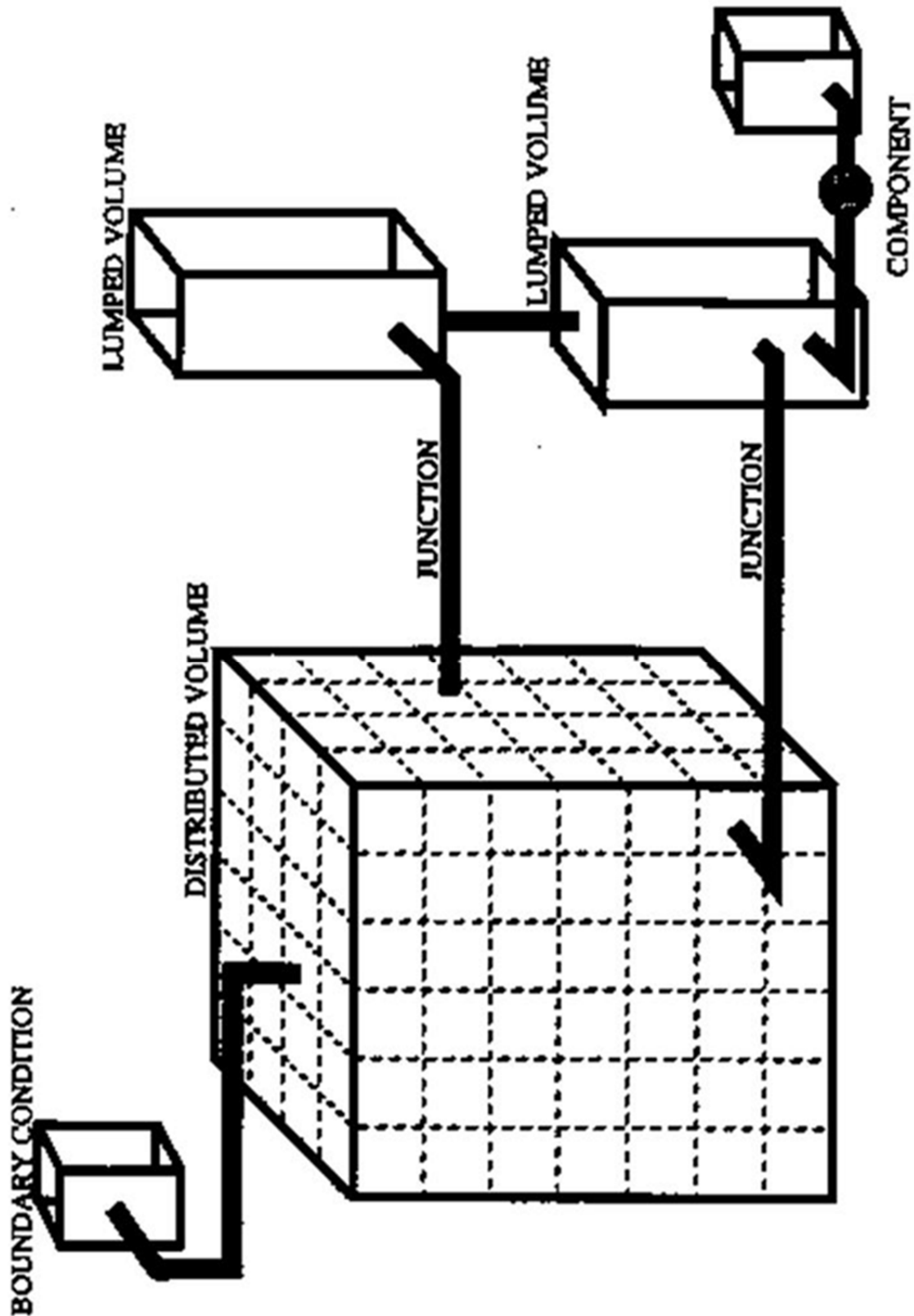


Figure 3-2. GOTHIC Modeling Features

The GOTHIC code also contains the options to model a large number of structures and components. These include, but are not limited to, heated and unheated conductors, heaters, coolers, pumps, fans, valves, and a variety of heat exchangers, and ice condensers. These components can be coupled to represent the various mitigation systems found in many containments. However, they are not used in the AP600 or **AP1000** peak containment pressure analyses to model any of the passive safety systems.

The GOTHIC code has an extensive validation history, which was an important consideration in the selection of the code for further development for modeling of the PCS. The GOTHIC code validation program includes both a comparison of code-calculated results with analytical solutions to specified standard problems and a comparison of code-calculated results with experimental data. The results of the Electric Power Research Institute (EPRI)-sponsored GOTHIC code validation program are presented in Reference 3.1, Enclosure 1. Table 3-1 lists some of the tests used in the GOTHIC code validation program. The phenomenological models validated by each test are cross-referenced and presented in Table 3-2. In addition, industry experience using GOTHIC in the lumped parameter mode, as well as attempts to improve results using multi-dimensional analyses, are described in Appendix 9.C.3.

Westinghouse purchased Version 3.4c of the GOTHIC code in 1991 and began modifying it to include mechanistic convection heat and mass transfer correlations, a liquid film tracking model, a one-dimensional wall conduction model, and wall-to-wall radiant heat transfer to model heat removal by the PCS. The code, with these modifications, is called Westinghouse-GOTHIC and is abbreviated as WGOTHIC.

The WGOTHIC development history is shown in Figure 3-3. The PCS heat and mass transfer models developed by Westinghouse were incorporated into the GOTHIC version 3.4c pre-processor and solver programs to create the WGOTHIC version 1.0 pre-processor and solver programs in 1993.

Between 1991 and 1993, while Westinghouse was developing the PCS heat and mass transfer models, GOTHIC version 3.4d underwent an EPRI-sponsored peer review. The purpose of the review was to establish a reference point for placing the GOTHIC code package under a 10 CFR 50, Appendix B Quality Assurance Program. The peer design review group reviewed the documentation, coding, convergence, pre-/post-processor, code qualification package, and the code's adequacy for containment analysis. The conclusions from the review are presented in Section 2.2 of the GOTHIC Design Review Final Report (Reference 3.2).

Overall, the GOTHIC containment analysis package was found to be adequate for containment analyses, and that the code package offered the ability to provide more accurate and mechanistic results than with other currently available containment codes. This conclusion was qualified with the statements that the nodal and junction treatment, as well as the range of the qualification database, need to be justified for each intended application; as was done via the large-scale (LST) and separate effects tests (SETs) (Reference 3.3) and various scale integral tests (Appendix 9.C.3) used to qualify WGOTHIC.

Table 3-1. GOTHIC Validation Tests

Battelle-Frankfurt Tests D-1, D-15, D-16	Modeling: 7 lumped parameter volumes, junctions Phenomena: Blowdown transients, subcompartment pressurization, wall differential pressures
Battelle-Frankfurt Test 6	Modeling: 1 distributed parameter volume (55 cells), conductors, junctions Phenomena: Hydrogen transport by convection and diffusion
Battelle-Frankfurt Tests 12, 20	Modeling: Combination of 5 lumped and 1 distributed parameter volumes (2 cells), conductors, junctions Phenomena: Hydrogen transport by convection and diffusion
Battelle-Frankfurt Tests C-13, C-15	Modeling: 10 lumped parameter volumes, conductors, junctions Phenomena: Main steamline break, pressure/temperature response
Hanford Engineering Development Laboratory Tests HM-5, HM-6	Modeling: 1 distributed parameter volume (300 cells), conductors, junctions Phenomena: Hydrogen mixing in a large, simulated containment
Light Water Reactor Aerosol Containment Experiments Tests LA-5, LA-6	Modeling: Combination of 1 lumped and 1 distributed parameter (2 cells) volumes, conductors, junctions Phenomena: Severe accident response to sudden containment failure
Marviken Full-Scale Containment Tests 17, 24	Modeling: 21 lumped parameter volumes, conductors, junctions Phenomena: Pressurized high temperature steam blowdown
Carolina's Virginia Tube Reactor Tests 3, 4, 5	Modeling: 2 lumped volume and a 2 distributed parameter volume (20 cells) models, conductors, junctions Phenomena: Steam blowdowns (T31.5 includes hydrogen/helium)
Heissdampfreaktor Tests V21.1, T31.1, T31.5, V44	Modeling: 37 lumped parameter volumes, conductors, junctions Phenomena: Steam blowdowns (T31.5 includes hydrogen/helium)

Table 3-2. GOTHIC Phenomenological Models Validated by Test

Item	BFMC	HEDL	LACE	MARV	CVTR	HDR
Fluid momentum	X		X	X		
Energy transport	X		X	X		
Non-condensable gases	X	X	X	X	X	X
Equations of state	X		X	X		
Pressure response	X	X	X	X	X	X
Temperature response	X	X	X	X	X	X
Humidity response	X	X	X	X	X	X
Hydrogen transport	X					
Energy sources	X	X	X		X	X
Subcompartment analysis	X			X		
High energy line breaks	X					
PWR standard containment			X			
BWR pressure suppression				X		
Fluid/structure interaction	X					
Conductors	X					
Subdivided volumes	X					
Turbulence	X					
3-D calculations	X	X		X		

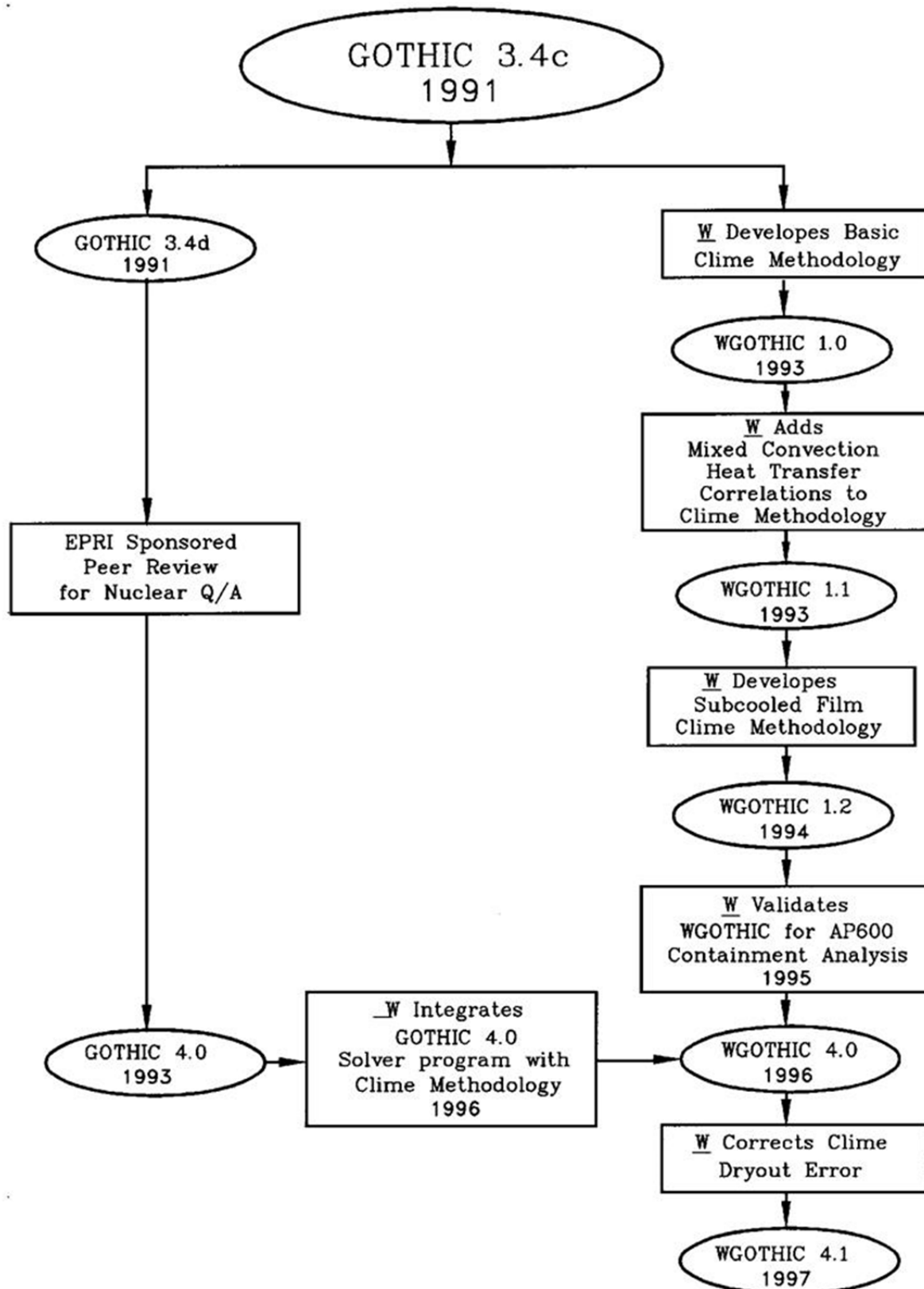


Figure 3-3. Summary of WGOTHIC Historical Development (Page 1 of 2)

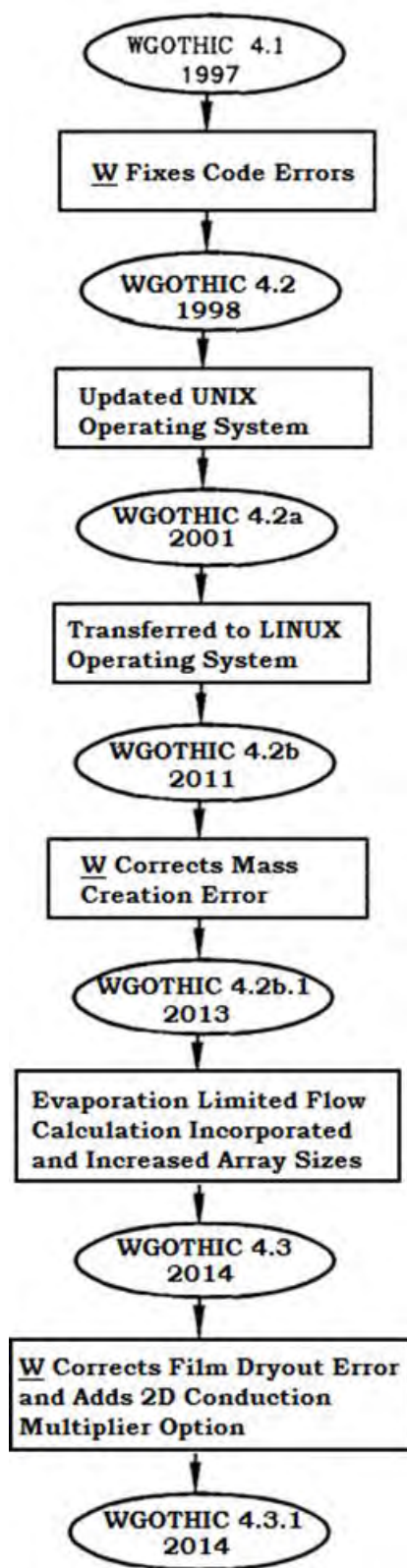


Figure 3-3. Summary of WGOTHIC Historical Development (Page 2 of 2)

The review group had three recommendations. The first was the addition of dynamic memory allocation, so that the code would not need to be recompiled for different sizes of models. The second was the inclusion of an iterated Newton method to aid in convergence. The third was to incorporate a fog model to simulate condensation of vapor when regions go from superheated to saturated.

As described in Reference 3.4, the conclusions and recommendations from the GOTHIC design review also apply to WGOTHIC. None of the recommended changes were incorporated in WGOTHIC. The first recommendation, dynamic memory allocation, wasn't incorporated in WGOTHIC, since it is a user convenience option and does not affect the solution technique. The second recommendation, to include an iterated Newton solution option to aid in convergence, was not incorporated in WGOTHIC, since satisfactory convergence was supported by the comparisons presented in the GOTHIC code qualification test report (Reference 3.1) and the WGOTHIC validation report (Reference 3.3). The third recommendation, to include a fog model, was not incorporated in WGOTHIC because it was concluded that, based on the GOTHIC Carolina's Virginia Tube Reactor (CVTR) qualification test case results (Reference 3.1) and an assessment of fog modeling as it relates to the AP600 (Reference 3.5, Sections 4.4.2D and 4.4.9C), it is conservative with respect to the prediction of containment temperature and pressure to not include the fog model.

Westinghouse updated the PCS models to account for subcooled films and incorporated the GOTHIC software error corrections that were provided by Numerical Applications, Inc. (NAI) to create WGOTHIC pre-processor version 2.0 and solver version 1.2 in 1994. Westinghouse validated this version of WGOTHIC for performing AP600 analyses in 1995 (Reference 3.3). The WGOTHIC validation program consisted of four parts:

1. The subset of GOTHIC validation tests that was identified as sensitive in the original acceptance tests was rerun with WGOTHIC. These tests were run with the same input options selected in the original GOTHIC validation calculation (that is, the PCS models were not exercised) to determine if any of the code changes made to incorporate the PCS models would affect the transient results. This comparison is presented in Appendix D of Reference 3.3. It shows that the code changes Westinghouse made to incorporate the PCS models do not affect the GOTHIC calculation results.
2. The PCS model one-dimensional conduction equation solution technique was validated by comparison with an analytical solution for a test problem. This comparison is presented in Section 4.1 of Reference 3.3. The code calculated results match the analytical solution.
3. The PCS model heat and mass transfer correlations were validated by comparison with separate effects test data from the Westinghouse Flat Plate Tests, the Westinghouse Large-Scale Tests, the Wisconsin Condensation Tests, and publicly available published reports. These comparisons are documented in Reference 3.6. The range of the important dimensionless parameters from the test program bounds both the AP600 and **AP1000** operating range, as shown in Table 3-3. The dimensionless parameters compared are the Prandtl number (Pr), the Schmidt number (Sc), the Reynolds Number (Re), and the Grashof Number (Gr). The percent differences reported for the enhanced shield building design (Reference 3.7) of the key scaling groups are small and negative indicating the PCS air flow path design changes are expected to slightly reduce the **AP1000** operating range from the previous shield building design. Therefore, the correlations are acceptable for modeling heat and mass transfer in both the AP600 and **AP1000** PCS.

4. WGOTHIC, including the PCS models and nodalization, was verified to be coded correctly by comparison with transient test data from the Westinghouse Large-Scale tests. Comparison with steady state test data from the LSTs assessed the ability of WGOTHIC to represent internal flow fields and noncondensable gas distributions and to calculate the net heat removal from the vessel in an integral system. The comparisons provided insight for the applicability of documented lumped parameter biases (Appendix 9.C.3) that are applied to the AP600 and **AP1000** containment Evaluation Models and identified a bounding approach to address compensating errors. This comparison is presented in Section 8 of Reference 3.3. Section 9, Table 9-1 summarizes how lumped parameter biases have been addressed.

In 1996, the source code for the PCS heat and mass transfer models for WGOTHIC solver version 1.2 and pre-processor version 2.0 was incorporated into the GOTHIC solver and pre-processor version 4.0 source code to create the WGOTHIC version 4.0 pre-processor and solver programs. This was done to incorporate all of the GOTHIC design review code changes into WGOTHIC.

A series of verification tests, including the most sensitive GOTHIC code qualifications test cases, were run to validate WGOTHIC version 4.0. The results of the GOTHIC code qualification test cases that were run using the WGOTHIC version 4.0 all compared very well with the results obtained using GOTHIC version 4.0, indicating that the incorporation of the Westinghouse PCS model did not significantly affect the GOTHIC calculations.

Version 4.1 of the WGOTHIC pre-processor, solver, and post-processor programs was created in 1997 to correct an error that was discovered in the PCS heat and mass transfer model and several other non-calculational code problems. The error caused the PCS heat removal to be over-predicted at the point of dryout. Verification test cases performed using WGOTHIC version 4.1 demonstrated that the dryout error was corrected. Version 4.1 of WGOTHIC has been used for all of the analysis results presented in this report except as specifically noted for sensitivity studies in Section 11.

Version 4.2 of the WGOTHIC code was created in 1998 to correct several errors that were discovered while using version 4.1. One error was caused by mixing both single and double precision variables within function and subroutine argument lists. Another error prevented the calculation of opposed mixed convection heat and mass transfer in the PCS. A third error was related to the cell centered velocity that is used in the clime heat and mass transfer calculations. It was determined that these errors did not have a significant effect on the code calculated output results; however, the code was updated to correct the errors and increase array dimensions to allow larger models to be created. Verification test cases that were performed using WGOTHIC version 4.2 demonstrated that the errors were corrected. Also, the changes that were made to create version 4.2 did not affect the results from the validation cases that were performed with version 4.1.

Version 4.2 was updated to Version 4.2a when the version of the UNIX operating system was upgraded in 2001. This version was used for the **AP1000** Design Control Document (DCD) analyses, Revision 15 through Revision 19.

Version 4.2a was updated to version 4.2b when the code was transferred from the UNIX operating system to the LINUX operating system in 2011. Version 4.2b.1 was created in 2013 to correct an error that would cause a small increase in the system mass over time. Although this error would not adversely affect the SSAR analyses, when integrated over several days, the mass error could become significant and affect the calculated results. The code output was also updated to allow the change in the mass and energy balances to be more easily tracked throughout the transient.

Version 4.3 of WGOTHIC was created in 2014 to incorporate an option to allow the evaporation-limited PCS flow calculations that are described in Section 7.5 to be automated within the code. This version also increased the array sizes, to allow more thermal conductor types, flow paths, and plot output time steps, along with providing plot output in binary files that can be read by another plotting program. These changes were made to improve the user experience and allow even larger models to be created. Validation testing of version 4.3 identified an error in the wet clime dry out calculation that affected the condensation rate inside containment. The error was introduced in version 4.2b.1 and only affected the version 4.3 results when the automated evaporation-limited PCS flow calculation option was not selected. No SSAR analyses were performed with version 4.3.

Version 4.3.1 was created in 2014 to correct the clime dry out error that was discovered during validation of version 4.3 and to add a 2-D conduction multiplier option to the automated evaporation-limited PCS flow calculation. The 2-D conduction multiplier that is used within WGOTHIC is described in Section 7.4.

Subsequent code version updates will be made to address changes in computing platforms, correction of errors, and updates to enhance the user experience without it being a change in methodology. Therefore, updates will not be made to this document unless a methodology-changing code change is made.

Table 3-3. Operating Range Comparison for AP600 and AP1000 Heat and Mass Transfer Parameters

Heat Transfer Correlation	Parameter	Composite of Test Data	AP600 Range	AP1000 Range	Percent Change for Enhanced AP1000 Shield Building
Internal Free Convection: $h = 0.13 \text{ k}/(\nu^2/g)^{1/3} [\Delta\rho/\rho]^{1/3} \text{ Pr}^{1/3}$	$\Delta\rho/\rho$	0.08 to 0.55	<0.40	<0.42	N/A
	Pr	0.72 to 0.90	0.72 to 0.90	0.72 to 0.90	N/A
	Sc	~0.52	~0.52	~0.52	N/A
External Mixed Convection: $\text{Nu}_{\text{force}} = 0.023 \text{ Re}_d^{0.8} \text{ Pr}^{1/3}$ $\text{Nu}_{\text{free}} = 0.13 (\text{Gr}_d \text{ Pr})^{1/3}$ For Opposed Mixed Convection: $\text{Nu}_{\text{mix}} = (\text{Nu}_{\text{force}}^3 + \text{Nu}_{\text{free}}^3)^{1/3}$ For Assisted Mixed Convection: $\text{Nu}_{\text{mix}} = \text{Max} \{(\text{Nu}_{\text{free}}^3 - \text{Nu}_{\text{force}}^3)^{1/3}, \text{Nu}_{\text{free}}, 0.75 * \text{Nu}_{\text{force}}\}$	Re_d Riser	<120000 evap. <500000 dry	<189000	<210000	-15%
	Re_d Downcomer		<151000	<190000	-7.0%
	Re_d Chimney		<1400000	<1800000	-13.0%
	Gr_d Riser	<7.0x10 ¹⁰ evap. <1.0x10 ¹¹ dry	<1.2 x 10 ⁹	<1.5 x 10 ⁹	-4.7%
	Gr_d Downcomer		<6.2 x 10 ⁹	<2.1 x 10 ¹⁰	
	Gr_d Chimney		<2.1 x 10 ¹²	<8.0 x 10 ¹²	2.9%
	Pr	~0.72	~0.72	~0.72	
	Sc	~0.52	~0.52	~0.52	
Liquid Film Heat Transfer: $\text{Nu}_{\text{turb}} = 0.0038 \text{ Re}^{0.4} \text{ Pr}^{0.65}$ $\text{Nu}_{\text{wavy laminar}} = 0.822 \text{ Re}^{-0.22}$	Re	<20000	<3200	<3500	
	Pr	1.77 to 5.9	1.5 to 3.0	1.5 to 3.0	

3.3 THE WGOTHIC CLIME MODEL

A solution technique that includes wall-to-wall radiation at the conditions expected for the passive plant design necessitates a close coupling of the participating walls. This coupling is accomplished by assigning boundaries that define the portions of the various walls that radiate to one another. Consistent with the basic formulation implemented for the GOTHIC code that considers conductors or heat sinks to be energy sink or source terms, code modifications that include wall-to-wall radiant heat transfer can be thought of as the addition of a special type of conductor group. This special conductor type or group consists of a set of walls that radiate to each other and interface with GOTHIC fluid cells through mass and energy source terms. The term *clime*, meaning *region*, is used to differentiate and distinguish this special conductor type from those already existing in GOTHIC terminology.

For the passive containment model, a clime is a horizontal slice of the containment structure consisting of the following:

[

] ^{a,c}

A representative three-conductor clime is shown schematically in Figure 3-4. The internal containment vessel volume, riser air flow channel volume, downcomer air flow channel volume, and environment volume are separate computational cells or fluid volumes in the model. The shell, baffle, and shield building walls are one-dimensional conductors representing solid wall structures between the

computational cells. These conductors are further subdivided into regions of different materials with different mesh sizes. Each conductor surface may have a liquid film present (not shown) depending on thermodynamic conditions.

The climes are stacked vertically through the PCS to model the effects of changing properties both inside and outside the containment shell. Usually there are at least two stacks of climes a wet stack and a dry stack. The only difference between a wet and dry stack is that a time-dependent, water flow rate boundary condition can be specified for each conductor surface of the top clime in a wet stack. Because condensation can occur on either wet or dry conductor surfaces, an initially dry stack of climes could contain some wet conductor surfaces and/or a partially wet conductor surface due to condensation. Likewise, an initially wet stack of climes could contain some dry conductor surfaces and/or a partially dry conductor surface due to evaporation. However, for the evaporation-limited option that was incorporated into WGOTHIC version 4.3, the wet and dry clime stacks are paired. As the water evaporates from the outside of the containment vessel wall wet clime, the corresponding area is moved to the dry clime. There can still be condensation on the inside surface of both a wet and a dry clime. See Section 7.5 and Section 13.5 for more information on the implementation of the clime modeling in the **AP1000** containment EM.

The user must specify values for the area and circumferential perimeter for each conductor of each clime in both the wet and dry stacks. The input values for the area and circumferential perimeter for the clime conductors in the wet stacks are based on measurements of the water coverage from the full-scale Water Distribution Tests. The PCS film coverage model, which conservatively bounds results from several test facilities, is described in Section 7.

The WGOTHIC clime model calculates the temperature, flow rate, and thermal resistance of the water films on the various conductor surfaces of a clime. Liquid mass is conserved whenever the film reaches the bottom clime in a stack or a conductor surface dries out. The clime model takes the film flow rate from each conductor surface of the previous clime in the stack as input, then adds the local condensation rate, or subtracts the local evaporation rate to determine the output water flow rate on each of its corresponding conductor surfaces. Any liquid film remaining on the conductor surfaces of the last clime in a stack is added to the liquid field of the GOTHIC cell in contact with the conductor surface, or an alternate drain cell specified by user input.

Dryout occurs when either the film flow rate is low enough or the heat flux is high enough to result in complete evaporation of the film before it can exit the conductor. The clime model calculates the evaporation heat and mass transfer and the location of the dryout elevation; the remainder of the conductor surface below the dryout elevation is treated as a dry surface.

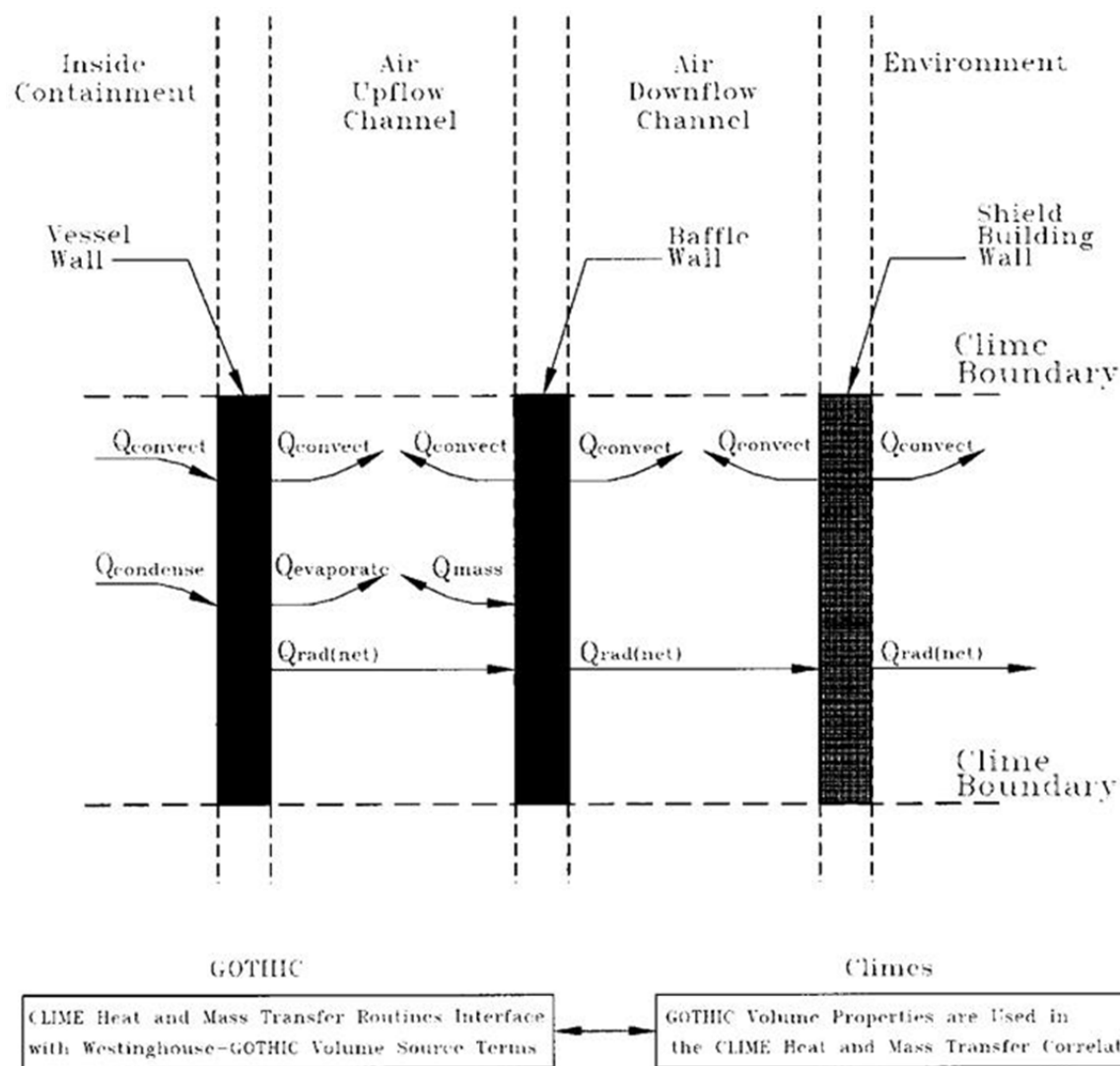


Figure 3-4. Westinghouse-GOTHIC Clime Wall Source Term Models

3.4 GENERAL CLIME EQUATIONS

Starting with WGOthic version 4.3, there are two options for modeling the PCS water flow rate and coverage. In the first option, the user specifies constant values for the area and wetted perimeter of the wet and dry climes, and an external calculation is performed to determine the evaporation-limited PCS flow rate. This is the standard coverage model option; it typically requires several iterations to converge and is consistent with all previous versions of WGOthic. In the second option, the user specifies the water coverage fraction for the first two climes as a function of the PCS flow rate (assuming no evaporation), and the evaporation-limited PCS flow rate is calculated within WGOthic. This is the automated evaporation-limited PCS flow and coverage model option. The general clime equations for both options are described next.

3.4.1 Standard PCS Flow and Coverage Model Option

The energy equation for the film must balance the heat from the wall into the film, the heat conduction through the film, and the heat and mass transfer from the film surface to the ambient, with the change in energy of the flowing film. Assuming constant fluid properties over the node surface, one-dimensional film flow along the wall, one-dimensional conduction across the film, and that the viscous dissipation term can be neglected, the general energy transport equation for the film can be written in terms of temperature as:

$$\frac{\partial T}{\partial t} = \frac{k}{\rho c_p} \frac{\partial^2 T}{\partial x^2} - v_z \frac{\partial T}{\partial z} \quad (3-1)$$

For computational purposes, the water film is divided into 3 control volumes as shown in Figure 3-5. The boundary control volume of the film includes the outer 1/2 layer of the wall and its temperature equals the wall temperature. The outer surface of the outer control volume touches the atmosphere and its temperature is coupled to the temperature of the atmosphere through the heat and mass transfer boundary layer correlations. The temperature in the central control volume represents the average heat stored in the film. Note that all convected energy is transported in the central control volume. This simplification improves numerical stability.

By convention, mass and energy entering a control volume are assigned positive values and mass and energy leaving a control volume are assigned negative values. Referring to Figure 3-5, the central control volume has a thickness of $\delta x_{\text{film}}/2$ and the film energy transport equation for this control volume can be expressed in a finite difference form as follows:

$$\frac{T_{\text{avg}} - T_{\text{avg,old}}}{\Delta t} = \frac{4k_{\text{film}}}{\rho_{\text{film}} c_{p,\text{film}}} \frac{T_{\text{surf},1} - 2T_{\text{avg}} + T_{\text{wall},1}}{\delta x_{\text{film}}^2} + v_z \frac{T_{\text{in}} - T_{\text{out}}}{\Delta z} \quad (3-2)$$

where,

k_{film}	=	film thermal conductivity (Btu/ft-sec-°F)
δx_{film}	=	film thickness (ft)
$c_{p,\text{film}}$	=	film specific heat (Btu/lbm-°F)
ρ_{film}	=	film density (lbm/ft ³)
T_{in}	=	inlet temperature of film at the top of the clime (°F)
T_{out}	=	exit temperature of film at the bottom of the clime (°F)
T_{avg}	=	temperature of the center of the film (°F)
$T_{\text{wall},1}$	=	temperature of first wall node (°F)
$T_{\text{surf},1}$	=	film surface temperature (°F)
ΔZ	=	height of the clime (ft)
v_z	=	film velocity (ft/sec)

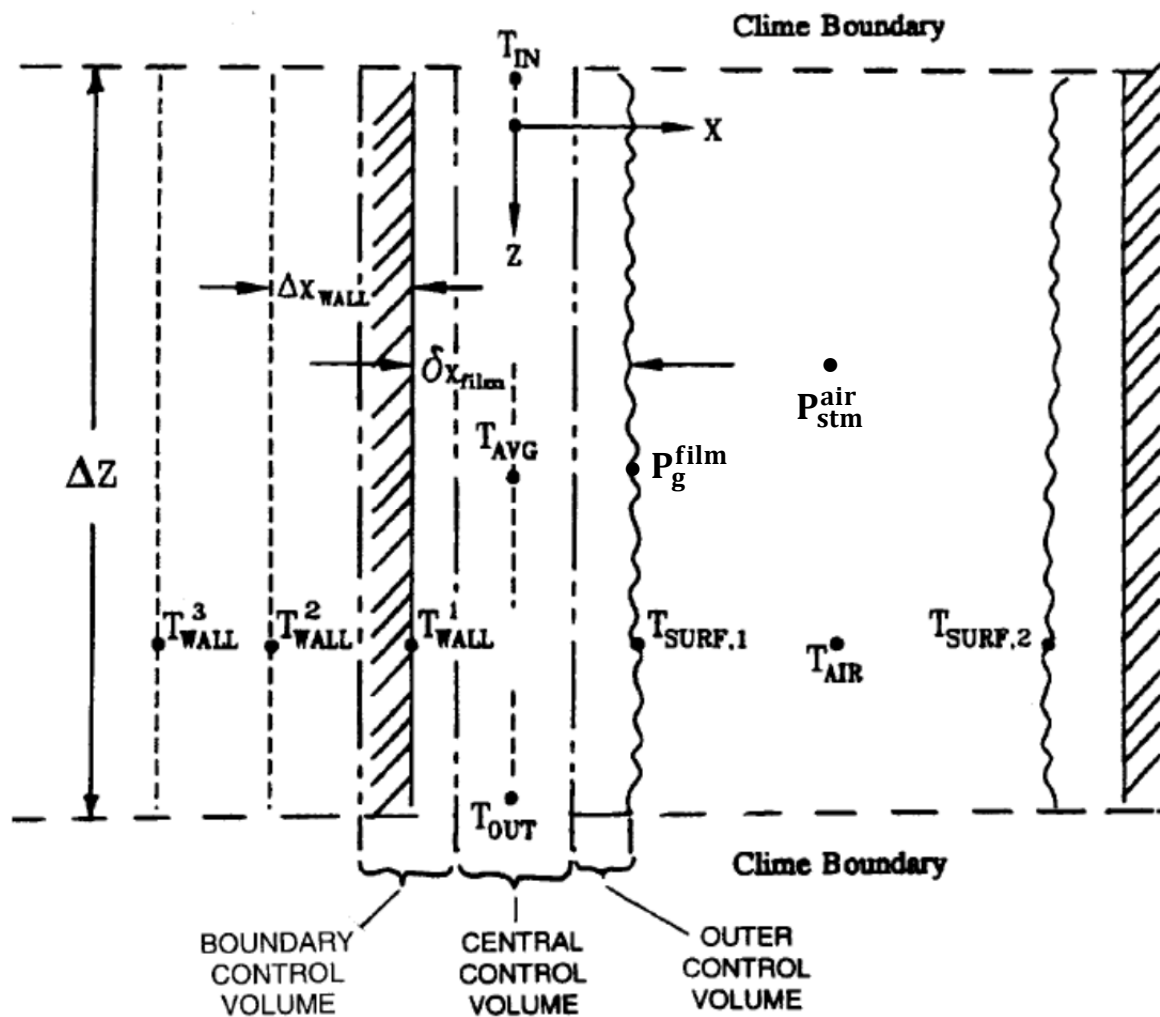


Figure 3-5. Clime Finite Difference Model Definitions

The film inlet temperature is given, either from a boundary condition or from the outlet temperature of the preceding clime in the stack. To ensure stability, the film outlet temperature is defined to be the same as the average temperature.

$$T_{out} = T_{avg} \quad (3-3)$$

The inner film surface boundary condition forces the heat flux from the outer surface of the conductor wall to equal the heat flux into the film. The solid film interface boundary condition is:

$$-k_{wall} \left. \frac{\partial T}{\partial x} \right|_{wall} = -k_{film} \left. \frac{\partial T}{\partial x} \right|_{film} \quad (3-4)$$

where k_{wall} is the wall thermal conductivity (Btu/ft-sec-°F).

The outer film surface boundary condition equates the energy leaving the outer film layer surface to the energy entering the atmosphere. The energy entering/leaving the film surface may leave/enter the atmosphere through a combination of convection, evaporation, and radiation. The outer film surface boundary condition is:

$$-k_{film} \left. \frac{\partial T}{\partial x} \right|_{film} = h_c (T_{surf,1} - T_{air}) + h_M h_{fg} (p_g^{film} - p_{stm}^{air}) + \epsilon \sigma (T_{surf,1}^4 - T_{surf,2}^4) \quad (3-5)$$

where,

h_c	=	convection heat transfer coefficient from the film to the air (Btu/sec-ft ² -°F)
$T_{surf,1}$	=	film surface temperature in (°F) in first right term, in (°R) in the last term
T_{air}	=	air temperature (°F)
h_M	=	mass transfer coefficient (lbm/sec-ft ² -psi)
h_{fg}	=	latent heat of vaporization of the film (Btu/lbm)
p_{stm}^{air}	=	partial pressure of steam in the air (psi)
p_g^{film}	=	saturation pressure of steam at the film surface temperature, $T_{surf,1}$ (psi)
ϵ	=	emissivity of film surface
σ	=	Stefan-Bolzman constant = 4.761×10^{-13} (Btu/sec-ft ² -°R)
$T_{surf,2}$	=	temperature of second radiative surface (°R)

The four film equations are:

$$\frac{T_{avg} - T_{avg,old}}{\Delta t} = \frac{4k_{film}}{\rho_{film} c_{p,film}} \frac{T_{surf,1} - 2T_{avg} + T_{wall,1}}{\delta x_{film}^2} + v_z \frac{T_{in} - T_{out}}{\Delta z} \quad (3-6)$$

$$-k_{wall} \left. \frac{\partial T}{\partial x} \right|_{wall} = -k_{film} \left. \frac{\partial T}{\partial x} \right|_{film} \quad (3-7)$$

$$-k_{\text{film}} \left. \frac{\partial T}{\partial x} \right|_{\text{film}} = h_c (T_{\text{surf},1} - T_{\text{air}}) + h_M h_{fg} (p_g^{\text{film}} - p_{\text{stm}}^{\text{air}}) + \epsilon \sigma (T_{\text{surf},1}^4 - T_{\text{surf},2}^4) \quad (3-8)$$

$$T_{\text{out}} = T_{\text{avg}} \quad (3-9)$$

The wall conduction equation is tightly coupled to these film equations. For points within the wall, the conduction equation is simply a one-dimensional partial differential equation:

$$\frac{\partial T}{\partial t} = \frac{k}{\rho c_p} \frac{\partial^2 T}{\partial x^2} \quad (3-10)$$

By replacing the derivatives with finite differences, this partial differential equation is replaced with a system of algebraic equations. The subscript “n” identifies the point (node) at which the derivatives are to be calculated.

$$\frac{T_{\text{wall},n} - T_{\text{wall},n,\text{old}}}{\Delta t} = \frac{k_{\text{wall}}}{\rho_{\text{wall}} c_{p,\text{wall}}} \frac{T_{\text{wall},n+1} - 2T_{\text{wall},n} + T_{\text{wall},n-1}}{\Delta x_{\text{wall}}^2} \quad (3-11)$$

where,

$$\begin{aligned} \rho_{\text{wall}} &= \text{wall density (lbm/ft}^3\text{)} \\ c_{p,\text{wall}} &= \text{wall specific heat (Btu/lbm-}^\circ\text{F)} \\ \Delta x_{\text{wall}} &= \text{wall node thickness (ft)} \end{aligned}$$

This equation, along with Equations (3-6 through 3-9), can be considered to be the system of equations for a clime.

Although the differential boundary condition Equation (3-7) is mathematically complete and correct, numerical stability in a finite difference formulation is improved by defining an alternate control volume containing the boundary between solid and liquid. As shown in Figure 3-5, the boundary control volume is defined to contain the wall material from the surface to a point halfway between the surface and the first internal calculational point (that is, between wall nodes 1 and 2) into the control volume and the inner quarter of the film thickness. The energy balance equation for the boundary control volume is:

$$\left[\rho_{\text{wall}} c_{p,\text{wall}} \frac{\Delta x_{\text{wall}}}{2} + \rho_{\text{film}} c_{p,\text{film}} \frac{\delta x_{\text{film}}}{4} \right] \frac{dT_{\text{wall},1}}{dt} = k_{\text{wall}} \frac{T_{\text{wall},2} - T_{\text{wall},1}}{\Delta x_{\text{wall}}} - 2k_{\text{film}} \frac{T_{\text{wall},1} - T_{\text{avg}}}{\delta x_{\text{film}}} \quad (3-12)$$

The film convective energy transport has been neglected for the boundary control volume. Because the film velocity at the wall is zero, the effect of neglecting this is small. A similar control volume and heat flux equation is defined for the outer quarter of the film thickness to model the air/film interface. In this case, the film surface heat flux is the sum of the convection, radiation, and mass transfer heat fluxes.

$$\rho_{\text{film}} c_{p,\text{film}} \frac{\delta x_{\text{film}}}{4} \frac{dT_{\text{surf}}}{dt} = 2k_{\text{film}} \frac{T_{\text{avg}} - T_{\text{surf}}}{\delta x_{\text{film}}} - h_c (T_{\text{surf},1} - T_{\text{air}}) - h_M h_{fg} (p_g^{\text{film}} - p_{\text{stm}}^{\text{air}}) - \epsilon \sigma (T_{\text{surf},1}^4 - T_{\text{surf},2}^4) \quad (3-13)$$

Most of the convective energy transport by the film as it flows down the shell is carried in the central flow region of the film. At the wall, the film velocity is zero so there is little transport next to the wall even though the temperature gradient is greatest there. At the film surface, the vertical temperature gradient is smallest because the film surface temperature is strongly coupled to the surrounding atmosphere which has a relatively small vertical temperature gradient.

In the WGOTHIC Containment Evaluation Model, most of the water film on the outside of the containment is expected to evaporate. The latent heat of evaporation of water is around 1000 Btu/lbm. Compare this with the heat required to heat water from its initial temperature to the dewpoint temperature of the surrounding air which is around 20-50 Btu/lbm. At most, the subcooling of a completely evaporating film accounts for about 5 percent of the total energy removal. The numerical error introduced by neglecting the transport in the control volumes at the wall and on the film surface is estimated to be less than 20 percent for the completely evaporated film. Thus, the total energy imbalance introduced by neglecting these transport terms is less than 1 percent of the total energy removal from containment.

On the inside of containment, the water film temperature is very closely tied to the partial pressure of steam. During the large-scale tests, the internal steam concentration vertical gradient was observed to be nearly zero. The numerical error in the transport equation on the inside is smaller than the 1 percent of total energy on the outside of containment.

In principle, the effects of the numerical modeling assumptions could be reduced more by including the film surface vertical convective energy transport term. During the development of the model, this term was included and appeared to be linked to an instability that arose through the interaction between the transport energy and the non-linear radiation and convective heat and mass transfer models. As a result, a decision was made to accept the small numerical error to maintain the stability of the model.

The second numerical assumption made is that the film instantly covers the containment as soon as film flow is introduced in the code, i.e., no tracking of a film front is performed. The film flow is initiated by a high-pressure signal inside containment. At this time, the outer surface of the containment is still cold. It takes several minutes for the film to entirely cover the containment. It also takes about 10-15 minutes for the outer surface of the containment to heat sufficiently for the heat and mass transfer models to start to have any effect. As a result, by the time evaporation could contribute to heat removal, the containment would be covered with water anyway. The only other time that this could have an impact on transient results would be if there is a step change in the flow. Given that the transient involving large changes in the film flow occur over a period of more than a day, the error in assuming an instantaneous step change instead of a change over several minutes can be considered to be small. In addition, it can be compensated for by ramping the flow rate over a period of several minutes instead of introducing the step change.

Equations 3-6, 3-9, and 3-11 through 3-13 represent the complete system of equations for a clime as used in WGOTHIC. See Sections 4 and 13 for a description of how climes are implemented for the AP600 and **AP1000** Containment Evaluation Models.

3.4.2 Automated Evaporation-Limited PCS Flow and Coverage Option

The equations above have been modified for the automated evaporation-limited PCS flow and coverage option. This option was originally intended to model 2D heat conduction between the wet and dry sections of the containment shell. However, some problems were encountered during the code development process, so a 1D conduction solution using the DLSODE solver with an optional 2D conduction heat transfer multiplier has been incorporated in WGOTHIC version 4.3. The 2D conduction heat transfer multiplier option is described in Section 7.6.

[

] ^{a,c}

[

] ^{a,c}

[

] ^{a,c}



Figure 3-6. Wetting Fraction vs. Elevation

3.5 INTEGRATION OF THE WESTINGHOUSE CLIME MODEL INTO GOTHIC

The Westinghouse clime model is composed of a set of subroutines. These subroutines were added to the GOTHIC solver program to create the WGOTHIC solver program. The GOTHIC solver program logic was modified to incorporate the clime model as follows:

- A call to the subroutine that reads the clime input was added
- A call to the subroutine “gshell”, the main calling routine for the clime model, was added
- A call to the subroutine that generates the clime output was added

The standard clime model flow control outline is shown in Figure 3-7. Subroutine “gshell” is the main calling routine for the other subroutines of the clime model. Separate subroutines in the clime model compute the heat and mass transfer coefficients between the conductor surfaces and the corresponding volumes, the surface-to-surface radiation heat transfer, the conductor wall temperature distribution, and the changes to the source terms for the GOTHIC mass and energy conservation equations.

The flow control outline for the automated evaporation-limited PCS flow and coverage model option is shown in Figure 3-8. Subroutine “gshell2” is the main calling routine for the other subroutines in this model. Note, the 2D conduction solution logic has not yet been implemented. If the 2D conduction multiplier option is selected, those multipliers are calculated and applied to the heat and mass transfer coefficients that are input to the DLSODE solver.

The interface between the clime model and GOTHIC takes place through the source terms for the GOTHIC mass and energy conservation equations. The GOTHIC vapor mass and energy source terms are updated to include the mass and energy transfer due to convection, radiation, evaporation, and condensation within the climes. The GOTHIC liquid mass and energy source terms are updated to include the liquid mass and energy transfer due to runoff or stripping of the liquid film from the climes.

a,b,c

Figure 3-7. Clime Routines Flow Control Outline

a,b,c

Figure 3-8. Clime Routines Flow Control Outline

3.6 REFERENCES

- 3.1. Westinghouse Letter NTD-NRC-95-4563, B.A. McIntyre to Quay (NRC), "GOTHIC Version 4.0 Documentation," September 21, 1995.
- 3.2. Westinghouse Letter NTD-NRC-95-4462, N.J. Liparulo to T.R. Quay (NRC), EPRI Report RA-93-10, "GOTHIC Design Review, Final Report," May 15, 1995.
- 3.3. WCAP-14382, "WGOTHIC Code Description and Validation," M. Kennedy, et al., May 1995.
- 3.4. Westinghouse Letter NTD-NRC-95-4595, B.A. McIntyre to Quay (NRC), "AP600 WGOTHIC Comparison to GOTHIC," November 13, 1995.
- 3.5. WCAP-14812, Rev. 2, "Accident Specification and Phenomena Evaluation for AP600 Passive Containment Cooling System," April 1998.
- 3.6. WCAP-14326, Rev. 2, "Experimental Basis for the AP600 Containment Vessel Heat and Mass Transfer Correlations," F. Delose, et al., April 1998
- 3.7. APP-GW-GLR-096, Rev. 3, "Evaluation of the Effect of the AP1000[®] Enhanced Shield Building Design on the Containment Response and Safety Analyses," R. Ofstun, June 13, 2011.

4 DESCRIPTION OF AP600 PLANT GEOMETRY IN WGOTHIC EVALUATION MODEL

This entire section (4) is proprietary to Westinghouse Electric Company (a,c).

5 INITIAL AND BOUNDARY CONDITIONS

5.1 INTRODUCTION

The purpose of this section is to describe a series of sensitivity analyses performed using the AP600 containment model to examine the effect of initial conditions on containment pressure response for the LOCA and MSLB events. Sensitivity evaluations are performed on initial containment humidity, pressure, and temperature, as well as ambient (outside containment) humidity and temperature. In addition, a sensitivity to drop modeling assumptions – a boundary condition for LOCA – is presented in this section.

Initial conditions assumed in the WGOTHIC Evaluation Model are conservatively set to maximize containment pressure response and are consistent with Technical Specifications and site interface parameter limits. Initial conditions assumed in the sensitivity evaluations are set at the opposing end of the Technical Specifications and site interface parameter limits for all sensitivity cases in this section except for the external temperature sensitivity, which was examined over a more limited range to be consistent with the film temperature range.

5.2 INITIAL CONDITION SENSITIVITY CASES

The initial conditions considered in the sensitivity studies are summarized in Table 5-1. The relative humidity inside containment is set to 0% for the containment EM. The input for the other initial conditions for the plant licensing analyses will be defined by the Technical Specifications and site parameters, in the direction of conservatism determined by these sensitivities.

Table 5-1. Initial Conditions

Initial Condition	Reference Value	Sensitivity Value	Direction of Conservatism for Evaluation Model
Containment Relative Humidity, %	0	100	Low
Containment Pressure, psia	15.7	14.5	High
Containment Temperature, °F	120	50	High
Ambient (Outside) Relative Humidity (Based on maximum wet bulb temperature coincident with maximum dry bulb temperature), %	22	0	High
Ambient (Outside) Temperature (Based on maximum dry bulb temperature), °F	115	40	High
Water Film Temperature on Outside Shell Surface, °F	120	40	High

The sensitivity cases considered for the LOCA and MSLB transients are summarized in Table 5-2 with the initial condition parameters assumed in each case. Only values noted in Table 5-2 were varied in each of the cases. The reference cases for the LOCA and MSLB are described in Sections 4.5.2.1 and 4.5.2.2, respectively. The mass and energy releases are the same for all LOCA and MSLB cases. A summary of the pressure results are summarized in Table 5-3 for the LOCA and Table 5-4 for the MSLB. A discussion of each sensitivity case is provided in the following sections.

Table 5-2. Initial Conditions Sensitivity Analysis Cases

Case	Inside Containment					Outside Containment		
	Transient	T-air (°F)	P (psia)	RH (%)	T-ht. sink (°F)	T-air (°F)	T-film (°F)	RH (%)
Reference		120	15.7	0	120	115	120	22
1	LOCA	120	15.7	100	120	115	120	22
2	LOCA	120	14.5	0	120	115	120	22
3	LOCA	50	15.7	0	50	115	120	22
4	LOCA	120	15.7	0	120	115	120	0
5	LOCA	120	15.7	0	120	40	40	100
6	LOCA	120	15.7	0	120	40	40	0
7	LOCA	120	15.7	0	120	115	40	22
8	MSLB	120	15.7	100	120	115	120	22
9	MSLB	120	14.5	0	120	115	120	22
10	MSLB	50	15.7	0	50	115	120	22
11	MSLB	120	15.7	0	120	115	120	0
12	MSLB	120	15.7	0	120	40	40	100
13	MSLB	120	15.7	0	120	40	40	0
14	MSLB	120	15.7	0	120	115	40	22

Table 5-3. Summary of Pressure Results for LOCA Initial Condition Sensitivity Studies

	Peak Pressure during Blowdown (psig)	Peak Post-Blowdown Pressure (psig)	Pressure at 24 Hours (psig)
Eval. Model	34.4	43.9	18.9
Case 1	34.0	42.5	16.6
Case 2	33.0	42.1	17.2
Case 3	35.2	42.5	19.4
Case 4	34.4	43.9	18.9
Case 5	34.4	43.7	16.6
Case 6	34.4	43.7	16.6
Case 7	34.4	43.7	16.6

Table 5-4. Summary of Pressure Results for MSLB Initial Condition Sensitivity Studies

	Peak Pressure (psig)
Evaluation Model	44.8
Case 8	43.6
Case 9	42.9
Case 10	44.6
Case 11	44.7
Case 12	44.7
Case 13	44.7
Case 14	44.7

5.3 INITIAL CONTAINMENT HUMIDITY

The purpose of this sensitivity analysis is to illustrate the effect of initial containment humidity on containment pressure response. Initial humidity affects the initial mass of air in the containment and the concentration of air inside containment during the accident. In general, the presence of non-condensable gases reduces the effectiveness of internal heat sink structures to absorb energy, since the condensing vapor must diffuse through the gas before it can condense on the surface.

The upper and lower bounds on relative humidity are 100 percent and 0 percent, respectively. The minimum, initial containment relative humidity (0 percent) is used for the Evaluation Model, since this value produces a higher peak containment pressure. The maximum relative humidity (100 percent) is assumed for the sensitivity case in order to quantify the effect of initial containment relative humidity on containment pressure response.

The sensitivity of containment pressure to initial containment humidity is illustrated in Figure 5-1 for the LOCA (Case 1) and Figure 5-2 for the MSLB (Case 8). The sensitivity and reference cases are compared, corresponding to 100 percent and 0 percent relative humidity, respectively. A higher containment pressure response is predicted for zero percent relative humidity than for the sensitivity case at 100 percent relative humidity. The effect of relative humidity on containment pressure is explained by the influence of air on the rate of condensation on internal heat sink structures, and the additional mass of air in containment. Lower relative humidity corresponds to lower vapor partial pressure and hence, to lower water vapor concentration. Since the total initial pressure is fixed, the partial pressure and, therefore, the concentration of air is greater at 0 percent than at 100 percent relative humidity. The higher mass of air also contributes to the pressurization as it heats up in thermal equilibrium with the steam. A greater quantity of air in the condensing vapor also results in greater resistance to heat transfer, since the vapor must diffuse through the gas before it can condense on the surface. This factor reduces the overall heat removal capability of internal heat sink structures, and results in greater containment pressures for the initial 0 percent relative humidity case.

5.4 INITIAL CONTAINMENT PRESSURE

Initial containment pressure directly affects the containment pressure response. The range of initial containment pressures is bounded by the Technical Specifications limits. The initial internal containment pressure is set to the maximum Technical Specifications limit of 15.7 psia (1.0 psig) in the Evaluation Model. The lower bound (sensitivity case) initial containment pressure is set at the minimum Technical Specification limit of 14.5 psia (-0.2 psig).

The sensitivity of containment pressure to the initial containment pressure is shown in Figure 5-3 for the LOCA (Case 2) and Figure 5-4 for the MSLB (Case 9). As expected, greater initial containment pressure results in greater containment pressure response throughout the transient. A higher initial pressure results in a greater mass (and hence concentration) of air and results in higher containment pressures.

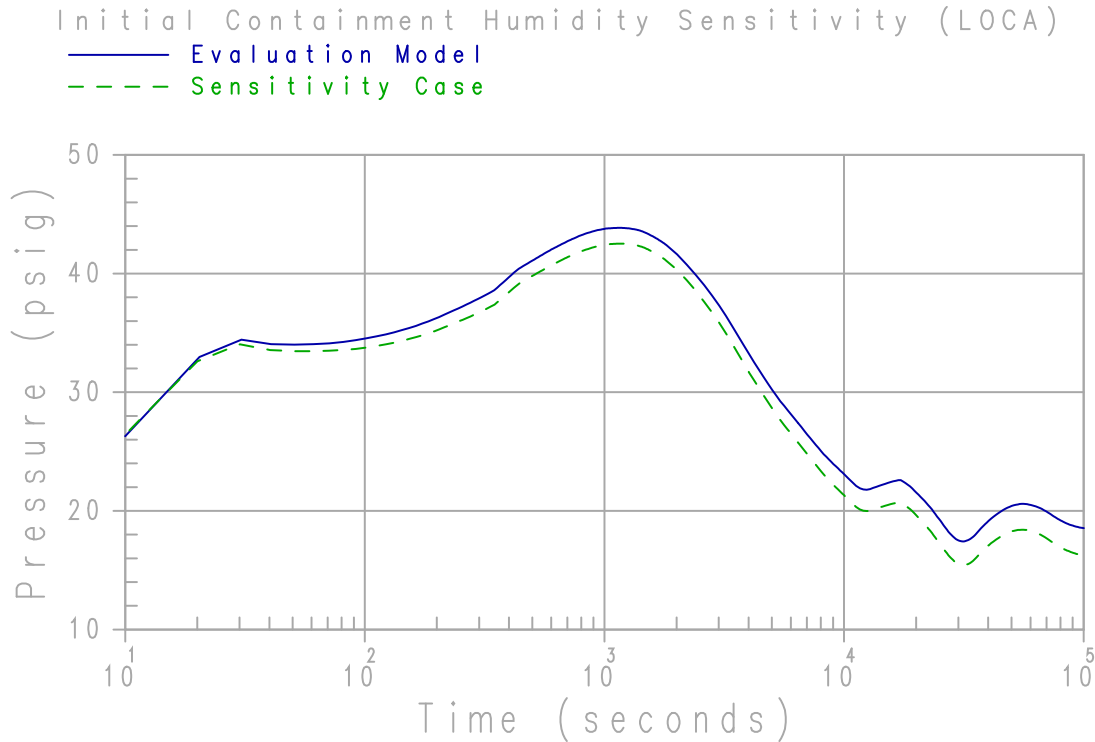


Figure 5-1. Case 1 – Initial Containment Humidity Sensitivity – LOCA

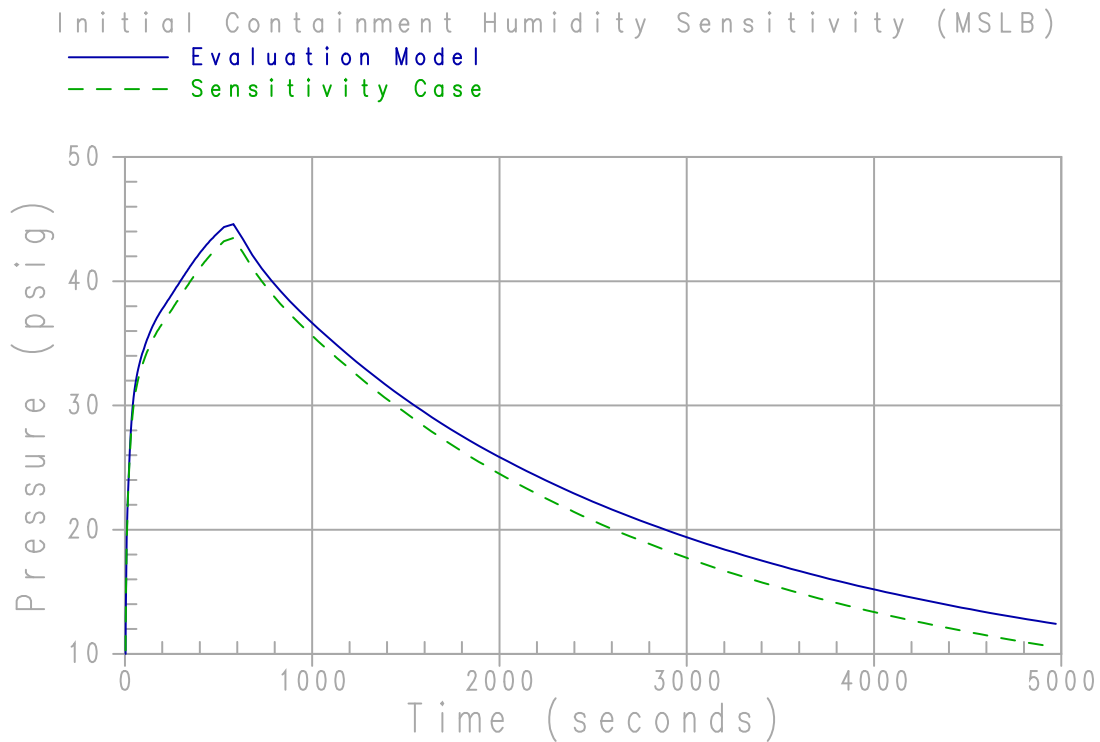


Figure 5-2. Case 8 – Initial Containment Humidity Sensitivity – MSLB

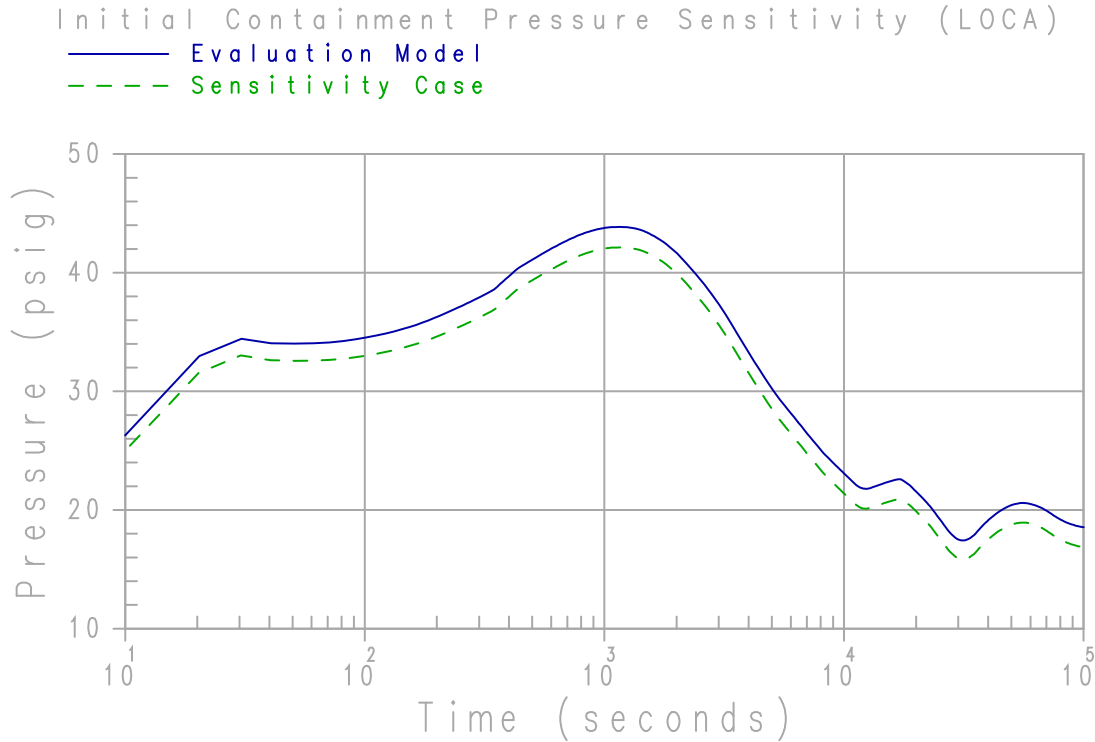


Figure 5-3. Case 8 – Initial Containment Humidity Sensitivity – MSLB

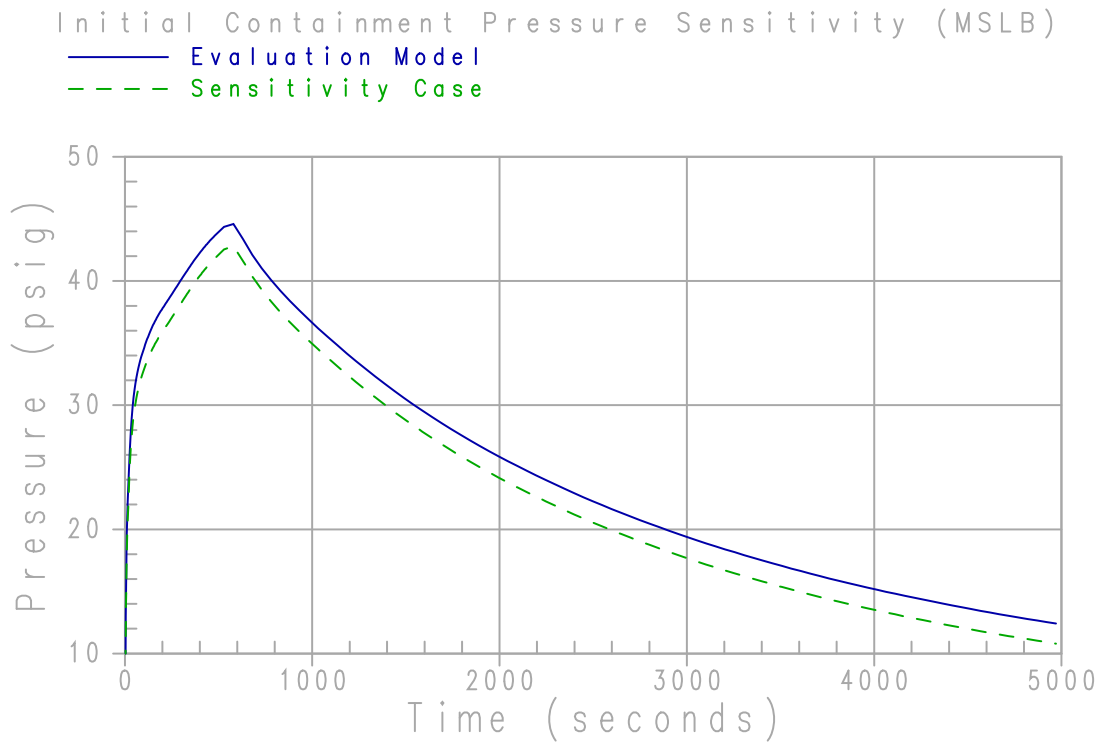


Figure 5-4. Case 9 – Initial Containment Pressure Sensitivity – MSLB

5.5 INITIAL CONTAINMENT TEMPERATURE

The purpose of this sensitivity analysis is to quantify the effect of initial containment temperature on containment pressure response. Containment air, internal heat sink, and containment shell initial temperature are simultaneously varied. A change in the initial air temperature affects the concentration of air inside containment. A change in the initial containment heat sink temperature directly affects the heat absorption capacity of these structures.

The initial containment temperature is set to the maximum Technical Specification limit of 120°F in the Evaluation Model. The lower bound (sensitivity case) initial containment temperature is set to a value of 50°F.

The sensitivity of containment pressure to initial containment temperature is shown in Figure 5-5 for the LOCA (Case 3) and Figure 5-6 for the MSLB (Case 10). As indicated, a higher peak containment pressure is predicted for the Evaluation Model case at 120°F, than for the sensitivity case at 50°F initial temperature. As illustrated in Figure 5-5, the pressure is higher for the 50°F initial temperature case during the blowdown phase of the transient, lower at the time of maximum pressure, and higher beyond approximately 5000 seconds. For the MSLB case shown in Figure 5-6, the peak pressure is slightly lower for the 50°F initial temperature case, but is higher during the initial pressure rise and beyond approximately 2000 seconds.

This pressure response behavior is predominately due to two competing influences: (1) the effect of initial temperature on the amount of air in the containment, and (2) the effect of initial temperature on the heat absorption capacity of internal heat sink structures. A lower initial temperature results in a higher air mass which contributes to the pressurization as the containment heats up. The increased concentration inhibits condensation of vapor on internal heat sinks and results in higher containment pressures. In contrast, a lower initial temperature results in increased heat absorption capacity of internal heat sinks that tend to lower containment pressures. Initially the non-condensable gas concentration factor dominates, and the sensitivity case exhibits a slightly higher containment pressure. When the heat absorption capacity of internal heat sinks becomes the more dominant factor, a higher containment pressure results for the Evaluation Model case. As the internal heat sinks saturate, the air concentration factor again becomes the governing influence, and the pressure for the sensitivity case exceeds that for the Evaluation Model. The Evaluation Model uses the maximum temperature assumption in order to maximize the more limiting post-blowdown peak containment pressure.

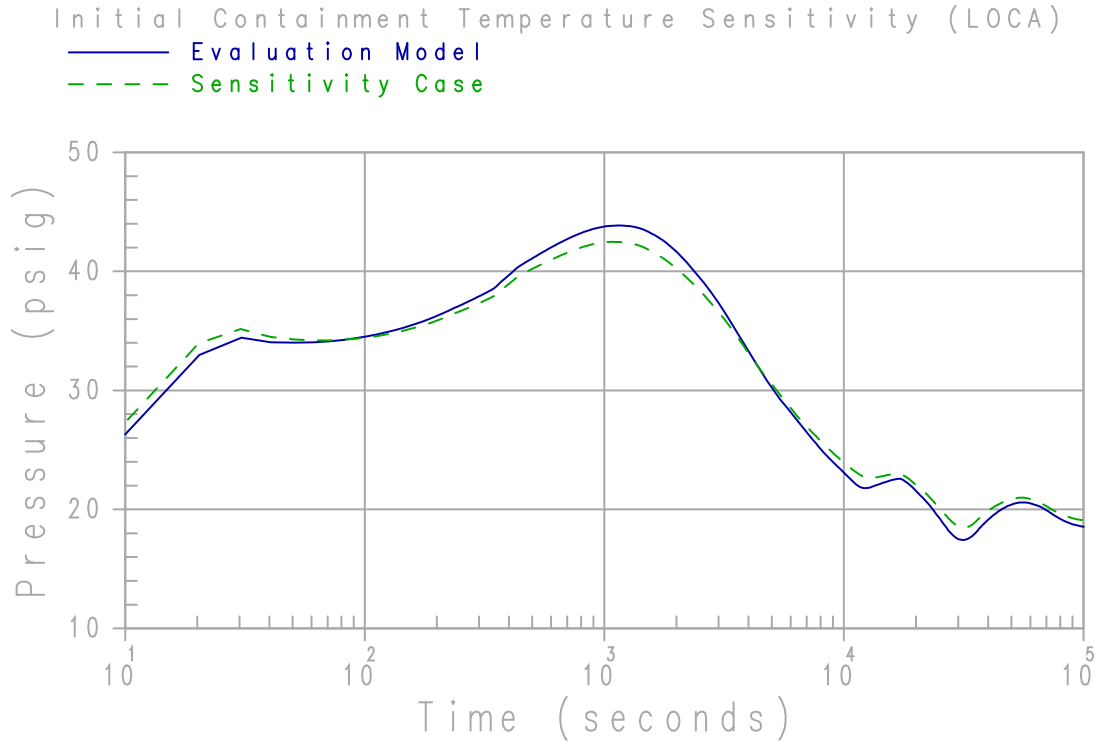


Figure 5-5. Case 3 – Initial Containment Temperature Sensitivity – LOCA

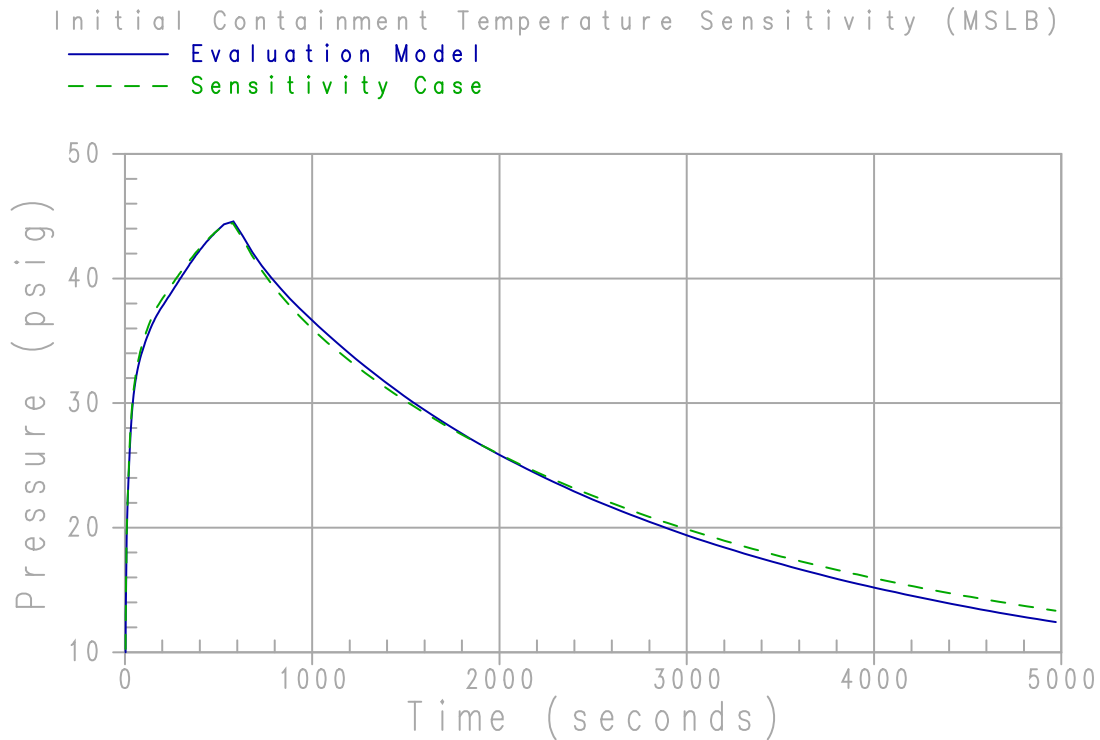


Figure 5-6. Case 10 – Initial Containment Temperature Sensitivity – MSLB

5.6 AMBIENT HUMIDITY

Heat is removed from the containment atmosphere by condensation and convection heat transfer to the shell, where it is conducted through the shell and rejected to the atmosphere on the outside of containment. Heat rejection to the atmosphere is achieved by convection to the buoyant cooling air, radiation to the baffle, and evaporation of the external PCS film to the cooling air. Evaporation of PCS water is the most significant of these heat removal mechanisms. Evaporation mass transfer is driven by the concentration gradient, or equivalently, the vapor partial pressure difference between the film and riser air. Changes in ambient or outside atmospheric conditions (e.g., relative humidity) can influence, to some degree, the vapor partial pressure difference. The purpose of this sensitivity analysis is to evaluate the effect of ambient humidity on containment pressure response.

The upper limit of ambient humidity is defined by the site interface parameters to be a maximum wet bulb temperature of 80°F for the AP600 plant. This corresponds to a relative humidity of 22 percent when the ambient temperature is 115°F. These boundary conditions are assumed in the Evaluation Model.

Two sets of sensitivities to relative humidity are presented. The first provides a comparison of the Evaluation Model to the case with 0 percent relative humidity at an ambient temperature of 115°F. The second sensitivity compares relative humidity of 0 percent and 100 percent at an ambient temperature of 40°F.

The sensitivity of containment pressure to ambient humidity is depicted in Figure 5-7 for the LOCA (Case 4) and Figure 5-8 for the MSLB (Case 11). The sensitivity and reference cases are compared corresponding to 0 and 22 percent relative humidity, respectively. These figures illustrate that containment pressure is not sensitive to initial inlet humidity. This result is consistent with the small effect of inlet humidity on the main factors governing the process of evaporation between the wetted shell and the riser air flow. The rate of evaporation is principally driven by the concentration gradient or, equivalently, the difference in vapor partial pressure between the film interface and the bulk air mixture. The partial pressure of vapor at the film interface is equal to the saturation pressure at the film temperature. Because the concentration of water vapor in the bulk air mixture is small in comparison, the partial pressure gradient is essentially given by the saturation pressure at the film interface. Consequently, initial inlet humidity has no significant effect on the rate of film evaporation or on containment pressure.

The sensitivity performed at 40°F, comparing 0 and 100 percent relative humidity, exhibited the same behavior, indicating almost no sensitivity to ambient humidity. A comparison of Case 5 to Case 6 for LOCA, and Case 12 to Case 13 for MSLB indicates a nearly identical pressure response. A comparison plot for these cases is not provided. The differences in these cases compared to the Evaluation Model are due to ambient temperature differences which are discussed in the Section 5.7.

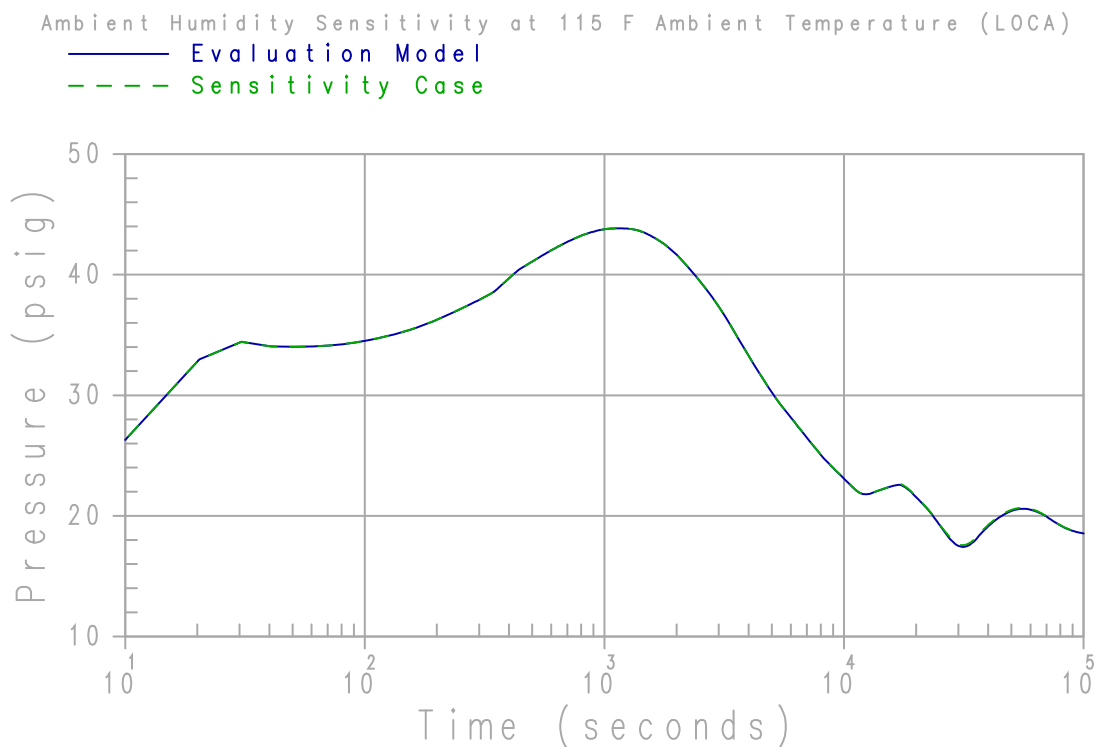


Figure 5-7. Case 4 – Ambient Humidity Sensitivity at 115°F Ambient Temperature – LOCA

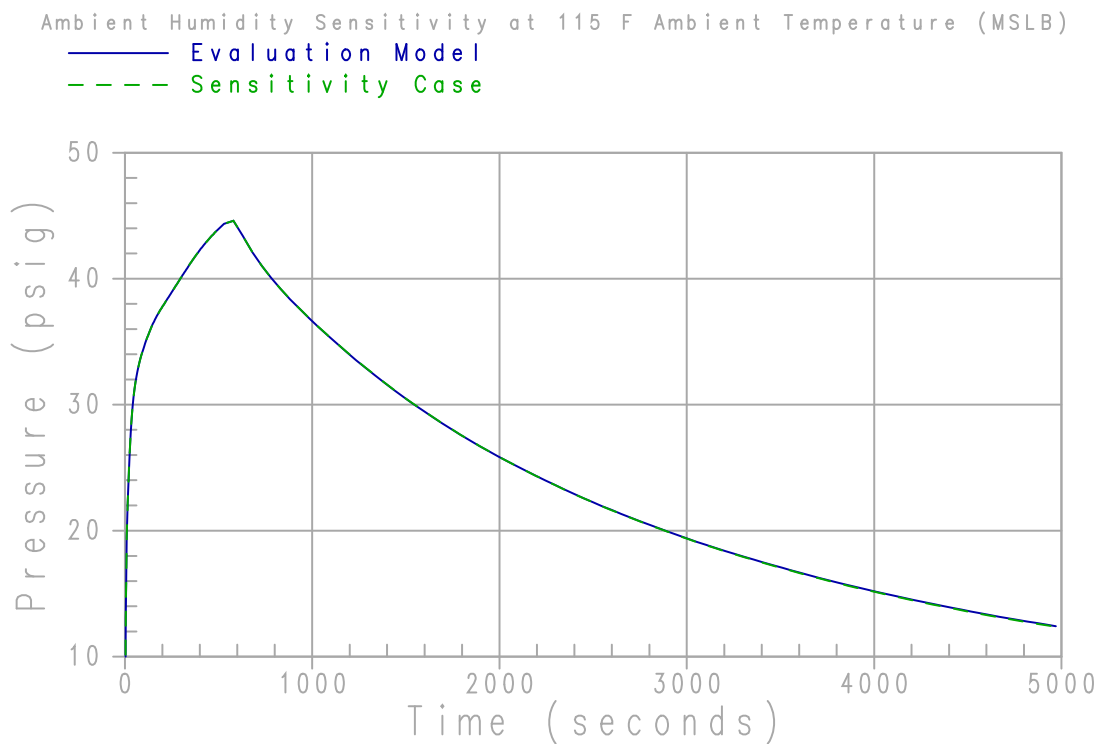


Figure 5-8. Case 11 – Ambient Humidity Sensitivity at 115°F Ambient Temperature – MSLB

5.7 AMBIENT TEMPERATURE

The purpose of this sensitivity analysis is to illustrate the effect of ambient temperature on containment pressure response. Cooling air and PCS water temperature are simultaneously and independently varied in order to investigate the effects. A change in the ambient air temperature primarily affects heat rejection by convection to the riser air flow. A change in the PCS water temperature affects the amount of energy absorbed by sensible heating.

The site interface parameter limits on ambient air temperature are 115°F and -40°F. The minimum PCS water temperature is limited by the Technical Specifications to a value of 40°F. Since a higher ambient temperature and PCS water temperature produces a slightly greater containment pressure, the maximum ambient temperature (115°F) and PCS water temperature (120°F) are assumed for the Evaluation Model. The temperature for both inlet air and PCS water (sensitivity case) is set equal to 40°F.

The sensitivity of containment pressure to ambient temperature is shown in Figure 5-9 for the LOCA (Case 5) and Figure 5-10 for the MSLB (Case 12). As indicated, lower containment pressures are predicted for the sensitivity case at lower ambient temperatures late in the transient for the LOCA case. There is little impact on the peak pressure or pressure early in time. The containment pressure for an MSLB is less sensitive to external conditions and therefore, there is a smaller impact on pressure for the entire transient.

The reduction in the long-term pressure is primarily attributed to liquid subcooling with a small contribution due to forced convection heat transfer effects. The external liquid film absorbs sensible heat from the point of PCS flow application to the point where significant film evaporation occurs. The subcooled heat capacity is dependent on water source temperature and external water flow rate. A lower source temperature results in greater subcooled heat capacity of the external film and, hence, more energy removed from containment. Forced convection heat transfer exists in the riser post-wetting as a result of the high buoyancy-driven air flow rate. The rate of energy transfer by forced convection is dependent on the heat transfer coefficient and the temperature difference between the liquid film and bulk air. Of these parameters, the temperature difference is influenced to a greater extent by bulk air temperature. A lower bulk air temperature results in greater forced convection heat transfer and, therefore, more energy removal from containment. The combined energy absorbed by liquid subcooling and forced convection represents a small fraction of the total energy removed from containment. Consequently, lowering the ambient air and source water temperatures to 40°F results in more total energy removed from containment, and, therefore, results in a decrease in containment pressure relative to the Evaluation Model.

Case 7 (LOCA) and Case 14 (MSLB) considered only the change in PCS water temperature, shown in Figures 5-11 and 5-12, respectively. These cases confirm that the air temperature impact is less important than the PCS water temperature.

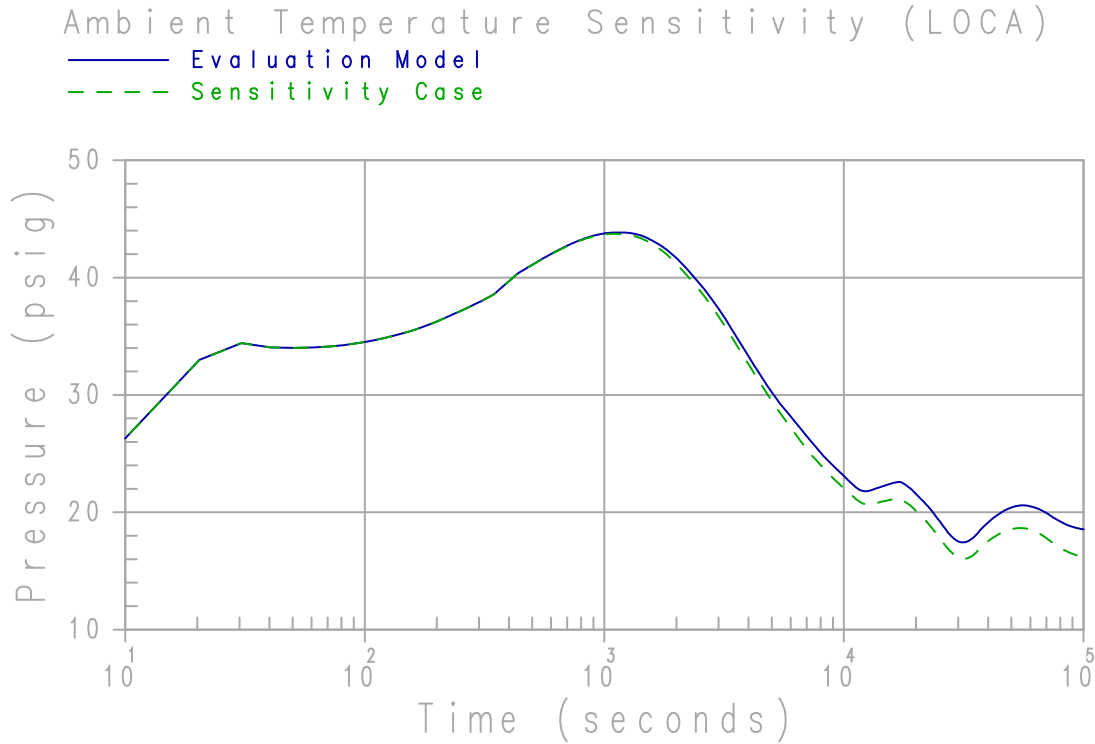


Figure 5-9. Case 5 – Ambient Temperature Sensitivity – LOCA

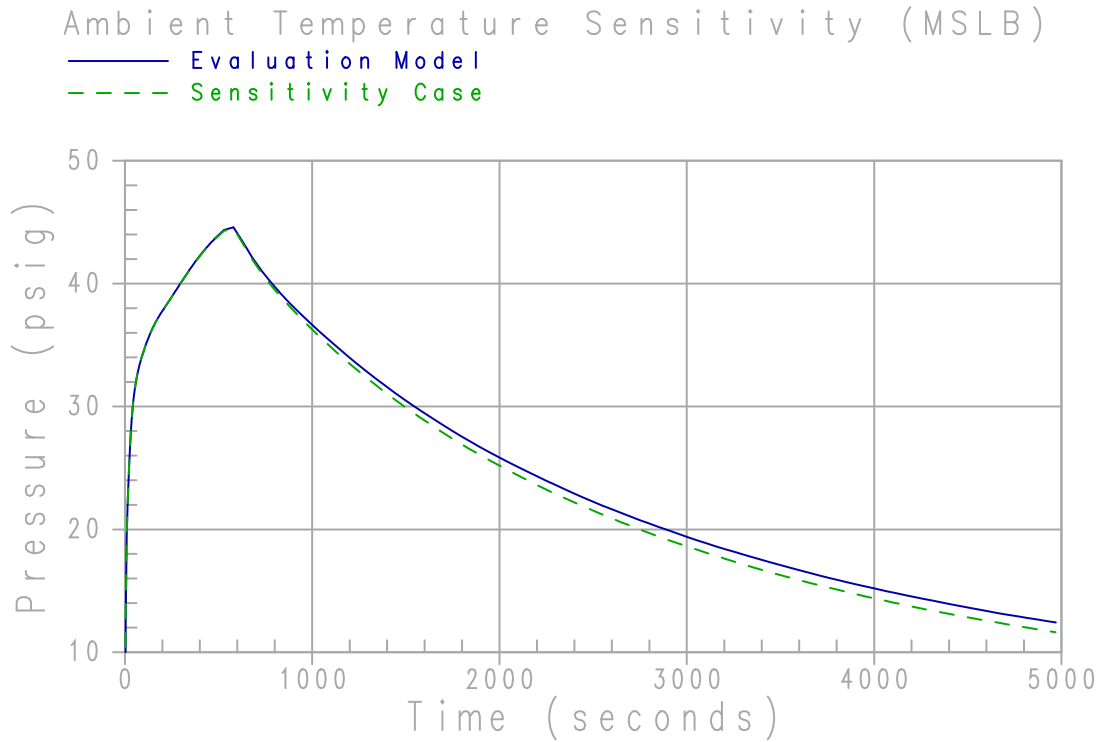


Figure 5-10. Case 12 – Ambient Temperature Sensitivity – MSLB

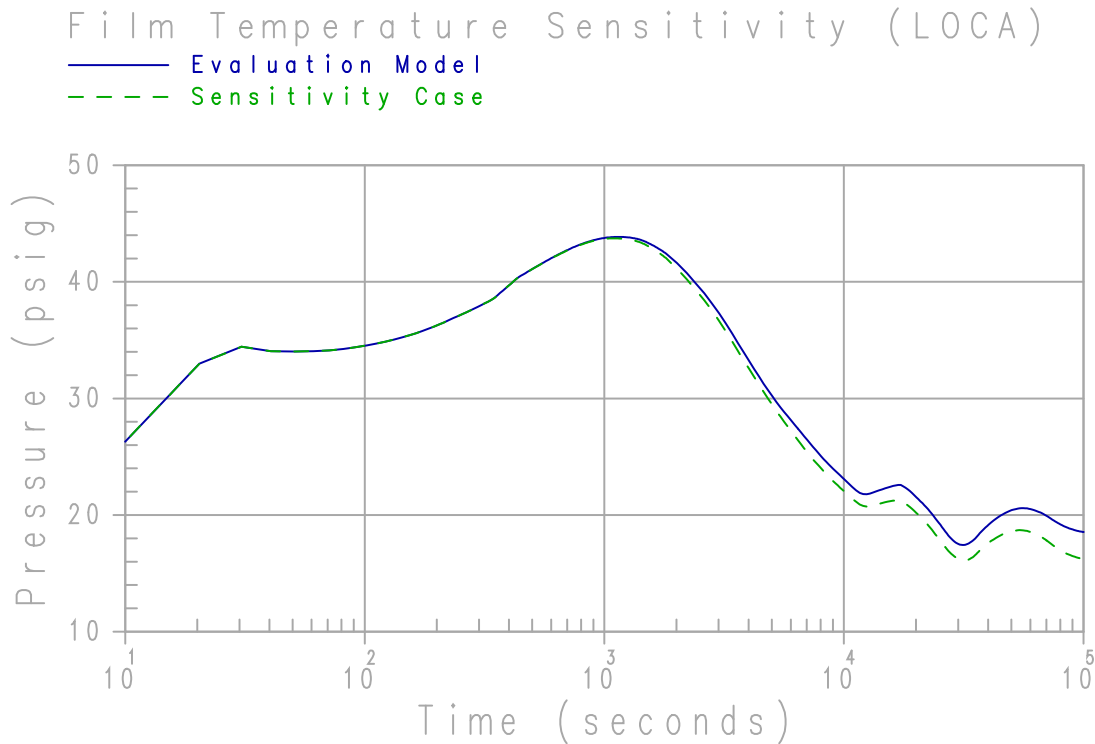


Figure 5-11. Case 7 – Film Temperature Sensitivity – LOCA

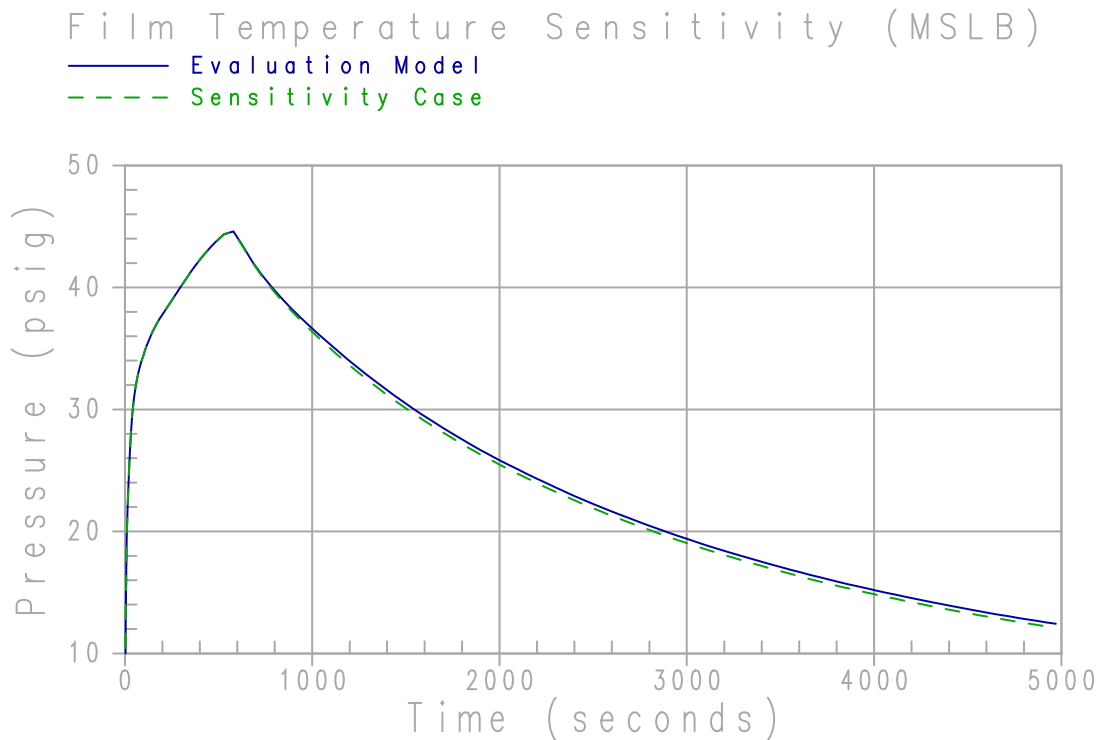


Figure 5-12. Case 14 – Film Temperature Sensitivity – MSLB

5.8 SENSITIVITY TO DROP MODELING ASSUMPTIONS

During a LOCA blowdown, the liquid and entrained droplets enter the atmosphere saturated at the containment total pressure where they are exposed to the containment gas mixture of air and steam at the steam partial pressure. Since the liquid and drops are initially superheated, they evaporate quickly to reach thermal equilibrium with the gas mixture. A sensitivity study was performed for the LOCA to determine the impact of the modeling assumption in WGOTHIC of the fraction of liquid converted to drops on the containment pressure. The mass released during the MSLB does not contain droplets.

The fraction of liquid assumed to be turned into droplets during the LOCA blowdown was varied from 0 to 100 percent. These sensitivities showed that the impact of assuming no droplets released, had a significant impact on the calculated pressure response compared to the cases where droplets were modeled. With no droplets assumed, the blowdown pressure was higher, but the peak pressure was lower. However, the sensitivity to the assumed fraction of droplets was very weak above a level of approximately 5 percent. The drops are strongly coupled to the containment atmosphere temperature due to the large surface area of the drops. The presence of drops in the atmosphere at approximately the 5 percent level maintains the atmosphere in a saturated condition and the presence of additional drops has little impact on containment pressure.

This sensitivity indicates that it is important to model the presence of drops in the containment atmosphere but the specific fraction assumed has a minor impact on the resulting pressure. The containment pressure response for assumed droplet fractions of 0 and 100 percent along with the Evaluation Model assumptions for drops (discussed in Section 4.5.2.1) is illustrated in Figure 5-13.

5.9 CONCLUSIONS

A series of sensitivity analyses has been carried out using the AP600 containment model to determine the effect of initial conditions on containment pressure response for the LOCA and MSLB events. Sensitivity evaluations were performed on initial containment humidity, pressure, and temperature, as well as ambient humidity and temperature and PCS water (film) temperature. These sensitivities demonstrate that the initial conditions assumptions in the Evaluation Model result in a conservative prediction of containment pressure. The containment pressure is more sensitive to internal conditions than to ambient conditions. The sensitivity to internal conditions is due primarily to the effect of these conditions on the amount of air in the containment.

A sensitivity was performed for the LOCA to determine the impact of the drop modeling assumption in WGOTHIC on the calculated containment pressure. The results show that it is important that the droplet formation be modeled, but at fractions above approximately 5 percent, the fraction assumed to be released as drops has a small impact on the calculated pressure.

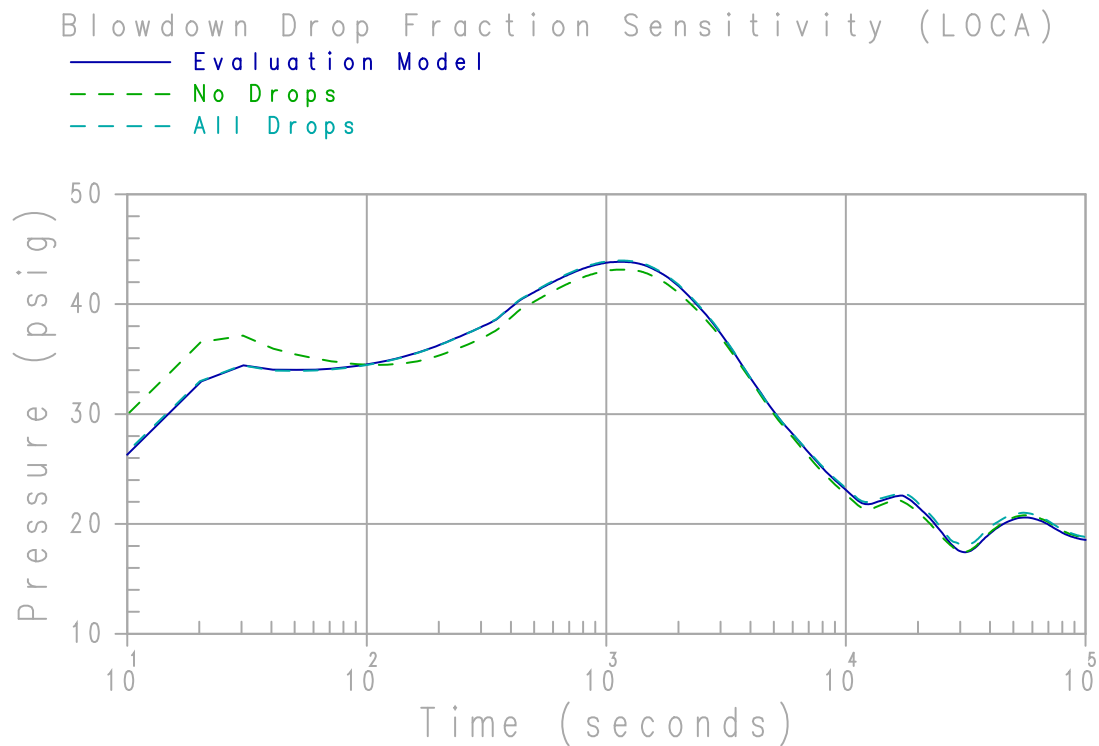


Figure 5-13. Blowdown Drop Fraction Sensitivity – LOCA

6 METEOROLOGICAL EFFECTS ON PCS PERFORMANCE

6.1 INTRODUCTION

Meteorological conditions which could be postulated to degrade the performance of the PCS design have been investigated. The design includes, within the chimney, a shield plate which protects the containment surface from direct impingement of rain. Screens on the PCS inlets and around the entrance to the chimney protect the PCS from birds or larger debris which may be blown by wind. Meteorological effects that are evaluated, are wind-induced turbulence and the potential for recirculation due to wind or temperature inversions. This chapter shows that the assumption of a quiescent atmosphere in the evaluation model conservatively neglects enhancements to heat and mass transfer due to wind. It is also shown that the potential effects of recirculation produce a negligible effect on containment pressure.

6.2 WIND-INDUCED TURBULENCE

6.2.1 Summary of Wind Tunnel Tests

A goal of the containment building design is that wind not adversely impact heat removal from the building. The PCS is designed for wind to either have a nominal effect on PCS flow (wind neutral) or enhance PCS flow (wind positive). To verify the wind positive performance, a series of wind tunnel tests were performed. The wind tunnel tests, performed at the Boundary Layer Wind Tunnel Laboratory at the University of Western Ontario (UWO), were designed to test the aerodynamic response of air flow past the AP600 containment under a variety of conditions. The tests occurred in four phases.

Phase 1 testing (~1:100 scale) examined the effects of various design options on the wind-induced pressures. In Phase 1 testing, although the flow through the building annulus was not modeled, the pressure difference between inlets and chimney, ΔP , was measured. The inlet-minus-chimney ΔP is the pressure driving flow through the PCS, and a pressure coefficient, c_p , is defined based on free stream wind velocity and ΔP :

$$\Delta P = \frac{1}{2} c_p \cdot \rho_{amb} \cdot V_{roof}^2$$

where,

ρ_{amb}	=	ambient air density
V_{roof}	=	free stream wind velocity

In Phase 2 tests, the air flow path was modeled for two different building designs: the most wind-neutral design found in Phase 1 testing and the current design of the building. The purpose of the Phase 2 testing was to provide information for the design of the baffle wall. Buoyancy was not considered in the wind tunnel tests, since the driving pressure due to buoyancy amounts to only about 1 to 5 percent of the wind-induced driving pressure for the design wind cases.

At the end of Phase 2 of the wind tunnel program, several questions remained. In Phase 3, analysis was used to address the potential effects of wind and thermal inversion on recirculation of the chimney effluent back into the inlet, using available literature from mechanical and natural draft cooling towers.

Three additional questions were addressed with testing in Phase 4. The first question regards the effect of Reynolds number on the results. Reynolds number effects could only be addressed definitively by testing a larger model (1:30 scale) in a higher wind speed tunnel, such that the Reynolds numbers were in the same range as expected full-scale values. The second question was the effect of a tornado wind profile (near uniform) on the results. Tornado profile effects could be obtained using the same test model as in previous phases, but with a uniform flow model. The third question addressed the blockage effects of a hyperbolic cooling tower relative to the UWO wind tunnel size. Cooling tower blockage could be addressed by testing the model in a larger wind tunnel where blockage would be small.

The final question, the effect of severe terrain, was the subject of Phase 4 testing, in which a smaller scale (1:800 scale) was chosen to allow modeling of larger areas around the site.

Test results indicated that the AP600 design was wind positive for average PCS flow. The testing included a variety of terrain and conditions, including open country terrain, tornado loading, modeling of the cooling tower(s), and simulation of several types of severe terrain. Open country terrain yielded the most beneficial results for PCS heat removal, indicating a significant contribution to PCS air flow due to wind-induced driving pressures. The effect of the cooling tower, however, was to reduce static pressure at both the chimney and the inlets, resulting in lower mean wind ΔP . Thus, the likelihood of flow in the PCS changing direction (flow reversal) was greater when the plant was in the wake of the cooling tower, giving the least positive mean PCS driving force due to wind.

The three Phase 4 severe terrain scenarios included an escarpment with mountain backdrop, a river valley site, and a river valley site with two cooling towers. Each terrain scenario caused durations and magnitudes of negative wind ΔP , which could lead to flow reversals within the PCS flow path.

The wind-positive response of the PCS has been shown (Reference 6.1) to be beneficial for containment heat removal for the limiting terrain configuration. Increased wind speed drives more flow through the PCS annulus and increases heat and mass transfer coefficients. Three questions have been addressed regarding the results of the wind tunnel tests:

- The model scale aerodynamic response versus full-scale response
- The effects of wind-induced flow oscillations on PCS heat removal and containment pressure response
- The effect of near-zero average wind ΔP for certain wind angles in some of the severe terrain tests

Due to the shape of the containment shield building (sharp edges initiate flow separation), the model-to-full-scale aerodynamic response is relatively insensitive to model size in the range tested. A review of the literature has indicated that pressure oscillations in heat transfer generally improve heat transfer rates. In addition, time constants associated with the containment shell and internal volume minimize any benefit or penalty on containment pressure due to oscillations. The effect of wind-induced pressure oscillations has been evaluated with simple calculations.

6.2.2 Tracking of a Wind-Driven Particle

Using the measured pressure coefficients, density of air, and design wind speed of 214 mph, wind ΔP was calculated and converted into annulus velocities using the momentum equation, which balances the driving force with the unrecoverable losses. Figure 6-1 presents the calculated path of the first element to travel from the inlet to the outlet of the PCS. Figure 6-1 also presents the path of the element neglecting the wind, and using an assumed buoyancy-driven annulus velocity of 15 ft/sec. Note that the wind-driven element shows a net positive flow response to pressure oscillations (net flow is from the inlet to the chimney).

6.2.3 Containment Time Constants

A review of the literature has indicated that oscillating flows generally increase heat transfer. The effect of the wind ΔP oscillations on the containment post-LOCA pressure response is limited by time constants associated with the containment shell and the containment volume. The shell time constant gives the response of the containment shell to changes in its environment. Using a lumped mass approach, the time constant compares the thermal capacitance of the shell to the heat removal rate from its surface and has a value of about []^{a,c}. The shell time constant is significantly higher than the frequency of pressure fluctuations, which are on the order of several seconds for high wind speed cases. The time constants show that the thermal response of the containment shell is sufficiently slow so that high speed oscillations will not significantly affect PCS heat removal. At lower wind speeds, oscillations are much slower. However, at lower wind speeds, the wind ΔP is much lower. As wind speed reduces, the wind ΔP decreases rapidly, as a function of the square of the wind velocity. Thus, oscillations will not have a significant impact on PCS heat removal. Since PCS heat removal is relatively unaffected, containment pressure response to a postulated LOCA will not be significantly affected by pressure oscillations. Thus, heat transfer fluctuations occur relatively faster than the ability of the wall material to transmit oscillations through the shell.



Figure 6-1. Particle Path through the AP600 PCS with and without Wind

6.2.4 Wind-Induced Oscillation Effect on Heat Transfer Coefficient

Pressure fluctuations affect the heat transfer coefficient on the containment surface. In particular, oscillations result in short periods where the heat transfer coefficient may be lower than the value assumed in the no-wind case, followed by periods of higher heat transfer coefficients. The heat transfer response to wind oscillations has been investigated using a 1-D plane wall conduction model. The conduction model was used to estimate the effect of pressure oscillations on heat transfer through the containment shell. The model simulates the containment shell and a liquid water film on the outside of the shell. The 1-D conduction model was subjected to the heat and mass transfer coefficient on the outside of the plane wall calculated from the time-varying annulus velocity. Only forced convection correlations were used, so that heat and mass transfer rates on the outside of the plane wall approached zero as annulus velocities approached zero. The use of a forced convection correlation is conservative since, even as velocities in the annulus pass through zero, heat transfer would still occur. To further impose a conservative bias in the calculation, heat and mass transfer rates on the outside of the wall were assumed to be zero whenever the annulus velocity was negative.

The response of the containment shell to the imposed velocity was calculated. Figure 6-2 presents the surface temperature of the inside of the plane wall versus time. The figure compares the response of the wall to the annulus velocity oscillations versus the response assuming a steady buoyancy-driven annulus velocity. Note that, despite neglecting heat removal from the wall during periods of negative annulus velocity, the temperature of the inside of the plane wall is still about the same as a typical steady velocity case, showing that the response of the containment shell is limited by the time constants discussed in previous sections.

a,b

Figure 6-2. 1D Containment Shell Model Inside Temperature Results

6.2.5 WGOTHIC Evaluation Model Basis

The wind tunnel testing of the AP600 indicates that the average wind ΔP tends to be positive under a variety of conditions. Wind flowing towards and over the containment building will tend to increase average flow rates through the PCS. The wind-induced flow rate increase will improve heat transfer rates in the PCS.

In addition to the open-country terrain, several highly turbulent severe terrain scenarios were tested to obtain data on the AP600 subjected to limiting site conditions. For the severe terrain, positive wind ΔP that averages near zero may be seen. In addition, the wind ΔP tends to oscillate, giving periods of negative wind ΔP . Negative pressures indicate the possibility of flow reversals within the PCS annulus. Assessment of the current literature has indicated that flow oscillations will tend to increase heat transfer primarily by enhancing mixing across the riser annulus flow channel. While periods of negative pressure may result in short periods of flow reversal within the annulus, the literature indicates that turbulent conditions may continue to exist. Turbulent conditions would continue to provide significant heat transfer

rates despite the oscillating flow. Time constants were calculated for the containment shell which indicated that the shell time constants were of significantly higher magnitude than the period of the pressure oscillations. Thus the pressure oscillations in the annulus would be damped in their effects on the containment heat removal rates at the inside of the containment shell. A 1-D conduction model of the containment shell, subjected to oscillating heat transfer rates, was solved using the wind Δp from a particularly turbulent angle of the limiting test site. The 1-D conduction calculation used the forced convection correlation to conservatively determine heat transfer rates in the annulus. Heat transfer was also assumed to be zero when the flow reversed. The results of the calculation indicate a slight benefit in PCS heat removal and containment pressure due to wind for the limiting case. The effect of the containment shell was to dampen the oscillations occurring on one side of the shell. Thus, a conservative calculation of the passive containment response to a LOCA could assume a quiescent atmosphere.

6.3 RECIRCULATION OF CHIMNEY EFFLUENT

After the PCS cooling air flow passes over the containment shell surface, the air and evaporated water exhaust through an opening in the roof of the shield building and through the chimney. The potential for recirculation of the chimney effluent back to the PCS inlets, due to temperature inversions or strong winds has been evaluated (Reference 6.2) through a review of literature and shows the negligible effect of a conservatively high assumed recirculation.

6.3.1 Summary of Literature Review

Many references were found in the literature to address potential recirculation due to strong winds or thermal inversions. References are available for natural draft hyperbolic cooling towers, typically hundreds of feet tall, and for mechanical draft cooling towers, typically 10 to 20 feet tall.

Strong winds can cause the formation of a recirculation cavity on the leeward side of a building or cooling tower. It was found that there are some intermediate wind speeds which can be sufficient to bend the plume horizontally, yet not strong enough to carry all the effluent away. Analytical and experimental research in the literature was conducted to determine the extent of the recirculation cavity behind a natural draft cooling tower and its effect on the plume. Curves are provided in the literature based on a normalized temperature difference that indicates the increase in the mixed mean ambient inlet temperature due to mixing with the plume. Such curves suggest a maximum normalized temperature increase of 10 percent for recirculation. Similar studies for mechanical draft towers suggest recirculation of 3 to 7 percent reaching a maximum of 15 percent.

Thermal inversions, and combinations of wind and temperature inversions were cited. Results showed that an inversion, by itself, does not induce the downflow necessary to recirculate chimney effluent. Adverse inversion conditions are associated with calm or light winds. Using simplified plume rise equations, the approximate effluent conditions resulted in plume rise above the shield building chimney for stable atmospheric conditions (inversions). The plume rise was sufficient to raise the plume, in light wind, above the recirculation zone of structures the size of those associated with the passive containment design. Consequently, the maximum expected recirculation would be determined from the strong wind case.

Based on the literature review and evaluations of the AP600, the upper limit for recirculation of the passive containment chimney effluent is []^{a,c}. To account for the uncertainty in choosing a value for recirculation, the more conservative value of []^{a,c} has been assessed, which would result in the mixed mean ambient inlet temperature increasing from the safety analysis basis of 115°F to []^{a,c}.

6.3.2 Evaluation of Effect of Recirculation

The effect of a recirculation ratio of []^{a,c} has been assessed with WGOTHIC sensitivity calculations. The base case calculation used an inlet temperature of 115°F and inlet humidity of 20 percent. Two sensitivities were run: one with only the inlet temperature increased, based on the recirculation ratio, and one with both the inlet temperature and inlet humidity increased. Results show that the pressure transient is insensitive to temperature and humidity in this range due to the self-regulating performance of the PCS.

The base case used for recirculation sensitivity differs from the evaluation model in the details of internal nodding, azimuthal segregation of the annulus into quadrants, modified mass and energy releases, the use of 22 percent relative humidity, an initial PCS flow profile starting at 220 gpm, and in the use of nominal heat and mass transfer correlations. Since these sensitivity results are used to examine relative effects of changes in the annulus inlet conditions, the sensitivity results are judged to provide a reasonable estimate of the potential effect of recirculation. The base case chimney outlet temperature reaches a maximum of []^{a,c} at about 2100 seconds and decreases almost linearly to []^{a,c} at about 8700 seconds, after which it gradually reduces to []^{a,c} at 24 hours. For simplicity, a conservative assessment of the potential effect can be based on an assumed chimney outlet temperature of []^{a,c}, which includes []^{a,c} to account for the increase in outlet temperature when the inlet temperature is increased in the sensitivity run. Using the definition of the recirculation ratio, the mixed mean inlet temperature, accounting for the effect of effluent recirculation, is

$$T_{in} = T_{\infty} + R (T_{out} - T_{\infty})$$
$$_{in} = 115 + []^{a,c}$$

So the inlet temperature to be assumed in the sensitivity cases is []^{a,c} which is applied for all annulus quadrants, consistent with the definition of R from the literature. The first sensitivity case used a constant []^{a,c} inlet temperature and essentially unchanged inlet humidity []^{a,c}. Results from the sensitivity show that the pressure transient changed by a negligible (<0.1 percent) amount due to the []^{a,c} increase in inlet temperature, and confirmed the initial guess for the corresponding increase in outlet temperature. The second sensitivity included the increase in inlet temperature combined with the inlet humidity set to 98 percent. Again, there is a negligible effect on the containment pressure. The lack of sensitivity of the pressure response is due to the self-regulating performance of the PCS. By comparing the annulus conditions in going from 20 to 98 percent inlet humidity, it is seen that the annulus mass flow rate increased by about []^{a,c}. The higher mass flow increases the capacity to move vapor out of the annulus and is due to the increase in vapor pressure at the annulus outlet from []^{a,c} of the approximately 14.7 psia total pressure. Since steam density is more sensitive to temperature increases than air density is, and steam density is less than air density at annulus conditions, the increased steam content provides a greater

density driving head for flow through the annulus. The increased mass flow results in a greater velocity through the annulus, which increases the PCS mass transfer coefficient. Thus, the mass flow increase offsets increases in inlet humidity. Similar, self-regulating performance results from an increase in inlet temperature alone.

It may be expected that an increase in inlet humidity would suppress the evaporation rate from the film. Such an effect is actually small since the driving force for evaporation is the difference between the vapor pressure of the film and the bulk saturation pressure in the annulus. Since the vapor pressure of the film is on the order of ten times that of the annulus, a relatively large percentage change to annulus humidity corresponds to a relatively small percent of the driving force.

Sensitivities to the effects of increasing both inlet temperature and humidity to account for potential recirculation show that there is a negligible effect on the containment pressure transient.

6.3.3 WGOTHIC Evaluation Model Basis

Since the effect of effluent recirculation is negligible, the WGOTHIC evaluation model does not consider any additional penalty due to recirculation.

6.4 APPLICABILITY TO THE AP1000 SHIELD BUILDING DESIGN

The **AP1000** shield building design increases the structural integrity, enhances the overall seismic safety margin, and simplifies construction. Some of the design changes impact the air flow rate through the PCS. [

^{a,c} In the **AP1000** air inlet design, a steel structure containing the fixed, always open louvers and screens has been added around the top of the shield building. The flow area through the modified louvers and screens is higher than what was through the original louvers, screens and inlet ducts. After passing through the screens, the air enters the common plenum that is formed by the steel structure and the outside of the concrete shield building and continues through the air inlet ducts. The air inlet ducts are arranged in two rows, and uniformly distributed around the circumference of the shield building. The flow area through the air inlet ducts is lower than it was through the original louvers, screens and inlet ducts. As in the previous design, air exiting these ducts enters a common plenum inside the shield building which transitions to the outer flow annulus.

The **AP1000** shield building design increases the overall resistance of the PCS flow path, reducing the natural circulation flow rate through the PCS air flow path. The impact of this change on the test results and scaling were examined. The operating range of the **AP1000** heat and mass transfer correlations is shown in Table 3-3. The percent differences caused by these design changes on the key scaling groups are small and negative indicating the **AP1000** PCS air flow path design is expected to slightly reduce the **AP1000** operating range. The wind tunnel tests included variations of the shield building design and concluded that the criteria of wind aiding in natural circulation of the PCS would be met. Therefore, the range of test data that was used to validate the **AP1000** PCS heat and mass transfer correlations remains acceptable and the conclusions in this section remain valid (Reference 6.3).

6.5 CONCLUSIONS

Wind-induced pressure oscillations have been shown to provide a benefit to PCS heat removal because of the wind-positive design; that is, wind induces more heat removal than a quiescent atmosphere. The effects of recirculation due to thermal inversions or strong winds has been shown to have a negligible impact on PCS heat removal. The WGOTHIC evaluation model bounds the postulated effects with no input modifications.

6.6 REFERENCES

- 6.1 NTD-NRC-95-4467, J. Narula, "Analysis of AP600 Wind Tunnel Testing for PCS Heat Removal," June 2, 1995.
- 6.2 NTD-NRC-94-4166, R. Haessler, "AP600 Passive Containment Cooling System Letter Reports," June 10, 1994.
- 6.3 APP-GW-GLR-096, Revision 3, R. Ofstun, "Evaluation of the Effect of the AP1000® Enhanced Shield Building Design on the Containment Response and Safety Analyses," June 13, 2011.

7 BASIS AND METHOD FOR CALCULATING THE PCS WATER EVAPORATION RATE FOR THE AP600 AND AP1000 CONTAINMENT DBA EVALUATION MODELS

7.1 INTRODUCTION

The energy released to the containment atmosphere following a postulated design basis high energy line break is removed from the exterior containment shell surface by a combination of convection and radiation from dry surface areas and by convection, radiation, and water evaporation from wetted surface areas, to a naturally circulating air stream. The energy removal due to water evaporation dominates the passive containment cooling system (PCS) total heat removal and is a function of the PCS flow rate, the wetted area, and the external shell temperature. Since these parameters vary with time, the energy removal rate due to evaporation also varies with time.

The containment shell outer surface is wetted with water that is stored in a tank located above the containment. Piping and three parallel valves provide a flow path from the tank to the top of the containment shell. The valves open upon receipt of a high-2 containment pressure signal, allowing water from the tank to drain by gravity through the piping to a central distribution bucket located above the center of the containment shell. This water flow fills the distribution bucket, overflows out onto the dome, and spreads outward on the nearly horizontal surface at the top of the containment shell. As the applied water spreads outward from the center of the dome, it runs down the increasingly sloped dome surface where it is collected and redistributed by weirs located at the ~24-foot and ~51-foot radius of the dome. These water distribution weirs reapply the collected water at a regular uniform spacing around the containment shell perimeter.

The PCS water flow rate into the distribution bucket and onto the containment surface is controlled by the inlet elevations of standpipes within the PCS water storage tank. As the tank drains and each standpipe is uncovered, the PCS flow to the containment surface is reduced in a step-wise fashion. The standpipes are located so that the PCS flow results in sufficient heat removal to match the decreasing rate of heat release to the containment, and to achieve the desired decrease in containment pressure.

Because the ability of the PCS to remove heat at a given containment pressure (temperature) is largely dependent on the amount of water applied and the surface area that is wetted, the method of water application and the behavior/stability of the liquid film are important. Therefore, this section describes the testing and analyses utilized to define a conservative water flow rate for the WGOTHIC Evaluation Model, including:

1. Water distribution testing used to demonstrate the weir design and how the resulting wetted surface area is affected by the applied water flow rate and surface irregularities in the containment shell structure.
2. PCS testing performed with heated wetted surfaces to determine how the water film is affected by post-accident containment operating conditions, including the steel shell surface temperature, the water film temperature, the water film mass flux (mass flow rate per foot of wetted perimeter, hereafter referred to simply as film flow rate), and cooling air flow velocity.

3. The method used to predict the containment shell wetted area and water film behavior conservatively compares with test data in order to conservatively calculate the amount of water than can be evaporated from the containment shell.
4. The method used to calculate the effect of heat conduction, the circumferential direction though the steel containment shell (2-D conduction), on the water evaporation rate from the surface with vertical wet stripes.

The liquid film application, flow rate, area wetted, and film behavior are factors in the conservative determination of the amount of supplied water that evaporates from the shell. The methodology bounds data from tests of an unheated, full-scale portion of the containment dome and 4 feet of sidewall, and from various scale heated tests. The evaporation-limited PCS water flow rate for the WGOTHIC Containment Evaluation Model is calculated using a simple model that is consistent with test observations and uses as inputs the parameters Γ_{dist} and Γ_{min} which are selected to conservatively bound test data. Γ_{dist} represents the film flow rate (mass flow rate per unit wetted perimeter) of water applied by the weir distribution system at the second weir. Γ_{min} represents the minimum stable film flow rate, below which water coverage is assumed to decrease, and is selected to bound heated film stability test data. The database from which conservative values for Γ_{dist} and Γ_{min} are determined is discussed, as well as how these parameters are implemented into the model.

The Evaluation Model conservatively neglects heat removal during the initial period from the first spillage from the bucket to the time when steady-state coverage has developed on the containment shell (Section 7.2.5). The time to develop steady-state coverage is conservatively estimated. The effects of surface temperature during the initial application are also addressed (Section 7.6.5).

The supporting tests for water coverage are shown to span the range of AP600 and **AP1000** non-dimensional parameters, so that the database is sufficient.

7.2 WATER APPLICATION AND DISTRIBUTION

The wetting characteristics of the containment coating and the application and distribution of water onto the containment steel shell outer surface are important design features of the passive containment design. The containment is covered with an inorganic zinc coating, and an assembly of devices on the containment dome are used to collect and redistribute water to maximize the containment surface wetted area at a given delivered water flow rate.

The Phase 3 Water Distribution Test (Reference 7.2) was performed to demonstrate the operation of the prototype of the AP600 water distribution devices on a full-scale sector of the containment dome. Other PCS tests were performed to quantify the heat removal capability of the PCS. The test results provided information to understand and characterize the behavior of water films on the outside of the containment surface. In addition to the containment coating and the water distribution devices, other parameters that characterize the water film behavior are the delivered water flow rate, the water film flow rate (per foot of wetted perimeter), the water film temperature, and the evaporative heat flux. The film Reynolds number provides a dimensionless measure of the film flow rate, and the Marangoni number is a dimensionless measure of heat flux. The range of dimensioned and dimensionless parameters for PCS testing used to understand and characterize containment surface wetting are summarized in Table 7-1.

Table 7-1. Ranges of the Film Coverage Parameters in the PCS Tests

a,c

7.2.1 Containment Shell Surface Coating

The containment shell surface is covered with an inorganic zinc coating for corrosion protection. Prototypical coated surfaces were obtained for testing by following the manufacturers' specifications for preparation of the metal surface and for application of the coating for each test article in the tests described in Sections 7.2.3 and 7.6.

- The surface was prepared for coating application according to the coating manufacturer's requirements by sandblasting to a white metal surface finish. The coating was then sprayed onto the surface to a thickness range within the required specification of 4 to 10 mils. Coating thickness measurements were taken to verify that the coating thickness was within specification.
- Local or spot recoating of the surfaces was performed if the surface of the test article was affected by changes to the facility, such as the installation of additional instrument penetrations.

Although no specific aging simulation of the surfaces was performed prior to testing, matrix tests were performed over a period of time using the original coated surface, where aging of the surfaces occurred due to operation and exposure to the environment. For example, the small-scale tests vessel was erected in 1986 and tests were performed until late 1992 using the same test vessel with the original coating. The large-scale test (LST) matrix tests were conducted from late 1991 until the end of 1993 and further operation took place through 1996, with the original coating. An estimate of the equivalent service time cannot be evaluated since a large number of tests were performed during this period. In each test facility, no noticeable degradation of the surface was noted during the testing.

In consideration of the above, the surfaces tested are considered prototypic of the AP600 and AP1000 containment shell exterior surfaces. Measurement and/or observations of film coverage on the prototypical surface were made in each of the PCS tests.

7.2.2 PCS Water Distribution Weir Description and Operation

An assembly of devices for distributing the water applied to the containment shell is provided to maximize the outside surface area of the containment shell that is wetted during PCS operation. The PCS water distribution devices include a distribution bucket located above the center of the containment dome, eight divider plates that extend radially from the center of the dome to the first set of water distribution weirs, the first set of water distribution weirs located []^{a,c}, and the second set of water distribution weirs located []^{a,c}.

The PCS water is delivered to the water distribution bucket at the center of the containment dome. The bucket has 16 vertical slots, such that two slots meter water flow to each of the eight pie-shaped segments on the dome created by the eight divider plates that originate at the distribution bucket and extend radially along the surface of the dome to the first distribution weir ring. These divider plates are required because the center of the dome is relatively flat, and maldistribution of flow due to localized imperfections in plate welds or alignment, or variations in the slope at the center of the dome could otherwise occur. Thus, the dividers distribute the water applied to each one-eighth dome segment and to the corresponding one of eight weir assemblies that comprise the first ring of weirs.

The first weir ring consists of eight weir assemblies located []^{a,c}. This radial position is just below [

] ^{a,c} Each of the eight first weir assemblies consist of two water collection dams that direct the applied water, in its one-eighth segment from the dome center, into a collection box. Each of the eight collection boxes meters flow to two distribution troughs, one on either side of the collection box. Each distribution trough meters the water from the collection box back onto the dome surface via nine V-notches spaced at 1-foot intervals. The eight weir assemblies are installed with the distribution boxes end-to-end, so that each forms one-eighth of the weir ring [

] ^{a,c}

The second weir ring is located [

] ^{a,c}. This assembly again corrects any uneven distribution of flow that may have occurred below the first weir ring due to weld discontinuities or deviations in the dome shape from the ideal shape. Also, since the containment dome is steeply sloped at this radial position, the water applied by this second weir ring is not significantly affected by local surface imperfections or deviations from ideal shape, since gravity rather than allowable surface variations becomes controlling. Thus, the second weir ring creates an even distribution over the rest of the dome and the vertical portion of the containment shell. The second weir ring consists of sixteen weir assemblies; each with two collection dams, a collection box, and two distribution troughs. The 16 weir assemblies are again arranged end-to-end to form a distribution system that completely circles the containment. Water that runs down the dome from each of the 16 distribution troughs in the first weir ring is collected by the dams, flows into the collection box, and is metered to two distribution troughs. [] ^{a,c}

Figure 7-1 is an illustration of a weir assembly. The dams collect all the water flowing from above them and direct this water into their corresponding collection box. As the water rises in the collection boxes, it overflows via three V-notches on either side of the top of the box, effectively dividing the collected water into six equal portions. Each portion of the water overflowing through the six collection box V-notches, flows into one of the three parallel flow channels in each of the two distribution troughs. As the parallel flow channels fill with water, each flow channel overflows via another set of V-notches arranged equidistantly along the back wall (facing the containment axial center-line) of the distribution trough, onto the containment shell. The eight weir assemblies comprising the first weir rang, have [

] ^{a,c} Note that in each weir assembly the spacing of the two streams, one on either side of the collection box, is greater than the uniform V-notch spacing along the distribution boxes.

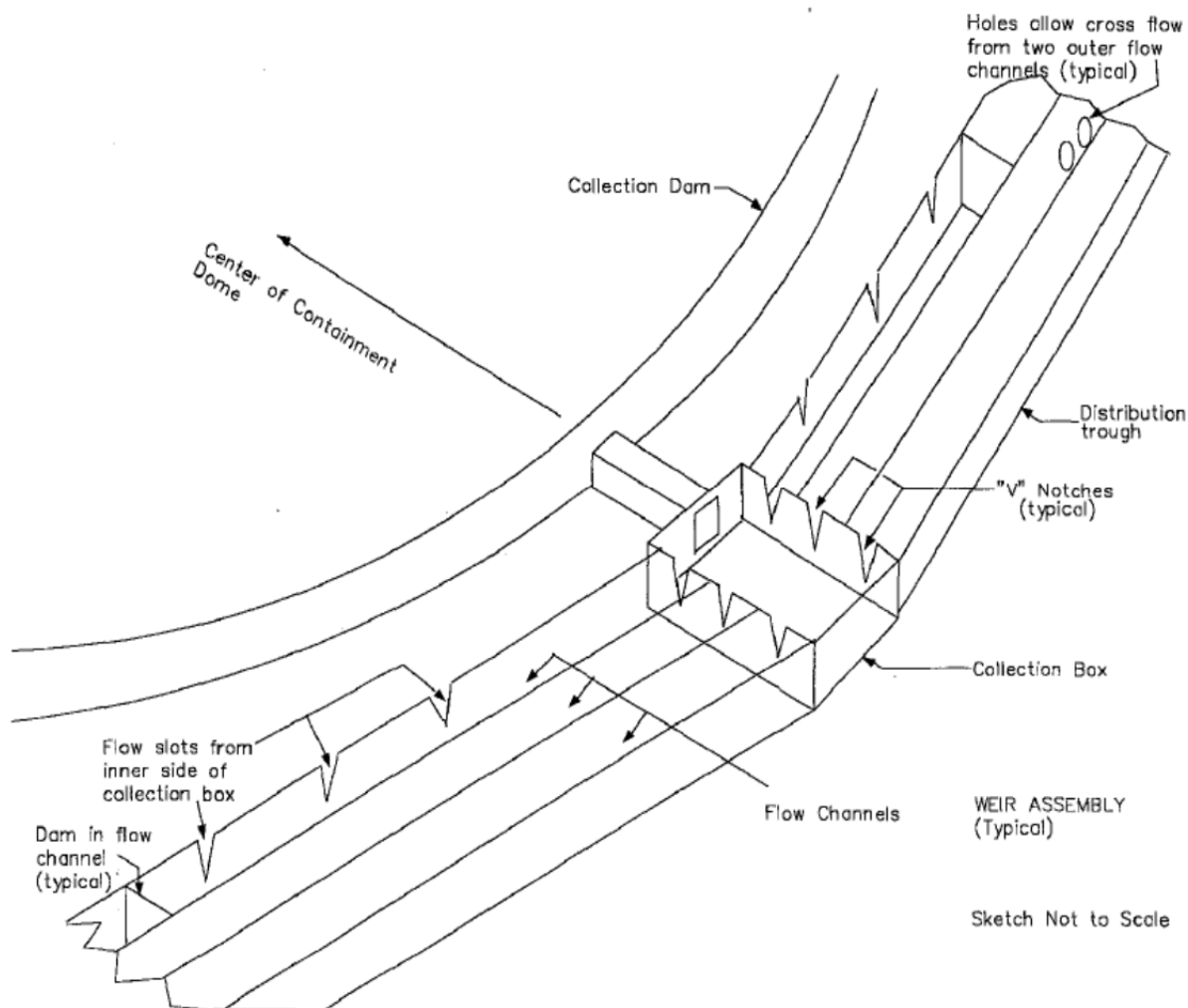


Figure 7-1. Illustration of PCS Water Distribution Weir Assembly

All components of the water distribution system are seismic category I, and designed to withstand thermal and pressure expansion/contraction of the containment without failure. The system is capable of functioning adequately during PCS accident operation under extreme low or high ambient temperatures. The weir distribution systems are constructed of stainless steel to limit concerns over blockage due to corrosion products or paint/coating degradation. The water distribution weir system is designated a safety class C component based on its containment cooling function.

7.2.3 PCS Water Distribution Testing Results

The Water Distribution Test (Reference 7.2) was used to determine the effectiveness of water distribution devices, to determine the water coverage as a function of the flow rate on the prototypical surface, and to determine the time to establish steady-state coverage. A full-scale test section, representing a 1/8 sector of the containment dome to the ~50 foot radius and a 1/16 sector of the full containment dome and a 4-foot long portion of the vertical sidewall, was built. The test section included both meridional and circumferential joints, with the maximum allowable plate misalignment, and was coated with the

prototypic inorganic zinc coating. Testing included simulation of the maximum allowable deviation in dome shape from ideal shape, by tilting the distribution troughs.

There was no source of heat to simulate mass and energy removal by evaporation for these tests. Two water distribution weir designs were tested. The final weir design was tested in Phase 3 of the Water Distribution Test (Reference 7.2) and is the weir described in Section 7.2.2.

These tests demonstrated that the water coverage just below the weirs consisted of discrete streams after the water was collected, redistributed, and re-applied at a fixed spacing around the containment dome perimeter by the water distribution weirs. These individual streams were sufficiently wide at the higher applied flows (35 and 27.5 gpm) to join just below the weirs and provide high water film coverage over the portion of the test section below the weir. However, at reduced applied water flow rates, the streams were sufficiently narrow in width that the water coverage consisted of vertical alternating wet and dry stripes. [

]^{a,c}

The water coverage was measured just above the second weir (at the 49-ft radius) and at the springline (65-ft radius at the top of the vertical sidewall). Measurements of stripe widths accounted for only the traverse where flowing water was observed, not the wider wetted traverse. The Phase 3 test data are summarized in Table 7-2, where the wetted perimeter of the flowing water was observed and is listed as a percent of total area or water coverage.

Table 7-2. Summary of the Phase 3 Water Distribution Test

^{a,c}

The coverage listed at 49-ft and 65-ft are the measured coverage just above the second weir and at the springline and for the water flow rates delivered in Phase 3 of the Water Distribution Test. The coverage decreases as the delivered flow rate decreases. The flow rate was not adjusted to account for the water lost at sampling points upstream of the springline. The correction would increase the water coverage percentages slightly.

The surface area that was wetted at a flow rate of 27.5 gpm (equivalent to 220 gpm on the full dome) was estimated to be []^{a,c} from the top of the dome down to the first weir, based on a review of the video tapes for the Phase 3 Water Distribution Tests. About []^{a,c} of the vessel was wet between the first and second weirs, and the entire vessel was wet at the bottom of the test section.

This test also demonstrated the time required to fill the prototypic water distribution devices and establish steady-state water coverage on the containment shell at a PCS flow rate equivalent to 220 gpm. [

] ^{a,c} Since the initial

PCS-delivered flow rate has been increased, the time required to achieve steady-state water coverage will be decreased, as discussed in Section 7.2.5.

7.2.4 Delivered PCS Water Flow Rate versus Time

The AP600 and AP1000 minimum delivered PCS water flow rates are shown as a function of time in Figure 7-2. The minimum delivered PCS water flow rate was calculated assuming only one of the parallel PCS tank discharge valves is open. This assumption reduces the gravity-driven flow rate by []^{a,c} since flow orifices in the discharge lines limit the flow rate from the tank.

The amount of water required for evaporative heat removal from the PCS shell decreases as the core decay heat decreases. Therefore, the PCS flow rate is designed to vary with time. The gravity-driven flow rate decreases as the water level in the PCS tank decreases. A series of standpipes are located within the PCS tank. The delivered PCS water flow rate decreases substantially whenever the water level falls below the top of a standpipe.

7.2.5 Time to Establish Steady State Water Coverage

Some period of time is required to establish steady state water coverage after the PCS has been actuated. This is an important input for the containment Evaluation Model. The delivered PCS water must fill the distribution bucket, two sets of distribution dam/weirs, and then cover the vertical containment shell.

The time needed to establish steady state water coverage was observed on the video tape recording of the 220 gpm equivalent full-scale PCS flow Water Distribution test. [

] ^{a,c}

As shown in Figure 7-2, the initial delivered PCS water flow rate is about twice as high as the tested value (440 gpm for AP600 and 469 gpm for the **AP1000** plant). Therefore, the time to establish steady state water coverage will be less than measured in the Water Distribution tests.

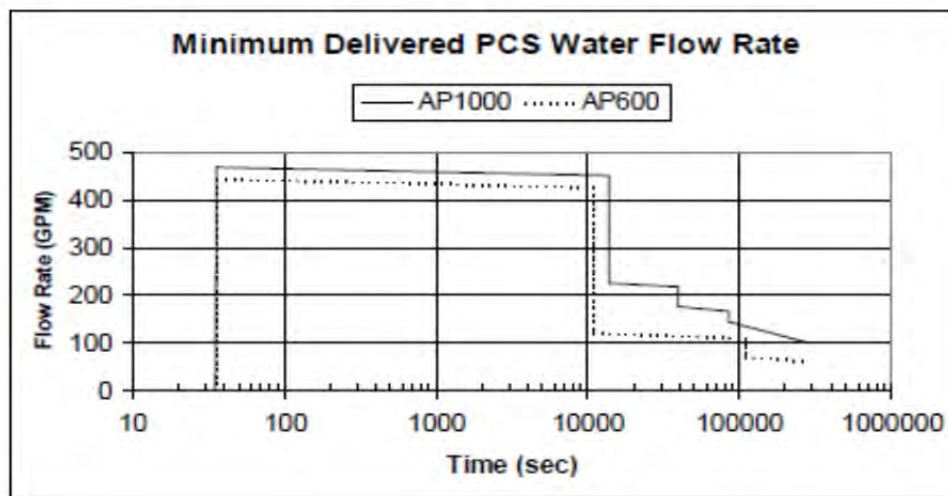


Figure 7-2. Minimum Delivered PCS Water Flow Rate from the Bucket

A simple analytical model was developed to estimate the weir outflow rates for a constant 440 gpm PCS water flow rate. The results are shown in Figure 7-3. This figure helps illustrate the various components of the time needed to establish steady state flow from the bucket, first, and second weirs. The steady state water coverage delay time input values for the AP600 and **AP1000** containment Evaluation Models are based on the actual prototype test results, rather than these calculations.

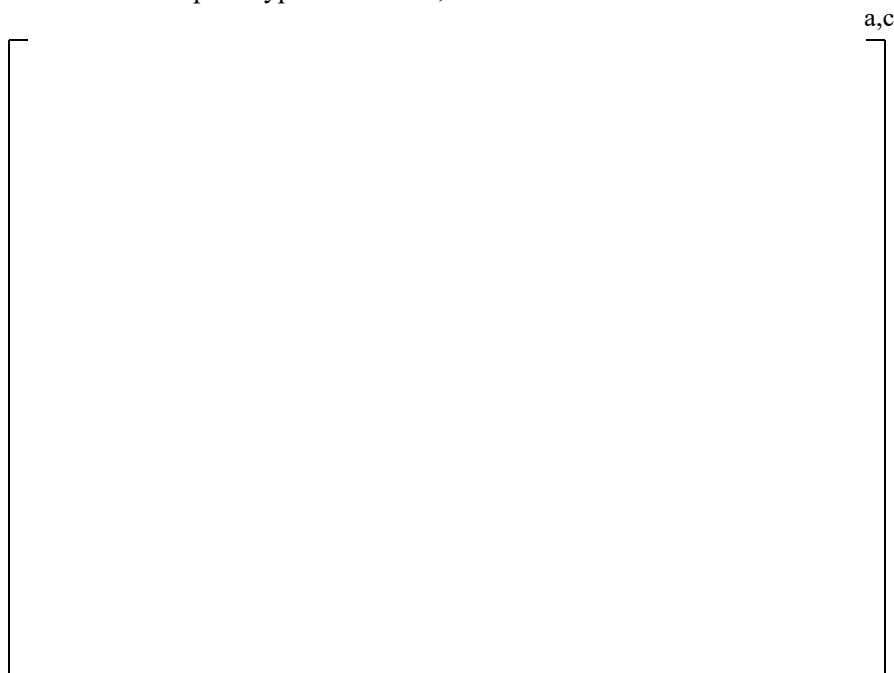


Figure 7-3. Weir Outflow

The time to establish steady state coverage is the sum of the time for the valve to open, the time to fill the lines and distribution bucket, the time to fill and spill over the two sets distribution dam/weirs, and the time to cover the vertical containment shell. The opening of the PCS isolation valve must bound electronic delays and the maximum valve stroke time. The higher flowrate for the AP600 and **AP1000** plants allows the bucket to fill up faster, which can be scaled from the test results based on [

] ^{a,c}

As described above, about [] ^{a,c} after flow initiation, a steady state flow and coverage pattern was observed in the 220 gpm equivalent full-scale PCS flow Phase 3 Water Distribution test. To estimate the time to fill the weirs and fully wet the containment sidewall for AP600 analyses, the test results were scaled [] ^{a,c}

The **AP1000** containment diameter, dome geometry, and water distribution system are the same as AP600, but the initial delivered PCS water flow rate for the **AP1000** plant is higher at 469 gpm. [

] ^{a,c}

[

]^{a,c}

Using a relationship between average film Reynolds numbers, the time to fill the weirs and wet the surface of the containment vessel can be determined. The steady state water coverage on the containment surface was estimated to occur within []^{a,c} for the test. Removing the time for the valve to open and the time to fill the bucket, the remaining []^{a,c} represents the time the film took to fill the weirs and wet the surface of the containment vessel. For the **AP1000** design, this is scaled as follows: [

]^{a,c}

Table 7-3 summarizes the time to reach steady state coverage. The total time is used in the Evaluation Model as a delay after the high-2 containment pressure setpoint is reached. No PCS water is credited until after the delay.

Table 7-3. Summary of Time to Reach Steady State Coverage

a,c

7.2.6 PCS Water Stripping from Baffle Supports

During pre-operational passive PCS flow tests, some water was observed as “raining” in the annulus rather than flowing down the containment vessel. It was postulated that this was due to stripping of the PCS water as it hit the baffle supports that are attached to the exterior surface of the containment vessel. To conservatively account for the loss of PCS water due to this effect, the safety analysis methodology was altered to remove all PCS water that interacts with the baffle supports on the cylindrical portion of the containment vessel. The assumptions and bases are summarized below.

Testing was performed for condensate return inside containment (Reference 7.14). The test facility consisted of a large, flat plate that could be positioned at an angle relative to the horizontal to simulate locations on the inside of the **AP1000** containment dome (i.e. 0-deg would represent the very top of the dome, and 90-deg would represent the vertical wall). The purpose of these tests was to determine the behavior of a liquid condensate film. While the tests were designed to simulate conditions inside the containment, some of the conclusions are applicable to the issue of film stripping by the baffle supports on the outside the containment.

A key conclusion from these tests was that the condensate losses from attachment plates that are located on the vertical wall are essentially zero as the film that contacts the support beams tends to flow around the beam and remain on the plate. The water film bypassed supports and remained attached to the containment vessel wall for the 90-deg test. This phenomenon was also observed at the bottom of the dome up to 86-deg inclination where film contacting the support beam tended to flow downward away from the wall and was lost. It should be noted that the film flow rates for the condensate on the inside of the containment vessel are significantly less than those expected on the outside, and this could result in higher losses on the outside. In addition, condensation on the relatively colder surfaces inside the containment vessel could impact the film behavior differently than evaporation off the relatively hot surface outside the containment vessel. However, these concerns are addressed by the bounding assumption of removing all of the PCS water film that interacts with the baffle supports on the vertical portion of the containment vessel. This bounding assumption also covers all other uncertainties regarding the non-uniformity of the evaporating PCS film.

Additional assumptions based on the condensation test observations:

- For obstructions on the dome section of the containment vessel that are angled upward (less than 90-deg), the water film would not separate from the obstruction, but would instead run over it. For the case of the baffle supports, the first row of supports is located on the dome above the spring line. Any water that might splash off this row would fall vertically downward and impact the dome below the support. Therefore, no losses are assumed for this row.
- Water film that interacts with the longitudinal welds along the supports will remain on the containment vessel wall. This is consistent with what was observed in the Phase 2 condensation tests, and is not expected to be affected by higher PCS water flow rates.
- Water that passes a row of baffle supports re-establishes into a uniform film flow that is reduced by the amount that is assumed to be stripped by the supports. Evaporation is also reducing the PCS water on the containment vessel wall.

7.3 WATER COVERAGE BASIS

The PCS film coverage model was developed to calculate the amount of water that evaporates from the AP600 shell, consistent with conservative models for film stability. The “film flow rate,” represented by the parameter Γ , is the water mass flow rate divided by the circumferential wetted perimeter, that is, $\Gamma = \dot{m}/W$. Water is distributed on to the containment shell by a series of streams around the circumference. At the high initial delivered PCS flow rate, these streams merge into a continuous film. After the first stand pipe uncovers and the delivered PCS flow rate decreases, the streams remain separate and flow down as stripes from the weirs. The stripes start with a film flow rate, Γ_{dist} and flow down the wall at a constant width until evaporation causes the film flow rate to reach the film stability limit, Γ_{min} . Once Γ_{min} is reached, film stability causes the width of the stripe to reduce as additional evaporation takes place. The bases for Γ_{dist} and Γ_{min} are presented in this section.

7.3.1 Water Distribution Film Flow Rate, Γ_{dist}

Values of water coverage at the springline were measured in Phase 3 of the Water Distribution Test (Reference 7.2). The data, presented in Figure 7-4, show the coverage increased with the total water flow rate to []^{a,b} percent coverage at 220 gpm, then increased to []^{a,b} percent at 280 gpm. Thus, a model that limits the coverage at the top of the side wall to []^{a,c} percent bounds the test data at flow rates greater than 280 gpm. Modeling the coverage at lower flow rates with a value of $\Gamma_{\text{dist}} = []^{\text{a,b}}$ lbm/hr-ft is a good estimate at 220 gpm and bounds the test data at 100 gpm and 55 gpm as shown in the figure below.

a,b

Figure 7-4. Comparison of Water Distribution Model to Phase 3 Water Distribution Test Results

The room temperature, isothermal Water Distribution Test data are applicable to both AP600 and AP1000 plants. The basis for using the data is that the water applied to the shell beyond the second weir during actual PCS operation is heated to the shell temperature while flowing down to the second weir. The AP600 scaling analysis estimated less than 1600 ft² of heat transfer surface area is required to heat up the subcooled water, whereas there is 4400 ft² of wetted surface area above the second weir (Reference 7.8, Section 7.6.6). Consequently, heated water is applied to a heated shell at approximately the same temperature at the second weir, so the water and shell are nearly isothermal, as in the Water Distribution Test. The decreased stability exhibited by the application of cold water to a hot surface (References 7.10 and 7.12) is not an issue in this case, so it is assumed that the coverage measured in the cold, isothermal tests is conservative for the nearly isothermal application below the second weir in both AP600 and AP1000 plant designs.

The room temperature (65° to 68°F) Water Distribution Test coverage's are a conservative basis for Γ_{dist} due to the effect of increased temperature on the film properties. The film spreads where the water spills from the weir V-notch and impinges on the shell surface. The spreading is a momentum-dominated process that is opposed by friction and surface tension. At higher temperatures, the film viscosity is decreased by a factor of 2 to 3, and the surface tension is decreased by 15-20 percent, while the impingement momentum is essentially unchanged. The reduction of the friction and surface tension both allow the film to spread more at high temperature than at low temperature.

7.3.2 Minimum Film Flow Rate, Γ_{min}

Observations of the evaporating film flow on heated surfaces show the film flows in constant width stripes until evaporation causes the film flow rate to reach a minimum value, Γ_{min} after which, the film width narrows with additional evaporation. Most of the LST, small scale test (SST), and Westinghouse Flat Plate tests produced constant width stripes, or constant coverage. The lowest values of film flow rate, Γ , either were above Γ_{min} , or at most were close to Γ_{min} . Consequently, the film measurement data for each of the tests is a record of values of $\Gamma \geq \Gamma_{\text{min}}$. Several of the lowest measured values of Γ are presented in Figure 7-5.

A conservative upper limit for the minimum stable film flow rate, Γ_{min} , is needed for the PCS film coverage model. The minimum stable film flow rate increases as the heat flux increases. As demonstrated by the work of Bohn and Davis (Reference 7.10). The Westinghouse test data cover a heat flux range that is greater than the maximum expected operating value for both the AP600 and AP1000 plants (see Table 7-11). A constant Γ_{min} value of []^{a,c} lbm/hr-ft was selected to bound the various Westinghouse test data as shown in Figure 7-5. The comparison presented in Figure 7-5 shows this value to be much higher than the lowest stable measured Γ values of each test.

Figure 7-5. Determination of Gamma-Min from LST, SST, and Flat Plate Data

7.4 EFFECT OF TWO-DIMENSIONAL (2-D) HEAT CONDUCTION THROUGH THE CONTAINMENT SHELL

The PCS transfers heat from the containment atmosphere to the outside environment. Cooling water is applied to the outside surface of the shell to facilitate the heat removal process by evaporation of the applied water. Early in the postulated event, the water applied to the shell exterior provides at least []^{a,b} percent coverage of the external surface. As the transient progresses, the applied flow rate is reduced and the water coverage of the external surface area of the shell is reduced as discussed in Sections 7.2 and 7.3.

As evidenced by test data, the flow distribution weirs develop alternating wet and dry vertical “stripes” on the containment surface. These stripes become clearly segregated as the applied water flow rate is reduced. Heat removal from the wetted areas is greater than from the dry areas and results in the wetted surface area being cooler than the dry surface (evaporative cooling in the wetted area is much greater than convection and radiation from the dry surface). This temperature difference results in heat conduction in the circumferential direction through the thickness of the containment shell. Thermal energy is conducted from the hotter dry stripe areas into the adjacent portions of the containment shell cooled by a wet stripe. The transfer of additional thermal energy to the wet stripe increases the temperature of the wetted steel which increases the water film temperature, which increases the water evaporation rate, the containment heat removal rate, and the use of the delivered water.

Since the water evaporation rate calculated by WGOTHIC only considers heat conduction in the radial direction through the containment steel shell, the effects of circumferential two-dimensional heat conduction can be credited by using multipliers applied to the PCS evaporation rate or the overall heat and mass transfer coefficients. A description follows of the method used to calculate the effect of circumferential two-dimensional heat conduction on the water evaporation. Section 7.5 describes how this is applied in the PCS film coverage model to calculate the evaporation-limited PCS water flow rate input for the Containment Evaluation Model.

7.4.1 Geometry of the Wet and Dry Vertical Stripes on the Containment Outside Steel Surface

The Water Distribution Tests, as discussed in Section 7.2.3, showed the outside surface of the containment shell will be partially wet when the PCS-delivered water flow rate is reduced below the high initial flow rate. At cold, unheated conditions, the observed side wall wetting was []^{a,c} percent with 100 gpm and []^{a,c} percent with 55 gpm equivalent delivered PCS flow. The limited percentages of wetted area were a consequence of the water being applied to the surface at discretely spaced locations, and the fact that the water spread to a stream width that resulted in a bounding Γ_{dist} of []^{a,b} lbm/hr-ft. Therefore, the observed stream width and wetted surface areas were directly proportional to the water flow rate. At these lower flow rates, the stream widths were observed to be less than the distance between weir slots and therefore alternating, vertical, dry and wetted stripes formed down the containment below the second distribution weir.

The occurrence of alternating wet and dry vertical stripes on the containment outside surface was also documented on a hot surface with evaporation in progress in the PCS large-scale test (Reference 7.7). In the LST, with heat transfer occurring, wet stripes were observed to flow vertically at constant width to the bottom of the sidewall unless almost all of the applied water was evaporated.

In the Water Distribution Test, the streams initiated by the second (lower) set of weirs had a center-to-center spacing on the vertical sidewall that corresponded to the spacing of applied water streams at the weir, multiplied by the ratio of the containment radius at the sidewall to the radius at the weir. For example, the 6-inch weir slot spacing at the ~50-foot radius of the dome produced stripes at a spacing of ~8-inches at the sidewall radius of 65 feet.

This evaluation of the effects of two-dimensional conduction on the wet steel surface temperature, and resulting water evaporation rate was based on the same alternating wet and dry stripe pattern and spacing produced by the weir(s) in the water distribution test. However, the location of the second weir ring and the weir ring slot spacing used were updated to correspond to the AP600 plant. Specifically, the weir slots on the backwall of the distribution troughs in the second weir ring are at the 50.7 foot radius, and the spacing between weir slots is 6.5 inches. This results in an 8.35-inch center-line to center-line stripe spacing at the vertical sidewall. In addition, a wider dry stripe directly under the 16-weir collection boxes was taken into account.

7.4.2 Heat Transfer Boundary Conditions for the 2-D Conduction Model

The boundary conditions used in the two-dimensional heat conduction model were established by a series of one-dimensional, steady-state calculations of the PCS heat transfer process performed at constant containment pressures ranging from 10 psig to 65 psig (24.7 to 79.7 psia). These calculations were performed using the same heat and mass transfer correlations as used in WGOTHIC. The heat transfer and the temperature differences from the steam/air mixture inside containment through the steel shell, and from the wet and dry outside containment surfaces to the air were provided. The heat transfer and temperature differences were used to establish heat transfer coefficients for each containment pressure condition for both the inside heat transfer to the inside water film, and for the outside heat transfer from the outside water film. These heat transfer coefficients were reduced based on the conservative multiplication factors (Reference 7.11, WCAP-15326, Rev. 1) applied in WGOTHIC, and were then further decreased to account for the water film and paint layer conductivities and thicknesses. The outside heat transfer coefficient versus the outside steel shell temperature obtained for each pressure condition for the wetted surface, was fitted using a second degree polynomial for use in the conduction model. A constant dry surface heat transfer coefficient (with a fixed outside cooling air temperature) that accurately modeled the pressure conditions analyzed, established the outside heat transfer boundary conditions. These boundary conditions were reviewed to assure that the heat transfer rates at all containment pressure/temperature conditions were higher than the corresponding heat transfer rates calculated by WGOTHIC in the containment analysis. This assures that any increase in heat transfer, as compared to the heat transfer with only radial conduction through the containment steel shell, is underpredicted.

7.4.3 2-D Conduction (ANSYS) Model Description

The effect of circumferential conduction through the AP600 steel containment shell on the shell surface temperatures and the resulting effects on the condensing heat transfer on the inside surface, the evaporative heat transfer on outside wetted surfaces, and the convective heat transfer from the dry outside surface were quantified using the ANSYS computer code. The ANSYS computer code is a multi-purpose, finite element program that has been used commercially since 1970. For this calculation ANSYS revision 5.3 was used.

The ANSYS calculation was a two-dimensional, thermal, steady-state analysis of a periodic half-cell (cross-section) that consisted of a two-dimensional block []^{a,c} thick and []^{a,c} wide; corresponding to the AP600 containment steel shell thickness and the spacing of water streams at the containment sidewall perimeter imposed by the PCS water distribution weirs. A thermal conductivity of 24 Btu/hr-ft-°F was used for the steel material. Adiabatic boundary conditions were used for the right and left side of the half-cell model to represent symmetry and periodicity of the cell.

For each steady-state containment pressure analyzed, a half-cell model was established for each water coverage fraction ranging from 0.05 to 0.95. The nodding density was increased on each side of the wet/dry interface on the outside surface to increase the accuracy of the heat transfer calculation near the wet/dry interface.

In addition to these partially wetted half-cell models, the heat transfer with a completely wetted and complete dry half-cell model was analyzed for each containment pressure using the same inside and outside boundary conditions. Since the half-cell has a 1-D solution when fully wet or dry, these cases provide the heat flux with only radial condition through the containment shell. The heat flux rate results of these fully wetted and fully dry cases were used to normalize the heat flux rate obtained from the partially wetted cases, where two-dimensional heat conduction occurs.

The ANSYS two-dimensional heat conduction results show that the temperature of the dry surface area is decreased compared to the dry surface temperature when only one-dimensional radial heat conduction is used. This results in less radiation and convection from the dry regions. Although WGOTHIC utilizes one-dimensional radial heat conduction, the dry area convection and radiation is not overpredicted because WGOTHIC must use a wet surface area that corresponds to the evaporated water flow rate calculated by the PCS film coverage model. The evaporated water flow rate calculated by the PCS film coverage model includes the enhanced evaporation characterized by the multiplier, M (Section 7.4). Thus, WGOTHIC must use more cooler wet surface area to evaporate the water flow rate from the PCS film coverage model. This results in less hotter dry surface area, and therefore, WGOTHIC underpredicts the net radiation and convection from the dry surface.

The WGOTHIC conservatism can be estimated using values from the ANSYS two-dimensional calculation, which is the best representation of the heat conduction through the shell. It is assumed the WGOTHIC temperatures and heat fluxes are the same as ANSYS one-dimensional cases.

- At containment pressures of 15 and 25 psig, and with 50 percent wet coverage, the two-dimensional ANSYS model predicts dry heat transfer (radiation and convection) is 73 and 82 percent respectively, of the one-dimensional value. WGOTHIC will predict 67 percent of the one-dimensional dry heat transfer, since it reduces the dry surface area available by 33 percent.
- For the same containment pressures, at 25 percent wet coverage, the two-dimensional model predicts the actual dry heat transfer (radiation and convection) is 83 to 91 percent of the one-dimensional value. WGOTHIC will predict 57 percent of the one-dimensional dry heat transfer, since it reduces the dry surface area by 43 percent. Thus, WGOTHIC again predicts less dry energy removal than two-dimensional model predicts.

It is concluded that the WGOTHIC model predicts less dry heat transfer than the two-dimensional ANSYS model.

7.4.4 Enhanced Evaporation due to 2-D Conduction

The heat flux from the wetted portion of the half-cell model was compared with the wetted heat flux that occurs when only radial heat conduction (one-dimension) is assumed. Figure 7-6 shows the water evaporation rate with two-dimensional conduction versus the fraction of wetted area, normalized to the evaporation rate, calculated with only radial heat conduction (one-dimensional) outward through the steel shell, for containment pressures of 10, 15, 20, and 25 psig. These calculational results are bounded by the following polynomial expression:

$$\left[\frac{M}{x} \right]^{a,c} \quad (7-1)$$

where,

M = the wetted area heat transfer rate enhancement or multiplication factor
x = fraction of containment surface wetted, = W/W_o

This multiplication factor is applied to the average evaporation flux from WGOTHIC in the spreadsheet calculation of the evaporation-limited PCS flow discussed in Section 7.5.2.1 to approximate the effects of 2-D conduction. Although there may be notable dry stripes at the lower elevations of the containment shell throughout the transient, the 2-D conduction multiplier is not credited until the PCS flowrate from the bucket has decreased such that the film width is narrowed below $\left[\frac{M}{x} \right]^{a,c}$ along the entire sidewall.

Several additional plots to illustrate the effect of two-dimensional conduction on the PCS heat transfer process are provided for the 20 psig containment pressure, 25 percent wetted case. A temperature distribution contour plot is shown for the ANSYS half-cell model in Figure 7-7, with the surface inside containment at the top of the page. Figure 7-8 shows the thermal flux from the inside to outside surface (y direction), perpendicular to the containment shell, and Figure 7-9 shows the total heat flux (x, y directions) that occur in the steel shell. Figure 7-10 and Figure 7-11 show the thermal flux distribution on the outside and inside surface of the wall, respectively.

a,c

Figure 7-6. Normalized Water Evaporation Rate (2-D/1-D) versus Overall Containment Wetted Fraction

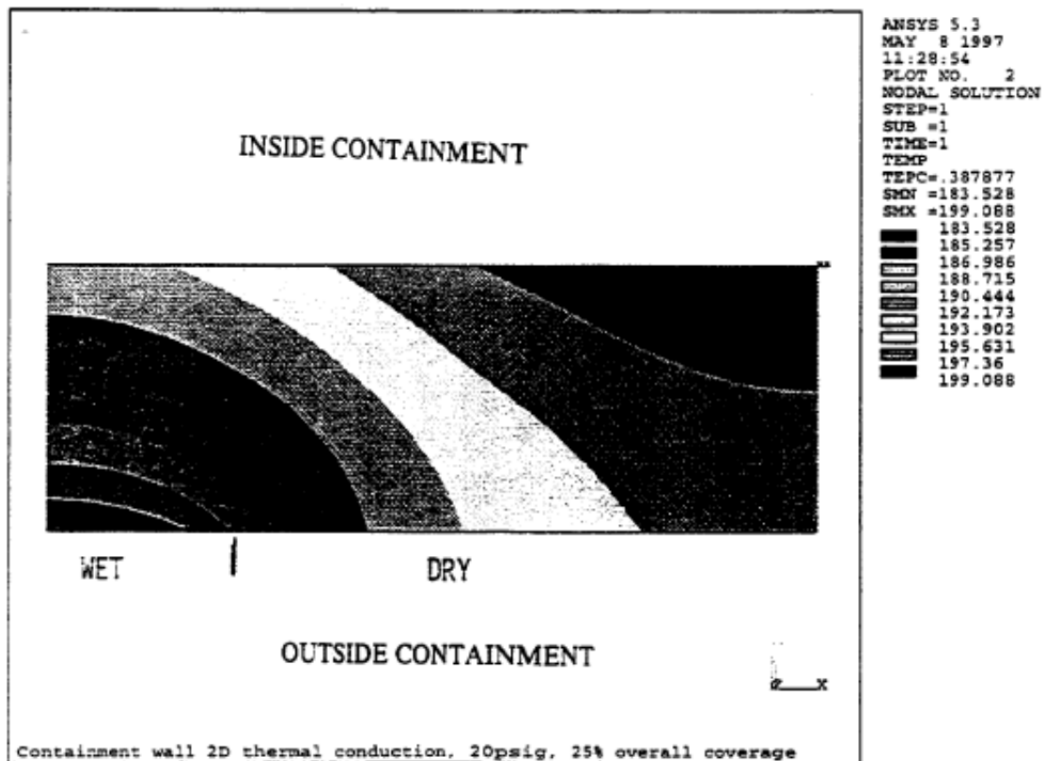


Figure 7-7. Containment Steel Shell Temperature Gradient (°F) with 2-D Heat Conduction; 20 psig, 25% Wetted

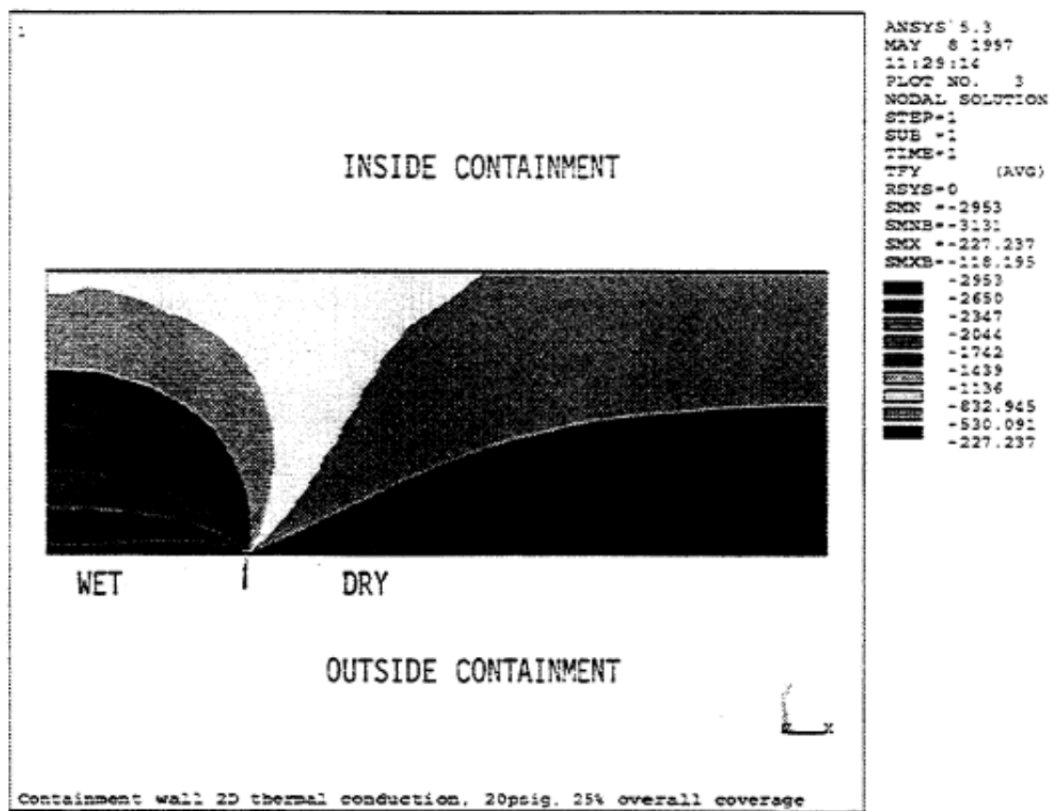


Figure 7-8. Containment Steel Shell Thermal Flux Gradients (Btu/hr-ft²) in Y-Direction; 20 psig, 25% Wetted

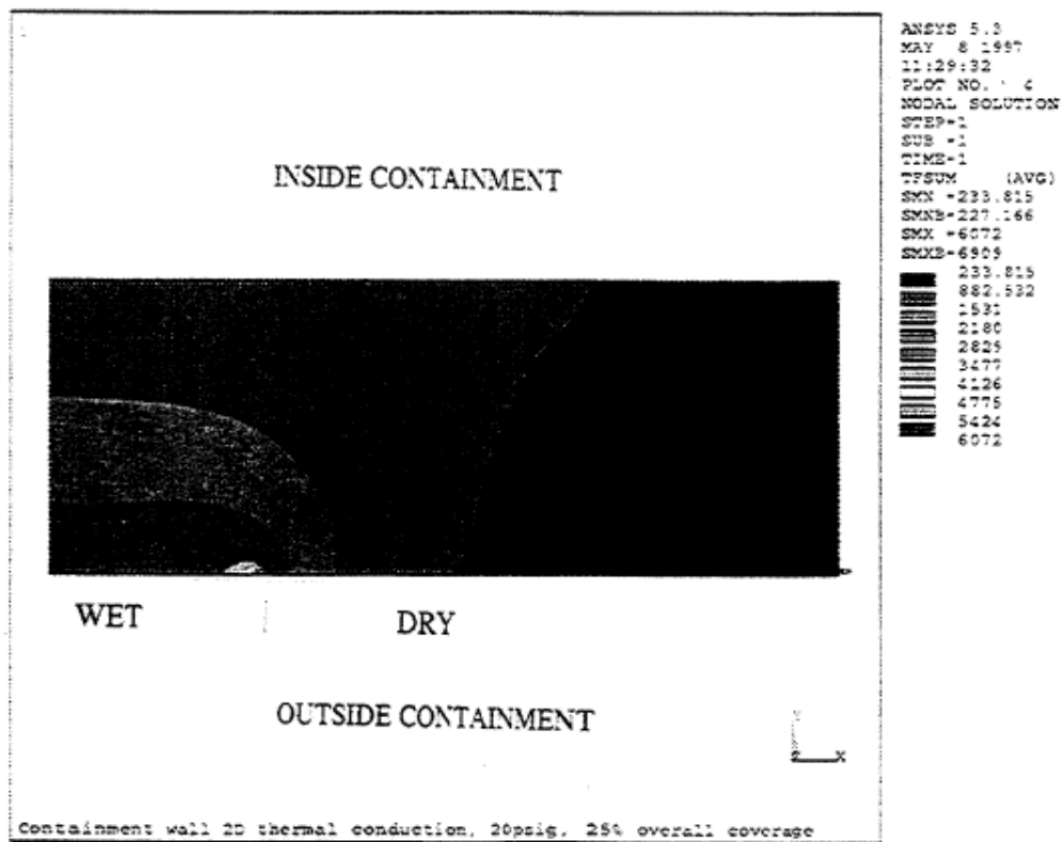


Figure 7-9. Containment Steel Shell Total Thermal Flux (Btu/hr-ft²); 20 psig, 25% Wetted

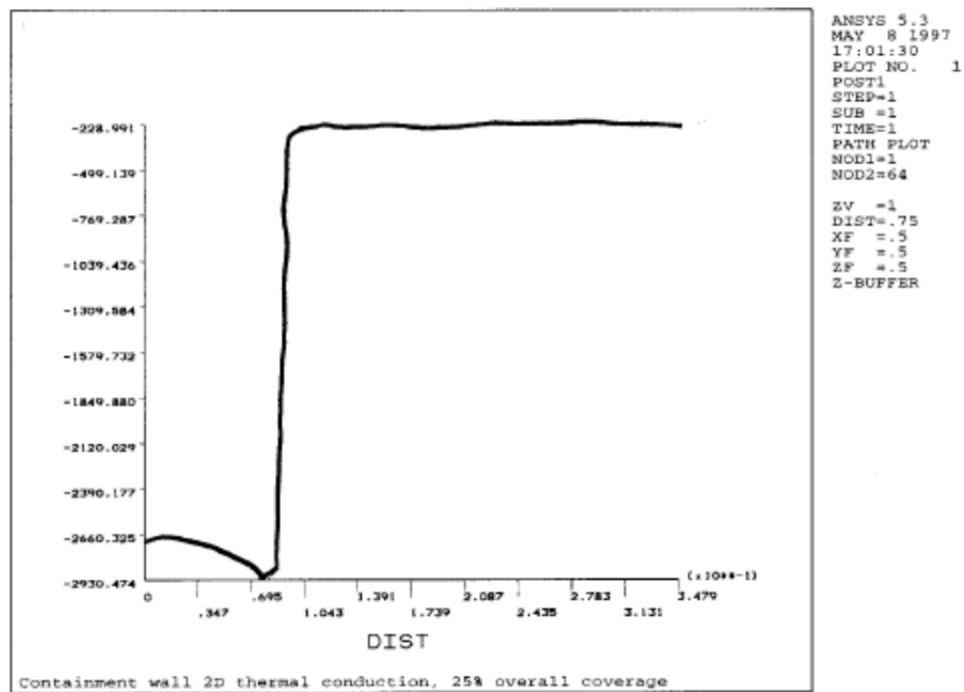


Figure 7-10. Thermal Flux in Y-Direction on Outside Surface of Containment Wall [Btu/hr-ft²]

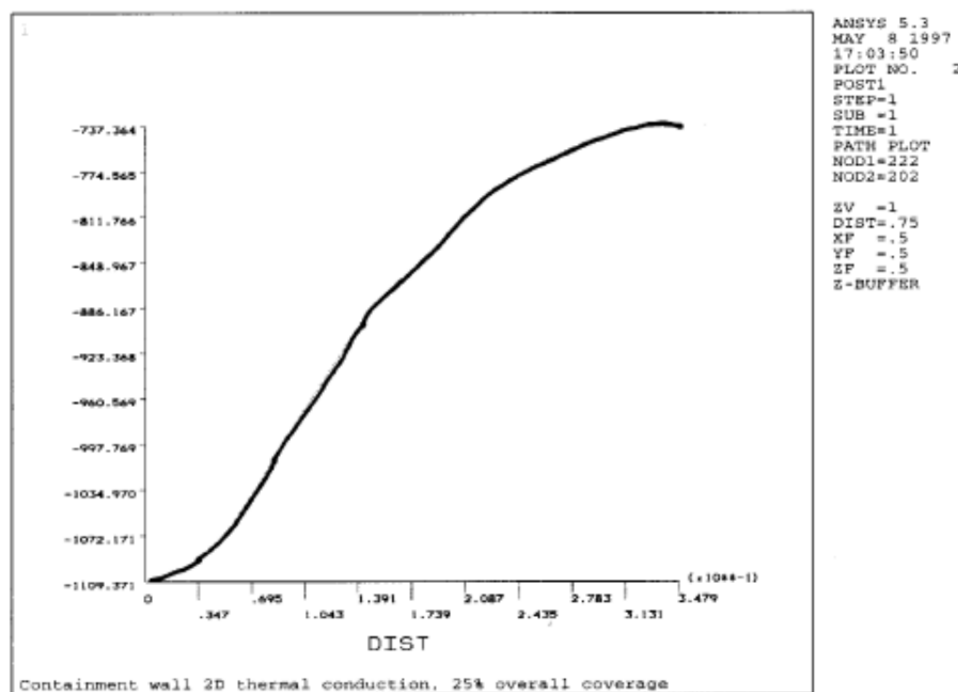


Figure 7-11. Thermal Flux in Y-direction on Inside Surface of Containment Wall [Btu/hr-ft²]

7.4.5 Enhanced Overall Heat and Mass Transfer Due to 2-D Conduction

As described in Section 7.4.4, the evaporation rate from the containment shell can be enhanced by including the effects of circumferential 2-D heat conduction by using a factor to increase the evaporation-limited PCS flowrate based on the fraction of the containment surface that is wetted. An alternate approach is to incorporate the effects of 2-D heat conduction by applying a multiplier on the overall heat transfer rate. The information in this section is developed from the same analyses that are the basis for the PCS evaporation factor in Section 7.4.4.

The conduction of heat from the hot dry region into the cooler wetted region of the containment shell will increase the overall heat transfer rate through the shell. Figure 7-12 shows the total heat transfer rate (wetted and dry areas combined) versus the fraction of wetted area, normalized to the heat transfer rates calculated with only radial heat conduction (one-dimensional) outward through the steel shell. [

^{a,c}

^{a,c}

Figure 7-12. Normalized Total Wet and Dry Heat Transfer (2-D/1-D Conduction) vs. Wetted Fraction

This alternate approach of modeling the effect of 2-D heat conduction is used with the evaporation-limited PCS option incorporated into the WGOTHIC code discussed in Section 7.5.2.2. Figure 7-13 shows [

$\Gamma^{a,c}$

$\Gamma^{a,c}$

Figure 7-13. 2-D Conduction Multiplier as a Function of Wetting Fraction

7.4.6 Insights from the PCS Large-Scale Testing

The large-scale PCS heat transfer tests were largely conducted with high water coverage fractions such that circumferential conduction would have little or no effect on the water evaporation rate. An exception is test run RC050C of matrix tests 213.1. A clear indication of 2-D conduction effects is seen by comparing the results of RC050C with test run RC048C of matrix test 212.1. In these tests, the containment pressure and other boundary conditions were essentially the same, with the exception that the amount of water applied to the external surface of the test vessel was []^{a,b} gpm in test RC048C and only []^{a,b} gpm in test RC050C.

The reduced water flow rate in test RC050C resulted in a reduction in the wetted area observed at the bottom of the test vessel sidewall, []^{a,b} percent for test RC050C versus []^{a,b} percent for test RC048C. In spite of the reduced wetted area in test RC050C, the total heat removed from the test vessel and the amount of water evaporated in this test was equal to test RC048C.

Furthermore, the lower portion of the vertical sidewall in test run RC050C was wetted with []^{a,b}. This stripe geometry is similar to that observed in the water distribution test discussed in Section 7.2.3 and assumed for the 2-D conduction model.

A comparison of the LST vessel shell wall temperatures for these two test runs using the thermocouple pairs (one thermocouple at the inside wall surface matched to a thermocouple at the outside wall surface), used to derive local heat flux rates, provides insight to the effect of circumferential conduction. Table 7-4 and Table 7-5 provide comparisons of the inside and outside LST shell temperatures, and the local heat flux derived from the temperature difference across the 7/8-inch thick steel shell; for the two lowest elevations on the LST sidewall.

Table 7-4 shows that at the Level D elevation in test run RC048C all the inside and outside wall temperatures are relatively uniform. This indicates that the outer wall is wetted at all the thermocouple pair locations. The average outside wall surface temperature is []^{a,b} °F, and the average local heat flux is []^{a,b} Btu/hr-ft² based on the thermocouple pair ΔT s. In comparison, only four of seven outside wall thermocouples appear to be wetted in test run RC050C (dry outside wall temperatures are very high, []^{a,b} °F, and the wall ΔT is small). In this test run the average wetted outside wall temperature is []^{a,b} °F, and the average wetted local heat flux is []^{a,b} Btu/hr-ft².

Similarly, Table 7-5 shows that at the Level E elevation (just above the runoff collection gutter) the test run RC048C uniformly wetted outside wall average temperature is []^{a,b} °F and the average heat flux is []^{a,b} Btu/hr-ft². In comparison, test run RC050C which is []^{a,b} percent wetted at this elevation; indicates that only two of the outside wall thermocouples are clearly wetted, and the average wetted outside wall temperature is []^{a,b} °F and the average heat flux is []^{a,b} Btu/hr-ft². Note that the test run RC050C thermocouples at the 240° circumferential location show an outside wall temperature and heat flux that is intermediate to the clearly wetted or dry locations. This thermocouple pair may be adjacent to a wet stripe, where circumferential heat conduction would cause these observed intermediate temperatures and ΔT .

These tables show that with the striped water coverage on the outside surface, the wall temperatures and heat flux of the wet portions of the shell are higher than when the outside surface is completely wet.

Table 7-4. Elevation D Heat Flux Comparison from PCS Large-Scale Tests RC048C and RC050C

a,c

Table 7-5. Elevation E Heat Flux Comparison from PCS Large-Scale Test RC048C and RC050C

a,c

7.5 THE CONTAINMENT EVALUATION MODEL TREATMENT OF WATER COVERAGE

The containment Evaluation Model includes a PCS film coverage model that determines the wetted area on the outside of the containment vessel. It accounts for the reduction in the wetted area down the side of the containment vessel as the PCS flowrate changes, due to the decreasing flowrate as the standpipes in the PCCWST uncover and due to the evaporation of the water. The model also determines the amount of PCS water that does not evaporate, and excludes the sensible heating of this runoff flow. Section 7.5.1 describes the equations that determine the wetted fraction, and Section 7.5.2 describes the implementation and interaction with the WGOTHIC code.

7.5.1 PCS Film Coverage Model

The PCS film coverage model, which is used to calculate the rate at which water evaporates from the sidewall of the containment shell, is described in this section. The model assumes water is delivered to the sidewall consistently with the initial distribution spreading data described in Section 7.3.1.

The PCS film coverage rate model starts with a simple definition that relates the total film flow rate, \dot{m} ; the containment circumference, W_o ; the wetted fraction of the circumference, or the fraction of the surface that is wet, f ; and the film flow, or mass flow rate per unit width, Γ . Each of these is a function of the parameter Z , the distance below the top of the sidewall. The equation is:

$$\dot{m}(Z) = \Gamma(Z)W_of(Z) \quad (7-2)$$

which, rearranged, also defines Γ . The derivative of the mass flow rate with respect to vertical distance is also used. Using the chain rule for derivatives:

$$\frac{d\dot{m}}{dZ} = W_of \frac{d\Gamma}{dZ} + \Gamma W_o \frac{df}{dZ} \quad (7-3)$$

The wetted coverage and runoff flow rate are calculated based on the following assumptions and boundary conditions:

- The delivered PCS water flow rate boundary condition at the top of the sidewall, \dot{m}_{on} is presented in Figure 7-2. The initial film flow rate at the top of the sidewall is specified to be $\Gamma = \dot{m}_{top}/(W_of)$, $f = []^{a,c}$. For delivered flow rates less than $[]^{a,b}$ gpm, the film flow rate at the top of the sidewall is specified to be $\Gamma_{dist} = []^{a,b}$ lbm/hr-ft. The other boundary condition, the width of coverage at the top is determined from $W_of_{top} = W_of$, $f = []^{a,c}$ or $W_of_{top} = \dot{m}/\Gamma_{dist}$, depending on the delivered flow rate.
- The water is assumed to flow in constant width stripes below each weir slot as long as the film flow rate Γ remains greater than Γ_{min} . The film flow rate decreases due to evaporation as the film travels down the sidewall. The constant width coverage model is described in Section 7.5.1.1.
- After the film flow rate reaches Γ_{min} , evaporation is assumed to cause the stripe width to narrow while Γ remains constant at Γ_{min} .

7.5.1.1 Constant Width Coverage

After the water distribution is established at the top of the sidewall by the weir, the film evaporates at mass flux, $\phi_m(Z)$, as it flows down the shell in stripes of constant width. The basis for the constant width stripe is the observations of the stripes on the LST, and the physical explanation in Appendix 7.A-3. For a constant wetted fraction $df/dZ = 0$, and $d\Gamma/dZ = \phi_m(Z)$. The rate of change equations for \dot{m} , Γ , and W_of for the constant width portion of the wetted area are:

$$\frac{d\dot{m}}{dZ} = -\phi_m(Z)W_of \quad (7-4)$$

$$\frac{d\Gamma}{dZ} = -\phi_m(Z) \quad (7-5)$$

$$W_o \frac{df}{dZ} = 0 \quad (7-6)$$

With the boundary conditions listed above, and Equations 7-4, 7-5, and 7-6, the water mass flow rate, \dot{m} , and the film flow rate, Γ , can be calculated for the constant width evaporation portion of the coverage. For the case with $\phi_m = \text{constant}$, the simple analytical expression for the mass flow rate is:

$$\dot{m}(Z) = \dot{m}_{top} - \phi_m W_o f_{top} Z \quad (7-7)$$

Equation (7-4) can be written in terms of difference equations for a numerical solution where $\Delta \dot{m} = \dot{m}_2 - \dot{m}_1$, $\Delta Z = Z_2 - Z_1$, and ϕ_m is a variable:

$$\Delta \dot{m} = -W_o f_{top} \phi_m \Delta Z \quad (7-8)$$

or

$$\dot{m}_2 = \dot{m}_1 - W_o f_{top} \phi_m (Z_2 - Z_1) \quad (7-9)$$

Knowing \dot{m} , the film flow rate is determined from Equation (7-2) where $\Gamma = \Gamma_{dist} = \dot{m}_{top} / (W_o f)$.

The value of Z when Γ reduces to Γ_{min} is Z_{min} . The value of Z_{min} can be determined from Equation (7-7) when ϕ_m is constant:

$$Z_{min} = \frac{(\dot{m}_{top} / W_o f_{top}) - \Gamma_{min}}{\phi_m} \quad (7-10)$$

7.5.1.2 Constant Γ_{min} Coverage

When $\Gamma = \Gamma_{min}$, the wetted width, $W_o f$, begins to narrow, while Γ_{min} is maintained at a constant value. The resulting rate of change equations for \dot{m} , Γ , and $W_o f$ for this portion of the stripe are:

$$\frac{d\dot{m}}{dZ} = -\phi_m(Z) W_o f(Z) \quad (7-11)$$

$$\frac{d\Gamma}{dZ} = 0 \quad (7-12)$$

$$\frac{df}{dZ} = -\frac{\phi_m(Z) f(Z)}{\Gamma(Z)} \quad (7-13)$$

When $\phi_m = \text{constant}$ and $\Gamma = \Gamma_{min} = \text{constant}$, the solution to Equation 7-13 is the simple exponential function:

$$f(Z) = f_{top} e^{-\phi_m(Z - Z_{min}) / \Gamma_{min}} \quad (7-14)$$

Knowing from Equation (7-14), the mass flow rate at any Z is simply calculated from Equation (7-2). The runoff flow rate is $\dot{m}_{off} = W_o f_{bot} \Gamma_{min}$, where $W_o f_{bot}$ is the wetted circumference at the bottom of the containment shell, $Z = Z_{max}$.

By inspection of Equation (7-14), it is noted that $W_o f$, the wetted width, is always greater than zero. Thus, for constant values of ϕ_m and Γ_{min} , Equation (7-14) always predicts some water runs off the wall without

evaporating. However, from experimental observations, all the water delivered to the containment shell is evaporated for some transient conditions. Thus, the preceding calculation method is conservative in its execution.

7.5.2 Interaction of the PCS Film Coverage Model with WGOTHIC

There are two processes that can be used to implement the PCS film coverage model. The first is a spreadsheet that is used iteratively with WGOTHIC runs. The second is fully contained within the WGOTHIC code. This section provides an overview of the WGOTHIC clime modeling as it relates to the PCS flow modeling followed by detailed summaries of the two process for determining the PCS film coverage and the evaporation-limited flowrate.

The WGOTHIC code uses a special type of heat conductor called a “clime” to model the convection, radiation, conduction, evaporation, and condensation heat and mass transfer processes from the inside of containment to the outside of containment. Each clime consists of a horizontal slice of the shell, riser, baffle, downcomer, and shield building of the PCS. []^{a,c} climes are used to represent the PCS in the AP600 containment design basis accident (DBA) Evaluation Model. []^{a,c} climes are used to represent the PCS in the **AP1000** containment DBA Evaluation Model. Details of the climes in the WGOTHIC AP600 containment model are described in Section 4.4; the clime portion of the WGOTHIC **AP1000** containment Evaluation Model is described in Section 13.5.

The maximum wetted area for each clime is input to the WGOTHIC model. The wetted area input values for the WGOTHIC Model are based on the measured water coverage values from the Phase 3 Water Distribution Tests on the dome, and []^{a,c} percent of the shell circumference wetted on the sidewall. The wetted area for the top of the dome down to the first weir is estimated from the video tapes of the Phase 3 Water Distribution test. The wetted coverage area change over the diverging area between the first and second weirs. The wetted perimeter specified for this region is based on the average of the value just below the first weir and the minimum measured value just above the second weir. The wetted perimeter does not change much over the steeply sloped region between the second weir and the top of the vertical sidewall. The wetted perimeter input values are the same for each clime representing the vertical sidewall.

The percent of the perimeter wetted is summarized in Table 7-6. The values listed represent the measurements at the []^{a,c} flow rate (which is equivalent to a []^{a,c} PCS water flow rate). The use of these wetted perimeter percentages for the higher initial PCS flow rate is a conservatism in the containment Evaluation Model.

Table 7-6. Clime Wetted Perimeter and Basis for WGOTHIC Evaluation Model

Clime	Percentage	Location	Method of Determination
[]		[] ^{a,c}	Visual inspection and calculation
[]		[]	Measured
[]		[]	Measured

The application of the PCS water flow is delayed based on the estimated time required to reach steady-state coverage at the full delivered PCS flow rate, as described in Section 7.2.5. No PCS water is credited until after the time that the containment sidewall is wet to the bottom elevation. The evaporation-limited PCS flow rate is calculated by the PCS film coverage model, using either the spreadsheet process or the option within WGOTHIC, as described in Section 7.5.2.1 and Section 7.5.2.2, respectively. Section 7.5.2.3 addresses the PCS water stripping from the baffle supports on the vertical surface of the containment vessel that was described in Section 7.2.6.

7.5.2.1 Spreadsheet Calculation of the PCS Film Coverage

The equations developed in Section 7.5.1 are solved in a spreadsheet for both one-dimensional and two-dimensional shell heat transfer. The use of the spreadsheet is an iterative process that requires preliminary WGOTHIC runs that assume a PCS flowrate, then the evaporation flux from WGOTHIC is determined, and that flux is used as input to the spreadsheet.

The containment evaluation model uses the following input to compute the evaporation heat removal rate from the shell: the evaporation-limited PCS water flow rate, the PCS water temperature, and the wetted area for each clime. The vertical variation in the wetted perimeter and the resulting wetted area are conservatively calculated by the PCS film coverage model; the WGOTHIC code does not calculate the change in these values as a function of time or position. The evaporation-limited PCS flow rate that is determined by the PCS film coverage model spreadsheet calculation must be input to WGOTHIC to account for changes in the evaporation rate due to anticipated changes in the coverage area with time and location on the shell.

The clime model allows the water to flow at constant width until it reaches the next lower clime, or it evaporates entirely. When it evaporates entirely before reaching the bottom of the clime, the code tracks the distance traveled and breaks the clime vertically into wet and dry portions with temperatures calculated using the appropriate wet or dry heat and mass transfer models.

Iteration between WGOTHIC runs and the PCS film coverage model spreadsheet is necessary to converge on the same evaporation rate in both. The iteration proceeds as follows:

1. An average evaporation mass flux, ϕ_m , at selected times is determined from the WGOTHIC output for climes below the second weir by summing the evaporation mass from each wet clime and dividing it by the total wetted area for each time step.
2. The evaporation mass flux, ϕ_m , is input to the spreadsheet, which solves the equations presented in Section 7.5.1. At each time step, the delivered flowrate is applied to the top of the containment shell, and the evaporation rate and PCS film width is tracked down the elevation of the sidewall. The run-off flow at the bottom is excluded, and \dot{m}_{evap} , the evaporation-limited PCS flowrate, is defined.
3. The evaporation-limited PCS flowrate calculated by the spreadsheet is compared to the PCS flowrate that was credited in the WGOTHIC run at each time step. Iterations are done until the flowrates are similar, with it being conservative for the spreadsheet \dot{m}_{evap} to be greater than or equal to the PCS flowrate input in the WGOTHIC run. If this condition is not met, a revised

evaporation-limited PCS flowrate is used as input to WGOTHIC and a new iteration round is performed.

The above process is done for the entire transient, with the evaporation-limited flow rate calculated at each selected time step.

The spreadsheet calculation has an option to include the effects of two-dimensional conduction. During the initial high flow PCS period, only one-dimensional heat transfer is credited. However, as the standpipes in the PCCWST uncover, the delivered PCS flow rate is reduced and the wetted circumference at the top of the containment shell is predicted to decrease. The effects of two-dimensional conduction are not credited until the uncover of the second standpipe, which occurs several hours after the start of PCS flow.

The two-dimensional conduction model discussed in Section 7.4 calculated the evaporation rate for a range of wet stripe widths for both one- and two-dimensional conduction. The calculation used the same overall temperature difference (and steam partial pressure difference) between the bulk containment and the bulk riser as boundary conditions for both cases. The effective heat transfer coefficients, for mass transfer, were determined for each case. The comparison shows for a given stripe width, the enhancement of the evaporation rate when the real physical case of two-dimensional conduction is considered. It was found that the enhancement varied with stripe width, but had little effect on the overall temperature difference between the bulk containment and riser. Consequently, the family of curves representing the bulk temperature difference were lower bounded, thereby eliminating the dependence on the bulk temperature difference. The only dependent variable is the wet stripe width. The enhancement of evaporation is characterized by the multiplier, M , that is a polynomial function of the wet stripe width. M is defined by Equation 7-1. The multiplier, M is used in the spreadsheet as a multiplier on ϕ_m to produce a better estimate of the actual evaporation flux from the film stripes and the evaporation-limited PCS flow rate that is used as input to the containment evaluation model.

7.5.2.2 WGOTHIC Automated Evaporation-limited PCS Flow Model

Starting with version 4.3, the WGOTHIC code includes an option to implement the evaporation-limited PCS flow model. This option automates the iterative process that is needed with the PCS film coverage model to calculate the evaporation-limited PCS flow rate. With the evaporation-limited PCS flow option, the PCS flow delivered from the bucket is input by the user. The code then performs the function of the spreadsheet described above, accounting for the narrowing of the water stripes down the containment shell and not crediting the sensible heating of the runoff flow. The incorporation of this calculation into the WGOTHIC code has the advantage of removing the manual iterations between the code and the spreadsheet. In addition, the WGOTHIC code more accurately calculates the evaporation-limited flowrate, without having differing margin at each time step, which occurs with the spreadsheet calculation and iteration.

[

] ^{a,c}

[

]^{a,c}

In summary, the evaporation-limited PCS flow option in WGOTHIC eliminates the need for an analyst to manually perform iterations between the code and a spreadsheet. The spreadsheet calculation does not converge the same at each time step or for each run, and causes varying margin between the credited PCS flow and the WGOTHIC evaporation calculation. The evaporation-limited flow option in WGOTHIC takes away this variability, using criteria that establish the same degree of conservatism each time step. The automated code option also does quadrant-specific calculations rather than the spreadsheet tracking the evaporation for the containment as a whole. The top clime, which is the dome region of the containment vessel, is specified with a wetted fraction of []^{a,c} in the WGOTHIC input for both PCS evaporation-limited calculation, but the spreadsheet calculation []^{a,c} of the top clime. A factor to credit the effects of 2-D conduction between wet and dry stripes is available as an option that can be turned in both the spreadsheet and the option built in to WGOTHIC. The factor is similar, but the spreadsheet applies it as a direct multiplier on the evaporation rate while the evaporation-limited PCS flow option puts a multiplier on the heat flux.

7.5.2.3 Application of PCS Water Stripping from Baffle Supports

As discussed in Section 7.2.6, some of the PCS water was observed as “raining” in the annulus rather than flowing down the containment vessel during a pre-operational PCS flow test. To conservatively account for this

effect, termed as rainout, the safety analyses will not credit any PCS water that encounters the baffle supports on the cylindrical portion of the containment vessel. It is assumed that PCS water hits the baffle supports in proportion to the fraction of the containment vessel circumference that is obstructed by the baffle supports, and that all of this PCS water is lost. The elevation of the baffle support affects the amount of rainout as the PCS flowrate decreases at lower elevation because of evaporation. In addition, the wetted fraction, which may decrease at lower elevations, affects the rainout because if a baffle support is in a dry stripe, there will obviously be no rainout due to the baffle support. Both the PCS flowrate and wetted fraction change not only down the elevation of the containment, but these parameters vary throughout the safety analysis transients. Thus, rainout is not modeled as a single fraction but is a transient factor that is expected to range between $[\quad]^{a,c}$ and $[\quad]^{a,c}$ of the PCS flow.

The rainout calculation tracks the PCS water for each quadrant as a function of elevation. The rainout at higher elevations, evaporation, narrowing of water stripes (see Section 7.5.1.2), and the changing wetted fraction are accounted for in determining how much PCS water hits a set of baffle supports. Because this issue arose after the evaporation-limited model was incorporated into WGOTHIC, the detailed rainout calculation was developed to interface only with this model (Section 7.5.2.2). The evaporation and wetted fraction of each clime is calculated by WGOTHIC and is used to calculate the rainout flowrate based on the geometric information (number, width, and location) of the baffle supports. The PCS flow delivered from the bucket to the top of the containment vessel, which is a WGOTHIC input, is reduced by the rainout flowrate. Although the water is stripped from the containment at various elevations, the rainout-adjusted PCS flowrate is used as the bucket-delivered PCS flowrate input to WGOTHIC. This method ignores the rainout water for all elevations, which has a small conservative effect on the wetted fraction and dryout calculations.

The evaporation-limited PCS flowrate that is credited for heat removal excludes any sensible heat removal by the water that runs off. $[\quad]^{a,c}$

7.6 SUMMARY OF SUPPORTING TESTS AND SELECTED ANALYSIS

This section provides a summary of the PCS tests and data that are relevant to water film coverage and film behavior, and which support the Evaluation Model. In addition Section 7.6.4 provides an estimate of the range of film coverage parameters that can occur in the AP600 and **AP1000** plants, and compares this parameter range to a composite of the ranges tested.

Section 7.6.5 summarizes an estimate of the heatup of the AP600 and **AP1000** containment shell versus time. This heatup versus time is utilized in the sensitivity study of PCS flow initiation time presented in Section 7.7.3.

7.6.1 Westinghouse Wet Flat Plate Test

The primary purpose of the Westinghouse wet flat plate test was to generate heat and mass transfer data for evaporative cooling with parameters that bound the expected conditions on the AP600 containment

shell. A secondary purpose was to observe the film hydrodynamics including possible formation of dry patches due to surface tension instabilities. The test article is described in Reference 7.3.

Tests were performed in two orientations, vertical (to represent the sidewall) and 15 degrees from horizontal (to represent the upper portion of the dome) with various combinations of air velocity, film flow rate, and heat flux. A stable, wavy laminar water film was formed easily on the hot, coated, steel surface, even in the vertical orientation. A description of the test section and results from the various tests are given in Reference 7.3. The test data are summarized in Table 7-7.

Two of the heated flat plate tests were run with very low film flow rates at relatively high heat flux (6000-8000 BTU/hr-ft²) to force the film to completely evaporate before reaching the end of the test section. The observations given in Reference 7.3 state the following: "The upper part was 80 percent wetted and fingers of water film extended down 4 feet to within 2 feet of the end of the heated plate. The bottom of the fingers slowly moved up and down. The dry patch between fingers was between 1/4-inch and 1-1/2 inches wide. As the width varied in time, the lateral, slow flow of liquid could be seen feeding the thinnest parts of evaporating film. These two tests showed that the end point of water films on the containment would still be stable film evaporation, even with very thin films and high heat fluxes."

7.6.2 Small-Scale Tests

The small-scale tests were designed to provide heat and mass transfer data for both the inside and outside of the test vessel. The test apparatus consisted of a 3-foot diameter, 24-foot high steel pressure vessel filled with air at atmospheric pressure into which steam was supplied to maintain various pressures. Water was applied to the external surface to simulate evaporation in the PCS annulus. The pressure vessel was surrounded by a clear, plexiglass shield that formed a 15-inch wide annulus for either forced or natural circulation-driven air flow and allowed observation of the applied external film flow.

The tests were conducted with varying steam supply flow rates, water film flow rates, water film temperatures, cooling air flow rates, and cooling air inlet temperature and humidity. Instrumentation was provided to measure internal steam condensation rates, external water evaporation rates, inner and outer wall temperatures, film temperatures, air velocity, temperatures, and humidity. A summary of the test data from Reference 7.4 (for tests with measured water coverage) is provided in Table 7-8.

The following observations and conclusions (with respect to the water film) were drawn from these tests:

- A stable, uniform, wavy laminar film was formed on the inorganic zinc-coated steel surface using simple weirs.
- The film remained stable and uniform on the vertical sidewall of the vessel at average evaporating heat fluxes in the range of those expected on the AP600.

7.6.3 Large-Scale Tests

The Westinghouse large-scale PCS test facility was built to provide heat and mass transfer test data for a geometrically similar model of the AP600 containment vessel. The tests provided experimental data used for evaluating the physics in containment, determining the relative importance of various parameters that

affect heat and mass transfer, and validating computer codes and models. The following provides a discussion focused on the use of LST data to develop a bounding film coverage model.

Three series of tests were run at the Westinghouse large-scale PCS test facility. The steady-state pressure, annulus air flow rate, external water flow rate, injected steam flow rate, injection velocity, location and orientation, and non-condensable gas concentration were varied between the tests. Test conditions were selected to provide heat and mass transfer validation over a range of post-accident containment operating conditions for the AP600.

Table 7-7. Summary of Westinghouse Science and Technology Center (STC) Heated Flat Plate Tests

a,c

[illegible]

Table 7-8. Summary of Small-Scale Tests

[illegible]

The large-scale PCS test facility is a 20-foot tall, 15-foot diameter pressure vessel that simulates the AP600 containment vessel. The geometry is approximately a 1/8-scale of the AP600 containment vessel. A plexiglass cylinder is installed around the vessel to form the air cooling annulus. Air flows upward through the annulus via natural convection to cool the vessel, resulting in condensation of the steam inside the vessel. A fan is located at the top of the annulus shell to provide the capability to induce higher air velocities than can be achieved with purely natural convection. Water is applied to the elliptical dome surface by two rings of J-tubes. This method of application resulted in a series of spaced, wavy laminar flow stripes. At low test pressures the stripes spread within a few inches of their application point to form a continuous wavy laminar film. At high pressure the continuous film separated to form discrete stripes.

The following important observations with respect to film behavior were made during the tests:

- The J-tubes resulted in a non-uniform distribution of water on the surface of the LST, similar to that observed in the Water Distribution Test.
- Some J-tubes dripped and others had noticeably lower flow rates. This resulted in some regions of the dome and sidewall that were just wet or had a very low film flow rate.
- As the pressure and temperature increased inside the pressure vessel, dry spots first began to form in the wet, but low flow regions on the dome and sidewall.
- With increased pressure and heat flux, the dry spots grew vertically (both upward from the gutter and downward from the dome, between dripping or low flow J-tubes), separating the original continuous film into wavy laminar flow stripes. At higher heat fluxes, dry spots also formed just below, and in line with the J-tube location. A typical coverage pattern for high heat flux and high flow rate is shown in Figure 7-14.
- The central, wavy laminar flow region of the individual film stripes was surrounded by a region of laminar flow (with no visible waves). The thickness of the laminar flow region appeared to continually decrease out to the very edge (or bottom) of the film stripe.
- The widths of both the wavy laminar and laminar flow regions of the stripe were observed to decrease with increasing heat flux. At high flow rates, the width of the stripe was observed to remain relatively constant with elevation as the film flowed down the vertical sidewall. At lower flow rates, the stripe width was observed to taper uniformly with elevation as the film flowed down the vertical sidewall.
- The film stripes remained stable (i.e., they did not split or bunch up to form thick, narrow rivulets) as they evaporated on the vertical sidewall.

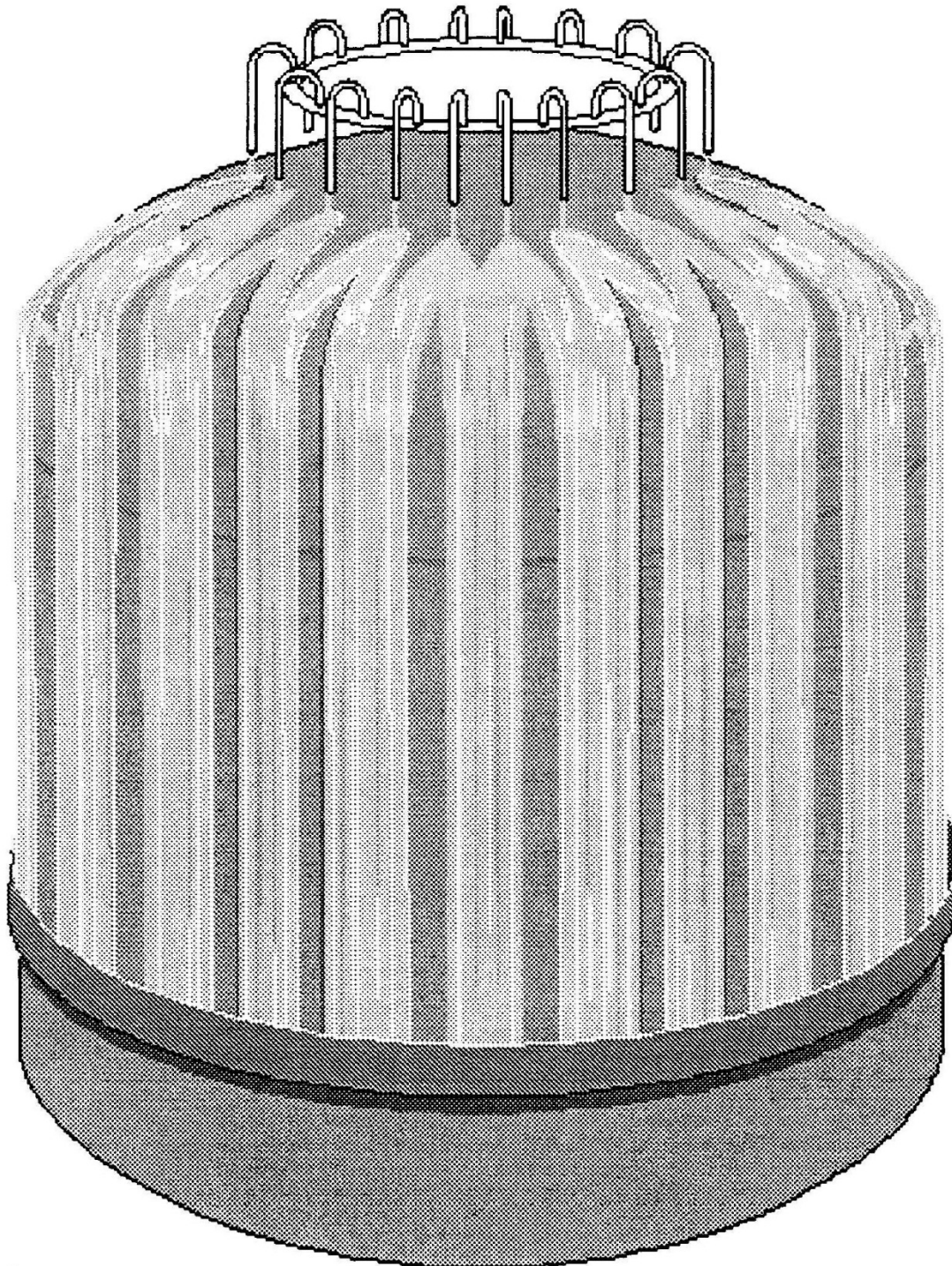


Figure 7-14. Large-Scale Test Water Coverage Pattern

The applied PCS flow rate was observed to vary or oscillate at a slow but regular period during some tests. This phenomenon was the result of sharing a common water source with a boiler feedwater valve that opened every two minutes, thereby reducing the PCS flowrate to the J-tube header. From observations made during testing, the flow oscillations had an effect on the water coverage fraction; it was most noticeable at the bottom of the sidewall. The length of the narrow film stripes and the width of the wider film stripes both decreased when the flow was observed to decrease. The dryout point of the narrow film stripes was observed to rise up and fall down the sidewall as the flow oscillated. At no time were the stripes observed to become unstable due to the oscillations; the process remained well-behaved and repeated itself with the periodicity of the applied flow.

After the Baseline LSTs were completed, instrumentation was added so the transient inlet and outlet cooling water flow rates could be measured and recorded by the data acquisition system. All of the Phase 2 and Phase 3 tests, with the exception of the blind test, (220.1, RC062) were included in the evaluation. The steam injection location, velocity, and initial pressure were much different in the Phase 3 tests, and subsequently, the level of stratification within the vessel was different than the Phase 2 tests. The differences in stratification resulted in changes in the coverage from the top to the bottom of the vessel; the top was less well covered than the bottom during some of the Phase 3 tests. The test numbers that were evaluated are listed in Table 7-9.

Measurements of the dry stripes on the vessel were taken just above the gutter during the defined steady-state periods of each test. The time the measurement was recorded on the data sheets for each test. This could have been either the time the measurement was started or finished. In test 221.1B, the time of measurement does not match with the stated steady-state time period. The test engineer postulated the recorded time to be one hour off, i.e., 12:45 was recorded as 1:45 by mistake. The following assesses the effects of variations in flow during the time taken to record coverage data at the gutter.

From recorded test data the maximum and minimum exit mass flow rates were determined over the approximate time the wetted perimeter measurement was made. The time taken to perform these measurements was related to the number of dry stripes; more stripes took longer to measure. A 15-minute band on either side of the stated time of measurement was used in this evaluation to bound the time it took to make the measurement.

The maximum and minimum exit film flow rates were calculated by dividing the maximum and minimum mass flow rate by the measured wetted perimeter value. Because the film flow rate is calculated by dividing the mass flow rate by the wetted perimeter, if the wetted perimeter were slightly less than measured (due to a reduction in the mass flow rate), the film flow rate would be higher than calculated with this method.

Table 7-9. Summary of Large-Scale Tests

a,c

[illegible]

a,c

[illegible]

Similarly, if the wetted perimeter were slightly higher than measured (due to an increase in the mass flow rate), the film flow rate would be lower. In either case, the difference between the maximum and minimum film flow rates would be smaller than calculated. The maximum and minimum film flow rates for the tests are tabulated in Table 7-9.

An evaluation of the LST data (Reference 7.5) yielded some additional important conclusions with respect to film coverage and heat removal:

- Evaporation is the primary mode of heat removal from the outside of the vessel. Sensible heating of the subcooled liquid film, convection, and radiation are second order.
- Striped film coverage provided better heat removal than forced quadrant coverage for the same wetted coverage.
- The highest heat flux occurred near the top of the dome at the elevation where the external film was applied for all of the wetted LSTs (except the horizontal, high-velocity, steam jet injection case). Although the dome represents about 30 percent of the heat transfer surface area, approximately 40 percent of the total heat removal occurred on the dome and 60 percent on the cylindrical sidewalls.
- Injection of high-velocity steam (similar to a steamline break) resulted in a well-mixed vessel (both above and below the operating deck), and thus, a relatively uniform wall temperature and heat flux over the evaporating surface.

The test data related to water coverage from References 7.6 and 7.7 are summarized in Table 7-9. Tests 207.1, 207.3, 208.1, 216.1A, and 216.1B were conducted with water coverage by quadrants and are not representative of AP600 conditions and are therefore excluded from the table. The data of Table 7-9 are used to develop a bounding film stability model as described in Section 7.3.2.

7.6.4 Estimated Range of Film Coverage Parameters

The estimates for the maximum and minimum values for the range of AP600 and **AP1000** film coverage parameters during a DBA are calculated using the simple approach described below. The range of film coverage parameters is compared with the range of the PCS tests and is shown in Table 7-11.

To determine a maximum sidewall film flow rate, none of the initial PCS water is assumed to evaporate on the dome. Measurements from the unheated, Phase 3 Water Distribution Tests indicate that approximately []^{a,c} percent of the perimeter at the top of the sidewall will be wetted with 220 gpm, assuming this same wetted parameter at the higher actual PCS delivered flow rate results in an estimated maximum sidewall film flow rate of []^{a,c} lbm/hr-ft for AP600 and **AP1000** plants respectively. The maximum sidewall Re_{film} would be []^{a,c} respectively at the estimated maximum 200°F film temperature. The liquid film Reynolds numbers range up to []^{a,c} in the test data (Reference 7.11).

The shell heat flux provides the boundary conditions for the evaporating film. The steady-state, shell average heat flux and film temperature were estimated for the subcooled, evaporating, and dry portions of the shell, assuming an initial ambient air and film temperature of 120°F. These estimates were made at the containment design pressure to bound conditions at the expected DBA peak pressure and at half containment design pressure, for conditions representative of 24 hours after blowdown. The results are presented in Table 7-10.

Table 7-10. Estimated Shell Heat Flux and Film Temperature

Containment Pressure (psig)		Avg. Subcooled		Avg. Evaporating		Avg. Dry	
		Heat Flux (BTU/hr-ft ²)	Film Temp (°F)	Heat Flux (BTU/hr-ft ²)	Film Temp (°F)	Heat Flux (BTU/hr-ft ²)	Shell Temp(°F)
AP1000	59	9500	160	4800	195	400	275
AP600	45	7500	155	3800	190	320	250
AP1000	29.5	6000	150	2800	180	290	240
AP600	22.5	3500	150	1500	170	165	215

To account for stratification, the maximum wet shell heat flux is estimated to be 50 percent higher than the average subcooled value. The minimum wet shell heat flux would be 0 BTU/hr-ft².

The initial PCS film temperature will be between 40°F and 120°F. The 120°F value is used in the DBA Evaluation Model to minimize the benefit of heat removed by heating the subcooled film. The film temperature will increase as the film flows down the dome. The maximum evaporating film temperature was estimated to be less than 212°F.

The resulting estimated range of the AP600 film parameters during a DBA is summarized in Table 7-11 and compared with the composite test data range.

The test data parameter ranges are sufficient for evaluating the film stability model. It is important for the test data to cover the higher range of heat flux and the lower range of the sidewall film Reynolds number for evaluating the film stability model. Films with high Reynolds number values on low heat flux surfaces are more stable than films with low Reynolds number values on high heat flux surfaces. The maximum tested heat flux is almost 50% higher than the estimated maximum **AP1000** value. Tests were run at low film flow rates and to dryout, so the lower range of film Reynolds numbers are also covered.

Table 7-11. Comparison of the Range of Film Coverage Parameters

a,c

7.6.5 Containment Shell Heatup Analysis

This section summarizes an analysis of the heatup of the containment shell versus time. This analysis will be utilized in the sensitivity study on the importance of the time at which PCS flow is put on the containment dome following a DBA (see Section 7.7.3).

The shell surface temperature begins to increase following a LOCA or secondary line break inside containment. The time for the dry outer shell to reach a given temperature is a function of the internal containment gas temperature, the internal energy transfer coefficient, and the shell thickness. The time can be calculated using the properties of the steel shell and Figure 4-8 from Kreith (Reference 7.9).

The initial shell temperature is assumed to be 120°F. The time for the dry external shell surface temperature to reach the boiling point (212°F) can be calculated with the following input:

$$\begin{aligned}
 T &= 212^{\circ}\text{F (external shell surface temperature)} \\
 T_i &= 120^{\circ}\text{F (initial shell temperature)} \\
 T_{\infty} &= 250^{\circ}\text{F (internal containment gas temperature for AP600)} \\
 T_{\infty} &= 270^{\circ}\text{F (internal containment gas temperature for AP1000)} \\
 \zeta &= (T - T_{\infty}) / (T_i - T_{\infty})
 \end{aligned}$$

So, $\zeta = 0.292$ for AP600 and $\zeta = 0.387$ for **AP1000**.

The Biot number is given by

$$Bi = h * L / k$$

where,

h is the heat transfer coefficient on the inside wall, Btu/hr-ft²-°F
k is the thermal conductivity of the shell

and

L is the shell thickness

The Fourier number is given by

$$Fo = \alpha * t / L^2$$

where,

α is the thermal diffusivity and is given by

$$\alpha = k / (\rho * c_p)$$

ρ is the shell density

c_p is the shell specific heat

and

t is the time to reach the target temperature

The properties of the steel shell are given below:

k	=	23.6 BTU/hr-ft-°F (AP1000)
	=	25 BTU/hr-ft-°F (AP600)
L	=	[] ^{ac} ft (AP1000)
	=	[] ^{ac} ft (AP600)
	=	490 lbm/ft ³
c_p	=	0.107 BTU/lbm-°F (AP1000)
	=	0.104 BTU/lbm-°F (AP600)

By assuming a heat transfer coefficient on the inside wall, the Biot number is calculated then used to determine the Fourier number and the time for the outer surface to reach 212°F.

h (BTU/hr-ft ² -°F)	$1/Bi$		Fo		t (sec)	
	AP600	AP1000	AP600	AP1000	AP600	AP1000
5	36.9	32.4	43	28	5792	4373
10	18.5	16.2	22	18	2963	2811
50	3.7	3.2	5	3.5	673	547
100	1.8	1.6	2.6	2.2	350	344

The shell internal heat transfer coefficient is likely in the range of 50-100 BTU/hr-ft²-°F. Thus, the external shell surface temperature is estimated to reach 212°F between 350 and 670 seconds for AP600 and between 340 and 550 seconds for the **AP1000** plant. The containment shell material properties in the **AP1000** WGOthic EM differ from the preliminary values listed above, but this calculation remains a valid illustration of the time for the outside of the containment vessel to reach 212°F. A lower thermal conductivity results in longer timing.

The WGOTHIC AP600 Evaluation Model calculated shell surface temperatures at the top of the dome, before application of the PCS film, can be compared to the hand calculated results. During the initial 5.5 minutes of the transient, the containment gas temperature (and therefore the maximum possible internal shell surface temperature) is maintained at about 250°F by condensation on the heat sinks inside containment. The dome surface temperature is predicted to be 174°F at 337 sec, and without external water is projected to reach 212°F at 500 sec, which is in reasonable agreement with the estimates above. The heatup rate from the WGOTHIC calculation is about 0.2°F/sec and falls between the 50 and 100 BTU/hr-ft²-°F internal energy transfer coefficient values assumed in the hand calculation.

The calculated temperature increase in the AP600 dry external shell surface is compared to water coverage events as a function of time in Table 7-12.

At the maximum time delay for initial water application to the shell (36 seconds, from Table 7-12), the outer shell temperature is calculated to increase less than 4°F. The temperature increase of the dry portion of the outer shell is less than 70°F at the time the weirs are filled and steady-state coverage is established (337 seconds, from Table 7-12). Therefore, the external shell surface temperature is less than 190°F at the time steady-state coverage is established for the AP600 plant. For the **AP1000** plant, the calculations above show that the heat-up will be a little faster and the steady-state coverage is not established until almost 400 seconds, but the external shell surface temperature remains well below 212°F at this time in the DECL LOCA analysis.

For a steamline break DBA postulated to occur at the highest elevation of the steamline inside containment and with no liquid entrained in the break effluent, there is a greater heatup of the containment gas and the containment shell than discussed above for the LOCA event. Application of the calculational method above, for an inside containment gas temperature of approximately 350°F, predicts the outside of the containment shell is 212°F before 200 seconds. The **AP1000** steamline break analysis confirms this timing. However, water coverage is not adversely affected by application of the film to a hot, dry, shell surface. Both the STC wet flat plate tests and the LSTs verified the ability of the water film to wet and rewet a hot, dry surface (temperature exceeding 240°F) with the inorganic zinc coating. Video tape records of the Westinghouse wet flat plate tests show the initial wetting, dryout, and re-wetting of a hot, dry plate in both a vertical and inclined position. The dry plate temperature was estimated to be about 240°F (based on the maximum heating fluid temperature). An applied wavy laminar film quickly covered the hot, dry plate. As the flow rate was reduced, the waves in the film became smaller and eventually disappeared. The plate remained visibly wet until after the film flow was turned off, then dry patches appeared and grew in circumference as the plate dried out. Video tapes also show the initial wetting of the LST vessel. The measured shell surface temperature was about 260°F at the time the water was applied. The film front was observed to “sizzle” as it quickly advanced downward and covered the surface of the elliptical dome.

Table 7-12. Transient Dry Shell Temperature Increase

Event	Time (sec)	Increase in Dry, External Shell Temp. (°F)
Signal Actuation	0	0
Valve Strokes Open	20	0
Piping Fills	34	2
Bucket Fills & Spills	36	4
Weirs are filled and steady-state coverage is established	337	68

7.7 AP600 CONTAINMENT DBA EVALUATION MODEL FILM COVERAGE SENSITIVITIES

Sensitivity analyses performed with the AP600 containment DBA Evaluation Model are provided in this section. The model's sensitivity to the PCS film flow rate and water coverage are studied. An estimate of the conservatism in the assumed time delay for PCS film application is also studied.

7.7.1 Sensitivity of the Evaluation Model to the Input PCS Film Flow Rate

Calculations were performed using the WGOTHIC code with the AP600 containment Evaluation Model described in Section 4. The delivered PCS flow rate presented in Figure 7-2 was applied to the WGOTHIC model. Sensitivity calculations were performed by decreasing the input PCS flow rates to 75, 60, 50, and 25 percent of the nominal value. Recalling that the time it takes to fill the headers and weirs is inversely proportional to the film flow rate, the time of film application was adjusted in each case to account for the decreased film flow rate. The water wetted perimeter input value was kept the same for each case, assuring the difference in calculational results was due only to applied PCS flow.

Figure 7-15 presents the change in peak containment pressure as a function of percent change in applied PCS flow rate. As expected, the peak containment pressure increases as PCS flow rate decreases from its nominal value. Decreasing the PCS flow rate results in the following;

- The time of film application is increased.
- The heat removed from the containment to heat the cool applied PCS water is reduced.
- The amount of evaporation from the containment shell decreases.

The containment pressure increase is very modest until the applied flowrate is significantly decreased. This is because the initial decreases in applied flow only decrease the runoff flow rate, the amount of water evaporated remains constant.

7.7.2 Sensitivity to the Water Coverage Area

A sensitivity study was performed to determine the effect that the PCS water coverage area has on the AP600 peak containment pressure for a DBA loss of coolant accident (LOCA) as calculated by WGOTHIC. The AP600 containment Evaluation Model described in Sections 4 and 7.5 was used to

perform the calculations with only one-dimensional heat conduction through the shell. The sensitivity study considered a range of sidewall water coverage fractions from 20 to 100 percent. These input coverage fractions were kept constant over the entire transient. The delivered PCS water flow rate shown in Figure 7-2 was used in each case.

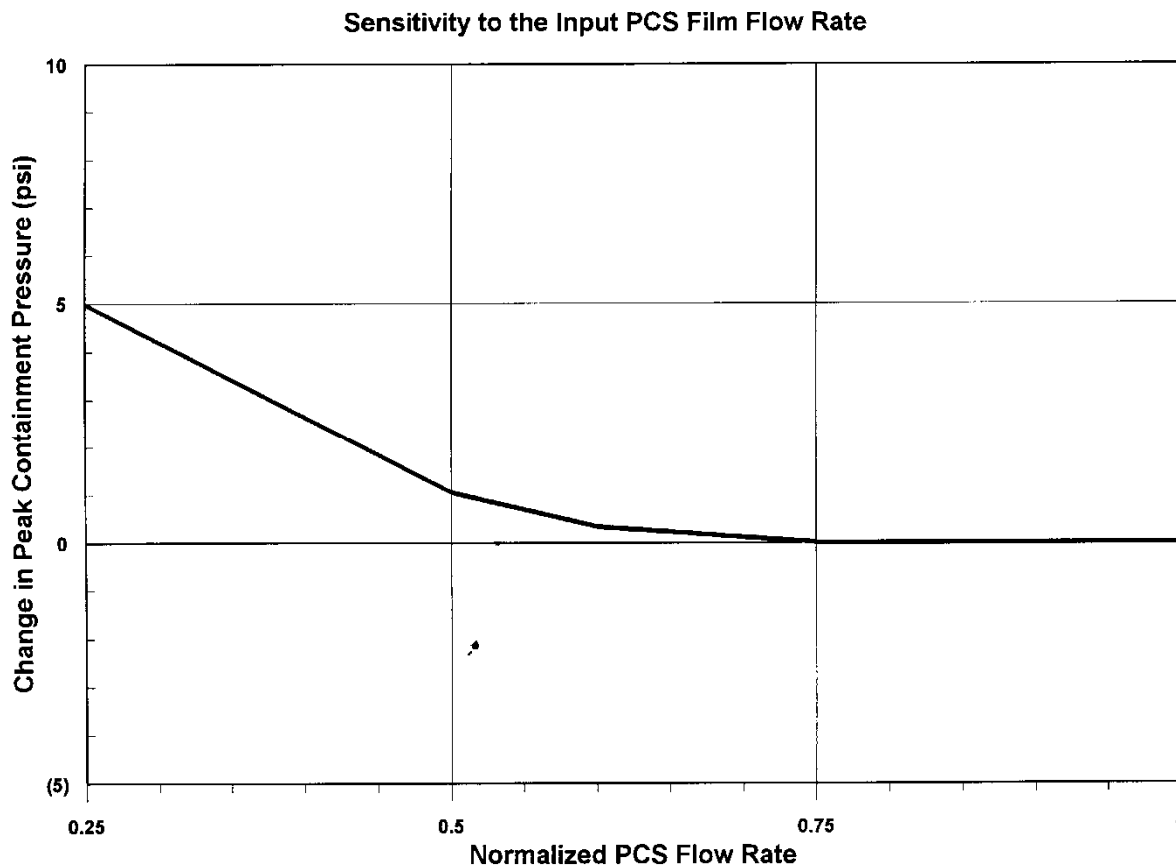


Figure 7-15. Sensitivity to the Input PCS Film Flow Rate

The transient pressure comparison is shown in Figure 7-1616. As the water coverage fraction decreases, the peak containment pressure increases. For the 100 percent coverage case, the peak pressure is about 43 psig. The containment design pressure limit, 45 psig, is exceeded at 70 percent and lower coverage.

Decreasing the coverage fraction results in a decrease in the amount of evaporation at a given containment pressure (temperature). As the coverage fraction decreases, the reduced evaporative heat removal causes the containment pressure to increase until the evaporation rate per unit area increases sufficiently to remove enough heat to match the energy input into containment.

The transient PCS runoff flow rate is shown in Figure 7-1717. The runoff flow rate is the difference between the PCS delivered flow rate and the evaporation rate. As the input coverage area decreases, the amount of evaporated water decreases and the runoff flow increases.

Figure 7-1818 presents a comparison of the pressure transients for the 50 and 100 percent coverage cases to the Evaluation Model.

The level in the PCS water storage tank drops below the first standpipe at about 10,800 seconds causing a substantial reduction in the PCS flow rate (from 423 gpm to 123 gpm). For the 100 and 50 percent coverage cases, this results in a large decrease in the runoff flow rate, but no change in the evaporation rate, which is dictated by the containment pressure (temperature). Note that all the delivered water is not being used. Pressure continues to decrease, although at a slower rate in both the constant coverage cases since in both cases evaporation is removing more heat than is being released to containment. But in the Evaluation Model, the containment pressure increases when the delivered flow decreases. This occurs because the PCS film coverage model decreases the wetted perimeter, (i.e., the wetted surface area is decreased in accordance with the decrease in the applied water flow rate). The increase in pressure reflects the increase in the evaporation rate required to achieve a balance between the heat removed from and the heat input to the containment. Therefore, the Evaluation Model containment pressure approaches the same pressure as the 50 percent fixed coverage case. Pressure then begins to decrease again when the evaporative heat removed at the area dictated by the delivered flow rate exceeds the heat input.

At about 40,000 seconds, the in-containment refueling water storage tank (IRWST) is predicted to empty. After the IRWST empties, the flow for core cooling is provided by the sump, which is assumed to be at saturation. Since most of the internal heat sinks (except concrete) are saturated, the PCS is the primary heat sink at this time and must now absorb the energy that had previously been absorbed by sensible heat addition to the cool IRWST water. The containment pressure increases until the heat removal rate (primarily evaporation from the PCS) exceeds the heat generation rate. The pressures for all three cases remained below the 24-hour goal of 1/2 design pressure.

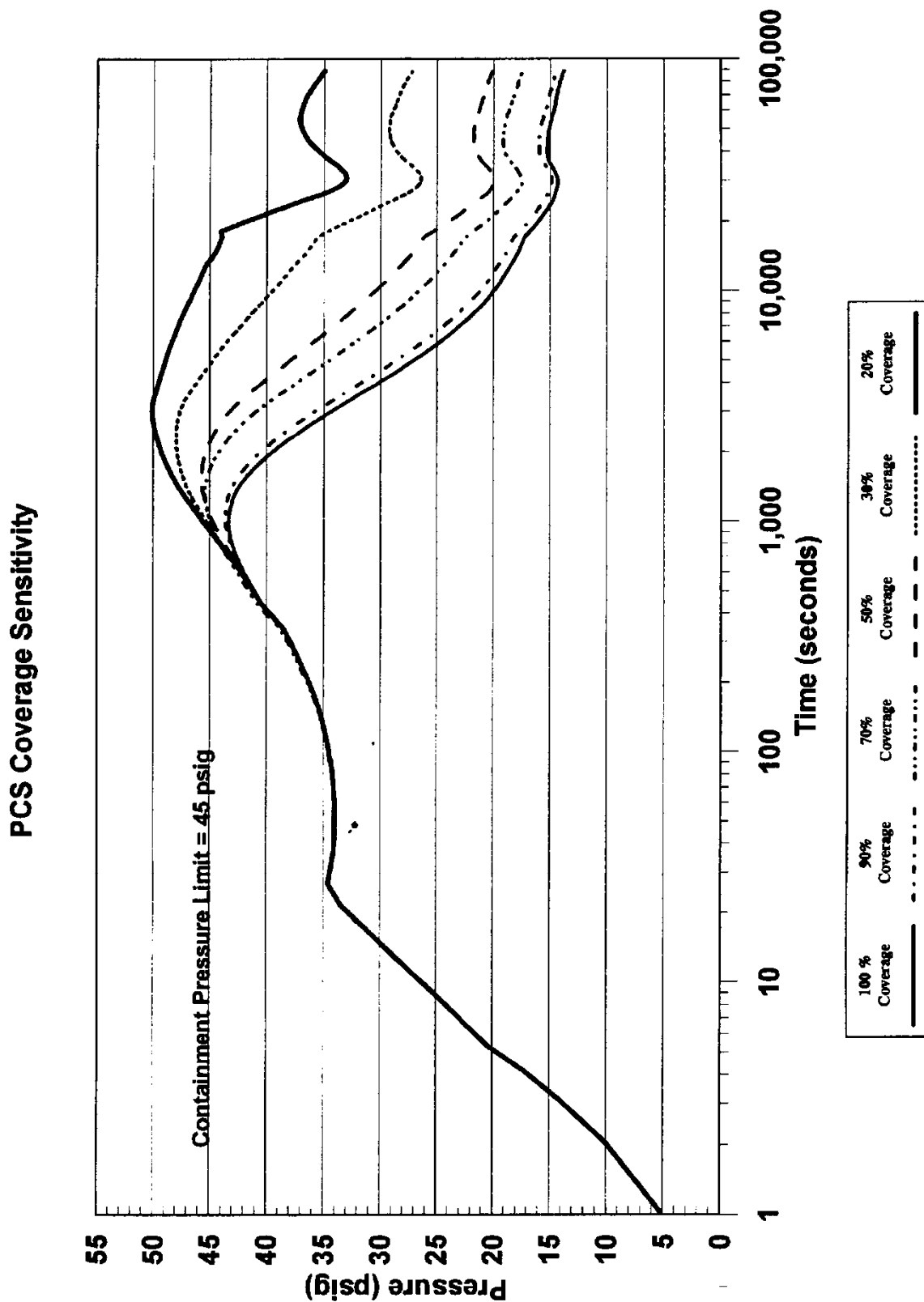


Figure 7-16. Comparison of Peak Containment Pressure as Function of PCS Coverage Area

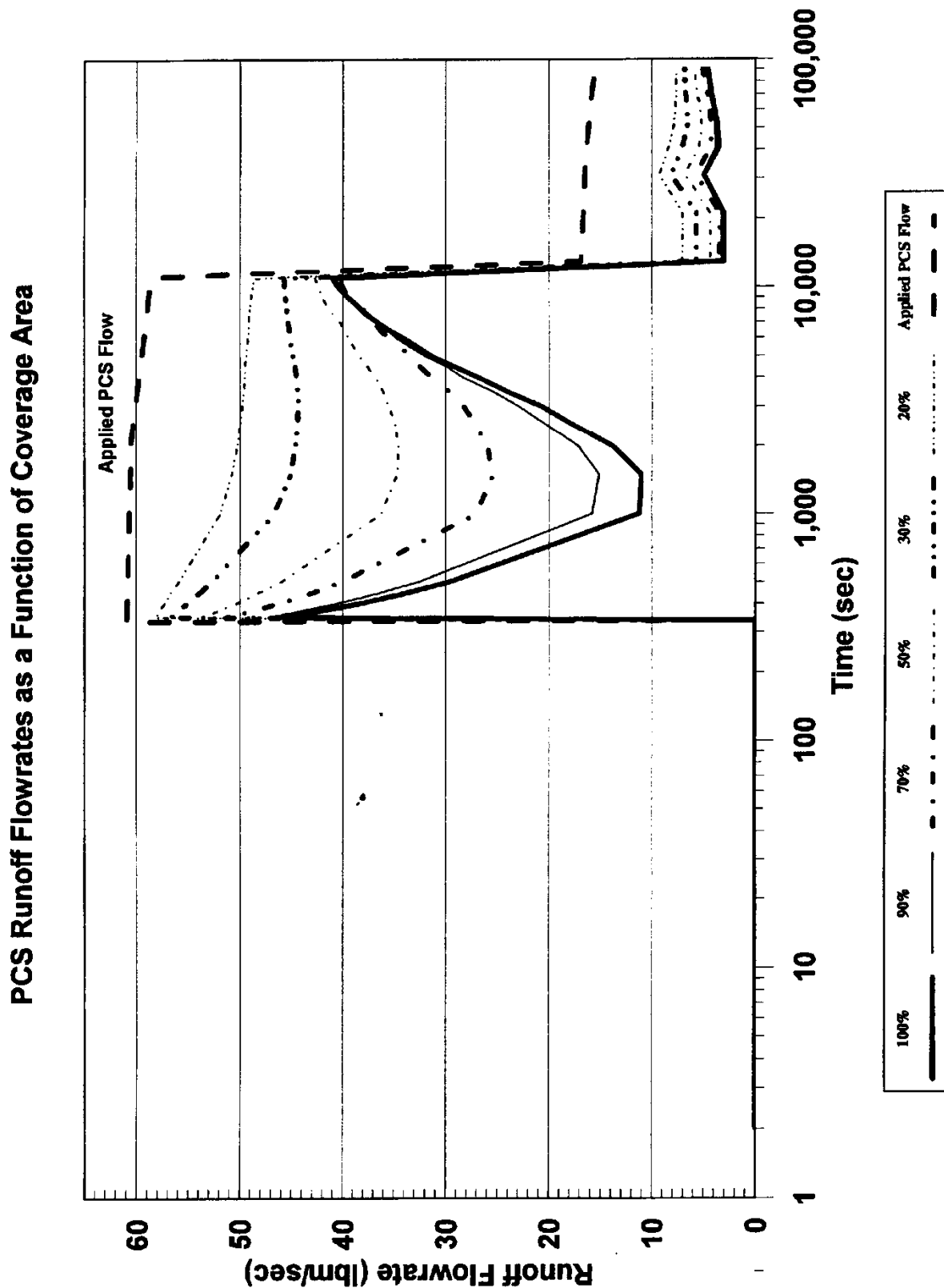


Figure 7-17. PCS Runoff Flow Rates as a Function of Coverage Area

Comparison of Evaporation Model Peak Pressure with 100% and 50% Constant Coverage Models

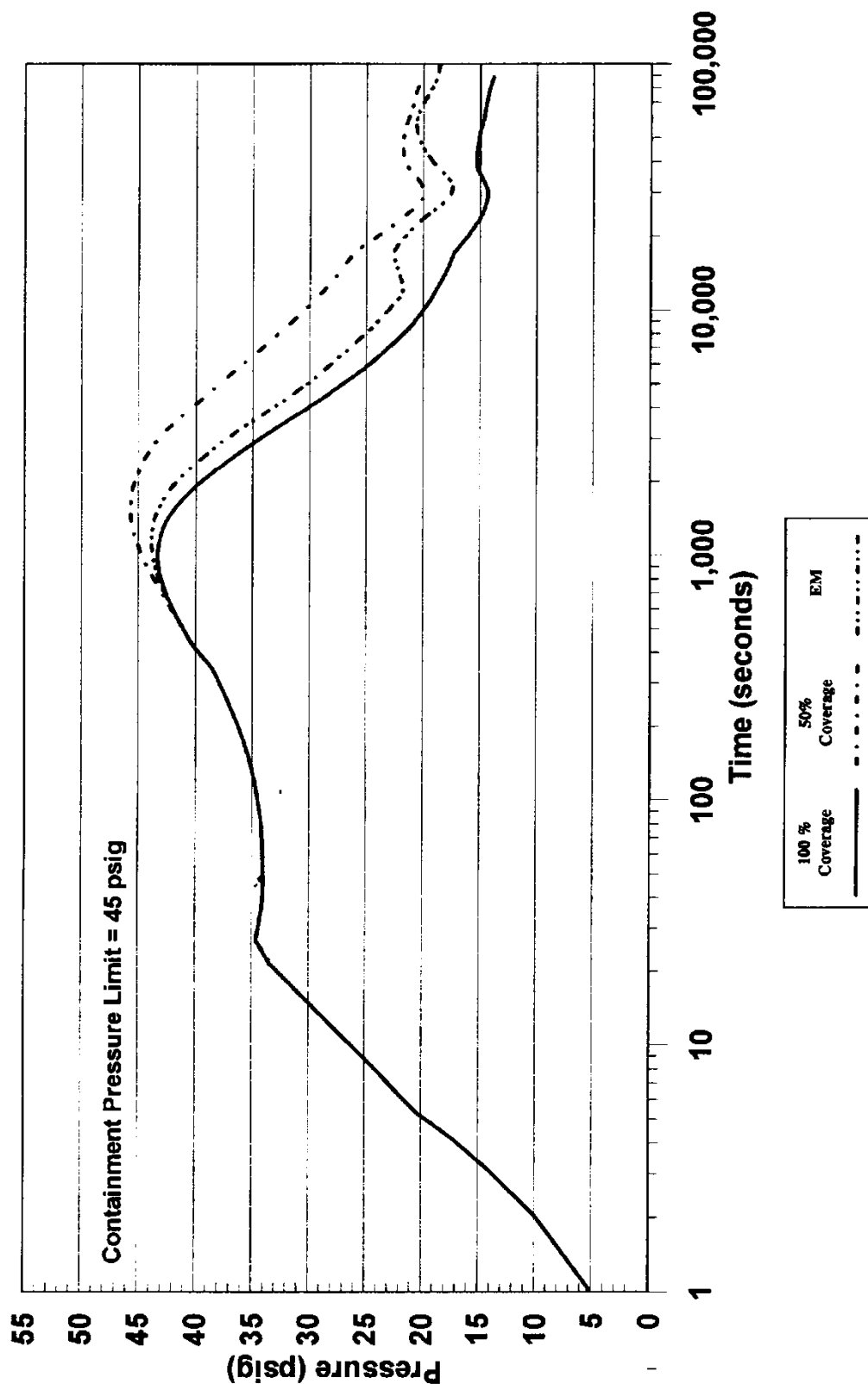


Figure 7-18. Comparison of Evaporation Model Peak Pressure with 100% and 50% Constant Coverage Models

The transient runoff flow rate for these three cases is shown in Figure 7-1919. The runoff flow rate for the 50 percent coverage case is higher than the 100 percent coverage case. The lower evaporative heat removal in this case results in a sustained higher containment energy content and subsequently higher pressure. Note that there is virtually no runoff flow in the Evaluation Model case since the water coverage portion of the model limits the applied water to the amount that can evaporate.

7.7.3 Conservatism in the Assumed Time Delay for Application of the PCS Film

A delay in application of the PCS film is assumed in the DBA Evaluation Model to cover the time it takes to fill the weirs and establish steady-state coverage, as described in Section 7.2. The coverage delay time is conservative in that it neglects energy removal from the shell while steady-state film coverage is being developed. The following assessment shows the amount of conservatism in the predicted energy removal is small.

To quantify the amount of energy removal neglected during the development of steady-state film coverage, the WGOTHIC calculation used to access the heatup of the containment shell, described in Section 7.6 was extended to 1,800 seconds. The heat removal results from this case with the water film applied at 337 seconds were compared to the results from a second case in which the assumed water coverage delay time was reduced to 35 seconds. The same input water coverage fractions were used in both cases.

Note that the WGOTHIC Evaluation Model assumes that steady-state water coverage develops instantaneously after a specified time required to fill the weirs and develop steady-state coverage. The 35-second delay case is a more realistic estimate of the film application delay time for the top of the dome, but will overestimate heat removal from the rest of the dome and sidewall. Therefore, only the heat removal from the top of the dome will be compared for the two cases to estimate the effect on heat removal.

Figure 7-2020 compares the integrated energy removal rate from the top of the dome as a function of time. There is very little difference in the energy removal rates for either case. This is because the time required to significantly heat the containment external shell is much greater than the 33-second delay time for water application. Recall that, from Table 7-12, the external shell surface is calculated to heat up about 68°F after ~5 minutes when steady flow conditions develop.

The energy release difference at the lower portions of the dome and sidewalls will be even less. Therefore, the assumed water coverage delay time, although conservative, has a minor effect on containment pressure.

Comparison of Evaporation Model PCS Runoff Flow Rate with 100% and 50% Constant Coverage Models

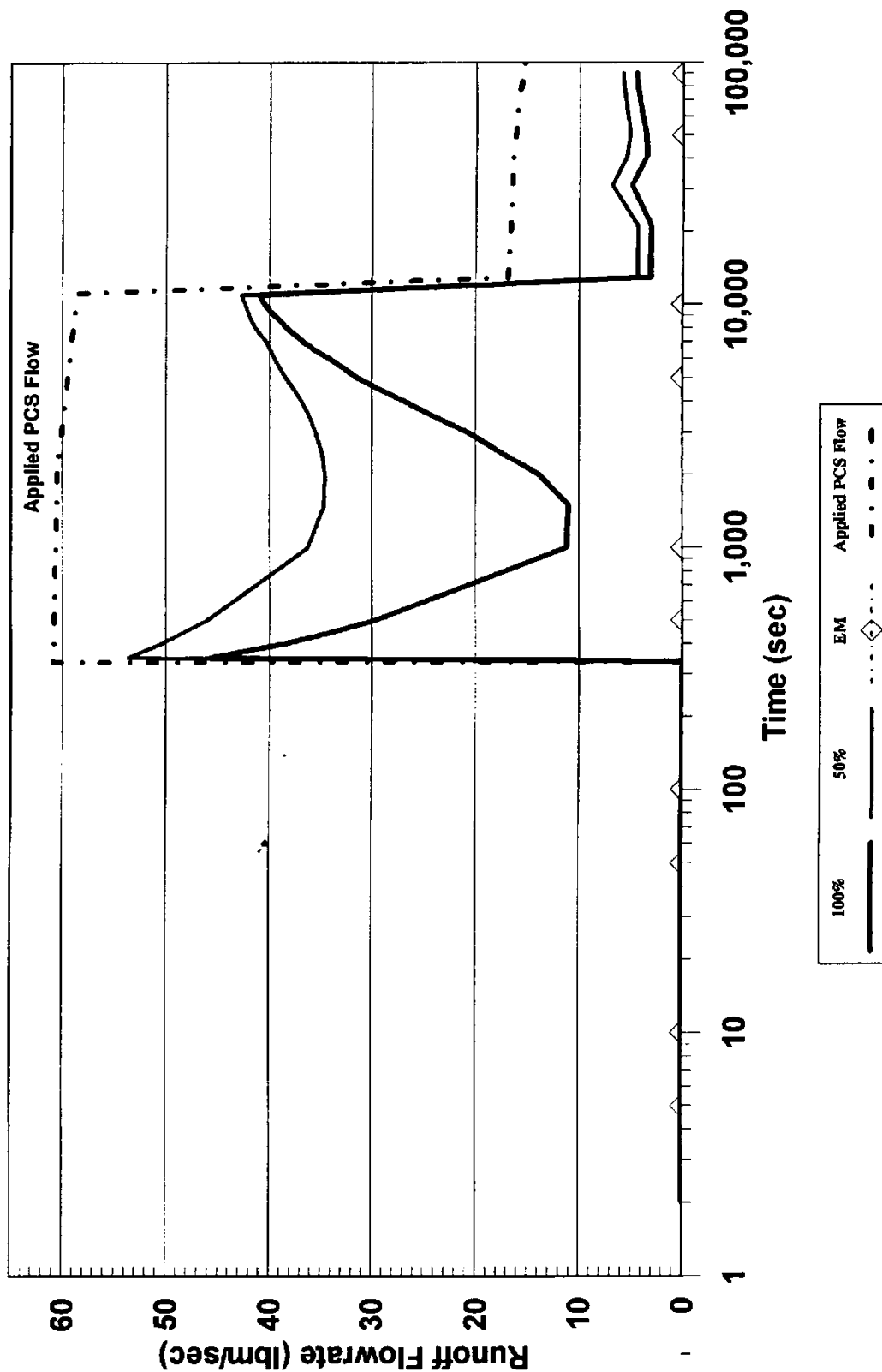


Figure 7-19. Comparison of Evaporation Model PCS Runoff Flow Rate with 100% and 50% Constant Coverage Models

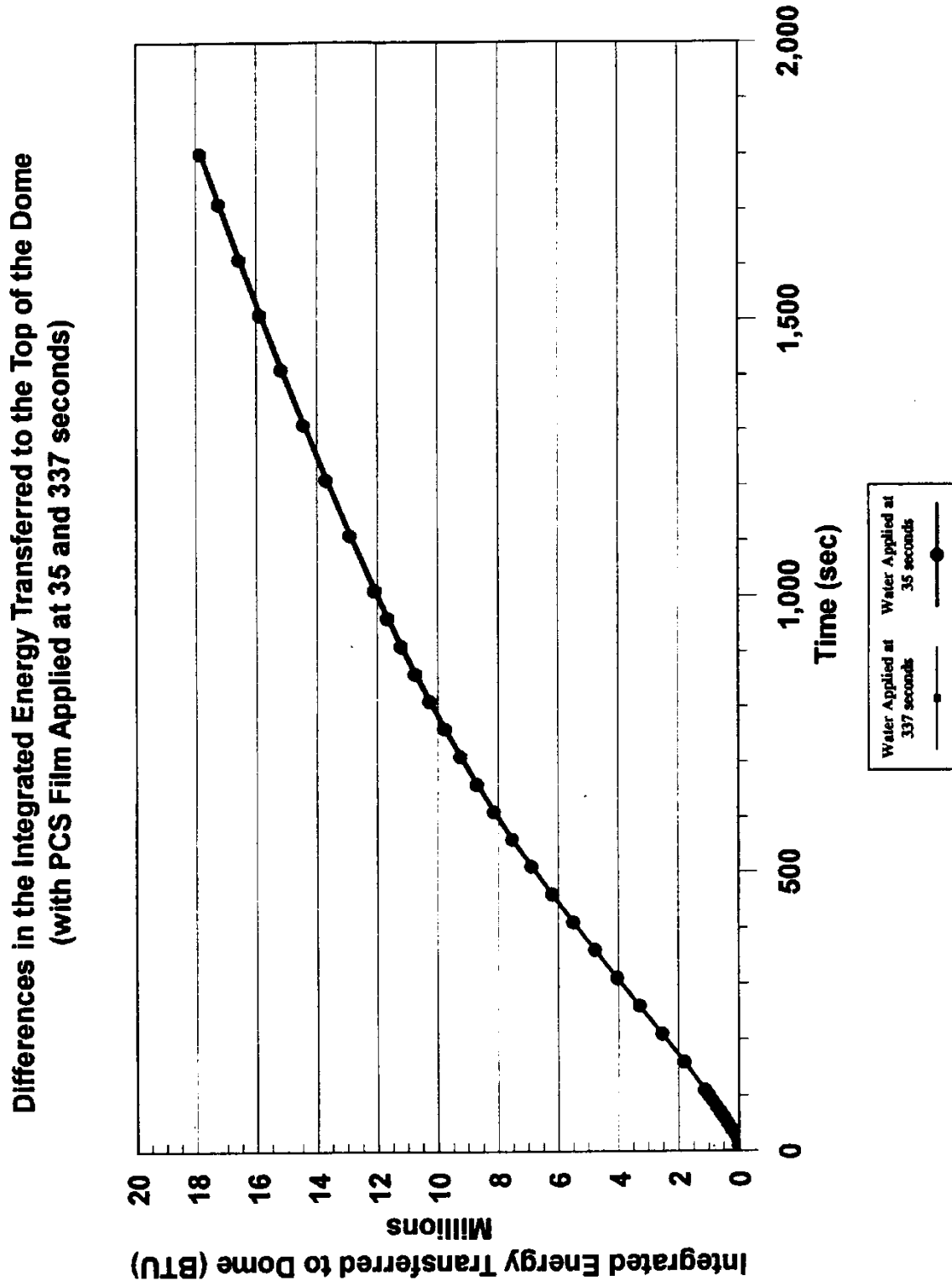


Figure 7-20. Difference in the Integrated Energy Transferred to the Top of the Dome
(with PCS Film Applied at 35 and 337 Seconds)

7.8 CONCLUSIONS AND SUMMARY

The basis and calculational method used to determine the amount of water that is evaporated from the AP600 containment steel shell during the operation of the passive containment water cooling system is conservative; both with respect to the individual elements of the WGOTHIC code and the PCS film coverage model, as well as the method of combining these elements in the Evaluation Model.

The amount of water that can be evaporated is the important input parameter to the WGOTHIC portion of the Evaluation Model. The amount of water evaporated determines the effectiveness of the PCS in limiting peak containment pressure, as well as the capability of the PCS to reduce and maintain low containment pressure following postulated limiting design basis events.

The basis for determining the evaporation-limited PCS flow rate input for WGOTHIC has been developed based on PCS test data and observations, and includes the following:

- The portion of the containment shell perimeter that is wetted versus the amount of water being delivered from the PCS water storage tank to the containment dome has been based on data from the Phase 3 Water Distribution Test. This test was performed with prototypic water distribution devices on a full sized segment of the dome and top of sidewall. The relationship of wetted perimeter to delivered flow is conservatively bounded by the linear equation,

$$\Gamma_{\text{dist}} = \text{Delivered Flow/Wetted Perimeter}$$

where,

$$\Gamma_{\text{dist}} \text{ is a constant} = [\quad]^{\text{a,c}} \text{ lbm/hr-ft for PCS flow rates less than 220 gpm}$$

The wetted perimeter used in the PCS film coverage model is limited to []^{a,c} percent of the containment circumference.

- The several PCS tests performed with hot evaporating surfaces have demonstrated that the value for Γ_{dist} obtained with cold water on a cold surface conservatively bounds the Γ_{dist} that will occur with heated water on a heated surface during operation of the PCS.
- In the heat flux range of PCS operation, water streams on the containment surface are observed to become narrower in width only when most of the water in the stream has been evaporated. The Evaluation Model uses a Γ_{min} of []^{a,c} lbm/hr-ft, as the film flow rate at which water streams will become narrower. This minimum film flow rate conservatively bounds the observed minimum film flow rates observed in the PCS tests over the entire range of anticipated heat fluxes.
- Water or streams of water on the containment below the second water distribution weir ring and on the vertical containment sidewall are always observed to flow downward, following the natural fall line of the dome surface.

The calculational methods for determining the amount of water evaporated have been developed and are consistent with or conservatively bound PCS test data and observations, and include the following:

- The evaporation of water due to the conduction of heat in the circumferential direction through the containment steel shell has been calculated for the alternating, vertical, wetted and dry stripes that were observed in the PCS testing at reduced delivered water flow rates.
- The reduction in dry surface convective and radiative heat transfer that is calculated to occur with alternating, vertical, wet and dry stripes on the containment shell has been determined to be conservatively considered in the WGOTHIC portion of the Evaluation Model.

Bounding assumptions and conservatisms for the operational characteristics of the PCS delivering and applying water to the containment surface have been incorporated in the Evaluation Model as summarized in Section 13.5.2.

7.9 NOMENCLATURE

Dimensionless Groups

Biot Number:

$$Bi = \frac{\text{Convection}}{\text{Conduction}} = \frac{h \cdot L}{k}$$

Marangoni Number:

$$Ma = \frac{\text{Surface Tension Force}}{\text{Viscous Force}} = \frac{\partial \sigma}{\partial T} * \frac{\partial T}{\partial L} * \frac{\delta^2}{\mu * \alpha}$$

Reynolds Number:

$$Re = \frac{\text{Momentum Force}}{\text{Viscous Force}} = \frac{4 \cdot \Gamma}{\mu}$$

Parameters

g	=	gravitational constant
h	=	convection heat transfer coefficient
k	=	conductivity
L	=	characteristic length,
\dot{m}	=	mass flow rate M=multiplier representing the ratio of 2-D to 1-D heat transfer
\dot{q}''	=	surface heat flux
T	=	film temperature;
W	=	width of water film stripe
Z	=	vertical distance from top of sidewall

Greek Characters

α	=	thermal diffusivity,
β	=	surface angle of inclination relative to horizontal
Γ	=	film flow rate = mass flow rate per unit width of film,
δ	=	film thickness,
ρ	=	liquid density
σ	=	liquid surface tension
ϕ	=	heat or mass flux
θ	=	contact angle between the surface and film
μ	=	liquid viscosity

7.10 REFERENCES

- 7.1 A. T. Pieczynski, W. A. Stewart, WCAP-13884, "Water Film Formation on AP600 Reactor Containment Surface," February 1988.
- 7.2 J. E. Gilmore, WCAP-13960, "PCS Water Distribution Phase 3 Test Data Report," December 1993.
- 7.3 W. A. Stewart, A. T. Pieczynski, L. E. Conway, WCAP-12665 Rev. 1, "Tests of Heat Transfer and Water Film Evaporation on a Heated Plate Simulating Cooling of the AP600 Reactor Containment," April 1992.
- 7.4 R. E. Batiste, WCAP-14134, "AP600 Passive Containment Cooling System Integral Small-Scale Tests Final Report," August 1994.
- 7.5 R. P. Ofstun and D. R. Spencer, PCS-T2R050, "Large-Scale Test Data Evaluation," May 1995, Westinghouse Electric Corporation.
- 7.6 F. E. Peters, WCAP-13566, "AP600 1/8th Large-Scale Passive Containment Cooling System Heat Transfer Test Baseline Data Report," October 1992.
- 7.7 F. E. Peters, WCAP-14135, Rev. 1, "Final Data Report for PCS Large-Scale Tests, Phase 2 and Phase 3," April 1997.
- 7.8 D. R. Spencer, WCAP-14845, Rev. 3, "Scaling Analysis for AP600 Containment Pressure During Design Basis Accidents," March 1998.
- 7.9 Frank Kreith, "*Principles of Heat Transfer*," 3rd Edition, 1973.
- 7.10 M. S. Bohn and S. H. Davis, "Thermocapillary breakdown of Falling Liquid Films at High Reynolds Numbers," *International Journal of Heat and Mass Transfer*, Vol. 36, pp 1875-1881 (1993).
- 7.11 F. Delose, R. P. Ofstun, D. R. Spencer, WCAP-14326, Rev. 2, "Experimental Basis for the AP600 Containment Vessel Heat and Mass Transfer Correlations," April 1998, Westinghouse Electric Corporation.
- 7.12 T. Fujita and T. Ueda, "Heat Transfer to Falling Liquid Films and Film Breakdown Parts I and II," *International Journal of Heat and Mass Transfer*, Vol. 21, pp. 97-108 and 109-118 (1978).
- 7.13 D.W. Green, R.H. Perry; "Perry's Chemical Engineers' Handbook", (8th Edition) McGraw-Hill, 2008.
- 7.14 TFD-FSE-15-1, Revision 0, "AP1000® Containment Vessel Inner Surface Condensate Return Test Facility Description Report," May 2015.

APPENDIX 7.A

PHYSICS OF LIQUID FILMS ON THE AP600 AND AP1000 CONTAINMENT SHELLS

7.A.1 INTRODUCTION

The total evaporation from the external shell is the parameter of interest for mass transfer, the dominant means of removing heat from the containment. Total evaporation is equal to the integral of the mass flux over the covered, or wetted, area. The mass flux for a given set of parameters (surface and film temperature, film flow rate, annulus conditions) is given by correlations presented in Reference 7.A.1. The subject of this appendix is the wetted area of the external shell surface, and how the wetted area is limited by film stability effects.

Note that the initial application of water to the external surface at safety analysis basis surface temperatures is discussed in Section 7.6.5, so that quasi-steady water coverage is assumed to be established in the discussions of this appendix.

The introduction and Section 7.2 provide a brief overview of the PCS design, as it relates to film stability considerations. The test program is discussed in Section 7.6, where it is shown that the range of non-dimensional parameters for AP600 and **AP1000** is adequately covered in the test program. Subsequent Appendix 7A sections give a summary of literature findings on film stability, a discussion of the contact wetting angle that addresses the wettability of the coated surface in the context of surfaces studied in the literature, and a description of LST observed liquid film behavior for high and low flow tests. The physics summarized in this appendix were considered in the development of the PCS film coverage model. The PCS film coverage model is biased to conservatively bound test data that include cold full-scale tests and smaller-scale heated surface tests.

The double dam-weir system is designed to evenly distribute the PCS water onto the surface of the dome. The elliptical shape of the dome and corresponding area divergence helps spread the stripes of water flowing from the individual V-notches in the weirs. Water coverage on the top of the dome is the most difficult to quantify, but water coverage on this portion of the dome is also the least important to the successful operation of the PCS; the area between the top of the dome and the second weir is only about 20 percent of the total shell external surface area and is neglected in the PCS film coverage model calculation of the evaporation-limited PCS flow rate input for the WGOTHIC model.

The distribution system applies water to the shell in discrete, evenly spaced streams. Water from the PCCWST discharge header falls into a bucket suspended just above the center of the dome. Slots on the side of the bucket allow water to spill at discrete locations around the circumference onto the containment dome. From there, the water flows outward and downward, spreading due to the area divergence, until it is collected and redistributed by a series of two weir rings. Weir outflow rates as a function of time, including the initial filling of the bucket and dams, are shown in Figure 7-3. The method of water application, by weir slots, induces discrete water streams that can remain discrete at low PCS water flow rates and merge to form continuous circumferential water coverage at higher PCS water flow rates.

The initial application of water flowing from a weir slot hits the surface and spreads until surface tension and skin friction dissipate the momentum. If the film is significantly subcooled relative to the surface at that point, thermocapillary effects (see Section 7.A.2.2) may also affect how wide the stripe is as it flows down from the point of application. The PCS water distribution system employs two weir rings on the dome. By the time the water exits the second weir ring, the water has been heated to a temperature relatively close to that of the shell, so that thermocapillary effects are less important. Therefore, the focus for film stability is on evaporating film stability.

Evaporation of the PCS water results in a reduction of the mass flow rate as the film advances down the containment structure from the second weir. As the mass flow rate decreases, the wetted perimeter of the stable film also changes. From observation of tests, the wetted perimeter typically decreases only after the mass flow rate decreases below a certain point. The physical processes that limit the amount of stable film coverage on the containment shell are discussed in this appendix.

7.A.2 SUMMARY OF GENERAL LIQUID FILM BEHAVIOR

This section provides a summary of available literature on models and data for liquid films and provides a discussion of the various aspects of liquid film behavior.

7.A.2.1 Literature Summary

The study of movement in a fluid interface has been studied over 150 years. In studying the spreading of a drop of alcohol on the surface of water, British engineer and physicist James Thompson correctly explained the phenomena as a surface-tension-driven flow. The name of Italian physicist Carlo Marangoni has been associated with two distinct but related surface effects. The first is motion in a fluid interface caused by local variations in interfacial tension which were, in turn, caused by differences in composition or temperature. The second phenomenon is a conjugate of the first; it is the departure from equilibrium surface tension that is produced by the extension or contraction of an interface. Both of these phenomena are important to the understanding of the behavior of liquid films.

The stability of liquid films has been studied by many analysts and experimenters within the last 50 years. These studies may be grouped in two general categories;

1. Determining the minimum flow rate required to rewet a stable dry patch.
2. Examining the thermocapillary breakdown of a thin film.

Films are generally categorized as saturated films or subcooled films, due to differences in stability, or wetting performance. Films that are applied at or near the temperature of the surface are typically referred to as “saturated films.” Such films, when applied to heated surfaces as is done on AP600 and **AP1000**, have a significant evaporation component and are thus called “evaporating films.” Norman and McIntyre (Reference 7.A.2) reported data showing that a large increase in the minimum film wetting rate was required as the temperature difference between the surface and film was increased (that is, subcooling of the liquid film relative to the surface was increased). Hallet (Reference 7.A-3) also observed this phenomenon and developed a film breakdown correlation that was related to the film surface tension difference, the wave number, and the heat transfer coefficient. Fujita and Ueda (Reference 7.A-4) measured the breakdown of both subcooled and saturated liquid films on heated, vertical, polished,

stainless steel tubes. A comparison of the results from their tests also showed that the highly subcooled films are unstable at flow rates several times higher than that observed for saturated films. More recently, Bohn and Davis (Reference 7.A-5) measured the breakdown of subcooled water films on heated, vertical, polished, stainless steel tubes and developed a film breakdown correlation that was dependent on thermocapillary effects. Thus, there is clearly a basis for separately considering film stability for subcooled and evaporating films.

The conclusion that thermocapillary effects influence the early breakdown of subcooled films is based on the following. Subcooled films having liquid temperatures much lower than the solid surface temperature absorb heat, causing the film temperature to increase. Evaporating films that are more nearly in thermal equilibrium with the solid surface, transfer mass and energy from the film surface to the gas atmosphere. Thus, one explanation for the apparent reduced stability of subcooled films is the existence of significantly higher temperature gradients through the film that give rise to increased thermocapillary forces (see Section 7.A.2.2).

The manner in which data has been presented in the literature is also of interest. In general, the surface heat flux is recognized as the dominant independent parameter, and properties have a strong influence on film behavior. The literature presents data most often as film flow rate (mass flow rate per unit wetted perimeter) versus heat flux. To account for the effect of viscosity on wettability, the Westinghouse test data reduction uses film Reynolds number as the dependent parameter, with surface heat flux as the independent parameter.

The performance of the coated surface to be used for AP600 and **AP1000** can be compared to the performance of the typical surfaces studied in the literature, polished steel and polished copper. The use of polished materials in laboratory tests allows careful characterization of the important parameter, the wetting angle. The coated surface does not lend itself to characterization of a single local wetting angle (Section 7.A.3.2). Therefore, the data for film flow rate versus heat flux give an appropriate means of comparison of film stability data. Stable film flow rates on the order of 20 to 50 lbm/hr-ft are noted on the LST and other test surfaces, even with heat fluxes up to 10,000 Btu/hr-ft². Comparison to Fujita-Ueda data shows that the coated surface is significantly better at wetting, and is less sensitive to heat flux than the polished surfaces.

The list of papers reviewed and considered for application to the containment Evaluation Model is extensive and will not be given here. However, in a summary article (Reference 7.A-6), Bankoff provided an extensive list of relevant papers. The current state of the art is focused on the "moving contact line," which was also considered for application to the containment Evaluation Model, but is generally not very practical for engineering application.

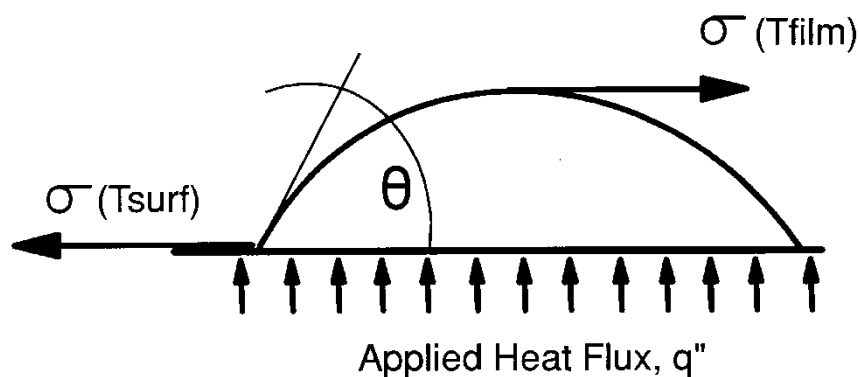
7.A.2.2 Thermocapillary Effect

Based on discussions with Bankoff (Reference 7.A-8), the thermocapillary effect is a result of the variation of surface tension with temperature in moving from the contact line to the free film surface (see Figure 7.A-1). For a stable stripe shape, the forces in the horizontal direction must sum to zero. The surface tension decreases as temperature increases, so the minimum stable film flow rate has to be greater to prevent the hotter liquid at the surface from causing the film stripe width to contract. The thermocapillary effect on the force balance is sometimes estimated (as in Equation 7.A-2) by replacing the actual $\sigma(T)$ function with a much simpler function using the temperature drop through the film which can be related to the heat flux as

$$\sigma_{surf} - \sigma_{film} \geq \sigma_{surf} - \left(\sigma_{surf} + \frac{d\sigma}{dT} * \Delta T_{film} \right) \geq - \frac{d\sigma}{dT} * \frac{q''}{k_{film}}$$

This simplification becomes increasingly inaccurate as the film subcooling increases, since the sensible temperature increase of the film invalidates the approximation q''/k , used to estimate the film surface temperature.

Overall, investigators have identified momentum, surface tension, body (hydrostatic) force, thermocapillary, and vapor thrust as the dominant forces affecting film stability. These forces are typically expressed as functions of flow rate, heat flux, fluid properties, and wetting angle. Vapor thrust can be neglected in AP600 and AP1000 because the heat flux is low, less than 10,000 BTU/hr-ft². Consequently, film stability may be considered to be controlled by a balance between momentum, surface tension, hydrostatic, and thermocapillary forces.



$$T_{surf} > T_{film}$$

$$\sigma_{surf} < \sigma_{film}$$

Figure 7.A-1. Variation in Surface Tension over the Surface of a Heated Liquid Film

7.A.2.3 Available Theoretical Analytical Models

The available analytical theoretical models have not been found to be practical for determining the film coverage on the passive containment design. Rather, the Evaluation Model includes a film coverage model that is consistent with the physics of liquid films, and is developed to provide a conservatively bounded total water coverage. However, models proposed in the literature can be used to gain insight into film behavior.

The Zuber-Staub model (Reference 7.A-7) considers the stability of a dry patch located within a uniform, flowing film, i.e., the inability of the liquid film to rewet the dry patch. The mathematical formulation of the model includes three of the dominant terms identified above: momentum, surface tension, and thermocapillary. The model uses a vertical force balance at the tip of a postulated dry patch to determine the minimum uniform film thickness required to rewet the dry patch. This minimum film thickness is a function of the surface heat flux, the film properties (including the contact angle between the film and surface).

One of the Zuber-Staub formulations treats the film thickness as the dependent parameter from which film stability criteria can be derived. Although film thickness is not easily measured, film thickness is related to the film flow rate through continuity. Therefore, the discussions that follow will treat the film flow rate as the controlling parameter from which film stability criteria may be derived.

According to the Zuber-Staub model, if the film flow rate is greater than the minimum stability value, any dry patch created in the film would be washed over and would readily disappear after formation due to the momentum of the flowing film. Conversely, if the film flow rate was equal to or less than the minimum stability value, a dry patch, if formed, would be predicted to be stable (i.e., the film would not be able to recover the dry patch). The Zuber-Staub model does not consider the effects of waves in recovering the dry patch.

The concept of a force balance can be used to develop insight into controlling parameters for film stability. A force balance more specific to the passive containment design that includes momentum, surface tension, thermocapillary, and body forces (and thus, surface inclination angle, β) to account for spreading on the inclined surface of the elliptical dome, but neglects the vapor thrust term, may be written in terms of the film flow rate, Γ . Since the relationship is for a stable film width, equilibrium between the various forces is assumed. If the film flow rate is greater than the value of Γ in the equation, the film will wash over any dry patch which happens to form. The equation, which can be used to examine the minimum stable film flow, Γ_{min} , is:

$$\frac{1}{15} * \left(\frac{9 * g * \sin \beta * \Gamma_{min}^2}{\rho * \mu} \right)^{\frac{2}{3}} + \left(\frac{3 * \rho * g^2 * \cos(\beta)^3 * \mu * \Gamma_{min}}{8 * \sin \beta} \right)^{\frac{1}{3}} = \frac{\sigma * (1 - \cos \theta)}{\left(\frac{3 * \mu * \Gamma_{min}}{g * \sin \beta * \rho^2} \right)^{\frac{1}{3}}} - \frac{d\sigma}{dT} * \frac{q''}{k} * \cos \theta \quad (7.A-2)$$

Note that the formulation given above assumes a laminar film with uniform film thickness and does not consider the effect of waves in wavy laminar flow. Waves in wavy laminar flow typically have a peak to valley distance of about 3 times the average film thickness, but occupy only a small fraction of the flowing volume. Waves carry momentum as they pass, but do not significantly affect the calculated average film thickness. Waves will wash through the region of flowing film, effectively wiping out any history effect of the method of application or other upstream effects. Therefore, film stability can be considered to be a local phenomenon, governed by local force balances at the point of interest on the contact line.

Equation 7.A-2 predicts higher values for the minimum stable film flow rate on surfaces that wet poorly, that is, those that have large contact angles, than for surfaces that wet readily. For surfaces that are heated, heat flux is destabilizing. The equation also shows that as the film heats up, it becomes more stable due to property changes.

Since the theoretical models available in the literature are not practical for determining the film coverage on the passive containment design, the insight gained from examining those approaches is used to support development of an empirical bulk coverage model. That is, the film stability can be characterized using a criterion for a minimum film flow rate, Γ_{\min} , that will maintain a stable stripe. Data from tests at different scales, wherein the range of AP600 and AP1000 dimensionless parameters is sufficiently covered, can be used to empirically derive a bounding value for Γ_{\min} . As discussed in 7.A.2.1, data can be represented using the film flow rate, and plotted against the dominant independent parameter, heat flux.

7.A.3 CONTACT ANGLE AND SURFACE WETTABILITY

A discussion of contact angles in general and observations from test coupons are provided to gain insight into the performance of the coated surface relative to surfaces in the literature. Finally, factors which can affect surface wettability are discussed.

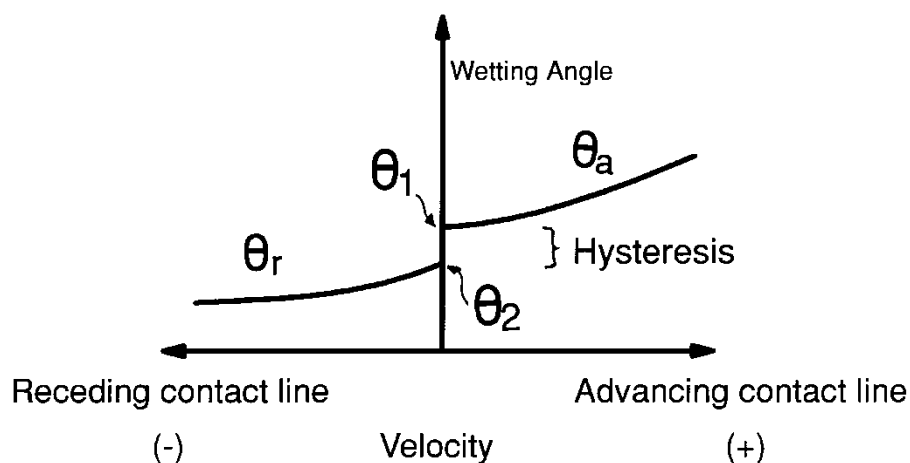
7.A.3.1 Advancing and Receding Contact Angles

The place where the wet and dry regions intersect is called the contact line. For example, in a liquid film flowing down a wall in a constant width stripe, the contact lines are the two vertical lines defining the width of the stripe. The contact angle is defined as the angle between the solid and the liquid surface at the contact line. The contact angle between a water film and the surface to which it is applied is an indication of the surface wettability. Typically, better wetting occurs on surfaces with small contact angles. In practice, contact angles are measured for both advancing and receding films. Usually the two values are quite different, with the advancing contact angle being much larger than the receding contact angle. The relation between contact angle and velocity is qualitatively depicted in Figure 7.A-2. Of interest is the hysteresis between advancing and receding contact angles. There is actually a range of stable contact angles for a static contact line. Thus, if a droplet starts out by spreading, such as when it is dropped onto the surface, it will spread to a diameter governed by the advancing contact angle. Then as the droplet evaporates, it may be expected to remain at a constant diameter, with the contact line anchored, until the mass lost contracts the droplet such that the receding contact angle is reached. Further evaporation would then cause the droplet diameter to decrease.

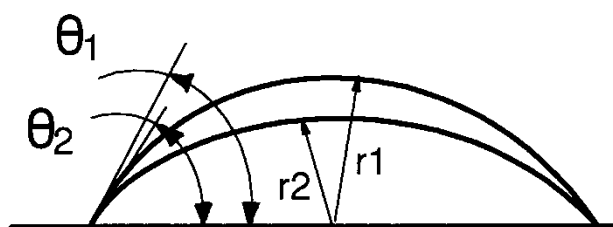
It is general practice to measure contact angles of a liquid on a smooth or polished surface, such as glass or polished steel having surface profiles measured in microns. High magnification is used to measure the contact angle as it meets the surface. The surface on the external containment shell is an inorganic zinc coating applied on a carbon steel structure. The surface of the inorganic zinc coating is not smooth, having a surface profile of several mils. With a surface profile of several mils, the magnified image shows significant peaks and valleys, making it impossible to measure a single contact angle that is applicable over the entire surface. Thus, the significance of a representative contact angle for the organic zinc coating used for the exterior of the containment shell is diminished. The interest is on bulk coverage performance over a large surface area, so larger scale integral tests are used. It is desired, however, to understand and relate the bulk wetting performance of the coated surface to that of surfaces in the literature. Therefore, measurements were taken to characterize a bulk static contact angle on the prototypic surface by observing a drop on sample coupons under various conditions as described below.

7.A.3.2 Static Contact Angle Measurements of Coated Surface

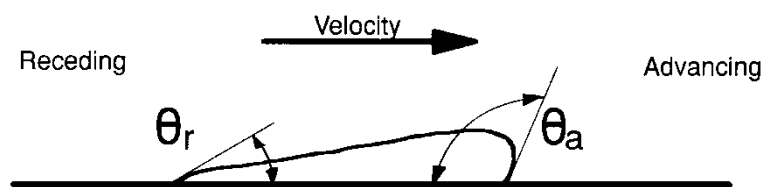
The bulk contact angle for a drop of water was measured as a function of temperature and age of the surface coating selected for the AP600 and **AP1000**. Two samples were prepared for these measurements. The first test coupon was supplied to Westinghouse by the coating vendor. This sample was prepared by the vendor and was not subjected to weathering. The second sample was a 12-in² section of a steel plate that was painted by Westinghouse and weathered for two years.



Contact Angle Behavior with Velocity



Static Contact Angle



Dynamic Contact Angle

Figure 7.A-2. Typical Qualitative Contact Angles for Advancing and Receding Contact Lines

The following procedure was used to determine the static contact angle for both samples at ambient conditions:

- The test coupons were cleaned per coating vendor specifications and dried.
- The test coupon was placed in a horizontal position.
- A drop of water was placed on the test coupon.
- Using an optical comparator, the average angle between the sample surface and the drop at the interface.
- Measurements were repeated using several drops to ensure repeatability and consistency in the measurements.

Additional measurements were taken with the test coupons held at different temperatures. This was done to evaluate the effect of the surface temperature on the contact angle. The test coupons were heated with either hot water or a heat gun.

The static contact angle measurements taken are summarized in Table 7.A-1. They show that the contact angle for inorganic zinc coated surface decreases both with an increase in age and an increase in temperature. At high temperatures, the contact angle was observed to be initially larger than that observed for lower temperatures. It was observed, however, that the drops quickly spread and flattened out to a quasi-steady shape, thereby reducing the measured contact angle.

From the measurements listed in Table 7.A-1, it is concluded that a representative bulk or average contact angle for the inorganic zinc coated containment shell surface is between []^{a,c} for a new surface, and between []^{a,c} after just two years of weathering.

Table 7.A-1. Summary of Test Results to Determine Static Contact Angle

Description of Test	Contact Angle	
	Weathered Sample	Unweathered Sample
1. Room Temperature, T=80°F	24°	30°
2. Heated, T=110°F	23°	33°
3. Heated, T=180°F t=0 sec	28°	53°
t=15 sec	23°	44°
t=30 sec	20°	35°
t=60 sec	20°	28°

A small drop of water spread around on the inorganic zinc-coated surface was not observed to contract, or snap back into a drop. This observation indicates that the receding contact angle for this surface is nearly zero. These observations also suggest that the film breakdown to form a dry spot occurs at a lower film Reynolds number than the critical Reynolds number for rewetting.

Static wetting angle measurements indicate that the coated surface is clearly more wettable than surfaces reported in the literature, and based on the force balance it is expected to be less sensitive to heat flux.

7.A.3.3 Relative Magnitude of Surface Tension Effects

A solid surface will be wet with liquid if the free surface energy of the solid is greater than the free surface energy of the liquid. Surface tension, σ , is defined as the work required to expand the surface of a liquid by a unit of area. It is a measure of the strength of the intermolecular forces in the fluid, similar to the latent heat of vaporization.

Hydrogen bonding is the strongest type of intermolecular force. Liquid water has relatively strong intermolecular forces due to the strong hydrogen bonds; 80 percent of the intermolecular attraction in water is attributed to hydrogen bonding. In a water molecule, the electrons spend more time in the vicinity of the oxygen atom than the hydrogen atoms because oxygen is more electro-negative than hydrogen (3.5 versus 2.1 for hydrogen on a scale of 4.0). This results in an electric dipole within the molecule. For this reason water is said to be a polar molecule.

As its temperature increases, the mean spacing between molecules in a liquid increases, causing the density to decrease and a reduction in the intermolecular forces. Therefore, both surface tension, σ , and the latent heat of vaporization, h_{fg} , decrease with increasing liquid temperature. For example, the surface tension of water is about 4.97×10^{-3} lbf/ft and the latent heat of vaporization is about 1054 BTU/lbm at room temperature. The value of these two parameters decreases to 4.0×10^{-3} lbf/ft and 970 BTU/lbm, respectively, at 212°F.

7.A.3.4 Factors Affecting Surface Wettability

The wetting of a solid surface by water is improved by reducing the surface tension of the water (by use of a wetting agent such as a detergent), by making the surface more porous (to improve the spreading by capillary action), or by using a polar surface (increasing the intermolecular forces between the surface and the polar liquid water). The use of a surfactant was examined during the Water Distribution Tests. It was found that surfactants offered no effective improvement in coverage. This has been postulated to be due to the turbulence of the flowing film which would not allow the surfactant to influence the surface of the film significantly. The porosity of the inorganic zinc coating is believed to be the primary factor affecting wetting early in the coating's life, adding a significant capillary effect at the contact line. It was postulated that the buildup of polar molecules (e.g., oxides of zinc) on the solid surface improved its wettability with age. Photographs were taken of both new and weathered surface coating samples using a scanning electron microscope with an energy dispersive X-ray spectrometer to identify the chemical species present on the surface. More oxides of zinc were found on the weathered surface than the new surface, supporting the hypothesis that the increase in wetting is due to the surface becoming more polar as it ages.

A buildup of some surface contaminants can result in a reduction in wettability. The worst surface contaminant for the inorganic zinc coating is silicone; it has both low surface energy and low polarity. Sources of silicone in air pollution are rare. Other surface contaminants that could result in reduced wetting include hydrocarbons such as oils, members of the PTFE family (Teflon), polypropylene, and polyethylene residues. To combat surface contaminants, the coatings vendor has developed and made available a standard cleaning procedure and a specially developed detergent that emulsifies these types of surface contaminants so they can be washed away.

Although the number of potential contaminants that would adversely affect wetting of the inorganic zinc coating surface is probably limited to a dozen or so, it would be very difficult to analytically predict the wetting degradation over time. The degradation of surface wettability would have to be estimated as a function of the concentration of each potential contaminant, the deposition rate of each as a function of the local or worst case atmospheric conditions, and the assumption that the degradation is additive, etc. Therefore, periodic in-service inspections will be performed to look for corrosion and surface contaminant buildups to assure surface wettability. The frequency and procedures for testing and the minimum acceptance criteria prior to cleaning the surface are defined in the Reliability Assurance Program.

7.A.3.5 Summary of Wetting Angle Assessment

The contact angle between a water film and the surface to which it is applied is an indication of the surface wettability. Although the surface provided by the inorganic zinc coating applied to the external surface of the containment is not smooth relative to other materials used to measure contact angles such as glass or polished steel, measurements were taken to characterize a bulk static contact angle of a spreading film on the prototypic surface to relate to literature data. The static angle was measured by observing the spreading of a drop on two coupons, one weathered and one not weathered, under ambient and heated conditions. Results showed that a surface weathered for two years is significantly more wettable []^{a,b} than surfaces for which data exists in the literature (in the range of 60 degrees).

7.A.4 DESCRIPTION OF LST OBSERVATIONS

LST observations to characterize wetting behavior were made during shakedown tests, video tapes were recorded, and sketches were made for the test records. During these shakedown tests, quasi-steady heat flux and water flow rate conditions were achieved, and then water flow was slowly valved down in stages with constant steam flow. At each stage, when quasi-steady conditions again were reached, observations and notes were taken. Subsequent similar cycles were done at several steam flows (heat fluxes). The objective was to observe the behavior of the liquid film as it varied from a moderately high flow down to nearly complete evaporation. Since the majority of the LST matrix tests were run with a high flow rate, the qualitative discussion starts with a description of water coverage on a high flow test. Finally, the water coverage on a low flow test is described. Observations are consistent with the physics of liquid films discussed above.

7.A.4.1 High Flow LST

As discussed in Section 7.6.3, the water is applied to the shell in stripes around the circumference of the test vessel. Stripe widths for a given steady state test were relatively constant, varying by fractions of an inch as the delivered flow rate varied (see Section 7.6.3). Based on Reynolds number, the flow regime is wavy laminar, which has been confirmed by test observations. The wavy laminar regime is discussed in the literature. A simple sketch is provided in Figure 7.A-3, showing qualitative characteristics observed for a representative film stripe on a heated LST surface with a high flow rate. High flow rate LST typically exhibited constant width stripes, as discussed further below. Stripe widths varied from an inch or less to complete circumferential coverage, depending on the test delivered flow and heat flux. Within a stripe, the majority of the width is flowing water with wavy laminar conditions. In that portion, waves are generated by upstream disturbances and advance down the stripe with a velocity faster than the average film speed, consistent with continuity flow theory. The waves generally alternate with slight left and right horizontal velocity components.

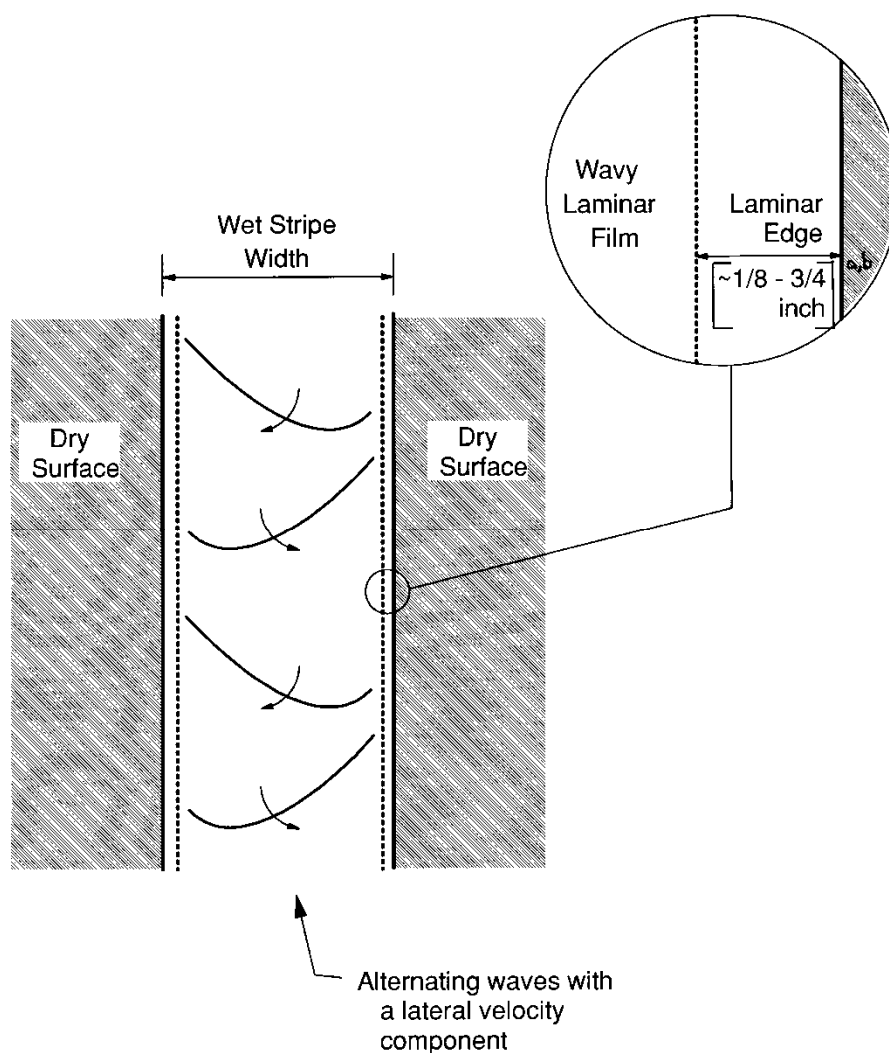


Figure 7.A-3. Sketch of Qualitative Wave Laminar Film Flow Characteristics on Heated LST Shell Water Stripe

Water stripe edges exhibited a narrow []^{a,b} region of laminar flow. Visual observation indicated that the edges were wetted but not obviously flowing. When an obstruction was placed within a wet edge, a “bow wave” built up above the obstruction, confirming that indeed liquid was flowing downward in that region. The film flow, and thus thickness, in that region is small enough that viscous forces damp out any disturbances. For example, the waves are damped by viscous forces in the stripe edge. Note that the laminar edge was also observed to occur on stripes which narrowed as their film flow rates decreased due to evaporation. This indicates that there is a very thin layer near a stripe edge, or in fact the equivalent wetting angle at the contact line is very small. This is consistent with the consideration in 7.A.3 that the receding wetting angle likely governs film stability of an evaporating stripe on the containment shell.

Since the water is applied as stripes at the dome with J-tubes (see Figure 7.A-4), and there is significant liquid film subcooling over much of the LST dome for high flow tests, the width of stripes that reach the vertical sidewall is less than can be supported by a stable film at the given film flow rate. Therefore, it can be postulated that the initial width at the top of the vertical sidewall is sufficiently greater than the evaporating film stability limit and that evaporation from the stripes does not cause the receding contact angle to be reached. Rather the film stripes in high flow LST tests are believed to remain within the region of hysteresis over the entire height, consistent with the observed constant width stripes.

7.A.4.2 Low Flow LST

Figure 7.A-5 shows a composite of typical film characteristics on a portion of the LST shell at relatively low flows typical of the water flow applied to LST 213.1. The tests described here have film flows that are low enough that evaporation causes the receding contact angle to be reached, and further evaporation leads to narrowing of the stripes.

As for the high flow LST, the water is delivered to the vessel shell surface via J-tubes, as a subcooled film. The application method and subcooled film stability set the initial stripe width, similar to the high flow tests. However, the film heats up to become an evaporating film before it reaches the sidewall. Observations were made of shakedown tests at conditions (steam flow, external water flow) similar to those for LST 213.1. During the initial setup prior to heating the vessel, the film flow was established and gradually valved down. As very low flows were reached, some J-tubes were seen to stop delivering water before others, indicating that there was some asymmetry in delivered flow per stream. This is consistent with observations of heated tests that indicated stripe widths and vertical extents varied around the circumference of the vessel.

In Figure 7.A-5 the width of the two outer stripes shown remain approximately constant down to a certain elevation, varying only as the delivered flow rate varied. At some elevation on the sidewall, which may be different for different stripes, the film width began to narrow until the gutter was reached.

For some stripes, shown as the two innermost stripes in Figure 7.A-5, the delivered flow was low enough that the stripes completely evaporated before reaching the gutter elevation.

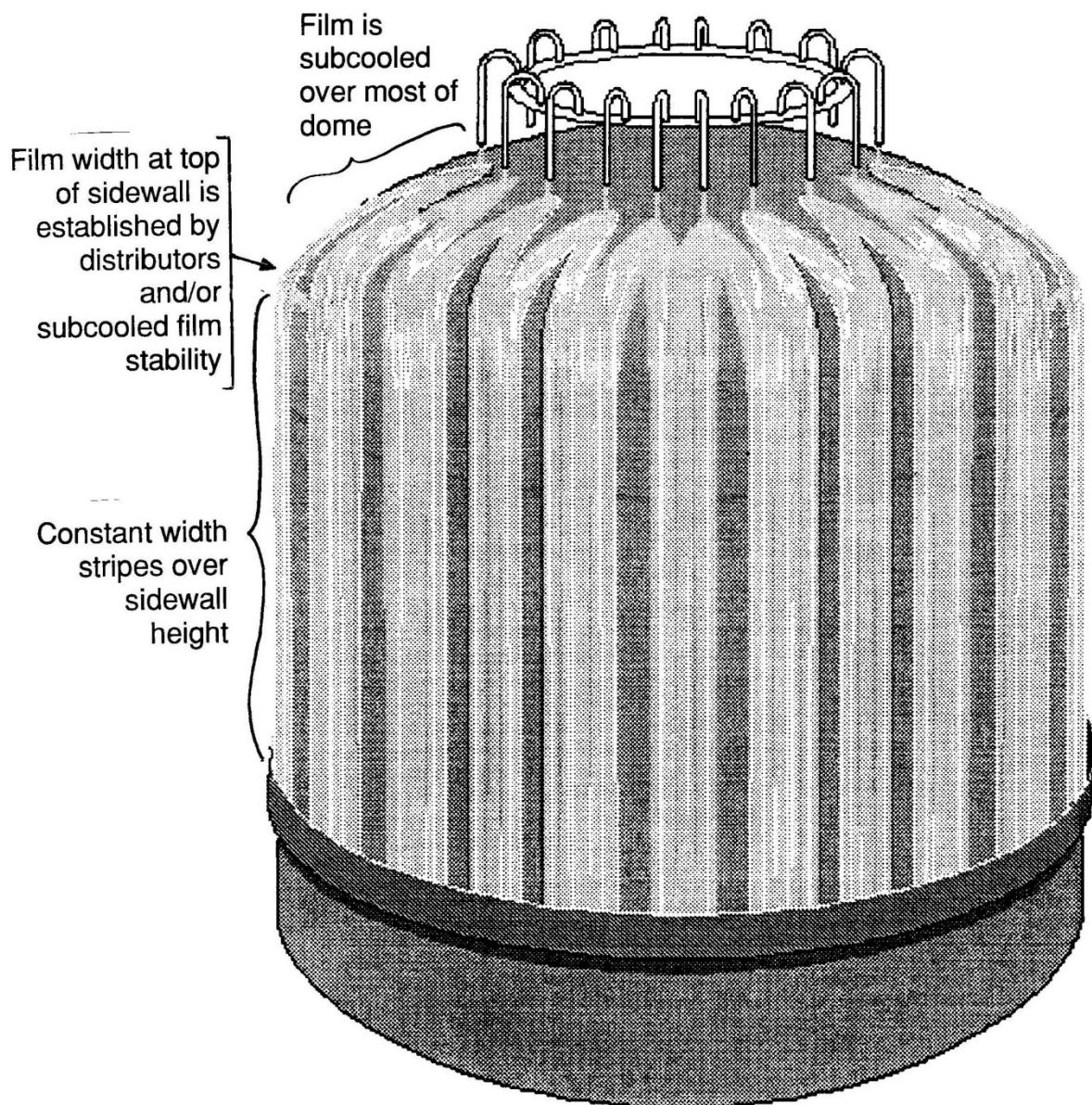


Figure 7.A-4. Large-Scale Test Water Coverage Pattern at High PCS Flows

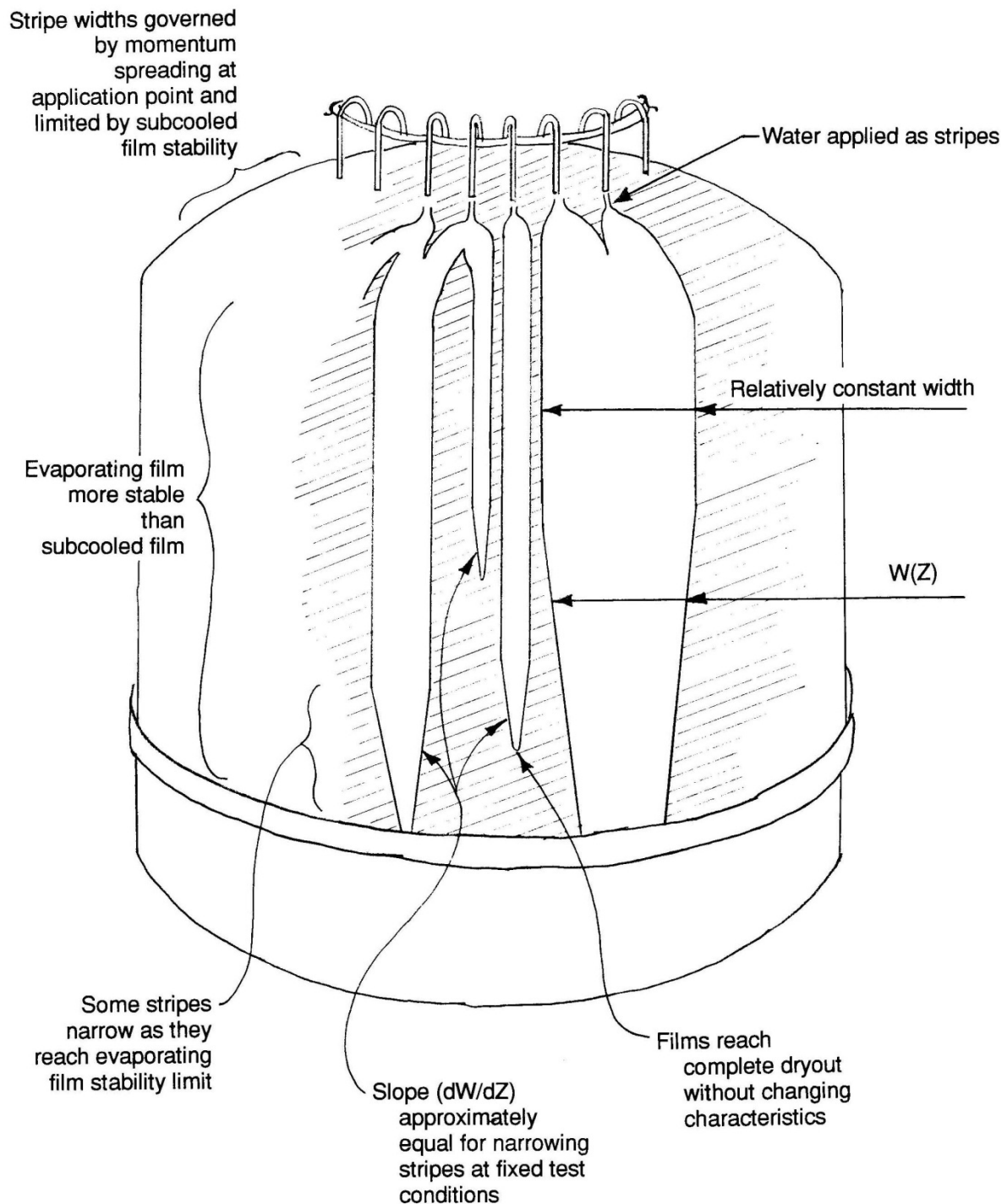


Figure 7.A-5. Sketch of LST Observation of Vessel Exterior at Water Flows Similar to LST 213.1 Showing Complete Dryout of Some Stripes

The slope of the changing width as a function of height, dW/dZ , was carefully observed. Qualitative observation indicated that the dW/dZ of each stripe around the circumference was nearly constant at a specific quasi-steady-state test condition.

Of most interest in these tests, relative to water coverage, is the fact that stripes that evaporated completely did so without changing their characteristics near the point of complete dryout. Thus, for the surface tested, the liquid films did not snap, or draw up, into a thick film. The edges of the film, including the bottom edge remained as wavy laminar film up to within a fraction of an inch from the edge, including the lower edge. As the water flow rate was valved down, the bottom edge moved gradually up, and when the flow was increased to its original value, the vertical extent of the stripe returned to a consistent elevation. Therefore, the film was well behaved as it completely evaporated.

7.A.5 CONCLUSIONS

A comparison of coated surface data with polished surface data from the literature shows the coated surface is more wettable.

Models from the literature are not sufficiently developed to be considered reliable. The literature provides an indication of the appropriate parameters to study film breakdown data: Re_{film} or Γ and heat flux. A practical approach taken to bound the data from the various tests is to establish a minimum stable film flow rate, Γ , that can be used to define a minimum coverage.

History effects are washed out by waves, so breakdown can be considered to be a local phenomenon. Therefore, LST (Section 7.6.3), SST (Section 7.6.2), and heated flat plate tests (Section 7.6.1) can be said to represent the bottom portions of liquid film stripes on the containment shell that dry out due to evaporation.

Observations of tests are explained based on physics of liquid films on heated surfaces. At high enough applied flows, the applied stripe maintains constant width until the film stability limit is reached, governed by the receding contact angle, then the stripe begins to narrow consistent with the minimum film flow rate required to maintain a stable film.

Observations of tests show that complete dryout occurs while maintaining a stable stripe geometry, gradually decreasing in width until it disappears.

7.A.6 REFERENCES

- 7.A.1 WCAP-14326, Revision 2, "Experimental Basis for the AP600 Containment Vessel Heat and Mass Transfer Correlations," April 1998.
- 7.A.2 W. S. Norman and V. McIntyre, "Heat Transfer to a Liquid Film on a Vertical Surface," *Trans. Inst. Chem. Engrs.* Vol. 38, pp 301-307 (1960).
- 7.A-3 V. A. Hallett, "Surface Phenomena Causing Breakdown of Falling Liquid Films During Heat Transfer," *International Journal of Heat and Mass Transfer*, Vol. 9, pp 283-294 (1966).

- 7.A-4 T. Fujita and T. Ueda, "Heat Transfer to Falling Liquid Films and Film Breakdown Parts I and II," *International Journal of Heat and Mass Transfer*, Vol. 21, pp 97-108 and 109-118 (1978).
- 7.A-5 M. S. Bohn and S. H. Davis, "Thermocapillary breakdown of Falling Liquid Films at High Reynolds Numbers," *International Journal of Heat and Mass Transfer*, Vol. 36, pp 1875-1881 (1993).
- 7.A-6 S. G. Bankoff, "Dynamics and Stability of Thin Heated Liquid Films," *Transactions of the ASME – Journal of Heat Transfer*, Vol. 112, pp 538-546, (1990).
- 7.A-7 N. Zuber and F. W. Staub, "Stability of Dry Patches Forming in Liquid Films Flowing over Heated Surfaces," *International Journal of Heat and Mass Transfer*, Vol. 9, pp 897-905 (1966).
- 7.A-8 Dr. S. G. Bankoff, discussions held at Westinghouse Science and Technology Center during observations of LST, 1996.

8 CONTAINMENT PRESSURE SENSITIVITY DURING BLOWDOWN

8.1 INTRODUCTION

The purpose of performing the single-node WGOTHIC analysis is to show that the containment pressure during the blowdown phase (predicted using the WGOTHIC code) is essentially the same as if Standard Review Plan (SRP) methodologies were utilized for the analysis. This comparison supports the use of WGOTHIC during the analysis of the blowdown phase of the transient, since it is expected that the presence of external heat removal from the containment shell during the first 50 seconds of the transient has little impact on the pressure transient. The containment shell time constant is long, as compared to the transient time, and passive cooling system (PCS) film flow is assumed to be delayed until well after the end of blowdown.

The purpose of performing the sensitivity to heat sinks during blowdown is to confirm that volume compliance is the dominant means of mitigating pressure increase during blowdown.

8.2 METHOD

The AP600 evaluation model (EM) described in Section 4 was used for comparison in this study. The EM was converted to a single-node containment model, consistent with SRP 6.2.1 methodology and comparable to the licensed Westinghouse methodology by the following input modifications:

- All of the climes were removed.
- All of the flow paths, except for those associated with the mass and energy release forcing functions, were deleted. The mass and energy forcing functions were not changed.
- All control volumes which represent the outside containment regions were deleted.
- A single-node containment control volume, containing all of the thermal conductors from the base case and the two mass and energy release forcing functions, was created.
- A conductor representing the containment shell was added to the single-node containment control volume.
- The Uchida heat transfer correlation with revaporization was used on the shell and conductors.

The EM was modified to eliminate heat removal from the containment gas volume by internal heat sinks and the steel shell. The only modification to the EM was to delete all thermal conductors within containment and to effectively eliminate the clime conductors for the shell itself by assuming an adiabatic inner surface.

8.3 ANALYSIS

The blowdown phase pressure results for the single-node analysis are compared to the EM containment pressure in Figure 8-1.

The blowdown phase pressure response without heat sinks is compared to the EM results in Figure 8-2.

8.4 CONCLUSIONS

The conclusion of the blowdown nodding sensitivity is that the single-node model (utilizing SRP 6.2.1 methodologies) essentially provides the same results during the blowdown phase as the EM.

The conclusion of the sensitivity to eliminating heat sinks during blowdown shows a relative pressure increase at the end of blowdown of only 3.6 psi relative to the EM. This compares to the EM pressure increase of about 33 psi during the blowdown phase, which confirms the dominant pressure mitigation during blowdown is energy storage due to pressure increase of the volume, or volume compliance.

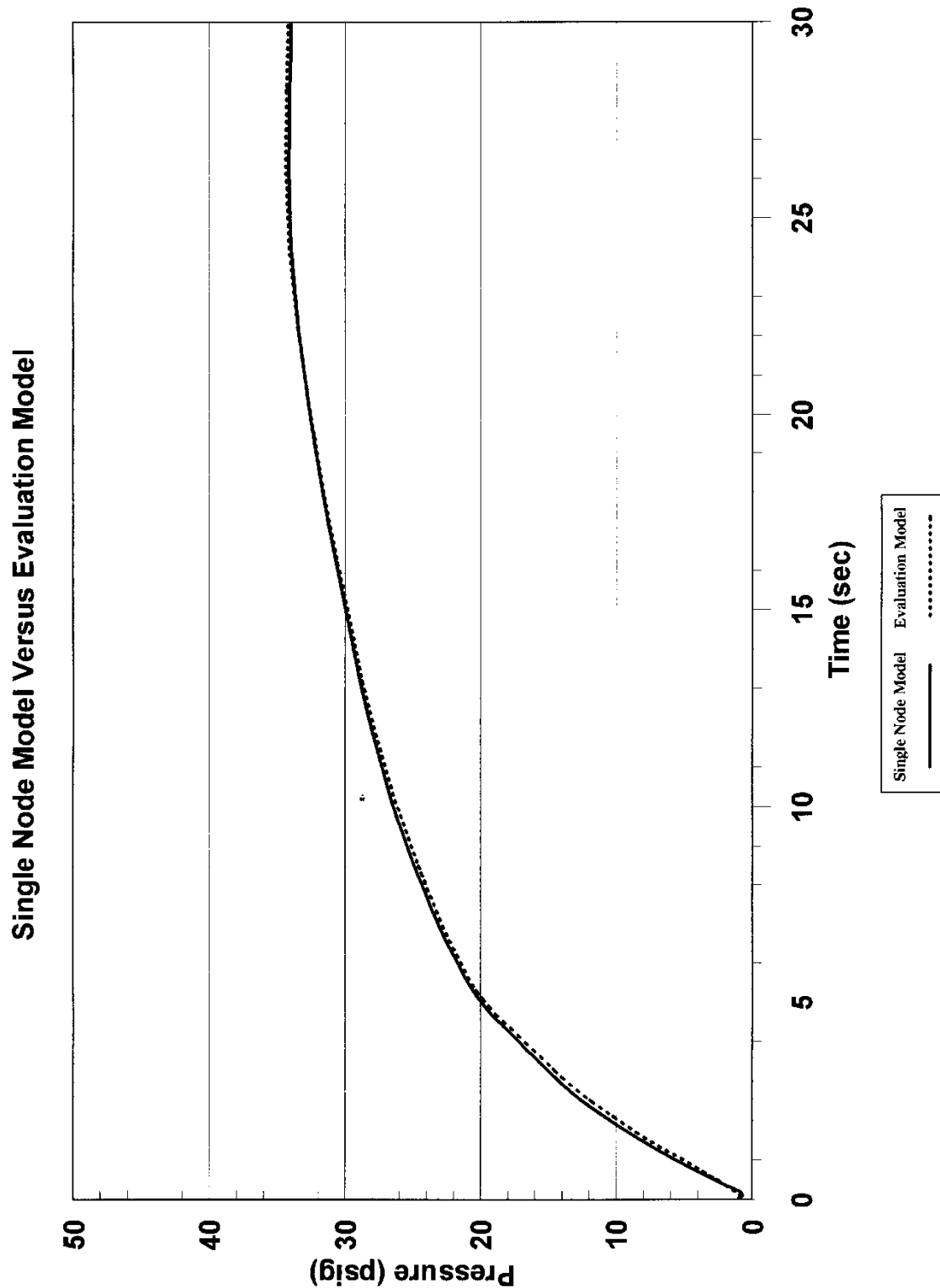


Figure 8-1. Comparison of Single-Node Model with EM Pressure Curve

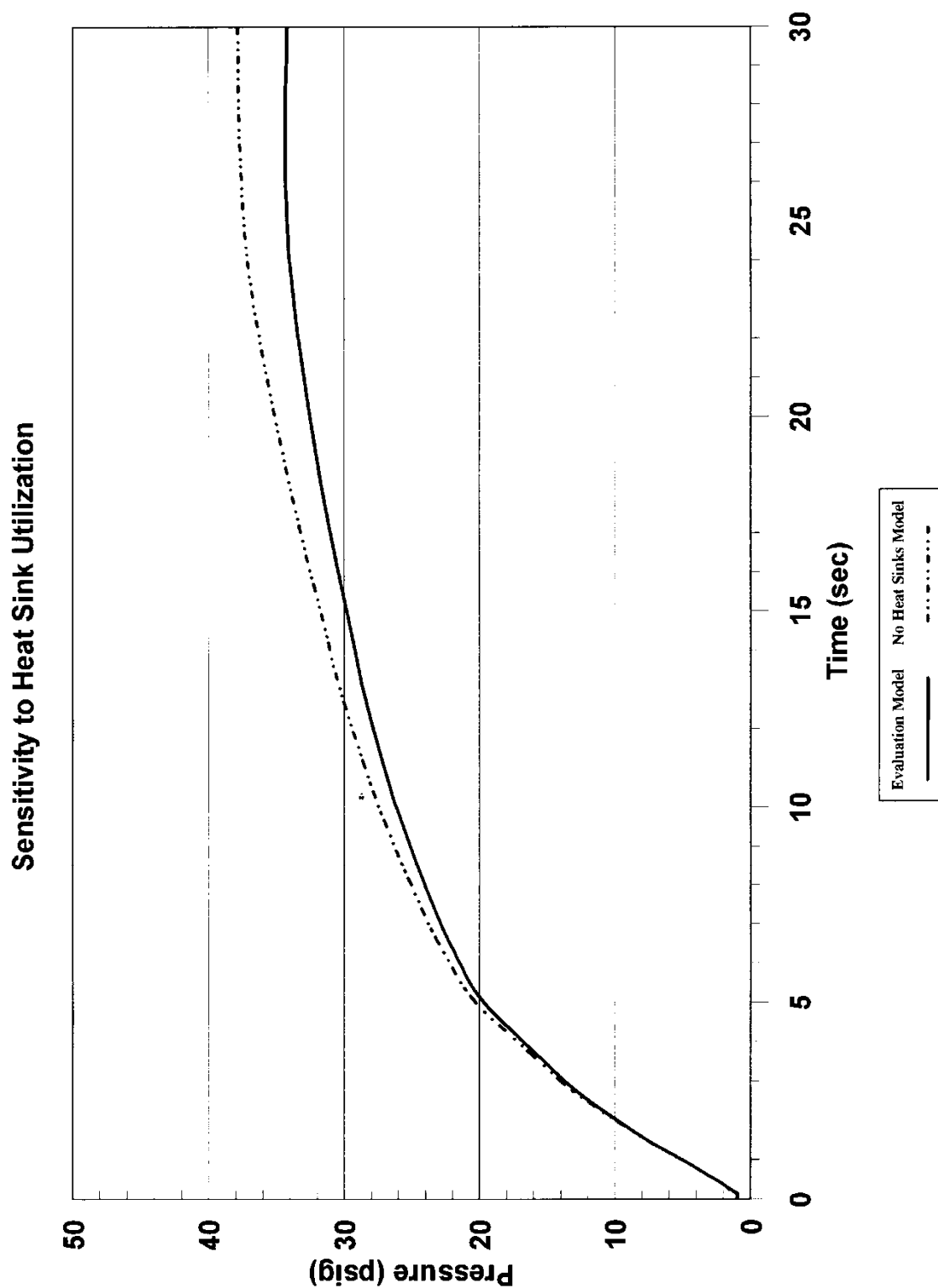


Figure 8-2. Comparison of Response with No Heat Sinks to EM Response

9 CIRCULATION AND STRATIFICATION WITHIN CONTAINMENT

Design basis accident (DBA) evaluations of AP600 and **AP1000** containment pressurization transients follow an approach that bounds uncertainties in parameters important for containment response. In this regard, the assessment of circulation and stratification examined a range of possible break elevations, orientations, and momentum to determine the worst case set of assumptions. A summary of the evaluation results and a cross reference to supporting subsections is given in Table 9-1.

The effect of break parameters on mass transfer to heat sinks, the dominant means of pressure mitigation, is evaluated. The evaluation results in both the selection of a limiting scenario for large-scale circulation, and also a conservative handling of potential effects of stratification. The objective is to perform a bounding, or worst case analysis. The effects of circulation and stratification do not lend themselves readily to quantification of a bias and distribution for uncertainty, such as would be done for a best-estimate analysis. For example, it would be very difficult to quantify the probability of a break being directed in any particular direction. Rather the simplest DBA approach is to examine the range of possible break conditions, to select a limiting scenario, and use modeling techniques to bound the potential for reduced heat sink mass transfer.

For equipment qualification (SSAR Appendix 3D.5.5.1.5), the simple bounding approach is taken which uses the maximum temperature from all control volumes inside containment at each time step. This bounds the effects of temperature distributions. For containment pressure, the evaluation in this section has been performed, summarized as follows.

The containment pressure transient is potentially affected by parameters which influence the dominant heat removal mechanism, mass transfer. Mass transfer has as its primary parameters steam concentration, and, in the case of forced convection conditions, velocity. Large-scale circulation and entrainment into jets or plumes can drive circulation and can affect local values of steam concentration and velocity near heat transfer surfaces. Jet and plume entrainment within compartments or the above-deck region can also result in stratification, or the existence of a vertical steam concentration gradient. Therefore, an assessment of the effects of circulation and stratification should focus on how the steam concentration and velocity are affected. Since the Evaluation Model assumes only free convection inside the containment, the potential benefit of forced convection, when it exists, is neglected. Therefore, the assessment can be further focused on the potential effects on steam concentration distributions.

For the main steamline break (MSLB), the containment vessel shell never becomes the dominant heat removal mechanism before break releases are over; therefore, known biases inherent in the lumped parameter Evaluation Model are used to minimize the internal heat sink effectiveness. Lumped parameter model biases, supported with LST comparisons, are used to impose a conservative break release boundary condition location in the Evaluation Model for MSLB pressure responses.

For the loss of coolant accident double-ended cold leg guillotine break (LOCA DECLG), temporal partitioning has been used to further refine the evaluation for blowdown (0-30 sec.), refill (30 to 90 sec.), peak pressure (90 to 1200 sec.), and long-term (1200 sec. and beyond). During blowdown, volume pressurization is the dominant energy absorber, so the details of mixing and stratification effects are not dominant. During the long-term, the passive containment cooling system (PCS) is the dominant heat removal mechanism, so that increasing the concentration of noncondensables in the above-deck region

would reduce the PCS heat removal capability and result in higher calculated containment pressures. The peak pressure period, where both the below-deck heat sinks and the PCS surface are significant contributors, has been assessed by examining extreme release scenarios and examining the range of conditions to select a limiting scenario for peak pressure. The evaluation includes a logical sorting and organization of extreme break scenarios that are quantified by various analytical models and selected experimental results. The analytical models include hand calculations and the use of the WGOTHIC AP600 Containment Evaluation Model for sensitivities to the range of the extreme break scenarios considered.

Entrainment into a jet or plume and large-scale, density-driven circulation between compartments can force some degree of homogenization between and within compartments. Entrainment into a jet or plume can reduce the vertical density gradient occurring due to stratification because of the induced circulation. The assessment of large-scale circulation and compartment density gradients is summarized below.

Large-scale circulation is evaluated by examining a range of extreme release scenarios, including break location, elevation, orientation, and momentum. A limiting, large-scale circulation scenario for the peak pressure period can be shown to result from the assumption of dissipation of the break momentum within the steam generator compartment, at the elevation of the primary system pipe. The scenario is limiting because other scenarios were shown to have improved heat sink utilization, and thus lower peak pressures. For example, the extreme postulated scenario of an undissipated forced jet exiting the upper steam generator compartment opening would drive significantly more convection on the steel shell (PCS) surface, and data indicates that the kinetic energy exiting the steam generator compartment would drive circulation below deck. Mass transfer would be greater than that for a buoyant plume. For a buoyant source and a break low in containment, it is reasonable to use a lumped parameter formulation to model the large-scale, or intercompartment circulation. A review of possible release locations and the expected circulation patterns led to the selection of four potentially limiting cases for further evaluation. The lumped parameter WGOTHIC AP600 Containment Evaluation Model was then used to examine those potentially limiting buoyant source release locations. Results from the sensitivity cases were consistent with the expected circulation patterns in each case, which supports the use of the WGOTHIC lumped parameter model for those sensitivities. Results also showed that the postulated scenarios examined a wide range of possible transient evolutions of steam concentrations throughout the dominant circulating compartments. An assumption of a buoyant release within the broken steam generator compartment reduced the steam access to a large fraction of heat sinks compared to the other locations for a buoyant release, which reduced below-deck heat sink effectiveness and led to the maximum calculated containment pressure.

The use of lumped parameter models can introduce a bias in heat and mass transfer calculations when details within a compartment or region may be important. The simplified momentum formulation can lead to overmixing when multiple lumped parameter nodes are used to represent a single region, such as is done for the above-deck region in the Evaluation Model. Thus, density gradients larger than those predicted by the model in the above-deck region are expected and are assessed independently from the Evaluation Model. The calculation uses a single calculational node to represent each below-deck compartment. The single node representing each compartment allows only an average value of steam concentration for that compartment. For both above- and below-deck regions, density gradients larger than those predicted by the Evaluation Model are evaluated to gain insight into the effects of extreme gradients on heat sink utilization. Showing how sensitive the heat sink utilization is to extreme gradients

provides greater confidence that the simplifications inherent in the Evaluation Model have been conservatively bounded.

Since stratification within compartments is not considered explicitly in the WGOTHIC lumped parameter model, it has been evaluated for its effect on total compartment heat sink utilization. The potential for degraded heat sink effectiveness has been examined using a simple calculation for the vertical heat sink distribution and an extreme vertical density gradient. Results show that the total heat sink effectiveness within a compartment or region is affected by the assumed vertical gradients. Evaluations also showed that mass transfer to upward facing surfaces in circulating compartments may be degraded very early in the transient, and heat sink effectiveness within dead-ended compartments may be overestimated by the lumped parameter model after blowdown. Biases have been introduced into the Evaluation Model to bound these effects.

The conclusion of the circulation and stratification assessment provides specific guidelines for the Evaluation Model to bound the effects. The guidelines are summarized in Table 9-1, noted in the conclusions in Section 9.5, and are implemented as noted in Section 4 in the Special Modeling Assumptions subsection for each compartment or region.

9.1 INTRODUCTION

The rupture of the primary system or main steamline piping has the potential to release a significant amount of mass and energy into the containment atmosphere. The passive containment is designed to withstand a loss-of-coolant accident (LOCA) or a main steamline break (MSLB) through a combination of a high containment design pressure and passive heat removal mechanisms. The passive heat removal systems include energy absorption by internal heat sinks as well as heat removal by the passive containment cooling system (PCS).

A containment analysis is performed to verify the adequacy of the containment heat removal mechanisms to maintain post-accident containment pressure below the design limit. In this regard, the WGOTHIC code (Reference 9.1) has been developed as the containment code for performing the design basis containment analysis. Appropriate Evaluation Models (Sections 4 and 13) have been created. These models consider important input parameters such as mass and energy releases, containment volume, internal heat sinks, and PCS heat removal to calculate post-LOCA and post-MSLB containment pressure and temperature response.

To obtain a conservative containment analysis, the effects of circulation and stratification must be bounded by the Evaluation Model. Circulation and stratification are natural processes that occur inside the passive containment during postulated containment pressurization transients and have been identified as important phenomena to be addressed in support of the Evaluation Model for containment pressure calculations (Reference 9.2). The circulation and stratification that occur during a high energy pipe break transient, have the potential to reduce heat and mass transfer rates by transporting and concentrating noncondensables. The degradation of heat and mass transfer may reduce the effectiveness of the heat sinks and the PCS at mitigating the peak containment pressure. The effects of circulation and stratification must be addressed to justify the approach used in the containment Evaluation Model.

This section presents an overview of the effects of circulation and stratification for the containment Evaluation Model for the LOCA and MSLB events. The evaluation results are summarized in Table 9-1. As the table shows, the LOCA and MSLB events are evaluated separately. The LOCA event is divided into four temporal phases based on heat sink utilization: the blowdown phase, the refill phase, the peak pressure phase, and the long-term phase. During each of these phases, important phenomena, such as mass and energy release rates, break source direction, and heat removal mechanisms are considered for impact on circulation and stratification. Unlike the LOCA events, the MSLB events are not divided into temporal phases. The MSLB is characterized by a single, high-intensity blowdown phase. However, different piping rupture locations are considered in the MSLB evaluation.

Table 9-1. Circulation and Stratification Evaluation Summary

Element	Summary of Evaluation	Relevant PIRT Parameter ⁽¹⁾	WCAP-14407 Section Reference
General Approach			
	Circulation and stratification evaluated because of the potential to degrade heat sink effectiveness via the condensation parameters: <ul style="list-style-type: none"> • Steam concentration • Velocity 	Circulation/stratification (2A), condensation (3F, 7C)	9.0
	High kinetic energy sources, such as during LOCA blowdown and MSLB result in forced convection component of mass transfer	Circulation (2A), condensation (3F)	9.0
	Effects of velocity eliminated in calculation by assuming only free convection internally. Focus, therefore, is on impact of circulation and stratification on steam and noncondensable distributions	Circulation/stratification (2A)	9.0
	Equipment qualification temperature is conservatively taken from the maximum temperature from all control volumes inside containment to bound the effects of temperature distributions (containment pressure is therefore, the focus of the evaluation in Section 9)	Circulation/stratification (2A)	9.0
	For the DBA LOCA, volume compliance is the primary pressure mitigator during blowdown, internal heat sinks and the containment steel shell are the primary mitigators during the peak pressure phase, and the steel shell surface is the dominant mitigator during the long-term phase	Gas compliance (2C), condensation (3F, 7C)	9.0, 9.3, 9.3.2.1, 9.3.2.4
	For the DBA MSLB, the internal heat sinks are the dominant pressure mitigators.	Condensation (3F)	9.0, 9.4.3

Table 9-1. Circulation and Stratification Evaluation Summary (cont.)

Element	Summary of Evaluation	Relevant PIRT Parameter ⁽¹⁾	WCAP-14407 Section Reference
Test Data (cont.)			
A. Method to Address Distortions in the LST for Circulation and Stratification Assessment	Power to volume ratio: using only quasi-steady-state data for circulation and stratification, therefore, no impact of this distortion on these results.	Stratification (2A), int. heat sink conduction (3D), shell conduction (7F)	9.2.3
	Power to area ratio: <ul style="list-style-type: none">• Steam flow was ranged and external boundary conditions were ranged• Considering the matrix of the LST, a range of power-to-area (or condensation rate) ratios were considered, which minimizes the degree of the distortion• Distortion addressed by considering stratification and condensation data from LST matrix tests and supplementing LST with assessment of international test data for stratification	Circulation/Stratification (2A)	9.2.3, 1.4.1
	Circulation path impact on <i>circulation</i> : cannot use the LST data for assessment of circulation. Addressed by supplementing LST with assessment of international test data for circulation	Circulation (2A), intercmprt flow (2B)	9.2.3
	Circulation path impact on <i>stratification</i> : <ul style="list-style-type: none">• Lack of LST SG compartment circulation results in LST stratification more extreme than if a circulation path existed• Addressed by supplementing LST with assessment of using international test data for stratification	Stratification (2A), intercmprt flow (2B)	9.2.3

Table 9-1. Circulation and Stratification Evaluation Summary (cont.)

Element	Summary of Evaluation	Relevant PIRT Parameter⁽¹⁾	WCAP-14407 Section Reference
Test Data (cont.)			
B. Usage of LST Data for Circulation and Stratification Assessment	LST above-deck separate effects style data for condensation and stratification is considered	Mass and energy (1A), direction and elevation (1B), momentum (1C), Circulation/stratification (2A)	9.2.1, 9.2.2
	LOCA – applicable tests had diffuser under the SG, reference case had elevated diffuser. Key LST result – above-deck stratification data used to support development of a bounding stratification gradient for evaluation of heat sink utilization for peak pressure/long-term phases	Stratification (2A)	9.2.1
	MSLB – applicable tests had elevated 3" pipe pointing vertically/horizontally. Key LST results – kinetic energy drives circulation below-deck, forced convection significantly enhances mass transfer (factor of 1 to 10 over shell surface relative to free convection mass transfer)	Circulation/stratification (2A)	9.2.2
Lumped Parameter Biases Implemented in <u>W</u>GOTHIC Evaluation Model			
A. International/ Industry Experience	Lumped-parameter modeling uses a simplified momentum formulation, which biases calculated pressure with respect to circulation and stratification. These biases are evaluated and bounded by the Evaluation Model.	Circulation/stratification (2A)	9.1.2
	NUPEC modeling experience is applied to Evaluation Model compartment flow connections, resulting in reasonably predicted circulation patterns.	Circulation (2A) Inter-compartment Flow (2B)	9.2.4, Appendix C Section 9.C.3

Table 9-1. Circulation and Stratification Evaluation Summary (cont.)

Element	Summary of Evaluation	Relevant PIRT Parameter ⁽¹⁾	WCAP-14407 Section Reference
Lumped Parameter Biases Implemented in <u>WGOTHIC</u> Evaluation Model (cont.)			
B. LOCA Biases	The effects of stratification on heat sink utilization are negligible for compartments experiencing downflow of heavier ambient atmosphere mixture	Stratification (2A)	9.3.1.1
	<ul style="list-style-type: none">Dead-ended compartments with no assumed thermal gradients stratifyCondensation and convective heat transfer turned off in dead-ended compartments after 30 seconds	Stratification (2A)	9.3.2.1
	<ul style="list-style-type: none">Effect of stratification on steel shell condensation assessed with extreme gradientStratification effect bounded by removing upward facing surface of operating deck as a heat sink	Stratification (2A)	9.3.1.1
	<ul style="list-style-type: none">Effect of stratification on heat sinks in a below-deck compartment assessed with extreme gradientCMT room (most heat sinks) evaluated for case in which LOCA plume is rising in roomStratification effect bounded by removing floor as heat sink (bias applied in all compartments regardless of assumed break location)	Stratification (2A)	9.3.1.3
C. MSLB Biases	LST data indicates: <ul style="list-style-type: none">Kinetic energy drives some circulation below-deckForced convection is driven by high kinetic energy jet above-deckNo significant stratification above-deck, therefore no bias required	Circulation/stratification (2A)	9.4.2

Table 9-1. Circulation and Stratification Evaluation Summary (cont.)

Element	Summary of Evaluation	Relevant PIRT Parameter ⁽¹⁾	WCAP-14407 Section Reference
Lumped Parameter Biases Implemented in <u>WGOTHIC</u> Evaluation Model (cont.)			
C. MSLB Biases (cont.)	<p>Lumped parameter model code biases:</p> <ul style="list-style-type: none"> • Evaluation Model places break node at operating deck level minimizing circulation and steam access to below-deck heat sinks • Momentum dissipated in each node (Evaluation Model uses only free convection) • Density-driven circulation as plume rises resulting in relatively homogeneous region above modeled break node <ul style="list-style-type: none"> – Results in steam-rich region above modeled break node and steam-deficient region below modeled break node, which bounds effects of stratification – Conservatively, the LOCA stratification biases are included for the MSLB Evaluation Model 	Circulation/stratification (2A)	9.4.2

Table 9-1. Circulation and Stratification Evaluation Summary (cont.)

Element	Summary of Evaluation	Relevant PIRT Parameter ⁽¹⁾	WCAP-14407 Section Reference
LOCA Evaluation Results			
A. Considerations by Time Phase for Evaluation Model	<p>LOCA blowdown (0 to 30 seconds):</p> <ul style="list-style-type: none"> • Blowdown pressurizes compartments and drives significant circulation above and below-deck • Lumped parameter modeling adequate for pressure-driven flow • Containment pressure insensitive to nodding (multi-node vs. one-node model) • Low sensitivity to heat sinks because volume storage is dominant pressure mitigator • Fr indicates significant forced convection on steel shell, Evaluation Model conservatively assumes only free convection • Steam driven into dead-ended compartments. Assuming thermally uniform heat sinks results in no circulation, therefore, condensation and convection heat transfer in dead-ended compartments neglected after 30 seconds. 	<p>Intercompartment Flow (2B)</p> <p>Gas compliance (2C)</p> <p>Break source momentum (1C)</p>	<p>9.3.2, 9.3.2.1, 9.2.2</p>

Table 9-1. Circulation and Stratification Evaluation Summary (cont.)

Element	Summary of Evaluation	Relevant PIRT Parameter ⁽¹⁾	WCAP-14407 Section Reference
LOCA Evaluation Results (cont.)			
A. Considerations by Time Phase for Evaluation Model (cont.)	LOCA refill (30 to 90 seconds): <ul style="list-style-type: none"> Break releases are negligible Containment depressurizes during this phase Conservatively ignore containment pressure reduction by neglecting this phase to maximize initial pressure for the peak pressure phase 	Break source mass and energy (1A)	9.3.2.2
	LOCA peak pressure (90 to 1200 seconds): <ul style="list-style-type: none"> Steam source location changes to ADS Stage 4 valves in both SG compartments at approximately 1000 seconds Condensation on steel shell becomes dominant heat removal mechanism towards end of peak pressure phase Compartment filling reduces heat transfer for affected compartments during peak pressure phase and long-term phase (compartment filling is modeled by code) 	Break source (1B, 1C)	9.3.2.3

Table 9-1. Circulation and Stratification Evaluation Summary (cont.)

Element	Summary of Evaluation	Relevant PIRT Parameter ⁽¹⁾	WCAP-14407 Section Reference
LOCA Evaluation Results (cont.)			
A. Considerations by Time Phase for Evaluation Model (cont.)	LOCA long-term (1200 seconds to 24 hours): <ul style="list-style-type: none"> Condensation on steel shell remains dominant heat removal mechanism WGOTHIC predicted steam gradient becomes essentially homogeneous in less than 24 hours, excluding the SG compartments (due to ADS Stage 4 valves releasing steam) Evaluation using extreme stratification gradient shows nearly negligible increase in heat removal by the steel shell relative to homogeneous steam concentration case – bounded by removing the non-grating operating deck floors Evaluation using extreme stratification gradient shows a decrease in heat removal by the below-deck compartment heat sinks relative to the homogeneous steam concentration case – bounded by removing the compartment floor. 	Condensation (7C) Break pool filling (5F) Stratification (2A)	9.3.2.4
			9.3.1.3

Table 9-1. Circulation and Stratification Evaluation Summary (cont.)

Element	Summary of Evaluation	Relevant PIRT Parameter ⁽¹⁾	WCAP-14407 Section Reference
LOCA Evaluation Results (cont.)			
B. Range of Break Scenarios and Effects	Jet dissipated in SG East compartment <ul style="list-style-type: none"> Limiting scenario Post-blowdown flow into CMT room is downward with steam/air mixture 	Break source (1B, 1C)	9.3.1.1, 9.3.2.5
	Undissipated jet in SG East compartment <ul style="list-style-type: none"> Forced convection above-deck improves condensation on containment shell Significant kinetic energy-driven circulation below-deck Minimal stratification in above-deck region 	Break source (1B, 1C)	9.3.1.2
	Jet to RCDT cavity – dissipated plume rises in CMT North room <ul style="list-style-type: none"> Good steam access to below-deck room with most internal heat sinks 	Break source (1B, 1C)	9.3.1.3
	Jet to RCDT cavity – dissipated plume rises in SG West compartment <ul style="list-style-type: none"> Same scenario as dissipated jet rising in SG East compartment 	Break source (1B, 1C)	9.3.1.3
	Jet dissipates in RCDT cavity <ul style="list-style-type: none"> Flow split based on flow area and loss coefficients Better steam access to CMT room and SG West compartment compared to break in SG East compartment 	Break source (1B, 1C)	9.3.1.3

Table 9-1. Circulation and Stratification Evaluation Summary (cont.)

Element	Summary of Evaluation	Relevant PIRT Parameter ⁽¹⁾	WCAP-14407 Section Reference
LOCA Evaluation Results (cont.)			
C. Sensitivity Cases Run with the Evaluation Model	Break locations (all located low in containment): <ul style="list-style-type: none"> • Jet undissipated in SG East compartment – forced convection benefit on steel shell assessed to estimate effect of undissipated jet • Jet dissipated in SG East compartment – limiting case for maximum containment pressure • Jet into RCDT cavity - plume rises in CMT North room • Jet dissipated in RCDT cavity – plume rise determined by flow path resistances 	Intercompartment Flow (2B)	9.3.2.5
	Loss coefficients: <ul style="list-style-type: none"> • Loss coefficients for several flow paths changed to modify blowdown-predicted flow direction • Modeled dissipated jet in SG East compartment • End of blowdown conditions changed with negligible change to maximum containment pressure 	Intercompartment Flow (2B)	9.3.2.1

Table 9-1. Circulation and Stratification Evaluation Summary (cont.)

[illegible]

Table 9-1. Circulation and Stratification Evaluation Summary (cont.)

Element	Summary of Evaluation	Relevant PIRT Parameter ⁽¹⁾	WCAP-14407 Section Reference
LOCA Evaluation Results (cont.)			
D. Conclusions	<ul style="list-style-type: none"> Evaluation Model with dissipated break in SG East compartment is the limiting scenario <ul style="list-style-type: none"> Calculated containment pressure is not very sensitive to break location due to heat sink utilization prior to maximum pressure Biases included in Evaluation Model to bound effects of stratification 		9.2.3.5, 9.5
MSLB Evaluation Results			
A. Break Location Scenarios and Effects	<ul style="list-style-type: none"> Selected based on routing of steamline pipe MSLB above-deck <ul style="list-style-type: none"> High kinetic energy release with relatively short duration, which drives circulation below the source High Fr number (comparison provided to LST Fr number) LST data indicates forced convection enhancement to mass transfer (only free convection modeled) Break in MSLB Evaluation Model located in node just above-deck, which limits steam access to below-deck heat sinks 	Stratification (2A) Intercompartment Flow 2B) Break source (1B, 1C)	9.4, 9.4.1, 9.4.1.1, 9.4.2

Table 9-1. Circulation and Stratification Evaluation Summary (cont.)

Element	Summary of Evaluation	Relevant PIRT Parameter ⁽¹⁾	WCAP-14407 Section Reference
MSLB Evaluation Results (cont.)			
A. Break Location Scenarios and Effects (cont.)	<ul style="list-style-type: none"> MSLB in CMT North room <ul style="list-style-type: none"> Break in CMT room would significantly dissipate due to equipment in room and rise as a plume CMT room contains most of the internal heat sinks Good steam access to CMT room heat sinks, therefore case is expected to be less limiting 		9.4.1.2
B. Sensitivity Cases	<ul style="list-style-type: none"> MSLB located just above deck MSLB in CMT North room 		9.4.3
C. Conclusions	<ul style="list-style-type: none"> MSLB in CMT North room calculated containment pressure significantly less limiting MSLB located just above-deck used for the MSLB Evaluation Model 		9.4.3, 9.5

Note:

- PIRT parameters are identified in Reference 9.2, Table 4-1

9.1.1 Definitions

Several terms used to discuss circulation and stratification are defined, as they relate to containment analysis.

Stratification is a state characterized by strata, or horizontal layers, of different density. Stratification is stable when the lower layers are increasingly dense due to composition and/or temperature. The term stratification does not indicate the magnitude of the density gradient.

Mixing is a collective term for convective transport processes that reduce temperature and/or concentration differences within a volume or between volumes. Convective transport processes in containment include jets, plumes, wall layers, turbulent diffusion, and entrained flow. Molecular diffusion also contributes to mixing but is considerably less effective than convection, except in boundary layers. Diffusion also contributes to mixing in stratified conditions.

Circulation is a term used to describe gross, overall convective flow patterns that occur on a compartment scale and on a large scale (or containment scale). The compartment-scale circulation is due to wall layers, jets, plumes, and entrained flow. The large-scale circulation is due to interactions between compartments induced by pressure, density, elevation, and momentum differences such as intercompartment flow. The break source jet or plume can induce both compartment-scale and large-scale circulation.

Segregation is a state characterized by a different air/steam concentration in one compartment than in another. For example, the heavier air may reach different concentrations in separate compartments, especially the dead-ended compartments if the intercompartment circulation is low.

9.1.2 Lumped Parameter Biases and Capabilities

Lumped parameter biases and capabilities have been identified based on industry experience, as documented in the literature (Appendix 9.C, Section 9.C.3.4). The documented experience base includes facilities at different geometric scales, from that of the LST to nearly full-scale AP600 height (Appendix 9.C, Figure 9.C-24). The lumped parameter biases and capabilities, summarized below, have been reported consistently across the range of facilities, indicating that the biases and capabilities are applicable to the Containment Evaluation Model. The consistency across scales also indicates that the LST facility is a reasonable basis on which to study the biases and capabilities as they apply to AP600, reported in WCAP-14382 (Reference 9.1). The following provides a summary of the method used in the development of the Containment Evaluation Model to address each documented bias and capability.

1. Single node models were not capable of modeling stratification, or the passing of a stratification front through horizontal vents.

[

] ^{a,c}

2. Sump liquid level and sump temperature were not well predicted

[

] ^{a,c}

3. Some codes produced results which were not correct due to missing or oversimplifying buoyancy terms

[

] ^{a,c}

4. To account for recirculation flows, the applied lumped parameter model used double junctions in the horizontal direction. (This did not help in the case of an elevated release and resulting stratified containment.)

See discussion for item 3 above regarding the impact of lumped volume static pressure profile on the use of double junctions in the Evaluation Model. All of the LOCA cases have releases in the lower compartments (below the operating deck). This break location results in good circulation throughout containment. The main steamline break releases contain high kinetic energy. Therefore, the break node used in the lumped parameter model is a node that minimizes kinetic energy driven circulation to below-deck heat sinks, thus overestimating calculated containment pressure.

5. For releases low in containment, typical for the LOCA DECLG, the lumped parameter model well-predicted pressure, temperature, and helium concentrations inside the compartments, which were affected by the global circulation loop, while predictions needed improvements to account for postulated circulation effects inside dead-ended compartments

[

] ^{a,c}

6. Scenarios with homogeneous containment atmosphere (like HDR E11.4 and E11.5) can be simulated successfully with lumped parameter models. (Such conditions typically result from breaks located within the bottom 20 percent of the containment height.)

See discussion for item 5 regarding the use of lumped parameter models for bounding design basis analyses.

7. Circulation effects due to sump boiling (releases generated at the bottom of containment) were well-simulated.

Sump boiling is not a consideration for containment DBA, since long-term primary system energy rejection is through the ADS Stage 4 valves and the sump is therefore a relatively insignificant heat source.

8. The order of magnitude of computed velocities matches data and it can be concluded that trends in the direction of the flow are predicted well; however, predicted velocities differ by as much as a factor of two.

Calculated velocities using lumped parameter codes are strongly dependent on the noding used. Experience with validating the WGOTHIC lumped parameter model of the LST (Reference 9.1, Section 8.2) shows that the noding used can result in calculated velocities that differ from measured by an order of magnitude, showing that the particular test facility and noding used can have a strong influence on calculated velocities. Therefore, a bounding approach is used in the WGOTHIC Evaluation Model, as follows. The effects of predicted velocities in the containment pressure transient are eliminated by considering only free convection heat and mass transfer in the containment. This conservatively biases the Evaluation Model when forced convection would occur during the LOCA blowdown and the MSLB transients.

9. The lumped parameter method does not have the capability to predict the hydrogen distribution in a stratified containment atmosphere, as in HDR E11.2 with high-positioned release. In a break scenario with buoyant plume (released at about 50 percent of containment height), the steam and gas transport to the lower parts of the containment were over-predicted. (Artificial limitation of convective flows by decreasing flow areas improved predicted concentrations in the lower regions, but overestimated the containment pressure in upper compartments.)

Hydrogen distribution predictions are not a consideration for containment DBA (Reference 9.2, Section 4.4.2E).

9.2 LARGE-SCALE TEST RESULTS

In the passive containment design, interest is focused on how much the jet kinetic energy affects gradients inside containment. If the jet kinetic energy is sufficient to disrupt stable stratification, it may also be sufficiently energetic to virtually eliminate vertical gradients in the upper containment volume and to induce circulation between the above-deck and below-deck regions. The Westinghouse Large-Scale Test (LST) data was used to understand the effect of jet kinetic energy on stratification gradients above the operating deck.

The Westinghouse large-scale PCS test facility was built to provide integral test data for a geometrically similar model of the AP600 containment vessel and PCS. The tests provide experimental data that can be used for evaluating the physics in containment, determining the relative importance of various parameters that affect heat and mass transfer, and validating computer codes. Three series of tests (References 9.5 and 9.6) were run at the Westinghouse large-scale PCS test facility. The steady-state pressure, annulus air flow rate, water coverage, steam flow rate, injection velocity, location and orientation, and noncondensable gas concentration were varied between the tests.

It is desirable to use a Froude number formulation that relates momentum phenomena in both the AP600 and the LST to permit scaled inferences between the tests and the AP600. A volumetric Froude number can be defined as the square of the jet Reynolds number, divided by the containment Grashof number:

$$Fr_v = \frac{\rho_a * U_o^2 * d_o^2}{g * (\rho_a - \rho_o) * H^3}$$

where,

ρ_a	=	density of ambient containment
U_o	=	velocity of jet at source
d_o	=	hydraulic diameter of jet at source
g	=	gravitational acceleration
ρ_o	=	density of jet source
H	=	height of volume above steam source

The following sections first describe test configurations as they represent LOCA and MSLB configurations and then provide data that can be used to examine gradients in the above-deck region.

9.2.1 LOCA Configuration

Twenty-five LSTs were conducted in the LOCA configuration with the diffuser located under the steam generator model. A diffuser was used to provide a uniform velocity profile. The tests do not apply to the LOCA blowdown phase, but they do apply to the peak pressure and long-term phases. The volumetric Froude numbers ranged from approximately 5×10^{-6} to 5×10^{-3} . Steam concentrations just above the deck and below the deck near the bottom of the vessel are presented in Figure 9-1, which can be used to see test to-test variation in above-deck gradients. The plotted values are the ratios of the measured local steam partial pressure to the partial pressure of steam assuming perfect mixing. A value of 1.0 indicates perfect mixing. The values show the above-deck ratios generally range from 0.6 to 1.0 and below-deck values

range from 0.1 to 0.4. The below-deck values are an indication of the distortion in the LST due to lack of a simulated steam generator compartment flow path. The distortion leads to an air-rich mixture in the LST below-deck.

Stratification data for LSTs with the diffuser under the simulated steam generator compartment are shown in Figure 9-2 through Figure 9-25. Tests have been grouped by steam flow and plotted so that the temperature axis spans the same range for all the tests to simplify test-to-test comparison. For each group of tests, three plots are shown. First is the azimuthally-averaged temperature data from thermocouples located one inch inside the vessel shell, called the “fluid thermocouples.” Data is available from nine elevations above the operating deck; fluid thermocouple data was not taken below the deck. Second is a plot of the saturation temperature obtained based on the third plot of measured steam mole fractions, or pressure ratio (p_{stm}/P_{vessel}).

Also, a reference test to examine the physics of stratification (test 222.2), with an elevated diffuser, is included as Figure 9-26 through Figure 9-28. These test data are reviewed in Section 9.2.3 to develop insight into an appropriate bounding stratification gradient.

9.2.2 MSLB Configuration

Phase 3 of the LST program included a series of tests designed to simulate a main steamline pipe rupture. LST data from baseline and Phase 2 tests suggested that noncondensable concentrations increase dramatically below the elevation of steam injection with considerable steam mixing above the operating deck. One could postulate that the effect of the higher steamline elevation could be to create a larger volume of rich air mixture which extends above the operating deck, and reduces the active heat transfer area. Test series 222 addressed the impact of the elevation and direction of the steamline break on the response of the test vessel and included a high flow transient to a steady-state condition. The kinetic energy available in an MSLB is seen to be an important parameter.

The four configurations in this test series were:

- 222.1 Low velocity steam flow from under the operating deck
- 222.2 Low velocity steam flow above the operating deck (a reference condition to examine the physics, not a realistic AP600 configuration)
- 222.3 High velocity steam flow with horizontal discharge above the operating deck
- 222.4 High velocity steam flow above the operating deck directed upward

Stratification data for LSTs with high kinetic energy above the operating deck are shown in Figure 9-29 through Figure 9-34 also grouped by steam flow, and showing measured internal fluid temperature, saturation temperature, and measured steam pressure ratio, as described in Section 9.2.1 for the LOCA configuration. These data are referenced in the development of a bounding MSLB Evaluation Model (Section 9.4.2).

To understand the effects of kinetic energy on circulation and stratification, it is useful to note the stratification pattern observed for a test with a buoyant source (low Froude number) versus a test with a high Froude number. For example, test 222.4 can be used to assess the effects of steam releases with Froude numbers representative of an MSLB occurring above the steam generator. Test 222.4 is compared to test 222.2, which had a similar setup, but a diffuser was used to provide a low velocity elevated steam source.

The elevated buoyant source in test 222.2 produced a significantly stratified vessel, with very little steam penetration below the elevation of the break. In contrast, the high kinetic energy-elevated source of test 222.4 induced a substantial amount of circulation in the test vessel, including substantial steam ingress into the below-deck regions. The decrease in the steam concentration stratification for test 222.4 compared to test 222.2 is due to the high kinetic energy of the injected fluid because that is the only significant difference between the two tests.

Mass transfer data from LSTs with high velocity jets (forced convection) has been compared to that from the low velocity diffuser under the simulated steam generator (dominated by free convection) in Reference 9.9, Figure 3.9-5. The referenced figure includes shell condensation data above the operating deck for the elevated high momentum source LST compared to the mean of such data from the diffuser under the steam generator. The elevated diffuser LST is not included in the referenced figure due to its atypical condition of a low Froude number elevated source - the elevated releases which may be postulated for an MSLB are of a higher Froude number similar to that of the tests for which data are plotted, as described earlier in this section. Results indicate that in the LST forced convection effects enhanced the mass transfer rate by a factor of 1 to a factor of 10 in the direction the jet is directed.

9.2.3 Method to Address Distortions in LST Stratification Data

Internal momentum effects were distorted in the LST due to the lack of a simulated flow path for entrainment near the bottom of the steam generator compartment. Thus in the LOCA DECLG configuration, the LST effectively stratified into two regions – separated at the elevation of the steam generator compartment exit (Section 9.2.1). Therefore, the LST cannot be used to examine intercompartment circulation.

There is also a system level distortion in the LST with respect to power-to-volume and power-to-area (Reference 9.7, Section 11). Since only quasi-steady state data for circulation and stratification were used, there is no impact of power-to-volume distortion on this evaluation. The LST quasi-steady data was taken with a range of break flow rates, and the external wall boundary condition was ranged using controllable variables (turning external water and fan on and off). The internal release configuration also allowed varying the release elevation, momentum, and direction. Initial noncondensable content ranged from near vacuum to two atmospheres. Thus the LST provides a valuable database to examine the physics of potential stratification mechanisms that may be postulated to occur in a passive containment.

Because of the momentum-related distortions in the LST, available international test data has been reviewed (Appendix 9.C, Section 9.C.2) to supplement the database for examining stratification effects. The supplementing of LST data with additional tests at various scales, combined with the use of LST matrix tests, sufficiently addresses the system level power-to-area distortion. The following summarizes conclusions that may be drawn from LST and the international databases, leading to the selection of an extreme stratification gradient to be considered in thermal calculations of Appendix 9.B.

It is desired to gain insight into vertical steam concentration gradients that may occur within the region above the operating deck and within compartments below-deck during a LOCA. (The bounding approach for an MSLB is given in Section 9.4.2.) The region above the operating deck in the LST can be considered to be an enclosure with a plume and wall boundary layers (Appendix 9.C, Section 9.C.1.4.1). The relevant vertical profile data is presented in Figure 9-2 through Figure 9-25. Comparisons of internal fluid thermocouple data (1-inch inside the vessel wall) and steam concentration measurements show that the gas is within a few degrees of saturation, so that the vertical temperature profiles provide a good measure of the vertical steam concentration gradient during the LSTs. Clearly, for the diffuser under the steam generator model, there is only about a 3 to 12°F temperature gradient from the steam generator exit elevation to the dome. The plotted data is at the fluid thermocouple location. A review of the internal rake temperature data shows that the bulk fluid vertical temperature difference is equal to or several degrees less than that given by the fluid thermocouples.

Comparison of the vertical temperature profile from the elevated diffuser case in the LST (Figure 9-26) shows that the stratification in the above-deck region is more pronounced than that in any of the tests with the LOCA configuration. Such stratification from an elevated diffuser is similar to that observed in the CVTR tests (Appendix 9.C, Section 9.C.2.3) which had a similarly elevated, low momentum source. Tests in the much larger HDR and NUPEC facilities indicate that stratification gradients from diffuse releases low in containment in fact produce temperature gradients above the operating deck similar in magnitude to those quoted above in the LST with a low diffuser. However, because of the distortions in LST mentioned above and uncertainties in transferring stratification data from HDR and NUPEC to AP600 and **AP1000**, an extreme stratification gradient, well beyond that which would occur in a containment with natural convection and a low elevation release, has been considered for thermal calculations.

The steam concentrations used for thermal calculations presented in Appendix 9.B assume a three region distribution — nearly pure steam at the top (steam fraction 0.98), the average value at the middle (steam fraction 0.63), and the balance of the air content at the bottom (steam fraction 0.28). The elevated diffuser case in the LST shows a steam pressure ratio (equal to steam mole fraction) of 0.10 near the operating deck and 0.90 under the dome. The distribution chosen is consistent with that indicated by the LST elevated diffuser, considering that the Appendix 9.B calculation represents an average steam concentration calculated for AP600 transient conditions. It should be noted that the LST elevated diffuser test produces an extreme, or bounding, test configuration for the real situation of a buoyant plume released low in containment, such as for the LOCA DECLG post-blowdown. Thermal calculations in Appendix 9.B are used to develop appropriate biases to bound the effects of stratification within the AP600 and **AP1000** lumped parameter compartment nodes and the above-deck region.

9.2.4 Application of Modeling Methods Developed for NUPEC M-4-3 Lumped Parameter Model

The following is a brief summary of the experience gained in developing the WGOTHIC lumped parameter model of the NUPEC natural circulation test, M-4-3, and application of the experience to development of the WGOTHIC lumped parameter Evaluation Model. Justification is provided for using the lumped parameter Evaluation Model for performing sensitivity studies. The sensitivities are used to examine the effects of circulation in containment from a LOCA DECLG.

NUPEC Lumped Parameter Modeling Experience

Actual circulation was interpreted based on data provided by NUPEC for the detailed time history for gas temperature and hydrogen concentration as well as a video of processed data to aid visualization.

As shown in Figure 9.C-55 (flow pattern) and Figure 9.C-61 (data for one circulation loop) of Appendix 9.C, the break flow rose from the affected steam generator loop, spread through the upper portion of the large vertical opening into the adjacent steam generator loop, and rose from those two compartments into the dome. The large-scale natural convection loop continued with continuity driving circulation down through the opposite steam generator compartments and other openings through the operating deck, and then down to the level of the break release. From the break release level, the convection loop was closed by entrainment into the rising plume. This result is consistent with results of international tests at several scales and is rather simple and straightforward. However, careful development of the lumped parameter noding structure is necessary to allow the code to predict the observed qualitative behavior, as follows.

It should first be noted that for the M-4-3 calculations, best estimate condensation correlations were used to better isolate the biases of lumped parameter noding on predicted parameter distributions and the effect of those biases on containment pressure.

For general application of WGOTHIC lumped parameter, it is necessary that the vertical noding be defined by a set of horizontal planes that cut through the entire modeled region, as described in Reference 9.4, Section 16.12.1. This is done to prevent artificial flows driven solely by the method used to estimate a static pressure profile using the single value of density available within a lumped parameter cell. The successful elimination of such artificial circulation is confirmed when a new model is developed by running a null problem (uniform temperatures in heat sinks and volumes, and no heat or mass source) and verifying that there is no predicted circulation.

[

] ^{a,c}

Application of NUPEC Test Experience to Containment Evaluation Model

The Evaluation Model has been verified to have no significant artificial flows in a null problem. In the further development of the WGOTHIC lumped parameter nodding used in the containment pressure Evaluation Model, experience with the NUPEC tests was used qualitatively in representing the CMT compartment.

[

] ^{a,c}

Table 9-2. AP600 Flow Areas Connecting to North and South CMT Compartments (excluding Dead-Ended Compartment Connections)

[illegible]

[

] ^{a.c}

9.3 CIRCULATION AND STRATIFICATION ASSESSMENT FOR THE LOSS-OF-COOLANT ACCIDENT

The rupture of primary system piping can lead to a significant release of mass and energy into the containment. A containment analysis is performed to verify the ability of the passive containment systems to mitigate the consequences of a hypothetical LOCA. The WGOTHIC code, in conjunction with the Containment Evaluation Model, is used for the containment analysis. The effects of circulation and stratification must be bounded by the containment analysis calculations to ensure a conservative containment analysis. For purposes of evaluating the effects of circulation and stratification on the LOCA containment analysis, the LOCA event is divided into four temporal phases: the blowdown phase, the refill phase, the peak pressure phase, and the long-term phase, based on Section 3.4.2.2 of Reference 9.2.

The blowdown phase is the period immediately following the rupture of the primary system piping: For the design basis event, a double-ended, cold leg guillotine (DECLG) break is assumed, which results in the complete severance of the pipe. This phase is characterized by a rapid depressurization of the reactor coolant system (RCS), as the RCS inventory is expelled into the containment volume. The containment gas volume rapidly pressurizes due to the tremendous release of mass and energy. This phase is short in duration (about 30 seconds) and ends when the RCS pressure has equilibrated with containment.

The refill phase immediately follows blowdown. After blowdown, the accumulators refill the lower plenum of the reactor with a high flow rate of cold water. The resulting steam and water flow rates from the break are very low and increase with time. The mass and energy release rates are two orders of magnitude less than the blowdown rates, and can be approximated as 0 from approximately 30 to 90 seconds into the event. With a negligible steam source rate and a high condensation rate, the containment pressure drops by a few psi from its peak at the end of blowdown to the end of the refill phase at approximately 90 seconds. (It should be noted that the Evaluation Model used for sensitivity studies conservatively neglects the refill period.)

The phase following refill is the peak pressure phase. During the beginning of the peak pressure phase, a continuing pressurization of the containment building accompanies the release of mass and energy. Containment pressurization is mitigated by the containment volume and the presence of the substantial number of heat sinks inside containment. Hot steam condenses on the cold steel and concrete surfaces, which transfers energy into the heat sinks. As this phase continues, the temperature of the internal heat sinks increases and their effectiveness is reduced. By this time, however, water flow onto the containment shell has initiated. The PCS provides the path to the ultimate heat sink, and represents the only assumed path through which energy can be removed from inside the containment building. A key feature of the peak pressure phase is the second, more limiting, pressure peak. The combination of internal heat sinks and the PCS act to limit the containment pressurization, and containment pressure begins to drop. Later in this phase, the PCS becomes clearly dominant. The peak pressure phase extends from 90 seconds to about 1500 seconds when the containment pressure reaches its peak. During this phase, ADS Stage 4 actuates and becomes the source of mass and energy release.

The long-term phase is the period after the peak pressure occurs out to twenty-four hours and beyond. During the long-term phase, core decay heat continues to create steam, which exits the fourth stage automatic depressurization system (ADS) as a buoyant plume. The containment continues to depressurize

as a result of energy removed by the PCS. As containment pressure drops, internal heat sinks may begin to reject some of their heat back into the containment atmosphere. Thus the long-term phase depressurization is governed by PCS heat removal.

To facilitate an understanding of the relative positions of the various compartments, a simplified AP600 compartment diagram is provided in Figure 9-36. Figure 9-36 shows the relative location of various important compartments, such as the steam generator compartment, the core makeup tank (CMT) compartment, and the above-deck volume. Noding used to represent these compartments within the Evaluation Model is described in Section 4. The compartment features are discussed in Section 4 and summarized in Table 3-1 of Reference 9.2.

Figure 9-35 presents a diagram of the CMT compartment. The CMT room contains most of the below-deck containment heat sinks (approximately 52 percent of below-deck heat sinks by area). Although 48 percent of the heat sinks are not in the CMT room, no other single below-deck compartment contains as many heat sinks. Also, the CMT room is the largest (volume) of the below deck compartments and contains many flow paths. These flow paths mean that the CMT room is of significant importance with respect to both above- and below-deck circulation patterns. Therefore, the effect of circulation and stratification on heat sink utilization in the CMT room plays an important part in the transient pressure mitigation.

9.3.1 LOCA Break Scenarios

The DECLG rupture is the design basis LOCA event for the AP600 and AP1000. The circulation and stratification patterns associated with this break will depend on the direction of the break jet momentum. Although leak-before-break has been implemented, the conservative design basis analysis evaluation assumes the broken pipe can be pointed in any direction from its nominal position. Three scenarios may be postulated: the jet momentum is locally dissipated in the steam generator compartment, the jet exits undissipated up through the steam generator compartment, or the jet momentum is dissipated in the reactor coolant drain tank (RDCT) cavity (stairwell).

9.3.1.1 Jet Momentum Locally Dissipated in Steam Generator Compartment

During the blowdown phase, a tremendous amount of mass is released as shown in Figures 4-96 and 4-98 of Section 4.5.2 for AP600. For the case where the jet momentum is locally dissipated, the source flow rate is so high that it increases the local pressure by several psi. This results in a high-pressure source in the break compartment, with the fluid flow distribution governed by the relative resistances through flowpaths. This forces the source mixture through the RDCT cavity, CMT room, the steam generator compartments, and into the above-deck volume. Pressurization will also drive steam into dead-ended compartments during blowdown (See subsection 9.3.2.1). As the event progresses into the peak pressure phase, the source flow rate drops by two orders of magnitude. The jet momentum locally dissipates. This brings the source flow velocity to near zero, including a local pressure increase that is the same order of magnitude as the buoyant forces. The pressure source may be opposed or aided by buoyancy in other flow paths. The resulting flow pattern is the solution to the flow in a network with buoyancy and heat/mass transfer in the network branches. Superimposed on the large-scale flow, the mixture within a given compartment is most likely stratified (Reference 9-8).

Within compartments, the gas may stratify with air concentrating in lower regions and steam concentrating in upper regions, resulting in a vertical steam concentration gradient. If the circulation is sufficient to entrain significant bulk mixture, the gradient may be expected to be small.

Entrainment-driven circulation rates in the CMT room are shown, for example, in Section 9.3.1.3.

Significant circulation occurs over the height of the CMT room.

Stratification is expected in the containment based on LST data. Low Froude numbers during the long-term indicate a low kinetic energy buoyant plume source. This type of plume is not sufficiently energetic to disrupt stratification. The physics of buoyant plumes and wall layers leads to the existence of recirculating stratification (Appendix 9.C, Section 9.C.1.4.1) in the above-deck region. Plumes rise from the release point and entrain significant volume of mixture as they rise. The heavier bulk air/steam mixture is drawn through the top of the CMT and other deck openings and through compartments to be entrained into the rising plume. Stratification is assumed to have a negligible impact on heat removal in compartments which experience the already air-rich downflow. A very conservative assessment of the effects of stratification on heat removal through the steel shell by the PCS has been performed (Appendix 9.B). An extreme stratification gradient is assumed, to bound the potential for distortions in test data (9.2.3). The homogeneous case total heat sink utilization results are nearly equal to those for the stratified case, with the homogeneous case giving less than 0.5 percent less instantaneous heat removal rates. A simple bias of removing operating deck floors is included in the Evaluation Model to bound this effect.

The containment pressure was calculated for this case using the WGOTHIC AP600 Evaluation Model, (Section 4). It was assumed that the jet was dissipated in the East steam generator compartment, so no specific break orientation was modeled. The break was located in Volume []^{a,c} at elevation []^{a,c}. The results are discussed in Section 9.3.2.5.

9.3.1.2 Jet Directed Up With No Dissipation

A jet directed upward, that passes through the steam generator compartment undissipated, is considered unlikely. Releases are initially from the break and, later in the transient, releases exit from the fourth stage ADS and the break pipe is covered with liquid. The containment design calls for a steel plate to cover half the flow area in the steam generator compartment above the cold leg pipe and ADS Stage 4 valves. This plate and other structures in the steam generator compartment such as gratings, supports, and the steam generator itself make it doubtful that the break jet could pass through the steam generator compartment unobstructed. Despite the improbability of this scenario, it will be considered as an extreme case to support the selection of a limiting scenario for circulation and stratification.

For the case in which a jet is postulated to pass undissipated up through the steam generator compartment, there is no entrainment into the Steam Generator compartment due to chimney or momentum effects because these effects would act to dissipate the jet. An undissipated jet would enter the above-deck region at the top of the Steam Generator compartment with approximately the same diameter as the broken cold leg pipe. This scenario is similar to two of the LST MSLB configuration tests 222.3 and 222.4. To assess the effects relative to the mass transfer in the above-deck region, volumetric Froude numbers (Fr_v) for the undissipated jet are determined and compared to the LST. An examination of the magnitude of AP600 pressure improvements is provided with sensitivities, relative to condensation results discussed in Reference 9.9, Section 3.9.

For a LOCA DECLG, a postulated undissipated jet will have the same mass flow rate as the design basis LOCA DECLG exiting the top of the steam generator compartment. The two cases differ in the flow area and exit velocity. For the design basis case, the flow area is the area at the top of the Steam Generator compartment. For the undissipated jet, the flow area is the area of the cold leg pipe. For a constant mass flow rate, the product of the flow area times the exit velocity will be equal for the two cases ($U_{DECL} \times A_{DECL} = U_{UNDIS} \times A_{UNDIS}$, where U is the velocity, A is the area, subscript $DECL$ designates the design basis case, and subscript $UNDIS$ designates the undissipated jet case). Fr_v defined in Section 9.2 is proportional to $U^2 d^2$, and is therefore proportional to $U^2 A^2$. For the two cases, the other terms in the Fr_v equation will be the same and $Fr_{v-UNDIS}$ can be expressed in terms of Fr_{v-DECL} , using $U_{DECL} \times A_{DECL} = U_{UNDIS} \times A_{UNDIS}$. The relationship is $Fr_{v-UNDIS} = Fr_{v-DECL} (A_{DECL} / A_{UNDIS})^2$. The area of the top of the Steam Generator compartment is approximately $[]^{a,c}$, and the area of the cold leg pipe is approximately $[]^{a,c}$. This results in $Fr_{v-UNDIS} \approx Fr_{v-DECL} \times []^{a,c}$.

Reference 9.7, Section 6.5.2 presents Fr_v as a function of time for the design basis LOCA in Figure 6-2. At 24 hours Fr_v is approximately $3E-06$ (the minimum value during the transient excluding the refill phase). For an undissipated jet, Fr_v is estimated to be $3E-06 \times []^{a,c}$ which equals $[]^{a,c}$. This value is at the lower end of the LST Fr range in the MSLB configuration as shown in Reference 9.7, Figure 6-3. For such high values of Fr , data from the LST in the MSLB configuration (Section 9.2.2) shows that there is minimal deviation from a homogeneous steam concentration in the above-deck region. For the MSLB, Reference 9.9, Figure 3.9-5 shows that use of the Evaluation Model free convection correlation underpredicts condensation on shell surfaces by a factor of $[]^{a,c}$ for the LST. A multiplier of $[]^{a,c}$ is a reasonable factor to assess based on the data. To address postulated uncertainty in scaling the LST condensation results to AP600, a range of potential forced convection benefits in AP600 shell heat transfer are considered by examining the sensitivity of predicted containment pressure to condensation multipliers in the Evaluation Model. A sensitivity study examined the effects on containment pressure of using condensation multipliers of $[]^{a,c}$. These sensitivity cases show that taking credit for improved condensation provides a significant benefit in the calculated containment pressure. The results are discussed in Section 9.3.2.5.

9.3.1.3 Jet into RCDT Cavity (Stairwell)

During the blowdown phase, a jet into the RCDT cavity will create a pressure source in the RCDT cavity compartment. As with the jet dissipation in the East steam generator compartment, the high-pressure source will force fluid through all available openings. The source mixture will flow into the above-deck volume through both the CMT room and steam generator compartments. Following the blowdown phase, the source will rise from the RCDT cavity as a buoyant plume and split, based upon flow areas and resistances, with part of the flow rising through the West steam generator compartment and the remaining fluid flowing through the CMT compartment.

The post-blowdown flow split between the West steam generator and the CMT compartment will depend on flow areas and loss coefficients associated with both flow paths. A range of flow splits can be postulated varying from all the fluid rising through the steam generator compartments to all of the fluid rising through the CMT room and everything in between.

The first scenario is an extreme case which postulates that all the fluid rises through the West steam generator compartment. This scenario is identical to the scenario that assumes the jet momentum is locally dissipated in the East steam generator compartment. The case of the jet momentum dissipated in the East steam generator compartment is discussed in Section 9.3.1.1. The buoyant plume rising from the RCDT cavity into the West steam generator compartment is essentially the same scenario.

The second scenario is a split of the flow entering the RCDT cavity, with part of the break flow rising through the West steam generator compartment and part rising through the CMT compartment. The flow split is dependent on the relative flow path resistances. In this scenario, both the steam generator compartments and the CMT compartment would be subjected to a steam-rich break plume. The CMT and steam generator compartments contain the majority of the below-deck heat sinks. The flow split will result in good heat sink utilization subjecting both the steam generator compartments and the CMT compartment to the steam source. Thus, the case with the jet momentum dissipated in the RCDT cavity and a plume flow split between the CMT and steam generator compartments, will not be limiting. This is confirmed in the sensitivity calculations of Section 9.3.2.5.

The third scenario is an extreme case which postulates that the plume from the RCDT cavity rises into the CMT room. For this scenario, the buoyant plume rises from the floor to the ceiling of the CMT room, entraining gas from the bulk concentration present in the CMT room. An examination of entrainment into a CMT plume can be used to gain insight into the potential for stratification.

Calculation of CMT Room Plume Entrainment Rates

For the case of the LOCA jet being dissipated in the CMT room, the rate of entrainment of mixture in the CMT into the incoming break flow plume, Q_e , can be estimated based on the work of Peterson (Reference 9.15). In particular, Peterson gives the following relation for the volumetric entrainment rate into a buoyant plume,

$$Q_e = k_\mu * B^{1/3} * z^{5/3} \quad (9-1)$$

where k_μ is a constant equal to approximately 0.15, z is the height of the plume, and B is the buoyancy flux, given by:

$$B = g * \frac{(\rho_a - \rho_o)}{\rho_a} * Q_b \quad (9-2)$$

In this equation, g is acceleration due to gravity, ρ_a and ρ_o are the ambient fluid and injected fluid densities respectively, and Q_b is the volumetric flow rate from the plume source.

Substitution of equation (9-2) into equation (9-1) gives:

$$Q_e = k_\mu * \left[g * \frac{(\rho_a - \rho_o)}{\rho_a} * Q_b \right]^{1/3} * z^{5/3} \quad (9-3)$$

The ratio of entrained flow to break flow is therefore:

$$\frac{Q_e}{Q_b} = k_\mu * \left[g * \frac{(\rho_a - \rho_o)}{\rho_a} * \frac{1}{Q_b^2} \right]^{1/3} * Z^{5/3} \quad (9-4)$$

AP600 break flow rates for a LOCA DECLG at transient times of 460 seconds and 1,000 seconds are 1,070 ft³/sec and 266 ft³/sec respectively for steam. The injected fluid density is taken as the density of saturated steam at the CMT room pressure. These densities are 0.128 lb/ft³ (based on 54.6 psia at 460 seconds) and 0.135 lb/ft³ (based on 58 psia at 1,000 seconds). Ambient fluid density is taken as the total density of gas mixture in the CMT room at the times of interest. Inspection of the WGOTHIC output, from the sensitivity case which modeled the break in the CMT room (see Section 9.3.2.5), indicates densities of 0.158 lb/ft³ at 460 seconds and 0.165 lb/ft³ at 1,000 seconds in the CMT room. The height of the CMT room is 28.1 feet. Based on this data the applicable entrainment ratios, Q_e/Q_b , are 0.68 at $t=460$ seconds, and 1.7 at $t = 1000$ seconds.

An entrainment-driven circulation time constant for the CMT room is calculated by dividing the entrainment flow rate into the volume of the CMT. From above Q_e/Q_b is 0.68 when Q_b is 1066 ft³/sec and 1.7 when Q_b is 266 ft³/sec. Solving for Q_e gives a range of 725 to 452 ft³/sec for the entrainment rate. The volume of the CMT room is approximately 157200 ft³ and the resulting circulation time constant ranges from 217 seconds to 348 seconds (3.6 to 5.8 minutes). This range is relatively short compared to the time of ADS Stage 4 actuation (approximately 1000 seconds), when the steam source is relocated to the steam generator compartments.

Assessment of CMT Room Entrainment Circulation

The entrainment rate for this case is relatively large, increasing to over a factor of two relative to break flow later in time. Thus, a significant amount of CMT room mixture is entrained into the break as the plume rises to the ceiling. It may be concluded that vertical concentration gradients in the CMT room would be relatively small due to circulation within the room. It also may be concluded that the break flow circulates within the room, significantly increasing the room average steam concentration. Thus, high steam concentrations are expected in the CMT room compared to other break scenarios. The high steam concentrations for this scenario will result in high heat sink utilization for heat sinks in this important room.

With such low density mixture in the North CMT room, the chimney effect induces flow to the room from connecting flow paths at the floor elevation. Connecting flow paths from the Section 4 Evaluation Model are []^{a,c}, horizontally connecting to the steam generator compartments, and until the liquid level closes the path, []^{a,c} from the RCDT cavity (see Figure 9-47). The density head over almost 30 feet of height outside the CMT room strongly drives circulation through the CMT and upward in this scenario, suggesting that the flow should rise from the North CMT room into the above-deck region. There is little resistance to flow navigating past the CMT room pinch point to access the ceiling openings on the South CMT room opposite the stairwell, suggesting that flow would spread as it rises into the South CMT room, and then rise from all CMT deck openings. It is known from studies of building fires that very little pressure driving force is necessary to drive horizontal flow in a stratified room (References 9.10, 9.11, 9.12).

The effect of stratification on heat sink utilization is also evaluated. Room pressure, temperature, and steam concentrations were input into a separate calculation to assess the potential effect of stratification in the CMT room. For the calculation, the CMT room was divided vertically into three equal sections. Using free convection heat and mass transfer correlations, room heat sink energy removal was calculated for a room with a homogeneous steam concentration. The applied steam fraction was .63. For the second scenario, the CMT room was subjected to a stratified condition. The top region was assumed to be nearly all steam (steam fraction = 0.98), the middle region was assumed to have a nominal steam fraction (0.63), and the bottom region steam fraction was determined by conserving the total amount of steam in the total volume (0.28). Figure 9.B-3 shows the energy absorbed by the heat sinks in the CMT room for; 1) a stratified steam concentration with the CMT floor included, 2) a homogeneous steam concentration with the CMT floor included, and 3) a homogeneous steam concentration without the CMT floor included. As Figure 9.B-3 shows, the homogeneous concentration with the floor results in the most energy absorbed in the CMT room (top curve). The curve for the stratified concentration with the floor is close to the curve for the homogeneous concentration without the floor. The curve for the homogeneous concentration without the floor is more conservative (less energy absorbed) after 2000 seconds. Given the relative closeness of these two curves, and considering the extreme cases they represent, it is concluded that the lumped parameter Evaluation Model (which uses a homogeneous steam concentration in each volume) without floors provides a reasonably conservative model for heat sink utilization, accounting for the thermal effects of potential stratification. Information on the heat sink utilization calculations is presented in Appendix 9.B.

The break scenario with a buoyant plume flowing into the CMT compartment will not be a limiting scenario. The evaluation of this scenario has shown only small vertical concentration gradients are expected in the CMT compartment while a bias has nevertheless been implemented by removing the floor. Furthermore, high steam concentrations are expected in this compartment due to the large amount of entrainment and subsequent circulation driven by the break plume. The high steam concentrations will yield improved heat sink usage in this room. The scenario discussed in Section 9.3.1.1, with the jet momentum dissipated in the steam generator compartment, will have lower steam concentrations in the CMT room. Thus, the break scenario with a buoyant plume flowing into the CMT compartment will be bounded by the case with the break jet locally dissipated. To further confirm this conclusion, the results of a WGOTHIC analysis using the AP600 Containment Evaluation Model (Section 4), for a buoyant plume flowing into the CMT compartment, are discussed in Section 9.3.2.5. The analysis confirms that the buoyant plume rising into the CMT compartment is not a limiting scenario.

9.3.2 WGOTHIC Containment Evaluation Model for LOCA

The WGOTHIC Containment Evaluation Model uses lumped parameter nodding. Lumped parameter nodding simplifies the calculation by assuming homogeneous conditions in each network node. Lumped parameter formulation uses what may be called a scalar form of the momentum equations as follows. Here, momentum flow into each volume is parallel to the junction, and the terms perpendicular to the junction are discarded while junction momentum is dissipated within the volume. Momentum orientation is not tracked, and no turning losses are represented. During the LOCA blowdown phase, the high break mass flow pressurizes the steam generator compartment and flow exits based on relative loss coefficients. Such pressure-driven flows are reasonably modeled by the lumped parameter node-network formulation. Lumped parameter reasonably represents buoyancy and pressure-driven flows and the resulting large-scale circulations. The effects of stratification within each compartment or region can then be

superimposed on the large-scale circulation solution. The Containment Evaluation Models are described in Section 4 (AP600) and Section 13 (AP1000).

Comparison of lumped parameter GOTHIC results to test data, has shown lumped parameter nodding to be acceptable for LOCA breaks occurring in low zones of containment. Reference 9.13 discusses the test results and subsequent GOTHIC evaluation of the German Heissdampfreaktor (HDR) hydrogen mixing and distribution experiment E11.5. This experiment simulated a large-break LOCA in the lowest region of the HDR containment. The authors conclude that accident scenarios initiated by large-break LOCAs in the low zones of containments can be reliably predicted by the GOTHIC lumped parameter model using only a modest number of nodes (Appendix 9.C, Section 9.C.3.3). The DBA LOCA case models the break in []^{a,c} (lower East steam generator compartment) at the []^{a,c} elevation.

The conclusions concerning the use of a lumped parameter for low breaks modeled by GOTHIC, can be readily applied to WGOTHIC because of the similarity between the two codes. WGOTHIC is a descendant of the GOTHIC code. The difference between the two codes relates to the heat and mass transfer correlations applied to WGOTHIC by Westinghouse, to model the PCS phenomena for the passive containment design. Thus, since the LOCA scenarios of interest are breaks in the lower region of containment, it is reasonable to use WGOTHIC lumped parameter to model these events.

As discussed previously, the LOCA event is divided into four phases: the blowdown phase, the refill phase, peak pressure phase, and the long-term phase. These phases are discussed in Subsections 9.3.2.1 through 9.3.2.4.

9.3.2.1 Blowdown Phase (0 to 30 seconds)

The lumped parameter solution during blowdown is a node-network solution, governed by pressure differences and flow resistances between nodes. The mass and energy release in the Evaluation Model acts as a high-pressure source that forces the steam out through flowpaths connected to the source node. The Evaluation Model also assumes only free convection on inner containment surfaces. Based on high kinetic energy during blowdown (Reference 9.7, Figure 6-2) significant enhancement to mass transfer due to forced convection occurs (Section 9.2.2). The steam is driven into the below-deck region and the above-deck volume. Figure 9-37 shows the calculated steam concentration of various containment regions during the blowdown phase, using the Evaluation Model described in Section 4 with a dissipated break in the SG East compartment.

The paragraphs in this subsection describe several sensitivity cases and an evaluation performed to examine various aspects of the blowdown phase. The first sensitivity case examines the effect of modeling a containment with a homogeneous steam concentration on the calculated containment pressure. The second sensitivity case examines the effect of removing all internal heat sinks on the calculated containment pressure. Following this sensitivity case, an evaluation of heat sink utilization in dead-ended compartments is performed. The final sensitivity case examines the effect of varying the flow pattern and steam concentrations on the calculated containment pressure.

To show the relative insensitivity to stratification, or heat and mass transfer coefficient during blowdown, a comparison is needed between the containment pressure response predicted by this node-network solution, and the containment response predicted for a homogeneous containment. Section 8, Figure 8-1 compares the LOCA blowdown pressure results of a one-node WGOTHIC AP600 model to the node-network solution. The one-node model assumes the same total containment volume and containment heat sinks as the multi-node model. Both models predict essentially identical containment pressure responses during the blowdown phase. Therefore, the details of the flow connections and heat mass transfer rates for the multi-node Evaluation Model are not important with respect to the containment pressure results because volume compliance is the dominant pressure mitigator during blowdown.

During the blowdown phase, the mass and energy release is mitigated primarily by containment volume via the rapid pressurization of the containment building. Figure 8-2 shows a comparison of the AP600 Evaluation Model results for the blowdown phase versus an identical model with all internal heat sinks removed. At the end of blowdown (30 seconds), the difference between these two cases is about 3 psi, accounting for only 10 percent of the pressurization. Thus, in the Evaluation Model, the blowdown mass and energy release increases containment pressure by about 35 psi, while the containment heat sinks absorb approximately 3 psi worth of energy. Clearly, the dominant mechanism during blowdown is the pressurization of containment.

The heat sink effectiveness in the presence of a stratification gradient is evaluated in Appendix 9.B. To conservatively account for the reduced effectiveness of heat sinks in lower room areas, floors are eliminated in the WGOTHIC Containment Evaluation Model throughout the transient.

The effectiveness of heat sinks in dead-ended compartments is also evaluated. Since only one opening exists for these compartments, interaction with overall containment volume is expected to be minimal unless the compartments have non-uniform temperatures. During blowdown, these compartments pressurize along with the rest of containment. Steam/air mixture from the bulk containment volume flows into the dead-ended compartments during the initial pressurization. Once pressurized, additional steam/air flow into the dead-ended compartments only occurs to make up for steam condensing in the compartment. Analysis of the Nuclear Power Engineering Corporation (NUPEC) natural circulation test, M-4-3, showed that asymmetric heating of dead-ended compartment walls can lead to natural circulation flows within the compartment (Reference 9.14). However, a conservative evaluation of dead-ended compartments would consider no thermally driven circulation. In such a case, inside the compartments, the condensation of steam leaves behind a heavier air-rich mixture. The air flows to the bottom and blankets the lower heat sinks. The poor circulation within the dead-ended compartments leaves the air-rich layer relatively undisturbed. As steam continues to condense, the air-rich layer continues to build up and will result in significant stable stratification within the dead-ended compartments. Although the heat sinks in the dead-ended compartments will contribute somewhat to containment heat removal, to conservatively bound the effects of stratification, condensation and convection on the heat sinks in the dead-ended compartments are neglected after 30 seconds in the Evaluation Model.

Based on the results of the evaluation, it has been demonstrated that blowdown pressure history is relatively insensitive to the effects of circulation and stratification. The internal heat sinks do heat up during blowdown, however, as discussed above, containment volume pressurization is the dominant mechanism for absorbing the energy released. Since volume pressurization is the governing process, blowdown pressure response is not sensitive to circulation and stratification effects. The Evaluation

Model utilizes a conservative lower estimate of containment free volume. Thus, the uncertainties in heat and mass transfer or stratification, and flow path effects, do not significantly impact the LOCA blowdown pressure history and the Evaluation Model adequately models the LOCA blowdown phase.

To assess the effects of varying the steam concentrations and flow rates on the calculated containment pressure, a sensitivity was performed which varied several loss coefficients in the Evaluation Model. This sensitivity shows how changes in conditions during the blowdown phase affect the later phases and, in particular, the calculated containment pressure. For this sensitivity, the AP600 Containment Evaluation Model (Section 4), with a dissipated jet in the SG East compartment, was used and the loss coefficients [

] ^{a,c} Figure 9-38 shows the pressure transient for this sensitivity case. The maximum calculated pressure is 43.8 psig, which is 0.1 psi less than the 43.9 psig reported in Section 9.3.2.5.

Circulation plots for this sensitivity case are presented in Figure 9-39 through Figure 9-42. Compared to the circulation plots for the dissipated jet in the SG East compartment (Figure 9-47 through Figure 9-50), the effects of the revised loss coefficients are evident. At 20 seconds, Figure 9-39 shows that most of the break flow goes from the SG East compartment to the SG West compartment, and through the RCDT cavity to the North CMT room. At 1000 seconds (Figure 9-40), flow is rising from both SG compartments and a steam/air mixture is flowing down into the North and South CMT volumes. Figure 9-48, shows flow rising only from the SG East compartment. At 1550 and 80050 seconds (Figure 9-41 and Figure 9-42) the ADS Stage 4 valves are the source of the steam releases and the flow patterns are similar to those in Figure 9-49 and Figure 9-50. This sensitivity altered the flow patterns and steam concentrations early in the transient by changing some of the flow path loss coefficients. The change in calculated maximum pressure was negligible.

9.3.2.2 Refill Phase (30 to 90 seconds)

The refill phase immediately follows blowdown. After blowdown, the accumulators refill the lower plenum of the reactor with a high flow rate of cold water. The resulting steam and water flow rates from the break are very low and increase with time. The mass and energy release rates are two orders of magnitude less than the blowdown rates, and can be approximated as 0 from approximately 30 to 90 seconds into the event. With a negligible steam source rate and a high condensation rate, the containment pressure drops by a few psi from its peak at the end of blowdown to the end of the refill phase at approximately 90 seconds. For the calculation of maximum containment pressure, the Evaluation Model conservatively neglects the refill period.

9.3.2.3 Peak Pressure (90 to 1200 seconds)

During the peak pressure phase, the location of the steam releases changes from the break to the ADS Stage 4 valves in both steam generator compartments. The Evaluation Model includes this change in steam release location. In addition, the lower compartments begin to fill with liquid from the break. The reduced heat transfer area due to filling is accounted for in the Evaluation Model. Figure 9-43, for a jet dissipated in the SG East compartment, shows that the condensation on the steel becomes the dominant mechanism for heat removal towards the end of the peak pressure phase.

The evaluation of break scenarios in Section 9.3.1 led to the conclusion that the case with jet momentum dissipated in the steam generator compartment may lead to stratification within compartments after the blowdown phase. Given this possibility, it is necessary to show that the Evaluation Model bounds the possible effects of this stratification. Lumped parameter models assume no gradients within each volume of the network. Thus, in the Evaluation Model, all heat sinks within a compartment volume see identical environmental conditions. In contrast, actual conditions may lead to a stratified compartment with a region of higher steam concentration on top and lower steam concentration near the bottom. For the effects of stratification on heat sink utilization, the most significant heat sinks are the above-deck region (containment shell) and the CMT room (steel and jacketed concrete). The compartment features are discussed in Sections 4 and 13 and summarized in Table 3-1 of Reference 9.2. In Section 9.3.1.3, the CMT room was assessed for its sensitivity to stratification. In this calculation, heat sink usage was calculated for a homogeneous room and a severely stratified room. A bias has been defined to bound the potential effects of stratification in compartments as discussed in 9.3.1.3. In Section 9.3.1.1, the containment shell was assessed for its sensitivity to stratification. A bias has been defined to bound the potential effects of stratification above-deck as discussed in Section 9.3.1.1. Appendix 9.B discusses the calculations performed.

Based upon the results of the evaluation, a method to bound circulation and stratification effects for the peak pressure phase has been developed. In the Evaluation Model, all floors are neglected throughout the transient and condensation and convection on all heat sinks in dead-ended compartments are neglected after 30 seconds (refer to Section 9.3.2.1).

9.3.2.4 Long-Term Phase (1200 seconds to 24 hours)

Figure 9-43 shows the condensation on the steel shell remains the dominant mechanism for heat removal during the long-term. The results shown are from the AP600 Containment Evaluation Model (Section 4) with a dissipated jet in the SG East compartment. During early portions of the transient, internal heat sinks are the primary path of containment heat removal. As the transient progresses, the temperature of the heat sinks increases and their heat removal effectiveness is reduced. PCS heat removal, which dominates in the long-term, is dependent on steam concentrations. The effects of stratification on the containment shell heat removal have been evaluated in Section 9.3.1.1 and a bias of removing operating deck floors has been included in the Evaluation Model.

In addition, WGOTHIC predicts a slight gradient between the upper and lower compartments (excluding dead-ended compartments). Figure 9-44 shows WGOTHIC predicted steam concentrations for various compartments in the AP600, using the Evaluation Model (Section 4) with a dissipated jet in the SG East compartment. As Figure 9-44 shows, at 24 hours WGOTHIC predicts a homogeneous above-deck region. However, WGOTHIC predicts a slightly lower steam concentration below the operating deck, excluding the SG compartments which continue to have steam release through the ADS Stage 4 valves.

The trend over time for the WGOTHIC calculations leads to a very small steam density gradient between above- and below-deck compartments. The WGOTHIC predicted average steam concentration above the operating deck is approximately 0.47 at 24 hours. Below the operating deck, the average is approximately 0.46 at 24 hours excluding the SG compartments. The calculated steam concentration for a homogeneous condition between the above-deck region and the below-deck open compartments is approximately 0.468. There is a negligible change between the WGOTHIC calculated above-deck steam concentration and the

calculated homogeneous concentration (excluding dead-ended and SG compartments). Since the predicted stratification is slight, and since the volume of the above-deck regions is significantly greater than the below-deck open compartments, mixing the above-deck volume with the below-deck open compartments does not significantly change the above-deck steam concentrations. Thus, the WGOTHIC predictions as the transient calculation passes through 24 hours are essentially similar to the assumption of a homogeneous containment. It is conservative to not include the steam generator compartment steam concentration in the homogeneous calculation.

It is concluded that WGOTHIC predicts a slight segregation between the above- and below-deck regions, but the deviation from the homogeneous assumption is insignificant. Based upon the results of the evaluation, it has been shown that the Evaluation Model adequately bounds the effects of circulation and stratification during the long-term phase.

9.3.2.5 Evaluation Model Results

Sensitivities have been performed using the lumped parameter AP600 Containment Evaluation Model (Section 4) for several postulated, plausible break locations. An evaluation of the sensitivities leading to selection of a limiting scenario for design basis accident calculations follows.

It has been determined that to bound circulation and stratification effects, floors are neglected throughout the transient, and condensation and convection on all heat sinks in the dead-ended compartments are neglected after blowdown. The stratification of steam and air within compartments may reduce heat sink effectiveness. These biases are included in the Evaluation Model used to perform sensitivities.

Undissipated Jet Rising in SG East Compartment

The postulated, undissipated jet directed up the Steam Generator compartment results in increased heat and mass transfer, possibly as high as a factor of []^{a,b} over the steel shell surface based on the LST, compared to that using the free convection correlation in the Evaluation Model, as discussed in Section 9.3.1.2. To estimate the potential benefit for AP600, the heat transfer coefficient multipliers for the inner surfaces of the clime conductors (that is, only the steel shell mass transfer is enhanced) were increased to []^{a,c} times the Evaluation Model values. The Evaluation Model with the break in the steam generator East compartment was used for the sensitivity cases. The postulated, undissipated jet will only occur until the ADS Stage 4 valves are opened at approximately 1000 seconds. Therefore the containment pressure response is plotted for the first 1000 seconds of the LOCA. The containment pressure sensitivity results are shown in Figure 9-45, along with the Evaluation Model results. The results show that the pressure response during the blowdown phase is the same for all cases. This is expected because volume compliance is the dominant pressure mitigator during blowdown (Section 9.3.2.1). Compared to the Evaluation Model results at 1000 seconds, the calculated containment pressure for the []^{a,c}. These results show that a substantial benefit in containment pressure is gained when the heat transfer coefficient is increased to account for the forced convection from an undissipated jet. Therefore, this case will be less limiting than the other postulated break scenarios in which the jet is dissipated.

Dissipated Jet Rising in SG East Compartment

Another postulated break scenario, the design basis case, is a dissipated jet in the SG East compartment (Volume 107, elevation 100 ft.). Figure 9-46 shows the results of the WGOTHIC AP600 Containment Evaluation Model which includes the circulation and stratification biases. Assuming the break momentum is dissipated in the broken loop steam generator compartment, a maximum containment pressure of 43.9 psig is calculated, which is below the design pressure of 45 psig. The pressure transients for compartments directly connected to the SG East compartments are shown in Figure 9-46A. Figure 9-47 through Figure 9-50 show the circulation pattern predicted by WGOTHIC for this case at different times during the transient. The figures show the Evaluation Model flow path connections for the below-deck volumes, the flow rates and directions, volume steam pressure ratio, and liquid level. Figure 9-51 is a depiction of each of the flow connections to the above-deck volumes. In subsequent figures, total flows through the ceiling of each compartment are shown for simplicity. Flow paths that have been grouped have the same flow direction. Figure 9-47 presents data at 20 seconds which is near the end of blowdown. Flow is forced into all of the below-deck volumes and into the above-deck volumes from the East and West steam generator compartments and the North and South CMT rooms. Figure 9-48 presents data at 1000 seconds which is near the time of maximum pressure and prior to ADS Stage 4 valve actuation. Flow to the dead-ended compartments has stopped. The general circulation pattern is fluid from the break flowing up through the SG East compartment while a steam/air mixture is drawn into and through the SG West compartment, the North and South CMT rooms, and the RCDT cavity into the SG East compartment. At 1500 seconds, Figure 9-49 shows the change in circulation pattern due to the actuation of the ADS Stage 4 valves. The steam releases flow up through both steam generator compartments while a steam/air mixture is drawn into and through the CMT rooms and the RCDT cavity. This flow pattern develops less than 2 minutes after ADS Stage 4 activation. Figure 9-50 shows the circulation pattern near 24 hours. The flow rate out of the ADS Stage 4 valves is approximately one-fourth of the flow at 1500 seconds. The flow pattern remains out of the SG compartments and into the CMT rooms, however, flow through the RCDT cavity has ceased, due to liquid level rising above the top of the flow path.

Plume Rising in CMT Room

In Section 9.3.1.3, the LOCA with jet dissipation in the RCDT cavity was postulated. It was postulated that the entire buoyant plume rises into the North CMT compartment. The evaluation concluded this scenario was not limiting because of the higher steam concentrations expected in the CMT compartment, which would result in better internal heat sink utilization. Furthermore, the evaluation concluded that the relative steam densities would drive the steam to navigate the bend in the CMT compartment. This would lead to a steam-rich environment for the heat sinks in the south end of the CMT room opposite the stairwell. To confirm that this scenario is not bounding, a WGOTHIC calculation was performed using the AP600 Containment Evaluation Model (Section 4). The calculation assumed a LOCA where the jet plume dissipates and rises into the North CMT compartment. This was simulated by applying the break boundary conditions to the North CMT node (Volume 6, elevation 107 ft.), the only change made to the Evaluation Model. The circulation and stratification biases of neglecting floors throughout the transient and condensation and convection in dead-ended compartments following blowdown were included. The containment pressure results of this evaluation are shown in Figure 9-52. The maximum pressure was calculated to be 43.7 psig. As expected, this pressure is below the previous scenario where momentum is dissipated in the East steam generator compartment. The circulation pattern predicted by WGOTHIC is shown in Figure 9-53 and Figure 9-54.

Figure 9-53 presents data at 1000 seconds which is near the time of maximum pressure and prior to ADS Stage 4 valve actuation. Compared to Figure 9-48 (break in SG East compartment), Figure 9-53 shows flow out of the North and South CMT rooms into the above-deck region, while a steam/air mixture flows down into both SG compartments and up through the RCDT cavity into the North CMT room. Figure 9-54, at 1400 seconds, shows the change in flow pattern due to ADS Stage 4 valve actuation. The flow rates and pattern are similar to those in Figure 9-49, as expected. Figure 9-55 shows the heat sink utilization for this sensitivity case. As expected, Figure 9-55 shows a greater CMT room (Volumes 6 and 104) heat sink utilization than that shown in Figure 9-43 for a break in the SG East compartment. Both figures show that the PCS shell is the dominant heat sink at the time of maximum containment pressure and beyond.

Plume Rising in RCDT Cavity

In Section 9.3.1.3, a LOCA with jet dissipation in the RCDT cavity was postulated. This scenario assumed the break flow splits between the CMT and steam generator compartments. The evaluation concluded that good below-deck heat sink utilization is expected because of the high steam concentrations in the CMT and steam generator compartments. A WGOTHIC calculation was performed for this scenario using the AP600 Containment Evaluation Model (Section 4). The calculation simulated the flow split by placing the break boundary condition directly in the RCDT cavity []^{a,c}. The circulation and stratification biases were included. The pressure prediction from the evaluation is shown in Figure 9-56. The maximum pressure was calculated to be 43.4 psig. This pressure is below both of the previously discussed sensitivities. The WGOTHIC predicted circulation pattern is shown in Figure 9-57 and Figure 9-58.

Figure 9-57 presents data at 1000 seconds which is near the time of maximum pressure and prior to ADS Stage 4 valve actuation. With the break in the RCDT cavity, the bulk flow distribution is based on the path areas and loss coefficients. Consequently, at 1000 seconds, the steam flow from the break goes up through the CMT rooms, while a steam/air mixture flows down through both SG compartments and into the North CMT room and RCDT cavity. Figure 9-58, at 1500 seconds, shows the change in flow pattern due to ADS Stage 4 valve actuation. The flow rates and pattern are similar to those in Figure 9-49, as expected. Figure 9-59 shows the heat sink utilization for this sensitivity case. Compared to Figure 9-43 for a break in the SG East compartment, Figure 9-59 shows a small delay in the heat absorption from the SG East compartment and the CMT rooms. The heat absorption from the SG West compartment starts a little sooner in Figure 9-59. The effects are due to the break location differences. Consistent with the other cases, Figure 9-59 shows that the PCS shell is the dominant heat sink at the time of maximum containment pressure and beyond.

9.3.2.6 Evaluation of Drops During a LOCA

Drops, or fog particles, are created when the blowdown break source steam velocity is large enough to disperse a fraction of the break liquid along with the gas. As discussed in Reference 9.2, Section 4.4.2D and Reference 9.7, Section 7.1, drops will be formed during the LOCA blowdown phase. For the post-blowdown phases of a LOCA and for the main steamline break (MSLB), there will not be any significant drop formation. The thermal and circulation effects of drops on LOCA containment pressure are examined in Appendix 9.A and summarized below.

Drop fall times for various size drops were determined in Appendix 9.A, which only account for the gravitational effects on the drops. Fall times range from seconds to hours depending on the drop size and fall height. This provides an indication that the drops will exist long enough that their effect on containment pressure must be considered. In addition, Appendix 9.A estimated plume entrainment rates for 0 percent and 100 percent of the break liquid converted to drops. The entrainment rates and subsequent circulation time

constant for both 0 and 100 percent drops show that a large fraction of the containment volume will be entrained in the plume within a few minutes, which is relatively short compared to the time to reach maximum pressure (at approximately 1200 seconds), and very short compared to long-term cooling. A relatively large entrainment rate within the above-deck region indicates that the steam density gradients above-deck are not large whether drops exist or not. Therefore, the presence of drops will not significantly affect the general circulation and stratification patterns in the containment atmosphere.

Section 5.8 shows the results of sensitivity cases to assess the Evaluation Model treatment of the thermal effects of drops with respect to containment pressure. The results that show the Evaluation Model assumption of 50 percent of the break liquid being converted into drops provides essentially the same containment maximum calculated pressure as assuming 100 percent of the liquid is converted into drops.

The 50 and 100 percent drop fractions are both more limiting with respect to maximum pressure than assuming none of the break liquid is converted into drops.

The formation of drops during the LOCA blowdown phase is a physically real phenomenon which may influence the maximum containment pressure calculated by the Evaluation Model. Drop formation increases the effective density of the containment atmosphere due to the close coupling between small drops and gas by shear forces, making the post-blowdown releases relatively more buoyant. A small percentage ($\geq 5\%$) of the blowdown break liquid formed into drops is sufficient to saturate the containment atmosphere, at which point, additional drop density has a minor thermal effect. The Evaluation Model treatment of drops, as described in Section 4.5.2.1 and Section 13.6.2.1, provides a sufficiently bounding calculation for maximum and long-term containment pressure.

9.4 MAIN STEAMLINE BREAK (MSLB)

The main steamline transports steam from the steam generators within the containment building to the turbine generators in the auxiliary building. The main steamline path begins at the top of the steam generator, where it bends 180° and follows a downward path to the CMT room. In the CMT room, the steamline bends 90°, crosses through the CMT room, and exits the building through a penetration in the

containment shell. Rupture of the main steamline inside containment would release high energy steam into the containment. To confirm the design adequacy of the containment, various MSLB scenarios are examined to develop a conservative model accounting for the effects of circulation and stratification in the containment pressure calculations.

9.4.1 Break Locations

An evaluation of circulation and stratification must allow for the consideration of possible break locations. For the MSLB, two distinct break locations may be postulated: a break in the steamline above the operating deck or a break in the steamline in the CMT compartment.

9.4.1.1 MSLB Above the Operating Deck

An MSLB above the operating deck could occur anywhere in the steamline piping from the top of the steam generator to the operating deck penetration into the CMT compartment.

The design basis MSLB mass and energy releases for containment pressure assume a 1.388 ft² break (due to integral flow limiters). The MSLB event is characterized by a high energy release of short duration. Reference 9.7, Figure 6-3 shows the calculated Froude numbers for the event compared to Froude numbers calculated for the LST. The high Froude numbers indicate a high kinetic energy source which is expected to drive circulation above and below the jet source elevation. High Froude numbers also indicate that a significant forced convection enhancement to mass transfer occurs during an MSLB.

An examination of releases from smaller sized breaks in main steamlines indicates that the reduction in mass flow is more than offset by the reduction in exit flow area. Therefore, the larger size breaks have the lowest Froude numbers. The double-ended rupture MSLB has the limiting combination of mass and energy release and Froude numbers.

9.4.1.2 MSLB in the CMT Compartment

A steamline rupture in the CMT compartment would propel a high momentum steam jet into the CMT room. Since the break is within an enclosed compartment, momentum from the jet would be dissipated by the equipment, walls, floors, and ceilings of the CMT room. The effect would create a pressure source in the CMT compartment with the fluid following the path of resistance through the node network into adjacent compartments and the above-deck volume.

The steam source in the CMT compartment will create a steam-rich environment for this room which contains many heat sinks. The high steam concentration will result in excellent heat sink utilization for this scenario.

The MSLB in the CMT compartment case is bounded by the scenario of an MSLB occurring above the operating deck. While the break above the operating deck does produce substantial circulation, the steam concentrations in the CMT compartment will not approach the steam levels for a break directly within the CMT room. Thus, the MSLB in the CMT compartment is not the bounding scenario. To confirm this conclusion, Section 9.4.3 presents the results of a WGOTHIC analysis for a break in the

CMT compartment. As expected, the containment peak pressure is lower for the MSLB in the CMT compartment than for an MSLB above the operating deck.

9.4.2 WGOTHIC Containment Evaluation Model for MSLB

In creating an appropriate and conservative Evaluation Model, it is necessary to understand how the code handles circulation, to bias the model to produce bounding but reasonably representative results. Investigation of the lumped parameter AP600 Containment Evaluation Model (Section 4) has shown that this nodding structure tends to mix upwards from the break elevation.

The lumped parameter calculational bias may be attributed to the use of multiple, relatively large lumped parameter nodes to represent the above-deck region in the Evaluation Model. Lumped parameter formulation uses what may be called a scalar form of the momentum equations, as follows. Here, momentum flow into each volume is parallel to the junction, and the terms perpendicular to the junction are discarded while junction momentum is dissipated within the volume. Momentum orientation is not tracked, and no turning losses are represented. This momentum dissipation is the characteristic of the lumped parameter nodding which results in the calculated stratification above/below the jet. With momentum diffused throughout the volume node, the vigorous circulation from the high kinetic energy jet does not occur in the model. Circulation above the jet source in the lumped parameter model is driven by the density head terms in the momentum equation which cannot drive flow below the source. Thus, lumped parameter nodding predicts a steam-rich atmosphere above the assumed source elevation, and a steam-deficient atmosphere below this source elevation (simulating stratification).

With an understanding of both the physics, and lumped parameter model biases, a WGOTHIC representation is constructed which conservatively represents the accident scenario. The high kinetic energy of the MSLB will tend to circulate steam through the above-deck portion of the containment vessel and lead to forced convection conditions for the shell. The lumped parameter Evaluation Model, however, calculates a steam-rich region above the injection point and an air-rich region below this point. Figure 9-60 shows the steam concentration results of a WGOTHIC MSLB calculation using the AP600 Containment Evaluation Model with the source entering []^{a,c}, which is just above the operating deck (refer to Section 4.5.2.2). The model predicts a small steam density gradient above-deck, consistent with the expectation of only small gradients in the AP600, based on LST data (see Section 9.2.2). Evaluation has shown that the effect on shell mass transfer of even extreme stratification, beyond that expected for the AP600 or **AP1000** (see Section 9.3.1.3), is very small. Very little steam penetrates into the below-deck region in the model. Steam access into the below-deck compartments in the model is governed only by the volume pressurization. As the mass and energy releases pressurize the above-deck region, a steam/air mixture from above-deck is pushed into the below-deck compartments. The use of the WGOTHIC lumped parameter model, with an injection point just above the operating deck, results in a conservative Evaluation Model for the steam line break as a result of reduced steam access to the below-deck heat sinks. The reduced steam access is due to the momentum dissipation in the model which reduces the calculated circulation to the nodes below the operating deck. The Evaluation Model neglects any heat and mass transfer contribution from forced convection, so above-deck velocity predictions become unimportant. Mass transfer is seen to be underestimated by as much as a factor of []^{a,c} on the steel shell surface relative to forced convection in the LST. To add an additional conservative bias, the stratification heat sink biases developed for LOCA scenarios are also included

9.4.3 MSLB Sensitivity Results

Based on an evaluation of circulation and stratification, an MSLB Evaluation Model has been constructed to bound circulation and stratification effects. The limiting MSLB scenario assumes a pipe break above the operating deck. In this scenario, test data indicates that the high kinetic energy source jet induces circulation above and below the jet elevation, including substantial steam penetration into below-deck compartments. The lumped parameter Evaluation Model, that bounds circulation and stratification, places the break source directly above the operating deck []^{a,c}. This results in a well-circulated upper region with little steam access to the heat sinks below the operating deck. To further bound circulation and stratification effects, stratification heat sink biases developed for LOCA scenarios are included (see Table 9-1). Figure 9-61 shows the results of the AP600 WGOTHIC MSLB Evaluation Model described above. A containment peak pressure of 44.8 psig is calculated, which is below the design pressure of 45 psig.

In Section 9.4.1.2, the MSLB in the CMT compartment scenario was evaluated, concluding that increased circulation below the operating deck would reduce the calculated containment pressure. This scenario was determined not to be the limiting scenario, because of the high steam concentrations expected in the CMT compartment. The high steam concentration would result in improved heat removal rates by the heat sinks in the CMT compartment. To confirm this hypothesis, a WGOTHIC analysis was performed for a break in the CMT compartment []^{a,c}. As with the break above the operating deck, LOCA stratification biases were included. Figure 9-62 shows the results of the WGOTHIC calculation. A containment peak pressure of 43.2 psig is calculated, which is 1.6 psi less than the peak pressure for the MSLB above the operating deck. As expected, the Evaluation Model predicts the MSLB above-deck to be the limiting location.

9.5 CONCLUSIONS

A WGOTHIC Containment Evaluation Model is used which considers circulation and stratification in the calculation of LOCA and MSLB containment pressures and temperatures. The effects of circulation and stratification on the calculated containment pressure have been examined, and biases have been defined for the Evaluation Model. The Evaluation Model input deck and specific biases are described in Sections 4 and 13. In addition, break locations have been examined for LOCA and MSLB to determine the limiting location for each transient with respect to calculated containment pressure.

The following biases have been incorporated into the Evaluation Model for the LOCA analysis based on the circulation and stratification evaluations documented in this section:

- Heat and mass transfer from floors of compartments and the operating deck have been removed to bound the potential reduction in heat transfer due to stratification. Refer to Sections 9.3.1.1, 9.3.1.3, and Appendix 9.B.
- Condensation and convective heat transfer in dead-ended compartments are turned off after 30 seconds (i.e., after blowdown) to bound the potential reduction in heat transfer due to stratification. The basis for this bias is provided in Section 9.3.2.1.

- The lumped parameter Evaluation Model considers only free convection for internal heat sinks and shell surfaces and, therefore, conservatively neglects the increase in mass transfer to the containment steel shell due to forced convection during blowdown. Refer to Section 9.3.2.1.

Ranges of LOCA break locations and jet directions were evaluated to determine the limiting case with respect to containment pressure. The limiting scenario is the DECLG break in the East steam generator compartment with the jet momentum locally dissipated. Other break locations, or jet directions, result in increased heat sink utilization which results in lower calculated containment pressures. Based on the results presented in Section 9.3.5.2, the calculated maximum LOCA containment pressure from a dissipated jet is not very sensitive to the break location since internal heat sinks “reach maximum effectiveness” well before the time of maximum pressure.

The following biases have been incorporated into the Evaluation Model for the MSLB analysis based on the circulation and stratification evaluations documented in this section:

- The break is placed in a node at the operating deck level to minimize circulation and steam access to below-deck heat sinks, which bounds the potential reduction in heat transfer in below-deck compartments due to stratification. This is discussed in Section 9.4.2.
- The lumped parameter Evaluation Model considers only free convection for internal heat sinks and shell surfaces and, therefore, conservatively neglects the increase in mass transfer to the containment steel shell due to forced convection during the entire transient. Refer to Section 9.4.2.
- The above listed LOCA biases (relative to floors and dead ended compartments) have been included in the MSLB Evaluation Model to further conservatively bound potential reductions in heat transfer due to stratification. Refer to Section 9.4.3.

Based on the routing of the steamline pipe, two MSLB locations were evaluated; a break above the operating deck and a break in the CMT room. As discussed in Section 9.4.3, the break above-deck resulted in the higher calculated containment pressure. The break in the CMT room had increased heat sink utilization in the CMT room which resulted in the lower calculated containment pressure.

The above biases are incorporated into the Evaluation Model as described in Sections 4.2 and 13.2, subsections entitled “Special Modeling Assumptions.” Therefore, the effects of circulation and stratification have been conservatively bounded in the WGOTHIC containment pressure calculations.

9.6 REFERENCES

- 9.1 WCAP-14382, "WGOTHIC Code Description and Validation," May 1995.
- 9.2 WCAP-14812, "Accident Specification and Phenomena Evaluation for AP600 Passive Containment Cooling System," Revision 2, April 1998.
- 9.3 NTD-NRC-95-4563, "GOTHIC Version 4.0 Documentation, Enclosure 2: Technical Manual," September 21, 1995.
- 9.4 NTD-NRC-95-4563, "GOTHIC Version 4.0 Documentation, Enclosure 3: User Manual," September 21, 1995.
- 9.5 WCAP-13566, "AP600 1/8th Large-Scale Passive Containment Cooling System Heat Transfer Test Baseline Data Report," October 1992.
- 9.6 WCAP-14135, "Final Data Report for PCS Large-Scale Tests, Phase 2 and Phase 3," Revision 1, April 1997.
- 9.7 WCAP-14845, "Scaling Analysis for AP600 Containment Pressure During Design Basis Accidents," Revision 3, March 1998.
- 9.8 Wolf, L., Gavrilas, M., Mun, K., 1996, "Overview of Experimental Results for Long-Term, Large-Scale Natural Circulations in LWR-containments after Large LOCAs," DOE - Project, Order Number: DE-AP07-96ID10765, University of Maryland at College Park, July 1996.
- 9.9 WCAP-14326, "Experimental Basis for the AP600 Containment Vessel Heat and Mass Transfer Correlations," Revision 2, April 1998.
- 9.10 Jaluria, Y. "Buoyancy Driven Wall Flows in Enclosure Fires," Twenty-first Symposium (International) on Combustion, The Combustion Institute, 151-157 (1986).
- 9.11 Goldman, D., Jaluria, Y., "Effect of Opposing buoyancy on the Flow in Free and Wall Jets," Journal of Fluid Mechanics, 166, 41-56 (1986).
- 9.12 Jaluria, Y., Cooper, L.Y., "Negatively Buoyant Wall Flows Generated in Enclosure Fires," Progress in Energy and Combustion Science, 15, 159-182 (1989).
- 9.13 Fisher, K., Schall, M., and Wolf, M., "Simulations of GOTHIC Large-Scale Containment Experiments," published by Battelle Ingenieurtechnik GmbH, October 1995.
- 9.14 Ofstun, R.P., Woodcock, J., Paulsen, D.L., "Westinghouse – GOTHIC Modeling of NUPEC's Hydrogen Mixing and Distribution Test M-4-3," Third International Conference on Containment Design and Operation, October 1994, Toronto, Canada.
- 9.15 Peterson, P.F., "Scaling and Analysis of Mixing in Large Stratified Volumes," International Journal of Heat and Mass *Transfer*, Vol. 37, Suppl. 1, pp 97-106, 1994.

a,c

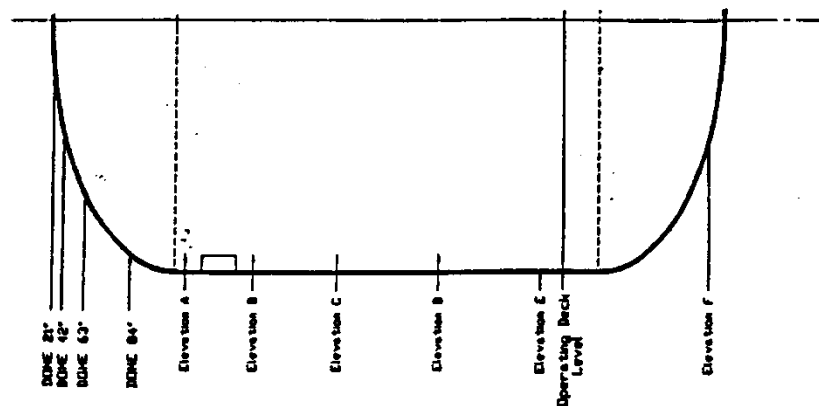
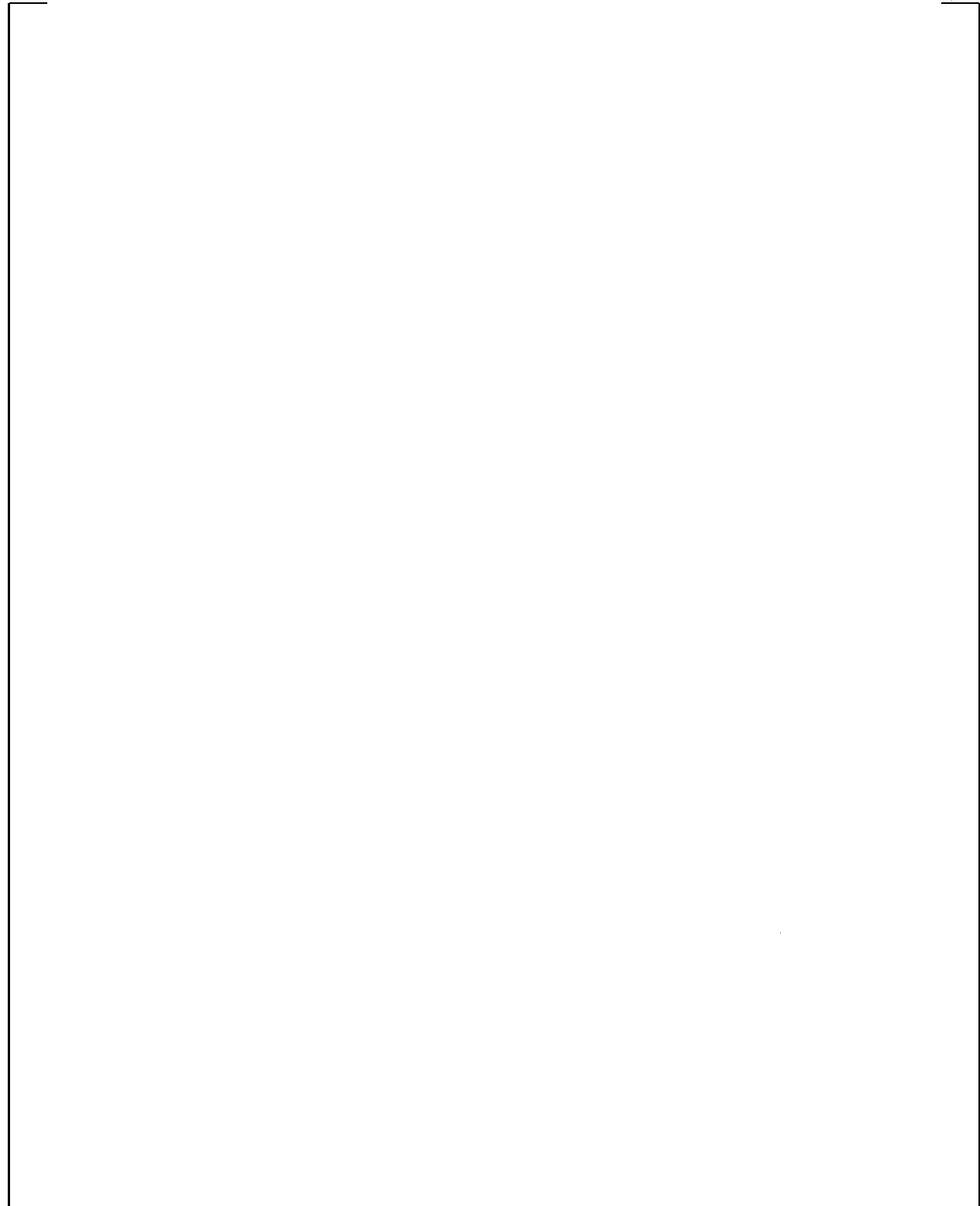


Figure 9-1. Measured Steam Concentrations for LST

a,c

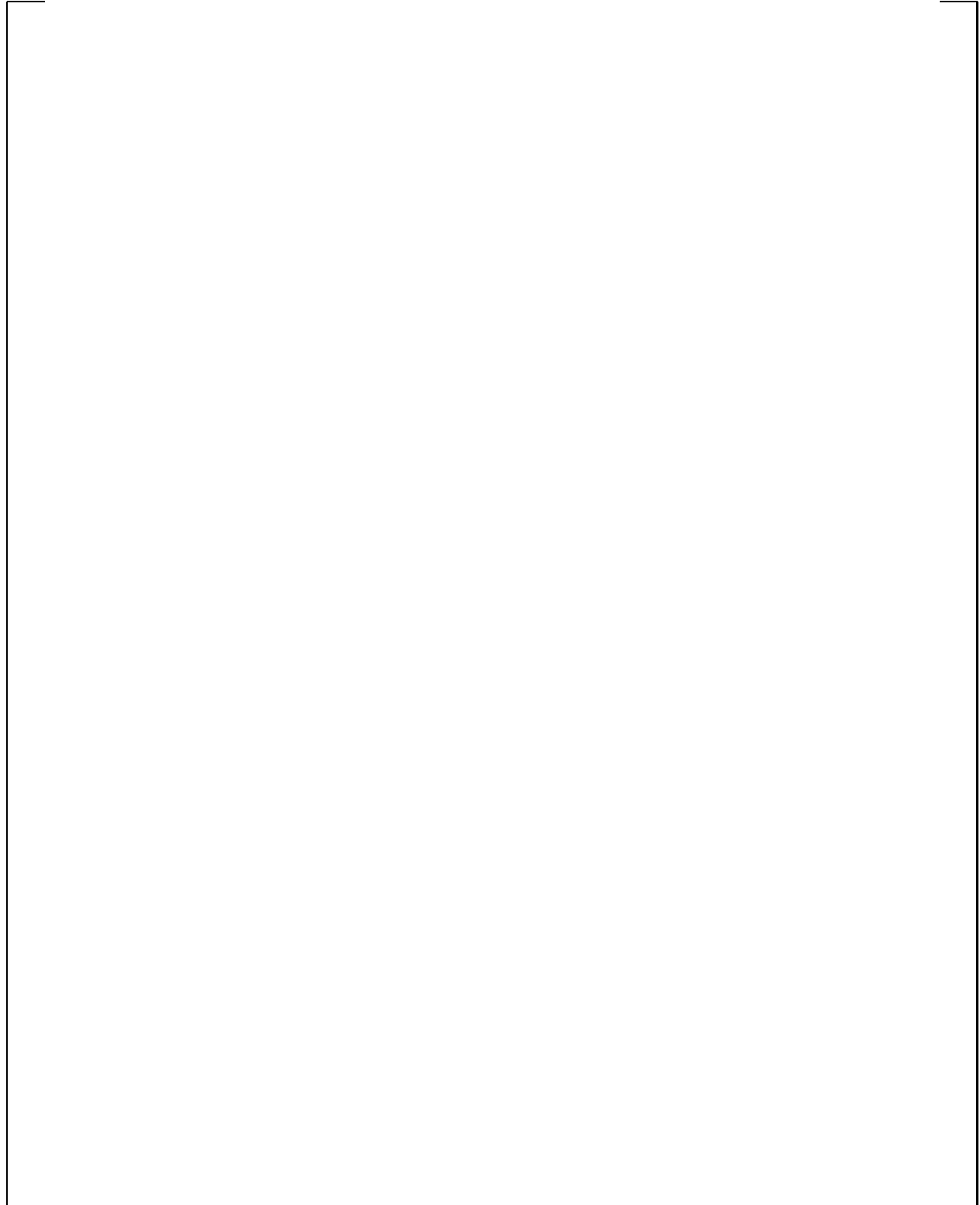


**Figure 9-2. LST with Diffuser Under Steam Generator – Steam Flow 0.11-0.17 lb/sec –
Internal Fluid Temperature – Group 1**

a,c

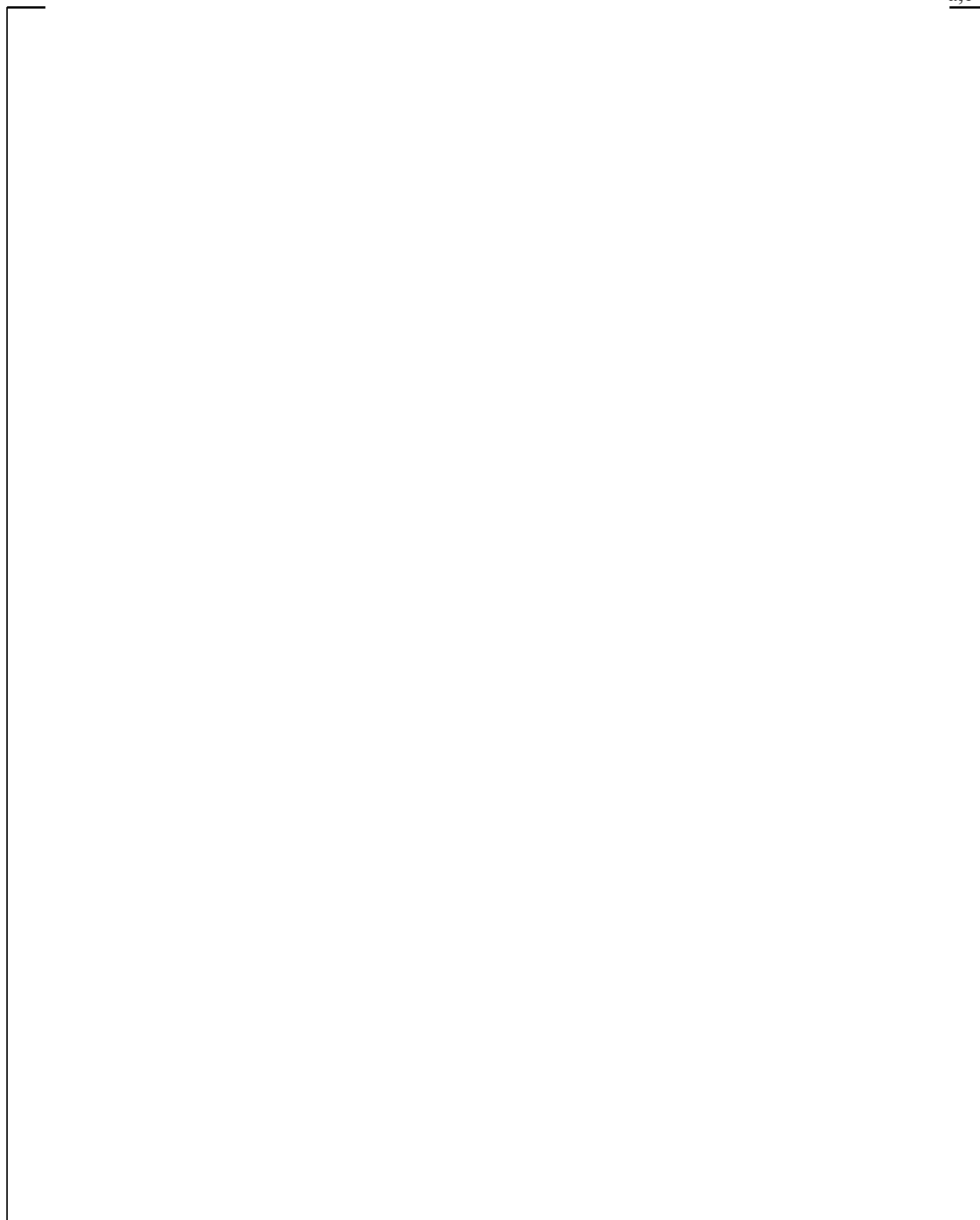


Figure 9-3. LST with Diffuser Under Steam Generator – Steam Flow 0.11-0.17 lb/sec – Saturation Temperature – Group 1



**Figure 9-4. LST with Diffuser Under Stream Generator – Steam Flow 0.11-0.17 lb/sec –
Internal Steam Pressure Ratio – Group 1**

a,c



**Figure 9-5. LST with Diffuser Under Steam Generator – Steam Flow 0.11-0.17 lb/sec –
Internal Fluid Temperature – Group 2**

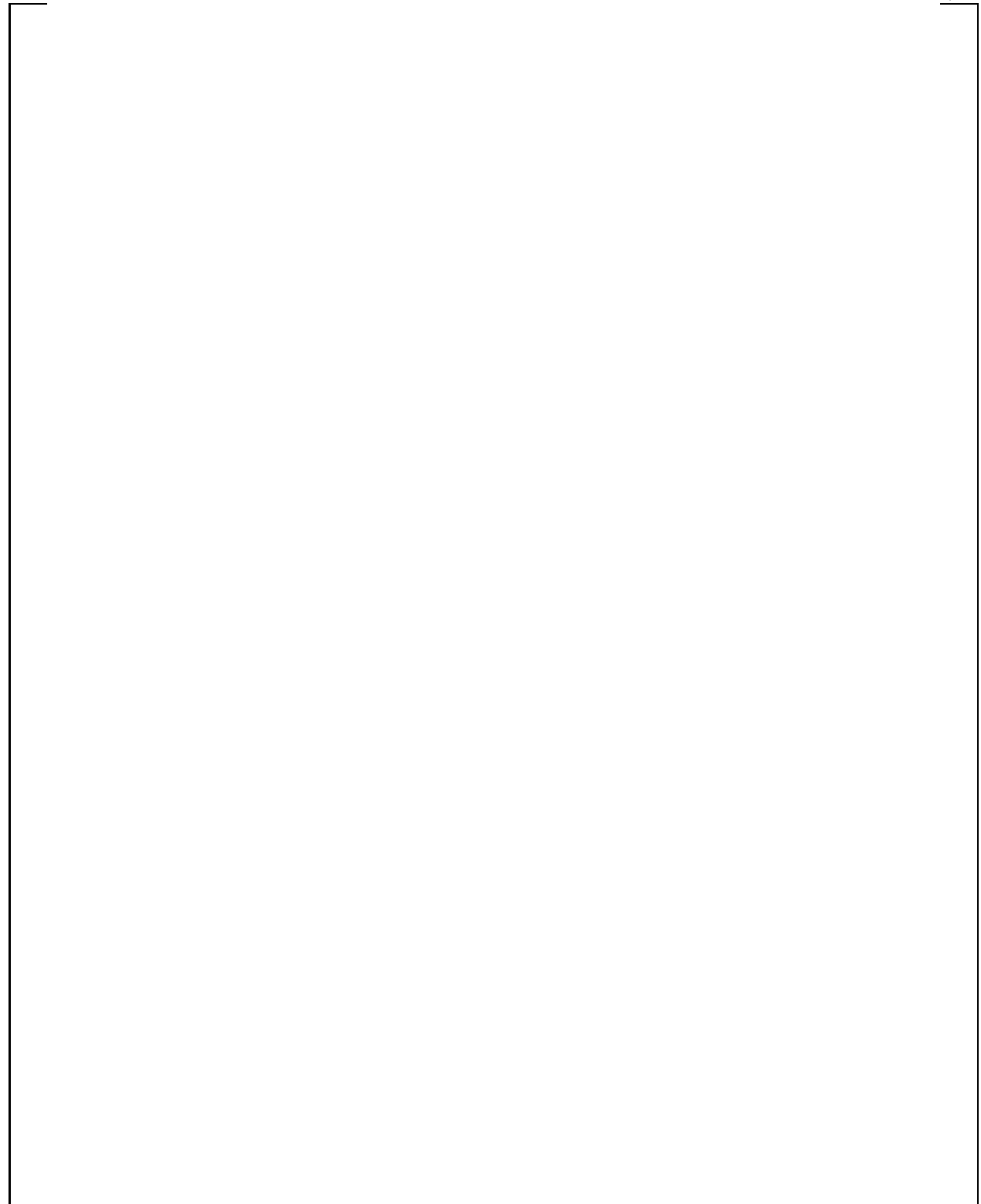
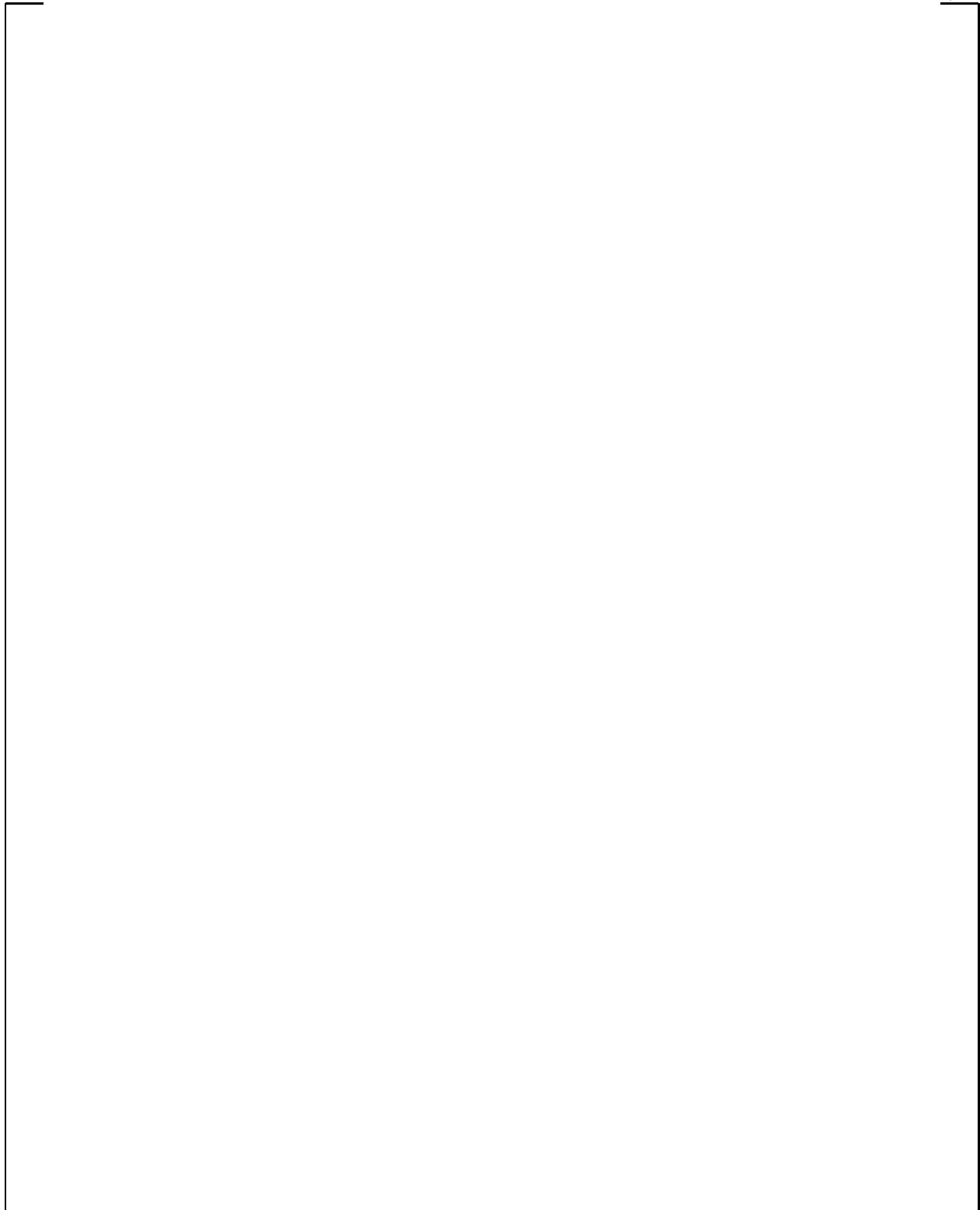


Figure 9-6. LST with Diffuser Under Steam Generator – Steam Flow 0.11-0.17 lb/sec – Saturation Temperature – Group 2

a,c



**Figure 9-7. LST with Diffuser Under Steam Generator – Steam Flow 0.11-0.17 lb/sec –
Internal Steam Pressure Ratio – Group 2**

a,c



**Figure 9-8. LST with Diffuser Under Steam Generator – Steam Flow 0.270.36 lb/sec –
Internal Fluid Temperature**

a,c

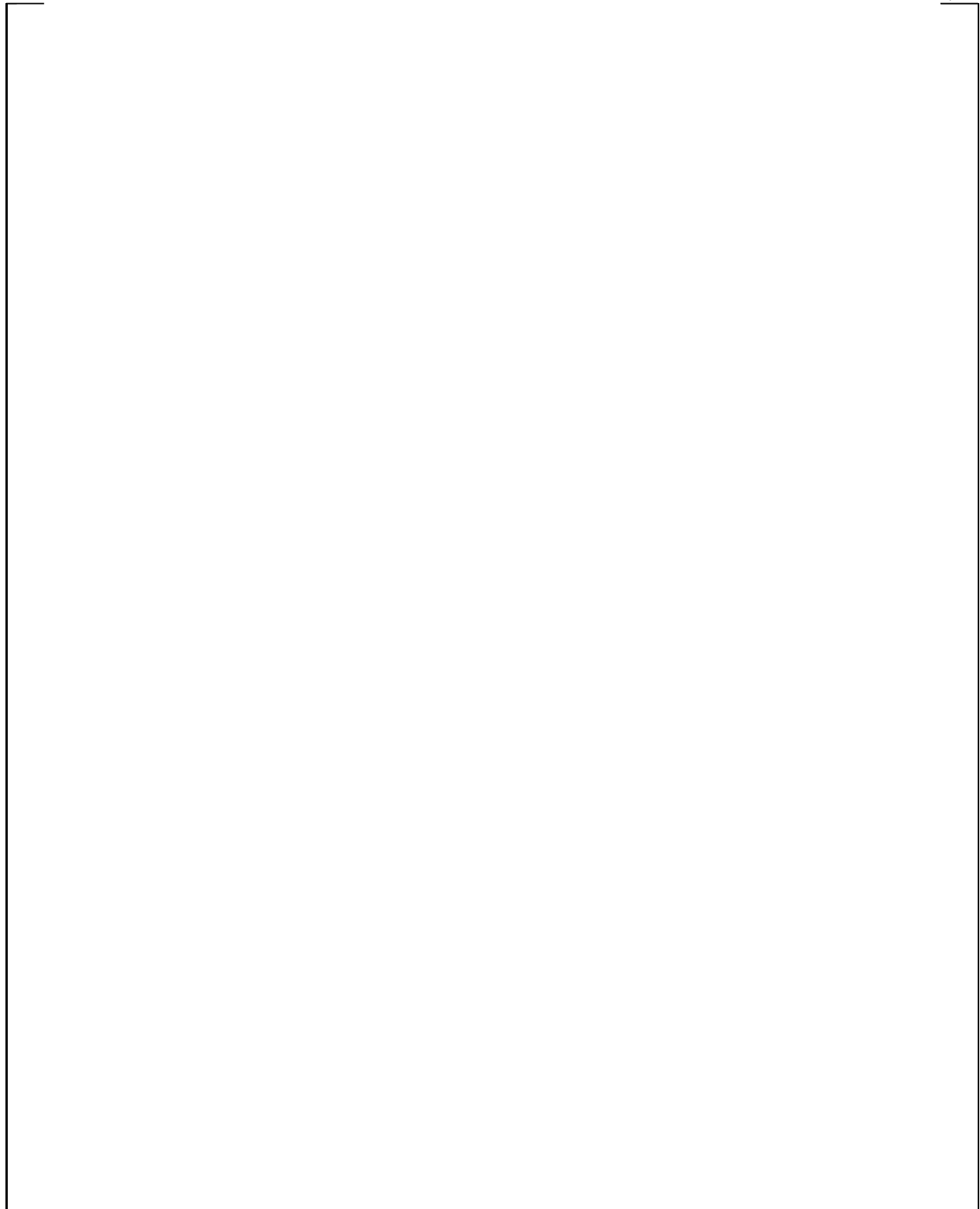
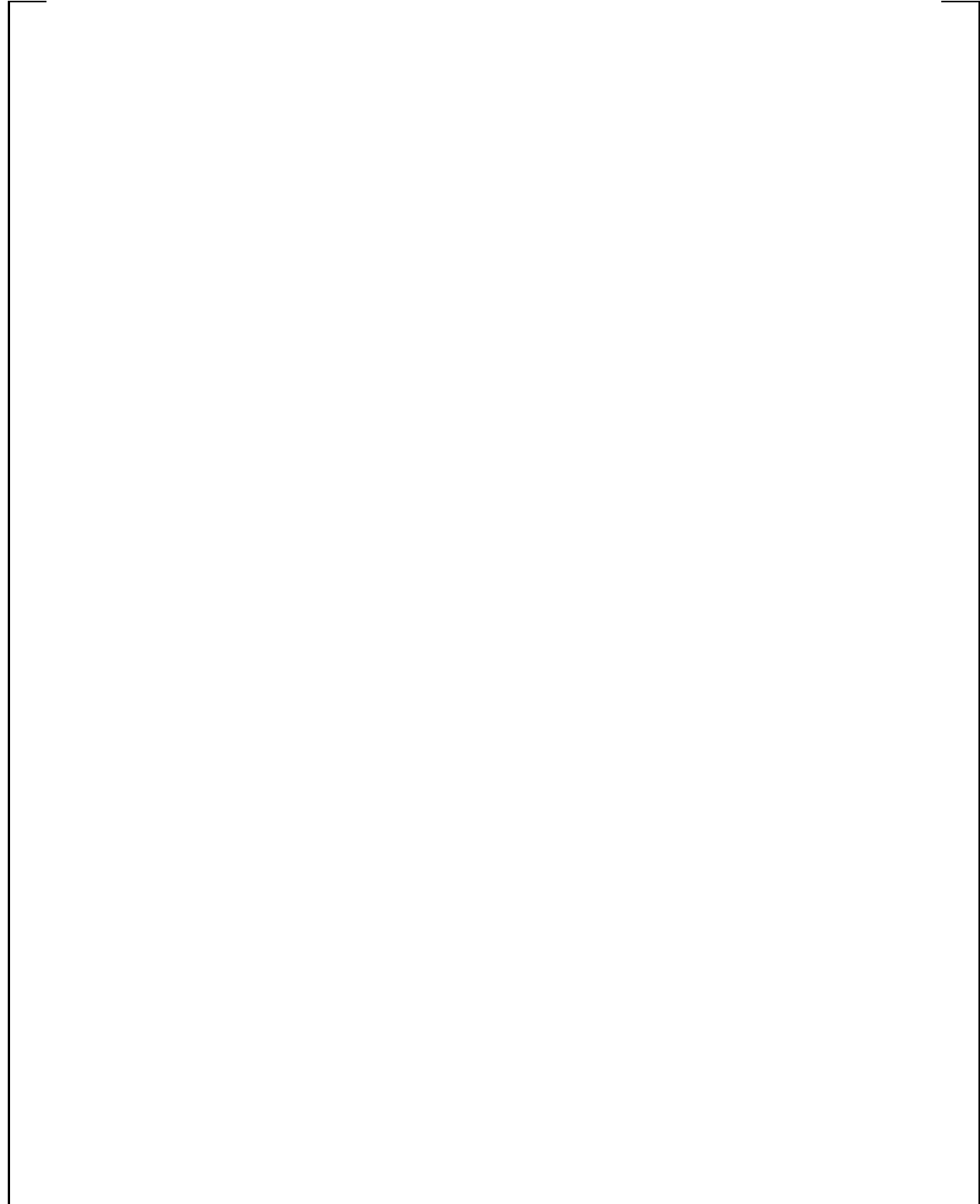


Figure 9-9. LST with Diffuser Under Steam Generator – Steam Flow 0.27-0.36 lb/sec – Saturation Temperature

a,c



**Figure 9-10. LST with Diffuser Under Steam Generator – Steam Flow 0.27-0.36 lb/sec –
Internal Steam Pressure Ratio**

a,c



**Figure 9-11. LST with Diffuser Under Steam Generator – Steam Flow 0.49-0.62 lb/sec –
Internal Fluid Temperature – Group 1**

a,c

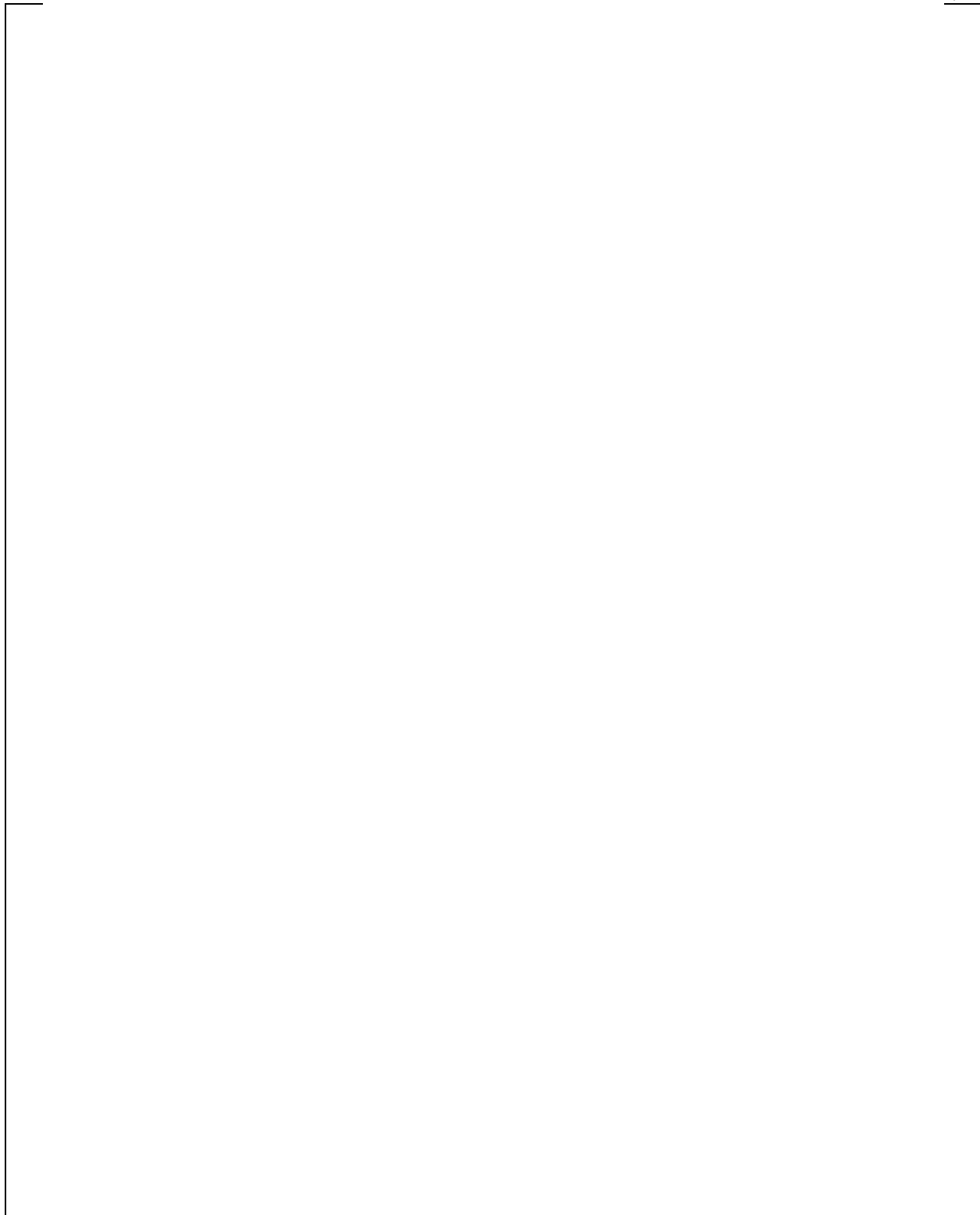
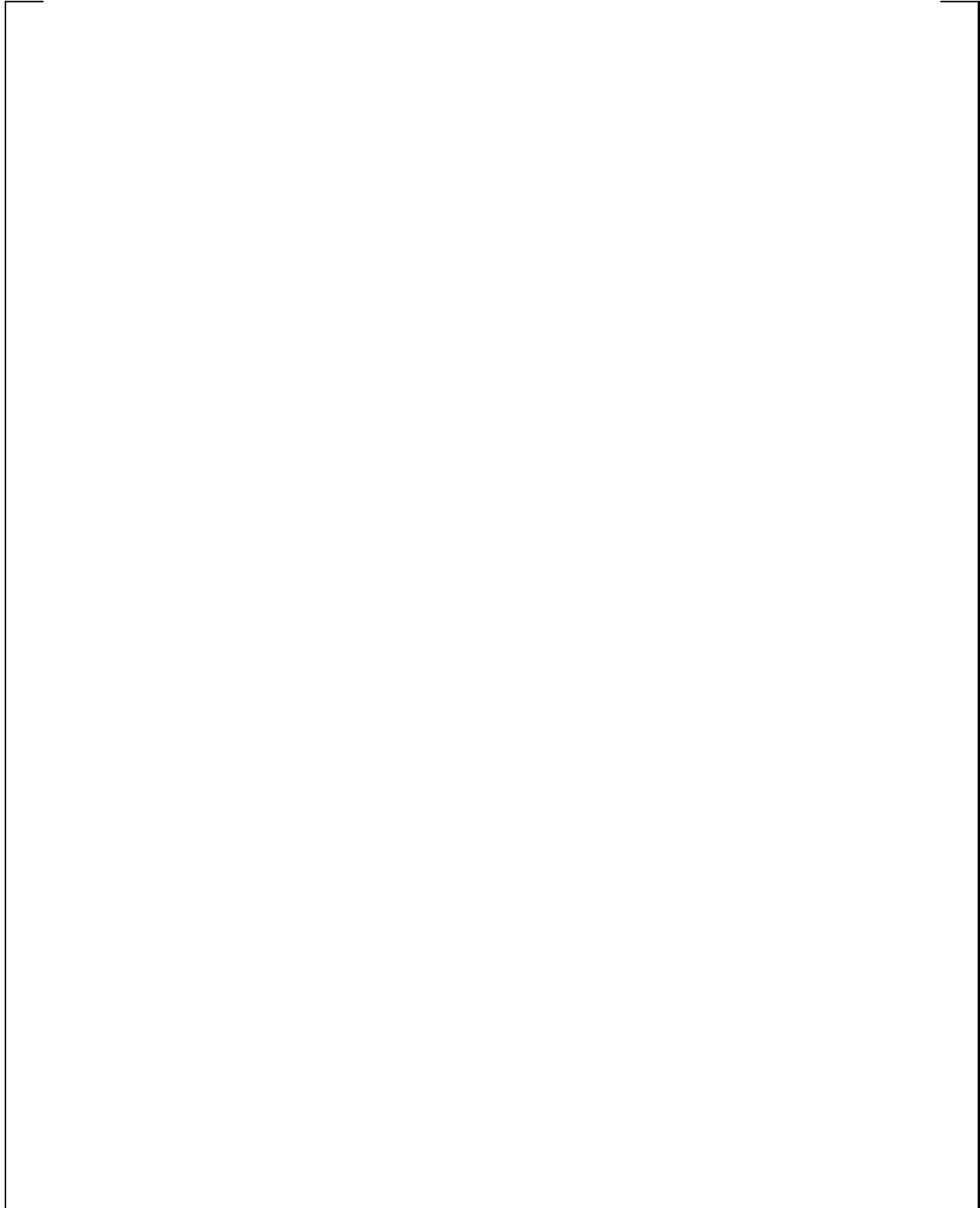
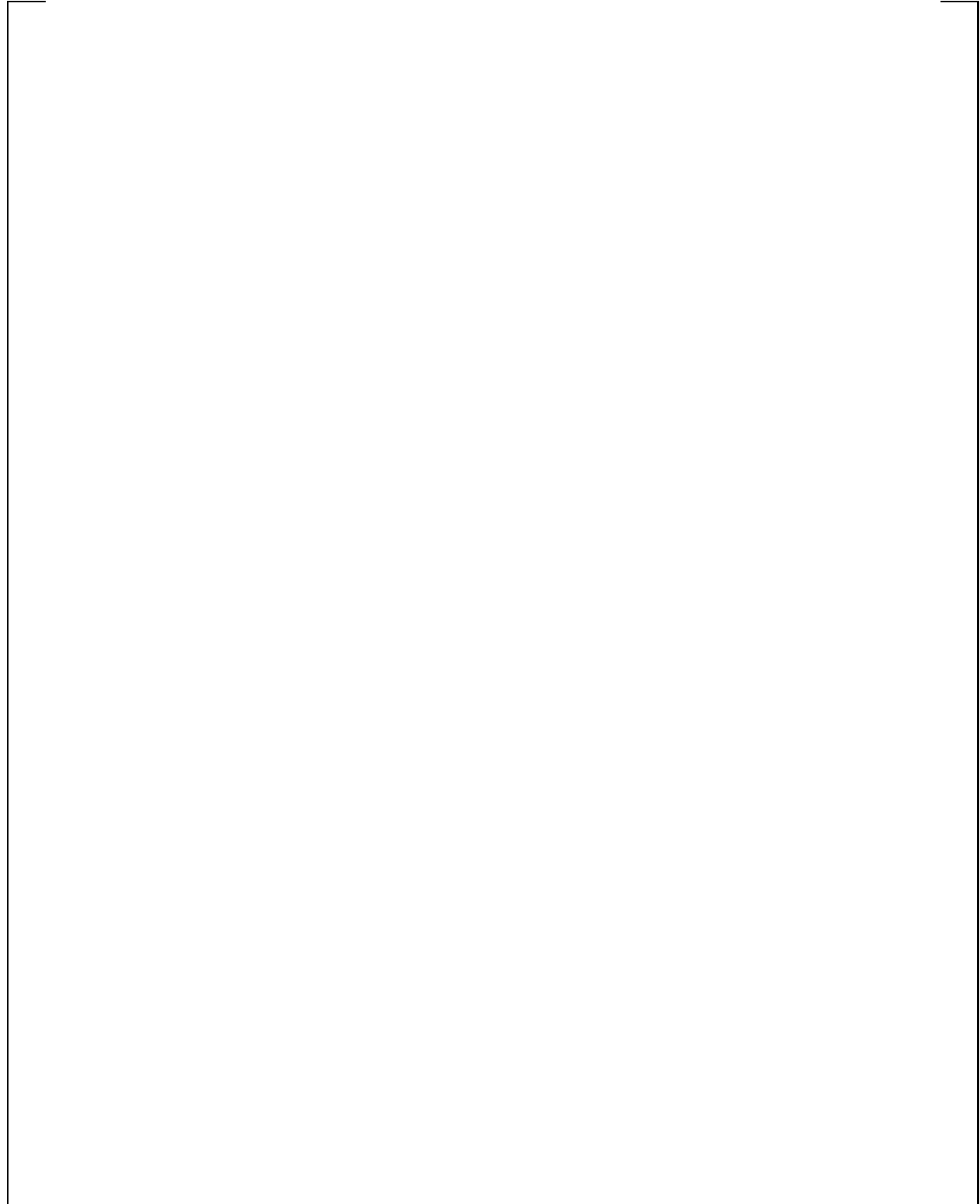


Figure 9-12. LST with Diffuser Under Steam Generator – Steam Flow 0.49-0.26 lb/sec – Saturation Temperature – Group 1

a,c



**Figure 9-13. LST with Diffuser Under Steam Generator – Steam Flow 0.49-0.62 lb/sec –
Internal Steam Pressure Ratio – Group 1**



**Figure 9-14. LST with Diffuser Under Steam Generator – Steam Flow 0.49-0.62 lb/sec –
Internal Fluid Temperature – Group 2**

a,c



**Figure 9-15. LST with Diffuser Under Steam Generator – Steam Flow 0.49-0.62 lb/sec –
Saturation Temperature – Group 2**

a,c

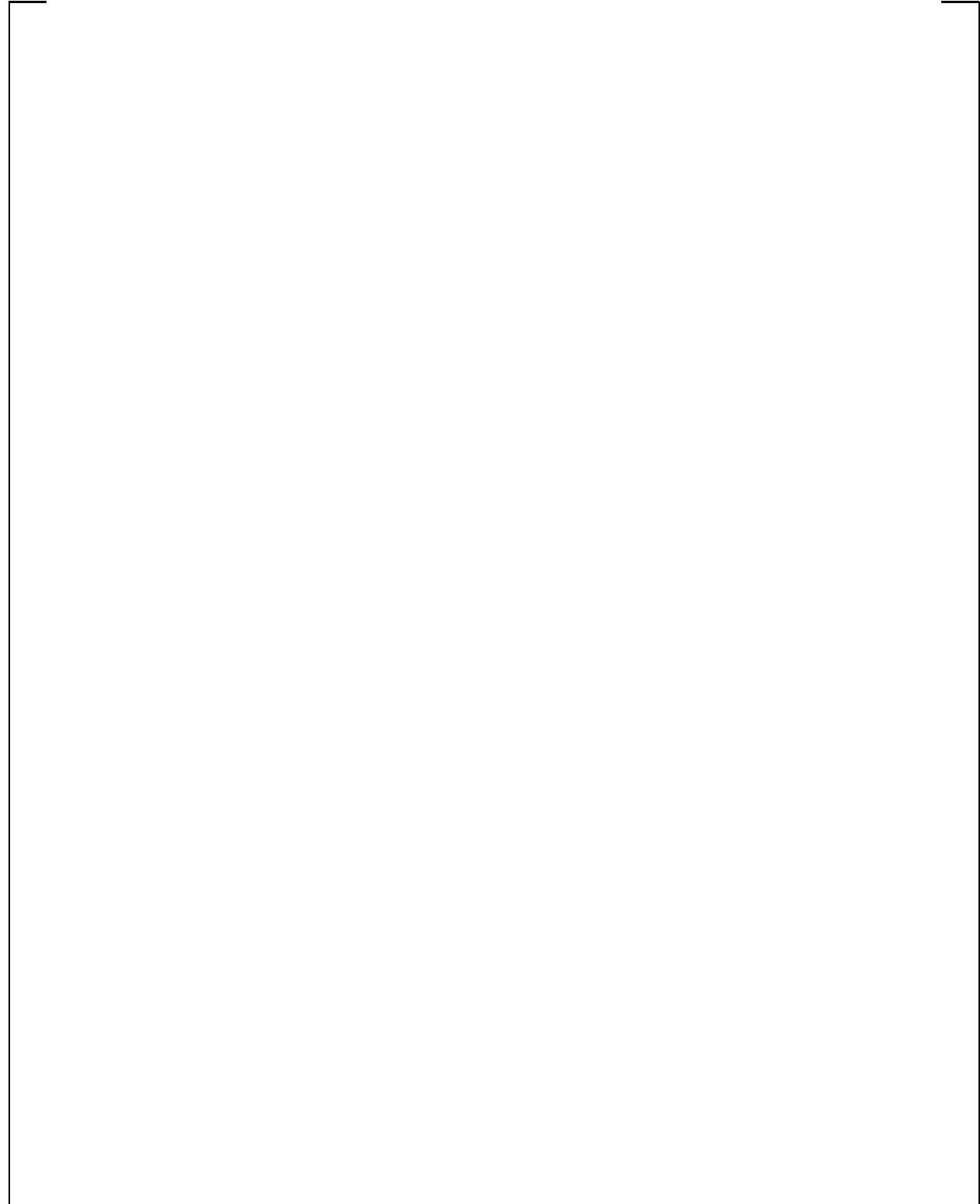


**Figure 9-16. LST with Diffuser Under Steam Generator – Steam Flow 0.49-0.62 lb/sec –
Internal Steam Pressure Ratio – Group 2**

a,c

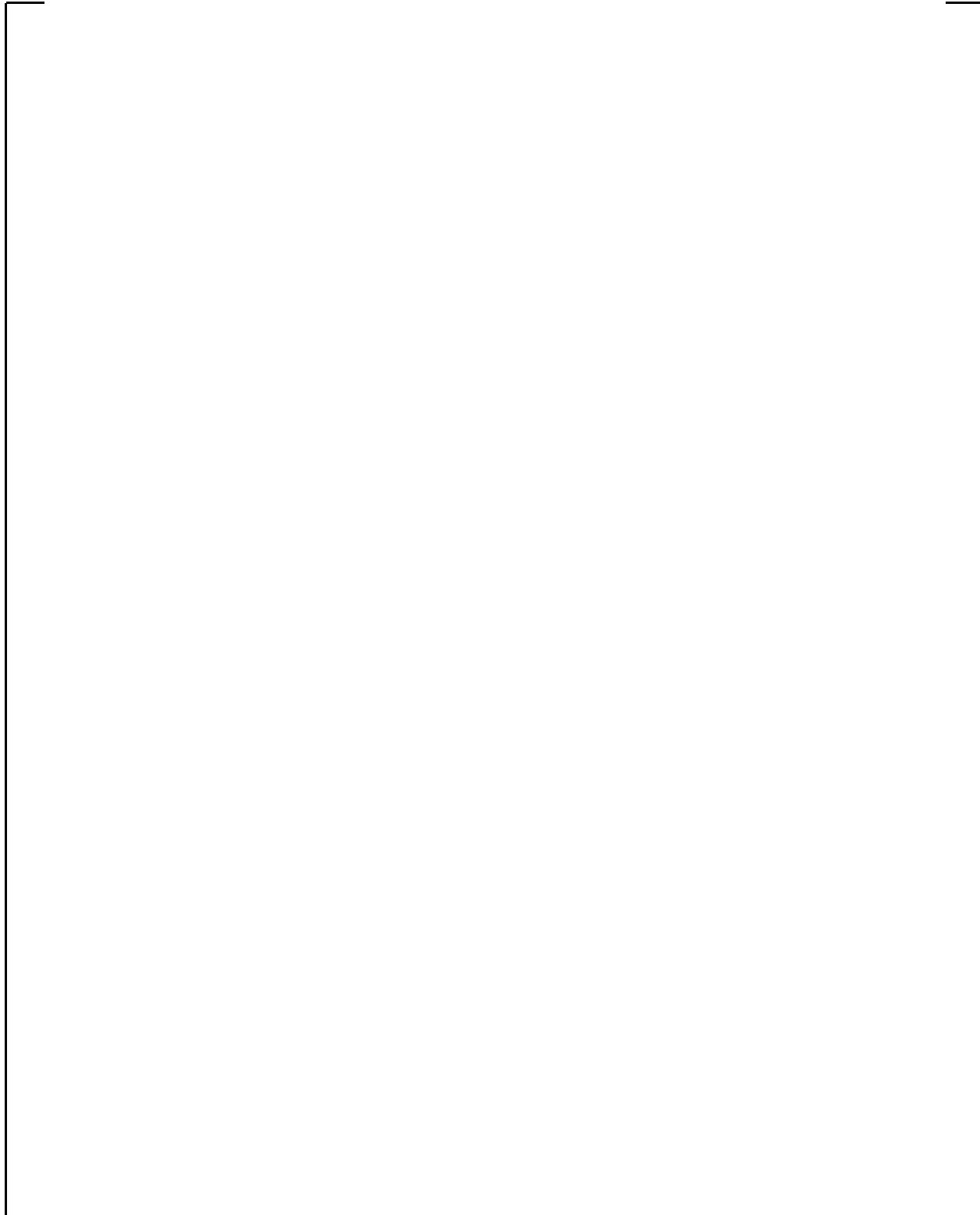


**Figure 9-17. LST with Diffuser Under Steam Generator – Steam Flow 0.76-0.84 lb/sec –
Internal Fluid Temperature**

a,c

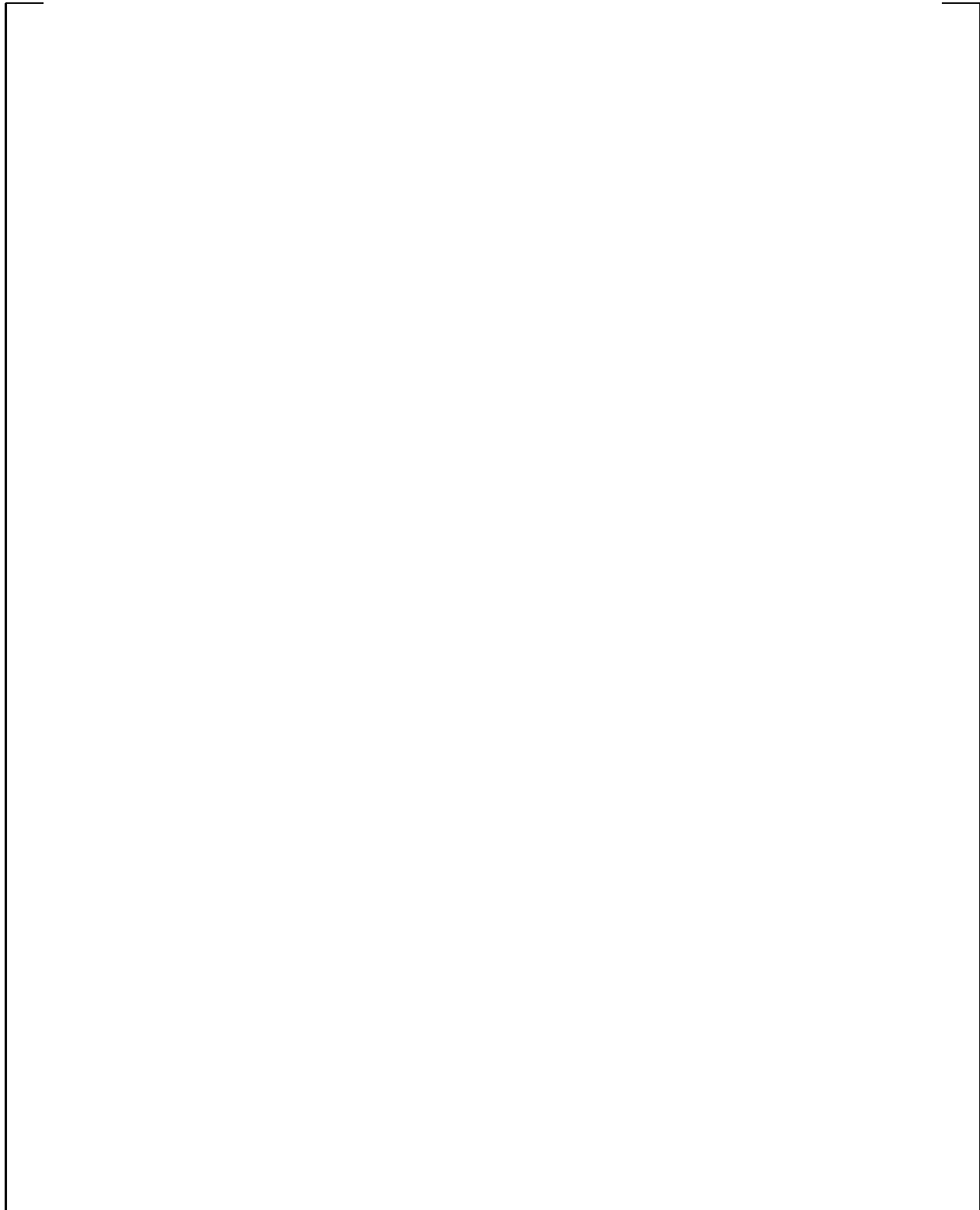
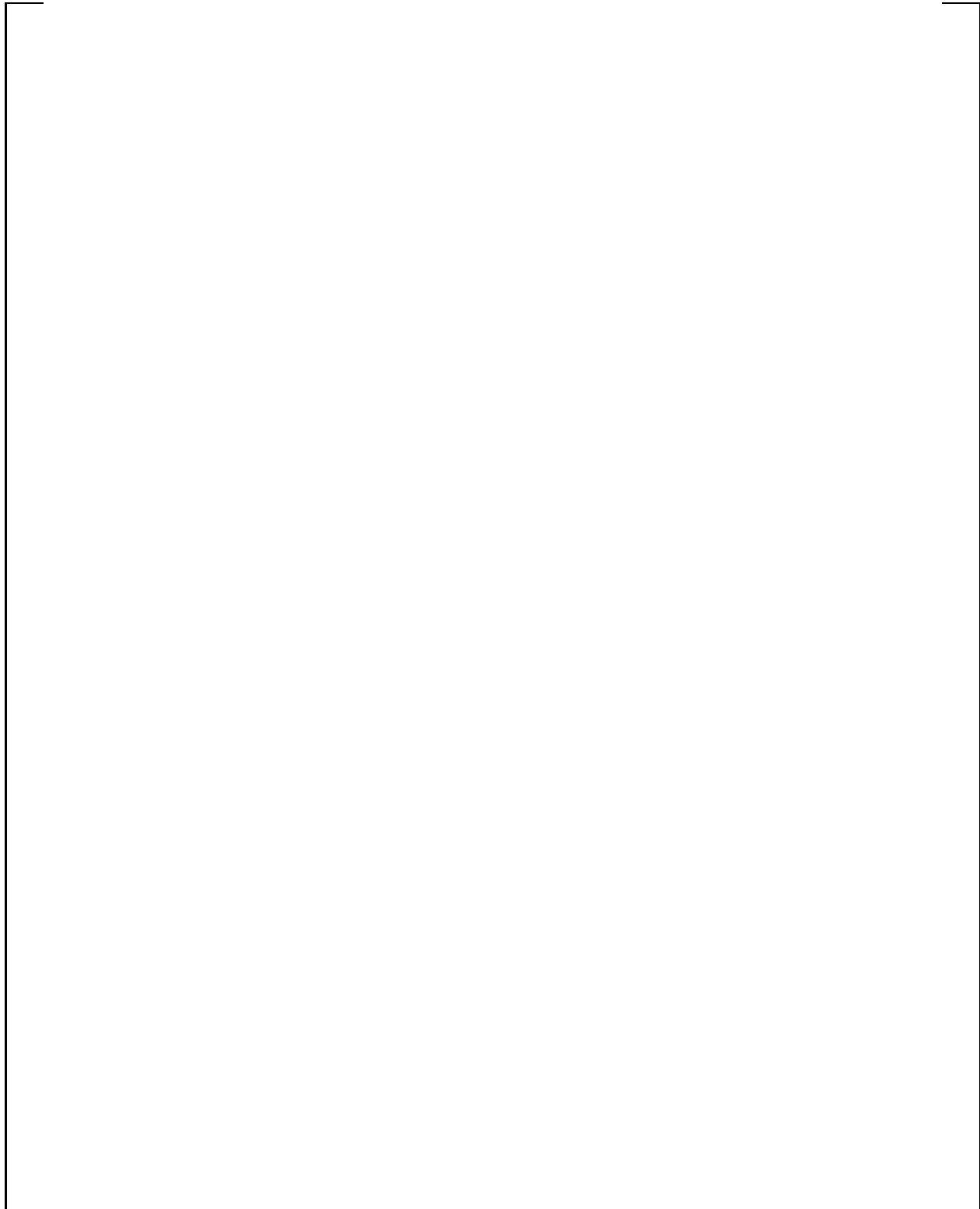


Figure 9-18. LST with Diffuser Under Steam Generator – Steam Flow 0.76-0.84 lb/sec – Saturation Temperature

a,c



**Figure 9-19. LST with Diffuser Under Steam Generator – Steam Flow 0.76-0.84 lb/sec –
Internal Steam Pressure Ratio**

a,c

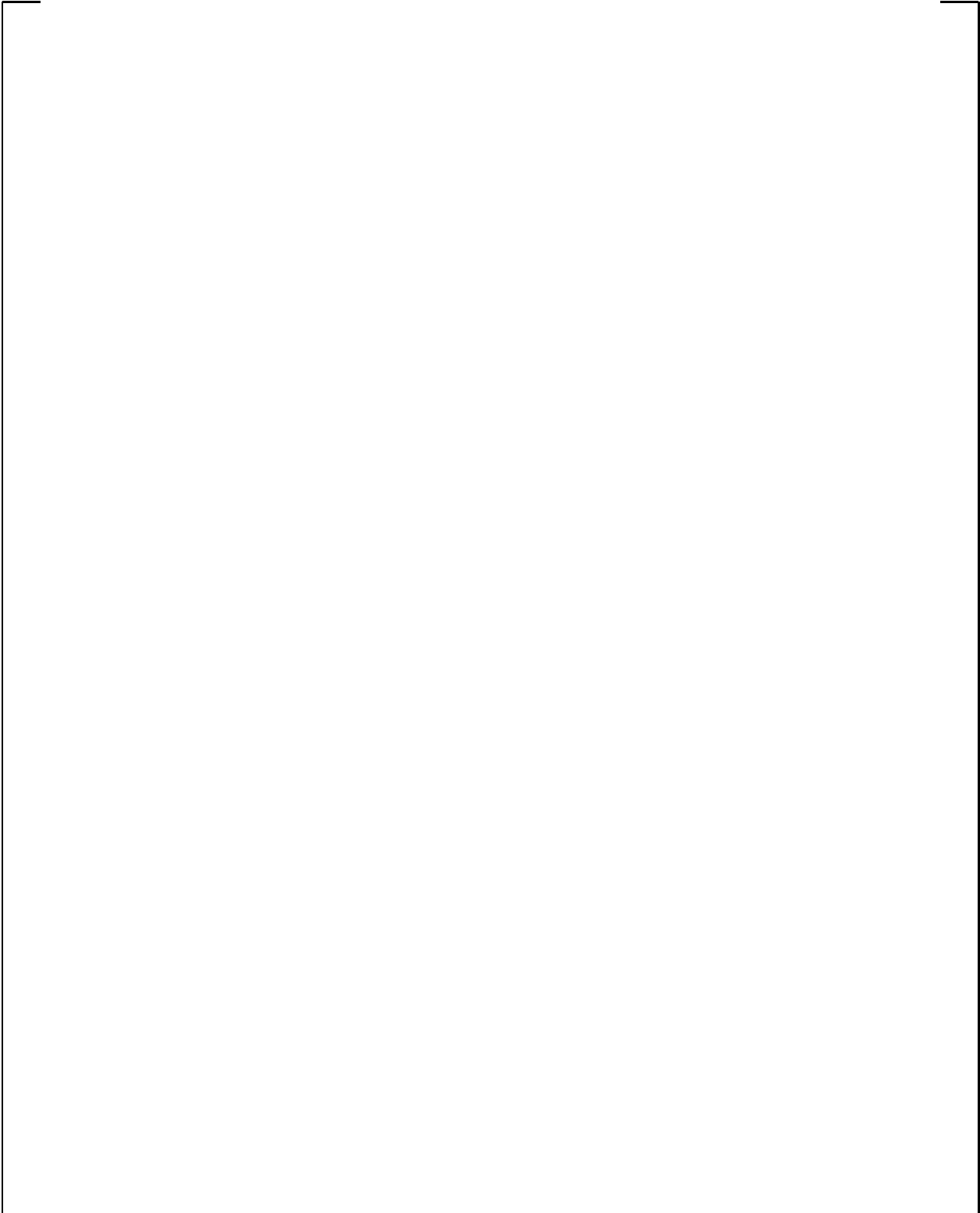


**Figure 9-20. LST with Diffuser Under Steam Generator – Steam Flow 1.10-1.20 lb/sec –
Internal Fluid Temperature**

a,c

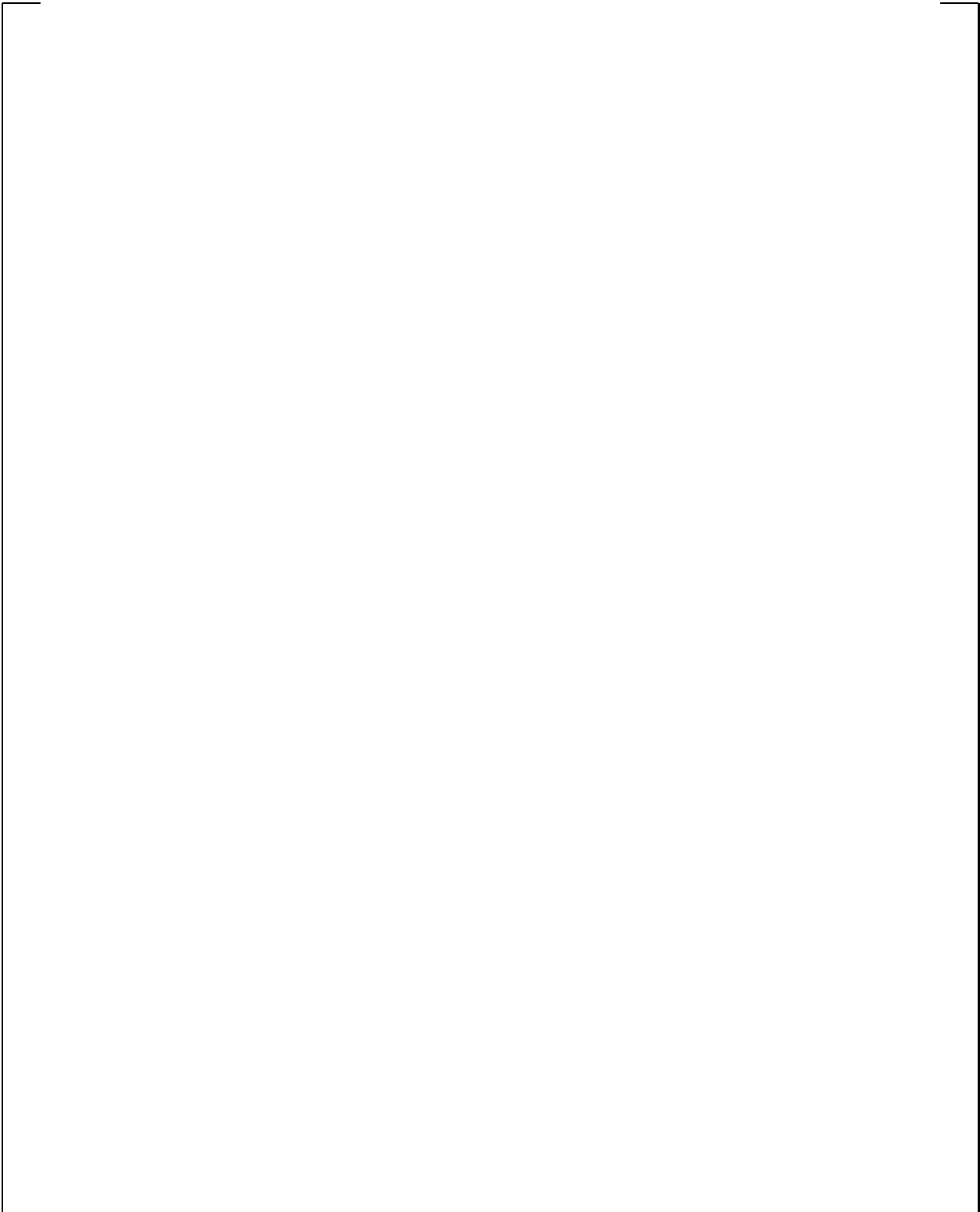
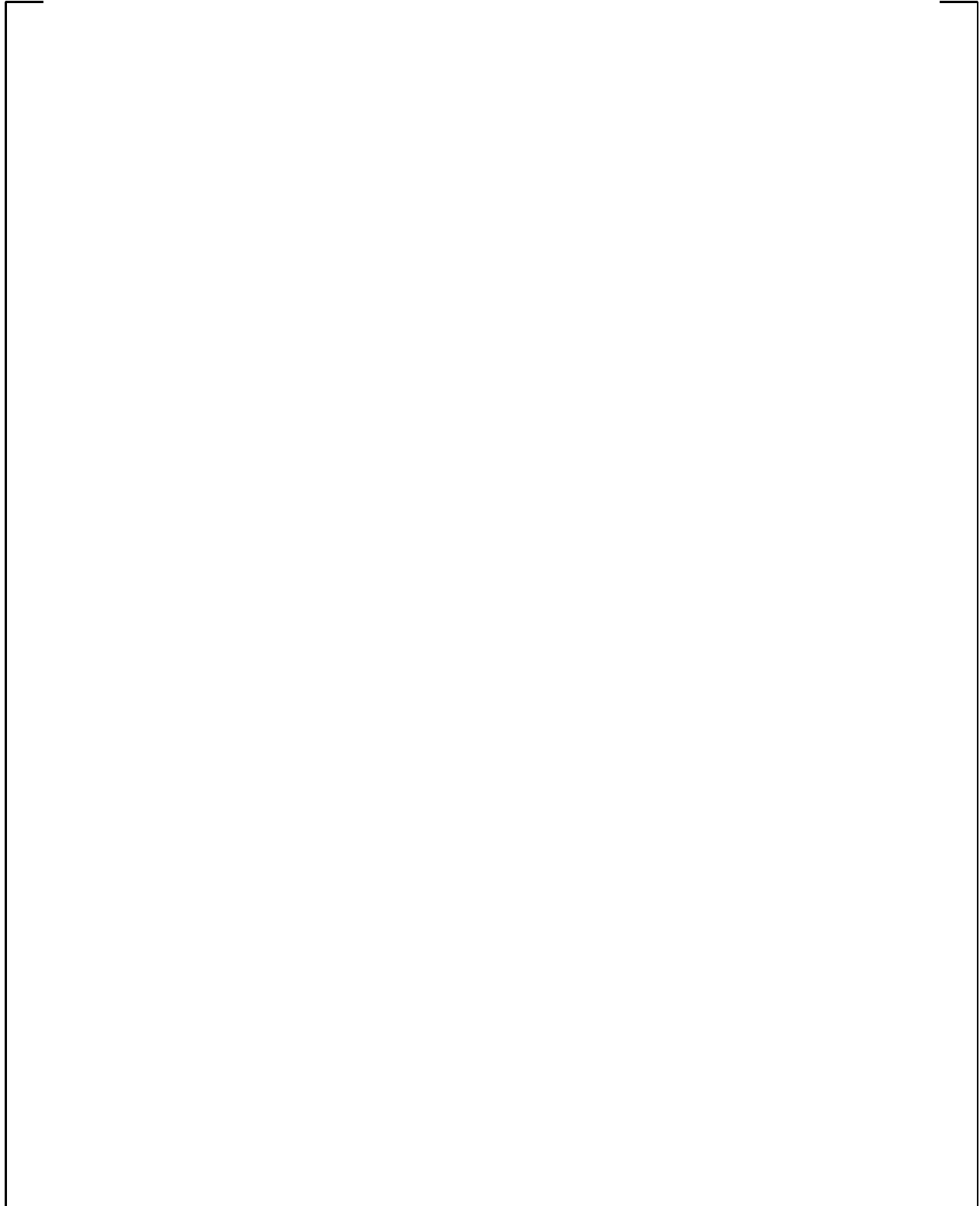


Figure 9-21. LST with Diffuser Under Steam Generator – Steam Flow 1.10-1.20 lb/sec – Saturation Temperature

a,c



**Figure 9-22. LST with Diffuser Under Steam Generator – Steam Flow 1.10-1.20 lb/sec –
Internal Steam Pressure Ratio**

a,c



**Figure 9-23. LST with Diffuser Under Steam Generator – Steam Flow 1.54-1.68 lb/sec –
Internal Fluid Temperature**

a,c



Figure 9-24. LST with Diffuser Under Steam Generator – Steam Flow 1.54-1.68 lb/sec – Saturation Temperature

a,c



**Figure 9-25. LST with Diffuser Under Steam Generator – Steam Flow 1.54-1.68 lb/sec –
Internal Steam Pressure Ratio**

a,c

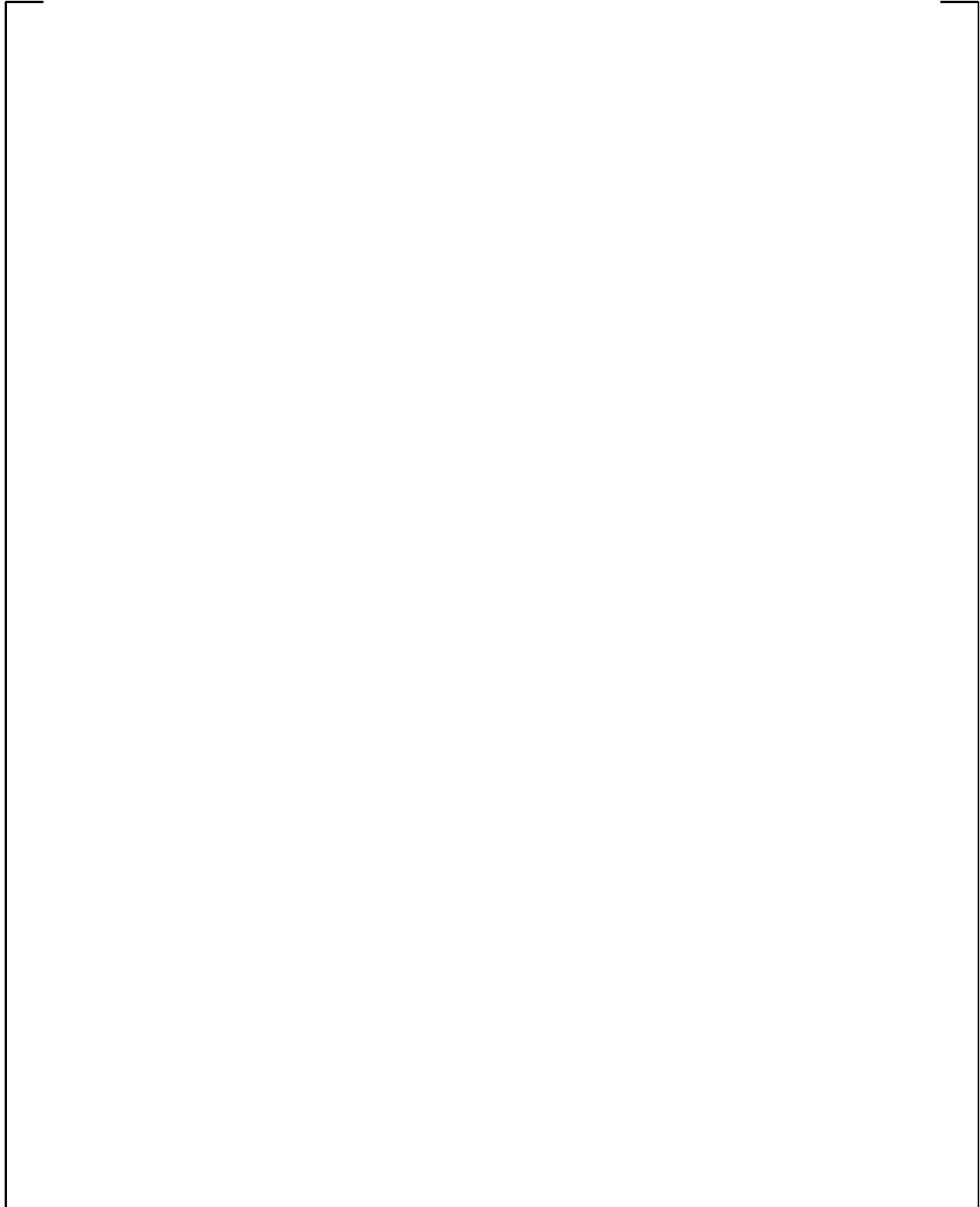


**Figure 9-26. LST with Diffuser Up 6 Feet – Steam Flow 0.76 & 1.68 lb/sec –
Internal Fluid Temperature**

a,c

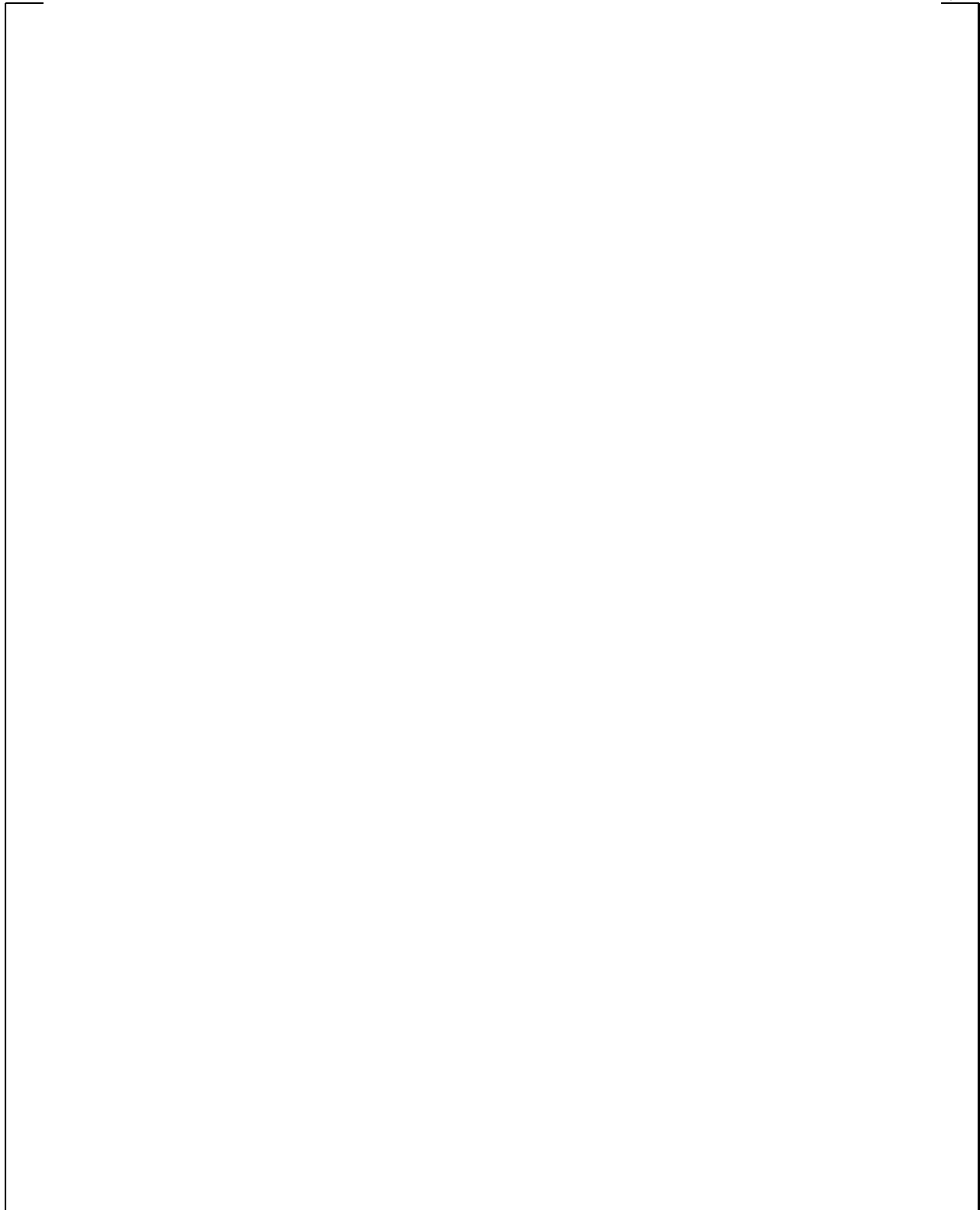
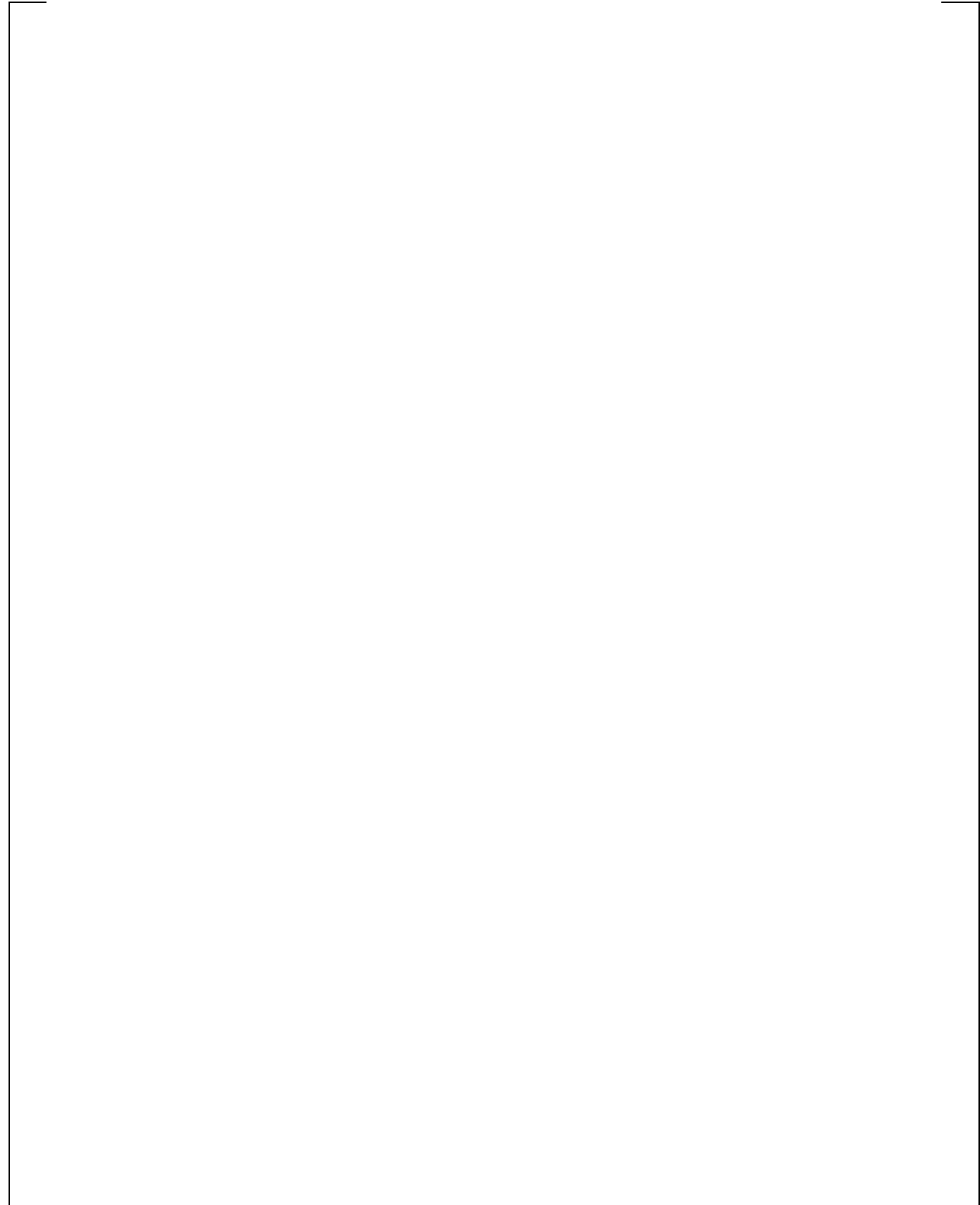


Figure 9-27. LST with Diffuser Up 6 Feet – Steam Flow 0.76 & 1.68 lb/sec – Saturation Temperature

a,c



**Figure 9-28. LST with Diffuser Up 6 Feet – Steam Flow 0.76 & 1.68 lb/sec –
Internal Steam Pressure Ratio**

a,c



**Figure 9-29. LST with Steam Injection: 3 Inch Pipe – Steam Flow 0.76 – 0.95 lb/sec –
Internal Fluid Temperature**

a,c

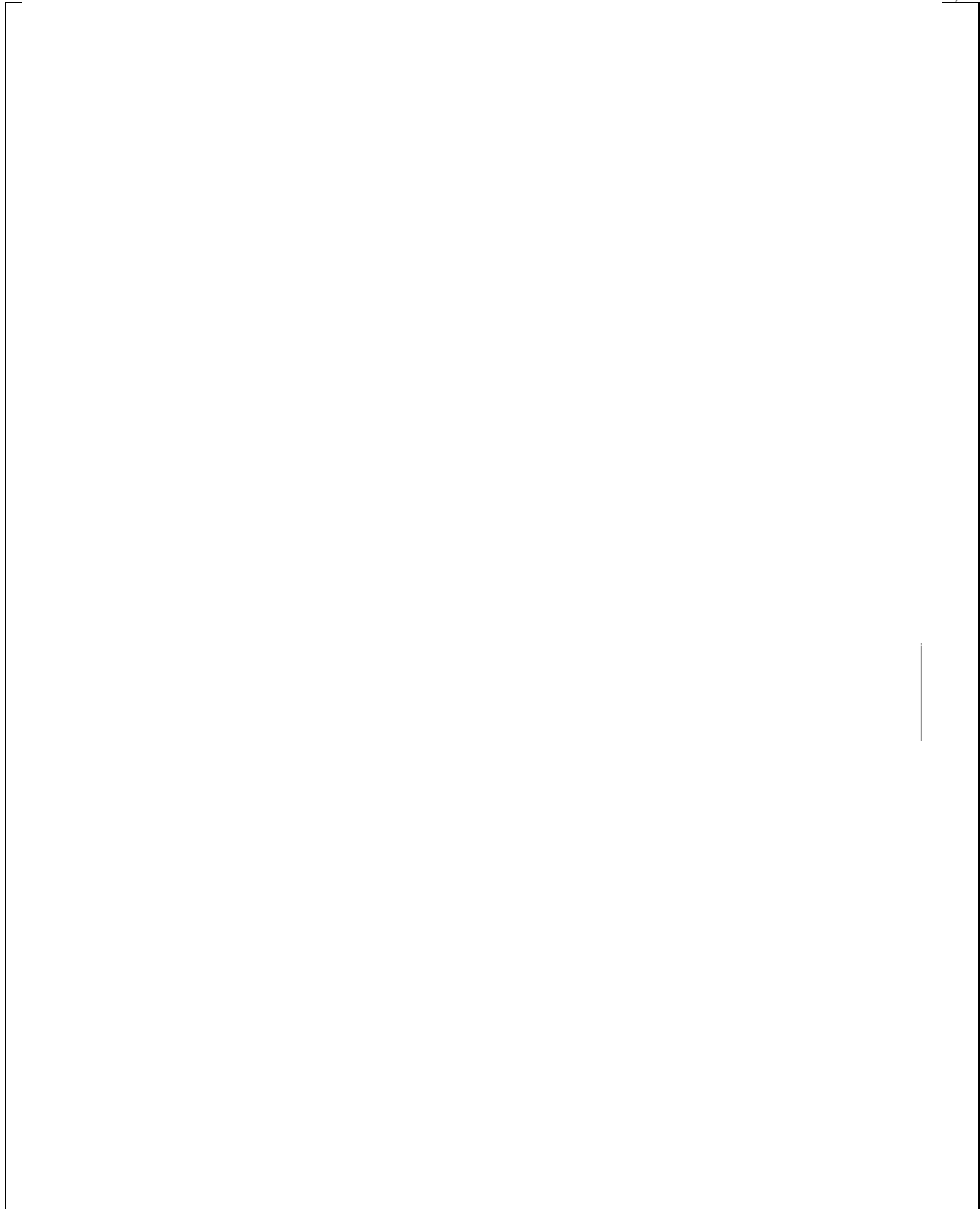
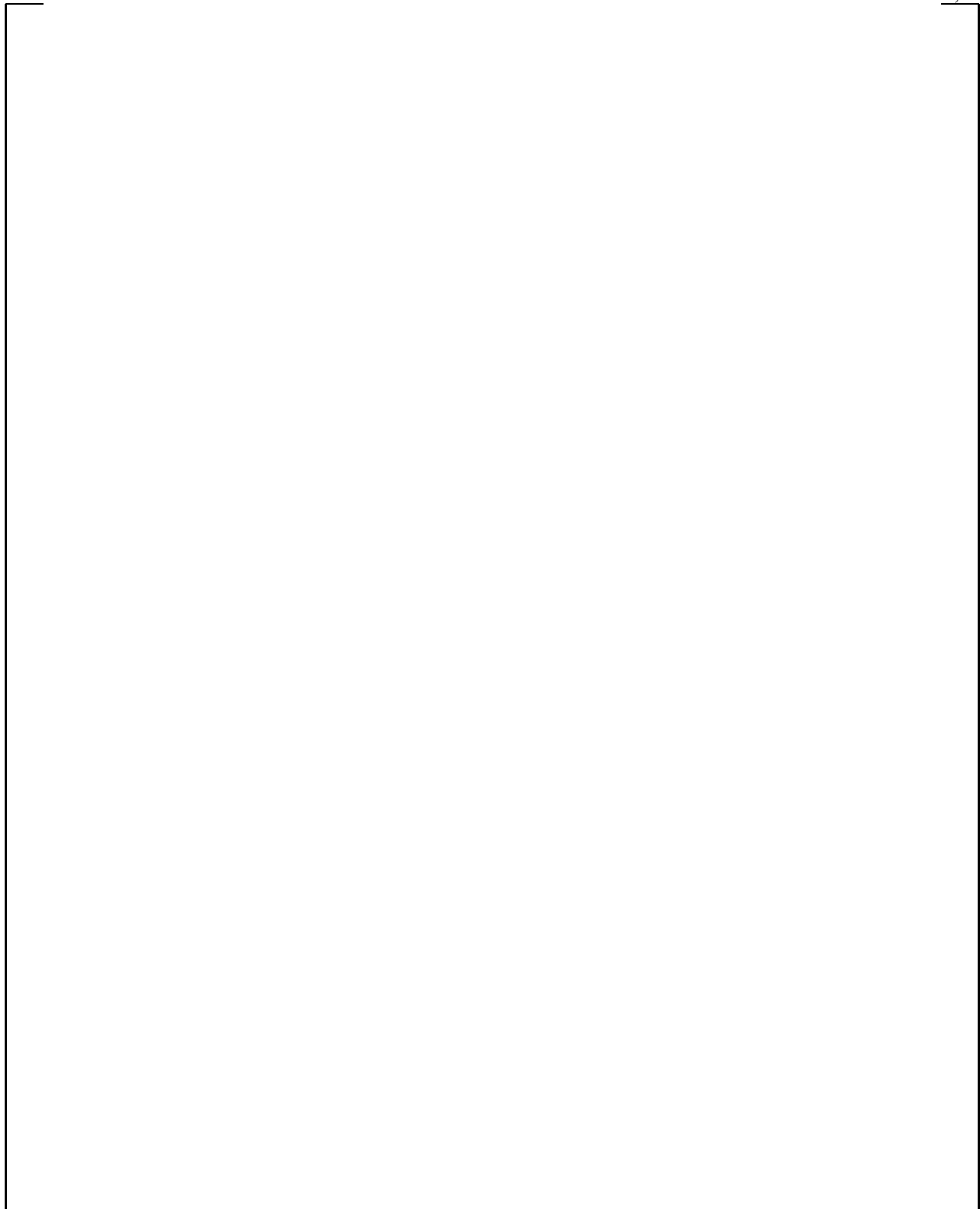


Figure 9-30. LST with Steam Injection: 3 Inch Pipe – Steam Flow 0.76 – 0.95 lb/sec – Saturation Temperature

a,c



**Figure 9-31. LST with Steam Injection: 3 Inch Pipe – Steam Flow 0.76 – 0.95 lb/sec –
Internal Steam Pressure Ratio**

a,c



**Figure 9-32. LST with Steam Injection: 3 Inch Pipe – Steam Flow 1.25 – 1.31 lb/sec –
Internal Fluid Temperature**

a,c



Figure 9-33. LST with Steam Injection: 3 Inch Pipe – Steam Flow 1.25 – 1.31 lb/sec – Saturation Temperature

a,c

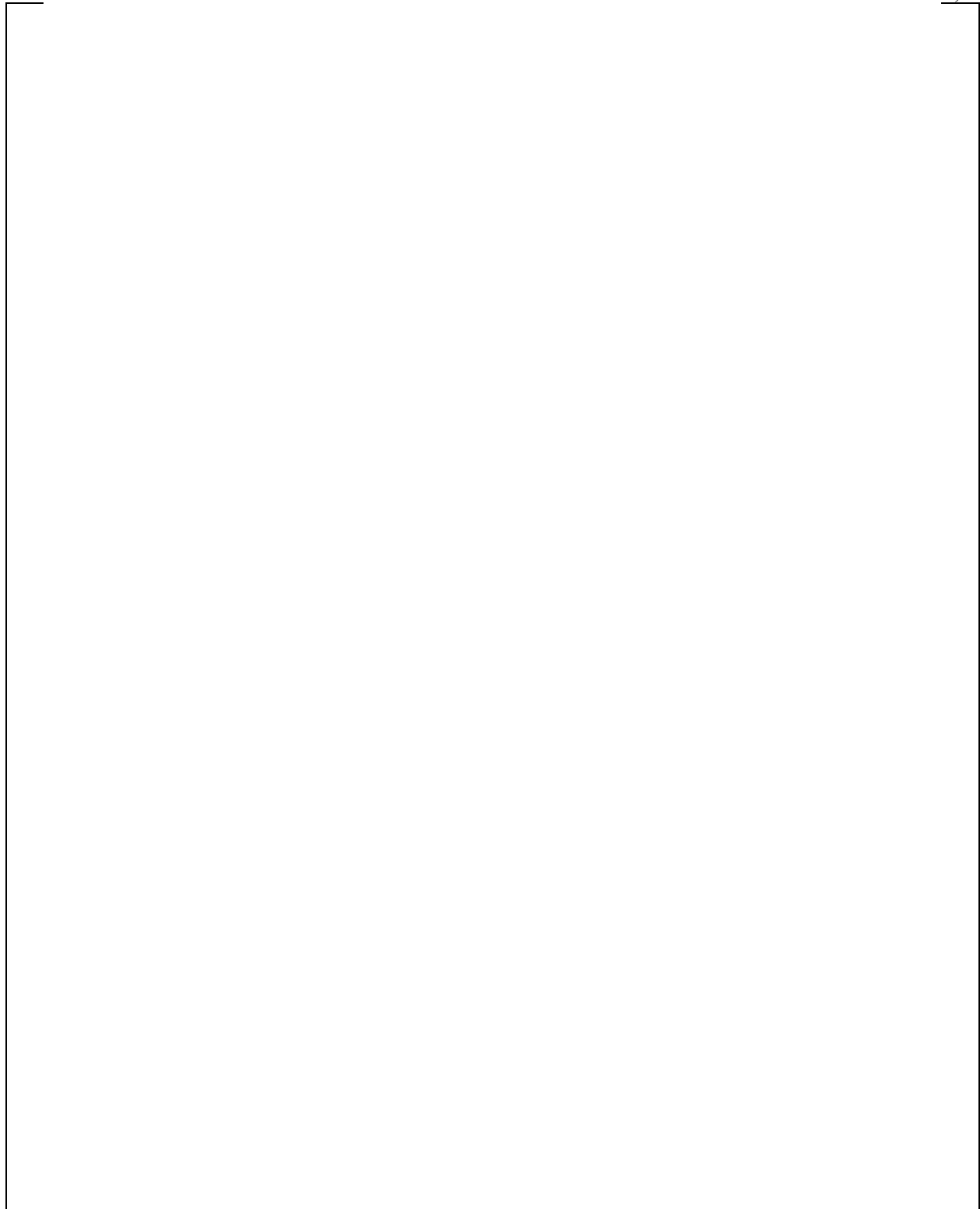


**Figure 9-34. LST with Steam Injection: 3 Inch Pipe – Steam Flow 1.25 – 1.31 lb/sec –
Internal Steam Pressure Ratio**

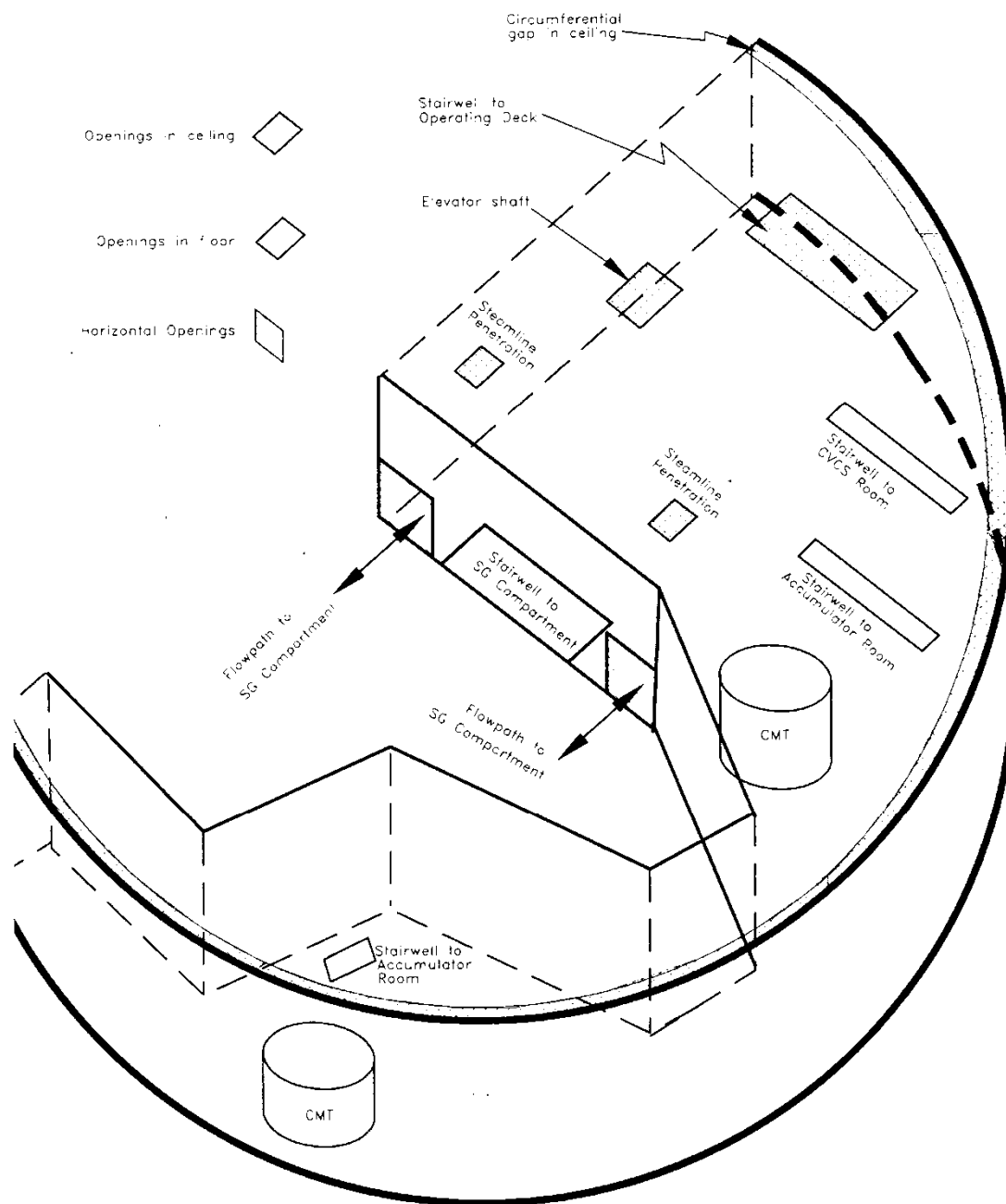


Figure 9-35. CMT Compartment Layout

a,c

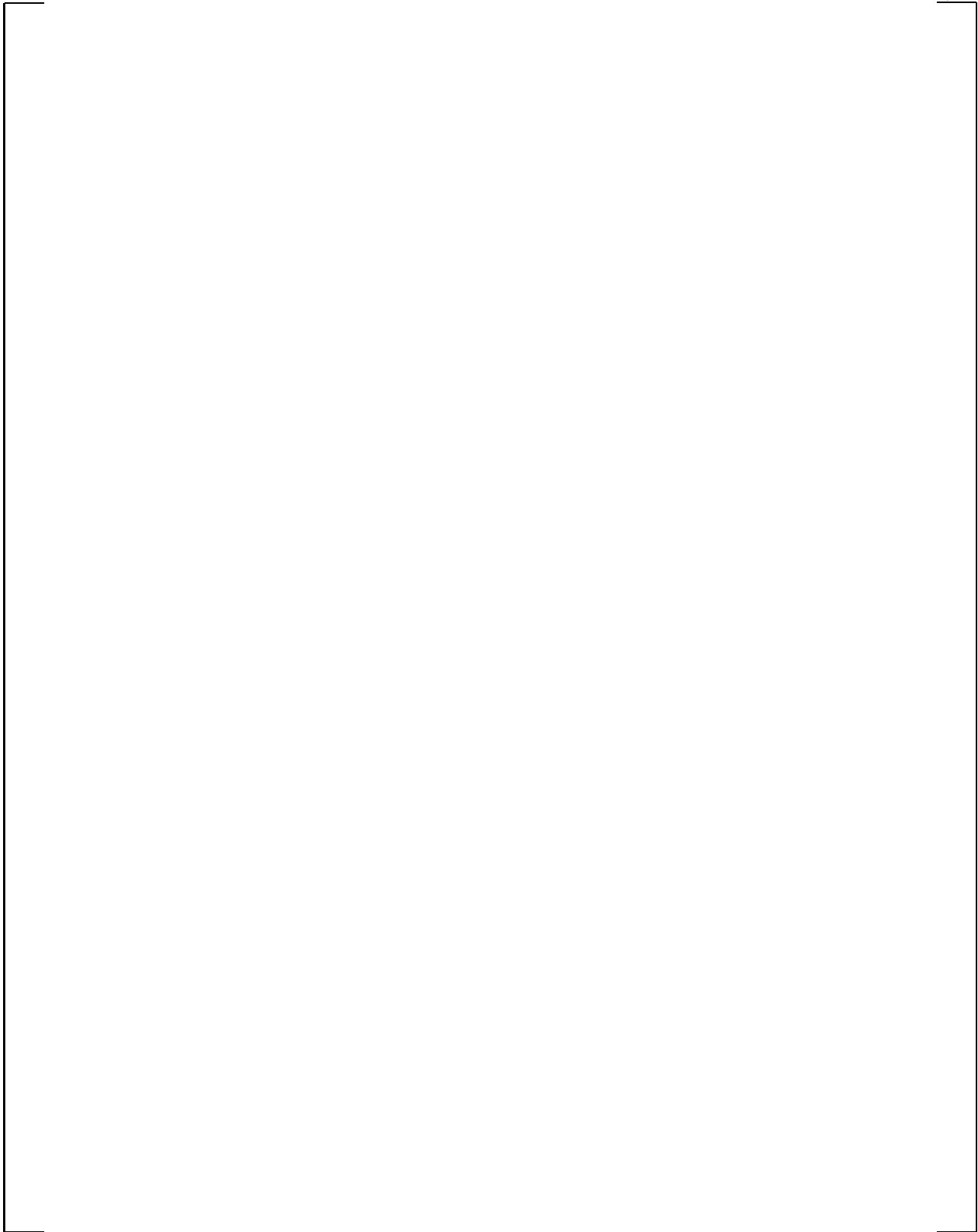


Figure 9-36. Simplified AP600 Containment Diagram

a,c

Figure 9-37. WGOTHIC Calculated LOCA Blowdown Steam Pressure Ratio for Jet Momentum Dissipated in SG East Compartment

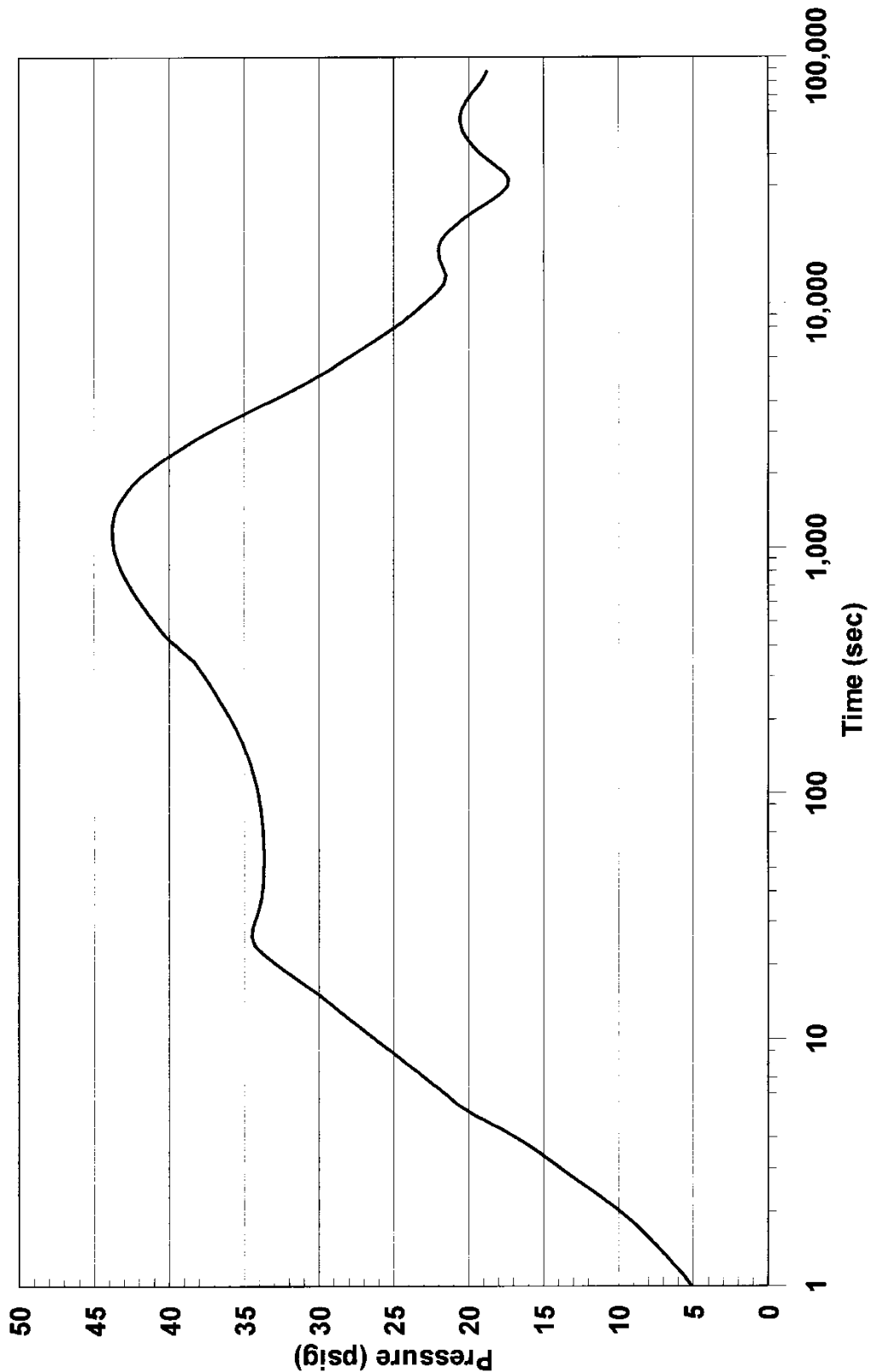


Figure 9-38. WGOthic Calculated AP600 Containment Pressure – Sensitivity to Loss Coefficients for LOCA Jet Momentum Dissipated in SG East Compartment

a,c

Figure 9-39. WGOTHIC Calculated Flow Pattern – Sensitivity to Loss Coefficients for LOCA Jet Momentum Dissipated in SG East Compartment at 20 Seconds

a,c

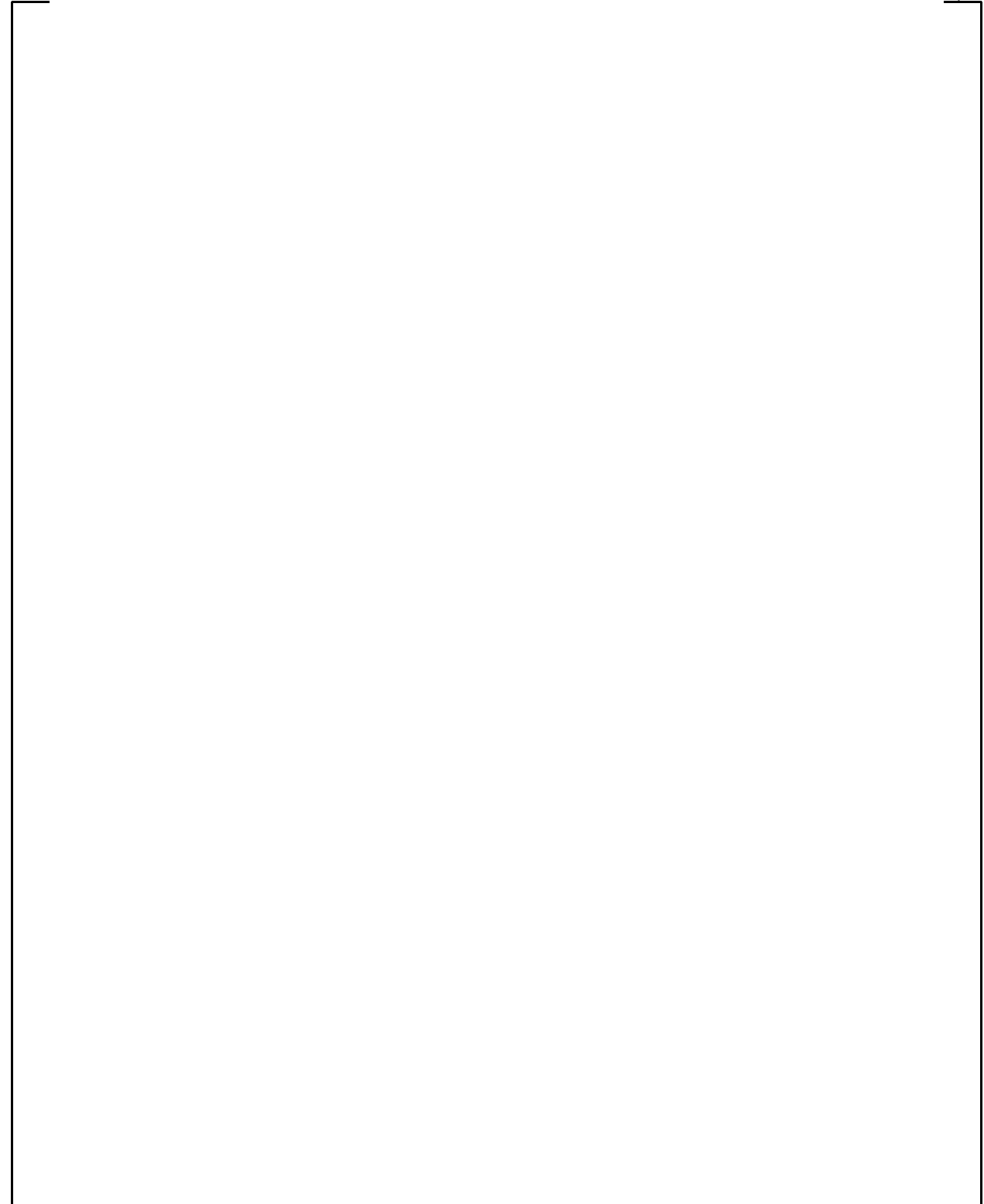


Figure 9-40. WGOTHIC Calculated Flow Pattern – Sensitivity to Loss Coefficients for LOCA Jet Momentum Dissipated in SG East Comp. at 1000 Seconds

a,c



Figure 9-41. WGOTHIC Calculated Flow Pattern – Sensitivity to Loss Coefficients for LOCA Jet Momentum Dissipated in SG East Comp. at 1550 Seconds

a,c



Figure 9-42. WGOTHIC Calculated Flow Pattern – Sensitivity to Loss Coefficients for LOCA Jet Momentum Dissipated in SG East Comp. at 80050 Seconds

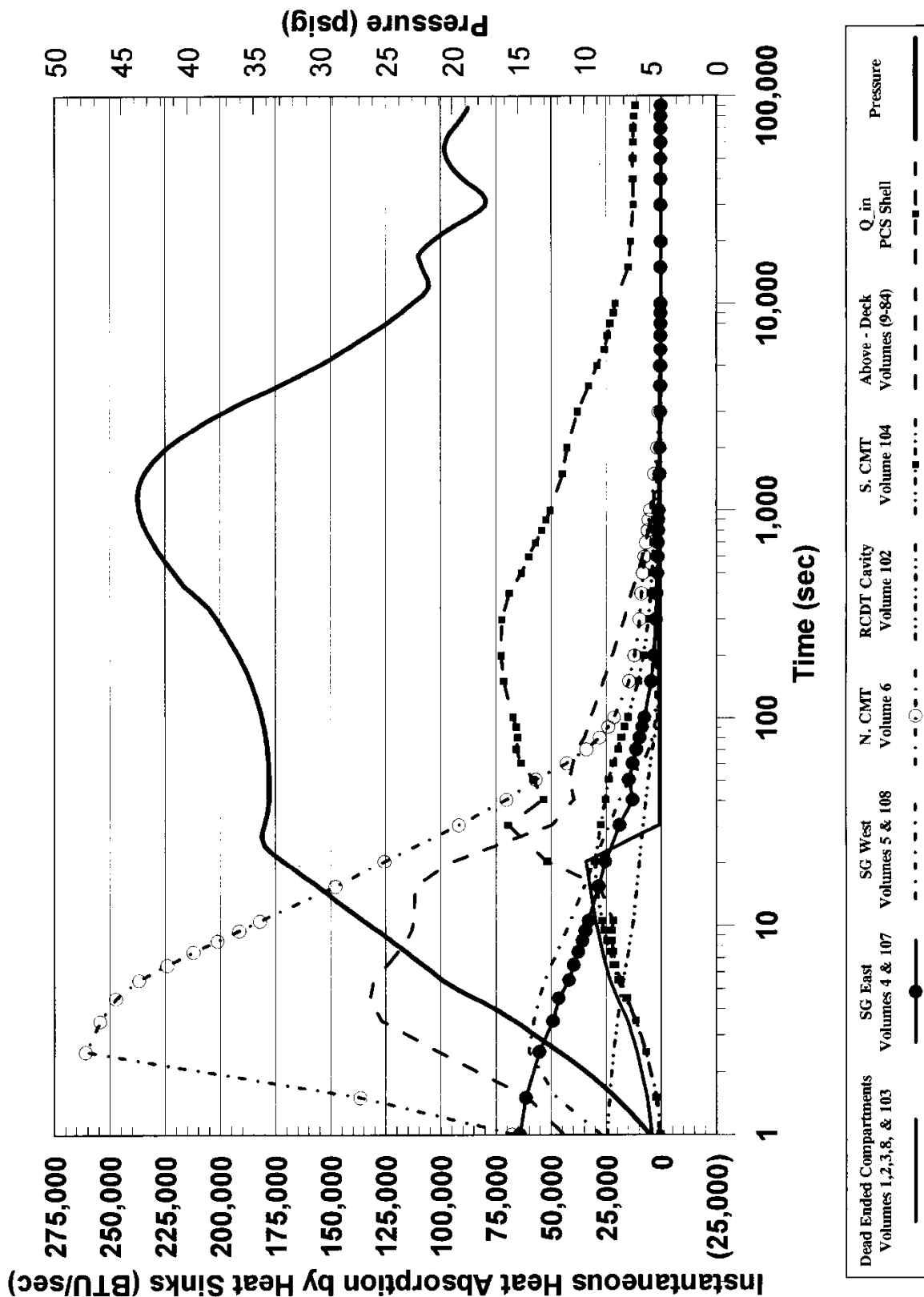


Figure 9-43. WGOthic Calculated AP600 Containment Heat Removal Rates – LOCA Jet Momentum Dissipated in SG East Compartment

a,c



Figure 9-44. WGOTHIC Calculated AP600 Containment Steam Pressure Ratio for LOCA Jet Momentum Dissipated in SG East Compartment

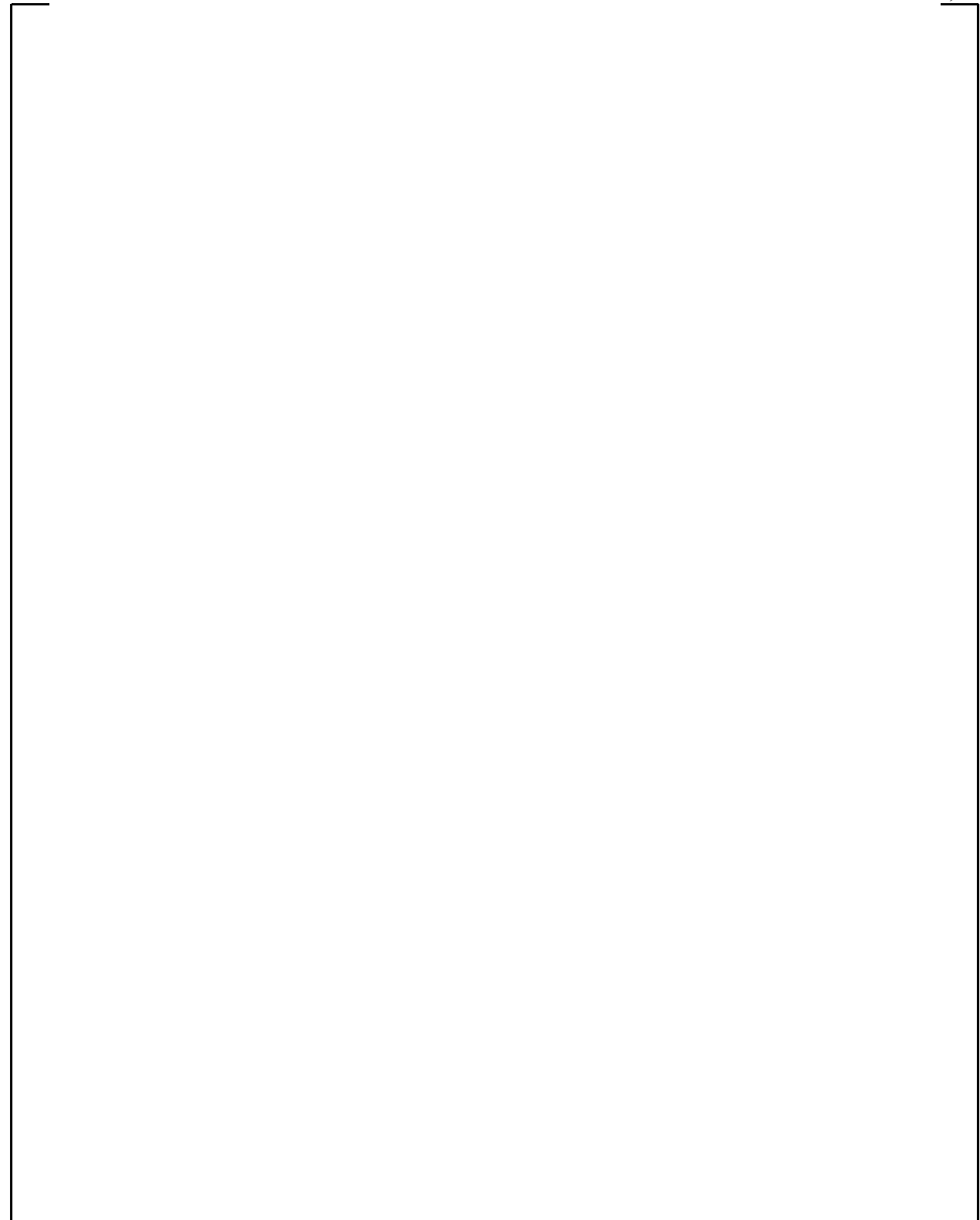


Figure 9-45. WGOTHIC Calculated AP600 Cont. Pressure – Sensitivity to Heat Transfer Coefficient for Study of Undissipated Jet Effects During a LOCA

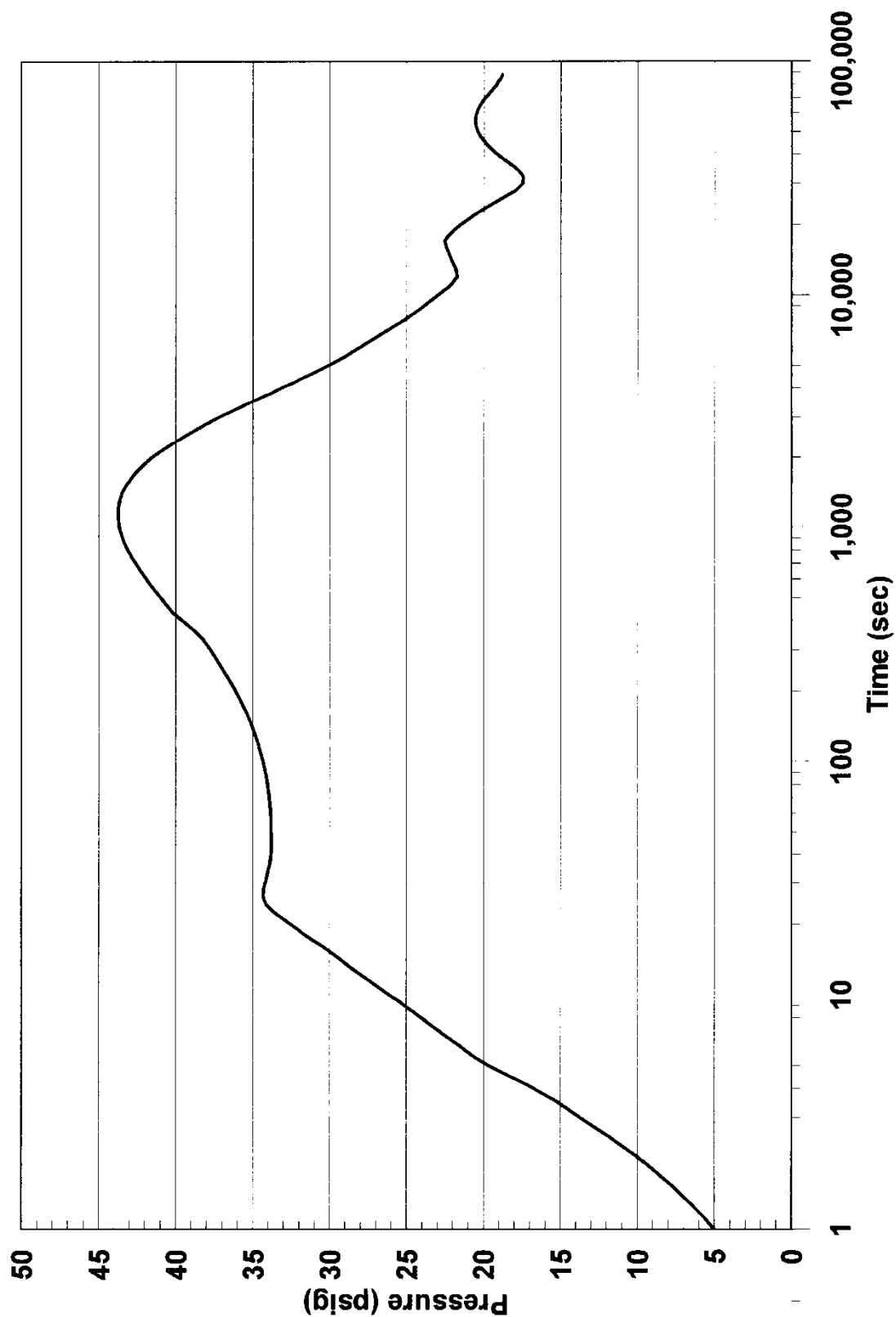


Figure 9-46. WGOthic Calculated AP600 Containment Pressure – LOCA Jet Momentum Dissipated in SG East Compartment

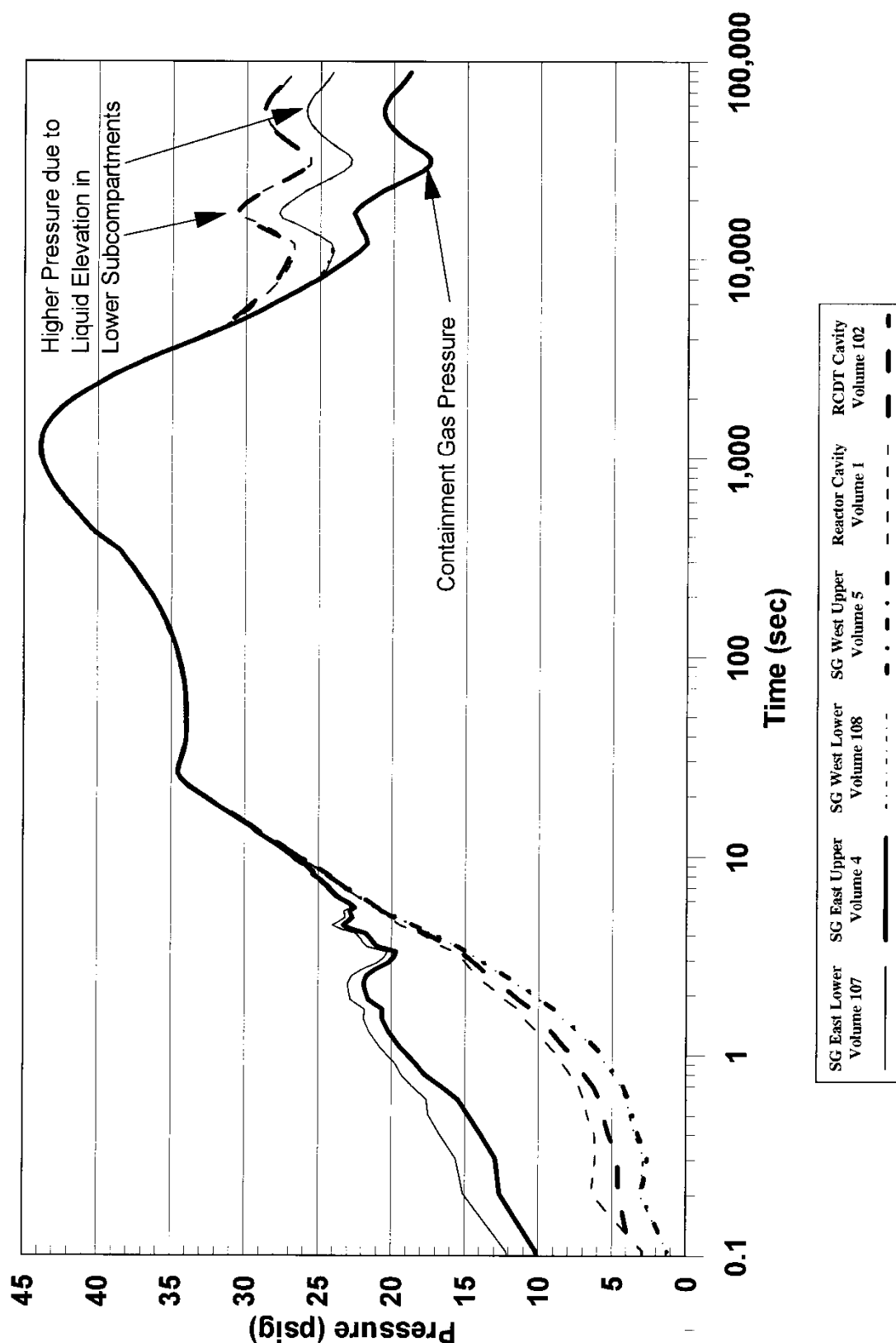


Figure 9-46A. WGOthic Calculated AP600 Containment Below-Deck Compartment Pressure for LOCA Jet Momentum Dissipated in SG East Compartment

a,c

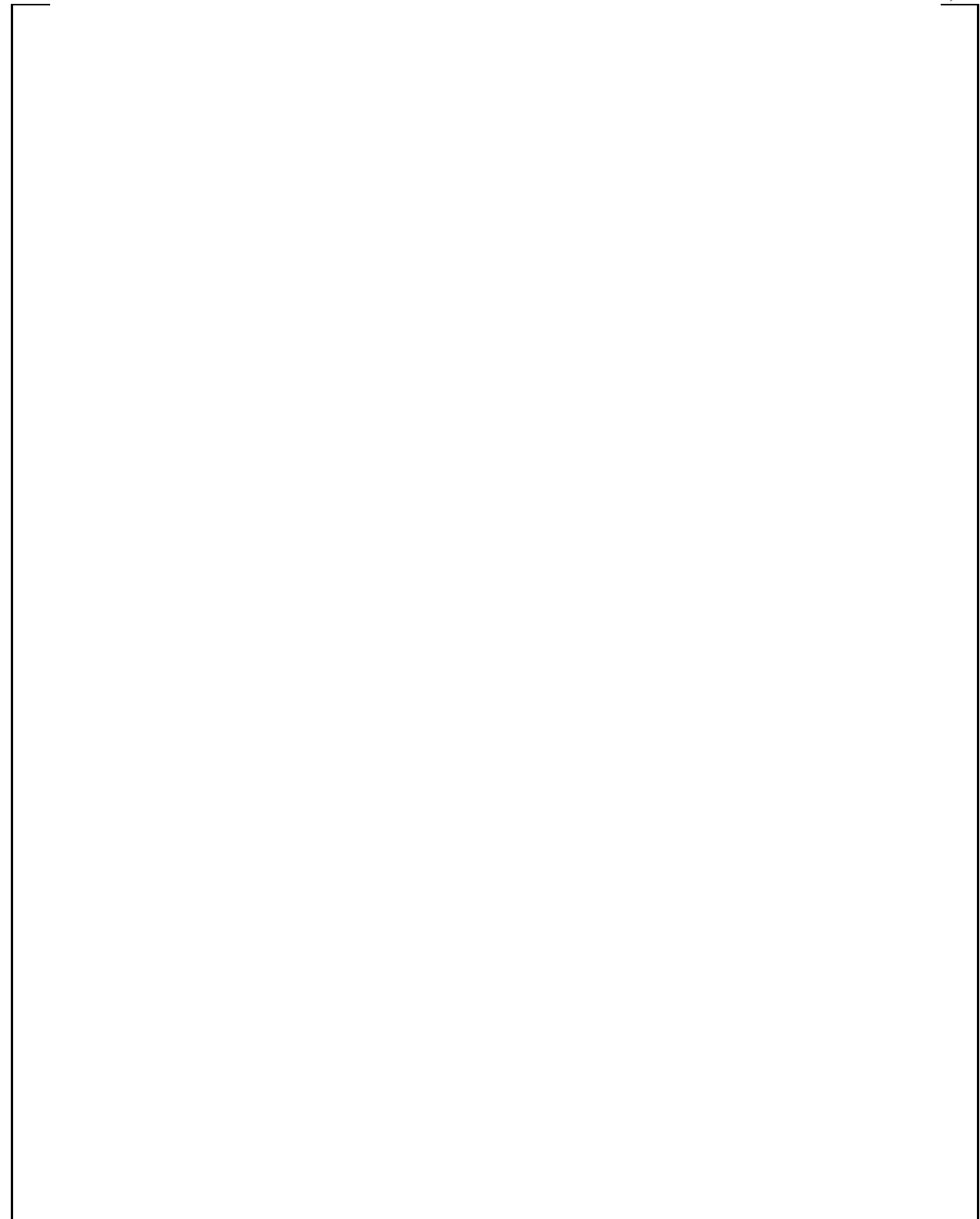


Figure 9-47. WGOTHIC Calculated Flow Pattern – LOCA Jet Momentum Dissipated in SG East Compartment at 20 Seconds

a,c

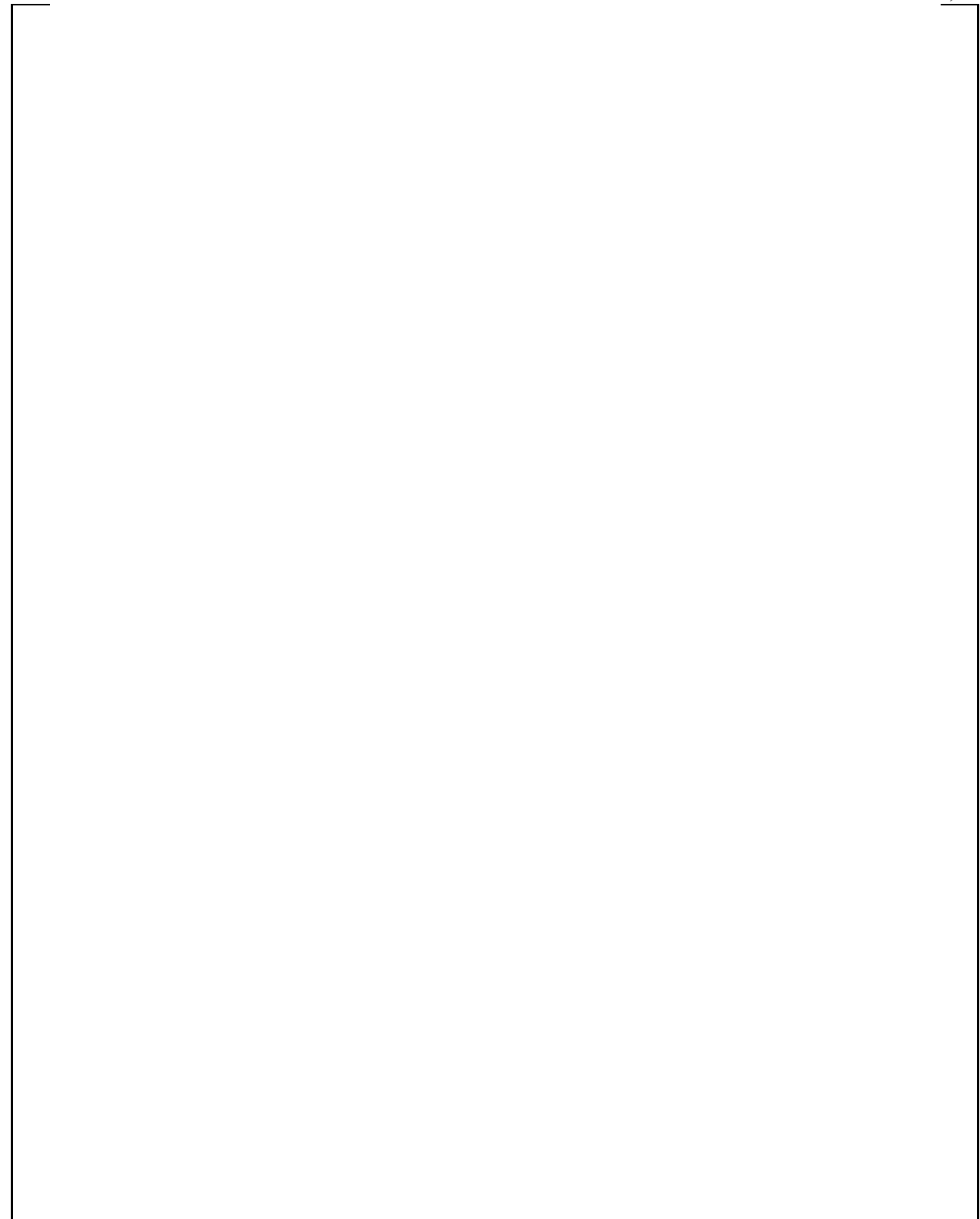


Figure 9-48. WGOTHIC Calculated Flow Pattern – LOCA Jet Momentum Dissipated in SG East Compartment at 1000 Seconds

a,c

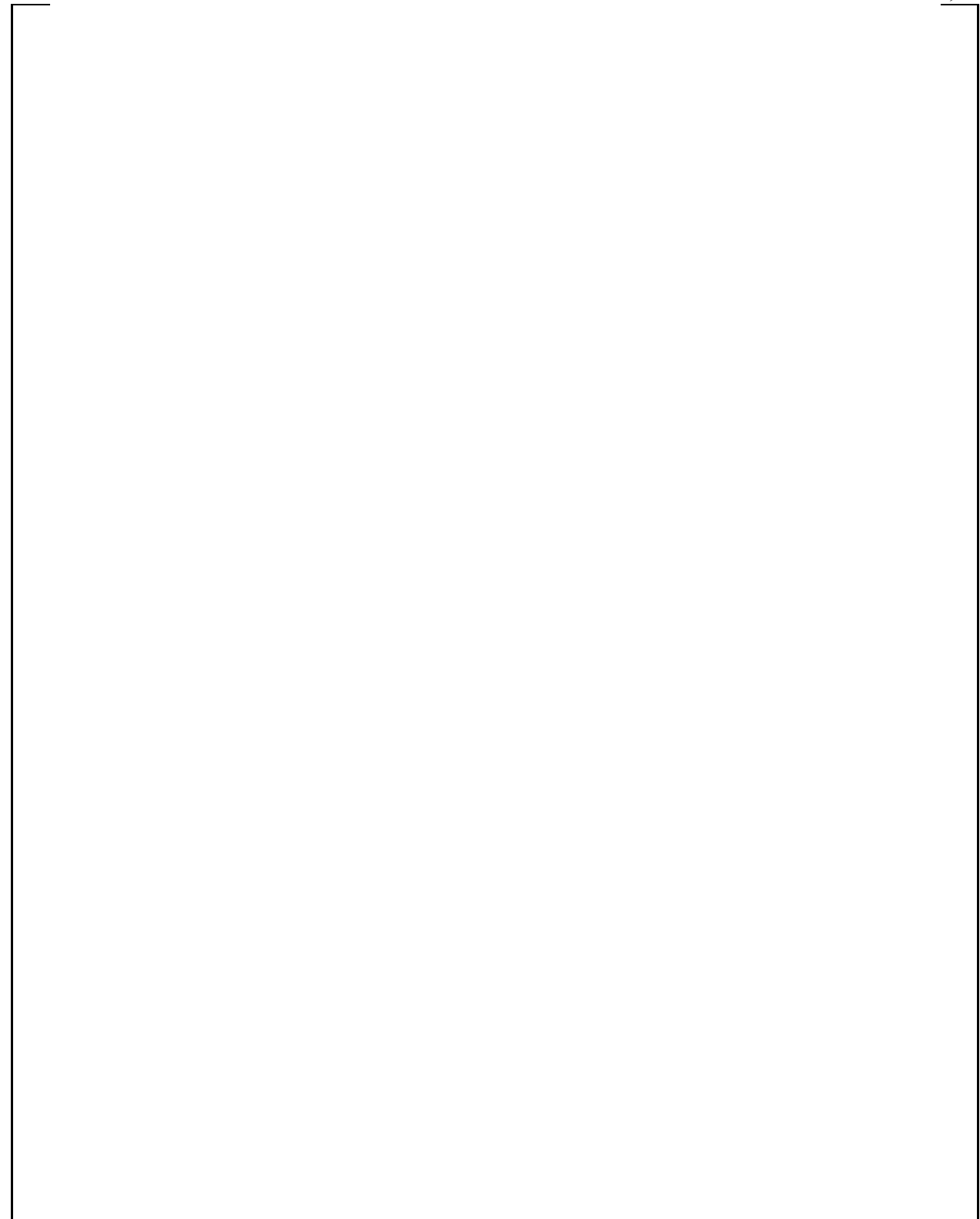


Figure 9-49. WGOTHIC Calculated Flow Pattern – LOCA Jet Momentum Dissipated in SG East Compartment at 1500 Seconds

a,c

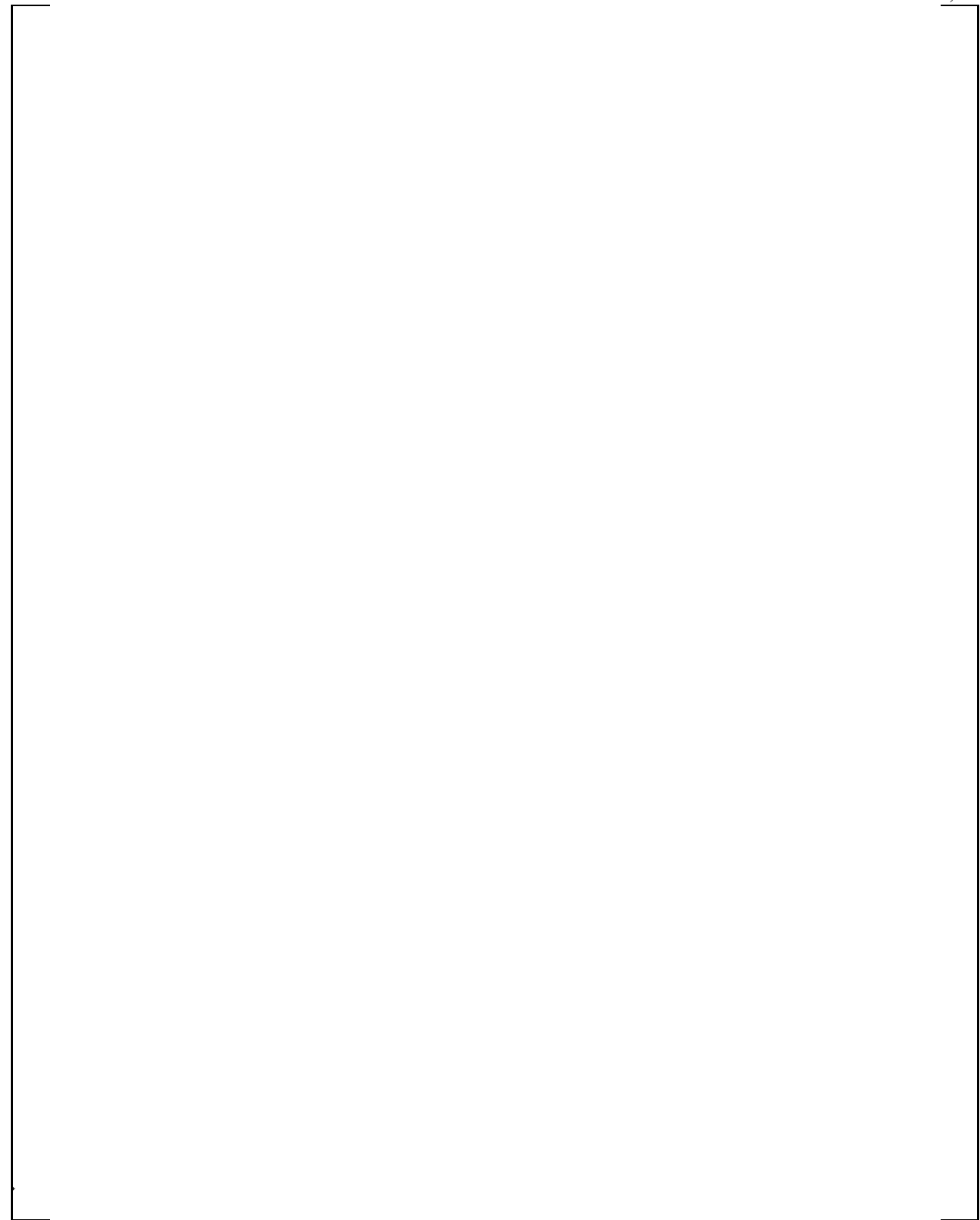


Figure 9-50. WGOTHIC Calculated Flow Pattern – LOCA Jet Momentum Dissipated in SG East Compartment at 8000 Seconds

a,c

A large rectangular frame, likely representing a diagram or figure, is positioned in the center of the page. It is defined by a thin black border. The interior of the frame is empty, suggesting that the content of the figure is not visible or has been redacted.

Figure 9-51. Details of WGOTHIC Flow Paths to Above-Deck Region from CMT, Refueling Canal, and IRWST

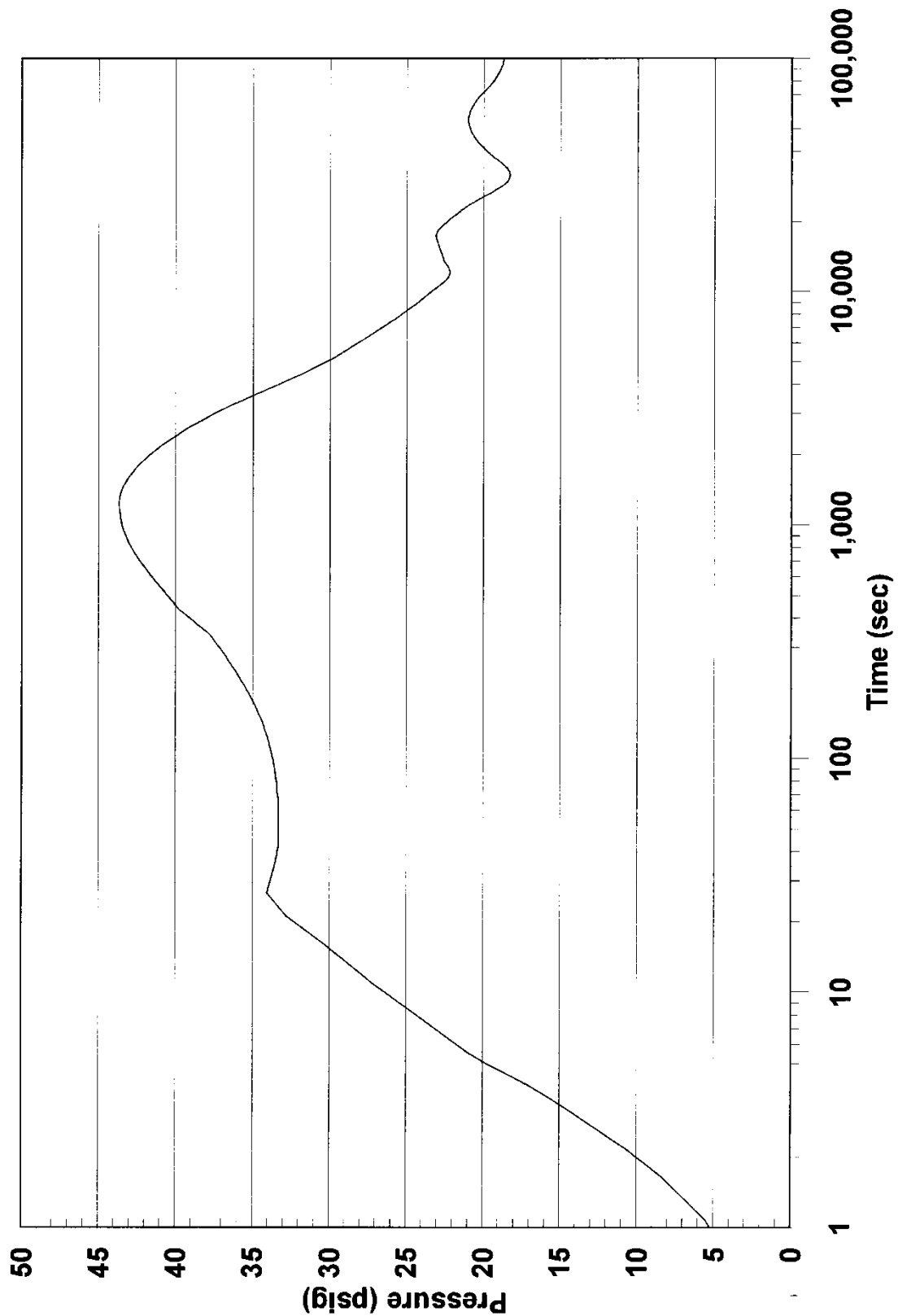


Figure 9-52. WGOTHIC Calculated AP600 Containment Pressure – LOCA Plume Rising into CMT Room

a,c

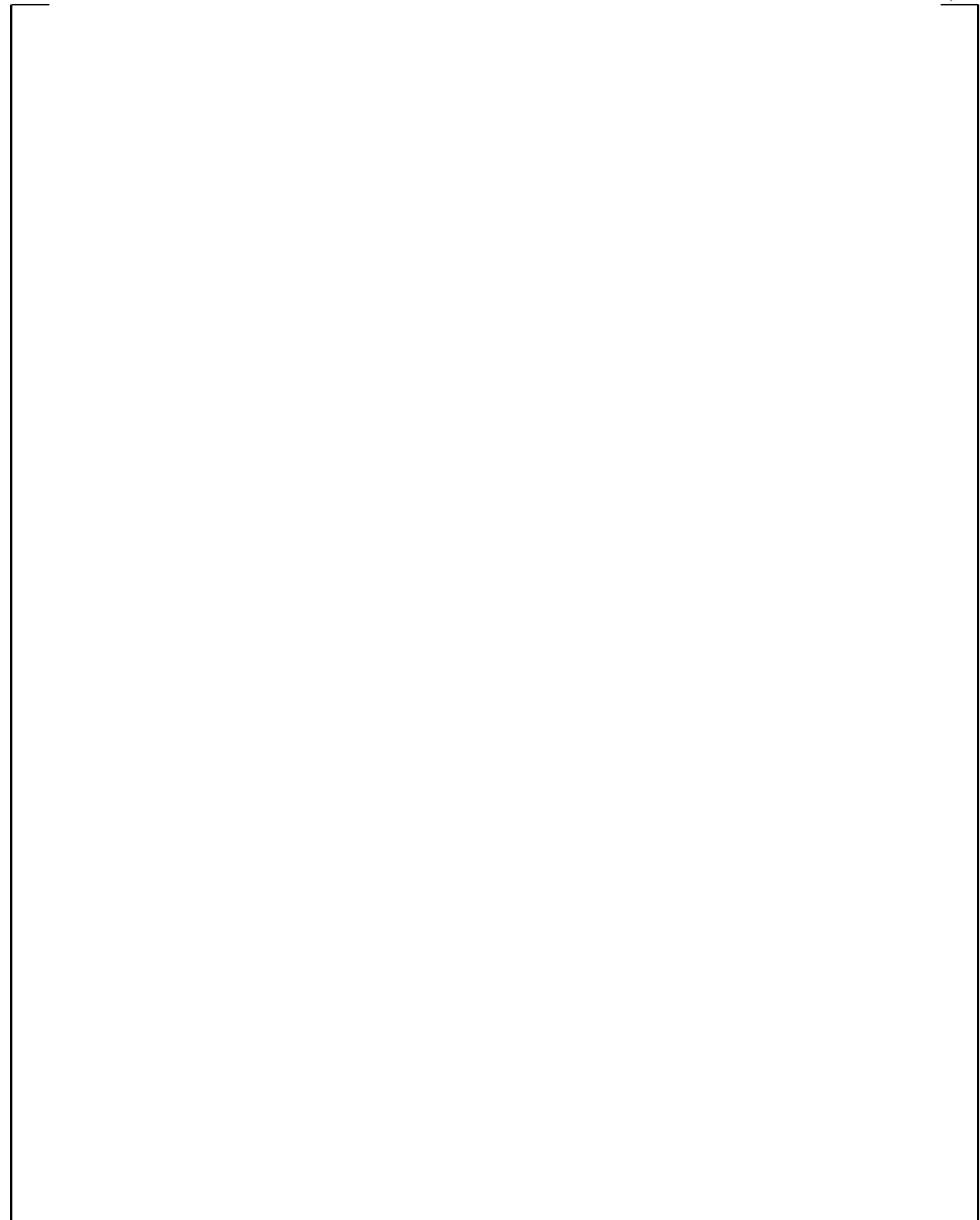


Figure 9-53. WGOTHIC Calculated Flow Pattern – LOCA Plume Rising into CMT Room at 1000 Seconds

a,c

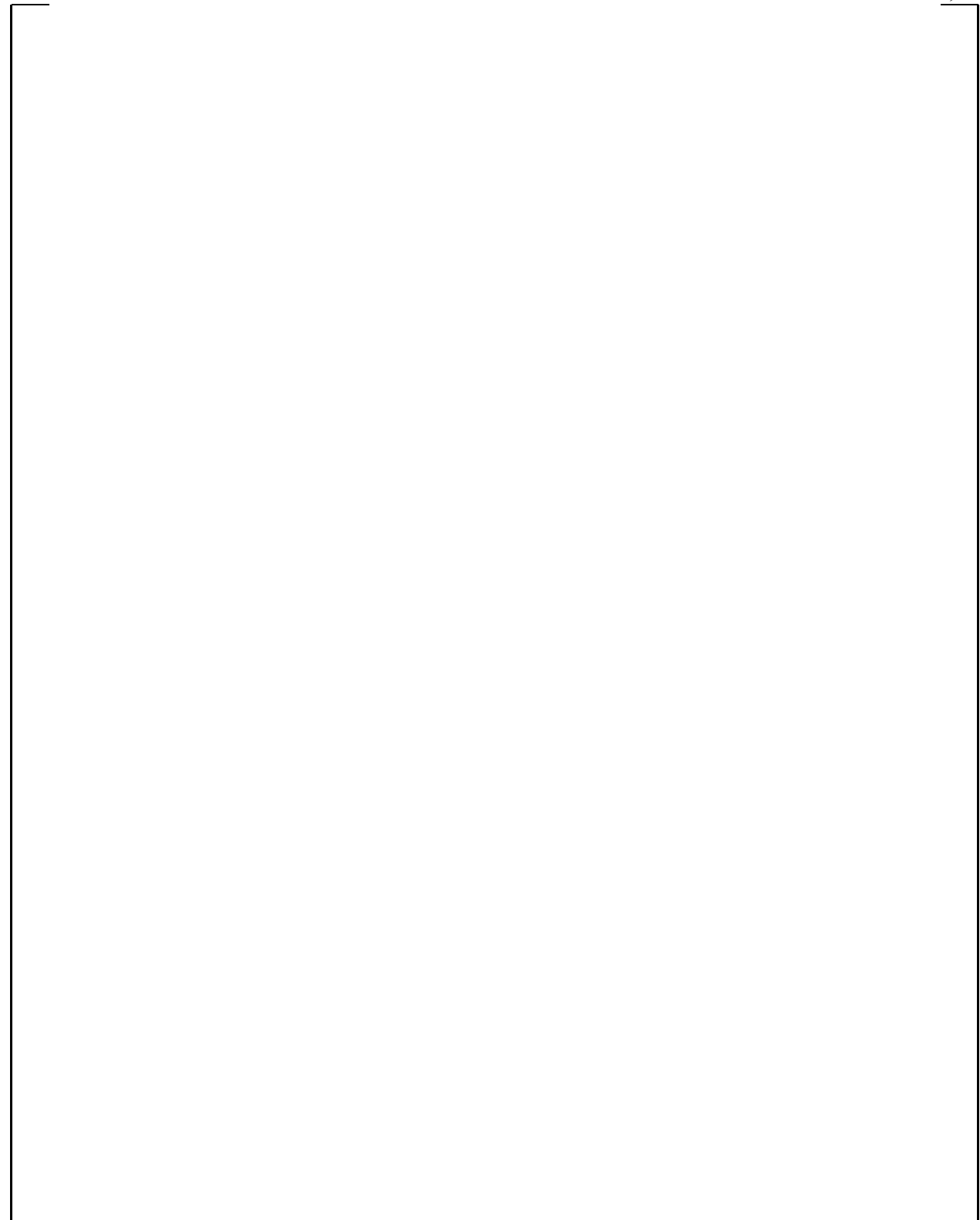


Figure 9-54. WGOTHIC Calculated Flow Pattern – LOCA Plume Rising into CMT Room at 1400 Seconds

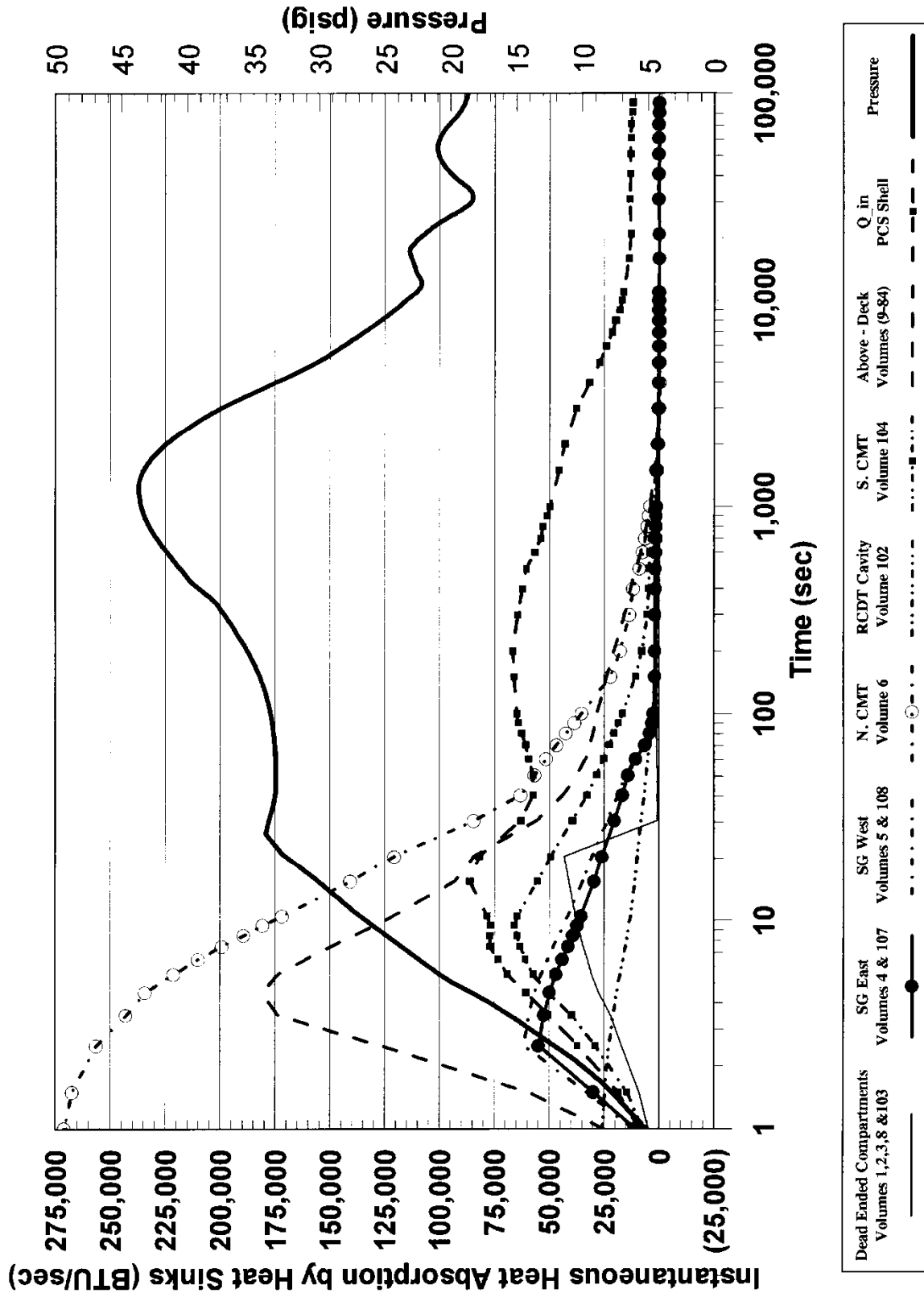


Figure 9-55. WGOthic Calculated AP600 Containment Heat Removal Rates – LOCA Plume Rising into CMT Room

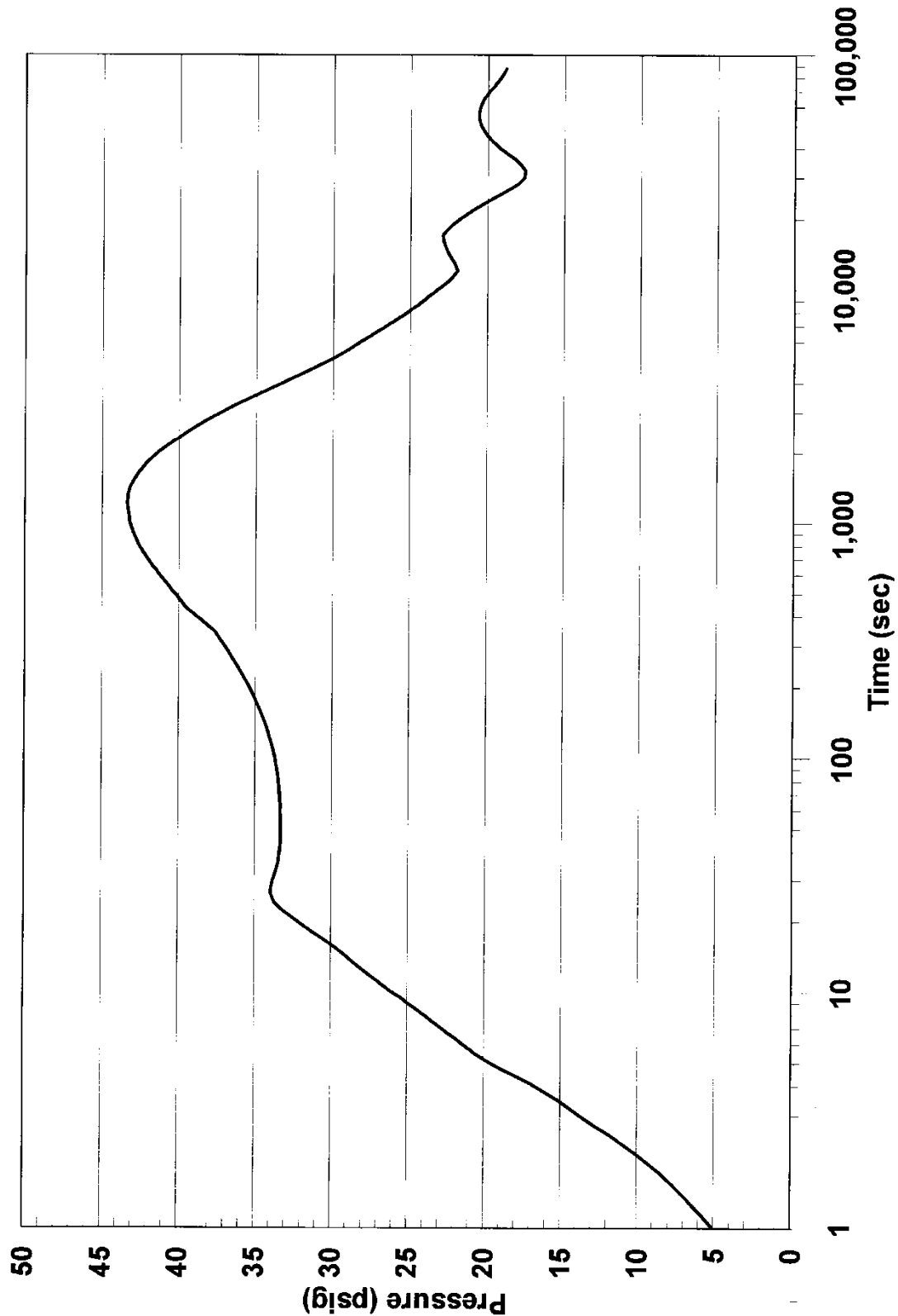


Figure 9-56. WGOTHIC Calculated AP600 Containment Pressure – LOCA Plume Rising into CMT Room and SG Compartments

a,c

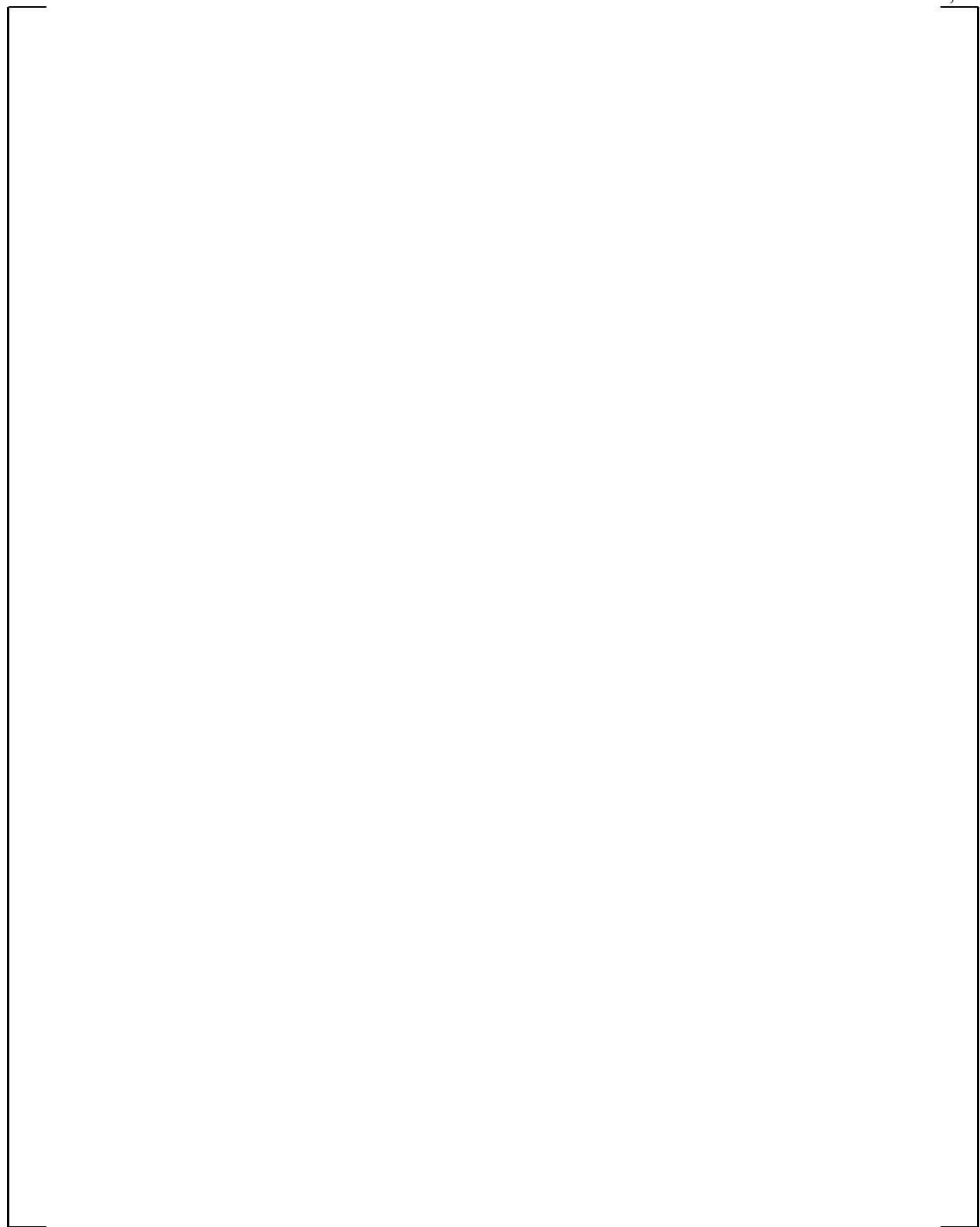


Figure 9-57. WGOTHIC Calculated Flow Pattern – LOCA Plume Rising into CMT Room and SG Compartment at 1000 Seconds

a,c



Figure 9-58. WGOTHIC Calculated Flow Pattern – LOCA Plume Rising into CMT Room and SG Compartments at 1500 Seconds

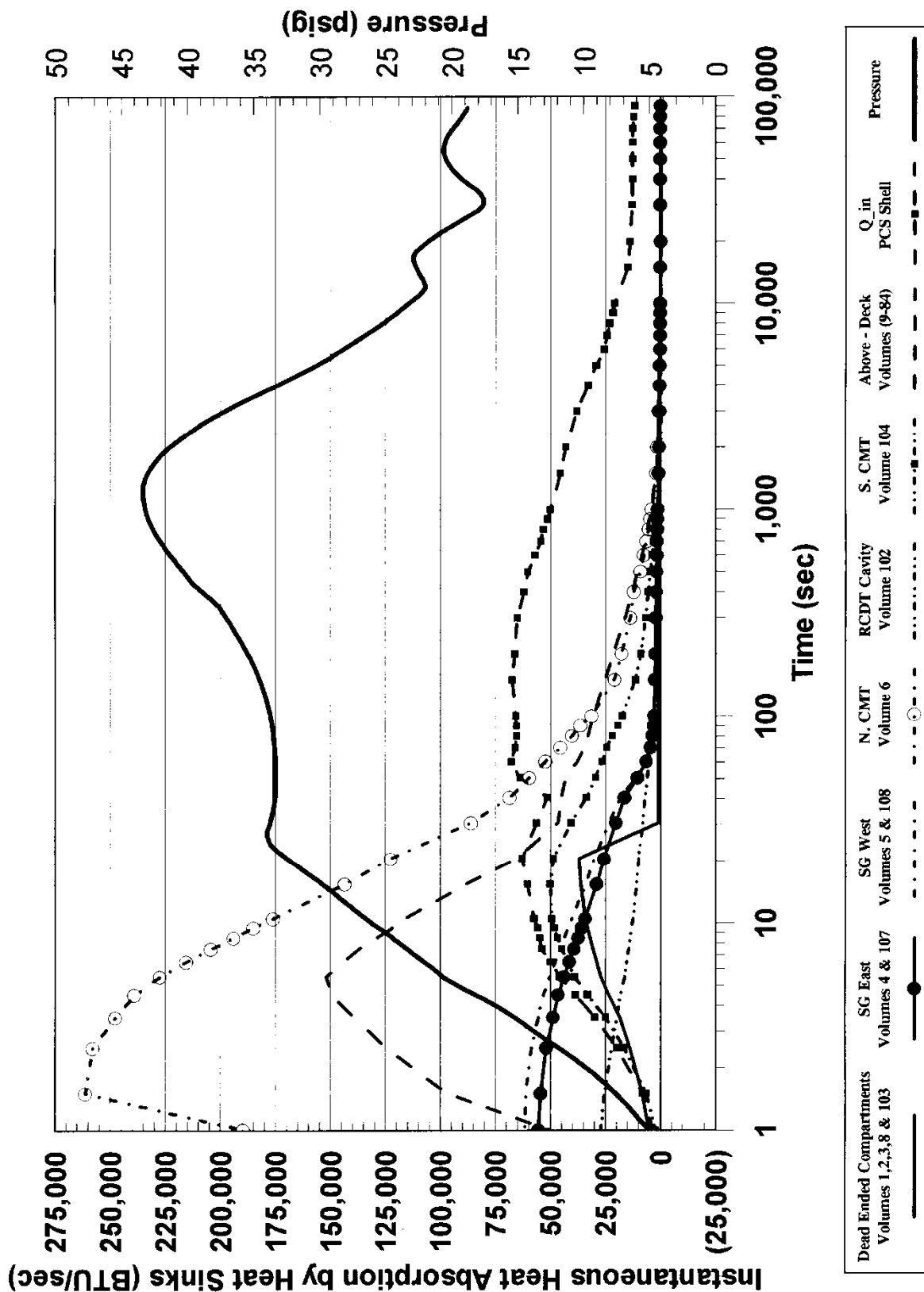
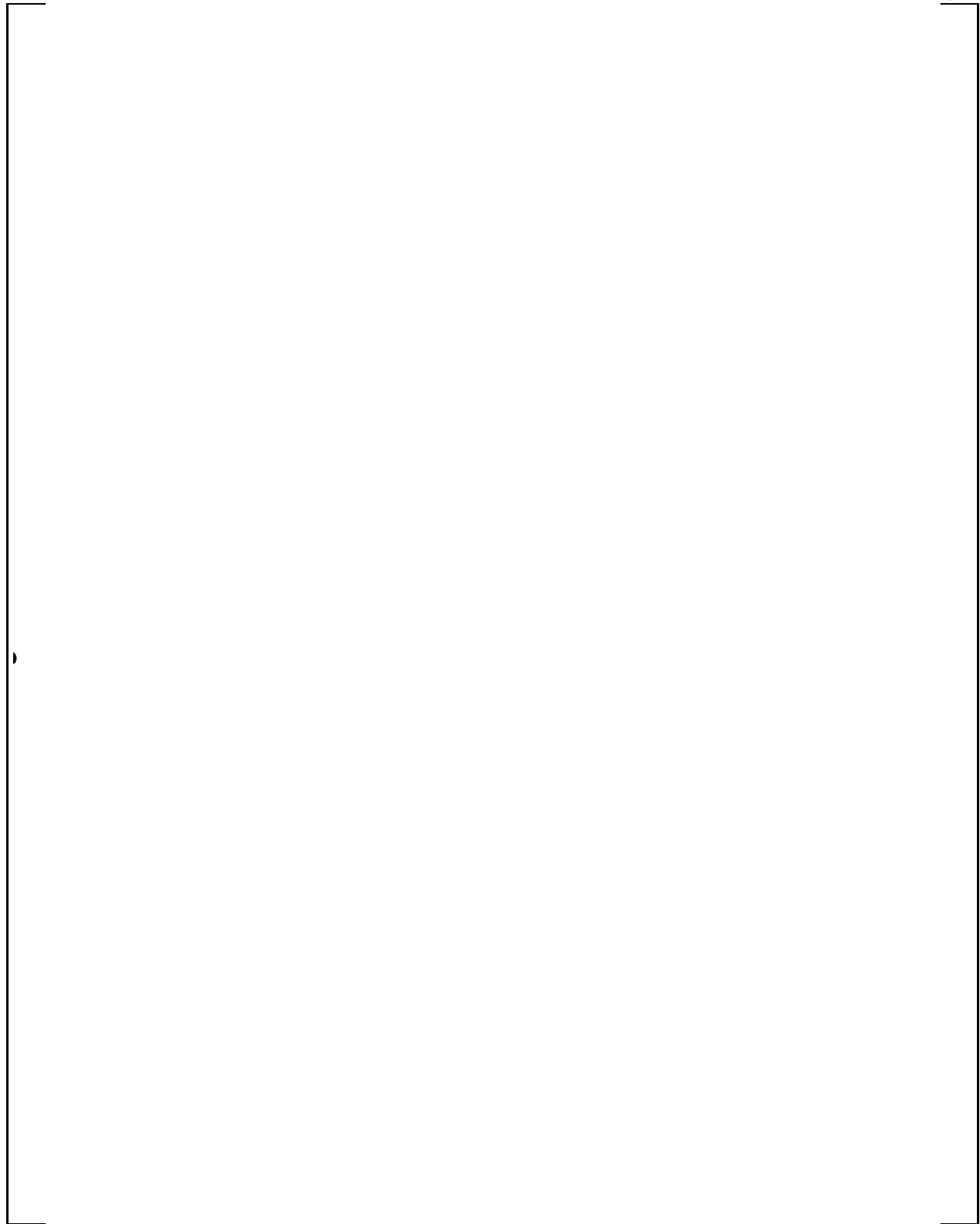


Figure 9-59. WGOOTHIC Calculated AP600 Containment Heat Removal Rates – LOCA Plume Rising into CMT Room and SG Compartments

a,c



**Figure 9-60. WGOTHIC Calculated AP600 Containment Steam Pressure Ratio for
MSLB Above-Deck**

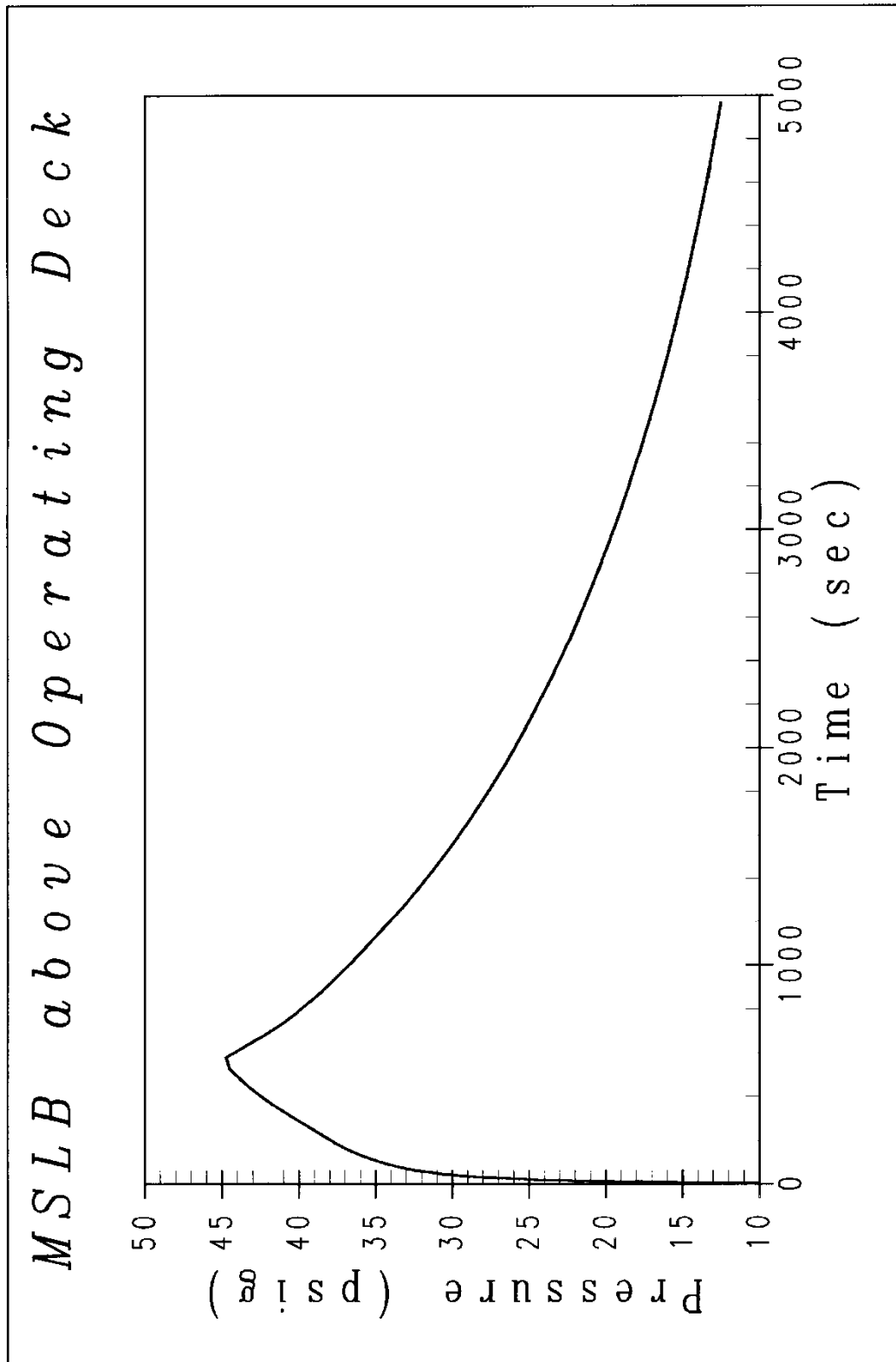


Figure 9-61. WGOTHIC Calculated AP600 Containment Pressure – MSLB Above Operating Deck

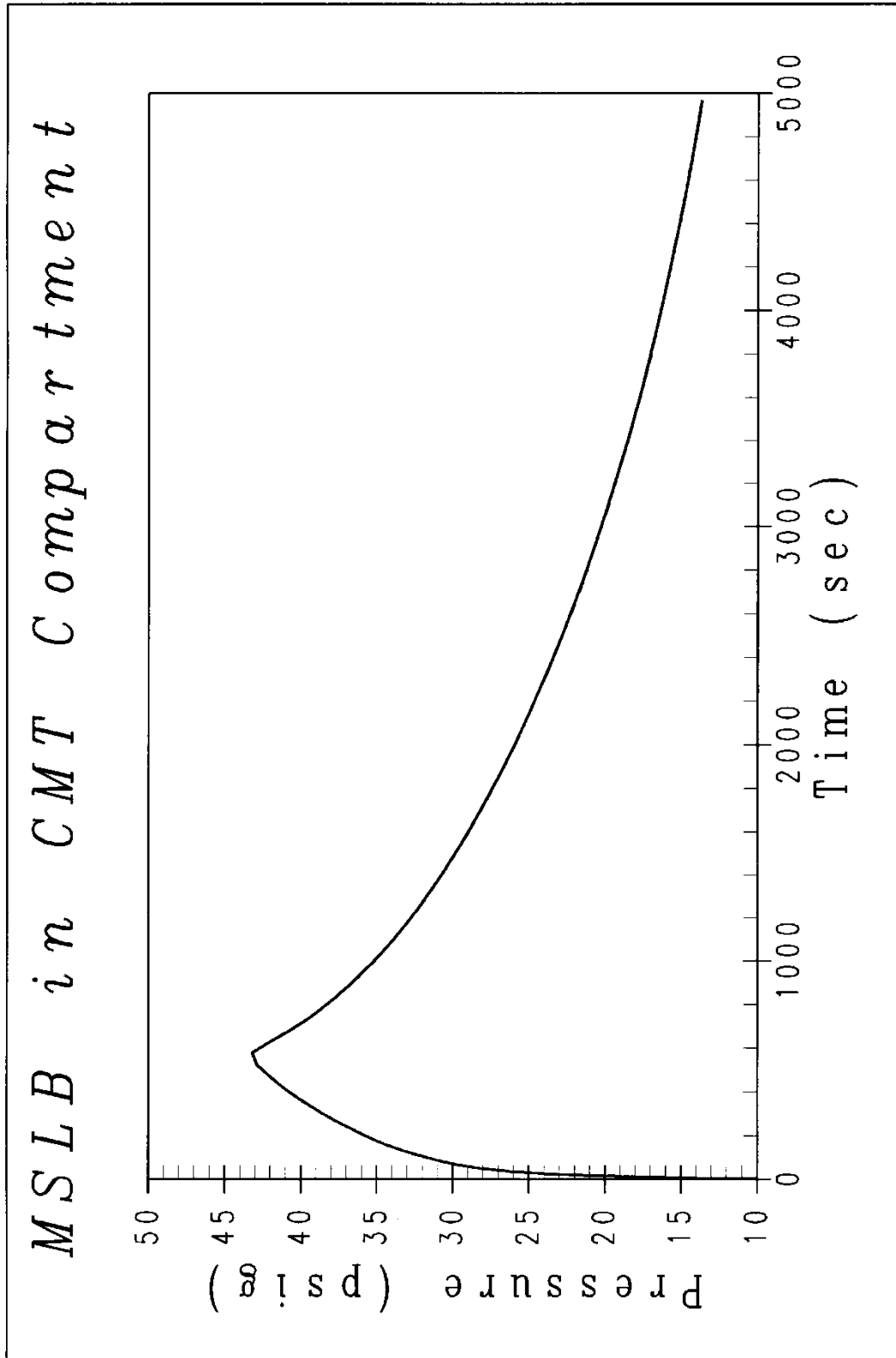


Figure 9-62. WGOTHIC Calculated AP600 Containment Pressure – MSLB in CMT Room

APPENDIX 9.A

THERMAL AND CIRCULATION EFFECTS OF DROPS DURING A LOCA

Drops, or fog particles, are created when the blowdown break source steam velocity is large enough to disperse a fraction of the break liquid along with the gas. As discussed in Section 4.4.2D of Reference 9.A.1 and Section 7.1 of Reference 9.A.2, drops will be formed during the LOCA blowdown phase. For the post-blowdown phases of a LOCA and for the MSLB, there will not be any significant drop formation. The thermal and circulation effects of drops on LOCA containment pressure are examined in this section.

The limiting DBA analysis LOCA is a DECLG break. The source flow from the reactor side of the break has more energy than the source flow from the steam generator side of the break, so more drops are expected from the reactor side. During blowdown, a range of drop sizes will be produced. The percentage of liquid converted to drops will also be within some range, the theoretical limits being 0 and 100 percent, although it is anticipated that a significant fraction of the liquid will form drops.

Many factors affect the length of time that the drops will be present in the atmosphere, such as shear coupling to the moving gas, coalescence, de-entrainment at walls and other surfaces, and the drop size (affecting its fall time). To estimate the fall time for various size drops, a simple calculation was performed which only accounts for the gravitational effects on the drops. Using the terminal velocity versus drop diameter information in Section 7.6 of Reference 9.A.3, fall times range from seconds to hours depending on the drop size and fall height. Table 9.A-1 shows estimated fall times for drops with diameters of 0.001, 0.01, and 0.1 inches. This provides an indication that the drops will exist long enough that their effect on containment pressure must be considered.

Table 9.A-1. Estimated Drop Fall Times

Drop Size (in)	Terminal Velocity (ft/sec)	Fall Time (sec)	
		30 ft	100 ft
0.001	.08	375	1250
0.01	8	3.8	12.5
0.1	20	1.5	5

Thermal Effects

The drops flash when they enter the containment atmosphere, reaching saturation very quickly. Section 7.1 of Reference 9.A.2 estimates 3.5 percent of a given drop flashes to steam. Section 7.1 also estimates that the drop diameter only decreases 5 percent due to evaporation in later phases. The drops are strongly coupled to the containment atmosphere temperature due to the large surface area of the total drop population. This strong coupling results in the drop temperature closely following the containment atmosphere temperature as it changes during the transient. Sensitivities using WGOTHIC show that if 5 percent or more of the liquid is converted into drops, then the containment atmosphere will be saturated

quickly. Given the high velocity of the blowdown releases, much greater than 5 percent is anticipated to be converted into drops. With the atmosphere saturated, thermal effects such as superheating will not occur and the effect of larger drop fractions does not significantly affect the pressure response. The effects of drops on the Evaluation Model calculation of containment pressure is investigated with a sensitivity study described in Section 5.8.

Circulation and Stratification Effects

The presence of drops increases the density of the containment atmosphere, which makes the post-blowdown steam release relatively more buoyant. An estimate of the effect of drops on circulation and stratification is made by calculating the plume entrainment rate and resulting circulation time constant for the conditions at the end of the blowdown phase of the DBA LOCA. As discussed in Section 7.1 of Reference 9.A.2, well-accepted models are not available to predict the mass of the drops created during blowdown, so the bounds of 0 percent and 100 percent of the liquid will be considered.

To estimate the volume entrained into the plume (Q_{ent} , in ft^3/sec), Peterson's equations (Reference 9.A.4) can be used:

$$Q_{ent} = 0.15 * B^{1/3} * Z^{5/3}$$

where,

- Z = elevation (ft.)
- B = $g * Q_{st} * (\rho_{amb} - \rho_{st}) / \rho_{amb}$
- g = gravitational acceleration = 32.2 ft/sec^2
- Q_{st} = volumetric steam flow (ft^3/sec)
- ρ_{amb} = containment ambient density (lbm/ft^3)
- ρ_{st} = steam density (lbm/ft^3)

The entrainment is calculated for a height of 100 feet above the top of the steam generator compartment, so $Z = 100 \text{ ft}$. The steam release at the beginning of the peak pressure phase is estimated to be $1870 \text{ ft}^3/\text{sec}$ (Q_{st}). For the case assuming 0 percent of the liquid is released as drops, the $(\rho_{amb} - \rho_{st}) / \rho_{amb}$ term is approximately 0.275. For the case assuming 100 percent of the liquid is released as drops, the density term is approximately 0.60. Using the above equation, the estimated entrainment rate is $Q_{ent} = 8239 \text{ ft}^3/\text{sec}$ (0 percent drops) and $10695 \text{ ft}^3/\text{sec}$ (100 percent drops). The estimated entrainment at the end of blowdown is approximately four times the steam flow (Q_{st}) for the case without drops, and slightly less than six times the steam flow for the case with drops.

Knowing the entrainment rate, a circulation time constant can be calculated for the containment free volume. This time constant will change with time, but it provides an indication of the amount of circulation expected for the releases after the refill phase. The circulation time constant is the volume divided by the entrainment rate, and for 0 percent drops it is 206 seconds and for 100 percent drops it is 159 seconds. It should be noted that the estimated times conservatively neglect volumetric entrainment into the wall layers. These time constants increase as the steam flow decreases, but this estimation shows that a large fraction of the containment volume will be entrained in the plume within a few minutes, which is relatively short compared to the time to reach maximum pressure (at approximately

1200 seconds), and very short compared to long-term cooling. A relatively large entrainment rate within the above-deck region indicates that the steam density gradients above-deck are not large whether drops exist or not. Therefore, the presence of drops will not significantly affect the general circulation and stratification patterns in the containment atmosphere.

Evaluation Model Drop Sensitivity Study

The AP600 Containment Evaluation Model, with the jet dissipated in the steam generator compartment, was used to determine the effect of drops on the calculation of containment pressure. The treatment of drops in the AP600 Containment Evaluation Model is described in Section 4.5.2.1. The Evaluation Model converts all of the liquid from the reactor side of the break to drops, and none of the liquid from the steam generator side of the break. Sensitivity cases were analyzed for comparison to the Evaluation Model results. The sensitivity cases are discussed in Section 5.8. One case modeled no drop formation and one case modeled 100 percent of the liquid converted into drops.

The containment pressure, as a function of time, was calculated for the sensitivity case. The maximum containment pressure, calculated with the Evaluation Model, is greater than the maximum pressure calculated assuming no drop formation. The presence of drops does have a slight influence on the Evaluation Model pressure calculation. Drop formation is expected during the blowdown phase and the sensitivity study indicates that drop formation should be modeled to provide a bounding calculation for containment pressure.

Conclusions

The formation of drops during the LOCA blowdown phase is a physically real phenomenon that may influence the maximum containment pressure calculated by the Evaluation Model. Drop formation increases the density of the containment atmosphere making the post-blowdown releases relatively more buoyant. A small percentage of the blowdown break liquid formed into drops is sufficient to saturate the containment atmosphere, at which point additional drop density has a minor thermal effect. The Evaluation Model treatment of drops provides a sufficient bounding calculation for maximum and long-term containment pressure.

References

- 9.A.1. WCAP-14812, "Accident Specification and Phenomena Evaluation for AP600 Passive Containment Cooling System," Revision 2, April 1998.
- 9.A.2. WCAP-14845, "Scaling Analysis for AP600 Containment Pressure During Design Basis Accidents," Revision 3, March 1998.
- 9.A.3. NTD-NRC-95-4563, "GOTHIC Version 4.0 Documentation, Enclosure 2: Technical Manual," September 21, 1995.
- 9.A.4. Peterson, P., "Scaling and Analysis of Mixing in Large Stratified Volumes," *International Journal of Heat and Mass Transfer*, Vol. 37, Supplement 1, pp 97-106, 1994.

APPENDIX 9.B

EFFECTS OF STRATIFICATION ON HEAT SINK UTILIZATION

9.B.1 INTRODUCTION

An analysis was performed to determine the impact of stratification on the relative effectiveness of containment heat sinks during a postulated LOCA. Models were developed to study transient heat conduction effects for steel and concrete structures under a variety of containment atmosphere boundary conditions. The models were then used to determine the effects of stratification of steam in the containment atmosphere on heat sink utilization in the CMT room and in the above-deck region.

9.B.2 HEAT SINK ANALYSIS

The condensation heat transfer in the containment atmosphere has been characterized as a function of the steam fraction, and has been used as boundary conditions to determine the transient heat absorption rate of the heat sink structures. The results of these analyses are used to estimate the relative effects of stratification on the heat sinks located on the PCS steel shell and in the CMT room.

The purpose of the analysis is to obtain relative effects of stratification for reasonably representative conditions to assess the magnitude of the bias. An extreme stratification gradient is assumed from which the relative effect of stratification on total heat sink energy removal in a region can be assessed. A bias is developed to bound the non-conservative effects of stratification.

9.B.3 CONDENSATION BOUNDARY CONDITIONS

These sensitivity calculations are performed to examine the relative effect of a gas mixture that is homogeneous (as in a lumped parameter node) and a gas mixture that is stratified. To keep the calculations simple, boundary conditions are assumed constant with time, and the following homogeneous atmosphere conditions are assumed:

$$\begin{aligned}T_{\text{atm}} &= 276^{\circ}\text{F} \\P_{\text{atm}} &= 59.7 \text{ psia} \\f_{\text{st}} &= 0.63 \text{ (homogeneous steam mole fraction)}\end{aligned}$$

These parameters represent approximately time-averaged values over the first hour of the LOCA, since the CMT room steam concentration is relatively constant (Figure 9-44).

The heat transfer from the containment atmosphere and the structure is assumed to be dominated by condensation so that convection and radiation are neglected. The condensation heat transfer is determined by first determining the mass transfer for turbulent free convection (Reference 9.B.1, Section 4.3):

$$m'' = 0.13 * \left[\frac{\rho_{\text{stm}} * D_v * \Delta P_{\text{stm}}}{\left(\frac{v^2}{g}\right)^{1/3} * P_{\text{lm,air}}} \right] * \left[\frac{\Delta \rho * S_c}{\rho} \right]^{1/3} \quad (9.B-1)$$

where,

- \dot{m}'' is the condensation mass flux
- ρ_{stm} is the density of steam at the total pressure and boundary layer temperature
- ΔP_{stm} is the difference in the steam partial pressure atmosphere - surface
- ν is the mixture kinematic viscosity
- g is gravity
- $P_{lm,air}$ is the log mean pressure difference atmosphere - surface
- $\Delta \rho$ is the mixture density difference atmosphere - surface
- ρ is the bulk mixture density
- Sc is the mixture Schmidt number (typically ~0.51)
- and D_v is the air-steam diffusion coefficient which is given by (Reference 9.B-1, Section 4.3.2)

$$D_v = 0.892 * \frac{14.2 \text{ psi}}{P} * \left(\frac{T_{surf} + T_{atm}}{2 * 460^\circ R} \right)^{1.81} \quad (9.B-2)$$

The steam partial pressure in the atmosphere is given by:

$$P_{stm_atm} = f_{st} * P \quad (9.B-3)$$

where f_{st} is the steam mole fraction in the atmosphere and P is the total pressure.

The steam partial pressure at the condensing surface is given by:

$$P_{stm_atm} = f_{st} * P \quad (9.B-4)$$

where P_{sat} is the saturation pressure corresponding to T_{surf} .

The log mean pressure difference between the atmosphere air pressure and the air pressure at the surface is given by:

$$P_{lm-air} = \frac{(P_{air-surf} - P_{air-atm})}{\ln \left(\frac{P_{air-surf}}{P_{air-atm}} \right)} \quad (9.B-5)$$

where $P_{air-surf}$ is the air partial pressure at the heat sink surface, $P - P_{stm-surf}$ and $P_{air-atm}$ is the air partial pressure in the atmosphere, $(1 - f_{st}) * P$.

The densities of air and steam at the atmospheric and surface pressures and temperatures are determined from the ideal gas law.

To determine the effect of the steam fraction, three distinct regions based on equal volume are assumed. The top region is assumed to be nearly all steam with $f_{st-top} = 0.98$. The middle region is assumed to be at the nominal conditions with $f_{st-mid} = 0.63$. The bottom region steam fraction is determined by conserving the total amount of steam in the total volume.

$$f_{st-bot} = 3 * f_{st-nom} - f_{st-top} - f_{st-mid} = 0.28 \quad (9.B-6)$$

Applying these three steam mole fractions along with the above containment atmosphere conditions, a relationship can be determined for the condensation heat transfer coefficient as a function of heat sink surface temperature. An equivalent condensation heat transfer coefficient is calculated from m'' for use as a boundary condition for heat sink condensation, described later. The equivalent condensation heat transfer coefficient is calculated by:

$$h_{cond} = \frac{m'' * h_{fg}}{(T_{atm} - T_{surf})} \quad (9.B-7)$$

where h_{fg} is the difference between the steam and liquid saturation enthalpy. The relationships for equivalent heat transfer coefficient are shown graphically Figure 9.B-1.

The condensation heat transfer coefficient varies considerably with respect to the steam fraction in the containment atmosphere, f_{st} , and the surface temperature, T_{surf} . For each steam fraction, the heat transfer coefficient increases with increasing T_{surf} until the saturation temperature that corresponds to the steam partial pressure at the surface is reached. At this point the condensation heat transfer drops to zero, and is zero for all surface temperatures greater than this temperature.

For the case of $f_{st} = 0.98$, $T_{sat} = 291^\circ\text{F}$, which is greater than the containment atmosphere temperature. Thus, the condensation heat transfer coefficient increases with surface temperature and no cutoff is reached. For the case of $f_{st} = 0.63$, $T_{sat} = 264^\circ\text{F}$, and the heat transfer coefficient drops to zero at this temperature. For the case of $f_{st} = 0.28$, 217°F , the heat transfer coefficient drops to zero.

9.B.4 HEAT CONDUCTION MODELS

Several models were developed to calculate heat transfer to the heat sinks. These include:

- Steel structures of varying thickness
- Concrete structures
- Steel-jacketed concrete structures
- Steel containment shell

A description of each model is given as follows.

Steel Structures

The one-dimensional model consists of a 1 ft. by 1 ft. section of steel, modeled by ten nodes of equal thickness, representing one-half the heat sink thickness. For example, for a one-half inch thick steel plate, the model has ten nodes, each 0.025 in. thick. A convective boundary condition is applied to one surface, while the other surface is assumed to be adiabatic. Connections between the nodes are defined by the area of the interface (1 ft²), and the distance from the node center to the interface (0.0125 in.). The properties for steel are listed below:

$$\begin{aligned}\rho &= 490.7 \text{ lbm/ft}^3 \\ C &= 0.107 \text{ Btu/lbm-}^\circ\text{F} \\ k &= 30 \text{ Btu/hr-ft-}^\circ\text{F}\end{aligned}$$

A zero-volume node is attached to the steel at the surface exposed to the atmosphere. The boundary conditions for the three steam fractions are described in the previous section.

Concrete Heat Sinks

The concrete heat sinks have much lower thermal conductivity and are modeled differently than the steel heat sink. The thermal properties of the concrete are given as:

$$\begin{aligned}\rho &= 140 \text{ lbm/ft}^3 \\ C &= 0.19 \text{ Btu/lbm-}^\circ\text{F} \\ k &= 0.83 \text{ Btu/hr-ft-}^\circ\text{F}\end{aligned}$$

Once again, ten nodes are used to represent one-half the concrete thickness. For this case, the nodes are not equal volume with the nodes nearest the convecting surface having small thicknesses, and the thickness increasing geometrically as the nodes progress inward to the adiabatic boundary. The thicknesses are summarized for each node in Table 9.B-1.

Table 9.B-1. Concrete Model Nodal Thickness

			a,c

As for the steel model, Node #1 is connected to a zero-volume surface node, which is in turn connected to the boundary temperature. The heat transfer coefficient is defined in the previous section as a function of the surface temperature for the three steam fractions considered.

Steel-Jacketed Concrete Heat Sinks

The steel-jacketed concrete heat sinks combines the two-foot thick concrete model previously described with a one-half inch steel plate. The condensation boundary condition is attached to the outside of the steel plate, that is represented by 10 nodes, 0.05 in thick. The inside steel node is attached to the first concrete node with an assumed gap of 0.036 in. The gap conductance is given by

$$h_{\text{gap}} = \frac{k_{\text{mix}}}{\delta_{\text{gap}}} \quad (9.B-8)$$

where δ_{gap} is the gap thickness

and k_{mix} is the thermal conductivity of the containment atmosphere mixture

$$k_{\text{mix}} = 0.5 * (k_{\text{air}} + k_{\text{stm}}) \quad (9.B-9)$$

For $T_{\text{atm}} = 276^{\circ}\text{F}$, and $f_{\text{st}} = 0.5$, $k_{\text{mix}} = 0.03 \text{ Btu/hr-ft}^{\circ}\text{F}$, and $h_{\text{gap}} = 10 \text{ Btu/hr-ft}^2\text{-}^{\circ}\text{F}$.

The concrete is represented by 10 nodes with thicknesses shown in Table 9.B-1.

Steel Containment Shell

The steel containment shell model is somewhat more complex in that the inside boundary condition is the same as the other models while the outside boundary condition is not adiabatic, but is representative of the outer shell evaporative heat transfer. The steel shell is assumed to be []^{a,c} thick. For this case, a []^{a,c}. The inner-most node is connected to a zero-volume node upon which the condensation boundary condition is assumed. The outer-most node is also connected to a zero-volume node upon which an evaporation boundary condition is assumed. The outside boundary temperature is assumed to be an average between the inlet air temperature at the bottom of the Passive Containment Cooling System annulus, and the outlet air temperature at the top.

$$T_{\text{air-avg}} = 142^{\circ}\text{F}$$

and $h_{\text{evap}} = 113 \text{ Btu/hr-ft}^2\text{-}^{\circ}\text{F}$

Note that the assumption of a constant value of h over the entire shell surface is very conservative, since in the stratified case, the shell adjacent to the steam-rich top would heat up and significantly increase the evaporation rate on the outside. No credit is taken in this analysis for the associated increase in external heat transfer coefficient.

For this model, there is a short period of time during which the shell heats up from the initial temperature. After this time, a steady-state condition is established as heat is transferred at a nearly constant rate from the inside to the outside of the shell.

9.B.5 RESULTS

For each of the models described above, three transient calculations were performed representing each of the three steam fraction conditions. The results of these calculations were used to examine heat absorption effects for each of the conditions. Since the models represent one square foot of heat sink area, the results can be used to estimate the heat sink behavior in a typical room by multiplying the integrated heat removal by the total area for a particular heat sink type.

Containment Steel Shell Heat Sink Stratification Sensitivity

Figure 9.B-2 shows the heat removal rate for the containment shell. The areas for the top, middle, and bottom of the shell are not weighted equally (as in Equation 9.B-10). The volume of the containment above the operating deck is divided into three regions of equal volume, and the associated surface area for each volume is used. For the AP600 containment,

Elevation of operating deck	=	135.25 ft
Elevation of spring line	=	218.71 ft
Elevation of top of dome	=	256.4 ft
Containment radius	=	65 ft
Gas Volume in dome	=	336,963 ft ³
Surface area of dome	=	15,552 ft ²
Total volume of gas above deck	=	1.45 x 10 ⁶ ft ³

The two lower regions both consist of a cylindrical gas volume = 481,582 ft³. This corresponds to a cylindrical section 36.28 feet in length with a surface area = 14,776 ft². The upper region gas volume is also 481,582 ft³, and consists of the dome and a cylindrical section 11.1 feet in length. The total surface area associated with this volume is 19,898 ft².

Thus, the equivalent integrated heat removal rate through one square foot of the shell is weighted by surface area as

$$Q_{3Region} = \frac{(19,898*Q_{Top} + 14,776*Q_{Mid} + 14,776*Q_{Bot})}{49,450} \quad (9.B-10)$$

The results show that the higher weighting of the upper, steam-rich region nearly compensates for the lower heat removal rates in the bottom region, and the heat removal rate is slightly (~0.5% after 200 seconds) higher for the homogeneous case.

Results for the steel shell assessment are presented in terms of instantaneous rate since the external boundary condition never allows the steel to saturate. The results also allow interpretation of stratification effects during the quasi-steady, long-term, while the steel shell is the dominant heat sink and the balance between instantaneous source and sink heat rates governs the containment pressure. Since the stratification penalty on the steel shell heat removal rate is nearly negligible, a simple bias is introduced into the Evaluation Model by removing the non-grating operating deck floors to bound the effect. The stratification effect is exaggerated due to the use of an extreme gradient, well beyond what has been observed in the LST (Section 9.2.1 and 9.2.3) and in the international containment database (Appendix 9.C.2).

Simulated Room Heat Sink Stratification Sensitivity

These models were applied to heat sinks which reasonably represent the AP600 CMT room. The heat sinks for the AP600 CMT room (North and South sections) are summarized in Table 9.B-2.

Table 9.B-2. AP600 Assumed Room Heat Sink Distribution

Heat Sinks in Simulated Room	Thickness	Surface Area	Region
Steel-Jacketed Concrete – Ceiling (single-sided)	0.5 in. / 24 in.	5398.87 ft ²	Top
Steel-Jacketed Concrete – Floors (single-sided)	0.5 in. / 24 in.	5601.44 ft ²	Bottom
Steel-Jacketed Concrete – Walls (double-sided)	0.5 in. / 24 in.	4596.11 ft ²	1/3 in each region
Steel-Jacketed Concrete – Wall (double-sided)	0.5 in / 48 in	673.99 ft ²	1/3 in each region
Concrete – Bulk (double-sided)	48 in.	3287.36 ft ²	1/3 in each region
Steel – CMT (single-sided)	4.874 in.	1848.8 ft ²	1/3 in each region
Steel – Containment Shell Wall (single-sided)	1.57 in.	11385.53 ft ²	1/3 in each region

Table 9.B-2. AP600 Assumed Room Heat Sink Distribution (cont.)

Heat Sinks in Simulated Room	Thickness	Surface Area	Region
Steel – Columns (double-sided)	0.39 in.	1656.5 ft ²	1/3 in each region
Steel – Floor Grating (double-sided)	0.39 in.	3781.69 ft ²	1/3 in each region
Steel – Elevator (double-sided)	0.2 in.	218.96 ft ²	1/3 in each region
Steel – Platform (double-sided)	0.144 in.	11254.2 ft ²	1/3 in each region
Steel – Stair & Rails (double-sided)	0.132 in.	181.59 ft ²	1/3 in each region

As was discussed previously, each heat sink was analyzed using three different steam fractions representing the top, middle, and bottom thirds of the room which is a bounding gradient when the plume rises through the CMT compartment. There is expected to be no significant stratification penalty in the CMT room with downflow in the Evaluation Model, where the plume rises from the steam generator compartment. For each individual heat sink, a homogeneous case and three-region averaged result was obtained for a 1 ft² section of the heat sink. The energy removal by each heat sink is determined by calculating the heat removal for 1 ft², and multiplying by the appropriate surface area.

Where appropriate, the heat sinks that are located in a specific volume (i.e., ceilings and floors) are not averaged for the three-region, but are analyzed solely with the steam fraction of that volume. This becomes important for the ceilings since these heat sinks are located within the high steam fraction volume and higher heat transfer is expected when the room is stratified. The opposite is expected when considering floors. Refer to Table 9.B-2 for the region designation.

Figure 9.B-3 shows the integrated heat removal by all the heat sinks in the CMT room for a one hour transient. As will be discussed below, the stratification bias for this case is a function of the total energy absorbed. This is because the adiabatic boundary condition results in heat sinks reaching a maximum thermal absorption governed by the saturation temperature for the given steam concentration in a volume. Therefore, results for this scenario are presented in terms of integrated total heat absorption.

The results show the CMT room heat sinks including the floors for the homogeneous and stratified cases. In addition, the case where the floors are not included for the homogeneous case is also shown. The stratified, three-region results are lower than the homogeneous case results by 10-15% when all heat sinks are considered. The homogeneous case with floors excluded is slightly conservative when compared to the stratified case with the floors included. Thus, the combination of assuming homogeneous conditions and neglecting the floors in the total heat sink area results in total heat sink utilization that is neutral at the time of peak pressure, and over the longer term is slightly conservative relative to the expected conditions.

The assessment of stratification effects is very conservative because a conservatively low benefit for the uppermost region is used, and the gradient is much more extreme than what has been observed in the LST (9.2.1 and 9.2.3) and in the international containment database (Appendix 9.C.2). The choice of stratified conditions to examine for this sensitivity are conservative and the results bound other, less extreme postulated stratification gradients. The room temperature is assumed to be 276°F in the stratified case, the same temperature as in the base case homogeneous room. One could, for example, postulate a less extreme, thermodynamically consistent, gradient of 0.77 for the top, 0.63 for the middle, and 0.49 for the bottom. The saturation temperature for a region at 59.7 psia and a steam mole fraction of 0.98 (psat of 58.5 psia) is 291°F. The upper region then would be about 15°F hotter than assumed. Therefore, the upper region conditions are thermodynamically inconsistent in a way that minimizes heat absorption in the upper region of the room, and thus maximizes the stratification bias.

The bias for the CMT room is governed by the air content in the lowest region. Results indicate that steel heat sinks, and the steel on jacketed concrete, reach a maximum for integrated heat absorption well within the one-hour time frame of the calculation. The concrete continues to absorb heat over a very long term, on the order of days. However, the transient skin temperature of concrete increases due to its relatively poor thermal conductivity and a gap between the steel jacket and concrete reduces concrete effectiveness, so that the magnitude of concrete heat absorption is not significant relative to the steel. The integrated heat absorption by heat sinks is then primarily a function of the maximum bulk steel temperature rise, which is related to the saturation temperature of the adjacent region. While a less severe assumed stratification gradient would result in less rapid heat absorption by sinks in the upper region, the upper heat sinks would still reach their maximum well within the one-hour time frame. The lower region integrated heat absorption is limited by the saturation temperature for the assumed steam concentration. Therefore, the stratification bias is controlled by the lower region steam concentration and is maximized by the assumption of the extreme stratification gradient.

Since the exaggerated effect of stratification for the case of a plume rising through the CMT shows a bias on total integrated heat removal, a bias is introduced into the Evaluation Model by removing heat sinks associated with floors in compartments. As an additional conservatism, that bias is retained for the Evaluation Model with a plume rising through the steam generator compartment, as well as all sensitivity cases performed, even though most situations result in downflow through the CMT compartment.

For the case of the steel containment shell above the operating deck, the dome surface area weights the upper, steam-rich volume more heavily than the lower volumes, and compensates for the lower heat removal rates. Thus, the homogeneous case results are nearly equal to those for the stratified case, with the homogeneous case giving less than 0.5% less instantaneous heat removal rates. A simple bias of removing operating deck floors is included in the Evaluation Model to bound this effect.

9.B.6 CONCLUSIONS

For the case of the steel containment shell above the operating deck, the dome surface area weights the upper, steam-rich volume more heavily than the lower volumes, and compensates for the lower heat removal rates. Thus, the homogeneous case results are nearly equal to the stratified case, with the homogeneous case giving less than 0.5 percent less instantaneous heat removal rates. A simple bias of removing operating deck floors is included in the Evaluation Model to bound this effect.

The results of the heat sink utilization analysis for below-deck compartments indicate that in general, the assumption of homogeneous compartment volumes predicts higher overall heat removal by the heat sinks compared to stratified volumes. This is primarily due to the propensity of the condensation heat transfer to fall off as the heat sink surface temperature approaches the local saturation temperature in the lower steam fraction volumes. Stratification gradients are not expected to be nearly as extreme as assumed in this evaluation. The results of the homogeneous case gives 15-20% higher integrated heat removal than the stratified results. Therefore, a bias is introduced in the Evaluation Model to account for this difference, implemented by removing heat sinks representing floors from the Evaluation Model.

References

- 9.B-1. WCAP-14845, "Scaling Analysis for AP600 Containment Pressure During Design Basis Accidents," Revision 3, March 1998.

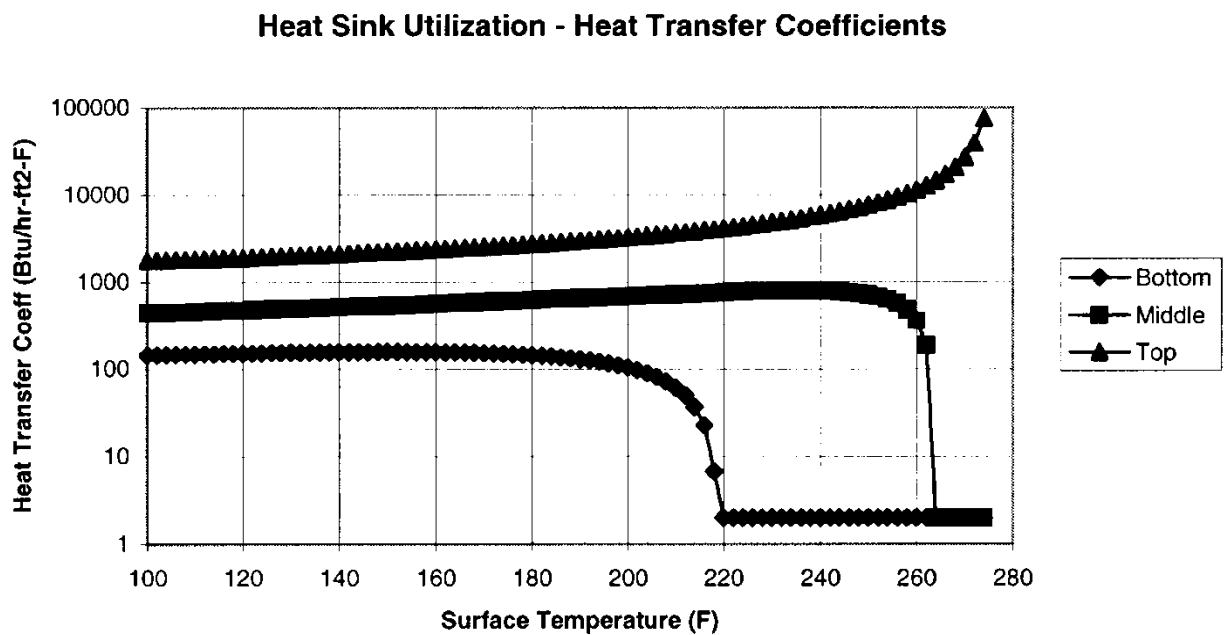


Figure 9.B-1. Condensation Heat Transfer Coefficients vs. T_{surf}

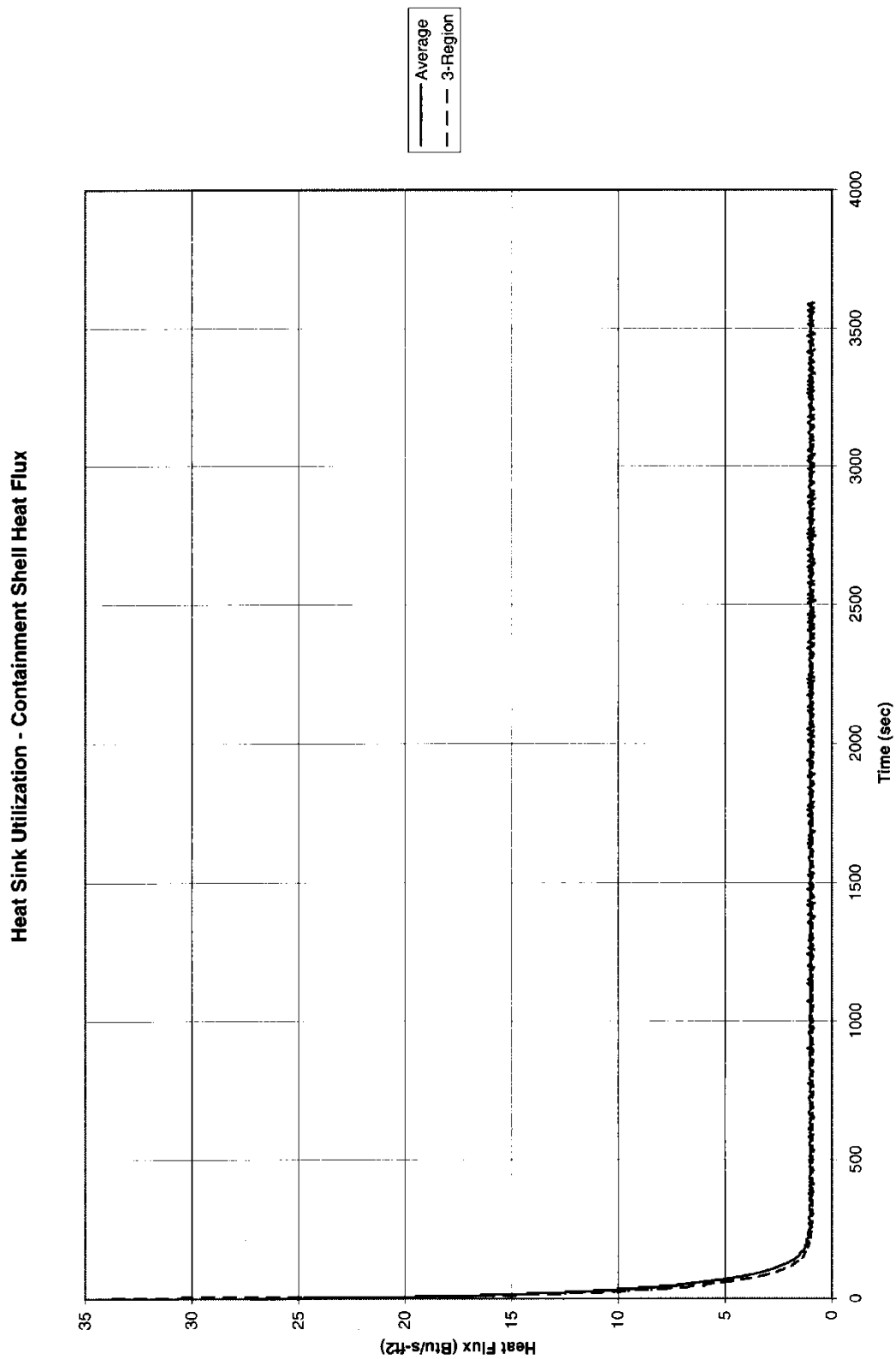


Figure 9.B-2. Containment Shell Heat Sink Results

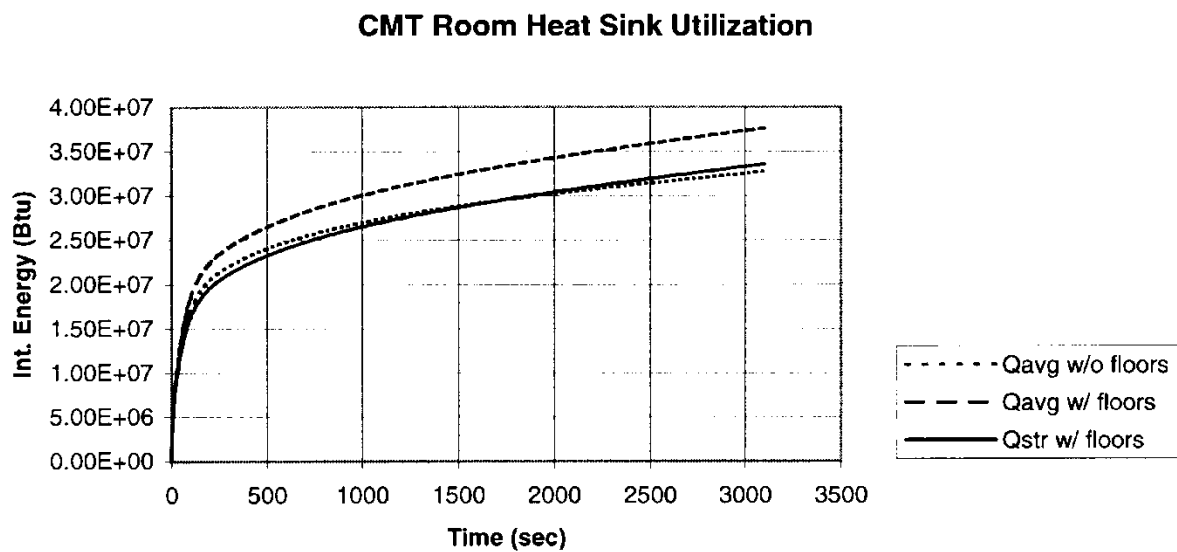


Figure 9.B-3. CMT Room Heat Sink Results

APPENDIX 9.C ADDITIONAL INFORMATION ON CONTAINMENT CIRCULATION AND STRATIFICATION

9.C.1 DEVELOPMENT OF EXPECTED FLOW PATTERNS FOR AP600 AND AP1000 BASED ON SEPARATE FLOW TESTS IN ENCLOSURES

9.C.1.1 Stratification Phenomena

Stratification is the formation of horizontal layers of constant density. Stratified layers are stable if the density of the layers decreases in the upward vertical direction (the gradients of density are negative in z direction according to Figure 9.C-1a) and if forced convection mixing is not sufficiently strong to disrupt the stable fluid layers.

Another more general definition of stratified conditions is that gradients of density in the horizontal direction are small, except in jets, buoyant plumes, and small regions near the vertical walls inside boundary layers (wall jets). In most of the volume, the density gradients in z direction are negative, while inside the jets, wall jets, and buoyant plumes they could be positive (see Figure 9.C-1b).

Stratification occurs as a consequence of the temperature or concentration gradients in the vertical direction. Increasing temperatures or decreasing concentrations of heavier mixture components with increasing elevation promote stratification. The existence of flow structures, such as jets, plumes, and vertical wall boundary layers, decreases the “steepness” of the vertical density gradients.

Examples of stratified conditions are numerous. Stratified layers are observed as large-scale geophysical phenomena (in lakes, sea, and oceans, in atmosphere - stratus clouds), as well as inside the enclosures. For example, warmer air tends to gather below ceilings in energy storage devices, nuclear reactors, solar collectors, and enclosures under the influence of the spread of fire and smoke.

This appendix discusses the stratification phenomena inside a nuclear reactor containment. Possible reasons for the stratification will be specified. Stratification may occur if:

1. The upper boundary is at the higher temperature than the lower boundary (see Figure 9.C-2 a), as well as for other similar combinations of temperature boundary conditions at the outside and inside surfaces (see Figure 9.C-2 b – d).
2. A higher concentration of the heavier or lighter components of the mixtures is maintained (by injecting and removing) near the lower or upper boundaries of the enclosure, respectively.
3. A lighter fluid is released (permanently, or from time to time) and captured below the ceiling of the containment.
4. The release point of the lighter/heavier fluid is closer to the top/bottom.
5. The shape of the enclosure promotes stratification (tall elongated enclosure).

6. The distribution of the non-complete vertical partitions suppresses fluid flow in the upper portions of the enclosure.
7. The distribution and size of the horizontal openings suppresses the fluid flow in vertical direction.
8. The internal heat sources (sinks) are positioned in the upper (lower) portions of the enclosure.

Under the conditions above (or a combination of them), the stratification may be stable. The presence of stratified layers inhibits circulation, that otherwise could be induced by a jet, plume, or boundary layers. The conduction and diffusion, heat and mass transfer processes, respectively, are dominant. As a result, the overall heat and mass transfer decreases and the heat transfer through the containment shell is slowed.

One way to avoid the stratification is to generate fluid flow patterns inside the enclosure using forced convection. Additional devices such as fans, sprays, or nozzles are necessary, as well as associated power supplies and controls.

Since the AP600 and **AP1000** rely on a passive containment cooling system (PCS), only the effects of fluid circulation due to the interaction of natural convection with the stratified field are discussed.

Modifications to the shape of the enclosure, the distribution and size of the internal partitions, and the openings could be made to avoid stratification. A different distribution of heat sources could also be applied to generate natural convection effects. The fluid flows due to natural convection promote better circulation inside the enclosure. The introduction of jets may also interrupt stably stratified layers through better mixing of the layers of various densities and concentrations. With a jet stratification may become unstable or, at least, the vertical gradient reduced. With only natural convection if the generated buoyancy forces are strong enough, the entire volume of the enclosure will be affected, resulting in the relatively uniform values of temperature and concentration fields. Natural convection heat transfer is dominant and the more intensive circulation improves the transfer of heat from the containment. Natural convection flow effects are generated spontaneously due to the gravity (buoyancy forces) when heated sources exist, so that additional control and other devices are not necessary.

9.C.1.1.1 Static Stratification

Static stratification occurs if the upper horizontal boundary of the domain is maintained at a higher temperature than lower boundary, as in Fig. 9.C.1-1a. Stratification also occurs if the concentration of heavy components is low in the mixture in the upper portion of the domain. The fluid layers are undisturbed and fluid motion is negligible. The temperature or density distribution in the vertical direction is linear. Heat transfer is predominantly governed by conduction, while mass transfer is driven by diffusion. The formed fluid layers are stable and communicate only with the neighboring upper and lower layers. The resulting heat and mass transfer rates are low.

Corresponding experimental results are found in Akino et al., 1989 and Hiller et al., 1988. In both papers, stable stratified layers are identified using various colors reflected by liquid crystals (suspended in the fluid).

Static stratification exists inside a containment vessel if the temperature distribution of the vertical walls is the same as in the surrounding stratified fluid (adiabatic vertical walls, as in Fig 9.C.1-1a). Since, the top of the passive containment, as well as the vertical walls, are exposed to the surrounding air and cooled by natural convection, stable stratification is not present. Even small temperature differences between the air inside and outside the containment produce large Grashof (Rayleigh) numbers, due to the height of the containment ($H_t=109$ ft). For example, a temperature difference of 9°F between the air at the deck level and the air below the dome ceiling results in $Gr_t = 2.2 \cdot 10^{13}$. This is in the range of chaotical turbulent flow, characterized by upward and downward plumes (see experimental results by Akino et al., 1989).

Static stratified layers are also generated by releasing a lighter gas, e.g., steam or hydrogen, into the upper portion of the containment and capturing the gas beneath the dome.

Hydrogen distribution experiments performed in the HDR facility, test group E11, combine high hydrogen release rates with superheated steam injection into the containment (see Wolf et al., 1994a). A comparison of influences of the axial break and gas release positions is obtained with E11.2 (high release position) and E11.4 (low release position) experiments. Although these two specific experiments simulate severe accident scenarios, comparison of results from the two experiments provides insights into the physics of stratification. The tests are characterized by boundary conditions that can promote circulation (especially test E11.4). They also show that relatively small concentration gradients can exist in the presence of circulation.

Steam release from small breaks generates thermal stratification for break positions located at the higher level, with the hot zone above the break locations. Two mechanisms are used to break up the established thermal stratification. The first mechanism used subsequent steam releases at positions lower than the original release to break up the established thermal stratification. This mechanism did not produce homogeneously mixed conditions. The second method is the application of external sprays on the upper dome. This causes condensation on the inner surface and a decrease in the temperature in the upper part of the dome. Convective flows form and affect the whole volume of the dome and lower compartments, resulting in a completely homogenized atmosphere.

As in the HDR E11.2 experiment, condensation on the dome of the passive containment breaks up stratification. The condensation on the vertical walls also contributes to breaking of stratified layers and to entrainment in the vertical boundary layers. The circulation inside the containment affects the lower compartments and promotes circulation due to the natural convection.

The shape of an enclosure could also promote stratification. One example is natural convection inside romb shaped enclosures (see Figure 9.C-3). Stratification is generated if the upper vertical side is at a high temperature and the inclined top and bottom sides are adiabatic (see, Dzodzo, 1993). The overall heat and mass transfer are suppressed by the presence of the stratified fluid in the upper and lower corners of the romb shaped enclosures. When the boundary conditions are reversed, i.e., the lower vertical side is at the higher temperature, the entire volume of the enclosure is effected by circulation. Heat transfer is intensified and stratified layers are not present in the upper and lower corners. A comparison of experimentally and numerically obtained temperature and velocity fields for these two cases is presented in Figure 9.C-4. An overview of the numerical results for various angles of the romb (parallelogram-shaped) enclosures, Prandtl numbers, and aspect ratios is presented by (Hyun and Choi, 1990).

Although the top of the passive containment is somewhat conical in shape, stratification in the upper portion of the dome would not exist because of the natural convection due to the lower temperatures of the ceiling and vertical walls. Stratification effects are promoted if the containment ceiling is insulated or at a higher temperature.

The distribution of the internal heat sources in the upper part and heat sinks in the lower part of enclosures promotes the formation of the stratified layers (see Figure 9.C-2 b, c, d). Examples of the influence of the position and distance between the heat source and heat sink are provided by A. Kurosawa et al., 1993 and C. J. Ho et al., 1994. An example of the influence of an array of discrete heat sources on natural convection is presented by T. J. Heindel et al., 1995.

Vertical non-complete partitions inside an enclosure contribute to the stratification. If the non-complete vertical partition is positioned near the ceiling, flow in the upper part of the enclosure is obstructed and a stagnant stratified region near the ceiling is formed (see Hanjalic et al., 1996, and Nowak and Novak, 1994 for examples of the two-dimensional numerical simulation, and T. Fusegi et al., 1992, for the three-dimensional simulation). This is of special interest for the analysis of the spread of fire and smoke inside the buildings. Such partitions do not exist above the operating deck level in the passive containment.

Narrow horizontal openings between upper and lower compartments also suppress circulation and cause stratification. The results of a two-dimensional numerical simulation (R. Frederick and A. Valencia, 1995) show the influence of the size of the horizontal openings on the natural convection inside the vertically connected enclosures.

The potential for stratification in compartments below the operating deck of containments, due to the various sizes of the openings is also studied (see Reference Wolf et al., 1994b).

9.C.1.1.2 Stratification and Circulation

Figure 9.C-1b illustrates conditions where a portion of an enclosure is stratified and other portions are affected by strong recirculation zones and currents. Due to the circulation effects, shallow vertical density gradients are present inside the stratified portion of the enclosure volume.

Convective heat and mass transfer that results from communication between the stratified and flow-affected zones, contributes to the mixing between the zones with different temperatures, concentrations, and densities. Flow inside the enclosure is promoted by the existence of the entraining wall layers (which are a consequence of the heat transfer), penetrating jets, and buoyant plumes (see Reference, Peterson, 1994 and Figure 9.C-1b).

To gain insight into passive containment physics, we will start with small-scale enclosure examples and progress to larger scale.

9.C.1.1.2.1 Interaction of Wall Jets (Boundary Layers) with Stratified Layers

One example of interaction of wall jets with stratified layers is the natural convection inside a square enclosure (see Figure 9.C-5). The opposite vertical walls of the enclosure are at the different temperatures and the horizontal walls are adiabatic (see Markatos and Pericleous, 1984 and Figure 9.C-5a). With high Rayleigh numbers (over 10^{+6}), $Pr=0.71$, turbulent flow exists inside the enclosure. Velocity and temperature gradients are large in the boundary layers. Velocities have maximum values near the walls, while inside the core of the enclosure they are small. The temperature (density) field in the core of the enclosure is stratified (see Figure 9.C-5). Communication exists between the boundary layer region and core of the enclosure through the vortices (see Figure 9.C-5b), which change in number, position, and intensity for various temperature differences between the opposite walls (various Ra numbers). Temperature gradients are highest in the boundary layers near the vertical and horizontal walls (see Figure 9.C-5c). For the laminar convection ($Ra=10^{+4}$ and $Ra=10^{+5}$), the temperature difference between the highest and lowest points at the vertical axis of the stratified core is $0.6*(T_h - T_c)$, while for the turbulent regime ($Ra=10^{+8}$, 10^{+12} , 10^{+16}) it is $0.4*(T_h - T_c)$. The decrease in the vertical temperature gradients inside the stratified core for the turbulent regime is the result of higher velocities and stronger circulation inside the cavity. The temperature field inside the core of the enclosure is stratified, while recirculation due to convection inside the enclosure is predominantly near the walls. Despite the presence of the stratified core, for high Ra numbers, a fluid particle travels the entire enclosure (due to the convection) and contributes to better mixing and decreases the vertical gradients inside the core.

The increase of the Rayleigh number corresponds with a decrease in the thickness of the boundary layers, an increase in the temperature gradients inside the boundary layers, and an increase in the heat transfer rate. The dependence of the average Nusselt numbers on the Rayleigh numbers is presented in Figure 9.C-6.

A similar two-dimensional flow pattern and stratified temperature (density) field is also obtained between two opposite vertical line jets (see Figure 9.C-7) as discussed in Baines and Turner, 1969.

A numerical analysis (Markatos and Pericleous, 1984) is performed for a two-dimensional plane, assuming that the influence of the front and back walls of real three-dimensional enclosures is not significant. For Rayleigh numbers greater than 10^6 , the $k-\epsilon$ turbulence model is used. Due to time-averaging, the numerical results do not show either the instability mechanisms during the transition from laminar to turbulent flow, or the resulting oscillations that would result from solving the time dependent Navier-Stokes equations.

Experimental and numerical results for three-dimensional enclosures are provided by Hiller et al. 1989, Mallinson and de Vhal Davis, 1977, respectively. The results indicate that observed vortices, which affect mixing inside the core of the enclosure, communicate between the front and back walls through the middle of the enclosure, thus enhancing mixing due to three-dimensional circulation effects (see Figure 9.C-8).

Reviews of various aspects of confined convective flows, including the interactions between boundary layers near the bounding walls and core and the effects of the cavity aspect ratio, inclination angle, and thermal boundary conditions on flow patterns, are presented by Ostrach 1972, 1982, Catton, 1978, Hoogendoorn, 1986 and Allard, 1992. A state of the art review of the analyses of two-dimensional and three-dimensional transient effects on the natural convection flows in sidewall heated enclosures is presented by T. Fusegi and J. M. Hyun, 1994.

R. J. Janssen and R.A.W.M Henkes, 1995 simulated the instability mechanisms and the transition from laminar to turbulent (oscillatory and finally chaotical) flow regimes inside a two-dimensional square enclosure with differentially heated vertical walls and adiabatic horizontal walls by solving the time-dependent Navier-Stokes equations. The results indicate that the transition from laminar to chaotic flow (for $Pr < 2.0$) is through periodic and quasi-periodic flow regimes. The periodic, quasi-periodic and chaotic flow regimes are established for Prandtl number 0.71 and Rayleigh numbers 2×10^8 , 3×10^8 and 7.5×10^8 . Internal waves corresponding to fluctuations in the temperatures at $Ra = 2 \times 10^8$ are presented in Figure 9.C-9. The temperature differences in the entire core of the enclosure are small, $0.004 \times (T_h - T_c)$. The predicted temperature differences inside the core of the enclosure are much smaller than those predicted by k- ϵ turbulence model (Markatos and Pericleous, 1984). This indicates that temperature gradients inside the boundary layers are greater (isotherms inside the thermal boundary layer are not presented in Figure 9.C-9) and heat transfer is more intensive than calculated by k- ϵ model.

Two instability mechanisms influence the transition to turbulent (chaotical) flow regime. The first instability is a Kelvin-Helmholtz type instability (as in a plane jet with inflection points in the velocity profile) in the fluid layer exiting from the corners (where the vertical boundary layers are turned horizontal). The second source of the instability is related to the instability in the boundary layer near the vertical walls. The instability inside the enclosure vertical boundary layers is mechanically (shear) driven. Both regions of the instability origins (hot and cold intrusions from corners and boundary layer waves) are presented in the Figure 9.C-10 (from S. Armfield and R. Janssen, 1996). The figure presents temperatures for the initial solution, i.e., immediately after setting the left and right vertical boundaries to $\Delta T/2$ and $-\Delta T/2$, respectively. For values of Rayleigh numbers greater than 10^9 , the turbulent oscillatory and chaotical flow affects the stratified layers inside the core of the enclosure. If the radius ($H_v = 65$ ft) of the containment is taken as a characteristic length (as a distance between the hot buoyant jet plume in the center and cold vertical wall boundary layers), a 9°F temperature difference results in a Grashof number $Gr_v = 4.7 \times 10^{12}$.

9.C.1.1.2.2 Interaction of Jets or Plumes with the Stratified Layers

The penetration of a stratified layer by a jet is another example where a portion of an enclosure is stratified and another portion is affected by strong recirculating zones (Figure 9.C-1b). Depending upon the strength of the jet and the depth of the stratified layers, portions of the enclosure are affected by interaction between the jet and stratified layers. A portion of the stratified fluid is entrained by the jet, decreasing the average jet velocity. The jet penetrates upward (Garrad and Patrick, 1983, So and Aksoy, 1993, and Porterie et al., 1996), or downward (Markatos and Pericleous, 1984, see Figure 9.C-5 b and c near the cool wall). A negatively buoyant jet, as presented in Kapoor and Jaluria, 1993, is also possible.

The upward penetrating jet is of interest for LOCA or MSLB accident scenarios. Scaling and analysis of mixing in large stratified volumes for the cases of upward penetrating jets is presented by Peterson, 1994. If the strength of the jet is strong enough, it produces fluid flow below the ceiling. After reaching the vertical side walls, the flow results in downward negatively buoyant jets (see Figure 9.C-11 a and b).

The downward, negatively buoyant penetrating jet (Kapoor and Jaluria, 1993, see Figure 9.C-11a and Figure 9.C-11b) is of interest for the analysis of the flow patterns inside the upper-deck region (Figure 9.C-11a), as well as for the compartments below the dome floor (Figure 9.C-11b). If the strength of the negatively buoyant jet is not high, it is not able to reach compartments below the deck. The direction of the flow changes as presented in Figure 9.C-11a. The redirection of the flow causes additional entrainment of the surrounding fluid, thus contributing towards the increase of the circulation (and mixing) inside the upper-deck region. The correlations for entrainment rates in the negatively buoyant jets are presented in Kapoor and Jaluria, 1993.

If the strength of the negatively buoyant jets is high, it is able to penetrate into the below-deck compartments. There are indications from large-scale tests conducted by Westinghouse (tests 222.3 and 222.4, 3-inch pipe, elevated 6 ft, pointed at the wall and up, respectively, see F. E. Peters, WCAP-14135, July 1994) which simulate the MSLB, that the entire volume of the containment has almost the same steam concentration. This occurs despite the fact that formation of the global circulation loop between the lower-deck compartments and upper dome regions is not possible. An explanation is that the kinetic energy of the jets is high enough to provide downward penetration of the negatively buoyant jets into the below-deck compartments.

Depending upon the distribution of compartments below the dome floor and the number, size and distribution of openings between the compartments and the dome region, various flow patterns are possible inside the compartments. A portion of the downward vertical plumes produced by natural convection (wall boundary layers) or the negatively buoyant jets produced by strong vertical upward penetrating jet into the dome region enters horizontal openings in the compartments, thus promoting circulation and flow inside the compartments below the deck. Fluid flows upward to the dome through other compartment horizontal openings to preserve overall mass continuity and to close the global circulation loop (see Figure 9.C-11b).

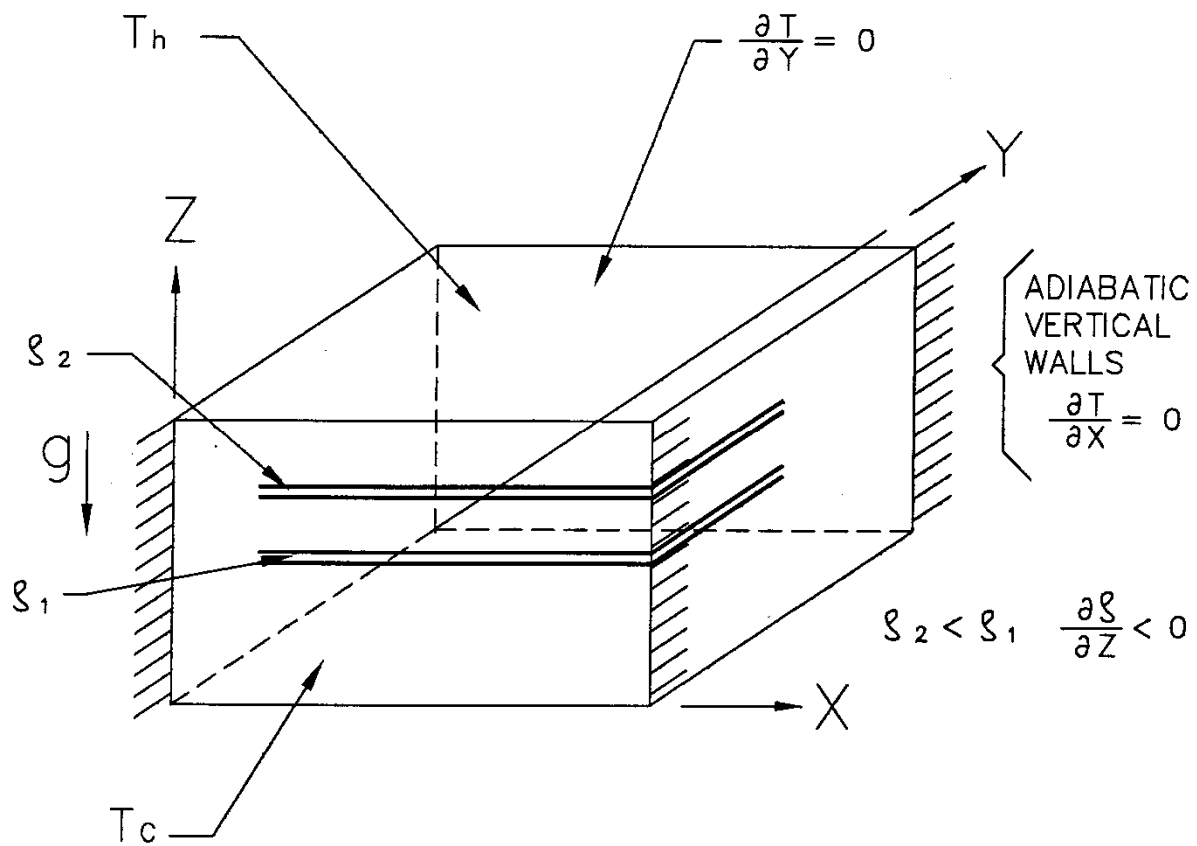
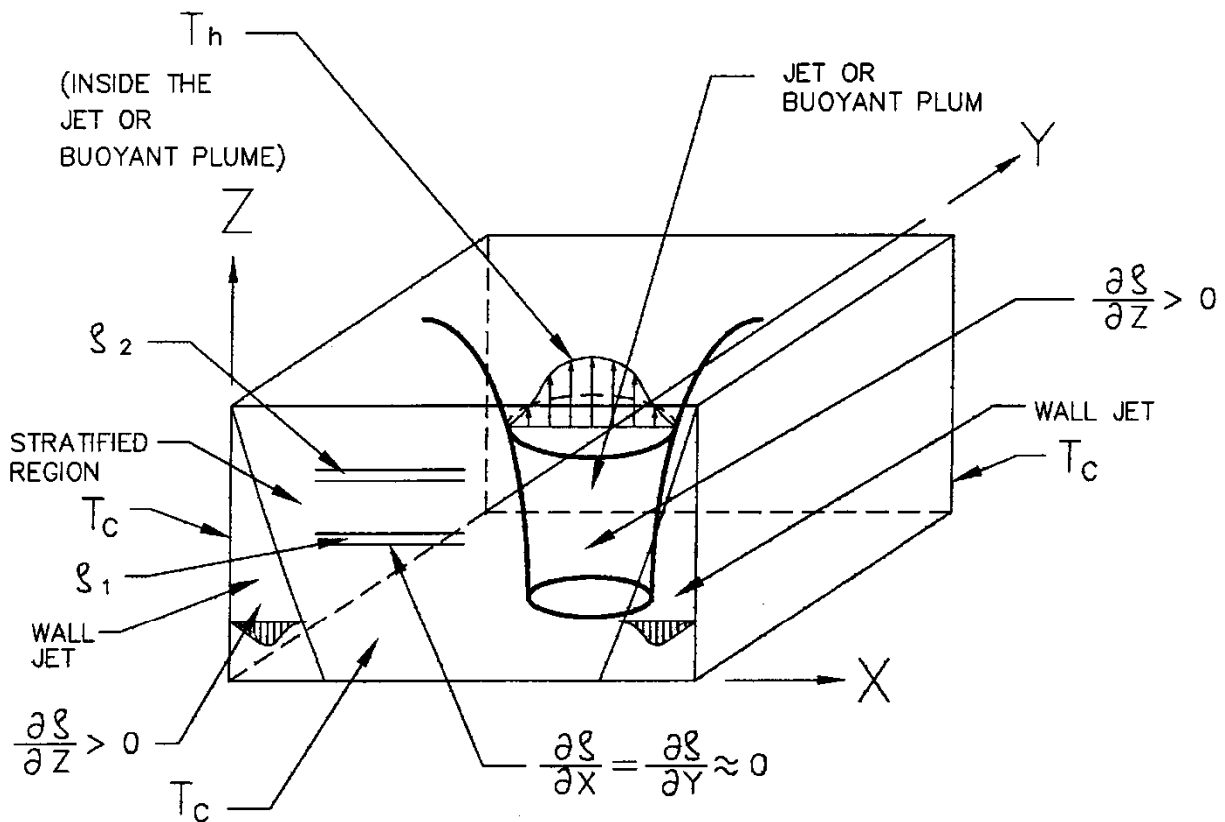


Figure 9.C-1a. The Formation of the Horizontal Layers of the Constant Density Due to the Stratification



STRATIFIED REGIONS $\left(\frac{\partial \rho}{\partial X} = \frac{\partial \rho}{\partial Y} = 0, \frac{\partial \rho}{\partial Z} < 0 \right)$ AND
 JET REGIONS $\left(\frac{\partial \rho}{\partial X} \neq 0, \frac{\partial \rho}{\partial Y} \neq 0, \frac{\partial \rho}{\partial Z} > 0 \right)$ INSIDE
 THE ENCLOSURE.

Figure 9.C-1b. Interaction of Jets, Plumes and Wall Boundary Layers with Stratified Regions

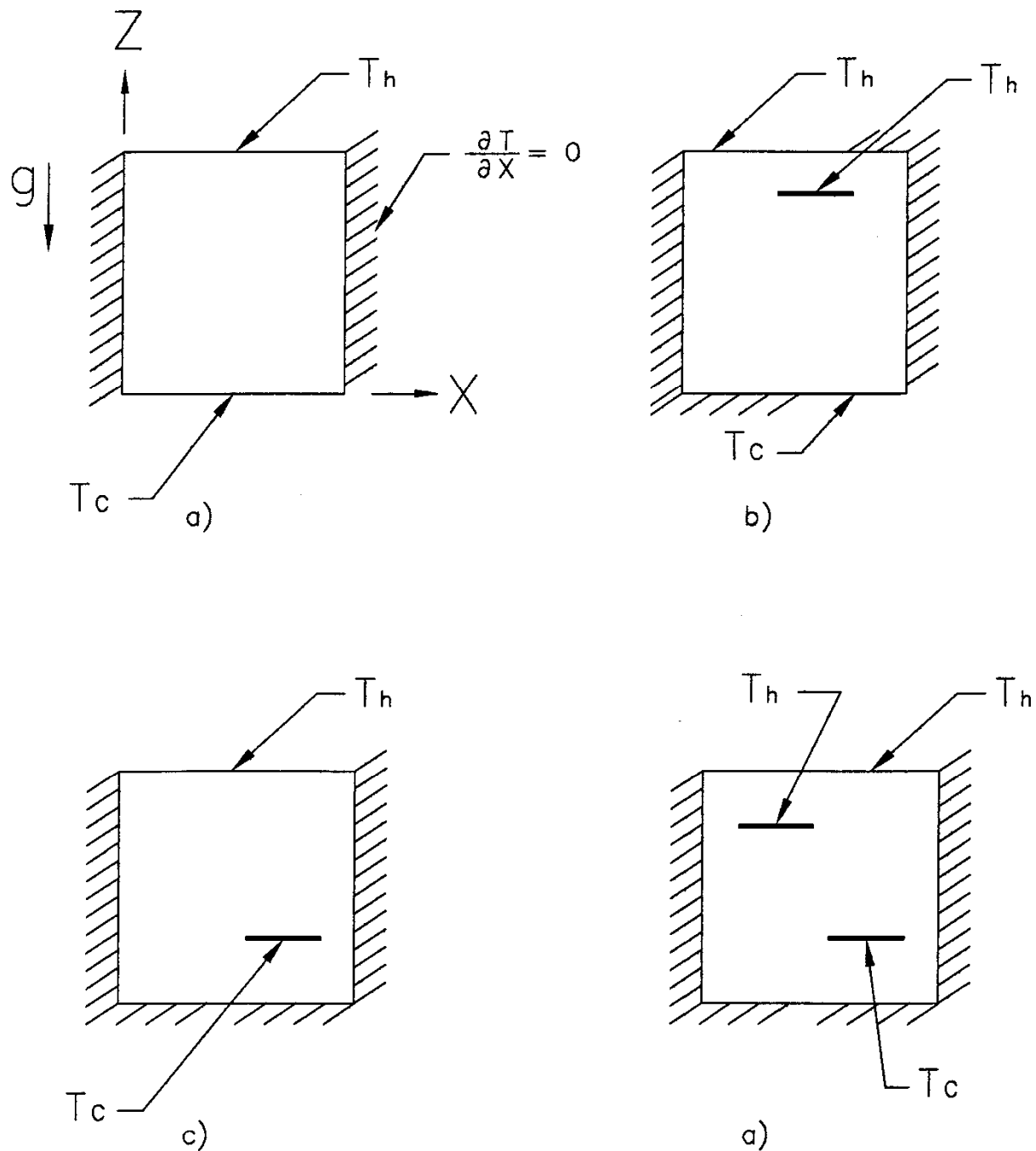


Figure 9.C-2. Combination of the Constant Temperature Boundary Conditions at the Outside and Inside Surfaces which will Produce Stratification Inside the Enclosure

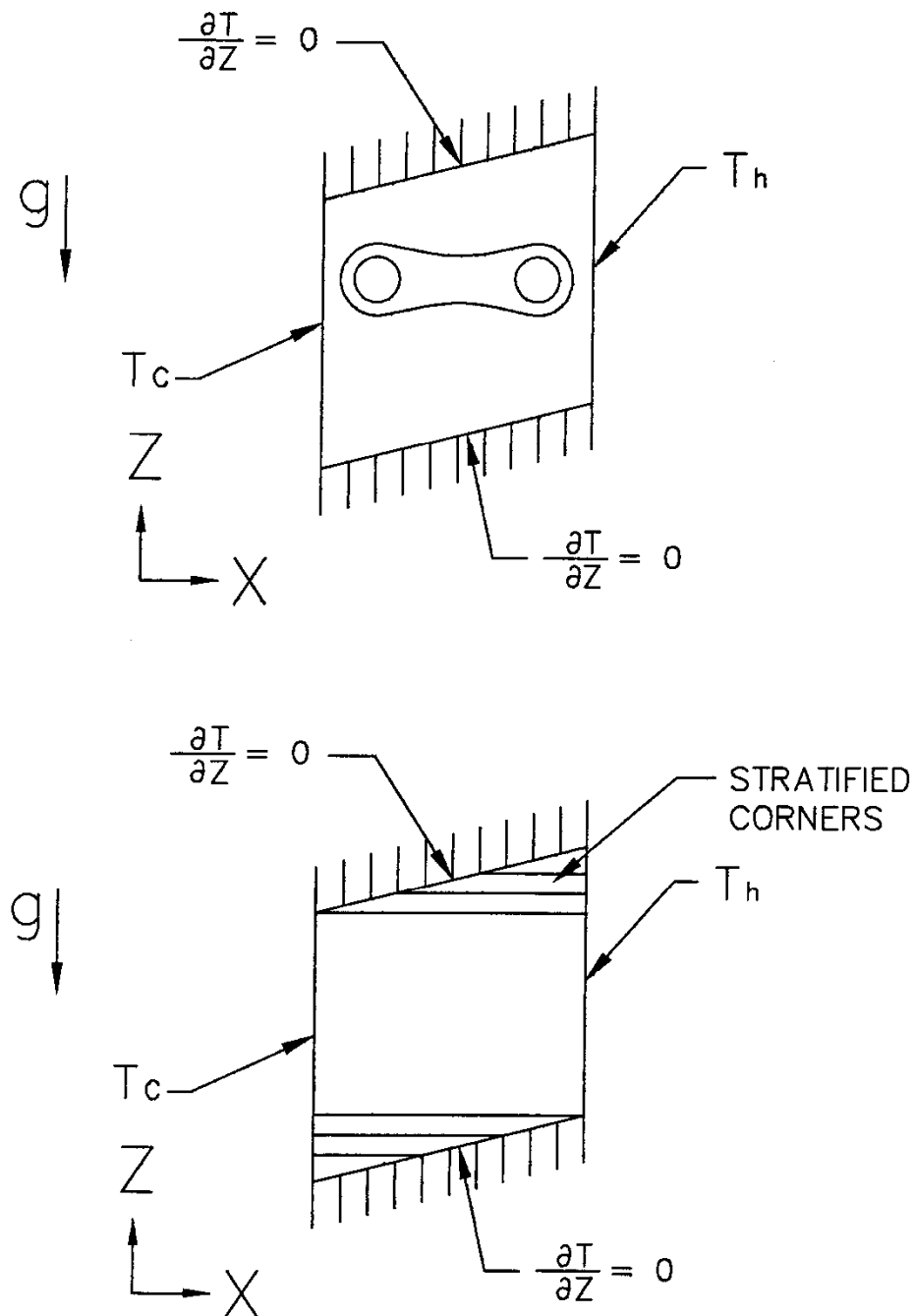


Figure 9.C-3. Stratification Inside the Upper and Lower Corners of the Romb-Shaped Enclosure

Example of the Stratification Caused by the Shape of the Enclosure and Distribution of the Boundary Conditions

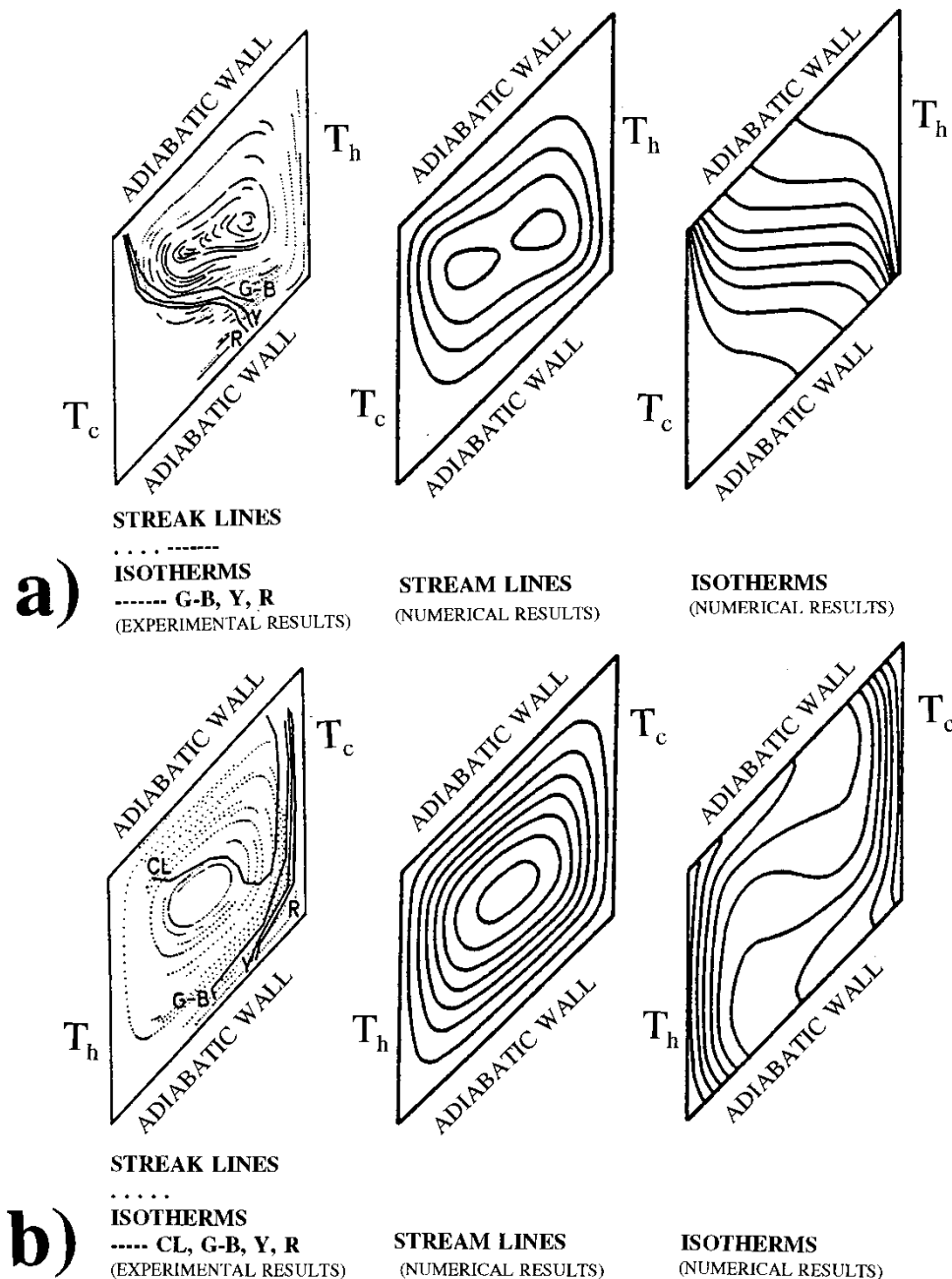
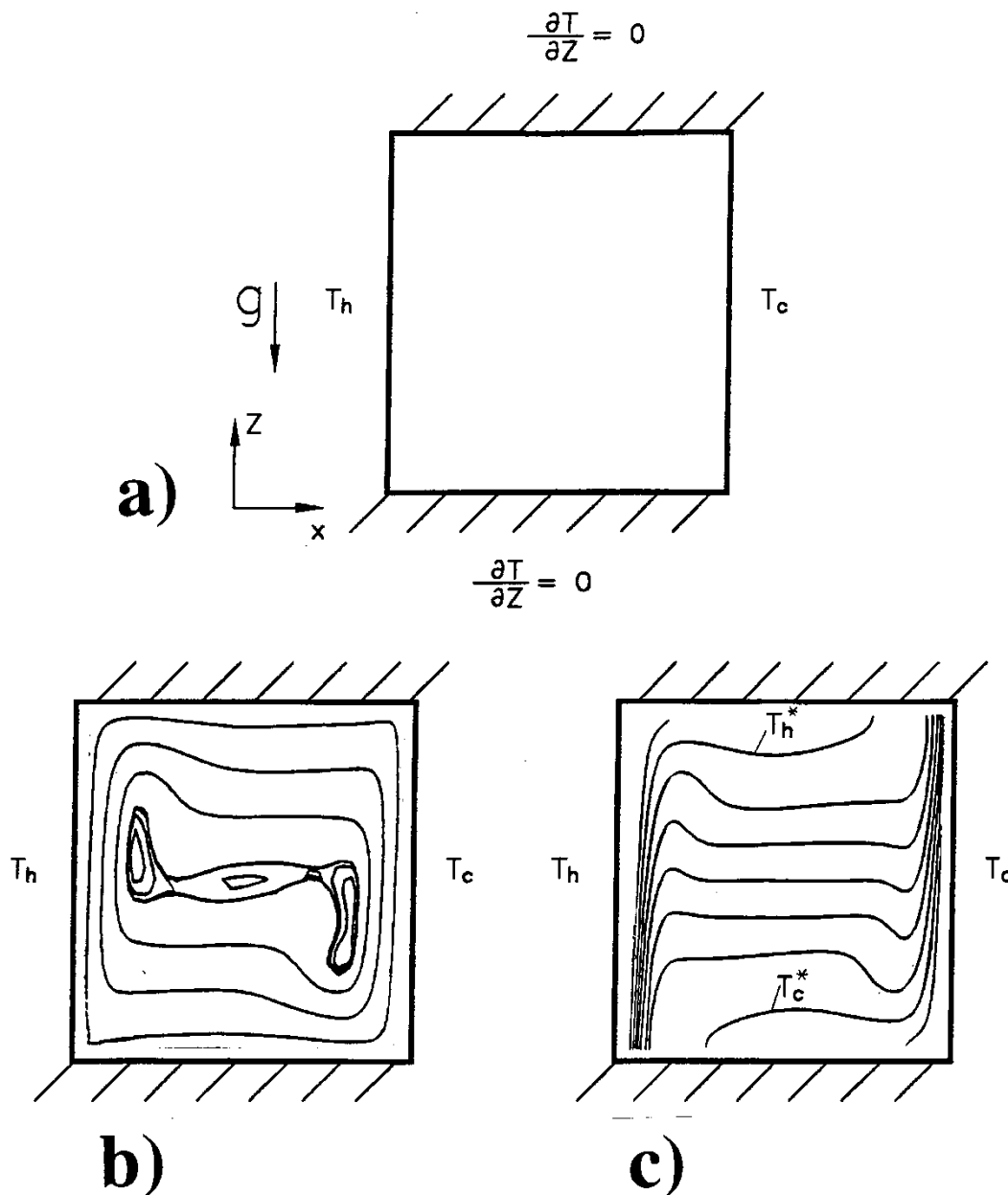


Figure 9.C-4. Experimental and Numerical Results for the Romb-Shaped Enclosure with the Romb Angle 44° and $Ra=3.5 \times 10^4$, $PR=5270$

- a) results for the upper vertical wall at the higher temperature
b) results for the lower vertical wall at the higher temperature

(Reprinted from: M.B. Dzodzo, "Visualization of laminar natural convection in romb-shaped enclosures by means of liquid crystals," in Imaging in transport processes (ed. S. Sideman and K. Hijikata), Begel House, Inc., 1993, pp. 183-193)



**Figure 9.C-5. a) The Square Enclose with Vertical Walls at the Different Temperatures and Horizontal Walls Adiabatic
b) Streamlines for $Ra=106$ and $Pr=0.71$,
c) Isotherms for $Ra=106$ and $Pr=0.71$**

“Reprinted from N.C. Markatos and K.A. Pericleous/Laminar and Turbulent Natural Convection in an Enclosed Cavity, Int. J. Heat Mass Transfer, Vol. 27, No. 5, pp. 755-772, 1984, Copyright 1984, Figure 9.C.5(d) and 6(d), with kind permission from Elsevier Science Ltd, The Boulevard, Langford Lane, Kidlington OX51GB, UK”

Ra	10^3	10^4	10^5	10^6	10^8	10^{10}	10^{12}	10^{14}	10^{16}
Nu	1.108	2.201	4.430	8.754	32.045	156.85	840.13	3624.4	11226

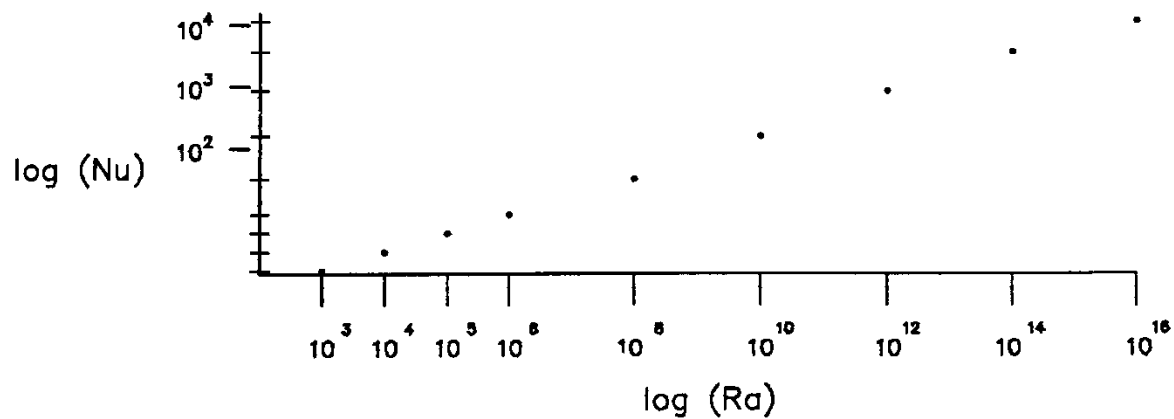
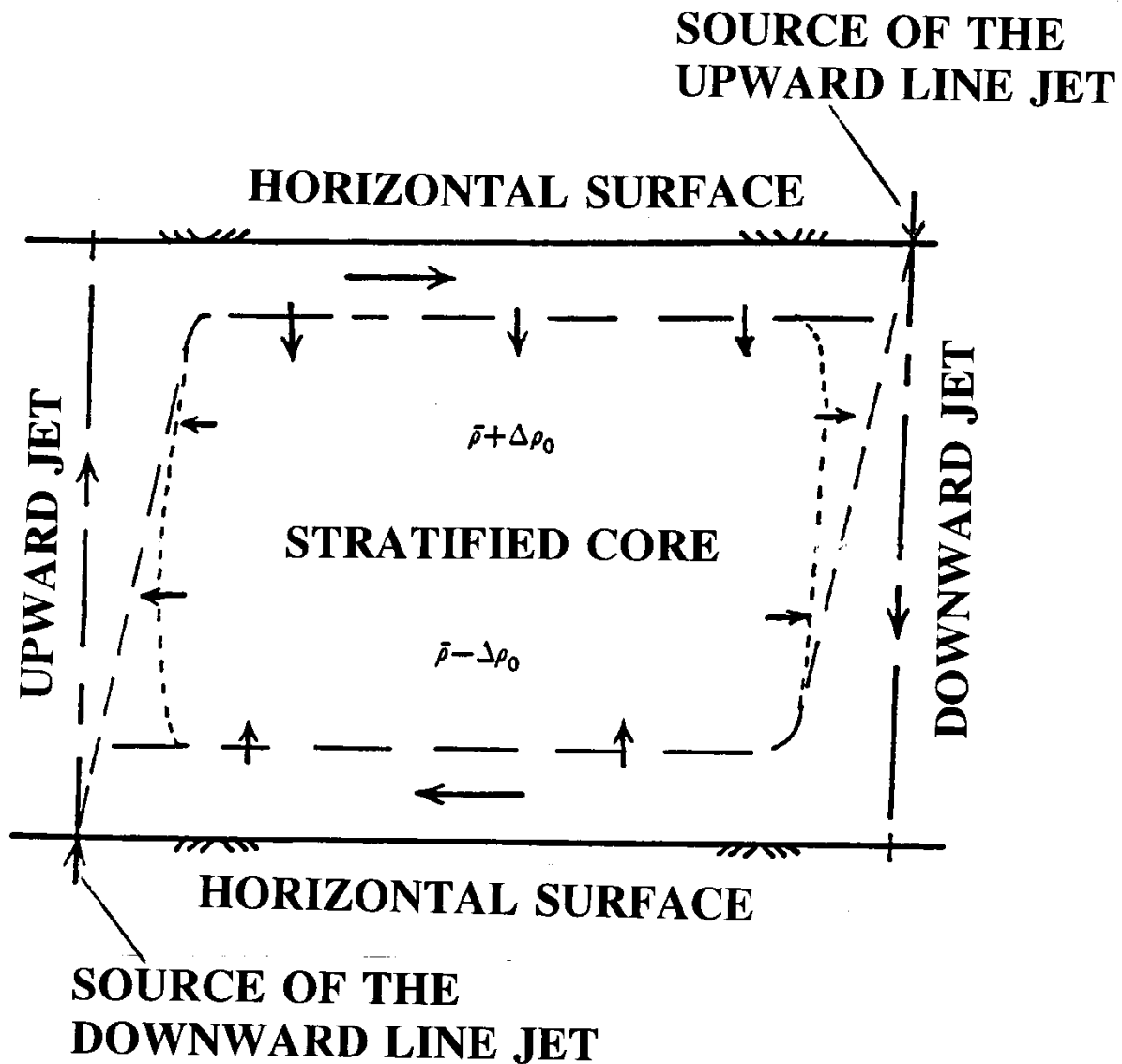


Figure 9.C-6. Average Nusselt Numbers as a Function of the Rayleigh Numbers for the Square Enclosure with Opposite Vertical Walls at the Different Temperatures and $Pr=0.71$ (air)

(according to N.C. Markatos and K.A. Pericleous/Laminar and Turbulent Natural Convection in an Enclosed Cavity, Int. J. Heat Mass Transfer, Vol. 27, No. 5, pp. 755-772, 1984)



**Figure 9.C-7. Formation of the Stratified Core in Between Two Opposite Vertical Line Jets
(after Baines and Turner, 1969)**

“Reprinted with the permission of Cambridge University Press from Baines W.D. and Turner, J.S./Turbulent buoyant convection from a source in a confined region, Journal of Fluid Mechanics, Vol. 37, 1969; pp. 51-80, Copyright 1969, Figure 9.C.10”

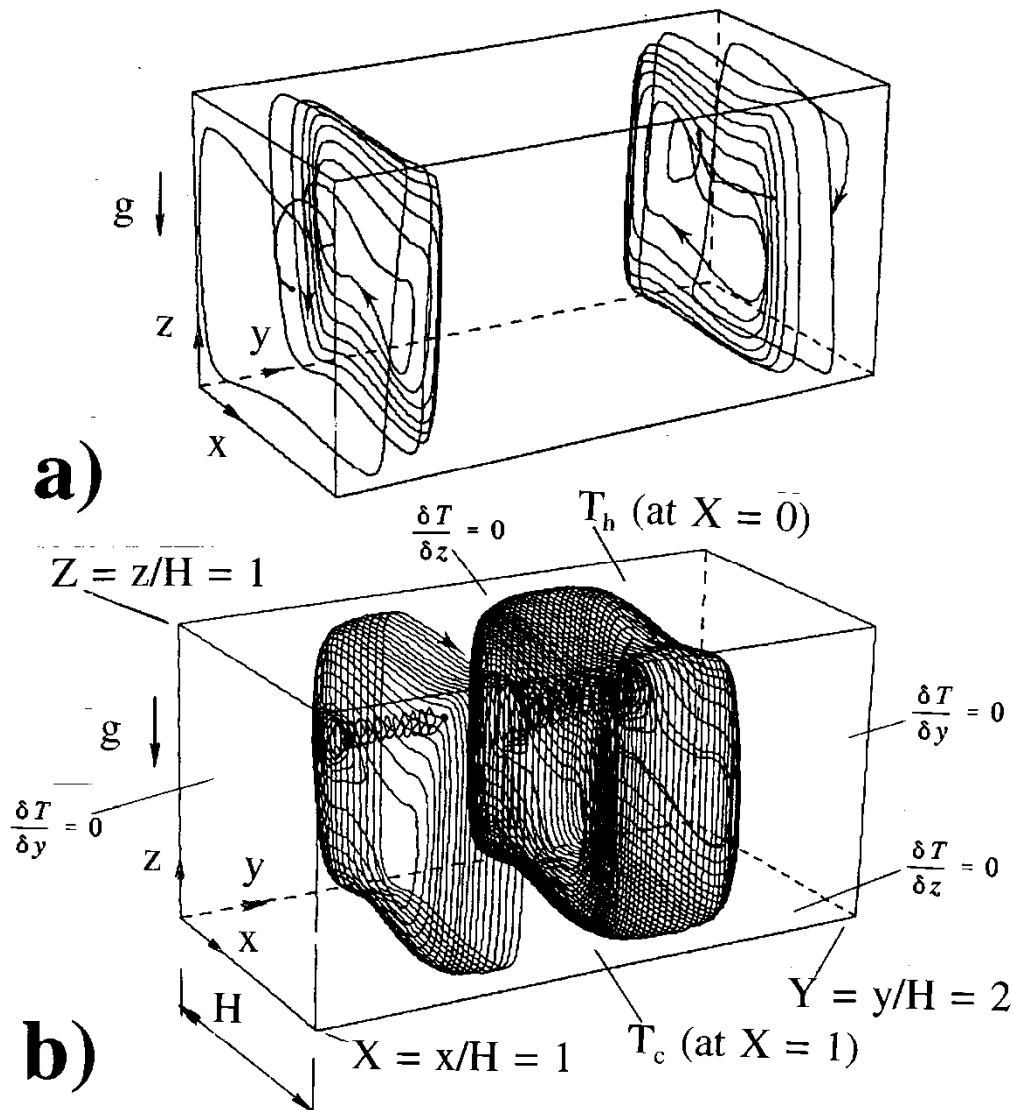


Figure 9.C-8. Flow in an Enclosure with Vertical Opposite Walls at Different Temperatures (Ra=105, PR=0.71)

- a) forward flow (towards $Y=0$ and $Y=2$) – streamlines through the points $(X=0.5, Y=0.1, Z=0.49)$ and $(X=0.5, Y=1.9, Z=0.49)$
- b) reverse flow (towards $Y=1.0$) – streamlines through the points $(X=0.3, Y=0.8, Z=0.65)$ and $(X=0.3, Y=1.2, Z=0.65)$ after (Mallinson and de Vahl Davis, 1977)

“Reprinted with the permission of Cambridge University Press from Mallinson G.D. and G. de Vahl Davis/Three-dimensional natural convection in a box; a numerical study, Journal of Fluid Mechanics, Vol. 83, 1977; pp. 1-31, Copyright 1977. Figure 9.C.8”

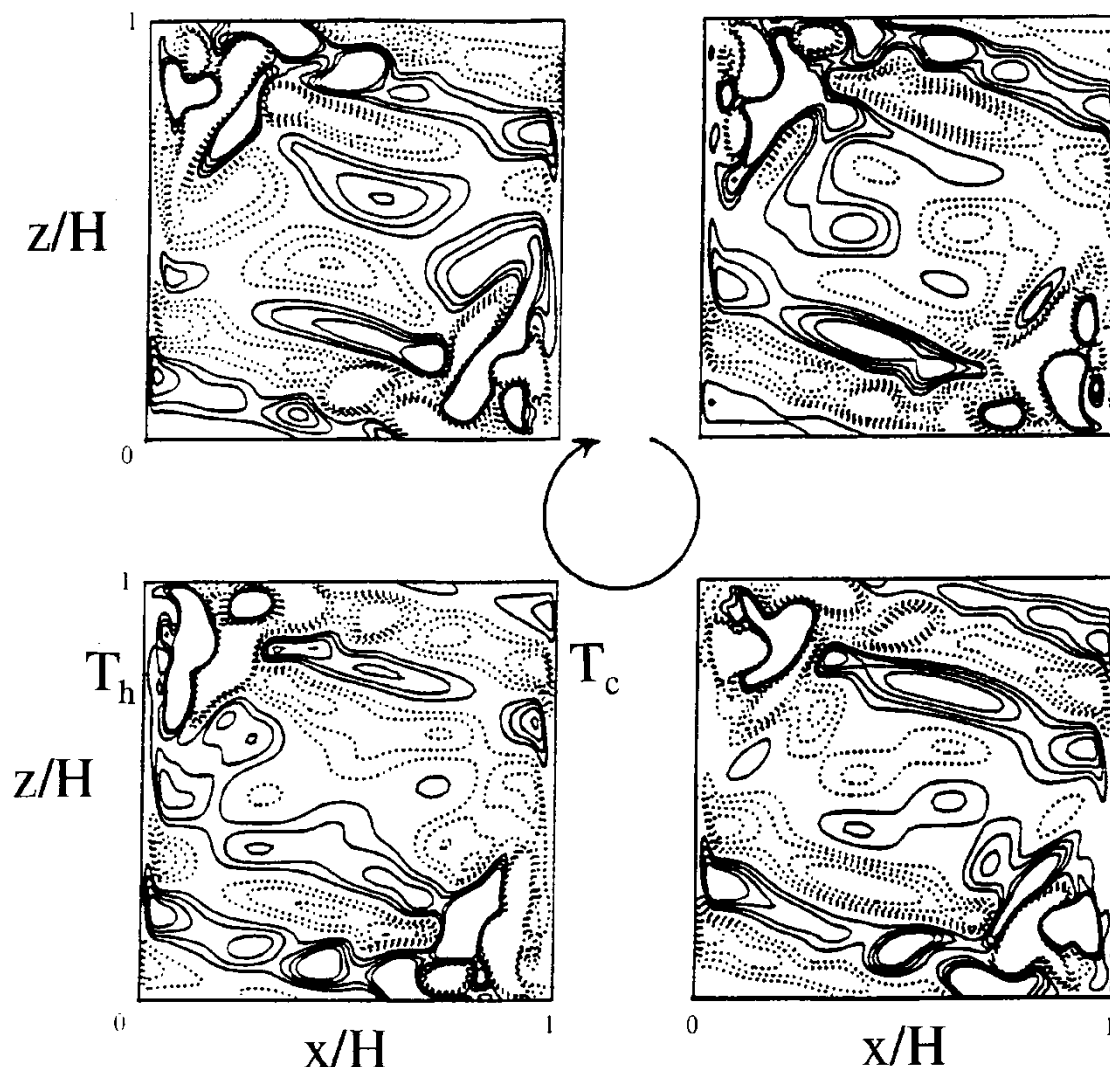


Figure 9.C-9. Internal Waves in the Square Cavity – Fluctuations in the Temperature Field at $Ra=2 \cdot 10^8$ and $PR=0.71$ (air)

Circle with the arrow (in the middle) presents the direction of the consecutive temperature fields. Contour lines correspond to $\pm 0.0005 \Delta T$, $\pm 0.001 \Delta T$, $\pm 0.0015 \Delta T$ and $\pm 0.002 \Delta T$ (the dotted contour lines correspond to negative values, where $T_b = \Delta T/2$ and $T_c = -\Delta T/2$). (After Jenssen and Henkes, 1995)

“Reprinted with the permission of Cambridge University Press from Jansenn, R.J.A. and R.A.W. Henkes/Influence of Prandtl number on stability mechanisms and transition in a differentially heated square cavity, Journal of Fluid Mechanics, Vol. 290, 1995; pp.319-344, Copyright 1995, Figure 9.C.4”

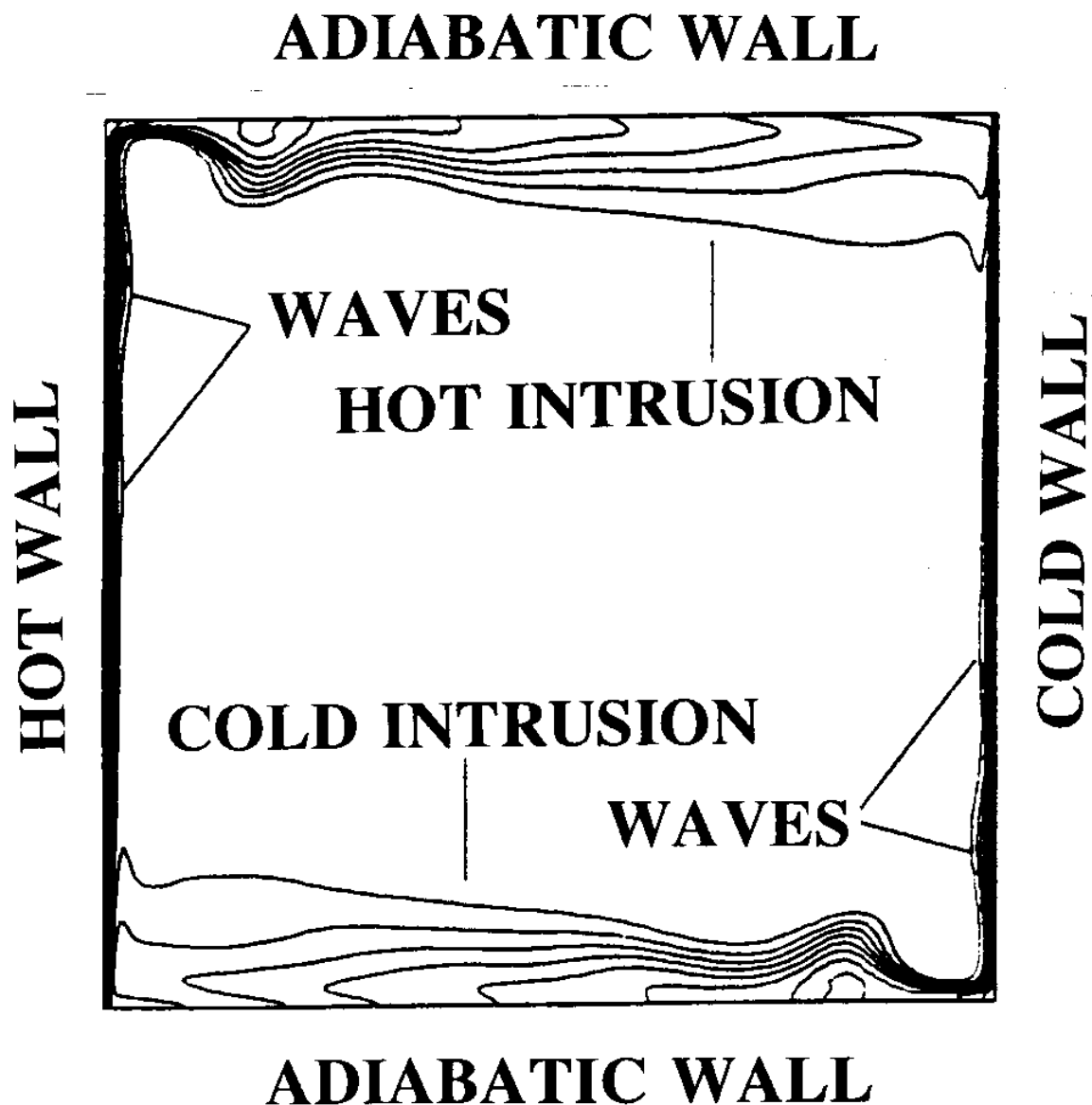


Figure 9.C-10. Temperature for the Initial Solution with the Hot and Cold Intrusions and Boundary Layer Waves Presented (after Armfield and Janssen, 1996)

“Reprinted with permission from Int. J. Heat and Fluid Flow, Vol. 17, S. Armfield and R. Janssen/A direct boundary-layer stability analysis of steady-state cavity convection flow, pp. 539-546, 1996. Elsevier Science Inc.”

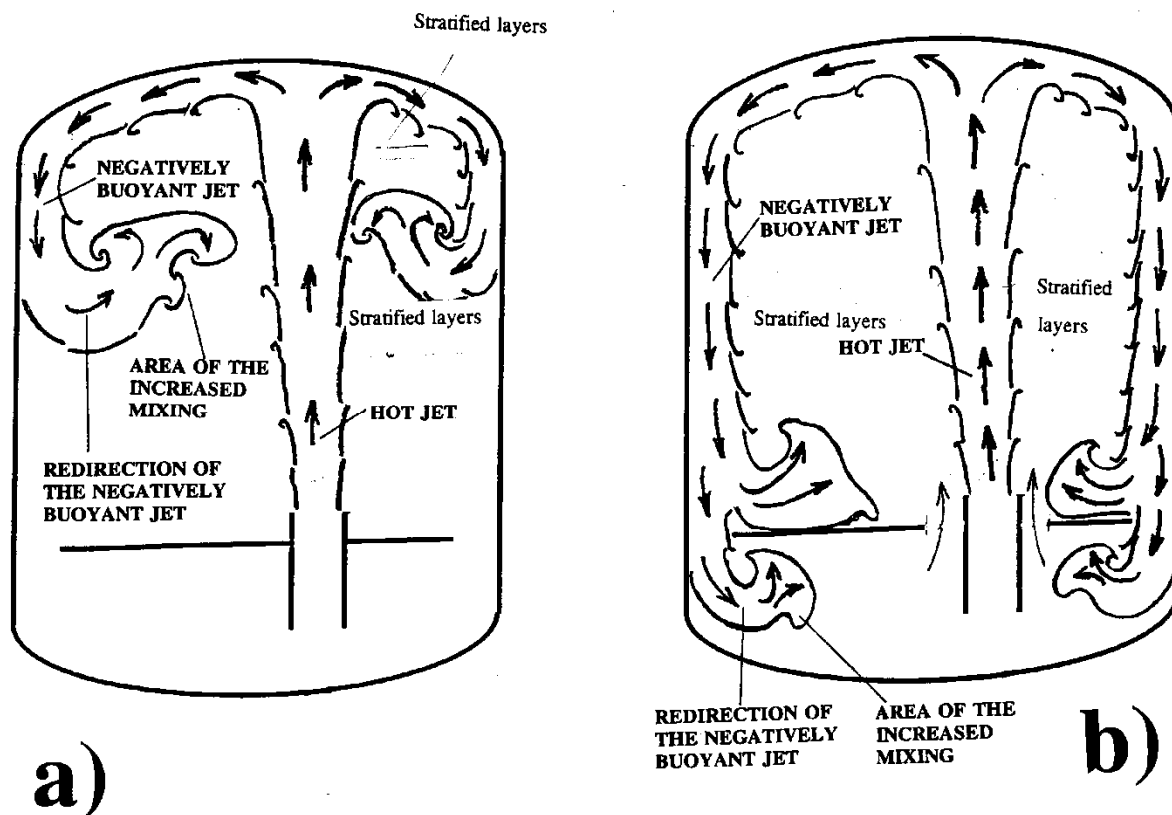


Figure 9.C-11. Formation of the Downward Negatively Buoyant Jets

- a) Negatively buoyant jet redirected inside the dome region
- b) Negatively buoyant jet penetrating the below deck region

9.C.1.1.3 References

1. Akino, N., Kunugi, T., Shiina, Y., Seki, M. and Okamoto, Y. (1989)
“Natural convection in a horizontal silicone oil layer in a circular cylinder heated from below and cooled from above,” (in Japanese), Trans. Jpn. Soc. of Mech. Eng. 55 509 no. 1989-1), no. 88-0901 B: 152-158, 1989.
2. Allard, F., (1992)
“Effects of thermal boundary conditions on natural convection in thermally driven cavities,” in-Turbulent Natural Convection in Enclosures, A Computational and Experimental Benchmark Study, (Eds.) R.A.W.M Henkes and C.J. Hoogendoorn, Editions Europeennes Thermique et Industrie, Paris, pp. 234-256.
3. S. Armfield and R. Janssen (1996)
“A direct boundary-layer stability analysis of steady-state cavity convection flow” Int. J. Heat and Fluid Flow, Vol. 17, No. 6, December 1996.
4. W.D. Baines and J.S. Turner (1969)
“Turbulent buoyant convection from a source in a confined region” J. Fluid Mech., Vol. 37, part 1, pp. 51-80.
5. Catton, I., (1978)
“Natural convection in enclosures” Proc. 6th Int. Heat Transfer Conf., Vol. 6, pp. 13-31.
6. Dzodzo M. B., (1993)
“Visualization of laminar natural convection in romb-shaped enclosures by means of liquid crystals” in “Imaging in transport processes”, (ed. S. Sideman and K. Hijikata), Chapter 15, pp. 183-193., Begel House, Inc., 1993.
7. R. Frederick and A. Valencia, (1995)
“Natural Convection in Central Microcavities of Vertical Pinned Enclosures of very High Aspect Ratios,” Int. J. Heat and Fluid Flow, Vol. 16, No. 2, April 1995, pp. 114-124.
8. T. Fusegi, J. M. Hyun, K. Kuwahara, (1992)
“Numerical simulations of natural convection in a differentially heated cubical enclosure with a partition” Int. J. Heat and Fluid Flow, Vol. 13, No. 2, June 1992, pp 176-183.
9. T. Fusegi, T. M. Hyun, (1994)
“Laminat and Transitional Natural Convection in an enclosure with complex and relistic conditions,” Int. J. Heat and Fluid Flow, Vol. 15, No. 4, August 1994, pp. 258-268.
10. A. D. Garrad and M.A. Patrick, (1983)
“The velocity field produced by a submerged jet directed upwards at a free surface” Int. J. Heat Mass Transfer, Vol. 26, No. 7, pp. 1029-1036.

11. K. Hanjalic, S. Kernjeres and F. Durst, (1996)
“Natural convection in partitioned two-dimensional enclosures at higher Rayleigh numbers”
Int J. Heat Mass Transfer, Vol. 39, No. 7, pp. 1407-1427, 1996
12. T. J. Heindel, S. Ramadhyani, and F. P. Incropera (1995)
“Conjugate natural convection from an array of discrete heat sources: part 1 – two and three-dimensional model validation” Int. J. Heat and Fluid Flow, Vol. 16, No. 6, December 1995, pp. 01-510.
13. Hiller W.J., Koch St., Kowalewski T.A., (1988)
“Simultane erfassung von temperatur und geschwindigkeitsfeldern in einer thermischen konvektionsstromung mit ungekapselten flussigkristalltracern, DGLR - Workshop, 2D-Mestechnik, 1988.
14. Hiller W.J., Koch St., Kowalewski T.A., (1989)
“Three-dimensional structures in laminar natural convection in a cube enclosure” Exp. Therm. Fluid Sci., Vol. 2, pp. 34-44.
15. C. J. Ho, Y. T. Cheng and C. C. Wang, (1994)
“Natural convection between two horizontal cylinders inside a circular enclosure subjected to external convection” Int. J. Heat and Fluid Flow, Vol. 15, No. 4, August 1994, pp 299-306.
16. Hoogendoorn, C.J., (1986)
“Natural convection in enclosures” Proc. 8th Int. Heat Transfer Conf., Vol. 1, pp. 111-120.
17. J.M. Hyun and B.S. Choi, (1990)
“Transient natural convection in a parallelogram-shaped enclosure,” Int. J. Heat and Fluid Flow, Vol. 11, No. 2, June 1990, pp. 129-134.
18. R. J. A. Janssen and R.A.W.M. Henkes, (1995)
“Influence of Prandtl number on instability mechanisms and transition in a differentially heated square cavity,” J. Fluid Mech., Vol. 290, pp. 319-344., 1995
19. K. Kapoor and Y. Jaluria, (1993)
“Penetrative convection of a plane turbulent wall jet in a two-layer thermally stable environment: a problem in enclosure fires” Int. J. Heat Mass Transfer, Vol. 36, No. 1, pp. 155-167, 1993.
20. A. Kurosawa, N. Akino, T. Otsuji, S. Kizu, K. Kobayashi, K. Iwahori, T. Takeda and Y. Ito, (1993)
“Fundamental study on thermo-hydraulic phenomena concerning passive safety of advanced marine reactor” Journal of Nuclear Science and Technology, Vol 30 [2], pp. 131-142, February 1993.
21. G.D. Mallinson and G. de Vahl Davis, (1977)
“Three-dimensional natural convection in a box: a numerical study” J. Fluid Mech., Vol. 83, pp. 1-31.

22. N.C. Markatos and K.A. Pericleous, (1984)
“Laminar and turbulent natural convection in an enclosed cavity” Int. J. Heat Mass Transfer, Vol. 27, No. 5, pp. 755-772.
23. E. S. Nowak and M. H. Novak, (1994)
“Vertical partitions in slender rectangular cavities” Int. J. Heat and Fluid Flow, Vol. 15, No. 2, April 1994, pp. 104-110.
24. Ostrach, S., (1972)
“Natural convection in enclosures” Advances in Heat Transfer, Vol. 8, Academic Press, New York, pp. 161-227.
25. Ostrach, S., (1982)
“Natural convection heat transfer in cavities and cells” Proc. 7th Int. Heat Transfer Conf., Vol 1, pp.365-379.
26. F.E. Peters, (1994)
WCAP-14135, “Final Data Report for PCS Large-Scale Tests, Phase 2 and Phase 3,” Revision 1, April 1997.
27. P.F. Peterson, (1994)
“Scaling and analysis of mixing in large stratified volumes” Int. J. Heat Mass Transfer, Vol. 37, Suppl. 1, pp. 97-106.
28. B. Porterie, M. Larini, F. Giroud and J.C. Loraud (1996)
“Solid-propellant fire in an enclosure fitted with a ceiling safety-vent” Int. J. Heat Mass Transfer, Vol. 39, No. 3, pp. 575-601.
29. R.M. C So and H. Aksoy, (1993)
“On vertical turbulent buoyant jets” Int. J. Heat Mass Transfer, Vol. 36, No. 13, pp. 3187-3200.
30. L. Wolf, H. Holzbauer, T. Cron, (1994a)
“Detailed Assessment of the HDR-Hydrogen Mixing Experiments E11” International Conference on New Trends in Nuclear System Thermohydraulics, Pisa, Italy, May 30th – June 2nd, Vol. 2, pp. 91-103.
31. L. Wolf, H. Holzbauer, M. Schall, (1994b)
“Comparisons between multi-dimensional and lumped-parameter Gothic-containment analyses with data” International Conference on New Trends in Nuclear System Thermohydraulics, Pisa, Italy, May 30th – June 2nd, Vol. 2, pp. 321 – 330.

9.C.1.2 Circulation Phenomena

Circulation processes inside enclosures are the result of natural or forced convection effects. Forced convection inside an enclosure is promoted using devices such as fans, nozzles, or sprays of liquid droplets. PCS applications are of primary interest, since no credit is taken for active systems in the design basis analysis.

A review of possible flow patterns due to natural convection effects is presented. Natural convection is generated if:

1. The upper boundary is at a lower temperature than the lower boundary or opposite vertical boundaries are at different temperature, as well as for other similar combinations of temperature boundary conditions (or imposed heat flux conditions) at the outside and inside surfaces.
2. A higher concentration of the lighter or heavier components of a mixture is maintained near the lower or upper boundaries of the enclosure, respectively.
3. A lighter fluid is released (permanently, or from time to time) from a source which is closer to the bottom of the enclosure.
4. The shape of the enclosure promotes natural convection (together with the distribution of other boundary conditions).
5. The distribution and size of the horizontal and vertical internal openings allows or enhances (as with a chimney or staircase effects) the formation of fluid flow patterns due to the natural convection.
6. If the internal heat sources (sinks) are positioned in the lower (upper) portions of the enclosure.

Under the conditions above (or a combination of them), natural convection causes circulation inside the enclosure. The convection increases the intensity of heat and mass transfer, therefore increasing the heat released from the containment. The intensity of heat transfer depends upon the location of the heat sinks and sources, which can exchange positions due to the transient effects. The velocity and temperature profiles inside the formed boundary layers (wall jets) influence the rate of heat transfer due to the convection. Wall jets entrain the surrounding atmosphere and contribute to better mixing. In the regions with a higher steam concentration, the increase in the heat transfer rate and the effects of entrainment occur due to the condensation inside the boundary layers.

Another contributing factor that promotes circulation inside an enclosure is the interaction of the enclosure atmosphere with the penetrating buoyant plumes or jets and wall layers. In the case of a containment vessel, the plumes or jets could be generated by a LOCA or MSLB. If the break position is inside a narrow corridor or surrounded by additional equipment, the kinetic energy of the jet is dissipated and steam rises in the form of a buoyant plume. The rising plume entrains the surrounding gas and results in circulation inside the volume of the enclosure.

If the break position is open and the jet is directed upward, both the kinetic energy of the jet and the buoyancy forces contribute to penetration into the atmosphere. The higher speeds of the jet affect a greater portion of the volume and both entrainment of the surrounding gas and circulation is stronger.

9.C.1.2.1 Circulation Phenomena Due to the Presence of Boundary Layers (Wall Jets) and Buoyant Plumes Formed as a Consequence of Natural Convection Effects

Natural convection flow is the most often generated by different temperatures or heat fluxes imposed on the boundaries of an enclosure. Various distributions on the boundaries produce various flow patterns and temperature fields.

Section 9.C.1.1 discusses boundary temperature distributions (upper/lower horizontal plates at the higher/lower temperatures) that produce static stratification. Section 9.C.1.2 discusses the case where vertical opposite sides are at constant, but different temperatures. If Rayleigh numbers are greater than 10^4 , this condition produces a recirculated region near the walls and a stratified core of the enclosure.

Figure 9.C-12 presents a case known as Rayleigh-Benard convection. The upper horizontal boundaries are at the lower temperatures (or cooled). The flow patterns formed depend upon the temperature difference and geometry of the enclosure (in fact the value of the Rayleigh number).

For the smaller Ra numbers, vortical cells are formed. An increase in the Ra numbers produces a greater number of vortical cells that start to oscillate, periodically changing the size and intensity. A further increase in the Ra number results in chaotic flow, and produces vertical plumes which reach the opposing horizontal sides of the enclosure. The flow patterns and possible bifurcations produced during the transition from the laminar to turbulent (chaotical) flow regimes are described in Koschmieder, 1993, Yang, 1988, and Ozawa et al., 1992. Some experimental results (flow patterns and temperature fields) are presented for laminar flow regimes by M. Dzodzo et al., 1994 and M.J. Braun et al., 1993. Flow patterns for turbulent and chaotic flow between two horizontal plates at different temperatures are described in Akino et al., 1989.

Flow in the Hele-Shaw cell is presented as an example of natural convection between two horizontal plates. A Hele-Shaw cell has a square cross-section, but it is narrow in one of the horizontal directions so that three-dimensional convection effects are suppressed (see Figure 9.C-13). The upper and lower horizontal sides are at the lower and higher temperatures, respectively.

Consecutive flow patterns and temperature fields for a Hele-Shaw cell with various Rayleigh numbers are presented in Figure 9.C-14 (after Buhler et al., 1987). If the value of the Rayleigh number is greater than 4×10^6 , oscillatory flow patterns with four vortical cells are present. The large and small vortices expand and contract periodically (see Figure 9.C-14). At high Rayleigh numbers (above 5.9×10^7), a reverse transition from the oscillatory to the steady flow patterns occurs. This phenomena is probably due to suppressed three-dimensional convection effects.

For cubic or cylindrical enclosures, with the upper and lower horizontal surfaces at the lower and higher temperatures, respectively, three-dimensional convection effects produce turbulent (chaotical) flow (see Figure 9.C-15). In the paper by Akino et al., 1989, the turbulent flow regime starts at a Rayleigh number of 2×10^6 ($Pr = 200$). For fluids with a Prandtl number close to one, the transition to turbulent flow regime occurs at a smaller Rayleigh number ($Ra \sim 10^4$).

The flow pattern consists of vertical buoyant plumes detached from the horizontal sides. The vertical plumes reach opposite sides of the enclosure and generate opposing plumes (see Figure 9.C-16). Temperature gradients near the horizontal surfaces are high, while temperatures in the core of the containment are almost uniform. Figure 9.C-17a illustrates an example where the temperature in the middle of the enclosure oscillates between 26 and 29°C with $Ra = 9.38 \times 10^7$ ($T_h = 35^\circ\text{C}$ and $T_c = 20^\circ\text{C}$). The highest temperature is registered during the rise of the hot plume and the lowest temperature is registered during the downward penetration of the cold plume. The amplitude of the temperature oscillations in the middle of the enclosure is three degree Celsius. The temperature interval between 26 and 29°C represents $0.2 \times (T_h - T_c)$ or 20 percent of the maximum temperature difference. The temperature in the middle of the enclosure is $(27.5^\circ\text{C}) \pm 1.5^\circ\text{C}$.

Rayleigh-Benard convection is relevant to the containment. In the case of a LOCA or MSLB, the upper portion of the dome and vertical sides are cooled. If the temperature below the ceiling is 9°F lower than temperature of the incoming steam (at the deck level), the Grashof number (based on the height of the containment, $H_t = 109$ ft) is $Gr_t = 2.2 \times 10^{13}$. This Grashof number is in the range of the chaotic flow, with the upward and downward plumes (because $Gr_t > 10^4/0.71$).

Maintaining the vertical walls of the containment at the lower temperature also promotes downward vertical plumes near the walls due to separation of the vertical boundary layers (see Figure 9.C-17b).

9.C.1.2.2 Circulation Phenomena Due to the Interaction With the Hot Buoyant Plumes and Jets

The presence of a hot buoyant plume or a jet of the hot steam during a LOCA or MSLB contributes to the circulation of the containment atmosphere by entraining the surrounding air and other gases. In the case of jet inflow, additional entrainment and circulation are generated by the jet kinetic energy.

Depending upon the strength (initial velocity and mass flow) and direction of the plume or jet, various flow patterns inside the containment are possible. Interaction of the vertical downward plumes generated due to the natural convection (cooling of the shell) produce turbulent flow. This results in good mixing of the dome atmosphere. Examples of vertical plumes and jets are presented by Garrad and Patrick, 1983, So an Aksoy, 1993, and Porterie et al. 1996. The scaling and analysis of circulation in large stratified volumes is presented by Peterson, 1994.

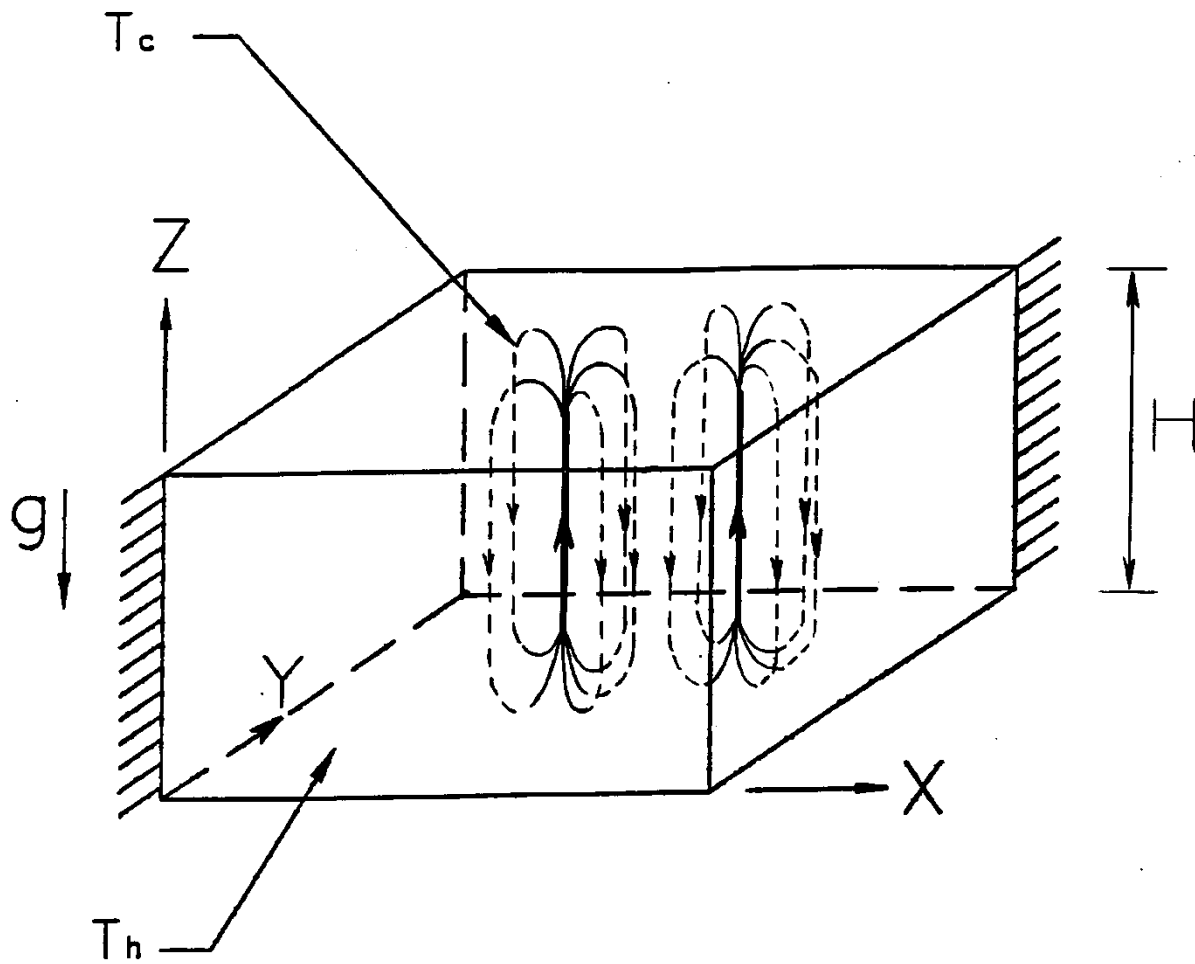


Figure 9.C-12. Rayleigh-Benard Convection Example

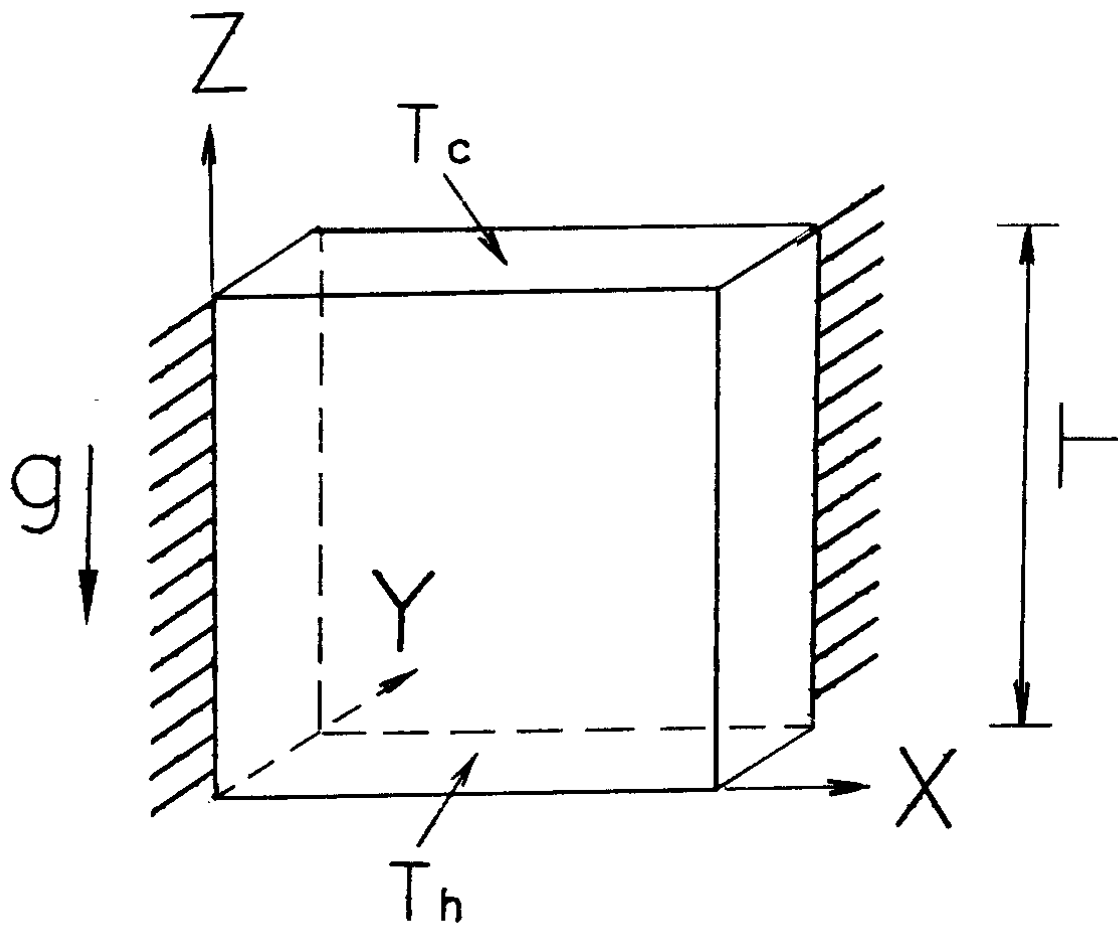


Figure 9.C-13. Hele-Shaw Cell

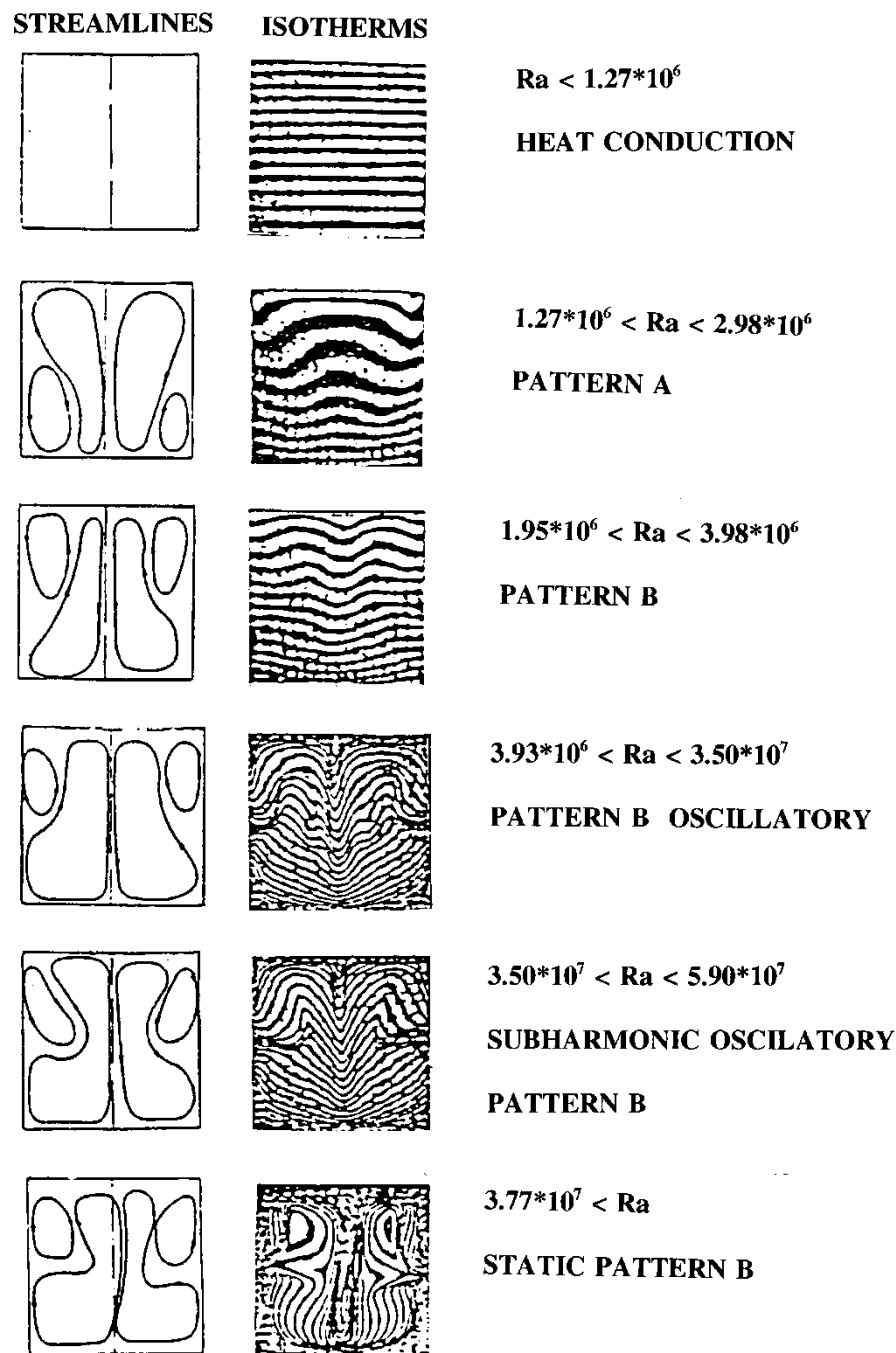
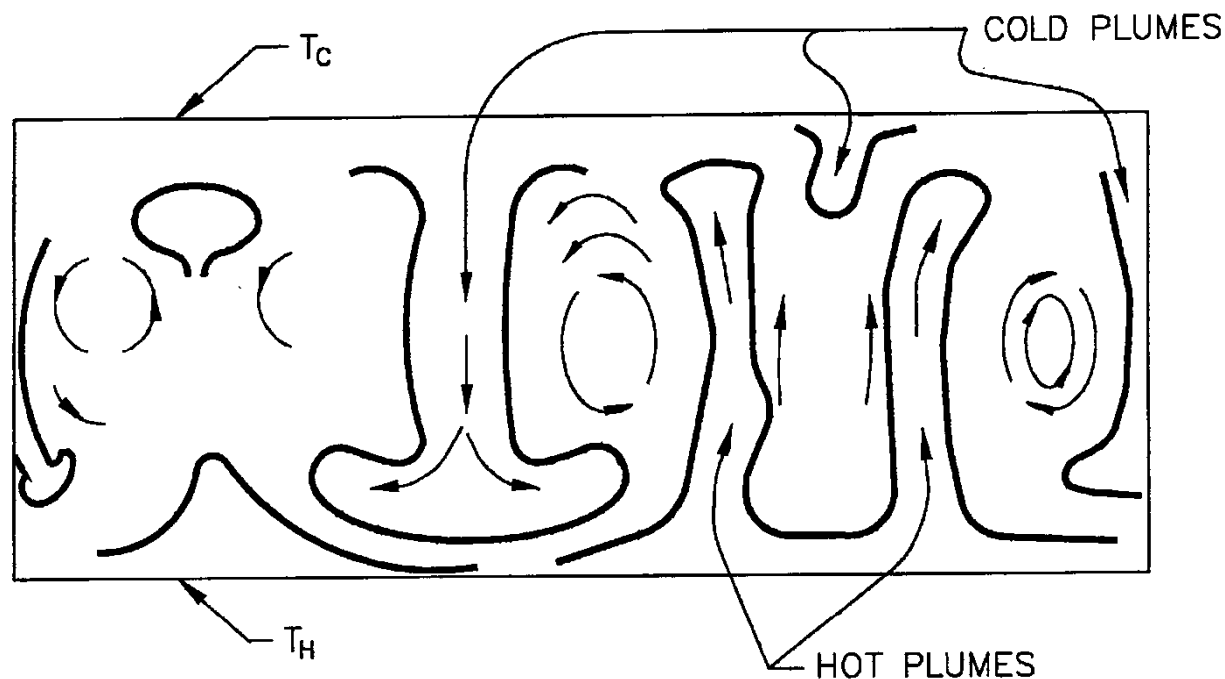


Figure 9.C-14. Steady and Oscillatory Convection in Hele-Shaw Cell (after Buhler et al., 1987)

“Reprinted from L. Buhler, P. Ehrhard, C. Gunther, U. Muller and G. Zimmermann/Natural convection in vertical gaps heated at the lower side – an experimental and numerical study, HTD-Vol.94, AMD-Vol. 89, Bifurcation Phenomena in Thermal Processes and Convection, Winter Annual Meeting of the American Society of Mechanical Engineers, Boston, Massachusetts, December 13-20, 1987”



**Figure 9.C-15. Turbulent (Chaotical) Flow without Hot and Cold Plumes Interactions
(Plane Cross-Section of the Three-Dimensional Enclosure is Presented)**

(according to Figure 6 in N. Akino, T. Kunugi, Y. Shiina, M. Seki, Y. Okamoto/Natural convection in a horizontal silicone oil layer in a circular cylinder heated from below and cooled from above," Trans. Jpn. Soc. Of Mech. Eng. 55 509 no. 1989-1), no. 88-0901 B;, pp. 152-158, 1989 – with permission from Norio Alkino)

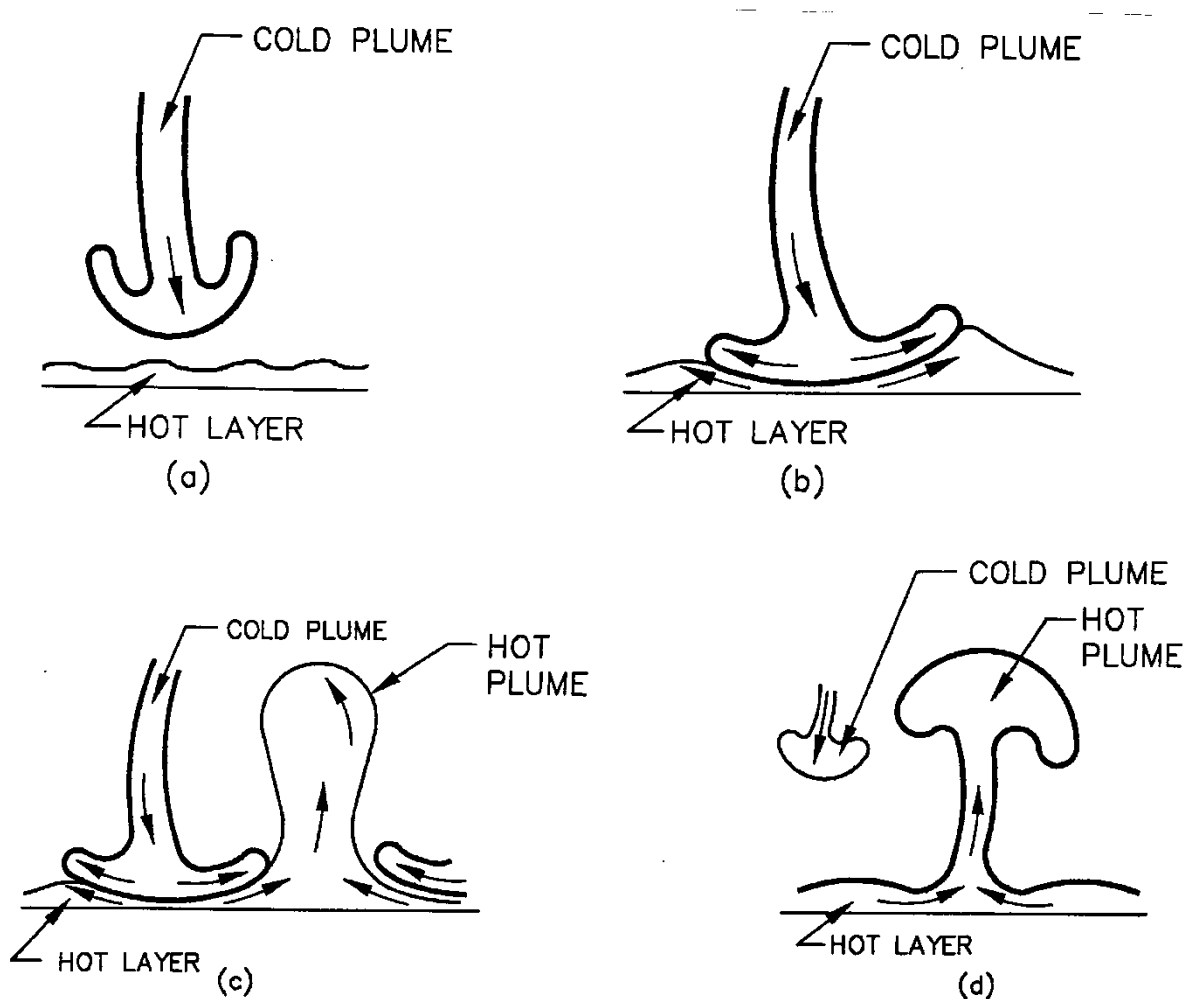


Figure 9.C-16. Interaction of Hot and Cold Plumes (after Aqino et al., 1989)

(according to Figure 12 in N. Akino, T. Kunugi, Y. Shiina, M. Seki, Y. Okamoto/Natural convection in a horizontal silicone oil layer in a circular cylinder heated from below and cooled from above," Trans. Jpn. Soc. of Mech. Eng. 55 509 no. 1989-1), no. 88-0901 B:, pp. 152-158, 1989 – with permission from Norio Akino)

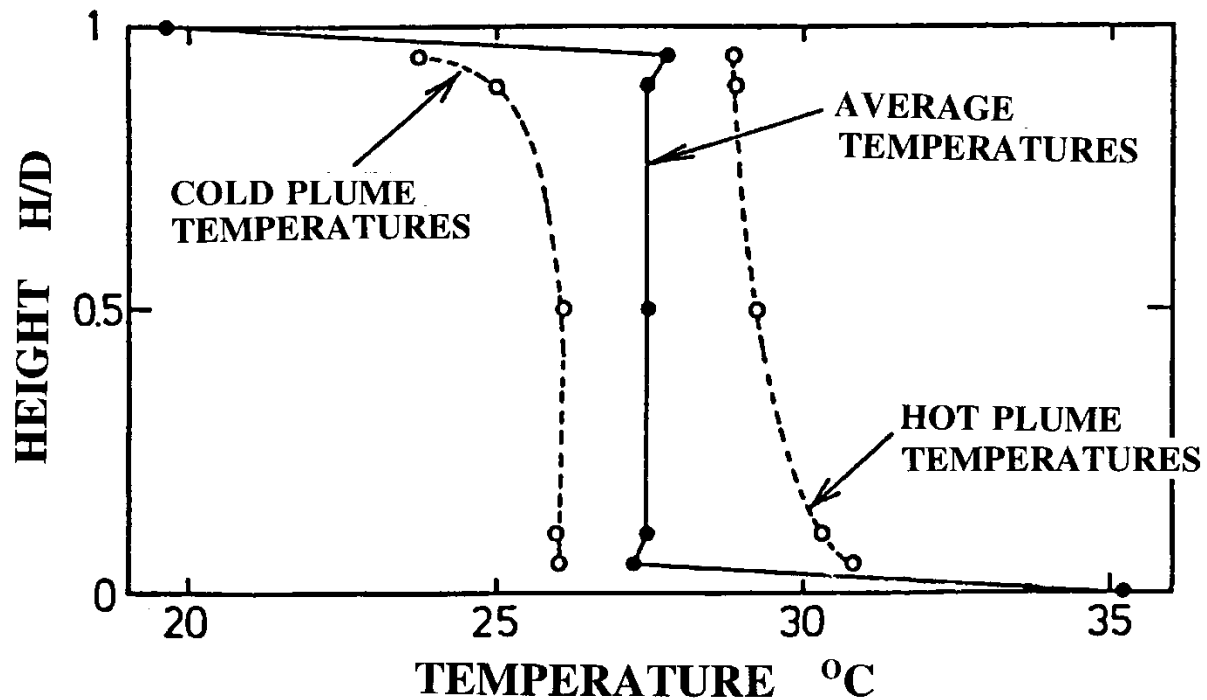


Figure 9.C-17a. Vertical Temperature Distribution inside the Cylindrical Enclosure with Lower and Upper Horizontal Plate at Higher and Lower Temperatures, Respectively ($Ra = 9.38 \times 10^7$, $Pr = 200$)

(according to Figure 14 in N. Akino, T. Kunugi, Y. Shiina, M. Seki, Y. Okamoto/Natural convection in a horizontal silicone oil layer in a circular cylinder heated from below and cooled from above," Trans. Jpn. Soc. of Mech. Eng. 55 509 no. 1989-1), no. 88-0901 B:, pp. 152-158, 1989 – with permission from Norio Akino)

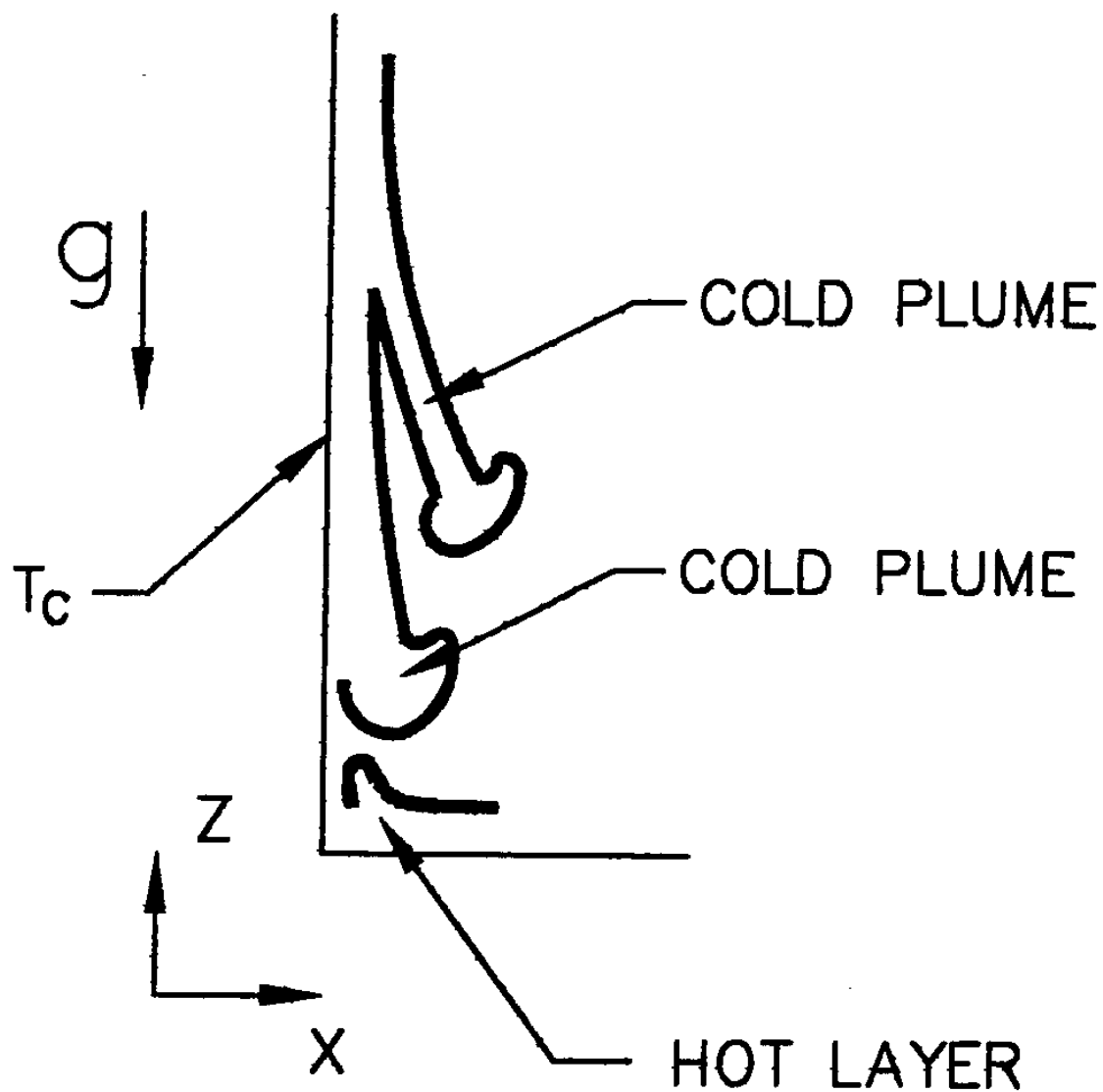


Figure 9.C-17b. Generation of the Cold Plumes Due to the Brake (Separation) of the Vertical Boundary Layers Near the Cold Vertical Walls

9.C.1.2.3 References

1. N. Akino, T. Kunugi, Y. Shina, M. Seki, Y. Okamoto, (1989)
“Natural Convection in a Horizontal Silicone Oil Layer in a Circular Cylinder Heated from Below and Cooled from Above” Nippon Kikai Gakkai Ronbunchyu, 55 Vol. 509 (1989-1), pp. 152 – 158.
2. M. J. Braun , M. B. Dzodzo, S. B. Lattime, (1993)
“Automatic computer based non-intrusive temperature measurements in laminar natural convection using thermochromic liquid crystals in enclosures with variable aspect ratio” FED-Vol. 172, Experimental and numerical flow visualization, The 1993 ASME Winter Annual Meeting, New Orleans, Louisiana, November 28 – December 3, 1993, pp. 111-119.
3. L. Buhler, P. Erhard, G. Gunther, U. Muller, G. Zimmermann, (1987)
“Natural convection in vertical gaps heated at the lower side – an experimental and numerical study. In: Bifurcation Phenomena in Thermal Processes and Convections (eds.H.M. Bau, L.A. Bertram, S.A. Lorpela) ASME, HTD-Vol. 94/AMD-Vol.89, 67-74.
4. M. Dzodzo, M.J. Braun, S.B. Lattime, (1994)
“A non-intrusive computer automated investigation of natural convection using thermochromic liquid crystals and comparison with numerical simulation” (ed. G.F. Hewitt) Proceedings of The Tenth International Heat Transfer Conference, Brighton, UK, Volume 2, 2-MT-6, pp. 225-230.
5. A.D. Garrad and M.A. Patrick, (1983)
“The velocity field produced by submerged jet directed upwards at a free surface”, Int. J. Heat Mass Transfer, Vol. 26, No. 7, pp. 1029-1036.
6. E. L. Koschmieder, (1993)
“Benard Cells and Taylor Vorticies” Cambridge University Press
7. M. Ozawa, U. Muller, I. Kimura and T. Takamori, (1992)
“Flow and temperature measurements of natural convection in a Hele-Shaw cell using a thermo-sensitive liquid-crystal tracer” Experiments in Fluids, Vol 12, pp. 213-222.
8. P.F. Peterson, (1994)
“Scaling and analysis of mixing in large stratified volumes” Int. J. Heat Mass Transfer, Vol. 37, Suppl. 1, pp. 97-106.
9. B. Porterie, M. Larini, F. Giroud and J.C. Loraud, (1996)
“Solid-propellant fire in an enclosure fitted with a ceiling safety-vent” Int. J. Heat Mass Transfer, Vol. 39, No. 3, pp. 575-601.
10. R.M.C. So and H. Aksoy, (1993)
“On vertical turbulent buoyant jets” Int. J. Heat Mass Transfer, Vol. 36, No. 13, pp. 3187-3200.
11. K.T. Yang, (1988)
“Transitions and Bifurcations in Laminar Buoyant Flows in Confined Enclosures” J. of Heat Transfer, November 1988, Vol. 110, pp. 1191-1204.

9.C.1.3 Important Dimensionless Groups

9.C.1.3.1 Important Dimensionless Groups for Stratification and Circulation Phenomena Inside Enclosures

For natural convection, the ratio of the buoyancy to viscosity forces is the most important dimensionless group. The Grashof number defines the ratio of the buoyancy to viscosity forces:

$$Gr = \frac{g * \beta * (T_h - T_c) * H^3}{\nu^2} = \frac{g * (\rho_c - \rho_h) * H^3}{\rho_c * \nu^2}$$

Natural convection correlations often use the Rayleigh number instead of Grashof number, where the Rayleigh number Ra is defined as:

$$Ra = \frac{g * \beta * (T_h - T_c) * H^3}{\alpha * \nu} = \frac{g * (\rho_c - \rho_h) * H^3}{\rho_c * \alpha * \nu} = Gr * \frac{\nu}{\alpha} = GrPr$$

Using the Rayleigh number reduces the number of dimensionless groups in the correlations for natural convection. The appearance of Prandtl number inside some correlations could be avoided.

The Prandtl number is based on fluid properties, i.e., the ratio of kinematic viscosity to thermal diffusivity.

$$Pr = \frac{\nu}{\alpha}$$

When considering the interaction between the hot buoyant plume and the cold vertical wall boundary layer, the Grashof and Rayleigh numbers are defined with H_v as the characteristic length.

$$Gr_v = \frac{g * (\rho_v - \rho_o) * H_v^3}{\rho_v * \nu^2}$$

This applies to flows generated inside the enclosures with the opposite vertical walls at the different temperatures. It also applies to flow caused by two opposing vertical jets (between the two horizontal plates). The AP600 and **AP1000** have a combination of the two cases.

Upward flow is caused by the buoyant plume, while downward flow is caused by the lower temperatures of the vertical wall. If the initial kinetic energy of the plume is small, this Grashof number gives an indication of the formed flow pattern and heat transfer due to the two opposing vertical flow paths. The formation of a recirculating stratified core between the vertical jets is related to this parameter as well.

When considering the interaction between the cold ceiling and the hot rising plume (at the bottom of the enclosure), the height of the upper-deck region H_t can be used as a characteristic length. The Grashof number is:

$$Gr_t = \frac{g * (\rho_t - \rho_o) * H_t^3}{\rho_t * \nu^2}$$

The value of this Grashof number indicates the status of the Rayleigh-Benard convection. If the values are above 10^4 , it is possible to form periodic vertical downward plumes which detach from the ceiling.

The conditions described above interact. The overall flow pattern is expected to be a superposition of the flow patterns described for enclosures with horizontal and vertical temperature gradients. The prevailing flow pattern is estimated from the ratio of the two Grashof numbers already defined:

$$\frac{Gr_t}{Gr_v} = \frac{(\rho_t - \rho_o) * H_t^3 * \rho_v}{(\rho_v - \rho_o) * H_v^3 * \rho_t}$$

Note that both dimensions of the large-scale test (LST) installation (H_t and H_v) are scaled to AP600 dimensions. Therefore, if the ratio of relative densities (in vertical and horizontal directions) is the same, the flow patterns obtained in LST experiments can be applied to the AP600.

Even small temperature differences between the shell and the atmosphere inside a containment produce large Grashof numbers. For example, a temperature difference of 9°F results in $Gr_t = 2.2 * 10^{13}$ and $Gr_v = 4.7 * 10^{12}$ for $H_t = 109$ ft and $H_v = 65$ ft, respectively.

In the case of LST, a temperature difference of 9°F results in $Gr_t = 3.9 * 10^{10}$ and $Gr_v = 7.2 * 10^9$ for $H_t = 13.2$ ft and $H_v = 7.5$ ft, respectively.

If the Grashof numbers are greater than 10^8 , the Nusselt number can be obtained by applying the correlation for turbulent free convection.

For jets and buoyant plumes that penetrate the containment, the ratio of inertia forces and buoyant forces influences the entrainment of surrounding gases. If the initial velocities are high, a constant spreading angle indicates a jet. As the jet velocities decrease, upward motion results from buoyant forces. Buoyant plume behavior is indicated by different spreading angles at each level.

The Froude number represents the ratio of the inertia to gravity forces, or the ratio of kinetic energy to potential energy:

$$\frac{Gr_t}{Gr_v} = \frac{(\rho_t - \rho_o) * H_t^3 * \rho_v}{(\rho_v - \rho_o) * H_v^3 * \rho_t}$$

For buoyant plumes and jets, the Froude number can be defined as:

$$Fr_{j,o} = \frac{\rho_o * U_o^2}{g * (\rho_a - \rho_o) * d_o}$$

where the characteristic length is the initial diameter of the jet or plume. The source velocity and density have the subscript (o), while the ambient density has the subscript (a). The elevation of the transition from a forced jet to a buoyant plume is calculated (Peterson, 1994 and Spencer, 1997) from the expression:

$$\frac{z_{trans}}{d_o} = Fr_{j,o}^{1/4} * \left(\frac{\rho_o}{\rho_a}\right)^{1/4}$$

The ratio of the square of the jet Reynolds number to the containment Grashof number is a volumetric Froude number:

$$Fr_v = \frac{\rho_a * U_o^2 * d_o^2}{g * (\rho_a - \rho_o) * H^3}$$

If the volumetric Froude numbers are much greater than one, the inertia forces dominate. The inertia forces unstabilize stratified layers, promote circulation inside the containment, and contribute towards the better mixing.

However, Peterson, 1994, proposes that the jet or plume is not able to disturb the stratified vertical density gradients if:

$$Fr_v < \left(1 + \frac{d_o}{4 * \sqrt{2} * \alpha * H}\right)^2$$

where (α) is Taylor's jet entrainment parameter and where $\alpha = 0.05 = \text{constant}$.

For volumetric Froude numbers less than one, the inertia forces are not dominant and are not able to unstabilize stratified layers inside the containment. Therefore, the buoyancy effects are more important than inertia effects. The reciprocal value of the Froude number or Richardson number is the appropriate dimensionless group.

$$Ri_v = \frac{g * (\rho_a - \rho_o) * H^3}{\rho_a * U_o^2 * d_o^2}$$

Since inertia effects of the plume are not important (Reynolds number of the plume is small), only Grashof numbers Gr_t and Gr_v will influence the flow pattern.

Another important factor is the position of the jet (plume) or heat source release location. The ratio of the release point level, H_r , to the height of the containment, H_t , describes the relative position of the jet (plume) or heat source:

$$\frac{H_r}{H_t}$$

If H_r/H_t is less than 0.2, the release location is considered low. A global circulation flow pattern affecting the entire containment is most likely formed. If H_r/H_t is greater than 0.5, the release elevation is high and stratification effects may occur in a portion of the volume. The result may be that only the upper portion of the enclosure is affected by global circulation, while the lower may be stratified. Such stratification may be stagnant. In stagnantly stratified regions, no entrainment into wall boundary layers or buoyant plumes occurs, and thus little or no vertical mixing occurs, while in recirculating stratified regions vertical mixing can be strong and can greatly reduce vertical density gradients.

Specified criteria for the H_r/H_t ratio are based on the international experimental database which is presented in the next chapter.

9.C.1.3.2 References

1. P. F. Peterson, (1994), "Scaling and Analysis of Mixing in Large Stratified Volumes," Int. J. of Heat and Mass Transfer, Vol. 37, Supplement 1, pp. 97-106, 1994.
2. D. R. Spencer, (1997), "Scaling Analysis for AP600 Containments Pressure During Design Basis Accidents," WCAP-14845, Revision 3, March 1998.

9.C.1.4 Expected Flow Patterns for AP600 and AP1000

9.C.1.4.1 Simplified Representation of Circulation Regions During Post-Blowdown LOCA in AP600 and LST

The AP600 containment and the large-scale test (LST) facility include five primary flow regions (Peterson, 1997 – letter to Woodcock). The regions are presented in Figure 9.C-18 showing a control volume that extends to the condensed fluid film surfaces. This figure is useful for structuring a discussion of circulation and stratification phenomena and for relating separate effects of enclosures tests to the various regions.

The volumetric flow rates presented in Figure 9.C-18 at "quasi-steady" conditions are:

- Q_o , the steam volumetric flow rate from the break,
- Q_e , the flow rate of fluid entrained from inside the below-deck region into the steam generator compartment (equivalent to the flow rate delivered to the below-deck region due to the penetration of a portion of the wall boundary layers through the deck gap near the walls),
- Q_p , the flow rate of fluid entrained into the plume in the above-deck region,

- Q_w , the flow rate of fluid entrained into the vertical wall boundary layers,
- Q_v , the flow rate of steam condensed on the vertical walls (shown leaving the control volume), and
- Q_t , the flow rate of steam condensed on the dome ceiling (shown leaving the control volume)

For the quasi-steady conditions, the steam flow rate entering in the containment volume Q_o is equal to the summation of the steam flow rates condensed on the dome ceiling Q_t and vertical walls Q_v .

The distances presented in Figure 9.C-18 are:

- H_t , the distance between the jet inflow position into the upper-deck region and the dome springline elevation (in vertical direction),
- H_{EF} , the distance between the break location and the jet inflow position into the upper-deck region (in vertical direction), and
- H_v , the distance between the vertical wall and the jet center (in horizontal direction).

The definitions of the regions relate well to the separate effects of the enclosure tests.

Region I is below the operating deck level. In the AP600 and **AP1000** configuration, connections exist between the below-deck compartments and the upper-deck region (dome). These connections allow the steam jet (plume) generated-entrainment into the break compartment to produce circulation through Region I. The volumetric flow from the lower to the upper deck regions is Q_e . Jet entrainment and the slots around the circumference of the deck floor enable this circulation (see Figure 9.C-19).

In the LST – LOCA experiments, the release point is also below the operating deck level. However, the compartment containing the release is not connected with the other below-deck compartments (see Figure 9.C-20). The simulated steam generator compartment is connected only with the upper portion (dome) of the containment. Therefore, the jet injection location for the LST LOCA experiments is effectively at the top of the simulated steam generator compartment, where the flow enters the above-deck region, and entrained volumetric flow Q_e is equal to zero (see Figure 9.C-20). The atmosphere in the below-deck compartment is a stably stratified region without recirculation. The heat and mass transfer in the below deck compartments are governed primarily by molecular diffusion.

Region II is defined as the volume between the springline elevation and a horizontal line above the operating deck elevation, and between the wall boundary layers (Region IV) and the plume (Region III). Two entrainment mechanisms remove fluid from Region II. Entrainments into the vertical jet (or buoyant plume) and the wall boundary layers are compensated for by the inflows from the upper and lower horizontal boundaries. In order to preserve mass continuity and to obtain inflow into Region II, the vertical velocity components (see Figure 9.C-21) are negative and positive at the upper and lower horizontal boundaries, respectively. The fluid inside the Region II is recirculating (see Figure 9.C-22), yet has a quasi-steady dp/dz maintained by balance between the buoyancy and the two entrainment mechanisms. Therefore, Region II can be called a recirculating stratified region. The horizontal density

and concentration gradients are small, but significant recirculation flow exists due to the entrainment into the free and wall jets (see Peterson, 1997). Region II can be considered as a region where the vertical density, temperature and concentration gradients are dependent on the values of the volumetric Froude numbers (for free jets or plumes) and Grashof (Rayleigh) numbers (for wall boundary layers). This is similar to the case of an enclosure with opposite vertical walls at different temperatures (see section 9.C.1.1.2.1). The recirculation and entrainment from the Region II contributes to a decrease in the vertical temperature, density, and concentration gradients.

Region III contains free jets (plumes) which transport fluid in the vertical direction. The upward motion of a jet (or plume) produces entrainment from Region II. As a result, the jet (or plume) spreads, reduces velocity, and dilutes (decreases the temperature and concentration difference between the core of the jet and the surrounding atmosphere – Region II).

Region IV contains wall boundary layers which also provide transport in the vertical direction. The entrainment into the wall boundary layer transports steam into Region IV. The entrainment from Region II into the wall boundary layers enhances recirculation inside the Region II. This contributes to a decrease in the vertical temperature, density, and concentration gradients inside Region II.

Region V, the dome region, is between the containment ceiling and the elevation of the springline. Because the temperature of the containment ceiling is lower than the temperature of the atmosphere below the ceiling, downward flowing “ceiling plumes” are formed (see the Rayleigh-Benard convection example of section 9.C.1.2.1). The difference in the steam concentrations between the top of the Region V (immediately below the ceiling where condensation occurs) and the top of Region II are small due to the circulation (interaction) within Region V, caused by cold plumes falling from the ceiling and the hot plume reaching the ceiling of the dome. The downward plumes increase circulation and reduce gradients inside the dome, Region V. The downward “ceiling plumes” interact with the uprising plume (from the Region III). If the strength of the jet (plume) from the Region III is high, interactions occur inside Region V and the influence of the downward plumes does not spread towards the lower regions.

However, if the plume from Region III is not strong enough to produce good mixing inside Region V, the penetration of the downward “ceiling plumes” into the lower regions can disturb (from time to time) the recirculating stratified layers inside Region II. This tends to reduce the vertical gradients within Region II.

If the plume is very weak or does not exist, the vertical downward “ceiling plumes” affect the entire volume of the upper-deck region. The flow patterns formed are the result of superposition of Rayleigh-Benard convection (described for the enclosure with cold upper and hot lower surface) and recirculating stratification (described for the enclosure with opposite vertical walls at different temperatures).

The cold dome ceiling produces downward vertical plumes as in Rayleigh-Benard convection case, while cold vertical walls produce downward wall boundary layers. Due to continuity, the downward wall boundary layers tend to generate upward flow in the middle of the above-deck region. The wall boundary layer and the upward flow in the middle of the containment form a recirculation zone. Between the wall boundary layers and the upward flow in the middle of the containment, a recirculating stratified core is formed. This is similar to enclosures with opposite vertical walls at different temperatures. Note that

although there is evidence from enclosure tests that a stable non-zero vertical density gradient could exist in Region II, entrainment flows cause circulation of fluid. Region II is not considered as stagnant.

The prevailing flow pattern can be postulated (Rayleigh-Benard or recirculating stratified) from the ratio of Grashof numbers Gr_t/Gr_v [defined for vertical $\Delta\rho$ and distance H_t (for Gr_t) and horizontal $\Delta\rho$ and distance H_v (for Gr_v)]. Note that turbulent Rayleigh-Benard convection starts at $Ra_t = Gr_t Pr > 10^4$ (for $Pr = 0.71$, based on 3D enclosure experiments – see section 9.C.1.2.1), while turbulent flow (with thin boundary layers and recirculating stratified but almost homogenized core) in enclosures with vertical walls at opposite temperatures starts at $Ra_v = Gr_v Pr > 10^8$ (for $Pr = 0.71$, based on 2D numerical simulations, see section 9.C.1.1.2.1). This indicates that for small values of Rayleigh numbers ($10^4 < Ra_v$ and $Ra_t < 10^8$), Rayleigh-Benard convection is dominant. Turbulent and chaotical flow are dominated by falling vertical plumes (see Figure 9.C-15).

For higher Rayleigh numbers (Ra_v and $Ra_t > 10^8$) combined with a weak source plume, in fact smaller Rayleigh number in horizontal direction, falling vertical plumes (see Figure 9.C-15) dominate the flow patterns. For the dominant jet (or plume), or high Rayleigh number in horizontal direction (Gr_v high) and moderate Froude number, a recirculating stratified flow pattern prevails in Region II (see Figure 9.C-5). Higher and similar magnitude values of both Rayleigh numbers (in vertical and horizontal direction) result in a flow pattern that is a superposition of the two described patterns (shown in Figure 9.C-15 and Figure 9.C-5). Finally, for the case of the momentum-dominated jet (with high Froude number), the circulation flow pattern will be present in the entire volume of the containment (see Figure 9.C-11).

9.C.1.4.2 A Qualitative Model for Recirculating Stratified Region II

A qualitative model of Region II is used to address the issue of recirculating stratification and circulation (Peterson, 1997). The model is a coarse, first-principle representation of the effects of various volumetric flows and entrainment rates. It qualitatively examines the influence of various parameters on the difference in steam concentrations from the bottom to the top of the Region II (ΔX).

Because of the complexity of the physics, two simplifying assumptions are used. It is assumed that Region II is not influenced by falling plumes from Region V and that the recirculation effects inside Region II can be neglected. Both assumptions cause overestimated vertical steam gradients ΔX . Interactions between Region II and Region V that result from the penetration of the cold falling plumes (from Region V), improve mixing and decrease vertical steam gradients ΔX . Recirculation inside Region II (established experimentally and numerically inside the core of enclosures) further decreases the vertical steam gradients.

Peterson, 1997, provides the following mass conservation equation for the thin horizontal layer inside Region II with area $A(z)$ (see Figure 9.C-23):

$$\rho(z) * A(z) * dv(z) = -\rho_p(z) * u_p(z) * p_p(z)dz - \rho_w(z) * u_w(z) * p_w(z)dz$$

where $v(z)$ is the vertical velocity, and $u_p(z)$ and $u_w(z)$ are the entrainment velocities into the steam plume and wall boundary layer, respectively. The vertical coordinate is z , while p_p and p_w are the perimeters of the plume (or jet) and wall boundary layer, respectively.

Since molar densities are dependent only on the temperature (assuming constant pressure in the entire volume), the differences between the molar densities $\rho(z)$, ρ_p and ρ_w are small. To simplify the analysis, the equation is written without densities. A balance of the volumetric flow rates is then used for the remainder of the analysis (instead of a mass balance).

To further simplify the analysis (considering only global effects), u_p , u_w , p_p , p_w , and A are assumed to be constant, or independent of z (Peterson, 1997). This assumption results in a linear, vertical velocity distribution. Although the actual entrainment varies with height, the integrated total should be reasonably close to the average constant values.

The calculations of the entrained volumetric flow into the plume Q_p and wall boundary layer Q_w are simplified as:

$$Q_p = \int_0^H u_p(z) * p_p(z) dz = u_p * p_p * H$$

and

$$Q_w = \int_0^H u_w(z) * p_w(z) dz = u_w * p_w * H$$

respectively. The total inflow to the top and bottom of Region II (see Figure 9.C-21) provides the boundary conditions for the vertical velocities $v(0)$ and $v(H)$ at the bottom and at the top of the Region II, respectively:

$$A * v(0) = Q_w - Q_v - Q_e$$

$$A * v(H) = -(Q_v + Q_p + Q_e)$$

where Q_e is the volumetric rate of flow into the below-deck region (see Figure 9.C-18 and Figure 9.C-19). Due to mass continuity (conservation) for the below-deck region, this flow rate is equal to the volumetric flow rate (Q_e) entrained into the steam generator compartment by the steam jet (plume).

The volumetric flow rate of steam condensed on the vertical wall is Q_v . Q_t is the flow rate of steam condensed on the dome. The total steam volumetric inflow into the containment is $Q_o = Q_v + Q_t$ (see Figure 9.C-18 and Figure 9.C-23).

The linear, vertical velocity distribution in Region II is:

$$A * v(z) = (Q_w - Q_v - Q_e) - \frac{z}{H} * (Q_p + Q_w)$$

Downflow exists in the top part of Region II, while in the lower portion, the velocities are positive (upwards flow). This agrees with the previous discussion of Region II inflow horizontal boundaries (see Figure 9.C-21). Because the continuity-driven velocities are assumed horizontally uniform upward at the bottom and downward at the top of Region II, there will be an elevation, z , where the two meet and vertical velocity is zero. The z coordinate where the vertical velocity is zero in this model is:

$$z = \frac{Q_w - Q_v - Q_e}{Q_p + Q_w} * H$$

The average gas mole fraction in Region II is:

$$\bar{x}_g = \frac{1}{V} * \int_0^H A(z) * x_g(z) dz = \frac{1}{H} * \int_0^H x_g(z) dz$$

The mole fraction of gas at the bottom of Region II is found from a mass balance on the wall boundary layer. (Note that Q_v is the volumetric flow of steam that condenses on the vertical wall. It contains no noncondensable gas.)

$$x_g(0) = \frac{\int_0^H x_g(z) * u_w(z) * p_w(z) dz}{Q_w - Q_v} = \frac{u_w * p_w * \int_0^H x_g(z) dz}{Q_w - Q_v} = \frac{u_w * p_w * H * \bar{x}_g}{Q_w - Q_v} = \frac{Q_w * \bar{x}_g}{Q_w - Q_v}$$

Similarly the gas mole fraction at the top of the Region II is:

$$\begin{aligned} x_g(H) &= \frac{x_g(0) * Q_e + \int_0^H x_g(z) * u_p(z) * p_p(z) dz}{Q_v + Q_p + Q_e} = \frac{\frac{Q_w * \bar{x}_g}{Q_w - Q_v} * Q_e + u_p * p_p * \int_0^H x_g(z) * dz}{Q_v + Q_p + Q_e} \\ &= \frac{\frac{Q_w * \bar{x}_g}{Q_w - Q_v} * Q_e + Q_p * \bar{x}_g}{Q_v + Q_p + Q_e} \end{aligned}$$

The relative difference in the concentrations from the bottom to the top of Region II is:

$$\frac{\Delta x}{\bar{x}_g} = \frac{x_g(0) - x_g(H)}{\bar{x}_g} = \frac{Q_w}{Q_w - Q_v} - \frac{\frac{Q_w * Q_e}{Q_w - Q_v} + Q_p}{Q_v + Q_p + Q_e}$$

The final form of the equation, which is more suitable for qualitative understanding of the influence of various volumetric flow rates, is:

$$\frac{\Delta x}{\bar{x}_g} = \frac{x_g(0) - x_g(H)}{\bar{x}_g} = \frac{Q_v * (Q_w + Q_p)}{(Q_w - Q_v)(Q_p + Q_v + Q_e)}$$

The influence of the various volumetric flow rates under various assumed conditions will now be examined.

9.C.1.4.2.1 Case 1: Strong Plume, Wall Boundary Layer and Plume Entrainments are Equal

If the entrainment volumetric flow rates are approximately equal ($Q_p \sim Q_w$) and are large compared to Q_v and Q_e , the relative concentration difference is simplified to:

$$\frac{\Delta x}{\bar{x}_g} = \frac{x_g(0) - x_g(H)}{\bar{x}_g} \geq \frac{Q_v * (2 * Q_w)}{(Q_w * Q_w)} = \frac{2 * Q_v}{Q_w}$$

These assumptions are valid for the case of the jet-dominated flow. The large plume and wall boundary layer entrainment volumetric flow rates act to reduce the relative, vertical steam concentration gradient.

Even if the flow pattern cannot be defined as jet-dominated (i.e., the equation for the relative difference in the concentration from the bottom to the top of Region II cannot be simplified), the recirculating stratified Region II interacts with the plume and wall jets, Regions III, and IV (see Figure 9.C-23). The relative concentration difference will still decrease if the entrainments in both the wall layer Q_w and plume Q_p are large.

It has been shown (Enclosure to Westinghouse Letter NSD-NRC-97-4978, February 7, 1997) that during the quasi-steady portion of a LOCA, jet entrainment rates (Q_p) in the AP600 are about a factor of 10 greater than the condensation rate ($Q_v + Q_t$).

9.C.1.4.2.2 Case 2: Equal Entrainment into the Wall Boundary Layer Q_w and the Rate of the Steam Condensed at the Vertical Walls Q_v

A small difference between the entrainment volumetric flow rate into the wall boundary layer Q_w and volumetric flow rate of the steam condensed at the vertical walls Q_v produces an increase in the relative difference of the concentrations. If all the steam entrained into the wall boundary layer is condensed at the vertical walls, nothing is left to be redistributed through the lower horizontal boundary of Region II and contribute towards a decrease in the vertical concentration gradients.

9.C.1.4.2.3 Case 3: High Dome Condensation Rate Q_t

The volumetric flow of the steam condensed on the dome of the containment Q_t does not directly affect the relative concentration difference in Region II (it is not present in the equation). However, indirect effects are possible. If the condensation on the dome is high, the ratio of Q_t/Q_v is high, and the volumetric flow of steam condensing on the vertical walls Q_v decreases. In contrast, a small ratio of Q_t/Q_v represents an increased volumetric flow rate condensing on the vertical walls, Q_v . A decrease in the rate of steam condensing on the vertical walls Q_v (in fact the increase of steam volumetric flow rate condensing on the dome, Q_t), decreases the relative concentration difference.

9.C.1.4.2.4 Case 4: Influence of the Below Deck Entrainment Q_e

Region I also interacts with the stratified Region II. The effects of this interaction on the relative concentration difference change are captured by the Q_e term. A large below-deck entrainment, Q_e , reduces the concentration difference. In the AP600 and AP1000, below-deck entrainment contributes to a decrease in the relative concentration difference. This effect is not present in the LST case, where $Q_e = 0$.

9.C.1.4.2.5 Case 5: Dominant Entrainment into the Wall Boundary Layer Q_w

If $Q_v = 0.5 Q_o$, as observed in phase 3 of the LST experiments where Q_v is between $0.4Q_o$ and $0.6Q_o$ (see WCAP-14135), and if $Q_w = 2Q_p$, i.e., the wall boundary layer entrainment is twice as strong as plume entrainment (weak plume scenario), if the entrainment in the below-deck region is negligible, $Q_e = 0$, and if we assume $Q_p = 10Q_o$ the relative steam concentration is:

$$\frac{\Delta x}{\bar{x}_g} = \frac{x_g(0) - x_g(H)}{\bar{x}_g} = \frac{0.5 * Q_o * (2 * Q_p + Q_p)}{(2 * Q_p - 0.5 * Q_o)(Q_p + 0.5 * Q_o + 0)} = 0.073$$

A further increase in the entrainment into the wall boundary layers causes an additional decrease in the relative difference between steam concentrations in the bottom and the top of Region II (e.g., if $Q_w = 3Q_p$, the relative concentration is 0.064). The increase in the entrainment into the wall boundary layers contributes to the homogenization of the containment atmosphere.

9.C.1.4.2.6 Conclusion

The expected circulation within the AP600 and **AP1000** containment is segregated into five regions that relate to separate effects tests (SETs) in enclosures. Given the presence of the externally cooled shell, which is assumed in a DBA analysis, there are no regions of stagnant stratification in containment.

The proposed conceptual model can be used to structure the containment into regions for comparison to relevant enclosures SETs. The mathematical representation provides insight into the influence of various volumetric flows on the axial steam concentration gradients in the AP600 and **AP1000**.

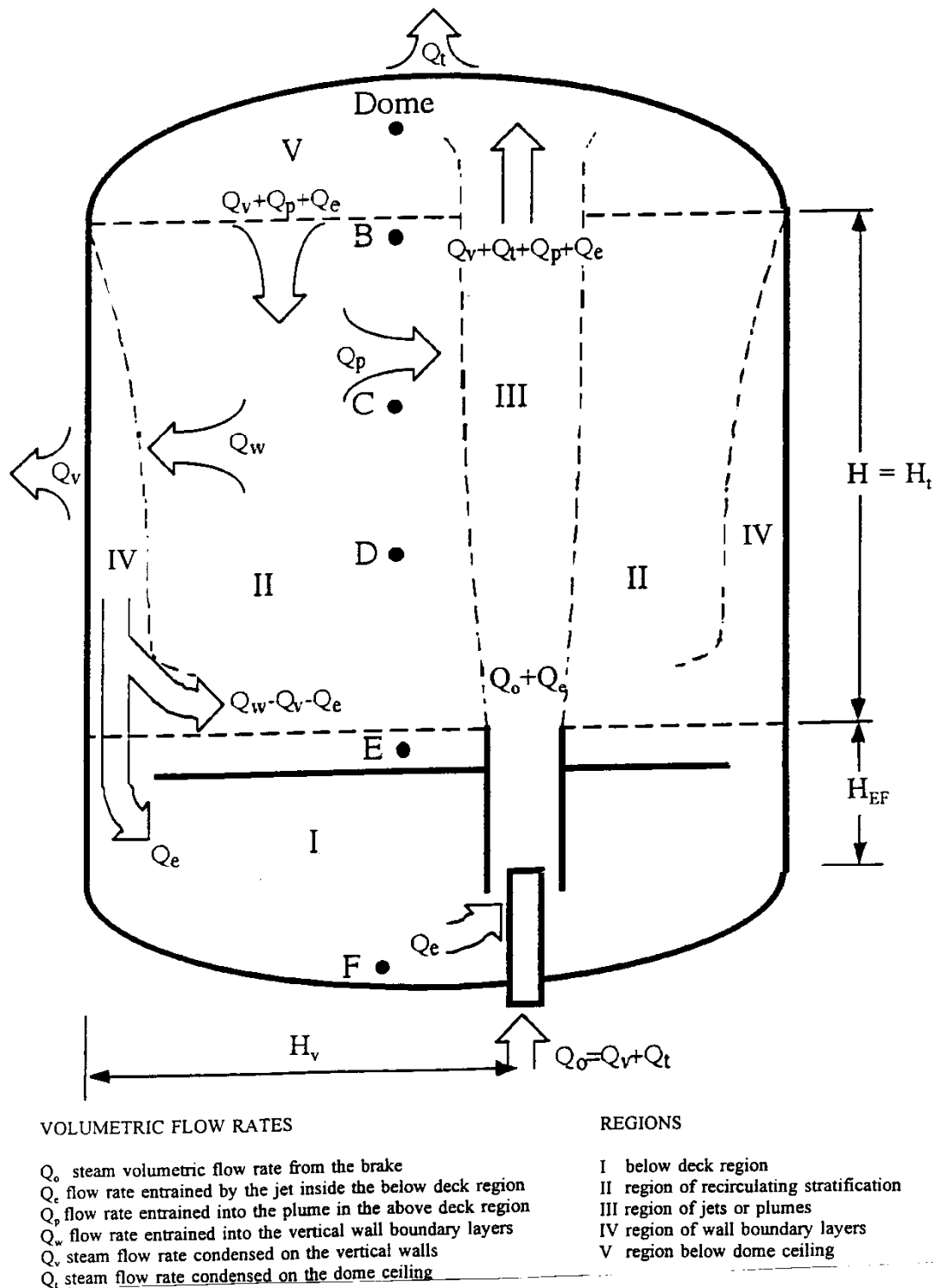


Figure 9.C-18. Primary Flow Regions and Volumetric Flow Rates for Quasi-Steady Containment Conditions

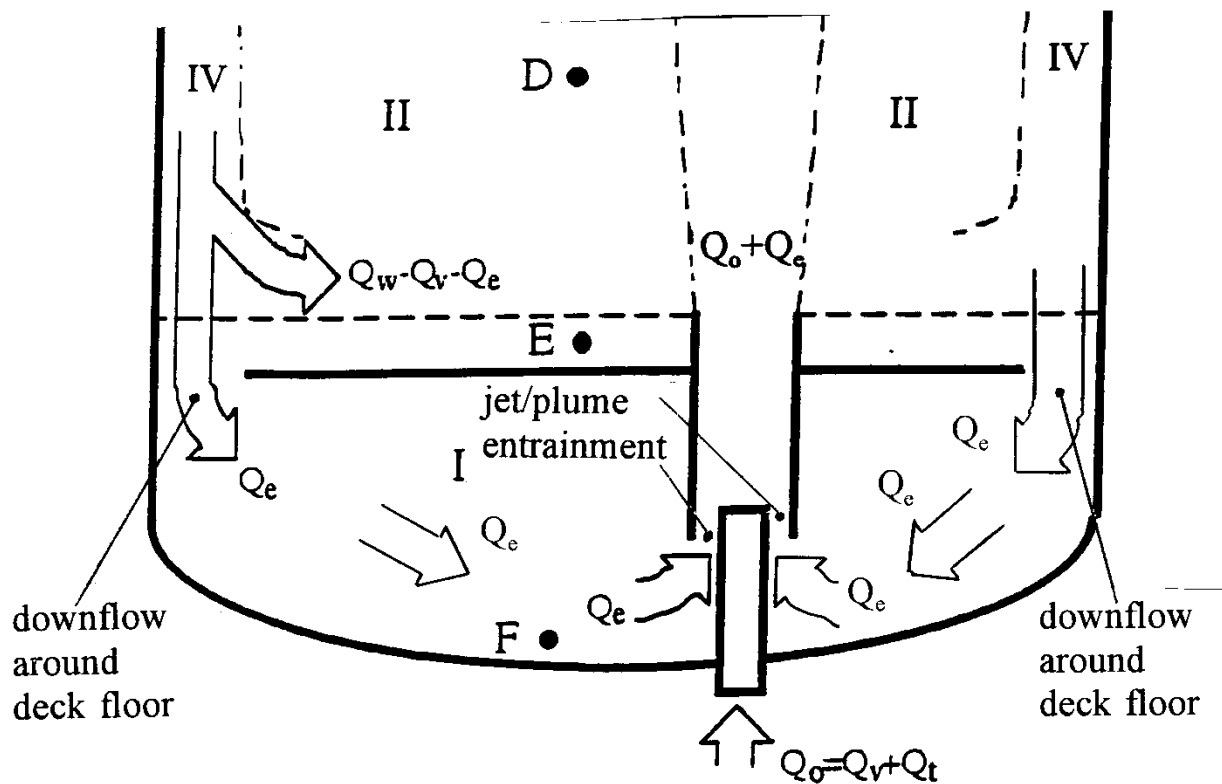


Figure 9.C-19. The Volumetric Flow between the Upper and Lower Deck Regions Q

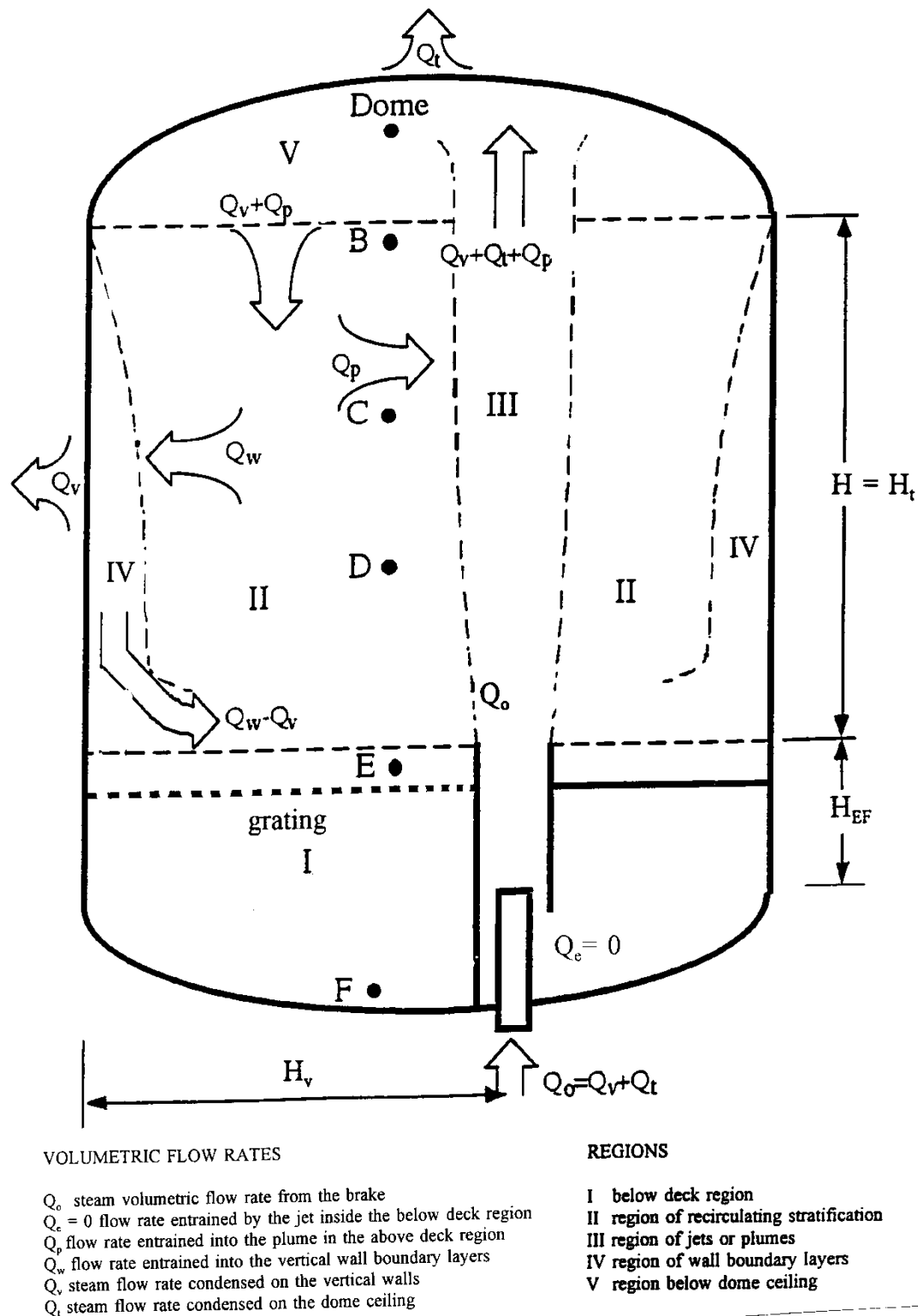


Figure 9.C-20. Primary Flow Regions and Volumetric Flow Rates for Quasi-Steady Containment Conditions in LST Case

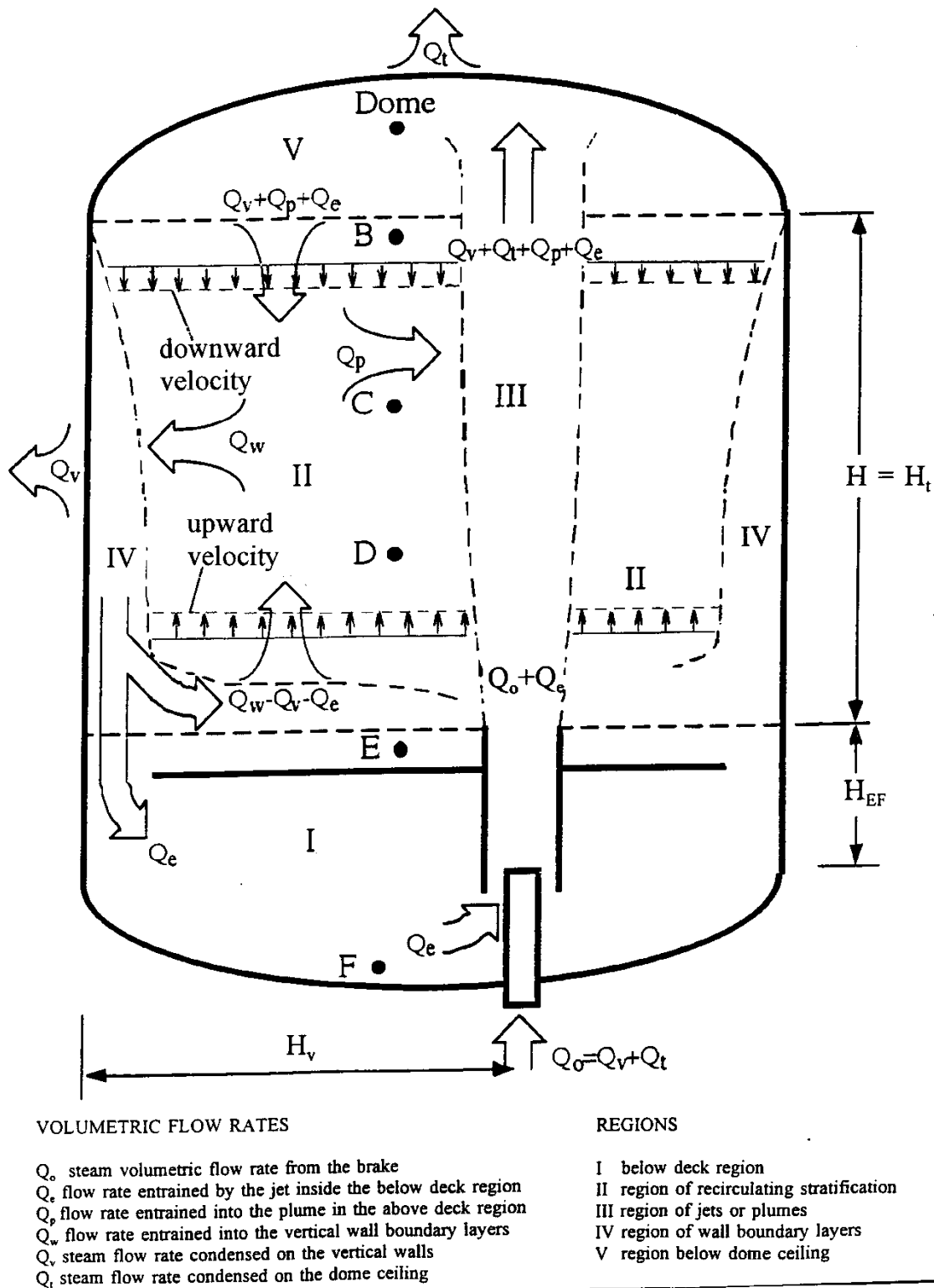
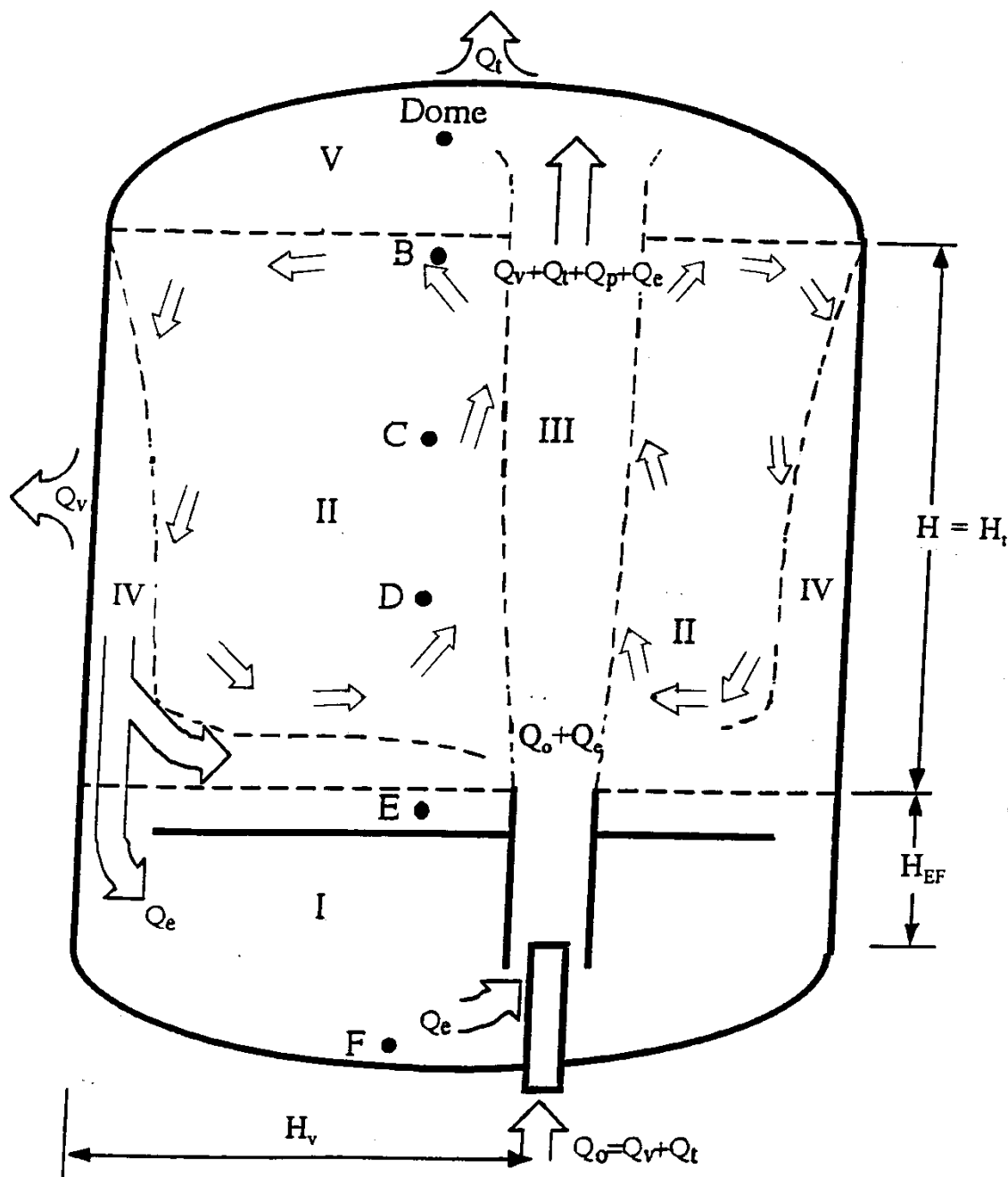


Figure 9.C-21. Inflows and Outflows from the Region II



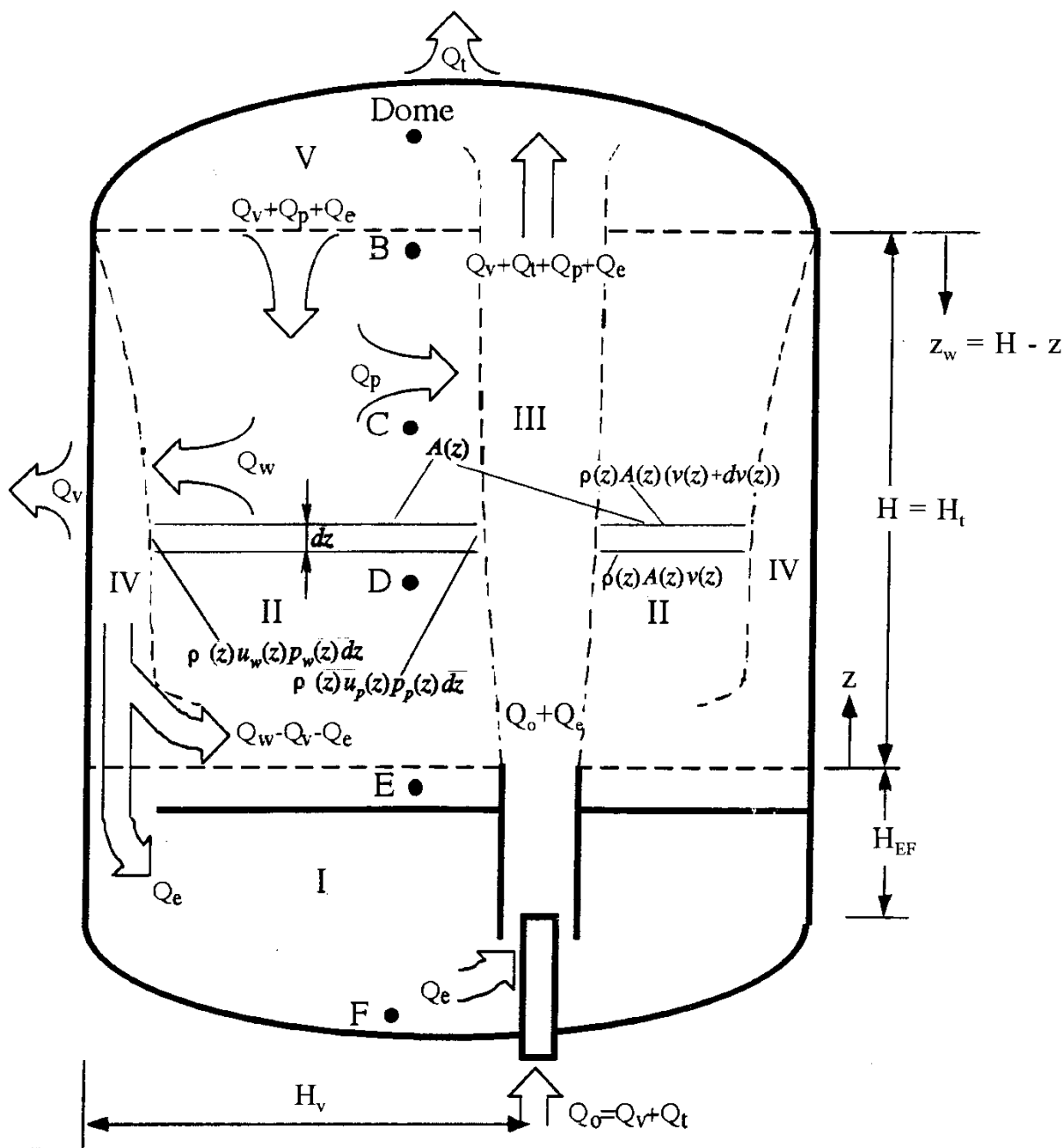
VOLUMETRIC FLOW RATES

- Q_b steam volumetric flow rate from the brake
- Q_e flow rate entrained by the jet inside the below deck region
- Q_p flow rate entrained into the plume in the above deck region
- Q_v flow rate entrained into the vertical wall boundary layers
- Q_c steam flow rate condensed on the vertical walls
- Q_t steam flow rate condensed on the dome ceiling

REGIONS

- I below deck region
- II region of recirculating stratification
- III region of jets or plumes
- IV region of wall boundary layers
- V region below dome ceiling

Figure 9.C-22. Recirculating Flow Paths Inside the Region II



VOLUMETRIC FLOW RATES

Q_o steam volumetric flow rate from the brake
 Q_e flow rate entrained by the jet inside the below deck region
 Q_p flow rate entrained into the plume in the above deck region
 Q_w flow rate entrained into the vertical wall boundary layers
 Q_v steam flow rate condensed on the vertical walls
 Q_t steam flow rate condensed on the dome ceiling

REGIONS

I below deck region
 II region of recirculating stratification
 III region of jets or plumes
 IV region of wall boundary layers
 V region below dome ceiling

Figure 9.C-23. Mass Conservation for Thin Horizontal Layer Inside the Region II

9.C.1.4.3 References

1. P.F. Peterson, 1997
LST Mixing Model Writeup - letter to J. Woodcock, 02/24/97
2. Enclosure to Westinghouse Letter NSD-NRC-97-4978
Subject: Position paper in support of the assumption of complete mixing of aerosols in the AP600 containment atmosphere following a loss of coolant accident February 7, 1997
3. WCAP-14135, F. E. Peters, April 1997
“Final Data Report for PCS Large-Scale Tests, Phase 2 and Phase 3,” Revision 1
Westinghouse Energy Systems

9.C.2 OVERVIEW OF THE INTERNATIONAL CONTAINMENT EXPERIMENTAL DATA BASE

Tests from the available international containment experimental database that are relevant to the passive containment design, are presented in this chapter. Some tests are very close to possible passive containment cases. Others are presented to emphasize the difference between the passive containment design and the test conditions that lead towards stratification.

Four experimental facilities are considered to supplement LST data. Table 9.C-1 specifies characteristics of each experimental facility and provides a comparison with the LST, the AP600 and the **AP1000**. A comparison of the sizes of various test facilities is provided in Figure 9.C-24. Scaled cross-sections of each facility are shown.

A list of the facilities and the overviewed experiments is provided in Table 9.C-2, as well as the main characteristics of each experiment.

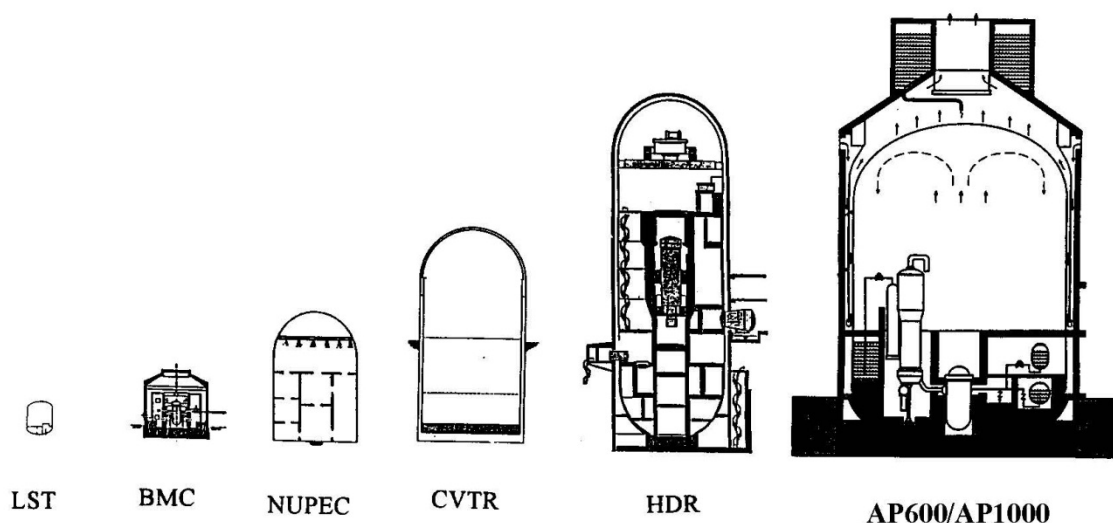


Figure 9.C-24. Comparison of Different Facilities

Table 9.C-1. Comparison of Various Facilities

Facility	LST	BMC	NUPEC	CVTR	HDR	AP600	AP1000
Volume m ³	83.1	640	1300 (used)	6428	11300	48710	58333
Height m	6.1	9	17.4	34.7	60	57.9	65.6
Diameter m	4.57	11.25	10.8	17.7	20	39.6	39.6
Number of compartments	3	9	25	3	62-72	11	11
Volume of the dome	79%		70%	41%	44%	81%	83%
Containment walls	steel	concrete	steel	concrete	steel shell concrete and steel	steel shell concrete and steel	steel shell concrete and steel

Table 9.C-2. Overviewed Tests from International Database

Facility	Experiment	Main Feature	Position of the Release Point and Other Relevant Data	Stratification or Circulation
BMC	F2 set First Phase	Stepwise steam addition	Release point is high Hr/Ht=0.444	Circulation through the majority of compartments, external annulus stratified
BMC	F2 set Phase 2	Inducing the natural circulation with steam injection	Steam release point is low Hr/Ht = 0.111	Circulation through the majority of compartments, external annulus stratified
BMC	F2 set Phase 3	Heater on in R6 to reverse circulation	Heat source location is low Hr/Ht = 0.111	Circulation through the majority of compartments, external annulus stratified
BMC	F2 set Phase 4	Steam injection in R6 compartment	Steam release point is low Hr/Ht = 0.111	Circulation through the majority of compartments, external annulus stratified
BMC	Test 2 Two compartments (Phase I)	Hydrogen injection, uniform initial temperature, orifice present, low feed rate	Low position of hydrogen source Hr/Ht = 0.06	Hydrogen uniformly distributed, circulation present

Table 9.C-2. Overviewed Tests from International Database (cont.)

Facility	Experiment	Main Feature	Position of the Release Point and Other Relevant Data	Stratification or Circulation
BMC	Test 4 Two compartments (Phase I)	Hydrogen injection, uniform initial temperature, no orifice	High position of hydrogen source $H_r/H_t = 0.57$	Concentration stratification occurs
BMC	Test 6 Two compartments (Phase I)	Hydrogen injection, stratified initial temperature, orifice present	Low position of hydrogen source $H_r/H_t = 0.06$	Stratification present, highest hydrogen concentration in the lower compartments
BMC	Test 12 Six compartments (Phase II)	Hydrogen injection in R2 room (high), uniform initial temperatures	High release point $H_r/H_t = 0.69$	Hydrogen uniformly distributed, circulation present
BMC	Test 20 Six compartments (Phase II)	Hydrogen injection in R6 room (low), stratified initial temperature	Low position of hydrogen source $H_r/H_t = 0.06$	Stratification present, highest hydrogen concentration in the lower compartments
BMC	RX4	Sump heat up and three hydrogen injections	Low position of the heat and hydrogen source $H_r/H_t = 0.0$	Circulation present, homogenization of temperature and concentrations
NUPEC	M-4-3	Simulated break inside the low steam generator compartment, steam and hydrogen release, containment shell insulated	Low position of the heat and hydrogen source $H_r/H_t = 0.0$	Circulation present during release, temperature stratifies and concentration homogenizes after the end of release
CVTR	First test without the internal water sprays	Steam release in the upper compartment, concrete shell	High position of the steam release $H_r/H_t = 0.525$	Temperature field stratifies
CVTR	The second and third test with internal water sprays	Steam release in the upper compartment, concrete shell	High position of the steam release $H_r/H_t = 0.525$	Temperature field stratifies but not as strong as in the previous case

Table 9.C-2. Overviewed Tests from International Database (cont.)

Facility	Experiment	Main Feature	Position of the Release Point and Other Relevant Data	Stratification or Circulation
HDR	E11.2	High positioned release point (small break) and active external spray	High position of the steam release $H_r/H_t = 0.555$	Stratification exists, external sprays promoted circulation
HDR	E11.3	Low positioned small break closed spiral stairway entrance		Global circulation pattern formed
HDR	E11.4	Low positioned release point (small break) and active external spray	Low position of the steam release $H_r/H_t = 0.18$	Global circulation formed almost uniform temperature distribution except below release point
HDR	T31.5	Simulates DBA large LOCA in the upper section of the containment	High position of the steam release $H_r/H_t = 0.526$	Temperatures and gas concentrations first stratify and latter homogenize
HDR	V21.1	Simulates DBA large LOCA in the middle section of the containment (in both staircases)	Middle position of the steam release $H_r/H_t = 0.38$	Equal heating of both staircases first suppressed circulation. Slight global circulation was generated later.
HDR	E11.5	Simulates DBA large LOCA in the lowest section of the containment with effects of dry heat release and sump boiling	Low position of the steam release $H_r/H_t = 0.18$	Global circulation due to the steam release, gas mixture injection and sump boiling contributed towards homogenization

9.C.2.1 Description of the Available Battelle Model Containment (BMC) Database

The objective of the Battelle Model Containment (BMC) tests is to obtain data to analyze design basis accidents (DBAs), hydrogen distribution, and aerosol depletion. The total volume of the containment is 640 m³ and represents 1/64 of the BIBLIS B containment. Its interior is divided into nine compartments and its walls are made of reinforced concrete. The sizes and locations of openings between the compartments can be adjusted by opening (or closing) the openings with steel plates or mobile concrete structures.

Three sets of tests are presented.

- The first set, the F2 experiments, tests natural convection as a function of release location and type of release (steam, air, dry heat).
- The second set of tests studies the influence of the initial temperature distribution, the location of hydrogen injection, the injection rates, and the size of the vent openings on hydrogen distribution, stratification and global circulation.
- The third set of tests examines the effect of sump heatup on global natural circulation.

9.C.2.1.1 Natural Convection Phenomena Inside the Multi-Compartment Containment (F2 Experiments)

The F2 experiments, performed by Kanzleiter in 1988, study natural convection inside a multi-compartment containment as a function of release location (room) and type (steam, air, dry heat). The BMC configuration used for experiment F2 is shown in Figure 9.C-25 and Figure 9.C-26. A 48-hour heatup period is the first phase of the experiment – see Figure 9.C-27, (Fischer et al., 1989, and Fischer et al., 1991). This is followed by a three-part, natural circulation phase (phases 2, 3, and 4) within the 48- to 75-hour time period see Figure 9.C-28, (Fischer et al., 1990 and Fischer et al., 1993).

An overview of the results and a comparison with analysis codes is presented by Wolf et al, 1996. Data for pressure, temperature, sump temperature, and liquid level, as well as partial steam pressure is presented for phases 1-4 (up to 75 hours).

9.C.2.1.1.1 F2 - Experiment Heatup Phase - Phase 1

Phase 1 is from 0-48 hours. A steam release inside the R2 compartment provides the heatup (see Figure 9.C-29 and Figure 9.C-27). The stepwise steam addition results in a stepwise increase of the containment pressure (see Figure 9.C-30 for GP 9117 location).

During the 48 hours of heatup, the atmosphere in the external annulus (the lower portion of R9 surrounding compartment) stratifies, Figure 9.C-31. Since there is no driving force for the circulation of steam into the lower air-rich regions of R9, the two experimental curves in Figure 9.C-31 (for temperatures GT9004 and GT9037) show that the heatup was delayed in lower positions in the external annulus behind the missile shield. The lower portion of R9 heats up over a longer period (Figure 9.C-31) because of global circulation induced by entrainment in the release. The entrainment is fed by flow from R9, R4 and R1.

Over a period of time, the atmosphere of the containment in the external annulus stratifies (after 16 hours it is already stratified). However, after 36 hours the stratification is not as pronounced, i.e., the temperature differences are not greater than 10°C in the external annulus. The initial stratification in the external annulus results from the high position of the steam release, which is inside the R2 compartment, and the closed circulation paths in the lower portion of the external annulus (see Figure 9.C-32).

The experimental curves for temperature histories of the other subcompartments (except for R4 and R3) are not presented in Wolf et al., 1996. However, consecutive phases of other experiments performed in the BMC indicate that natural circulation effects are present and contribute towards homogenization of the temperature fields among the majority of compartments. The only exception is the external annulus.

Application to the AP600 and AP1000

There is evidence that a release high in the steam generator compartment can induce global circulation flow by entrainment through the CMT room openings. It is difficult to compare time scales due to significant differences between the BMC and the passive containment compartment arrangement.

9.C.2.1.1.2 Phases 2-4 of the F2 Experiment (Natural Circulation)

After the heatup, the experiment continues through three additional phases (see Figure 9.C-27 and Figure 9.C-28 for phases 2, 3, and 4) that use the following methods to induce or amplify circulation:

- Steam injection to induce natural circulation,
- Activation of the heater to reverse circulation,
- Injection of steam to amplify reversed circulation.

Figure 9.C-28 illustrates four additional phases (5, 6, 7, and 8) that are not discussed. The circled numbers in Figure 9.C-28 represent the type of injection (see also Figure 9.C-27). The flow patterns formed during the particular injection are presented below the circled numbers. Figure 9.C-32 shows the two different locations for the steam injection, the location of the heater and the positions of the anemometers.

In addition to the measured velocities in the openings (see Table 9.C-3), the fluctuations in measured temperatures indicate natural circulation (see Figure 9.C-33 and Figure 9.C-34). Due to natural circulation, complex flow patterns form and temperatures in the compartments are nearly homogeneous (i.e., temperature differences are not greater than 4°C, see Figure 9.C-33 and Figure 9.C-34). The detailed temperatures and velocities during each subphase are given by Kanzleiter, 1988.

Figure 9.C-35 presents the thermodynamic states of the containment dome atmosphere at a high position ($H = 7.6$ m) during various time periods, while Figure 9.C-36 presents the conditions at a low position in the external annulus ($H = 1.0$ m). Except during air injection times, the steam partial pressure in the high position follows the shape of the total pressure curve (0.5 to 1.0 bar lower values than p_{tot}). At the low position, the steam partial pressure is almost constant (0.5 bar) after 60 hours. This indicates steam stratification inside the external annulus (lower portion of the R9 compartment) behind the missile shield.

The temperature distribution inside the external annulus is presented in Figure 9.C-37 for the second phase and in Figure 9.C-38 for the third and fourth phases. Both figures indicate stratification of the temperature fields. The temperature difference between the upper dome and the lowest position in the external annulus is 30°C at the end of the second phase and 18°C at the end of the fourth phase.

All other compartments have almost homogeneous temperatures (the greatest temperature differences are 4°C), which indicate the presence of the natural circulation (see Figure 9.C-33 and Figure 9.C-34).

The values of the measured velocities in the vent between the R3 and R6 compartments during the individual phases are presented in Table 9.C-3. The histories of the velocities in the R7-R9 and R3-R6 vent paths are presented in Figure 9.C-39 and Figure 9.C-40, respectively. The directions of the convective flow loops as a function of steam and air injections into the various compartments and the applications of the dry heater are presented in Figure 9.C-27 (arrow in R9 compartment represents positive flow loop direction). The upward (positive) velocities in Figure 9.C-39 produce a positive flow direction loop. The upward (positive) velocities in Figure 9.C-40 produce a negative flow direction loop.

The various injections and the application of the dry heat source generate natural circulation and homogenize temperatures in the majority of the containment compartments.

Table 9.C-3. Representative Velocity in [m/s] in Opening from R3 to R6 in the Different Experimental Phases of Experiment F2, Phases 2-4

	Phase No.										
	2.1	2.2	2.3	2.4	3.1	3.2	3.3	4.1	4.2	4.3	4.4
	0.35	-0.4	0.4	-0.4	+/-0.1	+/-0.1	+/-0.1	-0.35	0./0.6	0.35	-0.4

Reprinted from L. Wolf, M. Gavrilas, K. Mun, "Overview of experimental results for long-term, large-scale natural circulations in LWR-containments after large LOCAS," University of Maryland

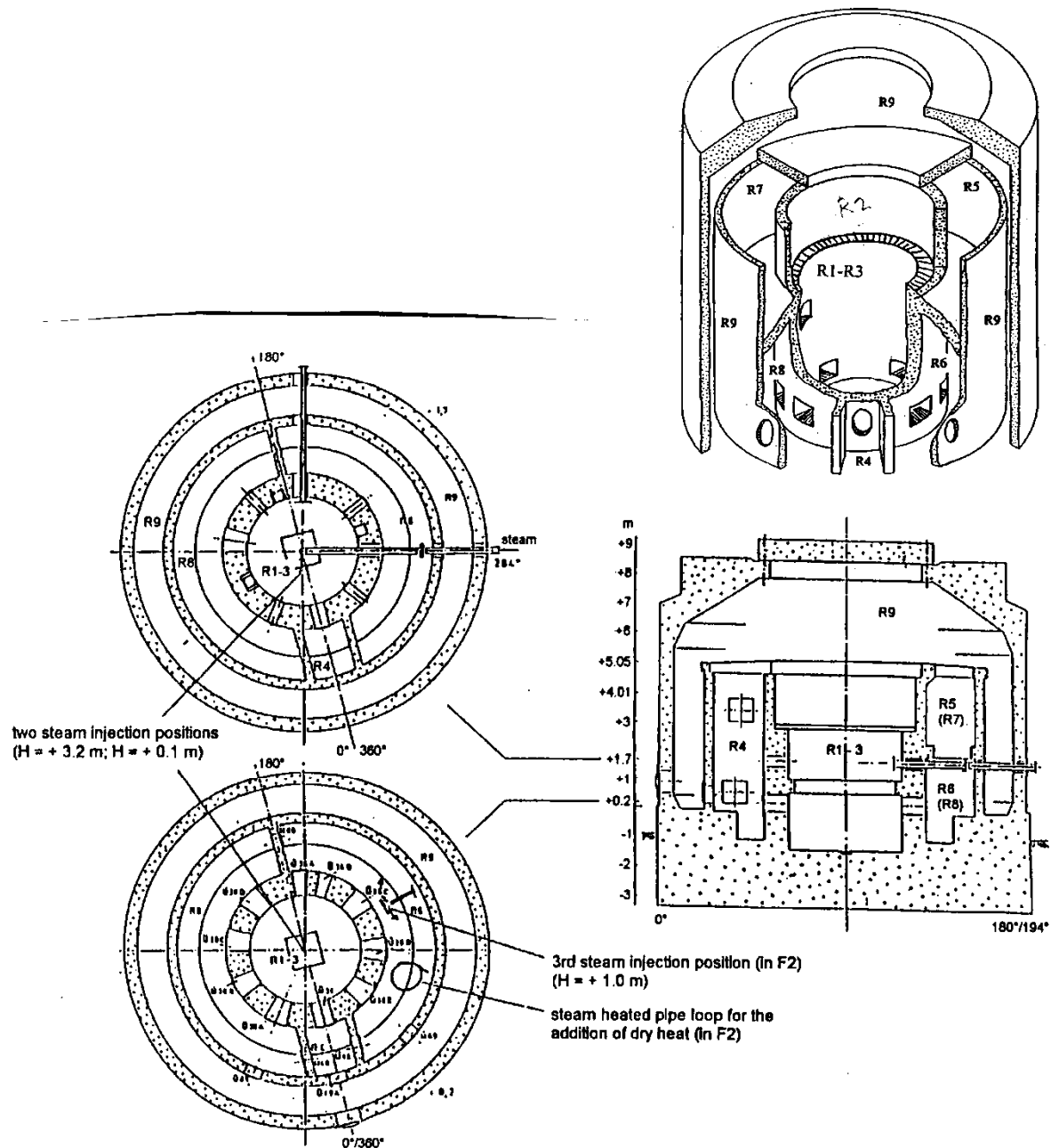


Figure 9.C-25. Model Containment: Vertical Cross-section 0/180; Horizontal Cross-sections at +0.2 m and +1.7m for Configuration in Experiment F2

(reprinted from L. Wolf, M. Gavrilas, K. Mun, "Overview of experimental results for long-term, large-scale natural circulations in LWR-containments after large LOCAs," University of Maryland at College Park, Final Report for DOE – Project, Order Number: DE-AP07-96ID10765")

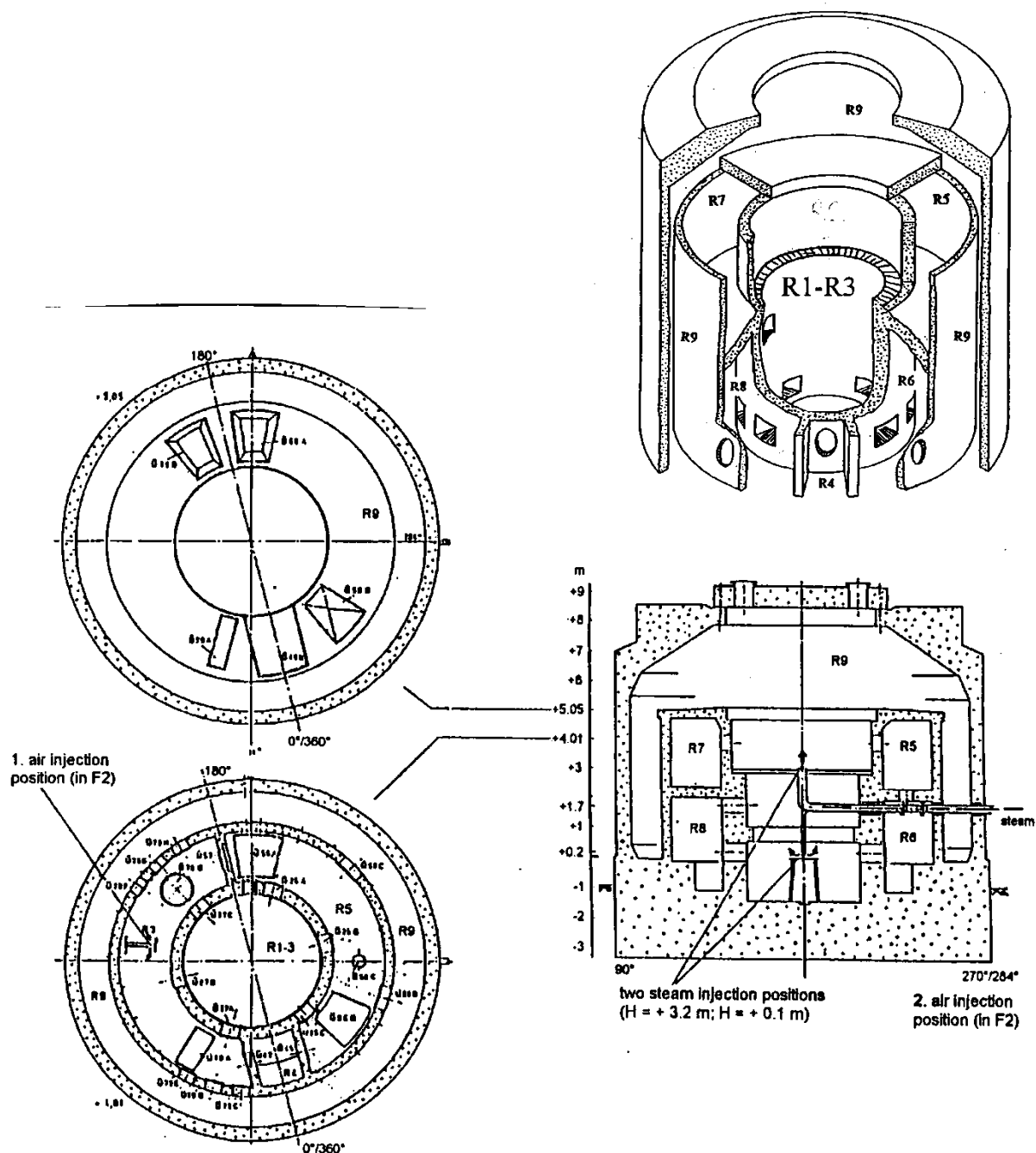


Figure 9.C-26. Model Containment: Vertical Cross-Section 0/180; Horizontal Cross-Sections at +4.01m and +5.05m for Configuration in Experiment F2

(reprinted from L. Wolf, M. Gavrilas, K. Mun, "Overview of experimental results for long-term, large-scale natural circulations in LWR-containments after large LOCAs," University of Maryland at College Park, Final Report for DOE – Project, Order Number: DE-AP07-96ID10765")

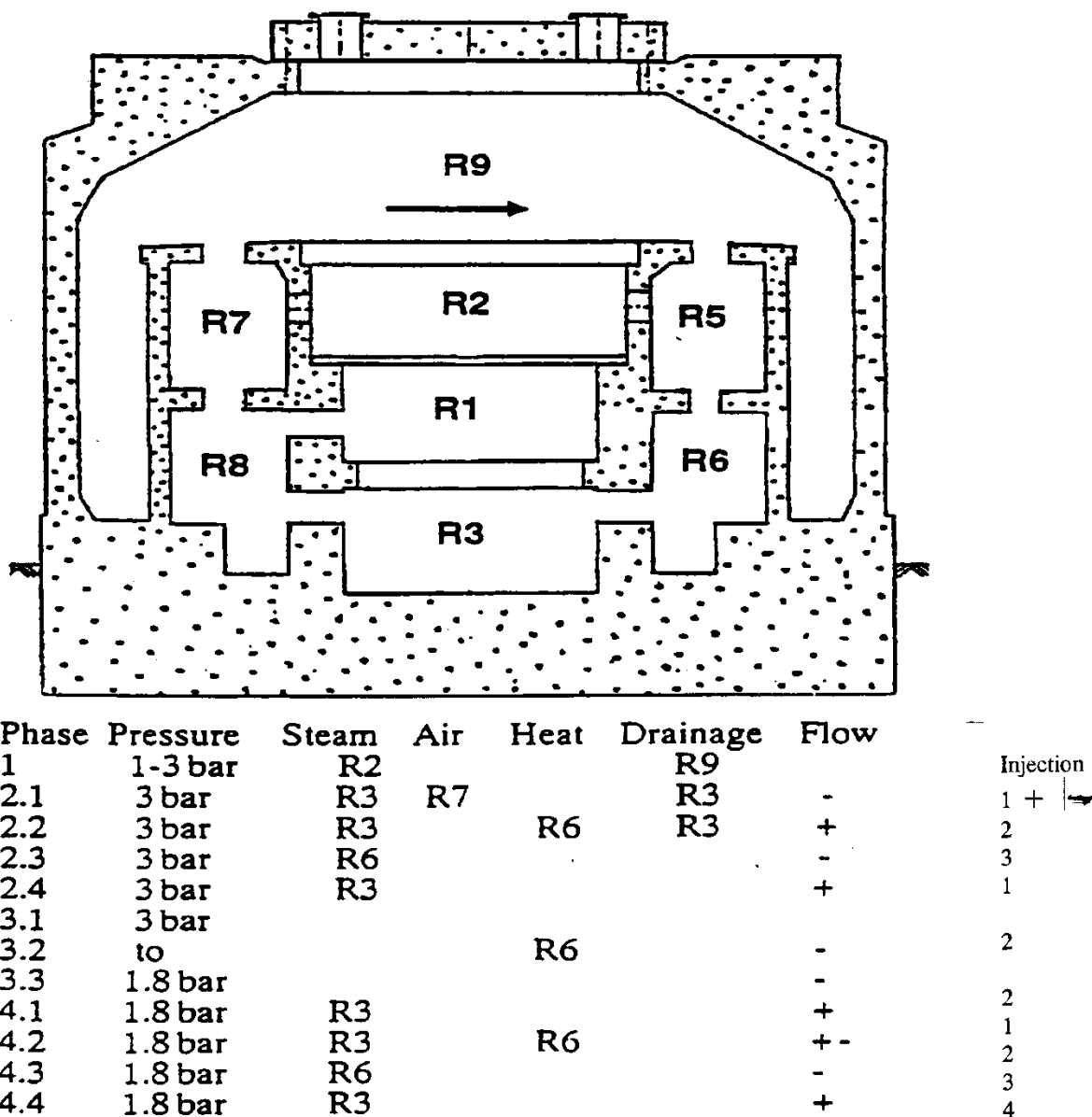


Figure 9.C-27. Injections and Convective Flow Loop Directions
(+ Sign for Flow Indicates the Same Direction of the Flow as Arrow in R9)

(reprinted from L. Wolf, M. Gavrilas, K. Mun, "Overview of experimental results for long-term, large-scale natural circulations in LWR-containments after large LOCAs," University of Maryland at College Park, Final Report for DOE – Project, Order Number: DE-AP07-96ID10765")

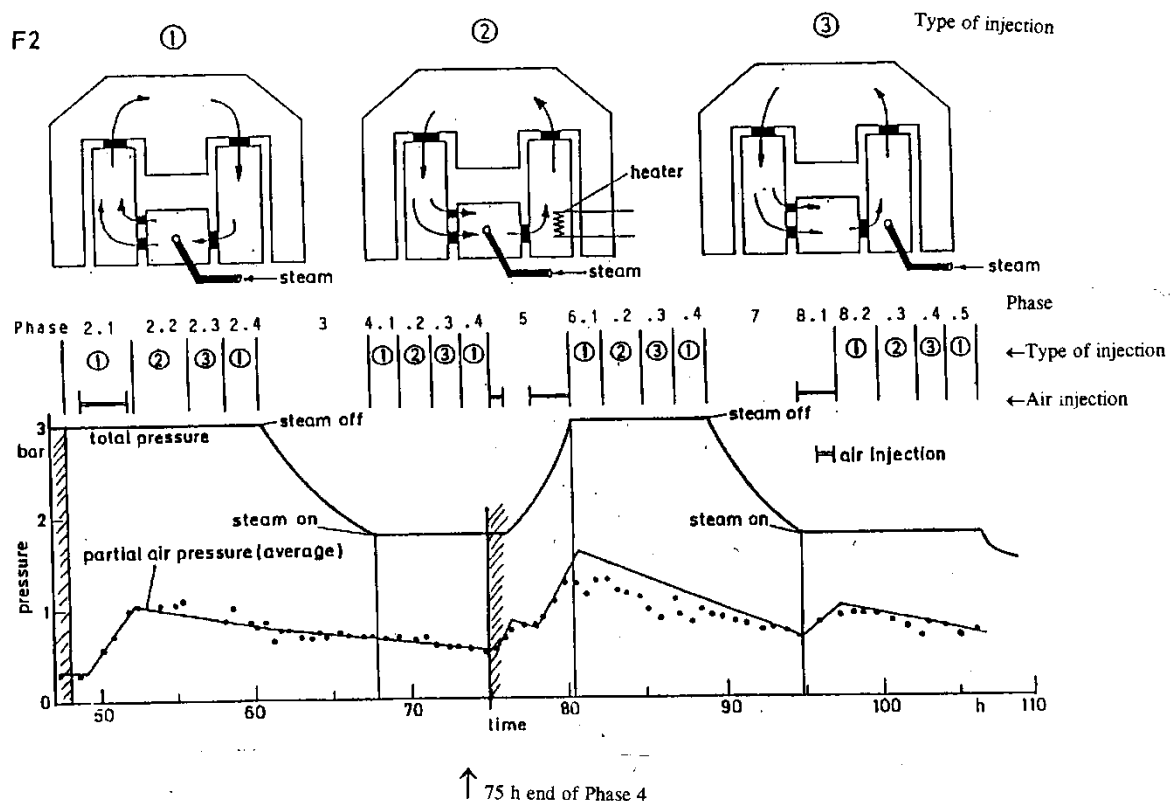


Figure 9.C-28. Experiment F2, Phase 2-8, Experimental Procedures, Total and Partial Pressures

(reprinted from L. Wolf, M. Gavrilas, K. Mun, "Overview of experimental results for long-term, large-scale natural circulations in LWR-containments after large LOCAs," University of Maryland at College Park, Final Report for DOE – Project, Order Number: DE-AP07-96ID10765")

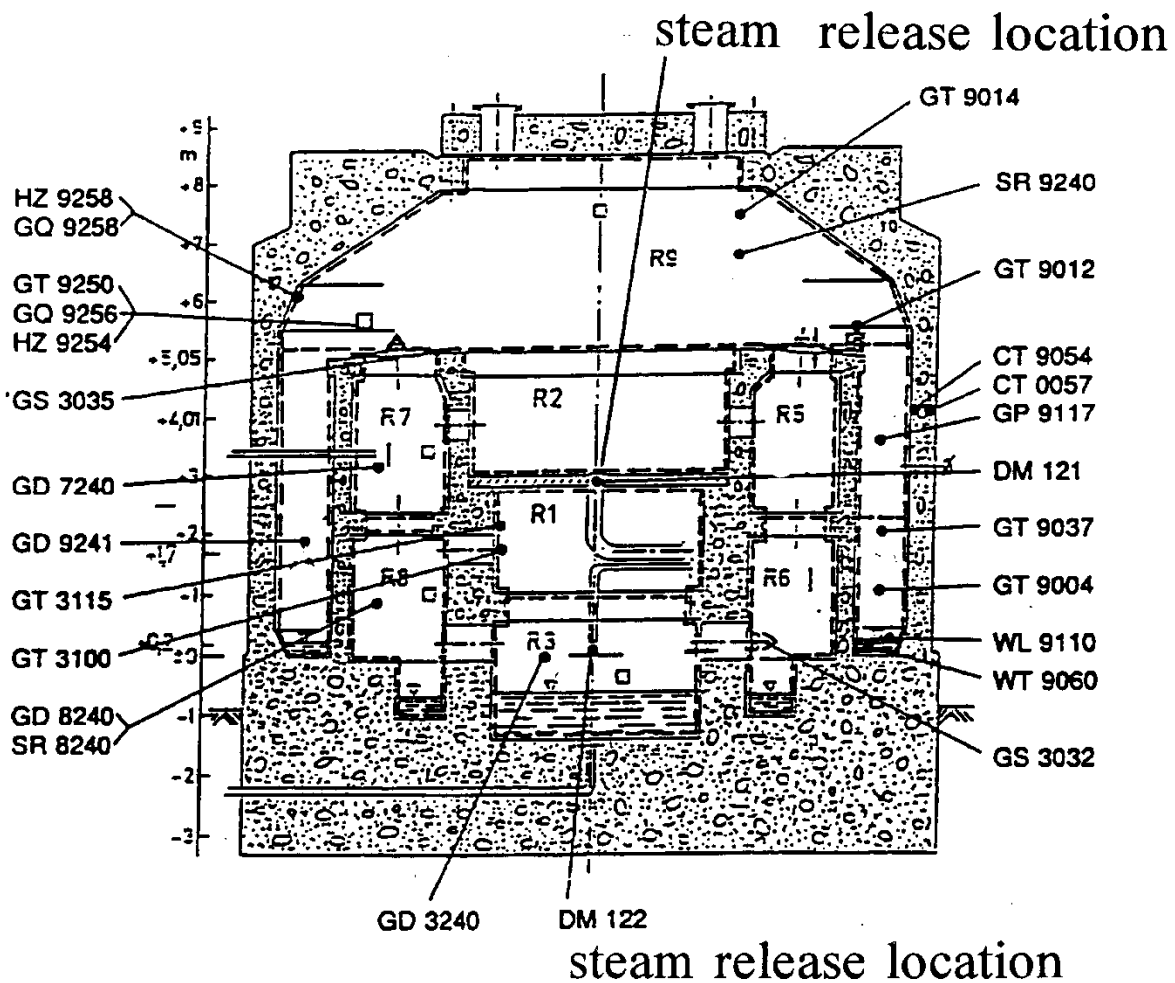


Figure 9.C-29. Number of Compartments, Locations of Measurement Transducers and Steam Releases

(reprinted from L. Wolf, M. Gavrilas, K. Mun, "Overview of experimental results for long-term, large-scale natural circulations in LWR-containments after large LOCAs," University of Maryland at College Park, Final Report for DOE – Project, Order Number: DE-AP07-96ID10765")

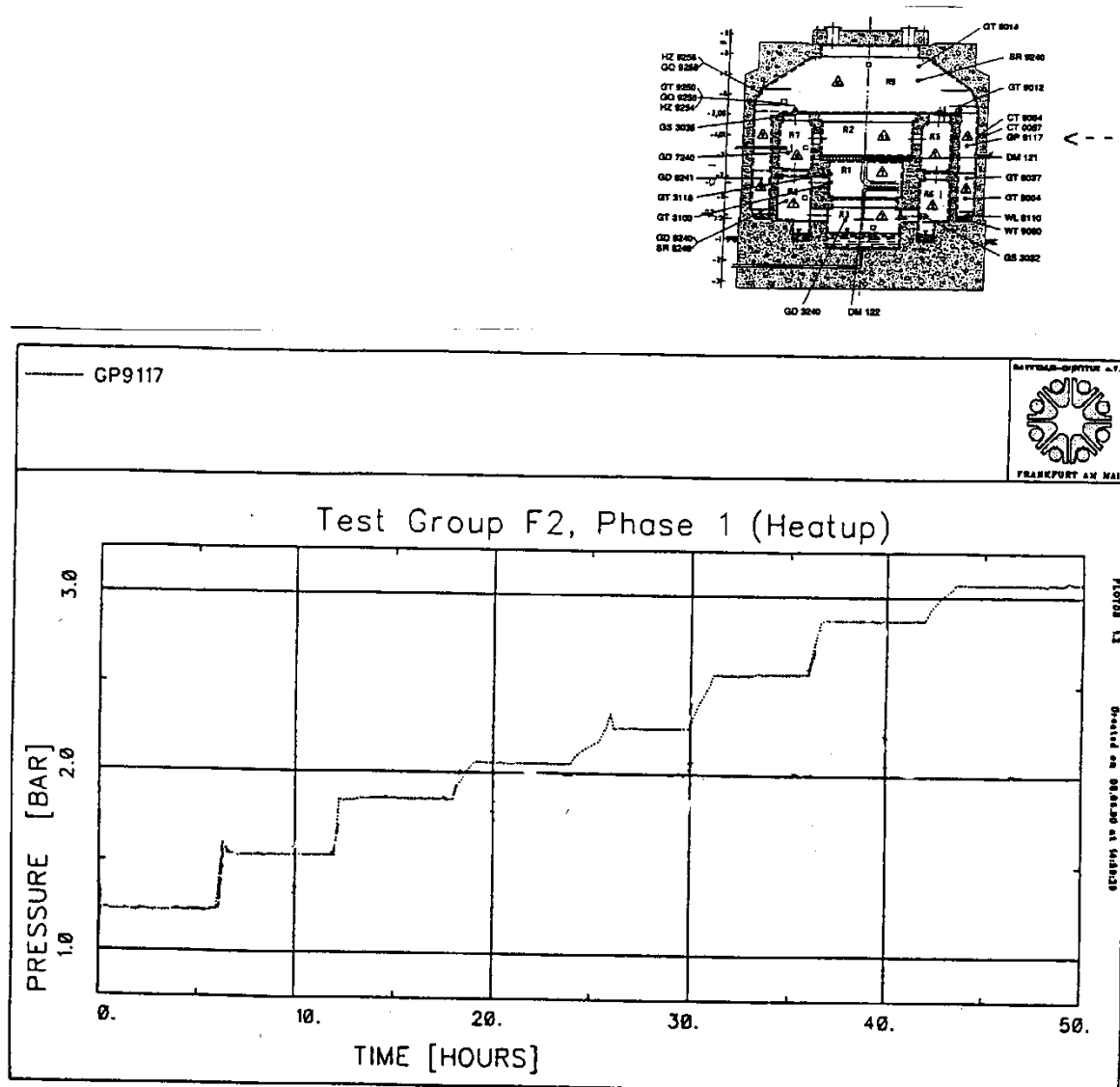


Figure 9.C-30. Test Group F2, Phase 1 (heatup), Total Pressure in the Containment

(reprinted from L. Wolf, M. Gavrilas, K. Mun, "Overview of experimental results for long-term, large-scale natural circulations in LWR-containments after large LOCAs," University of Maryland at College Park, Final Report for DOE – Project, Order Number: DE-AP07-96ID10765")

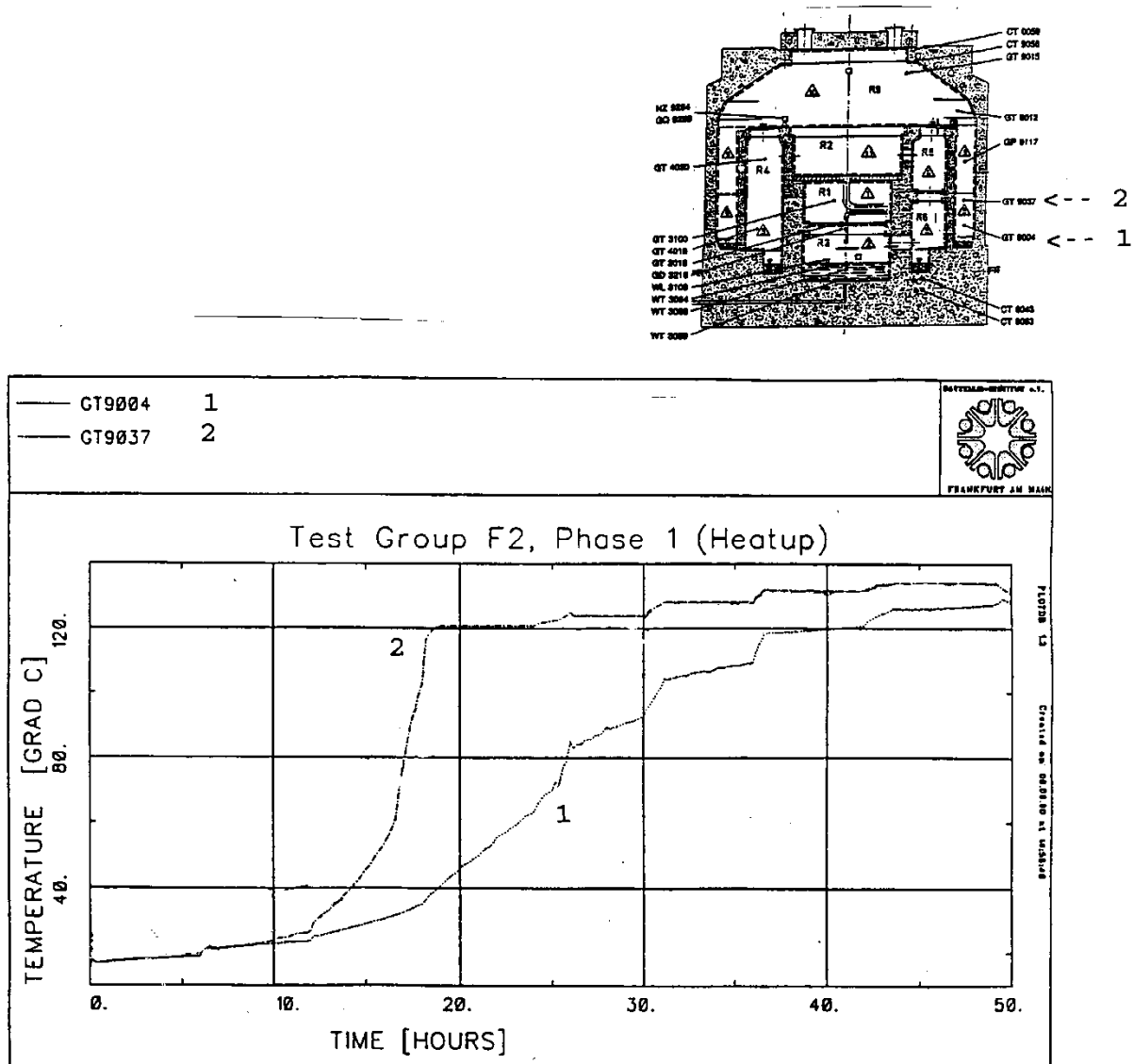
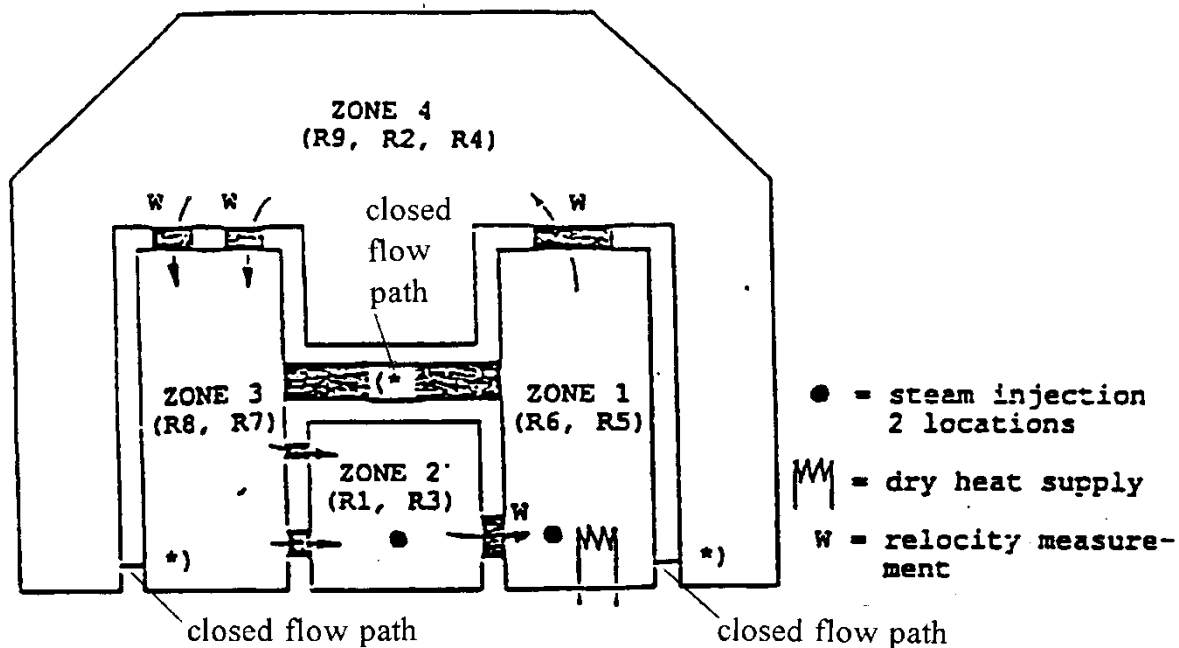


Figure 9.C-31. Test Group F2, Phase 1 (heatup), Atmospheric Temperature in the Compartment R9, H=1.0m and 2.1m.

(reprinted from L. Wolf, M. Gavrilas, K. Mun, "Overview of experimental results for long-term, large-scale natural circulations in LWR-containments after large LOCAs," University of Maryland at College Park, Final Report for DOE – Project, Order Number: DE-AP07-96ID10765")



circulation for phases 3 and 4 are shown

Figure 9.C-32. Scheme of Multi-Compartment Containment Geometry in Experiment F2

(reprinted from L. Wolf, M. Gavrilas, K. Mun, "Overview of experimental results for long-term, large-scale natural circulations in LWR-containments after large LOCAs," University of Maryland at College Park, Final Report for DOE – Project, Order Number: DE-AP07-96ID10765")

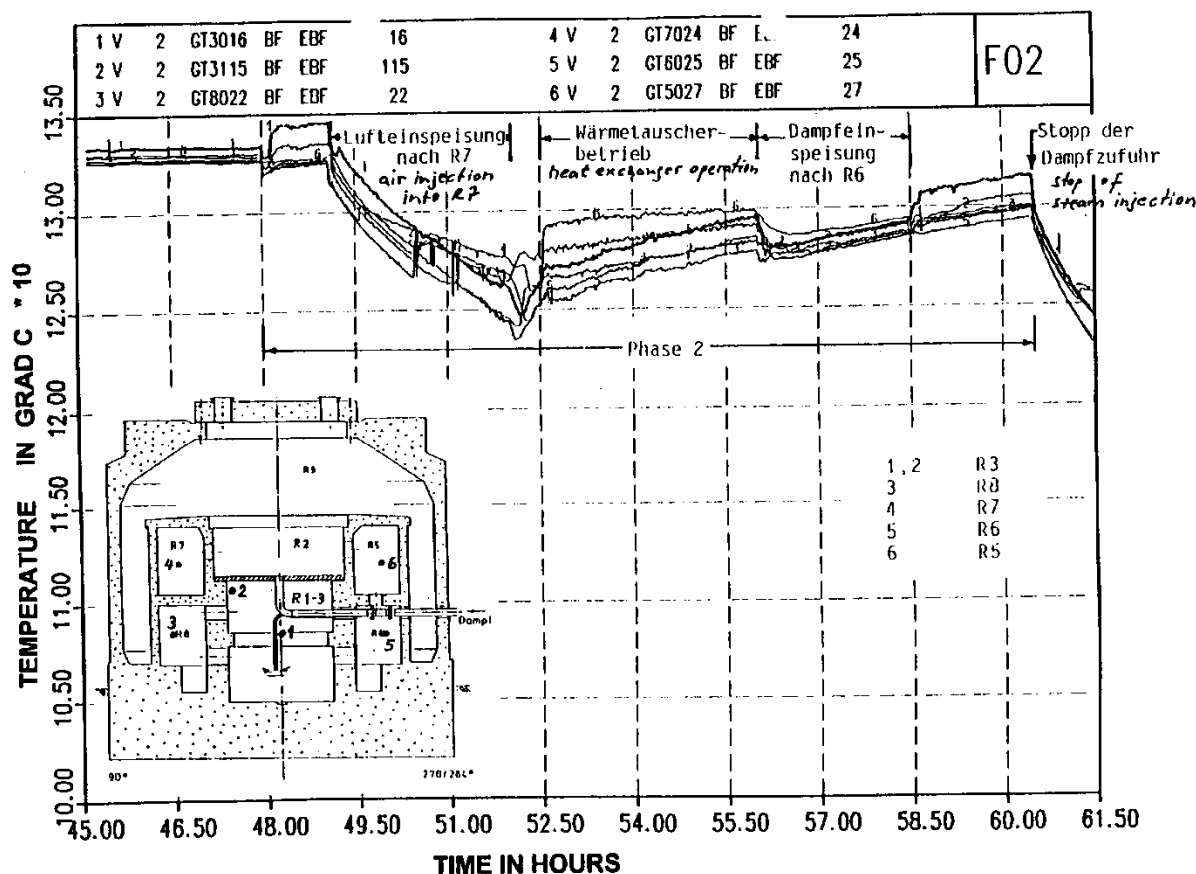


Figure 9.C-33. Test Group F2, Phase 2: Atmospheric Temperatures in Zones 1, 2 and 3 (R5 + R6, R1 + R4, R7 + R8)

(reprinted from L. Wolf, M. Gavrilas, K. Mun, "Overview of experimental results for long-term, large-scale natural circulations in LWR-containments after large LOCAs," University of Maryland at College Park, Final Report for DOE – Project, Order Number: DE-AP07-96ID10765")

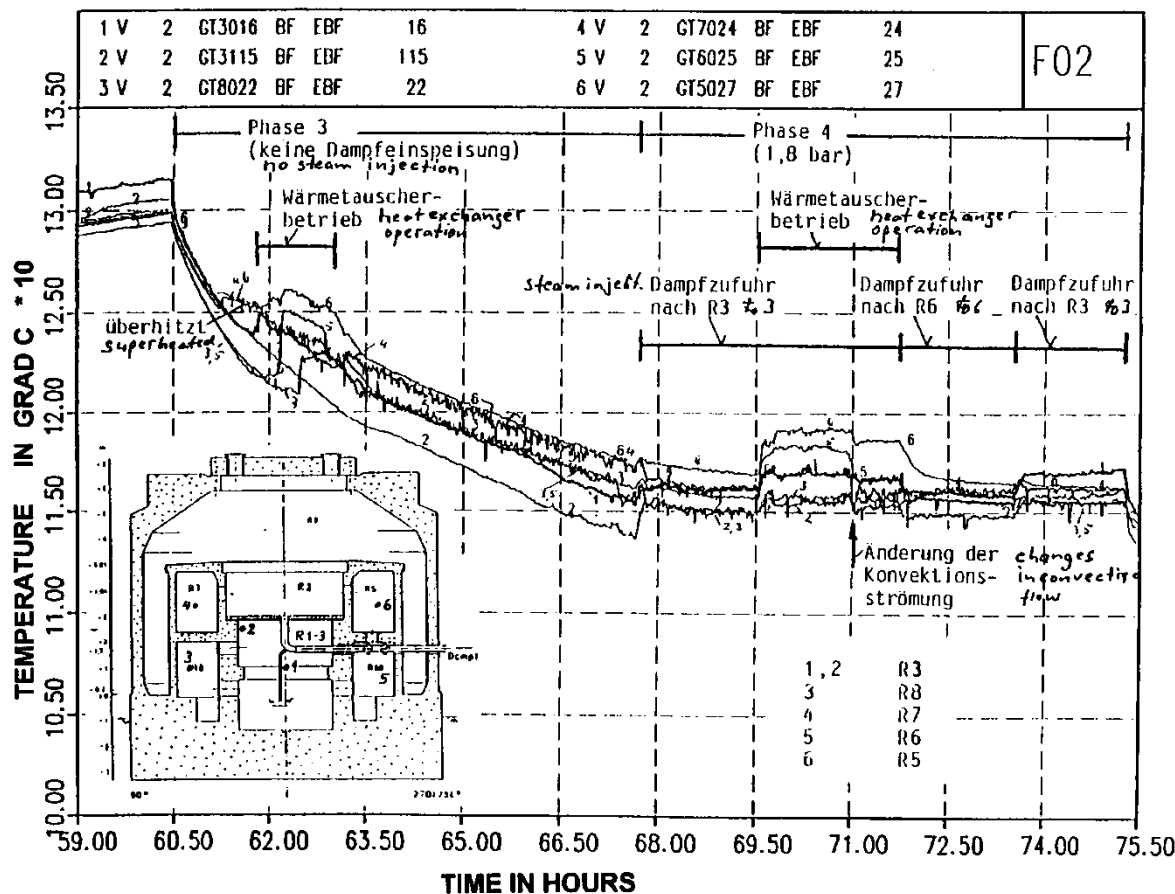


Figure 9.C-34. Test Group F2, Phase 3 and 4: Atmospheric Temperature in Zone 1, 2 and 3 (R5 + R6, R1 + R4, R7 + R8)

(reprinted from L. Wolf, M. Gavrilas, K. Mun, "Overview of experimental results for long-term, large-scale natural circulations in LWR-containments after large LOCAs," University of Maryland at College Park, Final Report for DOE – Project, Order Number: DE-AP07-96ID10765")

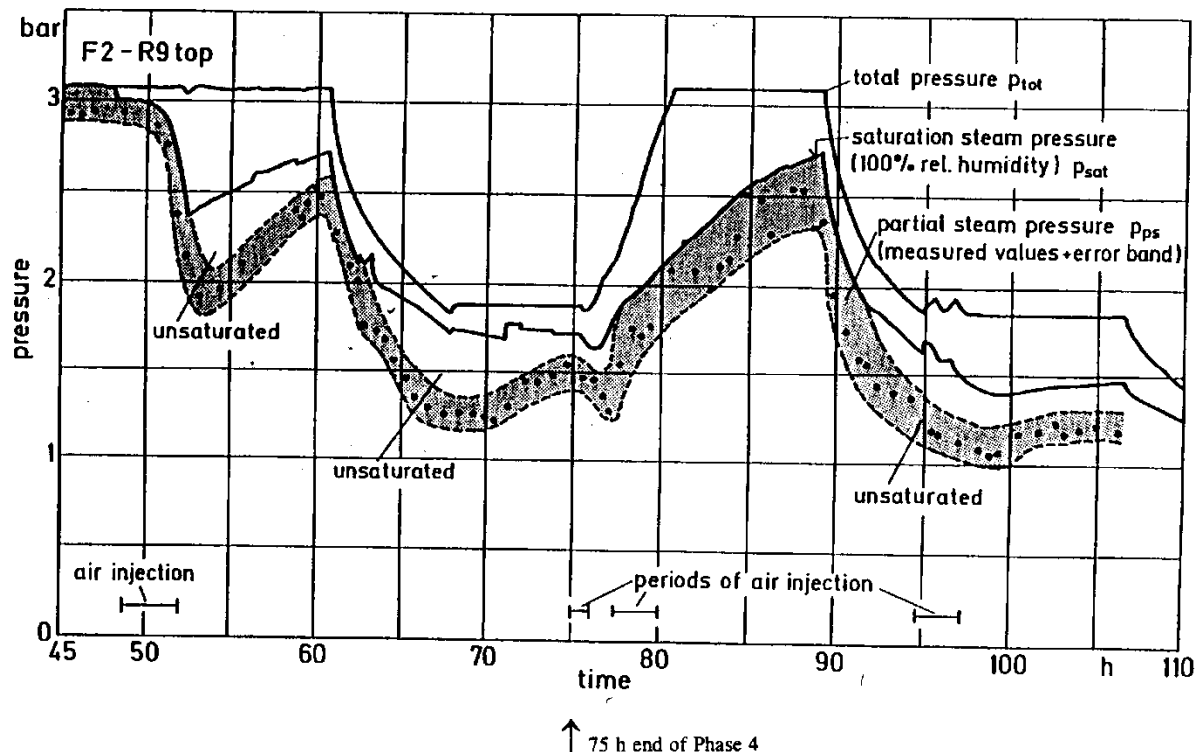


Figure 9.C-35. Thermodynamic State of Steam-Air Atmosphere in R9 top (H=7.6m)

(reprinted from L. Wolf, M. Gavrilas, K. Mun, "Overview of experimental results for long-term, large-scale natural circulations in LWR-containments after large LOCAs," University of Maryland at College Park, Final Report for DOE – Project, Order Number: DE-AP07-96ID10765")

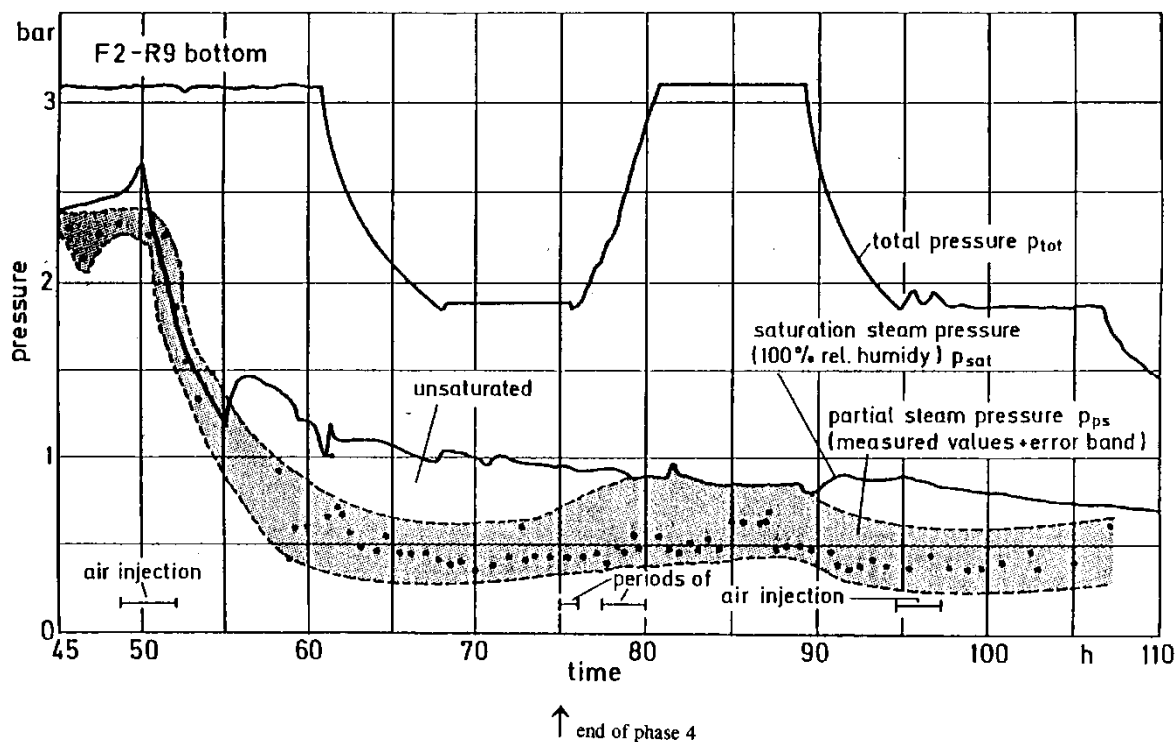


Figure 9.C-36. Thermodynamic State of Steam-Air Atmosphere in R9 Bottom (H=1 m)

(reprinted from L. Wolf, M. Gavrilas, K. Mun, "Overview of experimental results for long-term, large-scale natural circulations in LWR-containments after large LOCAs," University of Maryland at College Park, Final Report for DOE – Project, Order Number: DE-AP07-96ID10765")

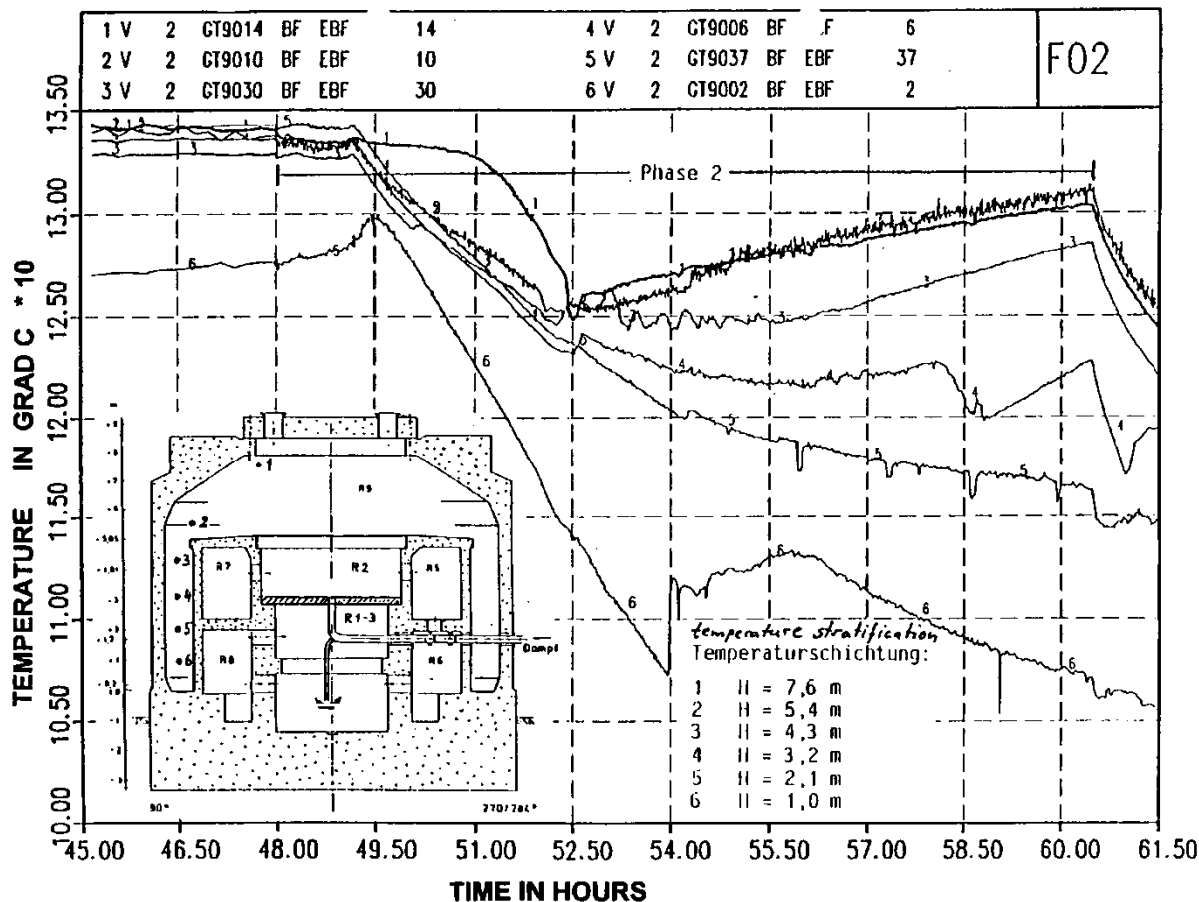


Figure 9.C-37. Test Group F2, Phase 2: Atmospheric Temperatures in R9 (Zone 4)

(reprinted from L. Wolf, M. Gavrilas, K. Mun, "Overview of experimental results for long-term, large-scale natural circulations in LWR-containments after large LOCAs," University of Maryland at College Park, Final Report for DOE – Project, Order Number: DE-AP07-96ID10765")

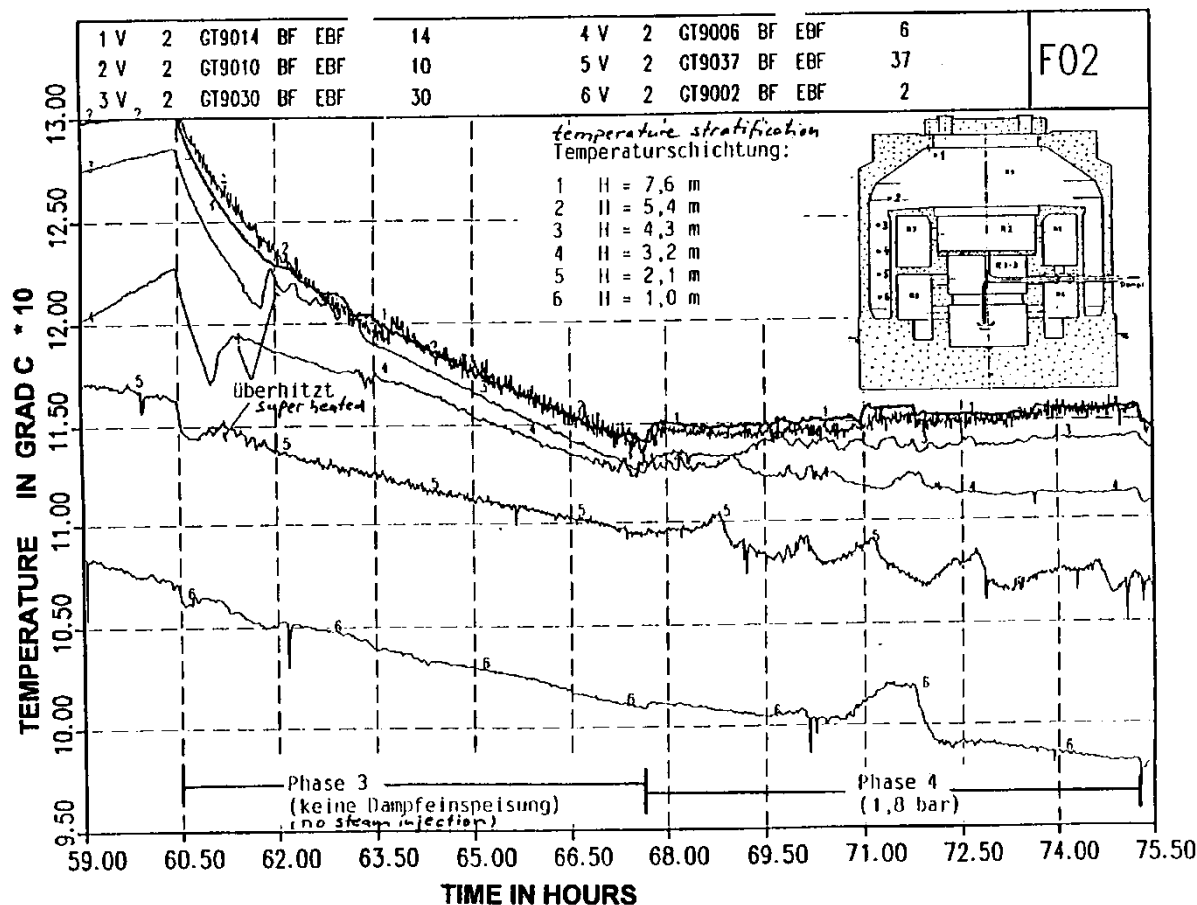


Figure 9.C-38. Test Group F2, Phase 3 and 4: Atmospheric Temperatures in R9 (Zone 4)

(reprinted from L. Wolf, M. Gavrilas, K. Mun, "Overview of experimental results for long-term, large-scale natural circulations in LWR-containments after large LOCAs," University of Maryland at College Park, Final Report for DOE – Project, Order Number: DE-AP07-96ID10765")

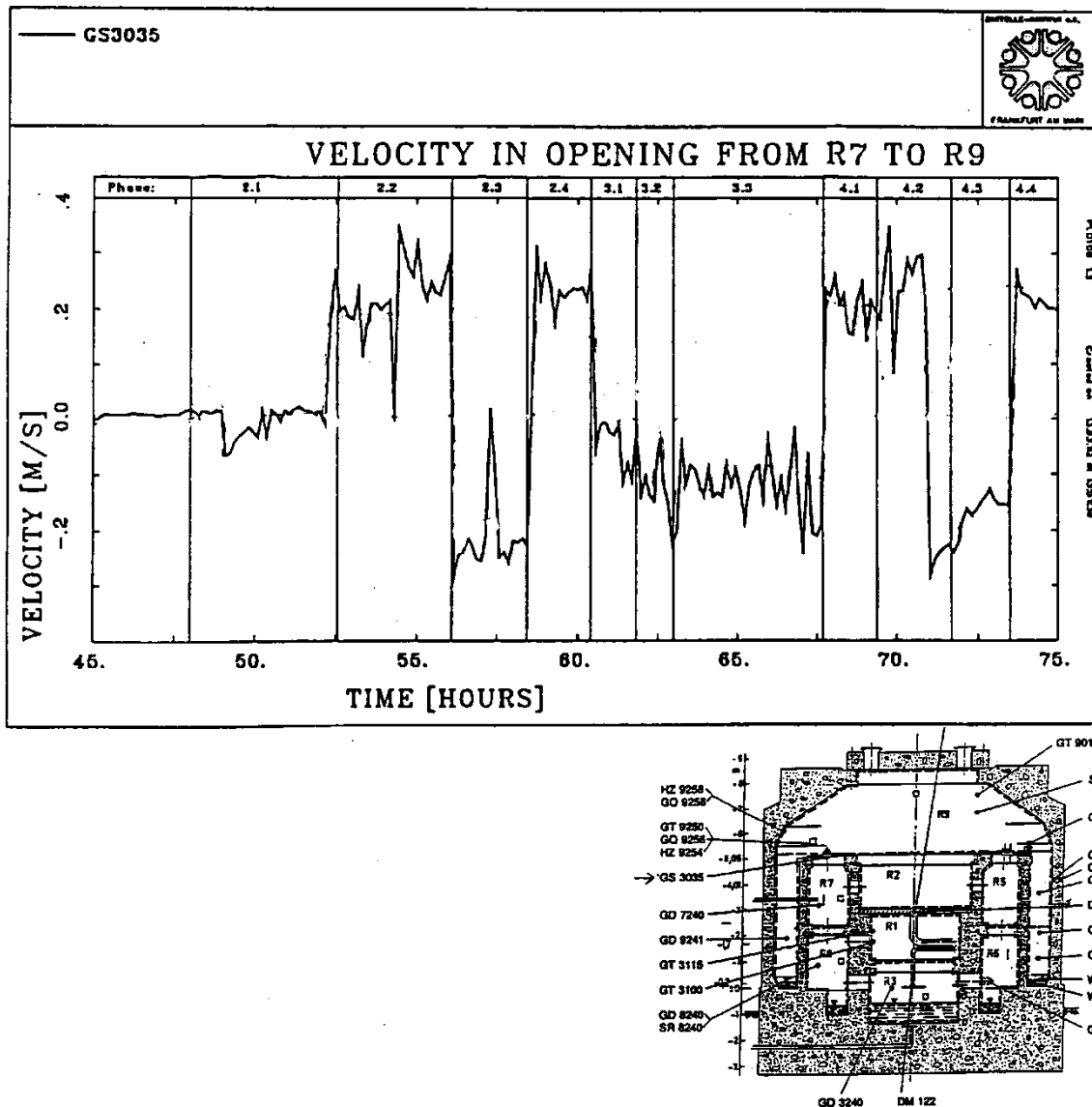


Figure 9.C-39. Velocities in Opening from Compartment R7 to Compartment R9

(reprinted from L. Wolf, M. Gavrilas, K. Mun, "Overview of experimental results for long-term, large-scale natural circulations in LWR-containments after large LOCAs," University of Maryland at College Park, Final Report for DOE – Project, Order Number: DE-AP07-96ID10765")

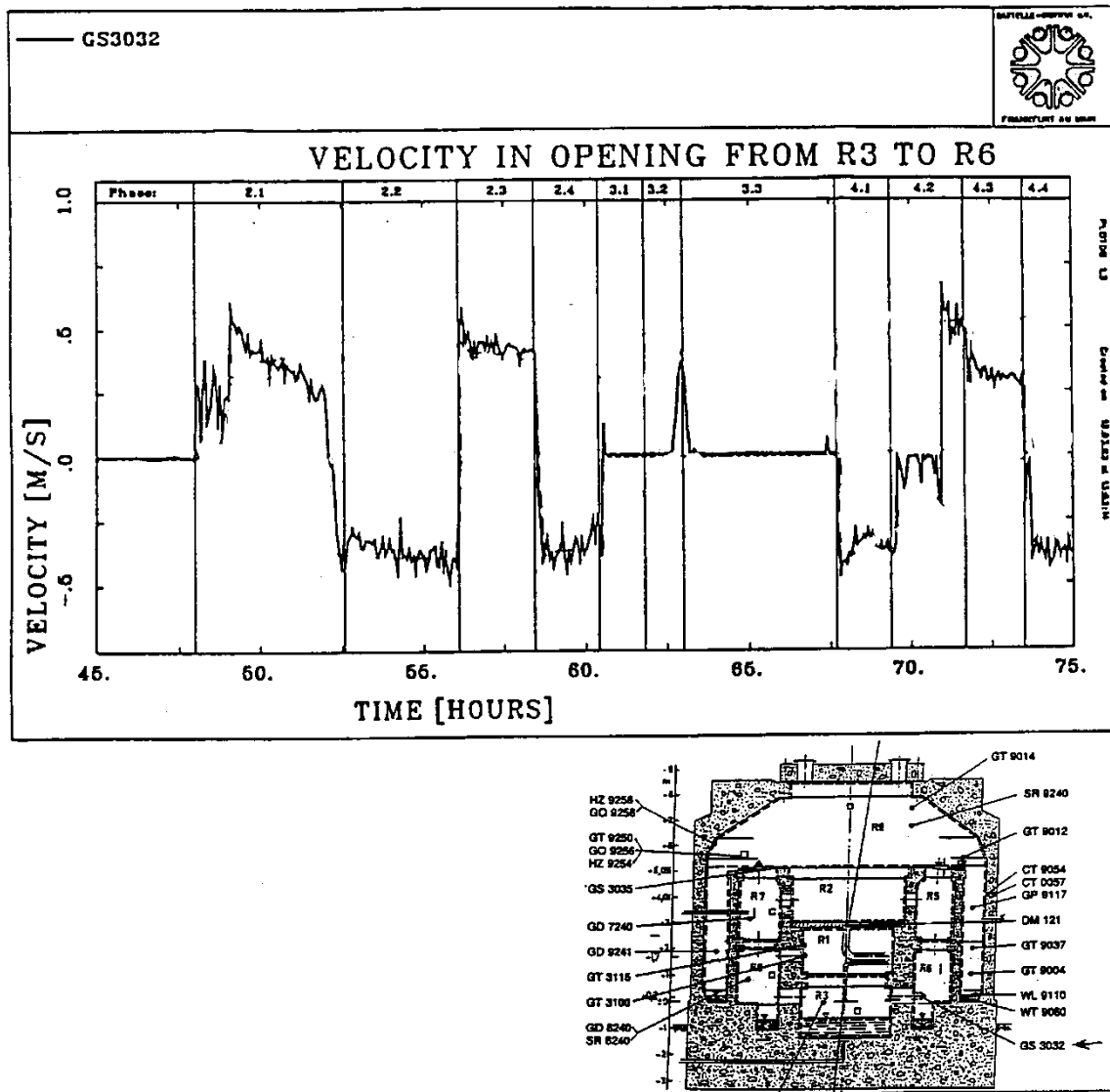


Figure 9.C-40. Velocities in Opening from Compartment R3 to Compartment R6

(reprinted from L. Wolf, M. Gavrilas, K. Mun, "Overview of experimental results for long-term, large-scale natural circulations in LWR-containments after large LOCAs," University of Maryland at College Park, Final Report for DOE – Project, Order Number: DE-AP07-96ID10765")

9.C.2.1.2 The Influence of Initial Temperature Distribution, Location of Hydrogen Injection, Duration of Injection, and Size of Vent Openings on the Hydrogen Distribution (BMC Tests 2, 4, 6, 12, and 20)

Another set of experimental results obtained in BMC is presented in Wolf et al., 1994. The temperature and hydrogen distribution are studied first for two compartments (Phase I) and later for the whole containment (Phase II). These experiments are not directly related to LOCA and MSLB situations, but contribute toward a better understanding of the influence of stratification and circulation phenomena on the hydrogen distribution inside containments. Although Wolf et al., 1994, compared the experimental results with the GOTHIC containment code, the comparisons are not discussed because of the non-prototypical nature of the experiment relative to the passive containment design.

The results of the experiments with only two compartments (upper and lower) are first presented by Langer et al., 1979. The total volume of the two compartments is 72 m³. The central compartments R1, R3 (from lower compartment) and R2 (upper – see Figure 9.C-25, Figure 9.C-26, and Figure 9.C-41) are used for the test. The opening size between the two compartments can be adjusted. Experiments are performed both with and without orifice (with an effective circular opening of 1 m²) between compartments R1 and R2 (see Figure 9.C-41). Uniform injection of hydrogen-nitrogen gas is provided by a flat circular plate with a diameter of 2.5 m. The upper containment is preheated with warm air for several days before the start of some experiments to provide stratification.

Tests 2, 4 and 6 (presented by Wolf et al., 1994) investigate the effects of the vertical hydrogen distribution. The measurement positions are located near the bottom (levels 1 m and 1.85 m) and at the top (levels 5 and 5.5 m) of the containment.

The experiments study the effects of

- The hydrogen injection rates
 - Test 2 has a longer time duration than test 6
- The locations of hydrogen injections
 - The hydrogen-nitrogen source is located above the pool surface in tests 2 and 6
 - The hydrogen-nitrogen source is at the 3.4 m elevation (above the mid-elevation of room R1) in test 4
- The vent flow area (between two compartments)
 - An orifice plate is present between R1 and R2 in tests 2 and 6
 - Test 4 is performed without the orifice plate

- The initial temperature distribution in the containment (homogeneous versus stratified)
 - A uniform temperature of 19°C is applied in test 2
 - The temperature is a uniform 22°C in test 4
 - A temperature stratification of 19°C in the R3 and R1 (lower rooms) and 35°C in the R2 (upper room) exist in test 6

The hydrogen pressure ratios at the top and bottom of the compartments are presented in Figure 9.C-42a, Figure 9.C-42b, Figure 9.C-42c for the second, fourth, and sixth experiments. A comparison of the hydrogen partial pressures shows the effects of the hydrogen release position (test 4) and the initially stratified temperature field (test 6) on the hydrogen concentration stratification.

The experimental findings presented in Wolf et al., 1994 are:

1. The hydrogen is homogeneously distributed through a compartment if the hydrogen source is at the floor and the feed rate is low, even if an orifice plate is installed (see the results for test 2, Figure 9.C-42a). Note that the feed rate in the second experiment is lower than in the fourth and sixth experiment. Also, hydrogen is released for 225 minutes in test 2 and for 125 minutes in test 4 and 6.
2. Vertical concentration stratification occurs if the source is located above the floor (see results for test 4, Figure 9.C-42b). For low kinetic energy, the diffusion process slowly equalizes concentrations.
3. If the openings between compartments are relatively small, the transport of hydrogen may be obstructed (see results for test 6, Figure 9.C-42b).
4. If an initial thermal stratification of air exists and an orifice is installed between the lower and upper compartments, the transport of the lighter H_2/N_2 gas mixture is prevented. The highest hydrogen concentrations exist in the lower, cooler part of the compartments, where circulation and mixing occurs (see results for test 6, Figure 9.C-42c). The initially stratified temperature field is provided by keeping the upper compartment R2 at a higher temperature (35°C) for several days before the start of the experiment.

Figure 9.C-42a (see results for test 2) shows that the buoyancy of the rising plume and the circulation resulting from entrainment into the introduced lighter H_2/N_2 gas mixture lead to a relatively homogenized atmosphere. Circulation and mixing are present in both the upper and lower compartments.

Test 4, with an elevated source and reasonably low kinetic energy (Fr is not reported for the tests), shows that there is no significant driving force for circulation below the break elevation. Stratification into two regions occurs, one below and one above the break elevation. The lower region is almost stagnant, while circulation and mixing is present in the upper region (see GOTHIC numerical simulation results by L. Wolf, H. Holzbauer, M. Schall, 1994).

In comparison, test 6, which includes an orifice between R1 and R2 and a stratified temperature field in the upper R2 compartment, shows an almost stagnant upper region. It also shows an increase in the concentration of the lighter H_2/N_2 gas mixture in the lower region (a result of the circulation and mixing in the lower regions R1 and R3). The lighter gas mixture is not able to penetrate into the upper stratified layers due to the presence of the narrow orifice. The circulation cell formed by the gas mixture injection into the lower compartments does not communicate with the stratified layers in the upper compartment (see also GOTHIC numerical simulation results by L. Wolf, H. Holzbauer, M. Schall, 1994).

Application to the AP600 and AP1000

These tests are not relevant to the passive containment design. The cold dome prevents the stratification that results from higher temperatures of either the vertical walls at the high elevations or the ceiling. In the BMC case, the higher temperatures of the wall surfaces are maintained for a long period of time due to the heat accumulated in the concrete walls (which are heated for several days before the start of the experiment). The passive containment shell is made of steel. Natural convection at the outer surface of the containment walls keeps their temperature low, so that a highly stratified initial temperature field is not possible. Even if initial stratification exists, the application of water on the outer containment surface decreases wall temperatures and causes circulation inside the containment.

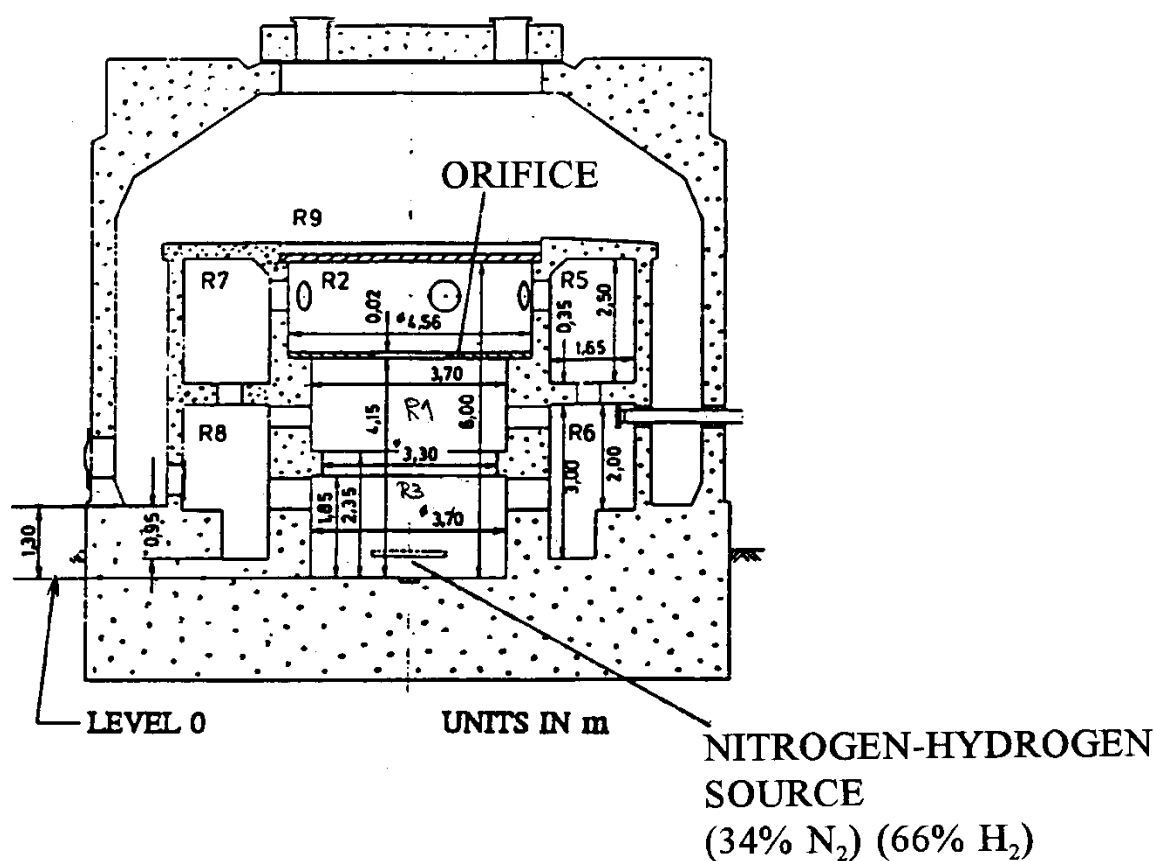
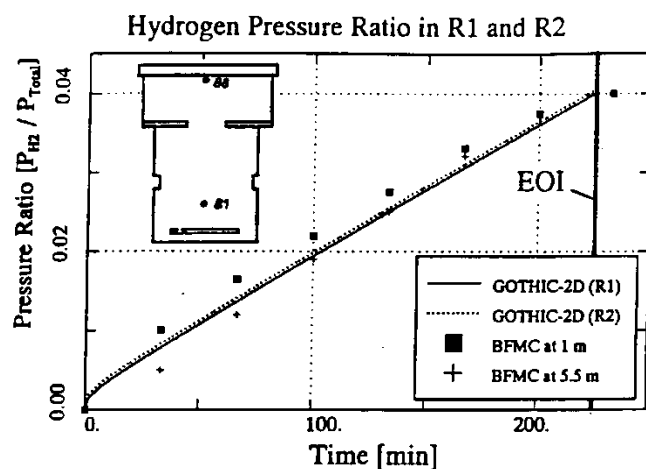


Figure 9.C-41. Vertical Cut through BMC with Orifice in Between R2 and R1

(reprinted with permission from authors from L. Wolf, H. Holzbauer, M. Schall, "Comparison between multi-dimensional and lumped-parameter GOETHIC-containment analyses with data," Proceedings, Volume II – Thermohydraulics of Containment and Severe Accidents, May 30th – June 2nd, 1994, pp. 321-330.)

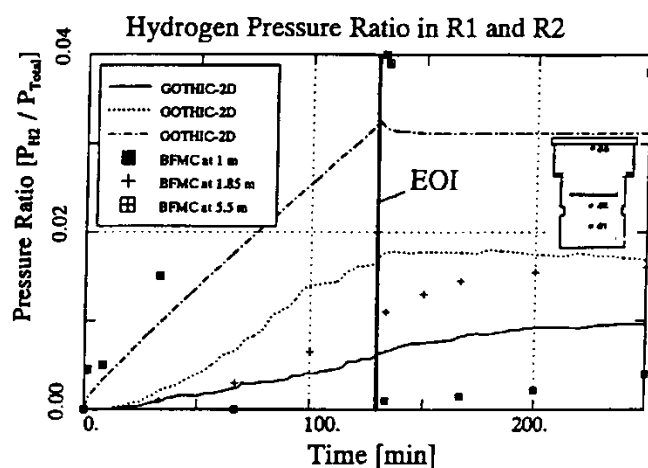


Battelle Test No. 2

EOI - End of Injection

Figure 9.C-42a. BMC Test No. 2: Comparison Between Experimental Data and 2-d GOTHIC Computations for Hydrogen Concentrations

(reprinted with permission from authors from L. Wolf, H. Holzbauer, M. Schall, "Comparison between multi-dimensional and lumped-parameter GOTHIC-containment analyses with data," Proceedings, Volume II – Thermohydraulics of Containment and Severe Accidents, May 30th – June 2nd, 1994, pp. 321-330.)

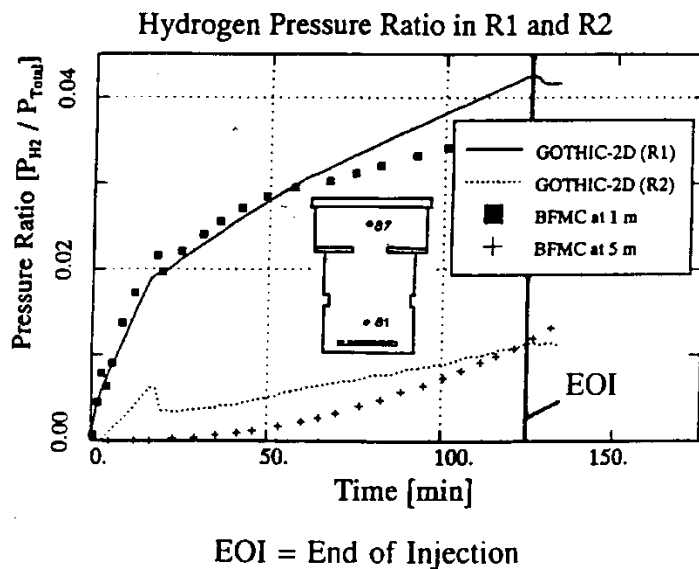


Battelle Test No. 4

EOI - End of Injection

Figure 9.C-42b. DMC Test No. 4: Comparison Between Experimental Data and 2-d GOTHIC Computations for Hydrogen Concentrations

(reprinted with permission from authors from L. Wolf, H. Holzbauer, M. Schall, "Comparison between multi-dimensional and lumped-parameter GOTHIC-containment analyses with data," Proceedings, Volume II – Thermohydraulics of Containment and Severe Accidents, May 30th – June 2nd, 1994, pp. 321-330.)



Battelle Test No. 6

Figure 9.C-42c. DMC Test No. 6: Comparison Between Experimental Data and 2-d GOTHIC Computations for Hydrogen Concentrations

(reprinted with permission from authors from L. Wolf, H. Holzbauer, M. Schall, "Comparison between multi-dimensional and lumped-parameter GOTHIC-containment analyses with data," Proceedings, Volume II – Thermohydraulics of Containment and Severe Accidents, May 30th – June 2nd, 1994, pp. 321-330.)

In the second phase (Langer and Baukal, 1982), the full model containment is used for experiments. The effects of: (1) the initial temperatures and humidities, (2) the geometry of the containment, and (3) the location and rate of hydrogen release are investigated.

The results of tests 12 and 20 are presented in Wolf et al., 1994 and are compared with the results of three GOTHIC modeling strategies. Tests 12 and 20 are performed with six compartments (R1-2, R5-8, see Figure 9.C-25 and Figure 9.C-26). The hydrogen-nitrogen mixture is injected into rooms R2 and R6 in tests no.12 and 20, respectively.

Test no. 12 is performed with a uniform initial temperature. It results in a homogenized hydrogen distribution in the containment (see Figure 9.C-43). The stratified initial temperature distribution in test 20 results in higher hydrogen distribution in the lower level compartments (R1, R6 and R8 – see Figure 9.C-44a, Figure 9.C-44b, Figure 9.C-44c). An explanation for this unexpected result is that the circulation cell formed by the injection of the lighter gas mixture is not able to penetrate upper stratified layers at the beginning of the experiment. This is similar to test 6, which includes an orifice and stratified initial temperature field in the upper compartment. After three hours, there is a tendency toward decreased gradients in the concentration field, especially between R1 and R2 compartments. This indicates that global circulation affects the upper stratified layers.

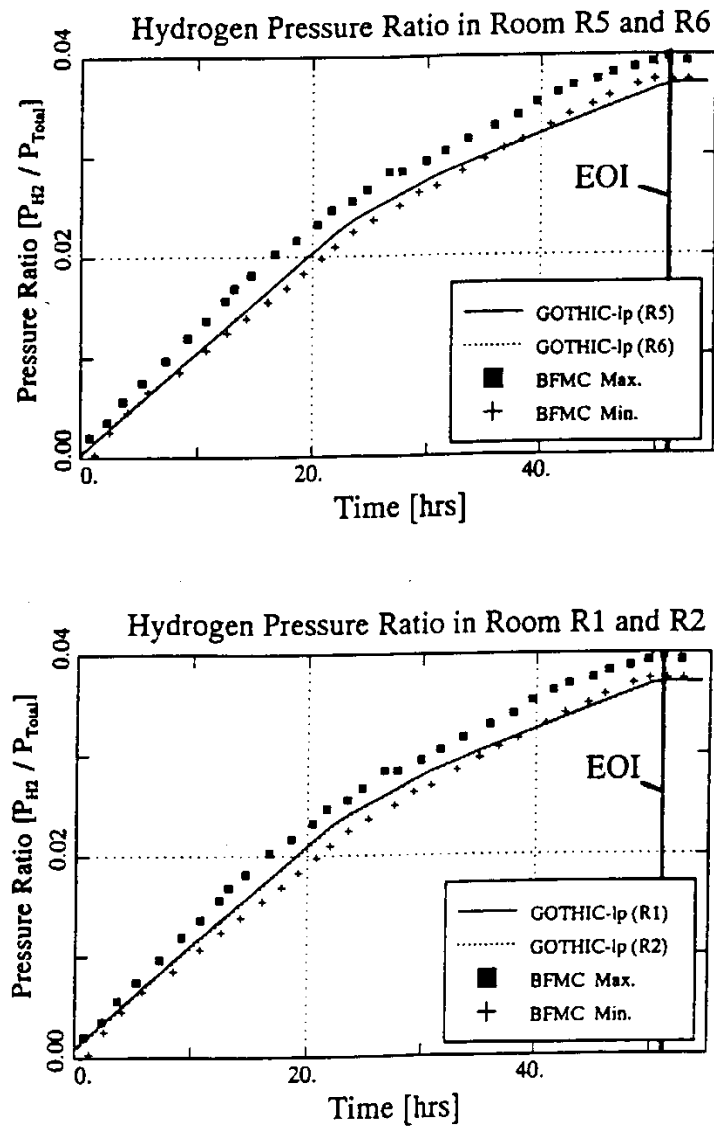
A summary of the experimental results is:

1. If the temperature field was uniform (test 12), hydrogen was homogeneously distributed inside the containments.
2. For an initially thermally stratified field (test 20), higher hydrogen concentrations are present in the lower (cooler) compartments at the beginning of the experiment.

Both groups of experiments indicate that good air circulation inside the containment (in fact a uniform temperature field) is crucial for homogeneous hydrogen distribution. Note that in the first group of tests, the stratification is obtained by preheating the upper room with warm air for several days before the start of the experiments.

A comparison between this experimental data and the numerical results obtained with GOTHIC (with lumped-parameter and multi-dimensional analyses) is presented in Wolf et. al, 1994.

Battelle Test No. 12



EOI = End of Injection

Figure 9.C-43. BMC Test No. 12: Comparison between Experimental Data and GOTHIC-lp Computations for Hydrogen Concentrations

(reprinted with permission from authors from L. Wolf, H. Holzbauer, M. Schall, "Comparison between multi-dimensional and lumped-parameter GOTHIC-containment analyses with data," Proceedings, Volume II – Thermohydraulics of Containment and Severe Accidents, May 30th – June 2nd, 1994, pp. 321-330.)

Battelle Test No. 20

Hydrogen Pressure Ratio in Room R1 and R2

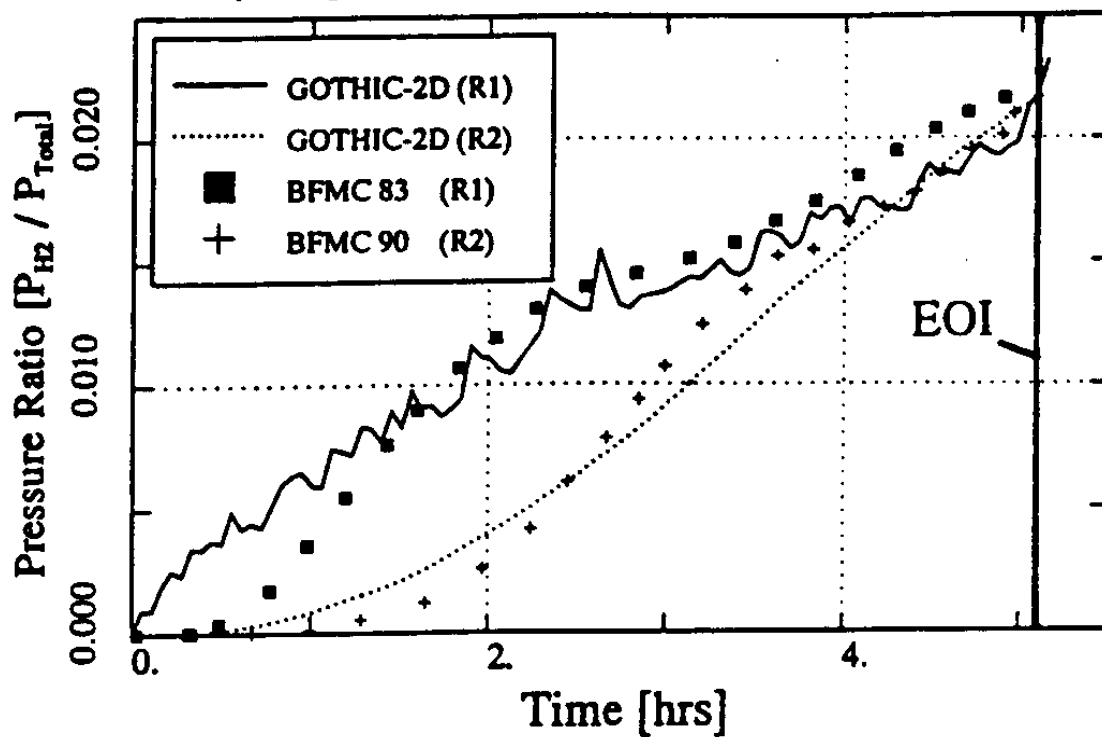


Figure 9.C-44a. BMC Test No. 20: Comparison Between Experimental Data and 2-d GOTHIC Computations for Hydrogen Concentrations

(reprinted with permission from authors from L. Wolf, H. Holzbauer, M. Schall, "Comparison between multi-dimensional and lumped-parameter GOTHIC-containment analyses with data," Proceedings, Volume II – Thermohydraulics of Containment and Severe Accidents, May 30th – June 2nd, 1994, pp. 321-330.)

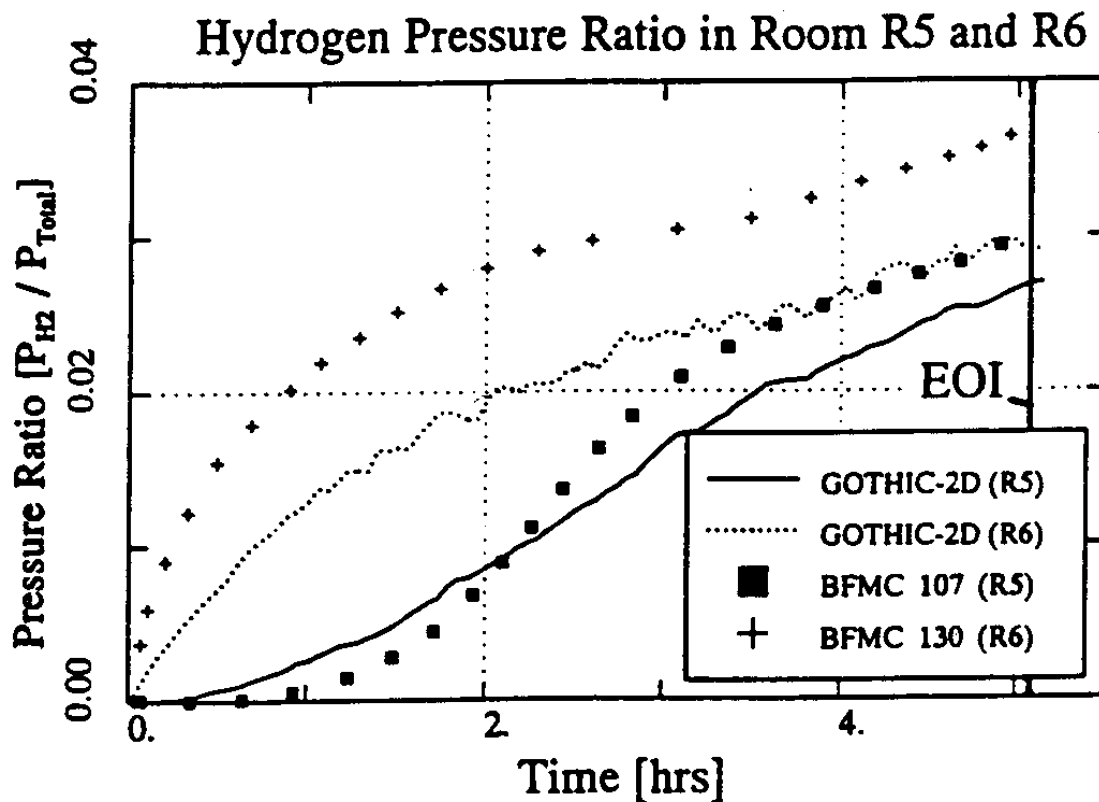


Figure 9.C-44b. BMC Test No. 20: Comparison Between Experimental Data and 2-d GOTHIC Computations for Hydrogen Concentrations

(reprinted with permission from authors from L. Wolf, H. Holzbauer, M. Schall, "Comparison between multi-dimensional and lumped-parameter GOTHIC-containment analyses with data," Proceedings, Volume II – Thermohydraulics of Containment and Severe Accidents, May 30th – June 2nd, 1994, pp. 321-330.

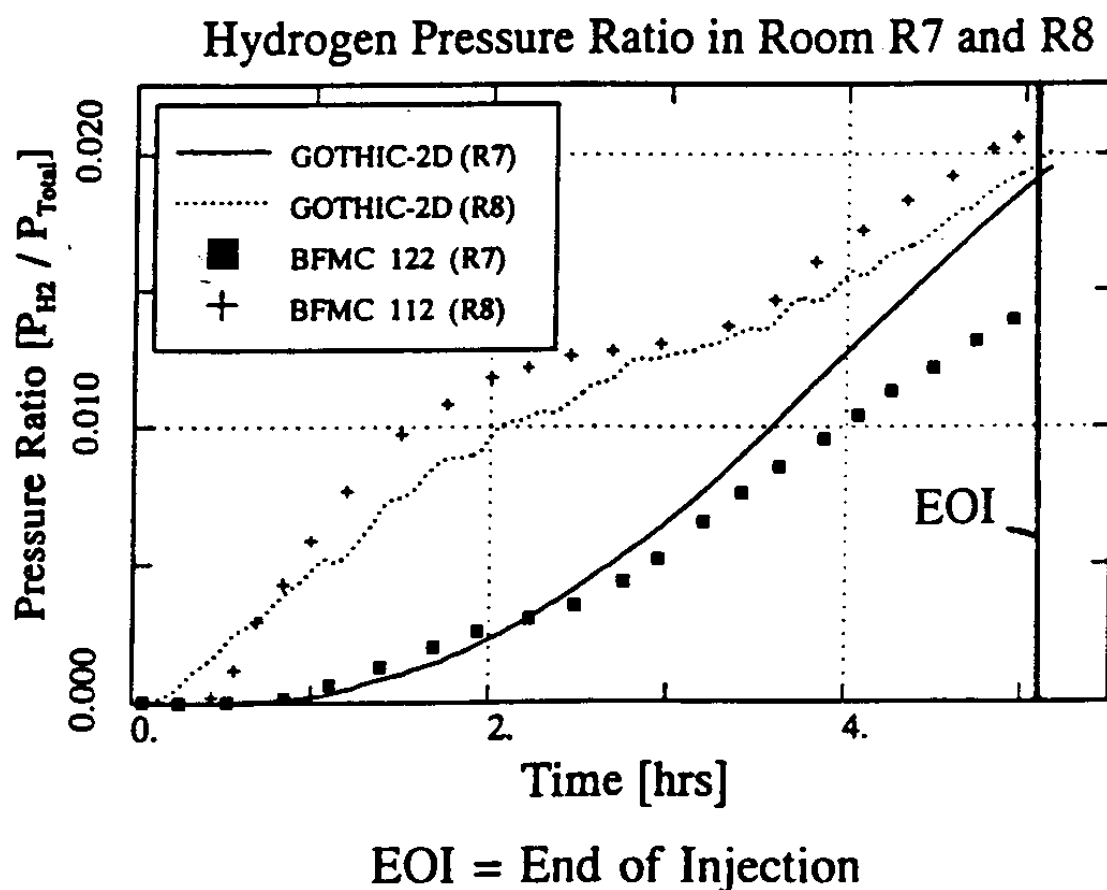


Figure 9.C-44c. BMC Test No. 20: Comparison Between Experimental Data and 2-d GOTHIC Computations for Hydrogen Concentrations

9.C.2.1.3 Effects of Sump Heatup on Global Natural Circulation (Experiments RX1 - RX5)

The third set of experiments performed in the BMC (Fischer et al., 1994 and Petersen et al., 1994) examine the effect of sump heatup on global natural circulation inside the containment. The starting and transient behavior of natural circulation for small temperature differences, the influence of natural circulation on mixing of hydrogen released during accident conditions, and the effects of stratification on the natural convection formation are also studied.

A total of five experiments are performed (RX1 to RX5) at atmospheric pressure. Temperatures are recorded in the sump, in the containment atmosphere, and in the concrete structures. The relative humidity, containment pressure, liquid sump level, velocities (in the vents), and hydrogen concentration are also measured.

The objective of long-term experiments is to establish at what sump temperature global circulation exists. During these experiments, the containment atmosphere, structure, and sump have nearly identical temperatures. Circulation effects inside the containment are already present with a sump temperature as low as 25°C. Experiments RX2 (without hydrogen injection) and RX4 (with multiple hydrogen injections) are performed as long-term tests. The respective initial and boundary conditions for all experiments are given in Table 9.C-4.

Results are provided for only the RX4 experiment, since the hydrogen distribution is available for this test. A summary of the results for the RX4 experiment, with the cold containment and multiple hydrogen injections, is presented in Wolf et al., 1996. The perspective view and cross-sections of the BMC containment, illustrating the compartment numbers and the location of the hydrogen injection, are presented in Figure 9.C-45 and Figure 9.C-46. The instrumentation plan for the RX4 test is specified in Figure 9.C-47.

At the beginning of the experiment, the temperatures of the structure range from 20-26°C. The sump temperature is 20°C (see Figure 9.C-48). Several consecutive characteristic periods evolve during the experiment. The sump heat up is divided into three periods:

1. 0 to 1:48 hr – the sump is heated to 50°C
2. 2:43 to 3:39 hr – continuation of sump heating to 60°C
3. 3:34 to 4:52 hr – continued sump heating to maintain the temperature at 60°C until the end of experiment (5 hr)

Three hydrogen injections occur:

1. 1:11-1:24 hr, 236 g of hydrogen is released
2. 2:11-2:23 hr, 215 g of hydrogen is released
3. 4:06-4:33 hr, 319 g of hydrogen is released

At the beginning of the sump heatup, the anemometers register velocities between 0.2-0.3 m/s (for sump temperatures 24-27°C), while at the end of the experiment, velocities are 0.6-0.8 m/s (see Figure 9.C-49). At the end, the temperature of the dome is 30°C (see Figure 9.C-50). Shaded areas in Figure 9.C-49 and Figure 9.C-50 represent periods of hydrogen injection. Velocities increase during periods of hydrogen injection.

Sump and atmosphere temperatures are presented in Figure 9.C-48, Figure 9.C-50, and Figure 9.C-51. Temperature differences in the area of the center compartment and dome are not greater than 2°C (Figure 9.C-50). The temperature difference in the external annulus is smaller than 3°C (Figure 9.C-51), indicating the presence of natural circulation effects.

Due to the natural circulation, the hydrogen distribution is almost uniform in the whole containment, see (Figure 9.C-52 and Figure 9.C-53). After two hours, the relative humidity of the whole containment atmosphere is 100 percent (see Figure 9.C-54). Even low natural circulation flows provide complete mixing of the hydrogen and steam (evaporated from sump). The heated sump provides sufficient buoyancy force for natural circulation flow.

Table 9.C-4. Test Matrix of Battelle Sump Heatup Experiments

Test No.	Containment-Atmosphere			Structure-Temperature [°C]	Sump-Temperature [°C]	H ₂ -Mass [g]
	Containment Media	Initial Temperature [°C]	Total Pressure [bar]			
RX1	air	23.5 – 28.5	1.011	24 – 26	1. ≈ 40 2. ≈ 50 3 ≈ 55 4. ≈ 60	-----
RX2	air	22 – 28.5	1.009	24.5 – 28	1. ≈ 40 2. ≈ 50 3. ≈ 60	-----
RX3	air + steam	48 – 58.5	1.008	42 – 61	60 - 100	-----
RX4	air + H ₂	24 – 27	1.014	22.5 – 26.5	1. ≈ 48 2. ≈ 60	1. 236 2. +215 3. +319
RX5	air + steam + H ₂	55 – 69	1.001	39 – 64	1. 62 – 49 2. 63 - 58	1. 371 2. +390 3. +406

(reprinted from L. Wolf, M. Gavrilas, K. Mun, “Overview of experimental results for long-term, large-scale natural circulations in LWR-containments after large LOCAS,” University of Maryland at College Park, Final Report for DOE – Project, Order Number: DE-AP07-96ID10765”)

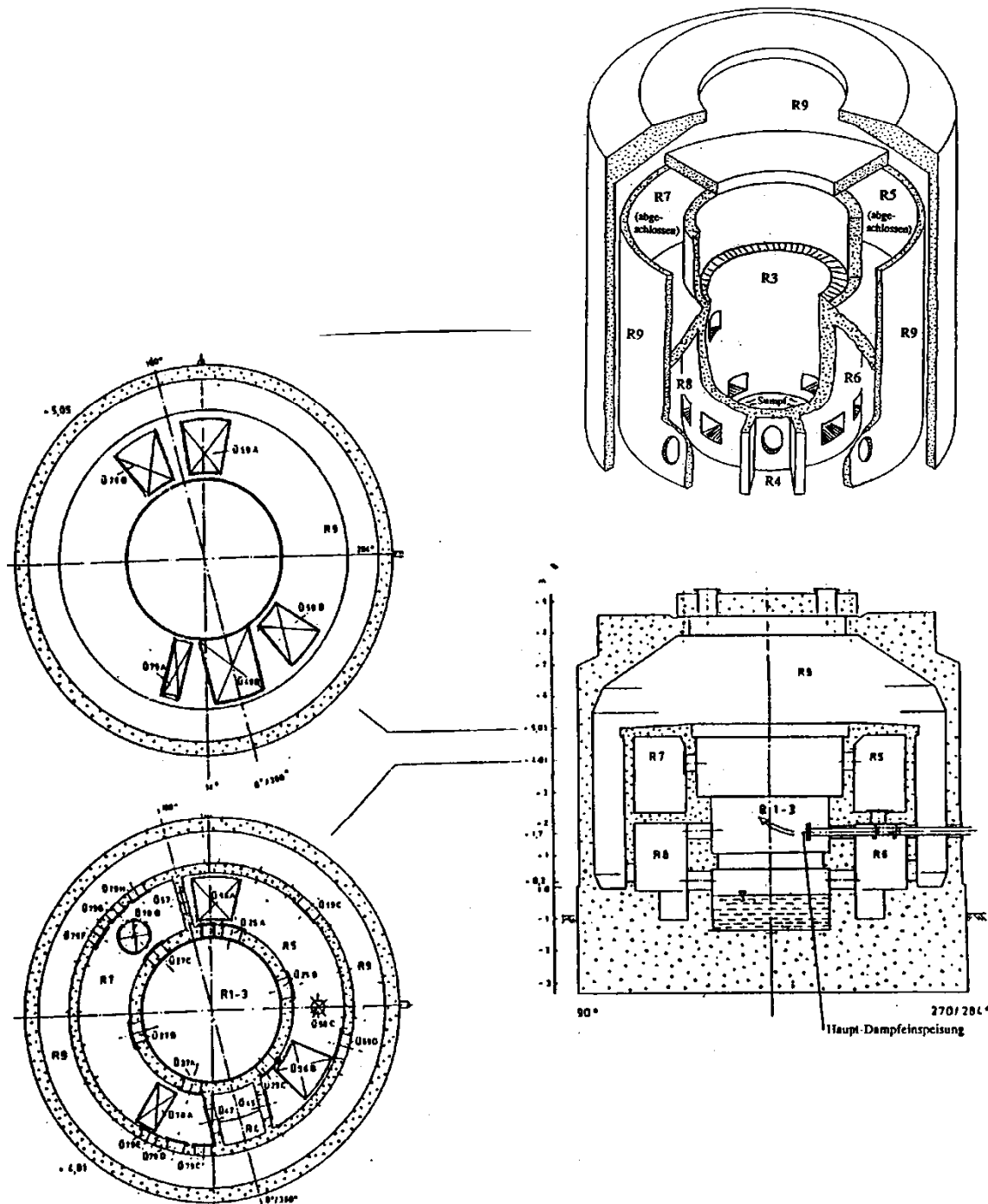


Figure 9.C-45. Perspective View, Vertical and Upper Horizontal Cross-Sections through BMC with Main Steam Feedline

(reprinted from L. Wolf, M. Gavrilis, K. Mum, "Overview of experimental results for long-term, large-scale natural circulations in LWR-containments after large LOCAs," University of Maryland at College Park, Final Report for DOE – Project, Order Number: DE-AP07-96ID10765")

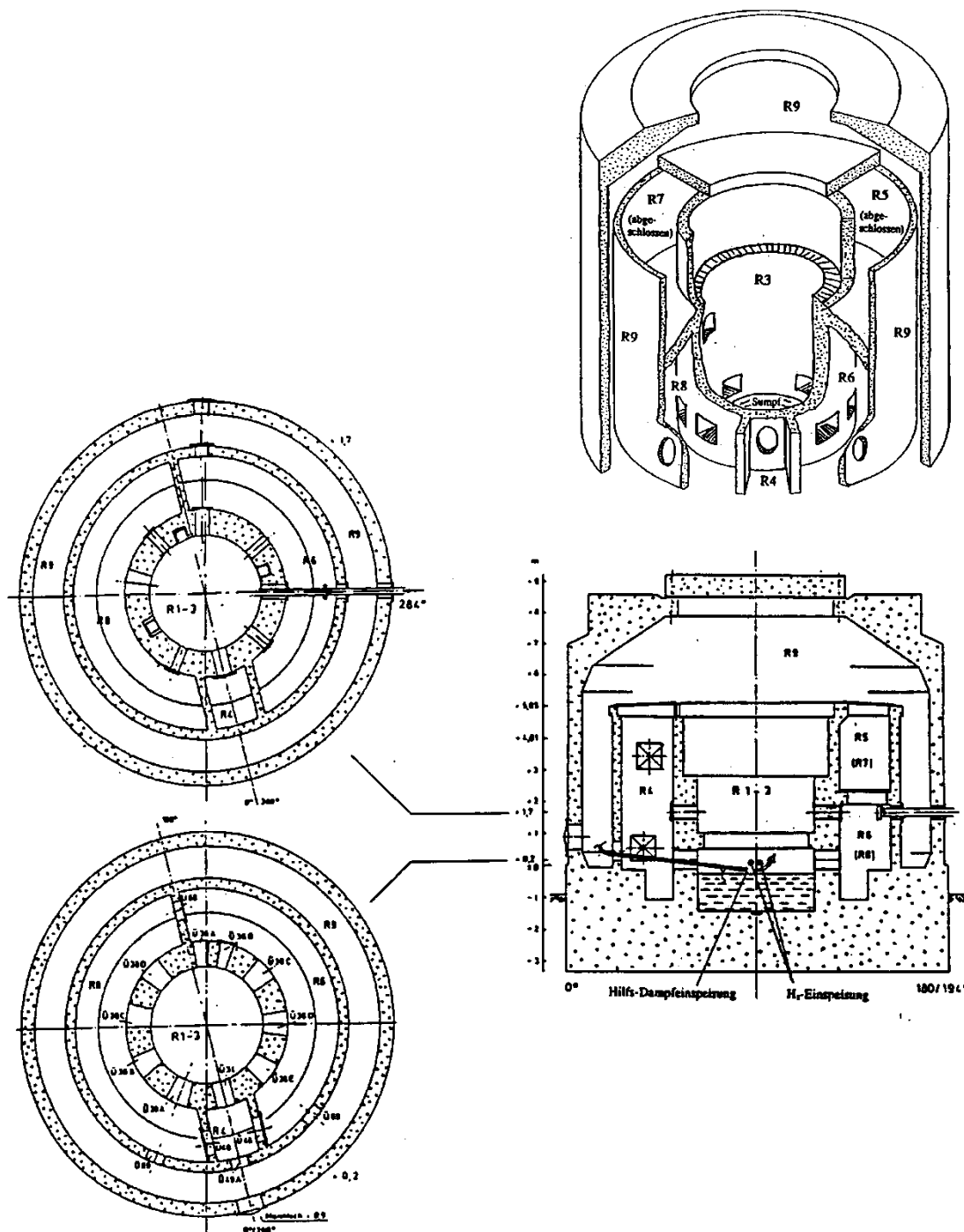


Figure 9.C-46. Perspective View, Vertical and Upper Horizontal Cross-Sections through BMC with Auxiliary Steam Feedline

(reprinted from L. Wolf, M. Gavriles, K. Mum, "Overview of experimental results for long-term, large-scale natural circulations in LWR-containments after large LOCAs," University of Maryland at College Park, Final Report for DOE – Project, Order Number: DE-AP07-96ID10765")

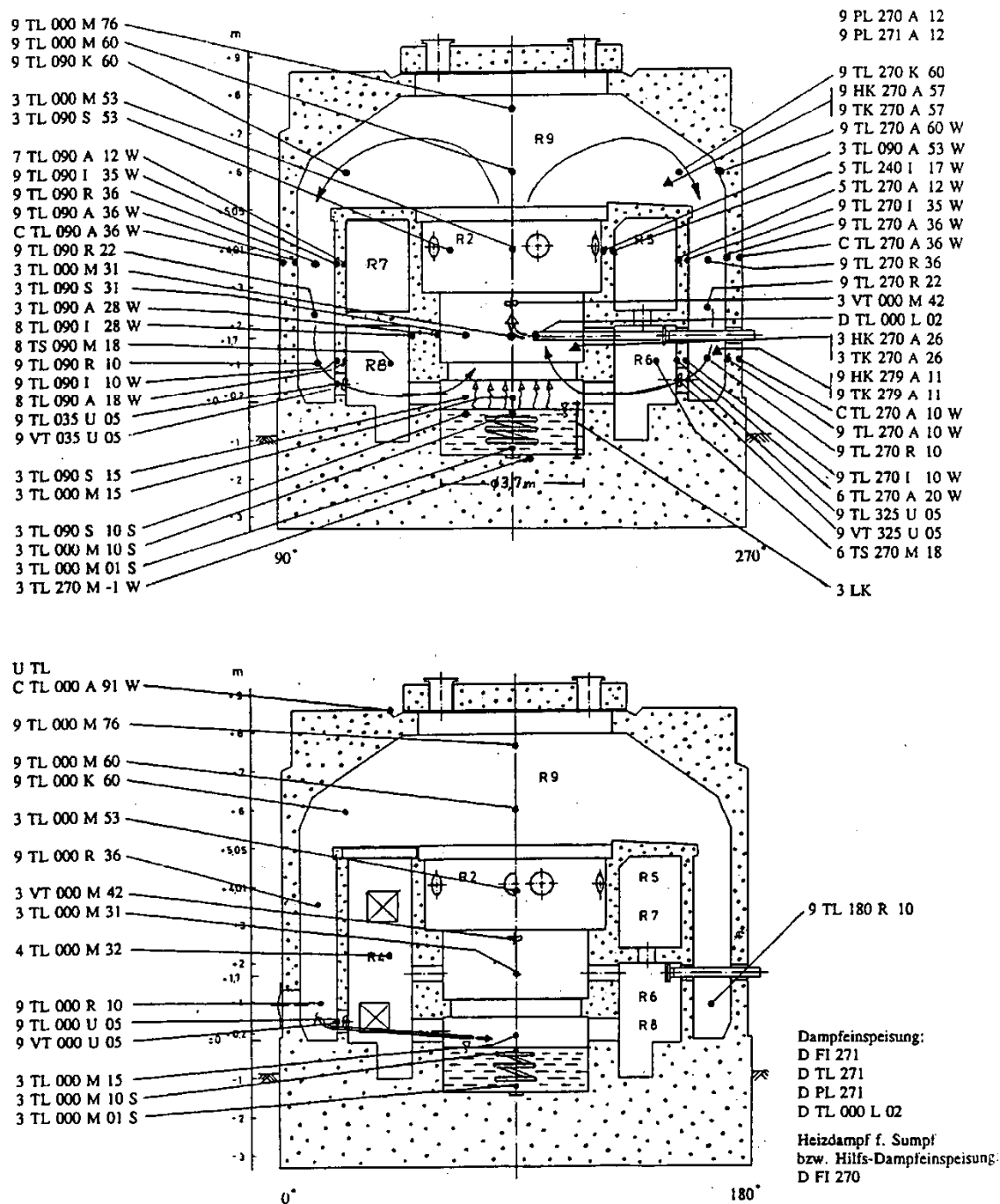


Figure 9.C-47. Instrumentation Plan for BMC – Sump Heatup Test RX4

(reprinted from L. Wolf, M. Gavriles, K. Mum, "Overview of experimental results for long-term, large-scale natural circulations in LWR-containments after large LOCAs," University of Maryland at College Park, Final Report for DOE – Project, Order Number: DE-AP07-96ID10765")

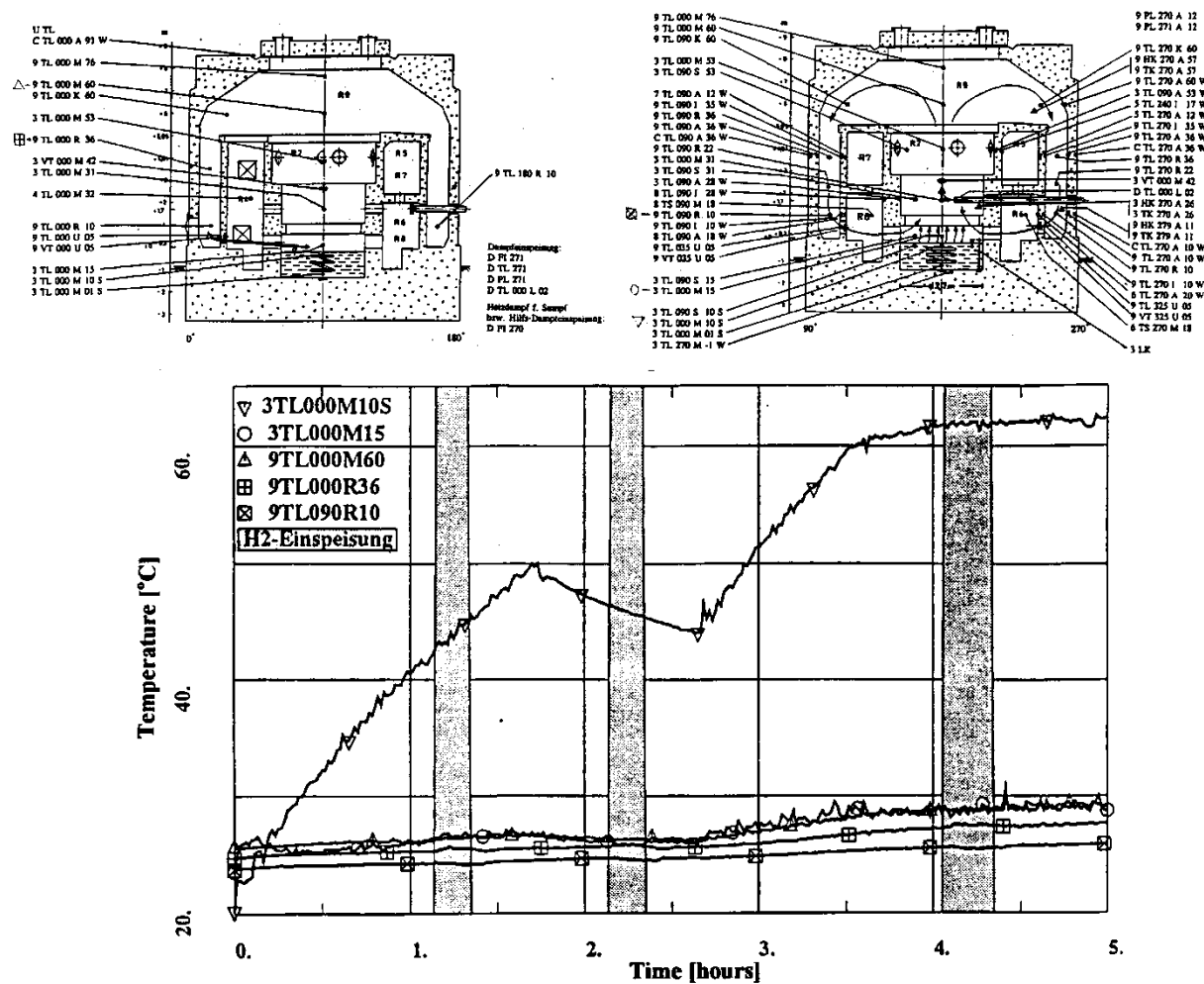


Figure 9.C-48. Battelle-Experiment RX4: Sump and Atmospheric Temperatures

(reprinted from L. Wolf, M. Gavriles, K. Mum, "Overview of experimental results for long-term, large-scale natural circulations in LWR-containments after large LOCAs," University of Maryland at College Park, Final Report for DOE – Project, Order Number: DE-AP07-96ID10765")

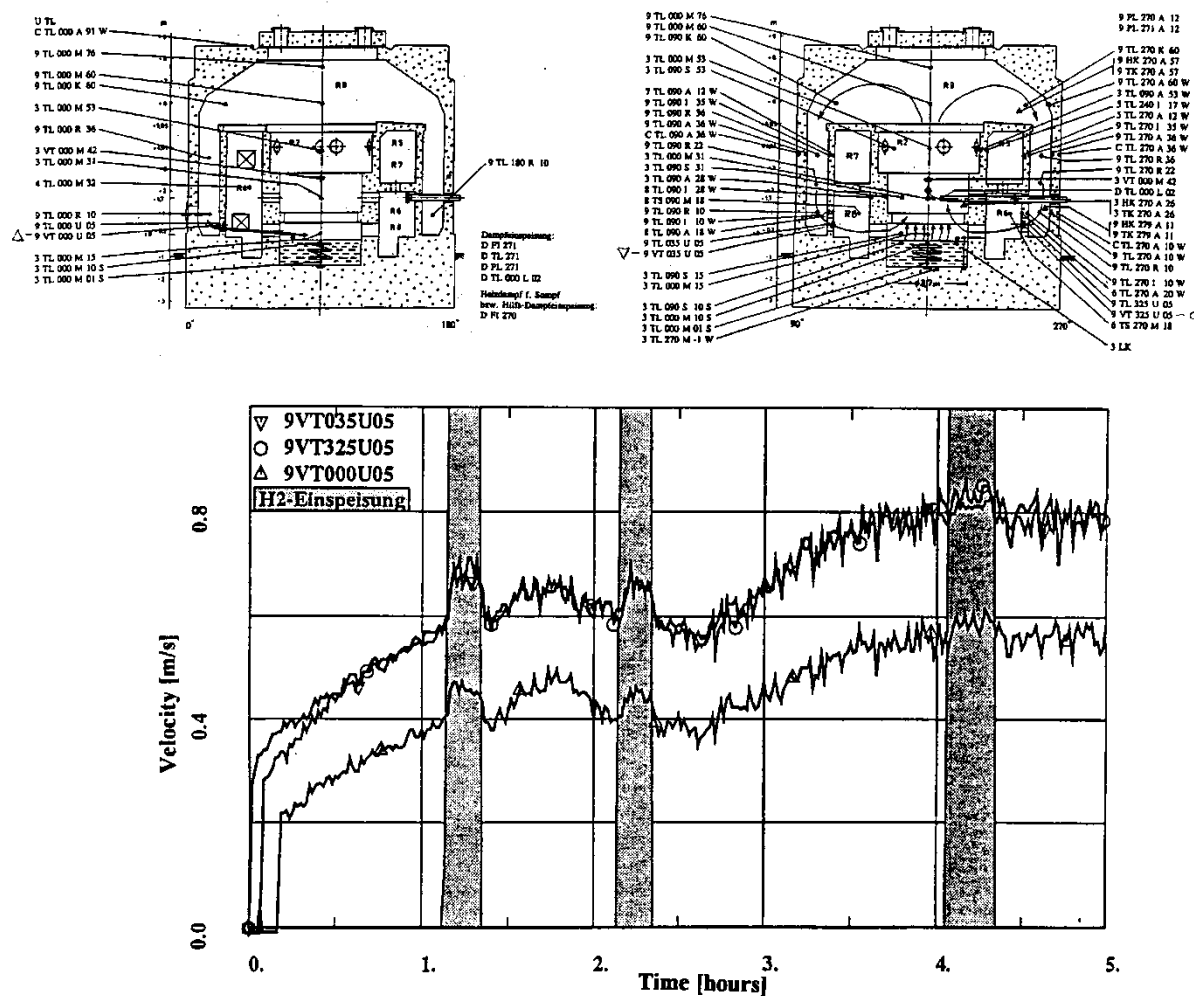


Figure 9.C-49. Battelle-Experiment RX4: Velocities in Side Vents

(reprinted from L. Wolf, M. Gavriles, K. Mum, "Overview of experimental results for long-term, large-scale natural circulations in LWR-containments after large LOCAs," University of Maryland at College Park, Final Report for DOE – Project, Order Number: DE-AP07-96ID10765")

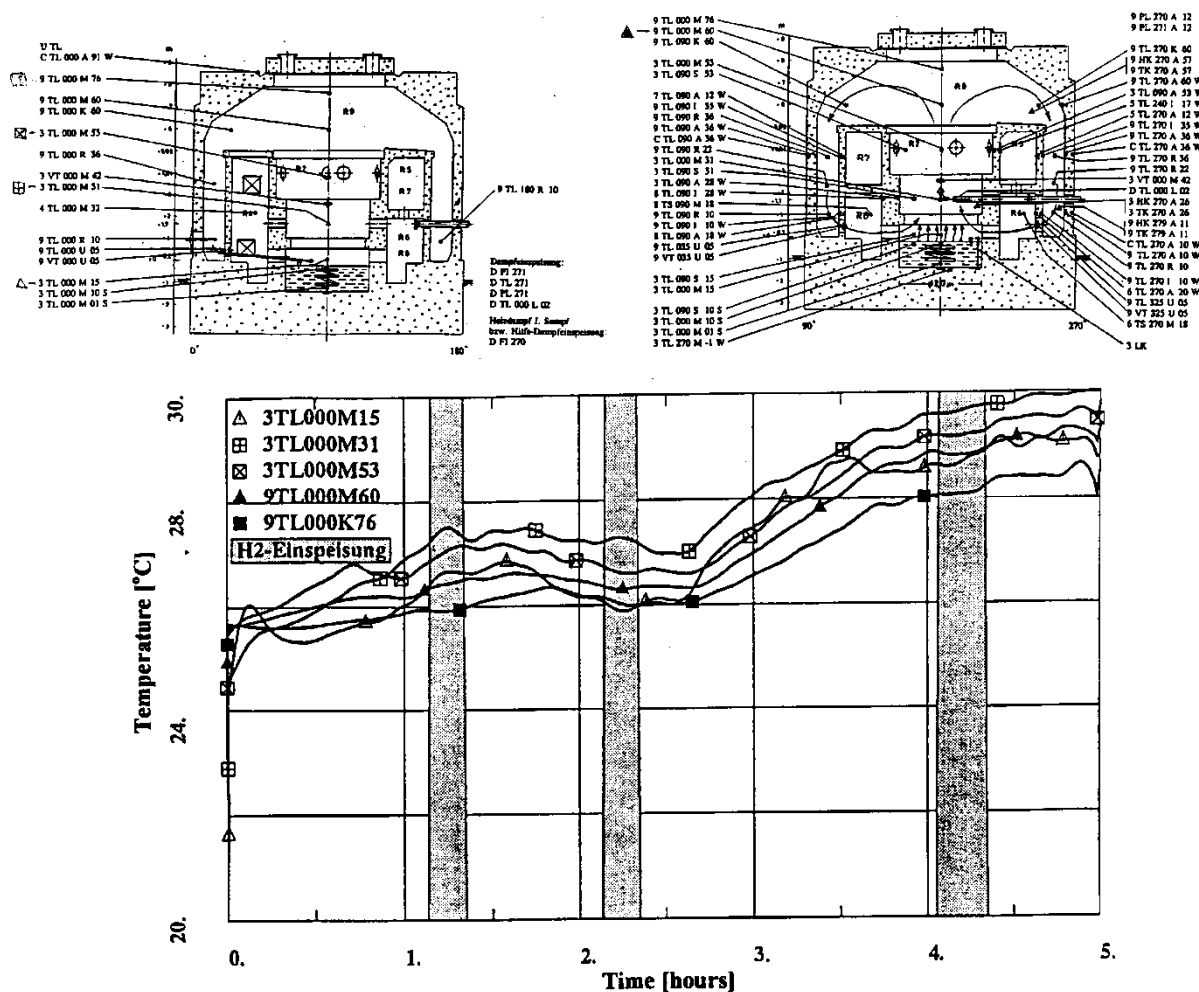


Figure 9.C-50. Battelle-Experiment RX4: Temperatures in Center Compartment and Dome

(reprinted from L. Wolf, M. Gavriles, K. Mum, "Overview of experimental results for long-term, large-scale natural circulations in LWR-containments after large LOCAs," University of Maryland at College Park, Final Report for DOE – Project, Order Number: DE-AP07-96ID10765")

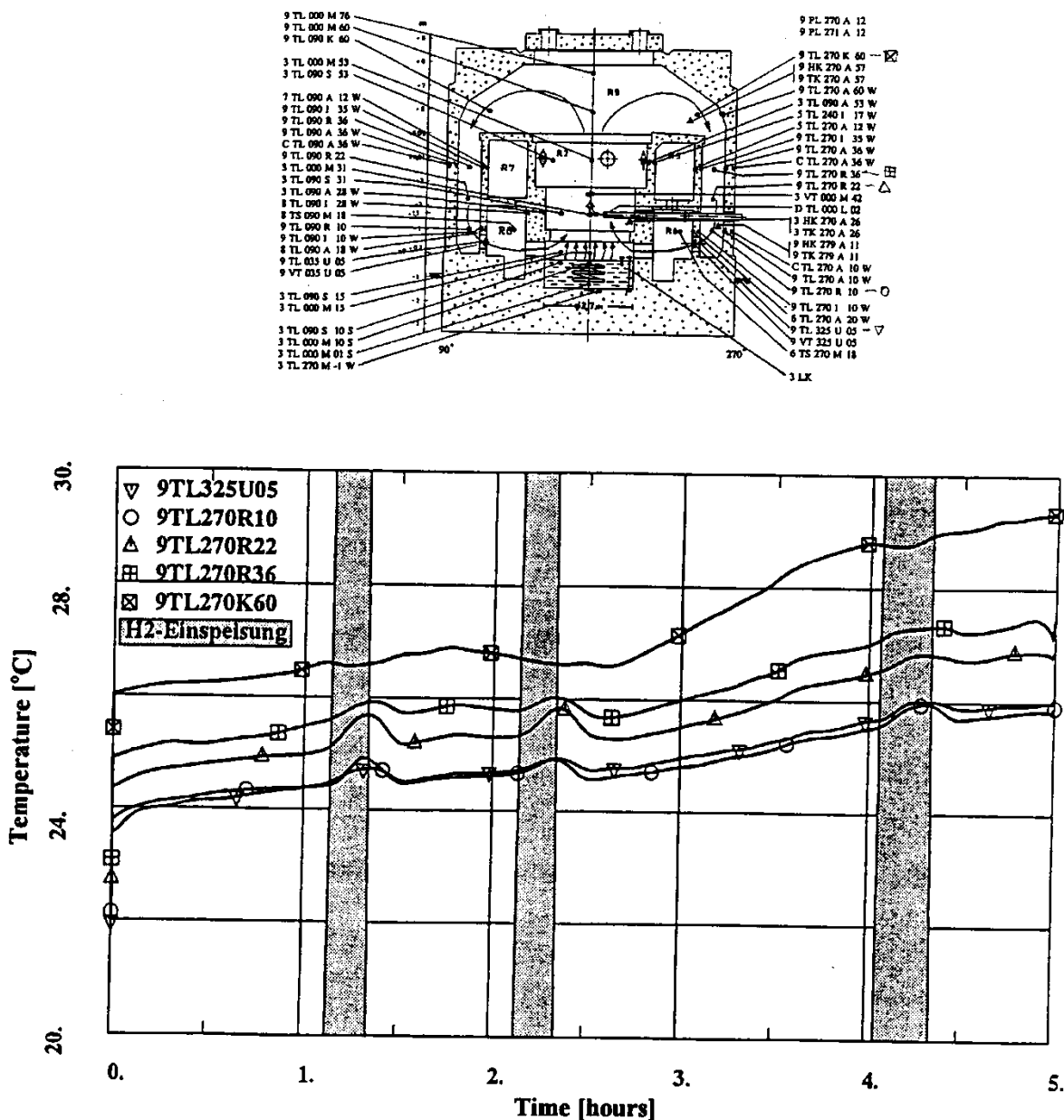


Figure 9.C-51. Battelle-Experiment RX4: Temperatures in External Annulus

(reprinted from L. Wolf, M. Gavriles, K. Mum, "Overview of experimental results for long-term, large-scale natural circulations in LWR-containments after large LOCAs," University of Maryland at College Park, Final Report for DOE – Project, Order Number: DE-AP07-96ID10765")

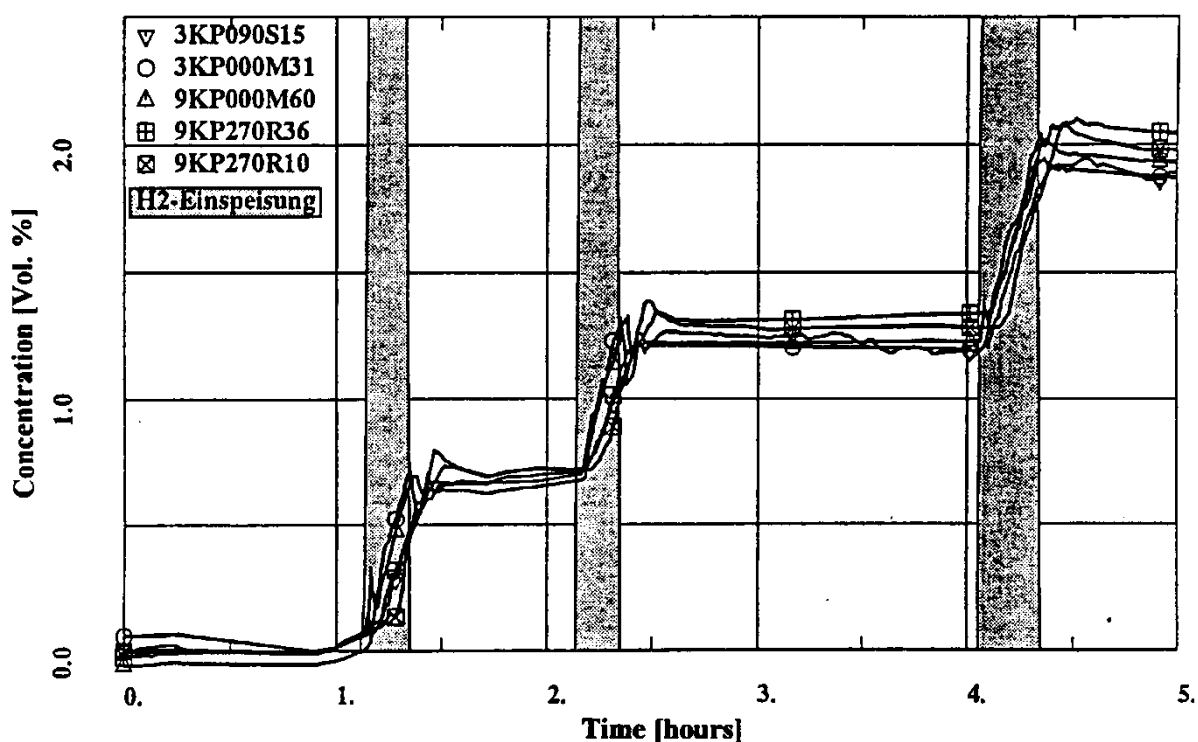


Figure 9.C-52. Battelle-Experiment RX4: Hydrogen Concentration Along Circulation Path

(reprinted from L. Wolf, M. Gavriles, K. Mum, "Overview of experimental results for long-term, large-scale natural circulations in LWR-containments after large LOCAs," University of Maryland at College Park, Final Report for DOE – Project, Order Number: DE-AP07-96ID10765")

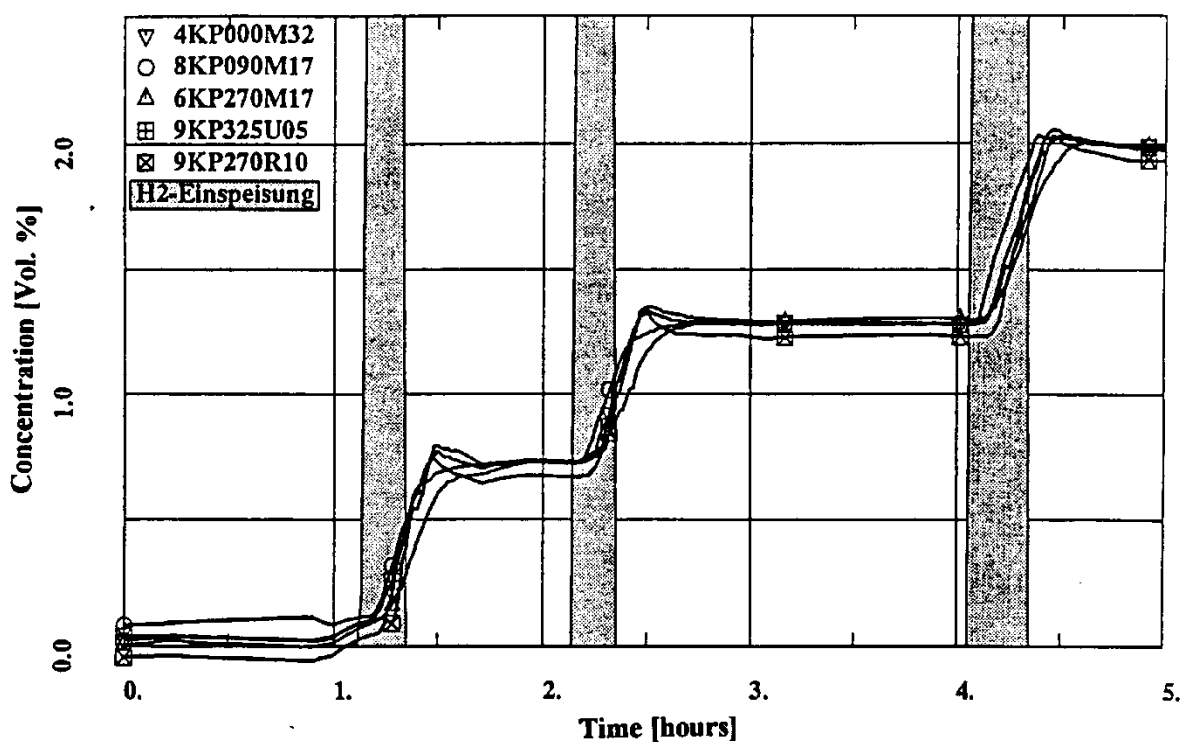


Figure 9.C-53. Battelle-Experiment RX4: Hydrogen Concentrations in Intermediate Subcompartments

(reprinted from L. Wolf, M. Gavriles, K. Mum, "Overview of experimental results for long-term, large-scale natural circulations in LWR-containments after large LOCAs," University of Maryland at College Park, Final Report for DOE – Project, Order Number: DE-AP07-96ID10765")

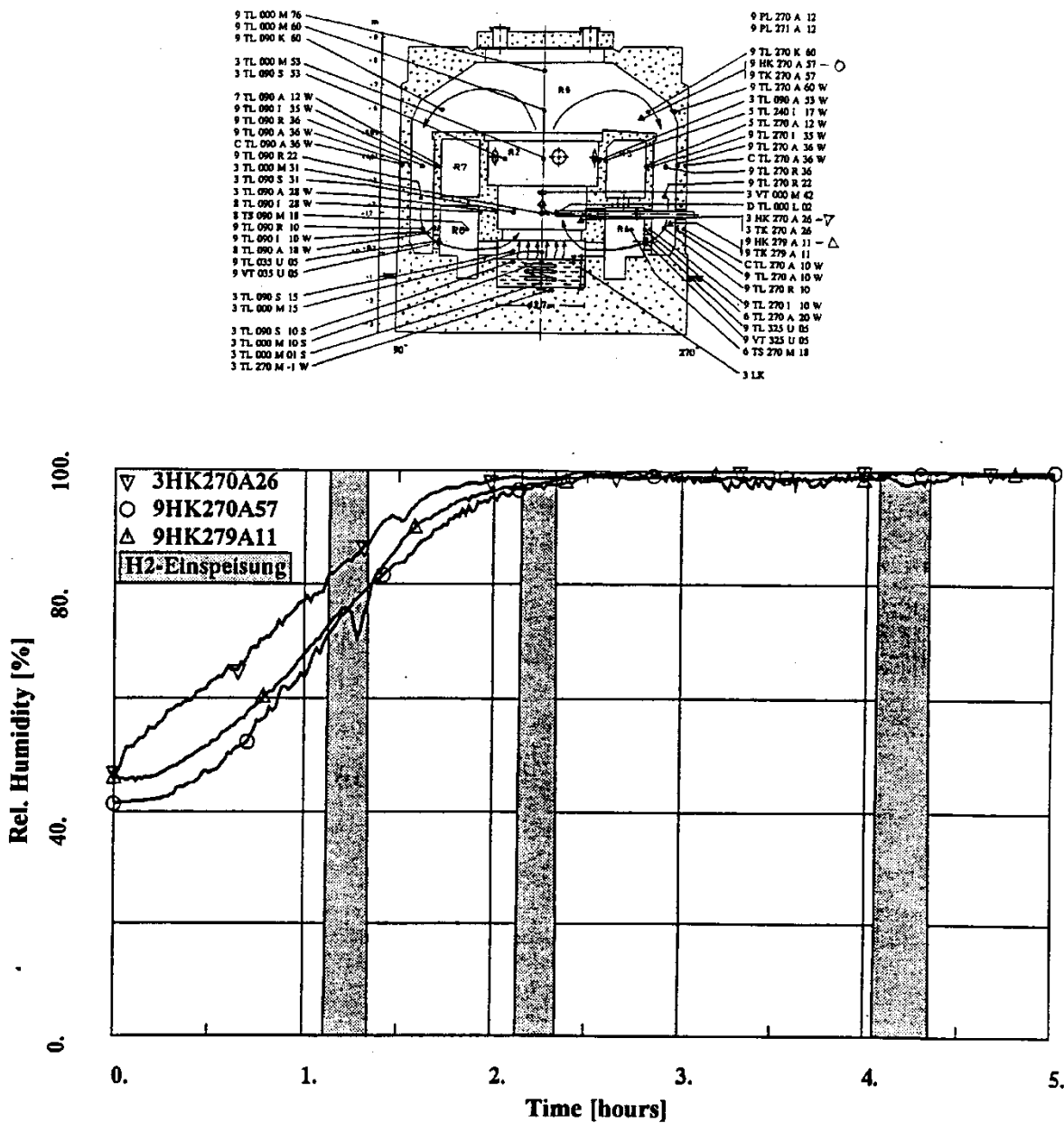


Figure 9.C-54. Battelle-Experiment RX4: Relative Humidity in the Containment Atmosphere

(reprinted from L. Wolf, M. Gavriles, K. Mum, "Overview of experimental results for long-term, large-scale natural circulations in LWR-containments after large LOCAs," University of Maryland at College Park, Final Report for DOE – Project, Order Number: DE-AP07-96ID10765")

9.C.2.1.4 References

1. Fischer, K., Kanzleiter, T., Schall, M., Wolf, L., 1989
“CEC Thermal-Hydraulic Benchmark Exercise on FIPLOC Verification Experiment F2 in BMC-Long-Term Heatup Phase – Specification for Phase I, Battelle-Institut e.V., Frankfurt/Main,” Germany, Sept. 1989
2. Fischer, K., T., Schall, M., Wolf, L., 1991
“CEC Thermal-Hydraulic Benchmark Exercise on FIPLOC Verification Experiment F2 in BMC-Long-Term Heatup Phase – Results for Phase I, Final Report,” EUR 13588 EN, 1991
3. Fischer, K., Kanzleiter, T., Schall, M., Wolf, L., 1990
“CEC Thermal-Hydraulic Benchmark Exercise on FIPLOC Verification Experiment F2 in BMC, Experimental Phases 2, 3, and 4 – Specification for Phase II, Battelle-Institut e.V., Frankfurt/Main,” Germany, July 1990
4. Fischer, K., T., Schall, M., Wolf, L., 1993
“CEC Thermal-Hydraulic Benchmark Exercise on FIPLOC Verification Experiment F2 in BMC, Experiment F2 in BMC, Experimental Phases – Results for Phase 2, 3 and 4, Results of Comparisons, Final Report,” EUR 14454 EN, 1993
5. Fischer, K., Hafner, W., Holzbauer, H., Kanzleiter, T., (1994)
“Experiments for Concerning Natural Convective Flows in Battelle Model Containment, Documentation of Measured Data” (In German), Battelle Ingenieurtechnik GmbH, Eschborn, Germany, Technical Report V68270.2, Oct. 1994
6. T. Kanzleiter, 1988
“FIPLOC-Verification Experiments,” (In German), Battelle-Institut e. V., Frankfurt/Main, Germany, Final Report BLeV-R-66.614-01, March 1988
7. Langer G., Jenior R., Wentlandt H.G., 1979
“Experimental investigation of the hydrogen distribution in the containment of a LWR following a LOCA” (In German), Battelle-Institut e. V., Frankfurt/Main, FRG, Report BF-R-63.363-3
8. Langer G., Baukal W., 1982
“Experimental investigation of the hydrogen distribution in a model containment (Preliminary Experiments II)” (In German), BMFT-Research Contract 150.375, Battelle-Institut e. V., Frankfurt/Main, FRG, Report BF-R-64.036-3
9. Petersen, K., Pamme, H., Seyffarth, L., Wolf, L., (1994)
“Hydrogen Mixing by Natural Convection in PWR Containments” (In German), atw 39 (1994), 758-769

10. L. Wolf, H. Holzbauer, M. Schall, 1994,
“Comparisons Between Multi-Dimensional and Lumped-Parameter GOTHIC Containment Analyses with Data” International Conference on New Trends in Nuclear System Thermohydraulics, Pisa, Italy, May 30th – June 2nd, Vol. 2, pp. 321 – 330.
11. L. Wolf, M. Gavrilas, K. Mun, 1996,
“Overview of Experimental Results for Long-Term, Large-Scale Natural Circulations in LWR-Containments after Large LOCAs” Final Report for DOE – Project, Order Number: DE-AP07-96ID10765, Department of Materials and Nuclear Engineering, University of Maryland at College Park, July 1996.

9.C.2.2 Description of the Available NUPEC Data Base

9.C.2.2.1 M-7-1 Test

NUPEC’s Hydrogen Mixing and Distribution Test M-7-1 is used as OECD/CSNI sponsored International Standard Problem Exercise ISP-35 (report NEA/CSNI/R(94)29) to compare and validate the performance of various computer codes. The WGOTHIC code is included among the codes that have been compared to this test (see Reference report NEA/CSNI/R(94)29). A detailed presentation of the M-7-1 test is not provided because the test is not directly applicable to the AP600 or **AP1000**. Internal sprays, which are not used in the passive containment design, are active during the M-7-1 test. A more relevant NUPEC experiment, the M-4-3 test (Reference T. Hirose, 1993), is performed without internal sprays. This test investigates the mixing behavior of hydrogen and steam injected into the lower containment compartment.

9.C.2.2.2 M-4-3 Test

The test facility represents one quarter of a linearly scaled PWR (four-loop) containment model with 25 inner compartments. The approximate volume is 1600 m³ with a height of 17.4 m and an inner diameter 10.8 m. Of the total volume, only 1300 m³ is used. The dome compartment is approximately 70 percent of the total volume. Twenty-four smaller compartments occupy from 0.1 percent to 4 percent of the total volume. The containment walls are made of steel plates (concrete structures are not present), so that the response of the heat sinks was very fast. The external containment wall is 12 mm thick steel and is insulated. Three floors are located at the 3.2, 5.4, and 7.3 m levels. A large sump is located below the lowest floor. A gas supply system for steam and helium, a containment internal spray supply system, and measuring systems for temperature, helium concentration, and pressure are installed.

The M-4-3 test simulates a break inside the lower D loop of the steam generator compartment. This compartment is at the first level of the containment. Figure 9.C-55, Figure 9.C-56, and Figure 9.C-57 illustrate the containment compartments and their corresponding numbers on each level. Figure 9.C-55 also shows the location of the break and typical circulation patterns.

The M-4-3 test starts with a pressure of 101.35 kPa and an initial containment temperature of 30°C. A mixture of steam and helium is injected at a constant flow rate during the first 30 minutes. The mass flow rates simulating a small break are 0.33 kg/s and 0.027 kg/s for the steam and helium, respectively. The inflow temperatures are 140°C and 20°C for the steam and helium, respectively.

Experimental data is recorded for 2 hours. The atmosphere and wall temperatures, the helium concentrations in the various compartments, and the pressure inside the dome are recorded. The pressure inside the dome increases almost linearly during the release and reaches 1.6 bar after 30 minutes (end of the release). The total mass of the steam released is 594 kg. Following the release, pressure decreases slowly to 1.5 bar (after 2 hours – see Figure 9.C-59). The dome temperature increases from 303 to 341°K during the release and then decreases to 334°K (see Figure 9.C-59). The dome helium concentration history is presented in Figure 9.C-60.

The temperature and helium concentrations increase first near the release point and the compartments above it, indicating an upward flow direction. This is followed by increases in the dome and steam generator compartments at the opposite side of the containment, indicating a downward flow loop direction. The global circulation loop is closed in the lower level of the containment. The consecutive positions of the higher temperatures and the helium concentration fronts indicate the flow path due to the global circulation during the break release (see Figure 9.C-61, from 0 – 1800 seconds).

A comparison of the temperatures and helium concentration histories in various compartments, Figure 9.C-61, shows the direction of the formed global circulation loop during the break release. One flow path starts in compartment 8, followed by compartments 15, 21, 25 (dome), 14, and 7. Following break release, the temperature field stratifies but the temperature difference between the dome and first floor level is not greater than 14°C at the end of the experiment. After the break release, the temperatures in all the compartments slowly decrease, despite the fact that the outer surface of the containment is insulated. Figure 9.C-61b shows that the concentration in the containment starts to homogenize after the end of the release (1800 seconds). This indicates that natural circulation effects are active after the end of release.

Note that the external walls of the containment are insulated and the interior walls are made of steel. This limits their ability to accumulate energy and act as a heat sources (which would promote natural circulation) later in the test. The natural circulation that exists after the end of release is most likely formed by the presence of the hot sump at the bottom of the containment.

Throughout the test, global circulation is present inside the containment and contributes to the homogenization of the atmosphere over time.

Application to AP600 and AP1000

This test is similar to the AP600 and **AP1000** plant configurations in both the position of the injection point (break at the low level) and the geometry of the containment (70 percent of the volume is dome). However, overriding the similarities are the absence of concrete structures (able to store heat and later act as heat sources) and cooling on the outer surface of the containment shell. These features make the test very dissimilar to the passive containment design. The external cooling and the hot concrete structures, positioned in the lower portion of the passive containment produce strong global circulation and decrease the effects of thermal stratification.

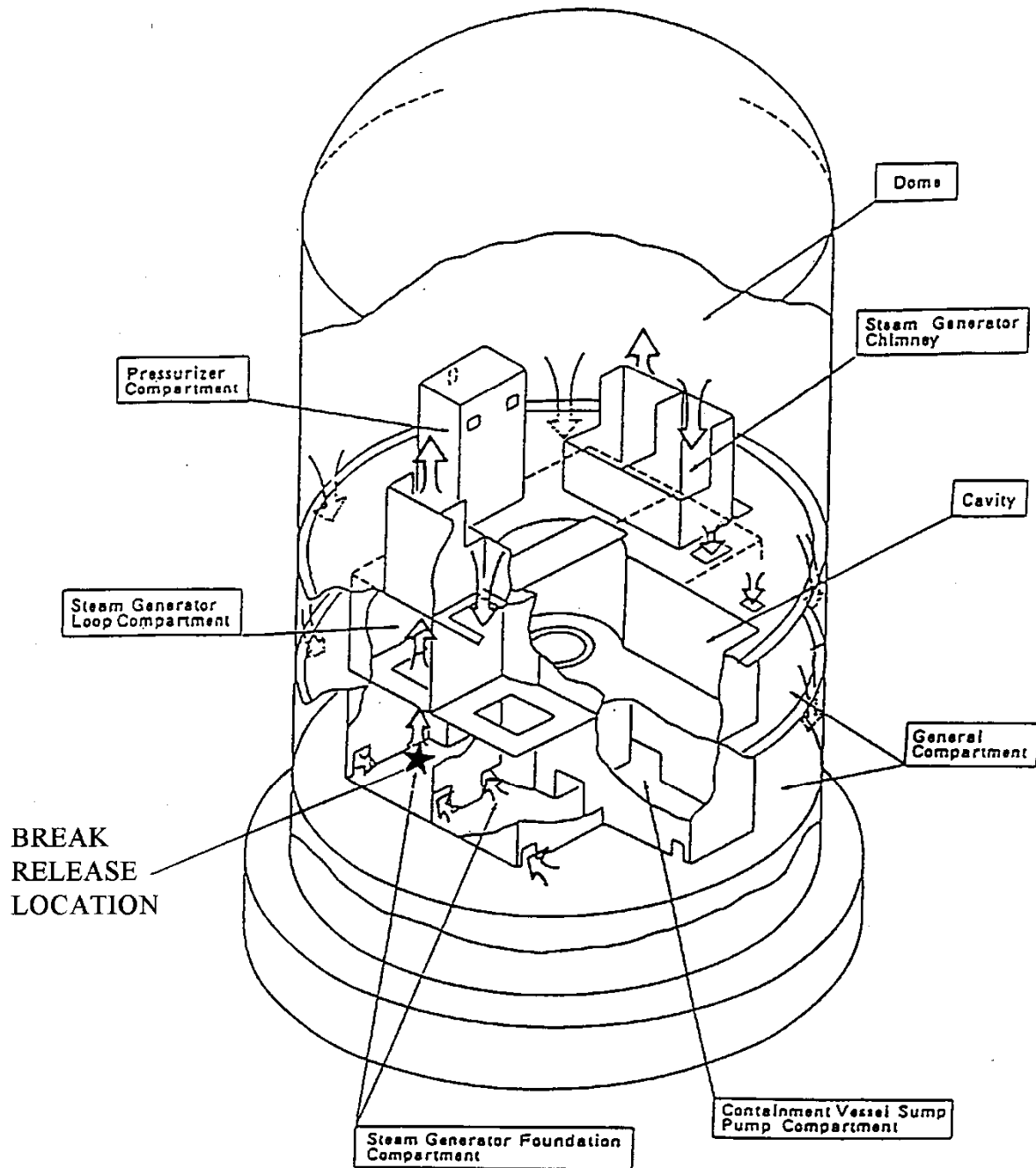


Figure 9.C-55. Model Containment used in the Test, Break-Release Position, and Circulation Flow Paths (See Arrows)

(Figure prepared according to T. Hirose documentation for M-4-3 test data, NUPEC Nuclear Power Engineering Corporation, ISP35-035, 30 April, 1993)

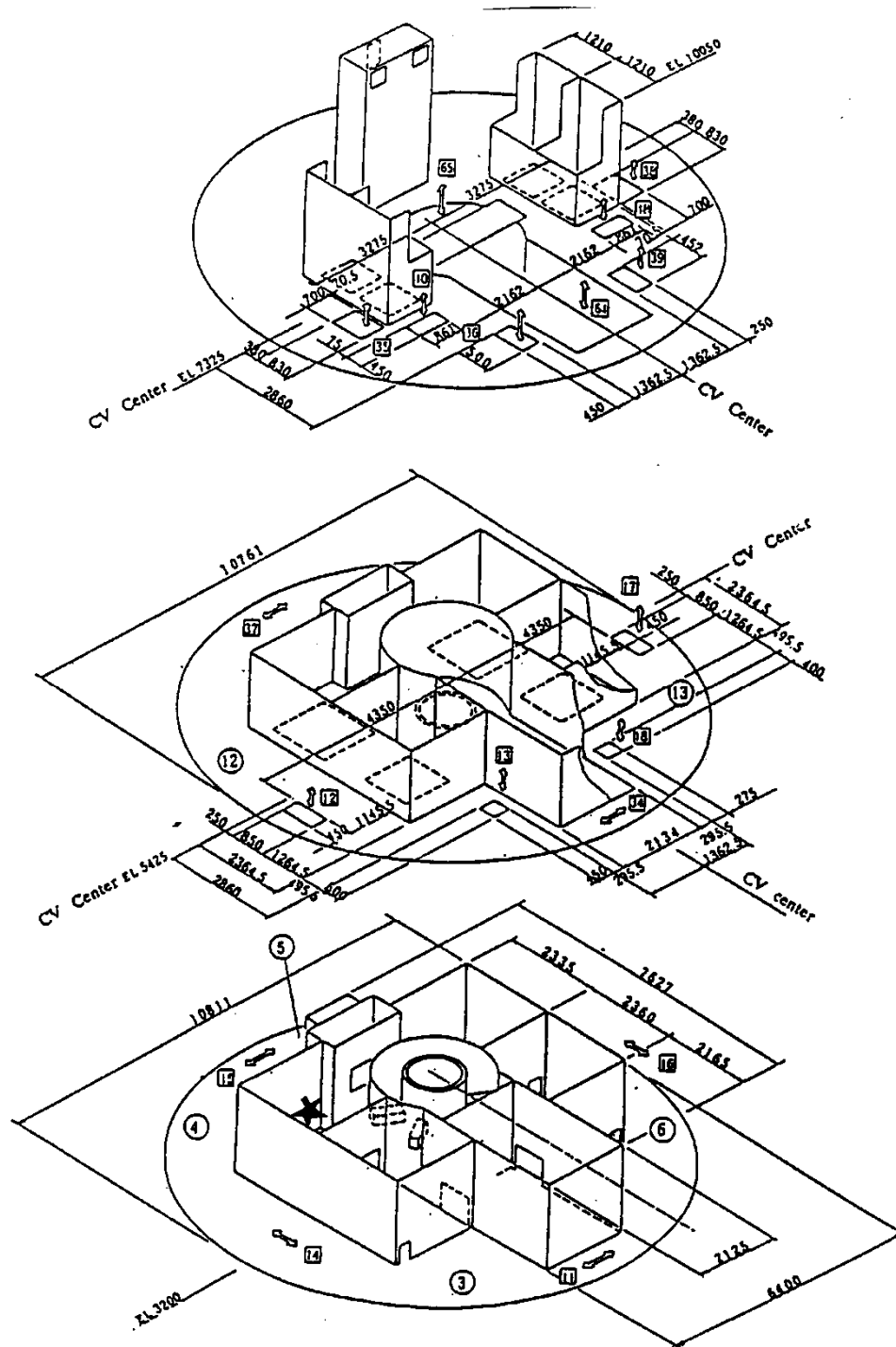


Figure 9.C-56. Detailed Arrangement of each Floor

(Figure prepared according to T. Hirose documentation for M-4-3 test data, NUPEC Nuclear Power Engineering Corporation, ISP35-035, 30 April, 1993)

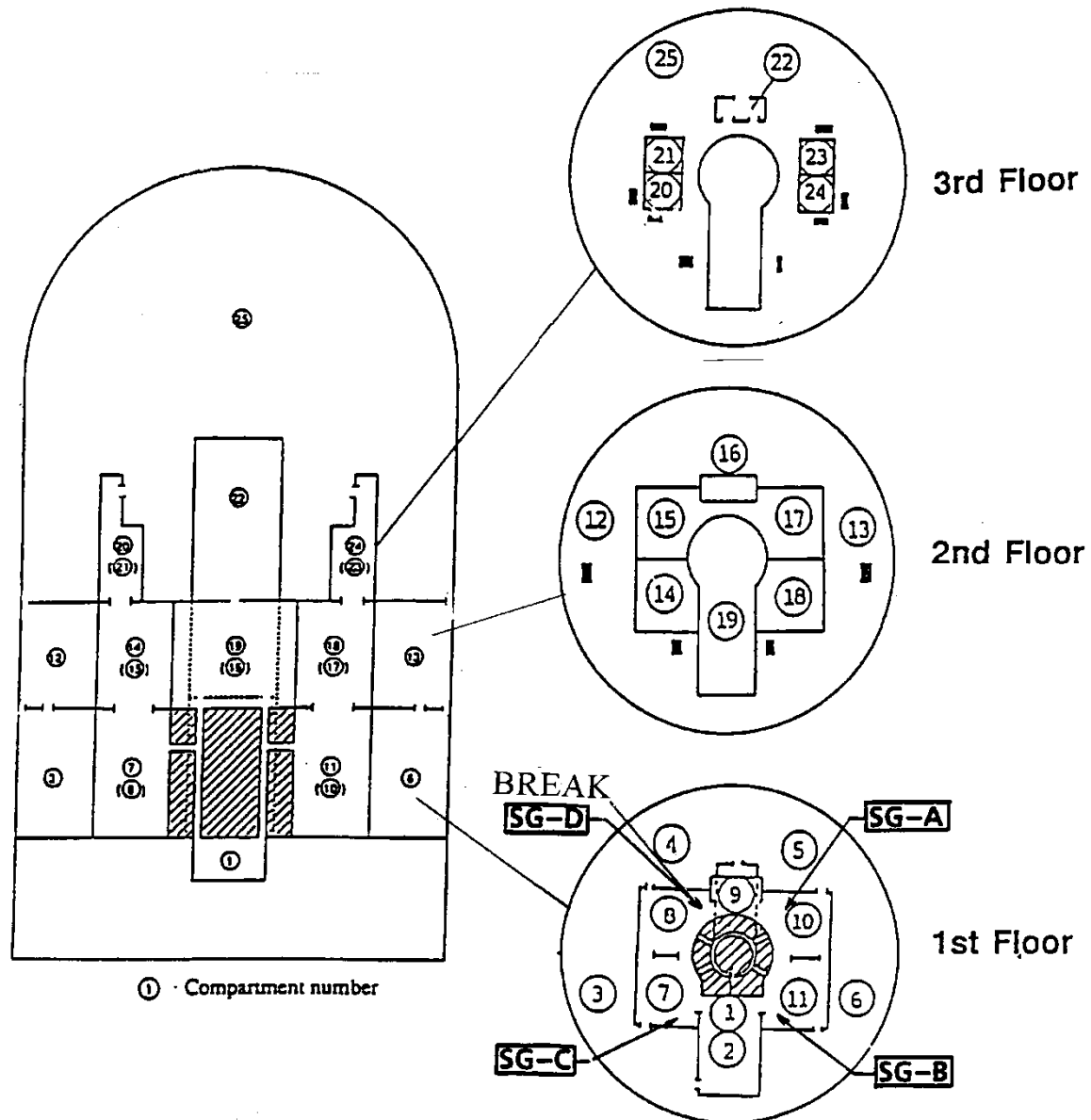


Figure 9.C-57. Distribution of the Compartments at each Floor

(Figure prepared according to T. Hirose documentation for M-4-3 test data, NUPEC Nuclear Power Engineering Corporation, ISP35-035, 30 April, 1993)

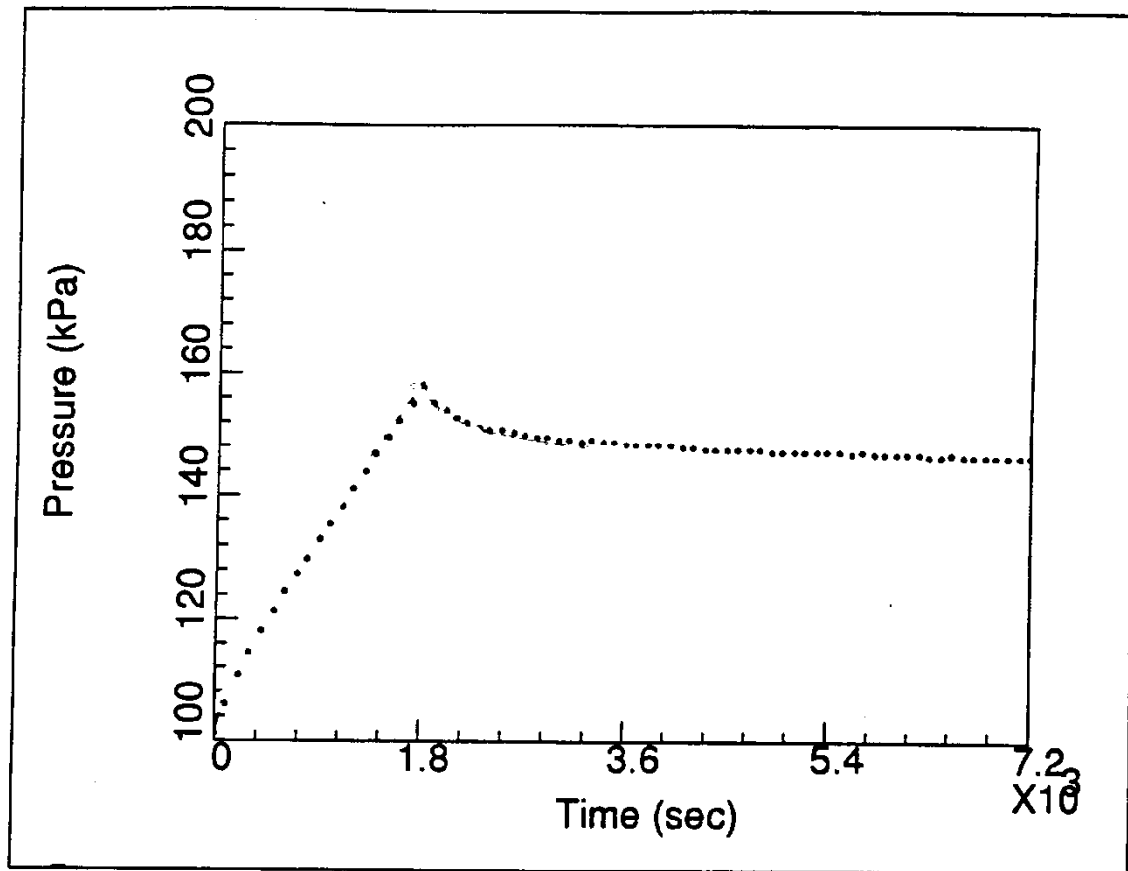


Figure 9.C-58. Pressure History

(Figure prepared according to T. Hirose documentation for M-4-3 test data, NUPEC Nuclear Power Engineering Corporation, ISP35-035, 30 April, 1993)

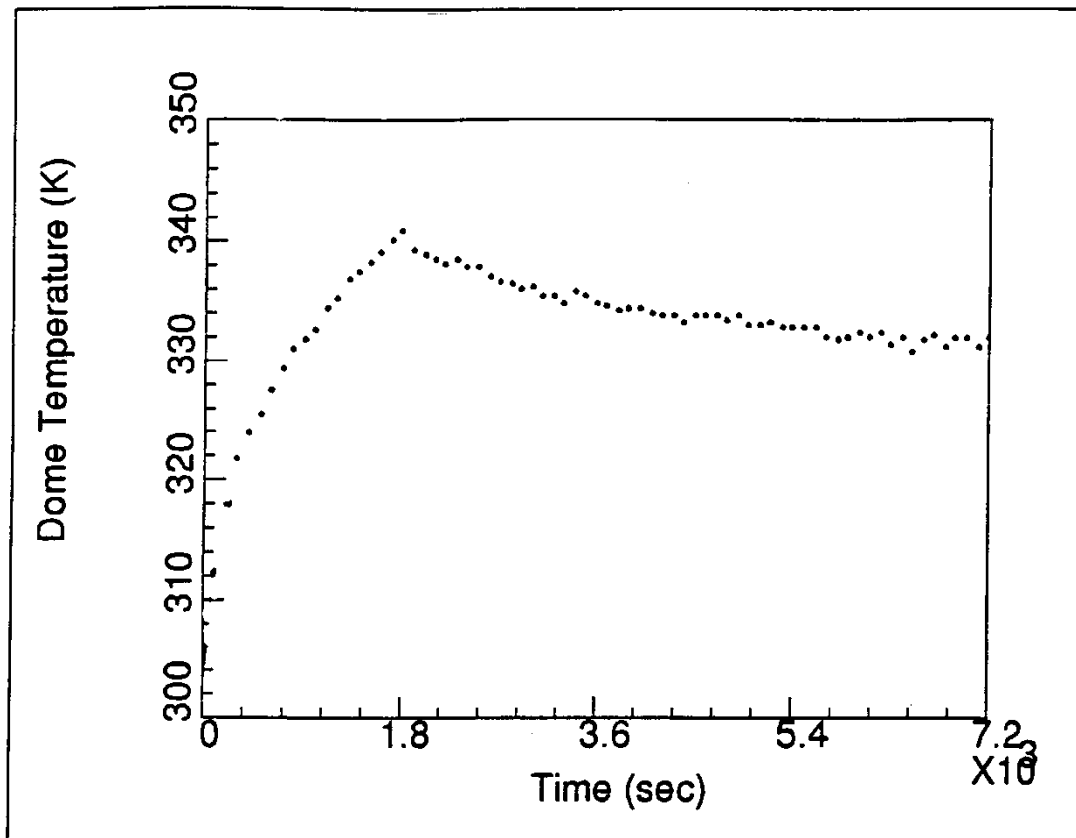


Figure 9.C-59. Dome Temperature History

(Figure prepared according to T. Hirose documentation for M-4-3 test data, NUPEC Nuclear Power Engineering Corporation, ISP35-035, 30 April, 1993)

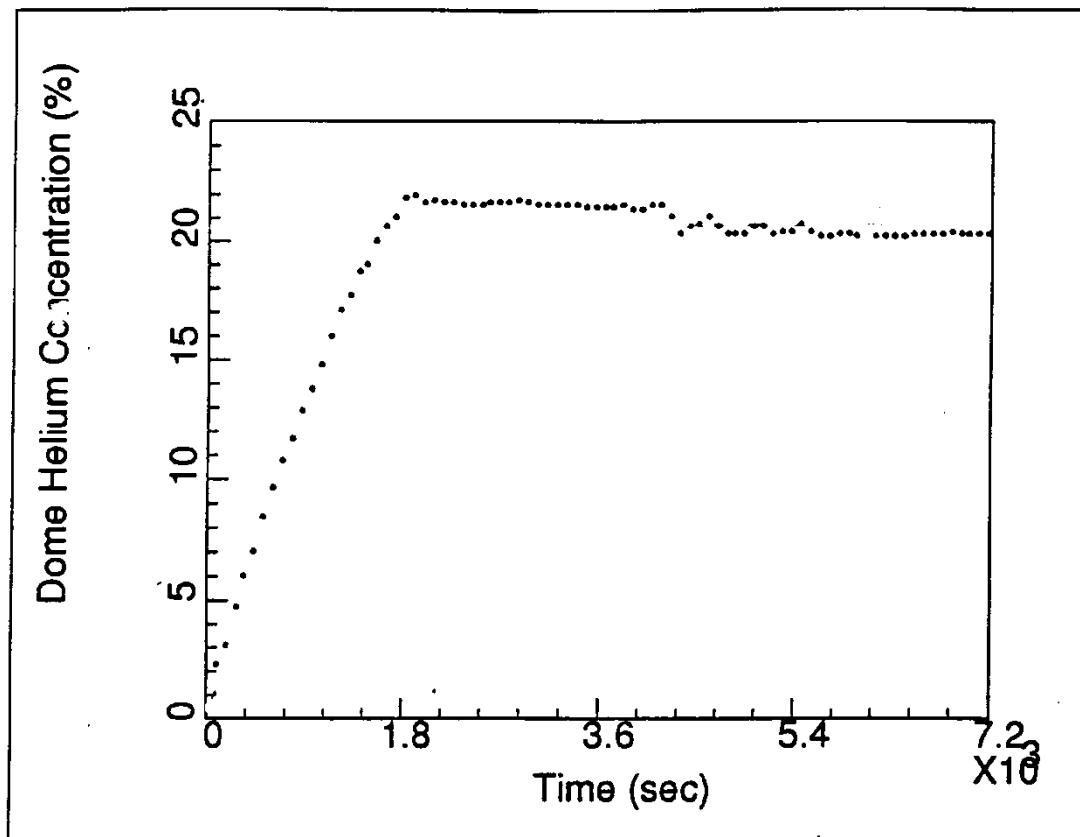


Figure 9.C-60. Dome Helium Concentration History

(Figure prepared according to T. Hirose documentation for M-4-3 test data, NUPEC Nuclear Power Engineering Corporation, ISP35-035, 30 April, 1993)

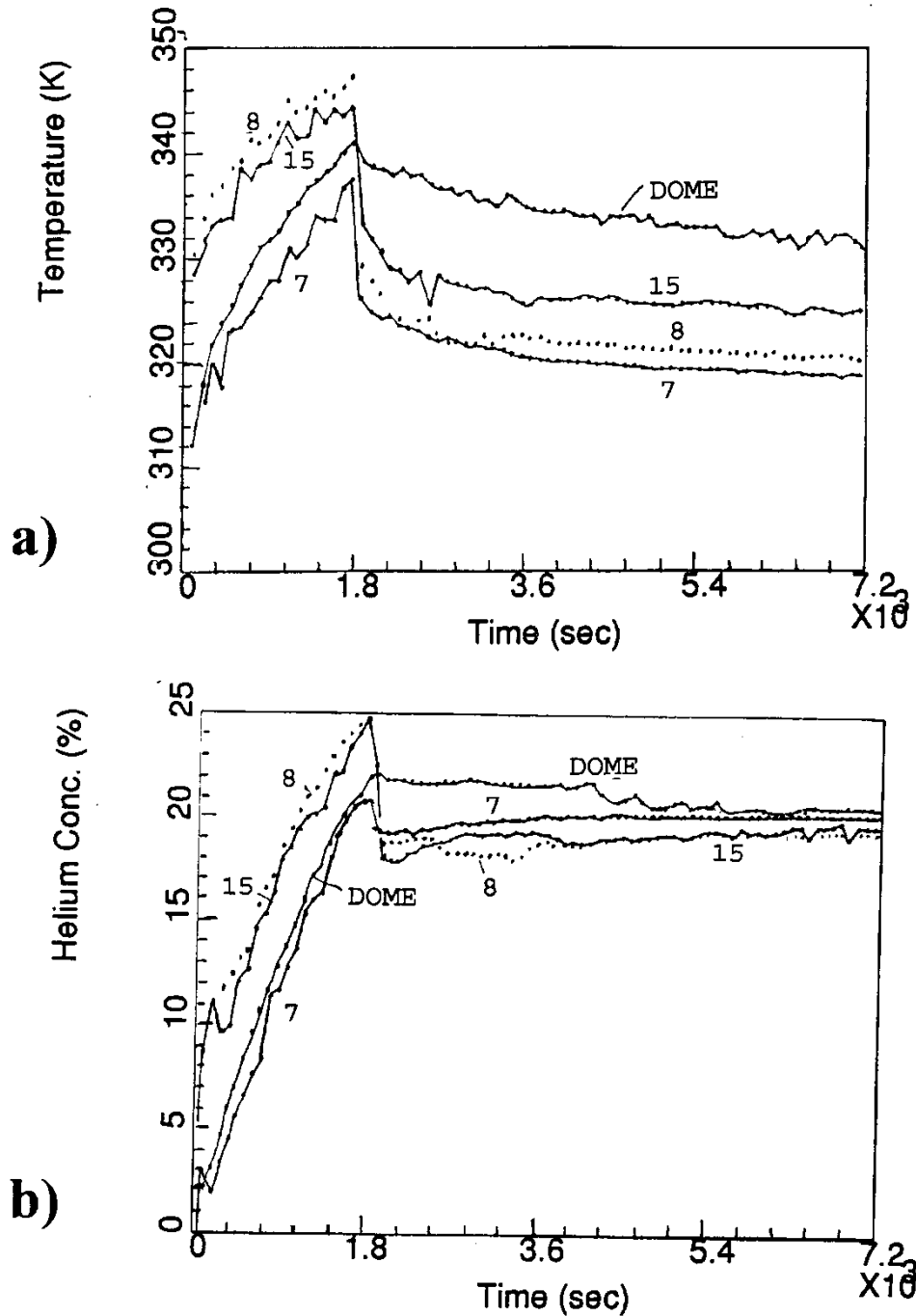


Figure 9.C-61. a) Temperature Histories for Compartments Forming a Circulation Path (8, 15, Dome and 7)

b) Helium Concentration Histories for Compartments Forming a Circulation Path (8, 15, Dome and 7)

(Figure prepared according to T. Hirose documentation for M-4-3 test data, NUPEC Nuclear Power Engineering Corporation, ISP35-035, 30 April, 1993)

9.C.2.2.3 References

1. NEA/CSNI/R(94)29: Final comparison report on ISP-35: NUPEC hydrogen mixing and distribution test (Test M-7-1), Committee on the safety of nuclear installations OECD Nuclear Energy Agency, December 1994
2. Tadashi Hirose (1993): Letter, floppy disk which contains the M-4-3 test data, an attached document, and a video-cassette, NUPEC Nuclear Power Engineering Corporation, ISP35-035, 30 April, 1993

9.C.2.3 Description of the Available Carolinas Virginia Tube Reactor Containment (CVTR) Database

The results of the simulated DBA of CVTR containment system are presented in (Schmitt et al., 1970). The CVTR containment is made of reinforced concrete (see Figure 9.C-62). It is cylindrical in shape with an internal diameter of 57 ft 11 - 1/2 in and an inside height of 114 ft. The cylindrical wall is 2 feet thick. At the top of the cylinder is a hemispherical dome made of 1/2-inch thick steel covered by 20.5 inches of concrete. The structure is divided in three regions (operating, intermediate, and basement). The free volume is about 227,000 ft³. A water spray system is installed at the 360 foot elevation (6 inches above the containment bend line).

Three simulated DBA tests are performed. The first test does not use the water sprays. The pressure and temperature histories are obtained to establish the effects of the sprays on pressure reduction. The remaining tests include active water sprays with flow rates 290 and 500 gpm, respectively. The water spray flow rate is adjusted by changing the total number of nozzles in the spray header. The spray flow is initiated 30 seconds after the end of steam injection and remains in operation for 12 minutes. The second and third tests are not applicable to passive containment DBA situations due to the spray effects.

Superheated steam, at approximately 10°F above the saturation temperature, is injected into the containment. The steam is released above the operating floor through a diffuser made of a 10 foot pipe installed vertically on the discharge nozzle of the steam line (see Figure 9.C-63). The end of the pipe is capped. The pipe contains approximately 126 holes (with 1-inch diameter) that direct the steam horizontally (see Figure 9.C-63). The injection continues until the containment pressure reaches 17.5 psig above the atmospheric pressure.

To obtain the containment response, measurements of the interior pressure are made using seven fast response pressure transducers and a Heise gauge. The containment atmospheric temperature is measured by 34 thermocouples and 15 resistance thermometers. Two additional thermocouples and pressure transducers are located in two partially isolated regions (the reactor header cavity and the refueling canal) to determine their thermal and pressure response. Twenty three thermocouples are positioned at the containment liner envelope and the interior surfaces to obtain the temperature response of the interior concrete sections. The heat transfer through the liner wall of the operating region of the containment is established using heat flow devices along with thermocouples that measure the temperature distribution in the cross-section of the wall. The weight of condensate collected from the selected areas of the cylindrical liner walls is also measured.

The mass flow rates of steam for the three DBA tests range from 360,000 to 380,000 lb/hr (see Figure 9.C-64a, Figure 9.C-64b, Figure 9.C-64c). The injection steam conditions are near to saturated conditions with an enthalpy of 1196 Btu/lb. The steam is injected in the operating region at 335 ft elevation. The duration of the release is approximately 180 seconds. The measurements are taken for approximately two hours, but only the first 50 minutes are presented in the report.

Containment pressure histories for the three DBA tests are presented in Figure 9.C-47. The influence of the spray application and the intensity of the sprays on the decrease of the containment pressure is obvious.

The containment vertical temperature profiles for various tests are presented in Figure 9.C-66, Figure 9.C-67 and Figure 9.C-68, respectively. For the first test, large vertical temperature gradients exist for the duration of the measurements (about two hours), indicating temperature stratification. The containment air recirculation system is activated one and half hours after the beginning of the first test and it decreases the vertical temperature gradients (but not so efficiently as water sprays).

The spray tests (tests 2 and 3 - which are not applicable for passive containment designs) contribute towards the uniformity of the containment atmosphere by decreasing the dome temperatures. After one hour, the dome temperatures were 177, 155, and 137°F for tests 1, 2, and 3, respectively.

One hundred minutes of test data from thermocouples mounted at the same horizontal level inside the operating region are analyzed. Significant temperature gradients are not established in the horizontal direction. This is consistent with the view that stratification gradients are mainly in a vertical direction, with negligible horizontal gradients, except near plumes and wall boundary layers.

Liner vertical temperatures are almost the same as the temperatures in the upper regions of the containment atmosphere, while they are higher than temperatures in the atmosphere of the lower regions (see Figure 9.C-69 and Figure 9.C-70 for lower regions). An explanation for the higher liner temperatures in the lower regions is that the steam, in its downward movement, passed through the annular gap near the containment wall (surrounding the operating floor) releasing heat predominantly to the wall instead of the atmosphere.

Data from six thermocouples embedded in concrete surfaces in the containment are presented in Figure 9.C-71 for the case without sprays. The operating region structures have a large temperature increase, while the basement region is almost unaffected. The results are in agreement with the atmospheric and liner temperature data and show stratification above the break elevation.

The results from two thermocouples installed in two partially isolated regions (the reactor header cavity and the fuel transfer canal) are presented in Figure 9.C-72. A small temperature increase is seen during the steam injection. After the injection, temperatures decrease very fast, resulting in the very small final temperature increase. The data also indicates that dead-ended compartments get some steam during the pressure increase.

The reasons for the established temperature stratification in the case of the CVTR containment test performed without internal sprays are:

- The position of the release point is above the 335 foot elevation of containment height see Figure 9.C-62). This could be considered as a release in the upper region of the containment ($H_r/H_t = 0.525$).
- The external walls and the dome of the containment were made of 23-3/4" thick concrete which accumulated a portion of the heat released in the upper regions (operational region and intermediate region – see Figure 9.C-71 for vertical temperature distribution inside the liner). The upper portions of the walls remain hot as containment cools, producing boundary conditions for a stable stratification.
- External spray cooling of the dome and walls (upper half exposed to the air) is not applied.
- The steam condensate is collected in the buckets so that weight of the condensate can be measured. This eliminated hot sump evaporation and heat source effects. The other experiments (BMC and HDR) indicate that even small temperature differences between the sump (as a heat source at the lowest level) and the containment atmosphere generate global natural circulation inside the containment.

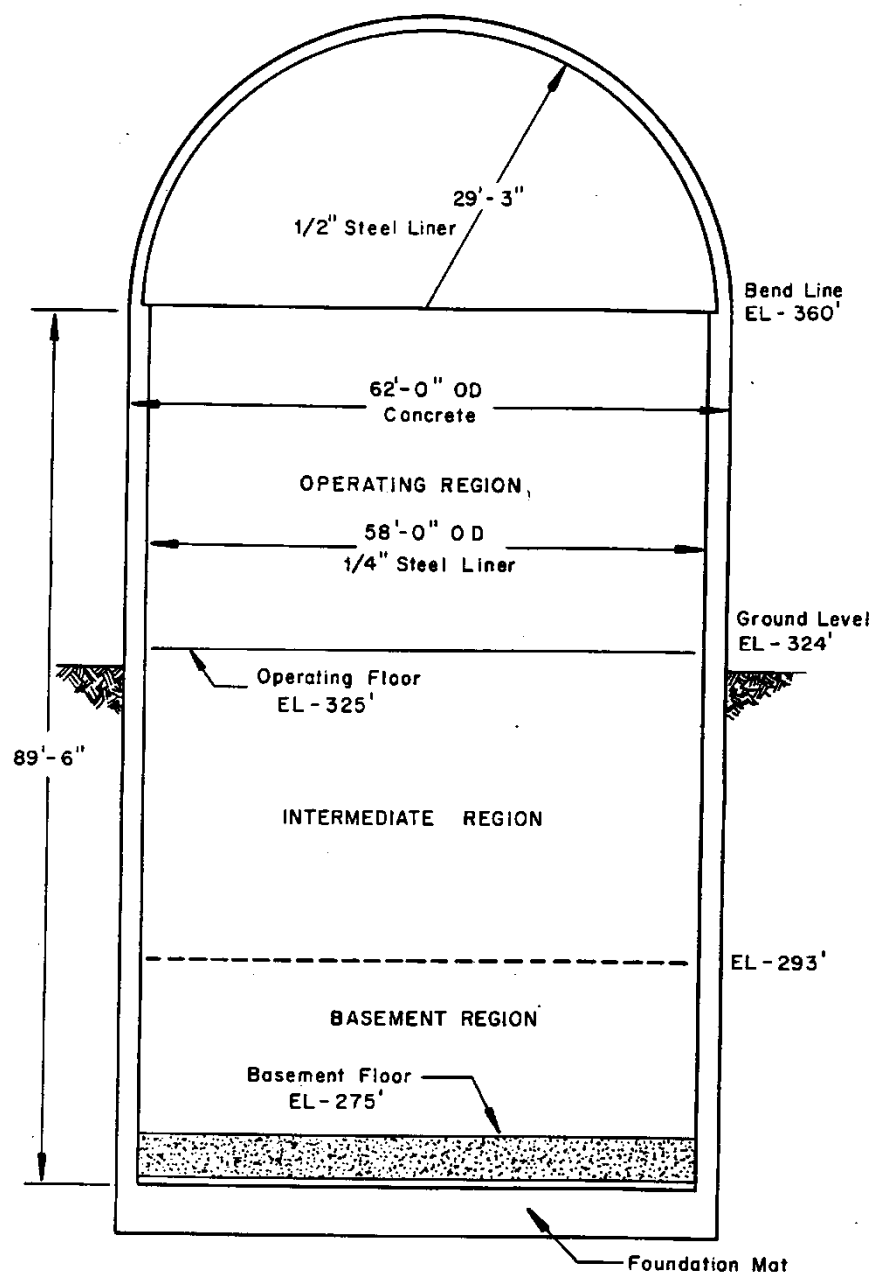


Figure 9.C-62. Carolinas Virginia Tube Reactor (CVTR) Containment Structure

(reprinted from: R.C. Schmitt, G.E. Bingham, J.A. Norberg, "Simulated design basis accident tests of the Carolinas Virginia Tube Reactor Containment – Final report," Prepared for the U.S. Atomic Energy Commission, Idaho Operations Office, Under Contract No. AT(10-1)-1230)

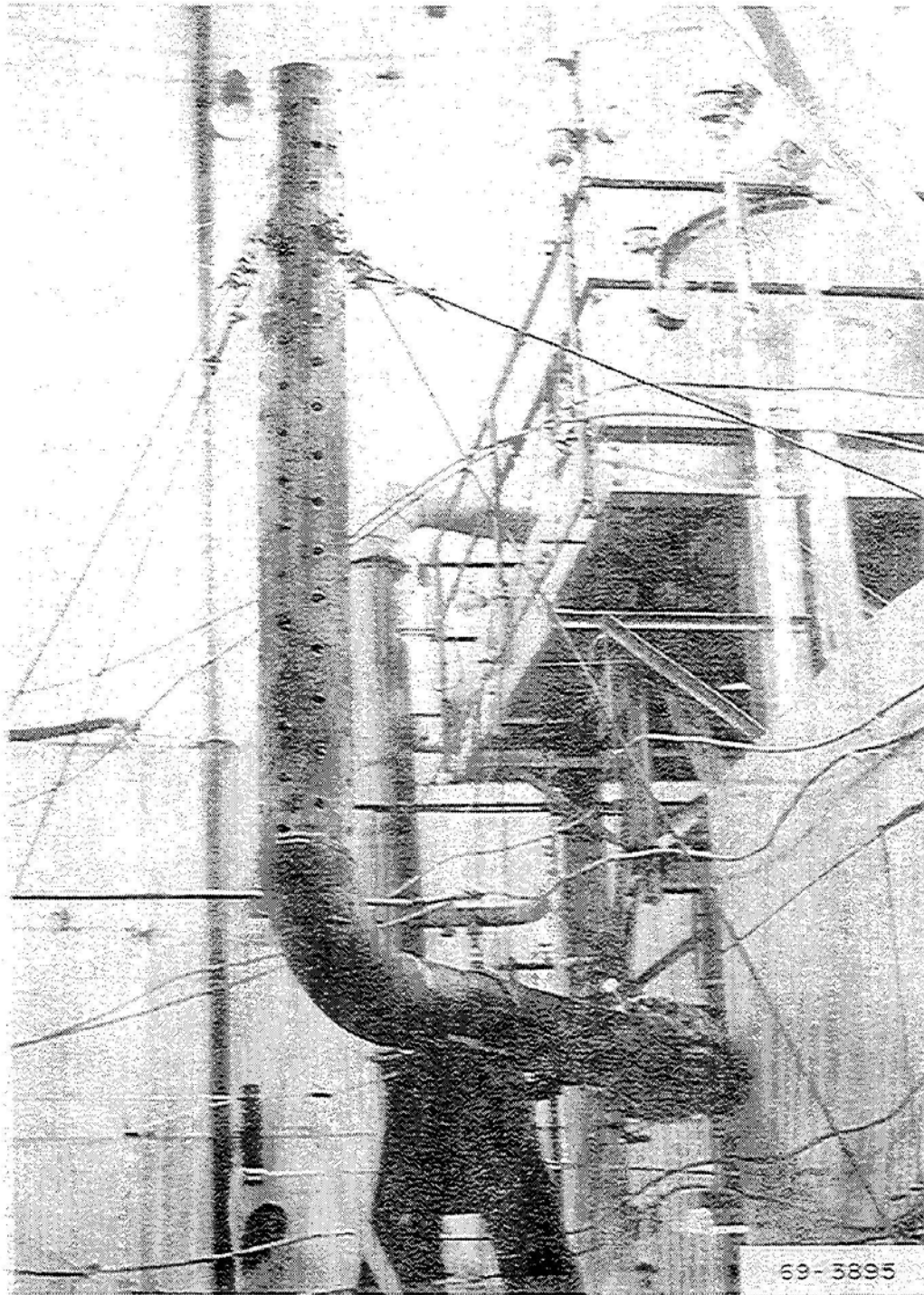


Figure 9.C-63. CVTR Steam Line Diffuser

(reprinted from: R.C. Schmitt, G.E. Bingham, J.A. Norberg, "Simulated design basis accident tests of the Carolinas Virginia Tube Reactor Containment – Final report," Prepared for the U.S. Atomic Energy Commission, Idaho Operations Office, Under Contract No. AT(10-1)-1230)

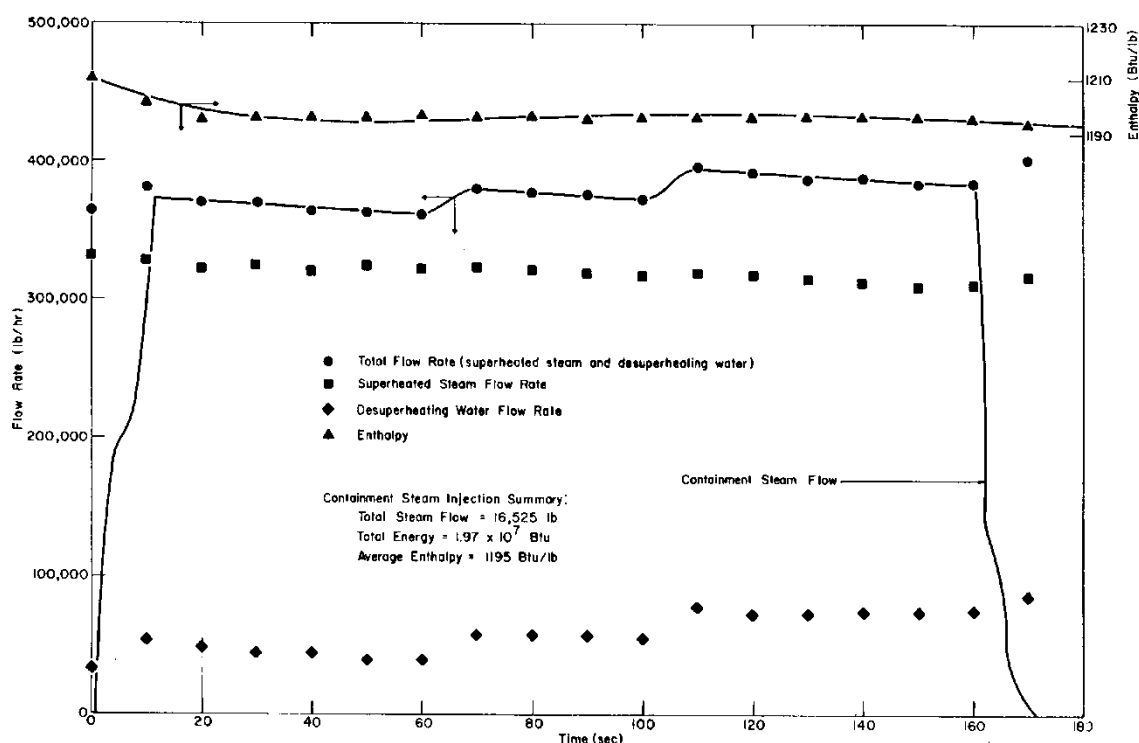


Figure 9.C-64a. Steam Injection Histories Test 1

(reprinted from: R.C. Schmitt, G.E. Bingham, J.A. Norberg, "Simulated design basis accident tests of the Carolinas Virginia Tube Reactor Containment – Final report," Prepared for the U.S. Atomic Energy Commission, Idaho Operations Office, Under Contract No. AT(10-1)-1230)

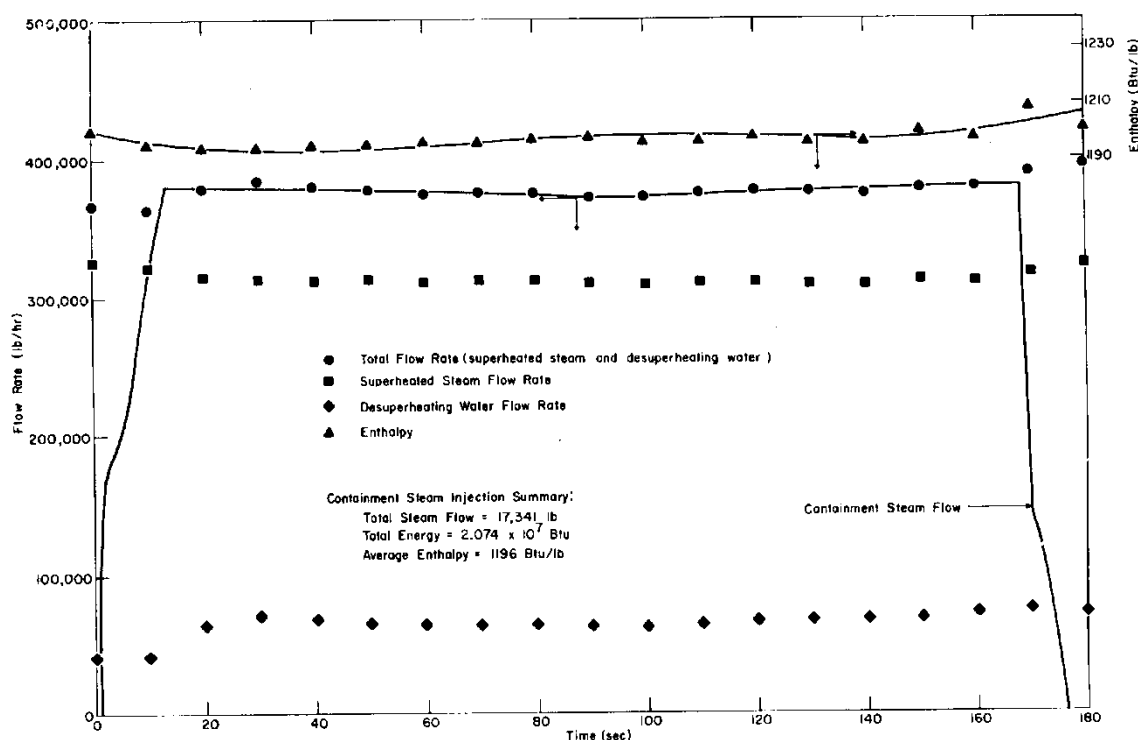


Figure 9.C-64b. Steam Injection Histories Test 2

(reprinted from: R.C. Schmitt, G.E. Bingham, J.A. Norberg, "Simulated design basis accident tests of the Carolinas Virginia Tube Reactor Containment – Final report," Prepared for the U.S. Atomic Energy Commission, Idaho Operations Office, Under Contract No. AT(10-1)-1230)

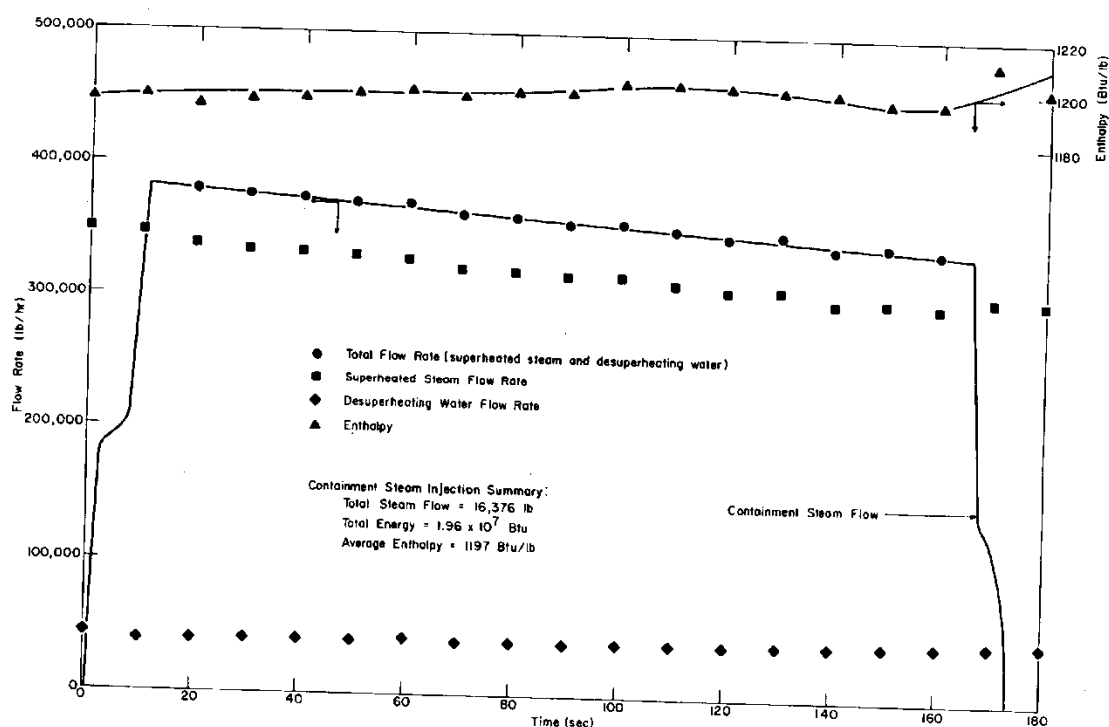


Figure 9.C-64c. Steam Injection Histories Test 3

(reprinted from: R.C. Schmitt, G.E. Bingham, J.A. Norberg, "Simulated design basis accident tests of the Carolinas Virginia Tube Reactor Containment – Final report," Prepared for the U.S. Atomic Energy Commission, Idaho Operations Office, Under Contract No. AT(10-1)-1230)

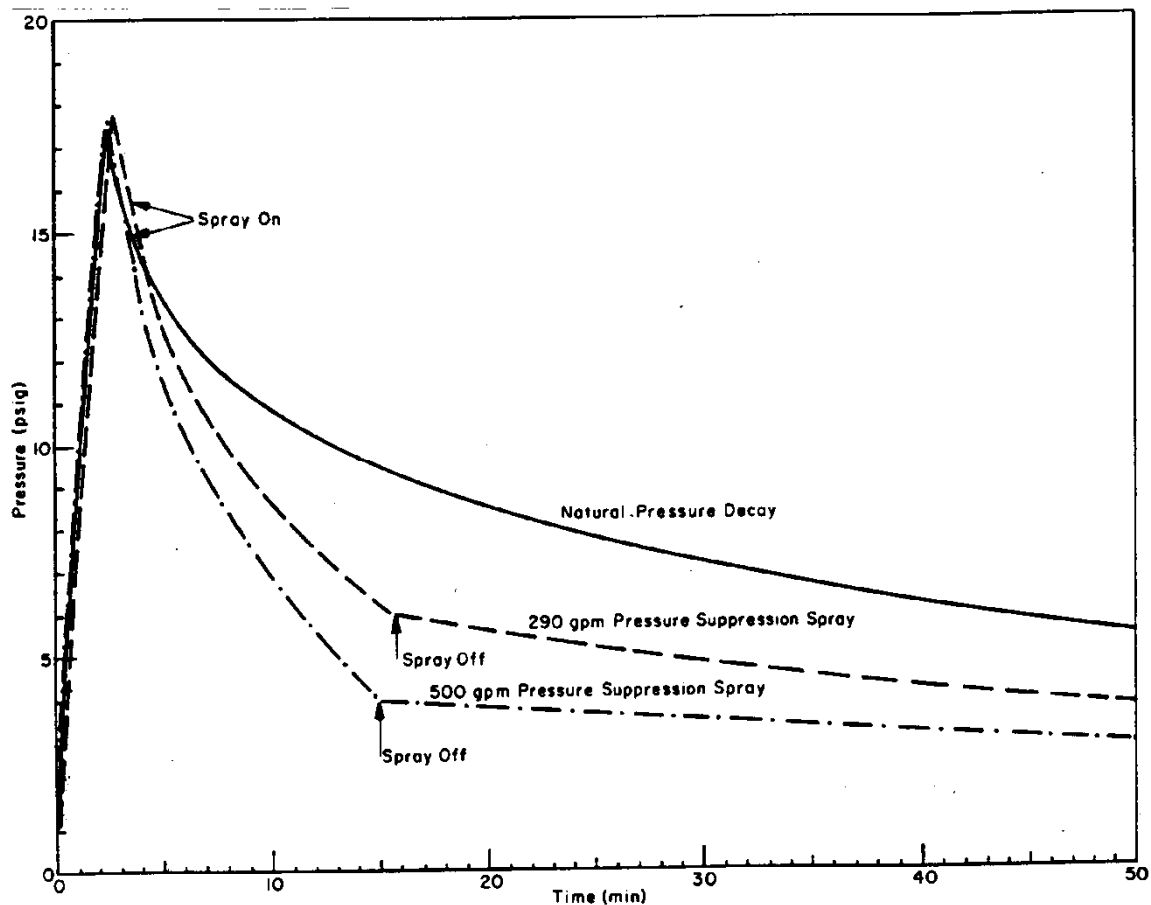


Figure 9.C-65. CVTR Containment Pressure Response (Heise Gauge)

(reprinted from: R.C. Schmitt, G.E. Bingham, J.A. Norberg, "Simulated design basis accident tests of the Carolinas Virginia Tube Reactor Containment – Final report," Prepared for the U.S. Atomic Energy Commission, Idaho Operations Office, Under Contract No. AT(10-1)-1230)

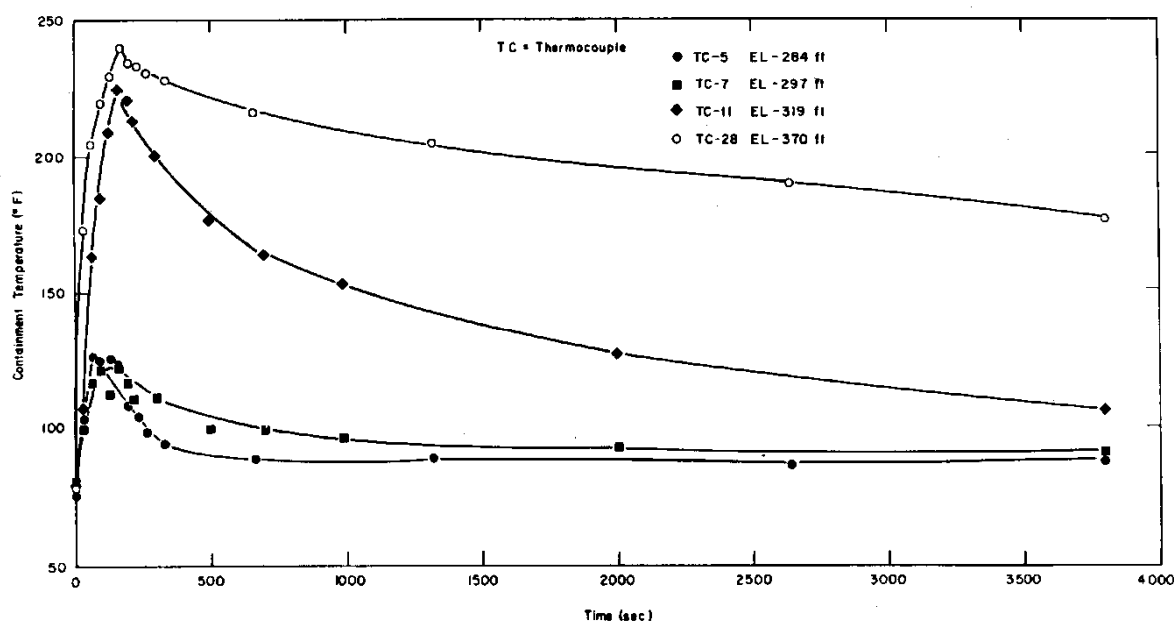


Figure 9.C-66. Atmospheric Vertical Temperature Profile, Test 1

(reprinted from: R.C. Schmitt, G.E. Bingham, J.A. Norberg, "Simulated design basis accident tests of the Carolinas Virginia Tube Reactor Containment – Final report," Prepared for the U.S. Atomic Energy Commission, Idaho Operations Office, Under Contract No. AT(10-1)-1230)

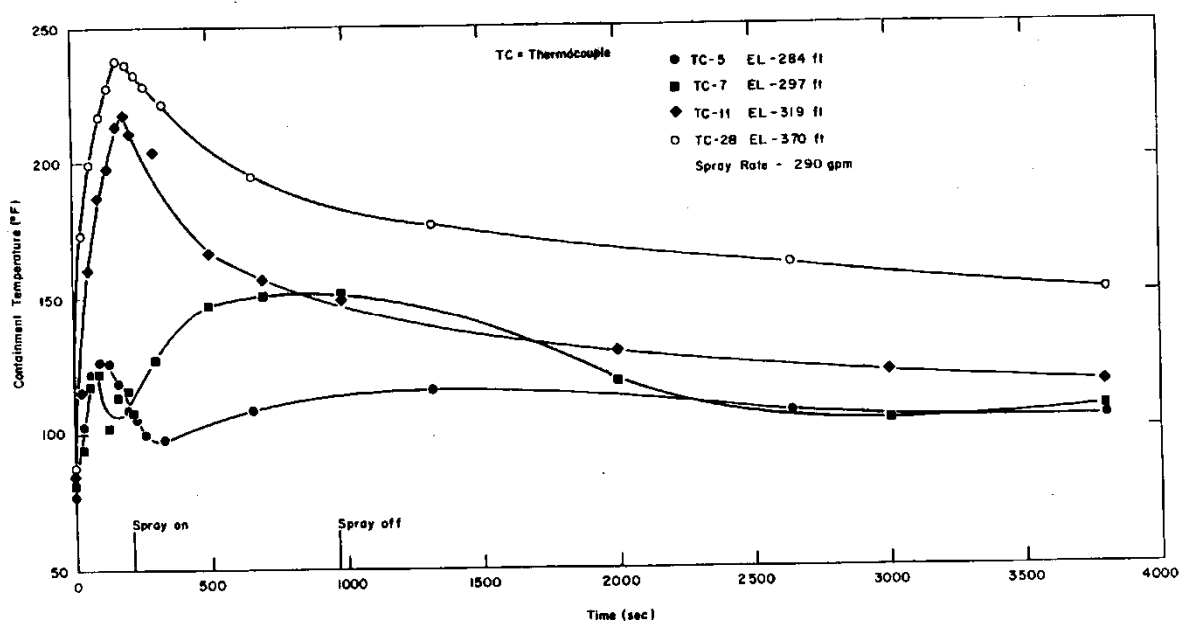


Figure 9.C-67. Atmospheric Vertical Temperature Profile, Test 2

(reprinted from: R.C. Schmitt, G.E. Bingham, J.A. Norberg, "Simulated design basis accident tests of the Carolinas Virginia Tube Reactor Containment – Final report," Prepared for the U.S. Atomic Energy Commission, Idaho Operations Office, Under Contract No. AT(10-1)-1230)

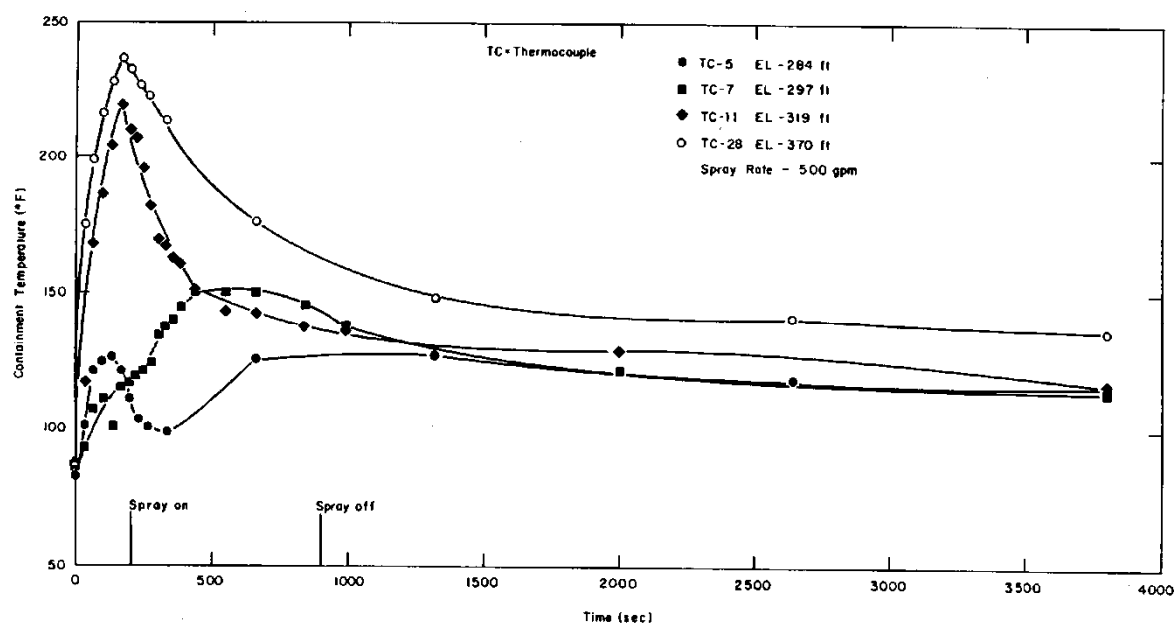


Figure 9.C-68. Atmospheric Vertical Temperature Profile, Test 3

(reprinted from: R.C. Schmitt, G.E. Bingham, J.A. Norberg, "Simulated design basis accident tests of the Carolinas Virginia Tube Reactor Containment – Final report," Prepared for the U.S. Atomic Energy Commission, Idaho Operations Office, Under Contract No. AT(10-1)-1230)

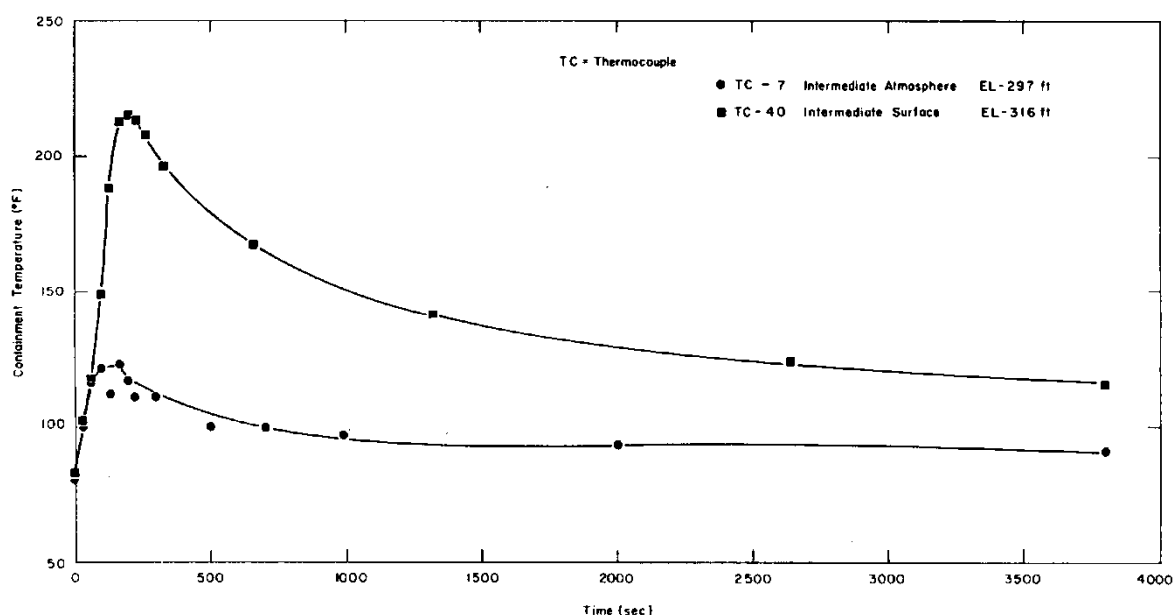


Figure 9.C-69. Surface and Atmosphere Temperatures – Intermediate Region, Test 1

(reprinted from: R.C. Schmitt, G.E. Bingham, J.A. Norberg, “Simulated design basis accident tests of the Carolinas Virginia Tube Reactor Containment – Final report,” Prepared for the U.S. Atomic Energy Commission, Idaho Operations Office, Under Contract No. AT(10-1)-1230)

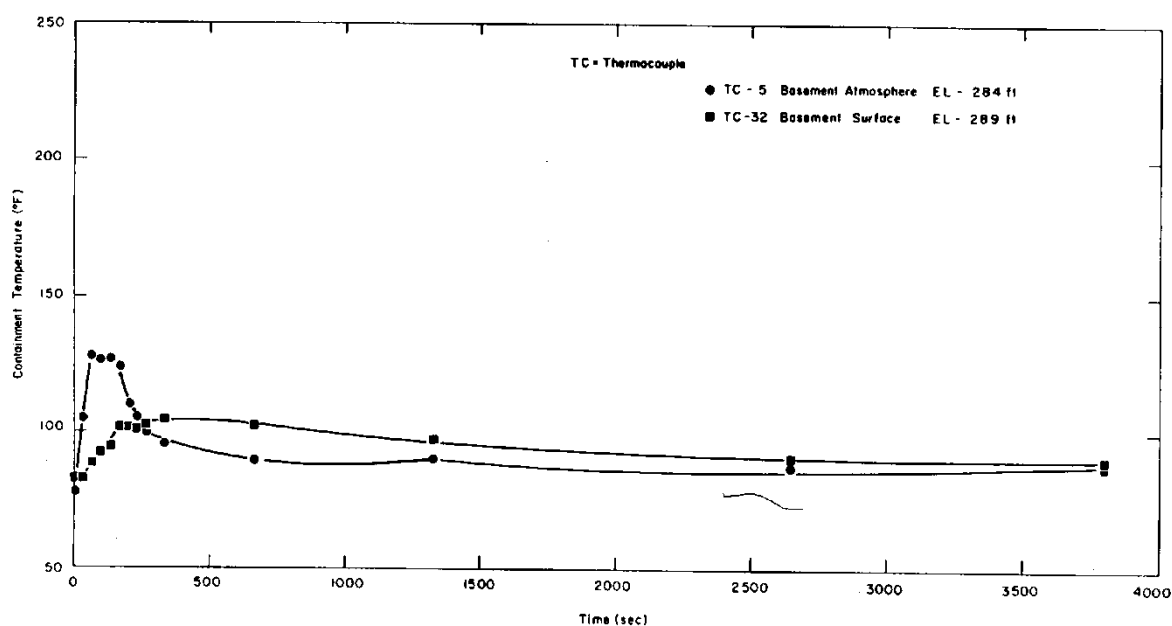


Figure 9.C-70. Surface and Atmosphere Temperatures – Basement Region, Test 1

(reprinted from: R.C. Schmitt, G.E. Bingham, J.A. Norberg, "Simulated design basis accident tests of the Carolinas Virginia Tube Reactor Containment – Final report," Prepared for the U.S. Atomic Energy Commission, Idaho Operations Office, Under Contract No. AT(10-1)-1230)

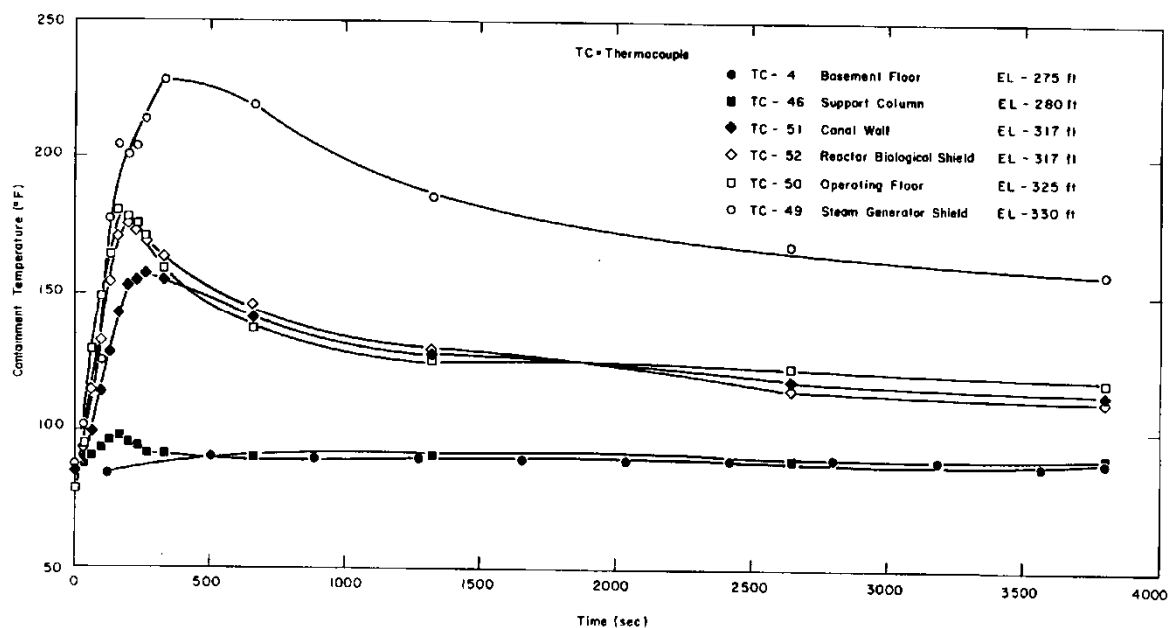


Figure 9.C-71. Concrete Surface Temperatures, Test 1

(reprinted from: R.C. Schmitt, G.E. Bingham, J.A. Norberg, "Simulated design basis accident tests of the Carolinas Virginia Tube Reactor Containment – Final report," Prepared for the U.S. Atomic Energy Commission, Idaho Operations Office, Under Contract No. AT(10-1)-1230)

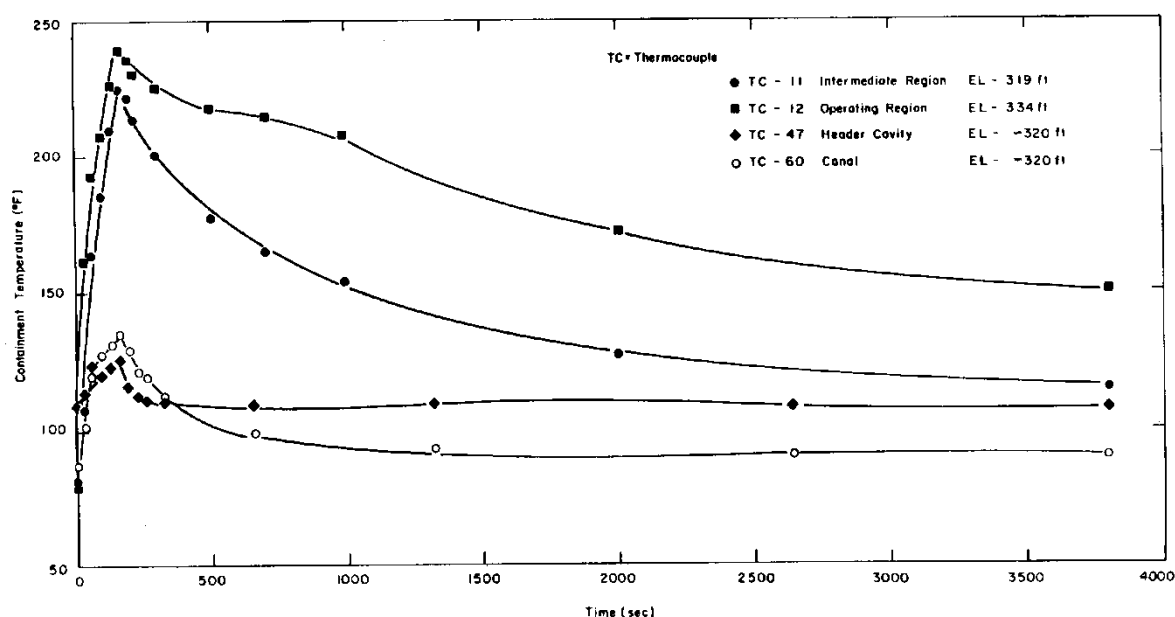


Figure 9.C-72. Isolated Containment Region Temperatures

(reprinted from: R.C. Schmitt, G.E. Bingham, J.A. Norberg, "Simulated design basis accident tests of the Carolinas Virginia Tube Reactor Containment – Final report," Prepared for the U.S. Atomic Energy Commission, Idaho Operations Office, Under Contract No. AT(10-1)-1230)

9.C.2.4 Description of the Available HDR Database

The HDR containment (Figure 9.C-73) is 20 m in diameter and 60 m high with a total free volume of 11,300 m³. It is made of steel and concrete with a total surface area of 30,000 m² available for heat transfer (condensation). The dome volume, including a crane structure, is about 42 percent of the total volume or 5,000 m³. The main and spiral staircase form the dominant vertical flow paths connecting the dome with sump. The containment can be subdivided into 62 to 72 subcompartments containing pipes, pumps, and valves etc. The subcompartments are interconnected by numerous openings. The numbers and locations of thermocouples and anemometers for the HDR-E test series are presented in Figure 9.C-74.

9.C.2.4.1 HDR E11 Test Series

Test group E11 (the hydrogen distribution and mixing experiments) is included as a part of the HDR-Safety Program Phase III that was conducted in the summer of 1989 (Cron and Schrammel, 1993). This test series simulated severe accident scenarios. The tests provide insights on DBA circulation and stratification. A review of the natural circulation flows formed in experiments E11.0 - E11.5 is presented in Wolf et al., 1996. Circulation is indicated by examination of the recorded temperatures and velocities.

Seven of the eight E11 experiments are initiated with small steam releases. The one exception, the E11.5 experiment, is initiated with a large-break, two-phase LOCA blowdown. The tests provide data for the transient and spatial distribution of the gas concentration (hydrogen/helium mixture) under various initial and boundary conditions.

The following features are considered:

- The large scale of the experimental facility and the multi-compartment geometry with a relatively large dome
- High hydrogen release rates typical of severe accidents
- Superheated steam injection into the containment - single and multiple steam and hydrogen injection phases
- Internal concrete and metal structures and surfaces
- Different axial positions for hydrogen and steam releases
- The efficiency of hydrogen mitigating features, including venting (for example blockage of one major vertical flow path)
- The impact of internal and external sprays
- Sump heat up effects
- Air heater operation effects

9.C.2.4.1.1 Experiment E11.0

Experiment E11.0 is performed with an external steam supply and without a gas mixture release. However, the external steam supply is not able to produce typical severe accident conditions. Therefore, a blowdown of the primary system is used for all other experiments. The results of E11.0 are not discussed here.

9.C.2.4.1.2 Experiment E11.1

Experiment E11.1 includes a high-positioned, small break LOCA, followed by additional steam and gas releases. The effectiveness of the internal spray for decreasing the pressure and temperature inside the containment is also tested. Since this experiment included internal sprays that are not a part of the passive containment design, the results are not discussed here.

9.C.2.4.1.3 Experiment E11.2

Experiment E11.2 also includes a high-positioned release point. However, instead of internal spray as in experiment E11.1, external spray is applied to the dome shell. A detailed presentation of this experiment is given in Wolf, Mun, Floyd, 1995. This experiment, together with E11.4, provides results used as benchmark problems to validate numerical models (Wolf et al., 1994). The verification of the GOTHIC code by Holzbauer and Wolf, 1994, is also based on E11.2 results.

Figure 9.C-75 provides the sequence of the experimental procedures. This includes the duration of the heatup and the blowdown of steam ($p=110$ bar and $T=318^{\circ}\text{C}$) in the compartment R1805 (in the main stairway at elevation 21.05-25.3 m, see Figure 9.C-74, right side). The consecutive steam and gas (mixture of 85 percent He and 15 percent H_2) injections are also presented in Figure 9.C-75. Compartment 1405, in the spiral stairway at elevation 4.5 m (see Figure 9.C-75 right side), receives steam at 770 minutes.

The change in the containment pressure with time is shown in Figure 9.C-76. The temperatures, steam concentrations, and He/ H_2 gas mixture concentrations at various axial positions of the main staircase are presented in Figure 9.C-77, Figure 9.C-78, and Figure 9.C-79, respectively. Temperature differences between the same axial positions of the two vertical flow paths (main and spiral staircases) are pronounced during the heatup phase. Later, temperature differences decrease and change signs. The crossing temperature histories in Figure 9.C-80, Figure 9.C-81, Figure 9.C-82, Figure 9.C-83 indicate a change in the flow directions.

A steep thermal gradient indicates the presence of the stratification that exists between the lower compartments and the containment dome (see Figure 9.C-84). Even an additional steam release in the lower portion of the containment (compartment R1405) at 770 minutes is not able to completely eliminate the vertical thermal gradient, although it is greatly reduced.

The injection of steam into the lower level, together with the effects of cooling the dome with the external spray, causes redistribution of the He/H₂ gas mixture (see Figure 9.C-79). The increase in the gas concentration in the upper part of the dome is a consequence of the steam condensation on the inside dome surface. Later, the decrease in temperatures in the upper dome promote global circulation (causing unstable stratification) and homogenize the dome atmosphere. Even after the external spray is stopped, global circulation affects the lower parts of the containment (see Figure 9.C-77, Figure 9.C-78, Figure 9.C-79). Overall, the external spray causes a reduction of 0.44 bar in the containment pressure (see Figure 9.C-76).

The application of external sprays at the dome surface promotes global circulation, homogenizes hydrogen concentrations, and decreases the containment pressure. The water film applied to the external surface of the AP600 and **AP1000** shell produces similar effects.

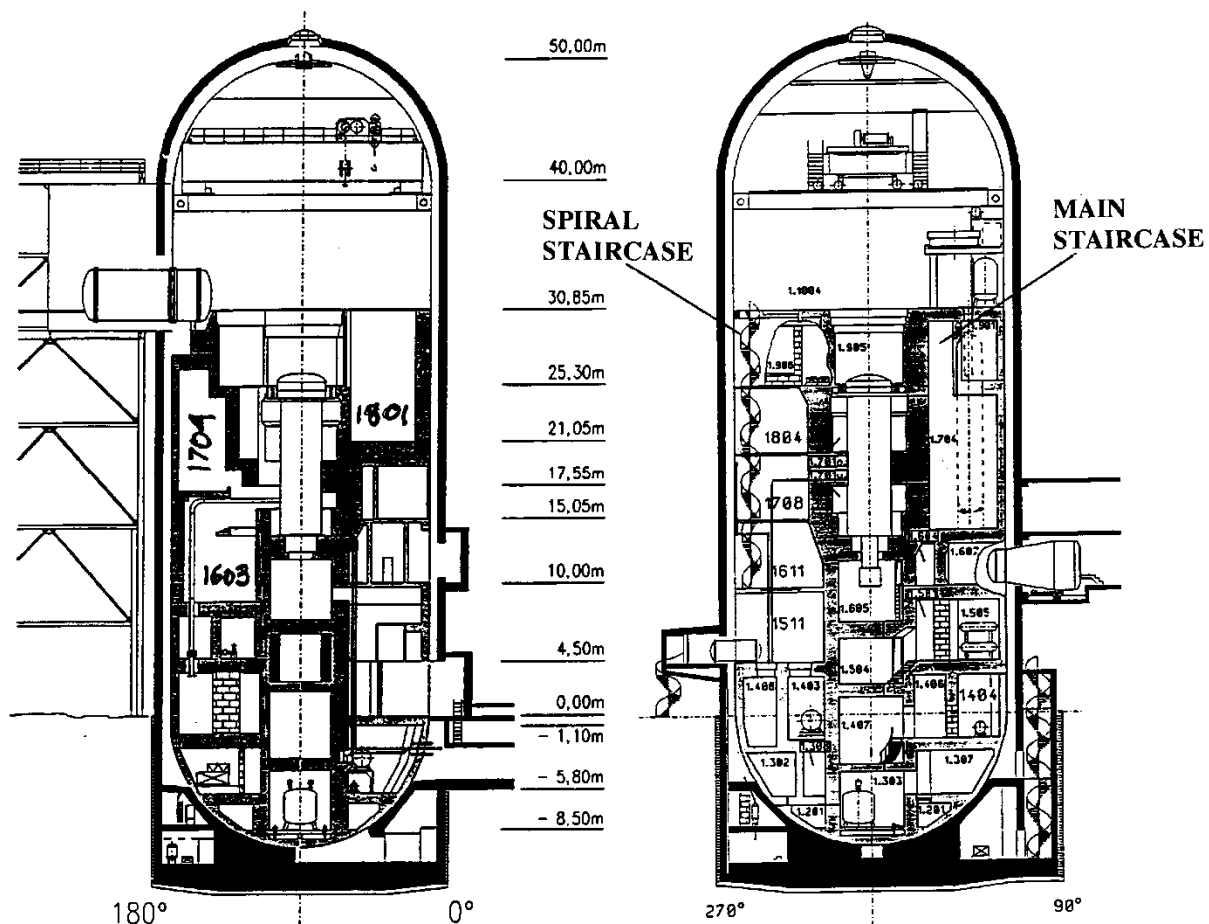


Figure 9.C-73. Cross-sections, Elevations and Numbers of Compartments of the HDR Containment, Left (180°-0°-cross-section), Right (270°-90°-cross-section)

(reprinted from: L. Wolf, K. Mun, J. Floyd, "HDR hydrogen mixing evaluation for containment safety evaluations" – Phase 1, University of Maryland at College Park, Final Report for DOE-Project Order Number: DE-AP07-95ID81401, July 1995)

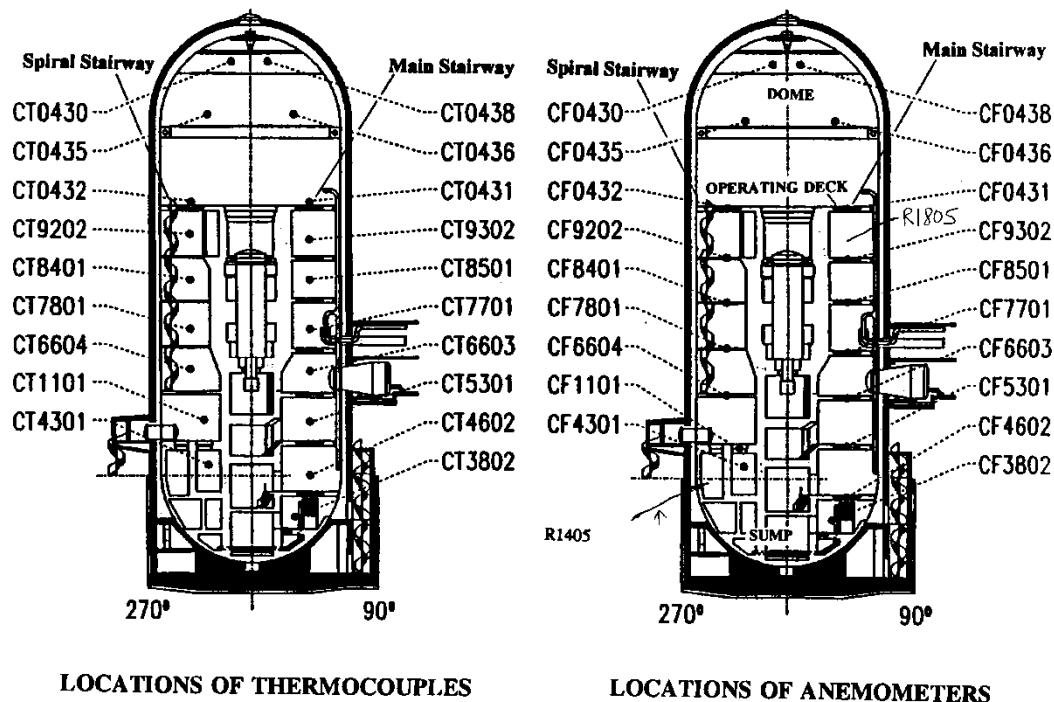
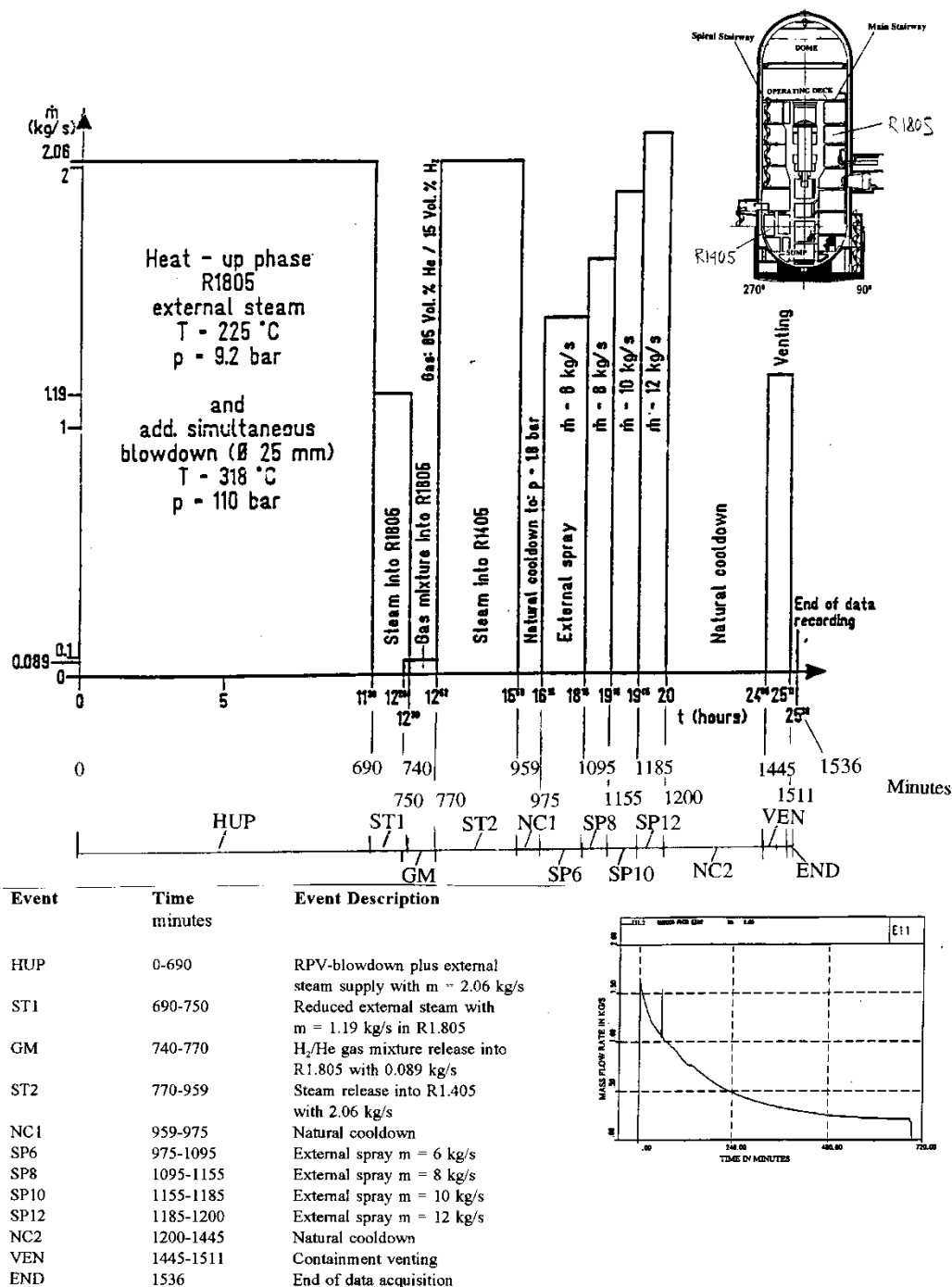


Figure 9.C-74. Locations and Enumerations of Thermocouple (left) and Anemometers (right) for HDR-E-Test Series

(reprinted from: L. Wolf, M. Gavrilas, K. Mun, "Overview of experimental results for long-term, Large-scale natural circulations in LWR-containments after large LOCAs," University of Maryland at College Park, Final Report for DOE – Project, Order Number: DE-AP07-96ID10765," July 1996)



(reprinted from: L. Wolf, K. Mun, J. Floyd, "HDR hydrogen mixing evaluation for containment safety evaluations" – Phase 1, University of Maryland at College Park, Final Report for DOE-Project Order Number: DE-AP07-95ID81401, July 1995)

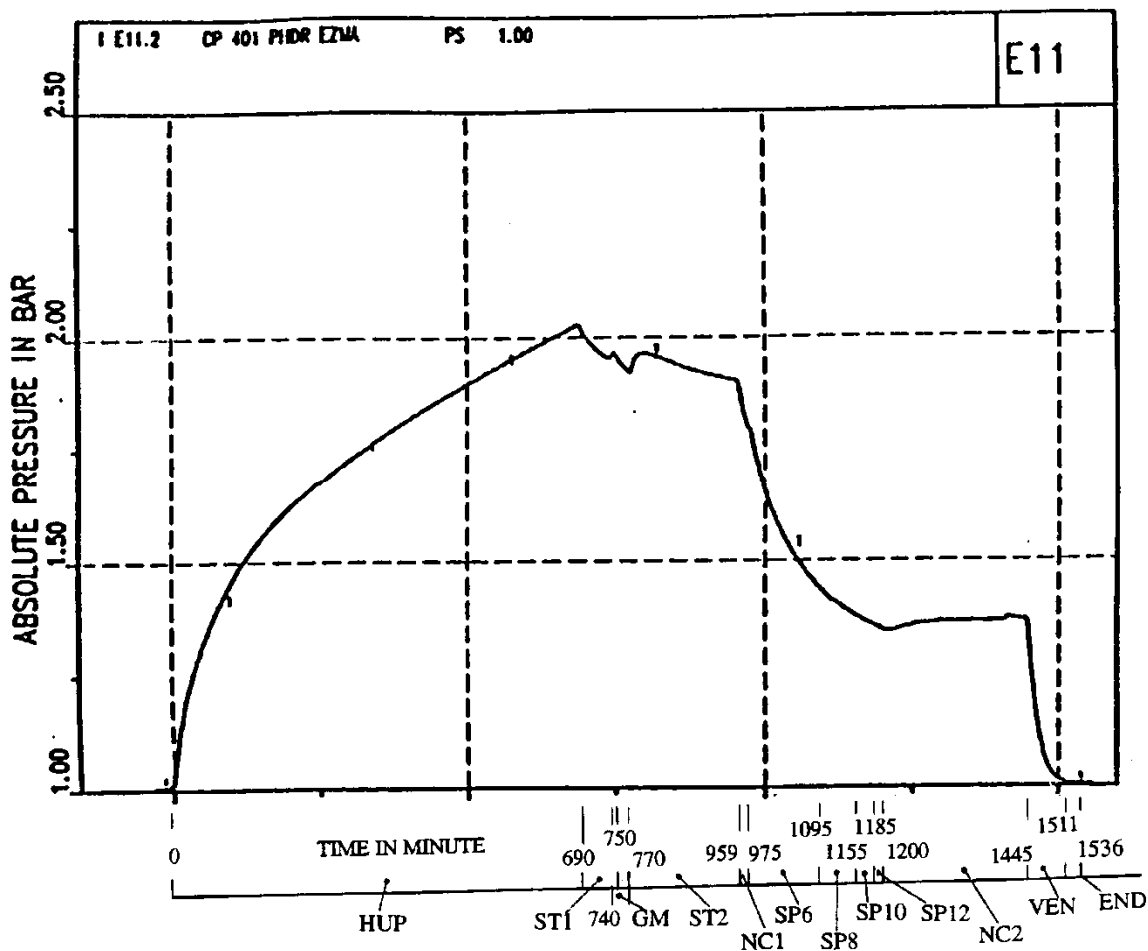


Figure 9.C-76. HDR-E11.2 Containment Pressure History

(reprinted from: L. Wolf, K. Mun, J. Floyd, "HDR hydrogen mixing evaluation for containment safety evaluations" – Phase 1, University of Maryland at College Park, Final Report for DOE-Project Order Number: DE-AP07-95ID81401, July 1995)

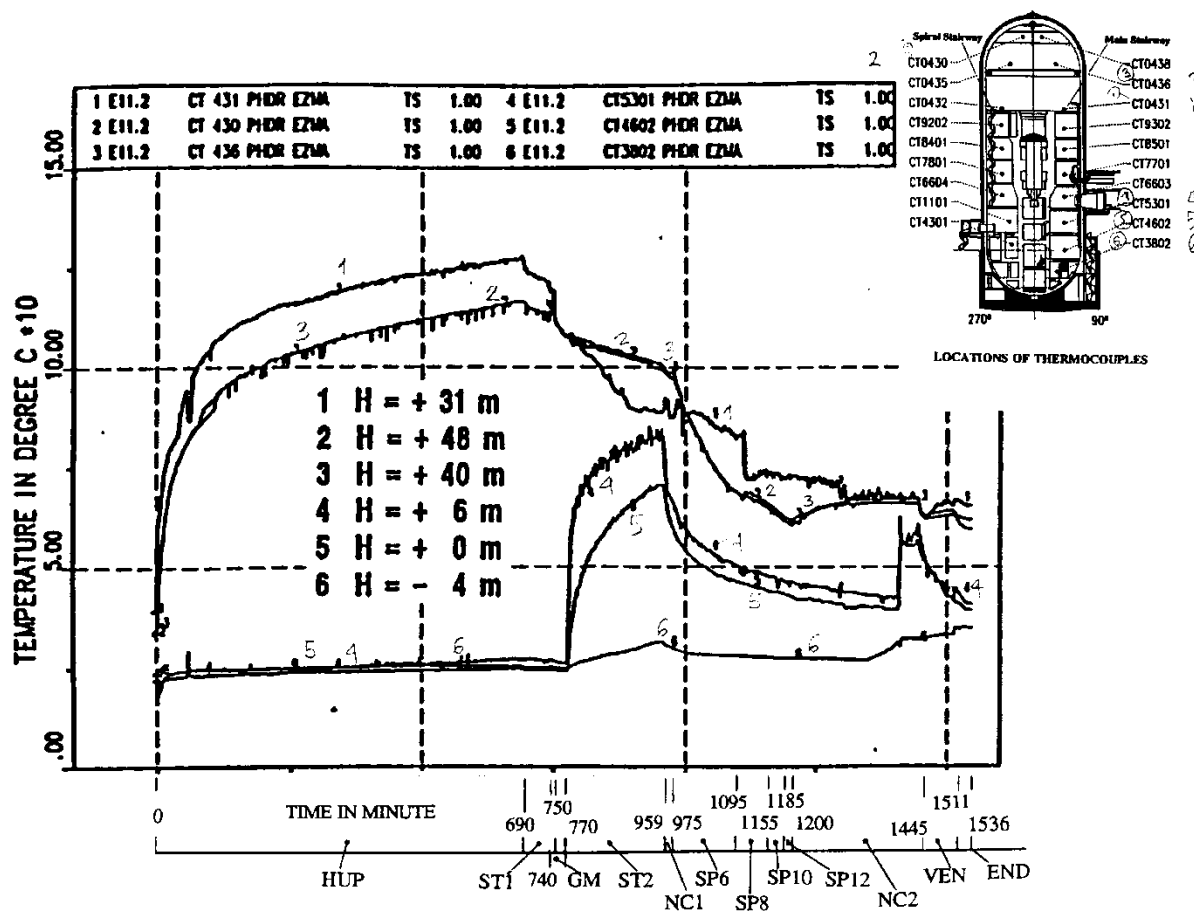


Figure 9.C-77. HDR-E11.2 Atmospheric Temperatures Along Main Stairway

(reprinted from: L. Wolf, K. Mun, J. Floyd, "HDR hydrogen mixing evaluation for containment safety evaluations" – Phase 1, University of Maryland at College Park, Final Report for DOE-Project Order Number: DE-AP07-95ID81401, July 1995)

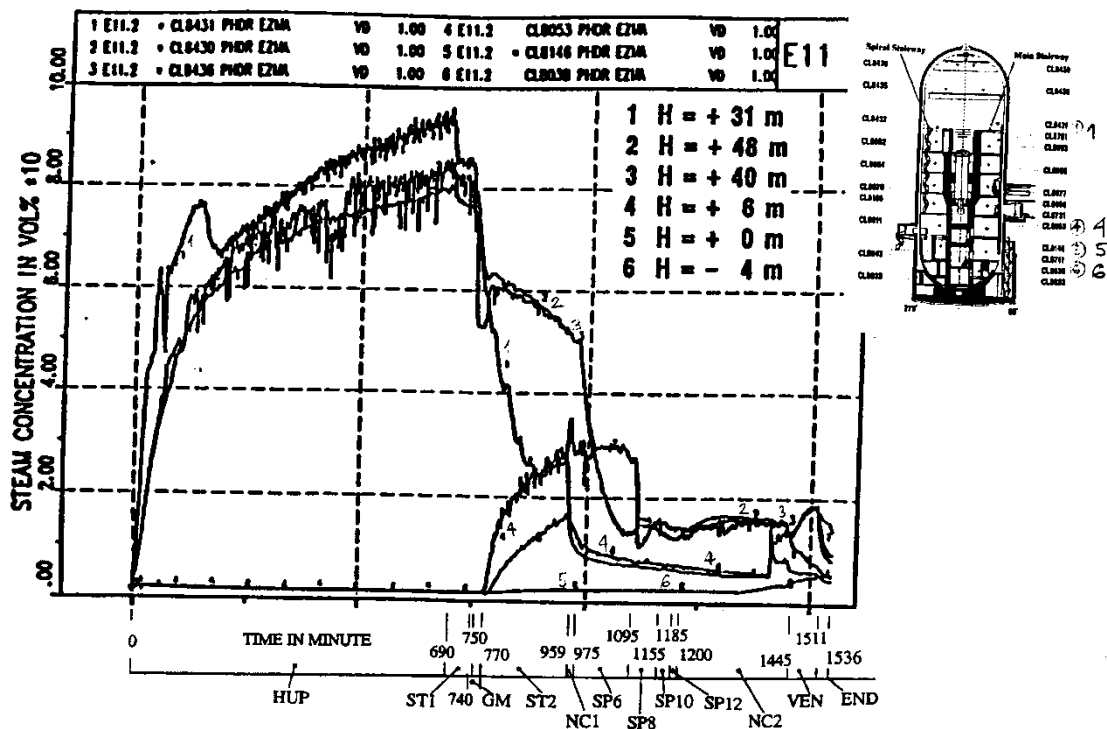


Figure 9.C-78. HDR-E11.2 Steam Concentrations Along Main Stairway

(reprinted from: L. Wolf, K. Mun, J. Floyd, "HDR hydrogen mixing evaluation for containment safety evaluations" – Phase 1, University of Maryland at College Park, Final Report for DOE-Project Order Number: DE-AP07-95ID81401, July 1995)

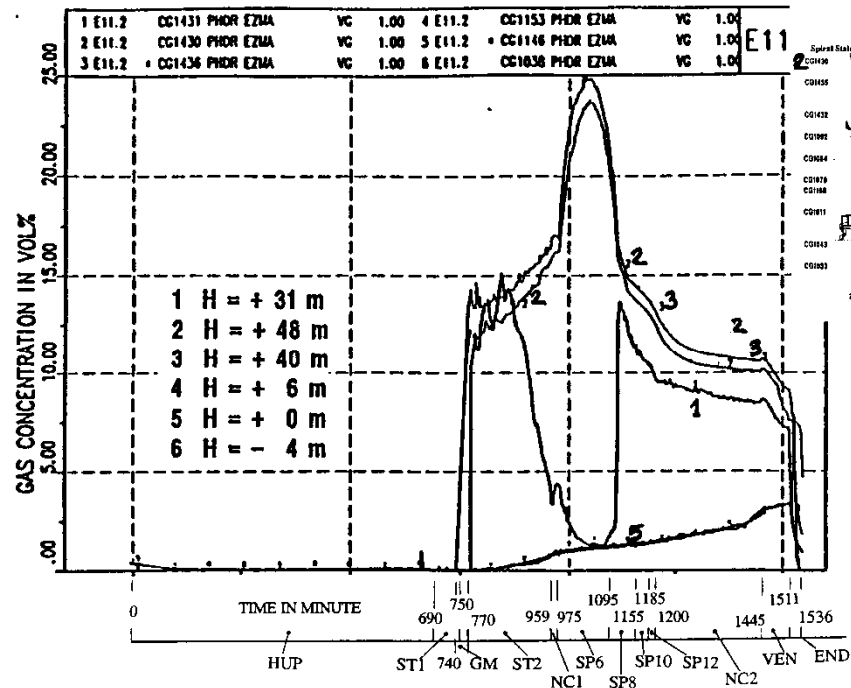


Figure 9.C-79. HDR-E11.2 H₂/He Gas Concentrations Along Main Stairway

(reprinted from: L. Wolf, K. Mun, J. Floyd, "HDR hydrogen mixing evaluation for containment safety evaluations" – Phase 1, University of Maryland at College Park, Final Report for DOE-Project Order Number: DE-AP07-95ID81401, July 1995)

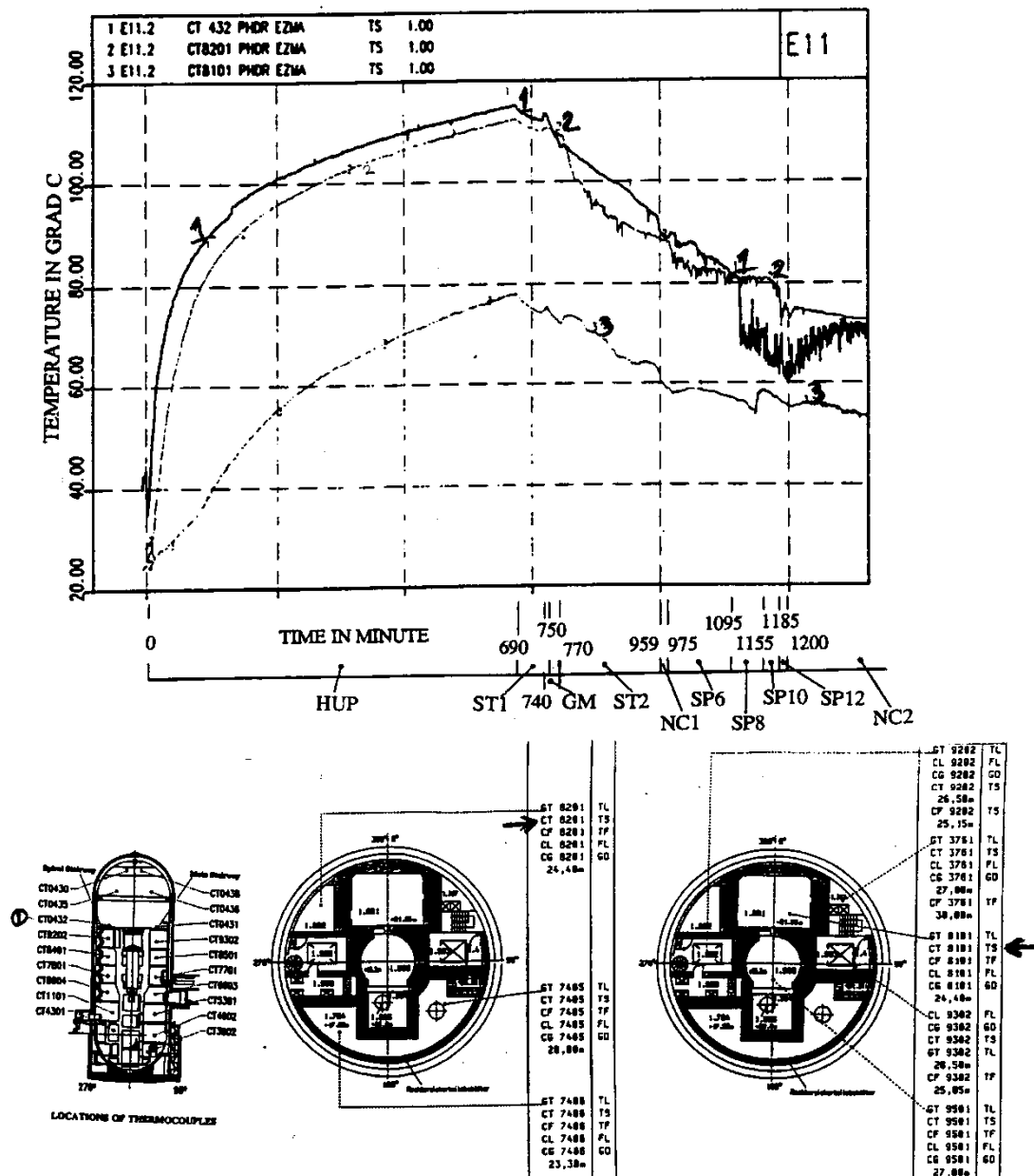


Figure 9.C-80. HDR-E11.2 Comparison Between Temperatures in Main and Spiral Stairways at +31.0 m Level

(reprinted from: L. Wolf, M. Gavrilas, K. Mun, "Overview of experimental results for long-term, Large-scale natural circulations in LWR-containments after large LOCAs," University of Maryland at College Park, Final Report for DOE – Project, Order Number: DE-AP07-96ID10765," July 1996)

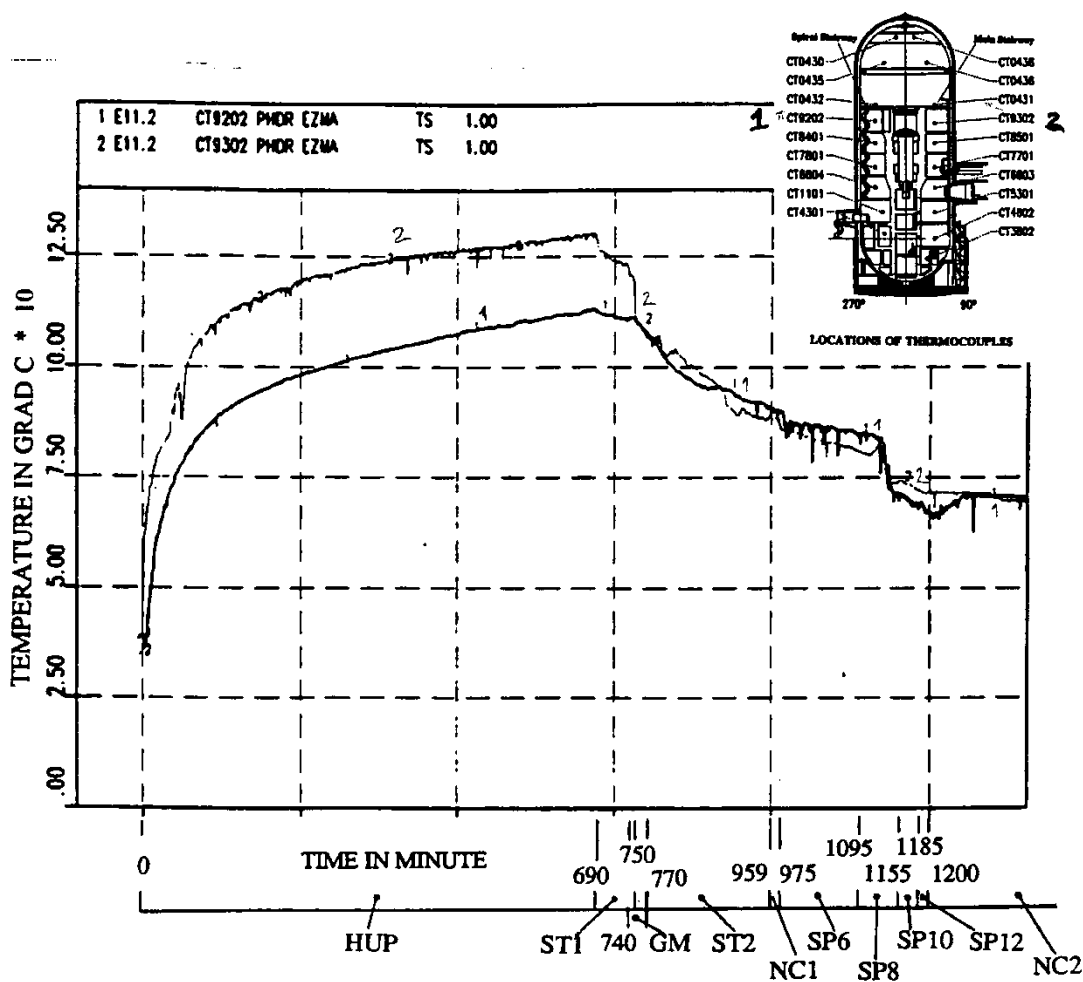


Figure 9.C-81. HDR-E11.2 Comparison Between Temperatures in Main and Spiral Stairways at +26.5 m Level

(reprinted from: L. Wolf, M. Gavrilas, K. Mun, "Overview of experimental results for long-term, Large-scale natural circulations in LWR-containments after large LOCAs," University of Maryland at College Park, Final Report for DOE – Project, Order Number: DE-AP07-96ID10765," July 1996)

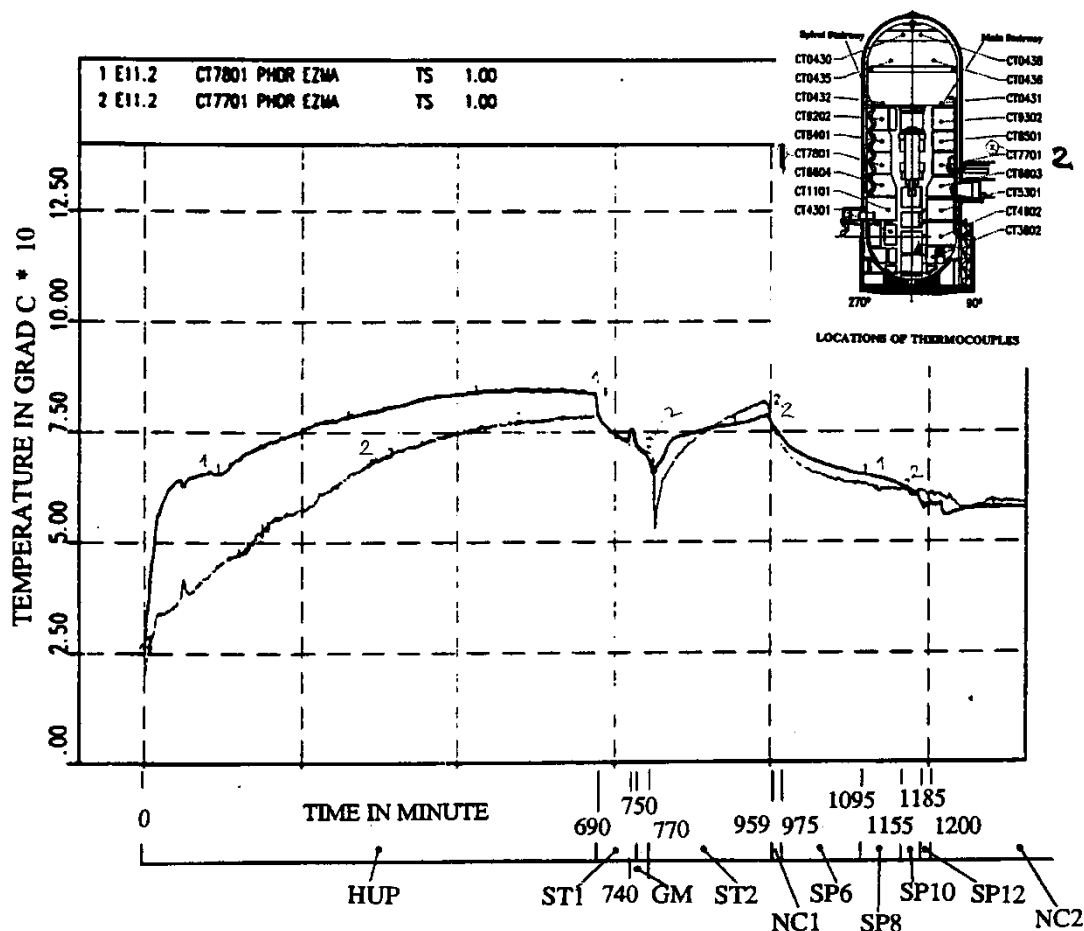


Figure 9.C-82. HDR-E11.2 Comparison Between Temperatures in Main and Spiral Stairways at +16.5 m Level

(reprinted from: L. Wolf, M. Gavrilas, K. Mun, "Overview of experimental results for long-term, Large-scale natural circulations in LWR-containments after large LOCAs," University of Maryland at College Park, Final Report for DOE – Project, Order Number: DE-AP07-96ID10765," July 1996)

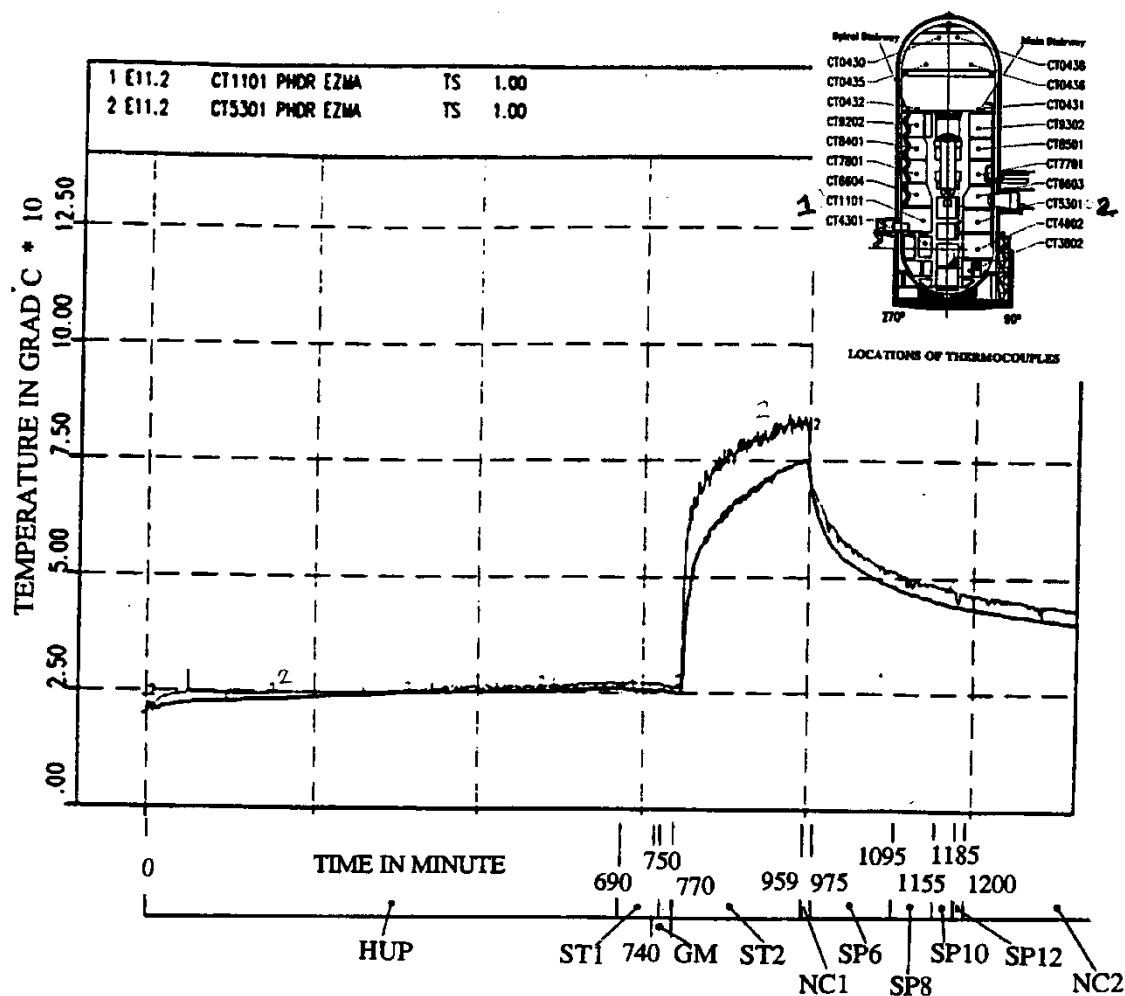


Figure 9.C-83. HDR-E11.2 Comparison Between Temperatures in Main and Spiral Stairways at +6 m Level

(reprinted from: L. Wolf, M. Gavrilas, K. Mun, "Overview of experimental results for long-term, Large-scale natural circulations in LWR-containments after large LOCAs," University of Maryland at College Park, Final Report for DOE – Project, Order Number: DE-AP07-96ID10765," July 1996)

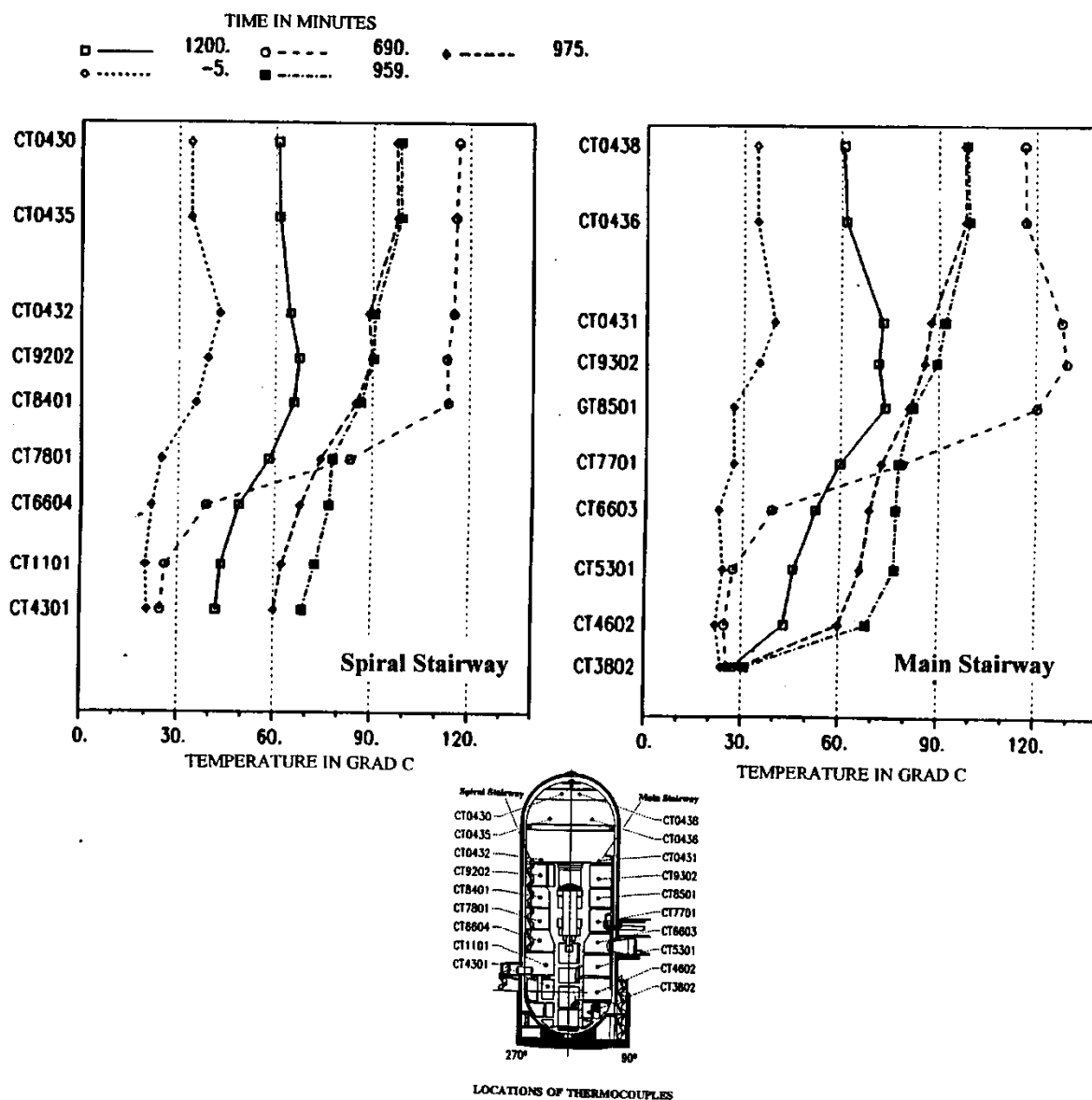


Figure 9.C-84. HDR-E11.2 Axial Temperature Profiles in Both Major Flow Paths at Specific Times, Left in Spiral Stairway, Right in Main Stairway

(reprinted from: L. Wolf, M. Gavrilas, K. Mun, "Overview of experimental results for long-term, Large-scale natural circulations in LWR-containments after large LOCAs," University of Maryland at College Park, Final Report for DOE – Project, Order Number: DE-AP07-96ID10765," July 1996)

9.C.2.4.1.4 Experiment E11.3

Experiment E11.3 includes a low-positioned small break and gas release, as well as a closed entrance to the spiral stairway at the upper-deck. Although detailed boundary conditions are not available in the literature, this case is included to qualitatively indicate the influence of the injection position on the formation of global circulation. Even with the main vertical flow path from the top of the spiral staircase to the dome closed, global circulation is generated through other horizontal connections between the compartments (see Figure 9.C-85 and Figure 9.C-86).

Temperature differences exist between the vertical axial flow channels during the heatup phase, the gas release phase, and the long cooldown period. The axial temperature profiles indicate that the temperature field was close to homogeneous with a ΔT of only 7°C , except for the region below the release, as indicated by CT8101 in Figure 9.C-87 (see Figure 9.C-87 to Figure 9.C-91).

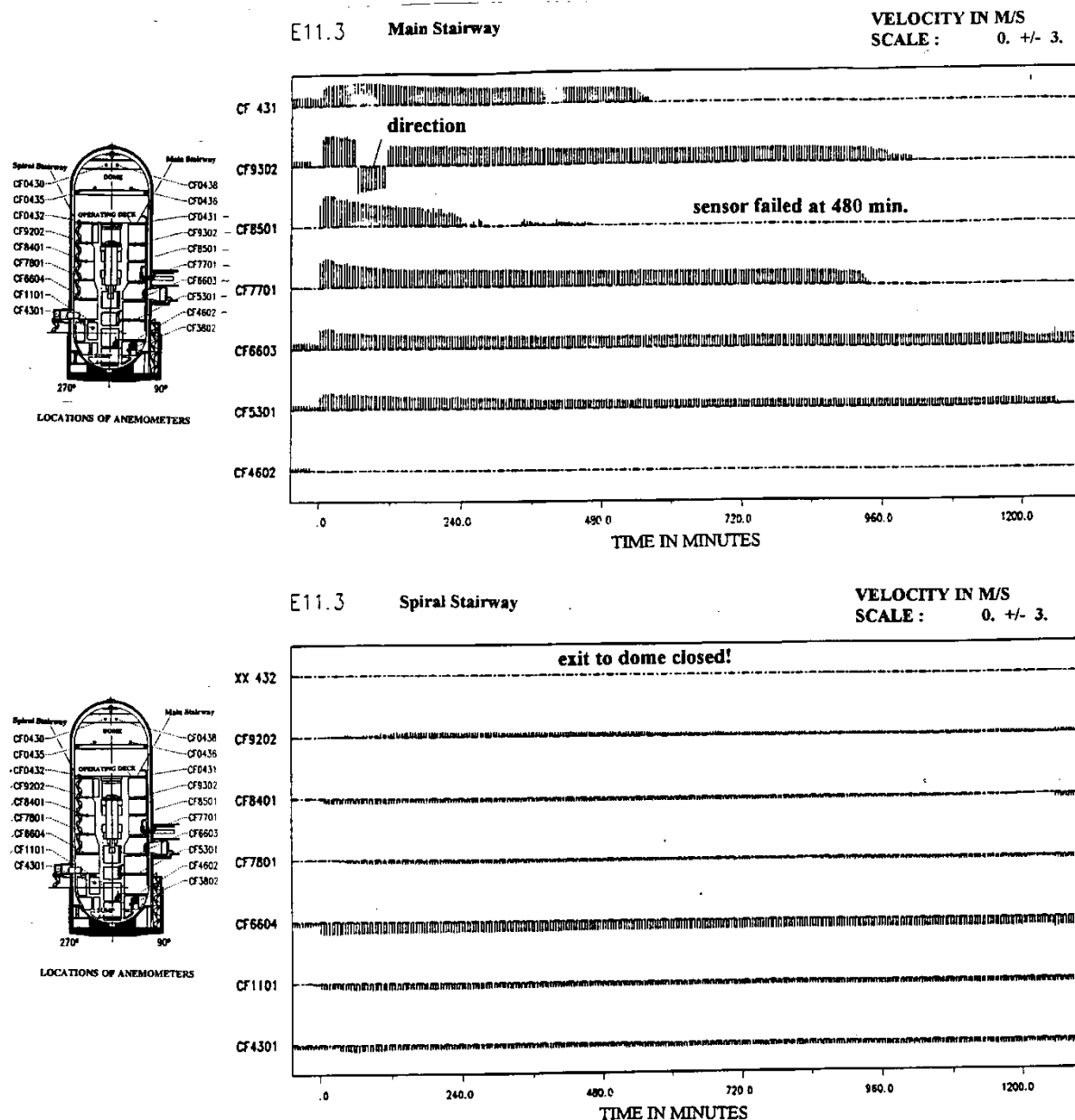


Figure 9.C-85. HDR-E11.3 Velocities in Both Major Flow Paths at Different Axial Positions During Containment Heatup

(reprinted from: L. Wolf, M. Gavrilas, K. Mun, "Overview of experimental results for long-term, Large-scale natural circulations in LWR-containments after large LOCAs," University of Maryland at College Park, Final Report for DOE – Project, Order Number: DE-AP07-96ID10765," July 1996)

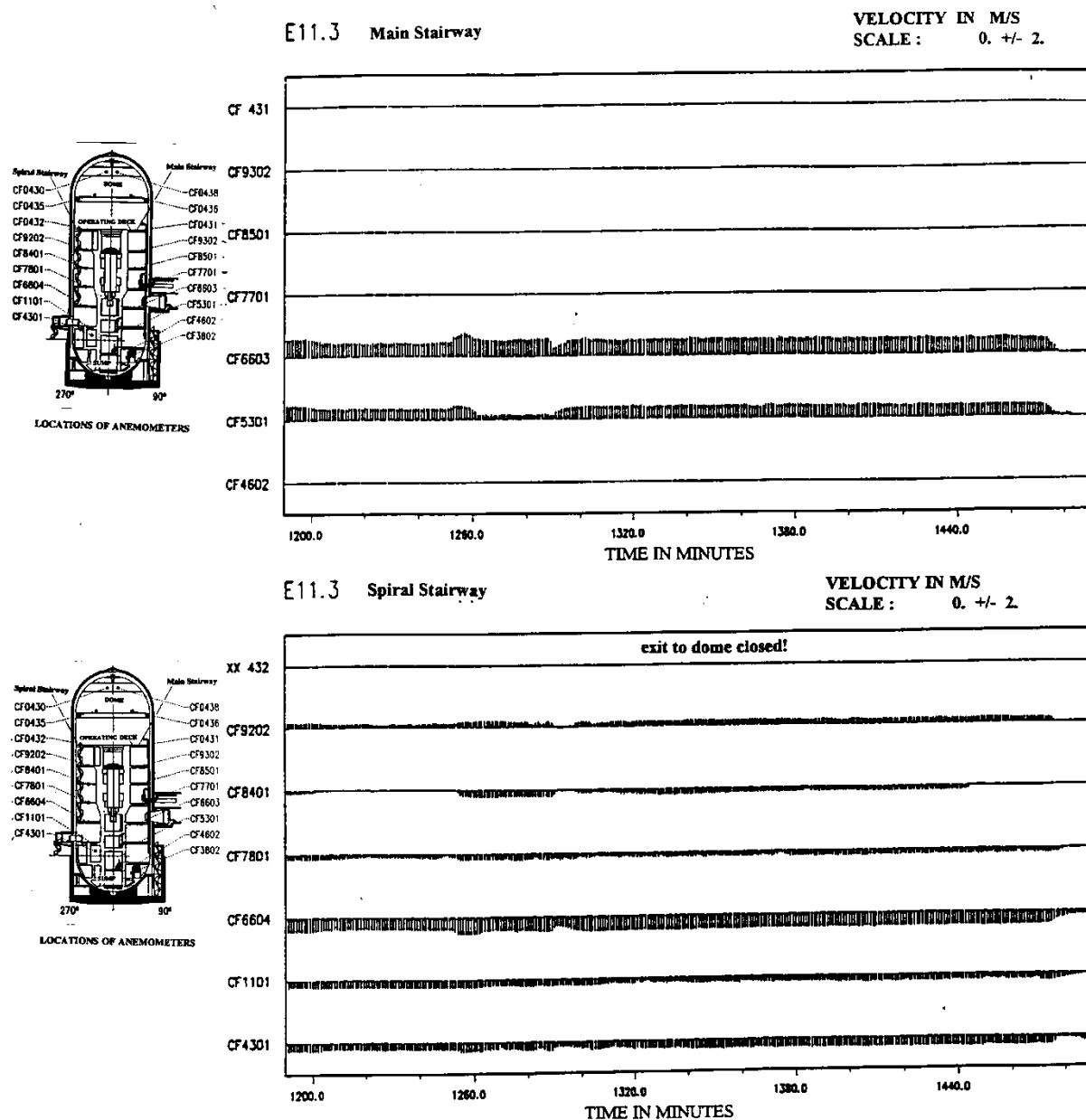
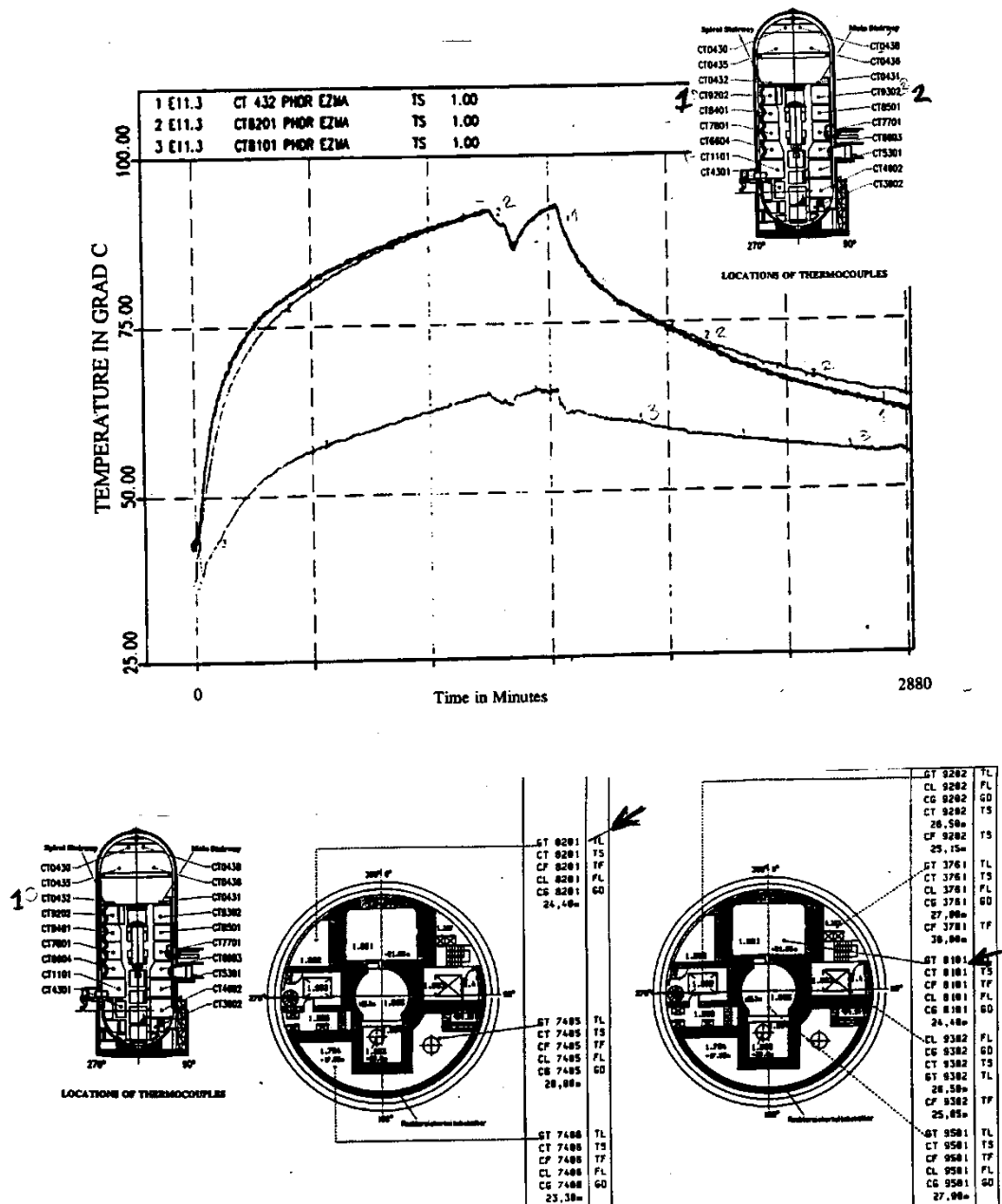


Figure 9.C-86. HDR-E11.3 Velocities in Both Major Flow Paths at Different Axial Positions During H₂/He Gas Mixture Release

(reprinted from: L. Wolf, M. Gavrilas, K. Mun, "Overview of experimental results for long-term, Large-scale natural circulations in LWR-containments after large LOCAs," University of Maryland at College Park, Final Report for DOE – Project, Order Number: DE-AP07-96ID10765," July 1996)



**Figure 9.C-87. HDR-E11.3 Comparison Between Temperatures in Main and Spiral Stairways
at +31.0 m Level**

(reprinted from: L. Wolf, M. Gavrilas, K. Mun, "Overview of experimental results for long-term, Large-scale natural circulations in LWR-containments after large LOCAs," University of Maryland at College Park, Final Report for DOE – Project, Order Number: DE-AP07-96ID10765," July 1996)

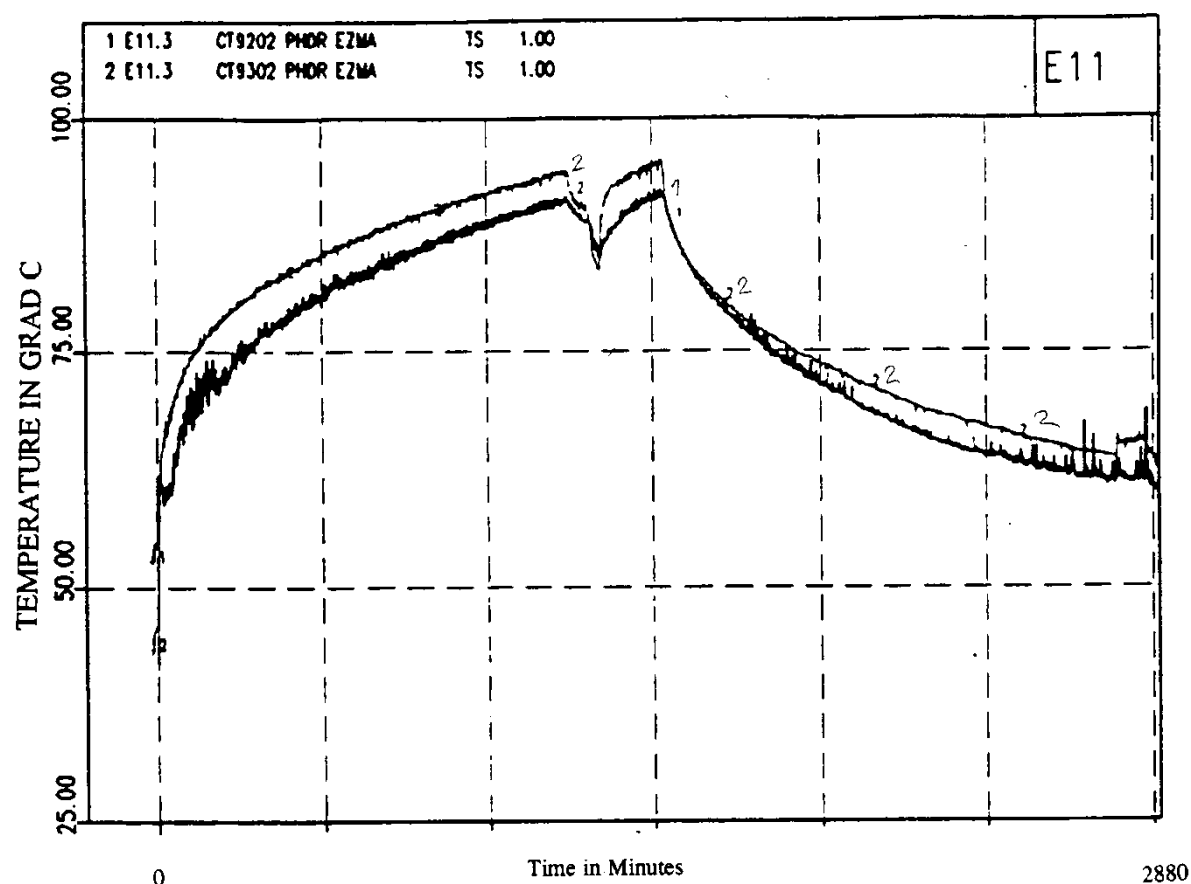


Figure 9.C-88. HDR-E11.3 Comparison Between Temperatures in Main and Spiral Stairways at +26.5 m Level

(reprinted from: L. Wolf, M. Gavrilas, K. Mun, "Overview of experimental results for long-term, Large-scale natural circulations in LWR-containments after large LOCAs," University of Maryland at College Park, Final Report for DOE – Project, Order Number: DE-AP07-96ID10765," July 1996)

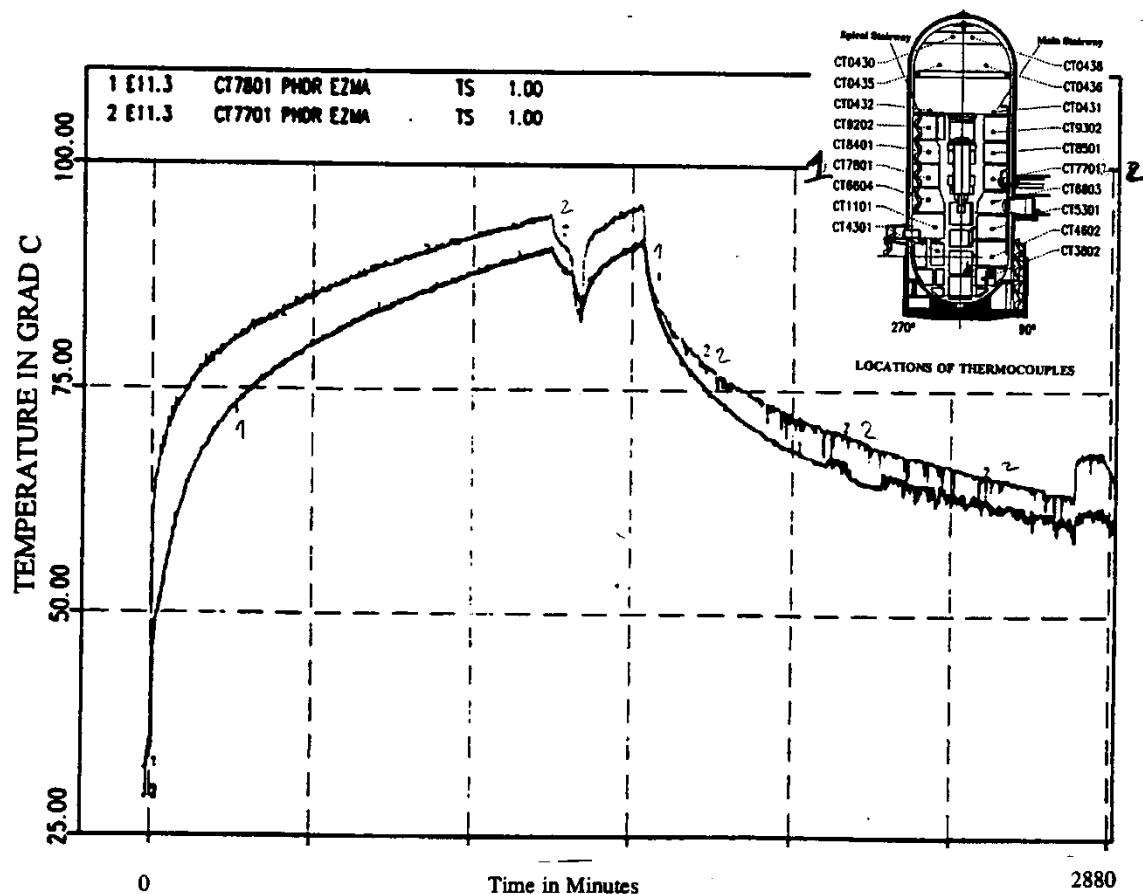


Figure 9.C-89. HDR-E11.3 Comparison Between Temperatures in Main and Spiral Stairways at +16.5 m Level

(reprinted from: L. Wolf, M. Gavrilas, K. Mun, "Overview of experimental results for long-term, Large-scale natural circulations in LWR-containments after large LOCAs," University of Maryland at College Park, Final Report for DOE – Project, Order Number: DE-AP07-96ID10765," July 1996)

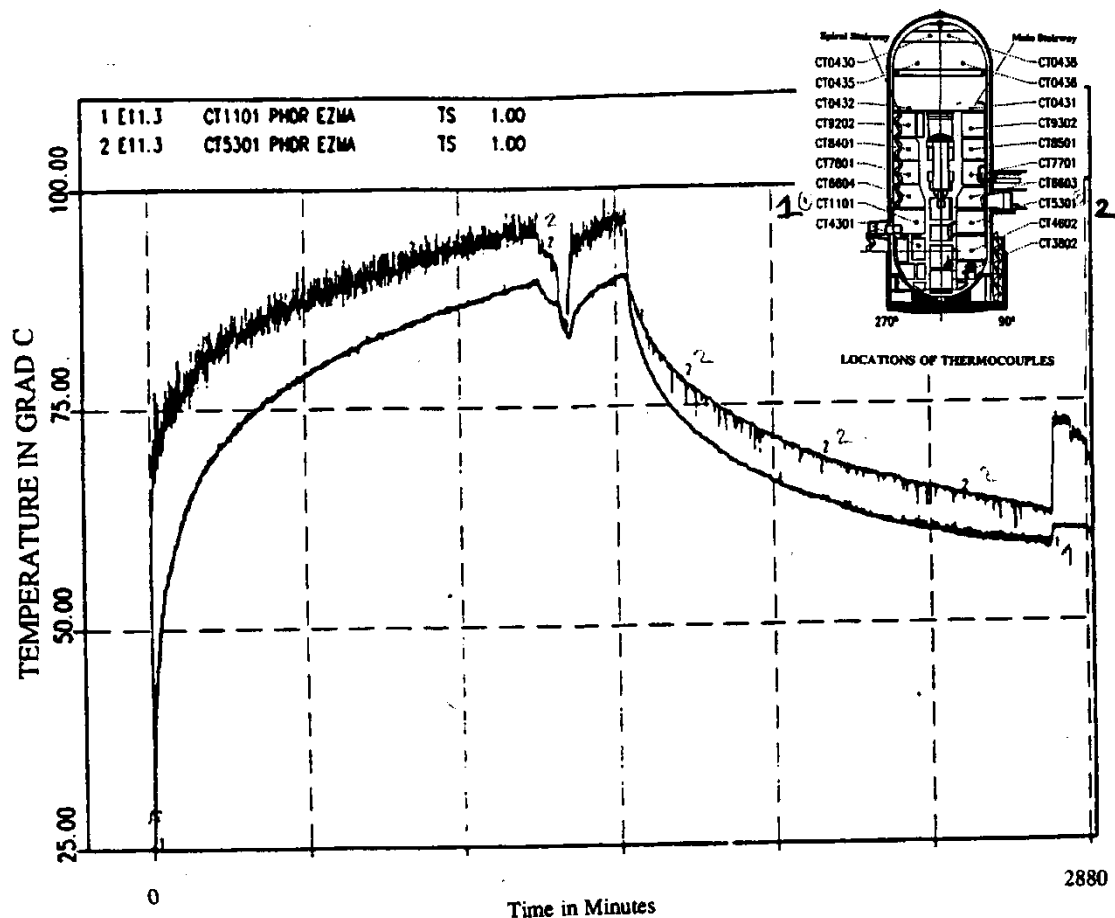


Figure 9.C-90. HDR-E11.3 Comparison Between Temperatures in Main and Spiral Stairwars at +6 m Level

(reprinted from: L. Wolf, M. Gavrilas, K. Mun, "Overview of experimental results for long-term, Large-scale natural circulations in LWR-containments after large LOCAs," University of Maryland at College Park, Final Report for DOE – Project, Order Number: DE-AP07-96ID10765," July 1996)

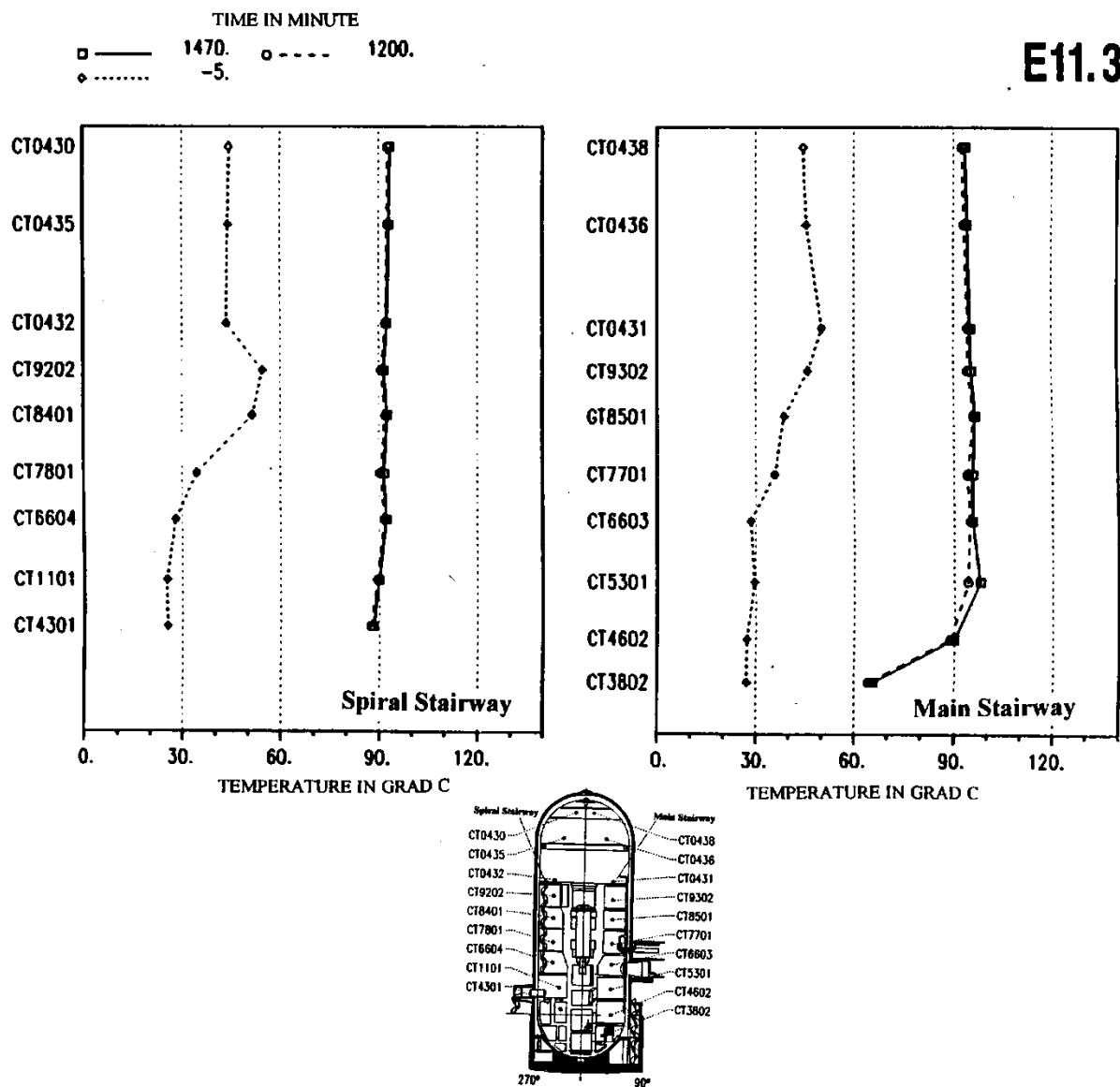


Figure 9.C-91. HDR-E11.3 Axial Temperature Profiles in Both Major Flow Paths at Specific Times, Left in Spiral Stairway, Right in Main Stairway

(reprinted from: L. Wolf, M. Gavrilas, K. Mun, "Overview of experimental results for long-term, Large-scale natural circulations in LWR-containments after large LOCAs," University of Maryland at College Park, Final Report for DOE – Project, Order Number: DE-AP07-96ID10765," July 1996)

9.C.2.4.1.5 Experiment E11.4

Experiment E11.4 includes a low-positioned break and an active external spray. The spiral stairway entrance to the dome is open. A detailed presentation of this experiment is given by Wolf, Mun, Floyd, 1995. Data from this test is used to validate various numerical containment codes (Wolf et al., 1994, Pisa and Holzbauer and Wolf, 1994, Pisa).

Figure 9.C-92 and Table 9.C-5 present the experimental procedure. This includes the duration of heatup and blowdown of steam ($p=110$ bar and $T=318^{\circ}\text{C}$ in the compartment R1405, (see Figure 9.C-74 and Figure 9.C-92) and the consecutive steam and gas injections.

The containment pressure history is shown in Figure 9.C-93. This figure shows the effects of the external spray application (after 2800 minutes) on the decrease of the containment pressure (by 0.25 bar).

Temperatures at the various axial positions in the main staircase are presented in Figure 9.C-94. Note that the shapes of the temperature curves for various levels are similar, but the values are different. Global circulation is indicated by the small temperature differences from the top to the bottom of the dome, $\Delta T=2\text{-}6^{\circ}\text{C}$, and from the dome to the sump, $\Delta T=10\text{-}26^{\circ}\text{C}$. Figure 9.C-95 and Figure 9.C-96 provide steam and gas concentration histories for the various levels in the main staircase.

During all phases of the experiment, temperature differences exist between the two vertical channels (main and spiral staircases) enabling the global circulation (see Figure 9.C-97 – Figure 9.C-100). The temperature differences decrease during the cooldown phase. As in experiment E11.3, the axial temperature distribution indicates a nearly uniform temperature profile, except below the release point (see Figure 9.C-101).

During the E11.4 test, the release into the lower-level compartment promotes global circulation and homogenizes the containment atmosphere. In addition, the application of the external sprays causes a decrease in the containment pressure (see Figure 9.C-93) and a reduction in the axial temperature gradient (see Figure 9.C-94, curves 1-6). The external spray also promotes a more uniform gas concentration (see Figure 9.C-96 from 2800 to 3000 minutes).

Table 9.C-5. Events for E11.4 Experiment

Event	Time (minutes)	Event Description
HUP	0-2040	RPV-blowdown plus external steam supply with $m = 2.06$ kg/s
ST1	2040-2100	Reduced external steam with $m = 1.19$ kg/s in R1.405
GM1	2090-2100	H ₂ /He gas mixture release into R1.405 with 0.089 kg/s
ST2	2120-2180	Steam release into R1.405 with 2.06 kg/s
DH	2180-2550	Dry heat addition into R1.308
GM2	2193-2195	H ₂ /He gas mixture release into R1.405 with 0.2 kg/s
GM3	2195-2205	H ₂ /He gas mixture release into R1.405 with 0.089 kg/s
ST3	2205-2505	Start of steam release into R1.405 with $m = 1.19$ kg/s
ST4	2550-2620	Steam release into R1.405 with $m = 2.06$ kg/s
SUB	2620-2800	Sump boiling
NC1	2800-2805	Natural cooldown
SP6	2805-2925	External spray $m = 6$ kg/s
SP8	2925-2985	External spray $m = 8$ kg/s
SP10	2985-3015	External spray $m = 10$ kg/s
SP12	3015-3016	External spray $m = 12$ kg/s
NC2	3016-3229	Natural cooldown
VEN	3229-3300	Containment venting
END	3360	End of data acquisition

(reprinted from L. Wolf, M. Gavrilas, K. Mun, "Overview of experimental results for long-term, large-scale natural circulations in LWR-containments after large LOCAS," University of Maryland at College Park, Final Report for DOE – Project, Order Number: DE-AP07-96ID10765")

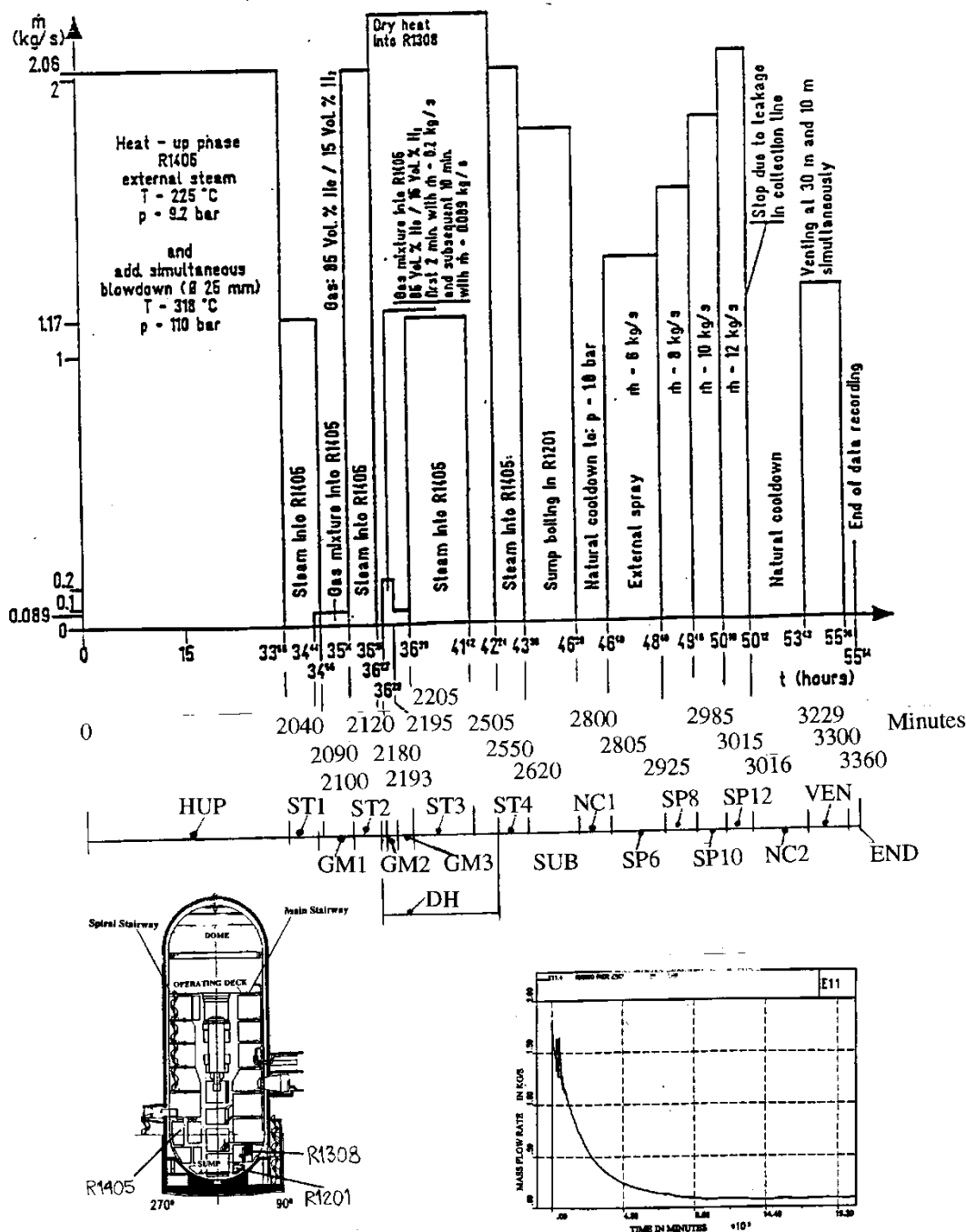


Figure 9.C-92. HDR-E11.4 Sequence of Experimental Test Procedures

(reprinted from: L. Wolf, K. Mun, J. Floyd, "HDR hydrogen mixing evaluation for containment safety evaluations" – Phase 1, University of Maryland at College Park, Final Report for DOE-Project Order Number: DE-AP07-95ID81401, July 1995)

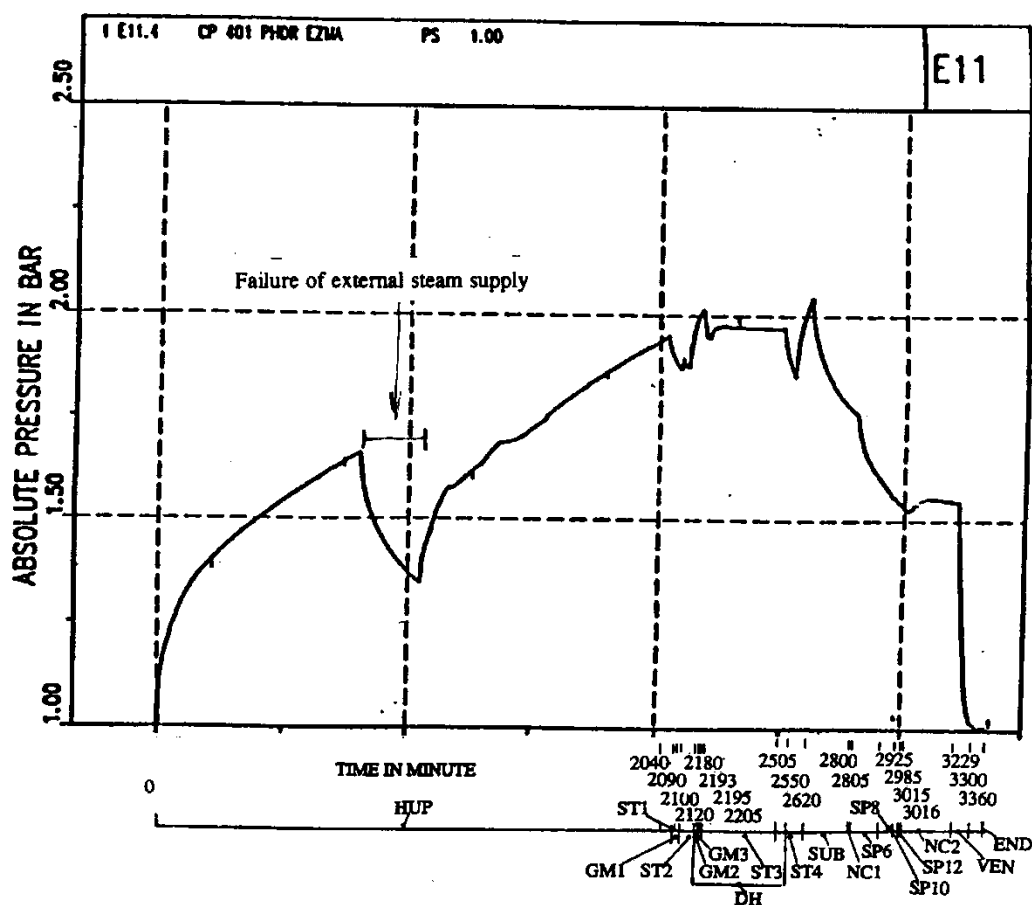


Figure 9.C-93. HDR-E11.4 Containment Pressure History

(reprinted from: L. Wolf, K. Mun, J. Floyd, "HDR hydrogen mixing evaluation for containment safety evaluations" – Phase 1, University of Maryland at College Park, Final Report for DOE-Project Order Number: DE-AP07-95ID81401, July 1995)

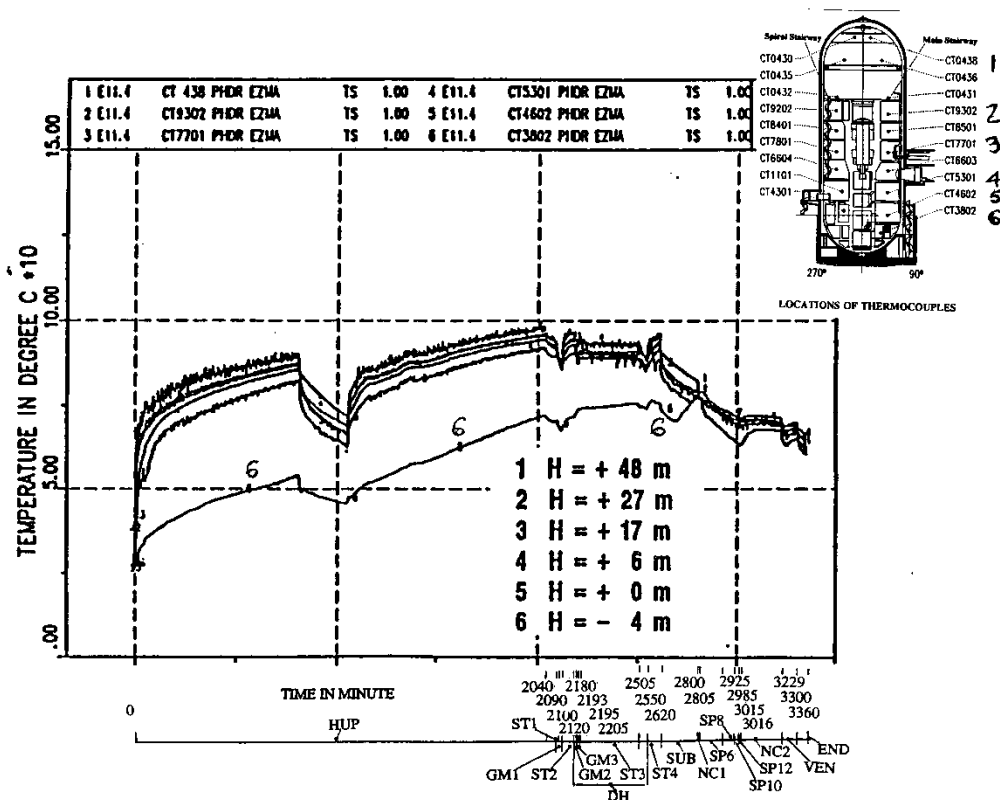


Figure 9.C-94. HDR-E11.4 Atmospheric Temperatures Along Main Stairway

(reprinted from: L. Wolf, K. Mun, J. Floyd, "HDR hydrogen mixing evaluation for containment safety evaluations" – Phase 1, University of Maryland at College Park, Final Report for DOE-Project Order Number: DE-AP07-95ID81401, July 1995)

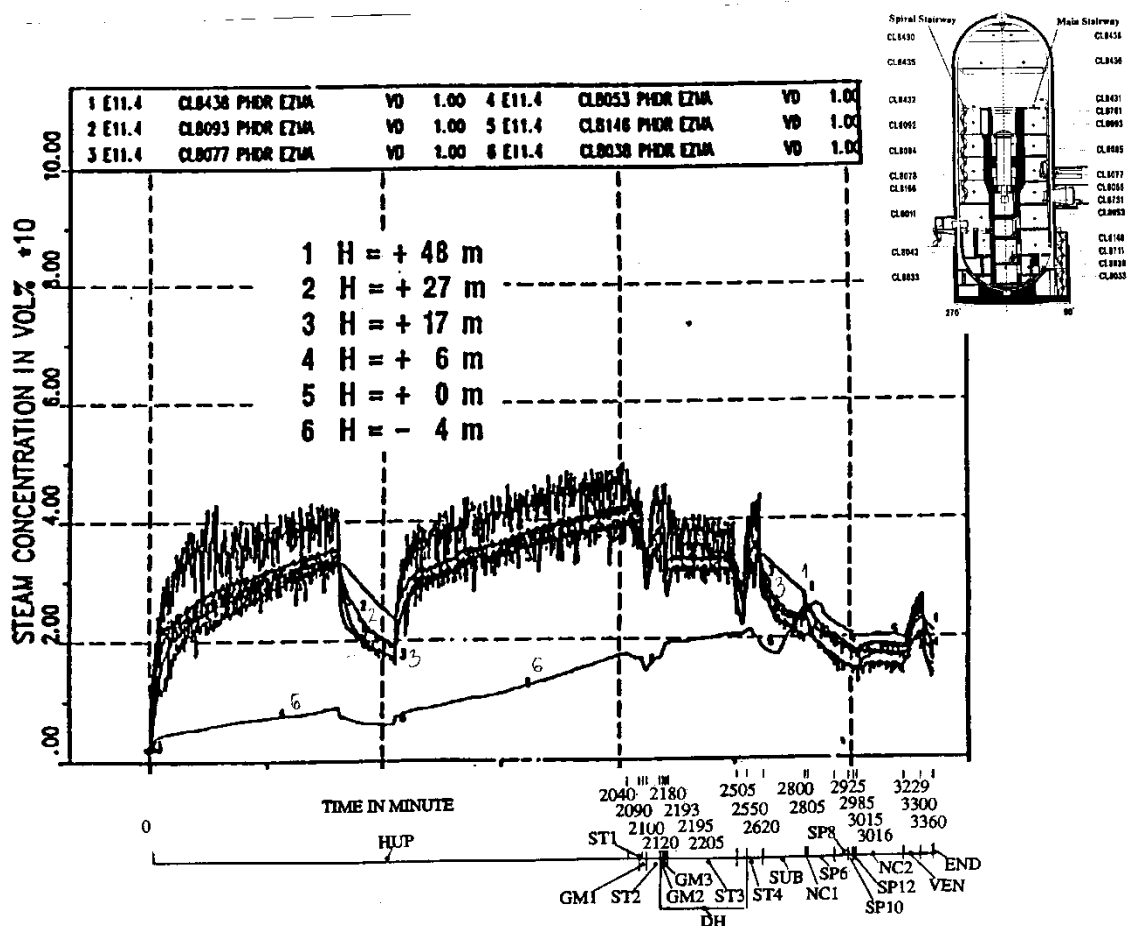


Figure 9.C-95. HDR-E11.4 Steam Concentration Along Main Stairway

(reprinted from: L. Wolf, K. Mun, J. Floyd, "HDR hydrogen mixing evaluation for containment safety evaluations" – Phase 1, University of Maryland at College Park, Final Report for DOE-Project Order Number: DE-AP07-95ID81401, July 1995)

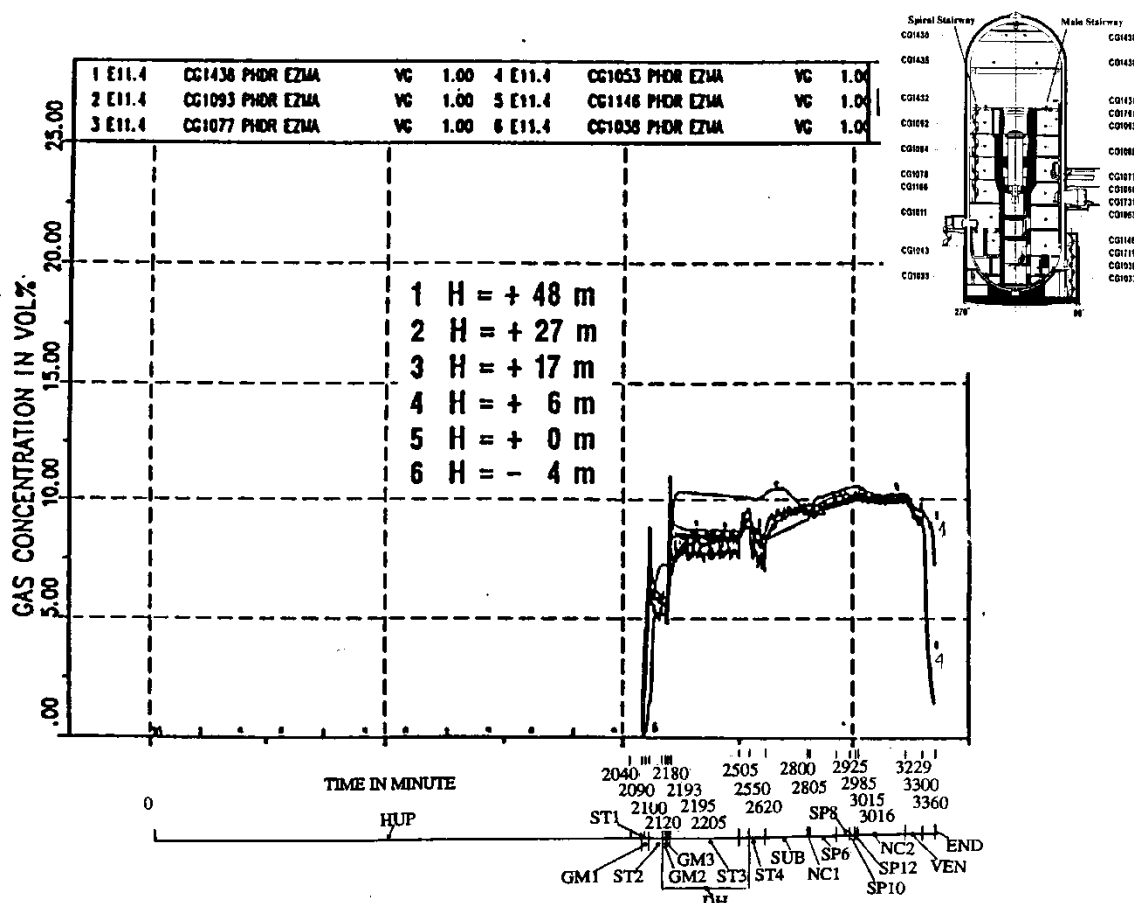


Figure 9.C-96. HDR-E11.4 H₂/He Gas Concentrations Along Main Stairway

(reprinted from: L. Wolf, K. Mun, J. Floyd, "HDR hydrogen mixing evaluation for containment safety evaluations" – Phase 1, University of Maryland at College Park, Final Report for DOE-Project Order Number: DE-AP07-95ID81401, July 1995)

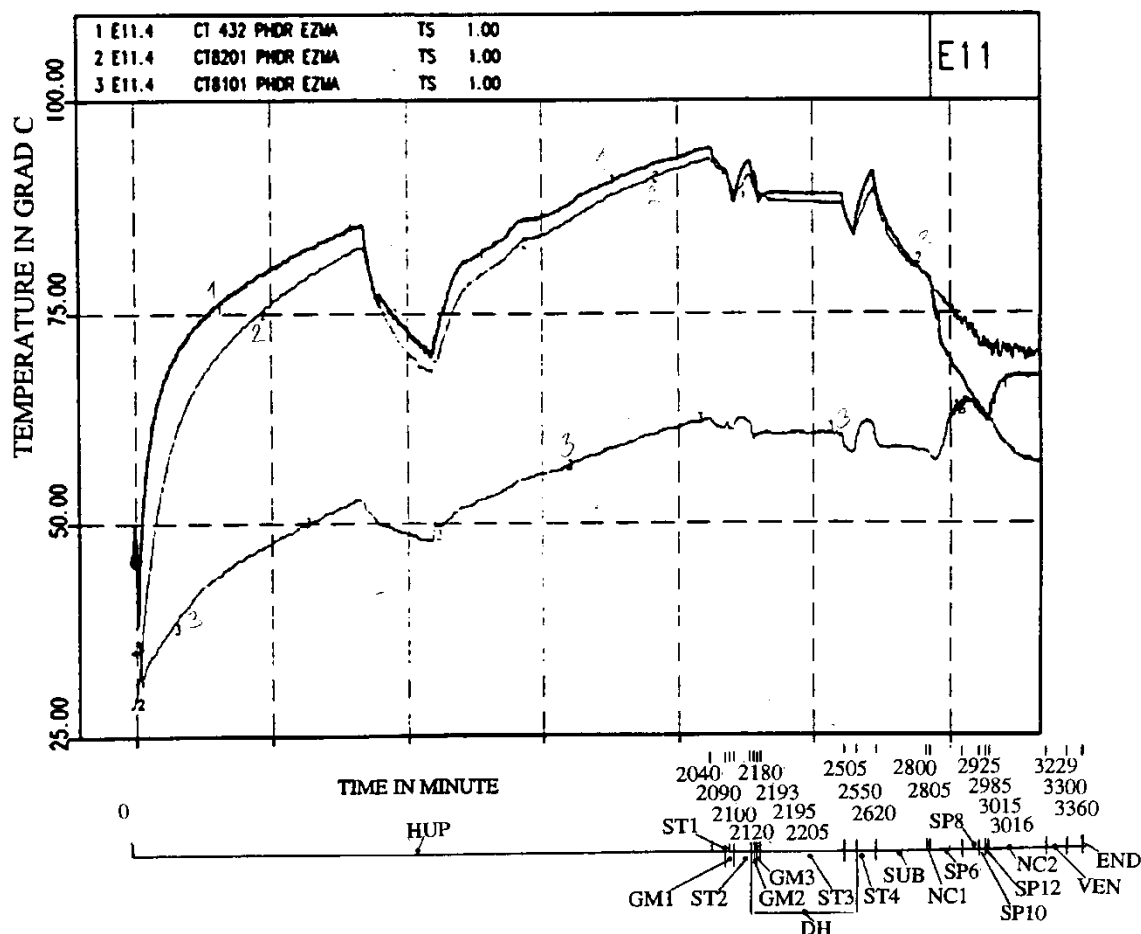


Figure 9.C-97a. HDR-E11.4 Comparison Between Temperatures in Main and Spiral Stairways at +31.0 m Level

(reprinted from: L. Wolf, M. Gavrilas, K. Mun, "Overview of experimental results for long-term, Large-scale natural circulations in LWR-containments after large LOCAs," University of Maryland at College Park, Final Report for DOE – Project, Order Number: DE-AP07-96ID10765," July 1996)

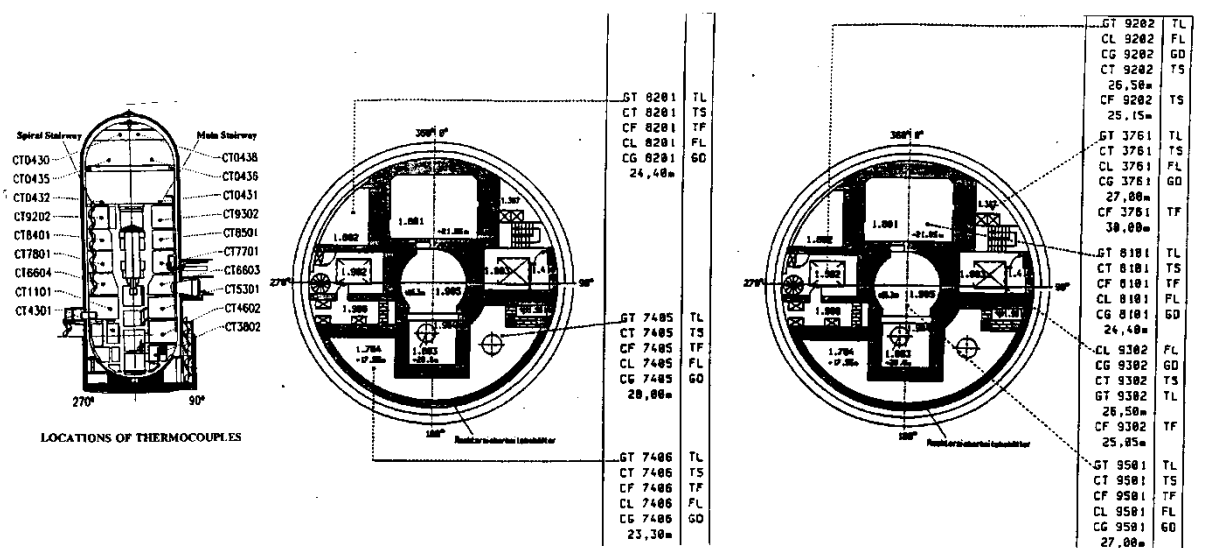


Figure 9.C-97b. HDR-E11.4 Comparison Between Temperatures in Main and Spiral Stairways at +31.0 m Level

(reprinted from: L. Wolf, M. Gavrilas, K. Mun, "Overview of experimental results for long-term, Large-scale natural circulations in LWR-containments after large LOCAs," University of Maryland at College Park, Final Report for DOE – Project, Order Number: DE-AP07-96ID10765," July 1996)

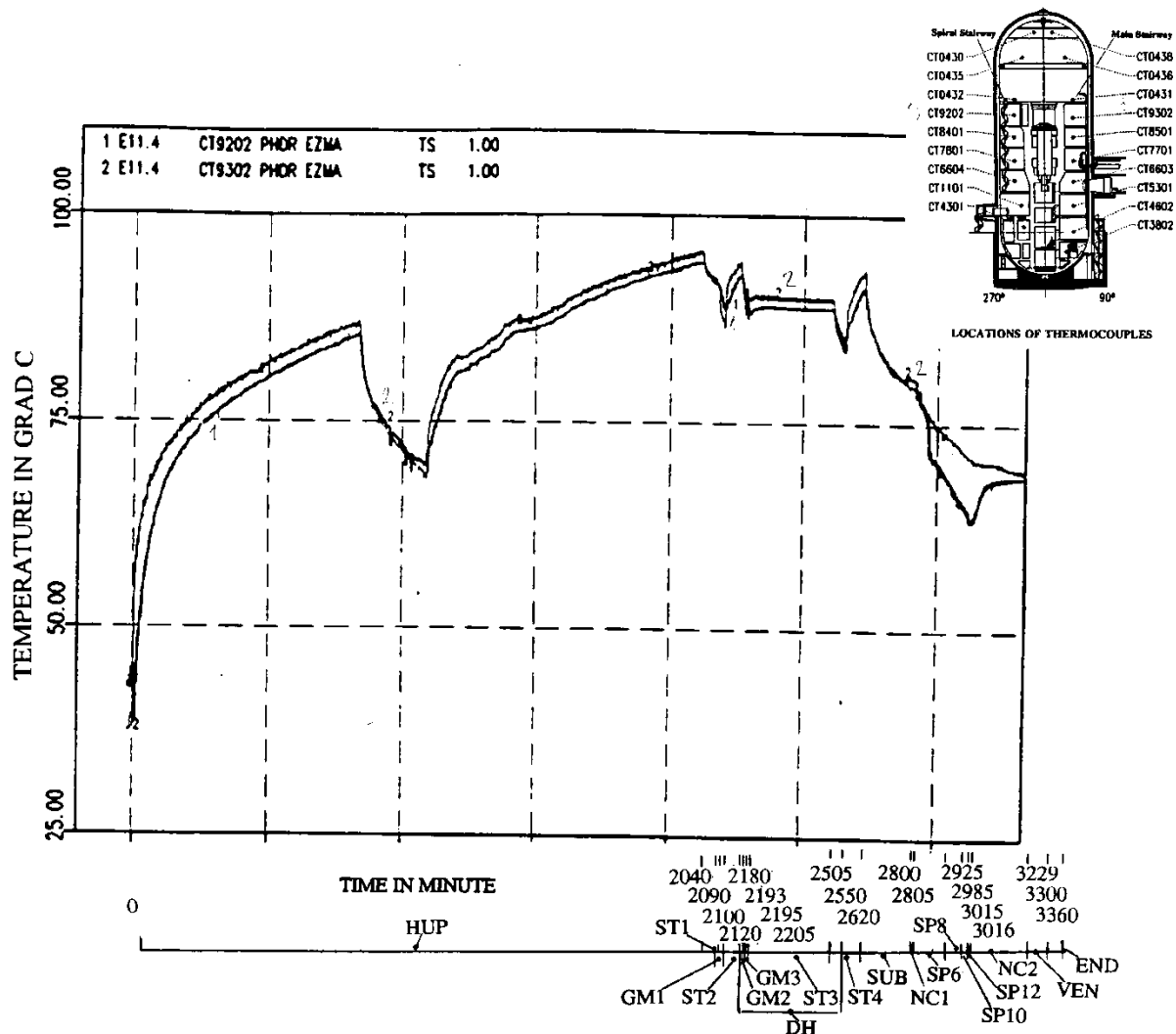


Figure 9.C-98. HDR-E11.4 Comparison Between Temperatures in Main and Spiral Stairways at +26.5 m Level

(reprinted from: L. Wolf, M. Gavrilas, K. Mun, "Overview of experimental results for long-term, Large-scale natural circulations in LWR-containments after large LOCAs," University of Maryland at College Park, Final Report for DOE – Project, Order Number: DE-AP07-96ID10765," July 1996)

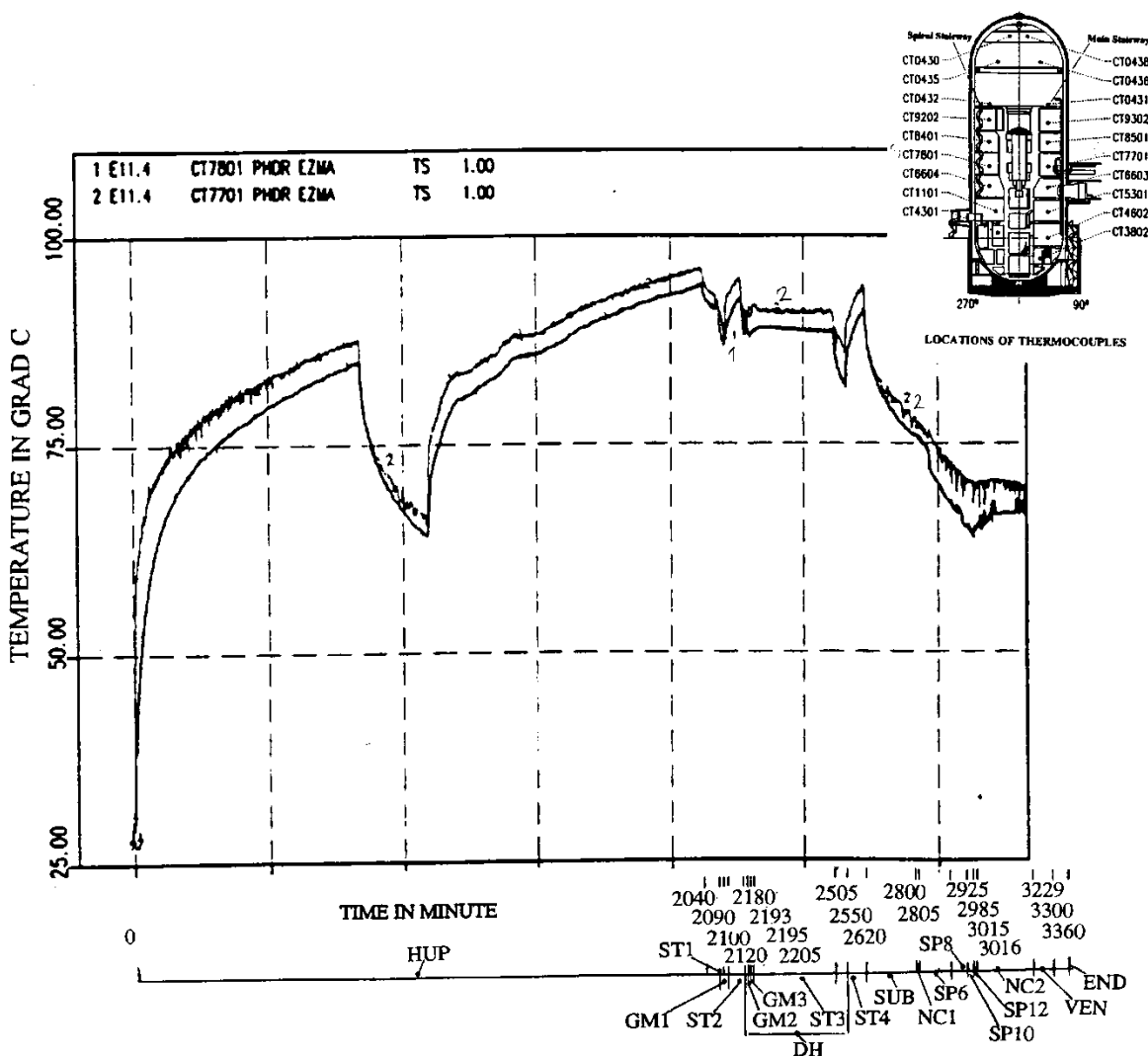


Figure 9.C-99. HDR-E11.4 Comparison Between Temperatures in Main and Spiral Stairways at +16.5 m Level

(reprinted from: L. Wolf, M. Gavrilas, K. Mun, "Overview of experimental results for long-term, Large-scale natural circulations in LWR-containments after large LOCAs," University of Maryland at College Park, Final Report for DOE – Project, Order Number: DE-AP07-96ID10765," July 1996)

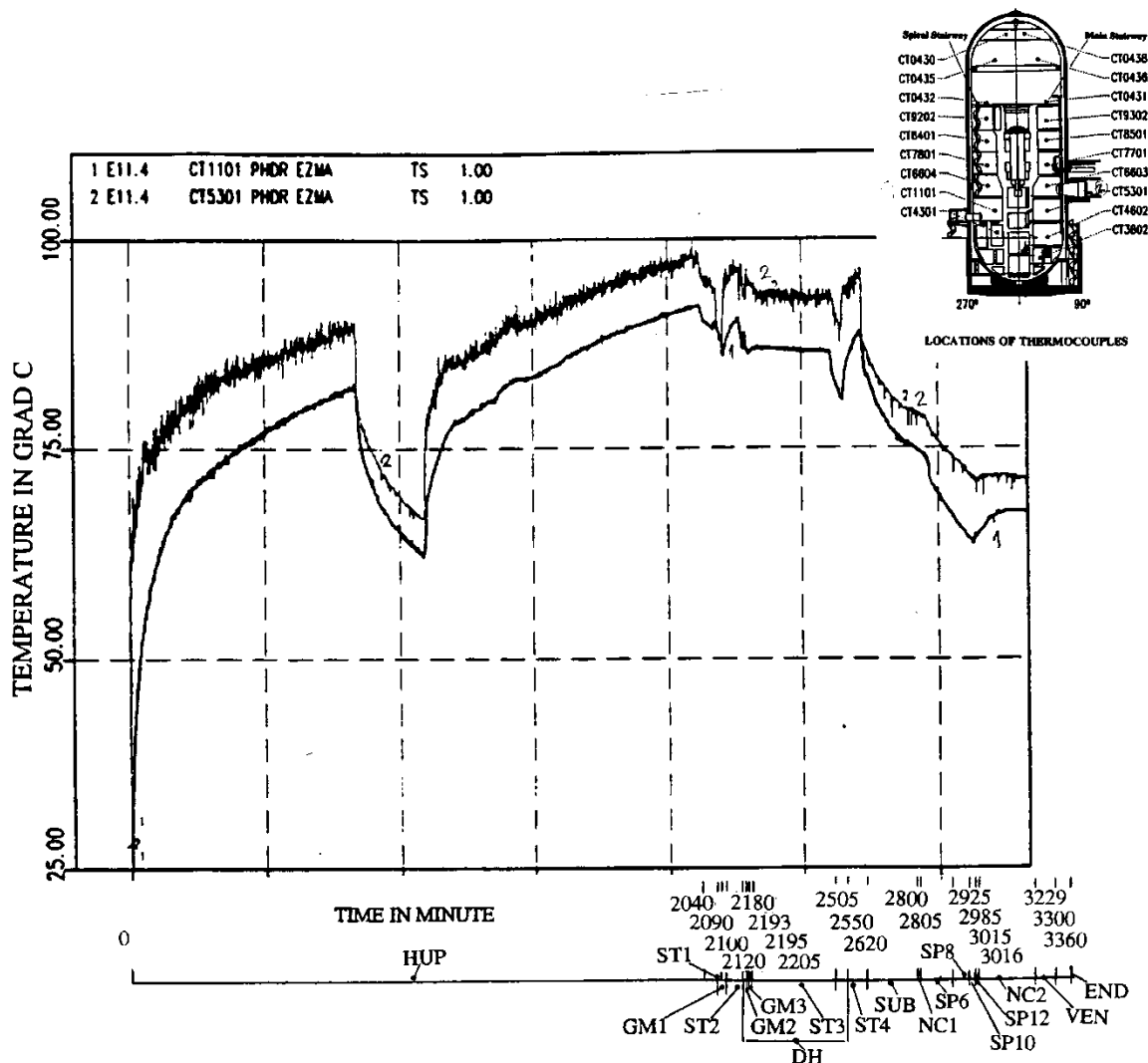


Figure 9.C-100. HDR-E11.4 Comparison Between Temperatures in Main and Spiral Stairways at +6 m Level

(reprinted from: L. Wolf, M. Gavrilas, K. Mun, "Overview of experimental results for long-term, Large-scale natural circulations in LWR-containments after large LOCAs," University of Maryland at College Park, Final Report for DOE – Project, Order Number: DE-AP07-96ID10765," July 1996)

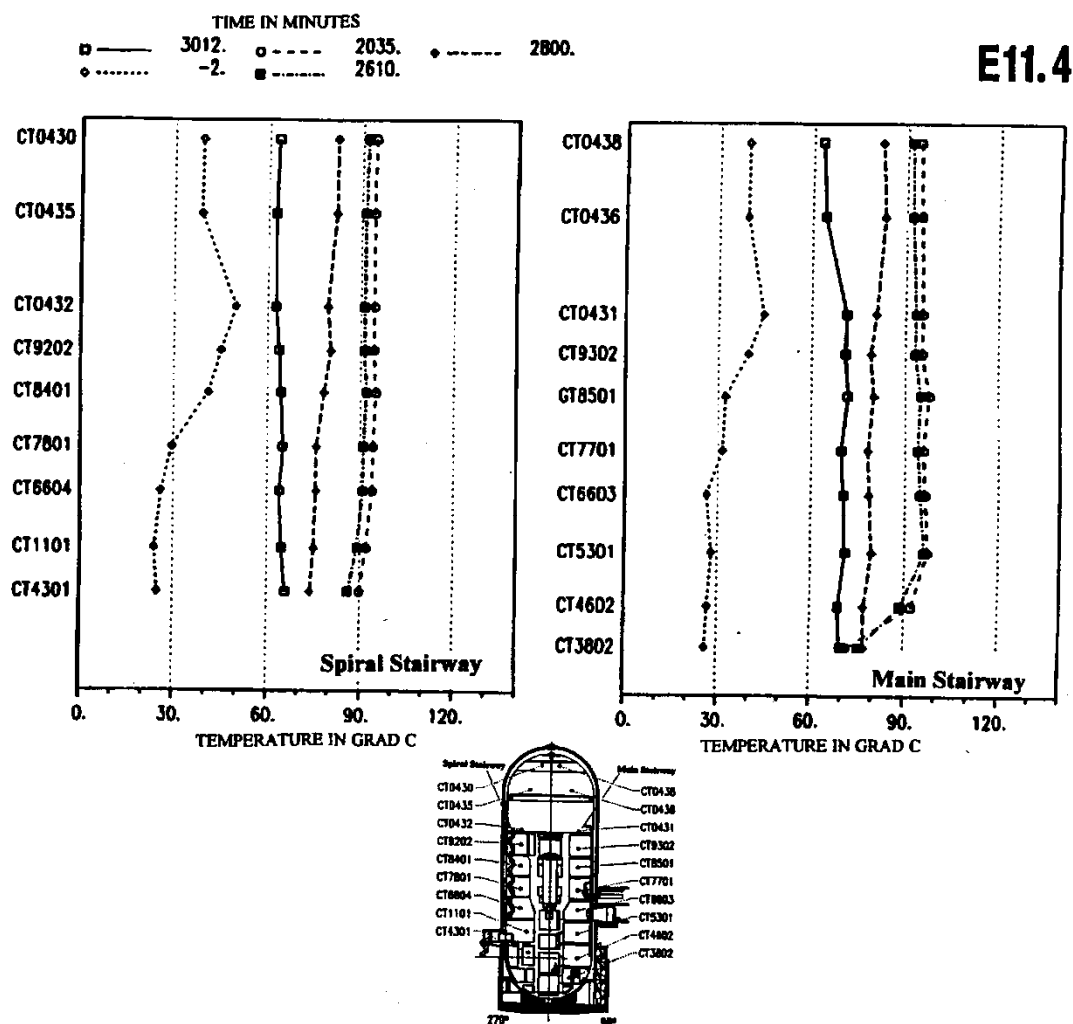


Figure 9.C-101. HDR-E11.4 Axial Temperature Profiles in Both Major Flow Paths at Specific Times, Left in Spiral Stairway, Right in Main Stairway

(reprinted from: L. Wolf, M. Gavrilas, K. Mun, "Overview of experimental results for long-term, Large-scale natural circulations in LWR-containments after large LOCAs," University of Maryland at College Park, Final Report for DOE – Project, Order Number: DE-AP07-96ID10765," July 1996)

9.C.2.4.1.6 Experiment E11.5

Experiment E11.5 includes a large-break LOCA at a low position, with subsequent small-break releases. The temperature differences between the vertical flow channels is large enough to obtain global natural circulation. The temperature difference changes sign at some axial positions during some phases.

A more detailed presentation of the E11.5 results will be given in the next chapter, together with the presentation of the other experiments related to large break LOCA.

Conclusions from the HDR E11 Test Series

Wolf, et al., 1996, concludes that global natural circulation patterns are established in all E11 experiments, despite the different release positions, the applications of internal and external sprays, and the changes to the flow path geometries. Also, an almost homogeneous temperature field is generated for the low position of the release points (experiments E11.3, E11.4 and E11.5). Higher release positions generated stratified temperature fields.

9.C.2.4.2 HDR Large LOCA Experimental Data Base

Experimental results for long-term, large-scale natural circulation in containments after large LOCAs presented by Wolf and Mun, 1996. An assessment of experiments T31.5, V21.1, V43, and E11.5 is provided.

Experiment T31.5 simulates a design basis large LOCA and hydrogen release in the upper section of the containment. Experiment V21.1 simulates a design basis large LOCA in the middle section of the containment, while experiment E11.5 simulates the release of steam and hydrogen in the lowest containment section. Experiment V21.1 is a subcooled blowdown, while all others use steam.

The influence of the break and hydrogen release locations on the containment atmosphere is established by comparing the results of these tests.

9.C.2.4.2.1 Experiment T31.5

The results of containment experiment T31.5 performed by Valencia, 1987 and Wenzel et al., 1987 are reported by Wolf and Valencia, 1988 and 1989. Experiment T31.5 includes a short-term, superheated steam blowdown followed by a long-term, low steam release rate and a H₂/He gas mixture injection. The short-term steam mass flow release into the room 1704 of the HDR-containment takes 25 seconds (with the approximate average flow rate of 1200 kg/s – see Figure 9.C-102). Room 1704 is at elevation 17.55-25.3 m in the upper section of the containment, near the spiral staircase (see Figure 9.C-73 and Figure 9.C-102). The large break position is at +22.3 m (about 8 m below the upper deck) and the blowdown pipe is pointing upward.

From 21 to 36 minutes, steam is released at an average mass flow rate 2.3 kg/s (see Figure 9.C-103). From 36 to 48 minutes, an H₂/He gas mixture is released into the containment with an approximate average mass flow rate of 0.24 kg/s (see Fig. 9.C.2-80). All the releases can be considered as steam blowdowns into a high-positioned compartment in the containment.

The containment pressure, temperature, hydrogen concentration, and velocities histories over 20 hours are presented in Figure 9.C-104 – Figure 9.C-108. The two pressure peaks correspond to the periods of steam injections (see Figure 9.C-104).

Temperature histories at various axial positions are presented in Figure 9.C-105. The axial temperature distribution is uniform above the break position, with the exception of local temperatures measuring the break plume. A linearly decreasing temperature (stratification) is present below the break position. The vertical temperature gradient decreases with time due to the global natural circulation, which develops both above and below the break location. The major vertical flow paths are through-compartments in the main and spiral staircases, where small temperature differences of about 5°C exist at equal heights. Horizontal connections exist at discrete elevations to provide circulation between the vertical flow paths.

The measured hydrogen concentration distributions at various times are presented in Figure 9.C-106. The H₂/He gas mixture concentration increases to a maximum value (13 percent volume, see Figure 9.C-107) in the regions above the release position. This concentration remains uniform over several hours in the upper portion of the dome (above 35 m – see Figure 9.C-107), while in the lower positions (34, 31, and 25m) it decreases after reaching maximum values. At the highest position of the dome (49 m), the decrease in the mixture concentration starts about 300 minutes after the start of the experiment and continues until about 360 minutes. After 360 minutes, the concentration above 12 m is a uniform mixture concentration of 10 percent vol. The steady-state profile of the mixture concentration is reached after 900 minutes.

For the first 12 minutes, upward and downward flows are present in the spiral and main staircases, respectively. The measured velocities are presented in Figure 9.C-108a and Figure 9.C-108b. The velocities are recorded again after the start of the steam injection (after 21 minute). Staircase flow starts again at approximately 200 minutes, at the same time that the mixture concentration in the upper portion of the containment starts to decrease. It then decreases again around 350 minutes, when upper region reaches a uniform concentration.

Interpretation of Data

Even for the case of the high release point with an initially stratified distribution, the final gas concentration through most of the containment is nearly homogenized due to the global natural circulation effects. Only a small, steady stratification gradient exists (about 1°C over the height of dome, about 18°C over 25 m below the break, gradient of about 7.5 to 8.8 percent H₂/He over the height of dome).

Applicability to the AP600 and AP1000

Since the AP600 and **AP1000** have significant cooling over the containment dome (which somewhat corresponds to the HDR dome region), additional driving forces for circulation above the operating deck exist.

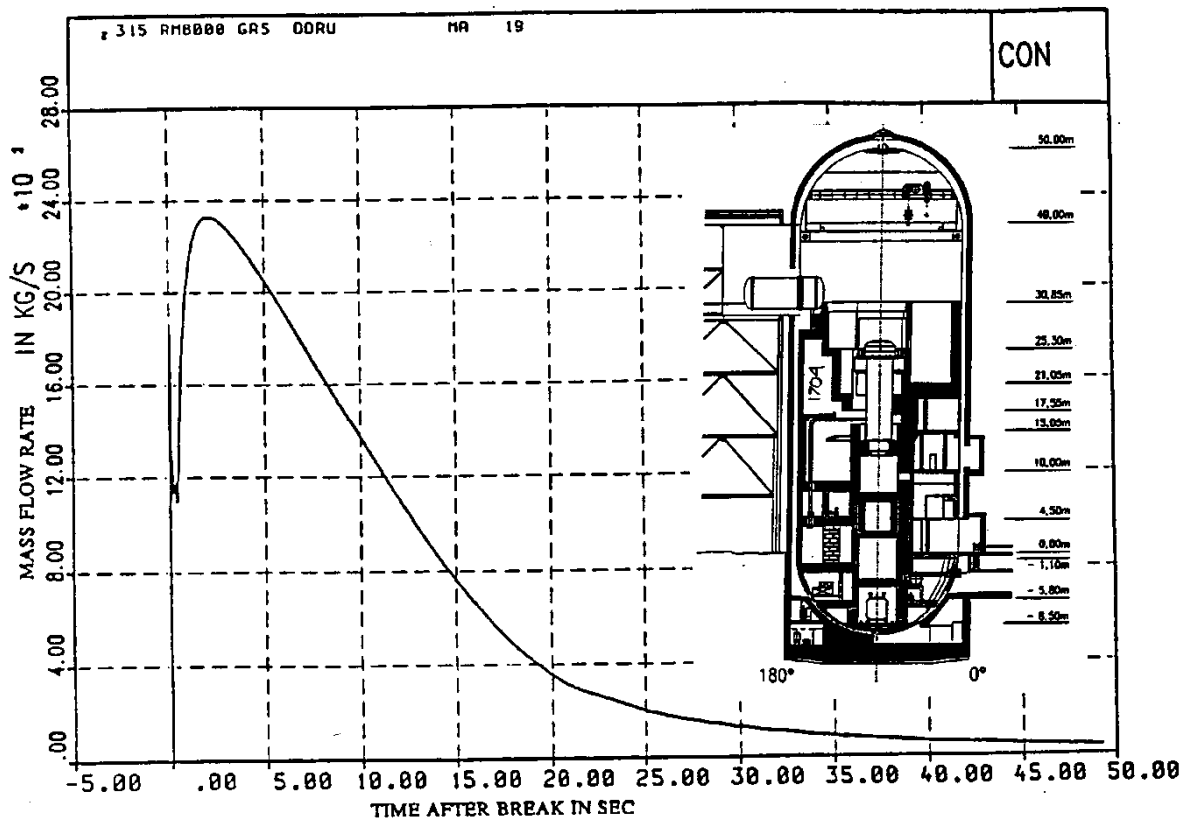


Figure 9.C-102. HDR-T31.5 Blowdown Mass Flow Rate into the Containment

(reprinted from: L. Wolf, K. Mun, "Overview of experimental results for long-term, Large-scale natural circulations in LWR-containments after large LOCAs, Vol. II: Assessment of HDR Experiments V21.1, V43, T31.5 and E11.5," University of Maryland at College Park, for DOE – Project HDR Hydrogen Mixing Evaluation for Containment Safety Evaluations natural Global Circulation, Order Number: DE-AP07-96ID10765," April 1996)

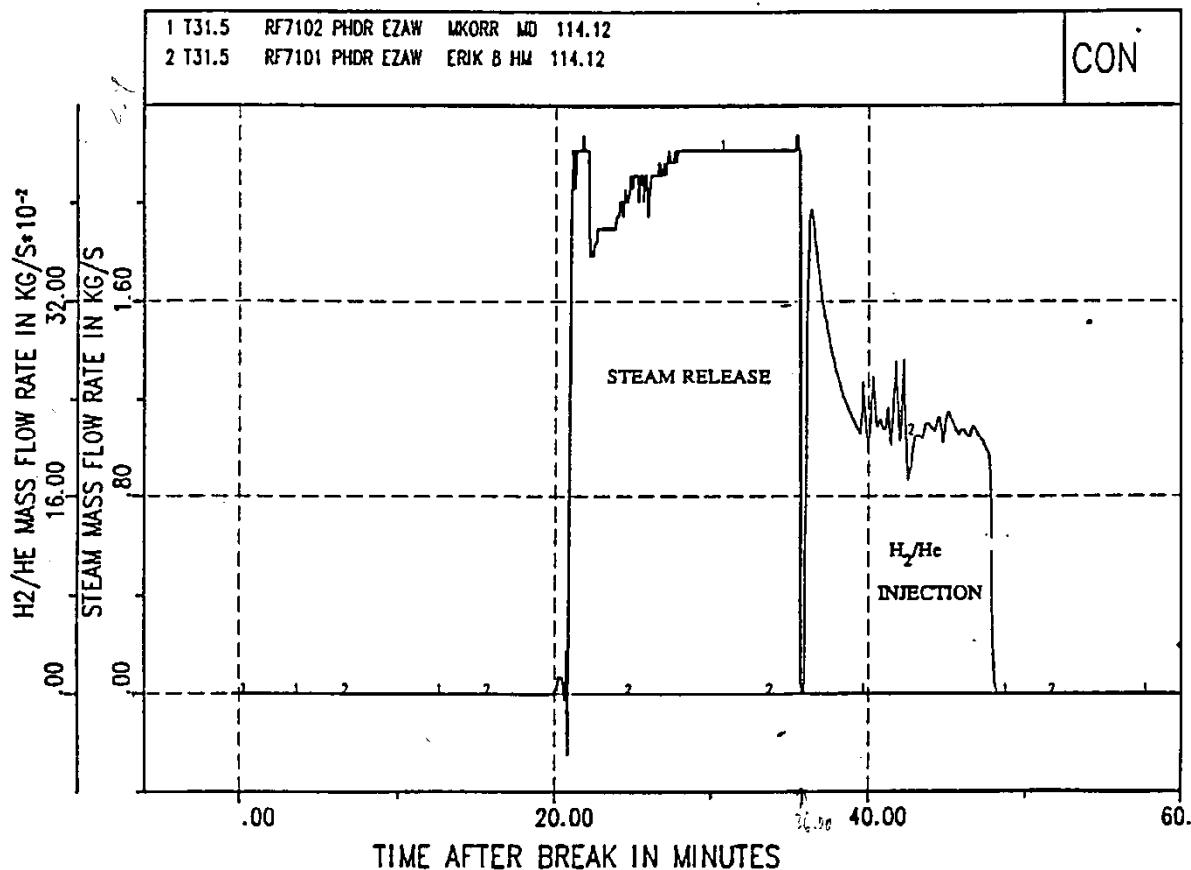


Figure 9.C-103. HDR-T31.5 Steam and H₂/He gas Mass Flow Rates into the Containment

(reprinted from: L. Wolf, K. Mun, "Overview of experimental results for long-term, Large-scale natural circulations in LWR-containments after large LOCAs, Vol. II: Assessment of HDR Experiments V21.1, V43, T31.5 and E11.5," University of Maryland at College Park, for DOE – Project HDR Hydrogen Mixing Evaluation for Containment Safety Evaluations natural Global Circulation, Order Number: DE-AP07-96ID10765," April 1996)

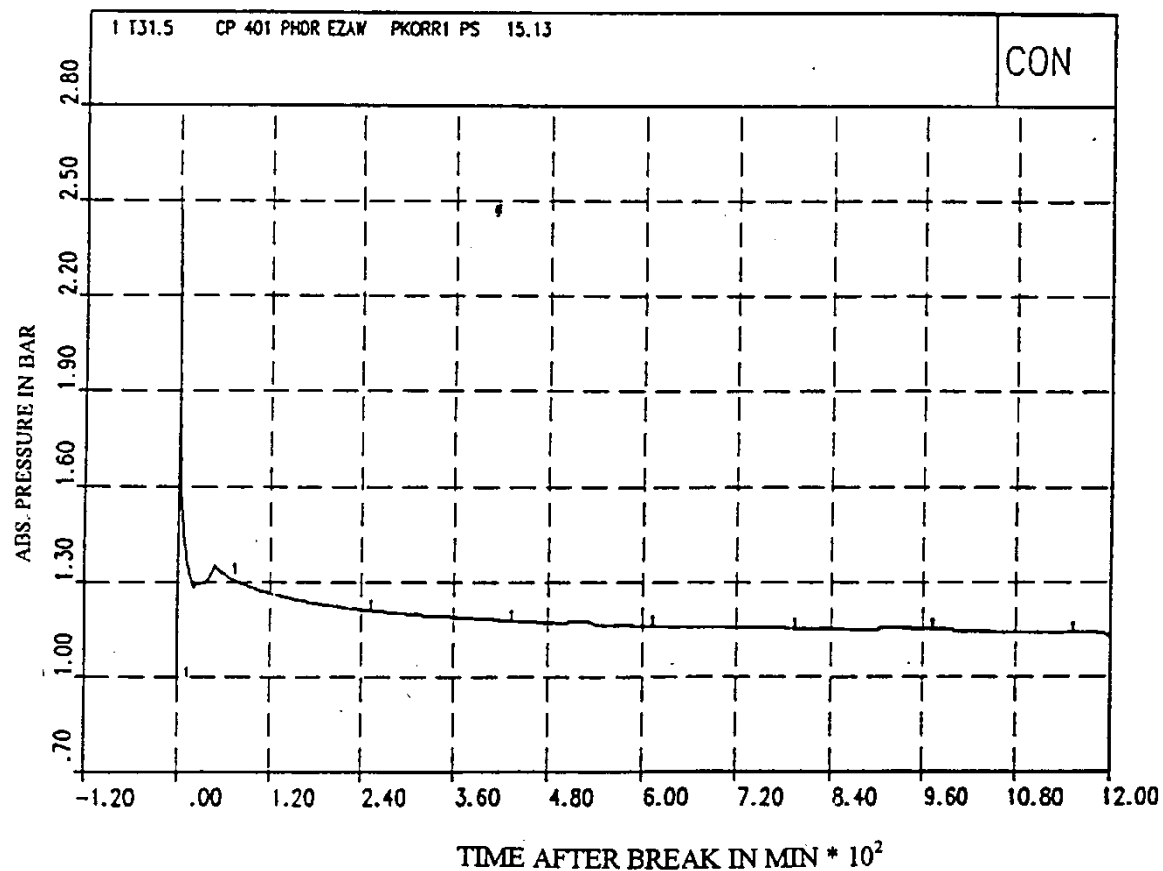


Figure 9.C-104. HDR-T31.5 Pressure History after Large LOCA over 1200 Minutes

(reprinted from: L. Wolf, K. Mun, "Overview of experimental results for long-term, Large-scale natural circulations in LWR-containments after large LOCAs, Vol. II: Assessment of HDR Experiments V21.1, V43, T31.5 and E11.5," University of Maryland at College Park, for DOE – Project HDR Hydrogen Mixing Evaluation for Containment Safety Evaluations natural Global Circulation, Order Number: DE-AP07-96ID10765," April 1996)

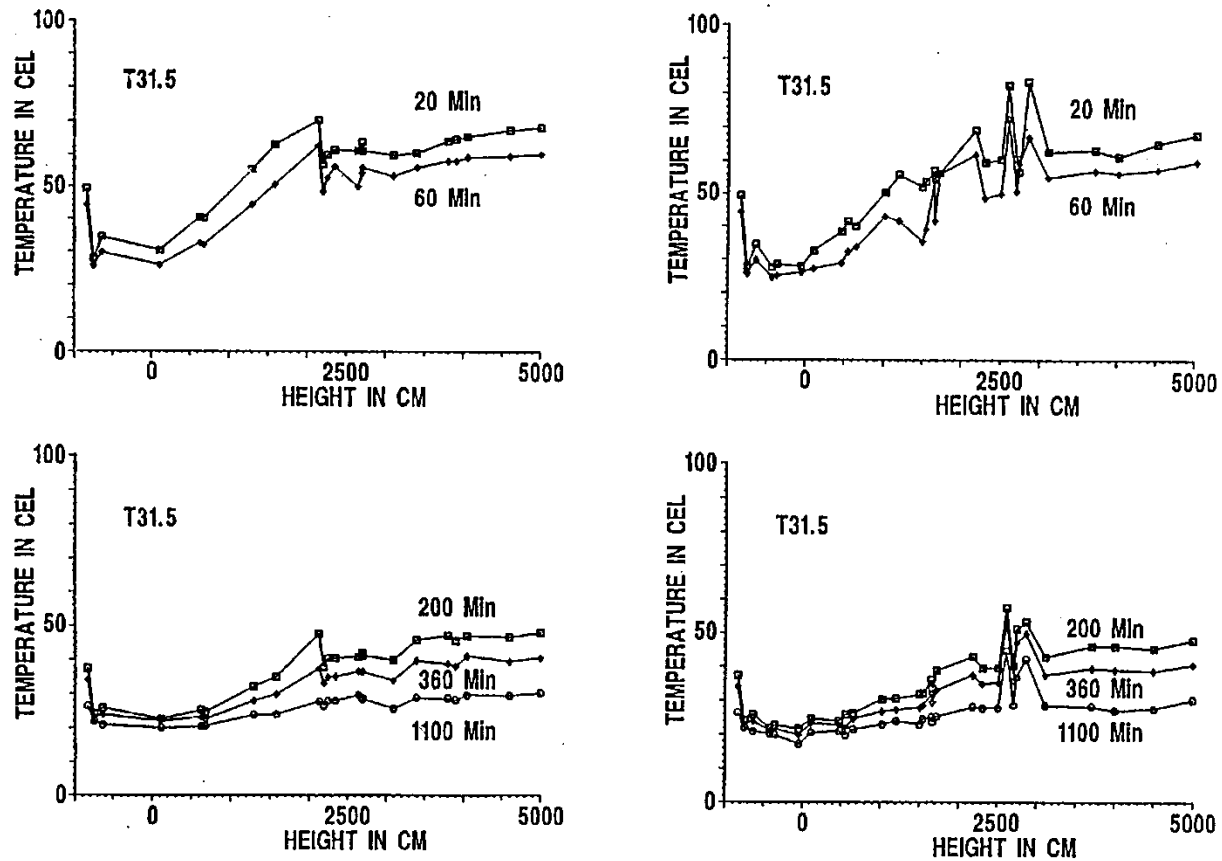


Figure 9.C-105. HDR-T31.5 Axial Temperature Profiles along Spiral Stairway (left) and Main Stairway (right) for Different Instants in Time

(reprinted from: L. Wolf, K. Mun, "Overview of experimental results for long-term, Large-scale natural circulations in LWR-containments after large LOCAs, Vol. II: Assessment of HDR Experiments V21.1, V43, T31.5 and E11.5," University of Maryland at College Park, for DOE – Project HDR Hydrogen Mixing Evaluation for Containment Safety Evaluations natural Global Circulation, Order Number: DE-AP07-96ID10765," April 1996)

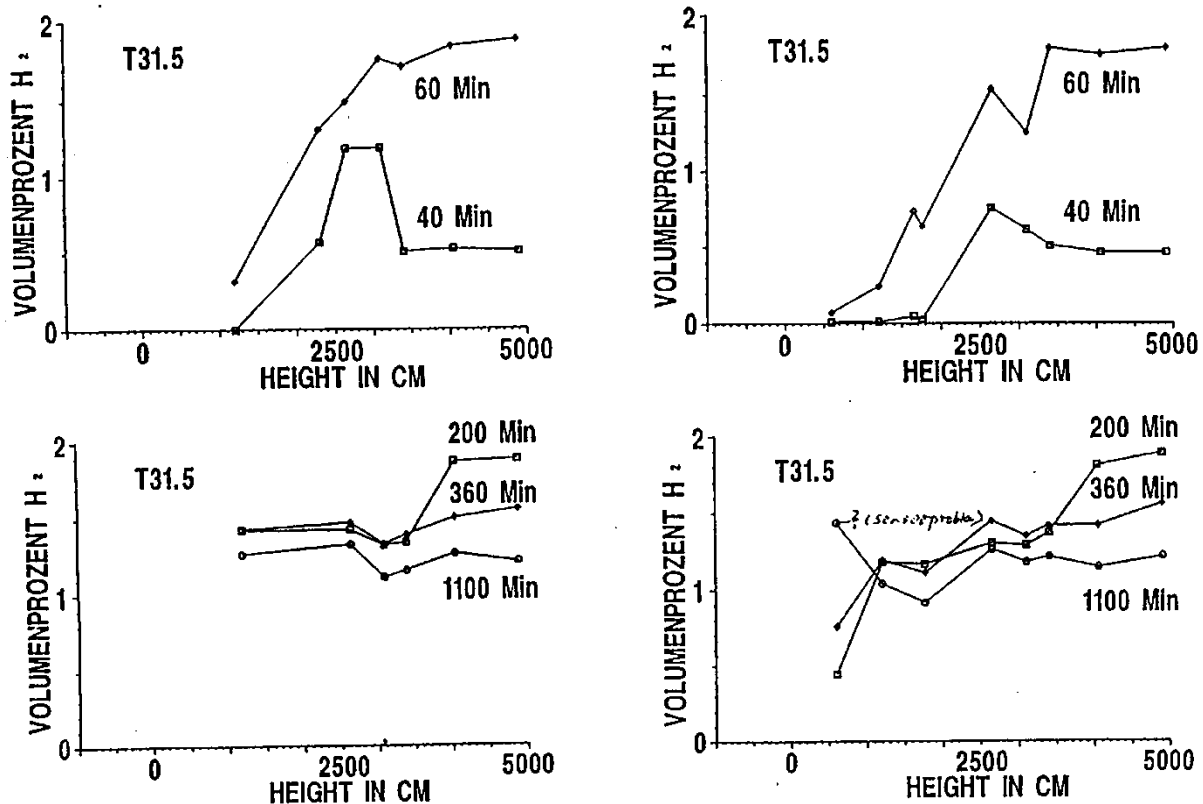


Figure 9.C-106. HDR-T31.5 Axial Gas Concentration Profiles along Spiral Stairway (left) and Main Stairway (right) in Upper Containment Region at Different Instants in Time

(reprinted from: L. Wolf, K. Mun, "Overview of experimental results for long-term, Large-scale natural circulations in LWR-containments after large LOCAs, Vol. II: Assessment of HDR Experiments V21.1, V43, T31.5 and E11.5," University of Maryland at College Park, for DOE – Project HDR Hydrogen Mixing Evaluation for Containment Safety Evaluations natural Global Circulation, Order Number: DE-AP07-96ID10765," April 1996)

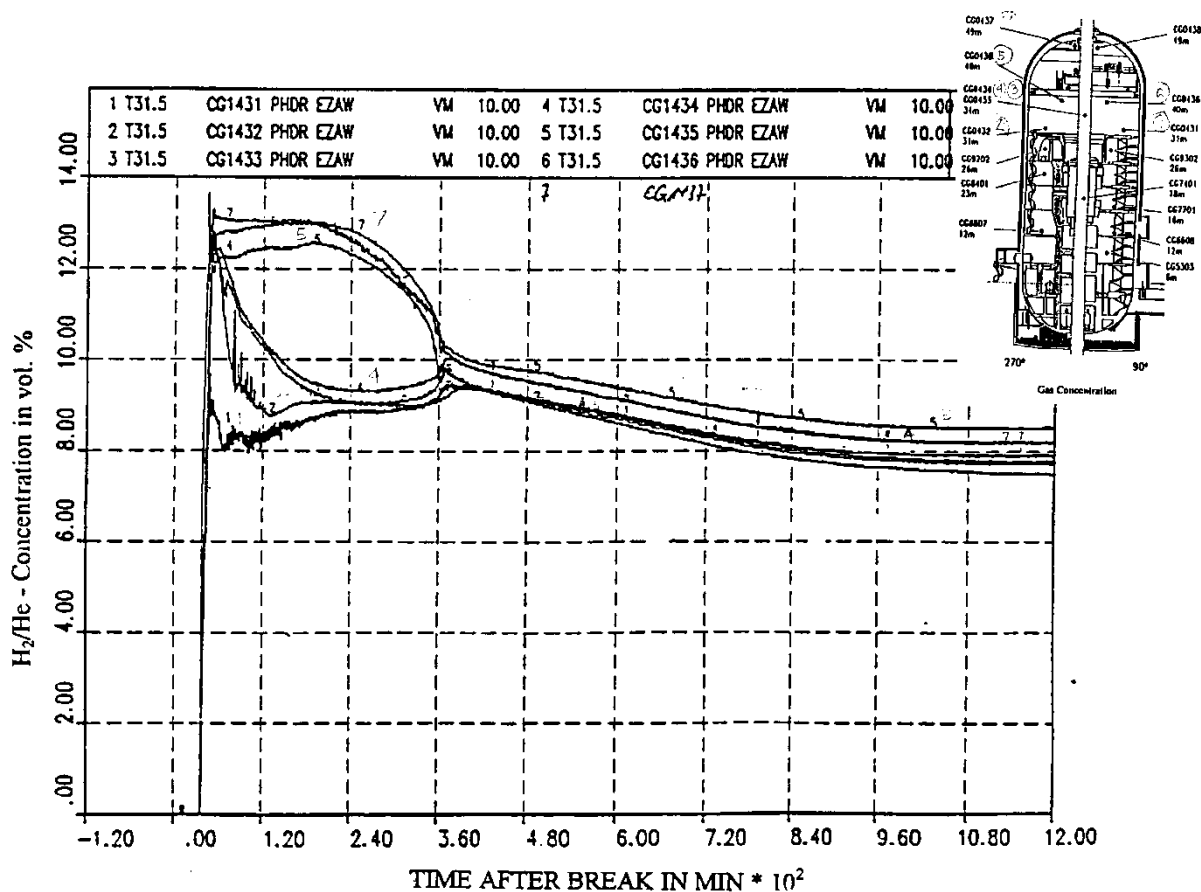


Figure 9.C-107. HDR-T31.5 Gas Concentrations Inside the Containment Dome

(reprinted from: L. Wolf, K. Mun, "Overview of experimental results for long-term, Large-scale natural circulations in LWR-containments after large LOCAs, Vol. II: Assessment of HDR Experiments V21.1, V43, T31.5 and E11.5," University of Maryland at College Park, for DOE – Project HDR Hydrogen Mixing Evaluation for Containment Safety Evaluations natural Global Circulation, Order Number: DE-AP07-96ID10765," April 1996)

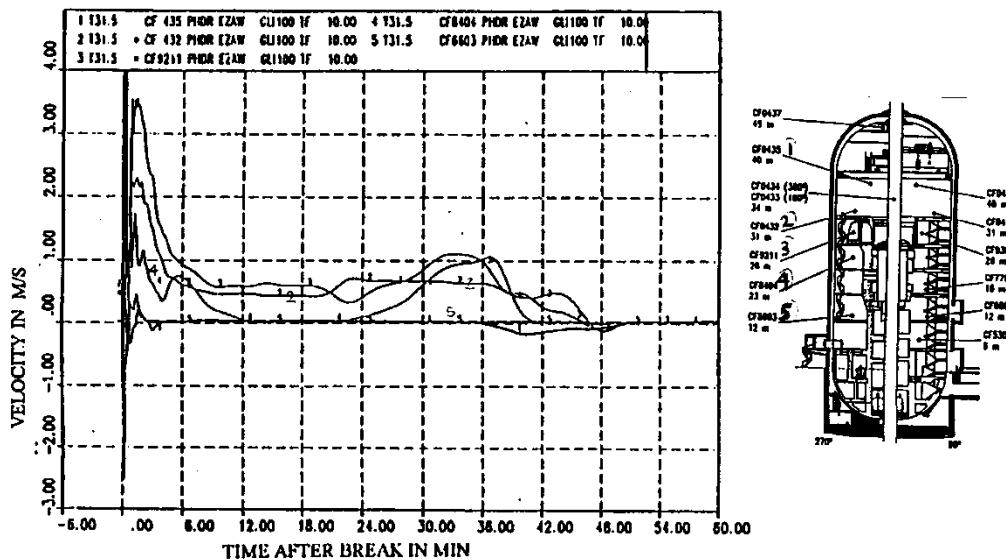


Figure 9.C-108a. HDR-T31.5 Velocities Over 60 Minutes along Spiral Stairways and Associated Dome Regions

(reprinted from: L. Wolf, K. Mun, "Overview of experimental results for long-term, Large-scale natural circulations in LWR-containments after large LOCAs, Vol. II: Assessment of HDR Experiments V21.1, V43, T31.5 and E11.5," University of Maryland at College Park, for DOE – Project HDR Hydrogen Mixing Evaluation for Containment Safety Evaluations natural Global Circulation, Order Number: DE-AP07-96ID10765," April 1996)

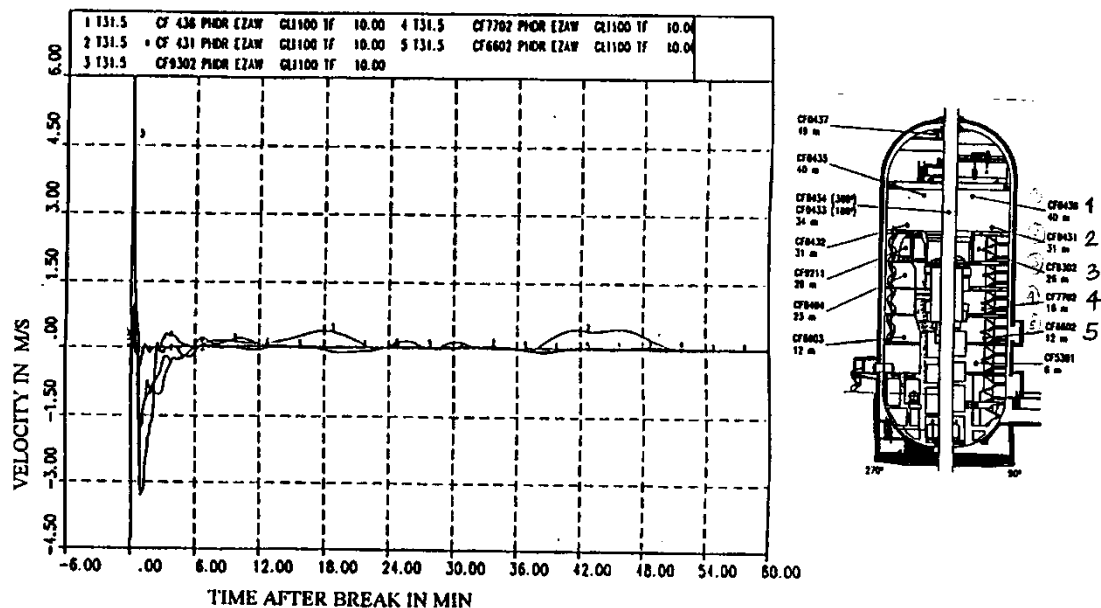


Figure 9.C-108b. HDR-T31.5 Velocities Over 60 Minutes Along Main Stairways and Associated Dome Regions

(reprinted from: L. Wolf, K. Mun, "Overview of experimental results for long-term, Large-scale natural circulations in LWR-containments after large LOCAs, Vol. II: Assessment of HDR Experiments V21.1, V43, T31.5 and E11.5," University of Maryland at College Park, for DOE – Project HDR Hydrogen Mixing Evaluation for Containment Safety Evaluations natural Global Circulation, Order Number: DE-AP07-96ID10765," April 1996)

9.C.2.4.2.2 Experiment V21.1

The blowdown for the V21.1 experiment (see Kanzleiter T., Valencia, L., 1984) is initiated inside the R1603 compartment, which is in the middle section of the HDR containment (see Figure 9.C-73 and Figure 9.C-109). The arrangement of reactor pressure vessel, blowdown pipe (break diameter 453 mm), and jet impingement plate for the subcooled water blowdown is shown in Figure 9.C-109. Other characteristics of the experiment are given in Table 9.C-6. The total mass and enthalpy of the exiting fluid are 50157 kg and 72320 MJ, respectively. The test could be characterized as a large break cross-section and a short-term blowdown (30 seconds). The maximum peak pressure was 3 bar because of the much higher mass and energy releases during the steam/liquid mixture blowdown (Figure 9.C-110). The transient atmospheric temperature for the dome, main and spiral stairway are presented in the Figure 9.C-111, Figure 9.C-112, and Figure 9.C-113.

At the beginning of the V21.1 experiment, the blowdown results in fairly uniform distribution of temperature in the dome (Figure 9.C-111). After about 10 seconds, a stratification gradient exists. The maximum temperature gradient over the above-deck height is 10°C at about 100 minutes. Until 420 minutes, the thermal stratification inside the dome volume exists (see Figure 9.C-111). At the end of the break release (after 30 seconds) the temperatures inside the dome are decreasing (slower near the top). After 420 minutes, temperature differences inside the dome volume are only around 2-3°C, indicating the presence of natural circulation. The natural circulation in the above-deck region acts to reduce the gradient with time.

The axial temperature distributions in the mean and spiral staircases are presented in Figure 9.C-112 and Figure 9.C-113. Immediately after the end of the blowdown, a stratification gradient develops. The transient histories of the temperatures at the same axial levels (in the spiral and main staircases) are presented in Figure 9.C-114. The large blowdown injected into the middle of the both staircases results in almost equal temperatures in both flow channels, therefore, global natural convection cannot be formed. A slightly higher temperature is recorded in the main staircase. A temperature difference of 1-2°C starts at 200 minutes and continues until 800 minutes.

Interpretation of Data

The large break with the blowdown penetrating into the middle of both staircases (mean flow paths) minimizes temperature differences among the same axial positions and suppresses the development of the natural circulation.

The small temperature differences of about 1°C (Figure 9.C-113) and the slight global natural circulation appear to be established later due to the different heat release rates of the various wall structures. These structures are heated to various temperatures during the early phase of the transient.

The large LOCA HDR tests described should be carefully applied to the passive containment design. The majority of the passive containment compartments are at the lower levels of the containment. Heating of the structures (walls, floors, and equipment) in the middle of the containment height or above is not possible because they do not exist. The formation of the stable stratified layers in the upper portion of the passive containment due to the accumulated heat (in fact the higher temperatures) in the concrete and steel structures is not possible. The temperature of the containment shell, which is the only solid structure in the upper portion of the containment, tends to be lower than the internal containment temperature. This promotes internal global circulation.

Application to AP600 and AP1000

Small temperature differences inside the dome, even without dome cooling or additional releases after blowdown, are sufficient to drive natural convection. This leads to more homogenous conditions over time.

Table 9.C-6. HDR-V21.1 Test Conditions

Measured Initial Conditions In Reactor Pressure Vessel	
Pressure	110.4 bar
Temperature	315 – 319°C
Liquid Level	filled
Liquid volume prior to blowdown	74.5 m ³
Liquid Mass prior to blowdown	50233 kg
Liquid level in reactor pressure vessel after blowdown	empty
Steam volume after blowdown	74.5 m ³
Steam mass after blowdown	76 kg
Mass of exiting fluid	50157 kg
Enthalpy of exiting fluid	72320 MJ
Jet impingement plate distance (LD)	2
Jet impingement plate inclination angle	0°
Break nozzle diameter	453 mm
Break nozzle length	6091 mm
Vent Flow Openings From Break Subcompartment	
UO140	open
UO143	closed
UO162	6.1 m ²
UO177	open
UO178	closed
External spray off (all the time)	

(reprinted from: L. Wolf, K. Mun, “Overview of experimental results for long-term, Large-scale natural circulations in LWR-containments after large LOCAs, Vol. II: Assessment of HDR Experiments V21.1, V43, T31.5 and E11.5,” University of Maryland at College Park, for DOE – Project HDR Hydrogen Mixing Evaluation for Containment Safety Evaluations Natural Global Circulation, Order Number: DE-AP07-96ID10765," April 1996)

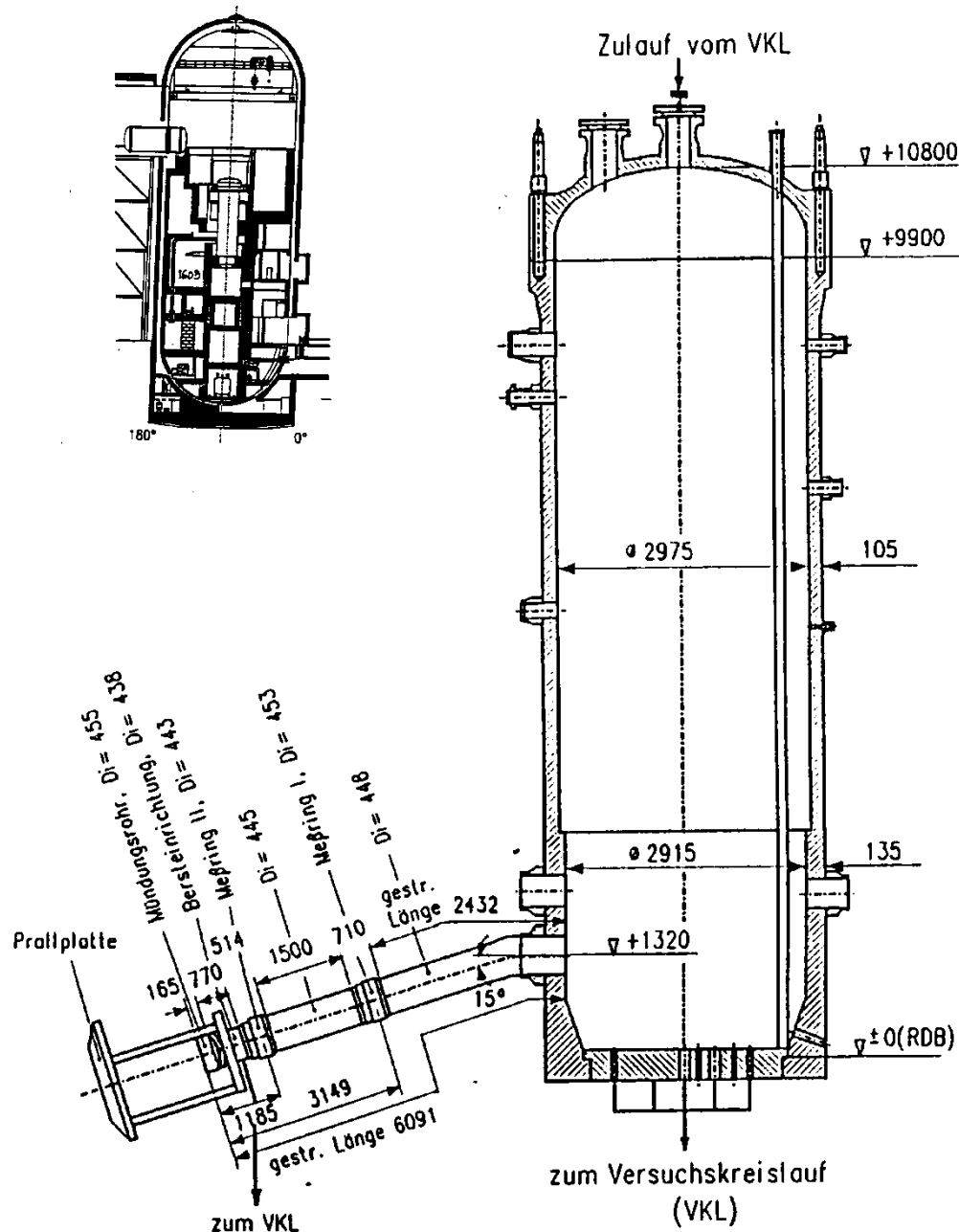


Figure 9.C-109. HDR-V21.1 Arrangement of Reactor Pressure Vessel, Blowdown Pipe and Jet Impingement Plate for Water Blowdown Test

(reprinted from: L. Wolf, K. Mun, "Overview of experimental results for long-term, Large-scale natural circulations in LWR-containments after large LOCAs, Vol. II: Assessment of HDR Experiments V21.1, V43, T31.5 and E11.5," University of Maryland at College Park, for DOE – Project HDR Hydrogen Mixing Evaluation for Containment Safety Evaluations natural Global Circulation, Order Number: DE-AP07-96ID10765," April 1996)

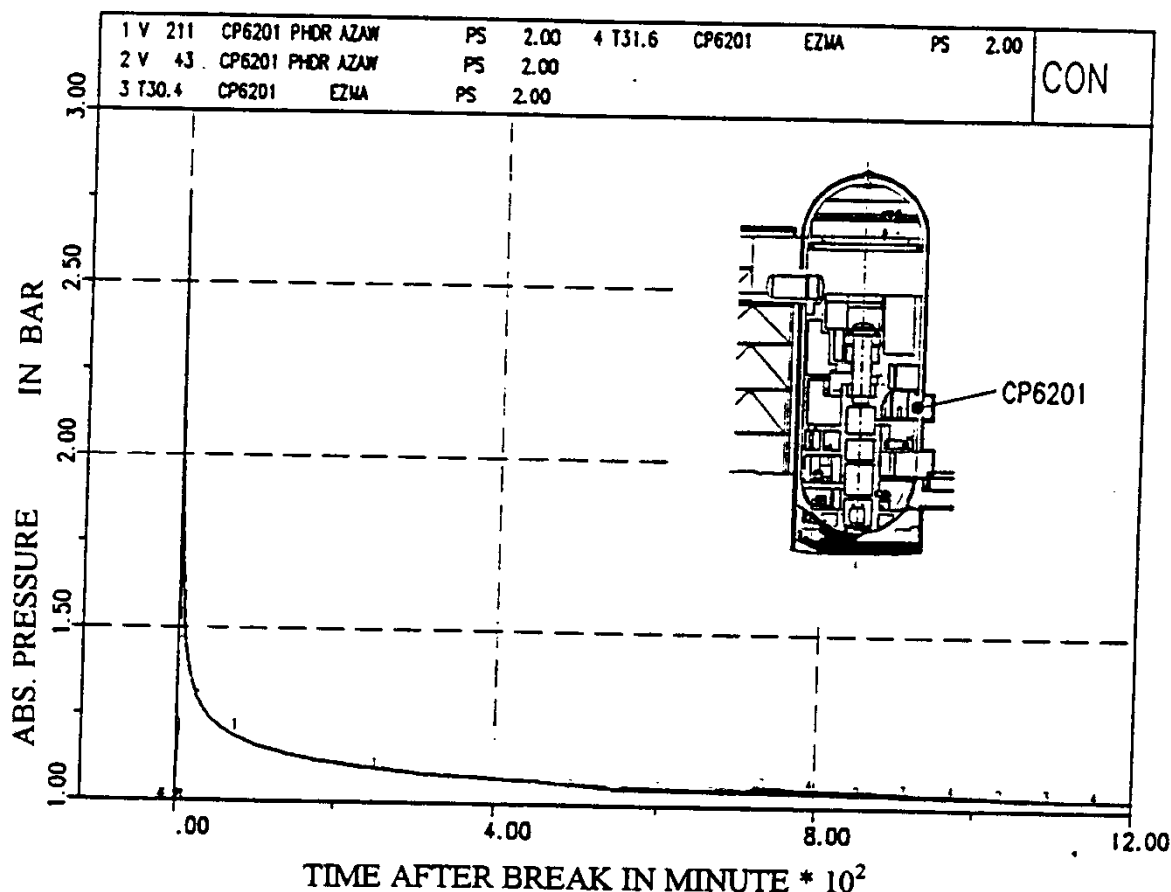


Figure 9.C-110. HDR-V21.1 Containment Pressure History

(reprinted from: L. Wolf, K. Mun, "Overview of experimental results for long-term, Large-scale natural circulations in LWR-containments after large LOCAs, Vol. II: Assessment of HDR Experiments V21.1, V43, T31.5 and E11.5," University of Maryland at College Park, for DOE – Project HDR Hydrogen Mixing Evaluation for Containment Safety Evaluations natural Global Circulation, Order Number: DE-AP07-96ID10765," April 1996)

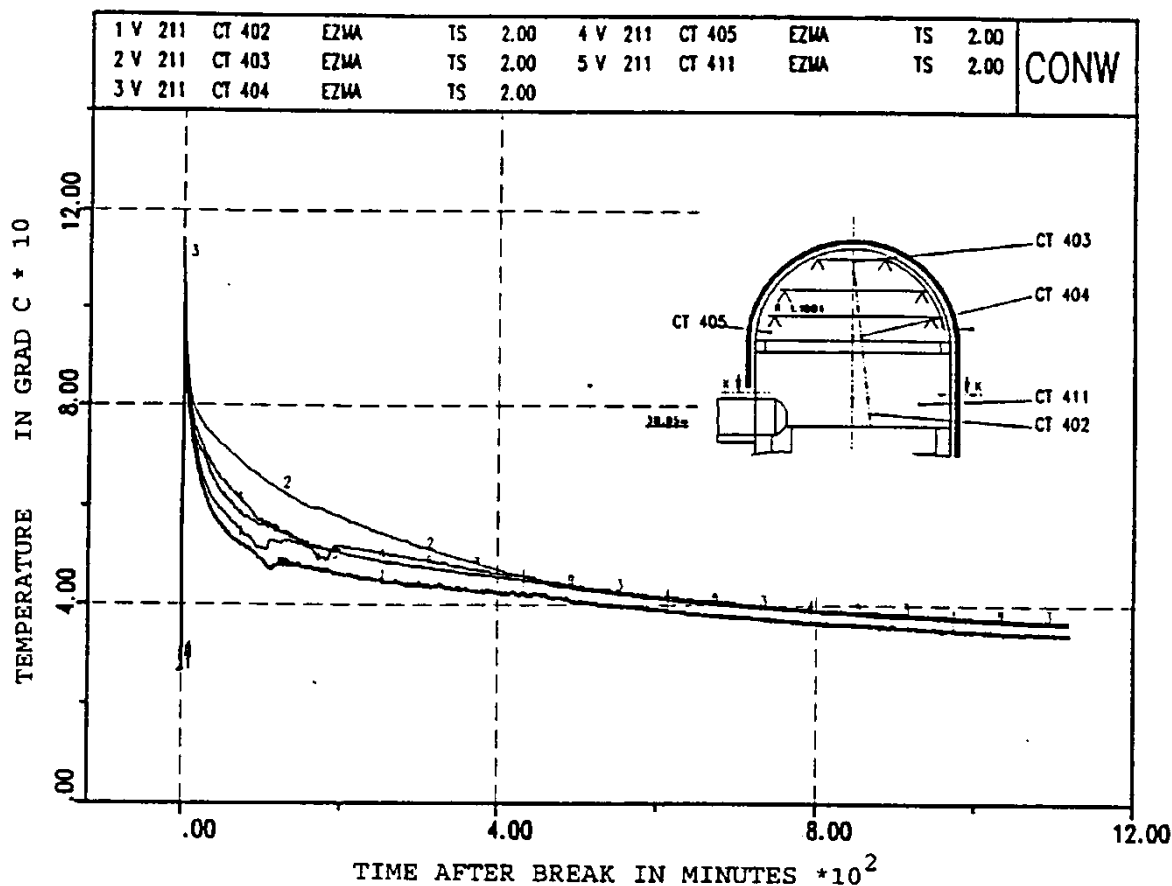


Figure 9.C-111. HDR-V21.1 Temperatures in the Containment Dome

(reprinted from: L. Wolf, K. Mun, "Overview of experimental results for long-term, Large-scale natural circulations in LWR-containments after large LOCAs, Vol. II: Assessment of HDR Experiments V21.1, V43, T31.5 and E11.5," University of Maryland at College Park, for DOE – Project HDR Hydrogen Mixing Evaluation for Containment Safety Evaluations natural Global Circulation, Order Number: DE-AP07-96ID10765," April 1996)

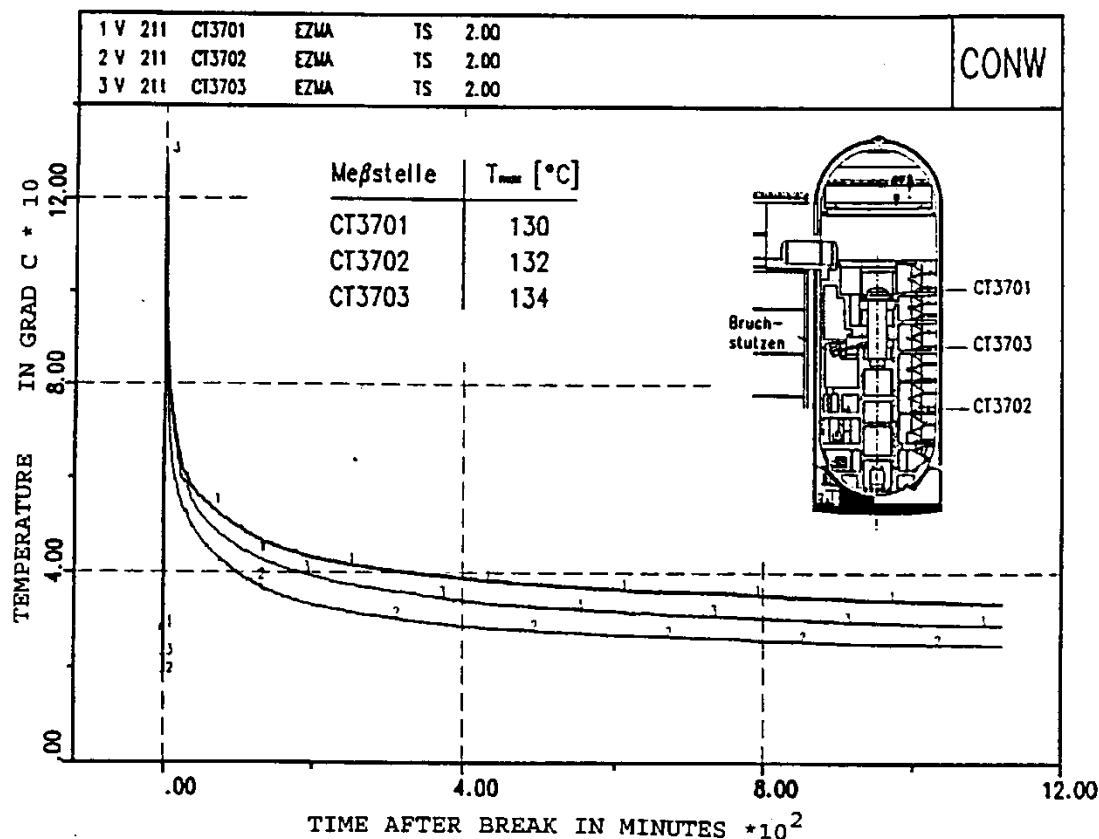


Figure 9.C-112. HDR-V21.1 Temperature Along the Main Staircase at Different Axial Positions

(reprinted from: L. Wolf, K. Mun, "Overview of experimental results for long-term, Large-scale natural circulations in LWR-containments after large LOCAs, Vol. II: Assessment of HDR Experiments V21.1, V43, T31.5 and E11.5," University of Maryland at College Park, for DOE – Project HDR Hydrogen Mixing Evaluation for Containment Safety Evaluations natural Global Circulation, Order Number: DE-AP07-96ID10765," April 1996)

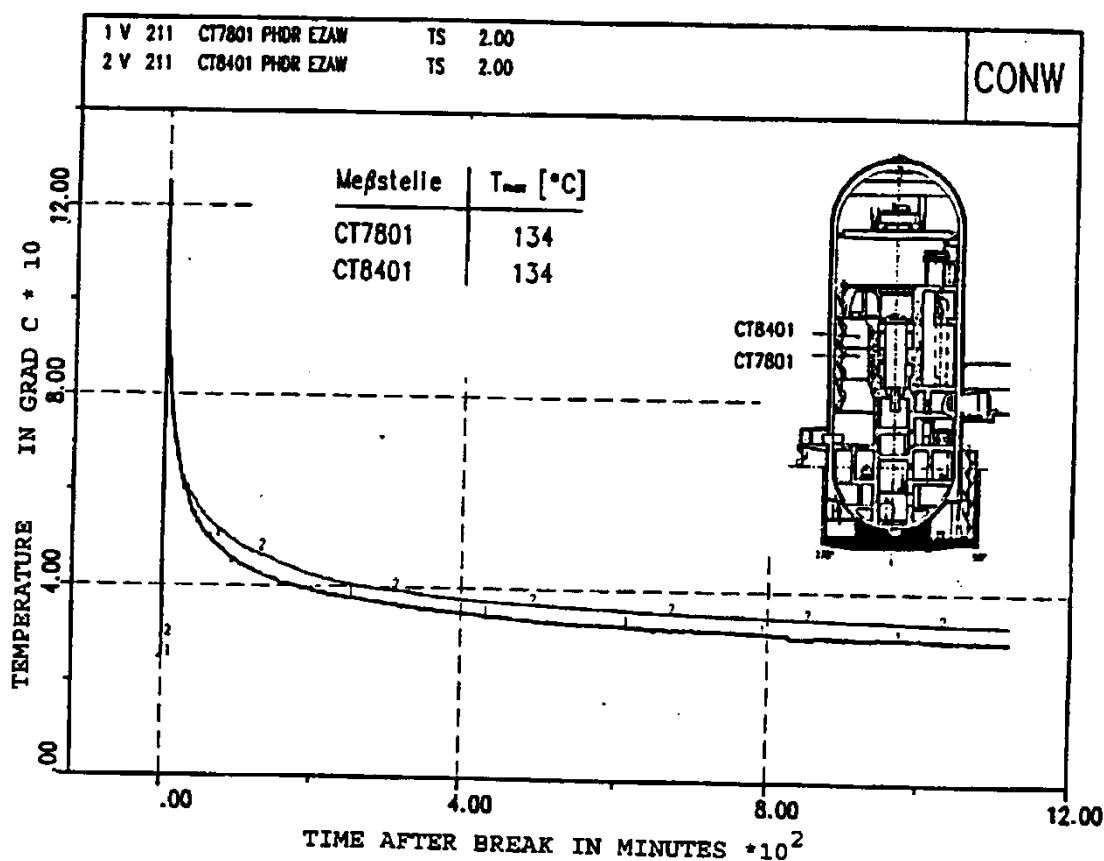


Figure 9.C-113. HDR-V21.1 Temperatures Along Spiral Staircase at Different Axial Positions

(reprinted from: L. Wolf, K. Mun, "Overview of experimental results for long-term, Large-scale natural circulations in LWR-containments after large LOCAs, Vol. II: Assessment of HDR Experiments V21.1, V43, T31.5 and E11.5," University of Maryland at College Park, for DOE – Project HDR Hydrogen Mixing Evaluation for Containment Safety Evaluations natural Global Circulation, Order Number: DE-AP07-96ID10765," April 1996)

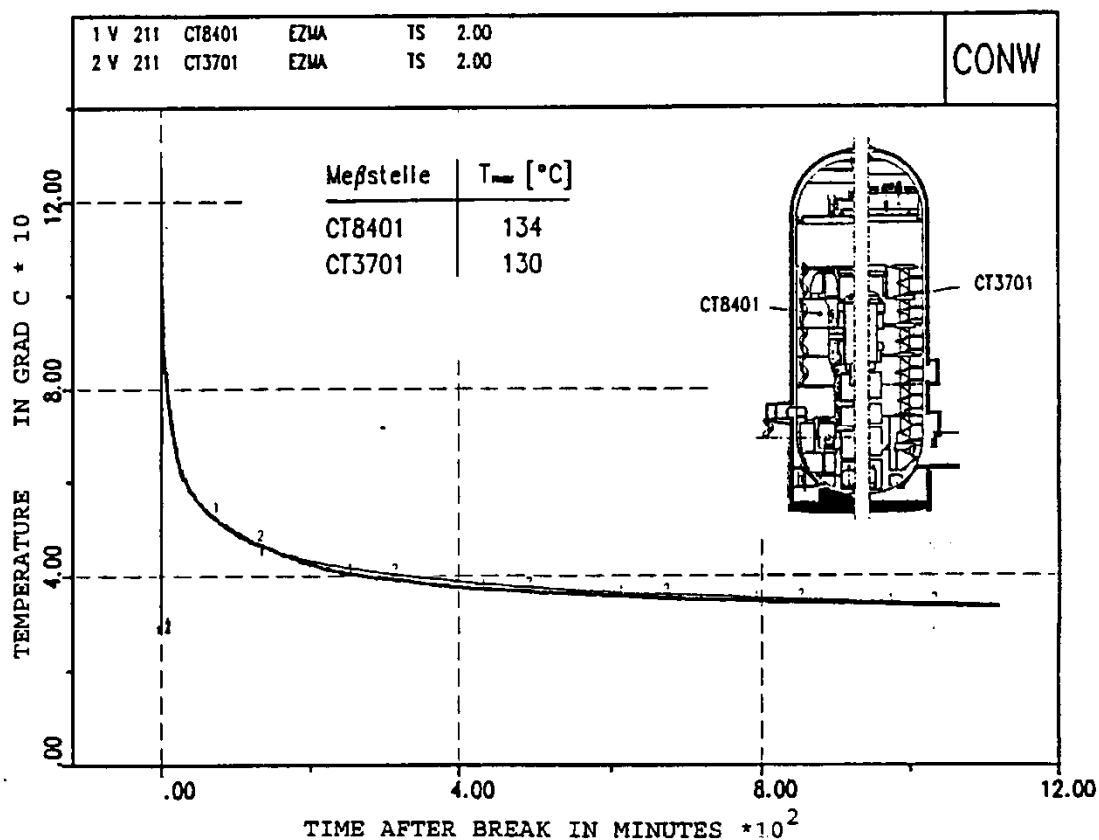


Figure 9.C-114. HDR-V21.1 Comparison Between Temperatures in Spiral Staircase (H=22.5 m) and Main Staircase (H = 25 m)

(reprinted from: L. Wolf, K. Mun, "Overview of experimental results for long-term, Large-scale natural circulations in LWR-containments after large LOCAs, Vol. II: Assessment of HDR Experiments V21.1, V43, T31.5 and E11.5," University of Maryland at College Park, for DOE – Project HDR Hydrogen Mixing Evaluation for Containment Safety Evaluations natural Global Circulation, Order Number: DE-AP07-96ID10765," April 1996)

9.C.2.4.2.3 Experiment E11.5

Experiment E11.5 is performed with a large break LOCA at the lowest possible position (room R1405) with subsequent small-break releases (see Figure 9.C-115). An overview of experimental results is presented by L. Wolf, K. Mun, 1996.

The containment pressure during the large break heatup phase is shown in Figure 9.C-116. At the end of the initial steam blowdown (50 seconds), the pressure reaches the peak of 2.56 bars (see Figure 9.C-116), then continuously decreases due to the condensation at the cold surfaces. Note that the external dome cooling is not applied during this experiment.

The 15-hour (900 minute) containment pressure history is presented in Figure 9.C-117. The gas release and steam injection following the initial blowdown slows the depressurization (see Figure 9.C-117). Over the time intervals 155-219 minutes, 245-545 minutes, and 695-820 minutes, the pressure slowly increases inside the containment due to the additional gas and steam releases. During the sump heating phase, the pressure first decreases and then increases. The increase in pressure coincides with the moment when the sump reaches saturated conditions and starts to evaporate. After reaching a second peak value of 1.6 bar at the end of the steam release into the subcompartment R1405, containment pressure decreases to atmospheric pressure. The containment depressurizes through the vent lines at the 0 m and 10 m elevations.

Temperatures along the main stairway during the heatup phase are presented in Figure 9.C-118. The combination of steam and gas releases during the heatup phase results in thermal stratification. This is shown by a 25°C temperature differential over the height of the containment after 80 minutes and a 12°C differential from top to bottom of the dome – see Figure 9.C-118.

Figure 9.C-119 presents the temperatures in both major flow paths (main and spiral staircases) at the same three axial positions. The temperature differences are relatively constant through time at each elevation, although smaller at the high elevations. Circulation is sufficient to keep the temperature difference between the two chimneys small (e.g., ΔT is approximately 5°C at the +16.5 elevation), for the various steam, dry heat, and sump boiling releases that occur in the lower portion of the containment.

The temperature distributions for the entire containment are presented in Figure 9.C-120 and Figure 9.C-121 over time intervals 2.0 to 75.0 minutes and 123 to 345 minutes, respectively. After the initial rise, the temperatures decrease quickly during the first 25 minutes (Figure 9.C-120). The decrease then continues at a slower rate (see Figure 9.C-121). The temperatures stratify in the main staircase, while in the spiral staircase they are almost uniform. Temperature differences between the top of the containment and the release level are approximately 10°C in the main staircase and 5°C in the spiral staircase. The temperature difference below the main stair case, between the level of the release and the bottom of the containment (between CT5301 and CT3802) is around 15°C.

The temperature decreases slowly in the upper region of the dome. The effects of the global circulation on the upper region of the dome are noticeable after the end of the steam release. This is evident from a comparison of the H₂/He concentrations during the gas mixture release (Figure 9.C-121). After the release, the temperature in the containment is relatively uniform, except for below the releases (see temperature distribution on the main stairway side).

During the sump heatup phase (but before the start of the boiling, 570 - 655 minutes), a convection circulation loop affects the region up to 15 m. This region has a uniform temperature gradient, while the region above is stagnant. After sump evaporation begins, the convection circulation loop affects the entire volume and homogenizes the temperatures.

The steam and gas concentrations over time correspond to the temperature distributions. Note that there are no large local changes in gas concentrations in the regions (radially) away from the two staircases, see Figure 9.C-122 and Figure 9.C-123

The flow patterns in the compartments may be inferred by comparing the velocities in the two staircases (see Figure 9.C-124, Figure 9.C-125, and Figure 9.C-126). Upward flow is recorded in both stairways at the early stage of the blowdown (first 30 seconds, see Figure 9.C-124). The upward flow in the spiral staircase is the result of the unplanned vent connection with the release point. A pressure wave destroyed the separating wall during the blowdown. This indicates that the break compartment pressurization forced flow out of all the openings in the break compartment.

After 80 seconds (end of blowdown is at 50 seconds), upward and downward flows are recorded in the main and spiral staircases, respectively (see velocities in Figure 9.C-124). During the steam releases ST1, ST2, ST3, ST4, and ST5 (see Figure 9.C-126 and Figure 9.C-127), upward flows are recorded in both staircases. During the gas mixture release phases GT1, GT2, and GT3, the flow is downwards in the spiral staircase (see Figure 9.C-126).

During the sump heatup phase the flow is upwards in the main staircase and downwards in the spiral staircase (see Figure 9.C-127). The weak circulation loop reaches the 15 m level before the start of sump boiling. After the start of sump boiling, the circulation loop extends over the total containment height and the flow velocities are higher (see Figure 9.C-127 for 655 – 695 minutes).

Various global circulation flow patterns are established during the E11.5 experiment as a result of the various steam and gas release phases, as well as the sump heatup and boiling phases. The temperatures, steam, and gas concentrations follow similar distributions. Global circulation effects contribute to reduced gradients in the vertical direction of temperature and concentration fields.

Application to AP600 and AP1000

The release position in experiment E11.5 is the closest to the possible AP600 and **AP1000** LOCA cases. However, in the HDR, chimney and heat storage effects (heat sink and source effects) along the two main flow paths cause dominant global circulation flow patterns below the operating deck. After the blowdown, the plume rises from the break compartment and entrains laterally, yielding global circulation.

In the passive containment, upward flow patterns are formed in the core of containment (depending on the break location). Downward flow is present near the vertical walls due to the relatively high cooling rates of the steel shell. The overall effects are shallower vertical density gradients in the above-deck region compared with E11.5 test. The shallow gradients are the result of the additional wall layer entrainment that is not present in HDR.

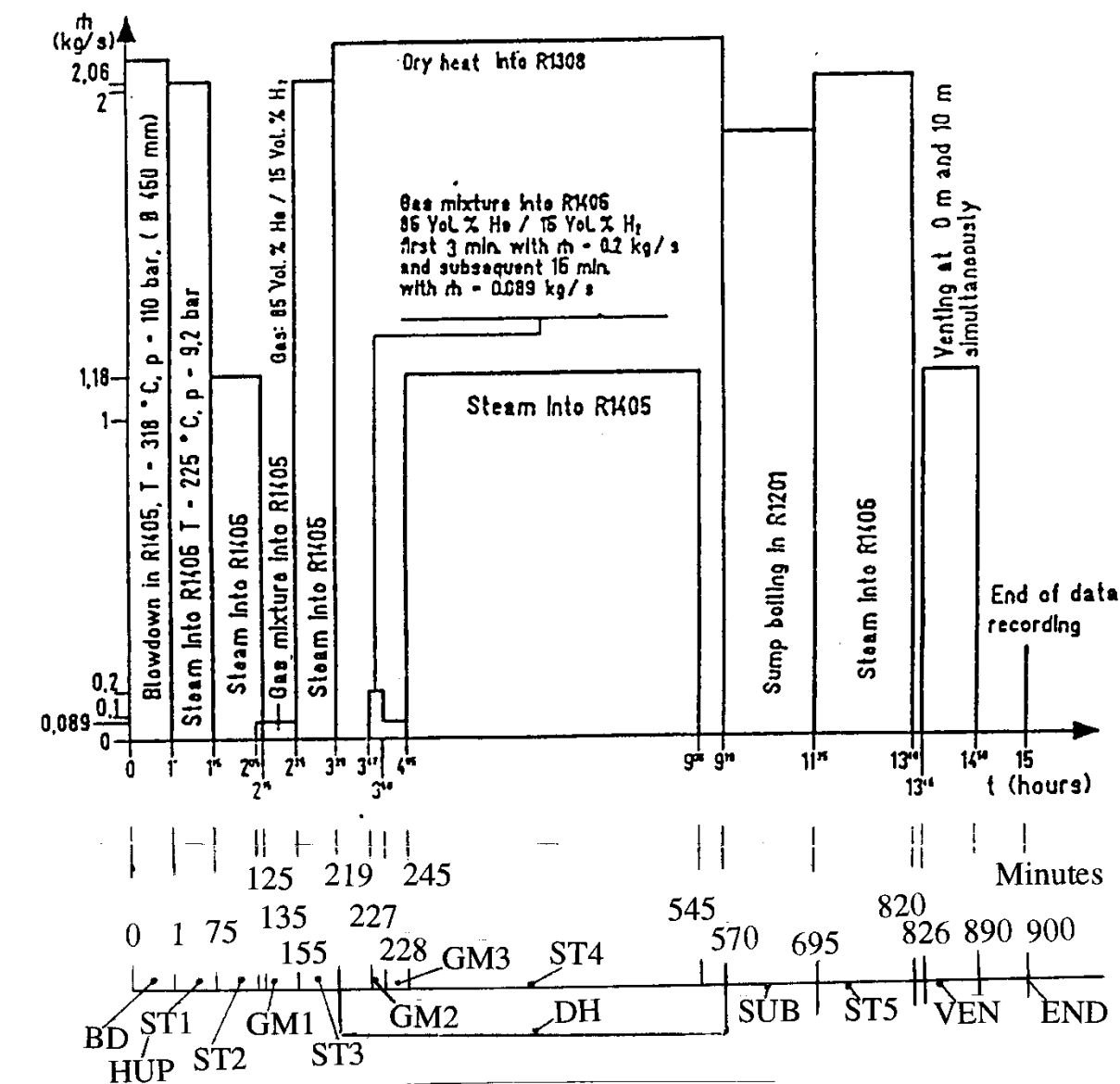


Figure 9.C-115a. HDR-E11.5 Sequence of Experimental Test Procedures

(reprinted from: L. Wolf, K. Mun, "Overview of experimental results for long-term, Large-scale natural circulations in LWR-containments after large LOCAs, Vol. II: Assessment of HDR Experiments V21.1, V43, T31.5 and E11.5," University of Maryland at College Park, for DOE – Project HDR Hydrogen Mixing Evaluation for Containment Safety Evaluations natural Global Circulation, Order Number: DE-AP07-96ID10765," April 1996)

Event	Time minutes	Event Description
BD	0-1	Blowdown in R1.405
HUP ST1	1-75	Steam supply with $m = 2.06 \text{ kg/s}$
ST2	75-135	Reduced external steam with $m = 1.18 \text{ kg/s}$ in R1.405
GM1	125-155	H_2/He gas mixture release into R1.405 with 0.089 kg/s
ST3	155-219	Steam release into R1.405 with 2.06 kg/s
DH	219-570	Dry heat addition into R1.308
GM2	227-228	H_2/He gas mixture release into R1.405 with 0.2 kg/s
GM3	228-245	H_2/He gas mixture release into R1.405 with 0.089 kg/s
ST4	245-545	Start of steam release into R1.405 with $m = 1.18 \text{ kg/s}$
SUB	570-695	Sump boiling
ST5	695-820	Steam release into R1.405 with $m = 2.06 \text{ kg/s}$
VEN	826-890	Containment venting
END	900	End of data acquisition

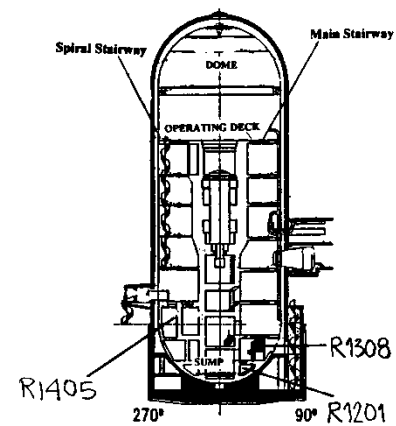


Figure 9.C-115b. HDR-E11.5 Sequence of Experimental Test Procedures

(reprinted from: L. Wolf, K. Mun, "Overview of experimental results for long-term, Large-scale natural circulations in LWR-containments after large LOCAs, Vol. II: Assessment of HDR Experiments V21.1, V43, T31.5 and E11.5," University of Maryland at College Park, for DOE – Project HDR Hydrogen Mixing Evaluation for Containment Safety Evaluations natural Global Circulation, Order Number: DE-AP07-96ID10765," April 1996)

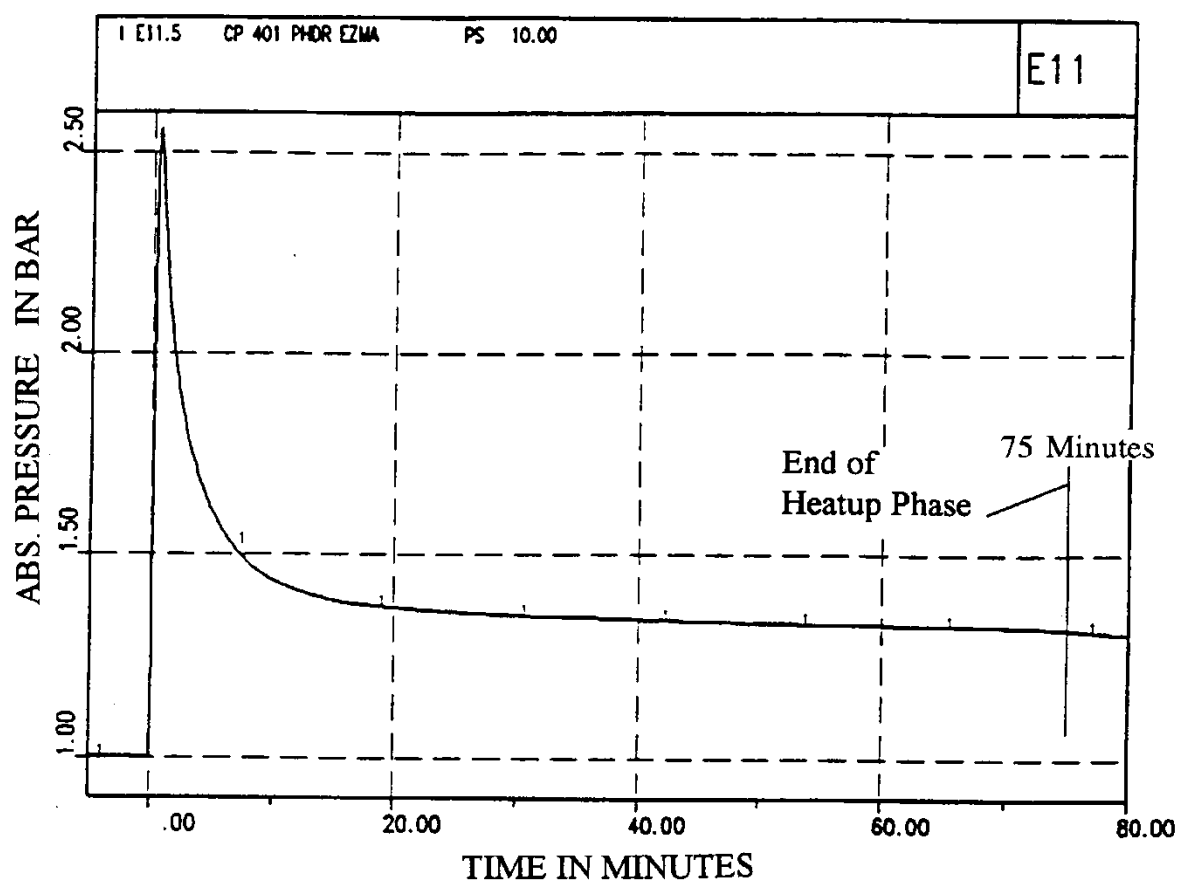


Figure 9.C-116. HDR-E11.5 Containment Pressure

(reprinted from: L. Wolf, K. Mun, "Overview of experimental results for long-term, Large-scale natural circulations in LWR-containments after large LOCAs, Vol. II: Assessment of HDR Experiments V21.1, V43, T31.5 and E11.5," University of Maryland at College Park, for DOE – Project HDR Hydrogen Mixing Evaluation for Containment Safety Evaluations natural Global Circulation, Order Number: DE-AP07-96ID10765," April 1996)

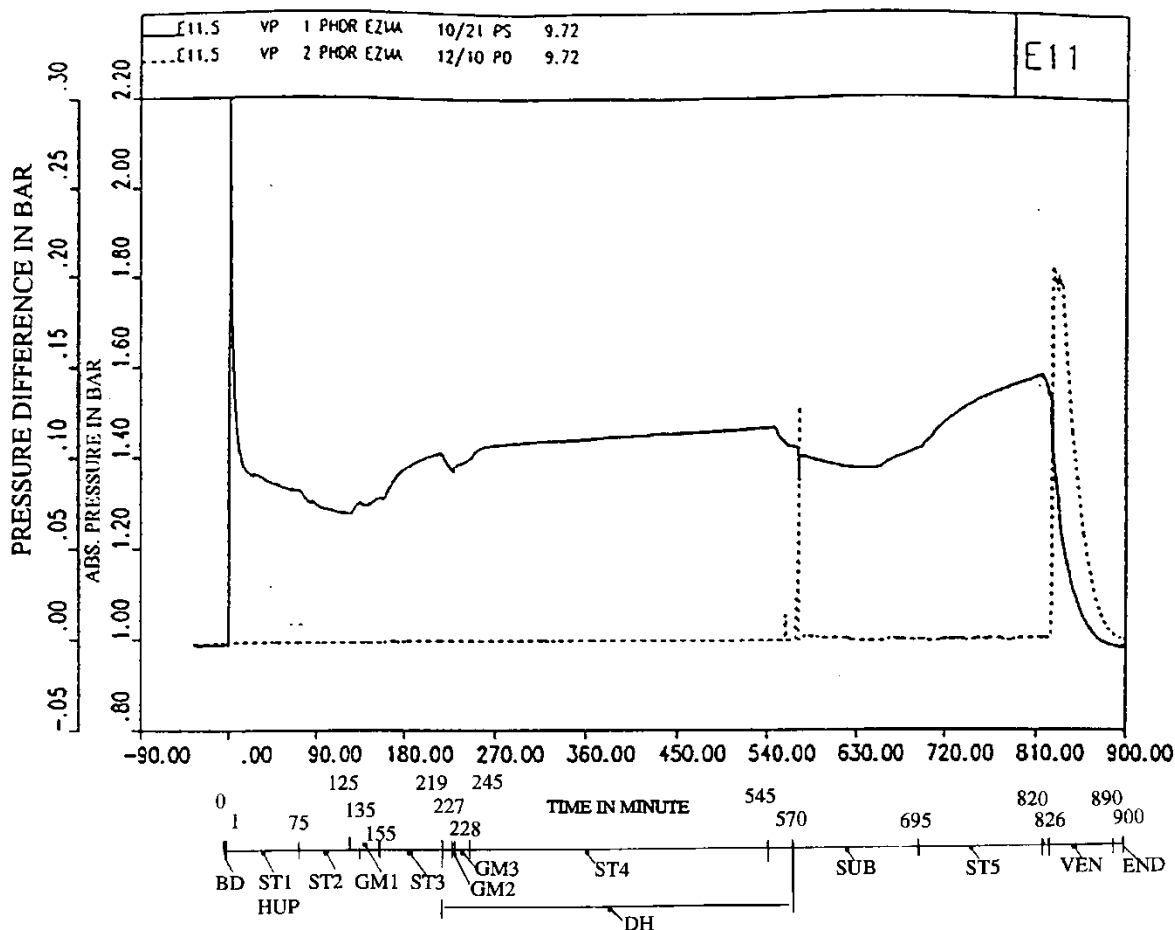


Figure 9.C-117. HDR-E11.5 Containment Pressure History

(reprinted from: L. Wolf, K. Mun, "Overview of experimental results for long-term, Large-scale natural circulations in LWR-containments after large LOCAs, Vol. II: Assessment of HDR Experiments V21.1, V43, T31.5 and E11.5," University of Maryland at College Park, for DOE – Project HDR Hydrogen Mixing Evaluation for Containment Safety Evaluations natural Global Circulation, Order Number: DE-AP07-96ID10765," April 1996)

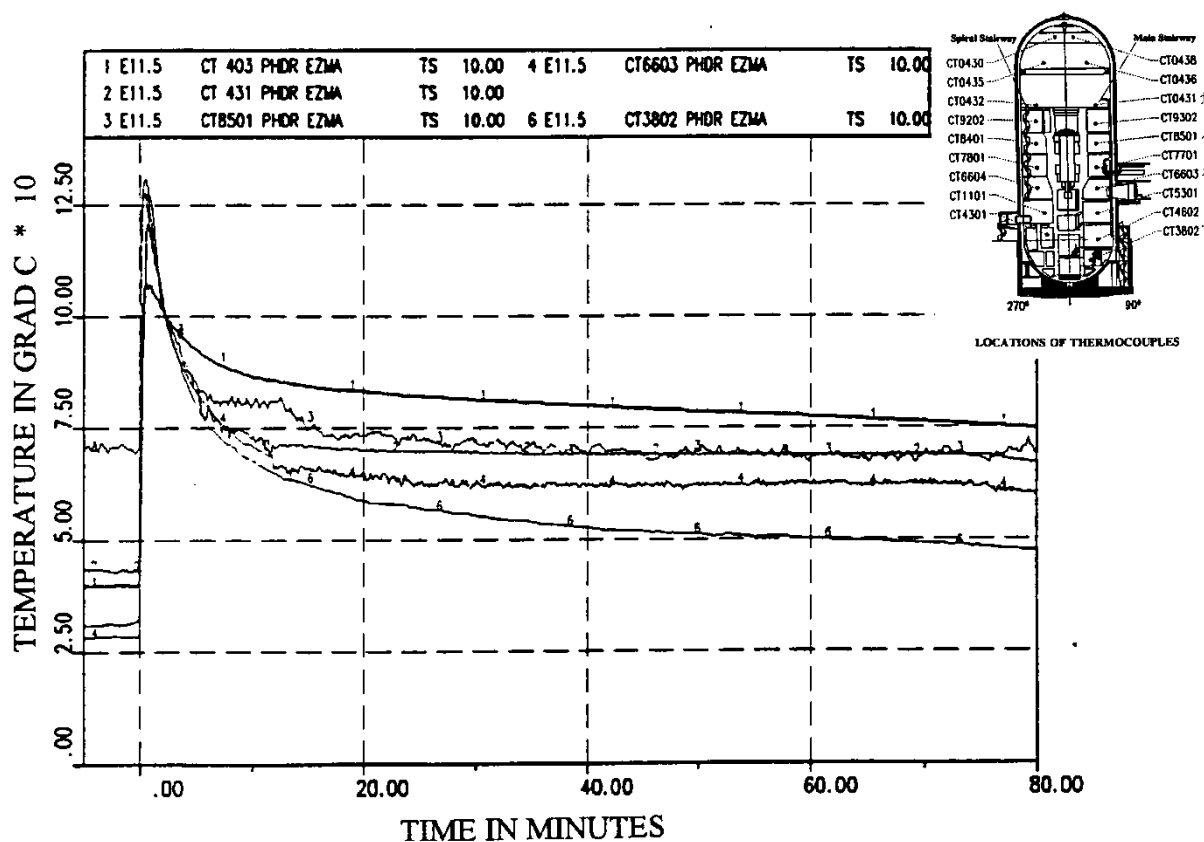


Figure 9.C-118. HDR-E11.5 Containment Temperatures Along main Stairway During Containment Heatup Phase

(reprinted from: L. Wolf, K. Mun, "Overview of experimental results for long-term, Large-scale natural circulations in LWR-containments after large LOCAs, Vol. II: Assessment of HDR Experiments V21.1, V43, T31.5 and E11.5," University of Maryland at College Park, for DOE – Project HDR Hydrogen Mixing Evaluation for Containment Safety Evaluations natural Global Circulation, Order Number: DE-AP07-96ID10765," April 1996)

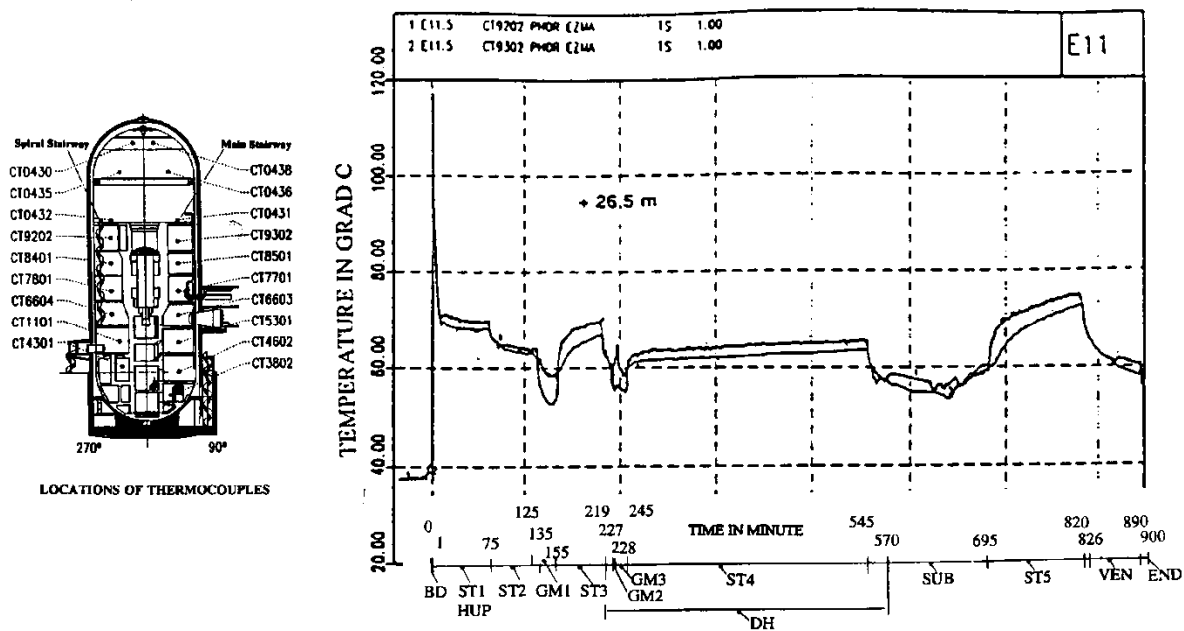


Figure 9.C-119a. HDR-E11.5 Temperatures in Both Major Flow Paths at the Same Axial Positions for Three Heights in the Containment

(reprinted from: L. Wolf, K. Mun, "Overview of experimental results for long-term, Large-scale natural circulations in LWR-containments after large LOCAs, Vol. II: Assessment of HDR Experiments V21.1, V43, T31.5 and E11.5," University of Maryland at College Park, for DOE – Project HDR Hydrogen Mixing Evaluation for Containment Safety Evaluations natural Global Circulation, Order Number: DE-AP07-96ID10765," April 1996)

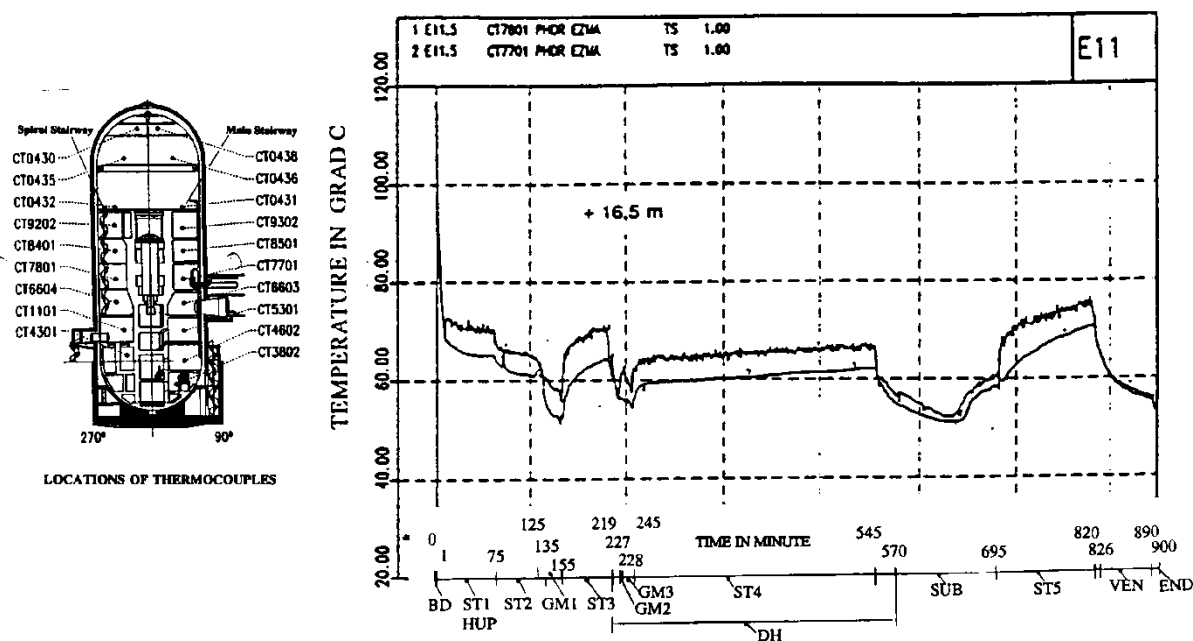


Figure 9.C-119b. HDR-E11.5 Temperatures in Both Major Flow Paths at the Same Axial Positions for Three Heights in the Containment

(reprinted from: L. Wolf, K. Mun, "Overview of experimental results for long-term, Large-scale natural circulations in LWR-containments after large LOCAs, Vol. II: Assessment of HDR Experiments V21.1, V43, T31.5 and E11.5," University of Maryland at College Park, for DOE – Project HDR Hydrogen Mixing Evaluation for Containment Safety Evaluations natural Global Circulation, Order Number: DE-AP07-96ID10765," April 1996)

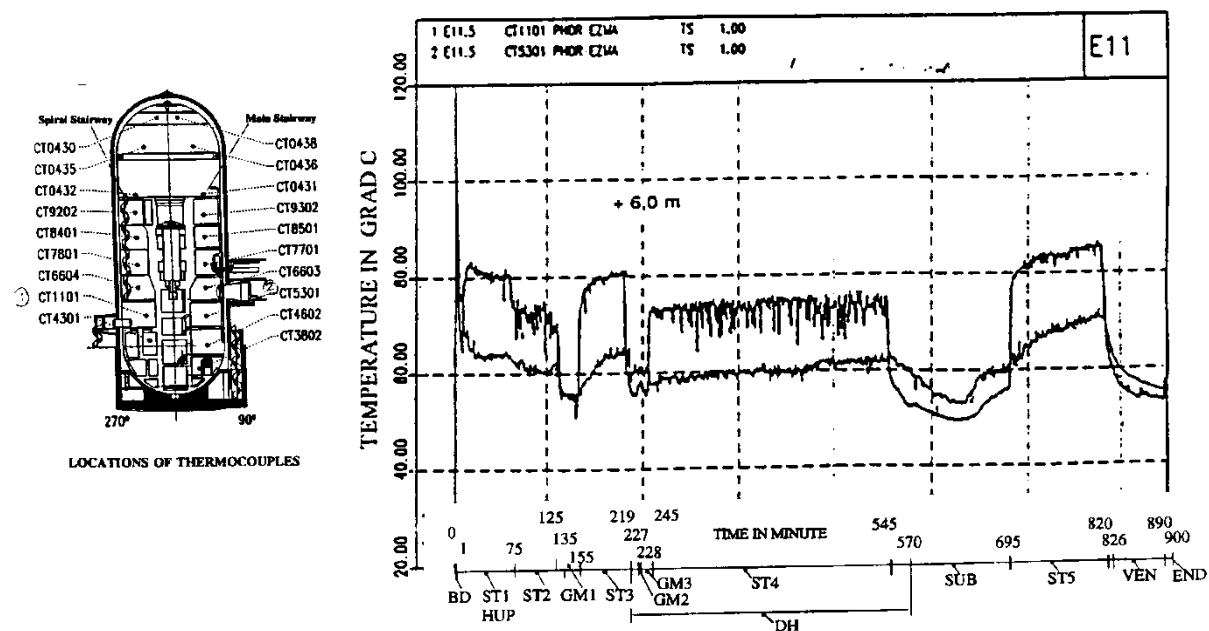


Figure 9.C-119c. HDR-E11.5 Temperatures in Both Major Flow Paths at the Same Axial Positions for Three Heights in the Containment

(reprinted from: L. Wolf, K. Mun, "Overview of experimental results for long-term, Large-scale natural circulations in LWR-containments after large LOCAs, Vol. II: Assessment of HDR Experiments V21.1, V43, T31.5 and E11.5," University of Maryland at College Park, for DOE – Project HDR Hydrogen Mixing Evaluation for Containment Safety Evaluations natural Global Circulation, Order Number: DE-AP07-96ID10765," April 1996)

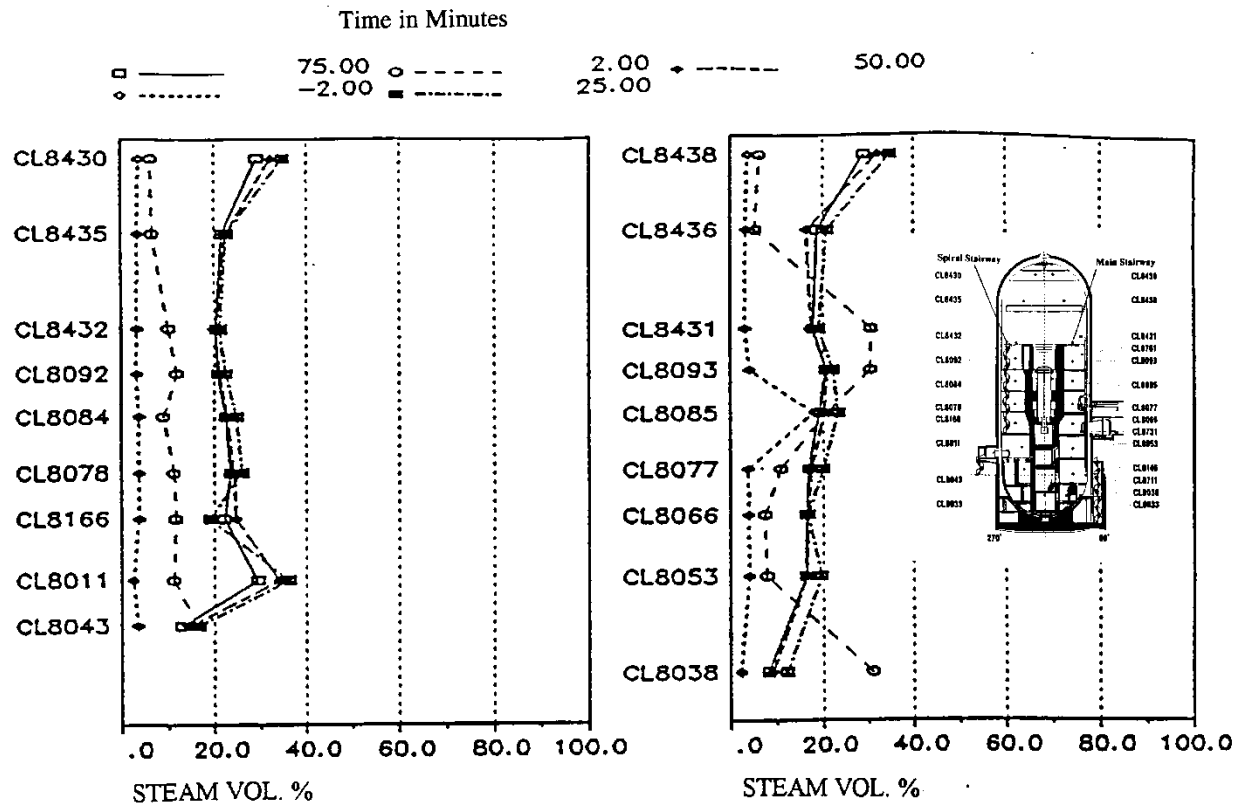


Figure 9.C-120a. HDR-E11.5 Axial Steam Concentration Profiles in Spiral (left) and Main (right) Stairways for Different Instants in time for Large Break LOCA release in Lower Containment Region

(reprinted from: L. Wolf, K. Mun, "Overview of experimental results for long-term, Large-scale natural circulations in LWR-containments after large LOCAs, Vol. II: Assessment of HDR Experiments V21.1, V43, T31.5 and E11.5," University of Maryland at College Park, for DOE – Project HDR Hydrogen Mixing Evaluation for Containment Safety Evaluations natural Global Circulation, Order Number: DE-AP07-96ID10765," April 1996)

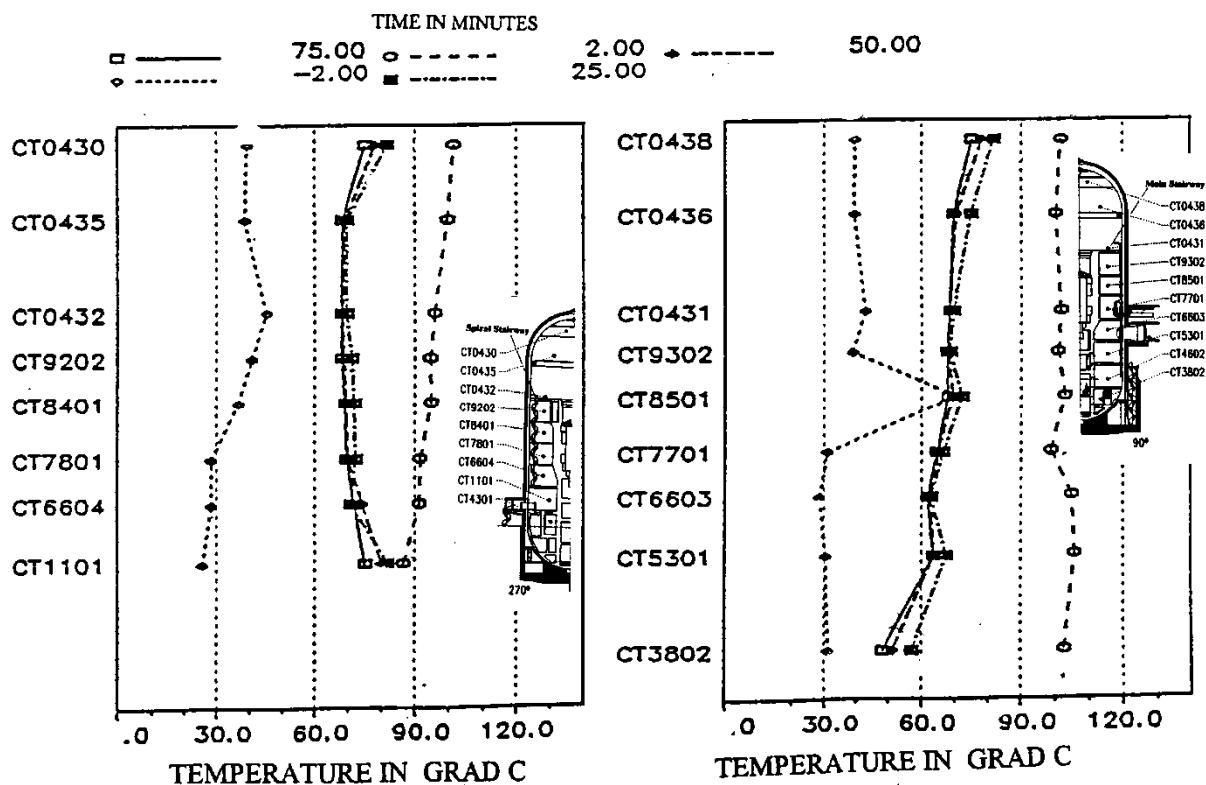


Figure 9.C-120b. HDR-E11.5 Axial Temperature Profiles in Spiral (left) and Main (right) Stairways for Different Instants in Time for Large Break LOCA Release in Lower Containment Region

(reprinted from: L. Wolf, K. Mun, "Overview of experimental results for long-term, Large-scale natural circulations in LWR-containments after large LOCAs, Vol. II: Assessment of HDR Experiments V21.1, V43, T31.5 and E11.5," University of Maryland at College Park, for DOE – Project HDR Hydrogen Mixing Evaluation for Containment Safety Evaluations natural Global Circulation, Order Number: DE-AP07-96ID10765," April 1996)

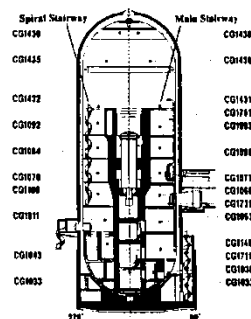
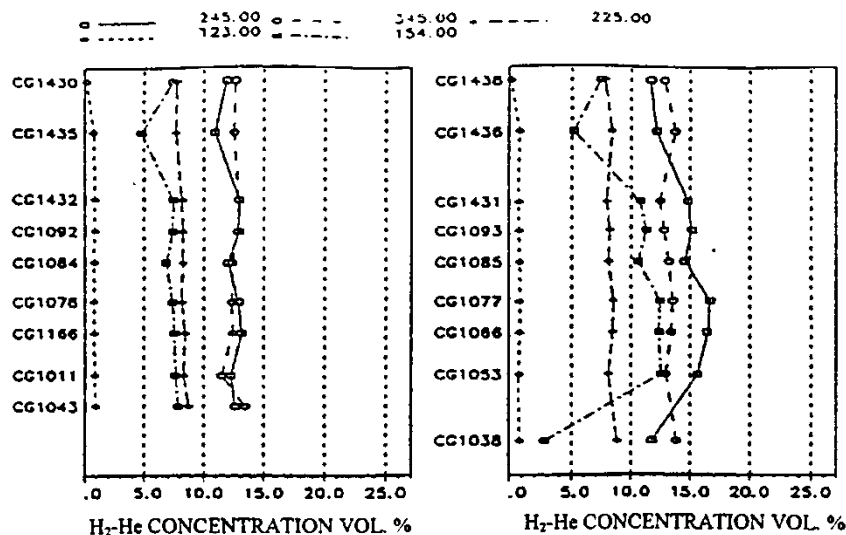


Figure 9.C-121a. HDR-E11.5 Axial H₂-He Gas Mixture Concentration Profiles along Spiral (left) and Main (right) Stairways During Gas Release Phase (Total Mass 291 kg)

(reprinted from: L. Wolf, K. Mun, "Overview of experimental results for long-term, Large-scale natural circulations in LWR-containments after large LOCAs, Vol. II: Assessment of HDR Experiments V21.1, V43, T31.5 and E11.5," University of Maryland at College Park, for DOE – Project HDR Hydrogen Mixing Evaluation for Containment Safety Evaluations natural Global Circulation, Order Number: DE-AP07-96ID10765," April 1996)

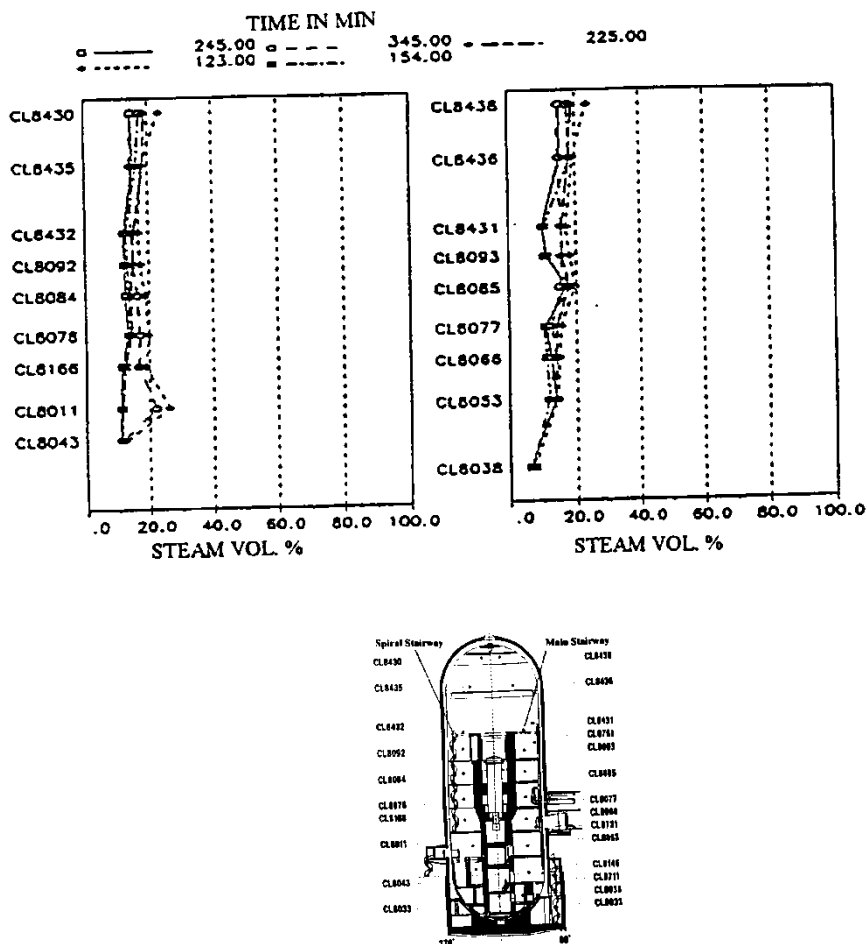


Figure 9.C-121b. HDR-E11.5 Axial Steam Concentration Profiles Along Spiral (left) and Main (right) Stairways During Gas Release Phase (Total Mass 291 kg)

(reprinted from: L. Wolf, K. Mun, "Overview of experimental results for long-term, Large-scale natural circulations in LWR-containments after large LOCAs, Vol. II: Assessment of HDR Experiments V21.1, V43, T31.5 and E11.5," University of Maryland at College Park, for DOE – Project HDR Hydrogen Mixing Evaluation for Containment Safety Evaluations natural Global Circulation, Order Number: DE-AP07-96ID10765," April 1996)

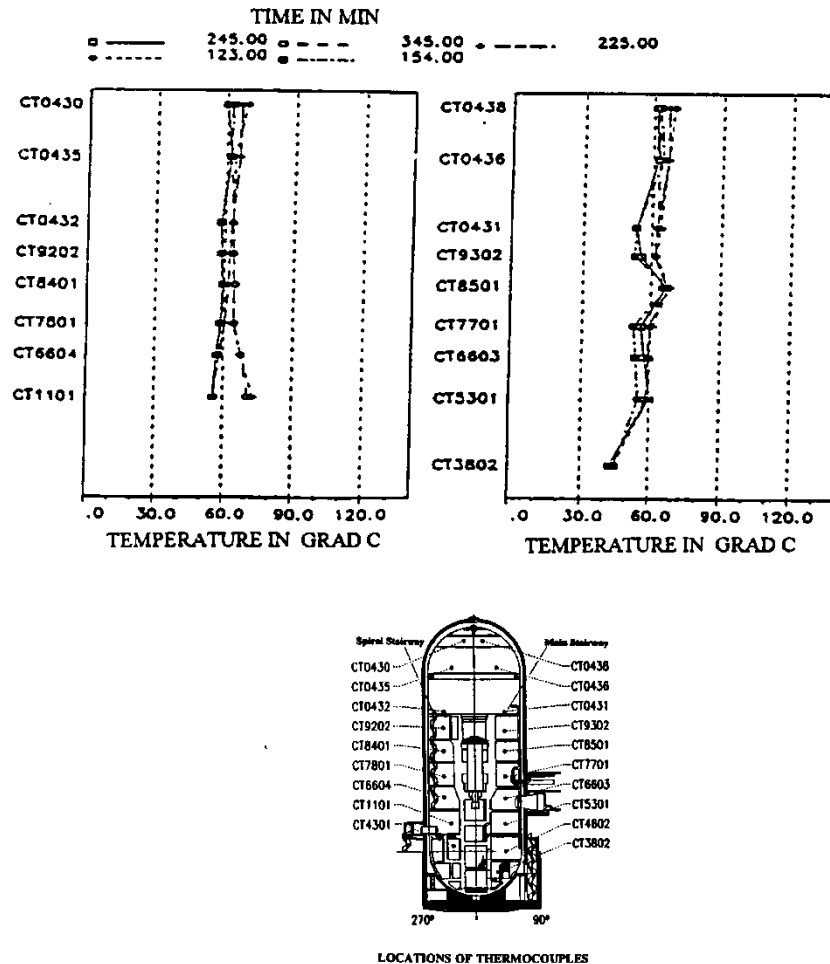


Figure 9.C-121c. HDR-E11.5 Axial Temperature Profiles Along Spiral (left) and Main (right) Stairways During Gas Release Phase (Total Mass 291 kg)

(reprinted from: L. Wolf, K. Mun, "Overview of experimental results for long-term, Large-scale natural circulations in LWR-containments after large LOCAs, Vol. II: Assessment of HDR Experiments V21.1, V43, T31.5 and E11.5," University of Maryland at College Park, for DOE – Project HDR Hydrogen Mixing Evaluation for Containment Safety Evaluations natural Global Circulation, Order Number: DE-AP07-96ID10765," April 1996)

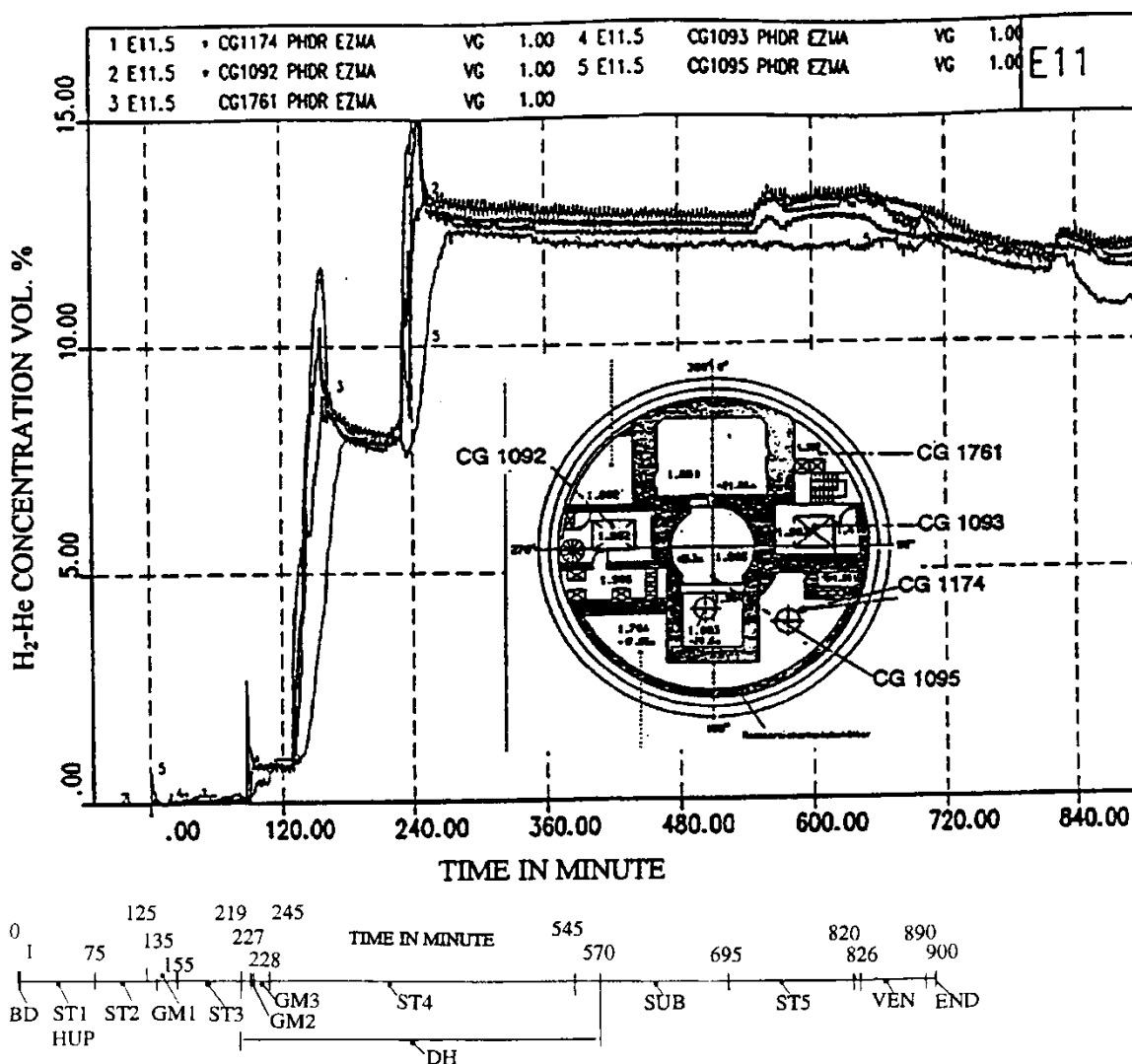


Figure 9.C-122a. HDR-E11.5 Gas Concentrations in the Major Flow Paths and in Regions and Subcompartments Away From the Stairways (H=22m up to 27 m)

(reprinted from: L. Wolf, K. Mun, "Overview of experimental results for long-term, Large-scale natural circulations in LWR-containments after large LOCAs, Vol. II: Assessment of HDR Experiments V21.1, V43, T31.5 and E11.5," University of Maryland at College Park, for DOE – Project HDR Hydrogen Mixing Evaluation for Containment Safety Evaluations natural Global Circulation, Order Number: DE-AP07-96ID10765," April 1996)

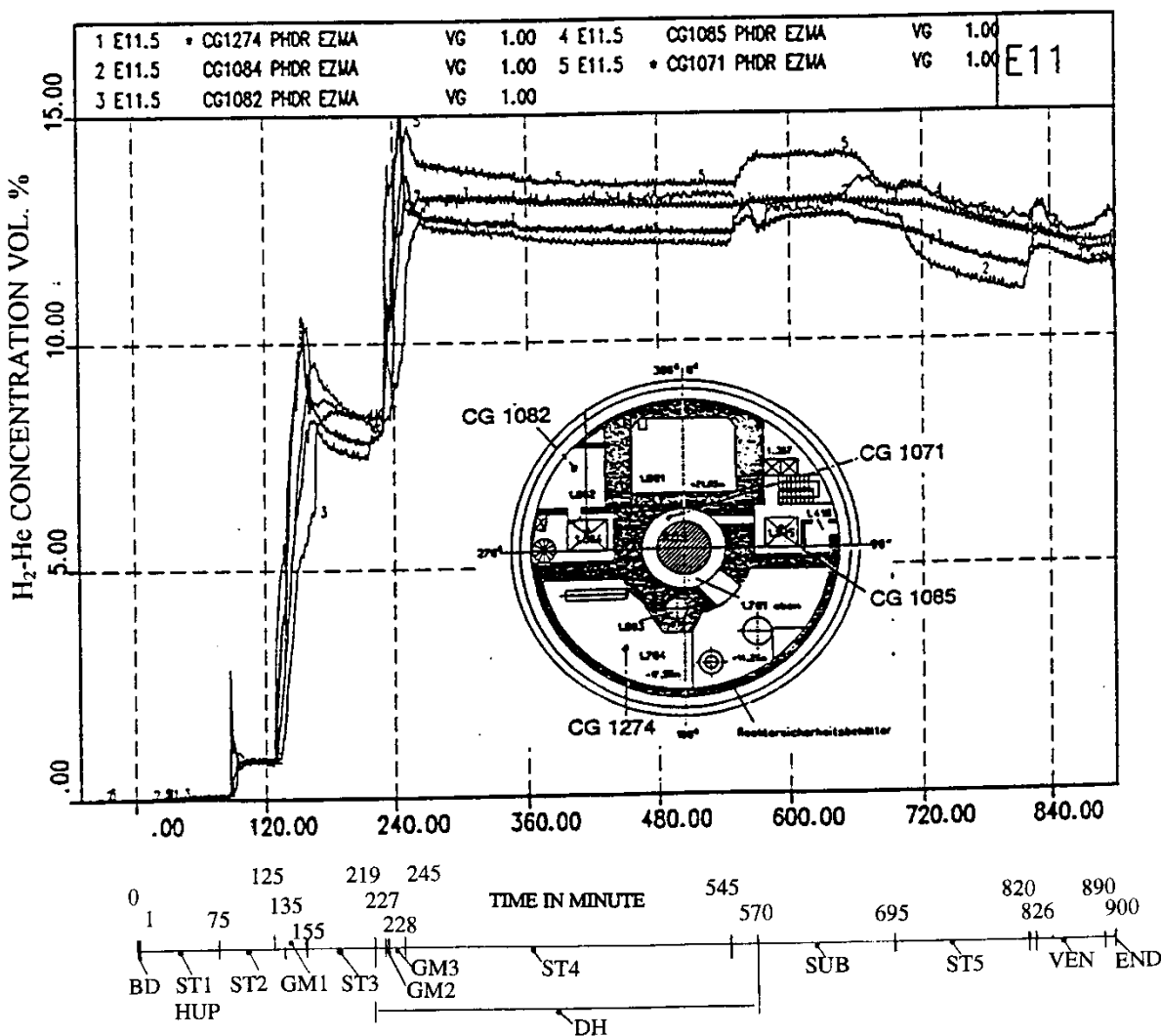


Figure 9.C-122b. HDR-E11.5 Gas Concentrations in the Major Flow Paths and in Regions and Subcompartments Away From the Stairways (H=22m up to 27 m)

(reprinted from: L. Wolf, K. Mun, "Overview of experimental results for long-term, Large-scale natural circulations in LWR-containments after large LOCAs, Vol. II: Assessment of HDR Experiments V21.1, V43, T31.5 and E11.5," University of Maryland at College Park, for DOE – Project HDR Hydrogen Mixing Evaluation for Containment Safety Evaluations natural Global Circulation, Order Number: DE-AP07-96ID10765," April 1996)

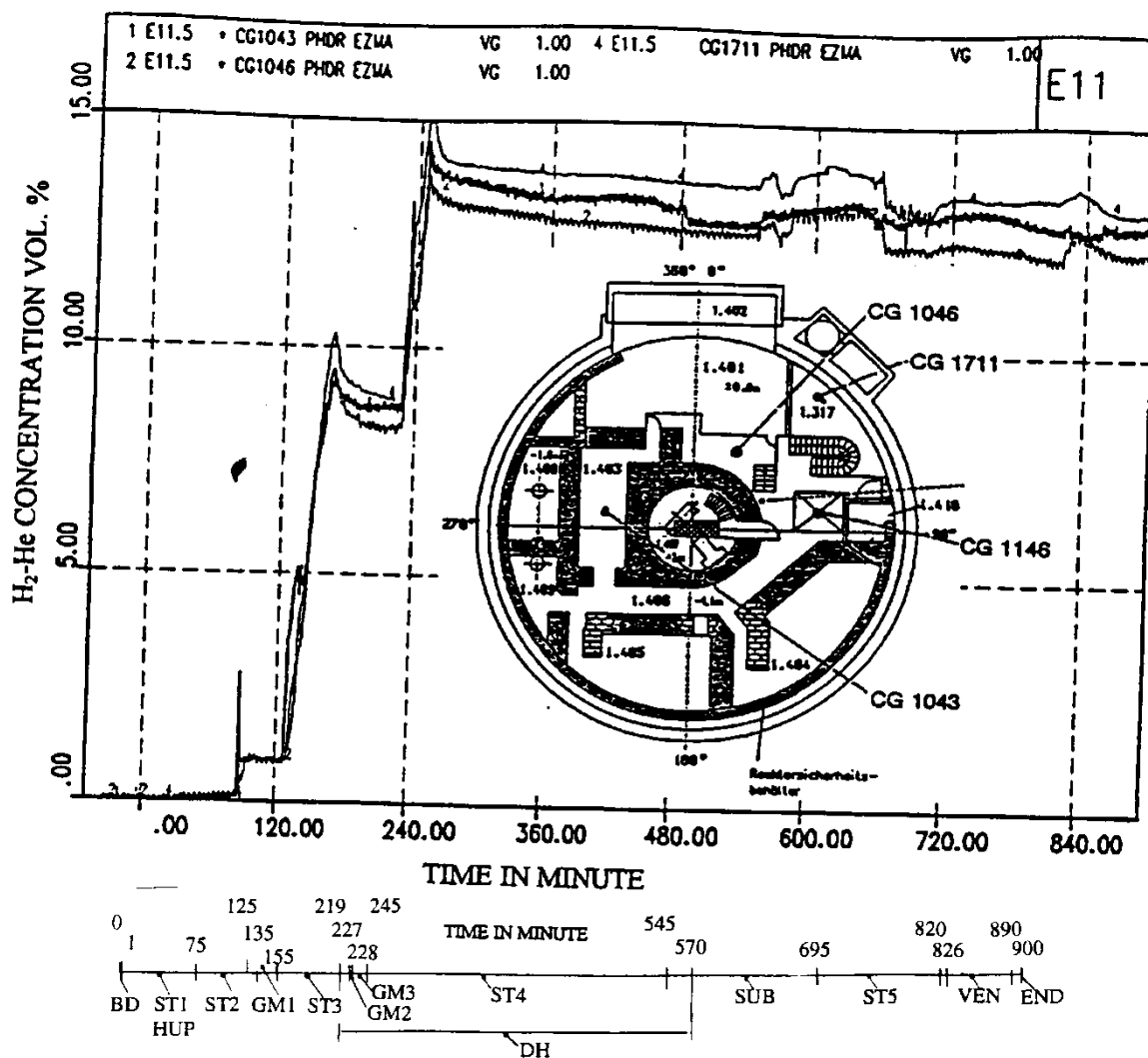


Figure 9.C-123a. HDR-E11.5 Gas Concentrations in the Major Flow Paths and in Regions and Subcompartments Away From the Stairways (H=-4.5m up to +2.0 m)

(reprinted from: L. Wolf, K. Mun, "Overview of experimental results for long-term, Large-scale natural circulations in LWR-containments after large LOCAs, Vol. II: Assessment of HDR Experiments V21.1, V43, T31.5 and E11.5," University of Maryland at College Park, for DOE – Project HDR Hydrogen Mixing Evaluation for Containment Safety Evaluations natural Global Circulation, Order Number: DE-AP07-96ID10765," April 1996)

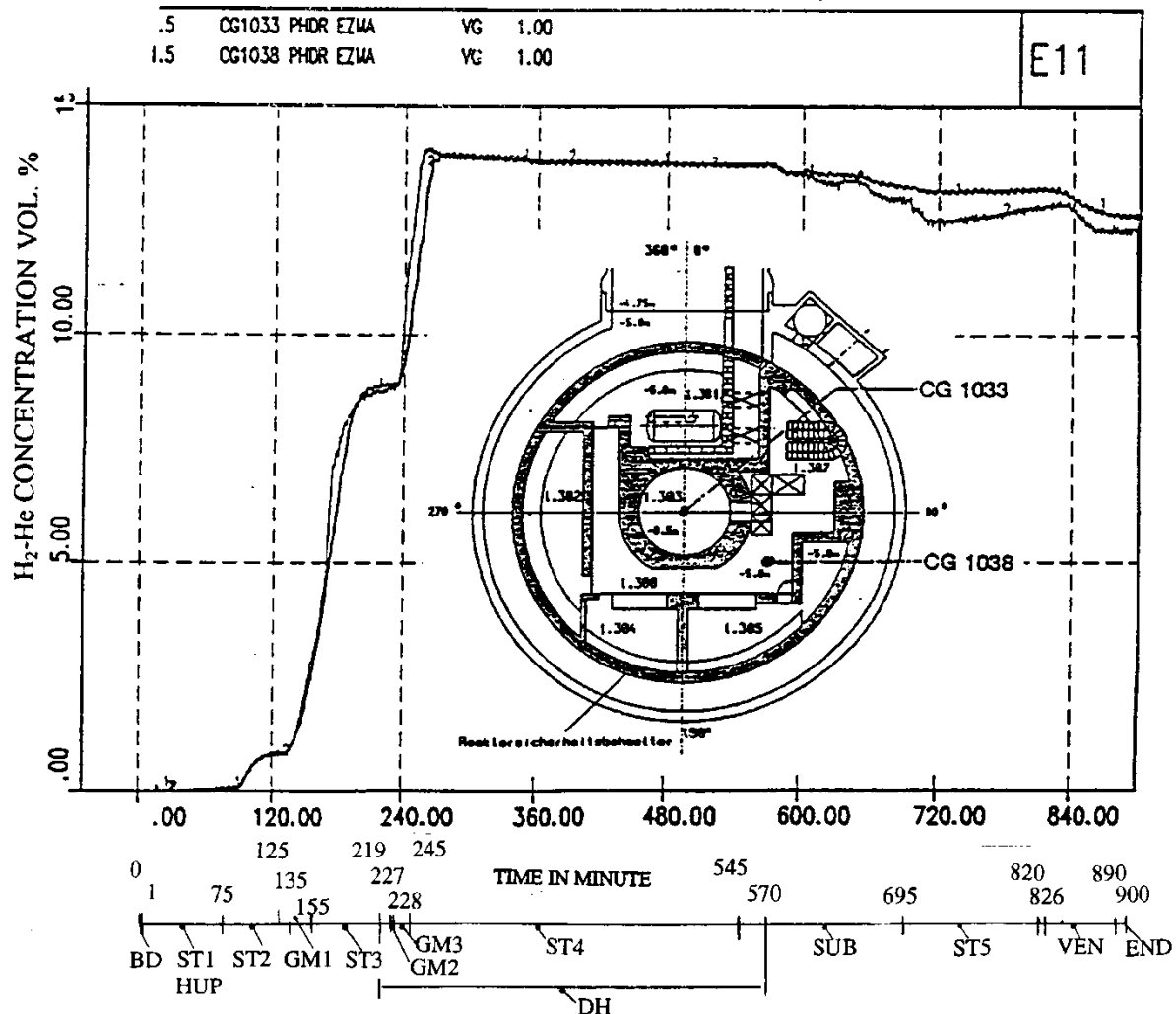


Figure 9.C-123b. HDR-E11.5 Gas Concentrations in the Major Flow Paths and in Regions and Subcompartments Away from the Stairways (H=-4.5m up to +2.0 m)

(reprinted from: L. Wolf, K. Mun, "Overview of experimental results for long-term, Large-scale natural circulations in LWR-containments after large LOCAs, Vol. II: Assessment of HDR Experiments V21.1, V43, T31.5 and E11.5," University of Maryland at College Park, for DOE – Project HDR Hydrogen Mixing Evaluation for Containment Safety Evaluations natural Global Circulation, Order Number: DE-AP07-96ID10765," April 1996)

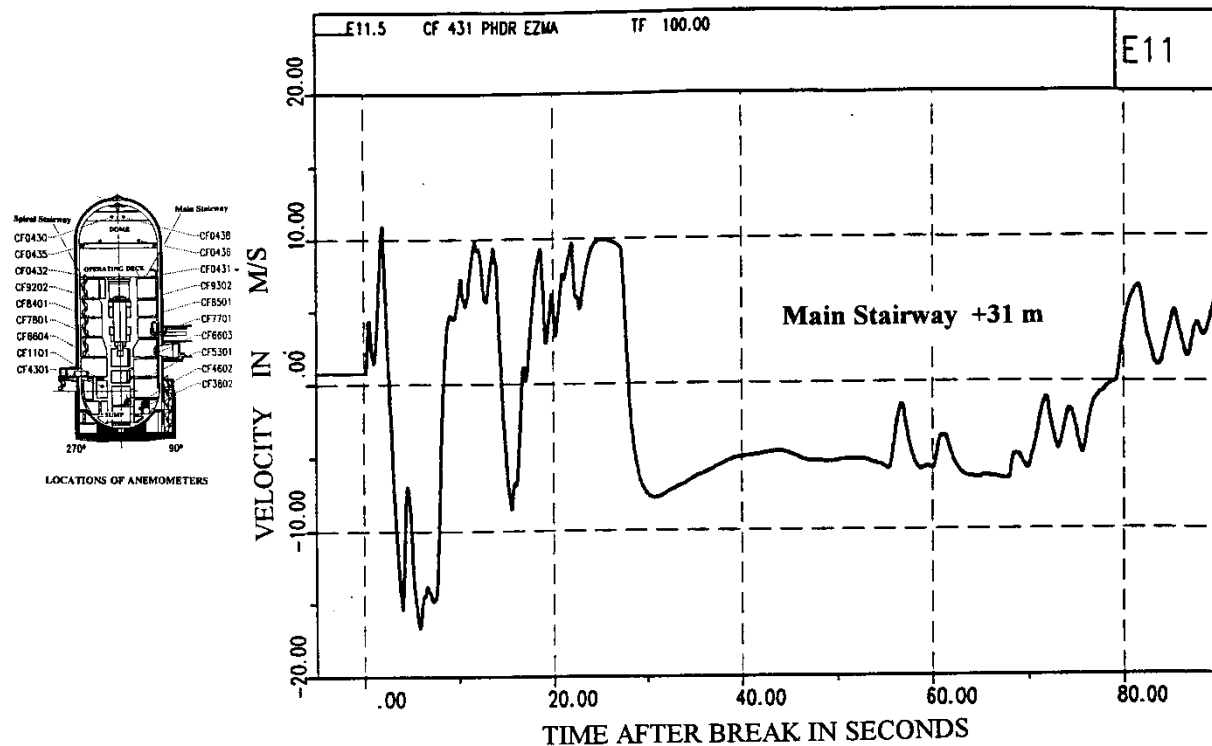


Figure 9.C-124a. HDR-E11.5 Velocities in the Main Stairway During Blowdown

(reprinted from: L. Wolf, K. Mun, "Overview of experimental results for long-term, Large-scale natural circulations in LWR-containments after large LOCAs, Vol. II: Assessment of HDR Experiments V21.1, V43, T31.5 and E11.5," University of Maryland at College Park, for DOE – Project HDR Hydrogen Mixing Evaluation for Containment Safety Evaluations natural Global Circulation, Order Number: DE-AP07-96ID10765," April 1996)

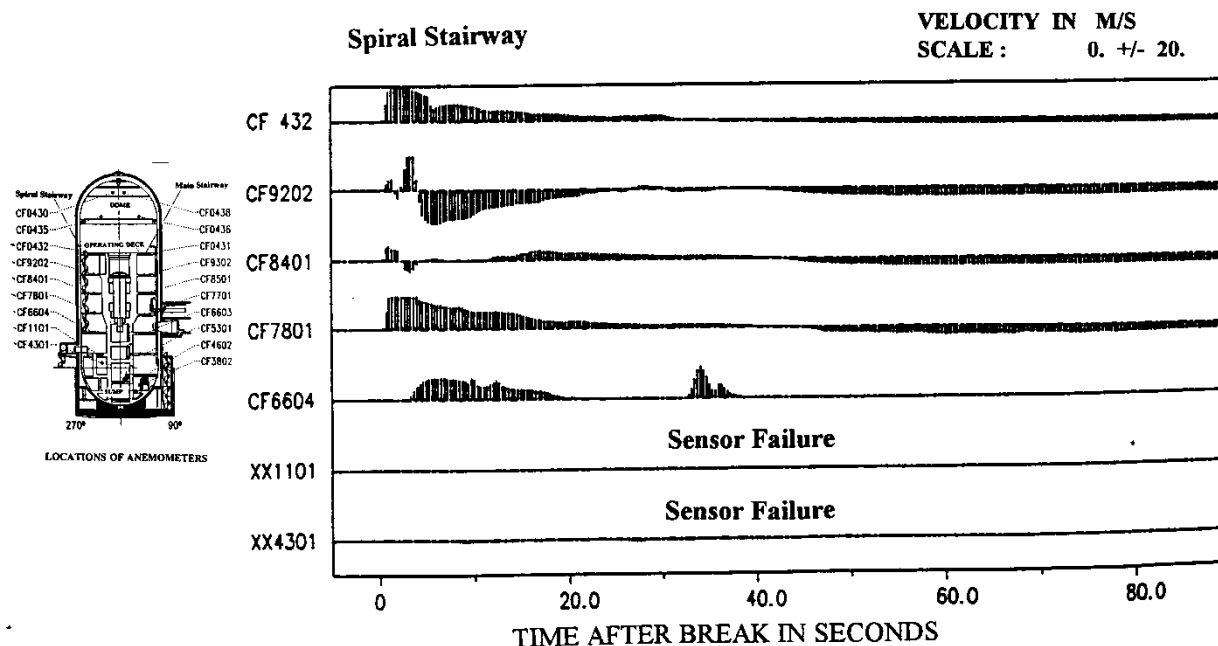


Figure 9.C-124b. HDR-E11.5 Velocities in the Spiral Stairway During Blowdown

(reprinted from: L. Wolf, K. Mun, "Overview of experimental results for long-term, Large-scale natural circulations in LWR-containments after large LOCAs, Vol. II: Assessment of HDR Experiments V21.1, V43, T31.5 and E11.5," University of Maryland at College Park, for DOE – Project HDR Hydrogen Mixing Evaluation for Containment Safety Evaluations natural Global Circulation, Order Number: DE-AP07-96ID10765," April 1996)

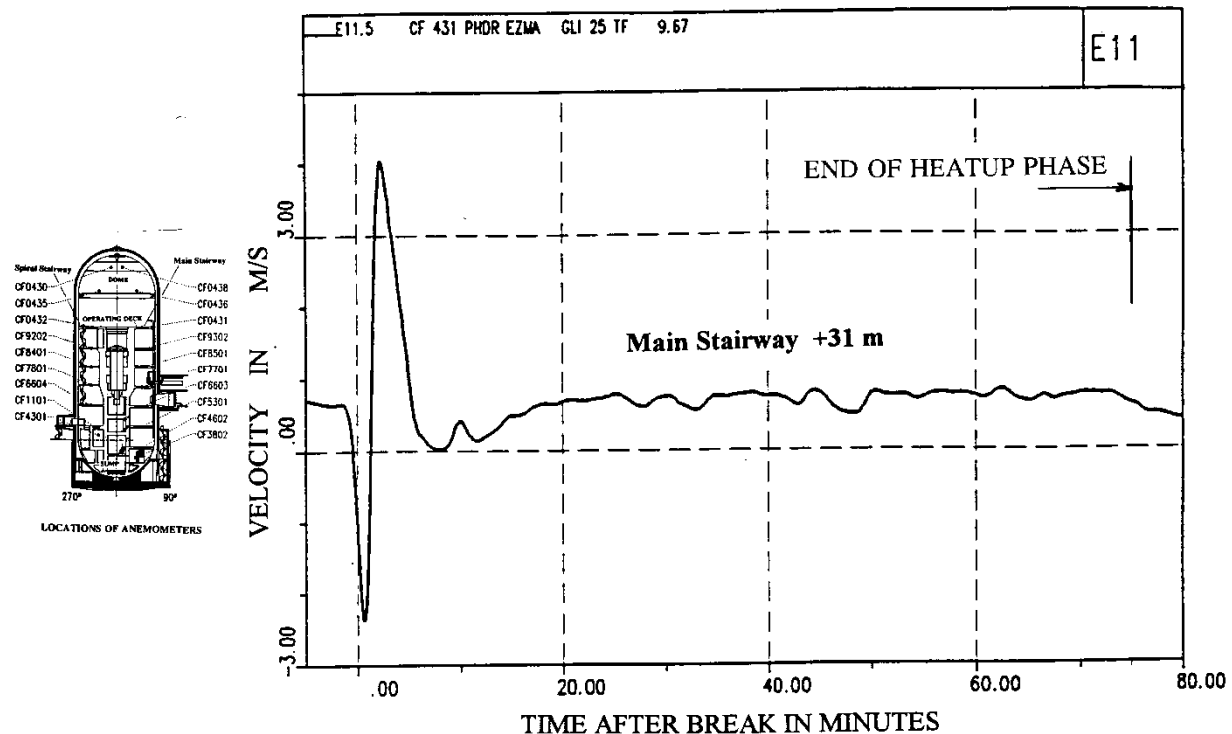


Figure 9.C-125a. HDR-E11.5 Velocities in the Main Stairway During Containment Heatup Phase

(reprinted from: L. Wolf, K. Mun, "Overview of experimental results for long-term, Large-scale natural circulations in LWR-containments after large LOCAs, Vol. II: Assessment of HDR Experiments V21.1, V43, T31.5 and E11.5," University of Maryland at College Park, for DOE – Project HDR Hydrogen Mixing Evaluation for Containment Safety Evaluations natural Global Circulation, Order Number: DE-AP07-96ID10765," April 1996)

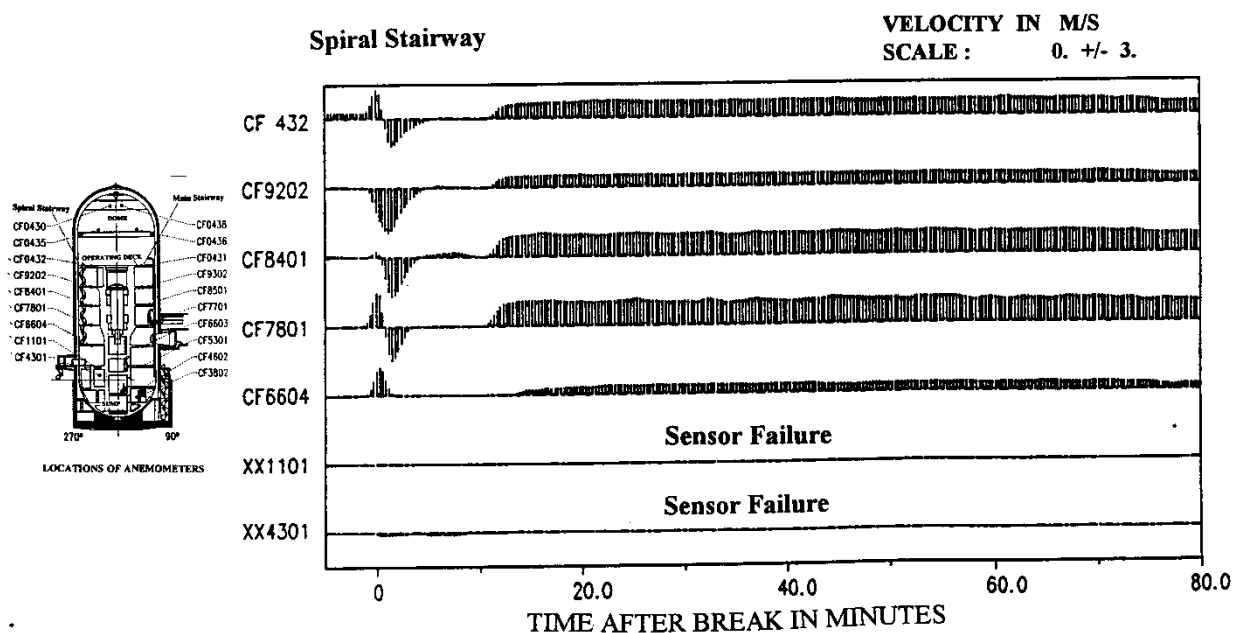


Figure 9.C-125b. HDR-E11.5 Velocities in the Spiral Stairway During Containment Heatup Phase

(reprinted from: L. Wolf, K. Mun, "Overview of experimental results for long-term, Large-scale natural circulations in LWR-containments after large LOCAs, Vol. II: Assessment of HDR Experiments V21.1, V43, T31.5 and E11.5," University of Maryland at College Park, for DOE – Project HDR Hydrogen Mixing Evaluation for Containment Safety Evaluations natural Global Circulation, Order Number: DE-AP07-96ID10765," April 1996)

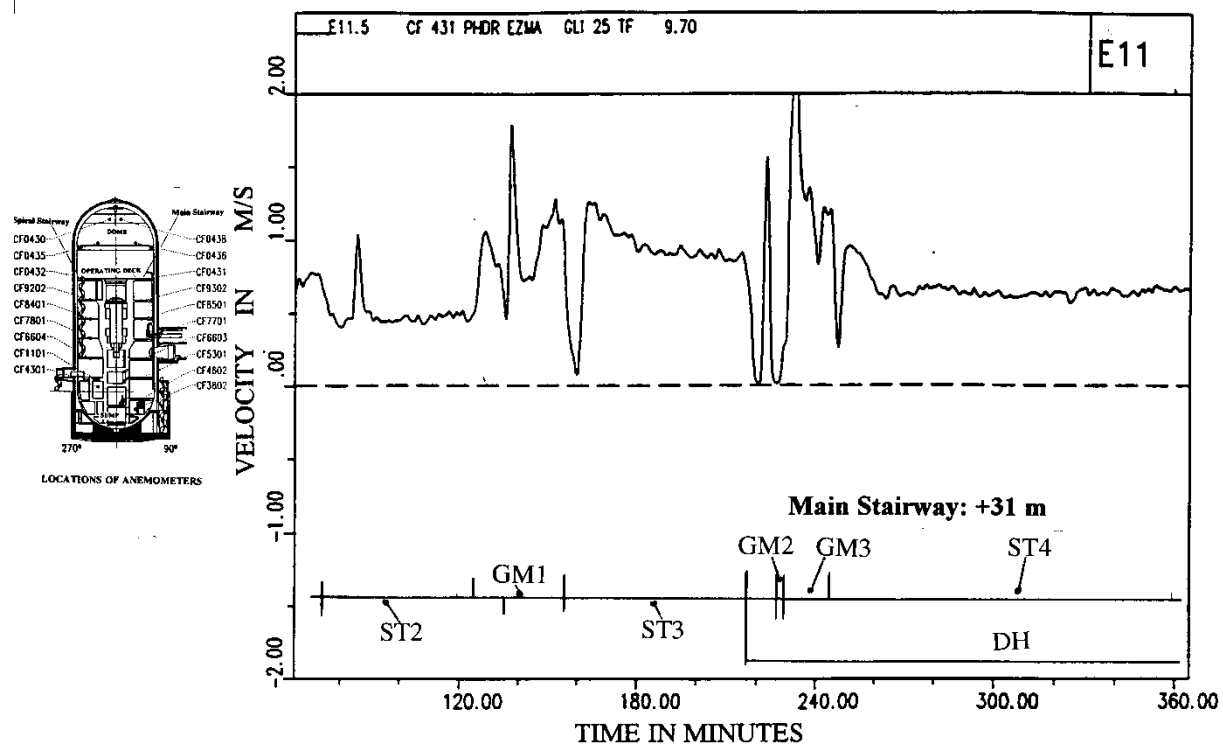


Figure 9.C-126a. HDR-E11.5 Velocities in the Main Stairway During H₂-He Gas Mixture Release Phase

(reprinted from: L. Wolf, K. Mun, "Overview of experimental results for long-term, Large-scale natural circulations in LWR-containments after large LOCAs, Vol. II: Assessment of HDR Experiments V21.1, V43, T31.5 and E11.5," University of Maryland at College Park, for DOE – Project HDR Hydrogen Mixing Evaluation for Containment Safety Evaluations natural Global Circulation, Order Number: DE-AP07-96ID10765," April 1996)

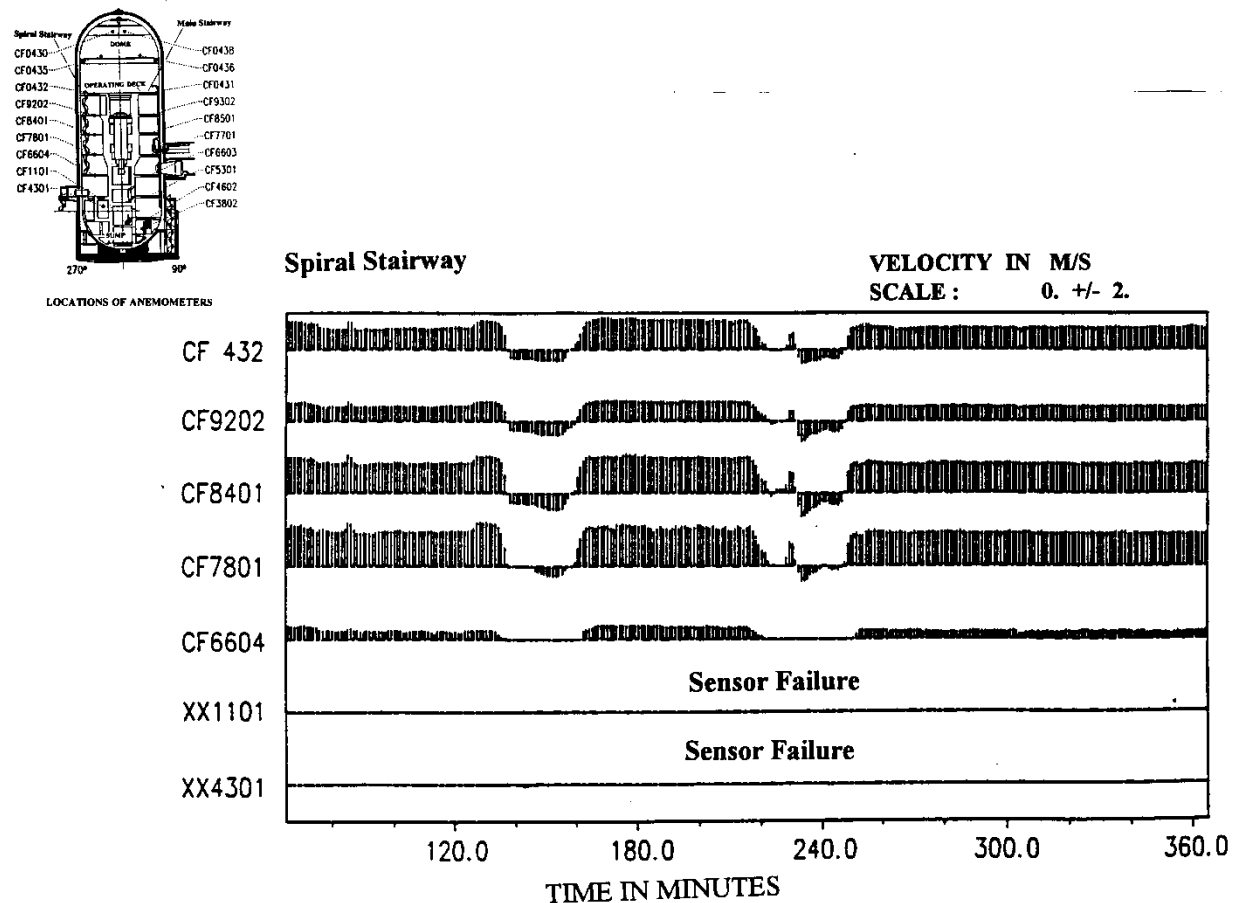


Figure 9.C-126b. HDR-E11.5 Velocities in the Spiral Stairway During H2-He Gas Mixture Release Phase

(reprinted from: L. Wolf, K. Mun, "Overview of experimental results for long-term, Large-scale natural circulations in LWR-containments after large LOCAs, Vol. II: Assessment of HDR Experiments V21.1, V43, T31.5 and E11.5," University of Maryland at College Park, for DOE – Project HDR Hydrogen Mixing Evaluation for Containment Safety Evaluations natural Global Circulation, Order Number: DE-AP07-96ID10765," April 1996)

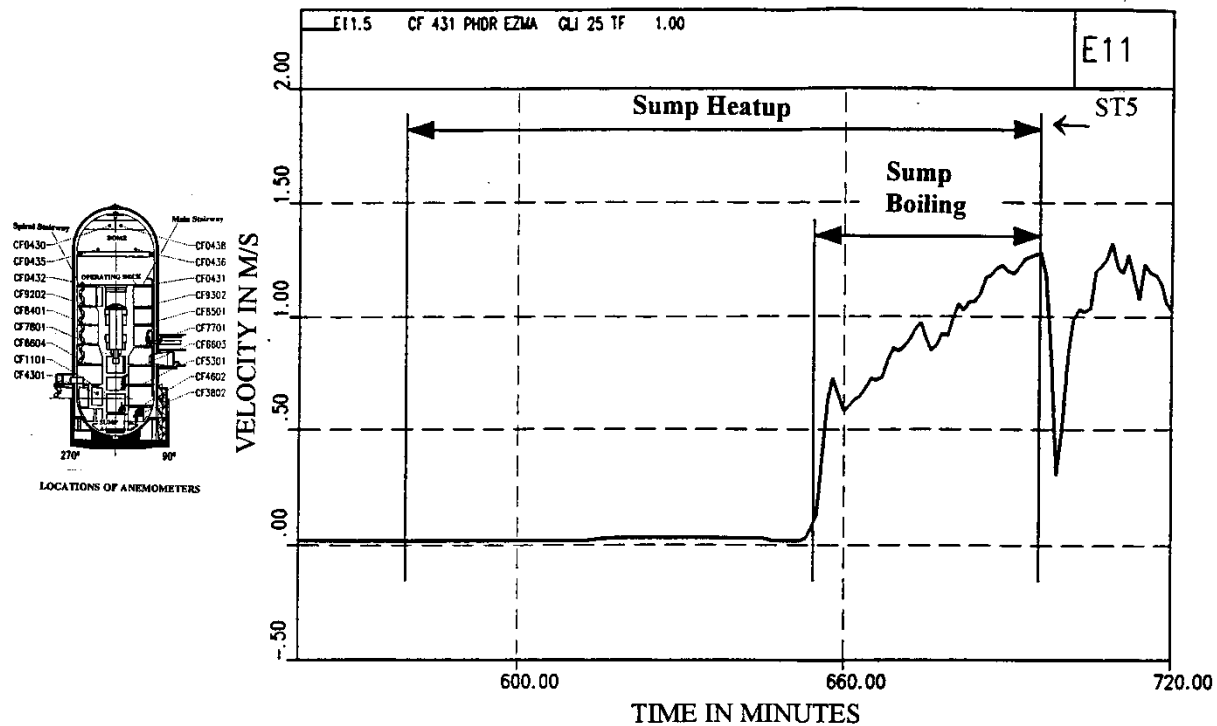


Figure 9.C-127a. HDR-E11.5 Velocities in the Main Stairway During Sump Heatup and Boiling Phase

(reprinted from: L. Wolf, K. Mun, "Overview of experimental results for long-term, Large-scale natural circulations in LWR-containments after large LOCAs, Vol. II: Assessment of HDR Experiments V21.1, V43, T31.5 and E11.5," University of Maryland at College Park, for DOE – Project HDR Hydrogen Mixing Evaluation for Containment Safety Evaluations natural Global Circulation, Order Number: DE-AP07-96ID10765," April 1996)

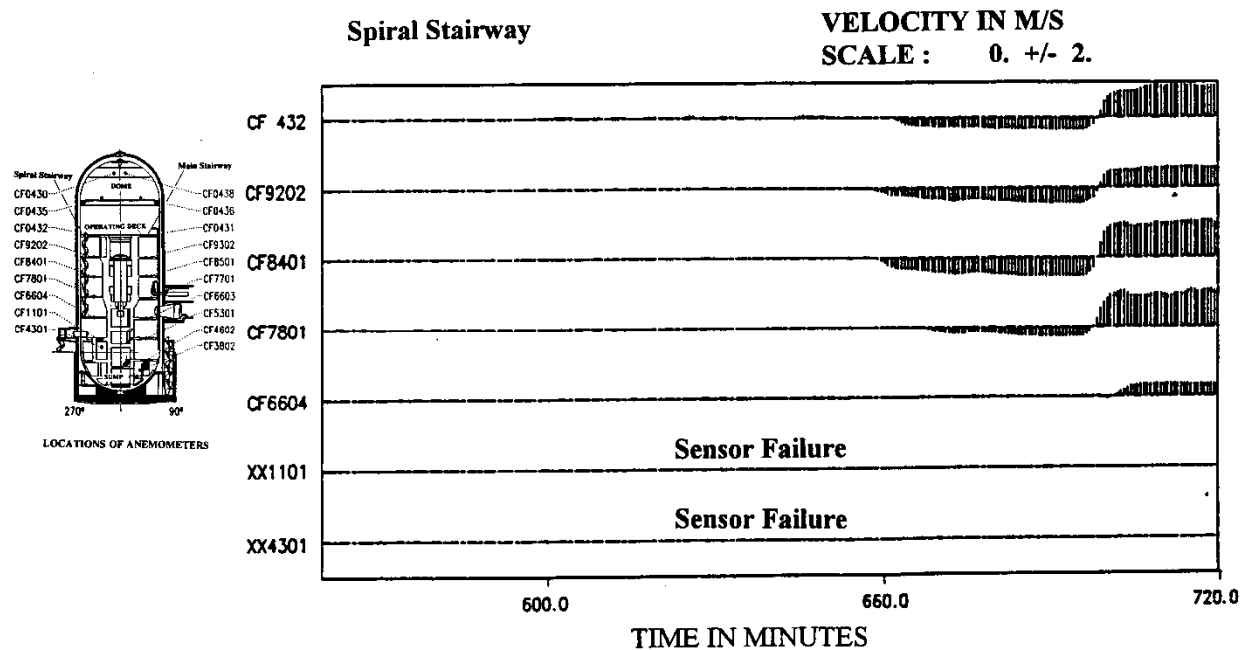


Figure 9.C-127b. HDR-E11.5 Velocities in the Spiral Stairway During Sump Heatup and Boiling Phase

(reprinted from: L. Wolf, K. Mun, "Overview of experimental results for long-term, Large-scale natural circulations in LWR-containments after large LOCAs, Vol. II: Assessment of HDR Experiments V21.1, V43, T31.5 and E11.5," University of Maryland at College Park, for DOE – Project HDR Hydrogen Mixing Evaluation for Containment Safety Evaluations natural Global Circulation, Order Number: DE-AP07-96ID10765," April 1996)

9.C.2.4.3 References

1. T. Cron, D. Schrammel, (1993)
“Investigations on Hydrogen Distribution in a Reactor Containment, Quick Look Report, Test Group E11, Experiments E11.0-6” (In German), PHDR Technical Report PHDR 111-92, 1993
2. H. Holzbauer, L. Wolf, (1994)
“GOTHIC verification on behalf of HDR-Hydrogen mixing experiments”
International Conference on New Trends in Nuclear System Thermohydraulics, Volume II, pp. 331-340., Pisa, Italy, May 30th - June 2nd, 1994
3. T. Kanzleiter, L. Valencia, (1984)
“Blowdown-Experiments in a Reactor Containment, Quick Look Report, Test Group CONW and COND, Experiments V21.1, V21.3, V45” (In German), Technical PHDR Report No. 49/84, Nuclear Center Karlsruhe, Germany, May, 1984
4. L. Valencia, (1987)
“Design Report, Blowdown and Hydrogen Distribution Experiments, HDR-Test Group CON, Experiments T31.4-5” (In German), PHDR-Working Report No. 3.516/87, Nov. 1987
5. H. H. Wenzel, R. Grimm, L. L’hr, (1987)
“Test Report, Blowdown and Hydrogen Distribution Experiments, HDR-Test Group CON, Experiments T31.5” (In German), PHDR-Working Report No. 3.520/88, Dec. 1987
6. L. Wolf, L. Valencia, (1988)
“Results of the Preliminary Hydrogen Distribution Experiment at HDR and Future Experiments for Phase III” 16th Water Reactor Safety Information Meeting, Gaithersburg, MD, USA, Oct. 24-27, 1988.
7. L. Wolf, L. Valencia, (1989)
“Experimental Results of the Preliminary HDR-Hydrogen Distribution Test T31.5” 4th Intl. Topical Mtg. on Nuclear Reactor Thermal-Hydraulics, Karlsruhe, Oct. 10-13, 1989, Vol. 2, pp. 967-973.
8. L. Wolf, H. Holzbauer, T. Cron, (1994)
“Detailed Assessment of the HDR-Hydrogen mixing experiments E11” International Conference on New Trends in Nuclear System Thermohydraulics, Volume II, pp. 91-103., Pisa, Italy, May 30th – June 2nd, 1994
9. L. Wolf, K. Mun, J. Floyd, (1995)
“HDR hydrogen mixing evaluation for containment safety evaluations,” Final Report, DOE-Project Order No.: DE-AP07-95ID81401, Dept. of Materials and Nuclear Engineering, University of Maryland, College Park, MD, Sept. 1995

10. L. Wolf, K. Mun, (1996)
“Overview of experimental results for long-term, large-scale natural circulations in LWR-containments after large LOCAS – Vol. II: Assessment of HDR Experiments V21.1, V43, T31.5 and E11.5” DOE – Project, HDR Hydrogen Mixing Evaluation for Containment Safety Evaluations Natural Global Circulation, Order Number: DE – AP07 – 96ID10765 University of Maryland at College Park, April 1996
11. L. Wolf, M. Gavrilas, K. Mun, (1996)
“Overview of experimental results for long-term, large-scale natural circulations in LWR-containments after large LOCAS” Final Report for DOE – Project, Order Number: DE - AP07 – 96ID10765 University of Maryland at College Park, July 1996

9.C.2.5 Conclusion

Eleven of the twenty experiments presented have a low release position $H_r/H_t < 0.2$. These experiments may be compared to the AP600 and **AP1000**.

They include the seven BMC experiments with a low release position (F2 set, Phase 2, 3 and 4, Test 2 – Phase I, Test 20 - Phase II and RX4), the NUPEC experiment M-4-3, and the three HDR experiments (E11.3, E11.4 and E11.5). Most of these tests (except two - BMC Test 20 and NUPAC M-4-3) have global circulation through the dome which contributes towards homogenization of temperature and concentration fields.

The two experiments with the low release position where stratification is recorded are BMC Test 20 and NUPEC M-4-3. As already noted, the stratification occurs due to the special circumstances (boundary conditions). BMC Test 20 stratifies due to the initially stratified temperature field. Upper compartments are maintained at the higher temperature for several days. Global circulation starts first in the lower compartments, resulting in higher concentrations of the released gas mixture being recorded. Later, the circulation flow path penetrates the upper thermally-stratified layers and the vertical concentration gradients are smaller.

In the M-4-3 NUPEC test, the temperature stratification occurs after the end of the release, although injected gas mixture homogenized slowly. The thermally insulated shell of the NUPEC containment could be one cause for thermal stratification. The homogenization of the gas mixture concentration indicates that some circulation inside of the containment existed, probably due to the presence of the sump.

The external cooling of the AP600 and **AP1000**, as well as the hot concrete structures positioned in the lower portion of the containment, will produce global circulation.

Seven experiments have high release positions ($H_r/H_t > 0.5$), two BMC (Test 4 and Test 12), all three CVTR experiments, and two HDR experiments (E11.2 and T31.5). Thermal stratification is present in six of the seven tests, with the exception of BMC Test 12. BMC Test 12 includes only hydrogen injection.

Due to the uniform initial temperature field (boundary conditions) and circulation patterns formed by hydrogen injection, the concentration field was uniform in BMC Test 12. In the second and third CVTR experiments, the application of the internal sprays decreases the pressure and vertical temperature gradients.

In HDR experiments E11.2 and T31.5, the temperature and concentration fields stratify at the beginning of the experiments. Later, the global circulation decreases the vertical gradients.

In experiment E11.2, additional steam release in the lower compartment and the application of external sprays generates global circulation and decreases vertical gradients.

A review of the tests indicates that global circulation and atmosphere homogenization will occur if:

1. The position of the steam or hydrogen release ($H_r/H_t < 0.2$) is low
2. External sprays are applied
3. Internal sprays are active
4. Openings between compartments are large
5. The temperature field is not initially stratified
6. Heat sources, such as hot concrete walls or a sump, are at the low positions
7. Compartments are connected (not dead-ended)

In the case of AP600 and **AP1000** passive containment designs, all conditions except 3) and partially 7) are satisfied.

9.C.3 APPLICATION OF LUMPED-PARAMETER CODES FOR MODELING LARGE CONTAINMENT FACILITIES

Results of codes using the lumped parameter approach are summarized in this chapter. The ability of the lumped parameter codes to model large facilities is assessed and guidelines to improve predictions are presented.

Tests from several facilities included in an international database are used to compare and validate the results of the lumped parameter containment analysis computer codes. Among the test facilities in the database are BMC, NUPEC, and HDR. Results from these experiments have been described in sections 9.C.2.1, 9.C.2.2, and 9.C.2.4, respectively.

9.C.3.1 Validation of the Lumped Parameter Containment Analysis Computer Codes Based on BMC Experimental Results

The BMC F2 tests are used to validate various containment codes (Fisher et al., 1991 and Fisher et al., 1993). BMC tests 2, 4, 6, 12, and 20 are used to compare various lumped parameter and distributed-parameter GOTHIC models (L. Wolf, H. Holzbauer, M. Schall, 1994).

9.C.3.1.1 F2 Experiments – Natural Convection Phenomena Inside the Multi-Compartment Containment

A comparison of the experimental results of the F2 experiments with the results of various codes is presented by L. Wolf, M. Gavrilas, K. Mun, 1996. The comparison is based on thermal-hydraulic benchmark exercises by Fisher et al., 1991 for Phase 1 and by Fisher et al., 1993 for Phases 2, 3, and 4. Many different codes including FUMO, JERICHO, FIPLOC, WAVCO, CONTAIN, MELCOR, and COBRA/FATHOMS are compared. The comparisons demonstrate the state of containment code development with respect to multi-compartment thermal-hydraulics.

Figures 1.17 through 1.37 (in Wolf et al., 1996) illustrate both the experimental data and the results of various containment analysis codes for F2-Experiment Heatup Phase (Phase I) over a long period of time (48 hours). Single-node models are specified for this exercise. This results in three main sources of deviations between measurement and code results:

1. **Single-node models are not able to model stratification** (due to the penetration of the steam front) inside the dead-end compartments.
2. **One-node lumped parameter models cannot model the stratification front passing through horizontal vents.** One-node models provide artificially perfect mixing between the connected compartments, while in reality only a portion of the vents are available for circulation.
3. **Sump liquid level and sump temperature are not predicted well due to the instantaneous** transport of high temperature condensate into sump and stratification phenomena inside the sump. (Note that the temperature of the condensate is too high.)

The influence of all three discrepancies between the experimental and numerical results can be decreased by applying a series of nodes in a vertical direction or subdivision, as in the GOTHIC distributed parameter model.

Figures 1.50 through 1.55 (in Wolf et al., 1996) compare the experimental data for the F2-Experiment Phase II with the results of various codes. All compartments except the external annulus have almost homogeneous temperatures due to the presence of the natural circulation. A comparison of the measured and predicted velocities through the vents is in agreement for the majority of the codes, which supports the conclusion (L. Wolf, M. Gavrilas, K. Mun, 1996) that containment codes based on lumped parameter models can predict fully-developed natural circulation flows.

However, some codes produced results that are not correct. It was established that the incorrect codes missed or oversimplified the buoyancy terms (see K. Fischer et al., 1993).

9.C.3.1.2 Influence of Initial Temperature Distribution, Location of Hydrogen Injection, Duration of Injection, and Size of Vent Openings on Hydrogen Distribution (BMC Tests 2, 4, 6, 12, and 20)

A comparison of the multi-dimensional and lumped parameter GOTHIC containment analyses and the BMC experimental data is presented in Wolf et al., 1994b. Tests 2, 4, and 6, described in Section 9.C.2.1.2, are performed with only the central compartments R1, R2, and R3. Only two-dimensional GOTHIC results are presented.

Three different models are used to compare the results with multi-compartment experiments 12 and 20. Test 12, which uses a uniform initial temperature distribution, results in homogenized hydrogen concentrations in the entire containment. The lumped parameter model simulates hydrogen concentration histories in the various compartments (see Figure 9 in Wolf et al., 1994b, see also Figure 9.C-43 in this appendix). **To account for recirculation flows, the applied lumped parameter model uses double-junctions in the horizontal direction.**

Test 20 has a stratified initial temperature distribution, which results in a higher hydrogen distribution in the lower rooms. The conventional lumped parameter model, with one junction connection between two subvolumes, results in a hydrogen concentration profile (in R1 and R2 rooms) that is opposite to that measured (see Figure 9 in L. Wolf, H. Holzbauer, M. Schall, 1994b). Also, the experimental results indicate a stratified hydrogen concentration during the first three hours, while the computed generated hydrogen distribution is more uniform. **The calculation performed with double-junction lumped parameter modeling (second model) does not improve results. This model also results in a high degree of hydrogen homogenization inside the containment.**

The third type of model uses a two-dimensional model (distributed parameter model) for all containment rooms except room R2 and uses double-junctions for horizontal connections. The results are presented in Figure 11 in L. Wolf, H. Holzbauer, M. Schall, 1994b and Figure 9.C-44 of this appendix. Improvement between experimental and computed results is obvious (except in the source room R6). A finer nodalization of the source compartment R6 could further improve the results, because the processes in this compartment affect the hydrogen distribution phenomena in all other portions of the containment. Therefore, a more complete momentum formulation, such as that in GOTHIC distributed parameters, is needed to accurately model H₂ distributions.

9.C.3.2 Validation of the Lumped Parameter Containment Analysis Computer Codes Based on Nupec Experimental Results

9.C.3.2.1 M-7-1 Test

A comparison of the M-7-1 test results with the various computer codes results is presented in report NEA/CSNI/R(94)29. The WGOTHIC (Westinghouse modified GOTHIC) code results are also included (see pages 125, 130, 135, blind test calculation results – pages 246-253, open test calculations – pages 322-327, preheating calculation - 374-378). However, the M-7-1 test is not directly applicable to the passive containment design, because internal sprays are active during the test.

9.C.3.2.2 M-4-1 Test

The experimental results of NUPEC M-4-3 test (T. Hirose, 1993) are used to validate various lumped parameter codes and to check the input geometry and boundary conditions, before applying them to blind and open comparisons with the NUPEC M-7-1 database. WGOTHIC is also compared with NUPEC M-4-3 experimental data. A comparison of the WGOTHIC results with the M-4-3 test, which is performed without internal sprays, is presented by R. P. Ofstun, J. Woodcock, D. L. Paulsen, 1994. The location of the break is at a low position in the first level of the containment. A mixture of steam and helium is injected at a constant flow rate during the first 30 minutes and experimental data is recorded for 2 hours.

A comparison of the experimentally and numerically obtained pressure of the dome is illustrated in Figure 9.C-128. Figure 9.C-129 through Figure 9.C-132 present comparisons of the temperatures and helium concentrations inside the compartments 8, 15, dome, and 7. These compartments are affected by the global circulation loop. Lumped parameter modeling methods developed for NUPEC M-4-3 are summarized in Section 9.2.4. Good agreement exists between the numerical and experimental results for the multiple, connected, lumped parameter compartments in the circulating regions.

However, a paper by R.P. Ofstun, J. Woodcock, D. L. Paulsen, 1994 shows a discrepancy between the measured and calculated (lumped parameter model) helium concentrations in dead-end compartments. Calculated values for in-core chase node and two pressurizer nodes (which are all dead-end compartments) are presented and compared with M-4-3 test data (see Figures 3-8, in R.P. Ofstun, J. Woodcock, D. L. Paulsen, 1994). The discrepancy shows that the lumped parameter model has difficulty predicting circulation effects within dead-end compartments.

It is postulated that asymmetric temperatures on the vertical walls of the dead-ended compartments induce a natural circulation within the compartment that is not modeled in the lumped parameter model. To improve the results for dead-end compartments, a WGOTHIC distributed parameter model is applied to the dead-ended compartments and interfaced to the lumped parameter model (see Figures 9 - 14 in R. P. Ofstun, J. Woodcock, D. L. Paulsen, 1994).

The lumped parameter model predicts pressure, temperature and helium concentrations inside the compartments affected by the global circulation loop. However, a distributed parameter model is necessary to improve predictions inside the dead-end compartments.

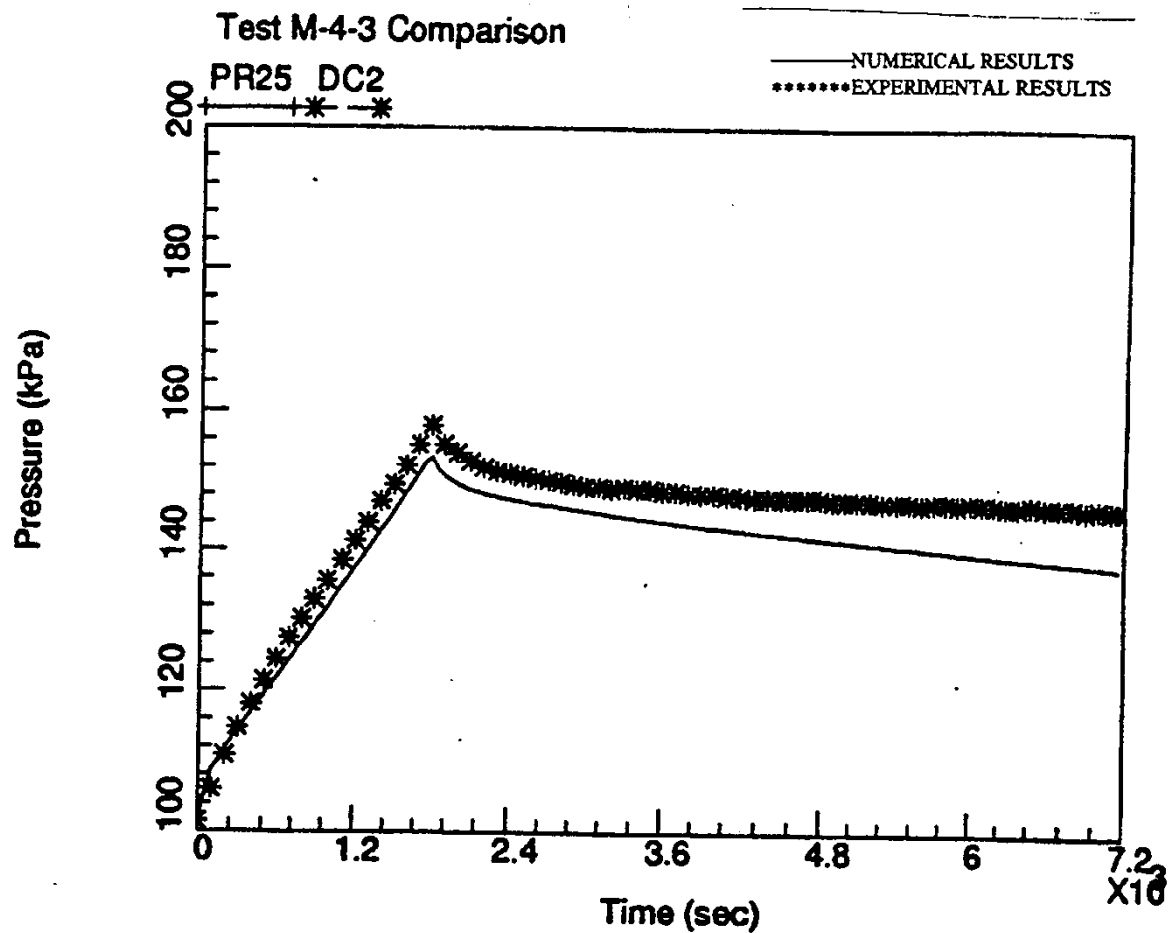


Figure 9.C-128. Dome Pressure History

(Numerical results are produced in the framework of: R.P. Ofstun, J. Woodcock, D.L. Paulsen, "Westinghouse-GOTHIC modeling of NUPEC's hydrogen mixing and distribution test M-4-3," The Third International Conference on Containment Design and Operations, Volume 1, Toronto, Canada, October 19-21, 1994)

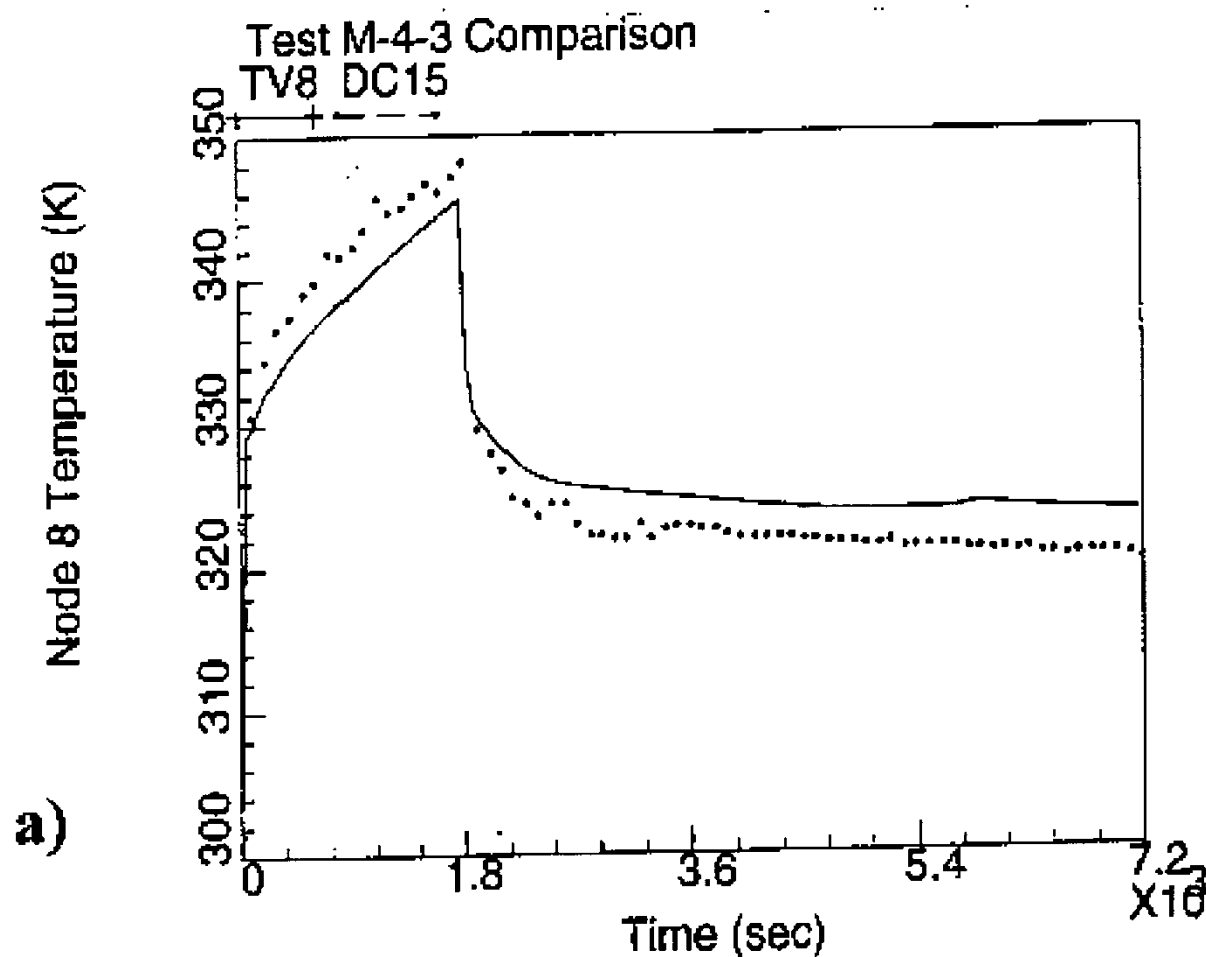


Figure 9.C-129a. Temperature History Inside Node 8

(Numerical results are produced in the framework of: R.P. Ofstun, J. Woodcock, D.L. Paulsen, "Westinghouse-GOTHIC modeling of NUPEC's hydrogen mixing and distribution test M-4-3," The Third International Conference on Containment Design and Operations, Volume 1, Toronto, Canada, October 19-21, 1994)

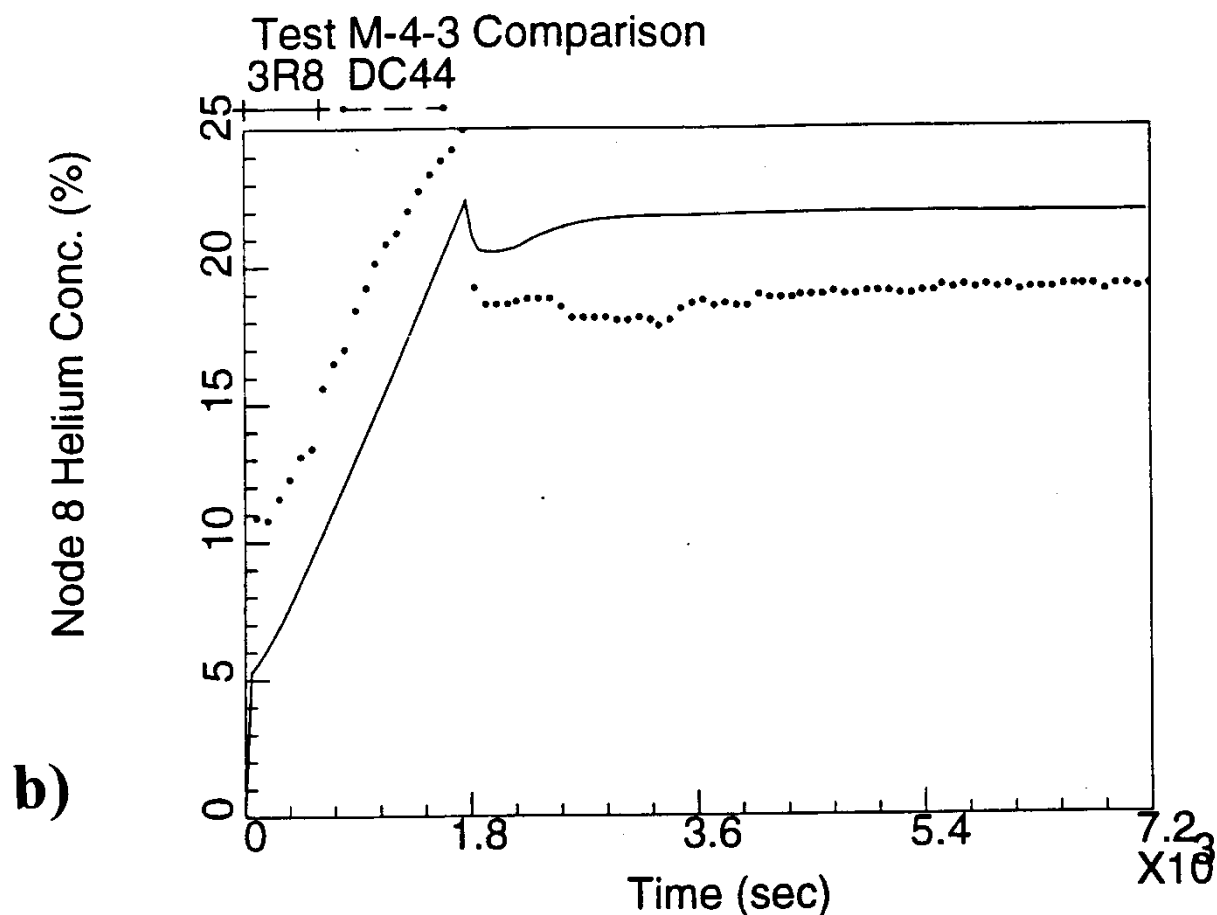


Figure 9.C-129b. Helium Concentration History Inside Node 8

(Numerical results are produced in the framework of: R.P. Ofstun, J. Woodcock, D.L. Paulsen, "Westinghouse-GOTHIC modeling of NUPEC's hydrogen mixing and distribution test M-4-3," The Third International Conference on Containment Design and Operations, Volume 1, Toronto, Canada, October 19-21, 1994)

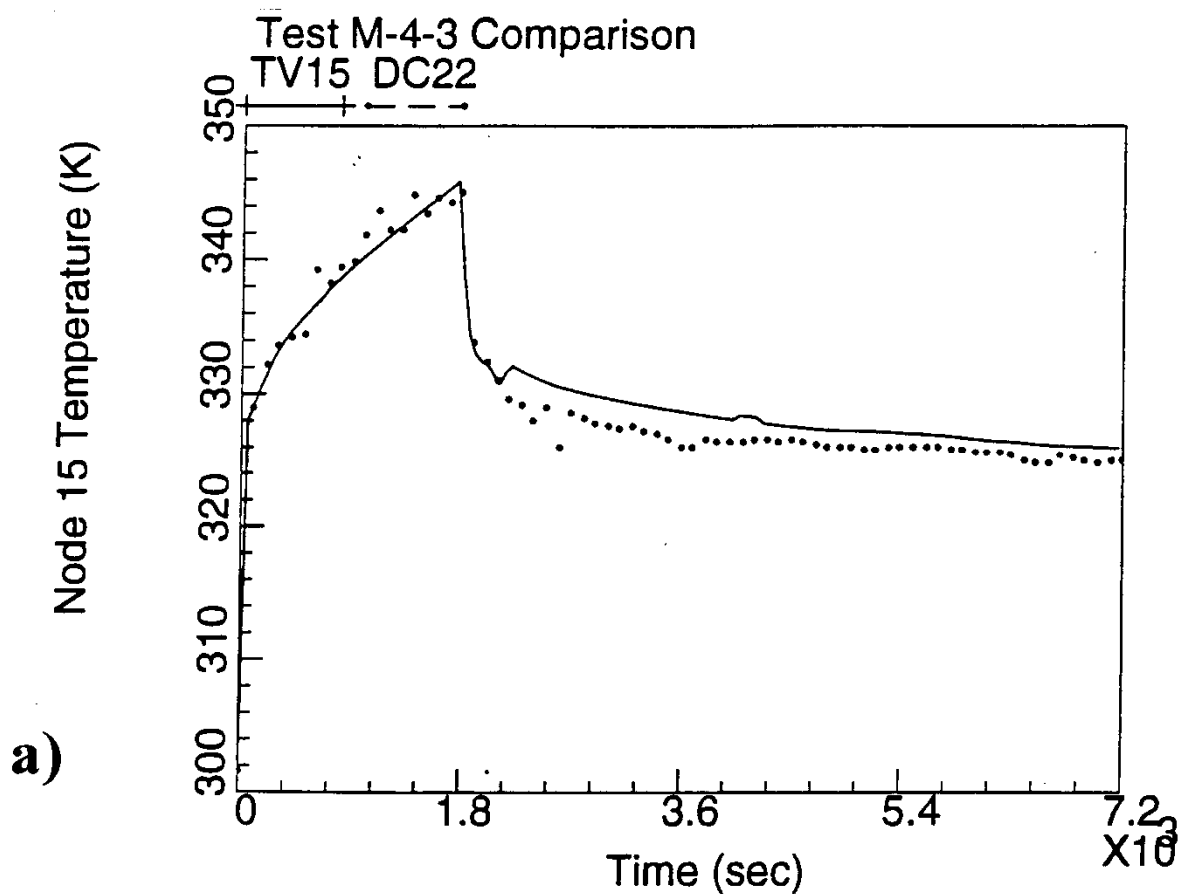


Figure 9.C-130a. Temperature History Inside Node 15

(Numerical results are produced in the framework of: R.P. Ofstun, J. Woodcock, D.L. Paulsen, "Westinghouse-GOTHIC modeling of NUPEC's hydrogen mixing and distribution test M-4-3," The Third International Conference on Containment Design and Operations, Volume 1, Toronto, Canada, October 19-21, 1994)

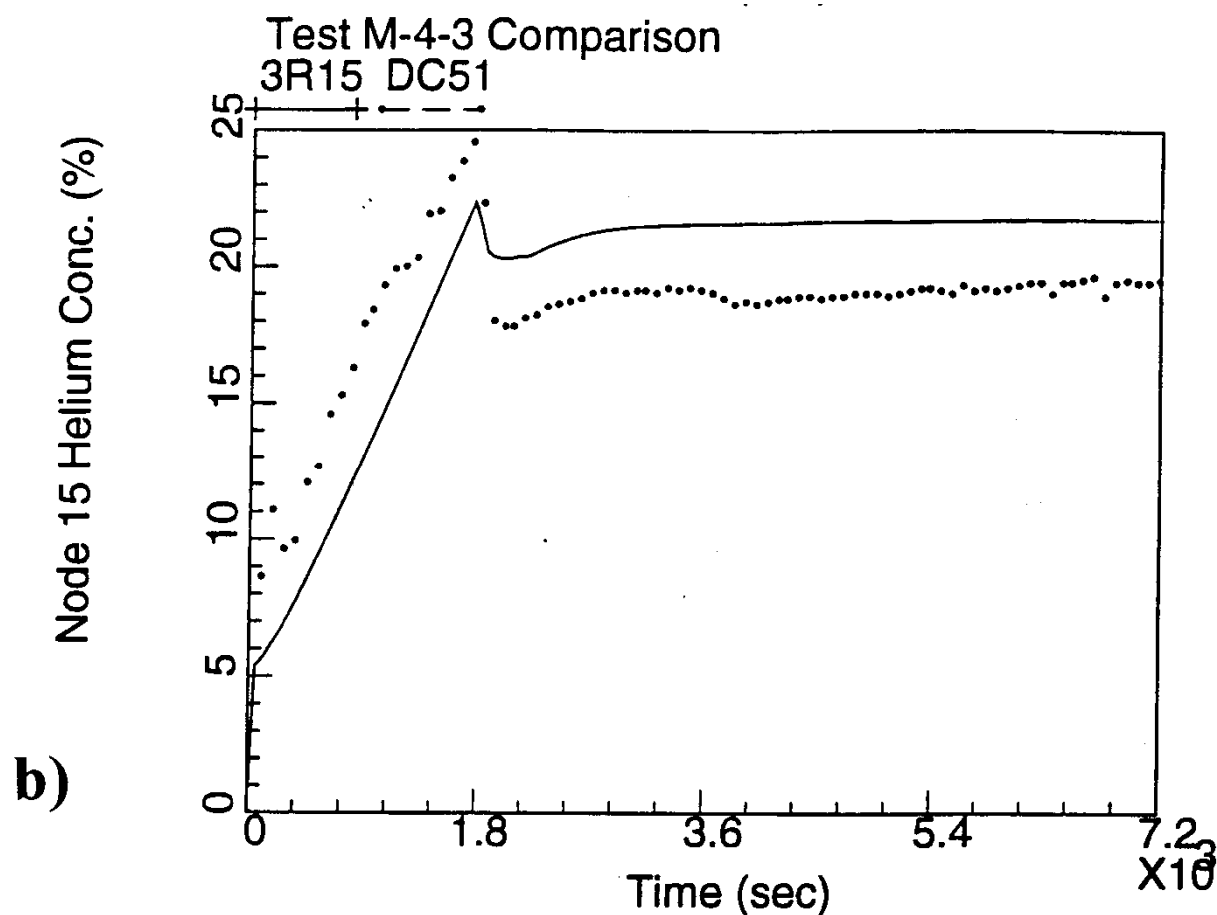


Figure 9.C-130b. Helium Concentration History Inside Node 15

(Numerical results are produced in the framework of: R.P. Ofstun, J. Woodcock, D.L. Paulsen, "Westinghouse-GOTHIC modeling of NUPEC's hydrogen mixing and distribution test M-4-3," The Third International Conference on Containment Design and Operations, Volume 1, Toronto, Canada, October 19-21, 1994)

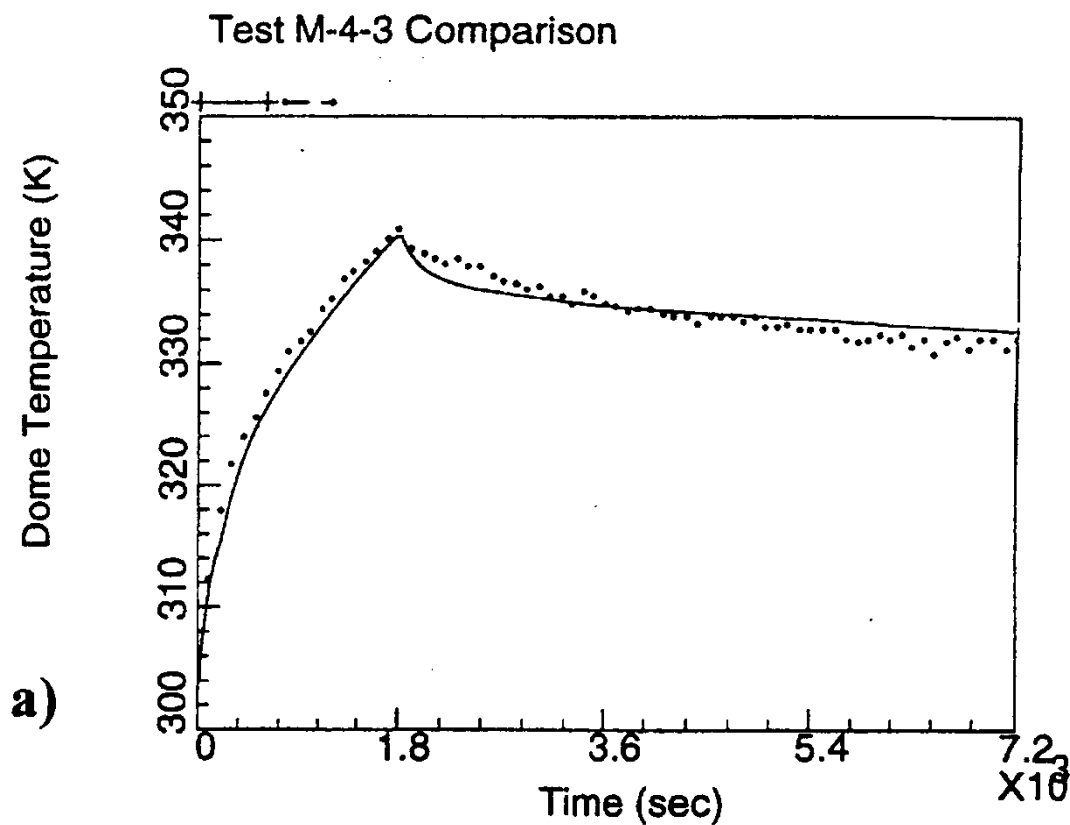


Figure 9.C-131a. Temperature History Inside Dome

(Numerical results are produced in the framework of: R.P. Ofstun, J. Woodcock, D.L. Paulsen, "Westinghouse-GOTHIC modeling of NUPEC's hydrogen mixing and distribution test M-4-3," The Third International Conference on Containment Design and Operations, Volume 1, Toronto, Canada, October 19-21, 1994)

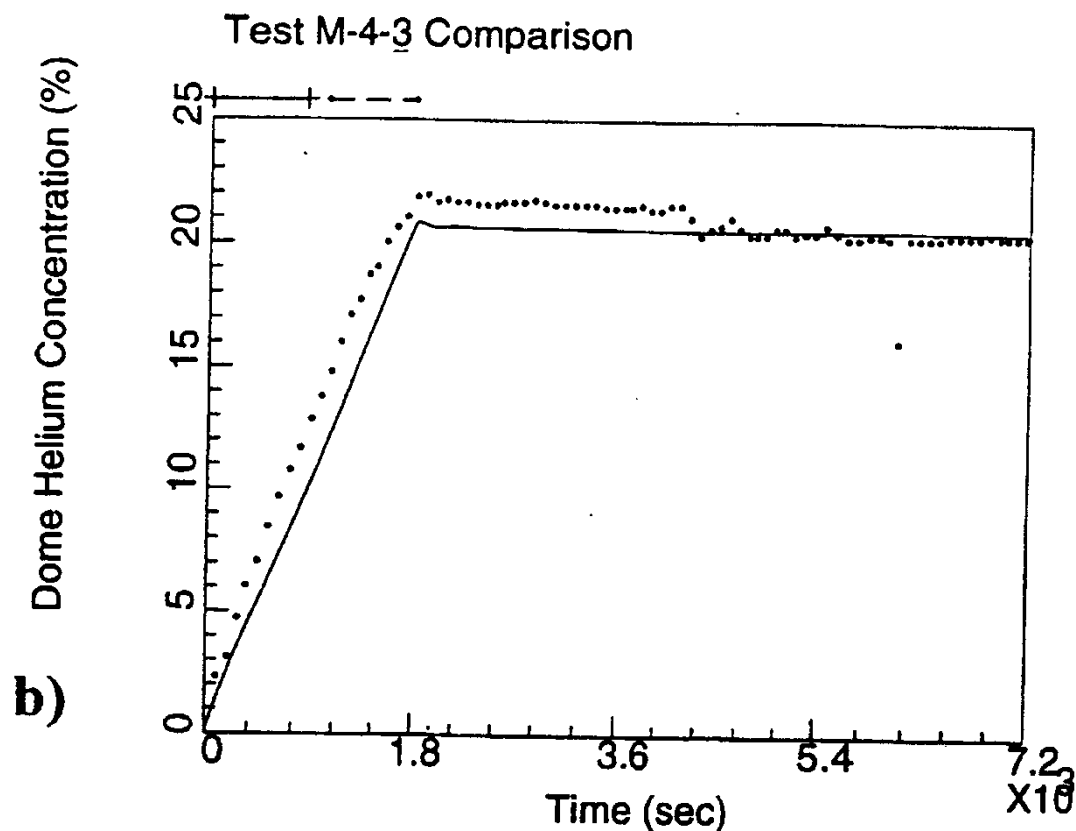


Figure 9.C-131b. Helium Concentration History Inside Dome

(Numerical results are produced in the framework of: R.P. Ofstun, J. Woodcock, D.L. Paulsen, "Westinghouse-GOTHIC modeling of NUPEC's hydrogen mixing and distribution test M-4-3," The Third International Conference on Containment Design and Operations, Volume 1, Toronto, Canada, October 19-21, 1994)

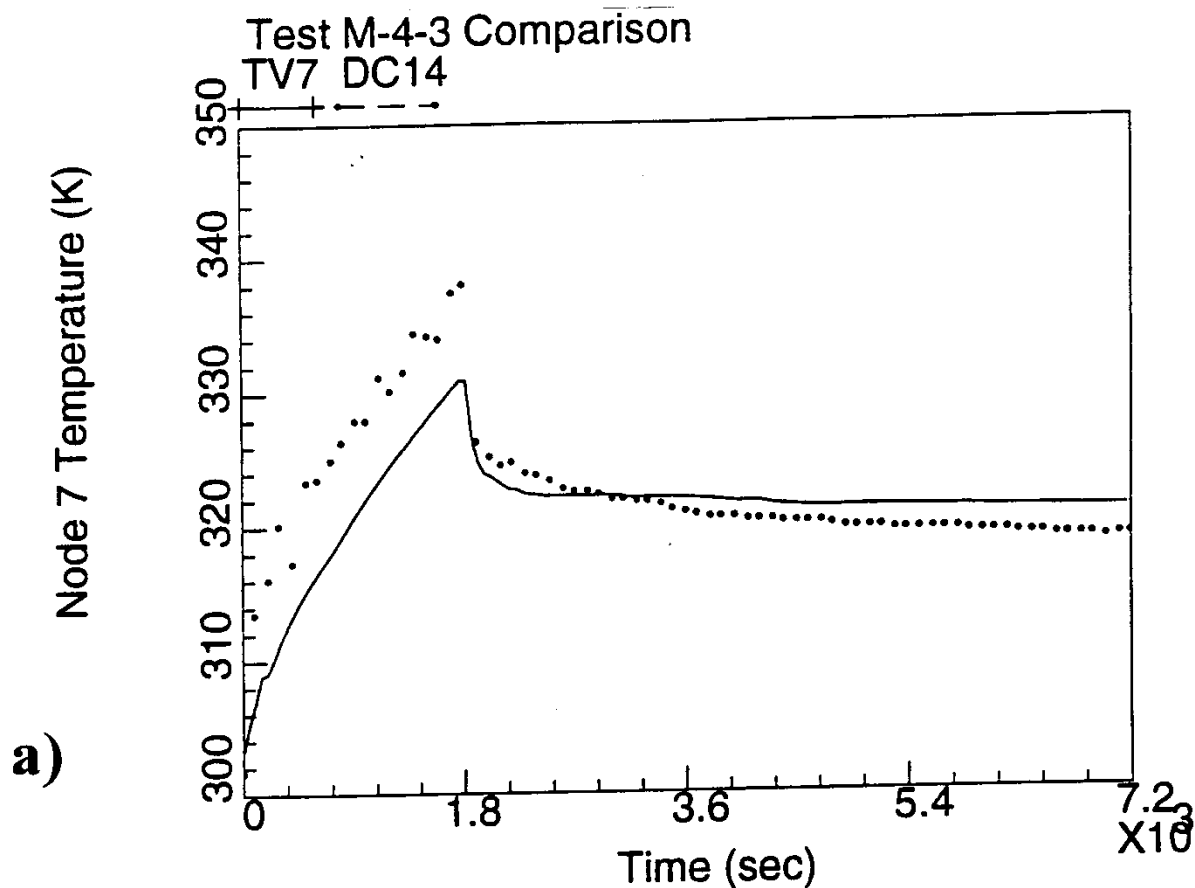


Figure 9.C-132a. Temperature History Inside Node 7

(Numerical results are produced in the framework of: R.P. Ofstun, J. Woodcock, D.L. Paulsen, "Westinghouse-GOTHIC modeling of NUPEC's hydrogen mixing and distribution test M-4-3," The Third International Conference on Containment Design and Operations, Volume 1, Toronto, Canada, October 19-21, 1994)

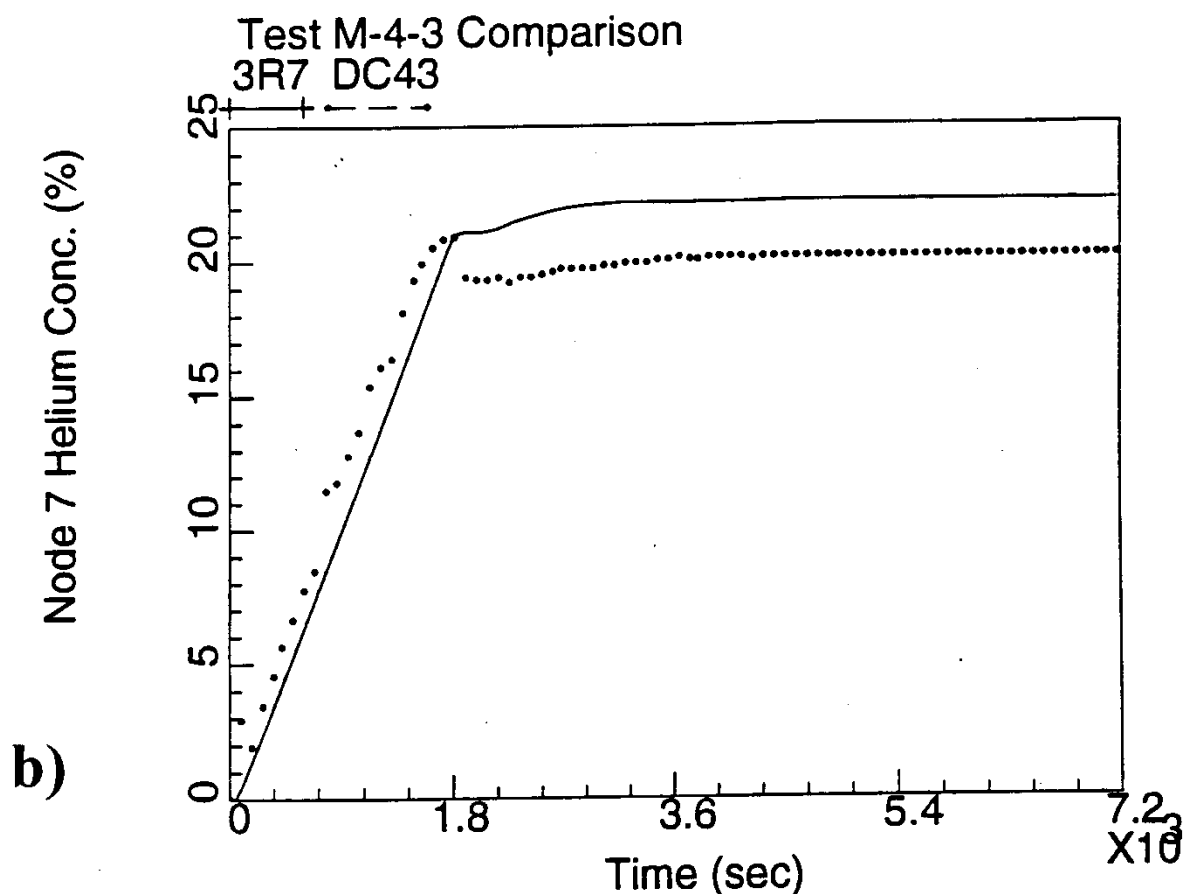


Figure 9.C-132b. Helium Concentration History Inside Node 7

(Numerical results are produced in the framework of: R.P. Ofstun, J. Woodcock, D.L. Paulsen, "Westinghouse-GOTHIC modeling of NUPEC's hydrogen mixing and distribution test M-4-3," The Third International Conference on Containment Design and Operations, Volume 1, Toronto, Canada, October 19-21, 1994)

9.C.3.3 Validation of the Lumped-Parameter Containment Analysis Computer Codes Based on HDR Experimental Results

Comparisons of the results of best-estimate open post-test predictions of various containment analysis computer codes (as RALOC, WAVCO, CONTAIN, MELCOR, and GOTHIC) for E11.2 and E11.4 HDR experiments presented by L. Wolf, H. Holzbauer and T. Cron, 1994a. Detailed comparisons and verifications of the blind and open GOTHIC results for the E11.2 and E11.4 HDR experiments are presented by H. Holzbauer and L. Wolf, 1994. More details about E11.2 and E11.4, and comparisons with the experimental results of large blowdown tests T31.5, V21.1, and E11.5, are presented in the report by K. Fischer, M. Schall, L. Wolf, 1995.

Following is a summary of observations from the comparison of the experiments with codes:

1. **Scenarios with homogeneous containment atmosphere (like E11.4 and E11.5) can be simulated successfully with lumped parameter models.**

The results of the E11.4 computation agree with the corrected experimental input data (open test – see Figures 17-21 in H. Holzbauer and L. Wolf, 1994).

The same conclusion is valid for accidents initiated by a large-break LOCA in the lower positions of containments, accompanied by subsequent steam and gas releases (as in E11.5). Good agreement has been achieved by the GOTHIC lumped-parameter model using a modest number of nodes (see Figures 10.9 – 10.22 in K. Fischer, M. Schall, L. Wolf, 1995). A comparison of the experimentally and numerically obtained pressure histories is presented in Figure 9.C-133. The calculated pressure history is slightly higher than the experimental results. Figure 9.C-134 presents a comparison for sump temperature. Note that the sump temperature sensor is exposed to the containment atmosphere for the first 8 hours. It is then submerged by higher sump water level. **The history of sump boiling is well simulated.** Comparisons of temperatures in main and spiral stairways at 6 m level are presented in Figure 9.C-135 and Figure 9.C-136, respectively. Gas mixture concentration comparisons for the same staircase elevation are presented in Figure 9.C-137 and Figure 9.C-138. The measured velocity in spiral stairway at 15 m elevation is presented in Figure 9.C-139. **Since the order of magnitude of the computed velocities matches the data, it can be concluded that trends in the direction of the flow are predicted well; however, predicted velocities differ by as much as factor of two.**

2. **The lumped parameter method is not capable of predicting the hydrogen distribution in a stratified containment atmosphere (as in E11.2 test with high-positioned release).**

The pressure history is well predicted after applying the correct steam inflow experimental data and accounting for energy sink of the sensors cooling system. Comparisons between the experimental data and the “optimized” post-test prediction for containment pressure are presented in Figure 9.C-140. GOTHIC lumped parameter results overpredict pressure by 0.25 bar (11%).

Temperatures, steam, and gas concentrations are underestimated and overestimated above and below the break location, respectively, (see Figures 7 and 8 in H. Holzbauer and L. Wolf, 1994). **Therefore, for a high-positioned release, the steam and gas transport to the lower parts of the containment are overpredicted.**

Artificial limitation of convective flows (by reduction of flow path areas) in all modeled flow paths improves the prediction of temperatures and gas concentrations in the lower containment regions (Figures. 13, 15, and 16 in H. Holzbauer and L. Wolf, 1994), but overestimates the containment pressure and temperatures in the upper containment (see results of parametric calculations NA15 and NA16, Figures 11 and 12 in H. Holzbauer and L. Wolf, 1994).

3. **Application of distributed parameter models may improve prediction of a stratified containment atmosphere (as in E11.2 test).**

A study of the influence of the number of nodes applied for a simple volume proportional to the HDR E11.2 facility volume using a distributed parameter model is presented by J.S. Narula and J. Woodcock, 1994. The authors conclude that in situations requiring detailed flow distribution in non-homogenous environments, a fine mesh may be required to obtain realistic results. A coarse mesh (small number of nodes) may reduce the accuracy of the results, despite a highly accurate containment model in all other aspects, including momentum representation.

A detailed study of the influence of the nodalization, and a comparison of the lumped parameter results with distributed parameter model results for E11.2 case are presented by K.K. Mun, 1996. This report also includes a comparison of the pressure, temperature, steam and hydrogen concentrations histories (see Figures 67 – 91 in K.K. Mun, 1996). The author concludes that, in general, the modeling approach of merging the distributed and lumped parameter models improves the prediction. However, to improve the prediction further, a proper distributed parameter nodalization for the lower break compartment and dome, together with the correct connections for the associated flow paths, are required.

All specified observations 1, 2, and 3 for GOTHIC applications are in agreement with comparisons of the results of other well-known codes (see L. Wolf, H. Holzbauer and T. Cron, 1994a).

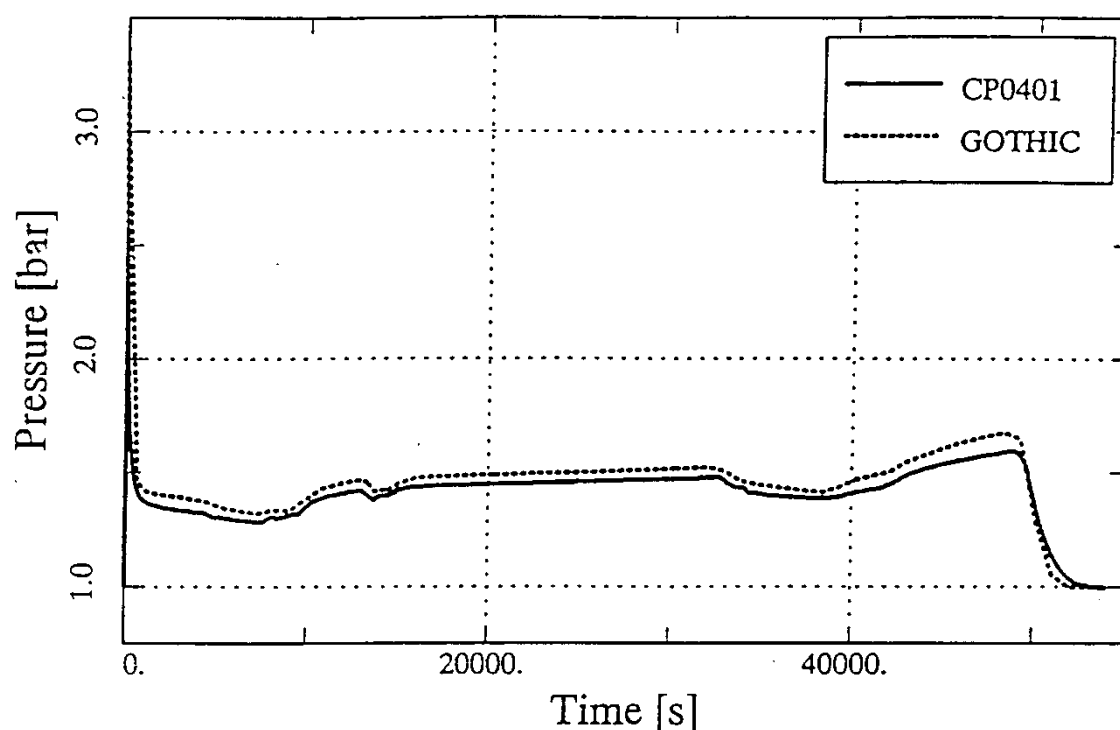


Figure 9.C-133. HDR-E11.5: Comparison Between Measured Long-Term Containment Pressure and GOTHIC Open Post-Test Prediction

Reproduced with permission from a report funded by the EPRI GOTHIC Advisory Group: K. Fischer, M. Schall, L. Wolf, "Simulations of GOTHIC Large Scale Containment Experiments," Battelle Ingenieurtechnik GnuBH, Eshborn, Fachbericht BF – V – 68317 – 01, October 1995)

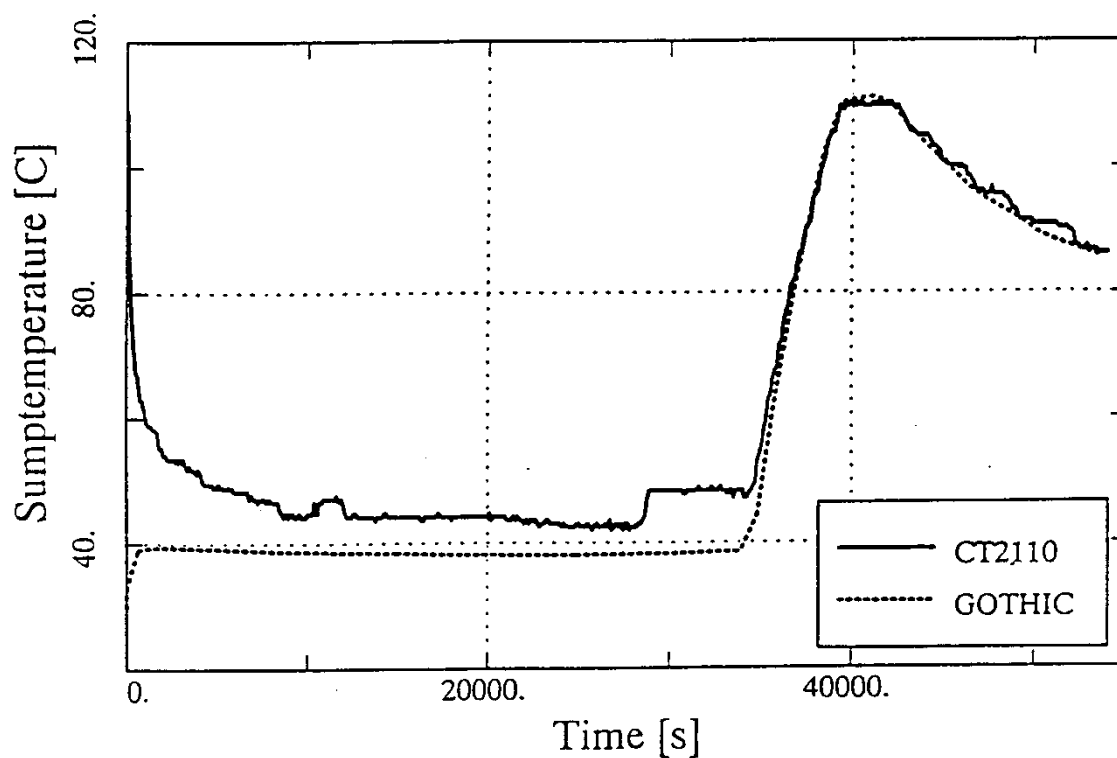


Figure 9.C-134. HDR-E11.5: Comparison Between Measured Sump Temperature and GOTHIC Open Post-Test Prediction

Reproduced with permission from a report funded by the EPRI GOTHIC Advisory Group: K. Fischer, M. Schall, L. Wolf, "Simulations of GOTHIC Large Scale Containment Experiments," Battelle Ingenieurtechnik GnuBH, Eshborn, Fachbericht BF – V – 68317 – 01, October 1995)

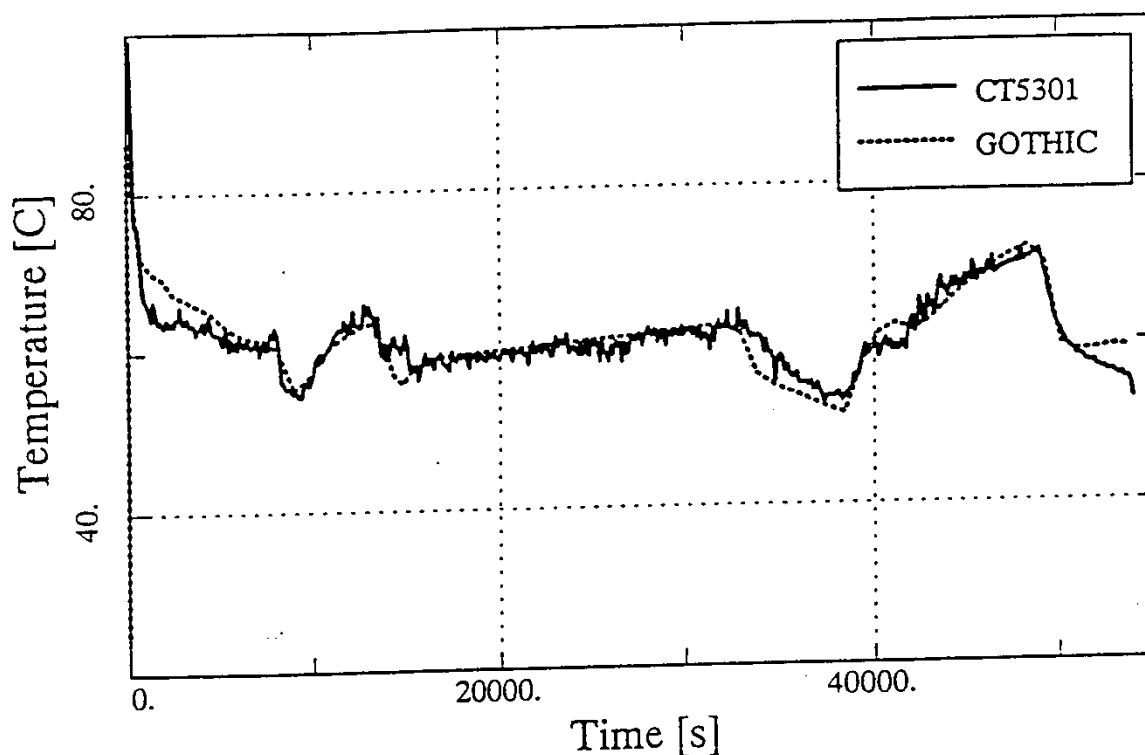


Figure 9.C-135. HDR-E11.5: Comparison Between Measured Temperature in Main Stairway (6m) and GOTHIC Open Post-Test Prediction

Reproduced with permission from a report funded by the EPRI GOTHIC Advisory Group: K. Fischer, M. Schall, L. Wolf, "Simulations of GOTHIC Large Scale Containment Experiments," Battelle Ingenieurtechnik GnuBH, Eshborn, Fachbericht BF – V – 68317 – 01, October 1995)

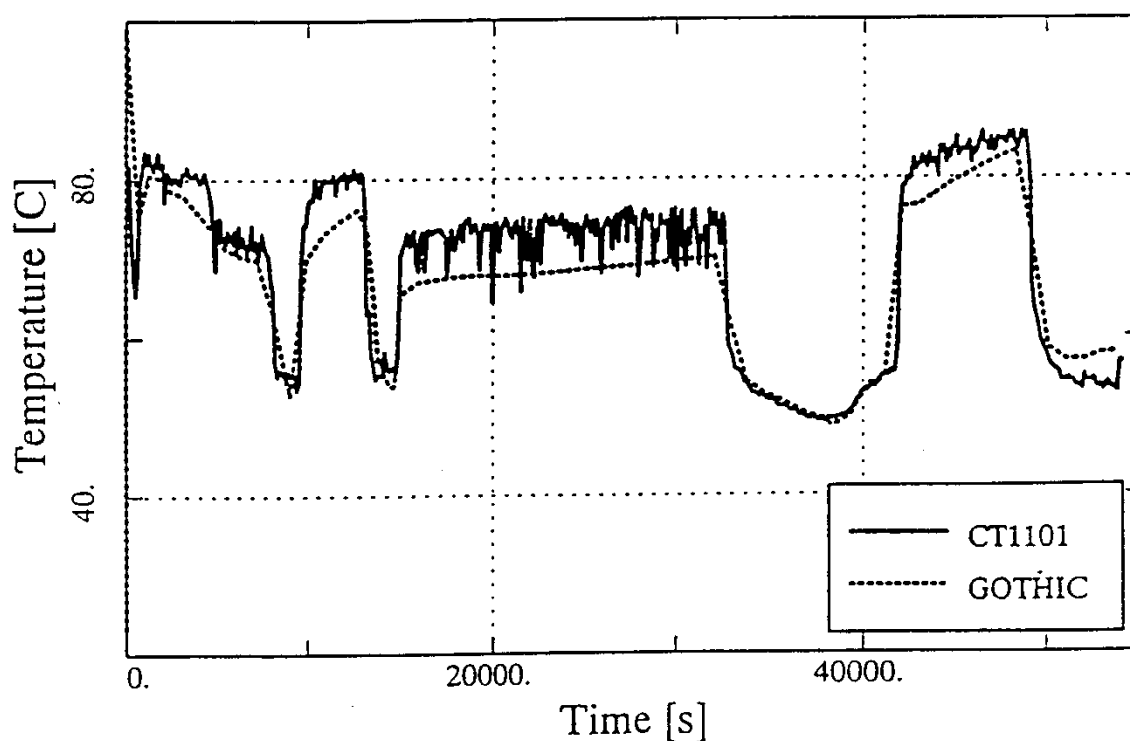


Figure 9.C-136. HDR-E11.5: Comparison Between Measured Temperature in Spiral Stairway (6m) and GOTHIC Open Post-Test Prediction

Reproduced with permission from a report funded by the EPRI GOTHIC Advisory Group: K. Fischer, M. Schall, L. Wolf, "Simulations of GOTHIC Large Scale Containment Experiments," Battelle Ingenieurtechnik GnuBH, Eshborn, Fachbericht BF – V – 68317 – 01, October 1995)

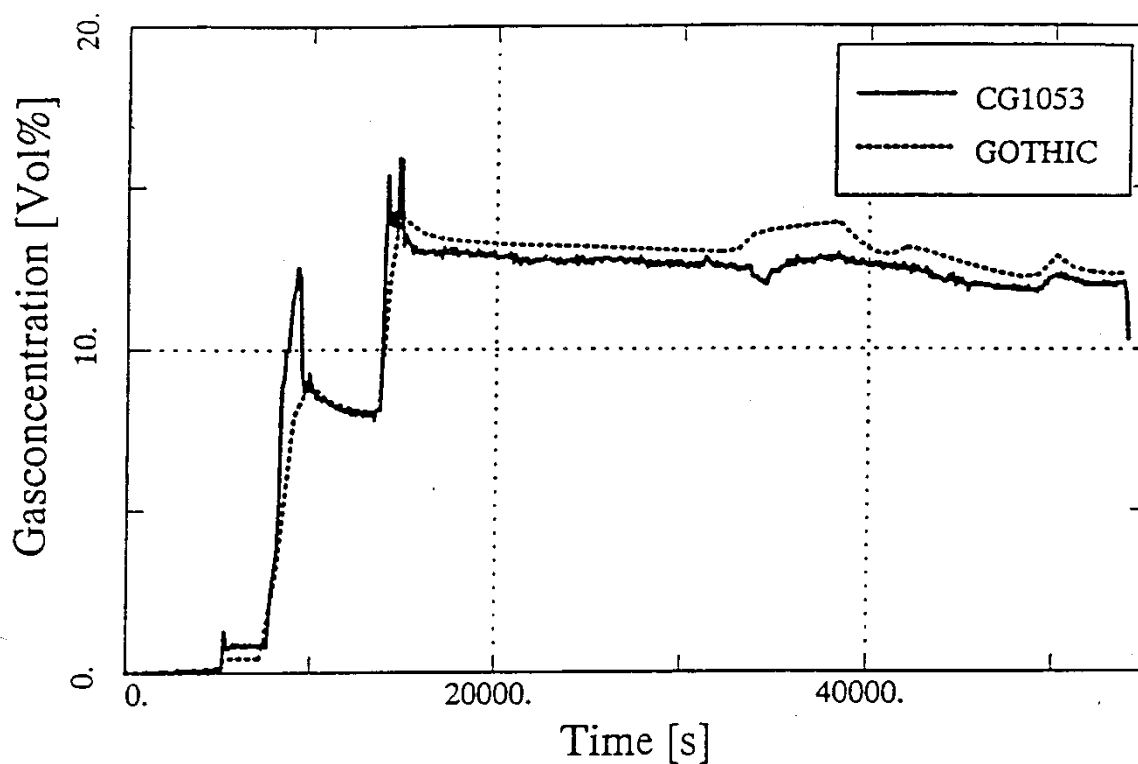


Figure 9.C-137. HDR-E11.5: Comparison Between Measured Gas Mixture Concentration in Main Stairway (6m) and GOTHIC Open Post-Test Prediction

Reproduced with permission from a report funded by the EPRI GOTHIC Advisory Group: K. Fischer, M. Schall, L. Wolf, "Simulations of GOTHIC Large Scale Containment Experiments," Battelle Ingenieurtechnik GnuBH, Eshborn, Fachbericht BF – V – 68317 – 01, October 1995)

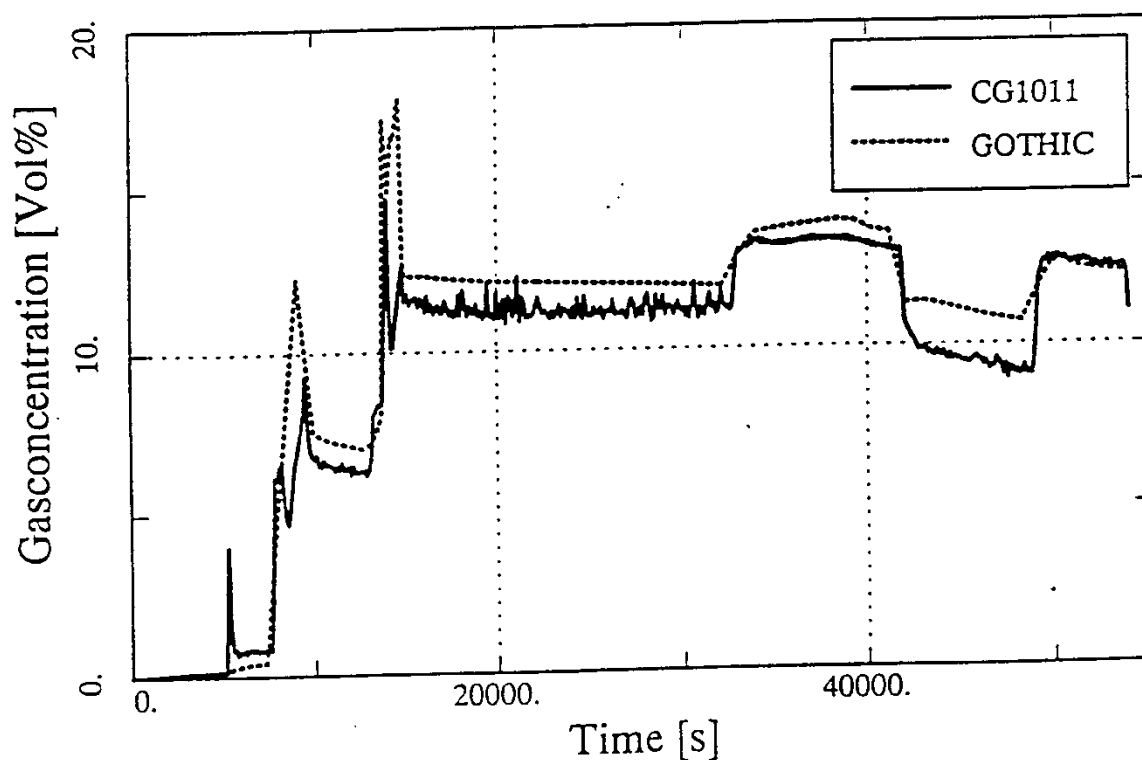


Figure 9.C-138. HDR-E11.5: Comparison Between Measured Gas Mixture Concentration in Spiral Stairway (6m) and GOTHIC Open Post-Test Prediction

Reproduced with permission from a report funded by the EPRI GOTHIC Advisory Group: K. Fischer, M. Schall, L. Wolf, "Simulations of GOTHIC Large Scale Containment Experiments," Battelle Ingenieurtechnik GnuBH, Eshborn, Fachbericht BF – V – 68317 – 01, October 1995)

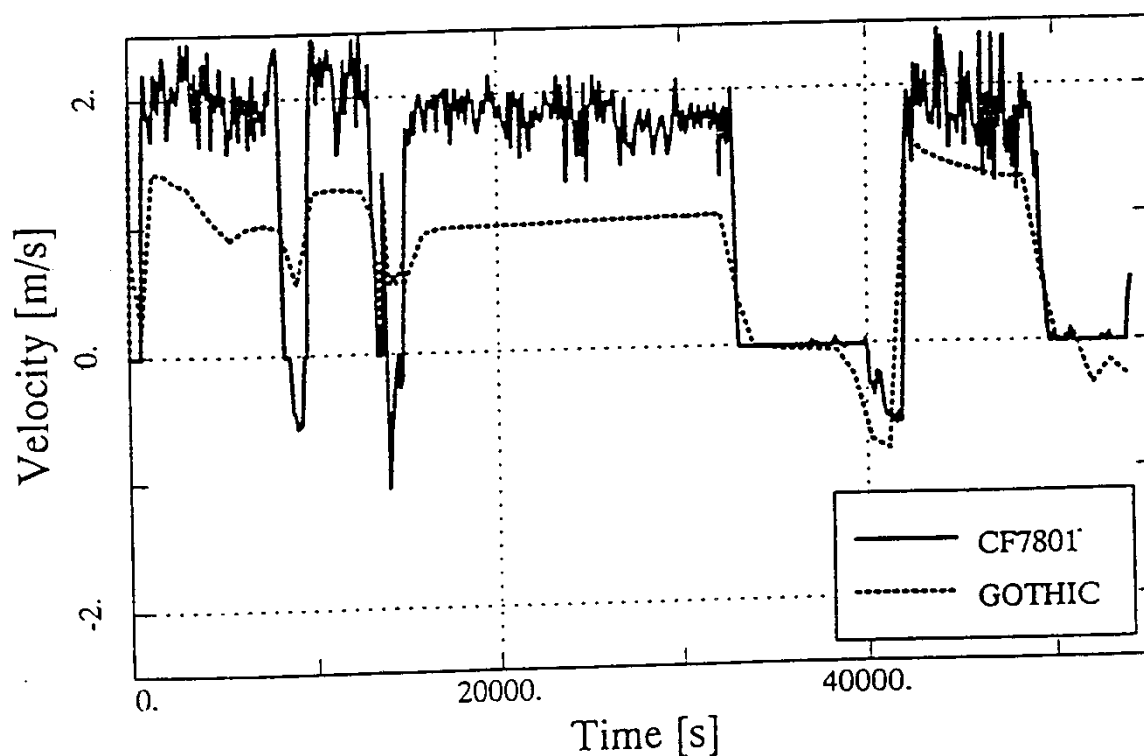


Figure 9.C-139. HDR-E11.5: Comparison Between Measured Velocity in Spiral Stairway (15m) and GOTHIC Open Post-Test Prediction

Reproduced with permission from a report funded by the EPRI GOTHIC Advisory Group: K. Fischer, M. Schall, L. Wolf, "Simulations of GOTHIC Large Scale Containment Experiments," Battelle Ingenieurtechnik GnuBH, Eshborn, Fachbericht BF – V – 68317 – 01, October 1995)

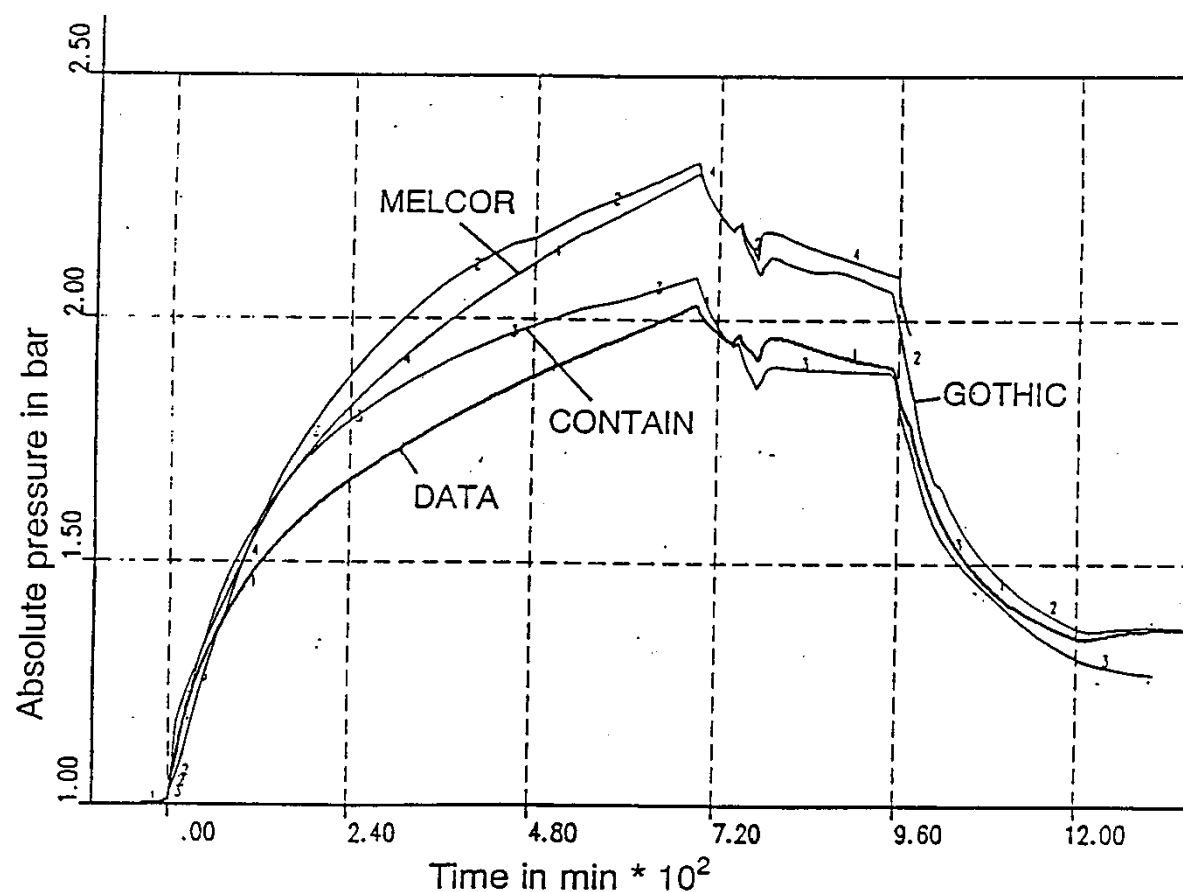


Figure 9.C-140. HDR-E11.2: Comparison Between Measured Long-Term Containment Pressure and Various “Optimized” Open Post-Test Predictions

Reproduced with permission from a report funded by the EPRI GOTHIC Advisory Group: K. Fischer, M. Schall, L. Wolf, “Simulations of GOTHIC Large Scale Containment Experiments,” Battelle Ingenieurtechnik GnuBH, Eshborn, Fachbericht BF – V – 68317 – 01, October 1995)

9.C.3.4 Conclusions

Lumped parameter models can predict pressure, and in some cases temperature, steam, and hydrogen concentrations inside the containment. Good predictions exist for the situations where the global circulation loop, which contributes towards the homogenization of atmosphere, is present inside the containment (see comparison with BMC F2 experiments and BMC test 12 experiments, NUPEC M-4-3 tests and HDR E11.4 and E11.5 tests). Additional improvements are possible if double-junctions between compartments in the horizontal direction are applied (allowing simulation of recirculation flows).

Single-node, lumped parameter models are not able to model stratification inside dead-end compartments due to the steam front penetration. They also do not include cases where the stratification front passes through horizontal vents, nor do they simulate sump liquid level, temperature, and stratification inside the sump. (See the BMC F2 experiments and the NUPEC M-4-3 results for dead-end compartments (R. Ofstun et al., 1994). The remedy can be an increase in the number of the nodes in the vertical direction or the application of distributed parameter model for dead-ended compartments (R. Ofstun et al., 1994).

For a stratified initial temperature distribution (BMC test 20) and a stratified containment atmosphere (HDR E11.2 test), the lumped parameter models do not predict the correct hydrogen distribution (they overmix the atmosphere). The artificial limitation of the size of the flow path areas in the HDR E11.2 test improved the prediction of temperatures and gas concentrations in the lower containment regions, but overestimated the containment pressure and temperatures in the upper levels.

Application of distributed parameter models may improve prediction capability. See BMC test 20 (L. Wolf, H. Holzbauer, M. Schall, 1994b; HDR E11.2 test - J. S. Narula and J. Woodcock, 1994; and K. K. Mun, 1996). All three publications conclude that proper distributed parameter nodalization for break and dome compartments is required to improve results. However, the increase of the number of nodes in all important regions of containment increases required memory and computing time beyond current practical limits.

The next step towards better space resolution and modeling would be the application of commercial CFD (Computational Fluid Dynamics) codes with built-in capabilities for multi-phase flows simulation, and multi-block, unstructured, or embedded grid options. Considering that three-dimensional transient multi-phase flow simulation would be required, only codes prepared for parallel multi-processor machines would produce results in a reasonable time. In addition, there are limitations related to noding convergence (see Gavrilas et al., 1997). Finally, an appropriate set of constitutive models (see Royl et al., 1997), such as condensation and sump evaporation, are not presently available in many CFD codes.

For the AP600 and **AP1000** with a low break release position and an established global circulation pattern that improves homogenization (see conclusion of the review of international experimental data base), a careful application of lumped parameter models could produce results which would be in agreement with test data.

In summary, biases that should be addressed when applying lumped parameter codes are:

1. Single-node models are not able to model stratification, or the passing of a stratification front through horizontal vents.
2. Sump liquid level and sump temperature are not predicted well.
3. Some codes produced results that are not correct due to missing or oversimplified buoyancy terms.
4. To account for recirculation flows, the applied lumped parameter model uses double junctions in the horizontal direction. (This does not help in the case of an elevated release and resulting stratified containment.)
5. For releases low in containment, typical for the AP600 and **AP1000** DECLG LOCA, the lumped parameter model predicts pressure, temperature, and helium concentrations inside the compartments that are affected by the global circulation loop. Improvements are needed to account for postulated circulation effects inside dead-ended compartments.
6. Scenarios with homogeneous containment atmosphere (HDR E11.4 and E11.5) are simulated successfully with lumped parameter models. (Such conditions typically result from breaks located below 20 percent of the containment height.)
7. Circulation effects due to sump boiling (releases generated at the bottom of containment) are well simulated.
8. The order of magnitude of computed velocities matches the experimental data. Trends in the direction of the flow are predicted well; however, predicted velocities differ by as much as a factor of two.
9. The lumped parameter method is not capable of predicting the hydrogen distribution in a stratified containment atmosphere, as in HDR E11.2 with high-positioned release. In a break scenario with a buoyant plume (released at about 50 percent of containment height), the steam and gas transport to the lower parts of the containment are over-predicted. (When convective flows are artificially limited by decreasing flow areas, predicted concentrations in the lower regions improve, but the containment pressure and temperatures in upper compartments are overestimated.)

9.C.3.5 References

1. Fischer, K., T., Schall, M., Wolf, L., 1991, "CEC Thermal-Hydraulic Benchmark Exercise on FIPLOC Verification Experiment F2 in BMC-Long-Term Heatup Phase – Results for Phase I," Final Report, EUR 13588 EN, 1991
2. Fischer, K., T., Schall, M., Wolf, L., 1993, "CEC Thermal-Hydraulic Benchmark Exercise on FIPLOC Verification Experiment F2 in BMC, Experiment F2 in BMC, Experimental Phases – Results for Phase 2, 3, and 4, Results of Comparisons," Final Report, EUR 14454 EN, 1993
3. K. Fischer, M. Schall, L. Wolf, 1995, "Simulations of GOTHIC Large-Scale Containment Experiments," Battelle Ingenieurtechnik GmbH, Eschborn Fachbericht BF – V - 68317 - 01, October 1995
4. M. Gavrilas, B. T. Mattingly, M.J. Driscoll, 1997, "WGOTHIC Noding and Parametric Studies of a Passively-Cooled Small Rating PWR Containment," Proceedings of the International Topical Meeting on Advanced Reactors Safety, Volume I, Orlando, Florida, June 1-5, 1997, pp. 549 – 560.
5. H. Holzbauer, L. Wolf, 1994, "GOTHIC Verification on Behalf of HDR-Hydrogen Mixing Experiments," International Conference on New Trends in Nuclear System Thermohydraulics, Volume II, pp. 331-340., Pisa, Italy, May 30th – June 2nd, 1994
6. T. Hirose, 1993, Letter, floppy disk which contains the M-4-3 test data, an attached document, and a video-cassette, NUPEC Nuclear Power Engineering Corporation, ISP35-035, 30 April, 1993
7. K. K. Mun, 1996, "Modeling of HDR Experiment E11.2 with the Distributed Parameter Feature of the GOTHIC – Code," M.S. Scholar's Paper, University of Maryland at College Park, September 1996
8. J. S. Narula, J. Woodcock, 1994, "Westinghouse – GOTHIC Distributed Parameter Modeling of HDR Test E11.2," The Third International Conference on Containment Design and Operation, Volume 1, Toronto, Canada, October 19 – 21, 1994
9. NEA/CSNI/R(94)29: Final Comparison Report on ISP-35: NUPEC Hydrogen Mixing and Distribution Test (Test M-7-1), Committee on the Safety of Nuclear Installations OECD Nuclear Energy Agency, December 1994
10. R. P. Ofstun, J. Woodcock, D. L. Paulsen, 1994, "Westinghouse - GOTHIC Modeling of HDR NUPEC'S Hydrogen Mixing and Distribution Test M-4-3," The Third International Conference on Containment Design and Operation, Volume 1, Toronto, Canada, October 19 – 21, 1994

11. P. Royl, Breitung, J.R. Travis, H. Wilkening, L. Seyffarth, 1977, "Simulation of Hydrogen Transport with Mitigation Using the 3D Field Code Gasflow," Proceedings of the International Topical Meeting on Advanced Reactors Safety, Volume I, Orlando, Florida, June 1-5, 1997, pp. 578 – 588.
12. L. Wolf, H. Holzbauer, T. Cron, 1994a, "Detailed Assessment of the HDR-Hydrogen Mixing Experiments E11," International Conference on New Trends in Nuclear System Thermohydraulics, Volume II, pp. 91-103., Pisa, Italy, May 30th – June 2nd, 1994
13. L. Wolf, H. Holzbauer, M. Schall, 1994b, "Comparisons Between Multi-dimensional and Lumped Parameter GOTHIC Containment Analyses with Data," International Conference on New Trends in Nuclear System Thermohydraulics, Volume II, pp. 321-330., Pisa, Italy, May 30th – June 2nd, 1994
14. L. Wolf, M. Gavrilas, K. Mun, 1996, "Overview of Experimental Results for Long-Term Large-Scale Natural Circulations in LWR-containments after Large LOCAS," DOE – Project, Order Number: DE - AP07 - 96ID10765, University of Maryland at College Park, July 1996

APPENDIX 9.D

BASIS FOR ASSUMING HOMOGENEOUS BULK CONDITIONS FOR AP600 AND AP1000 CONTAINMENT PRESSURE DESIGN BASIS ANALYSIS

9.D.1 INTRODUCTION

During the blowdown phase of a DECLG LOCA, forced jet momentum from the break source provides vigorous mixing of steam and air inside containment. The jet momentum helps establish homogeneous conditions within a few seconds (Reference 9.D-12, Section 10.2.1.5). Consequently, treating the containment as homogeneous or well-mixed during the blowdown phase is appropriate.

After the blowdown phase, however, the physical processes are different. The forced jet momentum quickly decreases and actually ceases for a brief period during the refill phase before the break source reestablishes itself as a buoyant plume. Although the forced jet momentum ceases during the refill phase of a DECLG LOCA, wall boundary layers are quickly established, on the order of seconds (see Reference 9.D-12, Section 4.8) and according to work by Hartley, quasi-isotropic turbulence resulting from the jet momentum continues mixing enclosed volumes for some time after the source jet ceases. The turbulent wall boundary layers provide entrainment of the bulk region inside containment and hence contribute to mixing of the containment atmosphere as well.

This appendix addresses the buoyant plume, wall boundary layers, and enclosure test data as they relate to mixing inside containment during the post-blowdown time period during a DECLG LOCA.

9.D.2 APPROACH

Thermal and concentration gradients in the horizontal direction, including the boundary layer next to the shell, are addressed using results of 1) theoretical, or first principles, calculations 2) LST temperature/concentration data, and 3) separate effects enclosure test data. The wall boundary layer steam concentration profile is examined using turbulent boundary layer models. Entrainment and boundary layer profile calculations are used to estimate the magnitude of the steam concentration in the wall layer and rising plume as compared to the bulk average steam concentration at a given elevation. Test data, where available, are used to support the conclusions.

Horizontal gradients in AP600 and **AP1000** during the post-blowdown LOCA periods are addressed for the base case scenario which assumes that the source mass rises from the east steam generator compartment as a buoyant plume, having lost its momentum as it passes around the equipment and structure in the compartment.

The potential magnitude of horizontal gradients are examined in three radial regions: (1) the turbulent buoyant plume (2) the bulk region between the plume and boundary layer and (3) the turbulent boundary layer. The three radial regions are depicted in Figure 9.D-1. This three-region approach is similar to that suggested by Peterson (Reference 9.D-1). In the region-wise discussions, area fractions are developed and processes which affect horizontal temperature and concentration gradients within each region are described.

The test bases for the discussions include the LST, as well as smaller scale separate effects natural convection enclosure tests. The general interaction between the regions via entrainment is then used to summarize how the integral system performs.

9.D.3 REGION 1 HORIZONTAL GRADIENTS ADDRESSED THROUGH TURBULENT BUOYANT PLUME ANALYTICAL MODEL

Referring to Figure 9.D-1, Region 1 is comprised of the rising plume and its entrained flow. In Region 1, the concentration profile within a turbulent buoyant plume is characterized by an exponential (i.e., $e^{-57(r/z)^2}$) profile at any given elevation, with the steam concentration at the boundary of the plume equal to that of the bulk (Region 2). Such a profile is summarized by Blevins (Reference 9.D-2). The turbulent buoyant plume analytical model, based upon Reference 9.D-2, shows that the plume centerline steam concentration at the exit of the plume is within 10 percent ($0.04/(1-0.6) = 0.10$) (see Section 9.D-7) of the bulk (Region 2), assuming uniform temperature and concentration in Region 2. With the assumption that the buoyant plume develops freely to the dome region, the plume occupies about 10 percent of the cross-sectional area at the top of containment. An axisymmetric round plume with a divergent angle of 7.5 degrees from the exit of the steam generator compartment is assumed. The calculated plume equivalent diameter at the top of containment is 38 feet based on the net exit area of the trapezoidal steam generator compartment opening, the containment radius of 65 feet, and plume height of 121 feet. It is recognized that negatively buoyant plumes may descend from the dome region and limit the free development height of the positively buoyant plume. However, since this phenomenon results in an additional mixing mechanism (i.e., counter-current plume mixing of positively and negatively buoyant plumes), it is conservatively neglected in the simple analytical plume model.

9.D.4 REGION 2 HORIZONTAL GRADIENTS ADDRESSED THROUGH LST TEMPERATURE DATA AND SEPARATE EFFECTS ENCLOSURE TEST DATA

The horizontal gradients in Region 2 can be assessed based on indications from LST temperature data and separate effects enclosure test data and by examining the postulated condition of a non-uniform horizontal gradient.

The LST has been examined for evidence of horizontal gradients outside the wall boundary layer. Time-averaged thermocouple rake data for LST tests in the LOCA configuration at two different steam flows (220.1 at 0.5 lbm/sec; 217.1 at 1.0 lbm/sec) show a near-zero horizontal temperature gradient except above the steam plume and over the distance within one inch of the wall (see Figure 9.D-6 and Figure 9.D-7). Since the convective processes operating in the bulk gas region mix temperature differences and gas species at about the same rate, the observation that there is no horizontal temperature gradient also shows that there is no horizontal gas concentration gradient, and therefore, no density gradient. The data show that all of the measurable temperature drop in the vessel wall boundary layer occurs between the wall and the thermocouple located one inch away from the wall. This is consistent with boundary layer calculations which indicate that the majority (60 percent) of the gradient occurs within the first 0.25 inch of the 7-inch boundary layer at the LST operating deck level.

LST thermocouple rake data at successive, incremental data collection times, shows evidence of buoyancy forces eliminating horizontal gradients. Data from the thermocouple rake was taken every 90 seconds during the LST matrix tests. The data at some point in time may show that the temperature at a

measurement location may deviate less than ten degrees Fahrenheit from the horizontal average. Data at the next time interval indicate that horizontal gradients are not maintained for more than the 90-second data acquisition interval. This is evidence that a perturbation which creates a nonhomogeneous density at a given elevation also creates a local relative density driving force which tends to level out the horizontal density gradient. This is to be expected since gravity will neutralize any gradients that attempt to form, tending to result in a time-averaged flat profile.

Separate effects enclosure test data show that as the Rayleigh number, Ra , increases from 3.5×10^4 to 1×10^6 , the circulation mechanism fully transitions to turbulent, and the horizontal gradient becomes primarily concentrated in the thin wall boundary layer (Section 9.C.1.1.2.1, see for example Figure 9.C-5). These tests show that at $Ra > 10^6$, the horizontal gradient in the bulk region is nearly zero in two-dimensional enclosures. Data from three-dimensional enclosures suggest that the transition to turbulence may occur at $Ra < 10^6$, due to vortices which affect mixing inside the enclosure by communicating between the front and back walls through the middle of the enclosure. The Rayleigh number between the plume centerline and the cooled wall for both AP600 and **AP1000** is 4.2×10^{12} based on a relatively low value of 9°F temperature difference. Therefore, both the AP600 and **AP1000** are fully turbulent and would be expected to show little or no horizontal gradient in Region 2.

Negatively buoyant falling plumes have been shown to occur with upper horizontal surfaces cooler than the enclosure and to result in an additional mixing mechanism (Figure 9.C-15 and Figure 9.C-16) which would further homogenize the containment gases. The presence of plumes of cooler gases descending from the underside of the dome, suggested by the large vertical Grashof number on the order of 2×10^{13} , based on a relatively low temperature difference of 9°F (Section 9.C.1.3.1), are conservatively ignored.

Separate effects enclosure test data span up to Ra equal to 10^9 . Numerical studies by Markatos and Pericleous predict that the heat transfer behavior is constant (Nusselt number linearly increases with length) at increasing Ra over many decades up through Ra of 10^{16} (Figure 9.C-6), suggesting that increased heat transfer is primarily a result of thinning of the boundary layer. The implication is that the Nusselt number varies monotonically over that range, and thus no unexpected performance is introduced at higher Ra values.

In a bulk region such as Region 2 in the AP600 or **AP1000**, while one may not rule out some minor transient horizontal temperature or concentration gradients, a horizontal gradient outside the relatively small volumes occupied by the plume and falling wall layer is difficult to sustain at high Ra number. That is, any postulated deviation from horizontal uniformity would tend to be readily flattened by buoyant forces. Therefore, horizontal gradients may be assumed to occur solely within the plume and wall layer.

9.D.5 REGION 3 HORIZONTAL GRADIENTS ADDRESSED THROUGH TURBULENT BOUNDARY LAYER ANALYTICAL MODEL

Region 3 consists of the negatively buoyant turbulent wall boundary layer. Equations for the velocity, temperature, and air concentration boundary layer profiles are presented in Section 9.D.9. The profiles are based on turbulent boundary layer 1/7 power laws, as used by Eckert and Jackson. More recent work in the area of turbulent boundary layer profiles has led to the refinement of the boundary layer into three or more layers, such as the viscous sublayer, logarithmic-law layer, and outer layer, to attempt to increase

accuracy. Such multi-layer models may indeed increase the accuracy; but results show the 1/7 power profile to be reasonable to use for simple calculations.

The results of the boundary layer calculation for the LOCA post-blowdown atmosphere are compared to calculations for the LST in the LOCA configuration, that is, having a diffuser below the steam generator compartment. The LST includes the effects of both temperature and concentration as driving forces for natural convection. Conclusions regarding the thin part of the boundary layer near the wall, over which most of the gradient occurs are consistent with observations of the internal thermocouple rake data from LST.

The normalized steam concentration profile versus normalized distance through the boundary layer is plotted in Figure 9.D-2a. The parameter, C , represents local boundary layer steam concentration, and the subscripted values represent: s for surface, and b for bulk. The normalized value, η , is x/δ , where x is distance from the wall and δ is the boundary layer thickness. From Figure 9.D-2a, it can be seen that the average steam concentration in the boundary layer is only 12.5 percent lower than the steam concentration in the bulk.

The maximum boundary layer thickness has been calculated from the Eckert and Jackson style model to be less than 31 inches at the operating deck level in AP600 (assuming that a turbulent boundary layer exists for the full AP600 containment height). From the calculated profile, it is found that 60 percent of the change from bulk to wall conditions occurs over the first 2½ percent of the boundary layer, or over less than the first

inch in AP600. Furthermore, these boundary layer calculations conservatively overpredict wall layer thickness due to neglecting the effects of suction at the boundary (velocity normal toward the wall due to condensation). The boundary layer occupies less than 9 percent of the AP600 cross-sectional area at the operating deck elevation, based on the boundary layer thickness calculations and the AP600 containment radius of 65 feet. The region of significant concentration difference occupies less than 0.5 percent of the AP600 and **AP1000** cross-sectional area.

9.D.6 COMPOSITE REGION DISCUSSION

Referring to Figure 9.D-1, Region 1 is comprised of the rising plume and its entrained flow; Region 2 is the bulk region of low velocity and nearly zero horizontal temperature/concentration gradient; and Region 3 is the falling turbulent wall boundary layer and its entrained flow.

Region 1 occupies about 10 percent of the cross-section at the top, and Region 3 occupies about 9 percent of the cross-section at the bottom, the maximum cross-section for each. Thus, it is reasonable to neglect momentum-related interaction between the rising plume and the falling wall layer in simple first principles calculations. Since the plume occupies about 10 percent of the cross-sectional area at the top, and even less at lower elevations, as a first approximation the effects of the enclosure walls and dome on plume entrainment over the plume height is neglected. Similarly, with the even smaller area occupied by the falling wall layer, the effects of the enclosure are neglected when calculating wall boundary layer entrainment rates.

At a given instant in time, the rising plume of Region 1 is supplied to the above-deck volume from the top of the steam generator cavity. Plume entrainment calculations (Section 9.D.8) show that 5 to 14 times the source flow is entrained from Region 2 over the height of a buoyant plume above the operating deck in AP600. Therefore, the plume average steam concentration would be expected to be near that of the bulk by the time it discharges to the top of Region 2. As discussed previously, entrainment is shown to result in a centerline plume steam concentration at the top that is within 10 percent of the bulk average steam concentration.

The flow leaving Region 1 spreads horizontally and feeds Region 2 at the top. Since higher order mixing mechanisms have been neglected, by continuity, the vertical flow velocity at the top of Region 2 is a low velocity net downward flow with a steam concentration reduced by condensation and heat transfer on the dome to a value lower than the steam concentration discharged from Region 1.

In Region 3, condensation develops a liquid film over the full height of the containment shell and a negatively buoyant gas boundary layer that grows with distance down the shell. Noting that at quasi-steady conditions, the volumetric condensation rate on the wall is just equal to the source flow rate, Q_o , wall boundary layer entrainment calculations (Section 9.D.8) show that the volume of steam condensed on the shell is only 1/6 to 1/13 of the volumetric flow rate of gas entrained into the falling wall layer. Such large entrainment rates relative to the condensation rate suggest that the average steam concentration exiting Region 3 would be near the bulk steam concentration of Region 2. These results are consistent with wall boundary layer profile calculations, discussed previously, which show that the average steam concentration through the boundary layer is only 12.5 percent below the steam concentration in the bulk.

Because global, or large-scale, circulation through the operating deck reduces stratification in the above-deck region (Section 9.C.1.4.2.4), global circulation through the operating deck is conservatively neglected for this discussion. By continuity, the flow exiting the bottom of Region 3 spreads out over the operating deck area, rising in Region 2 with a low net upward velocity and with the same steam concentration as the exit flow of Region 3. Because the top of Region 2 is fed by the plume and the bottom of Region 2 is fed by the wall layer, Region 2 will have a higher steam concentration at the top than at the bottom (neglecting negatively buoyant plumes in the dome region).

In this simplified model, as one moves from the top down in Region 2, entrainment into both the plume and the wall layer on either side of Region 2 steadily reduces the downward flow; similarly the upward flow from the bottom is reduced as one moves upward from the operating deck. There is, therefore, a neutral plane in Region 2 where the vertical velocity approaches zero.

A simplified representation summarizing horizontal gradients through the three regions, consistent with the above discussion, is shown in Figure 9.D-2b.

9.D.7 TURBULENT BUOYANT PLUME ANALYTICAL MODEL – SPECIES CONCENTRATION

This section addresses the assumptions, methodology, equations, and results for the turbulent buoyant plume analytical model - species concentration.

9.D.7.1 Time Period of Application

The turbulent buoyant plume analytical model is applicable in the post-refill phase (when break flow into containment is re-established) and beyond, as shown in Figure 9.D-3.

9.D.7.2 Nomenclature (See Figure 9.D-4)

u = velocity in plume
 C = concentration of air in plume
 T = temperature in plume
 u_{∞} = bulk velocity
 C_{∞} = bulk air concentration
 T_{∞} = bulk temperature
 C_{cl} = plume centerline air concentration

Subscripts:

∞ = bulk
 o = source
CL = centerline

9.D.7.3 Major Assumptions

1. Plume is turbulent and buoyant (i.e., density inside plume is less than the bulk region, Region 2).
2. Plume is not confined by wall surfaces or descending negatively buoyant plumes. It freely develops until it reaches dome region. It is recognized that descending negatively buoyant plumes may be generated in the dome region, and may limit the development height of the positively buoyant plume generated at the outlet of the steam generator compartment. However, the interaction of the positively and negatively buoyant plumes further enhances mixing, and therefore, this potential phenomenon is neglected in this simple analytical model.
3. Bulk conditions are uniform (i.e., homogeneous reservoir)
4. Plume is axisymmetric/round

9.D.7.4 Solution

The analytical solution to the turbulent, buoyant plume model with the above assumptions is already known, and the results are summarized in Table 9.D-1 (Reference 9.D-5, Table 9-7 – Turbulent Plumes in Constant Density Reservoirs).

9.D.7.5 Application of Turbulent Buoyant Plume Results to LST/AP600

Applying the plume centerline species concentration analytical solution, an expression for plume centerline air concentration, C_{CL} is obtained. (Note that C replaces T , and z replaces x from Table 9-7 of Reference 9.D-5)

$$C_{CL} = C_{\infty} - 11 * (Q_0 * \Delta C_0) * B^{-1/3} * z^{-5/3}$$

$$B = g * Q_0 * \left(\frac{\rho_{\infty} * \rho_{stm}}{\rho_{\infty}} \right) = \text{Buoyancy Flux}$$

where,

$$\begin{aligned} \Delta C &= \text{Difference in concentration of air in plume and ambient} \\ Q_0 &= \text{Volumetric flow rate of source} \end{aligned}$$

Applying the above expression to LST Test 213.1B and AP600 at the same total pressure (i.e., 29.8 psia) and air concentration (i.e., 0.60), the air concentration values near the top of containment can be obtained:

For LST Test 213.1B:

$$\begin{aligned} p_{\infty} &= 29.8 \text{ psia}, p_{\text{air}} = 17.9 \text{ psia}, p_{\text{stm}} = 11.9 \text{ psia}, T_{\infty} = 218^{\circ}\text{F}, z = 13.2 \text{ ft} \\ C_{\infty} &= p_{\text{air}}/p_{\infty} = 0.60, \rho_{\text{stm}} = 0.03 \text{ lbm/ft}^3, \rho_{\text{air}} = 0.073 \text{ lbm/ft}^3, \rho_{\text{stm},0} = 0.067 \text{ lbm/ft}^3 \end{aligned}$$

$$Q_0 = \frac{m_o}{\rho_{\text{stm},0}} = \frac{0.54 \text{ lbm/sec}}{0.067 \text{ lbm/ft}^3} = 8 \text{ ft}^3/\text{sec}$$

$$B = 32.2 \times 8 \times 0.35 = 90.2$$

$$\frac{\rho_{\infty} - \rho_{\text{stm},0}}{\rho_{\infty}} = 0.35$$

where,

$$\begin{aligned} \rho_{\infty} &= \rho_{\text{air}} + \rho_{\text{stm}} \\ \Delta C_0 &= C_{\infty} - 0 = 0.60 \\ \Delta C &= C_{\infty} \times 11 \times 8 \times (90.2)^{-1/3} \times (13.2)^{-5/3} = 0.16 \end{aligned}$$

For AP600: (assuming the same bulk air concentration as LST 213.1)

$$p_{\infty} = 29.8 \text{ psia}, p_{\text{air}} = 17.9 \text{ psia}, p_{\text{stm}} = 11.9 \text{ psia}, T_{\infty} = 202^{\circ}\text{F}, z = 110 \text{ ft}$$

$$C_{\infty} = p_{\text{air}}/p_{\infty} = 0.60, \rho_{\text{stm},0} = 0.0723 \text{ lbm/ft}^3$$

$$Q_o = \frac{m_o}{\rho_{\text{stm},0}} = \frac{15.4 \text{ lbm/sec}}{0.0723 \text{ lbm/ft}^3} = 213 \text{ ft}^3/\text{sec}$$

$$B = 32.2 \times 211 \times 0.305 = 2072$$

$$\frac{\rho_{\infty} - \rho_{\text{stm},0}}{\rho_{\infty}} = 0.305$$

$$\Delta C = 0.60 \times 11 \times 213 \times (2072)^{-1/3} \times (110)^{-5/3} = 0.04$$

Air Concentration, C_{CL} at the Top Centerline of Buoyant Plume

	Pressure (atm)	$\frac{\rho_{\infty} - \rho_{\text{stm},0}}{\rho_{\infty}}$	Q_o (ft ³ /sec)	C_{∞}	Z (ft)	B (ft ⁴ /sec ³)	ΔC	C_{CL}
LST	2	0.35	8	0.60	13.2	90.2	0.16	0.44
AP600	2	0.305	213	0.60	110	2072	0.04	0.56

9.D.7.6 Turbulent Buoyant Plume Conclusions

1. AP600 turbulent buoyant plume should provide better dilution of steam compared to LST due to the increased height above the source in AP600, and the $z^{-5/3}$ dependence for mixing/entrainment.
2. Based on the assumption of a well-mixed Region 2, the centerline concentration in the plume is close to ambient conditions for both AP600 and LST near the top of containment. Due to turbulent mixing, the average concentration in the plume should be even closer to the Region 2 bulk conditions.

9.D.8 ENTRAINMENT INTO THE BREAK PLUME AND WALL LAYER, AND THE EFFECT ON MASS TRANSFER RATE

The purpose of this calculation is to determine the volumetric entrainment rate into the break plume and into the negatively buoyant wall layer in AP600 containment during a large LOCA. The plume and buoyant wall layer entrainment models recommended by Peterson for mixing in large stratified volumes are used. The entrainment rates are used to calculate the dilution of the plume and buoyant layer to get the steam/air concentrations at the top (dome) and bottom (deck elevation) of containment. With the steam/air concentrations, the effect on the mass transfer rate in the dome region and at the operating deck level is determined.

9.D.8.1 Time Period of Application

The entrainment models for the buoyant plume are applicable in the post-refill period and beyond and models for the wall boundary layers are applicable to the post blowdown period and beyond, as shown in Figure 9.D-3.

9.D.8.2 Key Assumptions

- Bulk fluid (Region 2) is at a constant density

9.D.8.3 Entrainment into a Buoyant Plume

The volumetric flow rate entrained is:

$$Q_{ent} = 0.15 * B^{1/3} * Z^{5/3}$$

where,

- Z = 108 ft, the height of the plume (conservatively low value of height from steam generator cavity outlet to dome)
- B = $g Q_o(\rho_{amb} - \rho_o)/\rho_{amb}$, the buoyancy
- Q_o = the break steam volumetric flow rate
- ρ_o = the break steam density (assumed to be the saturation density at the total pressure)
- ρ_{amb} = density of the ambient gas, the same density as the entrained gas, ρ_{ent}

It is convenient to define the plume entrainment ratio:

$$r_p \equiv Q_{ent}/Q_o = 0.15 * g^{1/3} * \left(\Delta\rho/\rho\right)^{1/3} * Z^{5/3} * Q_o^{-2/3}$$

For entrainment into the plume, conservation of mass $\underline{m}_{out} = \underline{m}_{ent} + \underline{m}_o$ with $\underline{m} = Q\rho$, gives $Q_{out}\rho_{out} = Q_{ent}\rho_{ent} + Q_o\rho_o$. Conservation of mass for each species produces the relationships $Q_{out}\rho_{s,out} = Q_{ent}\rho_{s,ent} + Q_o\rho_{s,o}$ and $Q_{out}\rho_{a,out} = Q_{ent}\rho_{a,ent}$, where the s and a subscripts indicate the partial densities of the steam and air. With partial density and pressure $\rho_i = P_i/R_iT$, so mass conservation for each species becomes $Q_{out}P_{s,out}/T_{out} = Q_{ent}P_{s,ent}/T_{ent} + Q_oP_{s,o}/T_o$ and $Q_{out}P_{a,out}/T_{out} = Q_{ent}P_{a,ent}/T_{ent}$. Since the absolute temperature does not differ significantly throughout the system, the species equations can be approximated as $Q_{out}P_{s,out} = Q_{ent}P_{s,ent} + Q_oP_{s,o}$ and $Q_{out}P_{a,out} = Q_{ent}P_{a,ent}$. Note that the entrained flow is several times larger than the source flow, so the effect of the higher source temperature is not very significant. These latter equations permit the calculation of the steam and air concentration at the outlet of the plume.

Conservation of mass on a molar basis $\underline{n}_{out} = \underline{n}_{ent} + \underline{n}_o$. With $\underline{n} = \hat{u}A$, $\hat{u} = P/\bar{R}T$, and $Q = uA$, conservation of moles can be written $P_{out}Q_{out}/\bar{R}T_{out} = P_{ent}Q_{ent}/\bar{R}T_{ent} + P_oQ_o/\bar{R}T_o$. Since the total pressure, P is the same

for each, and the absolute temperature T only differs by a small amount, conservation of mass on a molar basis can be approximated as $Q_{out} = Q_{ent} + Q_o$.

With conservation of mass in terms of steam partial pressure, $P_{s,out} = (Q_{ent}P_{s,ent} + Q_oP_{s,o})/Q_{out}$, and $Q_{out} = Q_{ent} + Q_o$, the outlet steam partial pressure is $P_{s,out} = (Q_{ent}P_{s,ent} + Q_oP_{s,o})/(Q_{ent} + Q_o)$. Written in terms of the plume entrainment ratio r_p , $P_{s,out} = (r_pP_{s,ent} + P_{s,o})/(r_p + 1)$.

where,

\underline{m}	=	mass flow rate
\underline{n}	=	molar flow rate
$\hat{\underline{m}}$	=	molar density
Q	=	volumetric flow rate
ρ	=	mass density
R	=	gas constant
T	=	absolute temperature

Subscripts:

a	=	air
s	=	steam
ent	=	entrained
out	=	outlet
o	=	source
stm	=	steam
bl	=	boundary layer

Values for densities and break flow rates at different times using values representative of post-refill and peak pressure are as follows:

		90 sec	1200 sec	Units
ρ_{amb}	=	0.13584	0.16325	lbm/ft ³
ρ_o	=	0.10487	0.13373	lbm/ft ³
$P_{s,o}$	=	46	60	psia
$P_{s,ent}$	=	26.94	40.30	psia
$(\rho_{amb} - \rho_o)/\rho_{amb}$	=	0.2280	0.1808	
$\underline{m}_{g,brk,o}$	=	200	45	lbm/sec
$Q_0 = \underline{m}_{g,brk,o}/\rho_o$	=	1907	336.5	ft ³ /sec
$B = g Q_o(\rho_{amb} - \rho_o)/\rho_{amb}$	=	14,000	1959	ft ⁴ /sec ³
$Q_{ent} = 0.15 B^{1/3} Z^{5/3}$	=	8855	4597	ft ³ /sec
r_p	=	4.64	13.66	
$P_{s,out} = (r_pP_{s,ent} + P_{s,o})/(r_p + 1)$	=	30.32	41.64	psia

Solving the equations for AP600 at 90 seconds and at the time of peak pressure (1200 sec.) results in the following:

Steam Partial Pressure at Top of AP600 Plume from Entrainment Relations

Time sec	$\Delta p/\rho$	Q_o ft ³ /sec	Q_{ent} ft ³ /sec	r_p	$P_{stm,top}$ psia
90	0.2280	1,907	8,855	4.6	30.3
1200	0.1808	336.5	4,597	14	41.6

9.D.8.4 Entrainment into a Negatively Buoyant Wall Layer

The volumetric flow rate entrained is:

$$Q_{ent} = \frac{0.0979 * v * Gr_z^{2/5} p_{wall}}{(1 + 0.494 * Pr^{2/3})^{2/5} * Pr^{8/15}}$$

where,

Z = 121 ft, the height of the wall (deck to dome)

Gr_z = $g(\rho_{amb} - \rho_w)Z^3/(\rho_{amb}v^2)$, the Grashof number

Pr = the Prandtl number of the boundary layer

δ = boundary layer thickness

v = μ/ρ , the boundary layer kinematic viscosity based on the average of bulk and surface values of dynamic viscosity and density

p_{wall} = the wall perimeter (πD) = 408.4 ft

ρ_w = the total gas density adjacent to the liquid film surface

ρ_{amb} = the density of the ambient gas, the same density as the entrained gas, ρ_{ent}

V = volume

It is convenient to define the boundary layer entrainment ratio in terms of the entrained and condensed volumetric flow rates:

$$r_{bl} \equiv Q_{ent}/Q_{cond}$$

For entrainment into the boundary layer, the equations for conservation of mass $\underline{m}_{out} = \underline{m}_{ent} - \underline{m}_{cond}$, and on a molar basis $\underline{n}_{out} = \underline{n}_{ent} - \underline{n}_{cond}$ can be developed as was done for the plume. The results are the important relationships for the steam partial pressure at the outlet of the wall layer:

for volumetric flow $Q_{out} = Q_{ent} - Q_{cond}$, the outlet steam partial pressure is
 $P_{s,out} = (Q_{ent}P_{s,ent} - Q_{cond}P_{s,cond})/(Q_{ent} - Q_{cond})$. In terms of the plume entrainment ratio r_p ,
 $P_{s,out} = (r_p P_{s,ent} - P_{s,o})/(r_p - 1)$.

Values for densities and break flow rates at different times using representative values for post-refill (90 sec) and peak pressure (1200 sec) are as follows:

		90 sec	1200 sec	Units
ρ_{amb}	=	0.13584	0.16325	lbm/ft ³
ρ_w	=	0.19020	0.20229	lbm/ft ³
ρ_{cond}	=	0.10487	0.13373	lbm/ft ³
$P_{s,cond}$	=	46	60	psia
$P_{s,ent}$	=	26.94	40.30	psia
Pr	=	0.81	0.83	
μ	=	1.23×10^{-5}	1.24×10^{-5}	lbm/sec-ft
ρ	=	0.16302	0.18277	lbm/ft ³
$\nu = \mu/\rho$	=	7.55×10^{-5}	6.78×10^{-5}	ft ² /sec
$(\rho_w - \rho_{amb})/\rho_{amb}$	=	0.4001	0.2391	
$Gr_z = g(\rho_w - \rho_{amb})Z^3/(\rho_{amb}\nu^2)$	=	4.00×10^{15}	2.97×10^{15}	
$1 + 0.494 Pr^{2/3}$	=	1.4293	1.4363	
Q_{ent}	=	5098	4004	ft ³ /sec
$\underline{m}_{cond} = \underline{m}_{g,brk,o} \pi_{m,es}$	=	85	40.5	lbm/sec
$Q_{cond} = \underline{m}_{cond}/\rho_{cond}$	=	810.5	302.8	ft ³ /sec
$r_{bl} = Q_{ent}/Q_{cond}$	=	6.29	13.22	
$P_{s,out} = (r_{bl}P_{s,ent} - P_{s,cond})/(r_{bl} - 1)$	=	23.34	38.69	psia

Summary Tables:

Time, sec	P_{total} psia	$P_{\text{s,amb}}$ psia	Y ft ² /sec	$\Delta p/\rho$	Gr_z	Pr	Q_{cond} ft ³ /sec
90	46	26.9	7.55×10^{-5}	0.4004	4.00×10^{15}	0.81	810.5
1200	60	40.3	6.78×10^{-5}	0.2391	2.98×10^{15}	0.83	302.8

Time, sec	Q_{ent} ft ³ /sec	r_{bl}	$P_{\text{s,bot}}$ psia	δ_{bl} ft	V_{bl} ft ³
90	5098	6.3	23.34	2.2	63,200
1200	4004	13.221	38.69	2.3	65,500

9.D.8.5 Effect of Entrainment on Mass Transfer Rate

The condensation heat flux for given total pressure, steam partial pressure, and bulk-to-surface temperature difference is determined and used to calculate the influence of the concentration differences.

Representative bulk-to-surface temperature differences are:

		90 sec	1200 sec
T_{bulk}	=	244.2	267.7°F
T_{surf}	=	165.1	232.2°F
$\Delta T = (T_{\text{bulk}} - T_{\text{surf}})$	=	79.1	45.5°F

The refill time phase, from 30 to 90 sec., has no source, but does have a wall layer. Refill is represented by its end state that is assumed to have the same conditions as calculated at 90 sec, except that without a plume the steam partial pressure and heat flux at the top is the same as the ambient bulk conditions.

The steam partial pressure values at the top, middle, and bottom correspond to the steam partial pressure out of the plume, the bulk steam partial pressure, and the steam partial pressure out of the wall layer.

The average heat flux is a simple, unbiased average of the top, middle, and bottom values, that is

$$\bar{q} = q_{\text{top}}/4 + q_{\text{amb}}/2 + q_{\text{bot}}/4.$$

Summary of Mass Transfer Effects Due to Vertical Concentration Gradients

Time sec	P _{total} psia	ΔT °F	P _{stm,top} psia	P _{stm,amb} psia	P _{stm,bot} psia	q _{top} B/sec-ft ²	q _{amb} B/sec-ft ²	q _{bot} B/sec-ft ²	\bar{q} Average B/sec-ft ²
refill	46	79	26.9	26.9	23.3	1.85	1.85	1.4	1.74
90	6	79	30.3	26.9	23.3	2.25	1.85	1.4	1.84
1200	60	43	41.6	40.3	38.7	1.5	1.4	1.3	1.4

The results in this table show that the upper estimates of vertical concentration differences in AP600 result in a 6 percent reduction on the net heat transfer to the shell during refill and less than 1 percent effect on net heat transfer during the 90 to 1200 sec time period.

9.D.8.6 Boundary Layer Thickness and Volume

The thickness of the negatively buoyant wall layer can be calculated from the integral equations presented by Peterson (Reference 9.D-1).

$$\delta_{bl} = \frac{0.565 * (1 + 0.494 * Pr^{2/3})^{1/10} * z}{Gr_z^{1/10} * Pr^{8/15}}$$

The equation can also be integrated over its height, with the simplifying assumption that all properties are constant over the height, Z. This assumption is reasonable since the Prandtl number only changes a few percent over the range of conditions inside containment, and the only other parameters are contained in the term $\Delta\rho/(\rho v^2)$ which is estimated to change less than a factor of 2 over height, and when raised to the 1/10 power has only a 7 percent effect. Consequently, the product of the integral and the circumference gives a reasonable estimate of the boundary layer volume that can be used with the entrainment rate to estimate boundary layer transit times, or fill time.

The product of the circumference and the integral of the equation above is;

$$V_{bl} = \frac{0.565 * (1 + 0.494 * Pr^{2/3})^{1/10} * (v^2/g)^{1/10} * \pi * D}{(\Delta\rho/\rho)^{1/10} * Pr^{8/15}} * \int_0^H z^{0.7} dz$$

$$= \frac{0.565 * \pi * (1 + 0.494 * Pr^{2/3})^{1/10} * (v^2/g)^{1/10} * D * H^{1.7}}{1.7 * (\Delta\rho/\rho)^{1/10} * Pr^{8/15}}$$

Evaluating this equation with the values from Section 9.D.8.3;

		90 sec	1200 sec	Units
Pr	=	0.81	0.83	
v	=	7.55×10^{-5}	6.78×10^{-5}	ft ² /sec
$(\rho_w - \rho_{amb})/\rho_{amb}$	=	0.4001	0.2391	
$1 + 0.494 \text{ Pr}^{2/3}$	=	1.4293	1.4363	
V (Equation 4)	=	63436	64553	ft ³

Summary Table:

AP600 Boundary Layer Volume and Fill Times

Time, sec	V, ft ³	Q _{ent} , ft ³ /sec	Boundary Layer Fill Time, sec V/Q _{ent}
90	63436	5098	12.4
1200	64553	4004	16.1

9.D.8.7 Sublayer Penetration Time

A measure of the response time of the boundary layer temperature to a change in the environment is the sublayer penetration time. This represents the time it takes for steam to diffuse through the laminar sublayer, where most of the mass transfer resistance is located. The transient diffusion equation:

$$\frac{\partial \rho}{\partial t} = D_v \frac{\partial^2 \rho}{\partial y^2} \text{ becomes } \frac{\delta_m^2}{D_v \tau} \frac{\partial \rho^*}{\partial t^*} = \frac{\partial^2 \rho^*}{\partial y^{*2}}$$

with the substitutions:

$$\hat{\rho} = \hat{\rho}_\infty \hat{\rho}^* \quad y = \delta_m y^* t = \tau t^*$$

where,

$\hat{\rho}$	=	molar density
t	=	time
y	=	distance along the normal to the surface
δ_m	=	boundary layer thickness
D_v	=	air-steam gas diffusion coefficient
τ	=	time constant
∞	=	value at a large distance from surface
*	=	dimensionless variable

If the time constant is defined $\tau = \delta_m^2/D_v$, the coefficient on the left side of the dimensionless equation = 1, as required. The mass transfer sublayer thickness, δ_m , is related to the heat transfer sublayer thickness, δ_h , by $Nu/Sh = (Pr/Sc)^{1/3}$. The heat transfer sublayer thickness is $\delta_h = h/k$. Other assumed values are:

		90 sec	1200 sec	Units
h	=	2.61	2.51	Btu/hr-ft ² -°F
k	=	0.0164	0.0173	Btu/hr-ft-°F
D _v	=	0.537	0.464	ft ² /hr
Pr	=	0.81	0.83	
Sc	=	0.51	0.51	
$\delta_h = h/k$	=	0.0063	0.0069	ft
$\delta_m = \delta_h(Pr/Sc)^{1/3}$	=	0.0073	0.0081	ft
$\tau = \delta_m^2/D_v$	=	0.357	0.509	sec

Consequently, the sublayer penetration time is on the order of 1 sec or less. This is very rapid in comparison to the structure time constants that are on the order of 100 sec, and the system pressurization time constant that is on the order of 1000 sec. Even the boundary layer fill time of 16 sec is short compared to both the structure and pressure time constants.

9.D.9 TURBULENT BOUNDARY LAYER ANALYTICAL MODEL

This section addresses the assumptions, methodology, equations, and results for the turbulent boundary layer analytical model. The analytical model is not intended to be an independent verification of LST, rather, it is used to estimate boundary layer thickness and temperature/concentration profiles for AP600 containment and LST. Measured thermal/concentration boundary conditions from LST tests 217.1 and 220.1 are applied in the analytical model since these represent realistic conditions to apply to the boundary layer model.

9.D.9.1 Time Period of Application

The turbulent boundary layer analytical model (Figure 9.D-4) applies to the time period when quasi-steady conditions are established inside containment. The time period of applicability is shown in Figure 9.D-3.

9.D.9.2 Key Assumptions

- Surface is vertical flat plate
 - Containment shell radius of curvature is large so it can be treated locally as a flat plate.

- Velocity, temperature, concentration boundary layer profile is turbulent
 - This is appropriate since boundary layer is turbulent within a few feet of the top of the containment shell.
- Bulk (Region 2) fluid velocity $\cong 0$
 - This is true after blowdown period since the break source transitions from jet to buoyant plume and bulk containment area is large relative to plume/boundary layer.
- Condensate film is impermeable to noncondensable gases.
 - This is conservative since absorption by the film removes air from containment volume which enhances heat/mass transfer of steam.
- Condensate film is stationary relative to gas boundary layer.
 - This is appropriate since condensate film velocity is smaller than gas boundary layer velocity, and conservative because a moving film enhances heat transfer.
- Suction effect at wall is neglected.
 - This is conservative because suction thins the boundary layer.
- Thermal boundary layer thickness is the same as concentration boundary layer thickness.
 - This is appropriate since $Le^{1/3} = \left(\frac{Pr}{Sc}\right)^{1/3} \sim 1.0$.
- Saturation conditions exist at film surface.
 - This is appropriate since steam is condensing at the film surface.
- Bulk fluid (Region 2) temperature is uniform above the break source elevation.
 - Refer to LST test 217.1 and 220.1 temperature profiles in (Figure 9.D-6 and Figure 9.D-7).
- Bulk fluid (Region 2) concentration is uniform above the break source elevation.
- Surface Temperature is approximately constant for purposes of applying the simple analytical model.
- Wall heat flux is modeled as forced convection using equations from Reference 9.D-6.

9.D.9.3 Boundary Layer Profiles

The boundary layer profiles, used by Eckert and Jackson, are based on experimental data for turbulent boundary layers:

- Boundary Layer Velocity Profile (Reference 9.D-7, Equation 24)

$$u = U(1 - \eta)^4 * \eta^{\frac{1}{7}} \text{ where } \eta = \frac{r}{\delta}$$

where,

u = local velocity in boundary layer
 δ = boundary layer thickness
r = coordinate direction normal to condensing surface

- Boundary Layer Temperature Profile (Reference 9.D-7, Equation. 25)

$$T - T_{\infty} = (T_{\text{surf}} - T_{\infty})(1 - \eta^{\frac{1}{7}})$$

where,

T = temperature

- Boundary Layer Air Concentration Profile

$$C - C_{\infty} = (C_{\text{surf}} - C_{\infty})(1 - \eta^{\frac{1}{7}})$$

where,

C = air concentration

- Boundary Layer Thickness (Reference 9.D-8, Equation. 10.121b)

$$\delta = B * z^n$$

where,

B, n are constants to be determined

- Maximum Velocity in Boundary Layer (Reference 9.D-8, Equation. 10.121a)

$$U = A * z^m$$

A, m are constants to be determined

9.D.9.4 Governing Equations

- Momentum Equation

$$\frac{d \left[\int_0^\delta u * (T - T_\infty) dr \right]}{dz} = g * \int_0^\delta \beta * (T - T_\infty) dr - \frac{\tau_w}{\rho}$$

where,

τ_w	=	shear stress at condensing surface
β	=	volumetric thermal expansion coefficient
ρ	=	bulk density
g	=	local gravitation acceleration

- Energy Equation

$$\frac{d \left[\int_0^\delta u * (T - T_\infty) dr \right]}{dz} = \frac{q''_w}{\rho * C_p}$$

where,

C_p	=	specific heat at constant pressure
q''_w	=	wall heat flux

- Conservation of Mass Equation

Not used in this calculation since we are not calculating entrainment volumes/rates, but rather, temperature/concentration profiles.

- Boundary Conditions

Thermal and concentration boundary conditions are from LST tests are applied at the shell surface and in bulk (Region 2) locations because the boundary conditions are expected to be representative of AP600.

9.D.9.5 Boundary Layer Momentum Equation Development

Wall shear stress in the momentum equation is modeled using a correlation for forced turbulent convection. Eckert and Jackson argue the τ_w is similar to forced convection in the near surface region and can be represented as follows:

$$\frac{\tau_w}{\rho * U^2} = 0.0225 * \left[\frac{U * \delta}{\nu} \right]^{-1/4}$$

where,

ν = kinematic viscosity

$$\tau_w = 0.0225 * \rho * U^2 * \left(\frac{\nu}{U * \delta} \right)^{1/4}$$

where,

U = is a characteristic velocity interpreted by Eckert and Jackson as the maximum velocity in boundary layer.

The integral momentum equation then becomes:

$$\frac{d \left[\int_0^\delta u^2 dr \right]}{dz} = g * \int_0^\delta \beta * (T_\infty - T) dr - 0.0225 * U^2 * \left(\frac{\nu}{U * \delta} \right)^{1/4}$$

Applying turbulent velocity and thermal boundary layer profiles, it can be shown that:

$$\int_0^\delta u^2 dr = \delta \int_0^1 [U * (1 - \eta)^4 * \eta^{1/7}]^2 d\eta = 0.052315 * \delta * U^2$$

and

$$\int_0^\delta (T_\infty - T) dr = \delta * \int_0^1 (T_\infty - T_{surf}) \left(1 - \eta^{7/8} \right) d\eta = \frac{\delta}{8} * (T_\infty - T_{surf})$$

The boundary layer momentum equation becomes:

$$\frac{d}{dx} (0.052315 * U^2 * \delta) = g * \beta * (T_\infty - T_{surf}) * \frac{\delta}{8} - 0.0225 * U^2 * \left(\frac{\nu}{U * \delta} \right)^{1/4}$$

Applying Reynolds Analogy for heat/momentum transfer:

$$\frac{h}{\rho * C_p * U} = \frac{f_z}{2} * E_H \quad (\text{Reference 9.D-7, Equation 5})$$

where,

$$f_z = \text{local friction factor} = 0.045 * \left[\frac{\nu}{U * \delta} \right]^{1/4} \quad (\text{Reference 9.D-7, Equation 32})$$

E_H = ratio of turbulent eddy diffusivity of heat to that of momentum

h = heat transfer coefficient

from Colburn Analogy:

$$E_H = Pr^{-2/3} \quad (\text{Reference 9.D-7, Equation 6})$$

where,

$$Pr = \text{Prandtl number}$$

Therefore,

$$\frac{h}{\rho * C_p * U} = \frac{0.045}{2} * \left[\frac{v}{U * \delta} \right]^{1/4} * Pr^{-2/3} = 0.0225 * \left[\frac{v}{U * \delta} \right]^{1/4} * Pr^{-2/3}$$

Now, since

$$q''_w = \frac{q_w}{A_{surf}} = h * (T_\infty - T_w)$$

heat flux can be modeled as follows:

$$\frac{q''_w}{\rho * C_p} = 0.0225 * (T_\infty - T_{surf}) * U * \left[\frac{v}{U * \delta} \right]^{1/4} * Pr^{-2/3}$$

where,

$$A_{surf} = \text{heat transfer surface area}$$

Now,

$$\begin{aligned} & \int_0^\delta u * (T - T_\infty) dr \\ &= \delta * \int_0^1 \left[U * (1 - \eta)^4 * \eta^{1/7} \right] (T_\infty - T_{surf}) \left(1 - \eta^{1/7} \right) d\eta = 0.036633 * (T_\infty - T_{surf}) * \delta * U \end{aligned}$$

The boundary layer energy equation becomes:

$$\frac{d}{dz} [0.03663 * (T_\infty - T_{surf}) * \delta * U] = 0.0225 * Pr^{-2/3} * (T_\infty - T_{surf}) * U * \left[\frac{v}{U * \delta} \right]^{1/4}$$

Substituting expressions for U and δ into boundary layer momentum and energy equations, differentiating the resulting equations, solve for exponents m and n by matching exponents. This procedure results in m=1/2 and n=7/10 which can also be found in Reference 9.D-8, page 335.

Therefore:

$$U = A * z^{\frac{1}{2}} \text{ and } \delta = B * z^{\frac{7}{10}}$$

Substituting the expressions for U and δ into boundary layer equations and performing the differentiation, we obtain:

$$\left(\frac{17}{10}\right) [0.0252315 * A^2] = 0.125 * g * \beta * (T_{\infty} - T_{\text{surf}}) - 0.0225 * A^{\frac{7}{4}} * B^{-\frac{5}{4}} * v^{\frac{1}{4}}$$

and

$$\left(\frac{6}{5}\right) [0.03663 * A] * \text{Pr}^{\frac{2}{3}} = 0.0225 * A^{\frac{3}{4}} * B^{-\frac{5}{4}} * v^{\frac{1}{4}}$$

Solving for constants A and B, an expression for boundary layer thickness can be obtained:

$$\delta = B * z^{\frac{7}{10}} = 0.565 * z * \text{Gr}_z^{-\frac{1}{10}} * \text{Pr}^{-\frac{8}{15}} * [1 + 0.494 * \text{Pr}^{2/3}]^{-1/10} \text{ (Reference 9.D-7, Equation 36)}$$

The above equation agrees with that obtained in Reference 9.D-1, Equation 18.

From the expression for δ , the velocity, thermal and concentration boundary layer profiles can be calculated, where:

$$\text{Gr}_z = \frac{g * \beta * (T_{\infty} - T_{\text{surf}}) * z^3}{v^2} \quad \text{(Reference 9.D-7, Equation 29)}$$

9.D.9.6 Boundary Layer Thickness Results

Rather than calculate Gr_z and δ for a mixture, the calculation is done using air or steam properties to examine the range of possible values.

AP600 Prediction (for thermodynamic properties based on LST test 217.1)

The following parametric values are associated with LST test 217.1 and are used to calculate boundary layer thicknesses below:

Location	T_{∞}	T_{surf}	Pr (air)	v (air)
E	230°F	188°F	0.70	$0.84 \times 10^{-4} \text{ ft}^2/\text{sec}$

Based on AIR properties (Reference 9.D-10) and noting $\beta = 1/T$:

$$Gr_z = \frac{32.2 \frac{\text{ft}}{\text{sec}^2} * (230^\circ\text{F} - 188^\circ\text{F}) * \left(\frac{1}{690^\circ\text{R}}\right) * (110\text{ft})^3}{\left(0.84 \times 10^{-4} \frac{\text{ft}^2}{\text{sec}^2}\right)^2} = 3.7 \times 10^{14}$$

$$\delta = 0.565 * (110\text{ft}) * (3.7 \times 10^{14})^{-\frac{1}{10}} * (0.7)^{-\frac{8}{15}} * \left[1 + 0.494 * (0.7)^{\frac{2}{3}}\right]^{-\frac{1}{10}} = 30.5 \text{ in}$$

Based on STEAM properties:

$$Gr_z = \frac{32.2 * (230 - 188) * \left(\frac{1}{690}\right) * (110)^3}{(0.84 \times 10^{-4})^2} = 3.7 \times 10^{14}$$

$$\delta = 0.565 * (110\text{ft}) * (3.4 \times 10^{14})^{-\frac{1}{10}} * (1.1)^{-\frac{8}{15}} * \left[1 + 0.494 * (1.1)^{\frac{2}{3}}\right]^{-\frac{1}{10}} = 23.9 \text{ in}$$

LST Prediction (for thermodynamic properties based upon LST test 217.1)

Based on AIR properties:

$$Gr = \frac{32.2 * (230 - 188) * \left(\frac{1}{690}\right) * (13.2)^3}{(0.84 \times 10^{-4})^2} = 6.4 \times 10^{11}$$

at Point E in LST:

$$\delta = 0.565 [13.2 \text{ ft}] (6.4 \times 10^{11})^{-1/10} (0.70)^{-8/15} [1 + 0.494 (0.70)^{2/3}]^{-1/10} = 6.9 \text{ in.}$$

Based on STEAM properties ($Pr = 1.10$, $\nu = 0.87 \times 10^{-4} \text{ ft}^2/\text{sec}$):

$$Gr = \frac{32.2(230 - 188)\left(\frac{1}{690}\right)(13.2)^3}{(0.87 \times 10^{-4})^2} = 5.9 \times 10^{11}$$

at Point E in LST:

$$\delta = 0.565 * (13.2\text{ft}) * (5.9 \times 10^{11})^{-\frac{1}{10}} * (1.1)^{-\frac{8}{15}} * \left[1 + 0.494 * (1.1)^{\frac{2}{3}}\right]^{-\frac{1}{10}} = 5.4 \text{ in}$$

The following parametric values are associated with LST Test 220.1 and are used to calculate boundary layer thickness below:

Location	T_{∞}	T_{surf}	Pr (air)	ν (air)
E	200°F	155°F	0.70	$1.0 \times 10^{-4} \text{ ft}^2/\text{sec}$

Based on AIR properties:

$$\text{Gr} = \frac{32.2 * (200 - 155) * \left(\frac{1}{660}\right) * (13.2)^3}{(1.0 \times 10^{-4})^2} = 5.0 \times 10^{11}$$

at Point E in LST:

$$\delta = 0.565 * (13.2\text{ft}) * (5.0 \times 10^{11})^{-\frac{1}{10}} * (0.7)^{-\frac{8}{15}} * \left[1 + 0.494 * (0.7)^{\frac{2}{3}}\right]^{-\frac{1}{10}} = 7.1 \text{ in}$$

9.D.9.7 Concentration Profile Results

The concentration profile and integrated average in boundary layer are calculated from the turbulent analytical model for LST. The concentration at the surface is determined from inside surface temperature data and applying saturated conditions near the surface. See Figure 9.D-5 for relative measurement elevations. Radial positions are shown in Figure 9.D-6 and Figure 9.D-7.

LST Test 220.1 $P_{\text{total}} = 32 \text{ psia}$, $\dot{m} = 0.5 \text{ lbm/sec}$

Average LST Boundary Layer Air Concentration Based Upon Measured Bulk and Wall Conditions

Location	T_{surf} (measured) (°F)	T_{∞} (measured) (°F)	C_{surf} (calc)	C_{∞} (measured)	\overline{C}_{BL} (calc)
Dome	180	—	0.77	0.34	0.39
A	180	230	0.77	0.44	0.48
B	—	230	—	—	—
C	177	230	0.78	—	0.48
D	—	230	—	—	—
E	155	200	0.87	0.72	0.74

LST Test 217.1 $P_{\text{total}} = 43 \text{ psia}$, $\dot{m} = 1.0 \text{ lbm/sec}$ **Average LST Boundary Layer Air Concentration Based Upon Measured Bulk and Wall Conditions**

Location	T _{surf} (measured) (°F)	T _∞ (measured) (°F)	C _{surf} (calc)	C _∞ (measured)	\bar{C}_{BL} (calc)
Dome	200	–	0.73	0.33	0.38
A	210	260	0.67	0.35	0.39
B	207	260	0.67	–	0.39
C	205	260	0.70	–	0.395
D	198	260	0.74	–	0.40
E	188	240	0.79	0.67	0.69

Notes:

1. C_{surf} is calculated from applying Dalton's law of partial pressures, assuming saturation conditions exist at the condensing surface, and using measured surface temperatures and total pressure from LST tests.
2. \bar{C}_{BL} , which represents the average air concentration in the boundary layer, is calculated from performing an integrated average which results in $C_{BL} = (C_{\text{surf}} + 7 * c_{\infty})/8$
3. Refer to inside wall temperature data (Table 4.8-1 for LST test 217.1 and Figure 4.11-6 for LST test 220.1) in Reference 9.D-11 for surface temperature data.
4. Bulk fluid temperatures shown in the above tables represent spatially-averaged values based upon attached LST time-averaged temperature profiles for LST tests 220.1 and 217.1 at quasi-steady conditions.

9.D.9.8 Boundary Layer Concentration Profile Results – LST

1. Comparison of C_{∞} and \bar{C}_{BL} shows that the difference in air concentration is small (within 15 percent) in the radial (horizontal) direction for LST. This along with temperature profile data indicate that LST is well-mixed in the radial direction throughout the above-deck region, outside of the relatively thin laminar sublayer.
2. The measured bulk fluid temperature in both horizontal and vertical directions shows little difference (i.e. a few degrees) between the dome region and region D as seen in Figure 9.D-6 and Figure 9.D-7. There is however about 20°F difference in the bulk temperature between regions D and E, for LST test 217.1 and about 30°F difference for LST test 220.1. The data indicate some level of stratification between regions D and E, which is more pronounced in LST test 220.1. Since the LST does not have a flow connection from the simulated SG compartment, there is no global circulation. As a result, the stratification below the source elevation is not surprising.

3. Region E temperature/concentration is notably different than the regions above. This indicates an interface or gradient region exists between the higher temperature, steam-rich upper region (above the plane of the break) fed by the buoyant plume, and the lower temperature, air-rich region fed by the wall boundary layer.
4. Turbulent boundary layer mixing is significant such that boundary layer average properties are nearly at bulk conditions. It is expected that this will be the case for AP600.

9.D.9.9 Boundary Layer Analytical Model Results – Boundary Layer Thickness

1. The maximum boundary layer thickness calculated from the analytical model for LST turbulent boundary layer ~ 7 inches. (LST 217.1 and 220.1)
2. The maximum total boundary layer thickness calculated from the analytical model for AP600 at similar thermodynamic conditions ~ 31 inches.
3. The calculated boundary layer thicknesses are conservative because suction effects due to steam condensation at the wall were not included. It is well known that suction reduces boundary layer thickness (refer to Schlichting, Boundary Layer Theory). Therefore, actual boundary layers should be thinner than calculated.
4. The boundary layer horizontal profile is rather “flat” due to mixing effects of turbulence. Consequently, most of the horizontal boundary layer gradient is contained in the much smaller region near the condensing surface.

9.D.10 INFLUENCE OF HORIZONTAL GRADIENTS ON MASS TRANSFER COEFFICIENTS

Since only free convection is assumed throughout the design basis containment transients, the velocities calculated in the lumped parameter model are not used in calculating mass transfer rates. Therefore, justification of the approach taken for mass transfer is based on steam concentration gradients.

The horizontal concentration gradients in the post-LOCA containment atmosphere are consistent with the lumped parameter nodding and associated mass transfer coefficients used in the WGOTHIC Evaluation Model. The scale of significant concentration gradients near the wall are much less than the 2-foot thick calculation cell (node) used in the WGOTHIC Evaluation Model. Thus, the wall cell is large enough in the radial direction that cell properties can be used to represent the bulk condition for use with boundary layer heat and mass transfer correlations which are described in Reference 9.D-4.

9.D.11 CONCLUSION

The following conclusions apply to the containment atmosphere during the post blowdown period for a DECLG LOCA:

1. The turbulent buoyant plume (Region 1) entrains a significant volume from the bulk (Region 2) such that it is nearly at bulk thermal/concentration conditions in the dome region.
2. Based upon LST data and enclosure test data, the large bulk region (Region 2) is well-mixed horizontally and above the break source elevation, vertically as well.
3. The turbulent wall boundary layers entrain volume from the bulk region such that the average thermal/concentration in the boundary layer is nearly at bulk conditions.

9.D.12 REFERENCES

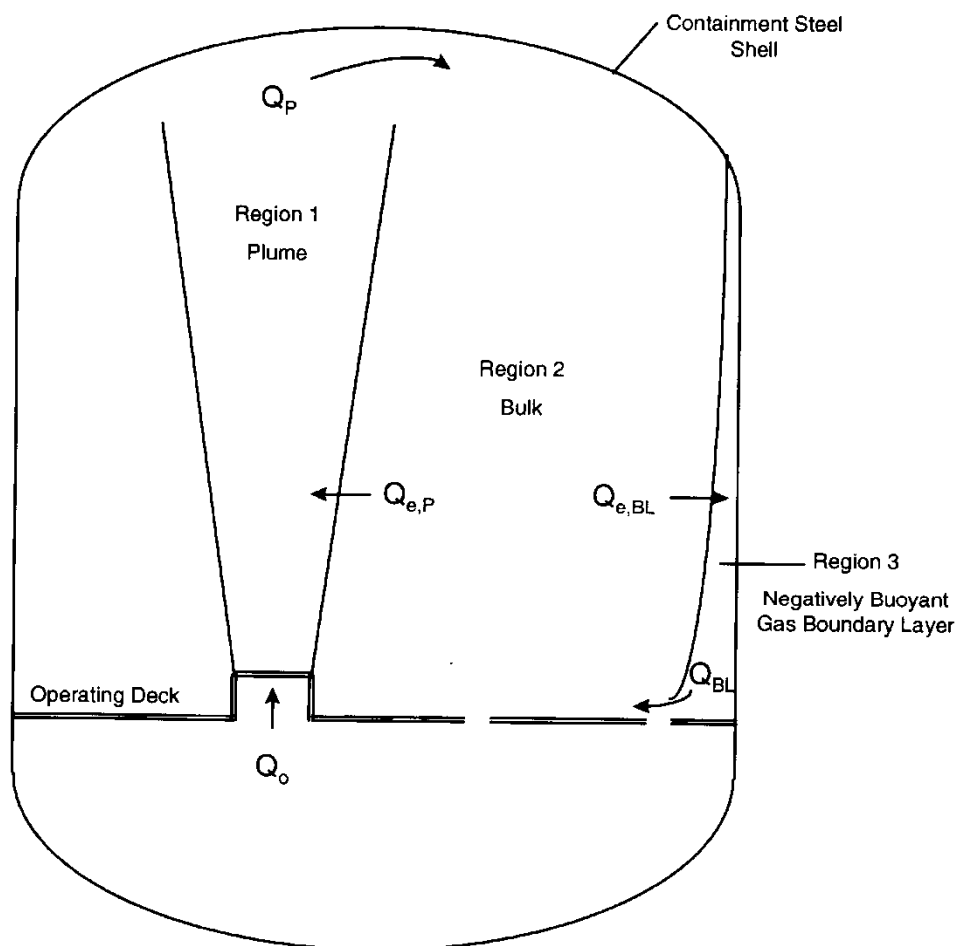
- 9.D-1 Peterson, P.F., "Scaling and Analysis of Mixing in Large Stratified Volumes," International Journal of Heat and Mass Transfer, Vol. 37, Suppl. 1, pp 97-106, 1994.
- 9.D-2 Blevins, "Jets, Plumes, Wakes, and Shear Layer," Applied Fluid Dynamics Handbook, 1984.
- 9.D-3 WCAP-14407, Rev. 2, "WGOTHIC Application to AP600," April 1998.
- 9.D-4 WCAP-14326, Rev. 2, "Experimental Basis for the AP600 Containment Vessel Heat and Mass Transfer Correlations," April 1998.
- 9.D-5 Blevins, "Jets, Plumes, Wakes, and Shear Layers," Applied Fluid Dynamics Handbook, 1984, pp. 247-251.
- 9.D-6 Eckert and Jackson, "Analysis Turbulent Free Convection Boundary Layer on a Flat Plate," NACA Report 1015, 1951.
- 9.D-7 Corradini, "Turbulent Condensation on a Cold Wall in the Presence of a Non-Condensable Gas," Proceedings on Nuclear Reactor Thermal Hydraulics, Vol. 1, 1983.
- 9.D-8 Kakac and Yener, Convective Heat Transfer, 2nd edition, CRC Press, 1995.
- 9.D-9 Kays and Crawford, Convective Heat and Mass Transfer, 3rd Edition, McGraw-Hill.
- 9.D-10 Kreith, "Principles of Heat Transfer," 3rd Edition, Appendix.
- 9.D-11 WCAP-14135, "Final Data Report for PCS Large-Scale Tests, Phase 2 and Phase 3," Revision 1, April 1997.
- 9.D-12 WCAP-14845, "Scaling Analysis for AP600 Containment Pressure During Design Basis Accidents," Revision 3, March 1998.

Table 9.D-1. Analytical Solution to the Turbulent Buoyant Plume Model
(Reference 9.D-5, Table 9-7)

Notation: b = half-width of the plume; i.e., transverse distance for the axial velocity to fall to one-half the centerline value; B = specific buoyancy flux, see Eqs. (9-50) and (9-54); Q = volume flow rate, per unit depth for plane plume; Q_0 = initial volume flow rate; r = radial distance from plume axis; ΔT = species concentration relative to reservoir level; ΔT_0 = initial relative species concentration; u = axial velocity; u_m = centerline axial velocity; v_e = transverse velocity of reservoir fluid into plume; x = axial distance from origin of the plume; y = transverse distance from center plane; ν = kinematic viscosity. (Refs. 9-1, 9-73.) The uncertainty in the coefficients is approximately $\pm 10\%$.

Plume Characteristic ^(a)	Plane Plume	Axisymmetric (i.e., round) Plume
1. Centerline velocity, u_m	$1.7 B^{1/3}$	$3.5 B^{1/3} x^{-1/3}$
2. Width, b	$0.097 x$	$0.11 x$
3. Axial velocity profile ^(b) , u/u_m	$e^{-74(y/x)^2}$	$e^{-57(r/x)^2}$
4. Volume flow rate, Q	$0.34 B^{1/3} x$	$0.15 B^{1/3} x^{5/3}$
5. Centerline species concentration, ΔT_m	$2.4 (Q_0 \Delta T_0) B^{-1/3} x^{-1}$	$11 (Q_0 \Delta T_0) B^{-1/3} x^{-5/3}$
6. Species concentration width, $b_{\Delta T}$	$0.13 x$	$0.10 x$
7. Species concentration profile ^(b) , $\Delta T/\Delta T_m$	$e^{-41(y/x)^2}$	$e^{-69(r/x)^2}$
8. Entrainment velocity, v_e	$0.10 u_m$	$0.041 u_m$
9. Reynolds number, $u_m b/\nu$	$0.17 \frac{B^{1/3} x}{\nu}$	$0.35 \frac{B^{1/3} x^{2/3}}{\nu}$

(a) In fully developed region.
(b) These are consistent with the corresponding width.



- Q_o = Source plume volumetric flow at exit of steam generator compartment
 $Q_{e,p}$ = Volumetric plume entrainment from Region 2
 $Q_{e,BL}$ = Volumetric wall boundary layer entrainment from Region 2
 Q_p = Volumetric plume flow feeding top of Region 2
 Q_{BL} = Volumetric boundary layer flow feeding bottom of Region 2

Figure 9.D-1. Interactions Between Containment Regions During Post-Blowdown LOCA (Low Momentum)

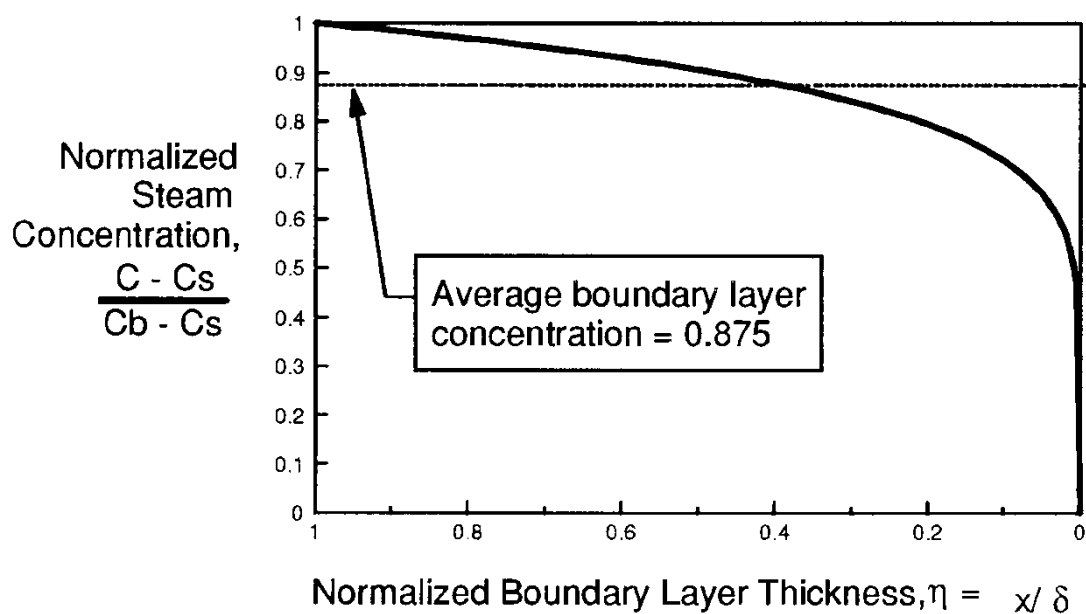


Figure 9.D-2a. Detail of Steam Concentration Distribution in Boundary Layer

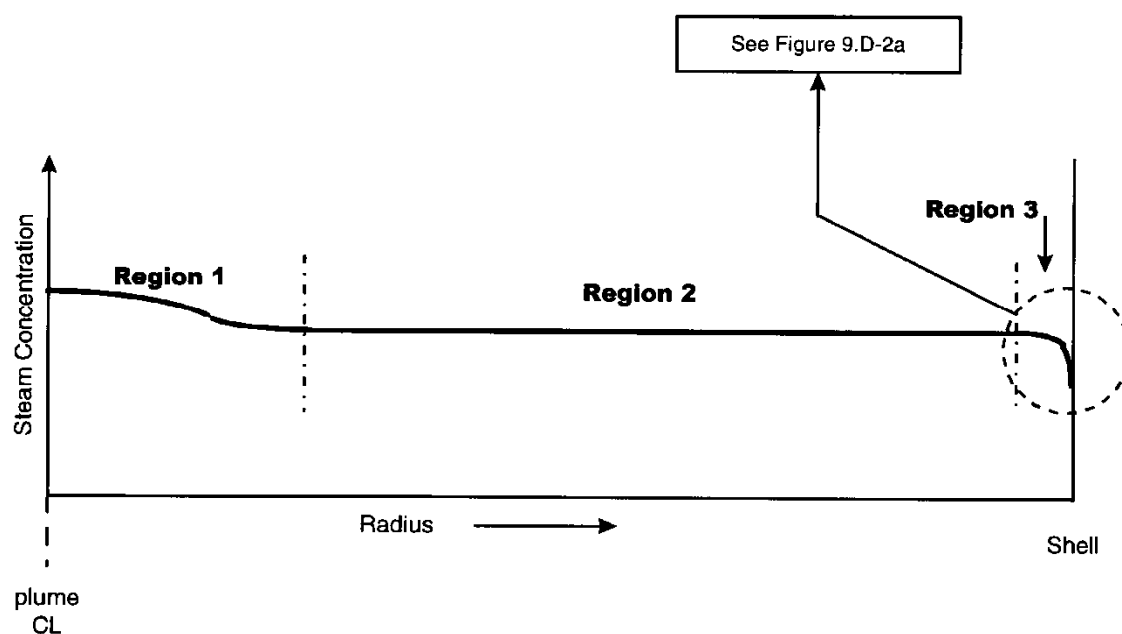


Figure 9.D-2b. Qualitative Radial Concentration Profile from Plume Centerline to Shell at Mid Elevation

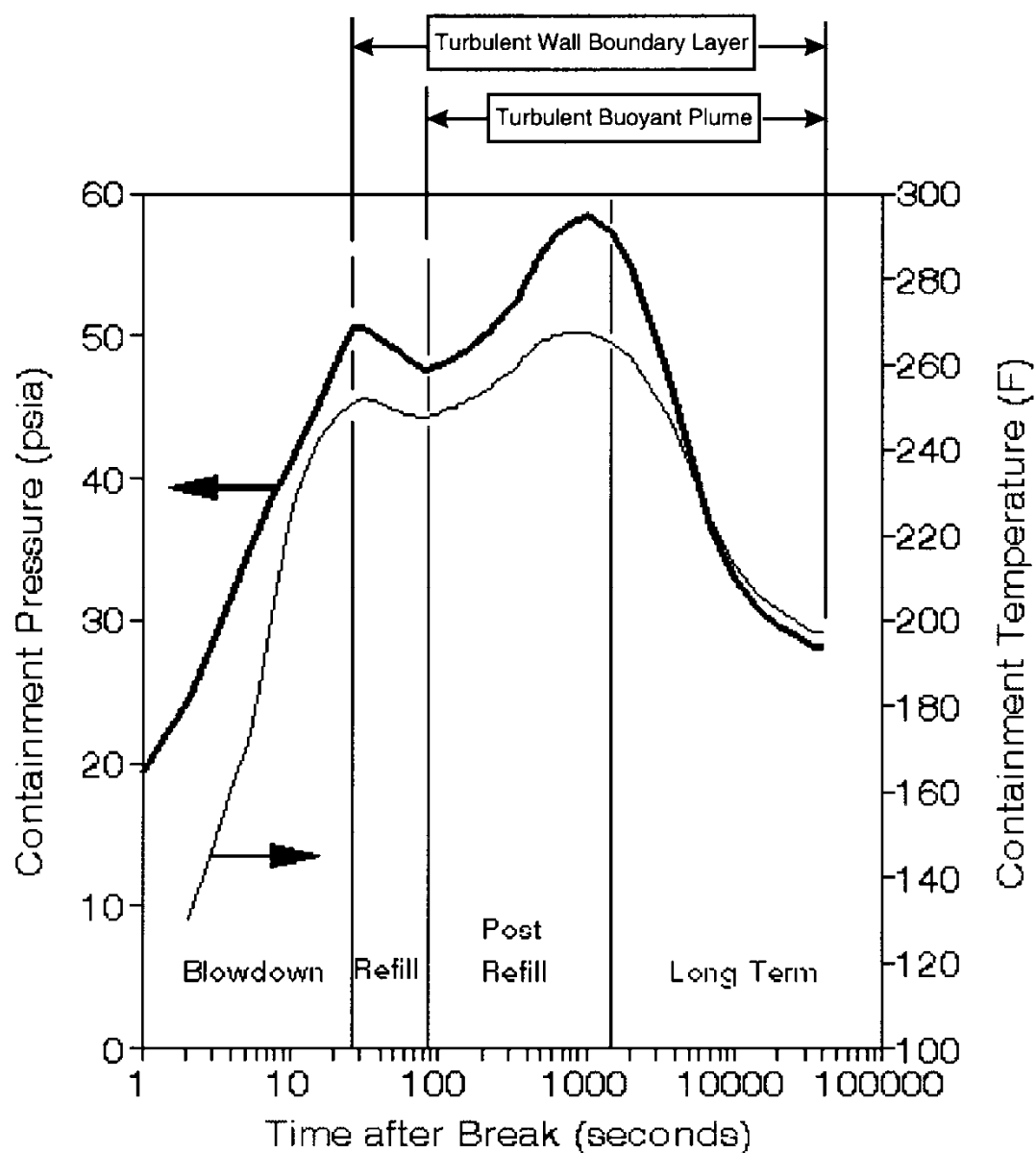


Figure 9.D-3. Period of Application of Analytical Models for Turbulent Wall Boundary Layer and Turbulent Buoyant Plume

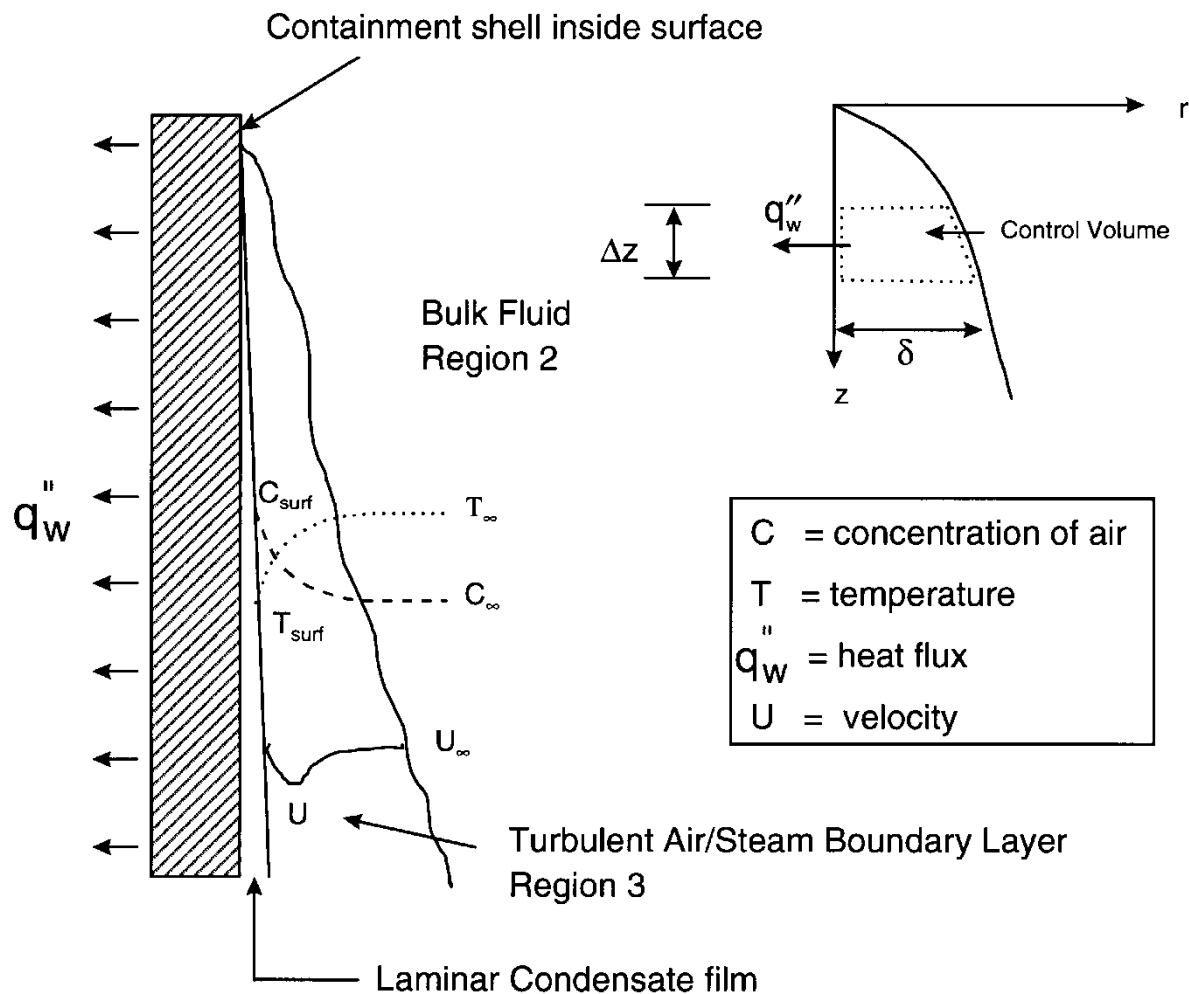


Figure 9.D-4. Turbulent Buoyant Plume Analytical Model

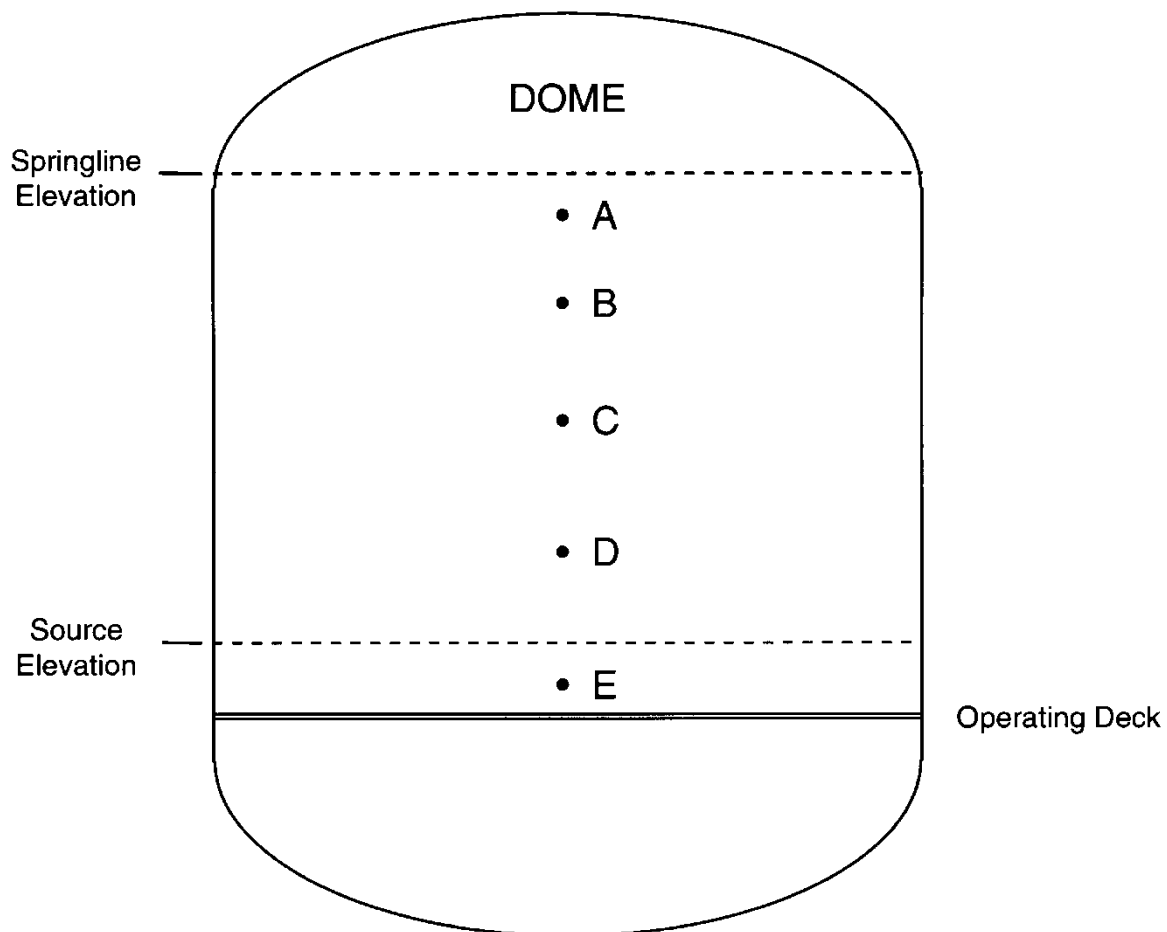


Figure 9.D-5. LST Measurement Locations

a,c

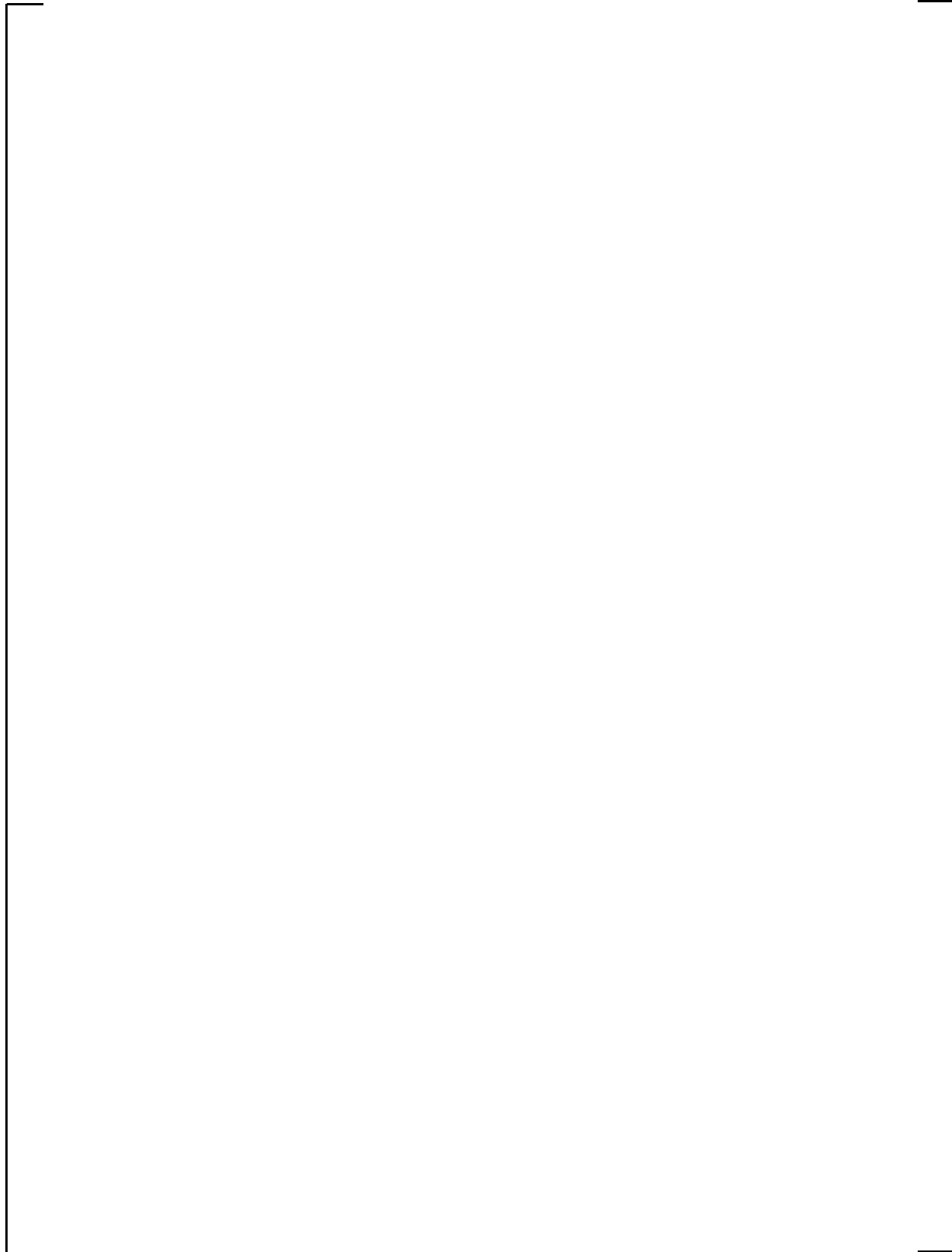


Figure 9.D-6. LST Temperature Profile – Test 220.1 @ Quasi-Steady Conditions

a,c

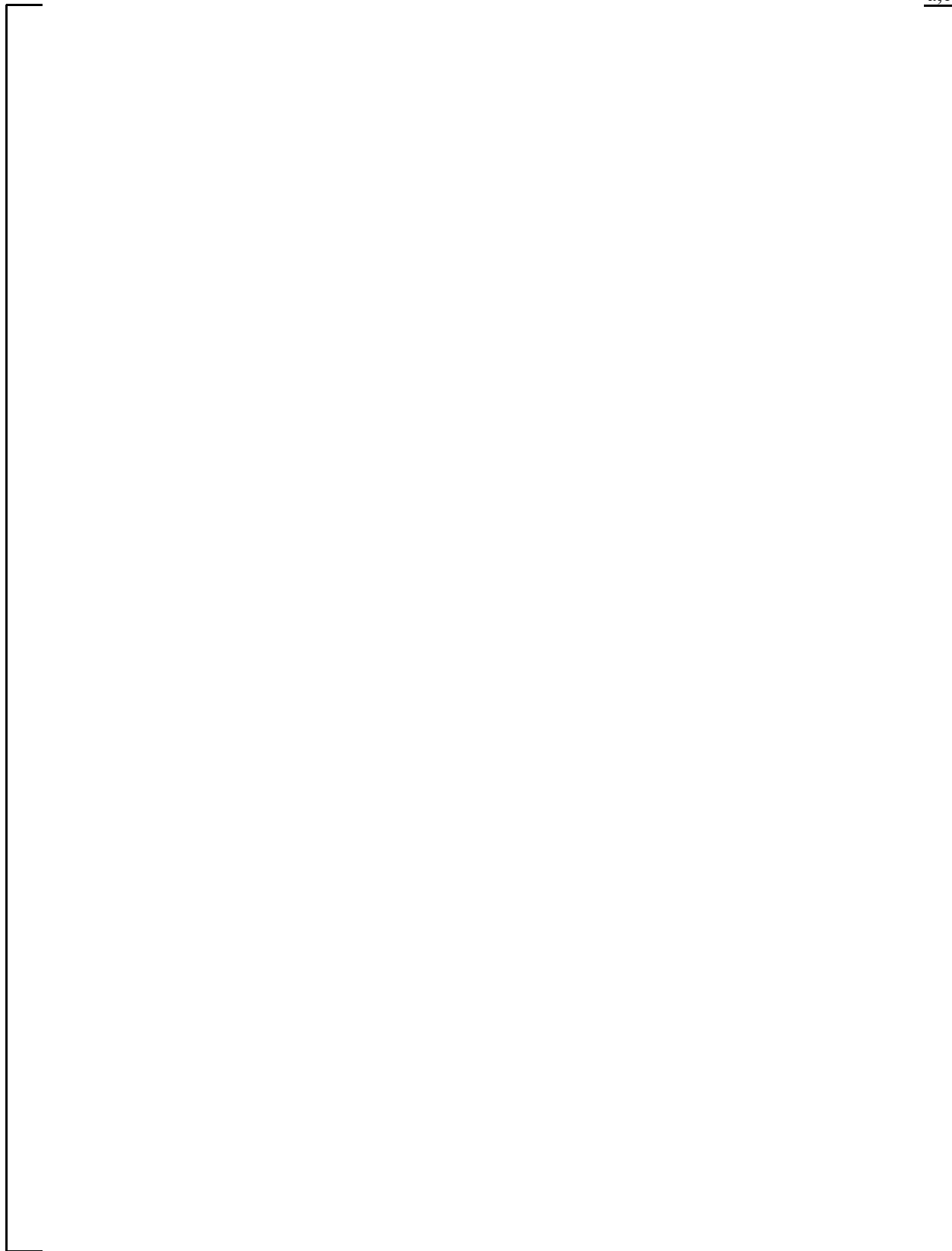


Figure 9.D-7. LST Temperature Profile – Test 217.1 @ Quasi-Steady Conditions

10 NOMINAL INPUTS AND CORRELATIONS SENSITIVITIES

10.1 INTRODUCTION

The input values for the WGOTHIC Evaluation Model have been biased to ensure a conservative prediction of containment pressure. A subset of these parameters has been selected to determine the impact of each parameter on the calculated pressure for the LOCA and MSLB transients, and to provide a quantification of the total conservatism in the Evaluation Model associated with these parameters. For these parameters, nominal values have been assumed.

Seven sensitivities were run for the LOCA transient to determine the additive sensitivity to each parameter. One sensitivity was run for the MSLB transient, which was a composite of six of the parameters investigated for the LOCA.

The results of these studies show that there is over 11.5 psi margin inherent in the AP600 Containment Evaluation Model for the LOCA peak pressure calculation due to the parameters studied. There is over 13 psi margin associated with the post-blowdown peak pressure, and for the final nominal case, the maximum pressure shifts to the blowdown phase. There is at least 4.9 psi margin in the MSLB calculation due to the parameters investigated. If nominal mass and energy releases were assumed for the MSLB case, even more margin would be shown.

10.2 SENSITIVITY STUDY RESULTS

An estimate of the amount of conservatism, quantified as the change in containment pressure and represented by some of the significant assumptions made for the Evaluation Model follows. These are not single-effect sensitivities. These results are cumulative, in that each additional modification is stacked upon those that immediately preceded it. These sensitivities provide insight into the effect of each parameter individually by comparison to the preceding case, as well as the total conservatism represented by these parameters.

The AP600 Containment Evaluation Model calculations for the LOCA and MSLB described in Section 4 were used as the basis for these studies, with the parameter changes described below, made in each succeeding case. Table 10-1 summarizes the basis for each case and the calculated pressure results for each case. Seven sensitivity cases were analyzed for the LOCA transient, as described below. Figure 10-1 shows a composite pressure curve for the LOCA cases. One MSLB sensitivity was run including all the parameters investigated for the LOCA, except for nominal mass and energy releases. Figure 10-2 shows the pressure results for the MSLB case.

Table 10-1. Nominal Inputs and Correlations Sensitivity Results

LOCA Sensitivities				
Case	Case Description	Blowdown Pressure (psig)	Post-Blowdown Peak Pressure (psig)	Pressure at 24 Hours (psig)
	AP600 Evaluation Model	34.4	43.9	18.9
1	Heat & Mass Transfer Multipliers on the Containment Shell	34.4	42.5	16.8
2	Nominal Initial and Ambient Conditions (plus case 1)	33.3	39.8	11.0
3	Nominal Clime Material Properties (plus Cases 1, 2)	33.3	39.0	10.4
4	Nominal Steel-to-Concrete Gap Thickness (plus Cases 1, 2, 3)	33.3	38.8	10.4
5	Nominal External Annulus Loss Coefficients (plus Cases 1, 2, 3, 4)	33.3	38.7	10.2
6	Condensation on Dead-Ended Compartment Heat Sinks Considered (plus Cases 1, 2, 3, 4, 5)	33.3	36.7	10.1
7	Nominal Mass and Energy Releases (plus Cases 1, 2, 3, 4, 5, 6)	32.4	30.6	9.2
	Total Conservatism Represented by Above Assumptions for LOCA Transient	2.0	13.3	9.7
MSLB Sensitivity				
Case	Case Description	Peak Pressure (psig)		
	Evaluation Model	44.8		
8	Nominal Inputs and Correlations with Conservative Mass and Energy Releases and Stratification Bias	39.9		
	Conservatism Shown	4.9		

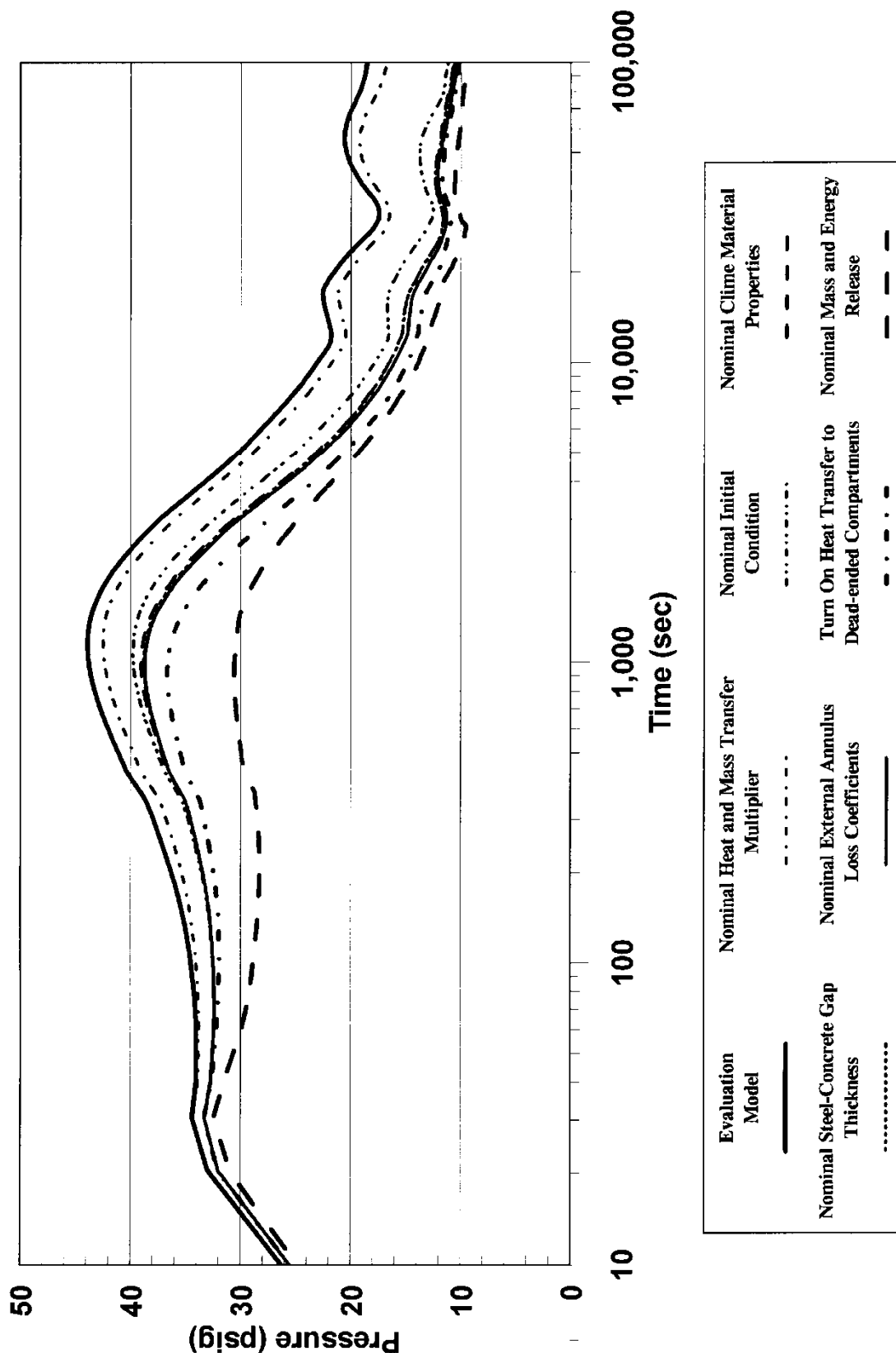


Figure 10-1. LOCA Sensitivities to Nominal Inputs and Correlations

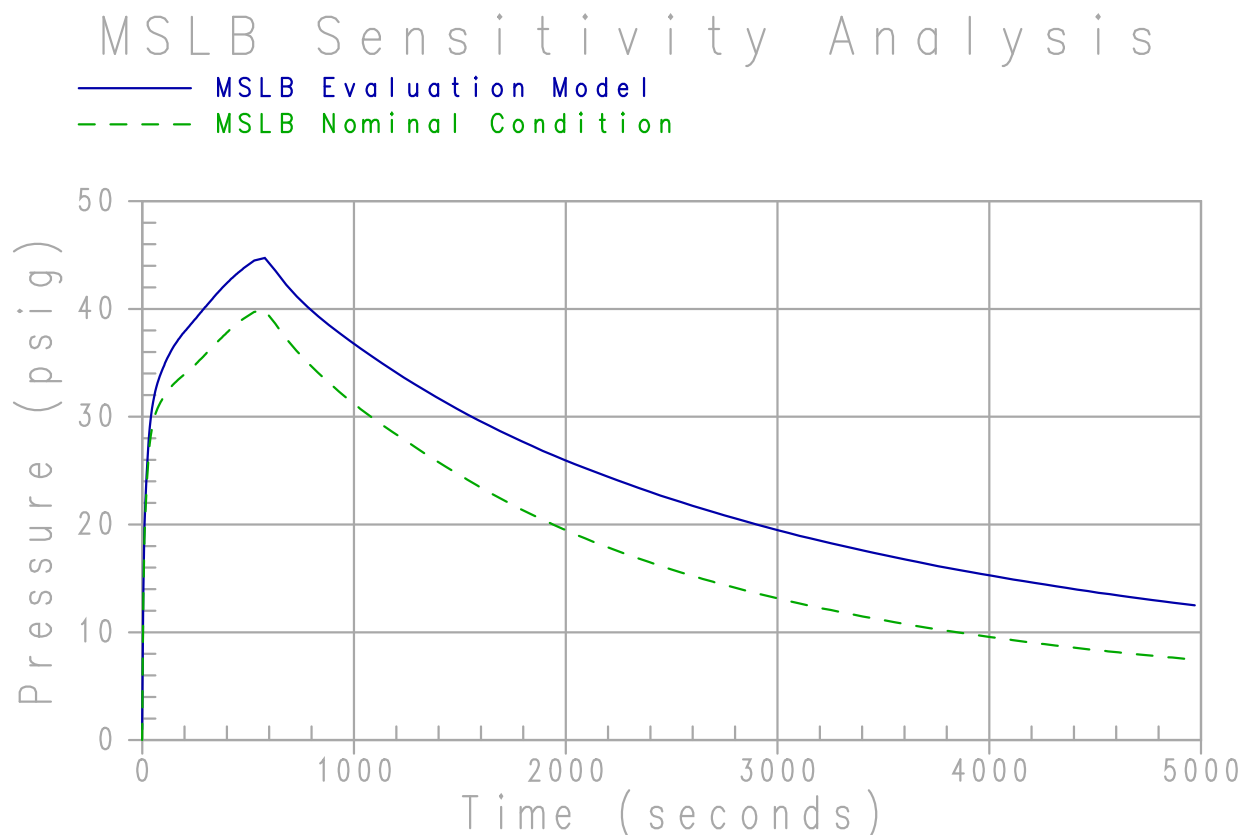


Figure 10-2. MSLB Sensitivity to Nominal Inputs and Correlations

10.2.1 Sensitivity Study Cases for LOCA

Case 1 considered nominal heat and mass transfer on the containment shell. Conservative multipliers have been applied to the heat and mass transfer coefficients calculated on the inside and outside surface of the containment shell in the Evaluation Model to ensure a conservative calculation. A multiplier of []^{a,c} is assumed on the inner surface, where free convection only is considered, and a multiplier of []^{a,c} is assumed on the outer surface, where mixed convection is considered. For this sensitivity, both multipliers were assumed to be 1.0, which represents a more nominal fit to the heat and mass transfer data with only a slight conservative bias remaining (Reference 10.1). The heat transfer regime assumptions were not changed.

The nominal heat and mass transfer modeling resulted in a 1.4 psi reduction in the post-blowdown peak pressure and a 2.1 psi reduction in the pressure at 24 hours. There was no significant impact on the peak blowdown pressure, since the heat removal from the shell has a small impact during this time period.

Case 2 considered the impact of nominal initial and ambient conditions. The parameters discussed in Section 5 were varied for this case, except they were set to a nominal set of conditions. The sensitivity case used initial conditions inside containment of 90°F, 14.7 psia, and 30 percent relative humidity as compared to 120°F, 15.7 psia, and 0 percent relative humidity in the Evaluation Model. The sensitivity case used ambient conditions of 70°F and 50 percent relative humidity compared to 115°F and 22 percent

relative humidity in the Evaluation Model. The sensitivity case PCS water temperature was set to 70°F compared to 120°F in the Evaluation Model. The initial temperature assumptions for the conductors in the containment and annulus were consistent with their environment. The individual contribution of each of these parameters is discussed in Section 5.

As discussed in Section 5, the internal containment conditions and the PCS water temperature have the most impact on containment pressure. This sensitivity case showed a 1.1 psi reduction in containment pressure during blowdown, a 2.7 psi reduction in the post-blowdown phase, and a 5.8 psi reduction at 24 hours.

Case 3 added the assumption of nominal material properties (thermal conductivity and emissivity) in the clime modeling. In the Evaluation Model (EM) the emissivities were reduced by 10 percent to bound the range found in the literature for the materials used, and the conductivity of the inorganic zinc paint was reduced by a factor of four to conservatively account for the effects of oxidation. In this sensitivity case the emissivities were increased to 0.9 (0.81 was used in the AP600 EM) and the conductivity of the inorganic zinc paint was set to its nominal value of 1.21 BTU/hr-ft-°F (0.302 BTU/hr-ft-°F was used in the AP600 EM). The factor of four decrease in the AP600 containment EM was a conservative factor based on engineering judgment rather than a mechanistic understanding of how thermal conductivity might change over time. The basis for the coatings thermal conductivity in the **AP1000** containment EM is addressed in Section 13.4.1.

The nominal clime property modeling resulted in a 0.8 psi reduction in the peak post-blowdown pressure and a 0.6 psi reduction in the pressure at 24 hours. There was no significant impact on the peak blowdown pressure, since the heat removal from the shell has a small impact during this time period.

Case 4 modified the assumption of the gap between the steel liner and the concrete on the applicable internal heat sinks.

The steel surface plates are one-half inch thick and are connected to each other by vertical trusses at 30-inch centers. The steel surface plates are connected to the concrete by embedding these trusses and also by six-inch long welded studs. The surface plates are stainless steel for the IRWST and refueling canal boundaries and are carbon steel elsewhere. The shear studs on the stainless steel plates are spaced at 10 inches horizontally and 8 inches vertically. The shear studs on the carbon steel plates are spaced at 10 inches horizontally and 9.6 inches vertically. The welded studs plus trusses result in a direct steel conduction path across the interface between the surface plate and the concrete. The contribution of this steel with much higher thermal conductivity has been neglected in the WGOTHIC Evaluation Model.

Concrete is placed into the structural modules and will initially bond to the surface plates. The wet concrete weight will load the steel plates and result in permanent outward deformation of the plates spanning between the trusses. Mechanical and thermal loading and shrinkage may break this bond due to relative motion. However, the welded studs will keep the surface plates in contact with the concrete at the stud locations and gaps between the studs would be very small. The Evaluation Model conservatively assumes a five mil gap for the steel-jacketed concrete heat sinks. A one mil gap was assumed for this sensitivity.

The results of this case show a 0.2 psi reduction in the post-blowdown peak pressure. The blowdown peak pressure was not affected significantly, since the heat capacity of the concrete has little impact on energy removal during this time. The pressure at 24 hours was not affected, since the heat sinks are effectively saturated at this time and the pressure is dictated by the balance between releases to the containment and heat removal via the PCS.

Case 5 included a modification to the pressure loss coefficient in the external annulus. The loss coefficient assumed in the Evaluation Model includes a 30 percent increase over the value derived from the test program. For this study, a loss coefficient 10 percent greater than measured was modeled.

The annulus loss coefficient has a small impact on the pressure, reducing the post-blowdown peak pressure by 0.1 psi and the pressure at 24 hours by 0.2 psi. There was no significant impact on the peak blowdown pressure since the heat removal via the PCS has a small impact during this time period.

Case 6 included the effects of heat sink utilization in the dead-ended compartments. As discussed in Section 9, condensation and convection on the heat sinks in the dead-ended compartments are not credited after blowdown to ensure a conservative treatment of their utilization. With only a small thermal asymmetry, convection would cause these heat sinks to continue to be exposed to steam after this time and would continue to provide a condensation surface. In this case, the structures were allowed to absorb energy based on conditions predicted by the WGOTHIC code. The WGOTHIC calculation limits the amount of steam entering these compartments, since circulation does not occur in lumped volumes, so the utilization of these heat sinks is not expected to be grossly over-predicted. It is therefore acceptable to include the utilization of these heat sinks in these sensitivities.

The additional heat absorption capability of the heat sinks in the dead-ended compartment, with an initial temperature of 90°F, resulted in a 2.0 psi reduction in the post-blowdown peak pressure. There was no change in the blowdown peak pressure since the Evaluation Model already considers condensation on these surfaces during blowdown. The reduction in the pressure at 24 hours was only 0.1 psi, since the heat sinks are effectively saturated at this time in both cases.

Case 7 includes the use of nominal mass and energy release rates. The nominal mass and energy release rates are compared to those used in the AP600 Evaluation Model (described in Section 4) in Figure 10-3 and Figure 10-4, respectively. The following modifications were made in the mass and energy release calculation:

- Nominal full-power temperatures and pressure without uncertainty
- Nominal RCS volume with no uncertainties (thermal expansion was considered)
- Core licensed power without adding 2 percent for calorimetric error
- Nominal core stored energy without adding 15 percent
- 1979 ANS decay heat standard without uncertainty for an 800 day average burnup

- Steam generator energy was assumed to be released over a period of one hour for the broken loop and two hours for the intact loop rather than thirty minutes and one hour, respectively
- The refill period was modeled
- No heat generation due to zirc-water reaction
- Nominal initial accumulator, CMT, and IRWST fluid temperatures were used in the post-blowdown releases

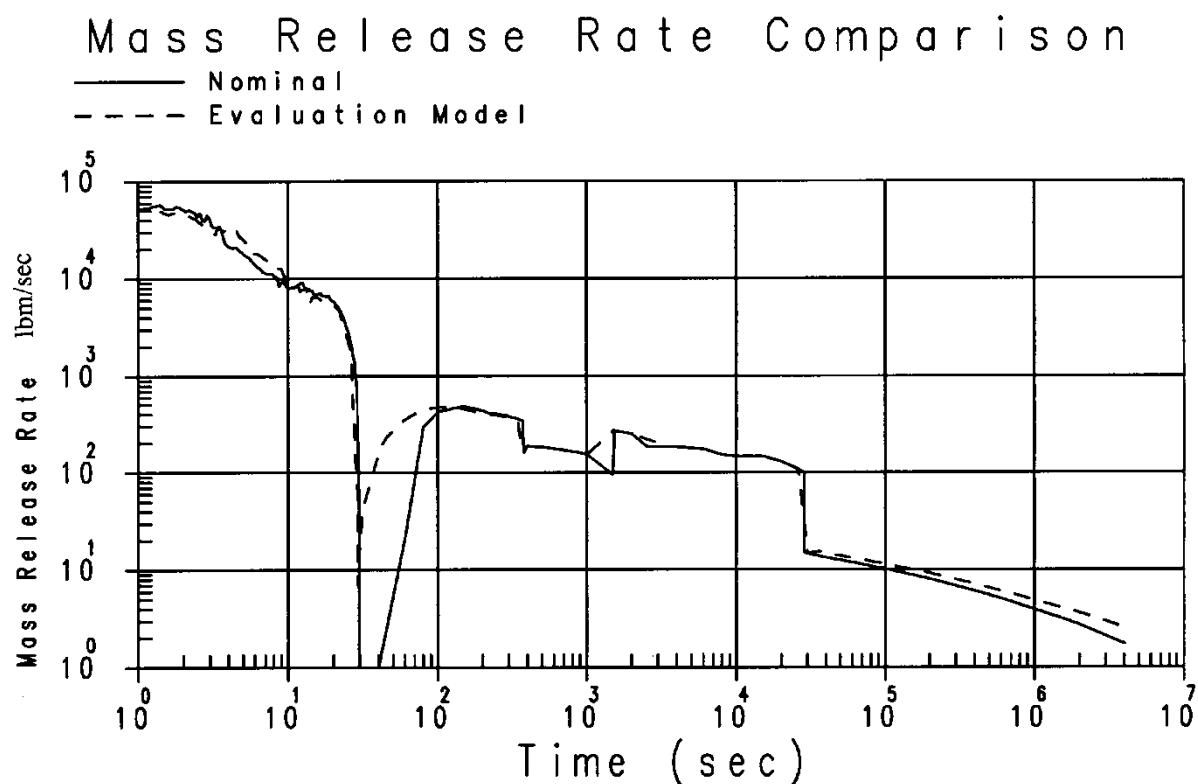


Figure 10-3. Comparison of Evaluation Model and Nominal Mass Release

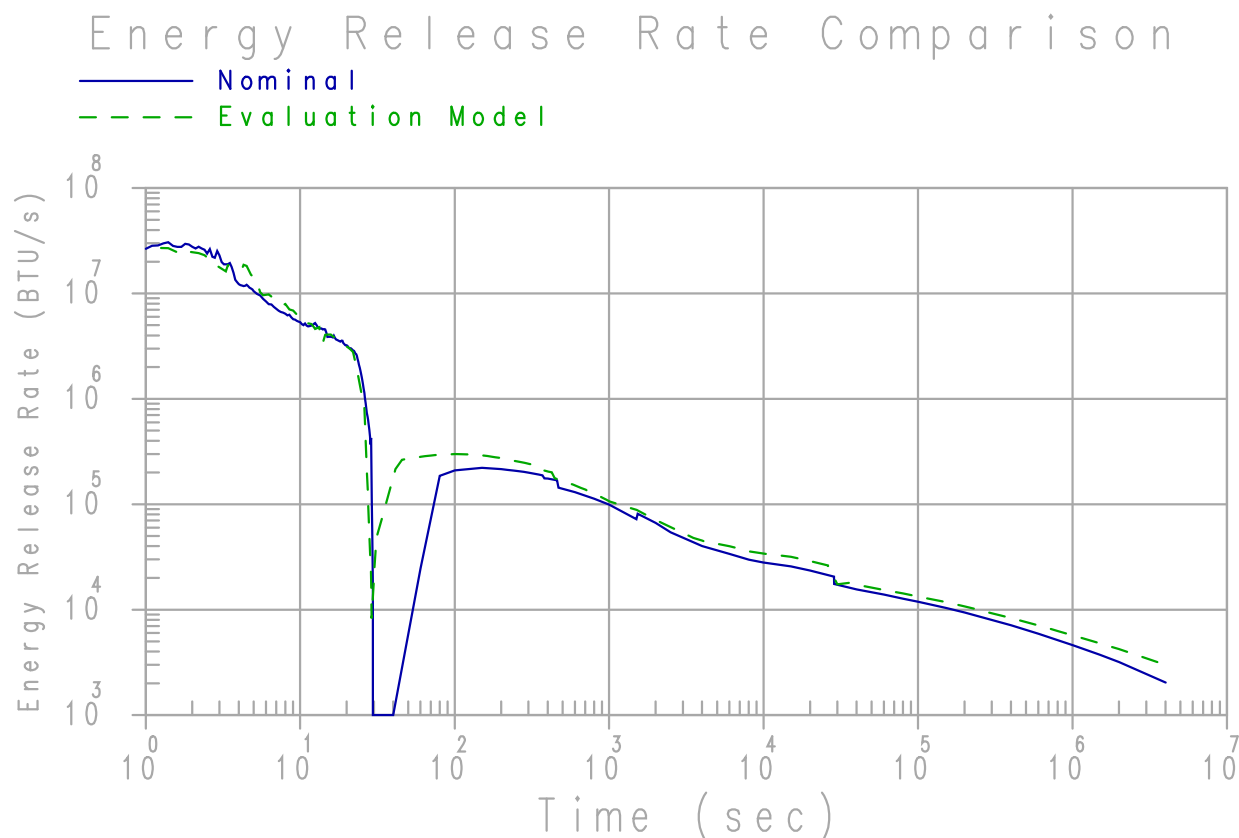


Figure 10-4. Comparison of Evaluation Model and Nominal Energy Release

This case demonstrates that the mass and energy input to the containment has the most impact on the resulting pressure and represents significant conservatism in the Evaluation Model. The blowdown peak pressure was reduced by 0.9 psi, the pressure during the post-blowdown period was reduced by 6.1 psi, and the pressure at 24 hours was reduced by 0.9 psi. The decrease in pressure is sufficient to shift the time of peak pressure for the entire transient from the post-blowdown phase to the blowdown phase. The large sensitivity during the post-blowdown phase is expected, since the mass and energy release models are deliberately biased to maximize the releases during this time in order to ensure that a conservative peak containment pressure is calculated.

10.2.2 Sensitivity Study Case for MSLB

A case was also run to provide quantification of the conservatism in some of the parameters for the MSLB transient. Case 8 included the nominal inputs and correlations embodied in cases 1 through 6 of the LOCA. Nominal mass and energy releases were not included in this calculation. The results of this case indicate that the conservative assumptions studied in the sensitivity case constitute 4.9 psi conservatism. Further reduction in containment pressure would result from the use of nominal mass and energy releases and a less conservative stratification bias. These results also do not credit the significant improvement to shell mass transfer, which would result from forced convection.

10.3 CONCLUSIONS

The results of the sensitivities in this section illustrate that the Containment Evaluation Model provides a conservative prediction of pressure. Some of the conservative nominal inputs and correlations in the Evaluation Model were removed to determine the impact on the calculated pressure for AP600 for the limiting LOCA and MSLB cases. These sensitivities are not intended to portray a best estimate calculation; other conservative features and modeling techniques have not been included that would further reduce the predicted pressure.

However, the conservatism represented by the parameters that were studied is significant. The LOCA cases investigated indicate a reduction of 2.0 psi during blowdown, 13.3 psi during the post-blowdown phase, and 9.7 psi at 24 hours. The summation of these cases switches the time of peak pressure from the post-blowdown period to the blowdown period. Comparison of the maximum pressures in the two cases shows 11.5 psi reduction in pressure. The MSLB case shows 4.9 psi margin due to nominal inputs included in this study. Incorporating other nominal conditions, such as mass and energy release rates and forced convection enhancements, would result in further pressure reduction.

10.4 REFERENCES

- 10.1 WCAP-14326, Revision 2, "Experimental Basis for the AP600 Containment Vessel Heat and Mass Transfer Correlations," April 1998.

11 TIMESTEP SENSITIVITY

11.1 INTRODUCTION

To establish WGOTHIC as an acceptable tool for use in the licensing process, it is necessary to perform a sensitivity to the time step size selected by the code. The timestep size determines how far the transient is permitted to progress from calculational step to calculational step. The algorithm that is used to determine the maximum allowable timestep size should produce a timestep value that results in a stable, suitably accurate solution without prohibitive computer execution times.

In the WGOTHIC code, the algorithm that is used to determine the maximum allowable timestep size is based on two stability criteria: the amount of time it would take to completely replace the mass within a given volume (Courant limit), and one half of the natural period of oscillation for a gravity-driven system (gravitational limit). In addition, the algorithm also includes limits on timestep growth, checks on nonphysical results, and limits on the rates of change of primary variables. These limits are all discussed in Reference 11.1, Enclosure 2, Section 12.7.

11.2 METHODOLOGY

Subroutine timstp.f in the WGOTHIC solver program contains the timestep selection algorithm. This subroutine calculates the maximum allowable timestep size that can be used in the WGOTHIC transient calculations.

Subroutine timstp.f was modified to perform the timestep sensitivity study. The maximum allowable timestep size was reduced to study the effect of using a smaller timestep on the results of the WGOTHIC transient calculations. Use of timesteps that are smaller than the maximum allowable value maintains numerical stability.

Two new versions of subroutine timstp.f were created; in WGOTHIC_S version 4.1.1, the maximum allowable timestep size was halved, and in version 4.1.2, it was quartered. The timestep selection process was not impacted by these changes and there were no other differences between the three versions of WGOTHIC_S.

The AP600 containment evaluation model input deck described in Section 4 was used for the timestep sensitivity analyses. The loss-of-coolant-accident (LOCA) transient was chosen since it contains both rapid and extended pressurization and depressurization transients. The LOCA is a long transient that relies on the PCS for a substantial amount of energy transfer to the environment.

11.3 RESULTS

The LOCA transient containment response analysis was performed with each of the three code versions. Table 11-1 indicates the number of calculational steps taken, the peak predicted pressure, and the predicted pressure at 24 hours for each code version.

Table 11-1. Timestep Sensitivity Results

WGOTHIC_S Code Version	Number of Computational Steps	Peak Pressure (psig)	Pressure at 24 Hours (psig)
Version 4.1 – 1.0* Δt	187380	43.85	18.86
Version 4.1.1 – 0.5* Δt	374414	43.76	18.88
Version 4.1.2 – 0.25* Δt	748680	43.72	18.85

The one-half timestep version of the code takes approximately twice the number of steps to complete the transient and the one-quarter-timestep version of the code takes about four times the number of steps to complete the transient. Since the timestep selection logic relies on the volume conditions at the end of each step, it is extremely difficult to get exactly twice or four times the number of steps. With the smaller timesteps, the changes in fluid conditions and other parameters used in the timestep selection process are smaller. The smaller changes permit larger timesteps to be allowed. As a result, slightly less than two times and four times the number of calculational steps are used in the modified versions of the code.

The reduced timestep versions predicted slightly lower peak pressures than the base version of the code. The predicted peak pressure for the quarter-timestep version was 0.04 psi lower than the one-half timestep version, and 0.13 psi lower than the full-timestep version. This indicates that the calculated peak pressure solution converges from above as the timestep is reduced.

In addition to the number of timesteps taken to complete the problem, the code output contains the number of times that a timestep was limited by some phenomenon. In all three cases, the timestep size was limited by either the phase change limit, the Courant limit, or the gravitational limit. Table 11-2 presents the number of times that the timestep was limited in each case.

Table 11-2. Timestep Limit Results

WGOTHIC_S Code Version	Courant Limit	Phase Change Limit	Gravitational Limit
Version 4.1 – 1.0 * Δt	4000	21	91612
Version 4.1.1 – 0.5 * Δt	8070	11	183305
Version 4.1.2 – 0.25 * Δt	16108	9	366639

During the pressurization phase of the LOCA transient, the timestep size was primarily limited by the Courant stability limit. This was not unexpected, since the volumetric break flow is so large during this phase. Since the circulation is primarily buoyancy-driven during the much longer depressurization phase, the time step size was primarily limited by the gravitational stability limit after the peak pressure was reached.

Note, the sum of the number of limiting timesteps in Table 11-2 does not add up to the total number of calculational timesteps given in Table 11-1 because, in some instances, the timestep size was not limited by any of the limits tracked in the output file. This could occur, for example, if the upper limit imposed by user input was less than the value calculated by the timestep selection algorithm.

The LOCA transient containment pressure predicted by each of the three code versions is shown in Figure 11-1. There is very little difference in the results. The transient results are further examined by comparing the differences in the predicted transient pressure from each of the three code versions. The percentage difference in the predicted transient pressure between the full-timestep version and the one-half-timestep version, and the percentage difference in the predicted transient pressure between the one-half timestep version and the one-quarter-timestep version is presented in Figure 11-2. The differences in the predicted transient pressure between successive versions of the code are very small (less than 1% over the entire 24-hour period).

11.4 SUMMARY

Two versions of WGOTHIC_S were created for this sensitivity study. The calculational timestep size was reduced to a value that was either one-half (Version 4.1.1) or one-quarter (Version 4.1.2) of the maximum allowable value calculated by the timestep selection algorithm.

A comparison of the predicted AP600 LOCA transient containment pressure response between the base version and the two versions created for the sensitivity study shows that there is very little difference in the results. Using smaller timesteps does not significantly affect the transient response. Therefore, the timestep selection algorithm produces a timestep value that results in a stable, suitably accurate solution.

Based on the timestep study results presented herein, it is concluded that the timestep selection logic for WGOTHIC_S is acceptable.

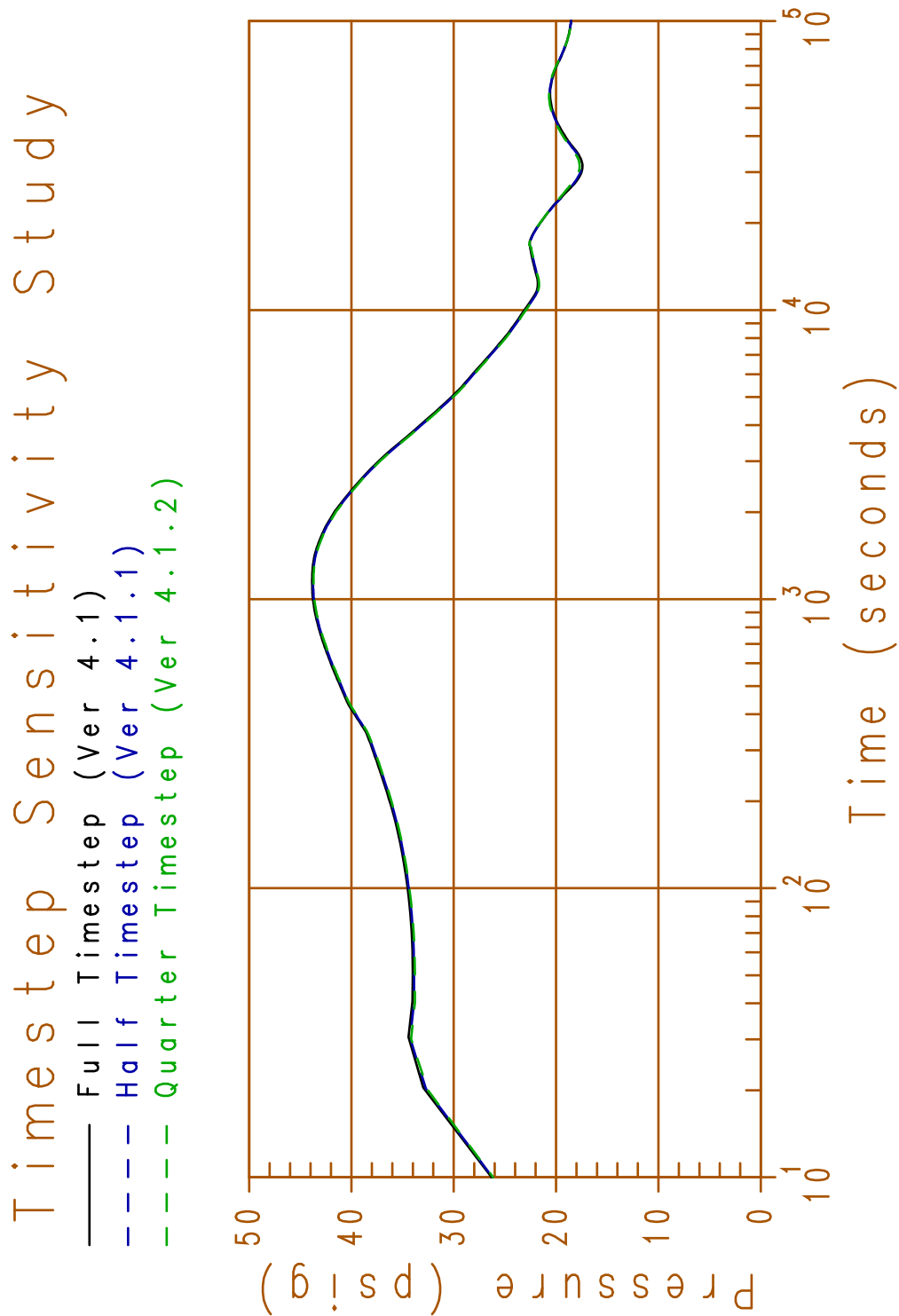


Figure 11-1. AP600 Containment LOCA Transient Pressure Prediction with Full, One-Half, and One-Quarter Timesteps

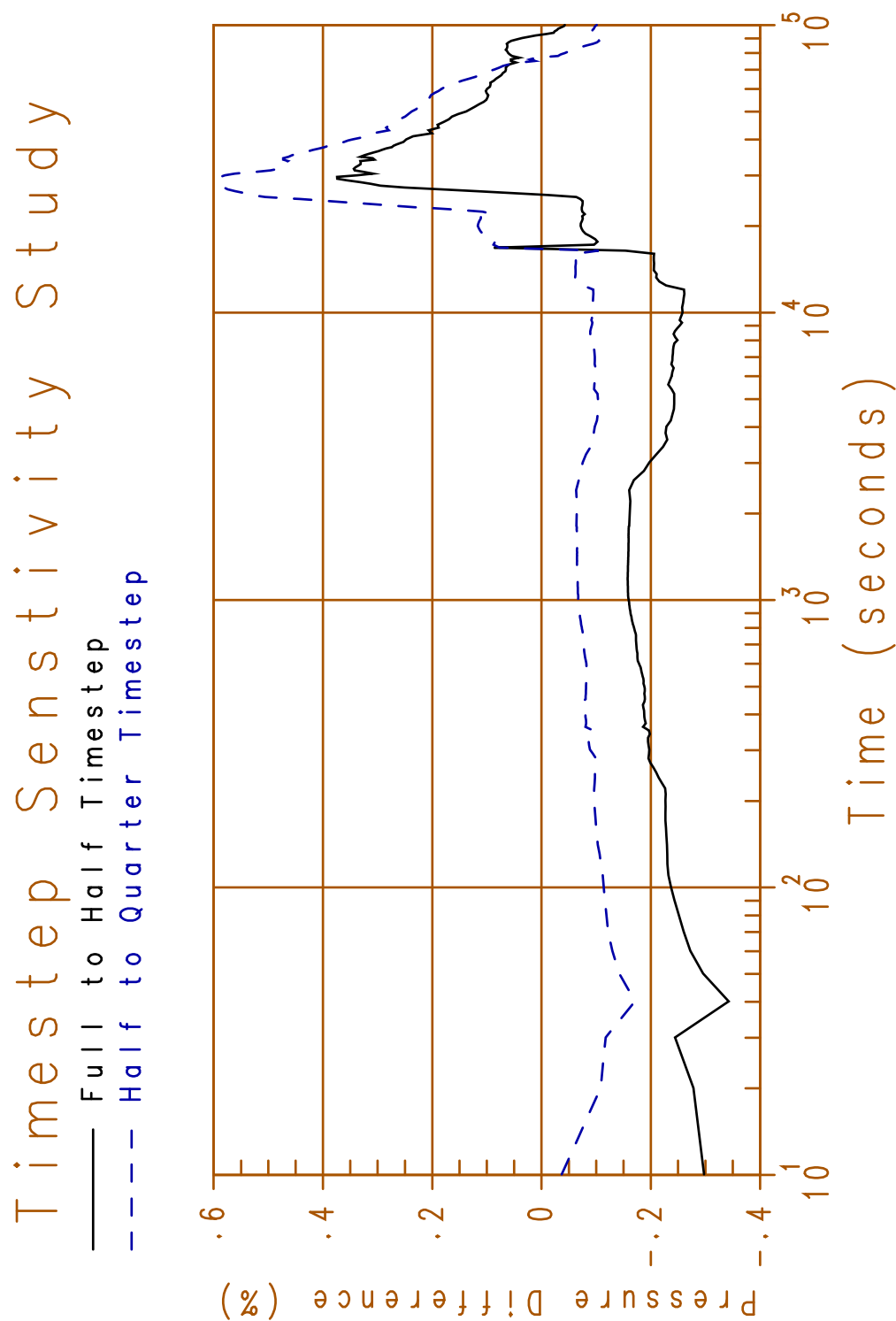


Figure 11-2. AP600 Timestep Comparison, Percentage Difference in Predicted Pressures between Successive Code Versions

11.5 REFERENCES

- 11.1 Westinghouse Letter NTD-NRC-95-4563, B. A. McIntyre to Quay (NRC), "GOTHIC Version 4.0 Documentation," September 21, 1995.

12 SENSITIVITY TO CLIME NODING

12.1 INTRODUCTION

This section provides background associated with the WGOTHIC clime model, a statement of the issue associated with the application of the clime methodology, a description of the approach developed and taken to address the issue, a summary of the results of the analyses and the conclusions drawn from a review of those analyses.

12.1.1 Background

The GOTHIC code (References 12.1 and 12.2) is a state-of-the-art program for modeling multi-phase flow for containment analysis. The code solves the integral form of the conservation equations for mass, momentum, and energy for multi-component, two-phase flow. The conservation equations are solved for three fields: continuous liquid, liquid drops, and a steam/gas phase. The three fields may be in thermal non-equilibrium within the same computational cell. Relative velocities are calculated for each field, as well as the effects of two-phase slip on pressure drop. Heat transfer between the phases, surfaces, and the fluid are also allowed.

As described in Section 3 of this report, the GOTHIC containment analysis code was modified by Westinghouse to include mechanistic convective heat and mass transfer correlations, a liquid film tracking model, a one-dimensional wall conduction model, and wall-to-wall radiant heat transfer to model heat removal by the PCS. The code with these modifications is called Westinghouse-GOTHIC, and is abbreviated as WGOTHIC.

A solution technique that includes wall-to-wall radiation at the conditions expected for the AP600 and **AP1000** plant designs necessitates a close coupling of the participating walls. This coupling is accomplished by assigning boundaries that define the portions of the various walls that radiate to one another. Consistent with the basic formulation implemented for the GOTHIC code that considers conductors or heat sinks to be energy and mass sink or source terms, code modifications that include wall-to-wall radiant heat transfer can be thought of as the addition of a special type of conductor group. This special conductor type or group consists of a set of walls that radiate to each other and interface with GOTHIC fluid cells through mass and energy source terms. The term *clime*, meaning *region*, is used to differentiate and distinguish this special conductor type from those already existing in GOTHIC terminology.

A three-conductor clime is shown schematically in Figure 12-1. For the containment model, a clime is a horizontal slice of the containment structure consisting of the steel shell, the baffle, and the shield building and liquid films which may form on those solid surfaces, and representing the following transport processes:

- The heat and mass transfer source terms from the containment volume to the shell
- Liquid film mass and energy conservation and thermal resistance on shell, baffle, or shield building surfaces

- Conduction through the shell
- Heat and mass transfer source terms from the exterior shell to the riser air flow channel
- Radiation from the exterior shell to the interior baffle
- Heat and mass transfer source terms to the interior baffle from the riser air flow channel
- Conduction through the baffle
- Heat and mass transfer source terms from the exterior baffle to the downcomer air flow channel
- Radiant heat transfer from the exterior baffle to the interior surface of the shield building
- Heat transfer source terms to the interior surface of the shield building from the downcomer air flow channel
- Conduction through the wall of the shield building
- Both radiant and convective heat transfer from the exterior surface of the shield building to the environment

As shown schematically in Figure 12-1, the internal containment vessel volume, riser air flow channel volume, downcomer air flow channel volume, and environment volume are separate computational cells or fluid volumes in the GOTHIC model. The shell, baffle, and shield building walls are one-dimensional conductors representing solid wall structures between the computational cells. These conductors are further subdivided into regions of different materials with different numerical mesh sizes.

The climes are stacked vertically through the PCS to model the effects of changing properties both inside and outside the containment shell. Usually there are at least two stacks of climes a wet stack and a dry stack. The only difference between a wet and dry stack is that a time-dependent, water flow rate boundary condition is specified for each conductor surface of the top clime in a wet stack. Because condensation can occur on either wet or dry conductor surfaces, an initially dry stack of climes could contain some wet conductor surfaces and/or a partially wet conductor surface due to condensation. Likewise, an initially wet stack of climes could contain some dry conductor surfaces and/or a partially dry conductor surface due to evaporation.

The user must specify values for the area and circumferential perimeter for each conductor of each clime in both the wet and dry stacks. The input values for the area and circumferential perimeter for the clime conductors in the wet stacks are based on measurements of the water coverage from the full-scale water distribution tests. The water coverage input calculation method for the containment Evaluation Model is described in Section 7.

The WGOTHIC clime model calculates the temperature, flow rate, and thermal resistance of the water films on the various conductor surfaces of a clime. Liquid mass is conserved whenever the film reaches the bottom clime in a stack or a conductor surface dries out. The clime model takes the film flow rate

from each conductor surface of the previous clime in the stack as input, then adds the local condensation rate, or subtracts the local evaporation rate to determine the output water flow rate on each of its corresponding conductor surfaces. Any liquid film remaining on the conductor surfaces of the last clime in a stack is added to the liquid field of the WGOTHIC cell in contact with the conductor surface, or an alternate drain cell specified by user input.

Dryout occurs when either the film flow rate is low enough or the heat flux is high enough to result in complete evaporation of the film before it can exit the conductor. The clime model calculates the evaporation heat and mass transfer and the location of the dryout elevation; the remainder of the conductor surface is treated as a dry surface.

The details of the clime equations and integration into the GOTHIC code are described in Sections 3.4 and 3.5.

12.1.2 Problem Statement

Simply stated, the objective of this effort is to demonstrate that the clime calculations are insensitive to increased numerical resolution relative to the noding pattern employed in the Evaluation Model.

12.1.3 Approach

The approach taken to address the problem statement given above is to:

- Perform sensitivity calculations using a simple two-channel annulus model with a constant temperature boundary condition. The simplified model is used to better isolate effects of clime noding. For this task, the number of climes in the model will vary from 4 to 16. Although not intended to simulate or scale to the AP600 or **AP1000** plants, this two-channel annulus model will provide for thermo-fluid conditions similar to those expected in the annulus of the passive plant, i.e., evaporation into a buoyancy-driven air flow.
- Perform sensitivity calculations with an AP600 containment model for which the number of climes, stacks, and conductor layers are varied to confirm the results of the simpler models.

12.1.4 Selected Parameters

The following thermal-hydraulic parameters are used in evaluating the comparison of various model predictions:

- Containment pressures (for the AP600 model only)
- Temperatures – cooling air and liquid film
- Heat fluxes and/or heat rates from the shell

These parameters are primary indicators of the heat transfer process and were selected as a basis for evaluating the sensitivity of the calculated results to noding patterns.

12.1.5 Success Criteria

The noding pattern used for a model may affect the results of a calculation. For the purpose of this study, the following success criteria are used to evaluate the significance of change in calculated results with increasing detail in clime noding:

- Success Criteria: The change between results calculated with two noding patterns is defined to be negligible; if:
1. The variation in results between two successive noding patterns is less than $[\quad]^{a,c}$ percent.
 2. The variation in results from successively finer noding patterns is decreasing.

[

$]^{a,c}$

Thus, the criteria listed above establish that the variation between results obtained from different noding patterns must be small, and the variation must be converging as the noding pattern is increased.

12.2 MODEL DESCRIPTIONS

The sensitivity of the thermo-fluid calculations of the WGOTHIC clime methodology to the number of nodes associated with the flow channel was investigated using a two-channel annulus model. This section presents descriptions of the model and the boundary conditions used in this investigation. This simplified two-channel model is not intended to scale to the plant. It is a simplified model with fixed boundary conditions that allows study of changes caused by clime noding detail. The fixed boundary conditions allow direct comparison of clime heat removal predictions. A detailed comparison of the results calculated for this model to those calculated in the AP600 or **AP1000** is not meaningful. However, the trends for the simple model, relative to the success criteria, are applicable to the passive plant design, as confirmed with the sensitivity calculations using an AP600 containment model as a basis (Section 12.3.2).

12.2.1 Simple Annulus Clime Model

Model Description

A simple two-channel model was developed to study the effects of increasing the number of climes over a wide range of film flow rates and film temperatures and is shown schematically in Figure 12-2. The modeled heated height was $[\quad]^{a,c}$ feet. This height was chosen to promote the calculation of velocities in the model representative of the lower bound of the range expected for AP600. The number of climes (and corresponding annulus cells) in the heated section of the model varied between 4 and 16. Figure 12-3 presents the noding structure for the 8 clime model. The noding pattern for the 4 and 16 clime models is similar to that of the 8 clime model, having one-half and double the number of axial cells, respectively.

The annulus clime model is connected to two stacks of lumped parameter cells, similar to the Evaluation Model. One stack represents the downcomer volume and the other represents the riser volume. The volumes of the riser and downcomer are []^{a,c} cubic feet and []^{a,c} cubic feet respectively. The downcomer volume was arbitrarily selected to be about twice the value of the riser volume. A set of equally spaced elevation planes crosses both the riser and downcomer to form the two stacks of lumped parameter cells. The volume, height, and vertical flow area of each cell in the riser stack and each cell in the downcomer stack is the same.

A natural draft flow of air from the downcomer through the riser develops as the riser channel is heated. Friction acts to retard the increase in air velocity. Except for the turning location and exit, the friction lengths for each flow path are equal to the cell height. The friction lengths at the riser entrance and exit are set to one half the cell height to conserve the total friction length and fL/D values between models. Loss coefficients of []^{a,c} at the downcomer entrance and []^{a,c} at the riser outlet are used to model the form losses representative of a contraction and an expansion, respectively.

For the 8 clime model shown in Figure 12-3, a thermal conductor located within the heat source (Volume 9), provides a []^{a,c} constant temperature boundary condition for the model. A single stack of climes is used to thermally connect the heat source with the riser and downcomer volumes. There is one clime per cell in the riser. An additional clime at the bottom of the stack is used to model the runoff film flow. The last clime in the stack is connected to three dummy volumes. This modeling is used to allow the runoff from the last clime to collect in the drain volume (Volume 18) without affecting the heat removal in the active section of the annulus.

Each clime has two conductors; the first one represents a []^{a,c} thick steel plate and the other represents an acrylic cover. The perimeter and heat transfer area is the same for each conductor on all climes.

To prevent the drain volume from overflowing, it is connected to a flow rate boundary condition. The boundary flow rate for the drain volume is controlled with trips based on the liquid level in the drain volume.

These features were also included in both the 4 and 16 clime models.

Boundary Conditions

Four cases were considered for this study. The independent variables for each case are listed in Table 12-1.

Table 12-1. Input Parameters for Annulus Clime Model Sensitivity Study

a,c

The film boundary conditions are selected to cover a range of temperatures and flow rates considered typical for the passive plant. For Case 4, the film mass flow rate is reduced to force the prediction of dryout about midway down the plate. Both the downcomer and riser are connected to a fixed pressure boundary set at []^{a,c} psia.

12.2.2 AP600 Containment Model

A schematic of the AP600 containment model clime noding pattern is shown in Figure 12-24. The dashed lines represent divisions between the []^{a,c} climes (and cells) in the annulus.

The AP600 clime noding sensitivity cases were performed using a preliminary Evaluation Model input deck. The differences between the AP600 containment model that was used for these sensitivity studies and the Evaluation Model, as described in Section 4, are irrelevant to the clime noding sensitivity study because each of the sensitivity cases used this same AP600 containment model as its basis. The major differences between the sensitivity model and the Evaluation Model, are summarized below:

- The mass and energy releases in the sensitivity model are lower during the peak pressure phase and higher during the long-term phase. The different phases of the LOCA containment pressurization transient are defined in Section 3.4.2.2 of Reference 12.3. []^{a,c}

] ^{a,c}

- The PCS flow rate input is higher in the sensitivity model for the first three hours, but lower for the remainder of time. [

]^{a,c}

- The internal nodding structure is different. [

]^{a,c}

- The annulus initial conditions in the sensitivity model (15.7 psia, 120°F) are different from those in the Evaluation Model (14.7 psia, 115°F).

- [

]^{a,c}

- The annulus loss coefficients are lower in the sensitivity model. [

]^{a,c}

The base case AP600 containment model was modified for the clime nodding sensitivity study to examine the following effects:

- Doubling the number of climes (or vertical segments) from []^{a,c} to []^{a,c} (see Figure 12-25)
- Doubling the number of stacks (or radial segments) from []^{a,c} to []^{a,c} (see Figure 12-26)
- Doubling the number of numerical mesh points through the thickness of the clime conductors (see Figure 12-27)

As with the simple annulus model nodding study described in Section 12.2.1, the heat transfer parameters identified in Section 12.1.4 were used to evaluate the sensitivity of the calculations to changes in the nodding pattern used for the calculations. In addition, plots comparing the annulus air pressure, density and velocity profiles are included for the vertical clime nodding sensitivity comparison.

12.3 RESULTS

12.3.1 Simple Annulus Clime Model

The four test cases described in Table 12-1 of Section 12.2.1 were run using WGOTHIC Version 4.1. Transient calculations were performed until the time when little or no change in one or more governing parameters (pressure, film temperature, etc.) was predicted. Since constant boundary conditions were used, a steady-state solution was eventually reached for each case. All four cases were run out to 2000 seconds of transient time.

Plots of the predicted heat removal rate from the plate surface, shown in Figures 12-4 through 12-7, indicate that the four cases were close to steady-state conditions at the end of the 2000-second transient period. The difference between the heat rejection rates of the 4 and 8, and 8 and 16 clime models is shown in Figures 12-8 through 12-11. From these plots, it is noted that the predicted transient heat removal rate is quite insensitive to the level of clime noding detail; a change of less than 1 percent is observed for increasing the axial nodal pattern from 4 to 8 climes. The difference observed when the axial nodal pattern is increased from 8 climes to 16 is even less.

A comparison of the predicted heat removal rate from the plate surface at the end of the transient is shown in Table 12-2.

Table 12-2. Predicted Heat Removal Rates for Various Clime Noding Schemes

a,c

For the first three tests (all dry or all wet), the steady-state heat removal rate increases slightly as the number of climes is doubled from 4 to 8. Doubling the number of climes from 8 to 16 increases the heat removal rate again, but by a much smaller amount. Therefore, for these cases, the predicted heat removal rate is converging from below.

For test case 4 (half wet), the steady-state heat removal rate decreases slightly as the number of climes is doubled from 4 to 8. Doubling the number of climes from 8 to 16 also decreases the heat removal rate, but by a smaller amount. Further comparisons show that the predicted heat removal rate decreases on the top []^{a,c} feet, but increases on the bottom []^{a,c} feet of the model surface as the number of climes is increased. The decrease on the top []^{a,c} feet is larger than the increase on the bottom []^{a,c} feet. Therefore, the total predicted heat removal decreases as the number of climes increases in case 4. At the low flow rate for this test, the increased resolution of the subcooled heat flux with more climes yields a slightly lower estimate of the predicted heat removal rate.

Figures 12-12 through 12-15 compare the calculated axial heat flux profiles, and Figures 12-16 through 12-19 compare the axial film temperature profiles at time $t = 2000$ seconds, where “film temperature” for the dry case represents the surface temperature. Note, the data from the 8 and 4 clime models is represented as 2 and 4 points respectively on the plots to match the 16 points from the 16 clime model.

For the wet tests, smoother axial heat flux and film temperature profiles are calculated as the number of climes increases. In the cold film tests (cases 2 and 4), the heat flux decreases and film temperature increases as the film flows from the first clime down. In the hot film test (case 3), the heat flux increases and the film temperature decreases as the film flows from the first clime down. The heat flux remains constant after the film reaches a temperature at which evaporation dominates. For the partially wet test (case 4), the heat flux decreases rapidly and the film temperature increases to the dry surface temperature in the clime where dryout occurs.

The heat flux and surface temperature profiles are adequately represented with either 4, 8, or 16 climes for the dry test (case 1). The heat flux decreases linearly from the entrance (last clime) to the exit (first clime) of the channel while the surface temperature remains essentially constant.

Figures 12-20 through 12-23 compare the calculated axial air temperature profiles at time $t=2000$ seconds. In all tests, the air temperature increases from the entrance (last clime) to the exit (first clime) of the heated channel.

12.3.2 AP600 Containment Model

The long-term mass and energy release input and PCS flow rate input were not finalized at the time the sensitivity cases were made, therefore, sensitivity results are presented up to the time the IRWST inventory was depleted (43500 seconds). This was a sufficient transient duration to determine if the AP600 containment model would be sensitive to doubling the number of climes, the number of stacks, or the conductor mesh points.

Clime Sensitivity Results

The number of climes and volumes in the annulus of the base AP600 containment model were doubled (while maintaining the same total volume and heat transfer area) and the case was run using WGOTHIC Version 4.1. Figure 12-28 shows a comparison of the transient pressure for the double clime case with the base case. There is essentially no difference between the two cases. Figures 12-29 and 12-30 present the axial wet heat flux profile for the []^{a,c} and []^{a,c} clime cases at transient time $t=0$, 30, 1500, and 43500 seconds. The profiles are similar, but the wet heat flux profile for the []^{a,c} clime case has better resolution of the subcooled region at the top of the dome at 1500 seconds and of the dryout elevation at 43500 seconds.

Figures 12-31 and 13-32 present the axial dry heat flux profile for the []^{a,c} and []^{a,c} clime cases at transient time $t=0$, 30, 1500, and 43500 seconds. The profiles are similar.

Figures 12-33 and 12-34 present the axial external film temperature profile for the []^{a,c} and []^{a,c} clime cases at transient time t=0, 30, 1500, and 43500 seconds. The profiles are similar, but the film temperature profile for the []^{a,c} clime case has better resolution of the subcooled region at the top of the dome at 1500 seconds and of the dryout elevation at 43500 seconds.

Figures 12-35 and 12-36 present the axial external dry surface temperature profile for the []^{a,c} and []^{a,c} clime cases at transient time t=0, 30, 1500, and 43500 seconds. The profiles are similar.

Figures 12-37 and 12-38 present the axial annulus air pressure profile for the []^{a,c} and []^{a,c} clime cases at transient time t=0, 30, 1500, and 43500 seconds. The pressure quickly decreases to the boundary condition value (14.7 psia) in both cases. The pressure at the bottom of the annulus is slightly higher than at the top due the density head.

Figures 12-39 and 12-40 present the axial annulus air temperature profile for the []^{a,c} and []^{a,c} clime cases at transient time t=0, 30, 1500, and 43500 seconds. The downcomer and riser air temperatures eventually establish similar profiles. The air temperature increases slightly as it flows downward, then increases rapidly (by about 30°F at 1500 and about 18°F at 43500 seconds) in the riser as it flows upward.

Figures 12-41 and 12-42 present the axial annulus air density profile for the []^{a,c} and []^{a,c} clime cases at transient time t=0, 30, 1500, and 43500 seconds. The profiles are similar.

Figures 12-43 and 12-44 present the axial annulus air velocity profile for the []^{a,c} and []^{a,c} clime cases at transient time t=0, 30, 1500, and 43500 seconds. The profiles are similar. The air velocity decreases at the top of the riser as it enters the large open area above the dome.

Comparisons of the transient heat rate and heat releases integrated over height of the model are shown in Figures 12-45 and 12-46. Again, there is essentially no difference between the two cases.

By this comparison, it is concluded that the transient pressure and shell heat removal rates calculated by the AP600 containment model are not sensitive to the number of climes.

Stack Sensitivity Results

The number of stacks of climes in the base model were doubled (while maintaining the same total heat transfer area) and the case was run using WGOTHIC, Version 4.1. Figure 12-47 shows a comparison of the transient pressure for the double stack case with the base case. There is essentially no difference between the two cases. Comparisons of the transient heat rate and heat releases integrated over the height of the model are shown in Figures 12-48 and 12-49. Again, there is essentially no difference between the two cases.

These comparisons show the transient pressure and shell heat removal rate calculated by the AP600 containment model are not sensitive to the number of stacks.

Clime Conductor Numerical Mesh Point Sensitivity Results

The number of numerical solution mesh points through the thickness of each of the three conductors (shell, baffle, and concrete) that make up each clime in the base model was doubled and the case was run using WGOTHIC Version 4.1. Figure 12-50 shows a comparison of the transient pressure for the double mesh case with the base case. There is essentially no difference between the two cases. Comparisons of the transient heat rate and heat releases integrated over the height of the model is shown in Figures 12-51 and 12-52. Again, there is essentially no difference between the two cases.

From these comparisons, it is concluded that the transient pressure and shell heat removal rates calculated by the AP600 containment model are not sensitive to the number of numerical mesh points within the conductors that comprise each clime.

12.4 SUMMARY

12.4.1 Simple Annulus Clime Model Noding Study

A two-channel annulus model was exercised over a range of film flow rates, and film temperatures with the code calculating air velocities associated with natural draft heating. For the cases considered, increasing the number of climes was observed to have no significant effect on the predicted heat removal rate. That is, the predicted heat removal rate was insensitive to the number of clime nodes used in the model. The predicted heat removal rate converges in all cases considered. Increasing the number of climes resulted in smoother axial heat flux and film temperature profiles for the wet tests. Adequate axial heat flux and temperature profiles were predicted without increasing the number of climes for the dry cases.

12.4.2 AP600 Containment Model Clime Noding Study

Using an AP600 containment model similar to, but not exactly the same as the Evaluation Model, the effect of doubling the number of clime nodes, doubling the number of stacks, and doubling the number of conductor mesh points was studied. In each case, code calculations were found to be unaffected by the variations in the model features.

These studies demonstrate that results obtained with the AP600 containment model are not sensitive to changes in the clime and annulus noding. Therefore, it is concluded that []^{a,c} climes are adequate to predict the PCS performance for the Evaluation Model.

12.5 REFERENCES

- 12.1 Westinghouse Letter NTD-NRC-95-4563, B. A. McIntyre to T. R. Quay (NRC), "GOTHIC Version 4.0 Documentation," September 21, 1995.
- 12.2 Westinghouse Letter NTD-NRC-95-4462, N. J. Liparulo to T. R. Quay (NRC), EPRI Report RA-93-10, "GOTHIC Design Review, Final Report," May 15, 1995.
- 12.3 WCAP-14812, Revision 2, "Accident Specification and Phenomena Evaluation for AP600 Passive Containment Cooling System," April 1998.

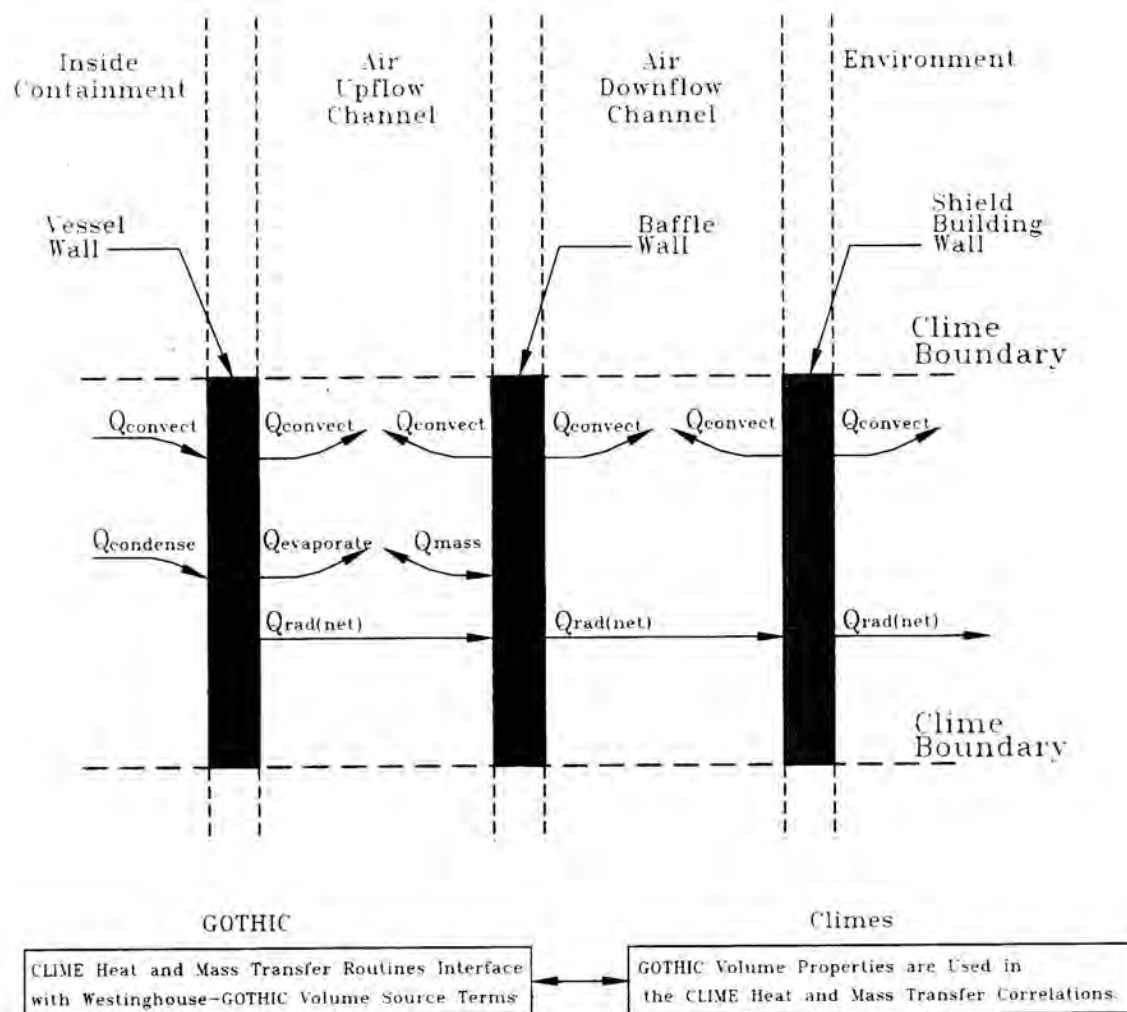


Figure 12-1. Westinghouse-GOTHIC Clime Wall Source Team Models

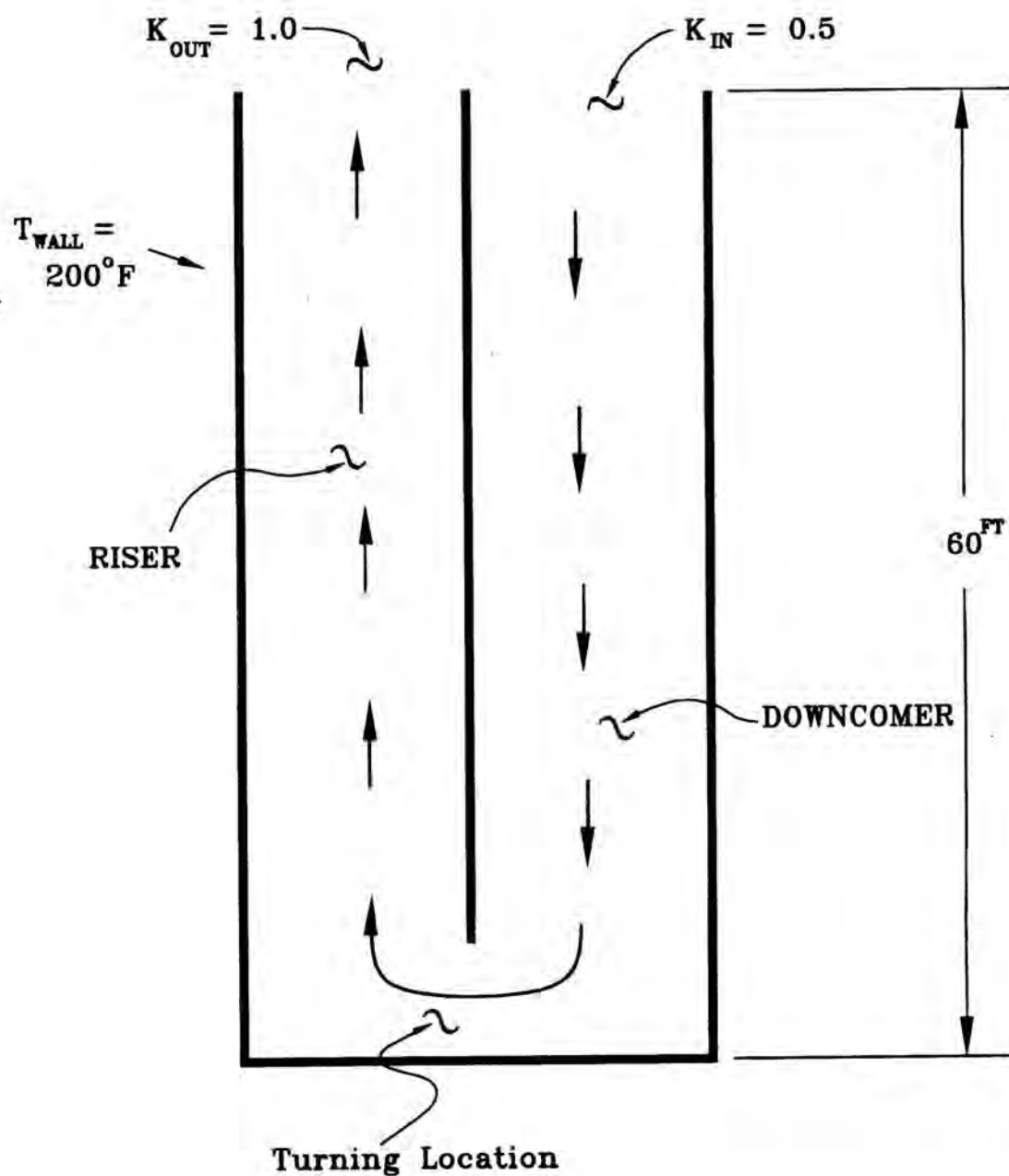


Figure 12-2. Simplified Line Diagram of Annulus Clime Model

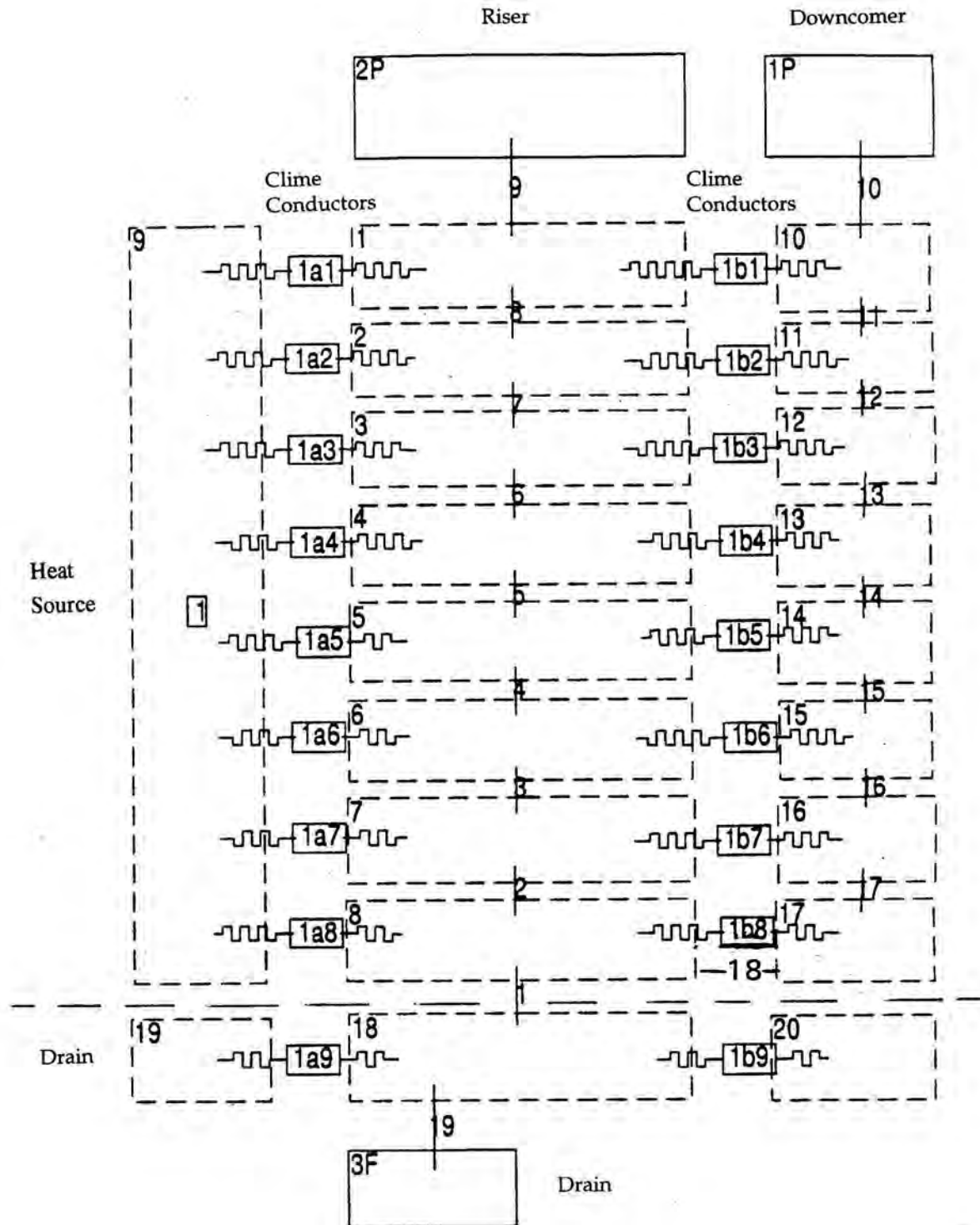


Figure 12-3. Noding Diagram, 8 Clime Node Model

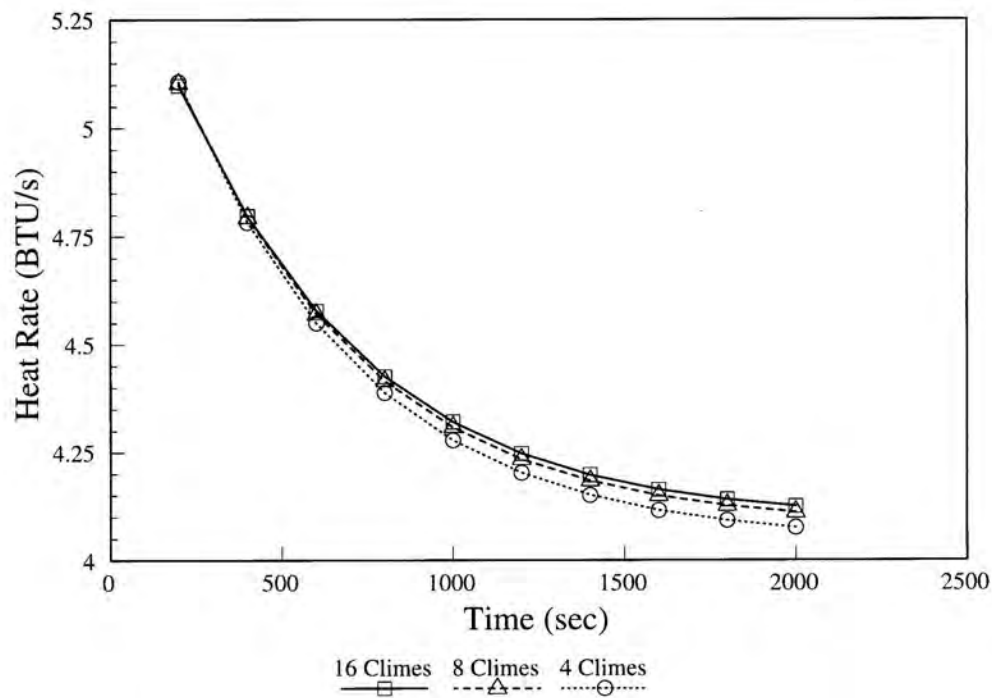


Figure 12-4. Comparison of Transient Heat Transfer Rates; Case 1

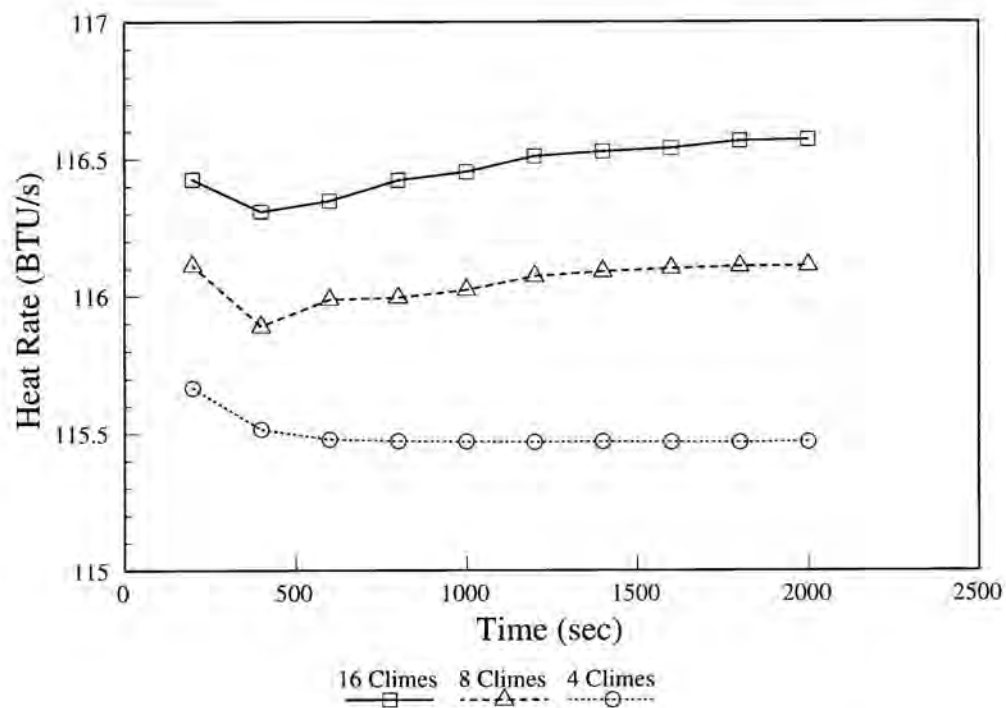


Figure 12-5. Comparison of Transient Heat Transfer Rates; Case 2

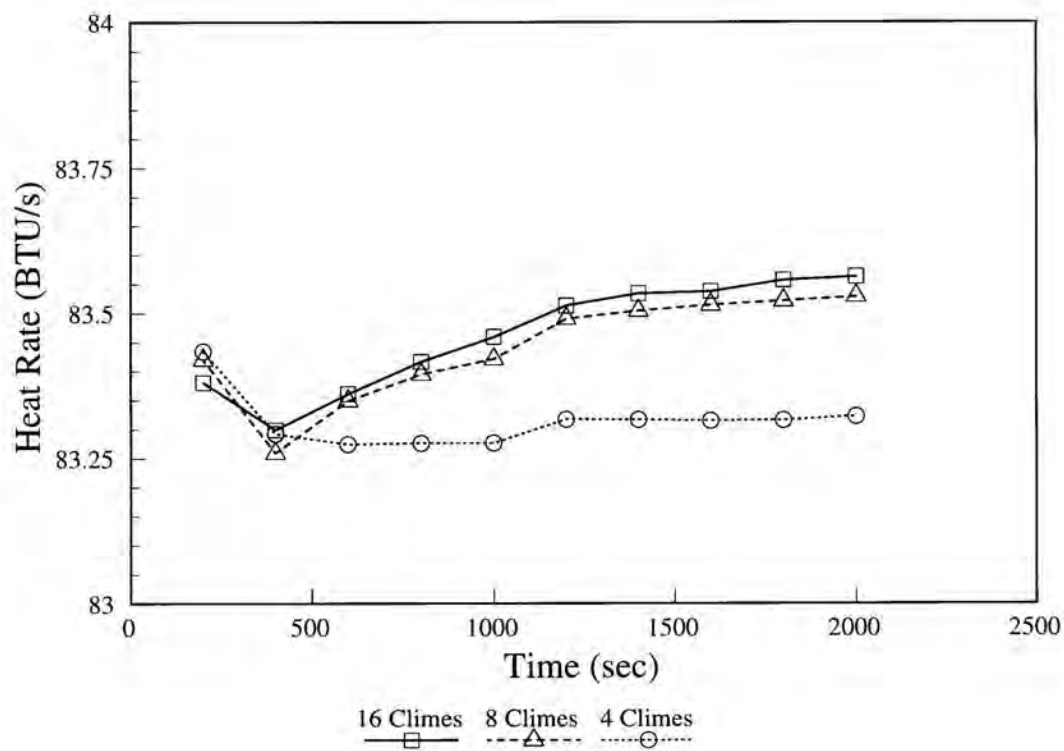


Figure 12-6. Comparison of Transient Heat Transfer Rates; Case 3

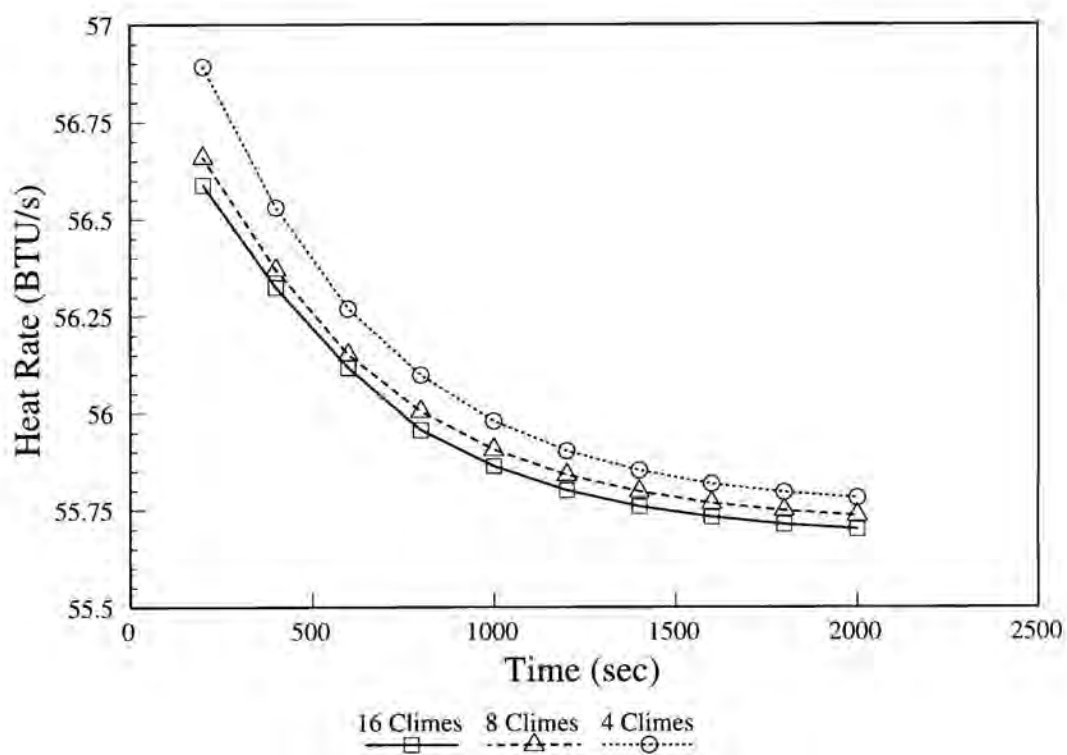


Figure 12-7. Comparison of Transient Heat Transfer Rates; Case 4

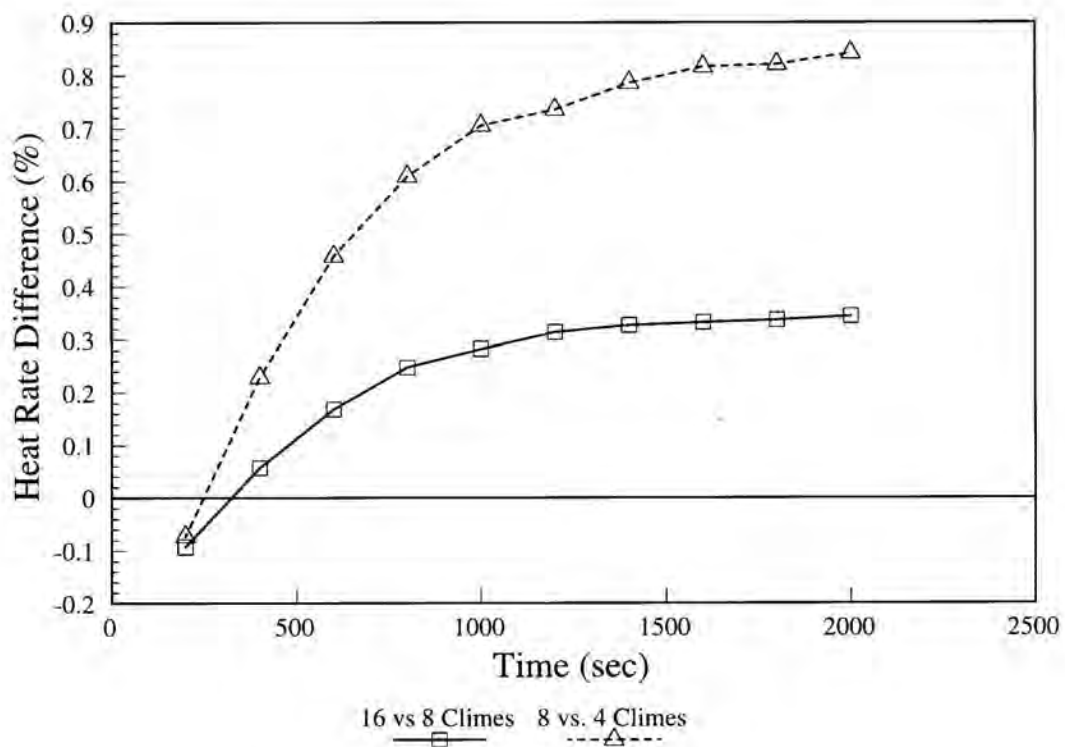


Figure 12-8. Comparison of Transient Heat Transfer Rate Differences; Case 1

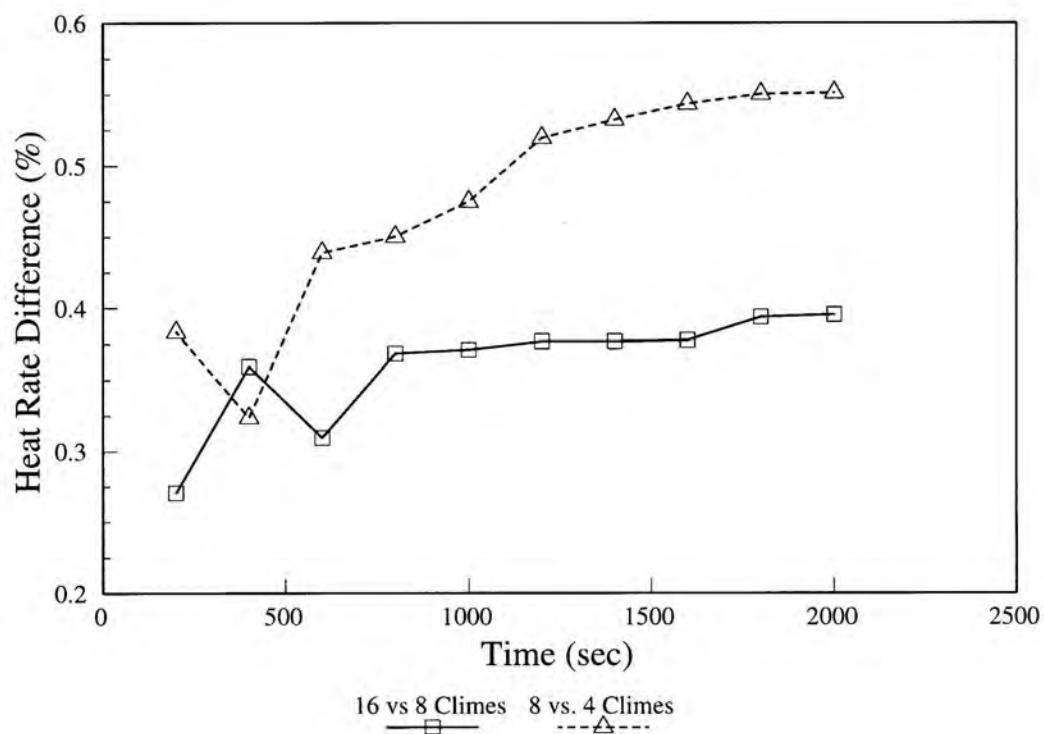


Figure 12-9. Comparison of Transient Heat Transfer Rate Differences; Case 2

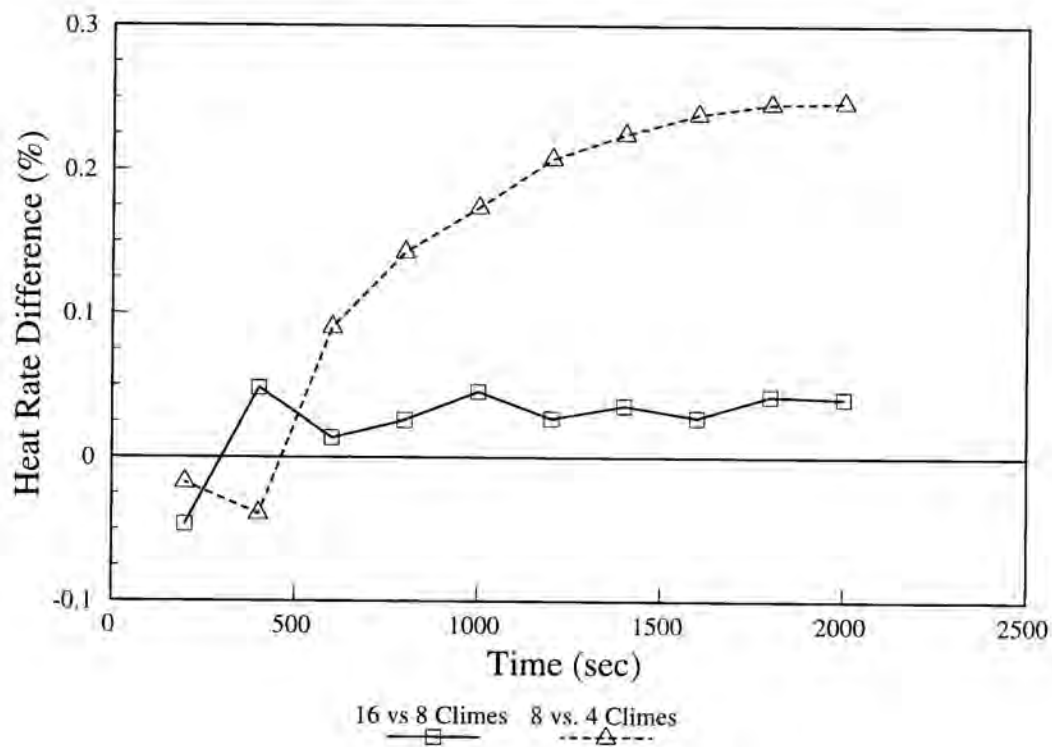


Figure 12-10. Comparison of Transient Heat Transfer Rate Differences; Case 3

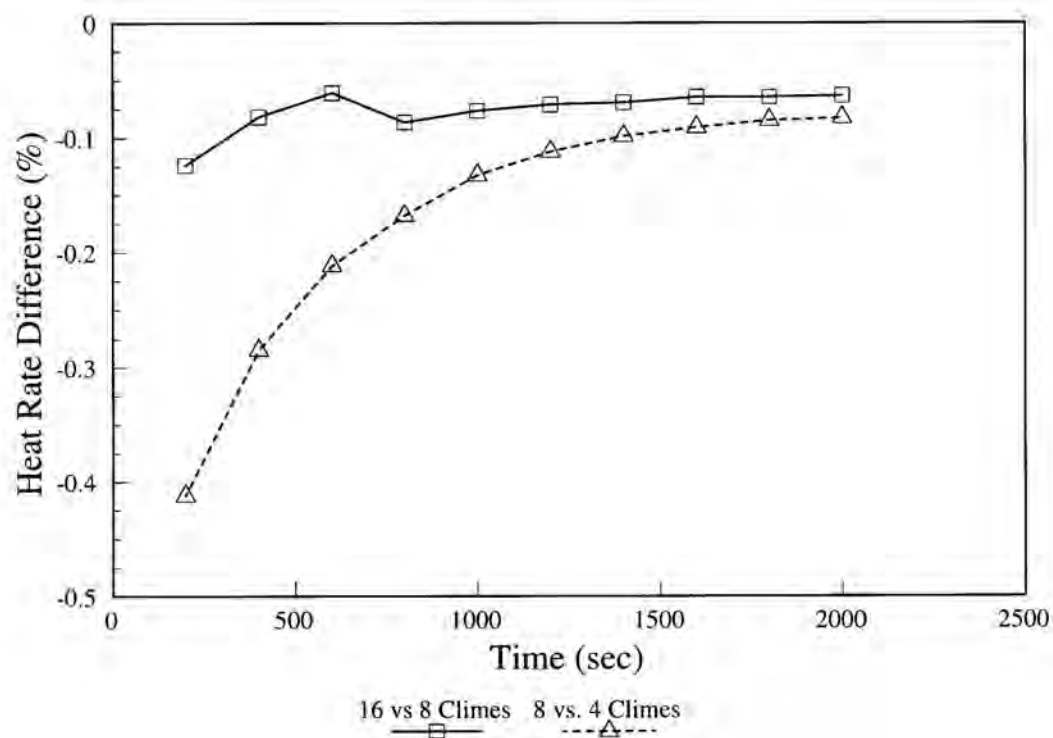


Figure 12-11. Comparison of Transient Heat Transfer Rate Differences; Case 4

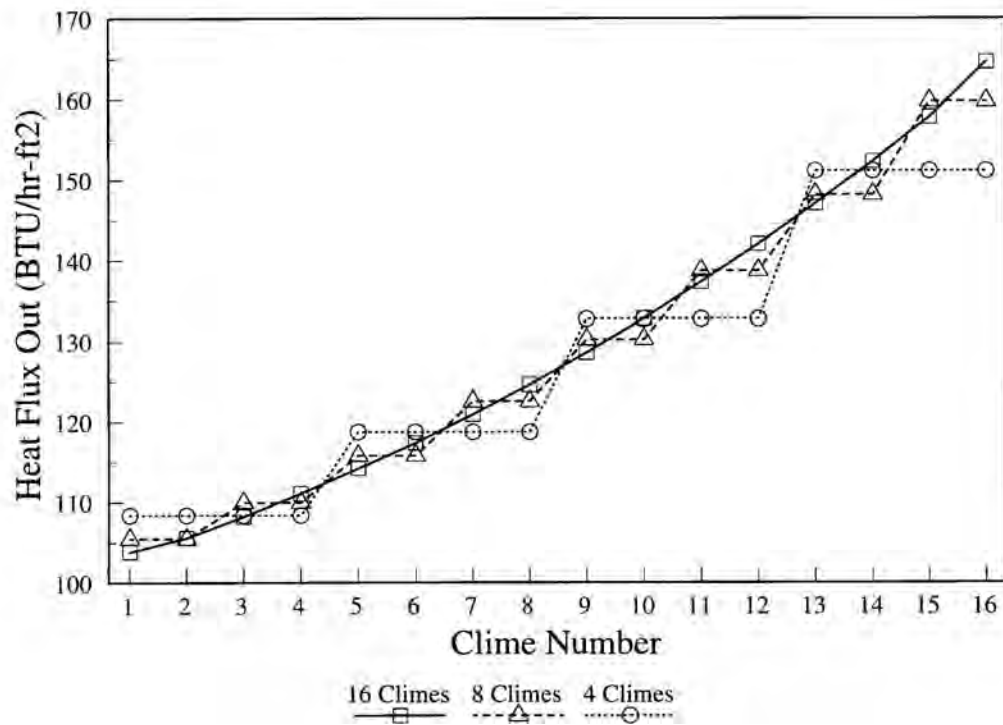


Figure 12-12. Comparison of Heat Flux Profiles; Time t=2000 Seconds; Case 1

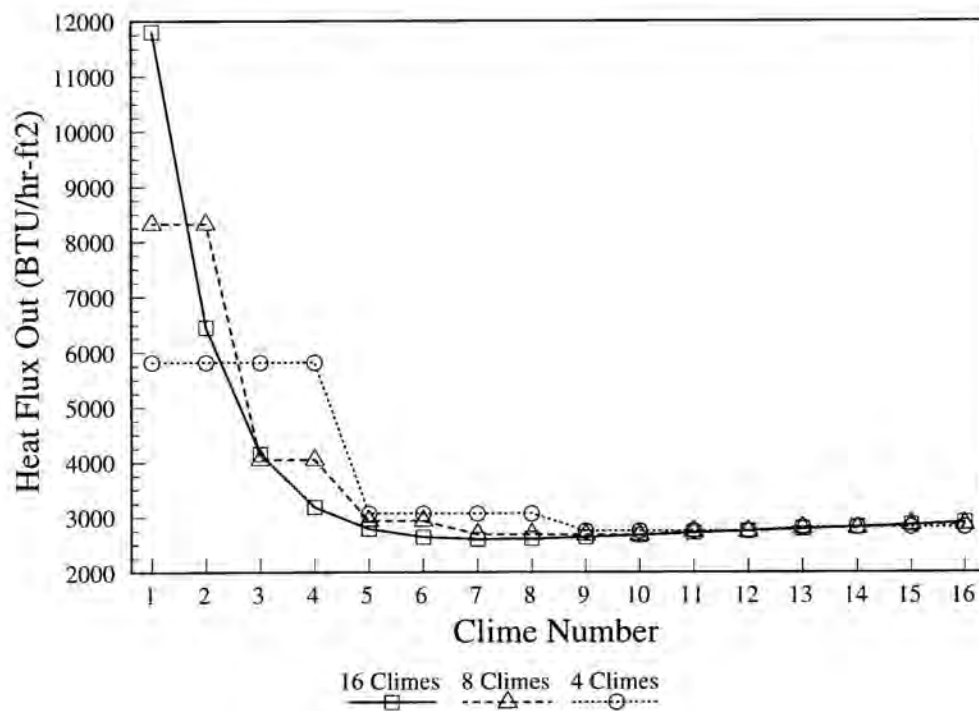


Figure 12-13. Comparison of Heat Flux Profiles; Time t=2000 Seconds; Case 2

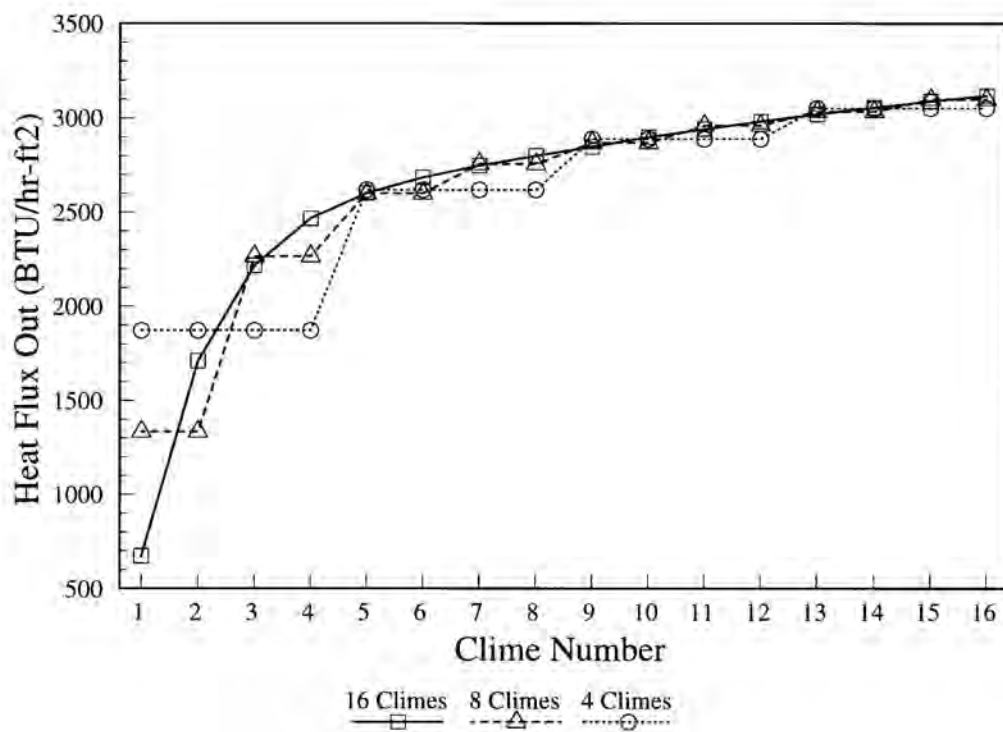


Figure 12-14. Comparison of Heat Flux Profiles; Time t=2000 Seconds; Case 3

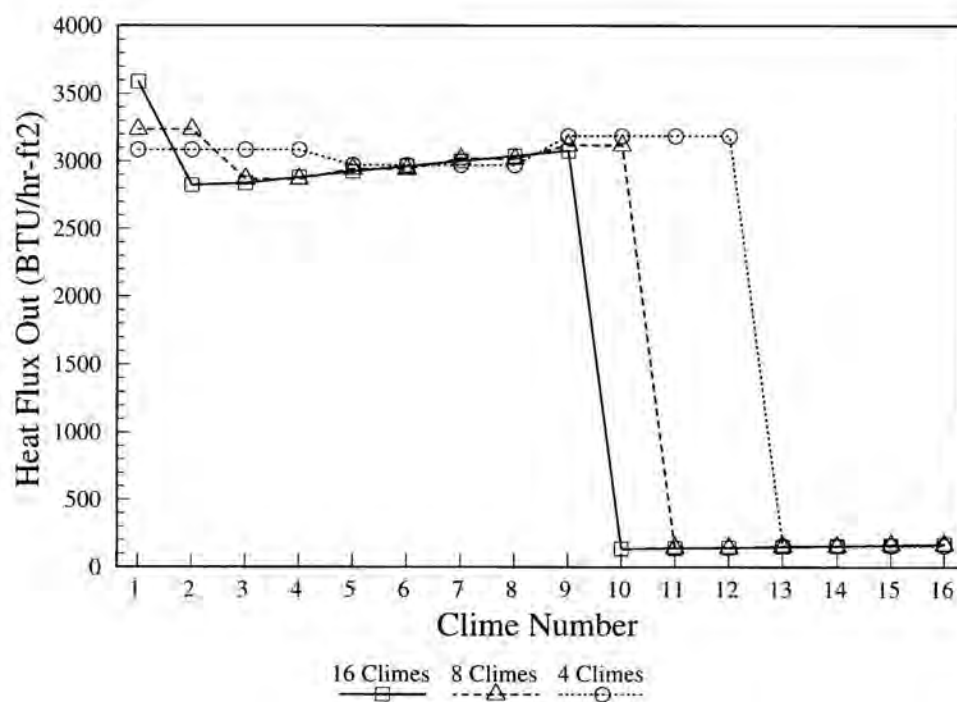


Figure 12-15. Comparison of Heat Flux Profiles; Time t=2000 Seconds; Case 4

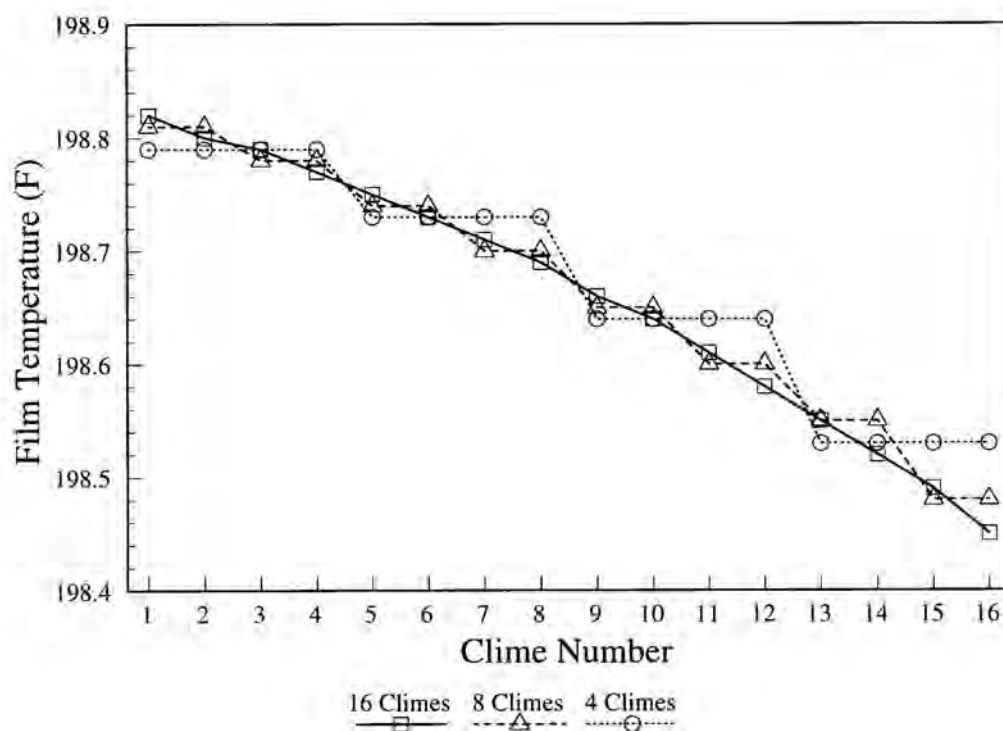


Figure 12-16. Comparison of Film Temperature Profiles; Time t=2000 Seconds; Case 1

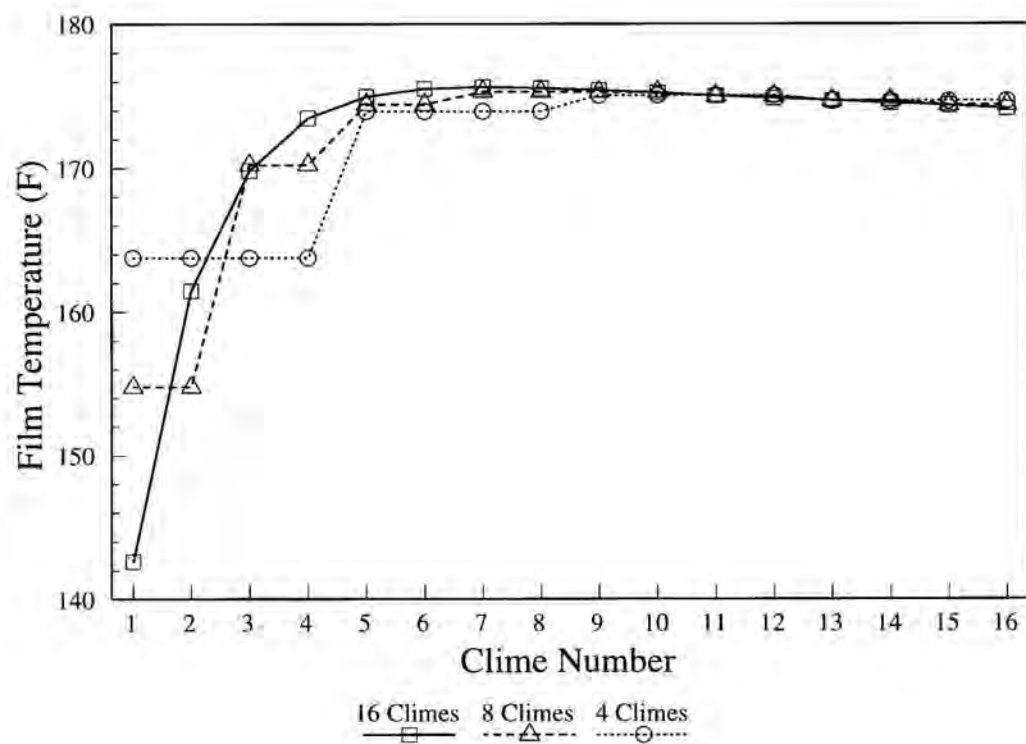


Figure 12-17. Comparison of Film Temperature Profiles; Time t=2000 Seconds; Case 2

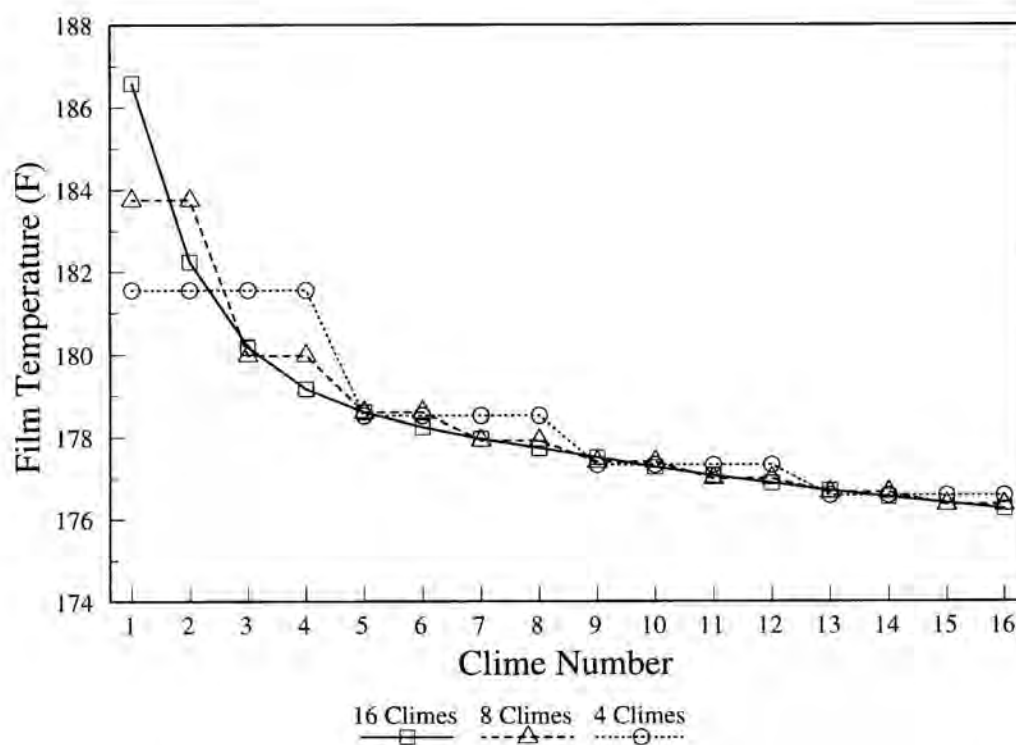


Figure 12-18. Comparison of Film Temperature Profiles; Time t=2000 Seconds; Case 3

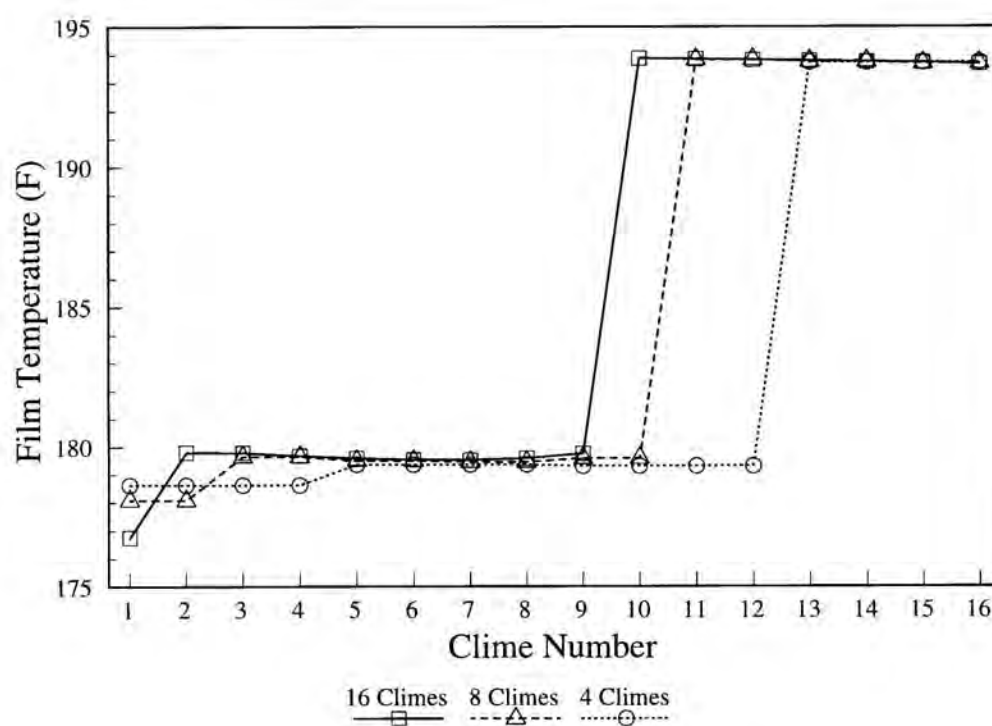


Figure 12-19. Comparison of Film Temperature Profiles; Time $t=2000$ Seconds; Case 4

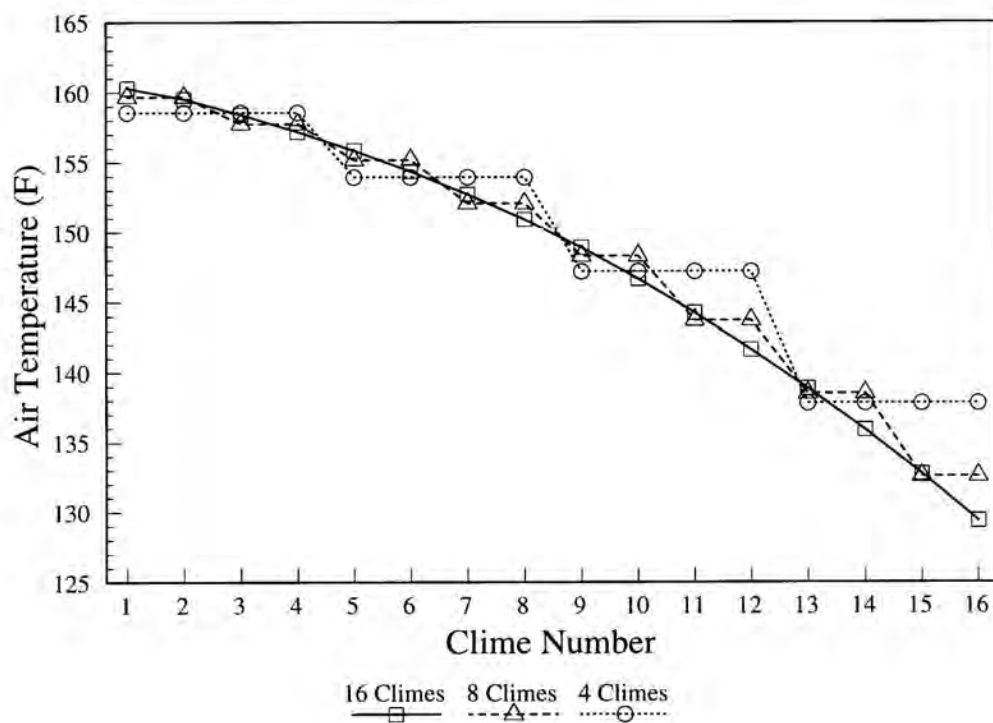


Figure 12-20. Comparison of Air Temperature Profiles; Time $t=2000$ Seconds; Case 1

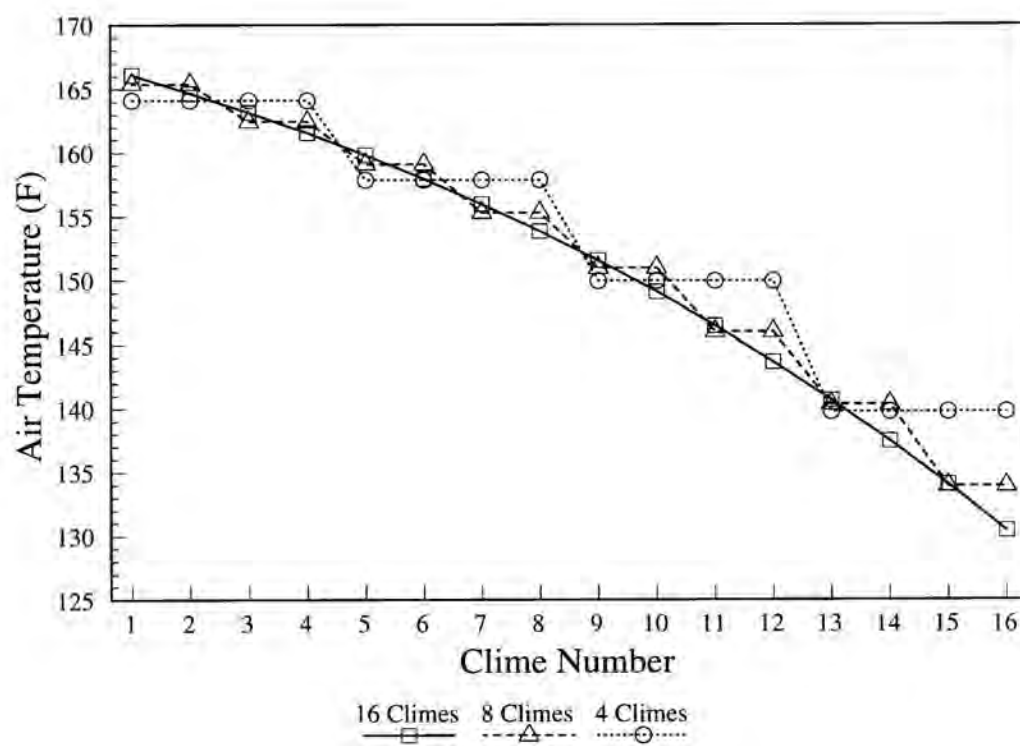


Figure 12-21. Comparison of Air Temperature Profiles; Time $t=2000$ Seconds; Case 2

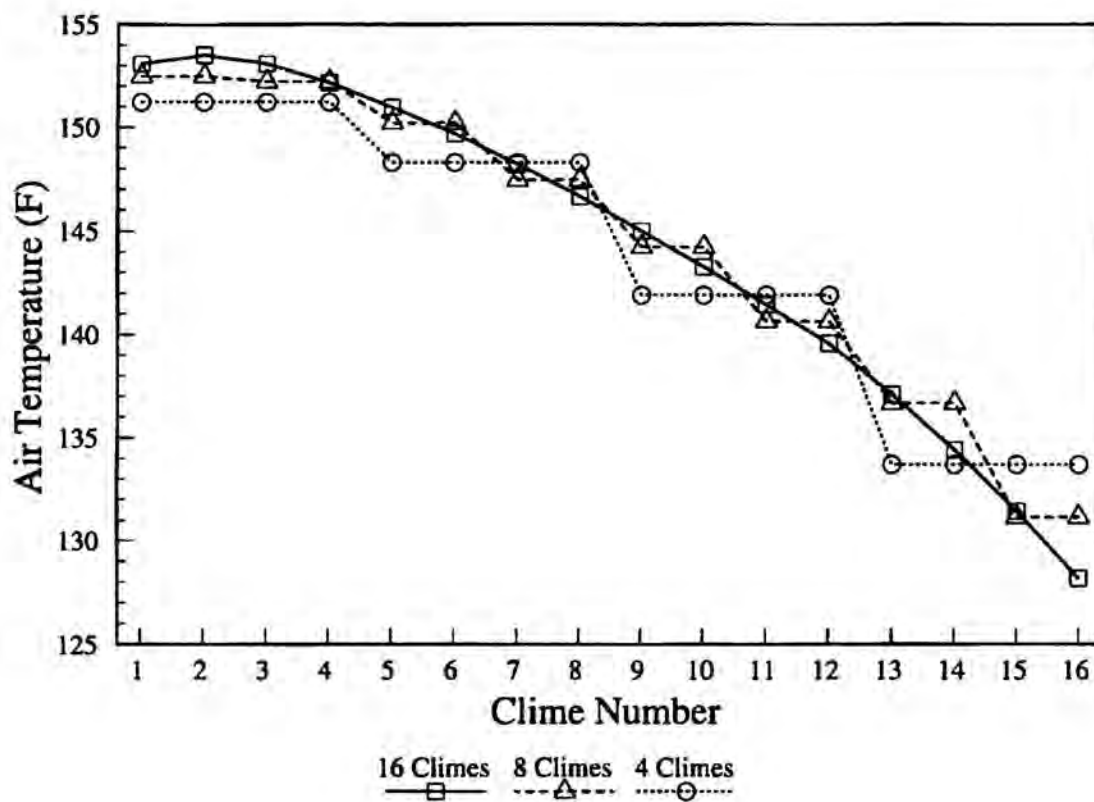


Figure 12-22. Comparison of Air Temperature Profiles; Time t=2000 Seconds; Case 3

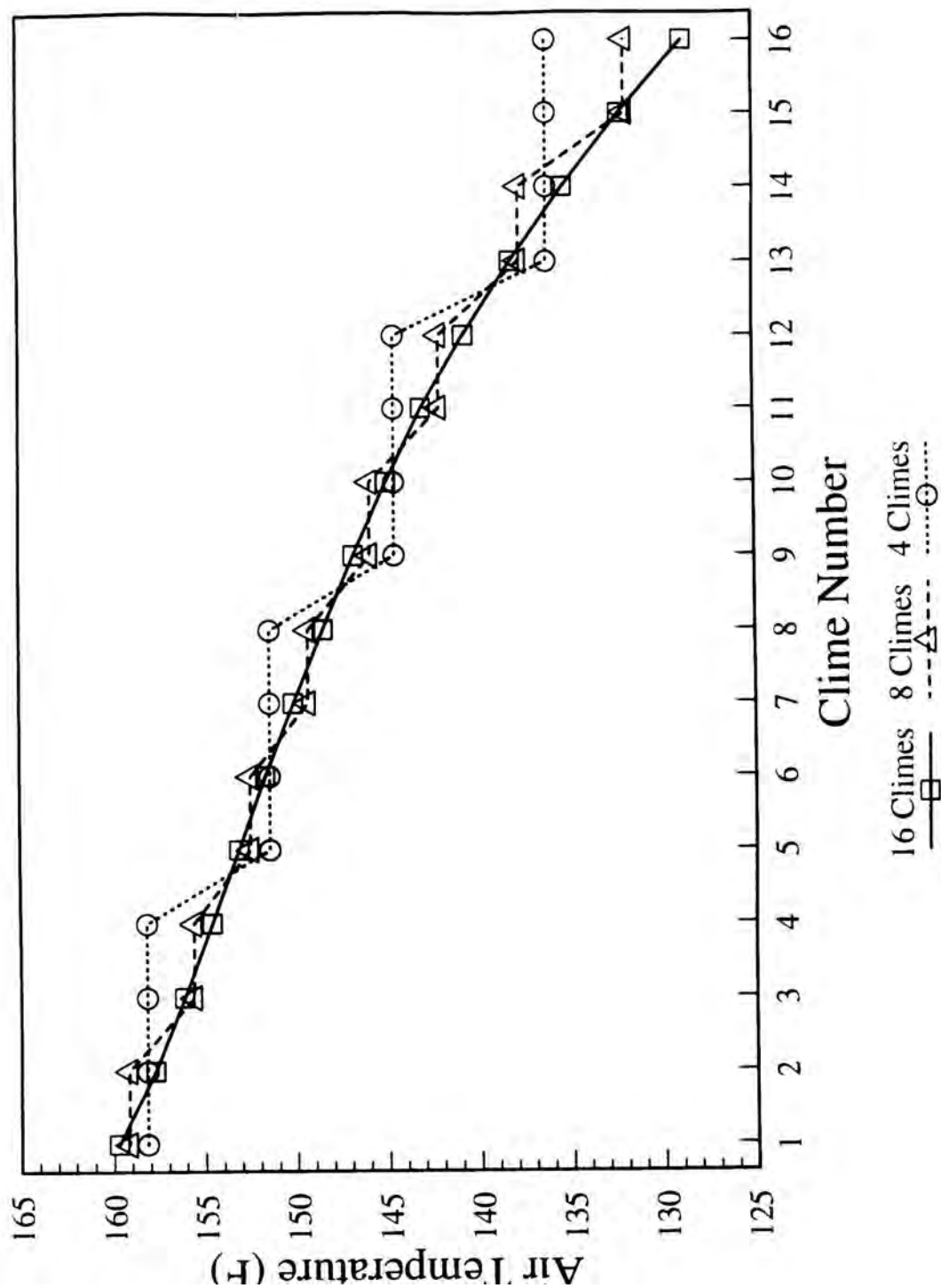


Figure 12-23. Comparison of Air Temperature Profiles; Time t=2000 Seconds; Case 4

a,c

Figure 12-24. AP600 Containment Model Clime Noding Pattern

a,c

Figure 12-25. AP600 Containment Model Double Vertical Clime Noding Pattern

a,c

Figure 12-26. AP600 Containment Model Double Stack Clime Noding Pattern

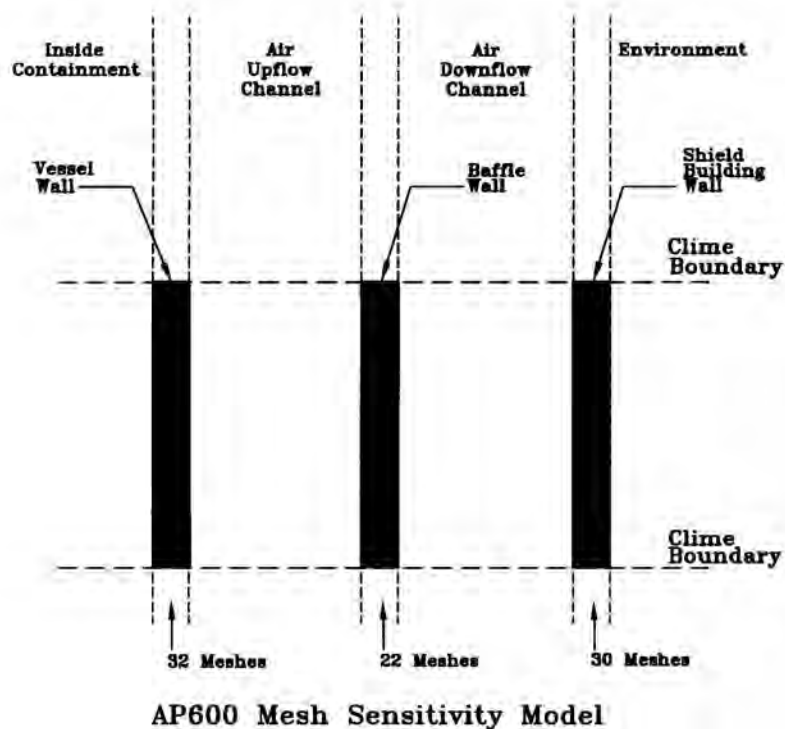
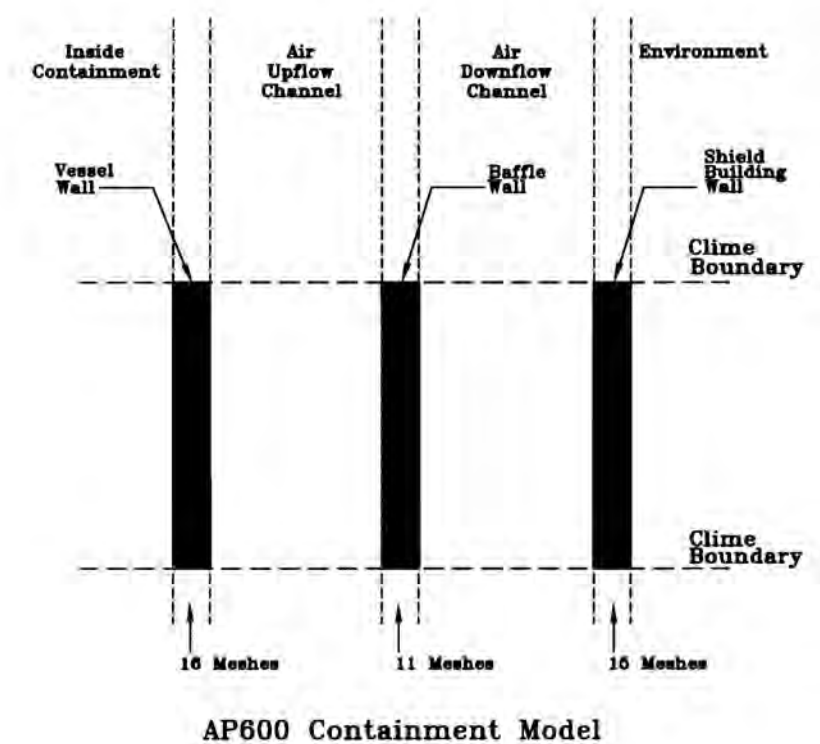


Figure 12-27. AP600 Containment Model Double Mesh Point Clime Noding Pattern

a,c

Figure 12-28. Pressure History, AP600 Containment Model; Double Clime

a,c

Figure 12-29. Wet Heat Flux vs. Clime; AP600 Containment Model, Base Case

a,c

Figure 12-30. Wet Heat Flux vs. Clime; AP600 Containment Model, Double Clime

a,c

Figure 12-31. Dry Heat Flux vs. Clime; AP600 Containment Model, Base Case

a,c

Figure 12-32. Dry Heat Flux vs. Clime; AP600 Containment Model, Double Clime

a,c

Figure 12-33. Film Temperature vs. Clime; AP600 Containment Model, Base Case

a,c

Figure 12-34. Film Temperature vs. Clime; AP600 Containment Model, Double Clime

a,c

Figure 12-35. Dry Surface Temperature vs. Clime; AP600 Containment Model, Base Case

a,c

Figure 12-36. Dry Surface Temperature vs. Clime; AP600 Containment Model, Double Clime

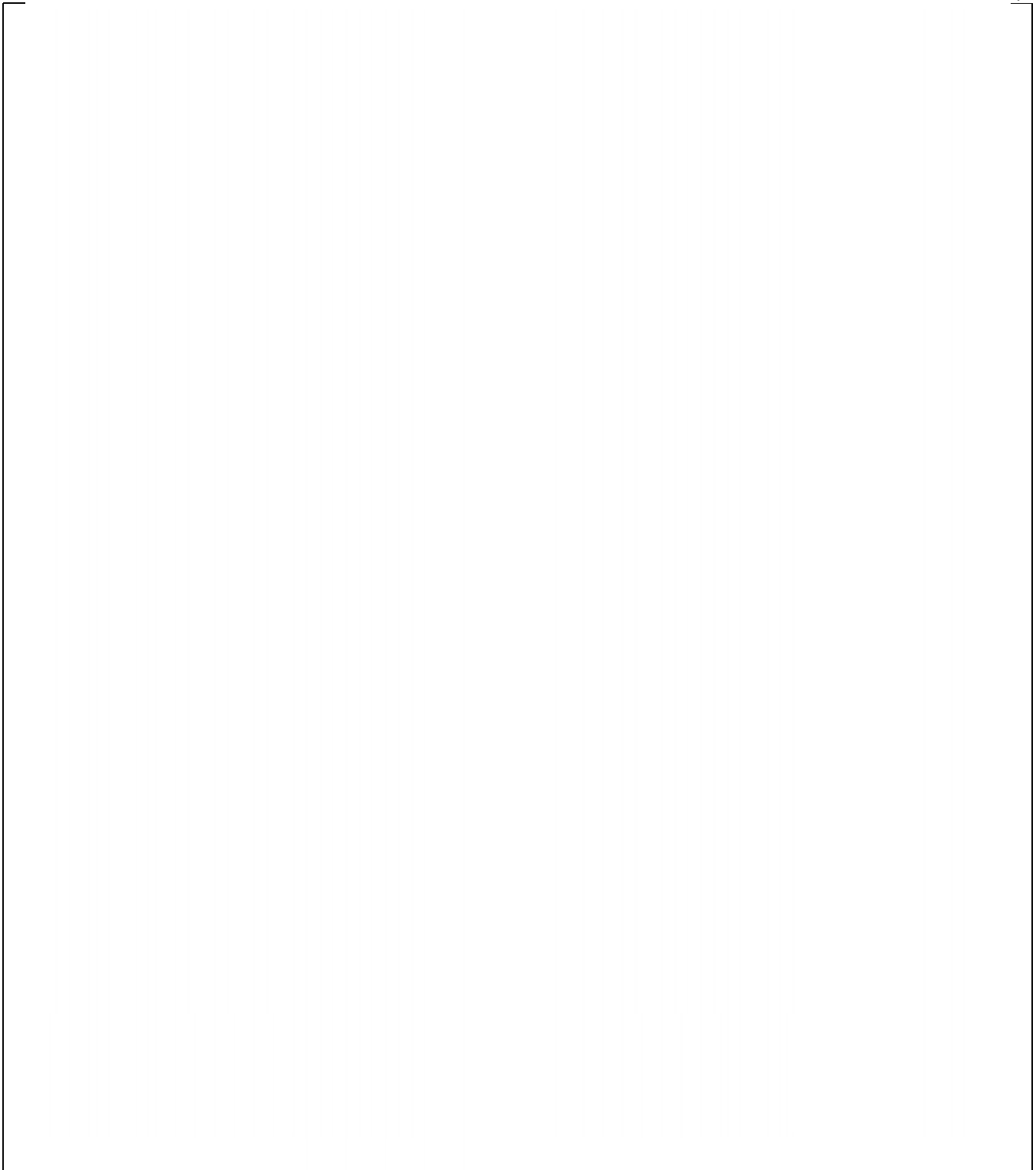


Figure 12-37. Annulus Pressure vs. Clime; AP600 Containment Model, Base Case

a,c

Figure 12-38. Annulus Pressure vs. Clime; AP600 Containment Model, Double Clime

a,c

Figure 12-39. Air Temperature vs. Clime; AP600 Containment Model, Base Case

a,c

Figure 12-40. Air Temperature vs. Clime; AP600 Containment Model, Double Clime

a,c

Figure 12-41. Air Density vs. Clime; AP600 Containment Model, Base Case

a,c

Figure 12-42. Air Density vs. Clime; AP600 Containment Model, Double Clime

a,c

Figure 12-43. Air Velocity vs. Clime; AP600 Containment Model, Base Case

a,c

Figure 12-44. Air Velocity vs. Clime; AP600 Containment Model, Double Clime

a,c

Figure 12-45. Heat Rejection History Comparison, AP600 Containment Model Double Clime Sensitivity Case

a,c

Figure 12-46. Integrated Heat Rejection Comparison, AP600 Containment Model; Double Clime Sensitivity Case

a,c

Figure 12-47. Pressure History Comparison, AP600 Containment Model; Double Stack Sensitivity Case

a,c

Figure 12-48. Heat Rejection History Comparison, AP600 Containment Model; Double Stack Sensitivity Case

a,c

Figure 12-49. Integrated Heat Rejection Comparison, AP600 Containment Model; Double Stack Sensitivity Case

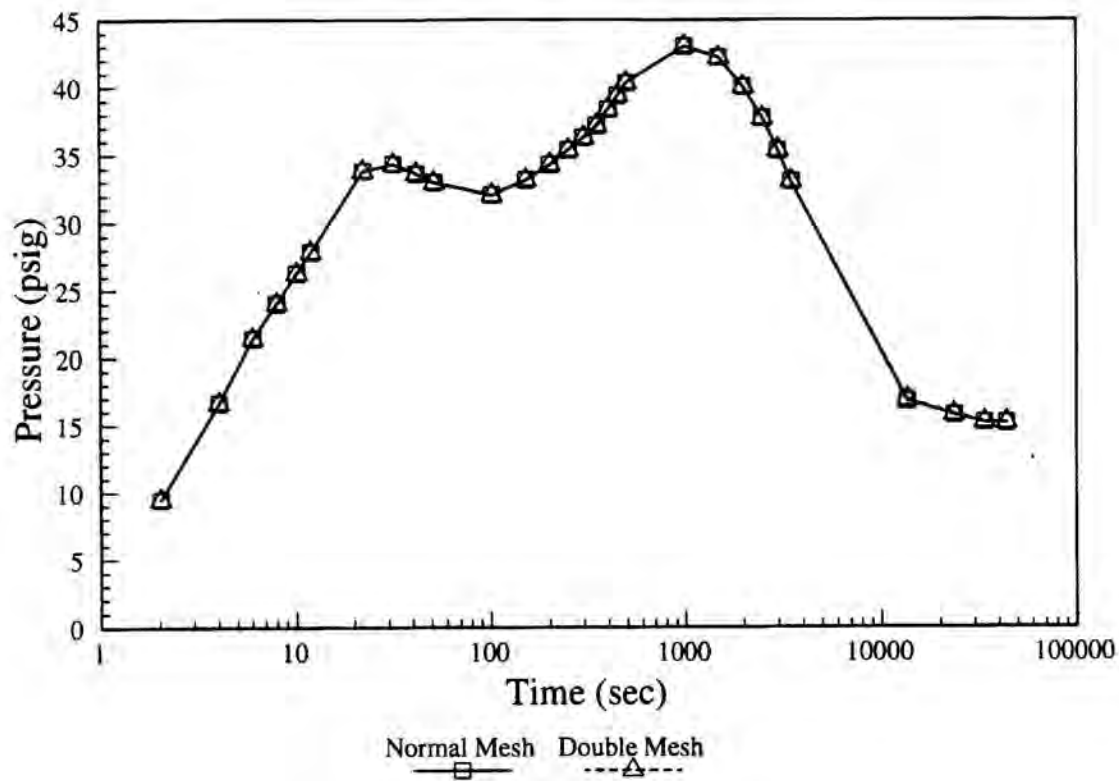


Figure 12-50. Pressure History Comparison, AP600 Containment Model; Double Mesh Sensitivity Case

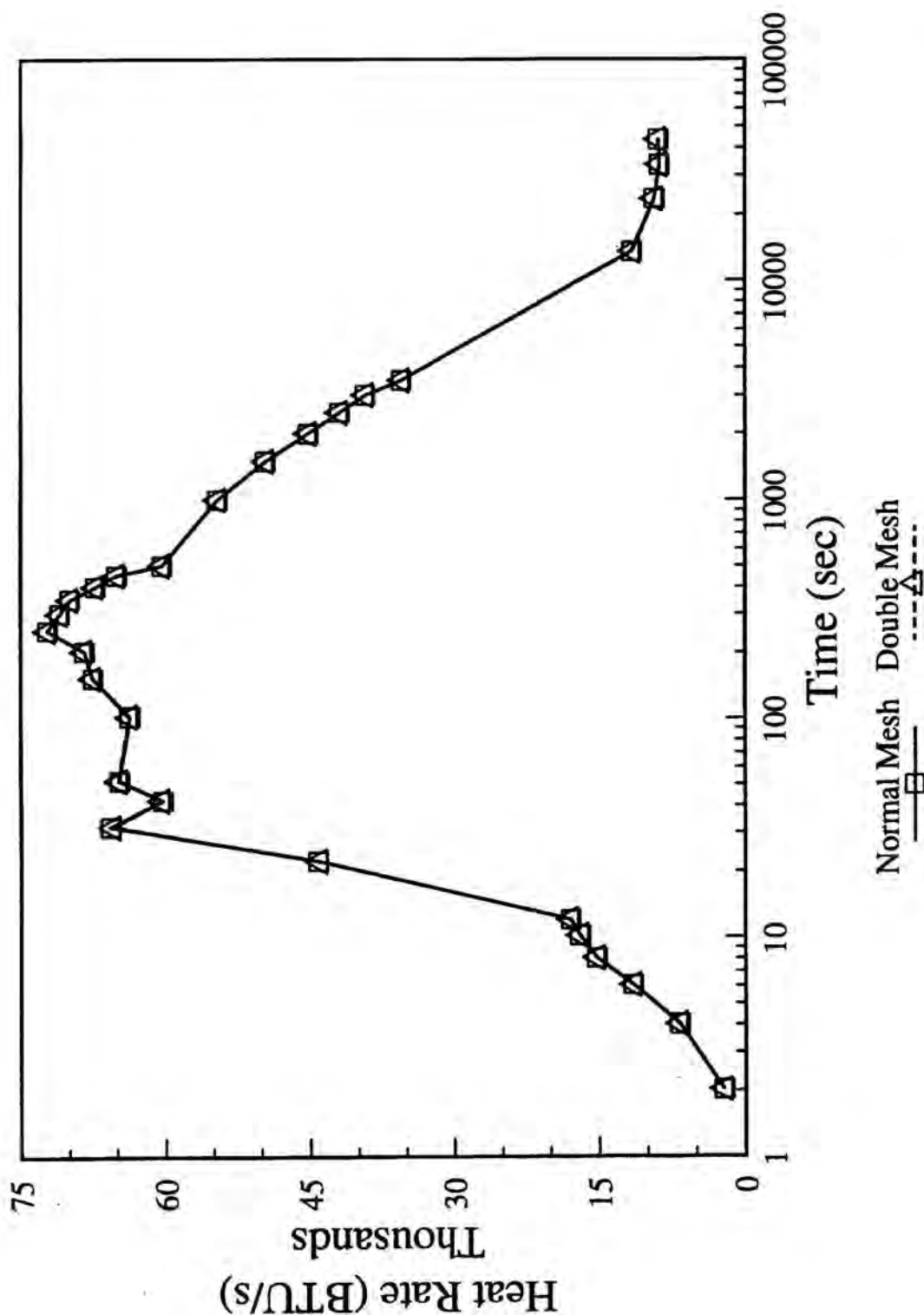


Figure 12-51. Heat Rejection History Comparison, AP600 Containment Model; Double Mesh Sensitivity Case

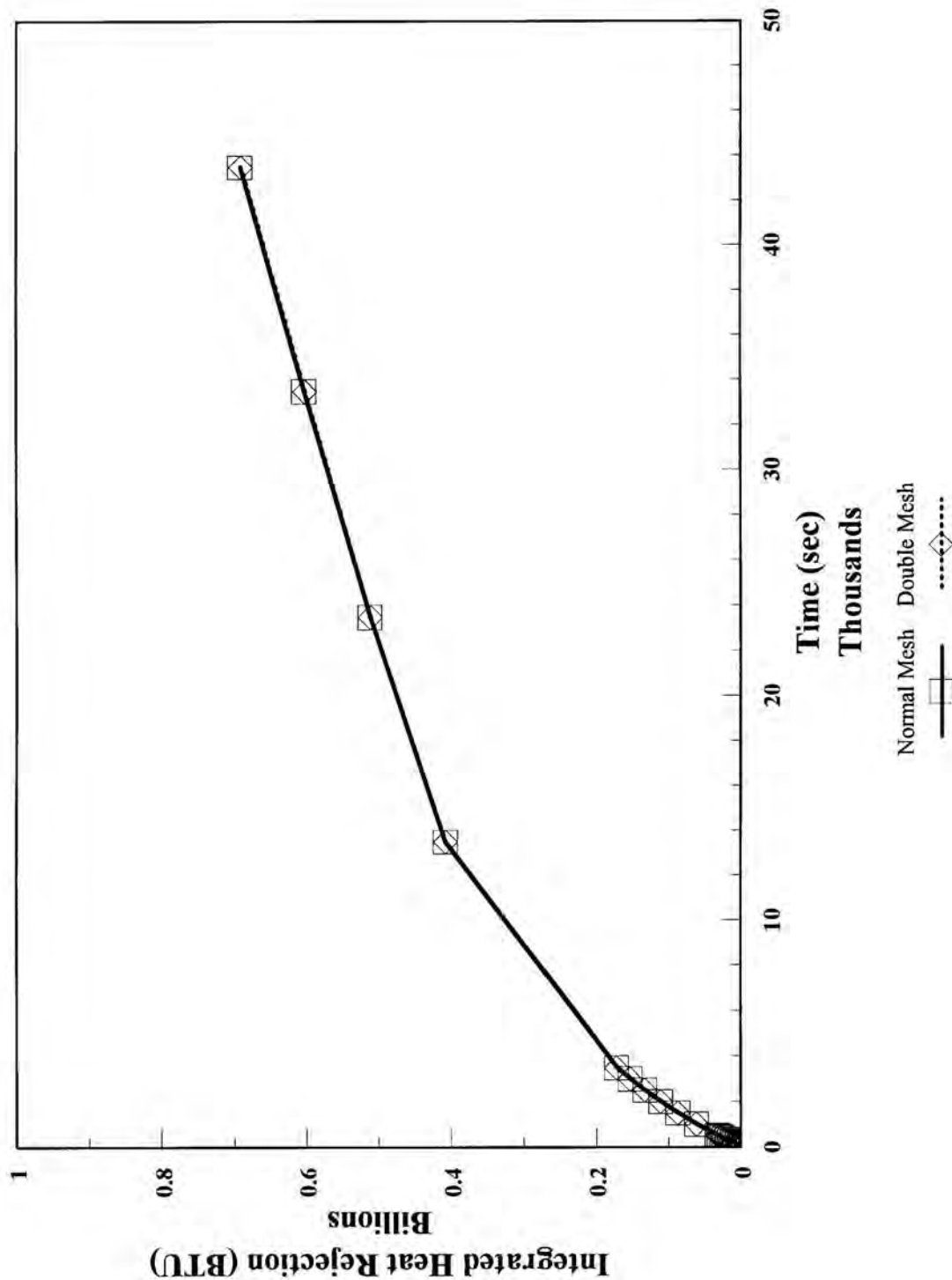


Figure 12-52. Integrated Heat Rejection Comparison, AP600 Containment Model; Double Stack Sensitivity Case

13 DESCRIPTION OF AP1000 PLANT GEOMETRY AND SUMMARY OF WGOthic EVALUATION MODEL

13.1 INTRODUCTION

The purpose of Section 13 is to describe the **AP1000** WGOTHIC Containment Evaluation Model (EM) that is used for containment integrity Design Basis Accident (DBA) analyses. The **AP1000** Containment Evaluation Model uses the WGOTHIC code (Section 3) and incorporates methodologies previously discussed in this document such as passive containment cooling system (PCS) liquid film stability (Section 7), circulation and stratification (Section 9), initial conditions (Section 5), and meteorological effects (Section 6).

The geometry of the plant is modeled with control volumes, flow paths, thermal conductors, and “climes” which are discussed in Sections 13.2, 13.3, 13.4 and 13.5, respectively. The climes are an addition to the standard GOTHIC code package that are used to model the **AP1000** PCS. The climes account for the condensation/evaporation mass transfer, the convection heat transfer, the radiative heat transfer, and the tracking of the mass and thermal resistance of the condensate and evaporative films on the containment shell.

Initial conditions and boundary conditions are summarized in Section 13.6. An overview of the loss of coolant accident (LOCA) and main steamline break (MSLB) transients is provided in Section 13.7. Section 13.8 summarizes changes that are made to the peak pressure EM for small-break LOCA analyses that minimize the containment pressure transient. Section 13.9 provides a high level summary of the EM methodology.

13.2 AP1000 PLANT WGOTHIC EVALUATION MODEL CONTROL VOLUMES

The WGOTHIC model of the **AP1000** plant consists of a network of lumped parameter control volumes. Control volumes are used to represent the inner free volume of the containment, the PCS annular flow path between the shield building and containment vessel, and the environment. The **AP1000** WGOTHIC Evaluation Model (EM) consists of []^{a,c} control volumes inside containment and []^{a,c} control volumes which represent the PCS annular flow path region. Control volumes are defined by their free volume, hydraulic diameter, pool area, elevation, and height.

The selection of volumes and flow paths corresponds with the lumped parameter model developed for the large-scale test (LST) vessel for validation of the WGOTHIC code. The LST model description and guidance on application of the LST model to the full-scale AP600 model are provided in Section 6 of WCAP-14382 (Reference 13.1). Based on this guidance, the volumes and flow paths of the AP600 Containment Evaluation Model, summarized in Section 4.6 of this report, were selected.

A comparison of the AP600 and **AP1000** containment evaluation model nodding elevations above the operating deck (135.25 ft elevation) is shown in Figure 13-1. An extra set of volumes was added above the operating deck to account for the extra 25.5 ft of elevation in the cylindrical portion of the **AP1000** structure. Other elevation divisions were shifted to be consistent with the physical basis of the divisions for AP600, as described below.

[

] ^{a,c}

[

]a,c

[

] ^{a,c}

a,c

Figure 13-1. Comparison of AP600 (left) and AP1000 (right) Above-Deck Containment Model Elevations for Nodalization

a,c

Figure 13-2. Plan View of Compartments Below 107' Elevation

a,c

Figure 13-3. Plan View of Compartments Immediately Below Operating Deck

a,c

**Figure 13-4. Plan View of Nodalization from 135.25' to 226' Elevation
(Pressurizer Compartment is Only Nodalized to 153' Elevation)**

a,c

Figure 13-5. Plan View of Nodalization from 226' Elevation to Top of Containment

a,c

Figure 13-6. Elevation View of Nodalization (Facing North)

a,c

Figure 13-7. Elevation View of Nodalization (Facing West)

a,c

[illegible]

Table 13-1. Inside Containment Volumes Listing (cont.)

Control Volume	Location	Elevation	a,c

Table 13-2. Outside Containment Volumes Listing

[illegible]

a,c

13.3 AP1000 PLANT WGOTHIC EVALUATION MODEL FLOW PATHS

The **AP1000** WGOTHIC control volumes discussed in Section 13.2 are connected by one or more flow paths. The inlet/outlet elevations, flow area, hydraulic diameter, inertia length, friction length, and loss coefficients are required input values for each flow path.

Flow paths represent physical openings between two volumes such as doorways, penetrations, stairwells, etc., but can also represent connections between volumes not defined by physical structures. Geometric information relating to the flow paths are obtained from general arrangement drawings or nominal dimensions on more detailed drawings, where available. However, the heights of all vertical flow flowpaths are set to 0.01 ft, consistent with the GOTHIC User's Guidance (Reference 13.2), [

] ^{a,c}.

The annulus region between the containment vessel and the baffle is a pathway for air to travel down the downcomer and up the riser. The air flow path is from the shield building inlet louvers downward to the annulus seal and then back upward along the external surface of the containment vessel and out of the chimney. Unrecoverable loss coefficients external to the containment are obtained from hydraulic tests of the external annular flow paths. The annulus loss coefficients are based on a 1/6 scaled test model [

] ^{a,c}.

Most flow paths below the operating deck represent physical openings between room compartments while the flow paths above the operating deck are not necessarily bounded by walls and physical boundaries. [

] ^{a,c}

Table 13-3 lists the flow paths in the **AP1000** containment Evaluation Model.

Table 13-3. Flow Path Listing

[illegible]

a,c

Table 13-3. Flow Path Listing (cont.)

[illegible]

a,c

Table 13-3. Flow Path Listing (cont.)

[illegible]

Table 13-3. Flow Path Listing (cont.)

[illegible]

Table 13-3. Flow Path Listing (cont.)

[illegible]

[illegible]

Table 13-3. Flow Path Listing (cont.)

[illegible]

Table 13-3. Flow Path Listing (cont.)

[illegible]

Table 13-3. Flow Path Listing (cont.)

[illegible]

a,c

[illegible]

Table 13-3. Flow Path Listing (cont.)

[illegible]

Table 13-3. Flow Path Listing (cont.)

[illegible]

Table 13-3. Flow Path Listing (cont.)

[illegible]

Table 13-3. Flow Path Listing (cont.)

[illegible]

a,c

[illegible]

Table 13-3. Flow Path Listing (cont.)

Flow Path Number	Description	Control Volume A	Control Volume B	Direction of Flow

a,c

13.4 AP1000 PLANT WGOTHIC EVALUATION MODEL THERMAL CONDUCTORS

Thermal conductors are one-dimensional slabs used to model structures that are at the ambient containment temperature and that are credited as heat sinks within the WGOTHIC Evaluation Model. The thermal conductors model the heat capacity of the structures, the heat transfer between the steam/gas mixture and these structures, and the heat transfer between control volumes via these structures. Any number of conductors can be assigned to a control volume. A thermal conductor can be fully contained within a control volume or it can be connected to two control volumes (e.g., walls, ceilings, floors). Thermal conductors cannot be connected to one another.

The inputs for the thermal conductors consist of the specification of the initial temperature, the exposed surface area, the thermal conductor type, and the heat transfer type. The thermal conductor type specifies the type and thickness of the material, and is further discussed in Section 13.4.1. The heat transfer type defines the characteristics of the credited heat transfer and is discussed in Section 13.4.2.

Thermal conductors are based on the metallic and concrete structures as defined on Certified for Construction drawings. [

] ^{a,c}

After the exposed surface area and volume of each material of the heat sinks are quantified, the information is converted into one-dimensional slab thermal conductors. The thermal conductors are specified with a surface area applicable to side A and the same surface area applicable to side B. For walls between control volumes, the surface area input corresponds to the surface area on each side of the wall. For structures that are contained within a control volume, the surface area of side A corresponds to the total exposed surface area, and side B is turned off for heat transfer. The volumes of the materials are implicitly defined through the effective thicknesses modeled in the thermal conductor types (Section 13.4.1). In the conversion of the exposed surface area and material volume to the evaluation model input, the volume of the materials is strictly conserved; the surface area input multiplied by the material thickness always equals the calculated material volume. The exposed surface areas are also preserved, although there are instances of small adjustments:

[

]^{a,c}

The temperature of all thermal conductors inside containment is set to the maximum containment operating temperature defined in the Technical Specifications.

Table 13-4 contains a list of all thermal conductors in the **AP1000** WGOTHIC containment Evaluation Model, sorted by location. Thermal conductors that are contained fully within one control volume have the associated control volume number listed for side A and side B. Wall thermal conductors that have each side exposed to a different control volume are listed twice, once indicating the side exposed to control volume A and once indicating the side exposed to control volume B. Thermal conductors listed at the end of Table 13-4 are ones developed for AP600 and remain in the WGOTHIC input file, but which are not used in the peak containment pressure EM for the AP1000 plant. Section 13.4.1 describes the thermal conductor types and material property modeling. Section 13.4.2 describes the heat transfer coefficients of the thermal conductors modeled in the **AP1000** WGOTHIC containment Evaluation Model.

Table 13-4. Thermal Conductor Listing

Description	Thermal Conductor Number	Control Volume A	Control Volume B

a,c

Table 13-4. Thermal Conductor Listing (cont.)

Description	Thermal Conductor Number	Control Volume A	Control Volume B

a,c

Table 13-4. Thermal Conductor Listing (cont.)

Description	Thermal Conductor Number	Control Volume A	Control Volume B

a,c

Table 13-4. Thermal Conductor Listing (cont.)

Description	Thermal Conductor Number	Control Volume A	Control Volume B

a,c

Table 13-4. Thermal Conductor Listing (cont.)

Description	Thermal Conductor Number	Control Volume A	Control Volume B

a,c

Table 13-4. Thermal Conductor Listing (cont.)

Description	Thermal Conductor Number	Control Volume A	Control Volume B

a,c

Table 13-4. Thermal Conductor Listing (cont.)

Description	Thermal Conductor Number	Control Volume A	Control Volume B

a,c

Table 13-4. Thermal Conductor Listing (cont.)

Description	Thermal Conductor Number	Control Volume A	Control Volume B

a,c

Table 13-4. Thermal Conductor Listing (cont.)

Description	Thermal Conductor Number	Control Volume A	Control Volume B

a,c

Table 13-4. Thermal Conductor Listing (cont.)

Description	Thermal Conductor Number	Control Volume A	Control Volume B

a,c

Table 13-4. Thermal Conductor Listing (cont.)

Description	Thermal Conductor Number	Control Volume A	Control Volume B

a,c

Table 13-4. Thermal Conductor Listing (cont.)

[illegible]

a,c

Table 13-4. Thermal Conductor Listing (cont.)

Description	Thermal Conductor Number	Control Volume A	Control Volume B

a,c

13.4.1 Thermal Conductor Type Descriptions

The thermal conductors in the **AP1000** WGOTHIC containment Evaluation Model are constructed of components referred to as thermal conductor types. Thermal conductor types are also used in the clime modeling discussed in Section 13.5. A thermal conductor type can be described as the cross-sectional composition of a given structure, defining both the material and effective thickness of each material. A single thermal conductor type can be used for multiple thermal conductors when the materials and thicknesses are the same. The WGOTHIC Evaluation Model of the **AP1000** plant utilizes []^{a,c} different thermal conductor types.

A thermal conductor type consists of a number of material regions divided into subregions to model and calculate conduction through the materials. Figure 13-8 illustrates the regions and subregions of a WGOTHIC thermal conductor type. The thermal conductor type shown in the example consists of four separate regions of variable thickness, subregions, and material types.

The following assumptions are used in the development of the **AP1000** containment Evaluation Model thermal conductor types:

- The effective thickness of each thermal conductor type material is specified so as to preserve the volume of each material when applied to the surface area input of the thermal conductor, as discussed in Section 13.4.
- Coatings are applied to carbon steel and concrete surfaces. The thickness of each layer of coating is maximized based on coatings application procedures to increase the resistance to heat transfer of the thermal conductors.
- []^{a,c}
- []^{a,c}

The properties of the materials used in the thermal conductor types are specified in the WGOTHIC Evaluation Model input. The properties used by WGOTHIC are thermal conductivity, volumetric heat capacity, and emissivity. The material properties are conservatively selected based on data available in literature and are consistent with the minimum coating test requirements. In addition the following conservatisms are applied:

- The thermal conductivity and volumetric heat capacity of all steel materials are reduced by 10% per the ASME standard to account for variability of alloy content.
- The thermal conductivity of inorganic zinc is reduced by a factor of two relative to the minimum test requirement. Although a sensitivity documented in Section 10.2.1 assumed a factor of four degradation in the thermal conductivity to address the effects of oxidation, later work in Reference 13.7 has shown that thermal conductivity will not decrease substantially as the coating ages, and may even increase slightly. The factor of two provides margin for variations in the coating composition and structure, corrosion product composition, and measurement uncertainties.
- Emissivity is reduced by 10% and is only input to credit radiation in the clime modeling of the outer surface of the containment vessel, the baffle and the shield building. All other emissivity input is set to 1E-10.

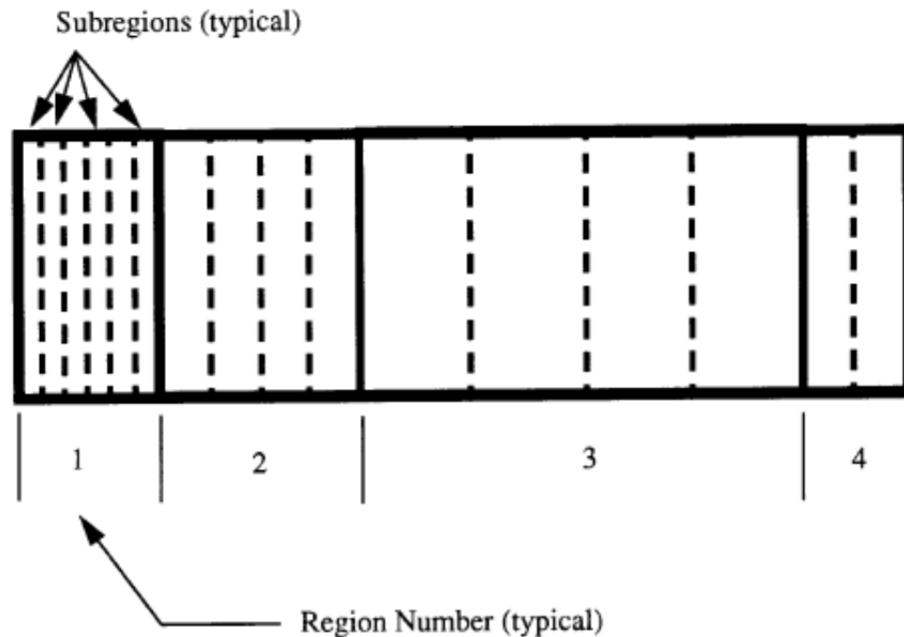


Figure 13-8. WGOTHIC Thermal Conductor Type Noding Example

13.4.2 Thermal Conductor Heat Transfer Coefficients

The heat transfer coefficient types define the surface heat transfer conditions of the thermal conductor for which they are modeled.

[

] ^{a,c}

[

] ^{a,c}

13.5 AP1000 PLANT WGOTHIC EVALUATION MODEL CLIMES

[

] ^{a,c}

a,c

Figure 13-9. Stack Configuration for the AP1000 WGOTHIC EM Clime Modeling

a,c

Figure 13-10. Clime Configuration for the AP1000 WGOTHIC EM

13.5.1 Clime Conductors

[

] ^{a,c}

a,c

Figure 13-11. WGOTHIC Clime Conductor Modeling

Table 13-5. Clime Modeling

a,c

[illegible]

Table 13-5. Clime Modeling (cont.)

a,c

13.5.2 Passive Cooling System Flow

One of the unique features of the **AP1000** plant is the cooling water film that is applied to the external surface of the steel containment shell. As stated in Section 13.5, []^{a,c} of the **AP1000** WGOTHIC containment Evaluation Model have PCS flow applied to them. The PCS flow rate in the **AP1000** Evaluation Model is a minimum flowrate versus time that is consistent with the minimum flowrate relative to the passive containment cooling water storage tank (PCCWST) water level at each standpipe elevation, which is confirmed through plant testing. The minimum delivered flowrate is based on only one of the passive containment cooling water flow paths being open. The amount of PCS flow credited is actually an “evaporation-limited” flow rate. The evaporation-limited PCS flow rate is derived by subtracting a conservatively calculated runoff flow rate from the total gravity-driven, delivered PCS water flow rate. The PCS film flow modeling is described in Section 7.

The PCS flow rate is input in the **AP1000** WGOTHIC containment Evaluation Model as a time-dependent boundary condition specified through a user-defined function. Two options are available to calculate a conservative evaporation limited flow, as discussed in Section 7.5.2. No evaporation of the film is credited prior to development of steady state PCS water coverage (Section 7.2.5). Table 13-6 summarizes the basis for the PCS inputs.

Table 13-6. Basis for PCS Inputs

Input Parameter	Basis for Value in Evaluation Model
Initial Temperature of Containment Shell	Containment shell initialized uniformly to maximum Technical Specification value for containment air temperature. Reference Technical Specification 3.6.5.
Applied External Film Flow Rate	Delivered film flow rate is based on one of three PCS tank discharge valves being open. Evaporation-limited flow is used in the Evaluation Model (Section 7).
External PCS Liquid Film Temperature	Film temperature set to upper bound of the PCCWST. This minimizes the subcooling benefit. Reference Technical Specification 3.6.6.
Film Coverage Fraction	Maximum coverage fraction is [] ^{a,c} , and reduces after the film stability limit is reached (Section 7).
PCS Coating Properties	Based on minimum coatings test requirements for most properties. Additional conservatism applied to the thermal conductivity of the Inorganic Zinc paint, crediting no more than 50% of the coatings test requirement (Section 13.4.1).
PCS Emissivity	Surface emissivity of Inorganic Zinc paint reduced to 90% of the coatings test requirement.
PCS Coatings Thickness	Maximum coating thicknesses used.

Table 13-6. Basis for PCS Inputs (cont.)

Input Parameter	Basis for Value in Evaluation Model
PCS Initial Delay Time	No credit is taken for partial film coverage prior to the development of steady state PCS water coverage. Conservatively neglects any cooling from the water as coverage develops (Section 7.2.5).
Internal Heat and Mass Transfer Correlation	[] ^{a,c}
External Heat and Mass Transfer Correlation	[] ^{a,c}

13.5.3 Condensate Film Stripping

[

] ^{a,c}

a,c

Figure 13-12. AP1000 WGOTHIC Evaluation Model Clime Stripping Diagram

13.6 AP1000 PLANT WGOTHIC EVALUATION MODEL INITIAL AND BOUNDARY CONDITIONS

The input for the **AP1000** WGOTHIC containment Evaluation Model also include a number of initial conditions used to define the temperatures and pressures, etc. at the beginning of the transient. Initial conditions assumed for the **AP1000** WGOTHIC containment Evaluation Model have been conservatively selected to maximize the containment pressure response for the DBA analyses, and are consistent with the Technical Specifications and site interface parameters limits described in Section 13.6.1.

In addition, there are boundary conditions that are used to drive the transients being analyzed. Section 13.6.2 describes the boundary conditions used in the base case LOCA and MSLB Evaluation Model calculations.

13.6.1 Initial Conditions

The initial conditions that are assumed for the base case LOCA and MSLB analyses are summarized below. Initial conditions are specified separately for regions inside and outside of containment. The outside containment initial conditions represent the conditions at the inlet to the PCS downcomer, the annulus region, the chimney region, and the surrounding environment. Sensitivities documented in Section 5 form the basis for most of the assumed initial conditions. Table 13-7 summarizes the initial conditions outside containment. The inside containment initial conditions are presented in Table 13-8.

Table 13-7. Outside Containment Initial Conditions

Input Parameter	Basis for Value in Evaluation Model	Reference to Applicable Sensitivity Studies
External Atmosphere Temperature	Set to maximum dry bulb air temperature limit defined by the site interface parameters.	WCAP-15846, Section 5.7
External Total Pressure	Set to standard atmospheric pressure (14.7 psia).	None
External Atmosphere Pressure Ratio (Relative Humidity)	A steam pressure ratio and relative humidity which bounds the limits defined by site interface parameters (wet bulb and dry bulb temperatures).	WCAP-15846, Section 5.6
External PCS Film Flow Temperature	Set to maximum PCCWST water temperature consistent with Technical Specification 3.6.6.	WCAP-15846, Section 5.7

Table 13-8. Inside Containment Initial Conditions

Input Parameter	Basis for Value in Evaluation Model	Reference to Applicable Sensitivity Studies
Internal Atmosphere/Containment Shell/Heat Sink Temperature	Set to maximum Technical Specification value. This maximizes the temperature of the internal heat sinks. Reference Technical Specification 3.6.5.	WCAP-15846, Section 5.5
Internal Total Pressure	Set to maximum Technical Specification value. This maximizes the initial pressure and amount of air initially inside containment and retards mass transfer. Reference Technical Specification 3.6.4.	WCAP-15846, Section 5.4
Relative Humidity-Humidity	Set to maximize the amount of air inside containment which is noncondensable and will reduce the effectiveness of internal heat sink structures to absorb energy.	WCAP-15846, Section 5.3
IRWST Liquid Volume Fraction	Set at minimum Technical Specification IRWST water volume. Reference Technical Specification 3.5.6.	Not Applicable
IRWST Water Temperature	Set at maximum Technical Specification IRWST water temperature. This minimizes heat storage capacity. Reference Technical Specification 3.5.6.	Not Applicable

13.6.2 Boundary Conditions

Boundary conditions provide communication between the WGOTHIC Evaluation Model and known conditions connected to the “boundaries” of the model. There are two types of boundary conditions, flow and pressure. Flow boundary conditions are addressed through WGOTHIC forcing functions and are used to prescribe flow into or out of a control volume. Flow boundary conditions are modeled on case specific bases for the LOCA and SLB cases. Pressure boundary conditions are used to model the atmosphere and/or environment attached to a fluid volume in the WGOTHIC model. In the **AP1000** WGOTHIC containment Evaluation Model, pressure boundary conditions model the PCS air outlet and inlet environmental conditions. These values are consistent with those in Table 13-7.

13.6.2.1 Base Case LOCA Boundary Conditions

[

]^{a,c}

[

] ^{a,c}

[

] ^{a,c}

13.6.2.2 Base Case MSLB Boundary Conditions

[

] ^{a,c}

13.7 SUMMARY OF EVALUATION MODEL TRANSIENT CALCULATIONS

This section provides an overview of the accident progression for the two limiting containment DBAs. The descriptions provided here do not define the containment peak pressure used as a licensing basis; licensing-specific results are provided in the DCD. Both of the transient events under consideration, double-ended cold-leg guillotine (DECLG) LOCA and MSLB, are assumed to start from the initial containment conditions as presented in Section 13.6.1. The boundary conditions vary for each event and are defined in Section 13.6.2.

13.7.1 LOCA Transient Response Overview

The high level sequence of events for the containment response to a DECLG LOCA event is shown in the bulleted list below and briefly described in the text below.

- Break occurs
- Blowdown phase complete, Reflood phase begins
- Begin PCS evaporation heat removal modeling (steady state coverage assumed)
- ADS-4 actuated (steam released in upper SG compartments, IRWST drain-down begins)
- Containment peak pressure occurs
- Broken cold leg covered with water
- Water begins flooding CMT compartment
- IRWST water level equilibrates with CMT/SG compartment water levels (IRWST drain-down ends, core boil-off of sump water begins)
- PCS tank stand-pipes begin uncovering sequentially

The blowdown of RCS fluid into the containment leads to a rapid rise in the containment pressure within the first thirty seconds. Energy that is stored in the RCS metal and steam generators, along with the core decay heat is released to containment by heating and boiling of the water that is supplied by the PXS. Condensation of steam by the relatively cold metal surfaces within the containment building is initially able to maintain containment pressure following the blowdown peak pressure; however, as the internal heat sink temperatures begin to increase, condensation becomes less effective and containment pressure begins to slowly increase.

The annulus between the steel containment shell and concrete shield building is continuously cooled by a natural draft of air that flows down along the inside surface of the shield building and upward along the warmer containment shell. Condensation of steam on the inside surface of the containment shell causes the shell temperature to increase. As heat is conducted through the shell, the external shell surface

temperature also increases. Heat transfer to the air in the riser section of the annulus causes the temperature and natural draft air flow rate to increase.

The passive PCS cooling water begins flowing onto the containment shell shortly after the initiation of the accident. As discussed in Section 7, the Evaluation Model does not credit external PCS water flow until such time as a fully-developed cooling water film forms on the containment shell. Evaporation increases the PCS heat removal capability and also increases the natural draft flow rate. The evaporation rate continues to increase as the shell temperature continues to increase.

The water level in the CMTs reaches the ADS-4 actuation setpoint at approximately 1200 seconds. After the ADS-4 relief valves open, steam generated by boiling in the core is able to vent through the large ADS-4 lines into the upper steam generator compartments inside containment. The ADS-4 actuation signal also opens valves that allow water to begin to gravity drain from the IRWST to the RCS.

At approximately 1600 seconds, the condensation rate on the containment shell and internal heat sinks exceeds the steam release rate through the LOCA break and ADS-4 flow paths and containment pressure begins to decrease.

Water spilled from the RCS has begun to fill the sump and lower steam generator compartments. The liquid levels in these compartments continue to increase as the IRWST drains to the RCS and spills from the break.

An open drain line, located between the refueling cavity and sump, allows some of the spill water to begin filling the lower refueling cavity. This helps slow the water level increase in the CMT and SG compartments. The curbs surrounding the openings to the accumulator and CVS compartments in the floor of the CMT compartment are sufficiently high to prevent water from flooding those compartments.

The IRWST gravity drain ceases after approximately 10,000 seconds when the CMT and IRWST compartment water levels equilibrate. After this, the water needed to make up for boiling in the core is supplied from the sump through the cold leg break. The flow through the open drain line between the sump and refueling cavity eventually causes the refueling cavity level to also equilibrate with the CMT and SG compartments.

The PCS flow rate decreases as the storage tank water level falls below the top of each successive stand-pipe. The first reduction in the PCS flow rate resulted in a significant reduction in the shell heat removal rate and significantly reduced the containment depressurization rate.

The containment pressure continued to slowly decrease over the remainder of the event as the only remaining energy source is the decay heat in the core. The continuous reduction in the shell evaporation rate caused the annulus air flow rate to slowly decrease and the annulus air temperature to slowly increase.

13.7.2 MSLB Transient Response Overview

Steam line breaks are postulated to occur at operating conditions ranging from hot shutdown to full power. Steam generator secondary-side mass decreases as the power level increases; while both the RCS and SG secondary side energy increase as the power level increases. Because of the opposing effects of changing power level on the steam line break releases, no single power level can be identified as always being the worst case initial condition for a steam line break event. Therefore, several different power levels spanning the operating range are analyzed.

The containment response to the MSLB event is determined by the magnitude and duration of the mass and energy releases, the containment volume, steam/air circulation to the heat sinks, and time response of the heat sinks. Due to the assumption of 0% humidity as the containment initial condition and saturated vapor mass and energy releases with no liquid entrained in the break effluent, the MSLB transient is characterized by the containment atmosphere being superheated throughout the transient.

Four different power levels are analyzed for the double-ended guillotine MSLB cases. Reactor trip, main feedwater isolation and main steamline isolation occur rapidly due to a low steamline pressure signal. The PCS water on the external surface of the containment vessel is credited after a high-2 containment pressure signal and a delay to account for the development of steady state PCS water coverage. Generally, the containment pressure continues to increase until the secondary side blowdown ends due to the SG fluid inventory depleting. The containment pressure decreases rapidly as the energy continues to be transferred to the environment by the PCS.

13.8 WGOTHIC CONTAINMENT MINIMUM PRESSURE CALCULATION FOR SMALL-BREAK LOCA AND LONG-TERM CORE COOLING

A conservative calculation of the containment pressure is needed to provide the containment boundary conditions for the **AP1000** small-break LOCA (SBLOCA) analysis and the long-term core cooling (LTCC) analysis. For these cases, containment backpressure results in enhanced gravity injection from the IRWST and the containment sump. For this reason, the WGOTHIC containment pressure calculation is biased to obtain the minimum containment pressure for a given event.

The WGOTHIC Evaluation Model is used to determine the peak containment pressure for design basis events and uses assumptions that are biased to maximize the containment pressure. The minimum containment pressure model for SBLOCA and LTCC reverses many of the biases to provide a set of assumptions to minimize the containment pressure. The assumptions for the minimum containment pressure model are summarized in Table 13-9. The assumptions are to minimize the calculated containment pressure and are not necessarily physically realistic or consistent with one another. For example, the containment shell area is not actually 10% higher than nominal, but this is a conservatism applied in the analysis. Also if the containment shell surface area is greater than the nominal value, the containment volume would not increase by the same percentage, yet this is a part of the conservative assumptions.

The assumptions minimize containment pressure in the following ways.

[

] ^{a,c}

Table 13-9. WGOTHIC Assumptions for SBLOCA Minimum Pressure Calculations

Parameter	Minimum Pressure Model
Containment volume	Nominal increased 10%
Containment shell heat transfer area	Nominal increased 10%
Shell heat and mass transfer correlations	Biased to increase heat and mass transfer
Heat sinks	All heat sinks active
Passive heat sink area	Nominal increased by factor of 1.35
Heat transfer correlation	Uchida increased by 20%
[] ^{a,c}	[] ^{a,c}
Passive heat sink structural air gaps in steel-jacketed concrete walls	Not modeled
Material properties	Volumetric heat capacity and thermal conductivity biased for maximum heat removal
Passive containment cooling system flow rates	Maximum system specified flows
PCS water temperature	Minimum to maximize evaporative cooling
Passive containment cooling system	Assumed to start at the beginning of the event
Fan coolers	Assumed to start 10 minutes after event initiation
Containment purge	Open, shuts on automatic safeguards actuation signal
Initial pressure inside containment	Set to the minimum operating air pressure defined by Technical Specification 3.6.4
Initial humidity inside containment	Maximized to minimize initial air quantity
Initial temperature inside containment	Set to the maximum operating air temperature defined by Technical Specification 3.6.5.
Initial environment temperature	Minimized based on maximum containment shell differential defined by Technical Specification 3.6.10

13.9 CONCLUSIONS

A summary of the key elements of the AP1000 containment EM methodology, as described within Section 13, is provided below.

[

] ^{a,c}

[

] ^{a,c}

13.10 REFERENCES

- 13.1 WCAP-14382, "WGOTHIC Code Description and Validation," May 1995.
- 13.2 NAI 8907-02, Rev. 4, "GOTHIC Containment Analysis Package User Manual," August 1994.
- 13.3 WCAP-14812, Rev. 2, "Accident Specification and Phenomena Evaluation for AP600 Passive Containment Cooling System," April 1998.
- 13.4 NTD-NRC-95-4563, "GOTHIC Version 4.0 Documentation," September 1995.
- 13.5 WCAP-14326, Rev. 3 "Experimental Basis for the AP600 Containment Vessel Heat and Mass Transfer Correlations," April 1998.
- 13.6 WCAP-10325-P-A, "Westinghouse LOCA Mass and Energy Release Model for Containment Design March 1979 Version," May 1983.
- 13.7 WCAP-15846-P, Addendum 1, "Effective Thermal Conductivity Model of Inorganic Zinc Coating for Application to **AP1000**," October 2013.

14 LOCA MASS AND ENERGY RELEASE CALCULATION METHODOLOGY

14.1 INTRODUCTION

This section describes the method used to calculate the loss-of-coolant accident (LOCA) mass and energy releases that are used to calculate the containment pressure response for the Design Basis Analysis (DBA). The method maximizes both the magnitude and the rate of the mass and energy release to containment. This introduces substantial conservatism in the prediction of the peak containment pressure and temperature response following a LOCA event.

Section 10, Figure 10-1 presents a comparison of the WGOTHIC AP600 Containment Evaluation Model sensitivity to various input values and correlations. These are not single-effect sensitivities; the results are cumulative. Each additional sensitivity case modification is stacked upon those that immediately preceded it. These sensitivities provide insight into the effect of each parameter, individually, by comparison to the preceding case, as well as the total conservatism represented by these parameters. Case 7 (the heavy dashed line in Figure 10-1) represents the effect of removing some of the conservatism in the input mass and energy releases.

For Case 7, the mass and energy release calculation input was modified as follows:

- The nominal (without adding 5°F uncertainty) full power RCS temperatures were used
- The nominal (without adding 30 psi) full power RCS pressure was used
- The nominal (without adding uncertainty) RCS volume was used
- The nominal (without adding 2% uncertainty) full core power was used
- The nominal (without adding 15%) full power core stored energy was used
- The nominal CMT, accumulator, and IRWST fluid temperatures were used.

In addition to the input changes described above, the following calculational changes were made during the post-blowdown phase:

- The 1979 ANS decay heat standard for an 800-day average burnup (without adding the 2 sigma uncertainty) was used
- The post-blowdown refill period was modeled
- The broken loop steam generator energy was assumed to be released over a 1-hour period
- The intact loop steam generator energy was assumed to be released over a 2-hour period
- No zirc-water reaction energy was added.

A comparison of the mass and energy releases for Case 7 and the AP600 Containment Evaluation Model is shown in Figures 10-3 and 10-4.

As shown in Figure 10-1, by eliminating only a portion of the conservatism in the calculation of the mass and energy releases, there is a substantial decrease in the post-blowdown peak pressure (about 6 psi). The calculated peak containment pressure is reduced from the previous case by about 4.3 psi and is shifted to the end of blowdown. The largest effect of any other single change to one of the containment model input values is a reduction of about 3 psi. Therefore, the conservatism in the mass and energy calculation outweighs any other single modeling parameter.

14.2 BLOWDOWN MASS AND ENERGY RELEASE CALCULATION

The primary differences between the conventional plant design and the passive plant design are the engineered safety features. The safety features of conventional operating plants include both passive and active systems; the AP600 and **AP1000** safety features are all passive. This difference only affects the long-term inventory makeup systems, not the system behavior during the blowdown phase.

The methodology for calculating the mass and energy release to containment during the blowdown phase is not affected by the passive safety systems. The only safety system that injects water during the blowdown phase is the accumulator system; the gravity-driven core makeup tanks (CMTs) cannot inject into the common direct vessel injection line against the pressure of the gas-charged accumulators. Accumulators are included in both the passive and active plant designs and are modeled with the NRC-approved DBA LOCA mass and energy release methodology. The AP600 uses spherical accumulators, whereas currently operating Westinghouse designed plants use cylindrical accumulators. The accumulator inventory is depleted well before the time of peak pressure so any difference in discharge rate associated with the different accumulator geometry would have an insignificant effect on the calculation for peak containment pressure.

The blowdown mass and energy releases are calculated using the SATAN-VI computer code. The SATAN-VI code, associated modeling assumptions and nodding structure for the mass and energy release calculations are documented in WCAP-10325-P-A (Reference 14.1). It has been reviewed and approved by the NRC for use in calculating the blowdown mass and energy releases for Westinghouse PWR containment integrity DBA. The blowdown phenomena modeled by the SATAN VI code are the same for all Westinghouse PWRs, including the AP600 design.

The variable nodding structure of the SATAN model allows the user to simulate current and advanced reactor coolant system geometry with generalized control volumes. The standard Westinghouse PWR reactor coolant system nodding structure is modified to specifically model the passive plant reactor coolant system geometry, which includes two cold legs in the coolant loops and a direct vessel injection (DVI) line to the downcomer.

14.3 POST-BLOWDOWN MASS AND ENERGY RELEASE CALCULATION

The post-blowdown phase consists of three periods: refill, reflood, and long-term cooling. The refill period occurs just after blowdown. During the refill period, the accumulators refill the downcomer and lower plenum of the vessel with water. There are little or no releases during the refill period. The reflood period occurs just after refill. During the reflood period, the core is refilled with a 2-phase mixture of steam and water. Following reflood, the RCS fluid inventory and long-term cooling are maintained by the pumped safety injection system and recirculation system (conventional plants) or the core makeup tanks and gravity draining of the IRWST (passive plants).

The approved codes for conventional plant post-blowdown mass and energy release analyses would have had to have been significantly modified for them to have been used for passive plant analyses. Instead, a calculational method was developed to conservatively predict the AP600 and **AP1000** post-blowdown mass and energy releases in a manner that is consistent with the current approved methods for DBA. A spreadsheet was used for the calculations to simplify accounting of the mass and energy sources and releases.

Mass Sources

Figure 14-1 illustrates the basic model for the AP600 and **AP1000** post-blowdown mass and energy release calculation. All of the injection sources (accumulators, CMTs, and IRWST) are assumed to be delivered to the DVI line at a mass flow rate, m_{inject} . Flow from both accumulators refills the vessel following blowdown. The CMTs begin to inject just before the accumulators empty. The IRWST begins to gravity drain to the vessel (and spill from break) just before the CMTs empty.

The injected liquid mass flow rate delivered to the DVI line is calculated with a simplified resistance network. Two cases were considered initially: one with the line resistances maximized (to produce the minimum accumulator, CMT, and IRWST flow rates) and one with the line resistances minimized (to produce the maximum accumulator, CMT, and IRWST flow rates). The resistance network also calculates a flow rate around the loops and a flow rate out the broken cold leg stub, however, these are not used in the mass and energy release spreadsheet calculation. Instead, as shown in Figure 14-1, all of the injection flow that is delivered to the DVI line is assumed to pass through the core, hot legs, steam generators and out of the break. This maximizes the SG heat release rate, and is a source of conservatism in the analysis.

J^{a,c}

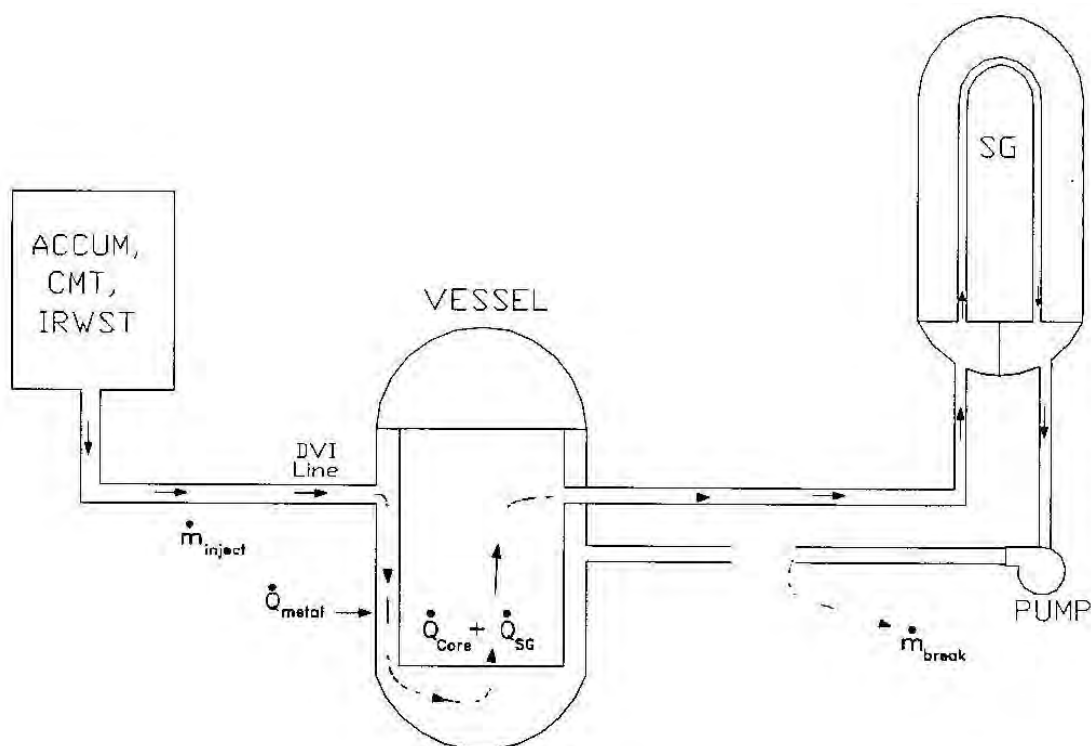


Figure 14-1. Spreadsheet Mass and Energy Release Schematic

a,c

Figure 14-2. WGOTHIC Draindown Model Noding Diagram

Energy Sources

The various sources of energy that are considered in the calculation, and their assumed release rates are summarized in Table 14-1. The release rates are biased to release energy (in the form of steam) to the containment early in the transient. The containment pressure response is dependent on the steam mass flow rate, so maximizing the steaming rate is conservative. The RCS metal energy release provides sensible heating of the injected liquid mass flow. The core decay heat and SG energy releases provide both sensible and latent heat to the injected liquid mass flow rate.

The SG equilibration time input value in the spreadsheet calculation is adjusted to maximize the steaming rate during the CMT injection phase. The SG equilibration times that are used for **AP1000** are longer than AP600 because both the core decay heat and SG stored energy are higher in the **AP1000**.

Table 14-1. DECLG LOCA Energy Release Modeling

Time Frame	Source of Energy	Energy Release Rate
Accident initiation to end of blowdown (30 seconds)	Core, RCS and SGs	SATAN VI Calculation
End of blowdown + 180 seconds	The Zr-H ₂ O Reaction Energy for 1% of the Fuel Cladding	Constant
End of blowdown to end of reflood (400 seconds)	Core stored energy	Constant
End of blowdown + SGB equilibration	SG energy - broken loop	Exponential
End of blowdown + SGI equilibration	SG energy - intact loop	Exponential
End of blowdown + 60 minutes	RCS metal energy	Exponential
End of blowdown to 72 hours	Fission Product Decay	ANS 1979 + 2 sigma

Description of Calculational Method

Three basic steps in the calculational method determine the DBA mass and energy releases as a function of time after the blowdown phase. First, the individual contributions for each of the various sources of energy are calculated. Second, the vessel internal mass and break mass flow rate are calculated. Third, the break mass flow rate is partitioned into a steam and a 2-phase component. A check for conservation of mass and energy is performed at the end of each time step. This method for calculating the mass and energy releases after the blowdown phase is described in more detail below.

Calculation of Sources of Energy

1. The 1979 decay heat standard with 2 sigma uncertainty, all U-235 fission, and 3 years full power operation is used to calculate the core decay heat energy release rate at each time step.

2. [

]^{a,c} The core stored energy is

released at a constant rate over the reflood period.

3. The Zr-H₂O reaction energy, corresponding to 1% clad oxidation, is released at a constant rate over the first 180 seconds of the reflood period.
4. The RCS metal energy is released exponentially. Using an exponential rate is conservative since this assumes the heat transfer rate is much larger than the rate of conduction through the metal. The equation for determining the stored metal energy as a function of time is:

$$Q(t) = Q_{final} + (Q_{initial} - Q_{final}) \cdot e^{-a \cdot (t-b)}$$

where,

Q_{final}	=	stored metal heat at equilibration (BTU)
$Q_{initial}$	=	stored metal heat at the end of blowdown (BTU)
a	=	inverse of the metal time constant (sec ⁻¹)
t	=	time (sec)
b	=	end of blowdown time (sec)

therefore, the release rate is:

$$\frac{dQ}{dt} = -a \cdot (Q_{init} - Q_{final}) \cdot e^{-a \cdot (t-b)}$$

The stored metal heat and time at the end of blowdown are obtained from the SATAN output tables. The stored metal heat at equilibration, Q_{final} , is determined by the metal heat capacity and the equilibration temperature, $M^*c_p \cdot T_{eq}$. The metal heat capacity, M^*c_p , is obtained from the SATAN input tables. The RCS temperature is assumed to reach an equilibrium value at the end of the reflood period. Using an equilibration temperature, T_{eq} , of []^{a,c} was found to produce good agreement between the spreadsheet calculational method and the code calculated mass and energy releases for a conventional plant. This equilibration temperature value corresponds to []^{a,c} the AP600 containment design pressure. A higher equilibration temperature value of []^{a,c} is used for **AP1000** since the containment design pressure is higher than AP600. The equilibration temperature is held constant for the post-blowdown calculation.

The metal time constant is the metal heat capacity divided by the heat transfer rate. Because the heat transfer rate is variable, the time constant is arbitrarily increased to release 99% of the RCS metal energy (in excess of the equilibration temperature) over 60 minutes.

5. The steam generator stored energy at the end of blowdown is released using the same equation shown above for the RCS metal energy release rate. The stored energy and time at the end of blowdown are obtained from the SATAN output tables. The stored energy at equilibration is determined by the metal and fluid heat capacity and the equilibration temperature, $\{(M \cdot c_p)_{\text{fluid}} + (M \cdot c_p)_{\text{metal}}\} \cdot T_{\text{eq}}$. The steam generator fluid and metal heat capacity input values are obtained from the SATAN input tables.

The stored energy in the broken loop and intact loop steam generators is released at different rates. The time constants for AP600 are set to values similar to standard plant analyses. Because the **AP1000** CMT injection flow rate limits the steaming rate, the **AP1000** time constants are adjusted to provide a more mechanistic representation of the steam generator energy release relative to the available core makeup flow, and to maximize the steaming rate during the CMT injection period.

Calculation of the Vessel Liquid Mass

6. During the reflood period, the mass of liquid in the vessel is assumed to increase exponentially according to the following equation:

$$M(t) = M_{\text{final}} + (M_{\text{initial}} - M_{\text{final}}) \cdot e^{-c \cdot (t-b)}$$

where,

M_{final}	=	RCS mass at the end of reflood (lbm)
M_{initial}	=	RCS mass at end of blowdown (lbm)
c	=	inverse reflood time constant (sec^{-1})
t	=	time (sec)
b	=	end of blowdown time (sec)

At the end of the reflood period, the RCS is assumed to be at a saturation temperature of []^{a,c} for the AP600 or []^{a,c} for the **AP1000** with a vessel void fraction of []^{a,c}. These assumptions were found to produce good agreement between the spreadsheet calculational method and the code calculated mass and energy releases for a conventional plant.

The RCS liquid mass at the end of the reflood period, M_{final} , is calculated using the following equation:

$$M_{\text{final}} = V \cdot (1 - \alpha) \cdot \rho$$

where,

V	=	Vessel volume (ft^3)
α	=	Vessel void fraction at end of reflood
ρ	=	Saturated liquid density at [] ^{a,c} (lbm/ft^3)

The temperature and amount of mass in the vessel at the end of reflood are held constant throughout the long-term cooling phase. These assumptions maximize the steam release rate because there is no additional filling of the vessel and, because the temperature does not decrease, the latent heat of vaporization does not increase.

An initial value for the RCS fluid mass is given in the SATAN summary table. The RCS initial mass input for the spreadsheet calculation, M_{initial} , is artificially instantaneously increased to eliminate the time delay associated with refilling the downcomer and lower plenum of the vessel. Eliminating the refill period shifts the mass and energy releases earlier in time and results in an increase in the predicted peak containment pressure.

The reflood time constant is related to the vessel volume, the injected mass flow rate and the steaming rate. The time constant is set to allow the vessel mass to reach 99% of the M_{final} value in approximately 400 seconds. This time frame is consistent with reflooding times for conventional Westinghouse PWR designs with similar vessel volume and injection rates.

Calculation of the Break Vapor and 2-Phase Mass Flow Rates

Steps 7 through 10 describe the method that is used to calculate the break mass flow rate and to partition it into the vapor and 2-phase flow components for input to the WGOTHIC Containment Evaluation Model.

7. The break mass flow rate is defined as the difference between the injected mass flow rate and the time derivative of the vessel liquid mass, as shown in the equation below:

$$m_{\text{break}} = m_{\text{inject}} - c \cdot (m_{\text{final}} - m_{\text{initail}}) \cdot e^{-c \cdot (t-b)}$$

Following the end of the reflood period (400 seconds), the total flow released from the break is equal to the injected flow; no additional inventory is stored in the RCS.

8. The core inlet enthalpy is calculated by dividing the RCS metal energy release rate by the injected liquid mass flow rate, and summing this with the enthalpy of the injected flow, $h_{\text{core}} = h_{\text{inject}} + Q_{\text{metal}}/m_{\text{inject}}$. After injection stops, the core inlet enthalpy is set to a constant value. This value is based on the upper bound fluid temperature in the containment sump.

9. The total break flow rate is partitioned into a steam and a 2-phase component. Because the containment pressure is dependent on the steam release, the steam mass flow rate is maximized by assuming 95% of the core energy and all of the steam generator energy is used to produce steam. The steam and 2-phase fluid break mass flow rates are calculated using the following equations:

$$m_{steam} = \min[m_{break}, (0.95 \cdot Q_{core} + Q_{SG}) / (h_g - h_{core})]$$

$$m_{2-phase} = m_{break} - m_{steam}$$

where,

Q_{core} = Sum of the core decay heat, stored energy and Zr-H₂O reaction release rates (BTU/s)

Q_{SG} = Sum of the broken and intact SG energy release rates (BTU/s)

h_g = Steam enthalpy at the equilibration temperature (BTU/lbm)

h_{core} = Core inlet enthalpy (BTU/s)

m_{break} = Total break mass flow rate (lbm/s)

Note, because the steam enthalpy is assumed to remain constant at the equilibration temperature, the steam generator energy is used to produce additional steam release, rather than superheat the steam. This maximizes the steam release rate.

10. The enthalpy of the 2-phase break fluid is calculated using the following equation:

$$h_{2-phase} = \min[h_g, (0.05 \cdot Q_{SG}) / (m_{2-phase})]$$

where all terms have been defined previously. The limit is applied to prevent the 2-phase enthalpy from exceeding h_g when the 2-phase mass flow rate is very small.

Check for Energy Conservation

11. Conservation of energy is checked at the end of each time step. [

]^{a,c}

14.4 COMPARISON OF SATAN/SPREADSHEET RELEASES WITH WCOBRA-TRAC CALCULATED RELEASES

The AP1000 DECL LOCA mass and energy releases calculated using the SATAN/spreadsheet method were compared to the best estimate WCOBRA-TRAC (WCT) code calculated results to demonstrate the amount of conservatism in the calculation. The comparison was run out 2000 seconds; this is beyond the calculated time of peak containment pressure. Although this version of the WCT code was not designed to produce LOCA mass and energy releases that would be conservative for use in calculating containment peak pressure, it should nevertheless mechanistically calculate a reasonable estimate of the releases.

A representative comparison of the blowdown mass and energy releases are shown in Figures 14-3 and 14-4. SATAN predicts a higher blowdown mass and energy release rate than WCT. The post-blowdown mass and energy comparison is shown in Figures 14-5 and 14-6. The spreadsheet method calculates a higher release rate than WCT because the spreadsheet releases the SG energy at a much higher rate than WCT.

The representative integrated mass and energy releases are compared in Figures 14-7 and 14-8. The SATAN/spreadsheet method predicts approximately a 50-percent higher integrated mass and energy release than WCT, by the time peak pressure occurs. This difference results in a 20 psi higher calculated peak pressure as shown in Figure 14-9.

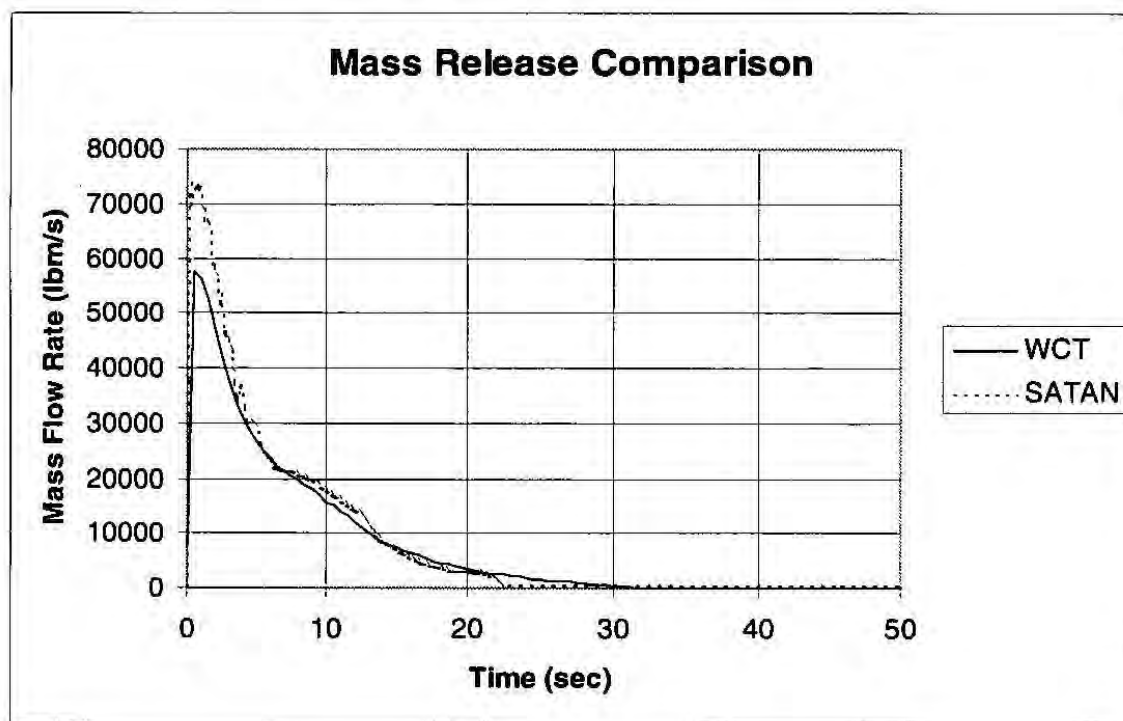


Figure 14-3. Mass Release Comparison

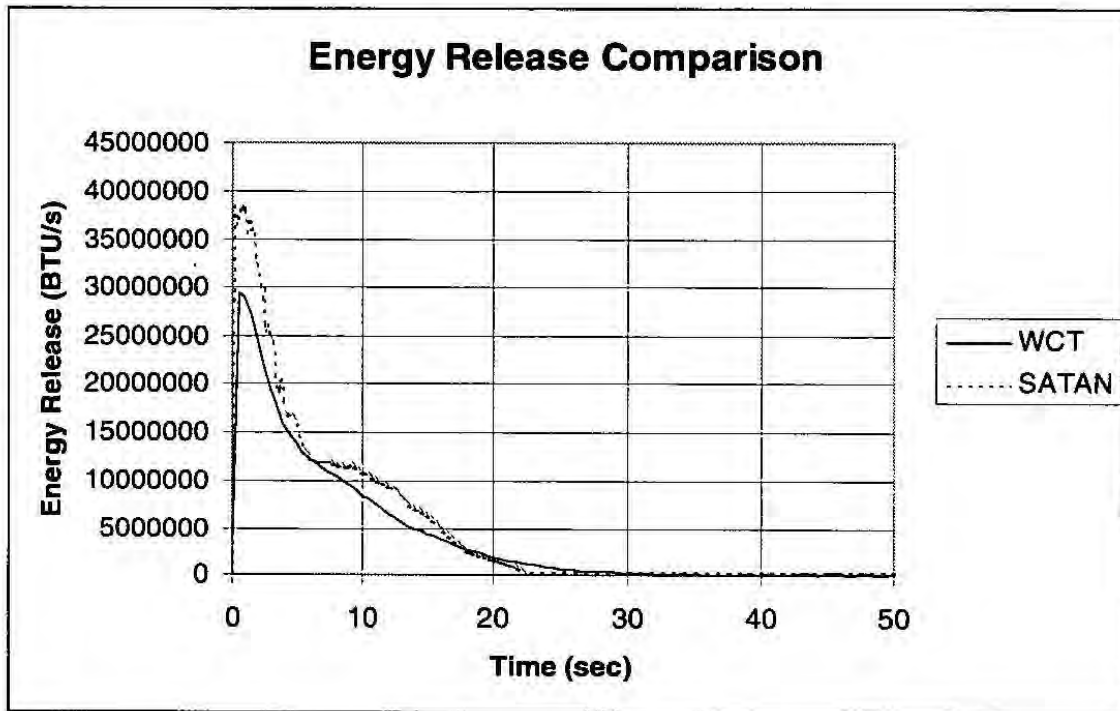


Figure 14-4. Energy Release Comparison

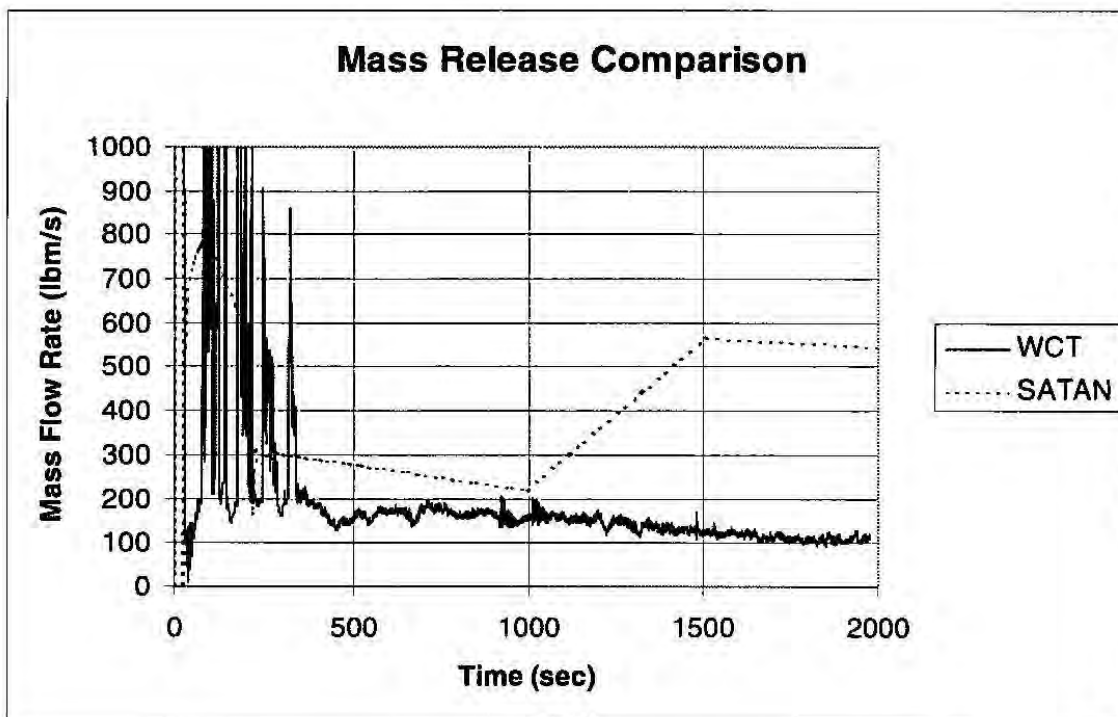


Figure 14-5. Mass Release Comparison

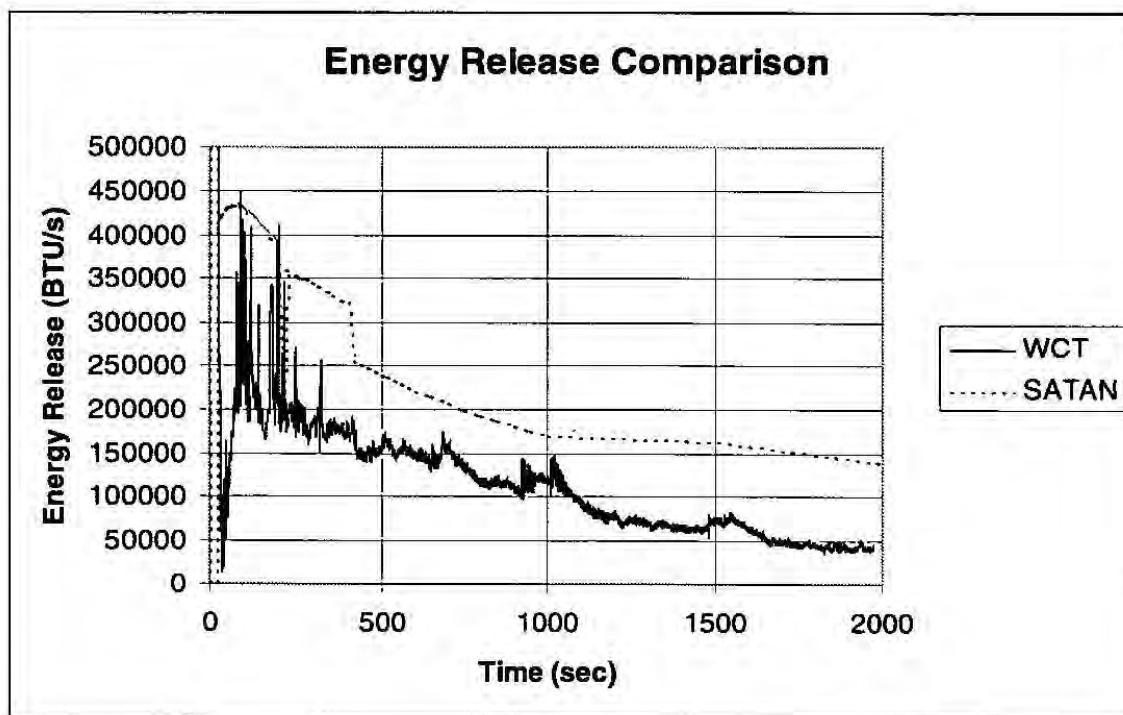


Figure 14-6. Energy Release Comparison

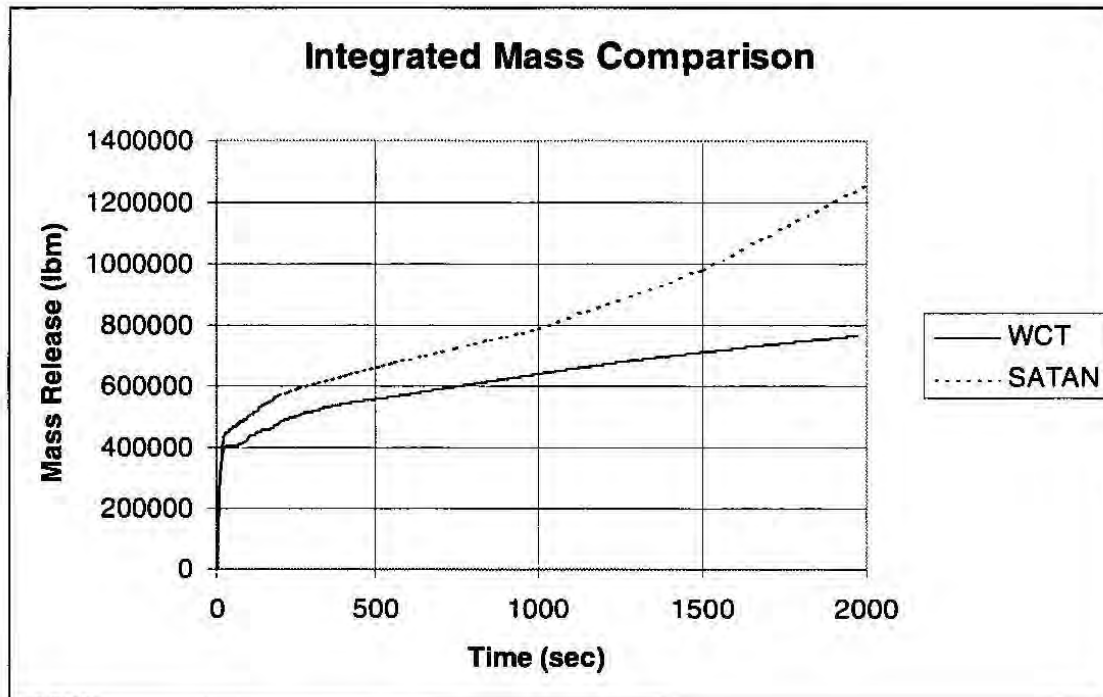


Figure 14-7. Integrated Mass Comparison

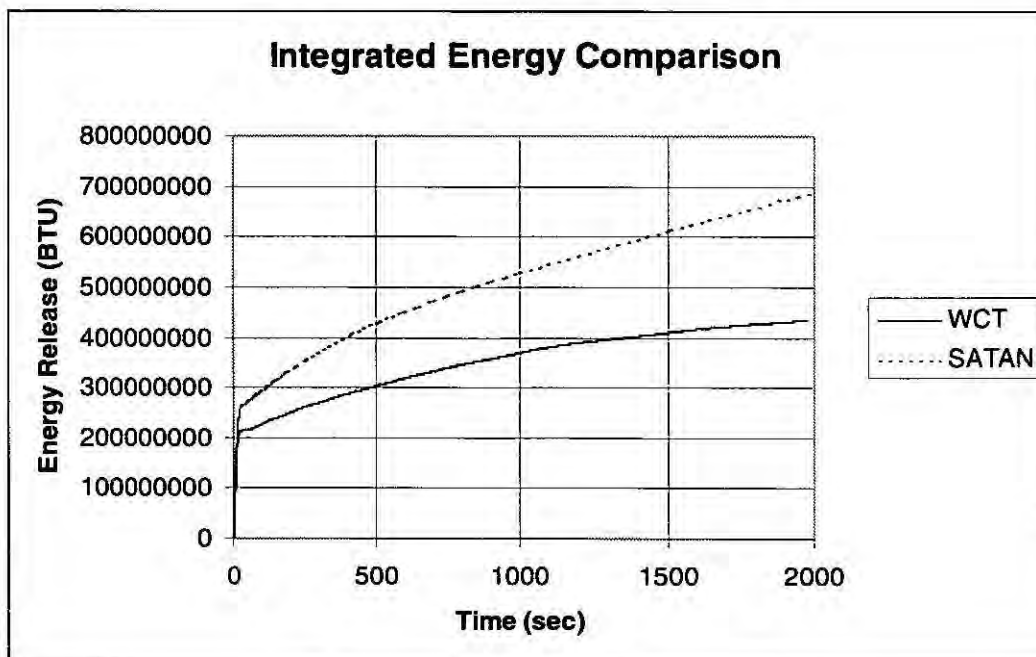


Figure 14-8. Integrated Energy Comparison

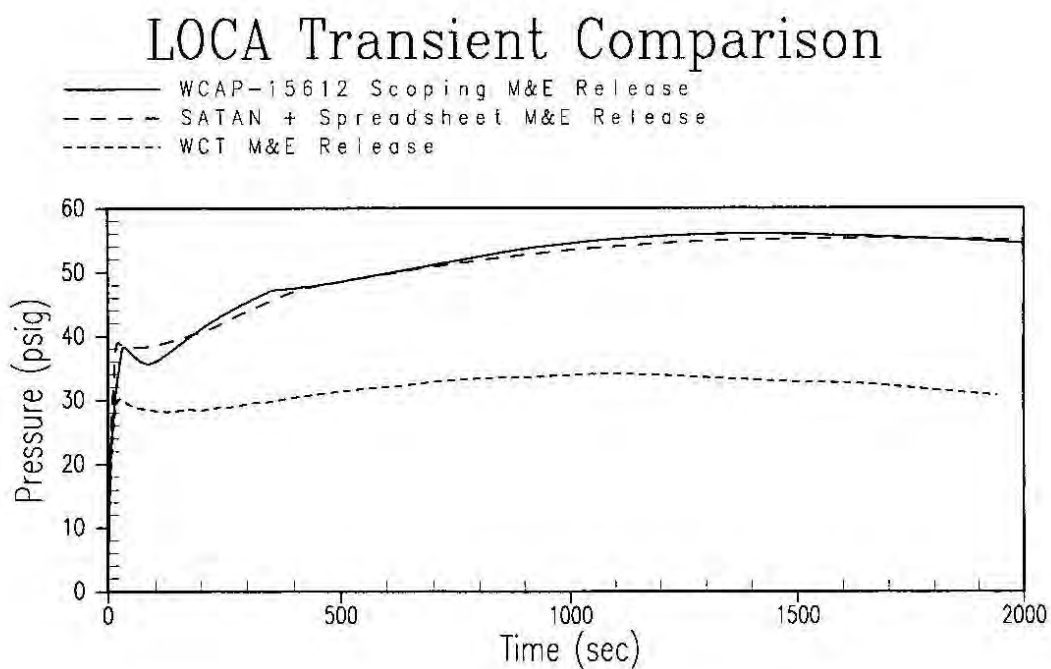


Figure 14-9. LOCA Transient Comparison

14.5 SUMMARY AND CONCLUSIONS

The methodology, used to predict mass and energy releases to the containment during the blowdown phase of the Large LOCA accident for the AP600 and **AP1000** containment DBA, is consistent with the methodology approved by the NRC for current operating plants. The approved methodology yields conservatively high total energy and energy release rates to the containment atmosphere, consistent with regulatory guidance for Design Basis Analyses.

A spreadsheet calculation method is applied to calculate the post-blowdown mass and energy releases for the AP600 and **AP1000**. Because the containment pressure is dependent on the steam release, the break steam mass flow rate is maximized in the calculation. The transient flow rates for the accumulators, CMTs and IRWST, are calculated using a resistance network. These flow rates, along with the conditions at the end of the SATAN blowdown mass and energy release analysis, are input to the spreadsheet. The spreadsheet accounts for the same sources of energy and uses similar energy release rates as the conventional plant analysis. A comparison of the releases predicted by the spreadsheet and the approved mass and energy release analysis codes/models show that the spreadsheet provides a conservatively high prediction of the release to containment. Therefore, the spreadsheet method for calculating the post-blowdown mass and energy releases used in the AP600 and **AP1000** containment analysis is consistent with the methodology approved by the NRC for current operating plants.

A summary outlining the design basis LOCA mass and energy release inputs and major assumptions is presented in Table 14-2.

Table 14-2. Basis for LOCA Mass and Energy Inputs

Input Parameter	Basis for Value in Evaluation Model
RCS Initial Conditions	Assumed to be at the maximum expected operating temperature and pressure. Includes allowances for error and instrument dead band.
RCS Volume	RCS coolant volumes increased by 1.4% for uncertainty and 1.6% for thermal expansion. As discussed in WCAP-10325-P-A, this model conservatism is chosen to maximize the available energy in the system.
Core Stored Energy	Core stored energy conservatively increased by 15%. As discussed in WCAP-10325-P-A, Core stored energy is maximized based upon the conditions at the most limiting time in life and maximum core fluid temperature.
Steam Generator Mass	Initial mass conservatively increased by 10%. As discussed in WCAP-10325-P-A, this model conservatism is chosen to maximize the available energy in the system.
Initial Power Level	Full technical specification power, accounting for calorimetric error. As discussed in WCAP-10325-P-A, this model conservatism is chosen to maximize the available energy in the system.
Zirc-Water Reaction	1% of the zirconium conservatively assumed to react. Bounds LOCA Chapter 15 results of no appreciable zirc-water reaction.
Blowdown Phase Calculation Methodology LOCA Mass and Energy Release	SATAN 78, WCAP-10325-P-A
Steam Generator Heat Release	Exponential decay constant adjusted to maximize steaming rate during CMT injection period.

14.6 REFERENCES

- 14.1 WCAP-10325-PA, "Westinghouse LOCA Mass and Energy Release Model for Containment Design March 1979 Version," May 1983.

Southern Nuclear Operating Company

ND-17-2074

Enclosure 9

Vogtle Electric Generating Plant (VEGP) Units 3 and 4

**Affidavit from Southern Nuclear Operating Company for Withholding Under 10 CFR 2.390
(LAR-17-043)**

(Enclosure 9 consists of 2 pages, excluding this cover page.)

Affidavit of Brian H. Whitley

1. My name is Brian H. Whitley. I am the Regulatory Affairs Director for Southern Nuclear Operating Company (SNC). I have been delegated the function of reviewing proprietary information sought to be withheld from public disclosure and am authorized to apply for its withholding on behalf of SNC.
2. I am making this affidavit on personal knowledge, in conformance with the provisions of 10 CFR Section 2.390 of the Commission's regulations, and in conjunction with SNC's filing on dockets 52-025 and 52-026, Vogtle Electric Generating Plant Units 3 and 4, Request for License Amendment and Exemption: Containment Pressure Analysis (LAR-17-043), also referred to as APP-FSAR-GLN-531, (Westinghouse LAR-079), Revision 0. I have personal knowledge of the criteria and procedures used by SNC to designate information as a trade secret, privileged or as confidential commercial or financial information.
3. Based on the reason(s) at 10 CFR 2.390(a)(4), this affidavit seeks to withhold from public disclosure Enclosures 5 and 7 of SNC letter ND-17-2074 for Vogtle Electric Generating Plant Units 3 and 4, Request for License Amendment and Exemption: Containment Pressure Analysis (LAR-17-043).
4. The following is furnished for consideration by the Commission in determining whether the information sought to be withheld from public disclosure should be withheld.
 - a. The information sought to be withheld from public disclosure has been held in confidence by SNC and Westinghouse Electric Company.
 - b. The information is of a type customarily held in confidence by SNC and Westinghouse Electric Company and not customarily disclosed to the public.

ND-17-2074

Enclosure 9

Affidavit from Southern Nuclear Operating Company for Withholding Under 10 CFR 2.390
(LAR-17-043)

- c. The release of the information might result in the loss of an existing or potential competitive advantage to SNC and/or Westinghouse Electric Company.
 - d. Other reasons identified in Enclosure 10 of SNC letter ND-17-2074 for Vogtle Electric Generating Plant Units 3 and 4, Request for License Amendment and Exemption: Containment Pressure Analysis (LAR-17-043), and those reasons are incorporated here by reference.
5. Additionally, release of the information may harm SNC because SNC has a contractual relationship with the Westinghouse Electric Company regarding proprietary information. SNC is contractually obligated to seek confidential and proprietary treatment of the information.
6. The information is being transmitted to the Commission in confidence and, under the provisions of 10 CFR Section 2.390, it is to be received in confidence by the Commission.
7. To the best of my knowledge and belief, the information sought to be protected is not available in public sources or available information has not been previously employed in the same original manner or method.

I declare under penalty of perjury that the foregoing is true and correct.



Brian H. Whitley

Executed on 12/21/17
Date

Southern Nuclear Operating Company

ND-17-2074

Enclosure 10

Vogtle Electric Generating Plant (VEGP) Units 3 and 4

**Westinghouse Authorization Letter CAW-17-4679, Affidavit, Proprietary
Information Notice and Copyright Notice**

(Enclosure 10 consists of 8 pages, excluding this cover page.)

ENCLOSURE 1 to CAW-17-4679

AFFIDAVIT

Westinghouse Non-Proprietary Class 3

CAW-17-4679

December 18, 2017


AFFIDAVIT

COMMONWEALTH OF PENNSYLVANIA:

SS

COUNTY OF BUTLER:

I, Jill S. Monahan, am authorized to execute this Affidavit on behalf of Westinghouse Electric Company LLC ("Westinghouse"), and declare that the averments of fact set forth in this Affidavit are true and correct to the best of my knowledge, information, and belief.



Jill S. Monahan, Manager
Licensing Special Programs

Date: 12-18-2017

Westinghouse Non-Proprietary Class 3

2

CAW-17-4679
December 18, 2017

- (1) I am Manager, Licensing Special Programs, Westinghouse Electric Company LLC (“Westinghouse”), and as such, I have been specifically delegated the function of reviewing the proprietary information sought to be withheld from public disclosure in connection with nuclear power plant licensing and rule making proceedings, and am authorized to apply for its withholding on behalf of Westinghouse.
- (2) I am making this Affidavit in conformance with the provisions of 10 CFR Section 2.390 of the Nuclear Regulatory Commission’s (“Commission’s”) regulations and in conjunction with the Westinghouse Application for Withholding Proprietary Information from Public Disclosure accompanying this Affidavit.
- (3) I have personal knowledge of the criteria and procedures utilized by Westinghouse in designating information as a trade secret, privileged or as confidential commercial or financial information.
- (4) Pursuant to the provisions of paragraph (b)(4) of Section 2.390 of the Commission’s regulations, the following is furnished for consideration by the Commission in determining whether the information sought to be withheld from public disclosure should be withheld.
 - (i) The information sought to be withheld from public disclosure is owned and has been held in confidence by Westinghouse.
 - (ii) The information is of a type customarily held in confidence by Westinghouse and not customarily disclosed to the public. Westinghouse has a rational basis for determining the types of information customarily held in confidence by it and, in that connection, utilizes a system to determine when and whether to hold certain types of information in confidence. The application of that system and the substance of that system constitute Westinghouse policy and provide the rational basis required.

Under that system, information is held in confidence if it falls in one or more of several types, the release of which might result in the loss of an existing or potential competitive advantage, as follows:

- (a) The information reveals the distinguishing aspects of a process (or component, structure, tool, method, etc.) where prevention of its use by any of

Westinghouse Non-Proprietary Class 3

3

CAW-17-4679
December 18, 2017

Westinghouse's competitors without license from Westinghouse constitutes a competitive economic advantage over other companies.

- (b) It consists of supporting data, including test data, relative to a process (or component, structure, tool, method, etc.), the application of which data secures a competitive economic advantage, e.g., by optimization or improved marketability.
 - (c) Its use by a competitor would reduce his expenditure of resources or improve his competitive position in the design, manufacture, shipment, installation, assurance of quality, or licensing a similar product.
 - (d) It reveals cost or price information, production capacities, budget levels, or commercial strategies of Westinghouse, its customers or suppliers.
 - (e) It reveals aspects of past, present, or future Westinghouse or customer funded development plans and programs of potential commercial value to Westinghouse.
 - (f) It contains patentable ideas, for which patent protection may be desirable.
- (iii) There are sound policy reasons behind the Westinghouse system which include the following:
- (a) The use of such information by Westinghouse gives Westinghouse a competitive advantage over its competitors. It is, therefore, withheld from disclosure to protect the Westinghouse competitive position.
 - (b) It is information that is marketable in many ways. The extent to which such information is available to competitors diminishes the Westinghouse ability to sell products and services involving the use of the information.
 - (c) Use by our competitor would put Westinghouse at a competitive disadvantage by reducing his expenditure of resources at our expense.

Westinghouse Non-Proprietary Class 3

CAW-17-4679

4

December 18, 2017

- (d) Each component of proprietary information pertinent to a particular competitive advantage is potentially as valuable as the total competitive advantage. If competitors acquire components of proprietary information, any one component may be the key to the entire puzzle, thereby depriving Westinghouse of a competitive advantage.
- (e) Unrestricted disclosure would jeopardize the position of prominence of Westinghouse in the world market, and thereby give a market advantage to the competition of those countries.
- (f) The Westinghouse capacity to invest corporate assets in research and development depends upon the success in obtaining and maintaining a competitive advantage.
- (iv) The information is being transmitted to the Commission in confidence and, under the provisions of 10 CFR Section 2.390, it is to be received in confidence by the Commission.
- (v) The information sought to be protected is not available in public sources or available information has not been previously employed in the same original manner or method to the best of our knowledge and belief.
- (vi) The proprietary information sought to be withheld in this submittal is that which is appropriately marked in APP-GW-GLR-801, Revision 0, "LAR-79 Supplementary Information for Updates to WGOTHIC Methodology (Proprietary)," and in APP-SSAR-GSC-587, Revision 5, "WGOTHIC Application to AP600 and AP1000," for submittal to the Commission, being transmitted by Southern Nuclear Operating Company letter. The proprietary information as submitted by Westinghouse is that associated with the NRC review of the Southern Nuclear Operating Company License Amendment Request in ND-17-2074 (WEC LAR-079, Southern LAR-17-043), and may be used only for that purpose.

Westinghouse Non-Proprietary Class 3

5

CAW-17-4679
December 18, 2017

- (a) This information is part of that which will enable Westinghouse to:
 - (i) Manufacture and deliver products to utilities based on proprietary designs.
- (b) Further this information has substantial commercial value as follows:
 - (i) Westinghouse plans to sell the use of similar information to its customers for the purpose of licensing of new nuclear power stations.
 - (ii) Westinghouse can sell support and defense of industry guidelines and acceptance criteria for plant-specific applications.
 - (iii) The information requested to be withheld reveals the distinguishing aspects of a methodology which was developed by Westinghouse.

Public disclosure of this proprietary information is likely to cause substantial harm to the competitive position of Westinghouse because it would enhance the ability of competitors to provide similar technical evaluation justifications and licensing defense services for commercial power reactors without commensurate expenses. Also, public disclosure of the information would enable others to use the information to meet NRC requirements for licensing documentation without purchasing the right to use the information.

The development of the technology described in part by the information is the result of applying the results of many years of experience in an intensive Westinghouse effort and the expenditure of a considerable sum of money.

In order for competitors of Westinghouse to duplicate this information, similar technical programs would have to be performed and a significant manpower effort, having the requisite talent and experience, would have to be expended.

Further the deponent sayeth not.

ENCLOSURE 2 to CAW-17-4679

PROPRIETARY INFORMATION NOTICE and COPYRIGHT NOTICE

CAW-17-4679
December 18, 2017

PROPRIETARY INFORMATION NOTICE

Transmitted herewith are proprietary and/or non-proprietary versions of documents furnished to the NRC in connection with requests for generic and/or plant-specific review and approval.

In order to conform to the requirements of 10 CFR 2.390 of the Commission's regulations concerning the protection of proprietary information so submitted to the NRC, the information which is proprietary in the proprietary versions is contained within brackets, and where the proprietary information has been deleted in the non-proprietary versions, only the brackets remain (the information that was contained within the brackets in the proprietary versions having been deleted). The justification for claiming the information so designated as proprietary is indicated in both versions by means of lower case letters (a) through (f) located as a superscript immediately following the brackets enclosing each item of information being identified as proprietary or in the margin opposite such information. These lower case letters refer to the types of information Westinghouse customarily holds in confidence identified in Sections (4)(ii)(a) through (4)(ii)(f) of the Affidavit accompanying this transmittal pursuant to 10 CFR 2.390(b)(1).

COPYRIGHT NOTICE

The reports transmitted herewith each bear a Westinghouse copyright notice. The NRC is permitted to make the number of copies of the information contained in these reports which are necessary for its internal use in connection with generic and plant-specific reviews and approvals as well as the issuance, denial, amendment, transfer, renewal, modification, suspension, revocation, or violation of a license, permit, order, or regulation subject to the requirements of 10 CFR 2.390 regarding restrictions on public disclosure to the extent such information has been identified as proprietary by Westinghouse, copyright protection notwithstanding. With respect to the non-proprietary versions of these reports, the NRC is permitted to make the number of copies beyond those necessary for its internal use which are necessary in order to have one copy available for public viewing in the appropriate docket files in the public document room in Washington, DC and in local public document rooms as may be required by NRC regulations if the number of copies submitted is insufficient for this purpose. Copies made by the NRC must include the copyright notice in all instances and the proprietary notice if the original was identified as proprietary.